Bioconjugate Chemistry

REVIEW

pubs.acs.org/bc

Theranostics: Combining Imaging and Therapy

Sneha S. Kelkar[§] and Theresa M. Reineke*[,§,†]

[§]Department of Chemistry and Macromolecular and Interfaces Institute Virginia Polytechnic Institute and State University, Blacksburg, Virginia 24060, United States

[†]Department of Chemistry, University of Minnesota, Minneapolis, Minnesota 55455, United States

ABSTRACT: Employing theranostic nanoparticles, which combine both therapeutic and diagnostic capabilities in one dose, has promise to propel the biomedical field toward personalized medicine. This review presents an overview of different theranostic strategies developed for the diagnosis and treatment of disease, with an emphasis on cancer. Herein, therapeutic strategies such as nucleic acid delivery, chemotherapy, hyperthermia (photothermal ablation), photodynamic, and radiation therapy are combined with one or more imaging functionalities for both *in vitro* and *in vivo* studies. Different imaging probes, such as MRI contrast agents (T_1 and T_2 agents), fluorescent markers (organic dyes and inorganic quantum dots), and nuclear imaging agents (PET/SPECT agents), can be decorated onto therapeutic agents or therapeutic delivery vehicles in order to facilitate their imaging and, in so doing, gain information about the trafficking pathway, kinetics of delivery, and therapeutic efficacy; several such strategies are outlined. The creative approaches being developed for these classes of therapies and imaging modalities are discussed, and the recent developments in this field along with examples of technologies that hold promise for the future of cancer medicine are highlighted.

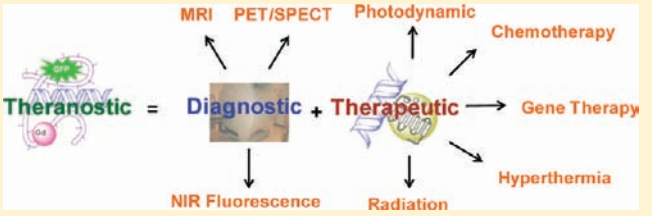

The term "theranostic" was coined in 2002 by Funkhouser[1] and is defined as a material that combines the modalities of therapy and diagnostic imaging. Thus, theranostics deliver therapeutic drugs and diagnostic imaging agents at the same time within the same dose. Before initiating treatment of various diseases such as cancer, it is essential to carry out diagnostic imaging to understand the cellular phenotype(s) and heterogeneity of the tumor.[2−4] In contrast to the development and use of separate materials for these two objectives, theranostics combine these features into one "package", which has the potential to overcome undesirable differences in biodistribution and selectivity that currently exist between distinct imaging and therapeutic agents. The ultimate goal of the theranostic field is to gain the ability to image and monitor the diseased tissue, delivery kinetics, and drug efficacy with the long-term hope of gaining the ability to tune the therapy and dose with heretofore unattainable control. Individualizing medicine, as opposed to adopting a 'one size fits all' approach, can move the field of nanomedicine forward toward an era of more effective and personalized treatment approaches.[5]

The most promising aspects of utilizing nanoparticles as therapeutics, diagnostics, and theranostics are their potential to localize (or be targeted) in a specific manner to the site of disease and reduce or eliminate the possible numerous untoward side effects. The nanometric size of these materials precludes them from being readily cleared through the kidneys, thereby extending circulation in the blood pool depending on their surface functionalization characteristics.[6] Also, when considering novel cancer treatments, blood vessels in many tumor types are irregular in shape, dilated, leaky, and can present fenestrations in endothelial cells. Due to the altered anatomy of tumor vessels, nanosized particles can easily extravasate from the blood pool into tumor tissues and be retained due to poor lymphatic drainage. This phenomenon of selective accumulation of nanosized particles near tumor tissues is termed the enhanced permeability and retention (or EPR) effect.[7,8] Additionally, nanoparticles have high surface area-to-volume ratios, yielding high loading capacities. Thus, nanoparticles can be loaded with therapeutic drugs and imaging agents; they may also be surface functionalized with targeting ligands and cloaking agents like poly(ethylene glycol) (PEG). Introduction of targeting ligands may help to increase the target-to-background contrast in imaging and improve the local concentration of the therapeutic at the target of interest, with the goal of reducing systemic toxicity.

In this review, we present an overview of some of the theranostic strategies developed for different types of cancer treatments, such as nucleic acid therapy, chemotherapy, hyperthermia treatment (photothermal ablation), photodynamic therapy, and radiation therapy. This review discusses syntheses and developmental studies of the novel multifunctional materials employed in this work, including linear and branched polymers, dendrimers, micelles, inorganic nanoparticles, and protein conjugates. In addition to their therapeutic uses, these materials have been functionalized with imaging agents to promote one or more diagnostic imaging techniques, such as magnetic resonance imaging, nuclear imaging (PET/SPECT/CT), and/or fluorescence imaging/optical imaging.

Received: March 24, 2011
Revised: July 14, 2011
Published: August 10, 2011

ACS Publications © 2011 American Chemical Society

Nucleic acid therapy holds promise in the treatment of both acquired and inherited diseases like Alzheimer's disease, cancer, adenosine deaminase deficiency, and cystic fibrosis. In addition to traditional "gene therapy", in which a defective copy of a gene is replaced with a functional (therapeutic one), other forms of nucleic acids exist as current and potential therapeutics, such as plasmids, antisense oligonucleotides, ribozymes, DNAzymes, aptamers, and small interfering RNA (siRNA). These polynucleotides can alter gene expression at the transcriptional or post-transcriptional level and may be effective to treat cancer, cardiovascular, inflammatory, and some forms of infectious diseases. The success of polynucleotide therapeutic modalities relies on their efficient delivery to the site of disease. Nucleic acids are large, negatively charged molecules that are highly susceptible to enzymatic degradation; they are not easily internalized by cells that contain a negatively charged plasma membrane. Injection of naked nucleic acids directly to the diseased areas (such as skeletal muscles, liver, thyroid, heart muscle, urological organs, skin, and tumor) via a physical method—such as electroporation, a "gene gun", or ultrasound—can be an effective mode of delivery.[9] However, systemic injection of naked DNA is largely ineffective due to the minimal amount of intact polynucleotide reaching the final intracellular destination. Direct injection of naked DNA holds limited promise toward efficient delivery, especially to the targets that are anatomically inaccessible (e.g., solid tumors).

Over the past several decades, tremendous effort has been put forth to design and develop delivery methods to produce highly efficient and efficacious delivery vehicles. These methods involve both viral and nonviral delivery vehicles. Virus-based therapeutic delivery involves the inactivation of viral genes that cause disease and incorporation of a copy of the therapeutic gene of interest—as RNA for retroviral and lentiviral vectors or as DNA for adenoviral or adeno-associated viral vectors.[10] Viral vectors can achieve high transfection efficiency and integration of the target gene into the chromosomal DNA of the recipient cell(s). Several clinical trials[11,12] with viral vectors have raised concerns due to undesirable interference with the host genome and the potential to elicit a severe immune response. To this end, in recent years, many researchers have focused on the development of new synthetic, nonviral vehicles, which have the potential to be nontoxic and less immunostimulatory, and can be more versatile for modification and carrying different types of drug payloads. Nonviral vehicles based on synthetic polymers, dendrimers, liposomes, cell-penetrating peptides, and inorganic nanoparticles have been developed and studied in detail.[9,13,14] These types of vehicles also possess the advantageous ability to be easily modified for theranostic purposes.

To design highly efficient gene delivery vectors, identification of the rate-limiting steps involved in the path of the delivery vehicle from its site of administration to the target of interest is crucial for success. Understanding trafficking of a nucleic acid from extracellular matrix, through the cell, and into the nucleus has traditionally been done by labeling the nucleic acid with one or more fluorescent dyes and monitoring colocalization signals with a fluorescent-labeled organelle at different time points. For example, Godbey et al.[15] investigated the intracellular trafficking of poly(ethyleneimine) (PEI) and PEI-DNA complexes (polyplexes) to the nucleus with the help of confocal laser scanning microscopy. PEI and DNA were labeled with Oregon Green 488 and rhodamine, respectively, and the yellow signal resulting from colocalization of green (PEI) and red (DNA) was monitored to understand trafficking of PEI-DNA complexes. They also studied trafficking of PEI and DNA individually by monitoring green and red fluorescence signals, respectively. They investigated the PEI-DNA polyplexes after endocytosis as well, revealing that PEI enters the nucleus along with the DNA. One of the major limitations of this approach for visualization (that is, separate labeling of polymer and DNA with fluorescent dyes and monitoring colocalization signal with fluorescent spectroscopy) is inherently low spatial resolution associated with the confocal microscopy technique. Fluorescence signals from each fluorophore may overlap in spite of the polymer and DNA not actually being associated with each other; that is, this approach is unable to provide potentially valuable details, such as more precise, real-time information about association−dissociation of the polymer from the polynucleotide.[16,17]

Recent studies in which both the delivery vehicle and DNA were labeled with organic dyes have allowed the use of more sophisticated imaging techniques, such as time-lapse microscopy, fluorescence resonance energy transfer (FRET),[18,19] and fluorescence correlation spectroscopy (FCS).[20] These approaches hold promise to provide more precise information regarding polyplex trafficking and dissociation and toward development of theranostic systems. For example, Lucas et al.[17] used dual-color fluorescence fluctuation spectroscopy (FFS) to monitor complexes comprising Cy5-labeled poly(L-lysine) (PLL) and pegylated poly[2-(dimethylamino)ethyl]methacrylate-*co*-aminoethyl methacrylate (pEG-pDMAEMA-*co*-AEMA, abbreviated as pDMAEMA) and rhodamine-labeled oligonucleotide (ON). FFS possesses high spatial and temporal resolution, which permits an enhanced ability to differentiate between associated and dissociated polyplexes. The authors' use of FFS led to novel and interesting findings, such as the observation that high molecular weight pDMAEMA (1700 kDa) dissociates from ON within the cytoplasm without entering the nucleus, whereas low molecular weight PLL (30 kDa) releases ON after nuclear entry.

Despite successes such as this, there remain several limitations associated with the use of fluorescent dyes for labeling the polymeric vehicle—such as photobleaching, fast fluorescence decay, and nonuniform labeling of the polymer.[21] Further, some research has also indicated that labeling the polymer with a fluorescent label can change its physiochemical properties. For example, Remaut et al.[22] have shown with the help of fluorescence correlational spectroscopy (FCS) that diblock PEI-PEG polymers lose their ability to bind to nucleic acids when labeled with a fluorescent dye, such as Cy5. For these reasons, other labeling strategies are being widely investigated to further improve understanding of delivery vehicle trafficking.

One set of well-studied alternative labeling agents are quantum dots (QDs). Advantages of QDs over fluorescent dyes include their high extinction coefficients, strong control over optical properties, and reduced susceptibility to photobleaching.[21,23] Many QDs form FRET pairs with fluorescent organic dyes and are useful for monitoring polyplex trafficking *in vitro*. FRET is a highly sensitive technique that provides information about intracellular interactions on the nanometer scale. Upon its excitation, the emission of one fluorescent species serves to excite a second species. Given the short distance over which the emission can propagate, detection of emission from the second species serves as a strong indicator of the close proximity (that is, molecular interaction) between the two indicators. When these two indicators are attached to separate molecules, a positive FRET

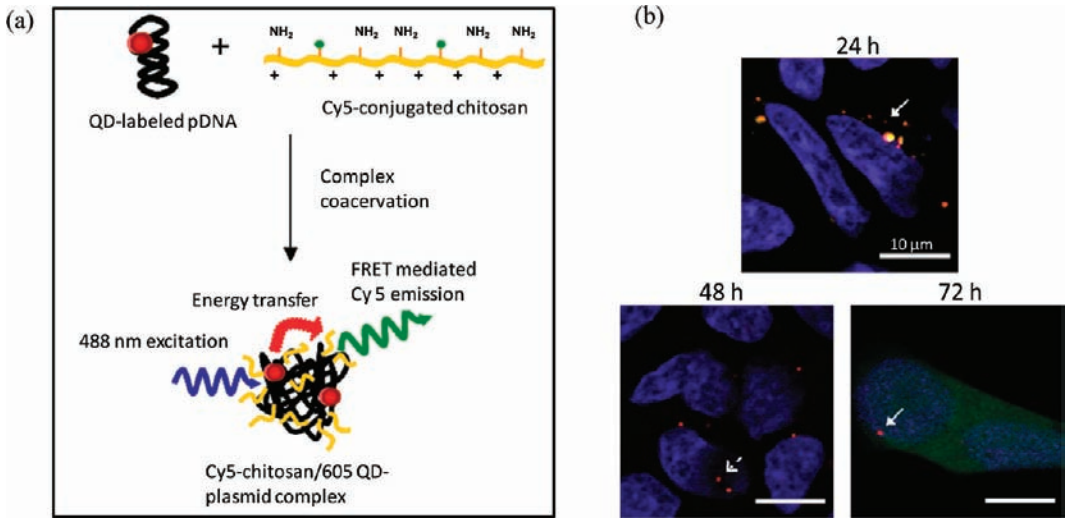

Figure 1. (a) Condensation of DNA and chitosan polymer to form compact nanocomplexes. Association of DNA and polymer was indicated by sensitized FRET signal from Cy5 upon excitation of QD-labeled DNA. (b) Confocal images showed localization of intact chitosan−DNA complexes (indicated by sensitized FRET signal from Cy5 in yellow/orange color) in the perinuclear region at 24 h, while the onset of DNA release (red) and its trafficking to the nucleus (blue) was observed at 48 and 72 h post-transfection (absence of Cy5 signal).
Figure reprinted from Ho, Y.-P., Chen, H. H., Leong, K. W., Wang, T.-H. (2006) Evaluating the intracellular stability and unpacking of DNA nanocomplexes by quantum dots-FRET, *J. Controlled Release 116*, 83-89 with permission, Copyright Elsevier (2006).

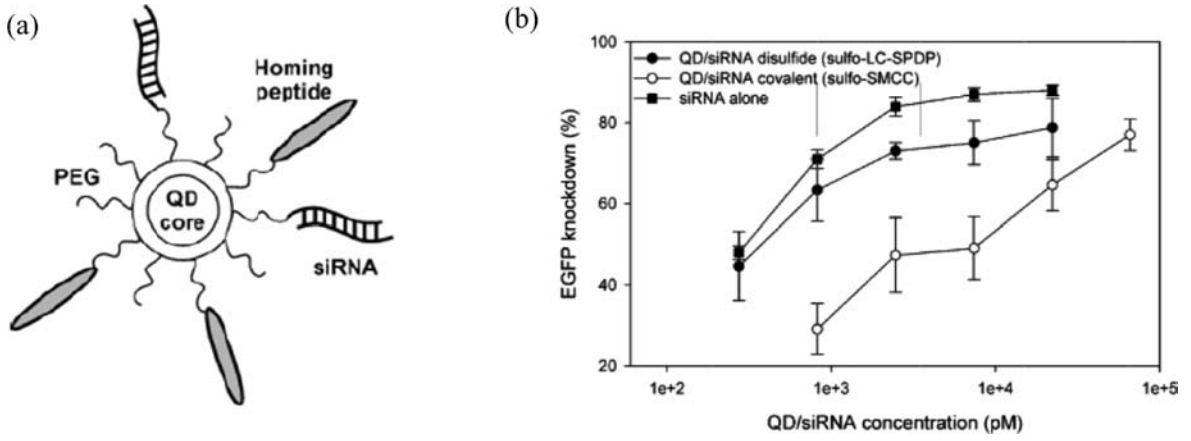

Figure 2. (a) Schematic representation of siRNA containing QD nanoparticles decorated with PEG and a targeting peptide. (b) Significantly greater EGFP knockdown was observed for the QD/siRNA complexes containing the reducible disulfide (sulfo-LC-SPDP) linker versus the nonreducible (sulfo-SMCC) linker.
Figure reprinted from Derfus, A. M., Chen, A. A., Min, D.-H., Ruoslahti, E., Bhatia, S. N. (2007) Targeted quantum dot conjugates for siRNA delivery. *Bioconjugate Chem. 18,* 1391-1396 with permission from the American Chemical Society (ACS).

signal (emission of the second indicator) is evidence of physical association of these two molecules at the time of signaling.

As an example, Ho et al.[16] demonstrated that the intracellular dissociation of polymer−pDNA complexes can be monitored via QD-FRET (Figure 1). In this study, streptavidin-functionalized, Cy5-labeled chitosan was conjugated to QD-labeled pDNA via biotin−streptavidin binding. QD-FRET analysis was performed using electron and confocal microscopy at 24, 48, and 72 h post-transfection in HEK293 cells to study unpackaging of chitosan−pDNA complexes. Their investigation indicated that at 24 h after transfection, polyplexes were localized in the perinuclear region, whereas at 72 h post-transfection, polyplexes were dissociated and DNA was located in the nucleus without any signal from chitosan (Cy5).

Commonly used techniques to visualize RNA interference (RNAi) experiments are cotransfection of siRNA with a fluorescent reporter gene (to monitor degree of reporter gene knockdown) and/or covalent end-modification of the sense strand on the siRNA to attach a fluorophore. Although above-mentioned strategies have some utility, these techniques are limited in that they are best suited for highly silenced genes and ignore moderately silenced genes, which might be of interest in some cases. Further, current transfection methods are incapable of discriminating among multiple siRNA molecules delivered simultaneously. Additionally, QDs do not photobleach and have longer fluorescence lifetimes compared to organic dyes. As an example, Bhatia and co-workers[24,25] synthesized near-infrared (NIR) QDs (emission max 655 or 705 nm) functionalized with

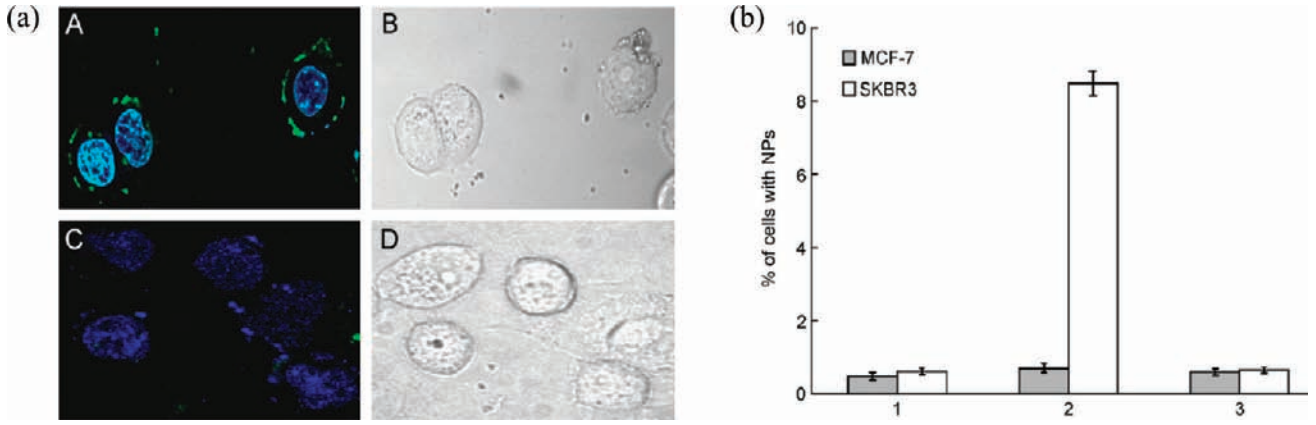

Figure 3. (a) Laser confocal microscopy images of SKBR3 cells showing HER2 siRNA-containing chitosan−QD nanoparticles (cyan) with (A) and without (C) anti-HER2 antibody labeling (green). Corresponding bright field microscopy images are shown in (B) and (D). (b) Cellular uptake of chitosan-QD-siRNA nanoparticles labeled with HER2-targeting antibody in SKBR3 and MCF-7 cell lines. "1" denotes control cell populations, "2" denotes cells exposed to HER2-targeted chitosan-QD-siRNA nanoparticles, and "3" denotes cells exposed to nontargeted chitosan-QD-siRNA nanoparticles. The role of HER2 targeting is revealed by the enhanced uptake of "2" by SKBR3 cells (vs MCF-7).
Figure adapted from Tan, W. B., Jiang, S., Zhang, Y. (2007) Quantum-dot based nanoparticles for targeted silencing of HER2/neu gene via RNA interference, *Biomaterials 28*, 1565-1571 with permission, Copyright Elsevier (2007).

PEG and amino groups and attached with an siRNA (designed to knock down expression of enhanced green fluorescent protein (EGFP)) and a cell-targeting moiety (tumor-homing F3 peptide; Figure 2) via reducible disulfide (sulfo-LC-SPDP) or nonreducible (sulfo-SMCC) linkers. The F3-peptide and siRNA were attached to the surface of the QD via reducible or nonreducible linkers and their effect on cell internalization and gene knockdown was compared. The resulting molecule was transfected into cultured cells with Lipofectamine 2000, a commercially available transfection reagent, and the EGFP expression was monitored by measuring the fluorescence intensity using flow cytometry.The use of reducible versus nonreducible cross-linker for the F3 peptide did not affect the cell internalization. However, the use of reducible disulfide linker (sulfo-LC-SPDP) for siRNA showed significantly higher gene knockdown, possibly due to a change in interaction of siRNA with the RNA induced silencing complex through release of the siRNA from the particle surface.

In another example, Tan et al.[26] developed a "self-tracking" siRNA delivery vehicle based upon chitosan-coated quantum dots (green fluorescent CdSe/ZnS) as a core. The negatively charged QD was coated with positively charged chitosan via electrostatic attraction and the surface of chitosan was complexed with negatively charged siRNA against human epidermal growth factor receptor 2 (HER2) to promote delivery of the nanoparticles to breast cancer cells (SKBR3 cells) in which HER2 is upregulated; a variation of these nanoparticles was also coated with an anti-HER2 antibody (via standard EDC/NHS chemistry). Cellular uptake studies were performed and confocal microscopy on both SKBR3 and MCF-7 (HER2 under-expressed) cell lines to validate the targeting efficacy of the HER2-targeting moiety on the nanoparticles in cellular uptake and target gene knockdown (Figure 3). The QD was encapsulated to probe the delivery of the siRNA−carrier system.

Prigodich et al.[27] have developed nanoconjugates that can both detect and regulate intracellular mRNA levels via monitoring an increase in fluorescence of a "flare" that is released upon successful binding of a therapeutic oligonucleotide to its target mRNA (Figure 4a). Nanoconjugates containing gold nanoparticles were functionalized with a therapeutic antisense oligonucleotide (a chimera of DNA and a linked nucleic acid (LNA)) which binds to a specific region of an mRNA suppressing expression of survivin, a well-known gene for cancer diagnosis and treatment. An additional complementary short oligonucleotide labeled with Cy5 was conjugated onto the nanoflare that is released upon binding to the target mRNA, thereby increasing the Cy5 fluorescence intensity. The mRNA detection technique is rapid (reaches completion in 10 min) and sensitive for single-base pair mismatch recognition. These nanoflares deplete mRNA levels in sequence- and dosage-dependent manners and, consequently, hold promise toward mRNA-directed theranostics (Figure 4b).

Our group has developed a new set of theranostic polymers for the combined delivery of nucleic acids and magnetic resonance imaging (MRI) contrast agents. [28] The macromolecule structures contain a lanthanide-binding domain (diethylenetriaminepentacetic acid or DTPA) and an oligoethyleneamine (PEI-like) domain that contain secondary amines, which are protonated at physiological pH and promote binding and compaction of nucleic acids into polyplexes (Figure 5a). The flexibility in this platform is that the lanthanide-binding domain can be chelated to either gadolinium (Gd), a MRI contrast agent for sub-micrometer to millimeter scale imaging or luminescent europium (Eu) for visualization on the nanometer to micrometer scale, which can be imaged with fluorescence microscopy. These polymeric delivery vehicles integrate both therapeutic delivery and diagnostic imaging functionalities into one system. Plasmid DNA (pDNA) transfection studies performed on polyplexes formed with these delivery beacons reveal that the Gd^{3+}-containing analogues show high image contrast (compared to untransfected cells) and Eu^{3+} analogues can be imaged with fluorescent microscopy inside the cell (Figure 5b,c). These polyplexes formed with these polymer beacons showed high cell internalization efficiency and a low toxicity profile, and they hold promise to individually monitor both the nucleic acid and the polymer vehicle during the delivery process. The use of a lanthanide metal, which luminesces (f-f transition) instead of fluoresces, as opposed to other common fluorescent markers (i.e., fluorescent dyes) eliminates concerns related to photobleaching and nonuniform labeling. Also, the

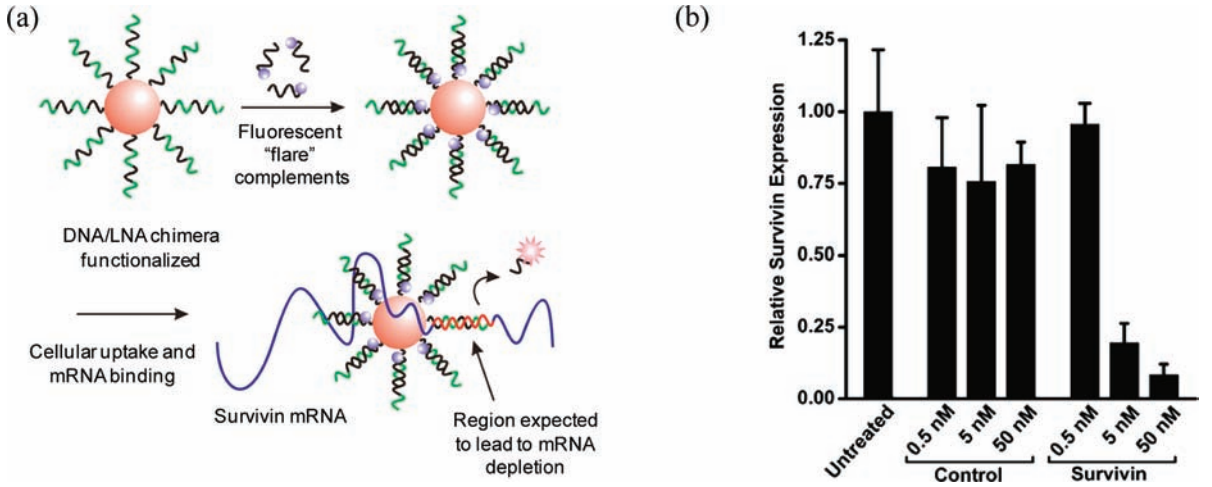

Figure 4. (a) Schematic of antisense oligonucleotide delivering gold nanoconjugates. (b) RT-PCR mRNA knockdown results for control and therapeutic (survivin) oligonucleotide delivery into HeLa cells normalized to untreated cells. Dosage-dependent knockdown was observed for survivin and no significant knockdown for controls at high therapeutic dosage.
Figure adapted from Prigodich, A. E., Seferos, D. S., Massich, M. D., Giljohann, D. A., Lane, B. C., Mirkin, C. A. (2009) Nanoflares for mRNA regulation and detection. *ACS Nano 3,* 2147-2152 with permission from ACS.

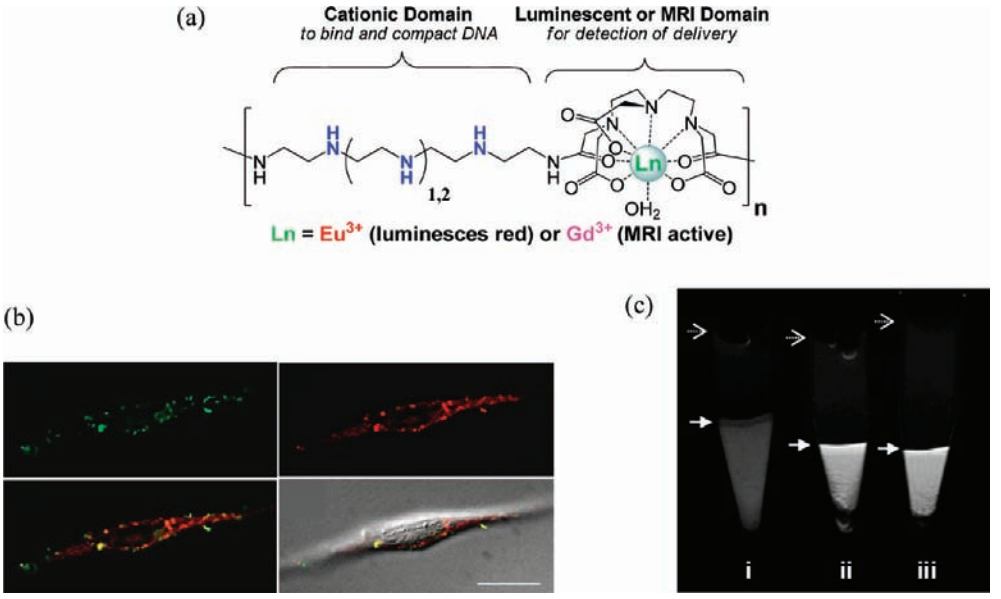

Figure 5. (a) Chemical structure of lanthanide- and oligoethyleneamine-containing theranostic polymers for nucleic acid delivery. (b) Deconvoluted confocal microscopy images of HeLa cells transfected with polyplexes containing Eu^{3+}-chelated polymer (red) and fluorescein isothiocyanate- (FITC−) labeled pDNA (green), and their overlay with DIC (differential interference contrast), shows accumulation of polyplexes in the perinuclear region and in cytoplasm. (c) Magnetic resonance (MR) images of cells transfected with two different Gd-containing polymers, (ii) and (iii), compared to untreated HeLa cells (i).
Figure adapted from Bryson, J. M., Fichter, K. M., Chu, W.-J., Lee, J.-H., Li, J., Madsen, L. A., McLendon, P. M., Reineke, T. M. (2009) Polymer beacons for luminescence and magnetic resonance imaging of DNA delivery. *Proc. Natl. Acad. Sci. U.S.A. 106,* 16913−16918, Copyright (2009) National Academy of Sciences, U.S.A.

long luminescence lifetime (on the order of milliseconds) characteristic of the lanthanides enables easy removal of background fluorescence via time-delayed measurements. Thus, FRET is a powerful technique for studying nanometer-scale molecular interactions. This phenomenon is called luminescence (or lanthanide-based) resonance energy transfer (LRET) and it offers several advantages over FRET.[29] Moreover, these lanthanides are known to form LRET pairs with some fluorescent dyes, such as tetramethyl rhodamine (TMR), Cy5, and some APC (allophycocyanin) dyes, which may be beneficial to monitor kinetics of polyplex association−dissociation via LRET. Current efforts are directed toward studying the effect of an increase in amine stoichiometry on transfection efficiency and toxicity and monitoring complex unpackaging via LRET with terbium- (Tb^{3+}-) containing analogues of these polymers.

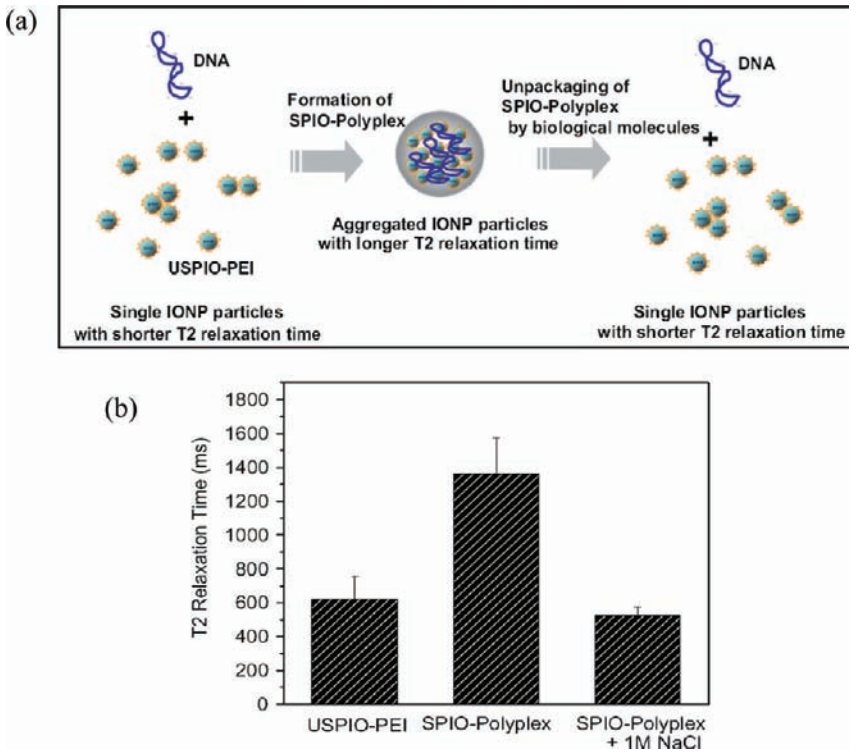

Figure 6. (a) Proposed mechanism of a "T_2 relaxation switch". (b) T_2 relaxation times upon formation of polyplexes and their subsequent dissociation upon addition of salt.
Figure adapted from Park, I.-K., Ng, C.-P., Wang, J., Chu, B., Yuan, C., Zhang, S., Pun, S. H. (2008) Determination of nanoparticle vehicle unpackaging by MR imaging of a T2 magnetic relaxation switch. *Biomaterials 29*, 724-732 with permission, Copyright Elsevier (2008).

Several interesting examples of *in vivo* administration of theranostics containing nucleic acid therapies have been reported previously; these materials are useful for the study of pharmacokinetic and biodistribution profiles of both the medicinal agent and the vehicle *in vivo*. Similar to the *in vitro* imaging discussed above, several labeling agents can be conjugated to the delivery vehicle and used for *in vivo* diagnostic imaging. Imaging agents such as NIR quantum dots (optical imaging), magnetic resonance contrast agents (MR imaging), and PET/SPECT (positron emission tomography/single photo emission computerized tomography) agents can be incorporated into the delivery system. Each of these imaging modalities has its advantages and disadvantages. For example, while MRI has good spatial resolution (10−100 μm), it is hampered by low sensitivity (micromolar quantities of paramagnetic agent must be used to see significant change in signal). Nuclear imaging techniques such as PET and SPECT imaging possess high sensitivity but are limited by low spatial resolution. Additionally, generating radionuclides in the cyclotron is expensive and exposure to ionizing radiation can be harmful in the long term.

In the case of MRI, to obtain high image contrast, significant accumulation of the contrast agents at the target site is necessary. This can be achieved by functionalizing contrast agents with suitable ligands that target various cell receptors, such as transferin receptor, folate receptor, and human/epidermal growth factor receptor 2, upregulated on the surface of various cancer cells. Both T_1 (positive) and T_2 (negative) contrast agents can be employed within theranostic materials. For *in vitro* imaging, iron oxide based nanoparticles (T_2 contrast agents) have been used and are discussed herein. Additionally, these particles can be functionalized with targeting ligands like human holo-transferin that are covalently attached to the dextran-coated monocrystalline iron oxide (Tf-MION) or cross-linked iron oxide (Tf-CFIO) and can easily be taken up by cells via receptor-mediated endocytosis.[30−32]

Park et al.[33] developed magnetic iron oxide-based nanoarchitectures that allow assessment of polyplex dissociation via tracking of changes in T_2 relaxation rates. Poly(ethyleneimine) (branched PEI, MW 10 kDa) that can bind to DNA via electrostatic interactions was covalently conjugated to ultrasmall superparamagnetic iron oxide (USPIO) to form higher-order structures (size ~100 nm). A "T_2 relaxation switch" (Figure 6a) was proposed as a tool for monitoring packaging and unpackaging of the polyplexes. When complexed with DNA, the nanoparticle carriers show longer T_2 relaxation times; conversely, upon dissociation, they reduce back to original values (Figure 6b). Increases or decreases in T_2 relaxation times upon formation or dissociation of polyplexes, respectively, can be attributed to changes in particle size, surface functional groups, and/or surface area available for water exchange from native USPIO. Salt (sodium chloride)-induced polyplex dissociation was studied via three different methods: (i) YOYO dye exclusion, (ii) turbidity measurement, and (iii) decrease in T_2 relaxation time. Plasmid-containing USPIO-PEI nanoparticles were less toxic to HeLa cells than PEI only (for 10 kDa and 25 kDa molecular weights at the same net PEI concentration) and showed higher luciferase gene expression (at N/P 15) than PEI alone.

Dubertret et al.[34] demonstrated that QDs encapsulated into phospholipid-block copolymer micelles (Figure 7) can be used as fluorescent probes for *in vitro* and *in vivo* imaging. ZnS-coated Cd−Se QDs encapsulated in the hydrophobic cavity of micelles

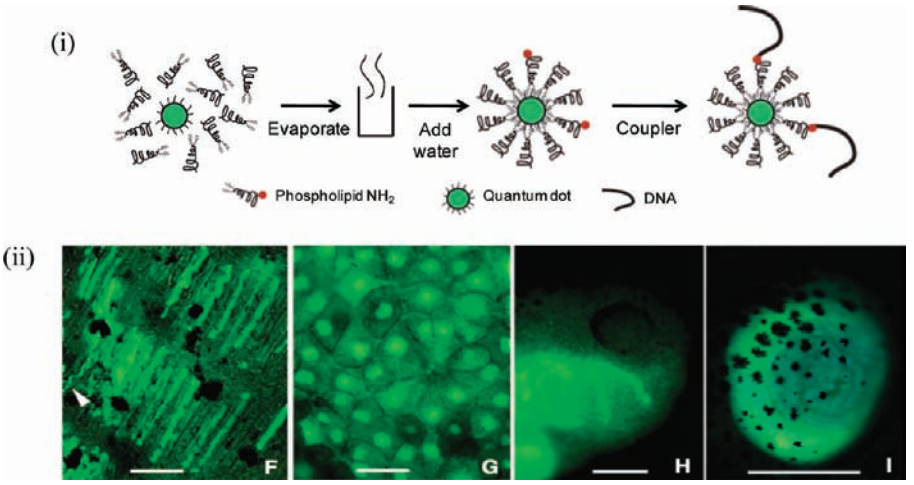

Figure 7. (i) Schematic of formation of a QD-micelle and its conjugation to single-stranded DNA (ssDNA). (ii) Fluorescence microscopy images of QD-micelles in different embryonic cells including: (F) axon (arrow) and somites at tadpole stage 40; (G) QDs localized in nucleus during midblastula stages; (H) neural crest cells; and (I) gut of an injected embryo. Scale bars: (F) and (G) 30 μm; (H) and (I) 0.5 mm.
Figure adapted from Dubertret, B., Skourides, P., Norris, D. J., Noireaux, V., Brivanlou, A. H., Libchaber, A. (2002) In vivo imaging of quantum dots encapsulated in phospholipid micelles. *Science 298*, 1759-1762 with permission from American Association for Advancement of Science.

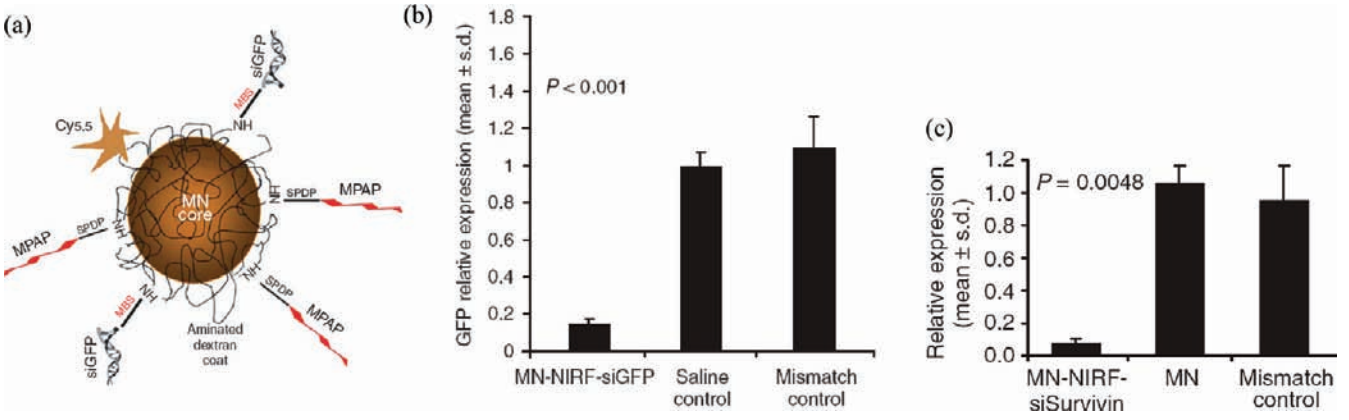

Figure 8. (a) Schematic of dextran-coated magnetic iron oxide nanoparticles containing siGFP, a NIR dye, Cy5, and a membrane translocation peptide, MPAP. Quantitative RT-PCR data of target mRNA levels in tumors of mice treated with MN-NIRF-siGFP (b) or MN-NIRF-siSurvivin (c) compared with controls.
Figure adapted from Medarova, Z., Pham, W., Farrar, C., Petkova, V., and Moore, A. (2007) In vivo imaging of siRNA delivery and silencing in tumors. *Nat. Med. 13*, 372-377 with permission from Nature Publishing Group.

formed with poly(ethylene glycol)-phosphatidylethanolamine (PEG-PE) and phosphatidylcholine (PC) were functionalized with primary amines to allow covalent binding to thiol-functionalized DNA. *In vivo* studies performed in *Xenopus* embryos revealed that these QD-micelles were able to label all types of embryonic cells without any aggregation, including somites, neurons, axonal tracks, ectoderm, neural crest, and endoderm. Additionally, QDs were found to be stable against photobleaching for as long as 80 min, a time at which rhodamine green dextran dye was completely photobleached. Toxicity studies indicated no abnormalities in the embryo at typical concentration ($<5 \times 10^9$ QDs/cell)—they showed unaltered phenotype and normal health.

Medarova et al.[35] synthesized dextran-coated superparamagnetic nanoparticles (MN) covalently attached to siRNA targeting green fluorescent protein (siGFP; five per particle), an NIR-emitting dye, Cy5.5 (NIRF; three per particle), and a membrane translocation peptide, myristolyated polyarginine peptide (MPAP; four per particle) to facilitate trafficking of nanoparticles inside the cytoplasm of target cells (Figure 8a). Cellular uptake of MN-NIRF-siGFP in 9 L-glioma cells (that stably expressed green fluorescent protein (GFP)) was monitored by fluorescence microscopy. These results were compared with red fluorescent protein (RFP)-expressing 9 L-glioma cells to test the specificity of siRNA target toward GFP; target mRNA levels were compared via quantitative RT-PCR. *In vivo* studies in tumor-bearing mice bilaterally implanted with 9 L-GFP- and 9 L-RFP-expressing glioma cells showed significant mRNA knockdown in 9 L-GFP tumors compared to saline only and mismatch controls (Figure 8b). After success of these proof-of-concept studies with GFP, MN-NIRF-MPAP-siSurvivin was developed to target survivin, a member of the inhibitor of apoptosis protein (IAP) family. MN-NIRF-MPAP-siSurvivin was injected into nude mice bearing subcutaneous human colorectal carcinoma tumors (LS174T) over a

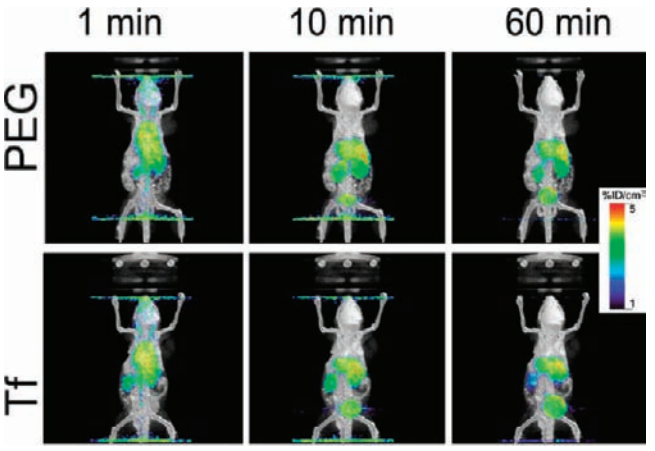

Figure 9. Fused micro-PET/CT images of transferrin-targeted (Tf) and nontargeted (PEG) nanoparticles injected into tumor-bearing mice and monitored at different time points (1, 10, and 60 min) after injection.
Figure adapted from Bartlett, D. W., Su, H., Hildebrandt, I. J., Weber, W. A., Davis, M. E. (2007) Impact of tumor-specific targeting on the biodistribution and efficacy of siRNA nanoparticles measured by multimodality in vivo imaging. *Proc. Natl. Acad. Sci. U.S.A. 104,* 15549−15554. Copyright (2007) National Academy of Sciences, U.S.A

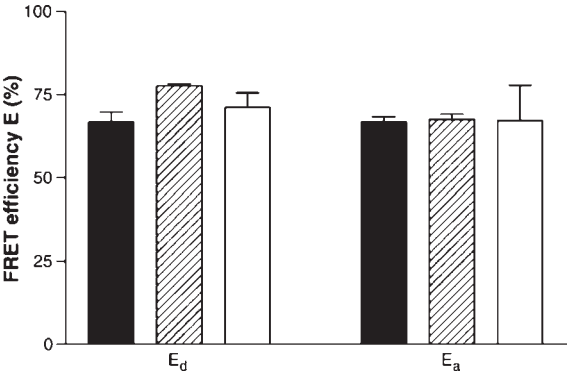

Figure 10. FRET efficiencies for donor (E_d) and acceptor (E_a) calculated based on three different measuring techniques: fluorimetry (solid bars), flow cytometry (hatched bars), and fluorescence microscopy (open bars) showed comparable results. The excitation wavelengths used for flow cytometry and fluorescence microscopy were 488 and 523 nm, respectively, and emission signals were monitored at 670 nm and above 650 nm, respectively.
Figure adapted from Schneider, S., Lenz, D., Holzer, M., Palme, K., Suess, R. (2010) Intracellular FRET analysis of lipid/DNA complexes using flow cytometry and fluorescence imaging techniques. *J. Controlled Release 145,* 289-296 with permission, Copyright Elsevier (2010).

2-week period and quantified by RT-PCR (Figure 8c)—strong reduction in survivin mRNA levels was observed. Additionally, *in vivo* studies with these particles indicated low cytotoxicity and a lack of immunostimulatory response (as monitored by aspartate aminotransferase (AST) and alanine aminotransferase (ALT) levels).

Davis and co-workers[36,37] have developed a series of linear cyclodextrin-containing polycations (CDPs) for *in vivo* delivery of nucleic acids. Their studies in mice have indicated, upon systemic injection, significant uptake (of polyplexes containing cyclodextrin polycations and siRNA against EWS-FLI1 gene to treat Ewing sarcoma) in the tumor microenvironment can be achieved due to the EPR effect; however, to maximize cellular internalization and specificity, the presence of a targeting ligand on the nanoparticles is crucial. Bartlett et al.[38] investigated the biodistribution and pharmacokinetics of polyplexes created by complexing CDP with siRNA via positron emission tomography (PET), computed tomography (CT), and bioluminescence imaging (BLI). The CDP delivery vehicles were conjugated to 1,4,7,10-tetraazacyclododecane-1,4,7,10-tetraacetic acid (DOTA), a chelator for [^{64}Cu], to introduce micro-PET/CT imaging functionality. *In vivo* biodistribution studies using micro-PET/CT in mice indicated that transferrin (Tf)-targeted and nontargeted nanoparticles have similar biodistribution and pharmacokinetic profiles (Figure 9). However, tissue analysis by bioluminescent imaging indicated that the targeted nanoparticles achieved greater target gene knockdown and thus had greater siRNA efficacy.

In a separate set of studies, Schneider et al.[39] studied intracellular trafficking of DNA/lipid complexes (lipoplexes) in rat smooth muscle cells (A10) via FRET. DNA and lipids were labeled with Cy3 and Cy5, respectively, and analyzed via flow cytometry, confocal microscopy, and fluorimetric techniques to calculate the donor- (E_d) and acceptor-based (E_a) efficiencies of energy transfer (Figure 10). Different optical settings (donor excitation wavelengths) were used for flow cytometry (excitation = 488 nm) and microscopy (excitation = 523 nm) to study the kinetics of lipoplex dissociation. Analysis of the efficiency of donor- and acceptor-based energy transfer studied at different time points (3, 5, 9, and 24 h) indicated that most of the DNA was released from the lipoplexes by 24 h post-transfection. These findings and techniques are crucial to understand the intracellular trafficking and mechanism of vehicle unpackaging, and their studies have highlighted the value of FRET to facilitate information acquisition with high spatial resolution inside the cell.

Several kinds of drug delivery vehicles have been developed over the years, such as polymeric micelles, block copolymers, liposomes, inorganic iron oxide nanoparticles coated with a biocompatible polymer, and quantum dot conjugates. These vehicles have been used to deliver a variety of hydrophobic/hydrophilic anticancer drugs such as paclitaxel, doxorubicin, methotrexate, and camptothecin. In addition to inclusion of these drugs, the delivery vehicles can be decorated with various imaging agents to simultaneously monitor the therapeutic delivery.

With the increasing concerns of nephrogenic system fibrosis due to gadolinium-based blood pool agents in patients with renal disease or with recent liver transplant,[40] several approaches[41,42] have been recently taken to substitute gadolinium with manganese (Mn). For example, Pan et al.[41] developed a fibrin-targeting "nanobialys"-based contrast agent and drug delivery vehicle containing a porphyrin which chelates Mn. "Nanobialys" are toroidal-shaped, nearly monodisperse reverse micellar structures formed from amphiphilic branched polyethyleneimine (PEI) in anhydrous chloroform with a core containing a porphyrin−Mn(III) complex, which is a T_1 contrast agent for MRI (Figure 11a). Amphiphilic PEI was modified by reaction of amines with hydrophobic linoleic acid (55% of primary amines were reacted) via EDC coupling. The core of the micelles was loaded with a hydrophobic (camptothecin) or hydrophilic (doxorubicin) chemotherapeutic drug, and the drug release profile was studied *in vitro* for 3 days (Figure 11c). The MR imaging of fibrin (Figure 11b) was performed with fibrin-rich clots supported on silk sutures in phosphate-buffered saline (PBS) with the help of sealed polystyrene test tubes. The MR imaging results for

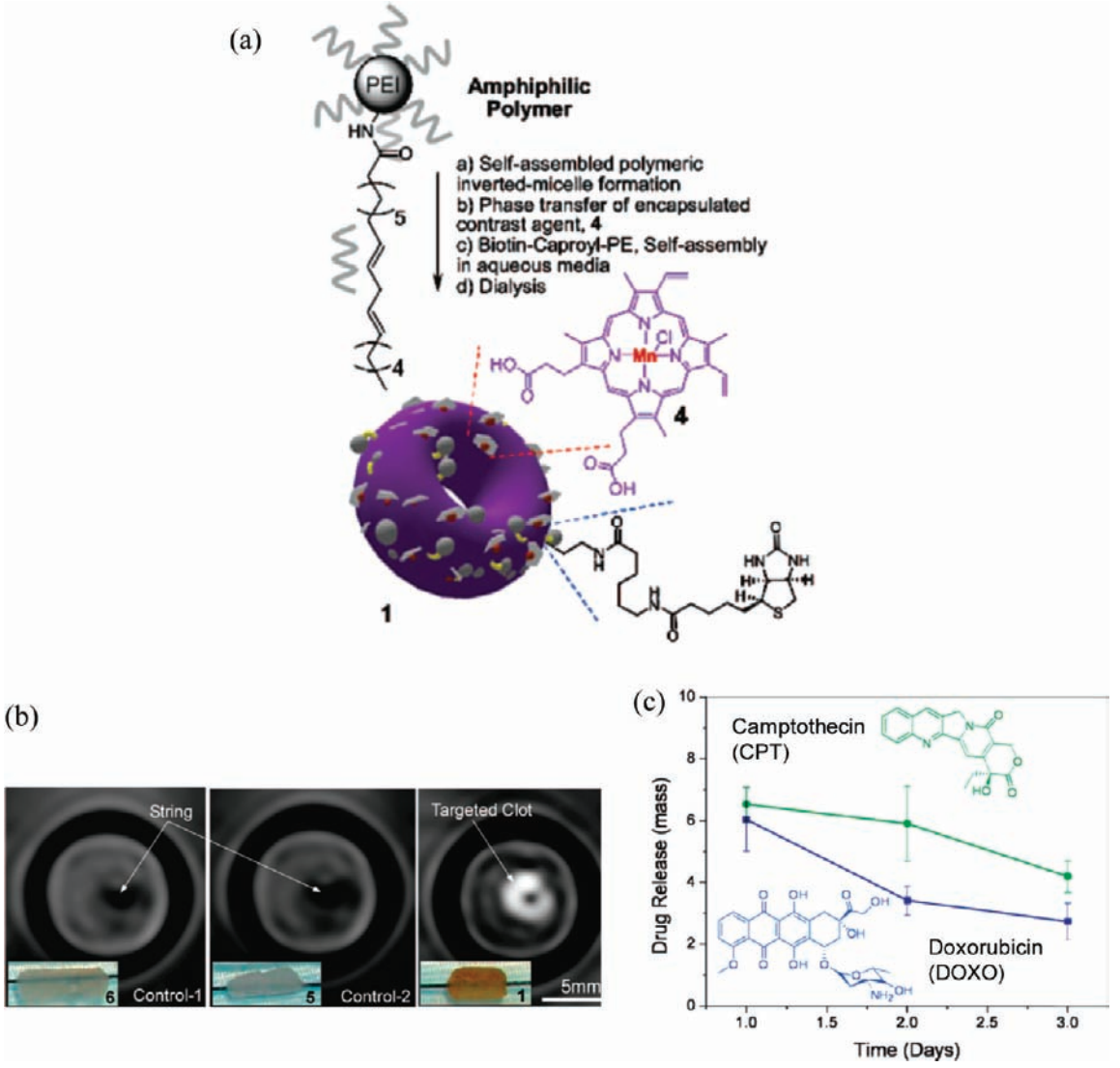

Figure 11. (a) Schematic of formation of nanobialys. (b) T_1-weighted MR images of Mn(III)-containing, fibrin-targeting nanobialys (right) compared with metal-free and nontargeted controls (left and center, respectively). (c) Drug (CPT or DOX) release from the nanobialys was monitored for 3 days.

Figure adapted from Pan, D., Caruthers, S. D., Hu, G., Senpan, A., Scott, M. J., Gaffney, P. J., Wickline, S. A., Lanza, G. M. (2008) Ligand-directed nanobialys as theranostic agent for drug delivery and manganese-based magnetic resonance imaging of vascular targets. *J. Am. Chem. Soc. 130,* 9186-9187. with permission from ACS.

targeted ligand-containing nanobialys (containing a fibrin-specific monoclonal antibody) were compared to nanobialys without any targeting ligand or without any metal inside as controls and demonstrated the role of the targeting agent in achieving contrast enhancement.

Shin et al.[42] developed manganese oxide-based hollow nanoparticles (HMONs) as dual (T_1 and T_2) MRI contrast and drug delivery agents. HMONs were synthesized by stabilization of manganese oxide nanoparticles with oleate, encapsulation with poly(ethylene glycol)-phospholipid, and selective removal of the manganese oxide core in acidic phthalate buffer solution (pH = 4.6) to dope it with doxorubicin (DOX). Cell culture studies indicated that these HMONs were efficiently taken up by cultured cancer cells and induced cell death. High T_1 and T_2 image contrast was obtained upon MR imaging of transfected cells as well as the brain of a mouse injected with HMONs (Figure 12).

It has been shown that, at very low concentrations, circulating iron can impart T_1 contrast to MR imaging; however, at concentrations that are commonly used for T_2-weighted imaging, T_2 contrast is the predominant effect.[43] Encapsulation of iron oxide within a hydrophobic matrix can abate the T_2 effect and, thereby, improve T_1 contrast; hence, this can enable one to develop positive contrast agents that are devoid of the gadolinium cation. Senpan et al.[43] developed vascular-targeted colloidal iron oxide nanocolloids for the detection of atherosclerotic ruptured plaques and antiangiogenic plaque therapy. These nanoparticles can be loaded with an antiangiogenic mycotoxin drug, fumagillin (Figure 13a). Colloidal iron oxide nanocolloids with phospholipids containing a partially cross-linked hydrophobic core and a low concentration of pure magnetite iron oxide particles (0.5% w/v) show high T_1 relaxivity (7 [Fe] mM^{-1} s^{-1}) compared to those with a mixed core (Fe_2O_3—Fe_3O_4 mixture,

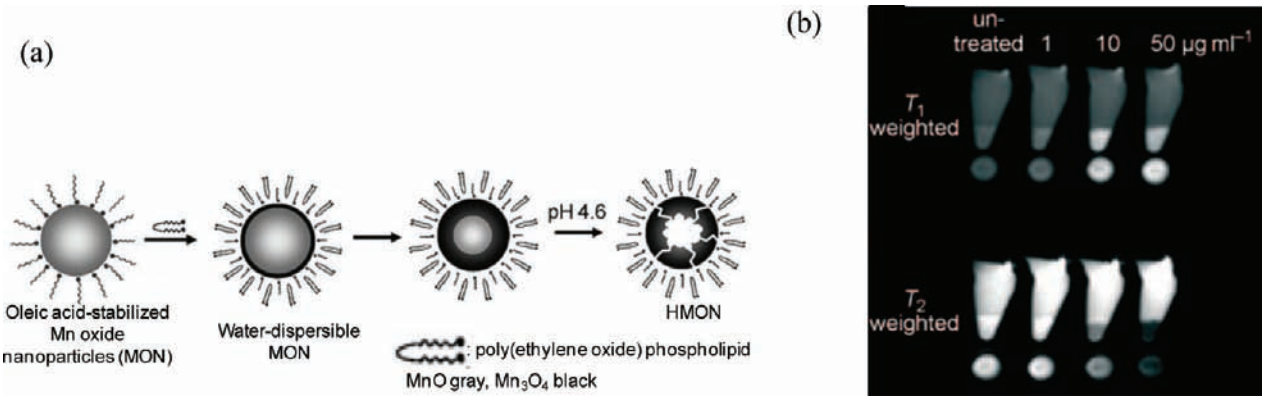

Figure 12. (a) Schematic of formation of HMON. (b) T_1- and T_2-weighted magnetic resonance images of DOX-loaded HMONs incubated with MCF-7 (human breast adenocarcinoma) cells at different concentrations and compared to untreated cells. A concentration-dependent increase in image contrast was observed.
Figure adapted from Shin, J., Anisur, R. M., Ko, M. K., Im, G. H., Lee, J. H., Lee, I. S. (2009) Hollow manganese oxide nanoparticles as multifunctional agents for magnetic resonance imaging and drug delivery. *Angew. Chem., Int. Ed. 48*, 321−324. Copyright Wiley-VCH Verlag GmbH & Co. KGaA. Reproduced with permission.

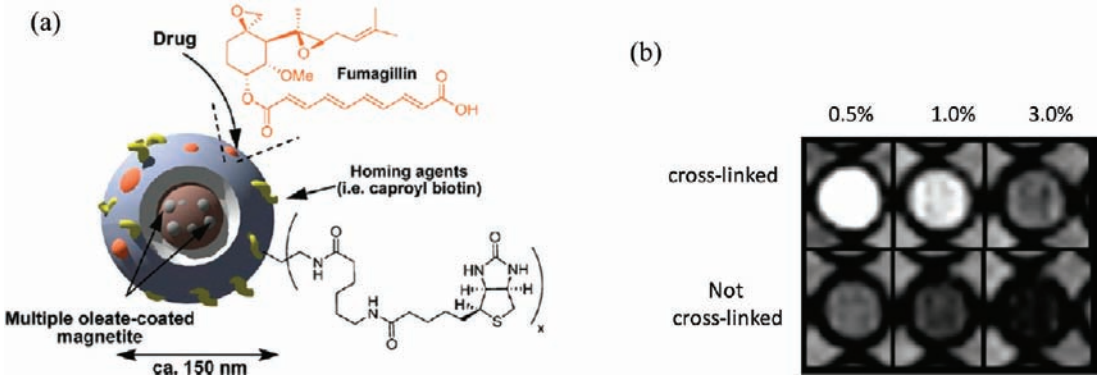

Figure 13. (a) Schematic of formation of fumagillin-loaded CION with a targeting ligand on the surface. (b) T_1-weighted MR imaging for colloidal iron oxide nanocolloids with (top row) and without (bottom row) surfactant cross-linking and with different extents of magnetite loading (0.5%, 1.0%, or 3.0% w/v). CIONs with the lowest magnetite loading evaluated showed the greatest image contrast.
Figure reprinted from Senpan, A., Caruthers, S. D., Rhee, I., Mauro, N. A., Pan, D., Hu, G., Scott, M. J., Fuhrhop, R. W., Gaffney, P. J., Wickline, S. A., Lanza, G. M. (2009) Conquering the Dark Side: Colloidal Iron Oxide Nanoparticles. *ACS Nano 3*, 3917-3926 with permission from ACS.

1.3 [Fe] mM^{-1} s^{-1}) and show potential as an alternative to gadolinium-containing agents (Figure 13b).

Calcium phosphate-based delivery vehicles can be effective for the delivery of hydrophobic, insoluble drugs such as ceramide and camptothecin. Calcium phosphate nanoparticles are relatively insoluble at physiological pH (pH = 7.4) but have improved solubility in acidic pH environments (pH = 6.5). Upon endocytosis, calcium phosphate will release the drug only in acidic compartments of the cell (endosomes and lysosomes), thus reducing the off-target toxicity in systemic administration. Researchers[44,45] have used this pH-tunable solubility to develop calcium phosphate-based vehicles for controlled, pH-triggered drug delivery. Kester et al. developed colloidally stable, amine carboxylate- and poly(ethylene glycol)-functionalized calcium phosphate nanoparticles (CPNPs) for delivery of ceramide (Cer6 and Cer10) and a fluorescent dye, rhodamine-water tracer (Rh-WT), to melanoma and breast adenocarcinoma cells.[45] Upon encapsulation into CPNPs, lifetimes and quantum properties of fluorescent dyes are believed to be improved.[46,47] Nanoparticles lacking any drug within were nontoxic (Figure 14) at low concentrations, and drug encapsulation induced apoptosis in neural, melanoma, and breast adenocarcinoma cells measured by MTS assay.

Barth et al. further modified CPNP with PEG groups and one of two different antibodies targeting the gastrin (gastrin-10-PEG-CPNP) and transferrin receptor (antiCD71-Avidin-CPNP), respectively.[44] These materials were created to study the *in vivo* biodistribution of CPNPs in murine models containing pancreatic (orthotopic) and breast (subcutaneous) cancer tumors. *In vivo* imaging using NIR microscopy (indocyanine green, ICG) on athymic female mice bearing tumor xenografts indicated greater tumor accumulation of targeted nanoparticles than non-targeted ones and penetration through the blood-brain barrier (Figure 15).

Langer and co-workers[48,49] developed poly(ethylene oxide) (PEO)-modified poly(β-amino ester) (PbAE)-based materials as novel, pH-responsive, nontoxic, and biodegradable nanoparticle drug carriers. Solid unprotonated PbAEs (Figure 16a) are insoluble at physiological pH; however, the solubility increases upon protonation of the amines along the backbone. Below

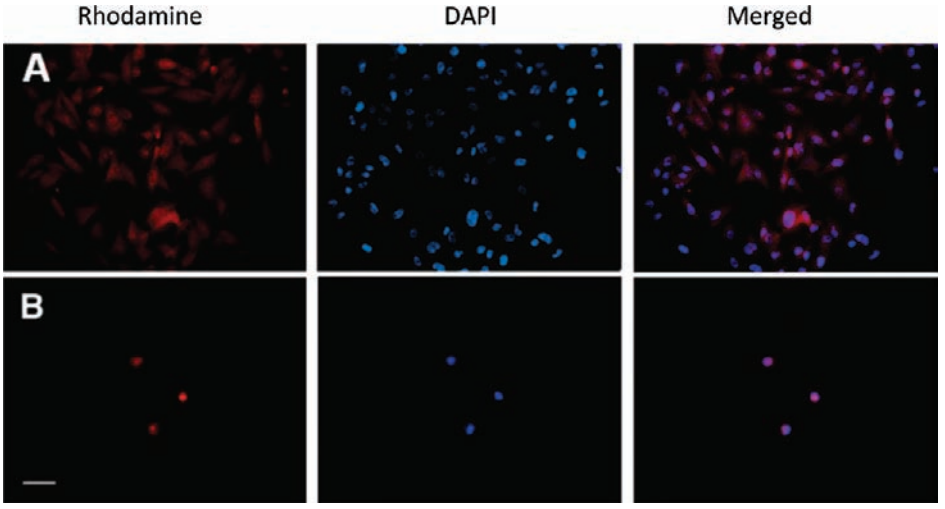

Figure 14. Cell images of cultured melanoma cells (UACC 903) exposed to Rh-WT-CPNPs with (B) or without (A) anticancer drug (Cer10). Cell nuclei stained with DAPI (blue). Cer10-containig CPNPs, unlike control CPNPs, induced melanoma cell death.
Figure adapted from Kester, M., Heakal, Y., Fox, T., Sharma, A., Robertson, G. P., Morgan, T. T., Altinoglu, E. I., Tabakovic, A., Parette, M. R., Rouse, S., Ruiz-Velasco, V., and Adair, J. H. (2008) Calcium phosphate nanocomposite particles for *in vitro* imaging and encapsulated chemotherapeutic drug delivery to cancer cells. *Nano Lett. 8*, 4116-4121with permission from ACS.

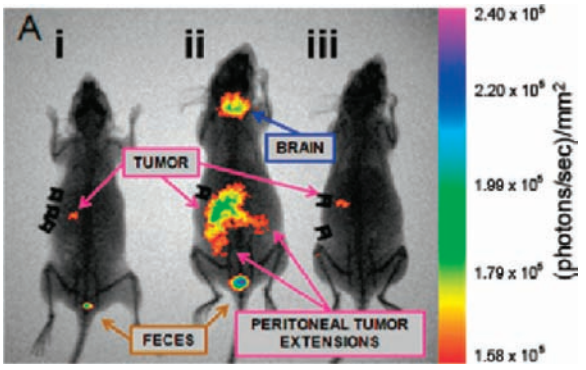

Figure 15. Human BxPC-3 pancreatic cancer cells were xenografted orthotopically in athymic nude mice. Biodistribution of indocyanine green (ICG) loaded PEG-CPNPs decorated with one of two different gastrin targeting groups (gastrin-10 (ii) and pentagastrin (iii)) was assessed *in vivo* using NIR imaging and compared to untargeted ICG loaded-PEG-CPNPs. Both nontargeted (i) and pentagastrin-targeted CPNPs showed some tumor accumulation; however, significantly higher accumulation was observed with gastrin-10-targeted PEG-CPNPs.
Figure adapted from Barth, B. M., Sharma, R., Altinoglu, E. I., Morgan, T. T., Shanmugavelandy, S. S., Kaiser, J. M., McGovern, C., Matters, G. L., Smith, J. P., Kester, M., Adair, J. H. (2010) Bioconjugation of calcium phosphosilicate composite nanoparticles for selective targeting of human breast and pancreatic cancers *in vivo*. *ACS Nano 4,* 1279-1287 with permission from ACS.

pH 6.5, PbAEs release their payload of chemotherapeutic drug, such as paclitaxel. *In vivo* biodistribution of encapsulated polymeric nanoparticles was studied in nude mice via radiolabeling using ^{111}Indium oxine (Figure 16b). When tumor-bearing (human ovarian adenocarcinoma) mice were evaluated 5 h after intravenous administration, 23-fold and 8.7-fold increases in tumor accumulation (compared to an aqueous solution of paclitaxel) were observed for paclitaxel-loaded PEO-PbAE nanoparticles and PEO-poly(caprolactam) (PCL) nanoparticles, respectively.

In another approach to theranostics, magnetoplasmonic nanoparticle assemblies (MPAs) combine both the magnetic and optical properties of metal nanoparticles and can be imaged with both magnetic resonance imaging and photoacoustic imaging. The general method for synthesizing these nanoparticles is by gradual reduction of gold nanoparticles in the presence of magnetic metal particles. The field of MPAs has been primarily restricted to hyperthermia or photothermal ablation treatment in cancer therapy thus far, and there have been few examples of incorporation of anticancer drugs within these nanoparticles. Chen et al.[50] synthesized magnetoplasmonic particles with a magnetic iron oxide (Fe_3O_4) core by coprecipitation—the core was coated with a porous, water-dispersible silica layer and then functionalized with gold nanoparticles, forming corona-like structures via surface amine functionality. This corona-like morphology was studied in MPAs containing curcumin, an anticancer drug (Figure 17a), using transmission electron microscopy (TEM) (Figure 17c); the particle size was determined to be ∼400 nm and ∼600 nm for MPA-curcumin and MPA-PEG-curcumin, respectively. The T_2 relaxation time of human leukemia cells (HL-60) transfected with MPA particles loaded with curcumin was lower than that of untransfected cells, as expected. Further, results of an MTT assay to examine therapeutic efficiency revealed that, while MPA-PEG-curcumin outperforms MPA-curcumin, both are potent inducers of apoptosis in HL-60 cells (Figure 17b).

Several research groups have introduced multimodal imaging functionalities into drug delivery vehicles. For example, Xie et al.[51] adapted a novel approach of treating iron oxide nanoparticles (IONPs) with dopamine to make them moderately hydrophilic, thereby allowing them to be doped into human serum albumin (HSA) matrices in a way very similar to that used for drug loading. Using this technique, IONPs were surface functionalized with Cy5.5 (fluorescence imaging) and [^{64}Cu] (PET imaging) via NHS ester-NH_2 coupling (Figure 18a). For *in vivo* and *ex vivo* imaging, animal models were prepared by subcutaneously injecting glioblastoma cells (U87MG) into the

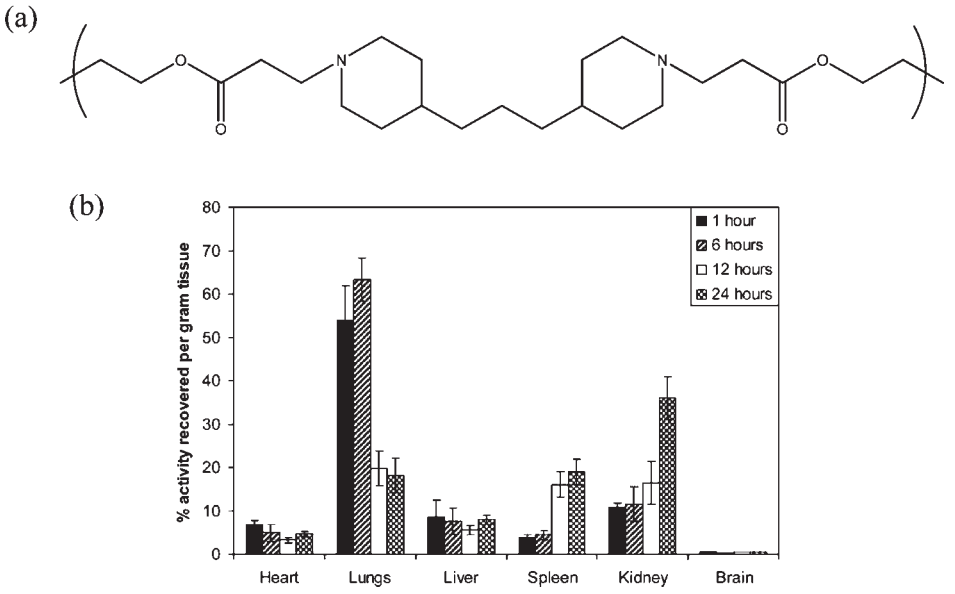

Figure 16. (a) Chemical structure of poly(β-amino ester) (PbAE). (b) Biodistribution of PEO-modified PbAE based nanoparticles loaded with gamma-emitter indium [^{111}In] oxine was examined in non-tumor-bearing mice at indicated time points (1, 6, 12, and 24 h postadministration) by comparing the percentage of recovered radioactivity within indicated organs.
Figures reprinted from Shenoy, D., Little, S.; Langer, R.; Amiji, M. (2005) Poly(ethylene oxide)-modified poly(beta -amino ester) nanoparticles as a pH-sensitive system for tumor-targeted delivery of hydrophobic drugs. 1. In vitro evaluations. *Mol. Pharm. 2,* 357−366; and Shenoy, D., Little, S., Langer, R., Amiji, M. (2005) Poly(ethylene oxide)-modified poly(beta -amino ester) nanoparticles as a pH-sensitive system for tumor-targeted delivery of hydrophobic drugs: Part 2. I*n vivo* distribution and tumor localization studies. *Pharm. Res. 22,* 2107-2114. with permission from ACS and Springer.

front flank of each mouse. Images were obtained at 1, 4, and 18 h postinjection for PET and NIRF imaging (Figure 18b) and at 18 h postinjection for MR imaging. MR imaging studies with HSA-IONPs indicated higher relaxivity (r_2) values and longer blood circulation half-life than a frequently used contrast agent, Feridex.

Liong et al.[52] synthesized mesoporous silica nanoparticles doped with superparamagnetic iron oxide nanocrystals and hydrophobic anticancer drugs, such as camptothecin (CPT) or paclitaxel (TXL), and functionalized with hydrophilic groups, like phosphonates, onto the surface to achieve high stability in aqueous solutions (Figure 19a). Incorporation of silica into theranostic nanoparticles like these can impart numerous desirable properties—silica nanoparticles are known to be endocytosed by cells, provide a mesoporous matrix capable of being doped with other inorganic metal particles (such as gold and iron oxide), and can be easily functionalized owing to silane linkers present on their surface. Additionally, a fluorescent dye, fluorescein isothiocyanate (FITC), and α-folate receptor-targeting folic acid groups were conjugated on the surface to promote uptake by tumor cells. Cellular uptake studies carried out in two types of pancreatic cancer cells, PANC-1 and BxPC3, indicated nanoparticles were internalized within 30 min of transfection. By comparison with drug-free nanoparticle controls, which were nontoxic, the toxicity of these nanoparticles was attributed to its drug payload (Figure 19b).

In order to achieve a high therapeutic concentration at the site of interest and to reduce off-target effects, several researchers have developed targeted theranostic agents to address specific receptors or proteins that are overexpressed in cancer targets, as has been mentioned above. In another example of this, Gao and co-workers[53,54] have developed targeted polymeric micellar architectures for drug delivery and magnetic resonance imaging. The core−shell morphology helps to introduce different hydrophobic functionalities (therapeutic and imaging) into the core, and the hydrophilic shell improves the stability in aqueous system and prevents aggregation. Polymeric micellar structures based on amphiphilic block copolymers maleimide-terminated poly(ethylene glycol)-*block*-poly(D,L-lactide) copolymer (MAL-PEG-PLA) and methoxy-terminated poly(ethylene glycol)-*block*-poly(D,L-lactide) copolymer (MPEG-PLA) were developed and loaded with doxorubicin (DOX) and superparamagnetic iron oxide (SPIO). Functionalization of these polymeric micelles was performed with $\alpha_v\beta_3$ integrin receptor-targeting cRGD peptide via thiol-maleimide reaction, and different extents of cRGD loading (0% vs 16%) were achieved through control of the amount of MPEG-PLA introduced into the system. Incorporation of the targeting group on polymeric micelles showed a concomitant change in cell uptake, MR image contrast (Figure 20a), and DOX-induced cytotoxicity (Figure 20b). Cellular uptake studies performed using flow cytometry and confocal laser scanning microscopy indicated that uptake of targeted particles was about 2.5 times higher than that of nontargeted analogues.

In a separate study, these polymeric micelles were modified with a lung cancer-targeting peptide (LCP) that binds specifically to $\alpha_v\beta_6$ receptors overexpressed on lung cancer cells. The specificity of LCP for $\alpha_v\beta_6$-expressing H2009 cells (lung cancer cells) was evaluated by comparative exposure to $\alpha_v\beta_6$-negative H460 cells and by using micelles containing a scrambled peptide (SP, a peptide with the same amino acid composition as LCP but scrambled sequence) in H2009 cells using [^{3}H] radioactivity measurements, confocal microscopy (Figure 21), and MRI.

The folate receptor is another surface molecule overexpressed on many cancer cells (such as lung, breast, and cervical cancer cells); consequently, numerous groups have imparted folate-receptor targeting in their theranostic nanoparticles. Santra et al.[55] developed a novel synthetic method to prepare biodegradable and

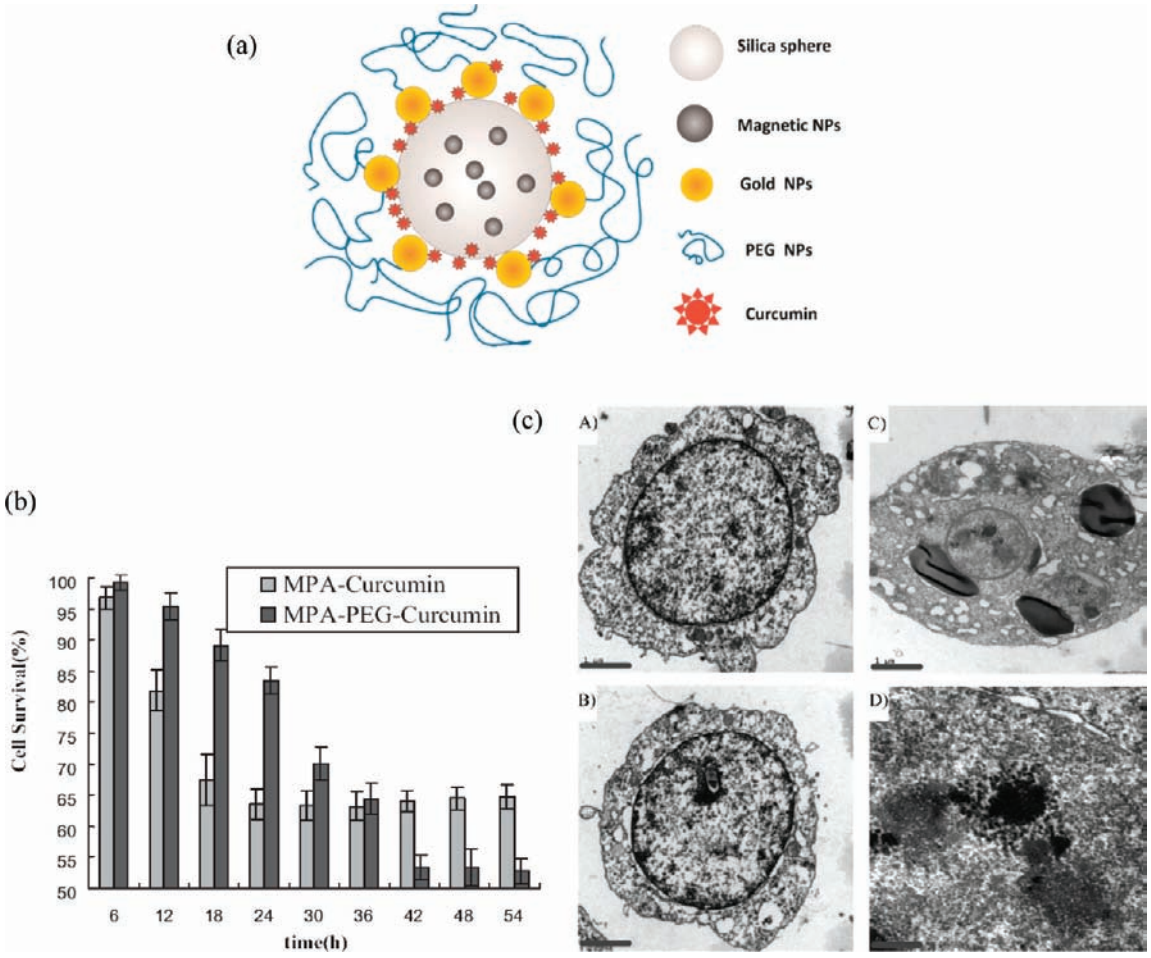

Figure 17. (a) Schematic of magnetoplasmonic nanoparticles containing magnetic iron oxide for anticancer drug delivery. (b) An MTT assay performed on human leukemia (HL-60) cells at various time points after treatment with curcumin-loaded MPA and MPA-PEG revealed significant, time-dependent induction of apoptosis for both preparations. (c) Transmission electron micrographs (TEMs) of HL-60 cells that were untreated (A), transfected with pure curcumin (B), or transfected with curcumin-loaded MPA-PEG (C). (D) This image is a magnified image of the circled portion of image (C). A change in cell morphology was observed upon treatment with curcumin-loaded MPA-PEG particles.
Figure adapted from Chen, W., Xu, N., Xu, L., Wang, L., Li, Z., Ma, W., Zhu, Y., Xu, C., and Kotov, N. A. (2010) Multifunctional magnetoplasmonic nanoparticle assemblies for cancer therapy and diagnostics (theranostics). *Macromol. Rapid Commun. 31*, 228−236. Copyright Wiley-VCH Verlag GmbH & Co. KGaA. Reproduced with permission.

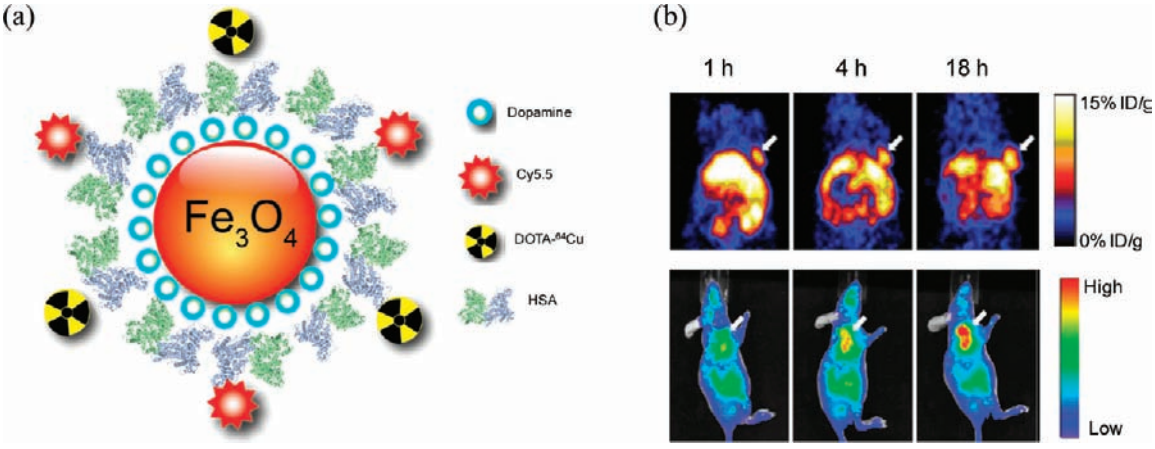

Figure 18. (a) Schematic of HSA-IONPs. (b) NIRF (bottom) and PET (top) images of a mouse containing a subcutaneous glioblastoma tumor taken 1, 4, and 18 h postinjection of HSA-IONPs. Significant tumor accumulation was observed via both imaging techniques, as indicated by an arrow.
Figure adapted from Xie, J., Chen, K., Huang, J., Lee, S., Wang, J., Gao, J., Li, X., and Chen, X. (2010) PET/NIRF/MRI triple functional iron oxide nanoparticles. *Biomaterials 31*, 3016-3022 with permission. Copyright Elsevier (2010).

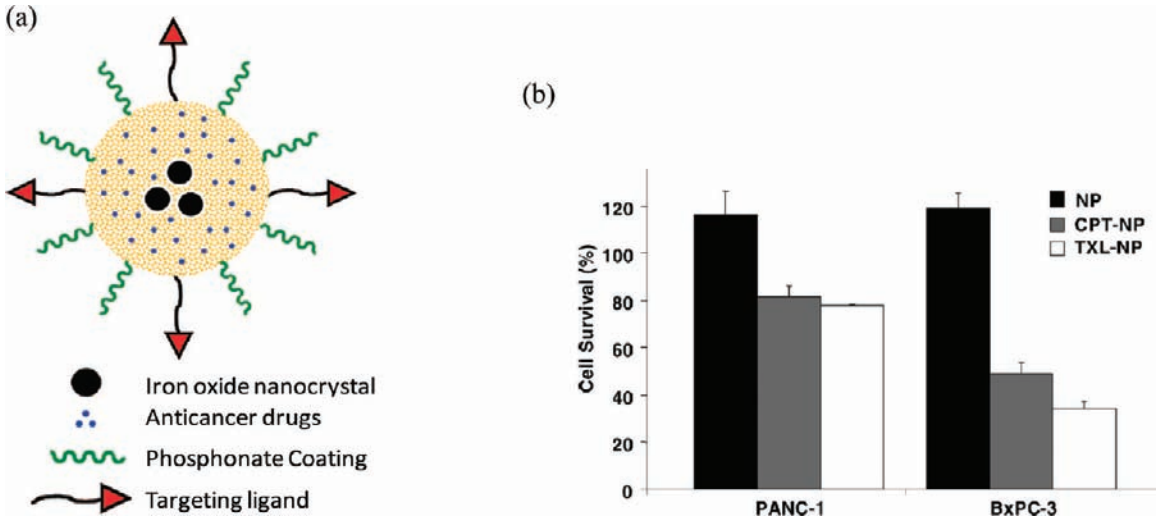

Figure 19. (a) Schematic of multifunctional iron oxide nanoparticles. (b) Cell growth inhibition assay results indicating relative therapeutic efficiency of CPT- or TXL-loaded nanoparticles in two different pancreatic cancer cell lines (PANC-1 and BxPC-3). Drug-free control nanoparticles were found to be nontoxic.
Figure reprinted from Liong, M., Lu, J., Kovochich, M., Xia, T., Ruehm, S. G., Nel, A. E., Tamanoi, F., and Zink, J. I. (2008) Multifunctional inorganic nanoparticles for imaging, targeting, and drug delivery. *ACS Nano 2*, 889-896 with permission from ACS.

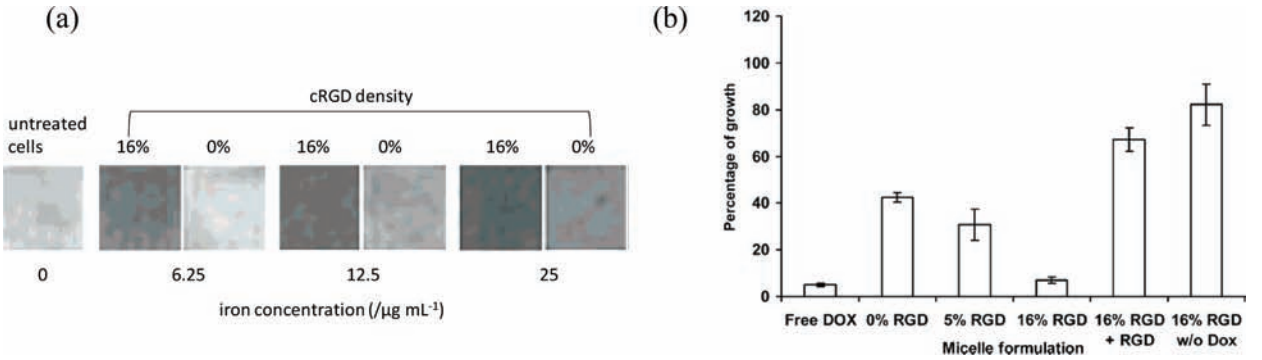

Figure 20. (a) Significant T_2-weighted image contrast was achieved for SLK endothelial tumor cells transfected with cRGD-containing micelles (16% cRGD density) compared to nontargeted (0% cRGD density) micellar analogues. (b) An increase in DOX induced-cytotoxicity in SLK cells was achieved upon incorporation of cRGD within the micellar nanoparticles.
Figure adapted from Nasongkla, N., Bey, E., Ren, J., Ai, H., Khemtong, C., Guthi Jagadeesh, S., Chin, S.-F., Sherry, A. D., Boothman David, A., and Gao, J. (2006) Multifunctional polymeric micelles as cancer-targeted, MRI-ultrasensitive drug delivery systems. *Nano Lett. 6*, 2427-2430 with permission from ACS.

biocompatible poly(acrylic acid)-iron oxide nanoparticles (PAA-IONPs). PAA-IONPs were functionalized with NIR dyes, DiR and DiL, and an anticancer drug, Taxol, by a solvent-diffusion method, then "click" chemistry was used to introduce a folate-receptor targeting ligand. Cytotoxicity and target specificity of folate-functionalized IONP were examined in lung carcinoma cells (A549, overexpress folate receptor) and cardiomyocytes (H9c2, do not overexpress folate receptor) via a MTT assay. The results from the MTT assay indicated almost 100% survival, for both A549 and H9c2 cells, when exposed to control Taxol-free PAA-IONPs. However, upon Taxol encapsulation in these PAA-IONPs, cell survival for A549 reduced to 20% after 3 h incubation, whereas cell viability for H9c2 cells remained unchanged. These results indicate specificity of PAA-IONPs toward tumor cells that overexpress folate receptor. Drug/dye release was only observed in acidic pH or in the presence of esterase, a degradative enzyme.

In another example of targeting of the folate receptor, Kohler et al.[56] covalently functionalized superparamagnetic iron oxide (SPIO) nanoparticles with an anticancer drug, methotrexate (MTX). MTX was incorporated via a peptide linkage that is reducible under acidic pH, thereby releasing the drug into the cell upon reaching the acidic environment of the endosome/lysosome. MTX is a reduced form of folic acid that inhibits dihydrofolate reductase, thereby stopping the folic acid cycle and inducing cellular toxicity. The delivery efficacy and cytotoxicity of MTX-loaded SPIO nanoparticles vs free MTX was tested in human cervical cancer cells (HeLa) and breast cancer cells (MCF-7). The endocytosis of these particles was confirmed to be folate-receptor-mediated, as determined by use of an acidic condition (to mimic lysosomes) and TEM.

Das et al.[57] synthesized N-phosphonomethyl iminodiacetic acid (PMIDA)-functionalized ultrasmall iron oxide nanoparticles

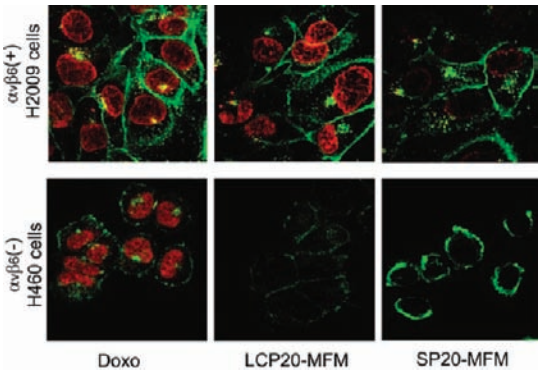

Figure 21. Evaluation of the cellular uptake of LCP-functionalized, doxorubicin (Doxo)-loaded multifunctional micelles (LCP20-MFM) in $\alpha_v\beta_6$-positive H2009 cells (top panels) and $\alpha_v\beta_6$-negative H460 cells (bottom panels) by fluorescence microscopy. Free Doxo (left panels) and MFM functionalized with a scrambled peptide (SP20-MFM, right panels) were used for comparison with LCP20-MFM (center panels). The cell membrane was stained with Alexa Fluor 350 and pseudocolored with green; Doxo fluorescence is indicated in red.
Figure adapted from Guthi, J. S., Yang, S.-G., Huang, G., Li, S., Khemtong, C., Kessinger, C. W., Peyton, M., Minna, J. D., Brown, K. C., and Gao, J. (2010) MRI-visible micellar nanomedicine for targeted drug delivery to lung cancer cells. *Mol. Pharm.* 7, 32-40 with permission from ACS.

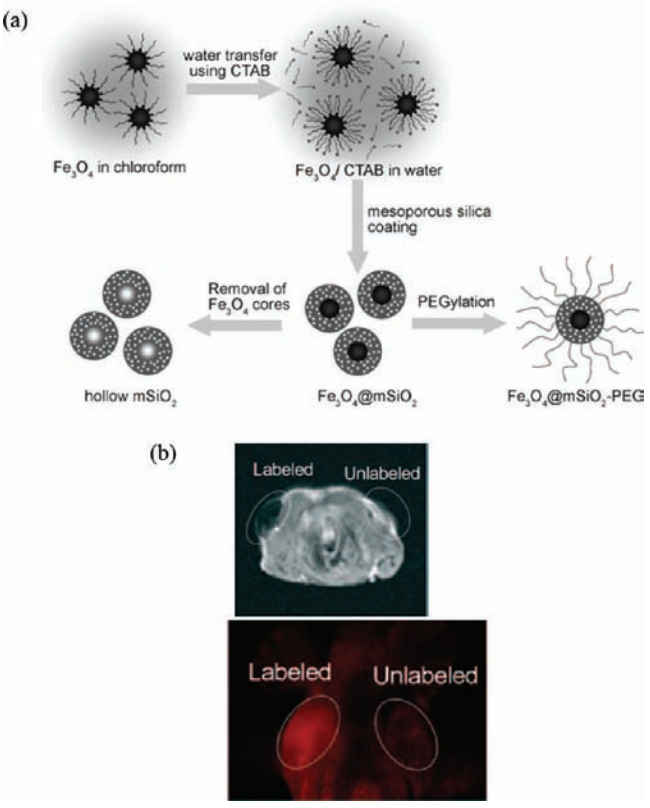

Figure 22. (a) Schematic for synthesis of $Fe_3O_4@mSiO_2$-PEG. (b) *In vivo* T_2-weighted MR imaging (top) and fluorescence microscopy imaging (bottom) of MCF-7 cells transfected with $Fe_3O_4@mSiO_2$-PEG, either unlabeled or labeled with rhodamine.
Figure adapted from Kim, J., Kim, H. S., Lee, N., Kim, T., Kim, H., Yu, T., Song, I. C., Moon, W. K., and Hyeon, T. (2008) Multifunctional uniform nanoparticles composed of a magnetite nanocrystal core and a mesoporous silica shell for magnetic resonance and fluorescence imaging and for drug delivery. *Angew. Chem. Int. Ed.* 47, 8438−8441. Copyright Wiley-VCH Verlag GmbH & Co. KGaA. Reproduced with permission.

(USPIO) equipped with (i) rhodamine B isothiocyanate (RITC) for optical imaging, (ii) a chemotherapeutic drug, methotrexate (MTX), and (iii) folic acid (FA) for targeting the folic acid receptor. They initially synthesized amine-functionalized iron oxide nanoparticles via a two-step process. First, the USPIOs were synthesized by an alkali-mediated chemical coprecipitation process in the presence of PMIDA containing one phosphonic and two carboxylic groups. This process creates stable nanoparticles with high interparticle repulsion due to negatively charged carboxylic and phosphonate groups on the surface. An amine-functionalized surface was then generated by reacting the terminal carboxylic acids with diamine (EDBE) in the presence of EDC and NHS. This amine functionality was further utilized to introduce MTX, RITC, and FA onto the particle to make USPIO-PMIDA-EDBE-RITC-FA. These authors were the first to functionalize an iron oxide surface with phosphonate groups (as opposed to solely using carboxylate groups, which is more common). The benefit of using phosphonate groups—instead of or in addition to carboxylate group—is that the phosphonate bond increases thermal stability and reduces susceptibility to enzymatic degradation. These targeted USPIO-PMIDA-EDBE-RITC-FA particles showed significantly higher cell uptake and MTX-induced cytotoxicity for folate receptor-expressing cancer (HeLa) cells than in nonfolate receptor-expressing (MG-63) cells.

In a final example of iron oxide-containing theranostic nanoparticles, Kim et al.[58] have developed a facile synthetic route (Figure 22a) with good control over size to synthesize monodisperse, discrete mesoporous silica materials (smaller than 100 nm) containing a single Fe_3O_4 nanocrystal as a core ($Fe_3O_4@mSiO_2$). Fluorescent dyes, rhodamine (R) or fluorescein (F) isothiocyanate, were covalently attached to the silica surface and doxorubicin (DOX) was encapsulated within the silica matrix. Next, the surface of the rhodamine-containing nanoparticles was functionalized with PEG groups ($Fe_3O_4@mSiO_2$(R)-PEG) to minimize nonspecific interactions and lengthen the blood circulation half-life. DOX-induced cytotoxicity was studied by transfecting SK-BR-3 cells with DOX-loaded $Fe_3O_4@mSiO_2$(R)-PEG nanoparticles. *In vivo* studies were performed by subcutaneously injecting MCF-7 cells pretreated with $Fe_3O_4@mSiO_2$(R)-PEG particles into the dorsal shoulder of nude mice. The MCF-7 cells containing $Fe_3O_4@mSiO_2$(R)-PEG particles were easily detectable as dark spots on T_2-weighted MR images and elicited significant rhodamine fluorescence when examined by fluorescence imaging (Figure 22b).

Quantum dots (QDs) are semiconductor materials with cadmium−selenium (Cd−Se) or cadmium−tellurium (Cd−Te) cores. As mentioned earlier, some of the major advantages of using QDs over fluorescent dyes are high extinction coefficients, control over optical properties, and reduced susceptibility to photobleaching. In addition, many QDs are known to form FRET pairs with fluorescent dyes, which allow them to be effectively used to understand intracellular trafficking and unpackaging of particles that contain them.[14,59−61]

Bagalkot et al.[62] have developed multifunctional nanoparticles for drug delivery based upon QDs that are capable of detecting

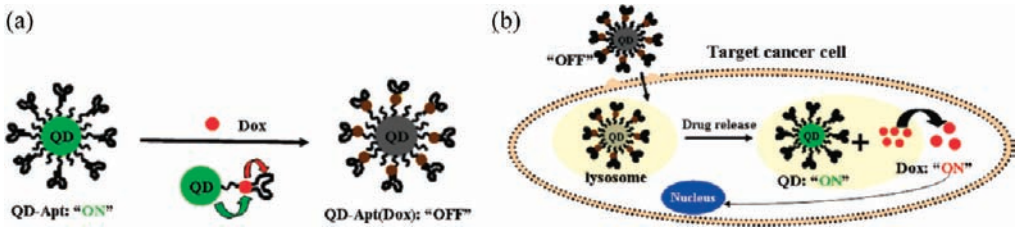

Figure 23. (a) Schematic of QD-Apt(Dox) conjugate in fluorescence "ON" state before conjugation to Dox, which leads to conversion to the "OFF" state due to Bi-FRET between two donor−acceptor (quencher) pairs. (b) Schematic of the proposed mechanism to monitor intracellular trafficking using Bi-FRET in QD-Apt (Dox) conjugates.
Figure adapted from Bagalkot, V., Zhang, L., Levy-Nissenbaum, E., Jon, S., Kantoff, P. W., Langer, R., and Farokhzad, O. C. (2007) Quantum dot-aptamer conjugates for synchronous cancer imaging, therapy, and sensing of drug delivery based on bifluorescence resonance energy transfer.*Nano Lett.* 7, 3065-3070 with permission from ACS.

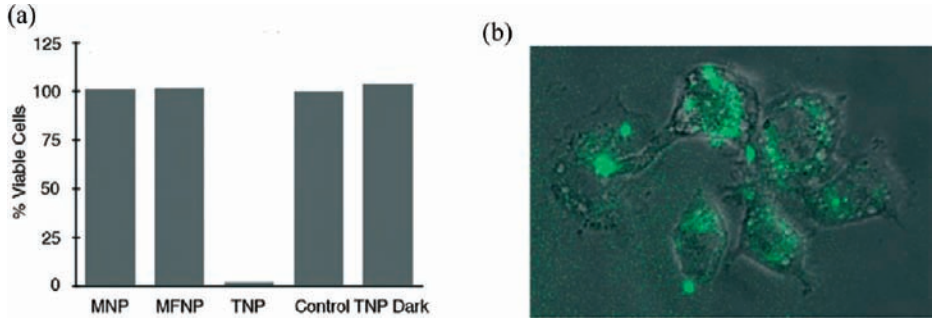

Figure 24. (a) Results from MTS assay of the viability of human macrophage (U937) cells upon transfection with indicated species and irradiation with a 646 nm laser for 1 h. "MNP" = magnetic nanoparticles (lack TPC and Alexa Fluor 750). "MFNP" = magnetofluorescent nanoparticles (lack TPC, contain Alexa Fluor 750). "TNP" = theranostic nanoparticles (contain TPC and Alex Fluor 750). "Control" = untransfected. "TNP Dark" = exposed to TNP but not irradiated. Unlike all other treatments, TNPs induced near-complete cytotoxicity upon irradiation. (b) Fluorescence microscopy images of murine macrophage (RAW 264.7) cells incubated with TNPs (green) for 3 h reveal intracellular accumulation of TNPs.
Figure adapted from McCarthy, J. R., Jaffer, F. A., and Weissleder, R. (2006) A macrophage-targeted theranostic nanoparticle for biomedical applications. *Small* 2, 983−987. Copyright Wiley-VCH Verlag GmbH & Co. KGaA. Reproduced with permission.

and treating cancer. They have created a novel, QD-targeting aptamer−doxorubicin conjugate (QD-Apt(Dox)) (Figure 23) that effectively targets prostate cancer cells via incorporation of an RNA aptamer (A10), which binds prostate-specific membrane antigen (PSMA). QD-Apt (Dox) systems were synthesized by first conjugating amine-terminated A10 aptamer with carboxylic group-functionalized QDs via EDC coupling and NHS activation chemistry. Once the aptamer is immobilized on the QD surface, Dox was introduced and conjugated by CG-sequence intercalation within the PSMA-targeting aptamer. The release of Dox from the delivery vehicle was detected from the conjugate via bimolecular FRET (Bi-FRET, Figure 23a,b). When the QD-Apt (Dox) conjugate is intact, both the QD and Dox fluorescence are in the "OFF" state—QD fluorescence is quenched by Dox, and Dox fluorescence is simultaneously quenched due to intercalation within the A10 aptamer. However, upon the dissociation of the conjugate/complex to release drug, the fluorescence is turned "ON"; hence, this system can be used to monitor intracellular vehicle unpackaging to release its cargo. The specificity of the A10 aptamer for PSMA was tested via MTT assay and confocal microscopy by transfecting QD-aptamer (Dox) conjugates into LNCaP (PSMA+) and PC3 (PSMA-) prostate adenocarcinoma cells. Minimal cytotoxicity resulting from QD-Apt(Dox)) was observed for PC3 cells compared to LNCaP cells, whereas comparable toxicity was achieved in these two cells for free Dox. These results together indicate successful targeting of these QD-containing theranostics to PSMA via inclusion of the A10 aptamer.

In photodynamic therapy (PDT), a photosensitizer-containing drug is delivered to the tumor cell that, upon light activation, generates "killer" singlet oxygen and free radicals (reactive oxygen species (ROS)) that induce apoptosis. PDT is currently being explored as a novel cancer treatment strategy. Three important things for the success of PDT are (i) minimized systemic toxicity, (ii) adequate oxygen permeability and drug (or O_2) diffusion in the diseased region, and (iii) sufficient concentration of photosensitizer in the region of interest (must have a high singlet oxygen quantum yield). These requirements are necessary to minimize the thermal damage due to photoirradiation and to avoid unwanted toxicity to neighboring healthy cells.

Porphyrin derivatives are the most commonly used photosensitizers in PDT. When irradiated with the required wavelength, the porphyrin produces cytotoxic singlet oxygen species via reaction of excited-state porphyrin with nearby molecular oxygen. In PDT, off-target toxicity can be prevented because generating the cytotoxic species only occurs at the site of illumination, which allows the therapy to be localized. This localized accumulation of the drug can further be enhanced by conjugation with targeting moieties and/or encapsulation in nanoparticles to increase concentration at the target site. Attachment of targeting groups can help to reduce one of the major limitations associated with PDT—increased patient photosensitivity due to prolonged accumulation of the drug within the skin.

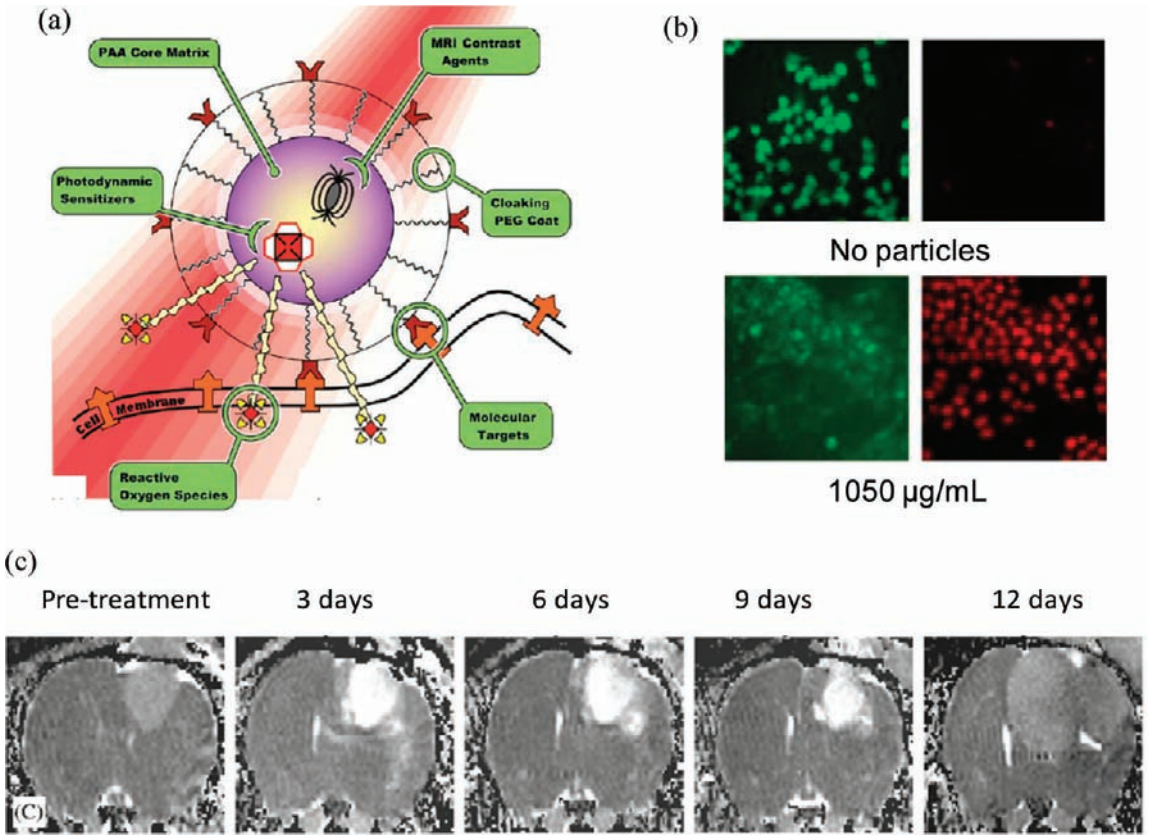

Figure 25. (a) Schematic of PAA-based multifunctional nanoparticles for photodynamic therapy. (b) *In vitro* cell kill test on 9 L glioma cells that were untreated (top) or transfected with 1050 μg/mL of PAA particles containing PHOTOFRIN (bottom). Live cells are stained with calcein acetoxymethylester (green) and dead cells with propidium iodide (red). (c) Diffusional MR imaging of rat 9 L gliosarcoma model treated with PAA nanoparticles containing PHOTOFRIN and irradiated with a laser for PDT. Treatment produced massive regional necrosis, demonstrated by large "bright" regions in the images, which resulted in shrinkage of the tumor mass. Regrowth occurred at 12 days post-treatment.
Figure adapted from Kopelman, R., Koo, Y-E. L., Philbert, M., Moffat, B. A., Reddy, R. G., McConville, P., Hall, D. E., Chenevert, T. L., Bhojani, M. S., Buck, S. M., Rehemtulla, A., and Ross, B. D. (2005) Multifunctional nanoparticle platforms for in vivo MRI enhancement and photodynamic therapy of a rat brain cancer. *J. Magn. Magn. Mater. 293*, 404-410 with permission, Copyright Elsevier (2005).

McCarthy et al.[63] developed macrophage-targeted theranostic nanoparticles (TNPs) for PDT application to cardiovascular diseases such as atherosclerosis and in-stent restenosis. Dextran-coated superparamagnetic iron oxide nanoparticles targeting the dextran receptor, SIGNR1, on macrophages were synthesized[64−68] and functionalized with a photosensitizer, 5-(4-carboxyphenyl)-10,15,20-triphenyl-2,3-dihydroxychlorin (TPC), and a fluorescent dye, Alexa Fluor 750, through covalent bonding with amine groups present on the surface of iron oxide particles. Cell uptake and light-induced phototoxicity studies carried out in a murine macrophage (RAW 264.7) cell line transfected with TNPs (0.1 mg Fe per mL) indicated only 35% cell survival after 1 h irradiation with a 646 nm laser. No toxicity was observed for TNPs without any photosensitizer loaded. TNPs (0.2 mg Fe per mL) caused as high as 100% cell death (Figure 24) after irradiation with a 646 nm laser for 1 h in human macrophage (U937) cells.

Kopelman et al.[69] have developed an extracellular PDT drug for imaging and treatment of brain tumors. This agent incorporates a photosensitizer, PHOTOFRIN (a complex mixture of porphyrin oligomers), into a polyacrylamide (PAA) core along with MRI contrast agents; it is further functionalized with PEG groups and the RGD targeting peptide on the surface of these nanoparticles (Figure 25a). Some of the major advantages of encapsulating PHOTOFRIN within a nanoparticle are that it (i) reduces the direct exposure of the drug to the physiological milieu, (ii) reduces cutaneous photosensitivity post-treatment, and (iii) significantly reduces the wait time (from 24 to 1 h) between intravenous injection of the drug and subsequent laser irradiation. The value of including a targeting ligand was demonstrated when RGD peptide-bearing nanoparticles showed higher accumulation in $\alpha_v\beta_3$-expressing cancer cells (MDA-435) than $\alpha_v\beta_3$-negative MCF-7 cells. *In vivo* pharmacokinetic behavior, studied in rats bearing 9 L gliosarcoma by diffusional MRI, indicated a 50-fold increase in circulation half-life of nanoparticles after PEGylation and a significant increase in the diffusion coefficient of the water surrounding tumor cells, indicating a decrease in rate of tumor growth and shrinkage of tumor mass (Figure 25b). The efficiency of PHOTOFRIN to generate killer singlet oxygen species and cause tumor cell death was also measured using a chemical test employing anthracene-9,10-dipropionic acid, disodium salt (ADPA)—in the presence of singlet oxygen species, the fluorescence of ADPA decays with time. Induction of cell death was also assessed by fluorescence microscopy on 9 L gliomas transfected with PAA nanoparticles containing PHOTOFRIN in varying amounts (Figure 25c). Overall, the nanoparticles were able to effectively kill brain tumors engrafted inside rats within 5 min of light exposure.

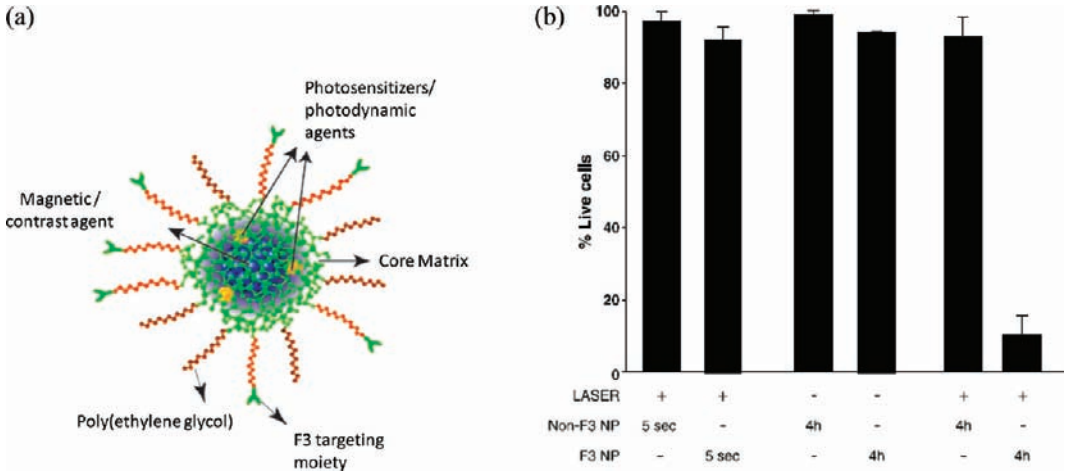

Figure 26. (a) Schematic of targeted PAA nanoparticles for PDT and diffusional MR imaging. (b) Cell viability studies performed on MDA-43 cells with PHOTOFRIN- and iron oxide-encapsulated nanoparticles lacking ("Non-F3 NP") or containing ("F3 NP") the F3 targeting ligand. Only the combination of F3-containing nanoparticles incubated for 4 h and laser irradiation significantly reduced the percentage of live cells.
Figure adapted and reprinted with permission from American Association for Cancer Research: Reddy, G. R., Bhojani, M. S., McConville, P., Moody, J., Moffat, B. A., Hall, D. E., Kim, G., Koo, Y.-E. L., Woolliscroft, M. J., Sugai, J. V., Johnson, T. D., Philbert, M. A., Kopelman, R., Rehemtulla, A., and Ross, B. D. (2006) Vascular targeted nanoparticles for imaging and treatment of brain tumors. *Clin. Cancer Res. 12*, 6677-6686.

Studies have shown that PDT can be promising for treatment of malignant brain tumors, for which more than 80% of the tumor growth recurs after therapy. Being a localized therapy, PDT has the potential to be very beneficial in this scenario.[70−74] A dose-dependent increase in survival rate of glioblastoma patients has also been shown, further suggesting that the future of this therapy is bright.

Reddy et al.[75] have synthesized PHOTOFRIN- and superparamagnetic iron oxide-encapsulated uniform poly(acrylamide) (PAA) nanoparticles (~40 nm) decorated with PEG groups and a vascular homing and cell-penetrating F3 peptide on the surface which targets brain cancer cells (Figure 26a). Laser irradiation (630 nm) for 5 min induced up to 90% cell death 4 h after transfection (Figure 26b). *In vivo* administration to 9 L glioma-bearing rats revealed that inclusion of PEG and targeting groups onto the surface increased the tumor half-life (from 39 to 123 min) and T_2-weighted image contrast compared to nontargeted analogues.

Another approach to introduce theranostic functionalities into a nanosystem is to covalently attach a palladium (Pd)-porphyrin chelate to mesoporous silica nanoparticles (MSNs) which are readily taken up by cells. Some of the important properties of MSNs are large surface area (~1000 m^2/g), uniform pore size (~3 nm), particle size (in the range ~70−100 nm), ease of functionalization, large payload capacity, high cellular uptake, and low cytotoxicity. Because of these properties, MSNs have several advantages over normal silica nanoparticles and, thus, are used in a wide array of applications, including chemical catalysis, drug delivery, controlled release of therapeutics, and cell labeling. Pd-porphyrin has a long phosphorescence lifetime and has been used for *in vivo* oxygen sensing and imaging.[76,77] Cheng et al.[78] synthesized (Figure 27a,b) phosphorescent Pd-meso-tetra (4-carboxyphenyl) porphyrin (PdTPP) covalently embedded in MSNs (MSN-PdTPP) as theranostic agents for the imaging and treatment of breast cancer. The energy required for phosphorescence imaging is only 10^{-4}−10^{-5} times that required for conventional PDT. Also, the concentration of singlet oxygen species generated during oxygen sensing/imaging is much lower compared to that during conventional PDT and, thus, by changing the energy of photoirradiation, the functionalities of MSN-PdTPP can be "switched" between a phosphorescence probe for oxygen sensing/imaging (diagnostics) and a photosensitizer for PDT (therapy). Breast cancer cells (MDA-MB-231) transfected with 25 μg MSN-PdTPP for 2 h at 37 °C, followed by photoirradiation (532 nm wavelength with energy 1.2 J/cm^2), showed a significant change in cell morphology and large extent of cell death indicated by high propidium iodide fluorescence (Figure 27c).

PDT is an FDA-approved first-line treatment for age-related macular degeneration and is routinely used for obstructive esophageal cancer and some forms of lung cancer.[79−81] One of the approaches for cancer treatment includes therapies that block or interrupt a specific cellular pathway or proteins involved in cell proliferation. One of these proteins is the K_i-67 protein (pKi-67), which is upregulated in highly proliferating cells during all active cell cycles (G1, S, and G2, as well as mitosis). Rahmanzadeh et al.[82] used a noncationic liposome-based vehicle for delivering fluorescently labeled (fluorescein isothiocyanate, FITC) antibodies, namely, TuBB-9 and MIB-1, that recognize K_i-67 protein in two different states. Twenty four hours after transfection in ovarian cancer cells (OVCAR-5), TuBB-9-FITC- and MIB-1-FITC-containing liposome particles (particle size ~180 nm) were found to be localized in the nucleolar regions (Figure 28a). Irradiation with a 488 nm laser (5 J/cm^2 laser power) resulted in a significant decrease in cell viability for cells incubated with TuBB-9-FITC-labeled liposomes, but not MIB-1-FITC-labeled liposomes (Figure 28b). As expected, no significant toxicity was observed for various controls, including liposome-treated cells that were not irradiated as well as irradiated cells treated with TuBB-9-FITC alone (without the liposomal carrier).

Hyperthermia, also called photothermal ablation, is a physical treatment for cancer involving the killing of cancer cells in the presence of heat. Hyperthermia leads to apoptotic cell death caused by heating of surrounding tissues or cells to a temperature of 42−46 °C; above 46 °C, photothermal ablation causes undesirable necrosis of the surrounding cells.[83,84] With no chemical payload to deliver, hyperthermia is less prone to toxic side effects that often accompany chemotherapeutic agents.

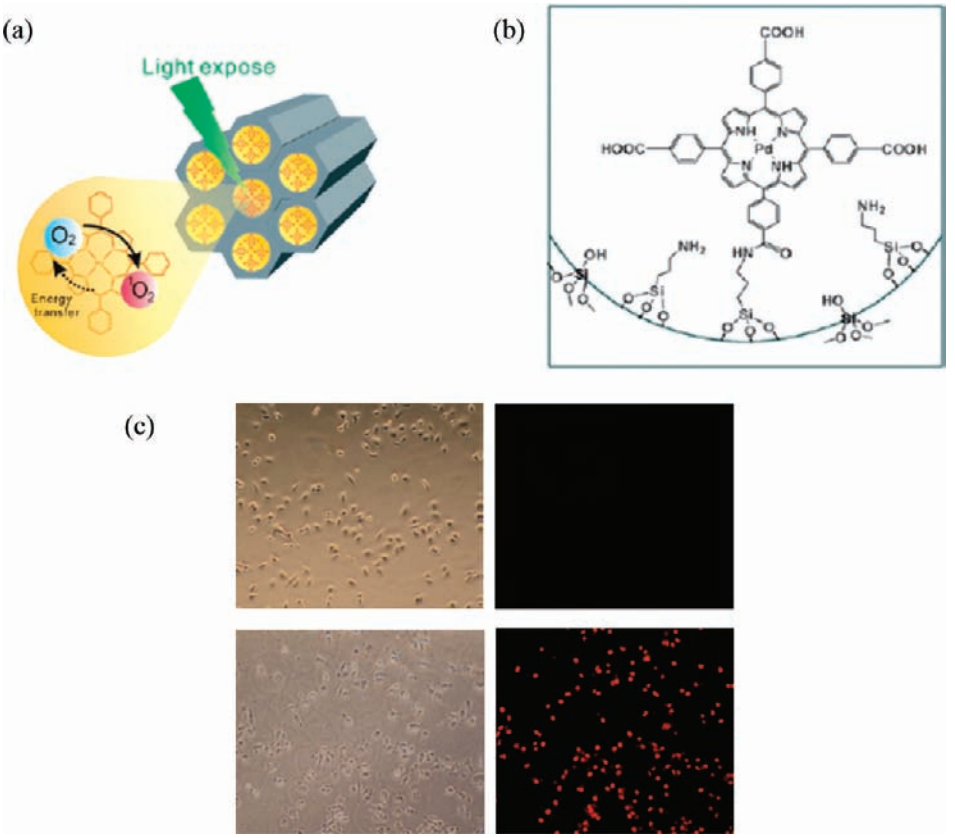

Figure 27. (a) Schematic of the mechanism of PDT with MSN-PdTPP. (b) Chemical structure of PdTPP covalently attached to MSN. (c) Propidium iodide (PI) staining of MDA-MB-231 cells treated with 25 μg of MSN-PdTPP at 37 °C for 2 h and then irradiated with a 532 nm laser. The left panels show the change in morphology of the cells before (top) and after (bottom) treatment, respectively. The right panels show red propidium iodide fluorescence (indicating dead cells) before (top) and after (bottom) treatment, respectively.
Figure adapted from Cheng, S.-H., Lee, C.-H., Yang, C.-S., Tseng, F.-G., Mou, C.-Y., and Lo, L.-W. (2009) Mesoporous silica nanoparticles functionalized with an oxygen-sensing probe for cell photodynamic therapy: Potential cancer theranostics. *J. Mater. Chem. 19*, 1252−1257. Reproduced by permission of The Royal Society of Chemistry.

Gold nanoparticles are more commonly used for hyperthermia than other heavy metals (such as silver or cobalt) due to the unique interaction of gold with light, which results in surface plasmon resonance (SPR). In the presence of oscillating electromagnetic radiations at a particular resonance frequency, free electrons in gold undergo collective coherent oscillations (SPR oscillations) which can decay via heat emission.[85,86] Changing the size, shape, and refractive index (RI) of the material changes its SPR frequency. Ideally, this frequency is tuned in the near-infrared (NIR) region. At NIR wavelengths, the absorption of innate biological fluorochromes and water is low,[87] and thus, the light can penetrate deeper into tissues without causing damage to surrounding healthy cells.

To combine imaging and therapy in the case of gold-containing nanoparticles, architectures with iron oxide cores and gold shells have been explored widely. Gold nanoparticles with iron oxide cores, such as magnetite (Fe_2O_4) or maghemite (γ-Fe_2O_4), can be imaged using MRI. The layer of gold surrounding the magnetic iron oxide particles helps to stabilize them from *in vivo* aggregation and reduces their toxicity. The desired NIR absorption frequency for gold nanoparticles can be achieved by coating them with silica, which has a high dielectric constant and, thus, helps to lower the absorption frequency toward NIR wavelengths.[85] Iron oxide particles impart a high T_2 relaxivity (good negative contrast for MRI) and, in the presence of a magnetic field, can be localized to the site of interest. This therapeutic targeting strategy is known as magnetic field-directed hyperthermia.[88]

As an example of magnetic field-directed hyperthermia, researchers have developed human epidermal growth receptor 2 (HER2)-targeted gold nanoparticles for breast cancer treatment. Kim et al.[89] designed magnetic gold nanoshells (Mag-GNS) consisting of a magnetic iron oxide (Fe_2O_4) and silica core surrounded by a 15 nm gold shell. For breast cancer targeting, Mag-GNS functionalized with an antibody targeting HER-2/neu receptor ($Ab_{HER2/neu}$), a cell surface molecule that is overexpressed on breast cancer cells. SKBR3 breast cancer cells and lung cancer cells (H520 cells, which do not overexpress HER2/neu) were treated with $Ab_{HER2/neu}$−containing Mag-GNS for 2 h at 37 °C. Upon subsequent exposure to a femtosecond-long laser (800 nm) pulse, Mag-GNS-transfected SKBR3 cells exhibited significant cell death. T_2-weighted MR images of transfected SKBR3 cells and H520 cells showed higher image contrast for targeted particles than untransfected cells (Figure 29), with SKBR3 cells exhibiting enhanced contrast relative to H520 cells, as expected.

In a related study, Lim et al.[90] synthesized core−shell-type structures in which 9−11 nm magnetic iron oxide cores were covered with 2−3 nm hollow gold nanoshells (HGNS); the resulting materials (Fe_3O_4@Au) were surface-functionalized

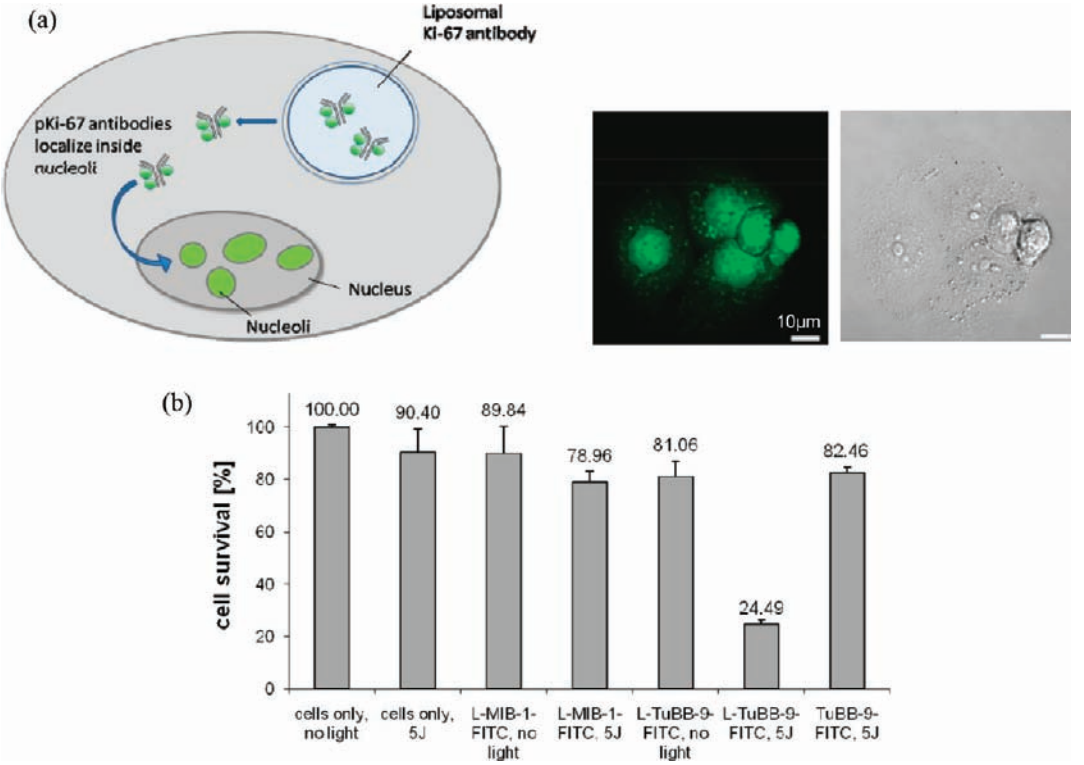

Figure 28. (a) Schematic and fluorescence micrograph of intracellular (nucleolar) localization of pKi-67-targeting liposomes. (b) MTT cell toxicity assay performed on ovarian cancer (OVCAR-5) cells incubated with TuBB-9-FITC-labeled liposomes (L-TuBB-9-FITC) indicated that more than 75% cells experienced death upon light irradiation (denoted 5J); minimal cell death was observed to upon treatment with various controls.
Figure adapted from Rahmanzadeh, R., Rai, P., Gerdes, J., and Hasan, T. (2010) Targeted light-inactivation of the ki-67 protein using theranostic liposomes leads to death of proliferating cells. *Proc. SPIE 7576*, 757602/757601-757602/757605 with permission from SPIE.

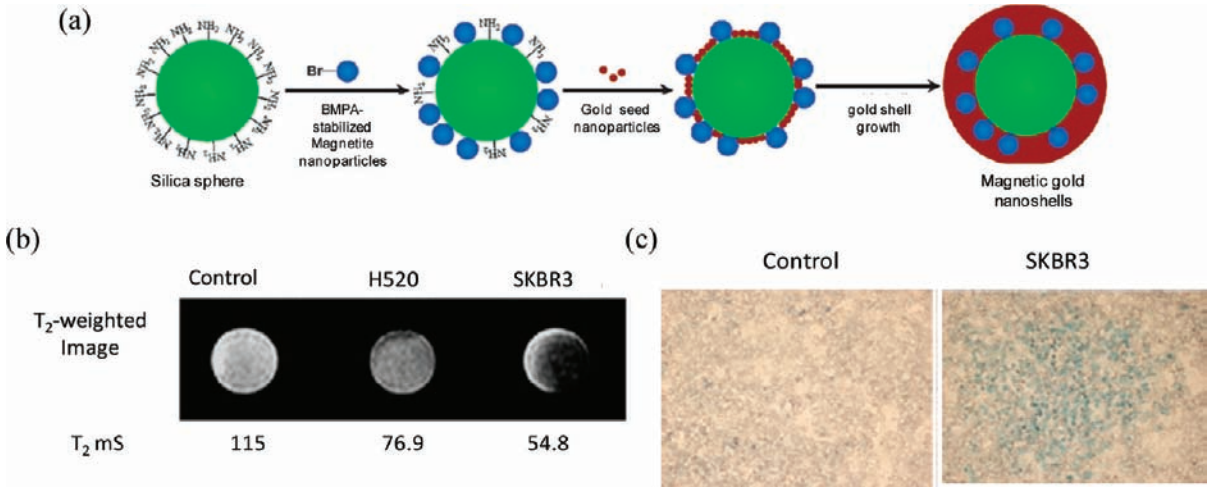

Figure 29. (a) Schematic of synthesis of magnetic gold-nanoshells (Mag-GNS); (b) T_2-weighted MR imaging of Mag-GNS-$Ab_{HER2/neu}$-transfected SKBR3 and H520 cells, compared to untransfected SKBR3 cells ("Control"). (c) Change in morphology of SKBR3 cells upon transfection with Mag-GNS-$Ab_{HER2/neu}$ and subsequent irradiation with a femtosecond-pulse laser (800 nm for 10 s); dead cells were stained with trypan blue.
Figure adapted from Kim, J., Park, S., Lee Ji, E., Jin Seung, M., Lee Jung, H., Lee In, S., Yang, I., Kim, J.-S., Kim Seong, K., Cho, M.-H., and Hyeon, T. (2006) Designed fabrication of multifunctional magnetic gold nanoshells and their application to magnetic resonance imaging and photothermal therapy. *Angew. Chem. Int. Ed. 45*, 7754−7758. Copyright Wiley-VCH Verlag GmbH & Co. KGaA. Reproduced with permission.

with anti-HER2 monoclonal antibodies (Figure 30a). The specificity of the antibody attached on the surface of HGNS (Fe_2O_3@Au) was tested in SKBR3 (HER2-positive) and MCF-7 (HER2-negative) cancer cells by further labeling these particles with tetramethyl rhodamine isothiocyanate (TRITC); TRITC fluorescence was only seen in SKBR3 cells, implicating HER2 engagement in the uptake of these nanoparticles. Photothermal therapy performed on treated SKBR3 cells with an 808 nm laser

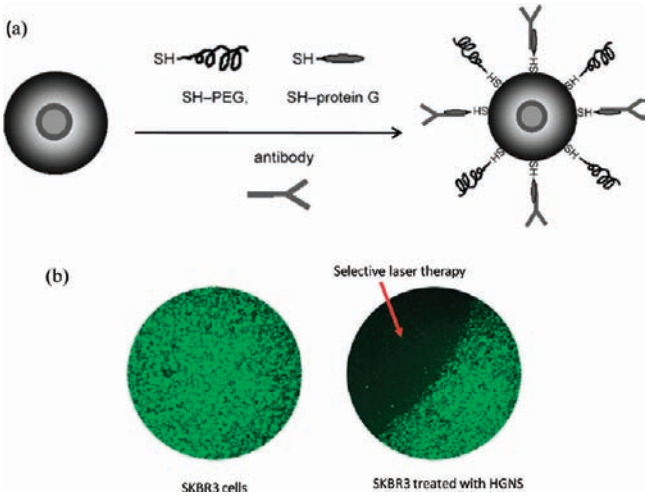

Figure 30. (a) Schematic of the synthesis of hollow gold nanoshells (HGNS) functionalized with iron oxide, a HER2-targeting antibody, and poly(ethylene glycol) (PEG). (b) SKBR3 cells incubated with the targeted HGNS (Fe_2O_3@Au) and stained with calcein-AM (green). Irradiation with an 808 nm laser resulted in a significant decrease in survival of treated cells.
Figure adapted from Lim, Y. T., Cho, M. Y., Kim, J. K., Hwangbo, S., and Chung, B. H. (2007) Plasmonic magnetic nanostructure for bimodal imaging and photonic-based therapy of cancer cells. *ChemBioChem 8*, 2204−2209. Copyright Wiley-VCH Verlag GmbH & Co. KGaA. Reproduced with permission.

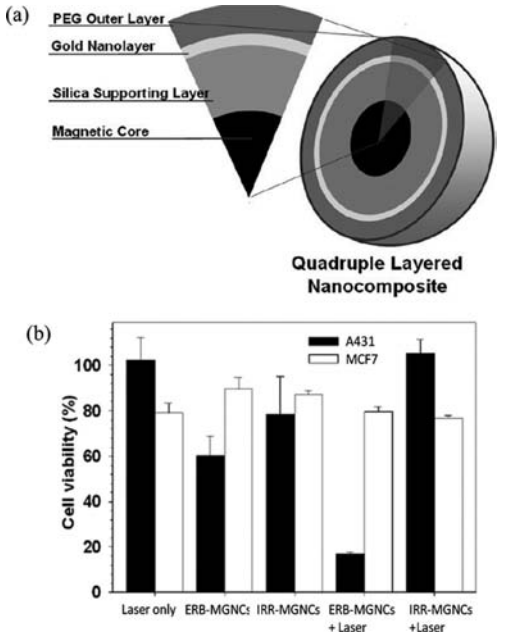

Figure 31. (a) Schematic of the quadruple-layered structure of magnetic-gold nanocomposites (MGNCs) targeting EGFR. (b) MTT assay shows the relative cell viability of A431 and MCF7 cells treated with ERB-MGNCs and IRR-MGNCs and irradiated with a NIR laser for 5 min. The combination of ERB-MGNCs in A431 cells resulted in the greatest observed reduction in cell viability.
Figure adapted from Lee, J., Yang, J., Ko, H., Oh, S. J., Kang, J., Son, J.-H., Lee, K., Lee, S.-W., Yoon, H.-G., Suh, J.-S., Huh, Y.-M., and Haam, S. (2008) Multifunctional magnetic gold nanocomposites: Human epithelial cancer detection via magnetic resonance imaging and localized synchronous therapy. *Adv. Funct. Mater. 18*, 258−264. Copyright Wiley-VCH Verlag GmbH & Co. KGaA. Reproduced with permission.

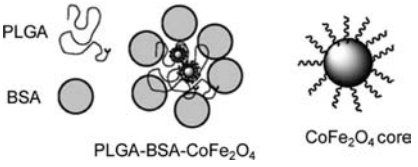

Figure 32. Schematic representation morphology of PLGA-BSA-$CoFe_2O_4$ nanoparticles for hyperthermia therapy.
Figure adapted from Comes Franchini, M., Baldi, G., Bonacchi, D., Gentili, D., Giudetti, G., Lascialfari, A., Corti, M., Marmorato, P., Ponti, J., Micotti, E., Guerrini, U., Sironi, L., Gelosa, P., Ravagli, C., and Ricci, A. (2010) Bovine serum albumin-based magnetic nanocarrier for MRI diagnosis and hyperthermic therapy: A potential theranostic approach against cancer. *Small 6*, 366−370.Copyright Wiley-VCH Verlag GmbH & Co. KGaA. Reproduced with permission.

resulted in cell death within 3 min of exposure without causing any damage to unexposed cells (Figure 30b).

Hybridization of $MnFe_2O_4$ with gold nanoparticles can help to combine MR imaging and hyperthermia treatment for cancer therapy. Recently, it has been shown that clustering of magnetic nanoparticles increases their MR properties.[91−93] Magnetic contrast agents consisting of magnetic kernels of manganese and iron oxide clusters were used to improve image contrast. Lee et al.[94] developed quadruple-layered theranostic agents (Figure 31a) for hyperthermia treatment by embedding a number of magnetic kernels in a silica layer, followed by coating with a layer of gold nanoparticles, and then finally incorporating a PEG layer and a targeting antibody, Erbitux (ERB), which binds to epidermal growth factor receptor (EGFR) that is overexpressed on certain cancer cells. T_2-weighted MR imaging of these multifunctional magnetic gold nanocomposites (MGNCs), performed on a 1.5 T magnetic scanner, indicated a dose-dependent increase in relaxivity upon increase in MGNC concentration. The specificity of the ERB antibody for EGFR-expressing tumor cells was tested via MTT assay by adding ERB- vs irrelevant antibody (IRR)-functionalized MGNCs to A431 (overexpress EGFR) and MCF7 (low EGFR expression) cells, followed by irradiation with a NIR laser (Figure 31b).

In 1957, Gilchrist and co-workers[88] first introduced the concept of magnetic fluid hyperthermia (MFH), whereby magnetic particles, in the presence of a magnetic field, produce heat by hysteresis loss and, thus, can be used for hyperthermia treatment. Comes Franchini et al.[95] employed this technique to develop (Figure 32) bovine serum albumin (BSA)- and poly(lactic-*co*-glycolic acid) (PLGA)-coated magnetic nanocarriers containing a cobalt−iron oxide (PLGA-BSA-$CoFe_2O_4$) core. In the presence of a high-frequency magnetic field (168 kHz, 21 kA/m), these particles can heat the surrounding cells up to 48 °C. At these conditions, an impressive 82% cell death is induced within 1 h of treatment. It is proposed that introducing structural anisotropy (such as via cobalt) into the iron oxide magnetic nanoparticles increases their hyperthermia efficiency and possibly also their magnetic contrast property. *In vivo* studies on the brain and liver of rats indicated that these PLGA-BSA-$CoFe_2O_4$ particles show higher image contrast compared to a commercial contrast agent, Endorem.

Radiation therapy uses high-energy radiations, such as X-rays, γ rays, and charged particles, to kill target cancer cells.[96]

Octreotide	D-Phe-Cys-Phe-D-Trp-Lys-Thr-Cys-Thr (ol)
[Tyr^3]octreotide	D-Phe-Cys-Tyr-D-Trp-Lys-Thr-Cys-Thr (ol)
[Tyr^3]octreotate	D-Phe-Cys-Tyr-D-Trp-Lys-Thr-Cys-Thr

Figure 33. Structures of somatostatin analogues: octreotide, Tyr^3-octreotide and Tyr^3-octreotate
Figure adapted from de Jong, M., Breeman, W. A. P., Kwekkeboom, D. J., Valkema, R., and Krenning, E. P. (2009) Tumor imaging and therapy using radiolabeled somatostatin analogues. *Acc. Chem. Res. 42*, 873-88 with permission from ACS.

Radiation can be received externally or internally, the latter occurring via a dosage of radioactive materials which emit radiation upon their decay. This high-energy ionizing radiation causes irreversible damage to DNA, thereby inducing cell death. Another mechanism involved may be generation of free radicals, which can also cause apoptosis of the cells. If employed without any cell surface targeting groups, radiation therapy does not have any specificity toward cancer cells over normal cells. Radiation therapy can be administered as a stand-alone therapy or in combination with other types of cancer treatment, such as chemotherapy or surgical intervention.

Due to increasing concerns associated with albumin-based radiopharmaceuticals (HIV, hepatitis C), Saatchi et al.[97] developed an alternative approach based on biodegradable poly(L-lactide) (PLL) microspheres. PLL microspheres (size 0.5−2 μm) were functionalized with a microSPECT/CT contrast agent, [^{99m}Tc], and decorated with PEG via a double-emulsion solvent evaporation technique. These PEGylated PLL microspheres showed significant accumulation in the liver and the reticuloendothelial system (RES), likely due to macrophage clearance of these large microspheres. When chelated to β-emitting radionuclides such as [^{90}Y], these microspheres can be utilized for radioembolization therapy of liver tumors, uterine fibroids, meningiomas, and arteriovenous malformations, as well as local treatments of leftover and recurring disease.

Radiation therapy can also be performed by delivering radionuclide-functionalized radiopeptides to the tumor cells. Radiopeptides are attractive options in the field of cancer therapeutics because they have rapid clearance, rapid tissue penetration, target accessibility, low antigenicity, and ease of synthesis. For patients with inoperable or metastasized tumors, selective receptor-targeting radiopeptides can be a useful therapy. Radiopeptides labeled with γ- or positron-emitting radionuclides can easily be visualized with diagnostic imaging techniques, like positron emission tomography (PET), or single-photon emission computed tomography (SPECT). These radiopeptides can be labeled with γ-emitters like indium-111 [^{111}In] or [^{99m}Tc] for SPECT imaging and/or positron emitters such as gallium-68 [^{68}Ga] or fluorine-18 [^{18}F] for PET imaging. In addition, when labeled with β-emitting species (such as yttrium-90 [^{90}Y] and lutetium-177 [^{177}Lu]), they can effectively eradicate the targeted tumor cells.[98]

Last, radiopeptides that target the somatostatin receptor (which is overexpressed on the surface of a majority of neuroendocrine tumors) show promise for both imaging and therapy of tumors in which other therapies are ineffective. Somatostatin analogues containing FDA-approved DTPA-octreotide (DTPA = diethylene triamine pentaacetic acid), DOTA-octreotide (DOTA = 1,4,7,10-tetraazacyclododecane-1,4,7,10-tetraacetic acid), DTPA-Tyr^3-octreotide/octreotate, and DOTA-Tyr^3-octreotide/octreotate have high binding affinity for the subtype 2 (sst_2) of somatostatin receptors (Figure 33).[99,100]

CONCLUSIONS

The field of theranostics remains relatively young but is developing at an incredibly fast rate. Researchers have created numerous nanoparticle-based systems that can be used for therapy, as in cases of hyperthermia or radiation therapy, and/or for delivery of chemotherapeutic drugs and diagnostic imaging agents. Several approaches include multi-imaging modalities that can facilitate tracking of nanoparticles both *in vitro* and *in vivo*. To monitor the therapy and response to therapy at a cellular level, the use of fluorescent labeling agents, such as organic fluorescent dyes or quantum dots, can permit achievement of high-resolution images delineating different organelles inside the cell. However, for *in vivo* purposes, modalities such as PET or SPECT agents and MRI contrast agents are preferred to overcome problems of background fluorescence and photobleaching.

Theranostic agents can play major roles both in early stage drug development and as clinical-stage therapeutic-containing drug candidates. *In vitro* imaging agents are important during early development, such as for modification of chemical structure and architecture to fine-tune drug properties. However, *in vivo* agents are important for advanced studies that may be promising for clinical trials. Until now, theranostics have not reached clinical trials; this field is, however, relatively young and issues related to ambiguity and/or difference between the optimum concentrations for the therapeutic and imaging agents are in the process of being resolved. For example, for systems with nuclear imaging agents, such as 2-[^{18}F]-2-deoxyglucose (FDG), and anticancer chemotherapeutics, such as doxorubicin, the dosages required for success of the individual modalities are vastly (several orders of magnitude) different. Systems with MRI agents based on gadolinium and therapeutic drugs can face similar problems because of the inherent low sensitivity of MRI. The minimum dosage required for Gd-based imaging agents, such as Magnevist, is 100 mg/kg, which is typically considerably higher than the appropriate therapeutic dose.[2] These mismatches can be overcome by exploring different combinations of diagnostic and therapeutic agents, developing new drugs that are potent at lower concentrations, and creating more advanced and sensitive imaging techniques that match the dose required for therapy and imaging. Research into theranostics that can overcome these obstacles and be suitable for important applications remains rich, and the time before theranostics begin clinical evaluation is likely to be short.

AUTHOR INFORMATION

Corresponding Author
*E-mail:treineke@umn.edu.

REFERENCES

(1) Funkhouser, J. (2002) Reintroducing pharma: Theranostic revolution. *Curr. Drug Discovery 2*.
(2) McCarthy, J. R. (2009) The future of theranostic nanoagents. *Nanomed. (London, England) 4*, 693–695.
(3) McCarthy, J. R. (2010) Multifunctional agents for concurrent imaging and therapy in cardiovascular disease. *Adv. Drug Delivery Rev. 62*, 1023–1030.
(4) Sumer, B., and Gao, J. (2008) Theranostic nanomedicine for cancer. *Nanomed. (London, England) 3*, 137–140.

(5) Warenius, H. M. (2009) Technological challenges of theranostics in oncology. *Expert Opin. Med. Diagn. 3*, 381–393.
(6) Alexis, F., Pridgen, E., Molnar, L. K., and Farokhzad, O. C. (2008) Factors affecting the clearance and biodistribution of polymeric nanoparticles. *Mol. Pharmaceutics 5*, 505–515.
(7) Iyer, A. K., Khaled, G., Fang, J., and Maeda, H. (2006) Exploiting the enhanced permeability and retention effect for tumor targeting. *Drug Discovery Today 11*, 812–818.
(8) Maeda, H., Greish, K., and Fang, J. (2006) The EPR effect and polymeric drugs: A paradigm shift for cancer chemotherapy in the 21st century. *Adv. Polym. Sci. 193*, 103–121.
(9) Niidome, T., and Huang, L. (2002) Gene therapy progress and prospects: Nonviral vectors. *Gene Ther. 9*, 1647–1652.
(10) Heilbronn, R., and Weger, S. (2010) Viral vectors for gene transfer: Current status of gene therapeutics. *Handb. Exp. Pharmacol. 197*, 143–170.
(11) Scollay, R. (2001) Gene therapy: A brief overview of the past, present, and future. *Ann. N.Y. Acad. Sci. 953*, 26–30.
(12) Thomas, C. E., Ehrhardt, A., and Kay, M. A. (2003) Progress and problems with the use of viral vectors for gene therapy. *Nat. Rev. Genet. 4*, 346–358.
(13) Akhtar, S. (2006) Non-viral cancer gene therapy: Beyond delivery. *Gene Ther. 13*, 739–740.
(14) Medintz, I. L., Uyeda, H. T., Goldman, E. R., and Mattoussi, H. (2005) Quantum dot bioconjugates for imaging, labelling and sensing. *Nat. Mater. 4*, 435–446.
(15) Godbey, W. T., Wu, K. K., and Mikos, A. G. (1999) Tracking the intracellular path of poly(ethylenimine)/DNA complexes for gene delivery. *Proc. Natl. Acad. Sci. U.S.A. 96*, 5177–5181.
(16) Ho, Y.-P., Chen, H. H., Leong, K. W., and Wang, T.-H. (2006) Evaluating the intracellular stability and unpacking of DNA nanocomplexes by quantum dots-FRET. *J. Controlled Release 116*, 83–89.
(17) Lucas, B., Remaut, K., Sanders, N. N., Braeckmans, K., De Smedt, S. C., and Demeester, J. (2005) Studying the intracellular dissociation of polymer-oligonucleotide complexes by dual color fluorescence fluctuation spectroscopy and confocal imaging. *Biochemistry 44*, 9905–9912.
(18) Matsumoto, Y., Itaka, K., Yamasoba, T., and Kataoka, K. (2009) Intranuclear fluorescence resonance energy transfer analysis of plasmid DNA decondensation from nonviral gene carriers. *J. Gene Med. 11*, 615–623.
(19) Stryer, L. (1978) Fluorescence energy transfer as a spectroscopic ruler. *Annu. Rev. Biochem. 47*, 819–846.
(20) Schwille, P. (2001) Fluorescence correlation spectroscopy and its potential for intracellular applications. *Cell Biochem. Biophys. 34*, 383–408.
(21) Resch-Genger, U., Grabolle, M., Cavaliere-Jaricot, S., Nitschke, R., and Nann, T. (2008) Quantum dots versus organic dyes as fluorescent labels. *Nat. Methods 5*, 763–775.
(22) Remaut, K., Lucas, B., Raemdonck, K., Braeckmans, K., Demeester, J., and De Smedt, S. C. (2007) Can we better understand the intracellular behavior of DNA nanoparticles by fluorescence correlation spectroscopy? *J. Controlled Release 121*, 49–63.
(23) Correa-Duarte, M. A., Giersig, M., and Liz-Marzan, L. M. (1998) Stabilization of CdS semiconductor nanoparticles against photodegradation by a silica coating procedure. *Chem. Phys. Lett. 286*, 497–501.
(24) Chen, A. A., Derfus, A. M., Khetani, S. R., and Bhatia, S. N. (2005) Quantum dots to monitor RNAi delivery and improve gene silencing. *Nucleic Acids Res. 33*, e190/191–e190/198.
(25) Derfus, A. M., Chen, A. A., Min, D.-H., Ruoslahti, E., and Bhatia, S. N. (2007) Targeted quantum dot conjugates for siRNA delivery. *Bioconjugate Chem. 18*, 1391–1396.
(26) Tan, W. B., Jiang, S., and Zhang, Y. (2007) Quantum-dot based nanoparticles for targeted silencing of HER2/neu gene via RNA interference. *Biomaterials 28*, 1565–1571.
(27) Prigodich, A. E., Seferos, D. S., Massich, M. D., Giljohann, D. A., Lane, B. C., and Mirkin, C. A. (2009) Nano-flares for mRNA regulation and detection. *ACS Nano 3*, 2147–2152.
(28) Bryson, J. M., Fichter, K. M., Chu, W.-J., Lee, J.-H., Li, J., Madsen, L. A., McLendon, P. M., and Reineke, T. M. (2009) Polymer beacons for luminescence and magnetic resonance imaging of DNA delivery. *Proc. Natl. Acad. Sci. U.S.A. 106*, 16913–16918.
(29) Selvin, P. R. (1996) Lanthanide-based resonance energy transfer. *IEEE Journal of Selected Topics in Quantum Electronics 2*, 1077–1087.
(30) Ichikawa, T., Hoegemann, D., Saeki, Y., Tyminski, E., Terada, K., Weissleder, R., Chiocca, E. A., and Basilion, J. P. (2002) MRI of transgene expression: Correlation to therapeutic gene expression. *Neoplasia (New York, NY, United States) 4*, 523–530.
(31) Moore, A., Josephson, L., Bhorade, R. M., Basilion, J. P., and Weissleder, R. (2001) Human transferrin receptor gene as a marker gene for MR imaging. *Radiology (Oak Brook, IL, United States) 221*, 244–250.
(32) Weissleder, R., Moore, A., Mahmood, U., Bhorade, R., Benveniste, H., Chiocca, E. A., and Basilion, J. P. (2000) In vivo magnetic resonance imaging of transgene expression. *Nat. Med. (New York) 6*, 351–354.
(33) Park, I.-K., Ng, C.-P., Wang, J., Chu, B., Yuan, C., Zhang, S., and Pun, S. H. (2008) Determination of nanoparticle vehicle unpackaging by MR imaging of a T_2 magnetic relaxation switch. *Biomaterials 29*, 724–732.
(34) Dubertret, B., Skourides, P., Norris, D. J., Noireaux, V., Brivanlou, A. H., and Libchaber, A. (2002) In vivo imaging of quantum dots encapsulated in phospholipid micelles. *Science (Washington, DC, United States) 298*, 1759–1762.
(35) Medarova, Z., Pham, W., Farrar, C., Petkova, V., and Moore, A. (2007) In vivo imaging of siRNA delivery and silencing in tumors. *Nat. Med. 13*, 372–377.
(36) Hu-Lieskovan, S., Heidel, J. D., Bartlett, D. W., Davis, M. E., and Triche, T. J. (2005) Sequence-specific knockdown of EWS-FLI1 by targeted, nonviral delivery of small interfering RNA inhibits tumor growth in a murine model of metastatic Ewing's sarcoma. *Cancer Res. 65*, 8984–8992.
(37) Pun, S. H., Tack, F., Bellocq, N. C., Cheng, J., Grubbs, B. H., Jensen, G. S., Davis, M. E., Brewster, M., Janicot, M., Janssens, B., Floren, W., and Bakker, A. (2004) Targeted delivery of RNA-cleaving DNA enzyme (DNAzyme) to tumor tissue by transferrin-modified, cyclodextrin-based particles. *Cancer Biol. Ther. 3*, 641–650.
(38) Bartlett, D. W., Su, H., Hildebrandt, I. J., Weber, W. A., and Davis, M. E. (2007) Impact of tumor-specific targeting on the biodistribution and efficacy of siRNA nanoparticles measured by multimodality in vivo imaging. *Proc. Natl. Acad. Sci. U.S.A. 104*, 15549–15554.
(39) Schneider, S., Lenz, D., Holzer, M., Palme, K., and Suess, R. (2010) Intracellular FRET analysis of lipid/DNA complexes using flow cytometry and fluorescence imaging techniques. *J. Controlled Release 145*, 289–296.
(40) Kuo, P. H. (2008) Gadolinium-containing MRI contrast agents: Important variations on a theme for NSF. *J Am. Coll. Radiol. 5*, 29–35.
(41) Pan, D., Caruthers, S. D., Hu, G., Senpan, A., Scott, M. J., Gaffney, P. J., Wickline, S. A., and Lanza, G. M. (2008) Ligand-directed nanobialys as theranostic agent for drug delivery and manganese-based magnetic resonance imaging of vascular targets. *J. Am. Chem. Soc. 130*, 9186–9187.
(42) Shin, J., Anisur, R. M., Ko, M. K., Im, G. H., Lee, J. H., and Lee, I. S. (2009) Hollow manganese oxide nanoparticles as multifunctional agents for magnetic resonance imaging and drug delivery. *Angew. Chem., Int. Ed. 48*, 321–324.
(43) Senpan, A., Caruthers, S. D., Rhee, I., Mauro, N. A., Pan, D., Hu, G., Scott, M. J., Fuhrhop, R. W., Gaffney, P. J., Wickline, S. A., and Lanza, G. M. (2009) Conquering the dark side: Colloidal iron oxide nanoparticles. *ACS Nano 3*, 3917–3926.
(44) Barth, B. M., Sharma, R., Altinoglu, E. I., Morgan, T. T., Shanmugavelandy, S. S., Kaiser, J. M., McGovern, C., Matters, G. L., Smith, J. P., Kester, M., and Adair, J. H. (2010) Bioconjugation of calcium phosphosilicate composite nanoparticles for selective targeting of human breast and pancreatic cancers in vivo. *ACS Nano 4*, 1279–1287.
(45) Kester, M., Heakal, Y., Fox, T., Sharma, A., Robertson, G. P., Morgan, T. T., Altinoglu, E. I., Tabakovic, A., Parette, M. R., Rouse, S., Ruiz-Velasco, V., and Adair, J. H. (2008) Calcium phosphate

nanocomposite particles for in vitro imaging and encapsulated chemotherapeutic drug delivery to cancer cells. *Nano Lett. 8*, 4116–4121.

(46) Morgan, T. T., Muddana, H. S., Altinoglu, E. I., Rouse, S. M., Tabakovic, A., Tabouillot, T., Russin, T. J., Shanmugavelandy, S. S., Butler, P. J., Eklund, P. C., Yun, J. K., Kester, M., and Adair, J. H. (2008) Encapsulation of organic molecules in calcium phosphate nanocomposite particles for intracellular imaging and drug delivery. *Nano Lett. 8*, 4108–4115.

(47) Muddana, H. S., Morgan, T. T., Adair, J. H., and Butler, P. J. (2009) Photophysics of Cy3-encapsulated calcium phosphate nanoparticles. *Nano Lett. 9*, 1559–1566.

(48) Shenoy, D., Little, S., Langer, R., and Amiji, M. (2005) Poly-(ethylene oxide)-modified poly(beta -amino ester) nanoparticles as a pH-sensitive system for tumor-targeted delivery of hydrophobic drugs: Part 2. In vivo distribution and tumor localization studies. *Pharm. Res. 22*, 2107–2114.

(49) Shenoy, D., Little, S., Langer, R., and Amiji, M. (2005) Poly-(ethylene oxide)-modified poly(beta -amino ester) nanoparticles as a ph-sensitive system for tumor-targeted delivery of hydrophobic drugs. 1. In vitro evaluations. *Mol. Pharmaceutics 2*, 357–366.

(50) Chen, W., Xu, N., Xu, L., Wang, L., Li, Z., Ma, W., Zhu, Y., Xu, C., and Kotov, N. A. (2010) Multifunctional magnetoplasmonic nanoparticle assemblies for cancer therapy and diagnostics (theranostics). *Macromol. Rapid Commun. 31*, 228–236.

(51) Xie, J., Chen, K., Huang, J., Lee, S., Wang, J., Gao, J., Li, X., and Chen, X. (2010) PET/NIRF/MRI triple functional iron oxide nanoparticles. *Biomaterials 31*, 3016–3022.

(52) Liong, M., Lu, J., Kovochich, M., Xia, T., Ruehm, S. G., Nel, A. E., Tamanoi, F., and Zink, J. I. (2008) Multifunctional inorganic nanoparticles for imaging, targeting, and drug delivery. *ACS Nano 2*, 889–896.

(53) Guthi, J. S., Yang, S.-G., Huang, G., Li, S., Khemtong, C., Kessinger, C. W., Peyton, M., Minna, J. D., Brown, K. C., and Gao, J. (2010) MRI-visible micellar nanomedicine for targeted drug delivery to lung cancer cells. *Mol. Pharmaceutics 7*, 32–40.

(54) Nasongkla, N., Bey, E., Ren, J., Ai, H., Khemtong, C., Guthi, J. S., Chin, S.-F., Sherry, A. D., Boothman David, A., and Gao, J. (2006) Multifunctional polymeric micelles as cancer-targeted, MRI-ultrasensitive drug delivery systems. *Nano Lett. 6*, 2427–2430.

(55) Santra, S., Kaittanis, C., Grimm, J., and Perez, J. M. (2009) Drug/dye-loaded, multifunctional iron oxide nanoparticles for combined targeted cancer therapy and dual optical/magnetic resonance imaging. *Small (Weinheim an der Bergstrasse, Germany) 5*, 1862–1868.

(56) Kohler, N., Sun, C., Wang, J., and Zhang, M. (2005) Methotrexate-modified superparamagnetic nanoparticles and their intracellular uptake into human cancer cells. *Langmuir 21*, 8858–8864.

(57) Das, M., Mishra, D., Dhak, P., Gupta, S., Maiti, T. K., Basak, A., and Pramanik, P. (2009) Biofunctionalized, phosphonate-grafted, ultrasmall iron oxide nanoparticles for combined targeted cancer therapy and multimodal imaging. *Small (Weinheim an der Bergstrasse, Germany) 5*, 2883–2893.

(58) Kim, J., Kim, H. S., Lee, N., Kim, T., Kim, H., Yu, T., Song, I. C., Moon, W. K., and Hyeon, T. (2008) Multifunctional uniform nanoparticles composed of a magnetite nanocrystal core and a mesoporous silica shell for magnetic resonance and fluorescence imaging and for drug delivery. *Angew. Chem., Int. Ed. 47*, 8438–8441.

(59) Gopalakrishnan, G., Danelon, C., Izewska, P., Prummer, M., Bolinger, P.-Y., Geissbuhler, I., Demurtas, D., Dubochet, J., and Vogel, H. (2006) Multifunctional lipid/quantum dot hybrid nanocontainers for controlled targeting of live cells. *Angew. Chem., Int. Ed. 45*, 5478–5483.

(60) Michalet, X., Pinaud, F. F., Bentolila, L. A., Tsay, J. M., Doose, S., Li, J. J., Sundaresan, G., Wu, A. M., Gambhir, S. S., and Weiss, S. (2005) Quantum dots for live cells, in vivo imaging, and diagnostics. *Science (Washington, DC, U. S.) 307*, 538–544.

(61) Yao, J., Larson, D. R., Vishwasrao, H. D., Zipfel, W. R., and Webb, W. W. (2005) Blinking and nonradiant dark fraction of water-soluble quantum dots in aqueous solution. *Proc. Natl. Acad. Sci. U.S.A. 102*, 14284–14289.

(62) Bagalkot, V., Zhang, L., Levy-Nissenbaum, E., Jon, S., Kantoff, P. W., Langer, R., and Farokhzad, O. C. (2007) Quantum dot-aptamer conjugates for synchronous cancer imaging, therapy, and sensing of drug delivery based on bi-fluorescence resonance energy transfer. *Nano Lett. 7*, 3065–3070.

(63) McCarthy, J. R., Jaffer, F. A., and Weissleder, R. (2006) A macrophage-targeted theranostic nanoparticle for biomedical applications. *Small (Weinheim an der Bergstrasse, Germany) 2*, 983–987.

(64) Denis, M. C., Mahmood, U., Benoist, C., Mathis, D., and Weissleder, R. (2004) Imaging inflammation of the pancreatic islets in type 1 diabetes. *Proc. Natl. Acad. Sci. U.S.A. 101*, 12634–12639.

(65) Jaffer Farouc, A., Nahrendorf, M., Sosnovik, D., Kelly Kimberly, A., Aikawa, E., and Weissleder, R. (2006) Cellular imaging of inflammation in atherosclerosis using magnetofluorescent nanomaterials. *Mol. Imaging 5*, 85–92.

(66) Kircher, M. F., Mahmood, U., King, R. S., Weissleder, R., and Josephson, L. (2003) A multimodal nanoparticle for preoperative magnetic resonance imaging and intraoperative optical brain tumor delineation. *Cancer Res. 63*, 8122–8125.

(67) Pande, A. N., Kohler, R. H., Aikawa, E., Weissleder, R., and Jaffer, F. A. (2006) Detection of macrophage activity in atherosclerosis in vivo using multichannel, high-resolution laser scanning flourescence microscopy. *J. Biomed. Opt. 11*, 021009/021001–021009/021007.

(68) Weissleder, R., Kelly, K., Sun, E. Y., Shtatland, T., and Josephson, L. (2005) Cell-specific targeting of nanoparticles by multivalent attachment of small molecules. *Nat. Biotechnol. 23*, 1418–1423.

(69) Kopelman, R., Koo, Y.-E. L., Philbert, M., Moffat, B. A., Ramachandra Reddy, G., McConville, P., Hall, D. E., Chenevert, T. L., Bhojani, M. S., Buck, S. M., Rehemtulla, A., and Ross, B. D. (2005) Multifunctional nanoparticle platforms for in vivo mri enhancement and photodynamic therapy of a rat brain cancer. *J. Magn. Magn. Mater. 293*, 404–410.

(70) Kaye, A. H., Morstyn, G., and Brownbill, D. (1987) Adjuvant high-dose photoradiation therapy in the treatment of cerebral glioma: A phase 1−2 study. *J. Neurosurg. 67*, 500–505.

(71) Kostron, H., Weiser, G., Fritsch, E., and Grunert, V. (1987) Photodynamic therapy of malignant brain tumors: Clinical and neuropathological results. *Photochem. Photobiol. 46*, 937–943.

(72) Muller, P. J., and Wilson, B. C. (2006) Photodynamic therapy of brain tumors--a work in progress. *Lasers Surg. Med. 38*, 384–389.

(73) Perria, C., Capuzzo, T., Cavagnaro, G., Datti, R., Francaviglia, N., Rivano, C., and Tercero, V. E. (1980) Fast attempts at the photodynamic treatment of human gliomas. *J. Neurosurg. Sci. 24*, 119–129.

(74) Popovic, E. A., Kaye, A. H., and Hill, J. S. (1995) Photodynamic therapy of brain tumors. *Semin. Surg. Oncol. 11*, 335–345.

(75) Reddy, G. R., Bhojani, M. S., McConville, P., Moody, J., Moffat, B. A., Hall, D. E., Kim, G., Koo, Y.-E. L., Woolliscroft, M. J., Sugai, J. V., Johnson, T. D., Philbert, M. A., Kopelman, R., Rehemtulla, A., and Ross, B. D. (2006) Vascular targeted nanoparticles for imaging and treatment of brain tumors. *Clin. Cancer Res. 12*, 6677–6686.

(76) Lo, L.-W., Koch, C. J., and Wilson, D. F. (1996) Calibration of oxygen-dependent quenching of the phosphorescence of Pd-meso-tetra (4-carboxyphenyl) porphine: A phosphor with general application for measuring oxygen zconcentration in biological systems. *Anal. Biochem. 236*, 153–160.

(77) Vinogradov, S. A., and Wilson, D. F. (1994) Phosphorescence lifetime analysis with a quadratic programming algorithm for determining quencher distributions in heterogeneous systems. *Biophys. J. 67*, 2048–2059.

(78) Cheng, S.-H., Lee, C.-H., Yang, C.-S., Tseng, F.-G., Mou, C.-Y., and Lo, L.-W. (2009) Mesoporous silica nanoparticles functionalized with an oxygen-sensing probe for cell photodynamic therapy: Potential cancer theranostics. *J. Mater. Chem. 19*, 1252–1257.

(79) Dougherty, T. J., Gomer, C. J., Henderson, B. W., Jori, G., Kessel, D., Korbelik, M., Moan, J., and Peng, Q. (1998) Photodynamic therapy. *J. Natl. Cancer Inst. 90*, 889–905.

(80) Price, M., Terlecky, S. R., and Kessel, D. (2009) A role for hydrogen peroxide in the pro-apoptotic effects of photodynamic therapy. *Photochem. Photobiol. 85*, 1491–1496.

(81) Hasan, T., Ortel, B., Solban, N., and Pogue, B. W. (2006) Photodynamic therapy of cancer. *Cancer Med. 7*, 537–548.

(82) Rahmanzadeh, R., Rai, P., Gerdes, J., and Hasan, T. (2010) Targeted light-inactivation of the ki-67 protein using theranostic liposomes leads to death of proliferating cells. *Proc. SPIE 7576*, 757602/757601–757602/757605.

(83) Hilger, I., Andra, W., Hergt, R., Hiergeist, R., Schubert, H., and Kaiser, W. A. (2001) Electromagnetic heating of breast tumors in interventional radiology: In vitro and in vivo studies in human cadavers and mice. *Radiology 218*, 570–575.

(84) Hilger, I., Fruhauf, K., Andra, W., Hiergeist, R., Hergt, R., and Kaiser, W. A. (2002) Heating potential of iron oxides for therapeutic purposes in interventional radiology. *Acad. Radiol. 9*, 198–202.

(85) Jain, P. K., Huang, X., El-Sayed, I. H., and El-Sayed, M. A. (2008) Noble metals on the nanoscale: Optical and photothermal properties and some applications in imaging, sensing, biology, and medicine. *Acc. Chem. Res. 41*, 1578–1586.

(86) Melancon, M. P., Lu, W., and Li, C. (2009) Gold-based magneto-optical nanostructures: Challenges for in vivo applications in cancer diagnostics and therapy. *MRS Bull. 34*, 415–421.

(87) Mahmood, U., and Weissleder, R. (2003) Near-infrared optical imaging of proteases in cancer. *Mol. Cancer Ther. 2*, 489–496.

(88) Gilchrist, R. K., Medal, R., Shorey, W. D., Hanselman, R. C., Parrott, J. C., and Taylor, C. B. (1957) Selective inductive heating of lymph nodes. *Ann. Surg. 146*, 596–606.

(89) Kim, J., Park, S., Lee, J. E., Jin, S. M., Lee, J. H., Lee, I. S., Yang, I., Kim, J.-S., Kim, S. K., Cho, M.-H., and Hyeon, T. (2006) Designed fabrication of multifunctional magnetic gold nanoshells and their application to magnetic resonance imaging and photothermal therapy. *Angew. Chem., Int. Ed. 45*, 7754–7758.

(90) Lim, Y. T., Cho, M. Y., Kim, J. K., Hwangbo, S., and Chung, B. H. (2007) Plasmonic magnetic nanostructure for bimodal imaging and photonic-based therapy of cancer cells. *ChemBioChem 8*, 2204–2209.

(91) Berret, J.-F., Schonbeck, N., Gazeau, F., El Kharrat, D., Sandre, O., Vacher, A., and Airiau, M. (2006) Controlled clustering of superparamagnetic nanoparticles using block copolymers: Design of new contrast agents for magnetic resonance imaging. *J. Am. Chem. Soc. 128*, 1755–1761.

(92) Lee, J.-H., Jun, Y.-W., Yeon, S.-I., Shin, J.-S., and Cheon, J. (2006) Dual-mode nanoparticle probes for high-performance magnetic resonance and fluorescence imaging of neuroblastoma. *Angew. Chem., Int. Ed. Engl. 45*, 8160–8162.

(93) Perez, J. M., Josephson, L., O'Loughlin, T., Hoegemann, D., and Weissleder, R. (2002) Magnetic relaxation switches capable of sensing molecular interactions. *Nat. Biotechnol. 20*, 816–820.

(94) Lee, J., Yang, J., Ko, H., Oh, S. J., Kang, J., Son, J.-H., Lee, K., Lee, S.-W., Yoon, H.-G., Suh, J.-S., Huh, Y.-M., and Haam, S. (2008) Multifunctional magnetic gold nanocomposites: Human epithelial cancer detection via magnetic resonance imaging and localized synchronous therapy. *Adv. Funct. Mater. 18*, 258–264.

(95) Comes Franchini, M., Baldi, G., Bonacchi, D., Gentili, D., Giudetti, G., Lascialfari, A., Corti, M., Marmorato, P., Ponti, J., Micotti, E., Guerrini, U., Sironi, L., Gelosa, P., Ravagli, C., and Ricci, A. (2010) Bovine serum albumin-based magnetic nanocarrier for MRI diagnosis and hyperthermic therapy: A potential theranostic approach against cancer. *Small (Weinheim an der Bergstrasse, Germany) 6*, 366–370.

(96) Kaplan, H. S. (1977) Basic principles in radiation oncology. *Cancer 39*, 689–693.

(97) Saatchi, K., and Hafeli, U. O. (2009) Radiolabeling of biodegradable polymeric microspheres with $[^{99m}Tc(CO)_3]^+$ and in vivo biodistribution evaluation using microspect/ct imaging. *Bioconjugate Chem. 20*, 1209–1217.

(98) de Jong, M., Breeman, W. A. P., Kwekkeboom, D. J., Valkema, R., and Krenning, E. P. (2009) Tumor imaging and therapy using radiolabeled somatostatin analogues. *Acc. Chem. Res. 42*, 873–880.

(99) Krenning, E. P., Kwekkeboom, D. J., Bakker, W. H., Breeman, W. A., Kooij, P. P., Oei, H. Y., van Hagen, M., Postema, P. T., de Jong, M., and Reubi, J. C. et al. (1993) et al. Somatostatin receptor scintigraphy with $[^{111}$In-DTPA-D-Phe1$]$- and $[^{123}$I-Tyr$_3]$-octreotide: The rotterdam experience with more than 1000 patients. *Eur. J. Nucl. Med. 20*, 716–731.

(100) Reubi, J. C., Schar, J.-C., Waser, B., Wenger, S., Heppeler, A., Schmitt, J. S., and Macke, H. R. (2000) Affinity profiles for human somatostatin receptor subtypes SST1-SST5 of somatostatin radiotracers selected for scintigraphic and radiotherapeutic use. *Eur. J. Nucl. Med. 27*, 273–282.

Bioconjugate Chemistry

COMMUNICATION

pubs.acs.org/bc

Novel Strategy for Microsphere-Mediated DNA Transfection

Jessica G. Borger,[#,†] Juan Manuel Cardenas-Maestre,[#,‡] Rose Zamoyska,[*,†] and Rosario M. Sanchez-Martin[*,‡,§]

[†]Institute of Immunology and Infection Research, School of Biological Sciences, University of Edinburgh, Ashworth Laboratories, King's Buildings, West Mains Road, Edinburgh, EH9 3JT, United Kingdom

[‡]School of Chemistry, University of Edinburgh, West Mains Road, Edinburgh, EH9 3JJ, United Kingdom

Supporting Information

ABSTRACT: A new approach for microsphere-mediated delivery of plasmid DNA has been developed and successfully evaluated. Basic molecular biology techniques were used to linearize and functionalize plasmid DNA by aminomodification, enabling efficient conjugation to carboxy-functionalized microspheres. A T cell hybridoma line was successfully transfected as determined by the efficient expression of a biologically relevant YFP fusion protein. Moreover, our data identified microsphere-mediated delivery of plasmid DNA as a noninvasive, nontoxic, and efficient gene delivery method with the potential to be applied to transfection-resistant, nondividing primary cells, including naïve T cells.

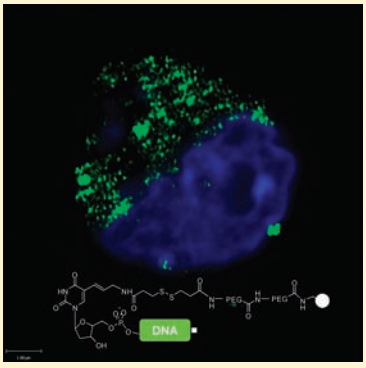

The development of an efficient carrier system for delivery of plasmid DNA (pDNA) into cells is a key technology for the progress of research in the biological sciences and medicine.[1] In the past few years, different technologies and methodologies have been developed in order to efficiently deliver nucleotides at the cellular level.[2] Examples include cell penetrating peptides,[3,4] cationic lipids,[5,6] nanodevices such as biodegradable nanoparticles[7] and nanotubes,[8] dendrimers,[9,10] polymer-mediated delivery including cationic polymers,[11] cationic amphiphiles,[12] and quantum dots,[13] in addition to more invasive techniques such as particle bombardment[14] and electroporation.[15] Even though all these approaches are currently available, there is still a need to improve transfection efficiency for specific cell lines that are difficult to transfect. We have previously reported that amino-functionalized, cross-linked polystyrene microspheres of highly defined sizes (200 nm to 2 μm) are efficient delivery agents, which can be taken up by a wide range of cell lines including adherent, suspension, primary, and stem cells.[16−18] We have achieved the effective microsphere-based delivery of siRNA[19] and proteins[20] among other biological cargos.[21−23] Recently, we reported the ability of palladium-loaded microspheres to carry out intracellular chemical reactions and their potential use to activate drugs and probes inside cells.[24] While the mechanism of uptake is not yet established, we have recently found that these microspheres are unlikely to enter cells through an endocytic pathway. The application of chemical inhibitors of endocytosis and extensive colocalization studies by microscopy and gene-expression profiling all argue against an endocytic mechanism. Instead, we have proposed an endocytosis-independent uptake mechanism that results in the uncompartmentalized, cytoplasmic localization of microspheres and their cargo.[25] The fact that these latex microspheres are easy to functionalize with high controllability over the cargo loading, in addition to showing no undesired cytotoxic effect, make them enormously attractive as a novel DNA carrier/delivery system.

Here, we describe a novel conjugation approach for microsphere-mediated delivery of pDNA inside cells resulting in expression of the encoded protein. pDNA was linearized and functionalized with 5-(3-aminoallyl)-2′′-deoxyuridine 5′′triphoshate dUTP (aminoallyl-dUTP) by an established molecular biological approach, to enable its conjugation to microspheres, which were subsequently used to transfect various cell lineages. To carry out this strategy, 200 nm polystyrene microspheres (**1**) were functionalized as described in Scheme 1 following a standard Fmoc solid-phase protocol, using Oxyma and *N*,*N*′-diisopropylcarbodiimide (DIC) as coupling reagents. The carboxy-linker (3,3′-dithiodipropionic acid), which contains a disulfide bond, enabled the efficient attachment of pDNA to microspheres to build construct (**3**) (Scheme 1). This is an efficient strategy for the delivery of the pDNA from the carrier by incorporation of cleavable bonds to enable controlled molecular release from the particle surface.The introduction of disulfide bonds into carrier molecules is an excellent approach to create an interactive delivery system that exploits the redox gradient between the extra- and intracellular compartments. Examples

Received: June 3, 2011
Revised: August 26, 2011
Published: September 07, 2011

ACS Publications © 2011 American Chemical Society

of delivery of bioactive cargos such as nucleic acid or proteins based on the introduction of disulfide bonds into carrier molecules such as chitosan or polymeric nanocapsules have been recently reported.[26,27] The efficiency of this strategy relies on the release of biological cargos from nanoparticles following cleavage of cargo−nanoparticle bonds inside biological systems. The stability associated with the disulfide bond linkage ensured that pDNA remained coupled to the microsphere during incubation in culture media. Upon cellular uptake, the nature of the disulfide bond ensured that it was cleaved within the cytosol, releasing the DNA to enable transcription and translation of the encoded protein. Additionally, microspheres were double-pegylated with a Fmoc monoprotected poly(ethylene glycol) spacer (Fmoc-PEG-OH) before being carboxyfunctionalized with a cleavable linker to give rise to microspheres (**2**) (Scheme 1).[28] There were two rationales to double-pegylate the microspheres: first, the addition of these units facilitated transport across the cell membrane by increasing bead biocompatibility, and second, the distance between the DNA and cellular vehicle was increased, which reduced the likelihood of unfavorable interactions.

The subsequent conjugation of linearized pDNA with carboxy-functionalized 200 nm polystyrene microspheres (**3**) (Scheme 1) involved the conjugation of a modified nucleotide aminoallyl-dUTP (**4**) to DNA (Scheme 2). Initially, pDNA encoding a yellow fluorescent protein (YFP)-tagged protein was linearized at a restriction endonuclease site upstream of the promoter region and amino-functionalized through the incorporation of a modified nucleotide to its 3′-end terminal. Specifically, aminoallyl-dUTP was incorporated into the pDNA by terminal deoxynucleotidyltransferase (TdT), a specialized DNA polymerase which catalyzes the addition of nucleotides to the 3′ terminus of a DNA molecule. The incorporation of an amino-reactive group onto the DNA strand enabled the conjugation of the pDNA to the carboxy-functionalized microsphere through formation of an amide bond. The aminoallyl modification enabled downstream reactions with amine-reactive compounds such as activated esters; thus, the aminoallyl-modified pDNA could be conjugated to carboxy-functionalized microspheres (**3**) in a single step as detailed in Scheme 2.

In order to validate beadfection as a novel technology for introduction and expression of DNA into transfection-resistant cell types, we selected immune cells as our model. Unlike other lineages, such as fibroblasts or endothelial cells, which are amenable to transfection by a variety of techniques, naïve T lymphocytes are small, nonproliferating, metabolically inert cells that are readily killed by most standard transfection protocols. T

Scheme 1. Microsphere Preparation for Conjugation to Linearized pDNA[a]

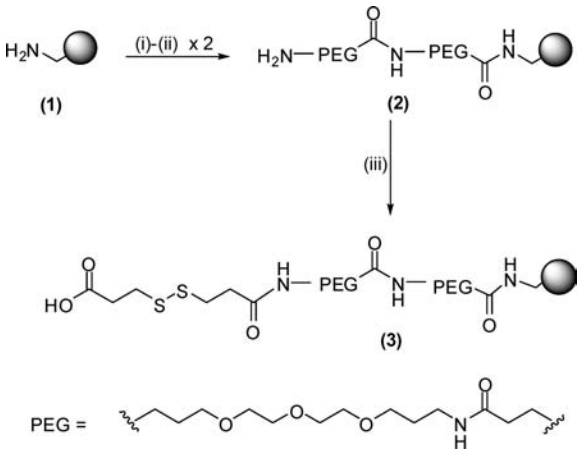

[a] Reagents and conditions: (i) Fmoc-PEG-OH spacer (5 equiv), Oxyma (5 equiv), DIC (5 equiv), DMF, 2 h, 60 °C; (ii) 20% piperidine in DMF, 3 × 20 min; (iii) 3,3′-Dithiodipropionic acid (5 equiv), DIC (5 equiv), DIPEA (0.1 equiv), DMF, 2 h, 60 °C.

Scheme 2. Strategy for Conjugation of DNA to Microspheres[a]

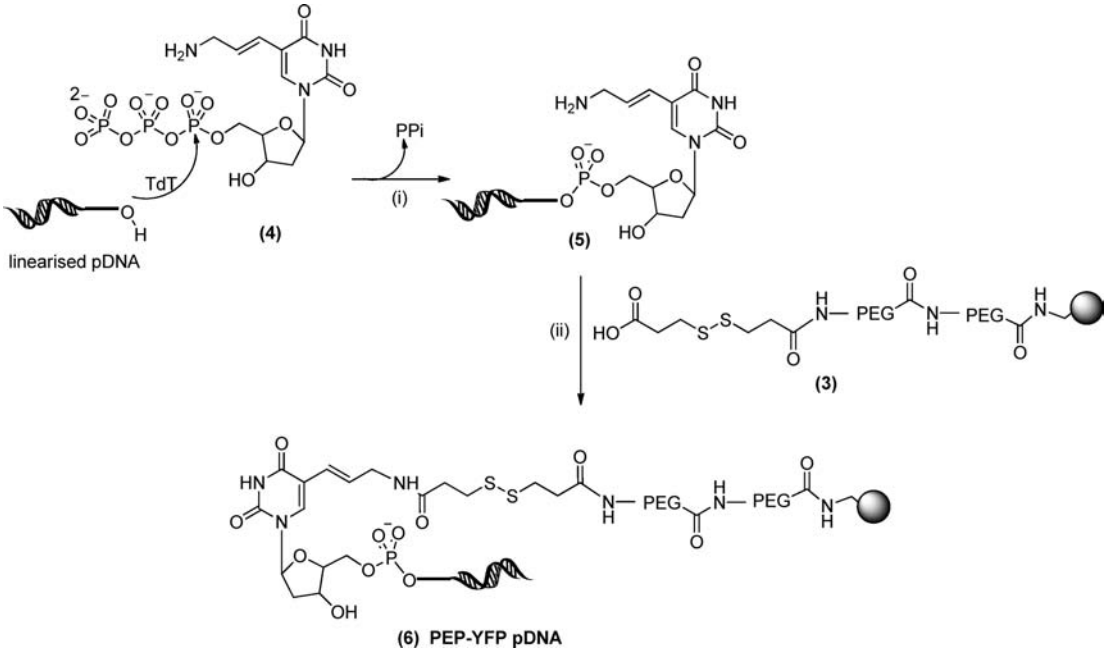

[a] Reagents and conditions: (i) TdT (20 units), 10× TdT buffer, $CoCl_2$, 37 °C, 20 min; (ii) 1. EDC, H_2O, rt, 4 h; 2. PBS pH 7.4, 18 h, rt.

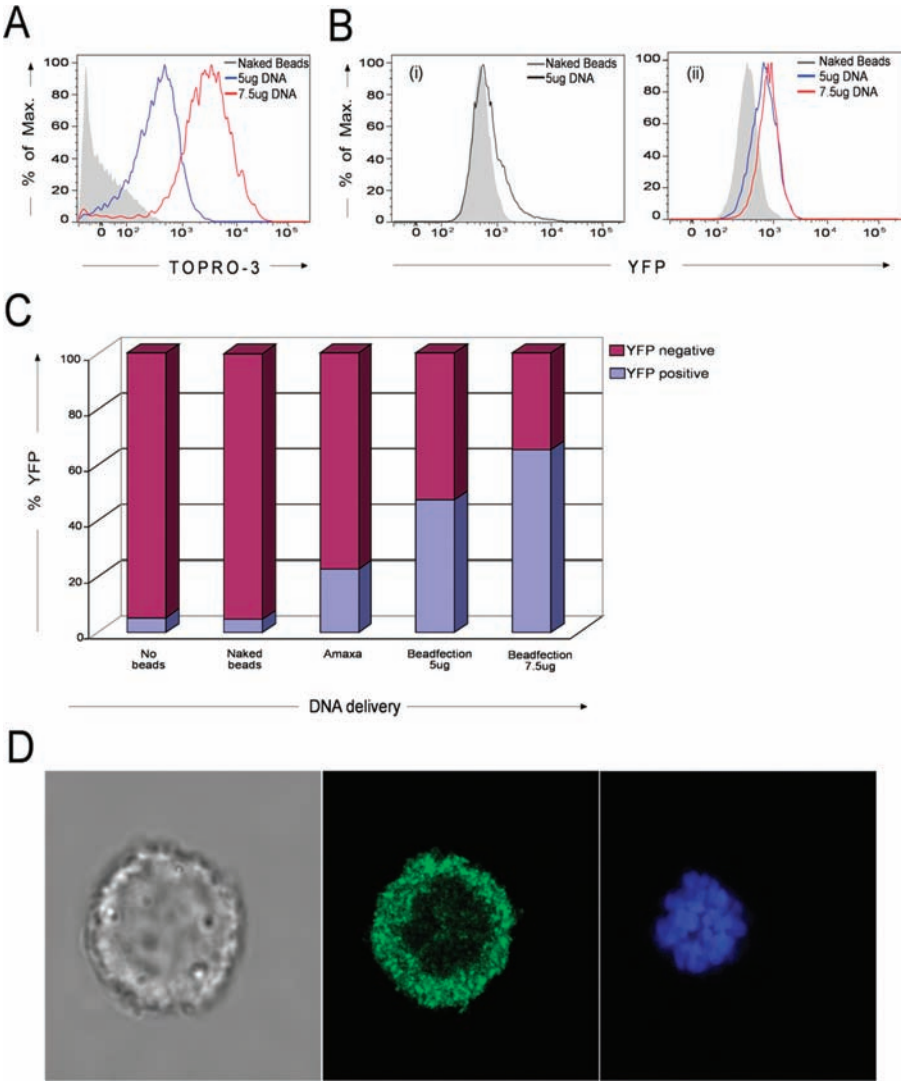

Figure 1. F5.BW hybridoma pDNA beadfection and protein expression. (A) Flow cytometric analysis of efficiency of pDNA conjugation to 200 nm microspheres by TOPRO-3 staining. (B) YFP protein expression observed 24 h after incubation: (i) Amaxa electroporation, (ii) beadfection. (C) Flow cytometric analysis of YFP expression in electroporated cells (Amaxa), pDNA-microsphere beadfected cells (Beadfection) and negative controls: untreated cells (No beads) and beads without pDNA conjugated (Naked beads). (D) Confocal microscopy image of a single T cell hybridoma (F5.BW) loaded with pDNA−microsphere conjugate **6** (DIC) expressing PEP-YFP (green). Image taken after 24 h at a 63× magnification, where nuclei are stained with DAPI.

lymphocytes can be activated *in vitro* by incubation with specific antigen or antibodies directed to the T cell receptor, whereupon they increase in cell size (from approximately 5−7 μM to ~12 μM) and enter into division. However, murine T lymphocytes, in particular, remain resistant to, and easily killed by, most standard DNA transfection methods. Development of an efficient and noninvasive system for gene delivery into nonproliferating, undifferentiating, or other transfection resistant immune cells would greatly facilitate research into the basic biology of lymphocytes that has been employed by other disciplines for many years. The ability to transfect naïve T lymphocytes remains a challenge that currently is not met by the relatively few transfection technologies available, all of which are associated with high toxicity, low efficiency, and relative lack of reproducibility.[29,30]

In order to test the beadfection protocol in T lymphocytes, we initially used an immortalized T cell hybridoma line (F5.BW). Given the relatively small size of T lymphocytes, we first evaluated the optimum size and number of microspheres that gave the most efficient delivery using fluorescein (FITC)-labeled microspheres following a previously described procedure[16] (see Supporting Information). After 24 h incubation, microspheres of 200 nm were found to be taken up most readily by the F5.BW hybridoma T cells, as the larger bead sizes were either less efficient (500 nm) or not taken up at all (900 nm) (Figure S1A-B, Supporting Information). Additionally, a linear increase in the efficacy of microsphere uptake was observed, which was proportional to the concentration of microspheres. In addition to microsphere uptake, cell viability was monitored by exclusion of a membrane-impermeable, DNA-intercalating dye, TO-PRO-3 Iodide (TO-PRO-3). Importantly, there was no change in the proportion of cells dying after incubation with the microspheres, although there was evidence of the association of smaller microspheres with dying cells (Figure S1C, Supporting Information). Analysis of the time course of microsphere uptake was carried out

(Figure S2A-B, Supporting Information), indicated that maximal uptake of 200 nm microspheres was already achieved by 4 h. Mean fluorescent intensity (MFI) was used as a measure of FITC-uptake, and these values remained unchanged following 8 h of incubation and were reduced only slightly at 24 h, which might be due to cell division and subsequent dilution of the numbers of microspheres per cell. Imaging of cells by confocal microscopy confirmed that the microspheres had entered the cell, localizing within the cytoplasm, excluding the possibility that the microspheres had simply adhered to extracellular membrane proteins (Figure S2C, Supporting Information).

To validate the use of these microsphere-based conjugates as a novel technology for DNA transfection of immune cells, we addressed whether pDNA could be delivered to F5.BW hybridoma T cells using microspheres as the transfection agent. For this purpose, pDNA encoding a lymphocyte-specific protein, proline-glutamine-serine-threonine-domain enriched phosphatase (PEP), fused at the carboxy-terminus to yellow fluorescent protein (PEP-YFP), was prepared as described in Scheme 1 and conjugated to microspheres as described in Scheme 2. To assess the efficiency of coupling of the pDNA to the microspheres, the DNA intercalator TO-PRO-3 was incubated with the microsphere suspension for 5 min after which the microspheres were washed and analyzed by flow cytometry for the presence of DNA. Figure1A shows that although the naked 200 nm microspheres stained with TO-PRO-3, covalent attachment of pDNA increased the MFI 10-fold, indicative of covalently coupled pDNA.Successful gene expression was achieved upon delivery of conjugate (**6**) (Scheme 2) to F5.BW hybridoma T cells as determined by the detection of YFP fluorescence by flow cytometry. As shown in Figure1Bii, the majority of the F5.BW hybridoma T cells expressed the PEP-YFP protein 24 h after transfection with pDNA conjugated microspheres (**6**). Coupling the microspheres with 7.5 μg of DNA rather than 5 μg provided a slight increase in transfection efficiency. As a positive control, F5.BW hybridoma T cells were transfected by the Amaxa (Lonza) electroporation method, currently the most efficient means of transfecting T lymphocytes.[31−33] Using the same relative concentration of DNA (5 μg/1 $\times$ 10^6 cells), F5.BW hybridoma T cells were Amaxa transfected and assessed by flow cytometry for YFP expression 24 h later (Figure1Bi) and 48 h later (Figure S3, Supporting Information). Notably, after 24 h beadfection led to a more uniform expression of PEP-YFP, as seen by a shift of the entire population of transfected F5.BW hybridoma T cells in Figure 1Bii. By comparison, only half as many cells were YFP^+ following Amaxa electroporation (Figure1C). However, protein expression decreased dramatically after 48 h in both the Amaxa-transfected and the beadfected cells (Figure S3). Endogenous PEP protein has previously been characterized by Western blot to reside wholly within the cytoplasm in T lymphocytes,[34] and transfected PEP was shown to localize within the cytoplasm in the nonimmune cell line HeLa.[35] Using confocal microscopy, we identified that the transcribed PEP-YFP protein similarly localized within the cytoplasm of F5.BW hybridoma T cells (Figure1D). These results show that a much higher efficiency of transfection is achieved into hybridoma T cells when the pDNA is delivered by beadfection rather than the traditional method of electroporation.

The efficient delivery of pDNA and subsequent rapid protein expression in hybridoma T cells led us to address whether naïve T lymphocytes isolated from murine lymph nodes could uptake microspheres. If so, this would identify a novel technique for the introduction of DNA into nondividing primary immune cells, which are resistant to more common transfection techniques including lipid carriers and calcium phosphate. Surprisingly, naïve $CD8^+$ T lymphocytes were as efficient in the uptake of FITC-labeled microspheres as the F5.BW hybridoma T cells (Figure S4AB), with a similar dependency on size and concentration of the microspheres. Two important considerations in the transfection of naïve T lymphocytes are whether the DNA delivery protocol leads to either cell death or cellular activation. We confirmed that neither occurred, as there was very little change in the proportion of dead cells (TO-PRO-3+, Figure S4C) and there was no expression on the cell surface of a marker of cellular activation, CD69 (Figure S4D). In contrast, the positive control for activation, which were naïve T lymphocytes stimulated with antibody to the T cell receptor (anti-CD3, Figure S4D) did show expression of CD69. Imaging of the cells by confocal microscopy confirmed that the microspheres had entered the naïve T lymphocytes and localized within the cytoplasm, as no fluorescence was observed within the nucleus (Figure S4E). These results show an efficient internalization of microspheres by naïve T lymphocytes, and consequently, they support the potential of this technology to carry out gene expression studies in this cell line and other resistant primary cells.

In conclusion, we have described a novel strategy of transfection, based on the delivery of pDNA by conjugation to microspheres. Following a simple protocol for the linearization and functionalization of the pDNA, this amino-modified DNA was successfully conjugated to 200 nm polystyrene microspheres and transfected into hybridoma T cells leading to successful expression of a biologically relevant protein fused to YFP. In addition, the microspheres were taken up by naive T lymphocytes, a primary cell which is difficult to transfect, with no associated toxicity. These data confirm the development of a novel, noninvasive, efficient, and controlled dose transfection methodology, specifically aimed at DNA delivery into transfection resistant cells that is not matched by currently available technology.

■ ASSOCIATED CONTENT

Ⓢ Supporting Information. Details of synthesis and experimental methods: Experimental procedures for preparation of functionalized microspheres, DNA linearization and aminoallyl-dUTP incorporation, DNA-microspheres conjugation and biological evaluation. Supplementary Figures: S1 to S4. This material is available free of charge via the Internet at http://pubs.acs.org.

■ AUTHOR INFORMATION

Corresponding Author

*Prof. Rose Zamoyska, E-mail: Rose.Zamoyska@ed.ac.uk, Tel: 44-131-651-3686, Fax: 44-131-650-6564. Dr. Rosario Maria Sanchez-Martin, E-mail: rosario.sanchez@ed.ac.uk, Tel: +44 (0) 131 650 4713, Fax: +44 (0) 131 650 6453.

Present Addresses

[§]Department of Medicinal and Organic Chemistry, Faculty of Pharmacy, University of Granada, Campus Universitario Cartuja s/n, 18071 Granada, Spain (rmsanchez@ugr.es).

Author Contributions

[#]These authors contributed equally to this work.

■ ACKNOWLEDGMENT

This work was supported by the Royal Society and the Medical Research Council (MRC) Ph.D. Fellowship (J.G.B). R.M.S.M would like to thank the Royal Society for a Dorothy Hogdkin Fellowship. J.M.C.M. thanks the School of Chemistry for a Ph.D. Fellowship.

■ REFERENCES

(1) Glover, D. J., Lipps, H. J., and Jans, D. A. (2005) Towards safe, non-viral therapeutic gene expression in humans. *Nat. Rev. Genet. 6*, 299–310.

(2) Mintzer, M. A., and Simanek, E. E. (2009) Nonviral vectors for gene delivery. *Chem. Rev. 109*, 259–302.

(3) Bertrand, J. R., Malvy, C., Auguste, T., Toth, G. K., Kiss-Ivankovits, O., Illyes, E., Hollosi, M., Bottka, S., and Laczko, I. A. (2009) Synthesis and studies on cell-penetrating peptides. *Bioconjugate Chem. 20*, 1307–1314.

(4) Diaz-Mochon, J. J., Bialy, L., Watson, J., Sanchez-Martin, R. M., and Bradley, M. (2005) Synthesis and cellular uptake of cell delivering PNA-peptide conjugates. *Chem. Commun.* 3316–3318.

(5) Martin, B., Sainlos, M., Aissaoui, A., Oudrhiri, N., Hauchecorne, M., Vigneron, J. P., Lehn, J. M., and Lehn, P. (2005) The design of cationic lipids for gene delivery. *Curr. Pharm. Res. 11*, 375–394.

(6) Unciti-Broceta, A., Moggio, L., Dhaliwal, K., Pidgeon, L., Finlayson, K., Haslett, C., and Bradley, M. (2011) Safe and efficient *in vitro* and *in vivo* gene delivery: tripodal cationic lipids with programmed biodegradability. *J. Mater. Chem. 21*, 2154–2158.

(7) Blum, J. S., and Saltzman, W. M. (2008) High loading efficiency and tunable release of plasmid DNA encapsulated in submicron particles fabricated from PLGA conjugated with poly-L-lysine. *J. Controlled Release 129*, 66–72.

(8) Singh, R., Pantarotto, D., McCarthy, D., Chaloin, O., Hoebeke, J., Partidos, C. D., Briand, J. P., Prato, M., Bianco, A., and Kostarelos, K. (2005) Binding and condensation of plasmid DNA onto functionalized carbon nanotubes: toward the construction of nanotube-based gene delivery vectors. *J. Am. Chem. Soc. 127*, 4388–4396.

(9) Diaz-Mochon, J. J., Fara, M. A., Sanchez-Martin, R. M., and Bradley, M. (2008) Peptoid dendrimers—microwave-assisted solid-phase synthesis and transfection agent evaluation. *Tetrahedron Lett. 49*, 923–926.

(10) How, S. E., Unciti-Broceta, A., Sanchez-Martin, R. M., and Bradley, M. (2008) Solid-phase synthesis of a lysine-capped bis-dendron with remarkable DNA delivery abilities. *Org. Biomol. Chem. 6*, 2266–2269.

(11) Peng, L., Liu, M., Xue, Y. N., Huang, S.-W., and Zhuo, R. X. (2009) Transfection and intracellular trafficking characteristics for poly(amidoamine)s with pendant primary amine in the delivery of plasmid DNA to bone marrow stromal cells. *Biomaterials 30*, 5825–5833.

(12) Zhang, X.- X., Prata, C. A. H., McInstoch, T. J., Barthelemy, P., and Grinstaff, W. (2010) The effect of charge-reversal amphiphile spacer composition on DNA and siRNA delivery. *Bioconjugate Chem. 21*, 988–993.

(13) Zhang, P., and Liu, W. (2010) ZnO QD@PMAA-co-PDMAEMA non viral vector for plasmid DNA delivery and bioimaging. *Biomaterials 31*, 3087–3094.

(14) Uchida, M., Li, X. W., Mertens, P., and Alpar, H. O. (2009) Transfection by particle bombardment: Delivery of plasmid DNA into mammalian cells using gene gun. *Biochim. Biophys. Acta 1790*, 754–764.

(15) Potter, H., and Heller, R. (2010) Transfection by electroporation. In *Current Protocols in Molecular Biology*, Units 9.3.1−9.3.10, Wiley On-line Library.

(16) Sánchez-Martín, R. M., Muzerelle, M., Chitkul, N., How, S. E., Mittoo, S., and Bradley, M. (2005) Bead-based cellular analysis, sorting and multiplexing. *ChemBioChem 6*, 1341–1345.

(17) Tsakiridis, A., Alexander, L., Gennet, N., Sanchez-Martin, R. M., Livigni, A., Li, M., Muzerelle, M, Cardenas-Maestre, J. M., Bradley, M., and Brickman, J. M. (2009) Microsphere-based tracing and molecular delivery in embryonic stem cells. *Biomaterials 30*, 5853–5861.

(18) Gennet, N., Alexander, L., Sanchez-Martin, R. M., Behrendt, J. M., Sutherland, A. J., Brickman, J. M., Bradley, M., and Li, M. (2009) Microsphere as a vehicle for biomolecule delivery to neuronal stem cells. *New Biotechnol. 25*, 442–449.

(19) Alexander, L. M., Sanchez-Martin, R. M., and Bradley, M. (2009) Knocking (anti)-sense into cells: the microsphere approach to gene silencing. *Bioconjugate Chem. 20*, 422–426.

(20) Sanchez-Martin, R. M., Alexander, L., Muzerelle, M., Cardenas-Maestre, J. M, Tsakiridis, A., Brickman, J. M., and Bradley, M. (2009) Microsphere-mediated protein delivery into cells. *ChemBioChem 10*, 1453–1456.

(21) Bradley, M., Alexander, L., and Sanchez-Martin, R. M. (2008) Cellular uptake of fluorescent labelled biotin-streptavidin microspheres. *J. Fluoresc. 18*, 733–739.

(22) Bradley, M., Alexander, L-, Duncan, K., Chennaoui, M., Jones, A. C., and Sanchez-Martin, R. M. (2008) pH sensing in living cells using fluorescent microspheres. *Bioorg. Med. Chem. Lett. 18*, 313–317.

(23) Sanchez-Martin, R. M., Cuttle, M., Mittoo, S., and Bradley, M. (2006) Microsphere-based real-time calcium sensing. *Angew. Chem., Int. Ed. 45*, 5472–5474.

(24) Yusop, M., Unciti-Broceta, A., Johansson, E., Sánchez-Martín, R. M., and Bradley., M. (2011) Palladium-mediated intracellular chemistry. *Nat. Chem. 3*, 239–243.

(25) Alexander, L., Pernagallo, S., Livigni, A., Sanchez-Martin, R. M., Brickman, J. M., and Bradley., M. (2010) Investigation of microsphere mediated cellular delivery by chemical, microscopic and gene expression analysis. *Mol. BioSyst. 6*, 399–409.

(26) Bauhuber, S., Hozsa, C., Breunig, M., and Gopferich, A. (2009) delivery of nucleic acids via disulfide-based carrier systems. *Adv. Mater. 21*, 3286–3306.

(27) Zhao, M., Biswas, A., Hu, B., Joo, K.- I., Wnag, P., Gu, Z., and Tang, Y. (2011) Redox-responsive nanocapsules for intracellular protein delivery. *Biomaterials 32*, 5223–5230.

(28) Song, A., Wang, X., Zhang, J., Marik, J., Lebrilla, C. B., and Lam, K. S. (2004) Synthesis of hydrophilic and flexible linkers for peptide derivatization in solid phase. *Bioorg. Med. Chem. Lett. 14*, 161–165.

(29) Gresch, O., Engel, F. B., Nesic, D., Tran, T. T., England, H. M., Hickman, E. S., Korner, I., Gan, L., Chen, S., Castro-Obregon, S., Hammermann, R., Wolf, J., Muller-Hartmann, H., Nix, M., Siebenkotten, G., Kraus, G., and Lun, K. (2004) New non-viral method for gene transfer into primary cells. *Methods 33*, 151–163.

(30) Magg, T., Hartrampf, S., and Albert, M. H. (2009) Stable non-viral gene transfer into primary human T cells. *Hum. Gene Ther. 20*, 989–998.

(31) Tahvanainen, J., Pykäläinen, M., Kallonen, T., Lähteenmäki, H., Rasool, O., and Lahesmaa, R. (2006) Enrichment of nucleofected primary human $CD4^+$ T cells: A novel and efficient method for studying gene function and role in human primary T helper cell. *J. Immunol. Methods 310*, 30–39.

(32) Goffinet, C., and Keppler, O. T. (2006) Efficient non viral gene delivery into primary lymphocytes from rats and mice. *FASEB J. 20*, 500–502.

(33) Zhao, Y., Zheng, Z., Cohen, C. J., Gattinoni, L., Palmer, D. C., Restifo, N. P., Rosenberg, S. A., and Morgan, R. A. (2006) High-efficiency transfection of primary human and mouse T lymphocytes using RNA electroporation. *Mol. Ther. 13*, 151–159.

(34) Davidson, D., Cloutier, J. F., Gregorieff, A., and Veillette, A. (1997) Inhibitory tyrosine protein kinase p50csk is associated with protein-tyrosine phosphatase PTP-PEST in hemopoietic and non-hemopoietic cells. *J. Biol. Chem. 272*, 23455–23462.

(35) Flores, E., Roy, G., Patel., D., Shaw, A., and Thomas, M. L. (1994) Nuclear localisation of the PEP protein tyrosine phosphatase. *Mol. Cell. Biol. 14*, 4938–4946.

Supporting Information for

Novel Strategy for microsphere-mediated DNA transfection

Jessica G. Borger,[¥,†] Juan Manuel Cardenas-Maestre,[¥, ‡] Rose Zamoyska[*,†] and Rosario M. Sanchez-Martin[*,‡,§]

1. Preparation of Fluorescein-labeled microspheres.

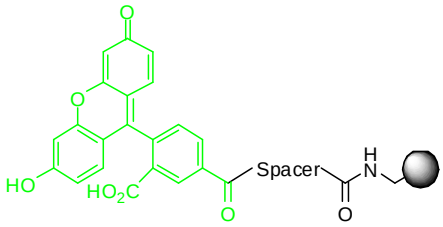

Amino functionalized microspheres (1 mL; 1 equiv) were washed in DMF (3 x 1 mL) and suspended in DMF (1 mL). Separately, 5(6)-carboxyfluorescein (5 eq) was dissolved in DMF (1 mL), then oxyma (5 eq; Apollo Scientific) was added and the solution mixture mixed for 4 minutes at rt before the addition of DIC (5 eq; Sigma-Aldrich) and mixed for 8-10 minutes at rt. The solution mixture was then added to amino microspheres and suspension mixed on the Thermomixer at 1400 rpm for 2 hours at 60°C.

2. Preparation of carboxy functionalised microspheres (3)

2.1. Synthesis of Fmoc-4,7,10-trioxa-1,13-tridecanediamine succinamic acid (polyethylene glycol type spacer, Fmoc-PEG-OH)

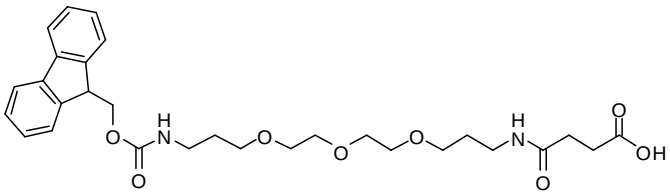

A solution of succinic anhydride (1 g, 10 mmol, 1 eq) dissolved in acetonitrile (25 mL) was added drop wise over 1 hour under strong magnetic stirring to 4,7,10- trioxa-1,13-tridecanediamine (2.2 g, 10 mmol, 1 eq) in acetonitrile (50 mL) and stirred for a further 3 hours. The liquid phase was decanted and discarded once the waxy product had settled. The product was redissolved by the addition of an acetonitrile:H2O (1:1) solution (100 mL) and the solution was chilled to 0°C prior to a drop wise addition of 9-fluorenylmethoxycarbony-succinimide (Fmoc-OSu) (4.38 g, 13 mmol, 1.3 eq) in acetonitrile (25 mL) under vigorous magnetic stirring during which time the pH was

kept at 8/9 by addition of DIPEA. After 12 hours reaction at room temperature the solvents were removed in vacuo and the residue was dissolved in a 5% NaHCO3 aqueous solution (100 mL) and washed with EtOAc (3 x 50 mL).

The aqueous phase was then acidified to pH 2 with 37% HCl, extracted with ethyl acetate (3 x 50 mL) and the organic phases were combined, washed with brine, dried over MgSO4 and concentrated in vacuo to afford a yellowish oil which was dissolved in hexane and purified by flash chromatography column (DCM:MeOH; 10:1) to afford the pure final compound as a sticky colorless product (3.51 g, 6.59 mmol, 65 %).

HPLC (S50D, λ=220 nm): purity 100%, retention time 8.4 minutes.

m/z (ES+) 565.5 (100%) [M+Na]+

1H NMR (500 MHz, CD3OD) δ (ppm): 1.71-1.78 (m, 4H), 2.46 (t, J = 6.54, 2H), 2.62 (t, J = 7.54, 2H), 3.26-3.34 (m, 4H), 3.49-3.65 (m, 12H), 4.20 (m, 1H), 4.38-4.44, (m, 2H), 5.30 (bs, 1H), 6.77 (bs, 1H), 7.29 (t, J = 7.41, 2H), 7.38 (t, J = 7.39, 2H), 7.59 (d, J = 7.48, 2H), 7.75 (d, J = 7.52, 2H). **13C NMR** (500 MHz, CD3OD) δ (ppm): 28.52, 29.34, 30.40, 30.98, 38.22, 38.80, 47.25, 66.40, 69.23, 69.88, 66.92, 70.02, 70.26, 70.35, 119.90, 125.02, 126.98, 127.61, 141.25, 143.95, 156.62, 172.58, 175.21.

2.2. Preparation of double PEGylated microspheres (2)

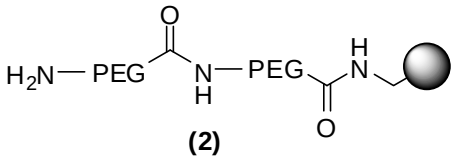

(2)

Amino functionalized microspheres **1** (1 mL; 1eq) were washed in DMF (3 x 1 mL) and suspended in DMF (1 mL). Separately, Fmoc-PEG-OH (5eq) was dissolved in DMF (1 mL), then DIC (5 eq) was added and the solution mixture mixed for 8-10 minutes at rt. The solution mixture was then added to amino microspheres and DIPEA (0.1 eq) was added. The suspension was mixed on the Thermomixer at 1400 rpm for 2 hours at 60°C. ***Fmoc deprotection*** was achieved by treating microspheres with 20% piperidine/DMF (1 mL; 3 x 20 minutes). Microspheres were obtained by centrifugation and subsequently washed with DMF (3 x 1 mL), MeOH (3 x 1 mL), deionised water (3 x 1 mL) and finally DMF (3 x 1 ml). Next, ninhydrin test was

performed to check the presence of primary amine. Then, the same protocol was repeated to give double PEGylated microspheres **2**.

2.3. Preparation of carboxy functionalised microspheres (3)

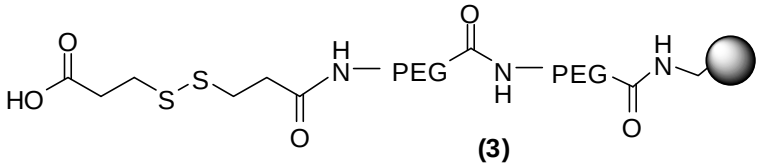

(3)

Amino functionalized microspheres **2** (1 mL; 1eq) were washed in DMF (3 x 1 mL) and suspended in DMF (1 mL). Separately, 3,3'-Dithiodipropionic acid (Sigma-Aldrich, 10 eq) was dissolved in DMF (1 mL), then DIC (5 eq) was added and the solution mixture mixed for 8-10 minutes at rt. The solution mixture was then added to amino microspheres and DIPEA (0.1 eq) was added. The suspension was mixed on the Thermomixer at 1400 rpm for 2 hours at 60°C. Microspheres were obtained by centrifugation and subsequently washed with DMF (3 x 1 mL), MeOH (3 x 1 mL), deionised water (3 x 1 mL).

3. DNA linearization and aminoallyl-dUTP incorporation

3.1. Plasmid DNA linearization

Gene sequences for PEP-YFP (J. Borger, University of Edinburgh) were encoded within the AMAXA pMax cloning vector (Lonza). Linearisation of 1µg DNA required 1U of restriction endonuclease and was incubated at 37°C overnight. Detailed protocol: A cocktail mix containing 1x digestion buffer, 1x BSA and 1U restriction enzyme/µg DNA in molecular biology grade water was prepared. pDNA (PEP-YFP) was added to the cocktail mix and incubated at 37°C for 18 hours. Digestion was stopped by inactivating the enzyme at 70°C for 10 min.

3.2. Analytical electrophoresis gel

Efficiency of restriction digest was analysed by agarose gel electrophoresis. Protocol: Agarose electrophoresis gel was performed on 1x Tris-Acetate-EDTA buffer. Samples were loaded at 0.5µg in 1x Blue juice loading dye where a 1 kb molecular weight DNA was used as ladder. Gel was visualised by UV.

3.3. Ethanol precipitation

Linear DNA (lDNA) was ethanol precipitated and resuspended in TE buffer. Protocol: To precipitate lDNA, 1/10 volume of 3M Sodium Acetate and 3 volumes of ethanol were added to the DNA solution. DNA was precipitated at -20°C for 18 hours. The DNA was pelleted by centrifugation, ethanol aspirated to allow the DNA to air-dry and then be resuspended in TE buffer at 1µg/µl.

3.4. Aminoallyl-dUTP incorporation

Terminal deoxynucleotidyl transferase (New England BioLabs) addition of 2 mM aminoallyl-dUTP (Yorkshire Bioscience Ltd) to the 3' end of the linear DNA was performed at 37°C for 20 min, with subsequent enzyme deactivation for 10 min at 70°C. ***Detailed Protocol:*** DNA was added to a solution containing 1x TdT buffer, $CoCl_2$, 10 mM aa-dUTP and 1U TdT/µg DNA and incubated at 37°C for 20 min. The enzyme was then inactivated by heating up to 70°C for 10min. The DNA was then ethanol precipitated as described above in 3.3.

4. DNA-microspheres conjugation

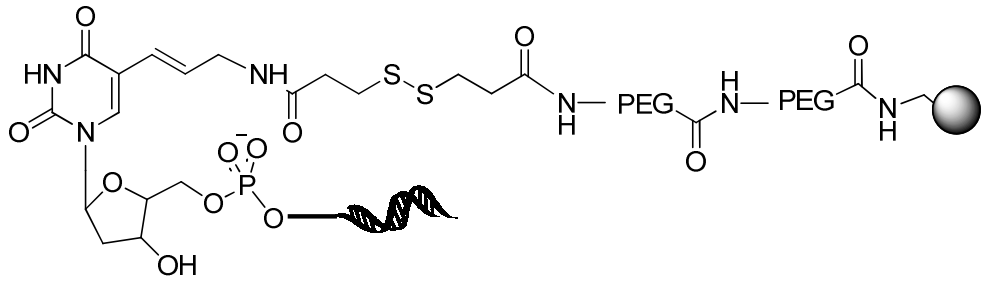

(6) PEP-YFP pDNA

Carboxy functionalised microspheres **(3)** (0.1 mL; 1eq) were washed in molecular biology grade water (0.1 mL x 3 times) and suspended in 0.1 M solution of EDC in water (0.1 mL) and solution mixed for 4 hours at rt. After mixing, microspheres were collected by centrifugation and microspheres resuspended in PBS pH 7.4, then DNA solution (0.1 mL) was added and the solution mixture mixed at room temperature for 18 hours to yield microspheres-DNA conjugates **6**. After mixing, it was found quite important not to perform any washing to the lDNA-microspheres conjugates.

5. Biological Evaluation

Cell culture conditions

Cells were cultured in RPMI medium 1640 supplemented with 5% FCS, L-glutamine, 100 U/ml penicillin and streptomycin (GIBCO) and 50 µM β-mercaptoethanol. F5 hybridoma T cells were additionally incubated in 500 µg/ml G418 for selection.

Microsphere incubation

Cells were seeded in a 24 well-plate at a density of 1 x 10^6 cells per well. Once cells settled as a monolayer, microspheres at varying concentrations ($5x10^{14}$, 10^{15}, $2x10^{15}$) and varying sizes (200 nm, 500 nm, 900nm) were incubated incubated for 4, 8 and 24 hours in supplemented media without b-mercaptoethanol at 37C with 5% CO_2. Cells were harvested into PBS at each time point, washed twice and resuspended in 2% FCS/PBS. T cells were stimulated with plate-bound 5 µg/ml anti-CD3 (145-2C11, BD Pharmingen) and 2 µg/ml anti-CD28 (37.51, BD Pharmingen) for 24 hours during incubation with microspheres.

Flow cytometry

Samples were collected on a flow cytometer (LSR II, BD) and analysed using FlowJo Version 8.8.6 software (Tree Star Inc.). At least 50,000 events per sample were analyzed. T cells were stained with antibodies CD8α-PerCP (53-6.7, BD Bioscience) and CD69-Pe (H1.2F3, eBiosciences). Cell viability was determined by staining with TOP-RO-3 Iodide (Invitrogen) in PBS (1:10000).

Confocal microscopy

Cells were diluted to 10^6/ml, aliquoted onto glass multiwell slides and incubated for 20 min at 37°C to adhere to the glass. Cells were fixed in 4% paraformaldehyde (PFA) for 30 minutes. Nuclei were stained with DAPI supplemented at 1 µg/ml in Prolong Anti-fade Gold (Invitrogen) mounting media. Samples were examined on the Leica SP5 II (Leica Microsystems) with lasers exciting at 405 and 488 with the 63× objective. Data was rendered and analysed using Volocity software (Improvision).

Supplementary Figures:

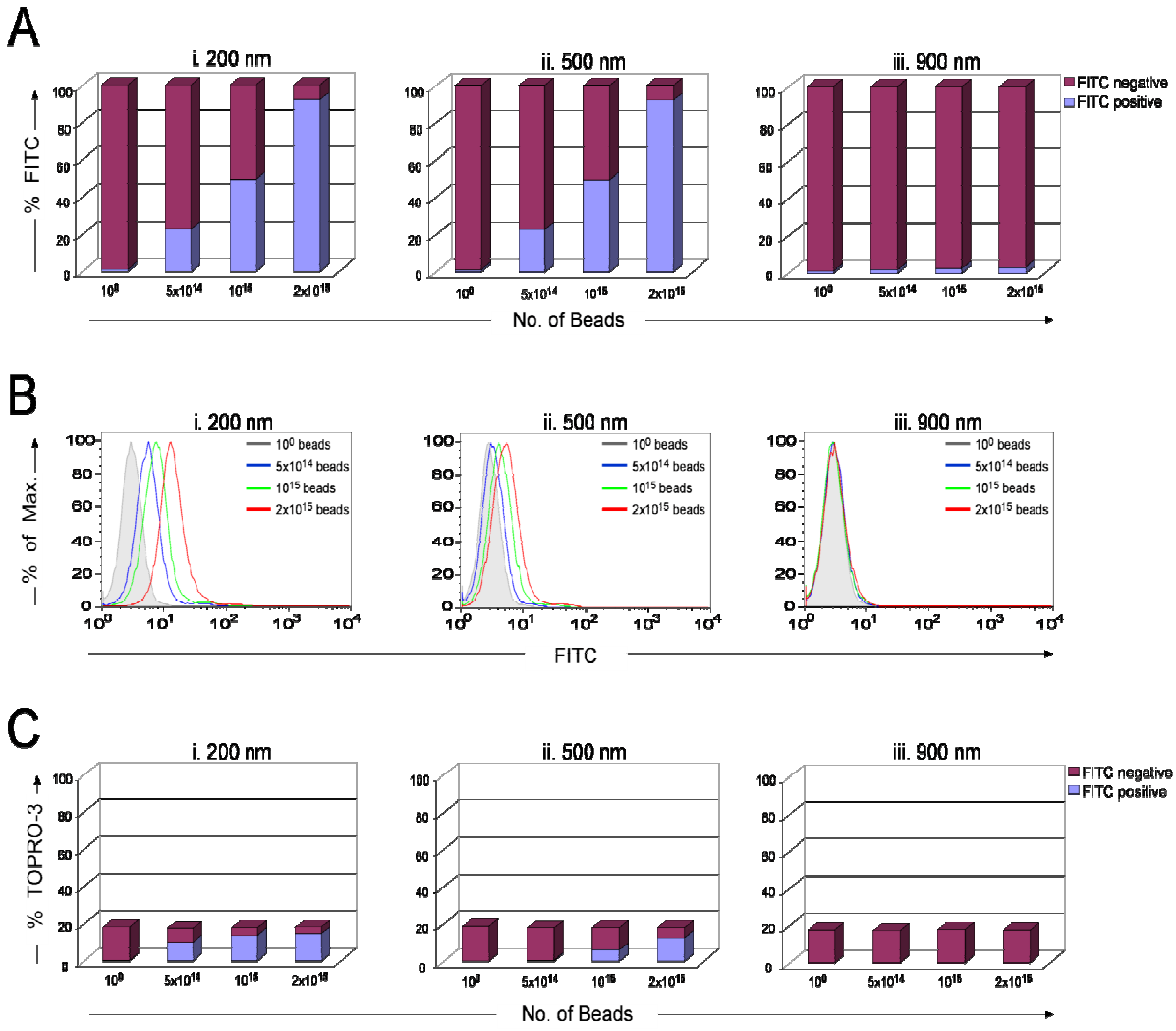

Figure S1. Flow cytometric analysis of T cell hybridoma (F5.BW) cellular uptake of microspheres of controlled sizes (A-B.i) 200 nm, (A-B.ii) 500 nm, (A-B.iii) 900 nm at different concentrations after 24 h incubation. Toxicity was measured by staining for TO-PRO-3 (C).

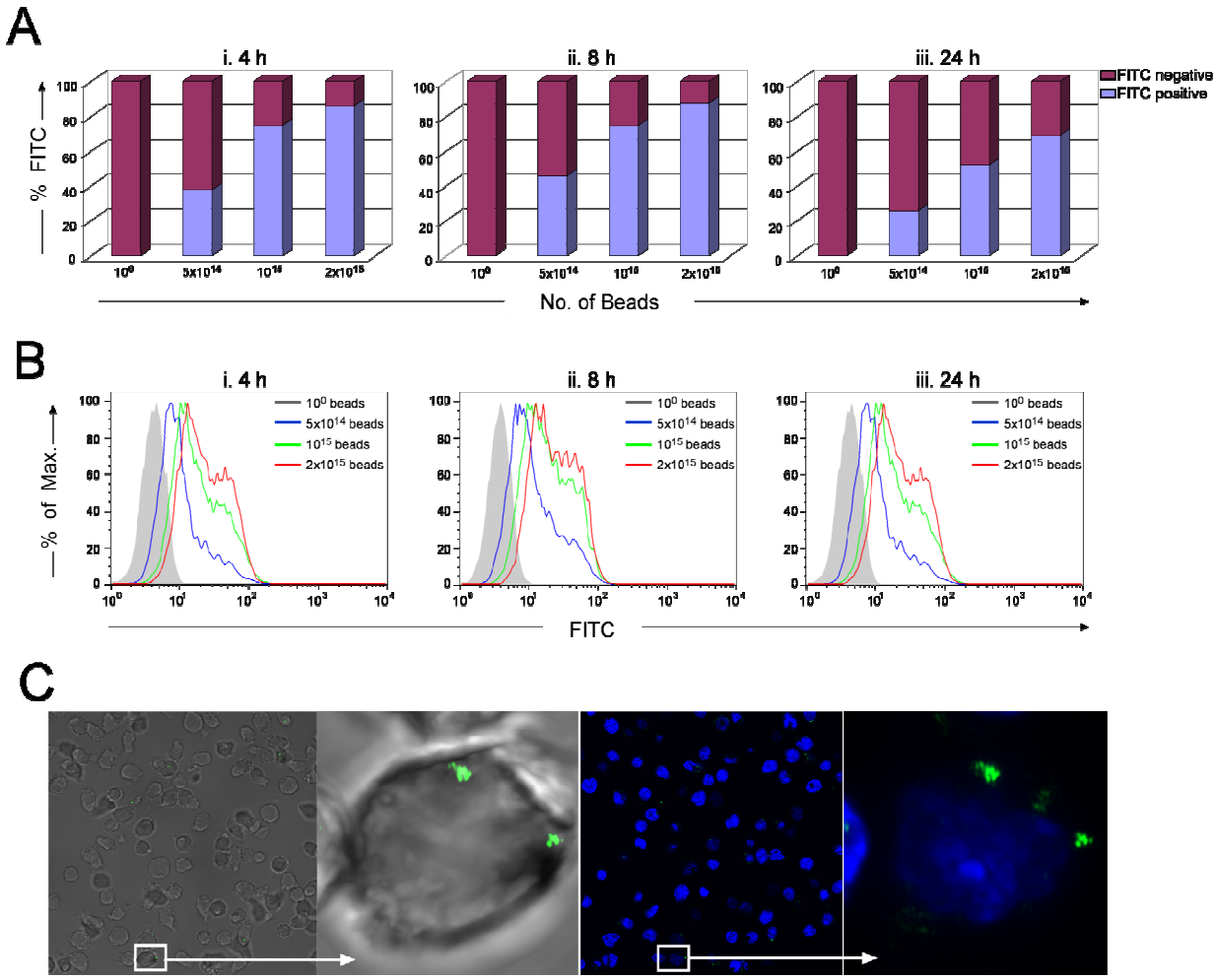

Figure S2. (A-B) Flow cytometric analysis of T cell hybridoma (F5.BW) cellular uptake of 200 nm microspheres at different concentrations over 4 h (i), 8 h (ii) and 24 h (iii). (C) Confocal image of T cell hybridoma (F5.BW) loaded with 200 nm microspheres (green), with boxed image representing 4x magnified single cell image. Images taken after 24 h at a 63x magnification, where nuclei are stained with DAPI.

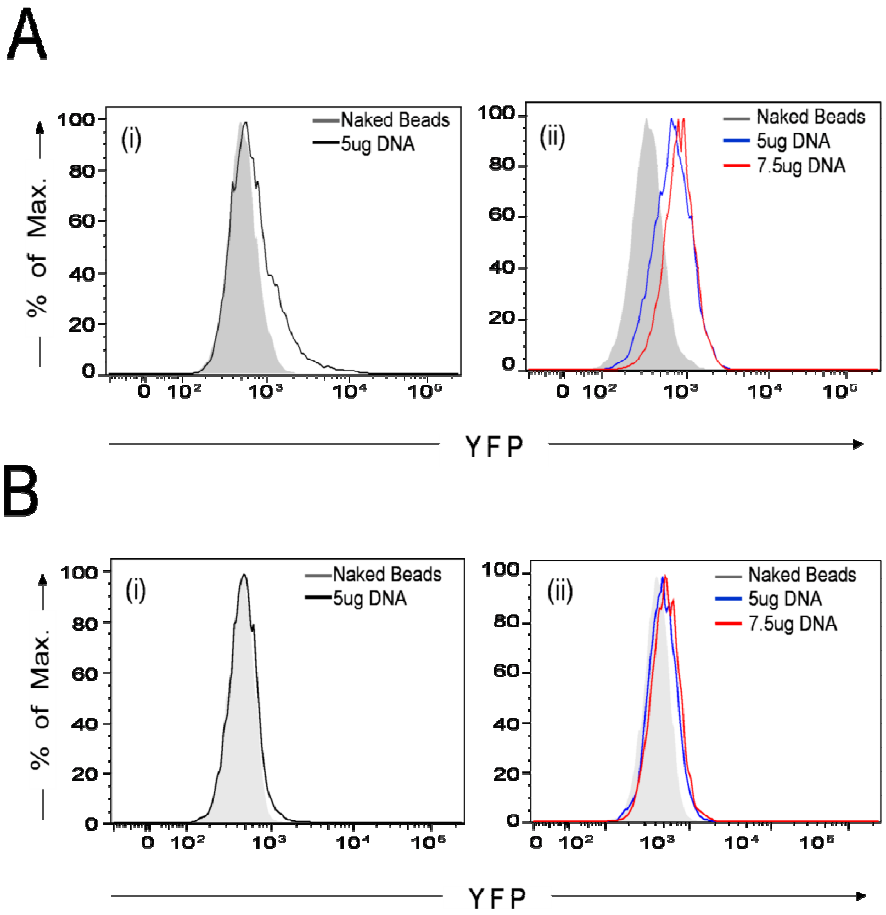

Figure S3. Time course of F5.BW hybridoma T cell pDNA beadfection and protein expression. Analysis of YFP fluorescence observed 24 h (A) and 48 h (B) after transfection: (i) Amaxa® electroporation, (ii) beadfection with conjugate **6**.

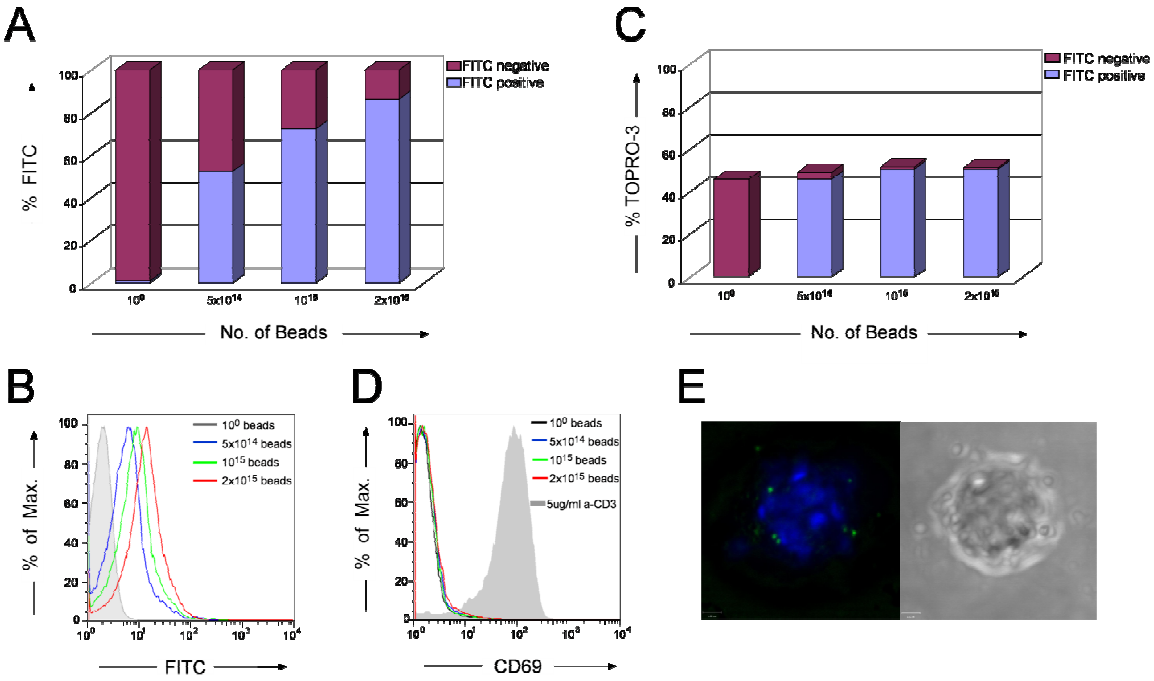

Figure S4. (A-B) Flow cytometric analysis of naïve T lymphocytes cellular uptake of 200 nm microspheres at different concentrations after 24 h incubation. (C) Toxicity was measured by staining for TO-PRO-3. (D) Cellular activation following 24 h incubation with different concentrations of 200 nm microspheres was gauged by upregulation of CD69 using a positive control of 5 µg/ml αCD3 stimulation. (E) Confocal image of naïve T lymphocyte loaded with 200 nm microspheres (green). Image taken after 24 h at a 63x magnification, where nuclei are stained with DAPI.

Bioconjugate Chemistry

ARTICLE

pubs.acs.org/bc

Dual Signal-Responsive Liposomes for Temperature-Controlled Cytoplasmic Delivery

Tomohiro Kaiden,[†] Eiji Yuba,[†] Atsushi Harada,[†] Yuichi Sakanishi,[‡] and Kenji Kono*[,†]

[†]Department of Applied Chemistry, Graduate School of Engineering, Osaka Prefecture University, 1-1 Gakuen-cho, Naka-ku, Sakai, Osaka 599-8531, Japan

[‡]Daicel Chemical Industries, Ltd., 2-1-4, Higashisakae, Ohtake, Hiroshima 739-0695, Japan

Supporting Information

ABSTRACT: For production of a new type of functional liposome whose destabilization can be triggered by a combination of a temperature signal and acidic pH signal, we prepared liposomes modified with hyperbranched poly(glycidol) derivatives having *N*-isopropylamide and carboxyl groups. HeLa cells incubated with the dual signal-responsive liposomes encapsulating a water-soluble fluorescent dye pyranine at 28 °C displayed punctate fluorescence of pyranine, indicating that the liposomes were trapped in endosome. However, after heating at 45 °C for 15 min, the same cells exhibited diffuse fluorescence of pyranine, indicating that destabilization of the liposomes in endosome with an acidic environment in combination with the brief heating caused efficient transfer of the contents into cytosol. The dual signal-responsive liposomes might have usefulness for site-specific delivery of membrane-impermeable molecules, which exhibit bioactivities in the intracellular spaces, such as siRNA and proteins.

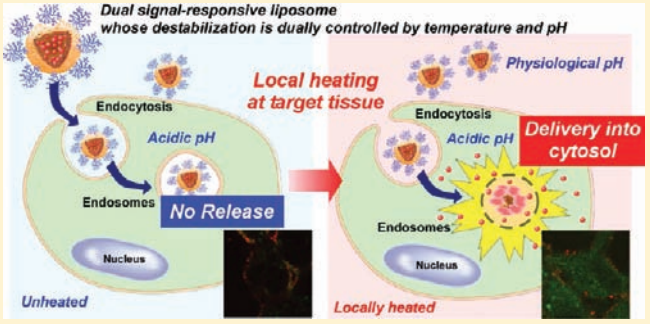

INTRODUCTION

Recent advances in molecular biology and biotechnology have introduced highly efficient therapeutic approaches based on specific interaction to target molecules, as shown in typical examples of siRNA for specific gene silencing and protein inhibitors and antibodies of various kinds for targeted therapy. Many of their target molecules exist in intracellular spaces. Therefore, to maximize their therapeutic effects, accurate delivery of these bioactive molecules, not only to target diseased tissues, but also into their intracellular spaces where their target sites exist, are highly necessary.

Various types of nanoparticles with stimuli-sensitive properties have been produced to increase local concentration of therapeutic molecules at the target tissues. Typical examples are temperature-sensitive liposomes, which release contents in response to elevated temperature.[1−3] These temperature-sensitive liposomes encapsulating membrane-permeable anticancer drugs, such as doxorubicin, exhibited efficient tumor growth suppression upon mild heating of tumor sites.[4,5] On the other hand, intracellular delivery of bioactive molecules, which cannot permeate cellular membranes, has been attempted using liposomes having pH-sensitive properties: so-called pH-sensitive liposomes.[6,7] Liposomes are generally taken up by cells through endocytosis and are trapped in endosome, which contains a weakly acidic environment in its interior. Therefore, those with pH-sensitive properties generate abilities to release bioactive molecules and promote their transfer into cytosol.[6−9]

On the basis of the functions of these temperature-sensitive and pH-sensitive liposomes, we attempted to develop a new type of liposome having a combination of these functions, which generate a membrane-destabilizing ability under conditions of mildly acidic pH with an elevated temperature. Their ability to respond to both pH and temperature signals might be useful for targeting tissue-specific intracellular delivery of membrane-impermeable molecules, because such dual-signal-responsive liposomes can destabilize and fuse with endosomes only when entrapped in endosomes of the target tissue, which has been mildly heated (Figure 1).

Recently, we synthesized hyperbranched poly(glycidol)s (HPGs) having *N*-isopropylamide (NIPAM) and succinylate (Suc) groups, which are, respectively, temperature-sensitive and pH-sensitive groups.[10] These polymers exhibited the dual-signal-sensitive property; their characteristics changed from hydrophilic to hydrophobic in response to both pH decreasing and temperature increasing.[10] For the present study, we incorporated these polymers onto stable egg yolk phosphatidylcholine (EYPC) liposomes to produce dual-signal-responsive liposomes. The pH-responsive and temperature-responsive properties of the HPGs-modified liposomes and their performance as intracellular delivery vehicles were investigated.

Received: January 19, 2011
Revised: July 14, 2011
Published: August 23, 2011

ACS Publications © 2011 American Chemical Society

dx.doi.org/10.1021/bc2000353 | *Bioconjugate Chem.* 2011, 22, 1909–1915

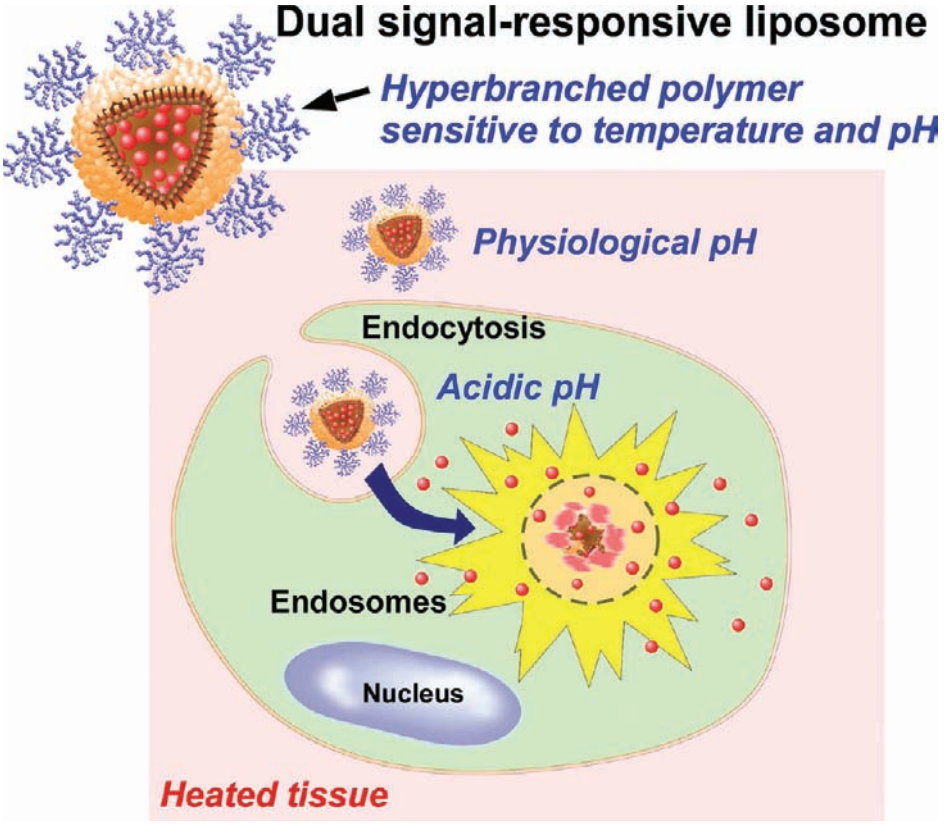

Figure 1. Design of dual-signal-responsive liposomes whose destabilization can be controlled by temperature and acidic pH. Dual-signal-responsive liposomes are expected to deliver contents into the cytosol of cells of target tissues, which are locally heated.

EXPERIMENTAL PROCEDURES

Materials. HPG with the polymerization degree of 40, which is designated as HPG40, was kindly donated by Daicel Chemical Industries, Ltd. (Osaka, Japan). Egg yolk phosphatidylcholine (EYPC) was kindly donated by NOF Co. (Tokyo, Japan). Pyranine, decylamine, and Triton X-100 were obtained from Tokyo Chemical Industries Ltd. (Tokyo, Japan). *p*-Xylene-bis-pyridinium bromide (DPX) and LysoTracker Red DND-99 were purchased from Molecular Probes (Oregon, USA). Lissamine rhodamine B-sulfonyl phosphatidylethanolamine (Rh-PE) was purchased from Avanti Polar Lipids (Birmingham, AL, USA). 4-(4,6-Dimethoxy-1,3,5-triazin-2-yl)-4-methyl morpholinium chloride (DMT-MM), isopropylamine, and *N*-methylpyrrolidone were from Wako Pure Chemical Industries Ltd. (Osaka, Japan). Succinic anhydride was obtained from Kishida Chemical Co., Ltd. (Osaka, Japan).

Synthesis of NIPAM-Suc-HPG. NIPAM-Suc-HPGs were prepared as previously reported.[10] A typical procedure was as follows. HPG40 (5.66 g) and an excessive amount of succinic anhydride (0.24 mol) were dissolved in pyridine (60 mL) and stirred at 65 °C for 7 h under an argon atmosphere. The polymer was washed with diethyl ether and was purified using a Sephadex LH-20 column with methanol to afford Suc-HPG40. The obtained Suc-HPG40 (0.82 g) was dissolved in *N*-methylpyrrolidone (8 mL), and DMT-MM (4.0 mmol) and isopropylamine (2.9 mmol) dissolved in *N*-methylpyrrolidone (1.2 mL) was added to the solution. The mixed solution was stirred at room temperature for 24 h under an argon atmosphere in the dark, and then, decylamine (0.48 mmol) dissolved in *N*-methylpyrrolidone (1 mL) was added to the solution. The mixture was stirred at room temperature for 3 days under an argon atmosphere in the dark. To the reaction mixture, acetic acid (3 mL) was added and stirred for 1 h. The polymer was precipitated with water and washed with diethyl ether. Then, the polymer was purified using a Sephadex LH-20 column with methanol to afford $NIPAM_{35}$-Suc_{55}-HPG. Compositions of polymers were estimated using ^1H NMR. ^1H NMR spectra for Suc-HPG40 and $NIPAM_{35}$-Suc_{55}-HPG were shown in Supporting Information Figure S1 A and B, respectively. Integration of peaks for these spectra indicated that essentially no hydroxyl groups remained in Suc-HPG40 (Figure S1 A) and the molar ratio of NIPAM, Suc, and *N*-decylamide (DA) groups was 34.9/55.3/9.8 in $NIPAM_{35}$-Suc_{55}-HPG (Figure S1 B).

Turbidity Measurements. Turbidity of NIPAM-Suc-HPGs dissolved in 10 mM phosphate and 150 mM NaCl solution (pH 5.0−7.4, 5 mg/mL) was measured at 700 nm using a Jasco model V-560 spectrophotometer equipped with a Peltier-type thermostatic cell holder coupled with an ETC-505T controller. The heating rate of the sample was 1.0 °C min^{-1}. The cloud points were taken as the initial break points in the resulting transmittance versus temperature curves.

Preparation of Liposomes. To a dry, thin membrane of EYPC (7 mg) and polymer (7 mg) was added 500 μL of aqueous 35 mM pyranine, 50 mM DPX, and 50 mM phosphate solution (pH 7.4), and the mixture was sonicated for 10 min using a bath-type sonicator. The liposome suspension was further hydrated by freezing and thawing repeatedly, and was extruded through a polycarbonate membrane with a pore size of 100 nm. The liposome suspension was dialyzed against 10 mM phosphate and 140 mM NaCl buffer (pH 7.4) at 4 °C for 2 days. Then,

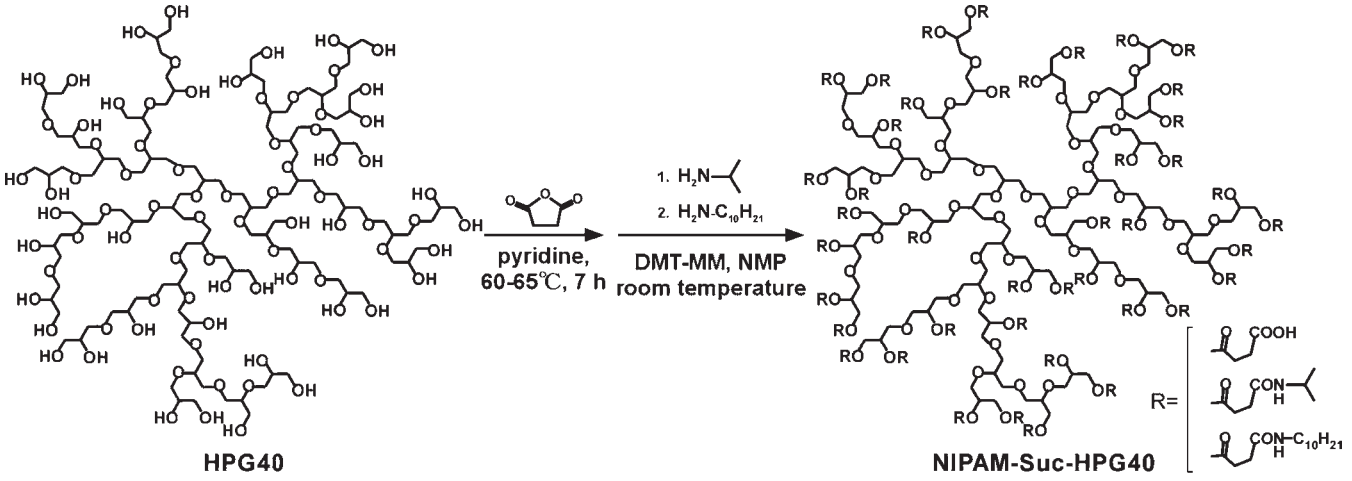

Figure 2. Preparation of NIPAM-Suc-HPG. DMT-MM and NMP represent 4-(4,6-dimethoxy-1,3,5-triazin-2-yl)-4-methyl morpholinium chloride and *N*-methylpyrrolidone, respectively.

liposome was ultracentrifuged twice at 55 000 rpm for 2 h to remove free pyranine and free polymer from the pyranine-loaded liposomes.

Pyranine Release from Liposomes. Release of pyranine from liposomes was measured as previously reported.[8,11] Pyranine fluorescence was quenched by DPX inside of the liposomes, but it exhibits intense fluorescence when released from the liposome. Polymer-modified liposomes encapsulating pyranine and DPX were suspended in 10 mM phosphate and 140 mM NaCl buffer of varying pHs (lipid concentration: 2.0×10^{-5} M) at varying temperatures, and fluorescence intensity at 512 nm of the suspension was followed with excitation at 416 nm using a spectrofluorometer (Jasco FP-6200). The percent release of pyranine from liposomes was defined as

$$release(\%) = (F_t - F_i)/(F_f - F_i) \times 100$$

where F_i and F_t mean the initial and intermediary fluorescence intensities of the liposome suspension, respectively. F_f is the fluorescence intensity of the liposome suspension after addition of Triton X-100 (final concentration: 0.1%).

Intracellular Distribution of Liposomes. The pyranine-loaded liposomes containing Rh-PE were prepared as described above except that DPX was not included in the pyranine solution and Rh-PE (0.1 mol %) was included as a liposome component. HeLa cells (2×10^5 cells) cultured in DMEM supplemented with 10% FBS and antibiotics for 2 days were washed with phosphate-buffered saline (PBS), and then incubated in DMEM without serum (500 μL). The pyranine-loaded liposomes (0.6 mM, 500 μL) were added gently to the cells and incubated for 4 h at 28 °C. After the incubation, the cells were washed with PBS three times and heated at 45 °C for 15 min. Confocal laser scanning microscopic (CLSM) analysis of these cells was performed using LSM 5 EXCITER (Carl Zeiss Co. Ltd.). The cells without the 15 min heating at 45 °C were also observed using CLSM (λ_{ex} = 485 nm). For inhibition of endosomal acidification, cells were preincubated with 100 μM chloroquine for 30 min before the incubation with liposomes.

RESULTS AND DISCUSSION

Preparation of Polymers for Liposome Modification. Hyperbranched poly(glycidol)s having NIPAM and Suc groups and decyl chains, which are anchors for their fixation onto liposomes, were prepared as presented in Figure 2 using HPG with the number average polymerization degree of 40 as previously reported.[10] The pH-sensitive and temperature-sensitive properties of the HPGs having NIPAM and Suc groups (NIPAM-Suc-HPGs) are dependent on their compositions.[10] Therefore, HPG-based polymers of five kinds having varying ratios of NIPAM and Suc groups were prepared for modification of liposomes (Table 1). We introduced decyl groups to about 10 unit % of the chain terminals of the polymers as anchors for their incorporation to liposomes. In addition, NIPAM-Suc-HPG having the NIPAM/Suc ratio of 64/36 without decyl groups, which is designated as $NIPAM_{64}$-Suc_{36}-HPG_{cont}, was synthesized as a control without anchors.

Table 1. Characterization of NIPAM-Suc-HPGs[a]

	molar ratio[b]		
polymer	NIPAM	Sue	DA
$NIPAM_0$-Suc_{89}-HPG	0	88.9	11.1
$NIPAM_{35}$-Suc_{55}-HPG	34.9	55.3	9.8
$NIPAM_{56}$-Suc_{33}-HPG	56.4	32.9	10.7
$NIPAM_{64}$-Suc_{27}-HPG	63.5	26.6	9.9
$NIPAM_{72}$-Suc_{17}-HPG	71.9	17.3	10.8
$NIPAM_{64}$-Suc_{36}-HPG_{cont}	63.8	36.2	0

[a] Suc-HPG40 was obtained by reacting HPG40 completely with excess succinic anhydride. And then NIPAM and DA groups were incorporated to Suc-HPG40 by condensation of a part of Suc groups with isopropylamine and decylamine. [b] Molar ratios of NIPAM, Suc, and DA groups in the polymers were evaluated based on ^{1}H NMR (see Supporting Information).

First, we examined pH-sensitive and temperature-sensitive properties of the NIPAM-Suc-HPGs by the detection of phase separation of their aqueous solutions (Figure 3). Figure 3A,B shows the optical transmittance of the $NIPAM_{65}$-Suc_{35}-HPG_{cont} and $NIPAM_{56}$-Suc_{33}-HPG solutions, respectively, at various pH values as a function of temperature. The solutions of these polymers were transparent at neutral pH in the experimental temperature region, indicating that their chains were highly hydrated irrespective of temperature at neutral pH. However,

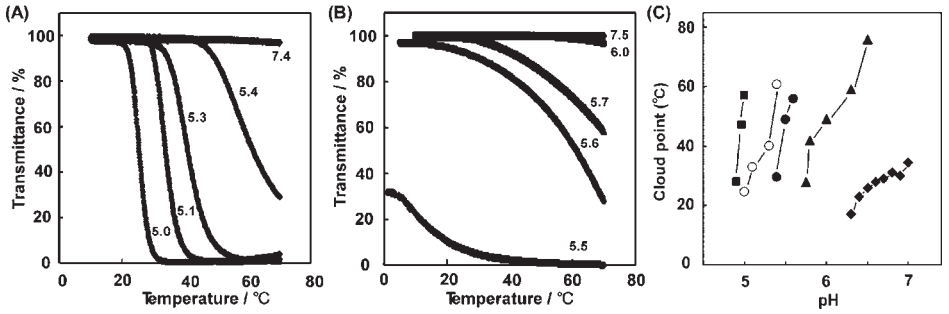

Figure 3. Temperature and pH-sensitive phase transition of NIPAM-Suc-HPGs. Temperature dependence of transmittance for solutions of $NIPAM_{64}$-Suc_{36}-HPG_{cont} (A) and $NIPAM_{56}$-Suc_{33}-HPG (B) at various pHs. (C) Cloud points of $NIPAM_{64}$-Suc_{36}-HPG_{cont} (open circles), $NIPAM_{35}$-Suc_{55}-HPG (squares), $NIPAM_{56}$-Suc_{33}-HPG (closed circles), $NIPAM_{64}$-Suc_{27}-HPG (triangles), and $NIPAM_{72}$-Suc_{17}-HPG (diamonds) as a function of pH.

these polymer solutions exhibited a temperature-dependent decrease in transmittance at pH 5−6, indicating that these polymers changed their characteristic from hydrophilic to hydrophobic depending on temperature in the weakly acidic pH region. These polymers showed the water-solubility change under similar temperature and pH regions, probably because these polymers have similar ratios of NIPAM units to succinylate units, which contribute, respectively, to temperature and pH sensitivities. Additionally, it is readily apparent that $NIPAM_{56}$-Suc_{33}-HPG changed its water-solubility with temperature gradually in broad temperature regions at weakly acidic pH compared to $NIPAM_{65}$-Suc_{35}-HPG_{cont}. For $NIPAM_{56}$-Suc_{33}-HPG, hydrophobic decyl chains connected to the polymer backbone might make its conformation more compact. Then, the polymer chains taking on a compact conformation would be unable to interact mutually as efficiently as $NIPAM_{65}$-Suc_{35}-HPG_{cont} taking on an expanded conformation, resulting in the transition in the broad temperature region for the anchor-carrying polymer.

We defined the cloud point of the polymer solution as the temperature at which the transmittance became 50%. Figure 3C shows cloud points of NIPAM-Suc-HPGs with various NIPAM/Suc ratios as a function of pH. Generally, the polymers exhibited cloud points between 20 and 60 °C. However, the pH region in which these polymers showed the cloud point tends to increase concomitantly with increase of the NIPAM/Suc ratio, indicating that their pH-sensitive and temperature-sensitive properties are controllable by adjusting their NIPAM/Suc ratio.

Dual Signal-Responsive Behaviors of Polymer-Modified Liposomes. To investigate production of dual signal-responsive liposomes, we examined the effect of modification of stable EYPC liposomes with the NIPAM-Suc-HPGs. On the basis of the result of Figure 3, we chose three kinds of HPG-based polymers with different NIPAM/Suc unit ratios, $NIPAM_{56}$-Suc_{33}-HPG, and $NIPAM_{72}$-Suc_{17}-HPG, as well as NIPAM-free $NIPAM_0$-Suc_{90}-HPG, to elucidate how the NIPAM/Suc unit ratio of the polymer affects pH- and temperature-sensitive properties of their modified liposomes. The liposomes were prepared by dispersing a mixture of egg yolk phosphatidylcholine (EYPC) and polymer in a phosphate solution containing water-soluble fluorescent dye pyranine and its quencher DPX and subsequent extrusion through a polycarbonate membrane with a pore size of 100 nm. The liposomes were purified by dialysis and subsequent ultracentrifugation. Their content release behaviors were investigated by following the fluorescence of pyranine, which become highly fluorescent when released from the liposome.[11,12] We confirmed that pyranine release from the unmodified EYPC was very low and that it was affected only slightly by pH and temperature under experimental conditions (see Figure S2). However, the liposomes modified with these polymers exhibited pyranine release depending on the ambient pH and temperature (Figure 4). The liposomes modified with $NIPAM_0$-Suc_{90}-HPG showed significant pH-responsive content release, which was significantly promoted below pH 5.5 and which achieved complete release at pH 4.5 (Figure 4A,D). However, these liposomes exhibited fundamentally equivalent pH-dependent release behavior irrespective of ambient temperature, indicating that they are responsive only to ambient pH.

On the other hand, the liposomes modified with $NIPAM_{56}$-Suc_{33}-HPG exhibited significant pH-responsive contents release at 37 and 45 °C, but they only slightly release the contents at 10 °C (Figure 4B,E). This fact indicates that these liposomes have sensitivity to both pH and temperature. Consequently, their function can be dually controlled by ambient pH and temperature. The $NIPAM_{72}$-Suc_{17}-HPG-modified liposomes showed the temperature-dependent enhancement of content release even at neutral pH, although they exhibited pH-dependent enhancement of content release below pH 6.0 to some degree (Figure 4C,F). Apparently, modification with the polymer having a high content of NIPAM moieties abolished pH-responsive properties of the liposomes and provided rather temperature-responsive properties to the liposomes.

Because the $NIPAM_{56}$-Suc_{33}-HPG-modified liposomes exhibited excellent response to both temperature and pH, we further examined the temperature-dependent enhancement of contents release at neutral pH and at pH 5.5, which respectively corresponds to the extracellular pH and the endosome pH.[13] As Figure 5 depicts, contents released from the liposomes were suppressed effectively, even at 50 °C under neutral pH condition, indicating that the liposomes retained pyranine at that pH. Similarly, under a weakly acidic condition, the liposomes retained contents less than 25 °C, but at greater than 30 °C, the liposomes enhanced the content release. On the basis of the result of Figure 2C, the $NIPAM_{56}$-Suc_{33}-HPG might change its character from hydrophilic to hydrophobic around 30 °C at pH 5.5. Therefore, the dehydrated polymer chains attached to the liposome surface might interact strongly with the liposome membrane and induce perturbation of the liposome membrane.

Control of Cytoplasmic Delivery by Dual Signal-Responsive Liposomes. We examined intracellular delivery mediated by the dual signal-responsive $NIPAM_{56}$-Suc_{33}-HPG-modified liposomes. The liposome membrane was labeled with Rh-PE to detect the location of liposomes in the cell. Plain EYPC

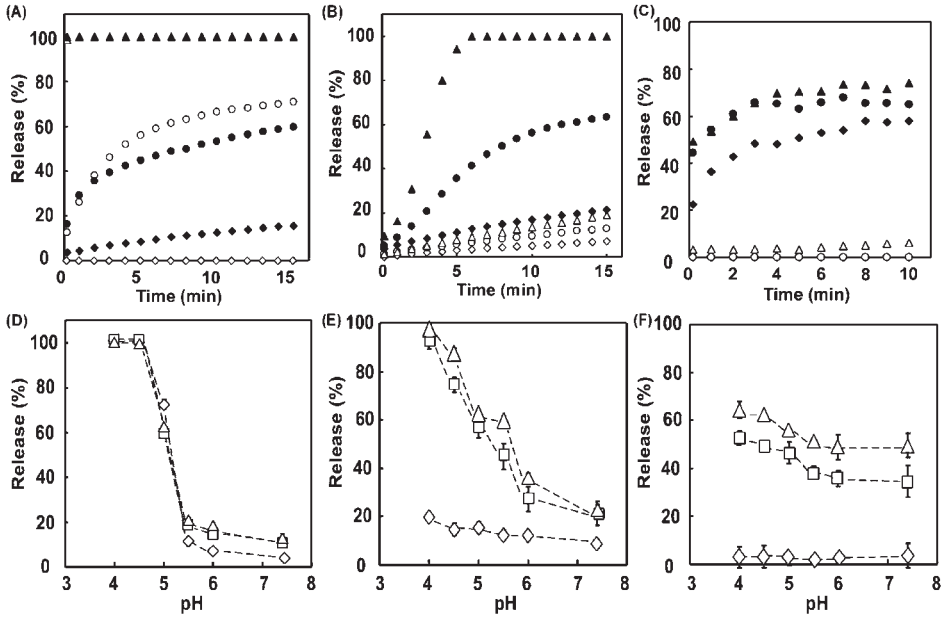

Figure 4. Typical profiles of pyranine release from liposomes modified with NIPAM$_0$-Suc$_{90}$-HPG (A), NIPAM$_{56}$-Suc$_{33}$-HPG (B), and NIPAM$_{72}$-Suc$_{17}$-HPG (C) at pH 7.4 (diamonds), pH 5.0 (circles), and pH 4.0 (triangles) at 10 °C (open symbols) or 45 °C (closed symbols). pH-Dependence of pyranine release from liposomes modified with NIPAM$_0$-Suc$_{90}$-HPG (D), NIPAM$_{56}$-Suc$_{33}$-HPG (E), and NIPAM$_{72}$-Suc$_{17}$-HPG (F). Percent release after 15 min incubation at 10 °C (diamonds), 37 °C (squares), or 45 °C (triangles) was shown.

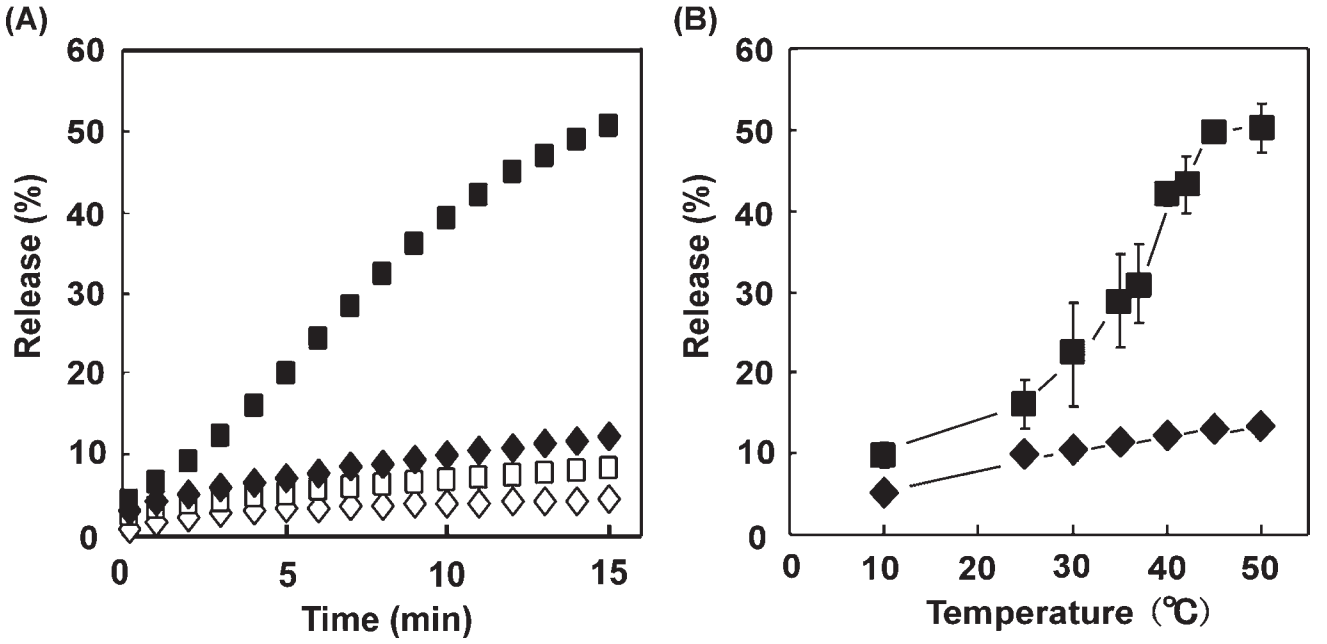

Figure 5. (A) Typical profiles of pyranine release from NIPAM$_{56}$-Suc$_{33}$-HPG-modified liposomes at pH 7.4 (diamonds) and pH 5.5 (squares) at 10 °C (open symbols) or 45 °C (closed symbols). (B) Temperature dependence of pyranine release at pH 7.4 (diamonds) and pH 5.5 (squares). Percent release after 10 min incubation was shown.

liposomes labeled with Rh-PE and loaded with pyranine were also examined as a control. These liposomes were incubated with HeLa cells for 4 h at 28 °C, where the NIPAM$_{56}$-Suc$_{33}$-HPG-modified liposomes were stable, even at weakly acidic pH (Figure 5B), then washed with PBS three times to remove free liposomes. The cells were additionally incubated in the culture medium at 28 or 45 °C for 15 min and observed using CLSM (Figure 6). As presented in Figure 6A, cells treated with the plain liposome at 28 °C displayed punctate fluorescence of Rh-PE and pyranine in the peripheral region of the cells at the same locations, suggesting that the liposomes retaining pyranine were trapped in early endosomes, which exist near the cellular surface. Because the cells were treated with the liposomes at 28 °C, the cellular activity might have been reduced. Consequently, internalization of the liposomes into the cells was limited largely to that taking place within the cellular membrane periphery. When

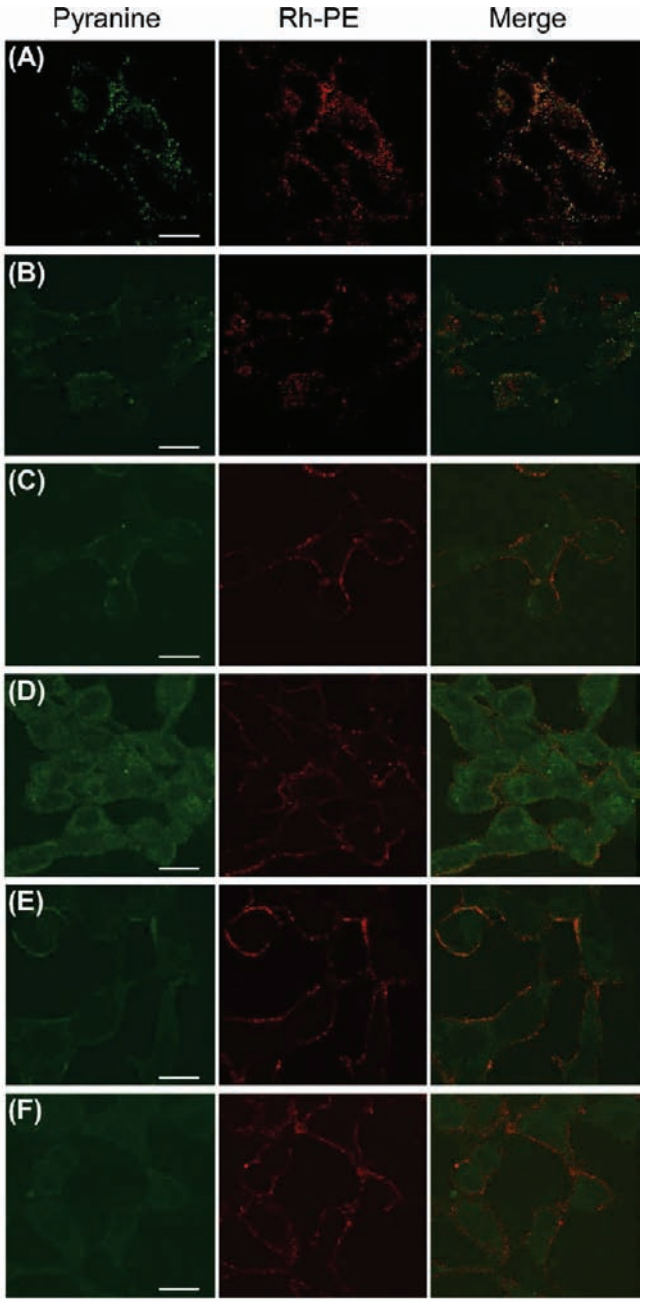

Figure 6. CLSM images of HeLa cells treated with pyranine-loaded plain (A,B) and $NIPAM_{56}$-Suc_{33}-HPG-modified (C−F) liposomes labeled with Rh-PE in the absence (A−D) or presence (E,F) of 100 μM chloroquine. Cells (2×10^5 cells) were incubated in the serum-free medium containing liposomes (0.3 mM) for 4 h at 28 °C and washed with phosphate-buffered saline three times. Then, the cells were additionally incubated at 28 °C (A,C,E) or 45 °C (B,D,F) for 15 min and were observed with CLSM. Bars represent 20 μm.

the cells were heated to 45 °C, the cells displayed the same fluorescence, indicating that the heat application did not affect the location of pyranine molecules in the cells (Figure 6B).

Similarly, cells treated with the dual signal-responsive $NIPAM_{56}$-Suc_{33}-HPG-modified liposomes at 28 °C mainly showed fluorescence around the cell surface (Figure 6C). However, when heated at 45 °C, the cells displayed the entirely different fluorescence of pyranine, which diffused in the cytosol, although Rh-PE fluorescence remained located around the cellular membrane. This fact indicates that pyranine molecules were released from liposomes and were introduced into cytosol upon heat application, although the liposomes were still in endosomes near the cellular membrane (Figure 6D). On the basis of Figure 5B, $NIPAM_{56}$-Suc_{33}-HPG chains attached onto the liposome surface strongly destabilize lipid membranes under a weakly acidic environment at temperatures higher than 35 °C. Therefore, it is likely that the polymer chains can cause significant destabilization of both the liposome and endosome membranes, enabling pyranine molecules to enter into the cytosol. Compared to the plain liposomes, the $NIPAM_{56}$-Suc_{33}-HPG-modified liposomes seemed to exhibit a tendency to remain in the peripheral region of the cellular membrane. The highly hydrated polymer chains covering the liposome surface may affect cellular processes, such as endocytosis, although the reason is unclear.

We also examined intracellular delivery mediated by the dual signal-responsive liposomes in the presence of chloroquine, which inhibits acidification of endosome.[14] As Figure 6F shows, cellular diffuse pyranine fluorescence was suppressed in the presence of chloroquine, indicating that a weakly acidic environment is required for temperature-induced triggering of liposome destabilization. These results demonstrate that destabilization of the dual signal-responsive liposomes can be triggered by mild heat application only for those trapped in weakly acidic compartments.

To confirm superiority of the dual signal-responsive liposomes, we further examined intracellular delivery using pH-sensitive but temperature-insensitive $NIPAM_0$-Suc_{90}-HPG-modified liposomes (Figure 4D) via the same incubation procedures. HeLa cells treated with the $NIPAM_0$-Suc_{90}-HPG-modified liposomes encapsulating pyranine exhibited mainly punctate fluorescence of pyranine around the periphery of cellular membrane irrespective of the temperature of the 15 min incubation (Supporting Information Figure S3). Because the cells were incubated with the liposomes for 4 h at 28 °C, which is much lower than the physiological temperature, reduced cellular activity might suppress the efficient lowering of pH in endosome. Considering that destabilization of $NIPAM_0$-Suc_{90}-HPG-modified liposomes was induced below pH 5.0 (Figure 4D), the liposomes trapped in endosome might not be efficiently destabilized, resulting in the limited extent of pyranine transfer into cytosol. This result suggests another merit of the dual signal-responsive liposomes, whose destabilization is efficiently induced through the synergy of protonated carboxyl groups and dehydrated NIPAM groups on the polymer chains.

CONCLUSION

We developed a new type of functional liposome whose destabilization can be dually controlled by pH and temperature using pH-sensitive and temperature-sensitive NIPAM-Suc-HPGs. The dual signal-responsive liposomes destabilized only when mildly heated under mildly acidic conditions. Therefore, only the liposomes taken up by cells and trapped in acidic compartments can be destabilized by mild heating. These liposomes destabilized in acidic endosome caused the transfer of contents into cytosol. To date, temperature-sensitive liposomes of various types have been developed. Their functions are focused only on temperature-induced control of drug release. Therefore, these liposomes may not be useful for delivery of membrane-impermeable molecules, such as siRNA and proteins, whose active sites exist in the intracellular space, because a large

fraction of the contents may be released from the liposomes in the extracellular space of the heated area. In contrast, the dual signal-responsive liposomes could release the contents only when trapped in the endosome of the cells in the heated area. Therefore, the dual signal-responsive liposomes might solve such problems of conventional temperature-sensitive liposomes and increase the efficacy and reliability of therapies based on these bioactive molecules. Attempts to adjust the temperature region in which the liposomes show response and to achieve sharp and drastic response upon signal applications are currently underway.

■ ASSOCIATED CONTENT

Supporting Information. ^{1}H NMR spectra of polymers (Figure S1), pyranine release from plain liposomes (Figure S2), and CLSM images of HeLa cells treated with $NIPAM_0$-Suc_{90}-HPG-modified liposomes (Figure S3). This material is available free of charge via the Internet at http://pubs.acs.org.

■ AUTHOR INFORMATION

Corresponding Author

*Tel: +81-722-54-9330; Fax: +81-722-54-9330; E-mail: kono@chem.osakafu-u.ac.jp.

■ REFERENCES

(1) Yatvin, M. B., Weinstein, J. N., Dennis, W. H., and Blumenthal, R. (1978) Design of liposomes for enhanced local release of drugs by hyperthermia. *Science 202*, 1290–1293.

(2) Gaber, M., Hong, K., Huang, S. K., and Papahadjopoulos, D. (1995) Thermosensitive sterically stabilized liposomes: formulation and in vitro studies on mechanism of doxorubicin release by bovine serum and human plasma. *Pharm. Res. 12*, 1407–1416.

(3) Kono, K. (2001) Thermosensitive polymer-modified liposomes. *Adv. Drug Delivery Rev. 53*, 307–319.

(4) Needham, D., Anyarambhatla, G., Kong, G., and Dewhirst, M. W. (2000) A new temperature-sensitive liposome for use with mild hyperthermia: characterization and testing in a human tumor xenograft model. *Cancer Res. 60*, 1197–1201.

(5) Kono, K., Ozawa, T., Yoshida, T., Ozaki, F., Ishizaka, Y., Maruyama, K., Kojima, C., Harada, A., and Aoshima, S. (2010) Highly temperature-sensitive liposomes based on a thermosensitive block copolymer for tumor-specific chemotherapy. *Biomaterials 31*, 7096–7105.

(6) Connor, J., Yatvin, M. B., and Huang, L. (1984) pH-sensitive liposomes: acid-induced liposome fusion. *Proc. Natl. Acad. Sci. U. S. A. 81*, 1715–1718.

(7) Karanth, H., and Murthy, R. S. R. (2007) pH-Sensitive liposomes-principle and application in cancer therapy. *J. Pharm. Pharmacol. 59*, 469–483.

(8) Yuba, E., Kojima, C., Harada, A., Tana, Watarai, , S., and Kono, K. (2010) pH-Sensitive fusogenic polymer-modified liposomes as a carrier of antigenic proteins for activation of cellular immunity. *Biomaterials 31*, 943–951.

(9) Fattal, E., Couvreur, P., and Dubernet, C. (2004) Smart delivery of antisense oligonucleotides by anionic pH-sensitive liposomes. *Adv. Drug Delivery Rev. 56*, 931–946.

(10) Kojima, C., Yoshimura, K., Harada, A., Sakanishi, Y., and Kono, K. (2009) Synthesis and characterization of hyperbranched poly(glycidol) modified with pH- and temperature-sensitive groups. *Bioconjugate Chem. 20*, 1054–1057.

(11) Yuba, E., Harada, A., Sakanishi, Y., and Kono, K. (2011) Carboxylated hyperbranched poly(glycidol)s for preparation of pH-sensitive liposomes. *J. Controlled Release 149*, 72–80.

(12) Yessine, M.-A., and Leroux, J.-C. (2004) Membrane-destabilizing polyanions: interaction with lpid bilayers and endosomal escape of miomacromolecules. *Adv. Drug Delivery Rev. 56*, 999–1021.

(13) Mellman, I. (1996) Endocytosis and molecular sorting. *Annu. Rev. Cell Dev. Biol. 12*, 575–625.

(14) Misinzo, G., Delputte, P. L., and Nauwynck, H. J. (2008) Inhibition of endosome-lysosome system acidification enhances porcine circovirus 2 infection of porcine epithelial cells. *J. Virol. 82*, 1128–1135.

Supporting Information

Dual Signals-Responsive Liposomes for Temperature-Controlled Cytoplasmic Delivery

Tomohiro Kaiden[1], Eiji Yuba[1], Atsushi Harada[1], Yuichi Sakanishi[2] and Kenji Kono[1]*

[1]Department of Applied Chemistry, Graduate School of Engineering, Osaka Prefecture University, 1-1 Gakuen-cho, Naka-ku, Sakai, Osaka 599-8531, Japan
[2]Daicel Chemical Industry, Ltd., 2-1-4, Higashisakae, Ohtake, Hiroshima 739-0695, Japan

***Corresponding author: Kenji Kono**
Department of Applied Chemistry, Graduate School of Engineering,
Osaka Prefecture University, 1-1 Gakuen-cho, Nakaku, Sakai, Osaka 599-8531, Japan
Tel: +81-722-54-9330; Fax: +81-722-54-9330; kono@chem.osakafu-u.ac.jp

A

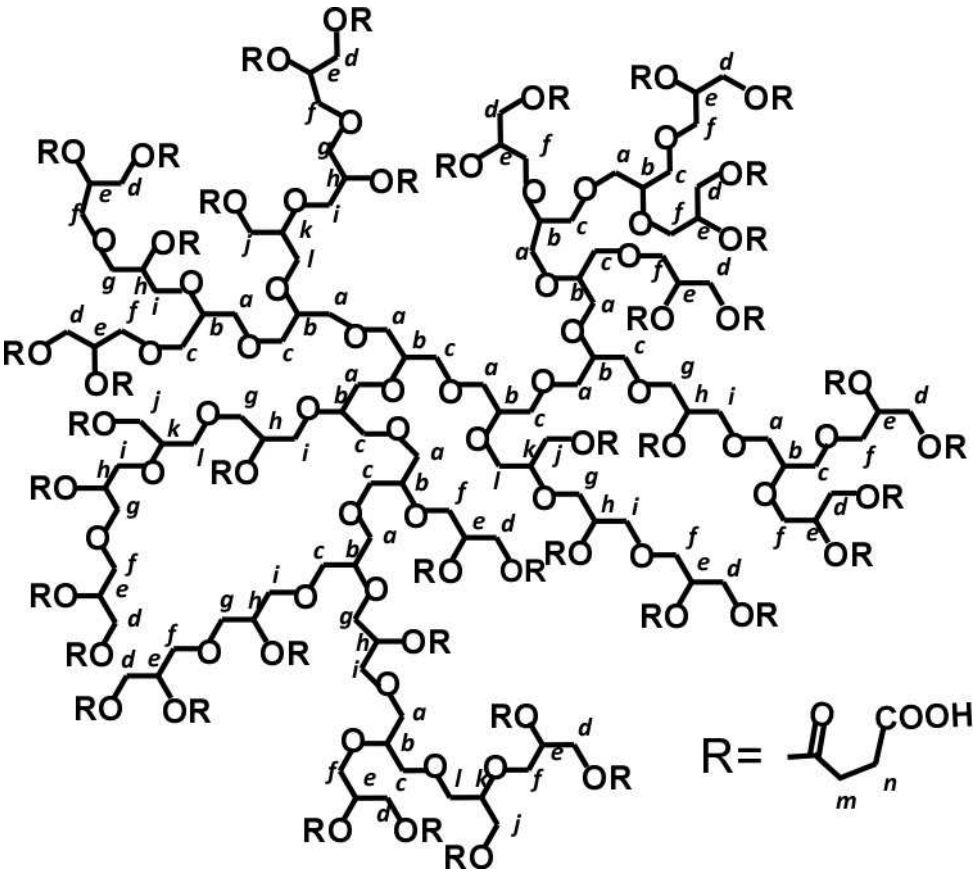

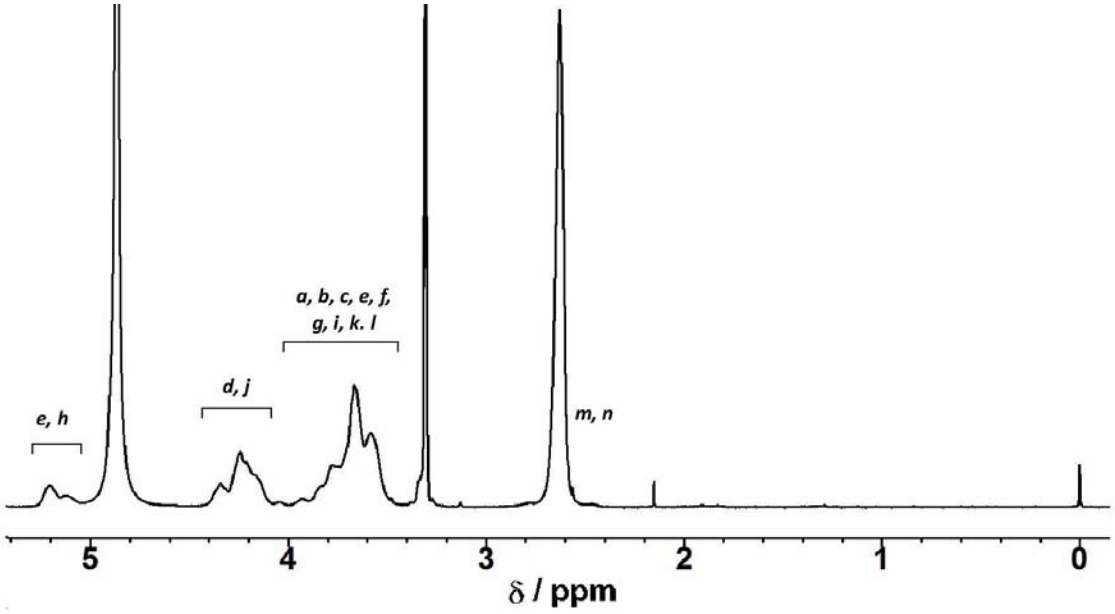

B

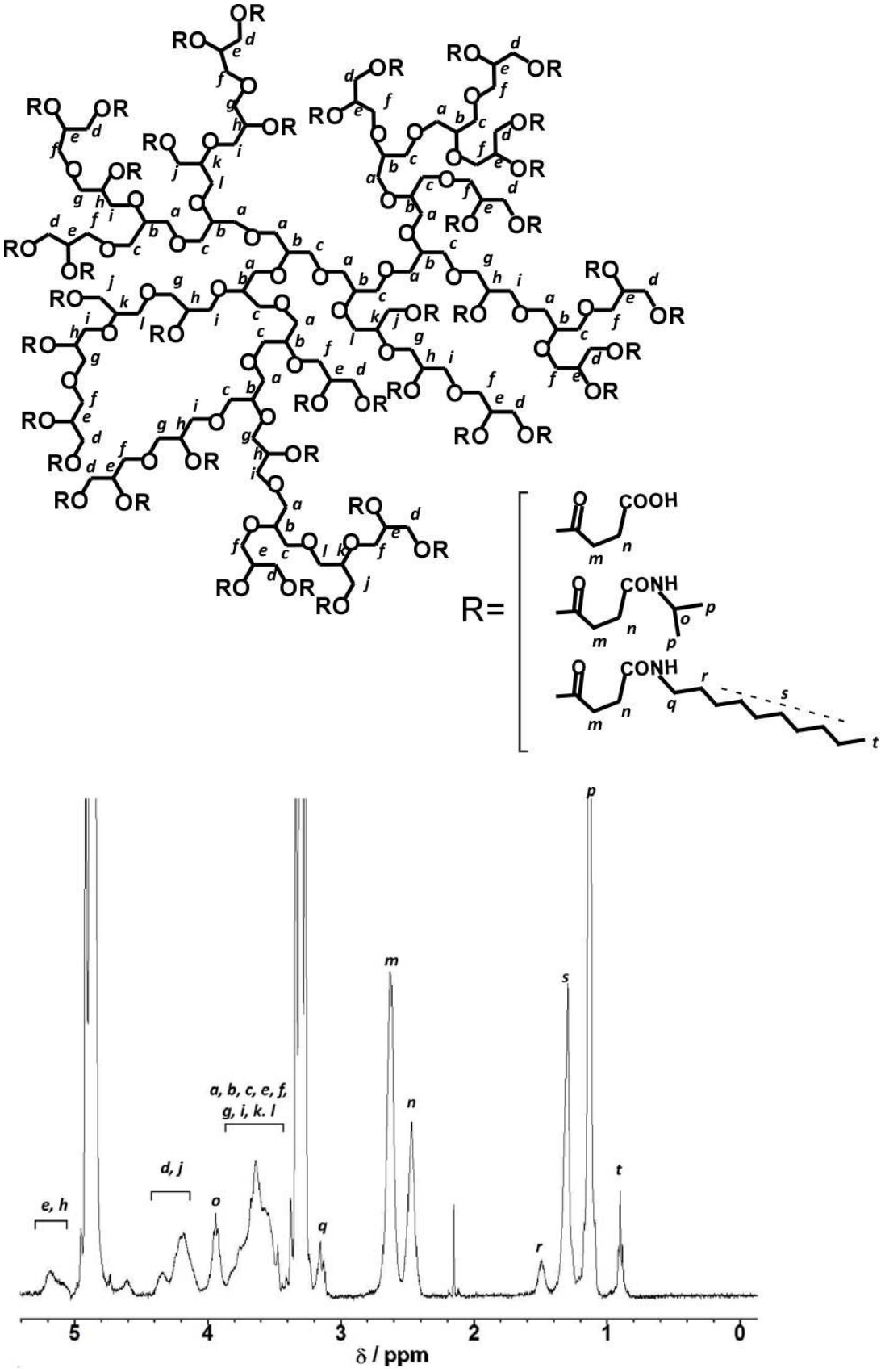

Figure S1. Chemical structures and ^{1}H NMR spectra for Suc-HPG (A) and $NIPAM_{35}$-Suc_{55}-HPG (B) in CD_3OD.

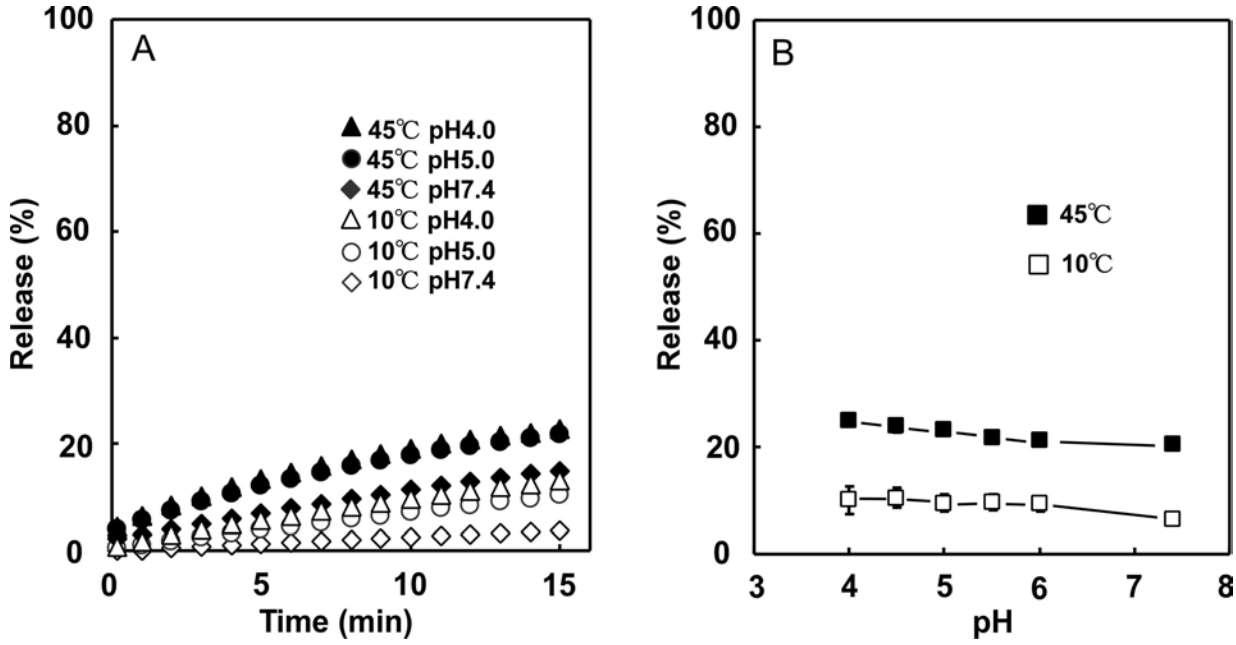

Figure S2. Release of pyranine from plain EYPC liposomes at varying pH and temperatures. (A) Time course. (B) pH-Dependence of pyranine release at 10 °C (diamonds) and 45 °C (triagles). Percent release after 10 min incubation was shown.

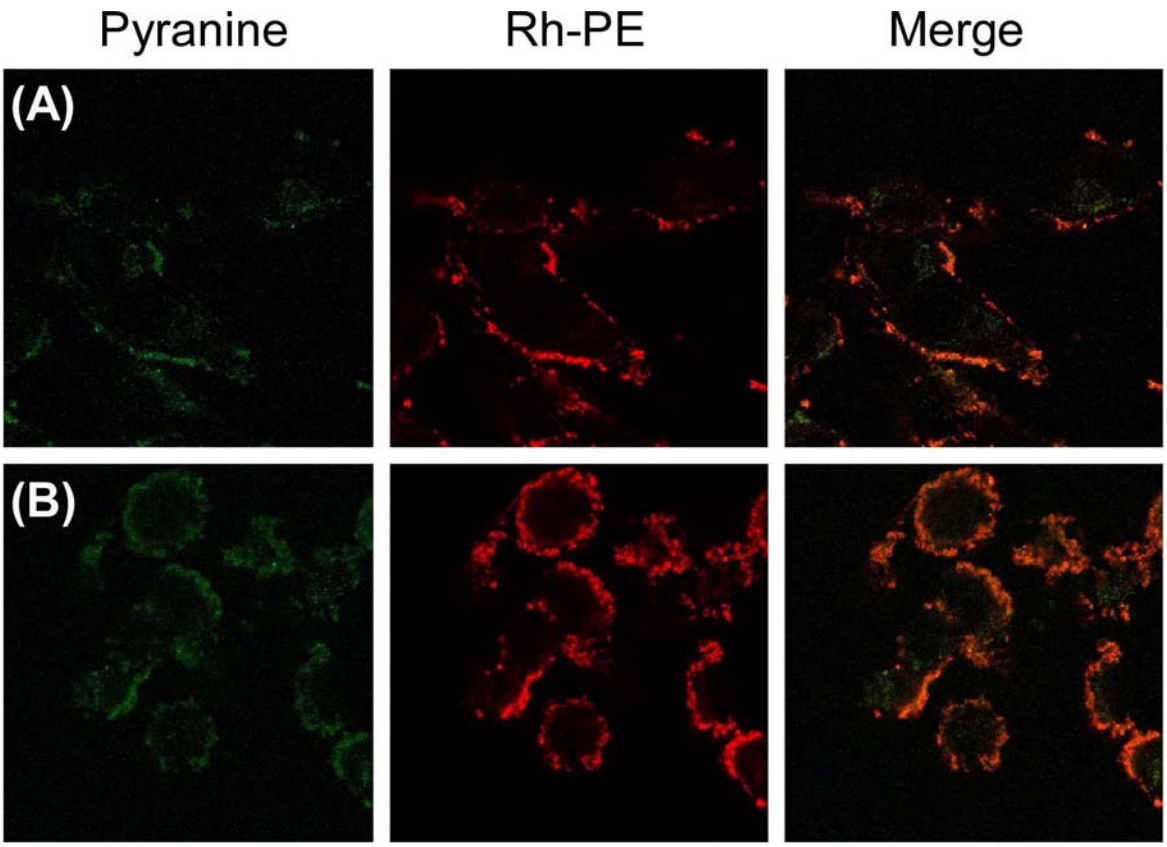

Figure S3. CLSM images of HeLa cells treated with $NIPAM_0$-Suc_{90}-HPG-modified liposomes labeled with Rh-PE and loaded with pyranine in the absence of serum. Cells ($2x10^5$ cells) were incubated in the serum-free medium containing liposomes (0.3 mM) for 4 h at 28 °C and washed with phosphate-buffered saline three times. Then, the cells were additionally incubated at 28 °C (A) or 45 °C (B) for 15 min and were observed with CLSM.

Bioconjugate Chemistry

ARTICLE

pubs.acs.org/bc

Cationic Polydiacetylene Micelles for Gene Delivery

Emmanuelle Morin,[‡,†] Marc Nothisen,[†] Alain Wagner,[*,‡] and Jean-Serge Remy[*,†]

[‡]Laboratory of Functional Chemo Systems and [†]Laboratory of Genetic Chemistry, CAMB, CNRS-UDS UMR 7199, Faculté de Pharmacie, Université de Strasbourg, 74 route du Rhin, BP60024, 67401 Illkirch, France

Supporting Information

ABSTRACT: Cationic surfactants easily interact with plasmid DNA to form small lipoplexes. However, their detergent behavior and associated biological toxicity limit their use as gene delivery vectors. We have incorporated a diacetylene motif in the hydrophobic chain of cationic surfactants. By using UV irradiation, the small cationic micelles (9 nm) obtained with diacetylenic detergents were photopolymerized into 40 nm spheres. Electrostatic interactions with plasmid DNA led to the formation of 45 nm lipoplexes at N/P = 5 ratio. *In vitro* transfection of the pCMV-Luciferase plasmid resulted in gene expression (>10^{10} RLU/mg protein) at the same ratio, comparable with the commercially available JetSi-ENDO gene delivery system. This new and versatile class of molecules could lead to a new generation of *in vivo* gene delivery vectors.

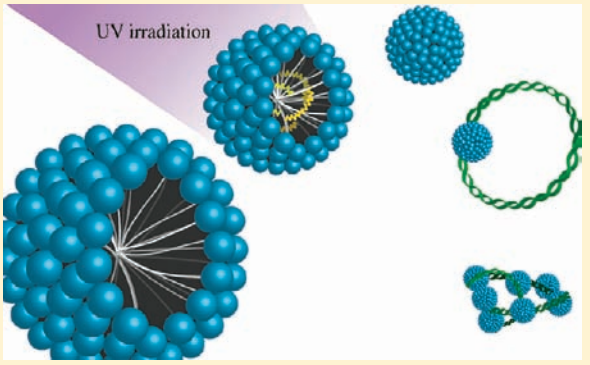

INTRODUCTION

Surfactants are a compound family, which show very interesting properties. Their amphiphilic nature allows them to self-organize and form various attractive supramolecular structures like micelles, liposomes, nanotubes,[1] fibers,[2] or more complex assemblies.[3−5] These cationic constructions have received a lot of attention, partly due to their use as synthetic supramolecular vectors for gene delivery.[6−8] Ordered cationic liposomes or micelles or cationic detergents spontaneously form lipoplexes with DNA, due to electrostatic interactions between the cationic head groups of detergents and the negatively charged phosphate groups of nucleic acids.[9−11] Among the large number of cationic amphiphiles, which induce effective gene transfer, amine- and ammonium-based detergents are still the most studied.[6,7] However, these organized structures have a very dynamic nature. Monomers constantly exchange between solution and self-assemblies, inducing instability and toxicity. Thus, it has been suggested that cross-linking, using amphiphiles bearing polymerizable groups, could improve the stability of these labile systems.[12,13] Core cross-linked micelles and shell cross-linked micelles are usually obtained from copolymers and show some interesting properties in drug delivery.[14,15] However, only a few studies describe the use of diacetylene micelles.

Diacetylene surfactants receive a lot of attention due to their polymerization properties upon exposition to ultraviolet radiations.[16] This leads to the formation of more rigid structures and could also provide some new supramolecular nanoconstructs.[17] The potential application range from biosensors,[18,19] nonlinear optical devices[20] through to drug delivery.[21,22] It has been shown that diacetylene formulations[23] or polymerized liposomes[24] can deliver genes, but to the author's knowledge, few studies have been conducted on micelles.

In this paper, we describe the synthesis and the characterization of two new photopolymerized cationic micelles as synthetic DNA vectors. These new ammonium-based structures were obtained from the commercially available 10,12-pentacosadiyonic acid (PCDA) and could easily be photopolymerized. We demonstrate that these self-assemblies form lipoplexes in the presence of pCMV-Luc plasmid and can efficiently mediate gene transfer. By comparing behaviors of polymerized and nonpolymerized DNA lipoplexes, we show that polymerization significantly improves transfection and reduces toxicity.

EXPERIMENTAL PROCEDURES

Synthesis of Pentacosa-10,12-diyn-1-ol (2). To a stirred suspension of lithium aluminum hydride (0.91 g, 20.02 mmol) in THF (100 mL), a solution of 10,12-pentacosadiynoic acid (5.00 g, 13.34 mmol) in THF (50 mL) was added at 0 °C under Ar atmosphere. The resulting mixture was stirred for 90 min at RT. The reaction was quenched by adding 1 N HCl solution (25 mL) and the mixture concentrated to dryness under reduced pressure. The aqueous layer was extracted with EtOAc (2 × 30 mL), and the combined organic layers washed with 1 N HCl (20 mL), dried over anhydrous Na_2SO_4, filtered, and evaporated under vacuum to afford **2** as a white solid (4.40 g, 91% yield).

Synthesis of Pentacosa-10,12-diynyl-4-methylbenzenesulfonate (3). To a stirred solution of pentacosa-10,12-diyn-1-ol (4.40 g, 12.20 mmol) in CH_2Cl_2 (60 mL) were successively added *p*-toluenesulfonyl chloride (3.49 g, 18.30 mmol),

Received: February 17, 2011
Revised: August 29, 2011
Published: September 16, 2011

ACS Publications © 2011 American Chemical Society

triethylamine (2.55 mL, 18.30 mmol), and catalytic amounts of DMAP. The resulting solution was stirred overnight at RT. A saturated solution of $NaHCO_3$ (25 mL) was added and the aqueous layer was extracted with CH_2Cl_2 (2 × 15 mL). The organic phases were combined, washed with a saturated solution of NaCl (15 mL), dried over anhydrous Na_2SO_4, filtered, and concentrated under reduced pressure. The residue was submitted to silica-gel chromatography to afford compound **3** as a white solid (5.58 g, 89% yield).

Synthesis of *N*,*N*-Diethyl-pentacosa-10,12-diyn-1-amine (4). To a stirred solution of pentacosa-10,12-diynyl-4-methylbenzenesulfonate (7.14 g, 13.86 mmol) and Na_2CO_3 (7.35 g, 69.3 mmol) in CH_3CN (150 mL) was added diethylamine (5.07 g, 69.3 mmol). The solution was stirred at 70 °C for 24 h. The solvent was removed under reduced pressure and the residue was poured into a saturated solution of $NaHCO_3$ (60 mL). The aqueous layer was extracted with CH_2Cl_2 (4 × 25 mL), and the organic layers were combined, washed with a saturated solution of NaCl (15 mL), dried over anhydrous Na_2SO_4, filtered, and concentrated under reduced pressure. The residue was purified by silica-gel chromatography (eluting with EtOAc/cyclohexane 5:95) to yield compound **4** as a colorless oil (3.54 g, 79% yield).

Synthesis of 4-(2-Aminoethyl)-1,7-bis(*tert*-butoxycarbonyl)-1,4,7-triazaheptane (6). To a stirred solution of tris(2-aminoethyl)-amine (1.47 g, 10.05 mmol) in THF (40 mL) at 0 °C was slowly added BocON (4.95 g, 20.11 mmol) in THF (50 mL). The solution was stirred overnight at RT. The solvent was removed under reduced pressure and the residue was poured into EtOAc (50 mL). The organic layer was washed with NaOH 1 M (2 × 10 mL). The aqueous layer was diluted into a saturated solution of NaCl (20 mL) and was extracted with EtOAc (3 × 10 mL). The organic layers were combined, dried over anhydrous Na_2SO_4, filtered, and concentrated under reduced pressure. The residue was purified by silica-gel chromatography (eluting with CH_2Cl_2/methanol 5:1) to yield compound **6** as a pale yellow oil (1.57 g, 45% yield).

Synthesis of Di-*tert*-butyl (((2-(tetracosa-10,12-diynamido)-ethyl)azanediyl)bis(ethane-2,1-diyl))dicarbamate (7). To a stirred solution of 10,12-pentacosadiynoic acid (1.00 g, 2.90 mmol) and *N*-hydroxysuccinimide (0.50 g, 4.33 mmol) in CH_2Cl_2 (20 mL) were added successively 1-ethyl-3-(3-dimethylamino-propyl) carbodiimide (0.83 g, 4.33 mmol) and *N*,*N*-diisopropylethylamine (757 μL, 4.33 mmol). The solution was stirred overnight at RT. The solvent was removed under reduced pressure and the residue was poured into EtOAc (20 mL). The organic layer was washed with H_2O (2 × 10 mL), dried over anhydrous Na_2SO_4, filtered, and concentrated under reduced pressure. The white solid was solubilized into THF (50 mL) with Et_3N (606 μL, 4.33 mmol) and 4-(2-aminoethyl)-1,7-bis(*tert*-butoxycarbonyl)-1,4,7-triazaheptane **4** (1.08 g, 2.90 mmol), and the solution was stirred overnight at RT. The solvent was removed under reduced pressure, and the residue was purified by silica-gel chromatography (eluting with EtOAc) to yield compound **7** as a white solid (1.57 g, 85% yield).

Synthesis of *N*-(2-(Bis(2-aminoethyl)amino)ethyl)tetracosa-10,12-diynamide (8). To a stirred solution of **7** (0.2 g, 0.28 mmol)) in CH_2Cl_2 (5 mL) was added trifluoroacetic acid (327 μL, 4.27 mmol). The solution was stirred 4 h at RT. The solvent was removed under reduced pressure and the residue was poured into EtOAc (10 mL). The organic layer was washed with NaOH 1 M (1 × 10 mL), dried over anhydrous Na_2SO_4, filtered, and concentrated under reduced pressure to yield compound **8** as a white solid (0.14 g, quantitative).

Polymerization. For the photopolymerization steps, quartz cuvettes containing 3 mL of micelles solution were placed into a Cross-Linker Bio-Link 254 from Fischer Bioblock. Photopolymerization was achieved at 254 nm and 48 W.

Photopolymerization was followed by UV−visible spectroscopy on a Varian Cary 100 Bio UV−visible spectrophotometer.

CMC Measurements. Surface tensions were measured by using the du Nouy ring, as follows. First, 15 mL of solution was prepared by diluting stock solutions of micelles. The solution were then transferred to the tensiometer vessel and was allowed to equilibrate at 25 °C for 5 min.

Dynamic Light Scattering (DLS). The hydrodynamic radii were determined *via* DLS measurements using a Malvern nano ZS apparatus with the following specifications: sampling time = 90 s; refractive index of medium, 0.1 M acetate buffer = 1.340; phosphate buffer = 1.340; refractive index of particles (RI) = 1.43; medium viscosity = 1.0140 cP; temperature = 25 °C. Data were analyzed using multimodal number distribution software included with the instrument. ζ potentials were measured with the same apparatus and with the following specifications: 20 measurements per sample; dielectric constant = 80; temperature = 25 °C; beam mode F(Ka) = 1.5 (Smoluchowski model).

Transmission Electron Microscopy (TEM). Images were taken with a TEM Phillips CM12 apparatus, onto 300 mesh copper grids (Ted Pella, 822-F, Formvar removed). Ten microliters of sample was allowed to adsorb for 1 min onto grids. Grids were wicked from one side, and placed for 30 s on a 50 μL drop of 2% uranyl acetate, wicked again, and air-dried before imaging.

Agarose Gel Electrophoresis. Twenty microliters of water containing 5% glucose or 150 mM NaCl, 0.4 μg pCMV-Luc, and increasing amount of polymerized and nonpolymerized cationic micelles were subjected (30 min of complexation time) to electrophoresis in a 1% agarose gel containing 1 mM EDTA, 40 mM Tris acetate buffer, and 0.5 μg/mL ethidium bromide for 90 min at 100 V. DNA was visualized with an UV transilluminator at 254 nm.

Cell Culture. HeLa cells were grown in Eagle's MEM supplemented with 10% FBS, L-glutamine (2 mM), penicillin (100 units/mL), and streptomycin (100 μg/mL). Cells were maintained at 37 °C in a 5% CO_2 humidified atmosphere and all experiments were done in triplicates. The day before experiment, cells were seeded in 24-multiwell plates at 5 × 10^4 cells/well in fresh complete medium (1 mL).

Lipoplex Formation for pCMV-Luc Delivery. The procedure is for a 24-multiwell plate experiment. Typically, an aqueous solution of polymerized and nonpolymerized micelles of compound **4** and **8**: $\mathbf{M_4P_{1h}}$, **M$_4$NP**, $\mathbf{M_8P_{1h}}$, and **M$_8$NP** (volume depending on N/P ratio), was diluted up to 50 μL in water containing 5% glucose or 150 mM NaCl. The solution was homogenized by vortexing and left for 10 min. Separately, an aqueous solution of pCMV-Luc (corresponding to 2 μg of pCMV-Luc) was diluted up to 50 μL in water containing 5% glucose or 150 mM NaCl. The solution was then homogenized and left for 10 min, after which the M_4P_{1h}, M_4NP, M_8P_{1h}, or M_8NP solution was added to the pCMV-Luc solution, and vigorously mixed (15 s). Finally, lipoplexes were incubated for 30 min at RT and added in each well by diluting with serum free cell culture medium (1 mL). Four hours later, serum (0.1 mL/well) was added. The gene expression profiles were analyzed 24 h after addition of lipoplexes. Transfection assays were also performed in the presence

Scheme 1. Synthesis of Amphiphile 4

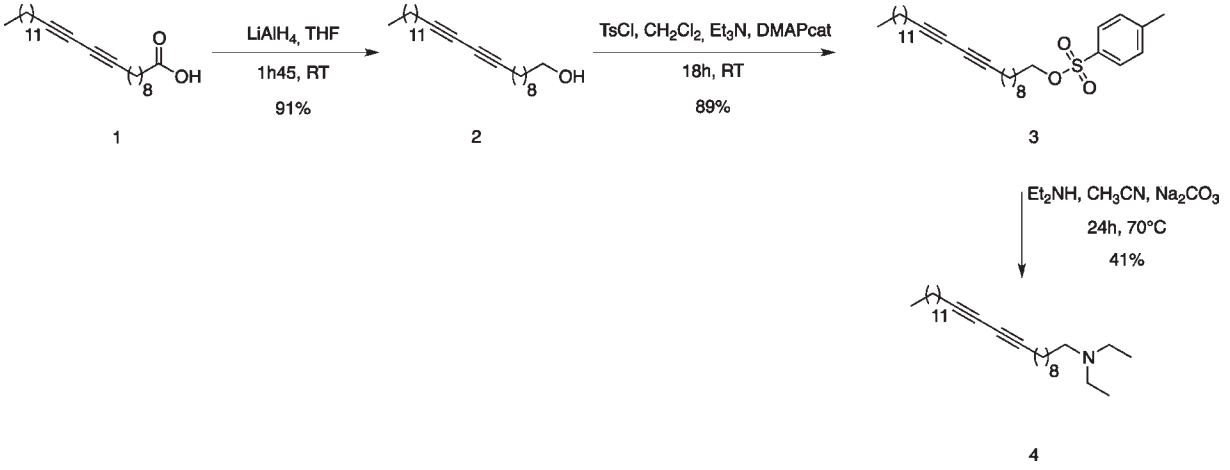

Scheme 2. Synthesis of Amphiphile 8

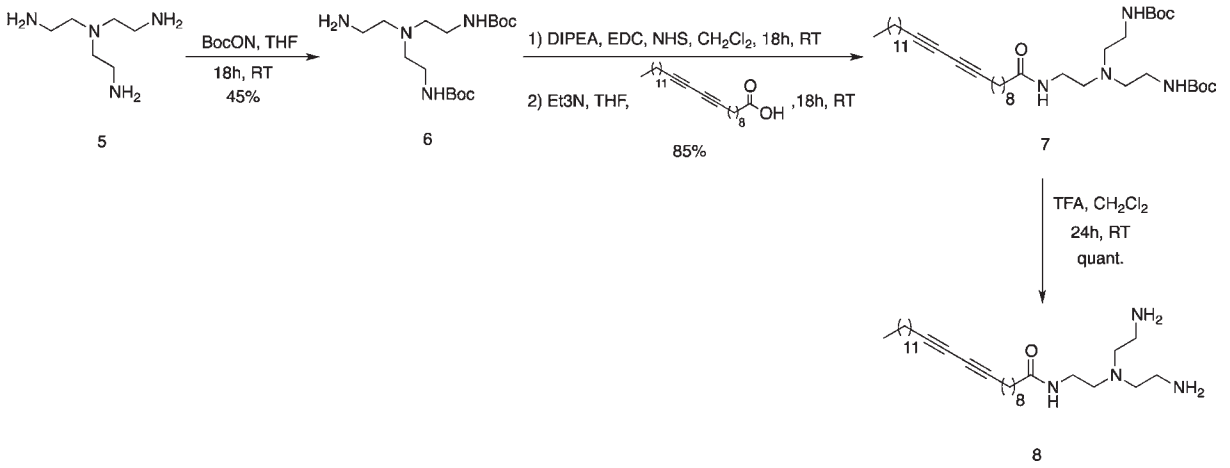

of serum: after incubation, lipoplexes were added in each well by diluting with complete cell culture medium (10% serum, 1 mL).

Quantification of the Luciferase Gene Expression. Luciferase gene expression was determined 24 h after delivery with a commercial kit, using manufacturer's protocol (Luciferase Assay System, Promega, Charbonnières, France). The luminescence was measured from 10 μL of lysate during 1 s with a luminometer (Centro LB960 XS; Berthold, Thoiry, France). Luciferase activity is expressed as the mean of light units integrated over 10 s (RLU) and normalized per mg of cell protein by using the BCA assay (Pierce, Brebières, France). The errors bars represent standard deviation derived from triplicate experiments. JetPEI and JetSi-ENDO are transfection reagents (Polyplus-Transfection, Illkirch, France), used according to manufacturer's instructions.

RESULTS

Design and Synthesis. The two new ammonium-based amphiphiles were easily obtained from the commercially available acid **1**. The synthesis of compound **4**, as depicted in Scheme 1, was prepared in three steps as previously reported.[3]

BOC protection of the two terminal amines of tris(2-aminoethyl)amine affords compound **6**, which is easily coupled to the starting acid **1** as described in Scheme 2. Treatment of **7** with an excess of TFA provides a high yield of compound **8**.

Micelle Characterization. Measurements of the surface tension of M_4NP and M_8NP solutions allowed us to access the critical micellar concentrations (CMC) of nonpolymerized solutions. Curves are presented in the Supporting Information. M_4NP and M_8NP solutions have CMC values of 12 μmol/L (0.0049 mg/mL) and 21 μmol/L, (0.011 mg/mL), respectively. Following polymerization, CMC could not be detected anymore. The self-assembly of amphiphiles **4** and **8** into micelles was then assessed by DLS. Experiments with compound **4** at 600 μM (0.25 mg/mL) in various buffer solutions showed the importance of pH and medium composition. In 0.1 M phosphate buffer (pH = 7.4), we observed no micellar structures but 400 nm aggregates were observed, while in 0.1 M acetate buffer (pH = 5), amphiphile **4** led to the formation of nonpolymerized micelles (M_4NP) of 9 nm diameter (see Supporting Information). Similarly, nonpolymerized micelles of compound **8** (M_8) at 500 μM (0.25 mg/mL) were only observed in 0.1 M acetate buffer. Micelle formation and size were confirmed by transmission electron microscopy

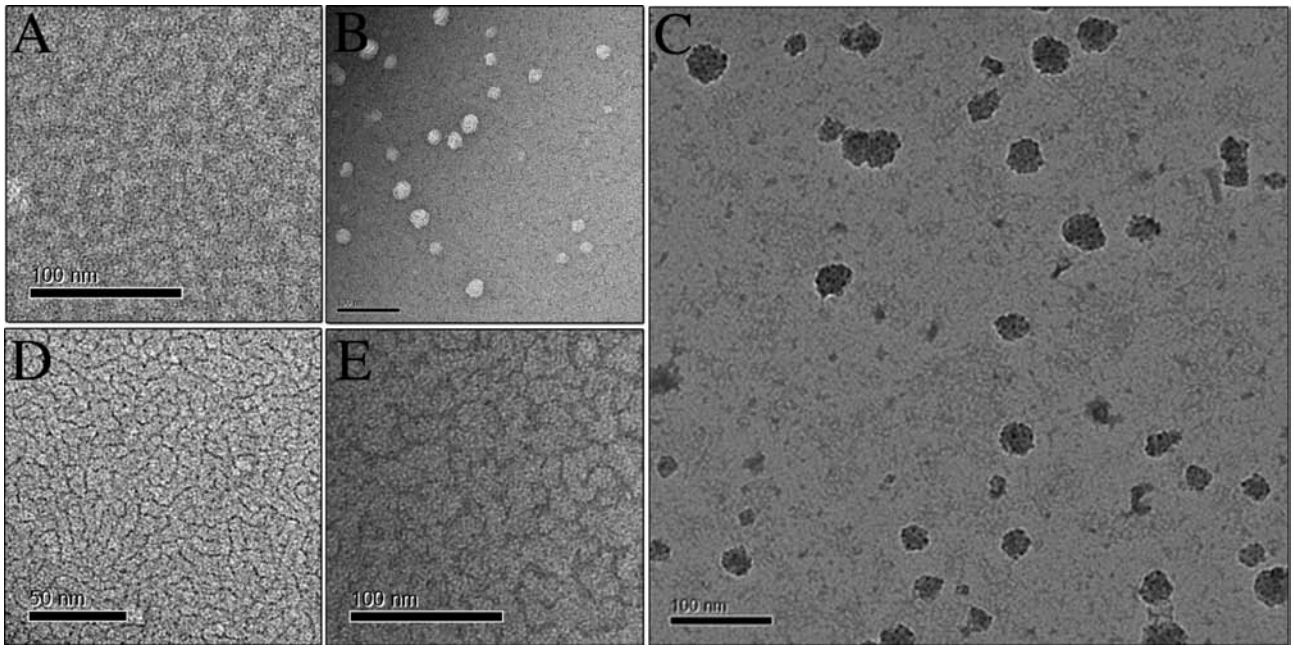

Figure 1. TEM images of M_4 and M_8 (C = 600 μM and 500 μM, respectively) in 0.1 M acetate buffer. A, M_4NP; B, M_4P_{1h}; C, M_4P_{1h} diluted to 60 μM in phosphate buffer; D, M_8NP; E, M_8P_{1h}. Scale bars: 100 nm (A, B, C, and E) and 50 nm (D).

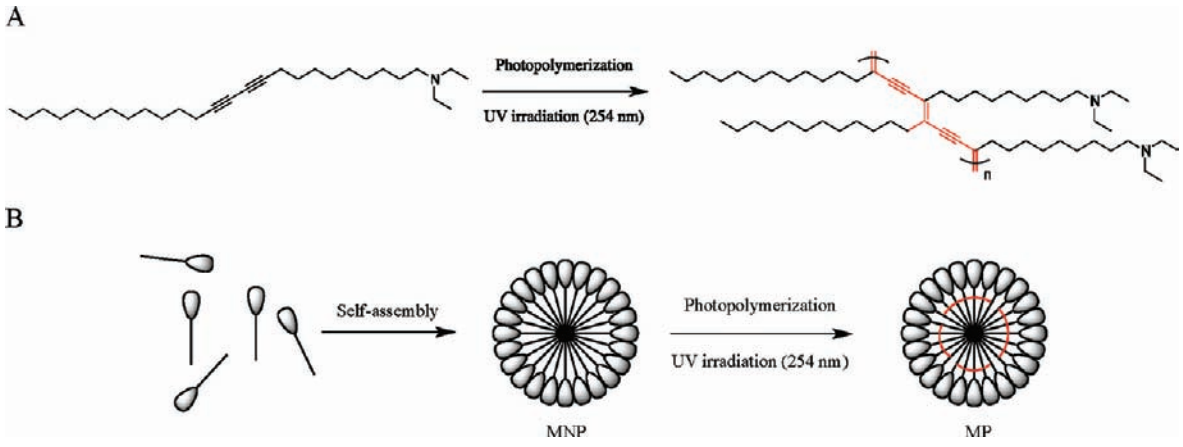

Figure 2. (A) Amphiphile **4** and corresponding polymer formula. (B) Schematic process of polymerization. Polar head groups are shown as gray balls, amphiphile chains by straight gray lines, and polymeric chains by curved red lines. (MNP: nonpolymerized micelles. MP: polymerized micelles.)

(TEM) experiments, as shown in Figure 1A,D, where elongated and tubular structures are visible.

Micelle Polymerization. Diacetylene polymerization (Figure 2) was initiated by 254 nm ultraviolet irradiation. This process was followed over time by DLS and TEM experiments. As shown in Supporting Information, the sizes of the assemblies of compound **4** increase over polymerization time. Beyond one hour, photopolymerization deeply affects the size of the structures: after four hours, objects present a 40 nm diameter, which increases up to 250 nm after 7 h. TEM only detected large aggregates. However, up to one hour of polymerization, assemblies kept the same diameter (9 nm) and still could be considered to be micelles (M_4P_{1h}). These small and spherical structures were also observed by TEM (Figure 1B), and as depicted in the Figure 1E, the same results were obtained with micelles of compound **8** polymerized for 1 h (M_8P_{1h}). The dilution of M_4P_{1h} micelles to 60 μM in phosphate buffer (Figure 1C) did not destroy their structure, and this demonstrates their resistance to dilution and pH changes, and consequently the effectiveness of the polymerization.

The polymerization process was followed every ten minutes for up to 90 min by UV−visible spectroscopy (spectra available in Supporting Information) in order to analyze the propagation process. In both cases, ene-yne bond elongation was shown by a characteristic absorption band between 250 and 300 nm. Its intensity increases over polymerization time and stabilizes at 20 min (Figure 3) showing an optimal propagation level into micelles. These analyses enabled us to choose the optimal condition taking into account self-assembly and micelle reticulation. For the rest of the study, photopolymerization time was one hour.

DNA Lipoplexes Characterization. Electrostatic interactions between plasmid DNA and nonpolymerized or polymerized micelles

were imaged by agarose gel electrophoresis of lipoplexes, which were made with increasing N/P (vector amine per DNA phosphate) ratios (Figure 4). The DNA was detected using ethidium bromide orange fluorescence.

M_4NP lipoplexes in isotonic 150 mM NaCl showed full DNA condensation at N/P 10 and the corresponding polymerized lipoplexes at N/P 2. This notable improvement was also observed for M_4 lipoplexes in iso-osmotic 5% glucose solutions in water. Thus, full DNA condensation was not observed with nonpolymerized lipoplexes in the range studied; however, it was observed at N/P 10 and above, for the polymerized lipoplexes.

A similar trend was observed for M_8 lipoplexes. DNA condensation occurred at N/P 2 in isotonic 150 mM NaCl and for N/P 3 in iso-osmotic 5% glucose solutions in water with nonpolymerized lipoplexes. A slight improvement was observed with polymerized lipoplexes.

It is interesting to note that lipoplexes formulated in 5% glucose solutions even these most compacted forms at high N/P ratio remain accessible to ethidium bromide.

Lipoplexes prepared in 5% glucose were further characterized by DLS. Size measurements on M_4P_{1h} lipoplexes (Figure 5A) showed that their diameter decreased when the N/P ratio was increased. The same behavior was observed for M_8P_{1h} lipoplexes, except at N/P 20. Both formulations showed an average diameter of 45 nm at N/P 5, which was confirmed by TEM experiments (Figure 6A,C). Zeta (ζ) potential measurements made on the above lipoplexes showed increasing positive surface charges with N/P ratio (Figures 5B). When prepared in 150 mM NaCl, lipoplexes at N/P 5 became micrometric structures made of aggregated spheres (see Supporting Information).

Transfection of Cells in Culture. pCMV-Luc gene delivery experiments were conducted with M_4 and M_8 lipoplexes on HeLa cells, prepared either in 5% glucose (Figure 7A) or 150 mM NaCl solutions (see Supporting Information).

Final monomer concentrations in wells were calculated as described in Table 1. Final plasmid concentration was fixed to 2 μg/mL.

In each case, the polymerized micelles exhibited higher transfection efficiency and lower toxicity than the nonpolymerized micelles.

N/P 5 was the optimal ratio for both M_4P_{1h} and M_8P_{1h}, and they have the same level of luciferase expression, between 10^{10} and 10^{11} RLU/mg of protein. This level is 1 order of magnitude lower than the JetPEI system, which is considered a "gold standard"

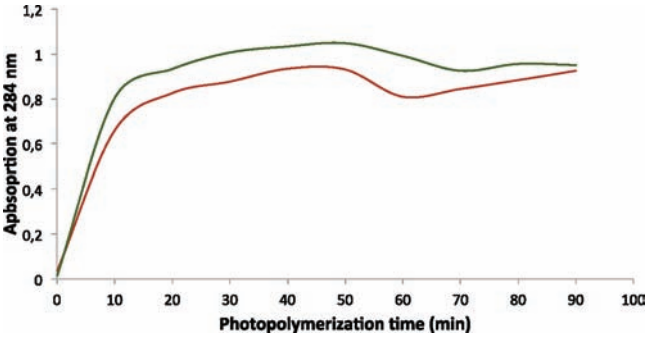

Figure 3. Absorption at 284 nm vs photopolymerization time. Green line: M_4 solution. Red line: M_8 solution.

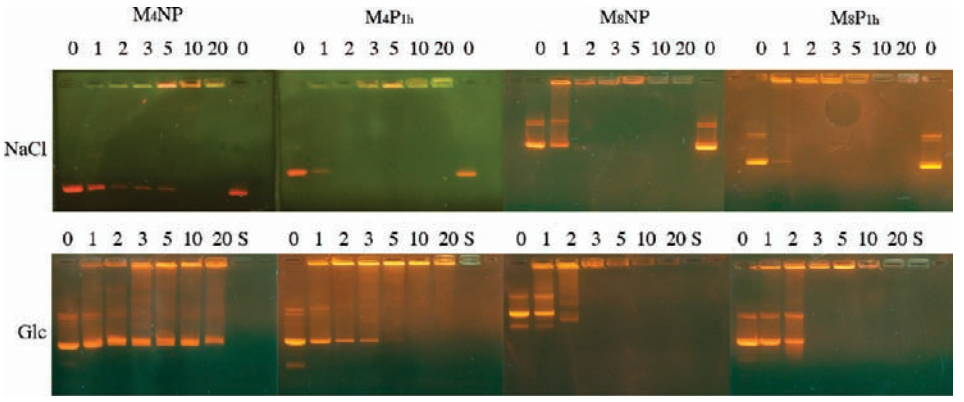

Figure 4. Agarose gels. Lipoplexes were prepared at N/P = 1 to 20; 0: pCMV-Luc without micelles; S: micelles without pCMV-Luc plasmid.

A

N/P	M_4P_{1h} (nm)	M_8P_{1h} (nm)
1	54	66
2	43	49
5	40	47
20	24	90

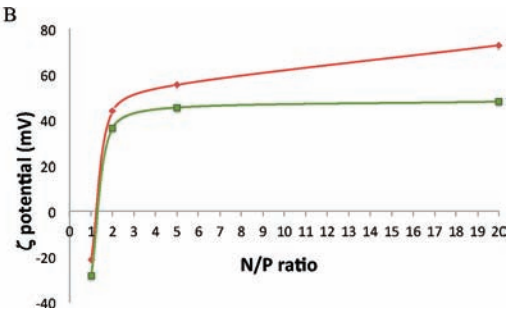

Figure 5. DLS results for M4P1h and M8P1h lipoplexes in 5% glucose aqueous solution. A: diameters at various N/P ratios. B: Zeta potentials. Green line: M_4P_{1h} lipoplexes. Red line: M_8P_{1h} lipoplexes.

in nonviral gene delivery; it is comparable to another commercially available gene delivery lipidic system, JetSi-ENDO, which is known for its high efficiency/toxicity ratio. However, M_4P_{1h} were found to be quite toxic, compared to M_8P_{1h} in optimal conditions. Transfection efficiencies were reduced by 1 to 3 orders of magnitude in the presence of 10% serum (see Figure 8), revealing deleterious interactions between the complexes and serum proteins. Thus, further developments (e.g., PEGylation and/or targeting ligands) will be necessary for effective *in vivo* gene delivery.

DISCUSSION

The application of polydiacetylene polymeric structures for gene delivery has never been studied. In a previous study, we have shown that amphiphiles formed by coupling diynic lipophilic tails and various polar headgroups spontaneously self-assembled into micelles in aqueous solution. In particular, coupling anionic, neutral, or cationic polar headgroups to 10,12-pentacosadiynoic acid led to amphiphiles with programmed pH-dependent self-assembly properties.[25] On the other hand, when we varied the length of the hydrophobic chain length containing a neutral polar headgroup, we found that, while 12 carbon chain was too short to enable the formation of micelles, 18 and 25 carbon chains led to stable micelles with CMC of 0.091 mg/mL and 0.082 mg/mL, respectively (unpublished results). Since it appears to form robust micelles and is readily available, we decided to use 10,12-pentacosadiynoic acid (C_{25}) as a lipophilic tail for this study. Cationic monomers were easily synthetized from PCDA and, as expected, self-assembled into micelles in a simple and spontaneous process. It is interesting to note that pH and medium composition are important parameters for micelle formation.

The photopolymerization state requires a perfectly calibrated process to ensure the size reproducibility of the polymerized micelle. Elongation creates covalent cross-linking between monomers into micelles to provide a three-dimensional network and more rigid assemblies as shown in Figure 1B. However, DLS experiments showed that, beyond one hour, polymerization provides larger aggregates than the initial micelles. This fact has already been observed in micelle polymerization[26] and in this study could be explained by geometric constraints imposed by the ene-yne backbone. It is well-known that photopolymerization of diacetylene groups occurs only in a highly ordered state.[16] In our case, the propagation of ene-yne bonds strongly alters the initial morphology, resulting in larger structures with lower radii of curvature.

Micelle structures were observed by DLS and TEM over one hour of polymerization, and UV spectrophotometric analysis showed a good level of elongation. One hour of polymerization

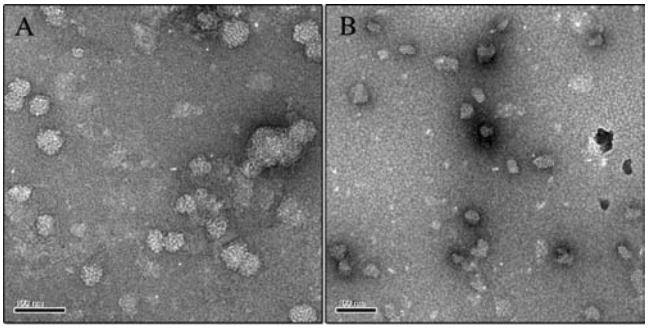

Figure 6. TEM images of micelles/pCMV-Luc lipoplexes at N/P 5 in water with 5% glucose. (A) M_4P_{1h}/pCMV-Luc lipoplexes. (B) M_8P_{1h}/pCMV-Luc lipoplexes. Scale bars: 100 nm.

Table 1. M_4 and M_8 Monomer Concentrations for Transfection Assays

N/P ratio	0	1	2	3	5	10	20
M_4 (μM)	0	6.1	12.1	18.2	30.3	60.7	121.3
M_8 (μM)	0	2.0	4.0	6.1	10.1	20.2	40.3

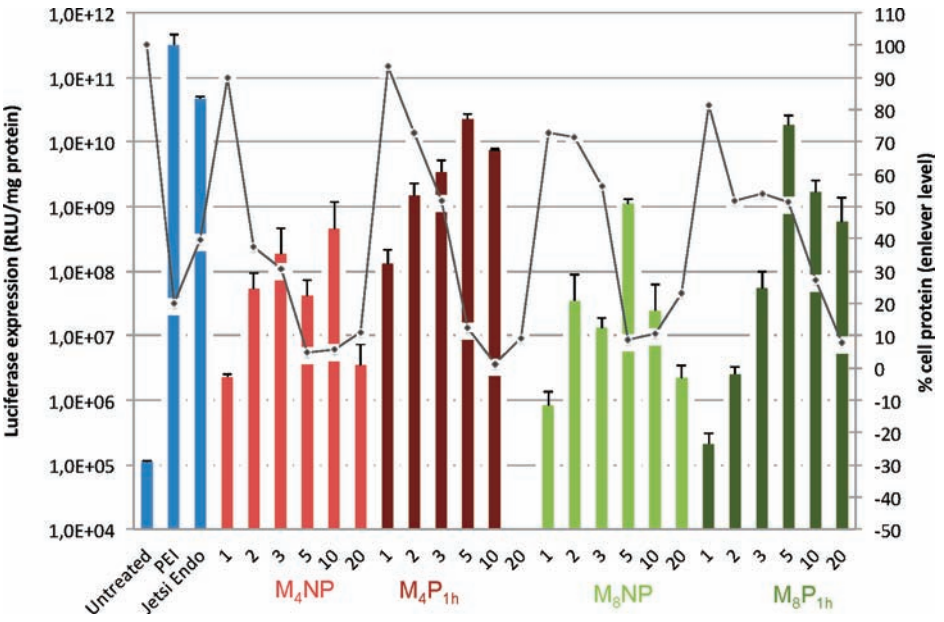

Figure 7. Gene delivery experiments of pCMV-Luc at various N/P (lipoplexes prepared in 5% glucose solution), without serum. Luciferase expression (bars) and percentage of total cellular proteins (line and circles) are given for negative control (untreated), positive control (JetPEI and JetSi-ENDO), M_4NP (light red), M_4P_{1h} (dark red), M_8NP (light green), and M_8P_{1h} (dark green). Means and sd of separate triplicates are given.

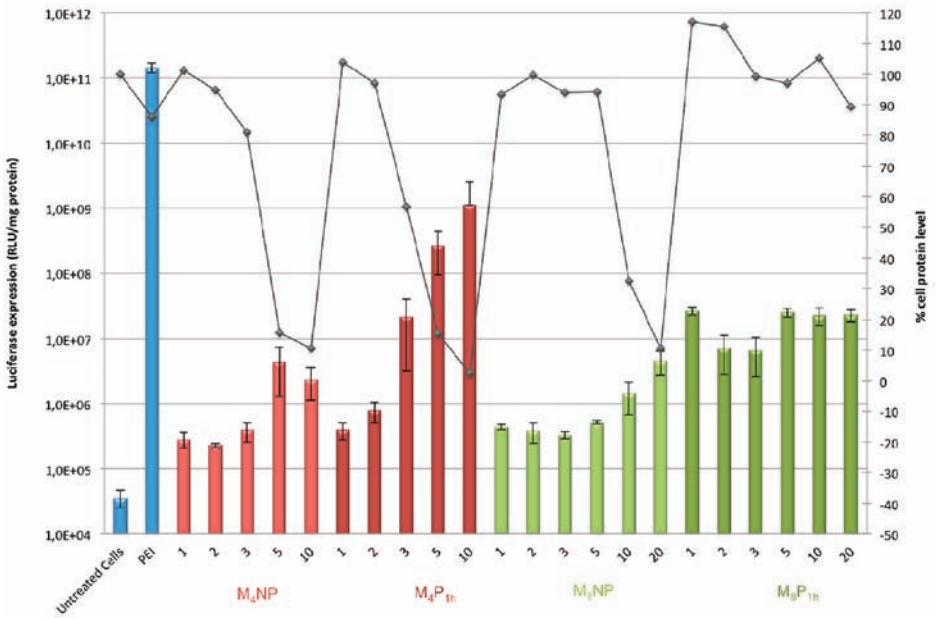

Figure 8. Gene delivery experiments of pCMV-Luc at various N/P (lipoplexes prepared in 5% glucose solution), with serum. Luciferase expression (bars) and percentage of total cellular proteins (line and circles) are given for negative control (untreated), positive control (JetPEI), M_4NP (light red), M_4P_{1h} (dark red), M_8NP (light green), and M_8P_{1h} (dark green). Means and sd of separate triplicates are given.

seemed to be the best compromise to retain the original structure, while having enough cross-linking to "freeze" the micelles. Diluting the micelles below their CMC in phosphate buffer (pH = 7) proved the efficiency of polymerization. Indeed, polymerized micelles were still observed after switching to neutral conditions, whereas nonpolymerized micelles were disrupted.

Agarose gel electrophoresis experiments showed the different behaviors of polymerized and nonpolymerized lipoplexes. Using either M_4 or M_8 complexes, the polymerized lipoplexes show full DNA condensation at lower N/P ratio than nonpolymerized lipoplexes. In polymerized micelles, the exchange of monomers between the micelle and its surroundings was strongly inhibited, and led to better DNA condensation and lipoplex stability. In isotonic 150 mM NaCl for N/P 20, no fluorescence due to the ethidium bromide staining was observed, reflecting very good DNA compaction into the lipoplexes. It has to be noted that polymerized micelles have their own green fluorescence, due to ene-yne bonds, which is absent in nonpolymerized micelles.

Lipoplexes were observed by DLS experiments in iso-osmotic 5% glucose solutions in water. A previous study showed that lipoplexes containing a single pCMV-Luc plasmid molecule have a size of about 25 nm.[27] In our case, size measurements, confirmed by TEM experiments, showed very small structures of about 40 nm, containing probably two to four plasmid molecules. This would allow further development of the lipoplexes for in vivo gene delivery because the size range should permit good tissue distribution.

In vitro transfection results showed that gene transfection potency is improved by photopolymerization, and as observed for agarose gel electrophoresis experiments, the best results are obtained for N/P 5, especially for M_8, which is considerably less toxic than M_4. This is expected since, at any given N/P ratio, the triamine M_8 concentration is only one-third of the monoamine M_4 concentration. At the optimal N/P ratio in 5% glucose solution, M_4P_{1h} and M_8P_{1h} transfection efficiencies are comparable, in serum-free serum conditions, to that of JetSi-ENDO, a cationic lipid transfection reagent. Synthesis of new amphiphilic molecules designed to be more effective for *in vivo* use, with poly(ethylene glycol) groups and targeting ligands, for example, should improve the robustness of our system.

In summary, we have prepared new cationic polydiacetylene micelles, with a reasonable *in vitro* gene transfection efficiency, and shown that photopolymerization significantly improves their transfection potency. These micelles are small, and their modular structure could lead to further developments. The use of functionalizable polar headgroups, for example, could allow addition of targeting ligands and/or poly(ethylene glycol). Alkyne polar headgroup could also lead to postfunctionalization by click-chemistry.

■ ASSOCIATED CONTENT

Supporting Information. Characterization and NMR spectra of compounds, UV/visible spectra, DLS experiments, TEM images and gene transfer experiments. This material is available free of charge via the Internet at http://pubs.acs.org.

■ AUTHOR INFORMATION

Corresponding Author

*remy@bioorga.u-strasbg.fr, wagner@bioorga.u-strasbg.fr.

■ ACKNOWLEDGMENT

We thank Christine Ruhlmann from the Structural Biology and Genomics Department of IGBMC for her help with TEM. E.M. received a grant from MESR.

■ REFERENCES

(1) Shimizu, T., Masuda, M., and Minamikawa, H. (2005) Supramolecular nanotube architectures based on amphiphilic molecules. *Chem. Rev. 105*, 1401–1444.

(2) Fuhrhop, J.-H., and Wang, T. (2004) Bolaamphiphiles. *Chem. Rev 104*, 2901–2938.
(3) Morin, E., Guenet, J.-M., Diaaz, D. D., Remy, J.-S., and Wagner, A. (2010) Fine-tuning the morphology of self-assembled nanostructures of propargyl ammonium-based amphiphiles. *J. Phys. Chem. B 114*, 12495–12500.
(4) Douliez, J.-P. (2005) Self-assembly of hollow cones in a bola-amphiphile/hexadiamine salt solution. *J. Am. Chem. Soc. 127*, 15694–15695.
(5) Richard, C., Balavoine, F., Schultz, P., Ebbesen, T. W., and Mioskowski, C. (2003) Supramolecular self-assembly of lipid derivatives on carbon nanotubes. *Science 300*, 775–778.
(6) Lasic, D. D., and Templeton, N. S. (1996) Liposomes in gene therapy. *Adv. Drug Delivery Rev. 20*, 221–266.
(7) Miller, A. D. (1998) Cationic liposomes for gene therapy. *Angew. Chem., Int. Ed. 37*, 1768–1785.
(8) Dauty, E., Remy, J.-S., Blessing, T., and Behr, J.-P. (2001) Dimerizable cationic detergents with a low cmc condense plasmid DNA into nanometric particles and transfect cells in culture. *J. Am. Chem. Soc. 123*, 9227–9234.
(9) Behr, J. P. (1993) Synthetic gene-transfer vectors. *Acc. Chem. Res. 26*, 274–278.
(10) Wong, F. M. P., Reimer, D. L., and Bally, M. B. (1996) Cationic lipid binding to DNA: characterization of complex formation. *Biochemistry 35*, 5756–5763.
(11) Zuidam, N. J., and Barenholz, Y. (1998) Electrostatic and structural properties of complexes involving plasmid DNA and cationic lipids commonly used for gene delivery. *Biochim. Biophys. Acta 1368*, 115–128.
(12) Durairaj, B., and Blum, F. D. (1989) Synthesis and dynamics of oligomeric micelles. *Langmuir 5*, 370–372.
(13) Cochin, D., Candau, F., and Zana, R. (1993) Photopolymerization of micelle-forming monomers. 1. Characterization of the systems before and after polymerization. *Macromolecules 26*, 5755–5764.
(14) Tomatsu, I., Hashidzume, A., and Harada, A. (2009) Photopolymerization of amphiphilic N,O-diacylated serine-based monomers in their micellar states for an encapsulation. *Macromol. Chem. Phys. 210*, 1640–1646.
(15) O'Reilly, R. K., Hawker, C. J., and Wooley, K. L. (2006) Cross-linked block copolymer micelles: functional nanostructures of great potential and versatility. *Chem. Soc. Rev. 35*, 1068–1083.
(16) Zhou, W., Li, Y., and Zhu, D. (2007) Progress in polydiacetylene nanowires by self-assembly and selfpolymerization. *Chem. Asian J. 2*, 222–229.
(17) Thauvin, C., Rickling, S., Schultz, P., Celia, H., Meunier, S., and Mioskowski, C. (2008) Carbon nanotubes as templates for polymerized lipid assemblies. *Nat. Nanotechnol. 3*, 743–748.
(18) Lee, J., Jun, H., and Kim, J. (2009) Polydiacetylene−liposome microarrays for selective and sensitive mercury(II) detection. *Adv. Mater. 21*, 3674–3677.
(19) Lee, J., Kim, H.-J., and Kim, J. (2008) Polydiacetylene liposome arrays for selective potassium detection. *J. Am. Chem. Soc. 130*, 5010–5011.
(20) Sarkar, A., Okada, S., Matsuzawa, H., Matsuda, H., and Nakanishi, H. (2000) Novel polydiacetylenes for optical materials: beyond the conventional polydiacetylenes. *J. Mater. Chem. 10*, 819–828.
(21) Perino, A., Klymchenko, A., Morere, A., Contal, E., Rameau, A., Guenet, J.-M., Mély, Y., and Wagner, A. (2011) Structure and behavior of polydiacetylene-based micelles. *Macromol. Chem. Phys. 212*, 111–117.
(22) FR0802390. (2008), Les Laboratoires Servier et Commissariat à l'Energie Atomique, invs.: Ogier, J., Doris, E., Lefoulon, F., and Thomas, A.
(23) Patel, M., Vivien, E., Hauchecorne, M., Oudrhiri, N., Ramasawmy, R., Vigneron, J.-P., Lehn, P., and Lehn, J.-M. (2001) Efficient gene transfection by bisguanylated diacetylene lipid formulations. *Biochem. Biophys. Res. Commun. 281*, 536–543.
(24) Yu, G. S., Choi, H., Bae, Y. M., Kim, J., and Choi, J. S. (2008) Preparation of cationic polydiacetylene nanovesicles for in vitro gene delivery. *J. Nanosci. Nanotechnol. 8*, 5266–5270.
(25) Thauvin, C., Perino, A., Contal, E., Morin, E., Schultz, P., Meunier, S., and Wagner, A. (2011) Programmed dispersions of MWNTs in aqueous media by coating with photopolymerizable synthetic amphiphiles. *J. Phys. Chem. C 115*, 7319–7322.
(26) Tajima, K., and Aida, T. (2000) Controlled polymerizations with constrained geometries. *Chem. Commun.* 2399–2412.
(27) Blessing, T., Remy, J.-S., and Behr, J.-P. (1998) Monomolecular collapse of plasmid DNA into stable virus-like particles. *Proc. Natl. Acad. Sci.U.S.A. 95*, 1427–1431.

Supporting Information

Cationic Polydiacetylene Micelles for Gene Delivery.

Emmanuelle Morin[#†], *Marc Nothisen*[†], *Alain Wagner**[#], *and Jean-Serge Remy**[†]

[#]Systèmes chimiques fonctionnels, Laboratoire CAMB, CNRS-UDS UMR7199, Faculté de Pharmacie, Université de Strasbourg, 74 route du Rhin, BP24, 67401 Illkirch (France), [†] Laboratoire de Chimie génétique, Laboratoire CAMB, CNRS-UDS UMR7199.

remy@bioorga.u-strasbg.fr, wagner@bioorga.u-strasbg.fr

Table of Contents

A. Materials and methods

General remarks

Unless stated otherwise, all starting materials and reagents were obtained from commercial suppliers and used without further purification. All solvents were of dry grade and purchased from Aldrich. All compounds were characterized using standard analytical and spectroscopic techniques. ^{1}H and ^{13}C spectra were obtained on a Brucker Advance III instrument (BBFO+ probe). Mass spectrometry was performed on a MS Bruker (Ion Trap, HCT Ultra, ESI) and a MS Agilent (QTof 6520, ESI) spectrometer. Unless otherwise indicated, the polarity/scan type used for ESI-MS was positive. NMR chemical shifts are reported in δ units (ppm) relative to tetramethylsilane and converted to the TMS scale using the residual proton of $CDCl_3$ (7.26 ppm for ^{1}H NMR, and 76.91 for ^{13}C NMR). Data are reported as follows: multiplicity (s = singlet, d = doublet, t = triplet, q = quartet, m = multiplet, br = broad), coupling constants, integration and assignment. Merck Silica Gel 60 F_{254} plates were used for analytical thin layer chromatography. TLC analysis was facilitated by the use of the following stains in addition to UV light (254 nm) with fluorescent-indicating silica-gel plates: vanillin/EtOH, $KMnO_4/H_2O$, or Ninhydrin/EtOH. Merck Silica gel 60 (particle: 40-63 μm) was employed for column chromatography. UV/vis. absorption spectra were recorded with a Varian Cary 100 bio spectrophotometer. The extinction coefficients (ε, $M^{-1}cm^{-1}$) are given as the average value obtained from three independent measurements at different concentrations (error value ± 5%). Melting points were measured in a Stuart Scientific SMP2 melting point apparatus 2 and are uncorrected.

B. Product characterization

Pentacosa-10,12-diyn-1-ol (2)

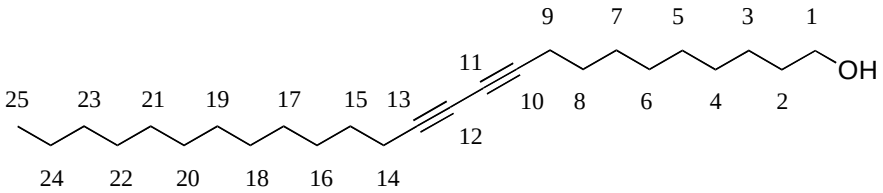

R_f = 0.32 (MeOH/CH_3Cl: 2/100); ^1H NMR (400 MHz, $CDCl_3$) δ 3.63 (t, J = 6.6 Hz, 2H, H_1), 2.24 (t, J = 7.0 Hz, 4H, $H_{9, 14}$), 1.58-1.25 (m, 34H, $H_{2-8, 15-24}$), 0.88 (t, J = 6.8 Hz, 3H, H_{25}); ^{13}C NMR (75 MHz, $CDCl_3$) δ 77.7 (1C, C_{10}), 77.6 (1C, C_{13}), 65.4 (2C, $C_{11,12}$), 63.2 (1C, C_1), 32.9 (1C, C_2), 32.1 (1C, C_{16}), 29.9-28.5 (13C, $C_{4-8,15,17-23}$), 25.9 (1C, C_3), 22.8 (1C, C_{24}), 19.4 (2C, $C_{9,14}$), 14.3 (1C, C_{25}); MS m/z (relative intensity) 360 $[M]^+$ (3.8); mp 62 ± 1 °C. UV/vis ($CHCl_3$): λ_{max} (log ε) = 244 (2.72) nm.

Pentacosa-10,12-diynyl-4-methylbenzenesulfonate (3)

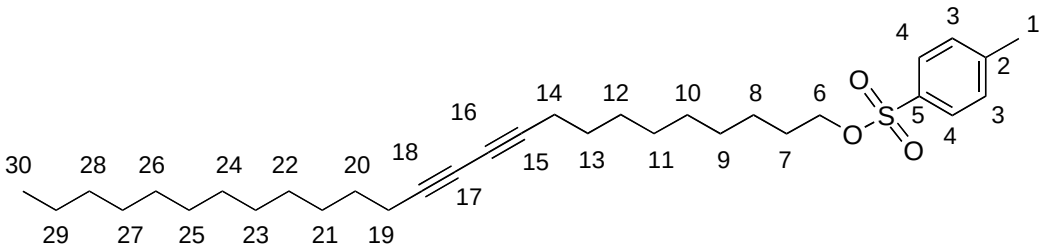

R_f = 0.68 (EtOAc/cyclohexane: 2/8); ^1H NMR (400 MHz, $CDCl_3$) **δ** 7.79 (dd, J_1 = 6.4 Hz, J_2 = 2.0 Hz, 2H, H_4), 7.34 (dd, J_1 = 8.4 Hz, J_2 = 0.8 Hz, 2H, H_3), 4.02 (t, J = 6.6 Hz, 2H, H_6), 2.45 (s, 3H, H_1), 2.23 (t, J = 7.2 Hz, 4H, $H_{14,19}$), 1.64 (m, 34H, $H_{5-13,20-29}$), 0.88 (t, J = 7.0 Hz, 3H, H_{30}); ^{13}C NMR (75 MHz, $CDCl_3$) δ 144.7 (1C, C_2), 133.47 (1C, C_5), 129.9 (2C, C_3), 128.0 (2C, C_2), 77.8 (1C, C_{15}), 77.6 (1C, C_{18}), 70.8 (1C, C_6), 65.5 (1C, C_{16}), 65.4 (1C, C_{17}), 32.1 (1C, C_{21}), 31.3 (1C, C_7), 29.9-28.4 (13C, $C_{9-13,20,,22-28}$), 25.4 (1C, C_8), 22.8 (1C, C_{29}), 21.8 (1C, C_1), 19.4 (2C, $C_{14,19}$), 14.3 (1C, C_{30}); MS m/z (relative intensity) 537 $[M+Na]^+$ (100); mp 56 ± 1 °C. UV/vis ($CHCl_3$): λ_{max} (log ε) = 241 (2.90) nm.

N,N-Diethyl-pentacosa-10,12-diyn-1-amine (4)

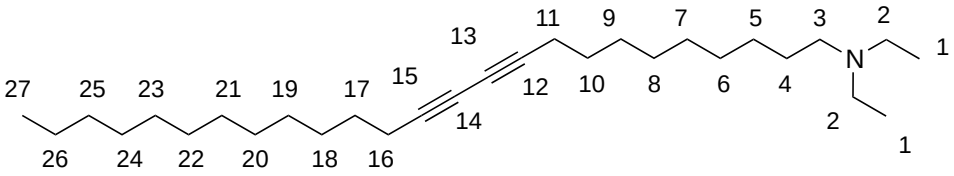

^{1}H NMR (400 MHz, $CDCl_3$) δ 2.51 (q, J = 7.5 Hz, 4H, H_2), 2.39 (t, J = 7.8 Hz, 2H, H_3), 2.23 (t, J = 7.0 Hz, 4H, $H_{11,16}$), 1.52-1.25 (m, 34H, $H_{4\text{-}10,17\text{-}26}$), 1.01 (t, J = 7.1 Hz, 6H, H_1), 0.88 (t, J = 6.9 Hz, 3H, H_{27}); ^{13}C NMR (75 MHz, $CDCl_3$) δ 77.5 (2C, $C_{12,15}$), 65.4 (2C, $C_{13,14}$), 53.1 (1C, C_3), 46.9 (2C, C_2), 31.9 (1C, C_{18}), 29.7-27.0 (15C, $C_{4\text{-}10,17,19\text{-}25}$), 22.7 (1C, C_{26}), 19.2 (2C, $C_{11,16}$), 14.1 (1C, C_{27}), 11.7 (2C, C_1); MS m/z (relative intensity) 416 $[M+H]^+$ (100). UV/vis ($CHCl_3$): λ_{max} (log ε) = 243 (2.43) nm.

4-(2-Aminoethyl)-1,7-bis(tert-butoxycarbonyl)-1,4,7-triazaheptane (6)

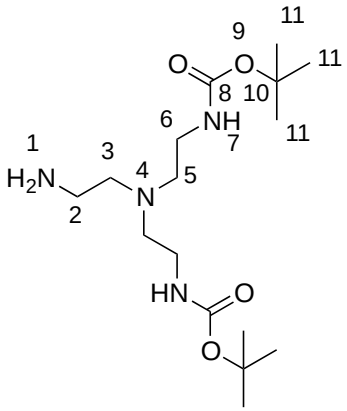

^{1}H NMR (400 MHz, $CDCl_3$) δ 3.16 (m, 4H, H_6), 2.72 (t, J = 5.8 Hz, 2H, H_2), 2.54 (t, J = 6.0 Hz, 4H, H_5), 2.49 (t, J = 6.0 Hz, 2H, H_3), 1.43 (s, 18H, H_{11}); ^{13}C NMR (75 MHz, $CDCl_3$) δ 156.3 (2C, C_8), 79.3 (2C, C_{10}), 57.1 (1C, C_3), 54.4 (2C, C_5), 40.0 (2C, C_6), 38.8 (1C, C_2), 28.6 (6C, C_{11}); MS m/z (relative intensity) 347 $[M+H]^+$ (100).

di-*tert*-butyl (((2-(tetracosa-10,12-diynamido)ethyl)azanediyl)bis(ethane-2,1-diyl))dicarbamate (7)

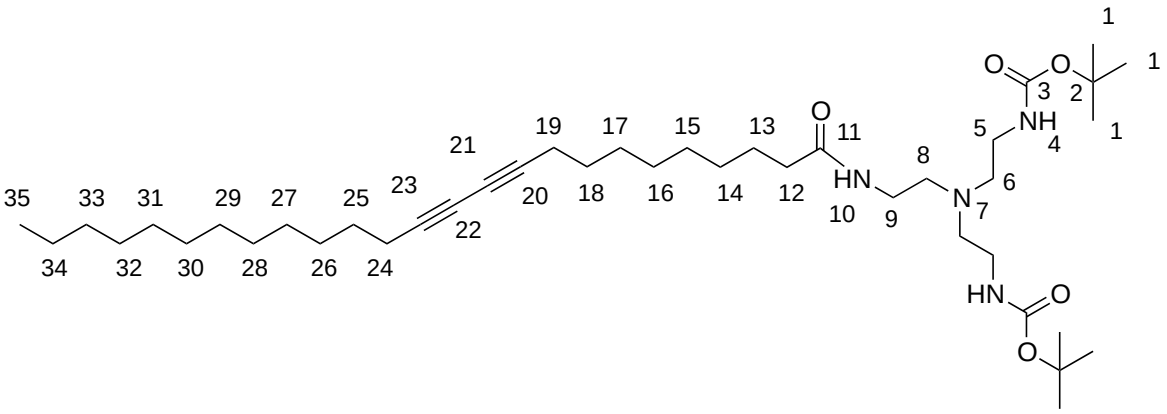

^{1}H NMR (400 MHz, $CDCl_3$) δ 6.81 (br s, 1H, H_{10}), 5.06 (br s, 2H, H_4), 3.27 (q, J = 5.3 Hz, 2H, H_{12}), 3.14 (q, J = 4.6 Hz, 4H, H_5), 2.55 (t, J = 5.6 Hz, 2H, H_8), 2.50 (t, J = 5.4 Hz, 4H, H_6), 2.25-2.21 (m, 6H, $H_{19,24,9}$), 1.44 (s, 18H, H_1), 1.39-1.23 (m, 32H, $H_{13\text{-}18,25\text{-}34}$), 0.87 (t, 6.8 Hz, 3H, H_{35}); ^{13}C NMR (75 MHz, $CDCl_3$) δ 173.8 (1C, C_{11}), 156.6 (2C, C_3), 79.5 (2C, C_2), 77.7 (2C, $C_{20,23}$), 65.4 (2C, $C_{21,22}$), 55.1 (2C, C_6), 54.2 (1C, C_8), 39.1 (1C, C_5), 37.5 (1C, C_9), 36.5 (1C, C_{12}), 32.0 (1C, C_{26}), 29.7-28.5 (12C, $C_{14\text{-}18,25,27\text{-}33}$), 28.6 (6C, C_1), 25.9 (1C, C_{13}), 22.8 (1C, C_{34}), 19.3 (2C, $C_{19,24}$), 14.2 (1C,C_{35}); MS m/z (relative intensity) 704 $[M+H]^+$ (100).

***N*-(2-(bis(2-aminoethyl)amino)ethyl)tetracosa-10,12-diynamide (8)**

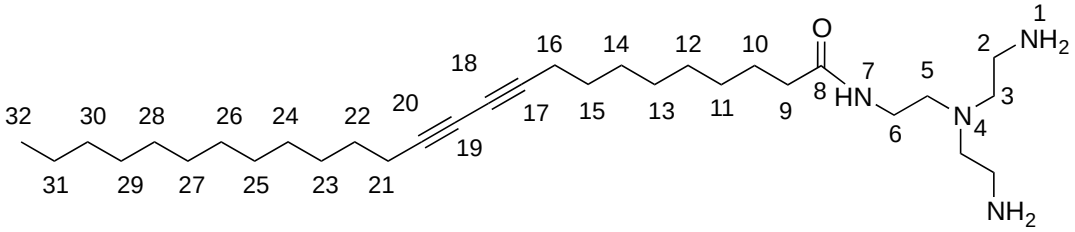

^{1}H NMR (400 MHz, $CDCl_3$) δ 7.06 (br s, 1H, H_7), 3.31 (q, J= 5.2 Hz, 2H, H_9), 2.79 (t, J = 5.8 Hz, 4H, H_2), 2.60 (t, J = 6.0 Hz, 2H, H_5), 2.56 (t, J = 5.8 Hz, 4H, H_3), 2.24 (t, J = 7.0 Hz, 4H, $H_{16,21}$), 2.16 (t, J = 7.6 Hz, 2H, H_6), 2.06 (br s, 4H, H_1), 1.62-1.22 (m, 32H, $H_{10\text{-}15,22\text{-}31}$), 0.88 (t, 7.0 Hz, 3H, H_{32}); ^{13}C NMR (75 MHz, $CDCl_3$) δ 77.8 (2C, $C_{17,20}$), 65.4 (2C, $C_{18,19}$), 56.8 (2C, C_3), 53.5 (1C, C_5), 39.7 (2C, C_2), 36.8 (1C, C_6), 32.1 (1C, C_{23}), 29.8-28.5 (15C, $C_{9,11\text{-}15,22,24\text{-}31}$), 26.0 (1C, C_{10}), 22.8 (1C, C_{31}), 19.3 (2C, $_{C16,21}$), 14.3 (1C, C_{32}) ; HRMS m/z (relative intensity) 503.5 $[M+H]^+$ (100).

C. NMR Spectra

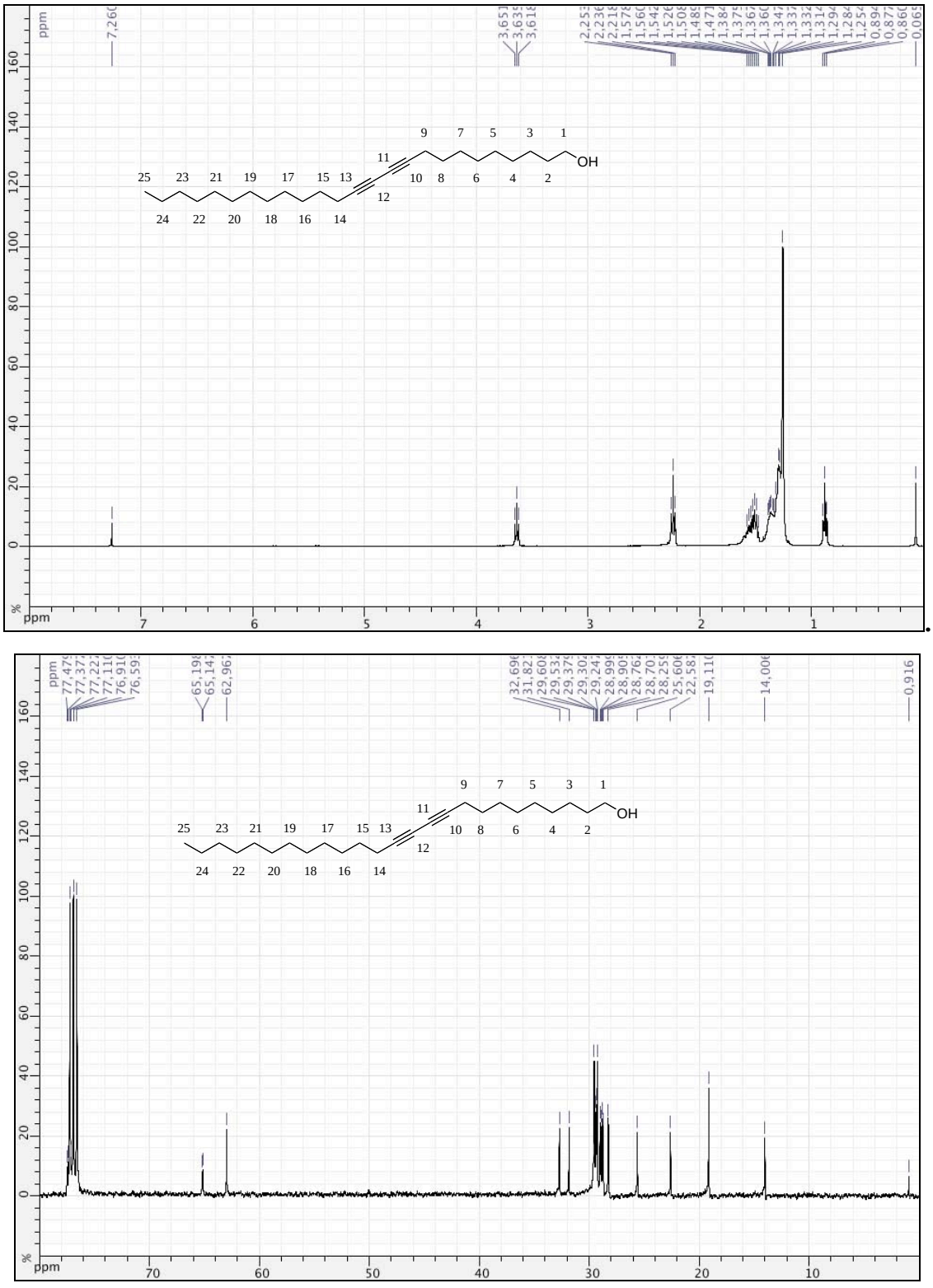

Figure S1. ^{1}H and ^{13}C NMR spectra of compound 2

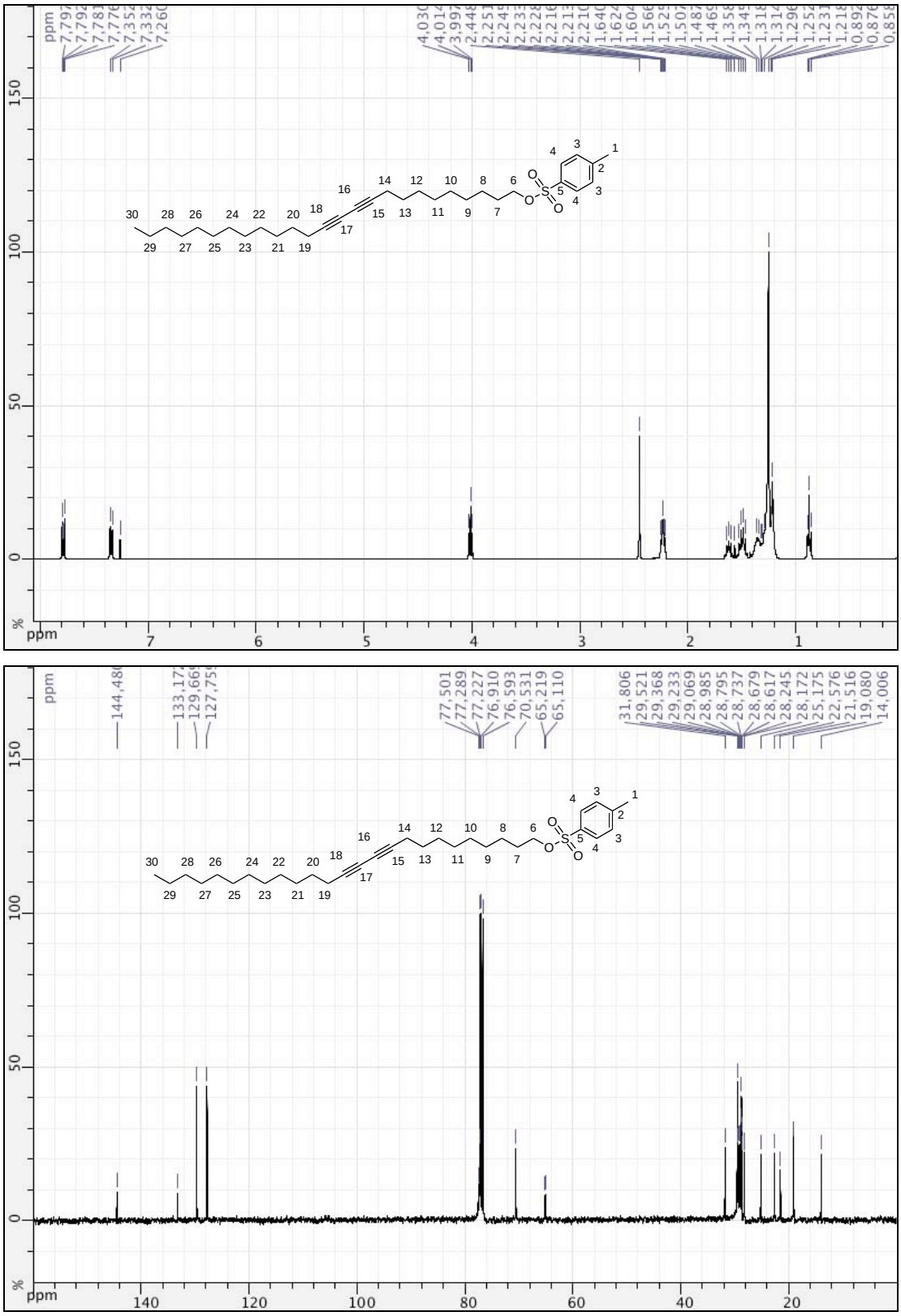

Figure S2. ^{1}H and ^{13}C NMR spectra of compound 3

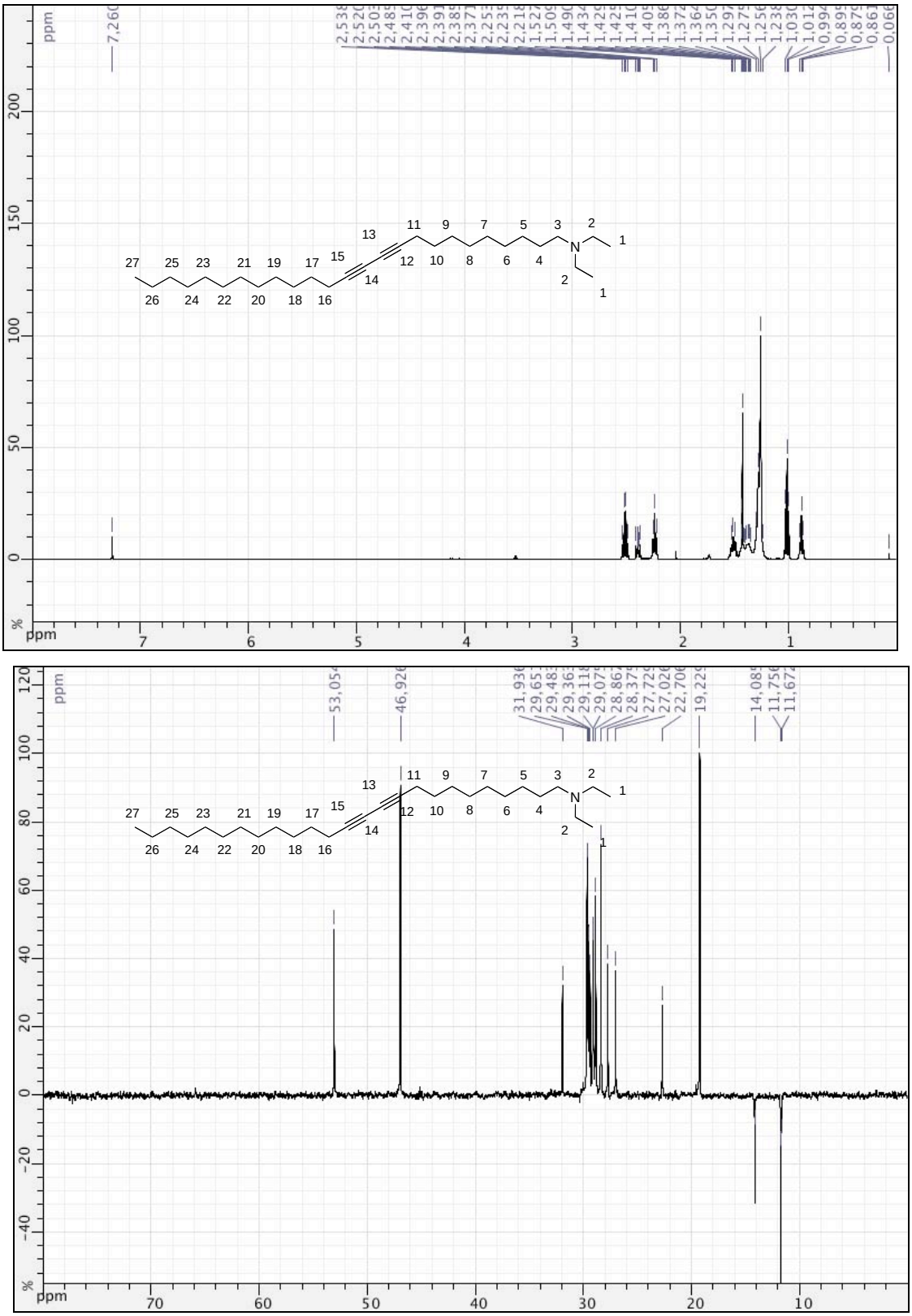

Figure S3. ^{1}H and ^{13}C NMR spectra of compound 4

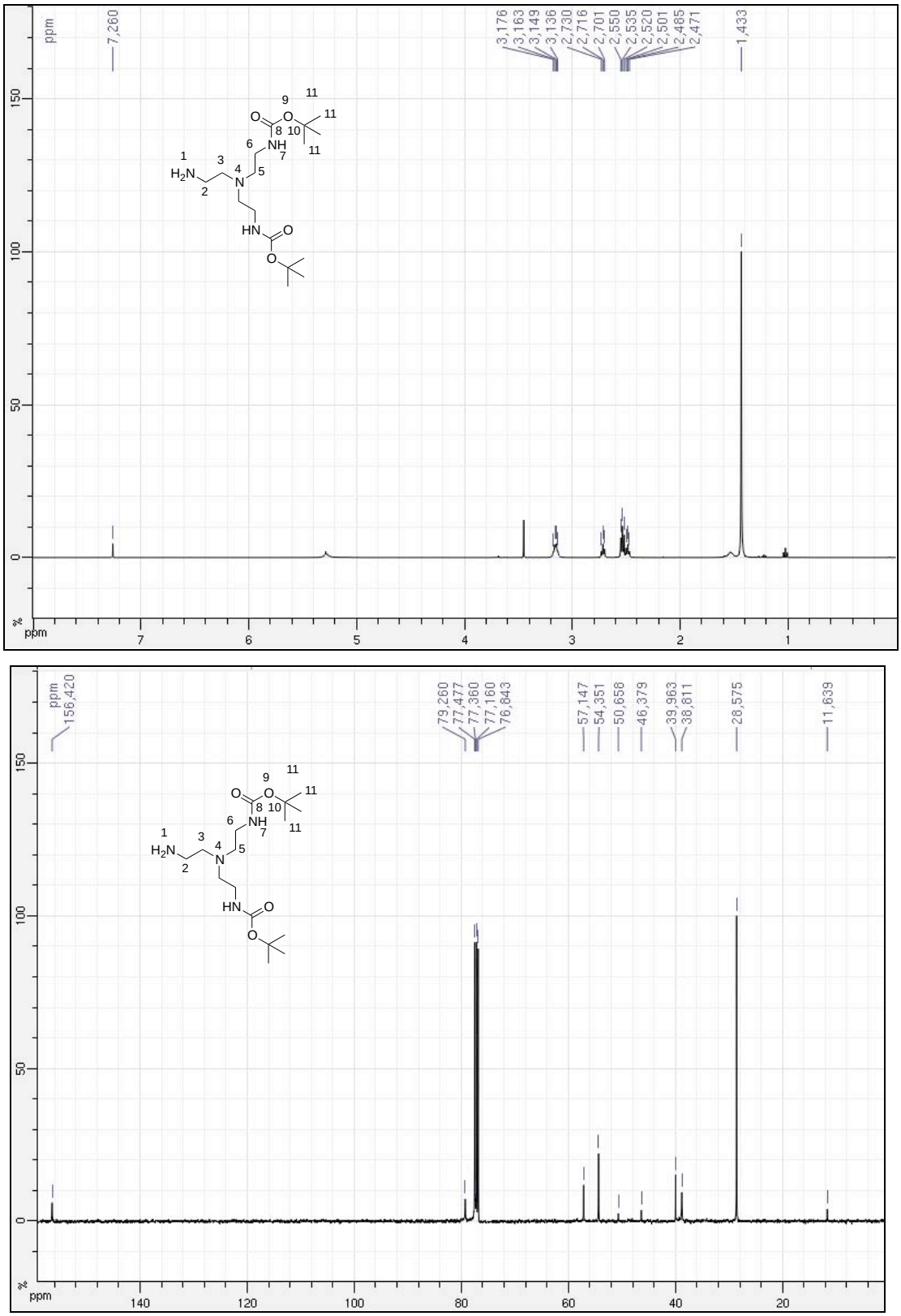

Figure S4. ^{1}H and ^{13}C NMR spectra of compound 6

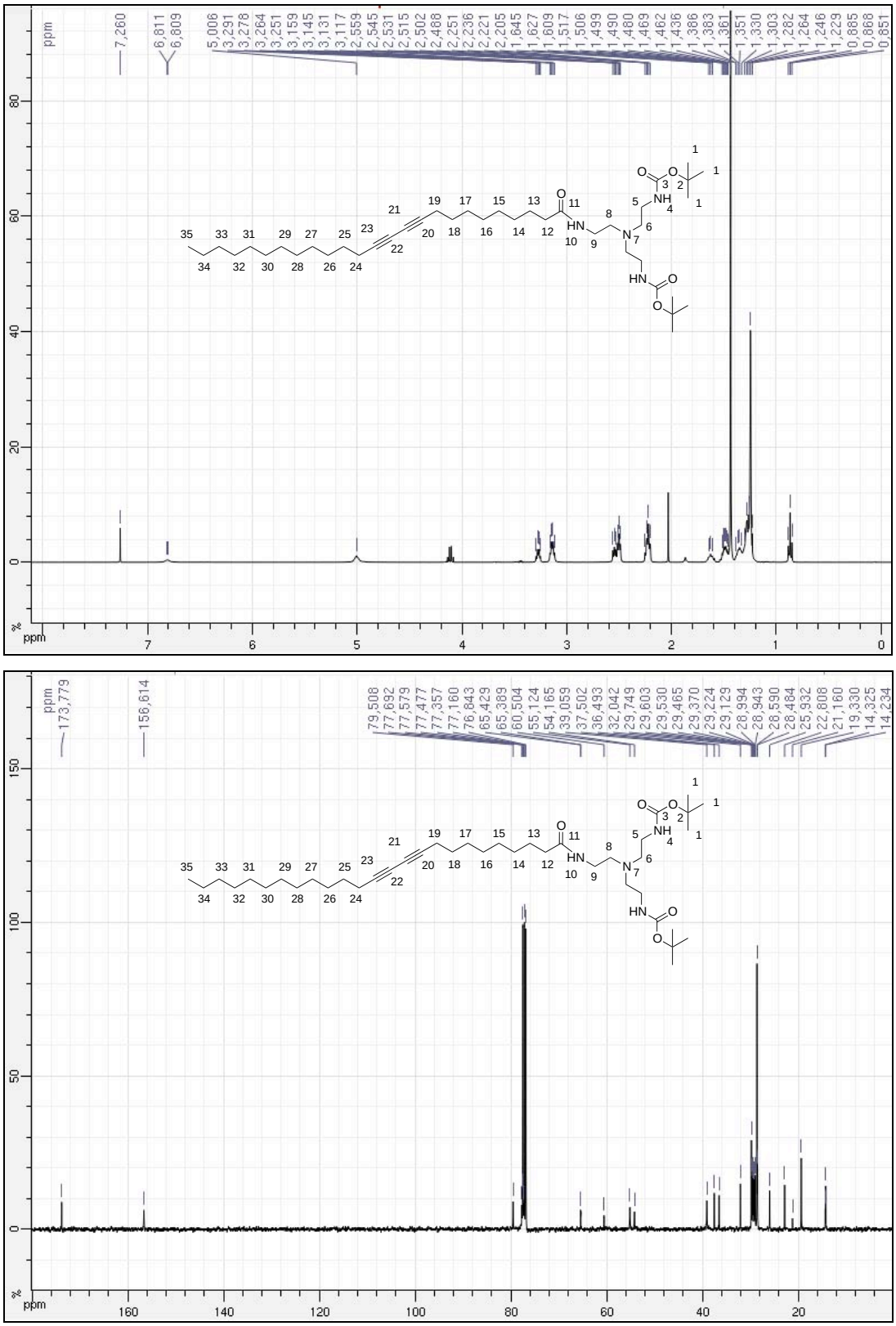

Figure S5. ^{1}H and ^{13}C NMR spectra of compound 7

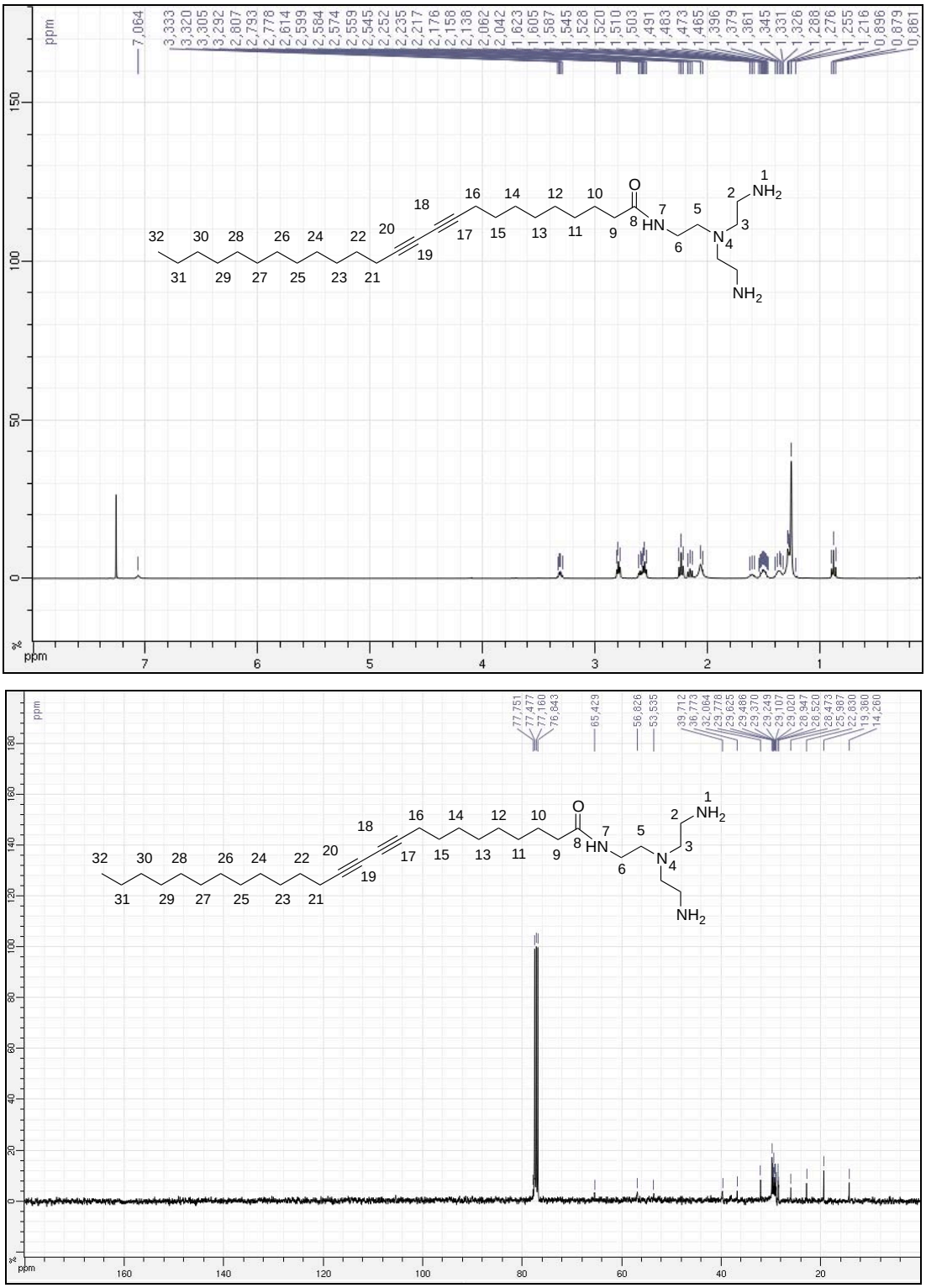

Figure S6. ^{1}H and ^{13}C NMR spectra of compound 8

D. Micelles

CMC measurements

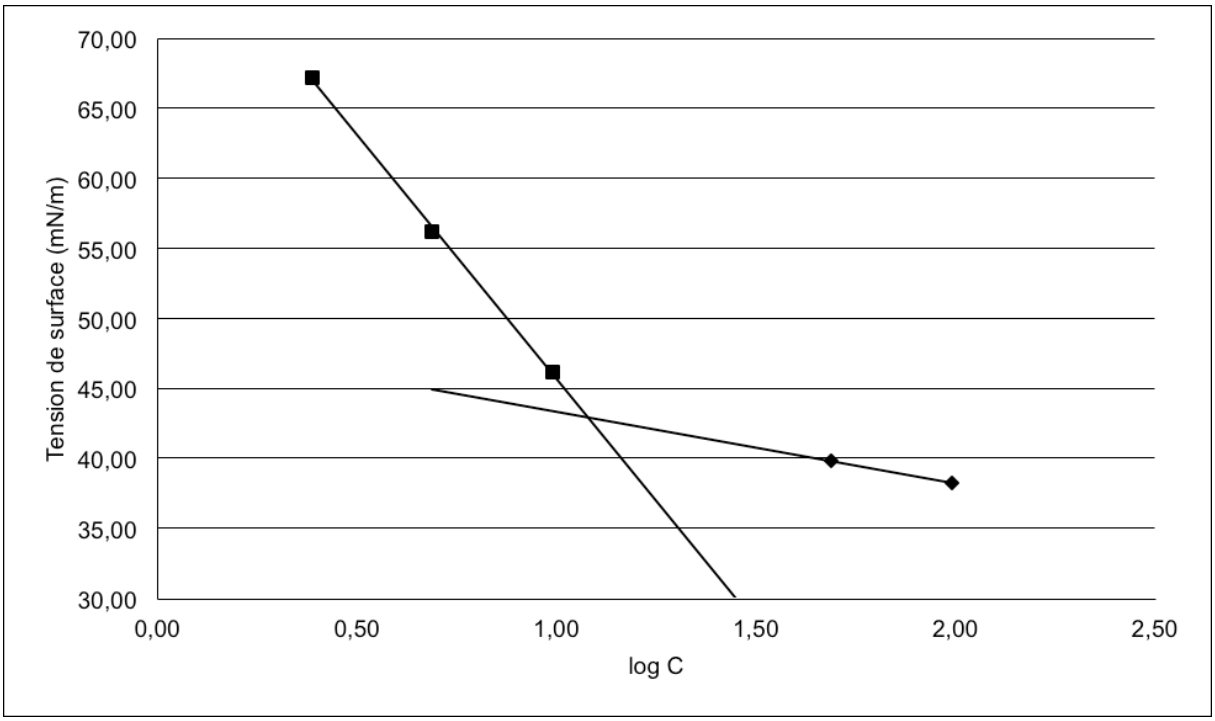

Figure S7. Surface Tension measurements of M_4NP solutions.

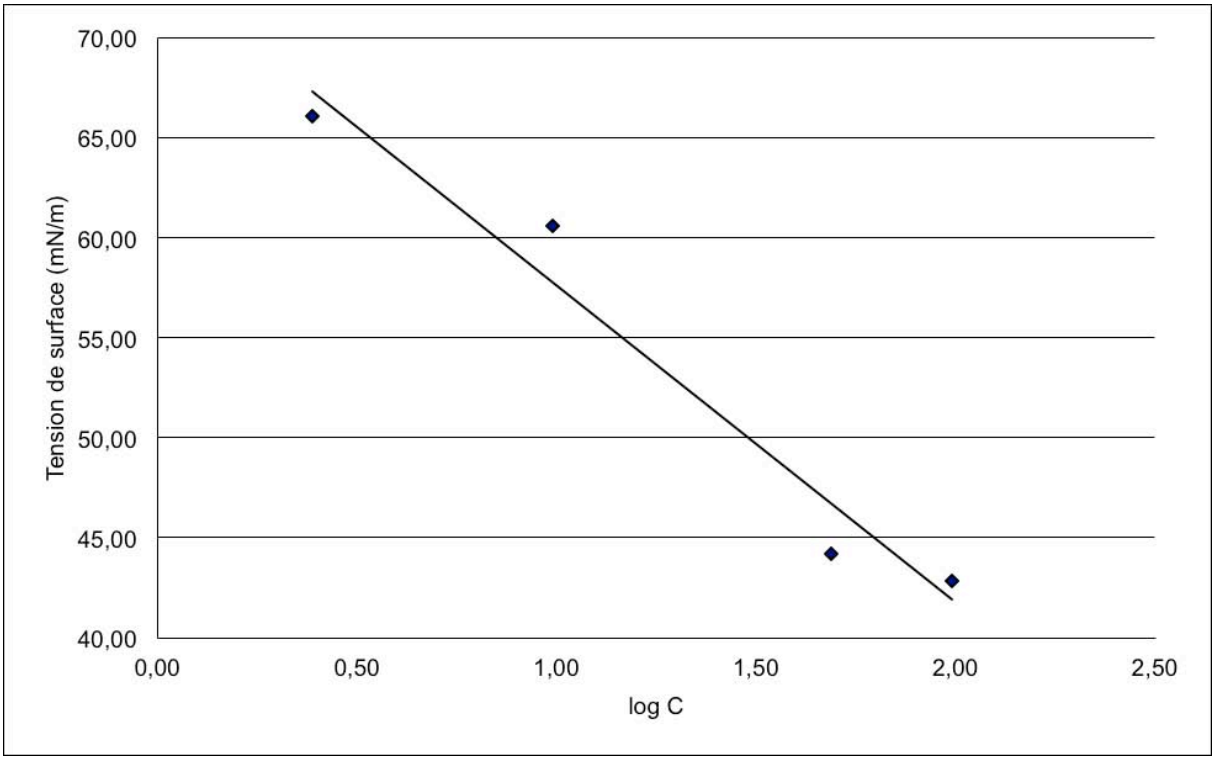

Figure S8. Surface Tension measurements of M_4P_{1h} solutions.

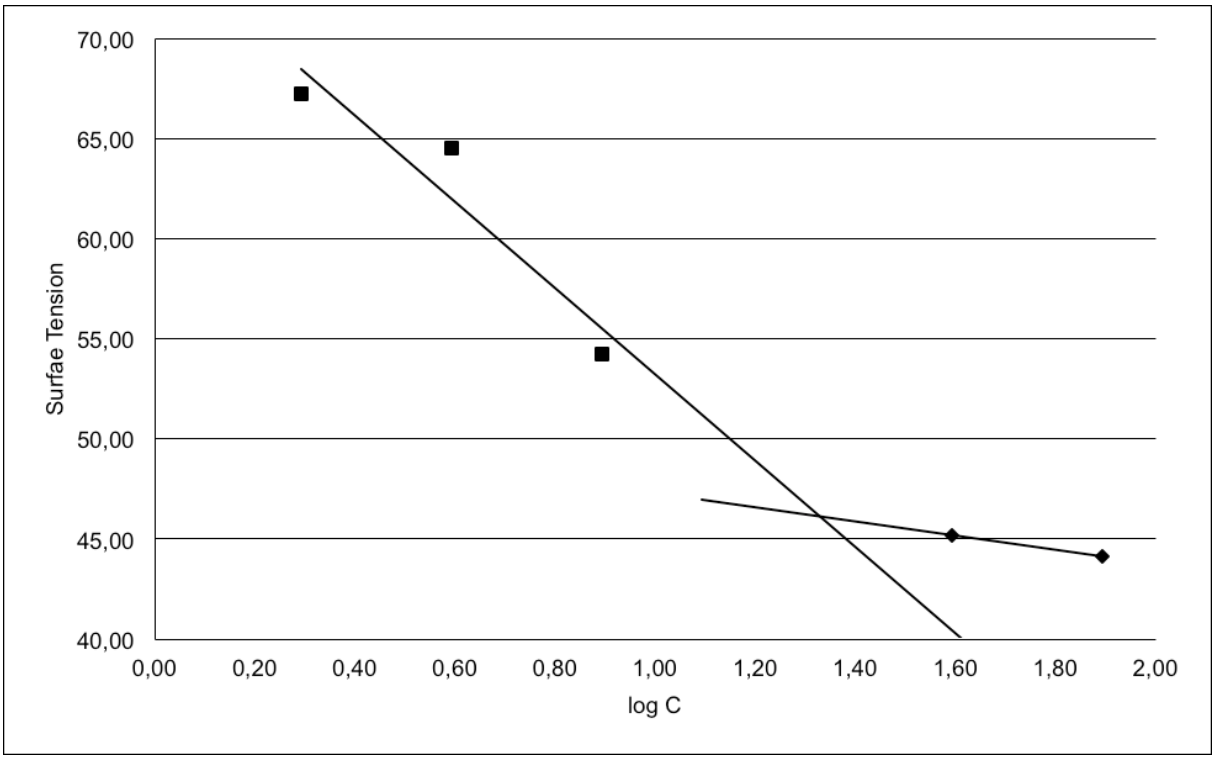

Figure S9. Surface Tension measurements of M_8NP solutions.

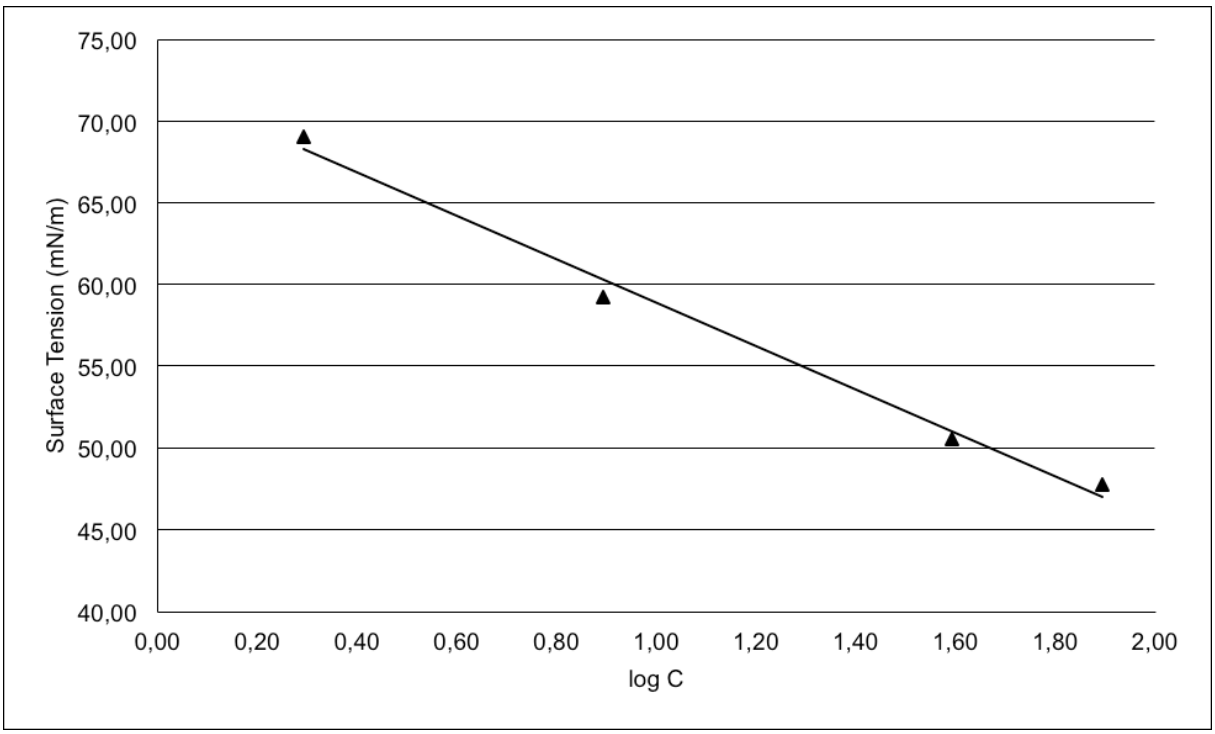

Figure S8. Surface Tension measurements of M_8P_{1h} solutions.

Polymerization.

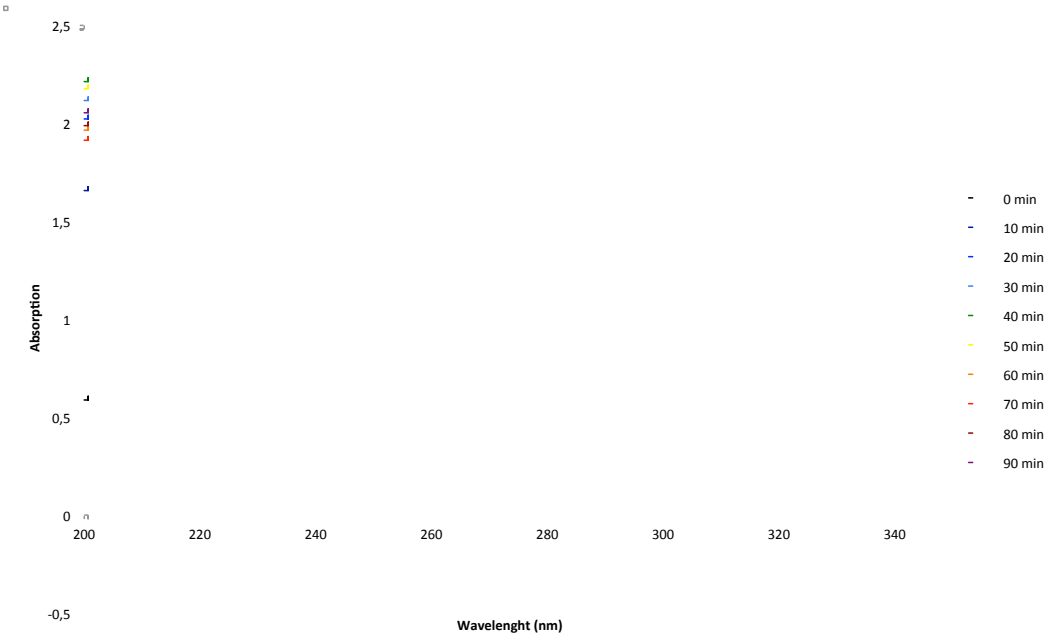

Figure S7. UV-Vis spectra of M_4 solutions (C = 0.25 mg/mL) with increasing photopolymerization time (0 – 90 minutes).

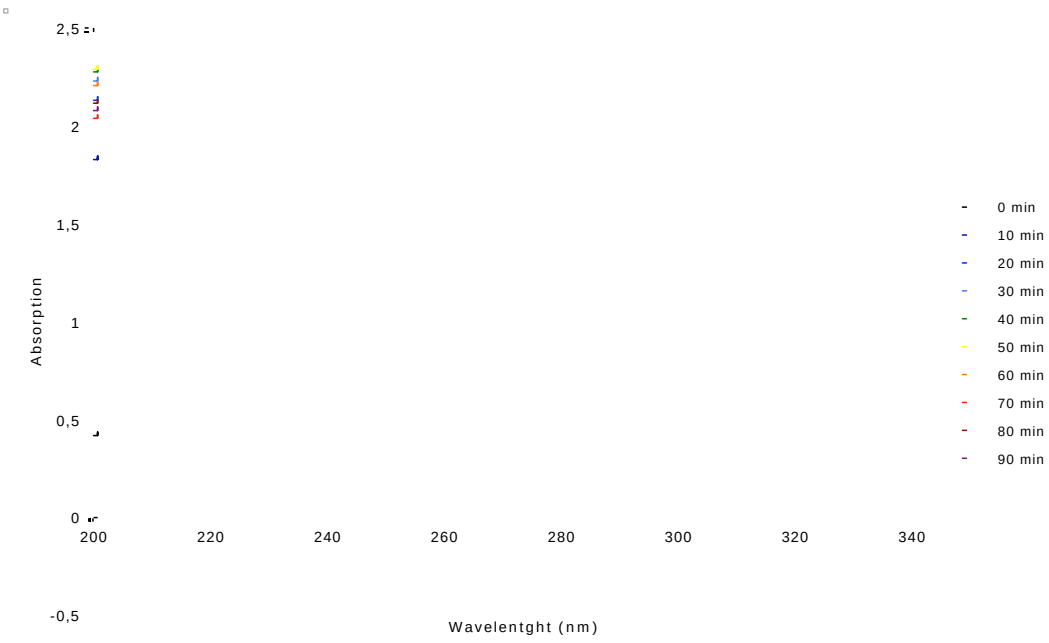

Figure S8. UV-Vis spectra of M_8 solutions (C = 0.25 mg/mL) with increasing photopolymerization time (0 – 90 minutes).

DLS, ζ potential.

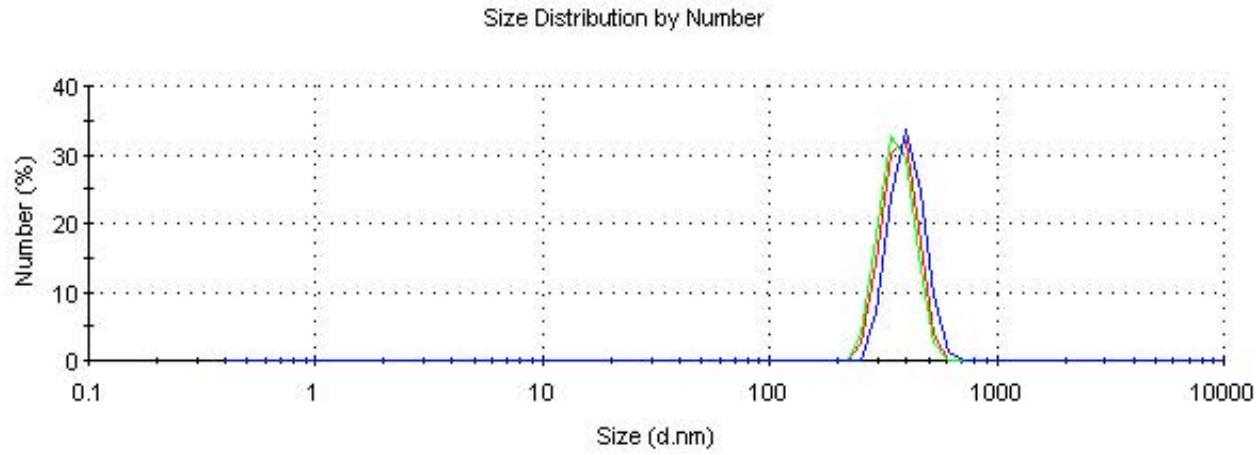

Figure S9. Size distribution of M_4NP at 1 mg/mL in 0.1 M phosphate buffer.

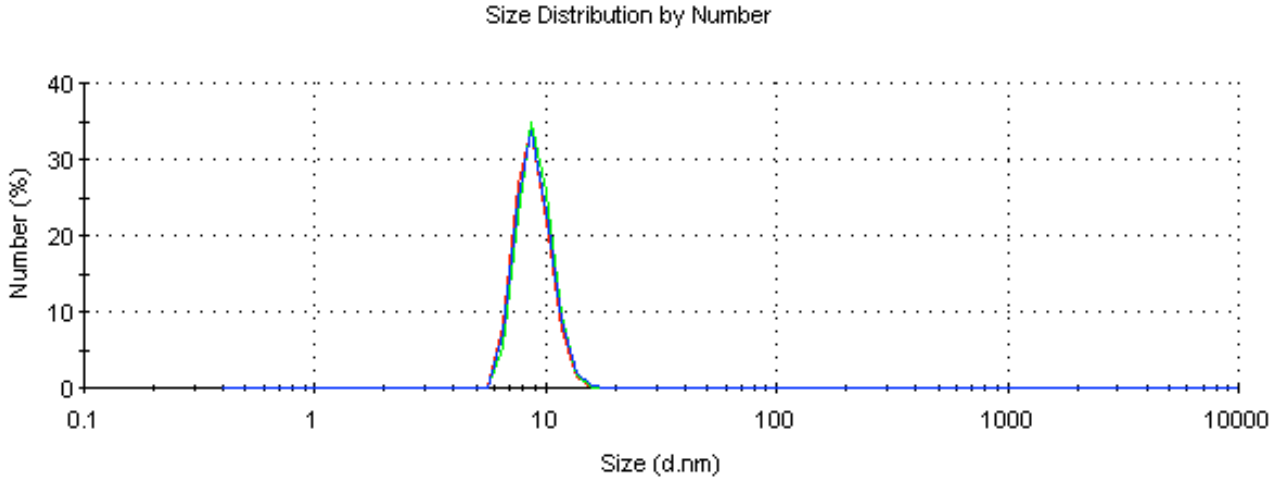

Figure S10. Size distribution of M_4NP at 0.25mg/mL in 0.1 M acetate buffer

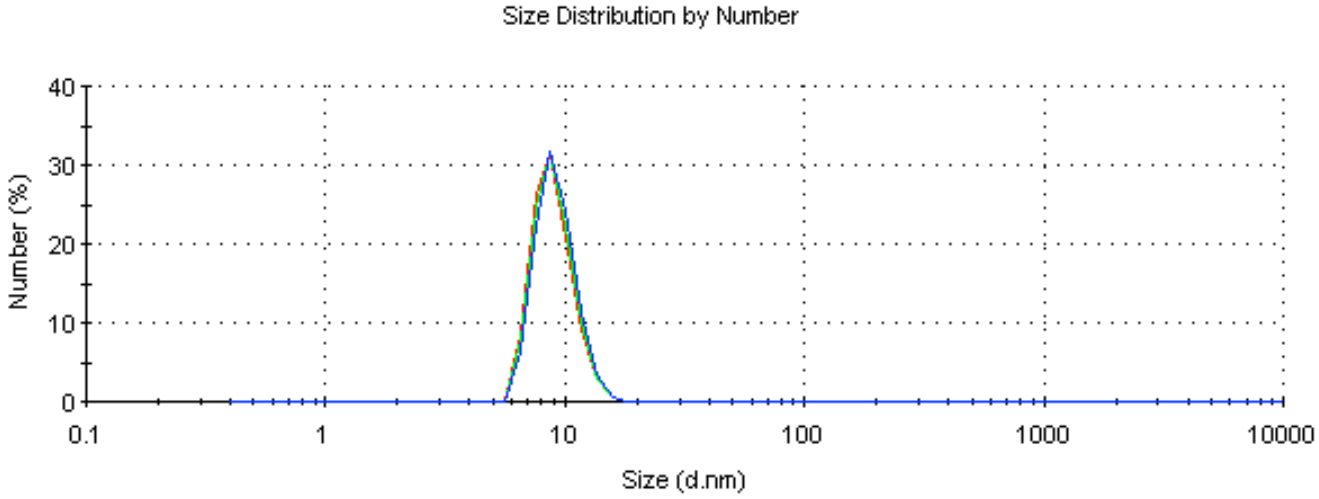

Figure S11. Size distribution of M_4P_{1h} at 0.25mg/mL in 0.1 M acetate buffer

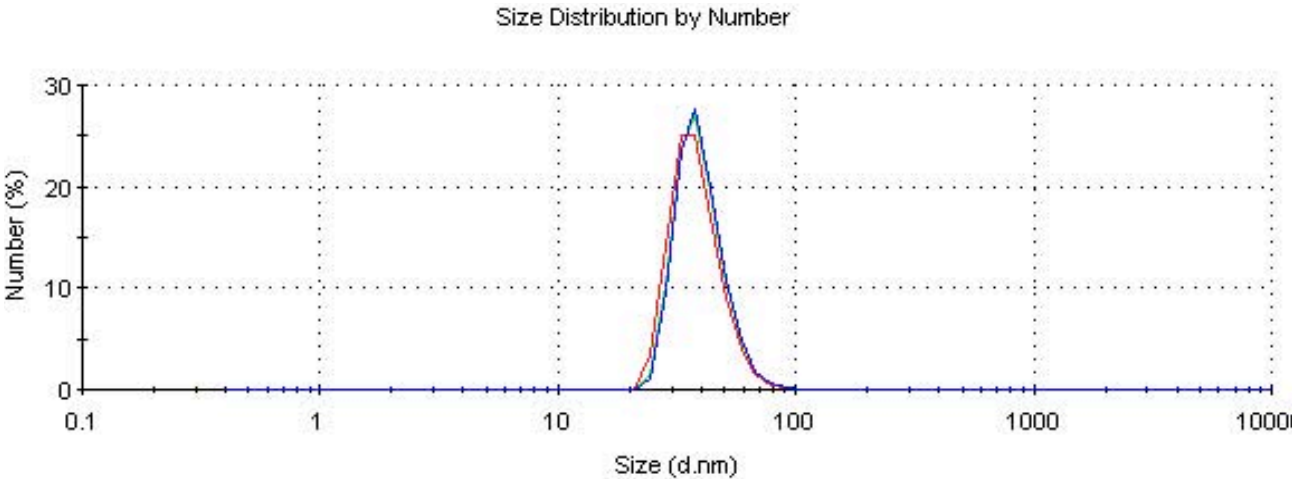

Figure S12. Size distribution of M_4P_{5h} at 0.25mg/mL in 0.1 M acetate buffer

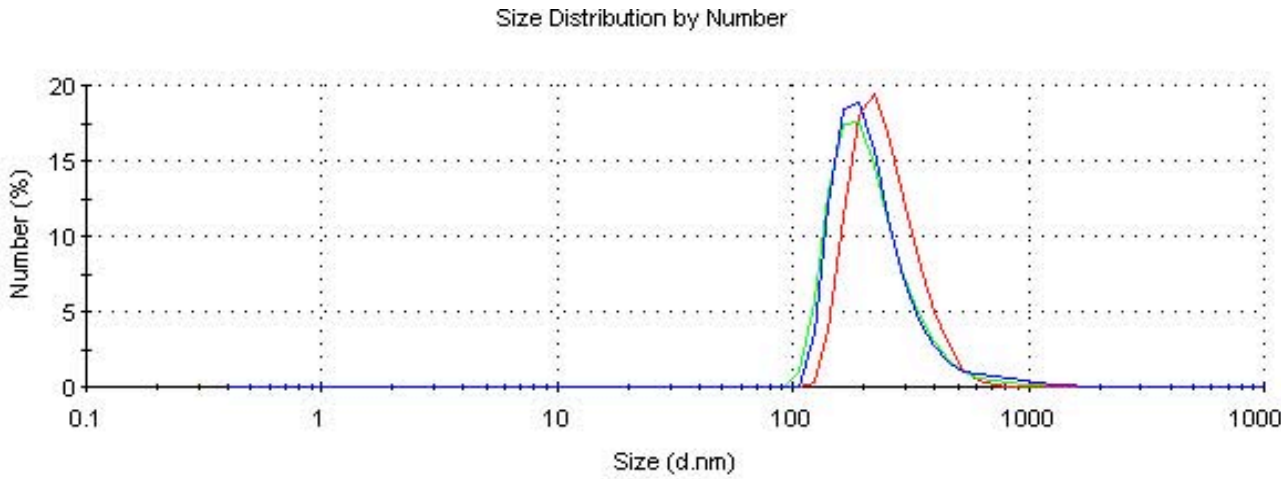

Figure S13. Size distribution of M_4P_{7h} at 0.25mg/mL in 0.1 M acetate buffer

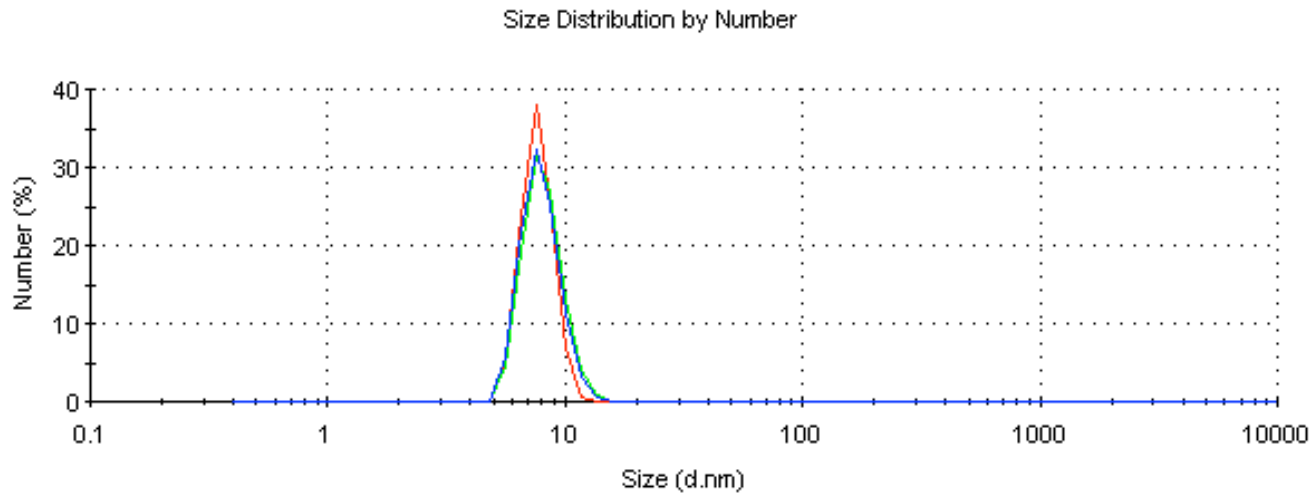

Figure S14. Size distribution of M_8NP at 0.25mg/mL in 0.1 M acetate buffer

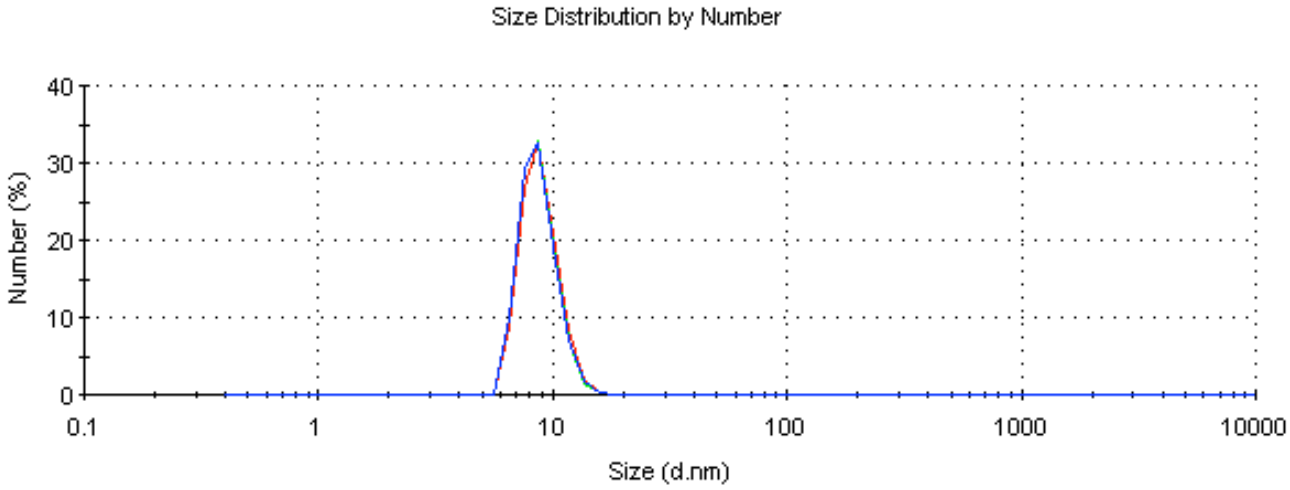

Figure S15. Size distribution of M_8P_{1h} at 0.25mg/mL in 0.1 M acetate buffer

Electron microscopy analysis.

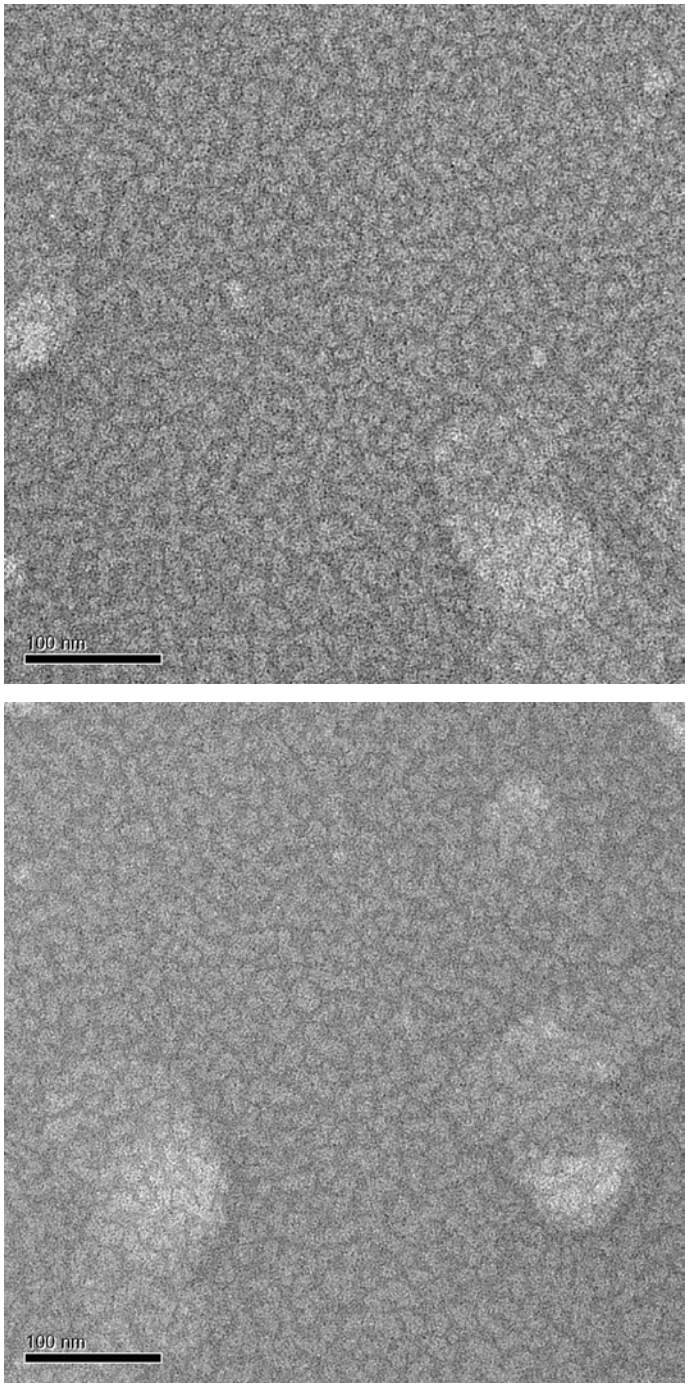

Figure S16. TEM images of M_4NP at 0.25 mg/mL in 0.1 M acetate buffer.

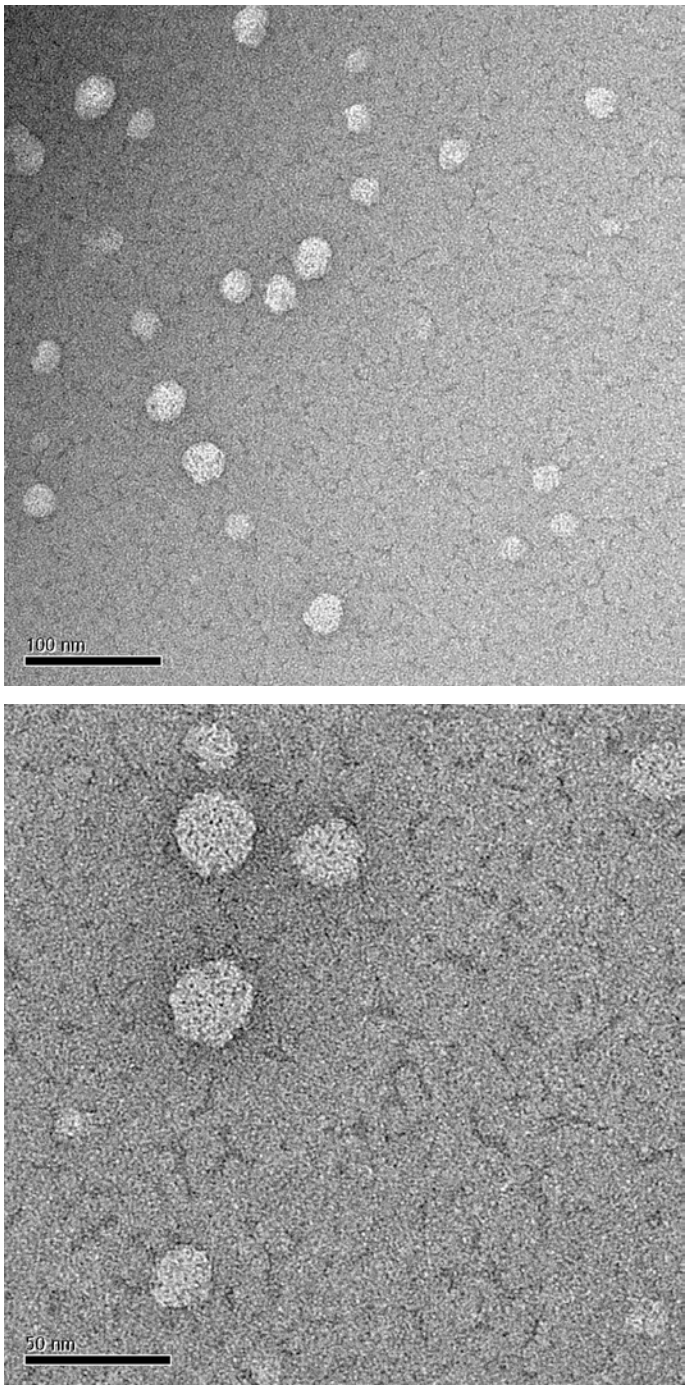

Figure S17. TEM images of M_4P_{1h} at 0.25 mg/mL in 0.1 M acetate buffer.

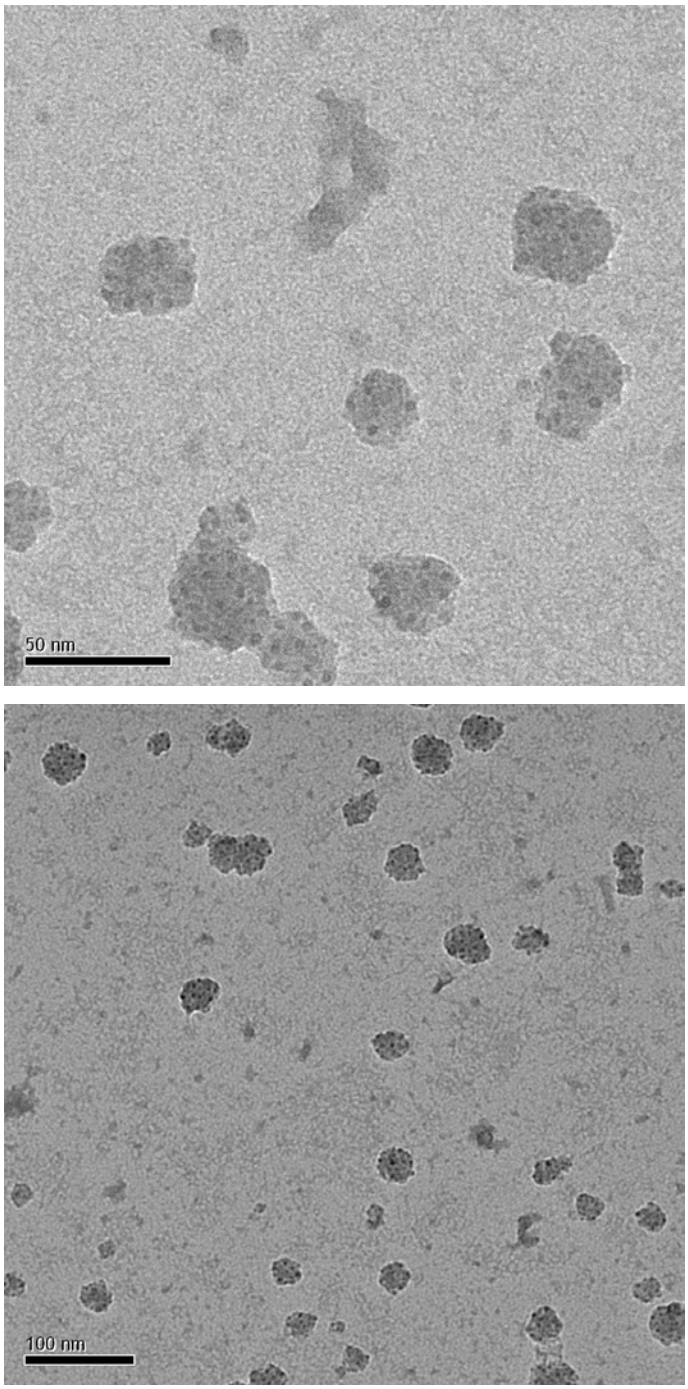

Figure S18. TEM images of M_4P_{1h} diluted to 0.025 mg/mL in 0.1 M PBS buffer.

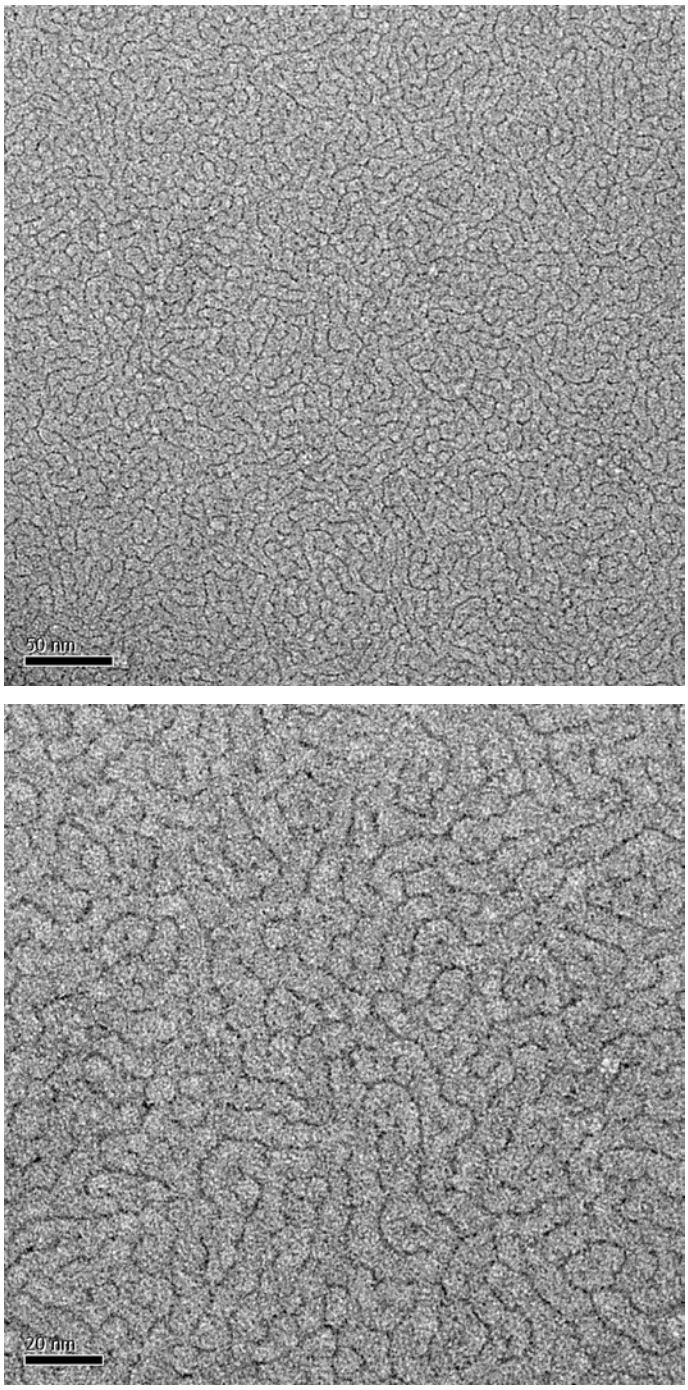

Figure S19. TEM images of M_8NP at 0.25 mg/mL in 0.1 M acetate buffer.

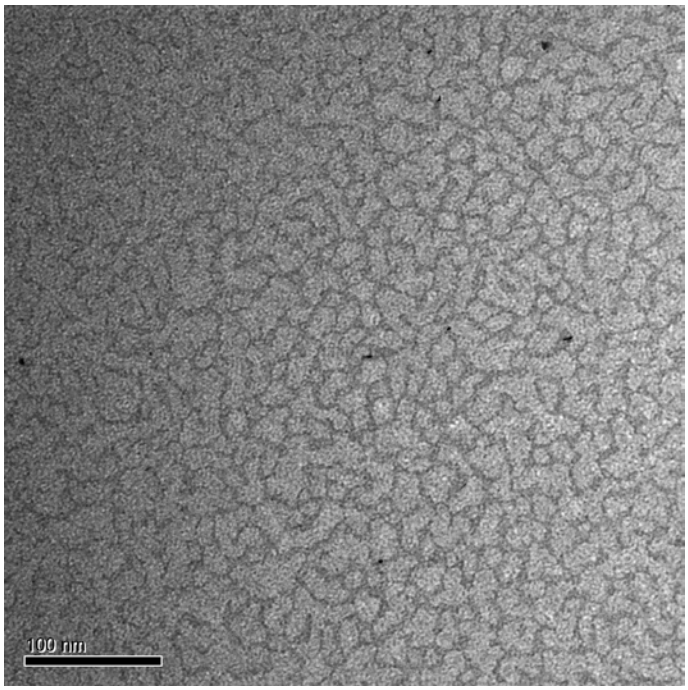

Figure S20. TEM images of M_8P_{1h} at 0.25 mg/mL in 0.1 M acetate buffer.

E. Micelle/pCMV-Luc lipoplexes

DLS, ζ potential.

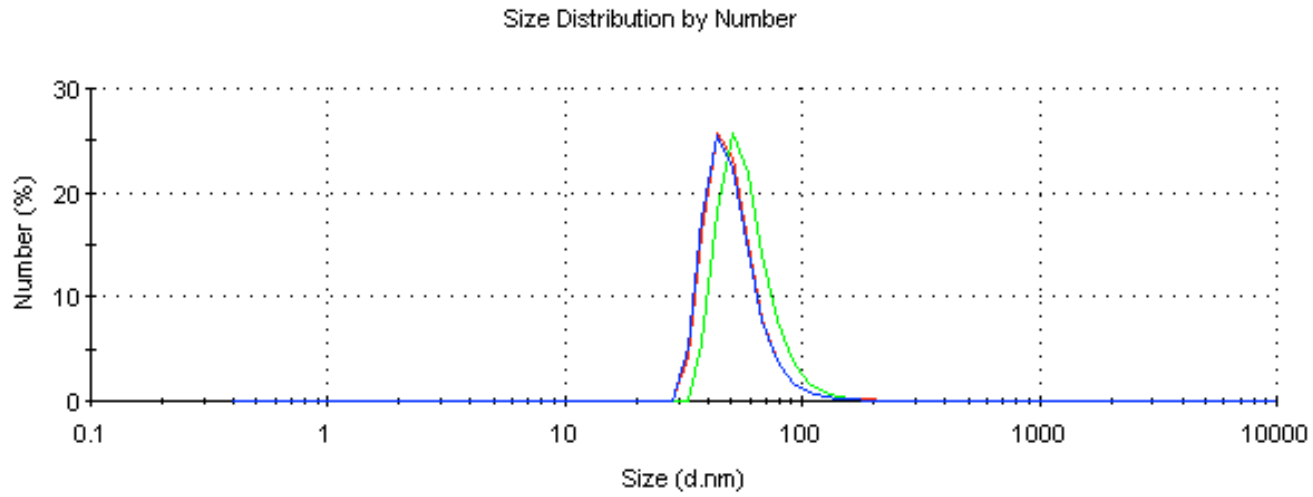

Figure S21. Size distribution of M_4P_{1h}/pCMV-Luc lipoplexes at N/P = 1 in water with 5% glucose.

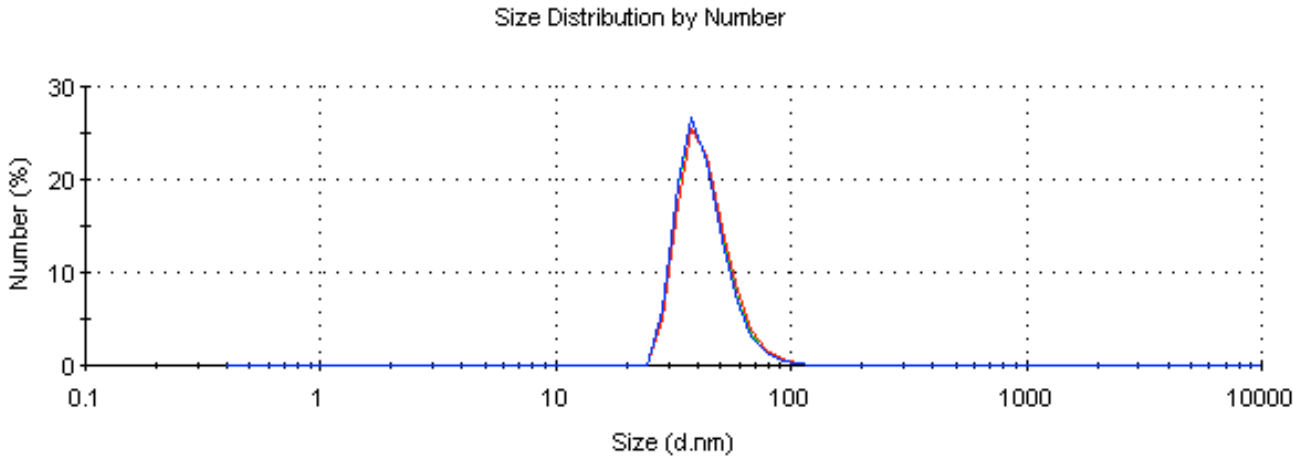

Figure S22. Size distribution of M_4P_{1h}/pCMV-Luc lipoplexes at N/P = 2 in water with 5% glucose.

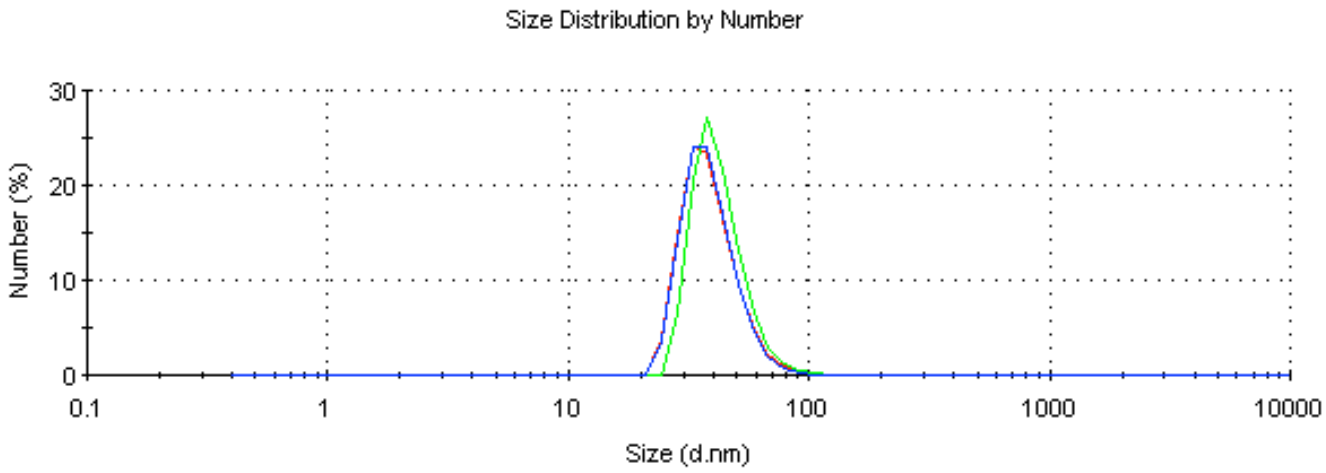

Figure S24. Size distribution of M_4P_{1h}/pCMV-Luc lipoplexes at N/P = 5 in water with 5% glucose.

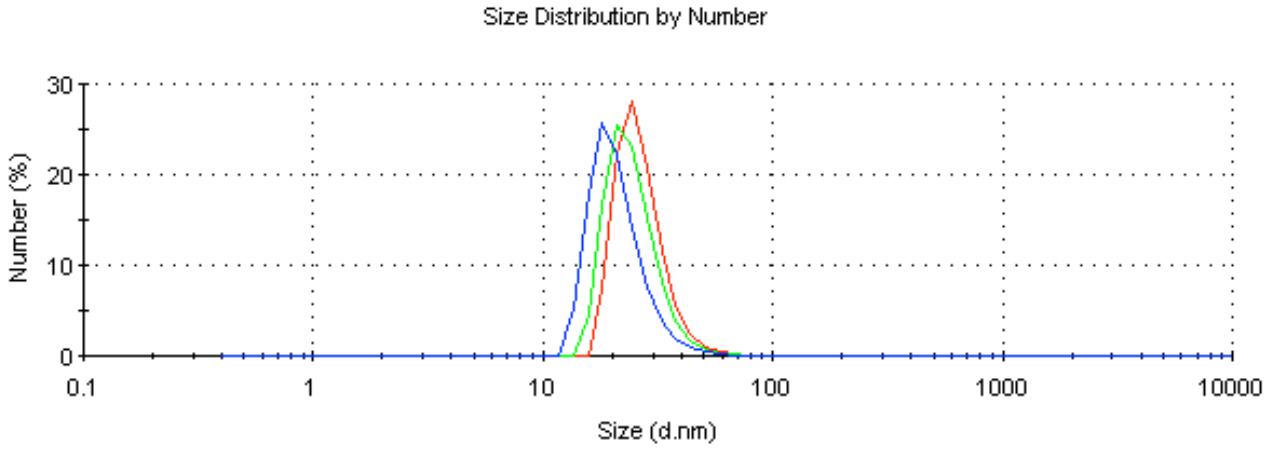

Figure S24. Size distribution of M_4P_{1h}/pCMV-Luc lipoplexes at N/P = 20 in water with 5% glucose.

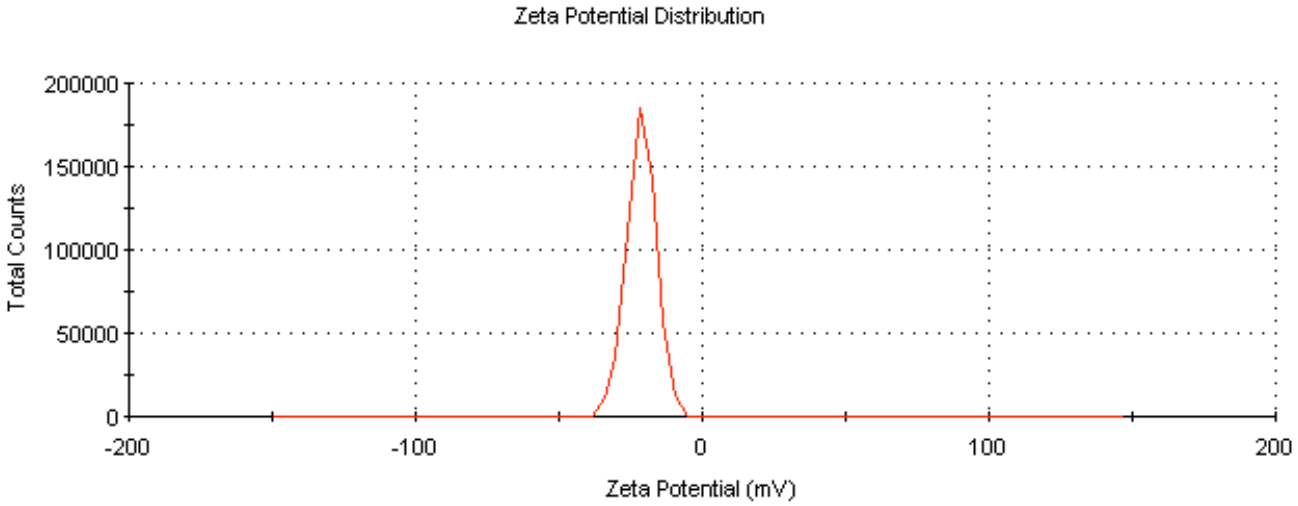

Figure S25. Size distribution of M_4P_{1h}/pCMV-Luc lipoplexes at N/P = 1 in water with 5% glucose.

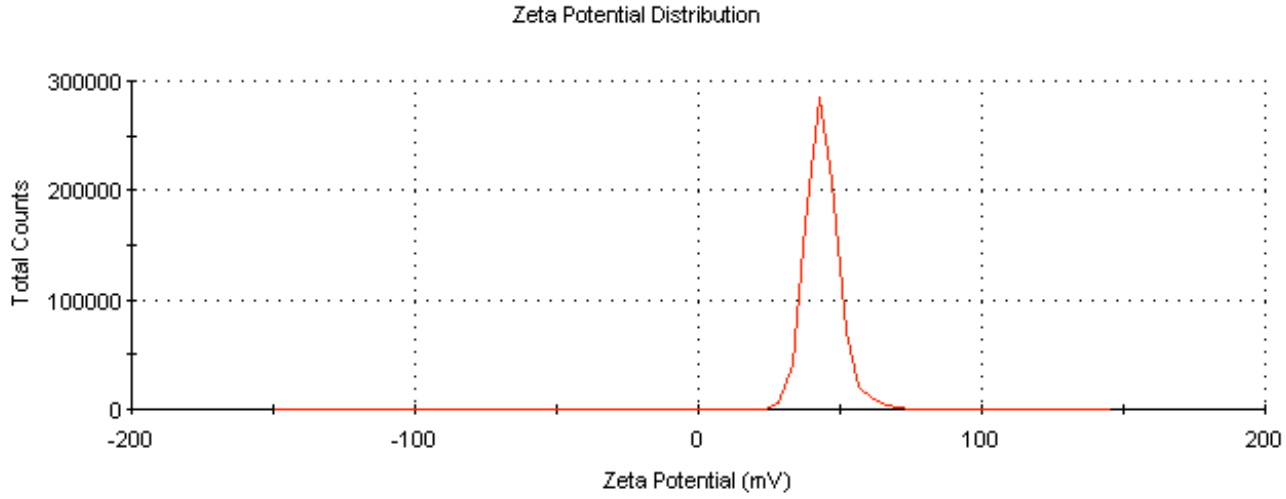

Figure S26. Size distribution of M_4P_{1h}/pCMV-Luc lipoplexes at N/P = 2 in water with 5% glucose.

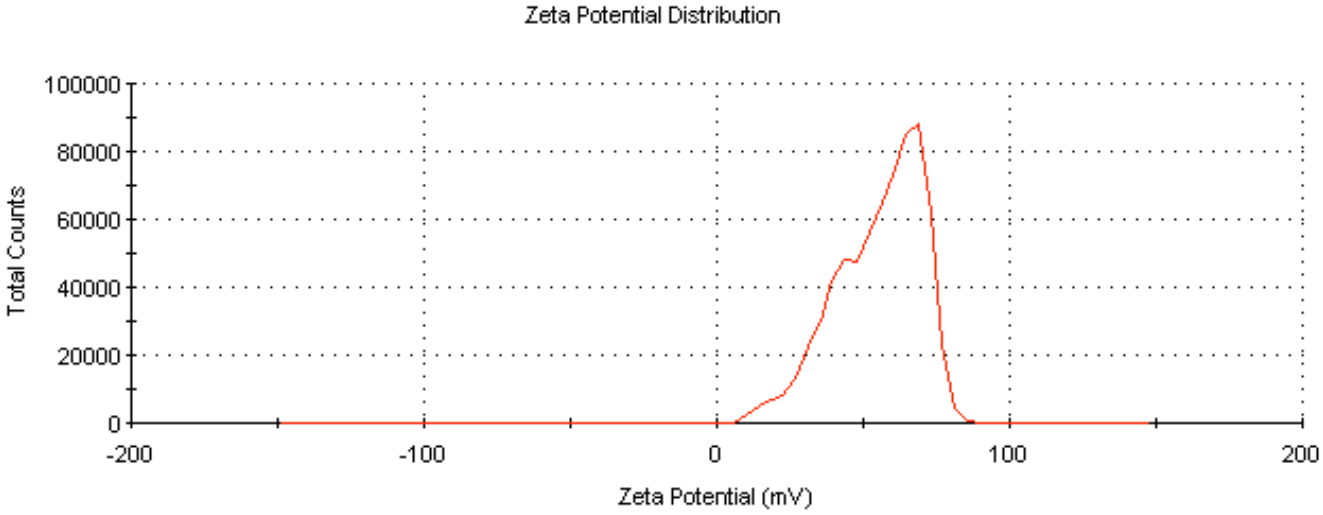

Figure S27. Size distribution of M_4P_{1h}/pCMV-Luc lipoplexes at N/P = 5 in water with 5% glucose.

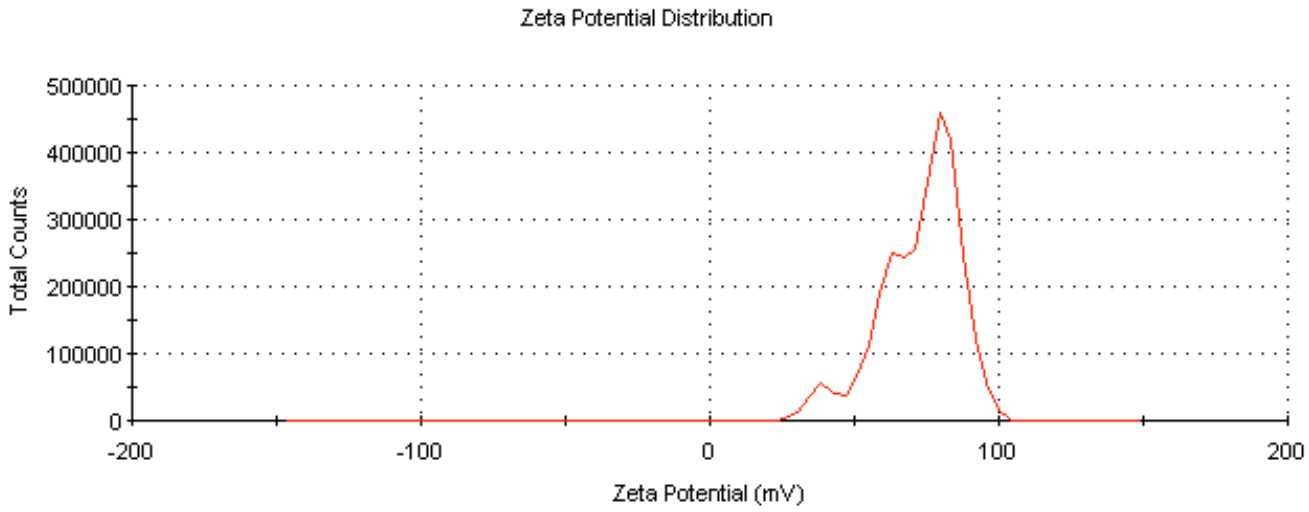

Figure S28. Size distribution of M_4P_{1h}/pCMV-Luc lipoplexes at N/P = 20 in water with 5% glucose.

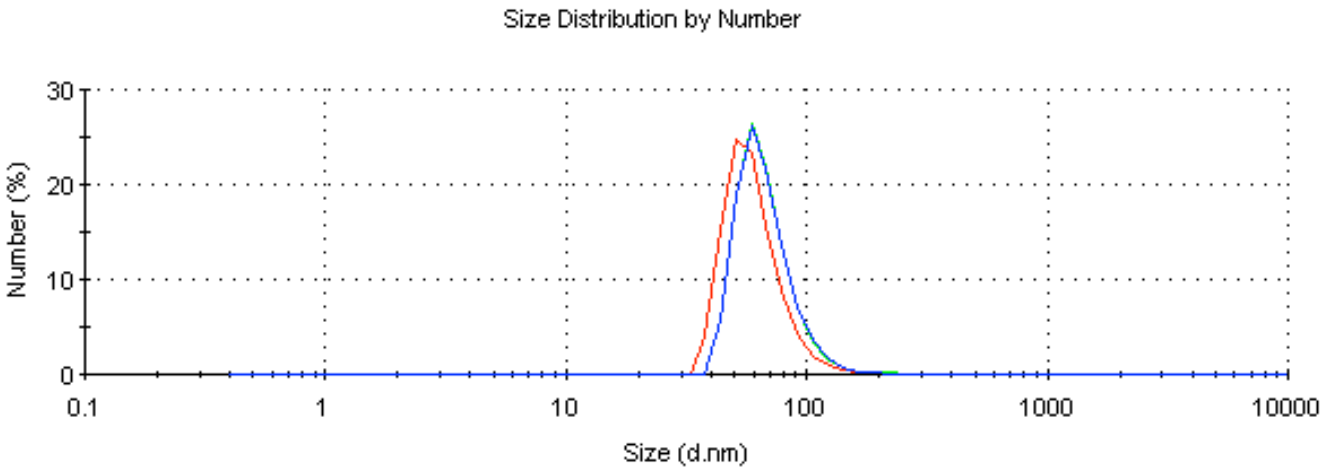

Figure S29. Size distribution of M_8P_{1h}/pCMV-Luc lipoplexes at N/P = 1 in water with 5% glucose.

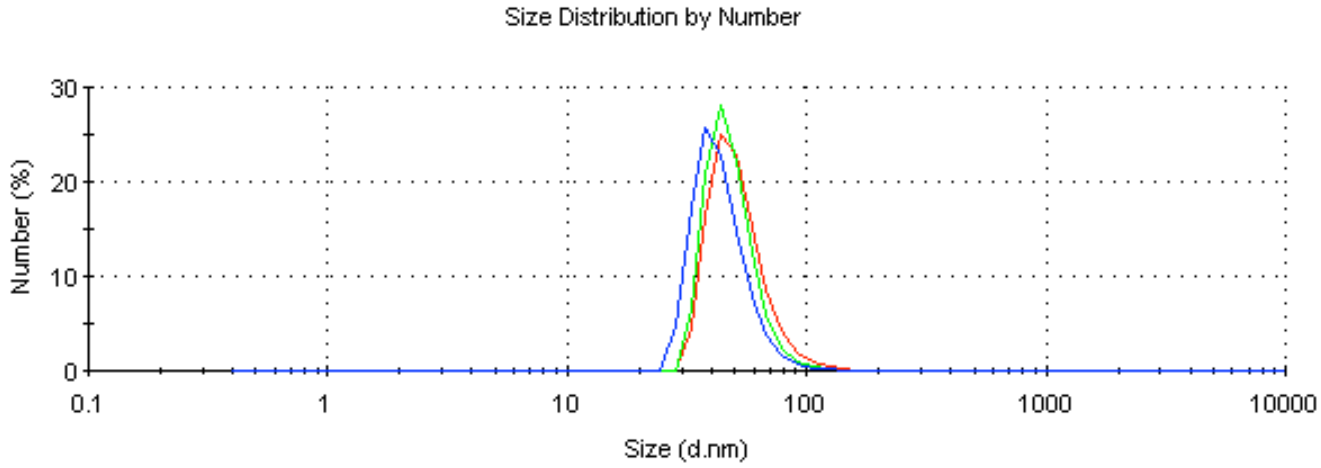

Figure S30. Size distribution of M_8P_{1h}/pCMV-Luc lipoplexes at N/P = 2 in water with 5% glucose.

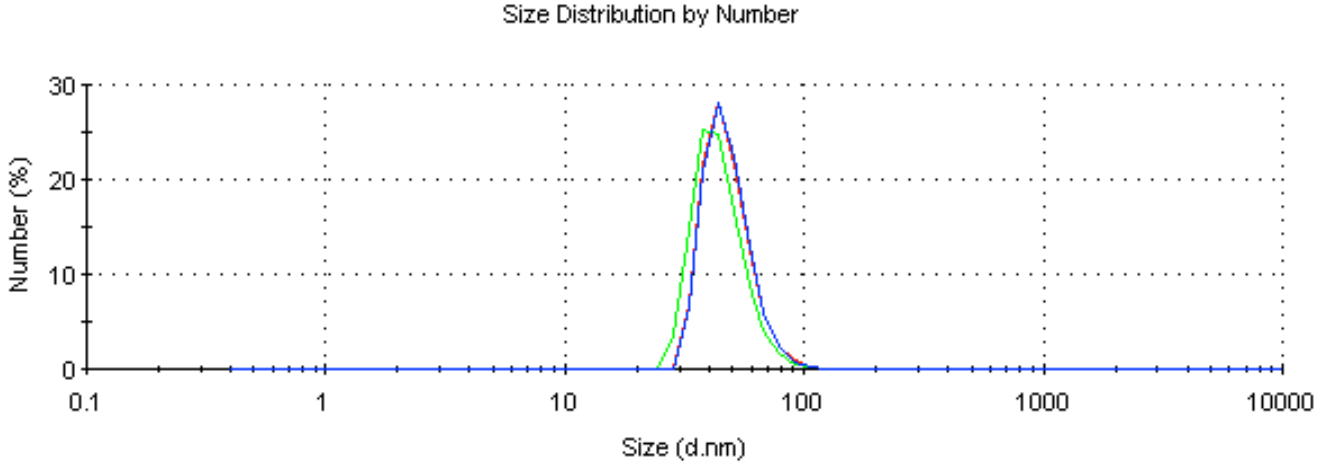

Figure S31. Size distribution of M_8P_{1h}/pCMV-Luc lipoplexes at N/P = 5 in water with 5% glucose.

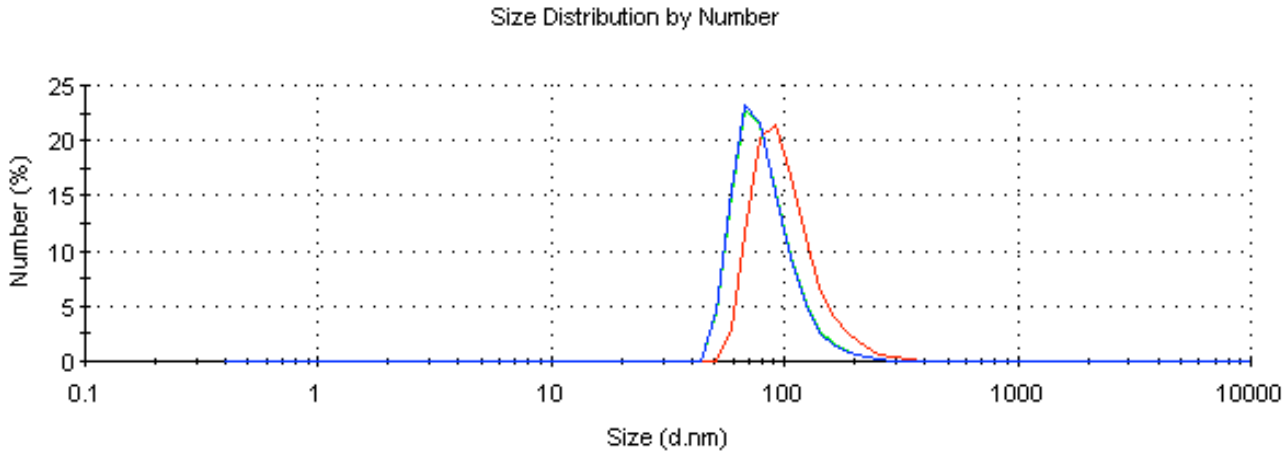

Figure S32. Size distribution of M_8P_{1h}/pCMV-Luc lipoplexes at N/P = 20 in water with 5% glucose.

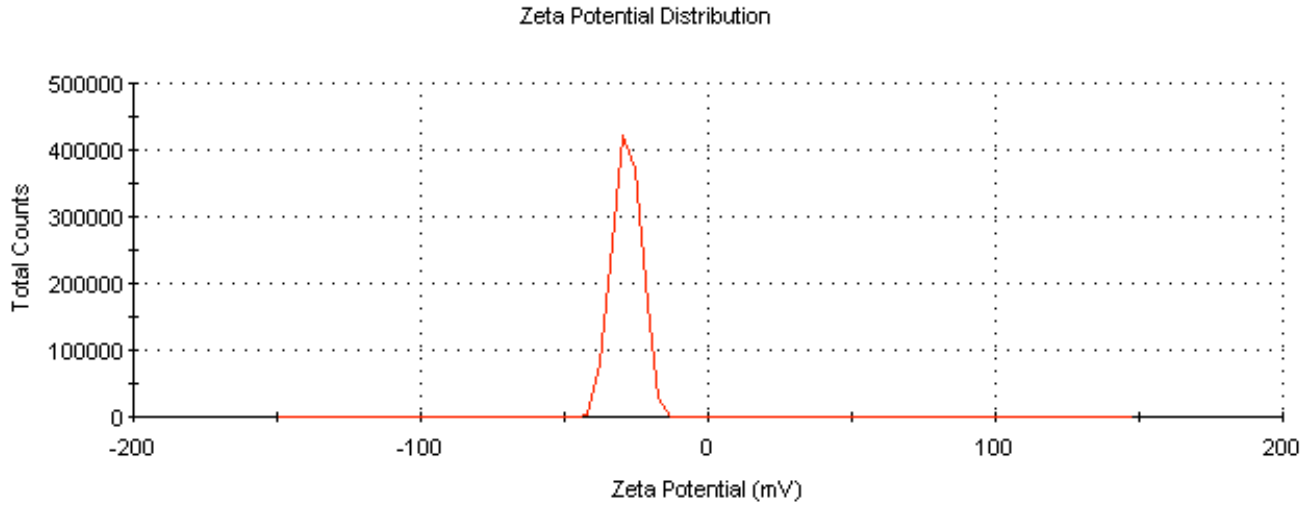

Figure S33. Zeta potential distribution of M_8P_{1h}/pCMV-Luc lipoplexes at N/P = 1 in water with 5% glucose.

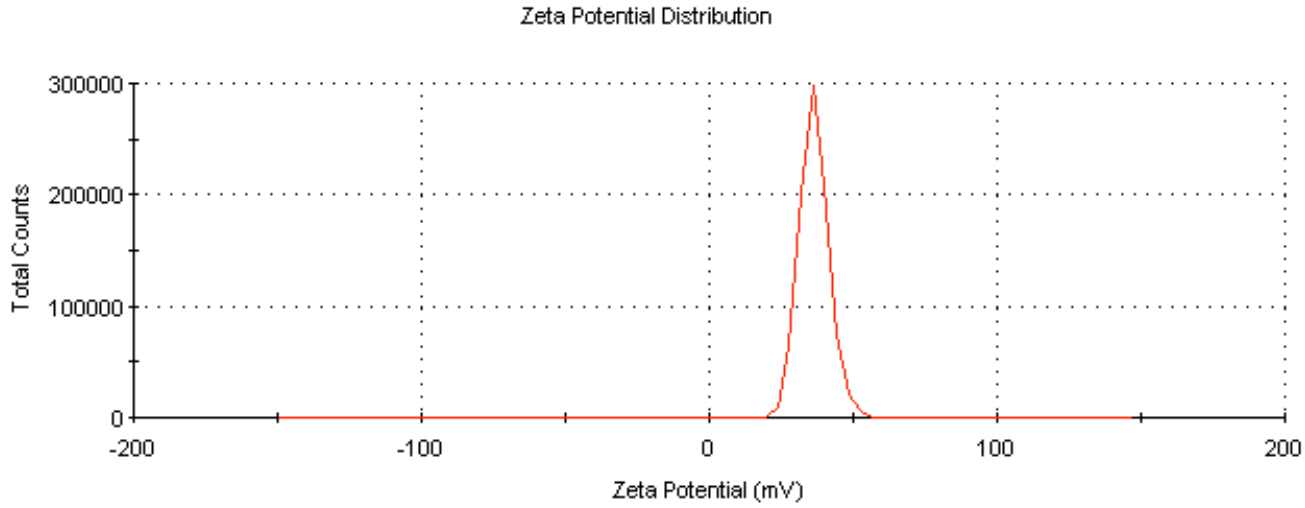

Figure S34. Zeta potential distribution of M_8P_{1h}/pCMV-Luc lipoplexes at N/P = 2 in water with 5% glucose.

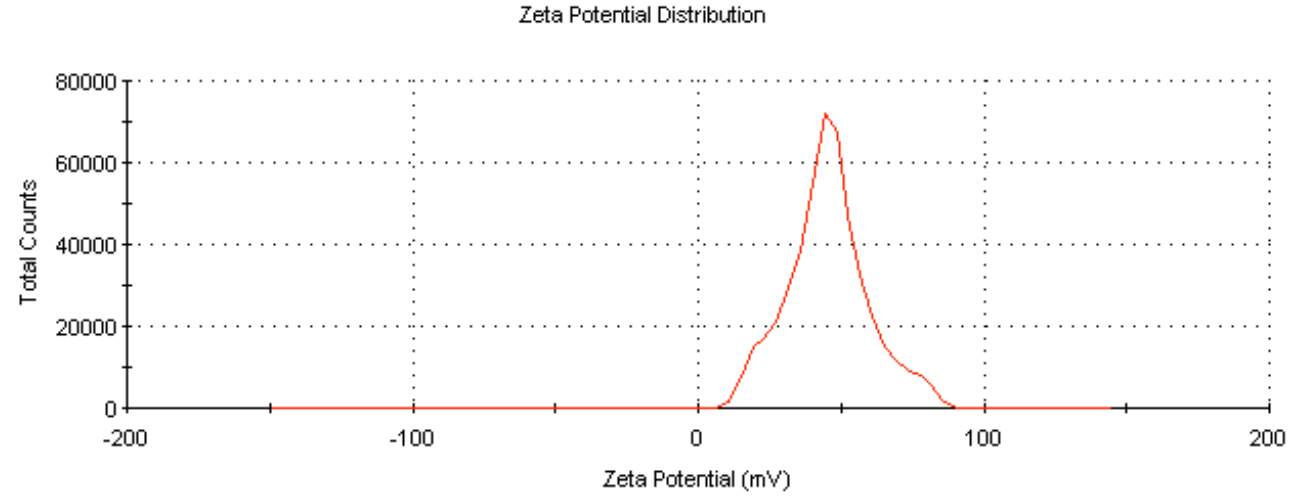

Figure S35. Zeta potential distribution of M_8P_{1h}/pCMV-Luc lipoplexes at N/P = 5 in water with 5% glucose.

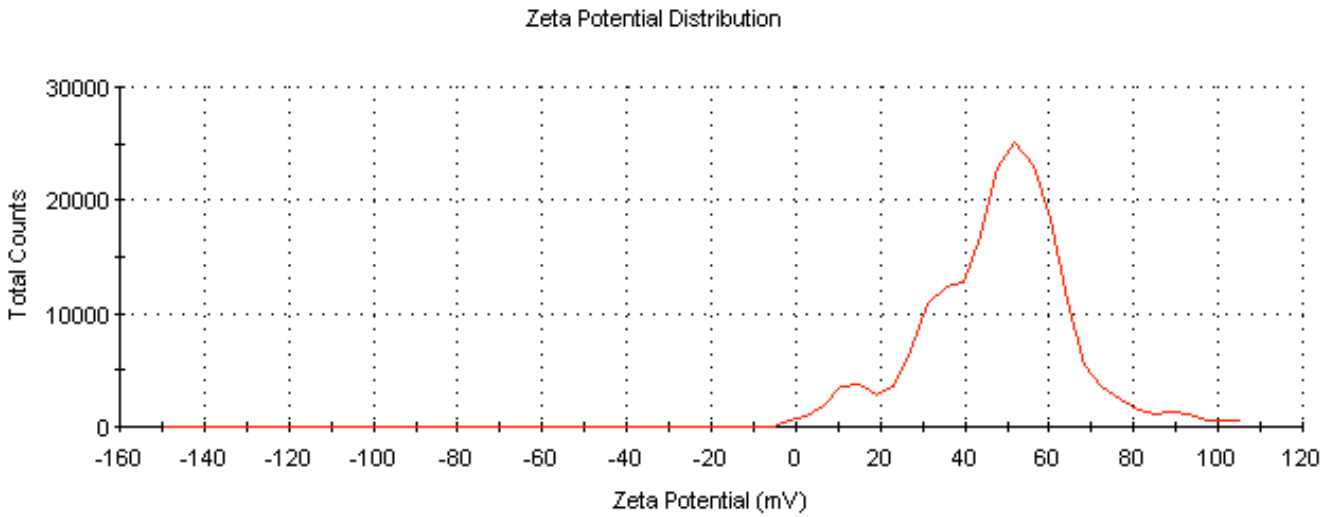

Figure S36. Zeta potential distribution of M_8P_{1h}/pCMV-Luc lipoplexes at N/P = 20 in water with 5% glucose.

Electron microscopy analysis.

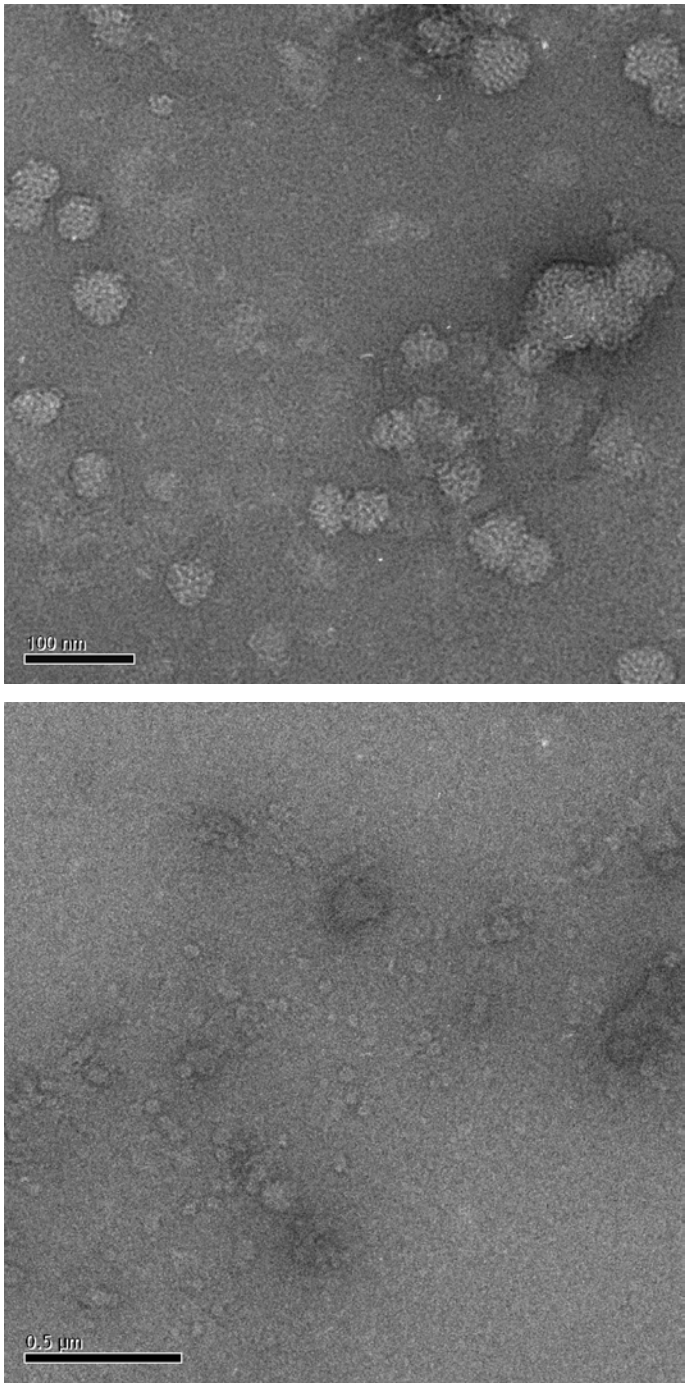

Figure S37. TEM images of M_4P_{1h}/pCMV-Luc lipoplexes at N/P = 5 in water with 5% glucose.

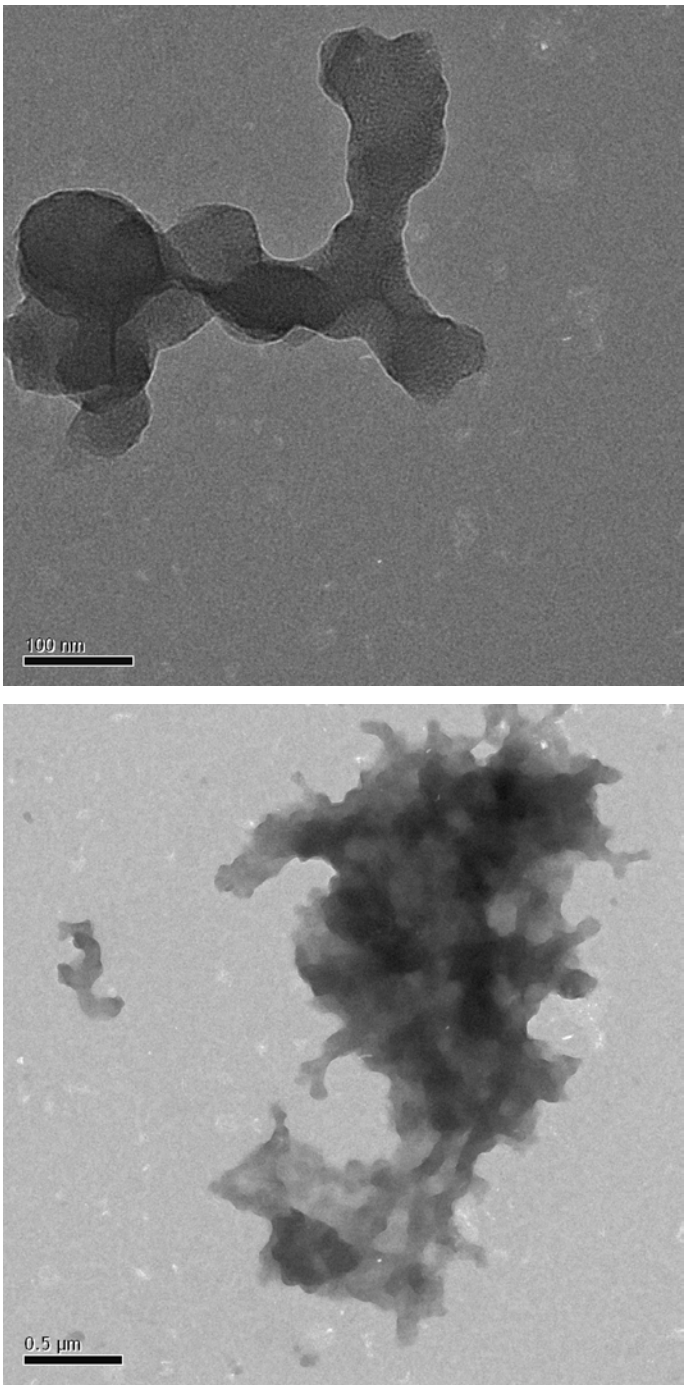

Figure S38. TEM images of M_4P_{1h}/pCMV-Luc lipoplexes at N/P = 5 in water with 150 mM NaCl.

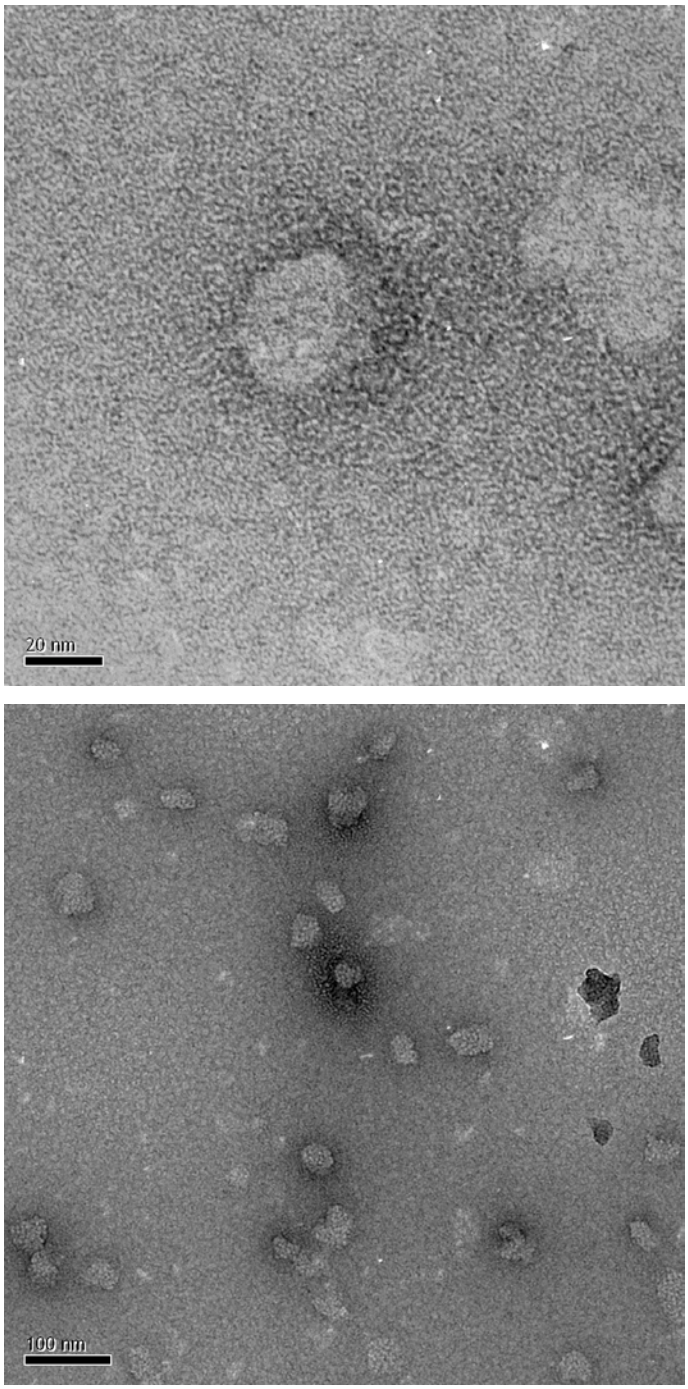

Figure S39. TEM images of M_8P_{1h}/pCMV-Luc lipoplexes at N/P = 5 in water with 5% glucose.

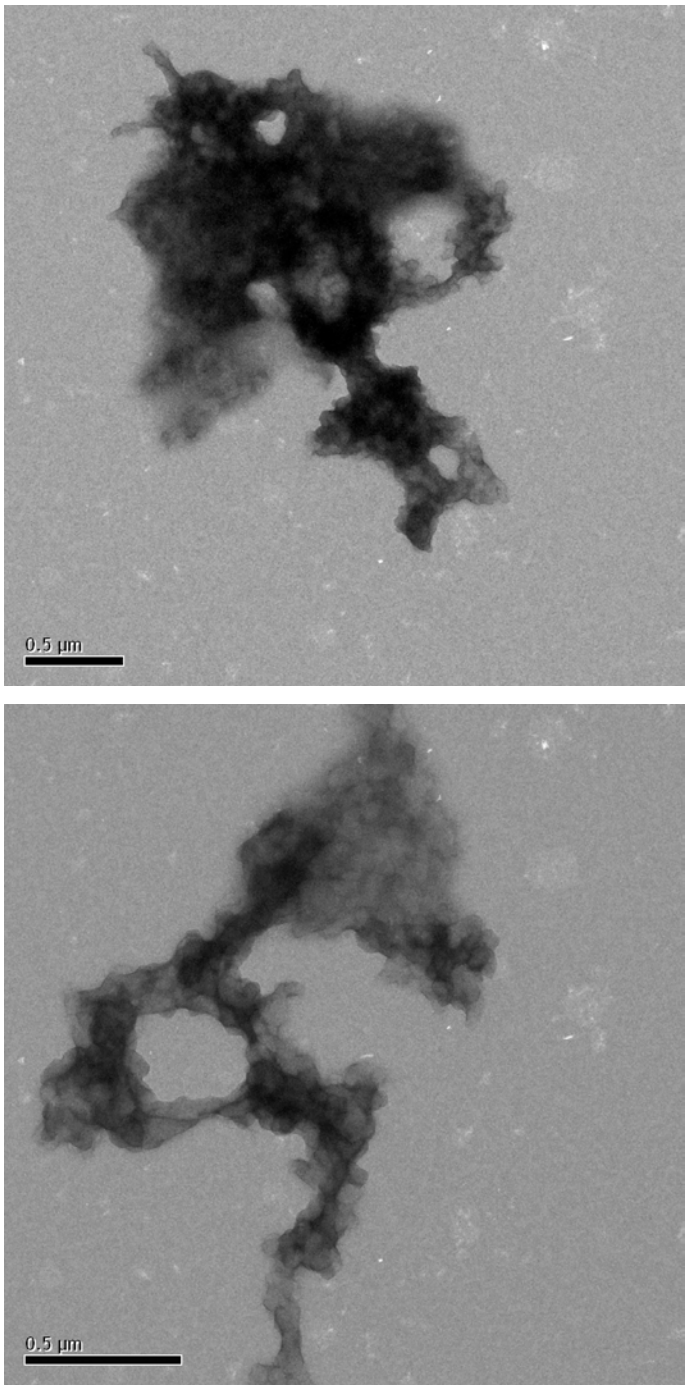

Figure S40. TEM images of M_8P_{1h}/pCMV-Luc lipoplexes at N/P = 5 in water with 150 mM NaCl.

F. Gene transfer experiments

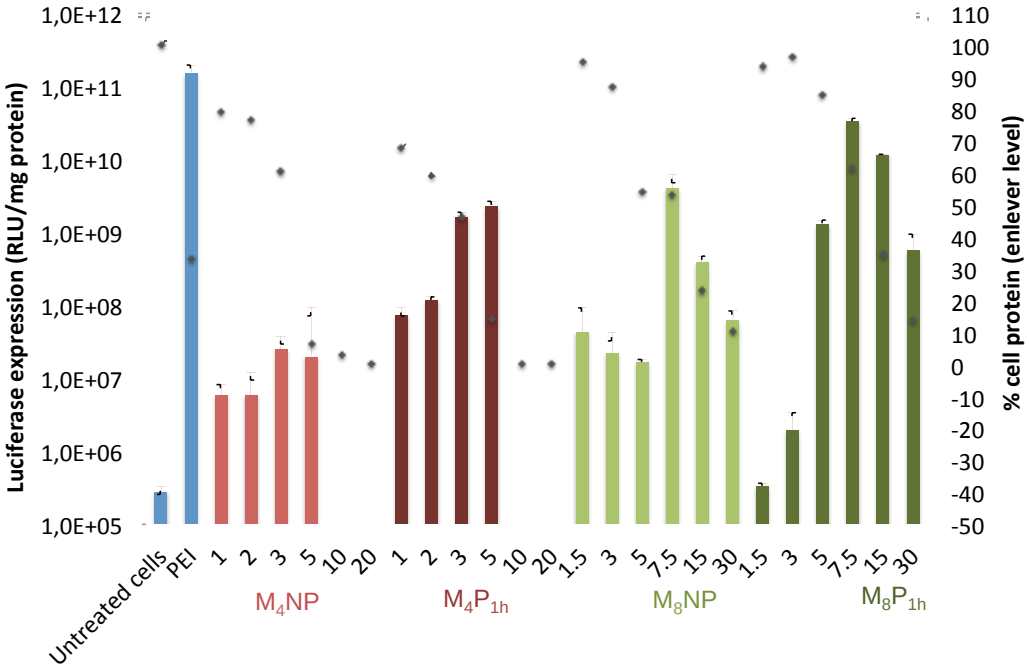

Figure S41. Luciferase expression and percentage of cell proteins after delivery experiments of pCMV-Luc at various N/P without serum (M_4 and M_8 Lipoplexes prepared in 150 mM NaCl solution)

Bioconjugate Chemistry

ARTICLE

pubs.acs.org/bc

Bioreducible Block Copolymers Based on Poly(Ethylene Glycol) and Poly(γ-Benzyl L-Glutamate) for Intracellular Delivery of Camptothecin

Thavasyappan Thambi,[†] Hong Yeol Yoon,[†] Kwangmeyung Kim,[‡] Ick Chan Kwon,[‡] Chang Kyoo Yoo,[*,§] and Jae Hyung Park[*,†]

[†]Theranostic Macromolecules Research Center, Department of Polymer Science and Engineering, Sungkyunkwan University, Suwon 440-746, Republic of Korea

[‡]Biomedical Research Center, Korea Institute of Science and Technology, Seoul 136-791, Republic of Korea

[§]Department of Environmental Science and Engineering, College of Engineering, Kyung Hee University, Gyeonggi-do 446-701, Republic of Korea

Supporting Information

ABSTRACT:

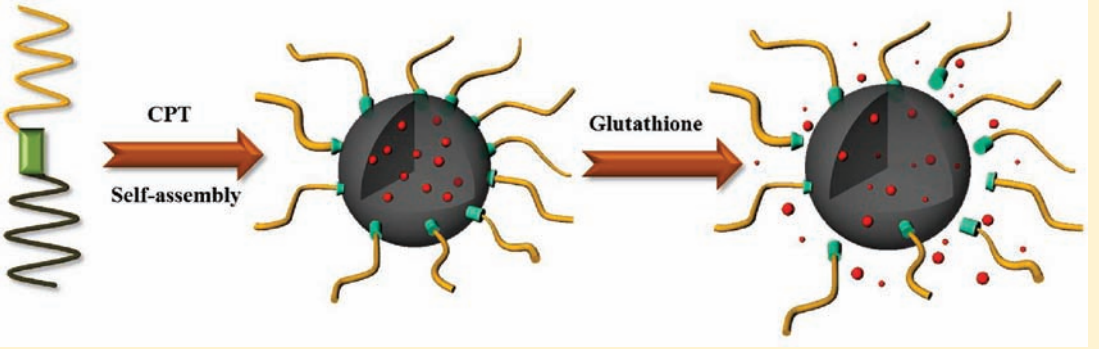

Poly(ethylene glycol)-*b*-poly(γ-benzyl L-glutamate)s bearing the disulfide bond (PEG-SS-PBLGs), which is specifically cleavable in intracellular compartments, were prepared via a facile synthetic route as a potential carrier of camptothecin (CPT). Diblock copolymers with different lengths of PBLG were synthesized by ring-opening polymerization of benzyl glutamate *N*-carboxy anhydride in the presence of a PEG macroinitiator (PEG-SS-NH_2). Owing to their amphiphilic nature, the copolymers formed spherical micelles in an aqueous condition, and their particle sizes (20−125 nm in diameter) were dependent on the block length of PBLG. Critical micelle concentrations of the copolymers were in the range 0.005−0.065 mg/mL, which decreased as the block length of PBLG increased. CPT, chosen as a model anticancer drug, was effectively encapsulated up to 12 wt % into the hydrophobic core of the micelles by the solvent casting method. It was demonstrated by the *in vitro* optical imaging technique that the fluorescence signal of doxorubicin, quenched in the PEG-SS-PBLG micelles, was highly recovered in the presence of glutathione (GSH), a tripeptide reducing disulfide bonds in the cytoplasm. The micelles released CPT completely within 20 h under 10 mM GSH, whereas only 40% of CPT was released from the micelles in the absence of GSH. From the *in vitro* cytotoxicity test, it was found that CPT-loaded PEG-SS-PBLG micelles showed higher toxicity to SCC7 cancer cells than CPT-loaded PEG-*b*-PBLG micelles without the disulfide bond. Microscopic observation demonstrated that the disulfide-containing micelle could effectively deliver the drug into nuclei of SCC7 cells. These results suggest that PEG-SS-PBLG diblock copolymer is a promising carrier for intracellular delivery of CPT.

INTRODUCTION

Self-assembled polymeric micelles, composed of amphiphilic block copolymers, have received attention as anticancer drug carriers because they can circulate in blood for long periods of time, followed by selective accumulation into tumor tissue via the enhanced permeation and retention (EPR) effect.[1−5] However, delivery of the drug into the intracellular compartments of the cancer cell is often insufficient due to the slow release of the drug from micelles.[6,7] For example, aliphatic polyester-based micelles, extensively studied as drug carriers, have shown sustained drug release over a period of days to weeks,[6−8] although dumping the drug into the intracellular compartments of the cell in tumor tissue can enhance therapeutic efficacy. In this regard, it is necessary to develop polymeric micelles that exhibit the rapid release of the drug, triggered by intracellular stimuli such as mildly acidic pH,[9] reductive agents,[10] and enzymes.[11] After reaching the tumor sites

Received: February 21, 2011
Revised: August 21, 2011
Published: September 07, 2011

ACS Publications © 2011 American Chemical Society

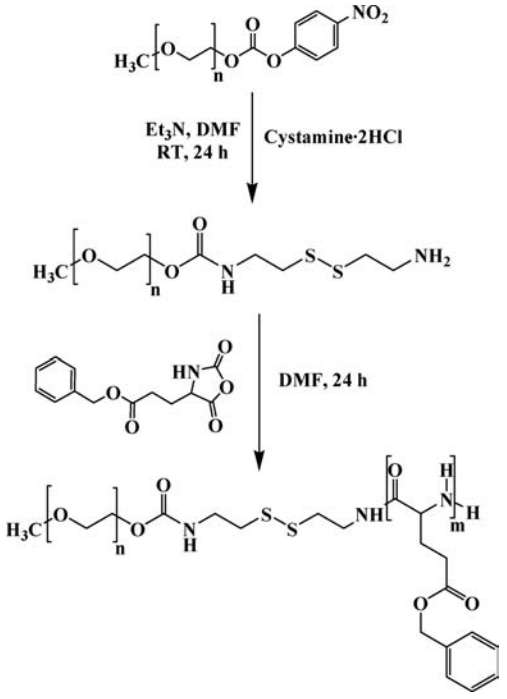

Figure 1. Synthetic route for PEG-SS-PBLG block copolymers.

via the EPR effect, such micelles can be internalized into tumor cells by endocytosis, followed by exposure to intracellular stimuli causing burst release of the drug.

Numerous polymers have been developed as biomaterials that are sensitive to various stimuli such as ultraviolet,[12] ultrasound,[13] pH,[14−16] and temperature.[17,18] In recent years, reduction-sensitive polymers have been extensively investigated for intracellular drug delivery, since they can rapidly release payloads under reductive environments that are similar to the intracellular compartments. Glutathione (GSH), a thiol-containing tripeptide capable of reducing disulfide bonds, is abundant in the cytoplasm of the cell (1−10 mM), whereas it is rarely present in blood plasma (~2 μM).[19,20] This unique feature of GSH has encouraged development of disulfide-bearing carriers for intracellular delivery of siRNA,[21] DNA,[22,23] and low molecular weight drugs.[10,24−29] However, syntheses of disulfide-bearing polymers are often complex and, in most cases, require thiol-exchange reactions to introduce disulfide bonds at the backbones or the side groups of polymeric carriers. A principal disadvantage of this method is the unstable nature of free thiols, which are readily oxidized even under ambient conditions, thus forming dimers instead of the desired product.[23]

In the present study, we developed reduction-sensitive and biodegradable amphiphiles for the intracellular delivery of camptothecin (CPT), an anticancer drug (Figure 1). Amphiphilic diblock copolymers, composed of poly(ethylene glycol) (PEG) and poly(γ-benzyl L-glutamate) (PBLG), were prepared with a facile synthetic method, i.e., ring-opening polymerization of benzyl glutamate *N*-carboxy anhydride (NCA) in the presence of a poly(ethylene glycol) macroinitiator (PEG-SS-NH_2). Three different diblock copolymers (PEG-SS-PBLGs) were obtained by varying the feed ratio of the macroinitiator to benzyl glutamate NCA. The physicochemical characteristics of PEG-SS-PBLGs were determined using ^{1}H NMR, dynamic light scattering (DLS), transmission electron microscopy (TEM), and fluorescence spectroscopy. The reduction sensitivity of the micelle was evaluated using an optical imaging technique in which the fluorescence signal of doxorubicin, quenched in the micelle, was monitored in the presence of different concentrations of GSH. In addition, the *in vitro* release behavior of CPT from micelles was measured in the presence and absence of GSH. The cytotoxicities of CPT-loaded micelles were tested by exposing them to the SCC7 cancer cells.

EXPERIMENTAL PROCEDURES

Materials. α-Methoxy-ω-amino PEG (mPEG-NH_2, M_n = 2000 g/mol) and mPEG-nitrophenyl carbonate (M_n = 2000 g/mol) were purchased from Laysan Bio Inc. (Arab, AL, USA). Doxorubicin· hydrochloride (DOX·HCl), CPT, benzyl glutamate, and triphosgene were purchased from Sigma-Aldrich Co. (St. Louis, MO, USA). Cystamine·dihydrochloride was obtained from Tokyo Chemical Industries (Tokyo, Japan). The water used in the experiments was prepared by an AquaMax-Ultra water purification system (Younglin Co., Anyang, Korea). All other chemicals were of analytical grade and used without further purification.

Synthesis of Benzyl Glutamate NCA. Benzyl glutamate NCA was synthesized by the Fuchs-Farthing method using triphosgene.[30] In brief, benzyl glutamate (2 g, 8.4 mmol) was suspended at 50 °C in THF. After triphosgene (1 g, 2.95 mmol) was slowly added to the solution, the reaction mixture was stirred for 3 h. The clear solution obtained was poured into *n*-hexane, cooled to −20 °C, and held overnight. After the precipitate was filtered, it was washed with *n*-hexane and dried at room temperature under vacuum.

Synthesis of PEG-SS-NH_2. Triethylamine (2.8 mL, 20 mmol) and cystamine·dihydrochloride (2.25 g, 10 mmol) were dissolved at 0 °C in DMSO. mPEG-nitrophenyl carbonate (4 g, 2 mmol) in DMSO was slowly added over 15 min under nitrogen atmosphere. The reaction mixture was stirred at room temperature for 24 h. Thereafter, the solution was purified with a dialysis membrane (MWCO = 1000 Da, Spectrum Laboratories, Inc., CA, USA) against distilled water for two days, followed by lyophilization.

Synthesis of Disulfide-Bearing Diblock Copolymers. PEG-SS-PBLG diblock copolymers were synthesized via ring-opening polymerization of benzyl glutamate NCA in the presence of a cleavable macroinitiator (PEG-SS-NH_2). Benzyl glutamate NCA (0.6 g, 2.3 mmol) was added to the PEG-SS-NH_2 (0.5 g, 0.23 mmol) solution in DMF under a nitrogen atmosphere and stirred for 24 h at 35 °C. The product was precipitated in diethyl ether, filtered, and dried at room temperature under vacuum. The PEG-*b*-PBLG diblock copolymer without the disulfide bond was prepared via an identical method and used as a control. The diblock copolymers, synthesized in this study, were coded depending on the degree of polymerization (DP) of the benzyl glutamate hydrophobic block. For example, PEG-SS-$PBLG_4$ indicates the diblock copolymer in which the DP of the hydrophobic block was 4.

Characterization. The chemical structures of the polymers were characterized using ^{1}H NMR (JNM-AL300, JEOL, Tokyo, Japan) operating at 300 MHz, for which the samples were dissolved in $CDCl_3$. The sizes of the micelles were determined at 25 °C using a FPAR-1000 fiberoptics particle analyzer (Otsuka Electronics, Osaka, Japan). The morphology of the particles was observed using a TEM (JEM-2100F, JEOL, Tokyo, Japan), operated at an accelerating voltage of 200 keV.

The critical micelle concentrations (CMCs) of the copolymers were evaluated using fluorescence spectroscopy in the presence of pyrene molecules.[31] In brief, a pyrene solution (12×10^{-7} M) was prepared in distilled water, which was then mixed with the

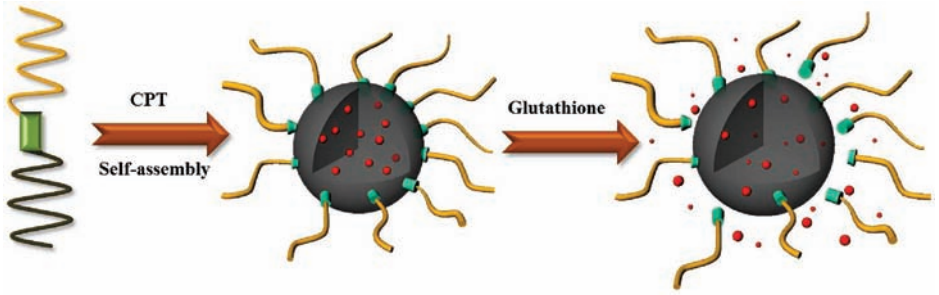

Figure 2. Schematic illustration of GSH-sensitive release of the drug from PEG-SS-PBLG micelles.

block copolymer solution to obtain a polymer concentration ranging from 1.0×10^{-4} to 1 mg/mL. The final concentration of pyrene in each sample was fixed at 6.0×10^{-7} M. The fluorescence spectra were recorded using an ISS K2 multifrequency phase and modulation fluorometer (ISS, Champaign, IL, USA). The excitation (λ_{ex}) and emission (λ_{em}) wavelengths were 336 and 390 nm, respectively.

Reduction Sensitivity of Micelles. The sensitivity of micelles to the reductive environment was estimated by exposing DOX-loaded micelles to different concentrations of GSH. DOX, which was chosen as a model fluorescence drug, was encapsulated into micelles by the solvent casting method as previously described.[32] The loading content of DOX was 6.7%, which was determined using a UV−vis spectrophotometer at 485 nm. After the DOX-loaded micelles were dispersed at various glutathione concentrations (0, 0.5, 1, 5, 10, and 20 mM), they were transferred into 96-well flat-bottomed plates and incubated for 1 h at 37 °C. The fluorescence image of DOX was obtained using a Kodak Image Station 4000MM equipped with a 12 bit CCD camera (New Haven, CT, USA).

Preparation of CPT-Loaded Polymeric Micelles. CPT-loaded micelles were prepared by the solvent casting method.[32] In brief, the PEG-SS-PBLG diblock copolymer was dissolved in a chloroform/methanol (1v:1v) mixture. CPT in chloroform and triethylamine (1v:1v) was added and stirred for 3 h. Then, the solvent was completely removed using a rotary evaporator to form a thin film. PBS (pH 7.4) was added and the solution was stirred for an additional 1 h, followed by filtration through a 0.45 μm filter to remove unloaded CPT. The solution was dialyzed against distilled water (MWCO = 1000 Da) for one day and lyophilized to obtain the CPT-loaded polymeric micelles (CPT-SS-PM). The same method was applied to the control sample to prepare CPT-loaded micelles (CPT-PM). The loading efficiency and content of CPT in polymeric micelles were determined using a UV−vis spectrophotometer (Optizen 3220UV, Mecasys Co., Ltd., Daejeon, Korea) at 370 nm.

***In Vitro* Release Behavior of CPT from Micelles.** CPT-loaded micelles (1 mg/mL) were dispersed in a PBS (pH 7.4), and the solutions were transferred to cellulose membrane tubes (MWCO = 1000 Da). The dialysis tubes were then immersed in PBS (pH 7.4) with or without GSH (10 mM). Each sample was gently shaken in a 37 °C water bath at 100 rpm. The medium was refreshed at predetermined time intervals, and the CPT concentration was determined using UV−vis spectroscopy at 370 nm.

Cytotoxicity and Intracellular Drug Release Tests. SCC7 (squamous carcinoma) cell lines, obtained from the American Type Culture Collection (Rockville, MD, USA), were cultured in RPMI 1640 medium (Gibco, Grand Island, NY, USA) containing 10% (v/v) fetal bovine serum and 1% (w/v) penicillin−streptomycin at 37 °C in a humidified 5% CO_2/95% air atmosphere. The cells were seeded at a density of 1×10^4 cells/well in 96-well flat-bottomed plates. After one day of growth, the cells were washed twice with a PBS (pH 7.4) and incubated for 12 h with various concentrations of samples. The cells were then washed twice with PBS to remove any remaining drug, and fresh culture medium was added. Twenty microliter aliquots of 3-(4,5-dimethylthiazol-2-yl)-2,5-diphenyltetrazolium bromide solution (5 mg/mL in PBS) were added to each well, and the cells were incubated for an additional 4 h at 37 °C. Subsequently, the medium was removed and the cells were dissolved in DMSO. The absorbance at 570 nm was measured using a microplate reader (VERSAmax, Molecular Devices Corp., Sunnyvale, CA, USA).

To observe the intracellular drug release from the micelle, the cells were incubated with DOX-loaded micelles (DOX-SS-PM and DOX-PM) for 12 h. The cells were then washed twice with PBS (pH 7.4) and fixed with 4% formaldehyde solution. For nuclear staining, the cells were incubated with 4,6-diamino-2-phenylinodole (DAPI) for 10 min at room temperature, followed by washing with PBS (pH 7.4). The intracellular localization of DOX-SS-PM and DOX-PM was observed using IX81-ZDC focus drift compensating microscope (Olympus, Tokyo, Japan).

RESULTS AND DISCUSSION

In an attempt to develop reduction-sensitive micelles, the disulfide bond was introduced between hydrophilic PEG and hydrophobic PBLG, as shown in Figure 1. Since the disulfide bond is specifically cleavable by GSH, which is abundant in the cell cytoplasm, the resulting micelles may have potential as carriers for selective delivery of the drug into the intracellular level (Figure 2). In particular, such micelles would be useful for the delivery of anticancer drugs because the intracellular concentrations of GSH in cancer cells are much greater than in normal cells .[19,20]

Synthesis and Characterization of PEG-SS-PBLG Diblock Copolymers. For facile synthesis of the disulfide-bearing diblock copolymer, PEG-SS-NH_2 was first prepared as the macroinitiator by reacting mPEG-nitrophenyl carbonate with cystamine. The ^{1}H NMR spectrum for PEG-SS-NH_2 indicated that the characteristic peaks of cystamine appeared at 1.8 ppm and 2.80−2.97 ppm (Figure 3). Alternatively, no peaks for the phenyl group were observed, suggesting complete removal of the nitrophenyl group at the chain end of mPEG. In the next step, PEG-SS-PBLG diblock copolymers were readily synthesized by ring-opening polymerization of benzyl glutamate NCA in the presence of PEG-SS-NH_2. Figure 3 shows the ^{1}H NMR spectrum of PEG-SS-$PBLG_9$ as the representative diblock copolymer, exhibiting

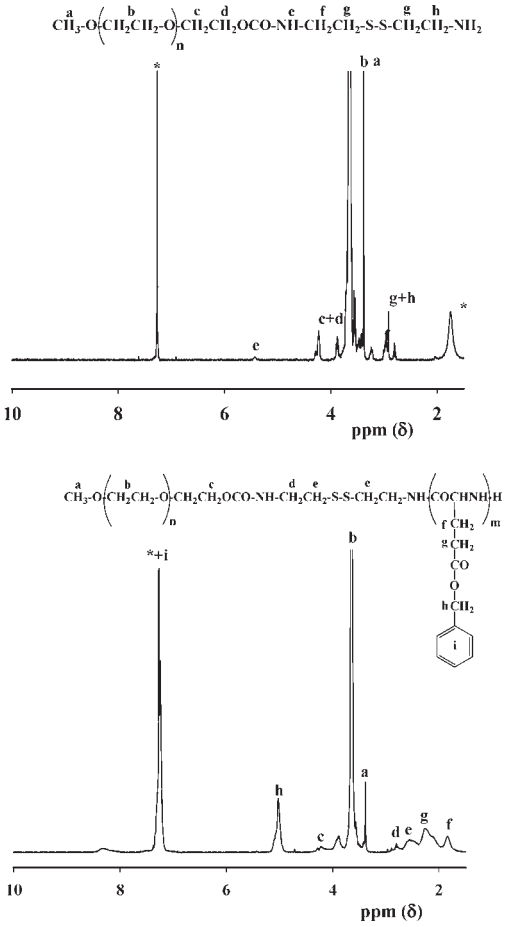

Figure 3. ^{1}H NMR spectra of PEG-SS-NH_2 and PEG-SS-$PBLG_9$.

the characteristic peaks of PEG and PBLG. The degree of polymerization of the PBLG block could be calculated based on the integration ratio of the proton peak appearing from the benzylic methylene of PBLG at 5.02 ppm and that from PEG at 3.60 ppm. As shown in Table 1, the molecular weights of the diblock copolymers were precisely controlled by varying the feed ratio of benzyl glutamate NCA to PEG-SS-NH_2. In general, the block length of PBLG in the copolymer increased as the feed ratio of benzyl glutamate NCA increased. It should be noted that, when the feed ratio was greater than 15, the resulting copolymer was barely soluble in water due to high hydrophobicity.

Owing to their amphiphilicity, PEG-SS-PBLG copolymers can form nanosized particles in aqueous environments. The size distribution and morphologies of PEG-SS-PBLG nanoparticles are shown in Figure 4. As expected, all the copolymers formed nanoparticles with unimodal size distributions. TEM images indicated that the nanoparticles were spherical in shape. The mean diameters of nanoparticles were in the range 20−127 nm, depending on the PBLG block length of the copolymer. The copolymer with the longer PBLG block formed larger nanoparticles, indicating that the size of the hydrophobic inner core is proportional to the PBLG length of the copolymer. The mean diameter of the nanoparticles did not significantly changed over the course of a week, implying high stability of the nanoparticles in an aqueous environment (data not shown).

CMCs of the copolymers were determined using pyrene as a fluorescent probe.[31] For all copolymers, the intensity ratios

Table 1. Physicochemical Characteristics of the Diblock Copolymers

sample	FR[a]	DP[b]	size (nm)[c]	M_n[d]
PEG_{45}-SS-NH_2	-	-	-	2180
PEG_{45}-SS-$PBLG_4$	5	4.0	19.6 ± 4.61	3065
PEG_{45}-SS-$PBLG_9$	10	8.5	51.3 ± 2.69	3761
PEG_{45}-SS-$PBLG_{13}$	15	13.2	126.9 ± 3.15	5101

[a] Molar feed ratio of [benzyl glutamate NCA] to [PEG-SS-NH_2]. [b] Degree of polymerization calculated using ^{1}H NMR. [c] Mean diameter measured using the particle analyzer. [d] Number- average molecular weight calculated using ^{1}H NMR.

(I_{338}/I_{334}) of the pyrene excitation spectra increased as the copolymer concentrations increased (see Supporting Information Figure S1). Since the increase in the intensity ratio indicates the aggregation of pyrene into the hydrophobic reservoirs of the copolymers, CMCs can be determined from the crossover point at low concentration ranges.[33] As summarized in Table 1, the CMCs of the PEG-SS-PBLG copolymers were in the range 0.005−0.065 mg/mL, which was less than those of some polymeric amphiphiles[34,35] and low molecular weight surfactants (e.g., 1.0 mg/mL for deoxycholic acid). Of the copolymers tested, PEG-SS-$PBLG_{13}$ demonstrated the lowest CMC values, indicating that the self-assembly of copolymers could be readily facilitated by longer PBLG.

For further experiments including the drug release and cytotoxicity tests, PEG-SS-$PBLG_9$ was chosen as the representative bioreducible block copolymer and PEG-*b*-$PBLG_9$ without the disulfide bond was used as the control to observe the effect of the disulfide bond as the linkage of the block copolymer. In fact, the micellar structure of PEG-SS-$PBLG_9$ was significantly affected by GSH inducing cleavage of the disulfide bond (see Supporting Information Figure S2). The PEG-SS-$PBLG_9$ in the buffer solution was readily precipitated in the presence of 10 mM GSH, implying formation of large aggregates. The precipitation might occur due to the cleavage of disulfide linkages, leading to disintegration of the micellar structure and formation of large aggregates by hydrophobic interaction between PBLG blocks detached from the micelles. On the other hand, no precipitates were observed in the control solution containing PEG-*b*-$PBLG_9$ and 10 mM GSH, suggesting high stability of the control polymer in the reductive environment.

Drug Release Pattern. In this study, CPT was chosen as a model anticancer drug because its applications have been limited by poor solubility in water, structural instability, and high toxicity to normal cells. In order to surmount these drawbacks of CPT, it is needed to develop a carrier that can increase the water solubility of CPT, preserve its chemical structure, and deliver it to the intracellular level of the cancer cell. Obviously, PEG-SS-PBLG diblock copolymers may have potential as the carrier of CPT, owing to their ability to form bioreducible nanoparticles that can imbibe hydrophobic drugs.

Table 2 shows the characteristics of CPT-loaded nanoparticles, prepared by the solvent casting method. In this experiment, PEG-SS-$PBLG_9$ copolymer was used to prepare bioreducible micelles, whereas PEG-*b*-$PBLG_9$ without disulfide bonds was used as the control. Three CPT-loaded PEG-SS-PBLG micelles (CPT-SS-PMs) were obtained by varying the feed amount of CPT. An increase in the feed amount of CPT decreased its loading efficiency. However, regardless of the feed amount of

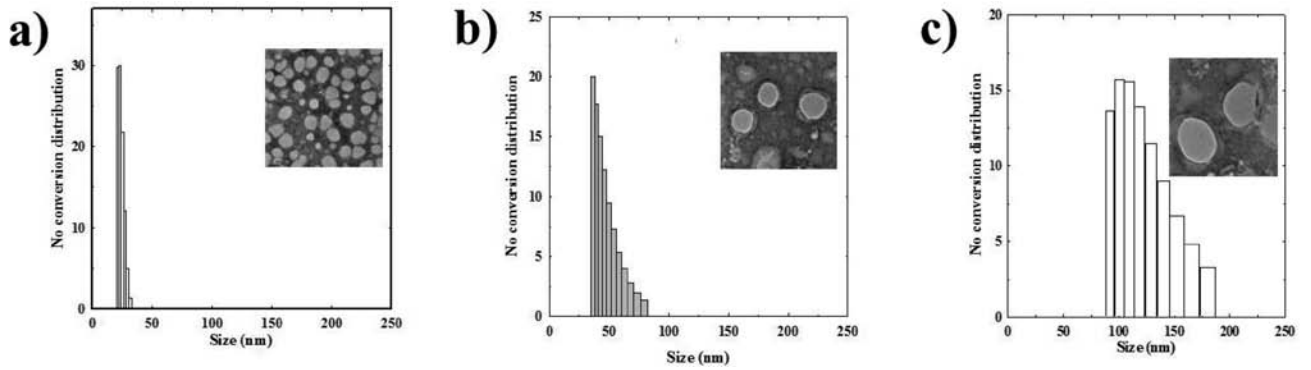

Figure 4. Size distribution of PEG-SS-PBLG nanoparticles: (a) PEG-SS-PBLG$_4$; (b) PEG-SS-PBLG$_9$; (c) PEG-SS-PBLG$_{13}$. The insets are for TEM images of each nanoparticle.

Table 2. Physicochemical Characteristics of CPT-Loaded Block Copolymers

sample name	CPT feed amount (%)	loading efficiency (%)[a]	loading content (%)[a]	mean diameter (nm)[b]
CPT5-SS-PM	5	83 ± 2.14	4.3%	76 ± 9.86
CPT10-SS-PM	10	79 ± 0.58	7.9%	94 ± 11.26
CPT20-SS-PM	20	60 ± 0.53	12.1%	120 ± 14.86
CPT10-PM	10	74 ± 2.30	7.4%	90 ± 6.60

[a] Determined using UV−visible spectrophotometer. [b] Determined using the particle analyzer.

CPT, its loading efficiencies were always greater than 60%, implying that CPT was effectively encapsulated into the micelles by the solvent casting method. The particle sizes of CPT-SS-PMs (77−120 nm) were higher than that of the bare PEG-SS-PBLG$_9$ micelle (51 nm), and the micellar size increased as the drug loading content increased. The loading efficiency and loading content of CPT for the PEG-*b*-PBLG$_9$ copolymer were comparable to those for the PEG-SS-PBLG$_9$ copolymer, suggesting that the disulfide bond did not affect the loading pattern of CPT.

The release behavior of CPT from the micelles was evaluated in the presence and absence of GSH (Figure 5). In this experiment, CPT10-SS-PM and CPT10-PM were used for investigation because they possessed similar amounts of CPT, as summarized in Table 2. In the absence of GSH, CPT10-SS-PM released 26% of CPT in the initial 3 h, after which its release rate decreased remarkably. In particular, after 10 h, no significant release of CPT occurred for the remaining period of time tested. On the other hand, in the presence of 10 mM GSH mimicking the intracellular environment, CPT was rapidly released from CPT10-SS-PM, resulting in complete release within 20 h. This might be due to the cleavage of the disulfide bond in the PEG-SS-PBLG copolymer, causing the disintegration of the micellar structure. It is of interest to note that the release behavior of CPT from CPT10-PM was not affected by GSH. Specifically, the release pattern of CPT from CPT10-PM was identical to that from CPT10-SS-PM in the absence of GSH. These results suggest that the disulfide bond in the copolymer was responsible for the rapid release of CPT, triggered by GSH.

The reduction sensitivity of micelles was investigated using DOX-loaded PEG-SS-PBLG$_9$ (DOX-SS-PM) and PEG-*b*-PBLG$_9$ (DOX-PM) in the presence of GSH as the reducing agent. Since DOX,

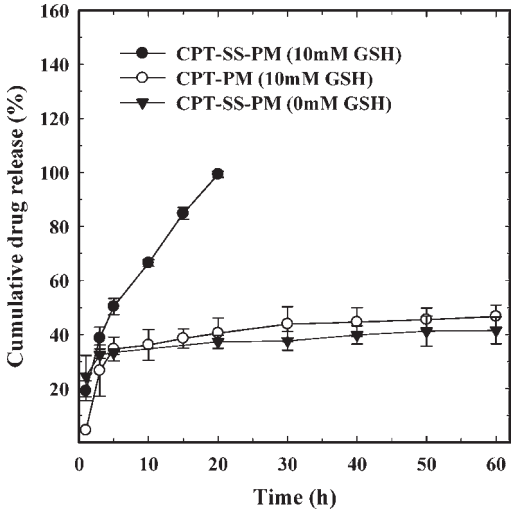

Figure 5. *In vitro* release behavior of CPT from PEG-SS-PBLG$_9$ in the absence and presence of GSH. The CPT-loaded PEG-*b*-PBLG$_9$ micelle (CPT-PM) was used as the control. The error bars in the graph represent standard deviations (n = 3).

an anticancer drug, is a hydrophobic fluorescent substance, it can be readily encapsulated into micelles in the quenched state.[9,36] Therefore, the release of DOX from micelles generates a fluorescent signal, and its intensity can be measured to estimate the concentration of DOX released. In this study, we aimed to evaluate the reduction sensitivity of micelles by observing the fluorescence images of DOX in micelles using the optical imaging technique. Figure 6 shows the fluorescence image of DOX as a function of the GSH concentration after a 1 h incubation of the DOX-loaded micelles in a PBS (pH 7.4) solution. In the absence of GSH, no significant fluorescence signals were observed for both DOX-PM and DOX-SS-PM, suggesting that most of the DOX existed in quenched states at the hydrophobic cores of the micelles. The fluorescent intensity of DOX-PM slightly increased as the GSH concentration increased, which might be due to the amphiphilic character of GSH that can weaken micellar integrity. Interestingly, DOX-SS-PM showed strong fluorescent signals at concentrations greater than 1 mM GSH, suggesting the rapid release of DOX from the micelles. These results imply that PEG-SS-PBLG micelles were highly susceptible to GSH, which is in good agreement with the release pattern of CPT in Figure 5.

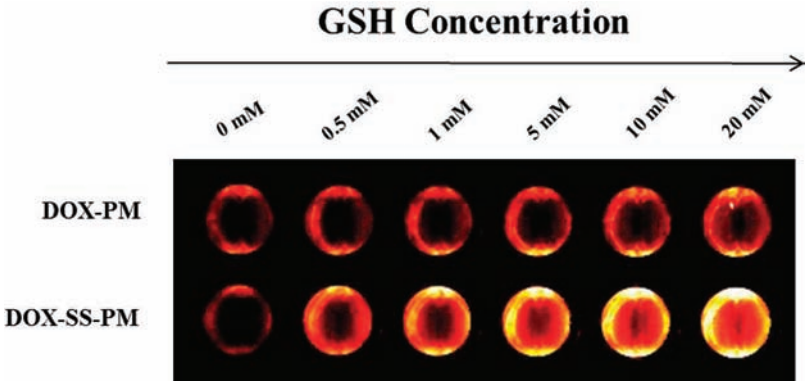

Figure 6. Fluorescent images of DOX-PM and DOX-SS-PM under different concentrations of GSH.

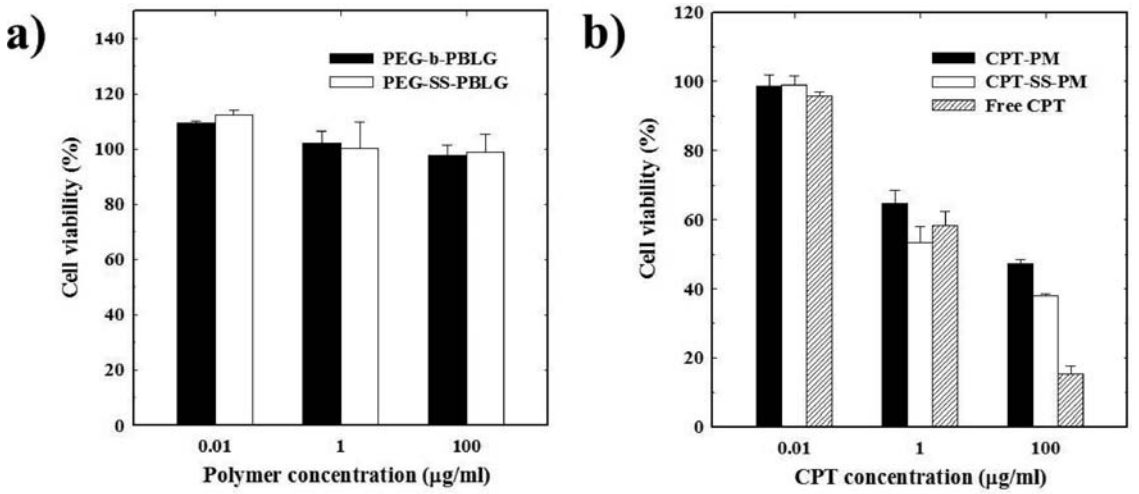

Figure 7. *In vitro* cytotoxicity of (a) bare micelles and (b) CPT-loaded micelles. The error bars in the graph represent standard deviations (n = 3).

***In Vitro* Cell Cytotoxicity and Cellular Uptake.** Figure 7 shows the cytotoxic effects of micelles with and without CPT on SCC7 cells, as evaluated using the MTT assay. Owing to their biocompatibilities, PEG-SS-PBLG$_9$ and PEG-*b*-PBLG$_9$ did not exhibit cytotoxicity to SCC7 cells. In particular, most cells were viable up to 100 μg/mL of PEG-SS-PBLG$_9$, indicating that the disulfide bond in the micelle was not harmful to the cells. Alternatively, due to the presence of the anticancer drug, both CPT10-SS-PM and CPT10-PM showed dose-dependent cytotoxicity to SCC7 cancer cells. It is important to note that the cytotoxicity of CPT-SS-PM to SCC7 cells was significantly greater than that of CPT-PM, which may be due to the rapid release of CPT from bioreducible micelles by cleavage of the disulfide bond in an intracellular environment (Figure 2).

To verify intracellular drug release, the DOX-loaded samples were monitored using the fluorescence microscope after they were treated with the SCC7 cancer cells. Since DOX interacts with DNA by specific intercalation, the fluorescence signal can be detected at the nucleus when the micelles release DOX. The results showed that, after a 12 h incubation of DOX-SS-PMs, strong fluorescence was observed at the nucleus of the cell, resulting from the rapid release of DOX from the micelles (Figure 8). On the contrary, for the reduction-insensitive control (DOX-PM), fluorescent signal was partially observed at the cytoplasm of the cell.

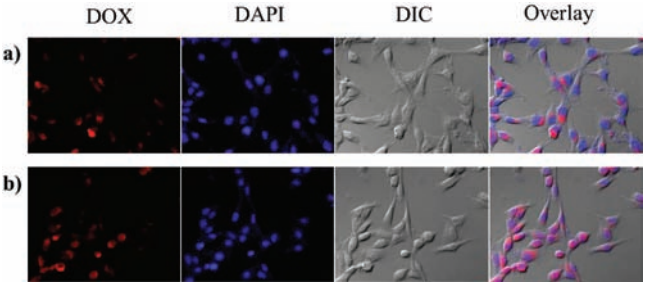

Figure 8. Fluorescent microscopic image of SCC7 cells incubated with (a) DOX-PM and (b) DOX-SS-PM. Each sample (50 μg/mL in PBS) was incubated with SCC7 tumor cells in a serum free medium for 12 h.

Therefore, it could be concluded that the DOX-SS-PMs, sensitive to GSH at the intracellular level, could effectively deliver the drug for enhanced therapeutic effect.

CONCLUSION

A series of PEG-SS-PBLG diblock copolymers, cleavable in intracellular environments, were synthesized as potential carriers of CPT for cancer therapy. The copolymers formed stable micelles in an aqueous solution and encapsulated CPT in hydrophobic

dx.doi.org/10.1021/bc2000963 |*Bioconjugate Chem.* 2011, 22, 1924–1931

inner cores with the high loading efficiency. The resulting bioreducible micelles could release CPT in the presence of GSH to mimic the reductive environment. As a consequence, CPT-loaded micelles exhibited high toxicity to SCC7 cancer cells. These results indicate that PEG-SS-PBLG block copolymers have promising potential as carriers of CPT for its selective delivery to the intracellular level of the cancer cells.

■ ASSOCIATED CONTENT

Supporting Information. Pyrene intensity as a function of the polymer concentration and photographical images of polymer solutions at 0 mM and 10 mM GSH. This material is available free of charge via the Internet at http://pubs.acs.org.

■ AUTHOR INFORMATION

Corresponding Authors

*Chang Kyoo Yoo, Ph.D., Department of Environmental Science and Engineering, College of Engineering, Kyung Hee University, Gyeonggi-do 446-701, Republic of Korea. Tel: +82-31-201-3824; fax: +82-31-202-8854; e-mail: ckyoo@khu.ac.kr. Jae Hyung Park, Ph.D., Department of Polymer Science and Engineering, College of Engineering, Sungkyunkwan University, Suwon 440-746, Republic of Korea. Tel: +82-31-290-7280; fax: +82-31-292-8790; e-mail: jhpark1@skku.edu.

■ ACKNOWLEDGMENT

This work was supported by the Conversing Research Program (20090081876) and Basic Science Research Programs (20100027955 and 20100015804) of MEST, National R&D Program for Cancer Control (0920120) of MW, and the BioImaging Research Center at GIST, Republic of Korea.

■ REFERENCES

(1) Kataoka, K., Harada, A., and Nagasaki, Y. (2001) Block copolymer micelles for drug delivery: design, characterization and biological significance. *Adv. Drug Delivery Rev. 47*, 113–131.

(2) Rösler, A., Vandermeulen, G. W. M., and Klok, H.-A. (2001) Advanced drug delivery devices via self-assembly of amphiphilic block copolymers. *Adv. Drug Delivery Rev. 53*, 95–108.

(3) Matsumura, Y., and Maeda, H. (1986) A new concept for macromolecular therapeutics in cancer chemotherapy: mechanism of tumoritropic accumulation of proteins and the antitumor agent smancs. *Cancer Res. 46*, 6387–6392.

(4) Maeda, H., Wu, J., Sawa, T., Matsumura, Y., and Hori, K. (2000) Tumor vascular permeability and the EPR effect in macromolecular therapeutics: a review. *J. Controlled Release 65*, 271–284.

(5) Gref, R., Minamitake, Y., Peracchia, M., Trubetskoy, V., Torchilin, V., and Langer, R. (1994) Biodegradable long-circulating polymeric nanospheres. *Science 263*, 1600–1603.

(6) Machida, Y., Onishi, H., Kurita, A., Hata, H., and Morikawa, A. (2000) Pharmacokinetics of prolonged-release CPT-11-loaded microspheres in rats. *J. Controlled Release 66*, 159–175.

(7) Musumeci, T., Ventura, C. A., Giannone, I., Ruozi, B., Montenegro, L., Pignatello, R., and Puglisi, G. (2006) PLA/PLGA nanoparticles for sustained release of docetaxel. *Int. J. Pharm. 325*, 172–179.

(8) Shuai, X., Ai, H., Nasongkla, N., Kim, S., and Gao, J. (2004) Micellar carriers based on block copolymers of poly([var epsilon]-caprolactone) and poly(ethylene glycol) for doxorubicin delivery. *J. Controlled Release 98*, 415–426.

(9) Bae, Y., Fukushima, S., Harada, A., and Kataoka, K. (2003) Design of environment-sensitive supramolecular assemblies for intracellular drug delivery: polymeric micelles that are responsive to intracellular pH change. *Angew. Chem., Int. Ed. 42*, 4640–4643.

(10) Koo, A. N., Lee, H. J., Kim, S. E., Chang, J. H., Park, C., Kim, C., Park, J. H., and Lee, S. C. (2008) Disulfide-cross-linked PEG-poly(amino acid)s copolymer micelles for glutathione-mediated intracellular drug delivery. *Chem. Commun.* 6570–6572.

(11) Duncan, R., Gac-Breton, S., Keane, R., Musila, R., Sat, Y. N., Satchi, R., and Searle, F. (2001) Polymer-drug conjugates, PDEPT and PELT: basic principles for design and transfer from the laboratory to clinic. *J. Controlled Release 74*, 135–146.

(12) Shamay, Y., Adar, L., Ashkenasy, G., and David, A. (2011) Light induced drug delivery into cancer cells. *Biomaterials 32*, 1377–1386.

(13) Zhang, H., Xia, H., Wang, J., and Li, Y. (2009) High intensity focused ultrasound-responsive release behavior of PLA-b-PEG copolymer micelles. *J. Controlled Release 139*, 31–39.

(14) Min, K. H., Kim, J.-H., Bae, S. M., Shin, H., Kim, M. S., Park, S., Lee, H., Park, R.-W., Kim, I.-S., Kim, K., Kwon, I. C., Jeong, S. Y., and Lee, D. S. (2010) Tumoral acidic pH-responsive MPEG-poly([beta]-amino ester) polymeric micelles for cancer targeting therapy. *J. Controlled Release 144*, 259–266.

(15) Oh, K. T., Yin, H., Lee, E. S., and Bae, Y. H. (2007) Polymeric nanovehicles for anticancer drugs with triggering release mechanisms. *J. Mater. Chem. 17*, 3987–4001.

(16) Gao, W., Chan, J. M., and Farokhzad, O. C. (2010) pH-responsive nanoparticles for drug delivery. *Mol. Pharmaceutics 7*, 1913–1920.

(17) Liu, S. Q., Tong, Y. W., and Yang, Y.-Y. (2005) Incorporation and in vitro release of doxorubicin in thermally sensitive micelles made from poly(N-isopropylacrylamide-co-N,N-dimethylacrylamide)-b-poly(d,l-lactide-co-glycolide) with varying compositions. *Biomaterials 26*, 5064–5074.

(18) He, C., Kim, S. W., and Lee, D. S. (2008) In situ gelling stimuli-sensitive block copolymer hydrogels for drug delivery. *J. Controlled Release 127*, 189–207.

(19) Jones, D. P., Carlson, J. L., Samiec, P. S., Sternberg, P., Mody, V. C., Reed, R. L., and Brown, L. A. S. (1998) Glutathione measurement in human plasma: Evaluation of sample collection, storage and derivatization conditions for analysis of dansyl derivatives by HPLC. *Clin. Chim. Acta 275*, 175–184.

(20) Saito, G., Swanson, J. A., and Lee, K.-D. (2003) Drug delivery strategy utilizing conjugation via reversible disulfide linkages: role and site of cellular reducing activities. *Adv. Drug Delivery Rev. 55*, 199–215.

(21) Matsumoto, S., Christie, R. J., Nishiyama, N., Miyata, K., Ishii, A., Oba, M., Koyama, H., Yamasaki, Y., and Kataoka, K. (2008) Environment-responsive block copolymer micelles with a disulfide cross-linked core for enhanced siRNA delivery. *Biomacromolecules 10*, 119–127.

(22) Takae, S., Miyata, K., Oba, M., Ishii, T., Nishiyama, N., Itaka, K., Yamasaki, Y., Koyama, H., and Kataoka, K. (2008) PEG-detachable polyplex micelles based on disulfide-linked block catiomers as bioresponsive nonviral gene vectors. *J. Am. Chem. Soc. 130*, 6001–6009.

(23) Zugates, G. T., Anderson, D. G., Little, S. R., Lawhorn, I. E. B., and Langer, R. (2006) Synthesis of poly(β-amino ester)s with thiol-reactive side chains for DNA delivery. *J. Am. Chem. Soc. 128*, 12726–12734.

(24) Kim, H., Kim, S., Park, C., Lee, H., Park, H. J., and Kim, C. (2010) Glutathione-induced intracellular release of guests from mesoporous silica nanocontainers with cyclodextrin gatekeepers. *Adv. Mater. 22*, 4280–4283.

(25) Navath, R. S., Kurtoglu, Y. E., Wang, B., Kannan, S., Romero, R., and Kannan, R. M. (2008) Dendrimer−drug conjugates for tailored intracellular drug release based on glutathione levels. *Bioconjugate Chem. 19*, 2446–2455.

(26) Sun, H., Guo, B., Cheng, R., Meng, F., Liu, H., and Zhong, Z. (2009) Biodegradable micelles with sheddable poly(ethylene glycol) shells for triggered intracellular release of doxorubicin. *Biomaterials 30*, 6358–6366.

(27) Sun, H., Guo, B., Li, X., Cheng, R., Meng, F., Liu, H., and Zhong, Z. (2010) Shell-sheddable micelles based on dextran-SS-poly(ε-caprolactone) diblock copolymer for efficient intracellular release of doxorubicin. *Biomacromolecules 11*, 848–854.

(28) Sun, Y., Yan, X., Yuan, T., Liang, J., Fan, Y., Gu, Z., and Zhang, X. (2010) Disassemblable micelles based on reduction-degradable amphiphilic graft copolymers for intracellular delivery of doxorubicin. *Biomaterials 31*, 7124–7131.

(29) Tang, L.-Y., Wang, Y.-C., Li, Y., Du, J.-Z., and Wang, J. (2009) Shell-detachable micelles based on disulfide-linked block copolymer as potential carrier for intracellular drug delivery. *Bioconjugate Chem. 20*, 1095–1099.

(30) Daly, W. H., and Poché, D. (1988) The preparation of N-carboxyanhydrides of [alpha]-amino acids using bis(trichloromethyl)carbonate. *Tetrahedron Lett. 29*, 5859–5862.

(31) Wilhelm, M., Zhao, C. L., Wang, Y., Xu, R., Winnik, M. A., Mura, J. L., Riess, G., and Croucher, M. D. (1991) Poly(styrene-ethylene oxide) block copolymer micelle formation in water: a fluorescence probe study. *Macromolecules 24*, 1033–1040.

(32) Ko, J., Park, K., Kim, Y.-S., Kim, M. S., Han, J. K., Kim, K., Park, R.-W., Kim, I.-S., Song, H. K., Lee, D. S., and Kwon, I. C. (2007) Tumoral acidic extracellular pH targeting of pH-responsive MPEG-poly([beta]-amino ester) block copolymer micelles for cancer therapy. *J. Controlled Release 123*, 109–115.

(33) Kwon, S., Park, J. H., Chung, H., Kwon, I. C., Jeong, S. Y., and Kim, I.-S. (2003) Physicochemical characteristics of self-assembled nanoparticles based on glycol chitosan bearing 5β-cholanic acid. *Langmuir 19*, 10188–10193.

(34) Kim, C., Lee, S. C., Kang, S. W., Kwon, I. C., Kim, Y.-H., and Jeong, S. Y. (2000) Synthesis and the micellar characteristics of poly(ethylene oxide)−deoxycholic acid conjugates1. *Langmuir 16*, 4792–4797.

(35) Saravanakumar, G., Choi, K. Y., Yoon, H. Y., Kim, K., Park, J. H., Kwon, I. C., and Park, K. (2010) Hydrotropic hyaluronic acid conjugates: Synthesis, characterization, and implications as a carrier of paclitaxel. *Int. J. Pharm. 394*, 154–161.

(36) Gillies, E. R., and Fréchet, J. M. J. (2005) pH-responsive copolymer assemblies for controlled release of doxorubicin. *Bioconjugate Chem. 16*, 361–368.

(Supplementary Information)

Bioreducible Block Copolymers Based on Poly(Ethylene Glycol) and Poly(γ-Benzyl L-Glutamate) for Intracellular Delivery of Camptothecin

Thavasyappan Thambi,[1] Hong Yeol Yoon,[1] Kwangmeyung Kim,[2]
Ick Chan Kwon,[2] Chang Kyoo Yoo[3,**], and Jae Hyung Park [1,*]

[1]Theranostic Macromolecules Research Center, Department of Polymer Science and Engineering, Sungkyunkwan University, Suwon 440-746, Republic of Korea
[2]Biomedical Research Center, Korea Institute of Science and Technology, Seoul 136-791, Republic of Korea
[3]Department of Environmental Science and Engineering, College of Engineering, Kyung Hee University, Gyeonggi-do 446-701, Republic of Korea

*Corresponding author:
Jae Hyung Park, Ph.D.
Department of Polymer Science and Engineering
College of Engineering
Sungkyunkwan University, Suwon 440-746, Republic of Korea
Tel: +82-31-290-7280; fax: +82-31-292-8790; e-mail: jhpark1@skku.edu

**Co-corresponding author:
Chang Kyoo Yoo, Ph.D.
Department of Environmental Science and Engineering
College of Engineering
Kyung Hee University, Gyeonggi-do 446-701, Republic of Korea
Tel: +82-31-201-3824; fax: +82-31-202-8854; e-mail: ckyoo@khu.ac.kr

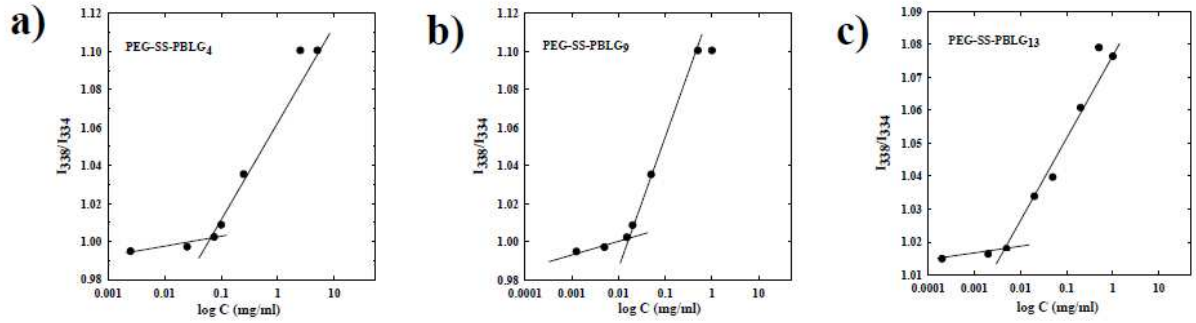

Figure S1. Plot of pyrene intensity versus polymer concentration: (a) PEG-SS-PBLG$_4$; (b) PEG-SS-PBLG$_9$; and (c) PEG-SS-PBLG$_{13}$.

a)

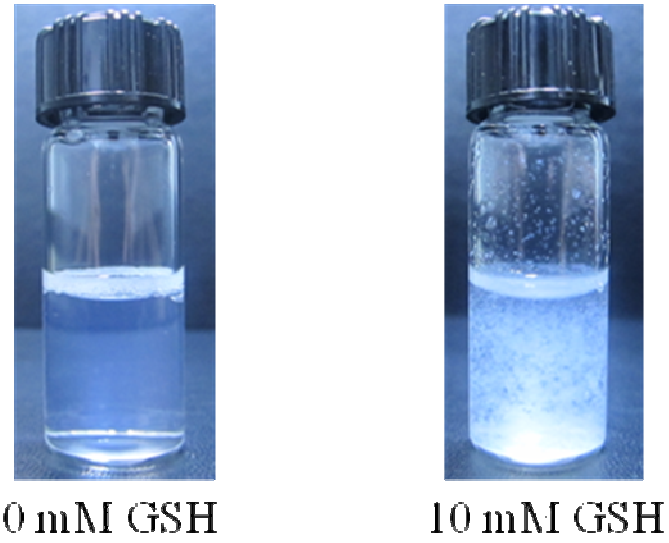

b)

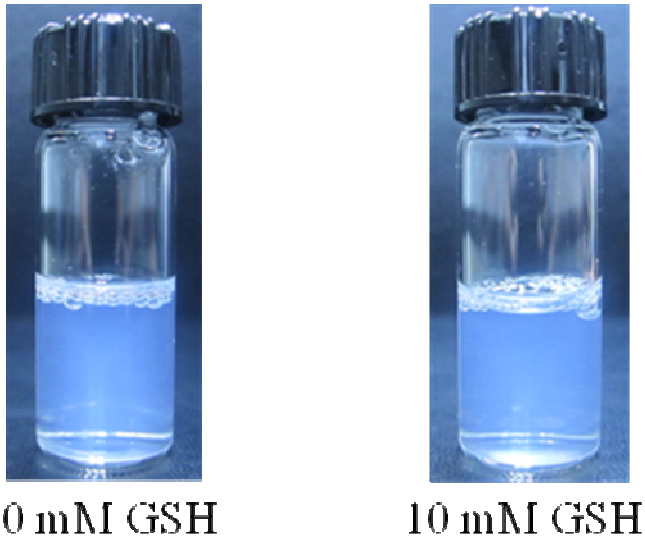

Figure S2. Photographical images of (a) PEG-SS-PBLG and (b) PEG-***b***-PBLG block copolymers at 0 m***M*** and 10 m***M*** GSH. The photographs were taken after 24 h.

Bioconjugate Chemistry

ARTICLE

pubs.acs.org/bc

Morpholinecarbonyl-Rhodamine 110 Based Substrates for the Determination of Protease Activity with Accurate Kinetic Parameters

Tatyana G. Terentyeva,[†] Wim Van Rossom,[†] Mark Van der Auweraer,[†] Kerstin Blank,*[,†,‡] and Johan Hofkens[†]

[†]Department of Chemistry, Katholieke Universiteit Leuven, Celestijnenlaan 200F, 3001 Heverlee, Belgium

[‡]Department of Molecular Materials, Institute for Molecules and Materials, Radboud University Nijmegen, Heyendaalseweg 135, 6525 AJ Nijmegen, The Netherlands

Supporting Information

ABSTRACT: Commonly used fluorogenic substrate analogues for the detection of protease activity contain two enzyme-cleavable bonds conjugated to the fluorophore. Enzymatic cleavage follows a two-step reaction with a monoamide intermediate. This intermediate shows fluorescence at the same wavelength as the final product complicating the kinetic analysis of fluorescence-based assays. Fluorogenic substrate analogues for α-chymotrypsin with one cleavable peptide bond have been prepared from morpholinecarbonyl-Rhodamine 110 (MC-Rh110). A comparison of their kinetic properties with the corresponding $(peptide)_2$-Rh110 derivatives revealed that these frequently used double-substituted substrate analogues yield only apparent K_m and k_{cat} values that are quite different from the kinetic parameters obtained from the monosubstituted MC-Rh110 based substrate analogues. Although both the monoamide intermediate and MC-Rh110 are monosubstituted Rhodamine 110 derivatives, they show different spectroscopic properties. The data from the spectroscopic analysis clearly show that these properties are directly related to the electron structure of the fluorophore and not to the previously proposed equilibrium between the lactone form and the open ionic form of the fluorophore. This knowledge about the determinants of the spectroscopic properties of monosubstituted Rhodamine 110 introduces a way for a more systematic development of new fluorogenic protease substrate analogues.

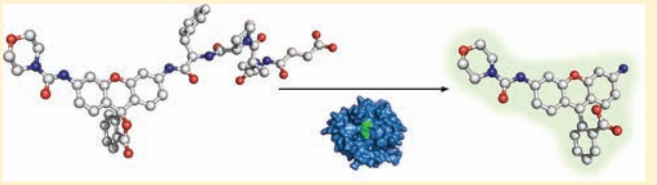

INTRODUCTION

Proteases and peptidases (EC 3.4) are enzymes that catalyze the hydrolysis of peptide bonds. They constitute approximately 2% of the human genome and are involved in many physiological processes such as cell-cycle progression, tissue remodeling, coagulation, wound healing, cell proliferation, and cell death, as well as the immune response.[1] Their involvement in these biological processes makes proteases very important drug targets. Furthermore, proteases are important biocatalysts for a wide range of industrial applications. Understanding the enzymatic mechanism and the factors determining their substrate specificity is therefore of crucial importance for the characterization of their medical relevance as well as for obtaining optimized biocatalysts.

To assay enzyme activity and substrate specificity, fluorogenic probes are commonly used.[2−4] The chemical modification of a fluorophore with one or two enzyme-cleavable bonds alters its photophysical properties and results in a nonfluorescent derivative. The fluorescence is recovered upon enzymatic cleavage. Peptide-based substrate analogues can further be designed based on photoinduced electron transfer[5] or fluorescence resonance energy transfer.[6,7] Fluorescence is often chosen as a detectable signal as it provides high sensitivity *in vitro*. Moreover, fluorescent probes also find widespread application in living cells and tissues where they provide high spatial and temporal resolution.

The choice of fluorophore is critical for the design of a good enzyme substrate analogue, and favorable fluorescent molecules have to meet several requirements: (i) high brightness to obtain high sensitivity, (ii) fluorescence excitation above 450 nm to reduce photodamage in biological molecules and to avoid interference with autofluorescence of biological samples, and (iii) no interference with the enzymatic reaction so that the kinetic parameters remain unaltered.[8] Although frequently used, Coumarin-based substrate analogues have a low brightness and are excited below 450 nm. Common fluorophores which possess the aforementioned properties and are often used for introducing an enzyme-cleavable bond are fluorescein, resorufin, and 7-hydroxy-9*H*-(1,3-dichloro-9,9-dimethylacridin-2-one) (DDAO) for esterases, phosphoesterases, and glycosidases. Fluorophores used for proteases are Rhodamine 110 and cresyl violet. The latter, however, yields only substrate analogues with insufficient stability to autohydrolysis in aqueous solutions.[9] Except for resorufin and DDAO, these substrate analogues contain two sites for conjugating the enzyme-cleavable group.[10−12] Using the double-substituted pro-fluorescent derivatives for kinetic measurements complicates a

Received: February 25, 2011
Revised: July 13, 2011
Published: September 12, 2011

ACS Publications © 2011 American Chemical Society

dx.doi.org/10.1021/bc2001038 | *Bioconjugate Chem.* 2011, 22, 1932–1938

quantitative analysis, since full fluorescence manifestation requires the cleavage of two bonds involving an intermediate with a different fluorescence intensity.

The difficulty of quantifying the kinetic constants of such a two-step reaction has been addressed in several studies, and solutions have been proposed to obtain the kinetic constants.[13,14] These approaches, however, always require the detection of the intermediate concentration, which is often not possible in a fluorescence measurement due to the overlap of the excitation and emission spectra of the intermediate and the final product. Other assays to determine the intermediate concentration such as HPLC might not be considered feasible especially in high-throughput assays or measurements in cellular systems. As a consequence, efforts are being made to synthesize monosubstituted substrate analogues, and a number of examples exist utilizing Rhodamine 110 (Rh110).

The most obvious solution might be to attach only one peptide to the Rh110 core. Although this yields a stable molecule, the applicability of such a monoamide Rh110 derivative is limited by its fluorescence, which is approximately still 10% relative to Rh110.[15] Hence, it is desirable to develop Rh110-based substrate analogues that have no intrinsic fluorescence while possessing only one enzyme cleavable bond. This has been achieved by modifying one of the amino groups with a nonhydrolyzable blocking group while attaching a peptide to the second amino group. Initially designed to increase cell permeability, a range of different blocking groups have been investigated, but they mostly yield dye molecules with a relative fluorescence intensity of only 5−15% compared to Rh110.[16−18] The best blocking group known to date, which preserves much of the high fluorescence of Rh110, introduces a urea functionality into Rh110.[19] Originally designed by Wang et al.,[20] morpholinecarbonyl-Rh110 (MC-Rh110) is a promising candidate for developing sensitive monoamide substrate analogues.

Although Rh110 has been used for many years to synthesize substrate analogues for proteases, the properties of the monosubstituted derivatives have never been investigated systematically. Double-substitution of Rh110 yields a nonfluorescent lactone. Consequently, it has been proposed in several reports that the fluorescence of monosubstituted Rh110 is determined by an equilibrium between a nonfluorescent monosubstituted lactone form and an open zwitterionic fluorescent form of the molecule. It was further suggested that the electron withdrawing character of the substituent influences this equilibrium and therefore the fluorescence intensity of the respective derivative.[18,20]

Using α-chymotrypsin as the model system, we determined the enzyme kinetic parameters for different MC-Rh110 based substrate analogues and compared them with conventional bisamide Rh110 substrate analogues. Furthermore, we performed a systematic analysis of the photophysical properties of MC-Rh110 and monoamide Rh110 in order to understand why different substituents on one of the amino-groups of Rh110 yield derivatives with different fluorescence intensity.

EXPERIMENTAL PROCEDURES

Synthetic Approaches. Unless stated otherwise, reagents were obtained from Sigma-Aldrich or Acros. The substrate analogues were purified on a Waters 996 HPLC with a Waters 600 controller. Reversed-phase C18 columns (Alltech Previal or Phenomenex Luna, both 15 cm long with 2.1 mm diameter and 5 μm particle size) were used. MPLC chromatography was performed using a Büchi Sepacore Flash apparatus. Mass spectra were run using Thermo Finnigan LCQ Advantage apparatus (ESI). NMR spectra were acquired on commercial instruments (Bruker Avance 300 MHz, Bruker AMX 400 MHz or Bruker Avance II+ 600 MHz with TXI probe or TCI CryoProbe) and chemical shifts (δ) are reported in parts per million (ppm) referenced to tetramethylsilane (^{1}H) or the internal (NMR) solvent signals (^{13}C). Rhodamine 110 (99% pure, laser grade, Acros) was used for the synthesis of the substrate analogues.

Chart 1

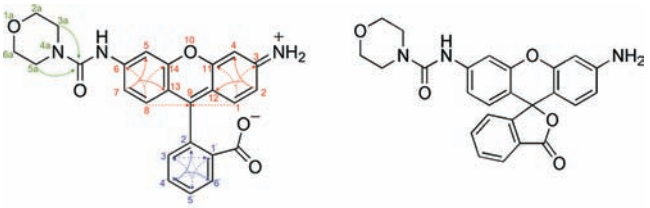

(suc-AlaAlaProPhe)$_2$-Rh110; (sucAAFP)$_2$-Rh110. The synthesis of (sucAAPF)$_2$-Rh110 was performed as described in the Supporting Information of De Cremer et al.[21] and verified by ESI and NMR spectrometry.

MC-Rh110. The synthesis of MC-Rh110 was based on the method described in the patent application by Diwu et al.[22] Since the described purification procedure using a silica gel column did not yield pure product, the dye was purified with MPLC using a mixture of EtOAc/$CHCl_3$/MeOH (50:47.5:2.5). Yield: 25%. MS (ESI+): 444 (MH^+). ^{1}H NMR (600 MHz, $CDCl_3$): δ (ppm) 7.99 (d, J = 7.9 Hz, 1H; H-6′), 7.65 (t, J = 7.5 Hz, 1H; H-5′), 7.59 (t, J = 7.5 Hz, 1H; H-4′), 7.50 (s, 1H; H-5), 7.15 (d, J = 7.6 Hz, 1H; H-3′), 6.83 (d, J = 6.8 Hz, 1H; H-7), 6.63 (d, J = 8.6 Hz, 1H; H-8), 6.53 (d, J = 8.3 Hz, 1H; H-1), 6.51 (s, 2H; H-4), 6.34 (d, J = 6.8 Hz, 1H; H-2), 3.90 (s_b, 2H; NH_2), 3.74 (t, J = 4.7 Hz, 4H; H-2a, 6a), 3.49 (t, J = 4.7 Hz, 4H; H-3a, 5a). ^{13}C NMR (125 MHz, $CDCl_3$): δ (ppm) 169.8 (C; COO), 154.7 (C; CO), 153.4 (C; C-6), 152.8 (C; C-11), 152.1 (C; C-14), 149.0 (C; C-3), 141.0 (C; C-2′), 135.1 (CH; C-4′), 129.7 (CH; C-1), 129.2 (CH; C-8), 128.5 (CH; C-5′), 126.9 (C; C-1′), 125.0 (CH; C-6′), 124.2 (CH; C-3′), 115.2 (CH; C-7), 113.6 (C; C-13), 111.7 (CH; C-2), 108.6 (C; C-12), 107.6 (CH; C-5), 101.6 (CH; C-4), 84.1 (C; C-9), 66.6 (CH_2; C-2a, 6a), 44.4 (CH_2; C-3a, 5a).

^{1}H NMR (600 MHz, D_2O + 5% DMSO-d_6): δ (ppm) 8.02 (d, J = 7.3 Hz, 1H; H-6′), 7.89 (s, 1H; H-5), 7.78 (t, J = 7.3 Hz, 1H; H-5′), 7.75 (t, J = 7.3 Hz, 1H; H-4′), 7.45 (d, J = 8.6 Hz, 1H; H-8), 7.44 (d, J = 8.6 Hz, 1H; H-1), 7.40 (d, J = 7.3 Hz, 1H, H-3′), 7.36 (d, J = 8.6 Hz, 1H; H-7), 7.00 (d, J = 10.6 Hz, 1H; H-2), 6.95 (s, 1H; H-4), 3.82 (t, J = 4.6 Hz, 4H; H-2a, 6a), 3.82 (t, J = 4.6 Hz, 4H; 3a, 5a). Carbon signals as derived from HSQC and HMBC NMR measurements (D_2O + 5% DMSO-d_6): δ (ppm) 164 (COO^-), 160.8 (C-3), 160 (C-14), 159.8 (C-11), 156 (CO), 155.1 (C-6), 147.6 (C-9), 137.8 (C-1′), 133 (C-1), 131.3 (C-2′), 130.4 (C-8), 130.2 (C-4′) 129.9 (C-5′), 129.6 (C-3′), 128.9 (C-6′), 118.7 (C-2), 118.1 (C-7), 116(C-13), 116.1 (C-12), 105.4 (C-5), 97.4 (C-4), 66.1 (C-2a, 6a), 44.3 (C-3a, 5a). (See Chart 1 for atom numbering and molecular structure in different solutions.)

suc-AlaAlaProPhe-Rh110-MC; sucAAPF-Rh110-MC. TBTU (*N,N,N′,N′*-tetramthyl-*o*-(benzotriazol-1-yl)uranium tetrafluoroborate) was obtained from Novabiochem and Boc-(L)-AlaAlaPro-OH from Bachem. A mixture of TBTU (215 mg, 0.7 mmol) and DIPEA (350 μL, 2 mmol) was dissolved in 1 mL of dry DMF and added to Boc-L-Phe-OH (180 mg, 0.7 mmol) dissolved in 2 mL of dry CH_2Cl_2 under Ar. MC-Rh110 (50 mg, 0.1 mmol) was dissolved in 1 mL dry CH_2Cl_2 and slowly added to the reaction. After 17 h of stirring, the solvents were evaporated and the crude mixture was directly purified by HPLC using an acetonitrile/water gradient (12−100% ACN). Yield: 40% (30 mg, 0.04 mmol) Boc-Phe-Rh110-MC. MS (ESI+): 692 (MH^+).

Deprotection of Phe was achieved by slow addition of 50/50 (v/v) TFA/CH_2Cl_2 (3 mL) to Boc-Phe-Rh110-MC (30 mg, 0.04 mmol) in CH_2Cl_2 (1.5 mL). After 3 h, the reaction was stopped and concentrated under vacuum. MS (ESI+): 592 (MH^+).

TBTU (32 mg, 0.1 mmol) and DIPEA (40 μL, 0.2 mmol) were dissolved in 1 mL of dry DMF and added to a solution of Boc-(L)-AlaAlaPro-OH (35 mg, 0.1 mmol in 3 mL dry THF), kept at 0 °C under Ar. The reaction mixture was stirred for 10 min after which it was left to warm to room temperature. The Phe-Rh110-MC was dissolved in 1 mL of dry THF and added to the above mixture. After stirring the reaction mixture at 37 °C for 12 h, the solvents were evaporated and the mixture was purified by HPLC (45% ACN in water; isocratic). Yield: 52% (21 mg, 0.02 mmol) Boc-AlaAlaProPhe-Rh110-MC. MS (ESI+): 931 (MH^+).

The Boc group was removed as described above and the deprotected product was succinylated in 4 mL THF using triethylamine (25 μL, 0.2 mmol) and succinic anhydride (10 mg, 0.1 mmol) at 37 °C for 10 h. The mixture was purified by HPLC (35% ACN in water; isocratic). Yield: 67% (14 mg, 0.015 mmol). MS (ESI+): 931 (MH^+), 953 (MNa^+). ^{1}H NMR (300 MHz, DMSO): δ (ppm) 9.98 (d, J = 5.4 Hz, 2H), 8.86 (s, 2H), 8.09−8.00 (m, 8H), 7.86 (dd, J = 1.7 Hz, J = 4.9 Hz, 2H), 7.80 (t, J = 7.3 Hz, 2H), 7.73 (t, J = 7.3 Hz, 2H), 7.68 (d, J = 1.9 Hz, 2H), 7.30−7.14 (m, 20H), 6.74 (d, J = 8.7 Hz, 2H), 6.66 (d, J = 8.7 Hz, 2H), 4.58 (dd, J = 1.7 Hz, J = 4.9 Hz, 2H), 4.51 (t, J = 7.0 Hz, 2H), 4.28−4.21 (m, 4H), 3.62 (d, J = 1.9 Hz, 2H), 7.30−7.14 (m, 20H), 6.74 (d, J = 8.7 Hz, 2H), 3.15 (dd, J = 4.7 Hz, J = 14.7 Hz, 2H), 2.93 (dd, J = 9.4 Hz, J = 13.7 Hz, 2H), 2.40−2.31 (m, 8H), 1.99−1.92 (m, 2H), 1.81−1.76 (m, 4H), 1.68−1.63 (m, 2H), 1.19−1.14 (m, 14H).

(suc-Phe)$_2$-Rh110; (suc-F)$_2$-Rh110. (Boc-Phe)$_2$-Rh110 was obtained as the product of the first step of the synthesis of (suc-AAPF)$_2$-Rh110. It was deprotected and succinylated as described above. After purification by HPLC (37% ACN in water; isocratic), the desired (suc-F)$_2$-Rh110 was obtained. MS (ESI+): 826 (MH^+). ^{1}H NMR (600 MHz, DMSO): δ (ppm) 10.39 (s, 2H), 8.38 (d, J = 7.9 Hz, 2H), 8.02 (d, J = 7.5 Hz, 1H), 7.88 (2s, 2H), 7.79 (t, J = 7.5 Hz, 1H), 7.72 (t, J = 7.5 Hz, 1H), 7.28−7.21 (m, 10H), 7.20−7.18 (m, 2H), 6.73 (d, J = 8.7 Hz, 2H), 4.62 (s, 2H), 3.07 (d, J = 9.4 Hz, 2H), 2.87 (t, J = 9.7 Hz, 2H), 2.38−2.24 (m, 8H). ^{13}C NMR (125 MHz, DMSO): δ (ppm) 173.8 (C), 171.3 (C), 170.8 (C), 168.5 (C), 150.6 (C), 140.8 (C), 137.4 (C), 135.4 (CH), 130.0 (CH), 128.9 (CH), 128.2 (CH), 127.9 (CH), 126.2 (CH), 125.6 (C), 124.7 (CH), 123.7 (CH), 115.5 (CH), 113.1 (C), 106.4 (CH), 81.6 (C), 54.8 (CH), 37.3 (CH_2), 30.0 (CH_2), 29.7 (CH_2).

suc-Phe-Rh110-MC; suc-F-Rh110-MC. Boc-Phe-Rh110-MC was obtained as the product of the first step of the synthesis of suc-AAPF-Rh110-MC. Deprotection and succinylation was performed as described above. The purified product was eluted from HPLC using 35% ACN in water (isocratic). MS (ESI+): 692 (MH^+). ^{1}H NMR (400 MHz, DMSO): δ (ppm) 10.51 (s, 1H), 8.78 (s, 1H), 8.39 (d, J = 6.5 Hz, 2H), 7.94 (d, J = 7.8 Hz, 1H), 7.90 (s, 1H), 7.72 (t, J = 7.3 Hz, 1H), 7.65 (t, J = 7.3 Hz, 1H), 7.59 (S, 1H), 7.38−7.35 (m, 1H), 7.21−7.17 (m, 5H), 7.12−7.09 (m 2H), 6.64 (S_{br}, 2H), 6.60 (t, J = 8.3 Hz, 4H), 4.50−4.48 (m, 1H), 3.54 (t, J = 4.3 Hz, 5H), 3.37 (t, J = 4.8 Hz, 5H), 3.07 (dd, J = 4.0 Hz, J = 13.7 Hz, 2H), 2.80 (dd, J = 9.8 Hz, J = 13.4 Hz, 2H), 2.6 (s, 1H), 2.26−2.01 (m, 5H).

Boc-Phe-Rh110; Boc-F-Rh110. During the synthesis of (Boc-Phe)$_2$-Rh110, monosubstituted Boc-F-Rh110 was obtained as a side product after silica chromatography. It was further purified by HPLC using an ACN/water gradient (10−100% ACN). MS (ESI+): 579 (MH^+). NMR: ^{1}H NMR (600 MHz, $CDCl_3$): δ (ppm) 7.99 (d, J = 7.5 Hz, 1H), 7.68−7.56 (m, 3H), 7.30 (d, J = 6.8 Hz, 1H), 7.29−7.21 (m, 3H), 7,14 (d, J = 6.8 Hz, 1H), 6.79 (s_b, 1H), 6.65 (d, J = 8.3 Hz, 1H), 6.55−6.51 (m, 2H), 6.34 (d, J = 7.9 Hz, 1H), 5.10 (s, 1H), 4.44 (s, 1H), 3.90 (s, 2H), 3.15 (s, 2H), 1.42 (s, 9H). ^{13}C NMR (125 MHz, $CDCl_3$): δ (ppm) 177.6 (C), 169.8 (C), 153.4 (C), 152.6 (C), 152.0 (C), 149.0 (C), 139.2 (C), 135.0 (CH), 129.7 (CH), 129.4 (CH), 129.3 (CH), 129.1 (CH), 128.7 (CH), 127.4 (CH), 127.0 (C), 125.1 (CH), 124.1 (CH), 115.2 (CH), 111.8 (CH), 108.6 (C), 108.0 (CH), 101.6 (CH), 100.1 (C), 83.5 (C), 56.8 (CH), 38.1 (CH_2), 28.4 (CH_3).

Boc-AlaAlaProPhe-Rh110; Boc-AAPF-Rh110. For the synthesis of this compound, the coupling of Boc-AlaAlaPro-OH to Phe-Rh110 was not possible, as the peptide might also react with the second amino group of Rh110. Instead, the 4 amino-acid-long peptide Boc-AlaAlaProPhe-OH was coupled to Rh110 directly. In the first step, the peptide Boc-AlaAlaProPhe-OH was synthesized. Boc-AlaAlaPro-OH (200 mg, 0.6 mmol) was dissolved in 10 mL of anhydrous THF at 0 °C. To this solution, a mixture of TBTU (180 mg, 0.6 mmol) and DIPEA (130 μL, 0.7 mmol), dissolved in 2 mL dry DMF, was added. After 10 min, the cooling bath was removed and the reaction mixture was allowed to warm to room temperature. Phe-OMe (160 mg, 0.7 mmol), dissolved in 4 mL dry DMF, was added slowly to the above mixture. After 20 h of stirring, the solvents were evaporated and the crude mixture was purified on a silica gel column using CH_2Cl_2/MeOH (9:1) as the eluent. Removal of the methyl group was carried out in CH_2Cl_2 and 0.3 M NaOH. After that, the reaction was neutralized by HCl and again purified on a silica gel column using CH_2Cl_2/MeOH (9:1) as the eluent. Yield: 83% (250 mg, 0.5 mmol). MS (ESI+): 527 (MNa^+).

Boc-AlaAlaProPhe-OH (53 mg, 0.1 mmol), TBTU (41 mg, 0.1 mmol) and DIPEA (75 μL, 0.4 mmol) were dissolved in 2 mL of dry DMF. To this mixture, Rhodamine 110 chloride (22 mg, 0.06 mmol in 1 mL dry DMF) was added and the solution was stirred overnight at 37 °C. The resulting mixture was evaporated and purified by HPLC (40% ACN in water; isocratic). The yield was only 2% (1.2 mg). MS (ESI+): 818 (MH^+). This low yield was expected, as it has been shown before that the coupling of the complete 4 amino-acid-long peptide is much less efficient than the sequential coupling of amino acids in a multistep reaction.[18]

Kinetic Measurements. Chymotrypsin (α-Chymotrypsin from bovine pancreas; Fluka) was dissolved in PBS (10 mM phosphate pH 7.4, 138 mM NaCl, 2.7 mM KCl; Sigma). Substrates were prepared as stock solutions in DMSO. Reactions were started by adding 190 μL of chymotrypsin in PBS to 10 μL of a substrate solution in the cuvette. The final enzyme

Scheme 1. Two-Step Enzymatic Hydrolysis of the Fluorogenic Substrate Analogue (suc-AAPF)$_2$-Rh110 into the Fluorescent Product Rhodamine 110 Showing the Production of the Less Fluorescent Intermediate

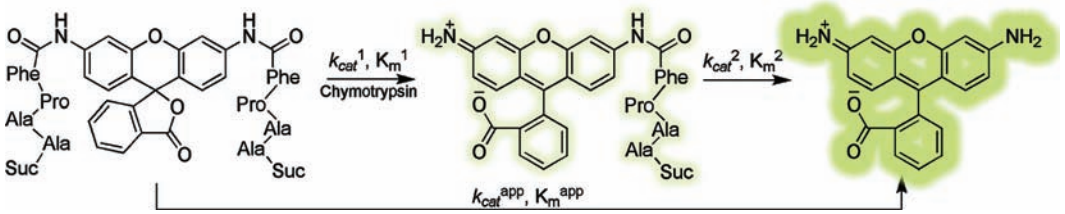

Scheme 2. One-Step Enzymatic Hydrolysis of the Fluorogenic Substrate Analogue (suc-AAPF)-Rh110-MC into the Fluorescent Product MC-Rh110

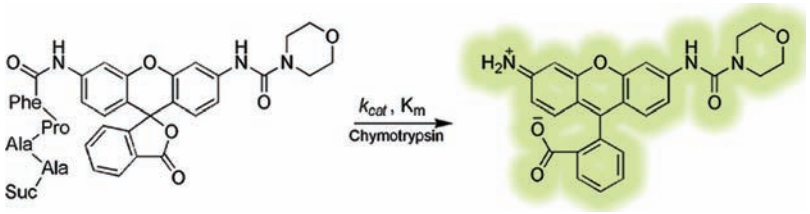

concentration was 3 nM for (suc-AAPF)$_2$-Rh110 and suc-AAPF-Rh110-MC or 900 nM for (suc-F)$_2$-Rh110 and suc-F-Rh110-MC. The substrate concentrations varied between 0.4 and 50 μM. Product formation was followed by recording fluorescence (λ_{ex} = 488 nm; λ_{em} = 520 nm) with a Photon Technology International fluorescence spectrometer. The emission intensity was converted into product concentrations using calibration curves of Rh110 or MC-Rh110, respectively. K_m, k_{cat}, and k_{cat}/K_m values were obtained by least-squares fitting of the data to the Michaelis−Menten equation using *Origin* (see Supporting Information).

Determination of the Absorption and Emission Spectra. Rhodamine 110 chloride (Bioreagent, Sigma) was used to study the photophysical properties. Absorption measurements were performed with a Lambda 40 UV/vis spectrometer (Perkin-Elmer). For the fluorescence measurements, a Photon Technology International fluorescence spectrometer was used.

Fluorescence Lifetime Measurements. Excited-state lifetimes were determined using time-correlated single photon counting (TCSPC). The instrument response function (IRF) was recorded using a LUDOX scattering solution and its fwhm amounted to ~40 ps. The fluorescence decay curves were analyzed by being fitted to a convolution of the IRF with a decay function for a δ-pulse using a TRFA Global Analysis Program based on a Marquard-Levenberg least-squares fitting. The quality of the fit was judged according the criteria published by Boens et al.[23]

Determination of the Quantum Yield. Quantum yield measurements were performed with an integrating sphere using a Fluorolog 3 fluorescence spectrometer (Horiba Jobin Yvon). The procedure as well as the calculations are described in the work of de Mello.[24] The measurements of the fluorophore solutions (absorption between 0.07 and 0.15) were performed in triplicate.

RESULTS AND DISCUSSION

For the enzyme activity measurements, the following substrate analogues were synthesized: (suc-AAPF)$_2$-Rh110, suc-AAPF-Rh110-MC, (suc-F)$_2$-Rh110, and suc-F-Rh110-MC. These molecules were nonfluorescent and stable in aqueous solution. No autohydrolysis could be detected. The bis-amide substrate analogues (suc-AAPF)$_2$-Rh110 and (suc-F)$_2$-Rh110 are hydrolyzed by the enzyme following the two-step reaction shown in Scheme 1. The hydrolysis of the monoamide substrate analogues suc-AAPF-Rh110-MC and suc-F-Rh110-MC follows the reaction of Scheme 2.

Enzymatic activity was measured over a range of substrate concentrations (at least 12 data points) in order to determine the kinetic constants. At least one reaction in each series was followed to completion. In this way, the final product concentration could be determined, which corresponds directly to the initial substrate concentration. This approach yields an accurate value of the substrate concentration even if the respective compound contains noncleavable components such as molecules with D-amino acids that have not been completely removed during purification.

The results (Table 1) clearly show that the activity of α-chymotrypsin is higher for the substrate analogues containing the AAPF sequence instead of phenylalanine only. It has been observed before that the activity of α-chymotrypsin increases with increasing length of the peptide.[25] More interesting are, however, the differences between the peptide-Rh110-MC and the bis-amide Rh110 substrate analogues. For both the 4 amino-acid-long and the 1 amino-acid-long peptides, the k_{cat} values for the peptide-Rh110-MC based substrate analogue are higher than for the (peptide)$_2$-Rh110 substrate analogue. This is expected when considering that the cleavage of the bis-amide substrate analogue (Scheme 1) involves the less fluorescent intermediate. When using the fluorescence of the product as the calibration, the actual number of cleaved bonds is underestimated due to the presence of the intermediate leading to a lower measured reaction velocity and k_{cat}^{app} value. The lower K_m^{app} values for the (peptide)$_2$-Rh110 substrate analogues can potentially result from a higher effective molarity of the cleavable

dx.doi.org/10.1021/bc2001038 |*Bioconjugate Chem.* 2011, 22, 1932–1938

bonds or rebinding of the intermediate after hydrolysis of the first bond. Although we cannot exclude that the MC-moiety influences the binding of the substrate analogues to the enzyme, it appears likely that the kinetic parameters obtained from the hydrolysis of the monoamide peptide-Rh110-MC substrate analogue represent the true kinetic constants related to peptide-bond cleavage. The result that the determined k_{cat}^{app} and K_m^{app} values for the double-substituted substrate analogue do not resemble the real kinetic constants is further supported by the observation that the two cleavage steps are characterized by different kinetic constants as has been shown for other fluorogenic substrate analogues before.[13]

Making several assumptions, we have also made an attempt to calculate the individual kinetic constants of the two-step hydrolysis reaction (see Supporting Information). While the calculated k_{cat}/K_m values for the individual reaction steps have a large error, they are clearly different from each other and from the apparent values. This further emphasizes the problem associated with obtaining kinetic constants for double-substituted substrate analogues. In summary, these results show that the apparent K_m^{app} and k_{cat}^{app} values determined for the double-substituted Rh110 substrate analogues are not the true rate constants characterizing the enzymatic reaction. Clearly, there is no accurate way to determine these from an assay purely based on fluorescence. Monosubstituted substrate analogues such as peptide-Rh110-MC are required for an accurate determination of K_m and k_{cat}.

In order to obtain a more detailed picture of the molecular mechanism determining the fluorescence of MC-Rh110, we also synthesized the monosubstituted peptide-Rh110 derivatives. We expected that a comparison of MC-Rh110 with Boc-F-Rh110 and Boc-AAPF-Rh110 as well as with Rh110 would give insight into the properties determining the high fluorescence intensity of MC-Rh110. The Boc-protected analogues were used instead of the succinylated peptides, because they are easier to obtain in high purity, which is essential for spectroscopic measurements. The Boc-group is not expected to affect the structural and photophysical properties as it has been shown before that only the amino acid closest to the fluorophore determines its properties.[26] The latter is confirmed by our measurements that show similar photophysical properties for Boc-F-Rh110 and Boc-AAPF-Rh110 (see Supporting Information).

For both MC-Rh110 and Boc-F-Rh110, we have observed that their solutions in chloroform do not absorb visible light. This suggests their presence in the nonfluorescent lactone form, which is confirmed by NMR spectra. The ^{1}H signals for protons 1, 2, 7, and 8 of the xanthene moiety are shielded, and the carbon ^{13}C signal at 84 ppm corresponds to carbon 9 (see Supporting Information). Combining the ^{13}C and DEPT spectra indicates that the number of carbons is compatible with the presence of a single molecular species. When these molecules are dissolved in water, however, they absorb in the blue region with a maximum absorption coefficient of 24 600 and 52 000 M^{-1} cm^{-1} for Boc-F-Rh110 and MC-Rh110, respectively. NMR measurements of MC-Rh110 in D_2O/DMSO (5%) confirm the formation of the open zwitterionic form and do not indicate the presence of more than one species. The carbon signals of the benzene ring and C-2, 3 of the xanthene moiety show very similar ppm values as for unsubstituted Rh110 (see Supporting Information).[27] X-ray diffraction analysis of MC-Rh110 single-crystals, obtained from the slow evaporation of a methanol solution, also revealed the open ionic conformation. Methanol as a medium corresponds to a polar environment just as in an aqueous solution. In conclusion, we suggest that the previously proposed conformational equilibrium of monosubstituted Rh110 molecules is completely shifted to the lactone form in a nonpolar solution. In contrast, all molecules adopt the open ionic form in a water solution. This result is further supported by the photophysical properties of Boc-F-Rh110 and MC-Rh110 that obviously suggest a different reason for the decrease in fluorescence intensity from Rh110 to MC-Rh110 and Boc-F-Rh110.

The data presented in Figure 1 and Table 2 show that the attachment of a substituent to one of the amino groups of Rh110 leads to a blue shift of the absorption maximum, a red shift of the emission maximum, an increased bandwidth, and vibrational progression in the absorption and emission spectra. This is accompanied by a decrease of the fluorescence quantum yield. This effect is more pronounced for Boc-F-Rh110 than for MC-Rh110. These results can be rationalized by considering the

Table 1. Kinetic Parameters for the α-Chymotrypsin Catalyzed Hydrolysis of the Substrate Analogues with One and Two Cleavable Peptide Bonds

substrate analogue	k_{cat} [s^{-1}]	K_m [μM]	k_{cat}/K_m [M^{-1} s^{-1}]
$(suc\text{-}AAPF)_2$-Rh110	0.43 ± 0.03	8.7 ± 1.6	(5.0 ± 1) × 10^4
apparent			
suc-AAPF-Rh110-MC	11 ± 1	68 ± 7	(16 ± 2) × 10^4
$(suc\text{-}F)_2$-Rh110 apparent	0.0035 ± 0.0003	31 ± 4	(1.1 ± 0.2) × 10^2
suc-F-Rh110-MC	0.054 ± 0.006	182 ± 23	(3.0 ± 0.5) × 10^2

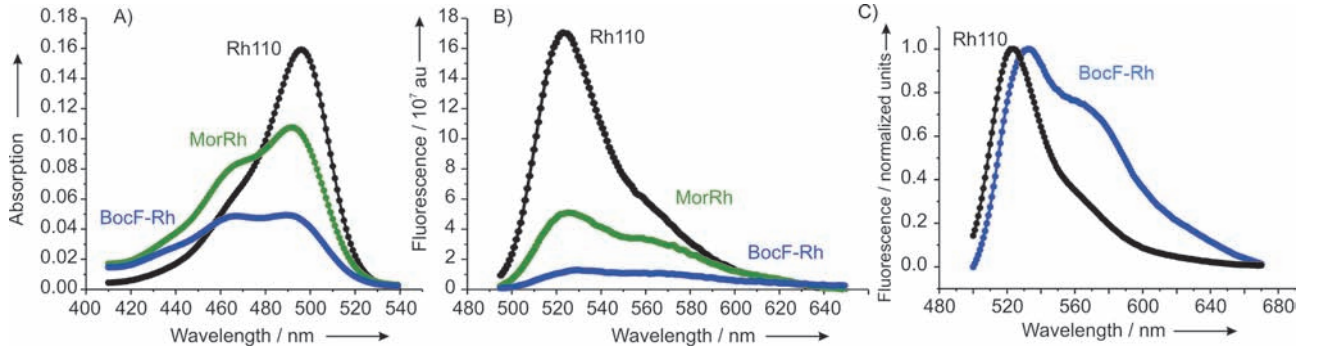

Figure 1. (A) Absorption and (B) emission spectra of Rhodamine 110, morpholinecarbonyl-Rh110, and BocF-Rh110; (C) normalized emission spectra of Rhodamine 110 and its monosubstituted peptide derivative.

Table 2. Spectroscopic Properties of Rhodamine110 and Its Monoderivatives

molecule	fluorescence lifetime [ns]	Φ_{488}	$\lambda_{max\ abs}$ [nm] $\lambda_{max\ em}$ [nm]	ε_{488} [M^{-1} cm^{-1}]	Fl. Int (rel)[a]
Rhodamine110	4.0	0.97	495	69 000	1
	$(2.4 \times 10^8)^b$	±0.05	523		
	$(7.5 \times 10^6)^c$				
MC-Rh110	3.6	0.60	492	52 000	0.3
	$(1.7 \times 10^8)^b$	±0.03	525		
	$(1.1 \times 10^8)^c$				
Boc-Phe-Rh110	2.8	0.31	489	24 600	0.1
	$(1.1 \times 10^8)^b$	±0.02	529		
	$(2.5 \times 10^8)^c$				

[a] λ_{ex} = 488 nm, λ_{em} = 520 nm. [b] k_f [s^{-1}]. [c] k_{nr} [s^{-1}].

resonance forms of the dyes. For Rh110, two equivalent and isoenergetic resonance forms exist with the positive charge on the left and right amino groups, respectively. For MC-Rh110, the attachment of an electron withdrawing amide moiety to one of the amino groups destabilizes the resonance form with the positive charge on the corresponding amino group. For Boc-F-Rh110, this resonance form is even more destabilized as the electron withdrawing character of the carbonyl is no longer attenuated by the electron donating morpholino moiety. As both resonance forms are no longer iso-energetic, there is an alternation of single and double bonds in the xanthenium cation leading to a blue shift of the absorption. Furthermore, the alternation of single and double bonds increases upon excitation which leads to increased electron phonon coupling and hence increased vibrational progression. The asymmetry furthermore leads to a dipole moment along the long axis of the molecule that is different in the excited state and the ground state. This difference in dipole moment leads to an increased Stokes shift and hence a red shift of the fluorescence. Furthermore, the increased asymmetry of the π-cloud results in a reduced transition dipole moment between the S_0 and S_1 states that is reflected in the fluorescent rate constant. The molar extinction coefficient at the maximum shows an even stronger decrease resulting from the combination of an increased electron phonon coupling and a decreased transition dipole moment. Finally, the increased electron phonon coupling also leads to an increase of the nonradiative decay rate from 7.5×10^6 s^{-1} in Rh110 over 1.1×10^8 s^{-1} in MC-Rh110 and 2.5×10^8 s^{-1} in Boc-F-Rh110. Finally, it should be noted that the fluorescence lifetimes measured at both maxima of Boc-F-Rh110 are the same, indicating that they must be attributed to the same emitting species. Overall, our results clearly suggest that the differences in fluorescence intensity do not originate from the proposed equilibrium between a lactone form and a zwitterionic form but result from differences in the electron structure of the monosubstituted Rh110 derivatives.

The absence of this equilibrium is important information for single molecule experiments, where it is essential that the fluorophore population studied is homogeneous. Thus, the chemical properties of MC-Rh110 in principle make it an ideal fluorophore for preparing substrate analogues with 1:1 stoichiometry for the analysis of enzyme kinetics at the single molecule level. However, not only the chemical properties ensure that each generated product molecule can be detected individually as a fluorescent signal.[21,28] MC-Rh110 further shows sufficient brightness to be detected at the single molecule level. It is therefore our next goal to investigate if suc-AAPF-Rh110-MC and $(suc\text{-}AAPF)_2$-Rh110 also yield different kinetic parameters in single molecule experiments where the intermediate is probably not detected due to its low brightness.

In conclusion, we have synthesized a series of fluorogenic substrate analogues for α-chymotrypsin. We have shown that only substrate analogues with one cleavable bond give access to the real kinetic constants of the enzymatic reaction. The origin of the relatively high fluorescence of the morpholine-carbonyl monosubstituted Rh110 was established. We anticipate that the fluorescence of monosubstituted fluorescein derivatives is determined by the same mechanism and that in aqueous solution xanthene dyes in general adopt an open ionic form. This information is vital for the development of the next generation of monosubstituted fluorogenic substrate analogues, e.g., with improved solubility or cell permeability, which might ultimately allow the study of single enzyme molecules in living systems.

■ ASSOCIATED CONTENT

Supporting Information. Calculation of the individual kinetic constants of the two-step hydrolysis reaction, and comparison of the fluorescent properties of monoamide Rh110 derivatives and NMR data. This material is available free of charge via the Internet at http://pubs.acs.org

■ AUTHOR INFORMATION

Corresponding Author

*Tel: (+) 31 (0) 24 365 2464. Fax: (+) 31 (0) 24 365 2929. E-mail: k.blank@science.ru.nl.

■ ACKNOWLEDGMENT

The authors thank Prof. Alan E. Rowan for helpful discussions, Kristof Van Hecke for the crystal structure analysis, and Karel Duerinckx for the NMR measurements. Financial support of the "Fonds voor Wetenschappelijk Onderzoek FWO" (Grant G.0402.09, G.0413.10, G.0697.11), the K. U. Leuven Research Fund (GOA 2011/03), the Flemish government (Long term structural funding – Methusalem funding CASAS METH/08/04), and the Federal Science Policy of Belgium (IAP-VI/27) is gratefully acknowledged. K. B. acknowledges support from a long-term fellowship from the Human Frontier Science Program (HFSP) and a VIDI grant from The Netherlands Organisation for Scientific Research (NWO).

REFERENCES

(1) Turk, B. (2006) Targeting proteases: successes, failures and future prospects. *Nat. Rev. Drug Discovery 5*, 785–99.

(2) Rotman, B. (1961) Measurement of activity of single molecules of beta-D-galactosidase. *Proc. Natl. Acad. Sci. U. S. A. 47*, 1981–1991.

(3) Chen, X., Sun, M., and Ma, H. (2006) Progress in spectroscopic probes with cleavable active bonds. *Curr. Org. Chem. 10*, 477–489.

(4) Lavis, L. D., and Raines, R. T. (2008) Bright ideas for chemical biology. *ACS Chem. Biol. 3*, 142–155.

(5) Marmé, N., Knemeyer, J.-P., Wolfrum, J., and Sauer, M. (2004) Highly sensitive protease assay using fluorescence quenching of peptide probes based on photoinduced electron transfer. *Angew. Chem., Int. Ed. 43*, 3798–3801.

(6) Matayoshi, E., Wang, G., Krafft, G., and Erickson, J. (1990) Novel fluorogenic substrates for assaying retroviral proteases by resonance energy transfer. *Science 247*, 954–958.

(7) Mitra, R. D., Silva, C. M., and Youvan, D. C. (1996) Fluorescence resonance energy transfer between blue-emitting and red-shifted excitation derivatives of the green fluorescent protein. *Gene 173*, 13–17.

(8) Boonacker, E., and Van Noorden, C. J. F. (2001) Enzyme cytochemical techniques for metabolic mapping in living cells, with special reference to proteolysis. *J. Histochem. Cytochem. 49*, 1473–1486.

(9) Boonacker, E., Elferink, S., Bardai, A., Fleischer, B., and Van Noorden, C. J. (2003) Fluorogenic substrate [Ala-Pro]2-cresyl violet but not Ala-Pro-rhodamine 110 is cleaved specifically by DPPIV activity: a study in living Jurkat cells and CD26/DPPIV-transfected Jurkat cells. *J. Histochem. Cytochem. 51*, 959–68.

(10) Rotman, B., Zderic, J. A., and Edelstein, M. (1963) Fluorogenic substrates for beta-D-galactosidases and phosphatases derived from flurescein (3,6-dihydroxyfluoran) and its monomethylether. *Proc. Natl. Acad. Sci. U. S. A. 50*, 1–6.

(11) Corey, P. F., Trimmer, R. W., and Biddlecom, W. G. (1991) A new chromogenic β-galactosidase substrate: 7-β-D-Galactopyranosyloxy-9,9-dimethyl-9H-acridin-2-one. *Angew. Chem., Int. Ed. 30*, 1646–1648.

(12) Van Noorden, C. J., Boonacker, E., Bissell, E. R., Meijer, A. J., van Marle, J., and Smith, R. E. (1997) Ala-Pro-cresyl violet, a synthetic fluorogenic substrate for the analysis of kinetic parameters of dipeptidyl peptidase IV (CD26) in individual living rat hepatocytes. *Anal. Biochem. 252*, 71–7.

(13) Hofmann, J., and Sernetz, M. (1983) A kinetic study on the enzymatic hydrolysis of fluoresceindiacetate and fluorescein-di-[beta]-galactopyranoside. *Anal. Biochem. 131*, 180–186.

(14) Huang, Z. J. (1991) Kinetic fluorescence measurement of fluorescein di-beta-D-galactoside hydrolysis by beta-galactosidase: intermediate channeling in stepwise catalysis by a free single enzyme. *Biochemistry 30*, 8535–40.

(15) Leytus, S. P., Melhado, L. L., and Mangel, W. F. (1983) Rhodamine-based compounds as fluorogenic substrates for serine proteinases. *Biochem. J. 209*, 299–307.

(16) Cai, S. X., Zhang, H.-Z., Guastella, J., Drewe, J., Yang, W., and Weber, E. (2001) Design and synthesis of Rhodamine 110 derivative and Caspase-3 substrate for enzyme and cell-based fluorescent assay. *Bioorg. Med. Chem. Lett. 11*, 39–42.

(17) Lorey, S., Faust, J., Mrestani-Klaus, C., Kahne, T., Ansorge, S., Neubert, K., and Buhling, F. (2002) Transcellular proteolysis demonstrated by novel cell surface-associated substrates of dipeptidyl peptidase IV (CD26). *J. Biol. Chem. 277*, 33170–7.

(18) Zhang, H. Z., Kasibhatla, S., Guastella, J., Tseng, B., Drewe, J., and Cai, S. X. (2003) N-Ac-DEVD-N′-(Polyfluorobenzoyl)-R110: novel cell-permeable fluorogenic caspase substrates for the detection of caspase activity and apoptosis. *Bioconjugate Chem. 14*, 458–63.

(19) Lavis, L. D., Chao, T.-Y., and Raines, R. T. (2006) Fluorogenic label for biomolecular imaging. *ACS Chem. Biol. 1*, 252–260.

(20) Wang, Z. Q., Liao, J., and Diwu, Z. (2005) N-DEVD-N′-morpholinecarbonyl-rhodamine 110: novel caspase-3 fluorogenic substrates for cell-based apoptosis assay. *Bioorg. Med. Chem. Lett. 15*, 2335–8.

(21) De Cremer, G., Roeffaers, M. B., Baruah, M., Sliwa, M., Sels, B. F., Hofkens, J., and De Vos, D. E. (2007) Dynamic disorder and stepwise deactivation in a chymotrypsin catalyzed hydrolysis reaction. *J. Am. Chem. Soc. 129*, 15458–9.

(22) Diwu, Z., Liao, J., Wang, Z. (2003) Luminogenic protease substrates. U.S. Patent application, WO2003099780.

(23) Boens, N., Qin, W., Basaric, N., Hofkens, J., Ameloot, M., Pouget, J., Lefevre, J. P., Valeur, B., Gratton, E., vandeVen, M., Silva, N. D., Jr., Engelborghs, Y., Willaert, K., Sillen, A., Rumbles, G., Phillips, D., Visser, A. J., van Hoek, A., Lakowicz, J. R., Malak, H., Gryczynski, I., Szabo, A. G., Krajcarski, D. T., Tamai, N., and Miura, A. (2007) Fluorescence lifetime standards for time and frequency domain fluorescence spectroscopy. *Anal. Chem. 79*, 2137–49.

(24) de Mello, J. C., Wittmann, H. F., and Friend, R. H. (1997) An improved experimental determination of external photoluminescence quantum efficiency. *Adv. Mater. 9*, 230–232.

(25) Case, A., and Stein, R. L. (2003) Mechanistic origins of the substrate selectivity of serine proteases. *Biochemistry 42*, 3335–48.

(26) Leytus, S. P., Patterson, W. L., and Mangel, W. F. (1983) New class of sensitive and selective fluorogenic substrates for serine proteinases. Amino acid and dipeptide derivatives of rhodamine. *Biochem. J. 215*, 253–60.

(27) Ramos, S. S., Vilhena, A. F., Santos, L., and Almeida, P. (2000) H-1 and C-13 NMR spectra of commercial rhodamine ester derivatives. *Magn. Reson. Chem. 38*, 475–478.

(28) Blank, K., De Cremer, G., and Hofkens, J. (2009) Fluorescence-based analysis of enzymes at the single-molecule level. *Biotechnol. J. 4*, 465–479.

Supporting Information

Morpholinecarbonyl-Rhodamine 110 based Substrates for the Determination of Protease Activity with Accurate Kinetic Parameters

Tatyana G. Terentyeva[†], Wim Van Rossom[†], Mark Van der Auweraer[†], Kerstin Blank[†,‡,] and Johan Hofkens[†]*

Department of Chemistry, Katholieke Universiteit Leuven, Celestijnenlaan 200F, 3001 Heverlee, Belgium, and Department of Molecular Materials, Institute for Molecules and Materials, Radboud University Nijmegen, Heyendaalseweg 135, 6525 AJ Nijmegen, The Netherlands.

[*] Corresponding author. Department of Molecular Materials, Institute for Molecules and Materials, Radboud University Nijmegen, Heyendaalseweg 135, 6525 AJ Nijmegen, The Netherlands.
Tel: (+) 31 (0) 24 365 2464. Fax: (+) 31 (0) 24 365 2929. E-mail: k.blank@science.ru.nl

[†] Department of Chemistry, KU Leuven, Belgium

[‡] Department of Molecular Materials, RU Nijmegen, The Netherlands

Determination of the kinetic parameters of the different substrate analogues

The enzymatic reaction of the "good" substrates $(suc\text{-}AAPF)_2$-Rh110 and suc-AAPF-Rh110-MC has been measured at 12 different concentrations between 400 nM and 25 µM using 3 nM α-chymotrypsin. For the substrates containing only Phe ($(suc\text{-}F)_2$-Rh110 and suc-F-Rh110-MC) a much higher enzyme concentration (900 nM) was required to obtain a measureable substrate conversion.

Product emission was measured every second and converted into the product concentration using calibration curves of Rh110 or MC-Rh110, respectively. The reaction velocity corresponding to the initial slope was obtained from linear regression to the first 100 – 150 data points measured. Before fitting the data to the Michaelis-Menten equation, the reaction velocity was converted into "enzymatic activity" by dividing the reaction velocity by the enzyme concentration. In this way K_m and k_{cat} could be obtained directly from least squares fitting to the Michaelis-Menten equation (Figure S1). The fit performed with Origin directly provided the standard deviations of the fitted parameters.

A)

Equation	y = P1*x/(P2 + x)		
Adj. R-Square	0.97565		
		Value	Standard Error
A	P1	0.43	0.03
A	P2	8.71	1.62

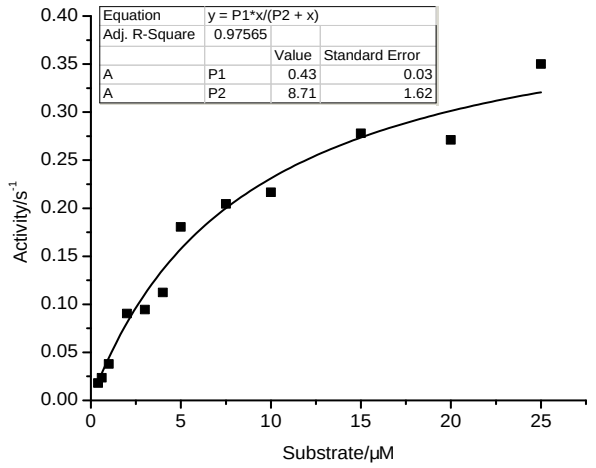

B)

Equation	y = P1*x/(P2 + x)		
Adj. R-Square	0.99876		
		Value	Standard Error
H	P1	10.7	0.9
H	P2	68.2	7.0

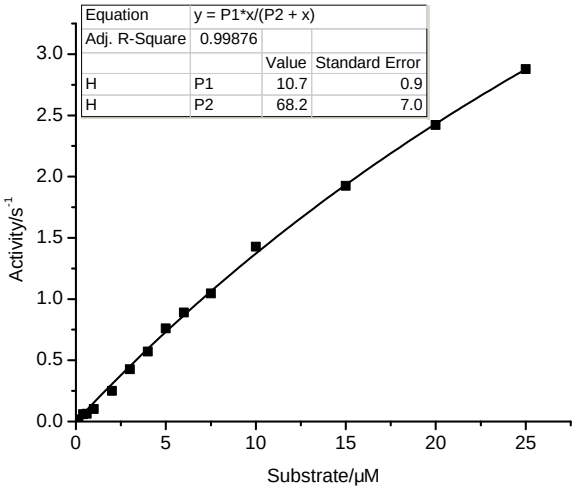

C)

Equation	y = P1*x/(P2 + x)		
Adj. R-Squar	0.9987		
		Value	Standard Error
H	P1	0.0035	0.0003
H	P2	31	3.4129

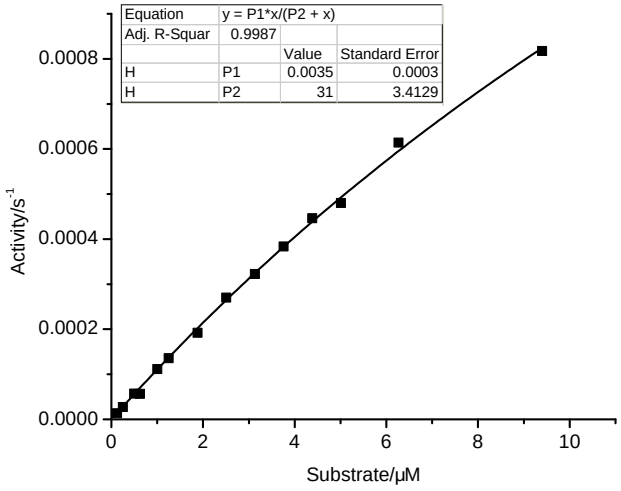

D)

Equation	y = P1*x/(P2 + x)		
Adj. R-Square	0.99901		
		Value	Standard Error
H	P1	0.054	0.006
H	P2	182.301	23.257

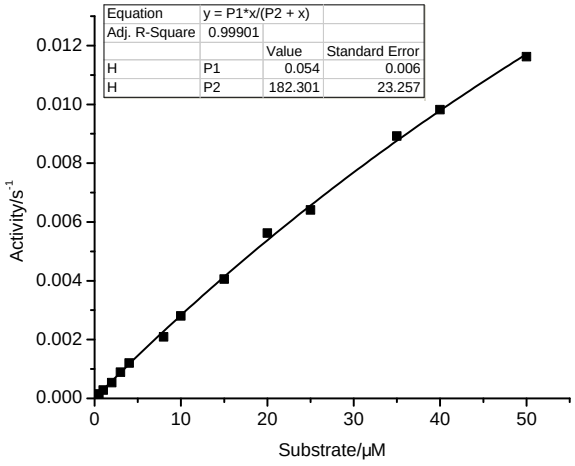

Figure S1. Michaelis-Menten plots of the 4 different substrate analogues (– fit to the Michaelis-Menten equation; P1 = k_{cat}, P2 = K_m). **A)** $(suc\text{-}AAPF)_2$-Rh110, **B)** suc-AAPF-Rh110-MC, **C)** $(suc\text{-}F)_2$-Rh110, **D)** suc-F-Rh110-MC.

Calculation of the individual kinetic constants of the two-step hydrolysis reaction

The appearance of a shoulder in the emission spectrum during the catalytic reaction together with the hydrolytic stability of the intermediate analogues Boc-AlaAlaProPhe-Rh110 and Boc-Phe-Rh110 clearly suggests the accumulation of a stable mono-amide intermediate, which can only be hydrolysed to the final product by the enzyme. Assuming Michaelis-Menten kinetics for the individual steps, the two-step reaction needs to be described by the following scheme:

$$E + S \underset{k_{-1}}{\overset{k_1}{\Leftrightarrow}} ES \overset{k_2}{\rightarrow} E + I + R$$

$$E + I \underset{k_{-1}^{'}}{\overset{k_1^{'}}{\Leftrightarrow}} EI \overset{k_2^{'}}{\rightarrow} E + P + R\,,$$

where S signifies substrate, I intermediate, P final product, E enzyme and R liberated peptide.

Assuming that no autohydrolysis of the substrate or intermediate takes place and that the reaction of the enzyme with either substrate or intermediate are independent, S and I can be seen as competitive inhibitors. For this case velocity equations for two-substrate kinetics are valid to describe the overall reaction:[1]

$$\frac{dS}{dt} = -\frac{k_2 \cdot E \cdot S}{K_m \cdot H + S}$$

$$\frac{dI}{dt} = -\frac{k_2^{'} \cdot E \cdot I}{K_m^{'} \cdot H_1 + I} - \frac{dS}{dt}$$

$$\frac{dP}{dt} = \frac{k_2^{'} \cdot E \cdot I}{K_m^{'} \cdot H_1 + I}$$

$$H = \frac{K_m^{'} + I}{K_m^{'}}$$

$$H = \frac{K_m + S}{K_m}\ .$$

This system of differential equations cannot be solved analytically so that only a numerical fit of the measured data is possible. When using these equations to fit the data obtained from the fluorescence measurements it needs to be considered that the fluorescence intensity of the intermediate is 10% of the Rh110 intensity. As a result, the fluorescent signal originates from two components: $signal = cf(Rh110) \cdot 0.1 \cdot I + cf(Rh110) \cdot P$ with $cf(Rh110)$ being the experimentally determined calibration factor for Rh110. Therefore, when converting the measured fluorescence signal into "product concentration" using *cf*(Rh110) the following correction needs to be made before fitting is possible. The overall concentration c of molecules contributing to the fluorescence signal corresponds to $c = signal / cf(Rh110) = 0.1 \cdot I + P$.

Using the above differential equations we have performed a numerical fit of several kinetic measurements using a 10 µM solution of $(suc\text{-}AAPF)_2$-Rh110 (Figure S2). To do so, we first calculated concentration changes starting from a 10 µM solution in time intervals of 0.25 s. We then performed least squares fitting of the measured to the calculated data set allowing the four parameters K_M, k_2, $K_M^{'}$ and $k_2^{'}$ to vary.

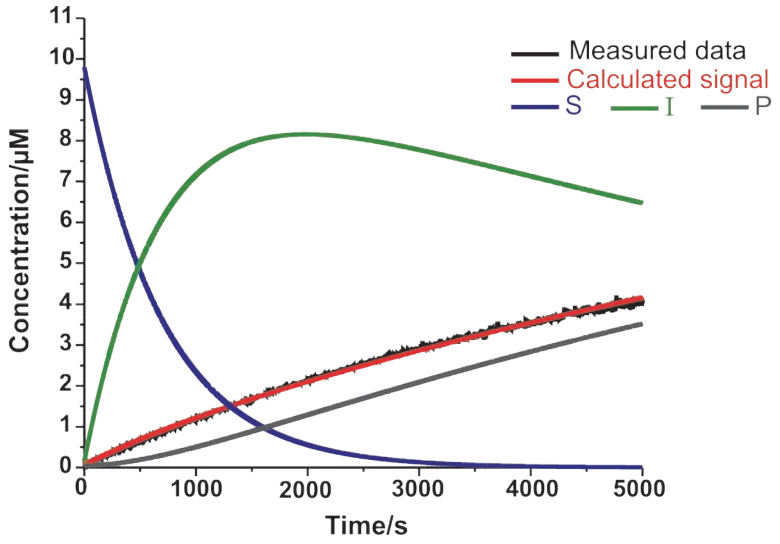

Figure S2. Measured and calculated kinetic data of the enzymatic hydrolysis of 10µM $(sucAAPF)_2$-Rh110. The numerical fit is also shown in the diagram (red line).

The fitting is not accurate due to the large number of variables and good fits can be obtained for a number of combinations of fit variables. Although variations in the individual parameters have been obtained (and k_{cat} and K_M can not be determined accurately) it was observed that the values obtained for k_2/K_m and k_2'/K_M' (i.e. k_{cat}/K_M) are obtained reproducibly and yield approximately $50 \cdot 10^4$ $M^{-1}s^{-1}$ and $4 \cdot 10^4$ $M^{-1}s^{-1}$, respectively. We would like to note here that good fits can only be obtained if $K_M \neq K_M'$ and $k_2 \neq k_2'$ clearly indicating that the rate constants for the two reaction steps need to be different.

Although the fits need to be seen critically due to their large error and the assumptions made initially, the result is still important information since it clearly shows that the two reaction steps are characterized by different kinetic constants and that the approximation of such a two step hydrolysis reaction with apparent k_{cat} and K_M values does not yield the true kinetic constants. It should further be noted that the first reaction step seems to proceed faster. The most likely explanation might be the higher effective molarity of cleavable bonds in the bis-amide substrate compared to the mono-amide intermediate.

Overall, having performed this fitting procedure with our data, it needs to be concluded that accurate fits are only possible if the intermediate concentration is known as it has been the case in the initial study by Hofmann & Sernetz.[1] This is an important result clearly showing that fluorescence experiments are not suited to obtain the rate constants for the individual steps and that the apparent rate constants obtained from fluorescence measurements do not represent the true values.

Comparison of the fluorescence properties of Boc-AlaAlaProPhe-Rh110 and Boc-Phe-Rh110

As described previously, the synthesis of Boc-AlaAlaProPhe-Rh110 is more difficult than the synthesis of Boc-Phe-Rh110. It was therefore preferable to perform the spectroscopic measurements with Boc-Phe-Rh110. To verify that the longer peptide in Boc-AlaAlaProPhe-Rh110 does not influence the fluorescence properties we have compared the absorption and emission spectra (Figure S3) as well as the fluorescence lifetimes of these two molecules. Both the absorption and emission spectra are almost identical. Further, the fluorescence decay curves, measured at the wavelengths 520, 530 and 563 nm, all fitted a monoexponential decay with a time constant of 2.8 ns for both Boc-AlaAlaProPhe-Rh110 and Boc-Phe-Rh110. These data clearly show that the length of the peptide doesn't influence the fluorescence properties and that only the first amino acid next to Rh110 defines these properties.

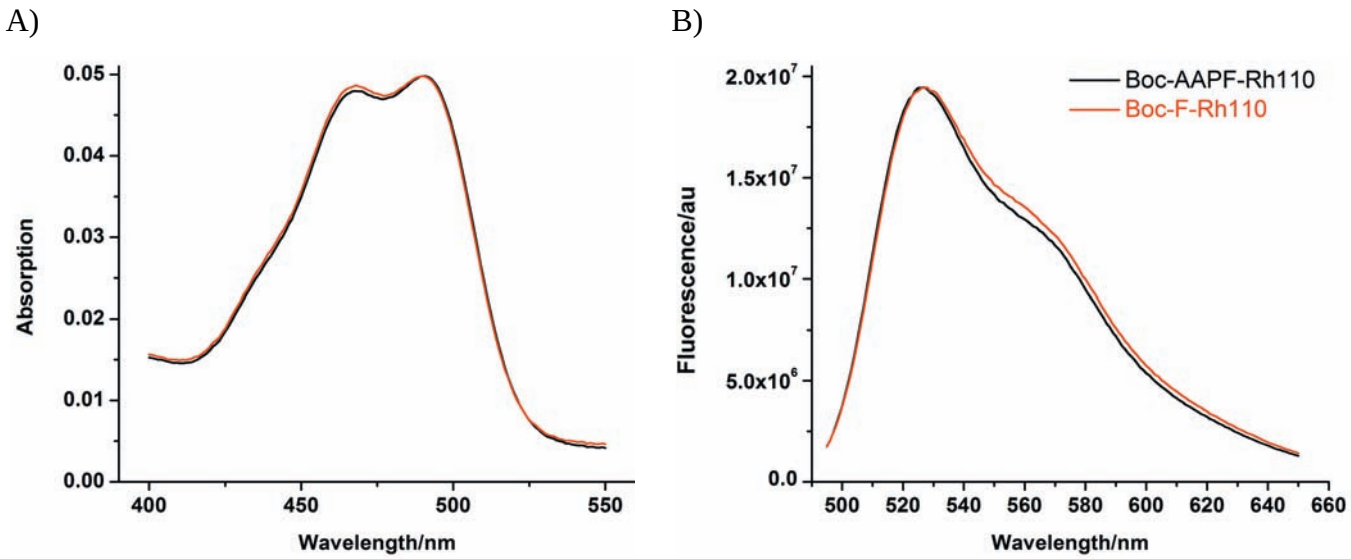

Figure S3. A) Absorption and B) emission spectra of a 2 μM solution of Boc-AlaAlaProPhe-Rh110 and Boc-Phe-Rh110 in PBS.

Crystals of MC-Rh110

Slow evaporation of methanol from a solution of MC-Rh110 resulted in small single-crystals. X-ray diffraction analysis did not yield enough resolution for publishing small molecule data but it clearly revealed the open ionic conformation presented in Figure S4.

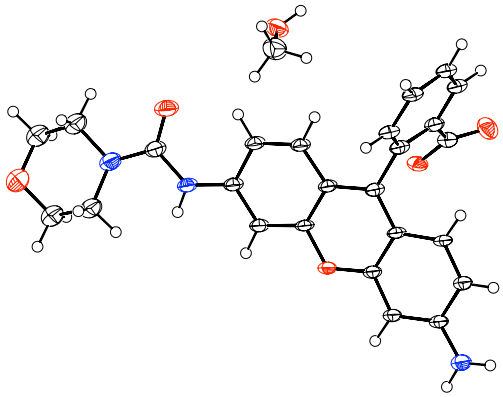

Figure S4. Crystal structure of MC-Rh110.

NMR measurements

Through NMR analysis a difference in molecular conformation of mono-substituted Rh110 was observed depending on the solvent used (apolar chloroform and polar water solution). Good spectra were obtained in $CDCl_3$ solution. Due to the low solubility of these compounds in H_2O, however, only a poor resolution ^{13}C NMR spectrum was achieved. The more sensitive two-dimensional HSQC and HMBC measurements performed for MC-Rh110 in D_2O + 5% DMSO-d_6 allowed the assignment of all carbon signals (Figure S8). The signals of the NMR spectra were assigned according to the generally accepted atom numbering of Rh110 as shown in Chart 1 of the article.

Rhodamine 110 chloride is known to be present in the open ionic form only, showing a signal for C-9 of the xanthene moiety at 158 ppm in $CDCl_3$. For both mono-substituted Rh110 derivatives BocF-Rh110

and MC-Rh110, however, a strong shielding of C-9 is observed placing the C-9 signal at 84 ppm, suggesting a lactone conformation, whereas no signal at 158 ppm is found of the open form. For Rh110 C3/6 give a signal at 156 ppm while substitution of the amine next to C-6 leads to a shift of C-3 to 149 ppm, which corresponds to the presence of an uncharged amine group (Figure S5, S6A). Combination of the ^{13}C and DEPT spectra suggests that for both BocF-Rh110 and MC-Rh110 the number of quaternary, tertiary and secondary carbons is compatible with the presence of a single conformation.

In a D_2O + 5% DMSO-d_6 solution of MC-Rh110, however, no carbon signal was observed at 84 ppm while a signal for C-9 is detected at 148 ppm and the signal for C-3 is deshielded to 161 ppm. This suggests the presence of the open ionic form in polar solutions (Figure S6). Also here the number of signals corresponds to the existence of only one conformation. In addition, ^1H NMR spectra show a stronger shielding for the protons of the xanthene moiety in chloroform solution than in water solution (Figure S7), which is expected assuming the presence of an amine group in chloroform and an ammonium group in water.

(S1) Hofmann, J., and Sernetz, M. (1983) A kinetic study on the enzymatic hydrolysis of fluoresceindiacetate and fluorescein-di-[beta]-galactopyranoside. *Anal. Biochem. 131*, 180-186.

A)

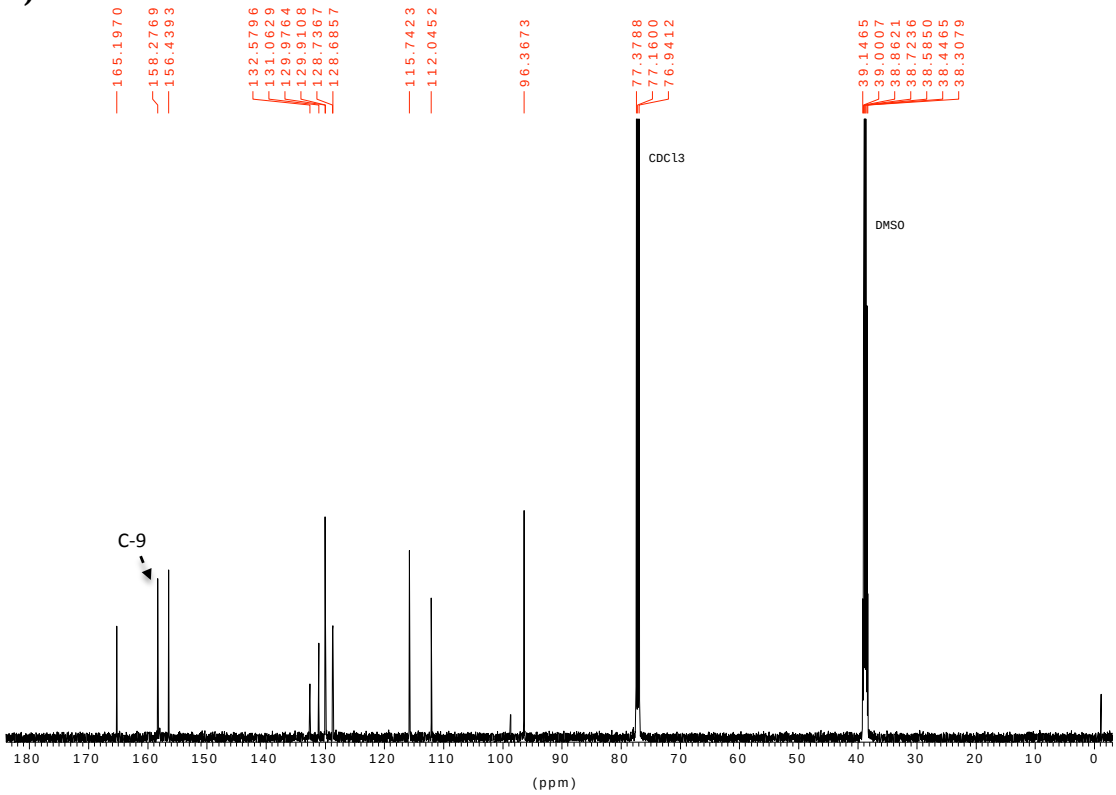

B)

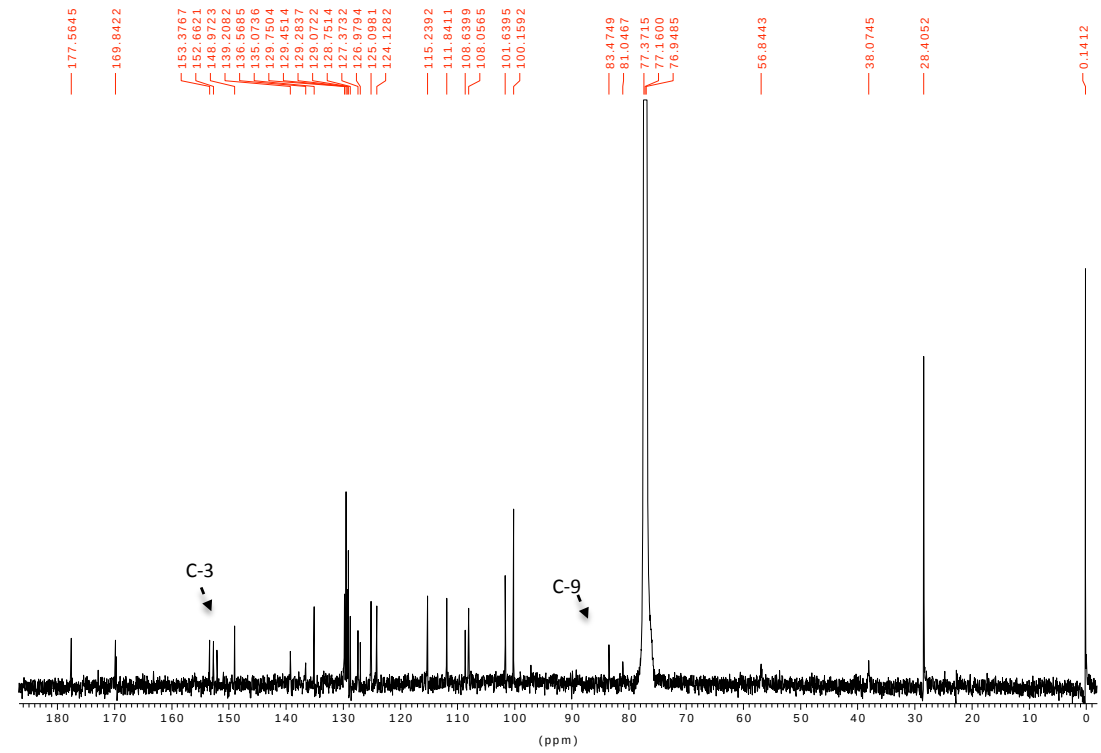

Figure S5. ^{13}C NMR spectra of Rh110 in $CDCl_3$ + drop of DMSO-d_6 (A) and Boc-Phe-Rh110 in $CDCl_3$ (B).

A)

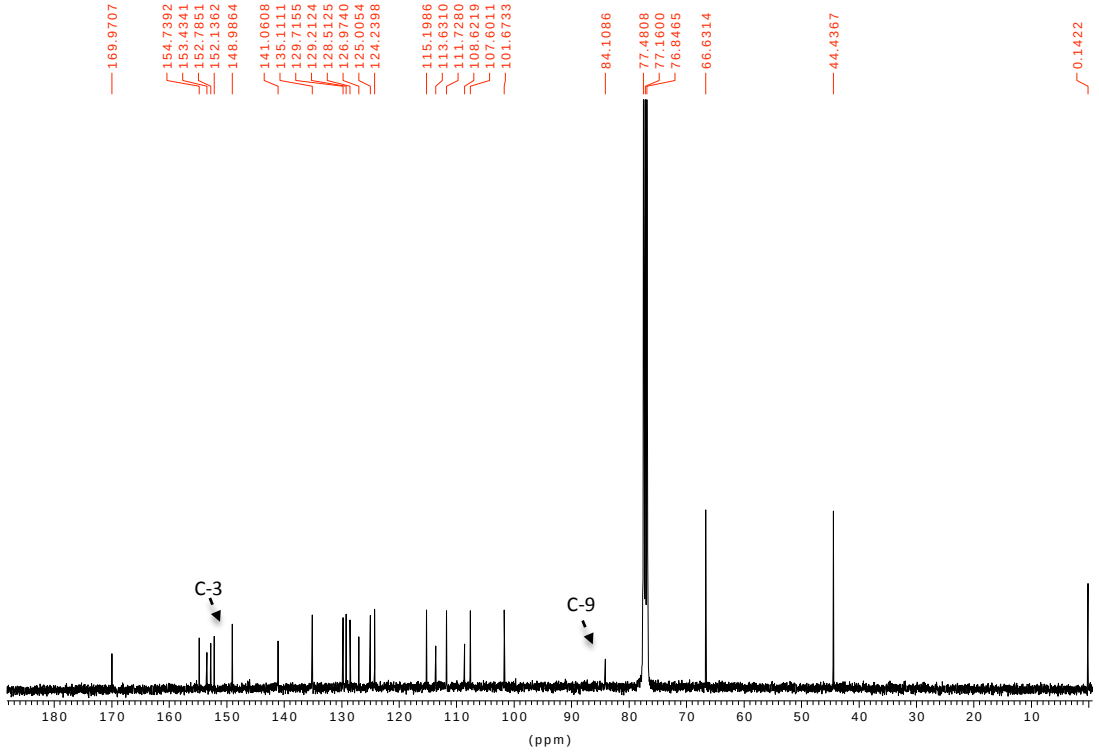

B)

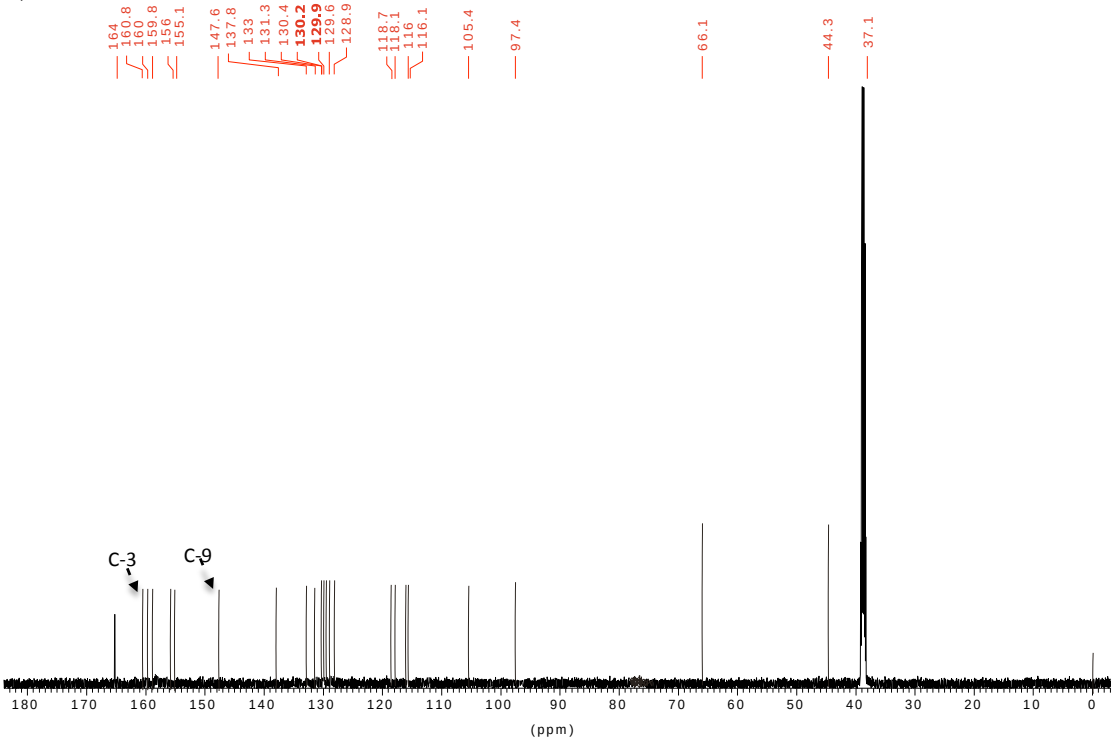

Figure S6. ^{13}C NMR spectrum in $CDCl_3$ (A) and simulated ^{13}C spectrum from HSQC and HMBC NMR measurements in D_2O + 5% DMSO-d_6 (B) of MC-Rh110.

A)

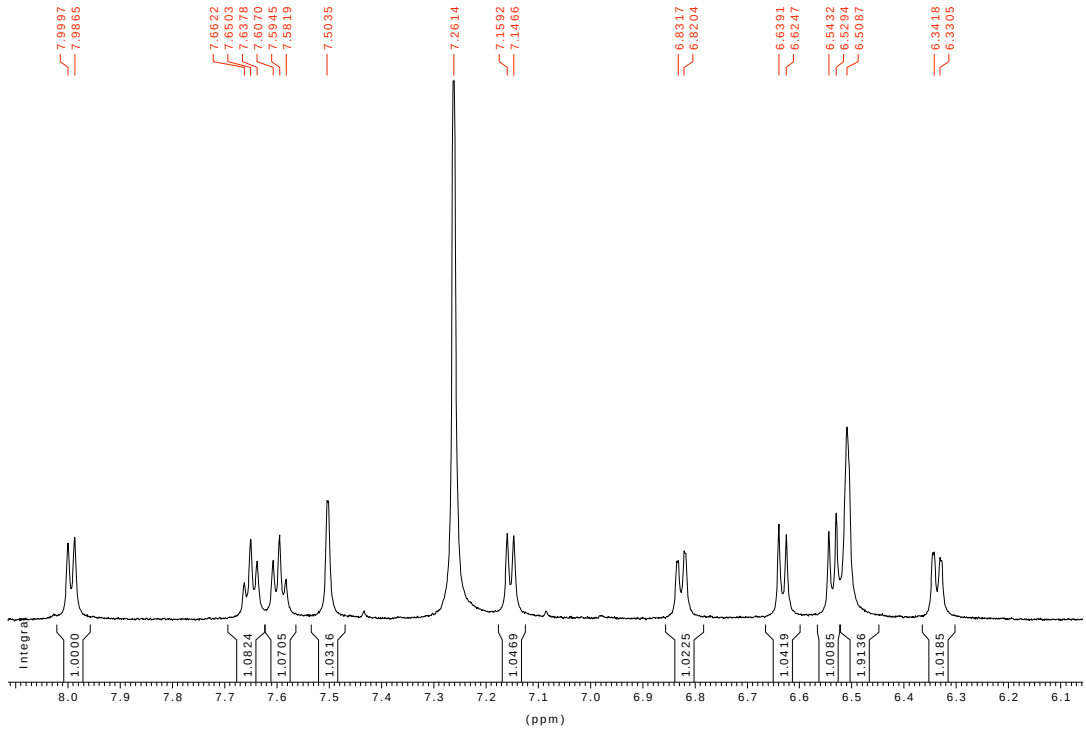

B)

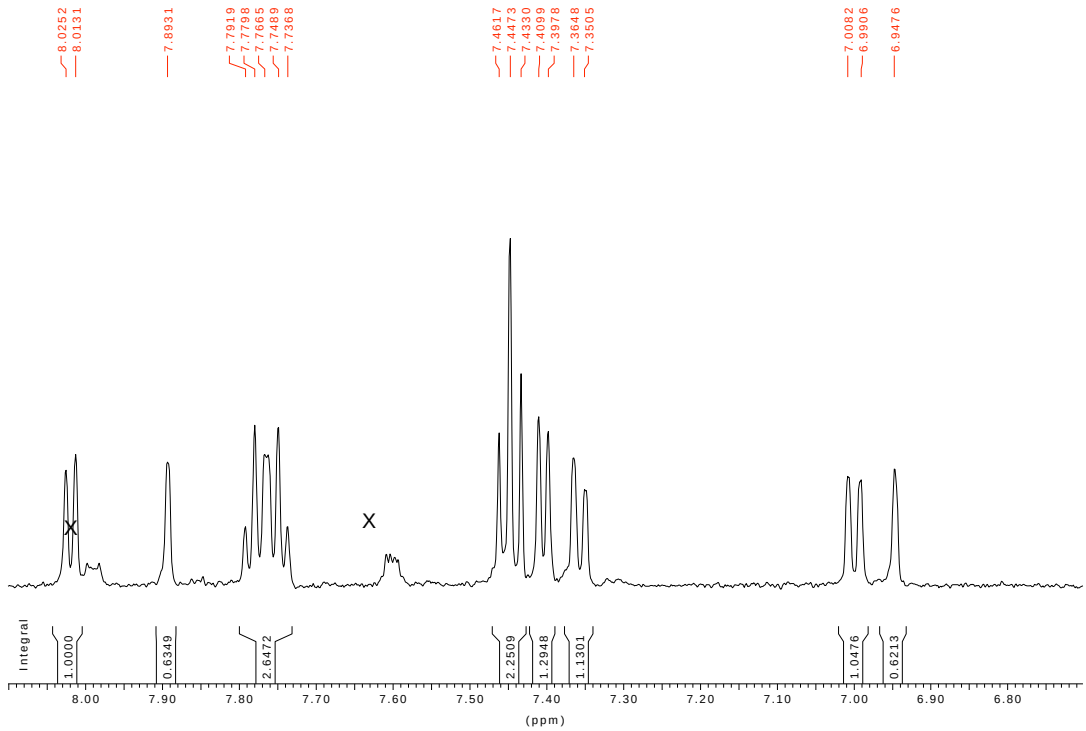

Figure S7. ^{1}H NMR spectra of MC-Rh110 in $CDCl_3$ (A) and D_2O + 5% DMSO-d_6 (B); X is an impurity since it does not couple to any other signals of the product .

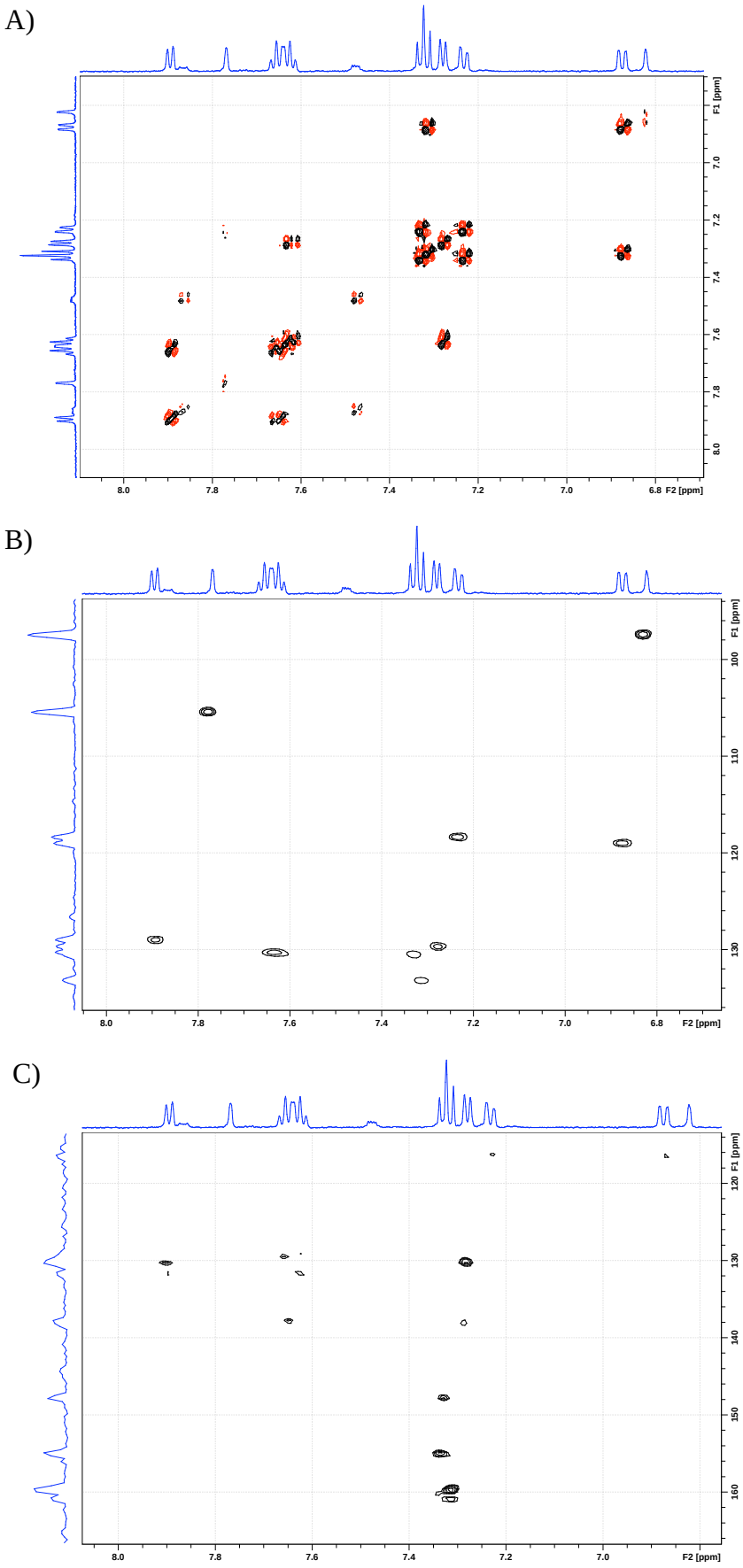

Figure S8. COSY (A), HSQC (B), HMBC (C) NMR spectra (aromatic region) of MC-Rh110 in D_2O + 5% DMSO-d_6.

Bioconjugate Chemistry

ARTICLE

pubs.acs.org/bc

Redox-Responsive Nanoparticles from the Single Disulfide Bond-Bridged Block Copolymer as Drug Carriers for Overcoming Multidrug Resistance in Cancer Cells

Yu-Cai Wang,[#,†] Feng Wang,[#,‡,⊥] Tian-Meng Sun,[‡,⊥] and Jun Wang*[,§,⊥]

[‡]Hefei National Laboratory for Physical Sciences at the Microscale, [§]CAS Key Laboratory of Brain Function and Disease, and [⊥]School of Life Sciences, University of Science and Technology of China, Hefei, Anhui 230027, P.R. China

[†]Department of Polymer Science and Engineering, University of Science and Technology of China, Hefei, Anhui 230026, P.R. China

ABSTRACT: Multidrug resistance (MDR) is a major impediment to the success of cancer chemotherapy. The intracellular accumulation of drug and the intracellular release of drug molecules from the carrier could be the most important barriers for nanoscale carriers in overcoming MDR. We demonstrated that the redox-responsive micellar nanodrug carrier assembled from the single disulfide bond-bridged block polymer of poly(ε-caprolactone) and poly(ethyl ethylene phosphate) (PCL-*SS*-PEEP) achieved more drug accumulation and retention in MDR cancer cells. Such drug carrier rapidly released the incorporated doxorubicin (DOX) in response to the intracellular reductive environment. It therefore significantly enhanced the cytotoxicity of DOX to MDR cancer cells. It was demonstrated that nanoparticular drug carrier with either poly(ethylene glycol) or poly(ethyl ethylene phosphate) (PEEP) shell increased the influx but decreased the efflux of DOX by the multidrug resistant MCF-7/ADR breast cancer cells, in comparison with the direct incubation of MCF-7/ADR cells with DOX, which led to high cellular retention of DOX. Nevertheless, nanoparticles bearing PEEP shell exhibited higher affinity to the cancer cells. The shell detachment of the PCL-*SS*-PEEP nanoparticles caused by the reduction of intracellular glutathione significantly accelerated the drug release in MCF-7/ADR cells, demonstrated by the flow cytometric analyses, which was beneficial to the entry of DOX into the nuclei of MCF-7/ADR cells. It therefore enhanced the efficiency in overcoming MDR of cancer cells, which renders the redox-responsive nanoparticles promising in cancer therapy.

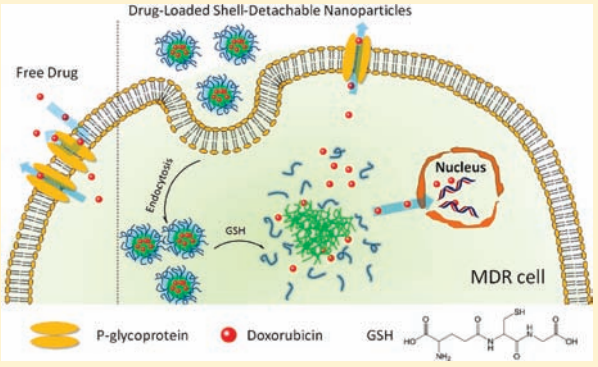

INTRODUCTION

Multidrug resistance (MDR) is a major impediment to the success of cancer chemotherapy.[1−3] Although cancer cells can acquire MDR through several molecular mechanisms, P-glycoprotein (P-gp) is the best known and is an important membrane transporter involved in MDR, being overexpressed in the plasma membrane of MDR tumor cells and capable of effluxing various anticancer drugs (e.g., doxorubicin and paclitaxel) out of the cells.[4−6] Nanoscale vehicles as drug carriers have shown the ability to target tumors and improve the anticancer efficacy of drugs, owing to their unique physical and biological properties,[7,8] and may provide opportunities for overcoming MDR.[9−14] Many nanobased drug delivery systems have been used for the inhibition of drug efflux mediated by P-gp.[15−21] Recently, it has been demonstrated that nanoparticles showing responsibility to intracellular stimulus are capable of delivering chemotherapeutic drugs to overcome MDR. Bae's group has carried out intensive studies on folic acid-conjugated polymer micelles, which are sensitive to early endosomal pH.[22−24] It has been suggested that MDR cancer cells may have limited capacity to defend themselves against cytotoxic chemicals.[23] In this sense, realizing a sufficiently high intracellular level of cytotoxic chemicals using an optimized delivery system might represent a novel tactic in overcoming the MDR of cancer cells, while the intracellular accumulation of drug and the intracellular release of drug molecules from the carrier could be the most important barriers for nanoscale carriers in overcoming MDR.

Nanoparticles based on diblock copolymer with a single disulfide bond in each polymer chain can be used as the intelligent drug carriers for promoted intracellular drug release.[25,26] In this study, we report that redox-responsive micellar nanoparticles based on disulfide-bridged PCL-*SS*-PEEP block polymer as a drug carrier can significantly overcome the two barriers in overcoming the MDR of cancer cells, thus reversing the multidrug resistance of cancer cells. On one hand, nanoparticles bearing a poly(ethyl ethylene phosphate) (PEEP) shell exhibit a high affinity to cells and are more efficiently internalized by cells, which help the drug escape from the pump-off by P-gp

Received: March 18, 2011
Revised: July 15, 2011
Published: August 25, 2011

ACS Publications © 2011 American Chemical Society

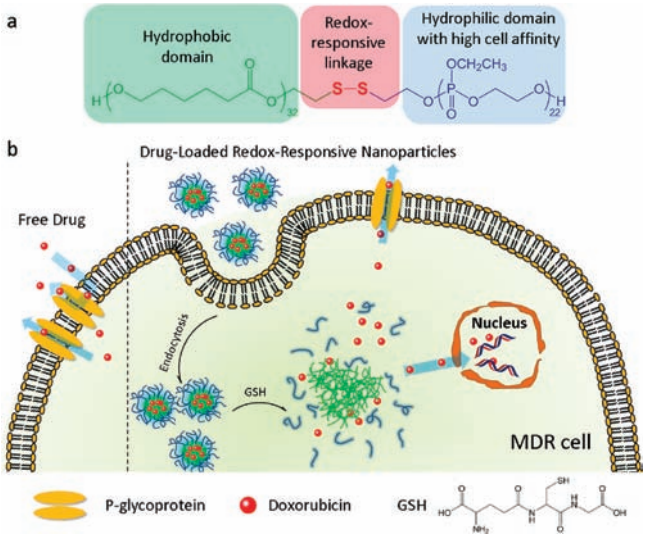

Figure 1. Chemical structure of disulfide-bridged PCL-*SS*-PEEP block copolymer (a) and schematic illustration of redox-responsive nanoparticles for overcoming multidrug resistance of cancer cells (b).

and lead to high levels of cellular drug accumulation. On the other hand, it is known that MDR in cancer cells is often associated with an elevation in the concentration of reductive glutathione (GSH).[27] Such shell-detachable nanoparticles are sensitive to the intracellular glutathione of MDR cancer cells, resulting in significantly enhanced intracellular drug release and rapid accumulation of free drug in MDR cancer cells (Figure 1).

MATERIALS AND METHODS

Syntheses of Block Copolymers. The block copolymers were synthesized as previously reported.[26,28] Briefly, block copolymer of poly(ε-caprolactone) and poly(ethylene glycol) (PCL-*b*-PEG) was synthesized by ring-opening polymerization of ε-caprolactone (Acros, USA) in bulk at 120 °C with polyethylene glycol monomethyl ether (PEG, MW 5000, Sigma-Aldrich, USA) as the initiator and stannous octoate as the catalyst, which was purified by precipitating its solution into ether.[29] The average molecular weights were 4900 and 5000 for PCL block and PEG block, respectively.

Block copolymer of poly(ε-caprolactone) and poly(ethyl ethylene phosphate) (PCL-*b*-PEEP) was synthesized by ring-opening polymerization of ethyl ethylene phosphate using poly(ε-caprolactone) as the initiator and stannous octoate as the catalyst at 30 °C in tetrahydrofuran.[28] The resultant polymer was purified by precipitation into ethyl ether/methanol (9/1, v/v). The average molecular weights of PCL and PEEP were 4650 and 4860, respectively.

Disulfide-bridged diblock copolymer of poly(ε-caprolactone) and poly(ethyl ethylene phosphate) (PCL-*SS*-PEEP) was synthesized through a coupling reaction between the thiol end group functionalized poly(ε-caprolactone) (PCL-SH) with the pyridyldisulfide groups at the end of poly(ethyl ethylene phosphate). The mixture was allowed to react for 24 h, concentrated, and precipitated into diethyl ether/methanol (10:1 v/v) three times. The precipitate was dried in vacuum, dialyzed against water at 4 °C for 3 days, and freeze−dried to obtain the product. The average molecular weights of PCL and PEEP were 3650 and 3480, respectively.[26]

The molecular weights of the polymers above were all calculated based on ^{1}H NMR analyses.

Preparation and Characterization of DOX-Loaded Nanoparticles. Doxorubicin hydrochloride (1 mg, DOX, Hisun Pharmaceutical Co., China) and block copolymer (10 mg) were dissolved in DMSO (1 mL), and then triethylamine (5 μL) was added. The mixture was stirred for 2 h at room temperature. Thereafter, the solution was added dropwise to ultrapurified water (5 mL) with stirring and transferred into Spectrum/Por dialysis membrane (M_w cutoff = 14 000 Da, Spectrum Laboratories Inc., CA, USA). It was dialyzed against water for 24 h at 4 °C. After ultrafiltration at 3000 *g* for 10 min using Amicon Ultra-4 centrifugal filter (M_w cutoff = 10 000 Da, Millipore, USA), the solution was resuspended to desired concentrations. The DOX concentration and drug loading contents were determined by HPLC analyses as previously reported.[26] Particle size and zeta potential of nanoparticles were characterized on a Malvern Zetasizer Nano ZS90 with a He−Ne laser (633 nm) and 90° collecting optics.

Cell Culture. The human breast adenocarcinoma (MCF-7) cell line was obtained from the American Type Culture Collection (ATCC, MD, USA), and the P-gp overexpressing human breast carcinoma cell line (DOX resistant MCF-7 cell line, MCF-7/ADR) was kindly provided by Prof. Tao Zhu of University of Science and Technology of China. The cells were cultured in RPMI 1640 medium, supplemented with 10% fetal bovine serum and L-glutamine (2 mM) at 37 °C using a humidified 5% CO_2 incubator. MCF-7/ADR cells were maintained with free DOX at 5 μg mL^{-1}.

Determination of Intracellular Accumulation or Retention of Doxorubicin. MCF-7 or MCF-7/ADR cells were seeded in 24-well plates at a density of 7×10^4 cells/well and incubated overnight. The cells were washed with Earle's Balanced Salt Solution (EBSS, Invitrogen Life Science Technologies) and treated with free DOX or DOX-loaded nanoparticles in EBSS with equivalent DOX at a concentration of 5 μg mL^{-1}. Cells were incubated at 37 °C for 0.5, 1, 2, 3, or 4 h, washed twice with ice-cold phosphate-buffered saline (PBS, 0.01 M, pH 7.4), and lysed in PBS containing 1% Triton X-100 at 37 °C for 30 min with three freeze−thaw cycles. DOX concentrations in cell lysates were measured by HPLC analyses as previously reported[26] and normalized to the total cellular protein content of the cells, which was measured with the BCA (bicinchoninic acid) Protein Assay (Pierce, IL, USA).

To determine the intracellular retention of DOX, MCF-7/ADR cells were cultured with either free DOX or DOX-loaded nanoparticles for 4 h, washed with PBS, and then incubated with EBSS at 37 °C for additional 0.5, 1, 2, 3, or 4 h. Cells were lysed and the DOX concentrations in cell lysates were measured as described above.

DOX Release from DOX-loaded PCL-*SS*-PEEP Nanoparticles Caused by the Reductive Condition. DOX-loaded PCL-*SS*-PEEP nanoparticles were incubated in PBS with or without DL-dithiothreitol (DTT, 10 mM). The fluorescence emission spectra of DOX-loaded PCL-*SS*-PEEP nanoparticles were recorded after different time intervals with excitation wavelength at 479 nm using a Shimadzu RF-5301PC spectrofluorophotometer.

To determine the drug release of DOX from DOX-loaded nanoparticles, the nanoparticles were suspended in PBS at 1 mg mL^{-1} in the dialysis membrane tubing (M_w cutoff = 14 000, Spectrum/Por), and immersed in PBS (15 mL) containing 0 mM or 10 mM GSH in a shaking water bath at 37 °C.

At predetermined time points, the external buffer was collected and it was replaced with equal volume of PBS containing 0 mM or 10 mM GSH. The collected release medium was freeze−dried and dissolved in acetonitrile−water (50:50, v/v) and the concentration of DOX was analyzed by HPLC analyses.

Flow Cytometric Analyses of MCF-7/ADR Cells Following Incubation with Free DOX or DOX-Loaded Nanoparticles. MCF-7/ADR cells were seeded in 24-well plates at 1×10^5 cells per well in 500 μL of complete RPMI 1640 medium containing 10% fetal bovine serum, and incubated at 37 °C in 5% CO_2 humidified atmosphere for 24 h. The medium was replaced with fresh medium containing either free DOX or DOX-loaded nanoparticles with equivalent DOX at a concentration of 5 μg mL^{-1}, and the cells were further incubated for various lengths of time. Cells were washed with PBS twice and harvested, then suspended in PBS (200 μL) for analyses using FACSCalibur flow cytometer. Cells with PBS treatment were used as the control. The data was analyzed using *WinMDI 2.9* software.

Confocal Laser Microscopic Observation of MCF-7/ADR Cells Following Incubation with Free DOX or DOX-Loaded Nanoparticles. MCF-7/ADR cells were seeded onto 12 mm coverslips in 24-well plates with 5×10^4 cells per well and allowed to grow until 60% confluence. Cells were washed twice with PBS, and then incubated with free DOX or DOX-loaded nanoparticles (with equivalent DOX at a concentration of 5 μg mL^{-1}) in a complete RPMI 1640 medium for 24 or 48 h at 37 °C. Cells were washed twice with ice-cold PBS and fixed with fresh 4% paraformaldehyde for 15 min at room temperature. The cells were counterstained with DAPI for cell nucleus and Alexa Fluor 488 phalloidin (Invitrogen Life Science Technologies) for cell membrane following the manufacturer's instructions. The coverslips were mounted on the glass microscope slides with a drop of antifade mounting media (Sigma-Aldrich Co., USA) to reduce fluorescence photobleaching. The intracellular localization of DOX nanoparticles was visualized under a laser scanning confocal microscope (LSCM; LSM 700 Meta, Carl Zeiss Inc., Thornwood, NY).

Cell Growth Inhibition Assay. MCF-7/ADR cells were seeded in 96-well plates at 5×10^3 cells per well in complete RPMI 1640 medium (100 μL), and incubated at 37 °C in 5% CO_2 humidified atmosphere for 24 h. The culture medium was then replaced with freshly prepared culture medium (100 μL) containing either free DOX or DOX-loaded nanoparticles at different concentration (from 1×10^{-3} to 1×10^2 μg mL^{-1}). The cells were further incubated for 24, 48, or 72 h, and MTT (25 μL, 3-(4,5-dimethylthiazol-2-yl)-2,5-diphenyltetrazolium bromide, Sigma-Aldrich Co., USA) stock solution (5 mg mL^{-1} in PBS) was added to each well to achieve a final concentration of 1 mg mL^{-1}, with the exception of the wells as blank, to which PBS (25 μL) was added. After incubation for another 2 h, extraction buffer (100 μL, 20% SDS in 50% DMF, pH 4.7, prepared at 37 °C) was added to the wells and incubated for another 4 h at 37 °C. The absorbance was measured at 570 nm using a Bio-Rad 680 microplate reader. The cell viability was normalized to that of MCF-7/ADR cells cultured in the complete culture medium. The half maximal inhibitory concentrations (IC_{50}) values were calculated based on the percentage of treatment over control.

RESULTS AND DISCUSSION

Preparation of Polymers and Nanoparticles. PCL-*SS*-PEEP is a disulfide-bridged diblock copolymer of poly(ε-caprolactone) and PEEP, which was prepared as previously reported.[26] The chemical structure is shown in Figure 1. It self-assembled into micellar nanoparticles in aqueous solution, encapsulating doxorubicin (DOX, in unsalted form) in the core with an average diameter of around 92 nm. We also made micellar nanoparticles of block copolymers poly(ε-caprolactone)-*b*-poly(ethyl ethylene phosphate) (PCL-*b*-PEEP) and poly(ε-caprolactone)-*b*-poly(ethylene glycol) (PCL-*b*-PEG) with similar particle size and size distributions for comparison, and encapsulated DOX into their hydrophobic cores at comparable drug loading contents (~6% w/w). Information about the nanoparticles is summarized in Table 1.

Table 1. Characterization of Doxorubicin-Loaded Nanoparticles

polymer	diameter [nm]	PDI[a]	zeta potential [mv]	DLC (%)[b]
PCL-*SS*-PEEP	91.7 ± 2.60	0.112	−30.6	6.53
PCL-*b*-PEEP	80.2 ± 2.27	0.105	−34.5	6.14
PCL-*b*-PEG	94.2 ± 0.93	0.135	−7.2	5.26

[a] Polydispersity index determined by dynamic light scattering. [b] Loading content of doxorubicin (w/w).

Intracellular Accumulation and Retention of DOX. We first incubated doxorubicin hydrochloride (free DOX) or DOX-loaded nanoparticles with either wild-type MCF-7 or DOX-resistant MCF-7/ADR breast cancer cells at drug doses of 5 μg mL^{-1}. The drug resistance of MCF-7/ADR cells was demonstrated by the overexpression of P-gp encoding the MDR1 gene and the reversal of DOX accumulation in the cells in the presence of verapamil hydrochloride, an inhibitor of P-gp (data not shown). At different time intervals, the intracellular DOX accumulation was quantitatively determined by analyzing the concentration of DOX in the cell lysate with high liquid performance chromatographic analyses, normalized to the total cellular protein content of the cells. Owing to the efflux of DOX by the P-gp of MCF-7/ADR cells, it was not surprising that intracellular accumulation of DOX in MCF-7/ADR cells was significantly lower than that in MCF-7 cells when the cells were incubated with free DOX (Figure 2A). However, the differences in cellular DOX levels between MCF-7 and MCF-7/ADR cells were much less prominent when the cells were incubated with DOX-loaded nanoparticles (Figure 2B−D), indicating that nanoparticles might not be the substrate of P-gp; thus, the DOX-loaded nanoparticles could be retained in the MDR cells after internalization.

On the other hand, although the use of poly(ethylene glycol) (PEG) as the shell material of nanoparticles has been the preferred strategy to help nanoparticles escape from protein opsonization and macrophage uptake in the reticuloendothelial system.[30,31] PEG also exhibits low affinity to cell membranes, behaving as an unexpected barrier to accessing the targeted cells.[32] As shown in Figure 2B, the cellular DOX level in MCF-7/ADR cells reached ~0.96 μg per mg protein when the cells were incubated with DOX-loaded PCL-*b*-PEG nanoparticles for 4 h, a value that was about 3.9 times higher when compared with treatment with free DOX. However, more DOX accumulated in MCF-7/ADR cells when the cells were incubated with DOX-loaded PCL-*SS*-PEEP or DOX-loaded PCL-*b*-PEEP nanoparticles, with the cellular DOX level in MCF-7/ADR cells reaching ~1.65 μg per mg protein after 4 h incubation, indicating that nanoparticles with PEEP shells showed greater affinity for

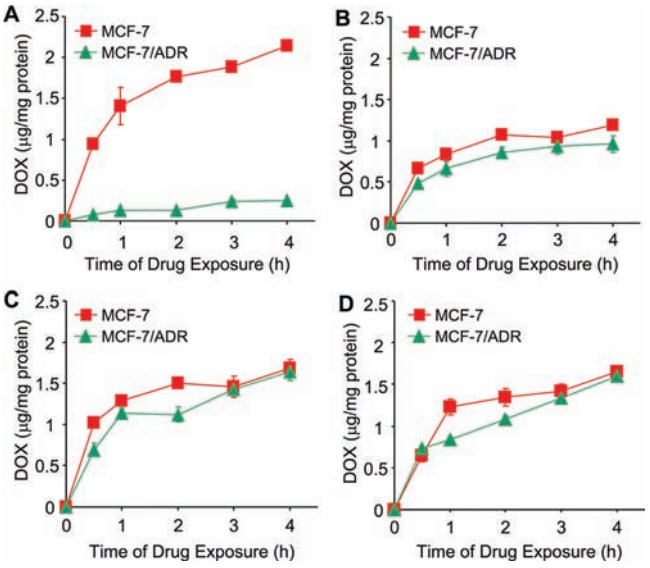

Figure 2. Doxorubicin (DOX) accumulation in wild-type MCF-7 and drug-resistant MCF-7/ADR breast cancer cells after incubation with free DOX (A), DOX-loaded PCL-*b*-PEG (B), DOX-loaded PCL-*b*-PEEP (C), and DOX-loaded PCL-*SS*-PEEP (D) nanoparticles.

cells. At the same time, it must be mentioned that no significant difference in the cellular DOX level was observed between treatments with DOX-loaded PCL-*SS*-PEEP and DOX-loaded PCL-*b*-PEEP nanoparticles (Figure 2C,D).

We next determined how DOX was retained in MCF-7/ADR cells with the delivery of different nanoparticles. MCF-7/ADR cells were incubated with either free DOX or DOX-loaded nanoparticles for 4 h, and subsequently washed with PBS to remove uninternalized free DOX or DOX-loaded nanoparticles. The cells were further incubated in fresh cell culture medium for different periods of time. It is noteworthy that we maintained the initial doses of DOX at 5 μg mL^{-1} in treatments with DOX-loaded nanoparticles but intentionally increased the initial concentration of DOX to 40 μg mL^{-1} in the free DOX treatment, to increase the initial cellular DOX level. As shown in Figure 3, as a result of drug efflux by P-gp, a fast decline in the cellular DOX level was observed in MCF-7/ADR cells preincubated with free DOX. Only 15% DOX was retained in the cells after 4 h incubation in the free DOX treatment. In contrast, the amount and rate of efflux of DOX were significantly lower when the cells were preincubated with DOX-loaded nanoparticles, and the cells retained about 50−62% DOX after 4 h incubation. These results demonstrated that encapsulation of DOX in the nanoparticles protected DOX against the pump-off by P-gp, and thus the nanoparticles increased the cellular retention of DOX in MCF-7/ADR cells.

DOX Release from DOX-Loaded PCL-*SS*-PEEP Nanoparticles Caused by the Reductive Condition. We thus demonstrated that more DOX can be accumulated and retained in MDR cells when delivered with nanoparticles, and that nanoparticles with a PEEP shell have a greater affinity for MDR cancer cells. We then focused on PCL-*SS*-PEEP nanoparticles in comparison with PCL-*b*-PEEP nanoparticles and studied intracellular DOX release in response to the endogenous reductive stimulus. The intracellular concentration of GSH is about 2−10 mM, and is often elevated in MDR cancer cells,[27] being significantly higher than the level outside the cells (ca. 2 μM).[33,34] Therefore, it is possible that PCL-*SS*-PEEP nanoparticles are subjected to rapid reductive degradation in MDR cancer cells.

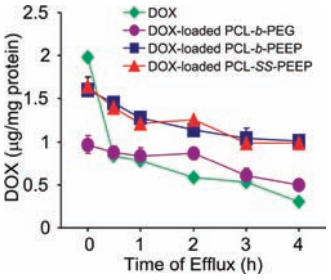

Figure 3. Retention of doxorubicin (DOX) in MCF-7/ADR cells after preincubation with free DOX (DOX), DOX-loaded PCL-*b*-PEG, DOX-loaded PCL-*b*-PEEP, and DOX-loaded PCL-*SS*-PEEP nanoparticles for 4 h. The concentration of DOX in the free DOX preincubation was 40 μg mL^{-1}, while it was 5 μg mL^{-1} for DOX-loaded nanoparticles.

We demonstrated that the detachment of the shell from the nanoparticles caused by the reductive condition accelerated drug release. The effect of PEEP shell detachment on DOX release from DOX-loaded PCL-*SS*-PEEP nanoparticles was directly observed by measuring the fluorescence spectrum of DOX in solution via treatment with 10 mM of DL-dithiothreitol (DTT). The DOX fluorescence of DTT-treated DOX-loaded PCL-*SS*-PEEP nanoparticles was remarkably enhanced (Figure 4A) whereas, in contrast, the fluorescence spectra of those without DTT treatment remained unchanged (inset in Figure 4A). It has been reported that incorporation of DOX in the hydrophobic core of micelles decreases the fluorescent intensity of DOX when compared with free DOX at the same concentration due to the self-quenching effect.[35] Therefore, the enhanced fluorescence should be due to the rapid release of drug from the nanoparticles. *In vitro* drug release was further quantitatively studied by incubating DOX-loaded PCL-*SS*-PEEP nanoparticles in GSH-containing medium. The results shown in Figure 4B revealed a slow and sustained release of 40% DOX from the nanoparticles over 4 d in the absence of GSH, probably due to the hydrophobic interactions between DOX and the PCL core. However, in the presence of 10 mM of GSH, much faster release of almost all the DOX was observed under otherwise identical conditions. These results demonstrated that cleavage of disulfide bridge linkages accelerated the rapid and complete release of the drug. It can be assumed that, in response to stimulation by GSH, the disulfide bridge linkages of PCL-SS-PEEP are reduced and broken, which destabilizes the micellar nanoparticles and results in accelerated DOX release. On the other hand, the release of DOX from DOX/PCL-*b*-PEEP nanoparticles was not affected by the addition of GSH to the release medium (Figure 4C).

Rapid Intracellular Release Caused by the Cellular Reductive Condition. To demonstrate our assumption that DOX-loaded PCL-*SS*-PEEP nanoparticles can release the drug more rapidly in response to the intracellular reduction condition in MDR cancer cells and in turn overcome drug resistance, we incubated free DOX or DOX-loaded nanoparticles with MCF-7/ADR cells, and analyzed the cells using flow cytometry at different time intervals. As shown in Figure 5A, low mean fluorescence intensity was observed when the cells were incubated with free DOX at all time intervals due to its poor cellular retention in MCF-7/ADR cells. On the contrary, higher cellular retention of DOX in MCF-7/ADR cells led to enhanced fluorescence of cells with preincubation of DOX-loaded

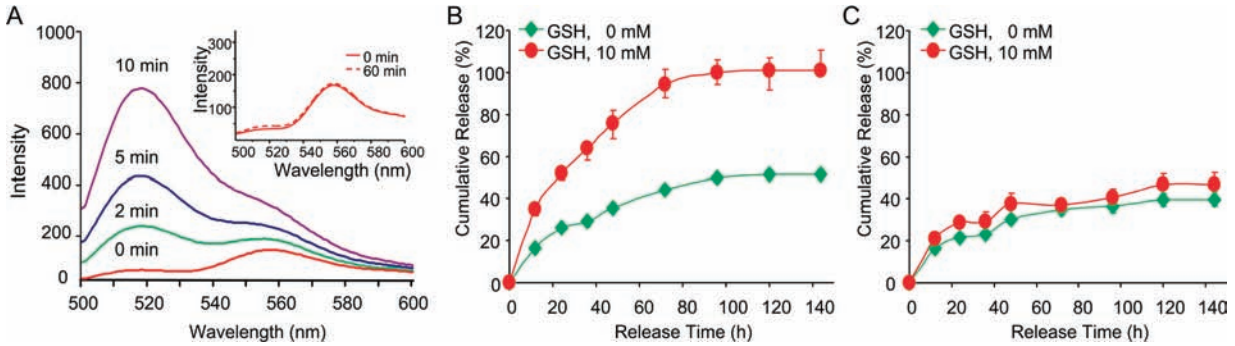

Figure 4. (A) Fluorescence spectra of DOX-loaded PCL-*SS*-PEEP nanoparticles with or without (inset) treatment of DTT for various lengths of time in PBS solution. (B) *In vitro* release of DOX from DOX-loaded PCL-*SS*-PEEP nanoparticles in PBS (pH 7.4) at 37 °C with or without GSH treatment. (C) *In vitro* release of DOX from DOX-loaded PCL-*b*-PEEP nanoparticles in PBS (pH 7.4) at 37 °C with or without GSH treatment.

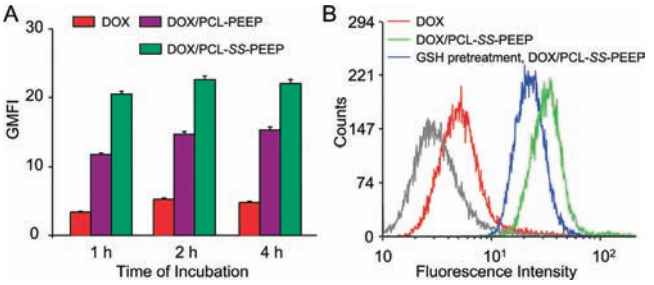

Figure 5. (A) Mean fluorescence intensity (GMFI) of MCF-7/ADR cells after incubation with free DOX, DOX-loaded PCL-*b*-PEEP (DOX/PCL-*b*-PEEP), or DOX-loaded PCL-*SS*-PEEP (DOX/PCL-*SS*-PEEP) nanoparticles for various lengths of times at a dose of 5 μg mL^{-1}. (B) Flow cytometric analyses of MCF-7/ADR cells after incubation with free DOX (DOX) or DOX-loaded PCL-*SS*-PEEP (DOX/PCL-*SS*-PEEP) nanoparticles with or without preincubation of GSH. The dose of DOX was 5 μg mL^{-1} in cell culture.

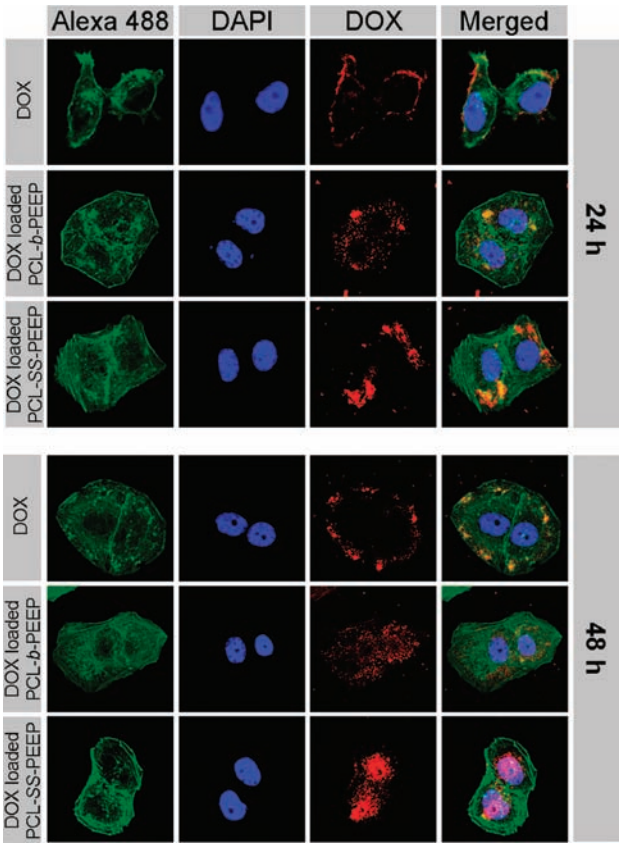

Figure 6. Confocal laser microscopic observation of MCF-7/ADR cells after incubation with free doxorubicin (DOX) or DOX-loaded nanoparticles for 24 or 48 h. The dose of DOX was 5 μg mL^{-1} in cell culture.

nanoparticles. However, although the cellular accumulation of DOX in MCF-7/ADR cells was similar between treatments with DOX-loaded PCL-*SS*-PEEP or DOX-loaded PCL-*b*-PEEP nanoparticles (Figure 2C,D), the fluorescence intensity of cells treated with DOX-loaded PCL-*SS*-PEEP was significantly higher than that in cells treated with DOX-loaded PCL-*b*-PEEP at all tested time intervals. Such enhancements should be due to the enhanced intracellular release of DOX following the cleavage of disulfide-bridges of PCL-*SS*-PEEP in MCF-7/ADR cells. As mentioned above, it was demonstrated that DOX released from the nanoparticles recovered its fluorescence, which was self-quenched in the hydrophobic PCL core of the nanoparticles. To further confirm that DOX-loaded PCL-*SS*-PEEP is effective in accelerated drug release under reductive conditions, we mixed DOX-loaded PCL-*SS*-PEEP or DOX-loaded PCL-*b*-PEEP nanoparticles with medium containing 20 mM GSH for 4 h, and then incubated this medium with MCF-7/ADR cells for 1 h. We observed a significant decline in cell fluorescence intensity with DOX-loaded PCL-*SS*-PEEP (Figure 5B) but not with DOX-loaded PCL-*b*-PEEP nanoparticles when compared with direct incubation of DOX-loaded nanoparticles that did not receive preincubation with GSH. The extracellular treatment of DOX-loaded nanoparticles with GSH led to partial extracellular release of DOX from PCL-*SS*-PEEP nanoparticles but not from PCL-*b*-PEEP nanoparticles. Nevertheless, the extracellular DOX could not be effectively retained in MCF-7/ADR cells due to the pump-off effect mediated by P-gp, resulting in the decline in cell fluorescence intensity.

Confocal Observations. We then examined whether the rapid intracellular release of DOX from DOX-loaded PCL-*SS*-PEEP nanoparticles would be beneficial to the entry of DOX into the nuclei of MCF-7/ADR cells, given that the interaction of DOX with DNA by intercalation in the nucleus is one of the major modes of action of DOX.[36,37] MCF-7/ADR cells were then incubated with free DOX, or DOX-loaded nanoparticles, and the cells were observed with confocal laser microscopy after 24 or 48 h incubation. As shown in Figure 6, DOX was mainly

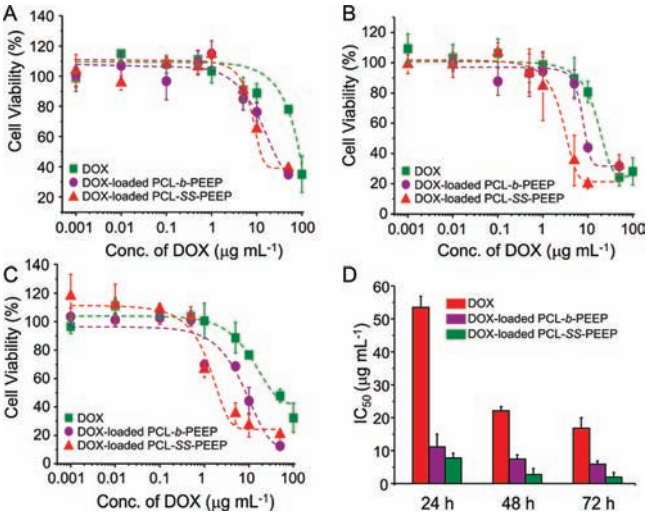

Figure 7. Viability of MCF-7/ADR cells after treatment with free DOX or DOX-loaded nanoparticles for 24 h (A), 48 h (B), and 72 h (C). (D) The half-maximal inhibitory concentration (IC_{50}) of DOX to MCF-7/ADR cells measured by MTT assay (n = 3).

located in the perimembrane region when MCF-7/ADR cells were cultured with free DOX at 5 μg mL^{-1} for 24 and 48 h, due to the action of P-gp. When DOX was incorporated into the nanoparticles, fluorescence signals were observed in the cells. Close scrutiny of the images revealed that the fluorescence signal from cells treated with DOX-loaded PCL-*SS*-PEEP was more dispersed when compared with cells treated with DOX-loaded PCL-*b*-PEEP nanoparticles, which displayed dotted red fluorescence signals. This difference indicated that shell shedding by DOX-loaded PCL-*SS*-PEEP nanoparticles might have taken place in the cells, accompanied by the rapid release of incorporated DOX. As a result, DOX was distributed mostly in the nuclei after 48 h when the cells were incubated with DOX-loaded PCL-*SS*-PEEP nanoparticles. On the contrary, only minimal amounts of fluorescence were detected in the nuclei of MCF-7/ADR cells after 48 h culture with DOX-loaded PCL-*b*-PEEP nanoparticles. Moreover, DOX signals were barely visible in cell nuclei when the cells were incubated with free DOX at the same dose.

Cytotoxicity to MCF-7/ADR Cells. The above results demonstrated that shell-detachable DOX-loaded PCL-*SS*-PEEP nanoparticles can enhance drug retention in MDR cells and more rapidly release the incorporated drug intracellularly. Therefore, delivery of DOX with PCL-*SS*-PEEP nanoparticles can rapidly increase the concentration of free drug in MCF-7/ADR cells, and is expected to improve its cytotoxicity and overcome the MDR of cancer cells efficiently. We then incubated free DOX, DOX-loaded PCL-*b*-PEEP, or DOX-loaded PCL-*SS*-PEEP nanoparticles at the equivalent DOX doses with MCF-7/ADR cells for 24 h, 48, or 72 h, and determined the half-maximal inhibitory concentration of DOX (IC_{50}) by MTT assay. The cytotoxicity to MCF-7/ADR in response to the doses of DOX was given in Figure 7A–C. As shown in Figure 7D, a significant decrease in the IC_{50} of DOX-loaded PCL-*b*-PEEP was observed when compared with free DOX treatment, owing to the accumulation effect of DOX. More importantly, the enhanced intracellular release of DOX from shell-detachable PCL-*SS*-PEEP nanoparticles significantly improved its cytotoxicity. The IC_{50} decreased to ~12% of that of free DOX and ~32% of DOX-loaded PCL-*b*-PEEP nanoparticles after 72 h incubation, demonstrating the potential of shell-detachable nanoparticles for overcoming multidrug resistance.

CONCLUSION

We have demonstrated that the rapid increase of the free drug concentration in MDR cancer cells via the delivery of shell-detachable nanoparticles is a novel strategy for overcoming the MDR of cancer cells. Our example of a nanoparticle based on disulfide-bridged diblock copolymer PCL-*SS*-PEEP exhibited high cell affinity, allowing enhanced drug accumulation and retention in MDR cells and rapid intracellular release of the incorporated cargo in response to the intracellular reductive environment. It therefore significantly enhanced the cytotoxicity of DOX to MDR cancer cells, and is therefore promising for overcoming multidrug resistance in cancer therapy.

AUTHOR INFORMATION

Corresponding Author

*Fax: (+86) 551 3600402, E-mail: jwang699@ustc.edu.cn.

Author Contributions

#Y. C. Wang and F. Wang contributed equally to this work.

ACKNOWLEDGMENT

This work was supported by the National Basic Research Program of China (973 Program, 2010CB934001, 2009CB930301), the Fundamental Research Funds for the Central Universities (WK2070000008), the National Natural Science Foundation of China (20974105, 50733003), and the Open Project of State Key Laboratory of Supramolecular Structure and Materials (SKLSSM201117).

REFERENCES

(1) Eckford, P. D. W., and Sharom, F. J. (2009) ABC efflux pump-based resistance to chemotherapy drugs. *Chem. Rev. 109*, 2989–3011.

(2) Kavallaris, M. (2010) Microtubules and resistance to tubulin-binding agents. *Nat. Rev. Cancer 10*, 194–204.

(3) Savage, P., Stebbing, J., Bower, M., and Crook, T. (2009) Why does cytotoxic chemotherapy cure only some cancers? *Nat. Clin. Pract. Oncol. 6*, 43–52.

(4) Fletcher, J. I., Haber, M., Henderson, M. J., and Norris, M. D. (2010) ABC transporters in cancer: more than just drug efflux pumps. *Nat. Rev. Cancer 10*, 147–156.

(5) Robey, R. W., To, K. K. K., Polgar, O., Dohse, M., Fetsch, P., Dean, M., and Bates, S. E. (2009) ABCG2: A perspective. *Adv. Drug Delivery Rev. 61*, 3–13.

(6) Wong, H. L., Bendayan, R., Rauth, A. M., Xue, H. Y., Babakhanian, K., and Wu, X. Y. (2006) A mechanistic study of enhanced doxorubicin uptake and retention in multidrug resistant breast cancer cells using a polymer-lipid hybrid nanoparticle system. *J. Pharmacol. Exp. Ther. 317*, 1372–1381.

(7) Park, K., Lee, S., Kang, E., Kim, K., Choi, K., and Kwon, I. C. (2009) New generation of multifunctional nanoparticles for cancer imaging and therapy. *Adv. Funct. Mater. 19*, 1553–1566.

(8) Petros, R. A., and DeSimone, J. M. (2010) Strategies in the design of nanoparticles for therapeutic applications. *Nat. Rev. Drug Discovery 9*, 615–627.

(9) Dong, X. W., and Mumper, R. J. (2010) Nanomedicinal strategies to treat multidrug-resistant tumors: current progress. *Nanomedicine 5*, 597–615.

(10) Jabr-Milane, L. S., van Vlerken, L. E., Yadav, S., and Amiji, M. M. (2008) Multi-functional nanocarriers to overcome tumor drug resistance. *Cancer Treat. Rev. 34*, 592–602.

(11) Lee, E. S., Kim, D., Youn, Y. S., Oh, K. T., and Bae, Y. H. (2008) A virus-mimetic nanogel vehicle. *Angew. Chem., Int. Ed. 47*, 2418–2421.
(12) Malam, Y., Loizidou, M., and Seifalian, A. M. (2009) Liposomes and nanoparticles: nanosized vehicles for drug delivery in cancer. *Trends Pharmacol. Sci. 30*, 592–599.
(13) Barraud, L., Merle, P., Soma, E., Lefrancois, L., Guerret, S., Chevallier, M., Dubernet, C., Couvreur, P., Trepo, C., and Vitvitski, L. (2005) Increase of doxorubicin sensitivity by doxorubicin-loading into nanoparticles for hepatocellular carcinoma cells in vitro and in vivo. *J. Hepatol. 42*, 736–743.
(14) Soma, C. E., Dubernet, C., Bentolila, D., Benita, S., and Couvreur, P. (2000) Reversion of multidrug resistance by co-encapsulation of doxorubicin and cyclosporin A in polyalkylcyanoacrylate nanoparticles. *Biomaterials 21*, 1–7.
(15) Dong, X. W., Mattingly, C. A., Tseng, M. T., Cho, M. J., Liu, Y., Adams, V. R., and Mumper, R. J. (2009) Doxorubicin and paclitaxel-loaded lipid-based nanoparticles overcome multidrug resistance by inhibiting P-glycoprotein and depleting ATP. *Cancer Res. 69*, 3918–3926.
(16) Kabanov, A. V., Batrakova, E. V., and Alakhov, V. Y. (2002) Pluronic((R)) block copolymers for overcoming drug resistance in cancer. *Adv. Drug Delivery Rev. 54*, 759–779.
(17) Meng, H. A., Liong, M., Xia, T. A., Li, Z. X., Ji, Z. X., Zink, J. I., and Nel, A. E. (2010) Engineered design of mesoporous silica nanoparticles to deliver doxorubicin and P-glycoprotein siRNA to overcome drug resistance in a cancer cell line. *ACS Nano 4*, 4539–4550.
(18) Cuvier, C., Roblottreupel, L., Millot, J. M., Lizard, G., Chevillard, S., Manfait, M., Couvreur, P., and Poupon, M. F. (1992) Doxorubicin-loaded nanospheres bypass tumor-cell multidrug resistance. *Biochem. Pharmacol. 44*, 509–517.
(19) deVerdiere, A. C., Dubernet, C., Nemati, F., Soma, E., Appel, M., Ferte, J., Bernard, S., Puisieux, F., and Couvreur, P. (1997) Reversion of multidrug resistance with polyalkylcyanoacrylate nanoparticles: Towards a mechanism of action. *Br. J. Cancer 76*, 198–205.
(20) Nemati, F., Dubernet, C., Deverdiere, A. C., Poupon, M. F., Treupelacar, L., Puisieux, F., and Couvreur, P. (1994) Some parameters influencing cytotoxicity of free doxorubicin and doxorubicin-loaded nanoparticles in sensitive and multidrug-resistant leukemic murine cells - incubation-time, number of nanoparticles per cell. *Int. J. Pharm. 102*, 55–62.
(21) Soma, C. E., Dubernet, C., Barratt, G., Nemati, F., Appel, M., Benita, S., and Couvreur, P. (1999) Ability of doxorubicin-loaded nanoparticles to overcome multidrug resistance of tumor cells after their capture by macrophages. *Pharm. Res. 16*, 1710–1716.
(22) Kim, D., Gao, Z. G., Lee, E. S., and Bae, Y. H. (2009) In vivo evaluation of doxorubicin-loaded polymeric micelles targeting folate receptors and early endosomal ph in drug-resistant ovarian cancer. *Mol. Pharmaceutics 6*, 1353–1362.
(23) Kim, D., Lee, E. S., Oh, K. T., Gao, Z. G., and Bae, Y. H. (2008) Doxorubicin-loaded polymeric micelle overcomes multidrug resistance of cancer by double-targeting folate receptor and early endosomal pH. *Small 4*, 2043–2050.
(24) Lee, E. S., Gao, Z. G., Kim, D., Park, K., Kwon, I. C., and Bae, Y. H. (2008) Super pH-sensitive multifunctional polymeric micelle for tumor pH(e) specific TAT exposure and multidrug resistance. *J. Controlled Release 129*, 228–236.
(25) Sun, H. L., Guo, B. N., Cheng, R., Meng, F. H., Liu, H. Y., and Zhong, Z. Y. (2009) Biodegradable micelles with sheddable poly(ethylene glycol) shells for triggered intracellular release of doxorubicin. *Biomaterials 30*, 6358–6366.
(26) Tang, L. Y., Wang, Y. C., Li, Y., Du, J. Z., and Wang, J. (2009) Shell-detachable micelles based on disulfide-linked block copolymer as potential carrier for intracellular drug delivery. *Bioconjugate Chem. 20*, 1095–1099.
(27) Balendiran, G. K., Dabur, R., and Fraser, D. (2004) The role of glutathione in cancer. *Cell Biochem. Funct. 22*, 343–352.
(28) Wang, Y. C., Tang, L. Y., Sun, T. M., Li, C. H., Xiong, M. H., and Wang, J. (2008) Self-assembled micelles of biodegradable triblock copolymers based on poly(ethyl ethylene phosphate) and poly(epsilon-caprolactone) as drug carriers. *Biomacromolecules 9*, 388–395.
(29) Huynh, D. P., Nguyen, M. K., Pi, B. S., Kim, M. S., Chae, S. Y., Kang, C. L., Bong, S. K., Kim, S. W., and Lee, D. S. (2008) Functionalized injectable hydrogels for controlled insulin delivery. *Biomaterials 29*, 2527–2534.
(30) Knop, K., Hoogenboom, R., Fischer, D., and Schubert, U. S. (2010) Poly(ethylene glycol) in drug delivery: pros and cons as well as potential alternatives. *Angew. Chem., Int. Ed. 49*, 6288–6308.
(31) Owens, D. E., and Peppas, N. A. (2006) Opsonization, biodistribution, and pharmacokinetics of polymeric nanoparticles. *Int. J. Pharm. 307*, 93–102.
(32) Hong, R. L., Huang, C. J., Tseng, Y. L., Pang, V. F., Chen, S. T., Liu, J. J., and Chang, F. H. (1999) Direct comparison of liposomal doxorubicin with or without polyethylene glycol coating in C-26 tumor-bearing mice: Is surface coating with polyethylene glycol beneficial? *Clin. Cancer Res. 5*, 3645–3652.
(33) Meng, F. H., Hennink, W. E., and Zhong, Z. (2009) Reduction-sensitive polymers and bioconjugates for biomedical applications. *Biomaterials 30*, 2180–2198.
(34) Saito, G., Swanson, J. A., and Lee, K. D. (2003) Drug delivery strategy utilizing conjugation via reversible disulfide linkages: role and site of cellular reducing activities. *Adv. Drug Delivery Rev. 55*, 199–215.
(35) Bae, Y., Fukushima, S., Harada, A., and Kataoka, K. (2003) Design of environment-sensitive supramolecular assemblies for intracellular drug delivery: Polymeric micelles that are responsive to intracellular pH change. *Angew. Chem., Int. Ed. 42*, 4640–4643.
(36) Fornari, F. A., Randolph, J. K., Yalowich, J. C., Ritke, M. K., and Gewirtz, D. A. (1994) Interference by doxorubicin with DNA unwinding in MCF-7 breast-tumor cells. *Mol. Pharmacol. 45*, 649–656.
(37) Ramachandran, C., Samy, T. S. A., Huang, X. L., Yuan, Z. K., and Krishan, A. (1993) Doxorubicin-induced DNA breaks, Topoisomerase-Ii activity and gene-expression in human-melanoma cells. *Biochem. Pharmacol. 45*, 1367–1371.

Bioconjugate Chemistry

ARTICLE

pubs.acs.org/bc

Tunable Degradation of Maleimide−Thiol Adducts in Reducing Environments

Aaron D. Baldwin[†] and Kristi L. Kiick[*,†,‡]

[†]Department of Materials Science and Engineering, 201 DuPont Hall, University of Delaware, Newark, Delaware 19716, United States

[‡]Delaware Biotechnology Institute, 15 Innovation Way, Newark, Delaware 19716, United States

Supporting Information

ABSTRACT: Addition chemistries are widely used in preparing biological conjugates, and in particular, maleimide−thiol adducts have been widely employed. Here, we show that the resulting succinimide thioether formed by the Michael-type addition of thiols to *N*-ethylmaleimide (NEM), generally accepted as stable, undergoes retro and exchange reactions in the presence of other thiol compounds at physiological pH and temperature, offering a novel strategy for controlled release. Model studies (^{1}H NMR, HPLC) of NEM conjugated to 4-mercaptophenylacetic acid (MPA), *N*-acetylcysteine, or 3-mercaptopropionic acid (MP) incubated with glutathione showed half-lives of conversion from 20 to 80 h, with extents of conversion from 20% to 90% for MPA and *N*-acetylcysteine conjugates. After ring-opening, the resultant succinimide thioether did not show retro and exchange reactions. The kinetics of the retro reactions and extent of exchange can be modulated by the Michael donor's reactivity; therefore, the degradation of maleimide−thiol adducts could be tuned for controlled release of drugs or degradation of materials at time scales different than those currently possible via disulfide-mediated release. Such approaches may find a new niche for controlled release in reducing environments relevant in chemotherapy and subcellular trafficking.

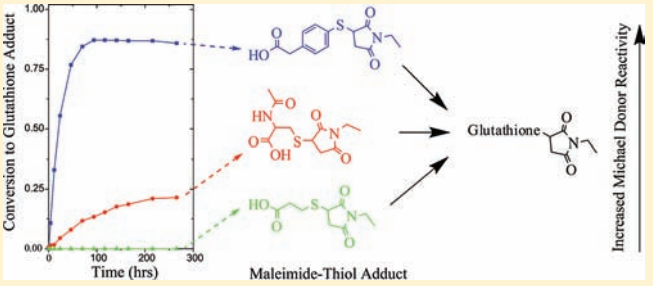

INTRODUCTION

Controlled release of drugs has been a key area of research in the field of polymeric biomaterials, owing to the need to sustain release in order to expand the therapeutic window and efficacy of known drugs. Many chemical degradation approaches have been used to control materials-based drug delivery including chemical hydrolysis,[1] enzymatic degradation,[2] and disulfide exchange.[3] The rate of nonspecific chemical hydrolysis depends mainly on aqueous pH and temperature, as well as on the hydrophobicity of the environment around the hydrolytically labile group. Enzymatic degradation, in contrast, occurs specifically at enzyme-recognized peptide sequences, although rates of degradation are dependent on the local enzyme concentration, activity, and accessibility to the substrate. Disulfide exchange is sensitive to reducing environments and has found use in drug delivery systems due to the weak reducing capacity of blood (ca. 2−20 μM glutathione) compared with that of reductive cellular compartments or highly reductive and hypoxic tumor tissues (ca. 0.5−10 mM glutathione).[4−9] Disulfide bonds have relatively short half-lives (<1 h) in highly reductive environments, while maintaining a degree of stability in circulation.[5,8] Although control of the cleavage kinetics is possible with variations in reducing agent concentration, only limited control of kinetics has been achieved by varying the disulfide's neighboring chemical substituents (half-lives ranging from 8 to 45 min).[8]

In contrast to disulfide-based drug conjugation and polymer network formation strategies, thiol-based Michael-type addition reactions have emerged as a widely employed strategy for covalent conjugation of proteins, peptides, and drugs (to various polymers and other molecules) by the reaction of free cysteine or thiols with acrylamides, acrylates, vinyl sulfones, and maleimides.[10] Maleimides have been commonly employed due to their specificity to thiols, fast aqueous reaction kinetics, lack of byproducts, and the stability of the thioether addition product.[11] Maleimides have thus been utilized in homobifunctional cross-linkers,[12] heterobifunctional cross-linkers,[13] fluorescent labels,[14,15] as well as in PEGylation reagents[16] and cross-linking of hydrogels.[17]

While the wide use of maleimide−thiol conjugation reactions have been motivated by the product stability, there have been limited reports indicating that select succinimide thioethers can undergo retro reactions at high temperatures (>300 °C)[18] and in some aqueous environments,[19−23] although the mechanisms and exact solution conditions for these retro reactions were not elucidated in great detail. Such reports are very limited, however, despite the fact that the reversibility of adducts of thiols with α,β-unsaturated carbonyls such as ethacrynic acid and 4-hydroxyalkenals has been long reported.[24−27] We have thus recently explored the

Received: March 24, 2011
Revised: July 30, 2011
Published: August 25, 2011

ACS Publications © 2011 American Chemical Society

Scheme 1. Proposed Exchange of Synthesized Maleimide Thiol Adducts (1) with Glutathione in Aqueous Solutions

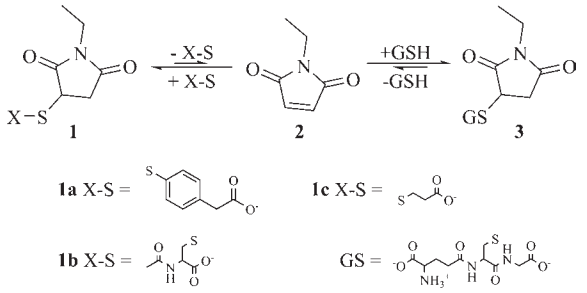

reversibility of maleimide−thiol conjugation reactions as a potential controlled degradation mechanism, which may have similar and complementary applications to the disulfide-mediated release of drugs in reducing environments. Scheme 1 illustrates the likely mechanism for the covalent bond transfer from the initial succinimide thioether compound (**1**) to a stable glutathione conjugate (**3**) in the presence of excess reductant. We have found that the rate and extent of this exchange, which is governed by the rate of the retro-addition, can be modulated by increasing or decreasing the Michael donor's reactivity.

EXPERIMENTAL PROCEDURES

Chemicals and General Methods. *N*-Ethylmaleimide (**2**), 4-mercaptophenylacetic acid (MPA), *N*-acetyl-L-cysteine (AcCys), 3-mercaptopropionic acid (MP), and glycine were purchased from Sigma-Aldrich (St. Louis, MO) and used without further purification. All other reagents including glutathione (GSH) and oxidized glutathione (GSSG) were purchased from Fisher Scientific (Pittsburgh, PA). Crude reactions were purified via reverse-phase chromatography on a Delta600 HPLC (Waters, Milford, MA) equipped with analytical (3.5 μm particle size, 4.6 × 75 mm) and preparative (5 μm particle size, 19 × 150 mm) Waters Symmetry300 C18 columns. Analytical linear gradients from 0% to 75% of solvent B were run over 20 min at 1 mL/min, where solvent A is 0.1% trifluoroacetic acid (TFA) in water and solvent B is 0.1% TFA in acetonitrile. Preparative-scale experiments utilized similar elution profiles determined from the analytical experiments, although with flow rates of 5 mL/min. Peaks were collected and analyzed via ESI-MS and ^{1}H NMR. ^{1}H NMR spectra were acquired under standard quantitative conditions at ambient temperature on a Bruker DRX-400 NMR spectrometer (Billerica, MA). The spectra of all purified compounds were recorded in either deuterated methanol or deuterium oxide.

Synthesis of Succinimide Thioether Compounds. Methanol-soluble mercapto-acids, MPA and MP (conjugates **1a** and **1c**), were dissolved at a concentration of 100 mg/mL in methanol and reacted with molar equivalents of **2**. A catalytic amount of triethylamine (0.01×) was added to the reaction mixture. The reaction was stirred for 30 min at room temperature. The crude product was diluted to 20 mL with solvent A and purified using RP-HPLC. Water-soluble thiol compounds AcCys and GSH (conjugates **1b** and **3**) were dissolved at a concentration of 50 mg/mL in deionized water. A molar equivalent of **2** was dissolved in MeOH (75 mg/mL) and added to the thiol solution. The unbuffered MeOH/aqueous solution had a final pH of ~4, retarding the maleimide−thiol addition reaction; therefore, the solution was stirred overnight at room temperature. The crude product was diluted to 5 mL with solvent A and purified using RP-HPLC. Purified fractions were collected and freeze−dried, with approximately 90% yield for all reactions. **1a** (Supporting Information Figure S1) ^{1}H NMR (MeOD): δ 0.96 (t, 3H), 2.63−2.69 (dd, 1H), 3.17−3.24 (dd, 1H), 3.39 (q, 2H), 3.61 (s, 2H), 4.13−4.17 (dd, 1H), 7.29 (d, 2H), 7.48 (d, 2H). ESI-MS: 338.1 $(M\text{-}1H+2Na)^+$, 338.0 calc'd ($C_{14}H_{14}NO_4SNa_2^+$). **1b** (Figure S2) ^{1}H NMR (MeOD): δ 1.16 (t, 3H), 2.03 (d, 3H), 2.42−2.55 (m, 1H), 2.93−2.99 (m, 0.5H), 3.15−3.28 (m, 2H), 3.52−3.58 (m, 2.5H), 3.96−4.00 (dd, 1H), 4.67−4.75 (m, 1H). ESI-MS: 289.1 $(M+H)^+$, 289.1 calc'd ($C_{11}H_{17}N_2O_5S^+$). **1c** (Figure S3) ^{1}H NMR (MeOD): δ 1.14 (t, 3H), 2.44−2.2.50 (dd, 1H), 2.69 (t, 2H), 2.91−2.99 (m, 1H), 3.09−3.23 (m, 2H), 3.53 (q, 2H), 3.91−3.94 (dd, 1H). ESI-MS: 276.0 $(M\text{-}1H+2Na)^+$, 276.0 9 calc'd ($C_9H_{12}NO_4SNa_2^+$). **3** (Figure S4) ^{1}H NMR (D_2O): δ 1.03 (t, 3H), 2.14 (m, 2H), 2.49 (m, 2H), 2.56−2.64 (m, 1H), 2.91−2.97 (dd, 0.5H), 3.06−3.28 (m, 2.5H), 3.45 (q, 2H), 3.89 (t, 1H), 3.93 (s, 2H), 3.94−4.00 (td, 1H), 4.60 (dt, 1H). ESI-MS: 455.2 $(M+Na)^+$, 455.1 calc'd ($C_{16}H_{24}N_4O_8SNa^+$).

NMR Analysis of MPA-NEM Retro Reactions. ^{1}H NMR spectroscopy with W5 water suppression[28] was used to monitor retro reactions of maleimide conjugates (Scheme 1). Samples of MPA were dissolved at a concentration of 3 mg/mL in 0.2 M phosphate buffer pH 7.4 with 10% D_2O. High buffer concentrations were needed (relative to those employed in the HPLC experiments below) in order to maintain a constant pH throughout the experiment, owing to the high concentration of MPA necessary for NMR investigation. After addition of compounds, the pH was adjusted to 7.4 if necessary. A molar equivalent of **2** was added to each NMR tube and the spectrum was recorded. Some samples were ring-opened by incubation at pH 8.0 @ 37 °C until ring-opening was complete (~5 days). Molar equivalents of GSH or glycine were added to ring-opened and non-ring-opened samples. Samples were incubated at 37 °C and spectra were recorded at time zero and at 24 hr.

HPLC Evaluation of Reaction Kinetics. Synthesized conjugates (**1**) were dissolved at a concentration of 0.1 mM in 50 mM phosphate buffers (pH 7.4) containing 10 mM GSH (and 5.0 mM, 0.5 mM, and 0.05 mM for GSSG). Lower buffer concentrations were employed to permit quantitative detection by HPLC, and these lower concentrations were sufficient to maintain a constant pH throughout the experiment. The kinetics of succinimide ring-opening were measured by monitoring reactions incubated without reductant. The pH values of all samples were verified and adjusted to 7.4 if needed before incubation at 37 °C. 150 μL samples were collected periodically and added to 150 μL of 0.5% formic acid solution to reduce the pH and quench the retro and ring-opening reactions. Samples were stored at −20 °C until analyzed. RP-HPLC injections were carried out under the above-defined conditions and areas of peaks were integrated to calculate conversion curves. The identities of the compounds present in each peak were determined using LC-MS or MS.

RESULTS AND DISCUSSION

NMR Analysis of MPA-NEM Retro Reactions. Our first experiments sought to validate that retro Michael-type additions were in fact a significant reaction route for select succinimide

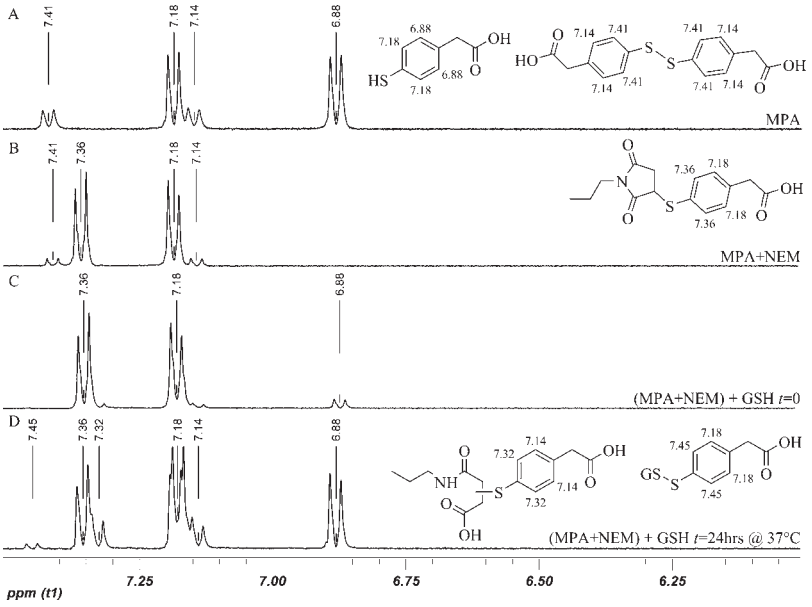

Figure 1. ^{1}H NMR of aromatic protons of (A) MPA, (B) after addition of NEM to MPA, (C) immediately after addition of GSH to (NEM+MPA) and (D) after incubation of (C) @ 37 °C for 24hrs. Evident in (D) are free MPA and small amounts of ring-opened **1a** (7.14, 7.32 ppm) and GS-MPA mixed disulfide (7.45, 7.18 ppm).

thioethers under reducing conditions. These experiments involved ^{1}H NMR analysis of the reaction of 4-mercaptophenylacetic acid (MPA) with *N*-ethylmaleimide (NEM, **2**) to yield (**1a**), with subsequent incubation with glutathione (GSH). The formation of the Michael-type adduct and its degradation via retro reactions were easily observed in the NMR experiment. Figure 1A shows the ^{1}H NMR spectrum for MPA in solution; this spectrum presents chemical shifts centered at 6.88 and 7.18 ppm, which result from the reduced MPA, as well as minor contributions from the oxidized form centered at 7.14 and 7.41 ppm. The chemical shifts of the thiophenyl aromatic protons are sensitive to the identity of the thiol substituents and thus provided a facile means to follow the addition and retro reactions (Figure 1B,C). A molar equivalent of **2** was added to the solution of MPA; upon addition of **2**, the aromatic protons shift downfield (to peaks centered at 7.18 and 7.36 ppm), indicating the production of the conjugate **1a** (Figure 1B). The resonances resulting from the small fraction of oxidized MPA (centered at 7.14 and 7.41 ppm) remained unchanged. A molar equivalent of GSH was added, resulting in immediate reduction of the unreacted MPA, indicated by a shift in the aromatic protons from 7.14 and 7.41 ppm (oxidized) to 6.88 and 7.18 ppm (Figure 1C). No other changes in the spectrum for conjugate **1a** were immediately apparent. After 24 h of incubation at 37 °C, however, MPA was liberated from **1a** as indicated by the increase in intensity of the MPA aromatic protons (centered at 6.88 and 7.18 ppm, Figure 1D). Under these conditions, a minor amount of ring-opening of the **1a** also occurred (resonances centered at 7.14 and 7.32 ppm), but the low intensity of these resonances indicates this occurs at a significantly slower rate than the retro reaction. Hydrolysis of the succinimide ring could occur on either carbonyl with respect to the thioether; however, the thiophenyl protons of either species were not distinct. Hydrolysis of the succinimide ring before incubation with GSH in these NMR experiments hindered the retro reaction as no exchange was observed over seven days incubation (data not shown). Furthermore, incubation of conjugate **1a** in the absence of reducing agents or in the presence of other nucleophiles such as glycine yielded only the ring-opened substituent (data not shown), clearly indicating that the equilibrium lies toward the Michael adduct and that formation of detectable quantities of free MPA only occurred when exogenous thiols were added to the reaction. Therefore, select succinimide thioethers should be sensitive to variations in reducing environments near physiological conditions.

HPLC Evaluation of Reactions Kinetics. We next sought to determine the selectivity of these retro and thiol-exchange reactions, as well as to obtain a quantitative measure of the time scales of these reactions, at biologically relevant concentrations of reductant. Such analysis required the quantification of small quantities of multiple compounds; HPLC and LC-MS were thus used to permit both quantification and identification. Various addition products were synthesized by reacting **2** with MPA (**1a**), *N*-acetylcysteine (**1b**), and 3-mercaptopropionic acid (**1c**). These thio-acids, which exhibit different thiol pK_a values (6.6,[29] 9.5,[30] 10.3,[31] respectively), were selected to determine how the rate of exchange may vary with the pK_a of the thio-acid. 0.1 mM of **1** was incubated in 10 mM GSH or 5.0 mM, 0.5 mM, and 0.05 mM GSSG (see below) in phosphate buffer at pH 7.4 and 37 °C; succinimide ring-opening hydrolysis rates were determined from solutions of **1** in buffer without addition of GSH. Rates of formation of the product **3** (Scheme 1), under these various conditions, were determined by monitoring changes of peak area in the HPLC experiment; the identity of the chemical species present in each fraction was confirmed by LC-MS (data not shown).

Figure 2 shows a typical set of traces obtained upon incubation of **1a** with excess GSSG, showing the location of all peaks and expanded regions highlighting relevant peaks. Arrows indicate the direction of peak growth or recession with increasing time. At time zero, a single peak was observed for compound **1a**. Over time, the peak for **1a** decreased in intensity, while peaks for compounds **3**, GS-MPA mixed disulfide, and $\mathbf{1a_{RO}}$ (ring-opened **1a**)

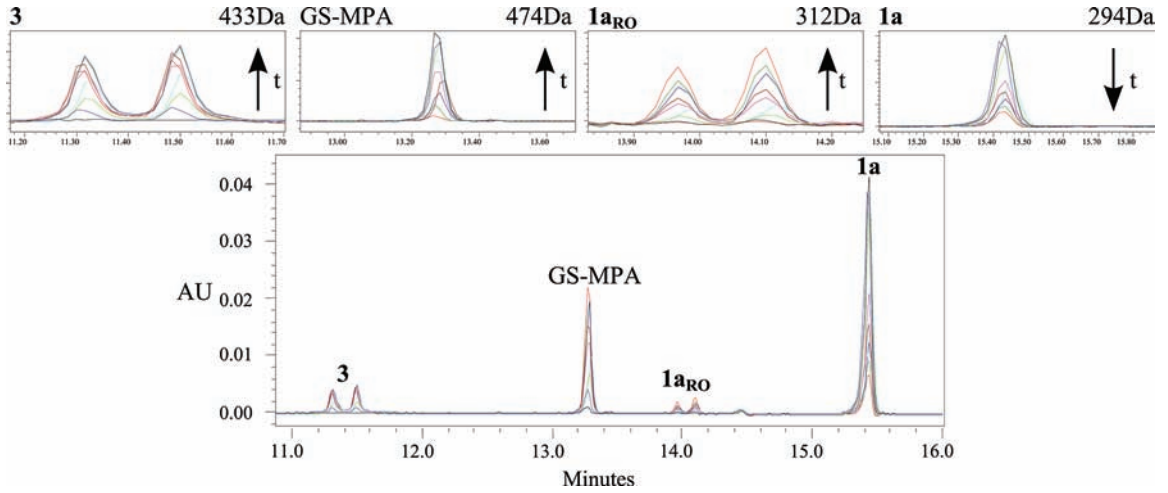

Figure 2. HPLC traces of degradation of **1a** in 50 mM phosphate buffer with 0.5 mM GSSG pH 7.4 @ 37 °C over a period of 6 days; masses obtained from LC-MS experiments are displayed for $(M+H)^+$. The peak area for **1a** decreases with time as peak areas for **3**, GS-MPA (mixed disulfide), and $\mathbf{1a_{RO}}$ increase with time, indicating the occurrence of the retro Michael-type reaction. Arrows indicate the direction of peak area growth or decline with time. Peak 3 consists of two equal peaks representing two diastereomers, while the two peaks of $\mathbf{1a_{RO}}$ evolve from ring-opening on either side of the succinimide with respect to the thioether.

Scheme 2. Complete Reaction Cycle of 1 in Solution with Oxidized or Reduced Thiols

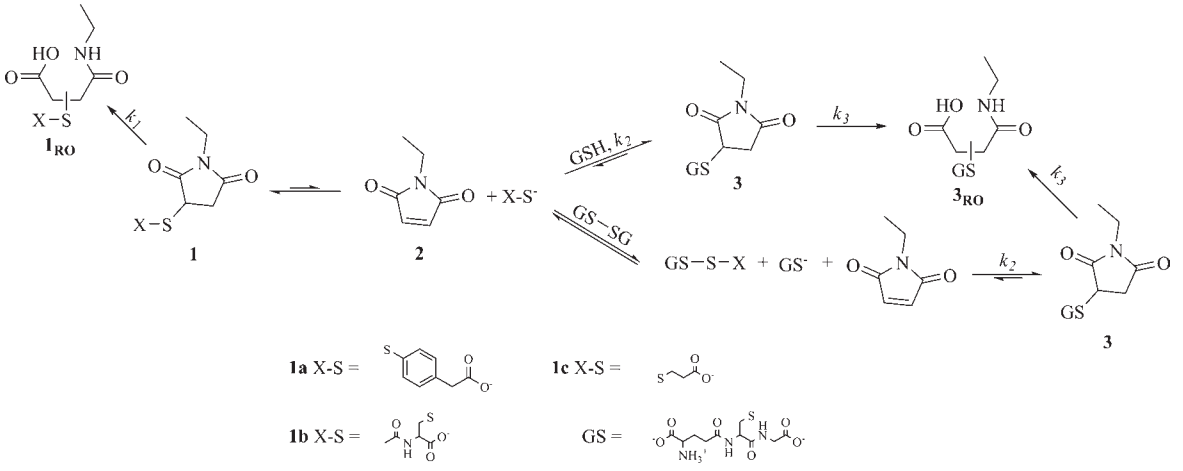

all increased in intensity. The loss of **1** occurred concomitantly with the generation of **3**. Peaks for **3** and **1aRO** are split into two equal peaks. Peak **3** is split as a result of the two diastereomers formed from the Michael addition of GSH to **2**[32] (verified by the equivalence of masses determined from LC-MS of the two different peaks), while **1aRO** is split depending on the side of succinimide ring-opening in relation to the thioether (also verified by the equivalence of masses determined from LC-MS of the two different peaks). Scheme 2 illustrates the likely reaction cycle for an initial conjugate **1** in the presence of excess thiols, showing ring-opening of conjugates, as well as the exchange with GSH or GSSG. Either GSH or GSSG causes exchange, with 5.0 mM GSSG yielding identical results as 10 mM GSH (Supporting Information, Figure S5). This observation suggests that the formation of **2** is the rate-limiting step in the overall reaction to **3** and is significantly slower than the disulfide exchange of the free thio-acid with excess GSSG; therefore, the oxidation state of GSH does not significantly impact the rate of formation of **3**.

Scheme 3. Simplified Reaction Cycle and Kinetics Constants for the Reaction of 1

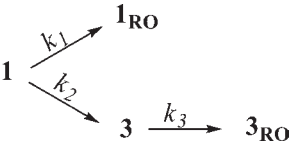

Throughout these experiments, no measurable amount of **2** was detected, confirming the widely known fact that the equilibrium greatly favors the succinimide thioether under the experimental conditions. Thus, by neglecting the kinetics of formation of **2** (and the thiol-exchange of GSSG to yield GSH as our above experiments validate), Scheme 2 can be simplified to the combination of a consecutive and parallel reactions (Scheme 3). Thus, pseudo first-order rate constants, k_1 and k_3, can be defined for the ring-opening of **1** and **3**, and k_2 can be defined as the pseudo first-order rate

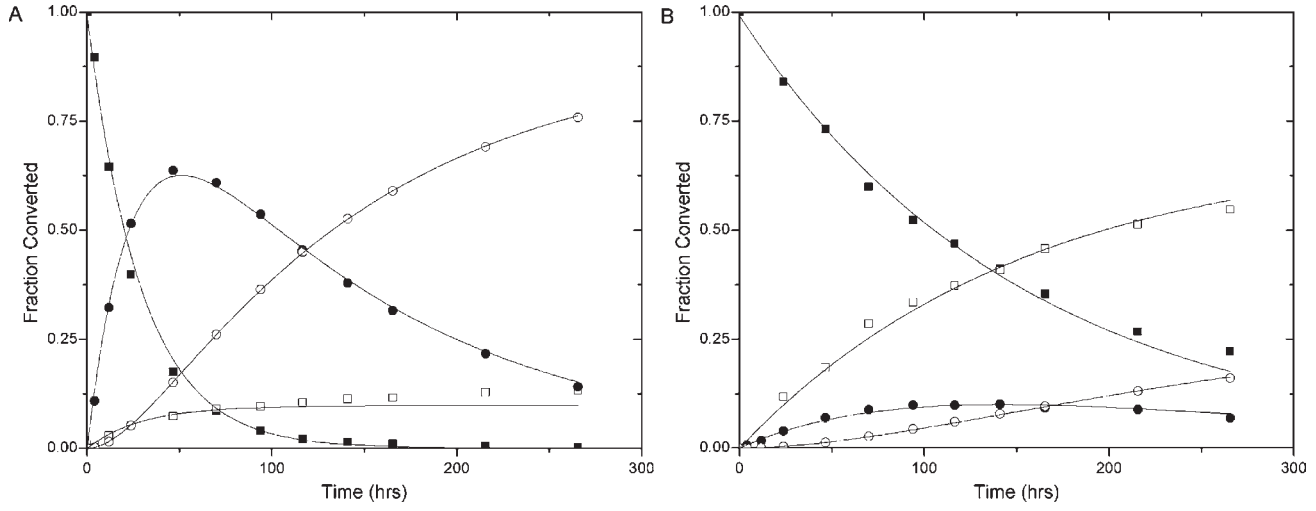

Figure 3. Relative HPLC measured concentrations for **1a** (panel A) and **1b** (panel B) over time, with constructed curves using derived rate constants and eqs 5−8 for (■) **1** (a or b), (□) $\mathbf{1}_{RO}$, (●) **3**, and (○) $\mathbf{3}_{RO}$.

constant for the retro and exchange reaction of **1** (to yield **3**) in the presence of a large excess of a thiol compound (10 mM GSH or 5 mM GSSG). Using the simplified Scheme 3, reaction rate equations (eqs 1−4)

$$\frac{d[\mathbf{1}]}{dt} = -k_1[\mathbf{1}] - k_2[\mathbf{1}] \quad (1)$$

$$\frac{d[\mathbf{1}_{RO}]}{dt} = k_1[\mathbf{1}] \quad (2)$$

$$\frac{d[\mathbf{3}]}{dt} = k_2[\mathbf{1}] - k_3[\mathbf{3}] \quad (3)$$

$$\frac{d[\mathbf{3}_{RO}]}{dt} = k_3[\mathbf{3}] \quad (4)$$

can be defined and converted to integrated rate laws (eqs 5−8)

$$[\mathbf{1}] = [\mathbf{1}]_0 e^{-(k_1 + k_2)t} \quad (5)$$

$$[\mathbf{1}_{RO}] = \frac{k_1[\mathbf{1}]_0}{k_1 + k_2}\left(1 - e^{-(k_1 + k_2)t}\right) \quad (6)$$

$$[\mathbf{3}] = \frac{k_2[\mathbf{1}]_0}{k_3 - k_2 - k_1}\left(e^{-(k_1 + k_2)t} - e^{-k_3 t}\right) \quad (7)$$

$$[\mathbf{3}_{RO}] = \frac{k_3 k_2[\mathbf{1}]_0}{k_3 - k_2 - k_1}\left(\frac{e^{-(k_1 + k_2)t} - 1}{-k_1 - k_2} + \frac{e^{-k_3 t} - 1}{k_3}\right) \quad (8)$$

Fractional concentrations of **1**, $\mathbf{1}_{RO}$, **3**, and $\mathbf{3}_{RO}$ measured by HPLC (relative to the initial concentration) were plotted as a function of time for **1a** (Figure 3A) and **1b** (Figure 3B). Equation 7 was employed to fit to the data for **3** (converted from **1a** and **1b** ($R^2 > 0.98$)), yielding k_1, k_2, and k_3 with values shown in Table 1, with their corresponding half-lives. Standard deviations for all values were calculated from the standard error from the fit.

Curves to plot the fractional concentrations of the other compounds as a function of time were constructed, as shown in Figure 3, by input of the appropriate rate constants into eqs 5−8. As clearly illustrated in the figure, the fits show exceptional agreement with collected data for all compounds. **1c** did not exhibit measurable retro and exchange reactions under these experimental conditions; therefore, only k_3 was determined. The fractional concentrations of **1** and $\mathbf{1}_{RO}$ as a function of time decreased and increased, respectively, as exponential decay functions with respect to k_1 and k_2, as shown in Figure 3. The dependence of the fractional concentrations of **3** and $\mathbf{3}_{RO}$ as a function of time were more complex, owing to the consecutive reaction mechanism, as shown by an initial increase and subsequent decrease in the fractional concentration of **3**; the fractional concentration of $\mathbf{3}_{RO}$ increased over time with a delayed onset. The extent of formation of $\mathbf{1}_{RO}$ and $\mathbf{3}_{RO}$ was directly related to the relative reaction rates of k_1 and k_2. In the reactions of **1a**, $k_2 > k_1$; therefore, the major product at equilibrium is $\mathbf{3}_{RO}$. Conversely, for **1b** $k_1 > k_2$; therefore, $\mathbf{1}_{RO}$ is the major product. Retro and exchange rates for **1a** were an order of magnitude greater than those for **1b**, with rate constants of 0.0371 ± 0.0038 versus 0.00207 ± 0.0002 h^{-1} and respective half-lives of 19 ± 2 versus 337 ± 27 h, while half-lives for ring-opening reactions of compounds **1** were the same order of magnitude (ca. 10^2) for all compounds. In comparison, half-lives for the glutathione-mediated cleavage of disulfide bonds under similar conditions range from 8 to 45 min (with pseudo first-order rate constants of 5 to 0.9 h^{-1}),[8] indicating that the use of maleimide−thiol adducts rather than disulfides may have advantages for producing more stable, yet degradable

Table 1. Pseudo-First-Order Rate Constants and Respective Half-Lives for Retro and Ring-Opening Reactions[a]

	retro reaction		ring-opening	
conjugate	k_2 (h^{-1})	half-life (h)	k_1 or k_3 (h^{-1})	half-life (h)
1a	0.0371 ± 0.0038	19 ± 2	0.0033 ± 0.0002 (k_1)	211 ± 15
1b	0.00207 ± 0.0002	337 ± 27	0.0044 ± 0.0003 (k_1)	157 ± 12
1c	n/a	n/a	0.0032 ± 0.0002 (k_1)	215 ± 11
3	--	--	0.0076 ± 0.0007 (k_3)	92 ± 2

[a] Standard deviations for all values were calculated from the standard error from fit.

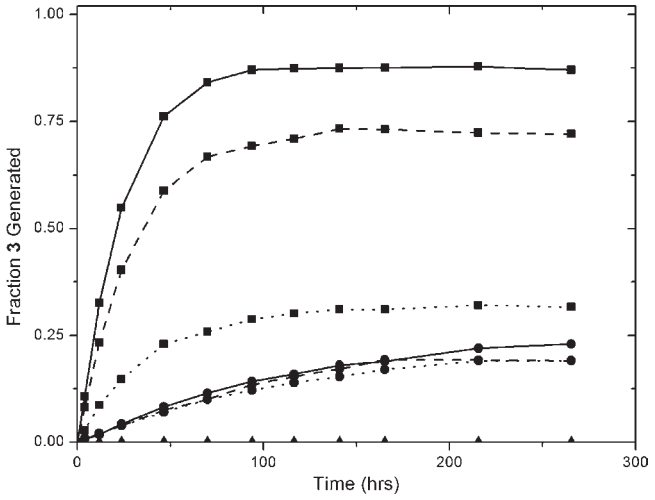

Figure 4. Fraction of **3** generated from (■) **1a**, (●) **1b**, and (▲) **1c** (at the baseline) in the presence of (—) 10 mM, (--) 1.0 mM, and (· ·) 0.1 mM GSH.

bioconjugates. Indeed, *in vivo* blood circulation stability has been shown to be as little as 4 h for disulfide-based immunotoxin-antibody conjugates, with circulation stability directly dependent on the kinetics of reduction by glutathione.[7,33,34] Accordingly, the decreased rate of exchange of the maleimide—thiol adduct with glutathione would increase compound circulation stability while maintaining cleavage sensitivity in highly reducing environments.

The release data from HPLC experiments illustrate the extent of turnover of the initial succinimide thioether under various reducing conditions, which is relevant to the use of these strategies for the liberation of drug conjugates or materials degradation. Thus, using these treatments, variations in the overall generation of **3** as a function of time (for different compounds and reductant concentrations) are presented in Figure 4 (calculations from obtained data are shown in the Supporting Information, Figures S6—S8). **1a** supported the greatest rate of conversion of the initial adduct, with conversion of nearly 85% after 70 h, followed by **1b** with much slower kinetics and substantially lower conversion, and then by **1c**, for which no measurable conversion was observed. The rate of exchange of the initial adduct is clearly impacted by the thiol pK_a, with higher pK_a decreasing the rate (Figure 4); the use of a Michael donor with sufficiently high pK_a (~10.3) can eliminate any impact of the retro reaction, as illustrated by the lack of conversion of **1c**.

Two other observations recommending the use of these strategies for tailoring the degradation of succinimide thioethers are indicated from these data. Importantly, the data in Figure 4 illustrate that the rate of thiol exchange varies with the concentration of reductant. **1a** showed the greatest dependence on reductant concentration with the total production of **3** ranging from 30% to 90% under these conditions. In contrast, conversion of **1b** showed little dependence, and that of **1c** showed no dependence, on reductant concentration; Michael donors can thus be selected for application on the basis of desired sensitivity to reductant. Additionally, the conversion to **3** can be impacted by the inactivation of **1** by ring-opening of certain adducts. The minimum half-lives for the retro reaction were approximately 19 h for **1a** and 337 h for **1b**, while those for inactivation of **1** by ring-opening were approximately 200 h. Thus, the inactivation by ring-opening became significant and limited the overall conversion to **3** for conjugates **1b** and **1c** (evidenced by the reduction in turnover of these compounds at later time points), which could be used to tailor initial release and long-term stability for specific conjugates.

The manipulation of the Michael-type addition has very limited precedent in literature, and there are no previous reports to our knowledge that seek to selectively utilize the retro reaction for a specific use. In studies by Lewis et al., in which a bis-maleimide was used to conjugate a chelating agent to a monoclonal antibody, it was determined that the resulting adduct was cleaved to some extent when exposed to fresh human serum.[19] Later, Alley et al. described mass spectrometry experiments that illustrated that an antibody—drug conjugate linked by maleimide—thiol chemistries had exchanged with rat serum albumin in vivo to yield albumin—drug adduct.[20] Concurrently, Lin et al. described studies indicating that maleimide—cysteine adducts disappeared in cells while similar iodoacetate adducts were stable.[21] The commonality in these reports stems from the use of the resulting succinimide thioether in environments containing reduced or oxidized thiol species, and although the mechanism underlying these previous observations was not discussed or determined, the reaction mechanism could proceed as suggested in Scheme 1, as supported by our experiments. More recently, Baker and co-workers have described the bromination of maleimides for reversible conjugation of thiols as a bioconjugate technique.[35—37] The process of bromination and subsequent elimination of HBr by the addition of a protected cysteine was found to be more rapid than the addition to maleimides. This bromomaleimide conjugate was found to be reversible by adding reducing agents such as GSH[36] or TCEP[37] with complete conversion within 4 h for incubation with excess GSH. In contrast, 70 h was required for 85% conversion of **2a**, indicating that the reduced reactivity of maleimides compared with bromomaleimides correlates with the rate of the retro reaction.

■ CONCLUSIONS

We have confirmed that succinimide thioethers undergo reversible addition in solutions and that exchange with nearby free thiols or disulfides can be manipulated under relevant physiological conditions. Reverse reactions of these kinds have not been reported for other Michael-type addition products such as thiol—acrylate conjugates, most likely due to the reduced Michael acceptor reactivity of acrylates compared to maleimides.[11] Glycine, substituted for GSH in control experiments, did not induce the reverse reaction under these conditions, although it has been shown that maleimides can be Michael acceptors for amine donors;[38,39] these observations suggest that the retro reaction may not be substantially affected by amine-bearing compounds present in vivo. Our data also indicate that ring-opening of the succinimide before the addition of GSH stabilizes the conjugate and will inhibit the liberation of free thio-acid and conversion to **3**. Hence, purposely ring-opening a succinimide thioether will stabilize bioconjugates for in vivo or in vitro assays if retro reactions are not desired, and ring-opening that would occur in vivo could be employed to dictate a lifetime over which a conjugated drug may be cleaved by GSH.

Importantly, thiophenyl conjugates were also sensitive to the reducing environment, with only approximately 30% converted at low reductant concentration within three days, versus 90% at high reductant concentration, potentially allowing for targeted

release/delivery. The slower 2w?>relative to disulfide-mediated release (e.g., half-lives >20 h for succinimide thioethers compared to minutes for disulfide-mediated release) may also allow for longer-term delivery of drugs in reducing environments. We note that the exchange and retro reactions kinetics discussed here were modulated by altering the thiol serving as the Michael donor; in many bioconjugates such alteration of the thiol reactivity would not be possible, particularly given that alkylthiols (i.e., cysteine) of natural proteins and peptides are common Michael donors in bioconjugation reactions. In cases in which Michael donor reactivity on proteins/peptides would be desirable, post-translational modification of natural proteins or peptides or non-natural amino acid incorporation could be employed for the addition of suitable thiols.[40] Other possibilities not investigated here rely on modulating the maleimide stability and reactivity as has been accomplished by addition of cyclohexyl or benzyl moieties to the nitrogen group to reduce the susceptibility of the maleimide ring to hydrolysis prior to addition reactions.[41] Albeit there are many different possibilities for tailoring retro reactions for use as delivery mechanisms, our observations expressed here could be exploited for both systemic and local administration of bioconjugated drugs or for imparting degradation sites in polymeric backbones or cross-linked biomaterials. Studies to test these potential opportunities are underway.

■ ASSOCIATED CONTENT

Supporting Information. Experimental procedures, characterization details, and data analysis are provided. This material is available free of charge via the Internet at http://pubs.acs.org.

■ AUTHOR INFORMATION

Corresponding Author

*Phone: +1 302 831 0201. Fax: +1 302 831 4545. E-mail: kiick@udel.edu.

■ ACKNOWLEDGMENT

This work was supported in part by the Nemours Foundation, the National Science Foundation (DGE-0221651) and the National Institutes of Health (5-P20-RR016472-10). The contents of the manuscript are the sole responsibility of the authors and do not necessarily reflect the official views of the National Institutes of Health nor of the National Center for Research Resources. The authors would like to thank Professor J. M. Fox and research group members for assistance with LC-MS experiments, as well as Dr. S. Bai for assistance with water suppression ^{1}H NMR techniques.

■ REFERENCES

(1) Uhrich, K. E., Cannizzaro, S. M., Langer, R. S., and Shakesheff, K. M. (1999) Polymeric systems for controlled drug release. *Chem. Rev. 99*, 3181–3198.

(2) Sakiyama-Elbert, S. E., Panitch, A., and Hubbell, J. A. (2001) Development of growth factor fusion proteins for cell-triggered drug delivery. *FASEB J. 15*, 1300–1302.

(3) Saito, G., Swanson, J. A., and Lee, K.-D. (2003) Drug delivery strategy utilizing conjugation via reversible disulfide linkages: role and site of cellular reducing activities. *Adv. Drug Delivery Rev. 55*, 199–215.

(4) Kuppusamy, P., Afeworki, M., Shankar, R. A., Coffin, D., Krishna, M. C., Hahn, S. M., Mitchell, J. B., and Zweier, J. L. (1998) In vivo electron paramagnetic resonance imaging of tumor heterogeneity and oxygenation in a murine model. *Cancer Res. 58*, 1562–1568.

(5) Bulmus, V., Woodward, M., Lin, L., Murthy, N., Stayton, P., and Hoffman, A. (2003) A new pH-responsive and glutathione-reactive, endosomal membrane-disruptive polymeric carrier for intracellular delivery of biomolecular drugs. *J. Controlled Release 93*, 105–120.

(6) Senter, P. D., Pearce, W. E., and Greenfield, R. S. (1990) Development of a drug-release strategy based on the reductive fragmentation of benzyl carbamate disulfides. *J. Org. Chem. 55*, 2975–2978.

(7) Thorpe, P. E., Wallace, P. M., Knowles, P. P., Relf, M. G., Brown, A. N. F., Watson, G. J., Knyba, R. E., Wawrzynczak, E. J., and Blakey, D. C. (1987) New coupling agents for the synthesis of immunotoxins containing a hindered disulfide bond with improved stability in vivo. *Cancer Res. 47*, 5924–5931.

(8) Trimble, S. P., Marquardt, D., and Anderson, D. C. (1997) Use of designed peptide linkers and recombinant hemoglobin mutants for drug delivery: *in vitro* release of an angiotensin II analog and kinetic modeling of delivery. *Bioconjugate Chem. 8*, 416–423.

(9) Meng, F., Hennink, W. E., and Zhong, Z. (2009) Reduction-sensitive polymers and bioconjugates for biomedical applications. *Biomaterials 30*, 2180–2198.

(10) Mather, B. D., Viswanathan, K., Miller, K. M., and Long, T. E. (2006) Michael addition reactions in macromolecular design for emerging technologies. *Prog. Polym. Sci. 31*, 487–531.

(11) Hermanson, G. T. (2008) *Bioconjugate techniques*, 2nd ed., Academic Press, San Diego, CA.

(12) Moore, J. E., and Ward, W. H. (1956) Cross-linking of bovine plasma albumin and wool keratin. *J. Am. Chem. Soc. 78*, 2414–2418.

(13) Yoshitake, S., Imagawa, M., Ishikawa, E., Niitsu, Y., Urushizaki, I., Nishiura, M., Kanazawa, R., Kurosaki, H., Tachibana, S., Nakazawa, N., and Ogawa, H. (1982) Mild and efficient conjugation of rabbit Fab' and horseradish peroxidase using a maleimide compound and its use for enzyme immunoassay. *J. Biochem. 92*, 1413–1424.

(14) Curtis, S. K., and Cowden, R. R. (1980) Demonstration of sulfhydryl and disulfide groups by a fluorescent maleimide procedure. *Histochem. Cell Biol. 68*, 23–28.

(15) Sekine, T., Ando, K., Machida, M., and Kanaoka, Y. (1972) Fluorescent thiol reagents: V. Microfluorometry of thiol compounds with a fluorescent-labeled maleimide. *Anal. Biochem. 48*, 557–568.

(16) Veronese, F. M. (2001) Peptide and protein PEGylation: a review of problems and solutions. *Biomaterials 22*, 405–417.

(17) Nie, T., Baldwin, A., Yamaguchi, N., and Kiick, K. L. (2007) Production of heparin-functionalized hydrogels for the development of responsive and controlled growth factor delivery systems. *J. Controlled Release 122*, 287–296.

(18) White, J. E., Snider, D. A., and Scaia, M. D. (1984) Synthesis and properties of some new polyimidosulfides with highly mobile backbones. *J. Polym. Sci.: Polym. Chem. Ed. 22*, 589–596.

(19) Lewis, M. R., and Shively, J. E. (1998) Maleimidocysteineamido-DOTA derivatives: new reagents for radiometal chelate conjugation to antibody sulfhydryl groups undergo pH-dependent cleavage reactions. *Bioconjugate Chem. 9*, 72–86.

(20) Alley, S. C., Benjamin, D. R., Jeffrey, S. C., Okeley, N. M., Meyer, D. L., Sanderson, R. J., and Senter, P. D. (2008) Contribution of linker stability to the activities of anticancer immunoconjugates. *Bioconjugate Chem. 19*, 759–765.

(21) Lin, D., Saleh, S., and Liebler, D. C. (2008) Reversibility of covalent electrophile-protein adducts and chemical toxicity. *Chem. Res. Toxicol. 21*, 2361–2369.

(22) Nampalli, S., McDougall, M. G., Lavrenov, K., Xiao, H., and Kumar, S. (2002) Utility of thiol-cross-linked fluorescent dye labeled terminators for DNA sequencing. *Bioconjugate Chem. 13*, 468–473.

(23) Wan, L., Zhang, X., Gunaseelan, S., Pooyan, S., Debrah, O., Leibowitz, M., Rabson, A., Stein, S., and Sinko, P. (2006) Novel multicomponent nanopharmaceuticals derived from poly(ethylene) glycol, retro-inverso-Tat nonapeptide and saquinavir demonstrate combined anti-HIV effects. *AIDS Res. Ther. 3*, 1–15.

(24) Esterbauer, H., Schaur, R. J., and Zollner, H. (1991) Chemistry and biochemistry of 4-hydroxynonenal, malonaldehyde and related aldehydes. *Free Radic. Biol. Med. 11*, 81–128.

(25) Koechel, D. A., and Cafruny, E. J. (1973) Synthesis and structure-activity relationship of some thiol adducts of ethacrynic acid. *J. Med. Chem. 16*, 1147–1152.

(26) Ploemen, J. H. T. M., Van Schanke, A., Van Ommen, B., and Van Bladeren, P. J. (1994) Reversible conjugation of ethacrynic acid with glutathione and human glutathione S-Transferase P1−1. *Cancer Res. 54*, 915–919.

(27) van Iersel, M. L. P. S., Ploemen, J.-P. H. T. M., Lo Bello, M., Federici, G., and van Bladeren, P. J. (1997) Interactions of α, β-unsaturated aldehydes and ketones with human glutathione S-transferase P1−1. *Chem.-Biol. Interact. 108*, 67–78.

(28) Liu, M., Mao, X.-a., Ye, C., Huang, H., Nicholson, J. K., and Lindon, J. C. (1998) Improved WATERGATE pulse sequences for solvent suppression in NMR spectroscopy. *J. Magn. Reson. 132*, 125–129.

(29) DeCollo, T. V., and Lees, W. J. (2001) Effects of aromatic thiols on thiol-disulfide interchange reactions that occur during protein folding. *J. Org. Chem. 66*, 4244–4249.

(30) Harman, B., and Sóvágó, I. (1983) Metal complexes of sulphur-containing ligands. V. Interactions of cobalt(II) ion with L-cysteine and its derivatives. *Inorg. Chim. Acta 80*, 75–83.

(31) Danehy, J. P., and Noel, C. J. (1960) The relative nucleophilic character of several mercaptans toward ethylene oxide. *J. Am. Chem. Soc. 82*, 2511–2515.

(32) Jemal, M., and Hawthorne, D. (1994) High performance liquid chromatography/ionspray mass spectrometry of N-ethylmaleimide and acrylic acid ester derivatives for bioanalysis of thiol compounds. *Rapid Commun. Mass Spectrom. 8*, 854–857.

(33) Arpicco, S., Dosio, F., Brusa, P., Crosasso, P., and Cattel, L. (1997) New coupling reagents for the preparation of disulfide cross-linked conjugates with increased stability. *Bioconjugate Chem. 8*, 327–337.

(34) Dosio, F., Arpicco, S., Adobati, E., Canevari, S., Brusa, P., De Santis, R., Parente, D., Pignanelli, P., Negri, D. R. M., Colnaghi, M. I., and Cattel, L. (1998) Role of Cross-linking agents in determining the biochemical and pharmacokinetic properties of MGR6−Clavin immunotoxins. *Bioconjugate Chem. 9*, 372–381.

(35) Schumacher, F. F., Nobles, M., Ryan, C. P., Smith, M. E. B., Tinker, A., Caddick, S., and Baker, J. R. (2011) In situ maleimide bridging of disulfides and a new approach to protein PEGylation. *Bioconjugate Chem. 22*, 132–136.

(36) Smith, M. E. B., Schumacher, F. F., Ryan, C. P., Tedaldi, L. M., Papaioannou, D., Waksman, G., Caddick, S., and Baker, J. R. (2010) Protein modification, bioconjugation, and disulfide bridging using bromomaleimides. *J. Am. Chem. Soc. 132*, 1960–1965.

(37) Tedaldi, L. M., Smith, M. E. B., Nathani, R. I., and Baker, J. R. (2009) Bromomaleimides: new reagents for the selective and reversible modification of cysteine. *Chem. Commun.* 6583–6585.

(38) Ishikawa, H., Suzuki, T., and Hayashi, Y. (2009) High-yielding synthesis of the anti-influenza neuramidase inhibitor (−)-oseltamivir by three "one-pot" operations. *Angew. Chem. 121*, 1330–1333.

(39) White, J. E., and Scaia, M. D. (1984) Polymerization of N,N′-bismaleimido-4,4′-diphenylmethane with arenedithiols. Synthesis of some new polyimidosulphides. *Polymer 25*, 850–854.

(40) Hohsaka, T., and Sisido, M. (2002) Incorporation of non-natural amino acids into proteins. *Curr. Opin. Chem. Biol. 6*, 809–815.

(41) Ishikawa, E., Kawai, T., Miyai, K. (1981) A more stable maleimide N-(4-carboxycyclohexylmethyl)maleimide, for enzyme labeling. *Enzyme Immunoassay* (Ishikawa, E., Kawai, T., and Miyazi, K., Eds.) pp 90−105, Igaku-Shoin, Tokyo.

Supporting Information

Tunable degradation of maleimide-thiol adducts in reducing environments

Aaron D. Baldwin[†] and Kristi L. Kiick[*,†,‡]

[†]Department of Materials Science and Engineering, 201 DuPont Hall, University of Delaware, Newark, DE 19716, United States

[‡]Delaware Biotechnology Institute, 15 Innovation Way, Newark, DE 19716, United States

[*]To whom correspondence should be addressed. Phone: +1 302 831 ***0201***. Fax: +1 302 831 4***545***. E-mail: kiick@udel.edu.

Table of Contents

[1]H-NMR Spectra of synthesized compounds

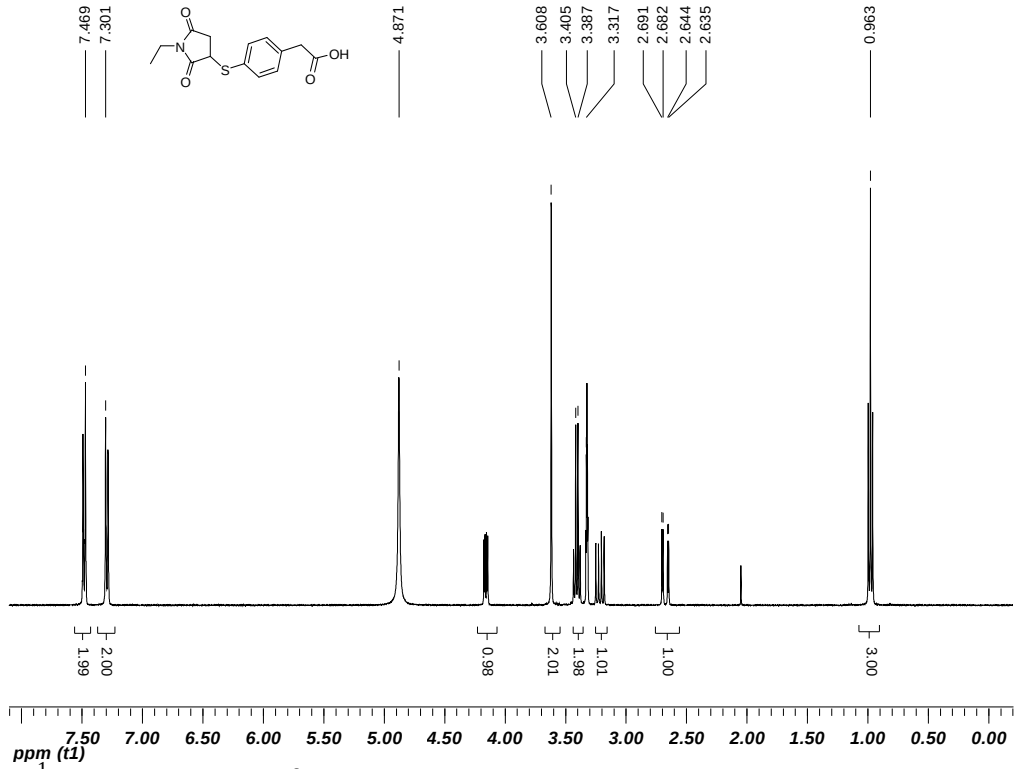

Figure S1. [1]H-NMR spectrum for compound **1a**

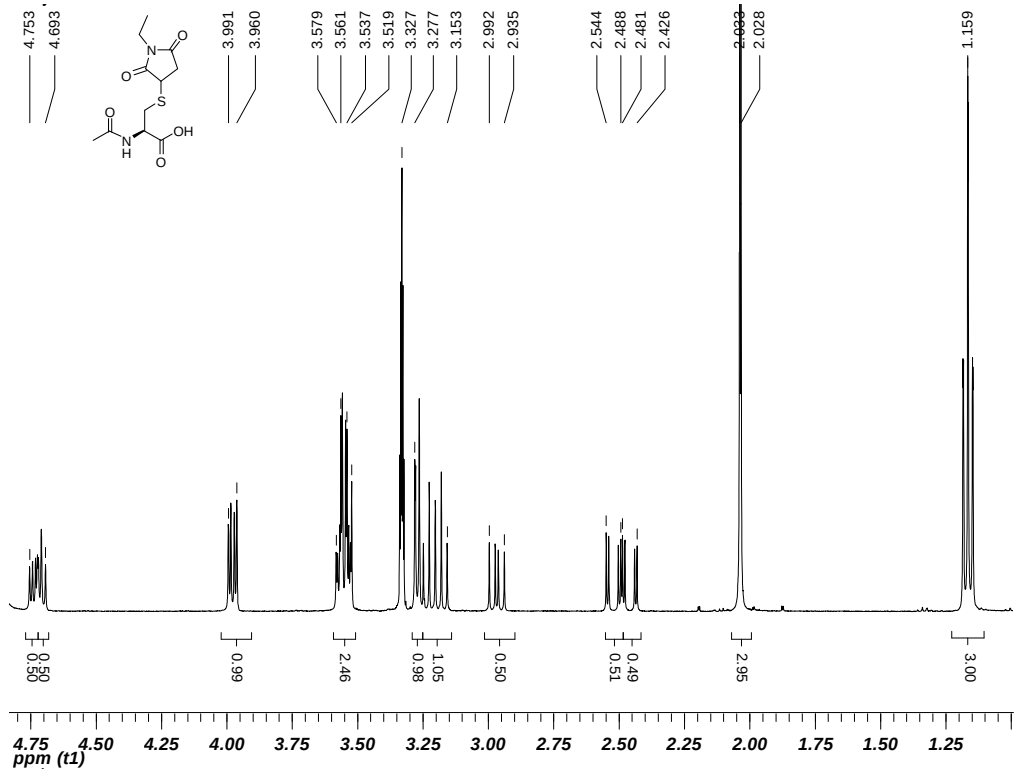

Figure S2. [1]H-NMR spectrum for compound **1b**

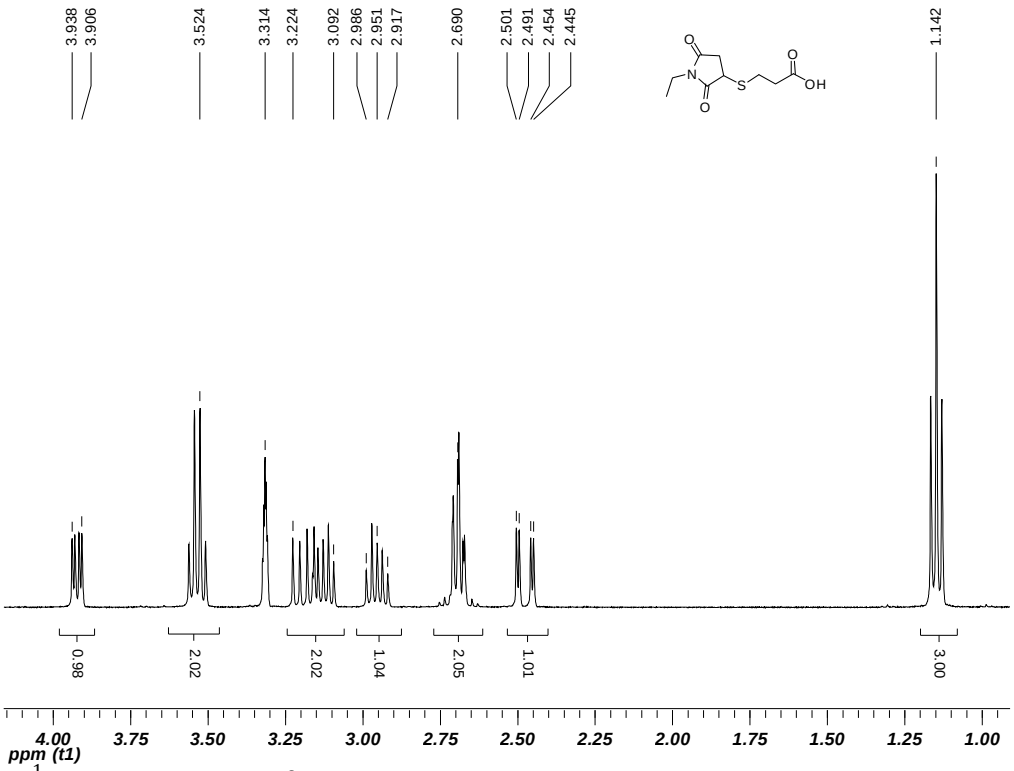

Figure S3. ^{1}H-NMR spectrum for compound **1c**

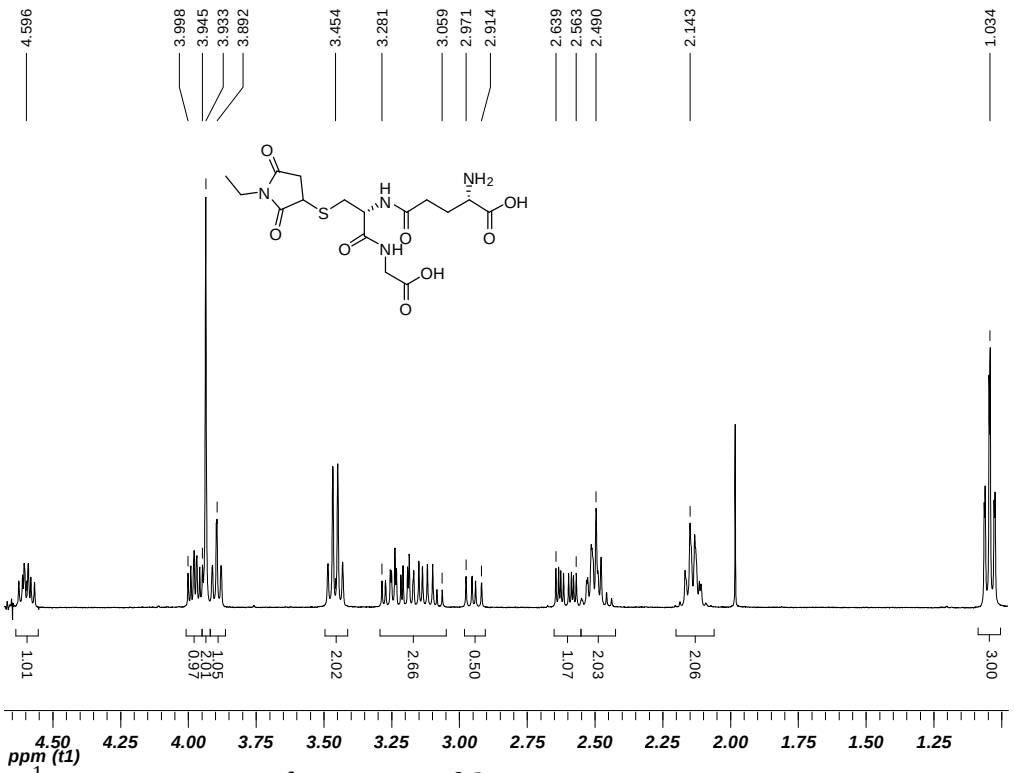

Figure S4. ^{1}H-NMR spectrum for compound **3**

Analysis of formation of 3, monitored by HPLC

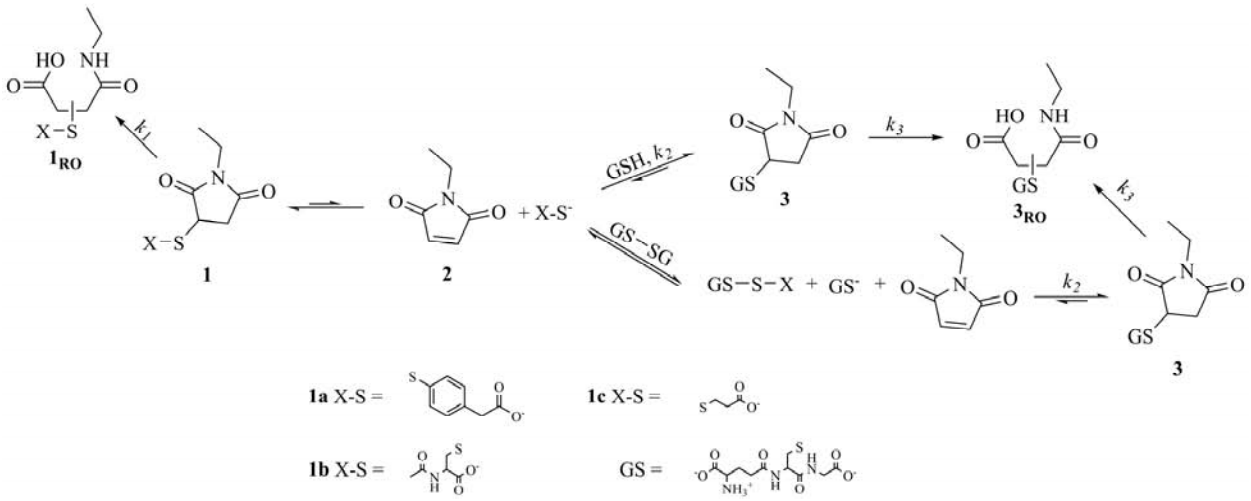

Scheme S1. Proposed exchange of the maleimide thiol adducts (**1**) with reduced (GSH) and oxidized glutathione (GSSG) and their ring opened byproducts ($\mathbf{1_{RO}}$ and $\mathbf{3_{RO}}$).

As discussed in the body of the manuscript it was found that the formation of **3** (Scheme S1) was independent of the oxidation state of glutathione, therefore a common kinetic parameter $\boldsymbol{k_2}$ was derived. Figure S5 displays the kinetic fit curves for solutions **1a** incubated with 10mM GSH and 5mm GSSG. The data points for each reading of 1a either in GSH or GSSG are similar, furthermore, fitting kinetic curves as described in the body of the manuscript to each trace yield a statistically indifferent $\boldsymbol{k_2}$.

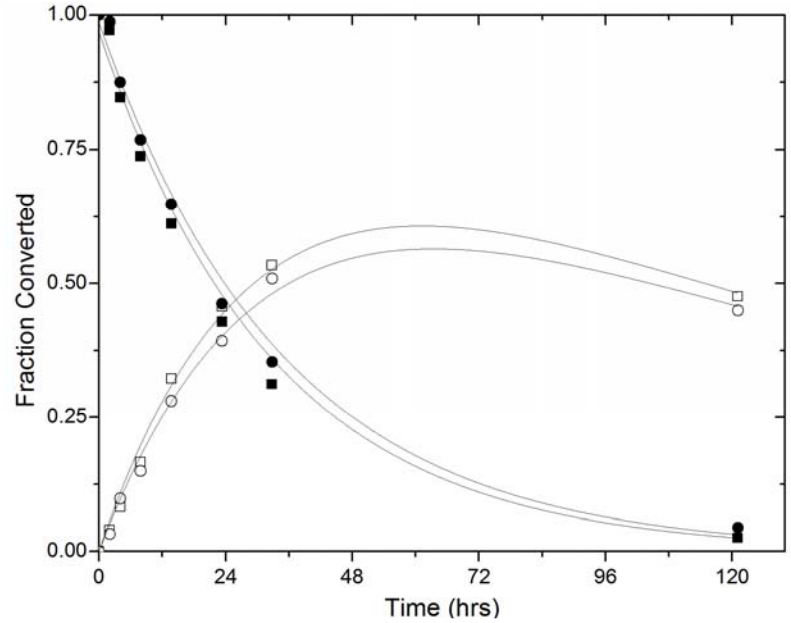

Figure S5. Relative HPLC measured concentrations for **1a** (solid) and **3** (open) in the presence of 10mM GSH (squares) and 5mM GSSG (circles) over time, with constructed curves using derived

rate constants and equations 5-8. Kinetic parameters statistically indifferent (2 sample t-test, p = 0.58, indicating no statistical evidence of a difference).

We demonstrated in the body of the manuscript our ability to predict the formation of all compounds in the reaction scheme. We present here the analysis of the total theoretical amount of **3** produced, obtained from data indicating the concentrations of relevant compounds in a select set of experiments (from **1a**). The value of this additional analysis is that it is based on confirmed measurements of the amounts of compounds of this specific set of reactions; such an analysis was not possible for all compounds studied. The procedure is as follows:

The amount of **1** converted to **3** was captured by the appearance of chromatic peak for **3** (Figure 2); monitoring the kinetics of this formation, however, was complicated by the fact that **3** ring-opens to form $\mathbf{3_{RO}}$, and that $\mathbf{3_{RO}}$ does not bind to the column and thus cannot be quantified. Therefore, a maximum, level plateau for the formation of **3** was not observed, and the data for monitoring the formation of **3** instead looked as presented in Figure S6. The loss of **3** (i.e., the amount of $\mathbf{3_{RO}}$ formed over a given time period) was estimated based on the ring opening kinetics observed when a solution of 0.1mM of **3** was incubated in buffer lacking any reductant (Figure S7). The pseudo first order rate constant, $\boldsymbol{k_3}$, for the ring-opening of **3** was determined to be 0.0076±0.0007 hr^{-1}. Computationally, the total concentration of $\mathbf{3_{RO}}$ ($[\mathbf{3_{RO}}]$) present at given time points throughout the experiment could be calculated by integrating the rate of ring-opening for **3** over time:

$$[\mathbf{3_{RO}}]\Big|_{t_1}^{t_2} = \int_{t_1}^{t_2} \boldsymbol{r} \cdot \boldsymbol{dt}$$

Where $\boldsymbol{r}$ is first order rate law equation:

$$\boldsymbol{r} = \frac{-\boldsymbol{d}[\mathbf{3}]}{\boldsymbol{dt}} = \boldsymbol{k}_3[\mathbf{3}]$$

The concentration of **3** ($[\mathbf{3}]$) over a short range of time can also be estimated by a line fit between two data points (e.g., between any given $\boldsymbol{t_1}$ and $\boldsymbol{t_2}$ data points in Figure S6) where the y-values are the integrated peak area of **3** determined from HPLC evaluation of the retro reaction, $\boldsymbol{m}$ is the slope and $\boldsymbol{b}$ is the y-intercept:

$$[\mathbf{3}] = \boldsymbol{mt} + \boldsymbol{b}$$

Overall, yielding a final equation for the amount of $\mathbf{3_{RO}}$ as:

$$[\mathbf{3_{RO}}]\Big|_{t_1}^{t_2} = \boldsymbol{k}_3 \cdot \int_{t_1}^{t_2} (\boldsymbol{mt} + \boldsymbol{b})\boldsymbol{dt}$$

Accordingly, the amount of $\mathbf{3_{RO}}$ was presented in the main manuscript as Figure 3A and 3B for compounds **1a** and **1b**. Furthermore, the summation of calculated $[\mathbf{3_{RO}}]$ values with the measured amount of **3** present at $\boldsymbol{t_n}$ yields the constructed conversion curve of **3** (total compound **1** converted **3**) presented in Figure 4 in the main manuscript.

The accuracy of estimating the total amount of converted **3** (via measurement of **3** and calculation of $\mathbf{3_{RO}}$) present as a function of time in the absence of ring opening was verified in a second set of experiments. In these experiments the amount of **3** formed from **1a** was determined on the basis of the known concentration **1a** (which is stoichiometrically equivalent to **3** in the absence of any ring opening, Scheme 1), and on the basis of conversion of **1a** to the ring-opened substituent $\mathbf{1a_{RO}}$ (which would reduce the concentration of **1a** in the reaction without conversion to **3**). Compound $\mathbf{1a_{RO}}$ bound to the HPLC column and could be quantified. Thus, the amount of **1a** and $\mathbf{1a_{RO}}$ were measured, and the amount of **3** anticipated was estimated on the basis of these measurements. This amount of **3** (determined based on these emipirical measurements) was compared to the amount of **3** estimated via the theoretical treatments above.

Because conversion of compound **1a** occurs both due to the formation **3**, and due to the ring-opening of **1a** to form $\mathbf{1a_{RO}}$, the total amount of compound **1a** converted to **3** at any point in time, t, would be:

$$[\mathbf{3}] = [\mathbf{1a}]_0 - [\mathbf{1a}]_t - [\mathbf{1a_{RO}}]_t$$

Where $[\mathbf{1a}]_0$ is the initial concentration of **1a** employed in the experiment, and $[\mathbf{1a}]_t$ and $[\mathbf{1a_{RO}}]_t$ are the measured concentrations of **1a** and $\mathbf{1a_{RO}}$ determined in the HPLC measurements at time t. Molar concentrations for **1a** and $\mathbf{1a_{RO}}$ were calculated from HPLC peak areas based on the extinction coefficients for **1a** and $\mathbf{1a_{RO}}$, which were experimentally determined from solutions of known concentration.

The measured (on the basis of the measured conversion of **1a**) and estimated (on the basis of the theoretical description above) values for the amount of **3** present as a function of time were in nearly perfect agreement (Figure S8), therefore it was assumed the above method for estimating the concentrations of conjugate **3** could be used for experiments for compounds **1b** and **1c** (whose ring-opened compounds were not possible to measure in the HPLC experiment).

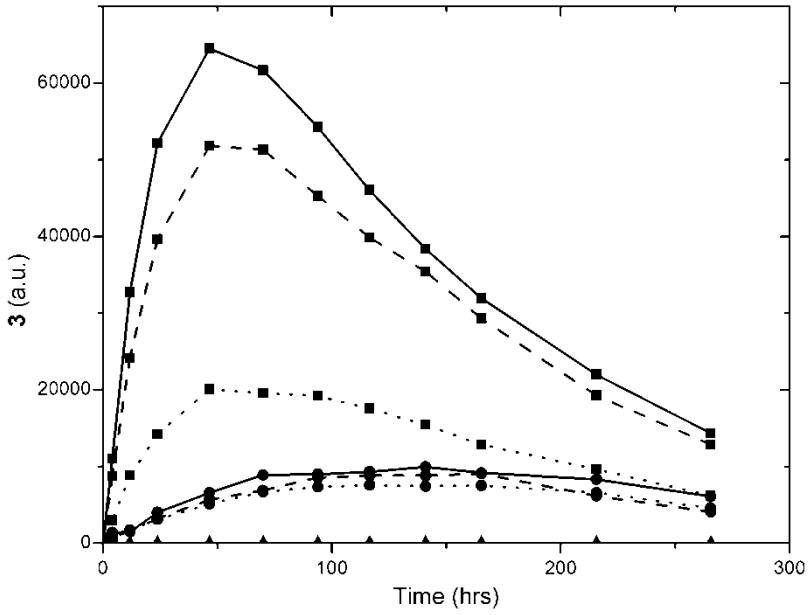

Figure S6. GS-NEM (3) formed from (■) **1a** (●) **1b** (▲) **1c** in the presence of (–) 5mM (--) 0.5mM (··) 0.05mM GSSG.

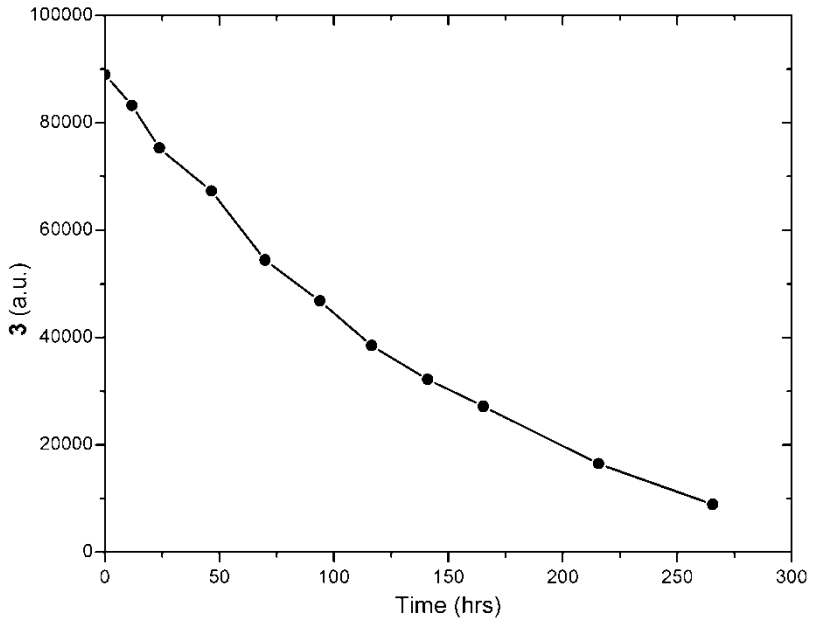

Figure S7. The concentration of **3** plotted as a function of time in the absence of added reductant. The reduction in the concentration of **3** over time is a result of ring opening, and thus this decrease indicates the rate of the ring opening.

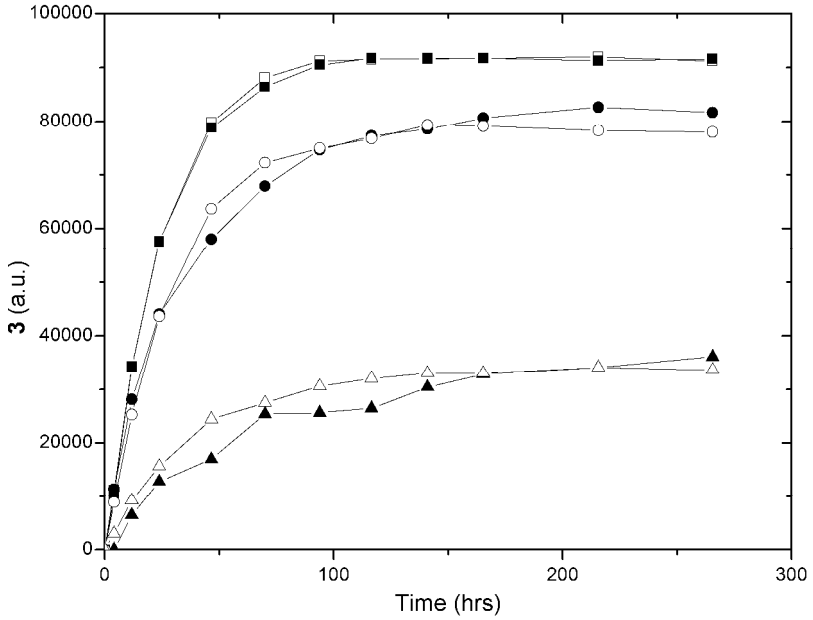

Figure S8. Comparison of measured (solid marks) and calculated (open marks) concentrations of **3** obtained from the retro addition and thiol exchange of **1a** (■) 5.0mM GSSG (●) 0.5mM GSSG (▲) 0.05mM GSSG. Trend lines are shown to aid in visualization.

Bioconjugate Chemistry

ARTICLE

pubs.acs.org/bc

4-Aminophenylalanine as a Biocompatible Nucleophilic Catalyst for Hydrazone Ligations at Low Temperature and Neutral pH

Adam R. Blanden, Kamalika Mukherjee, Ozlem Dilek, Maura Loew, and Susan L. Bane*

Department of Chemistry, Binghamton University, P.O. Box 6000, Binghamton, New York 13902, United States

Supporting Information

ABSTRACT: Hydrazone formation and similar reactions are highly versatile and specific, but their application to biological systems has been limited by their characteristically slow reaction kinetics at neutral pH. Catalysis of these reactions through imine formation with aromatic amines such as aniline has broadened the applicability of these reactions to biomolecular labeling. High concentrations of the catalyst are necessary, which may be incompatible with the native structure of certain proteins. In this study, we investigated the utility of 4-aminophenylalanine (4a-Phe) as a catalyst for these reactions. We find that 4a-Phe is nearly as effective as aniline in catalyzing hydrazone formation between the reactive amino acid 3-formyltyrosine (3f-Tyr) and hydrazine-containing fluorophores, both free in solution and incorporated into the protein tubulin. The catalyst 4a-Phe maintains ~70% of the catalytic efficacy of aniline and is less detrimental to the native structure of tubulin. Examination of the temperature dependence of imine formation between 3f-Tyr and 4a-Phe shows an increase in imine concentration accompanying a decrease in temperature, confirming the exothermic nature of the equilibrium reaction. Interestingly, decreasing the temperature of the 4a-Phe-catalyzed hydrazone reaction between 3f-Tyr and the fluorophore 7-hydrazinyl-4-methylcoumarin *increases* the overall rate of the reaction. This result indicates that the temperature dependence of the catalyst−aldehyde equilibrium is greater than the temperature dependence of the rate constant for hydrazone formation from this intermediate, and that the rate of hydrazone formation a direct function of the concentration of the intermediate imine. These results provide a platform for conducting nucleophilic catalysis under conditions that are more compatible with biomolecular targets than previously demonstrated, thereby expanding the utility of hydrazone ligations in biological systems.

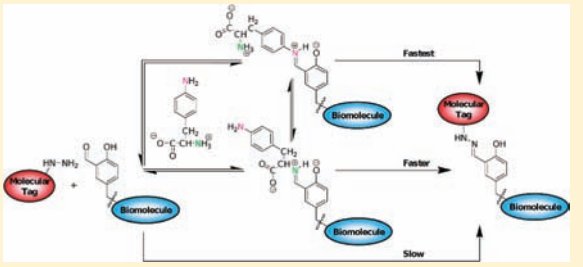

INTRODUCTION

Site-specific chemical modification of biomolecules relies on reactions of functional groups with reactivities that are orthogonal to endogenous moieties.[1] Ideally, such reactions occur rapidly under conditions that retain the native structure of the target; however, in practice most labeling systems fail to meet all criteria. Condensation reactions of aldehydes and ketones with nucleophiles such as hydrazines, hydrazides and hydroxylamines possess many attractive properties for ligations in biological systems.[2−4] They occur readily in aqueous solutions without major side reactions, and form covalent bonds with varying degrees of reversibility, tunable by the nature of the reactants. The usefulness of this class of reactions has been limited by its characteristic pH-sensitive kinetics—the rate of the condensation reaction is typically greatest near the pK_a of the nucleophile,[5] dropping off sharply at higher and lower pH.[6] Because of this kinetic profile, biomolecules that require neutral pH to maintain structural and functional integrity are not amenable to direct ligation reactions with the less basic members of this group.

Our laboratory has developed a hydrazine-tag aldehyde target-based labeling system that employs reaction of a protein containing 3-formyl-L-tyrosine (3f-Tyr), a synthetic tyrosine derivative, with a hydrazine-containing probe.[7] In this manifestation, the unnatural amino acid is appended to α-tubulin by a highly specific enzymatic reaction. Use of an aromatic hydrazine rather than a commercially available hydrazide as the nucleophile partially alleviated the problem of slow reaction at neutral pH owing to the greater basicity of the aromatic hydrazine. The aromatic hydrazine, a coumarin derivative synthesized in our lab, has an additional desirable feature, which is a red shift in its absorption and emission spectra accompanied by an increase in quantum yield upon hydrazone formation.

A wider variety of probes would increase the number of applications available for the labeled protein. However, our selection of probes has been limited precisely because our protein of interest, α,β-tubulin, is highly temperature and pH sensitive.[8−11] The commercial hydrazide-containing probes react too slowly at neutral pH and the protein is not stable at lower pH. Nucleophilic catalysis of these reactions using amines such as aniline and aniline derivatives (e.g., *p*-anisidine), which form a reactive imine intermediate with the target carbonyl, provides a potential solution to this problem. Aniline has been shown to be effective in aqueous buffered systems as well as with biomolecules and biomolecular conjugates.[3,12−15] However, it was not known at

Received: March 28, 2011
Revised: August 26, 2011
Published: September 20, 2011

ACS Publications © 2011 American Chemical Society

the outset of this investigation whether aniline catalysis would be amenable for use with fragile biomolecular targets such as tubulin. Millimolar concentrations of aniline are necessary to produce an appreciable amount of imine intermediate, as the equilibrium constant for imine formation is quite small (<10 M^{-1} for bisaryl imines).[16]

In this study, we explore the use of 4-aminophenylalanine (4a-Phe), a commercially available aromatic amine derivative of phenylalanine (Phe), as a catalyst for hydrazone ligations in aqueous buffer at neutral pH. We reasoned that the more hydrophilic zwitterionic molecule would be less likely to denature a protein but would retain the catalytic efficacy of aniline. Native but not denatured tubulin will assemble into microtubules, so the effect of the catalyst is assessed as the ability of the protein to form microtubules in the presence of the additive. The catalytic efficacies of aniline and 4a-Phe are compared with the protein and using a model system containing 3f-Tyr and 7-hydrazinyl-4-methylcoumarin (coumarin hydrazine, CH).

We also explore the effect of temperature on the catalytic reaction. Since bisaryl imine formation is exothermic,[17] the concentration of imine in solution can be increased by decreasing temperature. It was hoped that the increase in imine concentration would have a greater effect on the overall rate than the expected decrease in the rate of imine formation at the lower temperature. Finally, the ability of 4a-Phe to catalyze hydrazone formation with different fluorescent dyes is measured with both the model compound 3f-Tyr and 3f-Tyr-labeled tubulin. We find that 4a-Phe effectively catalyzes hydrazone formation between the unnatural amino acid and a variety of hydrazine-containing substrates, and that the labeling reaction is in fact enhanced at low temperature.

EXPERIMENTAL PROCEDURES

Reagents. Texas red hydrazide (TxRed, 90% single isomer) and 7-diethylaminocoumarin-3-carboxylic acid, hydrazide (DCCH) were purchased from Molecular Probes (Eugene, OR). CH and 3f-Tyr were synthesized as described previously.[7] The probe naphthalene-2-ylhydrazine (naphthalene hydrazine, NH) was synthesized as detailed in Supporting Information. Stock solutions of TxRed, DCCH, and NH were made in DMSO and stored at −20 °C. Stocks of CH were made fresh in PME buffer (100 mM PIPES, 1 mM $MgSO_4$, and 2 mM EGTA at pH 6.90) and discarded after 24 h. A stock solution of 3f-Tyr was made in PME and stored at 4 °C. Concentrations of TxRed, DCCH, and CH were determined spectrophotometrically using extinction coefficients of 109 000 M^{-1} cm^{-1} at 588 nm (TxRed, DMSO), 46 000 M^{-1} cm^{-1} at 420 nm (DCCH, DMSO), and 19 000 M^{-1} cm^{-1} at 346 nm (CH, PME).[7] The concentration of NH was determined by mass. The source of 4-amino-DL-phenylalanine hydrate (4a-Phe) was Sigma-Aldrich (>97% pure). All other chemicals were purchased from Sigma-Aldrich and were reagent grade or better. All experiments were performed in PME buffer unless otherwise noted. The reactions presented in this paper were conducted in PME at pH 6.9 for compatibility with tubulin. Many of these experiments were also performed in 0.1 M phosphate buffer at pH 7.0, and no difference in the results obtained with the two buffer systems was observed.

Spectral Characteristics and Kinetics of 3f-Tyr Imine Formation. Imine formation was monitored by absorption difference spectroscopy. Dual chambered cuvettes were loaded with identical volumes of 800 μM 3f-Tyr and 20 mM of aniline, Phe, or 4a-Phe. The cuvette was then placed in an HP 8453 UV−vis spectrophotometer equipped with a multicell thermostatted cuvette holder and equilibrated to 25 °C. After blanking, the solutions mixed rapidly by inversion, halving the concentration and doubling the path-length of each solution. Absorption difference spectra were collected at 30 s intervals. Steady state was reached in less than one hour, so the difference spectra of the equilibrated imine solution was also monitored at steady state. There was no change in the difference spectrum after steady state was achieved. The absorbance maximum at steady state (aniline: 440 nm, Phe: 405 nm, 4a-Phe: 415 nm) was then plotted as a function of time according to the following equation for a reversible pseudo first-order reaction approaching equilibrium:

$$-\ln(\Delta A_{eq} - \Delta A_t) = k_{obs}t$$

where ΔA_{eq} is the absorption difference at equilibrium, ΔA_t is the absorption difference at time t, and k_{obs} is the observed rate constant for approach to equilibrium, which is the sum of the forward and reverse rate constants. Values for k_{obs} were obtained from a linear fit done in *SigmaPlot 10.0* (Systat Software Inc., San Jose, CA).

Relative Initial Rates of Formation. For measurement of 3f-Tyr-4a-Phe imine formation kinetics, 800 μM 3f-Tyr and 20 mM 4a-Phe were loaded into either side of a dual-chambered cuvette as described above. The reaction vessels were equilibrated at 0 °C,

Chart 1. Structures of the Catalysts, Targets, and Probes

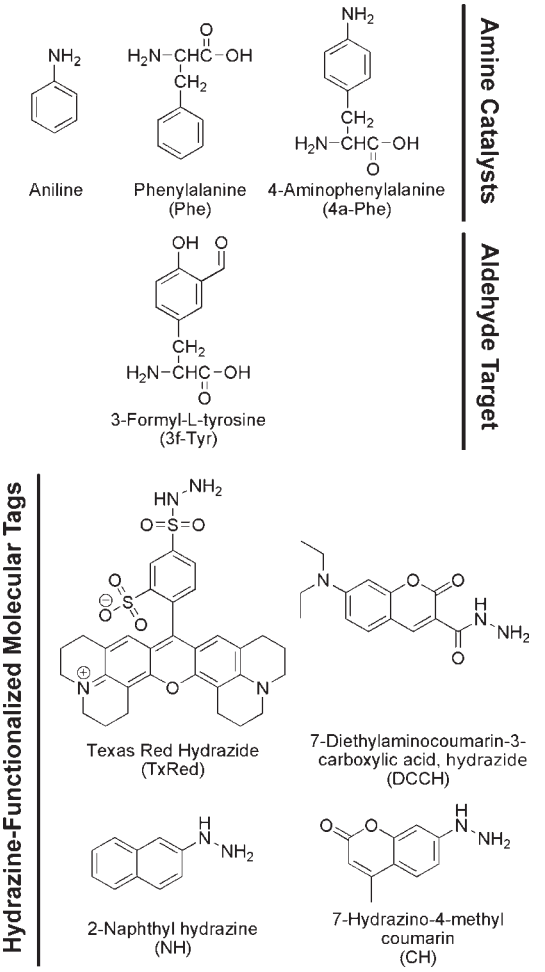

25 °C, or 37 °C before mixing and maintained those temperatures throughout the course of the reaction. Imine formation was monitored by the change in the absorption difference spectrum at 415 nm as a function of time. Reactions were compared based on initial rates, which were calculated for each reaction as the slope of the linear portion of the absorption vs time plot. The initial rate of each reaction was compared to its initial rate at 25 °C to yield a unitless relative initial rate.

Kinetics of Hydrazone Formation. Apparent pseudo first-order rate constants in the presence and absence the catalysts were determined by absorption difference spectroscopy in a CH and 3f-Tyr test system. Identical volumes of 800 μM 3f-Tyr and 80 μM CH were loaded into separate chambers of a dual chamber cuvette with or without 10 mM of aniline, Phe, or 4a-Phe in both chambers. (Note that including the catalyst in both chambers allows the concentration of catalyst to be constant throughout the experiment.) The solutions were allowed to equilibrate before the 3f-Tyr and hydrazine were mixed. The spectrophotometer was blanked, the solutions mixed, and reactions monitored as above at 400 nm. The resulting kinetic trace was then fit as a single pseudo first-order reaction according to the equation

$$\Delta A(t) = \Delta A_{\text{final}}(1 - e^{-k't})$$

where $\Delta A(t)$ is the absorption difference at time t, ΔA_{final} is the absorption difference at completion, and k' is the apparent pseudo first-order rate constant. These data are treated as an irreversible reaction because the hydrazones are not observed to dissociate under harsher reaction conditions (*vide infra*). Fitting was accomplished using *SigmaPlot 10.0*. For the reaction of TxRed, NH, and DCCH with 3f-Tyr, only 4a-Phe was used as a catalyst, and the wavelengths monitored were 610 nm (TxRed), 370 nm (NH), and 460 nm (DCCH); 4% DMSO was included in both chambers to solublize the probes and their hydrazones. The concentration of fluorophore was 40 μM after mixing in experiments with CH, TxRed, and NH. The concentration of DCCH was reduced to produce a final concentration of 20 μM due to low solubility of the hydrazone product from this reaction. Corroborating fluorescence experiments were conducted as previously described.[7]

Temperature-dependent rate constants were determined in the same manner, except the reactions were equilibrated at 0 °C or 37 °C in the thermostatted multicell holder prior to mixing and held at that temperature throughout the reaction and CH was the only probe used.

Temperature-Dependent Imine Formation. A mixture of 400 μM 3f-Tyr and 10 mM 4a-Phe in a 1 cm path length cuvette was placed in the thermostatted multicell holder, equilibrated to 25 °C, and allowed to react until equilibrium was achieved. The sample was then blanked, the temperature decreased to 0 °C, allowed to react until equilibrium, and a difference spectrum taken. The temperature was raised back to 25 °C, raised up to 37 °C, and finally cooled back to 25 °C, with a spectrum taken after the reactions reached equilibrium at every temperature. The criterion for equilibrium was no change in the difference spectrum for 2 min.

Tubulin Purification. Tubulin was isolated from bovine brains by two cycles of temperature-dependent polymerization and depolymerization followed by phosphocellulose ion-exchange chromatography.[18] The protein containing fractions were then pooled, drop-frozen, and stored in liquid nitrogen until use. Prior to use, frozen aliquots were gently thawed and desalted into PME buffer by the method of Penefsky.[19] The concentration was determined spectrophotometrically using an extinction coefficient of 114 000 M^{-1} cm^{-1} at 280 nm, which was calculated from sequence data as previously described with modification to account for the two bound guanosine nucleotides per tubulin dimer.[20] A detailed procedure can be found in Supporting Information.

Effect of Catalyst on Microtubule Formation. Tubulin (10 μM) was incubated with varying concentrations of the catalyst for 4 h at room temperature in PME. The samples were then equilibrated to 37 °C in 1 cm path length cuvettes in the UV−vis spectrophotometer in a thermostatted multicell holder and baselines taken. Polymerization was initiated by addition of 10% v/v DMSO and 1 mM GTP. Polymerization activity was monitored as apparent absorption increase at 400 nm, taking the plateau value to be polymerization extent. The plateau values were graphed on a semilog plot versus amine concentration and the IC_{50} value extracted from a nonlinear sigmoidal fit done in *SigmaPlot 10.0*.[21]

Preparation of 3f-Tyr Hybridized Tubulin. Tubulin was hybridized with 3f-Tyr using recombinant human tubulin−tyrosine ligase fused to glutathione transferase (GST-TTL) as previously described with minor modification.[7] Purified tubulin (40−80 μM) in PME buffer was treated with carboxypeptidase A (Sigma) for 30 min at 37 °C to remove the C-terminal tyrosine from α-tubulin. The reaction was stopped by addition of 20 mM DTT. Tubulin was equilibrated into TTL buffer (25 mM MES, 150 mM KCl, 27 μM $MgCl_2$, 2.5 mM ATP, 1 mM DTT, and 1.5% v/v glycerol at pH 6.8) by rapid gel filtration using Sephadex G-50. The protein was incubated with 1 mM 3f-Tyr and 0.45 mg mL^{-1} GST-TTL for 30 min at 37 °C. Excess ligand was removed by rapid gel filtration in Sephadex G-50 into PME buffer, and the concentration of tubulin determined spectrophotometrically as above, subtracting the absorbance due to the 0.45 mg mL^{-1} GST-TTL ($\varepsilon_{280\ \text{nm}}$ = 100 000 M^{-1} cm^{-1}, MW = 71 078). The extinction coefficient was calculated using the same method used for tubulin, and is detailed in Supporting Information.

Fluorescent Labeling of α-Tubulin. Tubulin hybridized with 3f-Tyr (40 μM) was incubated with 400 μM hydrazine-containing probe (CH, NH, DCCH, or TxRed) in the presence or absence of 10 mM 4a-Phe, along with an unmodified tubulin control. In the NH, DCCH, and TxRed reactions, 4% DMSO was also included. Reactions were allowed to progress for 15 and 60 min at either RT or 0 °C, and then immediately subjected to reducing SDS-PAGE without boiling. The gels were imaged under long-wavelength UV light. The same gels were then stained with Coomassie Brilliant Blue and imaged again under white light.

RESULTS AND DISCUSSION

The application of hydrazone ligations to biological systems has been limited by the slow kinetics of such reactions at neutral pH.[23] Rate enhancement of similar reactions by nucleophilic catalysis was first detailed by Jencks, who noted that certain amines were more effective catalysts of semicarbazone formation than predicted by a general acid catalysis mechanism and who then detailed the nucleophilic catalysis mechanism.[22,24] The recent application of this principle to biological systems by Dawson and co-workers has led to a plethora of new hydrazone and oxime ligations.[3,12−15,25−27] The work presented here

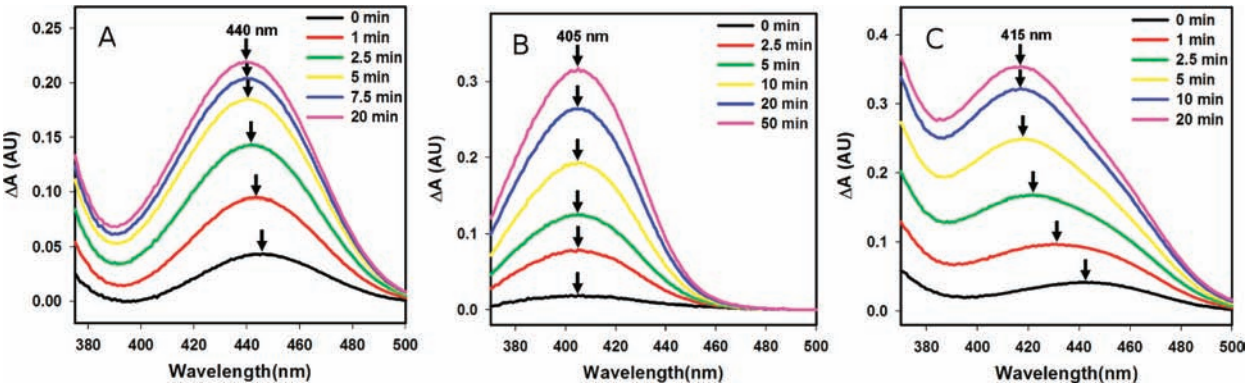

Figure 1. Time-dependent absorption difference spectra for aniline (A), Phe (B), or 4a-Phe (C) reacting with 3f-Tyr at 25 °C in PME buffer, pH 6.9. The concentration of 3f-Tyr was 400 μM and the concentrations of aniline, Phe, or 4a-Phe were 10 mM. Arrows indicate the wavelength at the maximum of the absorption difference spectrum at each time point. The peaks at $t = 0$ are due to the reaction that occurred during the seconds it took to mix the samples.

represents a continued expansion of nucleophilic catalysis in biological systems through the application of a catalyst that is more biocompatible than aniline.

Reactive Imine Formation. The catalyst 4a-Phe possesses two potential nucleophiles for imine formation: the aromatic amine of the side chain and the aliphatic α-amine. Therefore, the unmodified amino acid Phe was evaluated in parallel with aniline and 4a-Phe. Kinetics of imine formation between the three catalysts (aniline, Phe, and 4a-Phe) and the model compound 3f-Tyr were followed by absorption difference spectroscopy in aqueous buffer at neutral pH. All three catalysts formed imines with 3f-Tyr with distinct absorption difference characteristics (Figure 1, Table 1). The aniline imine peak (aromatic amine) in the absorption difference spectrum is significantly red-shifted from that of the Phe imine peak (α-amine) at equilibrium, presumably because of extended conjugation in the bisaryl product. The shape of the absorption difference spectrum of the Phe–3f-Tyr reaction is consistent throughout the reaction, indicating that a single product is formed. In the aniline–3f-Tyr reaction, the peak shape changes slightly during the reaction. The absorption maximum shifts slightly to the blue over the course of the reaction, which may be attributed to a small amount of imine formation between the α-amine and the aldehyde side chain of 3f-Tyr. The maximum of absorption difference spectrum of the 4a-Phe reaction shifts substantially during the course of the reaction, from the 445 nm (aromatic amino imine) region toward the 405 nm (α-amino imine) region. Taken together, these results indicate that imines with the *o*-hydroxybenzaldehyde moiety of 3f-Tyr form at both amino groups in 4a-Phe, and that the aromatic amino imine forms more quickly.

The relative rates at which each reaction approaches equilibrium were assessed by analyzing the data of absorbance change as a function of time as described under Experimental Procedures. The observed rate constants to equilibrium for each system are reported in Table 1. The wavelength of the absorption maximum at equilibrium was used in the calculation, since the goal was to assess equilibration rate of the entire system, which includes both α- and aromatic amines. Overall, it is observed that aniline approaches its equilibrium the fastest, Phe the slowest, and 4a-Phe at an intermediate rate.

Catalytic Efficacy and Protein Stability. The search for a more biocompatible catalyst was spurred by our interest in site-specific fluorescent labeling of the protein tubulin. When tubulin was exposed to 100 mM aniline, the concentration used in most studies currently aimed at adapting the catalysis to biomolecules; it was completely denatured and inactivated in less that 1 h (data not shown). We therefore investigated the effects of aniline, 4a-Phe, and Phe on the native structure of tubulin through polymerization activity assays. Native tubulin can be induced to assemble into microtubules, and denaturants inhibit this activity. Aniline is about 3-fold more damaging to tubulin's ability to polymerize than 4a-Phe; interestingly, unmodified Phe did not appear to affect the assembly process at equivalent concentrations (Table 2). The results suggest that the aminopropanoic acid moiety of Phe is compatible with the protein, and inclusion of this moiety in 4a-Phe protects the protein from the detrimental effects of aniline. On the basis of these results, the concentration of catalyst for subsequent experiments was fixed at 10 mM.

Table 1. Observed Rate to Equilibrium for Imine Formation with 3f-Tyr

amine	$k_{obs} \times 10^{-3}$ (s^{-1})[a]	λ_{max} (nm)[b]
Aniline	5.3 ± 0.2	445–440
4a-Phe	3.7 ± 0.1	443–415
Phe	1.4 ± 0.1	405

[a] Rate constant for equilibration of 400 μM 3f-Tyr and 10 mM of each substance at 25 °C in PME at pH 6.9, determined as described under Experimental Procedures. [b] Range of maximum wavelength of the absorption difference spectrum over the course of the reaction and monitored by absorption difference spectroscopy.

The relative catalytic efficacies of the molecules were evaluated by measuring the reaction rate of hydrazone formation between 3f-Tyr and CH as a function of catalyst. The reactants were selected because of their relevance to our tubulin labeling application, appropriate water solubilities of both the components and their resulting hydrazones, and reasonable uncatalyzed reaction kinetics for comparison.[7] Reactions were monitored by absorption difference spectroscopy as detailed in Experimental Procedures. A representative experiment is shown in Figure 2. An isosbestic point in the spectra is observed, which indicates that a single transformation is measured by the technique (i.e, hydrazine to hydrazone). Although the imine between the catalyst and 3f-Tyr absorbs in this region of the spectrum, its absorbance does not contribute to the observed difference spectrum. The 3f-Tyr/4aPhe

solution was allowed to equilibrate before the hydrazone reaction was initiated; thus, absorption due to the initial imine is eliminated by blanking the sample. The large excess of 3f-Tyr relative to CH ensures that the fractional change in imine concentration over the course of the reaction is small.

To further demonstrate that the absorption difference spectra are proportional to hydrazone formation, the reaction kinetics was monitored by fluorescence under the same experimental conditions. We have shown previously that the reaction between CH and 3f-Tyr produces a hydrazone with distinct absorption and emission properties, and that the fluorescence of the hydrazone can be observed without interference by unreacted hydrazine.[7] Figure 2C shows the kinetic trace of the fluorescence emission increase overlaid with absorption difference spectra data. The concurrence of the two data sets points to the fluorescence and absorbance signals corresponding to the same process, hydrazone formation. Calculated pseudo first-order rate constants for each signal are within experimental error of one another. In harmony with previous studies, all three catalysts increased the observed pseudo first-order rate constant for the formation of the 3f-Tyr-CH hydrazone (Table 2).[22] Aniline catalyzed the reaction most effectively (~19-fold), Phe the least effectively (~2-fold), and 4a-Phe was at an intermediate effectiveness (~13-fold). These data support the notion that the aromatic imine is the more reactive intermediate, and when both aromatic and α-amino groups are present, they may compete with each other, the net result of which is a decrease in the overall reaction rate (Scheme 1). However, this is counterbalanced by the increased concentrations of 4a-Phe that can be used because of its compatibility with the protein.

Table 2. Effect of Catalyst on the Native State of Tubulin and the Relative Efficacy of the Catalyst

catalyst	IC_{50} (mM)[a]	k (10^{-4}) (s^{-1})[b]
uncatalyzed	-	3.5 ± 0.2
aniline	28 ± 3	66 ± 0.8
4a-Phe	88 ± 13	45 ± 0.4
Phe	>100	5.5 ± 0.08

[a] IC_{50} for tubulin polymerization activity. Tubulin (10 μM) was incubated with varying concentrations of the catalyst in PME (pH 6.9) for 4 h at 25 °C and then polymerized at 37 °C. [b] Pseudo first-order rate constant for the reaction of 40 μM CH with 400 μM 3f-Tyr in the presence of 10 mM catalyst at 25 °C in PME (pH 6.9). Note the increased IC_{50} for 4a-Phe relative to aniline while still maintaining the majority of the rate enhancement for the reaction, indicating its utility as a biocompatible catalyst.

Alternative Tags. We also investigated the generalizability of 4a-Phe catalysis to varying classes of hydrazine-containing molecules using the model reaction. This was accomplished by calculating apparent pseudo first-order rate constants for reactions between 3f-Tyr and NH, DCCH, and TxRed (Table 3). The catalysis was effective for all three molecules, yielding rate enhancements of 9-, 130-, and 3-fold, respectively. Note that the rate of hydrazone formation with the more reactive aromatic hydrazines (CH and NH) is less affected by the catalyst than that of the less reactive hydrazide (DCCH). It is unclear why catalysis was less effective in the TxRed reaction. It may be that the increased sterics of the imine intermediate counteracts the greater reactivity of the iminium ion compared to the aromatic aldehyde.

Temperature Dependence of 4a-Phe and 3f-Tyr Reactions. A solution variable that frequently affects the stability of biological molecules is temperature. Proteins and nucleic acid polymers tend to be more stable at lower temperatures; the native conformation of tubulin is particularly sensitive to variations in temperature.[8,9] According to equilibrium thermodynamic parameters measured for related *o*-hydroxyl aldehyde-amine systems, imine formation is exothermic.[17] Therefore, a decrease in temperature would be expected to increase the concentration of imine in solution, which may then increase the overall efficacy of the catalyst.

Absorption difference spectroscopy was used to assess the effect of temperature on the relative equilibrium concentration of imine in a solution of the model compounds 3f-Tyr and 4a-Phe (Figure 3). The solution of the two components was equilibrated to room temperature (25 °C), and the spectrophotometer was blanked. The temperature was decreased to 0 °C, and absorption spectra were collected until no change in the spectrum was observed. A positive band was observed in the absorption difference spectrum that peaks near 440 nm, which is indicative of an increase in the concentration of the aromatic amino imine. This process was fully reversed when the temperature of the solution was restored to 25 °C. Subsequent warming of the solution to 25 °C caused a decrease in absorbance in the 440 nm region, which is consistent with dissociation of aromatic amino imine. This process was also fully reversed when cooled to 25 °C. Therefore, the imine concentration in the solution can be reversibly increased or decreased by lowering or raising the solution temperature.

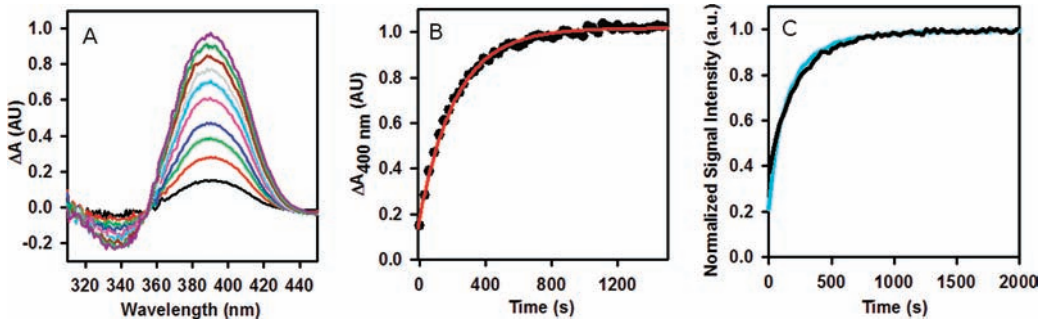

Figure 2. (A) Absorption difference spectra for the reaction of CH (40 μM) with 3f-Tyr (400 μM) at 25 °C in PME buffer, pH 6.9 in the presence of 4a-Phe (10 mM). (B) Absorption difference of the reaction shown in panel A at 400 nm as a function of time. Solid line: data fit as a single pseudo first-order reaction. (C) Kinetics of hydrazone formation catalyzed by 10 mM 4a-Phe monitored by absorption difference spectroscopy (black) and fluorescence spectroscopy (cyan). The signal data were normalized to arbitrary units to more clearly show the overlap of the kinetic traces.

Scheme 1. Proposed Reaction Pathway for 4a-Phe Catalyzed Hydrazine-Ligations with *o*-Hydroxyl Aromatic Aldehydes Attached to Biomolecules

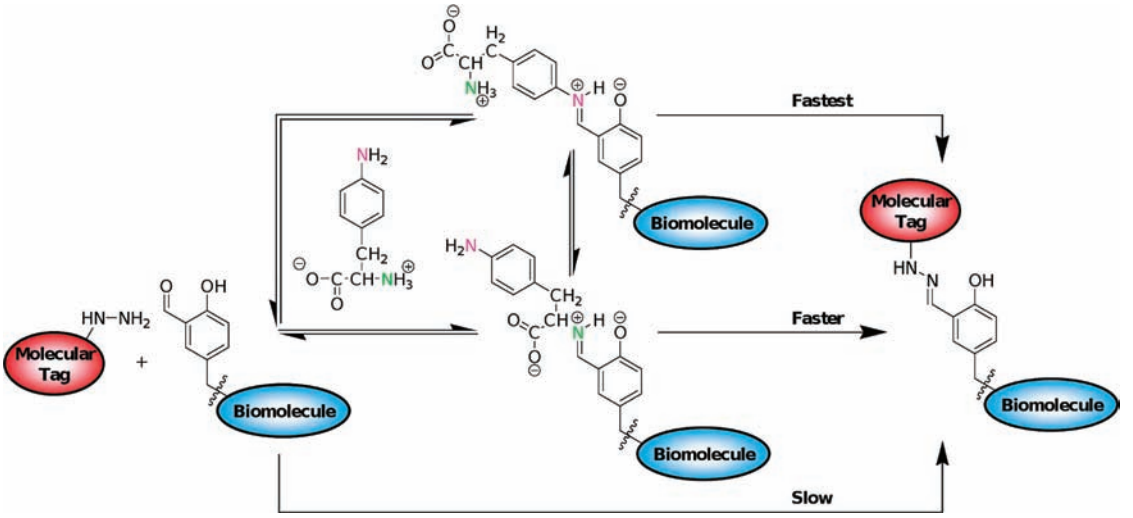

Table 3. Apparent Pseudo First-Order Rate Constants for Hydrazone Formation Between 3f-Tyr and Hydrazine-Containing Probes Catalyzed by 4a-Phe[a]

molecular tag	k_{uncat} (10^{-4}) (s^{-1})[b]	k_{cat} (10^{-4}) (s^{-1})[c]
NH	5.2 ± 0.3	45.2 ± 0.4
DCCH	0.11 ± 0.01	14.2 ± 0.04
TxRed	0.60 ± 0.12	1.8 ± 0.1

[a] Apparent pseudo first-order rate constants for the reaction of hydrazines with 3f-Tyr in the absence and presence of 4a-Phe. Experiments were performed with 400 μM 3f-Tyr with 40 μM molecular tag (20 μM in the case of DCCH) in the presence or absence of 10 mM 4a-Phe at 25 °C in PME (pH 6.9). [b] Absence of 4a-Phe. [c] Presence of 4a-Phe.

The temperature dependence of the kinetics of imine formation was assessed by measuring initial rates at the three temperatures. Table 4 compares the initial rates as a ratio of the initial rate of imine formation at 25 °C. At 0 °C, the initial rate of imine formation is about half of its value at room temperature, and at 37 °C, the initial rate is about 1-1/2 times faster.

The net effect of temperature on the catalytic ability of 4a-Phe was assessed empirically using a 3f-Tyr and CH test system. The rate of hydrazone formation was measured at the three selected temperatures in the absence or presence of 4a-Phe catalyst (Table 5). At 25 °C, 4a-Phe increased the observed rate constant by ~13-fold. At 0 °C, 4a-Phe caused a 28-fold increase in the apparent rate constant for hydrazone formation, more than double the rate enhancement observed at 25 °C (13-fold). Although there was a slight increase in observed rate constant when the temperature was increased to 37 °C (~10%), there was virtually no change in rate enhancement from 25 °C, which remained steady at 13-fold. The effect of temperature on the catalyzed reaction indicates that the effectiveness of 4a-Phe catalysis is governed by a mixture of thermodynamic and kinetic factors. We hypothesize that the thermodynamic favorability for imine formation at 0 °C is responsible for a marked increase in catalytic effectiveness by increasing intermediate imine concentration, which Cordes and Jencks determined to be a controlling factor governing the rate of imine-catalyzed semicarbazone formation.[22] It appears that

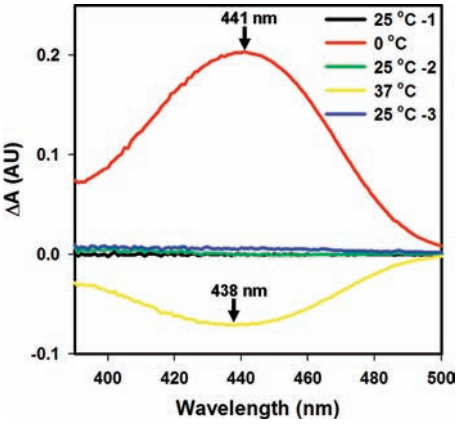

Figure 3. Effect of temperature on the absorption difference spectrum of 4a-Phe plus 3f-Tyr. A solution of 10 mM 4a-Phe and 400 μM 3f-Tyr in PME buffer (pH 6.9) was mixed at 25 °C and equilibrated until no change in the absorption spectrum was observed. The instrument was then referenced to this solution (black curve). Without removing the cuvette from the instrument, the temperature was decreased to 0 °C and the spectrum was monitored until no further change in the absorption spectrum was observed, at which point a spectrum was taken (red curve). The process of temperature change and equilibration was repeated on the same sample, which was not removed from the instrument. Green curve: After equilibration of 0 °C solution to 25 °C. Yellow curve: After equilibration of 25 °C solution to 37 °C. Blue curve: After equilibration of 37 °C solution to 25 °C. The fully reversible increase in the 440 nm region at 0 °C and decrease at 37 °C indicates aromatic amino imine concentration increases at 0 °C and decreases at 37 °C relative to the concentration at room temperature (25 °C).

kinetic favorability at 37 °C overcomes the thermodynamic disfavorability, possibly by regenerating the consumed imine intermediate more quickly. Although it is unclear how generalizable this effect is to molecules other than the *o*-hydroxyl aromatic aldehyde used in our system, it may be predicted by the energetic nature of the formation of the intermediate imine—if imine formation is sufficiently exothermic, decreasing the temperature will thermodynamically favor imine formation, thereby

Table 4. Relative Initial Rate of 4a-Phe/3f-Tyr Imine Formation at Various Temperatures[a]

temperature	$k_{i,\ app}/k_{i,\ app,\ RT}$
0 °C	0.4 ± 0.1
25 °C	1.0 ± 0.1
37 °C	1.6 ± 0.1

[a] Initial rates of formation imine at varying temperatures were determined as described under Experimental Procedures. A 400 μM solution of 3f-Tyr was reacted with 10 mM 4a-Phe at 0, 25, and 37 °C. Data are presented as the initial rate at 0, 25, or 37 °C divided by the initial rate at room temperature (25 °C).

Table 5. Effect of Temperature and 4a-Phe Catalyst on the Rate of CH/3f-Tyr Hydrazone Formation[a]

temperature	k_{uncat} (10^{-4}) (s^{-1})[b]	k_{cat} (10^{-4}) (s^{-1})[c]
0 °C	3.32 ± 0.04	94.4 ± 2.8
25 °C	3.52 ± 0.20	44.8 ± 0.4
37 °C	3.92 ± 0.08	51.6 ± 0.4

[a] Apparent pseudo first-order rate constants for the reaction of 400 μM 3f-Tyr with 40 μM CH in the absence or presence of 10 mM 4a-Phe at 0, 25, and 37 °C in PME (pH 6.9). [b] Absence of 4a-Phe. [c] Presence of 4a-Phe.

increasing imine concentration. If the rate constant of the subsequent transimination reaction has a smaller temperature dependence than the equilibrium constant for imine formation, as appears to be the case for the probes studied here (Figure 4, Table 5), then lowering the temperature of the reaction to increase its overall rate may be a general feature of these catalyzed reaction.

Application in Protein Labeling. To assess the applicability of 4a-Phe catalysis to protein labeling, we hybridized 3f-Tyr to α-tubulin as described previously[5] and allowed it to react with hydrazine-containing molecular tags. Identical reactions were performed in the presence and absence of catalyst at both 25 °C and at 0 °C. The protein was then subjected to SDS-PAGE (Figure 4) and visualized under long-wavelength UV light. It is clear that the catalysis effectively enhanced the labeling of the protein in most cases at both room temperature and 0 °C. The difference in the fluorescence intensities of the products in the catalyzed and uncatalyzed reactions are particularly evident at low temperature and short time points, consistent with the results in the model system. It should be noted that, although in this study the amino acid derivative 3f-Tyr is enzymatically appended to tubulin, the amino acid derivative suitable for incorporation into other proteins using unnatural amino acid mutagenesis (unpublished results) or via synthetic peptides. Therefore, the 4a-Phe-catalyzed hydrazone ligation reaction could be broadly applicable to protein labeling.

Hydrazone-containing conjugates have been criticized for biomolecular labeling because the reaction is an equilibrium process. It is feared that the reaction may not go to completion and that the reversibility renders the product too unstable. Equilibrium constants that have been measured for aromatic aldehyde—semicarbazide reactions in aqueous solution for aromatic semicarbazone formation in aqueous solution, which are analogous to the reactions presented here, are on the order of 10^5-10^6 M^{-1}.[28] Kalia and Raines argue that oximes are preferred over hydrazone linkages because of their superior resistance to hydrolysis.

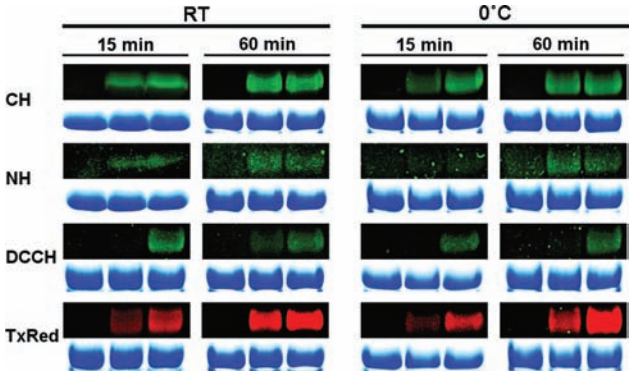

Figure 4. SDS-PAGE of α-tubulin labeled with hydrazine-containing fluorophores, visualized under long-wavelength UV light (top) and stained with Coomassie blue (bottom). Samples of tubulin (40 μM) in PME buffer were incubated with fluorophore (400 μM) for the specified time and temperature in the presence or absence of 10 mM 4a-Phe and immediately run on a gel. Each panel is from left to right: (1) Unmodified α-tubulin (control), (2) 3f-Tyr-α-tubulin, (3) 3f-Tyr-α-tubulin +4a-Phe. Note the increased fluorescence signal in most of the bands for the catalyzed reactions compared to the corresponding uncatalyzed reactions.

Their quantitative kinetic analyses show that the hydrolytic stability of hydrazone linkages is significantly affected by the structure of the hydrazone and pH at which the hydrolysis reaction is carried out. First-order rate constants of hydrazone hydrolysis decrease by 2—3 orders of magnitude from pD 5 to pD 9 in D_2O. These experiments illustrate what is generally known: hydrazone stability is dependent on structures of both reactants and pH of the medium.[29] The most pertinent question is whether a particular hydrazone is sufficiently stable for the biological application.

We have empirical observations to support our assertion that some hydrazones are well-suited for protein labeling. Tubulin labeled with this system does not observably lose the fluorophore in neutral pH buffer under conditions that retain the native structure of the protein. The hydrazone bond remains intact during SDS-PAGE (Figure 4). Moreover, SDS-PAGE gels of tubulin labeled with CH or TxRed do not noticeably lose fluorescence even after 2 weeks of storage in standard destaining solution (containing methanol, acetic acid, and water). The results suggest that the tubulin—fluorophore conjugates are stable under a variety of experimental conditions. Although the hydrazones are thermodynamically reversible, we believe that the 3f-Tyr-linked hydrazones remain intact because the products are kinetically trapped. Such behavior has been observed in hydrazone-containing dynamic covalent chemistry libraries.[30]

CONCLUSION

We conclude that 4a-Phe is a biocompatible catalyst for hydrazone ligations in aqueous buffer at neutral pH with catalytic efficacy about 70% of aniline but superior compatibility with proteins. We have applied the catalysis to a site-specific bioorthogonal labeling method for conjugating molecular labels to the C-terminus of α-tubulin under conditions that preserves the activity of the fragile protein. Importantly, we demonstrate that the reactions can be effectively conducted at 0 °C, successfully increasing the extent of labeling under conditions and time periods that are suitable for routine use with biomolecules.

■ ASSOCIATED CONTENT

Supporting Information. Synthesis and spectral characterization of NH and its corresponding hydrazones is available. The full sequence of the GST-TTL fusion protein and calculations of the extinction coefficients for tubulin and GTS-TTL are also presented. This material is available free of charge via the Internet at http://pubs.acs.org.

■ AUTHOR INFORMATION

Corresponding Author
*Phone: 607-777-2927. Fax: 607-777-4478. E-mail: sbane@binghamton.edu.

■ ACKNOWLEDGMENT

We thank David Tuttle for his excellent scientific photography, Dr. Rebecca Kissling for her expertise and assistance in organic synthesis, and P & N packing for bovine brains for tubulin isolation. This work was supported by NIH Grant R15GM093941.

■ REFERENCES

(1) Sletten, E. M., and Bertozzi, C. R. (2009) Bioorthogonal chemistry: fishing for selectivity in a sea of functionality. *Angew. Chem., Int. Ed. 48*, 6974–6998.

(2) King, T. P., Zhao, S. W., and Lam, T. (1986) Preparation of protein conjugates via intermolecular hydrazone linkage. *Biochemistry 25*, 5774–5779.

(3) Dirksen, A., and Dawson, P. E. (2008) Rapid oxime and hydrazone ligations with aromatic aldehydes for biomolecular labeling. *Bioconjugate Chem. 19*, 2543–2548.

(4) Kalia, J., and Raines, R. T. (2008) Hydrolytic stability of hydrazones and oximes. *Angew. Chem., Int. Ed. 47*, 7523–7526.

(5) Reeves, R. L. (1966) Condensations leading to double bonds. In , Ed., *The Chemistry of the Carbonyl Group* (Patai, S.) pp 567−619, Interscience Publishers, New York.

(6) Jencks, W. P. (1959) Studies on the mechanism of oxime and semicarbazone formation. *J. Am. Chem. Soc. 81*, 475–481.

(7) Banerjee, A., Panosian, T. D., Mukherjee, K., Ravindra, R., Gal, S., Sackett, D. L., and Bane, S. (2010) Site-specific orthogonal labeling of the carboxy terminus of α-tubulin. *ACS Chem. Biol. 5*, 777–785.

(8) Das, A., Sinha, S., Acharya, B. R., Paul, P., Bhattacharyya, B., and Chakrabarti, G. (2008) Deuterium oxide stabilizes conformation of tubulin: a biophysical and biochemical study. *BMB Rep. 41*, 62–67.

(9) Chakrabarti, G., Kim, S., Gupta, M. L., Barton, J. S., and Himes, R. H. (1999) Stabilization of tubulin by deuterium oxide. *Biochemistry 38*, 3067–3072.

(10) Burton, P. R., and Himes, R. H. (1978) Electron microscope studies of pH effects on assembly of tubulin free of associated proteins. Delineation of substructure by tannic acid staining. *J. Cell Biol. 77*, 120–133.

(11) Croom, H. B., Correia, J. J., and Williams, R. C. (1986) The effects of elevated pH and high salt concentrations on tubulin. *Arch. Biochem. Biophys. 249*, 397–406.

(12) Dirksen, A., Dirksen, S., Hackeng, T. M., and Dawson, P. E. (2006) Nucleophilic catalysis of hydrazone formation and transimination: implications for dynamic covalent chemistry. *J. Am. Chem. Soc. 128*, 15602–15603.

(13) Dirksen, A., Hackeng, T. M., and Dawson, P. E. (2006) Nucleophilic catalysis of oxime ligation. *Angew. Chem., Int. Ed. Engl. 45*, 7581–7584.

(14) Dirksen, A., Yegneswaran, S., and Dawson, P. E. (2010) Bisaryl hydrazones as exchangeable biocompatible linkers. *Angew. Chem., Int. Ed. 49*, 2023–2027.

(15) Bhat, V. T., Caniard, A. M., Luksch, T., Brenk, R., Campopiano, D. J., and Greaney, M. F. (2010) Nucleophilic catalysis of acylhydrazone equilibration for protein-directed dynamic covalent chemistry. *Nat. Chem. 2*, 490–497.

(16) Godoy-Alcántar, C., Yatsimirsky, A. K., and Lehn, J. (2005) Structure-stability correlations for imine formation in aqueous solution. *J. Phys. Org. Chem. 18*, 979–985.

(17) Saggiomo, V., and Lüning, U. (2009) On the formation of imines in water--a comparison. *Tetrahedron Lett. 50*, 4663–4665.

(18) Williams, R. C., and Lee, J. C. (1982) Preparation of tubulin from brain. *Methods Enzymol. 85 Pt B*, 376–385.

(19) Penefsky, H. S. (1979) Preparation of nucleotide-depleted F1 and binding of adenine nucleotides and analogs to the depleted enzyme. *Methods Enzymol. 55*, 377–380.

(20) Pace, C. N., Vajdos, F., Fee, L., Grimsley, G., and Gray, T. (1995) How to measure and predict the molar absorption coefficient of a protein. *Protein Sci. 4*, 2411–2423.

(21) Sharma, S., Poliks, B., Chiauzzi, C., Ravindra, R., Blanden, A. R., and Bane, S. (2010) Characterization of the colchicine binding site on avian tubulin isotype betaVI. *Biochemistry 49*, 2932–2942.

(22) Cordes, E. H., and Jencks, W. P. (1962) Nucleophilic catalysis of semicarbazone formation by anilines. *J. Am. Chem. Soc. 84*, 826–831.

(23) Prescher, J. A., and Bertozzi, C. R. (2005) Chemistry in living systems. *Nat. Chem. Biol. 1*, 13–21.

(24) Cordes, E. H., and Jencks, W. P. (1962) Semicarbazone formation from pyridoxal, pyridoxal phosphate, and their schiff bases. *Biochemistry 1*, 773–778.

(25) Yi, L., Sun, H., Wu, Y., Triola, G., Waldmann, H., and Goody, R. S. (2010) A highly efficient strategy for modification of proteins at the C terminus. *Angew. Chem., Int. Ed. 49*, 9417–9421.

(26) Byeon, J., Limpoco, F. T., and Bailey, R. C. (2010) Efficient bioconjugation of protein capture agents to biosensor surfaces using aniline-catalyzed hydrazone ligation. *Langmuir 26*, 15430–15435.

(27) Thygesen, M. B., Munch, H., Sauer, J., Cló, E., Jørgensen, M. R., Hindsgaul, O., and Jensen, K. J. (2010) Nucleophilic catalysis of carbohydrate oxime formation by anilines. *J. Org. Chem. 75*, 1752–1755.

(28) Volfenden, R. W., and Jencks, W. P (1961) The effect of o-substituents on benzaldehyde semicarbazone formation. *J. Am. Chem. Soc. 83*, 2763–2768.

(29) Smith, P. A. S. (1983) Derivatives of hydrazine and other hydronitrogens having N-N Bonds, Benjamin-Cummings Publishing Co., Subs. of Addison Wesley Longman, US.

(30) Beeren, S. R., Pittelkow, M., and Sanders, J. K. M. (2011) From static to dynamic: escaping kinetic traps in hydrazone-based dynamic combinatorial libraries. *Chem. Commun. 47*, 7359–7361.

SUPPORTING MATERIAL

Synthesis and Spectral Characterization of 2-Napthylhydrazine and Corresponding Hydrazone

Materials

Dry methanol, acetonitrile and THF were purchased from Acros Chimica and Aldrich and dried in our lab. Other solvents and reagents were also obtained from Acros or Aldrich and were used as received (regent grade or better). Deuterated solvents were obtained from Cambridge Isotope Laboratories. Non-deuterated solvents were degassed with argon before use.

General Procedures

^{1}H, ^{13}C spectra were recorded on instruments operating at a frequency of 360 MHz. ^{1}H NMR spectra were referenced to $CDCl_3$ (7.26 ppm). ^{13}C NMR spectra were referenced to the $CDCl_3$ (77.00 ppm). Chemical shift multiplicities are reported as s= singlet, d = doublet, t = triplet, q = quartet and m = multiplet. Flash column chromatography was performed using Baker silica gel 60-200 mesh or 200-400 mesh. Absorption spectra of all compounds were obtained by using a Hewlett-Packard 8453 diode array absorption spectrophotometer. Fluorescence emission spectra for were measured using Spex FluoroMax-3 spectrofluorometer. Reactions were monitored by thin layer chromatography using TLC plastic sheets, silica gel 60 $F_{254.}$

Fluorescence Quantum Yield Determination

The relative fluorescence quantum yields (ϕ_F) were determined in dilute solutions with an absorbance below 0.1 at the excitation wavelength. Quinine sulfate in 0.1 M H_2SO_4 (λex = 347 nm) was used as a standard, which has a quantum yield of 0.57.[1] Solvents were dried before use. The slit width was 2 nm for both excitation and emission. The relative quantum yields were

obtained by calculating the area under corrected emission spectrum of the sample and comparing these areas with the area under corrected emission spectrum of standard solution of quinine sulfate. Correction for the refractive index was also applied. All spectra were recorded at 23 °C. All the fluorescence integrals were calculated using SigmaPlot 10.0. The relative quantum efficiencies of fluorescence were obtained with the following equation:

$$\phi_F^{sample} = \phi_F^{standard} \times (F^{sample} - F^{solvent})/(F^{standard} - F^{solvent}) \times (\eta^{sample}/\eta^{standard}) \times (A^{standard}/A^{sample})$$

where F denotes fluorescence integral with respect to wavelength, A denotes the absorbance at the excitation wavelength, and η denotes the refractive index of the solvent.

2-Naphthylhydrazine hydrochloride (1)

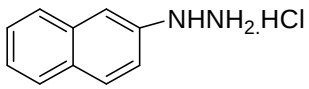

1

The procedure is modified from Portoghese et. al.[2] A stirred slurry of 2-naphthylamine (2 g, 0.01 mol) in concentrated hydrochloric acid (30 mL) was treated dropwise at -5 °C with sodium nitrite (0.89 g, 0.01 mol) in cold water (3 mL), care being taken not to allow the temperature to rise above 0 °C. After the addition of sodium nitrite, the diazotization reaction was continued for 1 hr. The solution was quickly filtered and the filtrate was poured in a thin stream into a solution of stannous chloride dihydrate (14 g, 0.05 mol) in cold hydrochloric acid (60 mL). After 1 hr, the reaction mixture was filtered and washed with water (20 mL), followed with alcohol (30 mL) and finally with ether (100 mL). The crude product was dried in the desiccator and stored under

nitrogen in the dark (1.1 g, 57%)); ^{1}H NMR (360 MHz, DMSO-d_6) δ 7.92 (d, 1H, ArH), 7.40 (t, 1H, ArH), 7.25 (t,1H, ArH), 7.20 (s, 1H, ArH), 7.15 (d, 1H, ArH), 3.85 (bs, 1H, NH); ^{13}C NMR (360 MHz, DMSO-d_6) δ 143.4, 133.6, 128.8, 127.6, 126.8, 126.5, 123.5, 117.1, 107.9.

(E/Z)-2-((2-(Naphthalen-2-yl)hydrazono)methyl)phenol (2)

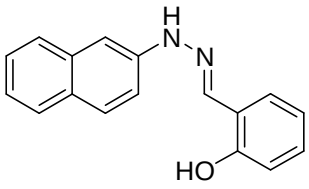

2

2-Naphthylhydrazine (1.42 g, 9 mmol) was dissolved in 5 mL of 95% ethanol. Salicylaldehyde (1.1 g, 9 mmol) was also dissolved in 5 mL of ethanol and added to the previous mixture. The solution was stirred for 1 hr at room temperature (a precipitate formed) and then cooled to -15 °C. The yellow-orange solid was collected by vacuum filtration and washed with ice cold ethanol. The product was recrystallized twice from ethanol to give pure product **2** (1.1 g, 47 %). R_f = 0.56 (CH_2Cl_2); ^{1}H NMR (360 MHz, DMSO-d_6) δ 10.62 (s, 1H, OH), 8.25 (s, 1H, CH), 7.79-7.73(m, 4H, ArH), 7.63 (d, 1H, ArH), 7.16-7.41 (m, 4H, ArH), 6.85-6.92 (m, 2H, ArH); ^{13}C NMR (360 MHz, DMSO-d_6) δ 171.8, 158.6, 153.6, 150.6, 145.3, 144.9, 143.9, 143.5, 143.1, 142.4, 142, 138.4, 136.5, 132.6, 131.9, 131.4, 120.6.

Table S1. Spectral Characteristics of 1 and 2.

Compound	Solvent	λ_{abs} max (nm)	λ_{em} max(nm)	ϕ_{rel}
1	MeOH	330	383	0.021
	DMSO	338	407	0.140
	Dioxane	345	391	0.059
2	MeOH	360	444	0.065
	DMSO	359	440	0.054
	Dioxane	355	461	0.048

The compounds show a significant red-shift upon hydrazone formation, indicating increased fluorophore conjugation through the pi system (Table S1).

Sequence of GST-TTL Fusion Protein

The sequence of our GST-TTL fusion protein was predicted from the sequence of the expression plasmid pReceiver05x (Genecopoeia, Maryland) using the Translate Tool hosted by the Swiss Institute for Bioinformatics (SIB) (http://ca.expasy.org/tools/dna.html). Molecular weight of this protein was then predicted from the predicted protein sequence using the Compute pI/Mw Tool hosted by the SIB (http://ca.expasy.org/tools/pi_tool.html) and confirmed by reducing SDS-PAGE (Data not shown). The results are shown in figure S1.

```
  1 MSPILGYWKIKGLVQPTRLLLEYLEEKYEEHLYERDEGDKWRNKKFELGLEFPNLPYYID 60
 61 GDVKLTQSMAIIRYIADKHNMLGGCPKERAEISMLEGAVLDIRYGVSRIAYSKDFETLKV 120
121 DFLSKLPEMLKMFEDRLCHKTYLNGDHVTHPDFMLYDALDVVLYMDPMCLDAFPKLVCFK 180
181 KRIEAIPQIDKYLKSSKYIAWPLQGWQATFGGGDHPPKSDLVPRSGENLYFQGASKEFGT 240
241 MYTFVVRDENSSVYAEVSRLLLATGHWKRLRRDNPRFNLMLGERNRLPFGRLGHEPGLVQ 300
301 LVNYYRGADKLCRKASLVKLIKTSPELAESCTWFPESYVIYPTNLKTPVAPAQNGIQPPI 360
361 SNSRTDEREFFLASYNRKKEDGEGNVWIAKSSAGAKGEGILISSEASELLDFIDNQGQVH 420
421 VIQKYLEHPLLLEPGHRKFDIRSWVLVDHQYNIYLYREGVLRTASEPYHVDNFQDKTCHL 480
481 TNHCIQKEYSKNYGKYEEGNEMFFKEFNQYLTSALNITLESSILLQIKHIIRNCLLSVEP 540
541 AISTKHLPYQSFQLFGFDFMVDEELKVWLIEVNGAPACAQKLYAELCQGIVDIAISSVFP 600
601 PPDVEQPQTQPAAFIKL 617

Blue = Open Reading Frame for GST Tag
Red  = Open Reading Frame for TTL

                Molecular Weight = 71077.57 (Predicted)
```

Figure S1. Predicted sequence of GST-TTL fusion protein. The molecular weight was confirmed by SDS-PAGE (data not shown). Unlabeled sequence from E227 to T240 contains a Tobacco Etch Virus protease site as well as transcript from a multiple restriction site in the expression plasmid.

Tubulin and GST-TTL Extinction Coefficients

Tubulin and GST-TTL extinction coefficients at 280 nm were calculated as described previously with minor modifications.[3] The number of the major amino-acid contributors to protein

absorbance at 280 nm (tryptophan, tyrosine, and cysteine) were determined from protein sequence data, multiplied by absorption coefficients for those residues at 280 nm, and summed according to the following equation:

$$\varepsilon(M^{-1}cm^{-1}) = (5{,}500\ M^{-1}cm^{-1})(n_{Trp}) + (1{,}490\ M^{-1}cm^{-1})(n_{Tyr}) + (125\ M^{-1}cm^{-1})(n_{Cys})$$

Where n_{Trp}, n_{Tyr}, and n_{Cys} are the number of tryptophan, tyrosine, and cysteine residues in a protein, and the corresponding coefficients are the average absorption coefficients for those residues in when in a protein. This equation assumes each cysteine represents one half a cystine. In the case of tubulin, a fourth term must be added to account for the absorbance of the two bound guanine nucleotides per dimer, yielding the following equation:

$$\varepsilon(M^{-1}cm^{-1}) = (5{,}500\ M^{-1}cm^{-1})(n_{Trp}) + (1{,}490\ M^{-1}cm^{-1})(n_{Tyr}) + (125\ M^{-1}cm^{-1})(n_{Cys}) + (7{,}760\ M^{-1}cm^{-1})(n_{GTP/GDP})$$

Where $n_{GTP/GDP}$ is the number of bound guanosine nucleotides (two in the case of a tubulin dimer) and its corresponding coefficient is the extinction coefficient for GTP/GDP in aqueous buffer at pH 6.9 as determined in our lab. The tubulin sequences used for bovine brain tubulin dimers were α_I and β_{II} as obtained from Swiss-Prot (P81947 and Q6B856 respectively). The sequence used for GST-TTL is reported in figure S1.

References

1. Lakowicz, J. R., and Masters, B. R. (2008) Principles of Fluorescence Spectroscopy, Third Edition. ***J. Biomed. Opt. 13***, 029901.
2. Portoghese, P. S., Sultana, M., and Takemori, A. E. (1990) Design of peptidomimetic delta opioid receptor antagonists using the message-address concept. ***J. Med. Chem. 33***, 1714-1720.

3. Pace, C. N., Vajdos, F., Fee, L., Grimsley, G., and Gray, T. (1995) How to measure and predict the molar absorption coefficient of a protein. ***Protein Sci. 4***, 2411-2423.

Bioconjugate Chemistry

ARTICLE

pubs.acs.org/bc

Multimerized siRNA Cross-linked by Gold Nanoparticles

Won Ho Kong,*[,†,‡] Ki Hyun Bae,[†] Cheol Am Hong,[†] Yuhan Lee,[†] Sei Kwang Hahn,[‡] and Tae Gwan Park[†,§]

[†]Department of Biological Sciences and Graduate School of Nanoscience and Technology, Korea Advanced Institute of Science and Technology, Daejeon 305-701, South Korea

[‡]Department of Materials Science and Engineering, Pohang University of Science and Technology, Pohang 790-784, South Korea

ABSTRACT:

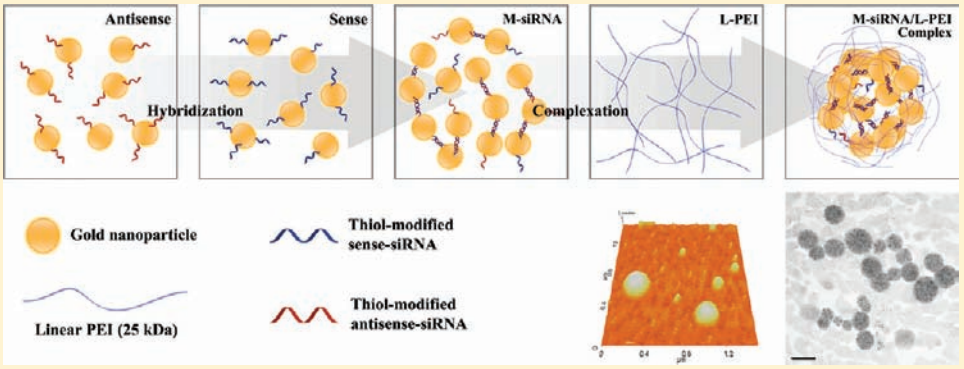

In this study, siRNAs terminated with thiol groups were multimerized and cross-linked using ~5 nm gold nanoparticles (AuNPs) via Au−S chemisorption that can be intracellularly reduced. AuNPs immobilized with single-stranded antisense siRNA were assembled with those with single-stranded sense siRNA via complementary hybridization or assembled with those with single-stranded dimeric sense siRNA. The multimerized siRNA cross-linked by AuNPs showed increased charge density and enhanced enzymatic stability, and exhibited good complexation behaviors with a polycationic carrier, linear polyethylenimine (L-PEI). The resultant multi-siRNA/AuNPs/L-PEI polyelectrolyte complexes exhibited far greater gene silencing efficiencies of green fluorescent protein (GFP) and vascular endothelial growth factor (VEGF) compared to naked siRNA complexes. They could also be visualized by micro-CT imaging. The results suggest that AuNP-mediated multimerization of siRNAs could be a rational approach to achieve both gene silencing and imaging at a target tissue simultaneously.

INTRODUCTION

Gold nanoparticles (AuNPs) have received significant attention as nanotemplates for biomolecular conjugates because of their excellent biocompatibility, controllable morphology and size dispersity, and easy surface functionalization via well-defined Au-thiol linkages.[1−4]

For diagnostic applications, AuNPs were functionalized with oligonucleotides for ultrasensitive detection of a target nucleic acid sequence via their unique surface plasmon optical properties generated upon hybridization.[5−7] For therapeutic applications, AuNPs were conjugated with therapeutic genes such as antisense oligodeoxynucleiotides (ODNs) and small interfering RNAs (siRNAs) for efficient cellular uptake and gene inhibition.[4−11]

More recently, siRNAs have been extensively utilized for gene silencing due to their extraordinary ability to specifically and efficiently block the gene expression of a target mRNA through an RNA interference mechanism. siRNAs hold great promise as a new class of therapeutic nucleic acid drugs for treating numerous diseases including cancer and other diseases from genetic disorders to viral infections.[12−16] Clinical applications of siRNAs have been limited mostly by the lack of efficient and biocompatible delivery carriers.[17,18] Since siRNA molecules have a low charge density with high stiffness as compared to plasmid DNA, they have to condense with an excess amount of cationic polymers and lipids to form stable nanocomplexes for facile endocytic cellular uptake.[19] Highly positively charged polymers such as branched polyethylenimine (bPEI) have been popular to stably complex siRNA, but their cytotoxicity remains a serious problem. Recently, multimeric siRNAs cross-linked via intracellularly cleavable disulfide linkages were proposed to increase the charge density of siRNA.[19,20] The reducibly multimerized siRNA was synthesized by forming covalent bonds between two or more siRNA monomers via bifunctional disulfide-containing cross-linkers (e.g., dithio-bis-maleimidoethane (DTME)). It was demonstrated that the one-dimensionally aligned siRNA molecules could significantly enhance electrostatic interactions with low-molecular-weight polycationic carriers that exhibit low cytotoxicity, generating stable and compact polyelectrolyte nanocomplexes. The multimeric siRNA showed greatly enhanced gene silencing efficiencies *in vitro* and *in vivo* as compared to naked

Received: April 4, 2011
Revised: August 30, 2011
Published: September 07, 2011

ACS Publications © 2011 American Chemical Society

siRNA, when complexed with linear PEI (L-PEI) at the same polymer nitrogen to siRNA phosphate (N/P) ratio.

Here, we demonstrate a facile synthetic route to multimeric siRNA species that are cross-linked by AuNPs via Au-thiol linkages. Thiolated single-stranded sense and antisense siRNA were separately anchored onto the surface of AuNPs, and they were subsequently annealed to produce multimeric siRNA cross-linked by AuNPs. In addition, single-stranded antisense siRNA/AuNPs were hybridized with a single-stranded sense dimeric and reducible siRNA as a spacing linker to control the distance between AuNPs. The resultant multi-siRNA/AuNPs are expected to regenerate naked siRNA species within cells by reductive cleavage of Au-thiol linkages. The multimeric siRNA/AuNPs were characterized in terms of their size, morphology, resistance to enzymes, and reducibility to glutathione, and condensed with L-PEI to form polyelectrolyte complexes for cellular uptake, gene silencing, and micro-CT imaging.

EXPERIMENTAL PROCEDURES

Materials. Tetrachlorohydrogenaurate ($HAuCl_4$), sodium citrate, sodium borohydride ($NaBH_4$), phosphine (4,4′-(phenylphosphinidene)bis-benzenesulfonic acid dipotassium salt), Triton X-100, and XTT based *in vitro* cytotoxicity assay kit were purchased from Sigma-Aldrich (St. Louis, MO). Linear polyethylenimine (L-PEI, M_w: 25 kDa) was purchased from Polysciences (Warrington, PA). All the chemicals were of analytical reagent grade. Dulbecco's modified eagle medium (DMEM), Roswell Park Memorial Institute (RPMI) 1640 medium, phosphate buffered saline (PBS), and fetal bovine serum (FBS) were purchased from Gibco-Invitrogen (Grand Island, NY). Enhanced green fluorescent protein (GFP) siRNA (sense strand: 5′-AACUUCAGGGUCAGCUUGC$(dT)_5$-3′; antisense strand: 5′-GCAAGCUGACCCUGAAGUU$(dT)_5$-3′), vascular endothelial growth factor (VEGF) siRNA (sense: 5′-GGAGUACCCUGAUGAGAUC$(dT)_5$-3′; antisense: 5′-GAUCUCAUCAGGGUACUCC$(dT)_5$-3′), alkanethiol-modified siRNA (the 3′-end of both the sense and antisense strands modified with thiol groups), and fluorescein-labeled single-stranded siRNA were provided from Bioneer Co. (Daejeon, Korea). RNase ONE ribonuclease was purchased from Promega Corporation (Madison, WI).

Synthesis of Phosphine-Capped Gold Nanoparticles (AUNPs). Citrate-stabilized AuNPs (5 nm in diameter) were prepared by direct reduction of Au (III) ions using citric acid.[21] Following the synthesis, the AuNPs were capped with phosphine and concentrated by precipitation and resuspension as described previously. [3] The resulting AuNPs were treated with 0.1% diethylpyrocarbonate (DEPC) followed by autoclaving at 121 °C for 20 min to yield sterile and RNase-free gold colloids.[5] The concentration of AuNPs was calculated using an extinction coefficient of 1×10^7 M^{-1} cm^{-1} at 520 nm.

AuNP-Mediated Assembly of Multimerized siRNA (M-siRNA). Phosphine-capped AuNPs were separately functionalized with single-stranded sense or antisense siRNA, according to the method described previously.[22] Either the sense or antisense-stranded thiol-modified siRNA (3.05 mol of siRNA relative to a mole of AuNPs) was added into a stirred solution of phosphine-capped AuNPs (500 nM). To promote the place-exchange reaction of siRNA at the polar defect site of the AuNPs, they were resuspended in 0.5 × TBE (45 mM Tris-base, 45 mM boric acid, 1 mM EDTA, pH 8.0)/100 mM NaCl buffer solution. The solution was further incubated for 40 h at room temperature. Unreacted siRNA was removed by centrifugation for 30 min at 50 000 × *g*. The resulting siRNA-functionalized AuNPs (obtained as red precipitates) were purified by successive dispersion/centrifugation in 0.3 M NaCl solution. In order to determine the number of siRNAs anchored onto the surface of a single AuNP, fluorescein-labeled siRNA was used for the preparation of siRNA-functionalized AuNPs.[23] The resultant siRNA-functionalized AuNPs were treated with 12 mM 2-mercaptoethanol in 0.1 M PBS solution (pH 7.4). After 12 h of incubation with gentle shaking, the solution containing the displaced siRNA was separated by centrifugation. The fluorescence in the supernatant was then analyzed using a LSM-AMINCO 8100 fluorophotometer (LSM instruments Inc., USA) with an excitation wavelength at 488 nm and an emission wavelength at 520 nm. The concentration of AuNPs in each sample was also quantified by measuring the absorbance at 520 nm using the NanoDrop ND-1000 spectrophotometer (Thermo Fisher Scientific, USA). The average number of siRNAs attached on each AuNP was calculated by dividing the amount of attached siRNA with the amount of AuNPs. M-siRNA was synthesized by annealing the sense siRNA-functionalized AuNPs with an equimolar amount of the antisense siRNA-functionalized AuNPs in 0.1 M phosphate-buffered saline (PBS) solution (pH 7.4) for 12 h at room temperature. M-siRNA having a longer spacing between AuNPs (M-siRNA-D) was also synthesized by hybridizing the antisense siRNA-functionalized AuNPs with a dimerized sense siRNA at the same molar concentration. The dimerized sense siRNA was prepared according to the previously reported procedure.[24] Briefly, 3′-end thiol-modified single-stranded sense siRNA (GFP; 5′-AACUUCAGGGUCAGCUUGC$(dT)_2$-3′) was reacted with dithio-bis-maleimidoethane, a homobifunctional thiol-reactive cross-linker, to prepare a single-stranded sense-dimer.

Physicochemical Characterization of M-siRNA. The size, shape, and spatial arrangement of AuNPs cross-linked in the M-siRNA and M-siRNA-D were investigated by transmission electron microscopy (TEM). Thirty microliters of the solution was deposited onto a 300 mesh Formvar/carbon-coated copper grid, air-dried, and then observed by a field-emission transmission electron microscope (FE-TEM, Philips TECNAI F20). The average center-to-center distance of AuNPs in the multimerized siRNA was determined by measuring more than 50 multi-siRNA/AuNPs clusters in the TEM image. UV−visible spectra of phosphine-capped AuNPs, siRNA-functionalized AuNPs, and M-siRNA were recorded from 450 to 650 nm using a Nano Drop ND-1000 spectrophotometer.

Glutathione-Responsive Release of siRNA from M-siRNA. Since the glutathione (GSH) concentration in the cytoplasm (1−10 mM) is substantially higher than in extracellular environments (2 μM in plasma), it was expected that M-siRNA would have an ability to selectively deliver siRNA into the cytoplasm.[29] Thus, to determine whether the cross-linked siRNA molecules were released from the M-siRNA in a reducible intracellular environment, the release of siRNA was examined at varying glutathione concentrations. In brief, M-siRNA (containing 1 μg equiv siRNA) was incubated in 0.1 M PBS solution (pH 7.4) containing 0, 100, 200, or 300 μM GSH at 37 °C. After incubation for 1 h, the released siRNA was separated from the AuNPs by centrifugation. Aliquots of the supernatant were diluted 2-fold with deionized water, and then analyzed by agarose gel electrophoresis for 10 min at 100 V in TAE buffer solution (40 mM Tris-HCl, 1% (v/v) acetic acid, 1 mM EDTA). After staining with ethidium bromide, the gel was imaged under UV illumination.

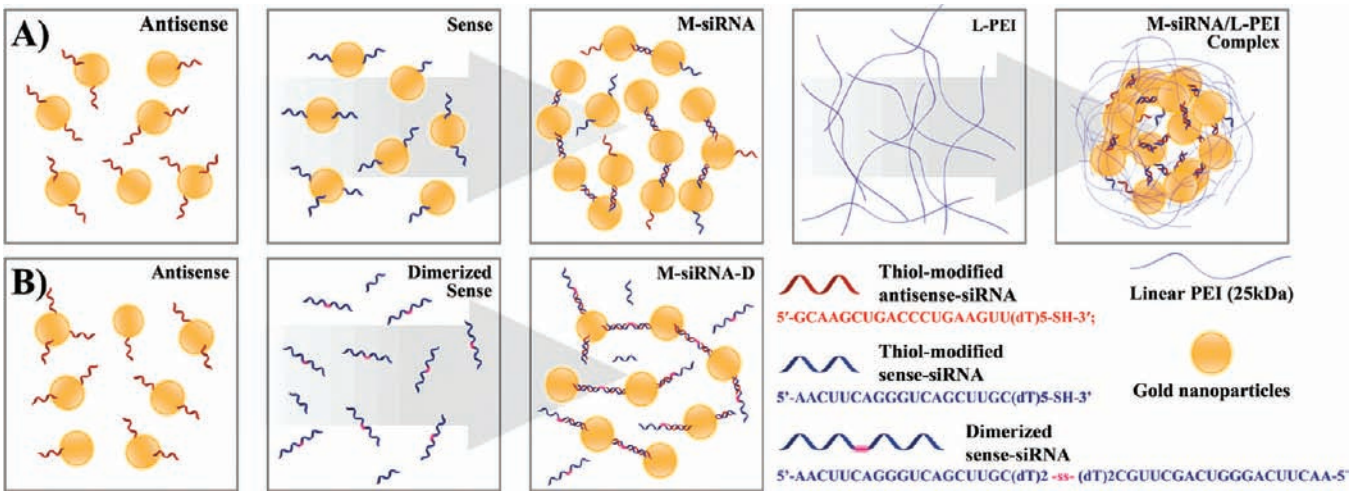

Figure 1. Schematic illustration of the formation of (A) AuNP-mediated multimerized siRNA (M-siRNA), collapsed complexes with L-PEI, and (B) another type of multimerized siRNA having a longer spacing between AuNPs (M-siRNA-D). The sequences of thiol-modified single-stranded siRNAs are 5′-AACUUCAGGGUCAGCUUGC$(dT)_5$-SH-3′ (sense) and 5′-GCAAGCUGACCCUGAAGUU$(dT)_5$-SH-3′ (antisense). The sequence of dimerized sense siRNA is 5′-AACUUCAGGGUCAGCUUGC$(dT)_2$-ss-$(dT)_2$CGUUCGACUGGGACUUCAA-5′.

Protective Effect of M-siRNA against Enzymatic Degradation. To evaluate the stability of siRNA against nuclease attack, M-siRNA and naked siRNA were treated with RNase ONE ribonuclease, which cleaves phosphodiester linkages between neighboring ribonucleotides. Two micrograms of siRNA or M-siRNA were incubated with 10 U RNase in 100 μL of the reaction buffer solution (10 mM Tris−HCl (pH 7.5), 5 mM EDTA, and 200 mM sodium acetate). In order to examine the effect of GSH on the enzymatic stability of M-siRNA, the samples were also simultaneously treated with 100 μM GSH. After incubation for 30 min at room temperature, the residual siRNA was detached from the surface of the AuNPs by treatment with 12 mM 2-mercaptoethanol in 0.1 M PBS solution (pH 7.4). Following centrifugation, the supernatant solution containing the detached siRNA was loaded on a 2% agarose gel. The remaining siRNA fraction was visualized by staining with ethidium bromide and analyzed using *Image J* software (NIH Image).

Preparation and Characterization of M-siRNA/L-PEI Polyelectrolyte Complexes. To form polyelectrolyte complexes, M-siRNA or monomeric siRNA (2 μg) dispersed in RNase-free water was mixed with L-PEI at various N/P ratios ranging from 1 to 10 in 0.1 M PBS solution (pH 7.4), and then incubated for 10 min at room temperature. The size, morphology, and internal structure of the polyelectrolyte complexes were examined using atomic force microscopy (AFM; PSIA XE-100, Park Systems, Korea) and TEM. In the AFM experiments, 100 μL of the sample solution was deposited onto a clean mica surface and images were obtained in a noncontact mode. The zeta potential values of the complexes were also measured using a dynamic light scattering instrument (Zeta-Plus, Brookhaven, NY) equipped with a He−Ne laser at a wavelength of 632 nm. The intensity-weighted particle size distribution data were collected at a scattering angle of 90° at physiological temperature, 37 °C. The zeta potential values of the complexes were measured in 0.1 M PBS solution (pH 7.4) in triplicate at 37 °C.

Evaluation of Gene Silencing Effect of M-siRNA/L-PEI Polyelectrolyte Complexes. A GFP-expressing human melanoma cell line (MDA-MB-435) was provided from Samyang Corp. (Daejeon, South Korea). The human prostate carcinoma cell line (PC-3 cells) was provided form the Korea Cell Line Bank (Seoul, South Korea). GFP-expressing MDA-MB-435 cells were seeded in a 24-well plate at a density of 2×10^5 cells per well and grown in RPMI medium supplemented with 10% (v/v) fetal bovine serum (FBS) for 24 h at 37 °C. The cells were then incubated with serum-deficient or 10% FBS-supplemented medium containing polyelectrolyte M-siRNA complexes formulated with L-PEI at N/P ratios ranging from 1 to 10. After 5 h of incubation, the culture medium was replaced with fresh medium containing 10% FBS, and further incubated for 48 h. As a control experiment, the cells were treated with only L-PEI at an equivalent concentration or monomeric siRNA/L-PEI complexes prepared at an N/P ratio of 10. To quantify the extent of GFP expression, the treated cells were washed with the PBS solution three times, and then lysed with 0.1% Triton X-100 solution in the PBS solution. After centrifugation at 4 °C, the GFP concentration in the supernatant was analyzed using a LSM-AMINCO 8100 fluorophotometer with an excitation wavelength at 488 nm and an emission wavelength at 509 nm. Relative GFP expression levels were calculated based on the GFP expression of untreated cells, which was set at 100%. To evaluate the VEGF gene silencing effect, PC-3 cells were transfected with the M-siRNA/L-PEI complexes at varying concentrations and then harvested. Total RNA was isolated using a Trizol reagent according to the manufacturer's protocol. Semiquantitative reverse transcriptase polymerase chain reaction (RT-PCR) was performed to measure the cellular VEGF mRNA levels according to our previous report.[25]

In Vitro Cytotoxicity Assay. The cytotoxicity of M-siRNA/L-PEI polyelectrolyte complexes was examined using an XTT-based *in vitro* cytotoxicity assay kit. Briefly, GFP-expressing MDA-MB-435 cells were seeded in a 48-well plate at a density of 2×10^4 cells per well, and then cultivated in RPMI medium supplemented with 10% (v/v) FBS for 24 h at 37 °C. The cells were then incubated with the M-siRNA/L-PEI complexes (siRNA concentration: 2 μg/mL), which were prepared at varying N/P ratios (N/P ratios ranging from 2 to 12), or naked siRNA (2 μg/mL) as a control. After incubation for 10 h, the cells were washed with the PBS solution, and then treated with a XTT

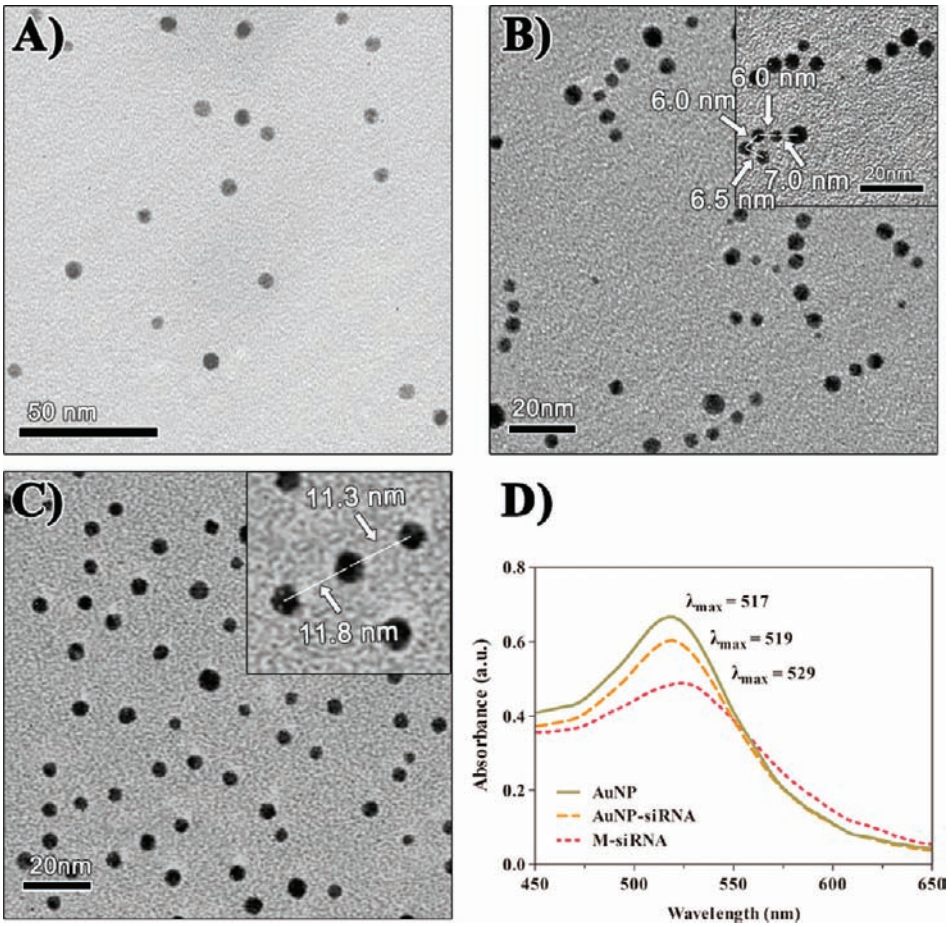

Figure 2. (A) TEM images of phosphine-capped AuNPs, (B) M-siRNA, and (C) M-siRNA-D. (D) UV−visible absorption spectra of phosphine-capped AuNPs (solid line), siRNA-AuNPs conjugates (dash), and M-siRNAs (dot).

reagent for 2 h. Cell viability was determined by measuring the absorbance at 450 nm using a Bio-Rad microplate reader, and then normalized with respect to the control population.

Micro-CT Imaging Procedures. GFP-expressing MDA-MB-435 cells were seeded in a 100 mm culture dish at a density of 1×10^6 cells per dish, and further grown for 24 h at 37 °C. The cells were then treated with the serum-deficient medium containing M-siRNA/L-PEI or monomeric siRNA/L-PEI polyelectrolyte complexes. Treatment was carefully carried out by adding the formulated complexes to the cells in a dropwise manner. After 5 h of incubation, the cells were washed three times with PBS solution, and detached using a trypsin−EDTA solution. The harvested cells were fixed with 1% formaldehyde in PBS solution. The cells were embedded in a 2% low-melting agarose gel, and then visualized through micro-CT imaging (Inveon Micro-CT, Siemens, USA).

RESULTS AND DISCUSSION

Synthesis of Phosphine-Capped AuNPs. Multimeric siRNA cross-linked by AuNPs (or AuNPs cross-linked by siRNA) was fabricated by complementary hybridization between sense and antisense single-stranded siRNA separately immobilized onto the surface of AuNPs via a Au-thiol linkage (Figure 1). In order to attain multimeric siRNA/AuNPs constructs with desired shape and morphological characters, the number of immobilized single-stranded sense or antisense siRNA molecules and their spatial distribution on the surface of negatively charged phosphine-capped AuNPs are highly important. When AuNPs were immobilized with two or more single-stranded sense or antisense siRNA molecules, they would produce linear, branched, or gel-like multimeric siRNA species by complementary hybridization, respectively. Since the number of siRNA molecules and their spatial orientation on the surface of AuNPs would primarily dictate the assembly pattern of AuNPs, the size of AuNPs is most critical in controlling the extent of siRNA immobilization. Depending on the surface area, curvature, and surface charge density of AuNPs, thiolated single-stranded sense or antisense siRNA could be bound on the surface to varying extents. To immobilize roughly two siRNA molecules on the surface, 5 nm AuNPs were prepared.[21] The size of the phosphine-capped AuNPs was 5.0 ± 1.8 nm as assessed through TEM image (Figure 2A). The UV−visible spectra showed a characteristic absorption peak near 520 nm (λ_{max} = 514 nm; data was not shown).

Multimerized siRNA Construct Formation. AuNPs were functionalized with single-stranded sense or antisense siRNAs terminated with a thiol group at their 3′ end. The thiolated 3′ end of siRNAs had an extended $(dT)_5$ overhang that could serve as a steric spacer to enhance the Au−S chemisorption of thiolated siRNA on the surface by reducing the tendency of Au-purine base interactions.[23,26−28] Because of the stiff nature of siRNA, the anchored siRNAs might be oriented perpendicularly onto the

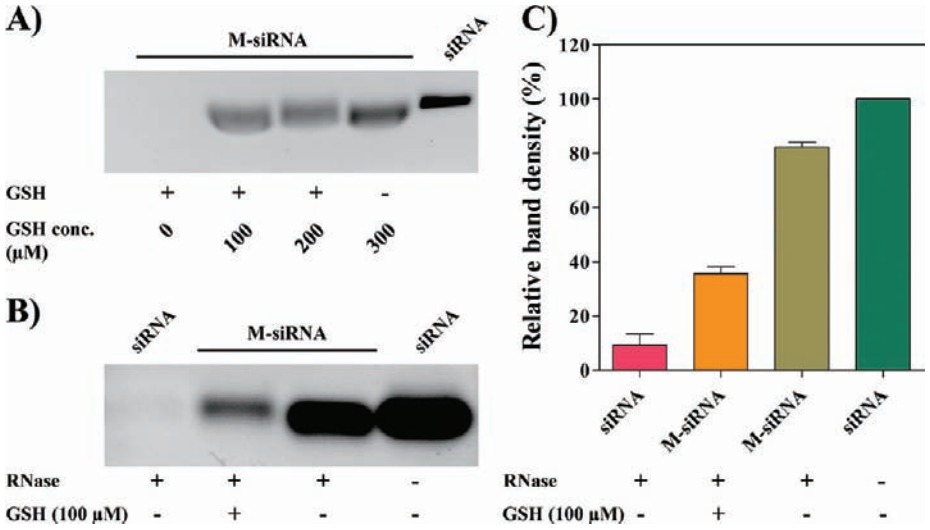

Figure 3. GSH triggered release of siRNA and resistance against RNase attack. (A) Gel electrophoresis showing GSH triggered release of siRNA as a function of GSH concentration (100, 200, 300, and 0 μM from the left). (B) Gel electrophoresis showing enzymatic degradation of siRNA (RNase concentration 10U/mL). (C) Densitometric analysis normalized to naked siRNA without RNase treatment.

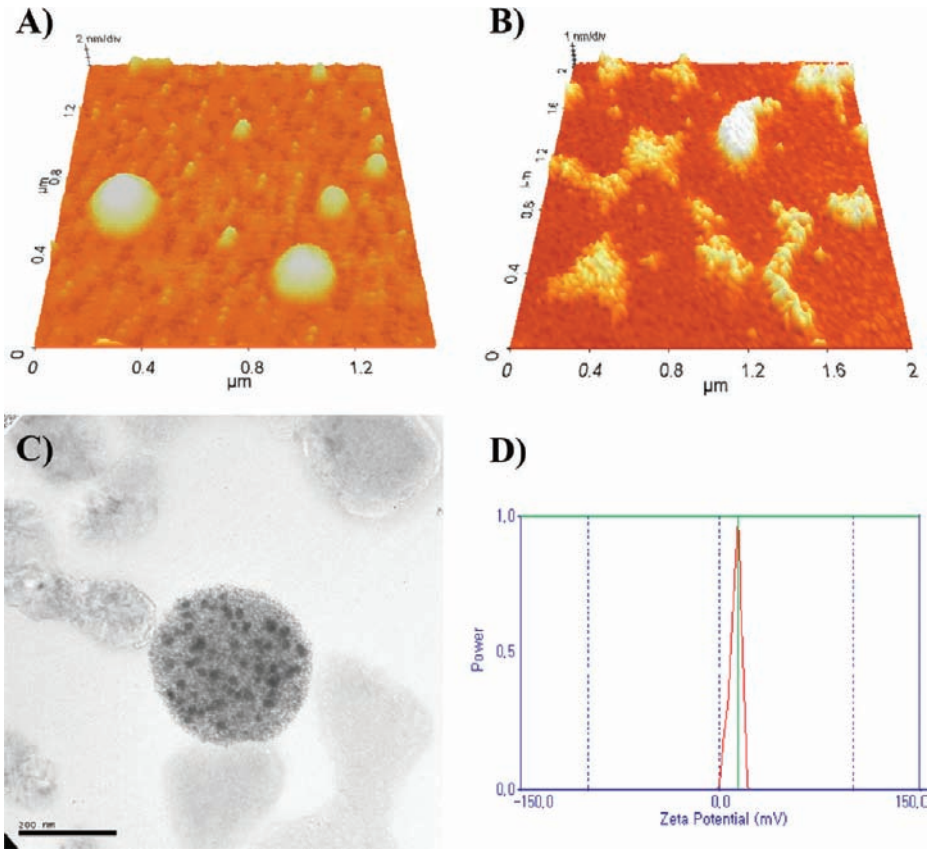

Figure 4. AFM and TEM images of M-siRNA/L-PEI complexes. (A) M-siRNA/L-PEI nanocomplex and (B) naked siRNA/L-PEI complex. (C) TEM image of M-siRNA/L-PEI nanocomplex. (D) Surface zeta potential of M-siRNA/L-PEI complex. N/P ratio of 10 was used in all measurements.

surface with a fully stretched structure, allowing for maximum hybridization with its complementary counterparts. The average number of siRNA onto the surface of an AuNP was controlled to be ~2 by adjusting a feed molar ratio of single-stranded siRNA to AuNPs at 3.05. The surface immobilization of siRNA on the Au surface was evidenced by observing a slight red shift of surface plasmon peak from 517 to 519 nm (Figure 2D). When the two separately prepared AuNPs immobilized with single-stranded sense and antisense siRNA were mixed, AuNPs were cross-linked by complementary hybridization, and they were consequently 1-D aligned with an average center-to-center distance of 6.5 ± 0.7 nm between the adjacent AuNPs (Figure 2B). The spacing

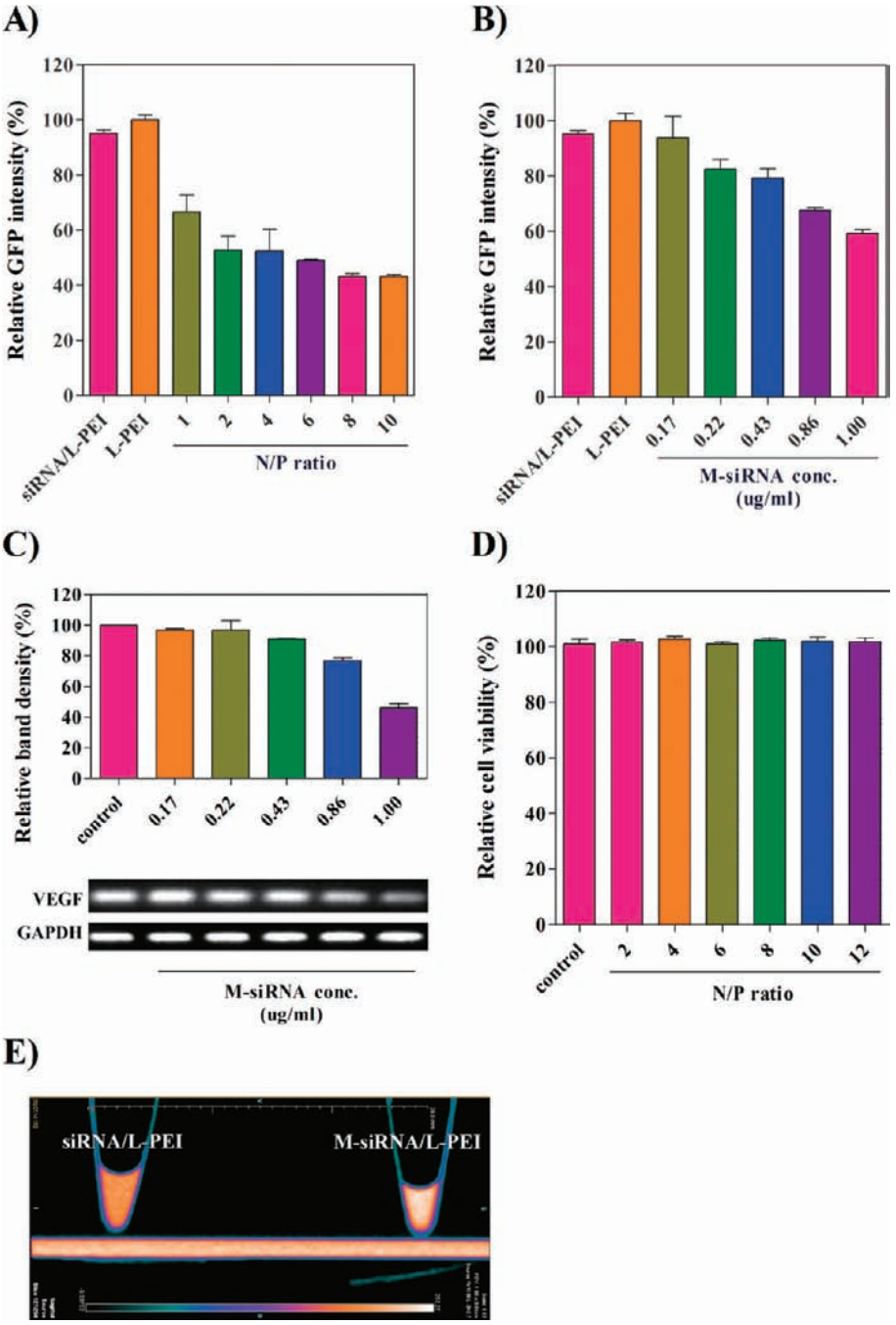

Figure 5. (A) Suppression of GFP gene expression by the M-siRNA/L-PEI complex at various N/P ratios (N/P ratio: 1−10) or the siRNA/L-PEI complex (N/P ratio: 10) under serum-deficient conditions. (B) GFP express level of MDA-MB-435 cells transfected with siRNA/L-PEI complexes, L-PEI, and M-siRNA/L-PEI complex as a function of siRNA concentration in serum-containing medium (N/P ratio: 10). (C)RT-PCR analysis (lower panel) and corresponding densitometric analysis (upper panel) of VEGF mRNA level in PC3 cells transfected with M-siRNA/L-PEI and complex (N/P ratio: 10) as a function of siRNA concentration. (D) Cytotoxicity of M-siRNA/L-PEI complexes at N/P ratios ranging from 2 to 12. (E) Micro CT imaging of agarose-embedded MDA-MB-435 cells transfected with siRNA/L-PEI (left) and M-siRNA/L-PEI (right) complexes, each complex was prepared at an N/P ratio of 10.

distance between the two neighboring AuNPs is well-matched with a calculated length of an siRNA duplex structure. The surface plasmon peak of 5 nm AuNPs was also significantly red-shifted to 529 nm after hybridization (Figure 2D), resulting from the spatial 1-D alignment of AuNPs. To further prove that the observed 1-D assembled M-siRNA was indeed formed by complementary hybridization, AuNPs immobilized with single-stranded antisense siRNA were hybridized with dimerized single-stranded sense siRNA to double the spacing distance between the AuNPs. As shown in Figure 1B, the center-to-center distance between the two adjacent AuNPs was 11.1 ± 0.2 nm, consistent with the calculated length of a dimeric siRNA structure (Figure 2C), proving that AuNPs were cross-linked by complementary hybridization between two sense and antisense siRNAs immobilized onto the surface of two separate AuNPs.

dx.doi.org/10.1021/bc200172p |*Bioconjugate Chem.* 2011, 22, 1962–1969

Glutathione-Triggered Regeneration of Monomeric siRNA from M-siRNA. M-siRNA was incubated with glutathione (GSH, final concentration: 0−300 μM) to verify the intracellular regeneration of naked siRNAs. The formation of monomeric siRNA was examined by agarose gel electrophoresis. The thiol-Au linkages could be reduced by intracellular reductive molecules such as GSH.[29,30] As shown in Figure 3A, the complete release of monomeric siRNA can be observed at elevated GSH concentrations. This result shows that the AuNPs-mediated multimerized siRNA (M-siRNA) could be reductively disassembled to form monomeric siRNAs within cells.

Stability of M-siRNA against Enzymatic Degradation. To evaluate the stability of M-siRNA against enzymatic degradation, the fabricated M-siRNAs were mixed with 10 units of RNase with or without 100 μM GSH. As shown in Figure 3B and C, M-siRNA survived 82.2 ± 1.4% of siRNA units even after treating with 10 units of nuclease (band 2 in Figure 3B), while naked siRNA was almost completely degraded in 30 min (band 1 in Figure 3B). In the presence of GSH (100 μM) and 10 units of nuclease, 35.6 ± 2.1% of siRNA units in the M-siRNA remained intact due to the GSH-triggered detachment of siRNA.

Polyelectrolyte Complex Formation with L-PEI. Since multimeric M-siRNA structures cross-linked by AuNPs have increased charge density as compared to monomeric siRNA, they could more readily form nanosized polyelectrolyte complexes with oppositely charged cationic polymers. Previously, we demonstrated that multimeric siRNA cross-linked by reducible disulfide linkages produced far more stable and compact polyelectrolyte complexes with cationic polymers compared to monomeric siRNA, resulting in promoted cellular uptake and enhanced gene silencing efficiency.[14,15] This was caused by enhanced electrostatic interactions between multimeric siRNA and cationic polymers. M-siRNA polyelectrolyte nanocomplexes were prepared using L-PEI (M_w 25 kDa). In the atomic force microscopy (AFM) images, the resulting M-siRNA/L-PEI polyelectrolyte complexes exhibited a compact and spherical morphology at the N/P ratio of 10 (average diameter: 289 ± 31 nm) (Figure 4A). On the other hand, monomeric siRNA/L-PEI complexes showed loosely packed aggregates at the same N/P ratio (Figure 4B). TEM image also showed that the M-siRNA/L-PEI complexes contained numerous embedded AuNPs within the complex particle (Figure 4C; average diameter of 319 ± 36.24 nm). The formation of nanosized M-siRNA polyelectrolyte complexes could be attributed mainly to ionic interactions of L-PEI with cross-linked siRNA units and, more importantly, highly anionic phosphine-capped AuNPs .[31−33] The resulting complexes had a zeta potential value of +13.2 ± 3.4 mV (Figure 4D).[34]

Gene Silencing. The gene silencing effect of M-siRNA/L-PEI nanocomplexes was examined at various N/P ratios using GFP-expressing MDA-MB-435 cells (siRNA concentration: 1 μg/mL) under serum-deficient conditions. As shown in Figure 5A, M-siRNA/L-PEI complexes exhibited enhanced GFP gene silencing efficiency down to 46.9 ± 0.9% at an N/P ratio 10. The dose-dependent silencing efficiency of M-siRNA/L-PEI complexes was further investigated at an optimal N/P ratio (N/P ratio: 10) in the media containing 10% serum. M-siRNA/L-PEI complexes showed the gradual decrease in GFP expression in a dose-dependent manner (Figure 5B), while naked siRNA/L-PEI complexes only showed slight gene inhibition under the same conditions. The gene silencing efficiency of M-siRNA/L-PEI complexes was further evaluated via semiquantitative RT-PCR using siVEGF (VEGF-silencing siRNA), one of the most widely studied antiangiogenic siRNA for cancer therapy. As shown in Figure 5C, when siRNA concentration was increased from 0.17 to 1.0 μg/mL, the relative band intensity of VEGF gradually decreased. The gene expression levels were quantified by a densitometric analysis. As shown in Figure 5C, when the siRNA concentration was increased from 0.17 μg/to 1.0 μg/mL, the relative band intensity of VEGF decreased proportionally from 99.5 ± 6.3% to 47.8 ± 5.8% in a dose-dependent manner. It seems that the enhanced gene inhibition effect of the M-siRNA/L-PEI complexes might result from the enhanced cellular uptake.

Cytotoxicity. We also examined the cytotoxicity of the M-siRNA/L-PEI complexes as a function of N/P ratio using monomeric siRNA/L-PEI complexes (at the N/P ratio of 10) as a control. As shown in Figure 5D, the M-siRNA/L-PEI complexes displayed no significant cytotoxic effects against MDA-MB-435 cells. This could be attributed to the use of relatively lower N/P ratio for M-siRNA complexation relative to that for monomeric siRNA complexation that normally requires the N/P ratio of 40 for gene silencing.

CT-Imaging. To visualize cellular uptake, MDA-MB-435 cells were transfected with M-siRNA/L-PEI or naked siRNA/L-PEI complexes (N/P ratio 10) under serum-deficient conditions, the transfected cells were imaged using micro-CT. AuNPs have been widely studied as CT contrast agents for detection of various tissues, because Au atoms have a high electron density, resulting in strong X-ray absorption.[35] The CT value for M-siRNA/L-PEI treated cells (129.6 HU) was more than 4-fold greater than that for monomeric siRNA/L-PEI treated cells (15.8 HU) (Figure 5E). These results clearly demonstrate the intracellular uptake of M-siRNA/L-PEI complexes.

■ CONCLUSIONS

We demonstrated that the formation of 1-D assembled and multimerized siRNA could be achieved via complementary hybridization between single-stranded sense and antisense siRNA immobilized AuNPs. The multimerized siRNA significantly improved the enzymatic stability of siRNA and exhibited superior complex forming ability with cationic polymers due to its substantially increased charge density. These results suggest the possibility that the AuNP-mediated siRNA multimerization could be used for efficient gene silencing.

■ AUTHOR INFORMATION

Corresponding Author

*Mailing address: Department of Materials Science and Engineering, POSTECH, Pohang 790-784, South Korea. E-mail: whkong@postech.ac.kr. Phone: +82-54-279-5433.

Notes

§The authors express their sincere condolences to family on the death (April 10, 2011) of Prof. Tae Gwan Park.

■ ACKNOWLEDGMENT

This work was supported by the Ministry for Health, Welfare and Family Affairs, and the World Class University project, Basic Science Research Program (2010-0027955), and the National Research Laboratory program from the Ministry of Education, Science and Technology, Republic of Korea.

REFERENCES

(1) Alivisatos, A. P., Johnsson, K. P., Peng, X., Wilson, T. E., Loweth, C. J., Bruchez, M. P., Jr., and Schultz, P. G. (1996) Organization of 'nanocrystal molecules' using DNA. *Nature 382*, 609–11.

(2) Mirkin, C. A., Letsinger, R. L., Mucic, R. C., and Storhoff, J. J. (1996) A DNA-based method for rationally assembling nanoparticles into macroscopic materials. *Nature 382*, 607–9.

(3) Aldaye, F. A., and Sleiman, H. F. (2007) Dynamic DNA templates for discrete gold nanoparticle assemblies: control of geometry, modularity, write/erase and structural switching. *J. Am. Chem. Soc. 129*, 4130–1.

(4) Ghosh, P., Han, G., De, M., Kim, C. K., and Rotello, V. M. (2008) Gold nanoparticles in delivery applications. *Adv. Drug Delivery Rev. 60*, 1307–15.

(5) Giljohann, D. A., Seferos, D. S., Prigodich, A. E., Patel, P. C., and Mirkin, C. A. (2009) Gene regulation with polyvalent siRNA-nanoparticle conjugates. *J. Am. Chem. Soc. 131*, 2072–3.

(6) Kim, J. Y., and Lee, J. S. (2009) Synthesis and thermally reversible assembly of DNA-gold nanoparticle cluster conjugates. *Nano Lett. 9*, 4564–9.

(7) Lee, J. S., Green, J. J., Love, K. T., Sunshine, J., Langer, R., and Anderson, D. G. (2009) Gold, poly(beta-amino ester) nanoparticles for small interfering RNA delivery. *Nano Lett. 9*, 2402–6.

(8) McMahon, K. M., Mutharasan, R. K., Tripathy, S., Veliceasa, D., Bobeica, M., Shumaker, D. K., Luthi, A. J., Helfand, B. T., Ardehali, H., Mirkin, C. A., Volpert, O., and Thaxton, C. S. (2011) Biomimetic high density lipoprotein nanoparticles for nucleic Acid delivery. *Nano Lett. 11*, 1208–14.

(9) Stobiecka, M., and Hepel, M. (2011) Double-shell gold nanoparticle-based DNA-carriers with poly-l-lysine binding surface. *Biomaterials 32*, 3312–21.

(10) Kim, D. W., Kim, J. H., Park, M., Yeom, J. H., Go, H., Kim, S., Han, M. S., Lee, K., and Bae, J. (2011) Modulation of biological processes in the nucleus by delivery of DNA oligonucleotides conjugated with gold nanoparticles. *Biomaterials 32*, 2593–604.

(11) Lee, S. K., Han, M. S., Asokan, S., and Tung, C. H. (2011) Effective gene silencing by multilayered siRNA-coated gold nanoparticles. *Small 7*, 364–370.

(12) van Rij, R. P., and Andino, R. (2006) The silent treatment: RNAi as a defense against virus infection in mammals. *Trends Biotechnol. 24*, 186–93.

(13) Dykxhoorn, D. M., and Lieberman, J. (2006) Running interference: prospects and obstacles to using small interfering RNAs as small molecule drugs. *Annu. Rev. Biomed. Eng. 8*, 377–402.

(14) Elbashir, S. M., Harborth, J., Lendeckel, W., Yalcin, A., Weber, K., and Tuschl, T. (2001) Duplexes of 21-nucleotide RNAs mediate RNA interference in cultured mammalian cells. *Nature 411*, 494–8.

(15) Caplen, N. J., Parrish, S., Imani, F., Fire, A., and Morgan, R. A. (2001) Specific inhibition of gene expression by small double-stranded RNAs in invertebrate and vertebrate systems. *Proc. Natl. Acad. Sci. U. S. A. 98*, 9742–7.

(16) Lares, M. R., Rossi, J. J., and Ouellet, D. L. (2010) RNAi and small interfering RNAs in human disease therapeutic applications. *Trends Biotechnol. 28*, 570–9.

(17) Kim, W. J., and Kim, S. W. (2009) Efficient siRNA delivery with non-viral polymeric vehicles. *Pharm. Res. 26*, 657–66.

(18) Oh, Y. K., and Park, T. G. (2009) siRNA delivery systems for cancer treatment. *Adv. Drug Delivery Rev. 61*, 850–62.

(19) Mok, H., Lee, S. H., Park, J. W., and Park, T. G. (2010) Multimeric small interfering ribonucleic acid for highly efficient sequence-specific gene silencing. *Nat. Mater. 9*, 272–278.

(20) Lee, S. Y., Huh, M. S., Lee, S., Lee, S. J., Chung, H., Park, J. H., Oh, Y. K., Choi, K., Kim, K., and Kwon, I. C. (2010) Stability and cellular uptake of polymerized siRNA (poly-siRNA)/polyethylenimine (PEI) complexes for efficient gene silencing. *J. Controlled Release 141*, 339–46.

(21) Zikich, D., Borovok, N., Molotsky, T., and Kotlyar, A. (2010) Synthesis and AFM characterization of Poly(dG)-poly(dC)-gold nanoparticle conjugates. *Bioconjugate Chem. 21*, 544–547.

(22) Hurst, S. J., Lytton-Jean, A. K., and Mirkin, C. A. (2006) Maximizing DNA loading on a range of gold nanoparticle sizes. *Anal. Chem. 78*, 8313–8.

(23) Demers, L. M., Mirkin, C. A., Mucic, R. C., Reynolds, R. A., 3rd, Letsinger, R. L., Elghanian, R., and Viswanadham, G. (2000) A fluorescence-based method for determining the surface coverage and hybridization efficiency of thiol-capped oligonucleotides bound to gold thin films and nanoparticles. *Anal. Chem. 72*, 5535–41.

(24) Devries, G. A., Brunnbauer, M., Hu, Y., Jackson, A. M., Long, B., Neltner, B. T., Uzun, O., Wunsch, B. H., and Stellacci, F. (2007) Divalent metal nanoparticles. *Science 315*, 358–61.

(25) Kim, S. H., Jeong, J. H., Lee, S. H., Kim, S. W., and Park, T. G. (2006) PEG conjugated VEGF siRNA for anti-angiogenic gene therapy. *J. Controlled Release 116*, 123–9.

(26) Bolcato-Bellemin, A. L., Bonnet, M. E., Creusat, G., Erbacher, P., and Behr, J. P. (2007) Sticky overhangs enhance siRNA-mediated gene silencing. *Proc. Natl. Acad. Sci. U. S. A. 104*, 16050–5.

(27) Parak, W. J., Pellegrino, T., Micheel, C. M., Gerion, D., Williams, S. C., and Alivisatos, A. P. (2003) Conformation of oligonucleotides attached to gold nanocrystals probed by gel electrophoresis. *Nano Lett. 3*, 33–36.

(28) Cardenas, M., Barauskas, J., Schillen, K., Brennan, J. L., Brust, M., and Nylander, T. (2006) Thiol-specific and nonspecific interactions between DNA and gold nanoparticles. *Langmuir 22*, 3294–9.

(29) Verma, A., Simard, J. M., Worrall, J. W., and Rotello, V. M. (2004) Tunable reactivation of nanoparticle-inhibited beta-galactosidase by glutathione at intracellular concentrations. *J. Am. Chem. Soc. 126*, 13987–91.

(30) Li, D., Li, G., Guo, W., Li, P., Wang, E., and Wang, J. (2008) Glutathione-mediated release of functional plasmid DNA from positively charged quantum dots. *Biomaterials 29*, 2776–82.

(31) Tierney, H. L., Baber, A. E., Sykes, E. C. H., Akimov, A., and Kolomeisky, A. B. (2009) Dynamics of thioether molecular rotors: effects of surface interactions and chain flexibility. *J. Phys. Chem. C 113*, 10913–10920.

(32) Maksymovych, P., Sorescu, D. C., Dougherty, D., and Yates, J. T., Jr. (2005) Surface bonding and dynamical behavior of the CH3SH molecule on Au(111). *J. Phys. Chem. B 109*, 22463–8.

(33) Reinhard, B. M., Sheikholeslami, S., Mastroianni, A., Alivisatos, A. P., and Liphardt, J. (2007) Use of plasmon coupling to reveal the dynamics of DNA bending and cleavage by single EcoRV restriction enzymes. *Proc. Natl. Acad. Sci. U. S. A. 104*, 2667–72.

(34) Kong, W. H., Sung, D. K., Shim, Y. H., Bae, K. H., Dubois, P., Park, T. G., Kim, J. H., and Seo, S. W. (2009) Efficient intracellular siRNA delivery strategy through rapid and simple two steps mixing involving noncovalent post-PEGylation. *J. Controlled Release 138*, 141–7.

(35) Hainfeld, J. F., Slatkin, D. N., Focella, T. M., and Smilowitz, H. M. (2006) Gold nanoparticles: a new X-ray contrast agent. *Br. J. Radiol. 79*, 248–53.

Bioconjugate Chemistry

ARTICLE

pubs.acs.org/bc

Mass Spectrometric Detection of Targeting Peptide Bioconjugation to *Red clover necrotic mosaic virus*

Ruqi Wang,[†] Dustin M. Lockney,[†] Michael B. Goshe,[*,‡] and Stefan Franzen[*,†]

[†]Department of Chemistry, [‡]Department of Molecular and Structural Biochemistry, North Carolina State University, Raleigh, North Carolina 27695, United States

Supporting Information

ABSTRACT:

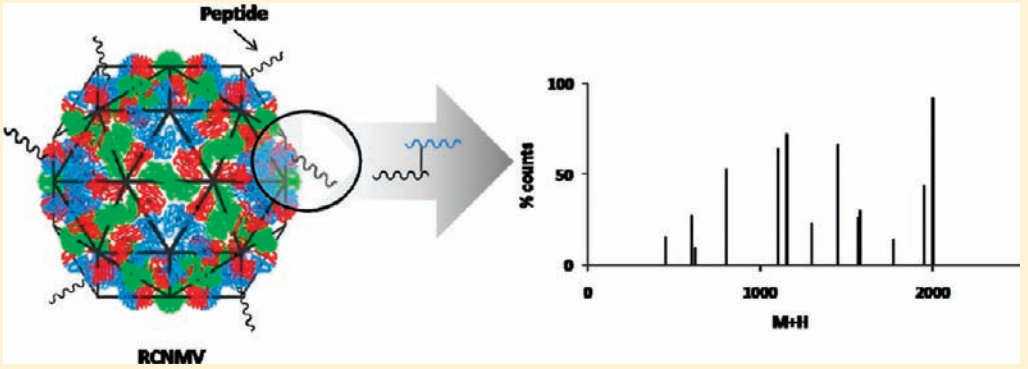

Plant virus nanoparticle (PVN) formulations constructed from *Red clover necrotic mosaic virus* by drug infusion and targeting peptide conjugation can be employed as drug delivery tools. In this investigation, we studied the cross-linked structures formed by application of sulfosuccinimidyl-4-(*N*-maleimidomethyl) cyclohexane-1-carboxylate (sSMCC) and succinimidyl-[(*N*-maleimido-propionamido)-hexaethylene glycol] ester (SMPEG) as heterobifunctional linkers in the bioconjugation process. The plant virus formulations using several targeting peptides cross-linked to the plant virus capsid were characterized by LC/MS^E analysis, which produced at least 69% sequence coverage using trypsin and chymotrypsin digestion. The results showed evidence for several types of modification located in three domains of the capsid protein. Extensive linker modifications on lysines or cysteines were detected in all the domains, including both intended peptide−capsid cross-links and unintended intracapsid cross-links. Surprisingly, the most extensive peptide modification was observed in the R domain, which is thought to be quite inaccessible to peptides and cross-linking reagents in solution, since it is on the interior of the virus. These results show that heterobifunctional linkers may not be the most efficient method for attachment of peptides to plant virus capsids. As an alternative conjugation strategy, maleimide peptides were used to conjugate with the virus in a one-step reaction. Analysis by LC/MS^E showed that these one-step maleimide coupling reactions were more specific, such as modifications of C154 and to a lesser extent C267, and provide a means for achieving more effective PVN formulations.

INTRODUCTION

Red clover necrotic mosaic virus (RCNMV) is a soil-borne plant virus that has a robust and stable capsomere, which is common for the members of family *Tombusviridae*. The capsid is a $T = 3$ icosahedron composed of 180 subunits of a 37 kDa capsid protein (CP) in one of three conformations.[1] RCNMV has two nonhomologous RNAs, 3.9 kb polycisronic RNA-1 encoding the 37-kDa CP, RNA polymerase, and related protein,[2,3] and 1.5 kb monocistronic RNA-2 encoding for movement protein (MP).[4] The packaging of RNA into CPs is mediated by the trans-activator sequence located on RNA-2.[5] Gold nanoparticles attached to RNA-2 have been shown to promote self-assembly of the capsid leading to internalization of the nanoparticle in the presence of RNA-1 and CP.[6] Upon depletion of divalent ions, such as Ca^{2+} and Mg^{2+}, the virus has been observed to exist in an open-pore state.[7] There are 60 pores located at the threefold axes of the icosahedral structure. The pores have a diameter of 1.3 nm, which is sufficient for the RNA genome to diffuse out in the cytosol of plant cells. We have previously shown that preparation of the open-pore state permits drug infusion. Specifically, we have shown that ~900 doxorubicin molecules can be infused into the interior of the virus.[8] Attachment of targeting peptides to the infused virus would then make the plant virus nanoparticles (PVN) an ideal vector for targeted drug delivery.

There are three domains in the capsid protein subunits of RCNMV, RNA-interacting (R), shell (S), and protruding (P)

Received: April 5, 2011
Revised: August 19, 2011
Published: August 22, 2011

ACS Publications © 2011 American Chemical Society

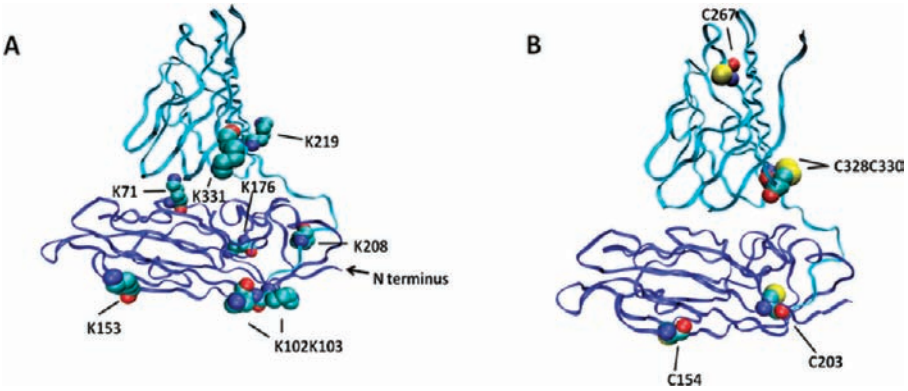

Figure 1. RCNMV capsid structure with locations of lysines and cysteines specified by number. The coordinates were determined using a combination of electron diffraction and homology modeling with all (A) Lys and (B) Cys residues shown.

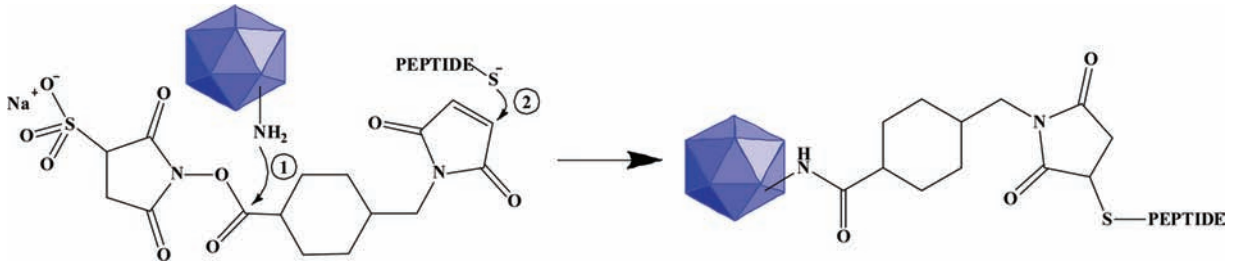

Figure 2. Scheme of a two-step reaction of PVN formulation. Step 1: lysines on RCNMV react with the NHS ester group on sSMCC. Step 2: cysteine on the conjugating peptide reacts with the RCNMV-sSMCC maleimide moiety.

domains (Figure 1). The R domain consists of a series of arginines and lysines, which function to bind the RNA on the interior of the assembled capsid due to their positive charge at pH 7 and below.[7] Due to the disorder in the structure, 47 residues of the R domain, which are located adjacent to the N-terminus, are not shown in the RCNMV model. The S domain is essentially the lower part of Figure 1 (colored in blue) and P domain starts at residue 205 and is the protrusion above the S domain (colored in cyan).

This study of plant viruses follows earlier work using gold nanoparticles designed to target cells.[9−11] A certain number of the targeting peptides and bioconjugation methods are the same as those used in this study, except that bovine serum albumin (BSA) was used for conjugation rather than the capsid peptide of RCNMV. One impetus to use a plant virus as a biological nanoparticle is the greater colloidal stability of an organic composition relative to gold.[12−14] A second reason is the ability to control the precise location of targeting peptides due to the defined structure of the capsid. However, the latter advantage must be established by a characterization method, and the present study represents a first step in this direction.

Our objective is to develop an RCNMV-based nanoparticle as a drug delivery tool for cancer therapy. This paper is focused on discussing conjugation efficiency of such a formulation. Our starting point was to attach targeting peptides to the capsid using sulfosuccinimidyl 4-[*N*-maleimidomethyl]cyclohexane-1-carboxylate (sSMCC), which is used widely as a protein conjugation reagent. The reactive groups of this heterobifunctional linker consist of an *N*-hydroxysuccinimide (NHS) ester on one end, which can react with primary amines (usually lysines), and maleimide on the other that can react with thiolate groups (usually cysteines) via a Michael addition as shown in Figure 2.

Liquid chromatography−mass spectrometry (LC/MS) analysis has been proven as an effective and important technique in protein identification and characterization.[15] Ultra Performance (UP) LC/MS^E methodology was used in this study. Unlike conventional data-dependent acquisition (DDA) MS/MS, MS^E is a data-independent acquisition (DIA) approach, which gives an unbiased characterization of proteins with better sequence coverage.[16] During LC/MS^E analysis, the low collision energy scan provides information for precursor ion mass and intensity, while the elevated collision energy scan provides fragment ion data, whose correspondence to a certain precursor ion at a certain retention time is almost guaranteed by well-resolved peaks from UPLC.[17,18] Thus, it is an ideal tool for capsid protein characterization.

MATERIALS AND METHODS

Sequencing grade-modified trypsin was purchased from Promega (Madison, WI, www.promega.com). Acetonitrile (HPLC grade) and formic acid (ACS reagent grade) were from Sigma/Aldrich/Fluka (www.sigmaaldrich.com). Water was distilled and purified using a High-Q 103S water purification system (www.high-q.com). Unless noted, other reagents were purchased from Fisher or Sigma. Peptides used in the conjugation reactions with the virus are listed in Table 1.

PVN Formulation. A molar ratio of 1:2000 of purified and dialyzed RCNMV (5 mg/mL) and sSMCC cross-linker (0.5 mg/mL)

Table 1. Peptides Conjugated to RCNMV[a]

peptide	sequence
GSGS	GSGSGC
RME[b]	NPVPYEDESGGGC
CD46[b]	AKRARLSTSFC
ADH304[c]	Ac-FHLRAHAVDINGNQVC-NH_2
maleimide	Ac-FHLRAHAVDINGNQV[Lys(Maleimide)]

[a] All the peptides were synthesized and characterized by GenScript. [b] Receptor-mediated endocytosis and nuclear localization sequences derived from human adenovirus fiber protein.[44] [c] ADH peptide containing the HAV tripeptide can be recognized by N-cadherin, the upregulation of which is a sign of tumor progression.[45]

(Pierce) was mixed in 50 mM phosphate buffer, pH 7.2, at room temperature for 30 min. The yield of cross-linkers and peptides was studied to ascertain that the ratio of 1:2000 is optimized. While this ratio may seem relatively large, we note that RCNMV has 180 copies of CP, and each CP has 16 lysines, so that 1 equiv of RCNMV contains a total of 2880 lysines. Of course, not all of the lysines are reactive and there is an excess of unreacted sSMCC. Excess cross-linkers were removed by buffer exchange using the same phosphate buffer and a NAP-25 desalting column (GE Healthcare). For maleimide peptide conjugation, the above step was omitted. The second step for conjugating peptides was carried out by adding peptide (0.5−1 mg/mL) to the above solution and incubating under the same conditions overnight. The sample was subjected to buffer exchange using the same phosphate buffer and a G-25 size exclusion column to remove excess peptide. Quantification of RCNMV was determined by UV spectroscopy with an extinction coefficient of 6.46 ml•mg^{-1}•cm^{-1} at 260 nm (1 mg/mL, 1 cm path length).[19] Bicinchoninic acid (BCA) protein assay kit (Thermo scientific) was also used for protein quantitation. PVN samples studied include RCNMV, RCNMV-linker (-SMCC or -SMPEG), RCNMV-SMCC-Peptide (-GSGS, CD46, ADH304, and RME) and RCNMV-maleimide peptide.

Digestion. Samples were prepared and analyzed on a 4−12% bis-tris gel (NuPAGE, invitrogen) to separate any cross-linked RCNMV capsid protein and other byproducts. Bands of interest were excised and washed with 50 mM ammonium bicarbonate (pH 8.0) acetonitrile (1:1, v/v). Reduction with 10 mM tris(2-carboxyethyl) phosphine at 37 °C and alkylation with 27.5 mM iodoacetamide at room temperature were conducted for 30 min. After dehydration, each gel band was incubated with either trypsin (Promega) or chymotrypsin (Promega) overnight using an enzyme-to-protein ratio of 1:50 in 50 mM ammoniuim bicarbonate (pH 8.0). After digestion, the peptides were extracted with 50% acetonitrile/0.1% formic acid, and reduced to a volume of 30 μL. All the samples were filtered prior to LC/MS^E analysis.

Mass Spectrometry. Mass spectrometric analysis was performed with a Waters nanoACQUITY ultraperformance liquid chromatograph coupled a Q-Tof Premier mass spectrometer equipped with a Nanolockspray ion source. An injection of 8 μL of each sample was loaded onto a Waters Symmetry C18 trapping cartridge (300 μm i.d. × 1 cm length) at a flow rate of 10 μL/min, and then peptides were separated by gradient elution using a 75 μm i.d. × 25 cm column packed with BEH C18 matrix, 1.7 μm particle size (Waters), at a flow rate of 0.300 μL/min. Mobile phase A (99.9% water and 0.1% formic acid) and B (99.9% acetonitrile and 0.1% formic acid) were employed to elute peptides over a 60 min linear gradient of 2−40% B. Glu-fibrinopeptide (Sigma) at a concentration of 200 fmol/μL (m/z 785.8426) was infused via the Nanolockspray ion source at a flow rate of 600 nL/min and sampled every 30 s as the external mass calibrant. For MS^E acquisitions, alternate scans (m/z 50−1990) of 4 V for low-energy (MS channel) and 15 to 30 V for high-energy (MS^E channel) were set for data collection every 2 s. Raw data were processed by Proteinlynx Global Server v 2.4 (PLGS2.4, Waters), and the resulting files were searched against a database containing the RCNMV, trypsin, chymotrypsin, and human keratin sequences using the ion accounting algorithm ($IDENTITY^E$). Searching parameters of precursor and product ion tolerance (default setting), minimum number of product ion matches per peptide (3), minimum number of peptide matches (1), maximum number of missed cleavage sites (2), and a false discovery rate (4%) were used. Fragment ions of cross-linked peptides were analyzed by MS3D,[20] which is a web portal providing analysis of mass spectrometry data for a variety of cross-link peptides. The annotation of identified fragment ions was performed as previously described.[21] Virus peptides and conjugating peptides were defined as the α and β chain, respectively. Reported precursor and product ion masses are charge-state reduced and analyzed for isotopomers using PLGS, with intensities corresponding to the integration of ESI chromatographic peak areas. It has been shown that, with the ion detection algorithm, the given signal (intensity) is reproducible and quantitatively related to the concentration of peptide/protein.[17,18] Therefore, our quantification of conjugation yield is primarily based on comparing the intensities of precursor ions from intact and modified samples.

RESULTS

Protein Sequence Coverage of Native RCNMV. To ascertain the conjugation sites, acceptable protein sequence coverage of RCNMV is required. As shown in Figure 3, LC/MS^E analysis is able to achieve 48.1% and 33.6% amino acid sequence coverage using tryptic and chymotryptic digestion, respectively, resulting in total sequence coverage of 69.9% (usually between 58% and 69%). Other enzymes like pepsin and GluC were also tried, but no additional coverage was obtained. The lysines covered include those at positions K33, K38, K45, K102, K153, K176, K219, and K331, where we have used the standard one letter code K for lysine. For elucidating conjugation sites, we considered specific cases where the linker, inter-, and intramolecular cross-linking modifications were detected.

Evidence for Linker Modifications at K102/K103. Modifications of both nonhydrolyzed and hydrolyzed SMCC or SMPEG were detected at K102/K103 for the peptide (101)LKKLTLR(107). Given that the peptides with hydrolyzed and nonhydrolyzed linkers tend to have similar ionization efficiencies, precursor ion intensities of those peptides indicate that about half of the sSMCC and SMPEG linkers were hydrolyzed (Table 2). For the sSMCC sample, product ion data indicated both K102 (modified b_2 ion LK, unmodified y_5 KLTLR) and K103 (modified y_5 ion KLTLR) were modified at a relative ratio of 1:2 for both the hydrolyzed and nonhydrolyzed forms (Supporting Information Figure S1). For the SMPEG-labeled sample, modifications (in this case, we are referring to both hydrolyzed and nonhydrolyzed forms) were detected primarily

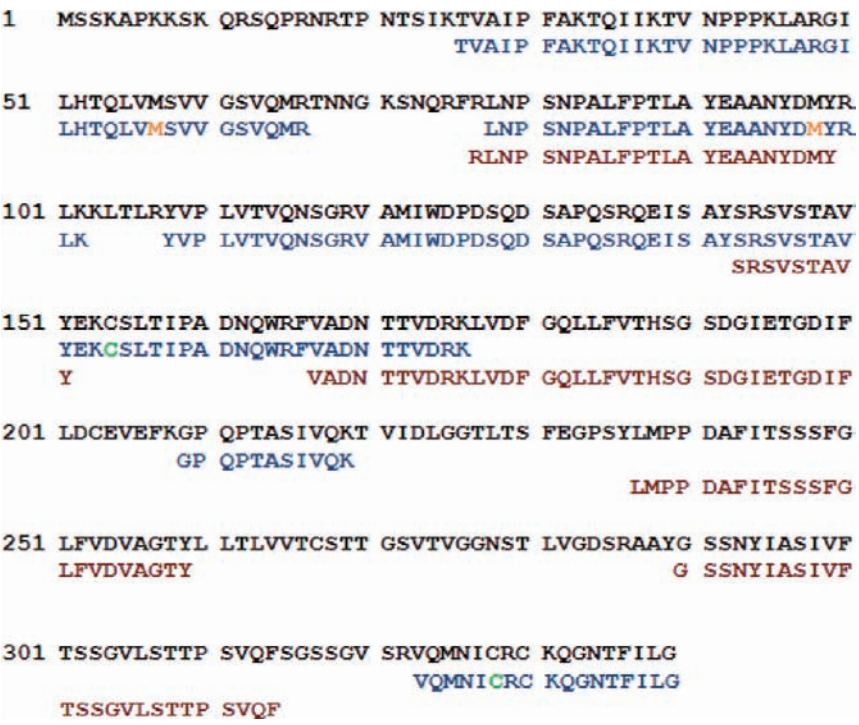

Figure 3. Coverage maps for native RCNMV. Sequence coverage for the tryptic (48.1%) and chymotryptic (33.6%) are colored in blue and purple, respectively. Oxidized methionine and alkylated cysteine are colored in orange and green, respectively.

Table 2. Intensities and Monoisotopic Masses of Precursor Ions for the Linker-Modified Capsid Peptide(101)LKKLTLR(107)

	SMCC		SMPEG	
precursor ion	intensity	$[M+H]^+$ cal/obs	intensity	$[M+H]^+$ cal/obs
nonhydrolyzed	4.27×10^4	1090.70/1090.70	1.17×10^4	1357.83/1357.64
hydrolyzed	3.92×10^4	1108.71/1108.71	1.05×10^4	1375.84/1375.84

at K103, indicating that K103 is more accessible to SMPEG than K102. These data together with the lack of identifying a conjugated peptide at K102 and K103 suggest that these residues are accessible and reactive to small molecules such as the sSMCC and SMPEG linkers, but not large molecules such as peptides.

Evidence for Intraprotein Cross-Linking at K153/C154. SSMCC is quite reactive, and it is therefore essential to determine the extent of side reactions in nanoparticle formulations where this reagent is used. For example, intramolecular cross-linking is possible when a lysine and a cysteine are sufficiently close to one another on the capsid surface. Identification of heterobifunctional cross-linker structural modifications at adjacent KC residues can be difficult because there are several possible fates for the bound sSMCC. As shown in Figure 4, the NHS-ester of sSMCC can amidate lysine (case 1) and the maleimidyl moiety can react with cysteine via a Michael addition (case 3). In either case, sSMCC can be hydrolyzed, as shown in cases 2 and 4, respectively. However, given the rapid hydrolysis rate of the ester, case 3 is not likely for the overnight incubations used in the method described here. Cysteines can also react with an NHS-ester and form a thioester bond (case 3), but since the bond is labile and susceptible to hydrolysis, this reaction is not considered important in our final preparation.[22] The final possibility is a cross-link between K and C on the same capsid protein (case 5).

All possibilities (Figure 4) can be divided into two groups according to their masses: cases 1 and 5 contain a nonhydrolyzed modification and cases 2 and 4 contain a hydrolyzed modification. Each type within the same group can be distinguished by examining the product ion spectrum generated from each precursor ion. Data from the sSMCC sample showed both modifications for the capsid peptide (145)SVSTAVYEKCSLTIPADNQWR(165). The hydrolyzed SMCC modification was assigned to cysteine because the y_{12} ion with the modification C(SMCC−OH)SLTIPADNQWR was present at a high abundance (~25%) relative to the other product ions (Supporting Information Figure S2). For the nonhydrolyzed SMCC modification, however, there was not a strong preference for case 1 or case 5 because no labeled b_9 ion or unlabeled y_{12} ion was detected, except for the occasional detection of some neutral losses that were close in mass to these ions. These results suggest that the sSMCC linker modifies either K153 or cross-links C154 and K153.

The analysis of the RCNMV sample conjugated with the SMPEG linker led to further insight regarding the possibility of cross-linking with a longer linker. In the SMPEG sample, only the hydrolyzed modification was found, and the labeled peptide

(152)EKCSLTIPADNQW(164) from the chymotryptically digested sample confirmed that the hydrolyzed linker on lysine (modified b_2) was present for the K153/C154 pair as opposed to an intraprotein cross-link between K153 and C154. This result supports the formation of an intraprotein cross-link at these residues by sSMCC. For SMPEG, the longer linker is statistically less likely to modify adjacent residues when one considers it as a freely jointed chain model.[23] The end-to-end length is equal to $\ell\sqrt{N}$ where ℓ is the PEG monomer spacing (the hypothetical bonds) and $N = 6$ for PEG6 (which is the SMPEG linker used in this study). This distance is significantly greater than the distance between the K153 amine nitrogen and the C154 sulfhydryl as estimated from the structure in the VIPER database (RCN7). These considerations agree with the lack of observed b_9 or y_{12} ions derived from the capsid peptide (145)SVSTAVYEKCSLTIPADNQWR(165) in the product ion spectra. The reason for the observed high hydrolysis yield of SMPEG can be found from studies performed in aqueous solution where it was shown that the high hydrophilicity of the PEG chain relative to the cyclohexane spacer in sSMCC[24] leads to near-complete hydrolysis of SMPEG. Intensities and scores of related precursor ions are shown in Table 3. Since the precursor ion of capsid peptide (145)SVSTAVYEKCSLTIPADNQWR(165) does not exist in the RCNMV sample, we have to use the other precursor ions (145)SVSTAVYEK(153) and (154)CSLTIPADNQWR(165) to quantify the modification. By comparing their intact precursor ion intensities for RCNMV and modified RCNMV samples, it can be estimated that about 30% of K153 and >90% of C154 are modified with sSMCC linker, while 75% of each residue was modified with the SMPEG linker.

Evidence for Intraprotein Cross-Linking at C330/K331. The adjacent amino acids C330 and K331 in the capsid peptide (330)CKQGNTFILG(339) displayed many of the features discussed above for K153/C154 residue pair. Peptide

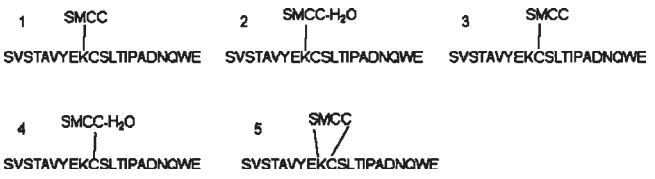

Figure 4. Schematic representation of five possible products for sSMCC conjugation of the peptide fragment (145)SVSTAVYEKCSLTIPADNQWR(165).

intensities of the unmodified peptides (330)CKQGNTFILG(339) and (332)QGNTFILG(339) (Table 3) from RCNMV and modified RCNMV samples were used to estimate the percentage of modification by sSMCC and SMPEG. The disappearance of the capsid peptide (330)CKQGNTFILG(339) in both samples suggested extensive modification. While peptide (332)QGNTFILG(339) can be generated from the capsid containing a modified C330 or unmodified CK, it is difficult to determine the accurate percentage of modification. In the sSMCC modified sample, at least 50% of K153 and C154 were modified. Similar to the K153/C154 residues, the SMPEG modification was observed only as the hydrolyzed form. Due to the lack of product ion formation for this region of the peptide, this modification can be on either K331 or C330. The increased intensity of (332)QGNTFILG(309) compared to the RCNMV sample indicated a significant amount of C330-modified sequence.

Overall, the stoichiometry of peptide conjugation of these two KC pairs is low (data not shown), partly due to severe cross-linking of these residues by sSMCC and hydrolysis of SMPEG. This is especially the case for K153/C154, since C154 is readily accessible to direct peptide conjugation (in the maleimide case shown below) but becomes protected if first exposed to the cross-linking reagents. While C330 is not accessible in the first place, the cross-linkers precluded the peptide conjugation step by modifying K331.

Extensive Modification of the R Domain Sites K33, K38, and K45. The R-domain contains a K-rich region from residues 26 to 48 with the sequence (26)TVAIPFAKTQIIKTVNPPPKLAR(48). Since trypsin cannot cleave at a modified lysine position, any identified peptides would be expected to contain one modified lysine in the middle of the peptide with an unmodified K or R at the N-terminus. For the K-rich sequence, there are three possible peptides, TVAIPFAKTQIIK, TQIIKTVNPPPK, or TVNPPPKLAR. Figure 5 shows the MS^E product ion spectra of the unmodified, sSMCC-modified, and sSMCC-GSGS peptide-modified peptide (26)TVAIPFAKTQIIK(38) at K33 obtained from the conjugated RCNMV sample. All three of the K-rich capsid peptides had similar fragmentation patterns with the most abundant ion being y_{13} (the precursor ion) at m/z 1429.88, 1648.97, and 2115.11, followed by y_9 and y_{11} ions, and then b_3 and b_4. By comparing intensities of intact precursor ions ((26)TVAIPFAK(33) and (26)TVAIPFAKTQIIK(38)) of native RCNMV to those of the conjugated sample (Table 4), it can be concluded that about 20% of K33 was modified with sSMCC, and 2/3 of those modifications also had an attached

Table 3. Intensities for the Precursor Ions of Capsid Peptide Sequences (152)SVSTAVYEKCSLTIPADNQWR(164) and (330)CKQGNTFILG(339) of RCNMV and RCNMV-Linker Samples[a]

precursor ion	RCNMV	RCNMV-SMCC	RCNMV-SMPEG
C(∼OH)SLTIPADNQWR	---	1.20×10^5	2.14×10^5
CSLTIPADNQWR	6.78×10^5	5.56×10^4	2.02×10^5
SVSTAVYEK(∼)CSLTIPADNQWR	---	1.06×10^5	1.43×10^5(∼OH)
SVSTAVYEKC(∼OH)SLTIPADNQWR	---	8.73×10^4	
SVSTAVYEK	2.03×10^6	1.36×10^6	5.63×10^5
CK(∼)QGNTFILG	---	1.64×10^4	---
CK(∼OH)QGNTFILG	---	9.64×10^4	1.22×10^4
CKQGNTFILG	1.73×10^5	---	---
QGNTFILG	4.29×10^5	2.85×10^5	8.14×10^5

[a] ∼ = linker, ∼OH = hydrolyzed linker.

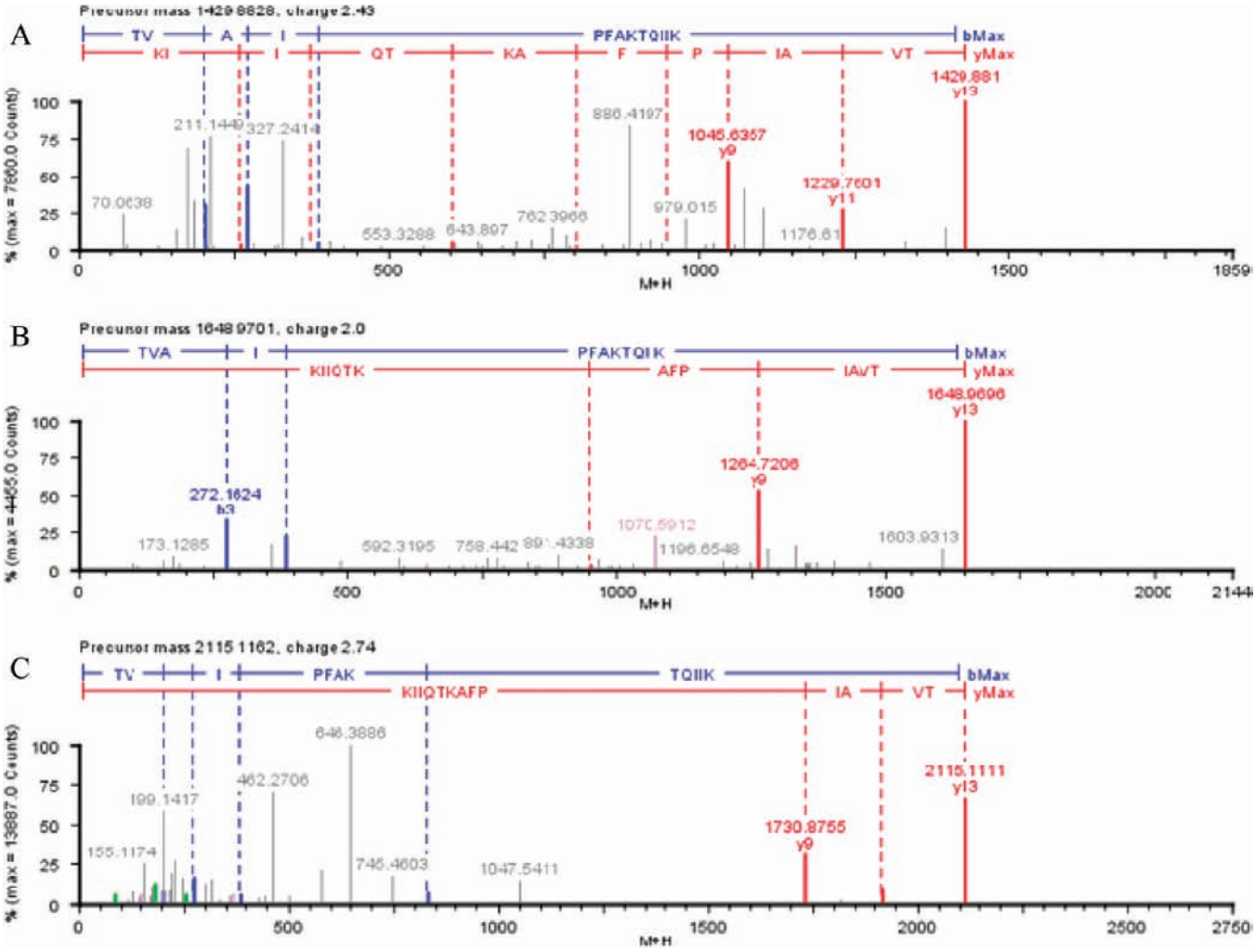

Figure 5. MS^E product ion spectra of (A) TVAIPFAKTQIIK, (B) TVAIPFAK(SMCC)TQIIK, and (C) TVAIPFAK(~GSGSGC)TQIIK obtained from the conjugated RCNMV-GSGS peptide sample.

Table 4. Intensities for the Precursor Ions Related to Capsid Peptide Sequence (26)TVAIPFAKTQIIK(38) of RCNMV and RCNMV-GSGS Peptide Samples[a]

precursor ion	RCNMV	RCNMV-GSGS peptide
TVAIPFAK	8.87×10^5	6.91×10^5
TVAIPFAKTQIIK	1.48×10^4	1.67×10^4
TVAIPFAK(-SMCC)TQIIK	n.d.	9.86×10^3
TVAIPFAK(-GSGS peptide)TQIIK	n.d.	2.16×10^4

[a] n.d., not detected.

GSGS peptide. Another sample containing the K33 modification with a peptide is RCNMV conjugated with the CD46 peptide. The precursor ion TVAIPFAK(~LSTSFC)TQIIK was identified manually with a calculated/observed m/z 2305.25/2305.26 (Supporting Information Figure S3). Representative product ions for the GSGS and CD46 conjugated peptides are listed in Table 5.

The modification of K38 in the sequence (34)TQIIKTVNPPPK(45) was even more extensive than K33. Several peptide sequences were conjugated at K38. In the CD46 sample, the precursor ion of peptide (TQIIK(~LSTSFC)TVNPPPK) was detected at the calculated/observed m/z 2211.17/2211.16 with an abundance that far exceeded the other fragment ions (Figure 6A) indicating that the collision energy settings used in the acquisition were not high enough to induce extensive fragmentation and generate highly abundant product ions. However, inspection of the product ions generated revealed

Table 5. List of Product Ion Intensities and Monoisotopic Masses for Peptide Conjugate (26)TVAIPFAK(~LSTSFC)TQIIK(38)[a]

	RCNMV-GSGS		RCNMV- CD46	
ions	normalized intensity (%)	$[M+H]^+$ cal/obs	normalized intensity (%)	$[M+H]^+$ cal/obs
prescursor ion	100	2115.12/2115.11	100	2305.25/2305.25
$y_{9\alpha}y_{6\beta}$	46.7	1730.88/1730.88	34.9	1921.02/1921.02
$y_{11\alpha}y_{6\beta}$	12.9	1914.98/1915.00		
$y_{13\alpha}y_{1\beta}$			11.7	1769.88/1769.88
$y_{9\alpha}y_{1\beta}$			9.6	1385.75/1385.74

[a] All intensities have been normalized to the value of the corresponding precursor ion.

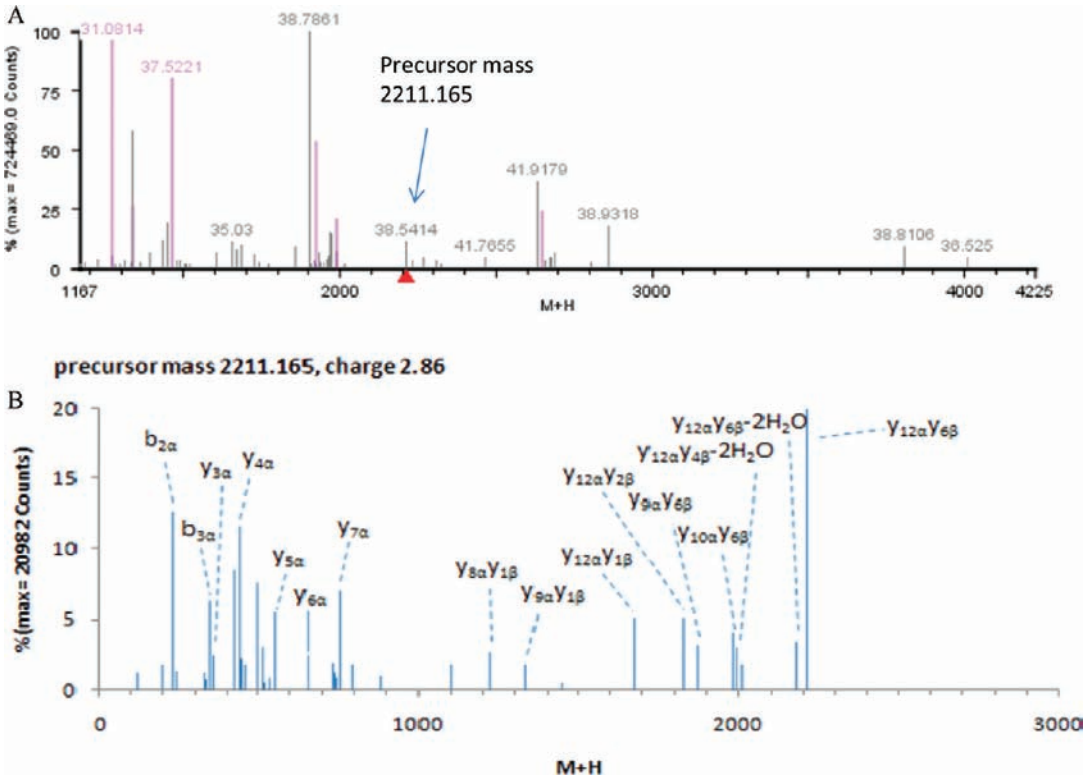

Figure 6. Detection of conjugated peptide TQIIK(~LSTSFC)TVNPPP from the CD46-labeled sample. (A) MS^E peptide mass chromatogram with the conjugated precursor mass and intensity as indicated. (B) A portion of the MS^E product ion spectrum pertinent to conjugate peptide identification.

Table 6. List of Product Ion Intensities and Monoisotopic Masses for Peptide Conjugates of (34)TQIIKTVNPPP(44)[a]

	RCNMV-GSGS		RCNMV-CD46		RCNMV-ADH304	
ions	normalized intensity (%)	$[M+H]^+$ cal/obs	normalized intensity (%)	$[M+H]^+$ cal/obs	normalized intensity (%)	$[M+H]^+$ cal/obs
precursor ion	100	2021.04/2021.04	100	2211.17/2211.17	100	2793.47/2793.46
$y_{12\alpha}y_{2\beta}$			5.18	1822.98/1822.97		
$y_{12\alpha}y_{1\beta}$			5.16	1675.91/1675.91	34.93	1674.93/1674.92
$y_{10\alpha}y_{6\beta}$	5.17	1791.93/1791.91	4.05	1982.07/1982.07		
$y_{8\alpha}y_{6\beta}$	4.34	1565.76/1565.76				
$y_{9\alpha}y_{6\beta}$			3.18	1868.98/1969.00		
$y_{8\alpha}y_{1\beta}$			2.69	1220.64/1220.61		

[a] All intensities have been normalized to the value of the corresponding precursor ion.

additional evidence for labeling at this position (Figure 6B). Fragment ions $y_{9\alpha}y_{6\beta}$ and $y_{10\alpha}y_{6\beta}$ (which contains the full LSTSFC peptide modification) were detected, as well as the $y_{12\alpha}y_{2\beta}$ and $y_{12\alpha}y_{1\beta}$ ions (which contain the intact capsid peptide). In addition, an extensive set of fragment ions from both the C- and N-terminus were observed, such as unmodified b_2-b_4 and y_2-y_7 ions for the capsid peptide (α chain). The virus sample conjugated with the ADH304 peptide TQIIK(~AHAVDINGNQVC)TVNPPPK showed a similar modification and fragmentation pattern to the CD46 labeled peptide, but was detected at a much lower intensity (Supporting Information Figure S5) at the calculated/observed m/z 2793.47/2793.48. The K38 residue was also modified with the GSGS peptide and was detected as TQIIK(~GSGSGC)TVNPPPK at the calculated/observed m/z 2021.06/2021.04. (Supporting Information Figure S4) Table 6 lists product ion intensities and monoisotopic masses for peptide conjugates of (34)TQIIKTVNPPP(44).

For the CD46 labeled sample, K45 was also found to be modified to some extent, as in the capsid peptide sequence (39)TVNPPPKLAR(48). The peptide TVNPPPK(~LSTSFC)LAR was the most abundant ion at the calculated/observed m/z 1968.02/1968.03. The fragmentation pattern of this particular cross-linked peptide (Figure 7) generated a series of moderately abundant y_α ions containing an uncleaved β peptide (i.e., viral peptide fragments containing the intact LSTSFC peptide) covered with moderately high intensity and a series of doubly fragmented product ions with both peptides cleaved, including $y_{8\alpha}y_{1\beta\text{-}4\beta}$, $y_{7\alpha}y_{1\beta\text{-}5\beta}$, $y_{6\alpha}y_{1\beta\text{-}4\beta}$; however, single peptide ions such as y_ω, b_ω and y_β were less numerous with diminished intensity.

On the basis of these data, K33, K38, and K45 are unequivocally modified. Among them, K38 had the greatest range of

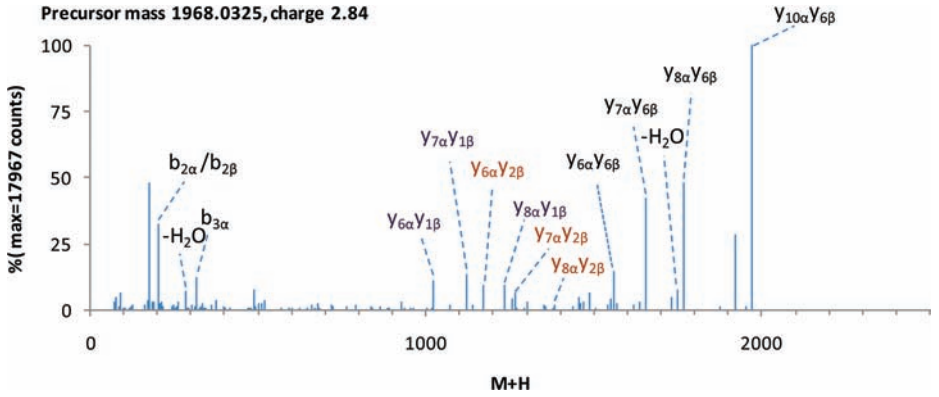

Figure 7. Portion of the MS^E product ion spectrum pertinent to conjugate peptide identification of TVNPPPK(~LSTSFC)LAR from the CD46 sample. Doubly fragmented product ions $y_{8\alpha}y_{1\beta\text{-}4\beta}$, $y_{7\alpha}y_{1\beta\text{-}5\beta}$, and $y_{6\alpha}y_{1\beta\text{-}4\beta}$ were detected, but only those with higher intensities are labeled.

Table 7. Precursor Ion Intensities of Capsid Peptides (209)GPQPTASIVQK(219) and (137)QEISAYSR(144) in Different Conjugation Samples

experiment	sample	GPQPTASIVQK	QEISAYSR
1	RCNMV	1.22×10^6	8.07×10^5
	RCNMV-SMCC	2.61×10^4	1.22×10^6
	RCNMV-GSGS	2.24×10^4	9.84×10^5
2	RCNMV	1.87×10^6	8.19×10^5
	RCNMV-CD46	1.72×10^5	7.17×10^5
	RCNMV-ADH304	6.59×10^5	5.61×10^5

conjugation including the GSGS, CD46, and ADH304 peptides, followed by K33, which was conjugated to the GSGS and CD46 peptides, while K45 was only conjugated to the CD46 peptide.

Indirect Evidence of Modification for K208 and K219. Examination of the coordinates of RCNMV in the VIPER database revealed that K208 and K219 are the two surface lysines in the P domain that appear most likely to be modified. However, it proved difficult to detect a modified lysine in this region because of poor sequence coverage. Aside from K208 and K219, there is no other Lys or Arg for tryptic digestion in the capsid sequence ranging from K176 to R286. Moreover, chymotrypsin lacks cleavage sites between residues 201 and 236. Given that trypsin only cleaves unmodified Lys residues, the capsid peptide (209)GPQPTASIVQK(219) can be observed only when both lysines are unmodified. If either lysine was modified, the abundance of this peptide would be reduced. Therefore, it was possible to infer that modification occurs in this region based on the relative intensities of (209)GPQPTASIVQK(219) in the modified and unmodified samples. Table 7 lists the intensities of the capsid peptide fragment ions detected for various conjugation samples. The coverage of fragment ions was sufficient for all of the samples that it was possible to detect the decrease in intensity that would be expected in a modified capsid peptide, which indicate that K208 and K219 must be modified to a significant extent. Table 7 also lists the intensities for (137)QEISAYSR(144), a reference capsid peptide that does not contain K or C residues. For each labeling reaction analyzed, the reference capsid peptide did not elicit a significant reduction in intensity for the sSMCC or peptide-conjugated samples compared to the intact RCNMV sample.

Evidence for Cysteine Labeling by Maleimide Peptide Modification. Given the cross-linking, aggregation, and hydrolysis issues of the sSMCC linker that were observed at the capsid sites discussed above, we turned to an alternative strategy for peptide labeling of the PVN. The characterization of cross-conjugated samples here correlated with modest targeting in samples studied using *in vitro* cell culture (data not shown). On the basis of these results, we adopted a different strategy using a maleimide-labeled ADH304 peptide which permitted the PVN-peptide conjugation reaction at Cys residues to be performed in a single step. Out of the five cysteines (154,203,267,328,330) in RCNMV, three (154,328,330) were contained in peptides identified from the unmodified RCNMV sample. Following conjugation with maleimide-modified ADH304, only C154 was detected as being labeled with the MS data appearing in Figure 8. The most abundant ion was the precursor ion at the calculated/observed m/z 2819.35/2819.37, which is consistent with the behavior of other cross-linked peptides observed using the LC/MS^E mode of acquisition. A series of y-ions for the virus peptide (α chain) were generated, including $y_{1\alpha}$ to $y_{5\alpha}$, $y_{8\alpha}$, $y_{10\alpha}$ and $y_{11\alpha}$. All b-ions of the ADH304 peptide (β chain) were produced except $b_{8\beta}$. Doubly fragmented ions were also detected as indicated in Figure 8C. Those ions that contain both one cleaved and one intact peptide, the $y_{12\alpha}y_{1\beta}$, $b_{4\alpha}y_{12\beta}$, and $y_{12\alpha}y_{2\beta}$ ions, had relatively high intensities, but also observed are ions containing cleavage events in both the capsid and ADH304 peptides with most of these ions having a single Cys or Lys residue (Lys preferred) attached to the linker, such as $b_{5\alpha}y_{1\beta}$, $b_{7\alpha}y_{1\beta}$, $b_{1\alpha}y_{11\beta}$, $b_{4\alpha}y_{1\beta}$. These data indicate that the fragmentation for this peptide cross-link is similar to that of a normal single peptide, which is expected due to the linker connecting the nitrogen side chain of the C-terminal Lys residue of the ADH304 peptide to the sulfhydryl side chain of the N-terminal Cys residue of the virus peptide. Thus, it is less likely that product ions containing both α and β peptides will be observed, particularly those with both incomplete peptide fragments. By comparing the intensity of the unmodified and modified RCNMV sample, we estimated that the percentage of ADH304 peptide conjugation is around 50%.

Overall Stability of the PVN Formulation. Modified PVN samples are prone to aggregation after more than two weeks of refrigeration at 4 °C. Figure 9 shows two distinct bands in the gel electrophoresis of the aged sample. The upper band has the same molar mass as the original virus capsid protein. The other

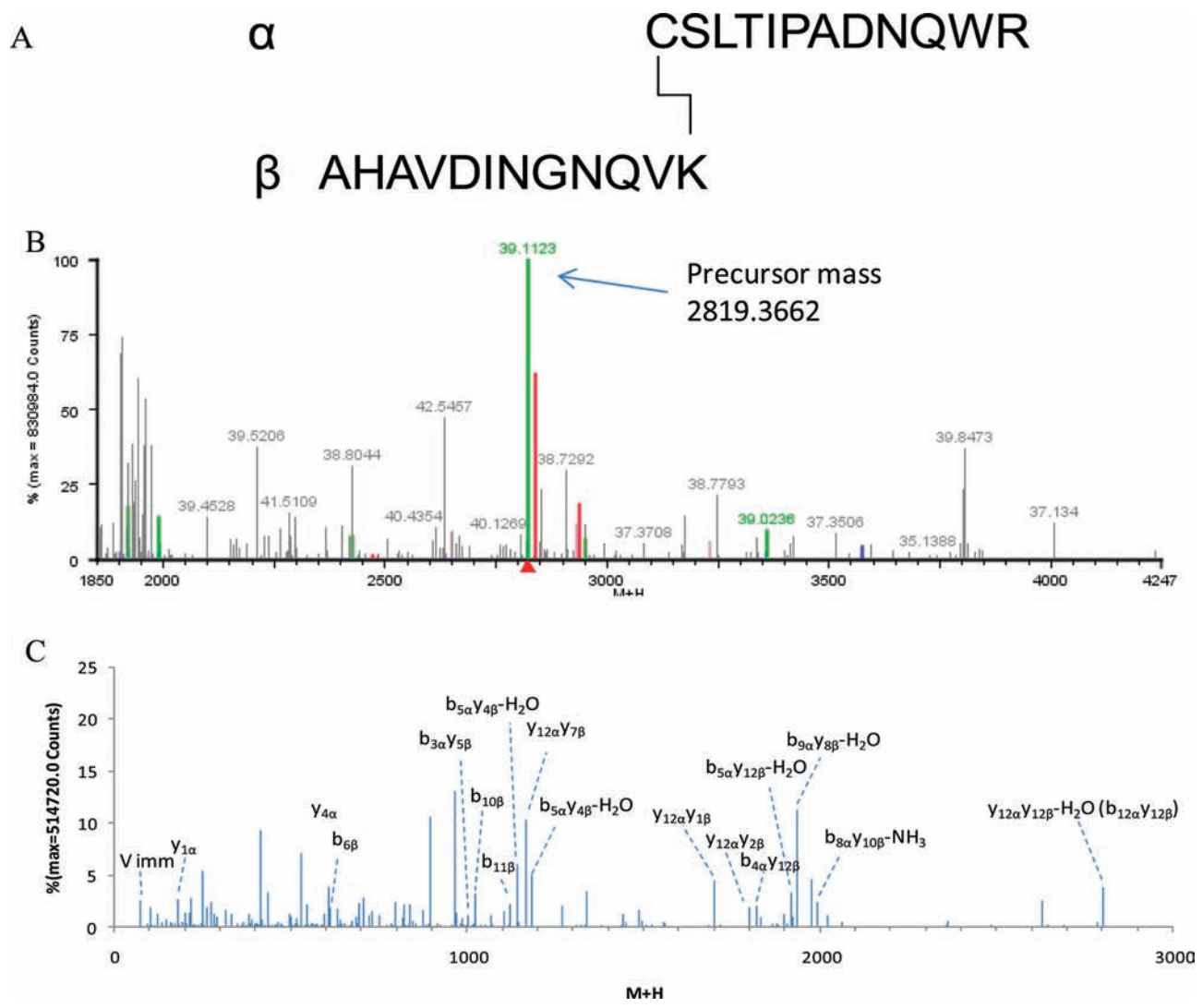

Figure 8. Detection of conjugated peptide C(ADH peptide)SLTIPADNQWR from the one-step labeling reaction of RCNMV with the maleimide-ADH304 peptide. (A) Scheme of cross-link between capsid peptide (α) and conjugated ADH peptide (β). (B) MS^E peptide mass chromatogram with the conjugated precursor mass and intensity as indicated. (C) A protion of the MS^E product ion spectrum pertinent to conjugate peptide identification.

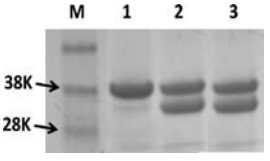

Figure 9. SDS page gel of the RCNMV capsid protein and its conjugation products with sSMCC and maleimide-ADH304 peptide labeling. M, marker; lane 1, RCNMV; lane 2, RCNMV-SMCC; and lane 3, RCNMV-peptide. Proteins were stained with Coomassie blue.

band of lower molar mass may be the product of an autodigestion of the capsid protein. While this phenomenon is observed to some extent in native RCNMV, it appears that the conjugation of linkers and peptides accelerates the process. The coverage map on the upper and lower bands are found to be similar: both of them have coverage at the C-terminus and no coverage at the N-terminus (data not shown), indicating that the degradation probably starts from N-terminus. The capsid protein modification resulting from the maleimide ADH304 peptide

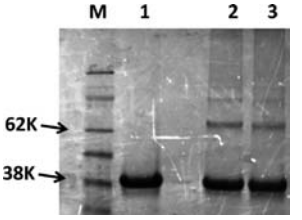

Figure 10. SDS page gel showing intercapsid cross-linking induced by treatment with sSMCC. M,marker; lane 1, RCNMV; lane 2, RCNMV-SMCC; and lane 3, RCNMV-CD 46. Proteins were stained with coomassie blue.

was observed in samples from the lower bands but not the upper bands.

DISCUSSION

The construction of plant virus nanoparticles for targeted drug delivery is a novel strategy, which has been described in a few reports. *Cowpea mosaic virus* (CPMV) has been conjugated with

a folic acid-PEG by Cu(I) catalyzed azide−alkyne cycloaddition (click chemistry[25]). Specific recognition of the resulting nanoparticle by tumor cells bearing the folate receptor was observed.[26] Doxorubicin loaded, folic acid conjugated *Hibiscus chlorotic ringspot virus* (HCRSV) nanoparticle was shown to increase the uptake and cytotoxicity of doxotubicin in ovarian cancer cells.[27] In addition, modification of antitumorgenesis peptide on the viral cage of *Cowpea chlorotic mottle virus* (CCMV) has been investigated and verified.[28] We have recently reported a similar strategy in RCNMV, where doxorubicin-loaded capsids[6] were functionalized with various targeting peptides using sSMCC.[26] The present study was motivated by the need for better process control during scale-up of the procedure for *in vivo* testing. Mass spectrometry analysis has been used to study virus−peptide conjugation using sSMCC and a variety of peptides. During the course of this work, it was realized that the complexity of the surface chemistry was hampering reproducibility and colloidal stability of the formulation. A simpler approach using a maleimide-modified peptide was employed and compared to bioconjugation using sSMCC.

The bioconjugation of peptides to a plant viral capsid is a key step in the development of a cell targeting technology. In our initial design for conjugation, we identified two surface lysines (K208 and K219) and one surface cysteine (C267) in the P-domain that were most accessible for bioconjugation. The data show that these sites are among the most difficult to detect by mass spectrometry due to poor sequence coverage in that region of the P-domain. Ironically, the R-domain (M1-L46) on the interior of the capsid is the region where modification by sSMCC and peptide conjugation was most easily detected by MS analysis. It was somewhat surprising that modification was so extensive in the R-domain. However, it is logical that the sheer number of lysines in the R-domain could influence the distribution of targeting peptides if they are accessible to some extent. For example, accessibility could arise from penetration of the capsid by relatively hydrophobic peptides. Alternatively, it is possible that capsid proteins may have alternative conformations that expose the R-domain. Conjugation in the S-domain (A47-E204) and P-domain (V205-G339) was also detected. However, in these regions the two cysteine−lysine pairs (K153/C154 and C330/K331) led to significant cross-linking or hydrolysis, and little conjugation of peptide. Residues K208 and K219 were observed indirectly using relative peptide intensities in conjugated and unconjugated samples. These sites did indeed show significant linker or peptide conjugation. On the basis of these MS results, we reasoned that a maleimide peptide coupling strategy would be superior to sSMCC and SMPEG cross conjugation. Indeed, coupling of a peptide to C154 was observed. Below, we discuss the relative efficiencies of the various sites and the issues of hydrolysis and cross-linking that were observed for the sSMCC and SMPEG linkers and finally conclude with a discussion of a maleimide peptide labeling strategy, which was ultimately used for both *in vitro* and *in vivo* studies.

Peptide Coupling Efficiencies. In this report, the effectiveness of sSMCC and SMPEG cross conjugation of RCNMV to the peptides CD46, GSGS, and ADH304 was explored by mass spectrometry analysis. The peptides were chosen as practical examples used in cell targeting experiments.[29] These peptides provided information on length and sequence-specific effects. Comparison of GSGS, CD46, and ADH304 peptides suggests that bioconjugation efficiency decreases as peptide length increases. One possible reason for this is a lower probability of approaching the conjugation site on the capsid surface due to steric hindrance. However, it must also be considered that the fragmentation for the larger $\alpha\beta$ peptide ions from the cross-linked peptide conjugate is less efficient, resulting in lower MS detection efficiency (see Supporting Information Figures S4−S6 for examples).

Most importantly, the MS results reveal aspects of capsid dynamics that are not evident from inspection of the structure. Peptide conjugation was mostly confined in the R domain, which is an inside region of the virus capsid according to the cryo-EM structure.[7] However, the R-domain may be accessible to the conjugating peptide because of a conformational change in the capsid that occurs under the labeling reaction conditions. Native RCNMV is most stable at pH 6.0, but while at pH 7.2 or even 8.0 during infusion, according to the observation of related viruses, it may swell and cause the disordered R domain to protrude out of the virion and become solvent exposed.[6,30,31] Results from MS analysis on degraded products also verify this hypothesis in that the N-terminus (R domain) is most likely responsible for degradation. In addition, the infusion step, as well as conjugation of linker/peptide on other sites, may also promote conformational changes and expose the R domain.

Unfavorable Side Reactions Observed Using sSMCC and SMPEG Linkers. sSMCC has been used as a cross-linker in various systems involving proteins/peptides,[32−34] especially in the field of nanotechnology where modification of nanoparticles such as quantum dots, virus, or virus particles are involved.[28,35−38] For example, sSMCC has been used to link bisphosphonate to synthetic salmon calcitonin, which is a 32 amino acid hormone with two lysines.[39] The reactions were monitored by MALDI-TOF analysis, and products with diverse numbers of SMCC/BP conjugates were observed.[39] Indeed, sSMCC has been effective in most cases, exemplified by bovine serum albumin, which contains numerous reactive lysines.[40,41] However, the application of sSMCC must be used with caution. It has been found that sSMCC destabilizes silica nanoparticles and causes aggregation.[42] There are several reports of both inter- and intra-cross-links by sSMCC in bioconjugation studies.[36,37] Our results also showed a significant degree of intercapsid cross-linking for RCNMV indicated by the gel shown in Figure 10 and the possibility of intracapsid cross-linking at position K153/C154 and C330/K331 based on LC/MS^E analysis, as discussed above.

Hydrolysis is also a problem for both the NHS ester and maleimide groups, which becomes overwhelming in the case of the SMPEG linkers. Since both NHS ester and maleimide groups on sSMCC can be hydrolyzed by hydroxide ions, it is very important to conduct the reaction at well-defined pH values to obtain the highest reaction efficiency. The nucleophilicity of lysine and cysteine is also quite pH-dependent, so there is a competition between the desired reactions of lysine and cysteine and the undesired hydrolysis reactions. For example, the ester is a very reactive group and may be hydrolyzed prior to reaction with lysines, which then may result in modification on cysteines. In the second hour-long incubation step, the maleimide may also be hydrolyzed. All of these factors can lead to the decrease of peptide conjugation efficiency. sSMCC is used instead of the uncharged variant SMCC because of the higher solubility conferred by a charged moiety. However, protocols call for the use of dimethylsulfoxide (DMSO) even when sSMCC is used. This fact underscores the issue of solubility of the reactant and possible lowered solubility of the bioconjugation product.

Finally, there was a significant amount of aggregation in the samples prepared using sSMCC that may have arisen from the bioconjugation chemistry. One cannot exclude the possibility that peptide modification itself reduces the colloidal stability of the plant virus, RCNMV. Of course, interprotein cross-linking is possible, which also reduces colloidal stability. These complexities led to consideration of an alternative strategy using a single site conjugation of a maleimide peptide.

Use of a Maleimide-Labeled ADH Peptide. A maleimide peptide was used to test whether a single-step conjugation to cysteine residues would result in a greater efficiency with fewer side reactions. Since a one-step reaction eliminates all the complex possibilities brought by the linker and with fewer virus reaction sites (five cysteines vs sixteen lysines), MS identification became much more straightforward. The results showed one out of three identified cysteines (C154) as being modified with the maleimide peptide. Although C267 appears to be quite solvent accessible based on the RCNMV structure, there is no direct evidence for coupling at this amino acid due to lack of capsid sequence coverage. However, we can infer that this amino acid is accessible based on analysis of the cysteines with spin labels. Electron paramagnetic resonance (EPR) analysis demonstrated the existence of the spin label on one cysteine residue of the virus, while MS showed negative results on the three covered cysteines of the RCNMV-spin labeled sample (data not shown). We deduce that the label has to be on one of two cysteines (C203 and C267) not covered by peptides obtained from the tryptic and chymotryptic digests. Since C267 is the more exposed cysteine, it is probably the one modified with the spin label, and there is reason to believe that the maleimide peptide may react with C267 as well.

Mass Spectrometry Assignments. Because of the specific nature of the peptide conjugation in RCNMV, and the difficulties associated with efficient fragmentation of large molecules using CID, the automated approach to MS data analysis was not always able to identify cross-links. As a result, we manually inspected product ion spectra especially in cases of peptide conjugation where a precursor ion was detected with sufficient abundance. Because the PLGS/ion accounting searching, described in the methods section, is only available for analysis of un-cross-linked peptides that contain modifications, the conjugated peptide to the virus must be treated as a fixed mass modification, and thus its fragmentation cannot be interpreted. In addition, the probability of identifying the conjugated peptide is reduced due to the preferred fragmentation of the peptide at residues distal to the cross-linked residues. Even in several cases where the cross-linked capsid peptide is identified due to its preferred fragmentation over that of the conjugated peptide, additional data acquisition using alternative CID energies will need to be developed to more confidently identify these peptide—peptide cross-links. As an alternative, we used MS3D to initially process the cross-link-peptide data and search for product ions, which was followed by manual inspection.

Automated software assignment can also fail when there is more than one modifiable residue in a capsid peptide. For instance, in the R domain where a capsid peptide contains two lysines, the software occasionally assigns a modification to the last K in the sequence, which is not possible if the peptide were generated by tryptic digestion (unless the lysine was the C-terminal residue of the protein). For example, in RCNMV samples conjugated with the GSGS peptide, capsid peptide (26)TVAIPFAKTQIIK(38) was found modified by sSMCC and the sSMCC-GSGS peptide. Software assigned the sSMCC modification on K33 and sSMCC-GSGS peptide modification on K38. The reason for the assignment was probably the presence of y_6 ion (K*TQIIK) containing the sSMCC modification and the b_8 ion (TVAIPFAK) without GSGS peptide modification. During CID, the peptide modification can be lost due to cleavage to produce an ion whose mass may match a b or y ion within the error tolerance used during automated database searching. This phenomenon is most frequently observed for modifications between capsid peptides and sSMCC. Thus, manual analysis of product ion spectra is necessary in these cases.

CONCLUSION

We have systematically investigated the conjugation of the capsid protein of RCNMV in formulations used as plant virus nanoparticles (PVNs). In these formulations, the capsid is sometimes infused with a chemotherapeutic cargo. Our focus here has been the chemical attachment of targeting peptides for *in vitro* and *in vivo* cell targeting applications. We have shown, by direct observation, that sSMCC, as a heterobifunctional linker, leads to attachment of peptides at several sites: K33, K38, and K45. Using the mass spectral data, we deduced that there is attachment at K208 and K219, although unfortunately we lack capsid sequence coverage to permit direct detection. However, there are significant disadvantages for the application of sSMCC as a heterobifunctional linker, which include intracapsid and intercapsid cross-linking and attachment of sSMCC to sites that peptides cannot access. The net effect of this unfavorable attachment is poor colloidal stability and unpredictable formulation conditions that depend strongly on the degree of hydrolysis of the sSMCC during the actual formulation. Since these factors are difficult to precisely control, sSMCC cannot be used for formulations of PVNs intended for clinical applications.

The present study also shows that a maleimide-peptide approach provides relatively efficient coupling and relatively high colloidal stability. Other than C154, the maleimide-peptide may also be attached at C267. However, this attachment could not be confirmed by mass spectrometry analysis due to the lack of capsid peptide coverage in the vicinity of C267. On the other hand, a parallel investigation using nitroxide spin-labeled RCNMV strongly suggests that C267 can be labeled. As a consequence of the present study, formulations of the maleimide-labeled ADH peptide were used for successful *in vivo* studies that will be discussed elsewhere.[43] As a result, the use of data-independent LC/MS^E has been established as a key method for the characterization of PVN formulations and will be valuable in future work using other formulations.

ASSOCIATED CONTENT

Supporting Information. Supplementary MS^E spectra of SMCC/peptide labeling on RCNMV and the description of proteases pepsin and gluC used for digestion of RCNMV are presented. This material is available free of charge via the Internet at http://pubs.acs.org.

AUTHOR INFORMATION

Corresponding Author

*Stefan Franzen, Department of Chemistry, NC State University; E-mail Stefan_Franzen@ncsu.edu, Phone 1-(919)-515-8915. Michael B. Goshe, Department of Molecular and Structural Biochemistry, NC State University; E-mail michael_goshe@ncsu.edu, Phone 1-(919)-513-7740.

■ ACKNOWLEDGMENT

The authors thank Nanovector, Inc., for supplying plant virus, peptides, and conjugation reagents used in this study. This work was supported in part by a grant from the National Science Foundation Major Research Instrumentation Grant Program (DBI-0619250). The authors thank the research agencies of North Carolina State University and the North Carolina Agricultural Research Service for continued support of our bioanalytical mass spectrometry research.

■ ABBREVIATIONS

MS, mass spectrometry; PVN, plant virus nanoparticles; RCNMV, *red clover necrotic mosaic virus*; sSMCC, sulfosuccinimidyl-4-(*N*-maleimidomethyl) cyclohexane-1-carboxylate; SMPEG, succinimidyl-[(*N*-maleimidopropionamido)-hexaethyleneglycol] ester; UPLC, ultra performance liquid chromatography

■ REFERENCES

(1) Hollings, M., and Stone, O. (1977) Red clover necrotic mosaic virus. *CMI/AAB Descriptions of Plant Viruses 181*.

(2) Xiong, Z., and Lommel, S. A. (1989) The complete nucleotide sequence and genome organization of red clover necrotic mosaic virus RNA-1. *Virology 171*, 543–554.

(3) Kim, K. H., and Lommel, S. A. (1994) Identification and analysis of the site of −1 ribosomal frameshifting in red clover necrotic mosaic virus. *Virology 200*, 574–582.

(4) Lommel, S. A., Westonfina, M., Xiong, Z., and Lomonossoff, G. P. (1988) The nucleotide sequence and gene organization of Red clover necrotic mosaic virus RNA-2. *Nucleic Acids Res. 16*, 8587–8602.

(5) Sit, T. L., Vaewhongs, A. A., and Lommel, S. A. (1998) RNA-mediated trans-activation of transcription from a viral RNA. *Science 281*, 829–832.

(6) Loo, L., Guenther, R. H., Basnayake, V. R., Lommel, S. A., and Franzen, S. (2006) Controlled encapsidation of gold nanoparticles by a viral protein shell. *J. Am. Chem. Soc. 128*, 4502–4503.

(7) Sherman, M. B., Guenther, R. H., Tama, F., Sit, T. L., Brooks, C. L., Mikhailov, A. M., Orlova, E. V., Baker, T. S., and Lommel, S. A. (2006) Removal of divalent cations induces structural transitions in Red clover necrotic mosaic virus, revealing a potential mechanism for RNA release. *J. Virol. 80*, 10395–10406.

(8) Loo, L., Guenther, R. H., Lommel, S. A., and Franzen, S. (2008) Infusion of dye molecules into Red clover necrotic mosaic virus. *Chem. Commun.* 88–90.

(9) Liu, Y. L., and Franzen, S. (2008) Factors determining the efficacy of nuclear delivery of antisense oligonucleotides by gold nanoparticles. *Bioconjugate Chem. 19*, 1009–1016.

(10) Tkachenko, A. G., Xie, H., Coleman, D., Glomm, W., Ryan, J., Anderson, M. F., Franzen, S., and Feldheim, D. L. (2003) Multifunctional gold nanoparticle-peptide complexes for nuclear targeting. *J. Am. Chem. Sco. 125*, 4700–4701.

(11) Tkachenko, A. G., Xie, H., Liu, Y. L., Coleman, D., Ryan, J., Glomm, W. R., Shipton, M. K., Franzen, S., and Feldheim, D. L. (2004) Cellular trajectories of peptide-modified gold particle complexes: Comparison of nuclear localization signals and peptide transduction domains. *Bioconjugate Chem. 15*, 482–490.

(12) Franzen, S. (2011) A comparison of peptide and folate receptor targeting of cancer cells: from single agent to nanoparticle. *Expert Opin. Drug Delivery, 8*, 281–298.

(13) Liu, Y. L., Shipton, M. K., Ryan, J., Kaufman, E. D., Franzen, S., and Feldheim, D. L. (2007) Synthesis, stability, and cellular internalization of gold nanoparticles containing mixed peptide-poly(ethylene glycol) monolayers. *Anal. Chem. 79*, 2221–2229.

(14) Xie, H., Tkachenko, A. G., Glomm, W. R., Ryan, J. A., Brennaman, M. K., Papanikolas, J. M., Franzen, S., and Feldheim, D. L. (2003) Critical flocculation concentrations, binding isotherms, and ligand exchange properties of peptide-modified gold nanoparticles studied by UV-visible, fluorescence, and time-correlated single photon counting spectroscopies. *Anal. Chem. 75*, 5797–5805.

(15) Croker, C., Pearcy, J., Stahl, D., Moore, R., Keen, D., and Lee, T. (2000) An expert virtual instrument approach to the automated, data dependent MS/MS and LC/MS/MS analysis of proteins. *J. Biomol. Techniques 11*, 135.

(16) Blackburn, K., Mbeunkui, F., Mitra, S. K., Mentzel, T., and Goshe, M. B. Improving protein and proteome coverage through data-independent multiplexed peptide fragmentation. *J. Proteome Res. 9*, 3621-3637.

(17) Silva, J., Gorenstein, M., Li, G., Vissers, J., and Geromanos, S. (2006) Absolute quantification of proteins by LCMSE. *Mol. Cell. Proteomics 5*, 144–156.

(18) Silva, J. C., Denny, R., Dorschel, C. A., Gorenstein, M., Kass, I. J., Li, G.-Z., McKenna, T., Nold, M. J., Richardson, K., Young, P., and Geromanos, S. (2005) Quantitative proteomic analysis by accurate mass retention time pairs. *Anal. Chem. 77*, 2187–2200.

(19) Lommel, S. A. (1983) University of California, Berkeley.

(20) Yu, E. T., Hawkins, A., Kuntz, I. D., Rahn, L. A., Rothfuss, A., Sale, K., Young, M. M., Yang, C. L., Pancerella, C. M., and Fabris, D. (2008) The collaboratory for MS3D: a new cyberinfrastructure for the structural elucidation of biological macromolecules and their assemblies using mass spectrometry-based approaches. *J. Proteome Res. 7*, 4848–4857.

(21) Schilling, B., Row, R. H., Gibson, B. W., Guo, X., and Young, M. M. (2003) MS2Assign, automated assignment and nomenclature of tandem mass spectra of chemically crosslinked peptides. *J. Am. Soc. Mass Spectrom. 14*, 834–850.

(22) Chih, H.-W., Gikanga, B., Yang, Y., and Zhang, B. Identification of amino acid residues responsible for the release of free drug from an antibody−drug conjugate utilizing lysine−succinimidyl ester chemistry. *J. Pharm. Sci. 100*, 2518−2525.

(23) Flory, P. (1989) *Statistical mechanics of chain molecules*, Oxford University Press, Oxford, U.K.

(24) Hermanson, G. T. (2008) Heterobifunctional Crosslinkers, in *Bioconjugate Techniques*, 2nd ed.) pp 276−335, Academic Press, New York.

(25) Kolb, H., Finn, M., and Sharpless, K. (2001) Click chemistry: diverse chemical function from a few good reactions. *Angew. Chem., Int. Ed. 40*, 2004–2021.

(26) Destito, G., Yeh, R., Rae, C. S., Finn, M. G., and Manchester, M. (2007) Folic acid-mediated targeting of cowpea mosaic virus particles to tumor cells. *Chem. Biol. 14*, 1152–1162.

(27) Ren, Y., Wong, S., and Lim, L. (2007) Folic acid-conjugated protein cages of a plant virus: A novel delivery platform for doxorubicin. *Bioconjugate Chem. 18*, 836–843.

(28) Gillitzer, E., Willits, D., Young, M., and Douglas, T. (2002) Chemical modification of a viral cage for multivalent presentation. *Chem. Commun. 2002*, 2390–2391.

(29) Lockney, D., Guenther, R., Loo, L., Overton, W., Antonelli, R., Clark, J., Hu, M., Luft, C., Lommel, S., and Franzen, S. (2010) The Red clover necrotic mosaic virus capsid as a multifunctional cell targeting plant viral nanoparticle. *Bioconjugate Chem.* 1532–1555.

(30) Robinson, I., and Harrison, S. (1982) Structure of the expanded state of tomato bushy stunt virus. *Nature 297*, 563–568.

(31) Tama, F., and Brooks, C., III (2002) The mechanism and pathway of pH induced swelling in cowpea chlorotic mottle virus. *J. Mol. Biol. 318*, 733–747.

(32) Anderson, D. C., Manger, R., Schroeder, J., Woodle, D., Barry, M., Morgan, A. C., and Fritzberg, A. R. (1993) Enhanced in vitro tumor cell retention and internallization of antibody derivatized with synthetic peptides. *Bioconjugate Chem. 4*, 10–18.

(33) Delforge, D., Gillon, B., Art, M., Dewelle, J., Raes, M., and Remacle, J. (1998) Design of a synthetic adhesion protein by grafting RGD tailed cyclic peptides on bovine serum albumin. *Lett. Pept. Sci. 5*, 87–91.

(34) Gauvreau, V., Chevallier, P., Vallieres, K., Petitclerc, E., Gaudreault, R. C., and Laroche, G. (2004) Engineering surfaces for bioconjugation: Developing strategies and quantifying the extent of the reactions. *Bioconjugate Chem. 15*, 1146–1156.

(35) Chatterji, A., Ochoa, W., Shamieh, L., Salakian, S. P., Wong, S. M., Clinton, G., Ghosh, P., Lin, T., and Johnson, J. E. (2004) Chemical conjugation of heterologous proteins on the surface of cowpea mosaic virus. *Bioconjugate Chem. 15*, 807–813.

(36) Peacey, M., Wilson, S., Baird, M. A., and Ward, V. K. (2007) Versatile RHDV virus-like particles: Incorporation of antigens by genetic modification and chemical conjugation. *Biotechnol. Bioeng. 98*, 968–977.

(37) Ionescu, R. M., Przysiecki, C. T., Liang, X. P., Garsky, V. M., Fan, J. A., Wang, B., Troutman, R., Rippeon, Y., Flanagan, E., Shiver, J., and Shi, L. (2006) Pharmaceutical and immunological evaluation of human papillomavirus viruslike particle as an antigen carrier. *J. Pharm. Sci. 95*, 70–79.

(38) Lee, J., Choi, Y., Kim, K., Hong, S., Park, H. Y., Lee, T., Cheon, G. J., and Song, R. (2010) Characterization and cancer cell specific binding properties of Anti-EGFR antibody conjugated quantum dots. *Bioconjugate Chem. 21*, 940–946.

(39) Bhandari, K. H., Newa, M., Uludag, H., and Doschak, M. R. (2010) Synthesis, characterization and in vitro evaluation of a bone targeting delivery system for salmon Calcitonin. *Int. J. Pharm. 394*, 26–34.

(40) Phaneuf, M. D., Berceli, S. A., Bide, M. J., Quist, W. G., and LoGerfo, F. W. (1997) Covalent linkage of recombinant hirudin to poly(ethylene terephthalate) (Dacron): creation of a novel antithrombin surface. *Biomaterials 18*, 755–765.

(41) Kim, F., Beeche, A., Hunter, J., Chin, D., and Hope, T. (1996) Characterization of the nuclear export signal of human T-cell lymphotropic virus type 1 Rex reveals that nuclear export is mediated by position-variable hydrophobic interactions. *Mol. Cell. Biol. 16*, 5147.

(42) Gubala, V., Le Guevel, X., Nooney, R., Williams, D. E., and MacCraith, B. (2010) A comparison of mono and multivalent linkers and their effect on the colloidal stability of nanoparticle and immunoassays performance. *Talanta 81*, 1833–1839.

(43) Lockney, D. M., Antonelli, R., Wang, R., Clark, J., Mei Hu, Oberhardt, B. J., Franzen, S. *Red clover necrotic mosaic virus* plant viral nanoparticle targeting of murine melanoma xenograft tumors (submitted).

(44) Zhang, F., Andreassen, P., Fender, P., Geissler, E., Hernandez, J., and Chroboczek, J. (1999) A transfecting peptide derived from adenovirus fiber protein. *Gene Ther. 6*, 171.

(45) Kelland, L. (2007) N-cadherin: a novel target for cancer therapy? *Drugs Future 32*, 925–930.

Supporting information for

Mass spectrometric detection of targeting peptide bioconjugation to *Red clover necrotic mosaic virus*

Ruqi Wang[1], Dustin M. Lockney[1], Michael B. Goshe[2]*, Stefan Franzen[1]*

1. Department of Chemistry, North Carolina State University, Raleigh, NC 27695

2. Department of Molecular and Structural Biochemistry, North Carolina State University, Raleigh, NC 27695

UPLC data and MS^E chromatograms

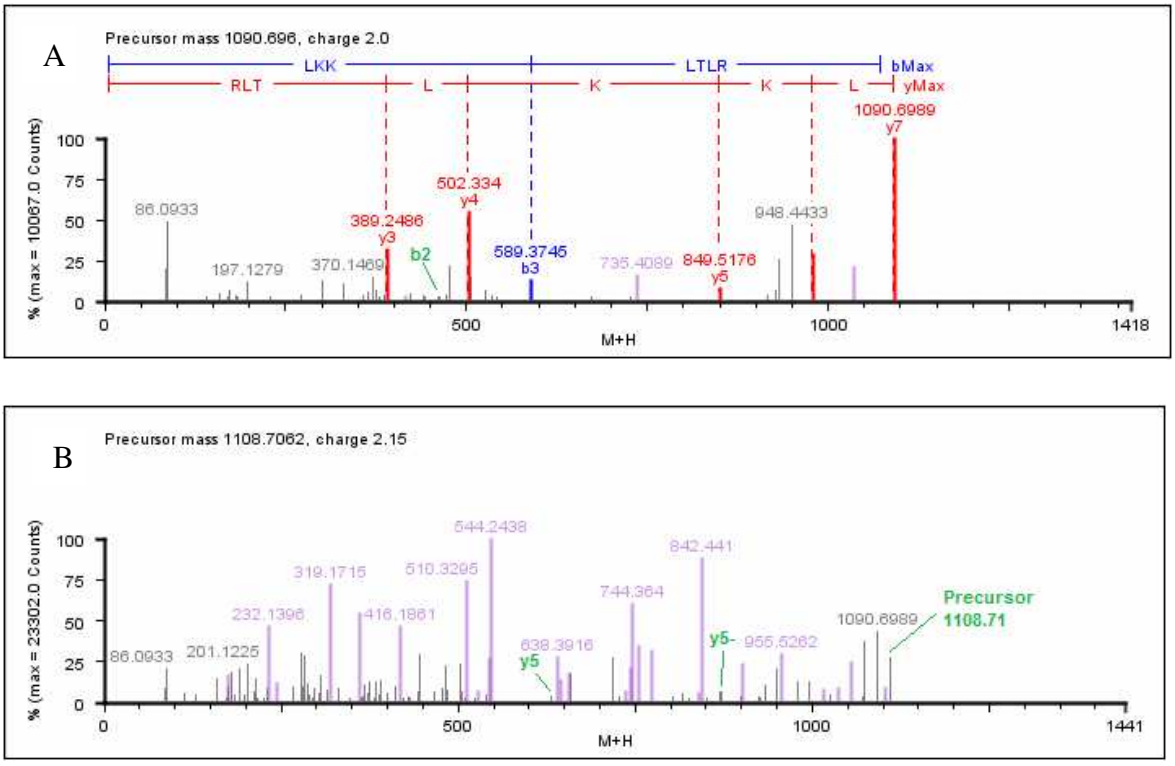

Figure S1. LC/MS^E analysis of SMCC labeling of RCNMV. (A) MS^E product ion spectrum of (101)LKK(SMCC)LTLR(107) with the b_2 ion containing the modification indicated in green. (B) MS^E product ion spectrum of (101)LKK(SMCC-OH)LTLR(107) with the y_5 ion without modification (lower mass value) and the y_5 ion with modification (higher mass value) indicated in green.

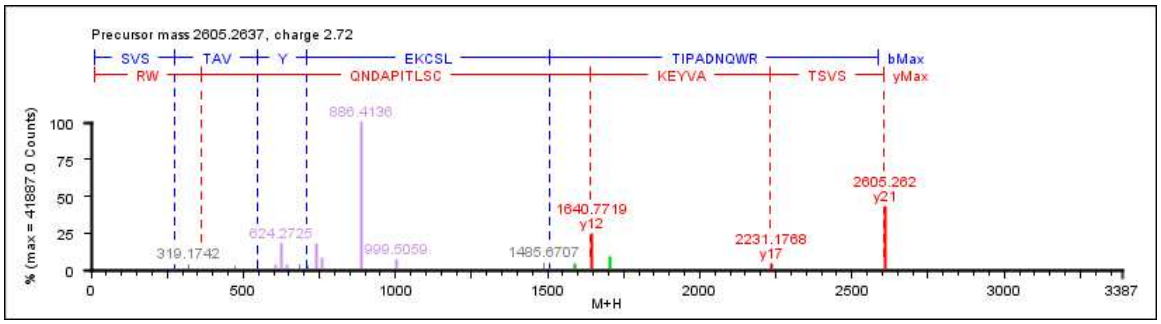

Figure S2. MS^E product ion spectrum of (145)SVSTAVYEKC(SMCCOH)SLTIPADNQWR(165) generated from the sSMCC conjugated RCNMV sample.

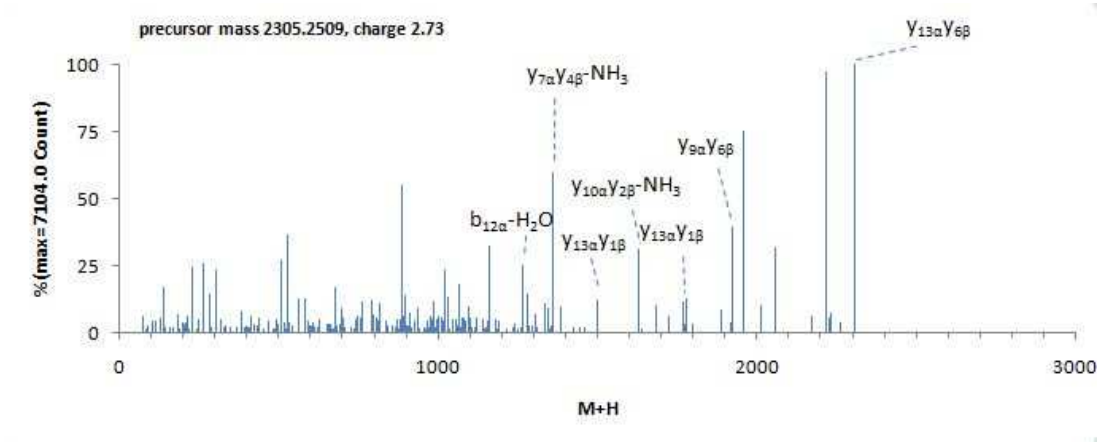

Figure S3. MS^E product ion spectrum of TVAIPFAK(~LSTSFC)TQIIK generated from the RCNMV conjugated with the CD46 peptide. The most abundant ion $[M+H]^+$ at *m/z* 2305.25 corresponds to the intact peptide conjugate. Representative crosslinked peptide product ions are shown. Although not labeled, single peptide ions $y_{1\alpha}$, $y_{5\alpha}$, and $b_{7\alpha}$ were dectected for the capsid protein.

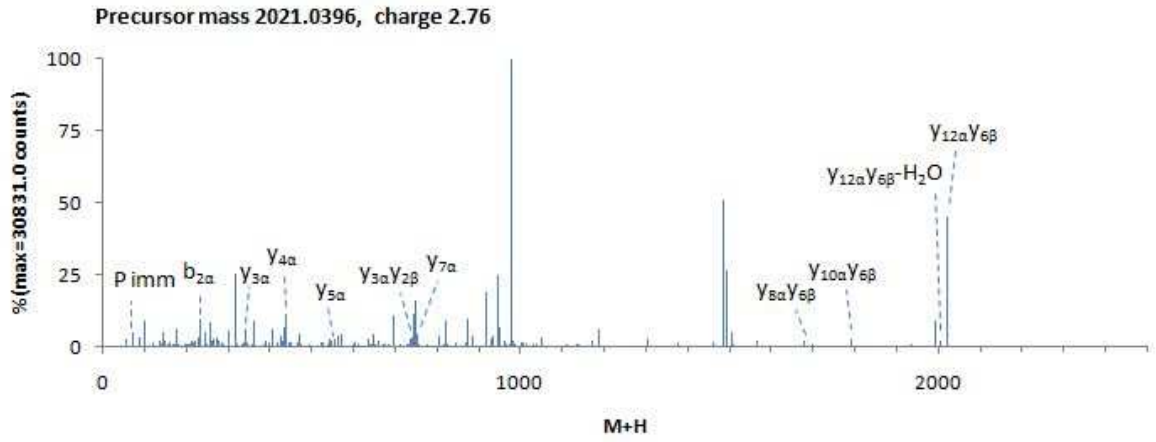

Figure S4. MS^E product ion spectrum of (26)TVAIPFAK(~GSGSC)TQIIK(38) generated from the RCNMV conjugated with the GSGS peptide. The most abundant ion $[M+H]^+$ at *m/z* 2021.04 corresponds to the intact peptide conjugate. Representative crosslinked peptide product ions and single peptide product ions are shown. Although not completely labeled, all b and y ions for the capside peptide (α chain) were detected except y_1, y_6, and b_4; all b ions for GSGS peptide (β chain) were detected.

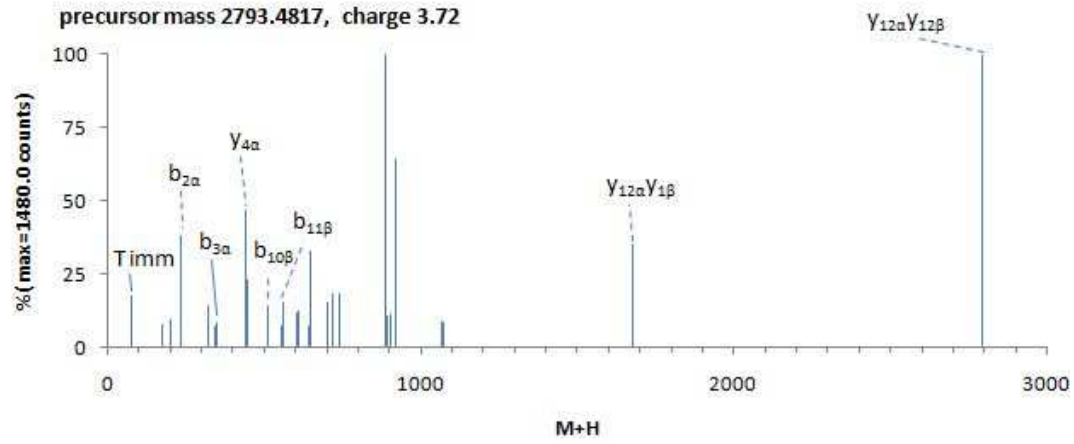

Figure S5. MS^E product ion spectrum of (34)TVAIPFAK(~AHAVDINGNQVC)TQIIK(45) generated from the RCNMV conjugated with the ADH304 peptide. The most abundant ion $[M+H]^+$ at *m/z* 2793.48 corresponds to the intact peptide conjugate. Representative crosslinked peptide product ions and single peptide product ions are shown. Although not labeled, product ions b_1, b_2, y_1, y_3-y_5 for capsid (α chain) were detected, and b_{10} and b_{11} ions for the ADH peptide (β chain) were detected.

Use of various proteases for digestion of RCNMV to extend peptide sequence coverage

In order to dectect capsid peptide sequencesnot covered by trypsin and chymotrypsin digestion, other enzymes were used. Pepsin has a primary digestion site at F, W, Y, E, and I residues, but further digestion can be random. Digestion was performed in 10 mM HCl, and after certain time, the reaction was quenched by adding 7uL of 100mM sodium phosphate buffer (pH~8.0) to increase the pH above 7. Then the sample

was frozen at -20℃ until further processing could be performed. Urea (8 M) or heating in

a boiling water bath (5 min) was used to unfold/denature the protein. The method was applied on bovine serum albumin (BSA) as a reference. Ratios of pepsin and RCNMV from 1:5 to 1:500 (wt: wt) were investigated.

The results of the pepsin digestion using a 1:100 ratio of pepsin:RCNMV (wt:wt) are shown in Figure 5. For the first few minutes, the virus was digested very quickly, but appeared to be arrested within 5 min as indicated by the large protein/peptide pieces that were left undigested. The reason for this result cannot be self-digestion or inactivation of the protease since pepsin was able to be detected in the control sample (Lane P). To attempt to circumvent this problem, additional pepsin was added at time points 15, 30 and 45 min after the initiation of the reaction to ensure that active pepsin was present in the solution during the course of the digestion. This approach promoted further digestion, but incomplete RCNMV digestion was still evident.

LC/MS^{E} analysis of RCNMV digested by pepsin did not provide reproducible results. Some samples had higher coverage but questionable peptide identications. By examining the masses of these peptides, we found that the majority of them are below 1000 Da which were difficult to identify due to the low number of product ions. This agrees with the SDS-PAGE results, in that pepsin seemed to digest only the solvent accessible part of the virus, but was not able further access the virus. In contrast, trypsin

(Lane Try) was able to more completely digest the virus except for the 6-10 kDa segments were no cleavage sites were available. In an attempt to obtain sequence information regarding this 6-10 kDa segment, in-gel digestion of this region was performed using pepsin but the small peptides generated precluded peptide detection.

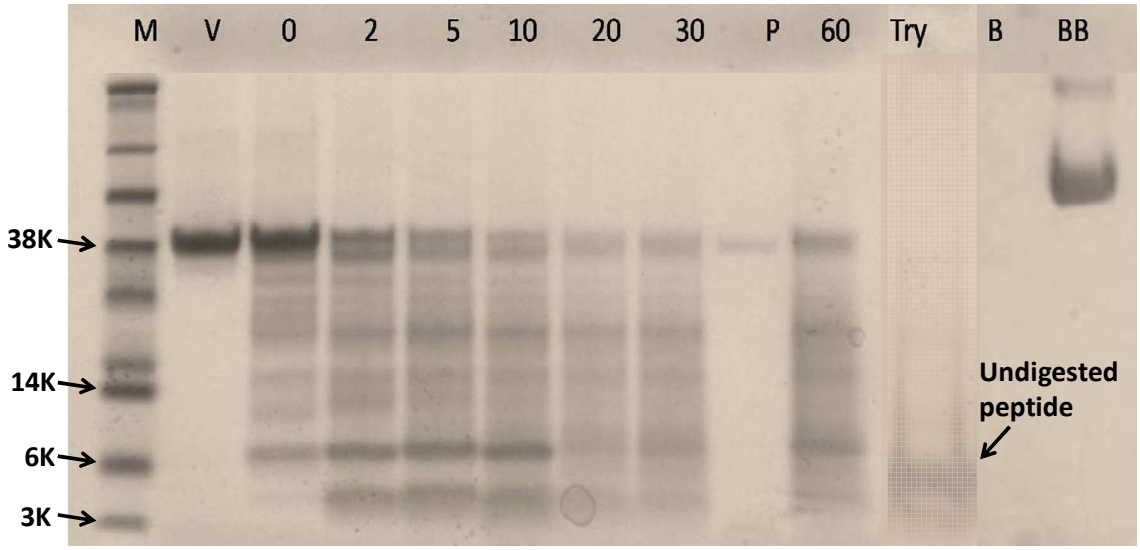

Figure S5. Combined SDS-PAGE analysis of RCNMV digestion using pepsin. For digestion, a ratio of 1:100 (pepsin:virus, wt:wt) was used. M=marker, V=virus, P=pepsin, Try= Trypsin digestion overnight, B=BSA, BB=BSA blank, and numbers=#minutes of digestion . Proteins were stained with coomassie blue.

GluC hydrolyzes proteins at glutamic acids and aspartic acids (much slower) in ammonium bicarbonate aspartic acids buffer at pH 4.0 or phosphate buffer at pH 7.8. GluC was explored as a possible avenue to increase capsid sequence coverage because there are several D and E residues in the region 176-286 where trypsin does not give adequate coverage. Unfortunately, GluC digestion did not meet our expectations. As indicated by SDS-PAGE analysis in Figure S6, GluC did not digest the capsid protein significantly in either buffer despite digesting overnight and using a 1:20 ratio of GluC:virus (wt:wt).In addition, no useful data were obtained by LC/MS^{E} analysis.

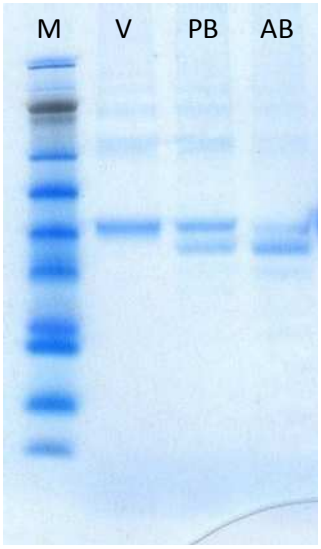

Figure S6. SDS-PAGE analysis of RCNMV digestion using GluC. For digestion, a ratio of 1:20 (GluC:virus, wt:wt) was used. M=marker, V=virus, PB=phosphate buffer, and AB= ammonium bicarbonate buffer. . Proteins were stained with coosmassie blue.

Bioconjugate Chemistry

ARTICLE

pubs.acs.org/bc

Novel Anticancer Polymeric Conjugates of Activated Nucleoside Analogues

Thulani H. Senanayake, Galya Warren, and Serguei V. Vinogradov*

Center for Drug Delivery and Nanomedicine and Department of Pharmaceutical Sciences, College of Pharmacy, University of Nebraska Medical Center, Omaha, Nebraska, United States

Supporting Information

ABSTRACT: Inherent or therapy-induced drug resistance is a major clinical setback in cancer treatment. The extensive usage of cytotoxic nucleobases and nucleoside analogues in chemotherapy also results in the development of specific mechanisms of drug resistance, such as nucleoside transport or activation deficiencies. These drugs are prodrugs; and being converted into the active mono-, di-, and triphosphates inside cancer cells following administration, they affect nucleic acid synthesis, nucleotide metabolism, or sensitivity to apoptosis. Previously, we actively promoted the idea that the nanodelivery of active nucleotide species, e.g., 5′-triphosphates of nucleoside analogues, can enhance drug efficacy and reduce nonspecific toxicity. In this study, we report the development of a novel type of drug nanoformulations, polymeric conjugates of nucleoside analogues, which are capable of the efficient transport and sustained release of phosphorylated drugs. These drug conjugates have been synthesized, starting from cholesterol-modified mucoadhesive polyvinyl alcohol or biodegradable dextrin, by covalent attachment of nucleoside analogues through a tetraphosphate linker. Association of cholesterol moieties in aqueous media resulted in intramolecular polymer folding and the formation of small nanogel particles containing 0.5 mmol/g of a 5′-phosphorylated nucleoside analogue, e.g., 5-fluoro-2′-deoxyuridine (floxuridine, FdU), an active metabolite of anticancer drug 5-fluorouracyl (5-FU). The polymeric conjugates demonstrated rapid enzymatic release of floxuridine 5′-phosphate and much slower drug release under hydrolytic conditions (pH 1.0−7.4). Among the panel of cancer cell lines, all studied polymeric FdU-conjugates demonstrated an up to 50× increased cytotoxicity in human prostate cancer PC-3, breast cancer MCF-7, and MDA-MB-231 cells, and more than 100× higher efficacy against cytarabine-resistant human T-lymphoma (CEM/araC/8) and gemcitabine-resistant follicular lymphoma (RL7/G) cells as compared to free drugs. In the initial *in vivo* screening, both PC-3 and RL7/G subcutaneous tumor xenograft models showed enhanced sensitivity to sustained drug release from polymeric FdU-conjugate after peritumoral injections and significant tumor growth inhibition. All these data demonstrate a remarkable clinical potential of novel polymeric conjugates of phosphorylated nucleoside analogues, especially as new therapeutic agents against drug-resistant tumors.

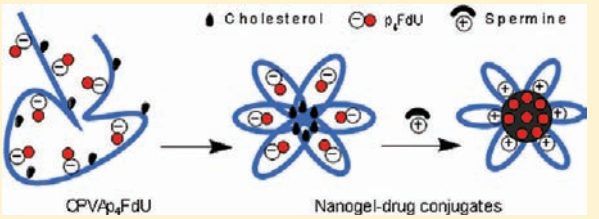

INTRODUCTION

Despite several decades of research and drug development, progress in the clinical struggle against cancer has been only moderate. Development of resistance by cancer cells to chemotherapeutic agents has currently become a major clinical problem, limiting the effectiveness of the treatment of hematological malignancies as well as solid tumors. Multiple studies have helped to identify many mechanisms of drug resistance, but in general terms, they can all be reduced to the prevention of a drug from entering cells, deactivation of drug molecules, or the enhanced resistance of cancer cells to apoptosis. The first group includes deficiencies in membrane nucleoside transporters or the overexpression of ATP-dependent drug efflux transporters like P-glycoprotein (MRP, BCRP) and other membrane proteins (MRP) responsible for drug efflux. In the second group, the drug metabolism/degradation and reduced levels of enzymatic drug activation should be mentioned. In the third group, the induction of antiapoptotic mechanisms, as well as the suppression of pro-apoptotic pathways, plays important roles in drug resistance.[1]

Cytotoxic nucleoside analogues belong to the important class of anticancer drugs, which are currently used as the first line of treatment of hematological malignancies and certain solid tumors.[2] These drugs act as antimetabolites by interfering with nucleic acid synthesis and enzymes of the nucleotide metabolism. The clinical efficacy of these drugs depends on higher metabolic activity and drug activation in rapidly proliferating cancer cells compared to normal cells. Activation of therapeutic nucleoside analogues occurs through the *de novo* synthesis of 5′-mono-, di-, and triphosphate derivatives, which interfere with the cellular pool of natural nucleosides. Nucleoside analogues require participation of specialized nucleoside transporter proteins such as hENT1, hENT2, or hCNT1 in order to accumulate in the cells. The integral drug uptake depends on the proper balance of the nucleoside transporters and drug efflux proteins presented on

Received: April 12, 2011
Revised: August 23, 2011
Published: August 25, 2011

ACS Publications © 2011 American Chemical Society

cellular membrane. Therefore, the drug accumulation is substantially reduced when the expression of such nucleoside transporters is deficient,[3,4] or the activity of drug efflux transporter proteins is elevated.[5,6] After entering cells, nucleoside analogues undergo phosphorylation into 5′-monophosphates with deoxycytidine kinase (dCK) or thymidine kinase (TK), a rate-limiting step in the intracellular activation of nucleosides, and are subsequently converted into active 5′-diphosphates and 5′-triphosphates by other nucleoside kinases.[3] The efficacy of nucleoside analogues may further be limited by additional factors such as metabolic deamination and intracellular dephosphorylation.[7,8]

In order to increase tumor accumulation of nucleoside analogues, various prodrug and drug delivery approaches have been developed, for example, the application of lipophilic nucleoside derivatives with an enhanced cellular membrane affinity. Many prodrugs with degradable lipophilic masking groups demonstrate the enhanced cell membrane permeability.[9] Early phase clinical trials have shown some improvements in the treatment of hematological malignancies, but these prodrugs were not effective in the treatment of solid tumors.[10] Moreover, lipophilic prodrugs have a reduced half-life in circulation due to the fast accumulation in liver. Various nanocarriers such as liposomes, biodegradable nanoparticles, polymeric micelles, and nanocapsules have been extensively for tumor delivery of chemotherapeutic drugs.[11] Many of these nanocarriers demonstrated advanced features, but have also shown serious shortcomings limiting their clinical usefulness. For example, liposomal formulations were unable to achieve effective drug concentration inside tumors because many anticancer drugs (cytarabine, 5-FU, etc.) diffused rapidly through the liposome bilayer.[12]

Recently, we introduced an alternative tumor treatment strategy using formulation and nanodelivery of activated drugs, nucleoside 5′-triphosphates, encapsulated in cationic nanogels.[17] Previously, several laboratories have attempted to achieve *in vivo* delivery of bioactive 5′-triphosphates of nucleoside analogue through encapsulation in liposomes,[13,14] nanoparticles,[15] or red blood cells.[16] Evidently, the success of this strategy depends on the advantages of nanoformulations in drug protection in biological milieu, controlled drug release, and the specific tumor targeting. Nanogel carriers have dramatically improved the delivery of activated phosphorylated nucleoside analogues into cancer cells and tumor growth inhibition effect.[18,19] However, the noncovalent nature of the encapsulation of anionic 5′-triphosphates in cationic nanogels was the reason for relatively fast drug release kinetics. Here, we report synthesis of novel types of drug-loaded nanogels, containing a polymer network with covalently linked phosphorylated nucleoside analogues, which are capable of sustained drug release and structurally different from the previously studied polymeric nanogels. Covalent drug attachment is an important factor in the controlled drug release, because it allows using specific chemistries. Various hydrolytically or enzymatically sensitive linkers, such as peptides, carboxylates, and so forth, have been previously evaluated with polymeric drug delivery systems.[20−22] In this study, drug conjugates were synthesized by the attachment of nucleoside analogues through a biodegradable tetraphosphate linker starting from amphiphilic polymers such as cholesterol-modified polyvinyl alcohol (PVA) or dextrin (DEX). The linker has strong advantage over other linkers, because the polymeric drug conjugates are able to release nucleoside analogues in active phosphorylated form in the result of its hydrolytic or enzymatic degradation,

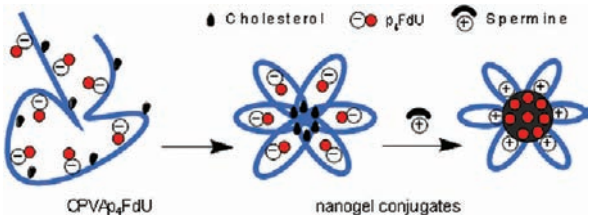

Figure 1. Formation of compact nanogels from polymer drug conjugates.

eventually showing an enhanced tumor growth inhibition efficacy against normal and drug-resistant cancer cells. These drug-containing polymer conjugates can form stable nanogels with a small hydrodynamic diameter after ultrasonication in aqueous media as demonstrated in Figure 1. Selection of biodegradable or mucoadhesive biocompatible polymers for preparation of polymeric conjugates might also reduce toxicity of chemotherapy and open potentials for oral administration of these nanoformulations.

MATERIALS AND METHODS

Materials. Most reagents, solvents, and polymers were purchased from Sigma Aldrich (St. Louis, MO) and Alfa Aesar (Wardhill, MA) with the highest available purity and used without purification unless otherwise stated. Thymidine, 3-[4,5-dimethylthiazol-2-yl]-2,5-diphenyltetrazolium bromide (MTT) and snake venom phosphodiesterase 1, type VI, from Carotalus adamanteus were purchased from Sigma (St. Louis, MO). Nucleoside analogues: 5-fluoro-2′-deoxyuridine (Floxuridine, FdU) was from SynQuest Laboratories (Alachua, FL), 2,2′-difluorocytidine (dFdC, Gemcitabine) was from Beta Pharma, Inc. (Branford, CT), and arabinosylcytosine (araC, Cytarabine) was from 3B Medical Systems, Inc. (Libertyville, IL). Centrifuge filter devices (MWCO 5000 Da) were purchased from Millipore (Bedford, MA).

All NMR spectra were recorded using a 500 MHz Varian NMR spectrometer. All chemical shift values are given in parts per million (ppm) and are referenced to a signal from $(CH_3)_4Si$ (0 ppm) for ^1H, DMSO-d_6 (39.7 ppm) for ^{13}C, and 85% phosphoric acid (0 ppm) for ^{31}P spectra at 25 °C. Hydrodynamic diameter, polydispersity, and zeta potential of nanogels and polymeric conjugates were measured using a dynamic light scattering instrument, the Zetasizer Nano-ZS90 (Malvern Instruments, Southborough, MA) at 25 °C. Monodisperse polystyrene dispersions were used as standards. UV absorbance of samples was measured by Biophotometer (Eppendorf, Hamburg, Germany). IR spectra were recorded using a Nicolet IR-200 FT-IR spectrometer (Thermo Scientific, Waltham, MA).

Cells. Human breast carcinoma MCF-7, human hepatocellular carcinoma HepG2, and human prostate adenocarcinoma PC-3 cells were obtained from ATCC (Rockville, MD). These cells were maintained in Dulbecco's Modified Eagle Medium (DMEM) supplemented with 10% fetal bovine serum (FBS), 1% L-glutamine, and 2% penicillin−streptomycin at 37 °C in a humidified atmosphere containing 5% CO_2. Human breast carcinoma MDA-MB-231 cell line was a gift from Dr. R. Singh (UNMC). These cells were maintained in DMEM/Nutrient mixture F-12 (DMEM/F12) with similar supplements and serum as above. Gemcitabine-resistant human follicular lymphoma RL7/G cell line, which is characterized by a reduced level of dCK enzyme,[23] was a gift from Dr. F. Bontemps (De Duve Institute, Bruxelles, Belgium). They were grown in the presence of 2 μM gemcitabine. Nucleoside

Table 1. Particle Characteristics of Polymeric Conjugates

polymeric conjugate[a]	d_h, nm (volume-averaged)	PDI	ζ, mV
CPVA31	35.00 ± 1.30	0.361 ± 0.01	0.00 ± 3.70
CPVA31-p_4FdU	42.12 ± 6.41	0.405 ± 0.04	−8.47 ± 3.60
CPVA13	12.52 ± 5.12	0.596 ± 0.03	−2.57 ± 3.40
CPVA13-p_4FdU	34.95 ± 5.43	0.417 ± 0.01	−34.0 ± 4.67
CDEX9	44.53 ± 8.34	0.458 ± 0.02	−8.00 ± 4.02
CDEX9-p_4FdU	26.23 ± 4.12	0.440 ± 0.03	−34.80 ± 5.06
CDEX9-p_4T	18.27 ± 2.01	0.508 ± 0.00	0.00 ± 4.52

[a] Particle size (d_h), polydispersity index (PDI), and zeta potential (ζ) were measured in 1% solutions in water after 2 h sonication. The results are average values ± SD of three measurements.

transport-deficient cytarabine-resistant human leukemic lymphoblast CEM/araC/8 cell line[24] was obtained from Dr. C. Galmarini (UFR Lyon-Sud, Oullins, France). The cells were grown in the presence of 0.5 μM cytarabine (araC). Both drug-resistant cell lines were grown in RPMI medium supplemented with 10% fetal bovine serum (FBS), 1% L-glutamine, and 2% penicillin−streptomycin at 37 °C in a humidified atmosphere containing 5% CO_2.

Synthesis of Cholesterol Conjugates. PVA was grafted with cholesterol moieties according to the procedures described below. Briefly, 2.1 g of PVA (M_w 13 kDa) was dried over phosphorus pentoxide *in vacuo* and dissolved in 50 mL of anhydrous DMSO at 70 °C. Triethylamine (0.8 mmol) was added to the cooled solution (25 °C) followed by 0.3 g (0.68 mmol) of cholesteryl chloroformate, and the final solution was stirred overnight at 25 °C. The reaction mixture was concentrated *in vacuo* and dialyzed (MWCO 3.5 kDa) against 20% aqueous ethanol three times for 24 h. The product (CPVA) was isolated after concentration *in vacuo* and freeze−drying with a yield of 80%. In another method, 2.1 g of PVA (M_w 13 kDa) was dissolved in 50 mL of anhydrous *N*-methyl pyrrolidone at 70 °C, then 0.3 g (0.68 mmol) of cholesteryl chloroformate was added, and the mixture was stirred for 4 h at 70 °C. The substituted CPVA was precipitated in diethyl ether (0.5 L) and dried *in vacuo*; the light yellow precipitate was obtained at a yield of 70%. ^{1}H NMR: 0.63 (s, 18H), 0.83 (m, 36H), 0.88 (m, 18H), 0.92 (s, 18H), 1.11−1.95 (m, 764H), 3.84−3.90 (m, 295H), 4.31 (brs, OH), 4.40 (s, 12H), 5.25 (s, 6H). Following the same protocol for PVA (M_w 31 kDa), we obtained CPVA with a yield of 85%. ^{1}H NMR: 0.65 (s, 18H), 0.83−0.85 (dd, J = 5.0, 1.6 Hz, 36H), 0.89 (d, J = 4.8 Hz, 18H), 0.94 (s, 18H), 1.07−1.98 (m, 1582H), 3.84 (m, 704H), 4.35 (12H and OH), 5.28 (s, 6H). IR: 3264, 2897, 1642, 1409, 1323, 1082, 915, 829.

The dextrin−cholesterol nanogel (CDex) was synthesized as follows. The water-soluble fraction of dextrin (M_w 9 kDa) was isolated by dialysis in a SpectraPor membrane tube (MWCO 2 kDa) followed by centrifugation. The supernatant was freeze−dried and used for nanogel synthesis. 1.0 g of the purified dextrin was dried over phosphorus pentoxide *in vacuo* and dissolved in 15 mL of anhydrous DMSO at 70 °C. After 0.3 g (0.68 mmol) of cholesteryl chloroformate was added, the reaction mixture was stirred for 24 h at 25 °C, concentrated *in vacuo*, and dialyzed (MWCO 3.5 kDa) against 20% aqueous ethanol three times for 24 h. The product (CDex) was isolated after concentration *in vacuo* and freeze−drying with a yield of 76%. ^{1}H NMR: 0.65 (s, 18H), 0.83−0.85 (dd, J = 5.0, 1.6 Hz, 36H), 0.89−1.51 (m, 211H), 3.24−3.64 (m, 333H), 4.28−5.10 (m, 122H), 5.23 (s, 6H), 5.37−5.62 (m, 55H).

Synthesis of Phosphorylating Reagent, CNEtOP(O)Im$_2$. The intermediate product CNEtOP(O)Cl_2 was synthesized by dissolving 18.6 mL (30.6 g, 0.2 mol) phosphorus (V) oxychloride and 20.6 mL (14.84 g, 0.147 mol) triethylamine in 40 mL anhydrous tetrahydrofuran (THF) at 0 °C. It was treated with 10 mL (10.45 g, 0.147 mol) 2-cyanoethanol in 5 mL THF while stirring at 0 °C. Stirring was continued for 30 min until white precipitate formed. The precipitate was carefully filtered with exclusion of moisture, and the resulting solution was concentrated *in vacuo* and distilled under argon. The product, CNEtOP(O)Cl_2, was recovered by distillation at 90 °C/1 mm with a yield of 60%.

The product, CNEtOP(O)Im_2, was synthesized by mixing 2.69 g (0.015 mol) CNEtOP(O)Cl_2 and 5.25 g (0.037 mol) *N*-trimethylsilyl-imidazole in 40 mL cold anhydrous toluene. The solutions were then incubated for 2 h at room temperature, concentrated *in vacuo* to a half-volume and placed in a freezer for 2 h at −20 °C. The precipitate of CNEtOP(O)Im_2 was recovered after centrifugation with a yield of 70%.[25]

Preparation of Polymeric Drug Conjugates. A solution of 3.3 g of dried cholesterol−polymer conjugates in 33 mL DMF was treated with a 2 M solution of CNEtOP(O)Im_2 in anhydrous DMF (2 mL) for 30 min at 25 °C. Then, a 1 M solution of tetra-*n*-butylammonium salt of pyrophosphate (PPi-TBA) in anhydrous DMF (4 mL) was added, and the reaction mixture was incubated for 1 h at 25 °C. In a separate flask, floxuridine (FdU, 490 mg, 2 mmol) was treated with a 2 M solution of CNEtOP(O)Im_2 in anhydrous DMF (1 mL) and allowed to stand for 20 min at 25 °C. Both solutions were then mixed and stirred for 40 min at 25 °C. The reaction mixture was treated with 1 mL of methanol and left overnight at 4 °C. Insoluble material was removed by filtration; the nanogel conjugate was purified three times over 24 h by dialysis (MWCO 3500 Da) against 20% aqueous ethanol, concentrated *in vacuo*, and precipitated as a sodium perchlorate in acetone. FdU content in the nanogel conjugate was measured by UV absorbance (ε_{260} = 7570). Drug loading: CPVA31, 0.51 μmol/mg; CPVA13, 0.50 μmol/mg; and CDex9, 0.44 μmol/mg.

Particle Size and Zeta-Potential Measurements. The hydrodynamic diameter and polydispersity of nanogels and polymeric conjugates were measured by dynamic light scattering (DLS) using a Zetasizer Nano-ZS90 with a 15 mV solid state laser operated at a wavelength of 635 nm. In brief, dry samples were resuspended in filtered deionized water, and then sonicated for 1 h at 4 °C to form a uniform dispersion of nanoparticles and centrifuged for 4 min at 10 000 × g. The size distribution in samples was characterized by polydispersity index. Zeta-potential was calculated based on electrophoretic mobility measurements performed with an electrical field strength of 15−18 V cm^{-1} at 25 °C using the instrument software. The data reported in Table 1 represent an average of three measurements.

Enzymatic Hydrolysis. Enzymatic stability and drug release from polymeric conjugates was assayed in 50 μL reaction mixtures containing: 100 mM Tris-HCl (pH 8.75), 2 mM $MgCl_2$, 0.5 mg of snake venom phosphodiesterase (VPDE), and 0.5 mg nanogel sample (FdU, 0.25 μmol). The reaction mixture was incubated at 37 °C and, at appropriate times, 5 μL aliquots were taken out and quenched with 1.5 μL of 1 M HCl. Nucleotide content was analyzed by ion-pair HPLC using an Ascentis C18 column (10 μm, 15 cm × 4.6 mm) at a flow rate of 1 mL/min. The elution was performed with buffer A: 40 mM KH_2PO_4, 0.2%

Scheme 1. Synthetic Steps in the Preparation of CPVA Conjugates

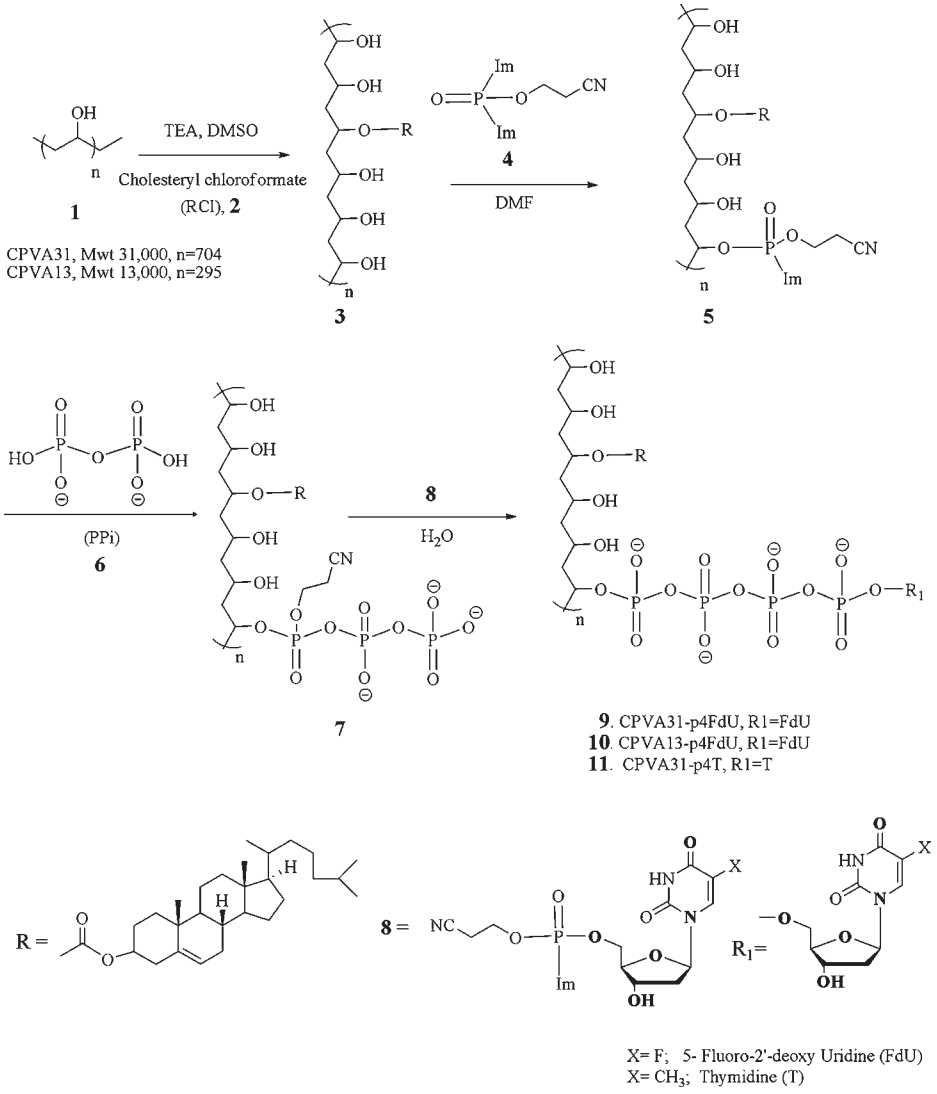

tetrabutylammonium hydroxide, pH 7.0, and buffer B: 30% acetonitrile, 40 mM KH_2PO_4, 0.2% tetrabutylammonium hydroxide, pH 7.0, in a linear gradient mode (100% B in 20 min).

***In Vitro* Drug Release.** *In vitro* drug release was investigated under different pH values. In short, 18 mg of CPVA31-p_4FdU or CDex9-p_4FdU conjugates was dissolved in 20 mL of PBS solution at pH 7.4, 4.0, and 1.0. These solutions were incubated at 37 °C and 0.5 mL aliquots were taken out every 24 h. The released nucleotides were separated from the rest of the polymeric conjugates by centrifugation at 7500 rpm for 25 min using an Amicon Ultra 0.5 centrifuge filter device (MWCO 3000 Da). The pH of the filtrate was adjusted to 7.4 and UV absorbance was measured at 260 nm.

Cytotoxicity Studies. Cytotoxicity of the polymeric conjugates was analyzed in different cancer cell lines by a standard MTT assay. Briefly, MCF-7, PC-3, HepG2, and MDA-MB-231 cells were seeded at a density of 10 000 cells/200 μL growth medium/well in flat-bottom 96-well plates; the corresponding suspensions of RL7/G and CEM/araC/8 cells were placed in round-bottom 96-well plates. Cells were allowed to grow overnight and appropriate amounts of drug, nanogels, or polymeric conjugates were added. Samples were incubated in full medium for 72 h at 37 °C, and the metabolic activity of each sample was determined by adding 20 μL of a 5 mg/mL of MTT stock solution in sterile PBS buffer to each well. The samples were then incubated for 2 h at 37 °C, the medium and the MTT dye were washed out by PBS, and 100 μL of extraction buffer (20% w/v SDS in DMF/water, 1:1, pH 4.7) was added to each well. Samples were incubated for 24 h at 37 °C. Optical absorbance was measured at 560 nm using a model 680 microplate reader (BioRad, Hercules, CA) and cytotoxicity was expressed as a percentage of survived cells relative to nontreated control cells. All samples were analyzed by an average of eight measurements (means ± SEM). These data were plotted versus drug/nanogel concentrations and converted into IC_{50} values (concentration of the 50% cell survival).

***In Vivo* Tumor Growth Inhibition Assay.** These experiments were performed using female nu/nu mice (RL7/G cells) or male nu/nu mice (PC-3 cells), aged 6−8 weeks (Charles River Laboratories, Wilmington, MA). Animal studies were carried out according to the Principles of Animal Care outlined by the National Institutes of Health, and protocols were approved by the Institutional Animal

Scheme 2. Synthesis of CDex-Conjugates (Compounds 1−11; see Scheme [1])

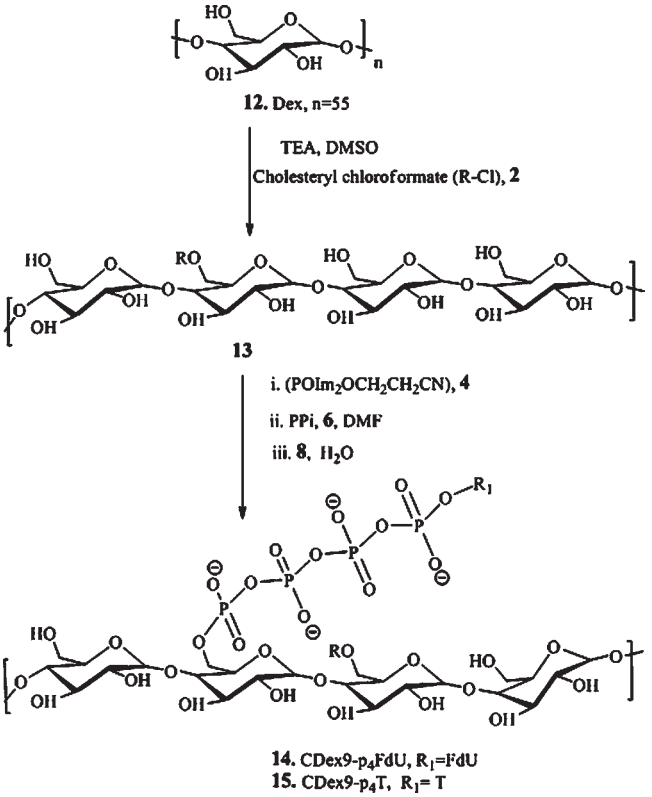

Care and Use Committee at the University of Nebraska Medical Center. The animals were randomly divided into groups of five per cage and maintained under sterile conditions and 12 h light/dark cycle in a temperature-controlled environment. All manipulations with animals were performed in a sterile laminar hood using sterile solutions. PC-3 and RL7/G cell suspensions of 5×10^6 cells/400 μL of medium containing 20% Matrigel (Becton-Dickinson, San Diego, CA) were injected subcutaneously in the right flank areas of mice. After tumors could be palpitated, the treatment solutions of CPVA31-p$_4$FdU were injected peritumorally (2×100 μL) twice a week at a dose of 12 mg FdU/kg. Tumor volume was measured by digital calipers and calculated based on the equation: $TV = L/2 \times W^2$, where L and W are length and width of tumor (mm).

RESULTS AND DISCUSSION

Synthesis of Nanogel Conjugates. Cholesterol is a well-known hydrophobic moiety used in many drug delivery applications in order to enhance the interactions of modified macromolecules or nanocarriers with the cellular membrane.[26,27] In our design of polymeric conjugates, we have exploited polymer modification with cholesterol for several reasons: (i) to render hydrophilic polymers soluble in organic solvents, (ii) to compel the modified polymers to form compact nanogels, and (iii) to increase membranotropic properties and ease transport of hydrophilic drug molecules across the cellular membrane. In aqueous solutions, at ultrasonication cholesterol-modified polymers form "flower-type" micelles with internally aggregated cholesterol moieties with the least association numbers 4−6.[28] We synthesized the cholesterol-modified polyvinyl alcohol (CPVA) containing six hydrophobic moieties per polymer chain by reaction of the corresponding PVA, M_w 13 and 31 kDa, with cholesterol chloroformate in dry DMSO in the presence of triethylamine at room temperature. The cholesterol-modified PVA polymers were isolated with a yield of 80−85%. In an alternative method, PVA was modified in *N*-methyl pyrrolidone at 70 °C, yielding the corresponding cholesterol-modified polymer at 70−75% as a white solid after precipitation in diethyl ether.[29] The cholesterol-modified PVA polymers were designated as CPVA13 and CPVA31 (Scheme 1). Similarly, as shown in Scheme 2, we synthesized a cholesterol-modified dextrin (CDex) with a high yield starting from dextrin (M_w 9 kDa). Four cholesterol moieties were attached to the smaller dextrin molecule. The flexibility of charged polymer chains was restricted by hydrophobic cholesterol groups aggregated in the core of nanogels. The nanogels bearing negatively charged phosphate groups formed even smaller spherical compacted particles following the addition of positively charged spermine molecules (Figure 1).

^{1}H NMR spectra showed that the cholesterol modification was nearly quantitative and amounted for six moieties per polymer chain in CPVA13 and CPVA31 and four per polymer chain in CDex9. Similarly, the formation of micelles in aqueous solutions by these polymers was also demonstrated by ^{1}H NMR spectroscopy. Figures S1 and S2 represent the spectra of CPVA13 and CDex9 in (a) D_2O and (b) DMSO-d_6, respectively (see Supporting Information). As shown in the spectra, proton signals of the cholesterol moiety (δ = 0.6−2.4 ppm) appeared in DMSO-d_6 (b), but completely disappeared or wide broadening of signals was observed in D_2O (a). This indicates the restricted molecular motion of cholesterol moieties upon self-aggregation. Our results confirmed the formation of a rigid core of hydrophobic cholesterol moieties and a relatively mobile shell consisting of hydrophilic PVA or Dex molecules in aqueous medium. The degree of cholesterol substitution (DS) was evaluated by calculating the ratio between the integrals of the protons in terminal CH_3-groups of cholesterol and methylene protons in CPVA or the protons of sugar monomers in CDex.

The hydroxyl functional groups in the cholesterol-modified polymers have been used as sites for the conjugation of the active phosphorylated nucleoside analogue, floxuridine (FdU), resulting in the formation of polymeric conjugates as anticancer drug carriers (Schemes 1 and 2). The 5′-hydroxyl group of the nucleoside analogue was chemically attached via a biodegradable tetraphosphate linker to nanogels using a 2-cyanoethyl-bis(imidazolyl)phosphate, CNEtOP(O)Im$_2$, as a phosphorylating reagent. As shown in Schemes 1 and 2, the polymers were phosphorylated with CNEtOP(O)Im$_2$ in DMF and then reacted efficiently with inorganic pyrophosphate in the form of tetra-*n*-butylammonium salt PPi-TBA(**6**) in order to form the polymeric triphosphate **7**. Separately, the 5′-hydroxyl group of the nucleoside was phosphorylated by CNEtOP(O)Im$_2$, and the activated 5′-phosphorylated nucleoside **8** was reacted in the next step with the polymeric triphosphate **7**.

In our preliminary experiments, we found that a similar phosphorylating agent, methyl-bis(imidazolyl)phosphate, MeOPOIm$_2$, reacted efficiently with the primary hydroxyl groups of nucleosides in the formation of activated 5′-monophosphates, but compared with CNEtOP(O)Im$_2$, this reaction was much slower. The relative efficacy of phosphorylation using these two reagents was compared based on the yields of nucleoside 5′-monophosphate analyzed by ion-pair HPLC. During the first hour of reaction, CNEtOP(O)Im$_2$ yielded 80% of monophosphate compared with only 10% when MeOPOIm$_2$ was used.

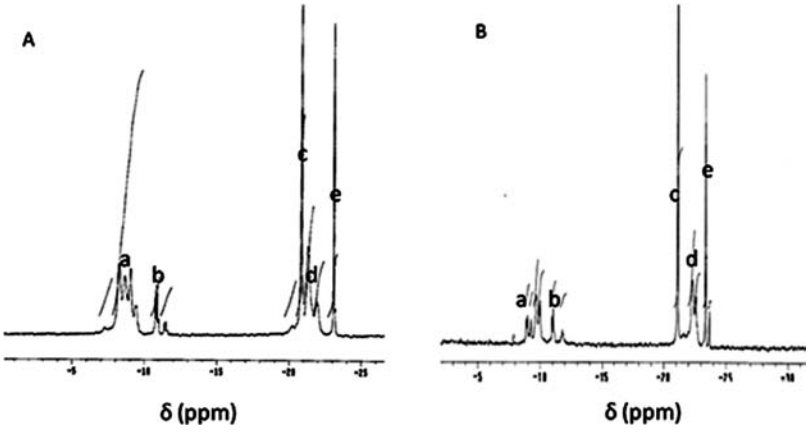

Figure 2. ^{31}P NMR spectrum of polymeric conjugates, CPVA31-p 4FdU (A) and CDex9-p4FdU (B) (phosphorus signals a−e are described in the text).

The electron donor effect of the methoxy group makes the phosphorus atom less electrophilic, which resulted in longer reaction times, especially with secondary hydroxyl groups. However, both phosphorylating agents formed the same final activated 5′-monophosphorylated nucleoside in our synthesis. Next, the activated imidazolyl-phosphate moiety in **8** readily reacted with polymer-triphosphate **7** and converted into nucleoside 5′-tetraphosphate anchored to CPVA, (**9**−**11**) or CDex (**14**, **15**). Initially, we used thymidine (T) as a model drug in this study. Polymeric conjugates were purified by extensive dialysis to remove all reactants. CPVA- and CDex-conjugated 5′-tetraphosphates of FdU were designated as CPVA13-p_4FdU, CPVA31-p_4FdU, CDex9-p_4FdU, and CDex9-p_4T and their properties are shown in Table 1. The amount of nucleoside attached to the polymer was determined by UV absorbance. We observed a high degree of nucleoside loading in nanogels, which was equal to 0.4−0.5 μmol/mg.

Covalent conjugation of the nucleoside to nanogels via a tetraphosphate linker was further verified by ^{31}P NMR and IR spectroscopy. ^{31}P NMR spectra confirmed the formation of tetraphosphate structures along with trace amounts of a triphosphate and polyphosphates such as a pentaphosphate (Figure 2). According to published chemical shifts,[30,31] upper field region of ^{31}P NMR spectra at −20 to −25 ppm corresponds to β- and γ-phosphates (peaks *c*, *d*, and *e*), while signals between −8 and −12 ppm correspond to terminal α- and δ-phosphates (peaks *a* and *b*). IR spectra of CPVA-p_4FdU have allowed us to observe conjugation of the FdU nucleoside to the CPVA nanogel (Supporting Information Figure S3). As is clearly shown in the spectra, the peak at 899 cm^{-1} corresponding to P-OR stretch, the peak at 1234 cm^{-1} corresponding to P═O stretch of phosphate, and the peak at 1708 cm^{-1} corresponding to C═O stretch of amide are clearly increased in the CPVA-p_4FdU products, while peaks at 1311−1417 cm^{-1} corresponding to O−H bonding of CPVA were reduced, confirming the formation of a polyphosphate linker between CPVA and FdU.

Particle Size and Zeta-Potential. Compact nanogel conjugates could be successfully formed as the result of self-organization of CPVA/CDex-p_4FdU molecules during ultrasonication in aqueous solutions. When sufficient energy was applied, the cholesterol moieties formed compact intramolecular clusters surrounded by a hydrophilic polymeric shell containing the embedded negatively charged drug molecules. The particle size, homogeneity, and morphology of CPVA/CDex-p_4FdU structures were measured by dynamic light scattering (DLS) and transmission electron microscopy (TEM). A single sharp peak in DLS profiles with a hydrodynamic diameter in the range of 12−45 nm implied the presence of a single population of small particles with a relatively low polydispersity index of 0.30−0.59 (Table 1). The high negative zeta-potential of CPVA/CDex-p_4FdU confirmed the presence of phosphates in the surface layer of polymeric conjugates. TEM pictures showed the spherical particle morphology with hydrodynamic diameters in the range 38−58 nm (Figure 3). We have also studied the change in particle size after neutralization of the negative charge in polymeric conjugates with the polyamine spermine (Figure 1). The addition of positively charged spermine at physiological conditions resulted in a 2−3-fold reduction in hydrodynamic and TEM-observed diameters and the change in morphology of particles, e.g., the appearance of a thicker electron-dense exterior layer surrounding these compacted polymeric conjugates.[32]

Enzymatic Hydrolysis. The formation of natural nucleoside 5′-phosphate bonds between nucleoside and nanogel backbone was further confirmed using enzymatic hydrolysis by snake venom phosphodiesterase I (VPDE). VPDE was able to catalyze the hydrolysis of esterified nucleoside 5′-phosphates into a nucleoside 5′-phosphate and also the cleavage of nucleoside 5′-phosphate from oligonucleotides with a free 3′-end.[33,34] This property of VPDE allows us to investigate the enzymatic stability of nanogel-bound nucleoside phosphates. Nanogels CPVA-p_4FdU and CDex-p_4FdU were incubated with VPDE at 37 °C and then analyzed by ion-pair HPLC (Figure 4). We observed the gradual disappearance of the initial wide peak with the elution time of 25−34 min (*a*) and the formation of a sharp peak at the elution time of ca. 5 min (*b*), which corresponded to control nucleoside 5′-phosphates (TMP or FdUMP). Structure of the released nucleoside products was further confirmed by comparison of UV spectra with initial nucleoside analogues. Our data demonstrated a nearly quantitative enzymatic release of nucleotide 5′-phosphate from polymeric conjugates within 12 to 24 h.

***In Vitro* Drug Release.** The *in vitro* release of FdU was monitored at 37 °C at different pH values (1.0, 4.0, and 7.4) in order to assess the stability of nanogel conjugates in the environments in the stomach, endosomal vesicles, and blood, respectively. Each nanogel, CPVA-p_4FdU or CDEX-p_4FdU, was placed into the appropriate buffer solution and incubated at 37 °C. Serial aliquots were removed at the appropriate times during hydrolysis, and the cleaved nucleoside/nucleotide was separated by ultrafiltration and quantified by UV absorbance.

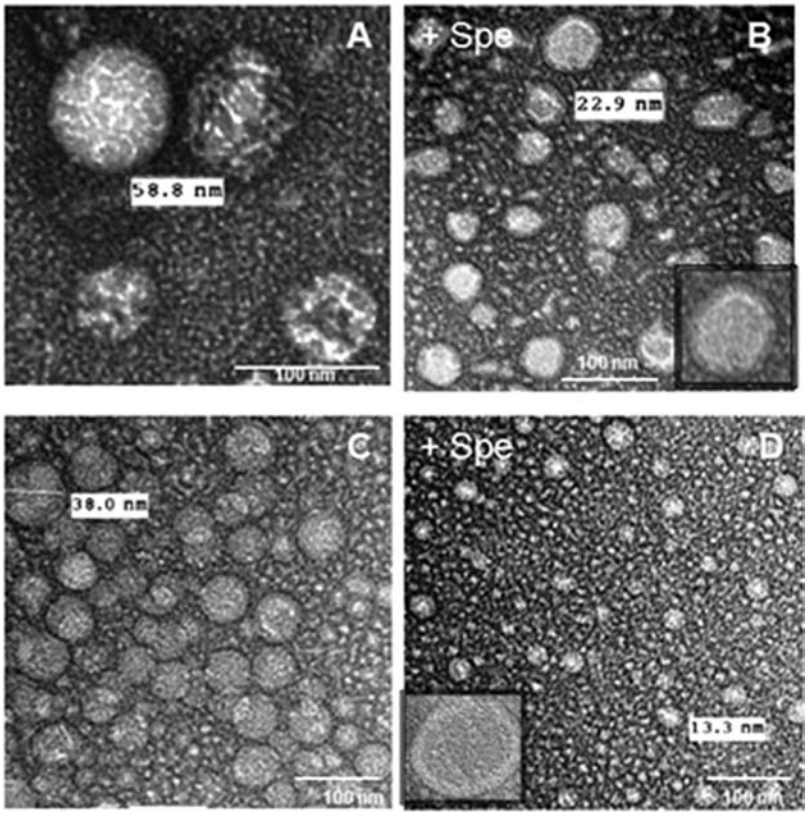

Figure 3. Transmission electron microscopy (TEM) images of nanogels formed from polymer conjugates: (A) CPVA31-p4FdU, (B) its spermine complex (Spe), (C) CDex9-p4FdU, and (D) its spermine complex. Samples were stained with vanadate.

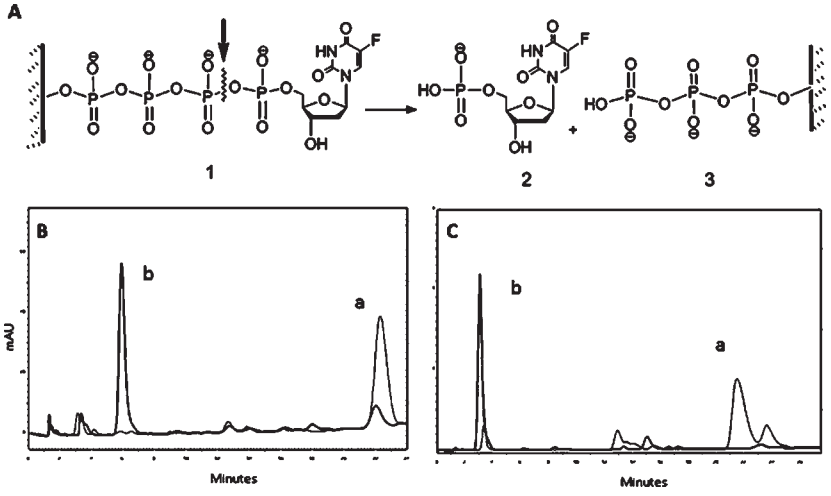

Figure 4. Enzymatic hydrolysis of polymeric conjugates by snake venom phosphodiesterase I (VPDE). (A) The enzyme hydrolyzes the P−O bond at α-phosphate group in nanogel conjugate resulting in nucleoside 5′-phosphate (2). (B) Ion-pair HPLC profiles of initial (a) and hydrolyzed (b) CPVA31-p4FdU. (C) Ion-pair HPLC profiles of initial (a) and hydrolyzed (b) CDex9-p4T after 24 h incubation with 0.01 units of VPDE enzyme.

The release profiles at different pH values are shown in Figure 5. In general, polymeric conjugates displayed linear first-order reaction kinetics of hydrolysis with slower drug release at pH 7.4 and pH 4.0 than at pH 1.0. At pH 4.0 and 7.4, drug release was 1−2% per day, while at pH 1.0 drug release reached 4% per day. These results are consistent with the pH-dependent degradation behavior of other dinucleoside polyphosphates, such as diadenosine-P**1**,P**3**-triphosphate and P**1**,P**4**-tetraphosphate.[35] However, CPVA/CDex-p_4FdU conjugates showed much slower drug release compared to diadenosine-P**1**,P**4**-tetraphosphate (25 days vs 3 days). The pH-dependent hydrolysis can be facilitated by a hydronium ion through the nucleophilic attack of protonated phosphate groups at lower pH, which results in an $S_N(P)$-type substitution, and then the formation of a penta-coordinated

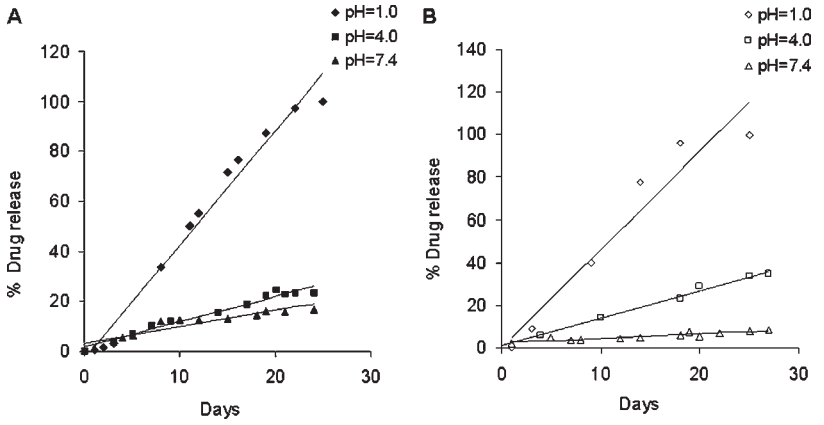

Figure 5. In vitro drug release from polymeric conjugates CPVA31-p4FdU (A) and CDex9-p4FdU (B) at different pH in buffered saline.

Scheme 3. Mechanism of Acidic Hydrolysis of Polymeric Conjugates and Release of Phosphorylated Nucleosides (R = cholesterol)

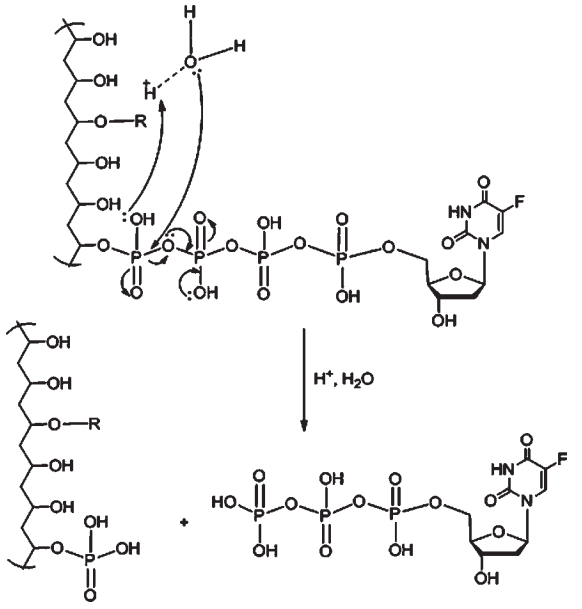

phosphorus transition state and nucleoside 5′-phosphates as final products (Scheme 3). Highly hydrated polymer coils surrounding the tetraphosphate linkers evidently create a steric hindrance and significantly slow down the process.

Evidently, the release of phosphorylated nucleosides in cancer cells would provide a strong therapeutic advantage to these polymeric conjugates, because the drug component does not have to pass through the phosphorylation step, which is known to be a rate-limiting step in biological activation of nucleoside analogues.[36] Our data show that this type of polymeric conjugates is capable of the sustained drug release during the extended period of time and can serve as active drug depot, significantly enhancing therapeutic effect against cancer cells. Peritumoral injections or systemic administration of polymeric conjugates would result in only minimal initial drug burst, a shortcoming of many drug delivery systems at systemic administration. Additionally, accumulation of nanocarriers from blood circulation through the enhanced permeability and retention (EPR) effect in leaking tumor neovasculature can potentially enhance the tumor growth inhibitory effect. Polymeric conjugates can also be considered as potential oral therapeutic formulations due to the observed slow drug release at low pH in the digestive tract (*in vivo* experiments are underway). We have also demonstrated that enzymatic hydrolysis of polymeric conjugates is at least 20−25 times faster than hydrolytic hydrolysis. Therefore, these polymeric conjugates, which have a slow, sustained drug release in tumor tissue and other organs in normal conditions *in vivo*, might be quickly activated by enzymatic activities present in the cytosol or subcellular compartments of proliferating cancer cells.[37] The most common type of hydrolytic enzymes in mammalian cells are cytosolic phosphodiesterases and nucleotide phosphatases, which can release active 5′-nucleotides from the polymeric conjugates.[38]

Cytotoxicity Assay. Drug resistance to nucleoside analogues is known to be an important clinical problem in the treatment of cancer. Therapeutic effects can be achieved with nucleoside analogues as a single agent or in combination with other drugs only at the increasingly higher dosage. Here, we have studied the cytotoxicity of several polymeric conjugates of activated analogues of 5-fluorouracyl as a model drug in various cancer cell lines including ones that are resistant to nucleoside analogues. The cytotoxicity of polymeric floxuridine conjugates CPVA13-p_4FdU, CPVA31-p_4FdU, and CDEX9-p_4FdU was determined in human prostate adenocarcinoma PC-3, breast carcinoma MCF-7 and MDA-MB-231, hepatic carcinoma HepG2, gemcitabine-resistant follicular lymphoma RL7/G, and cytarabine-resistant T-lymphoma CEM/araC/8 cells using a thiazolyl blue (MTT) dye reduction assay.[39] As shown in Figure 6 and Table 2, nanoconjugates showed considerably enhanced cytotoxicity and lower IC_{50} values (drug concentration resulting in 50% cell death) compared to free floxuridine in all of these cell lines. The enhancement factor (EF), which is equal to IC_{50}(drug)/IC_{50}(conjugate), was used as a measure of the increase in cytotoxicity of polymeric conjugates compared to free drug. Nanogels without conjugated drug demonstrated no cytotoxicity (IC_{50} > 10 mg/mL). All of these polymeric conjugates showed a higher EF in drug resistant cell lines, CEM/araC/8 and RL7/G, compared to other tumor cells. Specifically, CPVA13-p_4FdU and CDex9-p_4FdU exhibited an EF of 100 and 85 in CEM/araC/8 cells, while the EF showed by other cells was normally in the lower range of 3.5−50.

***In Vivo* Tumor Growth Inhibition.** The therapeutic efficacy of polymeric conjugates was evaluated in subcutaneous (s.c.) human prostate adenocarcinoma PC-3 and gemcitabine-resistant

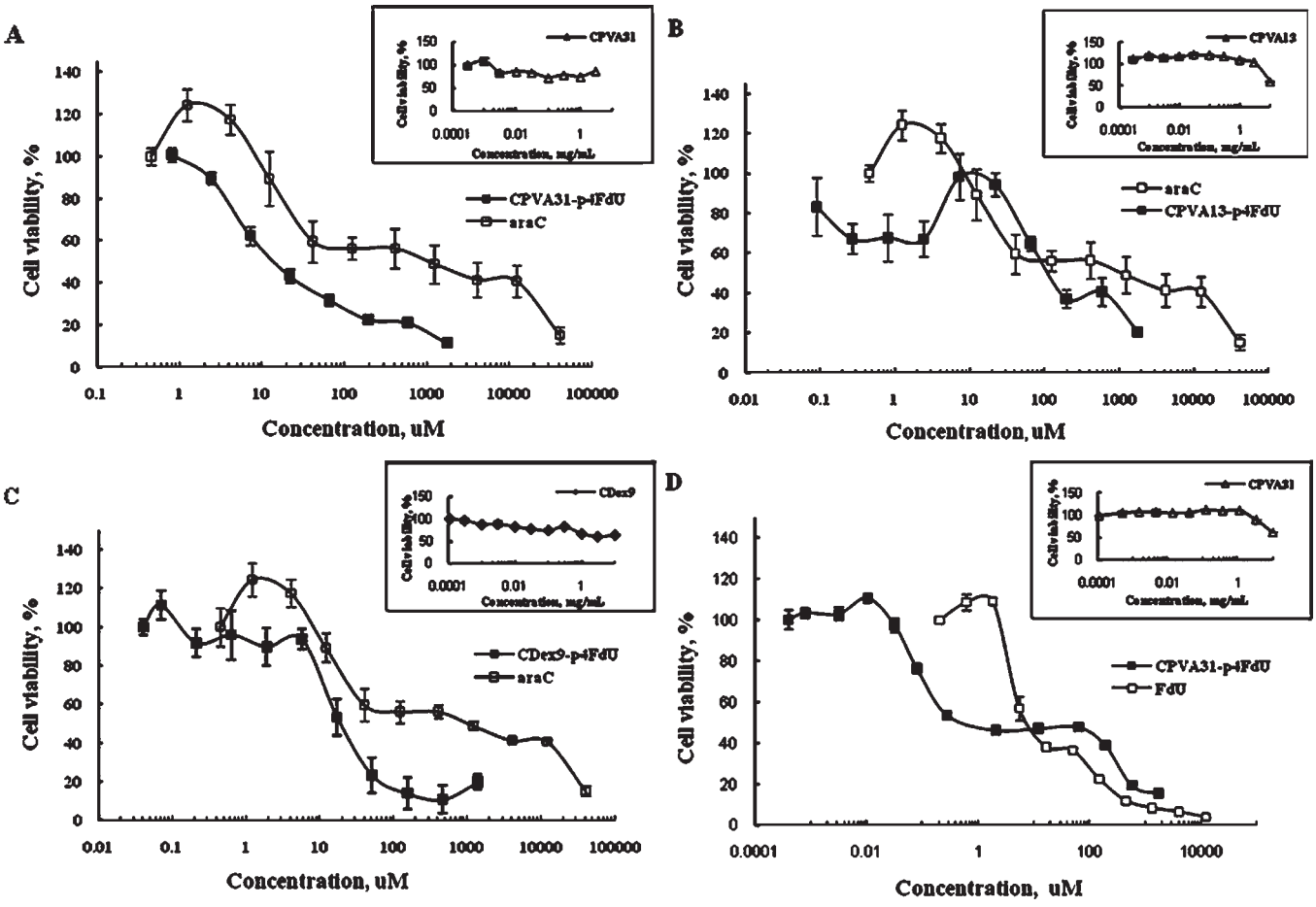

Figure 6. Cytotoxicity of polymeric conjugates in drug-resistant human T-lymphoma CEM/araC/8 cells (A−C) and prostate carcinoma PC-3 cells (D).

Table 2. Cytotoxicity of Cytotoxic Drugs, Polymeric Conjugates, and Drug Conjugates in Cancer Cells

	IC_{50} values (μM)[a]					
drug formulation	PC-3	MCF-7	HepG2	MDA-MB-231	CEM/araC/8	RL7/G
Floxuridine (FdU)	6.5	12195	2195	14.2		
Cytarabine (araC)					1234	
Gemcitabine (G)						19011
CPVA31	>10	>10	>10	>10	>10	>10
CPVA13	>10	>10	>10	>10	>10	>10
CDEX9					>10	>10
CPVA31-p_4FdU	0.4	2032	487	0.28	12.3	3802
	(EF=16)	(EF=6)	(EF=4.5)	(EF=50)	(EF=100)	(EF=5)
CPVA13-p_4FdU	81.3	813	609.7	0.6	102	950
		(EF=15)	(EF=3.6)	(EF=23)	(EF=12)	(EF=20)
CDEX9-p_4FdU					14.5	
					(EF=85)	

[a] Cytotoxicity was measured after 72-h treatment. IC_{50} of CPVA31, CPVA13, and CDEX9 in each cell line are given in mg/mL. EF = enhancement factor showing the efficacy compared to free drug.

follicular lymphoma RL7/G tumor xenograft mouse models. These tumors were established by s.c. injection of tumor cells in the lower flank areas of athymic nu−nu mice. After the observation of the initial tumors, animals were randomly separated into control and treatment groups ($n = 5-6$). Median tumor volume was measured by digital calipers twice a week simultaneously with peritumoral injections of polymeric conjugates with a dose of 80 mg/kg, which is equivalent to 10 mg FdU/kg. This way of administration allowed

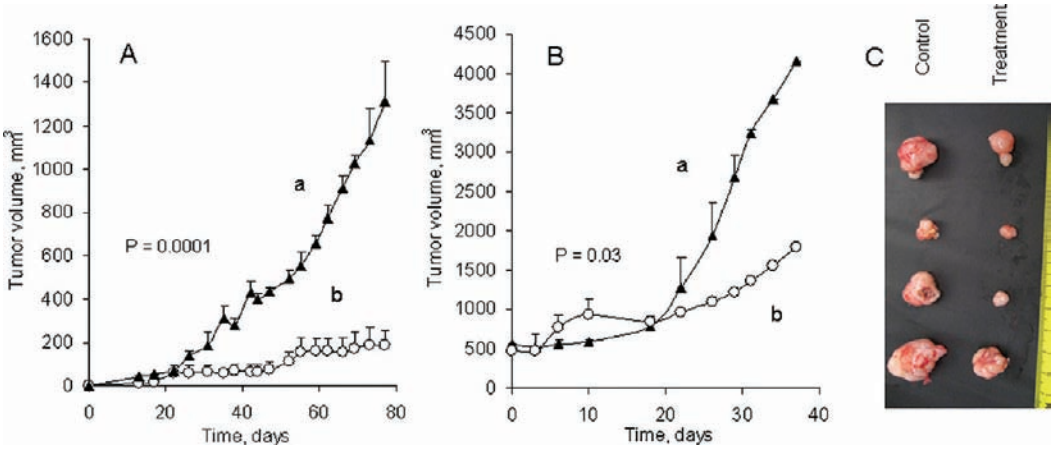

Figure 7. Tumor growth inhibition in mice with subcutaneous human prostate carcinoma PC-3 (A) and gemcitabine-resistant follicular lymphoma RL7/G (B) tumors following the peritumoral injections of the polymeric conjugate CPVA31-p4FdU (dose 80 mg/kg or 10 mg FdU/kg). The data were statistically significant with $P < 0.05$ between (a) control and (b) treatment groups. (C) Tumor photographs in the end of the experiment B taken from control and treatment groups.

a subcutaneous storage of the viscous polymer—drug conjugate and the sustained release of activated drug into the tumor. We observed a strong 6.5-fold tumor growth inhibition in human prostate carcinoma PC-3 model that confirms the high therapeutic potential of polymeric conjugates (Figure 7A). Although the observed 2-fold growth inhibition was lower in drug-resistant human follicular lymphoma RL7/G tumors compared to PC-3 tumors, the effect of the CPVA31-p_4FdU conjugate was statistically significant ($P < 0.05$) (Figure 7B). The significance of the experimental data was determined by a two-tailed Student's *t*-test. No significant weight loss or acute toxicity of polymeric conjugates was observed during the entire period of treatment. Tumors removed from experimental animals at the end of the experiments were clearly smaller than tumors in the control group (Figure 7C).

CONCLUSIONS

We have developed a novel type of covalently bound polymeric phosphorylated nucleoside analogues, polymeric conjugates, for a sustained delivery of the activated anticancer drugs into tumors. These carriers combine attractive properties of biocompatible polymers with an enhanced cytotoxic efficacy of activated nucleoside analogues and form compact drug-loaded polymeric nanoparticles. *In vitro* evaluation against various cancer cell lines, including drug-resistant cancer cells, demonstrated that the activated floxuridine conjugate has 50—100 times stronger cytotoxicity compared to free nucleoside analogue. Furthermore, the observed sustained drug release was a potential cause of the increased tumor growth inhibition following the peritumoral administration of polymeric conjugates in subcutaneous tumor xenograft models. This class of anticancer drug formulations also has features, which makes them a very promising vehicle for oral administration of activated phosphorylated nucleoside analogues.

ASSOCIATED CONTENT

Supporting Information. Analytical characteristics (^{1}H NMR and IR spectra, Figures S1—S3) of synthesized products. This material is available free of charge via the Internet at http://pubs.acs.org.

AUTHOR INFORMATION

Corresponding Author

*986025 Nebraska Medical Center, Omaha, NE 68198-6025. Phone: (402) 559-9362; Fax: (402) 559-9543; E-mail: vinograd@unmc.edu.

ACKNOWLEDGMENT

The financial support from National Cancer Institute (R01 CA136921 for S.V.V.) is gratefully acknowledged. The authors thank Tom Bargar of the Electron Microscopy Core Facility, Ed Ezell of the NMR Core Facility, and Marina Sokolsky-Papkov from Center for Drug Delivery and Nanomedicine (University of Nebraska Medical Center) for providing assistance with TEM microscopy, NMR and IR spectroscopy, respectively. We are grateful to Trevor Gerson for his help in the revision of the manuscript.

REFERENCES

(1) Johnstone, R. W., Ruefli, A. A., and Lowe, S. W. (2002) Apoptosis: a link between cancer genetics and chemotherapy. *Cell 108*, 153–164.

(2) Galmarini, C. M., Mackey, J. R., and Dumontet, C. (2002) Nucleoside analogues and nucleobases in cancer treatment. *Lancet Oncol. 3*, 415–424.

(3) Galmarini, C. M., Thomas, X., Calvo, F., Rousselot, P., Rabilloud, M., El Jaffari, A., Cros, E., and Dumontet, C. (2002) In vivo mechanisms of resistance to cytarabine in acute myeloid leukaemia. *Br. J. Hamaetol. 117*, 860–868.

(4) Ward, J. L., Sherali, A., Mo, Z. P., and Tse, C. M. (2000) Kinetic and pharmacological properties of cloned human equilibrative nucleoside transporters, ENT1 and ENT2, stably expressed in nucleoside transporter-deficient PK15 cells. Ent2 exhibits a low affinity for guanosine and cytidine but a high affinity for inosine. *J. Biol. Chem. 275*, 8375–8381.

(5) Crawford, C. R., Ng, C. Y., and Belt, J. A. (1990) Isolation and characterization of an L1210 cell line retaining the sodium-dependent carrier cif as its sole nucleoside transport activity. *J. Biol. Chem. 265*, 13730–13734.

(6) Crawford, C. R., Ng, C. Y., Noel, L. D., and Belt, J. A. (1990) Nucleoside transport in L1210 murine leukemia cells. Evidence for three transporters. *J. Biol. Chem. 265*, 9732–9736.

(7) Funato, T., Satou, J., Nishiyama, Y., Fujimaki, S., Miura, T., Kaku, M., and Sasaki, T. (2000) In vitro leukemia cell models of Ara-C resistance. *Leuk. Res. 24*, 535–541.

(8) Dumontet, C., Fabianowska-Majewska, K., Mantincic, D., Callet Bauchu, E., Tigaud, I., Gandhi, V., Lepoivre, M., Peters, G. J., Rolland, M. O., Wyczechowska, D., Fang, X., Gazzo, S., Voorn, D. A., Vanier-Viornery, A., and MacKey, J. (1999) Common resistance mechanisms to deoxynucleoside analogues in variants of the human erythroleukaemic line K562. *Br. J. Hamaetol. 106*, 78–85.

(9) Meier, C., and Balzarini, J. (2006) Application of the cycloSal-prodrug approach for improving the biological potential of phosphorylated biomolecules. *Antiviral Res. 71*, 282–292.

(10) Galmarini, C. M., Popowycz, F., and Joseph, B. (2008) Cytotoxic nucleoside analogues: different strategies to improve their clinical efficacy. *Curr. Med. Chem. 15*, 1072–1082.

(11) Zamboni, W. C. (2005) Liposomal, nanoparticle, and conjugated formulations of anticancer agents. *Clin. Cancer Res. 11*, 8230–8234.

(12) Crosasso, P., Brusa, P., Dosio, F., Arpicco, S., Pacchioni, D., Schuber, F., and Cattel, L. (1997) Antitumoral activity of liposomes and immunoliposomes containing 5-fluorouridine prodrugs. *J. Pharm. Sci. 86*, 832–839.

(13) Duzgunes, N., Simoes, S., Slepushkin, V., Pretzer, E., Flasher, D., Salem, I., Steffan, G., Konopka, K., and Pedroso de Lima, M. C. (2005) Delivery of antiviral agents in liposomes. *Methods Enzymol. 391*, 351–373.

(14) Oussoren, C., Magnani, M., Fraternale, A., Casabianca, A., Chiarantini, L., Ingebrigsten, R., Underberg, W. J., and Storm, G. (1999) Liposomes as carriers of the antiretroviral agent dideoxycytidine-5′-triphosphate. *Int. J. Pharm. 180*, 261–270.

(15) Vinogradov, S. V., Poluektova, L. Y., Makarov, E., Gerson, T., and Senanayake, M. T. (2010) Nano-NRTIs: efficient inhibitors of HIV type-1 in macrophages with a reduced mitochondrial toxicity. *Antivir. Chem. Chemother. 21*, 1–14.

(16) Magnani, M., Rossi, L., Fraternale, A., Casabianca, A., Brandi, G., Benatti, U., and De Flora, A. (1997) Targeting antiviral nucleotide analogues to macrophages. *J. Leukocyte Biol. 62*, 133–137.

(17) Vinogradov, S. V., Zeman, A. D., Batrakova, E. V., and Kabanov, A. V. (2005) Polyplex Nanogel formulations for drug delivery of cytotoxic nucleoside analogs. *J. Controlled Release 107*, 143–157.

(18) Vinogradov, S. V., Kohli, E., and Zeman, A. D. (2005) Cross-linked polymeric nanogel formulations of 5′-triphosphates of nucleoside analogues: role of the cellular membrane in drug release. *Mol. Pharm. 2*, 449–461.

(19) Galmarini, C. M., Warren, G., Kohli, E., Zeman, A., Mitin, A., and Vinogradov, S. V. (2008) Polymeric nanogels containing the triphosphate form of cytotoxic nucleoside analogues show antitumor activity against breast and colorectal cancer cell lines. *Mol. Cancer Ther. 7*, 3373–3380.

(20) Aryal, S., Hu, C. M., and Zhang, L. (2010) Combinatorial drug conjugation enables nanoparticle dual-drug delivery. *Small 6*, 1442–1448.

(21) Ferey, G. (2008) Hybrid porous solids: past, present, future. *Chem. Soc. Rev. 37*, 191–214.

(22) Ulbrich, K., Strohalm, J., and Kopecek, J. (1982) Polymers containing enzymatically degradable bonds. VI. Hydrophilic gels cleavable by chymotrypsin. *Biomaterials 3*, 150–154.

(23) Galmarini, C. M., Clarke, M. L., Jordheim, L., Santos, C. L., Cros, E., Mackey, J. R., and Dumontet, C. (2004) Resistance to gemcitabine in a human follicular lymphoma cell line is due to partial deletion of the deoxycytidine kinase gene. *BMC Pharmacol. 4*, 8.

(24) Ullman, B. (1989) Dideoxycytidine metabolism in wild type and mutant CEM cells deficient in nucleoside transport or deoxycytidine kinase. *Adv. Exp. Med. Biol. 253B*, 415–420.

(25) Sinha, N. D., Biernat, J., McManus, J., and Koster, H. (1984) Polymer support oligonucleotide synthesis XVIII: use of beta-cyanoethyl-N,N-dialkylamino-/N-morpholino phosphoramidite of deoxynucleosides for the synthesis of DNA fragments simplifying deprotection and isolation of the final product. *Nucleic Acids Res. 12*, 4539–4557.

(26) Vinogradov, S. V., Suzdaltseva, Y., Alakhov, V., and Kabanov, A. V. (1994) Inhibition of herpes simplex virus 1 reproduction with hydrophobized antisense oligonucleotides. *Biochem. Biophys. Res. Commun. 203*, 959–966.

(27) Nochi, T., Yuki, Y., Takahashi, H., Sawada, S., Mejima, M., Kohda, T., Harada, N., Kong, I. G., Sato, A., Kataoka, N., Tokuhara, D., Kurokawa, S., Takahashi, Y., Tsukada, H., Kozaki, S., Akiyoshi, K., and Kiyono, H. (2010) Nanogel antigenic protein-delivery system for adjuvant-free intranasal vaccines. *Nat. Mater. 9*, 572–578.

(28) Yusa, S., Kamachi, M., and Morishima, Y. (1998) Hydrophobic self-association of cholesterol moieties covalently linked to polyelectrolytes: Effect of spacer bond. *Langmuir 14*, 6059–6067.

(29) Gimenez, V., Reina, J. A., Mantecon, A., and Cadiz, V. (1999) Unsaturated modified poly(vinyl alcohol). Crosslinking through double bonds. *Polymer 40*, 2759–2767.

(30) Moreno, B., Urbina, J. A., Oldfield, E., Bailey, B. N., Rodrigues, C. O., and Docampo, R. (2000) 31P NMR spectroscopy of Trypanosoma brucei, Trypanosoma cruzi, and Leishmania major. Evidence for high levels of condensed inorganic phosphates. *J. Biol. Chem. 275*, 28356–28362.

(31) Warnecke, S., and Meier, C. (2009) Synthesis of nucleoside Di- and triphosphates and dinucleoside polyphosphates with cycloSal-nucleotides. *J. Org. Chem. 74*, 3024–3030.

(32) Chen, N., Murata, S., and Yoshikawa, K. (2005) Dramatic change in the tertiary structure of giant DNA without distortion of the secondary structure caused by pteridine-polyamine conjugates. *Chemistry 11*, 4835–4840.

(33) Razzell, W. E., and Khorana, H. G. (1959) Studies on polynucleotides. III. Enzymic degradation; substrate specificity and properties of snake venom phosphodiesterase. *J. Biol. Chem. 234*, 2105–2113.

(34) Garcia-Diaz, M., Avalos, M., and Cameselle, J. C. (1991) Methanol esterification reactions catalyzed by snake venom and bovine intestinal 5′-nucleotide phosphodiesterases. Formation of nucleoside 5′-monophosphate methyl esters from guanosine 5′-triphosphate and other nucleoside 5′-polyphosphates. *Eur. J. Biochem. 196*, 451–457.

(35) Mikkola, S. (2004) Hydrolytic reactions of diadenosine 5′,5′-triphosphate. *Org. Biomol. Chem. 2*, 770–776.

(36) Longley, D. B., Harkin, D. P., and Johnston, P. G. (2003) 5-fluorouracil: mechanisms of action and clinical strategies. *Nat. Rev. Cancer 3*, 330–338.

(37) Bender, A. T., and Beavo, J. A. (2006) Cyclic nucleotide phosphodiesterases: molecular regulation to clinical use. *Pharmacol. Rev. 58*, 488–520.

(38) Garcia-Diaz, M., Avalos, M., and Cameselle, J. C. (2006) Methanol esterification reaction catalyzed by snake venom and bovine intestinal 5′-nucleotide phosphodiesterases. *Eur. J. Biochem. 196*, 451–457.

(39) Hansen, M. B., Nielsen, S. E., and Berg, K. (1989) Re-examination and further development of a precise and rapid dye method for measuring cell growth/cell kill. *J. Immunol. Methods 119*, 203–210.

Supporting Materials

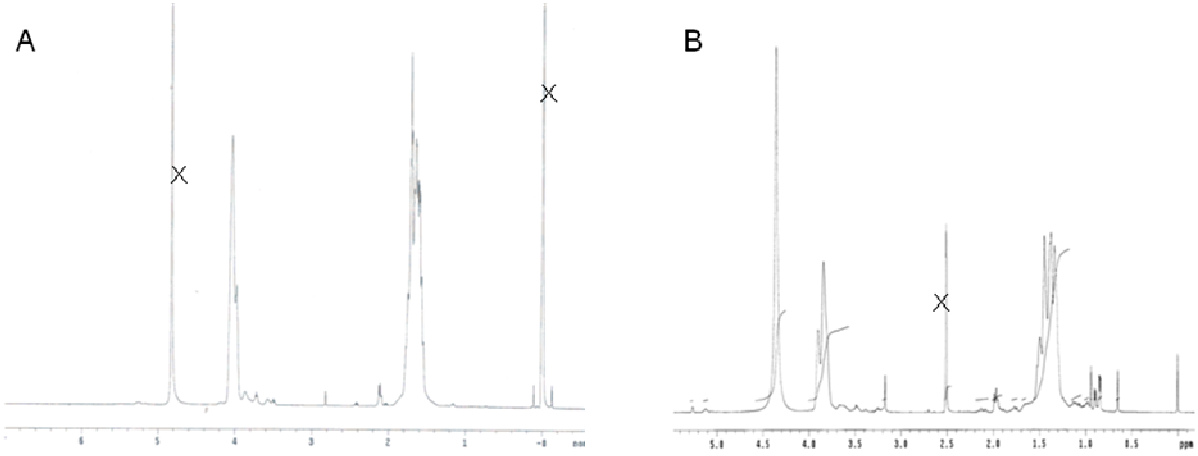

Figure S1. ^{1}H-NMR spectrum of CPVA31 in D_2O (A), in DMSO-$\boldsymbol{d_6}$ (B). Crossed peaks correspond to residual solvent peaks. Values on the x-axis are in ppm.

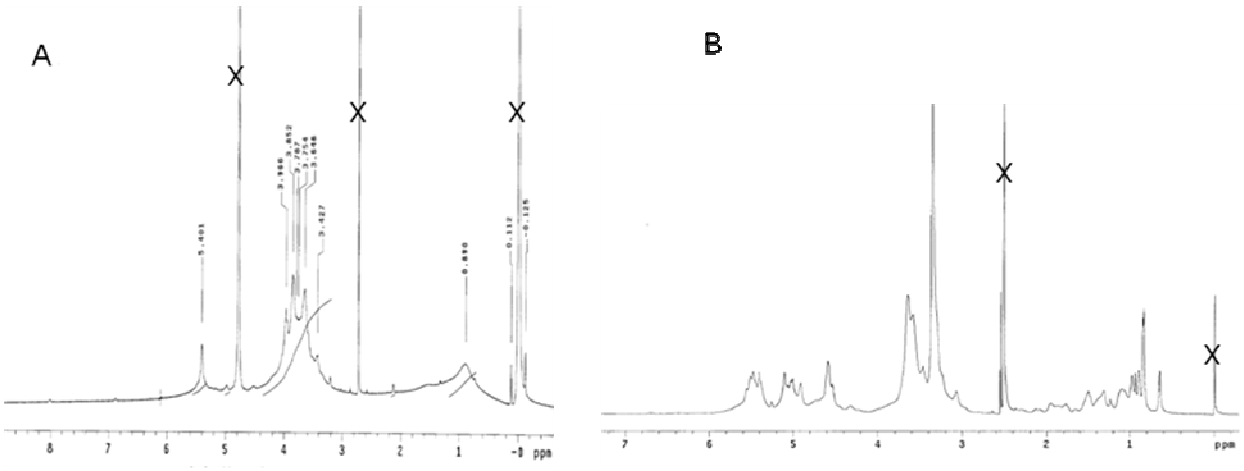

Figure S2. ^{1}H-NMR spectra of CDex9 in D_2O (A) and in DMSO-$\boldsymbol{d_6}$ (B). Crossed peaks correspond to residual solvent peaks. Values on the x-axis are in ppm.

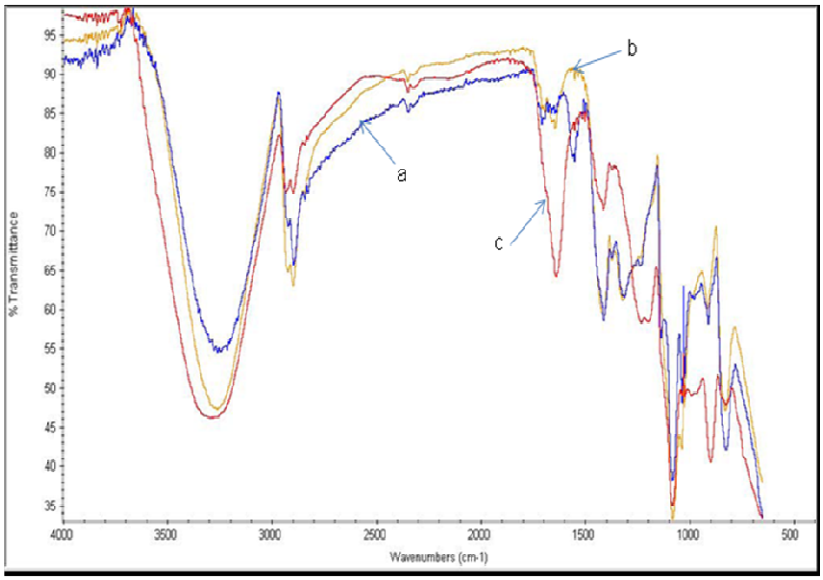

Figure S3. IR spectrum of (a) PVA31 polymer, (b) CPVA31 and (c) CPVA31-p_4FdU conjugates

Bioconjugate Chemistry

ARTICLE

pubs.acs.org/bc

Impact of Drug Conjugation on Pharmacokinetics and Tissue Distribution of Anti-STEAP1 Antibody–Drug Conjugates in Rats

C. Andrew Boswell,[†] Eduardo E. Mundo,[†] Crystal Zhang,[†] Daniela Bumbaca,[†] Nicole R. Valle,[‡] Katherine R. Kozak,[§] Aimee Fourie,[§] Josefa Chuh,[§] Neelima Koppada,[∥] Ola Saad,[∥] Herman Gill,[⊥] Ben-Quan Shen,[†] Bonnee Rubinfeld,[#] Jay Tibbitts,[†] Surinder Kaur,[∥] Frank-Peter Theil,[†] Paul J. Fielder,[†] Leslie A. Khawli,[*,†] and Kedan Lin[*,†]

[†]Department of Pharmacokinetic & Pharmacodynamic Sciences [‡]Department of Investigative Safety Assessment [§]Department of Assay & Automation Technology [∥]Department of BioAnalytical Research & Development [⊥]Department of Biomedical Imaging and [#]Department of Cancer Targets, Genentech Research & Early Development, South San Francisco, California 94080, United States

Supporting Information

ABSTRACT: Antibody–drug conjugates (ADCs) are designed to combine the exquisite specificity of antibodies to target tumor antigens with the cytotoxic potency of chemotherapeutic drugs. In addition to the general chemical stability of the linker, a thorough understanding of the relationship between ADC composition and biological disposition is necessary to ensure that the therapeutic window is not compromised by altered pharmacokinetics (PK), tissue distribution, and/or potential organ toxicity. The six-transmembrane epithelial antigen of prostate 1 (STEAP1) is being pursued as a tumor antigen target. To assess the role of ADC composition in PK, we evaluated plasma and tissue PK profiles in rats, following a single dose, of a humanized anti-STEAP1 IgG1 antibody, a thio-anti-STEAP1 (ThioMab) variant, and two corresponding thioether-linked monomethylauristatin E (MMAE) drug conjugates modified through interchain disulfide cysteine residues (ADC) and engineered cysteines (TDC), respectively. Plasma PK of total antibody measured by enzyme-linked immunosorbent assay (ELISA) revealed ~45% faster clearance for the ADC relative to the parent antibody, but no apparent difference in clearance between the TDC and unconjugated parent ThioMab. Total antibody clearances of the two unconjugated antibodies were similar, suggesting minimal effects on PK from cysteine mutation. An ELISA specific for MMAE-conjugated antibody indicated that the ADC cleared more rapidly than the TDC, but total antibody ELISA showed comparable clearance for the two drug conjugates. Furthermore, consistent with relative drug load, the ADC had a greater magnitude of drug deconjugation than the TDC in terms of free plasma MMAE levels. Antibody conjugation had a noticeable, albeit minor, impact on tissue distribution with a general trend toward increased hepatic uptake and reduced levels in other highly vascularized organs. Liver uptakes of ADC and TDC at 5 days postinjection were 2-fold and 1.3-fold higher, respectively, relative to the unmodified antibodies. Taken together, these results indicate that the degree of overall structural modification in anti-STEAP1-MMAE conjugates has a corresponding level of impact on both PK and tissue distribution.

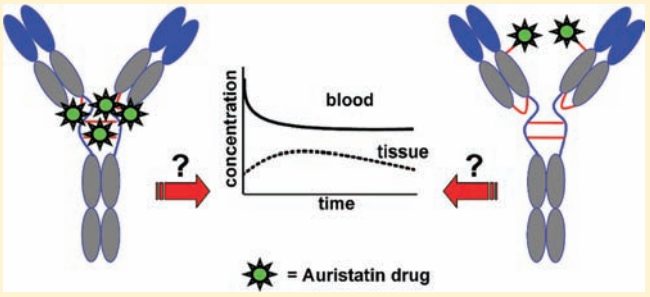

INTRODUCTION

Prostate cancer represents one-quarter of newly diagnosed cancer cases in men and is surpassed only by lung cancer in the number of male deaths.[1] Despite significant efforts toward improving the diagnosis[2,3] and treatment[4−7] of prostate tumors, there are few therapeutic options for metastatic prostate cancer, and developing effective treatments remains a critical priority. Antibody-based therapies are currently being developed against specific antigens that are expressed in prostate tumors. One such molecular target is the six-transmembrane epithelial antigen of the prostate 1 (STEAP1),[8] a cell-surface antigen that is overexpressed in the majority of human epithelial prostate cancers, but with restricted expression in normal tissues.[8−10] Although the normal functional role for STEAP1 is not fully understood, its restricted expression makes it an ideal antigen for antibody-mediated therapy.

The development of antibody–drug conjugates (ADCs) is a particularly promising therapeutic approach that combines the antigen targeting specificity of monoclonal antibodies with the cytotoxic potency of chemotherapeutic drugs.[11−20] Conjugation of cytotoxic drugs to antibodies can be achieved either through lysine side-chain amines or through cysteine sulfhydryl groups that are typically activated by reduction of interchain disulfide bonds. As such, a humanized IgG1 anti-STEAP1 conventional

Received: April 27, 2011
Revised: August 25, 2011
Published: September 13, 2011

ACS Publications © 2011 American Chemical Society

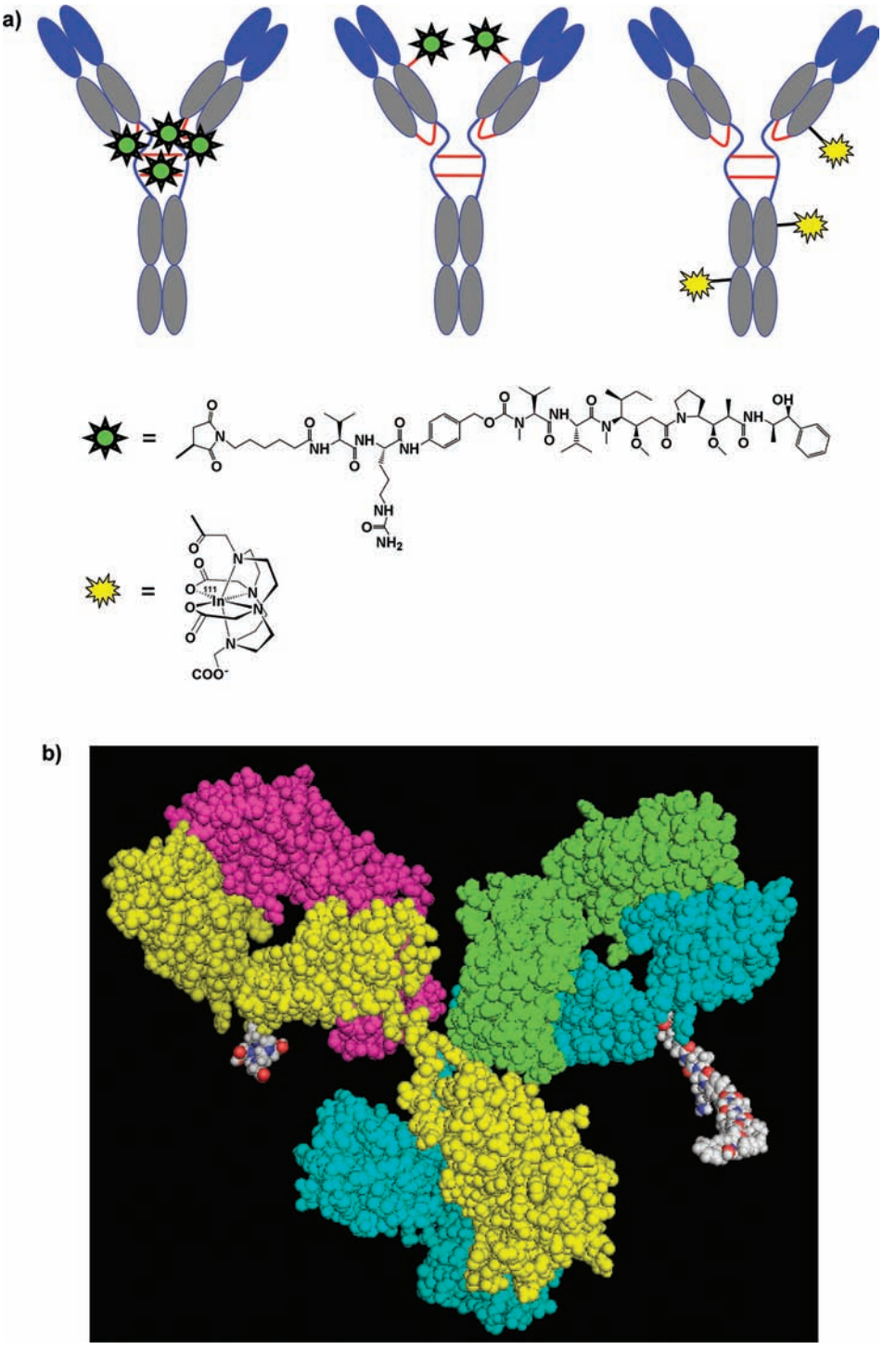

Figure 1. (a) Conceptual depiction of sites of anti-STEAP1 modification. The auristatin linker-drug, MC-vc-PAB-MMAE (green), was conjugated randomly through thioether bonds to cysteine thiols at the hinge region (left) or site-specifically to exactly two engineered thiols (center), while the radiometal chelate, DOTA (yellow), was randomly conjugated to lysine residues through amide bonds (right). (b) A space-filling three-dimensional model of an IgG1 (PDB code: 1igy) conjugated to a single molecule each of DOTA (left) and MC-vc-PAB-MMAE (right) is shown to depict the relative molecular sizes of the antibody, linker-drug, and chelate. Both MMAE and DOTA (without In^{3+}) were energy-minimized separately using the MM2 force field within *CambridgeSoft Chem3D Pro* version 7.0.0, exported as a PDB file, and merged with the IgG in the PyMOL Molecular Graphics System.[49] DOTA and MMAE are conjugated to LYS115 and CYS114 (mutated from ALA114 in 1igy), respectively. Carbons, oxygens, and nitrogens in DOTA and MMAE are colored white, blue, and red, respectively. Heavy chains bearing DOTA and MMAE are colored in yellow and blue, respectively.

antibody can be conjugated through cysteine residues to a potent antimitotic auristatin drug, monomethyl auristatin E (MMAE) via a protease-labile linker, maleimidocaproyl-valine-citrulline-*p*-aminobenzyloxycarbonyl (MC-vc-PAB, abbreviated as -vc-henceforth).[21−23] The peptidic vc-MMAE linker is designed to be stable in plasma, and has much improved stability in systemic

dx.doi.org/10.1021/bc200212a |*Bioconjugate Chem.* 2011, 22, 1994–2004

circulation compared to earlier chemically labile linkers such as hydrazone.[22] Drug conjugation in the presence of four sets of interchain disulfide bonds gives rise to a heterogeneous ADC mixture that can be described in terms of a drug to antibody ratio (DAR) distribution and an average DAR. For instance, the anti-STEAP1 ADC with an average DAR of 4 (illustrated in Figure 1) is just one possible molecular species of a mixture that may be composed of zero to eight drugs per antibody covalently attached via the -vc- linker. This heterogeneity may ultimately lead to different PK, efficacy, and toxicity properties of each fraction; for example, fractions with higher DAR have, in some cases, been reported to clear more rapidly and contributed to more severe toxicity.[24] Other reports have demonstrated, however, similar efficacy, tolerability, and PK between preparations having heterogeneous (0−8) and homogeneous (4) DAR.[25]

Recently, to control the heterogeneity of ADCs and to explore a novel strategy for potentially increasing the therapeutic window, a novel thio-anti-STEAP1 drug conjugate (TDC) was developed with site-specific conjugation through two engineered reactive thiols using ThioMab antibody technology.[15] The molecular structures in Figure 1a illustrate two ADC variants that differ in how the drug is covalently attached to anti-STEAP1. The linker-drug (vc-MMAE) is conjugated to the antibody through a thioether bond between the linker maleimide moiety and (i) a cysteine thiol that normally forms the interchain disulfide bond at the hinge region in the anti-STEAP1 ADC (Figure 1a left) or (ii) a site-specific, engineered thiol in the anti-STEAP1 TDC (Figure 1a center). The relative sizes of the antibody and MMAE are depicted in Figure 1b. Note that the theoretical drug load for the anti-STEAP1 ADC is a heterogeneous distribution of 0, 2, 4, 6, and 8 DAR, while the TDC is homogeneous with a DAR of 2. Anti-STEAP1 ADCs, including TDCs, have exhibited antitumor activity in explant and xenograft models and are being investigated for the treatment of prostate cancer.[26]

The present study investigates the potential impact of MMAE drug conjugation on antibody pharmacokinetics (PK) and tissue distribution of ADCs prepared through interchain thiol residues in a monoclonal antibody (mAb) or through site-specific, engineered cysteines in a ThioMab.[15] The anti-STEAP1 antibody and corresponding ADCs do not cross react with rat STEAP1; therefore, this species is suitable for evaluation of antigen-independent PK, biodistribution, and toxicity. In this context, the PK of four different molecular entities and biodistributions of their radiolabeled (via indium-111-DOTA, Figure 1) counterparts were compared following a single intravenous dose in rats. The rationale for selection of test molecules was to determine the potential effects of varying the site of drug conjugation and/or the DAR characteristics relative to unconjugated antibodies. Furthermore, we compared the PK profiles measured by both gamma counting and total antibody ELISA in order to bridge radiometric data from both terminal tissue distribution harvests and nonradioactive PK studies.

EXPERIMENTAL PROCEDURES

Antibody/ThioMab Production and MMAE Conjugation. The anti-STEAP1 antibody and anti-STEAP1-vc-MMAE conjugate (ADC) were prepared as previously described.[22] Briefly, the maleimido drug derivative was incubated with reduced mAbs for 1 h at 4 °C, followed by quenching with excess cysteine. Methods for construction and production of the thio-anti-STEAP1 (ThioMab) variant were reported previously.[15] Briefly, a cysteine residue was engineered at Ala114 position of the anti-STEAP1 heavy chain to produce its ThioMab variant from which the thio-anti-STEAP1-vc-MMAE conjugate (TDC) was produced. The DAR for each immunoconjugate was determined by hydrophobic interaction chromatography analysis as described earlier.[15]

DOTA Conjugation and Characterization. Proteins were conjugated to 1,4,7,10-tetraazacyclododecane-*N*,*N*′,*N*″,*N*‴-tetraacetic acid (DOTA) for indium-111 (^{111}In) complexation by random modification of lysine residues (Figure 1a right). Aliquots containing 2−6 mg of the fully human antibodies anti-STEAP1, thio-anti-STEAP1, and the corresponding vc-MMAE conjugates were exchanged from formulation buffer into aqueous 50 mM sodium borate, pH 8.5 using illustra NAP5 columns (GE Healthcare Life Sciences, Piscataway, NJ). A quantity of 5 mol equiv of the *N*-hydroxysuccinimidyl ester of DOTA in 0.68−1.66 μL of dimethylformamide was added to the 600 μL borate-buffered protein solutions. Reaction mixtures were gently agitated (300 rpm) for 1 h at 37 °C on a Thermomixer (Eppendorf North America, Hauppauge, NY). Reaction was terminated by promptly applying the mixtures to NAP5 columns pre-equilibrated in aqueous 0.3 M ammonium acetate buffer, pH 7.0. The resulting purified DOTA-mAb conjugates were stored at 4 °C. The binding specificity and affinity to STEAP1 for all four antibody variants were characterized by total antibody ELISA (see below).

Determination of the average number of covalently attached chelates for each DOTA conjugate by radiometric assay was performed by modification of previously reported procedures.[27,28] An aliquot of 10 μL of each mAb-DOTA conjugate (2−4 mg/mL in 0.3 M ammonium acetate pH 7.0) was added to 10 μL of a standardized $InCl_3$ solution (323 μM, 3.23 nmol, containing >150 000 cpm/μL of ^{111}InCl). The reaction was incubated at 37 °C for 3 h, after which 5 μL of 50 mM EDTA and 75 μL of 0.3 M ammonium acetate pH 7 were added, followed by further incubation for 5 min at 25 °C. The entire mixture was loaded onto a NAP5 column pre-equilibrated in PBS and allowed to settle, followed by an additional 400 μL of PBS. The radiolabeled antibody fraction was eluted separately with an additional 500 μL of PBS. The radioactivity in the eluent and remaining on the NAP5 column was measured using a 1480 WIZARD Gamma Counter (Wallac, Turku, Finland) in the energy window for the 245 keV photon peak of ^{111}In and with automatic background and decay correction. The number of chelates per antibody molecule was calculated from the ratio of counts in the eluted product to the total number of counts using the method of Meares and co-workers.[27]

The number of chelates per antibody was also estimated by LC-MS. Prior to analysis, all protein samples (100 μL, 0.25−0.5 mg/mL) were deglycosylated overnight at 37 °C using 2 μL peptide *N*-glycosidase (PNGase F, Prozyme). Anti-STEAP1 ADC samples were also further subjected to a reduction step using 10 μL of 200 mM dithiothreitol (DTT). Samples were injected onto a Pepswift Monolithic PS-DVB column (0.5 × 5 mm, ID 500 μm, Dionex) using an HTS PAL autosampler (LEAP Technologies) with a cooling stack set at 4 °C. The column temperature was maintained at 70 °C using a column heater (Keystone Scientific). The LC separation was conducted using an Express LC-100 liquid chromatography system (Eksigent Technologies, Dublin, CA) at a flow rate of 15 μL/min. Mobile phase A was water with 0.1% formic acid, and mobile phase B was acetonitrile with 0.1% formic acid. The gradient condition was maintained at 2% B for 4 min, ramped to 40% B in 8 min, kept at 40% B for 3 min, increased to 100% B in 1.5 min,

retained at 100% B for 1 min, returned back to 2% B in 0.8 min, and finally equilibrated for 0.7 min before the next injection (for a total run time of 15 min). For the first 6 min, the LC flow was diverted to waste. The eluate was then directed to a Q-STAR XL quadrupole time-of-flight (TOF) mass spectrometer (AB Sciex, Foster City, CA) operated with a turbo ionspray source maintained at 200 °C in the positive ion mode. The declustering potential (DP) and focusing potential (FP) were optimized at 100 and 300 V, respectively. Data analysis was performed using the *Analyst QS 1.1* software and a Bayesian Protein Reconstruct algorithm for mass spectral deconvolution (AB Sciex, Foster City, CA).

Radiochemistry. A 2 μL (820 μCi; 30.3 MBq) aliquot of ^{111}InCl (MDS Nordion, Ottawa, ON) was added to a 20 μL aliquot of each ammonium acetate-buffered DOTA−protein conjugate. Reaction mixtures were gently agitated (300 rpm) for 1 h at 37 °C on a Thermomixer. A 5 μL aliquot of 50 mM aqueous EDTA challenge solution was added, followed by an additional 73 μL aliquot of aqueous 0.3 M ammonium acetate buffer, pH 7.0. Each radiolabeled protein was purified using NAP5 columns pre-equilibrated in PBS. Purity of each radioimmunoconjugate was assessed by size-exclusion radiometric high-performance liquid chromatography (HPLC) (isocratic, PBS, 0.5 mL/min) on an Agilent 1100 series HPLC system operated through *ChemStation* software and equipped with a Biosep-SEC-S 3000 column (Phenomenex) and a raytest Ramona 90 radioactive flow monitor.

Pharmacokinetic Studies. All experimental animal studies were conducted according to protocols that were reviewed and approved by the Institutional Animal Care and Use Committees (IACUC) of Genentech Laboratory Animal Research (LAR). Male Sprague−Dawley rats ranging from 8 to 10 weeks old and weighing approximately 250−300 g at the initiation of the study were randomly assigned to 4 groups (n = 4 per group), and administered an intravenous bolus (5 mg/kg) of test article. Blood samples were collected from each animal via the femoral vein for up to 28 days and used to derive plasma for total and conjugated antibody concentration determination using an ELISA and the concentration of free MMAE released in vivo from anti-STEAP1 conjugates in plasma using LC-MS/MS detection (see below). Plasma concentration−time data were used to estimate relevant PK parameters using *WinNonlin* software (v 5.2.1 Pharsight Corporation, Mountain View, CA). To better compare the profile between radiometry and ELISA data, radiometric (In-111) blood PK data (see below) were normalized to the same dose level.

Tissue Distribution. Juvenile male Sprague−Dawley rats (Harlan) with weight range of 75−100 g received a single bolus intravenous injection of ^{111}In-labeled conjugates. Dosing solutions were prepared by mixing the ^{111}In-DOTA-labeled test articles with the corresponding non-DOTA-conjugated molecules to achieve a total protein dose of 10 mg/kg and radioactive dose of approximately 400 μCi/kg (14.8 MBq/kg) in no more than 200 μL of PBS. A 500 μL aliquot of whole blood was terminally collected at 1 h, 1 day, 2 days, 5 days, and 7 days in lithium heparinized tubes via cardiac puncture under inhaled isoflurane anesthesia. The following tissues were subsequently harvested: lungs, liver, kidneys, heart, spleen, right femur, gastrocnemius muscle, stomach, small intestine, and large intestine. All tissues were rinsed with PBS, blot-dried, weighed, frozen on dry ice, and stored at −70 °C. Blood, tissues, and 5 μL aliquots of dosing solution standards were counted for radioactivity using a 1480 WIZARD Gamma Counter in the energy window for the 245-keV photon peak of ^{111}In and with automatic background and decay correction. Average counts per minute (cpm) were converted to percentage of injected dose per gram of tissue (%ID/g) and plotted with standard deviations. Statistical significance was determined by one-way ANOVA followed by Tukey's post-test in *GraphPad Prism* v 5.04.

Total Antibody ELISA. Nunc MaxiSorp 384-well plates (Nalge Nunc International, Rochester, NY) were coated with either anti-idiotypic antibody 5093 (Genentech, South San Francisco, CA) or donkey antihuman Fc (Jackson ImmunoResearch Laboratories, Inc., West Grove, PA) and incubated overnight at 4 °C. The plates were washed 3 times with 0.05% Tween-20 in PBS buffer (pH 7.4). Diluted standards plasma samples were added to the wells and incubated on a shaker for 2 h at room temperature. The plates were washed 6 times and a detection antibody, either goat antihuman IgG antibody conjugated to horseradish peroxidase (Bethyl Laboratories, Montgomery, TX) or goat antihuman Fc conjugated to horseradish peroxidase (Jackson ImmunoResearch Laboratories, Inc., West Grove, PA), was added to the wells and incubated on a shaker for 1 h at room temperature. The plates were washed 6 times and developed using TMB peroxidase substrate (Moss Inc., Pasadena, Maryland). Both assay ranges were 0.164−40 ng/mL with a minimum dilution of 1:100 (limit of detection = 16.4 ng/mL). TDC assays were characterized as having acceptable (80-120%) DAR analyte recovery (data not shown). For ADC assays, DAR reagents were not available to characterize analyte recovery at the time of the original study sample analysis. However, data reported from the assay herein were confirmed using a more recent assay where DAR recovery was characterized and found to be acceptable) 80−120%; data not shown).

Conjugated Antibody ELISA. Nunc MaxiSorp 384-well plates were coated with anti-MMAE antibody (Seattle Genetics Inc., Bothell, WA) and incubated overnight at 4 °C. The plates were washed 3 times with 0.05% Tween-20 in PBS buffer (pH 7.4). Diluted standards and the ADC or TDC plasma samples were added to the wells and incubated for 2 h at room temperature. The plates were washed 6 times and a detection antibody, either goat antihuman IgG antibody conjugated to horseradish peroxidase (Bethyl Laboratories, Montgomery, TX) or goat antihuman Fc conjugated to horseradish peroxidase (Jackson ImmunoResearch Laboratories, Inc., West Grove, PA), was added on a shaker for 1 h at room temperature. All plates were developed using TMB peroxidase substrate. The ADC assay range was 0.0655-16 ng/mL with a minimum dilution of 1:100 (limit of detection = 6.6 ng/mL). The TDC range was 0.164−40 ng/mL with a minimum dilution of 1:100 (limit of detection = 16.4 ng/mL). TDC and ADC assays were characterized for DAR analyte recovery as described for the total antibody ELISA.

Free MMAE Assay. The concentration of free MMAE in plasma was determined by liquid chromatography tandem mass spectrometry (LC-MS/MS). Briefly, plasma samples were protein precipitated with 100 μL of 80/20 acetonitrile/water containing 2 nM monomethylauristatin F (MMAF) as an internal standard, and analyzed for MMAE by TurboIon Spray using an API 3000 mass spectrometer (Applied Biosystems, Foster City, CA). The HPLC system used for analysis was a Shimadzu HPLC LC-10Avp system (Shimadzu Scientific Instruments, Columbia, MD), equipped with a Short Hot Pocket column heater (Keystone Scientific, Inc., Bellefonte, PA) and analytical column (Phenomenex Synergi MAX-RP 80A, C12, 4 μm, 2.0 × 50 mm)

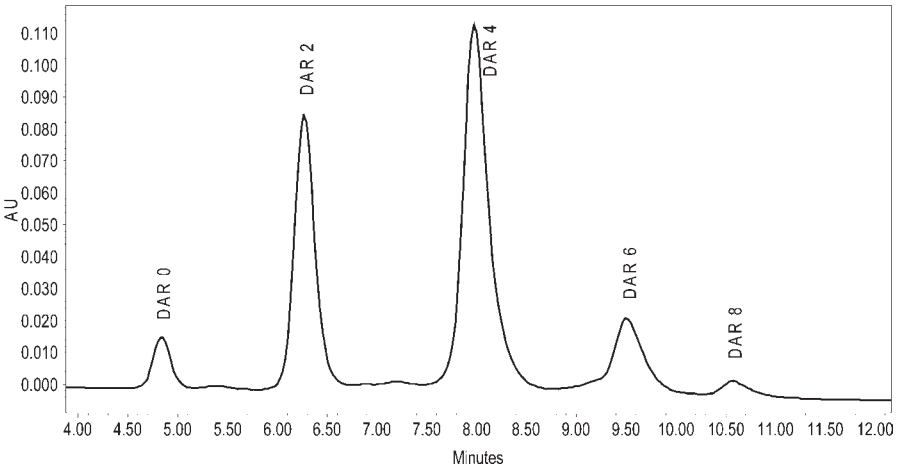

Figure 2. Representative hydrophobic interaction chromatography (HIC) of anti-STEAP1 ADC with average drug-to-antibody ratio (DAR) of approximately 3.5. The peak assignments are consistent with the conjugation of the linker−drug being primarily limited to the interchain cysteines of the antibody and leading to a DAR distribution of mainly 0, 2, 4, 6, or 8.

Table 1. Summary of Analytical Data Obtained during Characterization, DOTA Conjugation, and ^{111}In Radiolabeling of Anti-STEAP1 (mAb), Thio-anti-STEAP1 (ThioMab), and the Two Corresponding MMAE Conjugates (ADC and TDC)

test material	# MMAE (HIC)[a]	# DOTA (radiometric)[b]	# DOTA (MS)[c]	ELISA recovery (%)[d]	^{111}In labeling yield (%)[e]	^{111}In labeling purity (%)[f]
mAb	N/A	2.20 ± 0.148	2.6	73	82	98
ADC	3.1	1.50 ± 0.0787*	1.7	73	61	97
ThioMab	N/A	2.47 ± 0.273	3.2	80	84	98
TDC	1.7	1.67 ± 0.139*	2.3	82	78	99

[a] HIC: hydrophobic interaction chromatography. [b] Performed in triplicate. [c] Estimated from differences between mass spectrometry (MS) peaks before and after DOTA conjugation. [d] Measured by ELISA after DOTA conjugation to verify immunoreactivity. [e] Radiolabeling performed using ∼30 MBq ^{111}InCl and ∼40 mg DOTA-mAb in 0.3 M ammonium acetate pH 7 at 37 °C for 1 h. [f] Derived by integration of size exclusion radiochromatogram. * $P <$ 0.05 vs mAb by unpaired *t* test.

at 50 °C. Multiple reaction monitoring scan mode was used for quantitation. For MMAE quantitation, transition 732.7/170.3 was monitored for MMAF (internal standard) and 718.7/152.2 for MMAE. The LC-MS/MS assay had a lower limit of quantitation of 0.018 ng/mL (0.025 nM) with linearity demonstrable up to 18 ng/mL (25 nM) using a sample volume of 0.025 mL.

RESULTS

Antibody/ThioMab Production and MMAE Conjugation. The presence of a heterogeneous mixture of DAR species was demonstrated by hydrophobic interaction chromatography (HIC) as shown in a representative chromatogram for the anti-STEAP1 ADC (Figure 2). The calculated average DARs for the ADC and TDC used in PK and tissue distribution studies were 3.1 and 1.7 per mAb, respectively (Table 1).

DOTA Conjugation and Characterization. All four DOTA conjugates retained antigen binding, measured as percent recovery in a STEAP1-specific ELISA (Table 1). Radiometric measurement of the average number of DOTA chelates attached per antibody molecule gave values ranging from 1.5 to 1.7 for the drug conjugates and from 2.2 to 2.5 for the non-drug-conjugated molecules (Table 1). These values were in rough agreement with estimates based on shifts of mass peaks before and after DOTA conjugation, which showed a range of 1.7−2.3 for the drug conjugates and 2.6−3.2 for the non-drug-conjugated molecules (Table 1; see also Supporting Information).

Radiochemistry. Slightly lower radiochemical yields (Table 1) were obtained for the ADC (61%) and TDC (78%) than for the corresponding non-drug-conjugated antibody and ThioMab (82% and 84%, respectively). Size-exclusion HPLC demonstrated radiochemically pure (≥97%) products (Table 1) with no evidence of unconjugated ^{111}In (see Supporting Information).

Pharmacokinetic Studies. The anti-STEAP1 total antibody ELISA quantifies the antibody moiety irrespective of drug conjugation status, as the assay format is designed to capture both unconjugated antibody and ADC variants. The anti-STEAP1 conventional mAb and ThioMab showed similar PK profiles (Figure 3a), indicating that cysteine mutations had little impact on antibody clearance. Indeed, the clearances of the conventional mAb and ThioMab at rates of 7.27 ± 1.71 and 9.65 ± 2.33 mL/day/kg, respectively, were comparable (Table 2). The two drug conjugates had similar clearances, with 10.5 ± 1.42 and 9.56 ± 2.53 mL/day/kg for the ADC and TDC, respectively. The ADC total antibody cleared approximately 45% more rapidly than the corresponding unconjugated mAb at rates of 10.5 ± 1.42 and 7.27 ± 1.71 mL/day/kg ($P < 0.05$), respectively. In contrast, the TDC had a similar clearance compared with the ThioMab at rates of 9.56 ± 2.53 and 9.65 ± 2.33 mL/day/kg, respectively. This reflects the differential impact on the overall clearance of the antibody depending on site and degree of conjugation.

The anti-STEAP1 conjugate ELISA format is designed to measure any anti-STEAP1 antibody conjugated with one or more MMAE drugs. This assay is not sensitive to incremental

changes in drug load, but can estimate the overall complete drug loss from the ADC or TDC as unconjugated mAb is not measured. The anti-STEAP1 ADC and TDC showed markedly different conjugate PK profiles (Figure 4a). A summary of the PK parameters for both anti-STEAP1 total antibody and conjugate in plasma is presented in Table 2. The anti-STEAP1 ADC cleared 3 times as fast in terms of conjugated antibody relative to total antibody (33.6 ± 4.27 and 10.5 ± 1.42 mL/day/kg, respectively). However, it is difficult to distinguish whether biotransformation of ADC is dominated by MMAE release (deconjugation) versus proteolytic degradation of the antibody itself (total antibody clearance). In contrast, the TDC showed only 1.3 times faster clearance in terms of conjugated antibody compared to total antibody clearance (12.5 ± 2.41 and 9.56 ± 2.53 mL/day/kg, respectively). The clearance of the anti-STEAP1 ADC in terms of conjugated antibody was almost three times faster than that of the TDC (33.6 ± 4.27 and 12.5 ± 2.41 mL/day/kg, respectively). Overall, the volume of distribution (V_1) for all groups approximated to plasma volume in rats (31 mL/kg for a 250 g rat[29]), ranging from 39.4 ± 0.704 to 47.3 ± 8.82 mL/kg.

Plasma concentration−time profiles of free MMAE, measured by LC-MS/MS, following administration of the two MMAE-conjugated

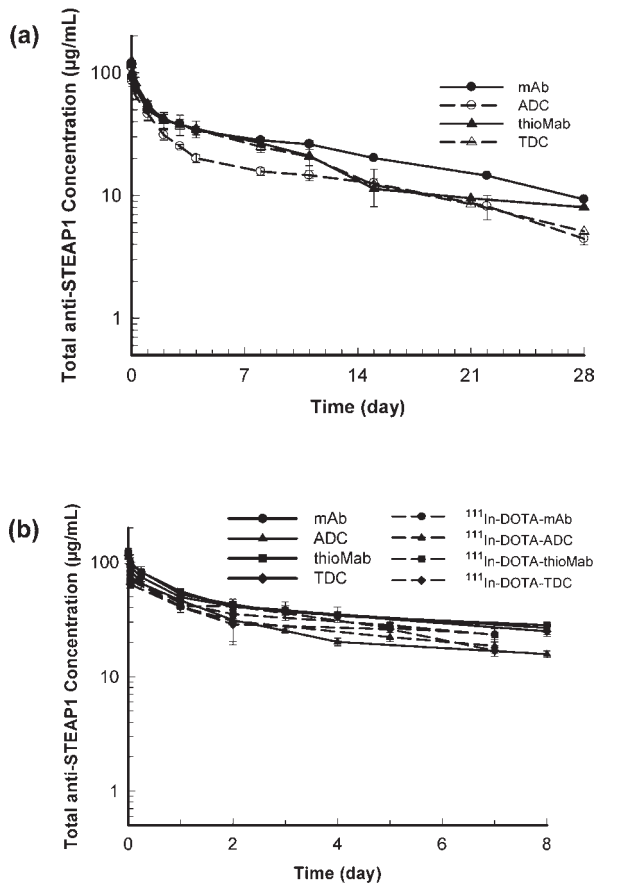

Figure 3. Mean total antibody concentrations in plasma of anti-STEAP1, thio anti-STEAP1, and the two corresponding MMAE drug conjugates in male rats following intravenous administration at 5 mg/kg. Error bars are standard deviations. Data from (a) ELISA-derived PK (solid lines) only and (b) both PK and radiometric tissue distribution (dotted lines) are included. Data for ^{111}In-labeled molecules in (b) was dose normalized to 5 mg/kg for comparison with ELISA-derived data.

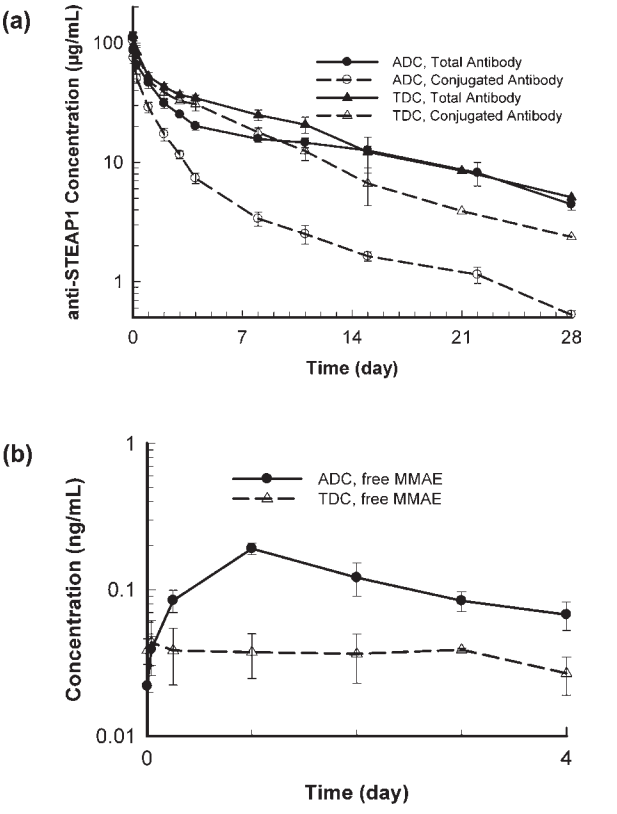

Figure 4. (a) Mean total and conjugated antibody concentrations (by ELISA) in plasma of anti-STEAP1 ADC and TDC in male rats following intravenous administration at 5 mg/kg. (b) Mean free MMAE concentrations (by LC-MS/MS) in plasma following administration of anti-STEAP1 ADC and TDC in male rats. Error bars in both (a) and (b) are standard deviations.

Table 2. Summary of Total Anti-STEAP1 Antibody Pharmacokinetics in Plasma of Anti-STEAP1 (mAb), Thio-anti-STEAP1 (ThioMab), and the Two Corresponding MMAE Drug Conjugates (ADC and TDC) in Male Rats (n =4)

test material	dose (mg/kg)	analyte	CL[a] (mL/day/kg)	V_1 (mL/kg)
mAb	5	total antibody	7.27 ± 1.71	41.4 ± 2.31
ADC	5	total antibody	10.5 ± 1.42*	44.8 ± 6.00
		conjugated antibody	33.6 ± 4.27*	47.3 ± 8.82
ThioMab	5	total antibody	9.65 ± 2.33	39.4 ± 0.704
TDC	5	total antibody	9.56 ± 2.53	42.9 ± 2.04*
		conjugated antibody	12.5 ± 2.41*	42.2 ± 1.79*

[a] Abbreviations: CL, clearance; V_1, volume of distribution of the central compartment (i.e., volume of initial dilution compartment). * $P < 0.05$ vs mAb by unpaired t test.

dx.doi.org/10.1021/bc200212a |Bioconjugate Chem. 2011, 22, 1994–2004

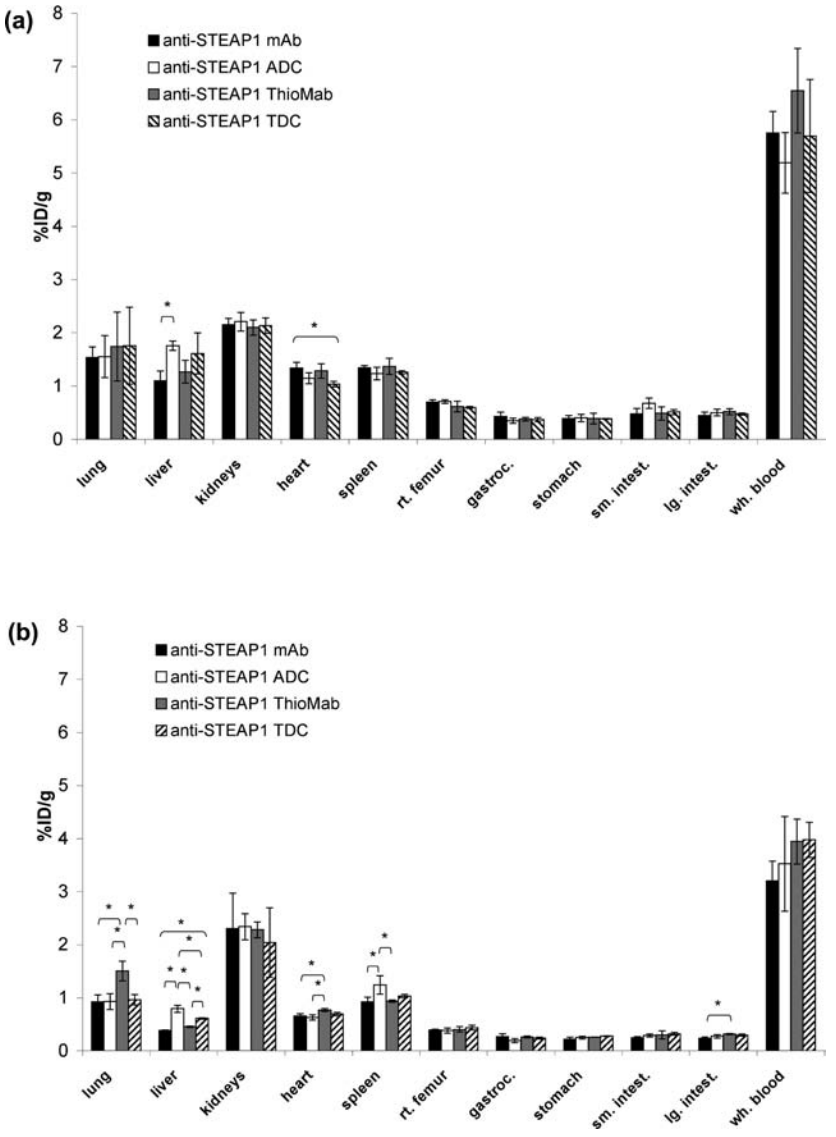

Figure 5. Tissue distribution of ^{111}In-DOTA-labeled anti-Steap1 (black), thio-anti-Steap1 (gray), and the corresponding MMAE conjugates (white and striped, respectively) in rats at (a) 24 h and (b) 120 h after intravenous injection. Data are presented as percentage of injected dose per gram of tissue (mean %ID/g ± SD for 3 rats per group). Statistically significant differences are indicated by brackets (*P < 0.05).

anti-STEAP1 antibodies are presented in Figure 4b. Although observed free MMAE concentrations were generally very low (~0.2 ng/mL or less) and detected only up to day 4 postdose for both conjugated antibodies, the anti-STEAP1 ADC showed a higher concentration of plasma MMAE at time points ranging from 6 h through 4 days. The observed free MMAE exposure measured by both C_{max} and AUC was approximately four times higher for the ADC than for the TDC (C_{max}: 0.19 ± 0.02 vs 0.04 ± 0.02 ng/mL; AUC: 0.45 ± 0.05 vs 0.14 ± 0.03 ng/mL days, respectively). These differences seem to exceed the roughly 2-fold expected difference based on DAR; however, it is difficult to distinguish between deconjugation versus total antibody catabolism in explaining greater drug loss from the ADC relative to the TDC.

Tissue Distribution. Radiometrically derived (dose-normalized) and ELISA-derived total antibody PK data were largely comparable (Figure 3b), indicating similar blood exposures of all four test articles. At 24 h postinjection, significantly (P < 0.05) higher hepatic uptake of ^{111}In was observed for anti-STEAP1 ADC (1.76 ± 0.0878) than for unconjugated anti-STEAP1 (1.10 ± 0.183%ID/g) (Figure 5a). Conversely, anti-STEAP1 TDC demonstrated lower cardiac uptake of ^{111}In at 24 h (1.04 ± 0.0497%ID/g) than unconjugated anti-STEAP1 (1.34 ± 0.108%ID/g).

At 120 h postinjection, elevated hepatic uptake of ^{111}In for anti-STEAP1 ADC relative to unconjugated anti-STEAP1 was maintained (0.791 ± 0.0648 vs 0.386 ± 0.00617%ID/g) with a similar but less pronounced trend for anti-STEAP1 TDC and its corresponding unconjugated ThioMab (0.610 ± 0.0155 vs 0.454 ± 0.0157%ID/g) (Figure 5b). Significantly (P < 0.05) higher uptake for anti-STEAP1 ADC (1.24 ± 0.173) relative to anti-STEAP1 (0.925 ± 0.0888) was also observed at 5 d in spleen. Meanwhile, thio-anti-STEAP1 uptake in both heart (0.768 ± 0.0252%ID/g) and lungs (1.50 ± 0.188%ID/g) was higher than for all other variants, which ranged from 0.628 ± 0.0476 to 0.691 ± 0.0323%ID/g in heart and from 0.923 ± 0.131%ID/g to 0.962 ± 0.0975%ID/g in lungs. Similar trends

were observed in additional tissue distribution data at 1, 48, and 168 h postinjection (see Supporting Information).

DISCUSSION

Considerable effort has been applied to understanding the PK,[30,31] tissue distribution,[20] metabolism,[32−34] and pharmacologic effects[19,35,36] of ADCs. Still, the inherent heterogeneity of these complex macromolecular entities remains a prominent challenge in understanding their properties in vivo during nonclinical development. For example, conjugation through interchain disulfides leads to ADCs with DAR ranging from 0 to 8, with each fraction potentially exhibiting a unique efficacy, PK, and toxicity profile. In addition, the existing analytical methods available for antibodies and small molecule drugs have inherent technical limitations for complex ADCs. For example, the performance of ELISA is sensitive to the heterogeneity of the analytes, and susceptible to variation in recovery of each DAR fraction.[31] Assays used in this study demonstrated 80-120% DAR analyte recovery (data not shown); however, it is not known if these analytes are structurally identical to DAR species formed in vivo.

The recent introduction of ThioMabs presents an opportunity to control the drug load and site of attachment of drug molecules, thereby limiting heterogeneity by conjugation through genetically engineered cysteine sites[15] and potentially improving the overall PK characteristics. In this context, the current single-dose study encompasses the evaluation of an anti-STEAP1 antibody, the corresponding ThioMab variant possessing engineered cysteines, and two corresponding thioether-linked MMAE conjugates (ADC and TDC, respectively) to assess the impact of conjugation site and drug load on PK and tissue distribution.

Plasma PK of anti-STEAP1 total antibody was measured by both ELISA and radiometric detection. Anti-STEAP1 total antibody clearances of the two unconjugated antibodies were similar, suggesting minimal impact on PK due to cysteine mutation (Figure 3). The PK profile comparison between unconjugated and conjugated variants reflects the impact of drug conjugation on PK and disposition of the antibodies. An increase in total antibody clearance of approximately 45% was observed for the anti-STEAP1 ADC, while no change in clearance was observed for the TDC, relative to their non-drug-conjugated counterparts. The exact magnitude of the increased clearance of the ADC may be somewhat affected by the inherent technical limitations of ELISA for mixture analysis; however, the trend is clearly apparent. Indeed, this trend toward faster plasma clearance of immunoconjugates relative to unconjugated antibodies (Figure 3a) is consistent with previous studies.[24] This suggests that controlled conjugation with lower DAR and without structural disruption of disulfide bonds (i.e., TDC) leads to minimal alteration in antibody PK behaviors. However, generalizations to other ADC platforms[37] should not be assumed, and the relationship between conjugation method and biological disposition must be independently established. In addition, a very good overall agreement existed between ELISA- and radiometrically derived PK, indicating that DOTA conjugation had no dramatic effect on disposition kinetics (Figure 3b).

The enzyme labile, peptidic vc-MMAE linker is designed to be stable in plasma, and has greatly improved stability in systemic circulation and a superior safety profile compared to chemically labile linkers such as hydrazone.[22] However, ADCs in blood may release some MMAE (i.e., deconjugate), resulting in changes in the DAR distribution of the drug-loaded species and the unconjugated antibody. To gain further mechanistic insights into ADC disposition and deconjugation, the plasma PK of conjugated antibody was measured by ELISA. The conjugate antibody assay format is designed to capture any antibody with at least one conjugated drug, such that the clearance encompasses both complete deconjugation and antibody clearance. Its comparison with total antibody clearance sheds light on the relative contribution of each process. The anti-STEAP1 ADC (average DAR = 3.1) showed a marked (approximately 3-fold) difference between conjugated antibody clearance and total antibody clearance. A similar trend between clearance rates of total antibody and conjugate for other immunoconjugates has been previously reported.[38] In contrast, deconjugation had much less impact (roughly 1.3-fold) on the overall clearance in TDC (Table 2 and Figure 4a).

Deconjugation from anti-STEAP1 ADC and TDC involves release of small molecules that may ultimately result in cytotoxic free MMAE in circulation. Very low levels of free MMAE (below 1 ng/mL) were detected for either ADC or TDC (Figure 4b). This, in part, reflects the stability of the linker and relatively limited deconjugation of MMAE from conjugated antibody; it is also likely that the result of the rapid distribution and clearance rates of MMAE in relation to its production. Alternatively, there may be additional drug catabolites other than free MMAE (e.g., Cys-MC-vc-PAB-MMAE) that are not detected by the MMAE-specific free drug assay. Although the absolute MMAE concentrations in plasma are very low, a correlation may exist between stability and MMAE levels in plasma. In this case, greater than 3-fold (based on AUC) higher free MMAE plasma levels were observed compared to the TDC. However, the higher initial drug load (roughly 2-fold) in the ADC likely contributes to the higher level of MMAE observed in plasma. Nevertheless, one plausible explanation for these observations is that conjugation through a precise number (two) of engineered cysteines induced fewer disturbances in the overall antibody structure relative to the unmodified antibody and a correspondingly more stable molecule.

Since most ADC targets are selected for their low and restricted expression in normal tissues, exploitation of the rat as a nonbinding species provides an initial assessment of antigen-independent disposition of ADCs. Overall, tissue distribution trends were similar for all four radiolabeled antibody platforms at all time points and were consistent with the expected behavior for a typical nonbinding humanized antibody in rats (Figure 5, see also Supporting Information). Concentrations in blood and in all tissues decreased over time, with the exception of kidneys, where nearly constant uptake values were sustained. This is likely due to the continual clearance of low molecular weight ^{111}In-labeled metabolites (e.g., ^{111}In-DOTA-lysine) being generated in liver and in other sites of IgG catabolism.[39] Elevated hepatic uptake for anti-STEAP1 ADC and TDC relative to the non-drug-conjugated proteins may be rationalized by higher hydrophobicities of the drug conjugates, resulting in greater reticuloendothelial system clearance. Blood-corrected uptake for liver and other tissues may be calculated from the %ID/g values reported herein based on reported fractional vascular volumes in rodents; however, this correction would affect antibodies and drug conjugates to the same extent due to similar blood exposures.[40,41]

Robust characterization of all four derivatives was necessary in order to ensure that observed differences, if any, in biological disposition were indeed due to drug conjugation, as opposed to inconsistencies in radiolabeling (Table 1). The lower observed

radiochemical yields for the ADC and TDC than for the corresponding non-drug-conjugated molecules may reflect the influence of MMAE in sterically blocking lysine residues for DOTA conjugation. Although approximately 80−90 lysine residues are present in a typical IgG1,[42] it is likely that many of these may not be solvent-accessible, especially following conjugation of MMAE. Even though slightly higher incorporation of DOTA was obtained for the non-MMAE-conjugated molecules, the effects should be minor given that much larger changes in isoelectric point (i.e., pI) would be necessary to invoke a difference in tissue distribution or PK.[42] Furthermore, the ADC and TDC herein were, in fact, modified on average by approximately one fewer molecule of DOTA than the respective non-MMAE-conjugated counterparts as measured by both radiometric assay and mass spectrometry (Table 1). If the differences in hepatic uptake (Figure 5), for instance, were due to DOTA conjugation, then the trend observed herein would be inconsistent with a previous report that overconjugation with DOTA causes increased hepatic accumulation.[43] It is therefore more likely that the conjugation of hydrophobic drug moieties, not the slightly lower DOTA conjugation yield, is responsible for the increased hepatic uptake of anti-STEAP1-MMAE conjugates relative to the mAb and ThioMab. Additionally, a STEAP1-specific ELISA confirmed that the immunoreactivities of the four variants were largely retained following DOTA conjugation (Table 1).

The choice of ^{111}In-DOTA as a probe was influenced by a desire to increase the likelihood of detecting any differences in tissue-specific uptake among the four tested platforms. Antibodies labeled with metal radionuclides via DOTA or other polyaminopolycarboxylate chelators tend to accumulate in antigen-expressing tissues following receptor-mediated endocytosis due to the residualizing properties of this charged, highly polar probe.[44] The exploitation of DOTA as a carrier for ^{111}In, a medium-energy gamma emitting radionuclide with a 2.7 day decay half-life,[45] and other metallic radionuclides is well-documented.[46−48]

Conjugation with a small molecule drug through specific sites on mAbs can potentially alter mAb hydrophobicity, charge, polarity, and PK.[42] ADCs with higher drug loads possess higher intrinsic potency; however, they may also exhibit faster blood clearance in terms of total antibody.[24] However, it should be emphasized that each antibody and drug platform should be considered on a case-by-case basis; for instance, a lysine-modified trastuzumab-maytansinoid ADC (DAR 3.3) showed similar PK compared with the analogous TDC (DAR 1.8) modified through engineered cysteines.[37] In addition, the increased release of free drug or toxic intermediates into systemic circulation or nontarget organs could potentially shrink the therapeutic window. The ability to define the DAR combined with the knowledge of PK and distribution will afford us new opportunities in optimizing ADCs.

In conclusion, an anti-STEAP1 antibody, a ThioMab variant possessing engineered cysteines, and two corresponding thioether-linked MMAE conjugates were studied in order to assess the impact of drug conjugation methodology on PK and tissue distribution. MMAE conjugation through native cysteine thiols comprising interchain disulfide bonds (average DAR 3.1) resulted in an accelerated clearance of total antibody, while conjugation through engineered cysteine thiols (average DAR 1.7) led to only a marginal difference in clearance. In addition, an ELISA assay specific for MMAE-conjugated antibody indicated that the ADC had faster clearance than the TDC, which is due in part to a greater magnitude of drug deconjugation from the ADC. Although very low in both cases, free MMAE measured in plasma was higher for the ADC relative to the TDC. Overall, modification by either method had a noticeable, albeit minor, impact on tissue distribution with a general trend toward increased hepatic uptake and reduced levels in other highly vascular organs. Taken together, these results indicate that the degree of overall structural modification of the antibody in an ADC has a corresponding level of impact on the PK behavior and stability in vivo. Accordingly, in addition to understanding the general chemical stability of the linker, it is important to consider the degree of structural modification of ADCs, the DAR distributions, and the sites of modifications to gain insight into the potential impacts on PK behavior and distribution.

■ ASSOCIATED CONTENT

Supporting Information. Size exclusion HPLC radiochromatograms of the radioimmunoconjugates used for tissue distribution. Additional tissue distribution data at 1 h, 2 days, and 7 days post intravenous injection. Mass spectrometry data before and after DOTA conjugation. This material is available free of charge via the Internet at http://pubs.acs.org.

■ AUTHOR INFORMATION

Corresponding Authors

*Kedan Lin, Ph.D., MS 463A, Genentech, Inc., South San Francisco, CA 94080. Tel. 650-225-8090; E-mail: lin.kedan@gene.com. *Leslie A. Khawli, Ph.D., MS 463A, Genentech, Inc., South San Francisco, CA 94080. Tel. 650-225-6509; E-mail: khawli.leslie@gene.com.

■ DISCLOSURE

All authors are employees of Genentech, a member of the Roche Group, and hold financial interest in Roche.

■ ACKNOWLEDGMENT

The authors would like to thank Michelle Schweiger, Kirsten Messick, Noore Kadri, Misia Bruski, Michael Reich, Jose Imperio, Sheila Ulufatu, Shannon Stainton, Cynthia Young, Nina Ljumanovic, Bernadette Johnstone, and Jason Ho for excellent animal studies support, Tracy Lou for assistance with study coordination, Jakub Baudys for assay support, and Paul Polakis for helpful scientific discussions.

■ REFERENCES

(1) Jemal, A., Siegel, R., Xu, J., and Ward, E. (2010) Cancer statistics, 2010. *CA Cancer J. Clin. 60*, 277–300.

(2) Hricak, H., Choyke, P. L., Eberhardt, S. C., Leibel, S. A., and Scardino, P. T. (2007) Imaging prostate cancer: a multidisciplinary perspective. *Radiology 243*, 28–53.

(3) Ravizzini, G., Turkbey, B., Kurdziel, K., and Choyke, P. L. (2009) New horizons in prostate cancer imaging. *Eur. J. Radiol. 70*, 212–26.

(4) Denmeade, S. R., and Isaacs, J. T. (2002) A history of prostate cancer treatment. *Nat. Rev. Cancer 2*, 389–96.

(5) Lin, G. A., Aaronson, D. S., Knight, S. J., Carroll, P. R., and Dudley, R. A. (2009) Patient decision aids for prostate cancer treatment: a systematic review of the literature. *CA Cancer J. Clin. 59*, 379–90.

(6) Rosenthal, S. A., and Sandler, H. M. (2010) Treatment strategies for high-risk locally advanced prostate cancer. *Nat. Rev. Urol. 7*, 31–8.

(7) Shepard, D. R., and Raghavan, D. (2009) Innovations in the systemic therapy of prostate cancer. *Nat. Rev. Clin. Oncol. 7*, 13–21.

(8) Hubert, R. S., Vivanco, I., Chen, E., Rastegar, S., Leong, K., Mitchell, S. C., Madraswala, R., Zhou, Y., Kuo, J., Raitano, A. B., Jakobovits, A., Saffran, D. C., and Afar, D. E. (1999) STEAP: a prostate-specific cell-surface antigen highly expressed in human prostate tumors. *Proc. Natl. Acad. Sci. U. S. A. 96*, 14523–8.

(9) Challita-Eid, P. M., Morrison, K., Etessami, S., An, Z., Morrison, K. J., Perez-Villar, J. J., Raitano, A. B., Jia, X. C., Gudas, J. M., Kanner, S. B., and Jakobovits, A. (2007) Monoclonal antibodies to six-transmembrane epithelial antigen of the prostate-1 inhibit intercellular communication in vitro and growth of human tumor xenografts in vivo. *Cancer Res. 67*, 5798–805.

(10) Ohgami, R. S., Campagna, D. R., McDonald, A., and Fleming, M. D. (2006) The Steap proteins are metalloreductases. *Blood 108*, 1388–94.

(11) Alley, S. C., Zhang, X., Okeley, N. M., Anderson, M., Law, C. L., Senter, P. D., and Benjamin, D. R. (2009) The pharmacologic basis for antibody-auristatin conjugate activity. *J. Pharmacol. Exp. Ther. 330*, 932–8.

(12) Carter, P. J., and Senter, P. D. (2008) Antibody-drug conjugates for cancer therapy. *Cancer J. 14*, 154–69.

(13) Chen, Y., Clark, S., Wong, T., Dennis, M. S., Luis, E., Zhong, F., Bheddah, S., Koeppen, H., Gogineni, A., Ross, S., Polakis, P., and Mallet, W. (2007) Armed antibodies targeting the mucin repeats of the ovarian cancer antigen, MUC16, are highly efficacious in animal tumor models. *Cancer Res. 67*, 4924–32.

(14) Ducry, L., and Stump, B. (2010) Antibody-drug conjugates: linking cytotoxic payloads to monoclonal antibodies. *Bioconjugate Chem. 21*, 5–13.

(15) Junutula, J. R., Raab, H., Clark, S., Bhakta, S., Leipold, D. D., Weir, S., Chen, Y., Simpson, M., Tsai, S. P., Dennis, M. S., Lu, Y., Meng, Y. G., Ng, C., Yang, J., Lee, C. C., Duenas, E., Gorrell, J., Katta, V., Kim, A., McDorman, K., Flagella, K., Venook, R., Ross, S., Spencer, S. D., Lee Wong, W., Lowman, H. B., Vandlen, R., Sliwkowski, M. X., Scheller, R. H., Polakis, P., and Mallet, W. (2008) Site-specific conjugation of a cytotoxic drug to an antibody improves the therapeutic index. *Nat. Biotechnol. 26*, 925–32.

(16) Lewis Phillips, G. D., Li, G., Dugger, D. L., Crocker, L. M., Parsons, K. L., Mai, E., Blattler, W. A., Lambert, J. M., Chari, R. V., Lutz, R. J., Wong, W. L., Jacobson, F. S., Koeppen, H., Schwall, R. H., Kenkare-Mitra, S. R., Spencer, S. D., and Sliwkowski, M. X. (2008) Targeting HER2-positive breast cancer with trastuzumab-DM1, an antibody-cytotoxic drug conjugate. *Cancer Res. 68*, 9280–90.

(17) Senter, P. D. (2009) Potent antibody drug conjugates for cancer therapy. *Curr. Opin. Chem. Biol. 13*, 235–44.

(18) Teicher, B. A. (2009) Antibody-drug conjugate targets. *Curr. Cancer Drug Targets 9*, 982–1004.

(19) Dornan, D., Bennett, F., Chen, Y., Dennis, M., Eaton, D., Elkins, K., French, D., Go, M. A., Jack, A., Junutula, J. R., Koeppen, H., Lau, J., McBride, J., Rawstron, A., Shi, X., Yu, N., Yu, S. F., Yue, P., Zheng, B., Ebens, A., and Polson, A. G. (2009) Therapeutic potential of an anti-CD79b antibody-drug conjugate, anti-CD79b-vc-MMAE, for the treatment of non-Hodgkin lymphoma. *Blood 114*, 2721–9.

(20) Mandler, R., Kobayashi, H., Hinson, E. R., Brechbiel, M. W., and Waldmann, T. A. (2004) Herceptin-geldanamycin immunoconjugates: pharmacokinetics, biodistribution, and enhanced antitumor activity. *Cancer Res. 64*, 1460–7.

(21) Bai, R. L., Pettit, G. R., and Hamel, E. (1990) Binding of dolastatin 10 to tubulin at a distinct site for peptide antimitotic agents near the exchangeable nucleotide and vinca alkaloid sites. *J. Biol. Chem. 265*, 17141–9.

(22) Doronina, S. O., Toki, B. E., Torgov, M. Y., Mendelsohn, B. A., Cerveny, C. G., Chace, D. F., DeBlanc, R. L., Gearing, R. P., Bovee, T. D., Siegall, C. B., Francisco, J. A., Wahl, A. F., Meyer, D. L., and Senter, P. D. (2003) Development of potent monoclonal antibody auristatin conjugates for cancer therapy. *Nat. Biotechnol. 21*, 778–84.

(23) Francisco, J. A., Cerveny, C. G., Meyer, D. L., Mixan, B. J., Klussman, K., Chace, D. F., Rejniak, S. X., Gordon, K. A., DeBlanc, R., Toki, B. E., Law, C. L., Doronina, S. O., Siegall, C. B., Senter, P. D., and Wahl, A. F. (2003) cAC10-vcMMAE, an anti-CD30-monomethyl auristatin E conjugate with potent and selective antitumor activity. *Blood 102*, 1458–65.

(24) Hamblett, K. J., Senter, P. D., Chace, D. F., Sun, M. M., Lenox, J., Cerveny, C. G., Kissler, K. M., Bernhardt, S. X., Kopcha, A. K., Zabinski, R. F., Meyer, D. L., and Francisco, J. A. (2004) Effects of drug loading on the antitumor activity of a monoclonal antibody drug conjugate. *Clin. Cancer Res. 10*, 7063–70.

(25) McDonagh, C. F., Turcott, E., Westendorf, L., Webster, J. B., Alley, S. C., Kim, K., Andreyka, J., Stone, I., Hamblett, K. J., Francisco, J. A., and Carter, P. (2006) Engineered antibody-drug conjugates with defined sites and stoichiometries of drug attachment. *Protein Eng. Des. Sel. 19*, 299–307.

(26) McKenna, T., Batson, J., Ross, S., Polakis, P., and Rubinfeld, B. (2007) Armed antibodies targeted to STEAP1 inhibit growth of human prostate xenografts in vivo. *AACR Meeting Abstracts 2007*, 4468.

(27) Meares, C. F., McCall, M. J., Reardan, D. T., Goodwin, D. A., Diamanti, C. I., and McTigue, M. (1984) Conjugation of antibodies with bifunctional chelating agents: isothiocyanate and bromoacetamide reagents, methods of analysis, and subsequent addition of metal ions. *Anal. Biochem. 142*, 68–78.

(28) Lewis, M. R., Kao, J. Y., Anderson, A. L., Shively, J. E., and Raubitschek, A. (2001) An improved method for conjugating monoclonal antibodies with N-hydroxysulfosuccinimidyl DOTA. *Bioconjugate Chem. 12*, 320–4.

(29) Davies, B., and Morris, T. (1993) Physiological parameters in laboratory animals and humans. *Pharm. Res. 10*, 1093–5.

(30) Lin, K., Lou, T., Ferl, G., Leipold, D., Graham, R., Kozak, K. R., Polakis, P., Tibbits, J., and Theil, F. P. (2009) Cross-species pharmacokinetic characterization of antibody drug conjugate TenB2-vc-E to understand target biology. *AAPS Meeting Abstracts* 2009.

(31) Stephan, J. P., Chan, P., Lee, C., Nelson, C., Elliott, J. M., Bechtel, C., Raab, H., Xie, D., Akutagawa, J., Baudys, J., Saad, O., Prabhu, S., Wong, W. L., Vandlen, R., Jacobson, F., and Ebens, A. (2008) Anti-CD22-MCC-DM1 and MC-MMAF conjugates: impact of assay format on pharmacokinetic parameters determination. *Bioconjugate Chem. 19*, 1673–83.

(32) Austin, C. D., Wen, X., Gazzard, L., Nelson, C., Scheller, R. H., and Scales, S. J. (2005) Oxidizing potential of endosomes and lysosomes limits intracellular cleavage of disulfide-based antibody-drug conjugates. *Proc. Natl. Acad. Sci. U. S. A. 102*, 17987–92.

(33) Doronina, S. O., Bovee, T. D., Meyer, D. W., Miyamoto, J. B., Anderson, M. E., Morris-Tilden, C. A., and Senter, P. D. (2008) Novel peptide linkers for highly potent antibody-auristatin conjugate. *Bioconjugate Chem. 19*, 1960–3.

(34) Perera, R. M., Zoncu, R., Johns, T. G., Pypaert, M., Lee, F. T., Mellman, I., Old, L. J., Toomre, D. K., and Scott, A. M. (2007) Internalization, intracellular trafficking, and biodistribution of monoclonal antibody 806: a novel anti-epidermal growth factor receptor antibody. *Neoplasia 9*, 1099–110.

(35) Zheng, B., Fuji, R. N., Elkins, K., Yu, S. F., Fuh, F. K., Chuh, J., Tan, C., Hongo, J. A., Raab, H., Kozak, K. R., Williams, M., McDorman, E., Eaton, D., Ebens, A., and Polson, A. G. (2009) In vivo effects of targeting CD79b with antibodies and antibody-drug conjugates. *Mol. Cancer Ther. 8*, 2937–46.

(36) Alley, S. C., Benjamin, D. R., Jeffrey, S. C., Okeley, N. M., Meyer, D. L., Sanderson, R. J., and Senter, P. D. (2008) Contribution of linker stability to the activities of anticancer immunoconjugates. *Bioconjugate Chem. 19*, 759–65.

(37) Junutula, J. R., Flagella, K. M., Graham, R. A., Parsons, K. L., Ha, E., Raab, H., Bhakta, S., Nguyen, T., Dugger, D. L., Li, G., Mai, E., Lewis Phillips, G. D., Hiraragi, H., Fuji, R. N., Tibbitts, J., Vandlen, R., Spencer, S. D., Scheller, R. H., Polakis, P., and Sliwkowski, M. X. (2010) Engineered thio-trastuzumab-DM1 conjugate with an improved therapeutic index to target human epidermal growth factor receptor 2-positive breast cancer. *Clin. Cancer Res. 16*, 4769–78.

(38) Xie, H., Audette, C., Hoffee, M., Lambert, J. M., and Blattler, W. A. (2004) Pharmacokinetics and biodistribution of the antitumor immunoconjugate, cantuzumab mertansine (huC242-DM1), and its two components in mice. *J Pharmacol. Exp. Ther. 308*, 1073–82.

(39) Rogers, B. E., Franano, F. N., Duncan, J. R., Edwards, W. B., Anderson, C. J., Connett, J. M., and Welch, M. J. (1995) Identification of

metabolites of ^{111}In-diethylenetriaminepentaacetic acid-monoclonal antibodies and antibody fragments in vivo. *Cancer Res. 55*, 5714s–5720s.

(40) Boswell, C. A., Ferl, G. Z., Mundo, E. E., Bumbaca, D., Schweiger, M. G., Theil, F. P., Fielder, P. J., and Khawli, L. A. (2011) Effects of Anti-VEGF on predicted antibody biodistribution: roles of vascular volume, interstitial volume, and blood flow. *PLoS One 6*, e17874.

(41) Boswell, C. A., Ferl, G. Z., Mundo, E. E., Schweiger, M. G., Marik, J., Reich, M. P., Theil, F. P., Fielder, P. J., and Khawli, L. A. (2010) Development and evaluation of a novel method for preclinical measurement of tissue vascular volume. *Mol. Pharm. 7*, 1848–1857.

(42) Boswell, C. A., Tesar, D. B., Mukhyala, K., Theil, F. P., Fielder, P. J., and Khawli, L. A. (2010) Effects of charge on antibody tissue distribution and pharmacokinetics. *Bioconjugate Chem. 21*, 2153–2362.

(43) Al-Ejeh, F., Darby, J. M., Thierry, B., and Brown, M. P. (2009) A simplified suite of methods to evaluate chelator conjugation of antibodies: effects on hydrodynamic radius and biodistribution. *Nucl. Med. Biol. 36*, 395–402.

(44) Kobayashi, H., Kao, C. H., Kreitman, R. J., Le, N., Kim, M. K., Brechbiel, M. W., Paik, C. H., Pastan, I., and Carrasquillo, J. A. (2000) Pharmacokinetics of ^{111}In- and ^{125}I-labeled antiTac single-chain Fv recombinant immunotoxin. *J. Nucl. Med. 41*, 755–62.

(45) Boswell, C. A., and Brechbiel, M. W. (2007) Development of radioimmunotherapeutic and diagnostic antibodies: an inside-out view. *Nucl. Med. Biol. 34*, 757–78.

(46) Boswell, C. A., Sun, X., Niu, W., Weisman, G. R., Wong, E. H., Rheingold, A. L., and Anderson, C. J. (2004) Comparative in vivo stability of copper-64-labeled cross-bridged and conventional tetraazamacrocyclic complexes. *J. Med. Chem. 47*, 1465–74.

(47) Bryan, J. N., Jia, F., Mohsin, H., Sivaguru, G., Miller, W. H., Anderson, C. J., Henry, C. J., and Lewis, M. R. (2005) Comparative uptakes and biodistributions of internalizing vs. noninternalizing copper-64 radioimmunoconjugates in cell and animal models of colon cancer. *Nucl. Med. Biol. 32*, 851–8.

(48) Lewis, M. R., Raubitschek, A., and Shively, J. E. (1994) A facile, water-soluble method for modification of proteins with DOTA. Use of elevated temperature and optimized pH to achieve high specific activity and high chelate stability in radiolabeled immunoconjugates. *Bioconjugate Chem. 5*, 565–76.

(49) DeLano, W. L. (2008) The PyMOL Molecular Graphics System, DeLano Scientific LLC, Palo Alto, CA, USA, http://www.pymol.org.

SUPPORTING INFORMATION

S1. Size exclusion HPLC radiochromatograms of the radioimmunoconjugates used for tissue distribution.

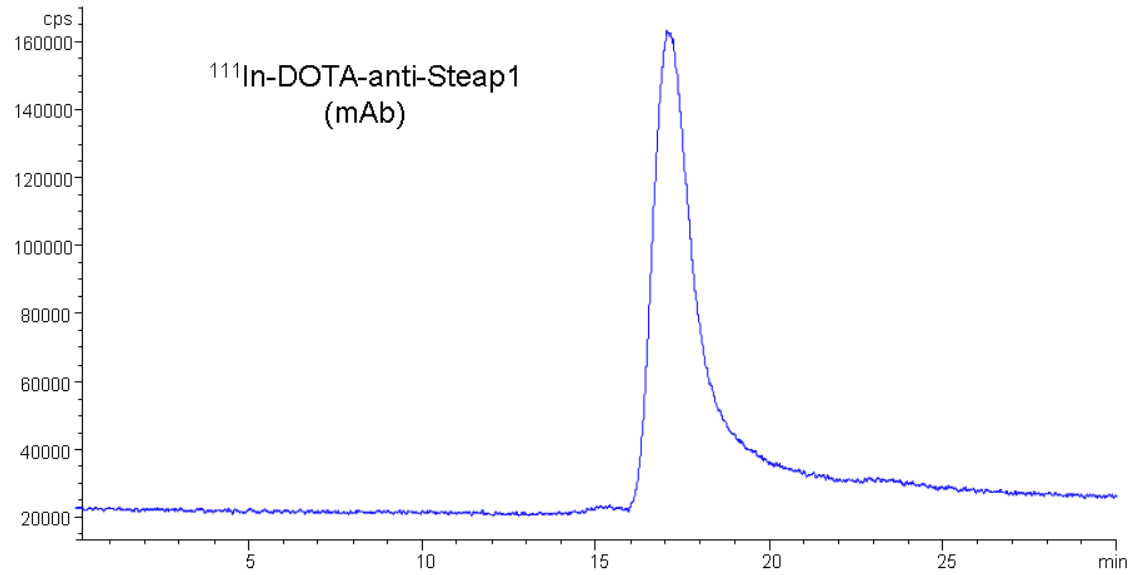

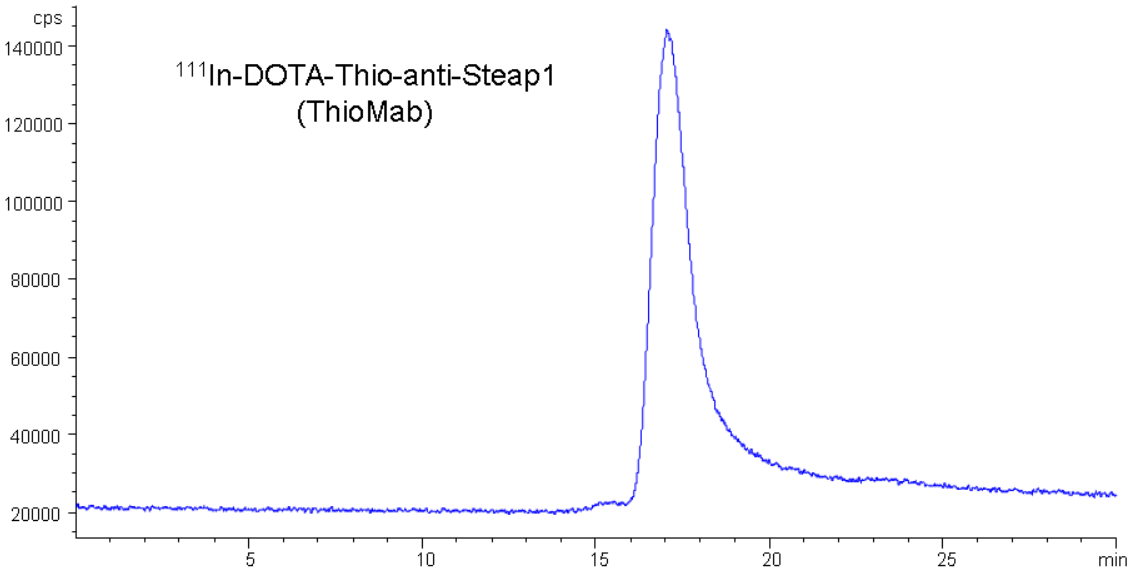

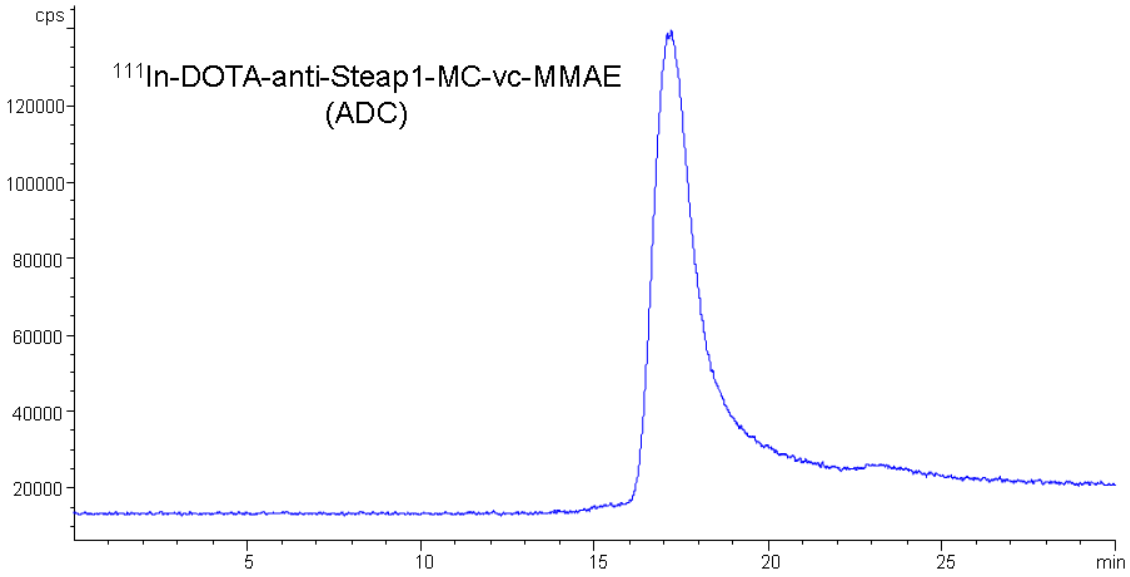
cps
120000
100000
80000
60000
40000
20000
111In-DOTA-anti-Steap1-MC-vc-MMAE
(ADC)
5
10
15
20
25
min

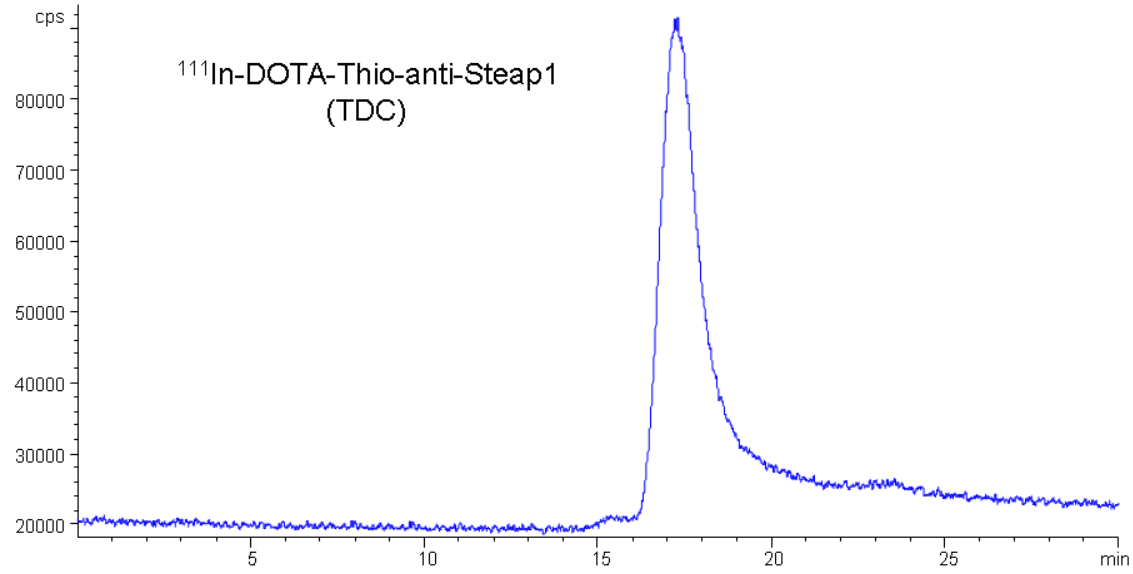
cps
80000
70000
60000
50000
40000
30000
20000
111In-DOTA-Thio-anti-Steap1
(TDC)
5
10
15
20
25
min

S2. Additional tissue distribution data at 1, 48, and 168 h post intravenous injection.

	anti-STEAP1			anti-STEAP1 ADC			thio-anti-STEAP1			anti-STEAP1 TDC		
1 hour	**%ID/g**	±	**SD**	**%ID/g**	±	**SD**	**%ID/g**	±	**SD**	**%ID/g**	±	**SD**
lung	2.40	±	0.47	3.53	±	0.82	4.27	±	1.14	3.12	±	1.15
liver	1.25	±	0.11	2.11	±	0.38	1.82	±	0.47	2.31	±	0.93
kidneys	1.80	±	0.59	2.11	±	0.40	1.84	±	0.27	1.88	±	0.17
heart	1.44	±	0.18	1.72	±	0.17	1.60	±	0.26	1.46	±	0.17
spleen	1.36	±	0.06	1.44	±	0.10	1.56	±	0.09	1.27	±	0.20
rt. femur	0.71	±	0.10	0.79	±	0.13	0.89	±	0.15	0.68	±	0.09
gastroc.	0.29	±	0.09	0.28	±	0.04	0.23	±	0.07	0.21	±	0.03
stomach	0.31	±	0.08	0.23	±	0.03	0.36	±	0.09	0.50	±	0.02
sm. intest.	0.51	±	0.11	0.58	±	0.17	0.60	±	0.04	0.46	±	0.12
lg. intest.	0.36	±	0.10	0.30	±	0.05	0.33	±	0.10	0.49	±	0.08
wh. blood	10.89	±	1.41	9.48	±	0.69	12.08	±	0.35	10.02	±	0.91
48 hour	**%ID/g**	±	**SD**	**%ID/g**	±	**SD**	**%ID/g**	±	**SD**	**%ID/g**	±	**SD**
lung	1.64	±	0.43	1.42	±	0.22	2.74	±	2.61	1.27	±	0.13
liver	1.14	±	0.38	1.61	±	0.03	0.93	±	0.15	1.35	±	0.13
kidneys	2.67	±	0.04	2.36	±	0.12	1.85	±	0.50	2.31	±	0.07
heart	1.02	±	0.05	0.97	±	0.04	1.04	±	0.12	0.97	±	0.08
spleen	1.34	±	0.12	1.28	±	0.07	1.22	±	0.07	1.19	±	0.12
rt. femur	0.55	±	0.07	0.50	±	0.07	0.50	±	0.05	0.55	±	0.04
gastroc.	0.33	±	0.08	0.32	±	0.03	0.30	±	0.01	0.30	±	0.06
stomach	0.41	±	0.06	0.36	±	0.04	0.37	±	0.08	0.36	±	0.02
sm. intest.	0.47	±	0.07	0.55	±	0.08	0.41	±	0.03	0.47	±	0.03
lg. intest.	0.46	±	0.11	0.44	±	0.08	0.45	±	0.10	0.45	±	0.09
wh. blood	6.42	±	0.27	5.49	±	0.69	6.01	±	0.77	5.78	±	0.54
168 hour	**%ID/g**	±	**SD**	**%ID/g**	±	**SD**	**%ID/g**	±	**SD**	**%ID/g**	±	**SD**
lung	0.83	±	0.14	0.88	±	0.08	0.83	±	0.00	0.82	±	0.35
liver	0.32	±	0.04	0.47	±	0.06	0.20	±	0.02	0.29	±	0.08
kidneys	2.61	±	0.27	2.27	±	0.37	2.23	±	0.21	1.83	±	0.22
heart	0.66	±	0.11	0.51	±	0.06	0.68	±	0.04	0.60	±	0.19
spleen	0.82	±	0.15	1.07	±	0.12	0.89	±	0.03	0.69	±	0.14
rt. femur	0.36	±	0.05	0.38	±	0.05	0.37	±	0.03	0.31	±	0.05
gastroc.	0.20	±	0.04	0.17	±	0.01	0.20	±	0.00	0.14	±	0.01
stomach	0.25	±	0.03	0.23	±	0.06	0.21	±	0.02	0.24	±	0.06
sm. intest.	0.22	±	0.03	0.29	±	0.09	0.26	±	0.04	0.29	±	0.08
lg. intest.	0.22	±	0.03	0.23	±	0.05	0.24	±	0.02	0.26	±	0.03
wh. blood	3.58	±	0.49	2.75	±	0.26	3.98	±	0.54	3.28	±	0.85

S3. Mass spectrometry data before and after DOTA conjugation.

(a) Anti-Steap1 mAb before (top) and after (bottom) DOTA conjugation, average DOTA incorporation of 2.6

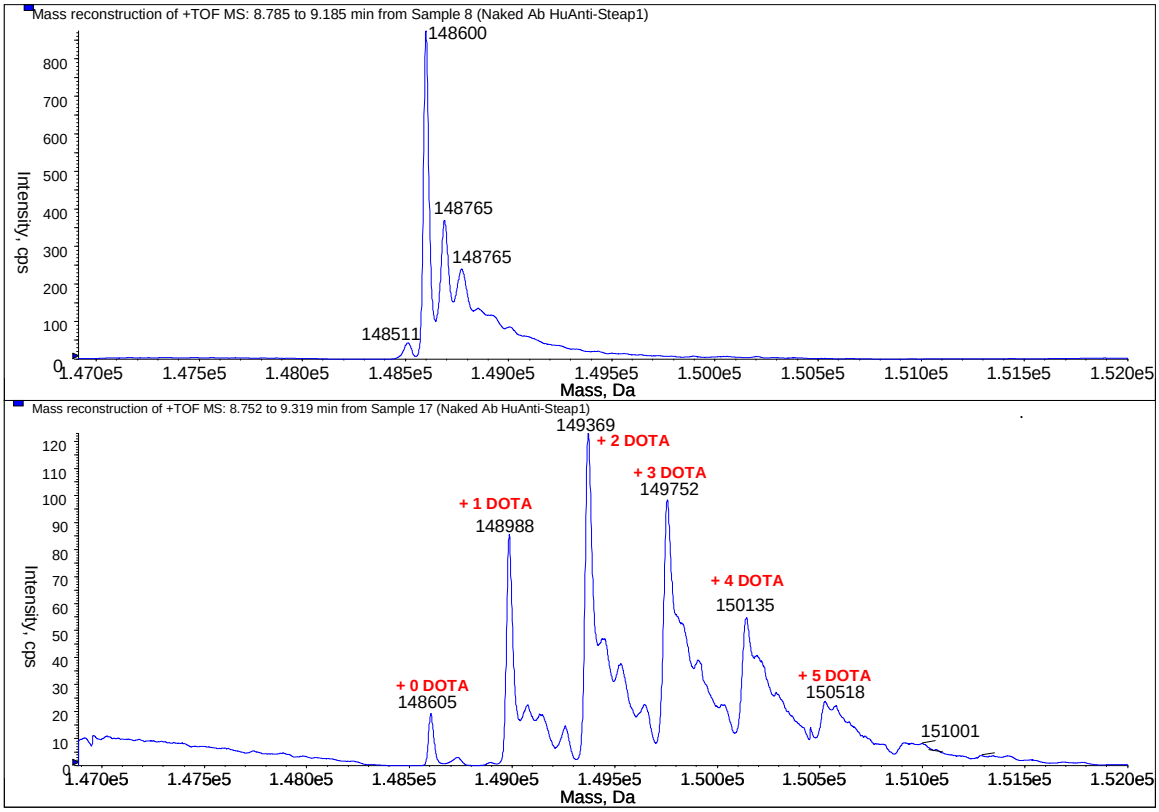

(b) Anti-Steap1 ThioMab before (top) and after (bottom) DOTA conjugation, average DOTA incorporation of 3.2

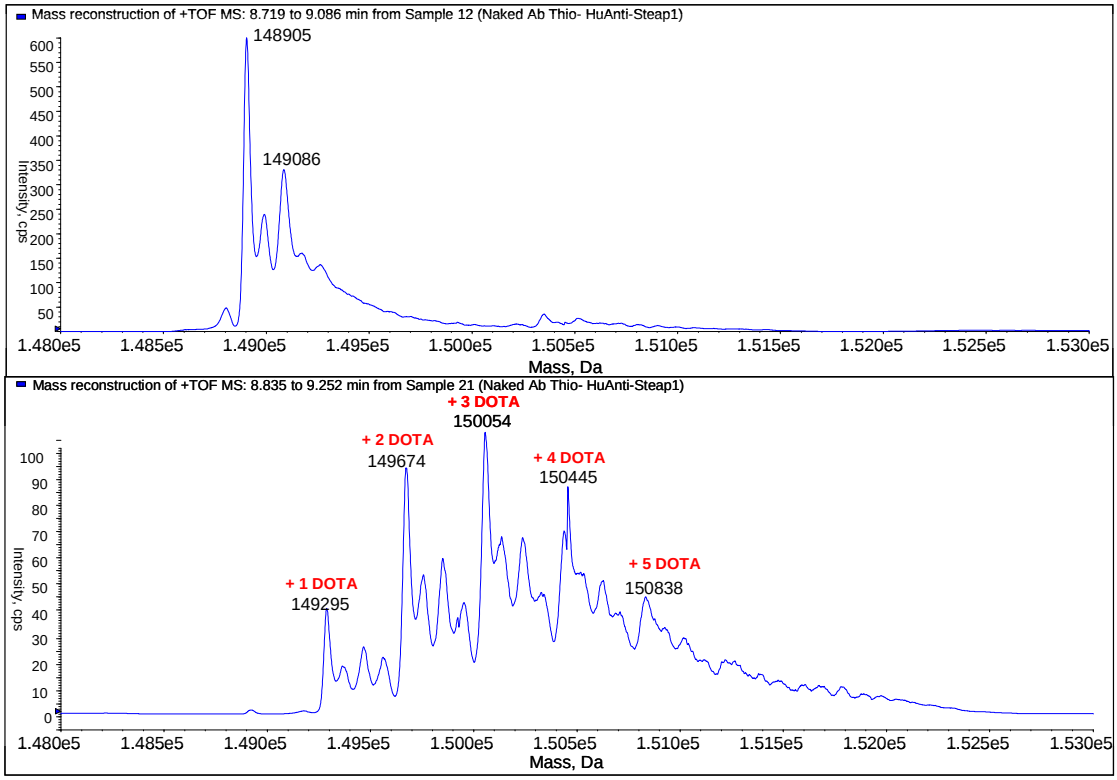

(c) Anti-Steap1 ADC before (top) and after (bottom) DOTA conjugation. Average DOTA incorporation per Ab of 1.7 (~0.16 per each LC, ~0.67 per each HC)

Note that samples were completely reduced prior to analysis for ADC due to conjugation of vcMMAE using interchain disulfide bonds

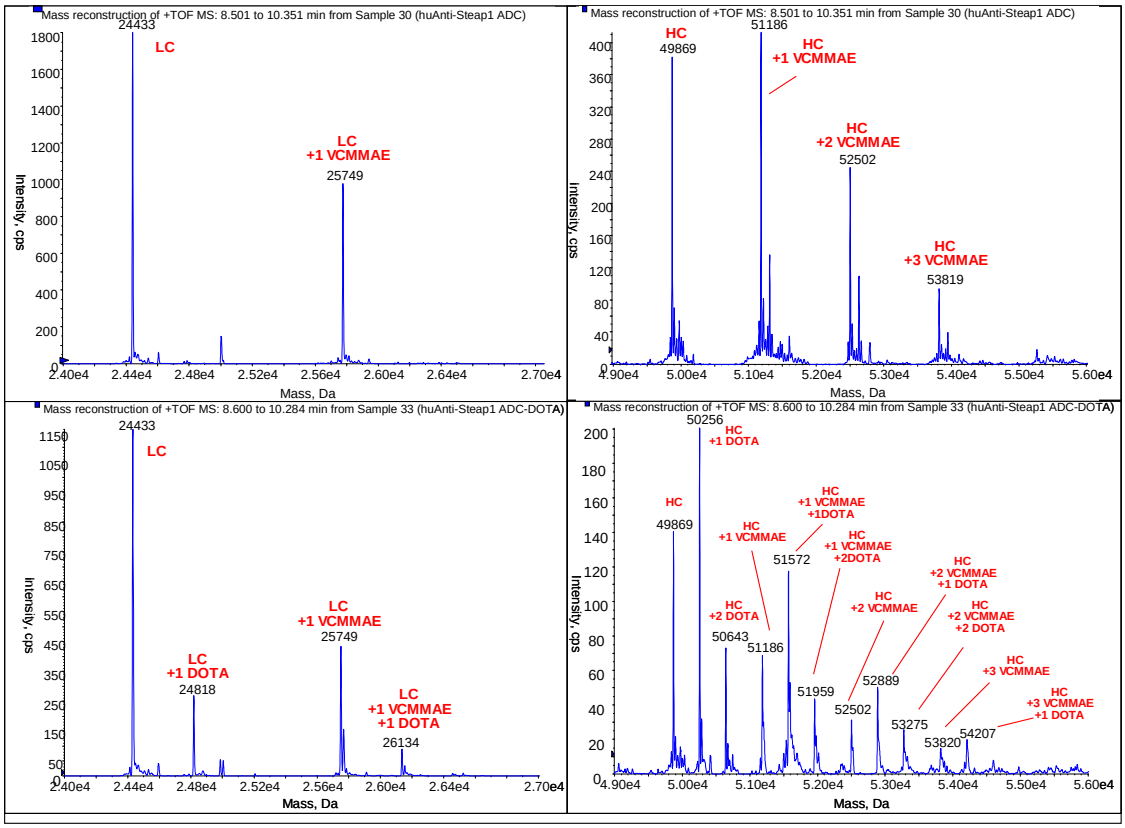

(d) Anti-Steap1 TDC before (top) and after (bottom) DOTA conjugation, average DOTA incorporation of 2.3

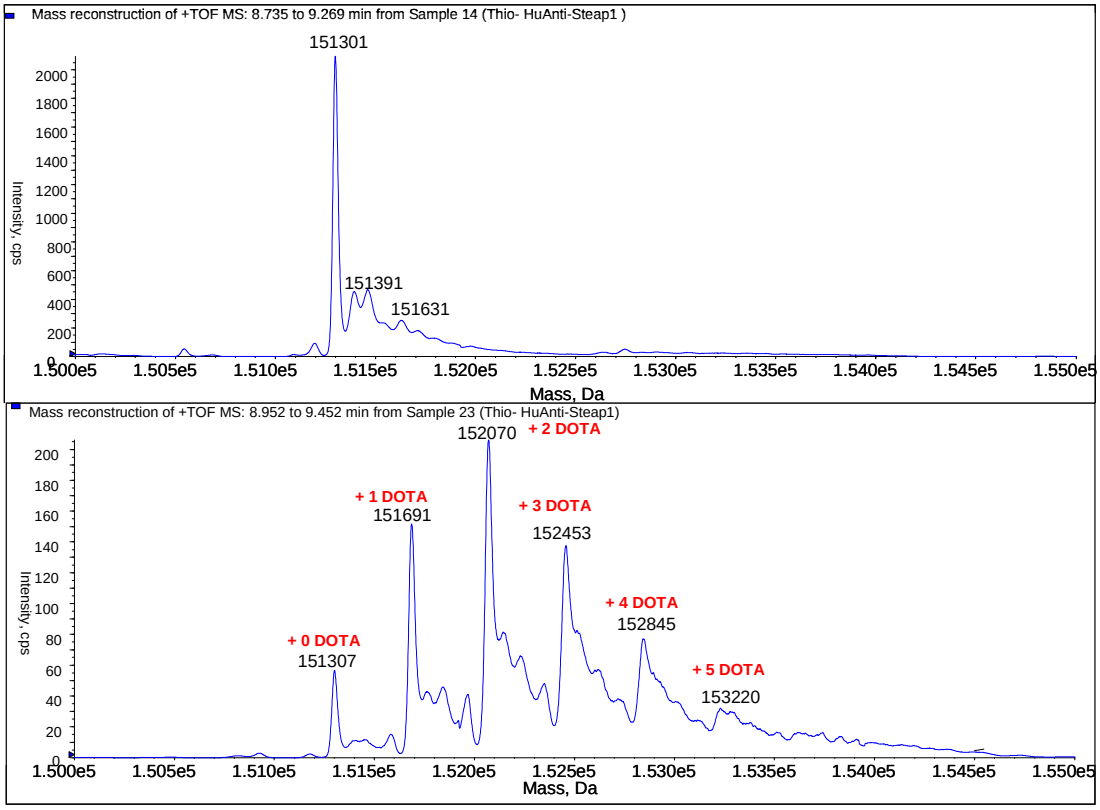

Bioconjugate Chemistry

ARTICLE

pubs.acs.org/bc

Development of the Novel PEG-PE-Based Polymer for the Reversible Attachment of Specific Ligands to Liposomes: Synthesis and in Vitro Characterization

Swati Biswas, Namita S. Dodwadkar, Rupa R. Sawant, and Vladimir P. Torchilin*

Center for Pharmaceutical Biotechnology and Nanomedicine, 360 Huntington Avenue, 312 Mugar Hall, Northeastern University, Boston, Massachusetts 02115, United States

ABSTRACT: Surface grafting of liposomes with the wide variety of ligands including antibodies and other proteins is a promising approach for targeted delivery of therapeutics. In this paper, we describe a simple method of synthesizing a hydrazine-functionalized poly(ethylene glycol)-phosphatidylethanolamine (PEG-PE)-based amphiphilic polymer which can conjugate a variety of ligands via a reversible, pH-cleavable bond. In this method, the targeting ligand is attached to the distal end of the PEG chain, which facilitates its easy access to the targeted site of interaction. The reversible attachment of targeting ligands is useful especially in multifunctional liposomal systems, whereafter successfully performing the function of targeting to the specific site, the bulky ligands, such as proteins or antibodies, are cleaved off in response to an environmental stimulus to expose some other functionalities such as ligands for intracellular penetration or organelle-specific targeting. To investigate the applicability of the protocol, the model ligands monoclonal antinucleosome antibody 2C5 and antimyosin antibody 2G4, and glycoproteins concanavalin A (Con-A) and avidin were conjugated to the synthesized polymer and incorporated into liposomes. In vitro assays including biochemical, enzyme-linked immunosorbent, fluorescence microscopy, and flow cytometry were used to confirm three key characteristics of the modified and/or liposome-attached proteins: successful conjugation of the targeting ligands to the polymer, preservation of specific activity of the ligands after the conjugation and liposome attachment, and the facile pH-sensitive ligand detachment. Monoclonal antibody 2C5 and 2G4, immobilized on the liposome surface, retained their binding affinity to corresponding antigens as confirmed by ELISA. The Con A-bearing liposomes showed significantly higher agglutination in the presence of its substrate mannan compared to plain liposomes (PL) and avidin-functionalized liposomes bound specifically with biotin−agarose. The study on the pH-dependence showed that almost 80% of the hydrazone bond was cleaved after rather brief preincubation of the immunoliposomes at pH 5 for 0.5 to 1 h. Fluorescence microscopy and flow cytometry analysis of cancer cells (HeLa and MCF-7) treated with cancer cell-specific targeting ligand mAb 2C5-bearing liposomes showed enhanced cellular binding. Studies at low pH clearly confirmed the easy cleavability of the targeting ligand from the liposomes resulting in significantly less or virtually no cellular association.

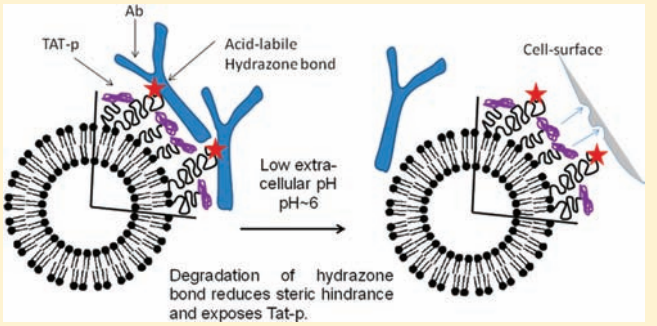

INTRODUCTION

Liposomes have served as an efficient drug delivery system for enhanced efficacy and decreased systemic toxicity of various biologically active molecules.[1,2] However, one of the major disadvantages of liposomal drug delivery systems (DDS) is that circulating liposomes are rapidly cleared when uptaken by cells of the reticuloendothelial system (RES) in the liver and spleen. To engineer liposomes capable of delivering therapeutic cargo to sites other than the RES, long-circulating polymer-coated (PEGylated) liposomes have been developed.[1,2] The modification of nanocarriers by conjugating PEG on the surface reduces many undesirable side effects triggered in vivo by various biological recognition mechanisms.[3] This property of prolonged systemic circulation also results in passive targeting of liposomes even in the areas with a compromised vasculature such as infarcts and tumors by the enhanced permeability and retention (EPR) effect.[4−9] Active targeting of liposomes to specific disease sites, such as tumors and infarcts, could be achieved by surface modification of the liposomes with various ligands, such as tumor-specific molecules including cancer cell-specific antinucleosome antibody (mAb 2C5), proteins (transferrin), peptides (RGD), and small molecules such as receptor ligands (folate) for anticancer therapy and antimyosin mAb (2G4) for the therapy of the myocardial infarction.[10−16] Thus, pharmaceutical nanocarriers can be endowed with the properties of both active and passive targeting.[17,18]

In the case of active targeting of PEGylated liposomes, the targeting moiety should be attached "above" the protective polymer

Received: April 27, 2011
Revised: August 18, 2011
Published: August 29, 2011

ACS Publications © 2011 American Chemical Society

dx.doi.org/10.1021/bc2002133 | *Bioconjugate Chem.* 2011, 22, 2005–2013

layer by coupling it to the distal end of a PEG chain to provide accessibility of the ligand to the target organ or tissue.[9,17,19] Liposomes can also be endowed with other functionalities such as enhanced intracellular penetration by surface attachment of cell-penetrating peptides (CPPs), as well as enhanced intracellular organelle recognition after cellular internalization by addition of specific ligands that target subcellular organelles such as mitochondria, lysozomes, or nuclei.[20,21]

Therefore, it is important to optimize such multifunctional nanocarriers by proper combination of several of the properties including longevity in the circulation, targetability, intracellular penetration, and organelle recognition to improve its efficacy.[22] Another approach to prepare "smart" multifunctional liposomes is to introduce the property of stimuli-sensitivity.[23,24] In our earlier study, we came up with a novel stimuli-sensitive multifunctional nanocarrier, a PEGylated TAT-p-modified pH-sensitive liposome.[23,24] The PEG chains which provide the longevity in systemic circulation for accumulation in a tumor or infarcted tissue by passive targeting were cleaved off at lowered pH environment of hypoxic areas to expose the previously hidden nonspecific cell penetrating function, such as TAT-p.

In our present study, we demonstrated a simplified synthesis of hydrazine-functionalized PEG-PE-based amphiphilic polymer, which could conjugate variety of ligands via the reversible, pH-cleavable bond. Although the concept of end-group-hydrazine-functionalized PEG−lipid conjugate has been reported,[25] in our study, we report a novel scheme of the modification of PEG-PE via only two facile reaction steps to prepare hydrazine-functionalized PEG-PE. The ligand−polymer conjugate was easily incorporated into the liposomes via its PE fragment. The targeting ligands were attached to the distal end of the PEG-chain to have sufficient freedom for various cellular interactions. Introducing a pH-sensitive linkage between bulky targeting ligand and liposome in the multifunctional liposomal system could be especially useful for drug delivery into tumors or infarcted regions with the lowered pH. After the successful target accumulation, lowered pH in such areas could cleave off the targeting ligands (and possible PEG) and expose other previously hidden (shielded) nonspecific functionalities. The model ligands used to confirm the applicability of our protocol were mAbs 2C5 and 2G4 and proteins Con-A and avidin. In this paper, we confirm that the suggested method of using stimuli-sensitive polymer for the ligand attachment can be successfully applied for the ligand conjugation, preservation of its specific activity, and further pH-dependent cleavage of these ligands attached to the liposomal surface.

EXPERIMENTAL PROCEDURES

Materials. 1,2-Distearoyl-*sn*-glycero-3-phosphoethanolamine-*N*-[methoxy(polyethylene glycol)-2000] (PEG_{2K}-PE), 1,2-dimyristoyl-*sn*-glycero-3-phosphoethanolamine-*N*-(lissamine rhodamine B Sulfonyl)(ammonium salt, Rh-PE), L-α-phosphatidylcholine (egg, chicken), and 1,2-distearoyl-*sn*-glycero-3-phophoethanolamine-*N*-[amino(polyethylene glycol)2000](ammonium salt) (DSPE-PEG_{2K}-Amine) were purchased from Avanti Polar Lipids Inc. (Alabaster, AL) and used without further purification. Cholesterol, chloroform-*d*, triethylamine, Con-A, avidin, α-methyl mannopyranoside, 5,5′-dithio-bis (2-nitrobenzoic acid) (DTNB), *N*-acetyl-L-cystein were purchased from Sigma (St. Louis, MO). Sephadex G 25 superfine medium was from GE Healthcare Biosciences Corp. (Piscataway, NJ, USA). 2-Iminothiolane-HCl (Traut's reagent), 4-(4-*N*-maleimidophanyl)butyric acid hydrazide−HCl (MPBH), fluorescein isothiocyanate (FITC-NHS), biotin-agarose, 2,4,6-trinitrobenzene sulfonic acid (TNBSA), 5% w/v solution in methanol, were purchased from Pierce (Rockford, IL). Paraformaldehyde was purchased from Electron Microscopy Sciences (Hatfield, PA). Fluoromount-G was from Southern Biotech (Birmingham, AL). The mAb 2C5 was produced in ascites via the i.p. injection of 1.5×10^6 hybridoma cells into pristane-primed 4-week-old BALB/c male mice. The production and purification of the mAb 2C5 were carried out by Harlan Bioproducts (Indianapolis, IL) using the cells from our laboratory. Cardiac myosin-specific mAb 2G4 of the immunoglobulin IgG class available in our laboratory was collected and purified from murine ascites according to the standard ammonium sulfate precipitation method.[15,26]

Cell Culture. Human cervical carcinoma (HeLa) cells and breast cancer cell line (MCF-7) were purchased from ATCC (Manassas, VA). Dulbecco's modified Eagle's media (DMEM), fetal bovine serum (FBS), and penicillin−streptomycin solution were from CellGro (Kansas City, MO). Cells were grown in DMEM supplemented with 10% FBS, 100 IU/mL of penicillin, streptomycin, and 250 ng/mL amphotericin-B at 37 °C and 5% CO_2.

Methods. *Synthesis, Purification, and Characterization of Synthesized Polymers. 1,2-Distearoyl-sn-glycero-3-phophoethanolamine-N-[thio(polyethylene glycol)2000](ammonium salt) (DSPE-PEG-$_{2K}$-SH).* 6.2 mg (45.05 μM) of Traut's reagent dissolved in 50 μL of methanol were added into the chloroform solution (25 mg/mL) of DSPE-PEG-$_{2K}$-amine (25 mg, 8.95 μM) at room temperature (RT). The reaction mixture was stirred at RT for 2 h. Chloroform was evaporated completely, the residue dissolved in PBS and dialyzed using a cellulose ester membrane (MWCO. 1 kDa, Spectrum Medical Industries, Houston, TX) overnight. The dialysate was freeze−dried, weighed, dissolved in chloroform at 5 mg/mL, and stored at −80 °C. The quantification of sulfhydryl groups was performed by DTNB assay using *N*-acetyl cysteine for the preparation of the standard SH calibration curve.[27] The yield of the reaction was calculated to be 60%. The freeze−dried product (5 mg) was dissolved in deuterated (*d*)-chloroform (1 mL) and analyzed by ^{1}H NMR using Varian 500 mHz.

1,2-Distearoyl-sn-glycero-3-phophoethanolamine-N-[hydrazido(polyethylene glycol)2000](ammonium salt) (DSPE-PEG-$_{2K}$-CONHNH$_2$). MPBH (13.1 mg, 36.9 μM) dissolved in PBS was added into the solution of DSPE-PEG-$_{2K}$-SH (17.7 mg, 6.2 μM) in PBS (pH 7.4). The reaction mixture was stirred at RT for 4 h and put for dialysis using cellulose ester bag (MWCO 2 kDa) against water overnight before freeze−drying. The hydrazide content of the freeze−dried product was determined by the TNBSA assay following the manufacturer's protocol and using the MPBH for the preparation of a standard calibration curve.[28] The freeze−dried fluffy solid was dissolved in chloroform at 10 mg/mL and stored at −80 °C. The solid product (5−10 mg) was dissolved in *d*-chloroform (1 mL) and characterized by ^{1}H NMR using Varian 500 mHz spectroscopy. The conjugates were not chromatographically isolated after the coupling steps. All polymers were purified by dialysis after the conjugation.

Liposome Preparation. *Activation of Antibodies (mAb 2C5, mAb 2G4) and proteins (Concanavalin A, Avidin).* Antibodies (mAbs 2C5, 2G4) and glycoproteins Con-A and avidin were aldehyde-activated using freshly prepared Na periodate. 100 μL of Na periodate (0.1 M) in water was added to 1.0 mL of the antibody or protein solution (10 mg/mL) in the dark and stirred for 10 min. The reaction was quenched by the addition of sodium sulfite at a 2× molar excess over the periodate added. The

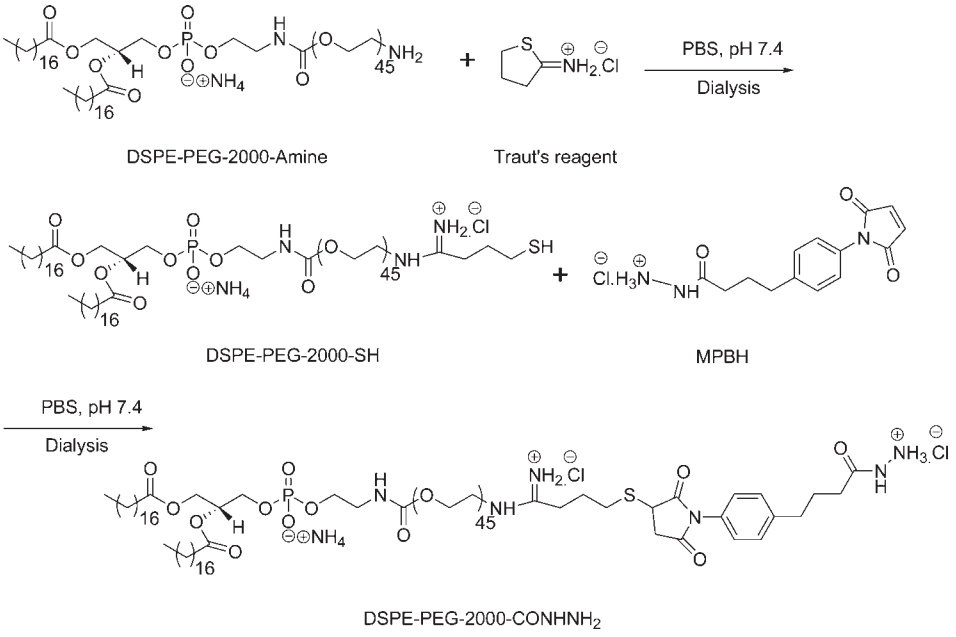

Figure 1. Synthesis of the novel polymer, DSPE-PEG-$_{2K}$-CONHNH$_2$.

aldehyde-activated antibodies or proteins were purified by gel filtration using a desalting spin column (Pierce) and used immediately.

Plain Liposomes (PL). Liposomes were prepared by the lipid film hydration technique. Briefly, a dry lipid film was prepared by rotary evaporation of a chloroform solution of all the ingredients including eggPC/cholesterol or eggPC/cholesterol/Rh-PE (in molar ratios of 65/30 or 64.5/30/0.5 with 5 mol % of DOPE-PEG-$_{2K}$) followed by the freeze−drying (Labconco, Freeze-dry system, Freezone) for at least 4 h to remove the traces of the solvent. The dry lipid film was hydrated in PBS, pH 7.4, at lipid concentration of 4 mg/mL. The hydrated mixture was vortexed vigorously for 5 min to form multilamelar vesicles and then extruded through the 200-nm-pore-sized polycarbonate membrane filters (Avanti Polar Lipids) 20 times to yield liposomes with uniform particle sizes of 150−200 nm mean diameter.

Antibody/Protein-Grafted Liposomes. Antibodies or proteins containing reactive aldehyde groups were incubated with DSPE-PEG-$_{2K}$-CONHNH$_2$ in PBS (pH 7.4) overnight at 0 °C to produce polymer−lipid conjugate-modified products. The freshly prepared loose micelles of antibody/protein conjugates (5 mol % of the total liposomal lipid) were incubated with preformed PL overnight at pH 7.4 for the transfer of the micelle components to liposomes via the postinsertion technique. The antibody or protein-grafted liposomes, 2C5-Hz-PEG-$_{2K}$-DSPE-modified liposomes (2C5-L), and 2G4-Hz-PEG-$_{2K}$-DSPE-modified liposomes (2G4-L), as well as avidin-Hz-PEG-$_{2K}$-DSPE-modified liposomes (avidin-L) and concanavalin-A-Hz-PEG-$_{2K}$-DSPE-modified liposomes (Con-A--L) were separated from unbound antibody/protein by extensive dialysis using cellulose ester membranes (MWCO 300 KDa) against PBS, pH 7.4, at 4 °C overnight.

Characterization of Liposomes. Zeta plus dynamic light scattering equipment (Brookhaven Instruments, Holtsville, NY) was used to determine the liposome size and size distribution. The zeta potentials of formulations were measured by zeta phase analysis light scattering (PALS) with an ultrasensitive zeta potential analyzer instrument (Brookhaven Instruments, Holtsville, NY). The liposome suspension was diluted as needed with water or a 1 M KCl solution to measure the particle size or zeta potential, respectively.

Determination of Immunoreactivity 2C5-L or 2G4-L by ELISA. An indirect ELISA (using an enzyme-tagged secondary Ab) was performed to assay the ability of the immunoliposomes to recognize the target antigens. ELISA microplates were coated with 50 μL of 10 μg/mL nucleosomes for testing 2C5-L, or with 50 μL of 10 μg/mL cardiac myosin for testing 2G4-L overnight at 4 °C. The plates were rinsed with the TBST buffer (Tris-buffered saline supplemented with 0.05% w/v Tween-20) and coated with 10% FBS in Tris-buffered saline. To the antigen-coated plates, 50 μL of 2C5-L or 2G4-L was added at antibody concentration of 10 μg/mL and incubated for 1 h at room temperature. Then, the plates were washed with TBST and coated with 50 μL/well horseradish peroxidase−antimouse IgG conjugate (ICN) at 1:5000 dilution. The conjugate was removed after 1 h incubation at room temperature, and the plates were again washed and incubated with enhanced Kblue TMB peroxidase substrate (Neogen Corporation, Lexington, KY) for 15 min. The microplates were read at dual wavelengths of 620 nm and at 492 nm using a Labsystems Multiskan MCC/340 microplate reader installed with GENESIS-LITE Windows-based microplate software.

Interaction of Avidin-L with Biotin. To examine the binding of Rh-PE-labeled avidin-L with biotin, two columns were prepared with the same quantity of biotin−agarose. The column was washed with PBS. Rh-labeled PL and avidin-L of same fluorescence intensity were passed through the column and first PBS and then avidin-denaturing guanidine-HCl buffer, pH 1.5, were used as eluents. The eluent was collected in 1 mL fractions. The fluorescent intensity of each fraction was measured using a multidetection microplate reader (Bio-Tek, Winooski, VT) at the 540/625 nm excitation/emission wavelengths. The degree of retention of the corresponding preparation on the column indicative of the preservation of the functional activity of the avidin to interact with biotin was estimated by following the decrease in the rhodamine fluorescence in the eluent.

dx.doi.org/10.1021/bc2002133 |*Bioconjugate Chem.* 2011, 22, 2005–2013

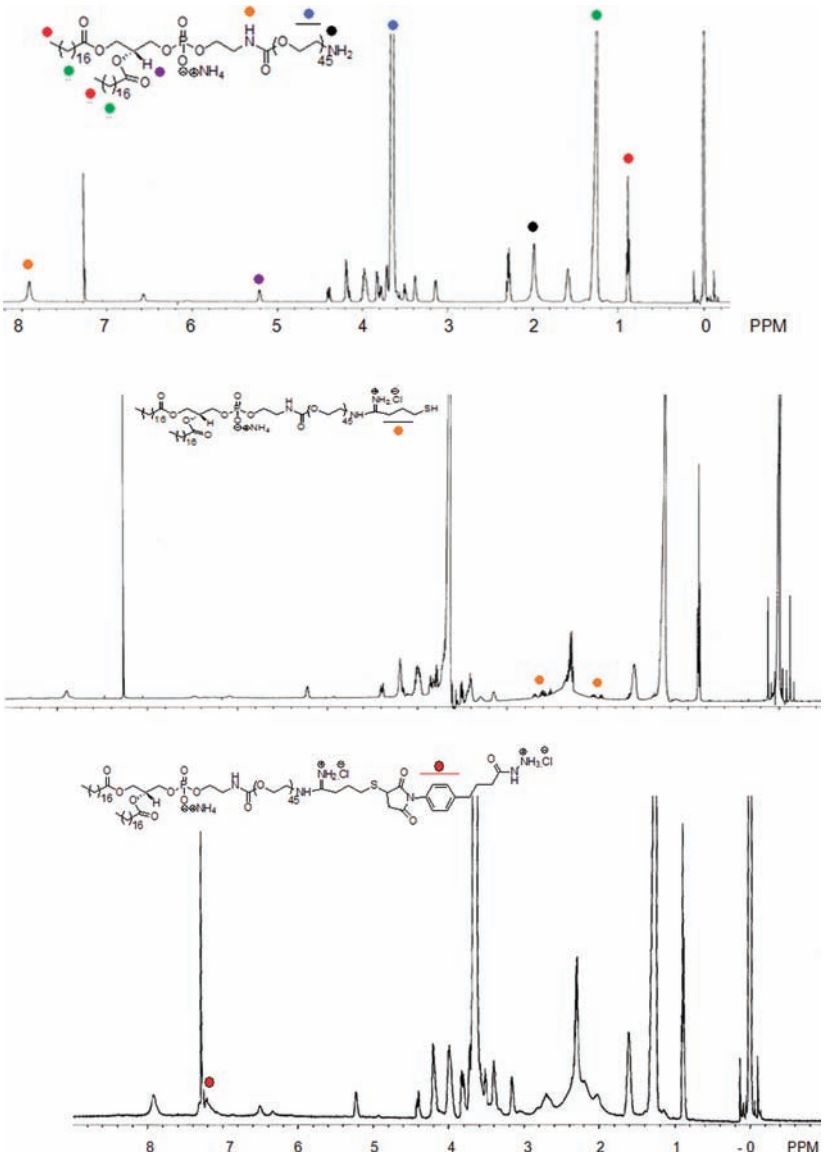

Figure 2. ^{1}H NMR spectra of DSPE-PEG-$_{2K}$-NH2, DSPE-PEG-$_{2K}$-SH, and DSPE-PEG-$_{2K}$-CONHNH$_2$.

Aggregation Assay for Con-A-L. The carbohydrate binding activity and specificity of the Con-A in Con-A-L was examined using an aggregation assay. The substrate for Con-A, mannan, was dissolved in PBS, pH 7.4, at different concentrations, and 100 μL aliquots of the solution were added to a 25 μL suspension of Con-A-L and PL in 96-well plates. The plates were shaken, incubated for 20 min at room temperature, and transferred to a Labsystems Multiskan MCC/340 microplate reader to be read at OD450 nm. Con-A in the presence of mannan aggregates, and the increase in the turbidity of the system is indicative of the preservation of Con-A's functional activity after the conjugation and immobilization on the liposome surface. The experiment was also performed in the presence of 100 μM of the competitive inhibitor, α-methyl mannopyranoside.

Labeling of Antibody (2C5) with Carboxyfluorescein (CF). A 50 μL aliquot of 2 mM 5-CF succinimidyl ester (Molecular Probes) in DMSO was added to 2 mL of a 12 μM solution of 2C5 in 50 mM TBS, pH 9.0. The mixture was incubated overnight at 4 °C, and free CF was removed by the dialysis against TBS.

The CF-labeled antibody was used to prepare 2C5-liposomes (CF-2C5-L) following above procedure. The pH of 200 μL of CF-2C5-L (1.2 μg of lipid/mL) in PBS, pH 7.4, was lowered to pH 5 by the addition of HCl (0.1 N). The mixture was incubated at the room temperature for 1 h and dialyzed against PBS using a 300 KDa MWCO cellulose ester membrane. Fluorescence intensity of the same amount of lipids in immunoliposomes was measured at pH 7.4. Both the solutions after dialysis at pH 7.4 and pH 5 were measured using a multidetection microplate reader (Bio-Tek, Winooski, VT) at 485/528 nm excitation/emission wavelengths.

Cell Experiments. Interaction of 2C5-L with cancer cells in vitro and pH-dependent cleavability of mAb 2C5. After the initial passage in tissue culture flasks, HeLa cells were grown on coverslips placed in 6-well tissue culture plates. After the cells reached 60−70% confluence, the plates were washed with PBS and incubated with 1% BSA in DMEM for 1 h at 37 °C, 5% CO_2. Rh-PE (Lissamine-rhodamine B-phosphatidyl ethanolamine)-labeled 2C5-L and Rh-PE-labeled PL, preincubated at pH 7.4 or pH 5 for 1 h, were added to a final lipid concentration of 0.1 mg/mL and

dx.doi.org/10.1021/bc2002133 |*Bioconjugate Chem.* 2011, 22, 2005–2013

incubated for 90 min at 37 °C, 5% CO_2. After the incubation, the cells were washed with PBS and the coverslips were mounted cell-side down on glass slides with fluorescence-free glycerol-based mounting medium (Fluoromount-G; Southern Biotechnology Associates) and studied with a Nikon Eclipse E400 microscope under the bright light or under the epifluorescence with a rhodamine filter.

Scheme 1. Schematic Representation of the Preparation of Antibody- or Protein-Grafted Liposomes Using DSPE-PEG-$_{2K}$-CONHNH$_2$ Polymer

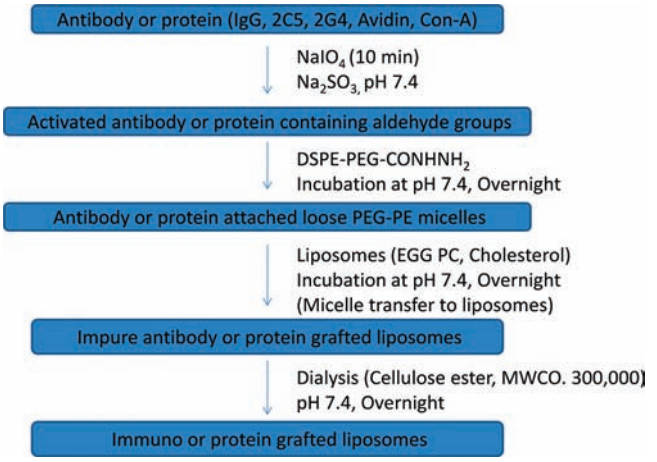

FACS Analysis. Approximately 200 000 HeLa and MCF-7 cells were seeded in 6-well tissue culture plates. After the cells reached 60−70% confluence, the plates were washed with PBS and incubated with 1% BSA in DMEM for 1 h. The immunoliposomes were preincubated for 1 h at pH 7.4 or pH 5 and treated with formulations at lipid concentration of 0.1 mg/mL for 90 min. The cells were centrifuged and washed with ice-cold PBS at least 3 times before analysis using a BD FACS Caliber flow cytometer. The cells were gated using forward versus side-scatter to exclude debris and dead cells before analysis of 10 000 cell counts. The data were analyzed with *BD Cell Quest Pro* Software.

Statistical Analysis. The data were tested for statistical significance using the paired Student's *t* test using *GraphPad Prism 4* (GraphPad Software, Inc.; San Diego, CA). Any *p* value less than 0.05 was considered statistically significant.

RESULTS AND DISCUSSION

Synthesis and Characterization of 1,2-Distearoyl-*sn*-glycero-3-phosphoethanolamine-*N*-[thio(polyethylene glycol)-2000](ammonium salt) (DSPE-PEG-$_{2K}$-SH) and 1,2-Distearoyl-*sn*-glycero-3-phophoethanolamine-*N*-[hydrazido(polyethylene glycol)2000](ammonium salt) (DSPE-PEG-$_{2K}$-CONHNH$_2$). The

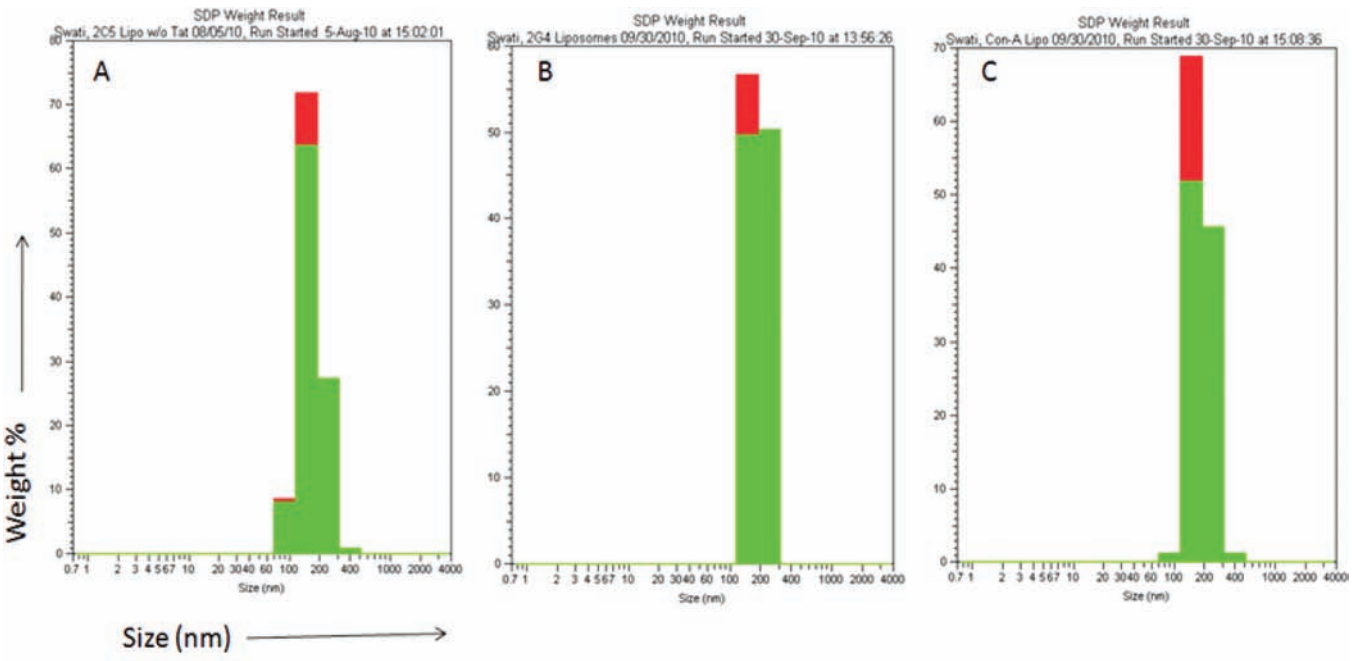

Liposomes	Mean diameter ± SD (nm) (n=3)	Polydispersity Index ± SD (n=3)
Plain Liposomes	188.1 ± 45	0.098 ± 0.07
IgG Liposomes	187.5 ± 53.1	0.131 ± 0.07
2C5 Liposomes	203.1 ± 56.3	0.157 ± 0.14
Con-A Liposomes	205.1 ± 50.1	0.081 ± 0.02
2G4 Liposomes	221.1 ± 39.9	0.051 ± 0.05

Figure 3. Size distribution of 2C5-L (A); 2G4-L (B) and Con-A-L (C) by the dynamic light scattering technique. A slight increase in size was observed after antibody or protein attachment. The table represents mean diameter and the polydispersity index. Values are mean ± standard deviation.

terminal hydrazine group-containing polymer DSPE-PEG-$_{2K}$-CONHNH$_2$ was synthesized following the scheme presented in the Figure 1. The starting polymer containing amine group was transformed into a thiol-modified polymer by the reaction using the Traut's reagent. The reaction yield was 60% by the DTNB assay. The next reaction with the cross-linking agent MPBH yielded 89% of DSPE-PEG-$_{2K}$-CONHNH2 calculated from the TNBSA assay.

The polymers were characterized by ^{1}H NMR in *d*-chloroform using Varian 500 MHz spectrophotometer (see the data in the Figure 2).

^{1}H NMR of DSPE-PEG-$_{2K}$-SH: δ 0.87−0.89 (t, 6H, (−CH_2-CH_3)$_2$), 1.25 (s, H from long chains of PE), 1.59−1.65 (m, 5H), 1.95−2.05 (m), 2.27−2.35 (m), 2.51−2.70 (m, −CH_2CH_2-CH_2SH), 3.14−4.4 (m), 5.2−5.24 (m, 1H), 7.89 (bs, 1H, −N*H*CO).

^{1}H NMR of DSPE-PEG-$_{2K}$-CONHNH$_2$: δ 0.87−0.89 (t, 6H, (−CH_2CH_3)$_2$), 1.25 (s), 1.58 (s), 2.02−2.69 (m), 3.14−4.4 (m), 5.21 (bs, 1H), 7.17−7.19 (m, 2H, Ar-*H*), 7.48−7.60 (m, 2H, Ar-*H*), 7.9 (bs, 1H, −N*H*CO).

Liposome Preparation and Characterization. Sizes of all types of liposomes prepared according to the general Scheme 1 (PL, 2C5-L, 2G4-L, Con-A-L, avidin-L) determined by the dynamic light scattering ranged between 150 and 200 nm (Figure 3). In all cases of the subsequent modification via the postinsertion technique, the incorporation of the added ligands into the liposomes was quantitative, since HPLC revealed no micelles of the free polymer-modified ligand in the system. To estimate the quantity of the protein bound to liposomes, the 2C5-L was used labeled with CF. Protein concentration per microgram of lipid was measured by the associated fluorescence at the excitation wavelength of 490 nm and emission wavelength of 520 nm. From the fluorescence data, approximately 150−200 protein molecules of antibody were bound to the surface of a single 200 nm liposome. The calculations were based on the fact that, while preparing the liposomes, the molar ratio of DSPE-PEG-$_{2K}$-CONHNH$_2$ per antibody was 32/1 and that number of phospholipid molecules per 200 nm liposomes was estimated to be 25×10^4.[29]

Activity of mAbs 2C5 and 2G4 in 2C5-L and 2G4-L by ELISA. To investigate whether various targeting ligands could be successfully attached to the liposomal surface by this reversible pH-sensitive hydrazone bond without losing their specific activity, the ELISA assay was performed to determine the interaction of 2C5-L and 2G4-L with specific antigens for the liposome-attached antibodies, nucleosomes, and cardiac myosin, respectively. Figure 4 represents the data of the direct binding assay of various preparations of liposomes with the corresponding antigens. The 2C5-L and 2G4-L bind to the monolayers of their corresponding antigens with the same efficiency as native free antibodies. Control IgG2a isotype-matching mAb UPC10 was attached onto the liposome surface following the same protocol. All controls—PL, IgG-bearing liposomes (IgG-L), and native IgG—demonstrated only a background binding to the antigens. These results indicate that the hydrazone bond used to attach the antibody was quite stable under the conditions used, and the antibodies' specific activity toward their antigens were completely preserved after covalent coupling to the distal tips of the PEG chains of liposomes via the hydrazone bonds.

Binding of Avidin-L with Biotin−Agarose. To further confirm the preservation of the specific properties of proteins attached to liposomes using the suggested scheme, Rh-PE-labeled PL and avidin-L were passed through the biotin−agarose

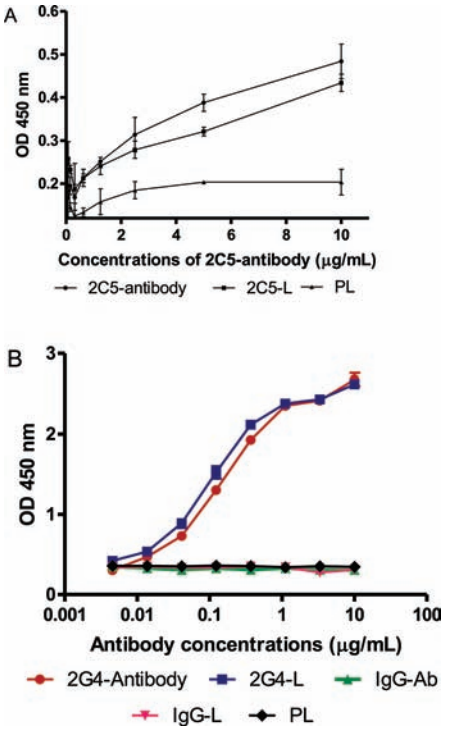

Figure 4. ELISA result for immunoliposomes. (A) Binding of 2C5-L to the monolayer of the antigen (nucleohistone) in comparison to the native mAb 2C5. (B) Binding of the 2G4-L to the monolayer of the antigen (porcine cardiac myosin) in comparison to the native mAb 2G4. The results show that the activity of the mAbs toward their antigens was retained after the conjugation on to the surface of liposomes.

column (Figure 5). The results showed the free passage of PL through the column (the fluorescence increase in initial fractions of the eluent at 540/625 excitation/emission wavelength) and complete retention of avidin-L on the column. In other words, the avidin in avidin-L was capable of strong binding with biotin. However, the treatment of the column with bound avidin-L with avidin-denaturing buffer, pH 5, released the major part of the fluorescence from the column via two possible mechanisms. First, the buffer denatured the avidin protein, which compromised the binding of avidin with the biotin−agarose and resulted in the release of Rh-labeled liposomes. Second, the lowered pH of this buffer could also degrade the hydrazone bond between avidin and liposomes and also cause the liposome release (fluorescence increase in the eluent). The result demonstrated that the avidin was successfully attached to the distal end of the polymer on the liposome surface and the specific activity of the protein was completely retained after the conjugation.

Agglutination of Con-A-L. One more test was done with Con-A-L and was based on the agglutination analysis of Con-A-L in the presence of ConA's polyvalent substrate mannan.[30,31] Figure 6 shows the turbidity changes measured by the increase in absorbance at OD450 nm in the suspensions of Con-A-L compared to PL in the presence of mannan. However, in the presence of the Con-A-specific low-molecular-weight competitive monovalent substrate, α-methyl mannopyranoside (100 μM), the turbidity rise was significantly inhibited. These data also show that, similar to avidin-L, the Con-A immobilized on the surface of liposome via the DSPE-PEG-$_{2K}$-CONHNH$_2$ polymer preserved its functional binding activity and carbohydrate specificity.

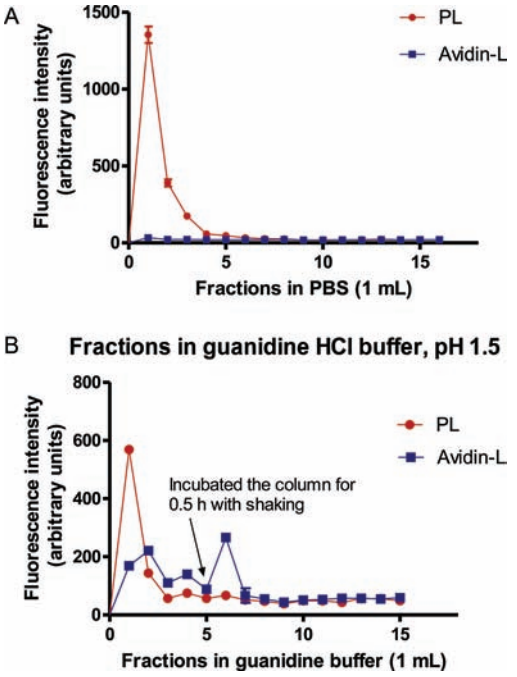

Figure 5. Binding of the Rh-PE-labeled avidin-L on biotin−agarose column compared to that of the Rh-PE-labeled PL. (A) Fluorescence intensity of the eluent collected in 1 mL fractions using PBS, pH 7.4, as mobile phase. Strong interaction of the liposome surface-attached avidin with biotin resulted in the complete retention of avidin-L in the column compared to PL. (B) Fluorescence intensity of eluent (avidin-denaturing buffer guanidine-HCl, pH 1.5) collected in 1 mL fraction. Slow release of avidin-L from the column is observed as the denaturation of the avidin progresses. The incubation of the column in denaturing buffer at room temperature resulted in an abrupt increase of the fluorescence in the eluent.

In Vitro Assay with CF-Labeled mAb 2C5 (pH-Dependent Degradation). To investigate the reversibility of the ligand attachment to the liposome surface via a pH-sensitive degradable bond at lowered pH values (mimicking to a certain extent intratumoral and/or intracellular environment), the in vitro degradation study of the ligand-modified liposomes at pH 5 was performed (Figure 7A). CF-labeled mAb 2C5 was conjugated at the distal end of the DSPE-PEG-$_{2K}$-CONHNH$_2$ and incorporated into liposomes (CF-2C5-L). The incubation of this liposome preparation at pH 5 degraded the hydrazone bond in the linker polymer and removed the labeled mAb 2C5 from the liposome, which resulted in marked decrease in cell-associated Rh-PE fluorescence. The result indicated that almost 80% of the hydrazone bond broke upon incubation of the preparation at pH 5, resulting in removing the surface-attached mAb. Dialysis, when continued at pH 5, provoked even more degradation to around 90%. This study proved the reversibility of the hydrazone bond between mAbs (or any other ligands) and liposomes, which is beneficial for the removal of the ligands attached via the proposed polymer linker from the liposome surface when it could become desirable at certain condition (for example, inside tumors or inside cells when other liposome-attached functionalities are required to become deshielded).

Fluorescence Microscopy and FACS Analysis: Interaction of 2C5-L with Cancer Cells in Vitro. Rhodamine-labeled 2C5-L were incubated with cervical cancer cells (HeLa) (Figure 7B). To enhance the cancer cell binding (eventual tumor accumulation),

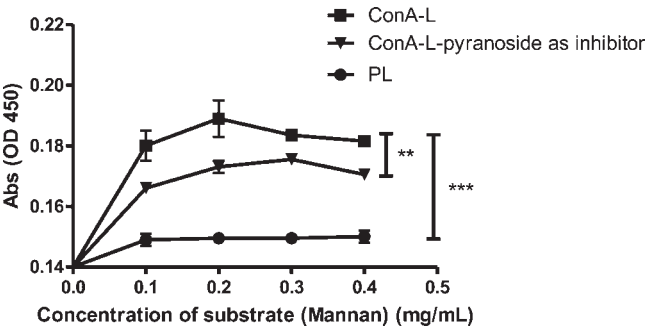

Figure 6. Agglutination analysis of Con-A-L in the presence of mannan and α-methyl mannopyranoside. The turbidity (agglutination) increases significantly with increasing concentration of mannan at OD 450 compared to PL (***$p < 0.001$, $n = 5$). In the presence of conA-specific competitive monovalent substrate α-methyl mannopyranoside (100 μM), a significant inhibition of the Con-A-L aggregation by the mannan was observed (**$p < 0.05$, $n = 5$). Results indicated the successful conjugation of Con-A onto the surface of liposome with full preservation of its specific activity.

the mAb 2C5 was used, which recognizes the surface of numerous tumor, but not normal cells via the tumor cell surface-bound nucleosomes.[15,32,33] Because mAb 2C5 binds to a broad variety of cancer cells, it may serve as a specific ligand for the delivery of drugs and drug carriers into tumors. The fluorescence microscopy result clearly demonstrated the successful recognition of HeLa cells by 2C5-L, which resulted in enhanced rhodamine fluorescence signal from the cell surface.

However, the preincubation of the 2C5-L at pH 5 resulted in loss of the antibody from the liposome surface, therefore preventing the liposome-to-cell association. PL did not show any cell association being kept at both pH values. The comparison of panels a and c in Figure 7B clearly indicates the successful conjugation of the targeting moiety (mAb 2C5) on the liposome surface, which resulted in more cellular association compared to PL. At the same time, the comparison of panels a and b shows that the action of the lowered pH eliminates the recognition phenomena (i.e., detach the antibody from the liposome because of linker degradation).

To further confirm the successful conjugation, the preservation of the functional specificity of the antibody as well as the cleavability of the hydrazone bond at lowered pH, flow cytometry-based experiments were performed with two cancer cell lines (HeLa and MCF-7) (Figure 8). FACS analysis confirmed the result obtained using the fluorescence microscopy and clearly demonstrated that the protocol used resulted in the successful conjugation of the antibody to liposomes and significantly better cellular association of 2C5-L compared to PL in both cell lines. And again, the pH-dependent linker degradation and antibody dissociation from the liposomal surface at lower pH (pH 5) was confirmed resulting in less cellular association compared to pH 7.4 in both cell lines.

Introducing a pH-sensitive linkage between a bulky targeting ligand and the liposome could be useful, for example, for drug delivery into tumors when decreased intratumoral pH after successful target accumulation could cleave off the targeting ligands and expose other functionalities such as ligands for enhanced cell penetration and intracellular trafficking to the organelles of interests.

In conclusion, an easy and simple method for synthesizing hydrazine-functionalized poly(ethylene glycol)-phosphatidyl

dx.doi.org/10.1021/bc2002133 |*Bioconjugate Chem.* 2011, 22, 2005–2013

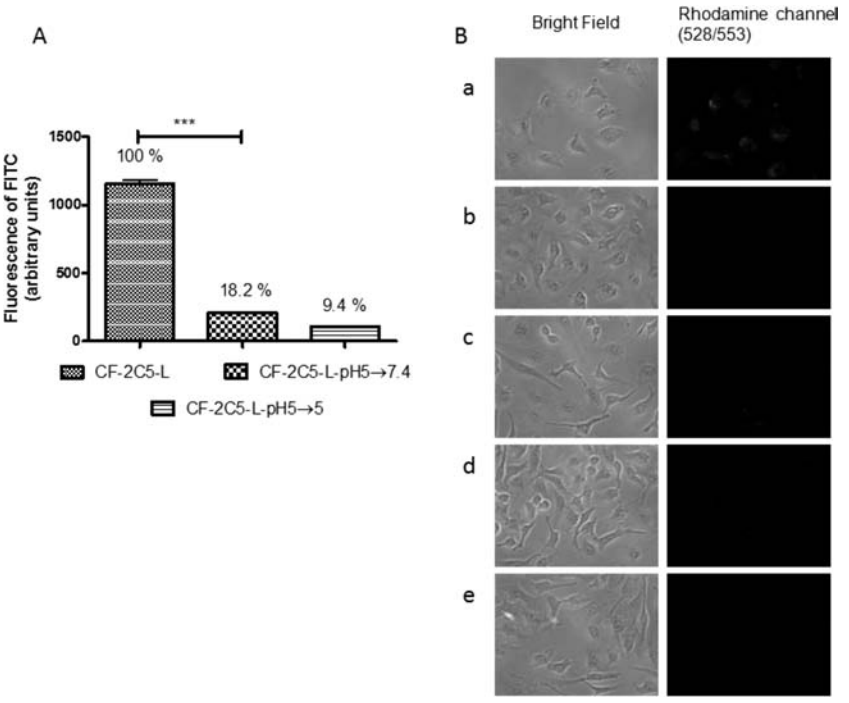

Figure 7. (A) Cleavability of CF-labeled mAb 2C5 from the liposome surface at low pH. The CF-2C5-L were preincubated at pH 5 for 1 h at room temperature and dialyzed (MWCO 300 000) against PBS at pH 7.4 and pH 5. The result clearly shows significantly (***$p < 0.001$, $n = 3$) less fluorescence after dialysis due to the hydrolysis of the hydrazone bond (around 80% and 90% fluorescence loss after the dialysis at pH 7.4 and 5, respectively) between mAb and liposome and release of free mAbs. (B) Effect of preincubation (at pH 5) of Rh-PE labeled 2C5-L on cellular association compared to 2C5-L at pH 7.4. Preincubation cleaved the antibody from the surface, thereby causing loss of the targeting potency of the liposomes, which resulted in virtually no cellular association: (a,b) 2C5-L, preincubated at pH 7.4 and 5, respectively; (c,d) PL, preincubated at pH 7.4 and 5; (e) untreated cells. Pictures of bright field and rhodamine channels are shown simultaneously for each treatment.

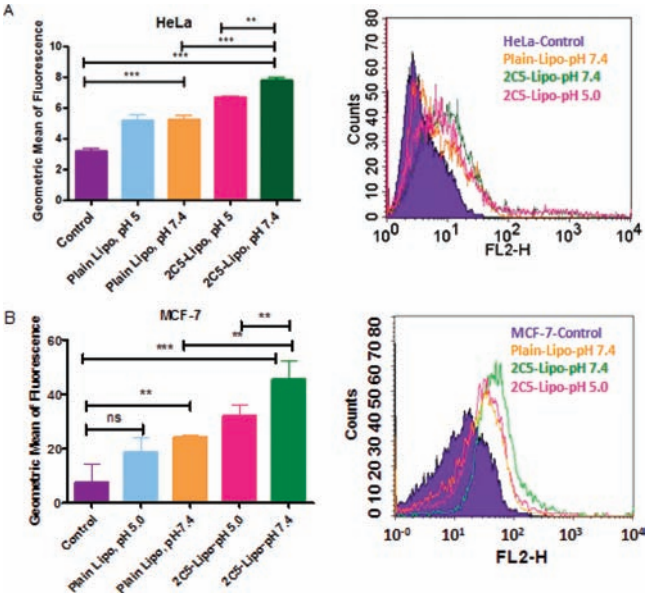

Figure 8. Flow cytometry analysis of Rh-PE-labeled 2C5-L and PL at different pH in (A) HeLa and (B) MCF-7 cell lines. The 2C5-L and PL were preincubated at pH 5 and pH 7.4 for 1 h before the incubation with the cells for 1 h. The result shows less targeting and less cellular uptake of 2C5-L after the preincubation at pH 5 than after the preincubation at pH 7.4 in both cell lines because of detachment of cell targeting antibody from the surface of the liposomes (***$p < 0.001$, **$p < 0.05$, $n = 3$).

ethanolamine polymer was developed. The polymer can readily conjugate various targeting ligands to pharmaceutical nanocarriers, such as liposomes, easily via a pH-responsive reversible hydrazone bond. Proteins avidin, Con-A, and monoclonal antibodies 2C5 and 2G4 were successfully immobilized on the liposome surface via the pH-responsive hydrazone bond. Various in vitro assays confirmed that the targeting ligands retain their specific functional activity. At the same time, the exposure of the ligand-bearing liposomes to a lowered pH results in the degradation of the hydrazone bond and detachment of the ligand.

AUTHOR INFORMATION

Corresponding Author

*E-mail: v.torchilin@neu.edu. Phone: 617-373-3206. Fax: 617-373-4201.

ACKNOWLEDGMENT

The work was supported by the NIH grants RO1 CA 121838 and RO1 CA 128486 to Vladimir P. Torchilin.

REFERENCES

(1) Muggia, F. M. (1997) Clinical efficacy and prospects for use of pegylated liposomal doxorubicin in the treatment of ovarian and breast cancers. *Drugs 54* (Suppl 4), 22–29.

(2) Valero, V., Buzdar, A. U., Theriault, R. L., Azarnia, N., Fonseca, G. A., Willey, J., Ewer, M., Walters, R. S., Mackay, B., Podoloff, D., Booser, D., Lee, L. W., and Hortobagyi, G. N. (1999) Phase II trial of

liposome-encapsulated doxorubicin, cyclophosphamide, and fluorouracil as first-line therapy in patients with metastatic breast cancer. *J. Clin. Oncol. 17*, 1425–1434.

(3) Zalipsky, S. (1995) Functionalized poly(ethylene glycol) for preparation of biologically relevant conjugates. *Bioconjugate Chem. 6*, 150–165.

(4) Maeda, H., Wu, J., Sawa, T., Matsumura, Y., and Hori, K. (2000) Tumor vascular permeability and the EPR effect in macromolecular therapeutics: a review. *J. Controlled Release 65*, 271–284.

(5) Palmer, T. N., Caride, V. J., Caldecourt, M. A., Twickler, J., and Abdullah, V. (1984) The mechanism of liposome accumulation in infarction. *Biochim. Biophys. Acta 797*, 363–368.

(6) Papahadjopoulos, D., Allen, T. M., Gabizon, A., Mayhew, E., Matthay, K., Huang, S. K., Lee, K. D., Woodle, M. C., Lasic, D. D., and Redemann, C. et al. (1991) et al. Sterically stabilized liposomes: improvements in pharmacokinetics and antitumor therapeutic efficacy. *Proc. Natl. Acad. Sci. U.S.A. 88*, 11460–11464.

(7) Woodle, M. C., and Lasic, D. D. (1992) Sterically stabilized liposomes. *Biochim. Biophys. Acta 1113*, 171–199.

(8) Senior, J., Delgado, C., Fisher, D., Tilcock, C., and Gregoriadis, G. (1991) Influence of surface hydrophilicity of liposomes on their interaction with plasma protein and clearance from the circulation: studies with poly(ethylene glycol)-coated vesicles. *Biochim. Biophys. Acta 1062*, 77–82.

(9) Klibanov, A. L., Maruyama, K., Beckerleg, A. M., Torchilin, V. P., and Huang, L. (1991) Activity of amphipathic poly(ethylene glycol) 5000 to prolong the circulation time of liposomes depends on the liposome size and is unfavorable for immunoliposome binding to target. *Biochim. Biophys. Acta 1062*, 142–148.

(10) Sapra, P., Tyagi, P., and Allen, T. M. (2005) Ligand-targeted liposomes for cancer treatment. *Curr. Drug Delivery 2*, 369–381.

(11) Torchilin, V. P. (2005) Recent advances with liposomes as pharmaceutical carriers. *Nat. Rev. Drug Discovery 4*, 145–160.

(12) Xiong, X. B., Huang, Y., Lu, W. L., Zhang, X., Zhang, H., Nagai, T., and Zhang, Q. (2005) Intracellular delivery of doxorubicin with RGD-modified sterically stabilized liposomes for an improved antitumor efficacy: in vitro and in vivo. *J. Pharm. Sci. 94*, 1782–1793.

(13) Willis, M., and Forssen, E. (1998) Ligand-targeted liposomes. *Adv. Drug Delivery Rev. 29*, 249–271.

(14) Torchilin, V. P. (2010) Passive and active drug targeting: drug delivery to tumors as an example. *Handb. Exp. Pharmacol.* 3–53.

(15) Khaw, B. A., Mattis, J. A., Melincoff, G., Strauss, H. W., Gold, H. K., and Haber, E. (1984) Monoclonal antibody to cardiac myosin: imaging of experimental myocardial infarction. *Hybridoma 3*, 11–23.

(16) Gabizon, A., Shmeeda, H., Horowitz, A. T., and Zalipsky, S. (2004) Tumor cell targeting of liposome-entrapped drugs with phospholipid-anchored folic acid-PEG conjugates. *Adv. Drug Delivery Rev. 56*, 1177–1192.

(17) Torchilin, V. P., Klibanov, A. L., Huang, L., O'Donnell, S., Nossiff, N. D., and Khaw, B. A. (1992) Targeted accumulation of polyethylene glycol-coated immunoliposomes in infarcted rabbit myocardium. *FASEB J. 6*, 2716–2719.

(18) Torchilin, V. P., Narula, J., Halpern, E., and Khaw, B. A. (1996) Poly(ethylene glycol)-coated anti-cardiac myosin immunoliposomes: factors influencing targeted accumulation in the infarcted myocardium. *Biochim. Biophys. Acta 1279*, 75–83.

(19) Torchilin, V. P., Omelyanenko, V. G., Papisov, M. I., Bogdanov, A. A., Jr., Trubetskoy, V. S., Herron, J. N., and Gentry, C. A. (1994) Poly(ethylene glycol) on the liposome surface: on the mechanism of polymer-coated liposome longevity. *Biochim. Biophys. Acta 1195*, 11–20.

(20) Gupta, B., Levchenko, T. S., and Torchilin, V. P. (2005) Intracellular delivery of large molecules and small particles by cell-penetrating proteins and peptides. *Adv. Drug Delivery Rev. 57*, 637–651.

(21) Lochmann, D., Jauk, E., and Zimmer, A. (2004) Drug delivery of oligonucleotides by peptides. *Eur. J. Pharm. Biopharm. 58*, 237–251.

(22) Torchilin, V. P. (2006) Multifunctional nanocarriers. *Adv. Drug Delivery Rev. 58*, 1532–1555.

(23) Kale, A. A., and Torchilin, V. P. (2007) "Smart" drug carriers: PEGylated TATp-modified pH-sensitive liposomes. *J. Liposome Res. 17*, 197–203.

(24) Sawant, R. M., Hurley, J. P., Salmaso, S., Kale, A., Tolcheva, E., Levchenko, T. S., and Torchilin, V. P. (2006) "SMART" drug delivery systems: double-targeted pH-responsive pharmaceutical nanocarriers. *Bioconjugate Chem. 17*, 943–949.

(25) Zalipsky, S. (1993) Synthesis of an end-group functionalized polyethylene glycol-lipid conjugate for preparation of polymer-grafted liposomes. *Bioconjugate Chem. 4*, 296–299.

(26) Khaw, B. A., Yasuda, T., Gold, H. K., Leinbach, R. C., Johns, J. A., Kanke, M., Barlai-Kovach, M., Strauss, H. W., and Haber, E. (1987) Acute myocardial infarct imaging with indium-111-labeled monoclonal antimyosin Fab. *J. Nucl. Med. 28*, 1671–1678.

(27) Ellman, G. L. (1959) Tissue sulfhydryl groups. *Arch. Biochem. Biophys. 82*, 70–77.

(28) Habeeb, A. F. (1966) Determination of free amino groups in proteins by trinitrobenzenesulfonic acid. *Anal. Biochem. 14*, 328–336.

(29) Enoch, H. G., and Strittmatter, P. (1979) Formation and properties of 1000-A-diameter, single-bilayer phospholipid vesicles. *Proc. Natl. Acad. Sci. U.S.A. 76*, 145–149.

(30) Chen, H., Torchilin, V., and Langer, R. (1996) Lectin-bearing polymerized liposomes as potential oral vaccine carriers. *Pharm. Res. 13*, 1378–1383.

(31) Torchilin, V. P., Levchenko, T. S., Lukyanov, A. N., Khaw, B. A., Klibanov, A. L., Rammohan, R., Samokhin, G. P., and Whiteman, K. R. (2001) p-Nitrophenylcarbonyl-PEG-PE-liposomes: fast and simple attachment of specific ligands, including monoclonal antibodies, to distal ends of PEG chains via p-nitrophenylcarbonyl groups. *Biochim. Biophys. Acta 1511*, 397–411.

(32) Iakoubov, L., Rokhlin, O., and Torchilin, V. (1995) Antinuclear autoantibodies of the aged reactive against the surface of tumor but not normal cells. *Immunol. Lett. 47*, 147–149.

(33) Iakoubov, L. Z., and Torchilin, V. P. (1998) Nucleosome-releasing treatment makes surviving tumor cells better targets for nucleosome-specific anticancer antibodies. *Cancer Detect. Prev. 22*, 470–475.

Bioconjugate Chemistry

ARTICLE

pubs.acs.org/bc

Development of a Diphtheria Toxin Based Antiporcine CD3 Recombinant Immunotoxin

Zhirui Wang,[*,†,‡] Raimon Duran-Struuck,[†] Rebecca Crepeau,[†] Abraham Matar,[†] Isabel Hanekamp,[†] Srimathi Srinivasan,[†] David M. Neville, Jr.,[§] David H. Sachs,[†,‡] and Christene A. Huang[†,‡]

[†]Transplantation Biology Research Center, Massachusetts General Hospital and Harvard Medical School, Boston, Massachusetts, United States

[‡]DF/HCC-MGH Recombinant Protein Expression and Purification Core, Boston, Massachusetts, United States

[§]Angimmune LLC, 9624 Parkwood Drive, Bethesda, Maryland 20814, United States

ABSTRACT: Anti-CD3 immunotoxins, which induce profound but transient T-cell depletion in vivo by inhibiting eukaryotic protein synthesis in CD3+ cells, are effective reagents in large animal models of transplantation tolerance and autoimmune disease therapy. A diphtheria toxin based antiporcine CD3 recombinant immunotoxin was constructed by fusing the truncated diphtheria toxin DT390 with two identical tandem single chain variable fragments (scFv) derived from the antiporcine CD3 monoclonal antibody 898H2−6−15. The recombinant immunotoxin was expressed in a diphtheria-toxin resistant yeast *Pichia pastoris* strain under the control of the alcohol oxidase promoter. The secreted recombinant immunotoxin was purified sequentially with hydrophobic interaction chromatography (Butyl 650 M) followed by strong anion exchange (Poros 50 HQ). The purified antiporcine CD3 immunotoxin was tested in vivo in four animals; peripheral blood CD3+ T-cell numbers were reduced by 80% and lymph node T-cells decreased from 74% CD3+ cells pretreatment to 24% CD3+ cells remaining in the lymph node following 4 days of immunotoxin treatment. No clinical toxicity was observed in any of the experimental swine. We anticipate that this conjugate will provide an important tool for in vivo depletion of T-cells in swine transplantation models.

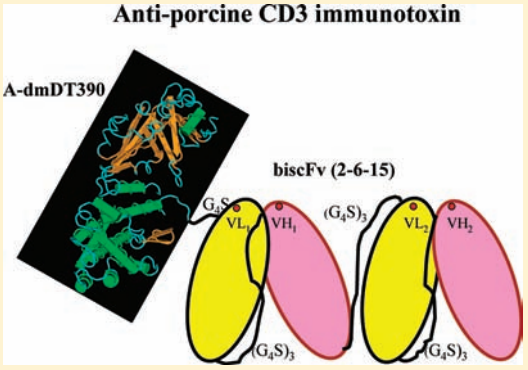

INTRODUCTION

Previous work has demonstrated that chemically conjugated antiporcine CD3 immunotoxin is a very effective T-cell depletion reagent in pigs,[1] and this reagent has played a role in the maintenance of long-term hematopoietic stem cell transplants in the absence of graft versus host disease.[2−4] The chemically conjugated immunotoxin was created by cross-linking the monoclonal antibody to a diphtheria toxin (DT) binding site mutant, CRM9, such that the binding site of the immunotoxin was dictated by the antibody moiety.[5] However, several problems were associated with the chemical conjugate including linkage heterogeneity, low yield, and strict limitations in dosage due to nonspecific neurological toxicity in pigs.[1,6]

Recombinant antihuman and antimonkey CD3 T-cell immunotoxins have been developed.[7,8] These immunotoxins contain a diphtheria toxin protein sequence that is truncated at amino acid residue 390. The antibody moiety is placed C-terminal to the truncated toxin DT390 to prevent any interference with the translocation of biologically active diphtheria toxin A chain.[9,10] However, it was found that when the scFv of an antihuman CD3 monoclonal antibody UCHT1 was fused to the C-terminus of DT390, its binding activity was dramatically reduced by a factor of 10. Adding a second scFv moiety separated with a $(G_4S)3$ linker resulted in a 10-fold increase in binding activity compared to a monovalent fusion immunotoxin. This fusion immunotoxin, designated A-dmDT390biscFv(UCHT1), displayed an increase in potency by 10- to 30-fold as compared with the corresponding chemically conjugated immunotoxin and depleted 2.4 logs of T-cells in the lymph node compartment of transgenic mice expressing human CD3ε.[11] The clinical trial for this immunotoxin in five patients with cutaneous T-cell lymphoma has shown promising results.[12]

In this paper, we present the development of the antiporcine CD3 recombinant immunotoxin, A-dmDT390biscFv(2−6−15). The VL (variable light chain) and VH (variable heavy chain) of the antiporcine CD3 monoclonal antibody 898H2−6−15[13] were cloned by PCR, and the resulting sequence was used to synthesize codon-optimized antiporcine CD3 scFv (2−6−15) DNA sequence suitable for the *Pichia pastoris* expression. The biscFv format antiporcine CD3 recombinant immunotoxin was expressed in a diphtheria-toxin resistant yeast *Pichia pastoris* strain and purified in a two-step chromatography protocol. The *in vivo* porcine CD3 T-cell depletion profile for this immunotoxin was assessed.

Received: May 3, 2011
Revised: July 20, 2011
Published: August 25, 2011

ACS Publications © 2011 American Chemical Society

Table 1. PCR Primers used for 2-6-15 VL and VH Amplification

MuIgVH5′-A:	GGGAATTCATGAACTTGTGG
	TTAAGCTGGGTTT
MuIgGVH3′-2:	CCCAAGCTTCCAGGGGCCAG
	GGGATAGACGGGTGG
2−6−15 Hr-1:	TGTTGTTTTGGCTGAGGAGA
2−6−15 Hr-3:	TCCATATAGT CCCCCCGTCTT
2−6−15 Hr-4:	TGTCCTCAGACCTCAGACTG
2−6−15 Hf-3:	GAGGCTTAGTGAAGCCTGGA
2−6−15 Hf-2:	TATACCATGTCTTGGGTTCGC
2−6−15 Hf-1:	TGGAGTGGGTCGCATACATTA
Ab Vk 5′:	ACCTATTACTGTCAGCACATTA
UMIgVK 5′:	GACATTCTGATGACCCAGTCT
MK-3Seq 3′:	TACAGTTGGTGCAGCATCAGC
2−6−15 Lr-1:	TTTCAGCTCCAGCTTGGTC
2−6−15 Lr-2:	TGAGCGGCAAGTTATCACTT
2−6−15 Lr-3:	AAGGAGCTTAGGAGGTTTCCC
2−6−15 Lf-3:	CAGATGCATAACCAGCACTGA
2−6−15 Lf-2:	GCTCCTTATTTCAGAAGGCAA
2−6−15 Lf-1:	ATTCTCCAGCAGTGGCTATGG

EXPERIMENTAL PROCEDURES

Cloning the VL and VH of the Antiporcine CD3 Monoclonal Antibody 898H2−6−15. To construct the antiporcine CD3 recombinant immunotoxin, the scFv DNA sequence of hybridoma 898H2−6−15 was obtained by RT-PCR. RNA was isolated from the antiporcine CD3 hybridoma cell line 898H2−6−15 developed and characterized in our lab[13] with the RNeasy kit (Invitrogen). cDNA was generated from DNase (Invitrogen) treated RNA using oligo dT primer and the Superscript III kit (Invitrogen). Preliminary VH sequence was isolated using a commercially available Mouse Ig Primer Set (EMD BioSciences), specifically primers MuIgVH5′-A and MuIgGVH3′-2. Gene-specific primers were designed and used for generating cDNA (2−6−15 Hr-1) and for 5′ rapid amplification of cDNA ends (RACE) PCR (2−6−15 Hr-3, 2−6−15 Hr-4) (5′ RACE Kit, Invitrogen). The sequence of the 3′ end was determined by 3′ RACE (Invitrogen) using gene-specific primers 2−6−15 Hf-3 for generating cDNA, as well as 2−6−15 Hf-2 and 2−6−15 Hf-1 for PCR. To circumvent the expression of aberrant light chain by hybridoma 898H2−6−15, saturating levels of a primer specific for the aberrant chain (Ab Vk 5′) along with the VL primers UMIgVK 5′ and MK-3Seq 3′ were used to amplify light chains.[14] As previously, 5′ sequence was determined by 5′ RACE using cDNA generated with gene-specific primers 2−6−15 Lr-1; 5′ RACE PCR was performed with 2−6−15 Lr-2 and 2−6−15 Lr-3 (5′ RACE Kit, Invitrogen). The sequence of the 3′ end was determined by generating cDNA with gene-specific primer 2−6−15 Lf-3 and 3′ RACE PCR with 2−6−15 Lf-2 and 2−6−15 Lf-1 (3′ RACE Kit, Invitrogen). All of the PCR primers used to amplify the VL and VH are listed in Table 1. The VL and VH DNA and derived amino acid sequences are shown in Figure 1 (VL GenBank accession: JF918977; VH GenBank accession: JF918978). The borders of 898H2−6−15 VL and VH were determined according to Kabat et al (1987).[18]

Plasmid Construction. Codon optimization is necessary to express DT390-based immunotoxins in *Pichia pastoris*.[8] We used the optimized DT390 nucleotide sequence described by

(A) 2-6-15 VL DNA and derived amino acid sequence

```
gaaacaactgtgacccagtctccagcatccctgtccatggctataggagaacaagtcacc
 E  T  T  V  T  Q  S  P  A  S  L  S  M  A  I  G  E  Q  V  T
atcagatgcataaccagcactgatattgatgatgatatgaactggtaccagcagaggcca
 I  R  C  I  T  S  T  D  I  D  D  D  M  N  W  Y  Q  Q  R  P
gggaaacctcctaagctccttatttcagaaggcaatactcttcgtcctggagtcccatcc
 G  K  P  P  K  L  L  I  S  E  G  N  T  L  R  P  G  V  P  S
cgattctccagcagtggctatggtacagattttgtttttacaattgaaaacatgctctca
 R  F  S  S  S  G  Y  G  T  D  F  V  F  T  I  E  N  M  L  S
gaggatgttgcagattactactgtttacaaagtgataacttgccgctcacgttcggtgct
 E  D  V  A  D  Y  Y  C  L  Q  S  D  N  L  P  L  T  F  G  A
gggaccaagctggagctgaaa
 G  T  K  L  E  L  K
```

(B) 2-6-15 VH DNA and derived amino acid sequence

```
gaagtgaagctggtggagtctgggggaggcttagtgaagcctggagggtccctgaaactc
 E  V  K  L  V  E  S  G  G  G  L  V  K  P  G  G  S  L  K  L
tcctgtgcagcctctggattcactttcagtagctataccatgtcttgggttcgccagact
 S  C  A  A  S  G  F  T  F  S  S  Y  T  M  S  W  V  R  Q  T
ccggagaagaggctggagtgggtcgcatacattagtagtggtggtagtaattcctactat
 P  E  K  R  L  E  W  V  A  Y  I  S  S  G  G  S  N  S  Y  Y
tcagacagtgtgaagggccgattcaccatctccagagacaatgccaggaacaccctgtac
 S  D  S  V  K  G  R  F  T  I  S  R  D  N  A  R  N  T  L  Y
ctgcaaatgagcagtctgaggtctgaggacacggccatgtattactgtgcaagacggggg
 L  Q  M  S  S  L  R  S  E  D  T  A  M  Y  Y  C  A  R  R  G
gactatatggactactggggtcaaggaacctcagtcaccgtctcctca
 D  Y  M  D  Y  W  G  Q  G  T  S  V  T  V  S  S
```

Figure 1. Antiporcine CD3 monoclonal antibody 898H2−6−15 variable light (VL) and variable heavy (VH) domain DNA and derived amino acid sequence.

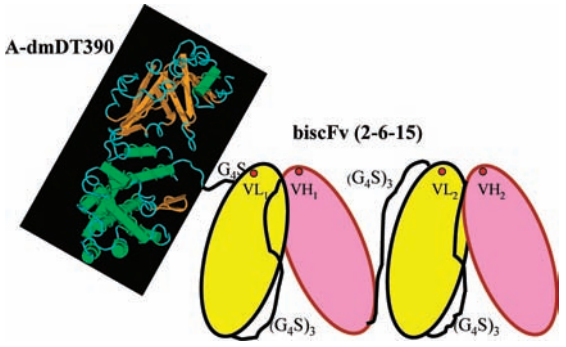

Figure 2. Schematic description of the antiporcine CD3 recombinant immunotoxin A-dmDT390biscFv(2−6−15). The putative antigen binding sites are shown as red spots.

Woo et al. (2002) for the DT390 domain in the new antiporcine CD3 immunotoxin. The DT390 has been modified to include an NH_2 terminal alanine (A) and double mutations (dm) to prevent glycosylation in the eukaryotic expression system, *Pichia pastoris*.[8,15] The antiporcine CD3 immunotoxin A-dmDT390biscFv (2−6−15) was constructed using the scFv derived from the antiporcine CD3 monoclonal antibody 898H2−6−15 following the strategy used to construct A-dm-DT390biscFv (UCHT1) in *Pichia pastoris*[8] except for the addition of an extra G_4S linker between A-dm-DT390 and biscFv (2−6−15) (Figure 2). The codon-optimized scFv (2−6−15) DNA was synthesized using the *Pichia pastoris* preferred codons.[16] Ten primers were designed for both the VL and the VH of the 2−6−15 scFv (Table 2). The primer length was limited to under 70 bases with a 21 base overlap between neighboring primers. Ten picomoles of the first and the last primers and 2 pmol of the rest of the primers were used in each PCR reaction (Pfu Turbo polymerase, Aglient, dNTP mixture at 2.5 mM each). The PCR program was 95 °C for 5 min, 25 cycles of 95 °C for 30 s, 55 °C for

Table 2. PCR Primers Used to Synthesize the Codon-Optimized scFv (2-6-15)

For 2−6−15 VL Domain
15L1a
5′ C ATG CCA TGG GGT GGT GGT GGT TCT GAG ACT ACT GTT ACT CAA TCT CCA GCT TCT TTG 3′
15L1b
5′ GGA AGA TCT GGT GGT GGT GGT TCT GAG ACT ACT GTT ACT CAA TCT CCA GCT TCT TTG 3′
15L2
5′ ACA TCT AAT AGT AAC TTG CTC ACC AAT AGC CAT AGA CAA AGA AGC TGG AGA TTG AGT 3′
15L3
5′ GAG CAA GTT ACT ATT AGA TGT ATT ACT TCT ACT GAC ATT GAC GAC GAC ATG AAC 3′
15L4
5′ CTT TGG TGG CTT ACC TGG TCT TTG TTG GTA CCA GTT CAT GTC GTC GTC AAT GTC 3′
15L5
5′ AGA CCA GGT AAG CCA CCA AAG TTG TTG ATT TCT GAG GGT AAC ACT TTG AGA CCA 3′
15L6
5′ GTA ACC AGA AGA AGA GAA TCT AGA TGG AAC ACC TGG TCT CAA AGT GTT ACC CTC 3′
15L7
5′ AGA TTC TCT TCT TCT GGT TAC GGT ACT GAC TTC GTT TTC ACT ATT GAG AAC ATG 3′
15L8
5′ CAA ACA GTA GTA GTC AGC AAC GTC CTC AGA CAA CAT GTT CTC AAT AGT GAA AAC 3′
15L9
5′ GTT GCT GAC TAC TAC TGT TTG CAA TCT GAC AAC TTG CCA TTG ACT TTC GGT GCT 3′
15L10
5′ CGC GGA TCC ACC ACC ACC AGA ACC ACC ACC ACC CTT CAA CTC CAA CTT AGT ACC AGC ACC GAA AGT CAA TGG CAA 3′
For 2−6−15 VH Domain
15H1
5′ GGA AGA TCT GGT GGT GGT GGT TCT GAG GTT AAG TTG GTT GAG TCT GGT GGT GGT TTG GTT AAG CCA GGT GGT TCT 3′
15H2
5′ AGA GAA AGT GAA ACC AGA AGC AGC ACA AGA CAA CTT CAA AGA ACC ACC TGG CTT AAC CAA 3′
15H3
5′ GCT TCT GGT TTC ACT TTC TCT TCT TAC ACT ATG TCT TGG GTT AGA CAA ACT CCA GAG AAG 3′
15H4
5′ AGA ACC ACC AGA AGA AAT GTA AGC AAC CCA CTC CAA TCT CTT CTC TGG AGT TTG TCT AAC 3′
15H5
5′ TAC ATT TCT TCT GGT GGT TCT AAC TCT TAC TAC TCT GAC TCT GTT AAG GGT AGA TTC 3′
15H6
5′ GTA CAA AGT GTT TCT AGC GTT GTC TCT AGA AAT AGT GAA TCT ACC CTT AAC AGA GTC 3′
15H7
5′ AAC GCT AGA AAC ACT TTG TAC TTG CAA ATG TCT TCT TTG AGA TCC GAG GAC ACT GCT 3′
15H8
5′ GTC CAT GTA GTC ACC TCT TCT AGC ACA GTA GTA CAT AGC AGT GTC CTC AGA TCT CAA 3′
15H9
5′ AGA AGA GGT GAC TAC ATG GAC TAC TGG GGT CAA GGT ACT TCT GTT ACT GTT TCT TCT 3′
15H10a
5′ CGC GGA TCC ACC ACC ACC AGA ACC ACC ACC ACC AGA AGA AAC AGT AAC AGA AGT 3′
15H10b
5′ CCG GAA TTC TTA AGA AGA AAC AGT AAC AGA AGT 3′

30 s, 72 °C for 1 min, and then extension for another 10 min. Amplification products were analyzed by electrophoresis in 1% agarose gels and purified using QIAquik Gel Extraction Kit (Qiagen). *Bam*HI digested VL PCR fragment was ligated to *Bgl*II digested VH fragment using T4 ligase for 6 h. The first scFv (2−6−15), amplified with primers 15L1a (carrying *Nco*I site) and 15 H10a (carrying *Bam*HI site), was cloned into pET27b. The second scFv (2−6−15), amplified with 15L1b (carrying *Bgl*II site) and 15H10b (carrying stop codon and *Eco*RI site), was cloned into pET17b. After sequence confirmation, the first and second scFv

(2−6−15) were subcloned into pwPICZα-DT390 (*Nco*I-*Bam*HI/*Bgl*II-stop codon-*Eco*RI).[8]

Protein Expression and Purification in *Pichia pastoris*. The linearized antiporcine CD3 immunotoxin construct, A-dmDT390-biscFv (2−6−15) in pwPICZα, was transformed into a diphtheria-toxin resistant yeast *Pichia pastoris* strain mutEF2JC307−8(2)[17] and the transformants were selected on YPD plates containing zeocin (100 μg/mL). Six colonies were randomly picked and cultivated in small tubes containing 5 mL YPD (1% yeast extract, 2% peptone, and 2% dextrose) at 30 °C at 250 rpm for 24 h as growth phase I, then in YPG (1% yeast extract, 2% peptone, 1% glycerol) at 30 °C at 250 rpm for another 24 h as growth phase II. The cultures were induced with methanol in 2 mL BMMYC (1% yeast extract, 2% peptone, 100 mM potassium phosphate, pH 7.0, 1.34% yeast nitrogen base without amino acids, 4×10^{-5} % biotin, 0.5% methanol, and 1% casamino acids) for 48 h at 25 °C at 225 rpm. Antifoam 0.02% (Emerald Performance Materials, cat # KFO673) was added in all of the growth and induction medium. 1 mM PMSF (Phenylmethanesulfonyl fluoride, Sigma) was added with methanol to inhibit the protein degradation during the induction phase. The culture supernatants were analyzed on SDS-PAGE under nonreducing condition. One clone (ZW130) was selected and cultivated to purify A-dmDT390-biscFv (2−6−15). Sodium sulfate (Fisher Scientific) was added to 1 L of culture supernatant to a final concentration of 200 mM. The sample was loaded onto 50 mL Butyl 650 M (Tosoh) in a 5 cm × 20 cm XK50 column (GE healthcare cat #18−1000−71). The bound A-dmDT390-biscFv (2−6−15) was eluted with TGE buffer (5% glycerol, 20 mM Tris HCl, pH 8.0, 1 mM EDTA, pH 8.0). Pooled fractions (Figure 3A, elution fraction #2 to #8, 50 mL per fraction) containing A-dmDT390-biscFv (2−6−15) were diluted 6-fold with TE (20 mM Tris-HCl pH 8.0, 1 mM EDTA pH 8.0) buffer and loaded directly onto 10 mL of Poros 50HQ (Applied Biosystems) in a 1.6 cm × 20 cm XK16 column (GE healthcare, cat #18−8773−01). The bound A-dm-DT390-biscFv (2−6−15) was eluted with 150 mM sodium borate in TGE buffer and 200 mM sodium borate +50 mM NaCl in TGE buffer. The immunotoxin containing elution fractions were mixed, concentrated down with Centricon Plus-70 (30 kDa cutoff, Millipore), dialyzed against PBS pH 7.4 + 5% glycerol, filter sterilized, and stored at 80 °C.

HPLC Analysis. A-dm-DT390biscFv (2−6−15) final protein product was analyzed with Shimadzu HPLC system using Superdex 200 size-exclusion column, 10/300 GL (GE healthcare, cat # 17−5175−01). The sample volume was 100 μL using 100 μL loop. The flow rate was 0.35 mL/min. The running time was 120 min and the running buffer was 90 mM $NaSO_4$, 10 mM $NaPO_4$, pH 8.0, 1 mM EDTA.

Porcine CD3 Depletion Study in vivo. Four miniature swine, aged two months, were brought to our AAALAC accredited animal facility and were allowed to acclimate to their new surroundings for one week. Three days prior to the start of treatment, they were bled for baseline blood values: complete blood counts, serum chemistry values, and flow cytometry analysis of CD3+ T-cell populations. They were then injected through a 23 g butterfly catheter, through a peripheral vessel, with an intravenous (IV) bolus of undiluted A-dmDT390biscFv (2−6−15) at a dose of 50 μg/kg, twice daily for 4 days. Prior to each day's injections, morning blood samples were taken to monitor the aforementioned blood values. Each day's values were then compared to the pretreatment values. The animals were also injected with 4 mg/kg diphenhydramine IV bolus immediately prior to immunotoxin infusion to prevent any unexpected anaphylactic reactions, of which none were observed. To ensure that the full volume of immunotoxin was administered to the animals, each dose was flushed with 10 mL of phosphate buffered saline (pH between 6.5 and 7.5). The animals were closely monitored for signs of change in clinical condition such as lethargy and significant weight loss and no signs of toxicity were seen in any animal. The animals were bled again on days 7 and 14 following the start of injections to monitor their T-cell recovery and any possible toxicity.

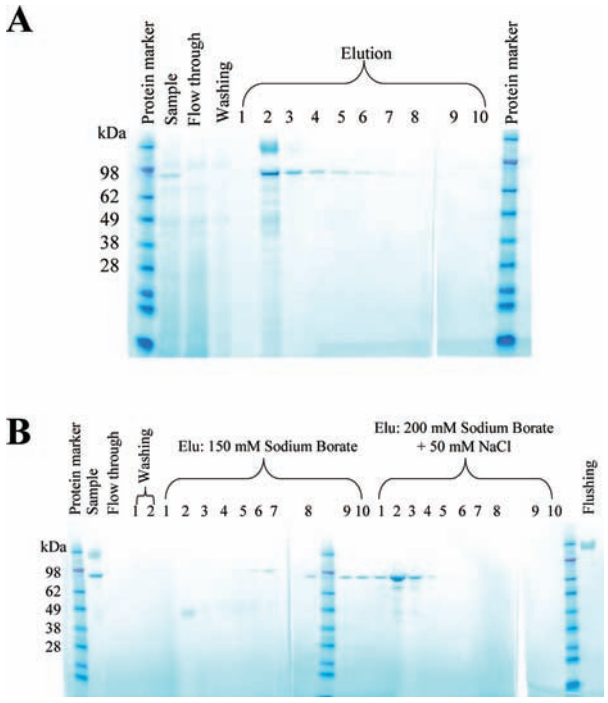

Figure 3. Two-step purification of the antiporcine CD3 immunotoxin A-dmDT390biscFv (2−6−15). (A) Capturing step with hydrophobic interaction resin Butyl 650 M. (B) Second step purification with strong anion exchange resin Poros 50HQ.

The percentage of CD3+ T-cells in the peripheral blood was determined by flow cytometry of heparinized whole blood samples after staining with FITC conjugated swine specific CD3 antibody (898H2−6−15, mouse IgGaK)[13] using BD FACS lysing solution whole blood staining procedure according to the manufacturer (BD Biosciences, San Jose, CA). The absolute T-cell count each day was calculated by multiplying the percentage of CD3+ cells in the peripheral blood by the white blood cell count. All experiments were approved by the Massachusetts General Hospital Institutional Animal Care and Use Committee.

RESULTS AND DISCUSSION

Plasmid Construction for the Antiporcine CD3 Recombinant Immunotoxin. The VL and VH DNA sequence and the deduced amino acid sequences of antiporcine CD3 mAb 898H2−6−15 are shown in Figure 1. According to Sreekrishna 1993,[16] we synthesized the codon-optimized scFv (2−6−15) and cloned it into the truncated diphtheria toxin DT390 containing yeast *Pichia pastoris* expression vector pwPICZα-A-dmDT390 between NcoI and *Eco*RI to replace the biscFv (UCHT1) portion.[8] Initially, we utilized the single chain foldback diabody format as in the

antimonkey CD3 immunotoxin construct,[7] but treatment with this recombinant immunotoxin did not result in depletion of porcine CD3+ T-cells in vivo (data not shown). We speculate that this could be because the single chain foldback diabody format is not suitable for binding the porcine CD3 epitope. Even though both 898H2−6−15 and FN18 recognize CD3 epsilon, it is likely that they bind different conformational CD3 epitopes. The traditional biscFv format, which was used in the antihuman CD3 recombinant immunotoxin (Figure 2),[8] was constructed. The bivalent immunotoxin is a multidomain protein containing the catalytic and translocation domains of DT and two VL and two VH of the antiporcine CD3 mAb 898H2−6−15. The VL and VH are joined by a 15 amino acid $(G_4S)_3$ linker (L) in the order of VL-L-VH-L-VL-L-VH.

Expression and Purification of the Antiporcine CD3 Recombinant Immunotoxin. The antiporcine CD3 recombinant immunotoxin A-dmDT390biscFv (2−6−15) was expressed using shaker flasks by scaling up from small tube expression as described in the Experimental Procedures. The scaled-up expression level is about 20 mg/L. The secreted antiporcine CD3 immunotoxin in the supernatant was captured directly by hydrophobic interaction chromatography resin Butyl 650 M (Figure 3A). For second-step purification, a strong anion exchange resin Poros 50 HQ was used. Sodium chloride alone did not work well for eluting the immunotoxin, as the glycosylated yeast host protein was coeluted with the immunotoxin.[19] Sodium borate was chosen, as it would separate the immunotoxin from the glycosylated yeast host protein and the aggregates. However, the maximal solubility for sodium borate is restricted to 200 mM, a concentration which is not strong enough to elute the majority of the immunotoxin. To overcome this problem, we added 50 mM NaCl to the 200 mM sodium borate elution buffer to increase the salt concentration. The majority of the immunotoxin was eluted with 200 mM sodium borate and 50 mM NaCl (Figure 3B). As shown in Figure 4, after two step purification we obtained the pure 95 kDa antiporcine CD3 recombinant immunotoxin. The purity reached around 95%. The final purification yield was ~13 mg per liter of the original harvested supernatant. As shown in Figure 4A, A-dmDT390biscFv (2−6−15) showed a second weak band migrating around 70 kDa. Western blots identified it as a breakdown product.

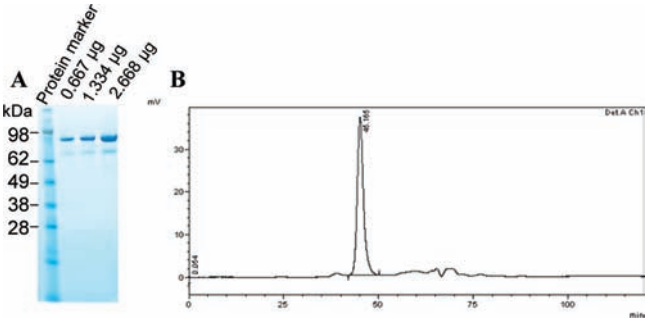

Figure 4. Antiporcine CD3 immunotoxin A-dmDT390biscFv (2−6−15) analysis. (A) NuPAGE 4−12% Bis-Tris gel analysis. (B) HPLC analysis.

Porcine CD3 T-cell Depletion in Vivo Using the Antiporcine CD3 Recombinant Immunotoxin. The CD3 T-cell depletion function of this recombinant immunotoxin was assessed in four MGH miniature swine, aged two months. Results are shown in Figure 5. This recombinant immunotoxin was given through IV bolus at a dose of 50 μg/kg, twice daily for four days. Complete blood counts, serum chemistry values, and CD3+ T-cell numbers were measured. The immunotoxin treatment decreased the number of CD3+ T-cells in the peripheral blood to approximately 20% of the pretreatment level (Figure 5A). There was no significant effect on the number of peripheral B cells (Figure 5B). The percent CD3+ T-cells in the lymph node decreased from 74% pretreatment to 24% following 4 days of

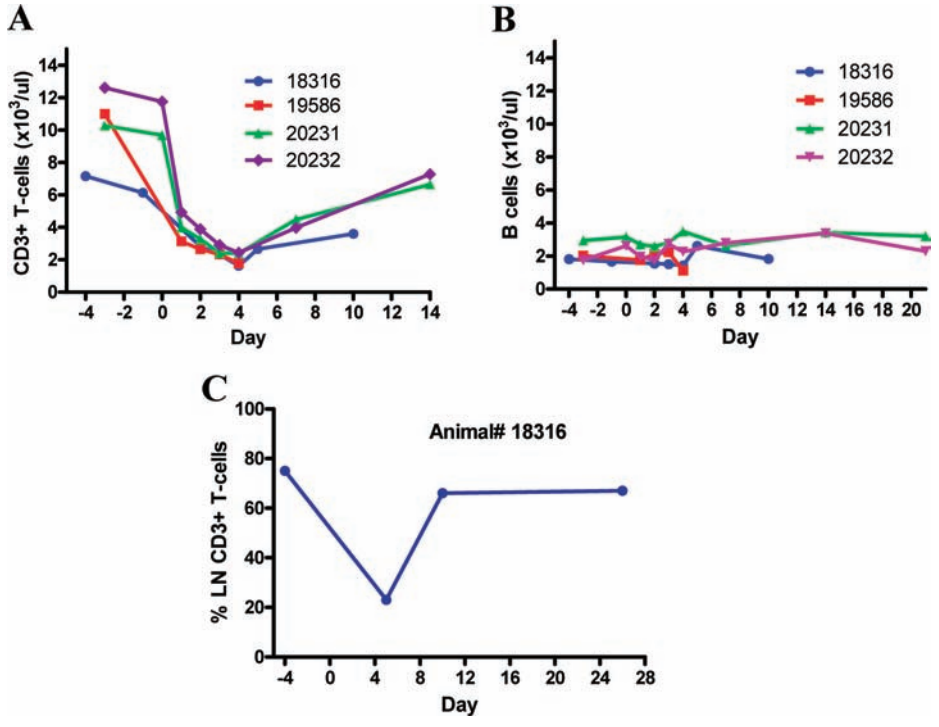

Figure 5. Porcine CD3 T-cell depletion profile in vivo for four animals using antiporcine CD3 immunotoxin, A-dmDT390biscFv (2−6−15). (A) Absolute number of CD3+ T-cells in the peripheral blood. (B) Absolute number of B cells in the peripheral blood. (C) Lymph node percent CD3+ T-cells.

immunotoxin treatment reversing the ratio of T:B cells in the lymph node (Figure 5C).

Clinically, no toxicities were observed in any of the treated animals. No anaphylactic reactions were observed. Kidney toxicity was not observed and renal values (blood urea nitrogen and creatinine) remained within normal limits. Two animals 18316 and 19586 developed mild increases of liver enzymes from baseline preimmunotoxin. Lactate dehydrogenase levels for animal 18316 increased from 1166 u/L to 1960u/L and for animal 19586 from 1722 u/L to 2017 u/L. Alkaline phosphatase levels for animal 18316 increased from 102 u/L to 204 u/L. No changes were observed in any of the other animals. Despite slight increases from baseline lactate dehydrogenase and alkaline phosphatase levels, these enzymes remained well within the normal limits in swine (575−3200 u/L for lactate dehydrogenase and 92−295 u/L for alkaline phosphatase). The transaminase remained normal and histopathology was unremarkable. In summary, we did not observe any side effect after the imunotoxin treatment. At the dose tested, the antiporcine CD3 recombinant immunotoxin did not deplete CD3 T-cells as well as its counterpart antihuman or antimonkey CD3 recombinant immunotoxins.[7,12] The dose used in swine was at least two times higher than the dose of its counterpart antihuman or antimonkey CD3 recombinant immunotoxins.[7,12] It is possible that miniature swine are more tolerant to the recombinant immunotoxin thereby allowing even further increased dosing for improved depletion effect. Given the absence of any signs of toxicity, we speculate that it is possible to increase the current daily dose or extend the administration days. A dosing study will need to be done to find the maximal safe dose and best dosing strategy for improved depletion. Since the half-life of recombinant antihuman CD3 immunotoxin is only 40 min,[12] it may not be necessary to spread 8 doses over 4 days. It is also possible that increasing the affinity of the scFv (2−6−15) similar to the affinity maturation approach used for the antimonkey CD3 recombinant immunotoxin may improve depletion function. Affinity maturation of the scFv (2−6−15) by yeast display[20] is currently in progress to isolate a higher affinity scFv (2−6−15) for improved porcine T-cell depletion in vivo.

Although CD3+ T-cell depletion following antiporcine CD3 recombinant immunotoxin treatment was not complete, in combination with other treatments, this reagent may provide sufficient T-cell depletion for certain applications.

Compared with the corresponding chemical conjugate antiporcine CD3 immunotoxin (pCD3-CRM9), this recombinant antiporcine CD3 immunotoxin [A-dmDT390biscFv(2−6−15)] has the following advantages: (1) high production level suitable for scale-up; (2) high purity and linkage homogeneity; (3) no neurological toxicity. In contrast, the chemical conjugate antiporcine CD3 immunotoxin caused significant dose-dependent neurotoxicity.[6] These finding suggest that the mutated DT binding domain of the chemical conjugate antiporcine CD3 immunotoxin can still bind to the porcine DT receptor. The recombinant antiporcine CD3 immunotoxin does not contain the DT binding domain (Figure 2). As expected, we did not observe any neurotoxicity in any of the animals treated with recombinant antiporcine CD3 immunotoxin. A-dmDT390biscFv (2−6−15) is a unique recombinant protein reagent that can be utilized in experimental porcine models of transplantation tolerance, autoimmune disease therapy, and T-cell leukemia treatment, as well as graft versus host disease studies.

AUTHOR INFORMATION

Corresponding Author

*Zhirui Wang, Ph.D., Transplantation Biology Research Center, Massachusetts General Hospital/Harvard Medical School MGH-East, Building 149-6113 13th Street, Boston, MA 02129, USA. Phone: +1-617-643-1957. Fax: +1-617-726-4067. E-mail: zhirui.wang@tbrc.mgh.harvard.edu.

ACKNOWLEDGMENT

The work was supported by National Institutes of Health (R01AI084657-02 to CAH) and Dana Farber/Harvard Cancer Center Core development grant. We thank Christina Hermanrud, Prashanth Vallabhajosyula, and Lauren L. Springett for their excellent technical assistance, and Bob Hawley and Sharon Germana for intensive manuscript review.

REFERENCES

(1) Huang, C. A., Yamada, K., Murphy, M. C., Shimizu, A., Colvin, R. B., Neville, D. M., Jr., and Sachs, D. H. (1999) *In vivo* T cell depletion in miniature swine using the swine CD3 immunotoxin, pCD3-CRM9. *Transplantation 68*, 855–860.

(2) Fuchimoto, Y., Huang, C. A., Yamada, K., Shimizu, A., Kitamura, H., Colvin, R. B., Ferrara, V., Murphy, M. C., Sykes, M., White-Scharf, M., Neville, D. M., Jr., and Sachs, D. H. (2000) Mixed chimerism and tolerance without whole body irradiation in a large animal model. *J. Clin. Invest. 105*, 1779–1789.

(3) Huang, C. A., Fuchimoto, Y., Scheier-Dolberg, R., Murphy, M. C., Neville, D. M., Jr., and Sachs, D. H. (2000) Stable mixed chimerism and tolerance using a nonmyeloablative preparative regimen in a large-animal model. *J. Clin. Invest. 105*, 173–181.

(4) Cina, R. A., Wikiel, K. J., Lee, P. W., Cameron, A. M., Hettiarachy, S., Rowland, H., Goodrich, J., Colby, C., Spitzer, T. R., Neville, D. M., Jr., and Huang, C. A. (2006) Stable multilineage chimerism without graft versus host disease following nonmyeloablative haploidentical hematopoietic cell transplantation. *Transplantation 81*, 1677–1685.

(5) Neville, D. M., Jr., Scharff, J., Hu, H. Z., Rigaut, K., Shiloach, J., Slingerland, W., and Jonker, M. (1996) A new reagent for the induction of T-cell depletion, anti-CD3-CRM9. *J. Immunother. Emphasis. Tumor Immunol. 19*, 85–92.

(6) Gargollo, P., Yamada, K., Esnaola, N., Fuchimoto, Y., Newell, K. L., Sachs, D. H., and Huang, C. A. (2001) Neuropathy in miniature swine following administration of the mutant diphtheria toxin based immunotoxin, pCD3-CRM9. *Transplantation 72*, 818–822.

(7) Kim, G. B., Wang, Z., Liu, Y. Y., Stavrou, S., Mathias, A., Goodwin, K. J., Thomas, J. M., and Neville, D. M., Jr. (2007) A fold-back single-chain diabody format enhances the bioactivity of an anti-monkey CD3 recombinant diphtheria toxin-based immunotoxin. *Protein Eng. Des. Sel. 20*, 425–432.

(8) Woo, J. H., Liu, Y. Y., Mathias, A., Stavrou, S., Wang, Z., Thompson, J., and Neville, D. M., Jr. (2002) Gene optimization is necessary to express a bivalent anti-human anti-T cell immunotoxin in Pichia pastoris. *Protein Expr. Purif. 25*, 270–282.

(9) Madshus, I. H., Olsnes, S., and Stenmark, H. (1992) Membrane translocation of diphtheria toxin carrying passenger protein domains. *Infect. Immun. 60*, 3296–3302.

(10) Hexham, J. M., King, V., Dudas, D., Graff, P., Mahnke, M., Wang, Y. K., Goetschy, J. F, Plattner, D., Zurini, M., Bitsch, F., Lake, P., and Digan, M. E. (2001) Optimization of the anti-(human CD3) immunotoxin DT389-scFv(UCHT1) N-terminal sequence to yield a homogeneous protein. *Biotechnol. Appl. Biochem. 34*, 183–187.

(11) Thompson, J., Stavrou, S., Weetall, M., Hexham, J. M., Digan, M. E., Wang, Z., Woo, J. H., Yu, Y., Mathias, A., Liu, Y. Y., Ma, S., Gordienko, I., Lake, P., and Neville, D. M., Jr. (2001) Improved binding

of a bivalent single-chain immunotoxin results in increased efficacy for in vivo T-cell depletion. *Protein Eng. 14*, 1035–1041.

(12) Frankel, A. E., Zuckero, S. L., Mankin, A. A., Grable, M., Mitchell, K., Lee, Y. J., Neville, D. M., Jr., and Woo, J. H. (2009) Anti-CD3 recombinant diphtheria immunotoxin therapy of cutaneous T cell lymphoma. *Curr. Drug Targets 10*, 104–109.

(13) Huang, C. A., Lorf, T., Arn, J. S., Koo, G. C., Blake, T., and Sachs, D. H. (1999) Characterization of a monoclonal anti-porcine CD3 antibody. *Xenotransplant 5*, 201–212.

(14) Yuan, X., Gubbins, M. J., and Berry, J. D. (2004) A simple and rapid protocol for the sequence determination of functional kappa light chain cDNAs from aberrant-chain-positive murine hybridomas. *J. Immunol. Methods 294*, 199–207.

(15) Liu, Y. Y., Gordienko, I., Mathias, A., Ma, A., Thompson, J., Woo, J. H., and Neville, D. M., Jr. (2000) Expression of an anti-CD3 single-chain immunotoxin with a truncated diphtheria toxin in a mutant CHO cell line. *Protein Expr. Purif. 19*, 304–311.

(16) Sreekrishna, K. (1993). Strategies for optimizing protein expression and secretion in the methylotrophic yeast Pichia pastoris. In *Industrial Microorganism: Basic and Applied Molecular Genetics* (Baltz, R. H., Hegeman, G. D., and Skatrud, P. L., Eds.) pp 119−126, American Society of Microbiology, Washington, DC.

(17) Liu, Y. Y., Woo, J. H., and Neville, D. M., Jr. (2003) Targeted introduction of a diphtheria toxin resistant mutation into the chromosomal EF-2 locus of Pichia pastoris and expression of immunotoxin in the EF-2 mutants. *Protein Expr. Purif. 30*, 262–274.

(18) Kabat, E. A., Wu, T. T., Reid-Miller, M., and Gottesman, K. S. (1987) *Sequences of proteins of immunological interest*, U.S. Department of Health and Human Services, U.S. Governmental Printing Office, Washington, DC.

(19) Woo, J. H., and Neville, D. M., Jr. (2003) Separation of bivalent anti-T cell immunotoxin from Pichia pastoris glycoproteins by borate anion exchange. *BioTechniques 35*, 392–398.

(20) Wang, Z., Kim, G. B., Woo, J. H., Liu, Y. Y., Mathias, A., Stavrou, S., and Neville, D. M., Jr. (2007) Improvement of a recombinant anti-monkey anti-CD3 diphtheria toxin based immunotoxin by yeast display affinity maturation of the scFv. *Bioconjugate Chem. 18*, 947–955.

Bioconjugate Chemistry

ARTICLE

pubs.acs.org/bc

Improved Tumor Targeting of Polymer-Based Nanovesicles Using Polymer−Lipid Blends

Zhiliang Cheng,[†] Drew R. Elias,[†] Neha P. Kamat,[†] Eric D. Johnston,[†] Andrei Poloukhtine,[‡] Vladimir Popik,[‡] Daniel A. Hammer,[†] and Andrew Tsourkas*[,†]

[†]Department of Bioengineering, University of Pennsylvania, Philadelphia, Pennsylvania 19104, United States

[‡]Department of Chemistry, University of Georgia, Athens, Georgia 30602, United States

Supporting Information

ABSTRACT: Block copolymer-based vesicles have recently garnered a great deal of interest as nanoplatforms for drug delivery and molecular imaging applications due to their unique structural properties. These nanovesicles have been shown to direct their cargo to disease sites either through enhanced permeability and retention or even more efficiently via active targeting. Here, we show that the efficacy of nanovesicle targeting can be significantly improved when prepared from polymer−lipid blends compared with block copolymer alone. Polymer−lipid hybrid nanovesicles were produced from the aqueous coassembly of the diblock copolymer, poly(ethylene oxide)-*block*-polybutadiene (PEO-PBD), and the phospholipid, hydrogenated soy phosphatidylcholine (HSPC). The PEG-based vesicles, 117 nm in diameter, were functionalized with either folic acid or anti-HER2/neu affibodies as targeting ligands to confer specificity for cancer cells. Our results revealed that nanovesicles prepared from polymer−lipid blends led to significant improvement in cell binding compared to nanovesicles prepared from block copolymer alone in both *in vitro* cell studies and murine tumor models. Therefore, it is envisioned that nanovesicles composed of polymer−lipid blends may constitute a preferred embodiment for targeted drug delivery and molecular imaging applications.

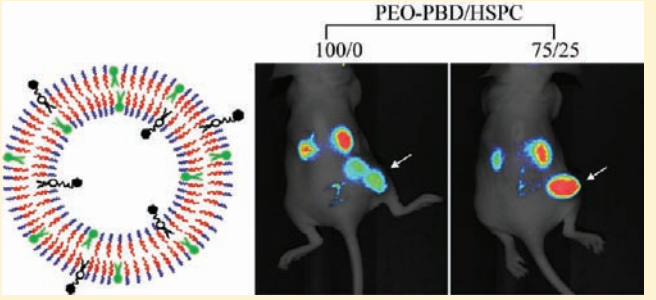

INTRODUCTION

For traditional drug delivery systems, only a small fraction of the therapeutic agents reach the disease site. Targeted drug delivery seeks to improve the accumulation of these agents in the tissues of interest while reducing their relative concentration in off-target sites. If successful, this would lead to a significant improvement in treatment efficacy, while reducing drug toxicity and/or dose. Accordingly, the use of nanoparticulate systems to facilitate the targeted delivery of therapeutic agents has been extensively explored in recent years.[1−10] Drug delivery nanoplatforms have included dendrimers, polymers, liposomes, micelles, emulsions, and silica nanoparticles. Beyond their enhanced targeting capabilities and ability to carry high drug payloads, nanoparticle-based drug delivery systems have also been shown to provide protection of some drugs against degradation and have enabled the efficient delivery of substances with poor inherent solubility or low membrane permeability.[2]

Among the many nanoparticulate systems that have been reported, hollow nanometer-sized vesicles are particularly attractive due to the increased functionality imparted by their amphiphilic structure. Specifically, hydrophilic compounds can be loaded into the aqueous lumen of the nanovesicles, the hydrophobic domain serves as a natural carrier environment for hydrophobic drugs, and the exterior surface can be functionalized with molecularly specific targeting ligands.

Polymer-based nanovesicles (i.e., polymersomes), prepared from high molecular weight diblock copolymers, have a thick hydrophobic domain, typically ∼6−10 nm.[11] This is significantly larger than the hydrophobic domain of most liposomes, which are typically ∼3 nm in thickness. Compared to liposomes, polymersomes possess several beneficial properties, including increased mechanical robustness and the ability to carry large quantities of hydrophobic and hydrophilic molecules.[11,12] The vast majority of polymersomes are formed from diblock copolymers with poly(ethylene glycol) (PEG) as the hydrophilic block. This creates a relatively inert, brush-like outer shell, which imparts "stealth"-like characteristics to the nanovesicles and allows them to effectively avoid the reticuloendothelial system, resulting in longer circulation times. Further, polymersomes can be finely tuned through polymer selection to yield vesicles with diverse functionality, i.e., biodegradability, biocompatibility, permeability, elasticity, and so forth.[13−15] As a result of all these characteristics, polymersomes have garnered a great deal of

Received: May 4, 2011
Revised: August 30, 2011
Published: September 07, 2011

ACS Publications © 2011 American Chemical Society

dx.doi.org/10.1021/bc200214g | *Bioconjugate Chem.* 2011, 22, 2021–2029

interest as nanoplatforms for a range of biomedical applications, including drug delivery, in vivo imaging, and cell mimicry.[13,16−18] For example, it has recently been shown that both hydrophobic paclitaxel and hydrophilic doxorubicin can be coloaded into polymersomes to effectively treat tumors,[13] porphyrins have been loaded into the hydrophobic domain of polymersomes creating highly fluorescent imaging agents,[19,20] and gadolinium-labeled dendrimers have been encapsulated within the lumen of polymersomes to create highly efficient magnetic resonance imaging (MRI) contrast agents.[16,17] When administered intravenously, polymeric vesicles generally maintain a long circulation time within the body and will nonspecifically accumulate within tumors due to enhanced permeability and retention (EPR). Although EPR can allow for a sufficient quantity of polymersomes to accumulate within tumors for effective treatment and/or imaging, it is generally desirable to develop actively targeted nanoplatforms to minimize nonspecific toxicity and/or enhance the efficiency of therapy.[21] Targeting, however, can often be compromised by the brush-like PEG coatings on the vesicle surface. Specifically, despite the benefits of pegylation in reducing polymer uptake by the reticuloendothelial system, it has been shown that the presence of PEG on vesicle surfaces can inhibit ligand-mediated targeting of the vesicle, due to steric effects.[22,23] Therefore, we hypothesized that the efficiency of polymersome targeting could be improved by diluting the surface density of PEG by integrating phospholipids into the membrane bilayer.

Recently, phospholipid−block copolymer hybrid nanoparticles have been reported and have drawn much attention.[17,24,25] The main components of these hybrid nanoparticles are the hollow polymeric scaffold with the incorporated phospholipid. Such hollow vesicles possess the structural stability and mechanical strength of polymer membranes and the biocompatibility and biofunctionality of phospholipid membranes. Owing to their unique structural properties, lipid−polymer hybrid vesicles may constitute a preferred nanoplatform for targeted drug delivery and molecular imaging applications. For example, Kanger and coworkers have prepared biofunctionalized lipid−polymer hybrid nanocontainers with controlled permeability for triggered delivery of drugs or imaging agents.[13,26]

In this study, we show that polymer-based nanovesicles prepared from polymer−lipid blends, as opposed to block copolymer alone, exhibit a significant improvement in tumor cancer cell binding. Specifically, lipid−polymer hybrid vesicles were produced from the aqueous coassembly of the diblock copolymer, poly(ethylene oxide)-*block*-polybutadiene, and the phospholipid, hydrogenated soy phosphatidylcholine (HSPC). The vesicles were functionalized with either folic acid or HER2/neu-targeted affibodies as targeting ligands to confer specificity for cancer cells. HER2-affibodies comprise a new class of high-affinity ligands based on a protein scaffold derived from the IgG-binding domains of staphylococcal protein A.[27] These small (6.5 kDa) robust molecules have been shown to exhibit remarkable specificity and affinity (pm range) for the HER2/neu receptor. The key features of the developed nanomaterials include nanometer-sized vesicles formed from self-assembly of amphiphilic diblock copolymers and phospholipids, brush-like PEG outer shell and tumor-targeting ligands conjugated onto hybrid nanovesicles, which serve to localize the therapeutic agent to the site of interest. Here, the design, assembly, characterization, and tumor-cell targeting of the polymer−lipid hybrid vesicles are discussed.

EXPERIMENTAL PROCEDURES

Materials. Poly(ethylene oxide)-*block*-polybutadiene copolymer (denoted PEO-PBD) was purchased from Polymer Source (Dorval, Quebec, Canada). Average molecular weights of the poly(ethylene oxide) and poly(butadiene) block were 600 and 1200, respectively. Hydrogenated soy phosphatidylcholine (HSPC), 1,2-dioleoyl-*sn*-glycero-3-phosphoethanolamine-*N*-(Lissamine rhodamine B sulfonyl) (Rhod-PE), 1,2-distearoyl-*sn*-glycero-3-phosphoethanolamine-*N*-[poly(ethylene glycol)2000-*N*′-carboxyfluorescein] (DSPE-PEG2K-CF), 1,2-distearoyl-*sn*-glycero-3-phosphoethanolamine-*N*-[amino(polyethylene glycol)-2000] (DSPE-PEG2000-Amine), and 1,2-distearoyl-*sn*-glycero-3-phosphoethanolamine-*N*-[folate(polyethylene glycol)-2000] (DSPE-PEG2000-Folate) were obtained from Avanti Polar Lipids (Alabaster, AL). ADIBO-dPEG4-NHS was synthesized in the lab (see Supporting Information). All other chemical were used as received. All buffer solutions were prepared with ultrapure grade water.

Preparation of Giant Vesicles. Giant vesicles were prepared by hydration of dry polymer/lipid films. Stock solutions of PEO-PBD and HSPC in chloroform were mixed in the following molar ratios: PEO-PBD/HSPC (100:0), PEO-PBD/HSPC (90:10), and PEO-PBD/HSPC (75:25). The total amount of PEO-PBD for each of the vesicle compositions was 1 mg. In all cases, a small amount of the fluorescent label, Rhod-PE, was also added for vesicle visualization. The solvent was removed using a direct stream of nitrogen prior to vacuum desiccation for a minimum of 4 h. Giant (micrometer-sized) vesicles were formed by adding 2 mL sucrose (285 mM) solution to dried film and incubating in a 65 °C water bath for more than 24 h.

Preparation of Nanometer-Sized Vesicles. Stock solutions of PEO-PBD and HSPC in chloroform were mixed in the following molar ratios: PEO-PBD/HSPC (100:0), PEO-PBD/HSPC (90:10), and PEO-PBD/HSPC (75:25). The total amount of PEO-PBD for each of the vesicle compositions was 1 mg. For folate-receptor targeting, DSPE-PEG2000-Folate (10 μL, 1 mg/mL in chloroform) was added to the PEO-PBD/HSPC mixture. Rhod-PE (2.5 μL, 1 mg/mL in chloroform) was also added as a fluorescent indicator for fluorescence microscopy images. For flow cytometric study, DSPE-PEG2K-CF (2.5 μL, 1 mg/mL in chloroform) instead of Rhod-PE was used for vesicle preparation. For Her2/neu-receptor targeting, DSPE-PEG2000-Amine (10 μL, 1 mg/mL in chloroform) was added to the PEO-PBD/HSPC mixture. The solvent was removed using a direct stream of nitrogen prior to vacuum desiccation for a minimum of 4 h. Vesicles were formed by adding an aqueous solution (0.1 M PBS, pH 7.4) to the dried film and incubating in a 65 °C water bath for 0.5 h and then sonicating for another 1 h at the same temperature. Samples were subjected to 10 freeze−thaw−vortex cycles in liquid nitrogen and warm H_2O (65 °C), followed by extrusion 21 times through two stacked 100 nm Nuclepore polycarbonate filters using a stainless steel extruder (Avanti Polar Lipids).

Micropipet Aspiration. The micropipet aspiration experiment was performed as described previously.[20,28] Briefly, micropipets made of borosilicate glass tubing (Friedrich and Dimmock, Milville, NJ) were prepared using a needle/pipet puller (model 720, David Kopf Instruments, Tujunga, CA) and microforged using a glass bead to give the tip a smooth and flat edge. Pipettes were filled with 290 mOsm PBS and mounted on a micromanipulator, and the pipet was connected via tubing to a manometer. A negative pressure, produced through the manometer using a

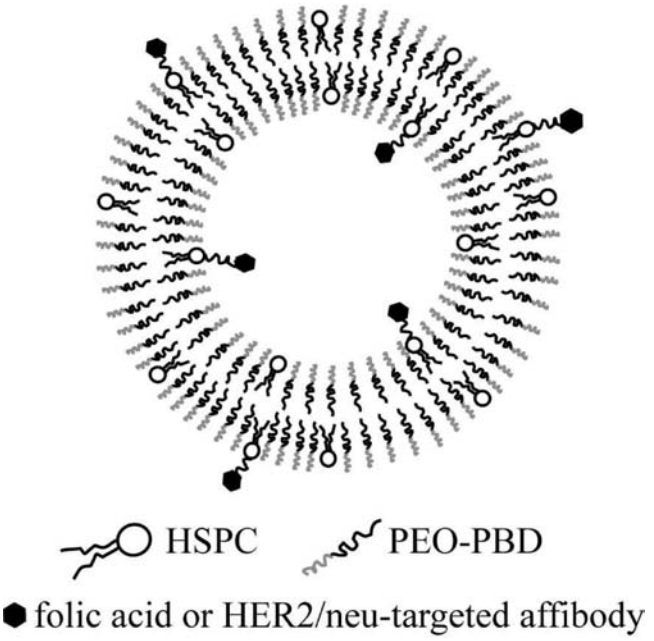

Figure 1. Schematic diagram of folate receptor or HER2/neu receptor-targeted, polymer−lipid hybrid vesicles. Nanovesicles were formed through the coassembly of the diblock copolymer PEO-PBD and the phospholipid HSPC. Folate receptor targeting was achieved by doping the vesicles with low percentage of PEG2000-DSPE-Folic acid. HER2/neu receptor targeting was achieved by conjugation of HER2/neu targeted affibodies to the vesicle surface via copper free click conjugation.

syringe, was created in the pipet to pick up a giant vesicle. The pressure applied to the vesicle was increased in stepwise increments (4 cm H_2O), and from this suction pressure (ΔP), the membrane tension (T) for a fluid membrane can be calculated from LaPlace's Law.[29] The length of the vesicle extension into the pipet in response to suction pressure was used to calculate the resulting vesicle area strain, $\alpha \equiv \Delta A/A_0$. The area elastic modulus was then measured by plotting α vs T in the high-tension regime ($T > 0.5$ dyn/cm) and calculating the slope of this tension−strain curve. Experiments were imaged using DIC optics with a 40× objective and a Cohu black-and-white CCD camera (Cohu, Inc., San Diego, CA). *ImageJ* software was used to measure membrane extensions and vesicle diameters.

Cloning and Expression of HER2-Affibody and Copper Free Click Conjugation. See Supporting Information.

Lipid Contents in Lipid−Polymer Hybrid Nanovesicles. Lipid−polymer hybrid nanovesicles, i.e., 10 mol % HSPC/90 mol % PEO-PBD and 25 mol % HSPC/75 mol % PEO-PBD, were lyophilized either before or after extrusion and purification. In these studies, samples were prepared in pure water. The residual solid was weighed and resuspended in pure water. Phospholipid content was determined by measuring the total content of phosphorus in the sample.[30] The polymer weight was calculated as the dry weight minus the lipid weight. The molar ratio of lipid to polymer was then calculated based on their respective molecular weights.

Quantification the Targeting Ligand Number on Vesicle Surface. The content of folate in the samples was determined by quantitative UV spectrophotometric analysis using the molar extinction coefficient value of 15 760 M^{-1} cm^{-1} at λ = 358 nm. Background absorbance measurements were determined using

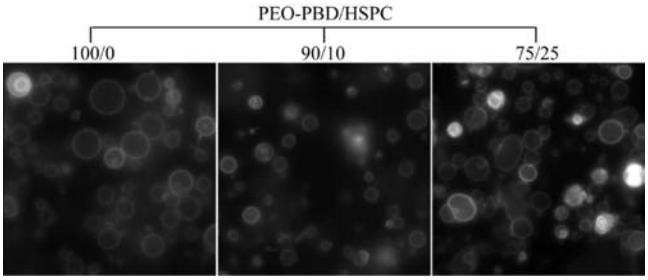

Figure 2. Fluorescent images of giant vesicles composed of PEO-PBD and HSPC at three different molar ratios. Vesicles composed of 100% PEO-PBD, 90% PEO-PBD/10% HSPC, or 75% PEO-PBD/25% HSPC were doped with a low amount (<1 mol %) of the fluorescent phospholipid Rhod-PE. Notably, it was observed that Rhod-PE was incorporated into all of the vesicles in each sample.

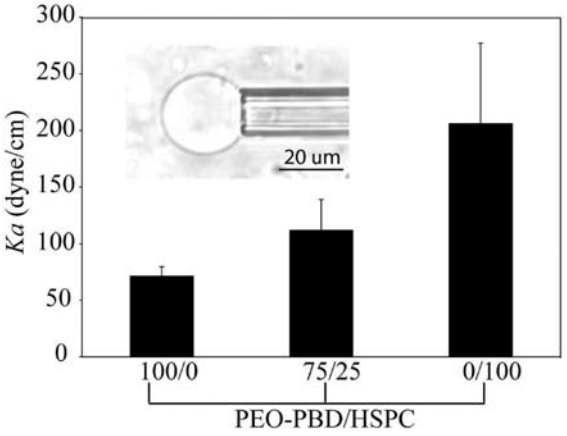

Figure 3. Elastic moduli of vesicles composed of PEO-PBD and HSPC at three different molar ratios. Micropipet aspiration was used to measure area elastic modulus (K_a) of giant vesicle formulations with different compositions of PEO-PBD and HSPC. Inset: Image of a giant polymerlipid hybrid vesicle (75 mol % PEO-PBD/25 mol % HSPC) during aspiration procedure.

analogous samples with no folate. To calculate the number of folate per vesicle, the number of vesicles in the purified sample was calculated based on the amount of polymer and phospholipid in each vesicle. For this calculation, the average diameter of each vesicle formulation was measured via dynamic light scattering. Further, the average area occupied by single polymer molecules in the bilayer was previously determined to be ~1 nm.[14] The average area occupied by single phospholipid molecules in the bilayer was previously determined to be ~0.65 nm,[31] and the thickness of the polymersome bilayer was considered to be ~6 nm based on previous study.[12] A similar approach was used to quantify the content of Rhod-PE in each vesicle. The molar extinction coefficient value used for Rhod was 93 000 M^{-1} cm^{-1} at λ = 568 nm.

Once the Rhod content per vesicle was established, it was possible to quantify the number of conjugated HER2−affibody per vesicle based on the ratio of absorbance of conjugated fluorescent-HER2 affibody relative to incorporated Rhod-PE. Notably, each HER2−affibody is labeled with a single near-infrared dye, Hilyte Fluor 750. The content of Hilyte Fluor 750 was determined by spectrophotometric analysis using the molar extinction coefficient value of 275 000 M^{-1} cm^{-1} at λ = 753 nm.

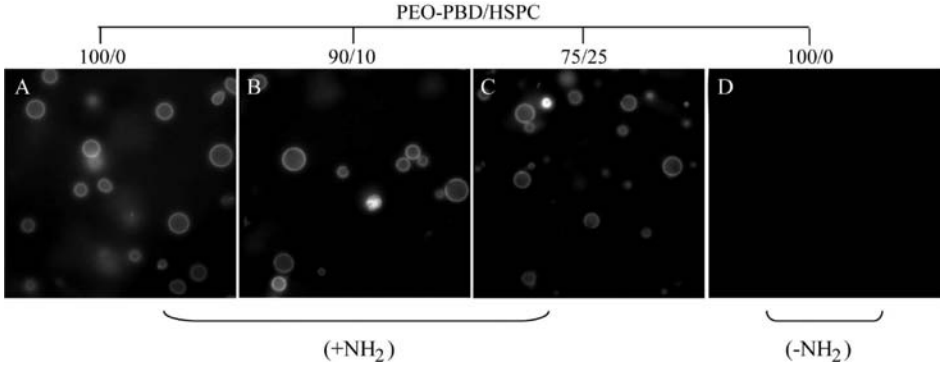

Figure 4. Fluorescent images of giant lipid−polymer vesicles following surface modification with a fluorescent dye. Vesicles prepared with (A) 100% PEO-PBD, (B) 90% PEO-PBD/10% HSPC, or (C) 75% PEO-PBD/25% HSPC were doped with low amount (<1%) of DSPE-PEG2K-NH2 and were subsequently labeled with NHS-ATTO740. (D) For comparison, 100% PEO-PBD vesicles were also prepared in the absence of DSPE-PEG2K-NH2 for NHS-ATTO740 surface conjugation.

Cell Culture. KB cells (human nasopharyngeal epidermoid carcinoma cells) were purchased from the America Type Tissue Collection (ATCC) and cultured in RPMI 1640 folic acid free media with 10% fetal bovine serum (FBS) and 1% penicillin/streptomycin at 37 °C in a humidified atmosphere containing 5% CO_2. T6−17 cells that were engineered to stably express the Her2/neu receptor (T6−17) were kindly provided by Mark Greene, MD/PhD (University of Pennsylvania). T6−17 cells were cultured and maintained in Dulbecco's modified Eagle's medium (DMEM), supplemented with 10% fetal bovine serum (FBS) and 1% penicillin/streptomycin at 37 °C and 5% CO_2.

Cell Viability via MTT Assay. NIH 3T3 cells were seeded in 96-well plates at a density of 10 000 cells per well. After incubation overnight (37 °C, 5% CO_2), the medium in each well was aspirated off and loaded with 100 μL of fresh medium containing nanovesicles with four different formulations including 100 mol % PEO-PBD, 10 mol % HSPC/90 mol % PEO-PBD, 25 mol % HSPC/75 mol % PEO-PBD, and 100 mol % HSPC. For PEO-based vesicles, the final polymer (PEO-PBD) concentration in the cultured media was 10 μM. For pure HSPC vesicles, the final HSPC concentration in the cultured media was also 10 μM. After incubation for 24 h, the nanoparticle containing medium in each well was aspirated off and replaced with 100 μL of medium and 10 μL of MTT reagent. The cells were incubated for 2 to 4 h, then 100 μL detergent reagent was added and left at room temperature in the dark for 2 h. The absorbance at 570 nm was measured using a microplate reader. Analogous viability studies were also conducted with the nanoparticle formulation consisting of 25 mol % HSPC/75 mol % PEO-PBD at PEO-PBD concentrations of 0, 5, 10, 50, 100, and 200 μM.

Fluorescence Microscopy. Cells plated in 8 glass well plates were washed once with PBS and then incubated in 200 μL of RPMI (for KB cells) or DMEM (for T6−17) containing vesicles for 2 h. For competitive inhibition experiments, cells were treated with the same vesicles but in the presence of 1 mM free targeting ligands in the media. The final PEO-PBD concentration in the cultured media was 5 μM for all imaging experiments. Prior to acquisition of fluorescence images, cells were washed with PBS three times. All microscopy images were acquired with an Olympus IX81 motorized inverted fluorescence microscope equipped with a back-illuminated EMCCD camera (Andor), an X-cite 120 excitation source (EXFO), and Sutter excitation and emission filter wheels. Images of the Rhod-PE were acquired using the filter set HQ545/30, HQ610/75, Q570LP. Images of FITC fluorescence were acquired using the filter set HQ480/40, HQ535/50, Q505LP. All filter sets were purchased from Chroma.

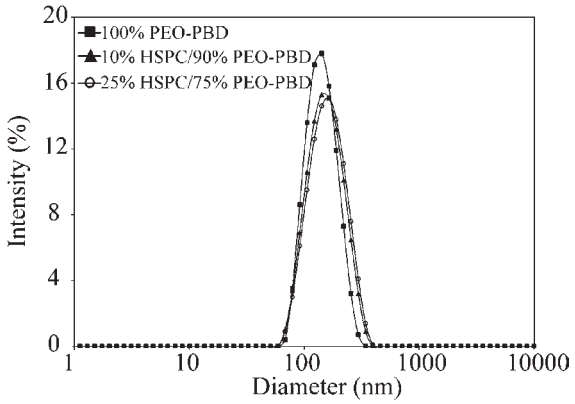

Figure 5. Intensity-weighted size distribution of three different vesicle formulations as measured by dynamic light scattering (DLS).

Flow Cytometric Analysis. Cells were dissociated from culture flasks using PBS-based enzyme free dissociation buffer and transferred to sterile 96-well plates at a final concentration of 50 000 cells per well. Targeted vesicles were added to the wells for 2 h at 37 °C. The final polymer (PEO-PBD) concentration in the cultured media was 5 μM for all flow cytometric experiments. For competitive inhibition experiments, cells were treated with the same vesicles but in the presence of 1 mM free targeting ligands in the media. Cells were transferred to 1.5 mL centrifuge tubes and washed in triplicate by pelleting cells at 1000 RCF for 3 min and then resuspending in PBS. Cells were resuspended in 250 μL of PBS and seeded in a 96-well plate (50 000 cells per well) and analyzed using a Guava Easycyte Plus system (Guava Technologies, Hayward, CA). Flow cytometry data were analyzed using *FlowJo* software (TreeStar Inc., San Francisco, CA).

***In Vivo* Imaging.** Approximately 6-week-old female Fox Chase SCID mice (Charles River Laboratory, Charles River, MS) were maintained in accordance with the Institutional Animal Care and Use Committee of the University of Pennsylvania. Mice were anesthetized via isoflurane and T6−17 cells were injected subcutaneously into the back right flank (2×10^6 cells in 0.2 mL PBS). Tumors were grown to an approximate size of 100 mm^3.

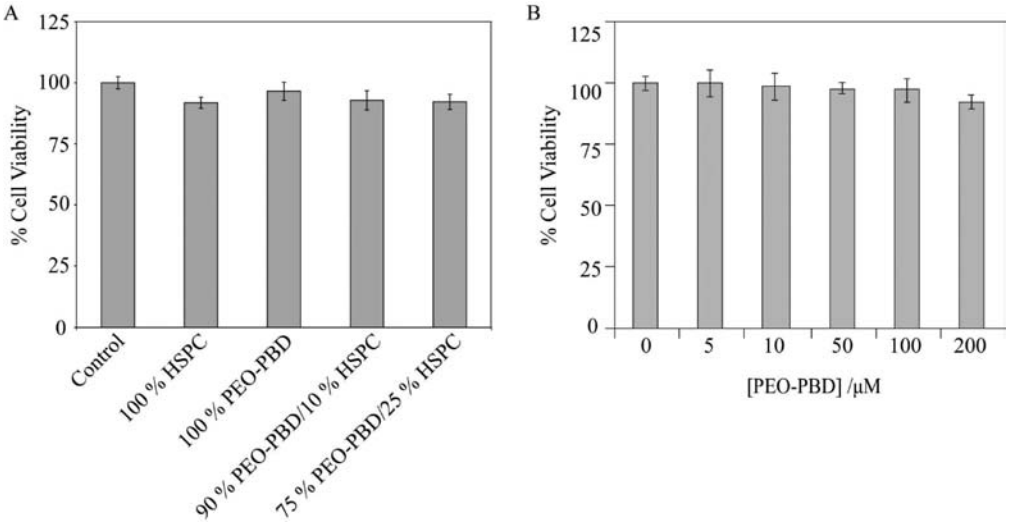

Figure 6. (A) Cell viability of NIH 3T3 cells incubated with nanovesicles with different lipid/polymer compositions. (B) Cell viability of NIH 3T3 cells incubated with 75% PEO-PBD/25%HSPC nanovesicles at different polymer concentrations. Viability was measured and normalized to cells grown in the absence of any particles based on an MTT assay.

Near-infrared (NIR) HER2-targeted nanovesicles were injected retro-orbitally (100 μM PEO-PBD in 0.2 mL PBS). Postcontrast images were collected 24 h postinjection. Fluorescent images were acquired using a Pearl NIR imaging system. Region of interest (ROI) analysis was performed using Pearl imaging software. Mean fluorescence of the tumor was measured after background subtraction.

Instrumentation. Dynamic light scattering (DLS) measurements were performed on a Zetasizer Nano from Malvern Instruments. The scattering angle was held constant at 90 °F. Fluorescence spectra measurements were acquired on a SPEX FluoroMax-3 spectrofluorometer (Horiba Jobin Yvon).

RESULTS AND DISCUSSION

Evidence of Forming Polymer−lipid Blends in Giant Vesicles. PEO-PBD are a class of synthetic amphiphilic diblock copolymers in which hydrophobic PBD is linked to hydrophilic PEG. When dispersed in aqueous medium, PEO-PBD with appropriate hydrophilic volume fractions can self-assemble to form polymeric vesicles.[11] As shown in Figure S1, the PEO-PBD selected for this study, PEO(600)-*b*-PBD(1200) (PEO-PBD), was capable of forming giant vesicles utilizing a classical swelling technique. Similarly, lipid−polymer hybrid nanovesicles could be formed from the aqueous coassembly of PEO-PBD and the phospholipid, hydrogenated soy phosphatidylcholine (HSPC). A schematic of a targeted lipid−polymer hybrid vesicle functionalized with either folic acid or HER2/neu-targeted affibodies as targeting ligands to confer specificity for cancer cells is shown in Figure 1. The ability to integrate phospholipids into the membrane of polymer-based vesicles was confirmed by preparing micrometer-sized lipid−polymer hybrid vesicles with a low molar percentage (0.5%) of fluorescent phospholipid 1,2-dioleoyl-*sn*-glycero-3-phosphoethanolamine-*N*-(lissamine rhodamine B sulfonyl) (Rhod-PE). As shown in Figure 2, incorporation of Rhod-PE into the vesicle membrane was evident at the resolution of the optical microscope, for vesicles doped with 0, 10, or 25 mol % HSPC. The phospholipid-based fluorescent probe within polymer−lipid hybrid giant vesicles did not exhibit any obvious amphiphile phase segregation on optically resolvable length scales. However, the possibility of forming nanoscale lipid domains below the length scale of optical resolution cannot be ruled out.[12,25,32]

Table 1. Vesicle Diameters and Number of Targeting Agents per Vesicle

vesicle composition	diameter (nm)	folate/ vesicle	HER2/ vesicle
100 mol % PEO-PBD	105	310	24
90 mol %PEO-PBD/10 mol % HSPC	112	261	22
75 mol %PEO-PBD/25 mol % HSPC	117	193	21

Membrane Elasticity. To provide evidence that HSPC was successfully incorporated into the vesicle bilyaer, the elastic modulus (K_a) for three types of vesicles, 100 mol % PEO-PBD, 25 mol % HSPC/75 mol % PEO-PBD, and 100 mol % HSPC, were obtained via micropipet aspiration. The K_a is a common mechanical parameter of vesicle membranes that measures the in-plane mechanical elasticity of the membrane, and reflects the interfacial tension of the membrane interface.[11] Because the interfacial tension is a function of the chemical composition of the membrane, subtle changes in membrane lipid/polymer composition can be detected through changes in the membrane area elastic modulus.[33,34] As shown in Figure 3, polymersomes made from pure PEO-PBD were more elastic, as illustrated by their significantly lower elastic modulus (K_a = 72 dyn/cm) than pure HSPC liposomes (K_a = 206 dyn/cm). When PEO-PBD and HSPC were blended at a molar ratio 75:25, the resulting vesicles exhibited an intermediate elastic modulus (K_a = 112 dyn/cm) between the K_a values of the pure lipid and pure polymer vesicles. This intermediate elastic modulus provides further support that the vesicles were indeed a blend of the polymer and lipid.

Surface Chemistry of Hybrid Polymer−Lipid Vesicles. To provide evidence that the outer surface of pure polymer and polymer−lipid hybrid nanovesicles (10% and 25% HSPC) could be modified with various functional molecules, a small percentage

of amine-terminated phospholipid, DSPE-PEG2K-NH_2, was first doped into membrane during fabrication. The surface amines were then labeled with the amine reactive dye ATTO740 (ATTO740-NHS ester) and visualized by fluorescence microscopy. Figure 4 shows the fluorescence images obtained for giant vesicles prepared from 100 mol % PEO-PBD, 10 mol % HSPC/90 mol % PEO-PBD, and 25 mol % HSPC/75 mol % PEO-PBD after conjugation of ATTO740. In all cases, conjugation of the ATTO740 into the vesicles membrane was evident. To ensure that the ATTO dye was specifically bound to the vesicle surface, the nanovesicles were also prepared in the absence of DSPE-PEG2K- NH_2, and then incubated with ATTO740-NHS ester. In contrast to the aminated nanovesicles, these control vesicles did not exhibit a fluorescent signal, suggesting that the bound ATTO dyes were conjugated through a surface chemical reaction and not from nonspecific absorption. This result indicates that biologically active molecules could be conjugated through the reactive groups on the hybrid polymer–lipid vesicle surface.

Nanometer-Sized Vesicles Using Polymer–Lipid Blends. Following the formation of micrometer-sized vesicles, the vesicle size was reduced to the ~100-nm-size range by subjecting the sample to multiple freeze–thaw cycles and extrusion through a 100 nm polycarbonate filter. Dynamic light scattering (DLS) presented in Figure 5 revealed that hybrid vesicles with 10 and 25 mol % HSPC had mean diameters of 112 and 117 nm, respectively, while pure PEO-PBD vesicles had a mean diameter of 105 nm. To confirm that the lipid-to-polymer molar ratio was unaffected by the extrusion and purification process, the lipid content in samples containing nano- or giant hybrid vesicles was determined by measuring the phosphorus content. The polymer content was calculated by subtracting the measured lipid weight from the total dry weight of the sample (see Experimental Procedures section for details). These measurements indicated that HSPC was incorporated into the hybrid membrane at the predetermined molar ratios and that there was no significant loss of HSPC during processing. To evaluate the ability to store lipid–polymer hybrid nanovesicles, the hydrodynamic diameter of the vesicles was measured by DLS for 10 days following suspension in PBS buffer (0.1 mM phosphate, pH 7.4). It was found that vesicles prepared with 10 and 25 mol % HSPC did not exhibit any significant change in hydrodynamic diameter over this time frame.

Viability. Prior to evaluating hybrid nanovesicles for targeting living cells or tissues, their cytotoxicity was examined in a MTT cell proliferation assay (MTT = 3-(4,5-dimethylthiazol-2-yl)2,5-diphenyl-tetrazoilum bromide). Specifically, four different vesicle samples, 100% HSPC, 100% PEO-PBD, 90% PEO-PBD/10% HSPC, and 75% PEO-PBD/25% HSPC, were incubated with NIH 3T3 fibroblasts for 24 h. Each vesicle was tested in triplicate. Cell viabilities were normalized to a control cell sample that was not incubated with any vesicles. As shown in Figure 6A, none of the vesicle formulations had any significant effect on the proliferation of NIH 3T3 cells at a PEO-PBD concentration of 10 μM. The average cell viability of NIH 3T3 remained unaffected for PEO-PBD concentrations up to 100 μM for the 75% PEO-PBD/25% HSPC vesicles and only a very slight loss in viability (<8%) was observed at 200 μM PEO-PBD (Figure 6B).

Targeting Efficiency of Lipid–Polymer Hybrid Vesicles *in Vitro*. To demonstrate the feasibility of utilizing hybrid lipid–polymer vesicles to target tumor cells, we developed two different types of polymer–lipid vesicles, one targeting the folate receptor and one targeting the HER2/neu-receptor. In the first approach, the small molecule folic acid (folate) was used for tumor targeting since folate specifically binds to folate receptors, which

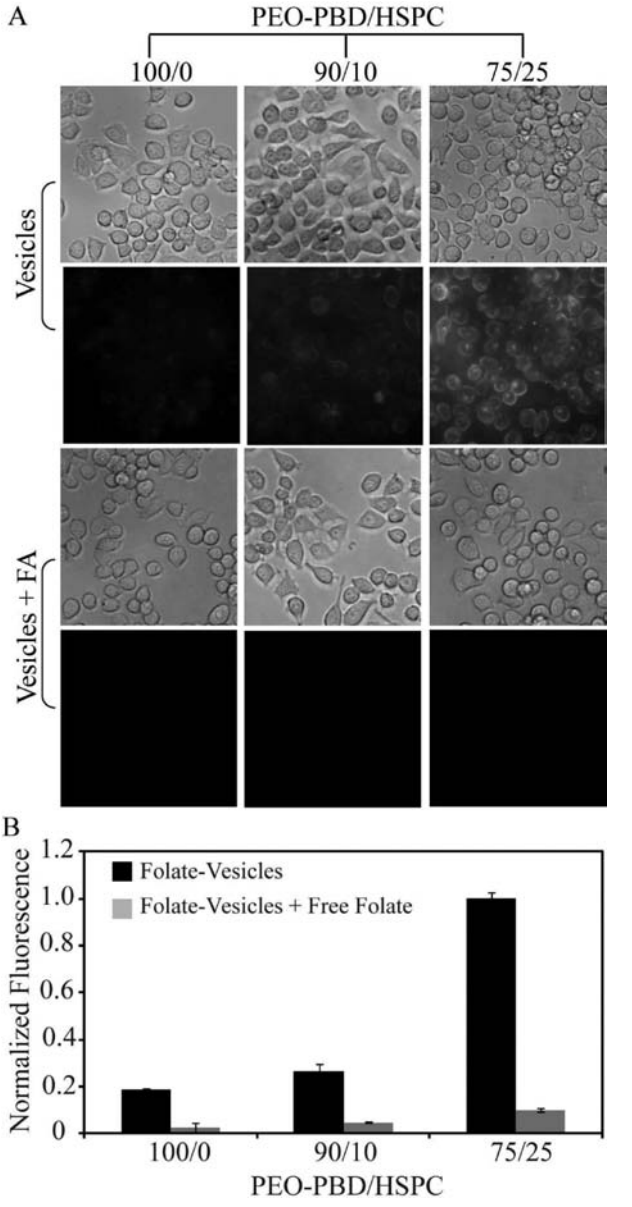

Figure 7. In cellulo analysis of folate receptor-targeted nanovesicles prepared with different lipid/polymer compositions. (A) Microscopy images of KB cells that have been incubated with various folate receptor-targeted vesicles prepared with PEO-PBD/HSPC at three different molar ratios. The top two rows show phase contrast and fluorescence images, respectively, collected in the absence of free folic acid in the media. The bottom two rows show images collected in the presence of 1 mM free folic acid in the media. All vesicles were incubated with KB cells for 2 h before images were acquired. Folate receptor targeting was achieved by doping the vesicles with low percentage of PEG2000-DSPE-Folic acid. All vesicles were also doped with a small amount of Rhod-PE. (B) Flow cytometric analysis of KB cells following incubation with folate receptor-targeted vesicles prepared with PEO-PBD/HSPC at three different molar ratios. Normalized mean fluorescent intensities are shown ± SD (n = 3). To confirm that cell binding was mediated through the folate receptor, competitive inhibition studies were performed by incubating KB cells with folate-targeted vesicles in the presence of excess free folic acid.

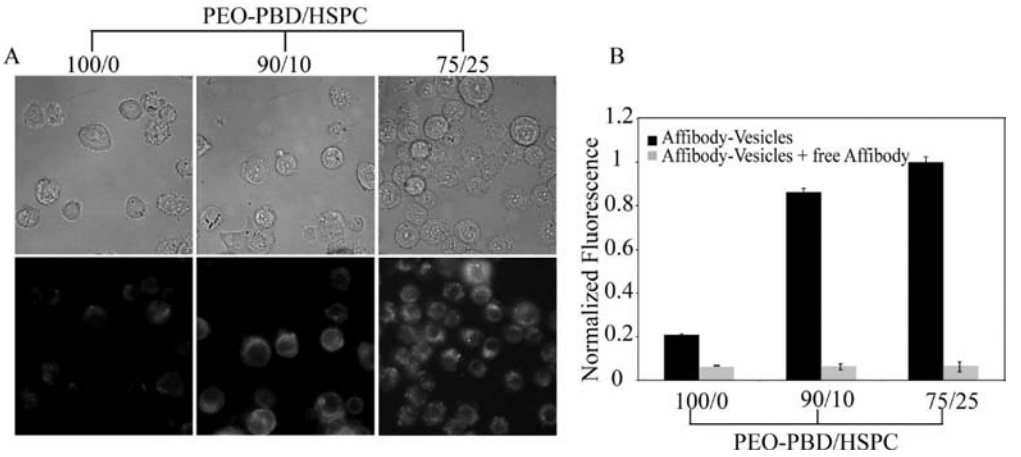

Figure 8. In cellulo analysis of Her2/neu receptor-targeted nanovesicles prepared with different lipid−polymer compositions. (A) Microscopy images of T6−17 cells that have been incubated with HER2/neu receptor-targeted vesicles prepared with PEO-PBD/HSPC at three different molar ratios. The top row shows phase contrast images, and the bottom row shows fluorescent images of the same cells. (B) Flow cytometric analysis of T6−17 cells following incubation with HER2/neu receptor-targeted vesicles prepared with PEO-PBD/HSPC at three different molar ratios. Normalized mean fluorescent intensities are shown ± SD (n = 3). To confirm that cell binding was mediated through the HER2/neu receptor, competitive inhibition studies were performed by incubating T6−17 cells with HER2/neu-targeted vesicles in the presence of excess free HER2/neu affibody.

are frequently overexpressed on tumor cancer cells. KB cells were used in this study as a model cell line to evaluate the targeting capabilities of folic acid-labeled nanovesicles since they are known to overexpress the folate receptor. Vesicles were prepared with 1,2-distearoyl-*sn*-glycero-3-phosphoethanolamine-*N*-[folate-(polyethylene glycol)-2000] (PEG2000-DSPE-Folate) and Rhod-PE at a fixed molar ratio of folic acid/Rhod per polymer. A summary of the number of targeting ligands on each vesicle is provided in Table 1. After a 2 h incubation with KB cells, fluorescent images were acquired. A bright fluorescent signal could be observed for KB cells incubated with polymer−lipid hybrid vesicles, especially PEO-PBD vesicles doped with 25% HSPC, as seen in Figure 7A. In contrast, very little fluorescence was observed from cells incubated with vesicles that did not contain HSPC. To verify that uptake of the vesicles was mediated through the folate receptor, competitive inhibition studies were performed by incubating the folate receptor-targeted vesicles with KB cells in the presence of excess free folic acid. Under these conditions, fluorescence was significantly reduced; confirming that cellular binding of the polymer−lipid hybrid vesicles was specifically mediated by the folate receptor. Analogous findings were also obtained via flow cytometry (Figure 7B). A clear shift in the mean cellular fluorescence was observed between cells incubated with folate-targeted lipid−polymer hybrid vesicles compared with cells incubated with folate-targeted vesicles that did not contain HSPC.

To confirm that the difference in targeting efficiency between pure polymer vesicles and lipid−polymer hybrid vesicles did not result from the differing number of targeting ligands on each vesicle, we further prepared 100 mol % PEO-PBD, 10 mol % HSPC/90 mol % PEO-PBD, and 25 mol % HSPC/75 mol % PEO-PBD vesicles with an equal number (n = 310) of folate ligands and fluorescent lipids on their surface. As can be seen in Supporting Information Figure S2, even at equal ligand densities, the lipid-doped nanovesicles exhibited a significantly higher degree of cell labeling than non-lipid-doped nanovesicles.

To evaluate whether polymer−lipid hybrid vesicles that had targeting agents conjugated to their outer surface also exhibited

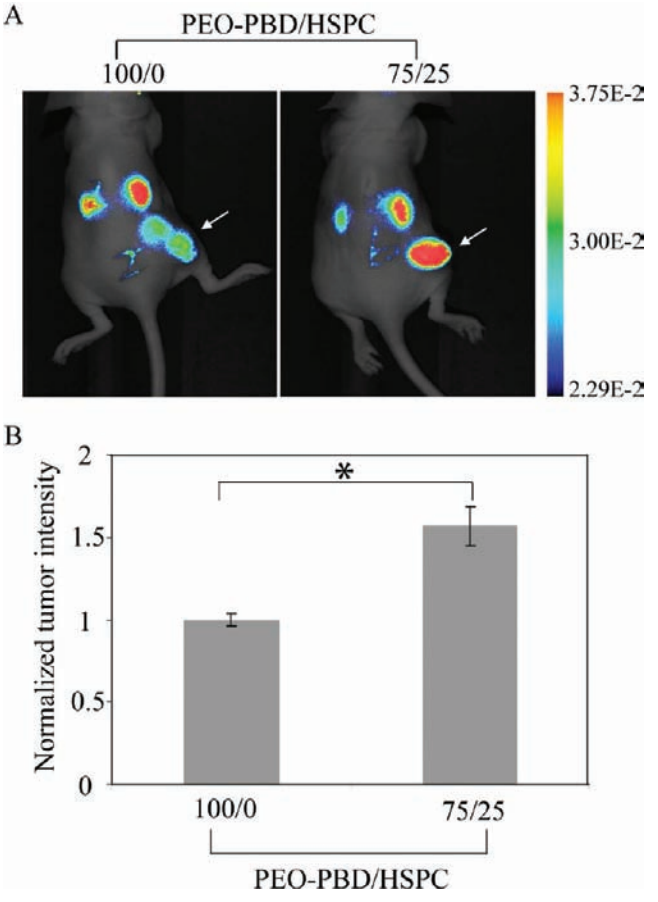

Figure 9. *In vivo* analysis of HER2/neu receptor-targeted nanovesicles prepared with different lipid/polymer compositions. (A) Fluorescence images of T6−17 tumor-bearing mice 24 h postinjection of NIR HER2/neu receptor-targeted vesicles prepared with PEO-PBD/HSPC at two different molar ratios. Tumors are indicated by white arrows. (B) Quantitative analysis of fluorescent images.

improved cellular binding, preformed vesicles were coupled to HER2/neu targeted affibodies via click conjugation.[35] After incubating the HER2-targeted nanovesicles with HER2/neu-positive T6−17 cells for 2 h, fluorescent images were acquired. As shown in Figure 8A, the HER2/neu-targeted nanovesicles composed of 25%HSPC/75%PEO-PBD exhibited a significantly higher degree of cell labeling than nanovesicles composed of 100%PEO-PBD. This was further supported by flow cytometric analysis (Figure 8B). Competitive inhibition studies using a molar excess of free HER2/neu affibody confirmed that the binding was specific for the HER2/neu receptor.

Targeting Efficiency of Lipid−Polymer Hybrid Vesicles *in Vivo*. To examine whether the incorporation of phospholipids into polymeric vessicles could be used to improve the targeting of HER2/neu-positive tumors in living subjects, near-infrared (NIR) fluorescent images of mice with T6−17 cell xenografts were acquired 24 h after retro-orbital injection of HER2-targeted lipid−polymer hybrid vesicles or HER2-targeted pure polymeric vesicles. As shown in Figure 9A, the HER2/neu-targeted nanovesicles composed of 25%HSPC/75%PEO-PBD exhibited a significantly higher signal in the tumor compared with nanovesicles composed of 100%PEO-PBD. Notably, some fluorescent signal was also observed in the kidney for both samples. Quantitative analysis of the NIR images revealed that HER2/neu-targeted nanovesicles composed of lipid−polymer blends exhibited more than a 1.5-fold improvement in tumor uptake compared with images from nanovesicles composed of 100% PEO-PBD (Figure 9B).

CONCLUSION

In summary, we have demonstrated that incorporation of HSPC into PEO-PBD-based nanovesicles can lead to a significant improvement in the efficiency of cell surface receptor targeting. It is hypothesized that incorporation of phospholipids into the vesicle bilayer diluted the density of the PEG-brush on the vesicle surface and as a result reduced the steric effect that PEG exerted on the targeting ligand. This is consistent with previous reports, which have also indicated that PEG-coatings can inhibit ligand-mediated targeting of the vesicle.[22,23] It is envisioned that the use of phospholipids can be extended to any polymer-based vesicles as a means to improve binding. Therefore, we believe that polymer−lipid hybrid vesicles constitute a promising nanoplatform for a broad variety of research areas, ranging from targeted drug delivery to molecular imaging.

ASSOCIATED CONTENT

Supporting Information. Synthesis of ADIBO-PEG$_4$-NHS Ester, Cloning and expression of HER2-Affibody, Expressed protein ligation, Copper free click conjugation, Image of giant vesicle prepared from 100% PEO-PBD (Figure S1), Flow cytometric analysis of KB cells following incubation with folate receptor-targeted vesicles with varying lipid-polymer ratios, but equal number of folate per vesicle (Figure S2). This material is available free of charge via the Internet at http://pubs.acs.org.

AUTHOR INFORMATION

Corresponding Author

*Phone: (215) 898-8167. Fax: (215) 573-2071. E-mail: atsourk@seas.upenn.edu.

ACKNOWLEDGMENT

This work was supported in part by the National Institute of Health (NCI) R21 CA125088 and (NIBIB) R21 EB013226, the American Cancer Society (RSG-07-005-01), the NSF (through a Graduate Research Fellowship to NK), and the DOD Breast Cancer Research Program of the Office of the Congressionally Directed Medical Research Programs (W81XWH-07-1-0457).

REFERENCES

(1) Alexis, F., Basto, P., Levy-Nissenbaum, E., Radovic-Moreno, A. F., Zhang, L., Pridgen, E., Wang, A. Z., Marein, S. L., Westerhof, K., Molnar, L. K., and Farokhzad, O. C. (2008) HER-2-targeted nanoparticle-affibody bioconjugates for cancer therapy. *ChemMedChem 3*, 1839–1843.

(2) Febvay, S., Marini, D. M., Belcher, A. M., and Clapham, D. E. (2010) Targeted cytosolic delivery of cell-impermeable compounds by nanoparticle-mediated, light-triggered endosome disruption. *Nano Lett. 10*, 2211–2219.

(3) Han, H. D., Mangala, L. S., Lee, J. W., Shahzad, M. M. K., Kim, H. S., Shen, D. Y., Nam, E. J., Mora, E. M., Stone, R. L., Lu, C. H., Lee, S. J., Roh, J. W., Nick, A. M., Lopez-Berestein, G., and Sood, A. K. (2010) Targeted gene silencing using RGD-labeled chitosan nanoparticles. *Clin. Cancer Res. 16*, 3910–3922.

(4) Liu, Y., Sun, J., Han, J. H., and He, Z. G. (2010) Long-circulating targeted nanoparticles for cancer therapy. *Curr. Nanosci. 6*, 347–354.

(5) Mei, H., Shi, W., Pang, Z. Q., Wang, H. F., Lu, W. Y., Jiang, X. G., Deng, J., Guo, T., and Hu, Y. (2010) EGFP-EGF1 protein-conjugated PEG-PLA nanoparticles for tissue factor targeted drug delivery. *Biomaterials 31*, 5619–5626.

(6) Murphy, E. A., Majeti, B. K., Barnes, L. A., Makale, M., Weis, S. M., Lutu-Fuga, K., Wrasidlo, W., and Cheresh, D. A. (2008) Nanoparticle-mediated drug delivery to tumor vasculature suppresses metastasis. *Proc. Natl. Acad. Sci. U. S. A. 105*, 9343–9348.

(7) Patil, Y., Sadhukha, T., Ma, L. N., and Panyam, J. (2009) Nanoparticle-mediated simultaneous and targeted delivery of paclitaxel and tariquidar overcomes tumor drug resistance. *J. Controlled Release 136*, 21–29.

(8) Petros, R. A., and DeSimone, J. M. (2010) Strategies in the design of nanoparticles for therapeutic applications. *Nat. Rev. Drug Discovery 9*, 615–627.

(9) Rivkin, I., Cohen, K., Koffler, J., Melikhov, D., Peer, D., and Margalit, R. (2010) Paclitaxel-clusters coated with hyaluronan as selective tumor-targeted nanovectors. *Biomaterials 31*, 7106–7114.

(10) Veiseh, O., Gunn, J. W., and Zhang, M. Q. (2010) Design and fabrication of magnetic nanoparticles for targeted drug delivery and imaging. *Adv. Drug Delivery Rev. 62*, 284–304.

(11) Discher, B. M., Won, Y. Y., Ege, D. S., Lee, J. C. M., Bates, F. S., Discher, D. E., and Hammer, D. A. (1999) Polymersomes: Tough vesicles made from diblock copolymers. *Science 284*, 1143–1146.

(12) Photos, P. J., Bacakova, L., Discher, B., Bates, F. S., and Discher, D. E. (2003) Polymer vesicles in vivo: correlations with PEG molecular weight. *J. Controlled Release 90*, 323–334.

(13) Ahmed, F., Pakunlu, R. I., Brannan, A., Bates, F., Minko, T., and Discher, D. E. (2006) Biodegradable polymersomes loaded with both paclitaxel and doxorubicin permeate and shrink tumors, inducing apoptosis in proportion to accumulated drug. *J. Controlled Release 116*, 150–158.

(14) Discher, B. M., Bermudez, H., Hammer, D. A., Discher, D. E., Won, Y. Y., and Bates, F. S. (2002) Cross-linked polymersome membranes: Vesicles with broadly adjustable properties. *J. Phys. Chem. B 106*, 2848–2854.

(15) Ghoroghchian, P. P., Frail, P. R., Susumu, K., Park, T. H., Wu, S. P., Uyeda, H. T., Hammer, D. A., and Therien, M. J. (2005) Broad spectral domain fluorescence wavelength modulation of visible and near-infrared emissive polymersomes. *J. Am. Chem. Soc. 127*, 15388–15390.

(16) Cheng, Z. L., Thorek, D. L. J., and Tsourkas, A. (2009) Porous polymersomes with encapsulated Gd-labeled dendrimers as highly efficient MRI contrast agents. *Adv. Funct. Mater. 19*, 3753–3759.

(17) Cheng, Z. L., and Tsourkas, A. (2008) Paramagnetic porous polymersomes. *Langmuir 24*, 8169–8173.
(18) Ghoroghchian, P. P., Frail, P. R., Susumu, K., Blessington, D., Brannan, A. K., Bates, F. S., Chance, B., Hammer, D. A., and Therien, M. J. (2005) Near-infrared-emissive polymersomes: Self-assembled soft matter for in vivo optical imaging. *Proc. Natl. Acad. Sci. U. S. A. 102*, 2922–2927.
(19) Christian, N. A., Milone, M. C., Ranka, S. S., Li, G. Z., Frail, P. R., Davis, K. P., Bates, F. S., Therien, M. J., Ghoroghchian, P. P., June, C. H., and Hammer, D. A. (2007) Tat-functionalized near-infrared emissive polymersomes for dendritic cell labeling. *Bioconjugate Chem. 18*, 31–40.
(20) Robbins, G. P., Jimbo, M., Swift, J., Therien, M. J., Hammer, D. A., and Dmochowski, I. J. (2009) Photoinitiated destruction of composite porphyrin-protein polymersomes. *J. Am. Chem. Soc. 131*, 3872–3873.
(21) Discher, D. E., and Ahmed, F. (2006) Polymersomes. *Annu. Rev. Biomed. Eng. 8*, 323–341.
(22) Gabizon, A., Horowitz, A. T., Goren, D., Tzemach, D., Mandelbaum-Shavit, F., Qazen, M. M., and Zalipsky, S. (1999) Targeting folate receptor with folate linked to extremities of poly(ethylene glycol)-grafted liposomes: In vitro studies. *Bioconjugate Chem. 10*, 289–298.
(23) Yamada, A., Taniguchi, Y., Kawano, K., Honda, T., Hattori, Y., and Maitani, Y. (2008) Design of folate-linked liposomal doxorubicin to its antitumor effect in mice. *Clin. Cancer Res. 14*, 8161–8168.
(24) Nam, J., Beales, P. A., and Vanderlick, T. K. (2011) Giant phospholipid/block copolymer hybrid vesicles: mixing behavior and domain formation. *Langmuir 27*, 1–6.
(25) Ruysschaert, T., Sonnen, A. F. P., Haefele, T., Meier, W., Winterhaltert, M., and Fournier, D. (2005) Hybrid nanocapsules: Interactions of ABA block copolymers with liposomes. *J. Am. Chem. Soc. 127*, 6242–6247.
(26) Dudia, A., Kocer, A., Subramaniam, V., and Kanger, J. S. (2008) Biofunctionalized lipid-polymer hybrid nanocontainers with controlled permeability. *Nano Lett. 8*, 1105–1110.
(27) Nilsson, F. Y., and Tolmachev, V. (2007) Affibody (R) molecules: New protein domains for molecular imaging and targeted tumor therapy. *Curr. Opin. Drug Discovery Dev. 10*, 167–175.
(28) Pangu, G., Johnston, E., Petkov, J., Parry, N., Leach, M., and Hammer, D. A. (2007) Targeted particulate adhesion to cellulose surfaces mediated by bifunctional fusion proteins. *Langmuir 23*, 10682–10693.
(29) Evans, E. A., Waugh, R., and Melnik, L. (1976) Elastic area compressibility modulus of red-cell membrane. *Biophys. J. 16*, 585–595.
(30) Zhou, X., and Arthug, G. (1992) Improved procedures for the deterination of lipid phosphorus by malachite green. *J. Lipid Res. 33*, 1233–1236.
(31) Heerklotz, H., Binder, H., Lantzsch, G., and Klose, G. (1994) Membrane water partition of oligo(ethylene oxide) dodecyl ethers and its relevance for solubilization. *Biochim. Biophys. Acta 1196*, 114–122.
(32) Le Meins, J. F., Sandre, O., and Lecommandoux, S. (2011) Recent trends in the tuning of polymersomes' membrane properties. *Eur. Phys. J. E 34*, 1–17.
(33) Bermudez, H., Brannan, A. K., Hammer, D. A., Bates, F. S., and Discher, D. E. (2002) Molecular weight dependence of polymersome membrane structure, elasticity, and stability. *Macromolecules 35*, 8203–8208.
(34) Mabrouk, E., Cuvelier, D., Pontani, L. L., Xu, B., Levy, D., Keller, P., Brochard-Wyart, F., Nassoy, P., and Li, M. H. (2009) Formation and material properties of giant liquid crystal polymersomes. *Soft Matter 5*, 1870–1878.
(35) Elias, D. R., Cheng, Z. L., and Tsourkas, A. (2010) An intein-mediated site-specific click conjugation strategy for improved tumor targeting of nanoparticle systems. *Small 6*, 2460–2468.

SUPPORTING INFORMATION for

Improved Tumor Targeting of Polymer-based Nanovesicles using Polymer-Lipid Blends

*Zhiliang Cheng,[1] Drew R. Elias,[1] Neha P. Kamat,[1] Eric D. Johnston,[1] Andrei Poloukhtine,[2] Vladimir Popik,[2] Daniel A. Hammer,[1] and Andrew Tsourkas[1,]**

[1]Department of Bioengineering, University of Pennsylvania, Philadelphia, PA 19104;

[2]Department of Chemistry, University of Georgia, Athens, GA 30602

Supplementary Materials and Methods.

Synthesis.

Scheme S1.[a] Synthesis of ADIBO-C3-amine.

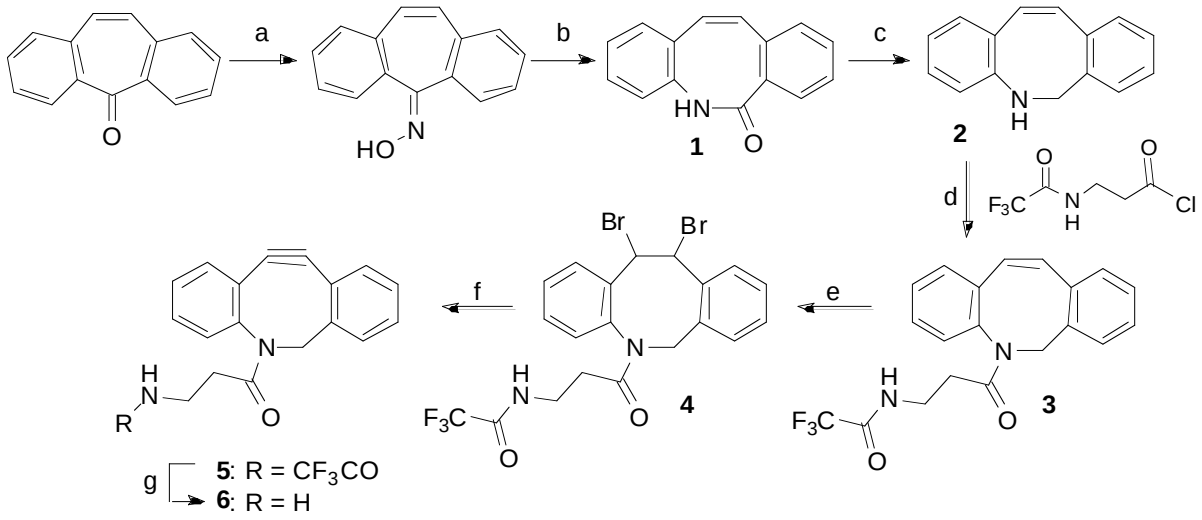

[a]*Reagents and conditions:* (a) $NH_2OH.HCl$, pyridine, 60%; (b) PPA, 125 °C, 73%; (c) $LiAlH_4$, ether, 58%; (d) pyridine, CH_2Cl_2, 71%; (e) pyridinium tribromide, 78%; (f) *t*-BuOK, THF, 88%; (g) K_2CO_3, aq MeOH, 58%.

5,6-Dihydrodibenzo[b,f]azocine (2). A solution of dibenzosuberenone (25 g, 121 mmol) and hydroxylamine hydrochloride (6.81 mL, 164 mmol) in pyridine (70 mL) was refluxed for 20 h. The reaction mixture was concentrated and poured into 5% aqueous hydrochloric acid (with crushed ice), stirred for 20 min, filtered, and dried in the air to provide 28.1 g of crude dibenzosuberenone oxime, as a white precipitate. Dibenzosuberenone oxime (16 g, 72.3 mmol) was added to 250 mL polyphosphoric acid at 125 °C, the reaction mixture was stirred for 60 min at this temperature, poured onto crushed ice (~700 mL), stirred for another 30 min, and filtered. The filter cake was washed with water, and dried under vacuum to provide crude dibenzo[*b,f*]azocin-6(5H)-one 1 (11.6 g, 52.4 mmol, 73%) as a grey powder.

A suspension of 1 (7.4 g, 33.4 mmol) and lithium aluminum hydride (2.494 ml, 66.9 mmol) in anhydrous ether (200 mL) was refluxed for 15 h. The reaction mixture was quenched by water, filtered, and the filter cake was washed with ether. The filter cake was dispersed in ether (100 mL), stirred for 10 min, and filtered. The combined organic layers were dried over $MgSO_4$, solvent was removed under vacuum, and the product purified by chromatography (hexanes:ethyl acetate 2:1) to provide 4.04 g (19.49 mmol, 58%) of 5,6-dihydrodibenzo[b,f]azocine (2). ^{1}H: 7.27-7.23 (m, 1 H), 7.2-7.1 (m, 3 H), 6.96-6.9 (m, 1 H), 6.9-6.8 (m, 1 H), 6.65-6.55 (m, 1 H), 6.54-6.48 (m, 1 H), 6.40 (d, *J* = 8 Hz, 1 H), 6.38-6.29 (m, 1 H), 4.51 (d, *J* = 6.8 Hz, 2 H), 4.2 (br s, 1 H); ^{13}C: 147.3, 139.3, 138.3, 134.9, 132.7, 130.3, 129.0, 128.1, 127.8, 127.6, 127.5, 121.8, 118.1, 117.9, 49.6. HRMS (ESI+) calcd for $C_{15}H_{14}N$ $[M+H]^+$ 208.1126, found 208.1120.

N-(6-(dibenzo[b,f]azocin-5(6H)-yl)-3-oxopropyl)trifluoroacetamide (3). 3-(trifluoroacetamido) propanoyl chloride (0.92 g, 4.52 mmol) was added to a solution of 2 (0.75 g, 3.62 mmol) and pyridine (0.859 g, 10.86 mmol) in CH_2Cl_2 (ca. 10 ml) at rt, and stirred for 30 min. The reaction mixture was diluted with CH_2Cl_2 (ca. 20 mL), washed with water (2x30 mL), dried over anhydrous $MgSO_4$ and the solvent was removed under reduced pressure. The residue was purified by chromatography (hexanes:ethyl acetate 2:3) to provide 958 mg (2.56 mmol, 71%) of 3 as yellowish oil.

N-(3-Trifluoroacetamidopropanoyl)-5,6-dihydro-11,12-didehydrodibenzo[b,f]azocine (5). Pyridine hydrobromide perbromide (0.948 g, 2.97 mmol) was added to a solution of 3 (958 mg, 2.56 mmol) in CH_2Cl_2 (4 ml) at rt, and the reaction mixture was stirred overnight. The reaction mixture was diluted with CH_2Cl_2 (20 mL), washed with 5% aqueous hydrochloric acid (20 mL), dried over $MgSO_4$, and solvent removed under vacuum. The residue was passed through a short pad of silica gel (CH_2Cl_2) to give 1.1 g of crude *N*-(3-trifluoroacetamidopropanoyl)-5,6,11,12-tetrahydro-11,12-dibromodibenzo[*b,f*]azocine (4) as an oil. Solution of crude 4 (1.1 g, 2.08

mmol) in THF (5 mL) was added to a solution of potassium t-butoxide (584 mg, 5.21 mmol) in THF (10 ml) at r.t., the reaction mixture was stirred for 1 h, diluted with ethyl acetate (20 mL), washed with 5% aqueous hydrochloric acid, brine, dried over $MgSO_4$, and the solvent was removed under reduced pressure. The crude product was purified by chromatography (hexanes:ethyl acetate, 2:1 to 1:1) to afford 685 mg (1.83 mmol, 88%) of 5 as brown oil.

N-(3-Aminopropionyl)-5,6-dihydro-11,12-didehydrodibenzo[b,f]azocine (ADIBO-C3-amine, 6). Solution of K_2CO_3 (2 g, 14.47 mmol) in 15 mL of water was added to a solution of N-(3-Trifluoroacetamidopropanoyl)-5,6-dihydro-11,12-didehydrodibenzo[b,f]azocine (5, 2.95 g, 7.12 mmol) in MeOH (30 mL) at rt and stirred overnight. Solvents were removed under reduced pressure, the residue was redissolved in CH_2Cl_2:ethyl acetate (1:4), washed with brine and water. The organic layer was dried over anhydrous Na_2SO_4, and concentrated in vacuum. The crude product was purified by chromatography (CH_2Cl_2:MeOH 10:1 to 10:4) to provide 1.14 g (4.11 mmol, 58%) of 6 as slightly yellow oil. ^{1}H NMR (500 MHz): 7.68 (d, *J* = 7.5 Hz, 1 H), 7.45-7.33 (m, 5 H), 7.29 (t, *J* = 7.5 Hz, 1 H), 7.25 (t, *J* = 7 Hz, 1 H), 5.15 (d, *J* = 14 Hz, 1 H), 3.16 (d, *J* = 14 Hz, 1 H), 2.82-2.67 (m, 2H), 2.45-2.35 (m, 1 H), 2.01-1.92 (m, 1 H), 1.6-1.4 (br s, 2 H); ^{13}C: 172.14, 151.48, 148.01, 132.12, 129.08, 128.29, 128.21, 127.99, 127.63, 127.01, 125.43, 122.85, 122.57, 114.97, 107.66, 55.25, 38.25, 38.15; HRMS (ESI+) calcd for $C_{18}H_{17}N_2O$ $[M+H]^+$ 277.1341, found 277.1339.

Scheme S2.[a] Synthesis of ADIBO-PEG_4-NHS Ester.

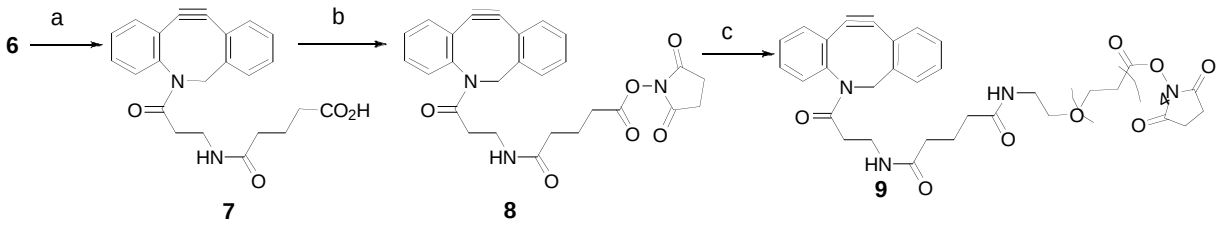

[a]*Reagents and conditions:* (a) Glutaric anhydride, $CHCl_3$, 59%; (b) *N*-hydroxysuccinamide, EDC, CH_2Cl_2; (c) 1) Amino-dPEG®4-acid, DIEA, CH_2Cl_2; 2) *N*-hydroxysuccinamide, EDC, CH_2Cl_2, 41%.

5-((3-(5,6-dihydro-11,12-didehydrodibenzo[b,f]azocin-5(6H)-yl)-3-oxopropyl)amino)-5-oxopentanoic acid (7). Glutaric anhydride (323 mg, 2.83 mmol) was added to solution of amine 6 (870 mg, 3.14 mmol) at r.t. in chloroform (20 ml) and the reaction mixture was stirred for 4 h at r.t. Solvent was removed in vacuum and the residue purified by chromatography (silica gel, CH_2Cl_2:MeOH 20:1) to provide carboxylic acid 7 (650 mg, 1.67 mmol, 59 %) as white waxy solid.

5-((3-(5,6-dihydro-11,12-didehydrodibenzo[b,f]azocin-5(6H)-yl)-3-oxopropyl)amino)-5-oxopentanoic acid N-hydroxysuccinamide ester (8). A solution of 7 (225 mg, 0.578 mmol), NHS (86 mg, 0.751 mmol), and EDC (150 mg, 0.780 mmol) in CH_2Cl_2 (ca. 2 mL) was stirred over overnight. The reaction mixture was diluted with CH_2Cl_2, washed with pH 6 buffer, dried over MgSO4 and concentrated. The residue was purified by chromatography on silica gel (CH_2Cl_2:MeOH 25:1) to provide 160 mg (0.32 mmol, 56 %) on NHS ester 8 as colorless oil.

ADIBO-PEG$_4$-NHS Ester (9). A solution of ADIBO-NHS ester (750 g, 1.538 mmol), amine-dPEG$_4$-acid (469 mg, 1.769 mmol), and DIEA (239 mg, 1.846 mmol) in CH_2Cl_2 (6 ml) was stirred for 1 h at r.t. EDC (442 mg, 2.308 mmol) was added to the reaction mixture followed by NHS (230 mg, 2 mmol). The reaction mixture was stirred for 3 h at r.t., diluted with CH_2Cl_2 (10 mL), washed with 5% aq. HCl, and dried over anhydrous $MgSO_4$. Solvent was removed in vacuum and the residue purified by chromatography (silica gel, CH_2Cl_2:iPrOH 20:1 to 10:1) to provide 460 g (0.626 mmol, 41 %) of ADIBO-PEG$_4$-NHS ester 9 as yellow-to-slightly orange oil. ^{1}H NMR (500 MHz): 7.67 (d, 1 H), 7.41-6.90 (m, 7H); 6.58 (br, NH), 5.18 (d, 1H), 3.76-3.41 (m,

21H), 2.84 (s, 4H), 2.68 (t, 2H), 2.45 (t, 2H), 2.31 (m, 4H), 2.08 (p, 2H); HRMS (ESI+) calcd for $C_{38}H_{47}N_4O_{11}$ $[M+H]^+$ 735.3241, found 735.3236.

Cloning and Expression of HER2-Affibody. The HER2-Affibody was cloned and expressed as previously reported.[1] Briefly, hybridized HER2-Affibody oligonucleotides were directly ligated with gel-purified *Nde*I-*Xho*I double digested pTXB1 vector (New England Biolabs, Inc) via the CloneEZ kit (Genscript). The pTXB1-HER2-Affibody vector was transformed in Rosetta™ 2(DE3)pLysS Competent Cells (Novagen). Bacterial cultures were grown to $OD_{600\ nm}$ = 0.6, and IPTG was added at a final concentration of 0.5 mM to induce T7 RNA polymerase-based expression. The cultures were allowed to express for 2 hours at 37 °C and were then pelleted by centrifugation at 10,000x g. Bacterial cell pellets were lysed by pulse sonication and HER2-Affibody complexes were isolated by centrifugation at 15,000x g. HER2-Affibodies were purified via affinity purification with a chitin bead column. HER2-Affibodies were eluted from the chitin bead column following an overnight incubation in 50 mM MESNA. Elutions were concentrated using an Ultracell 3,000 (Millipore, Billerica, MA) and then used for expressed protein ligation.

Expressed Protein Ligation. Expressed protein ligation was carried about between the thioester containing HER2-Affibody and an azido-fluorescent peptide (AzFP) with an N-terminal cysteine. The sequence of the AzFP was NH_2-CDPEK(5-FAM)DSG-D(Azi)-$CONH_2$. The K(5-FAM) represents a lysine with a fluorescein covalently attached to its ε-amino group and the D(Azi) represents a glycine with a azido group attached to its side-arm. The AzFP (0.1 mM) was incubated with approximately 0.01 mM HER2-Affibody. The EPL reaction was mixed overnight at room temperature. The EPL product and excess AzFPs were separated on a Superdex 30 chromatography column. A detailed experimental has been reported previously.[1]

Aza-Dibenzocyclooctene (ADIBO) Modification of Nanovesicles. Surface amines on nanovesicles were reacted with the amine-reactive ADIBO-dPEG$_4$-NHS, diluted 10 times from stock in dimethyl sulfoxide (DMSO), in 0.1 M sodium phosphate buffer, pH 9. The linker was added at 100 times molar excess to the nanovesicles. All nanovesicle solutions were mixed for overnight at room temperature. Nanovesicles were purified via superdex 200 chromatography columns (GE Healthcare, Piscataway, NJ).

Copper free click conjugation. Surface amines on nanovesicles were reacted with the amine-reactive ADIBO-dPEG4-NHS, diluted 10 times from stock in dimethyl sulfoxide (DMSO), in 0.1 M sodium phosphate buffer, pH 9. The linker was added at 100 times molar excess to the nanovesicles. All nanovesicle solutions were mixed for overnight at room temperature. Nanovesicles were purified via superdex 200 chromatography columns (GE Healthcare, Piscataway, NJ). ADIBO-modified nanovesicles were mixed with 30 μM of HER2-AzFP ligand in a pH neutral buffer. Reactions were mixed overnight at room temperature and then purified on Superdex 200 columns equilibrated with PBS.

HER2/neu-targeted near infrared (NIR) nanovesicles. To prepare HER2/neu-targeted nanovesicles for in vivo tumor imaging, expressed protein ligation was carried out between the thioester containing HER2-Affibody and an azido-NIR peptide (AzNIRP) with an N-terminal cysteine. Here, HiLyte Fluor™ 750 was used as NIR dye. HER2-AzNIRP was conjugated onto the surface of nanovesicles using similar procedures as those for the HER2-AzFP conjugation, as described above.

Supplementary Figures.

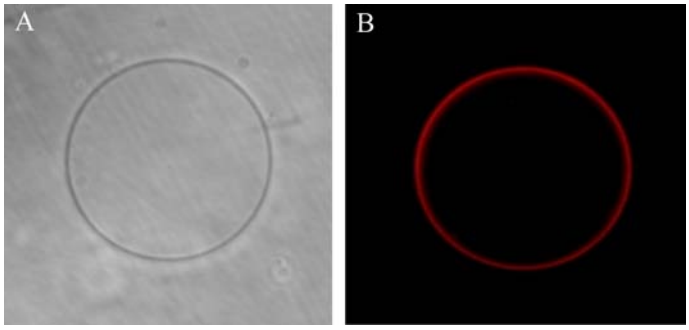

Figure S1. Microscopy images of giant vesicles composed of pure diblock copolymer PEO-PBD. The vesicles were fluorescently labeled by incorporating the phospholipid Rhod-PE into the membrane bilayer: (A) phase contrast image and (b) fluorescence image. Fluorescence is seen in an individual giant vesicle. The diameter of the vesicle is approximately 50 μm.

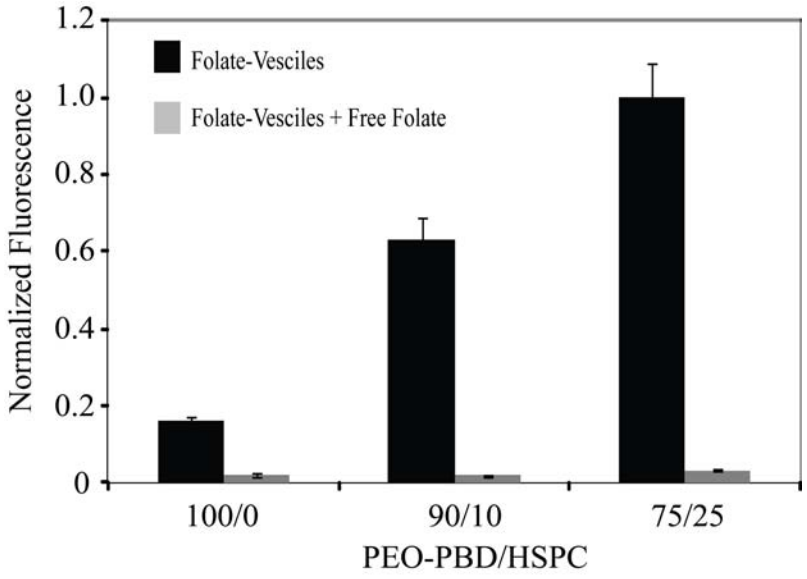

Figure S2. Flow cytometric analysis of KB cells following incubation with folate receptor-targeted vesicles prepared with PEO-PBD/HSPC at three different molar ratios. Normalized mean fluorescent intensities are shown ± S.D (n=3). Vesicles prepared with PEO-PBD/HSPC at

three different molar ratios have same number of folate ligands and fluorescent lipids (n=310) on their surface.

REFERENCE

1 Elias, D. R.; Cheng, Z. L.; Tsourkas, A. *Small* **2010,** 6, (21), 2460-2468.

Bioconjugate Chemistry

ARTICLE

pubs.acs.org/bc

Direct DNA Conjugation to Star Polymers for Controlled Reversible Assemblies

Saadyah Averick,[#] Eduardo Paredes,[#] Wenwen Li, Krzysztof Matyjaszewski,* and Subha R. Das*

Department of Chemistry and Center for Nucleic Acids Science and Technology, Carnegie Mellon University, 4400 Fifth Avenue, Pittsburgh, Pennsylvania 15213, United States

Supporting Information

ABSTRACT: Polymer biomolecule hybrids represent a powerful class of highly customizable nanomaterials. Here, we report star-polymer conjugates with DNA using a "ligandless" Cu(I) promoted azide−alkyne cycloaddition click reaction. The multivalency of the star-polymer architecture allows for the concomitant conjugation of other molecules along with the DNA, and the conjugation method provides control over the DNA orientation. The star-polymer DNA nanoparticles are shown to assemble into higher-order nanoassemblies through hybridization. Further, we show that the DNA strands can be utilized in controlled disassembly of the nanostructures.

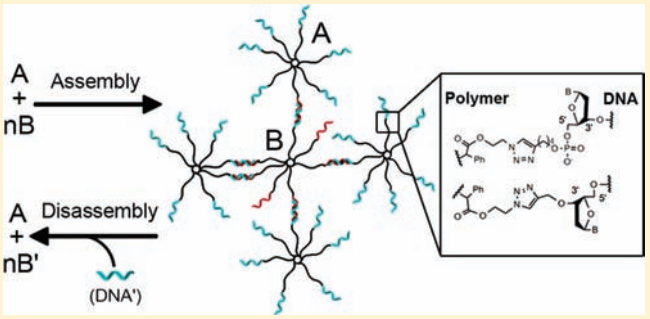

INTRODUCTION

The marriage of synthetic polymers with naturally occurring macromolecules has led to offspring that display complex biomacromolecular architectures thereby revolutionizing the field of bioconjugations.[1−6] Bioconjugates can be obtained from copolymers produced through atom transfer radical polymerization (ATRP), as well as other controlled radical polymerization (CRP) procedures, such as reversible addition−fragmentation chain transfer (RAFT) and nitroxide-mediated polymerization (NMP).[7−12] One of the key features of these CRP procedures is the ability to produce copolymers with well-defined polymer architectures, including linear, brush, and star-shaped molecules, with a high content of functional chain ends.[6,13−18] The polymer chain ends have recently been used in further conjugations to install biotin for avidin binding,[19−21] carbohydrate conjugates for lectin binding,[22,23] or direct protein−polymer hybrids.[4,24−36] A tetrafunctional RAFT initiator used in a "core-first" method of star synthesis yielded a tetrafunctional maleimide star polymer that was conjugated to lysozyme, generating a multiprotein star polymer hybrid. In another example, *tert*-butyl acrylate was polymerized from a tetra-functional ATRP initiator and its bromo-chain ends were substituted by reaction with sodium azide to produce azide-terminated star polymers that were conjugated to a peptide.[24] The ease of obtaining multivalent functional polymeric architectures by CRP techniques has enriched the field of bioconjugates and has the potential to lead to further novel materials.

Polymer−oligonucleotide hybrids, a relatively new class of biomacromolecules, are bioconjugates of significant promise. Maynard et al.[37] conjugated siRNA to a thiolated chain of a poly(oligo(ethylene oxide)methacrylate) prepared using RAFT. The disulfide linkage formed in this conjugate was labile under reducing conditions. A more robustly linked polymer−DNA hybrid was prepared from polymers synthesized using ATRP.[38] DNA synthesized on beads was directly coupled to a phosphoramidite-terminated polystyrene that has, in previous research, been used as an amphiphilic DNA block copolymer to encapsulate nanoparticles.[39] Reaction of maleimide chain ends yielded thioester-conjugated DNA aptamers. The aptamers, or single-stranded DNA sequences that bind small-molecules, retained *in vitro* functionality in binding to their target peptide. Proposed applications for these polymer−oligonucleotide (DNA or RNA) hybrids have mainly been therapeutic stabilization and delivery of detection agents. However, DNA can provide other functional and structural properties, *in vitro*, and *in vivo*,[40−42] that can be applied advantageously to polymer hybrids. Polymer−DNA conjugates would thus provide nanoscale macromolecules that could be controlled using sequence-specific hybridization and other functional properties of DNA that are highly tunable (Scheme 1).

DNA self-assembly and nanotechnology are well-developed fields and DNA can be used to create three-dimensional materials such as nanoscale objects,[43−45] macroscopic crystals,[46−48] and DNA-based gels.[49] DNA self-assemblies and origami[50] are now moving from static to dynamic systems.[51,52] However, although those designs are based solely or largely on DNA, ready access to large (nanoscale) three-dimensional objects and their manipulation, remains challenging. Large colloidal metal-based nanoparticles can be improved in their utility with a functional coating of DNA.[53−60] Although nanoparticle−DNA hybrids and nanoscale

Received: May 6, 2011
Revised: August 18, 2011
Published: August 26, 2011

ACS Publications © 2011 American Chemical Society

Scheme 1. Strategy for Star Polymer−DNA Hybrids by Direct Conjugation[a]

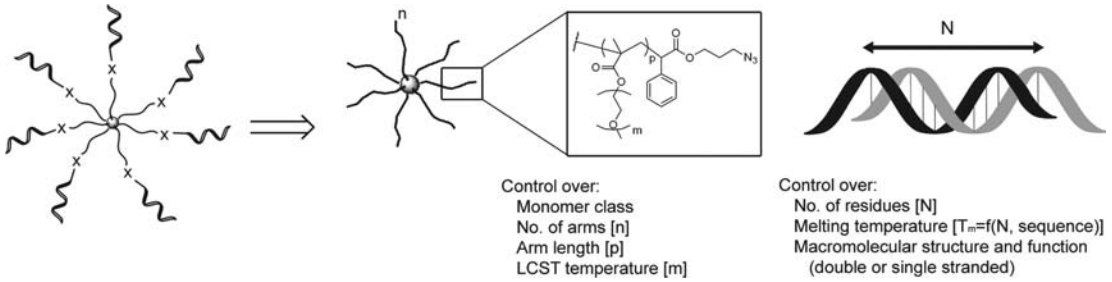

[a] These nanostructures would have high tunable control over design parameters. The star polymer−DNA conjugate would combine useful characteristics of each material into one molecule.

objects are both easily prepared and are useful, the DNA coating is nonspecific and the ability to custom tailor the coat and core is limited. A polymer nanoparticle would provide a highly customizable core material when used with DNA, including the possibility of concomitant molecules along with the DNA coat through the use of an appropriate conjugation methodology.

One of the most convenient conjugation strategies is the copper-catalyzed azide−alkyne cycloaddition (CuAAC) reaction.[61,62] This highly efficient reaction has risen to preeminence among the various "click" reactions[63] because the reacting azide and alkyne groups do not cross react with biologically abundant functional groups. The CuAAC reaction thus enables robust bio-orthogonal conjugations in aqueous media.[64,65] This click reaction has been extensively applied to the synthesis of polymers[66,67] and protein−polymer hybrids.[1,4,9,68] Besides the use with polymers and biomolecules, particularly proteins, click chemistry has been useful with synthetic and biochemically obtained DNA. DNA can be obtained with a high density of alkyne groups, and alkyne-modified DNA has been used with CuAAC for a wide variety of applications.[54,69−72] Although CuAAC has seen widespread use in both polymer chemistry and DNA supramolecular chemistry, the convergence of polymeric material and DNA through click conjugations is limited.[67,73−75]

We show that, by using CuAAC, ATRP based multivalent star polymers can be readily conjugated to functionalized DNA. Because click chemistry is used, simultaneous conjugation of these multivalent polymer cores with DNA, as well as other molecules, yields multicomponent-armed hybrids. We show that a polymer core armed with DNA provides a novel nanoscale material that can be designed quite simply, such that the DNA arms of the star can be used to engender function. While DNA can provide numerous useful functions, as a simple proof of principle for star-DNA hybrids, we demonstrate the use of hybridization properties of DNA to control the size of the star polymer nanoparticles. The self-assembly of star-DNA particles can be controlled and displacement with cDNA can reverse the assemblies. This preliminary study expands the scope of polymer−DNA hybrids by demonstrating how loading of DNA onto a multivalent architecture can provide control over self-assembly of polymer nanoparticles.

RESULTS AND DISCUSSION

Click Conjugations of DNA and Concomitant Molecules onto Star Polymers. Multiarm star polymers with peripheral functional azide-terminated arms were prepared by the macroinitiator "arm first" method. The macroinitiator was prepared using 3-azidopropyl 2-bromophenylacetate as an ATRP initiator for polymerization of $OEO_{300}MA$ (oligo(ethylene oxide) methacrylate with M_n = 300) targeting a degree of polymerization DP = 49. The macroinitiator was then copolymerized with ethylene glycol diacrylate (EGDA) under dilute conditions. The star polymers were analyzed using multiangle laser light scattering (MALLS) and determined to have M_n = 122 100, corresponding to average 7 arms per star. These star polymers with azide-terminated arms were conjugated with several different DNA strands that bore a reactive alkyne using click chemistry.

Table 1. DNA Sequences Used in This Study

		terminus	
name	sequence	5′-	3′-
DNA1	5′-cgc aag aag agc aaa cgc	Dy547	*O*-propargyl
DNA2	5′-gcg ttt gct ctt ctt gcg	Dy547	*O*-propargyl
DNA3	5′-ggc cga cgt gct tcg gct cgt	phosphohexynyl	OH
DNA4	5′-aat taa cga gcc gaa gca cgt	phosphohexynyl	OH
DNA5	5′-acg agc cga agc acg tcg gcc	OH	OH

Synthetic sequences of DNA with an alkyne, either at the 5′- or 3′-terminus, were obtained using commercially available reagents and protocols recommended by the manufacturer. For these studies, several DNA sequences were prepared with either a 5′-phosphohexynyl or 3′-*O*-propargyl group. In addition, some of the DNA strands included a terminal fluorescent dye that was incorporated during solid-phase synthesis using a commercially available phosphoramidite. A summary of the sequences used in this study is presented in Table 1.

Using recently optimized conditions to minimize DNA degradation and oxidation,[76] 3′-*O*-propargyl DNA strands (DNA1or DNA2) were initially clicked to the star polymer. Under these conditions, solutions of DNA and star-polymer in TRIS buffer (pH 7.5) with sodium ascorbate and acetonitrile (ACN) as a minor cosolvent (2%) were purged with argon gas, followed by addition of a $Cu_2SO_4 \cdot 5H_2O$ solution. The use of ACN helps stabilize Cu(I) and prevents DNA degradation due to oxidative damage under aqueous conditions, allowing successful conjugation of DNA (Scheme 2i). This "ligandless" method, using ACN, is in keeping with the philosophy of "click"-chemistry, which simplifies purification, as no additional triazole or other ligand molecules are used in the click conjugation. Following the click reaction, the

Scheme 2. Star Polymer Conjugation to DNA or DNA and Other Functional Molecules Using Click Chemistry[a]

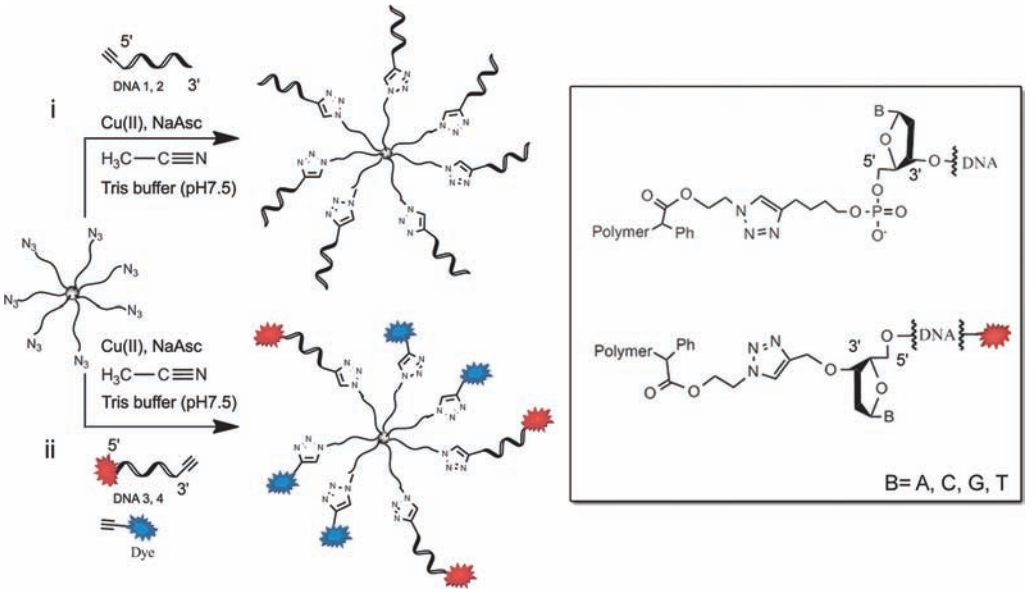

[a] The inset depicts the structure at the click linkages. The conjugations were performed using azide functionalized star polymers and 5′-alkyne (i) and 3′-alkyne [2] modifiers on the DNA, respectively. The 3′-alkyne modifiers allow for 5′-end modification of the DNA with useful probes.

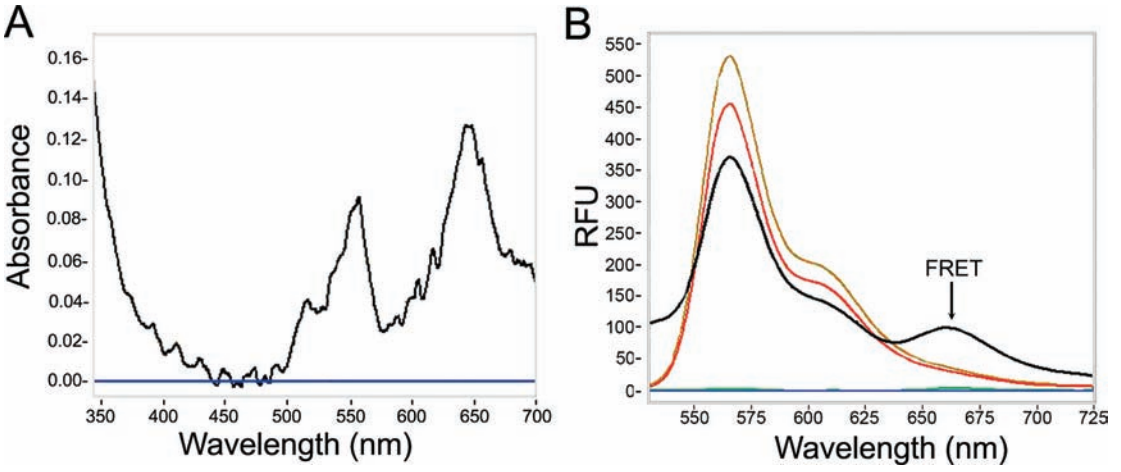

Figure 1. Click conjugation permits concomitant loading of molecules along with DNA onto a star polymer. (A) Absorption spectrum of Star/DNA1/Cy3 conjugate. (B) Fluorescence emission spectra showing FRET between fluorophores conjugated to the star polymer. All emission spectra were taken with an excitation wavelength at 470 nm. The emission spectra of Cy5 (green; on baseline), Cy3 (yellow), and a 1:1 Dy547:Cy5 solution (red) show no FRET between the fluorophores. Once DNA1 (carrying a Dy547 label) and Cy5 were conjugated to the star polymer, the emission spectrum of the conjugate (black) was a result of FRET in the fluorophore pair confirming that the two were attached to the same star polymer.

star−DNA conjugates were purified by filtration through a 10 kDa molecular mass cutoff nanosep filter that removes the solvent and ACN as well as unreacted DNA. The conjugation was verified using IR spectroscopy (Supporting Information Figure 1). Complete disappearance of the azide peak at 2200 cm^{-1} suggests that the star-polymers were essentially quantitatively conjugated to the DNA1 and DNA2.

Because star-polymers include multiple arms, we sought to demonstrate that click chemistry can be used to incorporate multiple groups onto these arms in a one-step process. Thus, DNA1, that included a 3′-*O*-propargyl group and 5′-flourescent dye, along with a second fluorescent dye bearing an alkyne were both used for the click reaction with the star polymer (Scheme 2ii). The two dyes—Dylight547 (Dy547; a Cyanine3(Cy3) equivalent) on the DNA and Cyanine5 (Cy5)—clicked on the star-polymer have known overlapping emission and absorbance regions, respectively, such that, when they are close enough, after excitation of the Dy547, the observed emission is from Cy5 due to Förster resonance energy transfer (FRET). Following the click reaction and purification of the stars to remove unreacted dyes and DNA, we could observe the absorbance peaks of both dyes (Figure 1A). As the Dy547 dye was at the 5′-terminus of the DNA and the click conjugation was at the 3′-terminus, the presence of the Dy547 absorbance peak indicated that the DNA strand remained intact. Furthermore, we were able to observe FRET emission of the multiconjugate star-DNA1-Cy5 (Figure 1B).

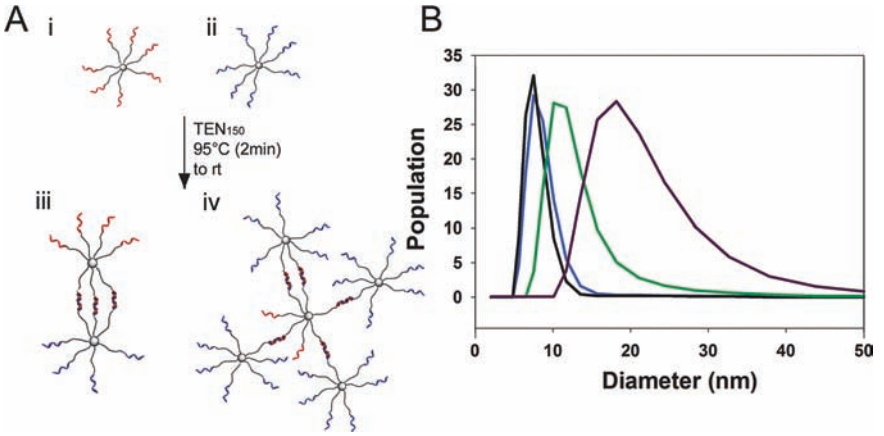

Figure 2. Controlled DNA self-assembly of star polymers. (A) Scheme for DNA directed self-assembly of star polymers. (B) DLS scans of star polymers click conjugated to DNA1 (black-Ai) and DNA 2 (blue-Aii). DNA directed hybridization of these two stars yield larger assemblies shown in a 1:1 star−DNA1/star−DNA2 ratio (green-Aiii) and in a 1:10 star−DNA1/star−DNA2 ratio (purple-Aiv) at 1 nM concentrations.

At the sample dilutions at which the fluorescence was measured, even if the statistically highly improbable reaction outcome produced star-polymer conjugates wherein some stars were only DNA-conjugated while other stars were only dye-conjugated, such a solution would not FRET. Solutions with only one dye or even both dyes in solution together do not result in the FRET emission peak. Thus, the emission due to FRET in the click-conjugate star-polymer solution strongly indicates that both DNA (with dye) and the dye molecule were click-conjugated concomitantly onto the same stars. This shows the power of the click chemistry approach to conjugate DNA as well as other molecules directly onto star-polymers together, taking advantage of the multivalency that the arms provide.

DNA-Directed Assembly of Soft Nanoparticle Hybrids. The ability to conjugate DNA by click chemistry onto star-polymers is significant as the functional properties of DNA can be harnessed. While there is a vast array of function that can be derived from DNA, we sought to demonstrate this quite simply by using the hybridization properties of DNA. Using star−DNA conjugates, star−DNA1 and star−DNA2, that include cDNA sequences, we obtained supra-molecular star−DNA architectures. DNA directed assembly was accomplished by heating solutions of mixtures of the two star−DNA conjugates (at 1 nM) at 95 °C in aqueous buffered salt solution and cooling to room temperature to anneal the DNA strands (Figure 2). We then tested for controlled hybridization behavior by altering the ratios of the star−DNA conjugates. Hybridization assembly of the nanoparticles was studied by dynamic light scattering (DLS). As expected, a relationship was found between hybridization ratio and size of the final self-assembled supramolecular architecture. Both star−DNA1 and star−DNA2 averaged approximately 4 nm. The resulting size of the 1:1 star−DNA1/star−DNA2 hybrid, Figure 2Aiii, was found to be approximately 9 nm, while a particle size of approximately 20 nm (purple) was observed in the 1:10 star−DNA1/star−DNA hybrid, Figure 2Aiv, system. No residual free stars were observed in the DLS traces thereby demonstrating the fidelity of cDNA hybridization.

These results indicate that self-assembled nanoscale structures can be readily created by using simple cDNA strands conjugated onto star polymers. By simply controlling the ratios of the star−DNA hybrids, one can control the size of the resulting particles. Star polymers provide a powerful tool for obtaining these large assemblies due to the controlled multivalent architecture unavailable to linear DNA systems. Through controlled hybridization, these stars can be used as templates for the design of more advanced DNA architectures. Additionally, nanoparticles with DNA of other functions can be designed and obtained.

Reversible Self-Assembly of Soft Nanoparticles using DNA Strand Invasion. The ability to controllably assemble star−DNA conjugate particles can be expanded by gaining control over the reverse disassembly process. The ability to control DNA self-assembly using strand invasion techniques has enabled DNA computation.[77−80] In this scheme, if one of the hybridized strands in a duplex includes a small, single-stranded overhang or "toehold", the duplex can be invaded by a cDNA strand that includes the toehold region under ambient conditions. This is typically done in linear DNA systems, and we extended this technique to the star−DNA hybrids. DNA3 and DNA4, that include partially complementary regions, were conjugated to star polymers, respectively. Additionally, the use of the 5′-phosphohexynyl-terminated DNA, rather than the 3′-*O*-propargyl DNA, demonstrated how readily the orientation of the conjugated DNA strand can be selected, thereby increasing the informational content loading. These DNA strands were designed such that, upon hybridization assembly of the star-DNA hybrids, a short unhybridized "toehold" region would remain available for an invading strand. DNA5, which is fully complementary to DNA3, can bind to the star−DNA3 conjugate displacing star−DNA4, in effect, disassembling the particles. This invasion takes place at room temperature and thus allows for detection using DLS.

Star−DNA3 and Star−DNA4 were hybridized (10 nM) at a 1:1 ratio at 95 °C in aqueous buffer (Figure 3; black and red bars). The resulting complex had a mean diameter of 70 nm by DLS (Figure 3B; green bar). This assembly of hybridized star−DNA3 to star−DNA4 at 10 nM concentrations is large, likely due to the flexibility of the nonbinding region that allows for a larger number of star−DNA to bind to one another. In contrast, the star−DNA1/star−DNA2 complexes that were hybridized at 1 nM concentration and where the strands were completely complementary with no flexible single-stranded region after hybridization formed smaller assemblies.

To evaluate control over the assembly, single-stranded DNA5 was used to disassemble the supramolecular structure.

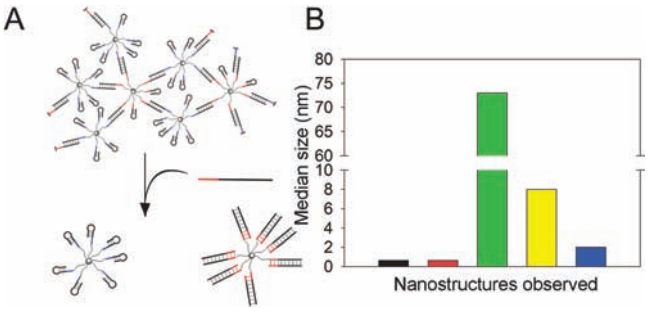

Figure 3. DNA controlled reversal of star polymer−DNA nanoassemblies. (A) Scheme for room-temperature disassembly of nanostructures using an invading DNA strand. (B) Mean area plots of DLS scans indicate a large nanoassembly (green bars) formed using a 1:1 ratio of smaller particles of star−DNA3 (black) and star−DNA4 (red) at 10 nM concentration can be subsequently gradually disassembled by an invading cDNA strand. The smaller assemblies, depicted in yellow and blue bars, are obtained at 1:100 star polymer/invading DNA and 1:300 star polymer/invading DNA ratios, respectively.

DNA5 was added in 100-fold excess over star−DNA3 to the star−DNA3/star−DNA4 hybrid complex to reduce the supramolecular assemblies from the 70 nm mean size to a hybrid of approximately 10 nm (yellow bar). The excess of invading DNA5 strand was to ensure adequate invasion of the crowded macromolecular complex at ambient temperature. When additional DNA5 was added, up to a 300-fold excess over star-DNA3 (1:300), the system reduced further in size to a mean of 2 nm (blue bar), close to that of the star−DNA complexes prior to assembly. Thus, the resulting particle corresponded to a totally disassembled star−DNA complex. The slightly larger mean size of the final complex can be attributed to the fact that this star−DNA complex is hybridized to DNA5. The phosphate backbone of the DNA caused the arms of the star to extend further due to charge repulsion, while in the parent nonhybridized stars, the single-stranded DNA collapsed into the star arms. Overall, these experiments demonstrate that assembled star−DNA hybrids can be selectively invaded. This can lead to star−DNA-based detection systems where not only the presence but also the concentration of an invading strand or other stimulus that DNA is sensitive to can be assayed.

CONCLUSIONS

This paper reports successful DNA−polymer conjugation to multifunctional star macromolecules using copper-catalyzed azide−alkyne cycloaddition. The application of click chemistry to the growing field of DNA−polymer hybrids represents a breakthrough because of the orthogonal control and high yields of this reaction. It is also useful because of ready availability of well-designed azide-terminated polymers, synthesized via CRP methodology.[81] DNA-based computing and self-assembly currently relies on either linear DNA with a toehold region[80,82] or hybrid macromolecules with an uncontrolled number of DNA arms formed by addition of DNA to nanoparticle templates.[83−85] This report demonstrates how DNA-based assembly, as well as polymeric systems, can be synergistically expanded in star polymer−DNA hybrids. We have developed a procedure that allows for preparation of star copolymers with a controllable number of azide-terminated arms per star. These peripheral functionalized stars can be clicked to alkyne DNA producing hybrids with a known number of DNA strands per star, as well as loading arms with DNA and other cargo simultaneously. The control over loading and size distribution is essential for the design and control over self-assembling nanoarchitectures.

EXPERIMENTAL SECTION

Star Polymer and DNA Synthesis. These were synthesized by standard methods. Details are included in Supporting Information.

Click Conjugation of 3′-*O*-Propargyl DNA and Cy5-Alkyne to Azide Star-Polymers. Stock solutions of $CuSO_4$, sodium ascorbate, and Tris-HCl (pH 7.5) buffer were degassed by bubbling argon through the solutions for 15 min prior to adding DNA. A reaction with 2 μM oligonucleotide in 500 mM Tris (pH = 7.5), 30 mg/mL of star polymer in THF (20 μL THF), 20 mM $CuSO_4$, and 40 mM sodium ascorbate in 3:1 water/ACN. The reaction was run for 2 h with shaking and purified with 10 K nanosep filter (Millipore). The reaction was confirmed by disappearance of the azide stretch at 2260 cm^{-1}on IR (Supporting Information Figure 1).

In the case of 3′-*O*-propargyl DNA-Dy547 and concomitant Cy5-alkyne conjugation to a single star polymer, 1.8 μM oligonucleotide and 0.2 μM Cy5-alkyne were introduced into the reaction mixture and the procedure as described above was followed. The resulting purified multivalent conjugate was analyzed using UV−vis spectroscopy (NanoDrop 1000) and emission spectroscopy (NanoDrop 3300). FRET controls were done using 100 nM Cy3 (Dy547 equivalent), 100 nM Cy5 solutions.

Hybridization Assembly of Star−DNA Conjugates. DNA-directed self-assembly of star polymers was achieved by heating solutions of 3 mg/mL (1 nM DNA) star−DNA polymer conjugates to 95 °C for 2 min in 100 mM Tris, 1 mM EDTA, and 150 mM NaCl (TEN_{150} buffer) and cooling to room temperature over 10 min. Following the hybridization cycles, star polymer assembly size was measured using dynamic light scattering (DLS) on a Zetasizer Nano spectrophotometer (Malvern Instruments Ltd.).

Controlled Disassembly of Star−DNA Nanoassemblies. Strand invasion studies were carried out at a concentration of 10 nM star−DNA. After star−DNA3 and star−DNA4 hybridization, DNA5 was added to a final concentration of 1 μM and 3 μM for a 100- and 300-fold excess over star−DNA3, respectively. Remeasurement of solutions following addition of the invading DNA5 strand was carried out after 30 s of incubation at room temperature.

ASSOCIATED CONTENT

Supporting Information. Information on chemicals, equipment (DLS, GPC, DNA synthesizer, UV−vis, fluorometer, and IR) and the synthesis of star polymers. This material is available free of charge via the Internet at http://pubs.acs.org.

AUTHOR INFORMATION

Corresponding Author

*K.M.: Fax (412) 268-6897; Tel (412) 268-3209; E-mail km3b@andrew.cmu.edu. S.R.D.: Fax (412) 268-1061; Tel (412) 268-6871; E-mail srdas@andrew.cmu.edu.

Author Contributions

#Authors contributed equally.

■ ACKNOWLEDGMENT

The authors of this paper would like to thank the CRP Consortium and NSF DMR09-69301 for funding. S.R.D. thanks the Department of Chemistry for startup funds.

■ REFERENCES

(1) Agut, W., Taton, D., and Lecommandoux, S. (2007) A versatile synthetic approach to polypeptide based rod-coil block copolymers by click chemistry. *Macromolecules 40*, 5653–5661.

(2) Liu, S., Maheshwari, R., and Kiick, K. L. (2009) Polymer-based therapeutics. *Macromolecules 42*, 3–13.

(3) Mei, Y., Beers, K. L., Byrd, H. C. M., Vanderhart, D. L., and Washburn, N. R. (2004) Solid-phase ATRP synthesis of peptide-polymer hybrids. *J. Am. Chem. Soc. 126*, 3472–3476.

(4) Reynhout, I. C., Cornelissen, J. J. L. M., and Nolte, R. J. M. (2009) Synthesis of polymer-biohybrids: from small to giant surfactants. *Acc. Chem. Res. 42*, 681–692.

(5) Borner, H. G. (2009) Strategies exploiting functions and self-assembly properties of bioconjugates for polymer and materials sciences. *Prog. Polym. Sci. 34*, 811–851.

(6) Shakya, A. K., Sami, H., Srivastava, A., and Kumar, A. (2010) Stability of responsive polymer-protein bioconjugates. *Prog. Polym. Sci. 35*, 459–486.

(7) Braunecker, W. A., and Matyjaszewski, K. (2007) Controlled/living radical polymerization: Features, developments, and perspectives. *Prog. Polym. Sci. 32*, 93–146.

(8) Klok, H. A. (2005) Biological-synthetic hybrid block copolymers: Combining the best from two worlds. *J. Polym. Sci., Polym. Chem. 43*, 1–17.

(9) Le Droumaguet, B., and Nicolas, J. (2010) Recent advances in the design of bioconjugates from controlled/living radical polymerization. *Polym. Chem. (U.K.) 1*, 563–598.

(10) Magnusson, J. P., Saeed, A. O., Fernandez-Trillo, F., and Alexander, C. (2011) Synthetic polymers for biopharmaceutical delivery. *Polym. Chem. (U.K.) 2*, 48–59.

(11) Matyjaszewski, K., and Xia, J. H. (2001) Atom transfer radical polymerization. *Chem. Rev. 101*, 2921–2990.

(12) Wang, J. S., and Matyjaszewski, K. (1995) Controlled living radical polymerization - atom-transfer radical polymerization in the presence of transition-metal complexes. *J. Am. Chem. Soc. 117*, 5614–5615.

(13) Barbey, R., Lavanant, L., Paripovic, D., Schuwer, N., Sugnaux, C., Tugulu, S., and Klok, H. A. (2009) Polymer brushes via surface-initiated controlled radical polymerization: synthesis, characterization, properties, and applications. *Chem. Rev. 109*, 5437–5527.

(14) Bunsow, J., Kelby, T. S., and Huck, W. T. S. (2010) Polymer Brushes: Routes toward Mechanosensitive Surfaces. *Acc. Chem. Res. 43*, 466–474.

(15) Lapienis, G. (2009) Star-shaped polymers having PEO arms. *Prog. Polym. Sci. 34*, 852–892.

(16) Sheiko, S. S., Sumerlin, B. S., and Matyjaszewski, K. (2008) Cylindrical molecular brushes: Synthesis, characterization, and properties. *Prog. Polym. Sci. 33*, 759–785.

(17) Lee, H. I., Pietrasik, J., Sheiko, S. S., and Matyjaszewski, K. (2010) Stimuli-responsive molecular brushes. *Prog. Polym. Sci. 35*, 24–44.

(18) Gao, H., and Matyjaszewski, K. (2009) Synthesis of functional polymers with controlled architecture by CRP of monomers in the presence of cross-linkers: From stars to gels. *Prog. Polym. Sci. 34*, 317–350.

(19) Liu, Y., Dong, Y., Jauw, J., Linman, M. J., and Cheng, Q. (2010) Highly sensitive detection of protein toxins by surface plasmon resonance with biotinylation-based inline atom transfer radical polymerization amplification. *Anal. Chem. 82*, 3679–3685.

(20) Siegwart, D. J., Oh, J. K., Gao, H. F., Bencherif, S. A., Perineau, F., Bohaty, A. K., Hollinger, J. O., and Matyjaszewski, K. (2008) Biotin-, pyrene-, and GRGDS-functionalized polymers and nanogels via ATRP and end group modification. *Macromol. Chem. Phys. 209*, 2180–2193.

(21) Vazquez-Dorbatt, V., and Maynard, H. D. (2006) Biotinylated glycopolymers synthesized by atom transfer radical polymerization. *Biomacromolecules 7*, 2297–2302.

(22) Chen, G. J., Tao, L., Mantovani, G., Geng, J., Nystrom, D., and Haddleton, D. M. (2007) A modular click approach to glycosylated polymeric beads: Design, synthesis and preliminary lectin, recognition studies. *Macromolecules 40*, 7513–7520.

(23) Vazquez-Dorbatt, V., Tolstyka, Z. P., Chang, C. W., and Maynard, H. D. (2009) Synthesis of a pyridyl disulfide end-functionalized glycopolymer for conjugation to biomolecules and patterning on gold surfaces. *Biomacromolecules 10*, 2207–2212.

(24) Skwarczynski, M., Zaman, M., Urbani, C. N., Lin, I. C., Jia, Z. F., Batzloff, M. R., Good, M. F., Monteiro, M. F., and Toth, I. (2010) Polyacrylate dendrimer nanoparticles: a self-adjuvanting vaccine delivery system. *Angew. Chem., Int. Ed. 49*, 5742–5745.

(25) Tao, L., Kaddis, C. S., Loo, R. R. O., Grover, G. N., Loo, J. A., and Maynard, H. D. (2009) Synthesis of maleimide-end-functionalized star polymers and multimeric protein-polymer conjugates. *Macromolecules 42*, 8028–8033.

(26) Bontempo, D., Heredia, K. L., Fish, B. A., and Maynard, H. D. (2004) Cysteine-reactive polymers synthesized by atom transfer radical polymerization for conjugation to proteins. *J. Am. Chem. Soc. 126*, 15372–15373.

(27) Heredia, K. L., Grover, G. N., Tao, L., and Maynard, H. D. (2009) Synthesis of heterotelechelic polymers for conjugation of two different proteins. *Macromolecules 42*, 2360–2367.

(28) Peeler, J. C., Woodman, B. F., Averick, S., Miyake-Stoner, S. J., Stokes, A. L., Hess, K. R., Matyjaszewski, K., and Mehl, R. A. (2010) Genetically encoded initiator for polymer growth from proteins. *J. Am. Chem. Soc. 132*, 13575–13577.

(29) Shi, W., Dolai, S., Averick, S., Fernando, S. S., Saltos, J. A., L'Amoreaux, W., Banerjee, P., and Raja, K. (2009) A general methodology toward drug/dye incorporated living copolymer-protein hybrids: (NIRF dye-glucose) copolymer-avidin/BSA conjugates as prototypes. *Bioconjugate Chem 20*, 1595–1601.

(30) Li, H. M., Bapat, A. P., Li, M., and Sumerlin, B. S. (2011) Protein conjugation of thermoresponsive amine-reactive polymers prepared by RAFT. *Polym. Chem. (U.K.) 2*, 323–327.

(31) Li, M., De, P., Li, H. M., and Sumerlin, B. S. (2010) Conjugation of RAFT-generated polymers to proteins by two consecutive thiol-ene reactions. *Polym. Chem.(U.K.) 1*, 854–859.

(32) Lowe, A. B. (2010) Thiol-ene "click" reactions and recent applications in polymer and materials synthesis. *Polym. Chem.(U.K.) 1*, 17–36.

(33) Matyjaszewski, K., Averick, S. E., Magenau, A. J. D., Simakova, A., Woodman, B. F., Seong, A., and Mehl, R. A. (2011) Covalently incorporated protein-nanogels using AGET ATRP in an inverse miniemulsion. *Polym. Chem.(U.K.) 2*, 1476–1478.

(34) Lele, B. S., Murata, H., Matyjaszewski, K., and Russell, A. J. (2005) Synthesis of uniform protein-polymer conjugates. *Biomacromolecules 6*, 3380–3387.

(35) Oh, J. K., Bencherif, S. A., and Matyjaszewski, K. (2009) Atom transfer radical polymerization in inverse miniemulsion: A versatile route toward preparation and functionalization of microgels/nanogels for targeted drug delivery applications. *Polymer 50*, 4407–4423.

(36) Oh, J. K., Drumright, R., Siegwart, D. J., and Matyjaszewski, K. (2008) The development of microgels/nanogels for drug delivery applications. *Prog. Polym. Sci. 33*, 448–477.

(37) Heredia, K. L., Nguyen, T. H., Chang, C. W., Bulmus, V., Davis, T. P., and Maynard, H. D. (2008) Reversible siRNA-polymer conjugates by RAFT polymerization. *Chem. Commun.* 3245–3247.

(38) Da Pieve, C., Williams, P., Haddleton, D. M., Palmer, R. M. J., and Missailidis, S. (2010) Modification of thiol functionalized aptamers by conjugation of synthetic polymers. *Bioconjugate Chem. 21*, 169–174.

(39) Chen, X. J., Sanchez-Gaytan, B. L., Hayik, S. E. N., Fryd, M., Wayland, B. B., and Park, S. J. (2010) Self-assembled hybrid structures of

DNA block-copolymers and nanoparticles with enhanced DNA binding properties. *Small 6*, 2256–2260.

(40) Liu, J. W., Cao, Z. H., and Lu, Y. (2009) Functional nucleic acid sensors. *Chem. Rev. 109*, 1948–1998.

(41) Modi, S., Swetha, M. G., Goswami, D., Gupta, G. D., Mayor, S., and Krishnan, Y. (2009) A DNA nanomachine that maps spatial and temporal pH changes inside living cells. *Nat. Nanotechnol. 4*, 325–330.

(42) Silverman, S. K. (2010) DNA as a versatile chemical component for catalysis, encoding, and stereocontrol. *Angew. Chem., Int. Ed. 49*, 7180–7201.

(43) Seeman, N. C. (2010) Nanomaterials based on DNA. *Annu. Rev. Biochem. 79*, 65–87.

(44) Lin, C., Liu, Y., and Yan, H. (2009) Designer DNA nanoarchitectures. *Biochemistry (U.S.) 48*, 1663–1674.

(45) He, Y., Ye, T., Su, M., Zhang, C., Ribbe, A. E., Jiang, W., and Mao, C. D. (2008) Hierarchical self-assembly of DNA into symmetric supramolecular polyhedra. *Nature 452*, 198–201.

(46) de Ilarduya, I. M., De Luchi, D., Subirana, J. A., Campos, J. L., and Uson, I. (2010) A geometric approach to the crystallographic solution of nonconventional DNA structures: helical superstructures of d(CGATAT). *Angew. Chem., Int. Ed. 49*, 7920–7922.

(47) Wang, T., Sha, R. J., Birktoft, J., Zheng, J. P., Mao, C. D., and Seeman, N. C. (2010) A DNA crystal designed to contain two molecules per asymmetric unit. *J. Am. Chem. Soc. 132*, 15471–15473.

(48) Winfree, E., Liu, F. R., Wenzler, L. A., and Seeman, N. C. (1998) Design and self-assembly of two-dimensional DNA crystals. *Nature 394*, 539–544.

(49) Xing, Y., Cheng, E., Yang, Y., Chen, P., Zhang, T., Sun, Y., Yang, Z., and Liu, D. (2011) Self-assembled DNA hydrogels with designable thermal and enzymatic responsiveness. *Adv. Mater. 23*, 1117–1121.

(50) Rothemund, P. W. K., Papadakis, N., and Winfree, E. (2004) Algorithmic self-assembly of DNA Sierpinski triangles. *PLOS Biol. 2*, 2041–2053.

(51) Gu, H. Z., Chao, J., Xiao, S. J., and Seeman, N. C. (2010) A proximity-based programmable DNA nanoscale assembly line. *Nature 465*, 202–208.

(52) Lund, K., Manzo, A. J., Dabby, N., Michelotti, N., Johnson-Buck, A., Nangreave, J., Taylor, S., Pei, R. J., Stojanovic, M. N., Walter, N. G., Winfree, E., and Yan, H. (2010) Molecular robots guided by prescriptive landscapes. *Nature 465*, 206–210.

(53) Cao, Y. W., Jin, R., and Mirkin, C. A. (2001) DNA-modified core-shell Ag/Au nanoparticles. *J. Am. Chem. Soc. 123*, 7961–7962.

(54) Cutler, J. I., Zheng, D., Xu, X. Y., Giljohann, D. A., and Mirkin, C. A. (2010) Polyvalent oligonucleotide iron oxide nanoparticle "click" conjugates. *Nano Lett. 10*, 1477–1480.

(55) Hurst, S. J., Hill, H. D., Macfarlane, R. J., Wu, J. S., Dravid, V. P., and Mirkin, C. A. (2009) Synthetically programmable DNA binding domains in aggregates of DNA-functionalized gold nanoparticles. *Small 5*, 2156–2161.

(56) Lee, J. S., Lytton-Jean, A. K. R., Hurst, S. J., and Mirkin, C. A. (2007) Silver nanoparticle-oligonucleotide conjugates based on DNA with triple cyclic disulfide moieties. *Nano Lett. 7*, 2112–2115.

(57) Li, Z., Zhang, Y., Fullhart, P., and Mirkin, C. A. (2004) Reversible and chemically programmable micelle assembly with DNA block-copolymer amphiphiles. *Nano Lett. 4*, 1055–1058.

(58) Seferos, D. S., Prigodich, A. E., Giljohann, D. A., Patel, P. C., and Mirkin, C. A. (2009) Polyvalent DNA nanoparticle conjugates stabilize nucleic acids. *Nano Lett. 9*, 308–311.

(59) Zheng, J. W., Constantinou, P. E., Micheel, C., Alivisatos, A. P., Kiehl, R. A., and Seeman, N. C. (2006) Two-dimensional nanoparticle arrays show the organizational power of robust DNA motifs. *Nano Lett. 6*, 1502–1504.

(60) Fischler, M., Sologubenko, A., Mayer, J., Clever, G., Burley, G., Gierlich, J., Carell, T., and Simon, U. (2008) Chain-like assembly of gold nanoparticles on artificial DNA templates via 'click chemistry'. *Chem. Commun.* 169–171.

(61) Tornoe, C. W., Christensen, C., and Meldal, M. (2002) Peptidotriazoles on solid phase: [1,2,3]-triazoles by regiospecific copper(I)-catalyzed 1,3-dipolar cycloadditions of terminal alkynes to azides. *J. Org. Chem. 67*, 3057–3064.

(62) Rostovtsev, V. V., Green, L. G., Fokin, V. V., and Sharpless, K. B. (2002) A stepwise Huisgen cycloaddition process: Copper(I)-catalyzed regioselective "ligation" of azides and terminal alkynes. *Angew. Chem., Int. Ed. 41*, 2596–2599.

(63) Kolb, H. C., Finn, M. G., and Sharpless, K. B. (2001) Click chemistry: Diverse chemical function from a few good reactions. *Angew. Chem., Int. Ed. 40*, 2004–2021.

(64) Sletten, E. M., and Bertozzi, C. R. (2009) Bioorthogonal Chemistry: fishing for selectivity in a sea of functionality. *Angew. Chem., Int. Ed. 48*, 6974–6998.

(65) Best, M. D. (2009) Click chemistry and bioorthogonal reactions: unprecedented selectivity in the labeling of biological molecules. *Biochemistry (U.S.) 48*, 6571–6584.

(66) Iha, R. K., Wooley, K. L., Nystrom, A. M., Burke, D. J., Kade, M. J., and Hawker, C. J. (2009) Applications of orthogonal "click" chemistries in the synthesis of functional soft materials. *Chem. Rev. 109*, 5620–5686.

(67) Golas, P. L., and Matyjaszewski, K. (2010) Marrying click chemistry with polymerization: expanding the scope of polymeric materials. *Chem. Soc. Rev. 39*, 1338–1354.

(68) van Dijk, M., Rijkers, D. T. S., Liskamp, R. M. J., van Nostrum, C. F., and Hennink, W. E. (2009) Synthesis and applications of biomedical and pharmaceutical polymers via click chemistry methodologies. *Bioconjugate Chem. 20*, 2001–2016.

(69) El-Sagheer, A. H., and Brown, T. (2010) Click chemistry with DNA. *Chem. Soc. Rev. 39*, 1388–1405.

(70) Seo, T. S., Li, Z. M., Ruparel, H., and Ju, J. Y. (2003) Click chemistry to construct fluorescent oligonucleotides for DNA sequencing. *J. Org. Chem. 68*, 609–612.

(71) Ustinov, A. V., Stepanova, I. A., Dubnyakova, V. V., Zatsepin, T. S., Nozhevnikova, E. V., and Korshun, V. A. (2010) Modification of nucleic acids using [3 + 2]-dipolar cycloaddition of azides and alkynes. *Russ. J. Bioorg. Chem. 36*, 401–445.

(72) Carell, T., Gierlich, J., Burley, G. A., Gramlich, P. M. E., and Hammond, D. M. (2006) Click chemistry as a reliable method for the high-density postsynthetic functionalization of alkyne-modified DNA. *Org. Lett. 8*, 3639–3642.

(73) Binder, W. H., and Sachsenhofer, R. (2009) *Click Chemistry on Supramolecular Materials*, John Wiley & Sons, Ltd.

(74) Gramlich, P. M. E., Warncke, S., Gierlich, J., and Carell, T. (2008) Click-click-click: Single to triple modification of DNA. *Angew. Chem., Int. Ed. 47*, 3442–3444.

(75) Pan, P., Fujita, M., Ooi, W.-Y., Sudesh, K., Takarada, T., Goto, A., and Maeda, M. (2011) DNA-functionalized thermoresponsive bioconjugates synthesized via ATRP and click chemistry. *Polymer 52*, 895–900.

(76) Paredes, E., and Das, S. R. (2011) Click chemistry for rapid labeling and ligation of RNA. *ChemBioChem 12*, 125–131.

(77) Chen, X., and Ellington, A. D. (2010) Shaping up nucleic acid computation. *Curr. Opin. Biotechnol. 21*, 392–400.

(78) Bi, S., Yan, Y. M., Hao, S. Y., and Zhang, S. S. (2010) Colorimetric logic gates based on supramolecular DNAzyme structures. *Angew. Chem., Int. Ed. 49*, 4438–4442.

(79) De Silva, A. P. (2005) Molecular computation - Molecular logic gets loaded. *Nat. Mater. 4*, 15–16.

(80) Frezza, B. M., Cockroft, S. L., and Ghadiri, M. R. (2007) Modular multi-level circuits from immobilized DNA-Based logic gates. *J. Am. Chem. Soc. 129*, 14875–14879.

(81) Sumerlin, B. S., and Vogt, A. P. (2010) Macromolecular engineering through click chemistry and other efficient transformations. *Macromolecules 43*, 1–13.

(82) Konry, T., and Walt, D. R. (2009) Intelligent medical diagnostics via molecular logic. *J. Am. Chem. Soc. 131*, 13232–13233.

(83) Sharma, J., Chhabra, R., Yan, H., and Liu, Y. (2007) pH-driven conformational switch of "i-motif" DNA for the reversible assembly of gold nanoparticles. *Chem. Commun.* 477–479.

(84) Katz, E., and Willner, I. (2004) Integrated nanoparticle-biomolecule hybrid systems: Synthesis, properties, and applications. *Angew. Chem., Int. Ed. 43*, 6042–6108.

(85) Ofir, Y., Samanta, B., and Rotello, V. M. (2008) Polymer and biopolymer mediated self-assembly of gold nanoparticles. *Chem. Soc. Rev. 37*, 1814–1823.

Supporting information for:

Direct DNA Conjugation of Star Polymers for Controlled Reversible Assemblies

Saadyah Averick, Eduardo Paredes, Wenwen Li, Krzysztof Matyjaszewski, and Subha Das

Chemicals and General Experimental

Commercially available compounds were used without further purification unless otherwise noted. $CuBr_2$ (98%), *N,N,N',N'',N''*-pentamethyldiethylenetriamine (PMDETA, 98%) were purchased from Aldrich. CuBr (98%, Acros) was purified by stirring in acetic acid, filtered, washed with 2-propanol and then dried under vacuum. Oligo(ethylene oxide) monomethyl ether methacrylate (average molecular weight ~300, OEOMA) and ethylene glycol diacrylate (EGDA, 90%) were purchased from Aldrich and purified by passing through a column filled with basic alumina to remove the inhibitor and/or antioxidant. Phosphoramidites with labile PAC protecting groups and appropriate reagents for solid phase synthesis of DNA were purchased from ChemGenes or Glen Research and the CPG columns for standard DNA synthesis were purchased from Biosearch. The 5'-phosphohexynyl modifier and Dylight 547 phosphoramidites were purchased from Glen Research. CPG columns for 3'-*O*-propargyl DNA were purchased from ChemGenes. Copper sulfate pentahydrate ($CuSO_4 \cdot 5H_2O$) was purchased from Sigma Aldrich. HPLC grade acetonitrile (ACN) was purchased from Fisher. Sodium ascorbate was purchased from Alfa Aesar. Other solvents and reagents not otherwise specified were purchased from Fisher.

Molecular weight and polydispersity were measured by GPC (Polymer Standards Services-PSS) columns (guard, 10^5, 10^3, and 10^2 Å), with THF eluent at 35 °C, flow rate 1.00 mL/min, and differential refractive index (RI) detector (Waters, 2410).

Toluene was used as the internal standard to correct for any fluctuation of the THF flow rate. The apparent molecular weights and polydispersity were determined with a calibration based on linear polystyrene standards using WinGPC 6.0 software from PSS. The detectors employed to measure the absolute molecular weights ($M_{w,MALLS}$) were a triple detector system containing RI detector (Wyatt Technology, Optilab REX), viscometer detector (Wyatt Technology, ViscoStar) and a multi-angle laser light scattering (MALLS) detector (Wyatt Technology, DAWN EOS) with the light wavelength at 690 nm. Absolute molecular weights were determined using ASTRA software from Wyatt Technology. DNAs were synthesized as described below. Infrared spectra (IR) were obtained on a JASCO FTIR 6300 instrument. UV-vis spectra were obtained on a NanoDrop 1000 spectrophotometer. Emission spectra were obtained on a NanoDrop 3300.

DNA synthesis

Solid phase oligonucleotide synthesis was performed on a MerMade 4 instrument (Bioautomation). Synthesis of the oligonucleotides was conducted on commercially available solid support columns and performed with standard commercially available phosphoramidites as directed by the manufacturer. Cleavage off the solid support and base deprotection of the oligonucleotides was performed by using ammonium hydroxide at 65°C for 2 h and standard protocols for PAC protected amidites as recommended by the manufacturer. Desalting and purification was conducted using a C18 columns (Waters) using protocols recommended by the manufacturer, with elution of the full length desired DNAs with ACN and water.

Star polymers synthesis and characterization

The azido group containing macroinitiator (N_3-POEOMA-Br MI) was obtained through ATRP of OEOMA from 3-azidopropyl 2-bromophenylacetate according to the procedure previously published[1] Number average molecular weight of linear N_3-POEOMA-Br MI M_n=14,700, average degree of polymerization, DP= 49.

The star polymer was prepared via arm-first method[2] The ratio of reagents $[N_3\text{-POEOMA-Br}]_0/[EGDA]_0/[CuBr]_0/[CuBr_2]_0/[PMDETA]_0$ was 1/10/0.9/0.1/1. A clean and dry Schlenk flask was charged with N_3-POEOMA-Br (0.31 g, 0.026 mmol initiating sites), EGDA (0.044 mL, 0.26 mmol), $CuBr_2$ (0.0006 g, 0.002 mmol), PMDETA (0.006 mL, 0.026 mmol) and 1.0 mL of DMF. The flask was degassed by five freeze-pump-thaw cycles, during the final cycle the flask was filled with nitrogen, and CuBr (3.6 mg, 0.025 mmol) was quickly added to the frozen mixture. The flask was sealed with a glass stopper and then evacuated and backfilled with nitrogen five times before it was immersed in an oil bath at 60 °C. Samples were withdrawn at timed intervals to measure polymer molecular weight by GPC. The reaction was stopped after 18 h via exposing the catalyst complex to air and dilution with THF. The solution was filtered through a column filled with neutral alumina to remove the copper complex, and then precipitated in diethyl ether to remove the unincorporated MIs. Apparent number average molecular weight of the purified star polymer is 43,000, and the absolute molecular weight of obtained star polymer determined by GPC MALLS is 122,100. The average arm number per star was calculated to be ~7, each arm has one azide group.

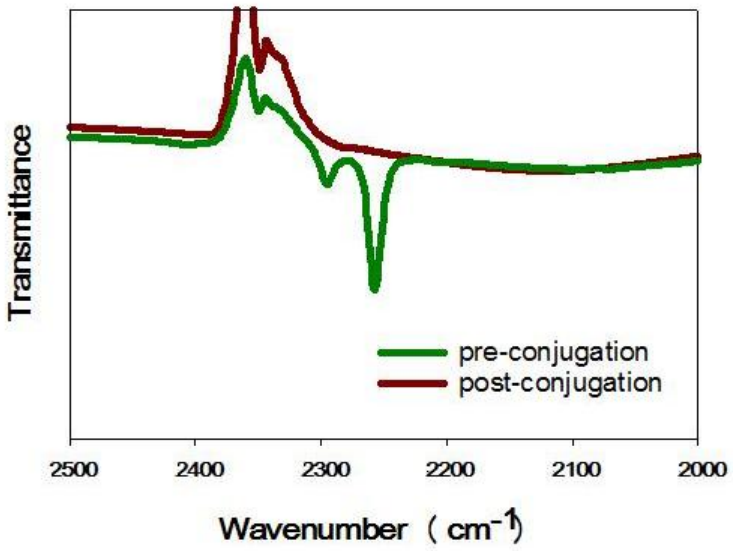

Supporting Figure 1. IR spectra of starpolymers before (green) and after (red) click reaction with alkyne DNA.

References:

1. Li, W.; Yoon, J. A.; Matyjaszewski, K., Dual-Reactive Surfactant Used for Synthesis of Functional Nanocapsules in Miniemulsion. *Journal of the American Chemical Society* **2010,** 132, (23), 7823-7825.

2. Gao, H.; Matyjaszewski, K., Arm-First Method As a Simple and General Method for Synthesis of Miktoarm Star Copolymers. *Journal of the American Chemical Society* **2007,** 129, (38), 11828-11834.

Bioconjugate Chemistry

ARTICLE

pubs.acs.org/bc

Construction of a bFGF-Tethered Extracellular Matrix Using a Coiled-Coil Helical Interaction

Eiry Kobatake,* Ryota Takahashi, and Masayasu Mie

Department of Biological Information, Graduate School of Bioscience and Biotechnology, Tokyo Institute of Technology B-28 4259, Nagatsuta, Midori-ku, Yokohama, 226-8501, Japan

Supporting Information

ABSTRACT: A novel method for construction of biomaterials for tissue engineering was developed. Noncovalent associations between extracellular matrix (ECM) and growth factors were achieved by engineering recombinant versions of both proteins that included helical peptides that could form a coiled-coil structure. The helix A peptide, which is capable of forming a coiled-coil helical structure, was fused with a matrix protein that contains a cell-adhesive RGD sequence. The helix B peptide, which is also capable of forming a coiled-coil helical structure, was fused with basic fibroblast growth factor (bFGF). Each protein retained its original activity of promoting cell adhesion and cell proliferation, respectively. These recombinant proteins associated noncovalently through coiled-coil helix formation between helix A and helix B. The resulting complex combined the functions of both proteins, and this method of joining proteins with different functionalities could be used to develop biomaterials for tissue engineering.

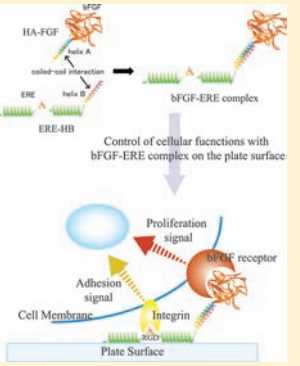

INTRODUCTION

Scaffolds with signaling molecules where cells can adhere, proliferate, and differentiate efficiently are essential for tissue engineering. Biomaterials providing such an environment for cells play an important role in most tissue engineering applications. In designing materials to allow specific cellular responses, recent strategies for tissue engineering applications have focused on the design of biomimetic materials. These biomaterials, which mimic functions of the extracellular matrix (ECM), are able to interact with surrounding tissues through specific molecular recognition motifs.[1,2] The incorporation of soluble signaling molecules such as growth factors and cell-binding properties into scaffold materials is one strategy to achieve biomolecular recognition of materials by cells.[3−6] In designing these strategies, supplementary steps for chemical or physical modification of the biomaterials are required. To avoid such troublesome processes, we previously constructed a fusion protein by genetic engineering, designated ERE-EGF, which is easy to immobilize onto hydrophobic surfaces and which also enhances cell adhesion and cell proliferation.[7,8]

Most signaling molecules are recognized and bound to their receptors on cell surfaces. After transducing signals into cells, they are internalized by endocytosis and digested. When the signaling molecule is immobilized on a scaffold by covalent bonding, some problems such as decreased recognition efficiency by the receptor, loss of activity, or malignant transformation caused by continuous signaling should be considered. One approach to overcome these problems is to utilize noncovalent bonding between the signaling molecule and the scaffold. Some experimental approaches include tethering of a growth factor to its substrate by engineering noncovalent bonding interactions between them. Boucher et al. utilized a coiled-coil interaction of E and K coils to immobilize epidermal growth factor (EGF) on a silicone surface.[9] A polyhistidine tag has been fused with EGF in order to immobilize EGF on a Ni^{2+}-bearing substrate.[10] Some growth factors have domains that bind to the ECM. Utilizing a similar approach, the collagen-binding domain from fibronectin has been introduced into growth factor proteins.[11−13] These fusion proteins had higher cell-growth activity when added to collagen than did soluble forms of the same proteins when they were added to cells on a collagen matrix. This method is effective for tissue engineering, which requires collagen as an ECM; however, other binding domains are needed to apply this method to other noncollagen ECM surfaces.

In order to immobilize signaling molecules to various types of ECM through noncovalent bonding interactions, the present study investigated proteins engineered to form coiled-coil dimers. Specifically, one peptide capable of forming a coiled-coil structure was fused with a growth factor protein, and another peptide with similar properties was fused with an ECM protein. A typical and well-studied coiled-coil dimer in nature is the leucine zipper of the yeast transcription factor GCN4.[14] However, this protein is a homodimer, and there is no interhelical ionic interaction. Another well-studied coiled-coil structure is the heterodimer of the Fos/Jun leucine zipper.[15] Unfavorable interhelical electrostatic interactions destabilize the homodimer form, thereby

Received: May 12, 2011
Revised: July 24, 2011
Published: August 06, 2011

ACS Publications © 2011 American Chemical Society

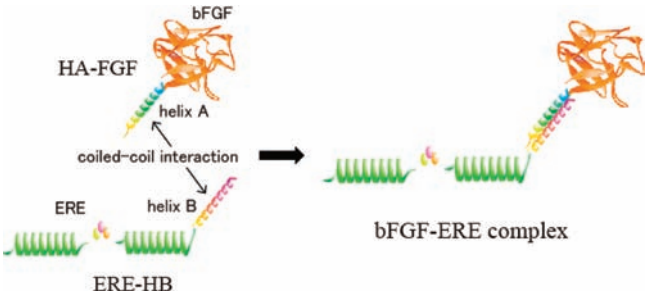

Figure 1. Design concept for the bFGF-ERE complex with a coiled-coil structure. Fusion proteins with helix A-bFGF (HA-FGF) and ERE-helix B (ERE-HB) were constructed, and they were noncovalently associated due to coiled-coil formation between the helix A and helix B moieties.

favoring heterodimer formation. On the basis of these studies, O'Shea et al. designed two peptides, designated ACID-p1 (helix A) and BASE-p1(helix B), which associate preferentially to form a stable, parallel, coiled-coil heterodimer with a leucine zipper and with favorable electrostatic interactions.[16]

In this study, the ERE protein, which has been described elsewhere,[7] was used as the ECM. In ERE, an RGD sequence found in the cell adhesion region was inserted between two other sequences, thus mimicking the ECM. Both of these peptide sequences contain 12 repeats of the polypeptide sequence Ala-Pro-Gly-Val-Gly-Val (APGVGV) designated as E. These kinds of sequence motif called elastin like polypeptides (ELPs) are found in elastin, which provides strength and flexibility in the ECM. ELPs have been paid attention as biomaterials for tissue repair.[17−19] On the other hand, basic fibroblast growth factor (bFGF) was used as a model signaling molecule since it has a wide variety of activities such as cell proliferation and differentiation. Helix A and helix B were fused at the N-terminus of bFGF and at the C-terminus of ERE, and the resulting proteins were designated as HA-FGF and ERE-HB, respectively. The structure of the complex formed between HA-FGF and ERE-HB through coiled-coil interactions is shown schematically in Figure 1. HA-FGF was immobilized via coiled-coil helix formation on a cell-culture plate whose surface was coated with ERE-HB, and the cell behavior on the surface was investigated.

EXPERIMENTAL PROCEDURES

Materials. Plasmid pBluescriptSKII (-) was obtained from Toyobo. Plasmid pET32c and *E. coli* Bl21 (DE3) were purchased from Novagen. *E. coli* KRX was obtained from Promega. Synthesized DNA fragments were purchased from Texas Genomics Japan. Synthesized oligopeptides were purchased form Sigma-genosis. Restriction enzymes and ligase were purchased from Toyobo and Takara Bio. All other chemicals were of analytical grade.

Construction of Plasmids. A pBS-FGF plasmid encoding a mouse bFGF gene was constructed previously. The DNA fragment encoding helix A was inserted at the 5′-end of the bFGF sequence of pBS-FGF. The helix A-bFGF fusion gene was inserted into pET32-c for expression, and the resulting plasmid was designated as pET-HA-FGF. A pBS-ERE plasmid encoding the ERE sequence was created as described elsewhere.[20] This plasmid has 12 repeats of APGVGV (E12) and RGD, as well as another E12 (the ERE sequence). The DNA fragment encoding (GGGS)4 as a linker peptide was inserted at the 3′-end of the ERE sequence of pBS-ERE. The DNA fragment encoding helix B was inserted into the pET32c expression vector (pET32c-helix B). The fusion gene of ERE and (GGGS)4 was inserted at the 5′-end of helix B of the pET32c-helix B. The resulting plasmid was designated as pET-ERE-HB. The DNA sequences of HA-FGF and ERE-HB with their translated sequences are shown in Supporting Information (Figure S1).

Protein Expression and Purification. *E. coli* KRX cells were transformed with plasmids and then were grown at 37 °C in an LB medium supplemented with ampicillin, to an OD_{660} = 0.6. After induction of protein expression with lamnose (0.1%) and isopropylthio-β-D-galactoside (1 mM), cells were cultured at 30 °C for another 4 h. Cells were harvested by centrifugation at 4 °C and then washed with PBS. After centrifugation, the cell pellet was resuspended in Bug Buster Reagent (Novagen) with benzonate nuclease (Novagen) and disrupted by gentle rotation. After centrifugation, the supernatant was applied to a TALON metal affinity resin (Clontech). After washing, the bound proteins were obtained by digesting with enterokinase (Novagen) for 16 h at room temperature. The enterokinase was removed by applying the digest onto EKapture agarose (Novagen).

Cell Proliferation Activity by Soluble HelixA-bFGF Fusion Protein. To investigate the growth factor activity of helixA-bFGF (HA-FGF), human umbilical vein endothelial cells (HUVEC) were utilized. The HUVEC cell line was purchased from Kurabo and maintained at 37 °C under 5% CO_2 in HuMedia EG-2 supplemented with 2% FBS, 10 ng/mL human EGF, 1 mg/mL hydrocortisone, 50 mg/mL gentamicin, 50 ng/mL amphotericin B, 5 ng/mL human bFGF, and 10 mg/mL heparin. HUVECs were seeded on a 96-well plate (coaster3595) at 2×10^3 cells/well, and HA-bFGF or bFGF was added to the HuMedia EG-2 without hFGF-b. The cells were incubated at 37 °C in a humidified atmosphere of 95% air and 5% CO_2. The culture medium was changed every 2 days. The day on which proteins were added was defined as day 0. The cell growth was observed every day under microscopy, and the numbers of cells on days 1, 3, 5, and 7 were estimated, using the Cell Counting Kit (CCK-8) (DOJINDO). The activity was evaluated at 450 nm as described in the CCK-8 kit.

Cell Adhesive Activity. Cell adhesion assays were performed in a 96-well plate (costor3361). The surfaces of the wells were coated with 10 nM of ERE-helix protein (ERE-HB). A fibronectin-coated surface was used as a positive control. BSA-coated and noncoated surfaces were used as negative controls. After incubation for 3 h at 37 °C, each well was washed with PBS, and then the wells were blocked with a 0.1% BSA solution for 2 h at 37 °C. HUVECs, prepared in a HuMedia-EG2 medium at 10^4 cells/well, were seeded in each plate. After 4 h of incubation at 37 °C, wells were washed with HuMedia-EG2. The remaining number of adhesive cells on the plate was examined using a CCK-8 kit.

Protein Binding Through a Coiled-Coil Structure. The surface of the wells of a 96-well plate (coster3361) was coated with 100 nM of ERE-HB and incubated for 3 h at 37 °C. After blocking with 0.1% BSA, various concentrations (10 nM, 100 nM, and 1 μM) of HA-FGF (100 μL) were added and the plates were incubated for 3 h at 37 °C. A solution of 100 μL of 1/5000 diluted rabbit anti-bFGF antibody (SIGMA) was reacted for 40 min at 30 °C. Finally, peroxidase-labeled antirabbit IgG antibody was reacted for 40 min at 30 °C. After thorough washing with PBS-T, HRP substrate (KPL) was added and the reaction was stopped after 2 min by adding 1 N HCl, then absorbance at 450 nm was measured using a microplate reader.

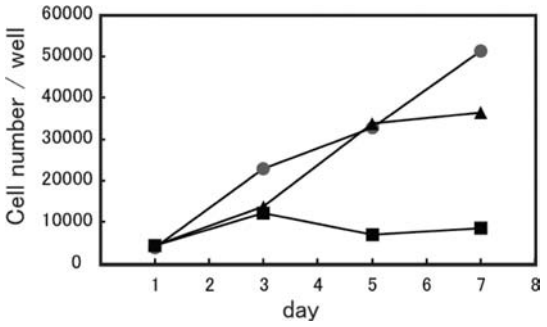

Figure 2. Cell growth with the soluble forms of the proteins. The cell growth activities of cultures with HA-FGF (▲), with bFGF (●), and without bFGF (■) were investigated by adding each protein to the HUVEC culture medium.

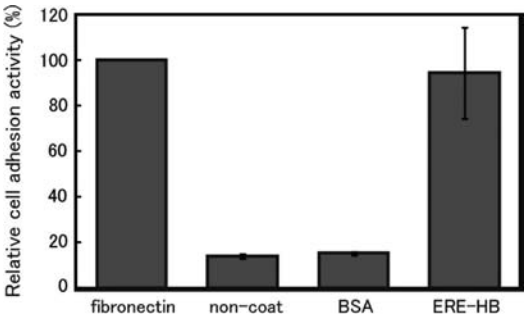

Figure 3. Cell adhesion activity of ERE-HB. Each protein was coated on a 96-well plate surface and HUVECs were then seeded. After 4 h of incubation at 37 °C, each well was washed and the remaining numbers of cells were determined. The positive control was fibronectin and samples were represented as the ratio of the number of cells attached to fibronectin-coated wells.

Growth Factor Activity of Adsorbed bFGF. The surface of wells of a 96-well plate was modified with HA-FGF by attaching a coiled-coil structure with ERE-HB as described in the previous section. HUVECs suspended in HuMedia-EG2 without bFGF at 2.0×10^3 cells/well were seeded on the plate. The culture medium was changed every 2 days. The numbers of cells on each day were counted using the CCK-8 kit. The growth kinetics of the remaining attached cells were followed for 5 days.

■ RESULTS AND DISCUSSION

Expression and Purification of Proteins. *E. coli* KRX was used as the host strain for the expression of the HA-bFGF and the ERE-HB thioredoxin fusion proteins. In our previous work, bFGF with a His-tag at the N-terminus was expressed in an insoluble fraction, and it had no bFGF activity even after refolding. Therefore, HA-bFGF was expressed as a fusion with thioredoxin at its N-terminus. LaVallie et al. reported that the fusion to thioredoxin increases the solubility of heterologous proteins synthesized in the *E. coli* cytoplasm, and that thioredoxin fusion proteins usually accumulate to high levels.[21] Also, in the case of expression of ERE-HB, thioredoxin was chosen as a fusion partner because the ERE-HB contains hydrophobic domains.[20] These fusion proteins with an attached helical peptide region were expressed at high levels in both the soluble and insoluble fractions. The proteins in the soluble fraction could be purified in a single step using a TALON metal affinity gel followed by the digestion with enterokinase to remove the His-tag and thioredoxin moieties. The expected sizes from their amino acid sequences of the HA-FGF and ERE-HB proteins after digestion with enterokinase are 21.1 kDa and 19.5 kDa, respectively. The estimated molecular weights of the proteins from SDS-PAGE (SI Figure S2) were a little larger than the expected sizes, but acidic protein[10] and elastin-like polypeptide[22] sometimes appeared larger than the calculated molecular weight in SDS-PAGE. Since the proteins bound to columns specifically and they were digested with enterokinase, we used them as objective proteins for the next experiments.

Growth Factor Activity of the Free Form of bFGF. Growth factor activities of HA-FGF and bFGF were investigated by adding 20 nM of each protein to the HUVEC culture medium. HUVECs are known to require the addition of bFGF as an essential factor for proliferation in low serum culture conditions. The growth curves of HUVEC with HA-FGF or bFGF are shown in Figure 2. HUVECs grew well in the presence of bFGF or HA-FGF, while the same cells did not grow at all without bFGF. Increased cell numbers were observed in culture with HA-FGF as well as bFGF. These results indicate that HA-FGF retained the cell growth activity of bFGF even after fusion with helix A.

Cell Adhesion Activity of ERE-HB. The HUVECs were seeded on ERE-HB-coated, fibronectin-coated, BSA-coated, and noncoated cell culture plates (Figure 3). After 4 h of incubation, the numbers of cells were counted in each plate. Cells were attached to the wells and spread on the fibronectin-coated plate, which was the positive control. However, cell attachment to the wells was barely observed on a BSA-coated plate or a noncoated plate (negative controls). In contrast, cells attached readily to the ERE-HB-coated plate (prepared with a coating concentration of 10 nM ERE-HB) as well as to a fibronectin-coated plate. Indeed, cells do not generally adhere to noncoated and BSA-coated plates, so the observed enhancement of cell adhesion to the ERE-HB-coated plates indicated that the ERE-HB protein itself must have adhered to the plate. The ERE protein adsorption to the plate surface was thus assumed but not examined further, given that this has already been reported elsewhere.[20] Because of the strong hydrophobicity of the repeated APGVGV sequence, the ERE adsorbed well onto a hydrophobic plate surface via hydrophobic bonding interactions. Even in this adsorbed state on the solid-phase surface, relatively hydrophilic regions of ERE-HB, such as the RGD sequence and the helix B sequence that was fused with an extremely hydrophilic sequence, retain their structure. The cell attachment on the ERE-HB-coated plate, according to our previous work,[20] should be attributed to the RGD sequence in ERE-HB.

Binding of HA-FGF Through Coiled-Coil Structure Formation with ERE-HB. Various concentrations of the HA-FGF were bound to the 96-well plate whose surface was coated with 100 nM of ERE-HB. The amounts of HA-FGF on the surface were indicated using an anti-bFGF antibody (rabbit) and HRP-labeled antirabbit IgG. As shown in Figure 4A, the amounts of HA-FGF bound on the surface increased in a concentration-dependent manner. However, the possibility of nonspecific adsorption of HA-FGF should be considered. To confirm the specific binding between HA-FGF and ERE-HB, ERE and bFGF without the attached helix domains were used for control experiments. In these experiments, 100 nM HA-FGF or bFGF was reacted with the surface coated with ERE-HB or ERE. The FGF moiety was detected as described above using an anti-FGF antibody, and the result is shown in Figure 4B. Among the four combinations

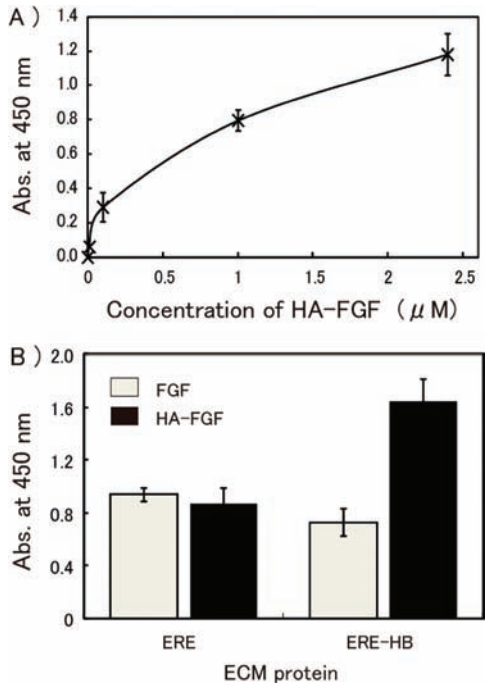

Figure 4. Binding of HA-FGF to ERE-HB with a coiled-coil structure on the solid-phase surface. (a) Various concentrations of HA-FGF were reacted with ERE-HB adsorbed on the 96-well plate surface, and the amounts of bound HA-FGF were determined using anti-bFGF antibody (rabbit) with an HRP-labeled antirabbit IgG secondary antibody. (b) The HA-FGF or bFGF was added to the surface coated with ERE-HB or ERE, and the amounts of immobilized bFGF moiety on each well were determined using an anti-bFGF antibody (rabbit) with an HRP-labeled antirabbit IgG secondary antibody.

tested, only the combination of HA-FGF and ERE-HB showed increased binding of bFGF. This indicates that the binding of HA-FGF to ERE-HB was specific. The FGF binding levels detected using the other three combinations were similar, and they should be considered background signals due to nonspecific adsorption.

In order to verify that the binding between HA-FGF and ERE-HB was due to the formation of a coiled-coil structure between helix A and helix B fused with their respective proteins, competitive inhibition of the binding of HA-FGF in the presence of helix A or helix B peptide was performed. A 100 nM HA-FGF solution was mixed with various concentrations (1 nM to 10 μM) of helix A or helix B, and the mixture was reacted with the ERE-HB-coated plate surface. The amounts of HA-FGF bound to the surface were determined as described above. The absorbance based on the bFGF surface signal was plotted against the concentration of helix A or helix B (Figure 5). The binding of bFGF was inhibited by addition of either helix A or helix B peptide in a concentration-dependent manner. These results indicated that the binding between HA-FGF and ERE-HB was due to formation of a coiled-coil structure between helix A and helix B from each protein.

bFGF Activity on the Plate Surface. HUVECs were seeded on the plate whose surface was modified with HA-FGF through coated-ERE-HB, and their growth curves were measured (Figure 6). On the ERE-HB-coated plate without HA-FGF, which was used as a negative control, clear cell growth was not observed (data not shown). As a control experiment, 100 nM

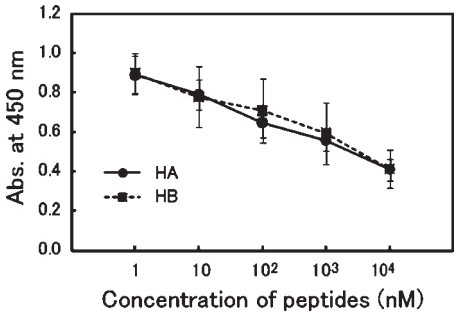

Figure 5. Competitive inhibition of binding of HA-FGF to ERE-HB using helixA and helix B peptides. The HA-FGF solution was mixed with various concentrations of helix A or helix B peptide, and the mixture was reacted to the ERE-HB-coated plate surface. The amounts of HA-FGF bound on the surface were determined using anti-bFGF antibody (rabbit) with an HRP-labeled antirabbit IgG secondary antibody.

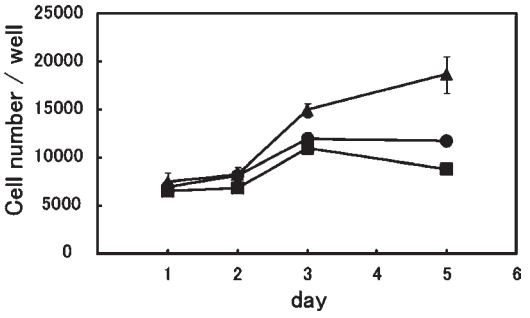

Figure 6. Cell growth with immobilized HA-bFGF. HUVECs were seeded on the plate whose surface was modified with HA-FGF through coated-ERE-HB (▲). bFGF without helix A peptide (●) or only buffer (■) was added to the culture medium at day 0 as a control experiment.

b-FGF without the attached helical peptide was added to the culture medium for seeding HUVECs. In this case, the growth curve was almost the same as that seen in the experiment without bFGF. A little growth was observed at 3 days of culture, but no cell growth was observed after that. Since the culture medium was exchanged at 2 days, bFGF that did not bind to ERE-HB should have been washed out. On the other hand, significant cell growth was observed when HA-FGF was immobilized on the ERE-HB-coated surface. The cells still grew well at 5 days of culture. These results suggest that the FGF moiety in the HA-FGF remained active even after immobilization on the plate surface, presumably through forming a coiled-coil structure with the ERE-HB. The effect of bFGF was sustained for a longer time period because the bFGF was retained in the matrix due to noncovalent bonding.

■ CONCLUSION

In this study, a novel method for construction of biomaterials for tissue engineering was developed. A designed extracellular matrix (ERE) and bFGF were combined with a noncovalent bonding by formation of coiled-coil structure. The resulting complex showed good cell adhesive and proliferation activities.

One advantage of this technique is that the growth factor or a matrix can be changed depending on the kind of target cell being studied. Preliminary experiments using a system that connected helix B with epidermal growth factor (EGF) yielded similar

dx.doi.org/10.1021/bc200249u |*Bioconjugate Chem.* 2011, 22, 2038–2042

encouraging results. In addition, we are beginning to apply this technique to construct an *in vitro* nerve system.

■ ASSOCIATED CONTENT

Supporting Information. Additional information as described in the text. This material is available free of charge via the Internet at http://pubs.acs.org.

■ AUTHOR INFORMATION

Corresponding Author

*Phone: +81-45-924-5760. Fax: +81-45-924-5779. E-mail: ekobatak@bio.titech.ac.jp.

■ REFERENCES

(1) Hubbell, J. A. (1999) Bioactive biomaterials. *Curr. Opin. Biotechnol. 10*, 123–129.

(2) Sakiyama-Elbert, S. E., and Hubbell, J. A. (2001) Functional biomaterials: design of novel biomaterials. *Annu. Rev. Mater. Res. 31* (2), 183–201.

(3) West, J. L., and Hubbell, J. A. (1999) Polymeric materials with degradation sites for proteases involved cell migration. *Macromolecules 32*, 241–244.

(4) Halstenberg, S., Panitch, A., Rizzi, S., Hall, H., and Hubbell, J. A. (2002) Biologically engineered protein-graft-poly (ethylene glycol) hydrogels: a cell adhesive and plasmin-degradable biosynthetic material for tissue repair. *Biomacromolecules 3*, 710–753.

(5) Gobin, A. S., and West, J. L. (2002) Cell migration through defined, synthetic ECM analogs. *FASEB J. 16*, 751–753.

(6) Lutolf, M. P., and Hubbell, J. A. (2003) Synthesis and physicochemical characterization of end-linked poly (ethylene glycol)-co-peptide hydrogels formed by Michael-type addition. *Biomacromolecules 4*, 713–722.

(7) Elloumi, I., Kobayashi, R., Funabashi, H., Mie, M., and Kobatake, E. (2006) Construction of epidermal growth factor fusion protein with cell adhesive activity. *Biomaterials 27* (18), 3451–3458.

(8) Elloumi, H. I., Nakamura, M., Mie, M., and Kobatake, E. (2009) Construction of multifunctional proteins for tissue engineering: Epidermal growth factor with collagen binding and cell adhesive activities. *J. Biotechnol. 139*, 19–25.

(9) Boucher, C., Ruiz, J.-C., Thibaut, M., Buschmann, M. D., Wertheimer, M. R., Jolicoeur, M., Durocher, Y., and Crescenzo, G. D. (2010) Human Corneal epithrial cell response to epidermal growth factor tethered via coiled-coil interactions. *Biomaterials 27*, 7021–7031.

(10) Nakaji-Hirabayashi, T., Kato, K., and Iwata, H. (2009) Surface-anchoring of spontaneously dimerized epidermal growth factor for highly selective expansion of neural stem cells. *Bioconjugate Chem. 20* (1), 102–110.

(11) Nishi, N., Matsushita, O., Yuube, K., Miyanaka, H., and Okabe, A. (1998) Collagen-binding growth factors: Production and characterization of functional fusion proteins having a collagen-binding domain. *Proc. Natl. Acad. Sci. U.S.A. 95*, 7018–7023.

(12) Andrades, J. A., Han, B., Becerra, J., Sorgente, N., Hall, F. L., and Nimni, M. E. (1999) A recombinant human TGF-b1 fusion protein with collagen-binding domain promotes migration, growth, and differentiation of bone marrow mesenchymal cells. *Exp. Cell Res. 250*, 485–498.

(13) Hall, F. L., Kaiser, A., Liu, L., Chen, Z. H., Hu, J., Nimni, M. E., Beart, R. W., Jr., and Gordon, E. M. (2000) Design, expression, and renaturation of a lesion-targeted recombinant epidermal growth factor-von Willebrand factor fusion protein: Efficacy in an animal model of experimental colitis. *Int. J. Mol. Med. 6*, 635–643.

(14) O'Shea, E. K., Klemm, J. D., Kim, P. S., and Alber, T. A. (1991) X-ray structure of the GCN4 leucine zipper, a two-stranded, parallel coiled coil. *Science 254*, 539–544.

(15) O'Shea, E. K., Rutkowski, R., Stafford, W. F., and Kim, P. S. (1989) Preferential heterodimer formation by isolated leucine zippers from Fos and Jun. *Science 245*, 646–648.

(16) O'Shea, E. K., Lumb, K. J., and Kim, P. S. (1993) Peptide 'Velcro': design of a heterodimeric coiled coil. *Curr. Biol. 3* (10), 658–667.

(17) Urry, D. W., Pattanaik, A., Xu, J., Woods, T. C., McPherson, D. T., and Parker, T. M. (1998) Elastic protein-based polymers in soft tissue augmentation and generation. *J. Biomater. Sci. Polym. Ed. 9* (10), 1015–1048.

(18) Betre, H., Setton, L. A., Meyer, D. E., and Chilkoti, A. (2002) Characterization of a genetically engineered elastin-like polypeptide for cartilaginous tissue repair. *Biomacromolecules 3*, 910–916.

(19) Lim, D. W., Nettles, D. L., Setton, L, A., and Chikoti, A. (2008) In situ cross-linking of elastin-like polypeptide block copolymers for tissue repair. *Biomacromolecules 9* (1), 222–230.

(20) Kobatake, E., Onoda, K., Yanagida, Y., and Aizawa, M. (2000) Design and gene engineering synthesis of an extremely thermostable protein with biological activity. *Biomacromolecules 1*, 382–386.

(21) La Vallie, E. R., DiBlasio, E. A., Kovacic, S., Grant, K. L., Schendel, P. F., and MaCoy, J. M. (1993) A thioredoxin gene fusion expression system that circumvents inclusion body formation in the E. coli cytoplasm. *Biotechnology (NY) 11*, 187–193.

(22) McPherson, D. T., Xu, J., and Urry, D. W. (1996) Product purification by reversible phase transition following *Escherichia coli* expression of genes encoding up to 251 repeats of the elastomeric pentapeptide GVGVP. *Protein Expr. Purif. 7*, 51–57.

DNA sequence

ATGAGCGATAAAATTATTCACCTGACTGACGACAGTTTTGACACGGATGTACTCAAAGCGGACGGGGCGA
TCCTCGTCGATTTCTGGGCAGAGTGGTGCGGTCCGTGCAAAATGATCGCCCCGATTCTGGATGAAATCGC
TGACGAATATCAGGGCAAACTGACCGTTGCAAAACTGAACATCGATCAAAACCCTGGCACTGCGCCGAAA
TATGGCATCCGTGGTATCCCGACTCTGCTGCTGTTCAAAAACGGTGAAGTGGCGGCAACCAAAGTGGGTG
CACTGTCTAAAGGTCAGTTGAAAGAGTTCCTCGACGCTAACCTGGCCGGTTCTGGTTCTGGCCATATGCA
CCATCATCATCATCATTCTTCTGGTCTGGTGCCACGCGGTTCTGGTATGAAAGAAACCGCTGCTGCTAAA
TTCGAACGCCAGCACATGGACAGCCCAGATCTGGGTACCGACGACGACGACAAGGCCATGGGAGCTCAAT
TAGAAAAAGAATTACAAGCATTAGAAAAAGAAAATGCGCAGCTGGAATGGGAACTGCAAGCCCTGGAGAA
AGAGCTCGCTCAAGGTATGGCTGCCAGCGGCATCACCTCGCTTCCCGCACTGCCGGAGGACGGCGGCGCC
GCCTTCCCACCAGGCCACTTCAAGGACCCCAAGCGGCTCTACTGCAAGAACGGCGGCTTCTTCCTGCGCA
TCCATCCCGACGGCCGCGTGGATGGCGTCCGCGAGAAGAGCGACCCACACGTCAAACTACAACTCCAAGC
AGAAGAGAGAGGAGTTGTGTCTATCAAGGGAGTGTGTGCCAACCGGTACCTTGCTATGAAGGAAGATGGA
CGGCTGCTGGCTTCTAAGTGTGTTACAGAAGAGTGTTTCTTCTTTGAACGACTGGAATCTAATAACTACA
ATACTTACCGGTCACGGAAATACTCCAGTTGGTATGTGGCACTGAAACGAACTGGGCAGTATAAACTCGG
ATCCAAAACGGGACCTGGACAGAAGGCCATACTGTTTCTTCCAATGTCTGCTAAGAGCCCATGA

Protein sequence

MSDKIIHLTDDSFDTDVLKADGAILVDFWAEWCGPCKMIAPILDEIADEYQGKLTVAKLNIDQNPGTAPK

YGIRGIPTLLLFKNGEVAATKVGALSKGQLKEFLDANLAGSGSGHMHHHHHHSSGLVPRGSGMKETAAAK

FERQHMDSPDLGT*DDDDK*AMGAQLEKELQALEKENAQLEWELQALEKELAQGMAASGITSLPALPEDGGA

AFPPGHFKDPKRLYCKNGGFFLRIHPDGRVDGVREKSDPHVKLQLQAEERGVVSIKGVCANRYLAMKEDG

RLLASKCVTEECFFFERLESNNYNTYRSRKYSSWYVALKRTGQYKLGSKTGPGQKAILFLPMSAKSP*

Figure S1 (A) DNA and protein sequences of HA-FGF with thioredoxin-tag. Blue, tag sequence including thioredoxin, histidine-tag, and enterokinase recognition site (italic); red: helix A sequence; underline, bFGF.

DNA sequence

ATGAGCGATAAAATTATTCACCTGACTGACGACAGTTTTGACACGGATGTACTCAAAGCGGACGGGGCGA
TCCTCGTCGATTTCTGGGCAGAGTGGTGCGGTCCGTGCAAAATGATCGCCCCGATTCTGGATGAAATCGC
TGACGAATATCAGGGCAAACTGACCGTTGCAAAACTGAACATCGATCAAAACCCTGGCACTGCGCCGAAA
TATGGCATCCGTGGTATCCCGACTCTGCTGCTGTTCAAAAACGGTGAAGTGGCGGCAACCAAAGTGGGTG
CACTGTCTAAAGGTCAGTTGAAAGAGTTCCTCGACGCTAACCTGGCCGGTTCTGGTTCTGGCCATATGCA
CCATCATCATCATCATTCTTCTGGTCTGGTGCCACGCGGTTCTGGTATGAAAGAAACCGCTGCTGCTAAA
TTCGAACGCCAGCACATGGACAGCCCAGATCTGGGTACCGACGACGACGACAAGGCCATGGGATATCTGT
GGATCCTGGCACCGGGTGTTGGCGTGGCACCGGGTGTTGGCGTGGCACCGGGTGTTGGCGTGGCACCGGG
TGTTGGCGTGGCACCGGGTGTTGGCGTGGCACCGGGTGTTGGCGTGGCACCGGGTGTTGGCGTGGCACCG
GGTGTTGGCGTGGCACCGGGTGTTGGCGTGGCACCGGGTGTTGGCGTGGCACCGGGTGTTGGCGTGGCAC
CGGGTGTTGGCGTGGCACCAAAGATCCTGGGCCGTGGTGACAGCAAGATCCTGGCACCGGGTGTTGGCGT
GGCACCGGGTGTTGGCGTGGCACCGGGTGTTGGCGTGGCACCGGGTGTTGGCGTGGCACCGGGTGTTGGC
GTGGCACCGGGTGTTGGCGTGGCACCGGGTGTTGGCGTGGCACCGGGTGTTGGCGTGGCACCGGGTGTTG
GCGTGGCACCGGGTGTTGGCGTGGCACCGGGTGTTGGCGTGGCACCGGGTGTTGGCGTGGCACCAAAGAT
CGGCGGTGGATCTGGCGGTGGATCTGGCGGTGGATCTGGCGGTGGATCTCAGATCCTAGCTCAATTAAAA
AAGAAATTACAGGCTTTAAAAAAAAAGAACGCTCAGCTGAAATGGAAGCTCCAAGCGTTAAAGAAAAAGT
TAGCTCAAGAGATCTTGTGA

Protein sequence

MSDKIIHLTDDSFDTDVLKADGAILVDFWAEWCGPCKMIAPILDEIADEYQGKLTVAKLNIDQNPGTAPK
YGIRGIPTLLLFKNGEVAATKVGALSKGQLKEFLDANLAGSGSGHMHHHHHHSSGLVPRGSGMKETAAAK
FERQHMDSPDLGT*DDDDK*AMGYLWILAPGVGVAPGVGVAPGVGVAPGVGVAPGVGVAPGVGVAPGVGVAP
GVGVAPGVGVAPGVGVAPGVGVAPGVGVAPKILGRGDSKILAPGVGVAPGVGVAPGVGVAPGVGVAPGVG
VAPGVGVAPGVGVAPGVGVAPGVGVAPGVGVAPGVGVAPGVGVAPKIGGGSGGGSGGGSGGGSQILAQLK
KKLQALKKKNAQLKWKLQALKKKLAQEIL*

Figure S1 (B) DNA and protein sequences of ERE-HB with thioredoxin-tag. Blue, tag sequence including thioredoxin, histidine-tag, and enterokinase recognition site (italic); underline, ERE; yellow, (GGGS)4 linker; red, helix B sequence

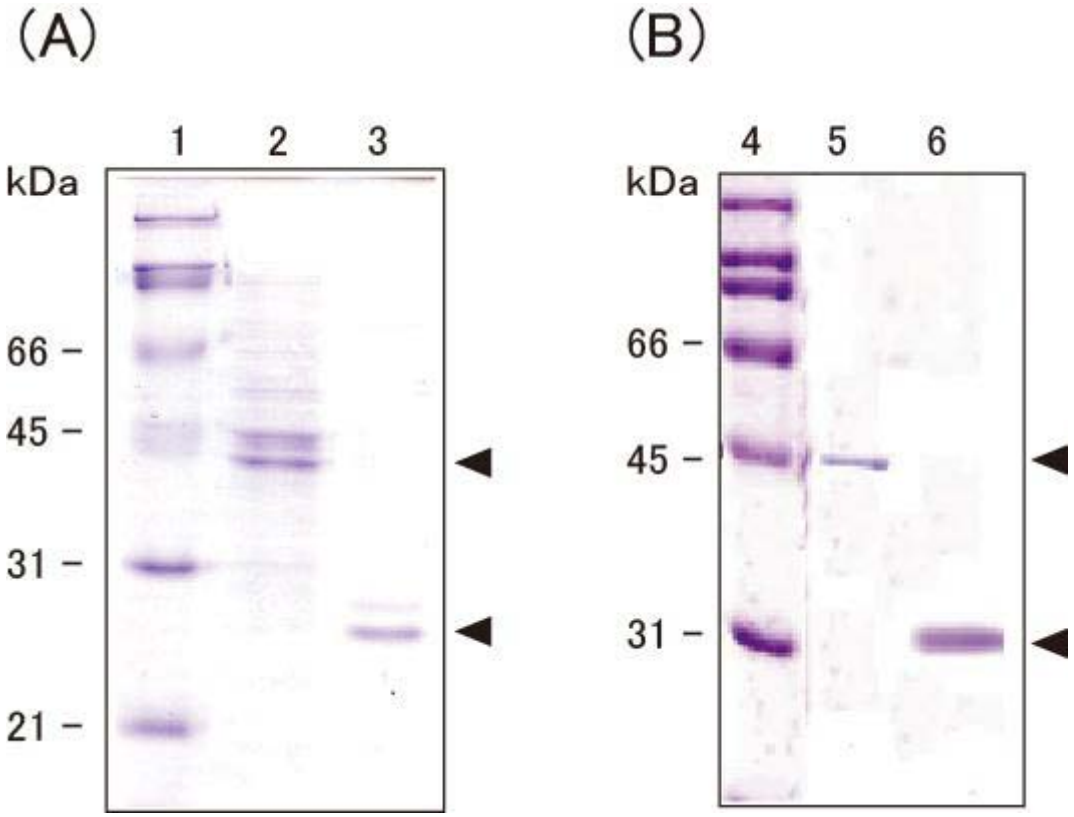

Figure S2 SDS-PAGE analysis of purified HA-FGF (A) and ERE-HB (B). The purified proteins were stained with coomasie brilliant blue. Lane 1 and 4, molecular mass standard proteins; lane 2, thioredoxin-HA-FGF; lane 3, HA-FGF; lane 5, thioredoxin-ERE-HB; lane 6, ERE-HB

Bioconjugate Chemistry

ARTICLE

pubs.acs.org/bc

G4-DNA-Coated Gold Nanoparticles: Synthesis and Assembly

Irit Lubitz and Alexander Kotlyar*

Department of Biochemistry, George S. Wise Faculty of Life Sciences and The Center of Nanoscience and Nanotechnology, Tel Aviv University, Ramat Aviv 69978, Israel

ABSTRACT: Here, we describe the preparation of stable 15 nm gold nanoparticles (Au-NPs) coated with parallel-stranded G-quadruplexes (G4-DNA), comprising phosphorothioate residues on both sides of the DNA. Phosphorothioate residues located on the surface of the coated particles can anchor them to noncoated ones. Their incubation with more than 20-fold excess of 15 nm citrate-stabilized Au-NPs leads to the formation of flower-shaped structures comprising a central noncoated particle and five to six G-quadruplex-coated ones at the periphery, as revealed by TEM imaging analysis. The absorption band of the structures is shifted toward long wavelengths compared to individual particles not connected to each other. We show a strong dependence of plasmon coupling strength on the length of the DNA connecting Au-NPs.

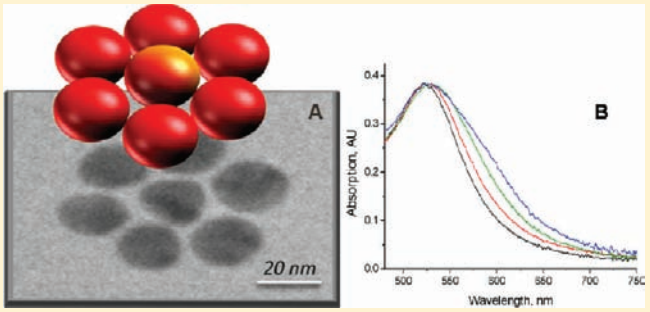

INTRODUCTION

Nanoparticle−DNA conjugates[1,2] are widely used in nanoassembly,[3,4] bionanotechnologies,[5−7] and nanoelectronics.[8,9] In a classical approach, thiol-containing DNA oligonucleotides are used to stabilize the Au-NPs. Covalent interaction between the thiol attached to the end of the DNA and noble metal atoms results in coating of the particle with DNA. These particles are stable and can bind particles coated with complementary sequences via hybridization. This reaction guided by DNA−DNA bimolecular recognition leads to the formation of various multiparticle structures.[2,10,11] We have recently reported the synthesis of stable conjugates between silver nanoparticles and four-stranded G-quadruplexes.[12] The conjugates were formed during incubation of silver particles with G-quadruplexes, containing phosphorothioate anchor residues at both ends of the DNA, at near-equimolar concentrations. In the conjugates, each pair of particles was connected by a G-quadruplex. Increasing the DNA-to-particle ratio in the incubation from 1 to 3−5 resulted in the formation of aggregates that fall out of solution.

Here, we report that incubation of 15 nm gold nanoparticles (Au-NPs) with more than 15-fold molar excess of the G-quadruplexes, comprising phosphorothioate residues at both ends of the DNA, unexpectedly yields stable nonaggregated DNA-coated Au-NPs. Phosphorothioate residues located on their surface can, however, anchor them to citrate-stabilized Au-NPs. Incubation of a 30-fold excess of the latter particles with former ones leads to the formation of flower-shaped structures in which a central citrate-stabilized Au-NP is surrounded by several (5−6) DNA-coated ones. Interparticle interactions in the structure lead to a shift of the surface plasmon absorption resonance, which strongly depends on the length of the DNA molecules connecting Au-NPs in the structure.

EXPERIMENTAL PROCEDURES

Unless otherwise stated, reagents were obtained from Sigma-Aldrich (USA) and were used without further purification.

DNA Samples. The deoxyoligonucleotides, $a_5G_5a_5$, $a_5G_{10}a_5$, $a_5G_{20}a_5$, were purchased from Alpha DNA (Montreal, Canada). The four-stranded G-quadruplexes composed of 5, 10, and 20 tetrad were prepared as described in our recent work.[12]

Synthesis of NPs. *15 nm Gold Nanoparticles.* Au-NPs with a diameter of 15 nm were prepared by the reduction of $HAuCl_4$ with sodium citrate essentially as described.[13] 100 mL of 1 mM $HAuCl_4$ solution was heated in a 250 mL round-bottom flask to boiling on the hot plate under reflux. Then, 10 mL of a 38.8 mM sodium citrate solution was added quickly under vigorously stirring. The solution turns deep red in approximately 5 min after the addition of citrate. The solution was refluxed with stirring for an additional 15 min. The mixture was cooled down to room temperature and centrifuged at 10 000 rpm for 20 min at 20 °C in a Sorval SS-34 Rotor. A clear supernatant was carefully discarded, and the pellet was suspended in 4−5 mL of residual supernatant. The resulting nanoparticles were screened for their size and uniformity by TEM, revealing an average diameter of 15 ± 2 nm. The UV−vis spectra showed a characteristic absorption peak at 520 nm. Concentration of the particles was calculated using an extinction coefficient (ε) of 4.2×10^8 M^{-1} cm^{-1} at 520 nm.[14]

60 nm Gold Nanoparticles. Au-NPs with a diameter of 60 nm were also prepared by the reduction of $HAuCl_4$ with sodium citrate.[13] 50 mL of 0.01% $HAuCl_4$ solution were heated in a 250 mL round-bottom flack to boiling on a hot plate under reflux.

Received: May 17, 2011
Revised: August 21, 2011
Published: September 07, 2011

ACS Publications © 2011 American Chemical Society

dx.doi.org/10.1021/bc200257e | *Bioconjugate Chem.* 2011, 22, 2043–2047

Then, 260 μL of 1% sodium citrate solution was added quickly under vigorously stirring. The solution turns purple in approximately 5 min after the addition of sodium citrate. The mixture was refluxed with stirring for additional 10 min and cooled down to room temperature. The particles were centrifuged at 4500 rpm for 5 min at 20 °C on a table Eppendorf centrifuge (model 5424). A clear supernatant was carefully discarded, and the pellet was suspended in 2 mL of residual supernatant. The resulting nanoparticles were screened for their size and uniformity by TEM, revealing an average diameter of 60 ± 5 nm. The UV−vis spectra showed a characteristic absorption peak at 536 nm. Concentration of the particles was calculated using an extinction coefficient (ε) of 5.3×10^{10} M^{-1} cm^{-1} at 536 nm.[15]

Gel Electrophoresis. The DNA-NP samples were loaded onto 1.5% agarose gel 7 × 7 cm^2 and electrophoresed at 4 °C at 130 V for 30 min. Tris-Acetate-EDTA (TAE) buffer, containing 40 mM Tris-Acetate and 1 mM EDTA, in addition to being used to prepare the agarose, also served as the running buffer.

TEM Measurement. A 5 μL aliquot of a sample solution in 20 mM TAE (pH 8.8) was dropped onto a carbon-coated copper grid (400 mesh). The grids (before depositing) were negatively glow-discharged using an Emitech K100X glow discharger. After incubation for 5 min at ambient temperature, the excess solution was removed by blotting with filter paper. TEM imaging was performed on a TEM JEM model 1200 EX instrument operated at an accelerating voltage of 120 kV.

Absorption Spectroscopy. Absorption spectra were recorded with a Jasco V-630 spectrophotometer (Japan).

RESULTS

Here, we used a four-stranded G-quadruplex DNA containing a central fragment flanked by phosphorothioated adenine residues on either side to coat Au-NPs. The parallel-stranded tetramolecular G-quadruplexes were prepared using oligonucleotides containing 5, 10, or 20 central G-base fragment flanked by two runs of 5 phosphorothioated adenines on either side as described in our recent publication.[12] Stable G-guadruplexes coated particles were obtained by gradually increasing NaCL concentration in a mixture of citrate-stabilized Au-NPs with 15-fold molar excess of the 10 tetrad quadruplexes as follows. The 15 nm particles (absorption is approximately equal to 30 at 520 nm) prepared as shown in the Experimental Procedures section were incubated at 42 °C with G-quadruplexes in the presence of 25 mM NaCL for 1 h. Then, the salt concentration in the incubation was increased to 100 mM, and then one hour later to 200 mM. The sample was incubated for another hour at 42 °C. No precipitate was formed during the incubation; the sample remained clear and red. In contrast, the incubation at DNA to particle ratios lying in the range from 2 to 5 leads to spontaneous aggregation of the particles and their precipitation out of the solution. These aggregates did not enter the gel (see Figure 1, lanes 1 and 2) in contrast to the particles obtained during the incubation at high (15 or higher) DNA to Au-NP ratios. The latter particles move as a relatively narrow single band in the gel (see Figure 1, lanes 3 and 4). We thus suggest that at high DNA concentrations (DNA to NP ratios) complete surface coverage is achieved before the particles collide and stick together (see schematic drawing in Scheme. 1). Due to steric reasons, the reactive phosphorothioate residues on the surface of a fully coated particle cannot bind to the metal core of another coated particle. No noticeable changes in the absorption spectrum were

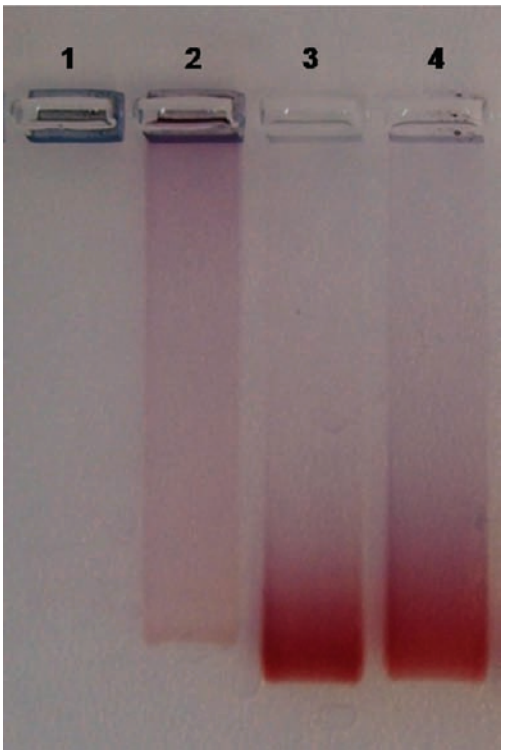

Figure 1. Electrophoresis of G-quadruplex-coated Au-NPs. 15 nm citrate-stabilized Au-NPs (absorption at 520 nm is equal to 30) were incubated with 2 μM (lane 1), 5 (lane 2), 15 (lane 3), and 20 μM (lane 4) 10 tetrad G-quadruplexes functionalized with phosphorothioated adenine residues at either side of the DNA molecule in the presence of 25 mM NaCL for 1 h at 42 °C. Then, the salt concentration was increased to 100 mM and one hour later to 200 mM. The samples were incubated for another hour at 42 °C and loaded onto a 1.5% agarose gel and electrophoresed at 130 V for 30 min at 4 °C.

Scheme 1. Schematic Drawing of Au-NPs (Red Spheres) Interaction with G-Quadruplexes (Four Closely Spaced Black Parallel Lines) Functionalized with Phosphorothioate Residues (Short Red Fragments at Each Sides of Each Black Line)[a]

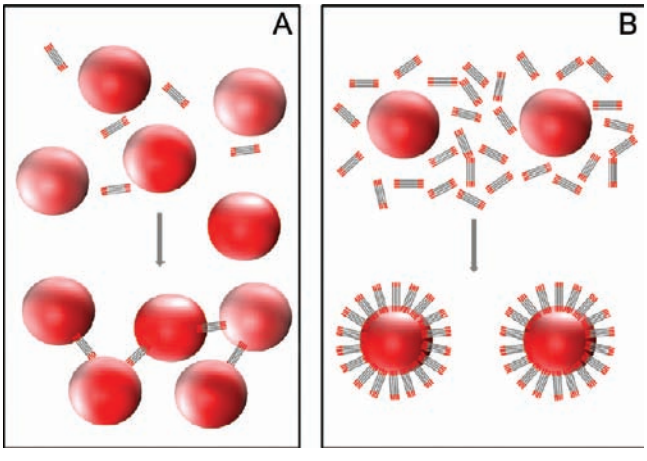

[a] (A) At near-stoichiometric concentrations, interaction of Au-NPs with the DNA molecules results in the formation of long nanoparticle chains. In the chain, the particles are connected by G-quadruplex molecules. (B) At high DNA concentrations (DNA to NP ratios), a complete surface coverage is achieved before the particles collide and stick together.

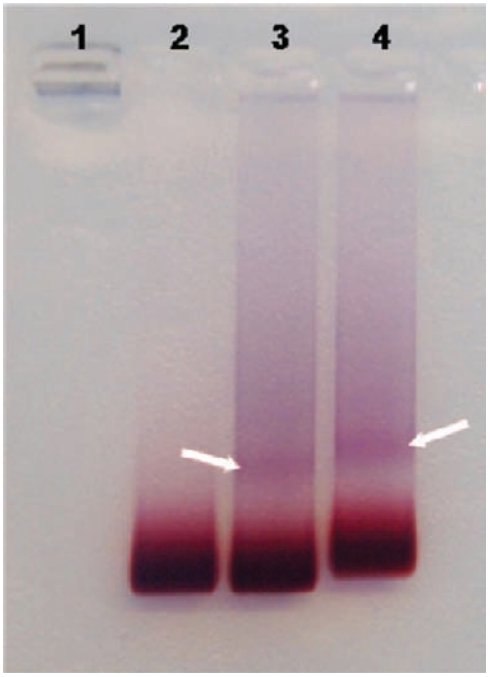

Figure 2. Electrophoretic purification of NP-flowers. Citrate-stabilized Au-NPs (lane 1) coated with 5 tetrad G-quadruplexes (lane 2) and products of 2 h incubation of citrate-stabilized Au-NPs with 30-fold excess of 5 (lane 3) and 10 tetrad (lane 4) coated Au-NPs in 50 mM Na-Pi buffer (pH = 7.4) at 42 °C. 20 μL aliquots of each sample were loaded onto a 1.5% agarose gel and electrophoresed at 130 V for 30 min at 4 °C.

observed during incubation of the particles for 14 h at 42 °C in the presence of 0.2 M NaCL. These particles can be chromatographed in contrast to citrate-stabilized ones, which precipitate in columns. High stability enabled us to use size-exclusion chromatography to purify the particles from nonbound DNA and from a minor fraction of multiparticle structures formed during the incubation. The size exclusion chromatography also enabled us to prepare particles with narrow size distribution. The particles were eluted from Sepharose CL-6B column (16 × 350 mm) in 10 mM Na-Pi (pH 7.4) in two peaks (data not presented). The first peak was eluted close to the void volume of the column and contained violet-colored multiparticle complexes. The second peak was eluted approximately 10 mL after the first one and contained individual red Au-NPs. The latter peak was collected and the particles were concentrated by centrifugation at 10 000 rpm for 20 min on a table centrifuge. The morphology of the particles was elucidated by TEM. As seen in Figure 3A, the particles are uniform and spherical with diameters of 15 ± 0.5 nm.

Despite their inability to interact with each other, the G-quadruplex-coated particles can efficiently bind to citrate-stabilized ones. Incubation of these two types of particles at near-equal concentrations yielded large multiparticle aggregates which do not enter the electrophoretic gel (data not shown). Incubation of 30-fold excess of the quadruplex-coated particles with citrate-stabilized ones, however, resulted in the formation of uniform structures that move as a narrow violet band through the gel (see Figure 2, lanes 3 and 4). The slice corresponding to the band was cut out of the gel with a razor blade. After electroelution into a dialysis bag, the sample was subjected to TEM analysis. As seen in the TEM image (see Figure 3B), the structures comprise a central particle and 5−6 ones in the periphery. They resemble

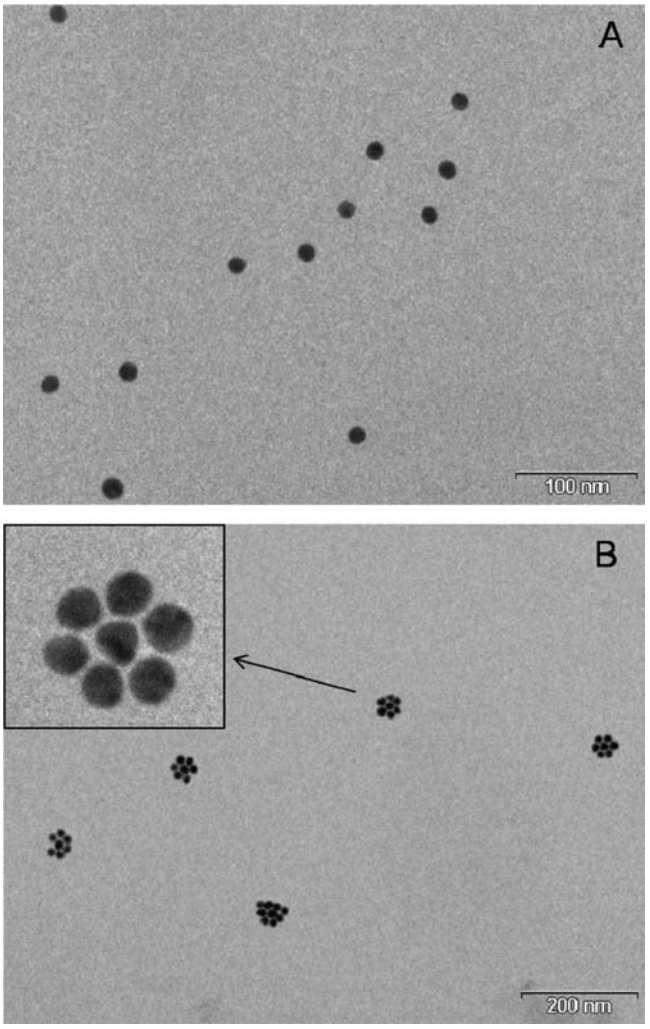

Figure 3. TEM images of (A) 15 nm G-quadruplex coated particles and (B) NP-flowers. The particles were prepared by incubation of 2 μM citrate-stabilized Au-NPs with 20 μM 10 tetrad G-quadruplexes functionalized with phosphorothioated adenine residues as shown in Figure 1. NP-flowers were prepared by incubation of citrate-stabilized Au-NPs with 30-fold excess of Au-NPs coated with 10 tetrad G-quadruplexes as shown in Figure 2. The slice corresponding to a violet band (see Figure 2, lane 4) was cut out of the gel with a razor blade, electroeluted into a dialysis bag, deposited on 400 mesh copper carbon grids, and visualized by TEM. The insert is an enlarged image of one of the flowers.

blue wildflowers, so we will refer to them as "NP-flowers" throughout the work. We have shown that the absorption spectrum of NP-flowers is red-shifted with respect to that of Au-NPs not connected to each other (compare blue and black curves in Figure 4). The red-shifted absorption is due to dipolar electromagnetic coupling between the plasmons of closely spaced nanoparticles in the flower. To investigate the dependence of the coupling strength on the distance between particles, we prepared Au-NPs coated with 5, 10, and 20 tetrad G-quadruplexes functionalized with phosphorothioated residues at both ends as described above (see Scheme 1). We have shown that the stability and the reactivity of Au-NPs are independent of the length of G-quadruplex molecules. To prepare NP-flowers, 15 nm citrate-stabilized Au-NPs were incubated with 30-fold excess of the 5, 10, or 20 tetrad quadruplex-coated 15 nm

Au-NPs. The products were separated by the electrophoresis. As clearly seen in Figure 2 (lanes 3−4), incubation of particles coated with 5 or 10 tetrad G-quadruplexes results in the appearance of a violet band corresponding to NP-flowers. We have shown by TEM (data not presented) that the average number of particles is independent of the length of DNA and is approximately equal to 6. The length of G-quadruplex molecules has, however, a noticeable effect on the shape of the absorption spectrum of the flowers. As seen in Figure 4, the spectrum of NP-flowers made of 20 tetrad G-quadruplexes is similar to that of Au-NPs not connected to each other (compare red and black curves). The spectrum of the 10 tetrad-based NP-flowers is, however, noticeably red-shifted compared to that of individual Au-NPs (compare green and black curves in Figure 4). The shift is even more pronounced for the 5 tetrad-based structures (blue curve in Figure 4). These results are in line with the dependence of plasmon coupling strength on the distance between metal particles (for review, see refs 16−18).

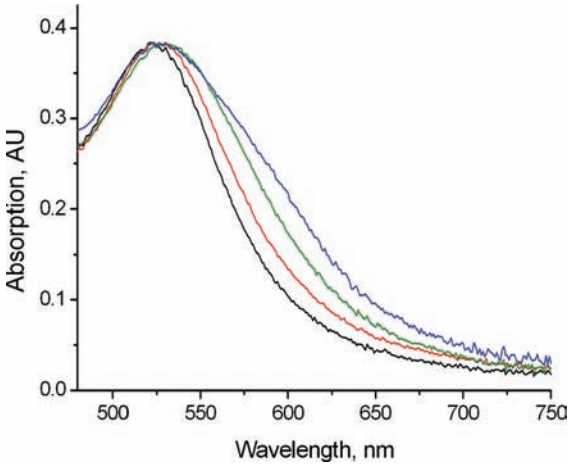

Figure 4. Absorption spectra of NP-flowers. 15 nm Au-NPs (black curve) and 20 (red curve), 10 (green curve), and 5 (blue curve) tetrad-based NP-flowers. The particles and the flowers were prepared as shown in Figures 1 and 2, respectively. The samples were electroeluted from the gel and measured.

We have also synthesized NP-flowers composed of a big (60 nm) central Au-NP particle and smaller (15 nm) peripheral ones. These flowers were prepared by incubation of a 30-fold molar excess of the 10 tetrad quadruplex-coated 15 nm Au-NPs with citrate-stabilized 60 nm ones using the experimental strategy described above. The reaction mixture was electrophoresed, the area of the gel corresponding to the blue band (see Figure 5A) was cut out of the gel, and the structures were electroeluted and analyzed by TEM. As can be clearly seen in the TEM image (see Figure 5B), the structures are composed of many peripheral particles surrounding a bigger central one. Some of peripheral particles are seen as dark spots on top of a central one. Image analysis of more than hundred individual structures revealed that the average number of particles in these NP-flowers is equal to 10 ± 5. As expected, the absorption plasmon band of the flowers is broader and red-shifted compared to that of the particles not connected to each other (compare red curve with blue and black ones in Figure 5C).

DISCUSSION

We have demonstrated that incubation of Au-NPs with a strong excess of G-quadruplexes, comprising phosphorothioate residues, yields stable nanoparticles. These particles do not aggregate even at relatively high (0.2 M) salt concentrations and can be purified and analyzed by electrophoresis and chromatography. Reactive phosphorothioate residues situated on the particle surface covalently bind to gold and silver atoms and can covalently attach the particles to metal electrodes, and other noncoated or weakly coated metal particles. This property can be used for covering metal surfaces and metal electrodes with densely packed particles. The particles can also be used to anchor long DNA molecules to metal surfaces. The method of nanoparticle coating described here is not limited to gold nanoparticles. We produce a similar coating protocol for coating silver particles as well as quantum nanodots.

These particles can be assembled into NP-flowers. We have shown that addition of a small amount (less than 10%) of citrate

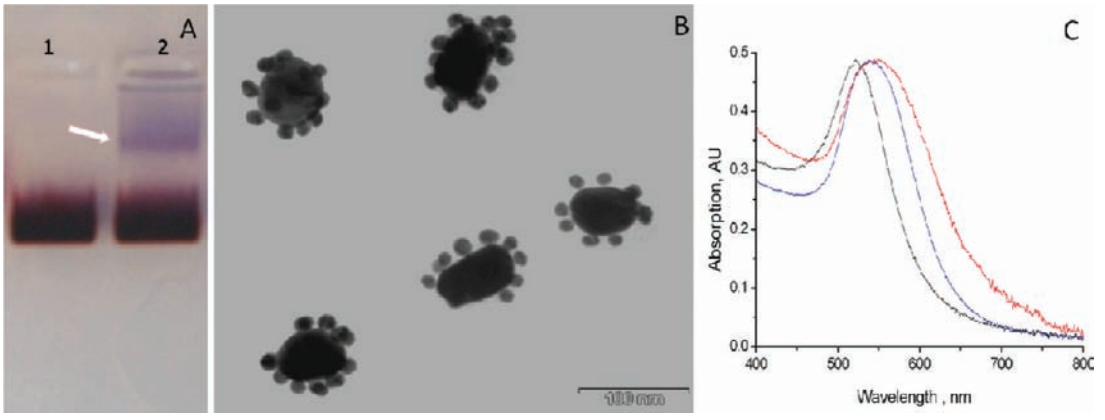

Figure 5. Preparation and properties of big NP-flowers: (A) Electrophoretic separation of NP-flowers from individual Au-NPs. 15 nm Au-NPs coated with 10 tetrad G-quadruplexes (lane 1) and products of 60 nm citrate-stabilized Au-NPs incubation with 30-fold excess of 15 nm Au-NPs coated with 10 tetrad G-quadruplexes (lane 2) in 50 mM Na-Pi buffer (pH = 7.4) for 2 h at 42 °C. 20 μL aliquots of each sample were loaded onto a 1.5% agarose gel and electrophoresed at 130 V for 30 min at 4 °C. (B) TEM image of the flowers. A slice corresponding to the violet band (A, lane 2) was cut out of the gel, and the structures were electroeluted, deposited on 400 mesh copper carbon grids, and visualized by TEM. (C) Absorption spectra of 15 nm Au-NPs coated with 10 tetrad G-quadruplexes (black curve), 60 nm citrate-stabilized Au-NPs (blue curve), and NP-flowers (red curve) electroeluted from the gel (see panel A, lane 2).

Au-NPs to G-quadruplex-coated particles results in the formation of NP-flowers. In the flower, the central citrate Au-NP is surrounded by several quadruplex-coated ones (see Figures 3B and 5B). The flowers composed of identical 15 nm particles are seen in the TEM image (see Figure 3) as planar 2D structures. We have analyzed hundreds of TEM images, but no structures containing additional particles on top of a central one have been found. In contrast, the "flowers" composed of 60 and 15 nm Au-NPs contain many smaller particles on top of a central bigger one (see Figure 5B). We can speculate that a planar arrangement is thermodynamically most favorable due to the repulsion of negatively charged peripheral particles in the NP-flower. We also cannot exclude the possibility that the preference of planar arrangement is governed by interaction of the NP-flower with the surface and that in aqueous solutions the flowers are shaped differently. Further theoretical and experimental studies are needed to address this issue.

We have demonstrated that the absorption spectrum of NP-flowers is red-shifted with respect to that of Au-NPs not connected to each other (see Figures 4 and 5C). The red shift is due to a strong dipolar electromagnetic coupling between the plasmons of closely spaced nanoparticles in the NP-flower. It is well-known that the coupling strength and extent of the coupling-induced red shift increases with decreasing interparticle distance within an individual structure.[19,20] Indeed, we have shown that the degree of the red shift strongly depends on the length of the G4-DNA linker connecting Au-NPs in the flower. G4-DNA structures are much more stable and rigid compared to canonical ds DNA. Even short G-quadruplexes composed of 5−10 tetrads are stable at room temperature in contrast to corresponding double-helical DNA molecules that dissociate into single strands. This enabled us to bring the particles very close together and to investigate plasmon coupling in NP-flowers.

The shift is very pronounced for NP-flowers composed of the particles coated with 5 tetrad G-quadruplexes, and is negligible for those composed of 20 tetrad G-quadruplex-coated ones (see Figure 4). This suggests that the strength of coupling in the flower drops with increasing interparticle separation distance from 1.6 (the length of the 5 tetrad G-quadruplex)[21] to 6.4 nm.

The shift in the plasmon absorption of the NP-flowers from 520 nm (absorption maximum of Au-NPs) to the direction of the biological window along with high stability of the structures make them potentially useful for laser photothermal diagnostics and therapy.

AUTHOR INFORMATION

Corresponding Author

*E-mail: s2shak@post.tau.ac.il.

ACKNOWLEDGMENT

This work was supported by European Commission FP6 Information Society Technologies program, grant "DNA- Based Nanodevices", and by the Israel Science Foundation, grant 172/10.

REFERENCES

(1) Alivisatos, A. P., Johnsson, K. P., Peng, X., Wilson, T. E., Loweth, C. J., Bruchez, M. P., Jr., and Schultz, P. G. (1996) Organization of 'nanocrystal molecules' using DNA. *Nature 382*, 609–11.

(2) Braun, E., Eichen, Y., Sivan, U., and Ben-Yoseph, G. (1998) DNA-templated assembly and electrode attachment of a conducting silver wire. *Nature 391*, 775–8.

(3) Fu, A., Micheel, C. M., Cha, J., Chang, H., Yang, H., and Alivisatos, A. P. (2004) Discrete nanostructures of quantum dots/Au with DNA. *J. Am. Chem. Soc. 126*, 10832–3.

(4) Goluch, E. D., Nam, J. M., Georganopoulou, D. G., Chiesl, T. N., Shaikh, K. A., Ryu, K. S., Barron, A. E., Mirkin, C. A., and Liu, C. (2006) A bio-barcode assay for on-chip attomolar-sensitivity protein detection. *Lab Chip 6*, 1293–9.

(5) Mirkin, C. A., Letsinger, R. L., Mucic, R. C., and Storhoff, J. J. (1996) A DNA-based method for rationally assembling nanoparticles into macroscopic materials. *Nature 382*, 607–9.

(6) Mitchell, G. P., Mirkin, C. A., and Letsinger, R. L. (1999) Programmed assembly of DNA functionalized quantum dots. *J. Am. Chem. Soc. 121*, 8122–8123.

(7) Nam, J. M., Stoeva, S. I., and Mirkin, C. A. (2004) Bio-bar-code-based DNA detection with PCR-like sensitivity. *J. Am. Chem. Soc. 126*, 5932–3.

(8) Nam, J. M., Thaxton, C. S., and Mirkin, C. A. (2003) Nanoparticle-based bio-bar codes for the ultrasensitive detection of proteins. *Science 301*, 1884–6.

(9) Park, S. J., Lazarides, A. A., Mirkin, C. A., Brazis, P. W., Kannewurf, C. R., and Letsinger, R. L. (2000) The electrical properties of gold nanoparticle assemblies linked by DNA. *Angew. Chem., Int. Ed. 39*, 3845–8.

(10) Laughlan, G., Murchie, A. I., Norman, D. G., Moore, M. H., Moody, P. C., Lilley, D. M., and Luisi, B. (1994) The high-resolution crystal structure of a parallel-stranded guanine tetraplex. *Science 265*, 520–4.

(11) Pal, S., Sharma, J., Yan, H., and Liu, Y. (2009) Stable silver nanoparticle-DNA conjugates for directed self-assembly of core-satellite silver-gold nanoclusters. *Chem, Commun. (Camb.)* 6059–61.

(12) Lubitz, I., and Kotlyar, A. (2011) Self-assembled G4-DNA-silver nanoparticle structures. *Bioconjugate Chem. 22*, 482–7.

(13) Kimling, J., Maier, M., Okenve, B., Kotaidis, V., Ballot, H., and Plech, A. (2006) Turkevich method for gold nanoparticle synthesis revisited. *J. Phys. Chem. B 110*, 15700–7.

(14) Demers, L. M., Mirkin, C. A., Mucic, R. C., Reynolds, R. A., Letsinger, R. L., Elghanian, R., and ViswanadhamA, G. (2000) Fluorescence-based method for determining the surface coverage and hybridization efficiency of thiol-capped oligonucleotides bound to gold thin films and nanoparticles. *Anal. Chem. 72*, 5535–41.

(15) Yguerabide, J., and Yguerabide, E. E. (1998) Light-scattering submicroscopic particles as highly fluorescent analogs and their use as tracer labels in clinical and biological applications. *Anal. Biochem. 262*, 137–56.

(16) Khlebtsov, N. G., and Dykman, L. A. (2010) Optical properties and biomedical applications of plasmonic nanoparticles. *J. Quant. Spect. Rad. Trans. 111*, 1–35.

(17) Romo-Herrera, J. M., Alvarez-Puebla, R. A., and Liz-Marzan, L. M. (2011) Controlled assembly of plasmonic colloidal nanoparticle clusters. *Nanoscale 3*, 1304–15.

(18) Moores, A., and Goettmann, F. (2006) The plasmon band in noble metal nanoparticles: an introduction to theory and applications. *New J. Chem. 30*, 1121–32.

(19) Su, K.-H., Wei, Q.-H., Zhang, X., Mock, J. J., Smith, D. R., and Schultz, S. (2003) Interparticle coupling effects on plasmon resonances of nanogold particles. *Nano Lett. 3*, 1087–90.

(20) Rechberger, W., Hohenau, A., Leitner, A., Krenn, J. R., Lamprecht, B., and Aussenegg, F. R. (2003) Optical properties of two interacting gold nanoparticles. *Opt. Commun. 220*, 137–41.

(21) Davis, J. T. (2004) G-quartets 40 years later: from 5′-GMP to molecular biology and supramolecular chemistry. *Angew. Chem., Int. Ed. Engl. 43*, 668–98.

Bioconjugate Chemistry

ARTICLE

pubs.acs.org/bc

Modular Strategy for the Construction of Radiometalated Antibodies for Positron Emission Tomography Based on Inverse Electron Demand Diels–Alder Click Chemistry

Brian M. Zeglis,[†] Priya Mohindra,[†] Gabriel I. Weissmann,[†] Vadim Divilov,[†] Scott A. Hilderbrand,[‡] Ralph Weissleder,[‡] and Jason S. Lewis*[,†]

[†]Department of Radiology and the Program in Molecular Pharmacology and Chemistry, Memorial Sloan-Kettering Cancer Center, New York, New York, United States

[‡]Center for Systems Biology, Massachusetts General Hospital/Harvard Medical School, Boston, Massachusetts, United States

Supporting Information

ABSTRACT: A modular system for the construction of radiometalated antibodies was developed based on the bioorthogonal cycloaddition reaction between 3-(4-benzylamino)-1,2,4,5-tetrazine and the strained dienophile norbornene. The well-characterized, HER2-specific antibody trastuzumab and the positron emitting radioisotopes ^{64}Cu and ^{89}Zr were employed as a model system. The antibody was first covalently coupled to norbornene, and this stock of norbornene-modified antibody was then reacted with tetrazines bearing the chelators 1,4,7,10-tetraazacyclo-dodecane-1,4,7,10-tetraacetic acid (DOTA) or desferrioxamine (DFO) and subsequently radiometalated with ^{64}Cu and ^{89}Zr, respectively. The modification strategy is simple and robust, and the resultant radiometalated constructs were obtained in high specific activity (2.7−5.3 mCi/mg). For a given initial stoichiometric ratio of norbornene to antibody, the ^{64}Cu-DOTA- and ^{89}Zr-DFO-based probes were shown to be nearly identical in terms of stability, the number of chelates per antibody, and immunoreactivity (>93% in all cases). *In vivo* PET imaging and acute biodistribution experiments revealed significant, specific uptake of the ^{64}Cu- and ^{89}Zr-trastuzumab bioconjugates in HER2-positive BT-474 xenografts, with little background uptake in HER2-negative MDA-MB-468 xenografts or other tissues. This modular system—one in which the divergent point is a single covalently modified antibody stock that can be reacted selectively with various chelators—will allow for both greater versatility and more facile cross-comparisons in the development of antibody-based radiopharmaceuticals.

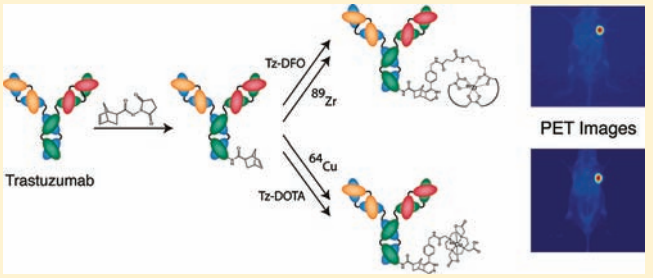

INTRODUCTION

Over the past two decades, radiopharmaceuticals based on antibodies have assumed an increasingly prominent role in both diagnostic and therapeutic nuclear medicine. This trend is particularly evident in the field of positron emission tomography (PET), in which a wide variety of effective antibody-based radiotracers have been developed against an array of cancer biomarkers.[1−3] Indeed, while some promising imaging agents have been labeled with long-lived nonmetallic radionuclides such as ^{124}I, the majority of antibody-based PET bioconjugates have employed positron-emitting radiometals, including ^{64}Cu, ^{86}Y, and, most recently, ^{89}Zr.[4−8] In these systems, radiometals offer significant advantages over their nonmetallic cousins, most notably decay characteristics that result in high image quality, radioactive half-lives that complement the biological half-lives of the antibody vectors, and enhanced control and ease of radiolabeling through the use of chelating moieties.

Despite their benefits, however, these chelating moieties are the source of a somewhat confounding issue in the study of radiometalated antibodies. Put simply, different radiometals require different chelators. For example, the small, hard ^{89}Zr^{4+} cation shows very high affinity for the multiple oxygen donors of the chelator desferrioxamine (DFO), while the larger and softer ^{64}Cu^{2+} cation exhibits higher thermodynamic and kinetic stability when bound to chelators bearing nitrogen donors in addition to oxygens, for example, 1,4,7,10-tetraazacyclo-dodecane-1,4,7,10-tetraacetic acid (DOTA) and 1,4,8,11-tetraazabicyclo[6.6.2]hexadecane-4,11-diyl)diacetic acid (CB-TE2A).[6,9] Further, different chelators often require dramatically different synthetic strategies for antibody couplings.[10] In an isolated case of one antibody and one radiometal, these facts do not present a problem. However, they do create a significant obstacle to the versatility of radiometalated bioconjugates. To wit, given a particular monoclonal antibody, the development of a ^{64}Cu-CB-TE2A-mAb conjugate for PET, a ^{89}Zr-DFO-mAb conjugate for PET, and a ^{225}Ac-DOTA-mAb conjugate for therapy would require three different routes

Received: June 4, 2011
Revised: August 22, 2011
Published: August 31, 2011

ACS Publications © 2011 American Chemical Society

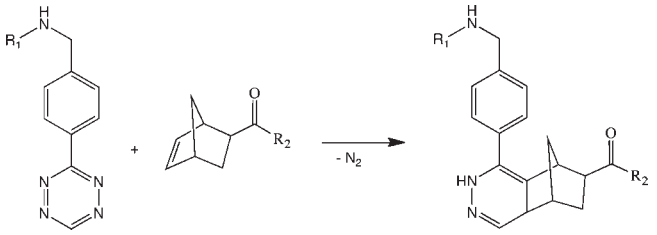

Figure 1. Tetrazine−norbornene ligation.

for antibody modification. Not only would this require additional time to develop and optimize each pathway, but the disparate routes would also mandate differing reaction conditions for each antibody, opening the door for differences in immunoreactivity and chelator/antibody ratio and ultimately making meaningful comparisons among the various radiopharmaceuticals more difficult. Consequently, a modular system—one in which the divergent point is a single covalently modified antibody stock that can be reacted selectively with various chelators—would resolve these issues and allow for more versatility and cross-comparisons in the development of antibody-based radiopharmaceuticals.

The chemical requirements of such a modular system—selectivity, biocompatibility, bioorthogonality—make it an almost perfect application for the use of click chemistry. Coined by K. Barry Sharpless, the term "click chemistry" broadly defines a group of chemical reactions by which two molecular components can be joined via a selective, rapid, clean, bioorthogonal, and biocompatible ligation.[11−13] By far, the most popular example of click chemistry is the Cu(I)-catalyzed [3 + 2] Huisgen cycloaddition between an azide and alkyne.[14] This reaction has already been widely employed in the development of radiotracers, particularly ^{18}F-based PET probes.[15−18] The application of this technology to radiometal-based probes has lagged behind, however, most likely due to concerns over metal contamination by the catalyst itself, though "clickable" chelators based on both the Cu(I)-catalyzed reaction and other Cu(I)-free systems have become more common in the literature in recent years.[19−22] Very recently, another promising "click" variant has come to light: the inverse electron demand Diels−Alder reaction between a tetrazine moiety and a strained alkene dienophile (Figure 1).[23−25] Like other click reactions, the ligation is selective, fast, biocompatible, and bioorthogonal, and unlike many Diels−Alder reactions, the coupling is irreversible, forming stable pyridazine products after the retro-Diels−Alder release of dinitrogen from the reaction intermediate. A number of different tetrazine-strained alkene pairs have been explored for the reaction, though the combination of 3-(4-benzylamino)-1,2,4,5-tetrazine (Tz) and either norbornene- or trans-cyclooctene-derivatives seems well-suited for biological applications. To date, the ligation has been employed in a variety of settings: the modification of oligonucleotides;[26] fluorescence imaging with small molecules, antibodies, and nanoparticles;[23,24,27,28] SPECT imaging with antibodies;[29] and ^{18}F-PET imaging with peptides.[30,31] However, to the best of the authors' knowledge, no application of this technology to positron-emitting radiometals has yet been made.

Herein, we report the development of a modular strategy for the construction of radiolabeled antibodies using the tetrazine-norbornene click reaction. The synthetic pathway involves three simple steps: (1) creation of a common stock of norbornene-modified antibody via peptide coupling; (2) ligation of a chelator-modified tetrazine moiety to the norbornene-modified antibody; and (3) radiolabeling of the resultant construct (Figure 2). For this proof of concept investigation, we have chosen the positron-emitting radiometals ^{64}Cu and ^{89}Zr, the chelators DOTA and DFO, and the antibody trastuzumab. ^{64}Cu and ^{89}Zr are the two most common radionuclides employed in antibody-based PET bioconjugates, and DOTA and DFO, respectively, are the most common chelators employed with these two metals.[6,9,10,32−34]

The antibody at hand, trastuzumab (Herceptin, Genentech), is an extremely well-characterized antibody specific to the human epidermal growth factor receptor 2 (HER2, also known as ERBB2). Overexpression of HER2 has been shown to be associated with augmented metastatic potential, increased tumor aggression, and poor prognosis for disease-free survival for patients with a variety of malignancies, most notably breast, ovarian, and colorectal cancer.[35−38] Trastuzumab alone has been employed as a therapeutic agent, and conjugates of both the antibody and its derivative fragments have been synthesized bearing a wide variety of radionuclides—including ^{64}Cu, ^{86}Y, ^{111}In, ^{124}I, ^{99m}Tc, and ^{89}Zr—for PET and SPECT imaging of HER2 expression.[39−47] It is our hope that this modular methodology will aid in both the expansion of the comparative study of antibodies labeled with different radionuclides and the development of novel antibody-based radiopharmaceuticals. Since more and more antibodies and dienophiles are being developed, this modular approach will likely lead to the rapid development of many novel imaging agents.[28] Importantly, while we have used positron-emitting radionuclides in this study due to our laboratory's area of expertise, this modular system need not be applied only to PET radiometals but rather can be used across the spectrum of metallic radionuclides, encompassing those employed for SPECT and radiotherapy as well.

EXPERIMENTAL PROCEDURES

Materials. All chemicals, unless otherwise noted, were acquired from Sigma-Aldrich (St. Louis, MO) and were used as received without further purification. All water employed was ultrapure (>18.2 MΩ cm^{-1} at 25 °C, Milli-Q, Millipore, Billerica, MA), and was passed through a 10 cm column of Chelex resin (Bio-Rad Laboratories, Hercules, CA) before use. DMSO was of molecular biology grade (>99.9%: Sigma, D8418), and all other solvents were of the highest grade commercially available. 1,4,7,10-Tetraazacyclododecane-1,4,7,10-tetraacetic acid mono-*N*-hydroxysuccinimidylester (DOTA-NHS) was purchased from Macrocyclics Inc. (Dallas, TX). *N*-Succinyldesferrioxamine B was prepared according to published procedures.[48] All instruments were calibrated and maintained in accordance with standard quality-control procedures.[49] UV−vis measurements were taken on a Cary 100 Bio UV−vis spectrophotometer. NMR spectroscopy was performed on a Bruker 500 MHz NMR with *Topsin 2.1* software for spectrum analysis. HPLC was performed using a Shimadzu HPLC equipped with a C-18 reversed-phase column (Phenomenex Luna analytical 4.6 × 250 mm or Semi-Prep 21.2 × 100 mm, 5 μm, 1.0 or 6.0 mL/min), 2 LC-10AT pumps, a SPD-M10AVP photodiode array detector, and a gradient of 0:100 MeCN/H_2O (both with 0.1% TFA) to 100:0 MeCN/H_2O over 15 min].

^{64}Cu was purchased from Washington University, St. Louis, where it was produced on the Washington University School of Medicine Cyclotron (model CS-15, Cyclotron Corp.) by the ^{64}Ni(p,n)^{64}Cu reaction and purified as previously described to

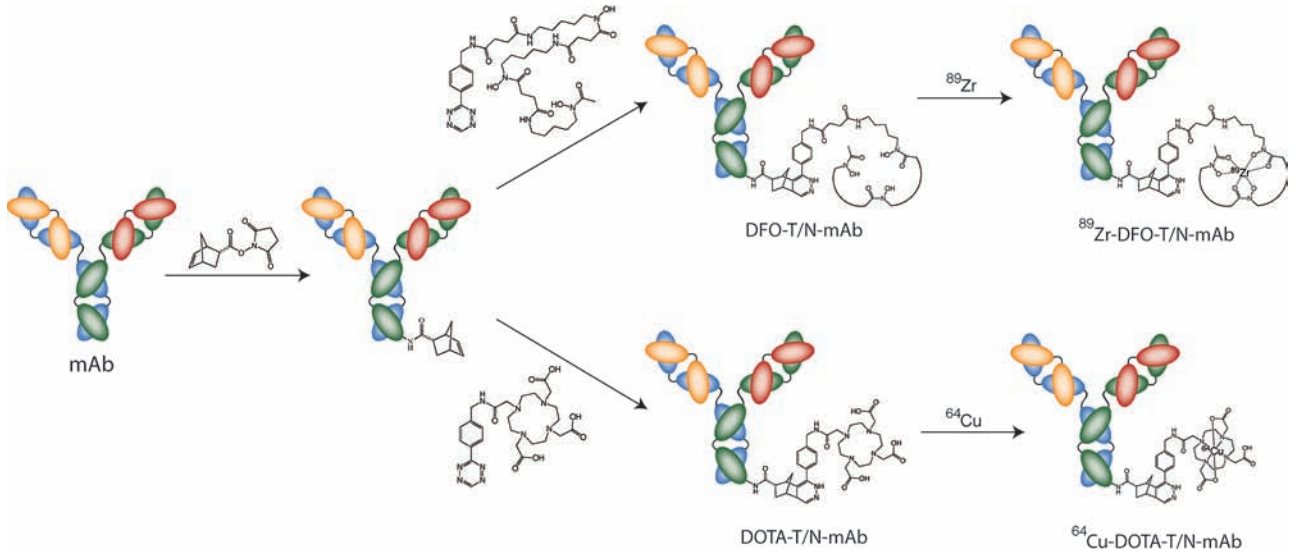

Figure 2. Schematic of a modular strategy for the construction of ^{89}Zr- and ^{64}Cu-modified antibody bioconjugates using the tetrazine-norbornene ligation.

yield [^{64}Cu]$CuCl_2$ with an effective specific activity of 200−400 mCi/μg (7.4−14.8 GBq/μg).[50] ^{89}Zr was produced at Memorial Sloan-Kettering Cancer Center on an EBCO TR19/9 variable-beam energy cyclotron (Ebco Industries Inc., British Columbia, Canada) via the ^{89}Y(p,n)^{89}Zr reaction and purified in accordance with previously reported methods to yield ^{89}Zr with a specific activity of 5.28−13.43 mCi/μg (195−497 MBq/μg).[51] All buffers used for ^{64}Cu and ^{89}Zr labeling were passed through Chelex resin before use. Activity measurements were made using a Capintec CRC-15R Dose Calibrator (Capintec, Ramsey, NJ). For accurate quantification of activities, experimental samples were counted for 1 min on a calibrated Perkin-Elmer (Waltham, MA) Automatic Wizard^2 Gamma Counter. Both ^{64}Cu and ^{89}Zr labeling reactions were monitored using silica-gel impregnated glass-fiber instant thin layer chromatography paper (Pall Corp., East Hills, NY) and analyzed on a Bioscan AR-2000 radio-TLC plate reader using Winscan Radio-TLC software (Bioscan Inc., Washington, DC). Human breast cancer cell lines BT-474 and MDA-MB-468 were obtained from the American Type Culture Collection (ATCC, Manassas, VA) and were grown by serial passage.

Synthesis of 3-(4-Benzylamino)-1,2,4,5-tetrazine (Tz). The protocol from Deveraj et al. was employed for the synthesis with slight modifications.[24] 4-(Aminomethyl)-benzonitrile hydrochloride (0.84 g, 0.005 mol) formamidine acetate (2.08 g, 0.02 mol), and elemental sulfur (0.16 g, 0.005 mol) were added to a dry, 50 mL round-bottom flask. Anhydrous hydrazine (2 mL) was then added to the flask, and the resultant orange reaction mixture was stirred for 20 h. After the allotted time, 1% $HCl_{(aq)}$ (50 mL) was slowly added to the reaction mixture, and the resultant solution was stirred for 10 min and subsequently filtered through a medium glass frit. The remaining orange solution was cooled in an ice bath to 0 °C, and a solution of 1.7 g of $NaNO_2$ in 15 mL of water was then added dropwise to the reaction mixture. While still cooled in an ice bath, acetic acid (50 mL) was added slowly, and the reaction mixture immediately turned bright pink. After allowing this solution to warm to room temperature over the course of 3 h, the solvent was evaporated at 50 °C and 20 Torr on a rotary evaporator. The resultant red crude solids were dissolved in 250 mL of water with 0.1% TFA. The aqueous solution was adsorbed onto a C_{18} column (Waters C_{18} Sep-Pak, Waters Corp., Milford, MA), washed with copious amounts of water, and eluted with acetonitrile. This bright pink, organic solution was evaporated to dryness, and the red crude was purified by flash chromatography (CombiFlash automated chromatography system, Teledyne Isco Inc., Lincoln, NE) using a gradient of 100% $CHCl_3$ (0.01% TFA) from 0 to 4 min followed by 0:100 MeOH (0.01%TFA)/$CHCl_3$ (0.01% TFA) to 30:70 (0.01%TFA)/HCl_3 (0.01% TFA) over 16 min. After the removal of solvent, the pure product was obtained in 35% yield (0.33 g, 0.0018 mol). ^{1}H NMR (500 MHz, D_2O), δ, ppm: 10.46 (s, 1H), 8.54 (d, 2H), 7.77 (d, 1H), 4.41 (s, 2H). ESI-MS: 188.1 $[M+H]^+$. HPLC t_R = 7.1 min.

Synthesis of N^1-(5-(4-((4-(1,2,4,5-Tetrazin-3-yl)benzyl)amino)-4-oxobutanamido)pentyl)-N^1-hydroxy-N^4-(5-(*N*-hydroxy-4-((5-(*N*-hydroxyacetamido)pentyl)amino)-4-oxobutanamido)pentyl)succinamide (Tz-DFO). 3-(4-Benzylamino)-1,2,4,5-tetrazine (8 mg, 0.045 mmol) was dissolved in DMSO (3 mL), and diisopropylethylamine (16 μL, 0.09 mmol) was added to this solution. After 15 min of stirring at RT, the pink DMSO solution was added to a second, premixed solution of *N*-succinyldesferrioxamine B (60 mg, 0.09 mmol) and benzotriazole-1-yl-oxy-tris-(dimethylamino)-phosphonium hexafluorophosphate (BOP, 53 mg, 0.12 mmol) in DMSO (3 mL). The combined reaction was stirred overnight and subsequently purified via C_{18} cartridge (Waters C_{18} Sep-Pak, Waters Corp., Milford, MA) and semipreparative reverse-phase HPLC. The purified product was obtained in 50% yield (molecular weight = 852.9, 19 mg, 0.023 mmol). ^{1}H NMR (500 MHz, DMSO-d_6), δ, ppm: 10.59 (s, 1H), 9.64 (s, 1H), 9.59 (s, 1H), 8.49 (m, 1H), 8.44 (d, 2H), 7.9−7.7 (m, 3H), 7.51 (d, 2H), 4.44 (d, 2H), 3.5−3.5 (m, 6H), 3.05−2.95 (m, 6H), 2.55 (t, 4H), 2.45−2.35 (m, 4H), 2.25 (t, 4H), 1.97 (s, 3H), 1.52−1.48 (m, 6H), 1.40−1.36 (m, 6H), 1.23−1.20 (m, 6H). ESI-MS: 831.5 $[M+H]^+$, 853.6 $[M+Na]^+$. HPLC t_R = 10.2 min.

Synthesis of 2,2′,2″-(10-(2-((4-(1,2,4,5-Tetrazin-3-yl)benzyl)amino)-2-oxoethyl)-1,4,7,10-tetraazacyclododecane-1,4,7-triyl)triacetic acid (Tz-DOTA). 3-(4-Benzylamino)-1,2,4,5-tetrazine (20 mg, 0.12 mmol) was dissolved in PBS (5 mL, pH 8.5), and diisopropylethylamine (40 μL, 0.24 mmol) was added

to this solution. This solution was then added to solid DOTA-NHS (50 mg, 0.065 mmol), and the resultant solution was stirred overnight at room temperature. The reaction was subsequently purified via C_{18} cartridge (Waters C_{18} Sep-Pak, Waters Corp., Milford, MA) and semipreparative reverse-phase HPLC. The purified product was obtained in 62% yield (molecular weight = 573.6, 23 mg, 0.04 mmol). ^{1}H NMR (500 MHz, DMSO-d_6), δ, ppm: 10.61 (s, 1H), 9.11 (br s, 1H), 8.50 (d, 2H), 7.62 (d, 2H), 4.50 (s, 2H), 4.42−4.38 (m, 4H), 3.65 (br s, 4H), 10.61 (s, 1H), 3.65−3.55 (m, 8H), 3.18−3.14 (m, 8H). ESI-MS: 574.5 $[M+H]^+$, 596.1 $[M+Na]^+$, 612.2 $[M+K]^+$. HPLC t_R = 8.1 min.

Antibody Modification. A protocol similar to that published by Devaraj et al. was employed for antibody modification.[24] 5-Norbornene-2-carboxylic acid (40 mg, 0.29 mmol) was incubated with 1.3 equiv of disuccinimidyl carbonate (100 mg, 0.39 mmol) and 1 equiv of pyridine (23 mg, 0.29 mmol) in dry acetonitrile (3 mL) for 2 h at room temperature. After 2 h, the solvent was removed via rotary evaporation, and the crude norbornene-succinimidyl ester product was recovered. Trastuzumab (purchased commercially as Herceptin, Genentech, San Francisco, CA) was purified using centrifugal filter units with a 30 000 molecular weight cutoff (Amicon Ultra 4 Centrifugal Filtration Units, Millipore Corp., Billerica, MA) and phosphate buffered saline (PBS, pH 7.4) to remove $\alpha-\alpha$-trehalose dihydrate, L-histidine, and polysorbate 20 additives. After purification, the antibody was taken up in PBS pH 8.0. Subsequently, 300 μL of antibody solution (150−250 μM) were combined with 100 μL PBS pH 8.0 and 1.5, 3, or 5 equiv of the crude norbornene-NHS ester in 10 μL of either DMF or DMSO. The reaction was incubated at room temperature for 2 h, followed by centrifugal filtration to purify the resultant antibody conjugate.

To perform the chelator ligation, 100 μL antibody solution (75−150 μM, PBS pH 7.4) was combined with 200 μL buffer (PBS pH 7.4) and a 10-fold molar excess of either Tz-DOTA or Tz-DFO in 10 μL DMSO (molar excess calculated based on initial norbornene reaction stoichiometry). The reaction was incubated at RT for 5 h and subsequently purified using centrifugal filtration to yield the completed DOTA- and DFO-modified antibodies. The final bioconjugates were stored in PBS pH 7.4 at 4 °C.

Labeling of DOTA-T/N-trastuzumab with ^{64}Cu. DOTA-T/N-trastuzumab (0.2−0.3 mg) was added to 200 μL labeling buffer (50 mM NH_4OAc, pH 5.5, though 50 mM NaOAc, pH 5.5 also is sufficient). $[^{64}Cu]CuCl_2$ (29.6−37 MBq, 800−1000 μCi) in approximately 1−3 μL 0.1 M HCl were then added to the antibody solution, and the resultant solution was incubated at room temperature for 1 h. After 1 h, the reaction progress was assayed using ITLC with an eluent of 50 mM EDTA, pH 5. The resultant ^{64}Cu-DOTA-T/N-trastuzumab was purified using either size-exclusion chromatography (Sephadex G-25 M, PD-10 column, 30 kDa, GE Healthcare; dead volume = 2.5 mL, eluted with 200 mL fractions of PBS, pH 7.4) or centrifugal column filtration. The radiochemical purity of the final radiolabeled bioconjugate was assayed by radio-TLC and was found to be >99% in all preparations. In the ITLC experiments, ^{64}Cu-DOTA-T/N-trastuzumab remains at the baseline, while $^{64}Cu^{2+}$ ions and $[^{64}Cu]$Cu-EDTA elute with the solvent front.

Labeling of DFO-T/N-trastuzumab with ^{89}Zr. DFO-T/N-trastuzumab (0.2−0.3 mg) was added to 200 μL buffer (PBS, pH 7.5). $[^{89}Zr]$Zr-oxalate (29.6−37 MBq, 800−1000 μCi) in 1.0 M oxalic acid was adjusted to pH 7.2−8.5 with 1.0 M Na_2CO_3. After evolution of CO_2(g) stops, the ^{89}Zr solution was added to the antibody solution, and the resultant mixture was incubated at room temperature for 1 h. After 1 h, the reaction progress was assayed using ITLC with an eluent of 50 mM EDTA, pH 5. The resultant ^{89}Zr-DFO-T/N-trastuzumab was purified using either size-exclusion chromatography (Sephadex G-25 M, PD-10 column, 30 kDa, GE Healthcare; dead volume = 2.5 mL, eluted with 200 mL fractions of PBS, pH 7.4) or centrifugal column filtration. The radiochemical purity of the final radiolabeled bioconjugate was assayed by radio-TLC and was found to be >99% in all preparations. In the ITLC experiments, ^{89}Zr-DFO-T/N-trastuzumab remains at the baseline, while $^{89}Zr^{4+}$ ions and $[^{89}Zr]$-EDTA elute with the solvent front.

Chelate Number. The number of accessible DFO and DOTA chelates conjugated to the antibodies was measured by radiometric isotopic dilution assays following methods similar to those described by Anderson et al. and Holland et al.[34,42,52,53] All experiments were performed in triplicate.

Immunoreactivity. The immunoreactivity of the ^{64}Cu-DOTA- and ^{89}Zr-DFO-T/N-trastuzumab bioconjugates was determined using specific radioactive cellular-binding assays following procedures derived from Lindmo et al.[54,55] To this end, BT-474 cells were suspended in microcentrifuge tubes at concentrations of 5.0, 4.0, 3.0, 2.5, 2.0, 1.5, and 1.0 × 10^6 cells/mL in 500 μL PBS (pH 7.4). Aliquots of either ^{64}Cu-DOTA- or ^{89}Zr-DFO-T/N-trastuzumab (50 μL of a stock solution of 10 μCi in 10 mL of 1% bovine serum albumin in PBS pH 7.4) were added to each tube (n = 4; final volume: 550 μL), and the samples were incubated on a mixer for 60 min at room temperature. The treated cells were then pelleted via centrifugation (3000 rpm for 5 min), resuspended, and washed twice with cold PBS before removing the supernatant and counting the activity associated with the cell pellet. The activity data were background-corrected and compared with the total number of counts in appropriate control samples. Immunoreactive fractions were determined by linear regression analysis of a plot of (total/bound) activity against (1/[normalized cell concentration]). No weighting was applied to the data, and data were obtained in triplicate.

Stability Measurements. The stability of the ^{64}Cu-DOTA- and ^{89}Zr-DFO-T/N-trastuzumab bioconjugates with respect to radiochemical purity and loss of radioactivity from the antibody was investigated *in vitro* by incubation of the antibodies in human serum for 48 h (^{64}Cu) or 7 d (^{89}Zr) at room temperature and 37 °C. The radiochemical purity of the antibodies was determined via radio-TLC with an eluent of 50 mM EDTA pH 5.0 (*vide supra*).

Cell Culture. Human breast cancer cell lines BT474 and MDA-MB-468 were obtained from the American Tissue Culture Collection (HTB-20 and HTB-132, respectively, ATCC, Bethesda, MD) and maintained in a 1:1 mixture of Dulbecco's Modified Eagle medium: F-12 medium, supplemented with 10% heat-inactivated fetal calf serum (Omega Scientific, Tarzana, Ca), 2.0 mM glutamine, nonessential amino acids, and 100 units/mL penicillin, and 100 units/mL streptomycin in a 37 °C environment containing 5% CO_2. Cell lines were harvested and passaged weekly using a formulation of 0.25% trypsin/0.53 mM EDTA in Hank's Buffered Salt Solution without calcium and magnesium.

Xenograft Models. All experiments were performed under an Institutional Animal Care and Use Committee-approved protocol, and the experiments followed institutional guidelines for the proper and humane use of animals in research. Six- to eight-week-old Athymic nu/nu female mice (NCRNU-M) were obtained from Taconic Farms Incorporated (Hudson, NY). Animals were

housed in ventilated cages, were given food and water *ad libitum*, and were allowed to acclimatize for approximately 1 week prior to treatment. Prior to tumor inoculation, mice were subcutaneously implanted with 0.72 mg 60 day release 17β-estradiol pellets (SE-121, Innovative Research of America, Sarasota, Florida) using a 10 gauge trocar. After several days, BT474 tumors were induced on the right shoulder by a subcutaneous injection of 3.0×10^6 cells in a 100 μL cell suspension of a 1:1 mixture of fresh media/BD Matrigel (BD Biosciences, Bedford, Ma). MDA-MB-468 tumors were induced on the left shoulder by a subcutaneous injection of 2.0×10^6 cells in the same manner (the number of cells injected was varied as described to compensate for cell growth rates and thus provide approximately the same tumor size at the time of radiopharmaceutical injection).

Acute Biodistribution. Acute *in vivo* biodistribution studies were performed in order to evaluate the uptake of the ^{64}Cu-DOTA- and ^{89}Zr-DFO-conjugated antibodies in mice bearing bilateral, subcutaneous BT-474 and MDA-MB-468 tumors (100−150 mm^3, 4 weeks postinoculation). Mice were randomized before the study and were warmed gently with a heat lamp for 5 min before administration of ^{64}Cu-DOTA-T/N-trastuzumab (0.74−1.11 MBq [20−30 μCi] in 200 μL 0.9% sterile saline) or ^{89}Zr-DFO-T/N-trastuzumab (0.56−0.74 MBq [15−20 μCi] in 200 μL 0.9% sterile saline) via intravenous tail vein injection (t = 0). Animals (n = 4 per group) were euthanized by CO_2(g) asphyxiation at 6, 12, 24, 36, 48, and 72 h (^{64}Cu) or 6, 24, 48, 72, 96, and 120 h (^{89}Zr). After asphyxiation, 13 organs (including both tumors) were removed, rinsed in water, dried in air for 5 min, weighed, and counted in a gamma counter calibrated for either ^{64}Cu or ^{89}Zr. Counts were converted into activity using a calibration curve generated from known standards. Count data were background- and decay-corrected to the time of injection, and the percent injected dose per gram (%ID/g) for each tissue sample was calculated by normalization to the total activity injected.

Small-Animal PET Imaging. PET imaging experiments were conducted on either a microPET Focus 120 (^{89}Zr) or a microPET R4 (^{64}Cu) rodent scanner (Concorde Microsystems).[56] Mice bearing bilateral, subcutaneous BT-474 (right shoulder) and MDA-MB-468 (left shoulder) tumors (100−150 mm^3, 4 weeks postinoculation) were administered ^{64}Cu-DOTA-T/N-trastuzumab (11.1−12.9 MBq [300−345 μCi] in 200 μL 0.9% sterile saline) or ^{89}Zr-DFO-T/N-trastuzumab (10.7−11.8 MBq [290−320 μCi] in 200 μL 0.9% sterile saline) via intravenous tail vein injection (t = 0). Approximately 5 min prior to the acquisition of PET images, mice were anesthetized by inhalation of 2% isoflurane (Baxter Healthcare, Deerfield, IL)/oxygen gas mixture and placed on the scanner bed; anesthesia was maintained using 1% isoflurane/gas mixture. PET data for each mouse were recorded via static scans at various time points between 6 and 120 h. A minimum of 20 million coincident events were recorded for each scan, which lasted between 10 and 45 min. An energy window of 350−700 keV and a coincidence timing window of 6 ns were used. Data were sorted into 2D histograms by Fourier rebinning, and transverse images were reconstructed by filtered back-projection (FBP) into a 128 × 128 × 63 (0.72 × 0.72 × 1.3 mm^3) matrix. The image data were normalized to correct for nonuniformity of response of the PET, dead-time count losses, positron branching ratio, and physical decay to the time of injection, but no attenuation, scatter, or partial-volume averaging correction was applied. The counting rates in the reconstructed images were converted to activity concentrations (percentage injected dose [%ID] per gram of tissue) by use of a system calibration factor derived from the imaging of a mouse-sized water-equivalent phantom containing ^{64}Cu or ^{89}Zr. Images were analyzed using *ASIPro VM* software (Concorde Microsystems).

Labeling Norbornene-Trastuzumab with [^{64}Cu]-Tz-DOTA. Tz-DOTA (5 μL of 1 mM solution in DMSO) was added to labeling buffer (50 mM NH_4OAc, pH 5.5), and [^{64}Cu]$CuCl_2$ (40.7−55.5 MBq [1100−1500 μCi]) in 0.1 M HCl were added to the reaction mixture. The resultant solution was incubated for 1 h at 85 °C, followed by purification via C_{18} cartridge (Waters C_{18} Sep-Pak, Waters Corp., Milford, MA) and radiochemical purity analysis via analytical HPLC (t_R = 10 min). The purified, radiolabeled [^{64}Cu]-Tz-DOTA was then added to a solution of norbornene-modified trastuzumab (0.4 mg, initial reaction stoichiometry of 5:1 norbornene/mAb) in PBS pH 7.4. The reaction mixture was allowed to incubate at 37 °C for 3 h. After 3 h, the progress of the reaction was assayed with radio-TLC using an eluent of 50 mm EDTA pH 5.0, and the radiolabeled antibody was purified with centrifugal filtration using centrifugal filter units with a 30 000 molecular weight cutoff (Amicon Ultra 4 Centrifugal Filtration Units, Millipore Corp., Billerica, MA) and phosphate buffered saline (PBS, pH 7.4). The radiochemical purity of the final radiolabeled bioconjugate was assayed again by radio-TLC and was found to be >99% in all preparations. In the radio-TLC experiments, ^{64}Cu-DOTA-T/N-trastuzumab remains at the baseline, while $^{64}Cu^{2+}$ ions, [^{64}Cu]Cu-Tz-DOTA, and [^{64}Cu]Cu-EDTA elute with the solvent front.

Statistical Analysis. Data were analyzed by the unpaired, two-tailed Student's t test. Differences at the 95% confidence level ($P < 0.05$) were considered to be statistically significant.

RESULTS AND DISCUSSION

Chemical Synthesis. 3-(4-Benzylamino)-1,2,4,5-tetrazine (Tz) was successfully synthesized through the reaction of 4-(aminomethyl)-benzonitrile hydrochloride, formamidine acetate, and elemental sulfur to form a dihydrotetrazine intermediate ((4-(1,2-dihydro-1,2,4,5-tetrazin-3-yl)phenyl)methanamine), followed by oxidation with $NaNO_2$ to form the aromatic tetrazine product. A method similar to that published by Devaraj et al. was employed; however, a number of small changes—for example, the use of 1% $HCl_{(aq)}$ rather than acetic acid in an intermediate step—were made and were found to considerably raise yields from the reported 20% to 35−40%. The product was characterized via UV−vis, ^{1}H NMR, ^{13}C NMR, and ESI-MS, and all data match that described in the original synthetic report.[24] Given the particularly promising nature of this cycloaddition reaction, the optimization of this synthesis was an important task. Tz was chosen as the particular tetrazine-based moiety for this line of experimentation due to its convenient, primary-amine coupling handle and its balance of reactivity and stability. To be sure, other tetrazine-based molecules with possible conjugation sites exist, but water instability (dimethyl 1,2,4,5-tetrazine-3,6-dicarboxylate), poor reactivity (1,2,4,5-tetrazine-3,6-diamine or 3,6-bis-(4-aminophenyl)-1,2,4,5-tetrazine), or instability (6-(6-(pyridin-2-yl)-1,2-dihydro-1,2,4,5-tetrazin-3-yl)pyridin-3-amine) render them unsuitable to the development of a modular system such as this.[29,57−59] Tz-DOTA and Tz-DFO (Scheme 1) were synthesized from Tz via simple peptide coupling reactions using the commercially available mono-NHS-ester of DOTA or *N*-succinyldesferrioxamine B and benzotriazole-1-yl-oxy-tris-(dimethylamino)-phosphonium hexafluorophosphate (BOP), respectively.

Scheme 1. Synthetic Route to Tz-DOTA and Tz-DFO

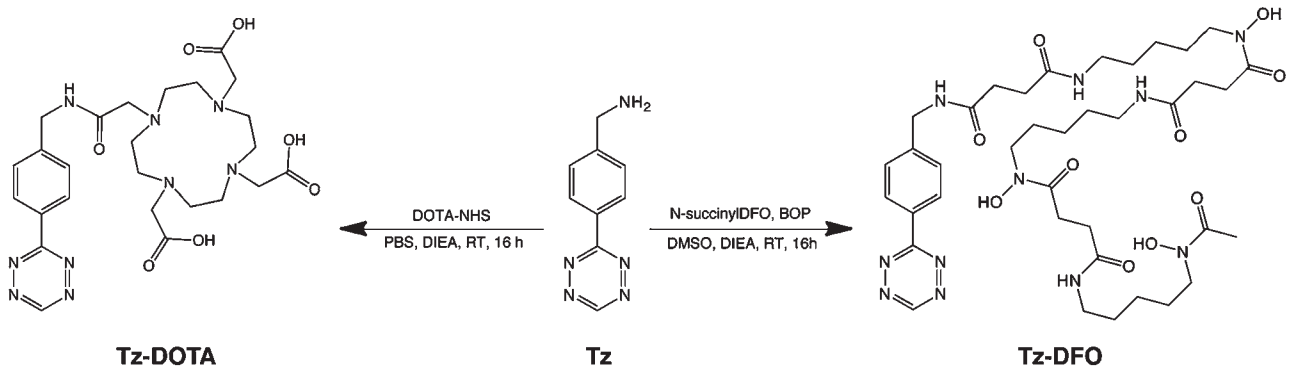

Table 1. Chemical and Biological Characterization Data for ^{64}Cu-DOTA-T/N- and ^{89}Zr-DFO-T/N-trastuzumab Bioconjugates

radionuclide	chelator	initial Nor/mAb reaction stoichiometry	chelates/mAb[a]	specific activity (mCi/mg)	immunoreactive fraction[b]	stability[c]
^{64}Cu	DOTA	1.5	1.0 ± 0.2	3.2 ± 0.4	0.96 ± 0.05	>98%
		3	2.3 ± 0.4	3.1 ± 0.2	0.95 ± 0.03	>96%
		5	3.7 ± 0.7	5.3 ± 0.5	0.94 ± 0.02	>96%
^{89}Zr	DFO	1.5	1.1 ± 0.3	2.7 ± 0.2	0.96 ± 0.03	>98%
		3	2.2 ± 0.3	2.9 ± 0.3	0.96 ± 0.04	>98%
		5	3.8 ± 0.9	4.3 ± 0.4	0.93 ± 0.05	>97%

[a] $n = 3$ for all experiments presented. [b] Determined prior to *in vivo* experimentation. [c] Calculated for incubation in human serum at 37 °C for 48 h (Cu) or 7 d (Zr).

Upon synthesis, both molecules were purified via reversed-phase HPLC and fully characterized by UV−vis, ^{1}H NMR, ^{13}C NMR, and ESI-MS. Importantly, Tz-DOTA exhibits high water solubility, but Tz-DFO does not. Consequently, DMSO was used as the stock solvent and delivery vehicle for both Tz-DOTA and Tz-DFO throughout the investigation in order to ensure that the antibodies in different branches of the modular pathway were exposed to exactly the same reaction conditions. Indeed, given the ease of synthesis of both Tz-DOTA and Tz-DFO, it is easy to envision the creation of a complete library of tetrazine-modified chelators—ranging from Tz-AmBaSar to Tz-HBED to Tz-DTPA—in order to maximize the utility and versatility of this modular construction strategy.

Antibody Modification, Radiolabeling, and Characterization. The radiolabeled trastuzumab bioconjugates were constructed via a modular three-step procedure (Figure 2). A common stock of norbornene-modified mAb was first produced via the room-temperature aqueous coupling of an NHS-ester of 5-norbornene-2-carboxylic acid with the exposed lysines of trastuzumab. After purification, the resultant norbornene-modified antibodies were then incubated for 5 h at room temperature with a 10-fold excess (based on norbornene loading) of the appropriate tetrazine-modified chelator—Tz-DOTA for ^{64}Cu or Tz-DFO for ^{89}Zr—and purified via centrifugal filtration or size exclusion chromatography. The bioconjugates were radiometalated with ^{64}Cu or ^{89}Zr at room temperature under either acidic (pH 5.5) or basic (pH 7.2−8.5) conditions, respectively. The crude radiochemical yields varied according to the initial norbornene loading of the antibody; however, after purification via centrifugal filtration, the ^{64}Cu-DOTA- or ^{89}Zr-DFO-T/N-trastuzumab conjugates were isolated with RCP >99% ($n = 3$ for each construct). The modification and radiolabeling strategy is simple, robust, and relatively rapid, and no antibody aggregation or precipitation issues were observed. Unlike other methods for the modification of mAbs with DOTA or DFO, overnight incubations, wide swings in buffer pH, and temperatures over room temperature are not required.[60−64] Importantly, we also observed that the tetrazine-norbornene ligation and subsequent radiolabeling proceeded almost identically whether performed the day of norbornene modification of the antibody or four weeks later (and likely after much longer periods of time, provided the antibody is stored at 4 °C). The radiolabeling of the DOTA- and DFO-modified trastuzumab conjugates is likewise robust, with the reaction providing similar yields with freshly prepared or four-week-old mAbs.

A number of chemical and *in vitro* tests were performed in order to characterize the chelator-modified and radiolabeled antibody constructs. Three different initial reaction stoichiometries of norbornene:mAb—1.5:1, 3:1, and 5:1—were employed to investigate the effect of different chelator loadings on the performance of the antibody. After the ligation of the variably norbornene-loaded antibodies with either Tz-DOTA or Tz-DFO, radiometric isotopic dilution experiments were performed in order to determine the number of accessible chelates on each antibody. The results, shown in Table 1, clearly illustrate that increasing initial loadings of norbonene result in higher numbers of chelates per antibody. Given the quantitative nature of the tetrazine/norbornene ligation and the proximity of the number of chelates per antibody to the initial modification stoichiometry in each case, calculating the loading of norbornenes per antibody was deemed unnecessary. The combined yield of the modification and ligation reactions is relatively consistent across all three

stoichiometries (~40−60%), and the results are generally consistent with antibody ligations using tetrazine/dienophile pairs reported by Devaraj et al., Haun et al., and Rossin et al.[23,28,29] Just as importantly, the number of chelates per antibody is, within error, identical for both the DOTA-T/N-trastuzumab and DFO-T/N-trastuzumab conjugates, a critical facet for such a modular system. Not surprisingly, the varying chelate numbers also played a role in the specific activities obtained for each antibody. All of the antibody conjugates were labeled in high specific activity (>2.0 mCi/mg). Interestingly, the specific activities of both the ^{64}Cu-DOTA-T/N-trastuzumab and ^{89}Zr-DFO-T/N-trastuzumab conjugates only roughly correlate with the number of chelates per antibody: those for ^{64}Cu-DOTA-T/N-trastuzumab range from 3.2 ± 0.4 mCi/mg to 5.3 ± 0.5 mCi/mg, though the specific activities for bioconjugates with initial nor/mAb ratios of 1.5:1 and 3:1 are within error of each other. Similarly, the specific activities of the ^{89}Zr-DFO-T/N-trastuzumab conjugates range from 2.7 ± 0.2 mCi/mg to 4.3 ± 0.4 mCi/mg, but again, the specific activities of the two conjugates with fewer DFO/mAb are statistically identical. Given the different specific activities of the original radiometals, comparisons between the specific activities of the two types of construct have little merit; however, the specific activities obtained in this investigation are consistent with those reported for other ^{64}Cu-DOTA-based and ^{89}Zr-DFO-based antibody bioconjugates in the literature.[6,10,34,42,45]

The immunoreactive fractions of the ^{64}Cu-DOTA- and ^{89}Zr-DFO-conjugates were determined via specific *in vitro* cellular association assays using the HER2/*neu* positive BT-474 breast cancer cell line.[54] Regardless of the number of chelates per antibody, all six conjugates exhibited immunoreactive fractions greater than 0.93 (n = 3 for each radiolabeled antibody). Blocking experiments performed with the addition of a vast excess (>500-fold) of unlabeled trastuzumab showed virtually no radioactive antibody binding and thus demonstrated the specificity of the ^{64}Cu-DOTA- and ^{89}Zr-DFO-T/N-trastuzumab. To assay the stability of radiolabeled bioconjugates, the ^{64}Cu-DOTA- and ^{89}Zr-DFO-T/N-trastuzumab formulations were incubated in human serum for 48 h and 7 d, respectively. Radio-TLC with an eluent of 50 mM EDTA (pH 5.0) illustrated that both sets of conjugates were >96% stable after the incubation period in all cases (Table 1).

Acute Biodistribution Studies. Acute biodistribution experiments and small animal PET imaging were performed in order to assay the *in vivo* efficacy of the ^{64}Cu and ^{89}Zr-bioconjugates. For all *in vivo* investigations, the trastuzumab bioconjugates with an initial nor/mAb stoichiometry of 5:1 were chosen, though similar results would be expected for all three ratios given the uniformly high immunoreactivity, stability, and specific activity observed in all of the constructs. In the biodistrubution experiment, nude mice bearing bilateral BT-474 (HER2-positive) and MDA-MB-468 (HER2-negative) were injected via tail vein with either ^{64}Cu-DOTA-T/N-trastuzumab (0.74−1.11 MBq [20−30 μCi] in 200 μL 0.9% sterile saline, specific activity: 5.1 mCi/mg) or ^{89}Zr-DFO-T/N-trastuzumab (0.56−0.74 MBq [15−20 μCi] in 200 μL 0.9% sterile saline, specific activity: 4.7 mCi/mg). Animals (n = 4 for each time point) were euthanized by CO_2(g) asphyxiation at 6, 12, 24, 36, 48, and 72 h (^{64}Cu) or 6, 24, 48, 72, 96, and 120 h (^{89}Zr). The organs (including tumors) of each animal were harvested and weighed, the amount of activity in each was counted on a gamma counter, and the %ID/g for each organ was calculated.

Table 2. Biodistribution Data of ^{64}Cu-DOTA-T/N-trastuzumab versus Time in Mice Bearing Bilateral s.c. BT-474 (HER2-positive) and MDA-MB-468 (HER2-negative) Xenografts (n = 4 for Each Time Point)

	6 h	12 h	24 h	48 h	72 h
blood	19.2 ± 5.2	16.2 ± 4.1	10.5 ± 3.6	11.2 ± 1.6	11.8 ± 1.3
HER2+ tumor	10.4 ± 4.6	23.9 ± 4.6	26.1 ± 4.8	44.0 ± 7.7	55.1 ± 2.3
HER2- tumor	6.2 ± 1.1	8.6 ± 2.7	9.0 ± 0.9	8.7 ± 2.5	11.7 ± 1.3
heart	4.9 ± 1.1	6.7 ± 2.7	4.3 ± 0.8	4.3 ± 1.2	5.7 ± 3.1
lungs	12.2 ± 1.2	9.5 ± 1.5	6.4 ± 2.3	8.0 ± 1.3	9.5 ± 0.4
liver	11.5 ± 2.0	10.1 ± 0.4	9.7 ± 1.3	6.4 ± 0.2	8.1 ± 0.9
spleen	11.1 ± 5.5	10.1 ± 1.4	10.6 ± 2.3	5.7 ± 0.4	6.9 ± 1.4
stomach	1.9 ± 0.7	1.0 ± 0.4	2.4 ± 0.3	1.3 ± 0.3	1.8 ± 0.2
sm intestine	3.5 ± 1.5	2.1 ± 0.3	3.5 ± 1.6	2.2 ± 0.1	2.6 ± 0.1
lg intestine	2.0 ± 0.3	1.7 ± 0.1	3.1 ± 1.7	1.4 ± 0.3	2.0 ± 0.4
kidney	5.5 ± 0.9	4.9 ± 1.0	2.9 ± 1.6	4.0 ± 0.4	4.5 ± 0.4
muscle	0.6 ± 0.2	0.7 ± 0.4	0.6 ± 0.3	1.0 ± 0.2	0.8 ± 0.1
bone	3.1 ± 2.7	1.4 ± 0.1	3.6 ± 0.4	1.1 ± 0.2	2.6 ± 1.1

In the ^{64}Cu-DOTA-T/N-trastuzumab biodistribution experiment (Table 2), high specific uptake is observed in the HER2-positive BT-474 tumor, with the %ID/g increasing from 10.4 ± 4.6 at 6 h to 55.1 ± 2.3 at 72 h (tumor/muscle ratios of 17.3 ± 7.1 and 68.8 ± 8.0, respectively). By comparison, far lower levels of ^{64}Cu-DOTA-T/N-trastuzumab uptake were seen in the HER2-negative MDA-MB-468 tumors. As expected, over the course of the experiment a concomitant decrease in the %ID/g in the blood (from 19.2 ± 5.2 at 6 h to 11.8 ± 1.3 at 72 h) also occurred. The organs with the highest background uptake were the lungs, liver, and spleen, though the uptake in these organs was at its highest point at 6 h, and by 72 h, the tumor/organ ratios for each of these organs were 5.8 ± 0.3, 6.8 ± 0.8, and 8.0 ± 1.6, respectively (see Supporting Information for complete table of tumor/organ ratios). Low levels of uptake were observed in the heart, stomach, small intestine, large intestine, kidney, muscle, and bone. Taken together, these results plainly indicate that ^{64}Cu-DOTA-T/N-trastuzumab is an effective imaging agent for the delineation of the HER2-positive BT-474 xenografts. Perhaps just as importantly, these results are consistent with those previously reported for ^{64}Cu-DOTA-T/N-trastuzumab conjugates, though the literature investigation used HER2-positive and HER2-negative non-small cell lung cancer cell lines.[65] Interestingly, far lower background liver uptake was observed in our study, and while comparisons between different tumor models systems may bear some risks, this discrepancy suggests a lower rate of ^{64}Cu decomplexation in our system.

Similarly positive results were observed in the ^{89}Zr-DFO-T/N-trastuzumab biodistribution experiments (Table 3). Initially very high blood activity levels decreased over the course of the experiment, from 42.2 ± 8.8%ID/g at 6 h to 18.2 ± 3.3%ID/g at 120 h. More importantly, high specific uptake was observed in the HER2-positive BT474 tumors, peaking at over 75%ID/g at 72 h postinjection (tumor to muscle ratio: 34.1 ± 12.7). In contrast, the uptake in the HER2-negative MDA-MB-468 tumors was significantly lower, starting at 11.2 ± 5.80%ID/g at 6 h and peaking at 120 h at 17.6 ± 3.9%ID/g. Highest background uptake was observed in the lungs, liver, spleen, and kidney, with uptake values ranging from 7 to 17%ID/g and typically decreasing over the course of the experiment. Maximum tumor to organ

Table 3. Biodistribution Data of ^{89}Zr-DFO-T/N-trastuzumab versus Time in Mice Bearing Bilateral s.c. BT-474 (HER2-positive) and MDA-MB-468 (HER2-negative) Xenografts (n = 4 for Each Time Point)

	6 h	24 h	48 h	72 h	96 h	120 h
blood	42.2 ± 8.8	37.4 ± 3.4	24.1 ± 6.1	24.1 ± 8.2	20.2 ± 2.1	18.2 ± 3.3
HER2+ tumor	22.9 ± 6.6	48.6 ± 6.9	64.0 ± 6.8	75.1 ± 7.6	72.2 ± 7.9	69.8 ± 3.9
HER2- tumor	11.2 ± 5.0	13.4 ± 4.1	14.5 ± 8.8	16.8 ± 2.7	16.7 ± 6.8	17.6 ± 1.7
heart	24.1 ± 5.7	17.7 ± 6.9	6.0 ± 3.2	9.6 ± 3.8	8.5 ± 3.2	10.4 ± 0.9
lungs	15.5 ± 2.4	15.8 ± 5.4	10.5 ± 4.6	11.9 ± 4.8	13.8 ± 8.1	12.9 ± 3.2
liver	24.2 ± 5.0	17.6 ± 4.7	16.0 ± 6.5	15.8 ± 1.4	12.8 ± 2.7	13.5 ± 7.3
spleen	11.3 ± 1.2	14.2 ± 5.3	15.0 ± 5.1	14.9 ± 5.2	12.6 ± 6.5	10.8 ± 5.3
stomach	6.7 ± 1.4	3.1 ± 0.2	2.5 ± 0.7	2.0 ± 0.5	1.9 ± 0.4	1.8 ± 0.3
small intestine	8.4 ± 1.7	6.3 ± 0.3	7.9 ± 2.9	4.8 ± 1.1	3.8 ± 0.9	4.4 ± 0.8
large intestine	4.5 ± 1.0	2.1 ± 0.6	1.7 ± 0.2	2.3 ± 0.9	1.0 ± 0.3	1.4 ± 0.5
kidney	15.9 ± 5.4	13.3 ± 1.2	7.0 ± 1.3	11.6 ± 2.6	10.2 ± 0.3	8.7 ± 2.9
muscle	2.2 ± 0.6	2.3 ± 0.2	1.6 ± 0.5	2.2 ± 0.4	2.2 ± 0.2	2.5 ± 0.2
bone	12.1 ± 0.8	13.2 ± 2.4	14.6 ± 3.8	15.2 ± 1.9	14.7 ± 3.1	15.1 ± 1.5

ratios for the lungs, liver, spleen, and kidney were 6.2 ± 2.6 (72 h), 5.6 ± 1.3 (96 h), 6.6 ± 3.2 (120 h), 9.8 ± 3.4 (72 h), respectively (see Supporting Information for complete table of complete tumor/organ ratios). As in the case of ^{64}Cu-DOTA-T/N-trastuzumab, after the earliest time points, only low levels of uptake were detected in the stomach, small intestine, large intestine, and muscle. Interestingly, distinct bone uptake is also observed, with %ID/g values ranging from 12.1 ± 0.8 at 6 h to 15.2 ± 1.9 at 72 h. This is certainly not a surprise, for residual bone uptake of ^{89}Zr has been reported on a number of occasions, and a recently publication by Abou et al. has shown that bone uptake is the *in vivo* fate of a number of species of ^{89}Zr, including [^{89}Zr]Zr-oxalate, [^{89}Zr]Zr-chloride, [^{89}Zr]Zr-citrate.[34,42,66] While a full discussion of the metabolic fate of ^{89}Zr-DFO-T/N-trastuzumab or ^{89}Zr-DFO is, of course, out of the scope of this work, it is interesting to note that the bone uptake does not increase dramatically over the course of the experiment, suggesting that the majority of ^{89}Zr deposition in the bone occurs very soon after injection.

Overall, these results are generally consistent with those previously reported for ^{89}Zr-trastuzumab bioconjugates by Munnink et al. and Holland et al.[42,43] No other data have been published on the uptake of ^{89}Zr-trastuzumab in HER2-negative MDA-MB-468 tumors; however, the uptake value obtained at 24 h in this study (13.4 ± 4.1%ID/g) is remarkably similar to the value obtained at the same time point in the blocking experiment (200 μg additional unlabeled trastuzumab) performed by Holland et al. with BT-474 cells: 13.5 ± 4.8%ID/g. While this latter experiment is not, of course, directly comparable, it does help establish a baseline for the nonspecific tumor uptake of radiolabeled antibody.

Overall, two key differences are evident upon comparing the biodistribution data obtained with ^{89}Zr-DFO-T/N-trastuzumab and ^{64}Cu-DOTA-T/N-trastuzumab. The first, increased bone uptake in the ^{89}Zr-DFO-T/N-trastuzumab experiment, is easily explained: free $^{89}Zr^{4+}$ is a bone-seeking radiometal, while free $^{64}Cu^{2+}$ has not been shown to accumulate in bone. Second, the HER2-specific tumor uptake and background signal (including initial blood levels) are higher in the ^{89}Zr-DFO-T/N-trastuzumab biodistribution than at the corresponding time points in the ^{64}Cu-DOTA-T/N-trastuzumab experiment. For example, at 6 h, the blood levels for ^{89}Zr-DFO-T/N-trastuzumab are 42.2 ± 8.8%ID/g, while they are 19.2 ± 5.2%ID/g for ^{64}Cu-DOTA-T/N-trastuzumab. Later, at 48 h, the uptake in the HER2-positive BT-474 tumor for ^{89}Zr-DFO-T/N-trastuzumab is 72.2 ± 7.9%ID/g, while for ^{64}Cu-DOTA-T/N-trastuzumab, it is 44.0 ± 7.7%ID/g. Moreover, at 48 h, the liver uptake of ^{89}Zr-DFO-T/N-trastuzumab stands at 12.8 ± 2.7%ID/g, while it is 6.4 ± 0.2%ID/g for ^{64}Cu-DOTA-T/N-trastuzumab at the same time point. It is possible that these variations in background uptake result from differences in the metabolism of the ^{89}Zr-DFO- and ^{64}Cu-DOTA-modified antibodies. The increase in HER2-specific uptake of the ^{89}Zr-DFO-T/N-trastuzumab is somewhat more puzzling, though these data are consistent with that obtained in other investigations of ^{64}Cu- and ^{89}Zr-trastuzumab.[42,65] In the case of small peptides, it has been previously reported that the identity of the radiometal may play a role in the uptake of otherwise identical radiopharmaceuticals;[67] however, given the vast size of antibodies, it is far less likely that the identity of the radiometal would exert as strong an influence in this case. Experiments are currently underway to further elucidate the origins of the differences between the pharmacodynamics of two conjugates.

Despite these differences, the biodistribution data plainly illustrate that both radiolabeled constructs are selectively and significantly taken up in the HER2-positive tumors. In addition, and perhaps more important in light of the goals of the investigation, the overall trends observed in uptake and tumor/organ ratio are strikingly similar in the two experiments.

Small Animal PET Imaging. Small animal PET imaging experiments were performed in order to further evaluate the *in vivo* behavior of the two radiometalated bioconjugates. In each case, nude mice (n = 5 for each construct) bearing bilateral BT-474 (HER2-positive) and MDA-MB-468 (HER2-negative) xenografts were injected via tail vein with either ^{64}Cu-DOTA-T/N-trastuzumab (11.1−12.9 MBq [300−345 μCi]) or ^{89}Zr-DFO-T/N-trastuzumab (10.7−11.8 MBq [290−320 μCi]). The animals were subsequently imaged periodically from injection (t = 0 h) to 48 h (^{64}Cu) or 120 h (^{89}Zr). The results clearly indicate that both constructs are taken up significantly and selectively in the HER2-positive BT-474 tumors (shown in Figures 3 and 4). In the case of ^{64}Cu-DOTA-T/N-trastuzumab, high blood pool activity and some background uptake are evident at the early time points, but over the course of the experiment, the

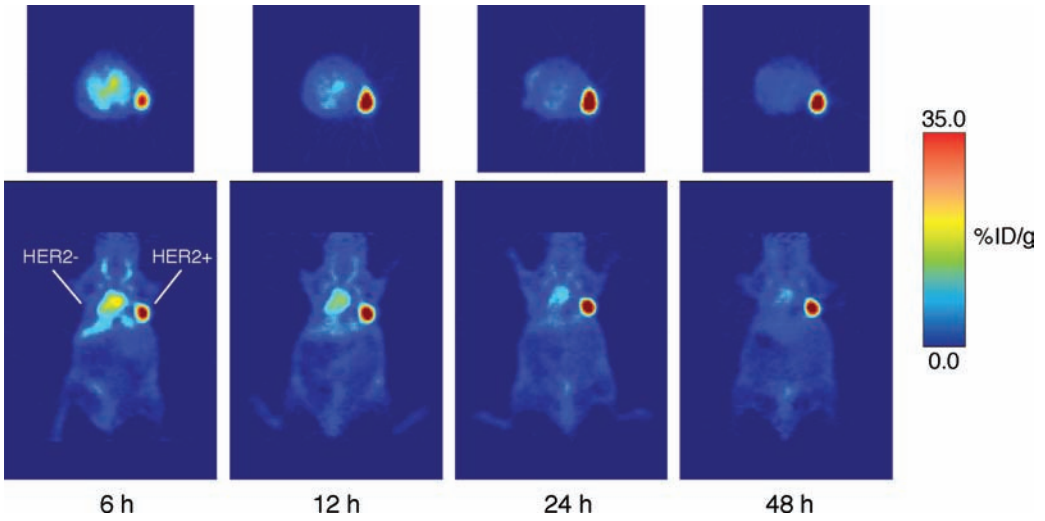

Figure 3. PET images of ^{64}Cu-DOTA-T/N-trastuzumab (11.1−12.9 MBq [300−345 μCi] in 200 μL 0.9% sterile saline) in mice bearing bilateral BT-474 (HER2-positive, right shoulder) and MDA-MB-468 (HER2-negative, left shoulder) tumors between 6 and 48 h postinjection. The transverse (top) and coronal (bottom) planar images intersect the center of the tumors.

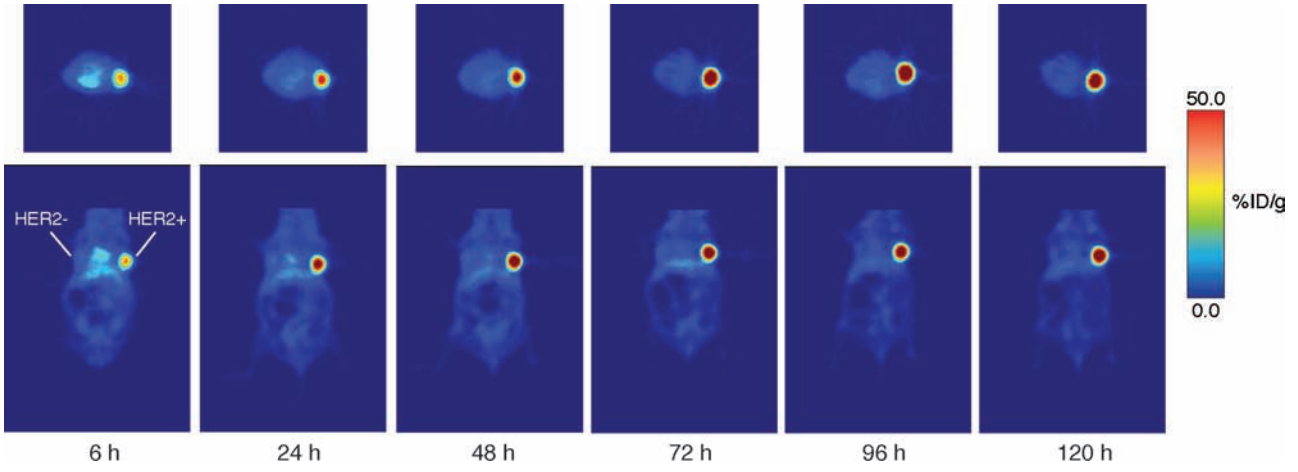

Figure 4. PET images of ^{89}Zr-DFO-T/N-trastuzumab (10.7−11.8 MBq [290−320 μCi] in 200 μL 0.9% sterile saline) in mice bearing bilateral BT-474 (HER2-positive, right shoulder) and MDA-MB-468 (HER2-negative, left shoulder) tumors between 6 and 120 h postinjection. The transverse (top) and coronal (bottom) planar images intersect the center of the tumors.

signal in the BT-474 tumor increases significantly to a point at which it is easily the most intense feature in the PET image. Similarly, for ^{89}Zr-DFO-T/N-trastuzumab, some blood pool activity is evident at the earliest time point, but the tumor uptake increases steadily in the subsequent time points along with a concomitant decrease in any background activity. The images produced by the two conjugates are very similar, a result that is consistent with the sum of the data collected in this investigation. In each case, very little background uptake is evident in either the HER2-negative MDA-MB-468 tumor or other organs. The only significant differences, as in the biodistribution experiments, are enhanced tumor and background uptake in the ^{89}Zr-DFO-T/N-trastuzumab images compared to those from ^{64}Cu-DOTA-T/N-trastuzumab and slight bone uptake of the former construct. The bone uptake is not evident in the images displayed in Figure 5 but can be spotted (though faint) in a maximum intensity projection (see Supporting Information). Just as important as the imaging similarities between the two constructs in this study, the images obtained here are consistent with those reported for other ^{89}Zr- and ^{64}Cu-trastuzumab radioagents in the literature.

Radiolabeling Trastuzumab with a Two-Step Ligation Strategy. The modular strategy described to this point comprises three simple steps: norbornene modification, tetrazine-chelator ligation, and radiometalation. However, the versatility of the tetrazine-norbornene ligation makes an alternate route possible as well: a two-step procedure in which a norbornene-modified antibody is reacted with a radiometalated, chelator-modified tetrazine (Figure 5). Indeed, similar ligations of dienophiles with radiolabeled tetrazines have already been employed with success with ^{18}F and ^{111}In, though in these cases, a transcyclooctene dienophile was employed rather than a norbornene.[29−31] To demonstrate the feasibility of such a strategy with PET radiometals, Tz-DOTA (5 nmol) was radiolabeled with ^{64}Cu (1.1−1.5 mCi) in 50 mM NH_4OAc pH 5.5 via incubation at 85 °C for 1 h (n = 3 trials). After the 1 h incubation, the labeling reaction was purified via radio-HPLC, and the product was obtained in an uncorrected

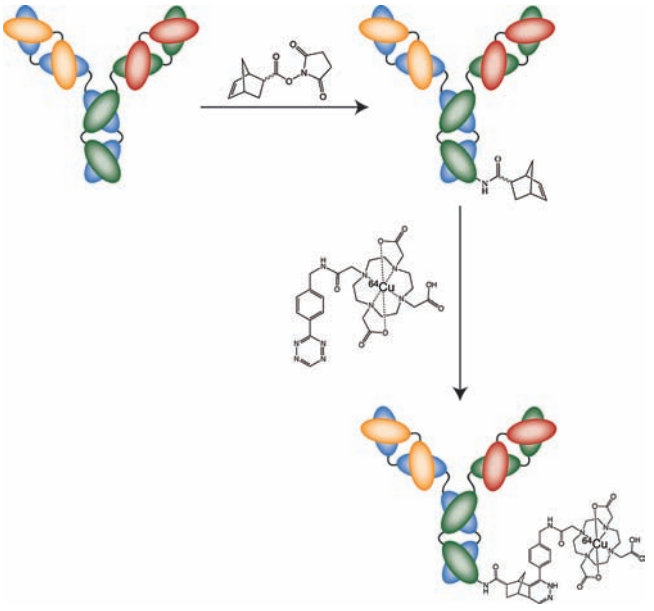

Figure 5. Schematic of the two-step radiolabeling strategy based on the ligation of norbornene-modified antibody and ^{64}Cu-labeled Tz-DOTA.

radiochemical yield of 80 ± 3% with greater than 99% radiochemical purity and a specific activity of 160 ± 5 mCi/μmol. Subsequently, this ^{64}Cu-Tz-DOTA was incubated with norbornene-modified trastuzumab (0.4 mg, 1.3 nmol, initial norbornene/mAb stoichiometry of 5:1) in PBS pH 7.4 (200 μL) at 37 °C. The progress of the reaction was monitored with radio-TLC, and after 3 h, the reaction was gauged to have reached completion. After purification via centrifugal filtration, the completed ^{64}Cu-DOTA-T/N-trastuzumab conjugate was isolated in ~75% radiochemical yield and in >99% radiochemical purity with a specific activity of 1.0 ± 0.4 mCi/mg. Granted, this specific activity is somewhat lower than that obtained with the three-step method; however, further optimization, though outside of the scope of the work at hand, could no doubt raise this specific activity to levels on par with that achieved with the three-step strategy.

Ultimately, it is our belief that the three-step method is preferable as a modular strategy for radiolabeling antibodies. This method holds the key advantage of only involving a single and relatively rapid radiochemical step, thereby minimizing the amount of radiochemistry needed for the creation of the bioconjugates while simultaneously maximizing specific activities. However, it is clear from the work currently in the literature —particularly that of Devaraj et al. and Rossin et al.—that the two-step method holds significant potential as a strategy for pretargeted antibody or peptide imaging.[23,24,27−29,31] In this application, a dienophile-modified biomolecule is first injected into a tumor-bearing animal and is permitted time to achieve its optimal biodistribution. Subsequently, a fluorophore- or radionuclide-modified tetrazine moiety is injected into the same animal and, due to the bioorthogonal nature of the tetrazine-dienophile ligation, could selectively react with the dienophile-modified biomolecule, resulting in specific localization of the marker. Indeed, both the optical and nuclear pretargeting strategies have shown very promising results. It is important to note, though, that the pretargeting systems described in the literature employ more reactive, less stable trans-cyclooctene dienophiles instead of the more stable, less reactive norbornene dienophile used in this study. Experiments are currently underway toward the creation of a pretargeting system for positron-emitting radiometals employing more reactive dienophiles.

CONCLUSION

In summary, herein we report the development of a modular system for the radiometalation of antibodies using the inverse electron demand Diels−Alder cycloaddition between tetrazine and norbornene. The strategy involves three facile, rapid, and biocompatible steps: modification of an antibody with norbornene, ligation of a chelator-modified tetrazine, and radiometalation. In this proof of concept investigation, the methodology was employed to create bioconjugates of the HER2-specific antibody trastuzumab bearing the positron-emitting radiometals ^{64}Cu and ^{89}Zr in high radiochemical purity and specific activity. For a given initial loading of norbornene, the DOTA- and DFO-modified constructs were shown to have identical numbers of chelates per antibody, and all of the radiolabeled ^{64}Cu-DOTA- and ^{89}Zr-DFO-bioconjugates displayed high serum stability and immunoreactivity. Finally, both radiolabeled bioconjugates were used in *in vivo* biodistribution and PET imaging studies with mice bearing HER2-positive (BT-474) and HER2-negative (MDA-MB-468) breast cancer xenografts. Both antibody constructs were shown to have significant and specific uptake in the HER2-positive tumor with low uptake in the HER2-negative tumor and other tissues.

This strategy does not necessarily offer a significant improvement in facility compared to popular DOTA-NHS or DFO-NCS antibody modification protocols; more importantly, however, it creates a modular platform in which a common, covalently modified antibody can be modified with a wide variety of chelators and radiometals. Given that different radiometals often require different chelators—and thus the use and optimization of different modification pathways—this methodology could no doubt aid in the rapid and robust construction of diverse radiopharmaceuticals from a single antibody stock. Further, this modular system could facilitate the creation of meaningful comparisons between bioconjugates labeled with different radiometals: as we have shown, because the chelator-modified antibodies are synthesized using identical ligation conditions, the immunoreactivity and chelator/antibody ratios of the resultant bioconjugates are likewise nearly identical regardless of the identity of the tetrazine−chelator pair.

Ultimately, therefore, this modular methodology has the potential not only to significantly aid in the synthesis and development of new radiometalated bioconjugates for PET, SPECT, and radiotherapy, but also to advance cross-pollination and constructive comparisons between radiopharmaceuticals employing diverse metallic radionuclides.

ASSOCIATED CONTENT

Supporting Information. Tables of tumor to muscle uptake ratios from ^{89}Zr-DFO-T/N-trastuzumab and ^{64}Cu-DOTA-T/N-trastuzumab biodistribution experiments and maximum intensity projection PET image of ^{89}Zr-DFO-T/N-trastuzumab indicating residual bone uptake. This material is available free of charge via the Internet at http://pubs.acs.org.

AUTHOR INFORMATION

Corresponding Author

*Phone: 1-646-888-3039. Fax: 1-646-888-3059. E-mail: lewisj2@mskcc.org.

ACKNOWLEDGMENT

The authors thank Dr. Jason P. Holland for insight and helpful conversations, Valerie Longo for aid with animal imaging experiments, Nicholas Ramos for aid in the purification of ^{89}Zr, and Alexander Veach for technical assistance. Services provided by the MSKCC Small-Animal Imaging Core Facility were supported in part by NIH grants R24 CA83084 and P30 CA08748. The authors also thank the NIH (Award 1F32CA1440138-01, BMZ; Award R01EB010011, RW) and the DOE (Award DE-SC0002184, JSL) for their generous funding.

REFERENCES

(1) van Dongen, G. A. M. S., Visser, G. W. M., Lub-de Hooge, M. N., de Vries, E. G., and Perk, L. R. (2007) Immuno-PET: a navigator in monoclonal antibody development and applications. *Oncologist 12*, 1379–1389.

(2) Wu, A. M. (2009) Antibodies and antimatter: The resurgence of immuno-PET. *J. Nucl. Med. 50*, 2–5.

(3) Zalutsky, M. R., and Lewis, J. S. (2003) Radiolabeled antibodies for tumor imaging and therapy. *Handb. Radiopharm.* 685–714.

(4) Verel, I., Visser, G. W. M., Vosjan, M. J. W. D., Finn, R., Boellaard, R., and Van Dongen, G. A. M. S. (2004) High-quality 124I-labelled monoclonal antibodies for use as PET scouting agents prior to 131I-radioimmunotherapy. *Eur. J. Nucl. Med. Mol. Imaging 31*, 1645–1652.

(5) Anderson, C. J., and Welch, M. J. (1999) Radiometal-labeled agents (non-technetium) for diagnostic imaging. *Chem. Rev. 99*, 2219–2234.

(6) Wadas, T. J., Wong, E. H., Weisman, G. R., and Anderson, C. J. (2010) Coordinating radiometals of copper, gallium, indium, yttrium, and zirconium for PET and SPECT imaging of disease. *Chem. Rev. 110*, 2858–2902.

(7) Nayak, T. K., and Brechbiel, M. W. (2009) Radioimmunoimaging with longer-lived positron-emitting radionuclides: potentials and challenges. *Bioconjugate Chem. 20*, 825–841.

(8) Divgi, C. R., Pandit-Taskar, N., Jungbluth, A. A., Reuter, V. E., Gönen, M., Ruan, S., Pierre, C., Nagel, A., Pryma, D. A., Humm, J., Larson, S. M., Old, L. J., and Russo, P. (2007) Preoperative characterisation of clear-cell renal carcinoma using iodine-124-labelled antibody chimeric G250 (124I-cG250) and PET in patients with renal masses: a phase I trial. *Lancet Oncol. 8*, 304–310.

(9) Wadas, T. J., Wong, E. H., Weisman, G. R., and Anderson, C. J. (2007) Copper chelation chemistry and its role in copper radiopharmaceuticals. *Curr. Pharm. Des. 13*, 3–16.

(10) Zeglis, B., and Lewis, J. S. (2011) A practical guide to the construction of radiometallation bioconjugates for positron emission tomography. *Dalton Trans.*

(11) Kolb, H. C., Finn, M. G., and Sharpless, K. B. (2001) Click chemistry: diverse chemical function from a few good reactions. *Angew. Chem., Int. Ed. 40*, 2004–2021.

(12) Lim, R. K. V., and Lin, Q. (2010) Bioorthogonal chemistry: recent progress and future directions. *Chem. Commun. 46*, 1589–1600.

(13) Sletten, E. M., and Bertozzi, C. R. (2009) Bioorthogonal chemistry: fishing for selectivity in a sea of functionality. *Angew. Chem., Int. Ed. 48*, 6973–6998.

(14) Moses, J. E., and Moorhouse, A. D. (2007) The growing applications of click chemistry. *Chem. Soc. Rev. 36*, 1249–1262.

(15) Glaser, M., and Robins, E. G. (2009) 'Click labelling' in PET radiochemistry. *J. Labelled Compd. Radiopharm. 52*, 407–414.

(16) Mindt, T. L., Muller, C., Stuker, F., Salazar, J. F., Hohn, A., Mueggler, T., Rudin, M., and Schibli, R. (2009) A "click chemistry" approach to the efficient synthesis of multiple imaging probes derived from a single precursor. *Bioconjugate Chem. 20*, 1940–1949.

(17) Nwe, K., and Brechbiel, M. W. (2009) Growing applications of "click chemistry" for bioconjugation in contemporary biomedical research. *Cancer Biother. Radiopharm. 24*, 289–301.

(18) Wang, C., Wang, N., Zhou, W., Shen, Y. M., and Zhang, L. (2010) Application of "click chemistry" in synthesis of radiopharmaceuticals. *Progress Chem. 22*, 1591–1602.

(19) Schultz, M. K., Parameswarappa, S. G., and Pigge, F. C. (2010) Synthesis of a DOTA-biotin conjugate for radionuclide chelation via Cu-free click chemistry. *Org. Lett. 12*, 2398–2401.

(20) Martin, M. E., Parameswarappa, S. G., O'Dorisio, M. S., Pigge, F. C., and Schultz, M. K. (2010) A DOTA-peptide conjugate by copper-free click chemistry. *Bioorg. Med. Chem. Lett. 20*, 4805–4807.

(21) Lebedev, A. Y., Holland, J. P., and Lewis, J. S. (2009) Clickable bifunctional radiometal chelates for peptide labeling. *Chem. Commun. 46*, 1706–1708.

(22) Knor, S., Modlinger, A., Poethko, T., Schottelius, M., Wester, H. J., and Kessler, H. (2007) Synthesis of novel 1,4,7,10-tetraazacyclodecane-1,4,7,10-tetraacetic acid (DOTA) derivatives for chemoselective attachment to unprotected polyfunctionalized compounds. *Chem.—Eur. J. 13*, 6082–6090.

(23) Devaraj, N. K., Upadhyay, R., Hatin, J. B., Hilderbrand, S. A., and Weissleder, R. (2009) Fast and sensitive pretargeted labeling of cancer cells through a tetrazine/trans-cyclooctene cycloaddition. *Angew. Chem., Int. Ed. 48*, 7013–7016.

(24) Devaraj, N. K., Weissleder, R., and Hilderbrand, S. A. (2008) Tetrazine-based cycloadditions: application to pretargeted live cell imaging. *Bioconjugate Chem. 19*, 2297–2299.

(25) Blackman, M. L., Royzen, M., and Fox, J. M. (2008) Tetrazine ligation: fast bioconjugation based on inverse electron demand Diels-Alder reactivity. *J. Am. Chem. Soc. 130*, 13518–13519.

(26) Schoch, J., Wiessler, M., and Jaschke, A. (2010) Post-synthetic modification of DNA by inverse-electron-demand Diels—Alder reaction. *J. Am. Chem. Soc. 132*, 8846–8847.

(27) Devaraj, N. K., Hilderbrand, S., Upadhyay, R., Mazitschek, R., and Weissleder, R. (2010) Bioorthogonal turn-on probes for imaging small molecules inside living cells. *Angew. Chem., Int. Ed. 49*.

(28) Haun, J. B., Devaraj, N. K., Hilderbrand, S., Lee, H., and Weissleder, R. (2010) Bioorthogonal chemistry amplifies nanoparticle binding and enhances the sensitivity of cell detection. *Nat. Nanotechnol. 5*, 660–665.

(29) Rossin, R., Verkerk, P. R., van den Bosch, S. M., Vulders, R. C. M., Verel, I., Lub, J., and Robillard, M. S. (2010) In vivo chemisry for pretargeted tumor imaging in live mice. *Angew. Chem., Int. Ed. 49*, 3375–3378.

(30) Li, Z., Cai, H., Hassink, M., Blackman, M., Brown, R. C. D., Conti, P. S., and Fox, J. M. (2010) Tetrazine-trans-cyclooctene ligation for the rapid construction of 18-F labeled probes. *Chem. Commun. 46*, 8043–8045.

(31) Reiner, T., Keliher, E. J., Earley, S., Marinelli, B., and Weissleder, R. (2011) Synthesis and in vivo imaging of a 18F-labeled PARP1 inhibitor using a chemically orthogonal scavenger-assisted high-performance method. *Angew. Chem., Int. Ed. 50*, 1922–1925.

(32) Meijs, W. E., Haisma, H. J., Klok, R. P., vanGog, F. B., Kievit, E., Pinedo, H. M., and Herscheid, J. D. M. (1997) Zirconium-labeled monoclonal antibodies and their distribution in tumor-bearing nude mice. *J. Nucl. Med. 38*, 112–118.

(33) Meijs, W. E., Herscheid, J. D. M., Haisma, H. J., and Pinedo, H. M. (1992) Evaluation of desferal as a bifunctional chelating agent for labeling antibodies with Zr-89. *Appl. Radiat. Isotop. 43*, 1443–1447.

(34) Holland, J. P., Divilov, V., Bander, N. H., Smith-Jones, P. M., Larson, S. M., and Lewis, J. S. (2010) Zr-89-DFO-J591 for immunoPET of prostate-specific membrane antigen expression in vivo. *J. Nucl. Med. 51*, 1293–1300.

(35) Hanahan, D., and Weinberg, R. A. (2000) The hallmarks of cancer. *Cell 100*, 57–70.

(36) Baselga, J., and Swain, S. M. (2009) Novel anticancer targets: revisiting ERBB2 and discovering ERBB3. *Nat. Rev. Cancer 9*, 463–475.

(37) Ellis, C. M., Dyson, M. J., Stephenson, T. J., and Maltby, E. L. (2005) HER2 amplification status in breast cancer: a comparison between immunohistochemical stainging and fluorescence in situ hybridisation using manual and automated quantitative image analysis scoring techniques. *J. Clin. Pathol. 58*, 710–714.

(38) Hanahan, D., Weinberg, R. A. Hallmarks of cancer: the next generation. *Cell 144*, 646-674.

(39) Slamon, D. J., Leyland-Jones, B., Shak, S., Fuchs, H., Paton, V., Bajamonde, A., Fleming, T., Eiermann, W., Wolter, J., Pegram, M., Baselga, J., and Norton, L. (2001) Use of chemotherapy plus a monoclonal antibody against HER2 for metastatic breast cancer that overexpresses HER2. *N. Engl. J. Med. 344*, 783–92.

(40) Tolmachev, V., Velikyan, I., Sandstrom, M., and Orlova, A. (2010) A HER2-binding Affibody molecule labelled with Ga-68 for PET imaging: direct in vivo comparison with the In-111-labelled analogue. *Eur. J. Nucl. Med. Mol. Imaging 37*, 1356–1367.

(41) Tang, Y., Wang, J., Scollard, D. A., Mondal, H., Holloway, C., Kahn, H. J., and Reilly, R. M. (2005) Imaging of HER2/neu-positive BT-474 human breast cancer xenografts in athymic mice using 111In-trastuzumab (Herceptin) Fab fragments. *Nucl. Med. Biol. 32*, 51–58.

(42) Holland, J. P., Caldas-Lopes, E., Divilov, V., Longo, V. A., Taldone, T., Zatorska, D., Chiosis, G., and Lewis, J. S. (2010) Measuring the pharmacodynamic effects of a novel Hsp90 inhibitor on HER2/neu expression in mice using Zr-89-DFO-trastuzumab. *PLOS One 5*.

(43) Munnink, T. H. O., de Korte, M. A., Nagengast, W. B., Timmer-Bosscha, H., Schroder, C. P., de Jong, J. R., van Dongen, G., Jensen, M. R., Quadt, C., Lub-de Hooge, M. N., and de Vries, E. G. E. (2010) Zr-89-trastuzumab PET visualises HER2 downregulation by the HSP90 inhibitor NVP-AUY922 in a human tumour xenograft. *Eur. J. Cancer 46*, 678–684.

(44) Dijkers, E. C. F., Kosterink, J. G. W., Rademaker, A. P., Perk, L. R., van Dongen, G. A. M. S., Bart, J., de Jong, J. R., de Vries, E. G. E., and Lub-de Hooge, M. N. (2009) Development and characterization of clinical-grade 89Zr-trastuzumab for HER2/neu immunolPET imaging. *J. Nucl. Med. 50*, 974–981.

(45) Niu, G., Li, Z., Cao, Q., and Chen, X. (2009) Monitoring therapeutic response of human ovarian cancer with 17-DMAG by noninvasive PET imaging with ^{64}Cu-DOTA-trastuzumab. *Eur. J. Nucl. Med. Mol. Imaging*.

(46) Smith-Jones, P. M., Solit, D. B., Afroze, F., Rosen, N., and Larson, S. M. (2006) Early tumor response to Hsp90 therapy using HER2 PET: Comparison with 18F-FDG PET. *J. Nucl. Med. 47*, 793–796.

(47) Garmestani, K., Milenic, D. E., Plascjak, P. S., and Brechbiel, M. W. (2002) A new and convenient method for purification of 86Y using a Sr(II) selective resin and comparison of biodistribution of 86Y and 111In labeled Herceptin. *Nucl. Med. Biol. 29*, 599–606.

(48) Verel, I., Visser, G. W. M., Boellaard, R., Stigter-van Walsum, M., Snow, G. B., and van Dongen, G. (2003) Zr-89 immuno-PET: Comprehensive procedures for the production of Zr-89-labeled monoclonal antibodies. *J. Nucl. Med. 44*, 1271–1281.

(49) Zanzonico, P. (2009) Routine quality control of clinical nuclear medicine instrumentation: a brief review. *J. Nucl. Med. 49*, 1114–1131.

(50) McCarthy, D. W., Shefer, R. E., Klinkowstein, R. E., Bass, L. A., Margeneau, W. H., Cutler, C. S., Anderson, C. J., and Welch, M. J. (1997) Efficient production of high specific activity Cu-64 using a biomedical cyclotron. *Nucl. Med. Biol. 24*, 35–43.

(51) Holland, J. P., Sheh, Y. C., and Lewis, J. S. (2009) Standardized methods for the production of high specific-activity zirconium-89. *Nucl. Med. Biol. 36*, 729–739.

(52) Anderson, C. J., Connett, J. M., Schwarz, S. W., Rocque, P. A., Guo, L. W., Philpott, G. W., Zinn, K. R., Meares, C. F., and Welch, M. J. (1992) Copper-64-labeled antibodies for PET imaging. *J. Nucl. Med. 33*, 1685–1691.

(53) Anderson, C. J., Schwarz, S. W., Connett, J. M., Cutler, P. D., Guo, L. W., Germain, C. J., Philpott, G. W., Zinn, K. R., Greiner, D. P., Meares, C. F., and Welch, M. J. (1995) Preparation, biodistribution, and dosimetry of copper-64-labeled anti-colorectal carcinoma monoclonal-antibody gragments 1A3-F(AB′)(2). *J. Nucl. Med. 36*, 850–858.

(54) Lindmo, T., Boven, E., Cuttitta, F., Fedorko, J., and Bunn, P. A., Jr. (1984) Determination of the immunoreactive fraction of radiolabeled monoclonal antibodies by linear extrapolation to binding at infinite antigen excess. *J. Immunol. Methods 72*, 77–89.

(55) Lindmo, T., and Bunn, P. A., Jr. (1986) Determination of the true immunoreactive fraction of monoclonal antibodies after radiolabeling. *Methods Enzymol. 121*, 678–91.

(56) Kim, J. S., Lee, J. S., Im, K. C., Kim, S. J., Kim, S.-Y., Lee, D. S., and Moon, D. H. (2007) Performance measurement of the microPET Focus 120 scanner. *J. Nucl. Med. 48*, 1527–1535.

(57) Kampchen, T., Massa, W., Overheu, W., Schmidt, R., and Seitz, G. (1982) Zur kenntnis von reaktionen des 1,2,4,5-tetrazin-3,6-dicarbonsaure-dimethylesters mit nucleophilen. *Chem. Ber. 115*, 683–694.

(58) Lin, C. H., Lieber, E., and Horwitz, J. P. (1954) The synthesis of syn-diaminotetrazine. *J. Am. Chem. Soc. 76*, 427–430.

(59) Solducho, J., Doskocz, J., Cabaj, J., and Roszak, S. (2003) Practical synthesis of bis-substituted tetrazine with two pendant 2-pyrrolyl or 2-thienyl groups, precursors of new conjugated polymers. *Tetrahedron 59*, 4761–4766.

(60) Vosjan, M., Perk, L. R., Visser, G. W. M., Budde, M., Jurek, P., Kiefer, G. E., and van Dongen, G. (2010) Conjugation and radiolabeling of monoclonal antibodies with zirconium-89 for PET imaging using the bifunctional chelate p-isothiocyanatobenzyl-desferrioxamine. *Nat. Protoc. 5*, 739–743.

(61) Verel, I., Visser, G. W. M., Boellaard, R., Stigter-van Walsum, M., Snow, G. B., and van Dongen, G. A. M. S. (2003) ^{89}Zr immuno-PET: comprehensive procedures for the production of ^{89}Zr-labeled monoclonal antibodies. *J. Nucl. Med. 44*, 1271–1281.

(62) Brouwers, A., Verel, I., Van Eerd, J., Visser, G., Steffens, M., Oosterwijk, E., Corstens, F., Oyen, W., Van Dongen, G., and Boerman, O. (2004) PET radioimmunoscintigraphy of renal cell cancer using Zr-89-labeled cG250 monoclonal antibody in nude rats. *Cancer Biother. Radiopharm. 19*, 155–163.

(63) Niu, G., Li, Z., Xie, J., Le, Q.-T., and Chen, X. (2009) PET of EGFR antibody distribution in head and neck squamous cell carcinoma models. *J. Nucl. Med. 50*, 1116–1123.

(64) Martin, S. M., O'Donnell, R. T., Kukis, D. L., Abbey, C. K., McKnight, H., Sutcliffe, J. L., and Tuscano, J. M. (2008) Imaging and pharmacokinetics of 64Cu-DOTA-HB22.7 administered by intravenous, intraperitoneal, or subcutaneous injection to mice bearing non-Hodgkin's lymphoma xenografts. *Mol. Imaging Biol. 11*, 79–87.

(65) Paudyal, P., Paudyal, B., Hanaoka, H., Oriuchi, N., Iida, Y., Yoshioka, H., Tominaga, H., Watanabe, S., Ishioka, N. S., and Endo, K. (2010) Imaging and biodistribution of Her2/neu expression in non-small cell lung cancer xenografts with 64Cu-labeled trastuzumab PET. *Cancer Sci. 101*, 1045–1050.

(66) Abou, D. S., Ku, T., and Smith-Jones, P. M. (2011) In vivo biodistribution and accumulation of 89Zr in mice. *Nucl. Med. Biol.* [Online early access].

(67) Antunes, P., Ginj, P., Zhang, H., Waser, B., Baum, R. P., Reubi, J. C., and Maecke, H. (2007) Are radiogallium-labeled DOTA-conjugated somatostatin analogues superior to those labeled with other radiometals? *Eur. J. Nucl. Med. Mol. Imaging 34*, 982–993.

A Modular Strategy for the Construction of Radiometallated Antibodies for Positron Emission Tomography Based on Inverse Electron Demand Diels-Alder Click Chemistry

Brian M. Zeglis, Priya Mohindra, Gabriel I. Weissmann, Vadim Divilov, Scott A. Hilderbrand, Ralph Weissleder, and Jason S. Lewis*

Supporting Information

Table of Contents

Table S1. Tumor to organ ratios obtained from data collected in biodistribution experiment employing ^{64}Cu-DOTA-T/N-trastuzumab in mice bearing bilateral s.c. BT-474 (HER2-positive) and MDA-MB-468 (HER2-negative) xenografts (n = 4 for each time point)

	6 h	**12 h**	**24 h**	**48 h**	**72 h**
HER2+/Blood	0.5 ± 0.3	1.5 ± 0.5	2.5 ± 1.0	3.9 ± 0.9	4.7 ± 0.5
HER2+/HER2-	1.7 ± 0.8	2.8 ± 1.0	2.9 ± 0.6	5.1 ± 1.7	4.7 ± 0.5
HER2+/Heart	2.1 ± 1.1	3.6 ± 1.6	6.1 ± 1.6	10.2 ± 3.4	9.7 ± 5.3
HER2+/Lungs	0.9 ± 0.4	2.5 ± 0.6	4.1 ± 1.6	5.5 ± 1.4	5.8 ± 0.3
HER2+/Liver	0.9 ± 0.4	2.4 ± 0.5	2.7 ± 0.6	6.9 ± 1.2	6.8 ± 0.8
HER2+/Spleen	0.9 ± 0.6	2.4 ± 0.6	2.5 ± 0.7	7.7 ± 1.5	8.0 ± 1.6
HER2+/Stomach	5.5 ± 3.1	23.9 ± 10.6	10.9 ± 2.4	33.8 ± 9.8	30.6 ± 3.5
HER2+/Sm. Inst.	3.0 ± 1.8	11.4 ± 2.7	7.5 ± 3.7	20.0 ± 3.6	21.2 ± 1.1
HER2+/Lg. Inst.	5.2 ± 2.4	14.1 ± 2.8	8.4 ± 4.9	31.4 ± 8.7	27.6 ± 5.6
HER2+/Kidney	1.9 ± 0.9	4.9 ± 1.4	9.0 ± 5.2	11.0 ± 2.2	12.2 ± 1.2
HER2+/Muscle	17.3 ± 9.6	34.1 ± 20.6	43.5 ± 23.2	44.0 ± 11.7	68.9 ± 8.9
HER2+/Bone	3.4 ± 3.3	17.1 ± 3.5	7.3 ± 1.6	40.0 ± 10.1	21.2 ± 9.0

Table S2. Tumor to organ ratios obtained from data collected in biodistribution experiment employing ^{89}Zr-DFO-T/N-trastuzumab in mice bearing bilateral s.c. BT-474 (HER2-positive) and MDA-MB-468 (HER2-negative) xenografts (n = 4 for each time point)

	6 h	**24 h**	**48 h**	**72 h**	**96 h**	**120 h**
HER2+/Blood	0.5 ± 0.2	1.3 ± 0.7	2.7 ± 1.1	3.1 ± 0.5	3.6 ± 0.5	3.8 ± 0.7
HER2+/HER2-	2.0 ± 1.1	3.6 ± 1.2	4.4 ± 2.7	4.5 ± 0.8	4.3 ± 1.8	4.0 ± 0.4
HER2+/Heart	1.0 ± 0.4	2.7 ± 1.1	10.7 ± 5.8	7.8 ± 3.2	8.5 ± 3.3	6.7 ± 0.7
HER2+/Lungs	1.5 ± 0.5	3.1 ± 1.1	6.1 ± 2.7	6.3 ± 2.6	5.2 ± 3.1	5.4 ± 1.4
HER2+/Liver	0.9 ± 0.3	2.8 ± 0.8	4.0 ± 1.7	4.8 ± 0.6	5.6 ± 1.3	5.2 ± 2.8
HER2+/Spleen	2.0 ± 0.6	3.4 ± 1.4	4.3 ± 1.5	5.0 ± 1.8	5.7 ± 3.0	6.5 ± 3.2
HER2+/Stomach	3.4 ± 1.2	15.7 ± 2.4	25.6 ± 7.7	37.6 ± 10.1	38.0 ± 8.9	38.8 ± 6.8
HER2+/Sm. Inst.	2.7 ± 1.0	7.7 ± 1.2	8.1 ± 3.1	15.6 ± 3.9	19.0 ± 4.9	15.9 ± 3.0
HER2+/Lg. Inst.	5.1 ± 1.9	23.1 ± 7.4	37.6 ± 5.9	32.7 ± 13.2	72.2 ± 22.9	49.9 ± 18.0
HER2+/Kidney	1.4 ± 0.6	3.7 ± 0.6	9.1 ± 2.0	6.5 ± 1.6	7.1 ± 0.8	8.0 ± 2.7
HER2+/Muscle	10.4 ± 4.1	21.1 ± 3.5	40.0 ± 13.2	34.1 ± 7.1	32.8 ± 4.6	27.9 ± 2.7
HER2+/Bone	1.9 ± 0.6	3.7 ± 0.8	4.4 ± 1.2	4.9 ± 0.8	4.9 ± 1.2	4.6 ± 0.5

Figure S1. Maximum intensity projection from PET image of ^{89}Zr-DFO-T/N-trastuzumab trastuzumab (0.56 – 0.74 MBq [15-20 μCi] in 200 μL 0.9% sterile saline) in a mouse bearing bilateral BT-474 (HER2-positive, right shoulder) and MDA-MB-468 (HER2-negative, left shoulder) at t = 96 h. The white lines are shown to illustrate the HER2-positive tumor, HER2-negative tumor, and residual bone uptake.

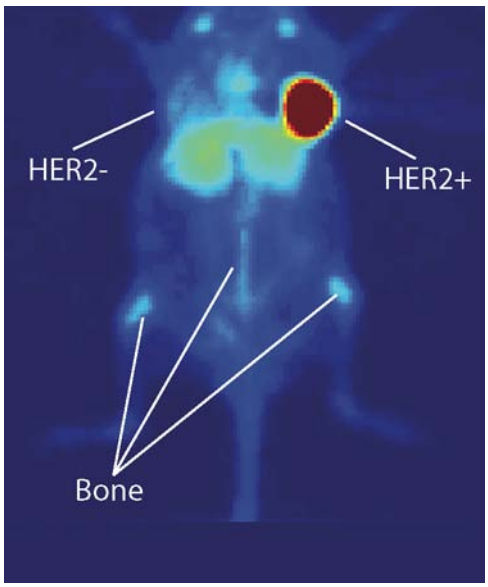

Bioconjugate Chemistry

Article

pubs.acs.org/bc

Two-Photon Fluorescence Vascular Bioimaging with New Bioconjugate Probes Selective toward the Vascular Endothelial Growth Factor Receptor 2

Carolina D. Andrade,[†] Ciceron O. Yanez,[†] Hyo-Yang Ahn,[†] Takeo Urakami,[§] Mykhailo V. Bondar,[∥] Masanobu Komatsu,[§] and Kevin D. Belfield*[,†,‡]

[†]Department of Chemistry and [‡]CREOL, The College of Optics and Photonics, University of Central Florida, P.O. Box 162366, Orlando, Florida 32816, United States

[§]Sanford-Burnham Medical Research Institute at *Lake Nona*, Orlando, Florida 32827, United States

[∥]Institute of Physics, Prospect Nauki 46, Kiev-28, 03094 Ukraine

Supporting Information

ABSTRACT: We report the synthesis and characterization of two amine reactive fluorescent dyes with efficient two-photon absorption (2PA) properties and high fluorescence quantum yields. Bioconjugation of these dyes with the DC-101 antibody proved to be useful for selectively imaging the vascular endothelial growth factor receptor 2 (VEGFR-2) in cells expressing this receptor *in vitro* and in "whole" mounted excised tumors (*ex vivo*) by two-photon fluorescence microscopy (2PFM). The penetration depths reached within the tumors by 2PFM was over 800 μm. In addition, the concentration of dye required for incubation of these bioconjugates was in the picomolar domain, the probes possessed very good photostability, and the 2PFM setup did not require any additional means of increasing the collection efficiencies of fluorescent photons to achieve the relatively deep tissue imaging that was realized, due, in large part, to the favorable photophysical properties of the new probes.

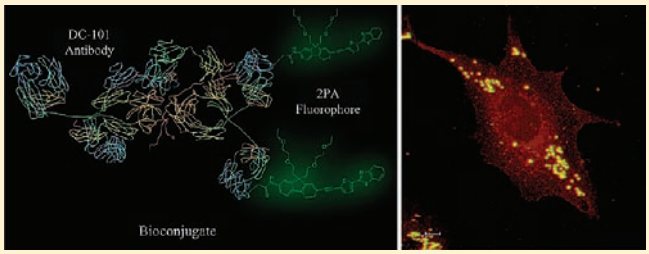

INTRODUCTION

The development of methodologies and materials to image cancer tumors is an area of increasing interest in the chemical and biomedical communities. The conjugation of fluorescent dyes with antibodies and peptides, used as targeting vectors, is a common strategy to selectively image tumors. In the interest of following tumor growth and drug efficacy, researchers have targeted the vasculature rather than the tumor itself to determine tumor size, morphology, and characteristics by different technologies (immunohistochemistry, fluorescence microscopy, photoacoustic microscopy, etc).[1−5]

Angiogenesis is the process of forming new blood vessels to support tissue growth. This fundamental physiological process promotes embryonic development, tissue repair, and fertility, although it also promotes chronic inflammation, tumor growth, and tumor metastasis.[6] Tumors, in particular, rely on angiogenesis for their continued growth. It has been demonstrated that solid tumors will not grow larger than 2−3 mm in diameter in the absence of new blood vessels and require angiogenesis to form metastases.[7] Vascular endothelial growth factor (VEGF) is a protein that stimulates vascular endothelial cell growth, survival, and proliferation. Thus, VEGF facilitates survival of existing vessels, contributes to vascular abnormalities that may impede effective delivery of antitumor compounds, and stimulates new vessel growth.[8−10]

The VEGF family consists of five members (VEGF-A, VEGF-B, VEGF-C, VEGF-D, and placental growth factor), which show different affinities for one of the three VEGF tyrosine kinase receptors (VEGFR-1, VEGFR-2, and VEGFR-3). VEGFR-1 and VEGFR-2 are expressed in vascular endothelial cells. Moreover, there is evidence that VEGFR-2 is the major mediator of VEGF-driven responses in endothelial cells and it has been considered to be crucial in angiogenic processes.[10]

In 2005, Backer and co-workers reported the use of a boronated polyamidoamine dendrimer able to target vasculature by means of a VEGF-containing bioconjugate that directed the dendrimer to a specific receptor (VEGFR). The incorporation of a near-infrared (NIR) dye (Cy5) was employed to track the bioconjugate. The targeting of tumor vasculature endothelial cells, rather than the tumor itself, was achieved, since endothelial cells in tumor neurovasculature express a significantly greater number of VEGFR-2 when compared to quiescent endothelial cells.[11] More recent work has demonstrated the use of VEGF bioconjugates containing

Received: June 8, 2011
Revised: August 31, 2011
Published: September 28, 2011

ACS Publications © 2011 American Chemical Society

NIR fluorescent dyes to study the possible expression of VEGFRs in bladder inflammation.[12]

The use of two-photon absorption (2PA) fluorophores offers several advantages over their one-photon NIR counterparts. In the nonlinear absorption process, the fluorescence emission is proportional to the square of the intensity of the incident light, providing the system with numerous intrinsic advantages, e.g., deeper penetration, more confined excitation areas, less scattering, and minimal photodamage outside of the focal volume.[13]

The scientific community has access to a wealth of efficient 1PA fluorescent dyes with emissions that range from the UV to the IR and that are commercially available. However, there is a need to develop new dyes with high fluorescence quantum yields and 2PA cross sections that meet the high photostability demands that two-photon fluorescence microscopy (2PFM) imposes for repeated three-dimensional (3D) imaging. We previously described a strategy to create 2PA amine reactive probes that can be conjugated to proteins or antibodies.[14,15] In this work, we introduce the synthesis and characterization of two new fluorescent amine reactive dyes based on a fluorenyl core. The fluorophore design was based on a small series of efficient 2PA dyes that were recently reported.[16] The architecture of the fluorophores involved a fluorenyl core flanked by a triple bond−thiophene bridge (π) that led to an electron withdrawing group on one side (A). On the other, the fluorenyl core was tethered to the anti-VEGFR-2 that served as a donor (D). This resulted in systems that have a D−π−A dipolar structure.

These probes were used to prepare VEGFR-2 antibody bioconjugates (anti-VEGFR-2) that selectively bound to the VEGFR-2 in vascular endothelial cells that overexpress this specific receptor in *in vitro* experiments. Furthermore, the conjugation of these new 2PA dyes to the VEGFR-2 antibody was used to image tumor vasculature of whole-mounted excised tumors by 2PFM (Figure 1). *In vitro*, and, more significantly, *ex vivo*, thick tumor 2PFM imaging was accomplished, revealing the 3D tumor microvasculature morphology.

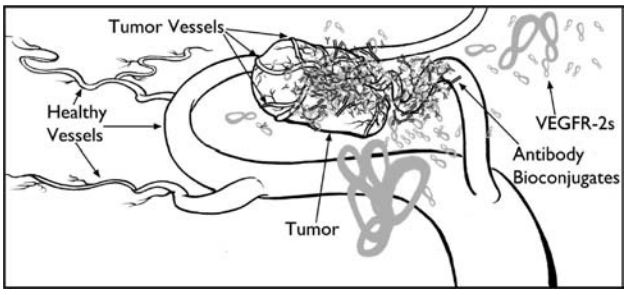

Figure 1. Depiction of a VEGFR-2 expressing tumor. Tumor cells induce the formation of new vasculature by expressing a higher concentration of VEGFR-2 which enables tumor growth. After they are treated with a 2PA fluorescent antibody bioconjugate, the tumor vessels can be imaged by 2PFM.

EXPERIMENTAL SECTION

Materials and Methods. Key intermediates **1**, **2**, and **7** were prepared as described in the literature.[15,16] All reactions were carried out under N_2. Microwave-assisted procedures were carried out in a CEM Discover unit microwave in 10 mL closed vessels; temperature, pressure, and power were programmed at a maximum value (as indicated), depending on the reaction. All other reagents and solvents were used as received from commercial suppliers. ^{1}H and ^{13}C NMR spectra were recorded in $CDCl_3$ on a Varian NMR spectrometer at 500 and 125 MHz, respectively. Mass analyses (APCI, atmospheric pressure chemical ionization) were performed at University of Florida. The analyses were carried out on a Finnigan LCQ—Quadrupole Ion Trap (Thermo Finnigan). Monoclonal antihuman VEGFR-2/KDR-Fluorescein isothiocyanate bioconjugate was obtained from R&D Systems and was used as a positive control without further treatment.

Synthetic Procedures and Characterization. *Synthesis of 2-(5-(9,9-Bis(2-(2-ethoxyethoxy)ethyl)-7-nitro-9H-fluoren-2-yl)thiophen-2-yl)benzothiazole (**3**).* In a 10 mL vessel, under nitrogen, 9,9-bis(2-(2-ethoxyethoxy)ethyl)-2-iodo-7-nitro-9H-fluorene (**1**; 200 mg, 0.335 mmol), 2-(5-(tributylstannyl)thiophen-2-yl)benzothiazole (**2**; 207 mg, 0.408 mmol), and $Pd(PPh_3)_2Cl_2$ (6 mg, 0.008 mmol) were dissolved in toluene (2 mL). The mixture was heated in the microwave for 25 min, at 130 °C, 150 psi, and 150 W, filtered through a Celite plug, and purified by column chromatography using as a solvent a mixture of hexane/ethyl acetate (2:1) to yield 216 mg (98%) of a light orange solid. mp 75.7−76.5 °C. ^{1}H NMR (500 MHz, $CDCl_3$) δ 8.26−8.34 (m, 2H, Ph-H), 8.06 (d, J = 8.06 Hz, 1H, Ph-H), 7.89 (d, J = 8.06 Hz, 1H, Ph-H), 7.73−7.84 (m, 4H, Ph-H), 7.69 (d, J = 3.93 Hz, 1H, Thy-H), 7.49−7.52 (m, 1H, Ph-H), 7.48 (d, J = 3.93 Hz, 1H, Thy-H), 7.38−7.42 (m, 1H, Ph-H), 3.34−3.40 (m, 4H, CH_2), 3.27−3.31 (m, 4H, CH_2), 3.15−3.22 (m, 4H, CH_2), 2.79−2.93 (m, 4H, CH_2), 2.45−2.56 (m, 4H, CH_2), 1.10 (t, J = 6.98 Hz, 6H, CH_3). ^{13}C NMR (125 MHz, $CDCl_3$) δ 161.1, 153.9, 152.1, 151.2, 147.7, 147.5, 146.3, 138.6, 137.0, 135.0, 134.8, 129.7, 126.8, 126.0, 125.6, 124.8, 123.9, 123.2, 122.2, 121.7, 121.0, 120.2, 119.3, 70.4, 69.8, 67.1, 66.8, 52.5, 39.6, 15.2. MS (APCI) m/z calcd $[M + H]^+$ 659.2244, found 659.2256.

*Synthesis of 7-(5-(Benzothiazol-2-yl)thiophen-2-yl)-9,9-bis(2-(2-ethoxyethoxy)ethyl)-9H-fluoren-2-amine (**4**).* In a 10 mL vessel, under nitrogen were dissolved 2-(5-(9,9-bis(2-(2-ethoxyethoxy)ethyl)-7-nitro-9H-fluoren-2-yl)thiophen-2-yl)-benzothiazole (**3**; 300 mg, 0.45 mmol) and 10% Pd/C (30 mg) in a 1:1 mixture of THF/EtOH (4 mL). $NH_2NH_2{\cdot}2H_2O$ (300 mg, 6.0 mmol) was added to the mixture dropwise at room temperature, and then the solution was heated in the microwave to 110 °C, 100 W, and 100 psi for 30 min. The mixture was filtered though a silica plug with ethyl acetate, and after the solvent was removed under reduced pressure, the material was purified by column chromatography using as a solvent ethyl acetate to yield 280 mg (97%) of a dark yellow solid. mp 120.8−121.4 °C. ^{1}H NMR (500 MHz, $CDCl_3$) δ 8.04 (d, J = 7.88 Hz, 1H, Ph-H), 7.86 (d, J = 7.88 Hz, 1H, Ph-H), 7.59−7.67 (m, 3H, Ph-H, Thy-H), 7.55 (d, J = 7.69 Hz, 1H, Ph-H), 7.45−7.50 (m, 2H, Ph-H), 7.34−7.40 (m, 2H, Ph-H, Thy-H), 6.75 (d, J = 7.99 Hz, 1H, Ph-H), 6.68 (dd, J = 7.99 Hz, J = 1.92 Hz, 1H, Ph-H), 3.38−3.44 (m, 4H, CH_2), 3.33−3.37 (m, 4H, CH_2), 3.21−3.26 (m, 4H, CH_2), 2.77−2.86 (m, 4H, CH_2), 2.31−2.46 (m, 4H, CH_2), 1.13 (t, J = 7.05 Hz, 6H, CH_3). ^{13}C NMR (125 MHz, $CDCl_3$) δ 161.3, 153.8, 151.1, 149.0, 148.8, 146.7, 141.6, 135.3, 134.6, 130.8, 130.7, 129.6, 129.6, 125.4, 125.1, 123.3, 122.8, 121.46, 121.1, 120.1, 119.0, 114.5, 109.8, 70.1, 69.7, 67.0, 66.6, 50.9, 39.9, 15.1. MS (APCI) m/z calcd $[M + H]^+$ 629.2502, found 629.2508.

Synthesis of 2-(5-(9,9-Bis(2-(2-ethoxyethoxy)ethyl)-7-isothiocyanato-9H-fluoren-2-yl)thiophen-2-yl)benzothiazole

*(**5**)*. In a two-neck round-bottom flask and under nitrogen, a solution of 7-(5-(benzothiazol-2-yl)thiophen-2-yl)-9,9-bis(2-(2-ethoxyethoxy)ethyl)-9*H*-fluoren-2-amine (**4**; 250 mg, 0.398 mmol) in chloroform (2 mL) was combined with an aqueous solution of $CaCO_3$ (103 mg, 1.03 mmol) in an ice bath. Thiophosgene (0.042 mL, 0.44 mmol) was added to the vial dropwise while stirring the mixture, and the reaction proceeded for 4 h. After completion, a 10% HCl solution was added until the gas formation ceased. The mixture was poured into water, extracted with methylene chloride, dried over magnesium sulfate, and purified by column chromatography using as a solvent a mixture of hexane/ethyl acetate (2:1) to yield 200 mg (74%) of a light orange solid. mp 103.2−104.0 °C. ^{1}H NMR (500 MHz, $CDCl_3$) δ 8.04 (d, J = 8.10 Hz, 1H, Ph-H), 7.86 (d, J = 8.10 Hz, 1H, Ph-H), 7.70−7.73 (m, 1H, Ph-H), 7.61−7.68 (m, 4H, Ph-H, Thy-H), 7.46−7.50 (m, 1H, Ph-H), 7.41 (d, 1H, J = 4.10 Hz, Thy-H), 7.34−7.39 (m, 1H, Ph-H), 7.32 (d, J = 1.68 Hz, 1H, Ph-H), 7.21 (dd, J = 7.97 Hz, J = 1.68 Hz, 1H, Ph-H), 3.36−3.42 (m, 4H, CH_2), 3.30−3.35 (m, 4H, CH_2), 3.18−3.23 (m, 4H, CH_2), 2.78−2.91 (m, 4H, CH_2), 2.38−2.47 (m, 4H, CH_2), 1.12 (t, J = 7.11 Hz, 6H, CH_3). ^{13}C NMR (125 MHz, $CDCl_3$) δ 161.0, 153.7, 151.1, 150.3, 148.0, 139.6, 139.0, 136.2, 135.4, 134.7, 133.1, 130.2, 129.6, 129.5, 124.2, 122.9, 121.5, 121.4, 121.1, 120.92, 120.85, 120.7, 120.6, 120.4, 70.1, 69.6, 66.9, 66.6, 51.8, 39.6, 15.1. MS (APCI) m/z calcd $[M + H]^+$ 671.2066, found 671.2068. UV−vis (DMSO) λ_{max} 397 nm.

*Synthesis of 1-(7-(5-(Benzothiazol-2-yl)thiophen-2-yl)-9,9-bis(2-(2-ethoxyethoxy)ethyl)-9H-fluoren-2-yl)-3-butylthiourea (**6**)*. In a small vial under nitrogen, a mixture of 2-(5-(9,9-bis(2-(2-ethoxyethoxy)ethyl)-7-isothiocyanato-9*H*-fluoren-2-yl)thiophen-2-yl)benzothiazole (**5**; 56 mg, 0.083 mmol) and *n*-butylamine (0.074 mL, 1.0 mmol) at room temperature was stirred for 1 h. The remaining *n*-butylamine was removed under vacuum, and the residue was purified by column chromatography with hexane/ethyl acetate (1:1) to yield 50 mg (80%) of a bright yellow solid. mp 67.0−68.0 °C. ^{1}H NMR (500 MHz, $CDCl_3$) δ 8.04 (d, J = 8.13 Hz, 1H, Ph-H), 7.84−7.94 (m, 2H, Ph-H, N−H), 7.67−7.73 (m, 4H, Ph-H), 7.66 (d, J = 4.01, 1H, Thy-H), 7.47−7.52 (m, 1H, Ph-H), 7.42 (d, 1H, J = 4.01 Hz, Thy-H), 7.35−7.40 (m, 1H, Ph-H), 7.32 (d, J = 1.46 Hz, 1H, Ph-H), 7.21 (d, J = 7.74 Hz, 1H, Ph-H), 6.34−6.39 (m, 1H, N−H), 3.62−3.69 (m, 2H, CH_2), 3.32−3.41 (m, 4H, CH_2), 3.24−3.30 (m, 4H, CH_2), 3.12−3.21 (m, 4H, CH_2), 2.78−2.98 (m, 4H, CH_2), 2.36−2.44 (m, 4H, CH_2), 1.57−1.65 (m, 2H, CH_2), 1.35−1.43 (m, 2H, CH_2), 1.10 (t, J = 6.96 Hz, 6H, CH_3), 0.95 (t, J = 7.55 Hz, 3H, CH_3). ^{13}C NMR (125 MHz, $CDCl_3$) δ 180.6, 161.1, 153.72, 153.71 150.1, 148.1, 140.1, 138.3, 136.1, 134.68, 134.67, 132.8, 129.5, 123.8, 122.9, 121.5, 121.4, 120.63, 120.61, 120.60, 120.48, 120.47, 120.0, 70.0, 69.6, 67.1, 66.5, 51.9, 39.6, 31.0, 20.2, 15.1, 15.0, 13.9. MS (APCI) m/z calcd $[M + H]^+$ 744.2958, found 744.2952. UV−vis (DMSO) λ_{max} 400 nm.

*Preparation of Bioconjugate **B1***. A mixture containing 1000 μL of monoclonal DC-101 antibody (4 mg/mL) and 1000 μL of $NaHCO_3$ (1 M) was combined with a fresh solution of isothiocyanate **5** in DMSO in a 1:6 molar protein/dye proportion and incubated for 1 h in the dark at room temperature. A mixture containing 100 μL of polyclonal VEGFR-2 antibody (1 mg/mL) and 100 μL of $NaHCO_3$ (1 M) was combined with a fresh solution of isothiocyanate **5** in DMSO in a 1:10 molar protein/dye proportion and incubated for 2 h in the dark at room temperature. The biconjugate was purified by using disposable PD-10 desalting columns from GE equilibrated and eluted with PBS buffer 7.4. Fractions containing the bioconjugate were identified using a spectrophotometer by monitoring bands at 280 and 400 nm. The degree of labeling was determined to be 3.

*Synthesis of 2-(5-((9,9-Bis(2-(2-ethoxyethoxy)ethyl)-7-nitro-9H-fluoren-2-yl)ethynyl)thiophen-2-yl)benzothiazole (**8**)*. In a 10 mL vessel, under nitrogen, 9,9-bis(2-(2-ethoxyethoxy)ethyl)-2-iodo-7-nitro-9H-fluorene (**1**; 413 mg, 0.725 mmol), 2-(5-ethynylthiophen-2-yl)benzothiazole (**7**; 175 mg, 0.725 mmol), $Pd(PPh_3)_2Cl_2$ (21 mg, 0.03 mmol), and CuI (5.7 mg, 0.03 mmol) were dissolved in a 1:4 mixture of Et_3N/toluene (3 mL). The mixture was heated in the microwave for 1 h, at 130 °C, 150 psi, and 150 W, filtered through a Celite plug, and purified by column chromatography using as a solvent a mixture of hexane/ethyl acetate (2:1) to yield 505 mg (74%) of a light orange solid. mp 105.0−106.5 °C. ^{1}H NMR (500 MHz, $CDCl_3$) δ 8.33 (d, J = 2.00 Hz, 1H, Ph-H), 8.26 (dd, J = 8.36 Hz, J = 2.00 Hz, 1H, Ph-H), 8.02 (d, J = 7.95 Hz, 1H, Ph-H), 7.85 (d, J = 7.95 Hz, 1H, Ph-H), 7.73−7.79 (m, 2H, Ph-H, Thy-H), 7.66−7.68 (m, 1H, Ph-H), 7.54−7.60 (m, 2H, Ph-H, Thy-H), 7.46−7.50 (m, 1H, Ph-H), 7.36−7.40 (m, 1H, Ph-H), 7.31 (d, J = 3.92 Hz, 1H, Thy-H), 3.35−7.42 (m, 4H, CH_2), 3.27−3.31 (m, 4H, CH_2), 3.15−3.21 (m, 4H, CH_2), 2.80−2.93 (m, 4H, CH_2), 2.43−2.54 (m, 4H, CH_2), 1.12 (t, J = 6.85 Hz, 6H, CH_3). ^{13}C NMR (125 MHz, $CDCl_3$) δ 160.5, 153.8, 151.1, 147.5, 146.0, 138.8, 138.6, 134.9, 133.3, 133.1, 128.6, 128.5, 126.9, 126.7, 126.6, 123.4, 123.3, 121.7, 121.4, 119.2, 119.1, 96.0, 84.2, 70.3, 69.7, 66.9, 66.7, 52.3, 39.4, 15.2. MS (APCI) m/z calcd $[M + H]^+$ 683.2244, found 683.2231.

*Synthesis of 7-((5-(Benzothiazol-2-yl)thiophen-2-yl)-ethynyl)-9,9-bis(2-(2-ethoxyethoxy)ethyl)-9H-fluoren-2-amine (**9**)*. In a 10 mL vessel, under nitrogen, 2-(5-((9,9-bis(2-(2-ethoxyethoxy)ethyl)-7-nitro-9H-fluoren-2-yl)ethynyl)-thiophen-2-yl)benzothiazole (**8**; 250 mg, 0.366 mmol) and 10% Pd/C (25 mg) were dissolved in a 1:1 mixture of THF/EtOH (4 mL). $NH_2NH_2{\cdot}2H_2O$ (220 mg, 4.4 mmol) was added to the mixture dropwise at room temperature, and then the solution was heated in the microwave to 110 °C, 100 W, and 100 psi for 30 min. The mixture was filtered though a silica plug with ethyl acetate, and after the solvent was removed under reduced pressure, the material was purified by column chromatography using as a solvent a mixture of hexane/ethyl acetate (1:3) to yield 200 mg (84%) of a light orange solid. mp 110−111 °C. ^{1}H NMR (500 MHz, $CDCl_3$) δ 8.03 (d, J = 8.09 Hz, 1H, Ph-H), 7.84 (d, J = 8.09 Hz, 1H, Ph-H), 7.52−7.57 (m, 2H, Ph-H, Thy-H), 7.43−7.52 (m, 4H, Ph-H), 7.35−7.39 (m, 1H, Ph-H), 7.28 (d, J = 4.09 Hz, 1H, Thy-H), 6.71−6.74 (m, 1H, Ph-H), 6.64−6.68 (m, 1H, Ph-H), 3.79 (s, 2H, NH_2), 3.39−3.46 (m, 4H, CH_2), 3.32−3.39 (m, 4H, CH_2), 3.20−3.26 (m, 4H, CH_2), 2.74−2.85 (m, 4H, CH_2), 2.29−2.44 (m, 4H, CH_2), 1.15 (t, J = 7.02 Hz, 6H, CH_3). ^{13}C NMR (125 MHz, $CDCl_3$) δ 160.6, 153.7, 151.3, 148.1, 147.1, 142.0, 137.7, 134.7, 133.0, 131.8, 130.6, 128.1, 127.4, 125.6, 125.5, 122.9, 121.7, 120.8, 118.9, 118.0, 115.1, 113.9, 110.2, 97.2, 82.2, 70.1, 69.7, 67.0, 66.7, 50.9, 39.9, 15.4. MS (APCI) m/z calcd $[M + H]^+$ 653.2502, found 653.2510.

*Synthesis of 2-(5-((9,9-Bis(2-(2-ethoxyethoxy)ethyl)-7-isothiocyanato-9H-fluoren-2-yl)ethynyl)thiophen-2-yl)-benzothiazole (**10**)*. In a two-neck round-bottom flask and under nitrogen, a solution of 7-((5-(benzothiazol-2-yl)-thiophen-2-yl)ethynyl)-9,9-bis(2-(2-ethoxyethoxy)ethyl)-9H-fluoren-2-amine (**9**; 178 mg, 0.273 mmol) in chloroform (2 mL) was combined with an aqueous solution of $CaCO_3$ (80

mg, 0.80 mmol) in an ice bath. Thiophosgene (0.026 mL, 0.34 mmol) was added to the vial dropwise while stirring the mixture, and the reaction proceeded for 4 h. After completion, a 10% HCl solution was added until the gas formation ceased. The mixture was poured into water, extracted with methylene chloride, dried over magnesium sulfate, and purified by column chromatography using as a solvent a mixture of hexane/ethyl acetate (2:1) to yield 170 mg (90%) of a bright yellow solid. mp 86−88 °C. ^{1}H NMR (500 MHz, $CDCl_3$) δ 8.05 (d, J = 7.97 Hz, 1H, Ph-H), 7.87 (d, J = 7.97 Hz, 1H, Ph-H), 7.63−7.67 (m, 2H, Ph-H), 7.53−7.61 (m, 3H, Ph-H, Thy-H), 7.47−7.52 (m, 1H, Ph-H), 7.37−7.42 (m, 1H, Ph-H), 7.30−7.33 (m, 2H, Ph-H), 7.21−7.24 (m, 1H, Ph-H), 3.39−3.45 (m, 4H, CH_2), 3.30−3.35 (m, 4H, CH_2), 3.18−3.23 (m, 4H, CH_2), 2.75−2.85 (m, 4H, CH_2), 2.34−2.45 (m, 4H, CH_2), 1.15 (t, J = 7.01 Hz, 6H, CH_3). ^{13}C NMR (125 MHz, $CDCl_3$) δ 160.4, 153.7, 151.2, 149.4, 139.8, 138.8, 138.1, 135.5, 134.7, 132.3, 130.5, 126.8, 126.5, 126.2, 124.9, 123.1, 123.0, 121.60, 121.58, 121.4, 121.2, 120.9, 120.6, 120.0, 96.4, 83.3, 70.1, 69.6, 67.3, 66.6, 51.7, 39.5, 15.1. MS (APCI) m/z calcd $[M + H]^+$ 695.2067, found 695.2076. UV−vis (DMSO) λ_{max} 391 nm.

Synthesis of 1-(7-((5-(Benzothiazol-2-yl)thiophen-2-yl)-ethynyl)-9,9-bis(2-(2-ethoxyethoxy)ethyl)-9H-fluoren-2-yl)-3-butylthiourea (11). In a small vial under nitrogen, a mixture of 2-(5-((9,9-bis(2-(2-ethoxyethoxy)ethyl)-7-isothiocyanato-9H-fluoren-2-yl)ethynyl)thiophen-2-yl)benzothiazole (**10**; 58 mg, 0.083 mmol) and *n*-butylamine (0.074 mL, 1.0 mmol) at room temperature was stirred for 1 h. The remaining amine was removed under vacuum, and the residue was recrystallized from hexane/ethyl acetate (9:1) to yield 48 mg (75%) of a light yellow solid. mp 118.5−119.5 °C. ^{1}H NMR (500 MHz, $CDCl_3$) δ 8.05 (d, J = 8.07 Hz, 1H, Ph-H), 7.88 (d, J = 8.07 Hz, 1H, Ph-H), 7.78 (s, 1H, N−H), 7.66−7.73 (m, 2H, Ph-H), 7.54−7.62 (m, 3H, Ph-H, Thy-H), 7.48−7.53 (m, 1H, Ph-H), 7.37−7.43 (m, 1H, Ph-H), 7.29−7.33 (m, 2H, Ph-H, Thy-H), 7.15−7.22 (m, 1H, Ph-H), 6.36 (s,1H, N−H), 3.62−3.71 (m, 2H, CH_2), 3.34−3.43 (m, 4H, CH_2), 3.22−3.32 (m, 4H, CH_2), 3.10−3.22 (m, 4H, CH_2), 2.74−2.97 (m, 4H, CH_2), 2.34−2.45 (m, 4H, CH_2), 1.61 (quintuplet, J = 7.05 Hz, 2H, CH_2), 1.40 (sextuplet, J = 7.05 Hz, 2H, CH_2), 1.13 (t, J = 7.05 Hz, 6H, CH_3), 0.96 (t, J = 7.83 Hz, 6H, CH_3). ^{13}C NMR (125 MHz, $CDCl_3$) δ 180.6, 168.1, 160.4, 153.7, 149.2, 140.4, 138.2, 138.1, 134.7, 132.9, 132.7, 128.5, 128.4, 126.9, 126.5, 126.5, 126.3, 123.1, 121.54, 121.5, 121.4, 121.3, 120.2, 120.1, 96.4, 83.1, 70.0, 69.6, 67.1, 66.5, 51.9, 45.5, 39.6, 30.9, 20.2, 15.1, 13.8. MS (APCI) m/z calcd $[M + H]^+$ 768.2958, found 768.3010. UV−vis (DMSO) λ_{max} 391 nm.

Preparation of Bioconjugate **B2**. A mixture containing 1000 μL of monoclonal DC-101 antibody (4 mg/mL) and 1000 μL of $NaHCO_3$ (1 M) was combined with a fresh solution of isothiocyanate **10** in DMSO in a 1:6 molar protein/dye proportion and incubated for 1 h in the dark at room temperature. The bioconjugate was purified by using disposable PD-10 desalting columns from GE equilibrated and eluted with PBS buffer 7.4. Fractions containing the bioconjugate were identified using a spectrophotometer by monitoring bands at 280 and 391 nm. The degree of labeling was determined to be 3.

Preparation of IgG Containing Bioconjugate. A mixture containing 190 μL of IgG antibody (21.16 mg/mL) in 890 μL of PBS buffer pH = 7.4 and 1000 μL of $NaHCO_3$ (1 M) was combined with a fresh solution of isothiocyanate **10** in DMSO in a 1:6 molar protein/dye proportion and incubated for 1 h in the dark at room temperature. The bioconjugate was purified by using disposable PD-10 desalting columns from GE equilibrated and eluted with PBS buffer 7.4. Fractions containing the bioconjugate were identified using a spectrophotometer by monitoring bands at 280 and 391 nm. The degree of labeling was determined to be 3.

Measurements. Spectra of amine reactive probes and model compounds were acquired in DMSO solutions with concentrations on the order of 10^{-6} M at room temperature using 1 cm quartz cuvettes. Absorption spectra were recorded with an Agilent 8453 UV−visible spectrophotometer. Steady-state fluorescence spectra were measured with a PTI Quanta-master spectrofluorimeter in the photon counting regime of the PMT using an L-format configuration. The fluorescence spectra were corrected for the spectral dependence of the PMT. Fluorescence quantum yields were determined relative to 9,10-diphenylanthracene in cyclohexane. Absorption spectra of bioconjugates **B1** and **B2** were measured in PBS buffer using 1 mm quartz cuvettes.

Two-photon absorption spectra were measured by the two-photon fluorescence (2PF) method relative to Rhodamine B in methanol,[17] using solutions with concentrations of approximately 10^{-4} M in spectroscopic grade DMSO following a previously reported methodology.[16]

Cell Culture and Incubation. PAE (porcine aortic endothelial) and PAE/KDR (commercially available porcine aortic endothelial expressing 2 × 10^5 VEGFR-2 per cell) were cultured in F-12 nutrient mixture (Ham's medium, Invitrogen) containing 10% fetal bovine serum (FBS) (Atlanta Biologicals) and 1% penicillin/streptomycin, at 37 °C, under a 5% CO_2 environment. Cells were cultured on no. 1 round 12 mm coverslips that were previously treated with poly-D-lysine. The treated coverslips were placed in 24-well plates, and 60,000 cells/well were seeded and incubated at the same conditions as indicated above until 75−85% confluency was reached on the coverslips. Cells were then fixed with a 3.7% solution of paraformaldehyde in pH = 7.4 PBS buffer for 10 min. The fixing agent was extracted and washed (2×) with PBS. To reduce autofluorescence, a fresh solution of $NaBH_4$ (1 mg/mL) in pH = 8 PBS buffer was used to treat the fixed cells (2x). Subsequently, cells were permeabilized with a 0.1% saponin solution in PBS containing 5% BSA. After permeabilization, PAE-KDR cells were incubated for 1 h at room temperature in a solution containing 0.4 μM solution of bioconjugate **B2** and the monoclonal antihuman VEGFR−2/KDR−fluorescein isothiocyanate bioconjugate (25 μg/mL) in culture media. PAE (negative control) and PAE-KDR cells were incubated for 2 h in a 0.4 μM solution of bioconjugate **B2** in PBS. The dye solutions were extracted by succion, and the coverslipped cells were washed abundantly with PBS (4×). The coverslipped cells were then washed with buffer PBS (2×) and mounted on microscope slides using Prolong Gold (Invitrogen) as a mounting media.

Tissue Immunofluorescence Staining. For the imaging of tumor endothelial cells, 10 μm thick sections were prepared from OCT-embedded frozen blocks. Tumor sections were incubated with rat antimouse CD31 antibody (BD Bioscience, San Diego, CA) and then Alexa Fluor 594-conjugated antirat Ig (Invitrogen).

Mouse Models and Tumor Excision. Lewis lung carcinoma cells were purchased from ATCC (Manassas, VA) and cultured in DMEM (Invitrogen) supplemented with 10% FBS. Experiments involving mice were done in accordance with

Scheme 1. Synthesis of B1

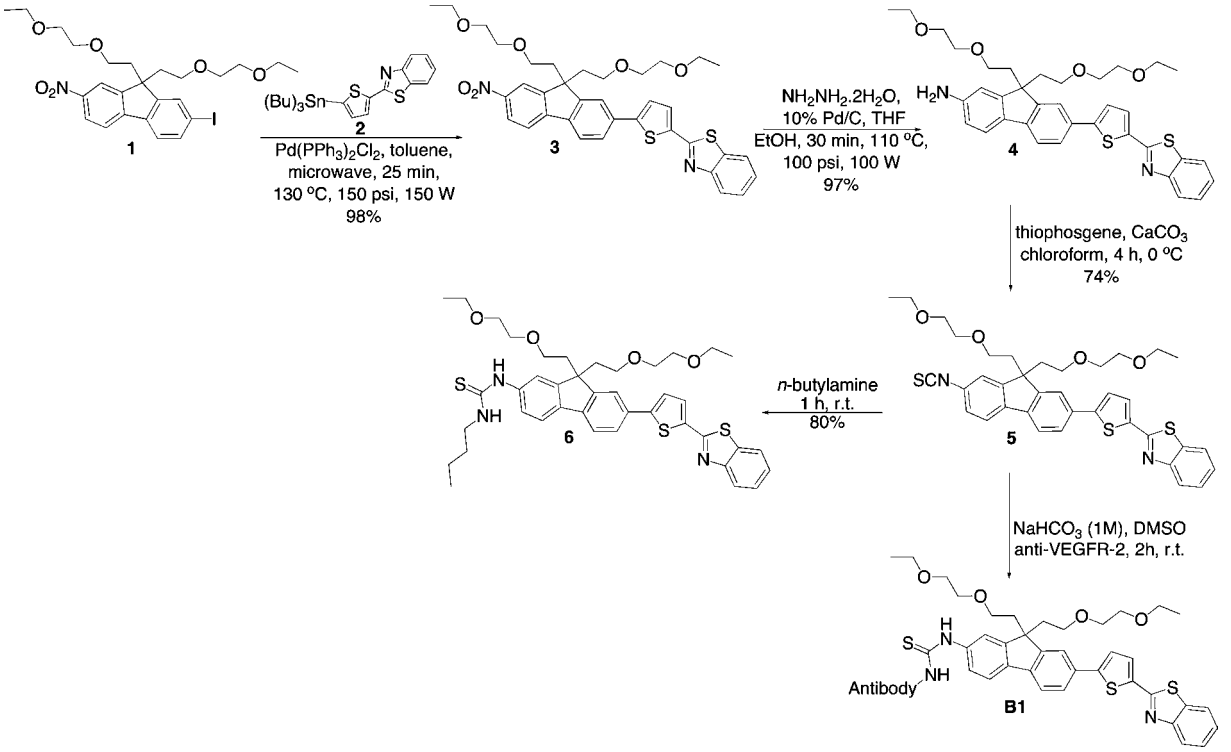

Scheme 2. Synthesis of B2

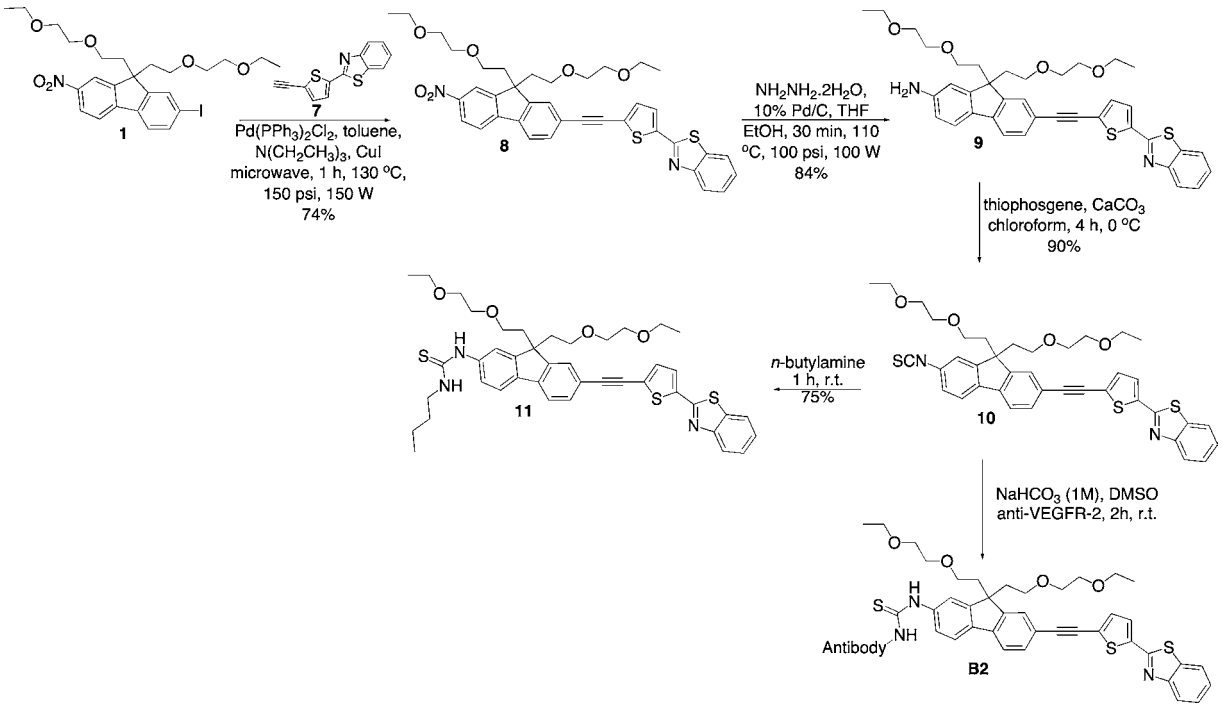

protocols approved by the Sanford-Burnham Medical Research Institutional Animal Care and Use Committee. Seven-week-old male C57BL/6 mice were purchased from Harlan Laboratories (Indianapolis, IN) and acclimated for 1 week upon delivery. Each mouse was injected subcutaneously into the right flank with 3×10^6 of Lewis lung carcinoma cells suspended in 0.1 mL of PBS. DC-101 antibody or mouse control IgG conjugated with 2PA probe (bioconjugate **B2**) was injected at a dose of 13.4 nmol (600 μg as a protein) per mouse via the tail vein 10 days after the inoculation of tumor cells. Two hours after the injection of the bioconjugate probe, mice were perfused with PBS and then 10% neutral-buffered formalin via the left ventricle under deep anesthesia with isoflurane. Tumors were excised and fixed with 10% neutral-buffered formalin for 18 h at 4 °C. After fixation, tumors were rinsed twice with PBS and cut into two pieces at the center of the tumors; one was used for

dx.doi.org/10.1021/bc200299z | *Bioconjugate Chem.* 2011, 22, 2060–2071

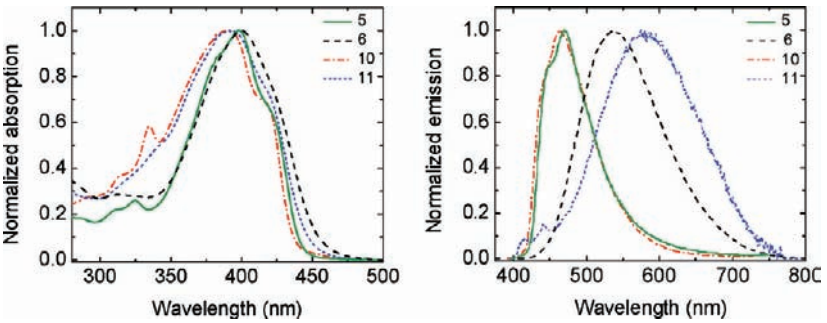

Figure 2. Normalized absorption (left) and fluorescence (right) spectra of compounds **5**, **6**, **10**, and **11** in DMSO.

Table 1. Linear Absorption Maximum (λ^{abs}_{max}), Emission Maximum (λ^{em}_{max}), Fluorescence Quantum Yield (Φ), Molar Absortivity Coefficient (ε^{max}), Fluorescence Lifetime (τ), Photodecomposition Quantum Yield (η), and Figure of Merit (F_M) of Compounds 5, 6, 10, and 11 in DMSO

compd	λ^{abs}_{max}, nm	λ^{em}_{max}, nm	Φ^a	ε^{max}, $\times 10^{-3}$ $M^{-1}\cdot cm^{-1}$	τ, ns	η, 10^6	F_M, $\times 10^{-6}$ GM
5	397 ± 1	469 ± 1	0.80 ± 0.05	61	0.95 ± 0.08		
6	400 ± 1	583 ± 1	1.00 ± 0.05	53	2.00 ± 0.08	4.23 ± 0.04	13 ± 2
10	391 ± 1	466 ± 1	0.70 ± 0.05	60	0.85 ± 0.08		
11	391 ± 1	580 ± 1	0.20 ± 0.05	54	0.79 ± 0.08	1.60 ± 0.02	23 ± 3

[a]Fluorescence quantum yield measured relative to 9,10-diphenylanthracene in cyclohexane.

3D two-photon fluorescence imaging, and the other was embedded in OCT compound (Sakura Finetek, Torrance, CA) for immunohistochemistry analysis.

One-Photon Fluorescence Imaging. *Cell Imaging.* One-photon confocal fluorescence microscopy was performed on a Leica SP5 II equipped with a spectral scanner. Micrographs of the fixed cells were taken under the following conditions: excitation of **B2** was done at 405 nm, excitation of the FITC anti-VEGFR-2 conjuagte was done at 476 nm; and fluorescence collection of both channels was done by setting the spectral window range from 490 to 620 nm. A water immersion, 63×, 1.3 N. A. objective was used for cell imaging.

Tissue Sections. One-photon fluorescence microscopy images were recorded on an Olympus IX-81 DSU microscope equipped with a Hamamatsu EM-CCD C9100 digital camera. One-photon fluorescence images were taken using a custom-made filter cube (Ex:377/50; DM:409; Em:525/40) for bioconjugates **B2**, a FITC filter cube (Ex:477/50; DM:507; Em:536/40) for FITC anti-VEGFR-2, and a TexRed filter cube (Ex:477/50; DM:507; Em:536/40) for the Alexa Fluor 594-CD31 antibody bioconjugate.

Two-Photon Fluorescence Imaging. Two-photon fluorescence microscopy (2PFM) imaging was performed on a modified Olympus Fluoview FV300 laser scanning microscopy system equipped with a broadband, tunable Coherent Mira Ti:sapphire laser (200 fs pulse width, 76 MHz repetition rate), pumped by a 10 W Coherent Verdi frequency doubled Nd:YAG laser. The Ti:sapphire laser, tuned and mode locked to 700 nm (for cell imaging) or to 820 nm (for "whole" tumor for imaging), was used as the two-photon excitation source. Two-photon induced fluorescence was collected by a 60× (UPLANSAPO, N.A. = 1.35 Olympus) or, for *ex vivo* tumor imaging, with a 10× (UPlanFl, N. A. = 0.30) microscope objective. A high transmittance (>95%) short-pass filter (cutoff 685 nm, Semrock) was placed in front of the PMT detector within the FV300 scanhead in order to filter off background radiation from the laser source (700 or 820 nm). The optical nonlinearity (quadratic dependence) for two-photon excitation was verified with dye **11**-doped poly(methyl methacrylate) films (see Figure S4 in the Supporting Information). The average laser power used for excitation of the tumors from mice injected with **B2** was 22 and 90 mW for all the control samples.

RESULTS AND DISCUSSION

Synthesis of New Fluorescent Probes and Preparation of Bioconjugates. The synthesis of the 2PA amine reactive probes **5** and **10** was achieved in short reaction times and high yields by using microwave-assisted synthesis, as illustrated in Schemes 1 and 2, respectively. Briefly, fluorene derivative **1** was coupled to intermediates **2** and **7** by either Stille or Sonogashira coupling to yield nitro derivatives **3** and **8**, respectively. These nitro derivatives were reduced to the corresponding amine intermediates **4** and **9**.[18] Transformation of these amines into the corresponding isothiocyanates **5** and **10** was performed by a previously reported method. [14,15,19]

In order to better understand the scope and properties of these probes, conjugation with *n*-butylamine was performed to generate model compounds **6** and **11**, which have optical properties closely resembling those of the bioconjugates. Once obtained, amine reactive probes and models were structurally and photophysically characterized.

The amine-reactive probes, isothiocyanates **5** and **10**, were conjugated to anti-VEGFR-2 for 2 h at room temperature in a 10:1 molar ration of dye/protein. Purification was achieved by using a commercially available, Sephadex packed, GPC column. The antibody of choice for this conjugation was DC-101, mainly because the epitiope for this antibody is extracellular. In these studies, where mice were going to be injected with the antibody conjugate, it was clear that the location of the antigenic determinant had to be on the surface of the endothelial cells of the tumor vessels in order to maximize the labeling efficiency of the bioconjuagte. Furthermore, DC-101 (Bevacizumab) has been FDA approved for the treatment of nonsmall cell lung cancer, colon cancer, and breast cancer and is currently being studied for the treatment of ovarian, prostate, renal, pancreatic, and liver cancers.

dx.doi.org/10.1021/bc200299z | *Bioconjugate Chem.* 2011, 22, 2060–2071

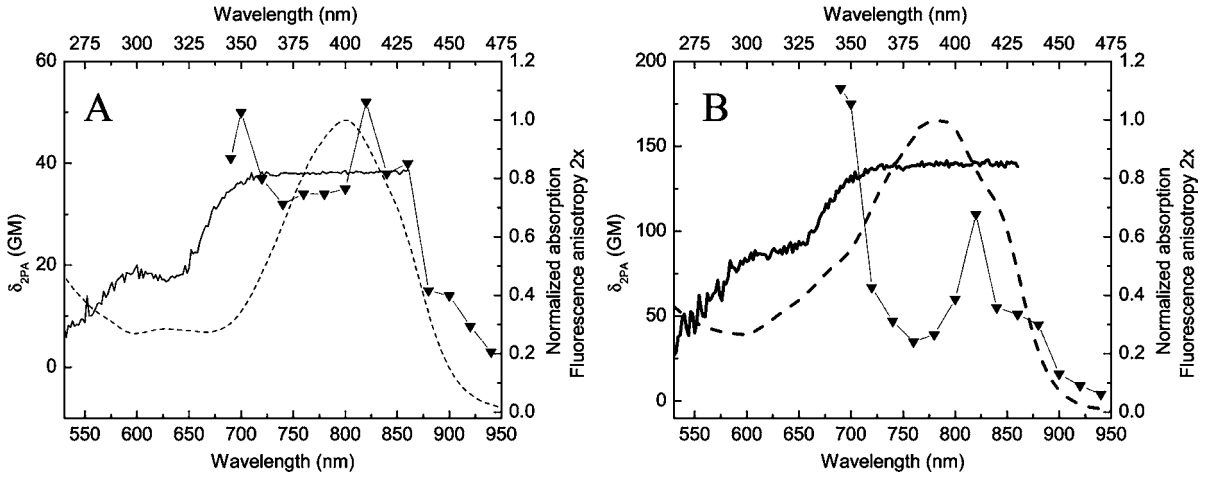

Figure 3. Normalized absorption (dash lines), two-photon absorption cross section (symbols and lines), and anisotropy (2×, solid lines) of model compounds **6** (A) and **11** (B).

Photophysical Properties. Photophysical characterization was performed for amine-reactive probes **5** and **10** and model compounds **6** and **11** (Figure 2). Table 1 reveals that there are intense absorption maxima for amine-reactive probes and model compounds located between 390 and 400 nm, whereas there was a red shift in the emission maxima when the dyes were conjugated to *n*-butylamine due to the dipolar nature of the model adducts. In addition, a larger Stokes shift was observed for the more conjugated model compound **11**.

In our previous studies, we observed that the presence of isothiocyanate groups in the fluorene system plays an important role by quenching the fluorescence of the dye, possibly by inducing intersystem crossing and allowing the molecule to relax by nonradiative pathways, but the fluorescence seems to be restored (switched on) upon conjugation.[14,15] Interestingly, in the case of these new dyes, this effect was not observed. For probe **5**, the quantum yield increased upon conjugation to the amine, as was observed previously for a similar molecule. However, for probe **10**, there was a significant decrease in the fluorescence quantum yield after conjugation with *n*-butylamine (Table 1). This important result suggests that luminescent properties cannot be predicted on the basis of only the similarities between structures.

In 2PFM applications where the upconverted fluorescence of the probe is directly interrogated, the efficiency of the probe depends on basically three parameters, namely the two-photon absorption cross section, the fluorescence quantum yield, and the quantum yield of photodecomposition. The first two parameters are of utmost importance and reflect the probability that the probe has to absorb two photons at a specific wavelength and the ratio of photons the molecule emits by means of fluorescence in relation to the photons it has absorbed, respectively. Combined, the two-photon absorption cross section and the fluorescence quantum yield constitute a parameter referred to as the action cross section, which is the product of these values ($\delta\Phi$). The parameter that is frequently overlooked is the photodecomposition quantum yield (η), which is a good indicator of how quickly a fluorofore photobleaches per photons absorbed. The figure of merit, F_M, is the action cross section normalized by the photodecomposition quantum yield ($F_M = \delta\Phi/\eta$) and is a more comprehensive parameter for evaluating the overall effiency of a fluorescent probe. In the particular case of compounds **6** and **11** (Table 1), the effiencies were quite favorable when compared to fluorescein ($F_M = 6 \times 10^6$ GM).

The lifetimes for these series of compounds were also measured in DMSO at concentrations of approximately 10^{-6} M, as shown in Table 1. A difference of 1.2 ns was found between the fluorescence lifetime of models **6** and **11**. Even though they have similar fluorescence maxima, with this difference in lifetime, it may be possible to distinguish between bioconjugates containing these dyes and different antibodies or vectors by fluorescence lifetime imaging microscopy (FLIM).

Anisotropy values of samples were measured under one-photon excitation in poly-THF at concentrations of approximately 10^{-6} M, while two-photon absorption (2PA) cross sections of model compounds were determined by the fluorescence method using DMSO solutions in concentrations of ca. 10^{-5} M. Rhodamine B in methanol was employed as a standard[17] (Figure 3). Both compounds have a significant 2PA cross section value within the measured range (700–940 nm). Anisotropy spectra exhibited a constant value at the wavelength where the maximum of linear absorption was located, corresponding to the first electronic transition $S_0 \rightarrow S_1$ (one-photon allowed); in this region, there is a decrease in the 2PA cross section value. The anisotropy began to decrease below 350 nm, reaching a minimum at around 325 nm leading to a second "plateau"; this may correspond to a higher electronic transition $S_0 \rightarrow S_n$, a two-photon allowed transition, resulting in a high 2PA cross section at this excitation wavelength.

A maximum in the 2PA spectra within the frame of the main linear absorption band was observed at around 820 nm for both model compounds. This transition correlated nicely to that responsible for the shoulder located at around 425 nm in the linear absorption spectrum. These dyes can be excited by 2PA at wavelengths as long as 850–900 nm, with the fluorescence emission ranging from 400 to 800 nm. These probes have great versatility because they can be efficiently excited over a range of wavelengths and their emission is in the visible to NIR range, required for deep tissue imaging.

After bioconjugation of the isothiocyanates with the selected antibody and purification by gel permeation chromatography, fractions containing the bioconjugates were analyzed by UV–vis spectrometry. Figure 4 shows the absorption spectra of isothiocyanate **10** (red) and biconjugate **B2** (green). The concentration of the protein in the bioconjugate was

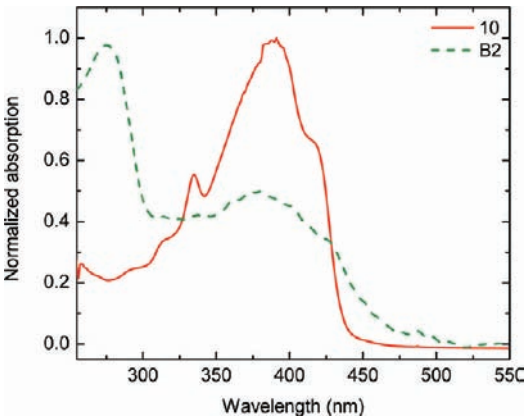

Figure 4. Normalized absorption of isothiocyanate **10** (red, solid line) and bioconjugate **B2** (green, dashed line).

determined to be ca. 50 μM, and the degree of labeling (DOL) was found to be 3. The concentration of the dye in the purified solution was estimated to be ca. 0.4 μM by using the extinction coefficient of the model compound. Preparation of bioconjugates following this method was performed more than once to evaluate the reproducibility of the method; repeated preparation of **B1** and **B2** generated these same results consistently.

Cell Imaging. To study the scope of the new bioconjugates, probes **B1** and **B2** were incubated with porcine aortic endothelial (PAE-KDR) cells that express VEGFR-2, as it is known that this receptor is found in higher concentrations when angiogenesis is occurring.[10] Preliminary studies demonstrated that fluorescence images obtained with **B2** were superior to those obtained with **B1** (not shown). Thus, bioconjugate **B2** was used for the subsequent experiments. PAE-KDR cells were coincubated with a commercially available fluorescent bioconjugate containing fluorescein isothiocyanate and a monoclonal VEGFR-2 antibody (DC101), as a positive control, and our DC101 bioconjugate **B2**. After 1 h of

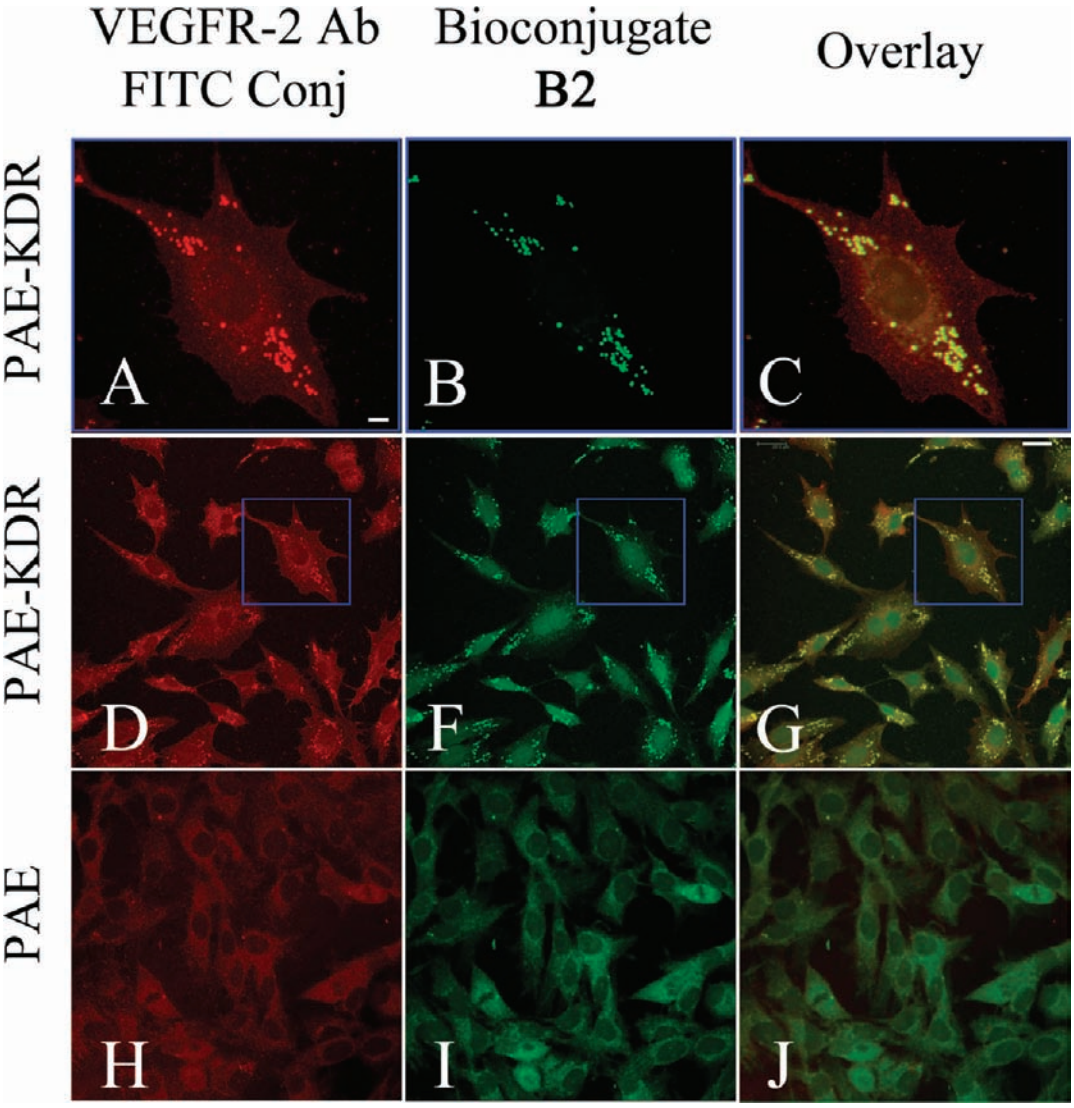

Figure 5. One-photon confocal micrographs of PAE-KDR and PAE cells. Cells were incubated with VEGFR-2 antibody-FITC conjugate (red) and DC101 bioconjugate (**B2**, green). Parts A, B, and C show the magnification of the area enclosed by the blue box in parts D, F, and G. Colocalization corroborates the VEGFR-2 selectivity (C and G) of **B2**. Fluorescence in negative control PAE cells (H and I) is much lower in intensity and less specific than that in PAE-KDR (A–G). Scale bars: 5 μm in A and 20 μm in part G.

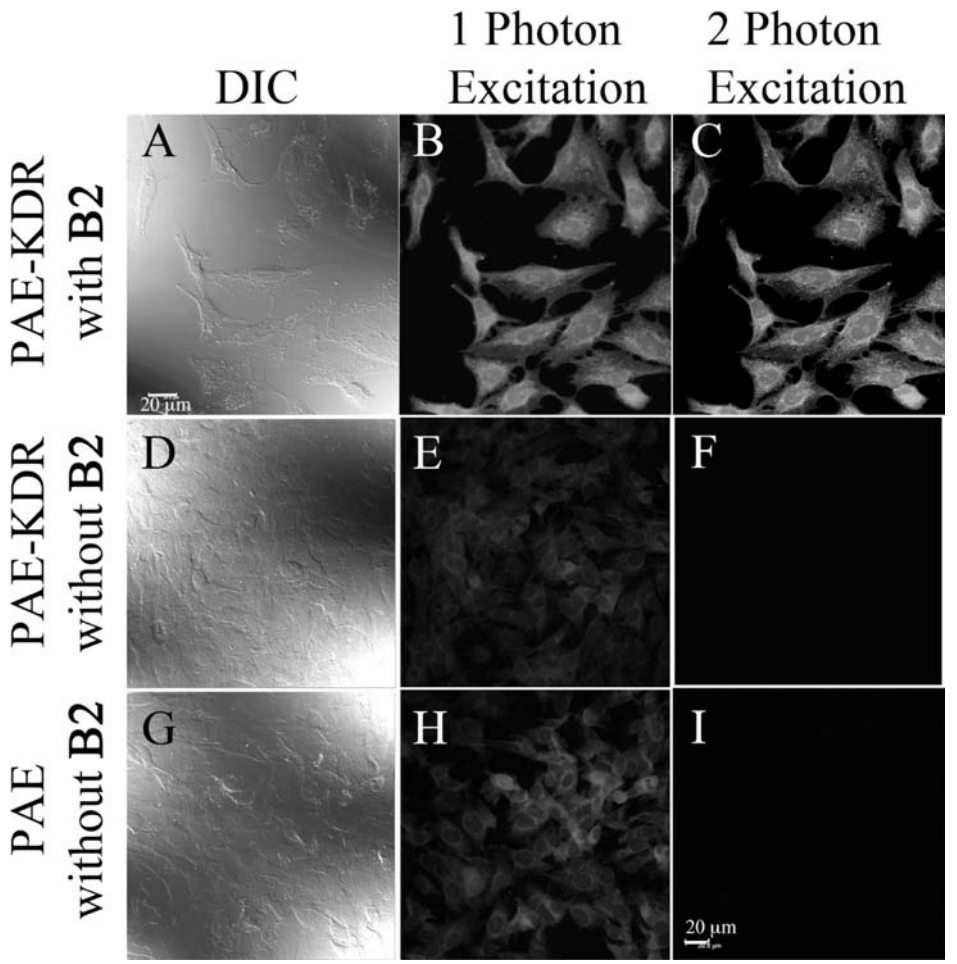

Figure 6. One- and two-photon fluorescence micrographs of PAE-KDR (porcine aortic endothelial cells expressing VEGFR-2) incubated with bioconjugate **B2** (15 μM, 45 min, A–C) and PAE-KDR; PAE cells without **B2** incubation (D–I) . A, D, and G are DIC images; B, E, and H are X–Y projections of one-photon confocal fluorescence (excitation, 405 nm; emission, spectral scanner window 480–620 nm). C, F, and I are X–Y projections along the Z-axis of two-photon fluorescence micrgraphs (excitation, 810 nm; emission, spectral scanner window 480–620 nm). The 20 μm scale bar in part A applies for parts B and C. The 20 μm scale bar in part I applies for D–I.

incubation, epifluorescence micrographs of the incubated cells revealed a high degree of colocalization between the two probes (Figures 5A–G). Figure 5C shows very good coloacalization of the commercial FITC antibody and bioconjugate **B2**. To examine the selectivity of bioconjugate **B2** toward the VEGFR-2, porcine aortic endothelial (PAE) cells that do not overexpress the receptor were used as a negative control. There is more evident autofluorescence in panel F; these are separate images. In panel B the field of view was reduced as a result of digitally zooming in that particular area; subsequently, the histograms of each micrograph are significantly different. This was particularly evident after no-neighbor deconvolution was performed on each micrograph. Micrographs of PAE cells showed little to no specific fluorescence when incubated with B2 (Figure 5I) or the VEGFR-2 antibody FITC conjugate (Figure 5H).

In the interest of comparing the difference resulting from exciting by one- versus two-photon absorption, PAE-KDR cells that had been previously incubated with **B2** were imaged by exciting at 405 and 810 nm, respectively. Collection of the one-photon fluorescence was confocal, as it was passed through a 120 μm pinhole (Figure 6 B). On the other hand, the upconverted fluorescence on the 2PFM was collected keeping the microscope pinhole completely open (Figure 6C). Fluorescence appeared to be much more localized in the 2PFM (Figure 6C) than in its one-photon counterpart. This is likely due to the fact that in the confocal image a significant proportion of the fluorescence being collected is autofluorescence, since the molecule is being excited at 405 nm. One the other hand, in 2PFM autofluorescence is not as much of a concern with excitation at 815 nm; that is, most of what is collected is fluorescence from bioconjuagte **B2**.

Whole Tumor *Ex Vivo* Imaging. Microscopy of biological specimens deep within the tissue is severely limited by scattering of visible light. However, many relevant physiological events occur within the tissue of living organisms. Imaging features deeper within tissue at micrometer resolutions has been possible by 2PFM because scattering decreases with increasing wavelengths. Within biological tissue only unscattered (ballistic) photons are effective in exciting molecules by the absorption of two-photons.[20,21] Efficient 2PA fluorophores with high two-photon absorption cross sections at near IR wavelengths have been previously reported.[16,22] Thus, 2PFM benefits from the use of near IR light that is less likely to be scattered in tissue. The maximum imaging penetration depth within biological tissue (z_{max}) has been estimated to be linearly dependent on the scattering length for excitation light in tissue, $l_s^{(ex)}$, but logarithmically dependent on the collection efficiency

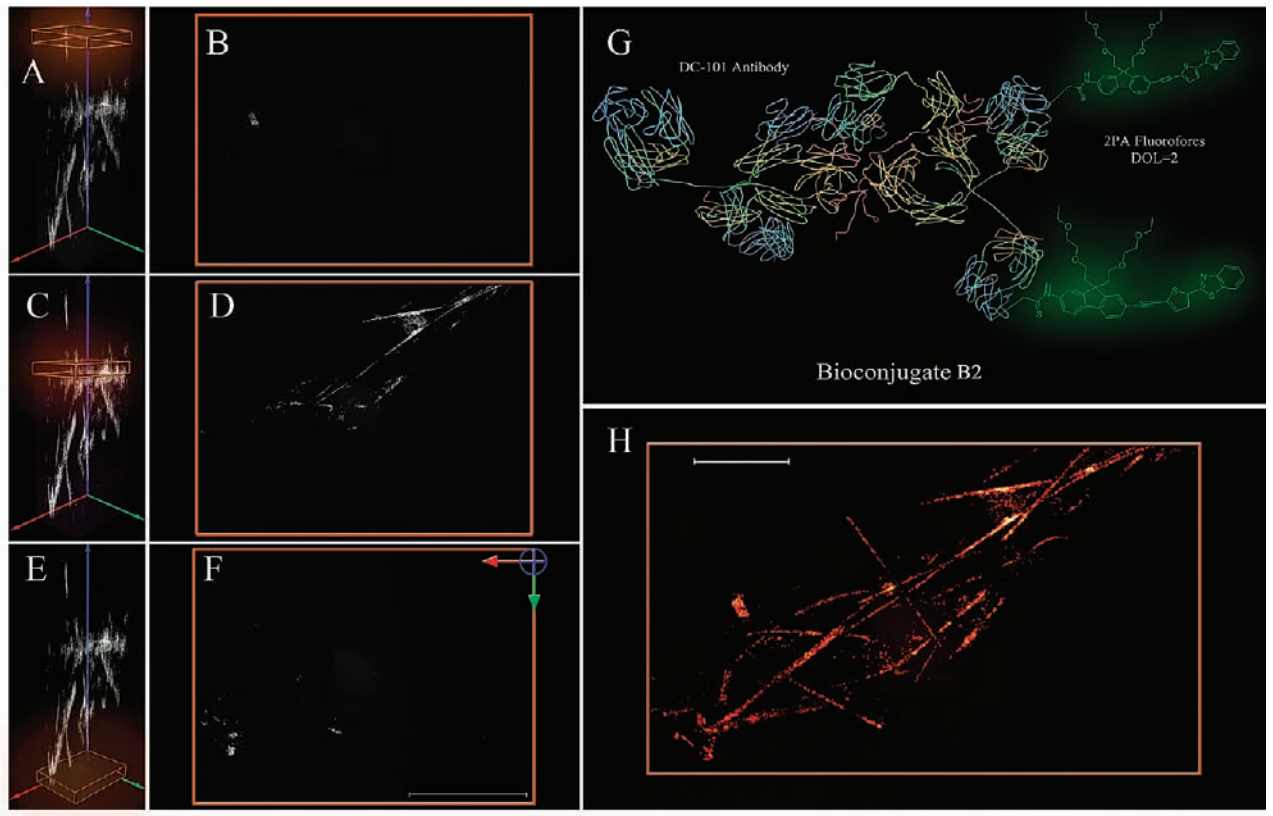

Figure 7. Whole mount tumor 2PFM micrographs of excised Lewis lung carcinoma excised tumors. Each mouse was tail vein injected with 400 μg of DC-101 bioconjugate **B2** (cartoon in G). Orange boxes (A, C, E) or squares (B, D, F) show 40 μm optical sections along the *Z*-axis. Parts B, D, and F are *X*−*Y* (red-green axes) plane projections along the *Z*-axis (blue) of optical sections centered at 740, 540, and 40 μm, respectively; parts A, C, and E show the relative position of the corresponding optical section in the *Z*-axis. The projection of the *X*−*Y* planes along the *Z*-axis (H) shows an image of chaotically intertwined vessels within the tumor. Micrographs were collected at 820 μm, 10×. Tissue penetration exceeded 830 μm. Scale bars: F, 20 μm; H, 10 μm.

of the system (fraction of fluorescent photons detected) and on the two-photon action cross section ($\delta\Phi$)[21,23] Limitations in most Ti:sapphire laser sources (1 W, 100 fs, 80 MHz, 680−1000 nm) restrict what can be done with these sources to increase imaging depth. These new, more efficient probes aim to increase the two-photon action cross section of the probe to enable imaging at greater depths in tissue.

Most efforts in improving the image quality and penetration depth of 2PFM have been oriented toward increasing the collection efficiencies of the emitted fluorescence photon,[24] microscope objective,[21] or repetition rates of the excitation source.[25] Herein, the focus has been to optimize the two-photon action cross section of fluorophores **6** and **11** in order to maximize the 2PFM imaging penetration within tumor tissue.[16] The optimal dye (**10**) was conjugated to the DC-101 antibody to facilitate observation of the formation of new vessels that overexpress VEGFR-2 receptor deep within the tumor.

A solid tumor is comprised of cancer cells and host stromal cells alike.[26,27] Neoplastic and host cells rely on blood vasculature to supply themselves with nutrients and get rid of toxins. All of these cells are exposed to hypoxic and acidic microenvironment that induces the production of positive or negative regulators of angiogenesis. In the past 20 years, more than 20 angiogenic stimulators have been discovered, with VEGF being one of the most important factors. Vascular function is key in determining the tumor microenvironment. Vasculature in healthy tissue is very well structured; in contrast, tumor vessels have very poor morphology and are conformed by immature cells in a meshlike architecture that confers a leaky property to the vessel. Because of its deep penetration, 2PFM offers an excellent means of monitoring tumor microenvironment, angiogenesis regulation, and normalization of tumor vasculature by antiangiogenic agents.[28,29]

The initial efficiency and selectivity of bioconjugate **B2** was evaluated in C57BL/6 male mice. Lewis lung carcinoma cells (3×10^6 cell/site) were implanted subcutaneously into the mice flanks. Eleven days postransplantation the tumor diameter had reached approximately 10 mm, and the mice were tail vein injected with 400 μg of the DC-101 bioconjugate **B2**. After 2 h the mice were perfused with PBS and sacrificed by formalin injection to the heart. Tumors were excised and fixed, and half was kept "whole" for tumor *ex vivo* microscopy and the other half for immunofluorescent histological experiments. The "whole" tumors were mounted on a glass coverslip and immobilized for imaging. 2PFM was conducted using both low (10×) and high (60×, oil immersion) N.A. objectives. The upconverted fluorescence was filtered prior to reaching the PMT (long pass 690 nm).

The whole tumor *ex vivo* 2PFM imaging experiments showed excellent results, allowing the visualization of vasculature over 800 μm deep in the tumor tissue (Figure 7). In Figure 7, the orange boxes (A−F) show layers corresponding to optical sections along the *Z*-axis (blue). The optical plane *X*−*Y* sections (*X*-axis in red, *Y*-axis in green) (Figure 7B, D, and F) at 738, 533, and 82 μm, respectively, show the fluorescence

dx.doi.org/10.1021/bc200299z | *Bioconjugate Chem.* 2011, 22, 2060−2071

contribution of these optical layers along the *Z*-axis. Fluorescence from two-photon excitation of the probe was recorded up 830 μm into the tumor. The relative position of these planes along the *Z*-axis can be seen in the micrographs shown in Figure 7A, C, and E, where the corresponding optical plane (orange square) is shown in the respective projection of the *X*−*Z* plane along the *Y*-axis. Projection of the *X*−*Y* planes along the *Z*-axis by the reconstruction of all of the optical planes (H) shows an image of chaotically intertwined vessels within the tumor where VEFGR-2 was overexpressed. The micrographs reveal how sensitive the 2PA phenomenon is to movements in the objective along the *Z*-axis and illustrates how useful this dye can be to reveal the formation of vasculature by 2PFM. Furthermore, the penetration that was achieved through a medium with such a wide distribution of refractive indices illustrates the potential of these efficient 2PA probes in monitoring the formation and development of vasculature in tumors by 2PFM imaging.

The selectivity of probe **B2** toward the tumor is evidenced by the excellent contrast observed in the micrographs in Figure 7; that is, there was very little nonspecific fluorescence within the tumors, mainly attributable to autofluorescence. The bioconjugate was also specific to tumors. This observation was verified by the 2PFM images of key organs of the mice that had been injected with **B2** (Supporting Information Figure S1). The organs and glands observed were kidneys, liver, heart, brain, lung, and spleen. Primarily only autofluorescence from native structures within each organ (e.g., elastin in muscle and actin in the heart) or residual dye that was being excreted (kidney) was observed.

Tissue sections (400 μm thick) of the tumors of the mice that had been injected with **B2** were costained with an Alexa Fluor 594-CD31 antibody to confirm, by fluorescence colocalization, that probe **B2** was, indeed, targeting vasculature (Figure 8). The tissue section was fixed and permeabilized for incubation with the Alexa Fluor 594-CD31 conjugate for 1 h at room temperature. Figure 8B shows the epifluorescence (1PA) corresponding to the sites where the DC-101 bioconjugate **B2** had accumulated 2 h following the tail vein injection. The vasculature was imaged by fluorescence of the Alexa Fluor 594 dye (Figure 8C). The overlay of micrographs B and C is shown in Figure 8D, where a high degree of colocalization can be observed for many vessels. As expected, not all vessels colocalized, presumably because some expressed higher levels of the VEGFR-2 than others.

The selectivity of the **B2** conjugate to the VEGFR-2 was also investigated by making an IgG conjugate with isothiocyanate **10**, which was injected in the same dose and conditions in control mice. Model compound **11** was also injected into different control mice under the same conditions to demonstrate the specificity of the monoclonal antibody **B2**. Only nonspecific fluorescence was observed from imaging these tumors by 2PFM (Supporting Information Figure S2).

CONCLUSIONS

We developed and synthesized new two-photon absorbing fluorescent amine reactive probes and bioconjugates. Photophysical characterization was performed for amine reactive probes, model compounds, and bioconjugates. The new probes demonstrated a number of desirable characteristics and optical properties, including high photostability and target selectivity. Successful imaging by one- and two-photon excitation with the bioconjugate **B2** in cells was performed, demonstrating that the new bioconjugates selectively bind VEGFR-2 in cell culture, tissue sections, and whole tumors. The DC-101 bioconjugate **B2** is a powerful new probe for selectively imaging the vascular endothelial growth factor receptor 2 (VEGFR-2) in cells expressing this receptor *in vitro* and in "whole" mounted excised tumors (*ex vivo*) by two-photon fluorescence microscopy (2PFM) imaging. This selectivity imparted excellent contrast in 2PFM micrographs that captured tumor vasculature features up to 800 μm within the tumor, despite the refractive index heterogeneity that is characteristic of this type of tissue. These images were recorded without having to increase the collection efficiency of fluorescent photons, without additional artifacts, and with a relatively low numerical aperture objective, fully exploiting the working distance of this objective. Since the tumors were "whole" mounted without prior treatment, the conditions are close to those of the *in vivo* environment. Hence, the new bioconjugate should be a candidate to continue with *in vivo* imaging of tumor models, through, e.g., a dorsal skinfold chamber where the first layers of tissue are significantly easier to access.

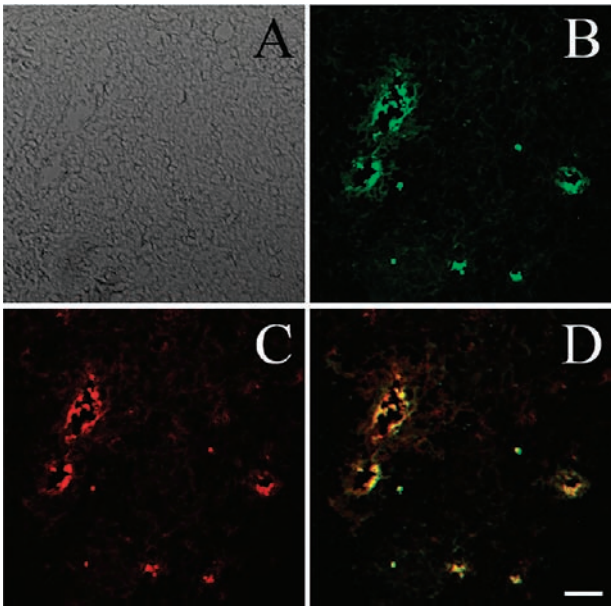

Figure 8. Micrographs of tissue sections (400 um thick) of tumors excised from a mouse injected with **B2**. The bright field image is shown in part A, and one-photon epifluorescence micrographs are shown parts B and C. An overlay of DC-101 bioconjugate **B2** (B) and Alexa Fluor 594-CD31 antibody conjugate (C) is shown in part D; colocalization confirms that probe **B2** targeted vasculature.

ASSOCIATED CONTENT

Supporting Information

^{1}H NMR and ^{13}C NMR data. Two-photon fluorescence micrographs of excised whole mount organs and glands of the mice that had been injected with bioconjuagte **B2** (negative control) and 2PFM of other negative controls are shown. A picture of the scanning process while taking a 2PFM micrograph is shown as is verification of the quadratic dependence of the microscope system for two-photon excitation, and a spectral scan vs solution emission spectrum of model probe **11**. This material is available free of charge via the Internet at http://pubs.acs.org.

AUTHOR INFORMATION

Corresponding Author

*Phone: 407-823-1028. Fax: 407-823-2252. E-mail: belfield@ucf.edu.

ACKNOWLEDGMENTS

We wish to acknowledge the National Institute for Biomedical Imaging and Bioengineering of the National Institutes of Health (1 R15 EB008858-01 to K.D.B.), the National Instutues of Health (1 R01 CA125255 to M.K.), the U.S. Civilian Research and Development Foundation (UKB2-2923-KV-07), the Ministry of Education and Science of Ukraine (Grant M/49-2008), and the National Science Foundation (CHE-0840431 and CHE-0832622).

REFERENCES

(1) Callagy, G., Dimitriadis, E., Harmey, J., Bouchier-Hayes, D., Leader, M., and Kay, E. (2000) Immunohistochemical measurement of tumor vascular endothelial growth factor in breast cancer—A more reliable predictor of tumor stage than microvessel density or serum vascular endothelial growth factor. *Appl. Immunohistochem. Mol. Morphol. 8*, 104−109.

(2) Tozer, G. M., Ameer-Beg, S. M., Baker, J., Barber, P. R., Hill, S. A., Hodgkiss, R. J., Locke, R., Prise, V. E., Wilson, I., and Vojnovic, B. (2005) Intravital imaging of tumour vascular networks using multi-photon fluorescence microscopy. *Adv. Drug Delivery Rev. 57*, 135−152.

(3) Gao, J. H., Chen, K., Xie, R. G., Xie, J., Yan, Y. J., Cheng, Z., Peng, X. G., and Chen, X. Y. (2010) In Vivo Tumor-Targeted Fluorescence Imaging Using Near-Infrared Non-Cadmium Quantum Dots. *Bioconjugate Chem. 21*, 604−609.

(4) Wang, L. V. (2009) Multiscale photoacoustic microscopy and computed tomography. *Nat. Photonics 3*, 503−509.

(5) Zhang, H. F., Maslov, K., Li, M. L., Stoica, G., and Wang, L. H. V. (2006) In vivo volumetric imaging of subcutaneous microvasculature by photoacoustic microscopy. *Opt. Express 14*, 9317−9323.

(6) Carmeliet, P. (2005) Angiogenesis in life, disease and medicine. *Nature 438*, 932−936.

(7) Asano, M., Yukita, A., Matsumoto, T., Kondo, S., and Suzuki, H. (1995) Inhibition of tumor-growth and metastasis by immunoneutralizing monoclonal-antibody to vascular endothelial growth-factor vascular-permeability factor (121). *Cancer Res. 55*, 5296−5301.

(8) Ellis, L. M., Curley, S. A., and Grothey, A. (2005) Surgical Resection After Downsizing of Colorectal Liver Metastasis in the Era of Bevacizumab. *J. Clin. Oncol. 23*, 4853−4855.

(9) Ferrara, N., and Kerbel, R. S. (2005) Angiogenesis as a therapeutic target. *Nature 438*, 967−974.

(10) Kowanetz, M., and Ferrara, N. (2006) Vascular Endothelial Growth Factor Signaling Pathways: Therapeutic Perspective. *Clin. Cancer Res. 12*, 5018−5022.

(11) Backer, M. V., Gaynutdinov, T. I., Patel, V., Bandyopadhyaya, A. K., Thirumamagal, B. T. S., Tjarks, W., Barth, R. F., Claffey, K., and Backer, J. M. (2005) Vascular endothelial growth factor selectively targets boronated dendrimers to tumor vasculature. *Mol. Cancer Ther. 4*, 1423−1429.

(12) Saban, M. R., Backer, J. M., Backer, M. V., Maier, J., Fowler, B., Davis, C. A., Simpson, C., Wu, X.-R., Birder, L., Freeman, M. R., Soker, S., Hurst, R. E., and Saban, R. (2008) VEGF receptors and neuropilins are expressed in the urothelial and neuronal cells in normal mouse urinary bladder and are upregulated in inflammation. *Am. J. Physiol. Renal Physiol. 295*, F60−72.

(13) Göppert-Mayer, M. (1931) Über Elementarakte mit zwei Quantensprüngen. *Ann. Phys. 401*, 273−294.

(14) Schafer-Hales, K. J., Belfield, K. D., Yao, S., Frederiksen, P. K., Hales, J. M., and Kolattukudy, P. E. (2005) Fluorene-based fluorescent probes with high two-photon action cross-sections for biological multiphoton imaging applications. *J. Biomed. Opt. 10*, 1−8.

(15) Morales, A. R., Schafer-Hales, K. J., Marcus, A. I., and Belfield, K. D. (2008) Amine-Reactive Fluorene Probes: Synthesis, Optical Characterization, Bioconjugation, and Two-Photon Fluorescence Imaging. *Bioconjugate Chem. 19*, 2559−2567.

(16) Andrade, C. D., Yanez, C. O., Rodriguez, L., and Belfield, K. D. (2010) A Series of Fluorene-Based Two-Photon Absorbing Molecules: Synthesis, Linear and Nonlinear Characterization, and Bioimaging. *J. Org. Chem. 75*, 3975−3982.

(17) Makarov, N. S., Drobizhev, M., and Rebane, A. (2008) Two-photon absorption standards in the 550−1600 nm excitation wavelength range. *Opt. Express 16*, 4029−4047.

(18) Belfield, K. D., Schafer, K. J., Mourad, W., and Reinhardt, B. A. (2000) Synthesis of new two-photon absorbing fluorene derivatives via Cu-mediated Ullmann condensations. *J. Org. Chem. 65*, 4475−4481.

(19) Morales, A. R., Yanez, C. O., Schafer-Hales, K. J., Marcus, A. I., and Belfield, K. D. (2009) Biomolecule Labeling and Imaging with a New Fluorenyl Two-Photon Fluorescent Probe. *Bioconjugate Chem. 20*, 1992−2000.

(20) Denk, W., and Svoboda, K. (1997) Photon upmanship: Why multiphoton imaging is more than a gimmick. *Neuron 18*, 351−357.

(21) Oheim, M., Beaurepaire, E., Chaigneau, E., Mertz, J., and Charpak, S. (2001) Two-photon microscopy in brain tissue: parameters influencing the imaging depth. *J. Neurosci. Methods 111*, 29−37.

(22) Wang, X. H., Nguyen, D. M., Yanez, C. O., Rodriguez, L., Ahn, H. Y., Bonder, M. V., and Belfield, K. D. (2010) High-Fidelity Hydrophilic Probe for Two-Photon Fluorescence Lysosomal Imaging. *J. Am. Chem. Soc. 132*, 12237−12239.

(23) Oheim, M., Beaurepaire, E., Chaigneau, E., Mertz, J., and Charpak, S. (2001) Two-photon microscopy in brain tissue: parameters influencing the imaging depth. *J. Neurosci. Methods 112*, 205−205.

(24) McMullen, J. D., Kwan, A. C., Williams, R. M., and Zipfel, W. R. (2010) Enhancing collection efficiency in large field of view multiphoton microscopy. *J. Microsc. 241*, 119−124.

(25) Beaurepaire, E., Oheim, M., and Mertz, J. (2001) Ultra-deep two-photon fluorescence excitation in turbid media. *Opt. Commun. 188*, 25−29.

(26) Jain, R. K., Munn, L. L., and Fukumura, D. (2002) Dissecting tumour pathophysiology using intravital microscopy. *Nat. Rev. Cancer 2*, 266−276.

(27) Fukumura, D., and Jain, R. K. (2007) Tumor microvasculature and microenvironment: Targets for anti-angiogenesis and normalization. *Microvasc. Res. 74*, 72−84.

(28) Garkavtsev, I., Kozin, S. V., Chernova, O., Xu, L., Winkler, F., Brown, E., Barnett, G. H., and Jain, R. K. (2004) The candidate tumour suppressor protein ING4 regulates brain tumour growth and angiogenesis. *Nature 428*, 328−332.

(29) Tong, R. T., Boucher, Y., Kozin, S. V., Winkler, F., Hicklin, D. J., and Jain, R. K. (2004) Vascular normalization by vascular endothelial growth factor receptor 2 blockade induces a pressure gradient across the vasculature and improves drug penetration in tumors. *Cancer Res. 64*, 3731−3736.

SUPPORTING INFORMATION

SYNTHESIS AND BIOIMAGING OF NEW FLUORESCENT TWO-PHOTON ABSORBING BIOCONJUGATES SELECTIVE TOWARDS VASCULAR ENDOTHELIAL GROWTH FACTOR RECEPTOR 2

Carolina D. Andrade,[§] *Ciceron O. Yanez,*[§] *Hyo-Yang Ahn,*[§] *Takeo Urakami,*[‡] *Mykhailo V. Bondar,*[⊥] *Masanobu Komatsu*[‡] *and Kevin D. Belfield*[§,£,]*

[§]Department of Chemistry and [£]CREOL, The College of Optics and Photonics, University of Central Florida, PO Box 162366, Orlando, FL 32816

[‡]Sanford-Burnham Medical Research Institute at *Lake Nona,* Orlando, FL 32827

⊥Institute of Physics, Prospect Nauki, 46, Kiev-28, 03094 Ukraine

E-mail: *belfield@ucf.edu

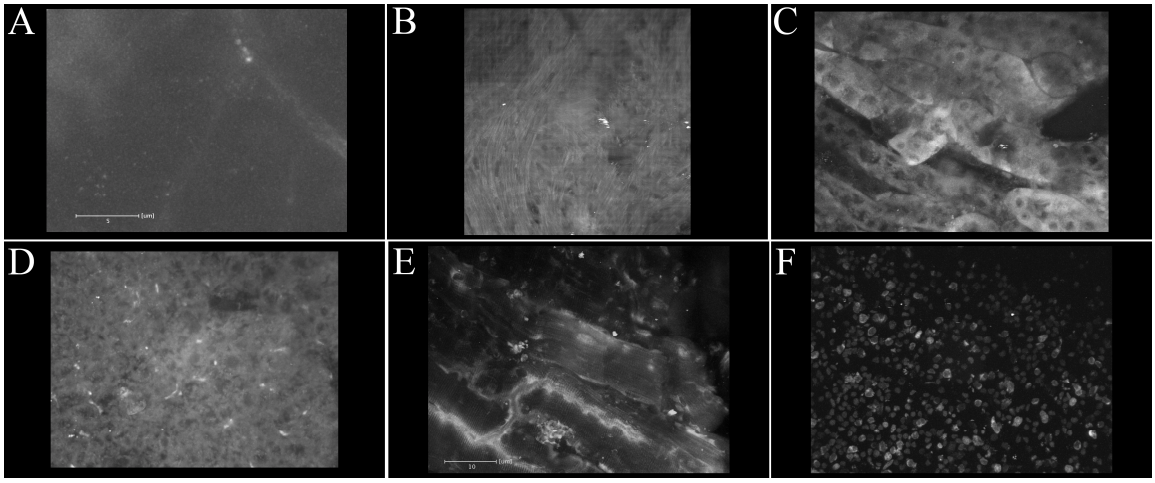

Figure S1. Two-photon fluorescence micrographs of excised whole mount organs and glands of the mice that had been injected with bioconjuagte **B2** (negative control)**.** Images were obtained from the Z-axis projection all X-Y plane optical sections of the organs**. A** brain; **B** heart; **C** kidney; **D** liver; **E** muscle; an **F** spleen. Micrographs were collected at 820 μm, 60 x. In these images mainly autofluorescence from native structures within each organ (elastin in muscle **E** and actin in the heart **B**, for example) or residual dye that was being excreted (kidney, **C**) was observed because very little to no conjugate resided in these organs (background was very modest). No vasculature formation was evidenced.

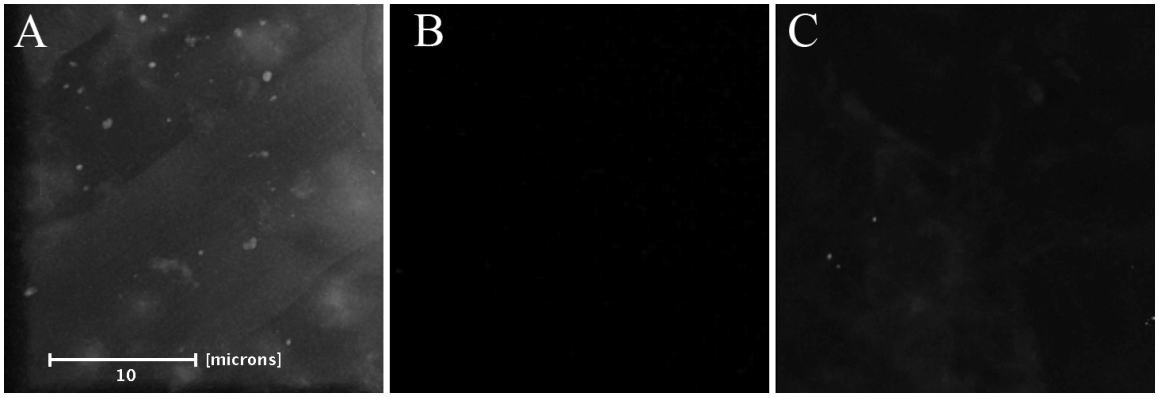

Figure S2. Whole mount tumor 2PFM micrographs of excised Lewis Lung Carcinoma excised tumors. Mice were tail vein injected 400 μg of IgG bioconjugate (**A** and **B**) or model dye **21** (**C**). Non specific fluorescence in **A** can be attributed to autofluorescence of the tissue and residual unbound dye.

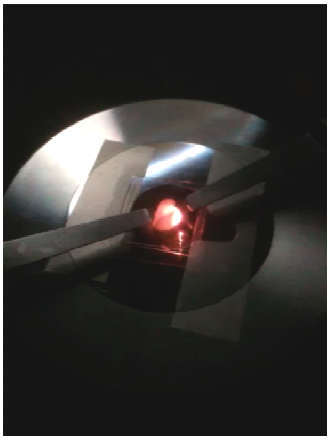

Figure S3. "Whole"-tumor mounted on microscope stage while being scanned by 810 nm, 200 fs excitation to excite the 2PA bioconjugate. In this inverted setup the tumor was immobilized between two cover slips and scanned layer by layer from below. Upconverted (two-photon induced) epifluorescence was collected either by a 10 or a 60x objective. 3-D reconstruction of the images was done in Amira 5.3 (Figure 7).

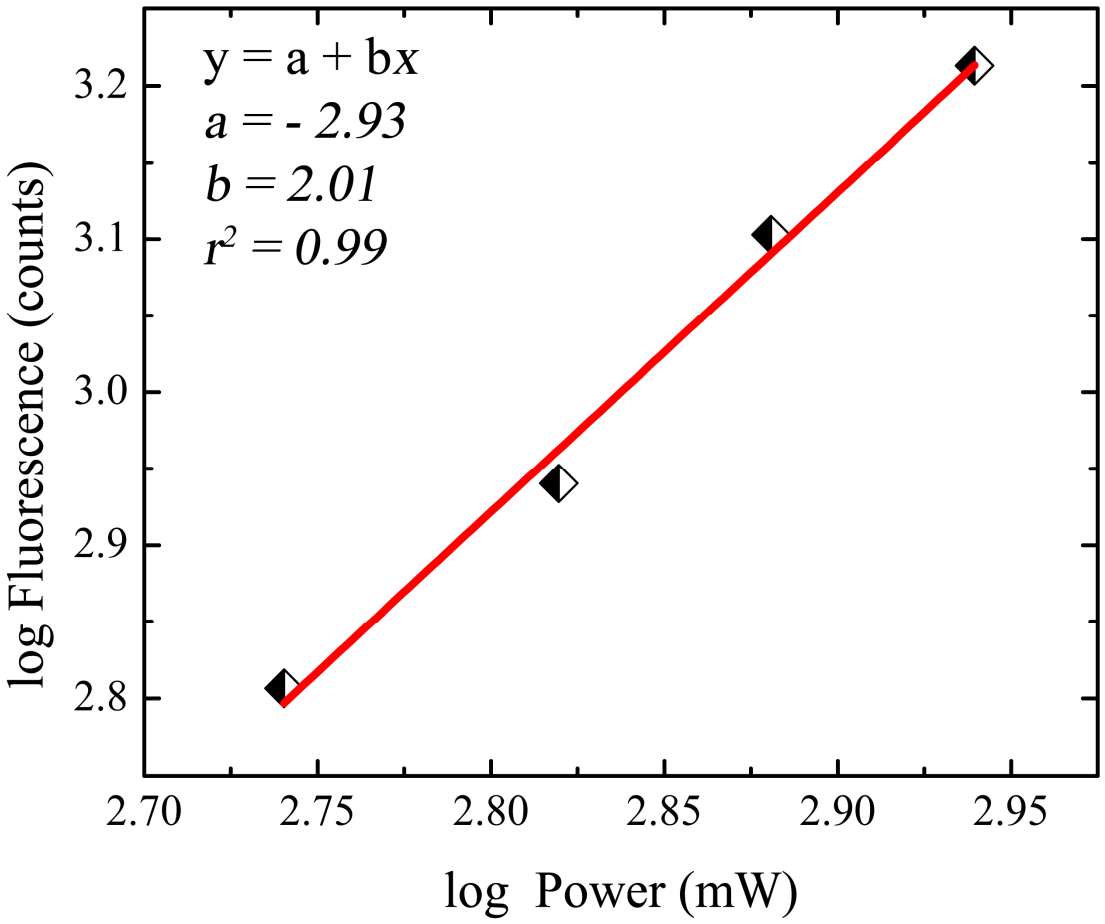

Figure S4. Quadratic dependence of the collected mean fluorescence on the average excitation. A solution of **11** in PMMA was excited at 815 nm at different powers.

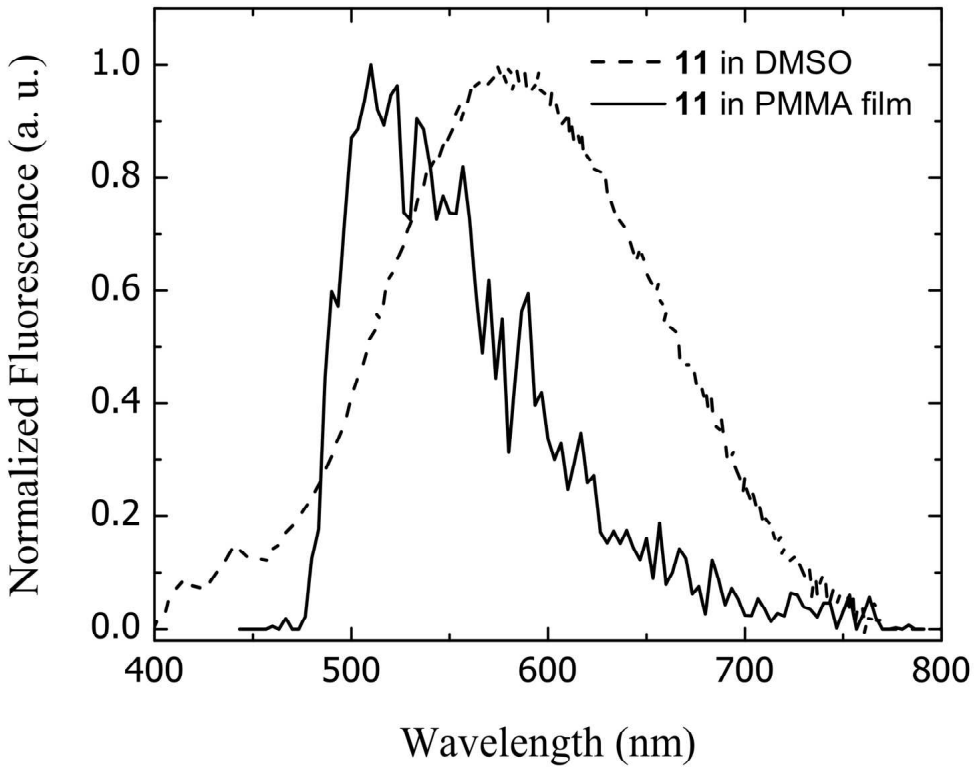

Figure S5. Emission spectra of bioconjugate **11** in DMSO (dashed line) and in a PMMA polymer film. The spectrum in DMSO solution was taken in a PTI spectrofluorimeter. The spectrum of **11** in the polymer film was taken on a Leica SP5 II equipped with a spectral scanner by taking a spectral scan of the region of interest (slit width 5 nm, step size 3 nm).

^{1}H NMR of **3**

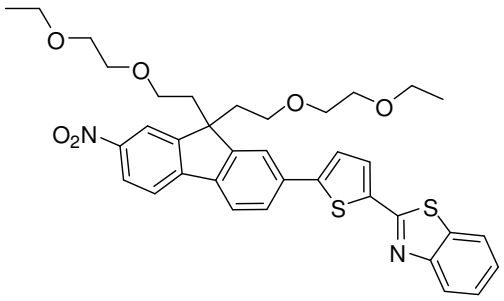
O
O
O
O
O
O_2N
S
S
N

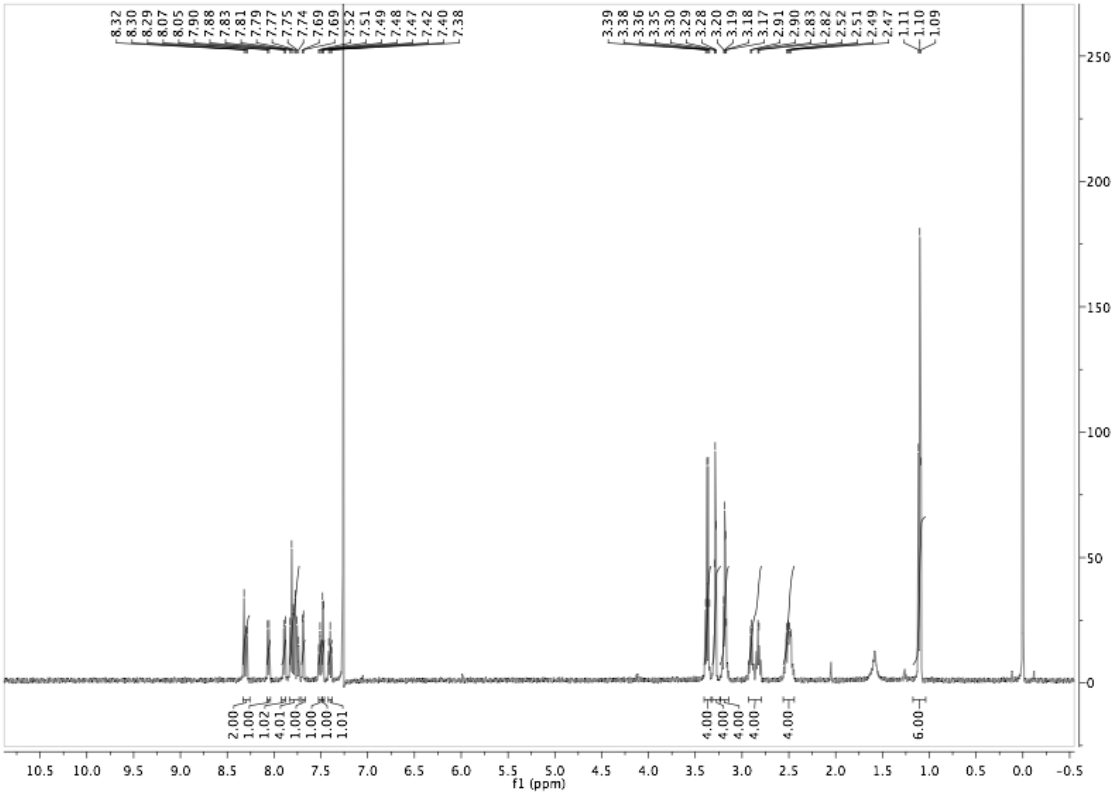
8.32
8.30
8.29
8.07
8.05
7.90
7.88
7.83
7.81
7.79
7.77
7.75
7.74
7.69
7.69
7.52
7.51
7.49
7.48
7.47
7.42
7.40
7.38
3.39
3.38
3.36
3.35
3.30
3.29
3.28
3.20
3.19
3.18
3.17
2.91
2.90
2.83
2.82
2.52
2.51
2.49
2.47
1.11
1.10
1.09
2.00
1.00
1.02
4.01
1.00
1.00
1.00
1.01
4.00
4.00
4.00
4.00
4.00
6.00
250
200
150
100
50
0
10.5 10.0 9.5 9.0 8.5 8.0 7.5 7.0 6.5 6.0 5.5 5.0 4.5 4.0 3.5 3.0 2.5 2.0 1.5 1.0 0.5 0.0 -0.5
f1 (ppm)

^{13}C NMR of **3**

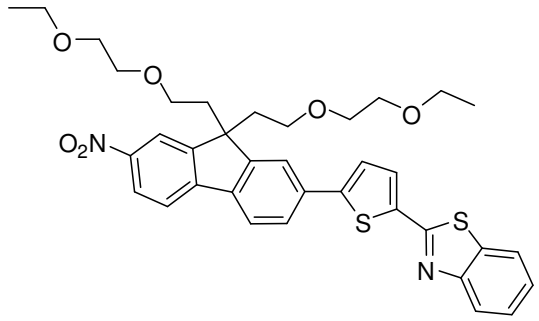
O
O
O
O
O
O_2N
S
S
N

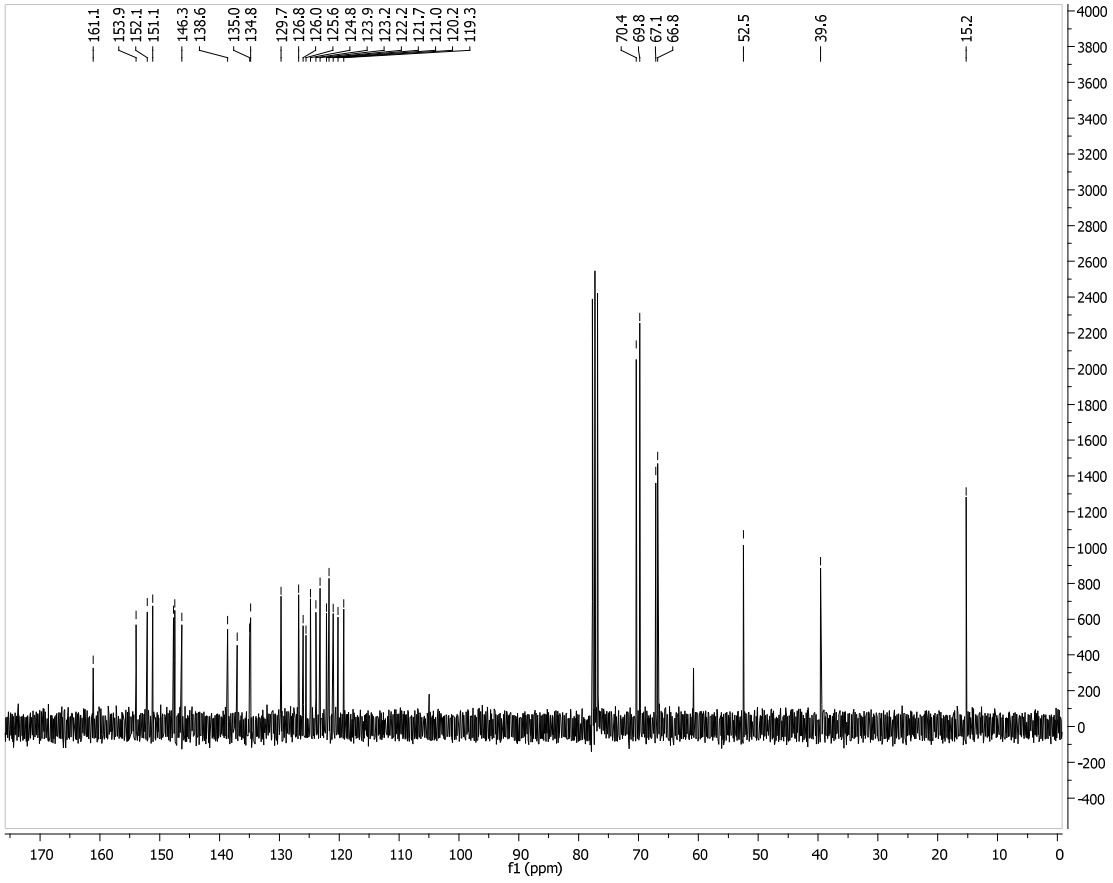
161.1
153.9
152.1
151.1
146.3
138.6
135.0
134.8
129.7
126.8
126.0
125.6
124.8
123.9
123.2
122.2
121.7
121.0
120.2
119.3
70.4
69.8
67.1
66.8
52.5
39.6
15.2
4000
3800
3600
3400
3200
3000
2800
2600
2400
2200
2000
1800
1600
1400
1200
1000
800
600
400
200
0
-200
-400
170
160
150
140
130
120
110
100
90
80
70
60
50
40
30
20
10
0
f1 (ppm)

^{1}H NMR of **4**

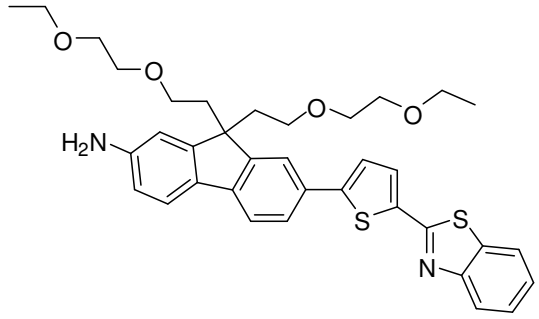
O
O
O
O
O
H_2N
S
S
N

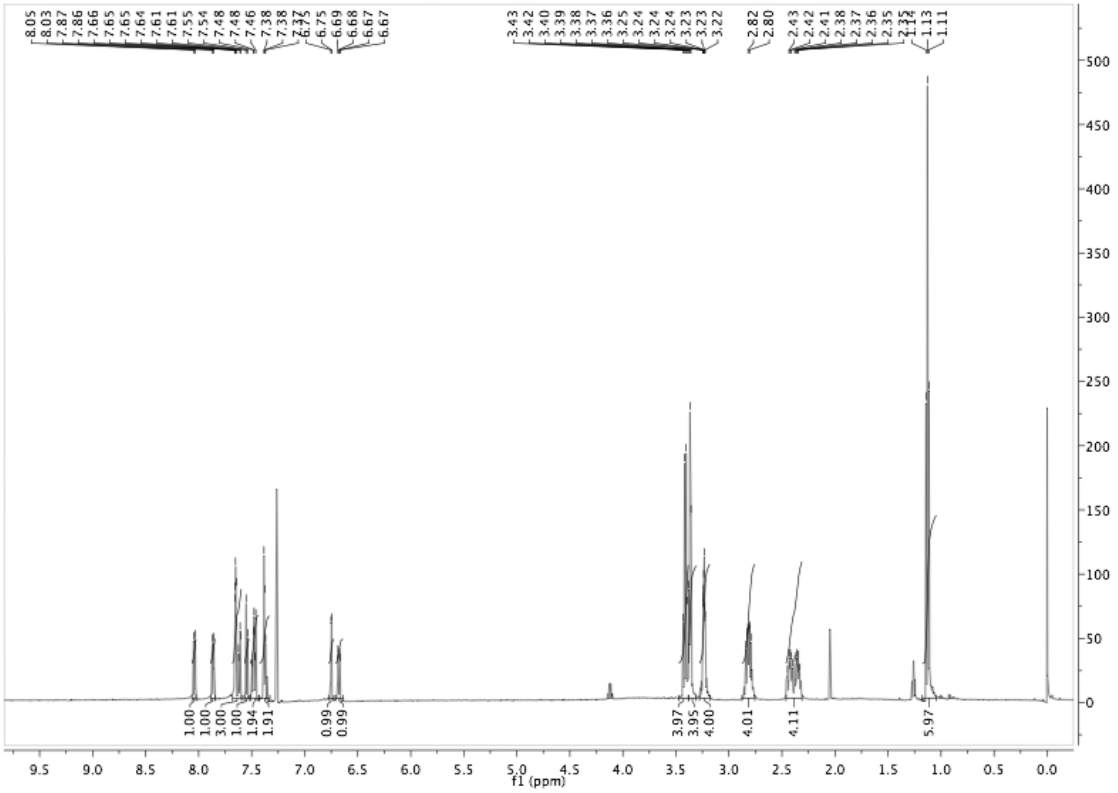
8.05
8.03
7.87
7.86
7.66
7.65
7.64
7.61
7.61
7.55
7.54
7.48
7.48
7.46
7.38
7.38
6.75
6.75
6.69
6.68
6.67
6.67
3.43
3.42
3.40
3.39
3.38
3.37
3.36
3.25
3.24
3.24
3.24
3.23
3.23
3.22
2.82
2.80
2.43
2.42
2.41
2.38
2.37
2.36
2.35
1.13
1.11
1.00
1.00
3.00
1.00
1.94
1.91
0.99
0.99
3.97
3.95
4.00
4.01
4.11
5.97
f1 (ppm)

^{13}C NMR of **4**

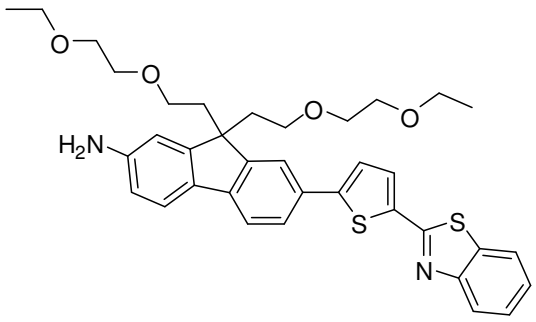
O
O
O
O
O
H_2N
S
S
N

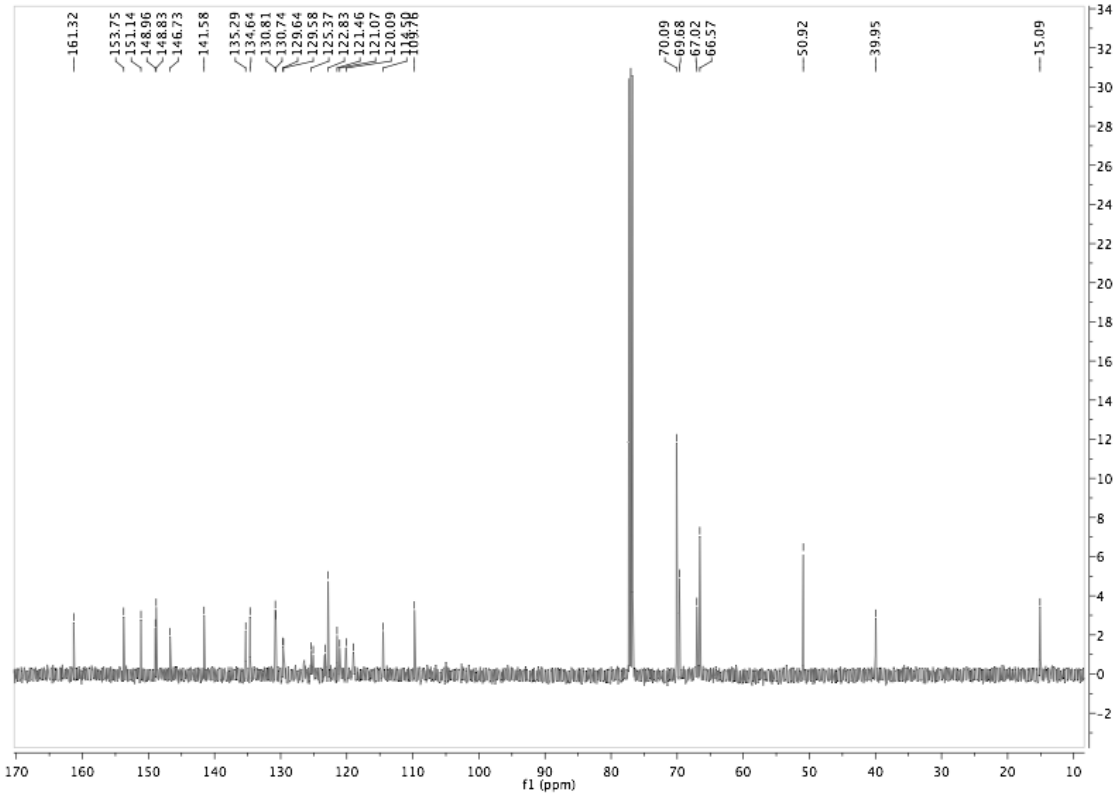
161.32
153.75
151.14
148.96
148.83
146.73
141.58
135.29
134.64
130.81
130.74
129.64
129.58
125.37
122.83
121.46
121.07
120.09
70.09
69.68
67.02
66.57
50.92
39.95
15.09
f1 (ppm)

^{1}H NMR of **5**

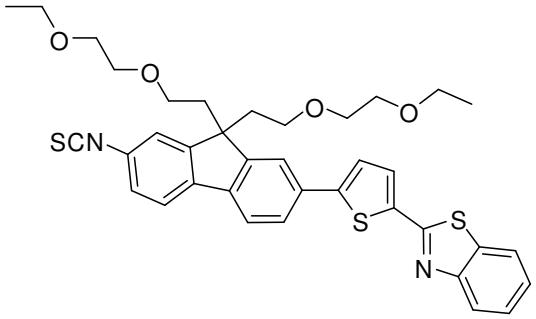

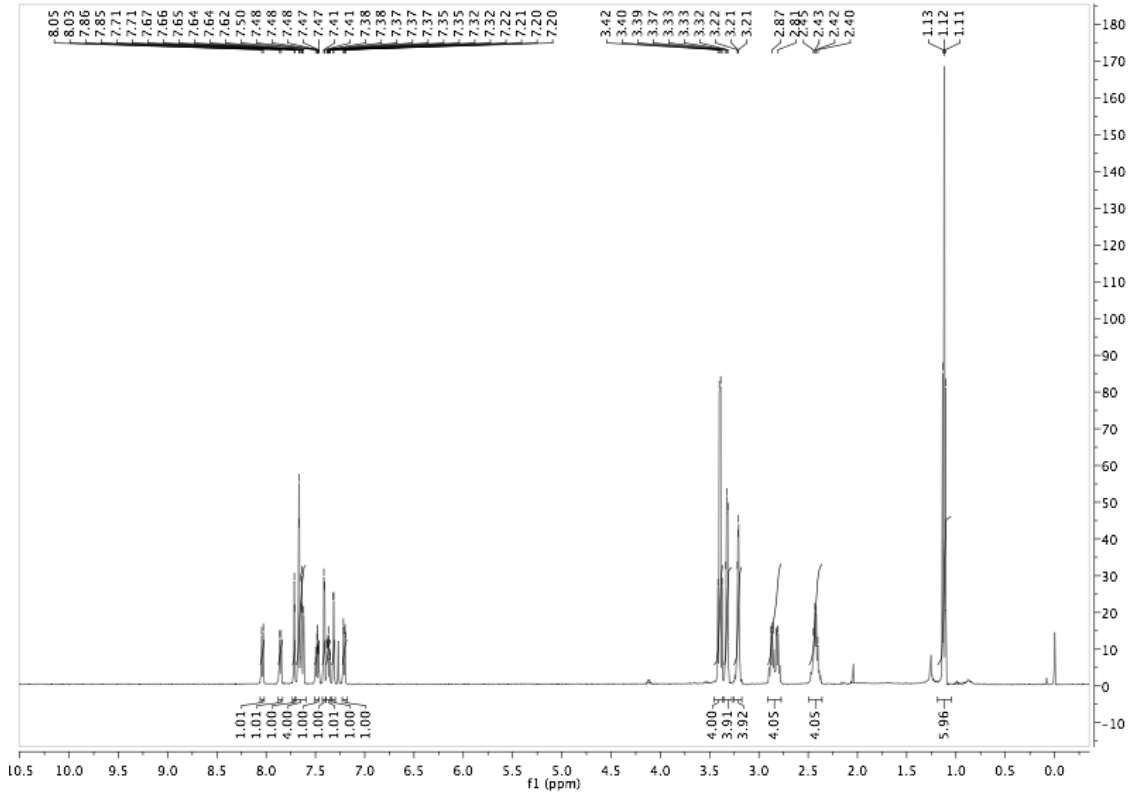

^{13}C NMR of **5**

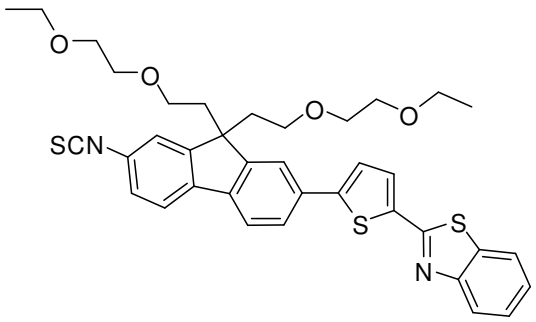
O
O
O
O
O
SCN
S
S
N

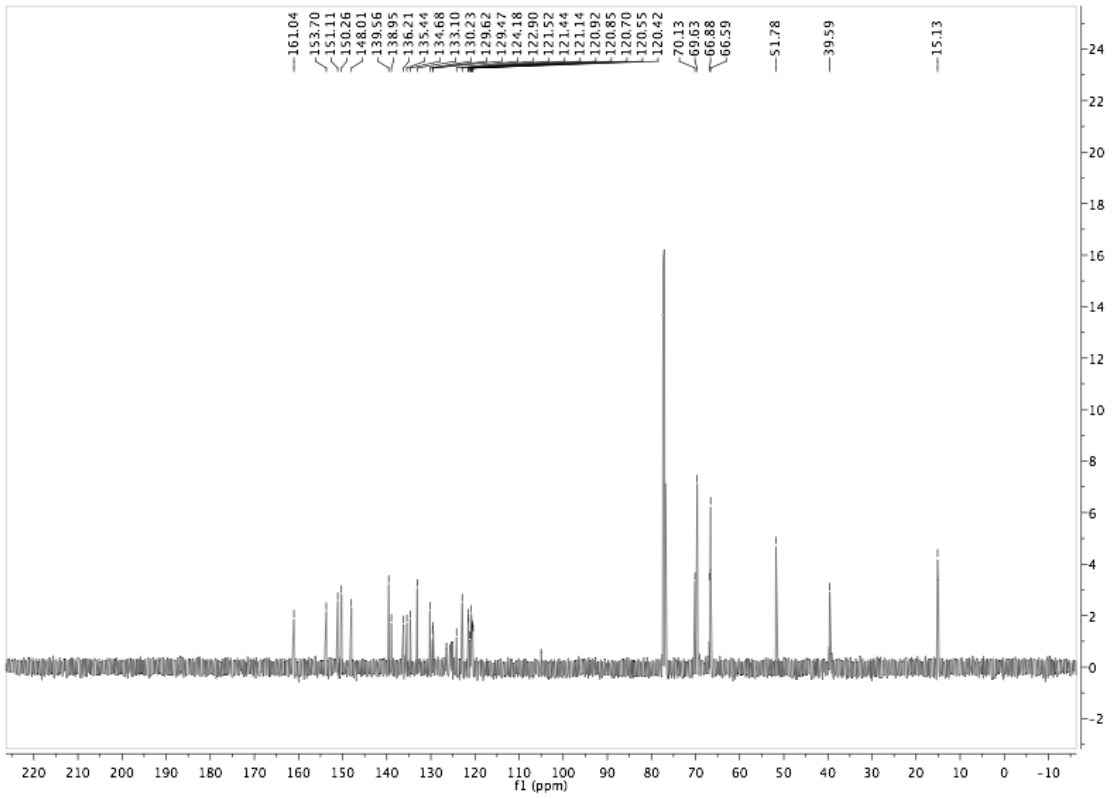
161.04
153.70
151.11
150.26
148.01
139.56
138.95
136.21
135.44
134.68
133.10
130.23
129.62
129.47
124.18
122.90
121.52
121.44
121.14
120.92
120.85
120.70
120.55
120.42
70.13
69.63
66.88
66.59
51.78
39.59
15.13
f1 (ppm)

^{1}H NMR of **6**

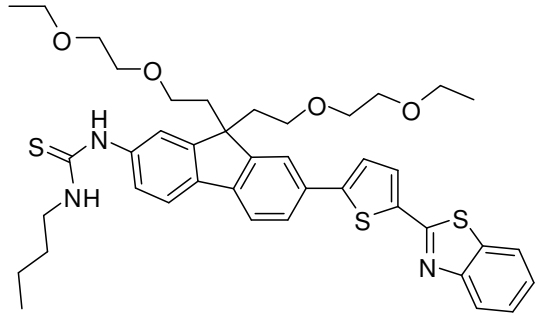

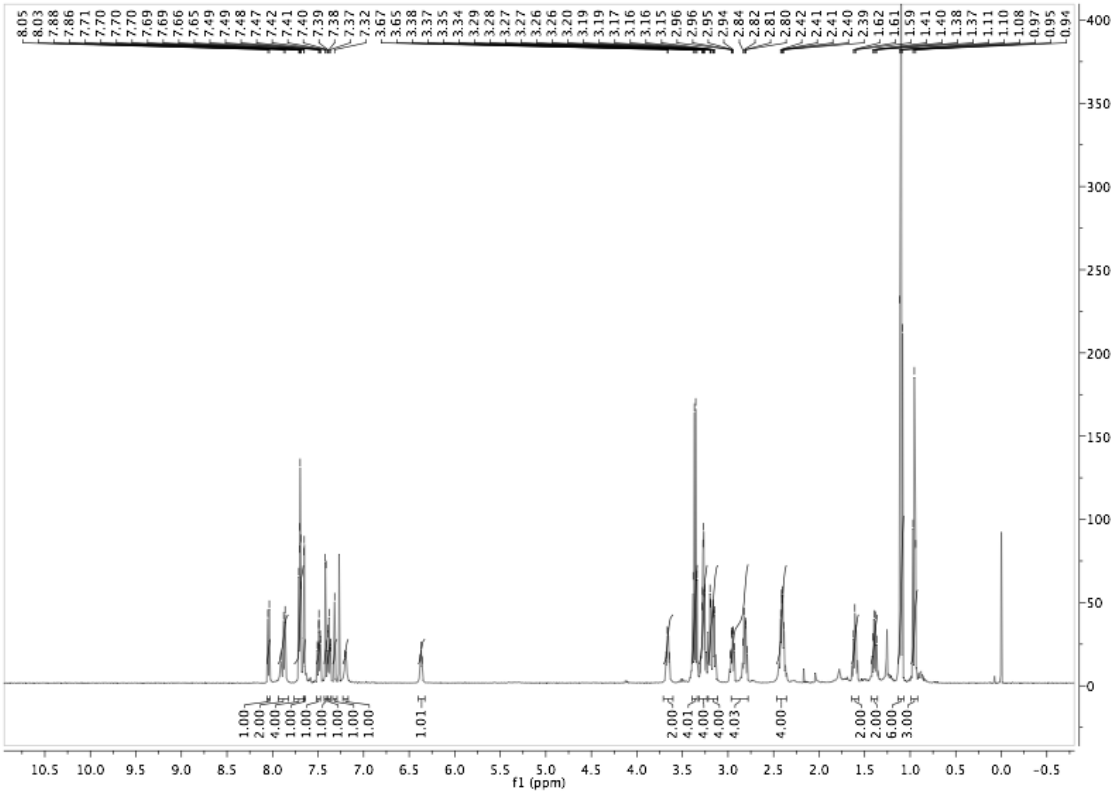

^{13}C NMR of **6**

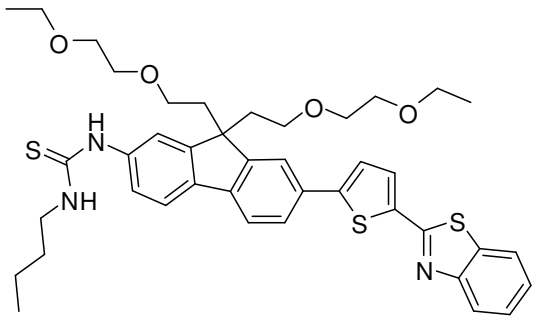
O
O
O
O
O
H
N
S
NH
S
S
N

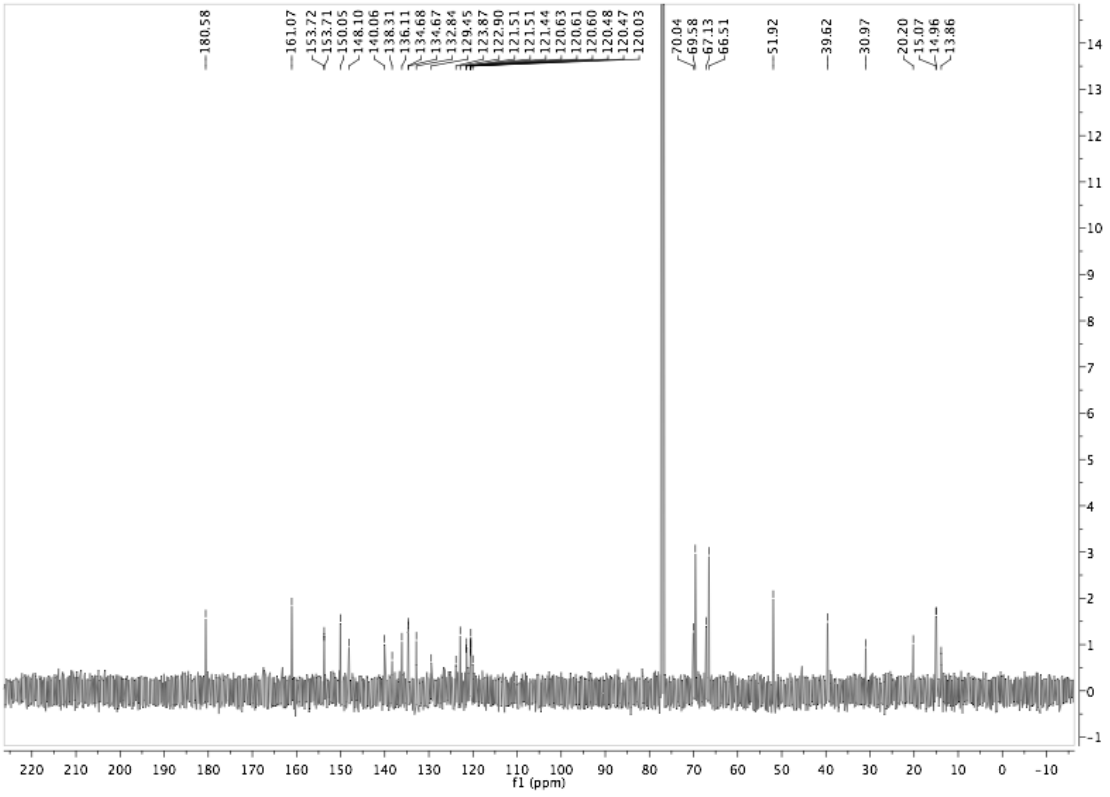
180.58
161.07
153.72
153.71
150.05
148.10
140.06
138.31
136.11
134.68
134.67
132.84
129.45
123.87
122.90
121.51
121.51
121.44
120.63
120.61
120.60
120.48
120.47
120.03
70.04
69.58
67.13
66.51
51.92
39.62
30.97
20.20
15.07
14.96
13.86
f1 (ppm)

^{1}H NMR of **8**

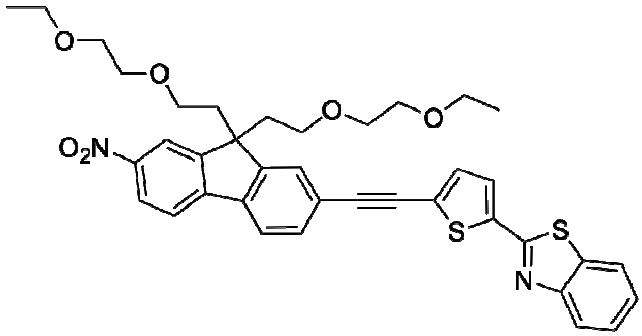
O
O
O
O
O
O_2N
S
S
N

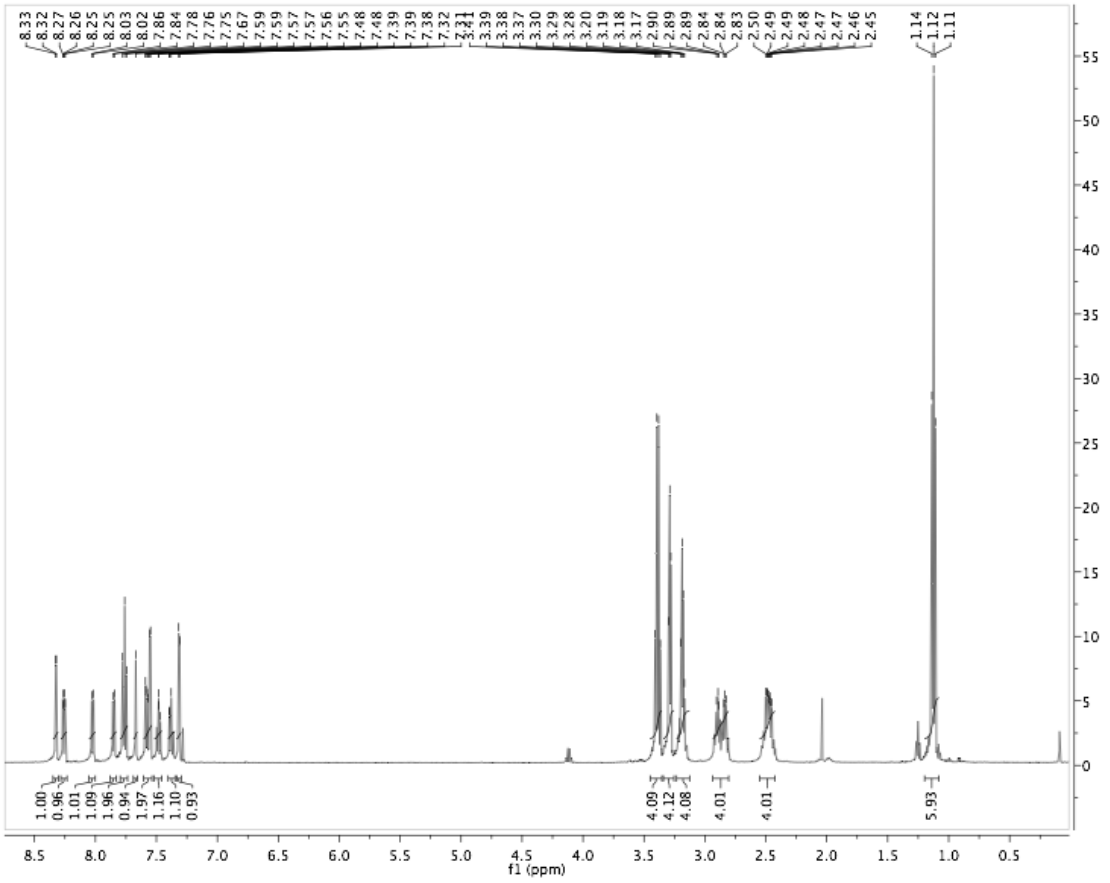
8.33
8.32
8.27
8.26
8.25
8.25
8.03
8.02
7.86
7.84
7.78
7.76
7.75
7.67
7.59
7.59
7.57
7.57
7.56
7.55
7.48
7.48
7.39
7.39
7.38
7.32
7.31
3.39
3.38
3.37
3.30
3.29
3.28
3.20
3.19
3.18
3.17
2.90
2.89
2.89
2.84
2.84
2.83
2.50
2.49
2.49
2.48
2.47
2.47
2.46
2.45
1.14
1.12
1.11
1.00
0.96
1.01
1.09
1.96
0.94
1.97
1.16
1.10
0.93
4.09
4.12
4.08
4.01
4.01
5.93
f1 (ppm)

^{13}C NMR of **8**

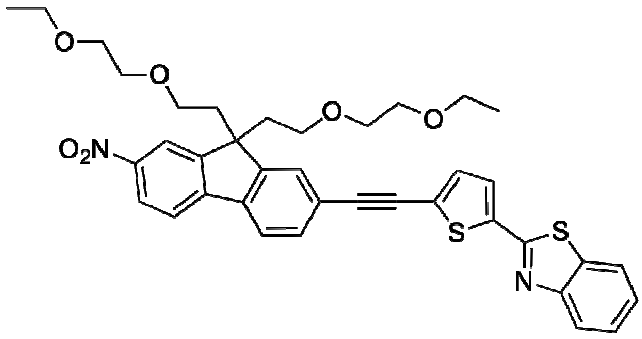
O
O
O
O
O
O_2N
S
S
N

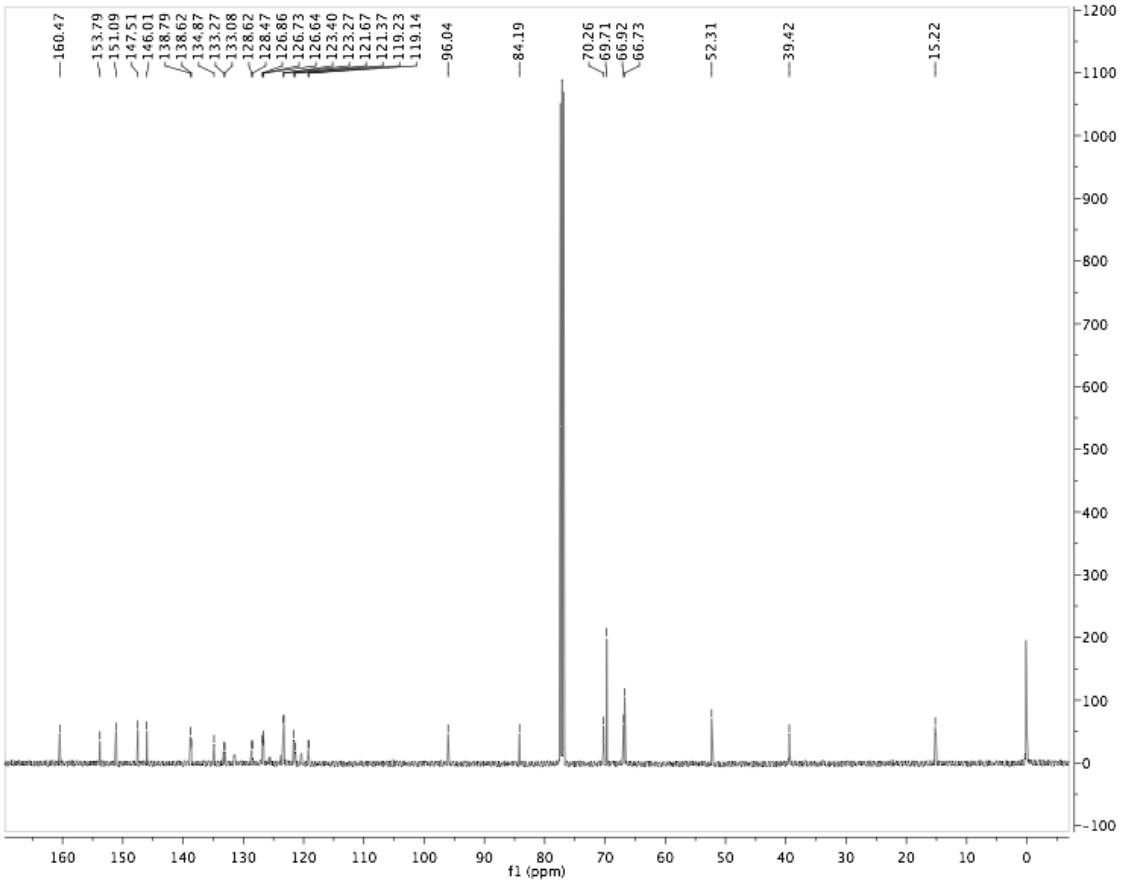
160.47
153.79
151.09
147.51
146.01
138.79
138.62
134.87
133.27
133.08
128.62
128.47
126.86
126.73
126.64
123.40
123.27
121.67
121.37
119.23
119.14
96.04
84.19
70.26
69.71
66.92
66.73
52.31
39.42
15.22
1200
1100
1000
900
800
700
600
500
400
300
200
100
0
-100
160
150
140
130
120
110
100
90
80
70
60
50
40
30
20
10
0
f1 (ppm)

^{1}H NMR of **9**

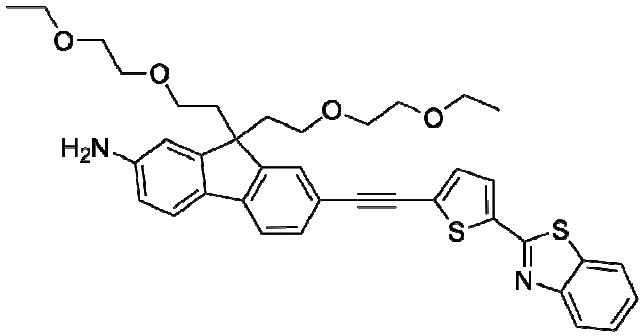
O
O
O
O
O
H_2N
S
S
N

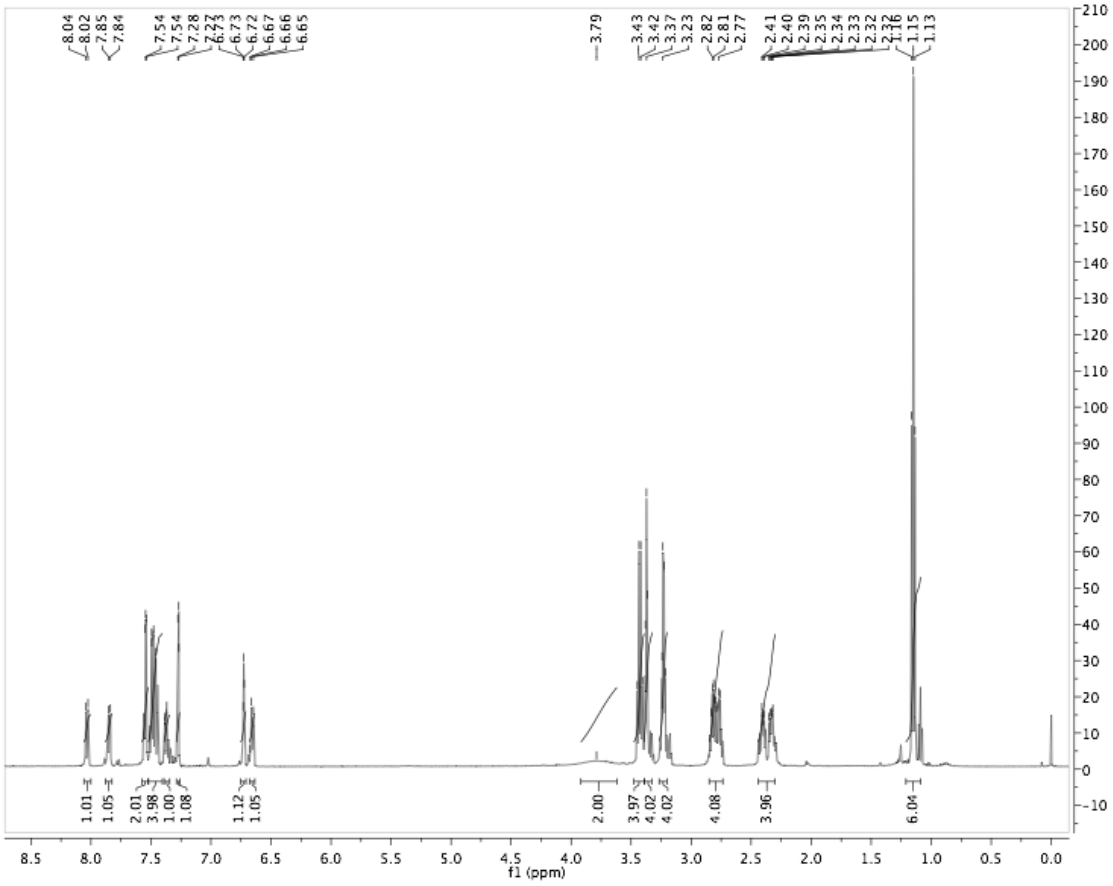
8.04
8.02
7.85
7.84
7.54
7.54
7.28
6.73
6.72
6.67
6.66
6.65
3.79
3.43
3.42
3.37
3.23
2.82
2.81
2.77
2.41
2.40
2.39
2.35
2.34
2.33
2.32
1.16
1.15
1.13
1.01
1.05
2.01
3.98
1.00
1.08
1.12
1.05
2.00
3.97
4.02
4.02
4.08
3.96
6.04
f1 (ppm)

^{13}C NMR of **9**

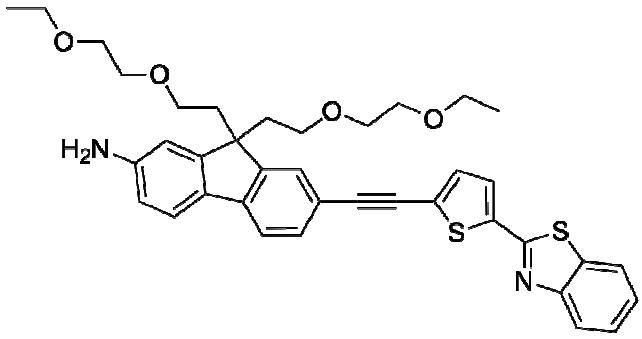
O
O
O
O
H2N
S
S
N

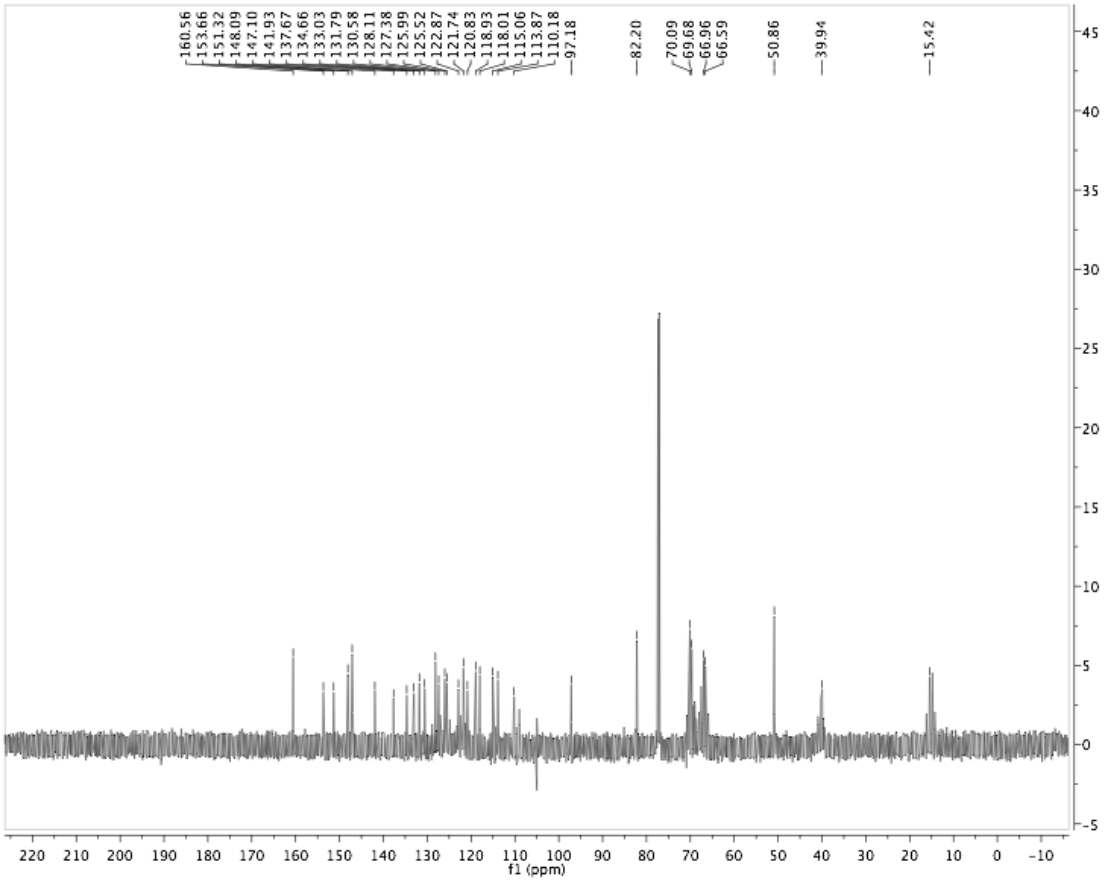
160.56
153.66
151.32
148.09
147.10
141.93
137.67
134.66
133.03
131.79
130.58
128.11
127.38
125.99
125.52
122.87
121.74
120.83
118.93
118.01
115.06
113.87
110.18
97.18
82.20
70.09
69.68
66.96
66.59
50.86
39.94
15.42
f1 (ppm)

^{1}H NMR of **10**

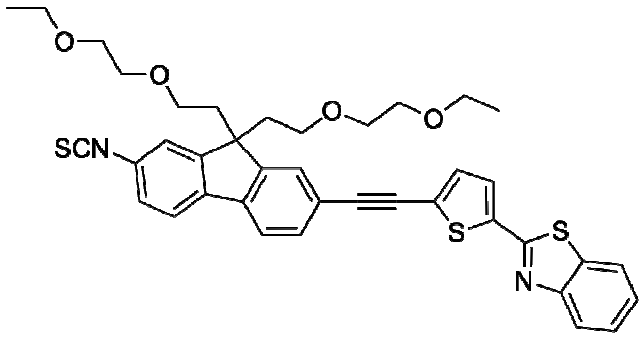

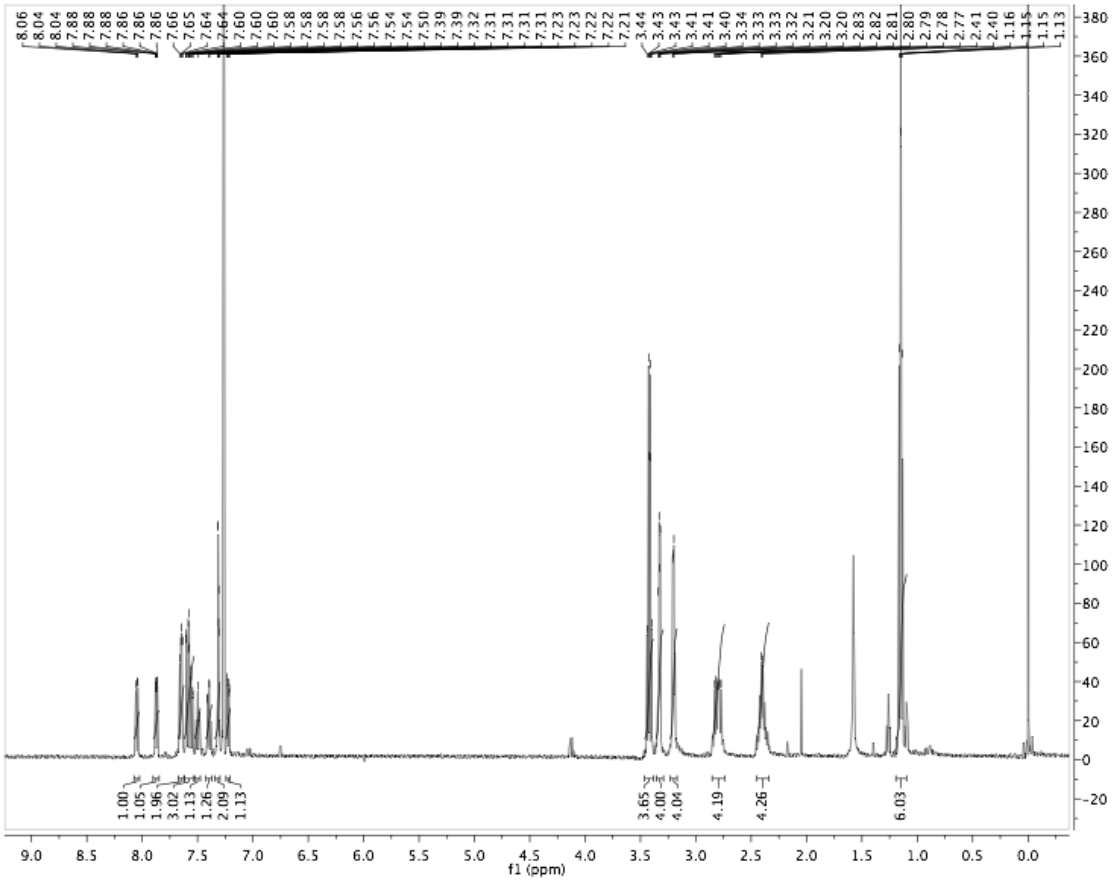

^{13}C NMR of **10**

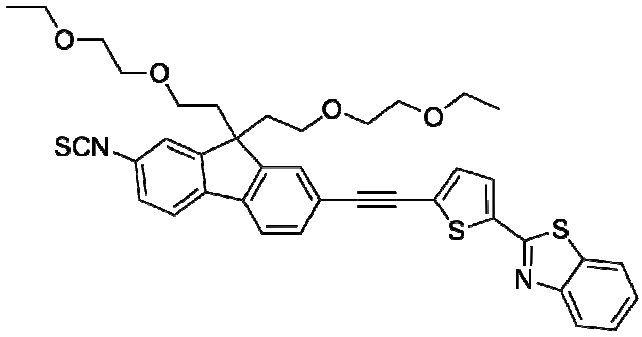
O
O
O
O
SCN
S
S
N

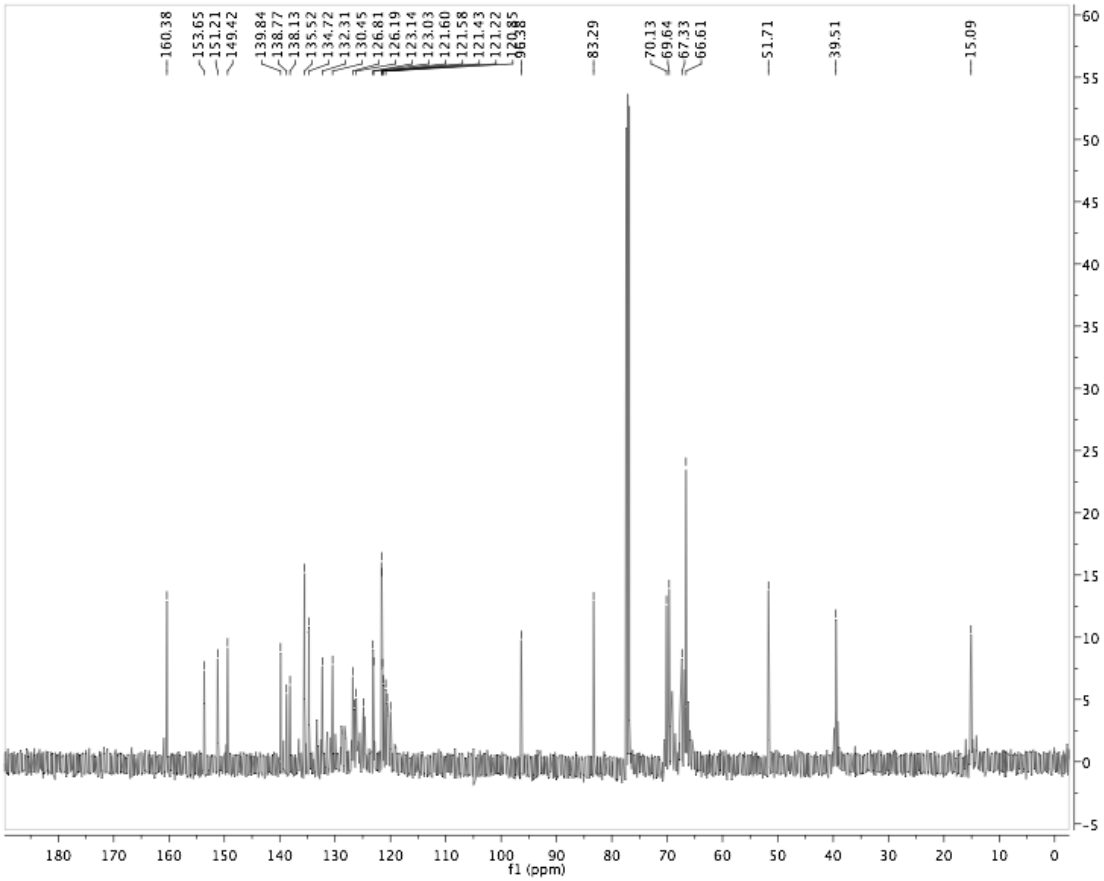
160.38
153.65
151.21
149.42
139.84
138.77
138.13
135.52
134.72
132.31
130.45
126.81
126.19
123.14
123.03
121.60
121.58
121.43
121.22
83.29
70.13
69.64
67.33
66.61
51.71
39.51
15.09
f1 (ppm)

^{1}H NMR of **11**

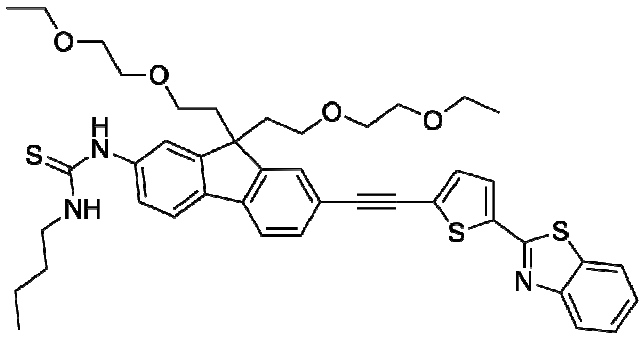

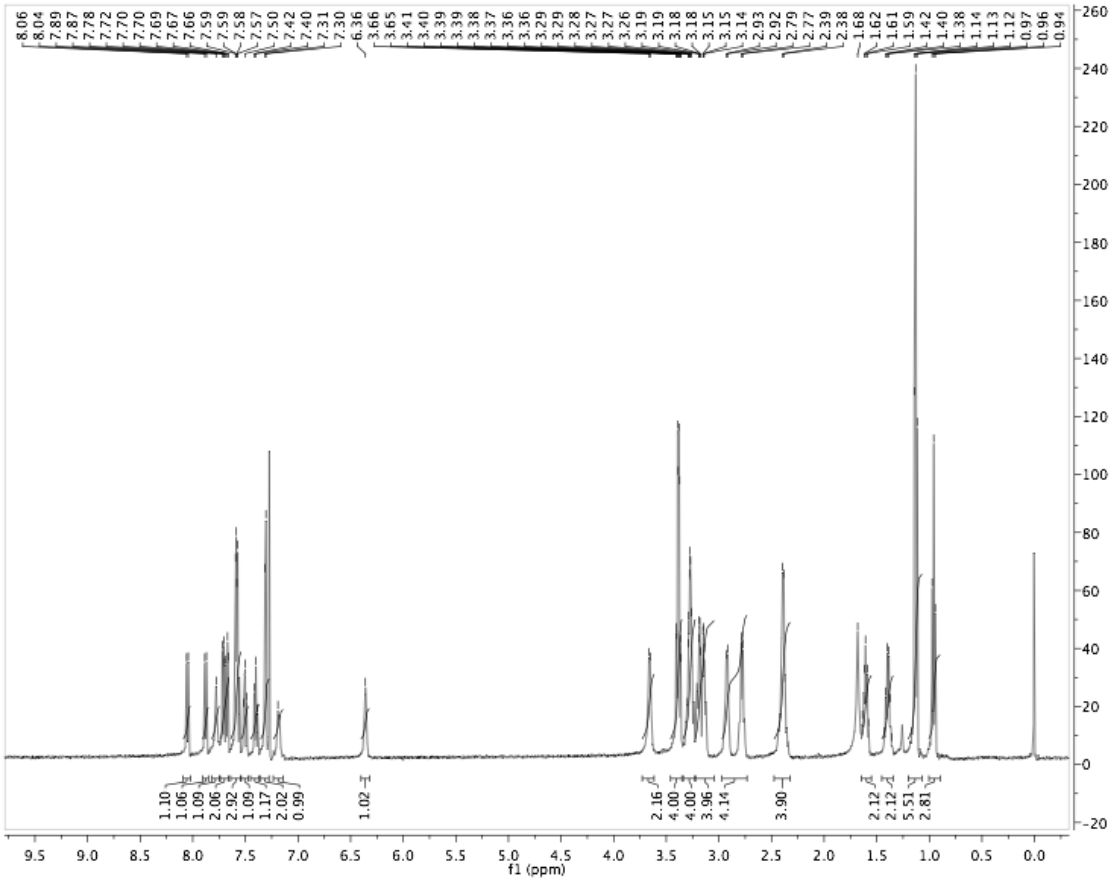

^{13}C NMR of **11**

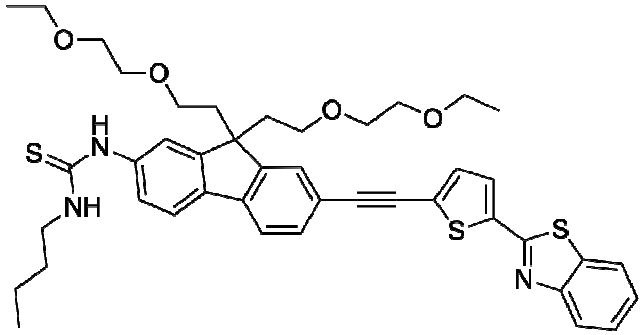
O
O
O
O
O
H
N
S
NH
S
S
N

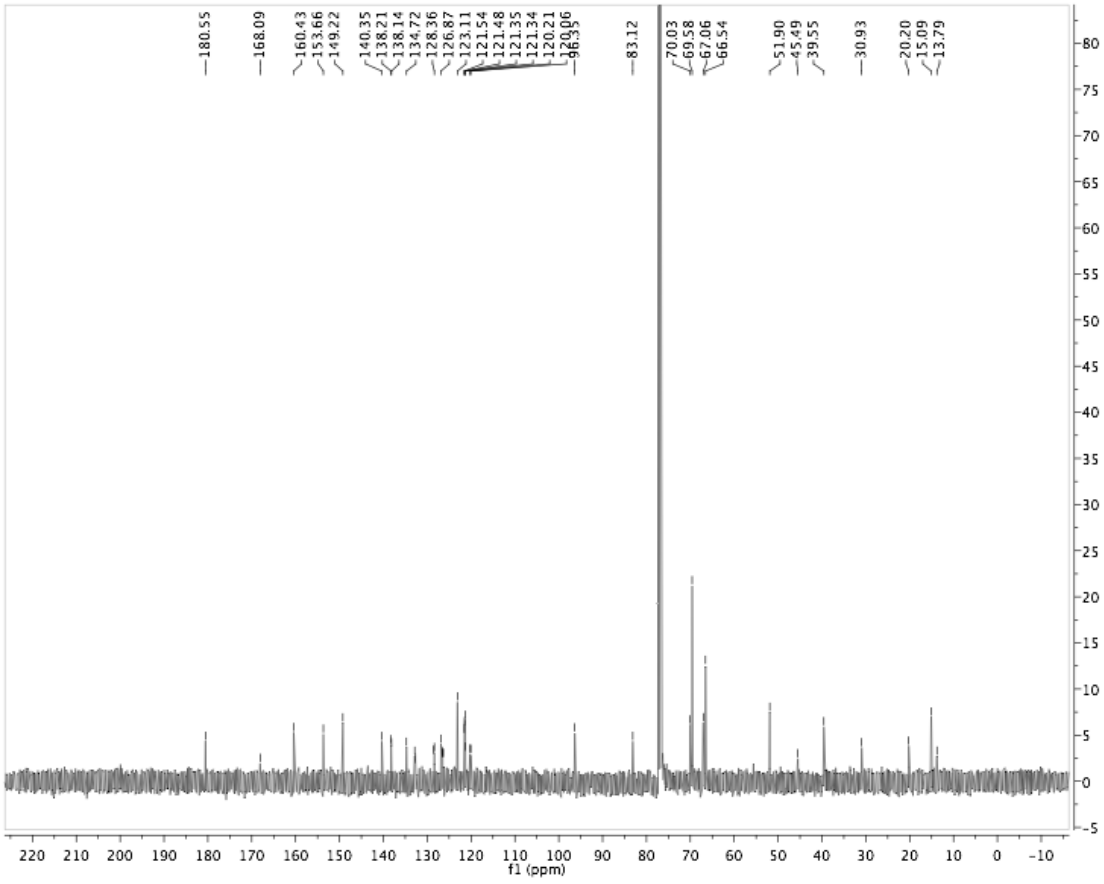
180.55
168.09
160.43
153.66
149.22
140.35
138.21
138.14
134.72
128.36
126.87
123.11
121.54
121.48
121.35
121.34
120.21
120.06
96.35
83.12
70.03
69.58
67.06
66.54
51.90
45.49
39.55
30.93
20.20
15.09
13.79
f1 (ppm)

Bioconjugate Chemistry

ARTICLE

pubs.acs.org/bc

Synthesis of Phosphine and Antibody−Azide Probes for *in Vivo* Staudinger Ligation in a Pretargeted Imaging and Therapy Approach

Danielle J. Vugts,*[,†,‡] Annelies Vervoort,[†,‡] Marijke Stigter-van Walsum,[†] Gerard W. M. Visser,[‡] Marc S. Robillard,[§] Ron M. Versteegen,[∥] Roland C. M. Vulders,[§] J. (Koos) D. M. Herscheid,[‡] and Guus A. M. S. van Dongen[†,‡]

[†]Department of Otolaryngology/Head and Neck Surgery, [‡]Department of Nuclear Medicine and PET Research, VU University Medical Center, Amsterdam, The Netherlands

[§]Biomolecular Engineering, Philips Research, Eindhoven, The Netherlands

[∥]SyMO-Chem BV, Eindhoven, The Netherlands

Supporting Information

ABSTRACT: The application of intact monoclonal antibodies (mAbs) as targeting agents in nuclear imaging and radioimmunotherapy is hampered by the slow pharmacokinetics of these molecules. Pretargeting with mAbs could be beneficial to reduce the radiation burden to the patient, while using the excellent targeting capacity of the mAbs. In this study, we evaluated the applicability of the Staudinger ligation as pretargeting strategy using an antibody−azide conjugate as tumor-targeting molecule in combination with a small phosphine-containing imaging/therapeutic probe. Up to 8 triazide molecules were attached to the antibody without seriously affecting its immunoreactivity, pharmacokinetics, and tumor uptake in tumor bearing nude mice. In addition, two ^{89}Zr- and $^{67/68}$Ga-labeled desferrioxamine (DFO)-phosphines, a ^{177}Lu-1,4,7,10-tetraazacyclododecane-1,4,7,10-tetraacetic acid (DOTA)-phosphine and a ^{123}I-cubyl phosphine probe were synthesized and characterized for their pharmacokinetic behavior in nude mice. With respect to the phosphine probes, blood levels at 30 min after injection were <5% injected dose per gram tissue, indicating rapid blood clearance. *In vitro* Staudinger ligation of 3.33 μM antibody−azide conjugate with 1 equiv of radiolabeled phosphine, relative to the azide, in aqueous solution resulted in 20−25% efficiency after 2 h. The presence of 37% human serum resulted in a reduced ligation efficiency (reduction max. 30% at 2 h), while the phosphines were still >80% intact. No *in vivo* Staudinger ligation was observed in a mouse model after injection of 500 μg antibody−azide, followed by 68 μg DFO-phosphine at t = 2 h, and evaluation in blood at t = 7 h. To explain negative results in mice, Staudinger ligation was performed *in vitro* in mouse serum. Under these conditions, a side product with the phosphine was formed and ligation efficiency was severely reduced. It is concluded that *in vivo* application of the Staudinger ligation in a pretargeting approach in mice is not feasible, since this ligation reaction is not bioorthogonal and efficient enough. Slow reaction kinetics will also severely restrict the applicability of Staudinger ligation in humans.

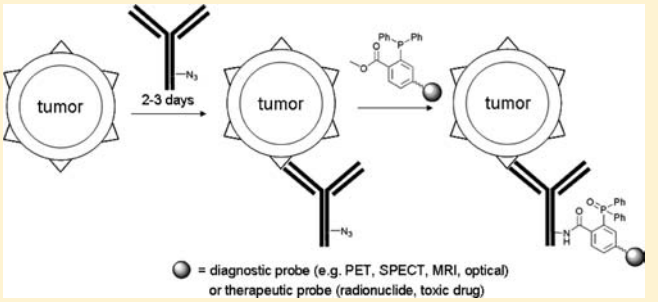

INTRODUCTION

Discovery of molecular targets on, e.g., cancer cells, has boosted the development of targeting agents. mAbs especially are gaining momentum for use in diagnosis and disease-selective therapy. At present, 5 mAbs have been approved by the FDA for diagnosis and 28 mAbs for therapy, either in naked form or conjugated to a toxic drug or radionuclide. Most of the approved therapeutic mAbs are intact immunoglobulins, and the majority are used for systemic treatment of cancer. In addition, hundreds of new mAbs are under development worldwide. Since intact mAbs have slow kinetics, it takes 3−6 days before optimal tumor-to-normal tissue ratios are obtained. When intact mAbs are used for nuclear imaging, imaging on the day of injection and at low radiation burden is virtually impossible, because low tumor uptake may be masked by high blood-pool activity. Furthermore, when mAbs are used for delivery of toxic agents like in radioimmunotherapy, highly radiosensitive bone marrow will be exposed continuously to a large fraction of the injected radioactivity resulting in dose-limiting myelosuppression. Clearly, achieving high tumor-to-blood ratios within a short time period after injection would provide benefit for both imaging and therapeutic applications. Strategies to prevent excessive exposure of normal tissues to toxin−mAb or radionuclide−mAb conjugates include the use of antibody fragments,[1] cleavable linkers,[2,3] local delivery,[4] antibody-directed enzyme prodrugs (ADEPT),[5] and pretargeting.[6−11] Several pretargeting approaches are under investigation: (strept)avidin−biotin,[12−14] hapten/antibody,[15] and DNA/DNA interactions.[16,17] All these pretargeting strategies

Received: June 8, 2011
Revised: August 19, 2011
Published: August 22, 2011

ACS Publications © 2011 American Chemical Society

Scheme 1. Schematic Presentation of a mAb-Based Pretargeting Strategy Using the Staudinger Ligation

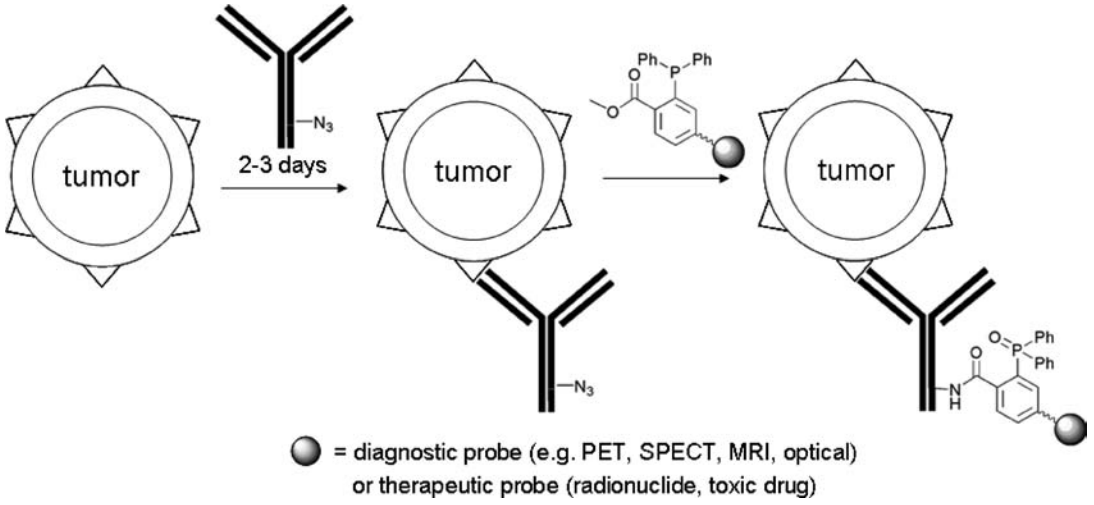

are based on biological interactions and suffer from several disadvantages, like the endogenous nature of the pretargeting ligand, the immunogenicity of the recognizing moiety, the large size of the recognizing moiety preventing fast imaging and effective therapy, and the weak binding of the interacting molecules. Using a covalent, nonbiological recognition system in a pretargeting approach could circumvent most of these drawbacks.

In the present study, we evaluated the possibility to use the Staudinger ligation[18−23] as the strategy for covalent conjugation in a pretargeting approach. The Staudinger ligation is a bioorthogonal reaction between a phosphine and an azide resulting in a covalent adduct with N_2 and methanol as byproducts. Next to the Staudinger ligation, other bioorthogonal reactions,[24−26] that might be applied in biological systems, are the ring-strain promoted azide−alkyne cycloaddition[27−30] and tetrazine ligation,[31−34] as published during the course of our studies.

To utilize the Staudinger ligation in a pretargeting strategy, a mAb needs to be functionalized with an azide handle. This azide handle should be relatively small and not alter the targeting properties of the mAb. The pretargeted mAb−azide will accumulate in target tissue by binding to a disease-specific antigen, while unbound mAb−azide will be cleared from the blood via the liver and spleen. Next, a small phosphine-containing diagnostic or therapeutic probe can be injected, which reacts covalently with the azide handle on the mAb (Scheme 1).

In this paper, we report on the coupling of triazide **1a** (Figure 1) to the anti-CD44v6 chimeric mAb (cmAb) U36 and the determination of the optimal triazide-to-mAb molar ratio for *in vivo* tumor targeting. To get a variety of imaging and therapeutic possibilities, DOTA and DFO-based phosphine derivatives were synthesized. DOTA can be used for labeling with Gd (MRI), ^{177}Lu (SPECT/therapeutic), ^{111}In (SPECT), ^{90}Y (therapeutic), and $^{67/68}$Ga (SPECT/PET) whereas DFO can be used for labeling with ^{89}Zr (PET), $^{67/68}$Ga, and ^{90}Nb (PET). In addition, an iodine-cubyl-phosphine was developed, which can be labeled with different PET, SPECT, or therapeutic iodine radionuclides. ^{89}Zr- and $^{67/68}$Ga-DFO-phosphines **2** and **3**, ^{177}Lu-DOTA-phosphine **4**, and ^{123}I-cubyl-phosphine **5** were prepared (Figure 1) and evaluated for their *in vitro* and *in vivo* ligation characteristics.

EXPERIMENTAL PROCEDURES

General Methods and Materials. The characteristics of the head and neck squamous cell carcinoma (HNSCC) cell lines HNX-OE and 11B, as well as the selection, production, and characterization of cmAb U36, have been described before.[35] cmAb U36 binds to the v6 region of CD44 (CD44v6), and is capable of selective tumor targeting of HNSCC as demonstrated in clinical trials.[36] ^{131}I (66.4 GBq/mL in 0.1 M NaOH) was obtained from Perkin-Elmer. The syntheses of triazide **1a** and phosphines **2**−**5** are described in the Supporting Information. Dialysis after reaction of triazide **1a** with cmAb U36 was performed with a Slide-a-Lyzer cassette from Pierce Biotechnology (cutoff 20 kDa) against PBS. mAb concentrations were measured by using the bicinchoninic acid (BCA) assay (Pierce) (UV-meter: Anthos 2001; data-analysis: Microwin) according to the suppliers instructions using naked cmAb U36 as a standard protein. HPLC analysis of antibody modification, ^{131}I-radiolabeled cmAb U36, antibody-Staudinger product stability, and *in vivo* Staudinger ligation were performed using a Jasco HPLC system equipped with a Superdex 200 10/30 GL size exclusion column (GE Healthcare Life sciences) using a mixture of 0.05 M sodium phosphate, 0.15 M sodium chloride (pH 6.8), and 0.01 M NaN_3 as the eluent at a flow rate of 0.5 mL/min. The radioactivity of the eluate was monitored using an inline NaI(Tl) radiodetector (Raytest Sockett). The ratios of triazide/cmAb U36 and phosphine/cmAb U36-triazide represent an average number of triazides or phosphines per mAb molecule, assuming Poisson distribution as generally observed in these types of mAb modifications.[37] Instant thin layer chromatography (iTLC) analysis of radiolabeled antibodies was carried out on silica impregnated glass fiber sheets (Pall Corp., East Hills, NY) using 20 mM citrate buffer (pH 5.0) as the mobile phase. Purification and isolation of ^{131}I-labeled cmAb U36-triazide conjugates and of cmAb U36-Staudinger product were performed with PD10 columns (GE Healthcare Life Sciences, NJ, USA). Gel electrophoresis was performed on a Phastgel system (Pharmacia Biotech, Amersham Biosciences) using preformed 7.5% SDS-PAGE gels under nonreducing conditions, followed by phosphor imager analysis (B&L-Isogen Service Laboratory). *In vitro* binding characteristics of the ^{131}I-cmAb U36-triazide conjugates were determined in an immunoreactivity assay essentially as described by Lindmo et al.,[38] using a serial dilution

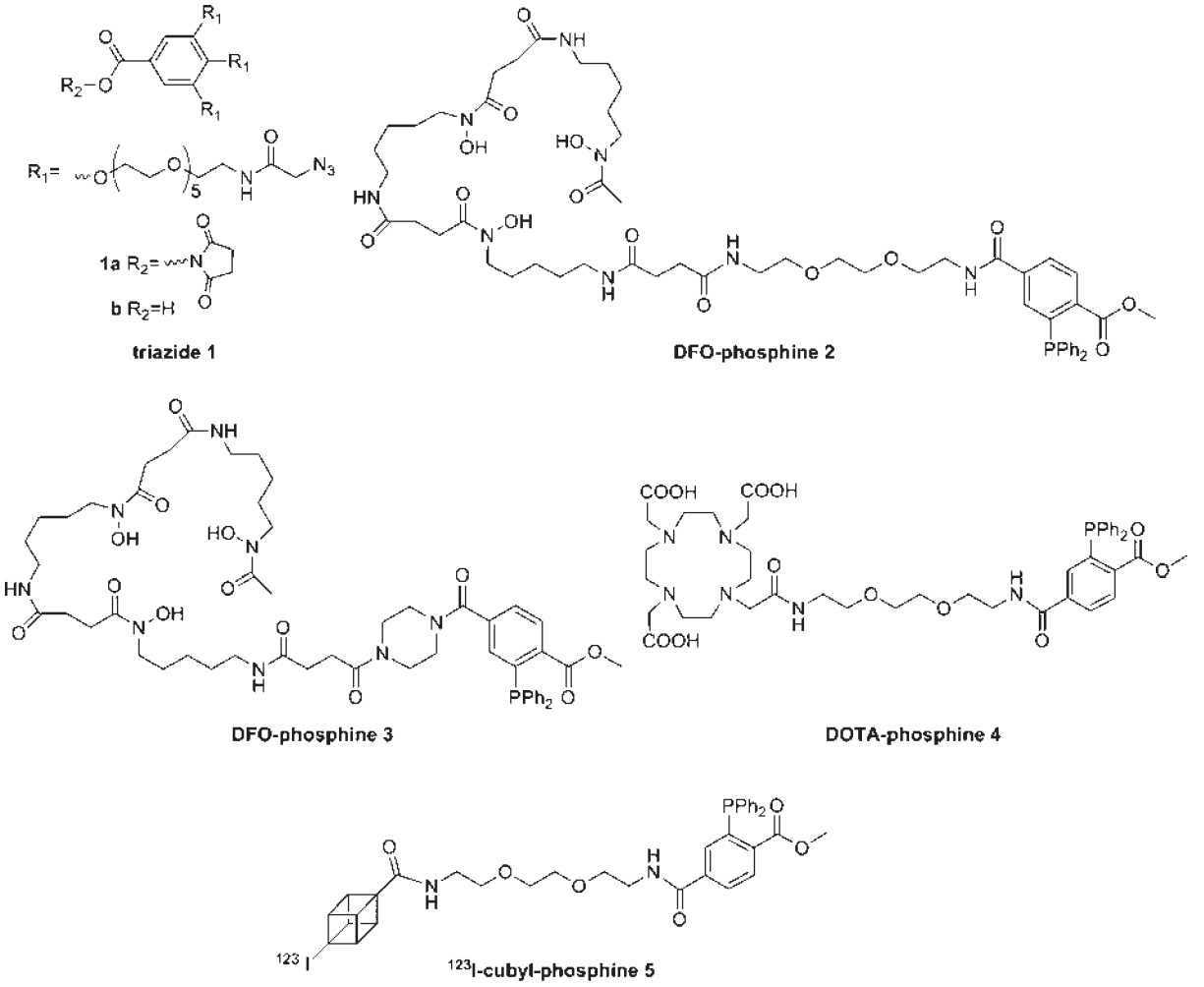

Figure 1. Selected pretargeting components for the Staudinger ligation as used in this study: triazide **1** for coupling to a mAb; DFO-phosphines **2** and **3** (for radiolabeling with ^{89}Zr and $^{67/68}$Ga), DOTA-phosphine **4** (for radiolabeling with ^{177}Lu), and ^{123}I-cubyl phosphine **5** as phosphine probes.

of 0.2% glutaraldehyde-fixed 11B cells and a fixed amount of ^{131}I-labeled cmAb U36-triazide conjugate (95 ng). After overnight incubation at 4 °C, the cell suspension was centrifuged and the specific binding calculated as the ratio of cell-bound radioactivity to the total amount of applied radioactivity. This was corrected for nonspecific binding, as determined with a 500-fold excess of non-radioactive U36-triazide. All binding assays were performed in triplicate. Single isotope counting was performed with a γ-well counter (Wallac LKB-CompuGamma 1282; Pharmacia) for ^{89}Zr, ^{67}Ga, ^{68}Ga, ^{123}I, ^{131}I, and ^{177}Lu.

cmAb U36 Modification with Triazide 1a and ^{131}I-Radiolabeling. cmAb U36 (4 mg; 11.53 mg/mL) was mixed with PBS (600 μL) and 1 M carbonate buffer pH 9.6 (30 μL) after which triazide **1a** (10, 15, 20, or 40 equiv) in DMF (20 μL) was added and incubated for 30 min at room temperature. The cmAb U36-triazide products were purified by dialysis until all unconjugated triazide was removed (assessed by HPLC-monitoring at 260 nm). After dialysis, the concentration of the cmAb U36-triazide product was determined by BCA assay. The average number of triazide molecules attached per mAb molecule was determined by HPLC using the UV absorption of triazide **1b** at 260 nm of the crude conjugation mixture. Next to the conjugation reaction, a mock reaction was performed without cmAb U36 resulting in fully hydrolyzed triazide **1b**. The difference in area corresponds to the amount of triazide **1** that was attached to cmAb U36 (see Supporting Information). ^{131}I-labeling of cmAb U36-triazide conjugates was done according to Tijink et al.[39] and is described in the Supporting Information. Radiochemical purity was determined by iTLC analysis, mAb integrity by HPLC and SDS-PAGE analysis followed by phosphor imaging, and immunoreactivity by a cell-binding assay.

Radiosynthesis of Phosphine Probes. Radiolabeling yield and percentage of oxidation were determined by HPLC analysis. The radiolabeling of the synthesized phosphine probes required extra precautions, because of the sensitivity of the phosphine for oxidation to phosphine oxide. Therefore, an appropriate antioxidant was used that did not affect the chelation itself. The preparation of ^{89}Zr- and $^{67/68}$Ga-DFO-phosphines **2** and **3**, ^{177}Lu-DOTA-phosphine **4**, and ^{123}I-cubyl-phosphine **5** are described in the Supporting Information.

Biodistribution of ^{131}I-cmAb U36-triazide Conjugates and Radiolabeled Phosphines 2−5. Radiolabeled cmAb U36-triazide conjugates were injected in nude mice bearing subcutaneously implanted xenografts of the tumor line HNX-OE, while radiolabeled phosphines were injected in tumor-free nude mice. Female mice (athymic nu/nu, 21−31 g; Harlan CPB), were 8−10 weeks old at the time of the experiment. All animal

experiments were performed according to National Institute of Health principles of laboratory animal care and Dutch national law ("Wet op de proefdieren". Stb 1985, 336). Five groups of four mice were injected via the retroorbital plexus with 185 kBq ^{131}I-cmAb U36-triazide conjugate (100 μg in 100 μL), in which the triazide was coupled to the cmAb at different molar ratios (triazide-to-mAb molar ratio 0, 4, 6, 8, and 15). The mean tumor size at start of the experiment was 104 ± 58 mm^3. Blood samples were taken at 5, 24, and 48 h post injection (p.i.). At 72 h p.i., the mice were anesthetized, bled, killed, and dissected. Blood, tumor, skin, tongue, sternum, heart, lung, liver, spleen, kidney, bladder, muscle, thighbone, colon (content), ileum (content), stomach (content), and thyroid were weighed and the amount of radioactivity in each tissue was assessed in a γ-well counter. Radioactivity uptake was calculated as the percentage of the injected dose per gram of tissue (%ID/g).

Six groups of four mice were injected intravenously (i.v.) via the tail vein with 0.4 MBq ^{89}Zr-DFO-phosphine **2** (1.52 μg, 1.3 nmol), 1.1 MBq ^{68}Ga-DFO-phosphine **2** (1.52 μg, 1.3 nmol), 0.4 MBq ^{89}Zr-DFO-phosphine **3** (1.52 μg, 1.4 nmol), 1.1 MBq ^{68}Ga-DFO-phosphine **3** (1.52 μg, 1.4 nmol), 0.4 MBq ^{177}Lu-DOTA phosphine **4** (1.50 μg, 1.7 nmol), or 0.8 MBq ^{123}I-cubyl-phosphine **5** (1.00 μg, 1.3 nmol). After 5, 10, 15, 30, 45, 60, and 90 min blood samples were taken and after 120 min, the mice were anesthetized, bled, killed, and dissected as described above.

***In Vitro* Staudinger Ligation.** Staudinger ligation efficiency was assessed by SDS-PAGE analysis of the reaction mixture followed by phosphor imager analysis. Equivalents of phosphine added for ligation were related to the reacting counterpart, the azide functionality. All Staudinger ligation experiments were performed with a cmAb U36-triazide conjugate containing on average 8 triazide **1** molecules (and thus 24 azide functionalities) and is further designated "cmAb U36-triazide". Standard reactions were performed with 1.67 nmol (0.25 mg, 40 nmol azide functionalities) cmAb U36-triazide and 1 equiv of phosphine (40 nmol, 44 μg) in 0.5 mL (6 v/v% ethanol) PBS at 37 °C for 2 h. The following characteristics were examined: (a) the *in vitro* stability of the phosphine probes **2** and **4** expressed as the chemical half-life; (b) the reactivity of phosphines **2** and **4** with cmAb U36-triazide in PBS; (c) the influence of the temperature on Staudinger ligation efficiency; and (d) the influence of the composition of the reaction medium on Staudinger ligation efficiency. The *in vitro* stability of the phosphine probes was examined by incubating 90 nmol/mL ^{89}Zr- or ^{67}Ga-DFO-phosphine **2** (10 MBq/mL) or ^{177}Lu-DOTA-phosphine **4** (7 MBq/mL) in PBS and in 10% or 37% freshly prepared human serum at 37 °C with 6 v/v% ethanol. At different time points (30, 75, and 120 min), aliquots were taken. Serum proteins were precipitated by the addition of a 2-fold excess (v/v) of acetonitrile, and after centrifugation, the supernatant was analyzed by radio-HPLC. The data obtained at 30, 75, and 120 min were plotted on a semi logarithmic scale, whereafter extrapolation to 50% decomposition gave the chemical half-life.

***In Vitro* Stability of cmAb U36-Staudinger Products.** For evaluation of the *in vitro* stability of the cmAb U36-Staudinger ligation products, samples containing 40 μg of the PD10 purified cmAb U36-Staudinger product, resulting from a reaction of cmAb U36-triazide with ^{89}Zr/^{67}Ga-DFO-phosphine **2** or ^{177}Lu-DOTA-phosphine **4**, were added to freshly prepared human serum, mouse serum or 0.9% NaCl (1:4 v/v dilution; sodium azide added to 0.02%) (n = 2). The samples were incubated at 37 °C in a CO_2-enriched atmosphere (5% CO_2). After 2, 24, and 48 h incubation, aliquots were taken and analyzed by radio-HPLC. Fractions of 0.5 mL were assessed for radioactivity in a γ-counter and used for determination of the recovery of the HPLC column.

***In Vivo* Staudinger Ligation.** Tumor-free nude mice were used for evaluation of *in vivo* Staudinger ligation in blood. By doing so, quantitative information about the ligation efficiency *in vivo* can easily be obtained. Three mice were injected with 500 μg cmAb U36-triazide (0.2 mL) via the retroorbital plexus followed by 68 μg ^{67}Ga-DFO-phosphine **2** two hours later via the tail vein. As control, three mice were injected only with 68 μg ^{67}Ga-DFO-phosphine **2**. At 5, 10, 15, 30, 60, and 90 min after injection of the phosphine probe, blood samples were taken; and after 5 h, the mice were anesthetized, bled, killed, and dissected as described above. Blood samples of 5 h p.i. of the phosphine were also analyzed by HPLC. To this end, the serum was separated from the blood by centrifugation and diluted to 25% serum with saline. HPLC-fractions of 0.5 mL were assessed for radioactivity in a γ-counter to determine whether *in vivo* Staudinger ligation had occurred.

Statistical Analysis. All values are given as mean ± SD. Statistical analysis was performed on pharmacokinetics, tissue uptake, and tumor-to-blood ratios between different groups of mice with the Student's t-test (SPSS) for paired data. Two-sided significance levels were calculated and $p < 0.05$ was considered statistically significant.

RESULTS

Synthesis of ^{131}I-cmAb-Triazide Conjugates and Their Biodistribution. cmAb U36 was reacted with 10, 15, 20, or 40 equiv of triazide **1a** in order to determine the maximum loading of triazide to cmAb U36 without affecting its integrity, immunoreactivity, and *in vivo* targeting behavior (Scheme 2). The average number of triazide molecules attached to the antibody was determined by UV-HPLC and appeared to be 4, 6, 8, and 15, respectively, which means that, within the applied stoichiometry, the efficiency of modification was 37−42%. Subsequent radiolabeling of these conjugates with ^{131}I resulted in overall radiolabeling yields of >70% after purification. As a control, cmAb U36 without any triazide groups was also radiolabeled. The radiochemical purity of all 5 products was >99%, and there was a gradual decrease of the immunoreactivity upon increase of the substitution ratio from 91% (^{131}I-cmAb U36 without triazide) to 87%, 85%, 79%, and 46% for cmAb U36 containing, respectively, 4, 6, 8, and 15 triazide molecules. SDS-PAGE analysis (Figure 2) showed an increased percentage of apparent high molecular weight product at higher substitution ratio (20% for cmAb U36−15 triazide), while also a change in the apparent molecular weight of the monomeric cmAb U36 (normally ∼150 kDa) was observed.

For assessment of the optimal triazide-to-mAb molar ratio for *in vivo* tumor targeting, five groups of four mice were injected with ^{131}I-cmAb U36-triazide conjugate with, respectively, 0, 4, 6, 8, and 15 triazide molecules attached. At 5, 24, 48, and 72 h p.i., blood samples were drawn to determine the pharmacokinetics. The blood clearance of the different ^{131}I-labeled cmAb U36-triazide conjugates did not show distinctive differences (p > 0.05), albeit the conjugate with the highest triazide-to-cmAb U36 molar ratio (cmAb U36−15 triazide) tended to exhibit a faster blood clearance (Figure 3). At 72 h p.i. the %ID/g in tumor, blood, normal tissue, and gastrointestinal contents was

Scheme 2. Modification Reaction of cmAb U36 with Triazide 1a Resulting in cmAb U36-Triazide Conjugates with, Respectively, 0, 4, 6, 8, and 15 Triazide 1 Molecules Attached

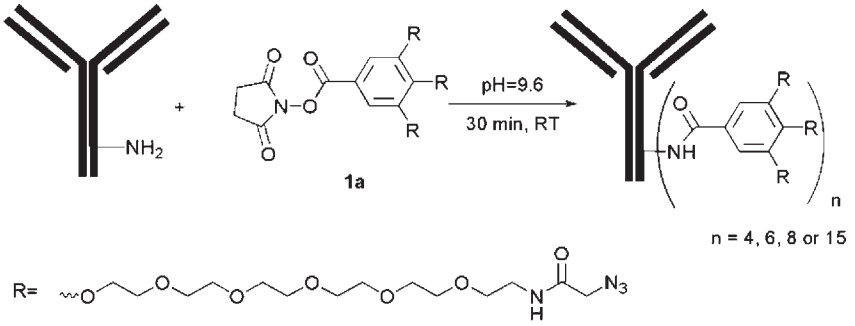

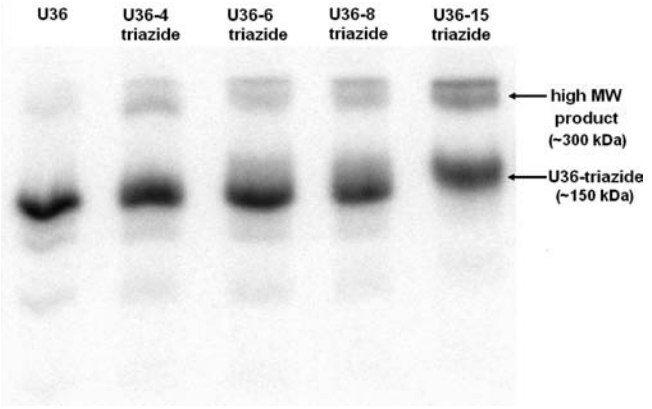

Figure 2. SDS-PAGE analysis of ^{131}I-cmAb U36-triazide conjugates with, respectively, 0, 4, 6, 8, and 15 triazide **1** molecules attached.

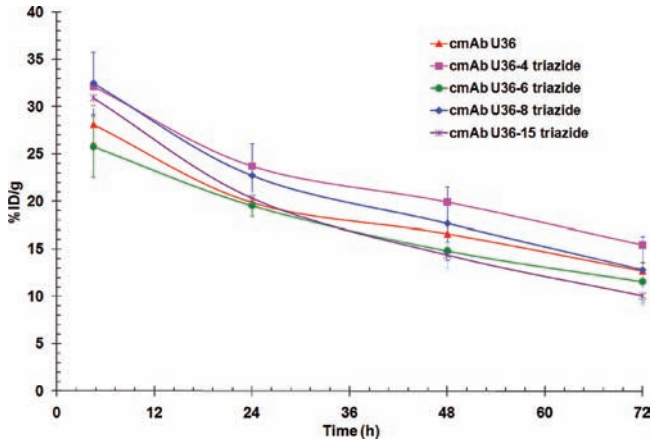

Figure 3. Pharmacokinetics of ^{131}I-cmAb U36-triazide conjugates containing, respectively, 0, 4, 6, 8, or 15 triazide **1** molecules in nude mice bearing HNX-OE tumors.

determined and depicted in Figure 4 for a selected panel of tissues. The tumor uptake of unconjugated ^{131}I-labeled cmAb U36 was 23.0 ± 3.5%ID/g, and was at the same level when 4 triazide groups were attached (23.1 ± 3.4%ID/g). However, tumor uptake tended to decrease at higher triazide-to-cmAb U36 molar ratio. A tumor uptake of 16.4 ± 3.7 and 18.7 ± 6.3%ID/g, respectively, was observed when 6 or 8 triazide groups were attached to cmAb U36. Tumor uptake of conjugates containing 15 triazide groups was 10.5 ± 1.9%ID/g, which is significantly lower than for all the other four conjugates ($p < 0.05$). No distinctive increased uptake in any of the normal organs was observed at higher triazide-to-cmAb U36 molar ratios. The ^{131}I-cmAb U36 conjugate with 15 triazide groups showed a significantly lower (1.05 ± 0.20) tumor-to-blood ratio than the other ^{131}I-cmAb U36-triazide conjugates (1.49 ± 0.24 to 1.81 ± 0.19) ($p < 0.05$). This parameter also indicates worse tumor targeting when too many triazide groups are attached to the mAb. The cmAb U36-triazide conjugate with 8 triazide groups was used in subsequent *in vitro* Staudinger ligation experiments and will be designated "cmAb U36-triazide" hereafter.

Biodistribution of Phosphine Probes. The pharmacokinetics and biodistribution of ^{89}Zr- and ^{68}Ga-DFO-phosphines **2** and **3**, ^{177}Lu-DOTA phosphine **4**, and ^{123}I-cubyl-phosphine **5** were examined in tumor-free nude mice. All six probes showed fast blood clearance, and after 30 min, less than 5%ID/g was still present in the blood (Figure 5). The phosphines are mainly excreted via the gastrointestinal and urinary tract with elevated uptake in liver (8.1 ± 1.8%ID/g) and spleen (3.2 ± 1.3%ID/g) for ^{177}Lu-DOTA phosphine **4**, and in kidney for ^{89}Zr-DFO-phosphine **2** (4.1 ± 0.6%ID/g), ^{89}Zr-DFO-phosphine **3** (2.0 ± 0.2%ID/g), and ^{177}Lu-DOTA-phosphine **4** (1.4 ± 0.2% ID/g) at 2 h p.i (Figure 6). The blood kinetics of ^{68}Ga-DFO-phosphine **2** and ^{68}Ga-DFO-phosphine **3** were comparable, while there was a difference between ^{89}Zr-DFO-phosphine **2** and ^{89}Zr-DFO-phosphine **3**, the latter clearing faster. ^{177}Lu-DOTA-phosphine **4** showed comparable blood kinetics to ^{89}Zr-DFO-phosphine **3**. ^{123}I-cubyl-phosphine **5** cleared significantly faster than the other probes and therefore this probe was not further evaluated in Staudinger ligation experiments.

Because the labeling of DFO-phosphine **3** resulted in a higher percentage of oxidation of the phosphine, it was decided to select DFO-phosphine **2** for Staudinger ligation experiments. For evaluation of the effect of the chelate on ligation efficiency, DOTA-phosphine **4** was also included.

***In Vitro* Staudinger Ligation in PBS.** The chemical half-life of ^{89}Zr- and ^{67}Ga-DFO-phosphines **2** and ^{177}Lu-DOTA-phosphine **4** in PBS in the absence of cmAb U36-triazide was examined at 37 °C. All three phosphines were only slowly oxidized in PBS with a chemical half-life of about 10 h. Staudinger ligation efficiency was investigated using cmAb U36-triazide in combination with each of the phosphine probes in aqueous solution. No significant difference in reactivity was observed for the three phosphines; Staudinger ligation efficiency was always between 20% and 25% after 2 h at 37 °C. The kinetics of

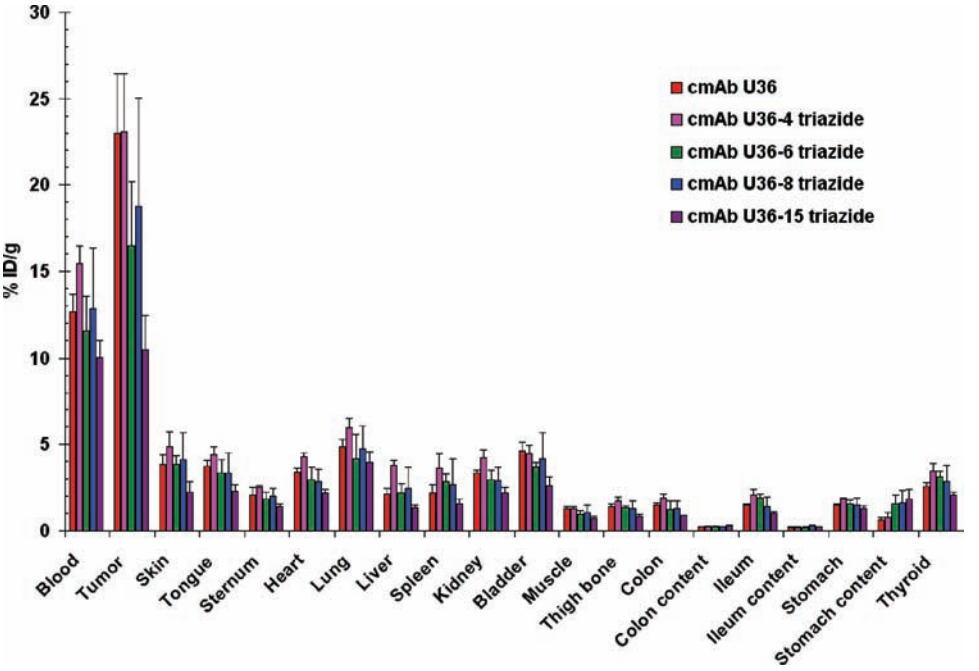

Figure 4. Biodistribution of ^{131}I-cmAb U36-triazide conjugates with, respectively, 0, 4, 6, 8, or 15 equiv of triazide **1** attached in nude mice bearing HNX-OE tumors at 72 h after injection.

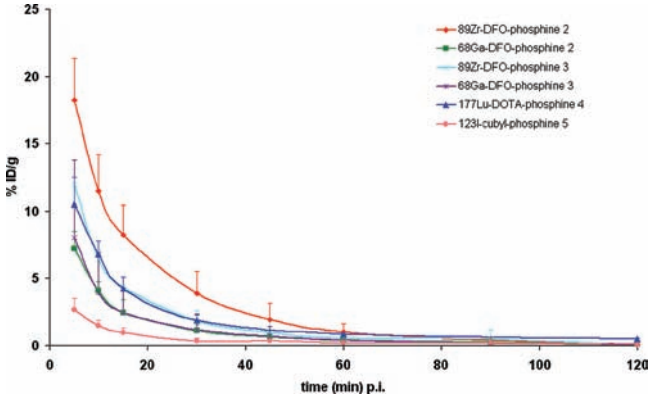

Figure 5. Pharmacokinetics of ^{89}Zr- and ^{68}Ga-DFO-phosphines **2**, ^{89}Zr- and ^{68}Ga-DFO-phosphine **3**, ^{177}Lu-DOTA phosphine **4**, and ^{123}I-cubylphosphine **5** in tumor-free nude mice.

the Staudinger ligation were determined with ^{67}Ga-DFO-phosphine **2** under standard conditions for shorter and longer periods. After 10 min, about 5% Staudinger ligation efficiency was observed, which increased to 32% after 5 h. Temperature dependency of the Staudinger ligation was examined with ^{177}Lu-DOTA phosphine **4** after 2 h incubation at 4 °C, room temperature, and 37 °C (standard temperature). The Staudinger ligation efficiency was found to be strongly temperature dependent, being 5% at 4 °C, 8% at room temperature, and 20% at 37 °C. Interestingly, when the reaction mixture contained 0.04% sodium dodecyl sulfate (SDS), the ligation efficiency was nearly twice as high (40−45% after 2 h at 37 °C).[24]

Once formed, the Staudinger products (^{89}Zr- and ^{67}Ga-DFO-Staudinger-cmAb U36 and ^{177}Lu-DOTA-Staudinger-cmAb U36) remained more than 93% intact upon 48 h incubation at 37 °C under the applied conditions (0.9% NaCl or 80% mouse or human serum). The ^{67}Ga-DFO-Staudinger cmAb-U36 product was the least stable in mouse serum (93% intact after 48 h incubation), while in human serum and 0.9% NaCl, the product was over 96% intact after 48 h incubation. The other two Staudinger ligation products were very stable in all three media for 48 h (>98% intact).

***In Vitro* Staudinger Ligation in Human Serum.** In the absence of cmAb U36-triazide, all three phosphine probes remained >90% intact in 10% human serum and >80% intact in 37% human serum after 2 h at 37 °C. Staudinger ligation took place in the presence of 10% and 37% human serum; however, the kinetics of all probes were slowed down with 30% compared with the reaction in PBS and with 50% for ^{89}Zr-DFO phosphine **2** in 37% human serum.

***In Vivo* Staudinger Ligation.** *In vivo* Staudinger ligation in blood of tumor-free mice was studied via the sequential administration of cmAb U36-triazide and ^{67}Ga-DFO-phosphine **2**. Blood kinetics and biodistribution of ^{67}Ga were not significantly different for mice which received cmAb U36-triazide plus phosphine in comparison with mice which did not receive cmAb U36-triazide, e.g., the blood levels at 5 h p.i. of the phosphine were 0.20 ± 0.04 vs 0.14 ± 0.05%ID/g. HPLC analysis of these blood samples did not reveal evidence for the presence of the cmAb U36-Staudinger product (Figure 7).

***In Vitro* Staudinger Ligation in Serum of Different Animal Species.** To explain the absence of Staudinger product formation in mice, *in vitro* Staudinger ligations experiments were performed in mouse serum and in serum of a panel of other animal species. ^{67}Ga-DFO-phosphine **2** was reacted with cmAb U36-triazide in 50% pig, goat, rabbit, human, and mouse serum for 2 h at 37 °C. In 50% mouse serum, Staudinger ligation was virtually absent (~95% reduction), and a side product was observed (Figure 8). The other sera did allow Staudinger ligation, although not as efficient as in PBS. Staudinger ligation in 50% human and goat

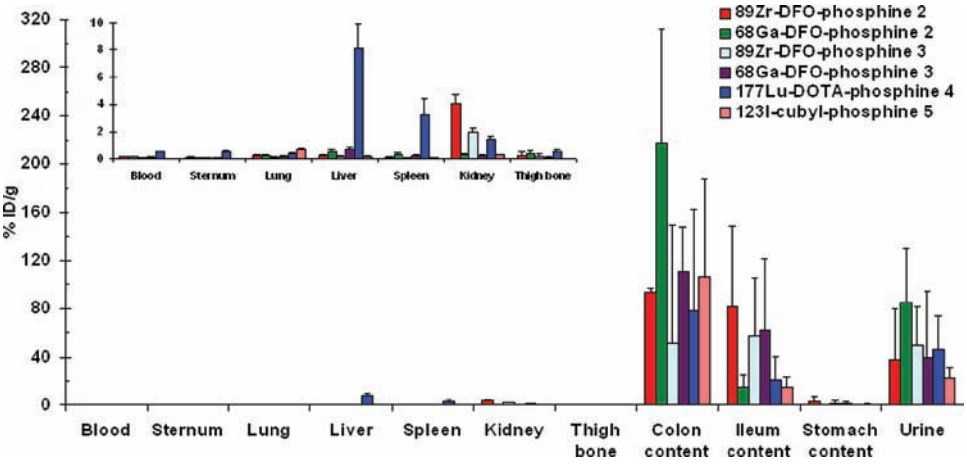

Figure 6. Biodistribution of ^{89}Zr-DFO-phosphine **2** (red bars), ^{68}Ga-DFO-phosphine **2** (green bars), ^{89}Zr-DFO-phosphine **3** (light blue bars), ^{68}Ga-DFO-phosphine **3** (purple bars), ^{177}Lu-DOTA-phosphine **4** (blue bars), and ^{123}I-cubyl-phosphine **5** (light salmon bars) in nude mice at 2 h after injection for a larger selection of tissues and a smaller selection of tissues (inset).

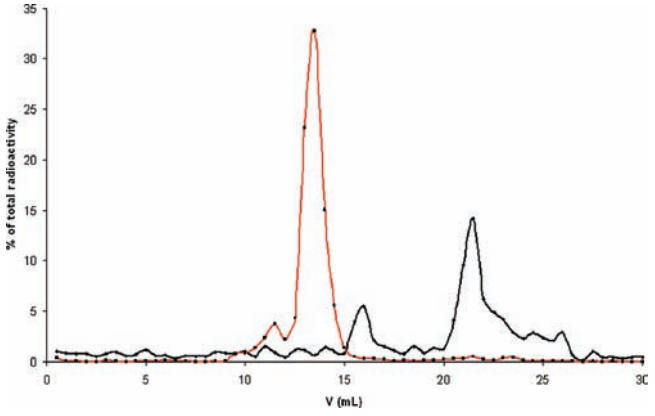

Figure 7. Representative HPLC diagram of mouse blood taken 5 h p.i. of the phosphine of a mouse that received cmAb U36-triazide and ^{67}Ga-DFO-phosphine **2** (black line). As a reference, the HPLC diagram of the *in vitro* prepared Staudinger product of this reaction is depicted (red line).

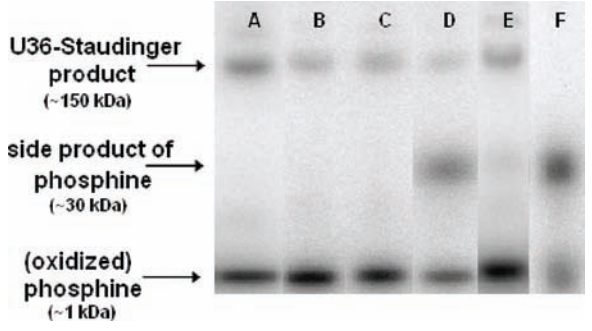

Figure 8. SDS-PAGE analysis of a Staudinger ligation reaction of cmAb U36-triazide with 1 equivalent of ^{67}Ga-DFO-phosphine **2** in the presence of 50% serum of different sources after 2 h at 37 °C: (A) PBS, no serum, (B) pig serum, (C) goat serum, (D) rabbit serum, (E) human serum, (F) mouse serum.

serum gave 30% reduction of ligation efficiency compared to PBS. Ligation efficiency in 50% pig and rabbit serum was, respectively, 50% and 75% reduced compared to PBS (Figure 8), the latter also showing the extra band on SDS-PAGE. Reduced ligation efficiency and the extra band were also observed when Staudinger ligation was performed in rat serum. Decreasing the percentage of mouse serum resulted in an increase in Staudinger ligation up to 4% efficiency in the presence of 37% mouse serum and 8% efficiency in 10% mouse serum. Reduced Staudinger ligation efficiency in mice was also observed when ^{177}Lu-DOTA-phosphine **4** instead of ^{67}Ga-DFO-phoshine **2** was used. In search for an explanation for the extra band on SDS-PAGE and the reduced Staudinger ligation efficiency in mouse serum, Staudinger ligation was also performed in the presence of mouse serum albumin. The ligation, however, was as efficient as in PBS. Dialysis of mouse serum before use (4.5 and 20 kDa cutoff) did not improve the low ligation efficiency and still gave the prominent extra band on SDS-PAGE. Finally, upon oxidation of the phosphine in advance, followed by incubation in mouse serum, no side product was observed by SDS-PAGE analysis.

DISCUSSION

The Staudinger ligation has until now been applied in the field of chemical biology and organic chemistry, but not in the field of radiochemistry nor in a pretargeting approach with mAbs. The Staudinger ligation is a bioorthogonal reaction, which implies that phosphine and azide react with each other and not with other bioavailable molecules in the body. Therefore, we investigated the applicability of this bioorthogonal reaction in a pretargeting concept with antibodies for tumor diagnosis and therapy. In the present paper, we developed the synthesis of mAb−azide conjugates and radiolabeled phosphines and evaluated their *in vivo* pharmacokinetic behavior as well as their *in vitro* and *in vivo* reactivity in Staudinger ligation.

cmAb U36 was chosen as the model mAb, because this mAb has shown high and selective tumor uptake in cancer patients. Moreover, cmAb U36 internalizes just to a limited extent, and this is expected to be a favorable characteristic for pretargeting. On the basis of the work of Bertozzi,[23] the amide containing azide **1a** was designed having a trivalent azide branch to increase the number of azides that are attached per lysine.[19,24] cmAb U36 was reacted with different amounts of triazide **1a** and subsequently radiolabeled with ^{131}I to evaluate the *in vivo* behavior. Since the

applied radiolabeling method does not impair the immunoreactivity and *in vivo* pharmacokinetic behavior of cmAb U36,[40] any change is caused by the number of triazide **1** groups that are attached to cmAb U36. A series of conjugates with, on average, 4, 6, 8, and 15 equiv of triazide **1** attached to cmAb U36 was produced (Scheme 2). The *in vitro* and *in vivo* evaluation revealed that up to 8 triazide **1** groups (24 azide functionalities) could be attached to cmAb U36 without substantially affecting the immunoreactivity, pharmacokinetics, tumor uptake, and tumor-to-blood ratio. These characteristics became clearly impaired, however, when 15 triazide **1** groups were coupled per mAb molecule, a phenomenon also observed earlier in the development of ^{186}Re-MAG3-labeled conjugates.[37]

Several radiolabeled phosphine probes were synthesized, differing in radioisotope, chelate, and linker. The major radiochemical challenge was the protection of the phosphine moiety against oxidation to phosphine oxide (see Supporting Information for experimental details). In the radiolabeling of DFO-phosphine **2** and **3** with ^{89}Zr, radiolytically formed oxidative species in the ^{89}Zr stock solution and in the reaction mixture needed to be scavenged. Sodium sulfite proved to be an excellent antioxidant. In this way, 45 μg/12 MBq/mL ^{89}Zr-DFO-phosphine **2** and **3** could be prepared with less than 10% oxidation caused by radiolabeling. Because ^{67}Ga was purified over a chromafix column just prior to use, the addition of an antioxidant was found to be unnecessary during the preparation of ^{67}Ga-DFO-phosphine **2**. However, for the *in vivo* experiment with a high dose ^{68}Ga-DFO-phosphine **2** and **3**, addition of an antioxidant to the reaction mixture appeared necessary. In this case, not sodium sulfite but a stannous sulfate containing gentisic acid solution proved adequate. A concentration of 270 μg/314 MBq/mL ^{68}Ga-DFO-phosphine **2** with 8% oxidation or ^{68}Ga-DFO-phosphine **3** with 13% oxidation could be prepared. Since addition of antioxidants like gentisic acid or ascorbic acid did not inhibit oxidation, the preparation of ^{177}Lu-DOTA phosphine **4** was restricted to the use of fresh ^{177}Lu and execution of the labeling at pH 8. In this way, oxidation caused by radiolabeling was limited to 15% and 91 μg/25 MBq/mL ^{177}Lu-DOTA-phosphine **4** could be prepared. ^{123}I-cubyl-phosphine **5** had to be synthesized from ^{123}I-cubyl carboxylic acid and linker−phosphine because direct labeling of a Br-analogue of **5** resulted in completely oxidized phosphine. Following this procedure, 95 μg/72 MBq/mL ^{123}I-cubyl-phosphine **5** could be prepared with less than 10% oxidation.

In vivo evaluation of the six radiolabeled phosphine probes revealed that blood clearance was very fast with a half-life time of less than 15 min. This means that the reaction of the phosphine probes with pretargeted mAb−triazide conjugate should be very fast for making Staudinger ligation an efficient option for *in vivo* pretargeting strategies.

The stability of ^{89}Zr- and ^{67}Ga-DFO-phosphine **2** and ^{177}Lu-DOTA-phosphine **4** in PBS was satisfactory, since the chemical half-life was about 10 h at 37 °C. However, their reactivity with cmAb U36-triazide was rather slow, taking the observed fast pharmacokinetics into account: after 2 h, Staudinger ligation efficiency was 20−25% at 37 °C, which means that per cmAb U36 molecule on average 5 to 6 out of 24 azide **1** groups have reacted. The presence of human serum did not affect the stability of the three probes, but their reactivity was reduced compared to PBS.

Although the circulation time of the probes was less than the reaction time *in vitro*, we speculated that it may still be enough to achieve conjugation *in vivo*. Therefore, we attempted to demonstrate *in vivo* Staudinger ligation in a pretargeting approach in tumor-free mice. HPLC analysis of the mouse blood revealed that the activity still present in the blood was not from cmAb U36-Staudinger product (Figure 7). To explain the complete absence of *in vivo* Staudinger ligation, we performed *in vitro* Staudinger ligation in mouse serum as well as in serum of other animal species. In the presence of mouse serum, the Staudinger ligation efficiency was severely reduced. SDS-PAGE analysis revealed that Staudinger ligation efficiency was primarily hampered by the formation of a side product. This side product was only formed when the phosphine was intact and not oxidized in advance. Identification of this side product was without success, and the molecular basis for the formation of this product is still not known. Apparently, larger molecules in mouse serum are involved, since in dialyzed mouse serum, the extra band on SDS-PAGE was still formed with concomitant reduction of Staudinger ligation efficiency. Tests in serum of other animals revealed that reduced Staudinger ligation efficiency and the formation of the extra band was not limited to mouse serum.

These results seem to be in contrast with those of the group of Bertozzi who reported on successful *in vivo* Staudinger ligation in mice.[20] In this study, azide groups were introduced on target cells by daily injection of the unnatural sugar peracetylated *N*-α-azidoacetylmannosamine (Ac_4ManNAz, 300 mg/kg) to mice for 7 days resulting in a total dose of about 52 mg azide per mouse (122 μmol), which is ∼3000 times more than we used in our research. Staudinger ligation in the splenocytes was confirmed by administration of 16 μmol phosphine-FLAG (∼300 times more than used here) 24 h after the last injection of Ac_4ManNAz. In this *in vivo* model system, in which pretargeting is not disease selective, the side reaction of the phosphine as we observed in mouse serum might be less dominant due to the very large amounts of azide and phosphine-FLAG used and the fact that intraperitoneal injections were applied. Therefore, in our opinion the results obtained in this way can not be directly translated to pretargeting approaches with mAbs.

Apart from not being bioorthogonal in rodents, chemical possibilities to increase the Staudinger ligation efficiency seem to be rather limited, and we have strong scientific doubts whether the Staudinger ligation can be made more efficient. Its kinetics are a function of subtle folding/defolding of the azide functionality at the mAb molecule and the accessibility and reactivity of the phosphorus atom within the triphenylphosphine methyl ester moiety. The mAb−triazide conjugate used was the best in the series of mono- to nonavalent azide, whereas removal of the amide next to the azide resulted in a 2-fold decrease of the efficiency (unpublished results). Variation around the phosphorus atom is very limited, since the triphenyl moiety is necessary for Staudinger ligation and to protect against oxidation of the phosphorus atom. And finally, introduction of an SDS moiety either in the triazide handle or in the phosphine probe is not expected to lead to a major breakthrough, because the observed increase in the presence of SDS in the reaction medium was only 2-fold. Therefore, we conclude that the Staudinger ligation is not the method of choice for pretargeting approaches in humans. We foresee that this also holds for the very recently reported so-called traceless Staudinger ligation.[41] This approach makes use of diphenylphosphines which are even more prone to oxidation than the triphenylphosphines used here for *in vivo* pretargeting. Possibly, the tetrazine ligation[34] is, because the reaction kinetics of this bioorthogonal reaction are reported to be at least 1000× faster than the Staudinger ligation.

■ ASSOCIATED CONTENT

Supporting Information. Synthesis and characterization of triazide **1a** and phosphine **2**−**5**, conjugation of triazide to cmAb U36 and determination of the average triazide to cmAb U36 ratio, and radiolabeling of cmAb U36 conjugates and phosphines. This material is available free of charge via the Internet at http://pubs.acs.org.

■ AUTHOR INFORMATION

Corresponding Author

*Danielle J. Vugts, Ph.D., Dept. of Otolaryngology/Head and Neck Surgery and Nuclear Medicine and PET research, VU University Medical Center, De Boelelaan 1085c, 1081 HV Amsterdam, The Netherlands, Tel +31-20-4445699, Fax +31-20-4449121, E-mail: d.vugts@vumc.nl.

■ ACKNOWLEDGMENT

We thank Marek Smoluch for measuring HRMS, Elwin Jansen for HPLC measurements of the modification of cmAb U36 with triazide **1a**, and Joost Verbeek for his help with the preparation of ^{123}I-cubyl-phosphine **5**.

■ ABBREVIATIONS

DFO, desferrioxamine; DOTA, 1,4,7,10-tetraazacyclododecane-1,4,7,10-tetraacetic acid; mAb, monoclonal antibody; PBS, phosphate buffered saline; PET, positron-emission tomography; SPECT, single-photon emission computed tomography; % ID/g, injected dose per gram tissue

■ REFERENCES

(1) Dancey, G., Begent, R. H., and Meyer, T. (2009) Imaging in targeted delivery of therapy to cancer. *Targ. Oncol. 4*, 201–217.

(2) Arano, Y., Wakisaka, K., Mukai, T., Uezono, T., Motonari, H., Akizawa, H., Kairiyama, C., Ohmomo, Y., Tanaka, C., Ishiyama, M., Sakahara, H., Konishi, J., and Yokoyama, A. (1996) Stability of a metabolizable ester bond in radioimmunoconjugates. *Nucl. Med. Biol. 23*, 129–136.

(3) Akizawa, H., and Arano, Y. (2002) Altering pharmacokinetics of radiolabeled antibodies by the interposition of metabolizable linkages - Metabolizable linkers and pharmacokinetics of monoclonal antibodies. *Q. J. Nucl. Med. 46*, 206–223.

(4) Grainger, D. W. (2004) Controlled-release and local delivery of therapeutic antibodies. *Expert Opin. Biol. Ther. 4*, 1029–1044.

(5) Tietze, L. F., and Krewer, B. (2009) Antibody-directed enzyme prodrug therapy: a promising approach for a selective treatment of cancer based on prodrugs and monoclonal antibodies. *Chem. Biol. Drug Des. 74*, 205–211.

(6) Goldenberg, D. M., Sharkey, R. M., Paganelli, G., Barbet, J., and Chatal, J. F. (2006) Antibody pretargeting advances cancer radioimmunodetection and radioimmunotherapy. *J. Clin. Oncol. 24*, 823–834.

(7) Boerman, O. C., van Schaijk, F. G., Oyen, W. J. G., and Corstens, F. H. M. (2003) Pretargeted radioimmunotherapy of cancer: Progress step by step. *J. Nucl. Med. 44*, 400–411.

(8) Liu, G., and Hnatowich, D. J. (2008) A semiempirical model of tumor pretargeting. *Bioconjugate Chem. 19*, 2095–2104.

(9) Goodwin, D. A., and Meares, C. F. (2001) Advances in pretargeting biotechnology. *Biotechnol. Adv. 19*, 435–450.

(10) Goldenberg, D. M., and Sharkey, R. M. (2007) Novel radiolabeled antibody conjugates. *Oncogene 26*, 3734–3744.

(11) Wu, A. M., and Senter, P. D. (2005) Arming antibodies: prospects and challenges for immunoconjugates. *Nat. Biotechnol. 23*, 1137–1146.

(12) Hnatowich, D. J., Virzi, F., and Rusckowski, M. (1987) Investigations of avidin and biotin for imaging applications. *J. Nucl. Med. 28*, 1294–1302.

(13) Goodwin, D., Meares, C., Diamanti, C., McCall, M., Lai, C., Torti, F., McTigue, M., and Martin, B. (1984) Use of specific antibody for rapid clearance of circulating blood background from radiolabeled tumor imaging proteins. *Eur. J. Nucl. Med. 9*, 209–215.

(14) Lesch, H. P., Kaikkonen, M. U., Pikkarainen, J. T., and Yla-Herttuala, S. (2010) Avidin-biotin technology in targeted therapy. *Expert Opin. Drug Delivery 7*, 551–564.

(15) Chang, C. H., Sharkey, R. M., Rossi, E. A., Karacay, H., McBride, W., Hansen, H. J., Chatal, J. F., Barbet, J., and Goldenberg, D. M. (2002) Molecular advances in pretargeting radioimunotherapy with bispecific antibodies. *Mol. Cancer Ther. 1*, 553–563.

(16) Liu, G. Z., Mang'era, K., Liu, N., Gupta, S., Rusckowski, M., and Hnatowich, D. J. (2002) Tumor pretargeting in mice using ^{99m}Tc-labeled morpholino, a DNA analog. *J. Nucl. Med. 43*, 384–391.

(17) Kuijpers, W. H. A., Bos, E. S., Kaspersen, F. M., Veeneman, G. H., and van Boeckel, C. A. A. (1993) Specific recognition of antibody-oligonucleotide conjugates by radiolabeled antisense nucleotides − a novel approach for 2-step radioimmunotherapy of cancer. *Bioconjugate Chem. 4*, 94–102.

(18) Saxon, E., and Bertozzi, C. R. (2000) Cell surface engineering by a modified Staudinger reaction. *Science 287*, 2007–2010.

(19) Saxon, E., Luchansky, S. J., Hang, H. C., Yu, C., Lee, S. C., and Bertozzi, C. R. (2002) Investigating cellular metabolism of synthetic azidosugars with the Staudinger ligation. *J. Am. Chem. Soc. 124*, 14893–14902.

(20) Prescher, J. A., Dube, D. H., and Bertozzi, C. R. (2004) Chemical remodelling of cell surfaces in living animals. *Nature 430*, 873–877.

(21) Prescher, J. A., and Bertozzi, C. R. (2005) Chemistry in living systems. *Nat. Chem. Biol. 1*, 13–21.

(22) Dube, D. H., Prescher, J. A., Quang, C. N., and Bertozzi, C. R. (2006) Probing mucin-type O-linked glycosylation in living animals. *Proc. Natl. Acad. Sci. U. S. A. 103*, 4819–4824.

(23) Kohn, M., and Breinbauer, R. (2004) The Staudinger ligation - A gift to chemical biology. *Angew. Chem., Int. Ed. 43*, 3106–3116.

(24) Agard, N. J., Baskin, J. M., Prescher, J. A., Lo, A., and Bertozzi, C. R. (2006) A comparative study of bioorthogonal reactions with azides. *ACS Chem. Biol. 1*, 644–648.

(25) Sletten, E. M., and Bertozzi, C. R. (2009) Bioorthogonal chemistry: fishing for selectivity in a sea of functionality. *Angew. Chem., Int. Ed. 48*, 6974–6998.

(26) Best, M. D. (2009) Click chemistry and bioorthogonal reactions: unprecedented selectivity in the labeling of biological molecules. *Biochemistry 48*, 6571–6584.

(27) Agard, N. J., Prescher, J. A., and Bertozzi, C. R. (2004) A strain-promoted [3 + 2] azide-alkyne cycloaddition for covalent modification of blomolecules in living systems. *J. Am. Chem. Soc. 126*, 15046–15047.

(28) Baskin, J. M., Prescher, J. A., Laughlin, S. T., Agard, N. J., Chang, P. V., Miller, I. A., Lo, A., Codelli, J. A., and Bertozzi, C. R. (2007) Copper-free click chemistry for dynamic in vivo imaging. *Proc. Natl. Acad. Sci. U. S. A. 104*, 16793–16797.

(29) Laughlin, S. T., Baskin, J. M., Amacher, S. L., and Bertozzi, C. R. (2008) In vivo imaging of membrane-associated glycans in developing zebrafish. *Science 320*, 664–667.

(30) Kolb, H. C., Finn, M. G., and Sharpless, K. B. (2001) Click chemistry: Diverse chemical function from a few good reactions. *Angew. Chem., Int. Ed. 40*, 2004–2021.

(31) Pipkorn, R., Waldeck, W., Didinger, B., Koch, M., Mueller, G., Wiessler, M., and Braun, K. (2009) Inverse-electron-demand Diels-Alder reaction as a highly efficient chemoselective ligation procedure: Synthesis and function of a BioShuttle for Temozolomide transport into prostate cancer cells. *J. Pept. Sci. 15*, 235–241.

(32) Blackman, M. L., Royzen, M., and Fox, J. M. (2008) Tetrazine ligation: Fast bioconjugation based on inverse-electron-demand Diels-Alder reactivity. *J. Am. Chem. Soc. 130*, 13518–13519.

(33) Devaraj, N. K., Upadhyay, R., Hatin, J. B., Hilderbrand, S. A., and Weissleder, R. (2009) Fast and sensitive pretargeted labeling of cancer cells through a tetrazine/*trans*-cyclooctene cycloaddition. *Angew. Chem., Int. Ed. 48*, 7013–7016.

(34) Rossin, R., Verkerk, P. R., van den Bosch, S. M., Vulders, R. C. M., Verel, I., Lub, J., and Robillard, M. S. (2010) In vivo chemistry for pretargeted tumor imaging in live mice. *Angew. Chem., Int. Ed. 49*, 3375–3378.

(35) Schrijvers, A. H. G. J., Quak, J. J., Uyterlinde, A. M., van Walsum, M., Meijer, C. J. L. M., Snow, G. B., and van Dongen, G. A. M. S. (1993) MAb U36, a novel monoclonal antibody successful in immunotargeting of squamous cell carcinoma of the head and neck. *Cancer Res. 53*, 4383–4390.

(36) Börjesson, P. K. E., Jauw, Y. W. S., Boellaard, R., de Bree, R., Comans, E. F. I., Roos, J. C., Castelijns, J. A., Vosjan, M. J. W. D., Kummer, J. A., Leemans, C. R., Lammertsma, A. A., and van Dongen, G. A. M. S. (2006) Performance of immuno-positron emission tomography with zirconium-89-labeled chimeric monoclonal antibody U36 in the detection of lymph node metastases in head and neck cancer patients. *Clin. Cancer Res. 12*, 2133–2140.

(37) van Gog, F. B., Visser, G. W. M., Klok, R., van der Schors, R., Snow, G. B., and van Dongen, G. A. M. S. (1996) Monoclonal antibodies labeled with rhenium-186 using the MAG3 chelate: Relationship between the number of chelated groups and biodistribution characteristics. *J. Nucl. Med. 37*, 352–362.

(38) Lindmo, T., Boven, E., Cuttitta, F., Fedorko, J., and Bunn, P. A. (1984) Determination of the immunoreactive fraction of radiolabeled monoclonal antibodies by linear extrapolation to binding at infinite antigen excess. *J. Immunol. Methods 72*, 77–89.

(39) Tijink, B. M., Perk, L. R., Budde, M., Stigter- van Walsum, M., Visser, G. W. M., Kloet, R. W., Dinkelborg, L. M., Leemans, C. R., Neri, D., and van Dongen, G. (2009) ^{124}I-L19-SIP for immuno-PET imaging of tumour vasculature and guidance of ^{131}I-L19-SIP radioimmunotherapy. *Eur. J. Nucl. Med. Mol. Imaging 36*, 1235–1244.

(40) Visser, G. W., Klok, R. P., Klein Gebbinck, J. W., ter Linden, T., van Dongen, G. A., and Molthoff, C. F. (2001) Optimal quality ^{131}I-monoclonal antibodies on high-dose labeling in a large reaction volume and temporarily coating of the antibody with IODO-GEN. *J. Nucl. Med. 42*, 509–519.

(41) Carroll, L., Boldon, S., Bejot, R., Moore, J. E., Declerck, J, and Gouverneur, V. (2011) The traceless Staudinger ligation of indirect ^{18}F-radiolabeling. *Org. Biomol. Chem. 9*, 136–140.

Supporting information for:

Synthesis of Phosphine and Antibody-azide Probes for *in vivo* Staudinger Ligation in a Pretargeted Imaging and Therapy Approach

Danielle J. Vugts[†‡*], Annelies Vervoort [†‡], Marijke Stigter-van Walsum[†], Gerard W.M. Visser[‡], Marc S. Robillard[§], Ron M. Versteegen[‖], Roland C.M. Vulders[§], J.(Koos) D.M. Herscheid[‡], Guus A.M.S. van Dongen[†‡]

[†] Dept. of Otolaryngology/Head and Neck Surgery, VU University Medical Center, Amsterdam, The Netherlands

[‡] Dept. of Nuclear Medicine and PET research, VU University Medical Center, Amsterdam, The Netherlands

[§] Biomolecular Engineering, Philips Research, Eindhoven, The Netherlands

[‖] SyMO-Chem BV, Eindhoven, The Netherlands

List of contents: Page

General methods and materials

All starting reagents and solvents were obtained from commercial sources and used without further purification unless otherwise stated. N-succinyl desferrioxamine (N-suc-DFO) **15**[1], t-butyl-2-(2-(2-aminoethoxy)ethoxy)ethylcarbamate (**19**)[2] and 4-iodocubane carboxylic acid[3] have been prepared according to literature procedures. Compounds **6**, **8**, **9**, **10, 18**, **26** and **27** have been prepared and isolated in slightly modified procedures as compared to those described, avoiding large excesses of hexa-ethylene glycol for the preparation of **8,** avoiding higher temperatures wth NaN_3 in the synthesis of **9** and improving the yield in the preparation of **18**. Analytical data of **6**, **8**, **9**, **10**, **18**, **26** and **27** are in line with those reported. Water was distilled and deionized (18 $m\Omega cm^{-1}$) by means of a milli-Q water filtration system (Millipore, USA). The labeling buffers for ^{177}Lu labeling of DOTA-phosphine **4** were treated with Chelex-100 resin (BioRad Laboratories, USA) overnight.

^{1}H, ^{13}C, ^{19}F and ^{31}P nuclear magnetic resonance (NMR) spectra were recorded on a Bruker AC, a Bruker Avance 250 MHz, a Bruker MSL 400 MHz, a Bruker 500 MHz spectrometer, a Varian Mercury Vx 400 MHz or a Varian Gemini 300 MHz spectrometer, where spectra were recorded at a temperature of 25 °C. Chemical shifts (δ) are given in ppm, internally referenced to residual solvent resonances (^{1}H: δ = 7.29 ppm, ^{13}C: δ = 77.0 ppm). ATR-FT-IR characterizations were done on a PerkinElmer Spectrum One machine. Mass spectrometry on isolated compounds was done using a Voyager DE-PRO MALDI-TOF-MS spectrometer (Perceptive Biosystems, USA), usually applying positive and reflector mode conditions and using α-cyano hydroxy cinnamic acid (CHCA) as matrix material. LC-MS/PDA analysis on prepared materials was carried out using a LC-10AD (Shimadzu, Japan) in combination with a Surveyor LCQ Fleet MS-spectrometer and a Surveyor PDA-plus detector (Thermo Fisher Scientific Inc., USA), and applying an Alltech Alltima HP C18 3µ column (Grace Alltech, USA). High resolution mass spectra (HRMS, ESI) were recorded on a micrOTOF-Q spectrometer (Capillary voltage: -4500V; collision energy: 5eV).

Column chromatography was performed with Baker 7024–02 silica gel (40 mm, 60 L) or Screening Devices 60Å silica gel or Merck standardized aluminum oxide 90. Thin-layer chromatography (TLC) was performed on Merck TLC-plates on aluminium sheets (Silica gel 60 F_{254} or neutral aluminium oxide 60 F_{254}) Compounds on the TLC plates were visualised by UV light. Preparative reversed phase (RP) chromatography was done on a Biotage SP1 flash purification system (Biotage AB, Sweden) using a SiliCycle C18 RP column (SiliCycle Inc., Canada) and applying linear gradients of MeCN in water.

HPLC analysis of the synthesis of phosphine **2** and **3** was done with a Chromspher 5 C18, 250x4.6 mm column (Varian) or a X-Terra MS C18 5 μm 3.9x150 mm column (Waters), using MeCN and 10 mM phosphate buffer (pH 6.0) as the eluent. The radioactivity of the eluate was monitored using an inline NaI radiodetector (Raytest Sockett). Sep-pak cartridges (Waters) were used to purify compound **16**, **22**, **24** and **30**.

^{177}Lu (9.25 GBq/mL in 0.05 M HCl) was obtained from Perkin-Elmer, ^{89}Zr (1 GBq/mL in 1 M oxalic acid) from IBA molecular, ^{67}Ga-citrate (74 MBq/mL) from Covidien, ^{68}Ga from a ^{68}Ge/^{68}Ga generator from Eckert & Ziegler Isotope Products, and ^{123}I (50 GBq/mL in 0.01M NaOH) from Cyclotron BV.

HPLC analysis of radiolabeled phosphines **2**, **3** and **4** was done with a Chromspher 5 C18, 250x4.6 mm column (Varian) or a X-Terra MS C18 5 μm 3.9x150 mm column (Waters), using MeCN and 10 mM phosphate buffer (pH 6.0) as the eluent for $^{67/68}$Ga-DFO-phosphine **2** and **3** and ^{177}Lu-DOTA-phosphine **4**, and MeCN and 50 mM phosphate buffer (pH 3.25) for ^{89}Zr-DFO-phosphine **2** and **3**. HPLC analysis of ^{123}I-cubyl-phopshine **5** was done with a Chromasil 100 C18 column (Phenomenex) using EtOH and water or MeCN, water and diisopropylamine as eluent. The radioactivity of the eluate was monitored using an inline NaI(Tl) radiodetector (Raytest Sockett). Light C18 sep-pak cartridges (Waters) were used to isolate ^{89}Zr-DFO-phosphine **2** and **3** from the labeling mixture. Single isotope counting was performed with a γ-well counter (Wallac LKB-CompuGamma 1282; Pharmacia) for ^{89}Zr, ^{67}Ga, ^{68}Ga, ^{123}I and ^{177}Lu.

Synthesis of azide **1a**

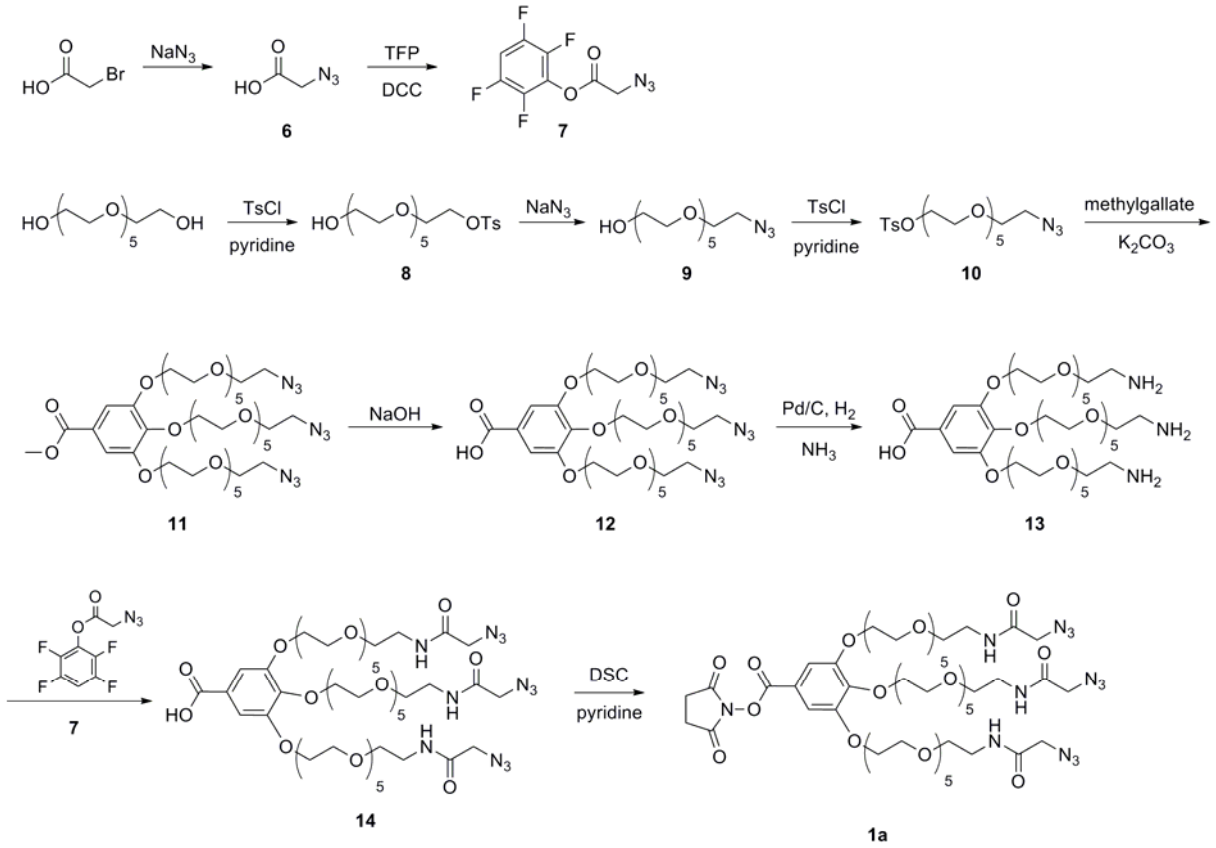

Scheme S1 Synthesis of azide **1a**

2-Azidoacetic acid (6)[4]

Bromo acetic acid (6.3 g; 45 mmol) was dissolved in dimethyl sulfoxide (DMSO) (15 mL) and NaN_3 was added in portions (3.6 g, 55 mmol) under stirring and cooling with an ice bath. After 10 min, the resulting gel was broken-up by adding DMSO (15 mL) and by vigorous stirring. The mixture was stirred overnight at room temperature (RT), then 1 M NaOH was added to increase the pH (>10), and the mixture was again stirred overnight. Water (300 mL) was added, the reaction mixture was acidified to pH<2 with 1 M HCl and was then extracted with diethyl ether (150 mL) (ethyl acetate is also possible[4], but we have observed that in time acid **6** gives transesterification in this solvent). The combined ether layer was washed with 1 M HCl (75 mL) and dried with Na_2SO_4. Addition of toluene and removal of the diethyl ether resulted in 26.7 g (87%) of a 15% (w/w) solution of **6** in toluene. A sample of the ether solution was evaporated down for analysis. ^{1}H-NMR (400 MHz, $CDCl_3$): δ = 10.7 (bs, 1H, COO<u>H</u>), 4.0 (s, 2H, C<u>H</u>$_2$N$_3$) ppm; ^{13}C-NMR ($CDCl_3$): δ = 174.4, 50.0 ppm.

2,3,5,6-Tetrafluorophenyl 2-azidoacetate (7)

A toluene solution of **6** (0.97 g of solute, 9.6 mmol), 2,3,5,6-tetrafluorophenol (TFP) (1.84 g, 11.1 mmol) in $CHCl_3$ (3 mL), and pyridinium p-toluene sulfonic acid (0.24 g; 0.96 mmol) were stirred at RT in a water bath. A solution of N,N'-dicyclohexylcarbodiimide (DCC) (2.34 g, 11.4 mmol) in $CHCl_3$ (3 mL) was added dropwise and the reaction mixture was stirred overnight under a N_2 atmosphere. The solvent was removed, MeCN (25 mL) was added and the resulting white suspension was stirred overnight at 4 °C. After filtration, solvent evaporation and silica column chromatography with a $CHCl_3$/heptane gradient, 1.6 g (67%) of pure product **7** was obtained. ^{1}H-NMR (400 MHz, $CDCl_3$): δ = 7.09–7.03 (m, 1H, Ph-H), 4.28 (s, 2H, CH_2N_3) ppm; ^{13}C-NMR (100 MHz, $CDCl_3$): δ = 164.5, 146.0 (d, ***J*** (FC) = 252 Hz), 140.4 (d, ***J*** (FC) = 234 Hz), 129.1, 103.9 (t, ***J*** (FC) = 22.8 Hz), 49.7 ppm; ^{19}F-NMR (375 MHz, $CDCl_3$): δ = -138.3, -152.7 ppm; ATR-FT-IR: ν = 2109 1797, 1645, 1523 cm^{-1}.

2-(2-(2-(2-(2-(2-Hydroxyethoxy)-ethoxy)-ethoxy)-ethoxy)-ethoxy)-ethyl p-tosylate (8)[5,6]

Tosyl chloride (18.0 g, 94.5 mmol) was added in portions to a stirred and ice-cooled solution of hexaethylene glycol (25.4 g, 90.0 mmol) in dry pyridine (35 mL). The mixture was stirred overnight under an argon atmosphere at 4 °C, then crushed ice and 10 M HCl (45 mL) were added, and the mixture was extracted with $CHCl_3$ (200 mL). The combined organic layer was washed with water (75 mL), dried with Na_2SO_4 and concentrated in vacuo to yield an oil containing mono- and difunctionalized hexaethylene glycol. Purification was performed on a silica column using a $CHCl_3$/MeOH gradient resulting in an oil. Yield: 16.5 g (42 %). ^{1}H-NMR (400 MHz, $CDCl_3$): δ = 7.79 (d, 2H, ***J*** = 8.7 Hz, Ph-H), 7.36 (d, 2H, ***J*** = 8.7 Hz, Ph-H), 4.18 (t, 2H, ***J*** = 4.7 Hz, CH_2OTs), 3.72–3.53 (m, 22H, OCH_2), 2.89 (bs, 1H, OH), 2.43 (s, 3H, Ph-CH_3) ppm; ^{13}C-NMR (100 MHz, $CDCl_3$): δ = 144.6, 132.8, 129.7, 127.8, 72.3, 70.5-70.1, 69.1, 68.5, 61.5, 21.4 ppm.

2-(2-(2-(2-(2-(2-Hydroxyethoxy)-ethoxy)-ethoxy)-ethoxy)-ethoxy)-ethyl azide (9)[5,6]

The tosylate **8** (16.5 g, 37.8 mmol), NaN_3 (3.5 g, 53.8 mmol) and dry DMSO (20 mL) were stirred at RT under an argon atmosphere for 3 days. Water (50 mL) and a few mL of a saturated $NaHCO_3$ solution were added to the reaction mixture and the aqueous solution was extracted with $CHCl_3$ (100 mL). The combined organic layer was washed with water (50 mL), dried with Na_2SO_4 and concentrated in vacuo to yield 11.1 g of oily product (95%). ^{1}H-NMR (400 MHz, $CDCl_3$): δ = 3.72–3.53 (m, 22H, OCH_2), 3.39 (t, 2H, ***J*** = 4.9 Hz, CH_2N_3), 2.78 (bs,

1H, O<u>H</u>) ppm; ^{13}C-NMR (100 MHz, $CDCl_3$): δ = 72.4, 70.5-69.9, 61.6, 50.6 ppm; ATR-FT-IR: ν = 2101 cm^{-1}.

2-(2-(2-(2-(2-(2-Azido ethoxy)-ethoxy)-ethoxy)-ethoxy)-ethoxy)-ethyl p-tosylate (10)[5,6]

Tosyl chloride (5.5g, 28.8 mmol) was added in portions to a stirred and ice-cooled solution of **9** (7.5 g; 24.4 mmol) in dry pyridine (10 mL). The mixture was stirred overnight under an argon atmosphere at 4 °C, then iced water (100 mL) was added and the mixture was stirred for 5-10 min. A 10 M HCl solution (10 mL) was added, and the aqueous solution was extracted with $CHCl_3$ (100 mL). The combined organic layer was washed with acidic water (1 M HCl, 75 mL), dried with Na_2SO_4 and concentrated in vacuo to give **10** (10.4 g, 92%) as a clear yellowish oil. ^{1}H-NMR (400 MHz, $CDCl_3$): δ = 7.80 (d, 2H, ***J*** = 8.7 Hz, Ph-<u>H</u>), 7.36 (t, 2H, ***J*** = 8.7 Hz, Ph-<u>H</u>), 4.16 (t, 2H, ***J*** = 4.7 Hz, C<u>H</u>$_2$OTs), 3.70–3.56 (m, 20H, OC<u>H</u>$_2$), 3.38 (t, 2H, ***J*** = 5.0 Hz, C<u>H</u>$_2$N$_3$), 2.43 (s, 3H, Ph-C<u>H</u>$_3$) ppm; ^{13}C-NMR (100 MHz, $CDCl_3$): δ = 144.6, 132.8, 129.7, 127.8, 70.5-70.3, 69.8, 69.1, 68.5, 50.5, 21.5 ppm.

Methyl-3,4,5-tris[2-(2-(2-(2-(2-(2-azidoethoxy)-ethoxy)-ethoxy)-ethoxy)-ethoxy)-ethoxy]-benzoate (11)

The tosylate **10** (10.4 g, 22.5 mmol), methyl gallate (1.24 g, 6.75 mmol), K_2CO_3 (9.2 g, 67 mmol), tetrabutyl ammonium bromide (70 mg) and dimethyl formamide (DMF) (67 mL) were heated overnight under argon atmosphere at 65 °C. The product was isolated by pouring the resulting suspension into a citric acid solution (1 M, 200 mL) and extracting the aqueous solution with several portions of $CHCl_3$ (300 mL). The combined organic layer was concentrated in vacuo and co-evaporated with toluene to give 9.6 g of a crude brown oil. Silica column chromatography with a dimethoxyethane/heptane gradient afforded **11** in quantitative yield (7.0 g). The product contained a small amount of alcohol **9** that was formed due to hydrolysis of the tosylate **10**. This contaminant was not removed from the mixture after this step, but after the next. ^{1}H-NMR (400 MHz, $CDCl_3$): δ = 7.31 (s, 2H, Ph-<u>H</u>), 4.24–4.16 (m, 6H, PhOC<u>H</u>$_2$), 3.88 (s, 3H, COOC<u>H</u>$_3$), 3.85 (t, 4H, ***J*** = 4.9 Hz, PhOCH$_2$C<u>H</u>$_2$), 3.79 (t, 2H, ***J*** = 4.9 Hz, PhOCH$_2$C<u>H</u>$_2$), 3.74–3.60 (m, 54H, C<u>H</u>$_2$O), 3.38 (t, 6H, ***J*** = 5.2 Hz, C<u>H</u>$_2$N$_3$) ppm; ^{13}C-NMR (100 MHz, $CDCl_3$): δ = 166.4, 152.1, 142.4, 124.8, 108.9, 72.2, 70.6-70.3, 69.8, 69.4, 68.7, 52.0, 50.5 ppm.

3,4,5-Tris[2-(2-(2-(2-(2-(2-azidoethoxy)-ethoxy)-ethoxy)-ethoxy)-ethoxy)-ethoxy]-benzoic acid (12)

The methyl ester **11** (2.1 g, 2.0 mmol) and NaOH (120 mg, 3.0 mmol) were stirred overnight at RT in a 8/1 MeOH/H_2O (10 mL) solution. MeOH was evaporated, the solution acidified with 1 M HCl (5 mL) and the product was extracted in $CHCl_3$ (25 mL). Drying with Na_2SO_4 and concentration in vacuo of the solution yielded 1.8 g of crude product that was purified over an alumina column (to remove the contaminant **9**), by applying an eluent mixture of $CHCl_3$/MeOH/H_2O 6/3/1. The fractions containing the product were pooled and concentrated. The oily residue was dissolved in $CHCl_3$ and the resulting solution was washed with a 1 M HCl solution (10 mL). Evaporation of the $CHCl_3$ yielded the product **12** as an oil (1.9 g, 91%). ^{1}H-NMR (400 MHz, $CDCl_3$): δ = 7.39 (s, 2H, Ph-H), 4.27–4.17 (m, 6H, PhOCH_2), 3.86 (t, 4H, ***J*** = 5.0 Hz, PhOCH_2CH_2), 3.79 (t, 2H, ***J*** = 5.1 Hz, PhOCH_2CH_2), 3.75–3.60 (m, 54H, CH_2O), 3.38 (t, 6H, ***J*** = 5.1 Hz, C$H_2$$N_3$) ppm; ^{13}C-NMR (100 MHz, $CDCl_3$): δ = 169.5, 152.0, 142.6, 124.7, 109.2, 72.2, 70.5, 70.4-70.3, 69.7, 69.4, 68.6, 50.4 ppm; ATR-FT-IR: ν = 2100, 1713, 1586 cm^{-1}. MALDI-TOF-MS: $[M+Na]^+$ = 1060.3.

3,4,5-Tris[2-(2-(2-(2-(2-(2-aminoethoxy)-ethoxy)-ethoxy)-ethoxy)-ethoxy)-ethoxy]-benzoic acid (13)

A solution of the acid **12** (200 mg) in dioxane (5 mL) and 28% ammonia in water (2 mL) was placed under an N_2 atmosphere. Pd/C (10%, ca. 20 mg) was added and the mixture was then shaken under a H_2 pressure of 50 psi until FT-IR analysis showed the absence of azide groups. The Pd/C was filtered off and the filtrate was concentrated to produce **13** as an oil (100 % yield). This was used in the next synthetic step without further purification. ^{1}H-NMR (400 MHz, $CDCl_3$): δ = 7.36 (s, 2H, Ph-H), 4.3 (bs, 6H, NH_2), 4.25 (t, 4H, ***J*** = 5.0 Hz, PhOCH_2), 4.19 (t, 2H, ***J*** = 5.1 Hz, PhOCH_2), 3.85 (t, 4H, ***J*** = 5.0 Hz, PhOCH_2CH_2), 3.79 (t, 2H, ***J*** = 5.1 Hz, PhOCH_2CH_2), 3.75–3.60 (m, 54H, CH_2O), 2.99 (t, 4H, ***J*** = 5.2 Hz, C$H_2$$NH_2$), 2.95 (t, 2H, ***J*** = 5.2 Hz, C$H_2$$NH_2$) ppm.

3,4,5-Tris[2-(2-(2-(2-(2-(2-(2-azidoacetamido)-ethoxy)-ethoxy)-ethoxy)-ethoxy)-ethoxy)-ethoxy]-benzoic acid (14)

The activated ester **7** (200 mg, 0.80 mmol) was added to a solution of **13** (185 mg, 0.19 mmol) and diisopropylethylamine (DIPEA) (250 mg) in $CHCl_3$ (3 mL). The reaction mixture was stirred overnight at RT and was then washed with 1 M HCl (2 mL). The solvent was evaporated and the residue was purified by RP-chromatography applying a SiliCycle C18 RP

column. The oily product **14** was isolated in 95% yield. ^{1}H-NMR (400 MHz, $CDCl_3$): δ = 7.35 (s, 2H, Ph-H), 7.00 (bs, 2H, NH), 6.95 (bs, 1H, NH), 4.27–4.17 (m, 6H, $PhOCH_2$), 3.95 (s, 6H, CH_2N_3), 3.85 (t, 4H, ***J*** = 5.0 Hz, $PhOCH_2CH_2$), 3.79 (t, 2H, ***J*** = 5.1 Hz, $PhOCH_2CH_2$), 3.75–3.60 (m, 54H, CH_2O), 3.45 (t, 6H, ***J*** = 5.1 Hz, CH_2NH) ppm; ^{13}C-NMR (100 MHz, $CDCl_3$): δ = 168.4, 167.1, 167.0, 152.1, 142.7, 124.7, 109.5, 72.3, 70.7, 70.5-70.3, 70.1, 69.6, 69.4, 68.8, 52.4, 39.1 ppm; ATR-FT-IR: ν = 2102, 1678 cm^{-1}; LC-MS: $[M+H]^+$ = 1209.3, $[M+2H]^{2+}$ = 605.50.

Succinimidyl 3,4,5-tris[2-(2-(2-(2-(2-(2-azidoacetamido)-ethoxy)-ethoxy)-ethoxy)-ethoxy)-ethoxy] benzoate (1a)

The acid **14** (250 mg; 0.21 mmol) and N,N'-disuccinimidyl carbonate (DSC) (75 mg; 0.29 mmol) were dissolved in MeCN (4 mL) and few drops of pyridine. After overnight stirring, a second portion of DSC (35 mg; 0.14 mmol) was added, and the mixture was stirred for 2 h more. At completion of the reaction, as confirmed by ^{1}H-NMR analysis, the solvent was evaporated and $CHCl_3$ (10 mL) was added. The organic solution was washed with an ice-cold aqueous solution of diluted HCl and NaCl (10 mL), dried with Na_2SO_4 and concentrated to give a turbid oil. Dissolution in 1/1 $CHCl_3$/diethyl ether, filtration and concentration of the filtrate in vacuo gave a quantitative amount of product **1a**. ^{1}H-NMR (400 MHz, $CDCl_3$): δ = 7.39 (s, 2H, Ph-H), 6.94 (bs, 3H, NH), 4.26 (t, 2H, ***J*** = 5.0 Hz, $PhOCH_2$), 4.20 (t, 4H, ***J*** = 4.9 Hz, $PhOCH_2$), 3.96 (s, 6H, CH_2N_3), 3.86 (t, 4H, ***J*** = 4.9 Hz, $PhOCH_2CH_2$), 3.79 (t, 2H, ***J*** = 4.8 Hz, $PhOCH_2CH_2$), 3.73–3.67 (m, 6H, CH_2O), 3.67–3.55 (m, 42H, CH_2O), 3.59 (t, 6H, ***J*** = 4.9 Hz, CH_2O), 3.48 (q, 6H, ***J*** = 5.3 Hz, CH_2NH), 2.91 (bs, 4H, CH_2CO) ppm; ^{13}C-NMR (100 MHz, $CDCl_3$): δ = 169.2, 166.9, 161.2, 152.4, 144.2, 119.3, 109.9, 72.4, 70.6, 70.5-70.3, 70.1, 69.4, 69.3, 68.9, 52.3, 39.1, 25.5 ppm; ATR-FT-IR: ν = 2103, 1738 cm^{-1}; MALDI-TOF-MS: $[M+Na]^+$ = 1328.6.

cmAb U36 modification with triazide **1a**

cmAb U36 (MW ~ 150 kDa, 4 mg, 27 nmol) was reacted with 10, 15, 20 and 40 equivalents (270, 405, 540 and 1080 nmol) of triazide **1a** (dissolved in DMF, max. 20 μL) in 1 mL total volume for 30 minutes. In parallel a mock reaction was performed with triazide **1a** without cmAb U36 resulting in fully hydrolyzed triazide **1b**. For determination of the average number of triazide **1** molecules attached per mAb molecule, the crude reaction mixtures were injected on HPLC equipped with a Superdex^{TM} 200 10/30 GL size exclusion column (GE healthcare Life sciences) using a mixture of 0.05 M sodium phosphate, 0.15 M sodium chloride (pH 6.8) and 0.01 M NaN_3 as the eluent at a flow rate of 0.5 mL/min. The retention times of the cmAb U36 was 25.6 min, of the hydrolyzed azide **1b** 40.1 min and of NHS 42.6 min. In the mock reaction the area of the hydrolyzed triazide **1b** at 40.1 min corresponded to the amount of triazide used in the reaction. In the modification reaction the area of the hydrolyzed triazide **1b** at 40.1 min corresponded to the amount of triazide that had not reacted. The percentage of triazide that had reacted, was be calculated for the difference of the hydrolyzed triazide between mock reaction and modification reaction.

^{131}I-labeling of cmAb U36-triazide compounds.

In short: 20 mL β-scintillation vials were coated with 25 μg iodogen (Pierce, Rockford, IL, USA) in dichloromethane, dried under a stream of N_2 gas, resulting in a thin coating of iodogen at the bottom surface of the vial. The vials were stored under N_2 atmosphere. To a iodogen-coated glass vial, successively 50 μL 0.5 M NaH_2PO_4 (pH 7.4), 450-X-Y μL 0.1 M Na_2HPO_4 (pH 6.8), X μL U36 and Y μL ^{131}I solution were added. After gentle shaking for 5 min, 0.1 mL ascorbic acid (25 mg/mL, pH 5) was added to reduce the iodogen, the SCl bonds and to protect cmAb U36 against radiation damage. After an additional 5 min, the reaction mixture was transferred to a syringe connected to a filter (0.22 μm Acrodisc, Gelman Sciences, Ann Arbor, MI, USA) followed by 0.4 mL 0.1 M Na_2HPO_4 (pH 6.8), used for an additional rinsing of the vial. This combined solution was filtered and purified on a PD10 column with 0.9% NaCl/ascorbic acid (5 mg/mL, pH 5) as eluent.

Synthesis of DFO-phosphine **2**

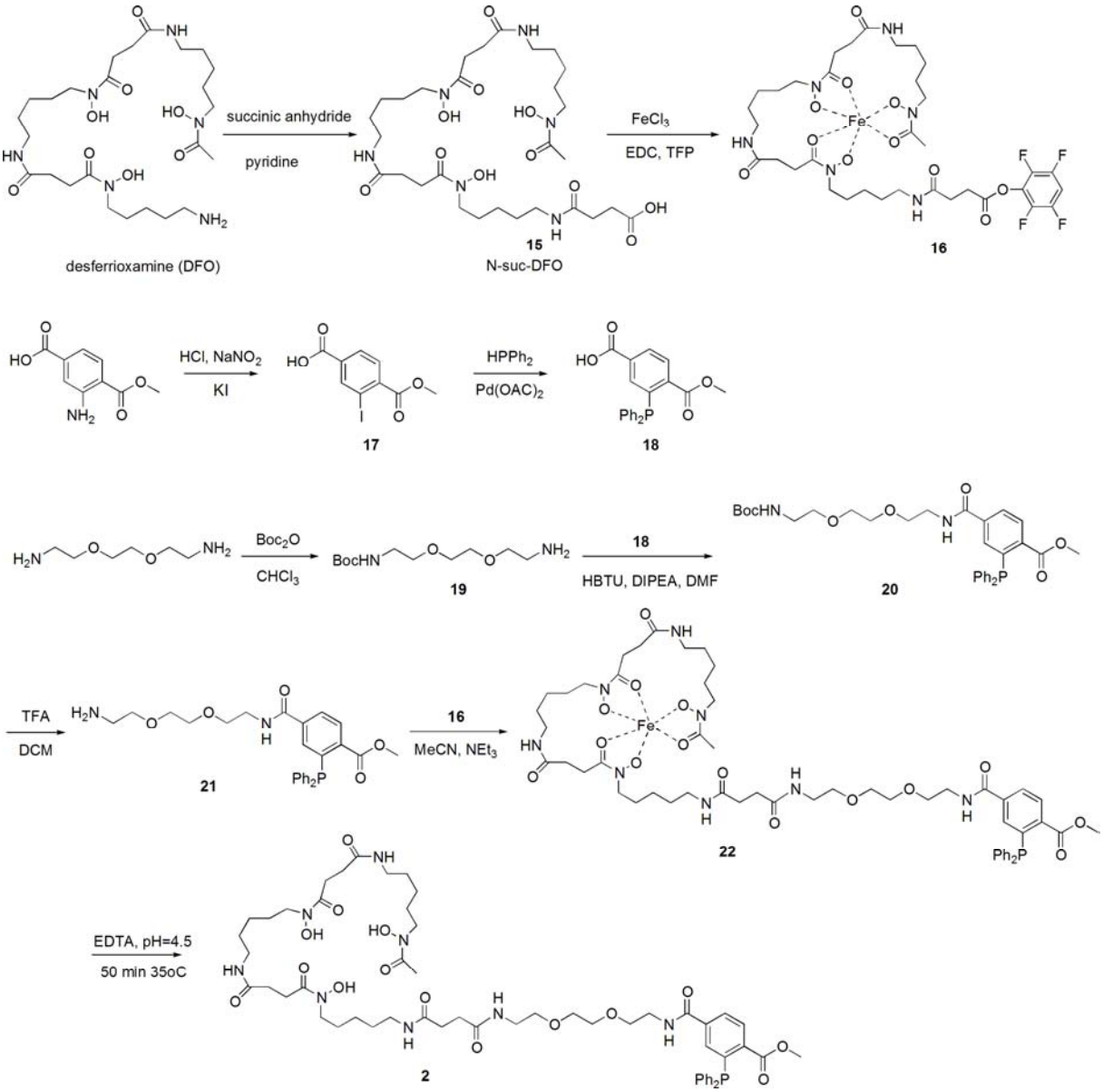

Scheme S2 Synthesis of DFO-phosphine **2**

TFP-N-suc-DFO-Fe ester (16)[1]

A stock solution of $FeCl_3$ (80 µL of 400 mg/mL in 0.5 M HCl, 32 mg, 0.20 mmol) was added dropwise to a solution of ***N*-suc-DFO** **15** (120 mg, 0.18 mmol) in 0.1 M Na_2CO_3 (2.64 mL) and 0.9 % NaCl (2.31 mL) while shaking. After 10 min 0.9 % NaCl (5 mL), MeCN (1.8 mL) and TFP solution (0.20 mL of 2 g/mL in MeCN, 0.40 g, 1.73 mmol) were added. Subsequently a first portion of 1-Ethyl-3-(3-dimethylaminopropyl)-carbodiimide (EDC) (0.50 g, 2.61 mmol) was added and incubated for 15 min, followed by a second portion of EDC (0.50 g, 2.61 mmol) and again incubated for 15 min. The resulting dark red solution was trapped on 2 double C18 sep-pak cartridges. The double sep-pak cartridges were washed with

60 mL H_2O each and subsequently eluted with 2 times 1.5 mL MeCN. Yield: 81% (estimated with HPLC at 430 nm).

1-Methyl-2-iodo-terephthalate (17)[7]

Hydrochloric acid (37%, 200 mL) was cooled on an ice bath, and 1-methyl-2-amino terephthalate was added. A solution of $NaNO_2$ (7.20 g; 0.104 mol) in 40 mL of H_2O was added dropwise, resulting in the evolution of a small amount of orange gas. The mixture was stirred for 30 min at 20°C and then filtered through a glass filter. The filtrate was subsequently added to a solution of potassium iodide (172 g; 1.04 mol) in H_2O (280 mL). The dark red solution was stirred for 1 h and then diluted with dichloromethane (DCM) (2 L) and washed with sat. Na_2SO_3 (2 times 400 mL), H_2O (800 mL), and sat. NaCl (400 mL). The combined aqueous layer was back extracted with DCM (500 mL). The combined organic layer was dried over Na_2SO_4 and concentrated in vacuo. The crude product was dissolved in hot MeOH (60 mL) and H_2O (20 mL) was added. Cooling to 4 °C and subsequent filtration afforded **17** as a bright yellow solid (18.92 g; 62%), mp=165-166°C. ^{1}H-NMR (400 MHz, $CDCl_3$): δ = 11.4 (br.s, 1H, O<u>H</u>), 8.69 (d, 1H, ***J*** = 1.6 Hz, Ph-<u>H</u> (H6)), 8.11 (dd, 1H, ***J*** = 1.6 Hz, J = 8.0 Hz, Ph-<u>H</u> (H4)), 7.83 (dd, 1H, ***J*** = 1.6 Hz, ***J*** = 8.0 Hz, Ph-<u>H</u> (H3)), 3.97 (s, 3H, C<u>H</u>$_3$) ppm; ^{13}C-NMR (400 MHz, $CDCl_3$): δ = 169.9, 166.5, 142.6, 140.1, 132.5, 130.5, 129.4, 93.4, 52.9 ppm; FT-IR (ATR): ν = 2957, 2845, 2646, 2535, 1737, 1693, 1552, 1480, 1417, 1248, 742 cm^{-1}.

1-Methyl-2-diphenylphosphino-terephthalate (18)[7]

To a flame dried flask was added MeCN (30 mL), NEt_3 (5.32 g; 52.3 mmol), compound **17** (3.06 g; 10.0 mmol) and palladium acetate (42 mg; 0.2 mmol). The mixture was degassed in vacuo. While stirring under an atmosphere of argon, diphenylphosphine (2.16 g; 11.6 mmol) was added to the flask via a syringe. The resulting solution was heated at 80°C for 3 d, and then allowed to cool to RT and concentrated in vacuo. The residue was dissolved in DCM (175 mL), washed with H_2O (175 mL), and 1 M hydrochloric acid (2 times 50 mL), and concentrated in vacuo. The crude product was dissolved in hot MeOH (100 mL) and cooled to 4°C. Filtration afforded the phosphine product as a golden yellow solid (2.87 g; 78%), mp=206°C. ^{1}H-NMR (400 MHz, $CDCl_3$): δ = 10.8 (br.s, 1H, O<u>H</u>), 8.07–8.00 (m, 2H, <u>H4 and H6</u>), 7.67 (d, ***J*** = 4.0 Hz, 1H, <u>H3</u>), 7.37-7.25 (m, 10H, Ph-<u>H</u>), 3.75 (s, 3H, C<u>H</u>$_3$) ppm; ^{13}C-NMR (100 MHz, $CDCl_3$): δ = 170.6, 166.7, 141.5 (d, ***J*** (PC) = 29.5 Hz), 138.9 (d, J (PC) =

19.1 Hz), 136.9 (d, ***J*** (PC) = 10.0 Hz), 135.6, 133.8 (d, ***J*** (PC) = 10.0 Hz), 131.9, 130.6, 129.7, 129.0, 128.7 (d, ***J*** (PC) = 7.1 Hz), 52.4 ppm; ^{31}P-NMR (80 MHz, $CDCl_3$): δ = -4.04 ppm; FT-IR (ATR): ν 2952, 2846, 2536, 1726, 1686, 1434, 1262, 1244, 1106, 1057, 743 cm^{-1}.

Phosphine 21

2-(1H-Benzotriazole-1-yl)-1,1,3,3-tetramethyluronium hexafluorophosphate (HBTU) (1.04 g; 2.74 mmol) was dissolved in dry (DMF) (12 mL) and DIPEA (0.96 mL; 5.48 mmol) and phosphine **18** (1.0 g; 2.74 mmol) were added. The mixture was stirred under argon at RT for 10 min, after which a solution of **19** (0.75 g; 3.0 mmol) in DMF (2.5 mL) was added. The mixture was stirred for 2 h and subsequently diluted with diethyl ether (165 mL), and washed with saturated $NaHCO_3$ (3 times 110 mL) and 0.1 M HCl (110 mL). The organic layer was dried with Na_2SO_4 and concentrated in vacuo to yield phosphine **20** as a yellow foam. This yellow foam was dissolved in DCM (7.5 mL) and trifluoroacetic acid (TFA) (7.5 mL) and stirred for 2 h at RT. The mixture was concentrated in vacuo and redissolved in DCM (37 mL). This organic solution was washed with saturated Na_2CO_3 (75 mL) and the aqueous layer was back extracted with DCM (20 mL). The combined organic solution was dried with Na_2SO_4 and concentrated in vacuo to yield a yellow oil. This crude product was purified by silica column chromatography using a gradient of $CHCl_3$/MeOH/NEt_3 of 100/1/0.1 to 10/1/0.1. Yield: 1.17 g (86 % over two steps). ^{1}H-NMR (200 MHz, $CDCl_3$): δ = 8.00 (dd, 1H, ***J*** = 8.0 Hz, ***J*** = 1.6 Hz, Ph-H), 7.78 (dd, 1H, ***J*** = 8.0 Hz, ***J*** = 3.6 Hz, Ph-H), 7.05–7.34 (m, 11H, Ph-H), 3.66 (s, 3H, CO_2CH_3), 3.41–3.52 (m, 10H, CH_2), 2.79 (t, 2H, ***J*** = 5 Hz, CH_2NH_2) ppm; ^{31}P-NMR (101 MHz, $CDCl_3$): δ = -3.7 ppm; HRMS (ESI): m/z = 495.2022 [M^+], calc. for $C_{27}H_{32}N_2O_5P$ = 495.2043.

Fe-DFO-phosphine 22

To a solution of TFP-***N***-suc-DFO-Fe ester **16** (103 mg, 0.12 mmol) in MeCN (4 mL) were added 3 eq. of NEt_3 (51 µL, 0.36 mmol) and 1 eq. of phosphine **21** (60 mg, 0.12 mmol) in MeCN (3 mL). The resulting solution was stirred overnight at RT, subsequently concentrated in vacuo and dissolved in 10% MeCN in H_2O and trapped on 2 sep-pak cartridges (C18). The sep-pak cartridges were washed with 60 mL H_2O and eluted with 5 mL MeCN. Yield: quantitative.

DFO-phosphine 2

To a solution of Fe-DFO-phosphine **22** (142 mg; 0.12 mmol) in MeCN (8 mL) was added ethylenediaminetetraacetic acid (EDTA) (75 mL of 25 mg/mL), H_2SO_4 solution (18.75 mL of pH=4.5) and MeCN (17 mL). The solution was heated at 35°C for 50 min. A white precipitate was formed during Fe^{3+} removal. This white precipitate was separated from the aqueous phase by centrifugation and washed with H_2SO_4 solution (pH=4.5, 20 mL) and H_2O (20 mL), followed by lyophilization. Yield: quantitative. Purity: >95 % according to HPLC. ^{1}H-NMR (500.23 MHz, DMSO): δ = 9.62 (s, 3H), 8.62 (dd, 1H, ***J*** = 5.5Hz, J= 5.5Hz), 8.01 (dd, 1H, ***J*** = 8.0 Hz, ***J*** = 1.5 Hz), 7.90 (dd, 1H, ***J*** = 8.0 Hz, ***J*** = 1.5 Hz), 7.86 (dd, 1H, ***J*** = 5.5 Hz, ***J*** = 5.5 Hz), 7.79–7.77 (m, 3H), 7.57–7.54 (m, 1H), 7.44–7.36 (m, 7H), 7.22–7.18 (m, 4H), 3.65 (s, 3H), 3.43–3.39 (m, 12H), 3.37–3.33 (m, 4H), 3.16–3.14 (m, 2H), 3.00–2.98 (m, 6H), 2.59–2.56 (m, 4H), 2.28–2.25 (m, 8H), 1.96 (s, 3H), 1.51–1.47 (m, 6H), 1.39–1.35 (m, 6H), 1.22–1.20 (m, 6H) ppm; ^{13}C-NMR (125.78 MHz, DMSO): δ = 172.0, 171.5, 171.3, 171.1, 170.1, 166.3, 165.3, 139.8 (d, ***J*** (PC) = 28.9 Hz), 137.2, 137.0 (d, ***J*** (PC) = 12.6 Hz), 136.3 (d, ***J*** (PC) = 20.1 Hz), 133.5 (d, ***J*** (PC) = 21.4 Hz), 133.2, 130.1, 129.0, 128.7 (d, ***J*** (PC) = 7.5 Hz), 126.8, 69.5, 69.1, 68.7, 52.1, 47.0, 46.7, 38.4, 30.7, 29.9, 28.8, 27.6, 26.0, 23.5, 20.4 ppm; ^{31}P-NMR (161.97 MHz, $CDCl_3$): δ = -5.3 ppm; HRMS (ESI): m/z = 1137.5580 [M^+], calc. for $C_{56}H_{82}N_8O_{15}P$ = 1137.5632.

Synthesis of DFO-phosphine **3**

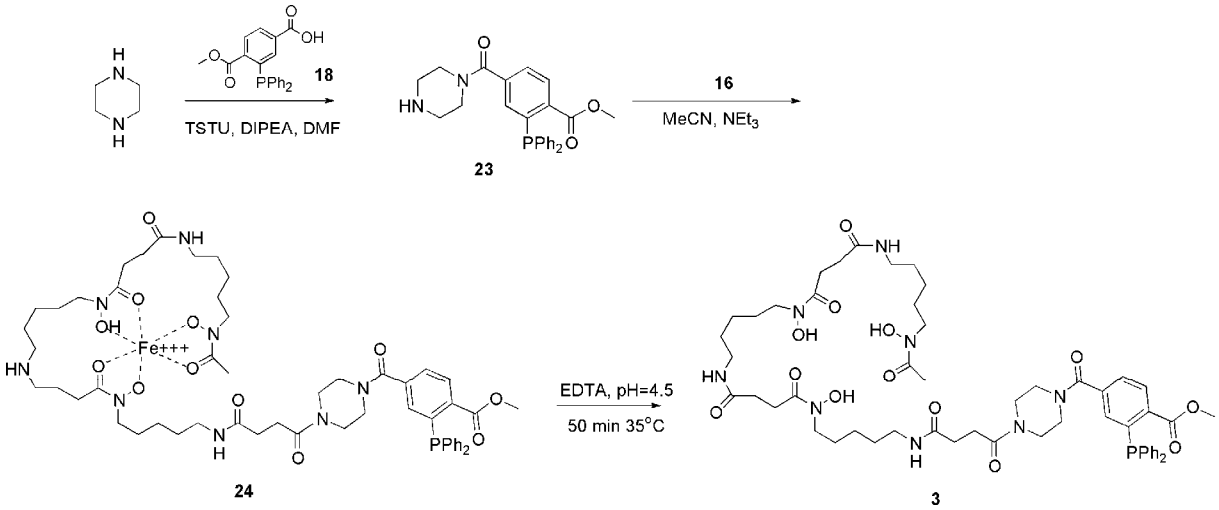

Scheme S3 Synthesis of DFO-phosphine **3**

Piperazine-phosphine 23

TSTU (110 mg, 0.37 mmol) was dissolved in dry DMF (1.15 mL) and DIPEA (96 µl, 0.55 mmol) and phosphine **18** (99 mg, 0.27 mmol) were added. The mixture was stirred under argon at RT for 10 minutes, and then a solution of piperazine (86 mg, 1 mmol) in 1.5 mL dry DMF was added. The mixture was stirred for 2 h, subsequently diluted with diethyl ether (20 mL) and washed with saturated $NaHCO_3$ (3 times 20 mL) and 0.1 M HCl (20 mL). To the aqueous layer was added ammonium hydroxide in water resulting in a basic layer, which was extracted with diethyl ether (25 mL). The combined organic layers were dried with Na_2SO_4 and concentrated in vacuo to yield the crude product. The crude product was purified with column chromatography with $CHCl_3$/MeOH/NEt_3 50/1/0.01 resulting in a slightly yellow solid. Yield: 73 mg (63 %). ^{1}H-NMR (500.23 MHz, $CDCl_3$): δ = 8.10 (dd, 1H, ***J*** = 8.0 Hz, ***J*** = 3.5 Hz, Ph-H); 7.54 (dd, 1H, ***J*** = 2.0 Hz, ***J*** = 8.0 Hz, Ph-H), 7.37–7.31 (m, 6H, Ph-H), 7.28–7.24 (m, 4H, Ph-H), 6.89–6.88 (m, 1H, Ph-H), 3.75 (s, 3H, CH_3), 3.65 (s, 2H, CH_2), 3.11 (s, 2H, CH_2), 2.85 (s, 2H, CH_2), 2.52 (s, 2H, CH_2) ppm; ^{13}C-NMR (125.8 MHz, $CDCl_3$) δ = 169.0, 166.6, 140.9 (d, ***J*** (PC) = 29.6 Hz), 138.4, 137.1 (d, ***J*** (PC) = 11.1 Hz), 135.4 (d, ***J*** (PC) = 19.2 Hz), 133.8 (d, ***J*** (PC) = 21.0 Hz), 132.4, 131.2 (d, ***J*** (PC) = 2.4 Hz), 129.0, 128.7 (d, ***J*** (PC) = 7.2 Hz), 127.6, 52.3, 48.1, 45.8, 45.4, 42.6 ppm; ^{31}P-NMR (101.25 MHz, $CDCl_3$): δ = -4.1 ppm; HRMS (ESI): m/z = 433.1687 [M^+], calc. for $C_{25}H_{26}N_2O_3P$ = 433. 1676.

Fe-DFO-piperazine-phosphine 24

To a solution of TFP-***N***-suc-DFO-Fe ester (**16**) (107 mg, 127 µmol) in 4.3 mL MeCN was added 3 eq. NEt_3 (53.3 µL, 0.38 mmol) and 1 eq. piperazine-phosphine **23** (54.7 mg, 127 µmol) in 1 mL MeCN. The resulting solution was stirred overnight at RT, subsequently concentrated in vacuo and diluted to 10% MeCN in water by the addition of 48 mL water and trapped on 2 sep-pak cartridges (C18). The sep-pak cartridges were washed with 60 mL water and eluted with 5 mL MeCN. Yield: quantitative

DFO-phosphine 3

To a solution of Fe-DFO-piperazine-phosphine **24** in MeCN (127 µmol, 12.4 mL) were added 73.8 mL EDTA (25 mg/mL), 18.45 mL H_2SO_4 buffer (pH=4.5) and 12.4 mL MeCN. The solution was heated at 35 °C for 50 minutes. The solution was extracted with DCM (3 times 120 mL) and dried with Na_2SO_4 and concentrated in vacuo and finally lyophilized. Yield: 103 mg (76%). Purity: >95 % according to HPLC. ^{1}H-NMR (500.23 MHz, $CDCl_3$): δ = 9.65 (s, 1H), 9.61 (s, 2H), 8.03 (dd, 1H, ***J*** = 7.7 Hz, ***J*** = 4.0 Hz), 7.86–7.77 (m, 3H), 7.63–7.56 (m, 2H), 7.43–7.37 (m, 5H), 7.25–7.20 (m, 4H), 6.91–6.82 (m, 1H), 3.65 (s, 3H), 3.46–2.99 (m, 22H), 2.57–2.50 (m, 4H), 2.28–2.25 (m, 6H), 1.96 (s, 3H), 1.50–1.48 (m, 6H), 1.39–1.36 (m, 6H), 1.22–1.19 (m, 6H) ppm; ^{13}C-NMR (125.78 MHz, DMSO): δ = 172.0, 171.3, 171.1, 170.2, 170.1, 167.9, 166.2, 139.9 (d, J (PC) = 29.2 Hz), 138.6, 136.9 (d, J (PC) = 11.6 Hz), 135.0 (d, J (PC) = 19.2 Hz), 133.5 (d, J (PC) = 20.9 Hz), 131.8, 130.6, 129.1, 128.8 (d, J (PC) = 7.2 Hz), 127.7, 52.1, 47.1, 47.1, 46.8, 38.4, 30.5, 30.3, 29.9, 28.8, 27.8, 27.6, 26.0, 23.5, 20.4 ppm; ^{31}P NMR (101 MHz, $CDCl_3$): δ = -5.4 ppm; HRMS (ESI): m/z = 1075.5218 [M^+], calc. for $C_{54}H_{76}N_8O_{13}P$ = 1075.5264.

Synthesis of DOTA-phosphine **4**

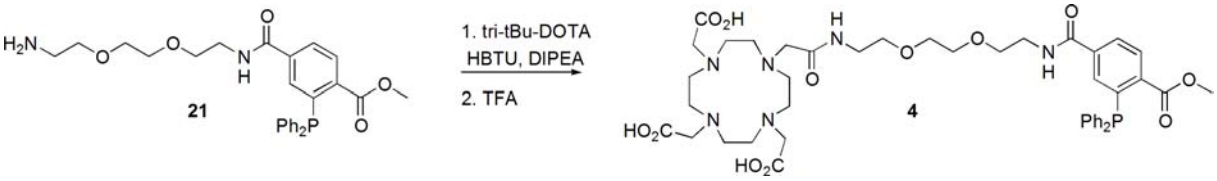

Scheme S4 Synthesis of DOTA-phosphine **4**

DOTA-phosphine 4

HBTU (1.32 g, 3.49 mmol) was dissolved in dry DMF (15 mL) and DIPEA (0.90 g; 6.98 mmol) and the DOTA tris(t-Bu) ester building block (2.00 g, 3.49 mmol) were added. The mixture was stirred under argon at RT for 10 min, and a solution of amine **21** (1.90 g, 3.84 mmol) in DMF (5 mL) was added. The mixture was stirred for 2 h, concentrated, redissolved in CH_2Cl_2 (100 mL), and subsequently washed with a saturated $NaHCO_3$ solution (3 times 50 mL), water, and 1 M NaOH (50 mL). The organic layer was dried with Na_2SO_4 and concentrated in vacuo. The crude product was purified by column chromatography on silica, by eluting with $CHCl_3$ and then with 5% (v/v) MeOH in $CHCl_3$. The purified tris-***tert***-butyl ester protected product was dissolved in CH_2Cl_2 (7 mL) and TFA (5 mL), and stirred at RT for 1 h. The mixture was concentrated, and again dissolved in CH_2Cl_2 (7 mL) and TFA (5 mL), and stirred for an additional 2 h. The mixture was concentrated and coevaporated (2x) with $CHCl_3$ (10 mL) and then concentrated in vacuo. The product was dissolved in water (30 mL) and lyophilized to yield **4** as a fluffy, yellow powder (1.16 g, 96%). ^{1}H-NMR (MeOD): δ = 8.04 (dd, 1H, ***J*** = 3.7 Hz, ***J*** = 8.1 Hz, Ph-H), 7.79 (dd, 1H, ***J***=1.7 Hz, ***J*** = 8.1 Hz, Ph-H), 7.45 (dd, 1H, ***J*** = 3.7 Hz, ***J*** = 1.7 Hz, Ph-H), 7.4–7.2 (m, 10H, Ph-H), 4.05–3.70 (br.m, 8H, CH_2), 3.68 (s, 3H, CH_3), 3.60–3.10 (br m, 28H, CH_2) ppm; ^{13}C-NMR (100 MHz, DMSO): 171.6, 168.6, 166.3, 165.6, 165.3, 158.2 (q, ***J*** (FC) = 43.7 Hz, TFA), 139.7 (d, ***J*** (PC) = 37.2 Hz), 137.1, 137.0 (d, ***J*** (PC) = 25.5 Hz), 136.3 (d, ***J*** (PC) = 27.0 Hz), 133.4 (d, ***J*** (PC) = 27.7 Hz), 131.3 (d, ***J*** (PC) = 13.1 Hz), 130.0, 128.8 (d, ***J*** (PC) = 23.3 Hz), 128.6, 126.7, 116.6 (q, ***J*** (FC) = 392.1 Hz, TFA), 69.5, 68.6, 54.7, 539, 52.6, 52.1, 50.5, 48.4, 48.0, 40.5–38.5 (m, DMSO-***d6*** + 2x CH_2NHCO). ^{31}P-NMR (MeOD): δ = 33.82 (oxidized phosphine, ca. 5%), -3.91 (phosphine 4, ca. 95%), -15.19 (t, HPO_2F_2, ***J*** = 953 Hz) ppm; ATR-FT-IR: ν = 3287, 3074, 2872, 2546, 1718, 1651, 1547, 1435, 1292, 1189, 1130, 745, 720, 698 $cm^{-1;}$ MALDI-TOF: m/z $[M + H]^+$ 881.4 Da.

Radiolabeling of DFO-phosphines **2** and **3** with ^{89}Zr and $^{67/68}$Ga

Radiosynthesis of ^{89}Zr-DFO-phosphine **2** and **3**:

The radiolabeling of DFO with ^{89}Zr was done according to Verel ***et al***.[1] with minor adjustments. In short: Radiolabeling of DFO-phosphine **2** for ***in vitro*** experiments: To ^{89}Zr in 1 M oxalic acid (500 µL, max. 500 MBq) a Na_2SO_3 solution was added (100 µL of 50 mg/mL in H_2O) and incubated for at least 2 h. Next, to 10-50 MBq of the Na_2SO_3 containing ^{89}Zr solution, adjusted to 200 µL 1 M oxalic acid, were added 0.9% NaCl (262-300 µL) and 2 M Na_2CO_3 (90 µL) and reacted for 10 min. Hereafter 0.5 M HEPES (1.2 mL of pH 7.2-7.4), DFO-phosphine (500 µg), EtOH (318 µL) and 0.9% NaCl (90 µL) were added (total volume 2.2 mL) and the reaction mixture was shaken for 30 min at RT. The radiolabeling yield was always >93% and the percentage of oxidation caused by radiolabeling was <10% (n>10). The reaction mixture was used as such for ***in vitro*** Staudinger ligation experiments.

Radiolabeling for ***in vivo*** experiments: the same conditions as for the ***in vitro*** experiments were applied using 26.7 MBq ^{89}Zr and 100 µg DFO-phosphine **2** or **3**. ^{89}Zr-DFO-phosphine **2** was prepared with 7% oxidation and ^{89}Zr-DFO-phosphine **3** with 8% oxidation caused by radiolabeling. The reaction mixture was diluted with a Na_2SO_3-solution (0.5 mL of 1 mg/mL in 0.9% NaCl) and the product was trapped on a light C18 sep-pak to remove chemical reagents like oxalic acid. The light C18 sep-pak was washed with the Na_2SO_3 solution (2 mL) and eluted with fractions of 100 µL of a 80/20 EtOH/Na_2SO_3 solution. The products eluted in fractions 2 and 3 with 81% overall yield. 100 µL (12 MBq, 48.9 µg DFO-phosphine **2** or 11.7 MBq, 49.0 µg DFO-phosphine **3**) of this solution was diluted with EtOH and 25 mg/mL hydroxypropyl-β-cyclodextrin in 0.04% tween-20, to solubilize the product without causing unacceptable oxidation of the phosphine. 50 µL of this solution was injected per mouse and contained 0.4 MBq/1.52 µg (1.3 nmol) ^{89}Zr-DFO-phosphine **2** (total: 15% oxidation of the

phosphine) or 0.4 MBq/1.52 μg (1 4 nmol) ^{89}Zr-DFO-phosphine **3** (total: 20 % oxidation of the phosphine) and 10% EtOH

Radiosynthesis of $^{67/68}$Ga-DFO-phosphine **2** and **3**:

Radiolabeling of DFO-phosphine **2** for ***in vitro*** experiments: ^{67}Ga-citrate was converted to $^{67}GaCl_4^-$ via a chromafix procedure[8]. ^{67}Ga in H_2O (35 μL, 10-70 MBq) was incubated with 3 M ammonium acetate buffer of pH 7 (100 μL) for 5 min. Hereafter, 0.25 M ammonium acetate buffer of pH 5.5 (100 μL), DFO-phosphine **2** (100 μg), EtOH (30 μL) and 0.9% NaCl (20 μL)) were added and reacted for 3 min. Radiolabeling yield was always >95% and the percentage of oxidation caused by radiolabeling was always <10% (n>10). The reaction mixture was used as such for ***in vitro*** Staudinger ligation experiments.

Radiolabeling for ***in vivo*** experiments on the kinetics of radiolabeled phosphine probes: ^{68}Ga was eluted from a ^{68}Ge/^{68}Ga generator according to the manufacturer protocol with ultra pure 0.1 M HCl solution (3.5 mL) and purified according to the method of Vosjan[8]. ^{68}Ga (70 μL, 116-120 MBq) was incubated with 3M ammonium acetate of pH 7 (100 μL) for 5 min. Then an anti-oxidant solution (25 μL of 100 mg/mL gentisic acid pH 3.4 + $SnSO_4$ (6 mg/mL)) was added and the mixture was left for 10-15 min. Subsequently, 0.25 M ammonium acetate of pH 8.5 (75 μL), DFO-phosphine **2** or **3** (100 μg), EtOH (60 μL) and 0.9% NaCl (40 μL) were added and reacted for 5 min (final pH 5.4). After dilution with 0.9% NaCl and EtOH, to a final concentration of 10% EtOH, 50 μL of this solution were injected per mouse and contained 1.1 MBq/1.52 μg (1.3 nmol) ^{68}Ga-DFO-phosphine **2** (7% oxidation of the phosphine, 98% labeling efficiency) or 1.1 MBq/1.52 μg (1.4 nmol) ^{68}Ga-DFO-phosphine **3** (13% oxidation of the phosphine, 98 % labeling efficiency).

Radiolabeling for ***in vivo*** Staudinger ligation experiments: ^{67}Ga in H_2O (140 µL, 56 MBq) was incubated with 0.5 M ammonium acetate buffer of pH 6.7 (800 µL) for 5 min. Hereafter DFO-phosphine **2** (520 µg), EtOH (120 µL) and 0.9% NaCl (80 µL)) were added and reacted for 3 min. 150 µL of this solution was injected per mouse and contained 7.4 MBq/68 µg (60 nmol) ^{67}Ga-DFO-phosphine **2** (9% oxidation of the phosphine, 100% labeling efficiency) and 10% EtOH.

Radiolabeling of DOTA-phosphine **4** with ^{177}Lu

To ^{177}Lu (10-50 MBq) in 0.05 M HCl (10 µL) were added 0.25 M ammonium acetate of pH 8.5 (140 µL) and DOTA-phosphine **4** (100 µg). The reaction mixture was incubated for 10 min at 45 °C. Radiolabeling yield was always >90% and the percentage of oxidation caused by radiolabeling was always <15% (n>10). For ***in vitro*** experiments the reaction mixture was used as such. Radiolabeling for ***in vivo*** experiment: to ^{177}Lu (16.9 MBq) in 0.05 M HCl (15 µL) were added 0.2 M ammonium acetate of pH 8.5 (660 µL) and DOTA-phosphine **3** (62 µg). The reaction was incubated for 10 min at 45°C. After dilution with 0.9% NaCl and EtOH, to a final concentration of 10% EtOH, 50 µL of this solution was injected per mouse and contained 0.4 MBq/1.50 µg (1.7 nmol) ^{177}Lu-DOTA-phosphine **4** (18% oxidation of the phosphine, 98% labeling efficiency).

(Radio)synthesis of I-cubyl-phosphine **5**

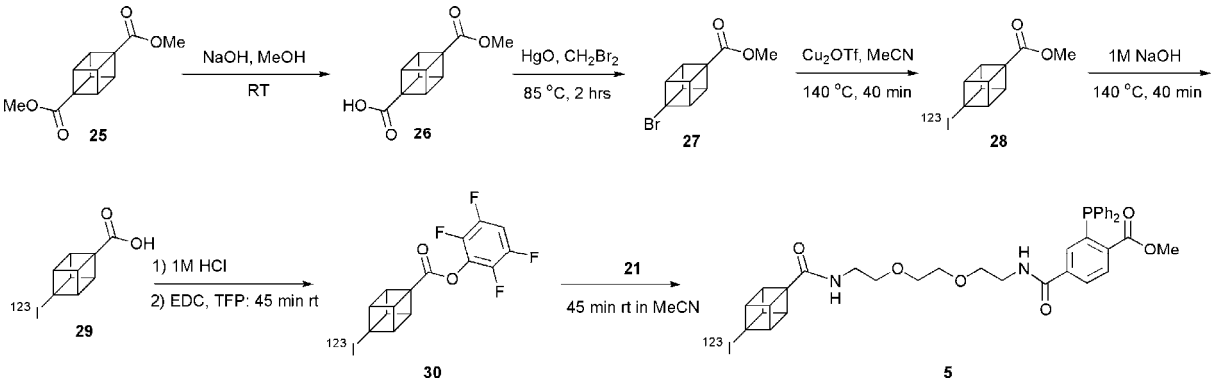

Scheme S5 Synthesis of ^{123}I-cubyl-phosphine **5**

4-(methoxycarbonyl)-1-cubanecarboxylic acid (26)[9]

To a solution of 1,4-bis(methoxycarbonyl)cubane **25** (2.25 g, 10.2 mmol) in THF (70 mL) was added dropwise a solution of 2.5 M sodium hydroxide in MeOH (4 mL, 10 mmol). After stirring overnight at RT the solvents were removed in vacuo without heating, after which H_2O (25 mL) was added. The aqueous layer was washed with $CHCl_3$ (3x25 mL) to remove unreacted starting materials, after which it was acidified with concentrated HCl to pH 3. The aqueous layer was extracted with $CHCl_3$ (3x25 mL). The combined organic layer was dried with $MgSO_4$ and concentrated in vacuo to give a white solid. Yield: 2 g (95%). Aanalytical data were according to literature[9].

Methyl-4-bromo-1-cubane carboxylate (27)[10]

To a suspension of **26** (1.64 g, 7.9 mmol) and HgO (2.5 g, 11.5 mmol) in CH_2Br_2 (47 mL) was added dropwise Br_2 (0.77 mL, 14.9 mmol) in CH_2Br_2 (5 mL). Subsequently the suspension was stirred for 2 h at 85°C, cooled down to RTand filtered to remove $HgBr_2$. The resulting solution was concentrated in vacuo and the solid was dissolved in hexane (40 mL) and washed with H_2O (3x20 mL). The organic layer was concentrated in vacuo and purified

by column chromatography with hexane:ethyl acetate 4:1 and crystallized from hexane resulting in a white solid. Yield: 1.16 g (61%). Analytical data were according to literature[10].

I-cubyl-phosphine (5) (cold reference compound)

HBTU (69 mg, 0.18 mmol) was dissolved in dry DMF (1 mL) and DIPEA (63 µL; 0.36 mol) and phosphine **21** (100 mg; 0.2 mmol) were added. The mixture was stirred under argon at RTfor 10 min, after which a solution of 4-iodocubane carboxylic acid[3] (50 mg; 0.18 mmol) in DMF (1 mL) was added. The resulting solution was stirred overnight at RT, followed by the addition of diethyl ether (20 mL). The organic layer was washed with saturated $NaHCO_3$ solution (3 x 15 mL) and 0.1 M HCl (15 mL) and dried over Na_2SO_4 and concentrated in vacuo. The crude product was purified by silica column chromatography using a gradient from 100% $CHCl_3$ to $CHCl_3$/MeOH/NEt_3 (10/1.5/0.1). Yield: 95 mg (70%). ^{1}H-NMR (250.13 MHz, $CDCl_3$): δ = 8.16 (dd, 1H, ***J*** = 8.0 Hz, ***J*** = 3.7 Hz, Ph-H), 7.89 (dd, 1H, ***J*** = 8.0 Hz, ***J*** = 1.6 Hz, Ph-H), 7.61–7.37 (m, 11H, Ph-H), 6.62 (s, 1H, NH), 6.21 (s, 1H**,** NH), 4.40–4.26 (m, 8H, CH_2CH_2NH), 3.72 (s, 3H, OCH_3), 3.72–3.44 (m, 10H, cubyl-H, CH_2O) ppm; ^{13}C-NMR (125.8 MHz, $CDCl_3$): δ = 171.1, 166.5, 166.3, 137.3, 136.5 (d, ***J*** (PC) = 17.9 Hz), 133.9, 133.8, 132.9, 131.8 (d, ***J*** (PC) = 10.4 Hz), 130.9 (d, ***J*** (PC) = 2.5 Hz), 129.3, 128.7 (d, ***J*** (PC) = 7.8 Hz), 128.5 (d, ***J*** (PC) = 13.0 Hz), 127.2, 70.2, 70.1, 69.8, 69.5, 57.9, 54.6, 52.4, 50.1, 39.8, 38.9, 36.2 ppm; ^{31}P-NMR (101.25 MHz, $CDCl_3$): δ = -4.1 ppm; HRMS (ESI): m/z = 751.1396 [M^+], calc. for $C_{36}H_{37}IN_2O_6P$ = 751.1428.

^{123}I-cubyl-phosphine (5)

To [^{123}I]-iodide in 0.01 N NaOH (~ 100 µL) was added 0.1 M H_2SO_4 (1 mL). The radioiodide was trapped on a platinum column under nitrogen atmosphere[11], washed with H_2O (5 mL), MeCN (5 mL) under nitrogen atmosphere and finally dried with nitrogen. ^{123}I was eluted with

MeCN and hydrogen gas resulting in > 90% recovery of the activity in less than 0.3 mL MeCN. Methyl-4-bromo-1-cubane carboxylate **27** (1.6 mg, 6.6 μmol) was reacted under anhydrous conditions with Cu_2OTf (10 μL of 1 mg/mL in MeCN), 1,4-dimethylpiperazine (10 μL of 10 mg/mL in MeCN) and ^{123}I in 100 μL total volume of MeCN at 140 °C in a closed vessel for 30 min. The reaction was allowed to cool down to RT, diluted with 45/55/0.2 MeCN/H_2O/diisopropylamine (DIPA) (0.5 mL), and purified by HPLC (flow 1 mL/min, eluent: 45/55/0.2 MeCN/H_2O/DIPA) resulting in methyl-4-^{123}Iodo-1-cubane carboxylate **28** in HPLC eluent in 65% yield. The collected product was hydrolyzed quantitatively by the addition of 1M NaOH (20 μL) and heating at 140 °C for 40 min in a closed vessel resulting in 4-^{123}Iodo-1-cubane carboxylic acid **29**. Hereafter, EDC (84.2 mg; 0.44 mmol) and TFP (300 μL of 200 mg/mL in MeCN) were added to the solution and reacted for 45 min at RT. The reaction mixture was diluted to 10 % EtOH with H_2O and trapped on a light C18 Sep-pak cartridge. The Sep-pak cartridge was washed with H_2O (15 mL) in order to remove excess TFP and EDC and eluted with MeCN resulting in TFP-ester **30** in 94% isolated yield. The purified TFP-ester **23** was reacted with phosphine **21** (1.2 mg; 2.4 μmol) in the presence of 3 equivalents diisopropylethylamine (DIPEA) for 30 min at RT resulting in ^{123}I-cubyl-phosphine **5**. ^{123}I-cubyl-phosphine **5** was diluted with 55/45/0.2 EtOH/H_2O/DIPA (0.5 mL) and purified with preparative HPLC (flow 1 mL/min, eluent: 55/45/0.2 EtOH/H_2O/DIPA) and collected in a stock solution of cold I-cubyl-phosphine **5** in EtOH (0.438 mg in 4.06 mL EtOH). Prior to injection the stock solution was diluted with 0.9% NaCl to arrive at a final concentration of 10% EtOH. 100 μL of this solution was injected and contained 0.77 MBq ^{123}I-cubyl-phosphine **5** (1 μg; 1.34 nmol) (5% oxidation of the phosphine).

References

(1) Verel, I., Visser, G. W. M., Boellaard, R., Stigter-van Walsum, M., Snow, G. B., and van Dongen, G. A. M. S. (2003) ^{89}Zr immuno-PET: Comprehensive procedures for the production of ^{89}Zr-labeled monoclonal antibodies, ***J. Nucl. Med. 44***, 1271–1281.

(2) Fyles, T.M. and Hu, C. (2001) The synthesis and membrane activity of linear oligoester, ester-amide, and oligoamide bolaamphiphiles, ***J. Supramol. Chem. 1,*** 207–215.

(3) Priefer, R., Farrell, P. G., and Harpp, D. N. (2002) Effective synthetic routes to cubylcarbinol derivatives, ***Synthesis***, 2671–2673.

(4) Banaszynski, L.A., Liu, C.W., and Wandless, T.J., (2005) Characterization of the FKBP-Rapamycin-FRB Ternary Complex***, J. Am. Chem Soc.***. ***127***, 4715–4721.

(5) Müller, M.K, and Brunsveld, L. (2009) A supramolecular polymer as a self-assembing polyvalent scaffold, ***Angew. Chem., Int. Ed***. ***28***, 2921–2924.

(6) Zych, A.J., and Iverson, B.L, (2000) Synthesis and conformational characterization of tethered, self-complexing 1,5-dialkoxynaphtalene/1,4,5,8-naphthalenetetracarboxylic diimide systems, ***J. Am. Chem. Soc. 122***, 8898–8909.

(7) Saxon, E., and Bertozzi, C.R. (2003) Chemoselective ligation, Patent US 2003/0199084

(8) Vosjan, M.J.W.D., Perk, L.R., Roovers, R.C., Visser, G.W.M., Stigter-van Walsum, M., van Bergen en Henegouwen, P.M., Van Dongen, G.A.M.S. (2011) Facile labelling of an anti-epidermal growth factor receptor Nanobody with ^{68}Ga via a novel bifunctional desferal chelate for immuno-PET, ***Eur. J. Nucl. Med. Mol. Imaging 38***, 753–763.

(9) Eaton, P. E., Xiong, Y., and Zhou, J. P. (1992) Systematic substition on the cubane nucleus:steric and electronic effects, ***J. Org. Chem. 57***, 4277–4281.

(10) Irngartinger, H., Strack, S., and Gredel, F. (1996) The cubane cage - A sensible probe for substituent effects on a four-membered ring, ***Liebigs Ann.***, 311–315.

(11) Braker, A. H., Moet, F. P., van der Zwart, R. E., Eersels, J. L. H., and Herscheid, J. D. M. (2002) Adsorption of radioiodine on platinum: a fast and simple column method to obtain concentrated and pure radioiodide in either water or anhydrous solvents, ***Appl. Radiat. Isot. 57***, 475–482.

Bioconjugate Chemistry

ARTICLE

pubs.acs.org/bc

Synthesis, Structure, and Biological Activity of Dumbbell-Shaped Nanocircular RNAs for RNA Interference

Naoko Abe,[†] Hiroshi Abe,[*,†] Chisato Nagai,[§] Mitsuru Harada,[†,‡] Hiroto Hatakeyama,[§] Hideyoshi Harashima,[§] Takahito Ohshiro,[∥] Mizuki Nishihara,[†] Kazuhiro Furukawa,[†,‡] Mizuo Maeda,[∥] Satoshi Tsuneda,[‡] and Yoshihiro Ito[*,†]

[†]Nano Medical Engineering Laboratory and [∥]Bioengineering Laboratory, RIKEN Advanced Science Institute, 2-1 Hirosawa, Wako-shi Saitama 351-0198, Japan

[‡]Department of Life Science and Medical Bio-Science, Waseda University, 2-2 Wakamatsu-cho, Shinjuku-ku, Tokyo 162-8480, Japan

[§]Faculty of Pharmaceutical Sciences, Hokkaido University, Kita12 Nishi6, Kita-ku, Sapporo Hokkaido 060-0812, Japan

Supporting Information

ABSTRACT: RNA interference (RNAi) is one of the most promising new approaches for disease therapy. The design of a dumbbell-shaped nanocircular RNA allows it to act as a short interfering RNA (siRNA) precursor. To optimize the design, we studied the relationship between the nanostructure and RNAi activity by synthesizing various RNA dumbbells. An RNA dumbbell with a 23-bp stem and 9-nt loops was the most potent. Sequence analysis by mass spectrometry showed that Dicer could edit RNA dumbbells to siRNA species. The reaction offered the slow release of siRNA species, which conferred prolonged RNAi activity. Introduction of DNA into the loop position significantly stabilized the dumbbell in biological fluid without any loss of RNAi activity. In-depth pharmacological evaluation was performed by introducing dumbbells into HeLa cells that stably express the target luciferase gene. The dumbbells provided a rapid silencing effect and retained this effect for a longer time even at a lower concentration than that at which standard siRNA completely lost RNAi activity. We conclude that an RNA dumbbell with DNA loops is the most promising design for in vivo applications for RNA medicine.

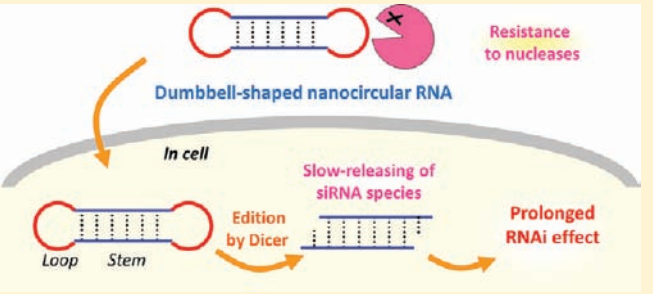

INTRODUCTION

RNA interference (RNAi) is a potent and highly specific gene-silencing phenomenon that was first reported for the nematode *Caenorhabditis elegans* by Fire and Mello in 1998.[1] They discovered that genes could be silenced by introducing double-stranded RNAs (dsRNAs) complementary to the mRNA sequences.[1] Since then, RNAi has been shown to be an evolutionarily well-conserved process that plays an important role in host defense and regulation of gene expression.[2] The RNAi pathway is initiated by the enzyme Dicer, an endoribonuclease in the RNase III family, which cleaves long dsRNA into short dsRNA fragments called short interfering RNA (siRNA). siRNA is a dsRNA molecule of about 20−23 nucleotides (nt) in length with 2-nt 3′ overhangs on either end. In the pathway, after being incorporated into a protein complex known as the RNA-induced silencing complex (RISC), the siRNA strand subsequently guides the RISC to the complementary mRNA molecule, where they cleave and destroy the cognate RNA.[3]

Much effort has been dedicated to the application of siRNAs as therapeutic agents, since they were shown to be effective in mammalian cells.[4−7] A wide variety of chemical modifications has been proposed to improve the stability of siRNAs in serum. For example, modification of the phosphate backbone with phosphorothioates or boranophosphates and modification of the ribose moiety with 2′-*O*-methyl, 2′-fluoro, or 4′-thio groups has been examined.[8−13] These chemical modifications can increase the stability of siRNAs, although they often decrease RNAi activity. There is also concern that unnatural RNA derivatives might be toxic in the body. A method to stabilize nontoxic natural RNA strands should be useful for applying RNAi technology in the development of therapeutic agents.

RNA molecules that can induce RNAi, but with different strand lengths or shapes than those of normally used canonical siRNA, have been reported recently.[14−21] Increasing the length of an siRNA duplex makes it a substrate for Dicer and has been found to increase its potency.[14] Changing the shape may also influence the RNAi activity; for example, the efficacy of an asymmetric dsRNA duplex, which was named asymmetric interfering RNA (aiRNA) and which comprises a 19-nt guide strand and 15-nt passenger strand, was reported.[16] In this report, aiRNA

Received: June 16, 2011
Revised: August 25, 2011
Published: September 07, 2011

ACS Publications © 2011 American Chemical Society

dx.doi.org/10.1021/bc2003154 | *Bioconjugate Chem.* 2011, 22, 2082–2092

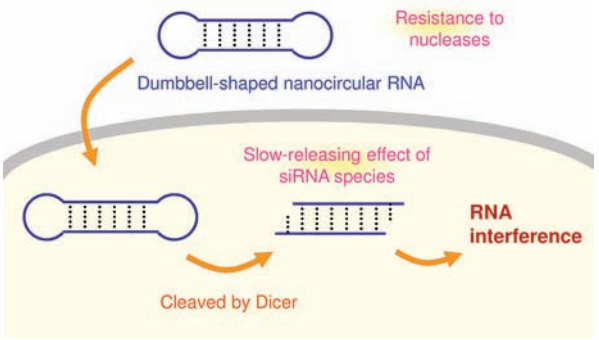

Figure 1. Proposed mechanism of the RNAi effect induced by a dumbbell-shaped nanocircular RNA.

was as efficient as conventional siRNA in silencing the target genes and was less prone to causing unwanted off-target effects.[16] Recently, we altered the structure of the siRNA molecule and produced dumbbell-shaped nanocircular RNAs that withstand enzymatic degradation and have a prolonged RNAi effect despite their natural RNA strand (Figure 1).[20] On the basis of the understanding that nucleases typically start by chewing at the loose ends of RNA,[22] we created circularized siRNA by designing a molecule that assembles into a stable dumbbell shape with a base-paired central stem connected by two loops at both ends. Closing off the ends limits the enzymatic activity of the exonuclease and confers greater stability of the RNA.[20]

Encouraged by these initial findings, we have been pursuing strategies to further increase the effectiveness of RNA dumbbells for RNAi. An important issue remaining is that of optimizing the loop structure of the RNA dumbbells. The mechanism shown in Figure 1 indicates that the loop can be cleaved by Dicer and is not necessary for the RNAi effect. However, in a previous study, we found that the single-stranded RNA loop is a weaker point than the stem in terms of stability because the loops can be cleaved by nucleases.[23,24] In addition, the loop and its related structure are also important for controlling the editing position by Dicer. To develop a more effective dumbbell structure, our current work focuses on modifying the loop sequences and structures. Here, we report on our systematic studies on the effect of changing the loop sequences and structures on RNAi activity. We also analyzed the dicing reaction of Dicer on an RNA dumbbell by comparing the reaction with RNAs of the related structure and by identifying the sequences using mass spectrometry (MS). We also synthesized RNA dumbbells that have loops containing deoxynucleotides or hexaethylene glycol linker to increase the biological stability. We confirmed their improved stability in both serum and cell lysates, and we found that they are good candidates for further study for clinical purposes.

EXPERIMENTAL PROCEDURES

RNA Synthesis and Purification Methods. RNA oligonucleotides were synthesized on a Gene World H-8-SE DNA synthesizer (Gene World, Tokyo, Japan) using 2′-*O*-TBDMS or 2′-*O*-TOM protected β-cyanoethyl phosphoramidites (Glen Research, Sterling, VA). 5′-Phosphorylation was performed on the synthesizer using Chemical Phosphorylation Reagent (Glen Research). Spacer Phosphoramidite 18 (Glen Research) or Spacer 18 Amidite (Biosearch Technologies, Novato, CA) was used as the hexaethylene glycol linker. Deprotection was performed according to the procedure provided by the supplier. Deprotected oligonucleotides were purified by 15% denaturing polyacrylamide gel electrophoresis (PAGE) and isolated by the "crush-and-soak" method.[25] Desalted RNAs were precipitated with sodium acetate (pH 5.2) and 2-propanol. siRNA-1 targeted 849−869 nucleotides,[26] and uGL3 targeted 153−173 nucleotides in the coding region of GL3 luciferase relative to the first nucleotide of the start codon.[4] All siRNA sequences were characterized by matrix-assisted laser desorption ionization - time-of-flight (MALDI-TOF) MS (RIKEN Brain Scientific Institute (BSI) Research Resources Center, Japan).

Enzymatic Synthesis of RNA Dumbbells using T4 RNA Ligase. The final composition of the reaction mixture was as follows: 2 μM 5′-phosphorylated-dsRNA, 0.05−0.4 units/μL T4 RNA ligase (Takara Bio, Otsu, Japan), 25% PEG 6000, 0.006% bovine serum albumin (BSA), 50 mM Tris-HCl (pH 7.5), 10 mM $MgCl_2$, 10 mM DTT, and 1 mM ATP. After the 5′-phosphorylated RNAs were annealed, PEG 6000, BSA, and T4 RNA ligase were added to the concentrations described above, and the reaction mixture was incubated at room temperature overnight. After extraction with chloroform, the RNA was precipitated by the addition of sodium acetate (pH 5.2) and 2-propanol. The ligated products were purified by preparative (1 mm thick) denaturing PAGE (10% polyacrylamide, 25% formamide, 7 M urea in 1× TBE). The bands were visualized by UV shadowing, and crushed and extracted with 0.2 M NaCl and 10 mM ethylenediaminetetraacetic acid (EDTA, pH 8.0). The eluate was desalted using a Sep-Pak cartridge (Waters, Milford, MA). The RNA dumbbells were precipitated with sodium acetate (pH 5.2) and 2-propanol.

Measurements of RNAi Activity of RNA Dumbbells by Dual-Luciferase Assay. All RNAs used were annealed at 5 μM concentrations in annealing buffer (100 mM potassium acetate, 30 mM HEPES-KOH at pH 7.4, 2 mM magnesium acetate) by heating at 90 °C for 3 min and then cooled slowly to room temperature. The solutions were incubated further at 4 °C overnight.

NIH/3T3 cells (RIKEN Cell Bank, Japan) were grown at 37 °C under 5% CO_2 in Dulbecco's modified Eagle's medium (DMEM; Invitrogen, Carlsbad, CA) supplemented with 10% fetal calf serum (FCS; Israel Beit Haemek, Israel). Cells were passaged regularly to maintain exponential growth. One day before transfection, cells were plated in 96-well plates (1.6×10^4 cells/100 μL per well). Cotransfection of the reporter plasmids and RNAs was performed using GeneSilencer (Genlantis, San Diego, CA) as described by the manufacturer for adherent cell lines. Just before cotransfection, the culture medium was replaced with 56 μL of DMEM without FCS, and 0.2 μg of pGL3-Control (Promega, Madison, WI), 0.2 μg of pRL-TK (Promega), and 2.5 pmol of RNA formulated into liposomes (44 μL) were added to each well. Four hours after the transfection, 100 μL of 20% FCS in DMEM was added to each well. Luciferase expression was monitored with the Dual-Luciferase Reporter Assay System (Promega) on a Wallac ARVO SX (PerkinElmer, Waltham, MA).

Atomic Force Microscopy (AFM) Imaging and Computer Modeling of the RNA Dumbbell Db-23. A drop of the RNA sample (200 pM in 10 mM Tris-HCl, pH 7.2, 12.5 mM $MgCl_2$, and 1 mM EDTA) was spotted on the mica, which was cleaved freshly and pretreated with 3 μL of 1 mM $NiCl_2$. After 30 s, the unbound RNA was removed by rinsing with Milli-Q water (Millipore, Billerica, MA). The sample was dried in a silica gel desiccator for one day, and AFM images were obtained under ambient conditions using a Nanoscope IIIa (Veeco Instruments Inc., Plainview, NY) in tapping mode with an SSS-NCH tip (NanoWorld AG, Neuchâtel, Switzerland). The three-dimensional

structure of Db-23 was energy-minimized using AMBER* in the *MacroModel* program.

Dicer Cleavage Reaction of RNAs with Various Structures. Annealed RNAs (2.5 μM) were incubated with 0.1 units/μL ColdShock-DICER (TmCspB and fragment of h-Dicer; cold shock protein from Thermotoga maritime (TmCspB) is added in this product to increase the dsRNA digestion efficiency; Takara Bio) in 20 mM Tris-HCl (pH 8.5), 150 mM NaCl, and 2.5 mM $MgCl_2$ at 37 °C. After 1, 6, and 18 h, aliquots (4.5 μL) were taken from the mixture, the reaction was stopped by mixing with 1.5 μL of 0.5 M EDTA (pH 8.0), and the samples were frozen. The samples were analyzed by 15% nondenaturing PAGE. siRNA Ladder Marker (Takara Bio) was used as the size marker for dsRNA. The total amount of RNA loaded was adjusted according to stem length to obtain uniform intensity for the bands. The gels were stained with SYBR Green I (Lonza, Rockland, ME), and visualized by scanning on a BioRad Molecular Imager FX (BioRad, Hercules, CA).

MALDI-TOF MS Analysis of the Products Produced by Dicer from the RNA Dumbbell Db-23. Db-23 (2.5 μM, 1250 pmol) was incubated with 0.1 units/μL ColdShock-DICER in 20 mM Tris-HCl (pH 8.5), 150 mM NaCl, and 2.5 mM $MgCl_2$ at 37 °C for 16 h. RNA was recovered from the reaction mixture by alcohol precipitation using sodium acetate (pH 5.2) and 2-propanol after phenol–chloroform extraction. Two-thirds of the precipitated RNA was purified by 15% nondenaturing PAGE. Each band was visualized by UV shadowing, excised, and extracted with 10 mM EDTA, pH 8.0 (0.5 mL × 2). The eluate was lyophilized, and the RNA was alcohol-precipitated using sodium acetate (pH 5.2) and 2-propanol. The MALDI-TOF MS spectra were measured on Microflex MALDI-TOF MS spectrometer (Bruker Daltonics, Billerica, MA) at RIKEN BSI Research Resources Center (positive mode, reflector mode, 3-hydroxypicolinic acid as the matrix).

Stability of Loop-Modified RNA Dumbbells in Bovine Serum. RNA (5 μM) was annealed in annealing buffer. Bovine serum (Invitrogen) was added to a final volume of 80% and the sample was incubated at 37 °C. After 0.5, 1, and 2 h, aliquots (5 μL) were taken from the mixture, mixed with 5 μL of 0.5 M EDTA (pH 8.0), and frozen. The samples were analyzed by 15% nondenaturing PAGE. siRNA Ladder Marker (Takara Bio) was used as the size marker for dsRNA. The gel was stained with SYBR Green I (Lonza) and visualized by scanning on a BioRad Molecular Imager FX.

Stability of Loop-Modified RNA Dumbbells in the Cell Lysate. HL60 cells (RIKEN Cell Bank) were grown at 37 °C in 5% CO_2 in RPMI 1640 medium (Invitrogen) supplemented with 10% FCS (Israel Beit Haemek) for three days to 100% confluency in a 75-mL flask. Cells were separated by centrifugation at 1000 × *g* for 2 min. Pelleted cells were resuspended in 1 mL of RPMI 1640 medium with 10% FCS and transferred to a 1.5 mL tube. After centrifugation at 1000 × *g* for 2 min, the supernatant was removed and the pellet was suspended in 400 μL of lysis buffer [10 mM sodium phosphate (pH 7.5), 10 mM $MgCl_2$, 150 mM NaCl, 1 mM DTT, 1% NP-40, and 0.2 mg/mL phenylmethylsulfonyl fluoride] and kept at −20 °C for 30 min.[27] After thawing, the cells were centrifuged at 14 000 × *g* for 15 min at 4 °C. The supernatant was separated, and its protein concentration was quantified by the Bradford method using BSA as a standard. The protein concentration was 16.8 mg/mL.

RNA (2.5 μM) was incubated with the cell lysate at a protein concentration of 10 mg/mL at 37 °C. After 0.5, 1, 2, and 4 h, aliquots (2 μL) were taken from the mixture, mixed with 5 μL of 0.5 M EDTA (pH 8.0), and frozen. They were analyzed by 15% nondenaturing PAGE. siRNA Ladder Marker (Takara Bio) was used as the size marker for dsRNA. The gel was stained with SYBR Green I (Lonza) and visualized by scanning on a BioRad Molecular Imager FX.

Time and Dose Dependency of RNA Dumbbells of the RNAi Effect. A multifunctional envelope-type nanodevice (MEND) was used as the model of a lipid nanoparticle; MEND was prepared as described previously.[28] Briefly, a lipid film comprising 1,2-dioleoyl-3-trimethylammonium propane (DOTAP)/dioleoylphosphatidyl ethanolamine (DOPE)/cholesterol (DOTAP, DOPE, and cholesterol were purchased from Avanti Polar Lipids, Inc., Alabaster, AL) was hydrated with 1 mL of 10 mM HEPES buffer (pH 7.4) and then incubated for 10 min at room temperature. The hydrated lipid film was sonicated using a probe-type sonicator to form small unilamellar vesicles (SUVs). RNA was complexed with stearyl octa-arginine (Kurabo Industries Ltd., Osaka, Japan) in 10 mM HEPES buffer (pH 7.4) at a nitrogen/phosphate ratio of 1.1. The RNA complex was then mixed with the SUV at a ratio of 1:2 (v/v) to coat the RNA complex with the lipid membrane. The average diameter and the ζ-potential of the prepared MEND were determined using a Zetasizer Nano ZS ZEN3600 (Malvern Instruments, Worcestershire, UK).

HeLa cells stably expressing luciferase (HeLa-Luc) were cultured in DMEM supplemented with 10% fetal bovine serum (FBS), penicillin (100 U/mL), streptomycin (100 μg/mL), and G418 (0.4 mg/mL) at 37 °C in an atmosphere of 5% CO_2 and 95% humidity. To examine the silencing effect of MEND, 4×10^4 HeLa-Luc cells were seeded in a 24-well dish one day before transfection. The MEND was suspended at the RNA concentration indicated in 0.25 mL of Opti-MEM (Invitrogen) without serum and added to the HeLa-Luc cells, and the mixture was incubated for 3 h at 37 °C. Next, 1 mL of DMEM supplemented with 10% FBS, penicillin (100 U/mL), streptomycin (100 μg/mL), and G418 (0.4 mg/mL) was added, and the mixture was incubated for 21 or 45 h. For further observation, the HeLa-Luc cells treated with MEND were collected and reseeded every two days as described above. The cells were washed and lysed with reporter lysis buffer (Promega). Luciferase activity in the cell lysate was measured using a luminometer (Luminescencer-PSN; ATTO, Tokyo, Japan) and luciferase assay reagent (Promega). The protein concentration was measured using a BCA Protein Assay Kit (Thermo Fisher Scientific, Waltham, MA). Luciferase activity was expressed as relative light units per mg of protein. The silencing effect was calculated as a percentage using the following equation:

$$\textit{Silencing effect}(\%) = [1 - (\mathrm{TEanti} - \mathrm{Luc}/\mathrm{TEnon})] \times 100$$

where TEanti-Luc and TEnon represent luciferase activity after transfection with MEND with and without antiluciferase RNA, respectively.

For statistical evaluation, comparisons between multiple treatments were made using one-way analysis of variance followed by the Bonferroni test. A *P*-value of <0.05 was considered significant.

RESULTS

Design and Synthesis of RNA Dumbbells to Optimize the Loop Sequences and the Stem Length. We reported recently on the synthesis of dumbbell-shaped nanocircular RNAs and their superior RNAi effect (Figure 1).[20] RNA dumbbells comprise a double-stranded stem region that contains an antisense sequence to the target mRNA and two loops at both ends of the stem. In the previous report, we used 9-nt sequences (UUCAAGAGA) as the loops, which are commonly used as the hairpin loop in the

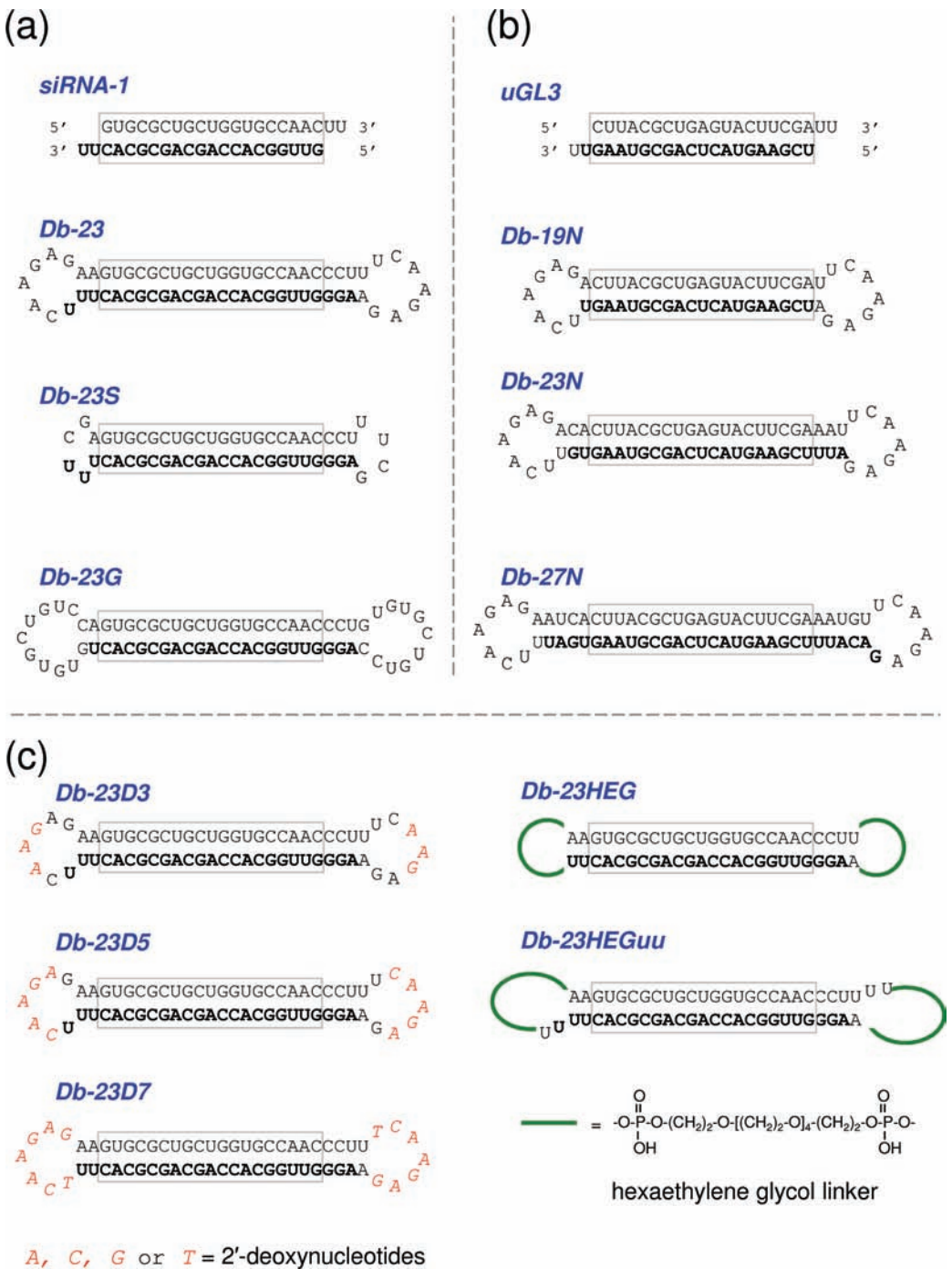

Figure 2. Sequences and structures of RNAs used in this study. Complementary sequences to the target mRNA are shown in bold. The stem regions of siRNA (19-bp) and the same sequences in the dumbbells are shown in the boxes. (a) RNA dumbbells with different loop sequences. siRNA sequences targeting GL3 luciferase corresponded to the coding regions 849−869. (b) RNA dumbbells with different stem lengths that target the coding regions 153−173 of GL3 luciferase. (c) RNA dumbbells with chemically modified loops by deoxyribonucleotides (red italic letters) or hexa(ethylene glycol) linker (green lines). They target the coding regions 849−869 of GL3 luciferase.

expression system of an RNA molecule.[29] We optimized the stem length of the dumbbells from 15 bp to 27 bp, and the RNA dumbbell with a 23 bp stem (Db-23) was found to have the best RNAi activity.[20] In this paper, we describe further studies on the structure−activity relationship of this RNA dumbbell.

First, to understand the influence of the loop sequences on their RNAi effect, two more RNA sequences in the loops were tested (Figure 2a). One of the RNA dumbbells, named Db-23S, has shorter 4-nt loops (UUCG).[30] The other, named Db-23G, has longer 11-nt loops (GUGUGCUGUCC)[26,31] compared with Db-23, which has 9-nt loops. These two other sequences were also adopted from the known sequences used in the expression system of shRNA. These RNA dumbbells were synthesized using the same method as that used to produce

dx.doi.org/10.1021/bc2003154 |*Bioconjugate Chem.* 2011, 22, 2082–2092

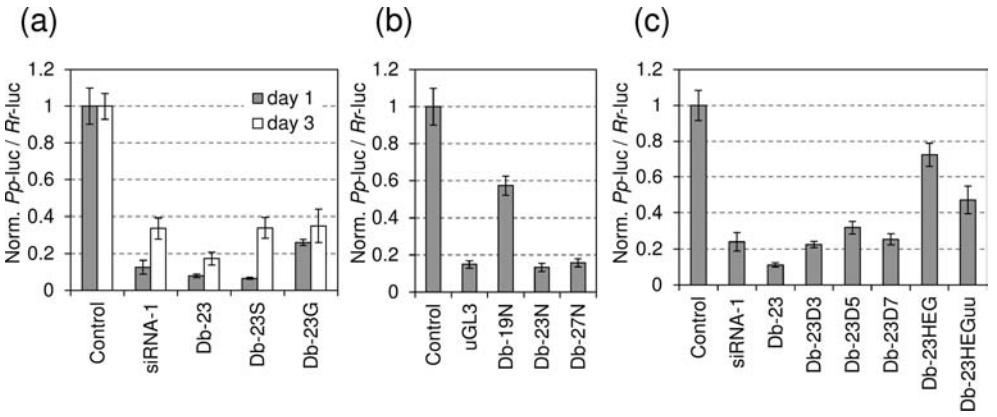

Figure 3. RNAi with RNA dumbbells. NIH/3T3 cells were cotransfected with RNA (at 25 nM) and the vectors. The expression of the two luciferase genes was measured after 24 h (day 1; gray bars) or three days (day 3, white bars). The ratios of the target to control luciferase were normalized to a control (no RNA). The plotted data are the means ± SD of four independent experiments. (a) RNAi by RNA dumbbells with different loop sequences (Figure 1a). (b) RNAi by RNA dumbbells with different stem lengths (Figure 1b). (c) RNAi by RNA dumbbells with loop-modified dumbbells (Figure 1c).

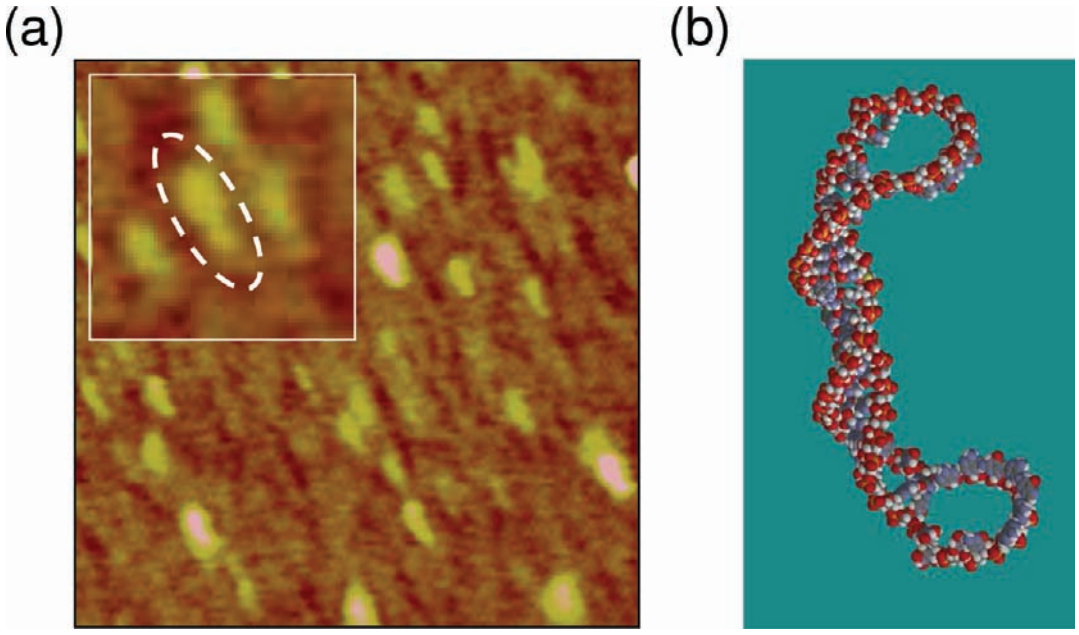

Figure 4. Three-dimensional structure of the RNA dumbbell Db-23. (a) AFM showing Db-23. The panel shows the area of 400 nm × 400 nm. The magnified image (60 nm × 60 nm) is shown in the inset. (b) Computer modeling by *MacroModel* software showing three-dimensional structure of Db-23.

Db-23. That is, the dumbbells were split in the loops and each strand was chemically synthesized (Supporting Information Figure S1). Nicks were ligated using T4 RNA ligase, and the RNA dumbbells produced were purified by denaturing PAGE.

We measured their RNAi activity by cotransfecting RNA and two distinct luciferase vectors using transfection reagent into NIH/3T3 cells, a mouse embryonic fibroblast cell line.[4]

As shown in Figure 3a, Db-23S and Db-23 showed similar interference activity 24 h after transfection, although Db-23G showed weaker activity. However, Db-23 showed better activity than Db-23S over the longer term, at three days after transfection. We selected the 9-nt loop sequences for further experiments.

Next, to determine whether the method can be generalized to other RNA dumbbells, we synthesized RNA dumbbells that target the other region of GL3 firefly luciferase mRNA. As shown in Figure 2b, these targeted sequences other than those shown in Figure 2a. The three differed in their stem lengths, and we confirmed the optimum length of the stem once again. As shown in Figure 3b, Db-23N showed better RNAi activity than Db-19N and comparable activity with Db-27N. We also synthesized two dumbbells with a 21-bp stem in these two distinct sequences (Supporting Information Figure S2a). We found better RNAi activity in dumbbells with a 23-bp stem than in those with a 21-bp stem (Figure S2b). We conclude that a 23-bp stem, not a 27-bp stem, is optimum when the 9-nt sequence UUCAAGAGA is used as the loops because the stem should be in a minimum length to avoid undesired effect such as interferon response.[32]

Three-Dimensional Structure of RNA Dumbbells. The structure of RNA dumbbells might be an important determinant

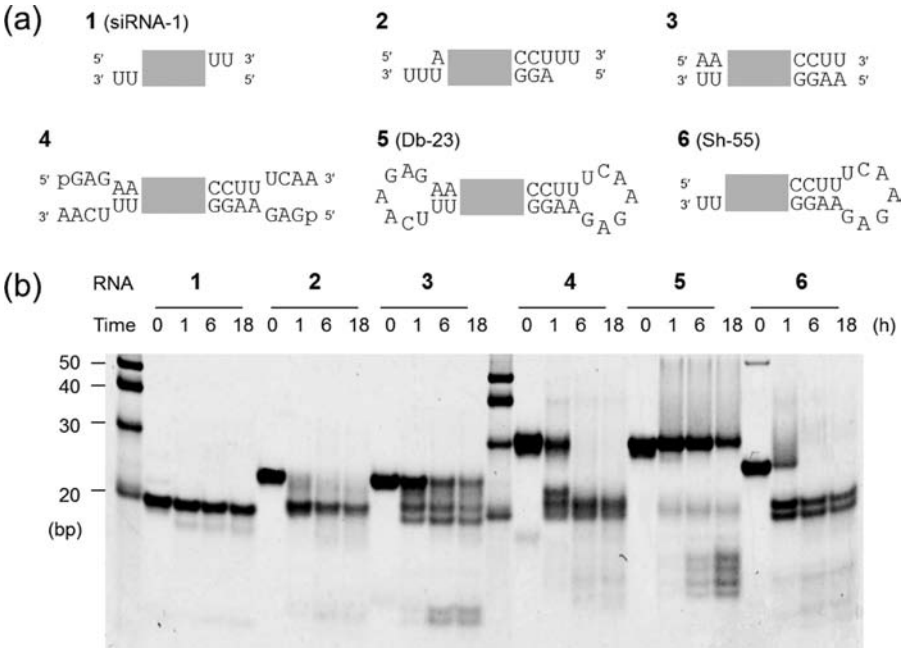

Figure 5. Processing of RNAs with the Dicer enzyme. (a) Structure of substrate RNAs used in this study. All substrate RNAs (**1** to **6**) contain an identical double-stranded 19-bp sequence, which is shown as a gray box in the structure. The sequences are 5′r(GUGCGCUGCUGGUGCCAACUU)3′ (upper) and 3′r(CACGCGACGACCACGGUUG)5′ (lower). The structural feature of RNAs are described as follows: (**1**) 21-nt dsRNA with 2-nt overhangs (siRNA-1), (**2**) 25-nt dsRNA with 2-nt overhangs, (**3**) 25-nt dsRNA with blunt ends (BL-23), (**4**) 32-nt dsRNA with frayed ends, a precursor of Db-23 (L-23) (ref [20]), (**5**) RNA dumbbell with a stem and two loops (Db-23), and (**6**) hairpin-shaped 55-nt ssRNA with 2-nt overhang (Sh-55). (b) Nondenaturing PAGE analysis of the digestion reaction of RNAs (**1** to **6**) with Dicer, visualized with SYBR Green I staining.

of the biological properties such as stability, intracellular distribution, and RNAi effect. We observed the structure of Db-23 directly using AFM; the results are shown in Figure 4a. The three-dimensional structural model of Db-23, which was optimized by *MacroModel* software, is shown for comparison in Figure 4b. In the AFM images,[33,34] the shape of Db-23 was observed as a rod. The observed height of Db-23 was 1.0 ± 0.55 nm, which is similar to the value in previous reports of RNA molecular images. Because the radius of the AFM tip was 2 nm, the estimated molecular length for Db-23 was 15.2 ± 3.6 nm, which is similar to the value of 11.2 nm that was calculated from the model structure. In addition, both ends of the RNA molecule in the AFM image protruded slightly, reflecting the looped structures of the molecules.

Dicer Processing of an RNA Dumbbell and Its Related RNAs. In our previous report, we showed that Db-23 is cleaved by Dicer and produces dsRNA of about 20-bp.[20] However, when compared with its nicked counterpart, the processing of Db-23 was slow. In this report, we examined in detail the cleavage reaction of Db-23 by Dicer with regard to the structure−activity relationship (Figure 5). In our previous study, we confirmed the production of 20-bp dsRNA only by PAGE.[20] In this paper, we directly analyzed the RNA sequences produced by Dicer by measuring their mass by MALDI-TOF MS (Figure 6).

As shown in Figure 5a, we compared the cleavage reaction of Db-23 (**5**) to that of several dsRNAs with various terminal structures, such as 21-nt dsRNA with 2-nt overhangs (**1**, siRNA-1), 25-nt dsRNA with 2-nt overhangs (**2**), 25-nt dsRNA with blunt ends (**3**), 32-nt dsRNA with frayed ends like an open dumbbell (**4**), or 55-nt hairpin-shaped ssRNA with a 2-nt overhang named Sh-55 (**6**). RNAs were treated with recombinant Dicer enzyme for up to 18 h, and the reaction mixtures were analyzed by PAGE at each time. All RNAs were digested to about 20 bp of dsRNAs, though RNA products shorter than 20 bp were more abundant when Db-23 was digested. However, the speed of digestion differed according to the structure. Dicer clearly preferred structures with an overhang over the blunt end because dsRNA (**2**) disappeared more rapidly than did dsRNA (**3**) (Figure 5b).[15,35] Although one side of the loop in Sh-55 (**6**) did not disturb the reaction, formation of dumbbell structure (**5**) by two loops greatly interfered with the activity (Figure 5b). After 18 h, 35% of Db-23 remained, although other RNAs disappeared completely. These experiments show that the design of a dumbbell structure characterized by the lack of an end should delay its cleavage by Dicer.

Next, we used MALDI-TOF MS to analyze the sequences of the digest produced from Db-23 by Dicer.[36] As a reference experiment, we analyzed the dicing reaction of Sh-55, which lacks one of the two loops of Db-23. As expected given the known action of Dicer,[37,38] four major peaks were found in the spectrum (Supporting Information Figure S3); these peaks were identified as two 21-nt and two 22-nt RNAs produced when Sh-55 was cleaved by Dicer. Next, the digest of the RNA dumbbell (Db-23) was analyzed. We purified the mixture of RNAs using nondenaturing PAGE to separate RNAs of about 20 bp (Figure 5b, Figure S4, lane 4). As shown in Figure 6a, the band gave a complex spectrum, suggesting the existence of multiple cleavage sites. However, these bands contained RNA strands of m/z 6600 to 7400, which correspond to sequences of 21- to 23-nt RNA. Several peaks were identified in its sequences (Figure 6b). These results show that cleavage occurred in the stem portion or in the middle of the loop portion. Although the identified sequences should have complementary sequences, the complexity of the spectrum prevented us from confirming this. Still, with this experiment, we confirmed that Dicer transformed the RNA dumbbell into 21- to

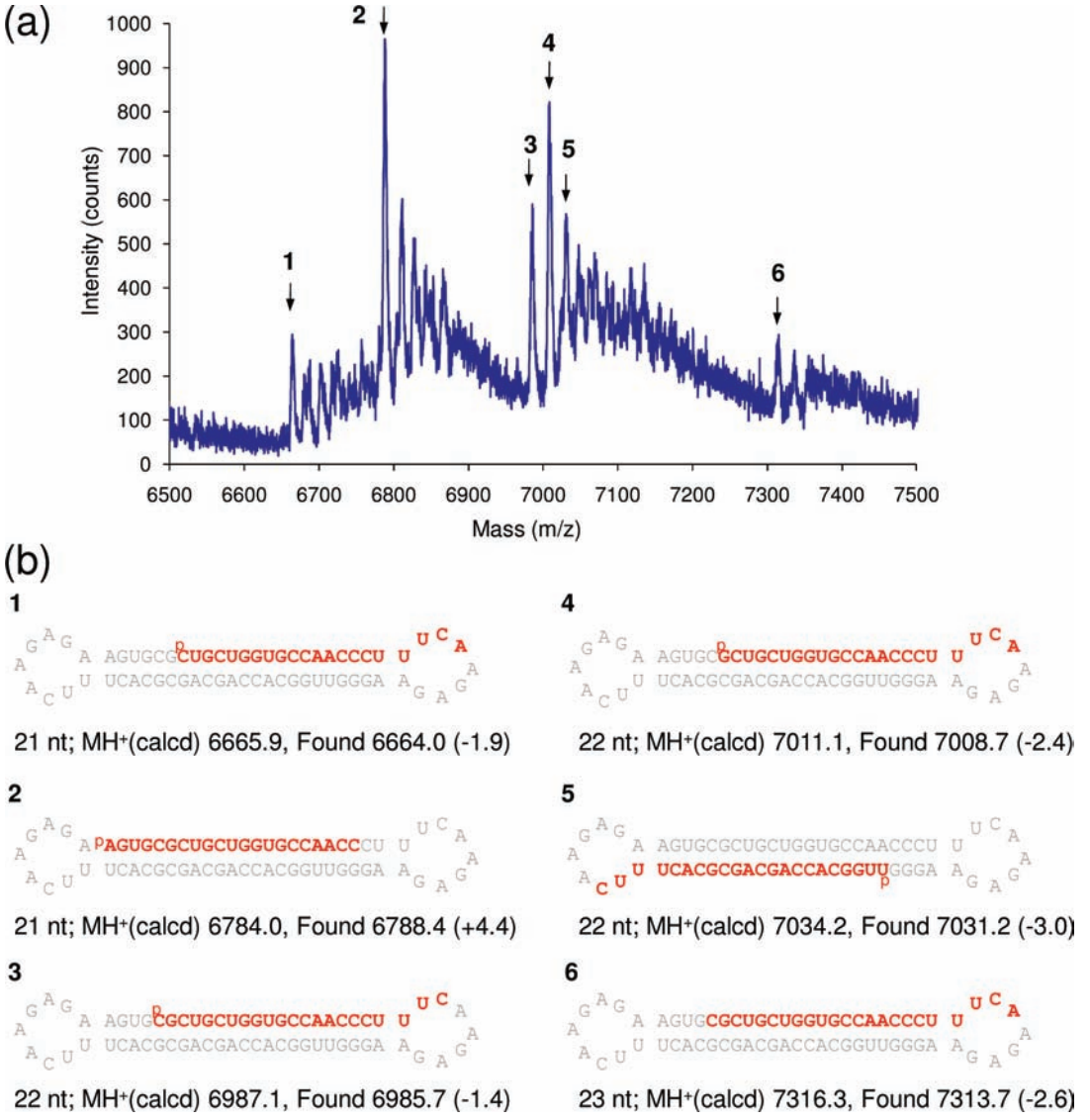

Figure 6. MALDI-TOF MS analysis of digestion products of Db-23 by Dicer. A band corresponding to about 20 bp in length in nondenaturing PAGE was excised, and RNAs were extracted from the gel and analyzed (Figure S4). (a) Mass spectrum of the digestion products. Peaks of the identified sequences are indicated by arrows and numbers **1** to **6**. (b) RNA sequences identified as peaks **1** to **6** in the spectrum shown in (a). Detected sequences are highlighted in red bold letters in the original dumbbell sequences (gray). Both the calculated mass (calcd) and the observed mass (found) are shown.

23-nt RNAs, which can be regarded as components of the siRNA species.

Synthesis of Loop-Modified RNA Dumbbells. An RNA dumbbell is stabilized against degradation in serum because of its termini-free structure.[20] However, we observed a nicking reaction in the single-stranded loop region as the first reaction when RNA dumbbell Db-23 was incubated in serum.[23,24] We decided to reinforce the loop moiety by introducing some modifications that are thought to be nontoxic. As shown in Figure 2c, ribonucleotides in the loop were replaced with their cognate 2′-deoxynucleotides, which comprise DNA, or with a hexaethylene glycol linker, which has been used to form folds and hairpins to bridge sections of oligonucleotides.[39−43] Deoxynucleotides are used in siRNAs, especially in the overhang regions, in the hope that this will make the siRNA resistant to nucleases.[4,44] In this study, we varied the number of 2′-deoxynucleotides introduced as three (Db-23D3), five (Db-23D5), or seven (Db-23D7) per one loop, to determine the optimum for substitution. These loop-modified RNA dumbbells were synthesized by ligating two chemically synthesized RNA strands using T4 RNA ligase (Figure S1g−k). To construct them, we preferred to make nicks in the single-stranded loop region if possible, because T4 RNA ligase works more efficiently on a single strand than on a double strand.[45] Ribonucleotide was then used as a nucleotide at the 3′-end (acceptor), because the ligation reaction is slowed with 2′-deoxynucleotide as an acceptor.[45] Ligation reactions to make these dumbbells proceeded well (Figure S5), although ligation in the double-stranded stem required more enzyme units, as expected.[45] After ligation, the dumbbells were purified by denaturing PAGE and used in further experiments.

The RNAi activity of these loop-modified RNA dumbbells was measured by a dual-luciferase assay 24 h after transfection in NIH/3T3 cells (Figure 3c). Substitution of ribonucleotides with 2′-deoxynucleotides in the loops (Db-23D3, Db-23D5, and

dx.doi.org/10.1021/bc2003154 |*Bioconjugate Chem.* 2011, 22, 2082–2092

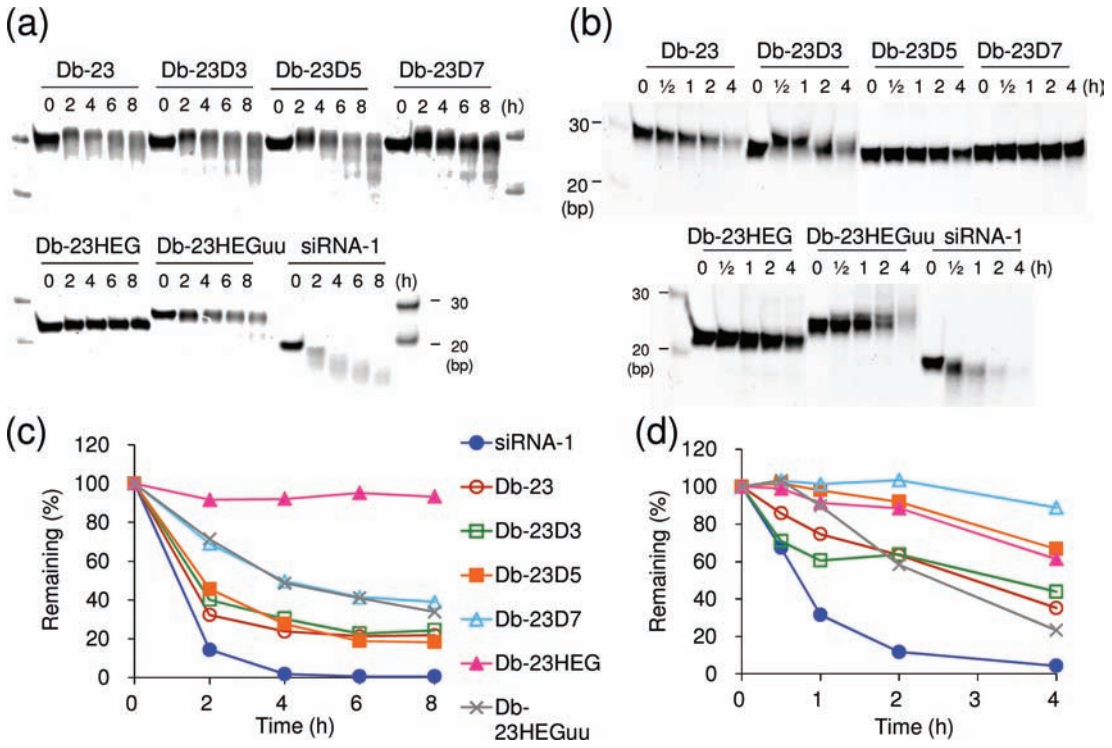

Figure 7. Stability of loop-modified RNA dumbbells. Nondenaturing PAGE analysis of digestion reaction with bovine serum (a) and with cell lysate of HL60 cell line (b). Remaining RNA sequences in the gel shown in (a) and (b) were quantified in (c) and (d), respectively.

Db-23D7) slightly decreased the activity compared with that of Db-23. In the substitutions with hexa(ethylene glycol) (Db-23HEG and Db-23HEGuu), the RNAi activity decreased more, compared with that of DNA-modified dumbbells. We concluded that dumbbells containing deoxynucleotides in the loops could be promising candidates in terms of retaining RNAi activity and adding biostability at the same time.

Stability of Loop-Modified Dumbbells in Serum and Cell Lysates. In clinical applications of RNAi, RNAs are injected into venous blood and must survive until reaching the target cells or organ.[46] Therefore, the biological stability of the RNA dumbbell is very important. To examine whether loop-modified RNA dumbbells become more stable in biological fluids, we incubated these modified dumbbells in bovine serum at 37 °C. As shown in Figure 7a, the reaction was analyzed by PAGE for up to 8 h, and the band intensity of undegraded RNA was quantified and plotted. We observed a stabilization effect of deoxynucleotides introduced into the loops, notably on Db-23D7 (Figure 7a,c). Db-23HEG, which has a hexa(ethylene glycol) linker and no unpaired nucleotide in the loop, was the most stable and almost no substantial degradation was detected in this reaction condition. The stability of Db-23HEGuu was clearly lower than that of Db-23HEG because of the presence of two uridine residues in the loops of Db-23HEGuu.

Increasing the stability of RNAs in living cells would extend the effective period of RNAi. To evaluate this ability, we examined the stability of RNA dumbbells in cell lysates.[27] Cell lysates were prepared from HL60 cells, a human promyelocytic leukemia cell line. Similar to the results in serum, RNA dumbbells were stabilized by introducing deoxynucleotides into the loops (Figure 7b,d). Interestingly, unlike in serum, Db-23D7 was more stable than Db-23HEG in cell lysates. These experiments confirmed that replacement of ribonucleotides with deoxynucleotides or hexa(ethylene glycol) in the loops confers significant biostability to RNA dumbbells.

Time and Dose Dependency of RNA Dumbbells in the RNAi Effect. Ideally, in clinical applications, a small dose of RNA should cause RNAi for a long time.[5] To investigate the ability of RNA dumbbells more thoroughly, the time and dose dependency of their RNAi were measured. RNA dumbbells Db-23, Db-23D3, Db-23D5, and Db-23D7 were introduced into HeLa cells stably expressing a firefly luciferase (HeLa-Luc), using the MEND method, in which RNA is complexed with a polycation followed by encapsulation by a lipid envelope.[28] The complexed RNA dumbbells were about 50 nm in diameter and had a −10 mV ζ-potential, values that are similar to those of the siRNA complex (siRNA-1: 53 nm and −14 mV). The observed diameter and ζ-potential of MENDs encapsulating the RNAs were 70−100 nm and 30−50 mV. To evaluate their silencing effect for up to eight days (192 h), the luciferase activity of the HeLa-Luc cells was measured with repeated passage after treatment with MENDs at a dose of 0.04 μM RNA. As shown in Figure 8a, the silencing effect of siRNA-1 reached a peak 48 h after the treatment. By contrast, RNA dumbbells retained their peak for longer, from 24 to 72 h. Introduction of 2′-deoxynucleotides into the loops (Db-23D3, Db-23D5, or Db-23D7) did not significantly change their RNAi activity, which was similar to that of Db-23. The silencing effect lasted longer for RNA dumbbells than for siRNA-1 (Figure 8a). Next, the dose dependency of the silencing effect was measured 24 and 144 h after the treatment (Figure 8b,c). At 24 h, RNA dumbbells exhibited a greater silencing effect than siRNA-1 at lower doses (Figure 8b). The differences in the silencing effect between RNA dumbbells and siRNA-1 expanded with longer incubation to 144 h after the treatment (Figure 8c). At lower doses, siRNA-1 did not show activity, but RNA dumbbells retained a significant effect. At both

dx.doi.org/10.1021/bc2003154 |*Bioconjugate Chem.* 2011, 22, 2082–2092

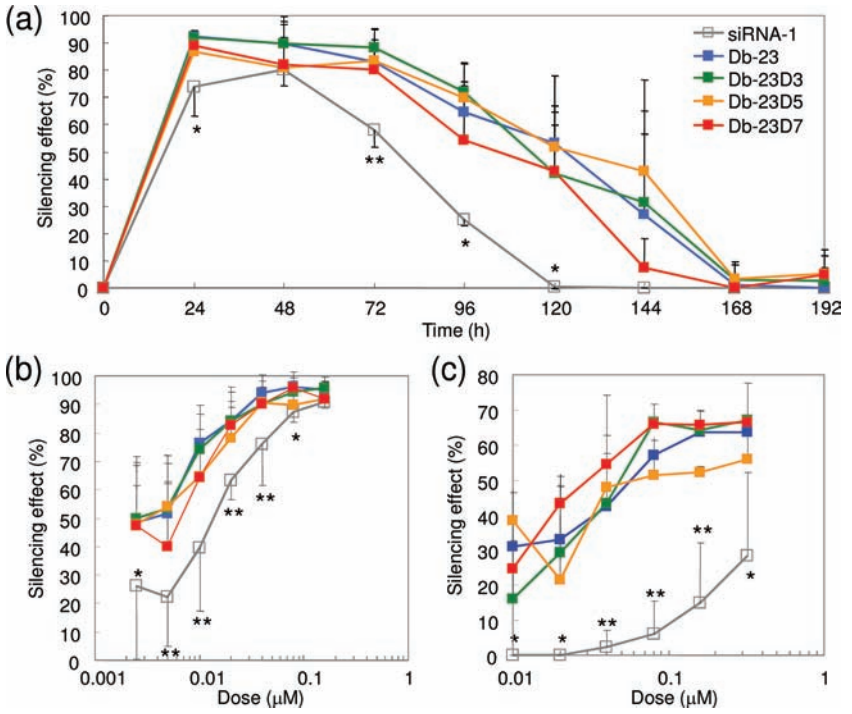

Figure 8. Time and dose dependency of RNA dumbbells of the RNAi effect. HeLa cells stably expressing luciferase were transfected with an MEND encapsulating siRNA-1 or an RNA dumbbell. Error bars were displayed in only one direction to prevent overlapping. (a) Time course of the silencing effect treated with MENDs at a dose of 0.04 μM of RNA. (b,c) Dose−response curves of MENDs at 24 h (b) and 144 h (c). The silencing effect is expressed as the mean ± SD (n = 3) $^{*}P < 0.05$, $^{**}P < 0.01$, RNA dumbbells vs siRNA-1.

times (24 and 144 h after treatment), the activity did not differ among the four kinds of RNA dumbbells. We should note that the silencing effect of Db-23D7 at 0.04 μM was 55% in Figure 8c but only 10% in Figure 8a at 144 h. The disagreement might be explained by the fact that the experimental errors became larger at later time points in Figure 8a, or simply because the two experiments were conducted independently. This discrepancy did not change the conclusion we obtained from the experiments shown in Figure 8. That is, the RNA dumbbells were stabilized in biological fluid by introduction of deoxynucleotides into the loops without any loss of RNA activity. These results show that RNA dumbbells can exert their silencing activity in mammalian cultured cells for longer than their canonical siRNA counterpart in a statistically significant way, presumably because RNA dumbbells retain their sequences longer after being delivered into the cytosol.

DISCUSSION

We optimized their loop sequences and stem length of RNA dumbbells (Figures 2 and 3). Our results suggest that the stem of 23 bp in length and 9-nt loop sequence UUCAAGAGA maximized the RNAi effect. With this design, an RNA dumbbell can be recognized by Dicer and produce siRNA species. Sequence analysis by MALDI-TOF MS confirmed the production of 21- to 23-nt RNAs that produced siRNA species after digestion with Dicer. dsRNAs are known to activate the innate immune response when introduced into cells.[47] In particular, siRNAs lacking dinucleotide 3′-overhangs activate the interferon system in cells because the overhang is a characteristic of endogenous Dicer products.[48] Considering this observation, we performed a preliminary experiment to test the ability to cause the interferon response by measuring the mRNA levels of interferon response-related genes (*OAS1* and *STAT1*) by quantitative real-time PCR after introducing RNA dumbbells into HeLa cells or HeLa S3 cells (Supporting Information Figure S6).[32,47] Various RNA dumbbells such as an all-RNA dumbbell (Db-23), dumbbells with DNA loops (Db-23D5 and Db-23D7), and dumbbells with an HEG loop (Db-23HEG and Db-23HEGuu) were examined and compared with standard siRNA (siRNA-1) or dsRNAs (BL-23 and L-23). In this experiment, we did not see any significant upregulation by the dumbbells; the mRNA levels of *OAS1* and *STAT1* were within 1.5-fold of those of mock-transfected cells (Figure S6). We concluded that dumbbell RNA does not cause a significant interferon response as does standard siRNA.

As shown in Figure 8c, RNA dumbbells caused a much more potent RNAi effect even at a lower concentration and for a longer time. Because RNAs are administered by injection through a vein in clinical applications, improving their stability in biological fluids will be valuable for delivering the RNAi effect within the target organ. Substituting ribonucleotide residues with 2′-deoxynucleotides in the loop position of the dumbbell significantly stabilizes it without the loss of RNAi activity (Figures 7 and 8). We conclude that an RNA dumbbell with DNA loops is the most promising design for in vivo applications.

The loop in the dumbbell can be modified to add various functions without affecting RNAi activity because the loop would be cleaved by Dicer and natural dsRNA as siRNA species is released eventually. For example, introduction of RNA or DNA aptamer, or even peptide, could confer membrane permeability or targetability in addition to biological stability. Interestingly, a nanoring such as a hexagon was constructed by assembling the RNA dumbbell through the interaction of a kissing loop.[49] The various nanostructures could be designed using RNA dumbbells

as an assembly unit, which might provide multiple functions. We plan to design and synthesize such highly functional dumbbells in the future.

In conclusion, we designed various RNA dumbbells to determine the optimum structure. A native RNA dumbbell with a 23 bp stem and 9-nt loops (UUCAAGAGA) had the most effective RNAi effect. Introduction of deoxynucleotides into the loops significantly stabilized the dumbbells in serum and cell lysates without loss of RNAi activity. The optimized RNA dumbbells showed longer silencing activity compared with the authentic siRNA counterpart.

■ ASSOCIATED CONTENT

Supporting Information. Additional figures and experimental procedures. This material is available free of charge via the Internet at http://pubs.acs.org.

■ AUTHOR INFORMATION

Corresponding Author

*E-mail addresses: h-abe@riken.jp (H.A.); y-ito@riken.jp (Y.I.).

■ ACKNOWLEDGMENT

We are grateful for the support of Mr. Masaya Usui and Ms. Kaori Otsuki for the mass spectrum analysis, and of Mr. Keisuke Fukumoto for the quantitative real-time PCR analysis (BSI Research Resources Center, RIKEN, Japan). This work was supported by National Institute of Biomedical Innovation (NIBIO) of Japan (to H.A.).

■ REFERENCES

(1) Fire, A., Xu, S. Q., Montgomery, M. K., Kostas, S. A., Driver, S. E., and Mello, C. C. (1998) Potent and specific genetic interference by double-stranded RNA in *Caenorhabditis elegans*. *Nature 391*, 806–811.

(2) Rana, T. M. (2007) Illuminating the silence: understanding the structure and function of small RNAs. *Nat. Rev. Mol. Cell Biol. 8*, 23–36.

(3) Bernstein, E., Caudy, A. A., Hammond, S. M., and Hannon, G. J. (2001) Role for a bidentate ribonuclease in the initiation step of RNA interference. *Nature 409*, 363–366.

(4) Elbashir, S. M., Harborth, J., Lendeckel, W., Yalcin, A., Weber, K., and Tuschl, T. (2001) Duplexes of 21-nucleotide RNAs mediate RNA interference in cultured mammalian cells. *Nature 411*, 494–498.

(5) Castanotto, D., and Rossi, J. J. (2009) The promises and pitfalls of RNA-interference-based therapeutics. *Nature 457*, 426–433.

(6) Hajeri, P. B., and Singh, S. K. (2009) siRNAs: their potential as therapeutic agents - Part I. Designing of siRNAs. *Drug Discovery Today 14*, 851–858.

(7) Singh, S. K., and Hajeri, P. B. (2009) siRNAs: their potential as therapeutic agents - Part II. Methods of delivery. *Drug Discovery Today 14*, 859–865.

(8) Harborth, J., Elbashir, S. M., Vandenburgh, K., Manninga, H., Scaringe, S. A., Weber, K., and Tuschl, T. (2003) Sequence, chemical, and structural variation of small interfering RNAs and short hairpin RNAs and the effect on mammalian gene silencing. *Antisense Nucl. Acid Drug Dev. 13*, 83–105.

(9) Hall, A. H. S., Wan, J., Shaughnessy, E. E., Shaw, B. R., and Alexander, K. A. (2004) RNA interference using boranophosphate siRNAs: structure-activity relationships. *Nucleic Acids Res. 32*, 5991–6000.

(10) Choung, S., Kim, Y. J., Kim, S., Park, H. O., and Choi, Y. C. (2006) Chemical modification of siRNAs to improve serum stability without loss of efficacy. *Biochem. Biophys. Res. Commun. 342*, 919–927.

(11) Watts, J. K., Choubdar, N., Sadalapure, K., Robert, F., Wahba, A. S., Pelletier, J., Pinto, B. M., and Damha, M. J. (2007) 2′-Fluoro-4′-thioarabino-modified oligonucleotides: conformational switches linked to siRNA activity. *Nucleic Acids Res. 35*, 1441–1451.

(12) Hoshika, S., Minakawa, N., Kamiya, H., Harashima, H., and Matsuda, A. (2005) RNA interference induced by siRNAs modified with 4′-thioribonucleosides in cultured mammalian cells. *FEBS Lett. 579*, 3115–3118.

(13) Watts, J. K., Deleavey, G. F., and Damha, M. J. (2008) Chemically modified siRNA: tools and applications. *Drug Discovery Today 13*, 842–855.

(14) Kim, D. H., Behlke, M. A., Rose, S. D., Chang, M. S., Choi, S., and Rossi, J. J. (2005) Synthetic dsRNA Dicer substrates enhance RNAi potency and efficacy. *Nat. Biotechnol. 23*, 222–226.

(15) Siolas, D., Lerner, C., Burchard, J., Ge, W., Linsley, P. S., Paddison, P. J., Hannon, G. J., and Cleary, M. A. (2005) Synthetic shRNAs as potent RNAi triggers. *Nat. Biotechnol. 23*, 227–231.

(16) Sun, X. G., Rogoff, H. A., and Li, C. J. (2008) Asymmetric RNA duplexes mediate RNA interference in mammalian cells. *Nat. Biotechnol. 26*, 1379–1382.

(17) Grimm, D. (2009) Asymmetry in siRNA design. *Gene Ther. 16*, 827–829.

(18) Bramsen, J. B., Laursen, M. B., Damgaard, C. K., Lena, S. W., Babu, B. R., Wengel, J., and Kjems, J. (2007) Improved silencing properties using small internally segmented interfering RNAs. *Nucleic Acids Res. 35*, 5886–5897.

(19) Chu, C. Y., and Rana, T. M. (2008) Potent RNAi by short RNA triggers. *RNA 14*, 1714–1719.

(20) Abe, N., Abe, H., and Ito, Y. (2007) Dumbbell-shaped nanocircular RNAs for RNA interference. *J. Am. Chem. Soc. 129*, 15108–15109.

(21) Abe, N., Abe, H., Ohshiro, T., Nakashima, Y., Maeda, M., and Ito, Y. (2011) Synthesis and characterization of small circular double-stranded RNAs. *Chem. Commun. (Cambridge, U. K.) 47*, 2125–2127.

(22) Shaw, J. P., Kent, K., Bird, J., Fishback, J., and Froehler, B. (1991) Modified deoxyoligonucleotides stable to exonuclease degradation in serum. *Nucleic Acids Res. 19*, 747–750.

(23) Chu, B. C. F., and Orgel, L. E. (1992) The stability of different forms of double-stranded decoy DNA in serum and nuclear extracts. *Nucleic Acids Res. 20*, 5857–5858.

(24) Abe, T., Takai, K., Nakada, S., Yokota, T., and Takaku, H. (1998) Specific inhibition of influenza virus RNA polymerase and nucleoprotein gene expression by circular dumbbell RNA/DNA chimeric oligonucleotides containing antisense phosphodiester oligonucleotides. *FEBS Lett. 425*, 91–96.

(25) Sambrook, J., and Russell, D. (2001) Isolation of DNA fragments from polyacrylamide gels by the crush and soak method. *Molecular Cloning: A Laboratory Manual*, 3rd ed.: pp 5.51−5.54, Chapter 5, Vol. 1, Cold Spring Harbor Laboratory Press, Woodbury, New York.

(26) Miyagishi, M., Sumimoto, H., Miyoshi, H., Kawakami, Y., and Taira, K. (2004) Optimization of an siRNA-expression system with an improved hairpin and its significant suppressive effects in mammalian cells. *J. Gene Med. 6*, 715–723.

(27) Bertrand, J. R., Pottier, M., Vekris, A., Opolon, P., Maksimenko, A., and Malvy, C. (2002) Comparison of antisense oligonucleotides and siRNAs in cell culture and in vivo. *Biochem. Biophys. Res. Commun. 296*, 1000–1004.

(28) Akita, H., Kudo, A., Minoura, A., Yamaguti, M., Khalil, I. A., Moriguchi, R., Masuda, T., Danev, R., Nagayama, K., Kogure, K., and Harashima, H. (2009) Multi-layered nanoparticles for penetrating the endosome and nuclear membrane via a step-wise membrane fusion process. *Biomaterials 30*, 2940–2949.

(29) Brummelkamp, T. R., Bernards, R., and Agami, R. (2002) A system for stable expression of short interfering RNAs in mammalian cells. *Science 296*, 550–553.

(30) Lee, N. S., Dohjima, T., Bauer, G., Li, H. T., Li, M. J., Ehsani, A., Salvaterra, P., and Rossi, J. (2002) Expression of small interfering RNAs targeted against HIV-1 rev transcripts in human cells. *Nat. Biotechnol. 20*, 500–505.

(31) Wakiyama, M., Matsumoto, T., and Yokoyama, S. (2005) Drosophila U6 promoter-driven short hairpin RNAs effectively induce

RNA interference in Schneider 2 cells. *Biochem. Biophys. Res. Commun. 331*, 1163–1170.

(32) Reynolds, A., Anderson, E. M., Vermeulen, A., Fedorov, Y., Robinson, K., Leake, D., Karpilow, J., Marshall, W. S., and Khvorova, A. (2006) Induction of the interferon response by siRNA is cell type- and duplex length-dependent. *RNA 12*, 988–993.

(33) Bustamante, C., Vesenka, J., Tang, C. L., Rees, W., Guthold, M., and Keller, R. (1992) Circular DNA molecules imaged in air by scanning force microscopy. *Biochemistry 31*, 22–26.

(34) Zenhausern, F., Adrian, M., Tenheggelerbordier, B., Emch, R., Jobin, M., Taborelli, M., and Descouts, P. (1992) Imaging of DNA by scanning force microscopy. *J. Struct. Biol. 108*, 69–73.

(35) Vermeulen, A., Behlen, L., Reynolds, A., Wolfson, A., Marshall, W. S., Karpilow, J., and Khvorova, A. (2005) The contributions of dsRNA structure to Dicer specificity and efficiency. *RNA 11*, 674–682.

(36) Rose, S. D., Kim, D. H., Amarzguioui, M., Heidel, J. D., Collingwood, M. A., Davis, M. E., Rossi, J. J., and Behlke, M. A. (2005) Functional polarity is introduced by Dicer processing of short substrate RNAs. *Nucleic Acids Res. 33*, 4140–4156.

(37) Sashital, D. G., and Doudna, J. A. (2010) Structural insights into RNA interference. *Curr. Opin. Struct. Biol. 20*, 90–97.

(38) MacRae, I. J., Zhou, K. H., Li, F., Repic, A., Brooks, A. N., Cande, W. Z., Adams, P. D., and Doudna, J. A. (2006) Structural basis for double-stranded RNA processing by Dicer. *Science 311*, 195–198.

(39) Durand, M., Chevrie, K., Chassignol, M., Thuong, N. T., and Maurizot, J. C. (1990) Circular-dichroism studies of an oligodeoxynucleotide containing a hairpin loop made of a hexaethylene glycol chain - conformation and stability. *Nucleic Acids Res. 18*, 6353–6359.

(40) Rumney, S., and Kool, E. T. (1992) DNA recognition by hybrid oligoether−oligodeoxynucleotide macrocycles. *Angew. Chem., Int. Ed. 31*, 1617–1619.

(41) Ma, M. Y. X., McCallum, K., Climie, S. C., Kuperman, R., Lin, W. C., Sumnersmith, M., and Barnett, R. W. (1993) Design and synthesis of RNA miniduplexes via a synthetic linker approach. 2. Generation of covalently closed, double-stranded cyclic HIV-1 TAR RNA analogs with high Tat-binding affinity. *Nucleic Acids Res. 21*, 2585–2589.

(42) Rumney, S., and Kool, E. T. (1995) Structural optimization of non-nucleotide loop replacements for duplex and triplex DNAs. *J. Am. Chem. Soc. 117*, 5635–5646.

(43) Pils, W., and Micura, R. (2000) Flexible non-nucleotide linkers as loop replacements in short double helical RNAs. *Nucleic Acids Res. 28*, 1859–1863.

(44) Elbashir, S. M., Martinez, J., Patkaniowska, A., Lendeckel, W., and Tuschl, T. (2001) Functional anatomy of siRNAs for mediating efficient RNAi in *Drosophila melanogaster* embryo lysate. *EMBO J. 20*, 6877–6888.

(45) Uhlenbeck, O. C., and Gumport, R. I. (1982) T4 RNA ligase. In *The Enzymes: Nucleic Acids*, 3rd ed. (Boyer, P. D., Ed.) pp 31−58, Vol. 15, Pt. B, Academic Press, New York.

(46) Soutschek, J., Akinc, A., Bramlage, B., Charisse, K., Constien, R., Donoghue, M., Elbashir, S., Geick, A., Hadwiger, P., Harborth, J., John, M., Kesavan, V., Lavine, G., Pandey, R. K., Racie, T., Rajeev, K. G., Rohl, I., Toudjarska, I., Wang, G., Wuschko, S., Bumcrot, D., Koteliansky, V., Limmer, S., Manoharan, M., and Vornlocher, H. P. (2004) Therapeutic silencing of an endogenous gene by systemic administration of modified siRNAs. *Nature 432*, 173–178.

(47) Sledz, C. A., Holko, M., de Veer, M. J., Silverman, R. H., and Williams, B. R. G. (2003) Activation of the interferon system by short-interfering RNAs. *Nat. Cell Biol. 5*, 834–839.

(48) Marques, J. T., Devosse, T., Wang, D., Zamanian-Daryoush, M., Serbinowski, P., Hartmann, R., Fujita, T., Behlke, M. A., and Williams, B. R. G. (2006) A structural basis for discriminating between self and nonself double-stranded RNAs in mammalian cells. *Nat. Biotechnol. 24*, 559–565.

(49) Grabow, W. W., Zakrevsky, P., Afonin, K. A., Chworos, A., Shapiro, B. A., and Jaeger, L. (2011) Self-assembling RNA nanorings based on RNAI/II inverse kissing complexes. *Nano Lett. 11*, 878–887.

Supporting Information

Synthesis, structure and biological activity of dumbbell-shaped nanocircular RNAs for RNA interference

Naoko Abe[1], Hiroshi Abe[*,1], Chisato Nagai[3], Mitsuru Harada[1,2], Hiroto Hatakeyama[3], Hideyoshi Harashima[3], Takahito Ohshiro[4], Mizuki Nishihara[1], Kazuhiro Furukawa[1,2], Mizuo Maeda[4], Satoshi Tsuneda[2] and Yoshihiro Ito[*,1]

[1]Nano Medical Engineering Laboratory, RIKEN Advanced Science Institute, 2-1 Hirosawa, Wako-shi Saitama 351-0198, Japan
[2]Department of Life Science and Medical Bio-Science, Waseda University, 2-2 Wakamatsu-cho, Shinjuku-ku, Tokyo 162-8480, Japan
[3]Faculty of Pharmaceutical Sciences, Hokkaido University, Kita12 Nishi6, Kita-ku, Sapporo Hokkaido 060-0812, Japan
[4]Bioengineering Laboratory, RIKEN Advanced Science Institute, 2-1 Hirosawa, Wako-shi Saitama 351-0198, Japan

Corresponding Auther: h-abe@riken.jp; y-ito@riken.jp

Experimental details:

Quantitative real-time PCR analysis of OAS1 and STAT1 levels in mammalian cultured cells after RNA transfection

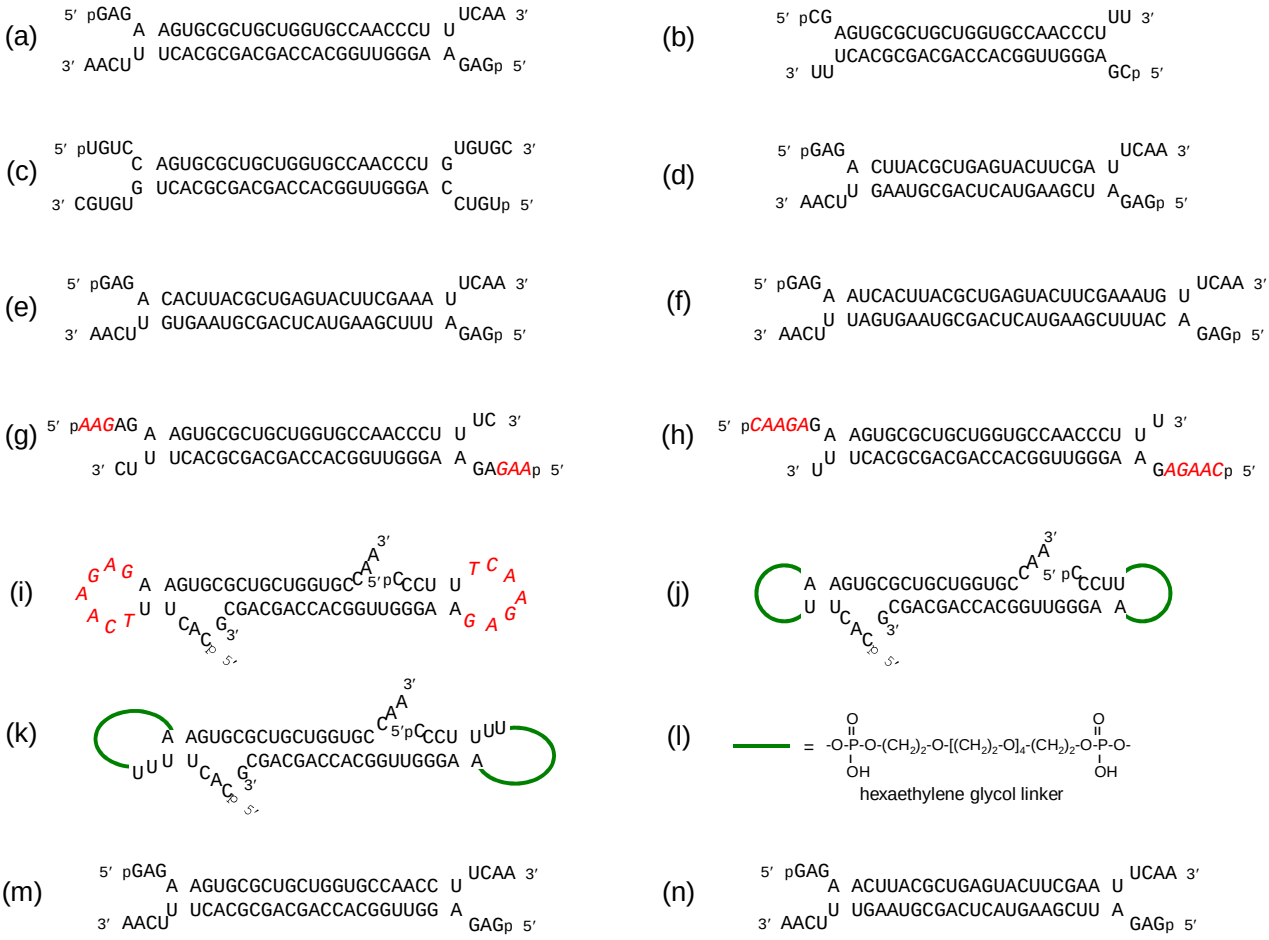

Figure S1. Chemically synthesized RNA sequences to be converted to a dumbbell by ligation reaction. They are ligated with T4 RNA ligase either at the single-stranded ends or at the nicks in the stem. All RNA oligos are 5′ phosphorylated (Letter p on 5′ -end means it is phosphorylated). Nucleobases written in red italic letters are replaced by deoxyribonucleotides (g, h and i). Green lines inserted into RNA sequences represent hexaethyleneglycol linker (l). The resulting RNA dumbbells are as follows: (a) Db-23, (b) Db-23S, (c) Db-23G, (d) Db-19N, (e) Db-23N, (f) Db-27N, (g) Db-23D3, (h) Db-23D5, (i) Db-23D7, (j) Db-23HEG, (k) Db-23HEGuu, (m) Db-21, (n) Db-21N.

(a)

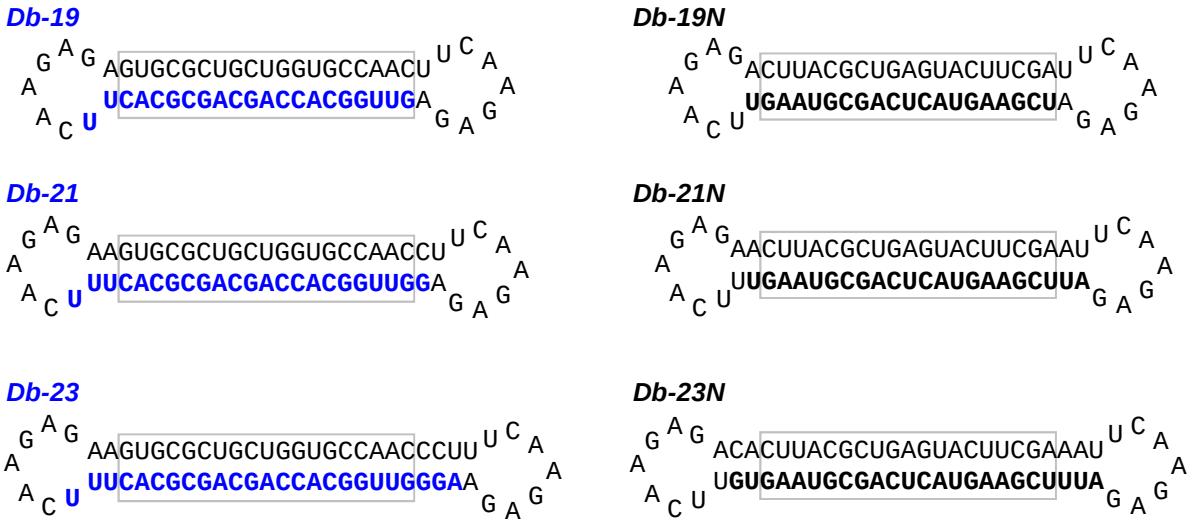

(b)

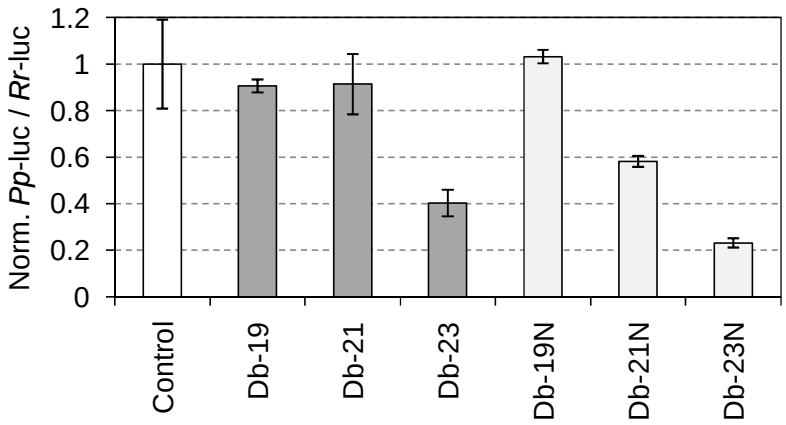

Figure S2. Optimization of the stem length of RNA dumbbells for RNA interference. (a) Sequences and structure of RNAs. Db-19, Db-21 and Db-23 target the coding regions 849– 869 of GL3 luciferase. Db-19N, Db-21N and Db-23N target the coding regions 153 – 173 of GL3 luciferase. Complementary sequences to the target mRNA are shown in bold. (b) RNA interference with RNA dumbbells. NIH/3T3 cells were cotransfected with RNA (at 25 nM) and the vectors. The expression of the two luciferase genes was assayed after 48 h. Ratios of target to control luciferase were normalized to a control (no RNA). The plotted data are the means ± S.D. of four independent experiments.

(a)

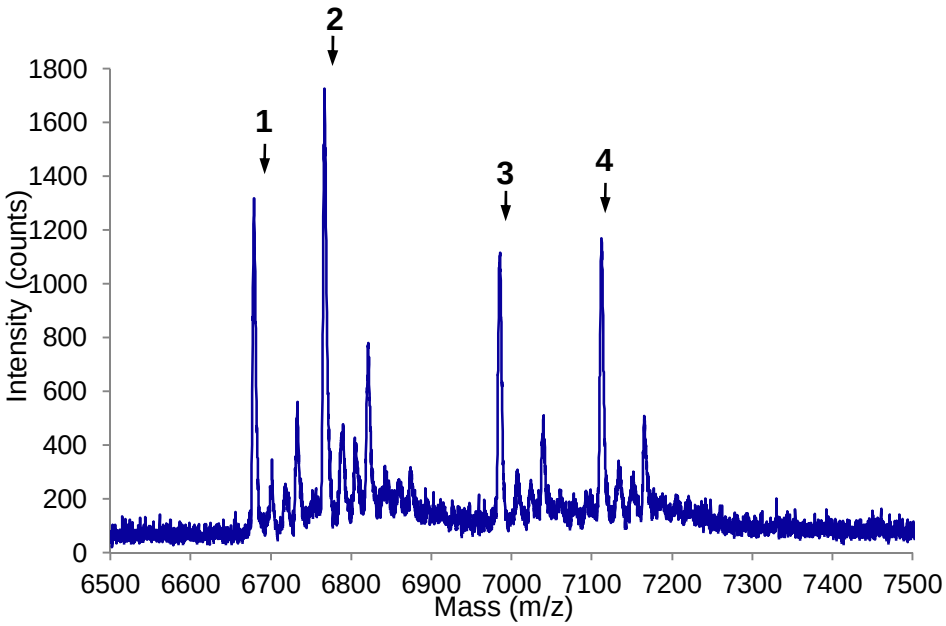

(b)

1 21 nt; MH^+ (calcd) 6680.0 , Found 6679.1 (-0.9)

5′ **GUGCGCUGCUGGUGCCAAC CC**U U U C A
3′ **UU CACGCGACGACCACGGUUG**pGGA A G A G A

2 21 nt; MH^+ (calcd) 6768.0, Found 6767.2 (-0.8)

3 22 nt; MH^+ (calcd) 6986.2, Found 6985.3 (-0.9)

5′ **GUGCGCUGCUGGUGCCAACC CU** U U C A
3′ **UU CACGCGACGACCACGGUUGG**pGA A G A G A

4 22 nt; MH^+ (calcd) 7113.2, Found 7112.5 (-0.7)

Figure S3. MALDI-TOF MS analysis of digestion products of a hairpin-shaped 55-nt RNA (Sh-55) by the Dicer. (a) Mass spectrum of the digestion products. Peaks of identified sequences are indicated by arrows and numbers **1** to **4**. (b) RNA sequences identified as peak **1** to **4** in the spectrum shown in (a). Detected sequences are highlighted in red bold letters in the original sequences (gray) and are phosphorylated. Both the calculated mass and the observed mass for the sequences are shown.

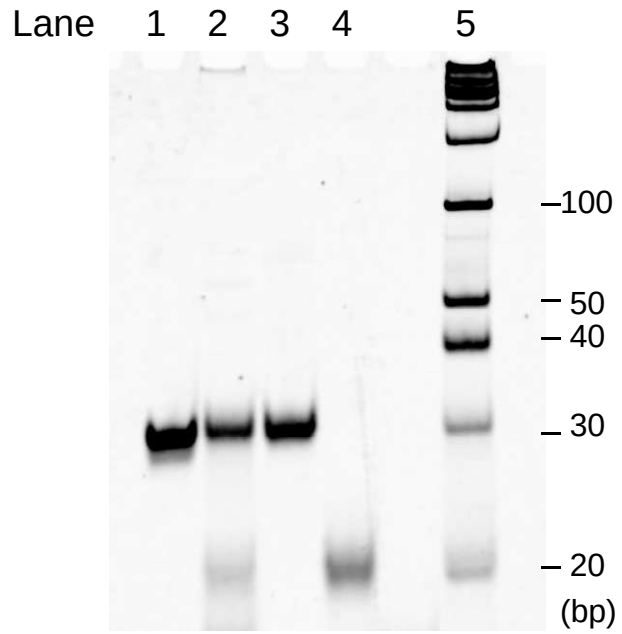

Figure S4. PAGE (10% non-denaturing) analysis of digestion products of RNA dumbbell Db-23 by the Dicer enzyme. Lane 1, Db-23; lane 2, digest of Db-23 by Dicer (reaction mixture); lane 3 and 4, isolated RNA after purification; lane 5, dsRNA size marker. The gel was visualized by SYBR Green I staining.

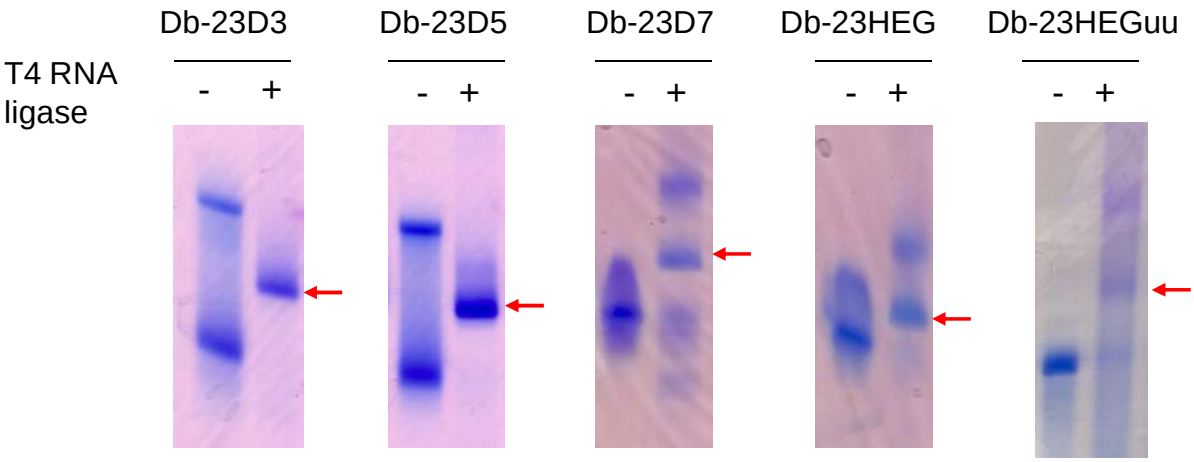

Figure S5. PAGE Analysis of ligation reactions to form loop-modified RNA dumbbells. Two chemically synthesized RNAs were annealed and ligated with T4 RNA ligase. Reaction mixture was analyzed by 10% denaturing PAGE (7 M urea, 25% formamide) and the gel was visualized by Stains-All staining. Red arrows point the ligated products (dumbbells).

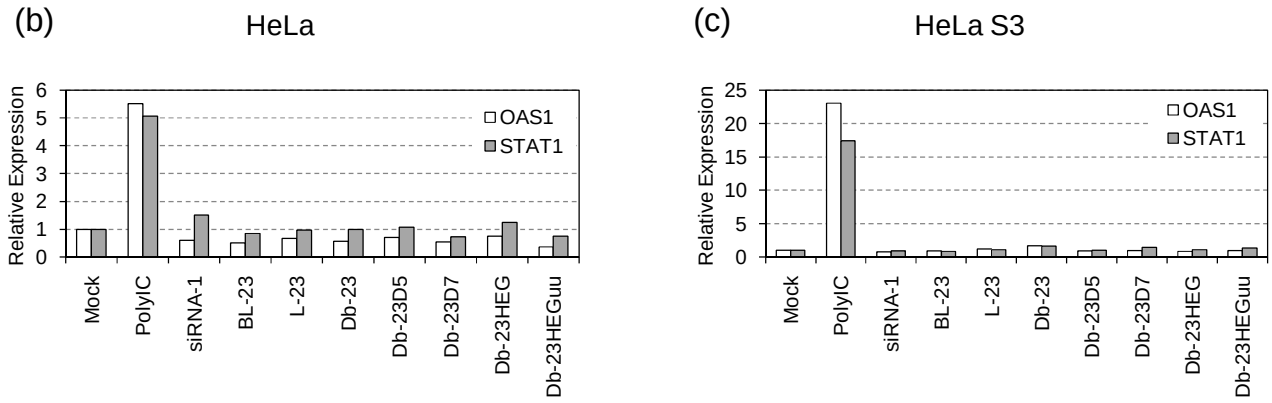

Figure S6. Quantitative real-time PCR analysis of OAS1 and STAT1 levels in mammalian cultured cells after RNA transfection. (a) Sequences and structures used in this study. (b)(c) HeLa cells (b) or HeLa S3 cells (c) were transfected with various RNAs at a concentration of 100 nM. OAS1, STAT1 and β–actin mRNA levels were measured 48 h after the transfection. Data are shown as ratios, target gene/β–actin and normalized to a mock transfected control (Mock). Polyinosinic-polycytidylic acid (PolyIC) was transfected to the cells at 0.21 μg/mL concentration.

Experimental details

Quantitative real-time PCR analysis of OAS1 and STAT1 levels in mammalian cultured cells after RNA transfection (interferon response assay)

All RNAs used were annealed at 5 μM concentrations in annealing buffer (100 mM potassium acetate, 30 mM HEPES-KOH at pH 7.4, 2 mM magnesium acetate) by heating at 90 °C for 3 min, then cooled slowly to room temperature. The solutions were further incubated at 4 °C overnight.

HeLa cells (RIKEN Cell Bank, Japan) were grown at 37 °C under 5% CO_2 in MEM (Sigma, MO) supplemented with 10% fetal calf serum (FCS; Israel Beit Haemek, Israel). HeLa S3 cells (RIKEN Cell Bank) were grown at 37 °C under 5% CO_2 in S-MEM (Invitrogen) supplemented with 10% fetal bovine serum (FBS). Cells were regularly passaged to maintain exponential growth. One day before transfection at 50 - 70% confluency, cells were plated in 48-well plates (2.5×10^4 cells/250 μL per well). Transfection of RNAs at 100 nM or polyIC (42 ng per well; Takara Bio, Japan) was carried out with GeneSilencer (Genlantis, CA) as described by the manufacturer. Just before transfection, the culture medium was replaced with 149 μL of medium without serum, and 20 pmol of RNA , 42 ng polyIC formulated into liposomes (51 μL) were added to each well. Four hours after the transfection, 200 μL of 20% serum in medium was added to each well. Two days after the transfection, cells were harvested and total RNA was extracted using RNeasy Mini Kit with DNase I treatment (Qiagen, CA). cDNA was produced using 75 ng of total RNA using PrimeScript RT reagent kit (Takara bio) and random hexamers in a 10 μL reaction according to the manufacturer's instructions. Expression of Stat1 and Oas1 was determined using real-time PCR at RIKEN BSI Research Resources Center (Japan) on Applied Biosystems 7900HT (Applied Biosystems, CA) by SYBR Green method. β-actin expression was used for normalization of the real-time PCR data. PCR reactions were run in duplicate and the data from these were confirmed to differ by < 0.5 threshold cycle. Sequences used for the primers were: STAT1, 5′-d(GCTGGCACCAGAACGAATGA) -3′ and 5′-d(TACCAAACCAGGCTGGCACA) -3′ ; OAS1, 5′-d(AGGTAGCTCCTACCCTGTGTGTGTG) -3′ and 5′-d(GAAGACAACCAGGTCAGCGTCA) -3′; β-actin, 5′-d(TGGCACCCAGCACAATGAA) -3′ and 5′-d(CTAAGTCATAGTCCGCCTAGAAGCA) -3′.

Bioconjugate Chemistry

ARTICLE

pubs.acs.org/bc

Gallium-68 Complex of a Macrobicyclic Cage Amine Chelator Tethered to Two Integrin-Targeting Peptides for Diagnostic Tumor Imaging

Michelle T. Ma,[†,‡] Oliver C. Neels,[§] Delphine Denoyer,[§] Peter Roselt,[§] John A. Karas,[‡] Denis B. Scanlon,[†,‡] Jonathan M. White,[†,‡] Rodney J. Hicks,[*,§] and Paul S. Donnelly[*,†,‡]

[†]School of Chemistry and [‡]Bio21 Molecular Science and Biotechnology Institute, The University of Melbourne, Parkville, Victoria, Australia

[§]The Centre for Molecular Imaging and Translational Research Laboratory, The Peter MacCallum Cancer Centre, Melbourne, Victoria, Australia

Supporting Information

ABSTRACT: Tumor-targeting peptides radiolabeled with positron-emitting ^{68}Ga are promising candidates as new noninvasive diagnostic agents for positron emission tomography (PET). The targeting peptides are tethered to a chelator that forms a stable coordination complex with Ga^{3+} that is inert to dissociation of Ga^{3+} *in vivo*. Metal complexes of macrobicyclic hexaamine "sarcophagine" (sar = 3,6,10,13,16,19-hexaazabicyclo[6.6.6]icosane) ligands exhibit remarkable stability as a result of the encapsulating nature of the cage amine ligand. A Ga^{3+} sarcophagine complex, $[Ga\text{-}(1\text{-}NH_3\text{-}8\text{-}NH_2\text{-sar})]^{4+}$, has been characterized using X-ray crystallography, demonstrating that Ga^{3+} is coordinated to six nitrogen atoms in a distorted octahedral complex. A bifunctional derivative of $(NH_2)_2$sar, possessing two aliphatic linkers with carboxylic acid functional groups has been attached to two cyclic-RGD peptides that target the $\alpha_v\beta_3$ integrin receptor that is overexpressed in some types of tumor tissue. This dimeric species can be radiolabeled with $^{68}Ga^{3+}$ in >98% radiochemical yield and $^{68}Ga^{3+}$ does not dissociate from the ligand in the presence of transferrin, an endogenous protein with high affinity for Ga^{3+}. Biodistribution and micro-PET imaging studies in tumor-bearing mice indicate that the tracer accumulates specifically in tumors with high integrin expression. The high tumor uptake is coupled with low nonspecific uptake and clearance predominantly through the kidneys resulting in high-quality PET images in animal models.

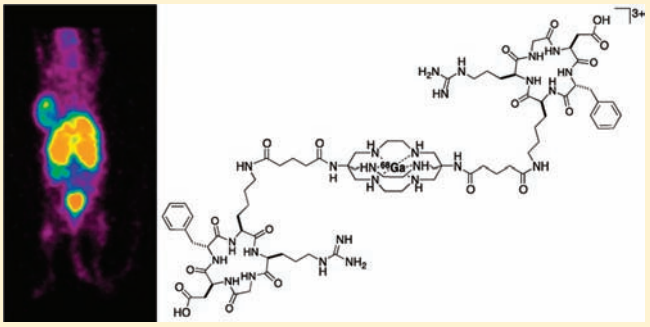

INTRODUCTION

Diagnostic imaging using positron emission tomography (PET) can provide clinicians with valuable information to guide and assess treatment regimes. PET relies on administering a tracer containing a positron-emitting isotope to a patient and then subsequently detecting the emitted radiation as the tracer passes through the body or accumulates within tissues as a function of biological processes. The radiolabeled glucose analogue FDG (^{18}F-fluoro-2-deoxy-D-glucose) is routinely used to probe glucose metabolism central to many cellular functions, but personalized and disease-specific diagnosis requires radiotracers that are designed to selectively target molecular characteristics of cells involved in the pathological process. ^{18}F is produced in a cyclotron and requires transport to imaging centers without an onsite facility. There are, therefore, potential advantages in using radiotracers that can be synthesized from generator-produced radioisotopes. Recently, the positron-emitting isotope, ^{68}Ga, has become available commercially by way of a ^{68}Ge/^{68}Ga generator.[1] The parent nuclide, ^{68}Ge, possesses a half-life of 271 days, and so ^{68}Ge/^{68}Ga generators can produce sufficient quantities of ^{68}Ga for up to one year. This generator system provides a relatively inexpensive and reliable source of a positron-emitting radionuclide without the need for a cyclotron. The favorable decay properties of ^{68}Ga (positron-emission, E_{max} 1.9 keV, 90%) coupled to a half-life of 68 min mean that the radionuclide is attractive for imaging applications based on peptide-targeted systems.[2,3]

Radioisotopes of gallium are already in use in nuclear medicine, for example, γ-emitting ^{67}Ga in the form of ^{67}Ga-citrate is used for single photon emission computed tomography scanning of lymphoma.[4] A ^{68}Ga complex bound to a peptide that targets neuroendocrine tumors is currently in clinical trials.[5] Peptide-targeted gallium containing imaging agents rely on a bifunctional ligand that complexes the gallium radioisotope into a coordination complex and also possesses a functional group to attach the targeting peptide to the gallium complex. It is important that the resulting Ga^{3+} complex is stable *in vivo*, as dissociation of $^{67/68}Ga^{3+}$ from the ligand can result in unwanted accumulation of activity in bone as well as prolonged circulation in the blood resulting in high background activity and inferior image quality.[6,7]

Received: June 19, 2011
Revised: August 22, 2011
Published: August 31, 2011

ACS Publications © 2011 American Chemical Society

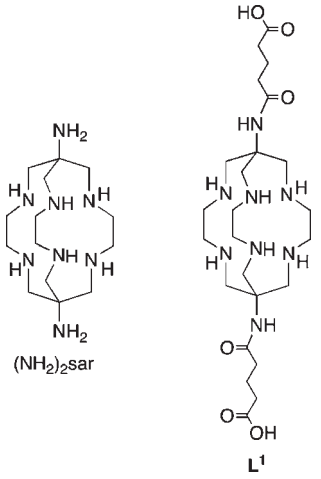

Figure 1. Structures of $(NH_2)_2$sar and $\mathbf{L^1}$.

Acyclic and cyclic bifunctional chelators have been investigated to coordinate $^{68}Ga^{3+}$ as well as the γ-emitting isotope $^{67}Ga^{3+}$. Currently, the most frequently employed cyclic chelators for attachment to targeting peptides are the macrocycles DOTA (1,4,7,10-tetraazacyclododecane-1,4,7,10-tetraacetic acid)[5,8−15] and NOTA (1,4,7-triazacyclononane-1,4,7-triacetic acid).[16−21] Tracers incorporating NOTA bind Ga^{3+} rapidly under mild conditions, and the gallium complexes exhibit a high degree of stability. However, ligands based on a DOTA framework require heating for prolonged periods of time to bind Ga^{3+}, and the resulting complexes are only moderately stable in the presence of competing ligands, such as transferrin.[6] More recently, a bifunctional linear chelator with an N_4O_2 binding mode[22] and a bifunctional tris-hydroxy(pyridinone) chelator[23] have demonstrated promising properties for gallium radiopharmaceutical application, including fast and quantitative radiolabeling at room temperature, high complex stability, and a favorable biodistribution profile that included a renal clearance pathway.

An alternative macrocyclic ligand framework to the triaza and tetraazamacrocycles is the macrobicyclic hexaamine ligand, 1,8-diamino-3,6,10,13,16,19-hexaazabicyclo[6.6.6]icosane, commonly referred to as "diaminosarcophagine" ($(NH_2)_2$sar) (Figure 1).[24,25] Metal complexes of $(NH_2)_2$sar exhibit high stability and are kinetically inert, largely due to the encapsulating nature of the cage-like ligand.[26,27] Metal complexes of $(NH_2)_2$sar and functionalized derivatives have been attached to biomolecules,[28,29] and a few bifunctional derivatives have been synthesized, primarily designed as ligands for ^{64}Cu-based radiopharmaceuticals.[30−41] Metal complexes of this class of ligand have been investigated extensively but there are no reports of Ga^{3+} complexes. To our knowledge, this is the first report of using a sarcophagine ligand to coordinate positron-emitting ^{68}Ga. A derivative of $(NH_2)_2$sar with two pendent acyl groups ($\mathbf{L^1}$) each containing a carboxylic acid functional group has been conjugated to two targeting peptides bearing an arginine-glycine-aspartate (RGD) motif. Cyclic peptides with the sequence cyclic-(RGDxK) (where x = DPhe(f) or DTyr(y)) bind with high affinity and specificity to the $\alpha_v\beta_3$ integrin receptor that is overexpressed in activated endothelial cells of cancer neovasculature and some types of tumors.[18−20,42−54] Visualization of $\alpha_v\beta_3$ integrin receptors by diagnostic imaging is of interest in characterizing tumor angiogenesis. In this work, two cyclic-(RGDfK) peptides have been attached to a single cage amine ligand, $\mathbf{L^1}$, to give a dimeric targeting molecule $\mathbf{L^1}(RGDfK)_2$, which has been radiolabeled with $^{68}Ga^{3+}$. The dimeric construct has the possibility of benefiting from superior binding to target cells due to a bivalent effect where a single radiolabeled tracer binds to two receptors on a single cell. Diagnostic tracers possessing two or more peptide groups have demonstrated increased tumor uptake relative to their monomeric analogues and, as a result, superior PET image quality.[49,51] The *in vivo* behavior of this new dimeric cyclic-RGD gallium-68 radiotracer has been investigated in tumor-bearing mice.

EXPERIMENTAL SECTION

Instrumentation. ESMS spectra were recorded in the positive ion mode on an Agilent 6510 Q-TOF LC/MS mass spectrometer coupled to an Agilent 1100 LC system (Agilent, Palo Alto, CA). Data were acquired and reference mass corrected via a dual-spray electrospray ionization source, using the factory-defined calibration procedure. Each scan or data point on the total ion chromatogram is an average of 9652 transients, producing 1.02 scans s^{-1}. Spectra were created by averaging the scans across each peak. Mass spectrometer conditions: fragmentor, 200−300 V; drying gas flow, 7 L/min; nebulizer, 30 psi; drying gas temp, 325 °C; V_{cap}, 4000 V; skimmer, 65 V; OCT R_fV, 750 V; scan range acquired, 150−3000 m/z.

HPLC-MS traces were recorded using an Agilent Poroshell 300SB-C18 column (5 μm, 2.1 × 75 mm) coupled to the Agilent 6510 Q-TOF LC/MS mass spectrometer described above. Aliquots (1−10 μL) of each sample were injected onto the column using the Agilent 1100 LC system, with a flow rate of 0.25 mL/min and a gradient mobile phase, which started with 100% 0.1% formic acid in water at 5 min to 100% 0.1% formic acid in acetonitrile at 25 min. Data acquisition parameters are the same as those described above for mass spectra.

Semipreparative HPLC purifications were performed using an Agilent 1200 series HPLC system. Solvent gradients and column specifications are described below. An automated Agilent 1200 fraction collector collected 2.5 mL fractions and fraction collection was time-based. Each fraction was analyzed using MS and analytical HPLC. Reverse-phase HPLC method 1 employed an Eclipse XDB-C18 5 μm 9.5 × 250 mm column with a flow rate of 3 mL min^{-1}. The gradient mobile phase started with 100% solvent A (0.1% trifluoroacetate in water) at 5 min to 100% solvent B (0.1% formic acid in acetonitrile) at 75 min. Reverse-phase HPLC method 2 employed an Eclipse XDB-C18 5 μm 9.5 × 250 mm column with a flow rate of 3 mL min^{-1}. The gradient mobile phase started with 100% solvent A at 5 min and increased at a rate of 1% B min^{-1} until all components had eluted. The 1850 MBq $^{68}Ge/^{68}Ga$ generator used in this study was obtained from IDB Holland BV, The Netherlands. Radio-TLC analyses were performed using a Raytest Rita-Star TLC scanner using Merck TLC silica gel 60F254 plates.

Radio-HPLC analyses were performed using a Shimadzu HPLC consisting of a SCL-10AVP system controller, a SIL-10ADVP autoinjector, a LC-10 ATVP solvent delivery unit, a FCV-10AL control valve, a DGU-14A degasser, and a SPD-10AVP UV detector. This was coupled to a radiation detector consisting of an Ortec model 276 Photomultiplier Base with Preamplifier, an Ortec 925-SCINT ACE mate Preamplifier, Amplifier, BIAS supply and SCA and a Bicron 1 M 11/2 Photomultiplier Tube. The reverse-phase radio-HPLC method utilized a Machery-Nagel Nucleosil 5 C18-AB 250 × 4 mm column, with a flow

rate of 1 mL min^{-1}. The gradient mobile phase started with 100% solvent A to 80% solvent B at 12 min, with 100% A from 12 to 15 min. The size exclusion radio-HPLC method employed a Waters Biosuite 125 5 μm HR SEC, 300 × 7.8 mm column with a flow rate of 1 mL min^{-1} of 0.1 M phosphate buffer (pH 7) for a data acquisition time of 20 min.

Micro-PET scanning and well-counter instrumentation is described below.

NMR spectra of $[Ga((NH_2)_2sar)](NO_3)_3$, $\mathbf{L^1}$ and $[Ga\mathbf{L^1}](NO_3)_3$ were acquired in D_2O on a Varian FT-NMR 500 spectrometer. ^1H NMR spectra were acquired at 500 MHz, and ^{13}C NMR spectra were acquired at 125.7 MHz. ^1H NMR and ^{13}C NMR spectral shifts were referenced to acetone (δ = 2.22 ppm, δ = 30.89 ppm, respectively). ^1H NMR spectra of $\mathbf{L^1}(RGDfK)_2$ and $[Ga(\mathbf{L^1}(RGDfK)_2)](C_2F_3O_2)_3$ were acquired at 25 °C on a Bruker 600 MHz Avance II spectrometer with a TCI cryoprobe. NMR solutions typically contained ~1 mg/mL peptide in 90% H_2O/10% D_2O without buffer, pH 2−4. TOCSY spectra were acquired over 6292 Hz with 2048 complex data points in F2, 512 increments in F1, and 16 scans per increment. For all experiments in 90%H_2O/10%D_2O, water suppression was achieved using presaturation. Spectra were processed using *TOPSPIN* v 1.3 (Bruker, Germany) software. The *t*1 dimensions of all TOCSY spectra were zero-filled to 2048 real data points with QSINE bell window functions applied in both dimensions followed by Fourier transformation and fifth-order polynomial baseline correction.

Materials and Synthesis. *Synthesis of $[Ga((NH_2)_2sar)]^{3+}$.* To a mixture of $(NH_2)_2$sar (14 mg, 0.003 mmol) dissolved in acetonitrile (2 mL) was added $Ga(NO_3)_3 \cdot xH_2O$ (9 mg) dissolved in methanol (2 mL) resulting in the immediate precipitation of a white solid. The solid was collected by filtration and washed with methanol. The solid was recrystallized from a water/ethanol mixture to give colorless needle-like crystals. A further recrystallization from water/acetone in the presence of HNO_3 (conc., 3 drops) gave colorless block-shaped crystals suitable for X-ray crystallography. MS: $[Ga(C_{14}H_{32}N_8)]^+$ 381.20 (experimental), 381.20 (calculated).

Crystal data: $[Ga((NH_2)_2sar)](NO_3)_3$ $Ga_2C_{28}H_{70}N_{24}O_{24}$, M = 1266.52, T = 130 (2) K, λ = 1.54184, monoclinic, space group $P21/n$, a = 10.3267 (3), b = 13.5498 (5), c =17.1407 (4) Å, β = 93.660(2)°, V = 2393.52 (13) Å^3, Z = 2, D_c = 1.757 mg M^{-3}, μ(Cu−Kα) 2.372, F(000) = 1320, crystal size 0.1930 × 0.1080 × 0.0360 mm^3. 9405 reflections measured, 4323 independent reflections (R_{int} = 0.043), the final R was 0.0328 [$I > 2\sigma(I)$] and $wR(F^2)$ was 0.0866.

The compounds $\mathbf{L^1}$ and $(t\text{-Boc})_5(Succ)_2\mathbf{L^1}$ were synthesized as previously reported.[33]

$[Ga\mathbf{L^1}](NO_3)_3$: A solution of ethanol (100 mL) containing $Ga(NO_3)_3 \cdot xH_2O$ (100 mg), $\mathbf{L^1} \cdot xHCF_3SO_3$ (150 mg) and sodium acetate (0.1 M) was heated at reflux overnight. Concentrated hydrochloric acid (5 mL) was added and the solution was applied to a DOWEX 50Wx2 cation exhange column (H^+ form, 10 × 5 cm). The column was washed with 1 M HCl solution (500 mL) and then eluted with 4 M HCl (350 mL) and the eluent was evaporated to dryness under reduced pressure at 45 °C to give a colorless residue. Yield: $[Ga\mathbf{L^1}](Cl)_3 \cdot xHCl$: 160 mg. The colorless residue was dissolved in deionized water (~5 mL) and several drops of nitric acid were added and the solution left to crystallize overnight. Colorless crystals were collected by filtration. MS: $[GaC_{24}H_{44}N_8O_6]^+$ 609.27 (experimental), 609.27 (calculated). ^1H NMR: δ 1.87, m, 4H, βCH_2 (with respect to COOH); 2.29, t, ^3J = 7.3 Hz, 4H, glutarate CH_2; 2.42, t, ^3J = 7.2 Hz, 4H glutarate CH_2; 2.96, d, ^3J = 9.5 Hz, 6H, cage CH_2; 3.43, d, ^3J = 13.4 Hz, 6H, cage CH_2; 3.61, d, ^3J = 9.5 Hz, 6H, cage CH_2; 3.91, d, ^3J = 13.4 Hz, 6H, cage CH_2. ^{13}C NMR: δ 23.1, 35.7, 37.7 (glutarate CH_2), 49.8, 52.4, 57.8 (cage), 178.8, 180.7 (CO).

$\mathbf{L^1}(RGDfK)_2$: Cyclic-(RGDfK) peptide was synthesized by solution cyclization of the linear protected peptide, H-Asp-(OtBu)-D-Phe-Lys(Boc)-Arg(Pbf)-Gly-OH, followed by deprotection using trifluoroacetic acid in the presence of triisopropylsilane and water followed by purification using semipreparative HPLC.[55] Cyclic-(RGDfK) peptide (3 mg) and $(t\text{-Boc})_5(Succ)_2\mathbf{L^1}$ (5 mg) were dissolved in dimethylformamide (400 μL) and diisopropylethylamine (3 μL) was added. This solution was stirred at ambient temperature for 2 h. Acetonitrile/water (50%/50%) (4 mL) was added and the solution applied to a C18 semipreparative HPLC column and separated using HPLC method 2. Fractions containing pure material were combined, frozen and lyophilized. $(t\text{-Boc})_5\mathbf{L^1}(RGDfK)_2$ (1 mg) eluted at 43 min. MS: $[C_{103}H_{166}N_{26}O_{28}]^{2+}$ 1108.12 (experimental), 1108.12 (calculated). Analytical HPLC: 14.24 min (0% to 100% B in 25 min). $(t\text{-Boc})_5\mathbf{L^1}(RGDfK)_2$ was dissolved in trifluoroacetic acid (1−2 mL) and stirred for ~2 h. The trifluoroacetic acid was evaporated under a stream of N_2 gas. Acetonitrile (1 mL) and water (1 mL) were added to redissolve the residue, and the solution frozen and lyophilized. The dried material was redissolved and purified using a C18 semipreparative HPLC column using HPLC method 2. $\mathbf{L^1}(RGDfK)_2$: MS $[C_{78}H_{126}N_{26}O_{18}]^{2+}$: 857.49 (experimental), 857.49 (calculated). Analytical HPLC: 11.84 min (0% to 60% B in 25 min).

$[Ga(\mathbf{L^1}(RGDfK)_2)]^{3+}$: An ethanol solution containing $\mathbf{L^1}(RGDfK)_2$ (~50 μg) and gallium nitrate (10 μg) with sodium acetate (0.1 M) was heated at 65 °C for one hour. Similarly, two reaction solutions containing the same components were incubated at room temperature and 35 °C for one hour. The mixture was diluted with deionized water and LCMS was acquired of an aliquot. A sample of $[Ga(\mathbf{L^1}(RGDfK)_2)]^{3+}$ for NMR analysis was synthesized in a similar manner and was subsequently isolated using HPLC method 2.

Radiochemical Synthesis. $^{68}GaCl_3$: ^{68}Ga was eluted from the generator where ^{68}Ge was attached to a tin dioxide column using 6 mL of 0.4 M HCl. The method for purifying $^{68}GaCl_3$ was adapted from a previously reported procedure.[56] A solution of $^{68}GaCl_3$ was eluted from the $^{68}Ge/^{68}Ga$ generator with aqueous HCl (5 mL, 0.4 M) and $^{68}GaCl_3$ was trapped on a cation exchange column (BioRad AG 50W × 4, 200−400 mesh). The cation exchange column was washed with a solution of 0.15 M HCl in acetone/water (80%/20%) (1 mL) and $^{68}GaCl_3$ was eluted with a solution of 0.05 M HCl in acetone/water (97.5%/2.5%) (0.4 mL).

$[^{68}Ga(\mathbf{L^1}(RGDfK)_2)]^{3+}$: An aliquot (0.05 M HCl in acetone/water (97.5%/2.5%), 200 μL) containing $^{68}GaCl_3$ (6−12 mCi) was added to $\mathbf{L^1}(RGDfK)_2$ (~50 μg) dissolved in a sodium acetate/ethanol solution (0.1 M, 2 mL). The mixture was heated at 85 °C for 30−35 min, at which point the solvent had evaporated. The remaining residue was dissolved in aqueous sodium chloride (0.9%, 2 mL). TLC analysis (0.1 M sodium citrate mobile phase): $[^{68}Ga(\mathbf{L^1}(RGDfK)_2)]^{3+}$ R_f < 0.1, 98.8%; $^{68}Ga^{3+}$ R_f > 0.8, 1.2%. Radio-HPLC analysis: Scintillation detector 9.68 min, 100%, UV−vis detector, 9.67 min.

Stability Studies. Stability studies using $[^{68}Ga(\mathbf{L^1}(RGDfK)_2)]^{3+}$: Radiolabeled $[^{68}Ga(\mathbf{L^1}(RGDfK)_2)]^{3+}$, synthesized as described above, was dissolved in phosphate buffer (800 μL, 1 M, pH 7.4) containing 6 mg of apo-transferrin. This solution was incubated

at 37 °C for 120 min. Aliquots were subjected to HPLC analysis using a size exclusion column after 0 and 120 min. UV−vis detector: apo-transferrin, 7.97 min. 0 min: TLC analysis: $[^{68}Ga(\mathbf{L^1}(RGDfK)_2)]^{3+}$ $R_f < 0.1$, 98.9%; $^{68}Ga^{3+}$ $R_f > 0.8$, 1.1%. Scintillation detector $[^{68}Ga(\mathbf{L^1}(RGDfK)_2)]^{3+}$, 13.19 min, 100%. 120 min: TLC analysis: $R_f < 0.1$, 97.7%; $^{68}Ga^{3+}$ $R_f > 0.8$, 2.3%. Scintillation detector: 13.41 min, 88.62%; 14.49 min, 11.38%.

Tumor Cell Line. Mouse mammary epithelial cell line, 66cl4β3, was a gift from Dr N. Pouliot (Peter MacCallum Cancer Centre, Melbourne, Australia). The cells have been genetically engineered to express high levels of integrin $\alpha_v\beta_3$.[57] The human squamous cell carcinoma line A431 was purchased at ATCC. Cells were maintained at 37 °C in a 5% CO_2 incubator and cultured in α-MEM medium supplemented with either 5% (66cl4β3 cells) or 10% (A431 cells) fetal calf serum.

In Vitro Studies. Cells (2.5×10^5 cells/well) were plated in 12-well plates and incubated overnight. Prior to addition of activity, the cells were washed three times with PBS and incubated at 37 °C for 15 min with 1 mL of uptake buffer (125 mM NaCl, 4.8 mM KCl, 1.3 mM $CaCl_2$, 1.2 mM $MgSO_4$, 25 mM HEPES, 1.2 mM KH_2PO_4, 5.6 mM glucose, pH adjusted to 7.4 with NaOH). The uptake buffer was then replaced by 0.5 mL uptake buffer containing 0.62 MBq/mL of $[^{68}Ga(\mathbf{L^1}(RGDfK)_2)]^{3+}$ and incubated at 37 °C for 30 min. Cells were washed three times with ice−cold PBS and solubilized in 0.5 mL sodium borate solution (10 mM) containing 1% sodium dodecyl sulfate. The lysates were transferred to tubes for well counting and ^{68}Ga disintegrations at 511 Kev ±15% were quantified in a well counter (187-950-A100 MCA; Biomedex Medical Systems) attached to a multichannel analyzer interfaced with *Atomlabs 950* software. For experiments at 4 °C, cells were placed on ice 15 min prior to addition of $[^{68}Ga(\mathbf{L^1}(RGDfK)_2)]^{3+}$ and during the course of the incubation period. Uptake medium containing $[^{68}Ga(\mathbf{L^1}(RGDfK)_2)]^{3+}$ was also cooled to 4 °C prior to addition to cells. All experiments were performed in quadruplicate and normalized to protein content (BCA method, Pierce). Results were expressed as the percentage of the added radioactive dose per mg of protein (%AR/mg).

Tumor Implantation and PET Imaging. Tumor xenografts were established in the shoulder of 6−8 week old anaesthetized (inhalation of 2.5% isoflurane [Abbott Laboratories] in 50% O_2 in air) Balb/c mice by injecting 10^5 66cl4β3 cells subcutaneously in 100 μL 1:1 PBS/Matrigel (BD Biosciences). When tumor volumes reached approximately 200 mm^3, a size at which partial volume effects are modest on the micro-PET system used for imaging, mice were injected with 15−22 MBq $[^{68}Ga(\mathbf{L^1}(RGDfK)_2)]^{3+}$ in 100 μL saline via lateral tail vein. Two hours after tracer injection, animals ($n = 5$) were anaesthetized as above and scanned for 10 min on a Mosaic small animal PET scanner (Philips Medical Systems, Ohio, USA; resolution 2.7 mm at the center of the FOV). An energy window of 450−700 keV and a 6 ns coincidence-timing window were used. Data were acquired in 3D mode and corrected for isotope decay and random disintegrations. Images were reconstructed with the 3D RAMLA algorithm and tracer uptake measured using the region of interest (ROI) software on the Mosaic workstation. Briefly, ROIs were drawn around tumors as well as background regions chosen to represent the mediastinal blood pool excluding regions of tracer accumulation such as kidneys and bladder. Tumor-to-background ratios were calculated by dividing the maximum pixel intensity within the tumor ROI by the average pixel intensity within the background ROI.

Biodistribution Studies. After 0.5, 1, 1.5, and 2 h, animals ($n = 3$ for each time point) were sacrificed and tumor and tissues were removed and weighted before analysis of retained radioactivity. Disintegrations at 511 Kev ±15% were quantified in a well counter (187−950-A100 MCA; Biomedex Medical Systems) attached to a multichannel analyzer interfaced with *Atomlabs 950* software. For blocking studies, animals ($n = 3$) were coinjected with 0.2 mg of cyclic-(RGDfK) peptide and sacrificed at 2 h and subjected to the same tumor and tissue analysis as described above. Linear regression models were used to estimate mean differences in uptake between blocked and unblocked animals, and the Wald test was used to obtain p-values for these differences.

RESULTS AND DISCUSSION

Synthesis of $\mathbf{L^1}(RGDfK)_2$. The bifunctional ligand $\mathbf{L^1}$ possesses two carboxylate groups and can be derivatized to give a sarcophagine−peptide dimeric species containing two biologically active peptide groups. The first dimeric construct of $\mathbf{L^1}$ a cage amine ligand tethered to two bombesin targeting peptides was reported recently, as well the characterization of the $^{64}Cu^{2+}$ complex.[58] A similar synthetic strategy was applied here to prepare a derivative with two cyclic-RGD peptide motifs linked to a single cage amine ligand, $\mathbf{L^1}(RGDfK)_2$. In the first step of the synthesis, the secondary amine groups of $\mathbf{L^1}$ were protected with *N-tert*-butoxycarbonyl (*t*-Boc) to give a derivative with five *N-tert*-butoxycarbonyl groups, $(t\text{-Boc})_5\mathbf{L^1}$ (Scheme 1). This protection step ensures selectivity in the peptide coupling reaction preventing any potential coupling between the secondary amine atoms of one cage amine ligand with the activated ester of another cage amine ligand. The reaction of $(t\text{-Boc})_5\mathbf{L^1}$ with *N*-hydroxysuccinimide in the presence of diisopropylethylamine allowed isolation of the activated N-succinimidyl ester, $(t\text{-Boc})_5(Succ)_2\mathbf{L^1}$. This activated ester was then reacted with cyclic-(RGDfK), the activated ester reacting with the amine side chain of lysine. Deprotection followed by purification by HPLC allowed isolation of $\mathbf{L^1}(RGDfK)_2$ (Scheme 1).

In at least one experiment of this type, the coupling reaction between $(t\text{-Boc})_5(Succ)_2\mathbf{L^1}$ and cyclic-(RGDfK) did not go to completion allowing the isolation of a product where only one of the activated esters had coupled to the peptide. Purification by HPLC enables the isolation of a compound where one peptide had formed an amide with the carboxylate functional group on one end of the ligand, but the second carboxylate functional group remained as an unreacted activated N-succinimidyl ester, $(t\text{-Boc})_5(Succ)\mathbf{L^1}(RGDfK)$. This species with a single activated ester remaining can be used to form heterodimeric sarcophagine derivatives as illustrated by the synthesis of $\mathbf{L^1}(RGDfK)(Lys^3$-bombesin1−14) (see Supporting Information). Lys^3-bombesin-(1−14) is a 14 amino acid peptide that binds to gastrin-releasing receptors that are overexpressed in certain cancers and radiolabeled derivatives have been used to image tumors. The isolation of this elegant heterodimeric cage amine ligand highlights the exciting possibilities for multimeric constructs synthesized from $\mathbf{L^1}$ as dual function radiotracers.

Synthesis of $[Ga(NH_2)_2sar)]^{3+}$, $[GaL^1]^{3+}$, and $[Ga(\mathbf{L^1}(RGDfK)_2)]^{3+}$. Sarcophagine ligands offer a flexible macrobicyclic cage amine framework with six secondary amine donors capable of encapsulating metal ions in a six coordinate environment with geometries varying between octahedral and trigonal prismatic.[59−61] Many metal complexes of sarcophagine and its derivatives have been structurally characterized by X-ray crystallography, but this is the

Scheme 1. Synthesis of $L^1(RGDfK)_2$

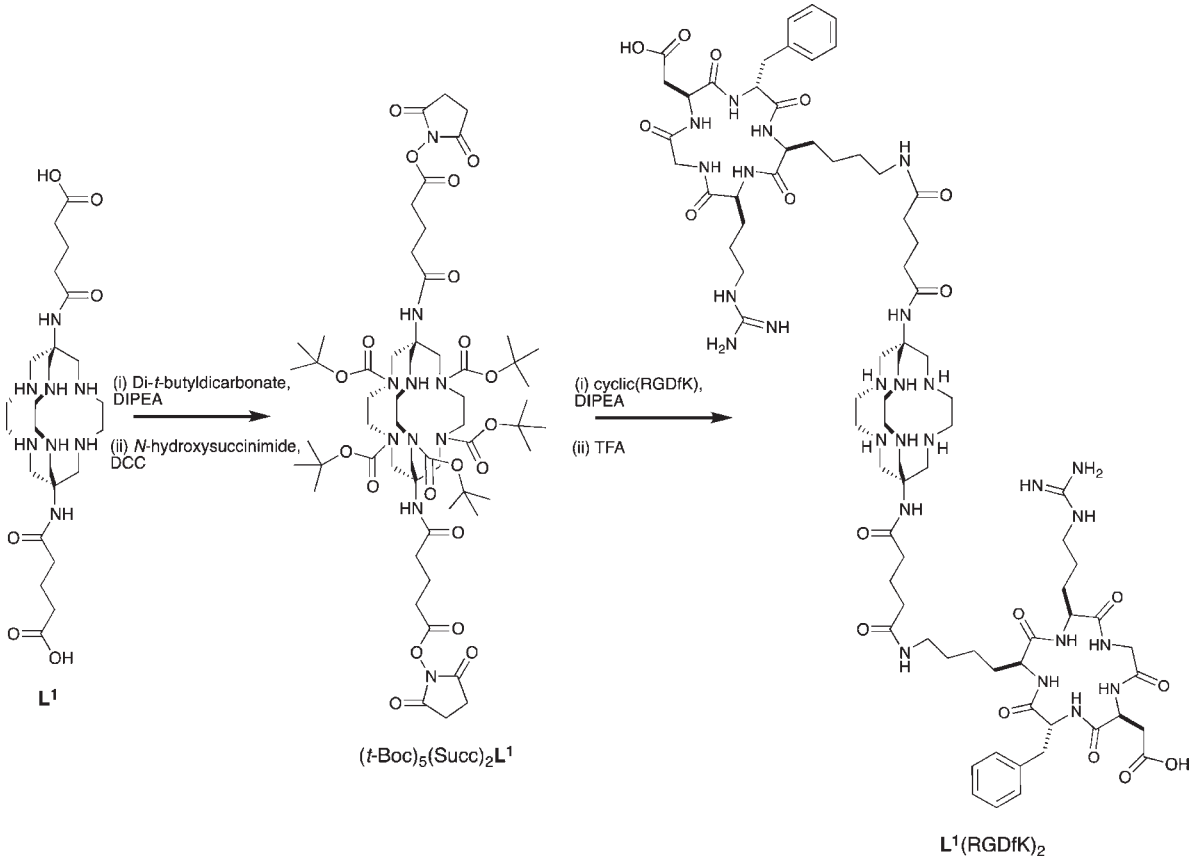

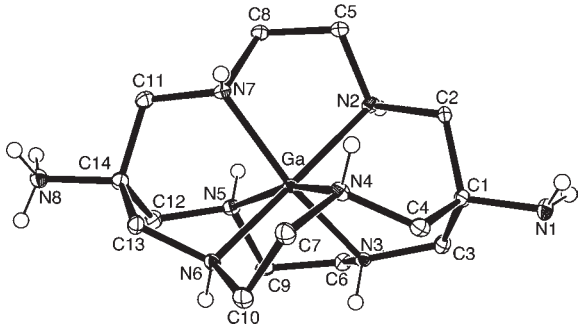

Figure 2. ORTEP representation of the cation present in $[Ga\text{-}(1\text{-}NH_3\text{-}8\text{-}NH_2\text{-}sar)](NO_3)_4$. Ellipsoids are shown at the 40% probability level. Hydrogen atoms attached to carbon are omitted for clarity.

first report of the molecular structure of a gallium sarcophagine complex. The gallium complex of $(NH_2)_2$sar was prepared by addition of $Ga(NO_3)_3$ to a solution of the ligand in acetonitrile at room temperature. Crystals of $[Ga((NH_2)(NH_3)sar)]^{4+}$ suitable for structural studies were grown from an aqueous solution after the addition HNO_3 (Figure 2). The gallium is six coordinate with a distorted octahedral geometry with trigonal distortions with both enantiomers present in the unit cell. The Ga−N bond lengths range 2.068(2)−2.114(2) Å. The encapsulating ligand adopts a relatively rare *lel*$_2$*ob* conformation where the terms *lel* and *ob* refer to either parallel or oblique orientations of the C−C bond of the five-membered chelate ring with respect to the C_3 axis.[30,60,61] The nitrate anions have several close contacts to NH residues of the cage amine ligand to form an intricate hydrogen bonding array within the lattice.[61]

Table 1. Crystallographic Data

	$[GaL^1](NO_3)_4$
formula	$Ga_2C_{28}H_{70}N_{24}O_{24}$
formula weight	1266.52
crystal system	monoclinic
space group	*P*21/*n*
a, *b*, *c* (Å)	10.3267 (3), 13.5498 (5), 17.1407 (4)
α, β, γ (deg)	90.00, 93.660(2), 90.00
cell volume (Å^3)	2393.52 (13)
Z	2
temperature (K)	130 (2)
λ (Å)	1.54184
reflections collected	9405
independent reflections	4323
R-factor (%)	3.28%

Efforts to form Ga^{3+} complexes of L^1 and $L^1(RGDfK)_2$ using nonradioactive naturally abundant gallium sources focused on conditions designed to be relevant to radiolabeling with $^{68}Ga^{3+}$ that is obtained from a $^{68}Ge/^{68}Ga$ generator that is normally eluted with hydrochloric acid. The coordination of Ga^{3+} to the diacylated ligand L^1 was monitored by ^1H NMR and ESMS revealing

dx.doi.org/10.1021/bc200319q |*Bioconjugate Chem.* 2011, 22, 2093–2103

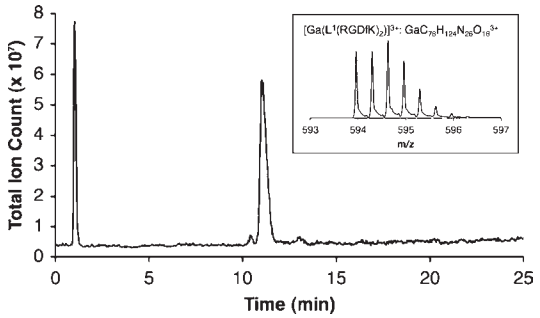

Figure 3. HPLC-MS chromatogram of $[Ga(\mathbf{L^1}(RGDfK)_2)]^{3+}$, R_t = 11.01 min (R_t = 1.01 min) corresponds to sodium acetate). Inset: ESMS of peak at R_t = 11.01 min = $[^{nat}Ga(\mathbf{L^1}(RGDfK)_2)]^{3+}$.

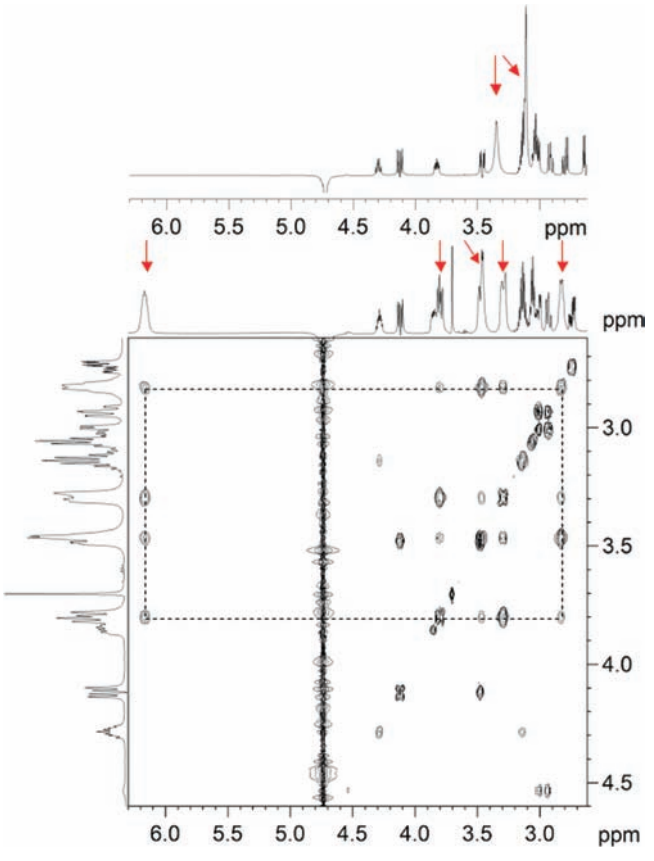

Figure 4. Top: ^{1}H 1D NMR spectrum of $\mathbf{L^1}(RGDfK)_2$ in H_2O/D_2O. Bottom: ^{1}H TOCSY spectrum of $[Ga(\mathbf{L^1}(RGDfK)_2)]^{3+}$ in H_2O/D_2O with ^{1}H 1D projections. Arrows indicate sarcophagine group proton signals.

that $[Ga\mathbf{L^1}]^{3+}$ forms quantitatively in ethanolic mixtures of sodium acetate (0.1 M). A ^{1}H NMR spectrum of $[Ga\mathbf{L^1}]^{3+}$ indicates that the metal ion is coordinated to the secondary amine nitrogen atoms of the sarcophagine ligand due to the appearance of four geminally coupled diastereotopic methylene signals of the sarcophagine ligand framework. The ESMS has a signal at m/z = 609.27 with the expected isotope pattern corresponding to the monocationic complex originating from deprotonation of the two carboxylic acids, of $[Ga\mathbf{L^1}\text{-}2H^+]^+$.

The gallium complex of $\mathbf{L^1}(RGDfK)_2$ can be prepared in ethanol containing sodium acetate (0.1 M) by heating at 65 °C for 30 min. The complex, $[Ga(\mathbf{L^1}(RGDfK)_2)]^{3+}$, was characterized

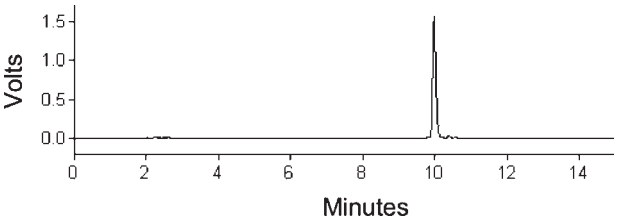

Figure 5. HPLC chromatogram of $[^{68}Ga(\mathbf{L^1}(RGDfK)_2)]^{3+}$ (detection of radioactivity).

by HPLC-MS with a single peak in the chromatogram with a signal in the ESMS at m/z = 594.63 with the expected isotope pattern corresponding to tricationic $[Ga(\mathbf{L^1}(RGDfK)_2)]^{3+}$ (Figure 3). The stability of the attached RGDfK peptide under these reaction conditions was confirmed by analysis by HPLC. Complexation at a lower temperature (35 °C) resulted in lower yields of $[Ga(\mathbf{L^1}(RGDfK)_2)]^{3+}$.

The coordination of Ga^{3+} within the encapsulating cage amine ligand rather than to the donor atoms of the cyclic-(RGDfK) peptide was confirmed by ^{1}H NMR spectroscopy. The ^{1}H NMR spectrum of $\mathbf{L^1}(RGDfK)_2$ in H_2O/D_2O (90%/10%) has two broad resonances between 3.0 and 3.5 ppm, each integrating to twelve protons (Figure 4, top, red arrows) due to the methylene groups of the sarcophagine framework. Resonances that could be attributed to the secondary amine atoms of the cage framework are not observed as a result of the rate of proton exchange relative to the NMR time scale under these conditions (H_2O, pH 3−5). A consequence of coordination and encapsulation of Ga^{3+} by the cage amine ligand is that the methylene protons become diastereotopic as observed in the ^{1}H NMR spectrum of $[Ga(\mathbf{L^1}(RGDfK)_2)]^{3+}$, confirming that the metal ion resides within the cage framework (Figure 4). Unlike the "free" ligand, it is possible to observe a resonance attributable to protons from the secondary amine groups of the cage in $[Ga(\mathbf{L^1}(RGDfK)_2)]^{3+}$ and the TOCSY spectrum shows that methylene cage protons and protons of the secondary amine groups are all coupled to each other (Figure 4).

$\mathbf{L^1}(RGDfK)_2$ Can Be Radolabeled with $^{68}Ga^{3+}$ to Give $[Ga(\mathbf{L^1}(RGDfK)_2)]^{3+}$ in High Radiochemical Purity. Solutions containing $^{68}GaCl_3$ were eluted from the $^{68}Ge/^{68}Ga$ generator using aqueous HCl solutions—in this case, 0.4 M HCl solution (5 mL).[56] Postelution preconcentration and purification results in solutions of $^{68}GaCl_3$ containing lower concentrations of HCl, lower concentrations of "other" metal ions including Zn^{2+} (decay product), $^{68}Ge^{4+}$ (break-through from generator), Fe^{3+} and Ti^{4+} (generator matrix), and smaller volumes of solution. The postelution purification method employed here yielded solutions of $^{68}GaCl_3$ (15−25 mCi) in 400 μL 0.05 M HCl in ~97.5% acetone/2.5% water.

Addition of this preconcentrated $^{68}GaCl_3$ solution to $\mathbf{L^1}$-$(RGDfK)_2$ (50 μg) in a solution of ethanol containing sodium acetate (0.1 M, 1 mL) and heating the mixture at 85 °C for 30 min resulted in the formation of $[^{68}Ga(\mathbf{L^1}(RGDfK)_2)]^{3+}$ in high radiochemical yield. During the heating period, the solvent evaporated and the residue was dissolved in saline for *in vivo* experiments. The radiochemical purity was greater than 98% with $\mathbf{L^1}(RGDfK)_2$ binding Ga^{3+} quantitatively to form a single radiolabeled product (Figure 5), as monitored by radio-TLC and radio-HPLC. The composition of the radiolabeled compound was confirmed by HPLC with coelution of the radiolabeled product with "cold" $[Ga((\mathbf{L^1}(RGDfK)_2)]^{3+}$ (detected at λ_{220}). This also confirmed that the conjugated peptide was stable under the radiolabeling conditions. Performing the radiolabeling at room

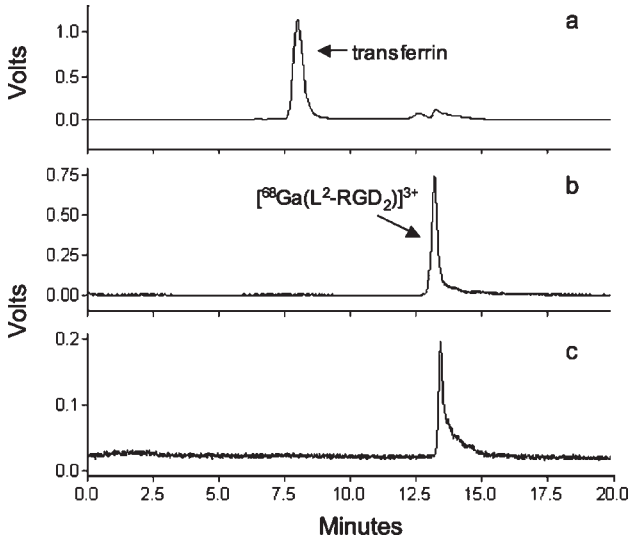

Figure 6. Size exclusion chromatography of (a) apo-transferrin protein (λ_{220}); (b) $[Ga(\mathbf{L}^1(RGDfK)_2)]^{3+}$ (with a radiation detector); (c) solution of $[^{68}Ga(\mathbf{L}^1(RGDfK)_2)]^{3+}$ incubated with apo-transferrin for 120 min (with a radiation detector).

temperature results in a lower radiochemical yield (30% after incubation for 30 min). The radiolabeling conditions described give a single radioactive product in high radiochemical yield allowing for minimal postprocessing of labeled species prior to *in vivo* administration.

$[Ga(L^1(RGDfK)_2)]^{3+}$ is Stable in the Presence of Transferrin. The endogenous protein transferrin is an iron transporter with two Fe^{3+} binding sites that is abundant in human serum (2.5 mg/mL, of which about 30% is occupied with Fe^{3+}). Transferrin binds Fe^{3+} with high affinity ($\log \beta_1 = 22.8$, $\log \beta_2 = 44.3$) but also displays high affinity for Ga^{3+} ($\log \beta_1 = 20.3$, $\log \beta_2 = 39.6$), which has a similar ionic radius to Fe^{3+}.[62] One of the major challenges in the design of any gallium radiopharmaceutical is to impart sufficient kinetic stability to the Ga^{3+} complex so that it can withstand competition in the presence of high serum levels of transferrin. The kinetic stability of $[^{68}Ga(\mathbf{L}^1(RGDfK)_2)]^{3+}$ was assessed by a challenge experiment with apo-transferrin (iron-free transferrin). A sample of $[^{68}Ga(\mathbf{L}^1(RGDfK)_2)]^{3+}$ was incubated at pH 7.0 at 40 °C for 2 h in the presence of apo-transferrin (7 mg/mL), and the mixture was analyzed by size exclusion chromatography. Under the size exclusion chromatographic conditions employed here, apo-transferrin elutes at 7.97 min (detected at λ_{220}) and $[^{68}Ga(\mathbf{L}^1(RGDfK)_2)]^{3+}$ elutes at 13.19 min (detected using a radiation detector) (Figure 6). After incubation with apo-transferrin for 2 h, >88% of the radioactive activity is associated with a species with a retention time of 13.41 min and the remaining activity, 11%, is associated with a species with a retention time of 14.49 min (Figure 6). Additionally, analysis by radio-TLC of the incubated sample indicated that only *ca.* 2.0% of ^{68}Ga activity could be attributed to ^{68}Ga not bound to peptide or protein. These data indicate the presence of a ^{68}Ga-bound peptide species, and importantly, there is no transfer of $^{68}Ga^{3+}$ to apo-transferrin indicating that the $^{68}Ga^{3+}$ sarcophagine complex is kinetically stable in the presence of apo-transferrin.

***In Vitro* Characterization of Cell Uptake of $[^{68}Ga(L^1(RGDfK)_2)]^{3+}$.** *In vitro* uptake of $[^{68}Ga(\mathbf{L}^1(RGDfK)_2)]^{3+}$ was compared in 66cl4β3 cells that have been engineered to express high levels of integrin $\alpha_v\beta_3$[57] and A431 human squamous cell carcinoma cells that do not express $\alpha_v\beta_3$.[63] Radioactivity counted

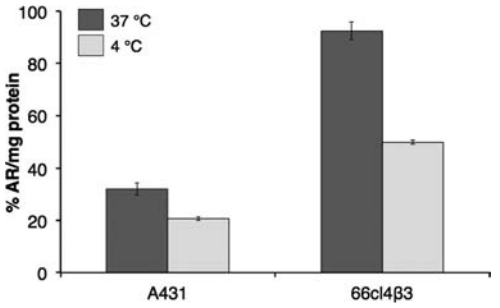

Figure 7. *In vitro* uptake of $[^{68}Ga(\mathbf{L}^1(RGDfK)_2)]^{3+}$ in $\alpha_v\beta_3$-positive 66cl4β3 cells vs $\alpha_v\beta_3$-negative A431 cells. Cells were incubated either at 37 or 4 °C for 30 min with 0.6 MBq $[^{68}Ga(\mathbf{L}^1(RGDfK)_2)]^{3+}$. Results are expressed as percentage of added radioactivity per mg of protein (%AR/mg protein) and represent mean ± standard error of four experiments.

in cells incubated at 37 °C represents cell surface-bound and internalized ^{68}Ga activity, whereas radioactivity counted in cells incubated at 4 °C largely represents only cell surface-bound activity. Activity for 66cl4β3 cells measured 92.5 ± 3.4 of % added radioactivity/mg protein (%AR/mg) at 37 °C, and 49.8 ± 0.9%AR/mg at 4 °C, indicating that over 40%AR/mg is internalized after 30 min incubation at 37 °C (Figure 7). This contrasts the observations for the negative control A431 experiments, where radioactivity measured 32.0 ± 2.3%AR/mg at 37 °C and 20.7 ± 0.7 at 4 °C, indicating that only ~10%AR/mg is internalized after 30 min incubation at 37 °C.

These *in vitro* results demonstrate that $[^{68}Ga(\mathbf{L}^1(RGDfK)_2)]^{3+}$ exhibits both significantly increased cell-surface binding and internalization in an $\alpha_v\beta_3$-positive cell line compared to an $\alpha_v\beta_3$-negative cell line, suggesting retention of activity toward $\alpha_v\beta_3$ receptors.[64] Nonetheless, in-depth biological characterization of this class of tracers is the focus of ongoing work.

Biodistribution and Tumor Uptake $[^{68}Ga(L^1(RGDfK)_2)]^{3+}$. Mice bearing subcutaneous 66cl4β3 tumors that express high levels of integrin $\alpha_v\beta_3$ were sacrificed 0.5, 1, 1.5, and 2 h after injection of 15−22 MBq $[^{68}Ga(\mathbf{L}^1(RGDfK)_2)]^{3+}$ in the tail vein. Primary tumor, blood, muscle, kidney, and liver were recovered, and the radioactivity in these tissues was measured by well counting (Figure 8). In the tumor, the percentage of injected dose per gram of tissue (%ID/g) reached an average value of 4.80 ± 1.38 at 0.5 h postinjection (PI) rising to 6.83 ± 0.47 at 1.5 h PI and remaining at 6.30 ± 0.45 at 2 h PI. Radioactivity cleared rapidly from the blood, reaching a peak of 1.23 ± 0.33%ID/g at 0.5 h PI that decreased to 0.25 ± 0.03%ID/g at 2 h PI. Muscle activity was low over the time course of the experiment (<1%ID/g at all time points). High levels of activity were observed in the kidney, with the highest activity seen at 1 h PI (40.23 ± 11.26% ID/g) decreasing by half by 2 h PI (19.96 ± 0.88%ID/g). Liver uptake was moderate, with activity measuring between 6 and 9% ID/g at all observed time points. Tumor/blood ratios gradually increased over the course of the experiment, consistent with rapid blood clearance and high tumor retention, increasing from 4.46 ± 2.06 at 0.5 h PI to 26.37 ± 5.38 at 2 h PI.

The high tumor uptake together with the low retention in nontarget organs observed soon after the tracer injection (from 1.5 h) makes $[^{68}Ga(\mathbf{L}^1(RGDfK)_2)]^{3+}$ eminently suitable for PET imaging using short-lived isotopes such as ^{68}Ga. These results also indicate that $[^{68}Ga(\mathbf{L}^1(RGDfK)_2)]^{3+}$ is predominantly eliminated through the kidneys and that the hepato-biliary clearance route contributes minimally to excretion of ^{68}Ga activity. Clearance

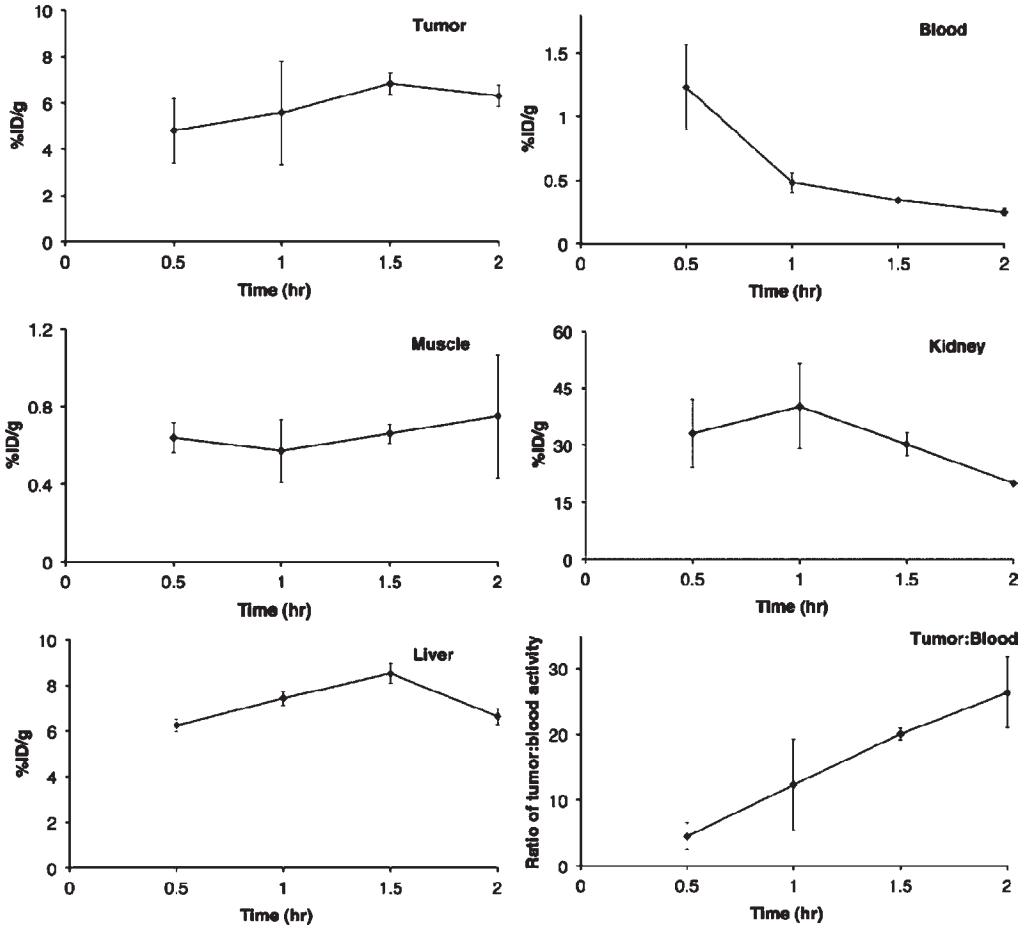

Figure 8. Time-dependent biodistribution of ^{68}Ga radioactivity in Balb/c mice bearing 66cl4β3 tumors administered with $[^{68}Ga(\mathbf{L^1}(RGDfK)_2)]^{3+}$. Results are expressed as percentage of injected dose per gram of tissue (%ID/g) and represent the mean ± SD from four separate experiments, each comprising three mice.

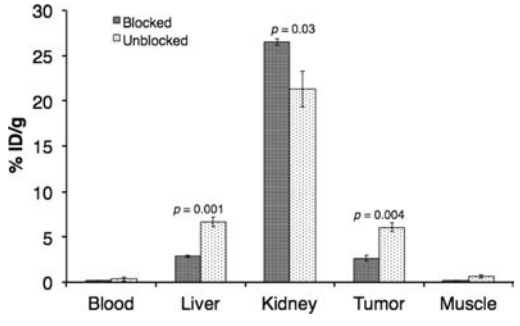

Figure 9. Biodistribution of ^{68}Ga activity in Balb/c mice bearing 66cl4β3 tumors 2 h postinjection with $[^{68}Ga(\mathbf{L^1}(RGDfK)_2)]^{3+}$ cyclic-(RGDfK) peptide ("blocked") or with $[^{68}Ga(\mathbf{L^1}(RGDfK)_2)]^{3+}$ ("unblocked"). Data presented are the mean ± standard error values of 3 mice, and p values were calculated using a Wald test of differences between means.

predominantly through the kidneys is favorable for diagnostic imaging purposes often leading to rapid clearance of activity in nontarget organs and tissue, resulting in low background levels for PET images.

To investigate the specificity of $[^{68}Ga(\mathbf{L^1}(RGDfK)_2)]^{3+}$ for $\alpha_v\beta_3$ integrin receptor, a "blocking" experiment was performed by coinjecting cyclic-(RGDfK) with $[^{68}Ga(\mathbf{L^1}(RGDfK)_2)]^{3+}$ (Figure 9). The specific blocking of $\alpha_v\beta_3$ resulted in a decrease of 56% of activity in the tumor at 2 h PI (6.07 ± 0.49%ID/g for a standard injection vs 2.64 ± 0.34%ID/g for a blocking experiment, p = 0.004), confirming that the peptide targeting group is indeed targeting receptors that bind the cyclic-(RGDfK) motif. Similarly, coinjection of cyclic-(RGDfK) resulted in a decrease of over half the measured activity in the liver at 2 h PI (6.66 ± 0.52%ID/g for a standard injection vs 2.87 ± 0.13%ID/g for a blocking experiment, p = 0.001), indicating that liver uptake of $[^{68}Ga(\mathbf{L^1}(RGDfK)_2)]^{3+}$ is most likely receptor-mediated. Taken together, these results clearly indicate that the tumor retention of $[^{68}Ga(\mathbf{L^1}(RGDfK)_2)]^{3+}$ is selective and receptor-mediated.

$[^{68}Ga(\mathbf{L^1}(RGDfK)_2)]^{3+}$ PET Imaging. Micro-PET scans of Balb/c mice bearing 66cl4β3 tumors were acquired at 2 h PI as ratios for tumor/kidney and tumor/blood were highest at 2 h PI (0.32 ± 0.01 and 26.37 ± 5.38, respectively). A representative micro-PET scan is included in Figure 10. In all scans, tumors could be easily delineated from normal tissue, with an average tumor/background intensity ratio of 2.68 ± 0.16. Consistent with biodistribution data, the kidneys and liver of each animal could also be delineated, along with the bladder. Notably, micro-PET scans indicate that skeletal uptake is low, which is consistent with the kinetic stability of $[^{68}Ga(\mathbf{L^1}(RGDfK)_2)]^{3+}$ *in vivo*.

SUMMARY

The encapsulating yet flexible sarcophagine ligands form kinetically and thermodynamically stable metal complexes with fast complexation kinetics, and have been demonstrated to be of particular interest in the development of copper radiopharmaceuticals.[33−35,37−39]

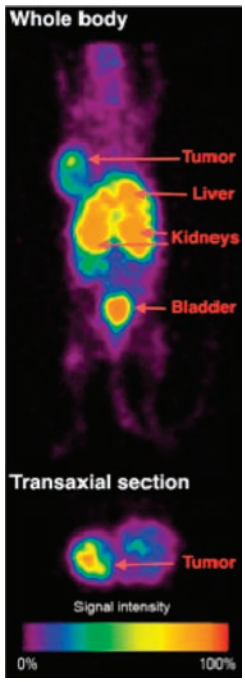

Figure 10. Micro-PET scan of a Balb/c mouse with selective uptake of $[^{68}Ga(\mathbf{L^1}(RGDfK)_2)]^{3+}$ in 66cl4β3 tumor. PET images were obtained 2 h post injection of 15−22 MBq $[^{68}Ga(\mathbf{L^1}(RGDfK)_2)]^{3+}$.

This work shows that bifunctional sarcophagine ligand systems also have the potential to be utilized as chelating agents for peptide targeted gallium radiopharmaceuticals that make use of the commercially available $^{68}Ge/^{68}Ga$ generator. A Ga^{3+} complex of a sarcophagine ligand has been structurally characterized by X-ray crystallography showing that the metal ion resides within the cavity of the cage amine ligand coordinated to six nitrogen atoms in a distorted octahedral environment. A macrobicyclic cage amine bifunctional chelator based on the sarcophagine ($\mathbf{L^1}$) framework has been conjugated to two cyclic-(RGDfK) peptides to give a dimeric bioconjugate with the potential for bivalent interactions with $\alpha_v\beta_3$ integrin receptors that are overexpressed on the cell surface of certain tumors. This new conjugate, $\mathbf{L^1}(RGDfK)_2$, binds Ga^{3+}, and the complex has been characterized by NMR spectroscopy and HPLC-mass spectrometry. It is possible to synthesize the radioactive analogue with positron emitting $^{68}Ga^{3+}$ in high radiochemical yields, and the resulting complex is kinetically stable with $^{68}Ga^{3+}$ remaining in the cage amine ligand when challenged with apo-transferrin. Biodistribution studies and micro-PET imaging in mice reveal high selective tumor uptake and clearance predominantly through the kidneys, and this is important for producing images with low background coupled to high tumor uptake. Furthermore, micro-PET images are consistent with the high stability of the $[^{68}Ga(\mathbf{L^1}(RGDfK)_2)]^{3+}$ complex during the imaging period demonstrating that $[^{68}Ga(\mathbf{L^1}(RGDfK)_2)]^{3+}$ is suitable for *in vivo* imaging of $\alpha_v\beta_3$ integrin receptors and has the potential to provide noninvasive diagnosis of tumors as well as monitoring of antiangiogenic or anti-$\alpha_v\beta_3$ targeted therapies.

■ ASSOCIATED CONTENT

Supporting Information. Includes the CIF for the X-ray structure of $[Ga\text{-}(1\text{-}NH_3\text{-}8\text{-}NH_2\text{-}sar)](NO_3)_4$ and the experimental procedures for the synthesis of $\mathbf{L^1}(RGDfK)(Lys^3\text{-bombesin1}-14)$. This material is available free of charge via the Internet at http://pubs.acs.org.

■ AUTHOR INFORMATION

Corresponding Author

*E-mail addresses: Rod.Hicks@petermac.org; pauld@unimelb.edu.au.

■ ACKNOWLEDGMENT

M.T.M. acknowledges Cancer Council Victoria for providing a Sydney Parker Smith Postdoctoral Cancer Research Fellowship; a Kaye Merlin Brutton Bequest. P.S.D. acknowledges funding from the Australian Research Council and National Health and Medical Research Council. The authors thank Dr. N. Pouliot from the Metastasis Research Lab at The Peter MacCallum Cancer Centre for gifting 66cl4β3 and 66cl4pBabe cells, Dr. Peter Eu for helpful discussions, Mr. Wayne Noonan for assistance with HPLC, Mr. David Muller from the Cancer Epidemiology Centre, Cancer Council Victoria for statistical analyses, and Dr. Brett Paterson for proof reading the manuscript.

■ REFERENCES

(1) Roesch, F., and Riss, P. J. (2010) The renaissance of the $^{68}Ge/^{68}Ga$ radionuclide generator initiates new developments in ^{68}Ga radiopharmaceutical chemistry. *Curr. Top. Med. Chem. 10*, 1633–68.

(2) Bartholoma, M. D., Louie, A. S., Valliant, J. F., and Zubieta, J. (2010) Technetium and gallium derived radiopharmaceuticals: Comparing and contrasting the chemistry of two important radiometals for the molecular imaging era. *Chem. Rev. 110*, 2903–20.

(3) Wadas, T. J., Wong, E. H., Weisman, G. R., and Anderson, C. J. (2010) Coordinating radiometals of copper, gallium, indium, yttrium, and zirconium for PET and SPECT imaging of disease. *Chem. Rev. 110*, 2858–902.

(4) Hicks, R. J. (2006) Ga-67 SPECT: ave atque vale! or have we bid a premature farewell to a trusted friend? *Leukemia Lymphoma 47*, 2440–2.

(5) Kayani, I., Bomanji, J. B., Groves, A., Conway, G., Gacinovic, S., Win, T., Dickson, J., Caplin, M., and Ell, P. J. (2008) Functional imaging of neuroendocrine tumors with combined PET/CT using ^{68}Ga-DOTATATE (DOTA-DPhe^1,Tyr^3-octreotate) and ^{18}F-FDG. *Cancer 112*, 2447–55.

(6) Ferreira, C. L., Lamsa, E., Woods, M., Duan, Y., Fernando, P., Bensimon, C., Kordos, M., Guenther, K., Jurek, P., and Kiefer, G. E. (2010) Evaluation of bifunctional chelates for the development of gallium-based radiopharmaceuticals. *Bioconjugate Chem. 21*, 531–6.

(7) Bandoli, G., Dolmella, A., Tisato, F., Porchia, M., and Refosco, F. (2009) Mononuclear six-coordinated Ga(III) complexes: A comprehensive survey. *Coord. Chem. Rev. 253*, 56–77.

(8) Meyer, G.-J., Maecke, H., Schuhmacher, J., Knapp, W. H., and Hofmann, M. (2004) ^{68}Ga-labelled DOTA-derivatised peptide ligands. *Eur. J. Nucl. Med. Mol. Imaging 31*, 1097–104.

(9) Kubicek, V., Havlickova, J., Kotek, J., Tircso, G., Hermann, P., Toth, E., and Lukes, I. (2010) Gallium(III) complexes of DOTA and DOTA-monoamide: Kinetic and thermodynamic studies. *Inorg. Chem. 49*, 10960–9.

(10) Brom, M., Oyen, W. J. G., Joosten, L., Gotthardt, M., and Boerman, O. C. (2010) ^{68}Ga-labelled exendin-3, a new agent for the detection of insulinomas with PET. *Eur. J. Nucl. Med. Mol. Imaging 37*, 1345–55.

(11) Cantorias, M. V., Figueroa, S. D., Quinn, T. P., Lever, J. R., Hoffman, T. J., Watkinson, L. D., Carmack, T. L., and Cutler, C. S. (2009) ^{68}Ga-labeled DOTA-rhenium-cyclized α-MSH peptide analog to target MC1 receptors overexpressed by melanoma tumors. *Nucl. Med. Biol. 36*, 505–13.

(12) Guo, H., Yang, J., Shenoy, N., and Miao, Y. (2009) Gallium-67-labeled lactam bridge-cyclized α-melanocyte stimulating hormone

peptide for primary and metastatic melanoma imaging. *Bioconjugate Chem. 20*, 2356–63.

(13) Tolmachev, V., Velikyan, I., Sandstroem, M., and Orlova, A. (2010) A HER2-binding affibody molecule labelled with ^{68}Ga for PET imaging: Direct in vivo comparison with the ^{111}In-labelled analogue. *Eur. J. Nucl. Med. Mol. Imaging 37*, 1356–67.

(14) Ujula, T., Huttunen, M., Luoto, P., Perakyla, H., Simpura, I., Wilson, I., Bergman, M., and Roivainen, A. (2010) Matrix metalloproteinase 9 targeting peptides: Syntheses, ^{68}Ga-labeling, and preliminary evaluation in a rat melanoma xenograft model. *Bioconjugate Chem. 21*, 1612–21.

(15) Shetty, D., Jeong, J. M., Ju, C. H., Kim, Y. J., Lee, J.-Y., Lee, Y.-S., Lee, D. S., Chung, J.-K., and Lee, M. C. (2010) Synthesis and evaluation of macrocyclic amino acid derivatives for tumor imaging by gallium-68 positron emission tomography. *Bioorg. Med. Chem. 18*, 7338–47.

(16) de Sa, A., Matias, A. A., Prata, M. I. M., Geraldes, C. F. G. C., Ferreira, P. M. T., and Andre, J. P. (2010) Gallium labeled NOTA-based conjugates for peptide receptor-mediated medical imaging. *Bioorg. Med. Chem. Lett. 20*, 7345–8.

(17) Velikyan, I., Maecke, H., and Langstrom, B. (2008) Convenient preparation of ^{68}Ga-based PET-radiopharmaceuticals at room temperature. *Bioconjugate Chem. 19*, 569–73.

(18) Li, Z.-B., Chen, K., and Chen, X. (2008) ^{68}Ga-labeled multimeric RGD peptides for microPET imaging of integrin $\alpha v\beta 3$ expression. *Eur. J. Nucl. Med. Mol. Imaging 35*, 1100–8.

(19) Liu, Z., Niu, G., Wang, F., and Chen, X. (2009) ^{68}Ga-labeled NOTA-RGD-BBN peptide for dual integrin and GRPR-targeted tumor imaging. *Eur. J. Nucl. Med. Mol. Imaging 36*, 1483–94.

(20) Liu, Z., Niu, G., Shi, J., Liu, S., Wang, F., Liu, S., and Chen, X. (2009) ^{68}Ga-labeled cyclic RGD dimers with Gly_3 and PEG_4 linkers: Promising agents for tumor integrin $\alpha v\beta 3$ PET imaging. *Eur. J. Nucl. Med. Mol. Imaging 36*, 947–57.

(21) Jeong, J. M., Hong, M. K., Chang, Y. S., Lee, Y.-S., Kim, Y. J., Cheon, G. J., Lee, D. S., Chung, J.-K., and Lee, M. C. L. (2008) Preparation of a promising angiogenesis PET imaging agent: ^{68}Ga-labeled c(RGDyK)-isothiocyanatobenzyl-1,4,7-triazacyclononane-1,4,7-triacetic acid and feasibility studies in mice. *J. Nucl. Med. 49*, 830–6.

(22) Boros, E., Ferreira, C. L., Cawthray, J. F., Price, E. W., Patrick, B. O., Wester, D. W., Adam, M. J., and Orvig, C. (2010) Acyclic chelate with ideal properties for ^{68}Ga PET imaging agent elaboration. *J. Am. Chem. Soc. 132*, 15726–33.

(23) Berry, D. J., Ma, Y., Ballinger, J. R., Tavare, R., Koers, A., Sunassee, K., Zhou, T., Nawaz, S., Mullen, G. E. D., Hider, R. C., and Blower, P. J. (2011) Efficient bifunctional gallium-68 chelators for positron emission tomography: tris(hydroxypyridinone) ligands. *Chem. Commun. 47*, 7068–70.

(24) Bottomley, G. A., Clark, I. J., Creaser, I. I., Engelhardt, L. M., Geue, R. J., Hagen, K. S., Harrowfield, J. M., Lawrance, G. A., Lay, P. A., Sargeson, A. M., See, A. J., Skelton, B. W., White, A. H., and Wilner, F. R. (1994) The synthesis and structure of encapsulating ligands: Properties of bicyclic hexamines. *Aust. J. Chem. 47*, 143–79.

(25) Geue, R. J., Hambley, T. W., Harrowfield, J. M., Sargeson, A. M., and Snow, M. R. (1984) Metal ion encapsulation: Cobalt cages derived from polyamines, formaldehyde, and nitromethane. *J. Am. Chem. Soc. 106*, 5478–88.

(26) Sargeson, A. M. (1996) The potential for the cage complexes in biology. *Coord. Chem. Rev. 151*, 89–114.

(27) Sargeson, A. M. (1986) Developments in the synthesis and reactivity of encapsulated metal ions. *Pure Appl. Chem. 58*, 1511–22.

(28) Conrad, D. W., and Scott, R. A. (1989) Long-range electron transfer in a cytochrome c derivative containing a covalently attached cobalt cage complex. *J. Am. Chem. Soc. 111*, 3461–3.

(29) Donnelly, P. S., and Harrowfield, J. M. (2002) Synthesis with coordinated ligands: Biomolecule attachment to cage amines. *J. Chem. Soc., Dalton Trans.* 906–13.

(30) Donnelly, P. S., Harrowfield, J. M., Skelton, B. W., and White, A. H. (2000) Carboxymethylation of cage amines: Control of alkylation by metal ion coordination. *Inorg. Chem. 39*, 5817–30.

(31) Donnelly, P. S., Harrowfield, J. M., Skelton, B. W., and White, A. H. (2001) Carboxymethylated cage amines: Coordination and lactamization. *Inorg. Chem. 40*, 5645–52.

(32) Ma, M. T., and Donnelly, P. S. (2011) Peptide targeted copper-64 radiopharmaceuticals. *Curr. Top. Med. Chem. 11*, 500–20.

(33) Ma, M. T., Karas, J. A., White, J. M., Scanlon, D., and Donnelly, P. S. (2009) A new bifunctional chelator for copper radiopharmaceuticals: A cage amine ligand with a carboxylate functional group for conjugation to peptides. *Chem. Commun.* 3237–9.

(34) Cai, H., Fissekis, J., and Conti, P. S. (2009) Synthesis of a novel bifunctional chelator AmBaSar based on sarcophagine for peptide conjugation and ^{64}Cu radiolabelling. *Dalton Trans.* 5395–400.

(35) Cai, H., Li, Z., Huang, C.-W., Shahinian, A. H., Wang, H., Park, R., and Conti, P. S. (2010) Evaluation of copper-64 labeled AmBaSar conjugated cyclic RGD peptide for improved microPET imaging of integrin $\alpha v\beta 3$ expression. *Bioconjugate Chem. 21*, 1417–24.

(36) Huang, C.-W., Li, Z., Cai, H., Shahinian, T., and Conti Peter, S. (2011) Biological stability evaluation of the $\alpha 2\beta 1$ receptor imaging agents: Diamsar and DOTA conjugated DGEA peptide. *Bioconjugate Chem. 22*, 256–63.

(37) Di Bartolo, N., Sargeson, A. M., and Smith, S. V. (2006) New ^{64}Cu PET imaging agents for personalised medicine and drug development using the hexa-aza cage. *Org. Biomol. Chem. 4*, 3350–7.

(38) Di Bartolo, N. M., Sargeson, A. M., Donlevy, T. M., and Smith, S. V. (2001) Synthesis of a new cage ligand, SarAr, and its complexation with selected transition metal ions for potential use in radioimaging. *J. Chem. Soc., Dalton Trans.* 2303–9.

(39) Voss, S. D., Smith, S. V., DiBartolo, N., McIntosh, L. J., Cyr, E. M., Bonab, A. A., Dearling, J. L. J., Carter, E. A., Fischman, A. J., Treves, S. T., Gillies, S. D., Sargeson, A. M., Huston, J. S., and Packard, A. B. (2007) Positron emission tomography (PET) imaging of neuroblastoma and melanoma with ^{64}Cu-SarAr immunoconjugates. *Proc. Natl. Acad. Sci. U. S. A.* 1–5.

(40) Lears, K. A., Ferdani, R., Liang, K., Zheleznyak, A., Andrews, R., Sherman, C. D., Achilefu, S., Anderson Carolyn, J., and Rogers, B. E. (2011) In vitro and in vivo evaluation of ^{64}Cu-labeled SarAr-bombesin analogs in gastrin-releasing peptide receptor-expressing prostate cancer. *J. Nucl. Med. 52*, 470–7.

(41) Wei, L., Ye, Y., Wadas, T. J., Lewis, J. S., Welch, M. J., Achilefu, S., and Anderson, C. J. (2009) ^{64}Cu-labeled CB-TE2A and diamsar-conjugated RGD peptide analogs for targeting angiogenesis: Comparison of their biological activity. *Nucl. Med. Biol. 36*, 277–85.

(42) Pierschbacher, M. D., and Ruoslahti, E. (1984) Cell attachment activity of fibronectin can be duplicated by small synthetic fragments of the molecule. *Nature 309*, 30–3.

(43) Xiong, J.-P., Stehle, T., Zhang, R., Joachimiak, A., Frech, M., Goodman Simon, L., and Arnaout, M. A. (2002) Crystal structure of the extracellular segment of integrin $\alpha V\beta 3$ in Complex with an Arg-Gly-Asp ligand. *Science 296*, 151–5.

(44) Brooks, P. C., Montgomery, A. M. P., Rosenfeld, M., Reisfeld, R. A., Hu, T., Klier, G., and Cheresh, D. A. (1994) Integrin $\alpha V\beta 3$ antagonists promote tumor tegression by inducing apoptosis of angiogenic blood vessels. *Cell 79*, 1157–64.

(45) Aumailley, M., Gurrath, M., Gerhard, M., Calvete, J., Timpl, R., and Kessler, H. (1991) Arg-Gly-Asp constrained within cyclic pentapeptides. Strong and selective inhibitors of cell adhesion to vitronectin and laminin fragment P1. *FEBS Lett. 291*, 50–4.

(46) Pfaff, M., Tangemann, K., Muller, B., Gurrath, M., Muller, G., Kessler, H., Timpl, R., and Engel, J. (1994) Selective recognition of cyclic RGD peptides of NMR-defined conformation by αIIb$\beta 3$ and $\alpha 5\beta 1$integrins. *J. Biol. Chem. 269*, 20233–8.

(47) Schottelius, M., Laufer, B., Kessler, H., and Wester, H.-J. (2009) Ligands for mapping $\alpha v\beta 3$-integrin expression in vivo. *Acc. Chem. Res. 42*, 969–80.

(48) Wangler, C., Maschauer, S., Prante, O., Schafer, M., Schirrmacher, R., Bartenstein, P., Eisenhut, M., and Wangler, B. (2010) Multimerization of cRGD peptides by click chemistry: Synthetic strategies, chemical limitations, and influence on biological properties. *ChemBioChem 11*, 2168–81.

(49) Liu, W., Hao, G., Long Michael, A., Anthony, T., Hsieh, J.-T., and Sun, X. (2009) Imparting multivalency to a bifunctional chelator: A

scaffold design for targeted PET imaging probes. *Angew. Chem., Int. Ed. 48*, 7346–9.

(50) Liu, Z., Li, Z.-B., Cao, Q., Liu, S., Wang, F., and Chen, X. (2009) Small-animal PET of tumours with ^{64}Cu-labeled RGD-bombesin heterodimer. *J. Nucl. Med. 50*, 1168–77.

(51) Shi, J., Kim, Y.-S., Zhai, S., Liu, Z., Chen, X., and Liu, S. (2009) Improving tumor uptake and pharmacokinetics of ^{64}Cu-labeled cyclic RGD peptide dimers with Gly_3 and PEG_4 linkers. *Bioconjugate Chem. 20*, 750–9.

(52) Li, Z.-b., Cai, W., Cao, Q., Chen, K., Wu, Z., He, L., and Chen, X. (2007) 64Cu-labeled tetrameric and octameric RGD peptides for small-animal PET of tumor $\alpha v\beta 3$ integrin expression. *J. Nucl. Med. 48*, 1162–71.

(53) Chen, X., Liu, S., Hou, Y., Tohme, M., Park, R., Bading James, R., and Conti Peter, S. (2004) MicroPET imaging of breast cancer αv-integrin expression with ^{64}Cu-labeled dimeric RGD peptides. *Mol. Imaging Biol. 6*, 350–9.

(54) Chin, F. T., Shen, B., Liu, S., Berganos, R. A., Chang, E., Mittra, E., Chen, X., and Gambhir, S. S. (2011) First experience with clinical-grade [^{18}F]FPP$(RGD)_2$: An automated multi-step radiosynthesis for clinical PET studies. *Mol. Imaging Biol.* DOI: 10.1007/s11307-011-0477-3.

(55) Haubner, R., Kuhnast, B., Mang, C., Weber, W. A., Kessler, H., Wester, H. J., and Schwaiger, M. (2004) [^{18}F]Galacto-RGD: synthesis, radiolabeling, metabolic stability, and radiation dose estimates. *Bioconjugate Chem. 15*, 61–9.

(56) Zhernosekov, K. P., Filosofov, D. V., Baum, R. P., Aschoff, P., Bihl, H., Razbash, A. A., Jahn, M., Jennewein, M., and Roesch, F. (2007) Processing of generator-produced ^{68}Ga for medical application. *J. Nucl. Med. 48*, 1741–8.

(57) Sloan, E. K., Pouliot, N., Stanley, K. L., Chia, J., Moseley, J. M., Hards, D. K., and Anderson, R. L. (2006) Tumor-specific expression of $\alpha v\beta 3$ integrin promotes spontaneous metastasis of breast cancer to bone. *Breast Cancer Res. 8*, R20.

(58) Ma, M. T., Cooper, M. S., Paul, R. L., Shaw, K. P., Karas, J. A., Scanlon, D., White, J. M., Blower, P. J., and Donnelly, P. S. (2011) Macrobicyclic cage amine ligands for copper radiopharmaceuticals: A single bivalent cage amine containing two Lys^3-bombesin targeting peptides. *Inorg. Chem. 50*, 6701–10.

(59) Comba, P., Sargeson, A. M., Engelhardt, L. M., Harrowfield, J. M., White, A. H., Horn, E., and Snow, M. R. (1985) Analysis of trigonal-prismatic and octahedral preferences in hexaamine cage complexes. *Inorg. Chem. 24*, 2325–7.

(60) Clark, I. J., Crispini, A., Donnelly, P. S., Engelhardt, L. M., Harrowfield, J. M., Jeong, S.-H., Kim, Y., Koutsantonis, G. A., Lee, Y. H., Lengkeek, N. A., Mocerino, M., Nealon, G. L., Ogden, M. I., Park, Y. C., Pettinari, C., Polanzan, L., Rukmini, E., Sargeson, A. M., Skelton, B. W., Sobolev, A. N., Thuery, P., and White, A. H. (2009) Variations on a cage theme: Some complexes of bicyclic polyamines as supramolecular synthons. *Aust. J. Chem. 62*, 1246–60.

(61) Harrowfield, J. (2006) Labile interactions and inert entities in supramolecular chemistry - the identification of recognition mechanisms for macrobicyclic amine complexes. *Supramol. Chem. 18*, 125–36.

(62) Harris, W. R., and Pecoraro, V. L. (1983) Thermodynamic binding constants for gallium transferrin. *Biochemistry 22*, 292–9.

(63) Haubner, R., Weber, W. A., Beer, A. J., Vabuliene, E., Reim, D., Sarbia, M., Becker, K.-F., Goebel, M., Hein, R., Wester, H.-J., Kessler, H., and Schwaiger, M. (2005) Noninvasive visualization of the activated $\alpha v\beta 3$ integrin in cancer patients by positron emission tomography and [^{18}F]Galacto-RGD. *PLoS Med. 2*, 244–52.

(64) Decristoforo, C., Gonzalez, H. I., Carlsen, J., Rupprich, M., Huisman, M., Virgolini, I., Wester, H.-J., and Haubner, R. (2008) ^{68}Ga- and ^{111}In-labelled DOTA-RGD peptides for imaging of $\alpha v\beta 3$ integrin expression. *Eur. J. Nucl. Med. Mol. Imaging 35*, 1507–15.

Tumor imaging with a gallium-68 complex of a macrobicyclic cage amine ligand tethered to two integrin-targeting peptides

Supporting Information

Michelle T. Ma,[ab] Oliver C. Neels,[c] Delphine Denoyer,[c] Peter Roselt,[c] John A. Karas,[b] Denis Scanlon,[ab] Jonathan M. White,[ab] Rodney J. Hicks[c]* and Paul S. Donnelly[ab]*

AUTHOR ADDRESS [a] School of Chemistry, The University of Melbourne, Parkville, Victoria, Australia; [b] Bio21 Molecular Science and Biotechnology Institute, The University of Melbourne, Parkville, Victoria, Australia; [c] The Centre for Molecular Imaging and Translational Research Laboratory, The Peter MacCallum Cancer Centre, Melbourne, Victoria, Australia.

AUTHOR EMAIL ADDRESS: Rod.Hicks@petermac.org; pauld@unimelb.edu.au

Synthesis of L^1(RGDfK)(Lys^3-bombesin(1-14))

(***t***-Boc)$_5$(Succ)$\mathbf{L^1}$(RGDfK): cyclic-(RGDfK) peptide (3 mg) and (***t***-Boc)$_5$(Succ)$_2$-$\mathbf{L^1}$ (5 mg) were dissolved in dimethylformamide (400 μL) and diisopropylethylamine (3μL) was added. This solution was stirred at ambient temperature for 2 hours. Acetonitrile/water (50%/50%) (4 mL) was added and the solution applied to a C18 semi-preparative HPLC column and separated using an Eclipse XDB-C18 5 μm 9.5 x 250 mm column with a flow rate of 3 mL min^{-1}. The gradient mobile phase started with 100% solvent A (0.1% trifluoroacetate in water) at 5 min to 100% solvent B (0.1% formic acid in acetonitrile) at 75 min. Fractions containing pure material were combined, frozen and lyophilised. (***t***-Boc)$_5\mathbf{L^1}$(RGDfK)$_2$ (1 mg) eluted at 43 min. (***t***-Boc)$_5$(Succ)$\mathbf{L^1}$(RGDfK) (2 mg) eluted at 49 min. MS: $[C_{80}H_{130}N_{18}O_{24}]^{2+}$ 863.48 (experimental) 863.48 (calculated); Analytical HPLC: 16.73 and 16.84 min (0 to 100% B in 25 min).

Lys^3-bombesin(1-14) (3 mg) and (***t***-Boc)$_5$(Succ)$\mathbf{L^1}$(RGDfK) (2 mg) were dissolved in dimethylformamide (400 μL) and diisopropylethylamine (3 μL) was added. This solution was stirred at ambient temperature for 5 – 10 mins. Acetonitrile/water (50%/50%) (4 mL) was added and the solution applied to a C18 semi-preparative HPLC column and separated using an Eclipse XDB-C18 5 μm 9.5 x 250 mm column with a flow rate of 3 mL min^{-1}. The gradient mobile phase started with 100% solvent A (0.1% trifluoroacetate in water) at 5 min to 100% solvent B (0.1% formic acid in acetonitrile) at 75 min. The fraction containing (***t***-Boc)$_5\mathbf{L^1}$(RGDfK)(Lys^3-bombesin(1-14)) eluted at 43 min. This was frozen and lyophilised. MS: $[C_{147}H_{236}N_{39}O_{39}S]^{3+}$ 1068.25 (experimental) 1068.24 (calculated); Analytical HPLC: 14.13 min (0 to 100% B in 25 min).

(***t***-Boc)$_5\mathbf{L^1}$(RGDfK)(Lys^3-bombesin(1-14)) was dissolved in trifluoroacetic acid (1 – 2 mL) and stirred for ~ 2 hours. The trifluroacetic acid was evaporated under a stream of N_2 gas. Acetonitrile (1 mL) and water (1 mL) were added to redissolve the residue, and the solution frozen and lyophilised. The dried material was redissolved and purified using a C18 semi-preparative HPLC column using an Eclipse XDB-C18 5 μm 9.5 x 250 mm column with a flow rate of 3 mL min^{-1}. The gradient mobile phase started with 100% solvent A (0.1% trifluoroacetate in water) at 5 min and increased at a rate of 1% B min^{-1} until all components had eluted. MS: $[C_{122}H_{195}N_{39}O_{29}S]^{2+}$: 1351.74 (experimental), 1351.74 (calculated); Analytical HPLC: 14.43 min (0 to 60% B in 25 min).

Scheme S1. Synthesis of **L**[1](RGDfK)(Lys[3]-bombesin(1-14)).

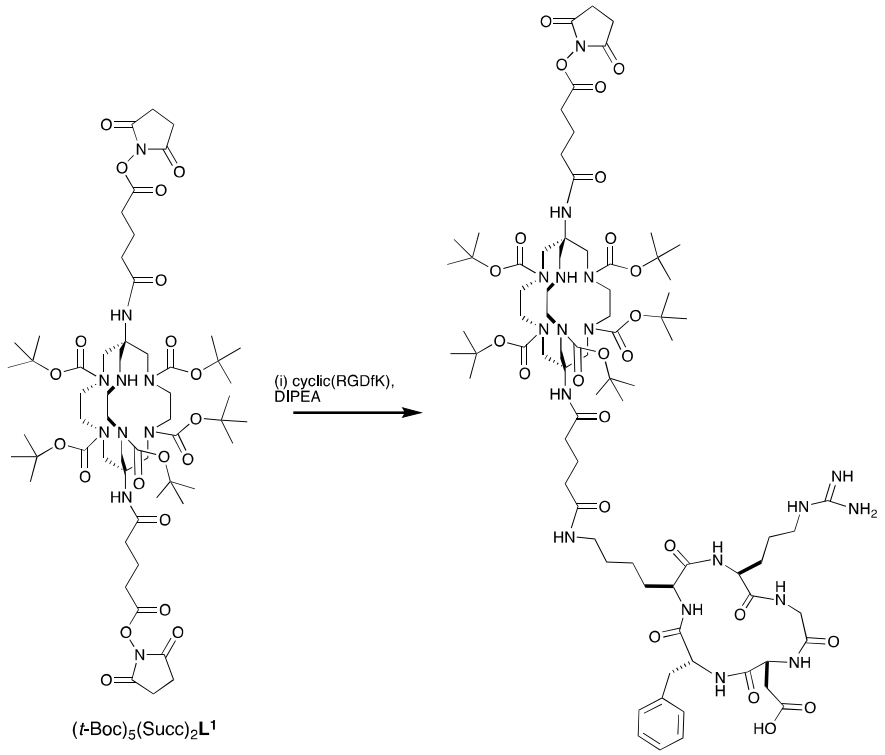

(*t*-Boc)$_5$(Succ)$_2$**L**[1]

(*t*-Boc)$_5$(Succ)**L**[1](RGDfK)

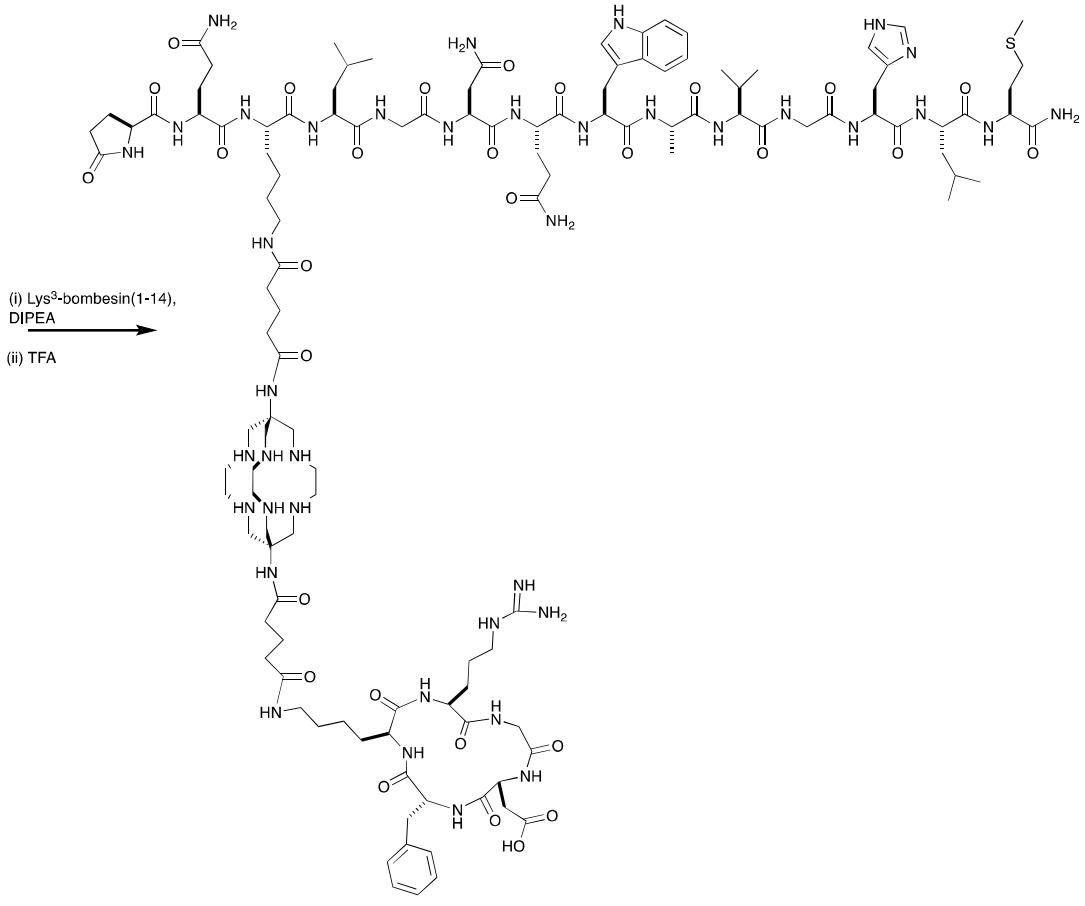

L[1](RGDfK)(Lys[3]-bombesin(1-14))

Bioconjugate Chemistry

ARTICLE

pubs.acs.org/bc

Relipidated Tissue Factor Linked to Collagen Surfaces Potentiates Platelet Adhesion and Fibrin Formation in a Microfluidic Model of Vessel Injury

Thomas V. Colace, Jannielle Jobson, and Scott L. Diamond*

Institute for Medicine and Engineering, University of Pennsylvania, Philadelphia, Pennsylvania, United States

ABSTRACT: Microfluidic devices allow for the controlled perfusion of human or mouse blood over defined prothrombotic surfaces at venous and arterial shear rates. To mimic in vivo injuries such a plaque rupture, the need exists to link lipidated tissue factor (TF) to surface-bound collagen fibers. Recombinant TF was relipidated in liposomes of phosphatidylserine/phosphatidylcholine/biotin-linked phosphatidylethanolamine (20:79:1 PS/PC/bPE molar ratio). Collagen was patterned in a 250-μm-wide stripe and labeled with biotinylated anticollagen antibody which was then bound with streptavidin, allowing the subsequent capture of the TF liposomes. To verify and detect the TF liposome−collagen assembly, individual molecular complexes of TF-factor VIIa on collagen were visualized using the proximity ligation assay (PLA) to produce discretely localized fluorescent events that were strictly dependent on the presence of factor VIIa and primary antibodies against TF or factor VIIa. Perfusion for 450 s (wall shear rate, 200 s^{-1}) of corn trypsin inhibitor (CTI, a factor XIIa inhibitor) treated whole blood over the stripe of TF-collagen enhanced platelet adhesion by 30 ± 8% ($p < 0.001$) and produced measurable fibrin (>50-fold increase) as compared to surfaces lacking TF. PS/PC/bPE liposomes lacking TF resulted in no enhancement of platelet deposition. Essentially no fibrin was formed during perfusion over collagen surfaces or collagen surfaces with liposomes lacking TF despite the robust platelet deposition, indicating a lack of kinetically significant platelet-borne tissue factor in healthy donor blood. This study demonstrates a reliable approach to link functionally active TF to collagen for microfluidic thrombosis studies.

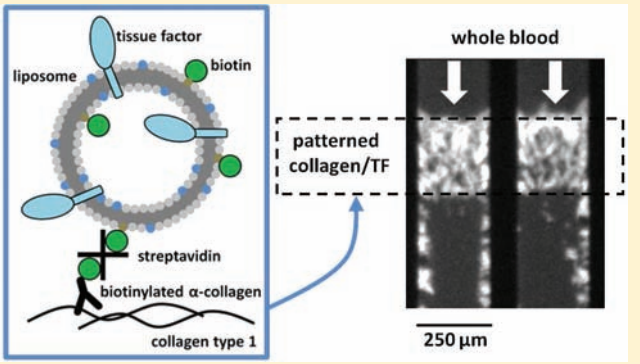

INTRODUCTION

Tissue factor (TF) in the vessel wall is exposed during injury or atherosclerotic plaque rupture and binds circulating factor VIIa. As a cofactor in this complex, TF dramatically enhances the catalytic activity of factor VIIa toward factor X and factor IX. Generation of factor Xa results in formation of the prothrombinase complex (Xa/Va) to generate thrombin. Thrombin, a potent activator of platelets, is necessary for the production of clot stabilizing fibrin.

The incorporation of TF into growing thrombi has been suggested to occur through a variety of mechanisms. While the presence of TF in platelets and other nonactivated blood cells in healthy blood has been an ongoing debate,[1−3] several studies have shown the localization of TF-bearing microparticles to sites of injury via the P-selectin/PSGL1 interaction,[4] and its synthesis by a variety of extracellular matrix cells in normal and atherosclerotic vessels.[5] For decades, various TF preparations have been used as a clinical laboratory reagent in the study of prothrombin times, but TF has rarely been deployed in microfluidic injury models. For microfluidic thrombosis models, it is critical to present both collagen to platelets as well as lipidated TF to the plasma. By simultaneously activating and capturing platelets with surface-bound collagen along with triggering of the coagulation protease cascade with surface-bound TF, the central biology of thrombosis and hemostasis is recreated. In contrast, addition of exogenous TF into blood absolutely fails to recreate the dynamical aspects of thrombosis reliant on the surface presentation of TF to flowing blood.

The activity of tissue factor relies on its insertion into a phospholipid membrane containing approximately 20% negatively charged phosphatidylserine.[6] Reliable techniques using readily available reagents have been developed to "relipidate" TF into phospholipid vesicles or membranes.[7] In vitro flow studies which include these designs are rare, however, and mainly focus on the dynamics of thrombin or fibrin production.[8] In traditional microfluidic studies, the roles of platelet adhesion and coagulation are commonly separated through the use of heparin or Phe-Pro-Arg-chloromethylketone (PPACK, an irreversible thrombin inhibitor) or through the perfusion of platelet-free plasma over a previously formed platelet surface.[9,10] When studied in vivo in the mouse laser injury model, however, platelet deposition and thrombin production occur simultaneously.[11] These models

Received: June 21, 2011
Revised: August 8, 2011
Published: September 08, 2011

ACS Publications © 2011 American Chemical Society

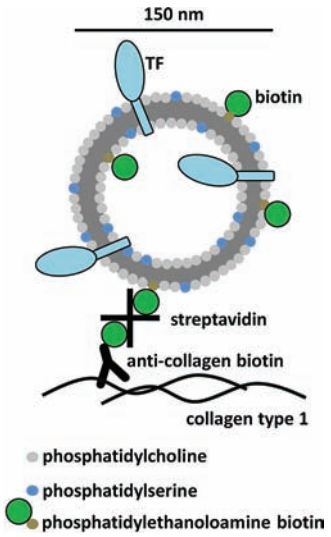

Figure 1. Tissue factor was relipidated in liposomes consisting of a molar ratio of 79:20:1 phosphatidylcholine to phosphatidylserine to biotinylated phosphatidylethanolamine in a lipid to TF ratio of 10 000:1. Dynamic light scattering indicated that the average vesicle radius was approximately 74.4 ± 28.0 nm. The liposomes were physically linked to collagen type 1 surface treated with a goat polyclonal antibody conjugated to biotin through a streptavidin linker.

have been helpful in defining a role for thrombin in platelet adhesion and fibrin generation in platelet plug stabilization; however, they lack characterization and control of the local hemodynamic conditions.[12]

In this study, we describe a method for generating reproducible surfaces of collagen and active tissue factor for use in microfluidic analyses of platelet function. We have modified the TF-bearing liposomes described by Smith et al.[7] to include a biotinylated lipid which we use to bind the vesicles to a collagen surface via a biotinylated anticollagen antibody and streptavidin (Figure 1). We have verified that these thrombogenic surfaces are functionally active leading to enhanced platelet deposition and measurable fibrin formation. Furthermore, we have characterized the surface through the use of the proximity ligation assay (PLA), a dual antibody immunodetection technique capable of visualizing individual molecule complexes based on molecular-scale proximity.

MATERIALS AND METHODS

Materials. Lipids, L-α-phosphatidylcholine (PC), L-α-phosphatidylserine (PS), and biotinylated phosphatidylethanolamine (bPE) were from Avanti Polar Lipids (Alabaster, AL, USA). Recombinant human tissue factor was from Haematologic Technologies Inc. (Essex Junction, VT, USA). Bio-Beads SM-2 (BioRad Laboratories, Hercules, CA, USA) were cleaned in methanol and stored under HEPES Buffered Saline (HBS, 20 mM HEPES, 150 mM NaCl, pH 7.4 [NaOH]) at 4 °C. The detergent, Triton X-100, was from Fisher Scientific (Fair Lawn, NJ, USA) Duolink proximity ligation assay (PLA) amplification and detection reagents were from O-Link Bioscience through distributor Axxora (San Diego, CA, USA). The primary monoclonal PLA antibody against tissue factor was from Haematologic Technologies and polyclonal primary against factor VIIa was from Abcam (Cambridge, MA, USA), as well as the biotinylated goat polyclonal anti collagen type 1 antibody. Streptavidin was from Sigma (St. Louis, MO, USA). Acid-insoluble collagen type 1 from equine tendon was from Chronolog Corp. (Havertown, PA, USA) and acid-soluble human collagen type 1 was from Advanced Biomatrix (San Diego, CA, USA). Poly(dimethylsiloxane), PDMS, for the microfluidic devices (Sylgard 184) was from Ellsworth Adhesives (Germantown, WI, USA) and Sigmacote used for hydrophobic treatment of glass slides was from Sigma. Finally, the anticoagulants corn trypsin inhibitor (CTI) and Pro-Arg-chloromethylketone (PPACK) were from Haematologic Technologies, and platelet labeling anti-CD41 antibody was from AbDSerotec (Raleigh, NC, USA). The fibrin-specific fluorescent monoclonal antibody was a generous gift from the Mortimer Poncz lab at the Children's Hospital of Philadelphia.

Blood Collection and Preparation. Blood was collected via venipuncture from healthy donors who were self-reported as free of medication for at least 10 days into CTI (40 μg/mL) for microfluidic assays or PPACK (100 μM) for TF detection assays. All volunteers provided informed consent in accordance with IRB approval and the Declaration of Helsinki. Whole blood was treated with Alexafluor 647-conjugated anti CD-41 monoclonal antibody for platelet detection in microfluidic assays 5 min prior to perfusion. PFP was generated for TF/VIIa complex detection assays by centrifugation of whole blood at 1000 *g* for 10 min. All blood samples were used within 1 h of the draw.

Preparation of Biotinylated TF Liposomes. Relipidation of recombinant tissue factor into liposomes was performed according to a previously described technique.[7] Briefly, PC, PS, and b-PE stored in chloroform were dried under vacuum in a 79:20:1 molar ratio, respectively. The dried film was resuspended in 1 mL of 4 mM Triton X-100 in HBS and allowed to hydrate for 30 min. Recombinant tissue factor was added and incubated for 10 min (10 000:1 lipid to TF). To this, 50 mg of Bio-Bead slurry was added and was gently agitated for 90 min, and then, 350 mg more of Bio-Bead slurry was added and gently agitated for the same amount of time. The beads were allowed to settle, and the supernatant was collected. The hydrodynamic radius of the resulting liposomes was determined by dynamic light scattering (Protein Solutions DynaPro, Wyatt Technology, Santa Barbara, CA, USA) to be 74.4 ± 28.0 nm.

Preparation of Collagen−Liposome Surfaces for Detection. Acid-soluble collagen was first neutralized to a pH of 7.4 with 1 M NaOH and then incubated on Sigmacote-treated glass slides for 2.5 h (300 μg/mL). The collagen surfaces were rinsed in HBS and treated with goat polyclonal anticollagen biotin (10 μg/mL) for 10 min and rinsed again. The droplet area was then treated with streptavidin (10 μg/mL) for another 10 min before rinsing. Ten microliters of the relipidated tissue factor liposome solution was added to the surface and allowed to rest for 1 h. A representation of the liposomes/collagen surface is presented in Figure 1. The relipidated tissue factor surfaces were finally treated with PFP (100 μM PPACK) for 30 min in order to generate TF/VII complexes.[13] When these surfaces were prepared for microfluidic assays, the steps were performed in a microfluidic patterning device which consisted of a single channel 250 μm wide as described in ref 14. Acid-insoluble collagen was used for these studies, as it better supports platelet adhesion. The final result was a strip of protein rather than a droplet. These surfaces were not treated with plasma, as they would be introduced to whole blood in the flow experiment.

Detection of TF/VIIa Complexes. Single tissue factor/factor VIIa complexes were detected on our thrombogenic surfaces

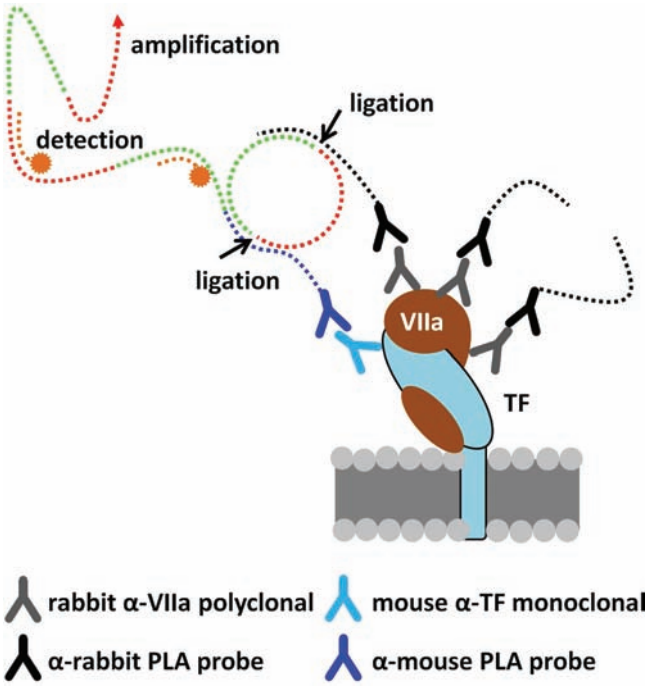

Figure 2. The Duolink proximity ligation assay is capable of detecting single molecule complexes. Primary antibodies directed against the components of the complex act to localize two "PLA probes", which are species-specific antibodies conjugated to short oligonucleotides. When the probes are brought together, they form a closed loop when complementary oligonucleotides are added. This loop is enzymatically ligated, which provides a template for rolling circle amplification. Small fluorescently labeled oligonucleotides hybridize with the amplified product producing a detection signal.

using the Duolink PLA.[15] Briefly, a mouse monoclonal antibody to tissue factor and a rabbit polyclonal antibody to factor VIIa were selected as primary antibodies. The binding of these antibodies to the TF/VIIa complex served as a localization site for two species-specific antibodies conjugated to short oligonucleotides (PLA probes). When the probes are in close proximity (i.e., bound to their antigens, which are bound to a protein complex), they may hybridize with two other oligonucleotides in solution, forming a loop. This loop is then ligated to create a closed circle which is an active site for rolling circle DNA amplification. Finally, fluorescently labeled oligonucleotides hybridize with the replication product to produce a detection signal. Figure 2 is an illustration of this technique.

Microfluidic Platelet Adhesion Model. Two sets of microchannels were designed in PDMS according to a previously described technique.[14,16] First, a patterning device consisting of a single channel 250 μm wide and 5 cm long was used to generate strips of thrombotic protein (collagen and tissue factor) according to the procedure above. This device was then removed and a flow device placed over the protein strip with perpendicular 250 μm channels resulting in a platelet/protein interaction zone measuring 250 × 250 μm^2 in each channel. The channels were blocked with 0.5% bovine serum albumin in HBS for 30 min prior to perfusion with whole blood. Blood was perfused through the channels at a wall shear rate of 200 s^{-1} via syringe pump (Harvard Apparatus PHD 2000, Holliston, MA, USA) and the interaction zone monitored via fluorescence microscopy (IX81, Olympus America Inc., Center Valley, PA, USA) in 15 s intervals.

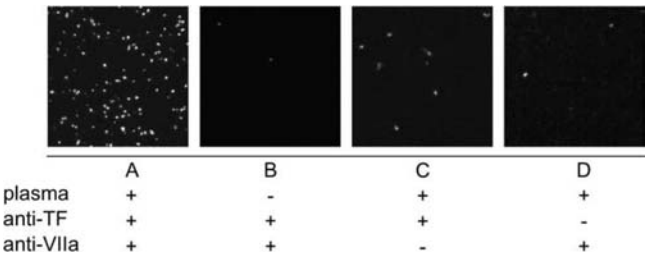

Figure 3. The PLA signal appears as 1 μm fluorescent dots (A). We have demonstrated that, in the absence of complexes (no factor VII from plasma [B]) or of either primary antibody (VIIa [C] or TF [D]), detection does not occur.

Images were captured using a CCD camera (ORCA-ER, Hamamatsu, Bridgewater, NJ, USA) illuminated with a mercury lamp (100 W, 620 nm Ex/700 nm Ex). Fluorescent intensity was evaluated using the freely available *ImageJ* software (NIH).

RESULTS

Detection of Single TF/VIIa Complexes. Tissue factor VIIa complexes were generated on a polymerized human collagen type 1 surface by linking relipidated tissue factor liposomes with 1% biotinylated-PE to a biotinylated anti-collagen antibody via streptavidin. We chose to use soluble collagen for this application as it creates a more uniform layer with less background fluorescence than fibrillar collagen surfaces. All surfaces were blocked in solutions of 0.5% BSA for 30 min prior to detection. The primary antibodies were used at a final concentration of 1 μg/mL and were incubated in open droplet reactions for 1 h at 37 °C. Following this, the PLA reaction was run according to the manufacturer's instructions.

The amplification product was observed as an approximately 1-μm-sized fluorescent dot (Figure 3) that was at least 3-fold brighter than the background. In order to confirm that we were detecting the desired complexes and not nonspecific antibody binding, two sets of controls were run. First, samples with linked tissue factor liposomes were either treated or untreated with plasma (±factor VIIa). Each sample was treated with both primary and secondary antibodies as well as all Duolink amplification and detection reagents. The images presented are representative of several 20× fields of view (Figure 3a,b). Identical samples with linked TF liposomes were incubated with human plasma and were treated with just the TF primary antibody or just the factor VIIa primary antibody (Figure 3c,d). These samples were treated according the unmodified Duolink procedure. The results demonstrate that the complete TF/VIIa complex must be present and that it must be treated with both primary antibodies for detection by PLA. Fluorescent staining observed under the negative control conditions is believed to be the result of nonspecific binding of the secondary PLA probes.

Effect of TF Liposomes under Flow Conditions. Fibrillar collagen surfaces with linked tissue factor liposomes were generated in a microfluidic model of thrombosis, as well as surfaces with liposomes lacking tissue factor. Whole blood anticoagulated with CTI (40 μg/mL), to inhibit the contact activation pathway, was perfused over the surfaces at an inlet wall shear rate of 200 s^{-1}. The experiment was performed in multichannel microfluidic device that allowed for 8 separate (but equal) adhesion events to be monitored simultaneously.[16] The data represented in Figure 4 are the fluorescent intensities of the surfaces captured in 15 s

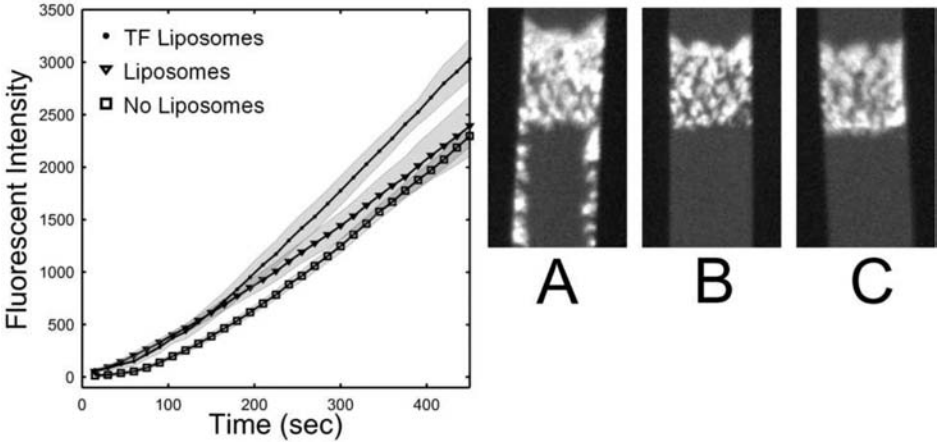

Figure 4. Tissue factor liposomes linked to collagen increased platelet deposition in a microfluidic injury model 30 ± 8.0% as compared to a similar surface with liposomes lacking TF or a control collagen surface. Whole blood was perfused over these surfaces at 200 s^{-1} in the presence of CTI (40 μg/mL). Each condition was performed in 8 separate channels and monitored simultaneously. The data represent the mass of platelets adhering at the collagen patch (in arbitrary units) and are presented ± STD. Representative images of platelet adhesion at 450 s are presented for each case ([A] TF liposomes, [B] liposomes, [C] control surface). Flow is from top to bottom. Platelet accumulation for the TF surface appears brighter, denser, and protrudes upstream. Platelets also adhere downstream of the main platelet mass when TF is present on the liposome/collagen surface, possibly as a result of fibrin deposition.

intervals over a 450 s period. The intensity represents the average mass of platelets aggregating on the surface. A significant increase (30 ± 8%, $p < .0001$) was observed in platelet deposition when the surface contained TF positive liposomes after 450 s of perfusion. Platelets also adhered downstream from the collagen patch, possibly on fibrin deposits (Figure 4a). Platelet adhesion to the liposome surface lacking tissue factor was undistinguishable from a control sample untreated with antibody, streptavidin, or liposomes after 450 s.

In a parallel experiment, unlabeled platelets in whole blood (40 μg/mL CTI) were perfused over a collagen surface treated with TF positive or negative liposomes in the presence of a fluorescently labeled fibrin-specific antibody (3 μg/mL). The data reveal that liposomes containing tissue factor are required for fibrin formation in the platelet mass during the 450 s perfusion. Detectable fibrin appears between 15 and 30 s into the TF liposome perfusion. Figure 5a shows the deposition of fibrin downstream from the collagen strip. When PS-PC-bPE liposomes lacking TF were attached to collagen, there was no increase in platelet deposition and no production of fibrin, consistent with the fact that PSPC liposomes do not trigger thrombin production in CTI-treated plasma.[17]

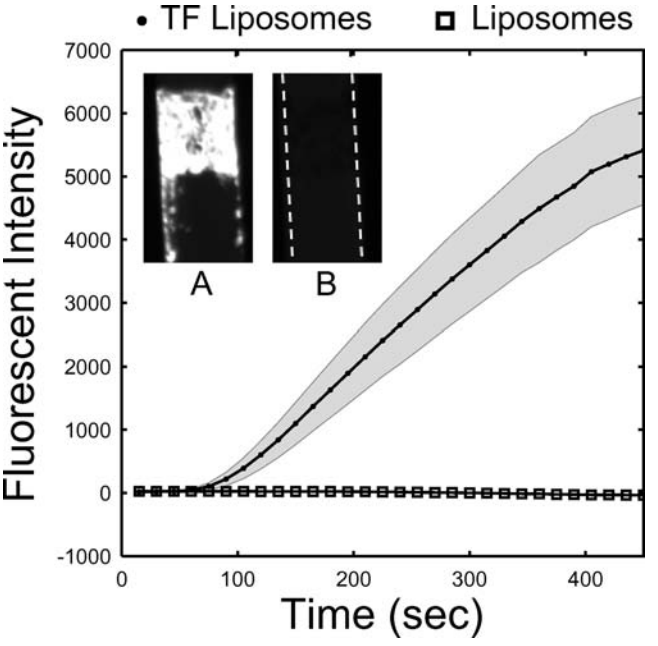

Figure 5. Whole blood treated with CTI (40 μg/mL) was perfused over a TF liposome/collagen surface or liposome/collagen surface at 200 s^{-1} in the presence of a fluorescently labeled fibrin specific monoclonal antibody. Each condition was performed and monitored simultaneously in 8 separate channels. Fluorescent intensity (in arbitrary units) of the fibrin mass accruing in the platelet mass is presented ± STD. The inset illustrates the two conditions after 450 s of perfusion (flow is from top to bottom). No fibrin deposition appears with the TF negative liposomes (B), while massive deposition appears for the positive liposomes (A). Fibrin deposition is detected downstream of the main thrombus as well.

DISCUSSION

Utilizing the tight binding between biotin and streptavidin, we have created a thrombogenic surface that consists of relipidated TF liposomes linked to an immobilized collagen surface. This construct produces a physiologically relevant hemostatic response which includes platelet activation, platelet adhesion, and coagulation, as is observed in vivo. The advantage of our ex vivo system, however, is that it allows for robust and reproducible control of hemodynamics, surface composition, and blood pharmacology. Furthermore, it represents a higher throughput and lower cost approach than animal models.

The results presented as part of this work were intended to verify the new TF liposome/collagen injury model against previous findings. Prior work in our lab conducted by Okorie et al., who spotted TF liposomes onto collagen features, demonstrated a 25% increase in platelet adhesion when the highest concentration of printed liposomes was used (25 molecules/μm^2).[18] In the new model, we observe a similar response (30% increase ± 8%) and capture the robust increase in fibrin formation reported in that study, as well. While we estimate a slightly lower TF concentration on our surface (see below) [0.1 to 1 molecules/μm^2], we may

explain the increased potency by the physical linking of liposomes to the collagen surface. The observation that platelet adhesion does not increase on liposome surfaces containing TF until ~200 s is supported by other groups who observed lag times in thrombin generation of >60 s,[19,20] as well as the lag time observed in fibrin generation in Figure 5. We also suggest that thrombin generation during primary adhesion has a less noticeable effect due to strong GPVI signaling generated by fibrillar collagen at early times.

In addition to platelet adhesion, the kinetics of fibrin deposition in our assay also compare well to other experimental models. In the mouse laser injury model, for example, measurable fibrin appears at 10−15 s after insult.[21] In these studies, the clotting response is triggered by activation of the endothelium and is driven by the exposure of tissue factor, not the subendothelium. Platelet adhesion is strongly dependent on PAR4 activation.[22] Therefore, a more relevant model may be the $FeCl_3$ injury, in which collagen and thrombin signaling play important roles regarding time to thrombus initiation and likelihood of vessel occlusion.[23−25] In these studies, FcγRII$^{-/-}$ or PAR4$^{-/-}$ mice, which lack collagen or thrombin signaling, respectively, have some protection from full vessel occlusion. Factor XIIa is not inhibited in the mouse models, whereas CTI is used in our in vitro perfusion studies with human blood.

We have demonstrated that our findings with the new TF/collagen assay compare well to other ex vivo and in vivo work. We have also used PLA to detect TF/factor VIIa complexes. However, quantifying fM to pM levels of surface TF is complex and is a drawback to other models as well.[8] With reasonable assumptions, we can provide an estimate of the [TF] range. Extensive characterization of tissue factor liposomes has been previously performed.[7] Using the relipidation technique described above, 80−90% of TF is recovered in liposomes, and approximately 50% of this TF is accessible. In our assay, these values predict that 5 molecules of TF per liposome are available (10 000:1 lipid to TF ratio). If we consider the results from PLA to represent a lower bound on the number of surface captured liposomes (PLA is known to have significantly less than 100% detection), we estimate 0.02 liposomes/μm^2. This value corresponds to 0.1 to 1 molecules TF/μm^2 for 100% or 10% PLA detection efficiency, respectively. These estimates compare well to our own prior work and relipidated TF patches created by other groups (0.3 molecules TF/μm^2).[26] Furthermore, we estimate that the random packing limit for spheres in 2 dimensions sets an upper bound of approximately 10^2 TF molecules/μm^2.

In vivo models of thrombosis have demonstrated the importance of coagulation in response to vessel injury. Using TF liposomes linked to a collagen surface, we have demonstrated an ex vivo system that is sensitive to both the coagulation and platelet aggregation components of the hemostatic mechanism.

AUTHOR INFORMATION

Corresponding Author

*E-mail: sld@seas.upenn.edu.

ACKNOWLEDGMENT

The authors would like to thank Dr. M. Poncz for the fibrin-specific monoclonal antibody. T. Colace was supported by a National Institutes of Health (NIH) Cardiovascular Training Predoctoral Fellowship. The authors acknowledge research support by NIH R01-HL-103419 (S.L.D).

REFERENCES

(1) Bouchard, B. A., Mann, K. G., and Butenas, S. (2010) No evidence for tissue factor on platelets. *Blood 116*, 854–5.

(2) Panes, O., Matus, V., Saez, C. G., Quiroga, T., Pereira, J., and Mezzano, D. (2007) Human platelets synthesize and express functional tissue factor. *Blood 109*, 5242–50.

(3) Giesen, P. L. A., Rauch, U., Bohrmann, B., Kling, D., Roque, M., Fallon, J. T., Badimon, J. J., Himber, J., Riederer, M. A., and Nemerson, Y. (1996) Blood-Borne tissue factor: Another view of thrombosis. *Proc. Natl. Acad. Sci. U.S.A. 96*, 2311–5.

(4) Falati, S., Liu, Q., Gross, P., Merrill-Skoloff, G., Chou, J., Vandendries, E., Celi, A., Croce, K., Furie, B. C., and Furie, B. (2003) Accumulation of tissue factor into developing thrombin in vivo is dependent upon microparticle P-selectin glycoprotein ligand 1 and platelet P-selectin. *J. Exp. Med. 197*, 1585–98.

(5) Wilcox, J. N., Smith, K. M., Schwartz, S. M., and Gordon, D. (1989) Localization of tissue factor in the normal vessel wall and in the atherosclerotic plaque. *Proc. Natl. Acad. Sci. U.S.A. 86*, 2839–43.

(6) Bach, R., Gentry, R., and Nemerson, Y. (1986) Factor VII binding to tissue factor in reconstituted phospholipid vesicles: Induction of cooperativity by phosphatidylserine. *Biochemistry 25*, 4007–20.

(7) Smith, S. A., and Morrissey, J. H. (2004) Rapid and efficient incorporation of tissue factor into liposomes. *J. Thromb. Haemost. 2*, 1155–62.

(8) Shen, F., Kastrup, C. J., Liu, Y., and Ismagilov, R. F. (2008) Threshold response of initiation of blood coagulation by tissue factor in patterned microfluidic capillaries is controlled by shear rate. *Arterioscler. Thromb. Vasc. Biol. 28*, 2035–41.

(9) Cosemans, J. M., Schols, S. E., Stefanini, L., de Witt, S., Feijge, M. A. H., Hamulyak, K., Deckmyn, H., Bergmeier, W., and Heemskerk, J. W. M. (2011) Key role of glycoprotein Ib/V/IX and von Willebrand factor in platelet activation-dependent fibrin formation at low shear flow. *Blood 117*, 651–60.

(10) Goel, M. S., and Diamond, S. L. (2001) Neutrophil enhancement of fibrin deposition under flow through platelet-dependent and -independent mechanisms. *Arterioscler. Thromb. Vasc. Biol. 21*, 2093–98.

(11) Falati, S., Gross, P., Merril-Skoloff, G., Furie, B. C., and Furie, B. (2002) Real-time in vivo imaging of platelets, tissue factor, and fibrin during arterial thrombus formation in the mouse. *Nat. Med. 8*, 1175–80.

(12) Rosen, E. D., Raymond, S., Zollman, A., Noria, F., Sandoval-Cooper, M., Shulman, A., Merz, J. L., and Castellino, F. J. (2001) Laser-induced noninvasive vascular injury models in mice generate platelet- and coagulation-dependent thrombi. *Am. J. Pathol. 158*, 1613–22.

(13) Ruf, W., Kalnik, M. W., Lund-Hansen, T., and Edgington, T. S. (1991) Characterization of factor VII association with tissue factor in solution. *J. Biol. Chem. 266*, 15719–25.

(14) Neeves, K. B., Maloney, S. F., Fong, K. P., Schmaier, A. A., Kahn, M. L., Brass, L. F., and Diamond, S. L. (2008) Microfluidic focal thrombosis model for measuring murine platelet deposition and stability: PAR4 signaling enhances shear-resistance of platelet aggregates. *J. Thromb. Haemost. 6*, 2193–201.

(15) Soderberg, O., Leuchowius, K. J., Gullberg, M., Jarvius, M., Weibrecht, I., Larsson, L. G., and Landegren, U. (2008) Characterizing proteins and their interactions in cells and tissues using the in situ proximity ligation assay. *Methods 45*, 227–32.

(16) Maloney, S. F., Brass, L. F., and Diamond, S. L. (2010) P2Y12 or P2Y1 inhibitors reduce platelet deposition in a microfluidic model of thrombosis while apyrase lacks efficacy under flow conditions. *Integr. Biol. 2*, 183–92.

(17) Goel, M. S., and Diamond, S. L. (2003) Neutrophil cathepsin G promotes prothrombinase and fibrin formation under flow conditions by activating fibrinogen-adherent platelets. *J. Biol. Chem. 278*, 9458–63.

(18) Okorie, U. M., Denney, W. S., Chatterjee, M. S., Neeves, K. B., and Diamond, S. L. (2008) Determination of surface tissue factor thresholds that trigger coagulation at venous and arterial shear rates: amplification of 100 fM circulating tissue factor requires flow. *Blood 111*, 3507–13.

(19) Fogelson, A. L., and Tania, N. (2005) Coagulation under flow: The influence of flow-mediated transport on the initiation and inhibition of coagulation. *Pathophysiol. Haemost. Thromb. 34*, 91–108.

(20) Van 't Veer, C., Hackeng, T. M., Delahaye, C., Sixma, J. J., and Bouma, B. N. Activated factor X and thrombin formation triggered by tissue factor on endothelial cell matrix in a flow model: effect of the tissue factor pathway inhibitor. *Blood 84*, 1132−42.

(21) Furie, B., and Furie, B. C. (2005) Thrombus formation in vivo. *J. Clin. Invest. 115*, 3355–59.

(22) Vandendries, E. R., Hamilton, J. R., Coughlin, S. R., Furie, B., and Furie, B. C. (2007) Par4 is required for platelet thrombus propagation but not fibrin generation in a mouse model of thrombosis. *Proc. Natl. Acad. Sci. U.S.A. 104*, 288–92.

(23) Dubois, C., Panicot-Dubois, L., Merrill-Skoloff, G., Furie, B., and Furie, B. C. (2006) Glycoprotein VI-dependent and -independent pathways of thrombus formation in vivo. *Blood 107*, 3902–6.

(24) Wang, L., Miller, C., Swarthout, R. F., Rao, M., Mackman, N., and Taubman, M. B. (2009) Vascular smooth muscle-derived tissue factor is critical for arterial thrombosis after ferric chloride-induced injury. *Blood 113*, 705–13.

(25) Sambrano, G. R., Weiss, E. J., Zheng, Y. W., Huang, W., and Coughlin, S. R. (2001) Role of thrombin signaling in platelets in haemostasis and thrombosis. *Nature 413*, 74–8.

(26) Kastrup, C. J., Shen, F., Runyon, M. K., and Ismagilov, R. F. (2007) Characterization of the threshold response of initiation of blood clotting to stimulus patch size. *Biophys. J. 93*, 2969–77.

Bioconjugate Chemistry

ARTICLE

pubs.acs.org/bc

Development of a Pterin-Based Fluorescent Probe for Screening Dihydropteroate Synthase

Ying Zhao,[†] Dalia Hammoudeh,[‡] Wenwei Lin,[†] Sourav Das,[†] Mi-Kyung Yun,[‡] Zhenmei Li,[‡] Elizabeth Griffith,[†] Taosheng Chen,[†] Stephen W. White,[‡] and Richard E. Lee*[,†]

[†]Department of Chemical Biology and Therapeutics, [‡]Department of Structural Biology, St. Jude Children's Research Hospital, 262 Danny Thomas Place, Mail Stop 1000, Memphis, Tennessee 38105, United States

Supporting Information

ABSTRACT: Dihydropteroate synthase (DHPS) is the classical target of the sulfonamide class of antimicrobial agents, whose use has been limited by widespread resistance and pharmacological side effects. We have initiated a structure-based drug design approach for the development of novel DHPS inhibitors that bind to the highly conserved and structured pterin subsite rather than to the adjacent *p*-aminobenzoic acid binding pocket that is targeted by the sulfonamide class of antibiotics. To facilitate these studies, a robust pterin site-specific fluorescence polarization (FP) assay has been developed and is discussed herein. These studies include the design, synthesis, and characterization of two fluorescent probes, and the development and validation of a rapid DHPS FP assay. This assay has excellent DMSO tolerance and is highly reproducible as evidenced by a high Z′ factor. This assay offers significant advantages over traditional radiometric or phosphate release assays against this target, and is suitable for site-specific high-throughput and fragment-based screening studies.

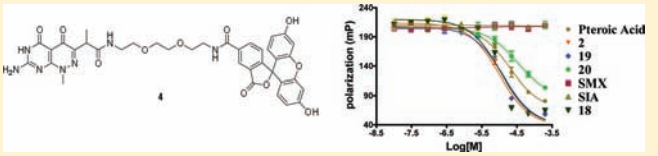

INTRODUCTION

There is a clear need to develop novel antimicrobial agents due to the widespread emergence of drug resistance.[1,2] Sulfonamides have been used as synthetic antibiotics since the 1930s to treat a wide variety of Gram-positive, Gram-negative, and protozoal infections, but their use has been greatly compromised by the emergence of resistance and the poor tolerance of certain patient populations.[2−7] Sulfonamides target the enzyme dihydropteroate synthase (DHPS) encoded by the *fol*P gene and function as competitive inhibitors of one of the DHPS substrates, *p*-amino benzoic acid (*p*ABA).[8] DHPS possesses a classic $(\beta/\alpha)_8$ TIM barrel structure, and the *p*ABA binding site is at the edge of the barrel and comprises loop regions where the mutations that confer sulfonamide resistance are found.[9,10] In contrast, the other substrate of DHPS dihydropterin pyrophosphate (DHPP) binds in a deep, structured pocket within the DHPS β-barrel. This pocket has a high degree of conservation between species, and no resistance mutations have been reported in or adjacent to the pterin binding site. Thus, we believe that the pterin binding site is an attractive alternative target for the design of novel antimicrobial agents.

Currently, the principal screening methods for DHPS are either radiometric or use coupled colorimetric phosphate release assays.[11−13] Although these assays do offer some advantages, they also suffer from a number of practical issues which pertain to their use for site-specific high-throughput screening: The instability and limited availability of the DHPP pterin substrate, the undesirable use of radioactive materials, the need for coincubation with pyrophosphatase and spectrometric interference in the colorimetric assays, and the lack of site specific inhibition information suitable for identifying the selective pterin-binding site inhibitors. In this paper, we report the design, development, and validation of a rapid, sensitive, and site-specific DHPS fluorescence polarization (FP) assay.[14]

A typical FP probe consists of a tracer derived from a high-affinity ligand, a spacing linker and a fluorophore. Previously, we reported structural studies of several small pterin-based inhibitors of DHPS,[15,16] and the two most potent inhibitors **1** and **2** were selected as candidate tracers to develop the FP probes (Figure 1a). The cocrystal structure of DHPS bound to compound **2** was used as a guide to determine the optimal linker length between the tracer and the fluorophore. The carboxylate group of **2** points away from the pterin binding site and was judged to be a suitable linking position. From visual inspection, the distance from the solvent-exposed surface to the carboxylate group was estimated to be approximately the length of two ethylene glycols (or aminoethanol). On the basis of this, three molecular probes with spacer lengths of 1, 2, and 3 ethylene glycols (or aminoethanol) were modeled into the cavity using Schrodinger Glide and our previously validated docking approach (see Supporting Information, Figure S1).[17] From these studies, both the amide-linked two and three glycol/aminoethanol-long probes were shown to bind well. The three-unit spacer would be

Received: June 30, 2011
Revised: August 23, 2011
Published: September 13, 2011

ACS Publications © 2011 American Chemical Society

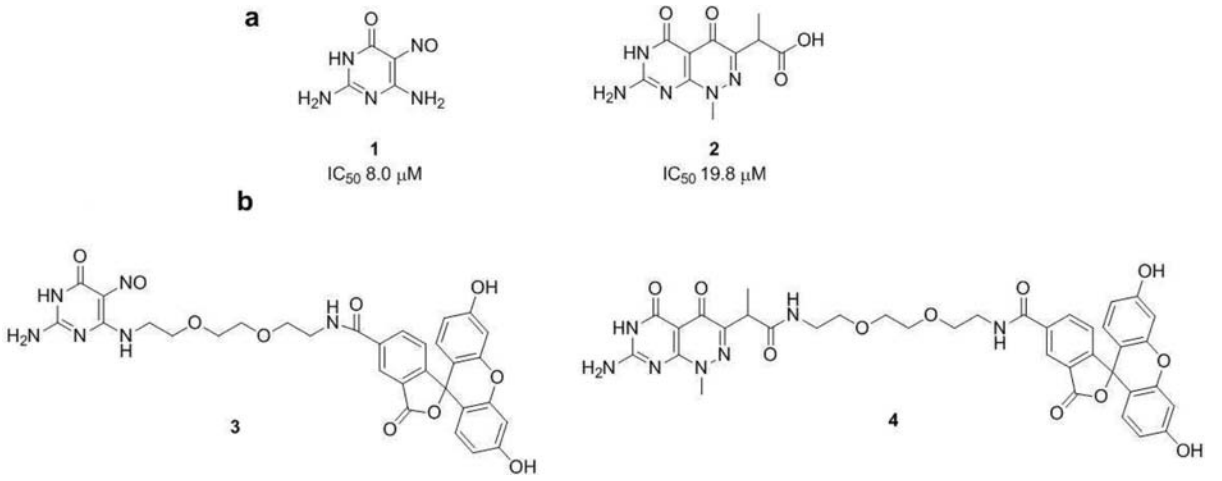

Figure 1. (a) Structures of pterin-based DHPS inhibitors **1** and **2**. (b) Structures of the designed FP probes **3** and **4**.

expected to improve solubility, and 2,2′-(ethane-1,2- diylbis-(oxy))diethanamine was therefore selected as the linker to offset the poor aqueous solubility of the pterin analogues that has previously been encountered.[18] Thus, **4** was chosen for synthesis and, using an analogues approach, probe **3** was also designed and selected for synthesis from **1** using a similar-sized linker (Figure 1b).

EXPERIMENTAL SECTION

Probe Synthesis. Methanol, trifluoroacetic acid (TFA), dichloromethane, triethylamine (TEA), acetone, *N*,*N*-dimethylformamide (DMF), tetrahydrofuran (THF), formic acid, and *tert*-butyl 2-(2-(2-aminoethoxy)ethoxy) ethylcarbamate **6** were purchased from Sigma-Aldrich (St. Louis, MO). 2,5-Dioxopyrrolidin-1-yl 3′,6′-dihydroxy-3-oxo-3*H*-spiro[isobenzofuran-1,9′-xanthene]-5-carboxylate **9** was purchased from OChem, Inc. (Des Plains, IL). *O*-(Benzotriazol-1-yl)-*N*,*N*,*N*′,*N*′-tetramethyluronium hexafluorophosphate (HBTU) was purchased from AK Scientific, Inc. (Union City, CA). Compounds **2** and **5** were prepared as previously reported.[16,19] The reactions were monitored by thin-layer chromatography (TLC) on precoated Merck 60 F254 silica gel plates and visualized by UV detection. The identity of final compounds was determined on a Waters Acquity UPLC MS C18 (H_2O + Formic → ACN + Formic) 5 min gradient, PDA (215−400 nm), ELSD, Acquity SQD ESI Positive MS. High-resolution mass spectra were determined on Waters Acquity UPLC C18 (H_2O → ACN gradient over 4 min) Xevo G2 Q-TOF ESI Negative, resolution mode, compound internally weighted to leucine enkephalin lock solution, calculated error of <3 ppm. The purity of final compounds was determined by UPLC/UV/ELSD/MS (see Supporting Information for UPLC/UV/ELSD/MS method). Both compounds **3** and **4** showed ELSD purity at 96% (see Supporting Information Figures S3 and S4). Melting points were obtained on an OptiMelt Automated Melting Point System (Lambda Photometrics, UK) and were uncorrected. All ^{1}H and ^{13}C spectra were recorded on a Bruker ULTRASHIELD 400 plus or Bruker 800/US^2. The chemical shift values are expressed in ppm (parts per million) relative to tetramethylsilane as internal standard; coupling constants (*J*) are reported in hertz (Hz).

tert-Butyl (2-(2-(2-((2-Amino-5-nitroso-6-oxo-1,6-dihydropyrimidin-4-yl)amino)ethoxy)ethoxy)ethyl)carbamate ***7***. A mixture of **5** (0.175 g, 0.938 mmol) and *tert*-butyl 2-(2-(2-aminoethoxy)ethoxy) ethylcarbamate **6** (0.233 g, 0.938 mmol) in methanol was heated at reflux for 20 h. After cooling, the reaction mixture was filtered. To the filtrate was added 2.5 g silica gel, and the solvent of filtrate was removed under reduced pressure to afford a dry plug, which was loaded on a silica gel column and eluted with chloroform/methanol (20:1). Fractions containing the product were pooled and evaporated to afford **7** as a brick red solid (0.21 g, 58%): R_f 0.4 ($CHCl_3$/CH_3OH = 5:1); mp 166−168 °C; ^{1}H NMR (400 MHz, DMSO-d_6) δ 1.36 (s, 9H), 3.07 (q, J = 5.9 Hz, 2H), 3.40 (t, J = 6.1 Hz, 2H), 3.55 (t, J = 4.5 Hz, 8H), 6.78 (t, J = 5.6 Hz, 1H), 7.08 (s, 1H), 8.19 (s, 1H), 10.96 (s, 1H), 12.49 (s, 1H); ^{13}C NMR (101 MHz, DMSO-d_6) δ 28.19 (s), 39.49, 68.17, 69.19, 69.44, 69.60, 77.53, 140.60, 152.21, 155.54, 156.37, 161.46; MS$^+$ 387.31.

2-Amino-6-((2-(2-(2-aminoethoxy)ethoxy)ethyl)amino)-5-nitrosopyrimidin-4(3H)-one ***8***. A solution of **7** (0.1 g, 0.259 mmol) in TFA/CH_2Cl_2 (v/v = 1:1, 6 mL) was stirred at room temperature for 1 h. The solvent was removed under reduced pressure. Any remaining TFA was removed by repeated coevaporation with methanol, ether, and acetone to give **8** as trifluoroacetic acid salt, a dark red solid (0.10 g, 97%): mp 200−204 °C; ^{1}H NMR (400 MHz, DMSO-d_6) δ 3.01−3.04 (m, 2H), 3.57−3.66 (m, 10H), 7.12 (s, 1H), 7.87 (s, 2H), 8.29 (s, 1H), 10.98 (s, 1H), 12.59 (s, 1H); ^{13}C NMR (101 MHz, DMSO-d_6) δ 38.72, 66.73, 67.94, 69.59, 140.23, 152.44, 156.50, 158.57 (q, J = 128 Hz), 161.16; MS$^+$ 287.26.

N-(2-(2-(2-((2-Amino-5-nitroso-6-oxo-1,6-dihydropyrimidin-4-yl)amino)ethoxy)ethoxy)ethyl)-3,6-dihydroxy-3′-oxo-3′H,10H-spiro[anthracene-9,1′-isobenzofuran]-5′-carboxamide ***3***. TEA (46.7 μL, 0.337 mmol) and 5-carboxyfluorescein *N*-hydroxysuccinimide ester **9** (0.044 g, 0.094 mmol) were added to a solution of **8** (0.03 g, 0.075 mmol) in acetone (4 mL). The reaction was stirred at room temperature for 4 h before being concentrated in vacuo. The crude residue purified by preparative HPLC using a Gemini 5 μ C18 110A AXIA column (50 × 30.00 mm, 5 μm) and a gradient of 20−85% MeOH+4%THF/10 mM ammonium bicabonate over 10 min period with the retention time of the product being 4.8 min. The respective fractions were pooled and concentrated to afford **3** as an orange solid (0.036 g, 75%): ^{1}H

NMR (400 MHz, DMSO-d_6) δ 3.47−3.59 (m, 12H), 6.42 (dd, J = 8.9, 2.2 Hz, 2H), 6.49 (d, J = 2.1 Hz, 2H), 6.62 (d, J = 8.9 Hz, 2H), 7.29 (d, J = 8.0 Hz, 1H), 8.12 (d, J = 8.0 Hz, 1H), 8.46 (d, J = 1.2 Hz, 1H), 8.88 (t, J = 5.5 Hz, 1H), 12.48 (s, 1H); ^{13}C NMR (201 MHz, DMSO) δ 68.33, 68.86, 69.62 (d, J = 11.6 Hz), 102.41, 109.85, 116.15, 125.35, 126.14, 129.57, 131.80, 135.51, 140.72, 152.61, 153.74, 158.36, 163.96, 165.25, 166.20, 166.61, 168.41; HRMS m/z [M-H]$^-$ calcd for $C_{31}H_{27}N_6O_{10}$: 643.5835, found: 643.1771.

tert-Butyl 2-(2-(2-(2-(7-amino-1-methyl-4,5-dioxo-1,4,5,6-tetrahydropyridazino[3,4-d]pyrimidin-3-yl)propanamido)ethoxy)-ethoxy)ethylcarbamate ***10***. To a solution of **2** (0.1 g, 0.377 mmol) and HBTU (0.157 g, 0.415 mmol) in DMF (5 mL), *tert*-butyl 2-(2-(2-aminoethoxy)ethoxy)ethylcarbamate **6** (0.112 g, 0.452 mmol) was added. The reaction mixture was stirred at room temperature for 3 h, diluted with water, and extracted with dichloromethane twice. The organic layer was dried with sodium sulfate; the solvent was evaporated to give a white solid at room temperature. The residue was washed with anhydrous ether and filtered to give **10** as a white solid (0.155 g, 83%): R_f = 0.35 ($CHCl_3$/CH_3OH = 5:1); mp 230 °C (dec); ^{1}H NMR (400 MHz, DMSO-d_6) δ 1.22−1.24 (d, J = 7.2 Hz, 3H), 1.36 (s, 9H), 3.03−3.08 (m, 2H), 3.13−3.20 (m, 2H), 3.35−3.37 (m, 4H), 3.48 (s, 4H), 3.74 (s, 3H), 3.85−3.91 (q, J = 7.2 Hz, 1H), 6.76 (t, J = 5.5 Hz, 1H), 7.83 (t, J = 5.6 Hz, 1H), 7.95 (bs, 2H), 10.84 (bs, 1 H); ^{13}C NMR (101 MHz, DMSO-d_6) δ 14.61, 28.19, 30.73, 35.74, 38.69, 41.00, 69.06 (d, J = 13.1 Hz), 69.48 (d, J = 13.6 Hz), 77.51, 155.54, 157.36, 162.25, 167.10, 171.95. MS$^+$ 496.33.

2-(7-Amino-1-methyl-4,5-dioxo-1,4,5,6-tetrahydropyridazino-[3,4-d]pyrimidin-3-yl)-N-(2-(2-(2-aminoethoxy)ethoxy)ethyl)-propanamide ***11***. Compound **10** (0.3 g, 0.6 mmol) was added to a solution of TFA/Cl_2Cl_2 (1:1 v/v). The reaction mixture was stirred at room temperature for 30 m. The solvent was removed under reduced pressure. Any remaining TFA was removed by repeated coevaporation with diethyl ether to afford **11** as trifluoroacetic acid salt as a white solid (0.246 g, 80%): mp 160 °C (dec); ^{1}H NMR (400 MHz, DMSO-d_6) δ 1.25−1.27 (d, J = 7.2 Hz, 3H), 1.36 (s, 9H), 3.00−3.03 (m, 2H), 3.09−3.27 (m, 2H), 3.39−3.43 (m, 4H), 3.53−3.60 (m, 2H), 3.64−3.72 (m, 2H), 3.78 (s, 3H), 3.93 (q, J = 7.2 Hz, 1H), 7.81 (t, J = 5.3 Hz, 1H); ^{13}C NMR (101 MHz, DMSO-d_6) δ 14.35, 41.19, 66.68, 68.91, 69.70, 100.69, 153.59, 155.46, 157.26, 158.11, 158.41, 160.19, 167.59, 171.70; MS$^+$ 396.26.

N-(2-(2-(2-(2-(7-Amino-1-methyl-4,5-dioxo-1,4,5,6-tetrahydro-pyridazino[3,4-d]pyrimidin-3-yl)propanamido)ethoxy)ethoxy)-ethyl)-3′,6′-dihydroxy-3-oxo-3H-spiro[isobenzofuran-1,9′-xanthene]-5-carboxamide ***4***. A solution of **11** (0.050 g, 0.098 mmol), 2,5-dioxopyrrolidin-1-yl 3′,6′-dihydroxy-3-oxo-3*H*-spiro-[isobenzofuran-1,9′-xanthene]-5-carboxylate **9** (0.058 g, 0.123 mmol), and TEA (61.2 μL, 0.442 mmol) in DMF (4 mL) was stirred at room temperature for 4 h. The crude product was purified by preparative HPLC using a Gemini 5 μ C18 110A AXIA column (50 × 30.00 mm, 5 μm) and a gradient of 20−85% MeOH + 4% THF/10 mM ammonium bicarbonate over 10 min period. The retention time of the product was 4.8 min. The respective fractions were pooled and concentrated to afford the title compound **4** as an orange solid (0.050 g, 68%): ^{1}H NMR (400 MHz, DMSO-d_6) δ 1.21−1.23 (d, J = 8 Hz, 3H), 3.38−3.62 (m, 12H), 3.73 (s, 3H), 3.86−3.91 (q, J = 8 Hz, 1H), 6.46−6.49 (m, 2H), 6.56−6.62 (m, 4H), 7.33 (d, J = 8.0 Hz, 1H), 7.85 (t, J = 5.6 Hz, 1H), 8.16 (d, J = 8.0 Hz, 1H), 8.48 (bs, 1H), 8.89 (t, J = 5.2 Hz, 1H); ^{13}C NMR (201 MHz, DMSO) δ 14.52, 38.77, 40.93, 68.71, 69.03, 69.55, 100.72, 102.38, 109.86, 115.38, 124.71, 125.75, 129.46, 135.70, 153.29, 153.79, 156.64, 157.57, 161.36, 165.08, 167.28, 168.16, 171.96; HRMS m/z [M-H]$^-$ calcd for $C_{37}H_{34}N_7O_{11}$: 752.7100, found: 752.2316.

Protein Preparation. *Bacillus anthracis* DHPS (*Ba*DHPS) was prepared as described previously.[16]

Probe Characterization—Isothermal Titration Calorimetry (ITC). The purified *Ba*DHPS protein was dialyzed against 50 mM HEPES, 5 mM $MgCl_2$, pH 7.6. ITC titrations were performed with an Auto-iTC200 Isothermal Titration Calorimeter (MicroCal) in 40 mM HEPES, 4 mM $MgCl_2$ at pH 7.6 and 25 °C over 19 2 μL injections each of 500 μM ligand into 20 μM *Ba*DHPS. Data were analyzed using *MicroCal Origin 7.0* software using a one-site binding model.

Probe Characterization—Fluorescence Polarization. The titration experiment was performed in triplicate with 6 nM of compounds **3** and **4** and 2-fold increasing concentrations of *Ba*DHPS (0.009 to 150 μM) in a 96-well plate with a final volume of 100 μL in 1× PBS buffer. Data were fit to a Langmuir isotherm

$$\mathrm{FP} = \mathrm{FP}^0 + \Delta\mathrm{FP} \cdot \left(\frac{1}{1 + K_D/[\mathrm{DHPS}]}\right)$$

To confirm pterin-pocket binding of **4**, inhibitor **2** was titrated (10 nM to 400 μM) against 6 nM of **4** and 6 μM of *Ba*DHPS in 1× PBS buffer to a final volume of 100 μL in a black polystyrene 96-well plate (Costar, Corning Inc.). The data were fit to the equation derived from the definition of dissociation constant with the approximation of a negligible concentration of fluorescent probe described in the Supporting Information.[20,21] All FP measurements were performed on a 2103 EnVision multilable reader (Perkin-Elmer) with excitation and emission wavelength filters of 450 ± 8 nm and 535 ± 40 nm, respectively.

High-Throughput Fluorescence Polarization Assay. In developing the FP assay for high-throughput screening purposes, we followed the NIH NCGC guidelines (http://www.ncgc.nih.gov/guidance/section5.html#practical-fluor-polar). FP measurements were performed as described previously, but using PMT sensitivity set to low and 100 readings per well. Assays were performed in flat-bottom, black polystyrene 384-well plates (3821 Costar, Corning Inc.) in 40 mM HEPES, 4 mM $MgCl_2$ at pH 7.6. The final assay volume was 20 μL/well. All measurements were performed in triplicate except for Z' determination assays in which 12 replicates were used in each group. The typical final DMSO concentration in tests was 2% except for DMSO tolerance experiments in which varied DMSO concentrations were used as indicated.

To optimize the assay, equilibrium binding experiments of **4** to *Ba*DHPS were performed under the following conditions: each individual well in a 384-well assay plate contained 2.7 μM **4** and increasing concentrations (from 0 to 16 μM) of *Ba*DHPS protein in assay buffer. The plate was mixed on a slow-moving shaker for the indicated times at 25 °C and the polarization signals were measured at room temperature. To test the signal stability, the FP of a plate containing samples was measured at different times over a period of 18 h. The assay equilibration time was determined by monitoring the FP signal at several time intervals as indicated. Between each reading, the plate was covered with a black lid to prevent photobleaching. For tracer specificity experiments, each individual well contained 2.7 μM **4** and 8 μM of *Ba*DHPS and DMSO; for competition experiments, each

Scheme 1. Synthesis of FP Probe 3[a]

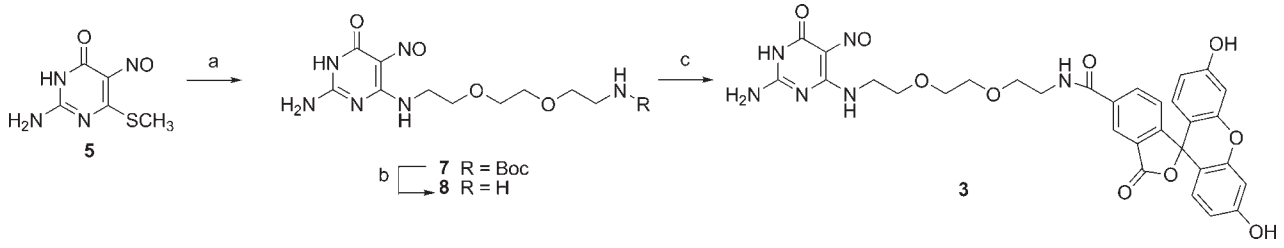

[a] Reagents and conditions: (a) *tert*-butyl (2-(2-(2-aminoethoxy)ethoxy)ethyl)carbamate **6**, CH_3OH, reflux, 20 h, 58%; (b) TFA, 97%; (c) 5-carboxyfluorescein *N*-succinimidyl ester **9**, DMF, TEA, 75%.

Scheme 2. Synthesis of Probe 4[a]

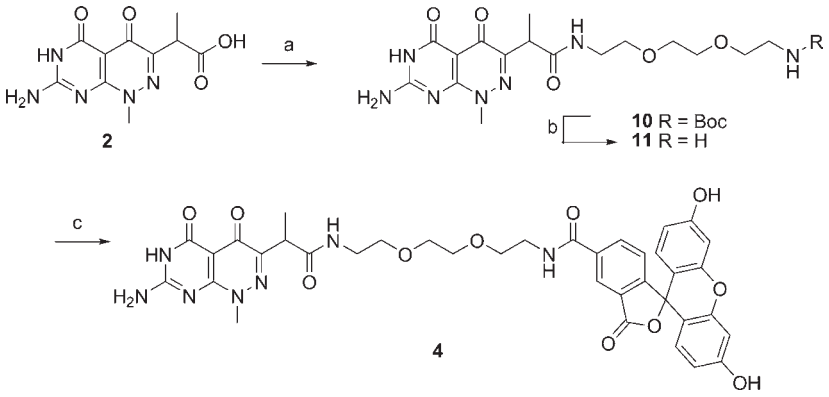

[a] Reagents and conditions: (a) *tert*-butyl (2-(2-(2-aminoethoxy)ethoxy)ethyl)carbamate **6**, HBTU, DMF, rt, 3 h, 83%; (b) TFA, 80%; (c) 5-carboxyfluorescein *N*-succinimidyl ester **9**, DMF, TEA, 68%.

individual well contained 2.7 μM **4**, 8 μM of *Ba*DHPS, 100 μM of **2** and DMSO; each control well contained 2.7 μM **4** and DMSO. The experiments were performed under conditions similar to those described above and the FP data were measured in triplicate. This experiment was repeated two more times on different days. To determine the effect of DMSO on the assay, DMSO tolerance experiments were performed under the above conditions with 2.7 μM **4**, 8 μM of *Ba*DHPS, and varying concentration of DMSO from 0.02% to10% (v/v). To determine the assay robustness, Z′-factor statistic experiments were implemented in triplicate in which 2 groups of samples, the high signal group and low signal group, were involved. The high signal group represents samples with protein and tracer. The low signal group represents samples with protein, tracer, and ligand **2** at 100 μM. This experiment was repeated two more times on different days. The Z′ factor is calculated using the equation $Z' = 1 - (3\sigma^+ + 3\sigma^-)/(\text{Mean}^+ - \text{Mean}^-)$, where σ^+ is the standard deviation of high signal group; σ^- is the standard deviation of low signal group; Mean^+ is the mean of high signal group; and Mean^- is the mean of low signal group. All experimental data were analyzed using *Microsoft Excel* (Microsoft Corporation, Redmond, WA) and *Prism 4.0* (Graphpad Software Inc., San Diego, CA).

Assay Validation—Competitive Displacement of 4 by Known DHPS Inhibitors. Competitive displacement studies were performed with DHPS inhibitors **2**, **18**, **19**, **20**, pteroic acid, SMX, and SIA. Stocks of these inhibitors were prepared in DMSO at 10 mM and serially diluted in assay buffer. FP assay was performed under following conditions: Corning black 384-well plate contained 2.7 μM probe **4**, 8 μM *Ba*DHPS protein, and each tested inhibitor at varying concentrations to a final volume of 20 μL. The plate was shaken for 25 min at room temperature and the FP values were recorded. The measured FP values (mP) were plotted against the $\log_{10}$ values of competitor concentration. Herein, the displacement data were empirically fit. In order to calculate accurate K_D values for hit compounds out of the HTS, where the approximation of a negligible concentration of fluorescent probe does not hold true due to experimental conditions, the exact analytical approach described by Wagner et al.[20,21] can be applied.

RESULTS AND DISCUSSION

The synthesis of FP probe **3** was achieved from 5-nitroso-6-methylpyrimidine **5**, [19] which was conjugated with *tert*-butyl 2-(2-(2-aminoethoxy)ethoxy)ethylcarbamate **6** in refluxing methanol to give **7**. [22] The Boc-protected **7** was converted to free terminal amine **8** by treatment with TFA. Coupling of **8** with 5-carboxyfluorescein *N*-succinimidyl ester **9** in the presence of TEA in DMF afforded the desired probe **3** in good yields. [23]

FP probe **4** was synthesized from **2**. Coupling of **2** with **6** in the presence of HBTU in DMF provided amide **10**, which then was treated with TFA to afford the free amine **11**. Coupling of **11** with **9** in the presence of TEA in DMF afforded the second FP probe **4** in good yields.

Prior to establishing the FP assay, the equilibrium dissociation binding constants (K_D) of the two probes were measured using two independent methods, isothermal titration calorimetry (ITC) and FP. Using ITC, the K_D values were found to be

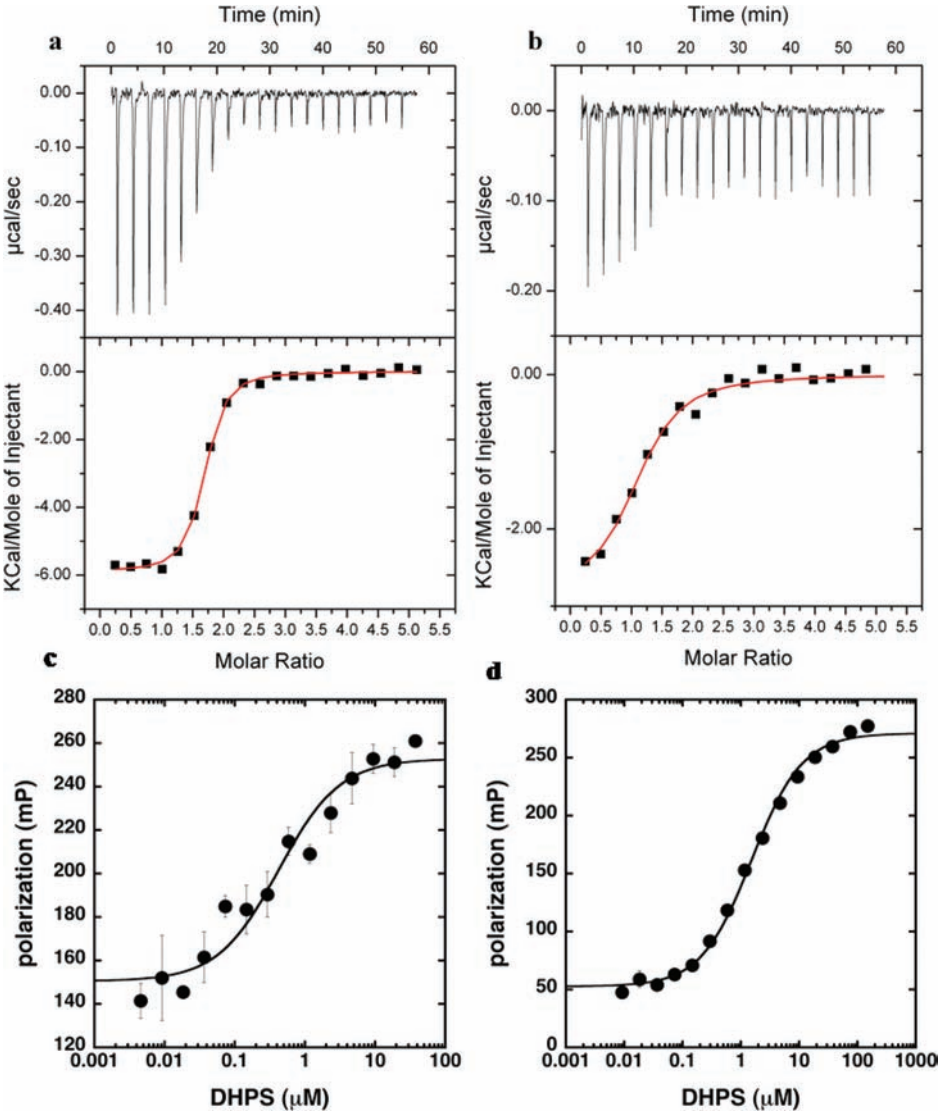

Figure 2. Measuring direct binding of compounds **3** and **4** to *Bacillus anthracis* DHPS (*Ba*DHPS). (a) ITC titration of 500 μM of **3** into a 20 μM *Ba*DHPS solution. Binding site $N = 1.59 \pm 0.0108$; ΔH is -5.9 ± 0.059 kcal/mol; ΔS is 0.0982 kcal/mol; K_D is 0.34 ± 0.043 μM. (b) ITC titration of 500 μM of **4** into a 20 μM *Ba*DHPS solution. Binding site $N = 1.09 \pm 0.0464$; ΔH is -2.8 ± 0.159 kcal/mol; ΔS is 0.16 kcal/mol; K_D is 2.7 ± 0.64 μM. (c) Direct binding of **3** to *Ba*DHPS by FP (average of 3 independent experiments). Error bars represent standard error of the mean; K_D is 0.37 μM $\pm$ 0.1 . (d) Direct binding of **4** to *Ba*DHPS by FP (average of 3 independent experiments). Error bars represent standard error of the mean; K_D is 1.5 ± 0.1 μM.

0.34 ± 0.043 μM for compound **3** and 2.7 ± 0.64 μM for compound **4** (Figure 2a,b). Using FP,[24,25] the K_D values were found to be in excellent agreement, 0.37 ± 0.1 μM for compound **3** and 1.5 ± 0.1 μM for compound **4** (Figure 2c,d). The affinities of both probes were found to be weaker than their corresponding parent inhibitors ($K_D = 0.124 \pm 0.017$ μM for **2** using ITC). This was anticipated and is likely due to some loss of receptor binding interactions from the introduction of the linker groups and the bulky fluorescein fluorophore. Comparison of the two probes showed that **3** has an apparently higher binding affinity than **4** to *Ba*DHPS, but the ITC and the FP data for **3** both showed that binding was not at a 1:1 ratio, whereas this was the case for **4** which has better FP signal. Further analysis by incubating **3** in 1% BSA showed that the FP absorbance of **3** was significantly reduced, which indicated that **3** is a nonspecific protein binder. Consequently, **3** was dropped from further study and **4** was selected to develop the DHPS FP binding assays.

Finally, to confirm pterin-binding pocket binding, we monitored the displacement of **4** by its parent compound **2** at low probe concentrations using an FP competition experiment. The binding signal of **4** disappeared within a narrow concentration range of **2** (Figure 3), and curve fitting (see Supporting Information) generated a K_D value for **2** of 0.24 ± 0.07 μM, which agrees well with the value obtained by ITC (0.124 ± 0.017 μM). It has already been confirmed by X-crystallography that **2** binds *Ba*DHPS at the pterin-binding site,[16] and this experiment therefore confirms that the FP probe **4** is a competitive binder with respect to **2** and binds at the pterin-binding pocket in *Ba*DHPS as expected.

To develop the high-throughput FP screening assay, it was necessary to determine the optimum protein concentration for competitive binding. Thus, **4** at its K_D (we chose the ITC value of 2.7 μM) was titrated with varying concentrations of *Ba*DHPS (Figure 4) and the FP signal monitored. In the absence of

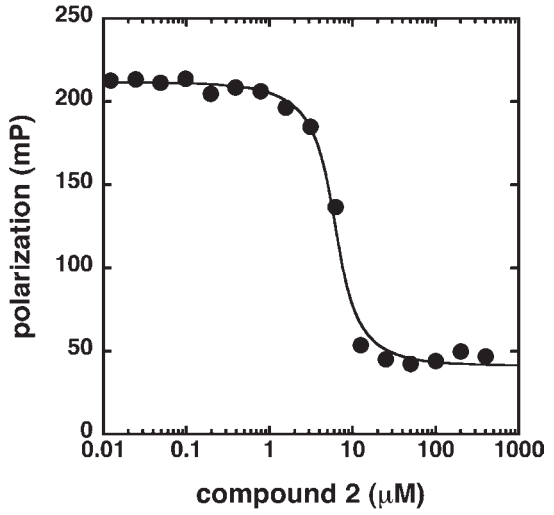

Figure 3. FP competition titration of nonfluorescent compound **2** (10 nM to 400 uM) against compound **4** (6 nM), and **6** μM *Ba*DHPS (average of 3 independent experiments). $K_D = 0.24 \pm 0.07$ μM.

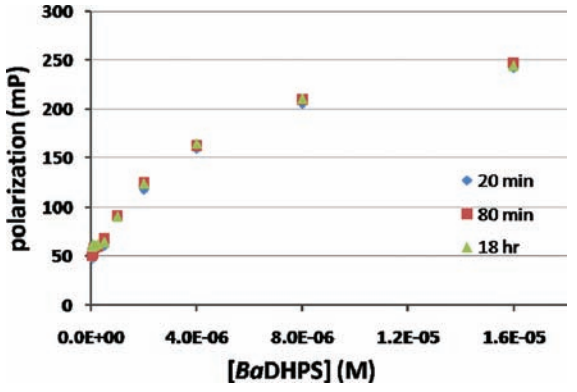

Figure 4. Titration of **4** (2.7 μM) with *Ba*DHPS monitored by FP. Increasing concentrations of *Ba*DHPS (0−16 μM) was incubated with **4** at 25 °C and the response measured at 20 min, 80 min, and 18 h.

protein, a low polarization value of 50 mP was observed, but with increasing concentrations of *Ba*DHPS protein, the FP signal progressively increased until it reached saturation. This revealed an assay window of up to 200 ΔmP which is a robust signal window for a FP assay. By examining the response curve (Figure 4), DHPS at 8 μM was selected for further assay development because this concentration yields an acceptable assay window of ΔmP ∼150 mP. This experiment was also used to evaluate the stability of the FP signal, which becomes an important parameter in the high-throughput screening of large number of compounds over long periods of time.[26] To this end, the probe was incubated with *Ba*DHPS for a period of 18 h within which the FP signal of the plate was read several times. The binding curves showed that the FP signal is very stable with little noticeable difference. In addition, incubation of the probe with protein reached signal saturation in a very short time (∼20 min), which is an added advantage (Figure 4).

DMSO is routinely used to dissolve or dilute compounds for screening assays; therefore, the effect of various DMSO concentrations on the FP signal was studied. Specifically, **4** was incubated with *Ba*DHPS in the presence of varying DMSO concentrations

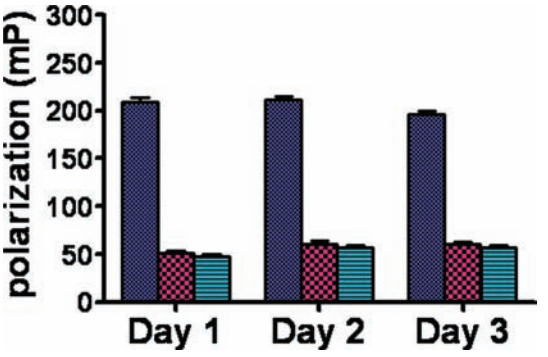

Figure 5. Tracer specificity test. blue bars: 2.7 μM of **4** with 8 μM of *Ba*DHPS in buffer; red bars: 2.7 μM of **4**, 8 μM of *Ba*DHPS, and 100 μM of **2** in buffer; green bars: 2.7 μM of **4** only in buffer.

up to 10% and the variation in FP signal was monitored (see Supporting Information Figure S2). This experiment showed that the FP binding assay tolerated DMSO well, up to a concentration of 10%, with less than 10% reduction of the FP signal, which remained stable for 18 h (higher DMSO concentrations were not tested because the DMSO concentration will not exceed 10% in a typical assay).

To evaluate the performance of the DHPS FP binding assay, the Z′ value was calculated for the assay carried out in a 384 well plate format.[27] In general, Z′ values between 0.5 and 1.0 are considered acceptable. Here, the Z′ values for the *Ba*DHPS FP binding assay obtained from three independent experiments were 0.87, 0.87, and 0.86, respectively (see Supporting Information Figure S3), and these values showed that the assay is highly reproducible. Furthermore, the FP assay with **4** was also tested against *Staphylococcus aureus* DHPS (*Sa*DHPS) using similar assay conditions, and this also performed remarkably well with a Z′ value at 0.84. This confirms that the assay is suitable for future high-throughput screening against multiple DHPS enzymes.

Finally, competitive displacement assays were performed with various known DHPS inhibitors to test the robustness of the developed FP assay and to validate its utility for detecting specific inhibitors that target the pterin-binding pocket. In an initial competition binding experiment in which *Ba*DHPS, probe **4**, and its parent inhibitor **2** were coincubated under high-throughput assay optimized conditions, the binding signal of **4** was completely abolished by an excess of **2** and the FP signal was almost identical to that for probe **4** in the absence of protein. The results were stable over a three-day period (Figure 5) and are consistent with the titration experiment shown in Figure 3. Seven inhibitors were then tested: **2**, **18** (an analogue of **2**), and **19** are DHPS inhibitors that are known to target the pterin-binding pocket,[16] sulfamethoxazole (SMX) and sulfanilamide (SIA) are two sulfonamides that bind the *p*ABA binding pocket, and **20** and pteroic acid are two DHPS inhibitors that engage both the pterin- and *p*ABA-binding sites simultaneously. The competition experiment (Figure 6) showed that all the compounds known to bind the pterin-binding site on DHPS (**2**, **18**, **19**, **20**, and pteroic acid) are able to compete off the FP probe **4** and are identified as hits in the current assay. However, SMX and SIA, which bind to the *p*ABA subsite, are not able to compete off the FP probe **4** and thus would not be identified as hits since the assay described herein specifically identifies compounds that bind to the pterin subsite.

In summary, two pterin-based fluorophores **3** and **4** were designed, synthesized, and evaluated as probes for the development

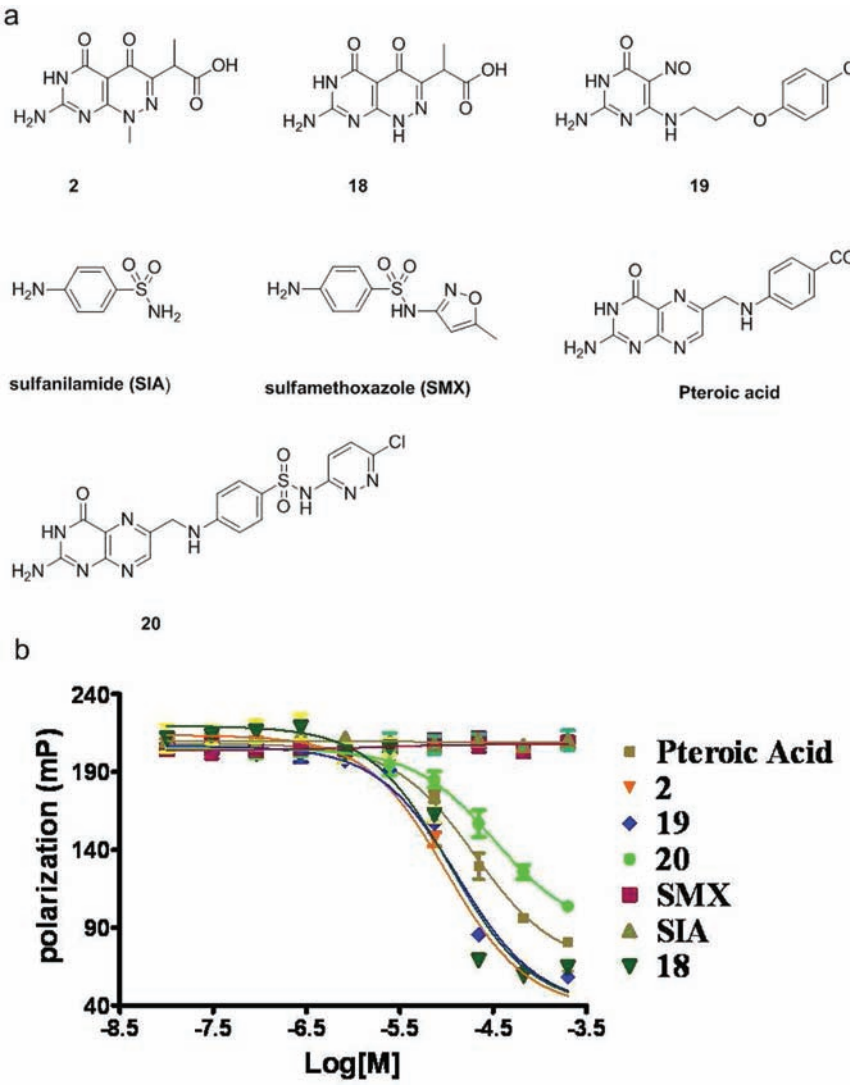

Figure 6. (a) Structure of small molecule inhibitors evaluated in FP competition experiment. (b) Competitive displacement of **4** from *Ba*DHPS by various DHPS inhibitors.

of a FP assay for screening against *Ba*DHPS and *Sa*DHPS. The FP assay described herein, in which **4** is used as probe, is rapid, accurate, robust, and reproducible as evidenced by an excellent Z′ factor. Furthermore, it has great tolerance with respect to the typical concentrations of DMSO used in small molecule screening and is suitable for identifying DHPS inhibitors that bind to the pterin subsite in a high-throughput format. Finally, **4** can be further used to subsequently derive K_D values for the pterin pocket inhibitors identified in the high-throughput FP assay.

■ ASSOCIATED CONTENT

Supporting Information. Additional figures as described in the text. This material is available free of charge via the Internet at http://pubs.acs.org.

■ AUTHOR INFORMATION

Corresponding Author

*E-mail: Richard.lee@stjude.org. Phone: 901 595 6617. Fax: 901 595 5715.

■ ACKNOWLEDGMENT

Funding for this research was provided by National Institutes of Health grants AI070721, Cancer Center core grant CA21765, and the American Lebanese Syrian Associated Charities (ALSAC). We thank Jerrod Scarborough, Drs. Lei Yang and Bing Yan from Department of Chemical Biology and Therapeutics at St Jude Children's Research Hospital for their help in analyzing and purification of final compounds, and Dr. David Smithson from Department of Chemical Biology and Therapeutics and Dr. Ariele Viacava Follis from Structure Biology at St Jude Children's Research Hospital for their assistance in the design of the FP assay and fitting of the data.

■ ABBREVIATIONS

DHPS, dihydropteroate synthase; FP, fluorescence polarization; *p*ABA, *p*-aminobenzoic acid; DHPP, dihydropterin pyrophosphate; ITC, isothermal titration calorimetry; *Ba*DHPS, *Bacillus anthracis* DHPS; *Sa*DHPS, *Staphylococcus aureus* DHPS; SIA, sulfanilamide; SMX, sulfamethoxazole

REFERENCES

(1) Silver, L. L. (2011) Challenges of antibacterial discovery. *Clin. Microbiol. Rev. 24*, 71–109.

(2) Payne, D. J., Gwynn, M. N., Holmes, D. J., and Pompliano, D. L. (2007) Drugs for bad bugs: Confronting the challenges of antibacterial discovery. *Nat. Rev. Drug Discovery 6*, 29–40.

(3) Brackett, C. (2007) Sulfonamide allergy and cross-reactivity. *Curr. Allergy Asthma Rep. 7*, 41–48.

(4) Huovinen, P., Sundstrom, L., Swedberg, G., and Skold, O. (1995) Trimethoprim and sulfonamide resistance. *Antimicrob. Agents Chemther. 39*, 279–289.

(5) Miller, A. K. (1944) Folic acid and biotin synthesis by sulfonamide-sensitive and sulfonamide-resistant strains of Escherichia coli. *Proc. Natl. Acad. Sci. U.S.A. 57*, 151–153.

(6) Skold, O. (2000) Sulfonamide resistance: Mechanisms and trends. *Drug Resist. Updates 3*, 155–160.

(7) Woods, D. D. (1940) The relationship of p-aminobenzoic acid to the mechanism of the action of sulphanilamide. *Br. J. Exp. Pathol. 21*, 74–90.

(8) Bermingham, A., and Derrick, J. P. (2002) The folic acid biosynthesis pathway in bacteria: evaluation of potential for antibacterial drug discovery. *Bioessays 24*, 637–648.

(9) Baca, A. M., Sirawaraporn, R., Turley, S., Sirawaraporn, W., and Hol, W. G. J. (2000) Crystal structure of Mycobacterium tuberculosis 6-hydroxymethyl-7,8-dihydropteroate synthase in complex with pterin monophosphate: New insight into the enzymatic mechanism and sulfa-drug action. *J. Mol. Biol. 302*, 1193–1212.

(10) Haasum, Y., Strom, K., Wehelie, R., Luna, V., Roberts, M. C., Maskell, J. P., Hall, L. M. C., and Swedberg, G. (2001) Amino acid repetitions in the dihydropteroate synthase of Streptococcus pneumoniae lead to sulfonamide resistance with limited effects on substrate K-m. *Antimicrob. Agents Chemother. 45*, 805–809.

(11) Azzopardi, P. V., O'Young, J., Lajoie, G., Karttunen, M., Goldberg, H. A., and Hunter, G. K. (2010) Roles of electrostatics and conformation in protein-crystal interactions. *PLoS ONE 5*, e9330.

(12) Kasekarn, W., Sirawaraporn, R., Chahomchuen, T., Cowman, A. F., and Sirawaraporn, W. (2004) Molecular characterization of bifunctional hydroxymethyldihydropterin pyrophosphokinase-dihydropteroate synthase from Plasmodium falciparum. *Mol. Biochem. Parasitol. 137*, 43–53.

(13) Triglia, T., Menting, J. G. T., Wilson, C., and Cowman, A. F. (1997) Mutations in dihydropteroate synthase are responsible for sulfone and sulfonamide resistance in Plasmodium falciparum. *Proc. Natl. Acad. Sci. U.S.A. 94*, 13944–13949.

(14) Burke, T. J., Loniello, K. R., Beebe, J. A., and Ervin, K. M. (2003) Development and application of fluorescence polarization assays in drug discovery. *Comb. Chem. High Throughput Screen. 6*, 183–194.

(15) Babaoglu, K., Qi, J., Lee, R. E., and White, S. W. (2004) Crystal structure of 7,8-dihydropteroate synthase from Bacillus anthracis: Mechanism and novel inhibitor design. *Structure 12*, 1705–1717.

(16) Hevener, K. E., Yun, M. K., Qi, J., Kerr, I. D., Babaoglu, K., Hurdle, J. G., Balakrishna, K., White, S. W., and Lee, R. E. (2010) Structural studies of pterin-based inhibitors of dihydropteroate synthase. *J. Med. Chem. 53*, 166–177.

(17) Hevener, K. E., Zhao, W., Ball, D. M., Babaoglu, K., Qi, J., White, S. W., and Lee, R. E. (2009) Validation of molecular docking programs for virtual screening against dihydropteroate synthase. *J. Chem. Inf. Model. 49*, 444–460.

(18) Qi, J., Virga, K. G., Das, S., Zhao, Y., Yun, M.-K., White, S. W., and Lee, R. E. (2011) Synthesis of bi-substrate state mimics of dihydropteroate synthase as potential inhibitors and molecular probes. *Bioorg. Med. Chem. 19*, 1298–1305.

(19) Lever, O. W., Bell, L. N., McGuire, H. M., and Ferone, R. (1985) Monocyclic pteridine analogs- Inhibition of escherichia-coli dihydropteroate synthease by 6-amino-5-nitrosoisocytosines. *J. Med. Chem. 28*, 1870–1874.

(20) Roehrl, M. H. A., Wang, J. Y., and Wagner, G. (2004) A general framework for development and data analysis of competitive high-throughput screens for small-molecule inhibitors of protein-protein interactions by fluorescence polarization. *Biochemistry 43*, 16056–16066.

(21) Roehrl, M. H. A., Wang, J. Y., and Wagner, G. (2004) Discovery of small-molecule inhibitors of the NFAT calcineurin interaction by competitive high-throughput fluorescence polarization screening. *Biochemistry 43*, 16067–16075.

(22) Lever, O. W., Bell, L. N., Hyman, C., McGuire, H. M., and Ferone, R. (1986) IInhibitors of dihydropteroate synthase substitutent effects in the side chain aromatic ring of 6-[[3-(aryloxy)propyl]amino]-5-nitrosoisocytosines and nitrosoisocytosines and synthesis and inhibitory potency of bridged 5-nitrosoisocytosine-para-aminobenzoic acid analogs. *J. Med. Chem. 29*, 665–670.

(23) Neres, J., Wilson, D. J., Celia, L., Beck, B. J., and Aldrich, C. C. (2008) Aryl acid adenylating enzymes involved in siderophore biosynthesis: Fluorescence polarization assay, ligand specificity, and discovery of non-nucleoside inhibitors via high-throughput screening. *Biochemistry 47*, 11735–11749.

(24) Nikolovska-Coleska, Z., Wang, R., Fang, X., Pan, H., Tomita, Y., Li, P., Roller, P. P., Krajewski, K., Saito, N. G., Stuckey, J. A., and Wang, S. (2004) Development and optimization of a binding assay for the XIAP BIR3 domain using fluorescence polarization. *Anal. Biochem. 332*, 261–273.

(25) Parker, G. J., Law, T. L., Lenoch, F. J., and Bolger, R. E. (2000) Development of high throughput screening assays using fluorescence polarization: Nuclear receptor-ligand-binding and kinase/phosphatase assays. *J. Biomol. Screen. 5*, 77–88.

(26) Seethala, R., Golla, R., Ma, Z., Zhang, H., O'Malley, K., Lippy, J., Cheng, L., Mookhtiar, K., Farrelly, D., Zhang, L., Hariharan, N., and Cheng, P. T. W. (2007) A rapid, homogeneous, fluorescence polarization binding assay for peroxisome proliferator-activated receptors alpha and gamma using a fluorescein-tagged dual PPAR[alpha]/[gamma] activator. *Anal. Biochem. 363*, 263–274.

(27) Zhang, J. H., Chung, T. D. Y., and Oldenburg, K. R. (1999) A simple statistical parameter for use in evaluation and validation of high throughput screening assays. *J. Biomol. Screen. 4*, 67–73.

Development of a Pterin-based Fluorescent Probe for Screening Dihydropteroate Synthase

Ying Zhao,[1] Dalia Hammoudeh,[2] Wenwei Lin,[1] Sourav Das,[1] Mi-Kyung Yun, [2] Zhenmei Li, [2] Elizabeth Griffith,[1] Taosheng Chen,[1] Stephen W. White[2] and Richard E. Lee[1*]

1. Department of Chemical Biology and Therapeutics, St. Jude Children's Research Hospital, 262 Danny Thomas Place, Mail Stop 1000, Memphis, TN 38105; 2. Department of Structural Biology, St. Jude Children's Research Hospital, Mail Stop 311, Memphis, TN 38105;

SUPPORTING INFORMATION

Kd fit equation for competition experiments:

The following equation derived from the definition of dissociation constant with the approximation of a negligible concentration of fluorescent probe:

$$FP = FP^{0} + \Delta FP \bullet \left\{ \frac{-\left[K_{comp} \bullet ([comp] - [DHPS]) + 2 \bullet [DHPS] + K_{D}\right] + \sqrt{\left[K_{comp} \bullet ([comp] - [DHPS]) + 2 \bullet [DHPS] + K_{D}\right]^{2} + 4 \bullet [DHPS] \bullet \left[K_{comp} \bullet ([DHPS] - [comp]) + K_{comp} \bullet K_{D} - [DHPS] - K_{D}\right]}}{2 \bullet \left[K_{comp} \bullet ([DHPS] - [comp]) + K_{comp} \bullet K_{D} - [DHPS] - K_{D}\right]} \right\}$$

where K_D is the dissociation constant between the probe and DHPS, K_{comp} is the ratio between dissociation constant between the K_D and the K_d of the competitor.

Method for HPLC/UV/ELSD/MS

LC-MS chromasolv grade methanol and ammonium bicarbonate were obtained from Sigma-Aldrich (St. Louis, MO). Milli-Q water as an ultrapure laboratory grade water was used in aqueous mobile phase.

Chromatographic separation was performed on an Acquity UPLC BEH C18 1.7 μm, 2.1 x 50 mm column (Waters Corporation, Milford, MA) using an Acquity ultra performance liquid chromatography system. Data were acquired using Masslynx v. 4.1 and analyzed using the Openlynx software suite. This was coupled to an Acquity photodiode array detector, which acquired UV data from 210-400 nm. The flow was then split, with half directed to an evaporative light scattering detector (ELSD) and half to an SQ mass spectrometer. The total flow rate was 0.7 mL/min. The sample injection volume was 2 μL. The UPLC column was maintained at 50 °C and the gradient program started at 90% A (10 mM ammonium bicarbonate in MilliQ H_2O), changed to 70% A over 0.2 min, to 95 % B (100% methanol) over 1.4 minutes, held for 0.35 minutes, then to 90% A over 0.05 minutes. The mass spectrometer was operated in positive-ion mode with electrospray ionization. The conditions were as follows: capillary voltage 3.4 kV, cone voltage 30 V, source temperature 130 °C, desolvation temperature 400 °C, desolvation gas 800 L/hr, cone gas 100 L/hr. A full scan range from m/z = 110-1000 in 0.2 s was used to acquire MS data. The ELSD-drift tube temperature was set at 52 °C.

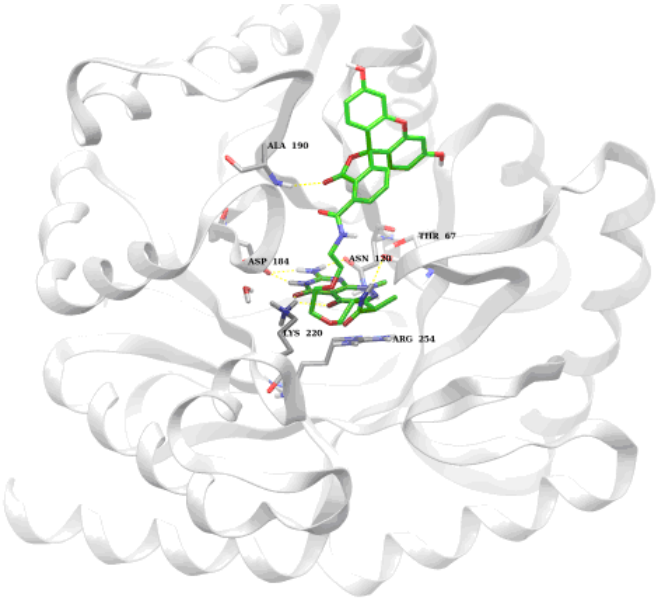

Figure S1 Probe 4 docked into DHPS active site

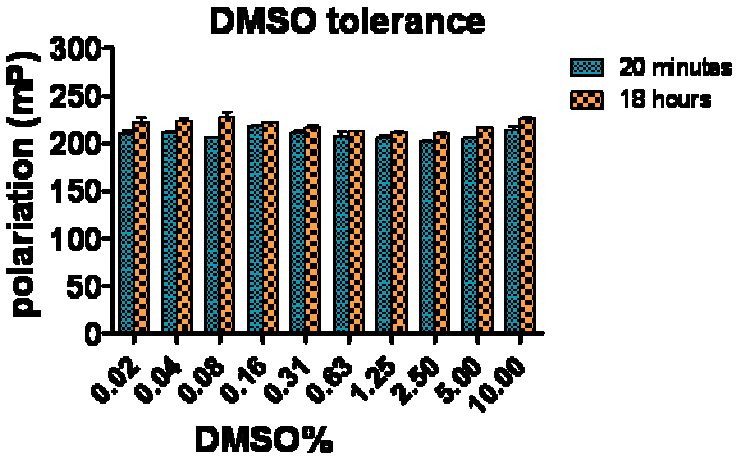

Figure S2: Effect of DMSO on binding experiments. 2.7 µM of **4** and 8 µM of ***Ba***DHPS were incubated with 10% in highest, 1-to-2 dilution for 10 concentration level, down to 0.02% of DMSO for 20 min and 18 hr.

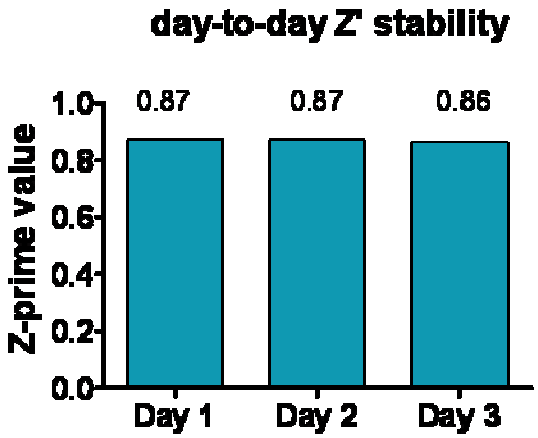

$$Z' = 1 - \frac{3\sigma^{+} + 3\sigma^{-}}{Mean^{+} - Mean^{-}}$$

Figure S3: Day-to-day Z' stability: In the equation, σ+ is the standard deviation of high signal group with protein and **4**; σ – is the standard deviation of low signal group with 100 µM of tracer **2**, protein and **4**; $Mean^{+}$ is the mean of high signal group with protein and **4** and $Mean^{-}$ is the mean of low signal group with 100 µM of tracer **2**, protein and **4**.

Openlynx Report - Page 1

Sample: 13 Vial:5:F,11 ID:070713
File:3 Date:08-Jul-2010 Time:16:38:03
Description:

Printed: Wed Jun 29 15:53:54 2011

Sample Report:

Sample 13 Vial 5:F,11 ID 070713 File 3 Date 08-Jul-2010 Time 16:38:03 Description

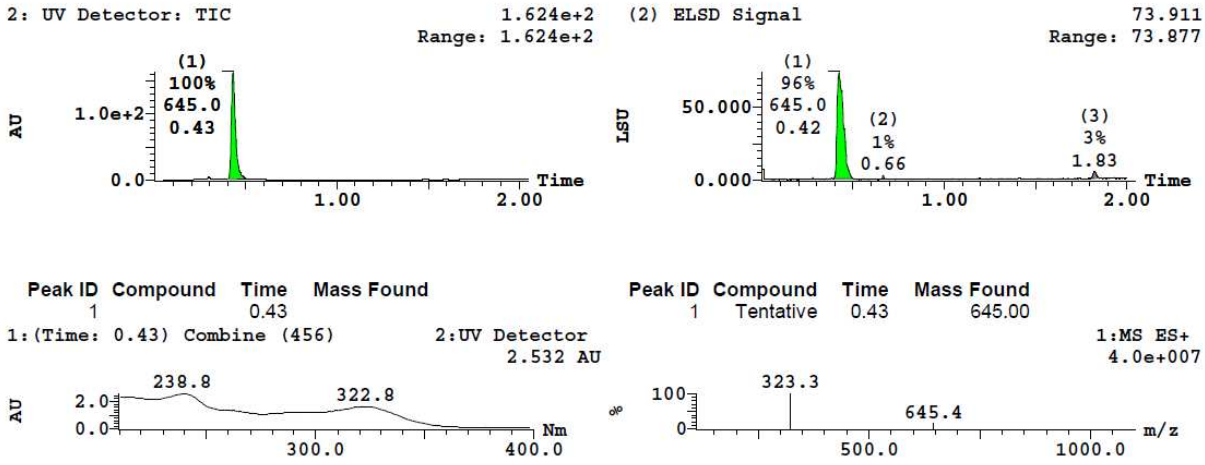

Peak ID	Compound	Time	Mass Found
1		0.43	

Peak ID	Compound	Time	Mass Found
1	Tentative	0.43	645.00

Figure S4: HPLC/UV/ELSD/MS analysis for **3**.

Sample: 14 Vial:5:F,12 ID:070713
File:4 Date:08-Jul-2010 Time:16:41:19
Description:

Printed: Wed Jun 29 15:53:54 2011

Sample Report (continued):

Sample 14 Vial 5:F,12 ID 070713 File 4 Date 08-Jul-2010 Time 16:41:19 Description

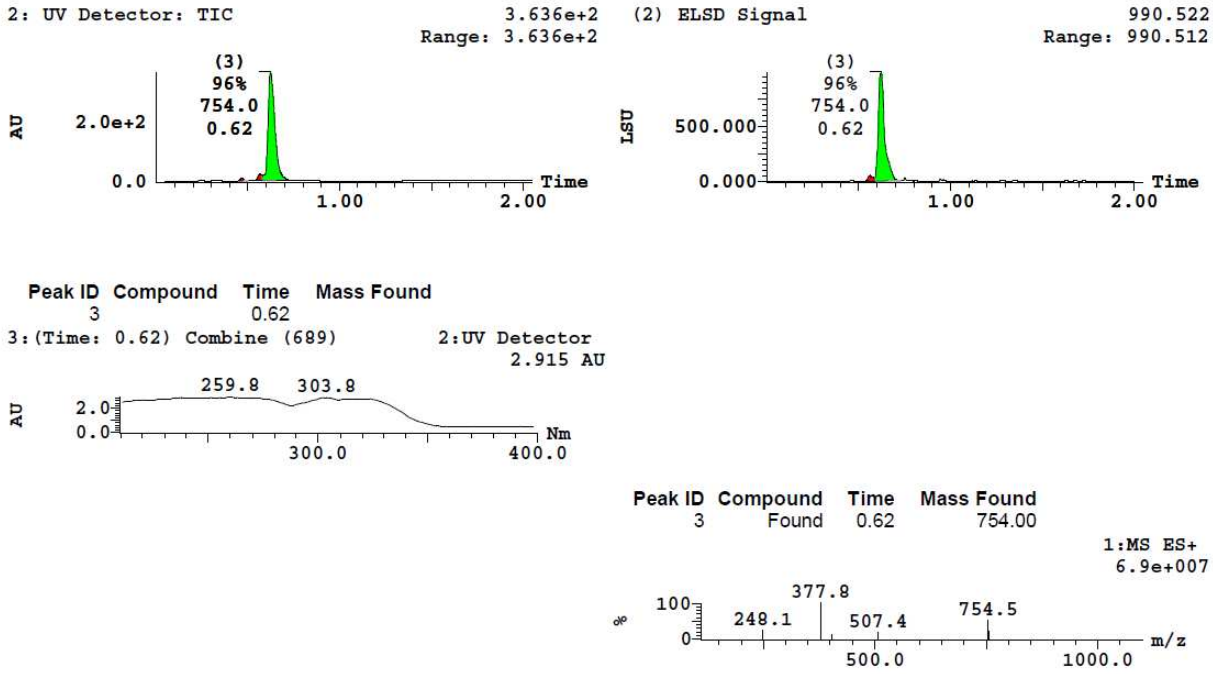

Figure S5: HPLC/UV/ELSD/MS analysis for **4**.

Bioconjugate Chemistry

ARTICLE

pubs.acs.org/bc

DOTA-Amide Lanthanide Tag for Reliable Generation of Pseudocontact Shifts in Protein NMR Spectra

Bim Graham,[†] Choy Theng Loh,[§] James David Swarbrick,[†] Phuc Ung,[†] James Shin,[†] Hiromasa Yagi,[§] Xinying Jia,[§] Sandeep Chhabra,[†] Nicholas Barlow,[†] Guido Pintacuda,[‡] Thomas Huber,[§] and Gottfried Otting*[,§]

[§]Research School of Chemistry, Australian National University, Canberra ACT 0200, Australia

[†]Medicinal Chemistry and Drug Action, Monash Institute of Pharmaceutical Sciences, Parkville VIC 3052, Australia

[‡]Centre de RMN à Très Hauts Champs, ENS-Lyon, 69100 Villeurbanne, France

Supporting Information

ABSTRACT: Structural studies of proteins and protein−ligand complexes by nuclear magnetic resonance (NMR) spectroscopy can be greatly enhanced by site-specific attachment of lanthanide ions to create paramagnetic centers. In particular, pseudocontact shifts (PCS) generated by paramagnetic lanthanides contain important and unique long-range structure information. Here, we present a high-affinity lanthanide binding tag that can be attached to single cysteine residues of proteins. The new tag has many advantageous features that are not available in this combination from previously published tags: (i) it binds lanthanide ions very tightly, minimizing the generation of nonspecific effects, (ii) it produces PCSs with high reliability as its bulkiness prevents complete motional averaging of PCSs, (iii) it can be attached to single cysteine residues, alleviating the need of detailed prior knowledge of the 3D structure of the target protein, and (iv) it does not display conformational exchange phenomena that would increase the number of signals in the NMR spectrum. The performance of the tag is demonstrated with the N-terminal domain of the *E. coli* arginine repressor and the A28C mutant of human ubiquitin.

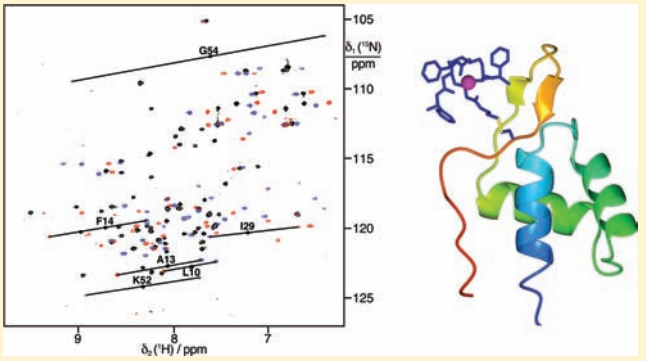

INTRODUCTION

Site-specific attachment of paramagnetic lanthanide ions to proteins produces large effects in NMR spectra that contain valuable long-range structural information.[1,2] Among the paramagnetic effects, pseudocontact shifts (PCS) stand out for their ease of measurement (as the difference in chemical shifts observed for samples labeled with, respectively, a paramagnetic or a diamagnetic lanthanide ion) and high information content (as PCSs can be observed for nuclear spins beyond 40 Å from the metal ion).

The PCS, $\Delta\delta^{PCS}$ (in ppm), of a nuclear spin can be described by[3]

$$\Delta\delta^{PCS} = \frac{1}{12\pi r^3}\left[\Delta\chi_{ax}(3\cos^2\theta - 1) + \frac{3}{2}\Delta\chi_{rh}\sin^2\theta\cos 2\varphi\right] \quad (1)$$

where $\Delta\chi_{ax}$ and $\Delta\chi_{rh}$ denote, respectively, the axial and rhombic components of the magnetic susceptibility anisotropy ($\Delta\chi$) tensor and r, and θ and φ are the polar coordinates of the nuclear spin with respect to the principal axes of the $\Delta\chi$ tensor. The limited number of parameters in eq 1 and the long-range nature of lanthanide-induced PCSs makes them powerful tools for structure determinations of protein−protein[4,5] and protein−ligand complexes (for recent reviews, see refs 6 and 7). In practice, eight parameters suffice to fit $\Delta\chi$ tensors to the 3D structure of a protein (x, y, z coordinates of the metal ion, three Euler angles to relate the orientation of the $\Delta\chi$ tensor to the frame of the protein atom coordinates, and the $\Delta\chi_{ax}$ and $\Delta\chi_{rh}$ parameters). Lanthanides are uniquely suited for PCS measurements, as different lanthanides produce different magnitudes of $\Delta\chi$ tensors while their chemical properties are very similar. This avoids chemical shift changes due to chemical differences among different paramagnetic and diamagnetic (La^{3+}, Y^{3+}, Lu^{3+}) ions.

A lanthanide ion can generate large PCSs only if it is site-specifically attached to the target protein in a rigid manner. If the tether between the lanthanide and the protein is flexible, the $\Delta\chi$ tensor associated with the lanthanide changes its orientation relative to the protein and the resulting averaging over positive and negative PCS values greatly reduces the magnitude of

Received: July 5, 2011
Revised: August 9, 2011
Published: August 31, 2011

 © 2011 American Chemical Society

observable PCSs. Therefore, no PCS may be observed if the tether allows substantial reorientation of the lanthanide ion with respect to the protein.

The problem of rigid lanthanide attachment can be addressed in different ways. Lanthanide chelates with two arms for attachment to two cysteine residues have been shown to minimize residual motion of the lanthanide relative to the protein.[8−10] A related strategy combines an N-terminal fusion with a lanthanide binding peptide (LBP) with a disulfide bond between the LBP and the target protein.[5,11] Engineering an LBP into the turn between two strands of a β-sheet similarly immobilizes lanthanides.[12] Another strategy coordinates the lanthanide by groups from two different sites of the protein. One group may be a small lanthanide binding tag attached to a cysteine residue, while the other group can be a carboxyl group of the protein.[13,14] Small tag molecules can also be attached to two cysteines with the aim of coordinating a single lanthanide between the two tags.[15,16] Finally, a lanthanide binding site can be engineered into the target protein by introducing amino acids with negatively charged side chains.[17] All these strategies rely on prior knowledge of the 3D structure of the target protein, at least at the site of modification.

To harness the power of PCSs for 3D structure determinations, however, it is necessary to use lanthanide tags that can be site-specifically attached without detailed knowledge of the 3D structure of the target protein. In this situation, tags with single attachment points have an advantage even if they may only incompletely immobilize the lanthanide ion. For example, LBPs with single cysteine residues have been shown to deliver large PCSs following attachment to the target protein via a disulfide bond.[18,19] The bulkiness of the tag restricts the amplitude of motion relative to the protein by steric constraints, preventing excessive averaging of the PCSs. Similarly, tags based on lanthanide complexes derived from cyclen (1,4,7,10-tetraazacyclododecane) can deliver PCSs of useful magnitudes, while providing exceptionally small dissociation constants of the lanthanide from the tag and robustness against extreme conditions of pH, temperature, and denaturants.[8,20] As a drawback, synthesis of cyclen tags can be expensive and arduous to prepare, and conformational equilibria can result in multiple sets of NMR signals.[20]

Lanthanide complexes of DOTA derivatives display two fundamental conformational equilibria.[21] The first affects the chirality of the cyclen ring. The second equilibrium affects the chirality of metal coordination by the acetate groups. Both equilibria are coupled. It has been shown that the equilibria can be pushed toward a single conformation of the lanthanide complex by incorporating chiral centers in the cyclene ring and its pendants[22] or, more simply, by turning the acetate groups of DOTA into amides with chiral amines.[23]

In the following, we present a new cyclen tag with three chiral amide groups and one nonchiral pendant for attachment to a cysteine residue of the target protein. We show that the three chiral amide pendants are sufficient to maintain a single enantiomeric conformation, as evidenced by a single set of peaks in the protein NMR spectrum, and that, even at 45 °C, the tag is free of complications arising from slow conformational exchange phenomena that have been reported for a different chiral DOTA tag.[20]

EXPERIMENTAL PROCEDURES

Tag Synthesis—(*S*)-2-Bromo-*N*-(1-phenylethyl)acetamide (1). Bromoacetyl bromide (12.7 g, 63 mmol) was added dropwise via syringe to a solution of (*S*)-1-phenylethanamine (15.3 g, 126 mmol) in DCM (200 mL) at 0 °C under nitrogen. Stirring was continued for a further 2 h at room temperature. The solution was washed with 2 N HCl (100 mL) followed by saturated brine (100 mL), then dried ($MgSO_4$), and solvent removed under reduced pressure to afford **1** (12.7 g, 83%) as a white solid. ^{1}H NMR (400 MHz, $CDCl_3$) δ 7.40−7.25 (m, 5H), 6.79 (br s, 1H), 5.12 (apparent p, J = 7.0 Hz, 1H), 3.95−3.82 (m, 2H), 1.55 (d, J = 6.9 Hz, 3H). ^{13}C NMR (101 MHz, $CDCl_3$) δ 164.7, 142.5, 128.9, 127.7, 126.2, 49.7, 29.4, 21.7. LRMS (ESI) m/z 244 (7%, $[M[^{81}Br]H]^+$), 242 (7, $[M[^{79}Br]H]^+$), 138 (10), 136 (9), 105 (100).

2,2′,2″-(1,4,7,10-Tetraazacyclododecane-1,4,7-triyl)tris-(*N*-((*S*)-1-phenylethyl)acetamide) (2). A solution of **1** (18.4 g, 76 mmol) in chloroform (500 mL) was added dropwise to a stirred mixture of cyclen (4.37 g, 25 mmol) and DIPEA (35 mL, 200 mmol) in chloroform (500 mL) under a nitrogen atmosphere at room temperature. The mixture was stirred for a further 24 h, then washed with water, and the organic phase dried over $MgSO_4$. After removal of the solvent, the residue was purified by flash chromatography (gradient from 90:10:1 to 80:20:2 EtOAc/MeOH/NH_3) to afford the product (10.2 g, 61%) as a thick, light yellow oil. ^{1}H NMR (400 MHz, DMSO) δ 8.36 (d, J = 8.0 Hz, 2H), 8.26 (d, J = 7.8 Hz, 1H), 7.33−7.26 (m, 12H), 7.25−7.16 (m, 3H), 4.98−4.85 (m, 3H), 3.15−3.00 (m, 6H), 2.73−2.43 (m, 16H), 1.41−1.30 (m, 9H). ^{13}C NMR (101 MHz, DMSO) δ 169.7(2), 169.6(8), 144.7, 144.4, 128.2, 128.2, 126.6, 126.5, 126.0, 126.0, 57.7, 55.9, 52.7, 52.3, 50.9, 47.7, 47.6, 46.4, 22.5, 22.4. LRMS (ESI) m/z 656 (85%, $[M+H]^+$), 329 (100, $[M+2H]^{2+}$).

2-Chloro-*N*-(2-(pyridin-2-yldisulfanyl)ethyl)acetamide (3). To a stirred solution of 2-(pyridin-2-yldisulfanyl)ethanamine hydrochloride (3.00 g, 13.5 mmol) and chloroacetic acid (1.28 g, 14 mmol) in 1:10 dichloromethane/acetonitrile (50 mL) was added DIPEA (7.0 mL, 400 mmol) and BOP (6.63 g, 15 mmol). The reaction mixture was stirred overnight at room temperature under nitrogen. Upon completion of the reaction, the solvent was removed under reduced pressure and the resulting crude product was dissolved in saturated $NaHCO_3$ solution (150 mL) and washed with ether (3 × 100 mL). The combined organic layers were washed with saturated brine, dried ($MgSO_4$), and the solvent removed under reduced pressure. Flash chromatography (30:70 ethyl acetate/petroleum spirit) afforded **2** (2.80 g, 79%) as a slightly yellow oil. ^{1}H NMR (400 MHz, $CDCl_3$) δ 8.56 (ddd, J = 4.9, 1.8, 0.9 Hz, 1H), 8.26 (br s, 1H), 7.60 (ddd, J = 8.0, 7.4, 1.8 Hz, 1H), 7.47 (dt, J = 8.1, 1.0 Hz, 1H), 7.14 (ddd, J = 7.4, 4.9, 1.1 Hz, 1H), 4.09 (s, 2H), 3.67−3.56 (m, 2H), 2.97−2.87 (m, 2H). ^{13}C NMR (101 MHz, $CDCl_3$) δ 166.3, 159.1, 150.2, 137.0, 121.5, 121.4, 42.9, 38.9, 37.6. LRMS (ESI) m/z 265 (40%, $[M[^{37}Cl]H]^+$), 263 (100, $[M[^{37}Cl]H]^+$).

2,2′,2″-(10-(2-Oxo-2-(2-(pyridin-2-yldisulfanyl)ethylamino)-ethyl)-1,4,7,10-tetraazacyclododecane-1,4,7-triyl)tris(*N*-((*S*)-1-phenylethyl)acetamide) (C1). A mixture containing **3** (1.40 g, 2.1 mmol), **2** (1.00 g, 3.8 mmol), and DIPEA (610 μL, 3.8 mmol) in acetonitrile (50 mL) was stirred at room temperature for 48 h. The resultant white precipitate was filtered and dried to afford C1 (0.65 g, 35%) as a white solid. Evaporation of the filtrate and purification of the residue by flash chromatography (90:10:1 DCM/MeOH/NH_3) afforded a further crop of the product (0.78 g, 41%). ^{1}H NMR (400 MHz, DMSO) δ 8.46−8.42 (m, 1H), 8.28 (t, J = 5.8 Hz, 1H), 8.19 (d, J = 8.1 Hz, 1H), 8.15 (d, J = 8.1 Hz, 2H), 7.83−7.76 (m, 1H), 7.73 (dt, J = 8.1, 1.0 Hz, 1H), 7.33−7.25 (m, 12H), 7.24−7.16 (m, 4H), 5.00−4.86 (m, 3H),

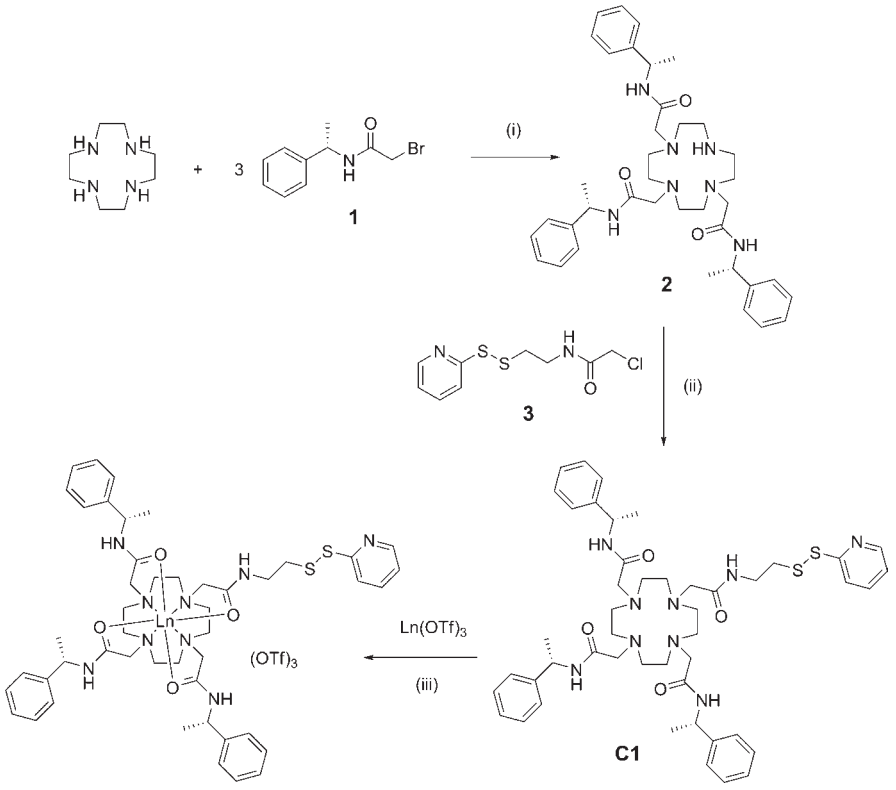

Figure 1. Synthesis of C1 tag and lanthanide complexes. Conditions: (i) DIPEA, chloroform, RT, O/N; (ii) DIPEA, acetonitrile, RT, 2 d; (iii) acetonitrile, reflux, O/N.

3.41−3.32 (m, 2H), 3.07−2.96 (m, 6H), 2.93−2.83 (m, 4H), 2.75−2.42 (m, 16H), 1.43−1.28 (m, J = 8.8, 7.1 Hz, 9H). ^{13}C NMR (101 MHz, DMSO) δ 170.6, 169.4, 169.4, 159.1, 149.6, 144.4, 144.3, 137.7, 128.2, 126.6, 126.0, 126.0, 121.2, 119.3, 58.1, 57.9, 57.6, 53.6, 53.3, 52.9, 47.6, 37.6, 37.4, 22.2, 22.1. HRMS (ESI): m/z: calcd for$[M+H]^+$ $C_{47}H_{64}N_9O_4S_2$: 882.4517, found: 882.4555.

Formation of Metal Complexes. As binding of lanthanides to DOTA-type cyclen derivatives is extremely slow and requires heating, we did not attempt to exchange the metal ion from tagged protein samples. To produce protein samples with different lanthanides, the C1 tag was prepared with different paramagnetic and diamagnetic ions (Tb^{3+}, Tm^{3+}, Yb^{3+}, Y^{3+}) by heating the tag in acetonitrile with a molar equivalent of the respective metal triflate salts overnight at 80 °C, followed by freeze−drying to afford off-white powders. Stock solutions of the C1−lanthanide complexes were prepared in water with concentrations of up to 20 mM.

Tagging Reaction. Uniformly ^{15}N/^{13}C-labeled samples of the N-terminal domain of the *E. coli* arginine repressor (ArgN) were produced on M9 minimum medium as described.[24] A 0.2 mM solution of ArgN in NMR buffer (20 mM MES, pH 6.6) was reduced by 5 equiv of DTT and subsequently washed with NMR buffer using a Millipore ultrafilter with a molecular weight cutoff of 3 kDa. The solution was added to a 3-fold excess of tag in NMR buffer to yield a total volume of 0.5 mL and the mixture was incubated at room temperature for 5 h. The reaction mixture was washed again with NMR buffer and concentrated to a final volume of 0.5 mL.

Uniformly ^{15}N-labeled samples of the mutant A28C of human ubiquitin were prepared as described.[15] DTT reduction of the thiol was as above for ArgN followed by passage over a PD10 column equilibrated with degassed NMR buffer (50 mM HEPES pH 7.5). A 15-fold excess of tag was added from a 20 mM stock solution in water to an approximately 50 μM solution of the protein and left for 3 h at room temperature and then overnight at 3 °C. Excess tag was removed by passage over a PD10 column and the sample concentrated using a Millipore ultrafilter to a final protein concentration of about 70 μM.

NMR Spectra. NMR spectra were recorded at 25 °C on 600 MHz NMR spectrometers equipped with cryogenic probes (Bruker Avance and Varian INOVA in the case of ArgN and ubiquitin(A28C), respectively). ^{15}N-HSQC, 3D HNCA, and HN(CO)CA spectra were recorded from differently tagged ArgN. ^{15}N-fast-HSQC spectra were recorded from differently tagged ubiquitin(A28C), and a 3D NOESY−^{15}N-HSQC spectrum was recorded from the ubiquitin(A28C)−C1-Y^{3+} complex. Resonance assignments of paramagnetic NMR spectra were supported by the program *Numbat*[25] to fit $\Delta\chi$ tensors to a set of unambiguously assigned PCSs and predict the PCSs of unassigned paramagnetic cross-peaks in several rounds of $\Delta\chi$ tensor fitting and resonance assignments.

Fitting of $\Delta\chi$ Tensors. $\Delta\chi$ tensors were fitted to the first conformer of the NMR structure of ArgN (PDB accession code 1AOY[24]) following a previously described protocol.[26,27] Briefly, the structure of ArgN with the C1 tag was modeled using the enantiomeric mirror image of the crystal coordinates of the DOTA-tetraamide Gd^{3+} complex with 1-phenylethyl amine (DOTAMPh, CSD accession code EQOZUF[28]). One of the 1-phenylethyl groups of the DOTAMPh molecule was changed to a 2-thioethyl group, which was connected via a disulfide bond to the sulfur of Cys68 of ArgN. 4×10^6 different conformations

were generated by randomly changing the χ_1 and χ_2 angles of Cys68 and the dihedral angles of the disulfide bond and ethylene tether, using dihedral angles of 60°, −60°, and 180° for the C−C bonds and dihedral angles of −90° or 90° for the S−S bond, with an uncertainty range of ±10°. Conformations producing steric clashes with the protein were excluded. The remaining 2287 conformers were used to fit $\Delta\chi$ tensors to the experimental PCSs. The final $\Delta\chi$ tensor was taken to be the one obtained with the conformation producing the best least-squares fit to the experimentally observed PCS data. As a measure of the precision of the $\Delta\chi$-tensors and metal positions, the fits to each of the 2287 model conformers were repeated 100 times, omitting 20% of the data from each metal ion in a Monte Carlo protocol.[25]

Fitting of $\Delta\chi$ tensors to the ubiquitin mutant A28C followed the same protocol as for ArgN. The fits used the first conformer of the NMR structure (PDB accession code 1D3Z[29]). 2897 conformers were obtained that were free of steric clashes between tag and protein.

RESULTS

Synthesis of the C1 Tag and Its Lanthanide Complexes. Figure 1 shows the synthetic route used to prepare the "conjugation ready" C1 tag from 1,4,7,10-tetraazacyclododecane (cyclen). This involved the sequential attachment of the three chiral amide groups and one nonchiral pendant via reaction with α-haloacetamide derivatives of (*S*)-1-phenylethanamine and 2-(pyridin-2-yldisulfanyl)ethanamine, respectively. Although chromatography was required at both stages to remove impurities, the synthesis avoided the need for protection groups and afforded the tag in good overall yield. The lanthanide complexes of C1 were readily prepared by refluxing 1:1 mixtures of the ligand and metal triflate salts, $Ln(OTf)_3$ (Ln = Dy^{3+}, Tb^{3+}, Tm^{3+}, Yb^{3+}, Y^{3+}), in acetonitrile overnight.

Tagging Reaction and Protein NMR Assignments. The C1 tag was attached to ArgN by adding the protein to a 3-fold excess of tag rather than adding tag to protein, to avoid the possibility of disulfide-bond formation between different protein molecules which could arise from disulfide exchange. The reaction reproducibly delivered tagged ArgN with greater than 95% yield. Samples were produced with tags loaded with different lanthanides (Dy^{3+}, Tb^{3+}, Tm^{3+}, Yb^{3+}) or a diamagnetic metal (Y^{3+}).

The C1 tag was attached to the ubiquitin mutant A28C using a similar protocol or a large excess of tag as described in the Experimental Procedures. Reaction yields increased with the duration of incubation (from hours to days) with the C1 tag. An overnight reaction at 3 °C (i.e., conditions suitable for less stable proteins) yielded 80−90% of tagged ubiquitin. Even the use of a large excess of tag produced no evidence for disulfide mediated protein dimerization.

The backbone NMR resonances of paramagnetic and diamagnetic ArgN-C1 complexes were assigned using 3D HNCA and HN(CO)CA spectra. The resonance assignments obtained are compiled in Supporting Information Table S1. Chemical shift changes in ArgN and ubiquitin(A28C) tagged with diamagnetic Y^{3+} tags were limited to amides in the vicinity of the cysteine residue, indicating that the tags did not significantly alter the protein structures. The resonance assignments of the diamagnetic ubiquitin(A28C)−C1−Y^{3+} complex were established by a 3D NOESY−^{15}N-HSQC spectrum. For either protein, resonance assignments of the paramagnetic samples were aided by the fact that the PCSs produced by different lanthanides

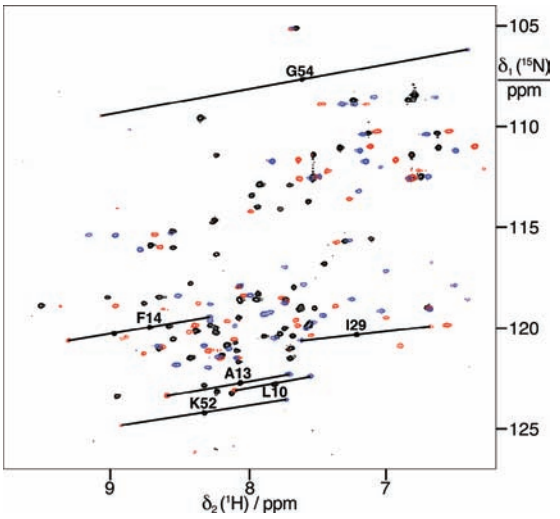

Figure 2. Superimposition of ^{15}N-HSQC spectra of 0.2 mM solutions of uniformly ^{13}C/^{15}N-labeled N-terminal domain of the *E. coli* arginine repressor ligated at Cys68 with the C1 tag loaded with Y^{3+} (black peaks), Tb^{3+} (red), or Tm^{3+} (blue). All spectra were recorded at 25 °C on a 600 MHz NMR spectrometer in a 20 mM MES buffer, pH 6.6. Selected diamagnetic cross-peaks are labeled with their resonance assignments and connected by lines with their paramagnetic partners.

displaced the cross-peaks along almost straight lines. Supporting Information Table S2 shows the experimentally determined PCSs of ubiquitin(A28C).

PCS Measurements and $\Delta\chi$ Tensors. Pronounced PCSs were observed in the complexes of ArgN and ubiquitin(A28C) tagged with C1 containing Dy^{3+}, Tb^{3+}, Tm^{3+}, or Yb^{3+}. All samples produced high-quality NMR spectra (Figure 2 and Supporting Information Figure S2). There was no evidence for conformational heterogeneity of the tag or slow conformational exchange, neither in the C1−Yb^{3+} tag alone (Figure S1) nor in the ubiquitin(A28C) mutant tagged with C1−Yb^{3+} and measured with high signal-to-noise ratio (Figure S3). No minor conformational species appeared at 45 °C (Figures S1 and S3).

$\Delta\chi$ tensors were fitted to the experimental PCSs using the first conformer of the NMR structure of ArgN[24] with the covalent structure of the tags crafted onto it via a disulfide bond linkage to Cys68. Table 1 shows the parameters of the fitted $\Delta\chi$ tensors. The tensors were sufficiently large to generate PCSs of up to 0.13 ppm at the site most remote from Cys68 (the amide proton of Asp39 in the C1(Tb)-tagged protein which is 32 Å from the site of the metal ion).

Fits of the $\Delta\chi$ tensors to the NMR structure of ubiquitin[29] produced smaller tensors than in the case of ArgN (Supporting Information Table S3), suggesting that the exposure of Cys28 on the surface of the protein permits a greater amplitude of motion for the tag (Figure S4; the calculated solvent accessibility of Cys68 of ArgN is about 7% and is 22% for Cys28 of ubiquitin(A28C)). As in the case of ArgN, however, the C1 tag produced significantly larger $\Delta\chi$ tensors than a previously used NTA derivative (N^{α},N^{α}-bis(carboxymethyl)-L-cysteine) that is a much smaller molecule with a shorter linker.[15]

Back-calculated and experimental PCSs correlated closely for ArgN and ubiquitin (Figure 3). Remarkably, the correlation was better for ubiquitin than for ArgN despite the greater conformational freedom of the C1 tag on the surface of ubiquitin, indicating that tag mobility is a lesser impediment to good fits of PCS data than structure quality.

Table 1. $\Delta\chi$ Tensors of Different Metal Ions Bound to ArgN-C1[a]

metal ion	$\Delta\chi_{ax}$ /10^{-32} m^3	$\Delta\chi_{rh}$ /10^{-32} m^3	Q^b	tensor axis	coordinates of tensor axes		
Dy^{3+}	−29	−11	0.08	x	−0.302	−0.248	0.921
	(−42/−25)	(−13/−7)		y	0.941	0.077	0.329
				z	−0.152	0.966	0.210
Tb^{3+}	−27	−4	0.14	x	−0.235	−0.064	−0.965
	(−37/−21)	(−9/−1)		y	−0.935	−0.240	0.261
				z	−0.249	0.969	0.001
Tm^{3+}	37	12	0.21	x	−0.833	−0.450	0.322
	(26/59)	(3/24)		y	0.439	−0.183	0.880
				z	−0.337	0.874	0.350
Yb^{3+}	13	3	0.18	x	−0.808	−0.444	0.388
	(10/19)	(0/7)		y	0.495	−0.154	0.855
				z	−0.320	0.883	0.344

[a] The tensors are listed in their unique tensor representation (UTR)[25] as obtained by fitting of the PCSs of Table S1 to ArgN (PDB ID 1AOY model 1)[24] simultaneously using the PCSs induced by Dy^{3+}, Tb^{3+}, Tm^{3+}, and Yb^{3+} and a common metal position. The fits used PCSs of amide protons in structurally well-defined regions of the protein (residues 8−20, 26−37, 43−52). The covalent structure of the tag was taken into account as described in the main text. The orientations of the tensor axes are given as unit vectors with respect to the origin (0, 0, 0). Uncertainty ranges (shown in brackets) were obtained by a Monte Carlo error analysis that randomly omitted 20% of the PCSs (100 trials for each of 2287 modeled tag conformations). The coordinates of the common metal position in the best fit using 100% of the PCSs were (13.705, 11.580, 0.445). A small fraction (9%) of the best solutions in the Monte Carlo trials positioned the metal in a group about 4 Å from this position. These solutions were omitted from the error analysis. In the remaining solutions, the metal was displaced by <1.9 Å. [b] Q-factor calculated as root-mean-square deviation between measured and predicted PCSs divided by the root-mean-square of the measured PCSs. The Q-factor of the simultaneous four-metal fit is 0.16.

DISCUSSION

Our results indicate that the C1 tag reliably produces PCSs following attachment to single cysteine residues. This is an important advantage over DPA tags[13,14,27] or IDA and NTA tags[15,16] that often generate vanishingly small PCSs if the metal ion is not coordinated by an additional carboxyl group from the protein, as mobility of the tether to the protein invariably reduces the magnitude of the PCSs observed in the protein. The reliability with which the C1 tag generates PCSs can be attributed to its bulkiness, which limits the amplitude of reorientational motions of the DOTA moiety relative to the protein. For comparison, no PCSs could be generated with lanthanides in the ubiquitin (A28C) mutant tagged with the much smaller 4MDPA tag[27] (data not shown), despite there being only a single rotatable bond in the linker between the lanthanide and the disulfide bond. Reliable generation of PCSs in the absence of structural information is an essential prerequisite before the power of PCS data can be harnessed for 3D structure determinations of proteins.

Generation of sizable PCSs in the target protein is greatly aided by an intrinsically large $\Delta\chi$ tensor of the lanthanide tag. Remarkably large paramagnetic shifts have been reported for the Yb^{3+} complex of the symmetrical parent compound of the C1 tag, DOTAMPh, which has 1-phenylethylacetamide pendants attached to all four nitrogens of the cyclen ring.[23] As the cyclen protons are separated from the lanthanide by only a few bonds, it is unclear, however, which fraction of the paramagnetic shifts in DOTAMPh must be attributed to contact shifts rather than PCSs. In a protein tagged with C1, however, contact shifts can be neglected for protons that are sufficiently far from the metal to yield observable NMR signals. Remarkably, the $\Delta\chi_{ax}$ value of 13 × 10^{-32} m^3 determined for the ArgN-C1(Yb^{3+}) complex (Table 1) is almost two times greater than any that has been reported for Yb^{3+} complexes of calbindin D_{9k},[30] CLaNP-5.2,[8,9] lanthanide binding peptides,[19] or DPA tags.[13,19,27] Correspondingly large residual dipolar couplings (RDC) could be observed on an 800 MHz NMR spectrometer, with $^1D_{HN}$ RDCs of up to 20.3 Hz measured for ArgN-C1(Tm^{3+}) at 25 °C. Maximal $^1D_{HN}$ RDC values greater than 20 Hz are hallmarks of the best lanthanide tags currently available.[8,20,31,32] Under the conditions of our RDC measurements, a maximal $^1D_{HN}$ value of about 20 Hz would be predicted for the $\Delta\chi_{ax}$ value of 37 × 10^{-32} m^3 associated with ArgN-C1(Tm^{3+}) (Table 1). This close agreement between predicted and experimental maximal RDC values would suggest that the tag has little conformational freedom. Large uncertainty ranges, however, were associated with the $\Delta\chi$ tensor determinations, which may be attributed to the fairly long distance of the metal from the protein surface (8 Å from the sulfur of the cysteine residue; Figure 4) and similar directions of the principal tensor axes of the different metals (Table 1).

In contrast to the situation encountered with RDCs, where the average of different alignment tensors can be represented by a single average tensor, an ensemble of different $\Delta\chi$ tensors from different metal positions cannot be approximated well by a single average tensor, at least not close to the metal ion, since PCSs are distance-dependent. At greater distances from the paramagnetic center, however, the approximation by an average $\Delta\chi$ tensor is much better, as different tag conformations have a smaller relative influence on the distance between nuclear spins and paramagnetic center. Therefore, even if mobility of the tag leads to a reduced average $\Delta\chi$ tensor, this tensor still yields useful structural restraints at greater distances from the metal ion, as long as it fits the experimentally observed PCSs in those regions of the protein. The large intrinsic $\Delta\chi$ tensor associated with the C1 tag thus makes it a useful tool for protein structure analysis even in the presence of substantial averaging as observed for the ubiquitin A28C mutant. Notably, PCSs could be measured for almost all peaks of ubiquitin (Supporting Information Figure S2) and even using all PCSs from residues 2−72 produced a better fit of back-calculated versus experimental PCSs for ubiquitin than for ArgN for which only a NMR structure determined by NOEs and J couplings is available (Figure 3).

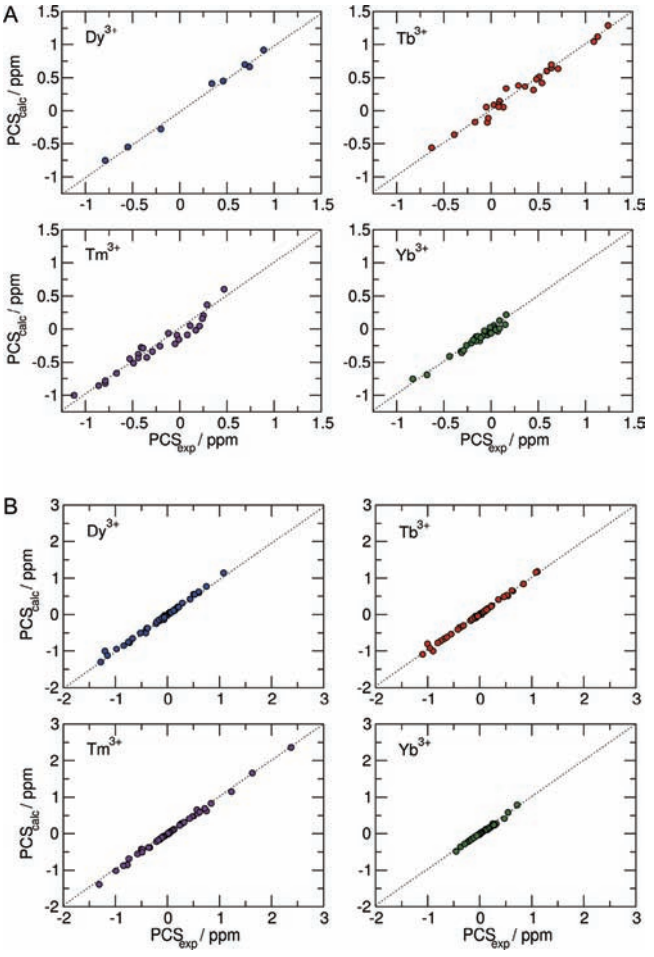

Figure 3. Correlations between back-calculated and experimental pseudocontact shifts of (A) the N-terminal domain of the *E. coli* arginine repressor and (B) ubiquitin obtained by the fits of Table 1 and Supporting Information Table S3, respectively.

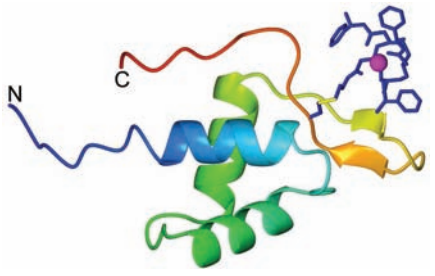

Figure 4. Model of the N-terminal domain of the *E. coli* arginine repressor with a C1-lanthanide complex bound to Cys68. The model represents the best fit of the PCSs to the first conformer of the NMR structures (PDB ID 1AOY[24]). The structure of the tag was derived from the crystal coordinates of a DOTA-tetraamide Gd^{3+} complex as described in the main text. The lanthanide ion is represented by a magenta sphere. The disulfide bond of the linker is highlighted in yellow. The N- and C-termini are labeled. The side chain of Cys68 and the tag are shown in a heavy atom representation.

$\Delta\chi$ tensor fits easily generate large uncertainty ranges for metal tags on protein surfaces, as the metal position must be determined along with five other tensor parameters (Euler angles and axial and rhombic components). For example, an unrealistically large distance of the metal from the protein can often be quite readily compensated for by a correspondingly larger tensor. To avoid such artifacts, we used a fitting procedure that explicitly restricts metal coordinates to positions that are compatible with the covalent structure of the tag and its steric requirements. Unless the tag is completely immobilized, however, the particular tag conformation producing the best fit must not be taken too literally, as the fitting does not consider the different rotamers of the linker moiety that may lead to the average metal position found.

The C1 tag carries the same ethylene thio linker as the previously published cyclen tags DOTA-M8[20] and CLaNP-5.1.[8] In the case of the DOTA-M8 tag, 15−20% of the tag was observed to assume a second conformation at 25 °C, which was tentatively attributed to cis−trans isomerization of the amide bond of the tether. This percentage rose to 50% at 50 °C.[20] In contrast, no second conformational species was reported for the CLaNP-5.1 tag[8] and we found no evidence for slow conformational exchange in the C1 tag either, not even at 45 °C (Supporting Information Figures S1 and S3). The C1 tag is thus suitable for measurements at elevated temperatures.

For the CLaNP-5.1 tag, data have been reported only for a single metal ion (Yb^{3+}) and protein site,[8] making comparisons difficult. We would expect the C1 tag to be less prone to PCS averaging because of its greater bulkiness. Compared to the even bulkier lanthanide binding peptides,[18,19] the C1 tag, like most DOTA-type tags, binds lanthanide ions much more tightly, is more resistant to unfolding under nonphysiological conditions, and is easier to use, as it is synthesized with an activated disulfide bond. The high lanthanide affinity of DOTA-type tags (dissociation constants of 100 pM have been reported for lanthanide complexes of cyclen with *N*-acetamide pendants, DOTAM[33]) is a decisive advantage for experiments with metalloproteins, where a kinetically less inert metal binding tag could lead to equilibration between the metals of the protein and the tag, for studies of compounds that display high natural affinities for lanthanides, such as DNA and RNA, and for EPR experiments with Gd^{3+} that depend on the absence of unbound Gd^{3+} ions.[34]

The parent compound of the C1 tag, DOTAMPh, forms a square antiprismatic complex[23] that completely encases the lanthanide ions except for a single coordination site for a water molecule.[35] The poor accessibility of the lanthanide is an advantage in interaction studies, where more solvent-exposed metal ions could produce misleading results by direct interactions between the metal and the interaction partner. The C1 tag thus carries great promise for lead compound development by fragment-based drug design, where PCSs observed for weakly binding fragments can be used to define their binding site, orientation, and structure.[36,37]

Using different lanthanides in the same protein-tag construct generates $\Delta\chi$ tensors of different magnitude, but the orientations of the principal axes of the tensors usually vary little.[13,30,38] It is a distinct possibility that a tag produced with opposite chirality (using (*R*)-1-phenylethanamine instead of (*S*)-1-phenylethanamine) may generate different tensor orientations relative to the protein. PCS data measured with both enantiomeric tags could thus deliver two independent sets of restraints to position nuclear spins relative to the protein.

In conclusion, the new lanthanide tag presented here displays an attractive combination of properties, including reliable generation of PCSs, conformational homogeneity, and tight lanthanide binding. We anticipate that it will become an important tool

for assessing the structure of biological macromolecules by NMR spectroscopy.

■ ASSOCIATED CONTENT

Supporting Information. ^{1}H NMR spectrum of the C1−Yb^{3+} complex, chemical shifts of ArgN tagged with C1 loaded with different metal ions, ^{15}N-HSQC spectra of ubiquitin (A28C) tagged with C1 loaded with different metal ions, PCSs of ubiquitin (A28C) tagged with C1 metal complexes, $\Delta\chi$ tensors of ubiquitin (A28C) tagged with C1 metal complexes, model of the C1 tag bound to Cys28 in ubiquitin (A28C). This material is available free of charge via the Internet at http://pubs.acs.org.

■ AUTHOR INFORMATION

Corresponding Author

*Gottfried Otting, Research School of Chemistry, Australian National University, Canberra, ACT 0200 (Australia). Fax: +61-2-61250750. E-mail: gottfried.otting@anu.edu.au.

■ ACKNOWLEDGMENT

Financial support by the Australian Research Council, including a Future Fellowship to T. H., is gratefully acknowledged.

■ REFERENCES

(1) Pintacuda, G., John, M., Su, X.-C., and Otting, G. (2007) NMR structure determination of protein-ligand complexes by lanthanide labelling. *Acc. Chem. Res. 40*, 206–212.

(2) Otting, G. (2008) Prospects for lanthanides in structural biology by NMR. *J. Biomol. NMR 42*, 1–9.

(3) Bertini, I., Luchinat, C., and Parigi, G. (2002) Magnetic susceptibility in paramagnetic NMR. *Prog. Nucl. Magn. Reson. Spectrosc. 40*, 249–273.

(4) Keizers, P. H. J., Mersinli, B., Reinle, W., Donauer, J., Hiruma, Y., Hannemann, F., Overhand, M., Bernhardt, R., and Ubbink, M. (2010) A solution model of the complex formed by adrenodoxin and adrenodoxin reductase determined by paramagnetic NMR spectroscopy. *Biochemistry 49*, 6846–6855.

(5) Saio, T., Yokochi, M., Kumeta, H., and Inagaki, F. (2010) PCS-based structure determination of protein-protein complexes. *J. Biomol. NMR 46*, 271–280.

(6) Keizers, P. H. J., and Ubbink, M. (2011) Paramagnetic tagging for protein structure and dynamics analysis. *Prog. Nucl. Magn. Reson. Spectrosc. 58*, 88–96.

(7) Otting, G. (2010) Protein NMR using paramagnetic ions. *Annu. Rev. Biophys. 39*, 387–405.

(8) Keizers, P. H. J., Desreux, J. F., Overhand, M., and Ubbink, M. (2007) Increased paramagnetic effect of a lanthanide protein probe by two-point attachment. *J. Am. Chem. Soc. 129*, 9292–9293.

(9) Keizers, P. H. J., Saragliadis, A., Hiruma, Y., Overhand, M., and Ubbink, M. (2008) Design, synthesis, and evaluation of a lanthanide chelating protein probe: CLaNP-5 yields predictable paramagnetic effects independent of environment. *J. Am. Chem. Soc. 130*, 14802–14812.

(10) Vlasie, M. D., Comuzzi, C., van den Nieuwendijk, A. M., Prudêncio, M., Overhand, M., and Ubbink, M. (2007) Long-range-distance NMR effects in a protein labeled with a lanthanide-DOTA chelate. *Chem.—Eur. J. 13*, 1715–1723.

(11) Saio, T., Yokochi, M., and Inagaki, F. (2009) Two-point anchoring of a lanthanide-binding peptide to a target protein enhances the paramagnetic anisotropic effect. *J. Biomol. NMR 44*, 157–166.

(12) Barthelmes, K., Reynolds, A. M., Peisach, E., Jonker, H. R. A., DeNunzio, N. J., Allen, K. N., Imperiali, B., and Schwalbe, H. (2011) Engineering encodable lanthanide-binding tags into loop regions of proteins. *J. Am. Chem. Soc. 133*, 808–819.

(13) Man, B., Su, X.-C., Liang, H., Simonsen, S., Huber, T., Messerle, B. A., and Otting, G. (2010) 3-Mercapto-2,6-pyridinedicarboxylic acid, a small lanthanide-binding tag for protein studies by NMR spectroscopy. *Chem.—Eur. J. 16*, 3827–3832.

(14) Su, X.-C., Man, B., Beeren, S., Liang, H., Simonsen, S., Schmitz, C., Huber, T., Messerle, B. A., and Otting, G. (2008) A dipicolinic acid tag for rigid lanthanide tagging of proteins and paramagnetic NMR spectroscopy. *J. Am. Chem. Soc. 130*, 10486–10487.

(15) Swarbrick, J. D., Ung, P., Su, X.-C., Maleckis, A., Chhabra, S., Huber, T., Otting, G., and Graham, B. (2011) Engineering of a bis-chelator motif into a protein α-helix for rigid lanthanide binding and paramagnetic NMR spectroscopy. *Chem. Commun. 47*, 7368–7370.

(16) Swarbrick, J. D., Ung, P., Chhabra, S., and Graham, B. (2011) An iminodiacetic acid based lanthanide binding tag for paramagnetic exchange NMR spectroscopy. *Angew. Chem., Int. Ed. 50*, 4403–4406.

(17) Lu, Y., Berry, S. M., and Pfister, T. D. (2001) Engineering novel metalloproteins: design of metal-binding sites into native protein scaffolds. *Chem. Rev. 101*, 3047–3080.

(18) Su, X.-C., Huber, T., Dixon, N. E., and Otting, G. (2006) Site-specific labelling of proteins with a lanthanide-binding tag. *ChemBioChem 7*, 1469–1474.

(19) Su, X.-C., McAndrew, K., Huber, T., and Otting, G. (2008) Lanthanide-binding peptides for NMR measurements of residual dipolar couplings and paramagnetic effects from multiple angles. *J. Am. Chem. Soc. 130*, 1681–1687.

(20) Häussinger, D., Huang, J., and Grzesiek, S. (2009) DOTA-M8: an extremely rigid, high-affinity lanthanide chelating tag for PCS NMR spectroscopy. *J. Am. Chem. Soc. 131*, 14761–14767.

(21) Parker, D., Dickins, R. S., Puschmann, H., Crossland, C., and Howard, J. A. K. (2002) Being excited by lanthanide coordination complexes: aqua species, chirality, excited-state chemistry, and exchange dynamics. *Chem. Rev. 102*, 1977–2010.

(22) Woods, M., Botta, M., Avedano, S., Wang, J., and Sherry, A. D. (2005) towards the rational design of MRI contrast agents: a practical approach to the synthesis of gadolinium complexes that exhibit optimal water exchange. *Dalton Trans. 2005*, 3829–3837.

(23) Dickins, R. S., Parker, D., Bruce, J. I., and Tozer, D. J. (2003) Correlation of optical and NMR spectral information with coordination variation for axially symmetric macrocyclic Eu(III) and Yb(III) complexes: axial donor polarisability determines ligand field and cation donor preference. *Dalton Trans. 2003*, 1264–1271.

(24) Sunnerhagen, M., Nilges, M., Otting, G., and Carey, J. (1997) Solution structure of the DNA-binding domain and model for the binding of multifunctional arginine repressor to DNA. *Nat. Struct. Biol. 4*, 819–826.

(25) Schmitz, C., Stanton-Cook, M. J., Su, X.-C., Otting, G., and Huber, T. (2008) Numbat: an interactive software tool for fitting $\Delta\chi$-tensors to molecular coordinates using pseudocontact shifts. *J. Biomol. NMR 41*, 179–189.

(26) Nguyen, T. H. D., Ozawa, K., Stanton-Cook, M., Barrow, R., Huber, T., and Otting, G. (2011) Pseudocontact shifts in protein NMR spectra generated using a genetically encoded Co^{2+}-binding amino acid. *Angew. Chem., Int. Ed. 50*, 692–694.

(27) Jia, X., Maleckis, A., Huber, T., and Otting, G. (2011) 4,4′-Dithiobis-dipicolinic acid: a small and convenient lanthanide-binding tag for protein NMR spectroscopy. *Chem.—Eur. J. 17*, 6830–6836.

(28) Parker, D., Puschmann, H., Batsanov, A. S., and Senanayake, K. (2003) Structural analysis of nine-coordinate lanthanide complexes: steric control of the metal-water distance across the series. *Inorg. Chem. 42*, 8646–8651.

(29) Cornilescu, G., Marquardt, J. L., Ottiger, M., and Bax, A. (1998) Validation of protein structure from anisotropic carbonyl chemical shifts in a dilute liquid crystalline phase. *J. Am. Chem. Soc. 120*, 6836–6837.

(30) Bertini, I., Janik, M. B. L., Lee, Y. M., Luchinat, C., and Rosato, A. (2001) Magnetic susceptibility tensor anisotropies for a lanthanide ion series in a fixed protein matrix. *J. Am. Chem. Soc. 123*, 4181–4188.

(31) Su, X.-C., and Otting, G. (2010) Paramagnetic labelling of proteins and oligonucleotides for NMR. *J. Biomol. NMR 46*, 101–112.

(32) Su, X.-C., and Otting, G. (2011) Erratum to: Paramagnetic labelling of proteins and oligonucleotides for NMR. *J. Biomol. NMR 50*, 99–100.

(33) Maumela, H., Hancock, R. D., Carlton, L., Reibenspies, J. H., and Wainwright, K. P. (1995) The amide oxygen as a donor group. Metal ion complexing properties of tetra-*N*-acetamide substituted cyclen: a crystallographic, NMR, molecular mechanics, and thermodynamic study. *J. Am. Chem. Soc. 117*, 6698–6707.

(34) Potapov, A., Yagi, H., Huber, T., Jergic, S., Dixon, N. E., Otting, G., and Goldfarb, D. (2010) Nanometer scale distance measurements in proteins using Gd^{3+} spin labeling. *J. Am. Chem. Soc. 132*, 9040–9048.

(35) Aime, S., Barge, A., Batsanov, A. S., Botta, M., Castelli, D. D., Fedeli, F., Mortillaro, A., Parker, D., and Puschmann, H. (2002) Controlling the variation of axial water exchange rates in macrocyclic lanthanide(III) complexes. *Chem. Commun. 2002*, 1120–1121.

(36) John, M., Pintacuda, G., Park, A. Y., Dixon, N. E., and Otting, G. (2006) Structure determination of protein-ligand complexes by transferred paramagnetic shifts. *J. Am. Chem. Soc. 128*, 12910–12916.

(37) Zhuang, T. D., Lee, H. S., Imperiali, B., and Prestegard, J. H. (2008) Structure determination of a Galectin-3-carbohydrate complex using paramagnetism-based NMR constraints. *Protein Sci. 17*, 1220–1231.

(38) Pintacuda, G., Park, A. Y., Keniry, M. A., Dixon, N. E., and Otting, G. (2006) Lanthanide labeling offers fast NMR approach to 3D structure determinations of protein-protein complexes. *J. Am. Chem. Soc. 128*, 3696–3702.

Supporting Information

A DOTA-amide lanthanide tag for reliable generation of pseudocontact shifts in protein NMR spectra

Bim Graham, Choy Theng Loh, James Swarbrick, Phuc Ung, James Shin, Hiromasa Yagi, Xinying Jia, Sandeep Chhabra, Nicholas Barlow, Guido Pintacuda, Thomas Huber, Gottfried Otting

Contents

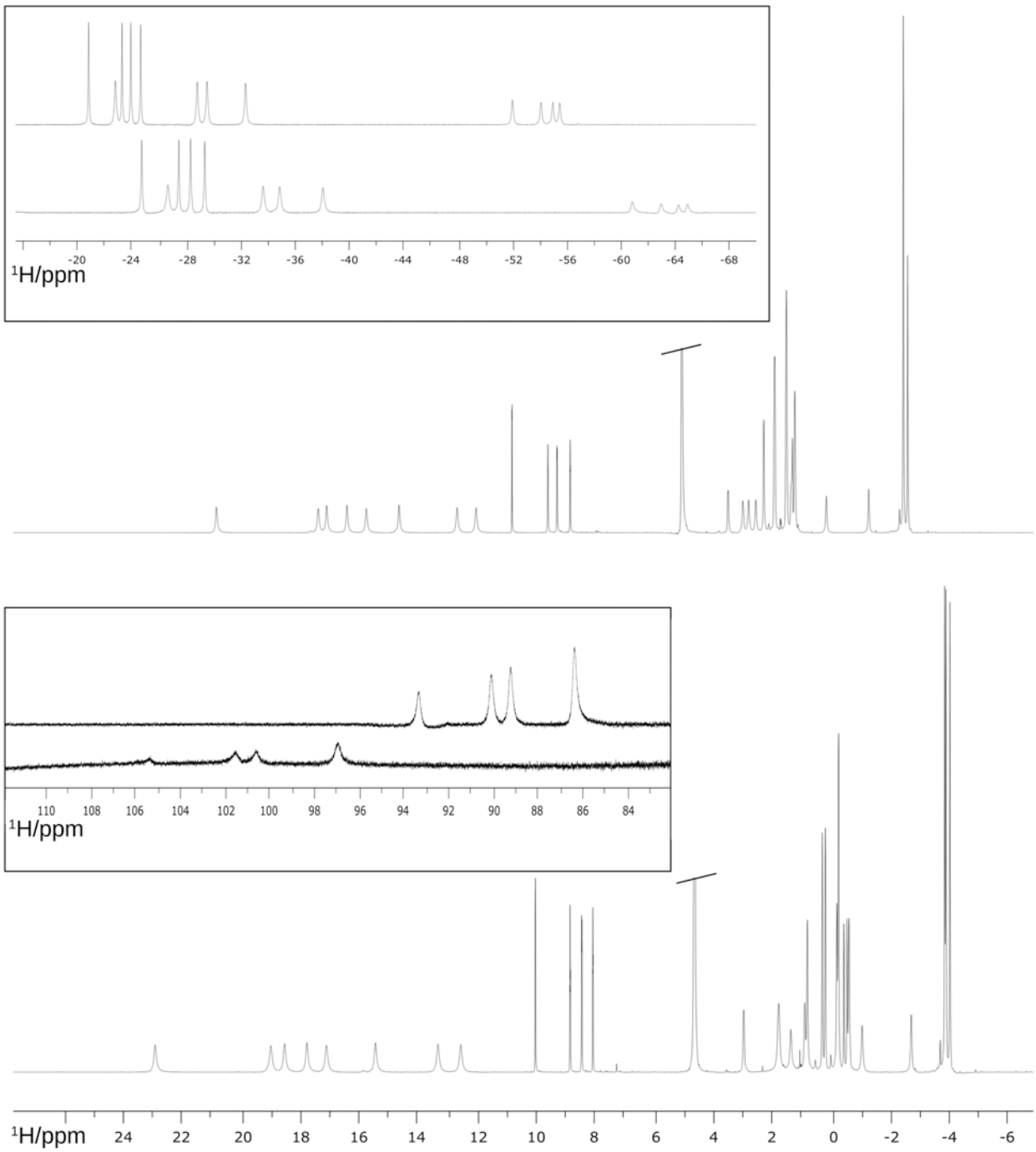

Figure S1. One-dimensional ^{1}H NMR spectra of the C1-Yb^{3+} complex in D_2O at 25 ^{o}C (lower traces) and 45 ^{o}C (upper traces), recorded on a 600 MHz Varian INOVA NMR spectrometer. The panels contain all the NMR signals observed. The signals with the largest paramagnetic shifts (inserts) come in groups of four inequivalent protons as expected for the symmetry of the cyclen ring in a single conformation. The absence of minor peaks attests to the purity of the compound and the absence of minor conformational species. The signals cluster closely at the chemical shifts detected for the parent compound $[Yb(DOTAMPh)]^{3+}$ at 17 ^{o}C (Dickins et al., 2003), namely 101.3, 17.8, 14.5 and -35.3 ppm for the signals of the cyclen ring, and -29.1 and -65.8 ppm for the methylene protons of the amide pendants. The signal intensities at extreme chemical shifts are weaker due to very large offset effects.

Table S1. Chemical shifts of $^{13}C/^{15}N$-labeled ArgN tagged with C1 with different metal ions in 20 mM MES, pH 6.6 at 25 ºC.

Residue		Diamagnetic (Y)				Paramagnetic (Tb)			
		CO	CA	N	H"	CO	CA	N	H"
4	Ser	171.848				172.051			
5	Ala	175.665	50.532	126.075	8.242	175.758	50.647	126.149	8.404
6	Lys	172.971	53.665	120.167	8.378		54.584	120.232	8.445
7	Gln	175.054	56.326	121.139	8.095	175.357			
8	Glu	176.282	56.468	118.478	8.646	176.565	56.606	118.926	8.982
9	Glu	175.650	55.960	119.509	8.081	175.900	56.332	119.871	8.409
10	Leu	175.034	55.488	122.819	7.824	175.450	55.787	123.111	8.114
11	Val	175.023	64.883	118.313	7.942	175.659	65.582	118.821	8.381
12	Lys	176.709	57.433	118.960	7.624	177.396	58.013	119.673	8.174
13	Ala	177.376	52.294	122.745	8.073	178.070	52.866	123.382	8.607
14	Phe	173.772	58.571	119.979	8.732	174.702	59.360	120.621	9.325
15	Lys	175.646	58.213	117.811	8.434	177.102	59.408	118.946	9.387
16	Ala	178.070	52.545	120.038	7.745	179.258	53.659	121.277	8.778
17	Lys	177.936	54.919	118.000	7.679		55.879	119.087	8.631
18	Leu	178.407	55.002	119.030	7.527				
19	Lys	174.624	55.568	120.734	8.103				
20	Glu	174.227	55.462	116.836	7.455				
21	Glu	172.398	54.474	113.432	7.989				
22	Lys	172.581	53.468	114.125	7.773				
23	Phe	172.582	56.754	120.256	8.247				
24	Ser	171.545	56.712	118.920	9.527				
25	Ser		53.782	114.024	7.947				
26	Gln	176.245							
27	Gly	174.259	44.593	107.182	8.939	173.779			
28	Glu	176.889	56.339	121.525	7.705	176.410	55.750	120.900	6.896
29	Ile	174.409	62.722	120.344	7.221	174.210	62.510	119.950	6.686
30	Val	174.592	64.353	118.590	8.078	174.475	64.284	118.548	7.769
31	Ala	177.339	52.380	119.104	7.639	177.208	52.245	118.933	7.373
32	Ala	178.151	52.340	120.418	7.687	178.239	52.341	120.385	7.552
33	Leu	177.313	55.123	117.958	8.075	177.314	55.121	117.990	8.087
34	Gln	178.399	56.974	121.042	8.665	178.503	56.949	120.990	8.644
35	Glu	175.265	56.492	121.369	8.205	175.294	56.699	121.498	8.216
36	Gln	172.973	53.792	115.706	7.302	172.992	53.817	115.792	7.367
37	Gly	171.893	42.362	105.145	7.662	172.027	42.378	105.193	7.698
38	Phe	172.541	55.756	119.955	7.584	172.491	56.056	119.896	7.651
39	Asp	173.637	52.008	120.871	8.168	173.595	51.781	121.131	8.303
40	Asn	172.113	50.593	115.231	8.566	172.051	50.499	115.409	8.691
41	Ile	170.305	55.944	118.641	7.953	170.380	55.984	118.425	8.046
42	Asn	168.342	48.778	119.007	6.699		48.725	119.027	6.687
43	Gln	176.543	54.472	120.017	8.254				
44	Ser	174.480	59.314	114.820	8.282	174.482			
45	Lys	176.143	56.635	121.713	8.084	176.396	56.801	121.492	8.094
46	Val	174.397	64.577	118.629	7.741	174.352	64.663	118.712	7.739
47	Ser	174.447	59.423	115.924	8.727	174.569	59.398	116.009	8.654
48	Arg	176.495	56.641	119.796	7.560	176.877	56.877	119.614	7.660
49	Met	175.005	57.346	120.439	7.896	175.452	57.815	120.594	8.117
50	Leu	176.294	56.361	119.940	8.592	177.013	56.983	120.479	8.912

51	Thr	174.806	63.425	113.754	7.573	175.637	64.126	114.231	8.000
52	Lys	175.462	56.596	124.255	8.333	176.480	57.354	124.846	8.936
53	Phe	172.552	55.905	112.915	7.929	174.415	57.443	114.098	8.975
54	Gly	172.003	44.023	107.693	7.616		46.148	109.506	9.093
55	Ala	174.655	50.249	118.700	8.068				
56	Val	171.321	56.516	116.026	8.561				
57	Arg	172.984	51.843	122.871	8.332				
58	Thr		57.337	120.299	8.993				
59	Arg	174.714							
60	Asn	174.207	48.274	120.576	8.560				
61	Ala	175.900	51.938	119.878	8.291				
62	Lys	172.757	52.777	115.618	7.118				
63	Met		53.581	111.467	8.241				
64	Glu	173.360							
65	Met	172.922	51.068	121.486	8.434				
66	Val	171.712	56.226	118.807	8.773				
67	Tyr	173.192	56.357	116.361	8.247				
68	Cys	170.747	51.388	118.497	9.041				
69	Leu		49.859	123.412	8.970				
70	Pro	173.601							
71	Ala	174.959	49.982	123.274	8.131				
72	Glu	173.593	53.665	120.217	8.401				
73	Leu	175.063	52.511	123.172	8.242				
74	Gly	171.070	42.527	109.610	8.365	170.202			
75	Val		57.010	120.324	7.781		56.219	119.502	7.003
76	Pro	174.409				173.292			
77	Thr	171.509	59.137	114.674	8.260	170.267	58.015	113.631	7.272
78	Thr		60.465	121.020	7.699		59.392	119.864	6.558

Residue		Paramagnetic (Tm)				Paramagnetic (Yb)			
		CO	CA	N	H"	CO	CA	N	H"
4	Ser	171.714							
5	Ala	175.418	50.069	125.883	8.119				
6	Lys		54.214	119.880	8.109				
7	Gln	174.857				174.987			
8	Glu	175.875	56.140	118.430	8.522	176.156	56.323	118.433	8.613
9	Glu	175.213	55.578	119.296	7.857	175.468	55.862	119.421	8.007
10	Leu	174.640	55.258	122.406	7.554	174.888	55.364	122.661	7.708
11	Val	174.429	64.498	117.870	7.609	174.823	64.859	118.147	7.818
12	Lys	176.285	56.930	118.610	7.252	176.568	57.299	118.836	7.482
13	Ala	176.915	51.879	122.306	7.713	177.216	52.134	122.582	7.937
14	Phe	173.065	58.154	119.486	8.296	173.488	58.439	119.772	8.562
15	Lys	174.503	57.165	117.023	7.738	175.221	57.805	117.495	8.173
16	Ala	177.152	51.722	119.180	7.032	177.714	52.270	119.732	7.480
17	Lys	176.977	54.229	117.209	7.002	177.538	54.694	117.712	7.427
18	Leu		53.511	117.907	6.501	177.618	54.551	118.593	7.138
19	Lys					173.710	54.687	119.900	7.456
20	Glu					173.573	54.862	116.158	6.886
21	Glu					172.248	53.871	112.684	7.184
22	Lys					172.975	53.609	114.102	7.674
23	Phe					173.196	57.120	120.563	8.449
24	Ser	173.466				172.269	57.468	119.550	10.060
25	Ser		55.010	115.402	9.173		54.272	114.580	8.405
26	Gln								
27	Gly	174.652				174.428			
28	Glu	177.175	56.788	121.997	8.300	176.956	56.498	121.683	7.921
29	Ile	174.473	62.996	120.629	7.622	174.421	62.832	120.439	7.361
30	Val	174.634	64.385	118.837	8.295	174.574	64.262	118.738	8.149
31	Ala	177.498	52.572	119.347	7.894	177.408	52.506	119.139	7.712
32	Ala	178.112	52.435	120.527	7.817	178.143	52.345	120.444	7.725
33	Leu	177.313	54.967	117.925	8.083	177.280	55.142	117.919	8.069
34	Gln	178.449	57.011	120.920	8.674	178.439	56.924	120.969	8.660
35	Glu	175.339	56.323	121.444	8.232	175.352	56.575	121.437	8.224
36	Gln	173.072	53.777	115.693	7.276	173.016	53.779	115.695	7.291
37	Gly	171.846	42.431	105.134	7.688	171.837	42.366	105.143	7.663
38	Phe	172.422	55.828	119.746	7.544	172.458	55.728	119.710	7.536
39	Asp	173.572	51.638	121.047	8.154	173.606	51.726	120.968	8.165
40	Asn	171.938	50.517	115.327	8.572	172.000	50.507	115.289	8.592
41	Ile	170.408	55.965	118.397	7.994	170.371	55.972	118.477	7.981
42	Asn		48.815	119.087	6.678	174.157	48.786	119.075	6.694
43	Gln					174.344	53.472	119.779	8.053
44	Ser	174.643				174.523	59.254	114.805	8.284
45	Lys	176.308	56.600	121.495	8.100	176.224	56.679	121.638	8.090
46	Val	174.285	64.540	118.795	7.741	174.337	64.608	118.684	7.743
47	Ser	174.401	59.436	116.138	8.799	174.481	59.438	116.011	8.752
48	Arg	176.276	56.337	119.392	7.461	176.407	56.458	119.658	7.529
49	Met	176.863	56.830	120.051	7.588	174.761	57.115	120.299	7.788
50	Leu	175.706	55.919	119.652	8.293	176.097	56.085	119.831	8.482

51	Thr	174.111	62.856	113.224	7.198	174.545	63.179	113.565	7.442
52	Lys	174.598	55.786	123.580	7.732	175.153	56.248	123.995	8.115
53	Phe	170.980	54.728	112.043	7.044	171.995	55.457	112.587	7.611
54	Gly	169.819	42.227	106.239	6.407	171.237	43.324	107.147	7.173
55	Ala		48.398	116.783	6.673	174.234	49.574	117.949	7.574
56	Val						57.491	115.605	7.900
57	Arg								
58	Thr								
59	Arg								
60	Asn								
61	Ala					175.425			
62	Lys						53.072	115.779	7.505
63	Met								
64	Glu								
65	Met								
66	Val					173.726			
67	Tyr						57.236	117.637	9.163
68	Cys					172.138			
69	Leu						54.139	123.967	9.366
70	Pro								
71	Ala					174.213			
72	Glu					173.639	53.487	119.781	8.025
73	Leu					175.334	52.857	123.251	8.245
74	Gly	171.623				171.264	42.751	109.826	8.553
75	Val		57.658	120.930	8.332		57.253	120.531	7.982
76	Pro	175.149				174.672			
77	Thr	172.359	59.989	115.444	8.987	171.821	59.475	114.965	8.527
78	Thr		61.223	121.847	8.538		60.766	121.339	8.013

Residue		Paramagnetic (Dy)	
		N	H^N
8	Glu	119.045	9.047
9	Glu	119.946	8.476
10	Leu	123.158	8.176
13	Ala	123.486	8.712
17	Lys	118.891	8.434
28	Glu	120.737	6.736
29	Ile	119.790	6.480
31	Ala	118.902	7.309
40	Asn	115.960	8.586
41	Ile	118.501	8.024
42	Asn	118.956	6.654
48	Arg	119.530	7.629
51	Thr	114.215	7.981
52	Lys	124.946	8.966

(Paramagnetic peaks of the ArgN-C1-Dy^{3+} sample were measured in a ^{15}N-HSQC spectrum.)

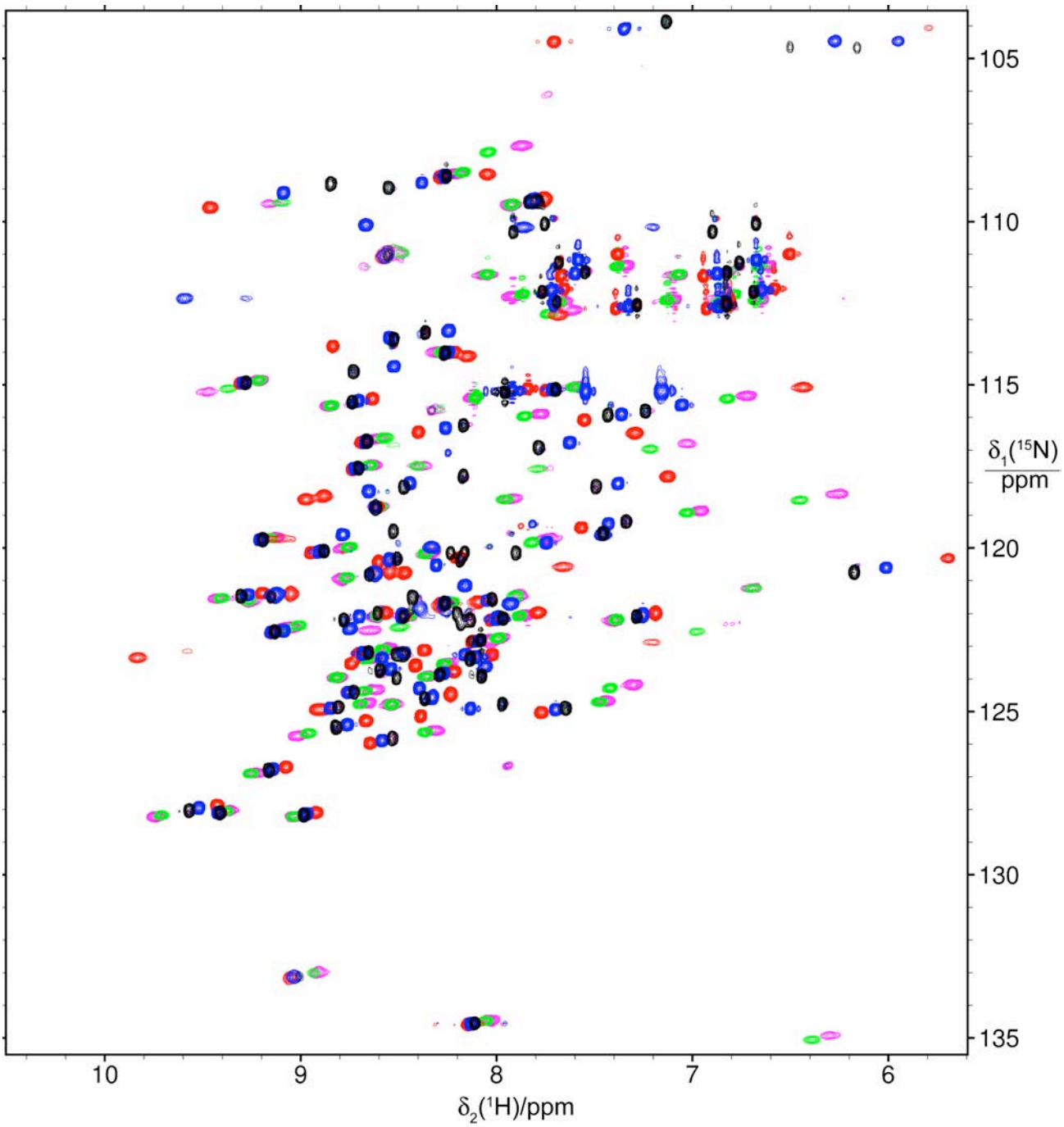

Figure S2. Superimposition of ^{15}N-HSQC spectra of about 70 μM solutions of the uniformly ^{15}N-labeled ubiquitin A28C mutant, ligated at Cys28 with the C1 tag loaded with Y^{3+} (black peaks), Yb^{3+} (blue), Tb^{3+} (green), Tm^{3+} (red), or Dy^{3+} (magenta). Judging by the intensities of the main peaks, the tagging yields varied between 80% and 100%. All spectra were recorded at pH 7.5 and 25 ^{o}C on a Varian INOVA 600 MHz NMR spectrometer.

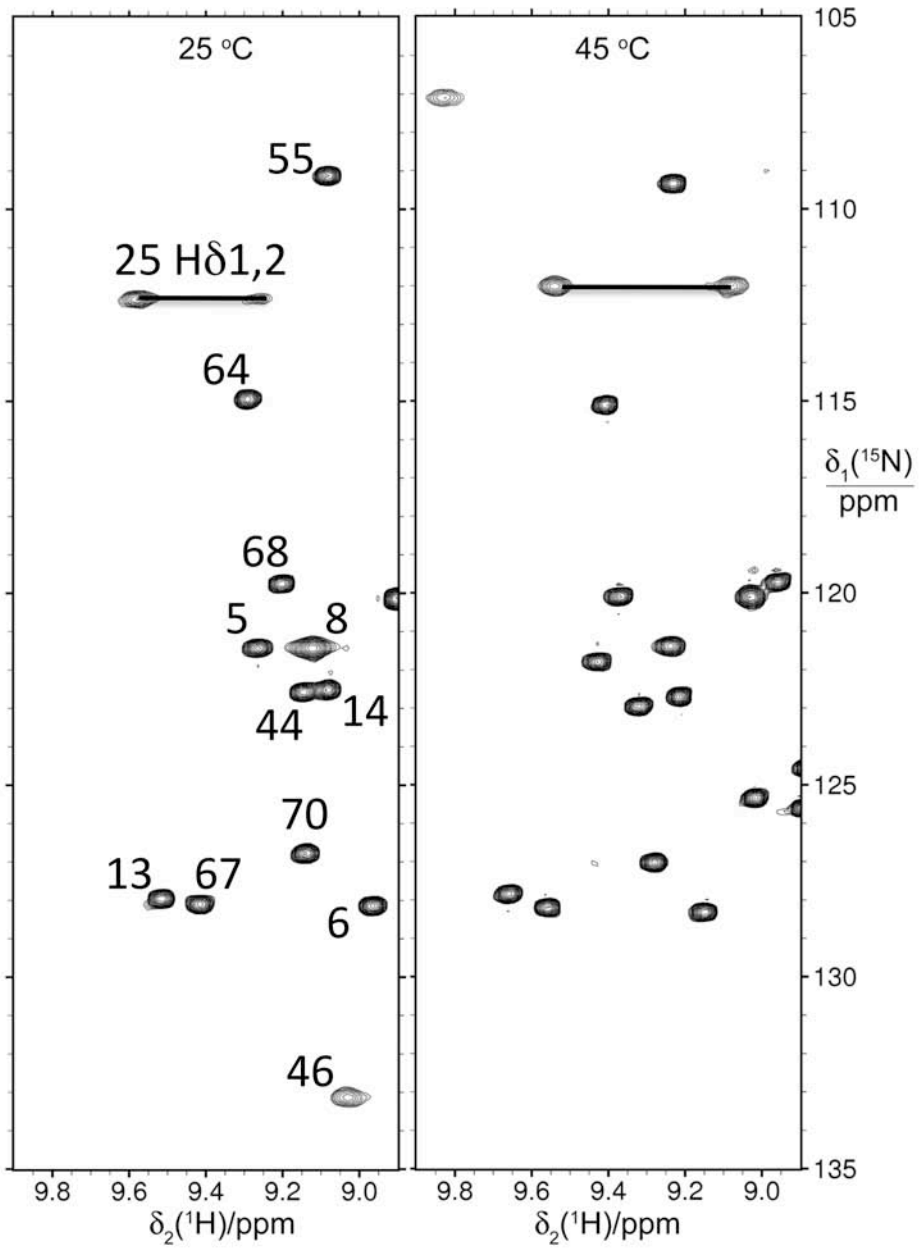

Figure S3. High-field spectral regions from ^{15}N-HSQC spectra of about 70 μM solutions of the uniformly ^{15}N-labeled ubiquitin A28C mutant, ligated at Cys28 with the C1 tag loaded with Yb^{3+} at pH 7.5 and two different temperatures. The signal-to-noise ratio for most peaks is better than 100:1. The lowest contour level was plotted at the height of the top noise peaks. No additional weak cross-peaks appear at either temperature, i.e. there is no evidence for slow conformational exchange phenomena of the C1 tag. The peaks in the left panel are labelled with the sequence number of the backbone amide protons. The side chain resonances of Asn25 are connected by a line.

Table S2. Pseudocontact shifts measured for backbone amide protons of ubiquitin(A28C) tagged with C1 and loaded with different lanthanides.[a]

		Dy^{3+}	Tb^{3+}	Tm^{3+}	Yb^{3+}
2	GLN	0.018	0.034	0.000	0.000
3	ILE	0.035	0.013	-0.041	-0.021
4	PHE	0.000	-0.015	-0.003	0.000
5	VAL	0.122	0.099	-0.106	-0.039
6	LYS	0.048	0.050	-0.057	-0.018
7	THR	0.115	0.106	-0.099	-0.034
8	LEU	0.120	0.116	-0.097	-0.035
9	THR	NA	NA	NA	NA
10	GLY	0.088	0.085	-0.074	0.000
11	LYS	0.112	0.101	-0.091	-0.031
12	THR	0.134	0.112	-0.099	-0.038
13	ILE	0.173	0.143	-0.136	-0.049
14	THR	0.285	0.231	-0.210	-0.082
15	LEU	0.199	0.144	-0.147	-0.058
16	GLU	0.505	0.360	-0.340	-0.142
17	VAL	-0.056	-0.089	0.030	0.003
18	GLU	-0.729	-0.685	0.502	0.179
20	SER	-0.839	-0.748	0.578	0.211
21	ASP	-1.282	-1.098	0.839	0.314
22	THR	NO	NO	2.375	0.718
23	ILE	NO	NO	1.229	0.472
24	GLU	NA	NA	NA	NA
25	ASN	NO	NO	NO	NO
26	VAL	NO	NO	1.630	0.545
27	LYS	NO	-0.897	0.567	0.250
28	ALA	NO	NO	NO	NO
29	LYS	NO	NO	-0.742	-0.223
30	ILE	NO	0.840	-0.771	NO
31	GLN	NO	NO	-1.312	-0.455
32	ASP	NO	NO	NO	NO
33	LYS	NO	1.107	-0.991	-0.369
34	GLU	0.749	0.637	-0.575	-0.206
35	GLY	0.605	0.541	-0.503	-0.174
36	ILE	0.524	0.518	-0.476	-0.162
39	ASP	1.079	1.080	-0.846	-0.290
40	GLN	0.600	0.617	-0.487	-0.165
41	GLN	0.435	0.464	-0.360	-0.117
42	ARG	0.139	0.163	-0.134	-0.031
43	LEU	-0.105	-0.055	0.032	0.018
44	ILE	-0.066	-0.046	0.025	0.016
45	PHE	-0.151	-0.118	0.087	0.032
46	ALA	-0.097	-0.074	0.060	0.022
47	GLY	-0.078	-0.055	0.047	0.014
48	LYS	-0.066	-0.088	0.064	0.026
49	GLN	-0.103	-0.075	0.070	0.025
50	LEU	-0.219	-0.167	0.120	0.053
51	GLU	-0.436	-0.385	0.261	0.145
52	ASP	-0.417	-0.366	0.283	0.122
53	GLY	NA	NA	NA	NA
54	ARG	-1.200	-1.003	0.750	0.289

55	THR	-0.978	-0.806	0.620	0.235
56	LEU	-1.153	-0.958	0.717	0.268
57	SER	-0.751	-0.630	0.478	0.178
58	ASP	-0.670	-0.550	0.421	0.159
59	TYR	-0.520	-0.421	0.318	0.119
60	ASN	-0.395	-0.314	0.236	0.088
61	ILE	-0.381	-0.313	0.234	0.089
62	GLN	-0.208	-0.177	0.129	0.047
63	LYS	-0.161	-0.144	0.099	0.035
64	GLU	-0.068	-0.068	0.034	0.010
65	SER	-0.108	-0.096	0.060	0.021
66	THR	-0.068	-0.056	0.036	0.017
67	LEU	-0.045	-0.028	0.009	0.002
68	HIS	-0.061	-0.038	0.013	0.007
69	LEU	0.058	0.071	-0.064	-0.020
70	VAL	0.070	0.091	-0.083	-0.025
71	LEU	0.121	0.134	-0.108	-0.034
72	ARG	0.215	0.221	-0.177	-0.061
73	LEU	0.168	0.167	-0.127	-0.045
74	ARG	-0.018	-0.030	0.000	0.000
75	GLY	0.052	0.071	0.025	0.011
76	GLY	0.158	0.147	-0.111	-0.037

[a] Data measured of about 70 μM solutions in (50 mM HEPES buffer) at pH 7.5 at 25 °C. The PCSs were determined as the chemical shift observed with paramagnetic lanthanides minus the corresponding chemical shift observed with ubiquitin(A28C)-C1 loaded with Y^{3+}. NA: not assigned; NO: not observed.

Table S3. $\Delta\chi$ tensors of different metal ions bound to the C1 tag on Cys28 of the ubiquitin mutant A28C.[a]

Metal ion	$\Delta\chi_{ax}$ /10^{-32} m^3	$\Delta\chi_{rh}$ /10^{-32} m^3	Q^b	Tensor axis	Coordinates of tensor axes		
Dy^{3+}	-10.8	-3.5	0.08	x	-0.830	0.526	-0.185
	(-13.3/-10.6)	(-5.4/-3.1)		y	-0.523	-0.619	0.586
				z	0.194	0.583	0.789
Tb^{3+}	-9.0	-2.3	0.08	x	-0.894	0.444	-0.066
	(-11.3/-8.9)	(-3.7/-2.1)		y	-0.390	-0.694	0.605
				z	0.223	0.567	0.793
Tm^{3+}	7.1	1.6	0.06	x	-0.852	0.514	-0.099
	(6.8/9.1)	(1.0/2.7)		y	-0.461	-0.648	0.606
				z	0.247	0.562	0.789
Yb^{3+}	2.4	0.5	0.11	x	-0.848	0.509	-0.146
	(2.2/3.0)	(0.1/0.8)		y	-0.475	-0.607	0.637
				z	0.236	0.609	0.757

[a] The tensors are listed in their unique tensor representation (UTR; Schmitz et al. 2008) as obtained by fitting of the PCSs of the structurally ordered residues 2-72 in Table S2 to the first conformer of the NMR structure of ubiquitin (PDB ID 1D3Z; Cornilescu et al. 1998) simultaneously using the PCSs induced by Dy^{3+}, Tb^{3+}, Tm^{3+} and Yb^{3+} and a common metal position. The covalent structure of the tag was taken into account as described in the main text. The orientations of the tensor axes are given as unit vectors with respect to the origin (0, 0, 0). Uncertainty ranges (shown in brackets) display the most extreme values identified among the family of fits obtained by a Monte Carlo error analysis that randomly omitted 20% of the PCSs. The coordinates of the common metal position in the best fit were (61.868, -91.284, -8.631). Relative to this position, the metal was displaced by up to 1.3 Å, when 20% of the PCSs were left off in the Monte Carlo error analysis.

[b] Q-factor calculated as root-mean-square deviation between measured and predicted PCSs divided by the root-mean-square of the measured PCSs. The *Q*-factor of the simultaneous four-metal fit is 0.07.

Figure S4. Model of the C1 tag bound to Cys28 in the ubiquitin mutant A28C. The model represents the best fit of the PCSs to the first conformer of the NMR structure (PDB ID 1D3Z (Cornilescu et al. 1998). The structure of the tag was derived from the mirror image of the crystal coordinates of the Gd^{3+} complex with 2,2',2'',2'''-(1,4,7,10-tetraazacyclododecane-1,4,7,10-tetrayl)*tetrakis*(*N*-((*R*)-1-phenylethyl)acetamide) (DOTAMPh, CSD accession code EQOZUF; Parker2003), as described in the main text. The lanthanide ion is represented by a magenta sphere. The disulfide bond of the linker is highlighted in yellow. The side chain of Cys28 and the tag are shown in a heavy atom representation.

References

Cornilescu, G., Marquardt, J. L., Ottiger, M., and Bax, A. (1998) Validation of protein structure from anisotropic carbonyl chemical shifts in a dilute liquid crystalline phase. *J. Am. Chem. Soc. 120*, 6836-6837.

Dickins, R. R., Parker, D., James, I. B., and Tozer, D. J. (2003) Correlation of optical and NMR spectral information with coordination variation for axially symmetric macrocyclic Eu(III) and Yb(III) complexes: axial donor polarisability determines ligand field and cation donor preference. *Dalton Trans. 2003*, 1264-1271.

Parker, D., Puschmann, H., Batsanov, A. S., and Senanayake, K. (2003) Structural analysis of nine-coordinate lanthanide complexes: steric control of the metal-water distance across the series. *Inorg. Chem. 42*, 8646-8651.

Schmitz, C., Stanton-Cook, M. J., Su, X.-C., Otting, G., and Huber, T. (2008) Numbat: an interactive software tool for fitting Dc-tensors to molecular coordinates using pseudocontact shifts *J. Biomol. NMR 41*, 179-189.

Sunnerhagen, M., Nilges, M., Otting, G., and Carey, J. (1997) Solution structure of the DNA-binding domain and model for the binding of multifunctional arginine repressor to DNA *Nat. Struct. Biol. 4*, 819-826.

Bioconjugate Chemistry

ARTICLE

pubs.acs.org/bc

Tuning G-Quadruplex vs Double-Stranded DNA Recognition in Regioisomeric Lysyl-Peptidyl-Anthraquinone Conjugates

Giuseppe Zagotto, Antonio Ricci, Elena Vasquez, Andrea Sandoli, Silvia Benedetti, Manlio Palumbo, and Claudia Sissi*

Department of Pharmaceutical Sciences, University of Padova, Via Marzolo 5, 35131 Padova, Italy

Supporting Information

ABSTRACT: Anthraquinone is a versatile scaffold to provide effective DNA binders. This planar system can be easily conjugated to protonable side chains: the nature of the lateral groups and their positions around the tricyclic moiety largely affect the DNA recognition process in terms of binding affinity and mode, as well as sequence and structure of the target nucleic acid. Starting from an anthracenedione system symmetrically functionalized with N-terminal lysyl residues, we incremented the length of side chains by introducing a Gly, Ala, or Phe spacer, characterized by different flexibility, lipophilicity, and bulkiness. Moreover, 2,6, 2,7, 1,8, and 1,5 regioisomers were examined to yield a small bis(lysyl-peptidyl) anthracenedione library. By merging spectroscopic, enzymatic, and cellular results, we showed that the proper combination of a basic aminoacid (Lys) with a more hydrophobic residue (Phe) can provide selective G-quadruplex recognition, in particular when side chains are located at positions 2,6 or 2,7. In fact, while these derivatives effectively bind G-quadruplex structures, they behave at the same time as rather poor double-stranded DNA intercalators. As a result, the Lys-Phe substituted anthraquinones are poorly cytotoxic but still able to promote a senescence mechanism in cancer cells. This combination of chemical and biological properties foresees potentially valuable applications in anticancer medicinal chemistry.

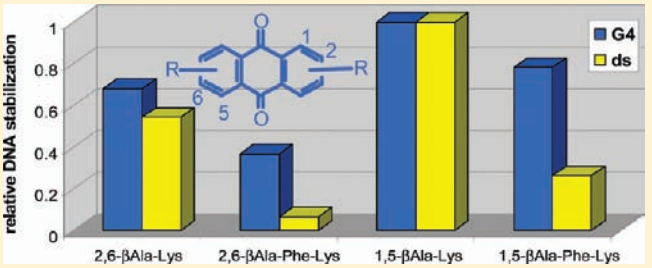

INTRODUCTION

Telomeres are specialized nucleoprotein structures localized at the end of chromosomes. They protect genomic information from degradation, fusion, and recombination and allow the DNA damage response machinery to discriminate between double-strand breaks and natural chromosome ends.[1] Telomeric DNA comprises several kilobases of tandem repeats of a G-rich DNA sequence (TTAGGG in humans) and are characterized by a single-stranded 3′ end (ca. 150−200 nucleotides). However, its length is progressively reduced in somatic cells due to the "end replication" problem.[2] When telomeres reach a critical length, cells enter a replicative senescence state and division no longer occurs.[3] On the contrary, over 80% of cancer cells maintain telomere integrity due to an up-regulation of a reverse transcriptase called telomerase.[4] This enzyme catalyzes the synthesis of telomeric DNA repeats, stabilizing telomeres length and contributing to cellular immortalization and oncogenesis.[5]

Due to its involvement in cell immortalization, telomerase represents a promising anticancer target.[6] Various strategies have been devised to directly target the enzyme or associated proteins. An alternative approach comprises derivatives directed toward the 3′ single-stranded end of telomeric DNA.[7] In this case, small molecules are used to induce nucleic acid folding into a noncanonical structure called the G-quadruplex, which is inaccessible to the RNA template component of telomerase.[8]

In the past decades, a large number of small molecules have been reported to efficiently bind G-quadruplex DNA and to inhibit telomerase.[9−11] Most of them are based on a polycyclic aromatic core that stacks by $\pi-\pi$ interactions over the terminal planar G-tetrads of a quadruplex. In addition, cationic side chains can interact with the negatively charged phosphate backbones in G-quadruplexes.

Properly substituted anthraquinones were early identified as potential effective G-quadruplex binders.[12−14] In particular, the substitution pattern with protonable side chains was shown to play a major role in driving selectivity toward double-stranded or G-quadruplex structures. In previous studies, we reported the modulation of G-quadruplex recognition by anthracenedione derivatives symmetrically disubstituted at 2,6 or 2,7 positions with one or two aminoacidic residues.[15,16] We showed the importance of the size of the planar surface, which was affected by reversal of the direction of the amide linkage connecting the anthracenedione to the side chains. Additionally, a significant role of ionic interactions was confirmed, since N-terminal protonable

Received: July 19, 2011
Revised: August 26, 2011
Published: September 12, 2011

ACS Publications © 2011 American Chemical Society

aminoacids (Lys, Arg) largely incremented G-quadruplex binding. Clearly, charged interactions simultaneously promote binding to double-stranded DNA too. However, taking into account the different geometries of the two DNA structures, it should be possible to optimize the relative position of the charged groups with reference to the aromatic core to preferentially drive the ligand toward one DNA fold.

Here, we synthesized and analyzed a small library of disubstituted peptidyl anthraquinones characterized by a lysyl N-terminal residue. We modulated its distance from the planar moiety by introducing mono- and dipeptidyl spacers, characterized by increasing steric hindrance and hydrophobicity (Gly, Ala, Phe). Additionally, the relative position of the two protonable groups was varied by considering the 2,6, 2,7, 1,8, and 1,5 regioisomers. These structural features should allow identifying the peptidyl anthraquinone requirements that grant selectivity for G-quadruplex vs duplex DNA by establishing distinct patterns of hydrogen bonding, hydrophobic, and charge interactions. In particular, preferential binding to G-quadruplex folded telomeric DNA would likely produce telomerase inhibition and cancer cell death without greatly affecting somatic cells.

EXPERIMENTAL PROCEDURES

Synthesis. All water- or air-sensitive reactions were carried out in oven-dried glassware under a nitrogen atmosphere with dry solvents, unless otherwise noted. All commercial reagents were purchased from Sigma-Aldrich and were used without further purification. The solvents were purchased from Fluka, WMC, and Carlo Erba; they were anhydrified as follows: *N*,*N*-Dimethylformamide (DMF) was distilled under reduced pressure over BaO; diisopropylethylamine (DIPEA) and piperidine were distilled over CaH_2. ^1H NMR spectra were recorded on a Bruker Avance AMX 300 spectrometer. Chemical shifts (δ) are expressed in parts per million relative to tetramethylsilane (ppm), and the following abbreviations were used for the multiplicities: s = singlet, d = doublet, dd = doublet doublets, t = triplet, dt = doublet triplets, tt = triplet triplets, q = quartet, m = multiplet, bm = broad multiplet, and bs = broad singlet. Mass spectrometric data were obtained using a Mariner API-TOF (Perseptive Biosystems Inc., Framingham, MA 01701, USA). Purities ($\geq$95%) of all tested compounds were established by HPLC using a Varian Pro Star equipped with an UV−vis detector (BioRad) and a Phenomenex C18 (4.6 × 250 mm, 5 μm) column. The mobile phase results from combination of (A) H_2O/TFA (99:1) and (B) MeOH/TFA (99:1). A gradient from 5% to 60% of solution B over 20 min followed by 5 min at the latter percentage was used; the flow rate was set at 1.0 mL/min. The signals were detected with a UV−vis detector at 254 nm. Within the experimental part, AQ stands for anthraquinone; in particular, AA-AQ stands for amino acid substituted anthraquinone.

General Procedure for the Synthesis of the Acyl Chloride Derivative of an Amino Acid. $SOCl_2$ (1 mol) was added to a solution of the desired Fmoc-amino acid (100 mmol) in 50 mL of DCM and heated at reflux under N_2 atmosphere for 4 h. The solvent was then removed by distillation and the crude white solid dried under high vacuum.

General Procedure for Peptide Coupling via Acyl Chloride. The acyl chloride derivative of the desired Fmoc-amino acid (100 mmol) was added to a solution of the required diaminoanthraquinone (25 mmol) in 15 mL of DMF. The solution thus obtained was stirred at RT under N_2 atmosphere for 3 h before pouring it into cold Et_2O (250 mL). The resulting precipitate was collected by centrifugation, washed with HCl 0.1 M (3 × 50 mL), isopropanol (20 mL), and Et_2O (50 mL), and dried under vacuum.

General Deprotection Procedure of the Fmoc Group. A solution of the desired AA-AQ derivative (10 mmol) in piperidine/DMF 10% (1 mL) was stirred at RT for 20 min and then poured into cold Et_2O (20 mL). The resulting precipitate was collected by centrifugation, washed with Et_2O (3 × 20 mL), MeOH (1 × 20 mL), and Et_2O (2 × 30 mL), and finally dried under vacuum.

General Procedure for Peptide Coupling via TBTU, HOBt, and DIPEA. A solution of the desired Fmoc-amino acid (40 mmol) in anhydrous DMF (5 mL) was introduced in a round-bottomed flask containing TBTU (42 mmol), HOBt (42 mmol), and DIPEA (128 mmol); the resulting solution was stirred for 15 min at RT under N_2 atmosphere. A solution of the desired AA-AQ (10 mmol) in anhydrous DMF (5 mL) was added and the mixture stirred at RT for 4 h under N_2 atmosphere. The mixture was poured in Et_2O (50 mL), and the resulting precipitate was collected by centrifugation, washed with Et_2O (3 × 50 mL), MeOH (2 × 10 mL), and Et_2O (50 mL), and finally dried under vacuum.

General Deprotection Procedure of the Boc Group. A solution of the desired Boc-AA-AQ (10 mmol) in TFA/H_2O 95% (5 mL) was stirred at RT for 20 min and then poured into Et_2O (30 mL). The resulting precipitate was collected by centrifugation, washed with Et_2O (3 × 30 mL), and dried under vacuum.

Synthetic Oligonucleotides. The labeled human telomeric sequence l-Tel23 5′-Dabcyl-AGGGTTAGGGTTAGGGTTAGGGT-FAM 3′ was synthesized and purified by ATDBIO (Southampton, UK). All other oligonucleotides were provided by Eurogentec (Belgium) (Tel22, AGGGTTAGGGTTAGGGTTAGGG; dsUP, 5′-FAM- GTGAGATACCGACAGAAG; dsDOWN CTTCTGTCGGTATCTCAC-Dabcyl 3′; 1GGG, TACAGATAGTTAGGGTTAGACTTA; 2GGG, TACAGATAGTTAGGGTTAGGGTTA; TS AATCCGTCGAGCAGAGTT; ACX: GTGCCCTTACCCTTACCCTTACCCTAA; TSNT: AATCCGTCGAGCAGAGTTAAAAGGCCGAGAAGCGAT; NT: ATCGCTTCTCGGCCTTTT; Tup:TGAGGATCCGCCTGGACAGCATGG-3′; Tdown: GTCGAATTCTCGGCGAGAAGCAGG).

Calf thymus DNA (ctDNA) was purchased from Sigma Aldrich (USA) and used with no further purification.

Fluorescence Melting Assay. Fluorescence melting curves were determined in a Roche LightCycler (λ_{ecc} 488 nm, λ_{em} 520 nm) in a total reaction volume of 20 μL containing 0.25 μM of l-Tel23 and increasing ligands concentrations in LiP buffer (10 mM LiOH, 50 mM KCl, pH 7.4 with H_3PO_4). In a typical experiment, the oligonucleotide was first denatured by heating to 95° at a rate of 0.1 °C s^{-1}, maintained at 95 °C for 5 min, and then annealed by cooling to 30 °C at a rate of 0.1 °C s^{-1}. Then, samples were maintained at 30° for 5 min before being slowly heated to 95 °C (1 °C/min) and annealed at a rate of 1 °C/min. When double-stranded DNA was used, dsUP and dsDOWN were mixed at equimolar concentrations, heated to 95 °C for 5 min, and then cooled to room temperature overnight before use. Recordings were taken during both the annealing and melting steps.

T_m values were determined from the first derivatives of the melting profiles using the Roche *LightCycler* software. Each curve

Scheme 1[a]

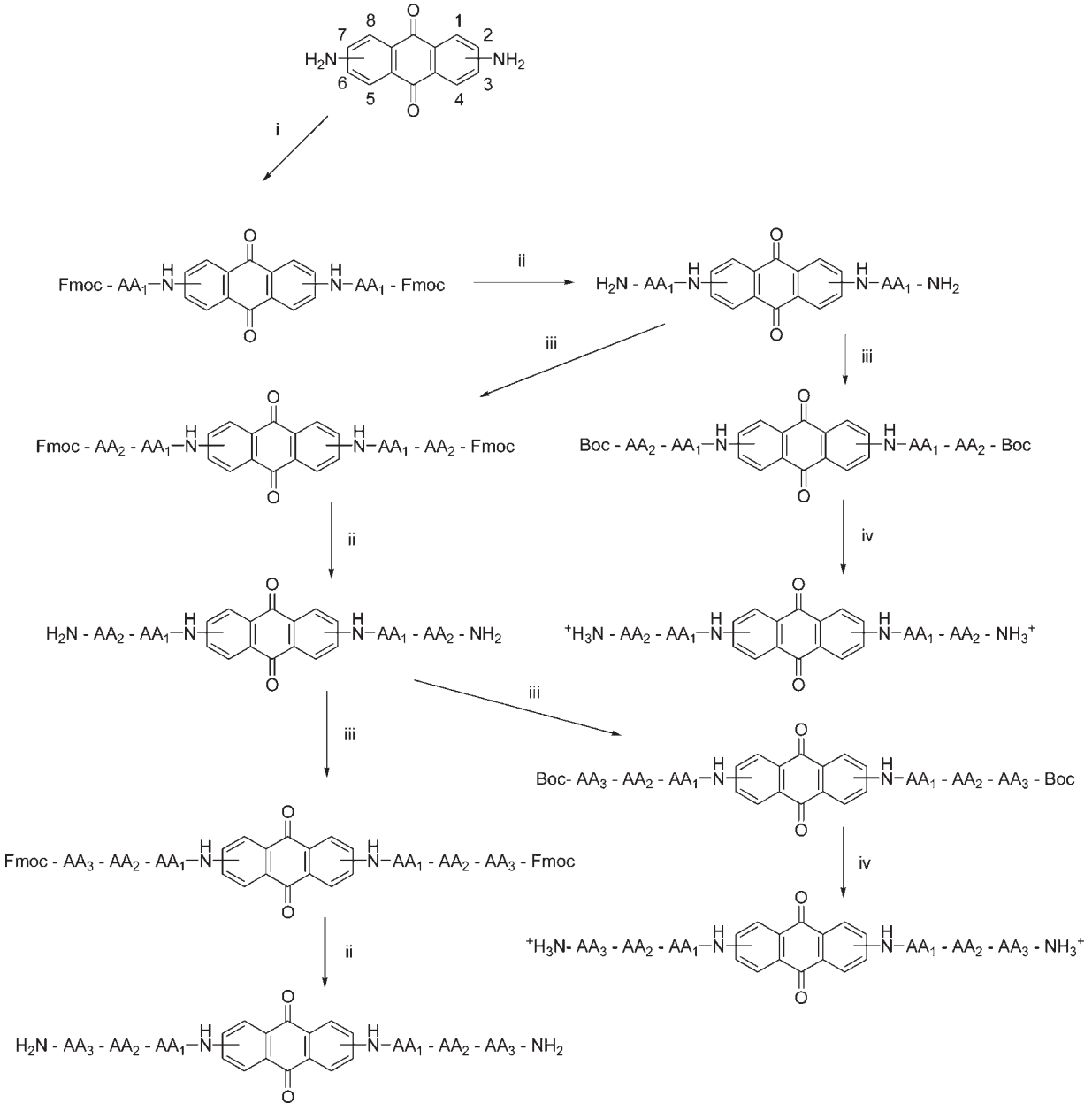

[a] Reagents: (i) AA_1-Cl, DMF, RT, N_2, 3 h. (ii) Piperidine/DMF 20%, RT, 20 min. (iii) $AA_{2,3,4}$, TBTU, HOBt, DIPEA, RT, N_2, DMF, 4 h. (iv) TFA/H_2O 90%, RT, 20 min.

was repeated at least three times and errors were ±0.4 °C. ΔT_m were calculated by subtracting the T_m value recorded in the presence of the ligand from the corresponding value in the absence of ligand.

Circular Dichroism Measurements. Circular dichroism spectra from 220 to 450 nm were recorded using 10 mm path length cells on a Jasco J 810 spectropolarimeter equipped with a NESLAB temperature controller and interfaced to a PC 100 in 10 mM Tris-HCl, 50 mM KCl pH 7.4. Before data acquisition, Tel22 solutions (4 μM) were heated at 95 °C for 5 min and left to cool overnight at room temperature. The reported spectrum of each sample represents the average of 3 scans recorded with 1 nm step resolution. Observed ellipticities were converted to mean residue ellipticity $[\theta] = \text{deg} \times \text{cm}^2 \times \text{d mol}^{-1}$ (Mol. Ellip.).

Electromobility Shift Assay. End-labeled single-stranded oligonucleotides were obtained by incubating the oligonucleotides with T4 polynucleotide Kinase and [γ-^{32}P] ATP for 30 min at 37 °C. The enzyme was then removed by extraction with phenol/chloroform/isoamylic alcohol (25:24:1). A mixture of purified labeled and unlabeled oligonucleotides (total final concentration 10 μM) was heated to 95 °C for 5 min in 10 mM Tris, 1 mM EDTA, 100 mM KCl, pH 8.0 buffer and allowed to cool overnight at room temperature. The folding of the starting material was monitored by native 16% polyacrylamide gel electrophoresis in 0.5× TBE (44.5 mM Tris base, 44.5 mM boric

acid and 1 mM Na_2EDTA) added of KCl (100 mM in buffer and 20 mM in gels).

Resolved bands on dried gels were visualized and quantified on a PhosphorImager (Amersham).

***Taq* Polymerase Assay.** Compounds were assayed with *Taq* polymerase reaction by using pBR322 (2.5 ng) as DNA template and appropriate primer sequences (T_{up} and T_{down}, 0.5 μM each) to amplify the 964−1064 plasmid sequence by PCR. The reaction was carried out in a Perkin-Elmer thermocycler performing 25 cycles of 30 s at 94 °C, 30 s at 65 °C, and 30 s at 72 °C. The reaction products were resolved on a 2% agarose gel in 1× TBE (89 mM Tris base, 89 mM boric acid, and 2 mM Na_2EDTA) and stained by ethidium bromide.

Telomerase Activity Assay (TRAP Assay). Telomerase activity was assayed using a modified telomere repeat amplification protocol (TRAP) assay. As a source of telomerase, the total cell lysates derived from human melanoma cell line HeLa were used. Protein concentration of the lysates was assayed using Bio-Rad protein assay kit using BSA as standard. A 50 μL TRAP reaction mix (50 μM of dNTPs, 0.2 μg of primer TS, 0.1 μg of return primer ACX, 500 ng of protein extract, 2 U *Taq* polymerase) was prepared in the presence/absence of increasing drug concentration in 20 mM Tris-HCl, pH 8.3, 68 mM KCl, 1.5 mM $MgCl_2$, 1 mM EGTA, 0.05% v/v Tween-20. An internal control template (0.01 mmol TSNT) with its return primer (1 ng NT) were added to the reaction mixture. Then, the telomerase elongation step has been performed (30 min at 30 °C) followed by a PCR amplification step (30 cycles of 30 s at 37 °C and 30 s at 58 °C). Telomerase products were resolved by 10% polyacrylamide gel electrophoresis in TBE 0.5× and visualized by staining with Sybr Green I.

MTT Assays. HeLa (human hepitelial) cell line was maintained in DMEM medium supplemented with 10% heat-inactivated fetal calf serum, 50 U/mL of penicillin G, and 50 μg/mL of streptomycin, at 37 °C in humidified atmosphere and 5% of CO_2.

To evaluate toxic profiles of the potential antitelomerase compounds, MTT assays were performed as described: cells were plated in 96 well plates at 10 000 cells/well, and cultured overnight. Afterward, compounds were added in triplicate and plates were incubated in the presence of the drug for 72 h. At the end of this period, MTT was added to a final concentration of 0.8 mg/mL, and two additional hours of incubation were performed. After that, medium was aspirated carefully and 150 μL of DMSO were added per well. Soluble formazan salts were homogenized by manual pipetting and absorbance at 540 nm was read. Curves consisted of 8 serial dilutions in triplicate in each case, and results were analyzed as sigmoidal dose−response curves.

Cell Senescence Assay. HeLa cells were plated in 6-well plates at 10 000 cells/well and cultured overnight. Afterward, compounds were added in triplicate (2.5 μM and 0.5 μM for C-16 and D-16, respectively) and plates were incubated in the presence of the drug for 240 h. Every 72 h, the medium was changed and new drug was added. At the end of the treatment, medium was removed and cells were washed once with 1 mL of PBS and fixed with 1 mL of 2% formaldehyde, 0.2% glutaraldehyde in PBS for 15 min at room temperature. After another washing step with PBS, cells were stained with 1 mL of 37.2 mM citric acid/sodium phosphate (pH 6.0), 140 mM NaCl, 1.8 mM $MgCl_2$, 5 mM $K_3Fe(CN)_6$, 5 mM $K_4Fe(CN)_6$ $3H_2O$, and 1 mg/mL X-gal in dimethylformamide. Plates were incubated overnight at 37 °C and then photographed with a light microscope.

Scheme 2

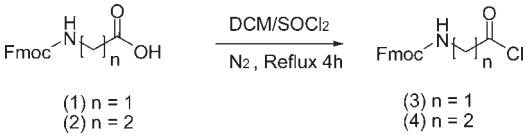

(1) n = 1
(2) n = 2

(3) n = 1
(4) n = 2

Table 1. Schematic Structures of the Synthesized 9,10-Anthracenedione-Aminoacyl Conjugates

		side chains		
regioisomer	compound	AA_1	AA_2	AA_3
2,6	**A-13**	Gly	Lys	
	A-14	Gly	Ala	Lys
	A-15	Gly	Gly	Lys
	A-16	Gly	Phe	Lys
2,6	**B-13**	βAla	Lys	
	B-14	βAla	Ala	Lys
	B-15	βAla	Gly	Lys
	B-16	βAla	Phe	Lys
2,7	**C-13**	βAla	Lys	
	C-14	βAla	Ala	Lys
	C-16	βAla	Phe	Lys
1,5	**D-13**	βAla	Lys	
	D-14	βAla	Ala	Lys
	D-16	βAla	Phe	Lys
1,8	**E-13**	βAla	Lys	
	E-14	βAla	Ala	Lys
	E-16	βAla	Phe	Lys

RESULTS

Chemistry. Starting materials for the synthesis of all derivatives were the appropriate diamino-substituted anthraquinones (AQ). While 2,6-diamino and 1,5-diamino AQ are commercially available, the 2,7-diamino and 1,8-diamino AQ were obtained via reduction of the corresponding dinitro derivatives.[17] In particular, the 2,7-dinitro AQ scaffold was obtained through a one-pot nitration−oxidation of commercial anthrone, as previously described.[16] The common synthetic route for all the disubstituted AQs is summarized in Scheme 1. Due to the low reactivity of the aryl amino groups, the first aminoacidic coupling (AA1) was efficiently carried out using the appropriate acyl chloride derivative (AA-Cl). These substrates were prepared treating the selected AA (Fmoc-glycine or Fmoc-β-alanine) with an excess of thionyl chloride in CH_2Cl_2 (Scheme 2). A first Fmoc deprotection of the amino groups, followed by salification with trifluoroacetic acid (TFA) led to the first group of compounds (**A-2**, **B-2**, **C-2**, **D-2**, and **E-2**). The salification step was performed to favor the solubility of the anthraquinone derivatives in water.

These compounds were used as starting blocks to synthesize several derivatives which can be divided into 5 related families: **A** and **B** where a glycine or a β-alanine was the AA_1 at positions 2 and 6, respectively; **C**, **D**, and **E** which correspond to the 2,7, 1,5, and 1,8 regioisomers of compound **B**.

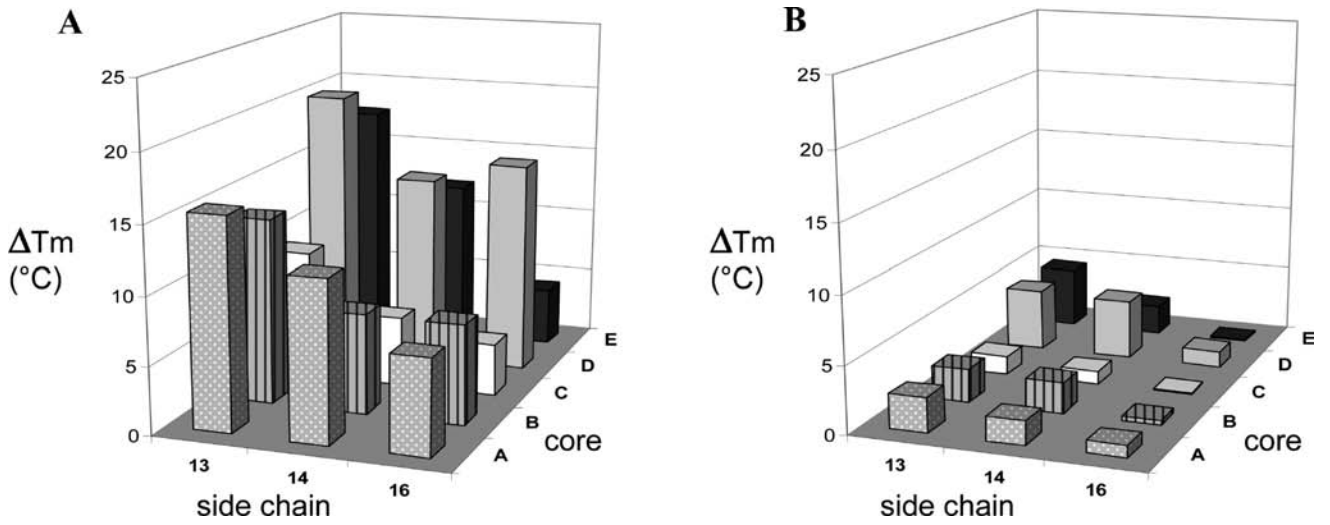

Figure 1. Variation of the melting temperature (ΔT_m) of a G-quadruplex folded telomeric sequence (A, 0.25 μM) or double-stranded DNA (B, 0.25 μM) upon addition of 1 μM selected anthraquinones in 50 mM KCl. Errors were ±0.4 °C.

The novel derivatives were prepared by standard peptide coupling of the free amino AA_1-AQ and the desired Fmoc- or Boc-protected AA_2 derivatives using TBTU, HOBt, and DIPEA as coupling reagents (Scheme 2). In the first case, basic deprotection led to the free amino derivatives, which were coupled with a third amino acid or salified with TFA to afford more water-soluble derivatives. In the case of the Boc-protected compounds, the acidic condition used to remove the Boc protective group directly led the desired trifluoroacetic salts derivatives. The side chains composition of the synthesized anthraquinones is reported in Table 1.

Fluorescence Melting Assays. All test derivatives were evaluated for their ability to bind and stabilize G-quadruplex structures by fluorescence melting measurements.

We used an oligonucleotide corresponding to the human telomeric sequence labeled at the 5′-end with a quencher (dabcyl) and at the 3′-end with a fluorophore (fluorescein). When the oligonucleotide folds into an intramolecular G-quadruplex, these groups are in close proximity, and as a consequence, the fluorescence is quenched. When DNA melts, the strands fall far apart and a large increase in fluorescence occurs. This system allows us to easily monitor DNA folding/unfolding processes upon temperature variation.[18,19] Drug binding to DNA affects nucleic acid stability, hence its melting temperature (T_m). Since a correlation exists between the observed T_m shift (ΔT_m) and the DNA binding affinity of structurally related binders, this allows us to build a relative G-quadruplex affinity ranking order.[20] Thus, the melting profile of the oligonucleotide (T_m in the absence of ligand 57.2 °C) was recorded in the presence of increasing anthracenedione concentration (0−20 μM, Supporting Information). The ΔT_m values determined for all derivatives at 1 μM concentration are included in Table 3. The behavior of the test ligands toward telomeric G-quadruplex is generally conserved among the 5 tested families (Figure 1A). In particular, it emerged that the introduction of an amino acid between AA_1 and the charged residue sensibly reduces the G-quadruplex stabilizing efficiency. This effect is more significant when shifting from Gly or Ala to become maximal with Phe. This suggests that the flexibility and bulkiness of the linker is relevant for G-quadruplex interaction, likely favoring the proper localization of the positive charge on the polyanionic target.

Fluorescence melting analysis was used also to evaluate the preference of the new derivatives for G-quadruplex structure vs duplex DNA arrangement by using a random double-stranded sequence (5′-GTGAGATACCGACAGAAG, T_m 52.8 °C). The ΔT_m value determined for all derivatives at 1 μM concentration are included in Table 3 and plotted in Figure 1B. All tested compounds stabilize double-stranded DNA to a considerably lesser extent than G-quadruplex. Interestingly, dsDNA recognition is more prominent for derivatives of the **D** and **E** families that bear substituents at positions 1,5 or 1,8. Comparison of melting data on different DNA folding underlines that for derivatives containing the Phe-Lys dipeptide (compounds with side chain -**16**) relevant thermal stabilization occurs only with the G-quadruplex structure, which suggests remarkable selectivity in the drug−DNA recognition process.

For a direct comparison of the ligand-mediated DNA stabilization on the two tested folds, melting profiles of the telomeric sequence were recorded in the presence of variable amounts of its complementary strand (Figure 2).[21] The results confirmed that the Phe-Lys containing analogues are the most selective for G-quadruplex structures. Indeed, they are the only derivatives able to increment the melting temperature of the quadruplex form when the double-stranded arrangement is highly favored (presence of an excess of complementary C-rich strand).

Circular Dichroism. The peculiar signature of the CD spectrum of the G-quadruplex folded telomeric sequence Tel22 is well-characterized. In potassium-containing buffer, it shows a positive band at 295 nm with a shoulder at 260 nm, which corresponds to a mixed type (antiparallel and parallel) strand arrangement.[22] Tel22 dichroic response was extensively modified in the presence of increasing concentrations of our ligands, thus confirming that they are effective binders (Figure 3). In particular, CD titrations confirmed a strong binding affinity for all tested compounds to G-quadruplex: saturation occurred at comparable drug/DNA ratio and indicated the binding of two anthraquinones per G-quadruplex unit (Figure 3C). In analogy to most of the known G-quadruplex interacting agents, this supports the stacking of one ligand on both terminal tetrads of the G-quadruplex.

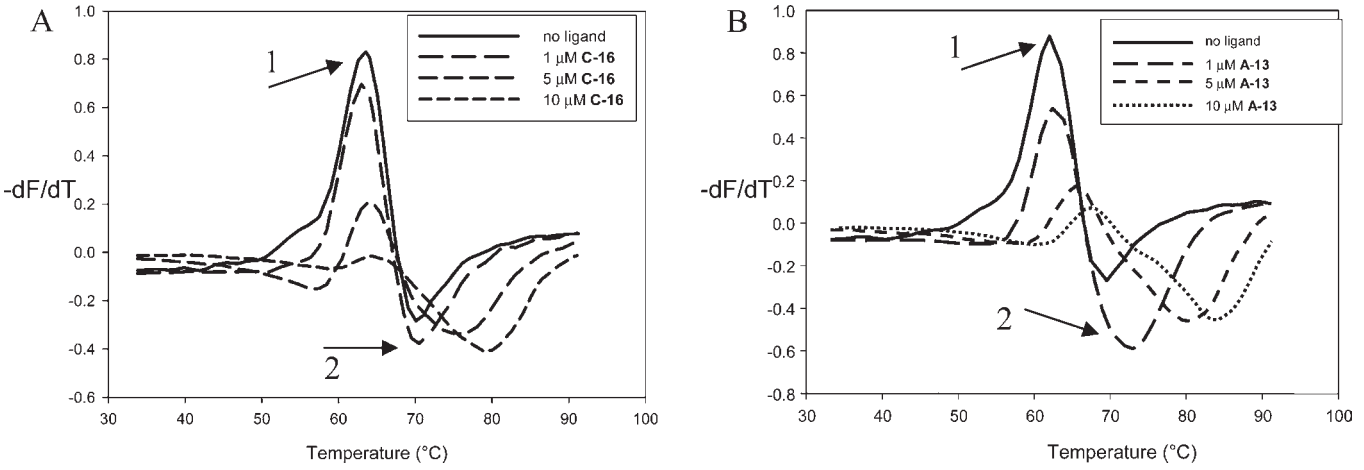

Figure 2. First derivatives of the melting profiles of a G-quadruplex folded telomeric sequence (0.25 μM) recorded in the presence of an excess (20-fold) of its complementary strand in 50 mM KCl. Arrows 1 and 2 indicate the shifts of the duplex and quadruplex melting transitions, respectively. Panels A and B refer to addition of **C-16** and **A-13**, respectively.

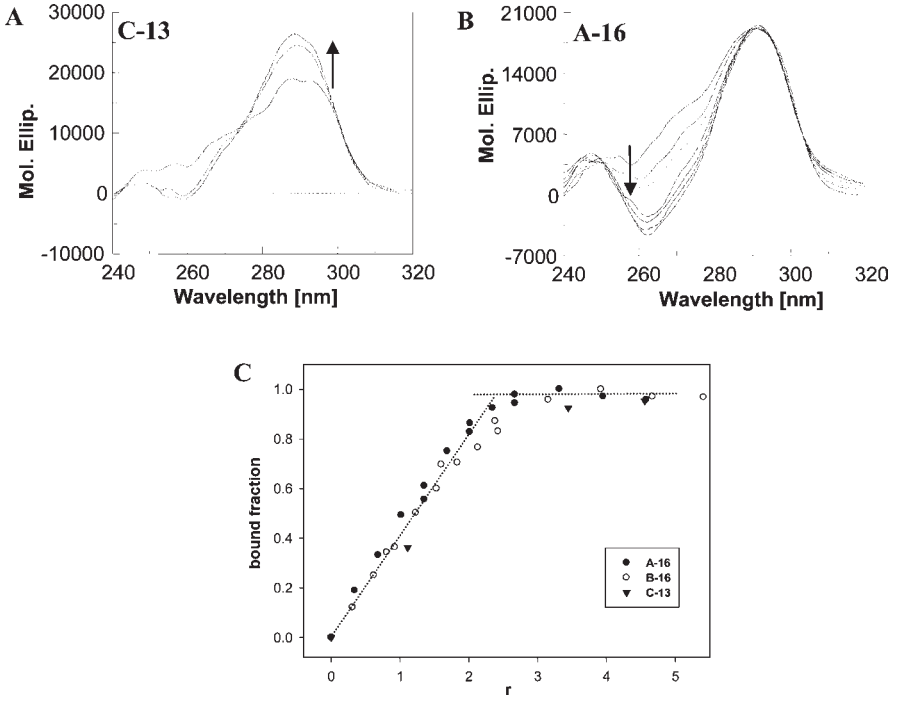

Figure 3. Circular dichroism spectra of Tel22 (4 μM) recorded in the presence/absence of anthraquinone derivatives in 10 mM Tris, 50 mM KCl, pH 7.4, 25 °C. Arrows indicate the changes induced by increasing concentrations of **C-13** (A) and **A-16** (B). The variation of the fraction of bound Tel22 upon increasing ligand/DNA ratio (r) determined by CD titrations is described in panel C.

Generally, an increment in the positive band at 295 nm is observed suggesting a stabilization of the antiparallel components of the G-quadruplex nucleic acid structure. Interestingly, the Phe-Lys substituted derivatives (compounds with side chain −**16**) induced the most notable variations at 260 nm. Since the tested derivatives showed comparable absorption spectra and, additionally, no significant induced CD in the drug absorption range, we are confident in assigning the observed differences primarily to slightly different binding modes.

When similar measurements were performed using a double-stranded DNA (we used calf thymus DNA, ctDNA, due to its similarity to the human nucleic acid composition) as the target, we still found odd behaviors for derivatives containing the Phe-Lys sequence (Figure 4B). In general (see, for example, the series -**13**, Figure 4A), an increment of the DNA dichroic intensity at 275 nm occurred which sustains intercalation into the double helix. On the contrary, all Phe-Lys containing derivatives showed a reduction in the DNA band intensities at both 275 and 245 nm (Figure 4B). Although this confirms a DNA−ligand interaction, it suggests that intercalation is probably not the principal binding mechanism. Generally, DNA intercalation of anthraquinone derivatives disubstituted at positions 1,5, 2,6, and 2,7 occurs by a threading mechanism with the planar system being oriented more or less perpendicularly to the base pair longest dimension

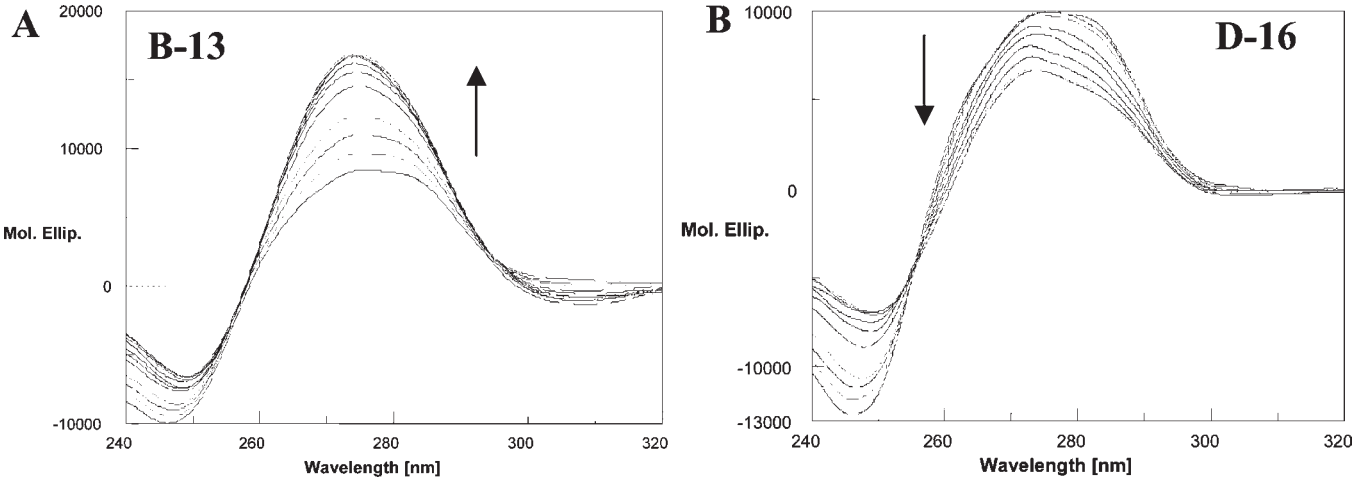

Figure 4. Circular dichroism spectra of ctDNA (88 μM) recorded in the presence of increasing concentrations of anthraquinone derivatives in 10 mM Tris, 50 mM KCl, pH 7.4, 25 °C.

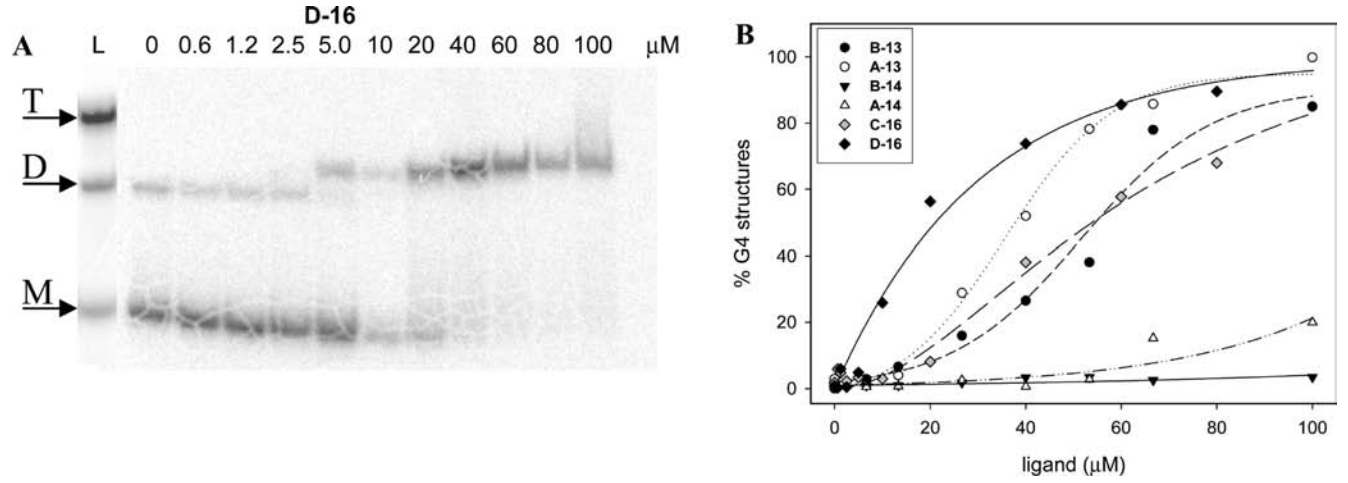

Figure 5. Induction of G-quadruplex structure by selected ligands in 10 mM Tris, 50 mM KCl, pH 7.4, 25 °C. Panel A: variation of the electrophoretic mobility of the unfolded oligonucleotide 2GGG (10 μM) upon addition of **D-16** due to its conversion into a dimeric G-quadruplex. A marker (L) for the monomeric (M), dimeric (D), or tetrameric (T) form is included. Panel B: plot of % of G-quadruplex forms promoted by increasing ligands concentrations.

and one side chain located in each DNA groove.[23] We can infer that the presence of the bulky Phe residue prevents threading of the side chains between the base pairs. As a result, an external binding mode promoted by the presence of highly charged residues in the side chains can be favored. This is particularly true for **B-16**, since it converts dsDNA into an insoluble compact form also at low ligand/DNA ratio.

Electromobility Shift Assay. Electromobility shift assays were performed to evaluate the ability of tested molecules to induce G-quadruplex folding of the human telomeric sequence (Figure 5).

In these experiments, we used an oligonucleotide which contains two repeats of the human telomeric sequence TTAGGG (2GGG). This sequence can form intermolecular (dimeric or tetrameric) G-quadruplex structures that migrate more slowly than the nonstructured single-stranded DNA (Figure 5A). None of our tested derivatives promoted the formation of tetrameric G-quadruplexes. However, some of them were able to promote induction of a dimeric G-quadruplex arrangement of the 2GGG sequence depending upon side chain composition.

Negligible conversion of oligomer 2GGG to an intermolecular G-quadruplex structure was observed when an amino acid is interposed between the AA_1 and the N-terminal Lys residue (compare compounds -**13** with homologues -**14**; Figure 5B). Interestingly, the presence of a Phe (compounds with side chain -**16**) that was observed to comparably reduce the thermal stability of the DNA—ligand complex, allows retention of effective G-quadruplex induction, the most successful being derivative **D-16** with side chains located at positions 1,5. These data further support a peculiar behavior associated to the presence of a Phe residue in the side chains.

Enzymatic Inhibition and Cell Toxicity Assays. To assess possible interference of test drugs with enzymatic processes involving DNA, we examined the effects of peptidyl anthraquinones upon DNA amplification and elongation mediated by *Taq* polymerase and telomerase, respectively. In addition, we determined the cytotoxic activity of our compounds by MTT assay on HeLa human cancer cells. The results are summarized in Table 2.

Table 2. *Taq* Polymerase Inhibition, Telomerase Inhibition and Cell Cytotoxicity (MTT on HeLa cell line) Produced by the Test Anthraquinone-Aminoacyl Conjugates

	IC_{50} (μM)		
compound	*Taq* polymerase[a]	telomerase[a]	HeLa
A-13	5	0.8	27 ± 1.2
A-14	30	1.9	25 ± 1.5
A-15	15	0.9	57 ± 1.1
A-16	15	7.0	41 ± 1.8
B-13	10	0.8	14 ± 2.0
B-14	22	6.5	28 ± 2.7
B-15	>40	3.8	49 ± 2.3
B-16	20	7.1	57 ± 2.7
C-13	2.5	1.5	31 ± 2.6
C-14	5	3	23 ± 5.0
C-16	20	10	18 ± 3.0
D-13	2.0	n.o.[b]	2.6 ± 0.3
D-14	5	2.5	27 ± 3.3
D-16	15	4	2.5 ± 0.2
E-13	5	n.o.	1.2 ± 0.3
E-14	>40	18	1.8 ± 0.1
E-16	>40	20	6.0 ± 0.2

[a] Experimental error ±4%. [b] n.o., not observed up to 40 μM.

Table 3. Increase of the Melting Temperature (ΔT_m °C) Produced by Tested Derivatives (1 μM) on a G-Quadruplex Folded Telomeric Sequence or Double-Stranded DNA in the Presence of 50 mM KCl[a]

compound	G-quadruplex telomeric sequence	double-stranded DNA
A-13	15.6	2.6
A-14	11.9	1.8
A-15	11.0	4.0
A-16	7.1	0.9
B-13	13.7	2.5
B-14	7.4	2.3
B-15	8.2	3.6
B-16	7.4	0.3
C-13	9.5	1.4
C-14	5.2	1.0
C-16	3.9	0.1
D-13	20.1	4.6
D-14	14.1	4.5
D-16	15.7	1.2
E-13	17.6	4.5
E-14	12.1	2.2
E-16	4.3	0.1

[a] DNA concentration was 0.25 μM, experimental error ±0.4°C.

For all active derivatives, inhibition of telomerase-mediated DNA elongation occurred generally at lower concentrations in comparison to DNA amplification. From these data, selective telomerase inhibition by our ligands cannot be firmly established from the present results, since competition between telomerase elongation and *Taq* polymerase amplification can occur.[24] In any event, the observed modulation of telomerase elongation is well-related to G-quadruplex binding thermodynamics as shown by the almost linear dependence of IC_{50} for telomerase inhibition from $\Delta T_m/T_m$, where T_m is the melting temperature in the presence of saturating amounts of the drug (Figure 6).[15] On the contrary, the G-quadruplex affinity data are poorly related to cell cytotoxicity.

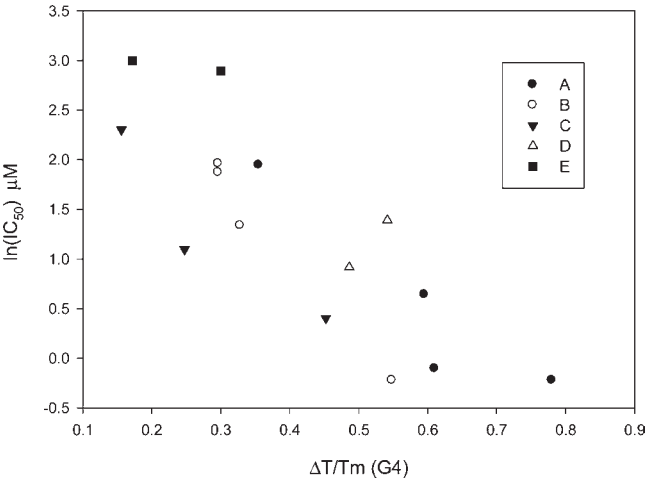

Figure 6. Correlation between Telomerase elongation inhibition (IC50) and thermal stabilization ($\Delta T_m/T_m$) of telomeric G-quadruplex measured for all tested derivatives.

In turn, *Taq* inhibition correlates with double-stranded DNA stabilization and, to a lesser extent, to cell cytotoxicity. In this case, the most active compounds are 1,5 and 1,8 derivatives that, indeed, were confirmed to be the most efficient DNA intercalators. We can infer that a short-term drug exposure causes an interference with processing of the nucleic acid that ultimately is translated into a cytotoxic signal.

Accordingly, poor dsDNA binders like **B-16** and **C-16** are poorly cytotoxic. Interestingly, however, both latter anthraquinones stimulated β-galactosidase activity in HeLa cells treated for 240 h at subcytotoxic concentrations without appreciably affecting cell growth (Figure 7), which is consistent with an induction of delayed senescence. However, when the more cytotoxic 1,5 regioisomer (**D-16**) was used in the same conditions, senescence induction was clearly coupled to a significant drop in cell growth. These results further emphasize the peculiar behavior of the Phe containing derivatives also at a cellular level.

DISCUSSION

The DNA binding properties of 9,10-anthracenedione derivatives have been extensively studied in the past,[25] highlighting that the nature of the side chains as well as their relative position are critical factors to address their DNA binding mode.[12,14] Conceivably, the presence of positively charged groups in the side chains greatly favors the binding process although generally regardless of the sequence/structure they bind to. However, provided that different DNA arrangements locate phosphate groups at different relative distances, in principle, charged interactions could be used for selective recognition if the binders' chains are appropriately positioned with reference to the macromolecule. Here, we showed for all test derivatives that increasing the distance of the lysyl residue from the anthracenedione ring system invariantly decreases G-quadruplex affinity. This is probably due to the fact that the positive charges are, on average, located more

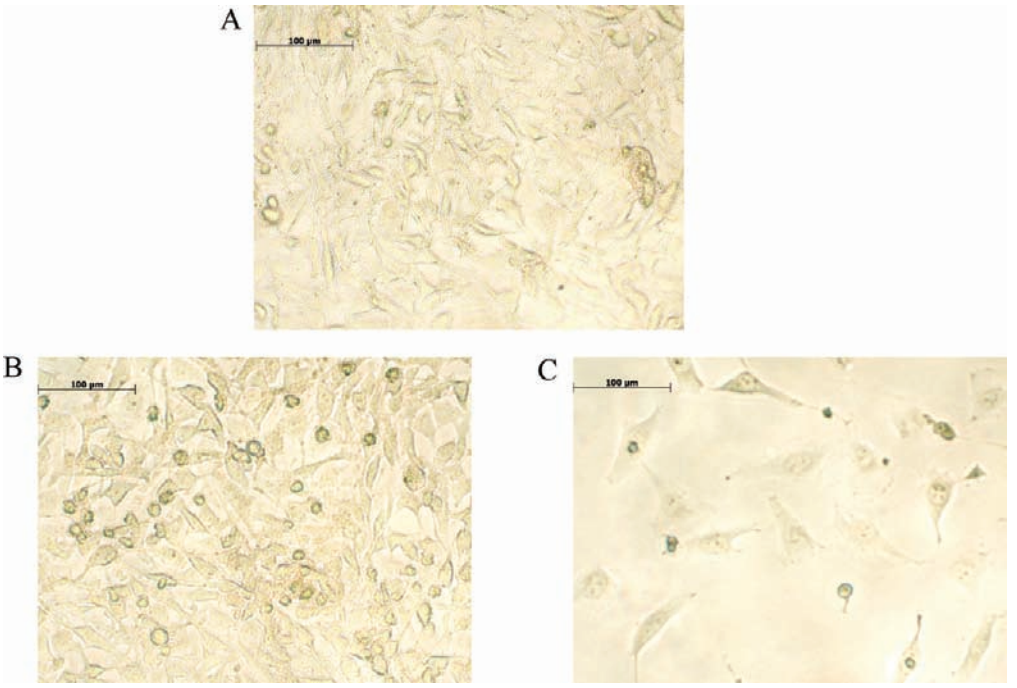

Figure 7. β-Galactosidase activity of HeLa cell when untreated (A) or treated with **C-16** (B) or **D-16** (C) for 144 h.

distant from the anionic sites of DNA. Hence, compounds having longer side chains with clear additional flexibility (possibly rendered less effective by the rigid peptide bonds) cannot get closer to the target counterions than the starting congeners. Apparently, introduction of the bulky Phe residue is even more detrimental than the presence of a glycine or alanine linker. However, Phe-containing derivatives turn out to be selective for G-quadruplex because, unlike other congeners, they hardly bind to double-stranded DNA, yet they are still able to stack on top of the terminal tetrads without requiring significant DNA distortion.

Shifting side chains from position 2,6 or 2,7 (families **A**, **B**, and **C**) to 1,5 (family **D**) or, to a lesser extent, to 1,8 (family **E**) helps increasing G-quadruplex stabilization, but at the same time, it promotes effective binding to dsDNA. Interestingly, this behavior is distinct from the one we reported for anthracene derivatives of the bisanthrene family.[26] In fact, among those anthracene derivatives, the shift of the side chains from 2,6 to 1,5 positions slightly incremented G-quadruplex recognition but remarkably disfavored double-stranded DNA binding. This suggests that the presence of the carbonyl groups causes different orientations of the anthracenedione vs anthracene ring when bound to G-quadruplex DNA.

As far as the biochemical and biological results, we found pronounced cell growth inhibition when the double-stranded DNA recognition process is efficient. On the other hand, the onset of senescence in cancer cells is particularly evident with the more telomerase-sensitive derivatives, which produce selective G-quadruplex stabilization. In conclusion, although we did not succeed in effectively improving G-quadruplex binding, we were able to remarkably uncouple quadruplex vs duplex affinity, which gives useful hints for future design of compounds exhibiting selectivity and efficient tetraplex-inducing properties at the same time.

■ ASSOCIATED CONTENT

Supporting Information. Structural properties, synthetic procedures, and analytical data (NMR, HRMS, and combustion) for new compounds. This material is available free of charge via the Internet at http://pubs.acs.org.

■ AUTHOR INFORMATION

Corresponding Author
*E-mail: claudia.sissi@unipd.it, tel.: +39-049 8275711.

■ ACKNOWLEDGMENT

This work was supported by AIRC (Associazione Italiana per la Ricerca sul Cancro) grant # 5286.

■ ABBREVIATIONS:

AA, amino acid; AQ, anthraquinones; β-Ala, β-alanine; TBTU, *O*-(benzotriazol-1-yl)-*N*,*N*,*N*′,*N*′-tetramethyluronium tetrafluoroborate; HOBt, hydroxybenzotriazole; DIPEA, diisopropylethylamine; TFA, trifluoroacetic acid; DMF, dimethylformamide; EGTA, ethylene glycol-*bis*(β-aminoethyl)-*N*,*N*,*N*′,*N*′-tetraacetic acid; DMSO, dimethylsulfoxide; FAM, fluorescein; T_m, melting temperature; CD, circular dichroism; MTT, (3-(4,5-dimethylthiazol-2-yl)-2,5-diphenyltetrazolium; PCR, polymerase chain reaction; TRAP, telomerase repeat amplification protocol

■ REFERENCES

(1) O'Sullivan, R. J., and Karlseder, J. (2010) Telomeres: protecting chromosomes against genome instability. *Nat. Rev. Mol. Cell Biol. 11*, 171–81.

(2) Watson, J. D. (1972) Origin of concatemeric T7 DNA. *Nat. New Biol. 239*, 197–201.

(3) Shay, J. W., Wright, W. E., and Werbin, H. (1991) Defining the molecular mechanisms of human cell immortalization. *Biochim. Biophys. Acta 1072*, 1–7.

(4) Shay, J. W., and Bacchetti, S. (1997) A survey of telomerase activity in human cancer. *Eur. J. Cancer 33*, 787–91.

(5) Greider, C. W., and Blackburn, E. H. (1985) Identification of a specific telomere terminal transferase activity in Tetrahymena extracts. *Cell 43*, 405–13.

(6) Folini, M., Gandellini, P., and Zaffaroni, N. (2009) Targeting the telosome: therapeutic implications. *Biochim. Biophys. Acta 1792*, 309–16.

(7) Neidle, S. (2010) Human telomeric G-quadruplex: the current status of telomeric G-quadruplexes as therapeutic targets in human cancer. *Febs J. 277*, 1118–25.

(8) Davis, J. (2004) G-quartets 40 years later: from 5′-GMP to molecular biology and supramolecular chemistry. *Angew. Chem. 43*, 668–698.

(9) De Cian, A., Lacroix, L., Douarre, C., Temime-Smaali, N., Trentesaux, C., Riou, J. F., and Mergny, J. L. (2008) Targeting telomeres and telomerase. *Biochimie 90*, 131–155.

(10) Neidle, S. (2009) The structures of quadruplex nucleic acids and their drug complexes. *Curr. Opin. Struct. Biol. 19*, 239–50.

(11) Monchaud, D., and Teulade-Fichou, M. P. (2008) A hitchhiker's guide to G-quadruplex ligands. *Org. Biomol. Chem. 6*, 627–36.

(12) Perry, P. J., Gowan, S. M., Reszka, A. P., Polucci, P., Jenkins, T. C., Kelland, L. R., and Neidle, S. (1998) 1,4- and 2,6-disubstituted amidoanthracene-9,10-dione derivatives as inhibitors of human telomerase. *J. Med. Chem. 41*, 3253–60.

(13) Perry, P. J., Read, M. A., Davies, R. T., Gowan, S. M., Reszka, A. P., Wood, A. A., Kelland, L. R., and Neidle, S. (1999) 2,7-Disubstituted amidofluorenone derivatives as inhibitors of human telomerase. *J. Med. Chem. 42*, 2679–84.

(14) Perry, P. J., Reszka, A. P., Wood, A. A., Read, M. A., Gowan, S. M., Dosanjh, H. S., Trent, J. O., Jenkins, T. C., Kelland, L. R., and Neidle, S. (1998) Human telomerase inhibition by regioisomeric disubstituted amidoanthracene-9,10-diones. *J. Med. Chem. 41*, 4873–84.

(15) Zagotto, G., Sissi, C., Lucatello, L., Pivetta, C., Cadamuro, S. A., Fox, K. R., Neidle, S., and Palumbo, M. (2008) Aminoacyl-anthraquinone conjugates as telomerase inhibitors: synthesis, biophysical and biological evaluation. *J. Med. Chem. 51*, 5566–74.

(16) Zagotto, G., Sissi, C., Moro, S., Dal Ben, D., Parkinson, G. N., Fox, K. R., Neidle, S., and Palumbo, M. (2008) Amide bond direction modulates G-quadruplex recognition and telomerase inhibition by 2,6 and 2,7 bis-substituted anthracenedione derivatives. *Bioorg. Med. Chem. 16*, 354–61.

(17) Dahan, A., Ashkenazi, T., Kuznetsov, V., Makievski, S., Drug, E., Fadeev, L., Bramson, M., Schokoroy, S., Rozenshine-Kemelmakher, E., and Gozin, M. (2007) Synthesis and evaluation of a pseudocyclic tristhiourea-based anion host. *J. Org. Chem. 72*, 2289–96.

(18) De Cian, A., Guittat, L., Kaiser, M., Sacca, B., Amrane, S., Bourdoncle, A., Alberti, P., Teulade-Fichou, M. P., Lacroix, L., and Mergny, J. L. (2007) Fluorescence-based melting assays for studying quadruplex ligands. *Methods 42*, 183–95.

(19) Risitano, A., and Fox, K. R. (2003) Stability of intramolecular DNA quadruplexes: comparison with DNA duplexes. *Biochemistry 42*, 6507–13.

(20) Crothers, D. M. (1971) Statistical thermodynamics of nucleic acid melting transitions with coupled binding equilibria. *Biopolymers 10*, 2147–60.

(21) Darby, R. A., Sollogoub, M., McKeen, C., Brown, L., Risitano, A., Brown, N., Barton, C., Brown, T., and Fox, K. R. (2002) High throughput measurement of duplex, triplex and quadruplex melting curves using molecular beacons and a LightCycler. *Nucleic Acids Res. 30*, e39.

(22) Ambrus, A., Chen, D., Dai, J., Bialis, T., Jones, R. A., and Yang, D. (2006) Human telomeric sequence forms a hybrid-type intramolecular G-quadruplex structure with mixed parallel/antiparallel strands in potassium solution. *Nucleic Acids Res. 34*, 2723–35.

(23) Tanious, F. A., Jenkins, T. C., Neidle, S., and Wilson, W. D. (1992) Substituent position dictates the intercalative DNA-binding mode for anthracene-9,10-dione antitumor drugs. *Biochemistry 31*, 11632–40.

(24) De Cian, A., Cristofari, G., Reichenbach, P., De Lemos, E., Monchaud, D., Teulade-Fichou, M. P., Shin-Ya, K., Lacroix, L., Lingner, J., and Mergny, J. L. (2007) Reevaluation of telomerase inhibition by quadruplex ligands and their mechanisms of action. *Proc. Natl. Acad. Sci. U. S. A. 104*, 17347–52.

(25) Lown, J. W. (1993) Anthracycline and anthraquinone anticancer agents: current status and recent developments. *Pharmacol. Ther. 60*, 185–214.

(26) Folini, M., Pivetta, C., Zagotto, G., De Marco, C., Palumbo, M., Zaffaroni, N., and Sissi, C. (2010) Remarkable interference with telomeric function by a G-quadruplex selective bisantrene regioisomer. *Biochem. Pharmacol. 79*, 1781–90.

Uncoupling of G-quadruplex and double stranded DNA recognition by symmetrically disubstituted anthraquinones

Giuseppe Zagotto, Antonio Ricci, Elena Vasquez, Andrea Sandoli, Silvia Benedetti, Manlio Palumbo, Claudia Sissi*

Department of Pharmaceutical Sciences, University of Padova, via Marzolo, 5, 30039, Padova, Italy

SUPPORTING INFORMATION

Table of Contents

Experimental Part.

Synthesis and characterization of compounds **A/B/C-1,2,3,4,7,8 A-5,6,13,15** and their precursor were described by us in a previous paper.[1]

Fmoc-glycine-Cl (3)

Obtained from **(1)** according to the general procedure for the synthesis of the acyl chloride of an aminoacid. Yield: 88%. **^{1}H-NMR** (d_6-DMSO; 300 MHz): δ 7.96 (d, 2H, J=7.2 Hz), 7.68 (d, 2H, J=7.2 Hz), 7.72 (t, 1H, J=6.1 Hz) 7.49 (t, 2H, J=7.2 Hz), 7.40 (t, 2H, J=7.2 Hz), 4.37 (d, 2H, J=6.4 Hz), 4.30 (t, 1H, J=6.4 Hz), 3.37 (d, 2H, J=6.1 Hz).

Fmoc-β-alanine-Cl (4)

Obtained from **(2)** according to the general procedure for the synthesis of the acyl chloride of an aminoacid. Yield: 85%. **^{1}H-NMR** (d_6-DMSO; 300 MHz): δ 7.89 (d, 2H, J=7.4 Hz), 7.68 (d, 2H, J=7.2 Hz), 7.41 (t, 2H, J=7.4 Hz), 7.32 (t, 2H; J=7.2 Hz), 4.28 (d, 2H, J=6.1 Hz), 4.2 (t, 1H, J=6.1 Hz), 3.20-3.17 (m, 2H), 2.37 (t, 2H, J=7.0 Hz).

1,5-[Fmoc-β-Alanine-amidyl]-anthracen-9,10-dione (D-1).

Obtained from 1,5-diaminoanthraquinone according to the general procedure for coupling ***via*** acyl chloride. Yield: 84%. **^{1}H-NMR** (d_6-DMSO; 300 MHz): δ 10.78 (s, 2H), 8.44 (d, 2H, J=2.2 Hz), 8.19 (d, 2H, J=8.6 Hz), 8.04 (dd, 2H, J=2.2 Hz, J=8.6 Hz), 7.88 (dd, 4H, J=0.9, J=7.4 Hz), 7.70 (dd, 4H, J=0.9 Hz, J= 7.4 Hz), 7.56 (t, 2H, J=5.7 Hz), 7.36 (td, 4H, J=0.9 Hz, J= 7.4 Hz), 7.25 (td, 4H, J=0.9 Hz, J=7.4 Hz), 4.82 (d, 4H, J=5.7 Hz), 4.23 (bt, 2H), 3.39 (m, 4H), 2.60 (t, 4H, J=6.6 Hz). **HRMS** (ESI) ***m/z*** for $C_{52}H_{42}N_2O_8$: ($[M+H^+]^+$) calcd 823.3014, found 823.3032; ($[M+2H^+]^{2+}$) calcd 412.1543, found 412.1578.

1,8-[Fmoc-β-Alanine-amidyl]-anthracen-9,10-dione (E-1).

Obtained from 1,8-diaminoanthraquinone according to the general procedure for coupling ***via*** acyl chloride. Yield: 85%. **^{1}H-NMR** (d_6-DMSO; 300 MHz): δ 10.82 (s, 2H), 8.47 (d, 2H, J=2.3 Hz), 8.16 (d, 2H, J=8.8 Hz), 8.06 (dd, 2H, J=2.3 Hz, J=8.8 Hz), 7.81 (dd, 4H, J=1.0, J=7.4 Hz), 7.68 (dd, 4H, J=1.0 Hz, J= 7.4 Hz), 7.53 (t, 2H, J=5.7 Hz), 7.40 (td, 4H, J=1.0 Hz, J= 7.4 Hz), 7.29 (td, 4H, J=0.9 Hz, J=7.4 Hz), 4.78 (d, 4H, J=5.7 Hz), 4.18 (bt, 2H), 3.32 (m, 4H), 2.62 (t, 4H, J=6.6 Hz). **HRMS** (ESI) ***m/z*** for $C_{52}H_{42}N_2O_8$: ($[M+H^+]^+$) calcd 823.3014, found 823.3033; ($[M+2H^+]^{2+}$) calcd 412.1543, found 412.1569.

1,5-[β-Alanine-amidyl]-anthracen-9,10-dione (D-2)

Obtained from **C-1** according to the general procedure for deprotection of the Fmoc group. Yield: 88%. ^{1}H-NMR (d_6-DMSO; 300 MHz): δ 10.80 (s, 2H), 8.49 (d, 2H, J=2.3 Hz), 8.23 (d, 2H, J=8.5 Hz), 7.89 (dd, 2H, J=2.3 Hz, J=8.6 Hz), 6.46 (bs, 4H), 3.36-3.25 (m, 4H). **HRMS** (ESI) ***m/z*** for $C_{22}H_{22}N_2O_4$: ($[M+H^+]^+$) calcd 381.1557, found 381.1575; ($[M+2H^+]^{2+}$) calcd 191.0815, found 191.0840.

1,8-[β-Alanine-amidyl]-anthracen-9,10-dione (E-2)

Obtained from **D-1** according to the general procedure for deprotection of the Fmoc group. Yield: 87%. ^{1}H-NMR (d_6-DMSO; 300 MHz): δ 10.76 (s, 2H), 8.49 (d, 2H, J=2.3 Hz), 8.23 (d, 2H, J=8.5 Hz), 7.89 (dd, 2H, J=2.3 Hz, J=8.6 Hz), 6.46 (bs, 4H), 3.36-3.25 (m, 4H). **HRMS** (ESI) ***m/z*** for $C_{22}H_{22}N_2O_4$: ($[M+H^+]^+$) calcd 381.1557, found 381.1569; ($[M+2H^+]^{2+}$) calcd 191.0815, found 191.0838.

1,5-[Alanine-β-Alanine-amidyl]-anthracen-9,10-dione (D-4)

Obtained from **D-3** according to the general procedure for deprotection of the Fmoc group. Yield: 89%. ^{1}H-NMR (d_6-DMSO; 300 MHz): δ 10.69 (s, 2H), 8.45 (d, 2H, J=1.9 Hz), 8.12 (d, 2H, J=8.5 Hz), 8.02 (dd, 2H, J=8.5 Hz, J=1.9 Hz), 4.05-3.93 (m, 2H), 3.46-3.35 (m, 4H), 2.59 (t, 4H, J=6.1 Hz), 1.27 (d, 6H, J=7.4 Hz). **HRMS** (ESI) ***m/z*** for $C_{26}H_{30}N_6O_6$: ($[M+H^+]^+$) calcd 523.2300, found 523.2313; ($[M+2H^+]^{2+}$) calcd 262.1186, found 262.1196.

1,8-[Alanine-β-Alanine-amidyl]-anthracen-9,10-dione (E-4)

Obtained from **E-3** according to the general procedure for deprotection of the Fmoc group. Yield: 91%. ^{1}H-NMR (d_6-DMSO; 300 MHz): δ 10.73 (s, 2H), 8.45 (d, 2H, J=1.9 Hz), 8.12 (d, 2H, J=8.5 Hz), 8.02 (dd, 2H, J=8.5 Hz, J=1.9 Hz), 4.05-3.93 (m, 2H), 3.46-3.35 (m, 4H), 2.59 (t, 4H, J=6.1 Hz), 1.27 (d, 6H, J=7.4 Hz). **HRMS** (ESI) ***m/z*** for $C_{26}H_{30}N_6O_6$: ($[M+H^+]^+$) calcd 523.2300, found 523.2317; ($[M+2H^+]^{2+}$) calcd 262.1186, found 262.1199.

2,6-[Glycine-β-Alanine-amidyl]-anthracen-9,10-dione (B-6)

Obtained from **A-5** according to the general procedure for deprotection of the Fmoc group. Yield: 91%. ^{1}H-NMR (d_6-DMSO; 300 MHz): δ 10.63 (s, 2H), 8.48 (d, 2H, J=1.7 Hz), 8.11 (d, 2H, J=8.6 Hz), 8.03 (dd, 2H, J=8.6 Hz, J=1.7 Hz), 3.54 (s, 4H, J=6.1 Hz), 3.39 (t, 4H, J=6.4 Hz), 2.62 (t, 4H, J=6.4 Hz). **HRMS** (ESI) ***m/z*** for $C_{24}H_{26}N_6O_6$: ($[M+H^+]^+$) calcd 495.1987, found 495.1992; ($[M+2H^+]^{2+}$) calcd 248.1030, found 248.1031.

1,5-[Phenylalanine-β-Alanine-amidyl]-anthracen-9,10-dione (D-8)

Obtained from **D-7** according to the general procedure for deprotection of the Fmoc group. Yield: 87%. ^{1}H-NMR (d_6-DMSO; 300 MHz): δ 10.76 (s, 2H), 8.42 (d, 2H, J=1.9 Hz), 8.10 (d, 2H, J=8.5 Hz), 8.03 (dd, 2H, J=8.5 Hz, J=1.9 Hz), 7.24-7.11 (m, 10H), 4.2 (td, 2H, J=3.4 Hz, J=10.3 Hz), 3.42 (m, 4H), 2.96 (dd, 2H, J=4.2 Hz, J=13.3 Hz), 2.79 (dd, 2H, J=10.3 Hz, J=13.3 Hz). **HRMS** (ESI)

m/z for $C_{38}H_{38}N_6O_6$: ($[M+H^+]^+$) calcd 675.2926, found 675.2942; ($[M+2H^+]^{2+}$) calcd 338.1499, found 338.1509.

1,8-[Phenylalanine-β-Alanine-amidyl]-anthracen-9,10-dione (E-8)

Obtained from **E-7** according to the general procedure for deprotection of the Fmoc group. Yield: 88%. ^{1}H-NMR (d_6-DMSO; 300 MHz): δ 10.78 (s, 2H), 8.42 (d, 2H, J=1.9 Hz), 8.10 (d, 2H, J=8.5 Hz), 8.03 (dd, 2H, J=8.5 Hz, J=1.9 Hz), 7.24-7.11 (m, 10H), 4.2 (td, 2H, J=3.4 Hz, J=10.3 Hz), 3.42 (m, 4H), 2.96 (dd, 2H, J=4.2 Hz, J=13.3 Hz), 2.79 (dd, 2H, J=10.3 Hz, J=13.3 Hz). **HRMS** (ESI) ***m/z*** for $C_{38}H_{38}N_6O_6$: ($[M+H^+]^+$) calcd 675.2926, found 675.2945; ($[M+2H^+]^{2+}$) calcd 338.1499, found 338.1512.

1,5-[Fmoc-Alanine-β-Alanine-amidyl]-anthracen-9,10-dione (D-3)

Obtained from **D-2** according to the general procedure for coupling ***via*** TBTU. Yield: 88%. ^{1}H-NMR (d_6-DMSO; 300 MHz): δ 10.78 (s, 2H), 8.45 (d, 2H, J=1.9 Hz), 8.10 (d, 2H, J=8.5 Hz), 8.02 (dd, 2H, J=8.5 Hz, J=1.9 Hz), 7.83 (d, 4H, J=7.3 Hz), 7.49 (d, 4H, J=7.3 Hz), 7.39 (t, 4H, J=7.3 Hz), 7.37 (t, 4H, J=7.3 Hz), 4.19 (d, 4H, J=5.4 Hz), 4.14 (t, 2H, J=5.4 Hz), 4.05-3.91 (m, 2H), 3.43-3.31 (m, 4H), 2.59 (t, 4H, J=6.1 Hz), 1.27 (d, 6H, J=7.4 Hz). **HRMS** (ESI) ***m/z***: for $C_{55}H_{48}N_6O_{10}$: ($[M+H^+]^+$) calcd 953.3505, found 953.3531.

1,8-[Fmoc-Alanine-β-Alanine-amidyl]-anthracen-9,10-dione (E-3)

Obtained from **E-2** according to the general procedure for coupling ***via*** TBTU. Yield: 86%. ^{1}H-NMR (d_6-DMSO; 300 MHz): δ 10.76 (s, 2H), 8.45 (d, 2H, J=1.9 Hz), 8.10 (d, 2H, J=8.5 Hz), 8.02 (dd, 2H, J=8.5 Hz, J=1.9 Hz), 7.83 (d, 4H, J=7.3 Hz), 7.49 (d, 4H, J=7.3 Hz), 7.39 (t, 4H, J=7.3 Hz), 7.37 (t, 4H, J=7.3 Hz), 4.19 (d, 4H, J=5.4 Hz), 4.14 (t, 2H, J=5.4 Hz), 4.05-3.91 (m, 2H), 3.43-3.31 (m, 4H), 2.59 (t, 4H, J=6.1 Hz), 1.27 (d, 6H, J=7.4 Hz). **HRMS** (ESI) ***m/z***: for $C_{55}H_{48}N_6O_{10}$: ($[M+H^+]^+$) calcd 953.3505, found 953.3531.

2,6-[Fmoc-Glycine-β-Alanine-amidyl]-anthracen-9,10-dione (B-5)

Obtained from 2,6-[β-Alanine-amidyl]-anthracen-9,10-dione according to the general procedure for coupling ***via*** TBTU. Yield: 87%. ^{1}H-NMR (d_6-DMSO; 300 MHz): δ 10.63 (s, 2H), 8.46 (d, 2H, J=1.9 Hz), 8.1 (d, 2H, J=8.6 Hz), 8.04 (dd, 2H, J=8.6 Hz, J=1.9 Hz), 7.97 (t, 2H, J=6.1 Hz), 7.86 (d, 4H, J=7.2 Hz), 7.68 (d, 4H, J=8.0 Hz), 7.53 (t, 2H, J=6.1 Hz), 7.39 (t, 4H, J=8.0, J=7.2 Hz), 7.30 (t, 4H, J=8.0 Hz, J=7.2 Hz), 4.25 (d, 4H, J=7.1 Hz), 4.19 (t, 2H, J=7.1 Hz), 3.58 (d, 4H, J=6.1 Hz), 3.39 (m, 2H), 2.65 (t, 4H, J=6.4 Hz). **HRMS** (ESI) ***m/z***: for $C_{53}H_{44}N_6O_{10}$: ($[M+H^+]^+$) calcd 925.3192, found 925.3201.

1,5-[Fmoc-Phenylalanine-β-Alanine-amidyl]-anthracen-9,10-dione (D-7)

Obtained from **D-2** according to the general procedure for coupling ***via*** TBTU. Yield: 86%. ^{1}H-NMR (d_6-DMSO; 300 MHz): δ 10.69 (s, 2H), 8.45 (d, 2H, J=1.9 Hz), 8.10 (d, 2H, J=8.5 Hz), 8.02

(dd, 2H, J=8.5 Hz, J=1.9 Hz), 7.83 (d, 4H, J=7.4 Hz), 7.62 (d, 4H, J=7.4 Hz), 7.37 (t, 4H, J=7.4 Hz), 7.23 (t, 4H, J=7.4 Hz), 7.22-7.13 (m, 10H), 4.23 (td, 2H, J=3.4 Hz, J=10.3 Hz), 4.12 (d, 4H, J=4.7 Hz), 4.02 (t, 2H, J=4.7 Hz), 4.02-3.88 (m, 2H), 2.96 (dd, 2H, J=4.2 Hz, J=13.3 Hz), 2.79 (dd, 2H, J=10.3 Hz, J=13.3 Hz), 2.59 (t, 4H, J=6.1 Hz). **HRMS** (ESI) ***m/z***: for $C_{67}H_{56}N_6O_{10}$: ($[M+H^+]^+$) calcd 1105.4131, found 1105.4156.

1,8-[Fmoc-Phenylalanine-β-Alanine-amidyl]-anthracen-9,10-dione (E-7)

Obtained from **E-2** according to the general procedure for coupling ***via*** TBTU. Yield: 87%. ^{1}H-NMR (d_6-DMSO; 300 MHz): δ 10.72 (s, 2H), 8.45 (d, 2H, J=1.9 Hz), 8.10 (d, 2H, J=8.5 Hz), 8.02 (dd, 2H, J=8.5 Hz, J=1.9 Hz), 7.83 (d, 4H, J=7.4 Hz), 7.62 (d, 4H, J=7.4 Hz), 7.37 (t, 4H, J=7.4 Hz), 7.23 (t, 4H, J=7.4 Hz), 7.22-7.13 (m, 10H), 4.22 (td, 2H, J=3.4 Hz, J=10.3 Hz), 4.12 (d, 4H, J=4.7 Hz), 4.02 (t, 2H, J=4.7 Hz), 4.02-3.88 (m, 2H), 2.96 (dd, 2H, J=4.2 Hz, J=13.3 Hz), 2.79 (dd, 2H, J=10.3 Hz, J=13.3 Hz), 2.59 (t, 4H, J=6.1 Hz). **HRMS** (ESI) ***m/z***: for $C_{67}H_{56}N_6O_{10}$: ($[M+H^+]^+$) calcd 1105.4131, found 1105.4143.

1,5-[Boc-Lysine(Boc)-β-Alanine-amidyl]-anthracen-9,10-dione (D-9)

Obtained from **D-2** according to the general procedure for coupling ***via*** TBTU. Yield: 86%. ^{1}H-NMR (d_6-DMSO; 300 MHz): δ 10.72 (s, 2H), 8.66 (t, 2H, J=5.4 Hz), 8.49 (d, 2H, J=2.0 Hz), 8.17 (d, 2H, J=8.8 Hz), 8.06 (dd, 2H, J=8.8 Hz, J=2.0 Hz), 3.30 (d, 4H, J=5.4 Hz), 3.08 (m, 6H), 2.76 (t, 4H, J=7.5 Hz), 1.70 (m, 4H), 1.52 (m, 4H), 1.39 (m, 4H), 1.35 (s, 36H). **HRMS** (ESI) ***m/z*** for $C_{52}H_{76}N_8O_{14}$: ($[M+H^+]^+$) calcd 1037.5554, found 1037.5571.

1,8-[Boc-Lysine(Boc)-β-Alanine-amidyl]-anthracen-9,10-dione (E-9)

Obtained from **E-2** according to the general procedure for coupling ***via*** TBTU. Yield: 87%. ^{1}H-NMR (d_6-DMSO; 300 MHz): δ 10.74 (s, 2H), 8.66 (t, 2H, J=5.4 Hz), 8.49 (d, 2H, J=2.0 Hz), 8.17 (d, 2H, J=8.8 Hz), 8.06 (dd, 2H, J=8.8 Hz, J=2.0 Hz), 3.30 (d, 4H, J=5.4 Hz), 3.12 (m, 6H), 2.76 (t, 4H, J=7.5 Hz), 1.70 (m, 4H), 1.52 (m, 4H), 1.39 (m, 4H), 1.35 (s, 36H). **HRMS** (ESI) ***m/z*** for $C_{52}H_{76}N_8O_{14}$: ($[M+H^+]^+$) calcd 1037.5554, found 1037.5568.

2,6-[Boc-Lysine-Alanine-Glycine-amidyl]-anthracen-9,10-dione (A-10)

Obtained from 2,6-[Alanine-Glycine-amidyl]-anthracen-9,10-dione according to the general procedure for coupling ***via*** TBTU. Yield: 79%. **^{1}H-NMR** (d_6-DMSO; 300 MHz): δ 10.63 (s, 2H), 8.55 (d, 2H, J=7.5 Hz), 8.48 (d, 2H, J=2.0 Hz), 8.17 (d, 2H, J=8.1 Hz), 8,05 (dd, 2H, J=8.1 Hz, J=2.05 Hz), 4.27-4.36 (m, 2H), 3.75 (t, 2H, J=6.1 Hz), 3.72 (d, 4H, J=5.4 Hz), 2.76 (t, 2H, J=7.5 Hz), 1.63-1.71 (m, 4H), 1.48-1.58 (m, 4H), 1.3-1.4 (m, 4H), 1.23 (d, 6H, J=7.5 Hz), 1.35 (s, 36H). **HRMS** (ESI) ***m/z***: for $C_{56}H_{82}N_{10}O_{16}$: ($[M+H^+]^+$) calcd 1151.5983, found 1151.5990.

2,6-[Boc-Lysine-Alanine-β-Alanine-amidyl]-anthracen-9,10-dione (B-10)

Obtained from 2,6-[Alanine-β-Alanine-amidyl]-anthracen-9,10-dione according to the general procedure for coupling ***via*** TBTU. Yield: 80%. **^{1}H-NMR** (d_6-DMSO; 300 MHz): δ 10.53 (s, 2H), 8.55 (d, 2H, J=7.5 Hz), 8.48 (d, 2H, J=2.0 Hz), 8.17 (d, 2H, J=8.1 Hz), 8.05 (dd, 2H, J=8.1 Hz, J=2.0 Hz), 4.36-4.27 (m, 2H), 3.75 (t, 2H, J=6.1 Hz), 3.52-3.42 (m, 2H), 2.76 (t, 2H, J=7.5 Hz), 2.59 (t, 4H, J=6.1 Hz), 1.63-1.71 (m, 4H), 1.58-1.48 (m, 4H), 1.42-1.36 (m, 4H), 1.32 (s, 36H), 1.25 (d, 6H, J=7.5 Hz). **HRMS** (ESI) ***m/z***: for $C_{58}H_{86}N_{10}O_{16}$: ($[M+H^+]^+$) calcd 1179.6296, found 1179.6299.

2,7-[Boc-Lysine-Alanine-β-Alanine-amidyl]-anthracen-9,10-dione (C-10)

Obtained from 2,7-[Alanine-β-Alanine-amidyl]-anthracen-9,10-dione according to the general procedure for coupling ***via*** TBTU. Yield: 82%. **^{1}H-NMR** (d_6-DMSO; 300 MHz): δ 10.58 (s, 2H), 8.55 (d, 2H, J=7.5 Hz), 8.48 (d, 2H, J=2.0 Hz), 8.17 (d, 2H, J=8.1 Hz), 8.05 (dd, 2H, J=8.1 Hz, J=2.0 Hz), 4.36-4.27 (m, 2H), 3.75 (t, 2H, J=6.1 Hz), 3.52-3.42 (m, 2H), 2.76 (t, 2H, J=7.5 Hz), 2.59 (t, 4H, J=6.1 Hz), 1.63-1.71 (m, 4H), 1.58-1.48 (m, 4H), 1.42-1.36 (m, 4H), 1.32 (s, 36H), 1.25 (d, 6H, J=7.5 Hz). **HRMS** (ESI) ***m/z***: for $C_{58}H_{86}N_{10}O_{16}$: ($[M+H^+]^+$) calcd 1179.6296, found 1179.6293.

1,5-[Boc-Lysine-Alanine-β-Alanine-amidyl]-anthracen-9,10-dione (D-10)

Obtained from **D-4** according to the general procedure for coupling ***via*** TBTU. Yield: 84%. **^{1}H-NMR** (d_6-DMSO; 300 MHz): δ 10.63 (s, 2H), 8.55 (d, 2H, J=7.5 Hz), 8.48 (d, 2H, J=2.0 Hz), 8.17 (d, 2H, J=8.1 Hz), 8.05 (dd, 2H, J=8.1 Hz, J=2.0 Hz), 4.36-4.27 (m, 2H), 3.75 (t, 2H, J=6.1 Hz), 3.52-3.42 (m, 2H), 2.76 (t, 2H, J=7.5 Hz), 2.59 (t, 4H, J=6.1 Hz), 1.63-1.71 (m, 4H), 1.58-1.48 (m, 4H), 1.42-1.36 (m, 4H), 1.32 (s, 36H), 1.25 (d, 6H, J=7.5 Hz). **HRMS** (ESI) ***m/z***: for $C_{58}H_{86}N_{10}O_{16}$: ($[M+H^+]^+$) calcd 1179.6296, found 1179.6299.

1,8-[Boc-Lysine-Alanine-β-Alanine-amidyl]-anthracen-9,10-dione (E-10)

Obtained from **E-4** according to the general procedure for coupling ***via*** TBTU. Yield: 84%. **^{1}H-NMR** (d_6-DMSO; 300 MHz): δ 10.68 (s, 2H), 8.55 (d, 2H, J=7.5 Hz), 8.48 (d, 2H, J=2.0 Hz), 8.17 (d, 2H, J=8.1 Hz), 8.05 (dd, 2H, J=8.1 Hz, J=2.0 Hz), 4.36-4.27 (m, 2H), 3.75 (t, 2H, J=6.1 Hz), 3.52-3.42 (m, 2H), 2.76 (t, 2H, J=7.5 Hz), 2.59 (t, 4H, J=6.1 Hz), 1.63-1.71 (m, 4H), 1.58-1.48 (m, 4H), 1.42-1.36 (m, 4H), 1.32 (s, 36H), 1.25 (d, 6H, J=7.5 Hz). **HRMS** (ESI) ***m/z***: for $C_{58}H_{86}N_{10}O_{16}$: ($[M+H^+]^+$) calcd 1179.6296, found 1179.6299.

2,6-[Boc-Lysine-Glycine-Glycine-amidyl]-anthracen-9,10-dione (A-11)

Obtained from 2,6-[Glycine-Glycine-amidyl]-anthracen-9,10-dione according to the general procedure for coupling ***via*** TBTU. Yield: 83%. **^{1}H-NMR** (d_6-DMSO; 300 MHz): δ 10.66 (s, 2H), 8.66 (t, 2H, J=5.4 Hz), 8.49 (d, 2H, J=2.0 Hz), 8.17 (d, 2H, J=8.8 Hz), 8.06 (dd, 2H, J=8.8 Hz, J=2.0 Hz), 3.80 (m, 6H), 3.30 (d, 4H, J=5.4 Hz), 2.76 (t, 4H, J=7.5 Hz), 1.70 (m, 4H), 1.52 (m, 4H),

1.39 (m, 4H), 1.35 (s, 36H). **HRMS** (ESI) ***m/z***: for $C_{54}H_{78}N_{10}O_{16}$: ($[M+H^+]^+$) calcd 1123.5670, found 1123.5682.

2,6-[Boc-Lysine-Glycine-β-Alanine-amidyl]-anthracen-9,10-dione (B-11)

Obtained from **A-6** according to the general procedure for coupling ***via*** TBTU. Yield: 79%. **^{1}H-NMR** (d_6-DMSO; 300 MHz): δ 10.66 (s, 2H), 8.66 (t, 2H, J=5.4 Hz), 8.49 (d, 2H, J=2.0 Hz), 8.17 (d, 2H, J=8.8 Hz), 8.06 (dd, 2H, J=8.8 Hz, J=2.0 Hz), 3.8 (m, 6H), 3.40 (q, 4H, J=6.8 Hz), 2.76 (t, 4H, J=7.5 Hz), 2.60 (t, 4H, J=6.8 Hz), 1.70 (m, 4H), 1.52 (m, 4H), 1.39 (m, 4H), 1.35 (s, 36H). **HRMS** (ESI) ***m/z***: for $C_{56}H_{82}N_{10}O_{16}$: ($[M+H^+]^+$) calcd 1151.5983, found 1151.5987.

2,6-[Boc-Lysine-Phenylalanine-Glycine-amidyl]-anthracen-9,10-dione (A-12)

Obtained from 2,6-[Phenylalanine-Glycine-amidyl]-anthracen-9,10-dione according to the general procedure for coupling ***via*** TBTU. Yield: 77%. **^{1}H-NMR** (d_6-DMSO; 300 MHz): δ 10.64 (s, 2H), 8.61 (d, 2H, J=7.5 Hz), 8.5 (d, 2H, J=2.0 Hz), 8.31 (t, 2H, J=5.4 Hz), 8.18 (d, 2H, J=8.1 Hz), 8.06 (dd, 4H, J=8.1 Hz, J=2.0 Hz), 7.12-7.2 (m, 8H), 7.2-7.28 (m, 2H), 4.49-4.57 (m, 2H), 3.72 (d, 4H, J=5.4 Hz), 3.7 (t, 2H), 2.97 (dd, 2H, J= 5.4 Hz, J=13.65 Hz), 2.83 (dd, 2H, J=8.8 Hz, J=13.6 Hz), 2.72 (t, 4H, J=7.5 Hz), 1.70 (m, 4H), 1.52 (m, 4H), 1.33 (m, 4H), 1.35 (s, 36H). **HRMS** (ESI) ***m/z***: for $C_{68}H_{90}N_{10}O_{16}$: ($[M+H^+]^+$) calcd 1303.6609, found 1303.6630.

2,6-[Boc-Lysine-Phenylalanine-β-Alanine-amidyl]-anthracen-9,10-dione (B-12)

Obtained from 2,6-[Phenylalanine-β-Alanine-amidyl]-anthracen-9,10-dione according to the general procedure for coupling ***via*** TBTU. Yield: 76%. **^{1}H-NMR** (d_6-DMSO; 300 MHz): δ 10.64 (s, 2H), 8.61 (d, 2H, J=7.5 Hz), 8.50 (d, 2H, J=2.0 Hz), 8.31 (t, 2H, J=5.4 Hz), 8.18 (d, 2H, J=8.1 Hz), 8.06 (dd, 4H, J=8.1 Hz, J=2.0 Hz), 7.28-7.12 (m, 10H), 4.57-4.49 (m, 2H), 3.70 (t, 2H), 3.52-3.41 (m, 4H), 2.97 (dd, 2H, J= 5.4 Hz, J=13.6 Hz), 2.83 (dd, 2H, J=8.8 Hz, J=13.6 Hz), 2.72 (t, 4H, J=7.5 Hz), 2.55 (t, 4H, J=5.4 Hz), 1.70 (m, 4H), 1.52 (m, 4H), 1.35 (s, 36H), 1.30 (m, 4H). **HRMS** (ESI) ***m/z***: for $C_{70}H_{94}N_{10}O_{16}$: ($[M+H^+]^+$) calcd 1331.6922, found 1331.6946.

2,7-[Boc-Lysine-Phenylalanine-β-Alanine-amidyl]-anthracen-9,10-dione (C-12)

Obtained from 2,6-[Phenylalanine-β-Alanine-amidyl]-anthracen-9,10-dione according to the general procedure for coupling ***via*** TBTU. Yield: 77%. **^{1}H-NMR** (d_6-DMSO; 300 MHz): δ 10.59 (s, 2H), 8.61 (d, 2H, J=7.5 Hz), 8.50 (d, 2H, J=2.0 Hz), 8.31 (t, 2H, J=5.4 Hz), 8.18 (d, 2H, J=8.1 Hz), 8.06 (dd, 4H, J=8.1 Hz, J=2.0 Hz), 7.28-7.12 (m, 10H), 4.57-4.49 (m, 2H), 3.70 (t, 2H), 3.52-3.41 (m, 4H), 2.97 (dd, 2H, J= 5.4 Hz, J=13.6 Hz), 2.83 (dd, 2H, J=8.8 Hz, J=13.6 Hz), 2.72 (t, 4H, J=7.5 Hz), 2.55 (t, 4H, J=5.4 Hz), 1.70 (m, 4H), 1.52 (m, 4H), 1.35 (s, 36H), 1.30 (m, 4H). **HRMS** (ESI) ***m/z***: for $C_{70}H_{94}N_{10}O_{16}$: ($[M+H^+]^+$) calcd 1331.6922, found 1331.6938.

1,5-[Boc-Lysine-Phenylalanine-β-Alanine-amidyl]-anthracen-9,10-dione (D-12)

Obtained from **D-8** according to the general procedure for coupling ***via*** TBTU. Yield: 80%. **^{1}H-NMR** (d_6-DMSO; 300 MHz): δ 10.70 (s, 2H), 8.61 (d, 2H, J=7.5 Hz), 8.50 (d, 2H, J=2.0 Hz), 8.31 (t, 2H, J=5.4 Hz), 8.18 (d, 2H, J=8.1 Hz), 8.06 (dd, 4H, J=8.1 Hz, J=2.0 Hz), 7.28-7.12 (m, 10H), 4.57-4.49 (m, 2H), 3.70 (t, 2H), 3.52-3.41 (m, 4H), 2.97 (dd, 2H, J= 5.4 Hz, J=13.6 Hz), 2.83 (dd, 2H, J=8.8 Hz, J=13.6 Hz), 2.72 (t, 4H, J=7.5 Hz), 2.55 (t, 4H, J=5.4 Hz), 1.70 (m, 4H), 1.52 (m, 4H), 1.35 (s, 36H), 1.30 (m, 4H). **HRMS** (ESI) ***m/z***: for $C_{70}H_{94}N_{10}O_{16}$: ($[M+H^+]^+$) calcd 1331.6922, found 1331.6946.

1,8-[Boc-Lysine-Phenylalanine-β-Alanine-amidyl]-anthracen-9,10-dione (E-12)

Obtained from **E-8** according to the general procedure for coupling ***via*** TBTU. Yield: 80%. **^{1}H-NMR** (d_6-DMSO; 300 MHz): δ 10.75 (s, 2H), 8.61 (d, 2H, J=7.5 Hz), 8.50 (d, 2H, J=2.0 Hz), 8.31 (t, 2H, J=5.4 Hz), 8.18 (d, 2H, J=8.1 Hz), 8.06 (dd, 4H, J=8.1 Hz, J=2.0 Hz), 7.28-7.12 (m, 10H), 4.57-4.49 (m, 2H), 3.70 (t, 2H), 3.52-3.41 (m, 4H), 2.97 (dd, 2H, J= 5.4 Hz, J=13.6 Hz), 2.83 (dd, 2H, J=8.8 Hz, J=13.6 Hz), 2.72 (t, 4H, J=7.5 Hz), 2.55 (t, 4H, J=5.4 Hz), 1.70 (m, 4H), 1.52 (m, 4H), 1.35 (s, 36H), 1.30 (m, 4H). **HRMS** (ESI) ***m/z***: for $C_{70}H_{94}N_{10}O_{16}$: ($[M+H^+]^+$) calcd 1331.6922, found 1331.6946.

1,5-[Lysine-β-Alanine-amidyl]-anthracen-9,10-dione tetra-trifluoroacetate (D-13)

Obtained from **D-9** according to the general procedure for for the deprotection of the Boc group. Yield: 94%. **^{1}H-NMR** (d_6-DMSO; 300 MHz): δ 10.70 (s, 2H), 8.50 (d, 2H, J=2.1 Hz), 8.17 (d, 2H, J=8.8 Hz), 8.03 (dd, 2H, J=8.8 Hz, J=2.1 Hz), 3.85 (m, 2H), 3.41 (q, 4H, J=6.6 Hz), 2.79 (t, 4H, J=7.5 Hz), 2.66 (t, 4H, J=6.6 Hz), 1.78 (m, 4H), 1.54 (m, 4H), 1.42 (m, 4H). **HRMS** (ESI) ***m/z*** for $C_{32}H_{44}N_8O_6$: ($[M+H^+]^+$) calcd 637.3457, found 637.3486; calcd ($[M+2H^+]^{2+}$) 319.1765, found 319.1804.

1,8-[Lysine-β-Alanine-amidyl]-anthracen-9,10-dione tetra-trifluoroacetate (E-13)

Obtained from **E-9** according to the general procedure for the deprotection of the Boc group. Yield: 92%. **^{1}H-NMR** (d_6-DMSO; 300 MHz): δ 10.73 (s, 2H), 8.50 (d, 2H, J=2.1 Hz), 8.17 (d, 2H, J=8.8 Hz), 8.03 (dd, 2H, J=8.8 Hz, J=2.1 Hz), 3.85 (m, 2H), 3.41 (q, 4H, J=6.6 Hz), 2.79 (t, 4H, J=7.5 Hz), 2.66 (t, 4H, J=6.6 Hz), 1.78 (m, 4H), 1.54 (m, 4H), 1.42 (m, 4H). **HRMS** (ESI) ***m/z*** for $C_{32}H_{44}N_8O_6$: ($[M+H^+]^+$) calcd 637.3457, found 637.3492; calcd ($[M+2H^+]^{2+}$) 319.1765, found 319.1793.

2,6-[Lysine-Alanine-Glycine-amidyl]-anthracen-9,10-dione tetra-trifluoroacetate (A-14)

Obtained from **B-14** according to the general procedure for the deprotection of the Boc group. Yield: 92%. **^{1}H-NMR** (d_6-DMSO; 300 MHz): δ 10.53 (s, 2H), 8.55 (d, 2H, J=7.5 Hz), 8.48 (d, 2H, J=2.0 Hz), 8.17 (d, 2H, J=8.1 Hz), 8.05 (dd, 2H, J=8.1 Hz, J=2.0 Hz), 4.27-4.36 (m, 2H), 3.75 (t, 2H, J=6.1 Hz), 3.72 (d, 4H, J=5.4 Hz), 2.76 (t, 2H, J=7.5 Hz), 1.63-1.71 (m, 4H), 1.48-1.58 (m,

4H), 1.3-1.4 (m, 4H), 1.23 (d, 6H, J=7.5 Hz). **HRMS** (ESI) ***m/z*** for $C_{36}H_{50}N_{10}O_8$: ($[M+H^+]^+$) calcd 751.3886, found 751.3897; ($[M+2H^+]^{2+}$) calcd 376.1979, found 376.1991.

2,6-[Lysine-Alanine-β-Alanine-amidyl]-anthracen-9,10-dione tetra-trifluoroacetate (B-14)

Obtained from **A-14** according to the general procedure for the deprotection of the Boc group. Yield: 92%. **^{1}H-NMR** (d_6-DMSO; 300 MHz): δ 10.54 (s, 2H), 8.55 (d, 2H, J=7.5 Hz), 8.48 (d, 2H, J=2.0 Hz), 8.17 (d, 2H, J=8.1 Hz), 8.05 (dd, 2H, J=8.1 Hz, J=2.0 Hz), 4.27-4.36 (m, 2H), 3.75 (t, 2H, J=6.1 Hz), 3.42-3.52 (m, 2H), 2.76 (t, 2H, J=7.5 Hz), 2.59 (t, 4H, J=6.1 Hz), 1.63-1.71 (m, 4H), 1.48-1.58 (m, 4H), 1.3-1.4 (m, 4H), 1.23 (d, 6H, J=7.5 Hz). **HRMS** (ESI) ***m/z*** for $C_{38}H_{54}N_{10}O_8$: ($[M+H^+]^+$) calcd 779.4199, found 779.4221; ($[M+2H^+]^{2+}$) calcd 390.2136, found 390.2147.

2,7-[Lysine-Alanine-β-Alanine-amidyl]-anthracen-9,10-dione tetra-trifluoroacetate (C-14)

Obtained from **C-14** according to the general procedure for the deprotection of the Boc group. Yield: 92%. **^{1}H-NMR** (d_6-DMSO; 300 MHz): δ 10.03 (s, 2H), 8.55 (d, 2H, J=7.5 Hz), 8.48 (d, 2H, J=2.0 Hz), 8.17 (d, 2H, J=8.1 Hz), 8.05 (dd, 2H, J=8.1 Hz, J=2.0 Hz), 4.27-4.36 (m, 2H), 3.75 (t, 2H, J=6.1 Hz), 3.42-3.52 (m, 2H), 2.76 (t, 2H, J=7.5 Hz), 2.59 (t, 4H, J=6.1 Hz), 1.63-1.71 (m, 4H), 1.48-1.58 (m, 4H), 1.3-1.4 (m, 4H), 1.23 (d, 6H, J=7.5 Hz). **HRMS** (ESI) ***m/z*** for $C_{38}H_{54}N_{10}O_8$: ($[M+H^+]^+$) calcd 779.4199, found 779.4217; ($[M+2H^+]^{2+}$) calcd 390.2136, found 390.2150.

1,5-[Lysine-Alanine-β-Alanine-amidyl]-anthracen-9,10-dione tetra-trifluoroacetate (D-14)

Obtained from **D-14** according to the general procedure for the deprotection of the Boc group. Yield: 91%. **^{1}H-NMR** (d_6-DMSO; 300 MHz): δ 10.03 (s, 2H), 8.55 (d, 2H, J=7.5 Hz), 8.48 (d, 2H, J=2.0 Hz), 8.17 (d, 2H, J=8.1 Hz), 8.05 (dd, 2H, J=8.1 Hz, J=2.0 Hz), 4.27-4.36 (m, 2H), 3.75 (t, 2H, J=6.1 Hz), 3.42-3.52 (m, 2H), 2.76 (t, 2H, J=7.5 Hz), 2.59 (t, 4H, J=6.1 Hz), 1.63-1.71 (m, 4H), 1.48-1.58 (m, 4H), 1.3-1.4 (m, 4H), 1.23 (d, 6H, J=7.5 Hz). **HRMS** (ESI) ***m/z*** for $C_{38}H_{54}N_{10}O_8$: ($[M+H^+]^+$) calcd 779.4199, found 779.4223; ($[M+2H^+]^{2+}$) calcd 390.2136, found 390.2147.

1,8-[Lysine-Alanine-β-Alanine-amidyl]-anthracen-9,10-dione tetra-trifluoroacetate (E-14)

Obtained from **E-14** according to the general procedure for the deprotection of the Boc group. Yield: 92%. **^{1}H-NMR** (d_6-DMSO; 300 MHz): δ 10.03 (s, 2H), 8.55 (d, 2H, J=7.5 Hz), 8.48 (d, 2H, J=2.0 Hz), 8.17 (d, 2H, J=8.1 Hz), 8.05 (dd, 2H, J=8.1 Hz, J=2.0 Hz), 4.27-4.36 (m, 2H), 3.75 (t, 2H, J=6.1 Hz), 3.42-3.52 (m, 2H), 2.76 (t, 2H, J=7.5 Hz), 2.59 (t, 4H, J=6.1 Hz), 1.63-1.71 (m, 4H), 1.48-1.58 (m, 4H), 1.3-1.4 (m, 4H), 1.23 (d, 6H, J=7.5 Hz). **HRMS** (ESI) ***m/z*** for $C_{38}H_{54}N_{10}O_8$: ($[M+H^+]^+$) calcd 779.4199, found 779.4226; ($[M+2H^+]^{2+}$) calcd 390.2136, found 390.2147.

2,6-[Lysine-Glycine-Glycine-amidyl]-anthracen-9,10-dione tetra-trifluoroacetate (A-15)

Obtained from **B-18** according to the general procedure for the deprotection of the Boc group. Yield: 91%. **^{1}H-NMR** (d_6-DMSO; 300 MHz): δ 10.63 (s, 2H), 8.66 (t, 2H, J=5.4 Hz), 8.49 (d, 2H, J=2.0 Hz), 8.17 (d, 2H, J=8.8 Hz), 8.06 (dd, 2H, J=8.8 Hz, J=2.0 Hz), 3.8 (m, 6H), 3.3 (d, 4H, J=5.4

Hz), 2.76 (t, 4H, J=7.5 Hz), 1.70 (m, 4H), 1.52 (m, 4H), 1.39 (m, 4H). **HRMS** (ESI) ***m/z*** for $C_{34}H_{46}N_{10}O_8$: ($[M+H^+]^+$) calcd 723.3573, found 723.3590; ($[M+2H^+]^{2+}$) calcd 362.1823, found 362.1850.

2,6-[Lysine-Glycine-β-Alanine-amidyl]-anthracen-9,10-dione tetra-trifluoroacetate (B-15)

Obtained from **A-18** according to the general procedure for the deprotection of the Boc group. Yield: 90%. **^{1}H-NMR** (d_6-DMSO; 300 MHz): δ 10.66 (s, 2H), 8.66 (t, 2H, J=5.4 Hz), 8.49 (d, 2H, J=2.0 Hz), 8.17 (d, 2H, J=8.8 Hz), 8.06 (dd, 2H, J=8.8 Hz, J=2.0 Hz), 3.8 (m, 6H), 3.4 (q, 4H, J=6.8 Hz), 2.76 (t, 4H, J=7.5 Hz), 2.60 (t, 4H, J=6.8 Hz), 1.70 (m, 4H), 1.52 (m, 4H), 1.39 (m, 4H). **HRMS** (ESI) ***m/z*** for $C_{36}H_{50}N_{10}O_8$: ($[M+H^+]^+$) calcd 751.3886, found 751.3892; ($[M+2H^+]^{2+}$) calcd 376.1979, found 376.1993.

2,6-[Lysine-Phenylalanine-Glycine-amidyl]-anthracen-9,10-dione tetra-trifluoroacetate (A-16)

Obtained from **B-22** according to the general procedure for the deprotection of the Boc group. Yield: 91%. **^{1}H-NMR** (d_6-DMSO; 300 MHz): δ 10.64 (s, 2H), 8.61 (d, 2H, J=7.5 Hz), 8.5 (d, 2H, J=2.0 Hz), 8.31 (t, 2H, J=5.4 Hz), 8.18 (d, 2H, J=8.1 Hz), 8.06 (dd, 4H, J=8.1 Hz, J=2.0 Hz), 7.12-7.2 (m, 8H), 7.2-7.28 (m, 2H), 4.49-4.57 (m, 2H), 3.72 (d, 4H, J=5.4 Hz), 3.7 (t, 2H), 2.97 (dd, 2H, J= 5.4 Hz, J=13.6 Hz), 2.83 (dd, 2H, J=8.8 Hz, J=13.6 Hz), 2.72 (t, 4H, J=7.5 Hz), 1.70 (m, 4H), 1.52 (m, 4H), 1.33 (m, 4H). **HRMS** (ESI) ***m/z*** for $C_{48}H_{58}N_{10}O_8$: ($[M+H^+]^+$) calcd 903.4512, found 903.4539; ($[M+2H^+]^{2+}$) calcd 452.2292, found 452.2306.

2,6-[Lysine-Phenylalanine-β-Alanine-amidyl]-anthracen-9,10-dione tetra-trifluoroacetate (B-16)

Obtained from **A-22** according to the general procedure for the deprotection of the Boc group. Yield: 91%. **^{1}H-NMR** (d_6-DMSO; 300 MHz): δ 10.64 (s, 2H), 8.61 (d, 2H, J=7.5 Hz), 8.5 (d, 2H, J=2.0 Hz), 8.31 (t, 2H, J=5.4 Hz), 8.18 (d, 2H, J=8.1 Hz), 8.06 (dd, 4H, J=8.1 Hz, J=2.0 Hz), 7.12-7.2 (m, 8H), 7.2-7.28 (m, 2H), 4.49-4.57 (m, 2H), 3.69-3.76 (t, 2H), 3.41-3.52 (m, 2H), 2.97 (dd, 2H, J= 5.4 Hz, J=13.6 Hz), 2.83 (dd, 2H, J=8.8 Hz, J=13.6 Hz), 2.72 (t, 4H, J=7.51 Hz), 2.55 (t, 4H, J=5.4 Hz), 1.70 (m, 4H), 1.52 (m, 4H), 1.33 (m, 4H). **HRMS** (ESI) ***m/z*** for $C_{50}H_{62}N_{10}O_8$: ($[M+H^+]^+$) calcd 931.4285, found 931.4288; ($[M+2H^+]^{2+}$) calcd 466.2449, found 466.2457.

2,7-[Lysine-Phenylalanine-β-Alanine-amidyl]-anthracen-9,10-dione tetra-trifluoroacetate (C-16)

Obtained from **C-22** according to the general procedure for the deprotection of the Boc group. Yield: 93%. **^{1}H-NMR** (d_6-DMSO; 300 MHz): δ 10.64 (s, 2H), 8.61 (d, 2H, J=7.5 Hz), 8.5 (d, 2H, J=2.0 Hz), 8.31 (t, 2H, J=5.4 Hz), 8.18 (d, 2H, J=8.1 Hz), 8.06 (dd, 4H, J=8.1 Hz, J=2.0 Hz), 7.12-7.2 (m, 8H), 7.2-7.28 (m, 2H), 4.49-4.57 (m, 2H), 3.69-3.76 (t, 2H), 3.41-3.52 (m, 2H), 2.97 (dd, 2H, J= 5.4 Hz, J=13.6 Hz), 2.83 (dd, 2H, J=8.8 Hz, J=13.6 Hz), 2.72 (t, 4H, J=7.51 Hz), 2.55 (t, 4H,

J=5.4 Hz), 1.70 (m, 4H), 1.52 (m, 4H), 1.33 (m, 4H). **HRMS** (ESI) ***m/z*** for $C_{50}H_{62}N_{10}O_8$: ($[M+H^+]^+$) calcd 931.4285, found 931.4294; ($[M+2H^+]^{2+}$) calcd 466.2449, found 466.2464.

1,5-[Lysine-Phenylalanine-β-Alanine-amidyl]-anthracen-9,10-dione tetra-trifluoroacetate (D-16)

Obtained from **D-22** according to the general procedure for the deprotection of the Boc group. Yield: 92. **^{1}H-NMR** (d_6-DMSO; 300 MHz): δ 10.64 (s, 2H), 8.61 (d, 2H, J=7.5 Hz), 8.5 (d, 2H, J=2.0 Hz), 8.31 (t, 2H, J=5.4 Hz), 8.18 (d, 2H, J=8.1 Hz), 8.06 (dd, 4H, J=8.1 Hz, J=2.0 Hz), 7.12-7.2 (m, 8H), 7.2-7.28 (m, 2H), 4.49-4.57 (m, 2H), 3.69-3.76 (t, 2H), 3.41-3.52 (m, 2H), 2.97 (dd, 2H, J= 5.4 Hz, J=13.6 Hz), 2.83 (dd, 2H, J=8.8 Hz, J=13.6 Hz), 2.72 (t, 4H, J=7.51 Hz), 2.55 (t, 4H, J=5.4 Hz), 1.70 (m, 4H), 1.52 (m, 4H), 1.33 (m, 4H). **HRMS** (ESI) ***m/z*** for $C_{50}H_{62}N_{10}O_8$: ($[M+H^+]^+$) calcd 931.4285, found 931.4297; ($[M+2H^+]^{2+}$) calcd 466.2449, found 466.2461.

1,8-[Lysine-Phenylalanine-β-Alanine-amidyl]-anthracen-9,10-dione tetra-trifluoroacetate (E-16)

Obtained from **E-22** according to the general procedure for the deprotection of the Boc group. Yield: 93%. **^{1}H-NMR** (d_6-DMSO; 300 MHz): δ 10.64 (s, 2H), 8.61 (d, 2H, J=7.5 Hz), 8.5 (d, 2H, J=2.0 Hz), 8.31 (t, 2H, J=5.4 Hz), 8.18 (d, 2H, J=8.1 Hz), 8.06 (dd, 4H, J=8.1 Hz, J=2.0 Hz), 7.12-7.2 (m, 8H), 7.2-7.28 (m, 2H), 4.49-4.57 (m, 2H), 3.69-3.76 (t, 2H), 3.41-3.52 (m, 2H), 2.97 (dd, 2H, J= 5.4 Hz, J=13.6 Hz), 2.83 (dd, 2H, J=8.8 Hz, J=13.6 Hz), 2.72 (t, 4H, J=7.51 Hz), 2.55 (t, 4H, J=5.4 Hz), 1.70 (m, 4H), 1.52 (m, 4H), 1.33 (m, 4H). **HRMS** (ESI) ***m/z*** for $C_{50}H_{62}N_{10}O_8$: ($[M+H^+]^+$) calcd 931.4285, found 931.4293; ($[M+2H^+]^{2+}$) calcd 466.2449, found 466.2459.

1 a) Zagotto, G.; Sissi, C.; Lucatello, L.; Pivetta, C.; Cadamuro, S. A.; Fox, K. R.; Neidle, S.; Palumbo, M. Aminoacyl-anthraquinone conjugates as telomerase inhibitors: synthesis, biophysical and biological evaluation. ***J. Med. Chem.*** **2008, *51***, 5566-5574.
b) Zagotto, G.; Sissi, C.; Moro, S.; Dal Ben, D.; Parkinson, G. N.; Fox, K. R.; Neidle, S.; Palumbo, M. Amide bond direction modulates G-quadruplex recognition and telomerase inhibition by 2,6 and 2,7 bis-substituted anthracenedione derivatives. ***Bioorg. Med. Chem.*** **2008, *16***, 354-361.

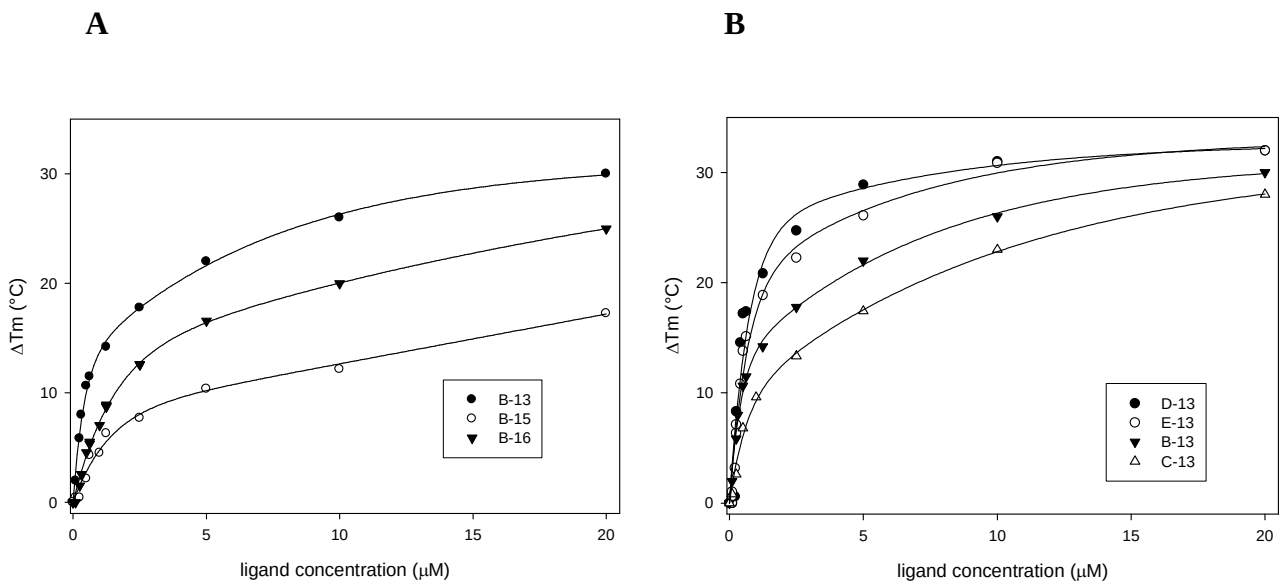

Figure S1. Variation of the melting temperature (ΔTm) of a G-quadruplex folded telomeric sequence (0.25 μM) upon increasing concentrations of selected anthraquinones in 50 mM KCl.

Bioconjugate Chemistry

ARTICLE

pubs.acs.org/bc

Stabilization and Photochemical Regulation of Antisense Agents through PEGylation

Jeane M. Govan, Andrew L. McIver, and Alexander Deiters*

Department of Chemistry, North Carolina State University, Campus Box 8204, Raleigh, North Carolina 27695, United States

Supporting Information

ABSTRACT: Oligonucleotides are effective tools for the regulation of gene expression in cell culture and model organisms, most importantly through antisense mechanisms. Due to the inherent instability of DNA antisense agents, various modifications have been introduced to increase the efficacy of oligonucleotides, including phosphorothioate DNA, locked nucleic acids, peptide nucleic acids, and others. Here, we present antisense agent stabilization through conjugation of a poly(ethylene glycol) (PEG) group to a DNA oligonucleotide. By employing a photocleavable linker between the PEG group and the antisense agent, we were able to achieve light-induced deactivation of antisense activity. The bioconjugated PEG group provides stability to the DNA antisense agent without affecting its native function of silencing gene expression via RNase H-catalyzed mRNA degradation. Once irradiated with UV light of 365 nm, the PEG group is cleaved from the antisense agent leaving the DNA unprotected and open for degradation by endogenous nucleases, thereby restoring gene expression. By using a photocleavable PEG group (PhotoPEG), antisense activity can be regulated with high spatial and temporal resolution, paving the way for precise regulation of gene expression in biological systems.

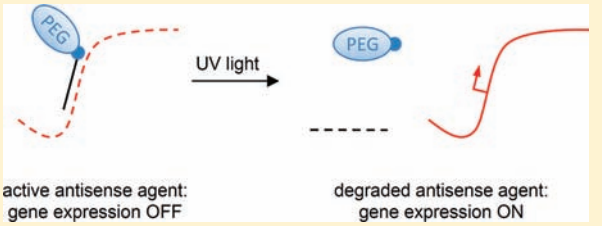

INTRODUCTION

Antisense oligonucleotides are extensively used in cell and developmental biology to inhibit gene expression. Site-specific hybridization of antisense agents to target mRNAs suppresses translation, either by degradation of the mRNA though an RNase H-dependent mechanism or by steric blocking of the ribosome.[1−3] Intracellularly, nonmodified DNAs are quickly degraded, mainly by 3′ exonucleases,[4] limiting the applicability of non-modified DNA as antisense agents. For the past two decades, modifications have been made to oligonucleotides to improve the pharmacokinetics and physicochemical properties. Various modifications to the phosphate backbone and the ribose have been developed to improve the stability and half-life of oligomers, including 3′-3′ inverted thymidines,[5] phosphorothioate linkages,[6] locked nucleic acids (LNA),[7] and 2′-*O*-methyl groups.[8]

PEGylation, the covalent attachment of a poly(ethylene glycol) polymer, enhances the pharmacokinetic properties of both oligonucleotides[9] and proteins[10−12] by shielding them from nucleases and proteases thus increasing their stability. Studies have also shown that PEGylation enhances the absorption, bioavailability, and biodistribution of biological macromolecules while reducing toxicity and immunological effects.[9] In addition, PEGylated triplex forming oligonucleotides and siRNAs have shown to be more efficiently taken up by cells and have displayed improved stability.[13,14]

We hypothesized that the combination of oligonucleotide PEGylation in conjunction with a light-cleavable linker group would enable photochemical control over antisense agent stability and activity. Light represents an ideal external control element for the study of gene expression and protein function with high spatial and temporal resolution.[15−18] Light-removable protecting groups ("caging groups") have been applied to the light-regulation of DNA function through the inhibition of the oligonucleotide's ability to undergo Watson−Crick base-pairing until the groups are removed through light irradiation.[19−31] Here, we propose that a PhotoPEGylated antisense agent will inhibit gene expression (Scheme 1A) until irradiation with nondamaging UV light removes the PEG group, leading to intracellular degradation of the oligonucleotide and subsequent activation of gene expression (Scheme 1B). Advantages of this approach compared to existing methods of photochemical regulation of antisense function are that (a) it can be easily applied to standard, commercially available DNA, (b) it stabilizes the DNA under physiological conditions, and (c) it enables the light-deactivation of antisense function and thus activation of gene expression.

EXPERIMENTAL PROCEDURES

Synthesis and Purification of PEGylated Oligonucleotides. A 3′ amino-modified phosphodiester DNA oligonucleotide (10 μM, Integrated DNA Technologies) was 5′ radiolabeled with ^{32}P-λ ATP (MP Biomedicals) using T4 polynucleotide kinase (New England Biolabs). The 5′ ^{32}P-DNA-NH$_2$ (2 μM) was reacted with *N*-hydrosuccinimide (NHS) ester PEG (200 μM, Laysan Bio, Inc.) in phosphate saline buffer (PBS, pH 8.0) and incubated for 4 h at 30 °C. Due to incomplete PEGylation, the

Received: July 27, 2011
Revised: September 12, 2011
Published: September 20, 2011

ACS Publications © 2011 American Chemical Society

Scheme 1. Photoregulation of Antisense Activity with Light-Removable PEG Groups[a]

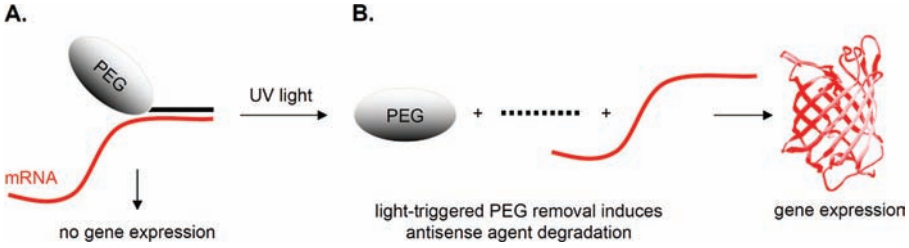

[a] (A) A PEGylated antisense agent binds to the mRNA target sequence, which recruits RNase H to the mRNA/DNA duplex leading to the degradation of the mRNA and thus gene silencing. (B) A PhotoPEG antisense agent is cleaved upon UV irradiation, leaving the DNA-based antisense agent susceptible to degradation by exonucleases, thereby allowing the translation of the mRNA and gene expression.

PEGylated DNA was gel purified, electro-eluted, and concentrated using a Millipore centricon (3000 Da molecular weight cutoff). The PEGylated DNA was quantified using a standard curve on a 20% denaturing PAGE gel, through scanning on a Typhoon FLA 7000 and measuring the band intensities using *ImageQuantTL*.

Melting Temperature Measurements. The melting temperature (T_m) of each PEGylated DNA/RNA duplex was measured using a Cary 100 Bio UV/vis spectrometer with a temperature controller (Varian). The PEGylated DNA antisense agent and RNA substrate (0.5 μM) were incubated in buffer (0.15 M NaCl, 0.05 M NaH_2PO_4, pH 7.2). The samples were heated to 100 °C for 2 min, and then cooled to 20 °C at a rate of 2 °C/min, held at 20 °C for 5 min, and then heated to 100 °C at a rate of 2 °C/min. Absorbance was recorded at 260 nm every 1 °C. The T_m was determined by the maximum of the first derivative of the absorbance vs temperature plot. Standard deviations were calculated from three independent experiments.

RNase H Assay. The RNase H assay was performed as described by Tang et al.[32] with the following modifications: PEGylated DNA (10 nM) and RNase H buffer were equilibrated, followed by the addition of radiolabeled RNA (^{32}P-γ ATP, 1 μM). The mixture was incubated at 37 °C for 20 min, and RNase H (New England Biolabs, 1 U) was added, followed by an additional incubation for 1 h at 37 °C. Samples were analyzed on a 10% denaturing PAGE gel and scanned on a Typhoon FLA 7000.

Photochemical Regulation of Antisense Activity in Mammalian Cells. HEK 293T cells were passaged into a poly-L-Lys coated 96-well plate, grown to 70% confluency, and transfected with pEGFP-N1 (Clontech, 150 ng), pDsRed-monomer (Clontech, 150 ng), and antisense agents (25 pmol) using X-tremeGENE (Roche). pEGFP-N1 encodes enhanced green fluorescent protein (EGFP) and served as the transfection control. pDsRed-monomer encodes a red fluorescent protein (DsRed) and was the targeted gene in this study. After 4 h, media was removed, the cells were irradiated on a transilluminator (365 nm, 25 W), and DMEM media was added. Following a 48 h incubation at 37 °C, 5% CO_2, the media was removed and the cells were imaged on a Jenco inverted microscope. The cells were lysed and the fluorescence was measured on a plate reader (EGFP 485/507 ex/em, DsRed 557/585 BioTek Synergy 4 Microplate Reader).

Spatial Control of Gene Expression in Mammalian Cells. NIH 3T3 cells were passaged into a black 96-well plate and grown to 75% confluency, followed by transfection with pEGFP-N1 (150 ng), pDsRed-monomer (150 ng), and antisense agent (25 pmol) using X-tremeGENE. After 4 h, the media was removed and half of the well was covered with an aluminum foil mask. The cells were irradiated for 2 min on a transilluminator (365 nm, 25 W) and DMEM media was added. Following a 48 h incubation, the media was removed and the cells were imaged on a Zeiss Axio Observer inverted microscope (5× magnification, filter sets 43 HE DsRed and 38 HE eGFP).

RESULTS AND DISCUSSION

First, the PEGylated DNA was synthesized through the acylation of 3′ amino-modified oligonucleotides with *N*-hydroxysuccinimide-activated poly(ethylene glycol)s of 5 kDa, 20 kDa, or 40 kDa (Scheme 2A). A DNA sequence targeting the DsRed gene was selected for subsequent cell-based reporter assays.[27,33] The PEGylated antisense agents were purified through gel electro-elution (Scheme 2C). In order to validate that the PEG group will stabilize the nonmodified DNA against nucleases, the 3′ PEGylated oligonucleotides were incubated in DMEM growth media (10% FBS). Upon conjugation of the 5 kDa PEG group to the deoxyoligonucleotide, the stability increased from 4 to 24 h. The 20 kDa PEG and the 40 kDa PEGylated oligonucleotides displayed similar trends with stabilizing DNA for a minimum of 24 h. The stability of the PEGylated oligonucleotides was also tested in the presence of exonuclease I, by measuring oligonucleotide integrity over time. A 15-, 30-, and 60-fold increased stability was found for DNA PEGylated with 5, 20, and 40 kDa PEG reagents, respectively. Thus, increasing the size of the bioconjugated PEG from 5 kDa to 40 kDa increases the stability of the oligonucleotide in both DMEM media and in the presence of an exonuclease (Supporting Information, Figures S1 and S2).

Melt curves of the PEGylated antisense agents were measured in the presence of target mRNA (5′ GCAGGAGGCCUCCUCCGAGAACGUCAUCACCGAGUUCAUCAAGGU 3′) to ensure that the PEG groups do not affect DNA/RNA hybridization. The non-PEGylated antisense agent had a T_m of 69 °C (Table 1). The conjugation of the 5 kDa PEG to the DNA phosphodiester oligonucleotide did not interfer with DNA/RNA hybridization as the T_m slightly decreased by 6 °C when compared to the non-PEGylated DNA. With an increasing PEG size to 20 kDa and 40 kDa, the T_m decreased by 13 and 19 °C, respectively, but hybridization was still detected (see Supporting Information, Figure S3). Therefore, all PEGylated deoxyoligonucleotides undergo DNA/RNA hybridization and thus have potential to function as antisense agents in live cells. The attachment of a smaller PEG group (5 kDa) had a less pronounced effect on melting point depression than larger PEG groups (20 kDa or 40 kDa).

Since the PEG groups do not affect DNA/RNA hybridization, the activity of the PEGylated DsRed antisense agents was

Scheme 2. PEGylation of 3′ Amino-Modified DNA[a]

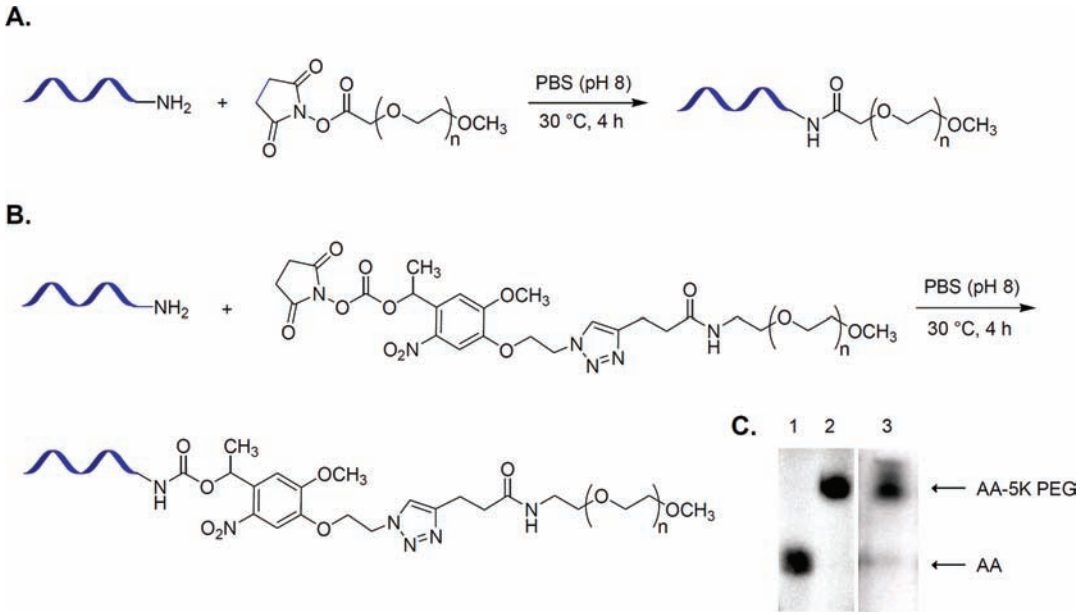

[a] (A) PEGylation reaction of 3′ amino-modified DNA with *N*-hydroxysuccinimide PEG. (B) PEGylation of DsRed targeting antisense DNA with the PhotoPEG reagent. (C) Representative PAGE analysis of purified, PEGylated DNA. Lane 1: non-modified antisense agent (AA). Lane 2: 5 kDa PEGylated antisense agent (AA-5 kDa PEG). Lane 3: 5 kDa photocleavable PEGylated antisense agent (AA-5K PhotoPEG).

Table 1. Sequences and Melting Temperatures of PEGylated DsRed Antisense Agents[a]

Name	DNA Sequence	T_m / °C
AA	5′ AACTCGGTGATGACGTTCTCGGAGGAG-NH_2	69.2 ± 0.7
AA-HP	5′ A A GCGCGCG GCGCGCG A A A CGCGCGCTACAACTCGGTGATGAGTTCTCGGAGGAGCGGCGCGCGC A	61.1 ± 0.8
AA-5K	5′ AACTCGGTGATGACGTTCTCGGAGGAG-NH-PEG_{5kDa}	63.4 ± 1.3
AA-20K	5′ AACTCGGTGATGACGTTCTCGGAGGAG-NH-PEG_{20kDa}	56.1 ± 1.5
AA-40K	5′ AACTCGGTGATGACGTTCTCGGAGGAG-NH-PEG_{40kDa}	50.9 ± 1.9

[a] Standard deviations were derived from T_m measurements conducted in triplicate.

determined in cell culture. Human embryonic kidney (HEK) 293T cells were co-transfected with pEGFP-N1, pDsRed-monomer, and the PEGylated antisense agents. The PEGylated antisense agents target the DsRed mRNA, while the enhanced green fluorescent protein (EGFP) served as a transfection control; therefore, DsRed fluorescence was normalized to EGFP fluorescence. The nonmodified antisense agent (AA) showed no knockdown of DsRed expression (Figure 1A), presumably due to a rapid intracellular degradation of the deoxyoligonucleotide (as discussed above). As a positive control, a hairpin loop-protected DsRed antisense agent that has previously been shown to successfully inhibit DsRed expression was used.[27,33] This hairpin-protected antisense agent (AA-HP) produced a 74% inhibition of DsRed expression (Figure 1B). Gratifyingly, all PEGylated antisense agents (AA-5K, -20K, and -40K) achieved similar levels of DsRed suppression (58−68%). Since the knockdown is not statistically different ($p \geq 0.15$), it can be concluded that even small PEG groups of 5−20K are sufficient for the protection of small deoxyoligonucleotides. Thus, the ability of nonmodified, PEGylated DNA to act as a translational-silencing antisense agent in tissue culture was demonstrated for the first time.

Antisense agents can inhibit gene function via two pathways: (a) the antisense agent can sterically block the translation of the mRNA or (b) the mRNA:DNA duplex can recruit RNase H to bind to the duplex and degrade the mRNA.[2] In order to determine by which mechanism the PEGylated antisense agent inhibits gene expression, an RNase H assay was performed. The DsRed mRNA target in the absence of antisense DNA was not affected by the addition of RNase H (Figure 2, Lanes 1−2). Nonmodified DsRed AA was incubated with its complementary mRNA sequence in the presence and absence of RNase H. As expected, only upon addition of RNase H was the mRNA

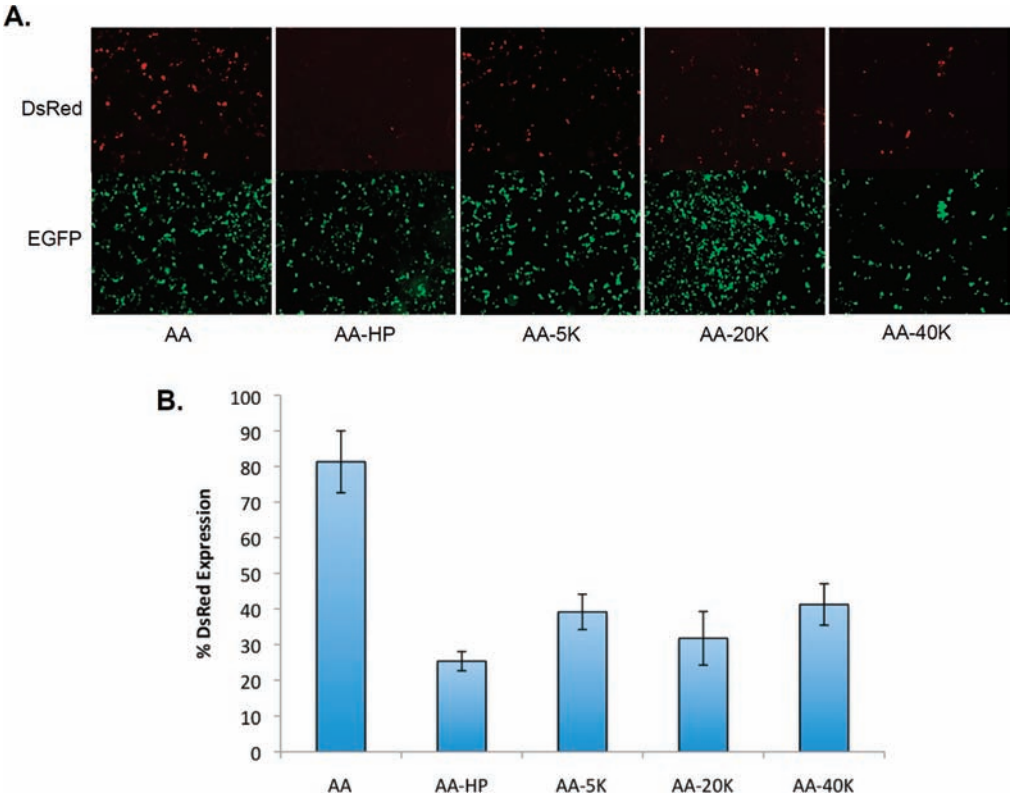

Figure 1. Inhibition of DsRed expression by PEGylated antisense agents. HEK 293T cells were transfected with pEGFP-N1, pDsRed-Monomer, and antisense agent. (A) After a 48 h incubation, the media was removed and the cells were imaged. The DsRed channel is shown above the EGFP channel. (B) Cells were subsequently lysed and the fluorescence was measured on a BioTek plate reader. DsRed (557/585 nm) fluorescence was normalized to EGFP (485/507 nm) fluorescence. Error bars represent standard deviatons from three independent experiments. AA: nonmodified antisense agent. AA-HP: hairpin-protected antisense agent. AA-5K: 5 kDa PEGylated antisense agent. AA-20 kDa: 20 kDa PEGylated antisense agent. AA-40: 40 kDa PEGylated antisense agent.

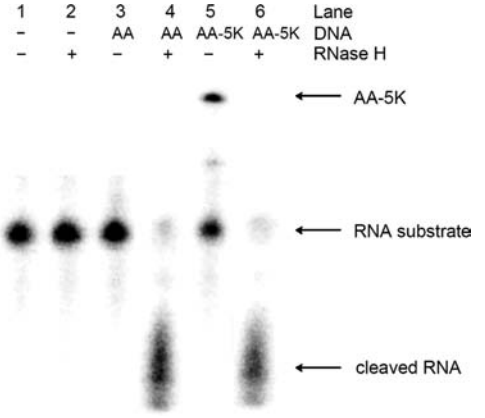

Figure 2. PEGylated antisense agent induces RNA degradation through an RNase H mediated mechanism. AA and AA-5K PEG were incubated with a radiolabeled RNA substrate and RNase H for 1 h at 37 °C. Samples were analyzed on a 10% denaturing gel and imaged with a Typhoon FLA 7000. AA: nonmodified antisense agent. AA-5K: 5 kDa PEGylated antisense agent.

degraded (Figure 2, Lanes 3−4). The same result was obtained for the PEGylated AA-5K DNA and RNase H (Figure 2, Lanes 5−6), indicating that the presence of the PEG group has no effect on the recruitment of RNase H. Thus, the PEGylated antisense oligonucleotide most likely inhibits gene expression intracellularly through RNase H-mediated degradation of mRNA.

On the basis of the results presented above, PEGylated oligonucleotides are active and stable antisense agents in cell culture, while the non-PEGylated DNA is quickly degraded. Thus, we hypothesized that we can photochemically inactivate an antisense agent by inserting a light-cleavable linker between the PEG group and the DNA (Scheme 2B). In order to test this hypothesis, we used a previously synthesized 5 kDa PhotoPEG reagent[34] and additionally synthesized a 20 kDa PhotoPEG group. The DsRed antisense DNA was PEGylated with the PhotoPEG group as shown in Scheme 2B.

The photoactivation of gene expression was conducted by transfection of the 5 kDa and 20 kDa PhotoPEGylated antisense agents with pEGFP-N1 and pDsRed-monomer into HEK 293T cells. The cells were irradiated for 2 min using a transilluminator (365 nm, 25 W), followed by incubation for 48 h. As in the previous cellular experiments, EGFP was used as a transfection control and DsRed fluorescence was normalized to EGFP fluorescence. The 5 kDa PhotoPEG antisense agent (AA-5K PhotoPEG) reduced DsRed expression by 52% (similar to earlier results shown in Figure 1), and after irradiation, DsRed expression was fully restored—comparable to the no antisense agent control (Figure 3A,B). The 20 kDa PhotoPEG antisense agent (AA-20K PhotoPEG) almost completely inhibited DsRed expression (80% inhibition), while after irradiation, fully restored DsRed expression was observed as well. Gene silencing with the

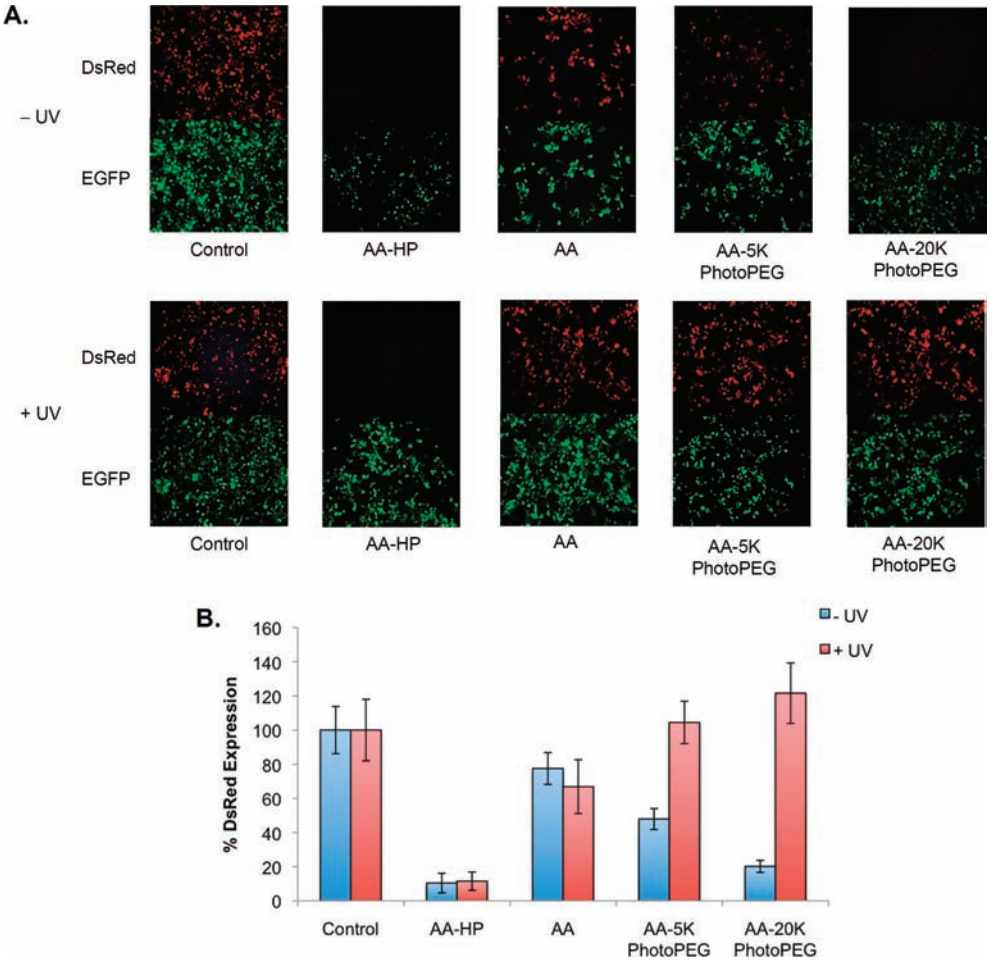

Figure 3. Light activation of gene expression using a PhotoPEGylated antisense agent. HEK 293T cells were transfected with pEGFP-N1, pDsRed-Monomer, and antisense agent. Cell were irradiated for 2 min (25 W, 365 nm) or kept in the dark. (A) Cells were imaged after 48 h. The DsRed channel is shown above the EGFP channel. (B) Cells were then lysed, and the fluorescence was measured on a BioTek plate reader. DsRed (557/585 nm) fluorescence was normalized to EGFP (485/507 nm) fluorescence. Error bars represent standard deviations from three independent experiments. AA-HP: hairpin-protected antisense agent. AA: nonmodified antisense agent. AA-5K PhotoPEG: 5 kDa photocleavable PEGylated antisense agent. AA-20K PhotoPEG: 20 kDa photocleavable PEGylated antisense agent.

AA-20K PhotoPEG reagent was more pronounced than what was previously observed for the simple PEG reagent without the light-cleavable linker (Figure 1). However, based on our cellular stability assays (see Supporting Information), the AA-20K PEG was more stable than the AA-5K PEG toward enzymatic degradation. This demonstrates the excellent switching from virtually complete inhibition of gene expression before irradiation to fully restored gene expression after irradiation. For the first time, nonmodified, standard DNA was conjugated with a photocleavable PEG group and used in the photochemical activation of gene expression.

Having successfully achieved light-activation of gene expression with an excellent off/on ratio by using the PhotoPEGylated antisense agent, we next investigated the possibility of spatial control over DsRed expression in mammalian cells. In a 96-well plate, the AA-20K PhotoPEG was cotransfected into NIH 3T3 cells with pEGFP-N1 and pDsRed-monomer. Only one-half of a well was then irradiated for 2 min (365 nm, 25 W), followed by incubation for 48 h. Consistent with earlier observations, the nonmodified antisense agent (AA) exhibited no inhibition of DsRed expression (Figure 4); conversely, the hairpin-protected antisense agent (AA-HP) completely inhibited DsRed expression. Cells transfected with the 20 kDa PhotoPEG antisense agent were only irradiated on the left half of the well and DsRed expression is only observed within the irradiated area. In the nonirradiated area, the right side of the micrograph, no DsRed expression is visible due to an intact PEGylated DsRed antisense agent. Thus, a high level of spatial control over gene activation was achieved.

In summary, PhotoPEG antisense agents were developed that enable precise activation of gene expression through UV irradiation. Traditionally, antisense agents are stabilized by various backbone and sugar modifications for applications in tissue culture and whole organisms. These modifications are often synthetically challenging and, moreover, prevent RNase H-catalyzed mRNA degradation. If RNase H cleavage of mRNA is desired, mixed modified/nonmodified deoxyoligonucleotides need to be synthesized. We discovered that simple PEGylation stabilizes nonmodified DNA intracellularly with minimal to no effect on antisense activity, DNA/RNA hybridization, and RNase H-catalyzed mRNA degradation, thus providing efficient and readily synthesized antisense agents. The application of a light-cleavable PhotoPEG linker inserted between the PEG polymer and the

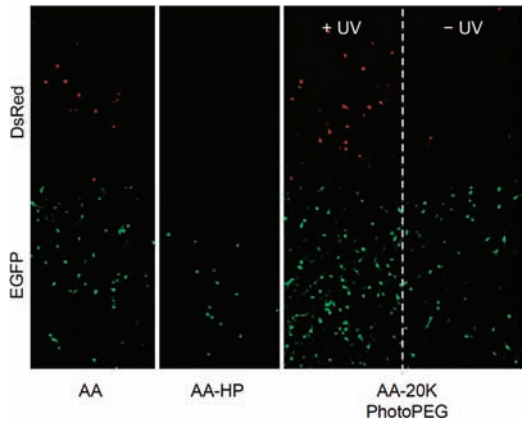

Figure 4. Spatial activation of gene expression using a PhotoPEGylated antisense agent. NIH 3T3 cells were transfected with pEGFP-N1, pDsRed-Monomer, and AA-20K PhotoPEG. Only one-half side of the well was irradiated for 2 min (25 W, 365 nm) and the cells were imaged after 48 h. The DsRed channel is shown above the EGFP channel. AA: nonmodified antisense agent. AA-HP: hairpin-protected antisense agent. AA-20K PhotoPEG: 20 kDa photocleavable antisense agent.

oligonucleotide enabled sequence-specific gene silencing until cells were briefly irradiated with UV light of 365 nm, inducing PEG cleavage and subsequent rapid, intracellular degradation of the antisense oligonucleotide. Degradation of the antisense agent then in turn activates the expression of the previously silenced gene of interest. Moreover, in addition to temporal control over gene expression, the developed methodology introduced a simple means for spatial control over gene activation through locally restricted irradiation of a monolayer of mammalian cells. This approach (light-*activation* of gene expression) is complementary to classical antisense caging methodologies (light-*deactivation* of gene expression). Due to the straightforward design of the reagents, only requiring standard deoxyoligonucleotides, the developed methodology can be readily applied in any chemical biology, cell biology, and molecular biology lab.

■ ASSOCIATED CONTENT

Supporting Information. PEGylated antisense agent stability assays and melt curves of DNA:RNA hybridization. This material is available free of charge via the Internet at http://pubs.acs.org.

■ AUTHOR INFORMATION

Corresponding Author

*1-919-515-7607 (phone), 1-919-515-5079 (fax), alex_deiters@ncsu.edu.

■ ACKNOWLEDGMENT

This research was supported in part by the National Institutes of Health (R01GM079114), the Beckman Foundation (Beckman Young Investigator Award for AD), and the Research Corporation (Cottrell Scholar Award for AD).

■ ABBREVIATIONS

PEG, poly(ethylene glycol); PhotoPEG, photocleavable poly(ethylene glycol); NHS, *N*-hydroxysuccinimide; PBS, phosphate saline buffer; HEK, human embryonic kidney cells; AA, antisense agents; AA-HP, hairpin-protected antisense agent; AA-5K, PEGylated 5 kDa antisense agent; AA-20K, PEGylated 20 kDa antisense agent; AA-40K, PEGylated 40 kDa antisense agent; AA-5K PhotoPEG, 5 kDa photocleavable PEGylated antisense agent; AA-20K PhotoPEG, 20 kDa photocleavable PEGylated antisense agent

■ REFERENCES

(1) Dean, N. M., and Bennett, C. F. (2003) Antisense oligonucleotide-based therapeutics for cancer. *Oncogene 22*, 9087–9096.

(2) Aboul-Fadl, T. (2005) Antisense oligonucleotides: the state of the art. *Curr. Med. Chem. 12*, 2193–214.

(3) Remaut, K., Lucas, B., Raemdonck, K., Braeckmans, K., Demeester, J., and De Smedt, S. C. (2007) Protection of oligonucleotides against enzymatic degradation by pegylated and nonpegylated branched polyethyleneimine. *Biomacromolecules 8*, 1333–40.

(4) Eder, P. S., DeVine, R. J., Dagle, J. M., and Walder, J. A. (1991) Substrate specificity and kinetics of degradation of antisense oligonucleotides by a 3′ exonuclease in plasma. *Antisense Res. Dev. 1*, 141–51.

(5) Schubert, S., Gul, D. C., Grunert, H. P., Zeichhardt, H., Erdmann, V. A., and Kurreck, J. (2003) RNA cleaving '10−23' DNAzymes with enhanced stability and activity. *Nucleic Acids Res. 31*, 5982–5992.

(6) Marcus-Sekura, C. J., Woerner, A. M., Shinozuka, K., Zon, G., and Quinnan, G. V. (1987) Comparative inhibition of chloramphenicol acetyltransferase gene expression by antisense oligonucleotide analogues having alkyl phosphotriester, methylphosphonate and phosphorothioate linkages. *Nucleic Acids Res. 15*, 5749–63.

(7) Wahlestedt, C., Salmi, P., Good, L., Kela, J., Johnsson, T., Hökfelt, T., Broberger, C., Porreca, F., Lai, J., Ren, K., Ossipov, M., Koshkin, A., Jakobsen, N., Skouv, J., Oerum, H., Jacobsen, M. H., and Wengel, J. (2000) Potent and nontoxic antisense oligonucleotides containing locked nucleic acids. *Proc. Natl. Acad. Sci. U. S. A. 97*, 5633–8.

(8) Lesnik, E. A., and Freier, S. M. (1998) What affects the effect of 2′-alkoxy modifications? 1. Stabilization effect of 2′-methoxy substitutions in uniformly modified DNA oligonucleotides. *Biochemistry 37*, 6991–7.

(9) Jäschke, A., Fürste, J. P., Nordhoff, E., Hillenkamp, F., Cech, D., and Erdmann, V. A. (1994) Synthesis and properties of oligodeoxyribonucleotide-polyethylene glycol conjugates. *Nucleic Acids Res. 22*, 4810–7.

(10) Jevsevar, S., Kunstelj, M., and Porekar, V. G. (2010) PEGylation of therapeutic proteins. *J. Biotechnol. 5*, 113–128.

(11) Pasut, G., and Veronese, F. M. (2009) PEG conjugates in clinical development or use as anticancer agents: An overview. *Adv. Drug Delivery Rev. 61*, 1177–1188.

(12) Joralemon, M. J., McRae, S., and Emrick, T. (2010) PEGylated polymers for medicine: from conjugation to self-assembled systems. *Chem. Commun. 46*, 1377–1393.

(13) Rapozzi, V., Cogoi, S., Spessotto, P., Risso, A., Bonora, G. M., Quadrifoglio, F., and Xodo, L. E. (2002) Antigene effect in K562 cells of a PEG-conjugated triplex-forming oligonucleotide targeted to the bcr/abl oncogene. *Biochemistry 41*, 502–10.

(14) Jung, S., Lee, S. H., Mok, H., Chung, H. J., and Park, T. G. (2010) Gene silencing efficiency of siRNA-PEG conjugates: Effect of PEGylation site and PEG molecular weight. *J. Controlled Release 144*, 306–313.

(15) Deiters, A. (2009) Light activation as a method of regulating and studying gene expression. *Curr. Opin. Chem. Biol. 13*, 678–686.

(16) Deiters, A. (2010) Principles and applications of the photochemical control of cellular processes. *ChemBioChem 11*, 47–53.

(17) Riggsbee, C. W., and Deiters, A. (2010) Recent advances in the photochemical control of protein function. *Trends Biotechnol. 28*, 468–75.

(18) Priestman, M. A., and Lawrence, D. S. (2010) Light-mediated remote control of signaling pathways. *Biochim. Biophys. Acta 1804*, 547–58.

(19) Young, D. D., Govan, J. M., Lively, M. O., and Deiters, A. (2009) Photochemical regulation of restriction endonuclease activity. *ChemBioChem 10*, 1612–1616.

(20) Young, D. D., Edwards, W. F., Lusic, H., Lively, M. O., and Deiters, A. (2008) Light-triggered polymerase chain reaction. *Chem Commun.* 462–464.

(21) Lusic, H., Lively, M. O., and Deiters, A. (2008) Light-activated deoxyguanosine: photochemical regulation of peroxidase activity. *Mol. Biosyst. 4*, 508–11.

(22) Young, D. D., Lusic, H., Lively, M. O., Yoder, J. A., and Deiters, A. (2008) Gene silencing in mammalian cells with light-activated antisense agents. *ChemBioChem 9*, 2937–2940.

(23) Kröck, L., and Heckel, A. (2005) Photoinduced transcription by using temporarily mismatched caged oligonucleotides. *Angew. Chem., Int. Ed. Engl. 44*, 471–3.

(24) Tang, X., Swaminathan, J., Gewirtz, A. M., and Dmochowski, I. J. (2008) Regulating gene expression in human leukemia cells using light-activated oligodeoxynucleotides. *Nucleic Acids Res. 36*, 559–69.

(25) Shestopalov, I. A., Sinha, S., and Chen, J. K. (2007) Light-controlled gene silencing in zebrafish embryos. *Nat. Chem. Biol. 3*, 650–651.

(26) Tang, X., Maegawa, S., Weinberg, E. S., and Dmochowski, I. J. (2007) Regulating gene expression in zebrafish embryos using light-activated, negatively charged peptide nucleic acids. *J. Am. Chem. Soc. 129*, 11000–1.

(27) Young, D., Lively, M., and Deiters, A. (2010) Activation and deactivation of DNAzyme and antisense function with light for the photochemical regulation of gene expression in mammalian cells. *J. Am. Chem. Soc. 132*, 6183–93.

(28) Deiters, A., Garner, R. A., Lusic, H., Govan, J. M., Dush, M., Nascone-Yoder, N. M., and Yoder, J. A. (2010) Photocaged morpholino oligomers for the light-regulation of gene function in zebrafish and Xenopus embryos. *J. Am. Chem. Soc. 132*, 15644–50.

(29) Tang, X. J., Su, M., Yu, L. L., Lv, C., Wang, J., and Li, Z. J. (2010) Photomodulating RNA cleavage using photolabile circular antisense oligodeoxynucleotides. *Nucleic Acids Res. 38*, 3848–3855.

(30) Rodrigues-Correia, A., Koeppel, M. B., Schäfer, F., Joshi, K. B., Mack, T., and Heckel, A. (2011) Comparison of the duplex-destabilizing effects of nucleobase-caged oligonucleotides. *Anal. Bioanal. Chem. 399*, 441–7.

(31) Mikat, V., and Heckel, A. (2007) Light-dependent RNA interference with nucleobase-caged siRNAs. *RNA 13*, 2341–2347.

(32) Tang, X., Swaminathan, J., Gewirtz, A. M., and Dmochowski, I. J. (2008) Regulating gene expression in human leukemia cells using light-activated oligodeoxynucleotides. *Nucleic Acids Res. 36*, 559–569.

(33) Abdelgany, A., Wood, M., and Beeson, D. (2007) Hairpin DNAzymes: a new toot for efficient cellular gene silencing. *J. Gene Med. 9*, 727–738.

(34) Georgianna, W. E., Lusic, H., McIver, A. L., and Deiters, A. (2010) Photocleavable polyethylene glycol for the light-regulation of protein function. *Bioconjugate Chem. 21*, 1404–7.

Supporting Information

Stabilization and Photochemical Regulation of Antisense Agents through PEGylation

Jeane M. Govan, Andrew L. McIver, and Alexander Deiters*

[1]*North Carolina State University, Department of Chemistry, Raleigh, NC 27695*
alex_deiters@ncsu.edu

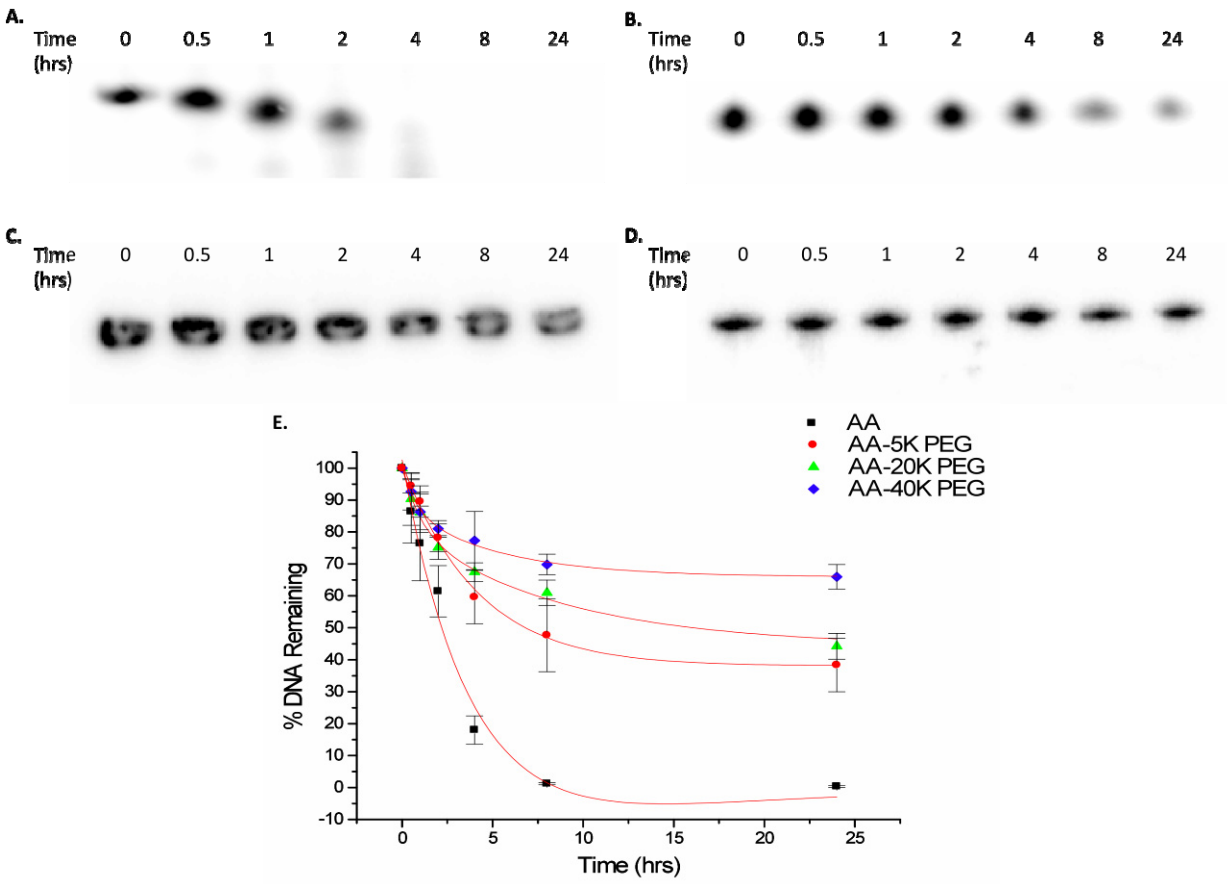

Supporting Figure S1. Stabilization of 3′ PEGylated DNA in DMEM media. (A) Non-modified DNA, (B) 5K PEGylated DNA, (C) 20K PEGylated DNA, and (D) 40K PEGylated DNA were incubated in DMEM (10% FBS) at 37 °C for up to 24 h. The assay was stopped by the addition of denaturing loading dye. Samples were analyzed on a 20% (DNA & 5K PEG), 15% (20K PEG) or 5% (40K PEG) denaturing PAGE gels. (E) Band intensities were quantified using ImageQuantTL and the percent DNA remaining was plotted against time. Error bars represent standard deviations from three independent experiments.

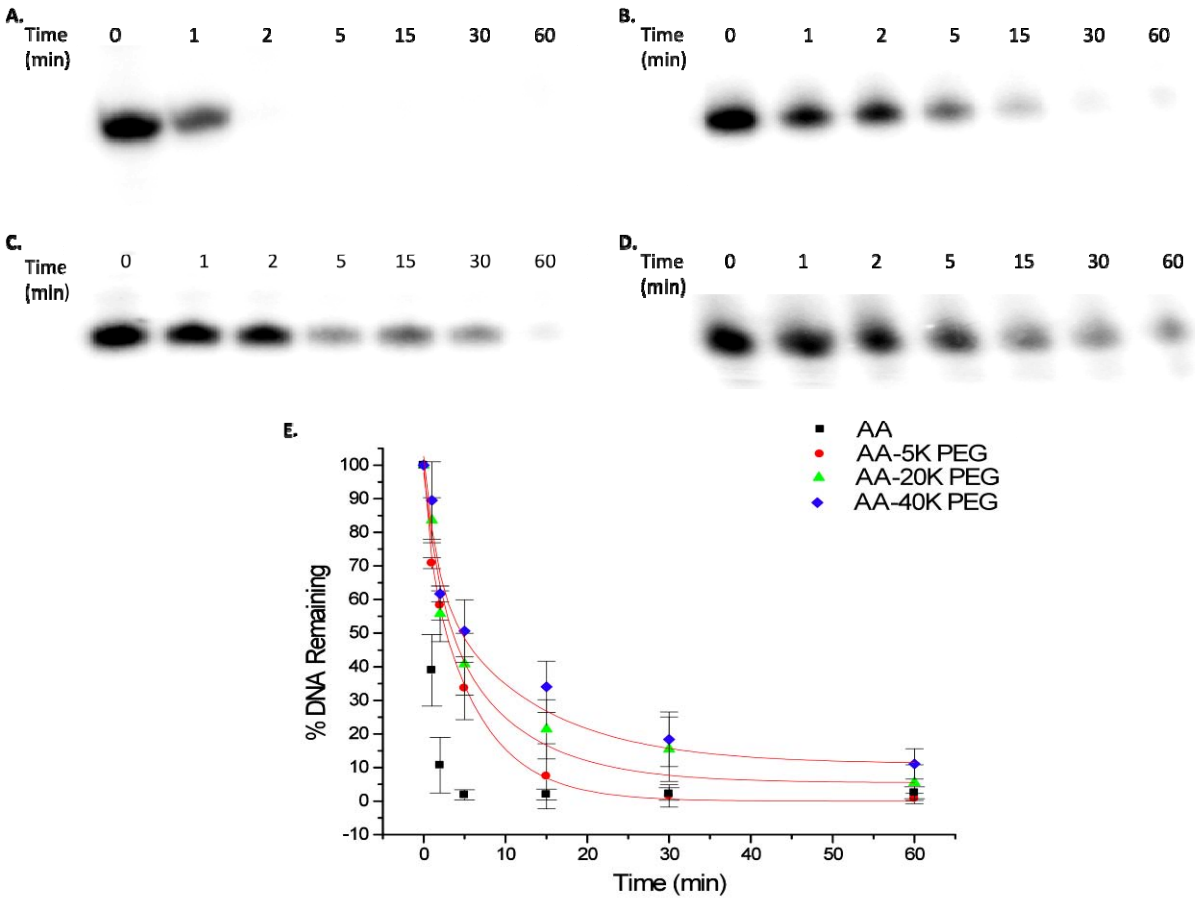

Supporting Figure S2. 3′ PEGylation of DNA protects against ExonucleaseI. Radiolabeled (A) non-modified DNA (B) 5K PEGylated DNA, (C) 20K PEGylated DNA, and (D) 40K PEGylated DNA was incubated with exonucleaseI (5U) at 37 °C for up to 1 h. Samples were heat inactivated at 80 °C for 20 min and then analyzed on a 20% (DNA & 5K PEG), 15% (20K PEG) or 5% (40K PEG) denaturing PAGE gels. (E) Band intensities were quantified using ImageQuantTL and the percent of DNA remaining was plotted against time. Error bars represent standard deviations from three independent experiments.

AA (T_m = 69.2 ± 0.7 °C)

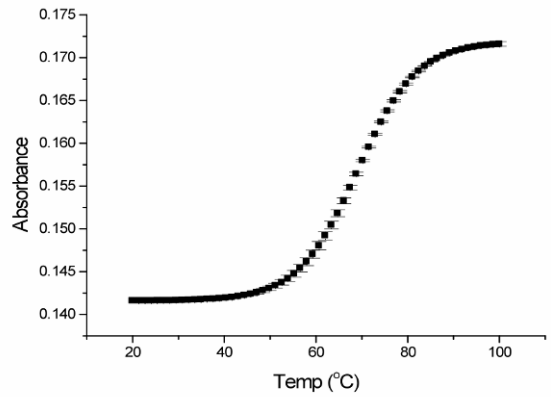

AA-HP (T_m = 61.1 ± 0.8 °C)

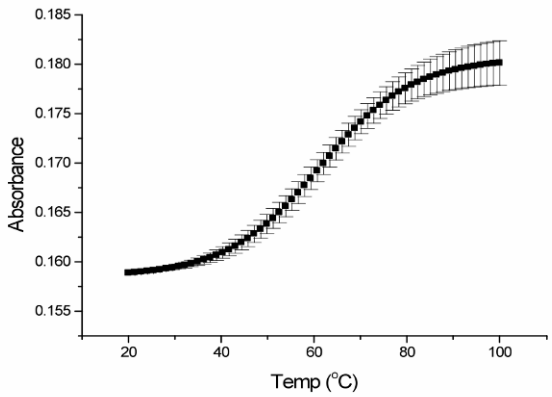

AA-5K PEG (T_m = 63.4 ± 1.3 °C)

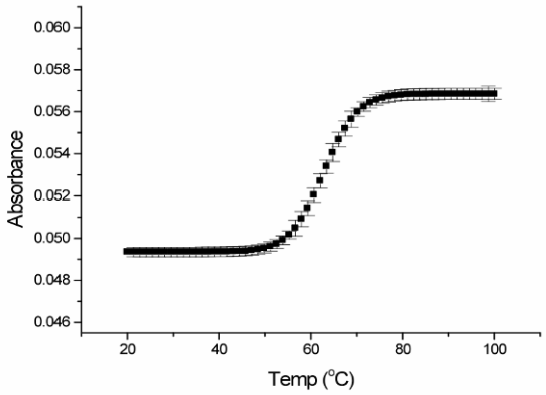

AA-20K PEG (T_m = 56.1 ± 1.5 °C)

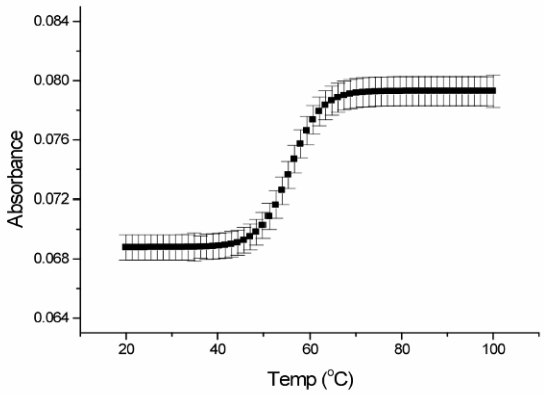

AA-40K PEG (T_m = 50.9 ± 1.9 °C)

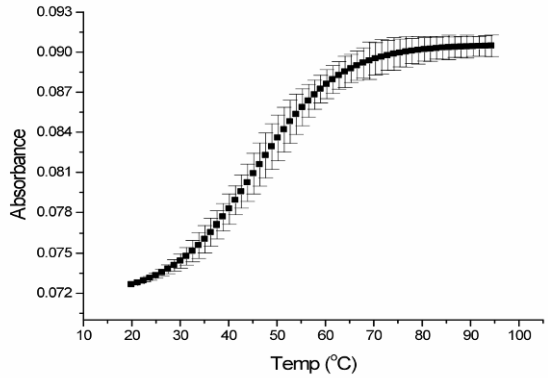

Supporting Figure S3. Melting curves of PEGylated DNA antisense agents with corresponding DsRed mRNA. PEGylated DNA and DsRed mRNA (0.5 μM) were incubated in a phosphate buffer (150 mM NaCl, 50 mM NaH_2PO_4, pH 7.4). Error bars represent standard deviations from three independent experiments.

Bioconjugate Chemistry

ARTICLE

pubs.acs.org/bc

Hydrazide Reactive Peptide Tags for Site-Specific Protein Labeling

Glenn M. Eldridge[†] and Gregory A. Weiss[*,†,‡]

[†]Department of Chemistry and [‡]Department of Molecular Biology and Biochemistry, University of California, Irvine, 1102 Natural Sciences 2, Irvine, California 92697-2025, United States

Supporting Information

ABSTRACT: New site-specific protein labeling (SSPL) reactions for targeting-specific, short peptides could be useful for the real-time detection of proteins inside of living cells. One SSPL approach matches bioorthogonal reagents with complementary peptides. Here, hydrazide reactive peptides were selected from phage-displayed libraries using reaction-based selections. Selection conditions included washes of varying pH and treatment with $NaCNBH_3$ in order to specifically select reactive carbonyl-containing peptides. Selected peptides were fused to T4 lysozyme or synthesized on filter paper for colorimetric assays of the peptide−hydrazide interaction. A peptide−lysozyme protein fusion demonstrated specific, covalent labeling by the hydrazide reactive (HyRe) peptides in crude bacterial cell lysates, sufficient for the specific detection of an overexpressed protein fusion. Chemical synthesis of a short HyRe tag variant and subsequent reaction with two structurally distinct hydrazide probes produced covalent adducts observable by MALDI-TOF MS and MS/MS. Rather than isolating reactive carbonyl-containing peptides, we observed reaction with the N-terminal His of HyRe tag **114**, amino acid sequence HKSNHSSKNRE, which attacks the hydrazide carbonyl at neutral pH. However, at the pH used during selection wash steps (<6.0), an alternative imine-containing product is formed that can be reduced with sodium cyanoborohydride. MSMS further reveals that this low pH product forms an adduct on Ser6. Further optimization of the novel bimolecular reaction described here could provide a useful tool for *in vivo* protein labeling and bioconjugate synthesis. The reported selection and screening methods could be widely applicable to the identification of peptides capable of other site-specific protein labeling reactions with bioorthogonal reagents.

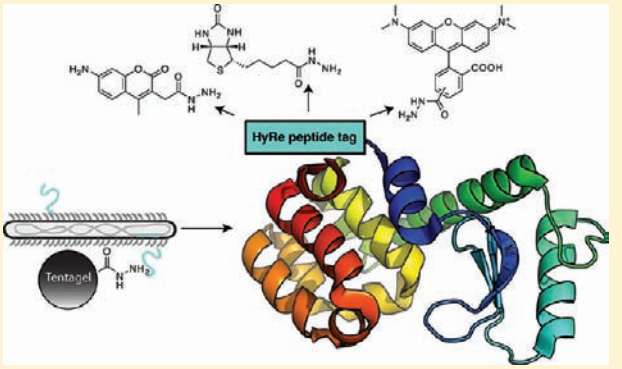

INTRODUCTION

Site-specific protein labeling (SSPL) provides a powerful tool for the *in vivo* tracking of protein localization, dynamics, and concentration.[1,2] SSPL enables visualization of specific proteins through conjugation to an appropriately functionalized probe. Genetically encoded fluorescent protein fusions provide a facile route to site-specific protein labeling[3] and are the current standard in labeling technology;[4] however, the large size and limitation to a fluorescent signal has stimulated a search for smaller and chemically flexible labeling strategies. One route, enzymatic labeling of genetically encoded peptide substrates, is useful in forming fluorescent conjugates *in vivo*, and has been reviewed recently.[5,6] Another powerful approach harnesses unique peptide sequences capable of forming covalent bonds with chemical probes. The latter approach does not require additional enzymes or reagents. Here, for example, we describe the selection, screening, and characterization of hydrazide reactive peptides (Figure 1).

Nonenzymatic SSPL reactions have revolutionized protein purification and visualization. For example, short polyhistidine peptides ("His-tags") selectively coordinate nickel (Ni^{2+}), or cobalt (Co^{2+}) chelated to a solid support. A genetically encoded His_6-tag enabled purification of dihydrofolate reductase from crude, *E. coli* cell lysate under both native and denaturing conditions.[7] Used by innumerable laboratories for protein purification, His-tags can also enable protein visualization via binding to a fluorescent, zinc-conjugated small molecule (HisZiFiT).[8] Another stand-alone, probe-reactive peptide, uses the tetracysteine motif (amino acid sequence CCXXCC) to selectively react with fluorogenic bisarsenical probes *in vitro* and *in vivo*.[9−11] Other short peptides are capable of being modified with fluorescent probes and include labeling of tetraserine motifs by bisboronic acids,[12] polyaspartic acids by zinc fluorophores,[13] and lanthanide binding peptides with lanthanide ions.[14,15]

Discovery of new SSPL peptide−probe pairs requires both a modestly reactive small molecule and a unique, complementary peptide. The small molecule must be stable to physiological conditions, yet reactive upon peptide binding. The partnering reactive peptide is ideally short enough to minimize misfolding and mislocalization of the fused protein, yet sufficiently long to ensure unique representation in the proteome. Suited for the identification of such complementary peptides, phage display enables the rapid sifting of vast libraries to identify peptides with affinity for essentially any target, including proteins,[16,17] small

Received: July 28, 2011
Revised: September 10, 2011
Published: September 12, 2011

ACS Publications © 2011 American Chemical Society

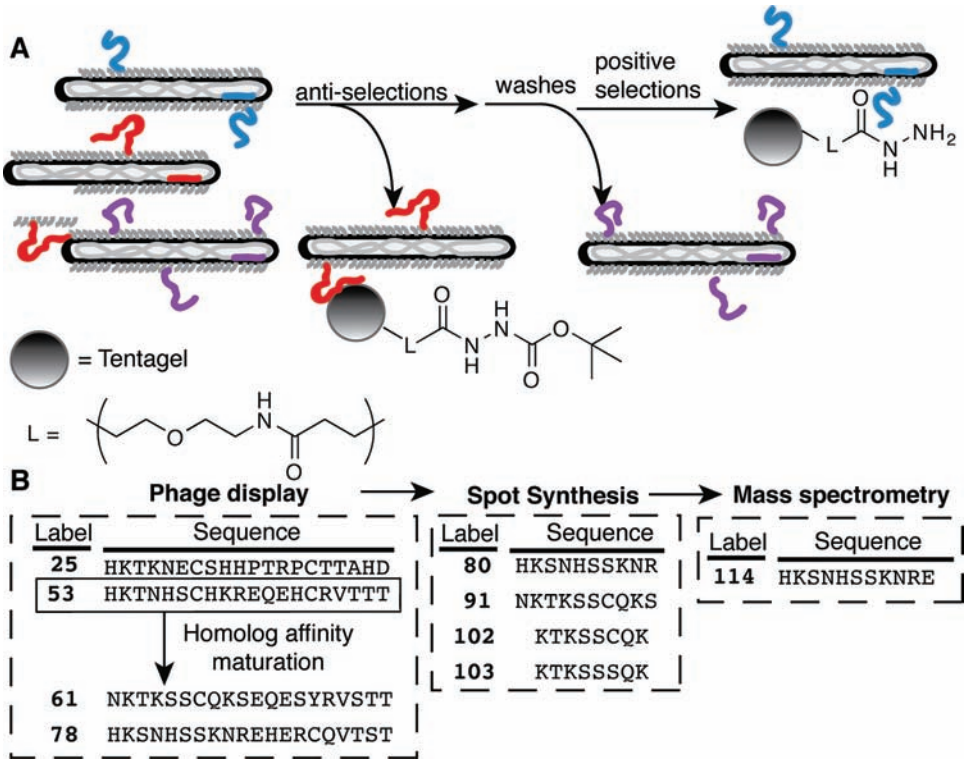

Figure 1. (A) Selections for hydrazide binding peptides included antiselections with Boc-protected hydrazide resin to remove nonspecific peptides (e.g., the red peptide), positive selections with hydrazide-derivatized resin to capture hydrazide interacting peptides (e.g., the blue peptide), and extensive wash steps to remove nonbinding peptides (e.g., the purple peptide). (B) Sequences of peptides discussed in the text from selections of phage-displayed peptide libraries, spot synthesis, and chemical synthesis followed by mass spectrometry analysis.

molecules,[1] and inorganic materials.[18] The filamentous bacteriophage used in phage display links the encoding DNA sequence to the displayed peptide, providing easy routes to both amplify and identify the selected peptides.[19,20]

Two examples illustrate the utility of phage display to identify either noncovalent or covalent SSPL peptide−probe pairs. First, conventional affinity-based phage display identified tightly binding peptides that modulate the fluorescence of Texas red.[21] After many rounds of optimization, a 38-residue peptide tethered via an intramolecular dimerization domain was developed that noncovalently bound a calcium-sensitive Texas red derivative with a K_D of 80 pM.[22] Second, reaction-based phage display targeted a diketone to isolate the 20-mer peptide rpf1368, which forms enaminones with various diketone-containing probes.[23] The reported peptides from the initial rounds of selection for both of these examples proved functional yet inefficient. Further optimization of the peptides through appending additional libraries to previously selected sequences and performing more stringent selections ultimately yielded tighter-binding or more reactive peptides.[22,23]

Other functionalities could be amenable to the discovery of bioorthogonal peptide−probe pairs using either affinity or reaction-based phage display. Side-chain modifying electrophiles, such as iodoacetamide and *N*-hydroxy succinamide are exceptional modifying agents for cysteine and lysine, respectively. These functionalities are insensitive to 3D sequence space, and can modify exposed side chains. Therefore, these reagents are restricted to use with purified proteins. Considering the nucleophilic nature of biopolymers, nucleophilic probes should be vastly more discriminating toward specific amino acid sequences. Thus, we focused on a nucleophilic functionality with known bioorthogonality toward proteins. Hydrazides do not react with unmodified biopolymers, but are used to label and isolate oxidized molecules with reactive carbonyls.[24] Reactive carbonyl-containing proteins, for example, can be purified from biological samples using biotin hydrazide and surface-bound avidin for mass spectrometry identification.[25,26]

Reactive carbonyls can also be introduced into protein sequences through enzymatic labeling of peptide substrates. Ligation of a ketone-containing probe to an acceptor peptide with biotin ligase generates a reactive carbonyl for modification with hydrazide probes.[27] Similarly, formylglycine-generating enzyme modifies cysteine in the sequence LCTPSR to generate a reactive carbonyl for subsequent hydrazide labeling.[28] These peptides are easily incorporated as fusions to proteins of interest for labeling with either hydrazide- or aminooxy-derivatized compounds, after treatment with the appropriate enzyme.[28,29] Unnatural amino acid incorporation can also introduce ketone-based amino acids.[30,31]

We sought to simplify protein labeling with hydrazide probes by identifying peptides with affinity for hydrazide, thus eliminating the need for the coexpression of a modifying enzyme. Hydrazides can interact with polypeptides in four different mechanisms (Figure 2). First, hydrazides would form hydrazones with reactive carbonyls present in oxidized peptides. A large number of spontaneous reactions introduce reactive carbonyls into protein sequences including conjugation to oxidized lipids and oxidation of susceptible amino acids (such as the side chains of arginine, histidine, lysine, or proline); both reactions occur during some age- and disease-related stresses.[32,33] In addition, peptides from a phage-displayed library could act as substrates for

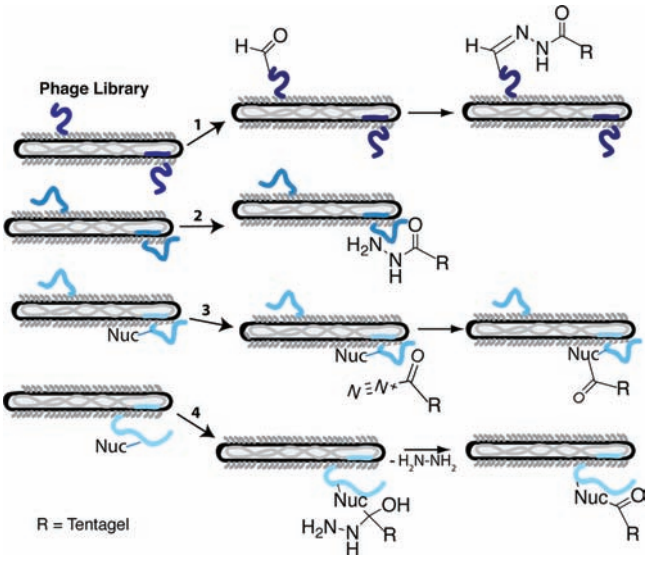

Figure 2. Potential mechanisms for the selection of hydrazide interacting peptides from phage-displayed libraries include oxidation of susceptible peptides (**1**) for capture with hydrazide-derivatized Tentagel via hydrazone bond formation. Additionally, phage-displayed peptides could form high-affinity noncovalent interactions with the hydrazide functionality (**2**). Alternatively, the hydrazide functional group could be oxidized and attacked by a peptide nucleophile liberating nitrogen gas (**3**). Lastly, a nucleophile from the displayed peptide could attack the carbonyl of the hydrazide functional group, displacing hydrazine (**4**).

carbonyl-forming enzymes such as the formylglycine-generating enzyme, described above.[34] Therefore, peptides susceptible to either enzymatic or atmospheric oxidation would react with hydrazide-based capture agents.

Alternatively, peptides could noncovalently bind to the probe, as was discovered for the Texas red binding peptides. However, the small size of the hydrazide group might preclude high-affinity binding. Contrary to peptide oxidation, the hydrazide functional group could be selectively oxidized, thereby presenting an electrophile for attack by a peptide nucleophile before displacement of nitrogen. The enzyme tyrosinase oxidizes acylhydrazide to an acyl diazene, to liberate nitrogen; and has been used as a chemical deprotection strategy.[35] In the fourth mechanism, a peptide nucleophile could attack the hydrazide carbonyl, exhibiting similar reactivity as cysteine proteases such as cathepsin K inhibition by acylhydrazide inhibitors. In this example, the active site cysteine attacks the carbonyl of the acylhydrazide resulting in a stabilized tetrahedral intermediate.[36]

Thus, reaction-based phage selections for peptides interacting with the hydrazide functional group could explore a number of different reaction possibilities to expand the palette of bioorthogonal peptide−probe pairs (Figure 1). After five rounds of selection and DNA sequencing of the selected phage to determine trends of the peptide interactions with the hydrazide functionality, one sequence was chosen for further affinity maturation by homologue shotgun scanning. The selected peptides were screened for interaction with hydrazide probes through fusion to T4 lysozyme. After homologue affinity maturation, the interaction of selected peptides with biotin hydrazide was compared through peptide spot synthesis and screening. The most promising short peptides identified by spot synthesis were chemically resynthesized, treated with hydrazide-containing probes, and analyzed by mass spectrometry. Given the reactivity of hydrazides with ketones and aldehydes, we expected to isolate oxidation-susceptible peptides. Instead, the isolated 20-mer peptides are nucleophilic toward certain hydrazide derivatives.

EXPERIMENTAL PROCEDURES

Selections for Hydrazide Binding Peptides. To remove background-binding peptides, an antiselection was performed by incubating a previously described, phage-displayed peptide library[37] with Boc-hydrazide Tentagel for 1 h at room temperature in a peptide reaction vessel. The unbound phage were next subjected to a positive selection through incubation with a new aliquot of deprotected, hydrazide Tentagel for 20−60 min with decreasing concentrations of resin in each round. The hydrazide-bound phage were washed three to six times with increasing volumes of PBS (from 10 to 50 mL) and times (from 2 to 20 min) for each subsequent round. Additional wash steps to enhance the stringency of selections included two washes with HCl (0.1 M, 1.5 mL) in rounds 1 and 2, and three to six washes of HCl (0.1 M, 50 mL) in rounds 4 and 5. The phage−resin mixture was then rebuffered with a wash of PBS (50 mL, 10 min) before being resuspended in PBS (1.5 mL) for storage and propagation. Half of the phage−Tentagel suspension was incubated with 10 mL of XL-1 blue *E. coli* (OD_{600} = 0.5−1.0) for 20 min with shaking at 37 °C. A small aliquot of the infected cells was titered on LB-carbenicillin-agar plates, and the remaining culture was transferred to 2YT (250 mL) supplemented with M13-KO7 helper phage before overnight incubation at 37 °C with shaking. Individual colonies from the titer plate were sequenced following PCR using M13 primers (Supporting Information).

Bacterial Subcloning and Overexpression of HyRe−Lysozyme Fusion. The selected peptides were subcloned into a plasmid encoding each peptide fused through a GGGSG linker to the N-terminus of T4 lysozyme (Supporting Information). Correctly ligated plasmids were transformed into heat shock competent BL21(DE3) *E. coli*. An overnight 37 °C culture (10 mL LB, 40 μg/mL kanamycin) was added to 1 L of LB media supplemented with kanamycin (40 μg/mL), and grown for an additional ∼2.5 h at 37 °C to an OD_{600} of 0.6. The addition of IPTG (1 mM) induced protein expression at 30 °C for 4 h. Following centrifugation and sonication, the crude supernatant was purified using cation exchange chromatography. Protein fusions were eluted with a gradient to 1 M NaCl and fractions containing the protein fusion were then combined and concentrated. Gel permeation chromatography further purified fusion proteins to >95% homogeneity (Figure S2 A in Supporting Information).

Biotin Hydrazide and Rhodamine B Hydrazide Binding Assay to HyRe 53-T4 Lysozyme Fusion. Following purification, the HyRe peptide **53**-T4 lysozyme fusion, the proteolyzed peptide **53**-T4 lysozyme fusion, or wild-type T4 lysozyme was treated with either biotin hydrazide (1 mM in PBS for 1 h at room temperature) or an equivalent volume of buffer (negative controls) before the addition of SDS loading dye (20% volume). The solution was then incubated at 95 °C for 3 min to denature the proteins. The denatured protein samples were added to two 15% SDS-page gels before electrophoresis at a voltage of 130 V for 90 min. One protein gel was Coomassie-stained, and the other gel was transferred to a nitrocellulose membrane via electrophoresis in transfer buffer (25 mM Tris base, 192 mM glycine, 20% methanol, 0.02% SDS, pH 8.3) at 100 V for 100 min. This

nitrocellulose membrane was blocked with 1.0% Tween 20 in PBS overnight at 4 °C. Biotinylation was assessed by incubating the membrane with SAV-AP at room temperature for 1 h. This membrane was washed five times with PT before visualization by treatment with 4-chloro-1-naphthol and 3,3′-diaminobenzidine, tetrahydrochloride (Pierce) before image capture. Binding to a hydrazine fluorophore was visualized by adding rhodamine B hydrazide (final concentration 1 mM) was added to crude lysates for 1 h at room temperature, before SDS-PAGE and electrophoretic transfer to nitrocellulose as before. The blot was then visualized using a GE Typhoon scanner (532 nm laser, 580 bp 30 filter, 400 PMT voltage).

Spot Synthesis and Assay of HyRe Peptide Variants. Peptides were synthesized as C-terminal adducts to filter paper, and deprotected as outlined in ref 47. A background-binding assay was completed by incubating the sheets of spot-synthesized peptides with SAV-HRP, before visualization with BCIP/NBT. The AP substrates, BCIP (135 mM in DMF) and NBT (61 mM in 70% DMF), were added to AP buffer (100 mM Tris, 100 mM NaCl, 2 mM $MgCl_2$, 0.05% Tween-20, pH 9.5) to a final concentration of 445 μM and 403 μM, respectively. This buffer was added to the spot-synthesized peptide cellulose sheets, and incubated for 5 min. After washing five times, images of the sheets were captured by digital photography under white light illumination. Peptides specifically binding to biotin hydrazide were then assayed by incubating biotin hydrazide (0.17 mM) in PBS for 2 h. The sheet was then washed five times (50 mL, 2 min each), before readdition of SAV-HRP, revisualization with BCIP/NBT, and reimaging.

HyRe Peptide Synthesis and Reaction with Hydrazide Derivatives. Peptides **103** and **114** were synthesized on a 0.2 mmol scale using standard solid-phase peptide synthesis with Fmoc-protected amino acids (Aroz technologies) on Rink amide resin (Novabiochem). The synthesized peptides were cleaved, purified, and characterized, using standard conditions (Figures S7 in Supporting Information). The purified peptides were resuspended in water before dilution into PBS to a 1 mM final concentration. The hydrazides dissolved in DMSO were then added to each peptide (1 mM final concentration), and incubated at room temperature for 1−3 h before desalting with C_{18} peptide desalting Zip-Tips (Varian; Palo Alto, CA) and characterized by MALDI-TOF MS.

RESULTS

Selections of Hydrazide Ligands from a Phage Library. The naïve, M13 phage-displayed peptide library included ∼2.5×10^{10} unique sequences fused to the major coat protein, P8. This collection of peptide sequences included 22 different configurations of disulfide-constrained peptide libraries and one linear peptide library, ranging in length from 8- to 20-mers[37,38] (Table S1 in Supporting Information).

Molecular display selections can sometimes fail due to deleterious amplification of "background binding" peptides; such peptides are selected for binding to either the solid support or blocking agents employed during selection, and do not specifically bind to the target. Background binding peptides are removed from the phage library through antiselections using similar selection conditions without the target. Thus, before each round of selection, an antiselection with Boc-hydrazide Tentagel removed peptides with an affinity for Tentagel. The antiselected phage library was added to a second aliquot of deprotected hydrazide Tentagel, and used to select phage-displayed peptides with affinity for hydrazide (Figure 1A). This water-miscible solid support enables stringent wash steps to remove nonspecific binding peptides during positive selections. Up to half a liter of different wash buffers was applied to 20 mg of resin during each round of selection. Additionally, in an effort to ensure capture of oxidized peptides, the phage library was subjected to treatment with sodium cyanoborohydride ($NaCNBH_3$), and washes of varying pH. The reactive carbonyl-hydrazide reaction is reversible at low pH,[39] which in round 1 provided a route to selectively elute bound phage from the Tentagel. Sodium cyanoborohydride will reduce hydrazones, [40] permanently linking the selected phage to the Tentagel. After five rounds of increasingly stringent selection conditions (including shorter reaction times, lower concentration of target resin, and increasing numbers of longer washes), the amino acid sequences of 74 phage-displayed, hydrazide interacting peptides were determined by DNA sequencing to yield 58 distinct sequences (Table S2 in Supporting Information).

In round 1, 4.4×10^7 phage were isolated, but more stringent conditions in round 2 reduced the phage titers to 6.6×10^5 plaque forming units, and 2.2×10^6 phage colonies in round 3. The titers then equilibrated to 1×10^7 for the final two rounds of selection. More importantly, 30% of the first round of selection was identified as empty phagemid by sequencing, whereas 0% of the selectants in rounds 2−5 were empty phagemid. The reduced presence of empty phagemid in the selected pool demonstrates a successful selection for functional phage-displayed peptides.

The success of molecular display selections can be gauged by sequence homology and other trends in the sequences of selectants.[41] In selections for binding to hydrazide Tentagel, hydrophilic amino acid side chains were enriched during selections, and hydrophobic amino acid side chains were almost entirely absent from the selected sequences. Furthermore, the sequences from selection rounds 3−5 were entirely derived from 2 of the 23 peptide scaffolds, $X_7CX_4CX_7$ and $X_6CX_7CX_5$ (where X represents any of the 20 naturally occurring amino acids). Several peptides appeared in multiple rounds of selection, including peptide **25**, identified in selection rounds 2 through 5, and peptide **53**, which accounted for ∼30% of the isolated sequences from the final 2 rounds of selection.

Next, peptides with potentially higher affinity for hydrazide were selected using homologue shotgun scanning. This method applies a protein-based, medicinal chemistry approach with a library composed of either the wild-type or closely homologous amino acid.[42,43] This library strategy focuses peptide diversity space, and selects for subtle side chain substitutions that can collectively contribute large effects to binding affinity. Additionally, conserved residues during these selections can indicate functionally important side chains.

Chosen for its high frequency among the initial selectants, peptide **53** formed the basis for a homologue shotgun-scanning library. Unlike previous homologue shotgun-scanning libraries, each amino acid position encoding His, Arg, or Lys was substituted with a library codon encoding His, Lys, Arg, Asn, Ser, Pro, or Gln. These additional amino acid residues were included for their observed importance in hydrazide binding from the initial library selectants. Reaction-based selections analogous to those described above isolated an additional 23 hydrazide interacting peptides (Table S2 in Supporting Information). Peptide **61** was identified in homologue shotgun scanning rounds 2 through 4, and peptide **78** dominated round 4,

accounting for 60% of the selectants. Additionally, valine at position 17 and glutamic acid at positions 11 and 13 were highly conserved, suggesting the importance of those residues for hydrazide binding (Figure S1C in Supporting Information).

Notably, highly enriched peptides, **61** and **78**, include only one cysteine residue. Thus, the intramolecular disulfide bonds engineered into the naïve libraries appeared unnecessary for hydrazide binding. This result contrasts with previous studies in which intramolecular disulfide bonds in peptides selected from phage-displayed peptide libraries contribute critical stability to peptide structure for target binding.[44,45] This observation presented the opportunity, explored below, to eliminate cysteine residues in chemically synthesized versions of the selected peptides.

Typically, screens examining the functionality of individual phage-displayed selectants quantify the relative binding abilities of selectants from a library. Conventional screens for hydrazide binding with phage-displayed peptides proved problematic due to cross-reactivity between biotin hydrazide and contaminants remaining in the phage solutions, likely oxidized proteins. Two screening approaches explored the capabilities of the selected hydrazide interacting peptides. First, the gene for peptide **53** was fused to a test protein T4 lysozyme for colorimetric assays. Second, peptides and peptide variants from both the original selections and the homologue shotgun scanning selections were spot-synthesized on filter paper.

Hydrazide Binding to Peptide-T4 Lysozyme Fusions. To test the reaction specificity of the selected peptides, the frequently selected peptide **53** was subcloned into an expression plasmid (pET-28c, Invitrogen) as an N-terminal fusion to the enzyme T4 lysozyme. The purified fusion protein was then treated with biotin hydrazide (1 mM) for two hours at room temperature in aqueous buffer (PBS at pH 7.2). SDS-PAGE and subsequent binding assay of the lysozyme fusions, either treated or untreated with biotin hydrazide, demonstrated that fusion to peptide **53** conferred biotin−hydrazide binding ability (Figure 3, lanes 1−2). Sustained affinity during the denaturing conditions required for SDS-PAGE (95 °C in SDS) can provide evidence for covalent labeling of peptide−probe interactions (e.g., the bis-arsenical tetracysteine peptide reaction).[10] Therefore, additional mass spectrometry-based experiments were performed to identify the covalent adducts formed by hydrazide reactive (HyRe) peptide **53** and its variants reacting with hydrazide derivatives.

As might be expected for fusions to a well-folded protein separated by a glycine linker (amino acid sequence of GGGSG), the peptide lysozyme fusions are susceptible to proteolysis (Figure 3, lanes 1−2). HyRe peptide **53** is completely removed from the N-terminus of lysozyme by endogenous protease activity (Figure 3, lanes 3−4), as confirmed by MALDI-TOF mass spectrometry (Figure S2 C in the Supporting Information). Proteolytic removal of the HyRe tag prevents reaction with biotin hydrazide (Figure 3B, lane 3), and no signal is observed in the biotin-binding assay. Comparable results are observed for the negative control, treatment of wild-type lysozyme with biotin hydrazide (Figure 3B, lanes 5−6). Selective proteolysis from the N-terminus of lysozyme demonstrates that biotin hydrazide reacts site-specifically with the HyRe tag and not with the other amino acids of lysozyme.

Additionally, rhodamine B hydrazide reacts exclusively with the **53**−lysozyme fusion protein in crude *E. coli* lysate (Figure 3D). Following SDS-PAGE and electrophoretic transfer to nitrocellulose of the crude lysate reaction mixture, the fluorescent probe labels only the fusion protein. Taken together, the experiments with lysozyme fusion show that two different hydrazide derivatives selectively label HyRe peptide **53**. Therefore, further characterization of the interaction between HyRe peptide tags and hydrazide-containing probes focused on a covalent reaction.

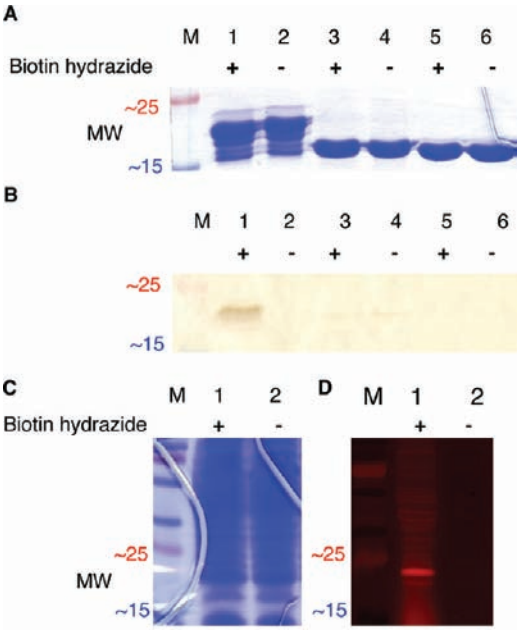

Figure 3. (A) SDS-PAGE of the purified **53**−lysozyme fusion protein (22.3 kDa in lanes 1−2), the fully proteolyzed **53**−lysozyme fusion protein (19.2 kDa in lanes 3−4), and wild-type lysozyme (18.6 kDa in lanes 5−6). Each sample was either treated (+) or untreated (-) with biotin hydrazide (1 mM) for 1 h at room temperature before electrophoresis. (B) Western blot analysis for biotin hydrazide labeling the purified **53**−lysozyme fusion protein. The protein gel and Western blot, excerpted for clarity here, are shown in full in Figure S2 in Supporting Information. (C) SDS-PAGE of the **53**−lysozyme fusion protein in crude *E. coli* lysates, either treated (+) or untreated (-) with 1 mM rhodamine B hydrazide before separation by SDS-PAGE. (D) The protein lysate shown in (C) was then transferred electrophoretically to nitrocellulose, and imaged by fluorescence scanning. "M" indicates molecular weight standards.

Spot Synthesis of Hydrazide-Interacting Peptides. Peptides **61**, **78**, and **53** and variants of all three were chemically resynthesized using spot synthesis. In this technique, each peptide is covalently attached as a C-terminal fusion to spatially segregated positions on a cellulose membrane.[46,47] Spot synthesis allows for the simultaneous fabrication and screening of hundreds of different peptides in a format free from biological contaminants such as post-translational modifications by enzymes (e.g., formylglycine-generating enzyme)[34] or reactive carbonyl-containing metabolites (e.g., pyridoxal phosphate).[48,49] The synthesized analogs of peptides **61** and **78** included sequential 10-mers and single-site alanine substitutions. Scanning sequential 10-residue peptides could identify smaller active sequence of the HyRe tag. The spot-synthesized variants of peptide **53** included all 1, 2, 3, and 4 contiguous amino acid deletions. Additionally, the homologue shotgun scanning results suggested substitution of serine for cysteine in the HyRe peptide tags. Three different spot synthesis cellulose sheets containing over 350 different variants were synthesized and screened for

binding to biotin hydrazide (Figures S3−S5 in Supporting Information).

Following deprotection of the spot-synthesized peptides, the relative binding affinity for biotin hydrazide was assayed by treatment with streptavidin conjugated to alkaline phosphatase (SAV-AP) and developed through addition of the AP substrates 5-bromo-4-chloro-3-indolyl phosphate (BCIP) and nitrotetrazolium blue (NBT). The levels of SAV-AP activity in each spot can provide an estimate of the efficiency of each peptide in the reaction with biotin hydrazide. However, many factors can influence the signal intensity at individual spots including peptide synthesis failure and purity.[50] Additionally, identical sequences in different locations on the filter paper produced slightly variant levels of reactivity with hydrazide (see HyRe tag **53** in Figure 4). Thus, the qualitative analysis of spot synthesis reported here focuses on trends and requirements for hydrazide−peptide reactivity.

Testing all possible contiguous 10-mers from both HyRe tags **61** (peptides 80−90) and **78** (peptides 91−101) revealed the importance of the N-terminal amino acids for reactivity with biotin hydrazide (Figure S6 in Supporting Information). The 10-residues at the N-terminus of peptide **78**, labeled peptide **80**, resulted in the highest overall signal intensity for reaction with biotin hydrazide on spot synthesis sheet 1, a result confirmed through duplicated synthesis and screens (Figure 4). However, peptide **80** also exhibited high background signal in the SAV-AP assay. This independent assay for background included all steps except treatment with biotin hydrazide, and measures peptide interaction with SAV-AP or the ability of the peptides to dephosphorylate BCIP.

The spot synthesis screens guided the synthesis of HyRe tags with both reactivity toward biotin hydrazide and reduced background binding. For example, HyRe peptide **91**, the N-terminal 10 residues of HyRe tag **61**, reacted efficiently with biotin hydrazide, but also had high background binding to SAV-AP. Further minimization via spot synthesis and screening identified HyRe peptide **102**, an 8-mer peptide derived from HyRe tag **61**, which resulted in the highest specific reactivity with biotin hydrazide relative to background levels. HyRe tag **102** includes one cysteine residue; therefore, the Cys7Ser substitution, peptide **103**, was also spot-synthesized. This cysteine-free 8-mer peptide produced a signal equivalent to peptide **102**, and also exhibited little background in the SAV-AP assay (Figure 4). Thus, as observed by homologue shotgun scanning, cysteine residues from the original selected HyRe tags can be omitted in homologue variants of peptide **53** without drastically reducing reactivity with biotin hydrazide.

Single-point alanine substitutions of every residue in HyRe **61** and **78** had little effect on the qualitative reactivity of HyRe peptides with biotin hydrazide. Given the relative insensitivity for single-point alanine substitutions, we next examined contributions made by each type of amino acid side chain to HyRe tag function by substituting all occurrences of each amino acid with alanine (Figure 4). For example, peptide **104** substituted all four threonines of peptide **53** with alanine. Subsequent reaction with biotin hydrazide and assay of the ten spot-synthesized peptides demonstrated the critical importance of arginine, histidine, and lysine side chains. Conversely, HyRe peptide **110** substituted Ala in place of both Glu residues, and resulted in increased background binding to SAV-AP. The importance of glutamic acid in position 11 also correlates to the conserved glutamic acids observed in homologue affinity selections (Figure S1 in Supporting Information). The spot-synthesis results guided the choice of peptides for large-scale synthesis.

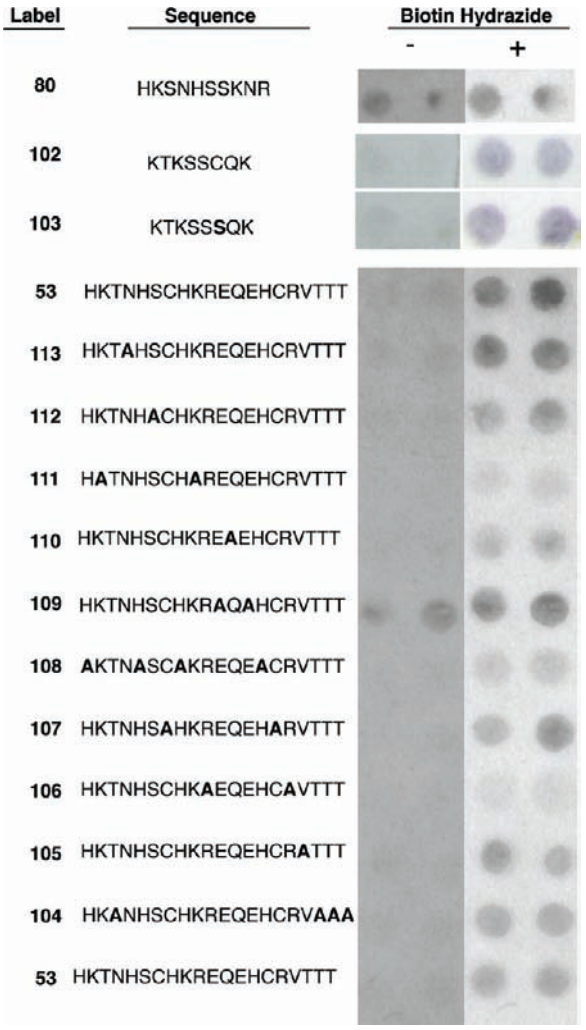

Figure 4. Variants of selectant peptides were spot-synthesized and either treated (+) or untreated (-) with biotin hydrazide before binding to SAV-AP and visualization through addition of the AP substrate. The N-terminal 10-mer from peptide **78** produces a nonspecific signal in the SAV-AP assay. An 8-mer from peptide **61** produces a specific signal for biotin hydrazide, as does the Cys7Ser substituted 8-mer, **103**. Each type of amino acid in peptide **53** was substituted with alanine to identify key side chain functionalities required for the interaction with biotin hydrazide, while the other residues of peptide **53** remained unchanged. Bold letters indicate substitutions in the selected peptides.

Synthesis and Mass Spectrometry Analysis of HyRe Peptides. Two peptides identified initially from phage selections with hydrazide Tentagel and then minimized by screening spot-synthesized peptides were chosen for additional analysis: peptide **114**, the N-terminal 11-residues from peptide **78** including the specificity determining Glu11, and peptide **103**, residues 2 through 9 with the Cys7Ser substitution of HyRe peptide **61**. After conventional solid-phase peptide synthesis, HPLC purification, and MALDI-TOF MS confirmation (Figure S7 in the Supporting Information), the synthesized HyRe peptides were treated with 12 different hydrazide-containing small molecules (structures shown in Figure S8) at equimolar concentrations (1 mM) in PBS, pH 7.2. The reactions were monitored by

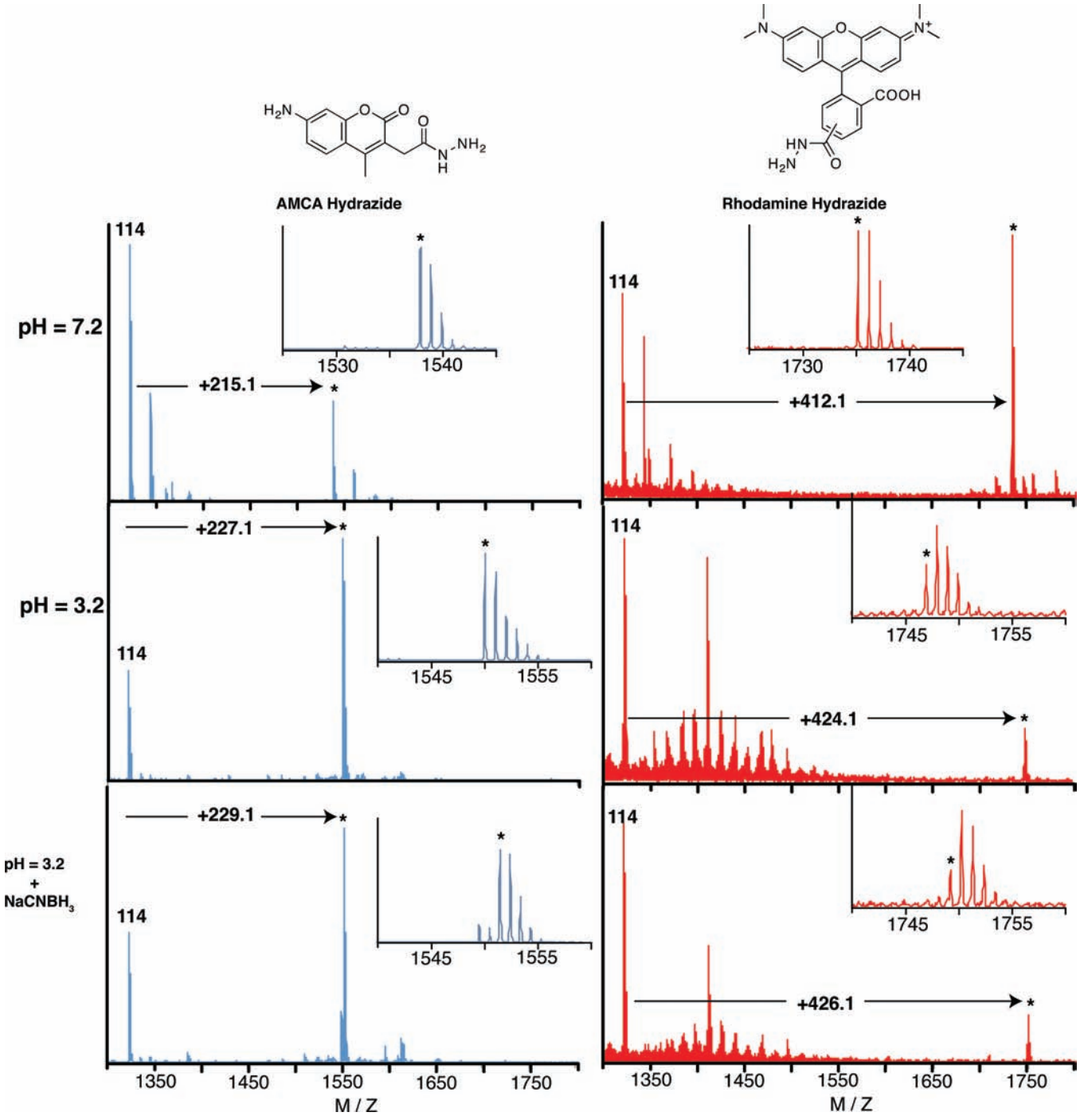

Figure 5. Treatment of peptide **114** with two hydrazide-containing probes. Treatment with AMCA hydrazide at pH 7.2 produces a species with an additional mass of 215 mass units. However, treatment at pH 3.2 produces an adduct with an additional 227 mass units, which can be reduced with $NaCNBH_3$. Treatment of **114** with rhodamine B hydrazide produces similar species at both pH 7.2 and 3.2, as well as upon reduction. The peaks marked with an asterisk (*) are the new adducts observed upon treatment with the hydrazide-containing probes.

MALDI-TOF mass spectrometry (Figure 5). Interestingly, only AMCA hydrazide (aminomethylcoumarin acetate hydrazide) and rhodamine B hydrazide produced new mass adducts with either peptide.

At pH 7.2, both HyRe peptides reacted with AMCA hydrazide to produce adducts with identical additional mass. The discussion here focuses on peptide **114**, though similar results were observed for reactions of AMCA hydrazide with HyRe peptide **103** (Figures S7 in Supporting Information). Treatment of HyRe peptide **114** with AMCA hydrazide, followed by analysis with MALDI-TOF mass spectrometry, identified a new compound with an additional mass of 215 amu (Figure 5). Similarly, treatment of peptide **114** with rhodamine B hydrazide produced a new compound with an additional mass of 412. Both probes yield products with masses 32 amu less than the sums of the peptides and probes. The observation of new probe-specific

Scheme 1. Proposed Mechanism for the Reaction between HyRe Tag 114 and AMCA Hydrazide[a]

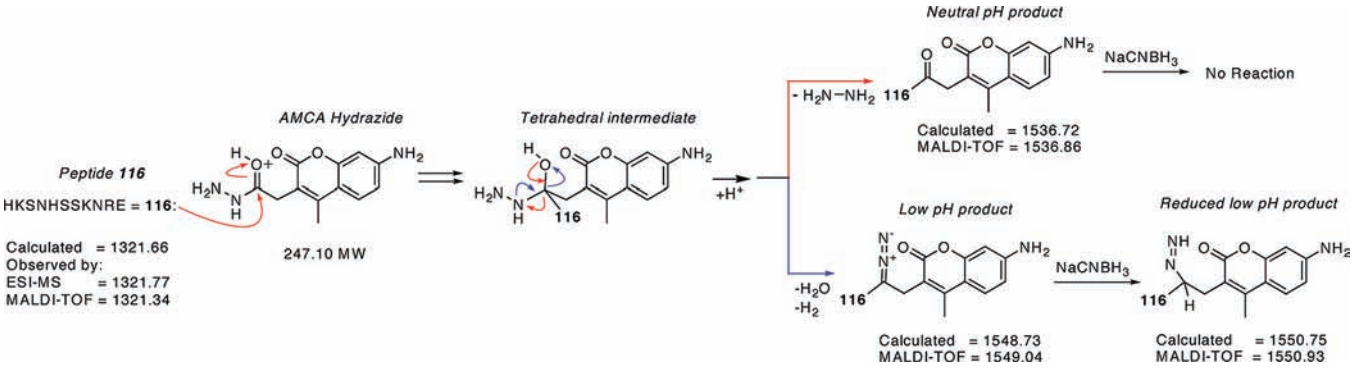

[a] At pH = 7.2, loss of hydrazine justifies the observed loss of 32 mass units. At acidic pH (3.2 to 6.0), the loss of 20 mass units most likely results from a dehydration plus additional oxidation, to yield a product capable of reduction by $NaCNBH_3$.

higher-molecular-weight adducts is evidence for a single, covalent bond-forming reaction between the selected peptide and hydrazide reagents. Furthermore, the difference in mass provides insight into the reaction mechanism.

MSMS analysis of the neutral pH peptide **114**-AMCA hydrazide reaction reveals that the modification was restricted to daughter ions containing His1 and was absent from fragments lacking this residue. For example, a modified b-ion of the first residue (m/z = 481.2) was observed, while the y″-ion corresponding to residues 2−11 (lacking His1) possessed zero modifications (m/z = 1185.6). Additionally, both modified and unmodified b ions are observed for every residue, while no modified y″ ions were observed. Therefore, the modification resides on the N-terminal histidine. This bond between AMCA hydrazide and the peptide is labile to MSMS conditions as some unmodified ions are observed in the mass spectrum. This result was also observed in the analysis of the reaction product between **114** and rhodamine B hydrazide.

Addition of the hydrazide derivatives to HyRe peptide **114** followed by loss of hydrazine (32 amu) could account for the observed mass of the product (Scheme 1). In this proposed mechanism, the imidazole of the N-terminal His attacks the hydrazide carbonyl. Subsequent collapse of the tetrahedral intermediate displaces hydrazine. Additionally, since the leaving group hydrazine has not been directly observed, oxidation of the hydrazine, prior to displacement, could contribute to the mechanism.

Notably, the HyRe peptide−hydrazide reaction takes place under mild conditions. The reaction occurs in aqueous buffer, at room temperature and physiological pH. No transition metal ions, organic solvents, and other proteins or cofactors are required. A peak corresponding to the adduct can be observed in the MALDI-TOF mass spectrum essentially immediately after the peptide and AMCA hydrazide are mixed, desalted, and applied to the mass spectrometer.

The reaction product could not be detected by reverse-phase HPLC or pH-neutral, ion-exchange chromatography. The reaction produces sufficient product for detection by fluorescence (peptide **53** fused to lysozyme in Figure 3), spot synthesis assays (Figure 4), and MS (peptide **114** in Figure 5). However, insufficient product is obtained for spectroscopic analysis, including HPLC detection. The MS analysis benefits from concentration by the desalting Zip-Tips for sample preparation. Furthermore, the Zip-Tips appear to enrich for the product of the reaction with hydrazide, as the very hydrophilic HyRe peptide **114** is incompletely retained by C_{18} Zip-Tips (data not shown). However, after modification with either of the hydrophobic hydrazide fluorophores, the peptides could be preferentially retained on the Zip-Tips. Alternatively, the covalent products from the hydrazide reaction could be initiated by the MS conditions; however, MS is typically used to characterize covalent bonding. Despite these caveats, the interaction between the HyRe peptides and hydrazide derivatives is sufficiently strong for various previously described assays.

The sensitivity of using MALDI-TOF mass spectrometry provided a method to investigate the basis for the selection of these peptides from the phage-displayed peptide libraries. As described above, the selections featured both washes with pH 5 buffer and the addition of $NaCNBH_3$ in an attempt to select reactive carbonyl containing peptides. However, the electrophilic modification of the N-terminal His complicates interpretation of the selection conditions. Specifically, the imidazole side chain should be largely protonated at pH values <6, thus preventing modification on this side chain at low pH.

MS screening of conditions between pH 3 and 11 identified a new product formed at low pH values. For pH values ≤6, a different product resulted from the treatment of peptide 114 with AMCA and rhodamine B hydrazide. AMCA hydrazide added 227 and rhodamine B hydrazide added 424 amu (Figure 5). Both modifications result from the loss of 20 amu following addition of the probe to the peptide. Such conjugates could result from a condensation (−18 amu) accompanied by an additional oxidation (−2 amu). Additionally, these products from the low pH reaction, unlike the analogous neutral pH products, are reducible upon addition of $NaCNBH_3$, producing new adducts with +2 additional atomic mass units (Figure 5 and Scheme 1).

MSMS of the products from the low pH reaction of peptide **114** with AMCA hydrazide reveals that the fluorescent probe covalently attaches to a different amino acid, than was observed for neutral pH (Figure 6). MSMS analysis of the products from the AMCA hydrazide reaction demonstrates modification of the Ser6 side chain. Thus, the modification has switched residues from His1 at neutral pH to Ser6 at pH 5. This observation suggests a different mechanism for the selection of HyRe peptides from the phage-displayed peptide libraries. Consistent with the observed $NaCNBH_3$ reduction, a diazo compound or other imine-containing isomer could be formed.

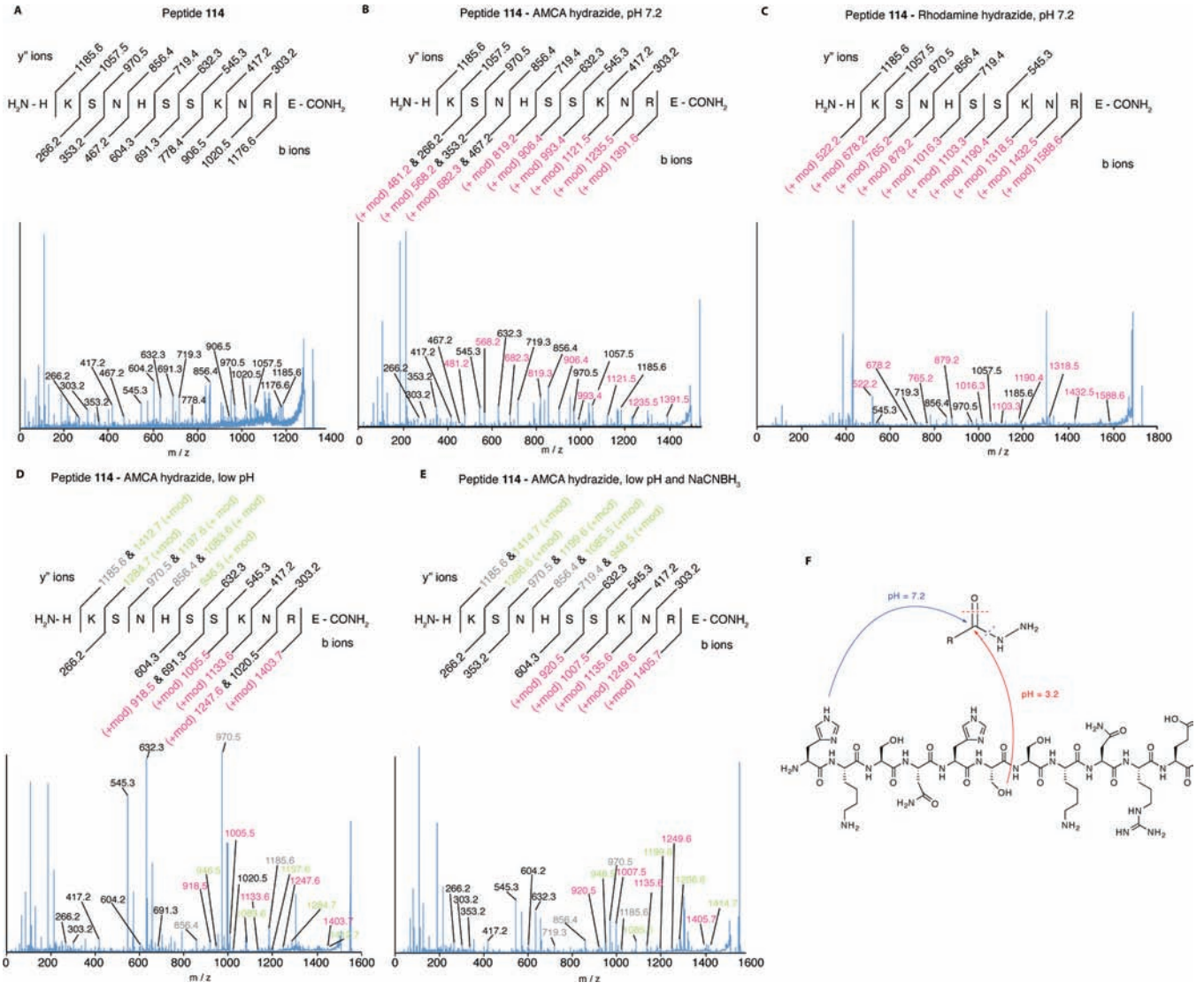

Figure 6. MSMS of products from the reaction of peptide **114** with AMCA and rhodamine B hydrazides. (A) MSMS of unmodified peptide 114 reveals all expected b and y″ ions. (B,C) MSMS of both the AMCA- and rhodamine-modified peptides reveals an unmodified set of y″ ions and a complete set of modified b ions indicating the covalent modification (+mod) occurs on the side chain of the N-terminal histidine. (D) MSMS of the reaction product at low pH and (E) following reduction with $NaCNBH_3$ product indicates that the covalent modification occurs on Ser6. The MSMS chromatogram of peptide **114** modified with rhodamine B hydrazide at low pH was dominated by rhodamine cleavage adducts (data not shown). (F) Schematic diagram for the observed covalent modifications.

In conclusion, as shown by the results in Figures 3−6 the selected peptides can react with hydrazide derivatives at a range of different pH values and with sufficient efficiency for detection by MS, spot synthesis, and fluorescence blot assays.

DISCUSSION

The identification of short, stand-alone peptides capable of directing SSPL reactions remains a major challenge in modern chemical biology. The HyRe peptides offer an important step toward the goal of short peptides composed of naturally occurring amino acids that can react with hydrazide-based probes without requiring additional enzymes or reagents. The short sequence length of the peptides identified here and the availability of hydrazide-containing chemical probes suggest that HyRe tags could be used in a large number of applications with minimal perturbation, if the sequences are further optimized. As demonstrated here, HyRe peptide tags are capable of selectively detecting fusions in crude cell lysates on Western blots (Figure 3).

Selection and screens required careful planning to minimize false positives. To avoid the selection of streptavidin-binding peptides, streptavidin was omitted from the selection protocols. Thus, no sequences commonly associated with streptavidin binding were observed (e.g., HPQ-based sequences).[41] Thus, any background binding in the spot synthesis results reflects nonspecific interactions with SAV-AP or other components of the binding assay. Furthermore, the spot synthesis results clearly demonstrate the importance of 20-mer peptides for high-specificity interactions between HyRe peptides and hydrazide derivatives. Shorter peptides were more likely to result in higher background assay levels.

Though the HyRe peptides react with different hydrazide bearing probes, the results reaffirm the adage, "you get what you

screen [and select] for."[51] The selection conditions targeted hydrazide-derivatized Tentagel, which includes a linker between the PEG and the surface-exposed hydrazides. The resultant HyRe peptides also required an additional carbonyl at the γ-carbon of the hydrazide, found in both AMCA and rhodamine B hydrazide, for the covalent reaction observed by MS. Thus, the selection conditions isolated peptides requiring a functionality analogous to the linker of the targeted Tentagel. Interestingly, amide linkers have been found to participate in other examples of reaction discovery.[52,53] Though designed to specifically capture reactive carbonyl-containing peptides, the selection conditions described here identified peptides that react with hydrazide derivatives at neutral and low pH values, and subsequently with $NaCNBH_3$.

Contrary to expectations, the selected peptides provide a nucleophile to react with the carbonyl of the hydrazide functionality. The HyRe tag-hydrazide reactivity reported here is analogous to acylhydrazide inhibitors of cathepsin K, in which an active site nucleophilic thiol forms a reversible covalent bond with the acylhydrazide carbonyl. Though the covalent bond in this example could be observed by X-ray crystallography, the lability of the resultant adduct prevented product isolation by both dialysis and HPLC. Similarly, the efficiency of the hydrazide reaction by our selected peptides was insufficient for detection by HPLC.

In conclusion, this report demonstrates the reactivity of HyRe peptides composed of naturally occurring amino acids, which were selected from two generations of combinatorial libraries. As fusions to filter paper and lysozyme, the HyRe peptides react with both biotin hydrazide and rhodamine B hydrazide, respectively, to provide detectable adducts. Such reactions can provide an immediately usable method for labeling a single protein in complex mixtures, such as the cell lysate in Figure 3D. In the future, the reaction of the HyRe tags with hydrazide derivatives could provide a powerful new tool for bioconjugate synthesis and *in vivo* protein labeling.

■ ASSOCIATED CONTENT

Supporting Information. Peptide sequences, spot synthesis assay results, and complete peptide characterization are available free of charge via the Internet at http://pubs.acs.org.

■ AUTHOR INFORMATION

Corresponding Author
*E-mail: gweiss@uci.edu.

■ ACKNOWLEDGMENT

We gratefully acknowledge support from the National Cancer Institute of the NIH (R01 CA133592-01 to G.A.W.). We thank Drs. John Greaves and Ben Berhane at the UCI Mass Spectrometry Center for mass spectrometry expertise, Professor Tadhg Begley for a helpful suggestion, and Professor Jennifer Prescher for helpful comments during manuscript preparation.

■ REFERENCES

(1) Marks, K. M., and Nolan, G. P. (2006) Chemical labeling strategies for cell biology. *Nat. Methods 3*, 591–596.

(2) O'Hare, H. M., Johnsson, K., and Gautier, A. (2007) Chemical probes shed light on protein function. *Curr. Opin. Struct. Biol. 17*, 488–494.

(3) Chalfie, M., Tu, Y., Euskirchen, G., Ward, W. W., and Prasher, D. C. (1994) Green fluorescent protein as a marker for gene expression. *Science 263*, 802–805.

(4) Dobbie, I. M., Lowndes, N. F., and Sullivan, K. F. (2008) Autofluorescent proteins. *Meth. Cell Biol. 85*, 1–22.

(5) Sletten, E., and Bertozzi, C. (2009) Bioorthogonal chemistry: fishing for selectivity in a sea of functionality. *Angew. Chem., Int. Ed. 48*, 6974–6998.

(6) Hackenberger, C. R, and Schwarzer, D. (2008) Chemoselective ligation and modification strategies for peptides and proteins. *Angew. Chem., Int. Ed. 47*, 10030–10074.

(7) Hochuli, E., Bannwarth, W., Dobeli, H., Gentz, R., and Stuber, D. (1988) Genetic approach to facilitate purification of recombinant proteins with a novel metal chelate adsorbent. *Nat. Biotechnol. 6*, 1321–1325.

(8) Hauser, C. T., and Tsien, R. Y. (2007) A hexahistidine-Zn2+-dye label reveals STIM1 surface exposure. *Proc. Natl. Acad. Sci. U.S.A. 104*, 3693–3697.

(9) Griffin, B. A., Adams, S. R., and Tsien, R. Y. (1998) Specific covalent labeling of recombinant protein molecules inside live cells. *Science 281*, 269–272.

(10) Adams, S. R., Campbell, R. E., Gross, L. A., Martin, B. R., Walkup, G. K., Yao, Y., Llopis, J., and Tsien, R. Y. (2002) New biarsenical ligands and tetracysteine motifs for protein labeling in vitro and in vivo: synthesis and biological applications. *J. Am. Chem. Soc. 124*, 6063–6076.

(11) Gaietta, G. M., Giepmans, B. N. G., Deerinck, T. J., Smith, W. B., Ngan, L., Llopis, J., Adams, S. R., Tsien, R. Y., and Ellisman, M. H. (2006) Golgi twins in late mitosis revealed by genetically encoded tags for live cell imaging and correlated electron microscopy. *Proc. Natl. Acad. Sci. U.S.A. 103*, 17777–17782.

(12) Halo, T. L., Appelbaum, J., Hobert, E. M., Balkin, D. M., and Schepartz, A. (2008) Selective recognition of protein tetraserine motifs with a cell-permeable, pro-fluorescent bis-boronic acid. *J. Am. Chem. Soc. 131*, 438–439.

(13) Ojida, A., Honda, K., Shinmi, D., Kiyonaka, S., Mori, Y., and Hamachi, I. (2006) Oligo-Asp Tag/Zn(II) complex probe as a new pair for labeling and fluorescence imaging of proteins. *J. Am. Chem. Soc. 128*, 10452–10459.

(14) Franz, K. J., Nitz, M., and Imperiali, B. (2003) Lanthanide-binding tags as versatile protein coexpression probes. *ChemBioChem 4*, 265–271.

(15) Nitz, M., Franz, K. J., Maglathlin, R. L., and Imperiali, B. (2003) A powerful combinatorial screen to identify high-affinity terbium(III)-binding peptides. *ChemBioChem 4*, 272–276.

(16) Kehoe, J. W., and Kay, B. K. (2005) Filamentous phage display in the new millennium. *Chem. Rev. 105*, 4056–72.

(17) Smith, G. P., and Petrenko, V. A. (1997) Phage display. *Chem. Rev. 97*, 391–410.

(18) Sarikaya, M., Tamerler, C., Schwartz, D. T., and Baneyx, F. (2004) Materials assembly and formation using engineered polypeptides. *Annu. Rev. Mater. Res. 34*, 373–408.

(19) Smith, G. P. (1985) Filamentous fusion phage: novel expression vectors that display cloned antigens on the virion surface. *Science 228*, 1315–1317.

(20) Scott, J. K., and Smith, G. P. (1990) Searching for peptide ligands with an epitope library. *Science 249*, 386–390.

(21) Rozinov, M. N., and Nolan, G. P. (1998) Evolution of peptides that modulate the spectral qualities of bound, small-molecule fluorophores. *Chem. Biol. 5*, 713–728.

(22) Marks, K. M., Rosinov, M., and Nolan, G. P. (2004) In vivo targeting of organic calcium sensors via genetically selected peptides. *Chem. Biol. 11*, 347–356.

(23) Tanaka, F., Fuller, R., Asawapornmongkol, L., Warsinke, A., Gobuty, S., and Barbas, C. S. 3rd (2007) Development of a small peptide tag for covalent labeling of proteins. *Bioconjugate Chem. 18*, 1318–1324.

(24) Shaper, J. H., and Stryer, L. (1977) Accessibility of the carbohydrate moiety of membrane-bound rhodopsin to enzymatic and chemical modification. *J. Supra. Struct. 6*, 291–299.

(25) Mirzaei, H., and Regnier, F. (2006) Creation of allotypic active sites during oxidative stress. *J. Proteome Res. 5*, 2159–2168.
(26) Madian, A. G., and Regnier, F. E. Profiling carbonylated proteins in human plasma. *J. Proteome Res. 9*, 1330−1343.
(27) Chen, I., Howarth, M., Lin, W., and Ting, A. Y. (2005) Site-specific labeling of cell surface proteins with biophysical probes using biotin ligase. *Nat. Methods 2*, 99–104.
(28) Wu, P., Shui, W., Carlson, B. L., Hu, N., Rabuka, D., Lee, J., and Bertozzi, C. R. (2009) Site-specific chemical modification of recombinant proteins produced in mammalian cells by using the genetically encoded aldehyde tag. *Proc. Natl. Acad. Sci. U.S.A. 106*, 3000–3005.
(29) Carrico, I. S., Carlson, B. L., and Bertozzi, C. R. (2007) Introducing genetically encoded aldehydes into proteins. *Nat. Chem. Biol. 3*, 321–322.
(30) Wang, L., Zhang, Z., Brock, A., and Schultz, P. G. (2003) Addition of the keto functional group to the genetic code of Escherichia coli. *Proc. Natl. Acad. Sci. U.S.A 100*, 56–61.
(31) Datta, D., Wang, P., Carrico, I. S., Mayo, S. L., and Tirrell, D. A. (2002) A Designed Phenylalanyl-tRNA synthetase variant allows efficient in vivo incorporation of aryl ketone functionality into proteins. *J. Am. Chem. Soc. 124*, 5652–5653.
(32) Stadtman, E. R. (1992) Protein oxidation and aging. *Science 257*, 1220–1224.
(33) Grimsrud, P. A., Xie, H., Griffin, T. J., and Bernlohr, D. A. (2008) Oxidative stress and covalent modification of protein with bioactive aldehydes. *J. Biol. Chem. 283*, 21837–21841.
(34) Schmidt, B., Selmer, T., Ingendoh, A., and Figurat, K. von. (1995) A novel amino acid modification in sulfatases that is defective in multiple sulfatase deficiency. *Cell 82*, 271–278.
(35) Muller, G. H., and Waldmann, H. (1999) The phenyl hydrazide as an enzyme-labile protecting group−Oxidative cleavage with mushroom tyrosinase. *Tetrahedr. Lett. 40*, 3549–3552.
(36) Thompson, S. K., Halbert, S. M., Bossard, M. J., Tomaszek, T. A., Levy, M. A., Zhao, B., Smith, W. W., Abdel-Meguid, S. S., Janson, C. A., D'Alessio, K. J., McQueney, M. S., Amegadzie, B. Y., Hanning, C. R., DesJarlais, R. L., Briand, J., Sarkar, S. K., Huddleston, M. J., Ijames, C. F., Carr, S. A., Garnes, K. T., Shu, A., Heys, J. R., Bradbeer, J., Zembryki, D., Lee-Rykaczewski, L., James, I. E., Lark, M. W., Drake, F. H., Gowen, M., Gleason, J. G., and Veber, D. F. (1997) Design of potent and selective human cathepsin K inhibitors that span the active site. *Proc. Natl. Acad. Sci. U.S.A. 94*, 14249–14254.
(37) Lamboy, J. A., Arter, J. A., Knopp, K. A., Der, D., Overstreet, C. M., Palermo, E. F., Urakami, H., Yu, T.-B., Tezgel, O., Tew, G. N., Guan, Z., Kuroda, K., and Weiss, G. A. (2009) Phage wrapping with cationic polymers eliminates nonspecific binding between M13 phage and high pI target proteins. *J. Am. Chem. Soc. 131*, 16454–16460.
(38) Lamboy, J. A., Tam, P. Y., Lee, L. S., Jackson, P. J., Avrantinis, S. K., Lee, H. J., Corn, R. M., and Weiss, G. A. (2008) Chemical and genetic wrappers for improved phage and RNA display. *ChemBioChem 9*, 2846–2852.
(39) Jencks, W. P. (1959) Studies on the mechanism of oxime and semicarbazone formation. *J. Am. Chem. Soc. 81*, 475–481.
(40) Borch, R. F., Bernstein, M. D., and Durst, H. D. (1971) Cyanohydridoborate anion as a selective reducing agent. *J. Am. Chem. Soc. 93*, 2897–2904.
(41) Devlin, J. J., Panganiban, L. C., and Devlin, P. E. (1990) Random peptide libraries: a source of specific protein binding molecules. *Science 249*, 404–406.
(42) Levin, A. M., Murase, K., Jackson, P. J., Flinspach, M. L., Poulos, T. L., and Weiss, G. A. (2007) Double barrel shotgun scanning of the Caveolin-1 scaffolding domain. *ACS Chem. Biol. 2*, 493–500.
(43) Cochran, J. R., Kim, Y.-S., Lippow, S. M., Rao, B., and Wittrup, K. D. (2006) Improved mutants from directed evolution are biased to orthologous substitutions. *Protein Eng. Des. Sel. 19*, 245–253.
(44) Murase, K., Morrison, K. L., Tam, P. Y., Stafford, R. L., Jurnak, F., and Weiss, G. A. (2003) EF-Tu binding peptides identified, dissected, and affinity optimized by phage display. *Chem. Biol. 10*, 161–168.
(45) Angelini, A., and Heinis, C. (2011) Post-translational modification of genetically encoded polypeptide libraries. *Curr. Opin. Chem. Biol. 15*, 355–361.
(46) Frank, R. (1992) Spot-synthesis: an easy technique for the positionally addressable, parallel chemical synthesis on a membrane support. *Tetrahedron 48*, 9217–9232.
(47) Hilpert, K., Winkler, D. F. H., and Hancock, R. E. W. (2007) Peptide arrays on cellulose support: SPOT synthesis, a time and cost efficient method for synthesis of large numbers of peptides in a parallel and addressable fashion. *Nat. Protoc. 2*, 1333–1349.
(48) Scheck, R. A, and Francis, M. B. (2007) Regioselective labeling of antibodies through N-terminal transamination. *ACS Chem. Biol. 2*, 247–51.
(49) Witus, L. S., Moore, T., Thuronyi, B. W., Esser-Kahn, A. P., Scheck, R. a, Iavarone, A. T., and Francis, M. B. (2010) Identification of highly reactive sequences for PLP-mediated bioconjugation using a combinatorial peptide library. *J. Am. Chem. Soc. 132*, 16812–16817.
(50) Hilpert, K., Volkmer-Engert, R., Walter, T., and Hancock, R. E. W. (2005) High-throughput generation of small antibacterial peptides with improved activity. *Nat. Biotechnol. 23*, 1008–1012.
(51) You, L., and Arnold, F. H. (1996) Directed evolution of subtilisin E in Bacillus subtilis to enhance total activity in aqueous dimethylformamide. *Protein Eng. Des. Sel 9*, 77–83.
(52) Momiyama, N., Kanan, M. W., and Liu, D. R. (2007) Synthesis of acyclic α,β-unsaturated ketones via Pd(II)-catalyzed intermolecular reaction of alkynamides and alkenes. *J. Am. Chem. Soc. 129*, 2230–2231.
(53) Kanan, M. W., Rozenman, M. M., Sakurai, K., Snyder, T. M., and Liu, D. R. (2004) Reaction discovery enabled by DNA-templated synthesis and in vitro selection. *Nature 431*, 545–549.

Supporting Information for:

Hydrazide-Reactive Peptide Tags for Site-Specific Protein Labeling

Glenn M. Eldridge[†] *and Gregory A. Weiss**[*,†,‡]

Departments of [†]Chemistry, [‡]Molecular Biology and Biochemistry,

University of California, Irvine CA 92697-2025 USA

Table of Contents **Page**

Labels used here in the supplemental are identical to those used in the main text.

Additional Experimental procedures

All reagents were purchased from Sigma Aldrich (Milwaukee, WI), and used without further purification. M13 phage display libraries were re-propagated using KO7 helper phage from New England Biolabs (Ipswich, MA). Boc-hydrazide Tentagel and nitrotetrazolium blue (NBT; a substrate for AP) were purchased from Acros Organics (Geel, Belgium). AMCA hydrazide, streptavidin conjugated to alkaline phosphatase, high-sensitivity streptavidin conjugated to horseradish peroxidase, and chloronapthol and diaminobenzidine (CN/DAB) (AP substrate) were purchased from Pierce (Piscataway, NJ). The gene for T4 lysozyme (mutant C54T and C97A) was a gift from Prof. Bryan Matthews (University Oregon). DNA sequencing was performed by GeneWiz (South Plainfield, NJ).

Primers used in this study:

LysPetR2 5'-ATAGCCCTCGAGCTATTACGGTAGATTTTTATACGCGTC-3'

LysPetF 5'-GAGGATCCGGAGATGAATATATTTGAAATGTTACGT-3'

LibPetF 5'-GGCTATCCATGGTTGCTACAAATGCCTATGCA-3'

LibPetR 5'-CAAATATATTCATTCCTCCGGATCCTCCACC-3'

M13F 5'-TGTAAAACGACGGCCAGT-3'

M13R 5'-CAGGAAACAGCTATGAC-3'

T7F 5'-TGTAAAACGACGGCCAGTTAATACGACTCACTATAGGG-3'

T7R 5'-CAGGAAACAGCTATGACGCTAGTTATTGCTCAGCGG-3'

Homolog**53** 5'-

GCTACAAATGCCTATGCAMRSMRSASCMASMRSASCTSCMRSMRSMRSGASMAS-

GASMRSTSCMRSGYGASCASCASCGGTGGAGGATCCGGA-3'

Degenerate bases in Homolog**53** are named in accordance with IUBMB conventions.

Construction of the homolog shotgun scanning library

The homolog shotgun scanning library of HyRe tag 53 was generated using Homolog**53** oligonucleotide targeting the pM1165a phagemid[1] for site-directed mutagenesis using previously reported protocols.[2]

Selections with homolog shotgun scanning library

The phage-displayed peptide library was incubated with Boc-hydrazide Tentagel (50 mg in 10 mL PBS) for 1 h at room temperature in a peptide reaction vessel. The filtrate was transferred to a new vessel, and incubated with hydrazide Tentagel for 20 to 60 min with decreasing concentrations of deprotected resin for each round of selection. The resin was washed six times with PBS (50 mL for 6 min). Additional washes included pH = 5.6 PBS (50 mL for 20 min) and HCl (0.1 M, 50 mL for 10 min). The phage-resin mixture was then pH-buffered with a final PBS wash (50 mL, 10 min), and were re-propagated and titered, as previously described.[2]

HyRe peptide fusions to T4 lysozyme

PCR with primers LibPetR and LibPetF amplified the genes encoding the peptides from the selected phage and incorporated an NcoI site at the 5'-terminus of the amplicon. The gene for T4 lysozyme with mutations C54A and C97T was amplified using primers LysPetF1 and LysPetR2, which incorporates a stop codon and an XhoI site at the 3'-terminus of the amplicon. The primers LibPetR and LysPetF both include complementary regions for gene synthesis by overlap extension PCR. The pET-28c(+) plasmid (Novagen) and the purified gene synthesis product were digested with the restriction enzymes NcoI and XhoI (New England Biolabs). The digested products were mixed and ligated using T4 DNA ligase (New England Biolabs) by incubation in ATP-supplemented buffer at 16 °C for 16 hours. The crude ligation product was transformed into

heat shock competent XL-1 *E. coli* cells, and plated onto Luria Broth (LB) agar plates supplemented with kanamycin (40 μg/mL) for overnight incubation at 37 °C. The DNA sequences of the resultant colonies were confirmed using T7 primers.

Synthesis of Rhodamine B hydrazide

Rhodamine B hydrazide was synthesized by adding tert-Butyl carbazat to NHS rhodamine B (Pierce), deprotecting with 50:50 TFA:DCM, and purifying by reverse phase HPLC.

Synthesis of HyRe peptides

The peptides **114** and **104** were synthesized on 0.2 mmol scale using standard solid-phase peptide synthesis with Fmoc-protected amino acids (Aroz technologies) on Rink amide resin (Novabiochem). The synthesized peptides with a carboxamide C-terminus were deprotected and cleaved from the resin using a mixture of 9.5 mL trifluoroacetic acid, 0.25 mL triisopropylsilane, and 0.25 mL of H_2O at room temperature for 4 h under N_2. The cleavage mixture was filtered from the resin, and precipitated in ice-cold diethyl ether for 20 min. The precipitate was next centrifuged at 3 krpm for 20 min at 4 °C, before being re-suspended in deionized H_2O. The peptides were purified by reverse-phase HPLC with a C_{18} column using a gradient from 100% solvent A (99.9% H_2O / 0.1%TFA) to 50% solvent B (95% acetonitrile / 4.9%H_2O / 0.1%TFA) over 40 min. Fractions containing the purified peptides were combined and concentrated using rotary evaporation, followed by vacuum centrifugation. Purified peptides were subjected to analytical HPLC and MALDI-TOF to verify purity (>80%), and confirm identity, respectively (**Supporting Figs. 7-8**).

MALDI-TOF sample preparation and analysis

After the peptides (1 mM) were treated with Aminomethylcoumarin acetate hydrazide (AMCA-hydrazide) (1 mM) in PBS for 2.5 h, the reaction mixtures were applied to a C_{18} Ziptip (Varian), washed with 0.1% TFA in deionized water, and eluted with a saturated solution of α-Cyano-4-hydroxycinnamic acid (CHCA) in 25% aqueous acetonitrile containing 0.1 % TFA. The eluates were deposited on a stainless steel target. An ABI SciEx TOF/TOF 5800 (Applied Biosystems) system with a reflectron using standard configurations and parameters was used to obtain the MALDI-TOF mass spectra. The averaged spectra were exported to Excel for analysis.

Table S1. Peptide Scaffolds Selected for Interaction with Hydrazide Tentagel.*

Scaffold	1st Round	2nd Round	3rd Round	4th Round	5th Round
CX5C					
CX5CX	1				
CX5XC2					
X2CX10CX2					
X2CX2CX2	1				
X2CX2CX3					
X2CX3CX2					
X2CX4CX2		1			
X2CX5C		1			
X2CX5CX2					
X2CX6CX2					
X2CX7CX2					
X2CX8CX2	2				
X2CX9CX2	1				
X4CX10CX4					
X4CX2GPX4CX4					
X5CX8CX5					
X5CX9CX4					
X6CX6CX6					
X6CX7CX5	4	9	4	8	8
X7CX4CX7	3	9	17	5	
X7CX5CX6					
X8					
SM	7				
Total Sequenced	19	20	21	13	8

*****Phage-displayed peptide library scaffolds used for the selection of hydrazide binding peptides and the number of selectants from each scaffold for each round. The sequences from each round of selection are found in Table S2.

Table S2. Peptide Sequences from Phage Selection Rounds (Rd.) 1 through 5 and Homolog Shotgun Scanning Rounds 1 through 4.*

Naïve Library Selectants			
Rd.	HyRe	aa sequence	sib
1	1	CEGSGACstop	
	2	HKREHNCDTPPPTPCFKANR	
	3	RPTKNNCDHTTHCTCHQQNQ	
	4	GTHDTNCHPPAHSKCRDSDY	
	5	PTPARKPCPKPPCPPTPKEQ	
	6	KPNTNHCTNNNQHDCKKATH	
	7	VLCTWCSM	
	8	TEPATPPCHHTTCKPRTGAD	
	9	QHKHHEHCKGPQCQKQHRKE	
	10	FYCREHSPVAGstopCV	
	11	GWCKYYLRSCHCMV	
	12	ATCNSYLYSALCSV	
2	3	RPTKNNCDHTTHCTCHQQNQ	
	13	TKNKPTHCGHHECTQPQHNS	
	14	APRHHQHCPTHACHAEAQEN	
	15	HDAPGKCKHPNHNHCQASHI	
	16	HTDHSKCRRDHTNSCANTEQ	
	17	HKTNPEPCKNHCCTGQPDNK	
	18	GKKNNQCPHRTPTSCLSNYQ	
	19	MLCGTTWCMG	
	20	HPNPRQDCHTHQCRTPTQDK	
	21	GICWLLDNC	
	22	KNSGKMCTTQDTSICSHKIR	
	23	TYRHDHCNPSRPYRCNHSPR	
	24	AKTHAHKCNTQTCQHERTHT	
	25	HKTKNECSHHPTRPCTTAHD	2
	26	TATNTLCHKHTHPKCGENSS	
	27	HQNPRTNCKTANCATHAPTN	
	28	TKPHDRDCHKQTCATHNHHR	
	29	NKTNSHQCATHACEHHKTNR	
	30	TGAPEPECPANRCTETNRQE	
3	25	HKTKNECSHHPTRPCTTAHD	2
	31	HQKADHTCAKHECQKKPHTR	
	32	KTNHEQQCHHNTCHEKGPSQ	
	33	KTHKPPNCPPEPCHQKAQPH	
	34	HKNEPPHCQQHKCEQHAPRP	
	35	KTPPPPACTKHECHRTGHTN	
	36	TEKHRTHCHEEQCQKTTPPP	
	37	SHKKRHKCRHHQCQTNETTT	
	38	HKQKAQNCTHKECHQTKAHT	
	39	HTPHRHECEHRHCEPKNRET	
	40	RPPKGEQCHHAHCRQTEKPP	
	41	EKTKHHKCPTTHCHEKTSPR	
	42	TSKHQHCEQTTSTDCKTKNT	
	43	HRNHHTKCPQDTCQQAPTKQ	
	44	KKAHEHRCAHTTCEDRQKPT	
	45	TKNHAQHCTTTQCPPTTRTH	
	46	DKSTHHQCKHTICTEQHDHK	
	47	KQHSPQACHQKHCQRHAPAK	
	48	HKGSPPCTTEHHKTCRMNPT	
	49	HKNTPAKCPTTTCQTEKTAQ	
4	3	RPTKNNCDHTTHCTCHQQNQ	
	25	HKTKNECSHHPTRPCTTAHD	3
	50	HSDHHKCGKPREPTCQRTNS	
	51	GEHHKEHCKPRQCTTATPQA	
	52	GAKDNKHCHHQECTHSKTRT	
	53	HKTNHSCHKREQEHCRVTTT	2
	54	KNARDHTCDNHHCHHHTAAA	
	55	HKQETPHCTSHHCTQPKTPA	
	56	HKTKTTQCTKHQCPTQKINP	
	57	KPPTHNPCHHNSCSKKTTDP	
5	25	HKTKNECSHHPTRPCTTAHD	
	50	HSDHHKCGKPREPTCQRTNS	
	53	HKTNHSCHKREQEHCRVTTT	5
	58	KQTDTRCQSQLHKHCKIVEN	

Homolog Shotgun Scanning			
Rd.	HyRe	aa sequence	sib
2	59	RRSQQSCSRHEKERSSVSSS	
	60	RRTKKSCRKKNQERCRASTS	
	61	NKTKSSCQKSEQESYRVSTT	
	62	HQSKNSCSKPDHDRCQVSTS	
	63	SSSHRSSSQHEHEHCRVTSS	
	64	KQSHSSYQHREQERCQVTST	
	65	KHSQHSCRSQEQERSQVTTS	
3	61	NKTKSSCQKSEQESYRVSTT	2
	66	NKSHHSCNKREQERCSVTST	
	67	KKSQHSCHHREQERCQVTTT	
	68	KSSQKSCHRQDQEQCRVTST	
	69	HRSQQTCNRQEHEPCQVSTS	
	70	KKSQNSCNRRDHEHCSVTTS	
	71	KSSHNSCSHREHDRSRVTTS	
	72	HRSHHTCSHQEQERCRVSSS	
	73	KSTHHSCNSREQDRCSVTTT	
	74	HNTQQTCRKQEQEHCKVSSS	
	75	KSTHHSCNSREQDRCSVTTT	
	76	SHTKKTCRHHEHERCHVTSS	
	77	KHTHSSSRQKEQERCQVSSS	
4	61	NKTKSSCQKSEQESYRVSTT	
	78	HKSNHSSKNREHERCQVTST	3
	79	NHTQRSCKHHEQESCRVSSS	

*The column “sib” indicates the number of siblings or identical sequences identified in the same round.

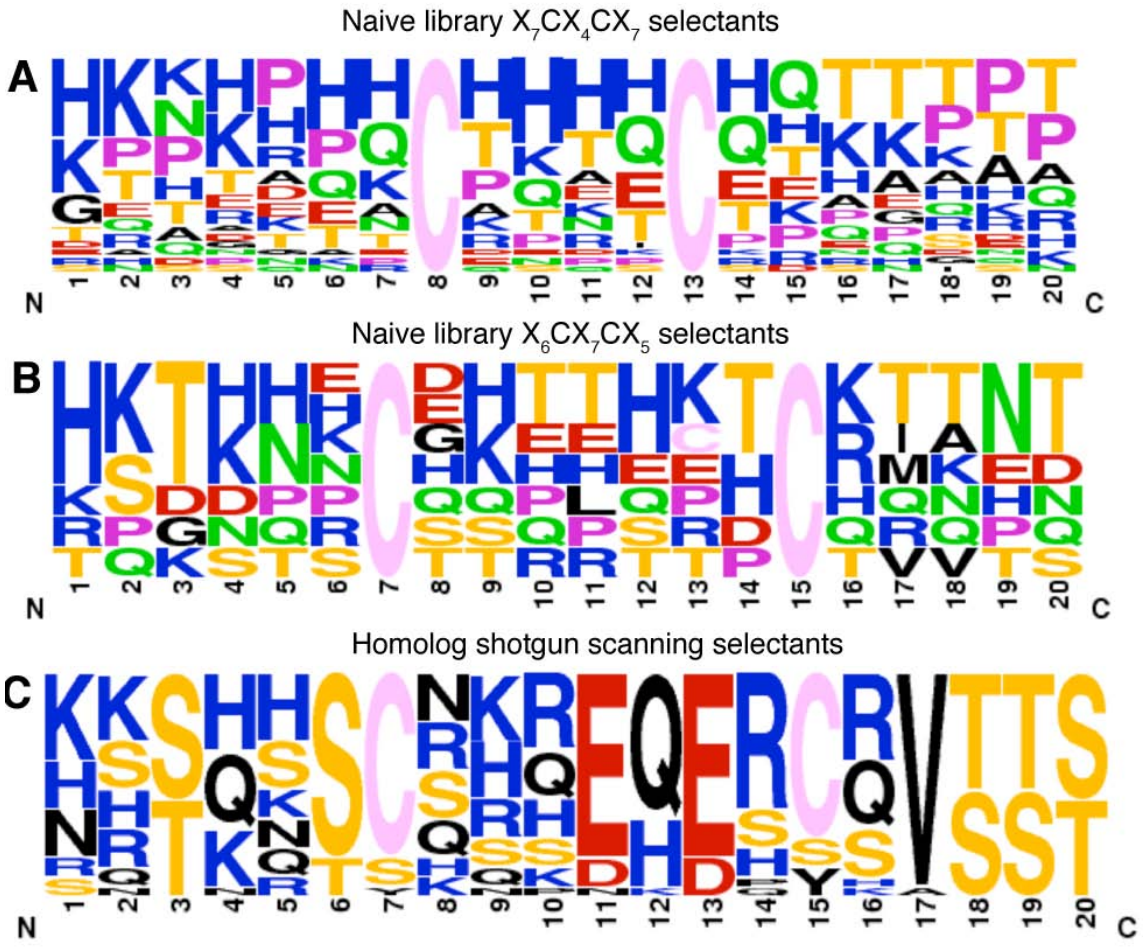

Figure S1. Sequence analysis of selectants from the naïve (A and B) and homolog shotgun scanning (C) libraries (weblogo.berkeley.edu).

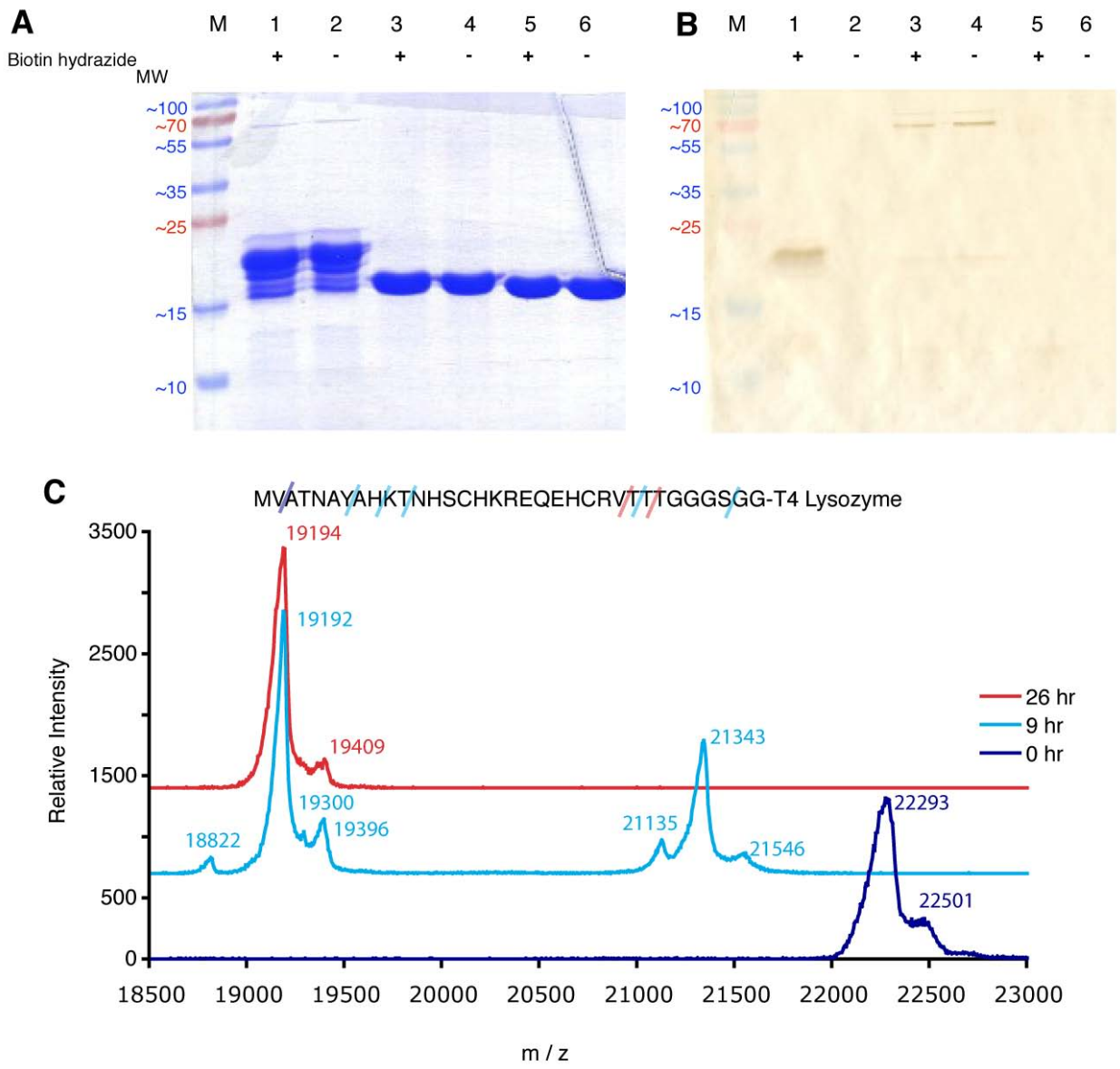

Figure S2. (A and B) The full SDS-PAGE and Western blot of the HyRe **53**-T4 lysozyme fusion excerpted in Figure 3. (C) MALDI-TOF of **53**-T4 lysozyme fusion incubated at room temperature for the indicated times. The MALDI-TOF results indicate that the HyRe tag is specifically cleaved from the fusion. These results also account for the partially proteolyzed fusion proteins after purification apparent in lanes 1 and 2 of the protein gel shown in (A).

A

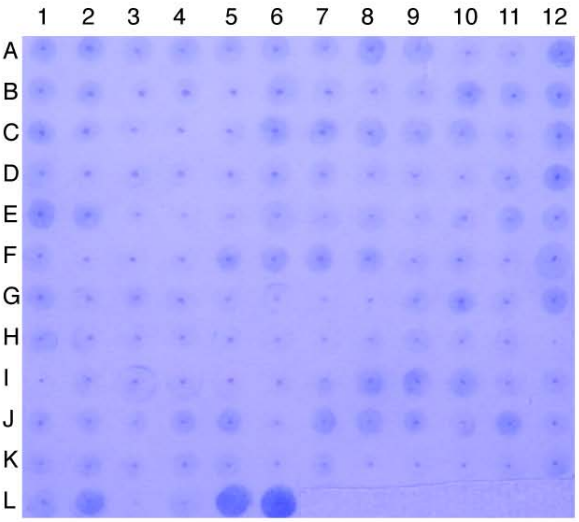

B

Spot	Sequence	Spot	Sequence	Spot	Sequence	Spot	Sequence
A1	HKTNHSCHKREQEHCRVTTT	C12	HKTNHSCHKREQEHCRTT	F11	HKTNHSCHKREQEHCT	I10	NKTKSSCQKS
A2	KTNHSCHKREQEHCRVTTT	D1	HKTNHSCHKREQEHCRVT	F12	HKTNHSCHKREQEHCR	I11	HKSNHSSKNREHERCQVTST
A3	HTNHSCHKREQEHCRVTTT	D2	NHSCHKREQEHCRVTTT	G1	HKTNHSCHKREQEHCRVTTT	I12	HKSNHSSKNREHERCQVTSA
A4	HKNHSCHKREQEHCRVTTT	D3	HHSCHKREQEHCRVTTT	G2	NKTKSSCQKSEQESYRVSTT	J1	HKSNHSSKNREHERCQVTAT
A5	HKTHSCHKREQEHCRVTTT	D4	HKSCHKREQEHCRVTTT	G3	NKTKSSCQKSEQESYRVSTA	J2	HKSNHSSKNREHERCQVAST
A6	HKTNSCHKREQEHCRVTTT	D5	HKTCHKREQEHCRVTTT	G4	NKTKSSCQKSEQESYRVSAT	J3	HKSNHSSKNREHERCQATST
A7	HKTNHCHKREQEHCRVTTT	D6	HKTNHKREQEHCRVTTT	G5	NKTKSSCQKSEQESYRVATT	J4	HKSNHSSKNREHERCAVTST
A8	HKTNHSHKREQEHCRVTTT	D7	HKTNHKREQEHCRVTTT	G6	NKTKSSCQKSEQESYRASTT	J5	HKSNHSSKNREHERAQVTST
A9	HKTNHSCKREQEHCRVTTT	D8	HKTNHSREQEHCRVTTT	G7	NKTKSSCQKSEQESYAVSTT	J6	HKSNHSSKNREHEACQVTST
A10	HKTNHSCHREQEHCRVTTT	D9	HKTNHSCEQEHCRVTTT	G8	NKTKSSCQKSEQESARVSTT	J7	HKSNHSSKNREHARCQVTST
A11	HKTNHSCHKEQEHCRVTTT	D10	HKTNHSCHQEHCRVTTT	G9	NKTKSSCQKSEQEAYRVSTT	J8	HKSNHSSKNREAERCQVTST
A12	HKTNHSCHKRQEHCRVTTT	D11	HKTNHSCHKEHCRVTTT	G10	NKTKSSCQKSEQASYRVSTT	J9	HKSNHSSKNRAHERCQVTST
B1	HKTNHSCHKREEHCRVTTT	D12	HKTNHSCHKRHCRVTTT	G11	NKTKSSCQKSEAESYRVSTT	J10	HKSNHSSKNAEHERCQVTST
B2	HKTNHSCHKREQHCRVTTT	E1	HKTNHSCHKRECRVTTT	G12	NKTKSSCQKSAQESYRVSTT	J11	HKSNHSSKAREHERCQVTST
B3	HKTNHSCHKREQECRVTTT	E2	HKTNHSCHKREQRVTTT	H1	NKTKSSCQKAEQESYRVSTT	J12	HKSNHSSANREHERCQVTST
B4	HKTNHSCHKREQEHRVTTT	E3	HKTNHSCHKREQEVTTT	H2	NKTKSSCQASEQESYRVSTT	K1	HKSNHSAKNREHERCQVTST
B5	HKTNHSCHKREQEHCVTTT	E4	HKTNHSCHKREQEHTTT	H3	NKTKSSCAKSEQESYRVSTT	K2	HKSNHASKNREHERCQVTST
B6	HKTNHSCHKREQEHCRVTT	E5	HKTNHSCHKREQEHCTT	H4	NKTKSSAQKSEQESYRVSTT	K3	HKSNASSKNREHERCQVTST
B7	HKTNHSCHKREQEHCRTTT	E6	HKTNHSCHKREQEHCRT	H5	NKTKSACQKSEQESYRVSTT	K4	HKSAHSSKNREHERCQVTST
B8	TNHSCHKREQEHCRVTTT	E7	HKTNHSCHKREQEHCRV	H6	NKTKASCQKSEQESYRVSTT	K5	HKANHSSKNREHERCQVTST
B9	HNHSCHKREQEHCRVTTT	E8	HSCHKREQEHCRVTTT	H7	NKTASSCQKSEQESYRVSTT	K6	HASNHSSKNREHERCQVTST
B10	HKHSCHKREQEHCRVTTT	E9	HSCHKREQEHCRVTTT	H8	NKAKSSCQKSEQESYRVSTT	K7	AKSNHSSKNREHERCQVTST
B11	HKTSCHKREQEHCRVTTT	E10	HKCHKREQEHCRVTTT	H9	NATKSSCQKSEQESYRVSTT	K8	EHERCQVTST
B12	HKTNCHKREQEHCRVTTT	E11	HKTHKREQEHCRVTTT	H10	AKTKSSCQKSEQESYRVSTT	K9	REHHRCQVTS
C1	HKTNHHKREQEHCRVTTT	E12	HKTNKREQEHCRVTTT	H11	NKTKSSCQKSEQESYRVSTT	K10	NREHERCQVT
C2	HKTNHSKREQEHCRVTTT	F1	HKTNHREQEHCRVTTT	H12	EQESYRVSTT	K11	KNREHERCQV
C3	HKTNHSCREQEHCRVTTT	F2	HKTNHSEQEHCRVTTT	I1	SEQESYRVST	K12	SKNREHERCQ
C4	HKTNHSCHEQEHCRVTTT	F3	HKTNHSCQEHCRVTTT	I2	KSEQESYRVS	L1	SSKNREHERC
C5	HKTNHSCHKQEHCRVTTT	F4	HKTNHSCHEHCRVTTT	I3	QKSEQESYRV	L2	HSSKNREHER
C6	HKTNHSCHKREHCRVTTT	F5	HKTNHSCHKHCRVTTT	I4	CQKSEQESYR	L3	NHSSKNREHE
C7	HKTNHSCHKREHCRVTTT	F6	HKTNHSCHKRCRVTTT	I5	SCQKSEQESY	L4	SNHSSKNREH
C8	HKTNHSCHKREQCRVTTT	F7	HKTNHSCHKRERVTTT	I6	SSCQKSEQES	L5	KSNHSSKNRE
C9	HKTNHSCHKREQERVTTT	F8	HKTNHSCHKREQVTTT	I7	KSSCQKSEQE	L6	HKSNHSSKNR
C10	HKTNHSCHKREQEHVTTT	F9	HKTNHSCHKREQETTT	I8	TKSSCQKSEQ		
C11	HKTNHSCHKREQEHCTTT	F10	HKTNHSCHKREQEHTT	I9	KTKSSCQKSE		

Figure S3. Spot synthesis examining variants of peptides **53**, **61**, and **78**. A) After treatment with biotin hydrazide the sheet was developed by exposure to SAV-AP, followed by washing and then addition of AP substrates. B) The synthesized peptide sequences include all single, double, triple, and quadruple contiguous amino acid deletions of HyRe peptide **53** (A2-F12). Variants of HyRe tags **61** and **78** include single alanine substitutions (G3-H10; and I12-K6) and all contiguous 10-mers (H12-I10; and K8-L6). The 10-mers for both peptides **61** and **78** are analyzed and compared in Supporting Figure S4.

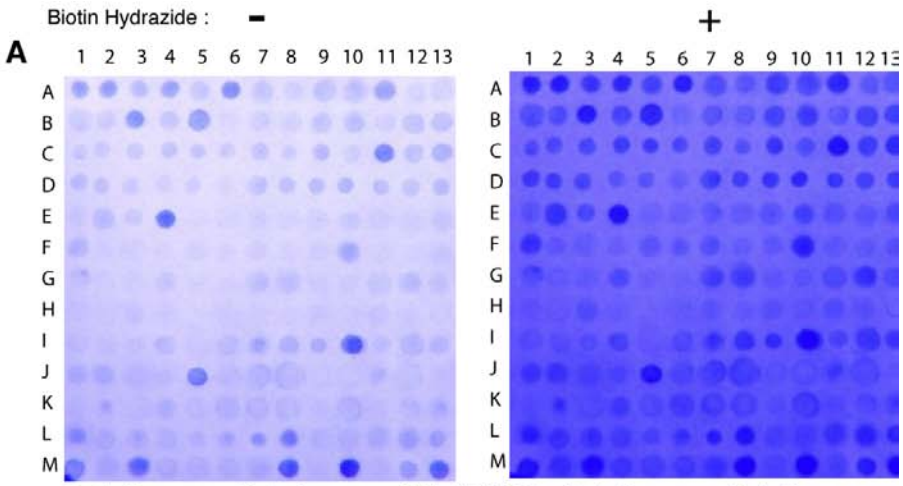

B

Spot	Sequence	Spot	Sequence	Spot	Sequence	Spot	Sequence	Spot	Sequence
A1	HKSNHSSKNR	C9	KSNHSSKRE	F4	KTSCQKSE	H12	TKSSCQKSEQ	K7	~~TICTEQHDHK~~
A2	KSNHSSKNR	C10	KSNHSSKNE	F5	KTKCQKSE	H13	EQEHCRVTTT	K8	HTICTEQHDH
A3	HKSNHSSKN	C11	KSNHSSKNR	F6	KTKSQKSE	I1	REQEHCRVTT	K9	KHTICTEQHD
A4	SNHSSKNR	C12	NHSSKNRE	F7	KTKSSKSE	I2	KREQEHCRVT	K10	CKHTICTEQH
A5	KSNHSSKN	C13	KHSSKNRE	F8	KTKSSCSE	I3	HKREQEHCRV	K11	QCKHTICTEQ
A6	HKSSSKNR	D1	KSSSKNRE	F9	KTKSSCQE	I4	CHKREQEHCR	K12	HQCKHTICTE
A7	NHNHSSK	D2	KSNSKNRE	F10	KTKSSCQK	I5	SCHKREQEHC	K13	HHQCKHTICT
A8	SNHSSKN	D3	KSNHKNRE	F11	KTKSSCQKSE	I6	HSCHKREQEH	L1	THHQCKHTIC
A9	KSNHSSK	D4	KSNHSNRE	F12	TKSSCQKSEQ	I7	NHSCHKREQE	L2	STHHQCKHTI
A10	HKSNHSS	D5	KSNHSSRE	F13	KSSCQKSEQ	I8	TNHSCHKREQ	L3	KSTHHQCKHT
A11	HSSKNR	D6	KSNHSSKE	G1	TKSSCQKSE	I9	KTNHSCHKRE	L4	DKSTHHQCKH
A12	NHSSKN	D7	KSNHSSKN	G2	SSCQKSEQ	I10	HKTNHSCHKR	L5	REPTCQRTNS
A13	SNHSSK	D8	HSSKNRE	G3	KSSCQKSE	I11	PTRPCTTAHD	L6	PREPTCQRTN
B1	KSNHSS	D9	KSSKNRE	G4	TKSSCQKS	I12	HPTRPCTTAH	L7	KPREPTCQRT
B2	HKSNHS	D10	KSSKNRE	G5	SCQKSEQ	I13	HHPTRPCTTA	L8	GKPREPTCQR
B3	HKSNHSSKNR	D11	KSNKNRE	G6	SSCQKSE	J1	SHHPTRPCTT	L9	CGKPREPTCQ
B4	KSNHSSKNRE	D12	KSNHNRE	G7	KSSCQKS	J2	CSHHPTRPCT	L10	KCGKPREPTC
B5	KSNHSSKNRA	D13	KSNHSRE	G8	TKSSCQK	J3	ECSHHPTRPC	L11	HKCGKPREPT
B6	KSNHSSKNAE	E1	KSNHSSE	G9	CQKSEQ	J4	NECSHHPTRP	L12	HHKCGKPREP
B7	KSNHSSKARE	E2	KSNHSSK	G10	SCQKSE	J5	KNECSHHPTR	L13	DHHKCGKPRE
B8	KSNHSSANRE	E3	KSNHSSKNRE	G11	SSCQKS	J6	TKNECSHHPT	M1	SDHHKCGKPR
B9	KSNHSAKNRE	E4	NKTKSSCQKS	G12	KSSCQK	J7	KTKNECSHHP	M2	HSDHHKCGKP
B10	KSNHASKNRE	E5	KTKSSCQKSE	G13	TKSSCQ	J8	HKTKNECSHH	M3	HKTNHSCHKR
B11	KSNASSKNRE	E6	TKSSCQKSE	H1	TKSSCQKSEQ	J9	TTCQTEKTAQ	M4	HKTKNECSHH
B12	KSAHSSKNRE	E7	KKSSCQKSE	H2	TKSSCQKSEA	J10	TTTCQTEKTA	M5	HKNTPAKCPT
B13	KANHSSKNRE	E8	KTSSCQKSE	H3	TKSSCQKSAQ	J11	PTTTCQTEKT	M6	DKSTHHQCKH
C1	ASNHSSKNRE	E9	KTKSCQKSE	H4	TKSSCQKAEQ	J12	CPTTTCQTEK	M7	~~HSDHHKCGKP~~
C2	KSNHSSKNRE	E10	KTKSSQKSE	H5	TKSSCQASEQ	J13	KCPTTTCQTE	M8	HKTNHSCHKR
C3	SNHSSKNRE	E11	KTKSSCKSE	H6	TKSSCAKSEQ	K1	AKCPTTTCQT	M9	TKSSCQKSEQ
C4	KNHSSKNRE	E12	KTKSSCQSE	H7	TKSSAQKSEQ	K2	PAKCPTTTCQ	M10	NKTKSSCQKS
C5	KSHSSKNRE	E13	KTKSSCQKE	H8	TKSACQKSEQ	K3	TPAKCPTTTC	M11	KTKSSCQKSE
C6	KSNSSKNRE	F1	KTKSSCQKS	H9	TKASCQKSEQ	K4	NTPAKCPTTT	M12	KSNHSSKNRE
C7	KSNHSKNRE	F2	KSSCQKSE	H10	TASSCQKSEQ	K5	KNTPAKCPTT	M13	HKSNHSSKNR
C8	KSNHSSNRE	F3	KSSCQKSE	H11	AKSSCQKSEQ	K6	HKNTPAKCPT		

Figure S4. Spot synthesis peptide sheet 2. A) Both before and after treatment with biotin hydrazide (indicated with a – or +), the sheet was developed by exposure to SAV-AP, followed by washing and then addition of AP substrates. B) The synthesized peptide sequences include contiguous 9, 8, 7, and 6-mers; single alanine substitutions, single, double and triple amino acid deletions of peptide **80** and **91**. Peptide variants of **80** reveal background binding or no activity. Some of the **91** variants reveal specificity for binding to biotin hydrazide, especially the 8-mer **102** (F10). Additionally, the contiguous 10-mers of original selectants **25**, **53**, **49**, **46** and **50** were also synthesized and screened (H13-M2). Scored through sequences were incorrectly synthesized.

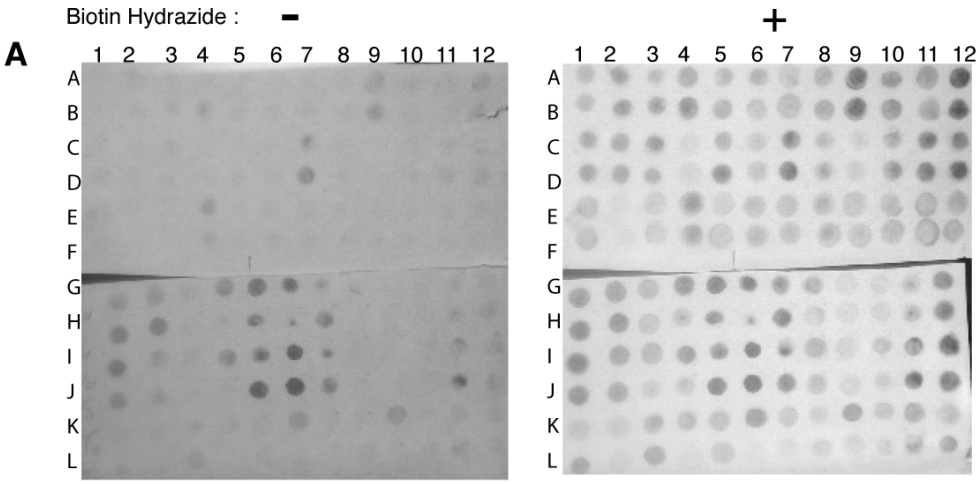

B

A1	HKTKNECSHHPTRPCTTAHD	D1	HKTNHSCHKREQEHCRVTTT	G1	SDHHKCGKPR	J1	SDHHKSGKPR
A2	HKTNHSCHKREQEHCRVTTT	D2	HKANHSCHKREQEHCRVAAA	G2	GKPREPTCQR	J2	GKPREPTSQR
A3	KQTDTRCQSQLHKHCKIVEN	D3	HKTNHSCHKREQEHCRATTT	G3	KNECSHHPTR	J3	KNESSHHPTR
A4	GAKDNKHCHHQECTHSKTRT	D4	HKTNHSCHKAEQEHCAVTTT	G4	HKTNHSCHKR	J4	HKTNHSSHKR
A5	HSDHHKCGKPREPTCQRTNS	D5	HKTNHSAHKREQEHARVTTT	G5	NKTKSSCQKS	J5	NKTKSSSQKS
A6	GEHHKEHCKPRQCTTATPQA	D6	AKTNASCAKREQEACRVTTT	G6	NHTQRSCKHH	J6	NHTQRSSKHH
A7	DKSTHHQCKHTICTEQHDHK	D7	HKTNHSCHKRAQAHCRVTTT	G7	HKSNHSSKNR	J7	HKSNHSSKNR
A8	HKNTPAKCPTTTCQTEKTAQ	D8	HKTNHSCHKREAEHCRVTTT	G8	KSSKNRE	J8	KSSKNRE
A9	GAKDNKHCHHQECTHSKTRT	D9	HATNHSCHAREQEHCRVTTT	G9	HSDHHKCGKP	J9	HSDHHKSGKP
A10	GEHHKEHCKPRQCTTATPQA	D10	HKTNHACHKREQEHCRVTTT	G10	HPTRPCTTAH	J10	HPTRPSTTAH
A11	HKQETPHCTSHHCTQPKTPA	D11	HKTAHSCHKREQEHCRVTTT	G11	TNHSCHKREQ	J11	TNHSSHKREQ
A12	HQKADHTCAKHECQKKPHTR	D12	HKTNHSCHKREQEHCRVTTT	G12	KTKSSCQK	J12	KTKSSSQK
B1	HKTKNECSHHPTRPCTTAHD	E1	DKSTHHQCKHTICTEQHDHK	H1	SDHHKCGKPR	K1	GEHHKEHCKP
B2	HKTNHSCHKREQEHCRVTTT	E2	DASTHHQCAHTICTEQHDHA	H2	GKPREPTCQR	K2	RQCTTATPQA
B3	KQTDTRCQSQLHKHCKIVEN	E3	DKSTHHQCKHTICTEQADAK	H3	KNECSHHPTR	K3	PRQCTTATPQ
B4	GAKDNKHCHHQECTHSKTRT	E4	AKSTHHQCKHTICTEQHAHK	H4	HKTNHSCHKR	K4	KPRQCTTATP
B5	HSDHHKCGKPREPTCQRTNS	E5	DKSTHHACKHTICTEAHDHK	H5	NKTKSSCQKS	K5	CKPRQCTTAT
B6	GEHHKEHCKPRQCTTATPQA	E6	DKSTHHQCKHTICTAQHDHK	H6	NHTQRSCKHH	K6	HCKPRQCTTA
B7	DKSTHHQCKHTICTEQHDHK	E7	DKSAHHQCKHAICAEQHDHK	H7	HKSNHSSKNR	K7	EHCKPRQCTT
B8	HKNTPAKCPTTTCQTEKTAQ	E8	DKSTHHQAKHTIATEQHDHK	H8	KSSKNRE	K8	KEHCKPRQCT
B9	GAKDNKHCHHQECTHSKTRT	E9	DKSTHHQCKHTACTEQHDHK	H9	HSDHHKCGKP	K9	HKEHCKPRQC
B10	GEHHKEHCKPRQCTTATPQA	E10	DKATHHQCKHTICTEQHDHK	H10	HPTRPCTTAH	K10	HHKEHCKPRQ
B11	HKQETPHCTSHHCTQPKTPA	E11	DKSTAAQCKATICTEQHDHK	H11	TNHSCHKREQ	K11	EHHKEHCKPR
B12	HQKADHTCAKHECQKKPHTR	E12	DKSTHHQCKHTICTEQHDHK	H12	KTKSSCQK	K12	GEHHKEHCKP
C1	HKTNHSCHKREQEHCRVTTT	F1	DKSTHHQCKHTICTEQHDHK	I1	SDHHKSGKPR	L1	GAKDNKHCHH
C2	HKANHSCHKREQEHCRVAAA	F2	DASTHHQCAHTICTEQHDHA	I2	GKPREPTSQR	L2	QECTHSKTRT
C3	HKTNHSCHKREQEHCRATTT	F3	DKSTHHQCKHTICTEQADAK	I3	KNESSHHPTR	L3	HQECTHSKTR
C4	HKTNHSCHKAEQEHCAVTTT	F4	AKSTHHQCKHTICTEQHAHK	I4	HKTNHSSHKR	L4	HHQECTHSKT
C5	HKTNHSAHKREQEHARVTTT	F5	DKSTHHACKHTICTEAHDHK	I5	NKTKSSSQKS	L5	CHHQECTHSK
C6	AKTNASCAKREQEACRVTTT	F6	DKSTHHQCKHTICTAQHDHK	I6	NHTQRSSKHH	L6	HCHHQECTHS
C7	HKTNHSCHKRAQAHCRVTTT	F7	DKSAHHQCKHAICAEQHDHK	I7	HKSNHSSKNR	L7	KHCHHQECTH
C8	HKTNHSCHKREAEHCRVTTT	F8	DKSTHHQAKHTIATEQHDHK	I8	KSSKNRE	L8	NKHCHHQECT
C9	HATNHSCHAREQEHCRVTTT	F9	DKSTHHQCKHTACTEQHDHK	I9	HSDHHKSGKP	L9	DNKHCHHQEC
C10	HKTNHACHKREQEHCRVTTT	F10	DKATHHQCKHTICTEQHDHK	I10	HPTRPSTTAH	L10	KDNKHCHHQE
C11	HKTAHSCHKREQEHCRVTTT	F11	DKSTAAQCKATICTEQHDHK	I11	TNHSSHKREQ	L11	AKDNKHCHHQ
C12	HKTNHSCHKREQEHCRVTTT	F12	DKSTHHQCKHTICTEQHDHK	I12	KTKSSSQK	L12	GAKDNKHCHH

Figure S5. Spot synthesis peptide sheet 3. A) Both before and after treatment with biotin hydrazide the sheet was developed by exposure to SAV-AP, followed by washing and then addition of AP substrates. B) The synthesized peptide sequences include full-length 20-mers from the original phage selections and were synthesized in duplicate (A1-B12). Each type of amino acid was substituted with alanine in HyRe peptides **53** and **46,** and synthesized in duplicate (C1-F12). The most interesting short peptides from spot synthesis peptide sheets 1 and 2 were re-synthesized in duplicate to determine background binding (G1-J12). Cysteine was substituted for alanine in the short 10-mers (I1-J12). The contiguous 10-mer variants from original selectants **51** and **52** were also tested (K1-L12).

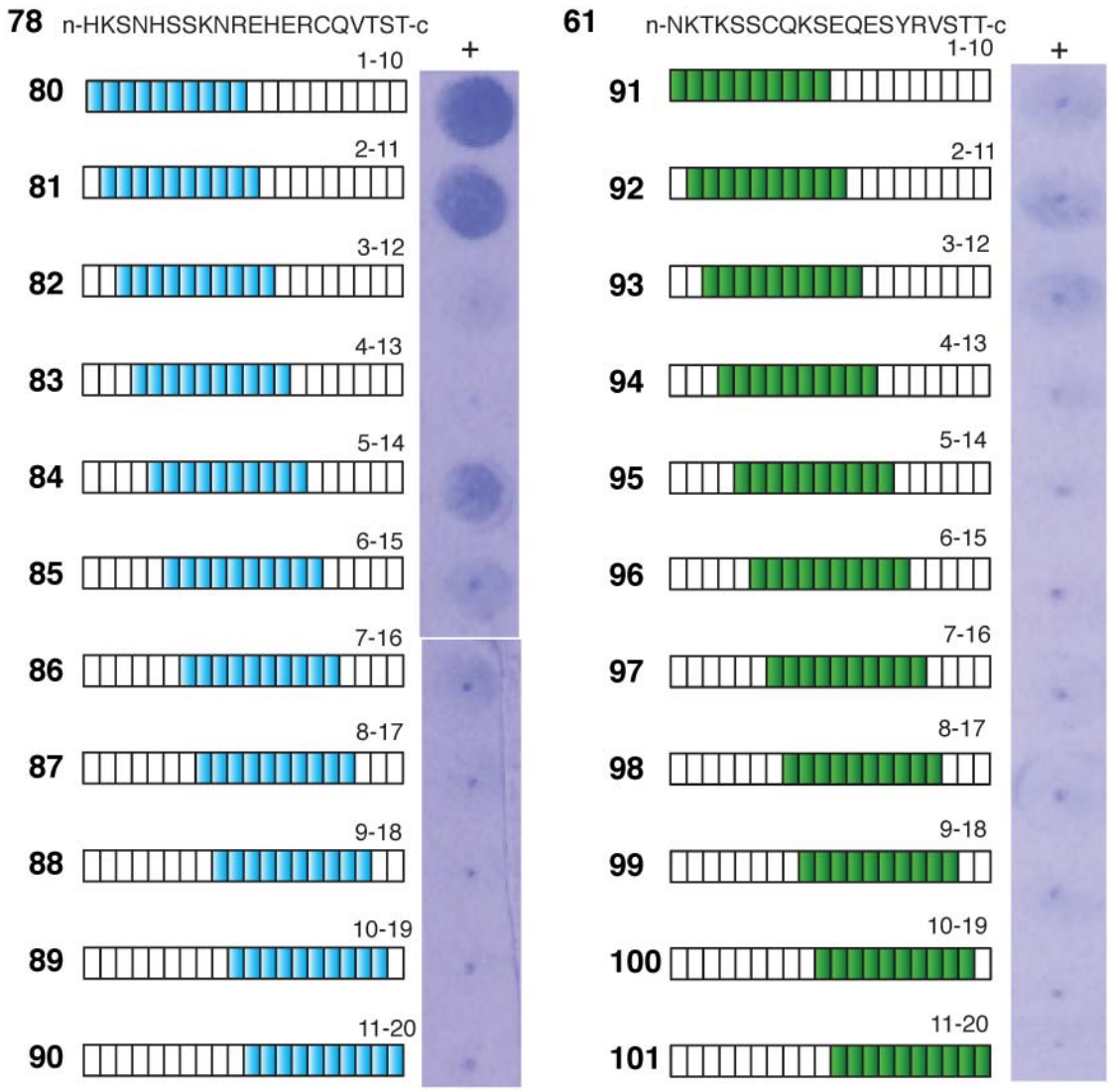

Figure S6. Analysis of contiguous 10-mer peptides **61** and **78** derived from HyRe peptide **53**. As shown by spot synthesis, the N-terminus of both peptides contributes critical residues to the peptide reactivity with biotin hydrazide at pH 7.

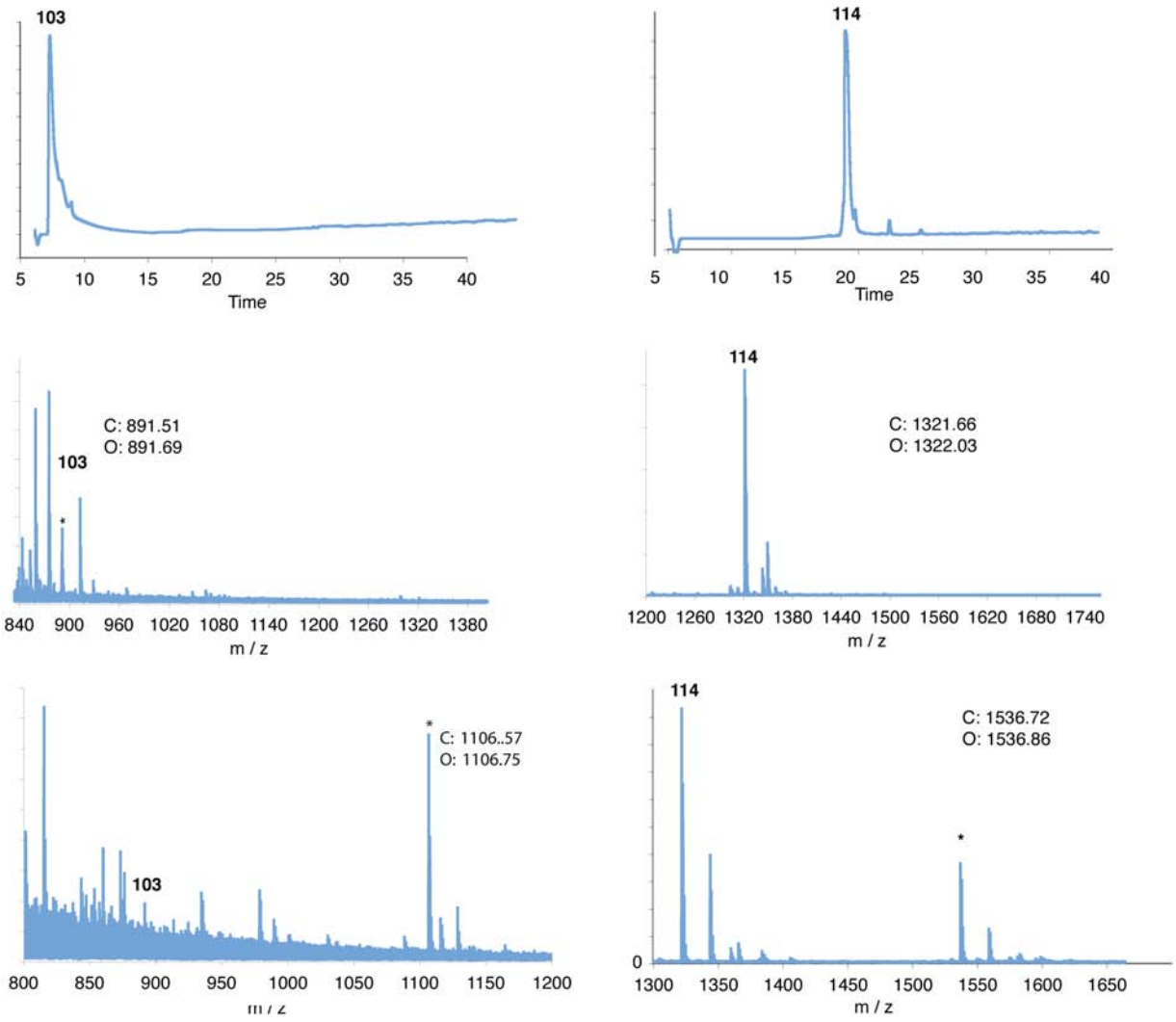

Figure S7. Analytical HPLC and MALDI-TOF MS analysis of synthesized and purified HyRe peptide **114** variants. The chromatograms (top) were monitored at 210 nm. MALDI-TOF MS analysis of purified HyRe tag variants (middle). MALDI-TOF MS analysis of the two peptides treated with AMCA hydrazide, revealing the +215 amu products (bottom). "C:" and "O:" indicate the calculated and observed (*) molecular weights, respectively.

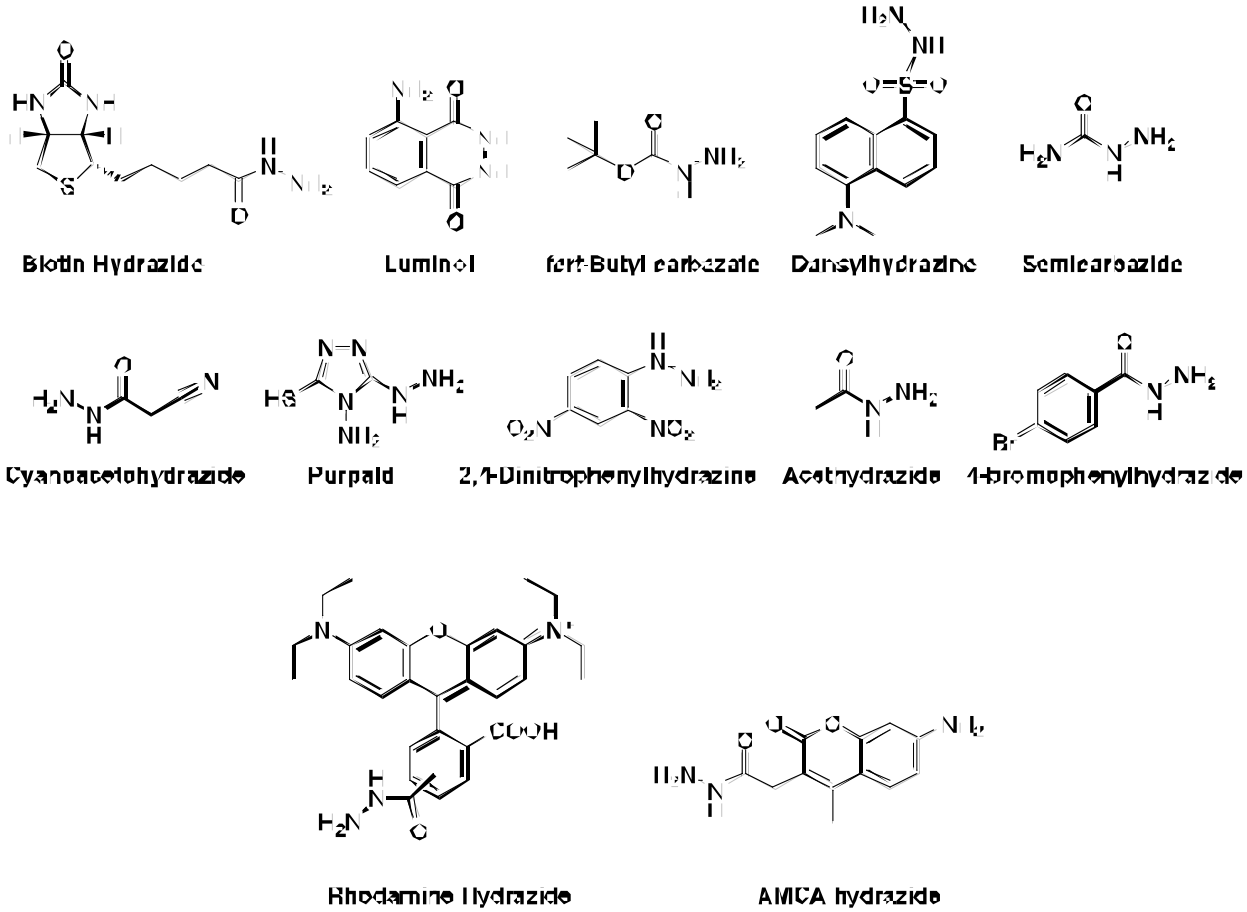

Figure S8. 12 unique hydrazides and hydrazine derivatives used to determine the generality of the reaction with peptide **114**. Only rhodamine B hydrazide and AMCA hydrazide produce the a covalent adduct upon reaction with the peptide at pH 7.

Additional references.

(1) Murase, K. *et al.* (2003) EF-Tu binding peptides identified, dissected, and affinity optimized by phage display. *Chem. Biol. 10,* 161-168.

(2) Sidhu, S.S., Weiss, G.A.. "Constructing phage display libraries by oligonucleotide-directed mutagenesis." In Phage Display. Lowman, H.L., and Clackson,T., Eds. Ch. 2 pg. 27-41 (Oxford University Press, Oxford, 2004).

Bioconjugate Chemistry

Article

pubs.acs.org/bc

A New Daunomycin–Peptide Conjugate: Synthesis, Characterization and the Effect on the Protein Expression Profile of HL-60 Cells *in Vitro*

Erika Orbán,[†] Marilena Manea,[‡,§] Andreas Marquadt,[∥] Zoltán Bánóczi,[†] Gabriella Csík,[⊥] Erzsébet Fellinger,[#] Szilvia Bősze,[†] and Ferenc Hudecz*[,†,▽]

[†]Research Group of Peptide Chemistry, Hungarian Academy of Sciences, Eötvös Loránd University, Budapest, Hungary

[‡]Laboratory of Analytical Chemistry and Biopolymer Structure Analysis, Department of Chemistry, University of Konstanz, Konstanz, Germany

[§]Zukunftskolleg, University of Konstanz, Konstanz, Germany

[∥]Proteomics Facility, University of Konstanz, Konstanz, Germany

[⊥]Department of Biophysics and Radiobiology, Semmelweis University, Budapest, Hungary

[#]Department of Anatomy, Cell and Developmental Biology, Eötvös Loránd University, Budapest, Hungary

[▽]Department of Organic Chemistry, Eötvös Loránd University, Budapest, Hungary

Supporting Information

ABSTRACT: Daunomycin (Dau) is a DNA-binding antineoplastic agent in the treatment of various types of cancer, such as osteosarcomas and acute myeloid leukemia. One approach to improve its selectivity and to decrease the side effects is the conjugation of Dau with oligopeptide carriers, which might alter the drug uptake and intracellular fate. Here, we report on the synthesis, characterization, and *in vitro* biological properties of a novel conjugate in which Dau is attached, via an oxime bond, to one of the cancer specific small peptides (LTVSPWY) selected from a random phage peptide library. The *in vitro* cytostatic effect and cellular uptake of Dau═Aoa-LTVSPWY-NH_2 conjugate were studied on various human cancer cell lines expressing different levels of ErbB2 receptor which could be targeted by the peptide. We found that the new daunomycin–peptide conjugate is highly cytostatic and could be taken up efficiently by the human cancer cells studied. However, the conjugate was less effective than the free drug itself. RP-HPLC data indicate that the conjugate is stable at least for 24 h in the pH 2.5–7.0 range of buffers, as well as in cell culture medium. The conjugate in the presence of rat liver lysosomal homogenate, as indicated by LC-MS analysis, could be degraded. The smallest, Dau-containing metabolite (Dau═Aoa-Leu-OH) identified and prepared expresses DNA-binding ability. In order to get insight on the potential mechanism of action, we compared the protein expression profile of HL-60 human leukemia cells after treatment with the free and peptide conjugated daunomycin. Proteomic analysis suggests that the expression of several proteins has been altered. This includes three proteins, whose expression was lower (tubulin β chain) or markedly higher (proliferating cell nuclear antigen and protein kinase C inhibitor protein 1) after administration of cells with Dau-conjugate vs free drug.

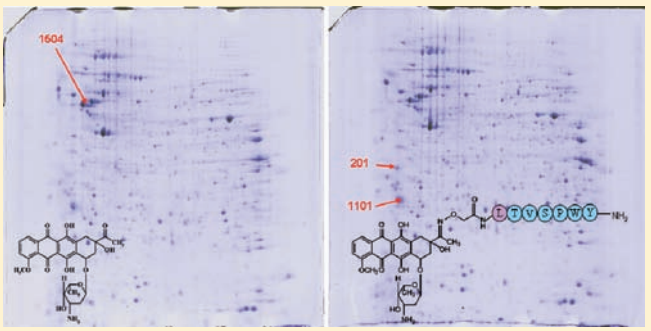

INTRODUCTION

Anthracyclines (e.g., daunomycin, doxorubicin, epirubicin, idarubicin) are antineoplastic agents widely used in the treatment of various types of cancer, such as osteosarcomas and acute myeloid leukemia.[1]

Daunomycin (Dau) is one of the anthracycline-type antitumor agents able to inhibit the division of the cells by intercalating to DNA or/and by inhibiting the topoisomerase-II.[2] Clinical application of Dau is limited by side effects such as nausea, vomiting, and lack of appetite, but the most severe side effect is cardiotoxicity.[3] The intrinsic or acquired resistance of tumor cells to daunomycin also reduces the response to the treatment.[4]

To investigate the effect of anthracyclines at the molecular level, a few proteomic studies were carried out. In these publications two types of studies are reported. In communications belonging to the first group, proteomics are used to identify proteins involved in the development of multidrug resistance.[5−7] Other authors studying the effects of anthracycline drugs (adriamycin, epirubicin, or daunomycin) on various tumor cells compared the protein expression profiles of treated and untreated cells. In these papers proteins were determined

Received: August 1, 2011
Revised: September 8, 2011
Published: September 28, 2011

ACS Publications © 2011 American Chemical Society

with altered expression due to the treatment with free drug. The authors observed these changes mainly in the expression level of cytoskeletal proteins and proteins involved in protein biosynthesis, metabolic pathways, and apoptosis.[8−12] In both types of studies various treatment schedules (time, concentration) and proteomic methods were used. It is important to note that—according to our knowledge—no studies were reported so far on changes of the protein expression profile after treatment of anthracycline−carrier conjugates in comparison with that of free drug treatment.

It has been shown that conjugation of anthracycline drug to different types of carrier (e.g., oligo- and polypeptides,[13,14] proteins,[15] polysaccharides,[16] polymers,[17,18] and dextran[19]) could improve the selectivity and decrease the side effects by utilizing different cellular uptake mechanism(s).

Daunomycin has four functional groups suitable for covalent conjugation (Figure 1). According to the literature data, the most frequently used site for conjugation is the primary amino group of the carbohydrate moiety even though the free amino group is critical for binding to DNA.[20] If this amino group is used for conjugation, the drug has to be released from the conjugate in order to generate the free amino function. Modification of anthracyclines is also possible on the 13-oxo group using different hydrazide[21−24] and *O*-alkyl-hydroxylamine[23,25] derivatives. The replacement of the methyl ether group on C-4 provides another option for conjugation. This strategy has recently been employed for the coupling of daunomycin to triplex forming oligonucleotides.[26]

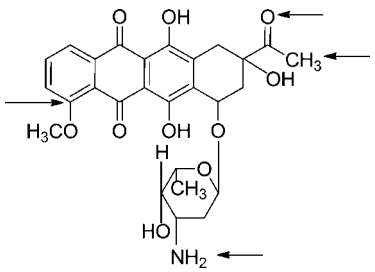

Figure 1. Structure of daunomycin. Four functions suitable for covalent conjugation are indicated by arrows.

Peptide conjugates of daunomycin were synthesized for various purposes: to reduce its side effects;[23] to circumvent the multidrug resistance;[27,28] and to increase the selectivity or target the molecule to a specific part of the body.[21,29−31]

It was found that the nature of the chemical bond between daunomycin and the peptide could markedly influence the chemical and biological properties of the conjugate and, thus, the efficacy of the drug. We described earlier that conjugates containing an oxime bond between daunomycin and the oligopeptide were chemically stable and also effective on HL-60 human leukemia and HepG2 human hepatoma cell lines.[32] On the basis of the observations in the present study, an oxime bond was utilized for the attachment of daunomycin to the targeting peptide.

Here, we describe the synthesis, chemical characterization, *in vitro* stability, cytotoxicity, cytostatic effect, and cellular uptake profile of a new conjugate in which daunomycin is conjugated to a tumor specific peptide via an oxime bond.

Tumor targeting peptides are often selected for their binding to cell surface proteins involved in biological functions such as cell surface receptors, growth factor receptors, and cell adhesion molecules. Members of the ErbB receptor tyrosine kinase family are central regulators of normal and tumor cell functions.[33] This family has four members: the epidermal growth factor receptor (EGFR), ErbB-2, ErbB-3, and ErbB-4.[34] ErbB-2 is a tumor-associated receptor responsible for tumor cell survival, proliferation, and metastases in many human cancers.[35−37] This tyrosine kinase-linked transmembrane protein is overexpressed in 30−50% of primary breast cancers.[38]

Using random phage peptide libraries, Shadidi and coworkers aimed to identify peptides that specifically or preferentially bind to breast cancer cells. The selected peptides did not bind to normal mammary epithelial cells but showed preferential binding and internalization into breast cancer cell lines.[39] One of the cancer-specific oligopeptides, peptide LTVSPWY, was identified as an ErbB-2-binding peptide. It was also shown that its GFP-fusion derivative was specifically internalized by SK-BR-3 human breast cancer cells.[35,40] This peptide was also chemically coupled to antisense oligonucleotides.[39,41]

Here we report on our findings related to the preparation and analysis of the relevant functional properties (e.g., *in vitro* cytotoxicity, cytostatic effect, cellular uptake) of the new Dau−peptide conjugate on cancer cells with different expression levels of ErbB-2. For these studies, cell lines with normal expression (e.g., MCF-7) or with overexpression of ErbB-2 (e.g., SK-BR-3)[42] were selected. In addition we have included HepG2 cells, which express the ErbB-2 receptor to some extent,[43] as well as HL-60 cells highly sensitive to daunomycin treatment. Data presented in this paper might also be useful to identify proteins with altered expression due to the treatment with Dau-conjugate and could be considered as future potential targets for rational design in cancer chemotherapy.

MATERIALS AND METHODS

Materials. Daunomycin hydrochloride was a gift from the Institute of Drug Research Institute (IVAX, Budapest, Hungary). The amino acid derivatives were obtained from Reanal (Budapest, Hungary) and IRIS Biotech (Marktredwitz, Germany). Rink-Amide MBHA resin (0.65 mmol/g) was purchased from Novabiochem (Darmstadt, Germany). Scavengers (thioanisole, ethanedithiol [EDT], phenol), coupling agents (*N*,*N*′-diisopropylcarbodiimide [DIC], 1-hydroxybenzotriazole [HOBt]), and cleavage reagents (piperidine, 1,8-diazabicyclo[5.4.0]undec-7-ene [DBU], trifluoroacetic acid [TFA]) were Fluka (Buchs, Switzerland) products. Acetonitrile [ACN], acetone, and *N*-methylpyrrolidone [NMP] were from Merck (Darmstadt, Germany). Dimethylformamide [DMF], dichloromethane [DCM], diethyl ether, NH_4OAc, and EtOAc were purchased from Reanal (Budapest, Hungary). 3-(4,5-Dimethylthiazol-2-yl)-2,5-diphenyltetrazolium bromide [MTT], RPMI-1640 medium, and fetal calf serum [FCS] were obtained from Sigma-Aldrich (Budapest, Hungary). HPMI buffer (HEPES buffered medium RPMI-1640 containing D-glucose, $NaHCO_3$, NaCl, HEPES, KCl, $MgCl_2$, $CaCl_2$, $Na_2HPO_4{\cdot}2H_2O$) and lysis buffer (0.15 M NaCl, 5 mM EDTA, 1% Triton-X100, 10 mM Tris-HCl pH = 7.4, 5 mM DTT, and protease inhibitor used according to the recommendation of the manufacturer) were prepared in our laboratory using ingredients purchased from Sigma-Aldrich (Budapest, Hungary). Rehydration buffer (7 M urea, 2 M thiourea, 4% CHAPS, 40 mM Tris, 2% servalyt) and equilibration buffer (6 M urea, 2% SDS, 30% glycerol, 2.5

dx.doi.org/10.1021/bc2004236|*Bioconjugate Chem.* 2011, 22, 2154−2165

mM Tris-HCl) were also prepared in our laboratory. IPG strips (pH 3−10 NL, 17 cm) were purchased from Bio-Rad Laboratories (Hercules, CA). Trichloroacetic acid (TCA) was obtained from Roth (Karlsruhe, Germany). The BCA assay kit was a Pierce product (Rockford, USA).

Synthesis of Dau═Aoa-Leu-OH and Dau═Aoa-LTVSPWY-NH_2 Conjugates. *Synthesis of Dau═Aoa-Leu-OH.* H-Leu-OH (0.1 mmol) was dissolved in 1.5 mL of 2 M K_2CO_3. This solution was diluted with 1.5 mL of DMF, and an equivalent amount of Boc-Aoa-OPcp (0.1 mmol) in 1.5 mL of DMF was added. The reaction proceeded at room temperature (RT) for 24 h. DMF was removed, and the remaining material was washed with diethyl ether and dissolved in water. The pH of the solution was adjusted to 2.0 with 1 M HCl. The compound was extracted with EtOAc, and the organic phase was dried over $MgSO_4$. The EtOAc was removed, and the oily compound was dried in a desiccator for 1 day. The Boc group was cleaved with TFA containing 5% distilled water at RT for 1 h. After the removal of the cleavage mixture, 2 mL of 0.2 M NH_4OAc was added. The daunomycin hydrochloride (1.5 equiv) was added to this solution. The coupling reaction was carried out at RT overnight. For semipreparative RP-HPLC purification, 2 mL of A eluent (water containing 0.1% TFA) was added to the reaction mixture and the solution was injected. The target compound was characterized by analytical RP-HPLC (as described below; R_t = 33.8 min) and ESI-MS (Bruker Esquire 3000+; M_{mo}[calcd] = 713.4; M_{mo}[exptl] = 714.4).

For the RP-HPLC analysis a laboratory-assembled Knauer HPLC system (Bad Homburg, Germany) was used with a Phenomenex Luna C18 column (250 mm × 4.6 mm, 5 μm particle size, 100 Å pore size) (Torrance, CA). The gradient elution system consisted of 0.1% TFA in water (eluent A) and 0.1% TFA in acetonitrile/water = 80/20 (v/v) (eluent B). First, the eluent B content was 0% for 5 min; then it was varied from 0 to 90% in 50 min at a flow rate of 1 mL/min at room temperature. The sample (20 μL) was injected, and peaks were detected at λ = 214 nm.

Synthesis of NH_2-O-CH_2-CO-LTVSPWY-NH_2. Peptide LTVSPWY was prepared manually by solid phase synthesis on Rink-Amide MBHA resin (0.65 mmol/g) using the Fmoc/^{t}Bu strategy. The following side chain protected amino acid derivatives were used: Tyr(^{t}Bu), Trp(Boc), Ser(^{t}Bu), Thr(^{t}Bu). The protocol of the synthesis was as follows: (i) Fmoc deprotection with piperidine/DBU/DMF (2:2:96 v/v) solution (4 times, 2 + 2 + 5 + 10 min); (ii) washing with DMF (5 × 1 min); (iii) coupling 3 equiv of Fmoc-amino acid derivative−DIC-HOBt dissolved in NMP (60 min); (iv) washing with DMF (5 × 1 min); (v) ninhydrin or isatin test. Boc-aminooxy-acetic acid was also coupled on the solid phase to the free *N*-terminal amino group of Leu using a DIC/HOBt coupling agent. The coupling time was 60 min. The peptide derivative was cleaved from the resin with a TFA/H_2O/thioanisol/EDT/phenol (10 mL/0.5 mL/0.5 mL/0.25 mL/0.75 g) mixture (2 h, RT). After the resin was filtered off, the peptide derivative was precipitated with cold diethyl ether and centrifuged. The pellet was solubilized in 0.1% TFA (aqueous solution), freeze-dried, and characterized by analytical RP-HPLC (as described below; R_t = 24.4 min) and ESI-MS (Bruker Esquire 3000+; M_{mo}[calcd] = 936.9; M_{mo}[exptl] = 936.6).

Conjugation of Daunomycin to NH_2-O-CH_2-CO-LTVSPWY-NH_2. Equal amounts of Dau hydrochloride and aminooxyacetyl peptide (NH_2-O-CH_2-CO-LTVSPWY-NH_2) were dissolved in a mixture of 0.2 M NaOAc/AcOH buffer (pH 5.0) and DMSO (85:15 v/v%). The reaction mixture was stirred at room temperature, and the reaction was monitored by analytical RP-HPLC using an Eurospher-100, C18 column (250 mm × 4 mm, 5 μm particle size, 300 Å) (Knauer, Bad Homburg, Germany), and an appropriate gradient (10% eluent B for 5 min, then 10−80% eluent B in 50 min; eluent A (0.1% TFA in water) and eluent B (0.1% TFA in acetonitrile/water = 80/20 (v/v)). The flow rate was 1 mL/min. The sample (20 μL) was injected, and peaks were detected at λ = 214 nm. The Dau═Aoa-LTVSPWY-NH_2 conjugate was formed in one day.

The crude product was purified by semipreparative RP-HPLC using a C18 Phenomenex Jupiter column (250 mm × 10 mm) packed with 10 μm silica (300 Å pore size) (Torrance, CA, USA) using the above-mentioned eluents and a linear gradient. The sample (6 mg in 2 mL of eluent A) was injected into the column at a flow rate of 4 mL/min. The purified conjugate was dissolved in 0.1% TFA (aqueous solution), freeze-dried, and characterized by analytical RP-HPLC (as described above; R_t = 33.7 min), ESI-MS (Bruker Esquire 3000+; M_{mo}[calcd] = 1446.5; M_{mo}[exptl] = 1446.0), and amino acid analysis after hydrolysis with 6 M HCl for 24 h at 110 °C (measured [calcd]: T 1.17 [1]; S 1.17 [1]; P 1.02 [1]; V 0.92 [1]; L 0.89 [1]; Y 0.84 [1]).

Stability/Degradation of Dau═Aoa-LTVSPWY-NH_2 Conjugate. For the stability studies, the conjugate was dissolved in 0.1 M sodium citrate/citric acid buffer (pH 2.5, 5.0, or 7.0) or in 10% FCS containing DMEM cell culture medium and incubated at 37 °C. Aliquots were taken from the solution after 3 and 24 h and analyzed in a analytical RP-HPLC system under the conditions described above for the analysis of the conjugate.

The degradation of the Dau═Aoa-LTVSPWY-NH_2 conjugate was determined in the presence of rat liver lysosomal homogenate prepared as previously described.[44] The protein concentration of the lysosomal fraction was determined by Pierce BCA protein assay (bicinchoninic acid) according to the manufacturer's protocol (Thermo Fisher Scientific, Rockford, IL, USA). Briefly, 100 μg of lysosomal homogenate was added to 100 μg of bioconjugate dissolved in 1 mL of 0.2 M sodium acetate buffer, pH 5.0 (bioconjugate/lysosomal homogenate ratio = 1:1, w/w). The reaction mixture was incubated at 37 °C, and aliquots of 50 μL were taken at 5 min and 2, 4, 6, 8, and 24 h. The reaction was terminated by adding 5 μL of acetic acid, and the composition of the mixture was determined by liquid chromatography in combination with mass spectrometry (LC-MS). A control experiment was performed with a conjugate solution in 0.2 M sodium acetate buffer (pH 5.0), which was incubated at 37 °C for 24 h and analyzed by LC-MS as previously described.[44]

Absorption and Emission Spectra of Dau═Aoa-Leu-OH and Dau═Aoa-LTVSPWY-NH_2 Conjugates. Ground-state absorption spectra were recorded with 1 nm steps and 2 nm bandwidth using a Cary 4E (Varian, Mulgrave, Australia) spectrophotometer. Spectra of Dau and its derivatives were recorded at 10 μM concentration in Tris buffer (pH 7.4) containing 20 mM Tris-HCl and 50 mM NaCl.

Corrected steady-state emission spectra of the compounds were obtained using a Fluorolog-3 (Yvon Jobin, France) spectrofluorimeter. The excitation wavelength was λ = 488 nm, and the emission was detected between 495 and 800 nm. The excitation wavelength was chosen because the laser of the BD-

LSR II flow cytometer used for cellular uptake studies operates at this excitation wavelength. The same content of the compound solution was used in the absorption studies.

DNA-Binding of Dau═Aoa-Leu-OH and Dau═Aoa-LTVSPWY-NH_2 Conjugates. The ratio of the integrated fluorescence intensity of daunomycin derivatives in the absence of DNA (I_0) and in the presence of DNA (I) was used to calculate the amount of bound compound according to the following equation:

$$c_{free} = c_t(I/I_0 - P)/(1 - P)$$

where c_t is the known added amount of compound and P is the ratio of the observed quantum yield of fluorescence of the totally bound compound to that of the free one; c_{bound} was then obtained by difference.[45] The ratio $P = I_\infty/I_0$ was obtained from the initial value of I and the plateau value of I at the highest DNA concentration.

Apparent binding constants were determined by the neighbor exclusion model[46] using the equation

$$\frac{r}{c_{free}} = K(1 - nr)\left[\frac{1 - nr}{1 - r(n - 1)}\right]^{n-1}$$

where r is the number of moles of bound compound per mole of DNA base pair, K is the intrinsic binding constant, and n is the exclusion parameter in base pairs. DNA concentration was calculated on the basis of the measured optical density at 260 nm.

Cells. HL-60 human leukemia cells (ATCC: CCL-240) and HepG2 human hepatoma cells (ATCC: HB-8065) were cultured in RPMI-1640 medium supplemented with 10% FCS (fetal calf serum, Sigma Ltd.), 2 mM L-glutamine, and 160 μg/mL gentamycin.[47] SK-BR-3 human breast cancer cells (ATCC: HTB-30) and MCF-7 human breast adenocarcinoma cells (ATCC: HTB-22) were maintained in DMEM (Sigma Ltd., St. Louis, MO) medium containing 10% FCS, L-glutamine (2 mM), gentamycin (160 μg/mL), 1 mM pyruvate, and nonessential amino acids (Sigma Ltd.). Cell cultures were maintained at 37 °C in a humidified atmosphere with 5% CO_2.

***In Vitro* Cytostatic and Cytotoxic Effect.** The *in vitro* cytostatic and cytotoxic effect of the compounds was evaluated by the 3-(4,5-dimethylthiazol-2-yl)-2,5-diphenyltetrazolium bromide-assay (MTT-assay).[48] For the experiment, 5×10^3 cells per well were plated on 96-well plates. After 24 h incubation at 37 °C, cells were treated for 3 h with the conjugate and control compounds dissolved in serum-free medium. The compounds were tested in the $(2.6 \times 10^{-4})-10^2$ μM concentration range. Cells treated with serum-free medium for 3 h were used as negative control. To determine the cytostatic effect, cells were washed twice with serum-free medium and cultured for a further 72 h in serum containing medium. To characterize the cytotoxicity of the compounds, MTT-assay was carried out directly after the 3-, 24-, 48-, or 72-h treatment: MTT solution was added to each well (final concentration: 367 μg/mL). After 3.5 h of incubation, purple crystals were formed by mitochondrial dehydrogenase enzyme of living cells. Cells were centrifuged for 5 min at 863 g, and the supernatant was removed. Crystals were dissolved in DMSO, and the optical density (OD) of the samples was measured at λ = 540 and 620 nm using an ELISA Reader (Labsystems MS reader, Finland). OD_{620} was subtracted from OD_{540}. The percent of cytostasis or cytotoxicty was calculated using the following equation:

$$\text{cytotoxicity \% or cytostasis \%} = [1 - (OD_{treated}/OD_{control})] \times 100$$

where $OD_{treated}$ and $OD_{control}$ correspond to the optical densities of treated and control cells, respectively. Cytostasis % or cytotoxicty % was plotted as a function of concentration, fitted to a sigmoidal curve, and based on this curve, the half maximal inhibitory concentration (IC_{50}) value was determined. IC_{50} represents the concentration of a drug that is required for 50% inhibition *in vitro* and expressed as micromolar units.

Cellular Uptake. To study the cellular uptake of the compounds, 10^5 cells per well were plated on a 24-well plate. After 24 h of incubation at 37 °C, cells were treated for 1.5 h with the compounds dissolved in serum-free medium in the 0.8−100 μM concentration range. Cells treated with serum-free medium for 1.5 h were used as negative control. After treatment and incubation, cells were washed with HPMI and treated with trypsin for 10 min. The effect of trypsin was stopped by the addition of HPMI supplemented with 10% FCS, and then the cells were transferred from the plate to FACS-tubes. After washing, cells were resuspended in HPMI, and the ratio of daunomycin-positive cells was determined by flow cytometry (BD LSR II, BD Bioscience, San Jose, CA, USA). Data were analyzed with the FACSDiVa software.

Two-Dimensional (2D) Gel Electrophoresis. In order to prepare cell lysates, 5×10^5 HL-60 cells per well were plated on 6-well plates. After 24 h of incubation at 37 °C, cells were removed from the plate and treated for 24 h with the conjugate (c = 9 μM) or daunomycin (c = 0.024 μM). These concentrations were chosen on the basis of *in vitro* cytotoxicity data. Cells treated with cell culture medium for the same period of time were used as control. After incubation, cells were washed with PBS and centrifuged at 220*g* for 5 min, and the supernatant was discarded. A volume of 40 μL lysis buffer was added per 10^6 cells, and samples were incubated for 30 min on ice and centrifuged for 20 min at 16000*g*. The protein content of the supernatant was determined spectrophotometrically by BCA assay according to the manufacturer's instructions using bovine serum albumin as a standard.

To remove salts and contaminants, proteins were precipitated by five volumes of ice-cold acetone at −28 °C for 3 h. Samples were centrifuged at 16000*g* for 20 min. The supernatant was discarded, and the pellet was dried with nitrogen gas and resuspended in rehydration buffer. After sonication for 10 min, samples were placed into a rehydration tray, and passive rehydration of 17 cm nonlinear IPG strips (pH 3−10) was carried out overnight. Approximately 0.5 mg of total protein was loaded on each gel. A Bio-Rad Protean IEF cell instrument was used for the isoelectric focusing. The steps of the isoelectric focusing were as follows: (i) 0−150 V in 3 min, (ii) 150 V for 30 min, (iii) 150−300 V in 15 min, (iv) 300 V for 30 min, (v) 300−3500 V in 150 min, (vi) 3500 V for 10 h. After isoelectric focusing, samples were equilibrated first in equilibration buffer I (containing DTT) for 20 min and then in equilibration buffer II (containing iodoacetamide) for 20 min. After washing, the IPG strips were placed on a 12% SDS gel and overlaid with 0.5% agarose. Gel electrophoresis was performed using a Bio-Rad PROTEAN II ix cell. The current was set to 25 mA/gel until the samples ran from the strip to the gel, and then 40 mA/gel was applied. After the run, gels were prefixed for 1 h with 12% TCA and stained with Coomassie Brillant Blue G-250-containing staining solution overnight. Gels

dx.doi.org/10.1021/bc2004236|*Bioconjugate Chem.* 2011, 22, 2154−2165

were destained with 25% methanol in Milli-Q water and scanned with a GS-800 calibrated densitometer (Bio-Rad) using QuantityOne software. From each sample two replicate gels were prepared and analyzed.

2D-Gel Image Analysis. On the gel images, spots were matched and the quantity of the proteins was compared with PDQuest 8 software (Bio-Rad). The computer analysis allowed automatic detection with manual corrections and quantification of protein spots, as well as matching between control gels and gels from treated samples. The significance of differences between protein spots was evaluated by Student's *t*-test, and $p < 0.05$ was considered as significant.

In-Gel Tryptic Digestion. Spots with significant quantitative differences were manually excised and transferred to siliconized tubes. Gel pieces were washed once with Milli-Q water for 15 min and then an acetonitrile–Milli-Q (3:2 v/v) solvent mixture was added. After 30 min, the acetonitrile–Milli-Q solvent mixture was removed, and the gel pieces were dried using a SpeedVac (Eppendorf). Gel pieces were rehydrated with 20 mM ammonium bicarbonate buffer (pH 8.0) for 15 min. This buffer was changed to an acetonitrile–Milli-Q (3:2) solvent mixture, and gels were incubated for 30 min. The steps after SpeedVac centrifugation were repeated until the gel pieces were transparent. After the last incubation with an acetonitrile–Milli-Q (3:2) solvent mixture, gels were dried in a SpeedVac (Eppendorf). To the dry gel pieces, 50 μL of 20 mM ammonium bicarbonate containing 12.5 ng/μL of sequencing grade modified trypsin solution (Promega, Madison, WI) was added. The samples were incubated at 4 °C for 45 min, and then the trypsin containing solution was changed to 20 mM ammonium bicarbonate buffer (pH 8.0) and incubated at 37 °C for at least 12 h. The tryptic peptides were extracted from the gel with a mixture of acetonitrile–0.1% TFA in Milli-Q (3:2, v/v).

Identification of Proteins. Tryptic peptide mixtures were analyzed by reversed-phase liquid chromatography nanospray tandem mass spectrometry (LC-MS/MS) using an LTQ-Orbitrap mass spectrometer (Thermo Fisher) and an Eksigent nano-HPLC. The characteristics of the reversed-phase LC column were 5 μm, 200 Å pore size C18 resin in a 75 μm i.d. × 10 cm long piece of fused silica capillary (Hypersil Gold C18, New Objective). After injecting the sample, the column was washed with 90% eluent A (0.1% formic acid, aqueous solution) and 10% eluent B (0.1% formic acid in acetonitrile) for 5 min. Peptides were eluted using a linear gradient of 10–50% eluent B in 25 min and then 50–80% eluent B in 5 min, at a 300 nL/min flow rate.

The LTQ-Orbitrap mass spectrometer was operated in a data dependent mode in which each full MS scan (30 000 resolving power) was followed by five MS/MS scans, where the five most abundant molecular ions were dynamically selected and fragmented by collision-induced dissociation (CID) using a normalized collision energy of 35% in the LTQ ion trap. Dynamic exclusion was allowed. Tandem mass spectra were searched against the SwissProt protein database using Mascot (Matrix Science) with the following parameters: "Trypsin" cleavage with one missed cleavage, cysteine alkylation by iodoacetamide as a constant modification, and methionine oxidation as a variable modification.

RESULTS

Synthesis and Chemical Characteristics of Dau=Aoa-Leu-OH and Dau=Aoa-LTVSPWY-NH_2 Conjugates. For the synthesis of Dau=Aoa-Leu-OH, the amino acid H-Leu-OH was reacted with the *N*-protected aminooxy-acetic acid active ester (Boc-Aoa-OPcp), followed by the removal of the *N*-terminal Boc protecting group of the amino acid derivative. The oxime bond formation between the free primary amino group of H-Aoa-Leu-OH and the C^{13} oxo function of Dau was achieved in solution with acceptable overall yield (55%). The crude product was purified by RP-HPLC, and the conjugate was characterized by analytical RP-HPLC (R_t = 33.8 min) and mass spectrometry (Bruker Esquire 3000+; M_{mo}[calcd] = 713.4; M_{mo}[exptl] = 714.4).

The strategy used for the preparation of daunomycin conjugate with peptide LTVSPWY is outlined in Figure 2.

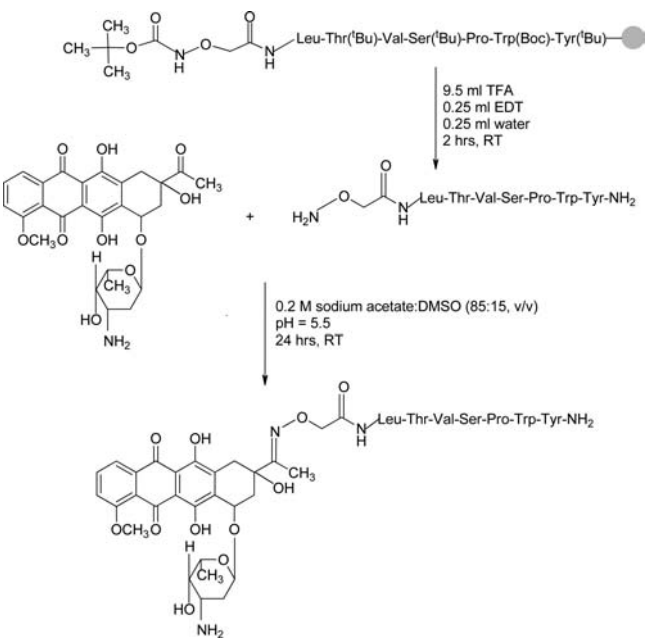

Figure 2. Outline of the synthesis of the Dau=Aoa-LTVSPWY-NH_2 conjugate.

First, the oligopeptide LTVSPWY was synthesized on solid phase using the Fmoc/^{t}Bu strategy and Rink-Amide MBHA resin to obtain the peptide amide. Boc-aminooxy-acetic acid was coupled on solid phase to the free *N*-terminal amino group of Leu using the DIC/HOBt based active ester strategy. The protected peptide derivative was cleaved from the resin, resulting in NH_2-O-CH_2-CO-LTVSPWY-NH_2 (Aoa-LTVSPWY-NH_2), which was used for the conjugation with daunomycin in solution using a buffer (pH 5.0) and DMSO (85:15 v/v) mixture. The product obtained in 24 h was purified by RP-HPLC and characterized by analytical RP-HPLC (R_t = 33.7 min), ESI-MS (Bruker Esquire 3000+; M_{mo}[calcd] = 1446.5; M_{mo}[exptl] = 1446.0), and amino acid analysis (measured [calcd]: T 1.17 [1]; S 1.17 [1]; P 1.02 [1]; V 0.92 [1]; L 0.89 [1]; Y 0.84 [1]). The analytical RP-HPLC chromatogram of the purified conjugate is shown in the Supporting Information (Figure S1).

Absorption and Emission Properties of Dau=Aoa-Leu-OH and Dau=Aoa-LTVSPWY-NH_2 Conjugates. First, the absorption spectra of the conjugates (Dau=Aoa-Leu-OH and Dau=Aoa-LTVSPWY-NH_2) and Dau were recorded at pH 7.4, and the shapes of these spectra were found to be similar. The corrected steady-state emission spectra of the compounds were obtained using a λ = 488 nm excitation

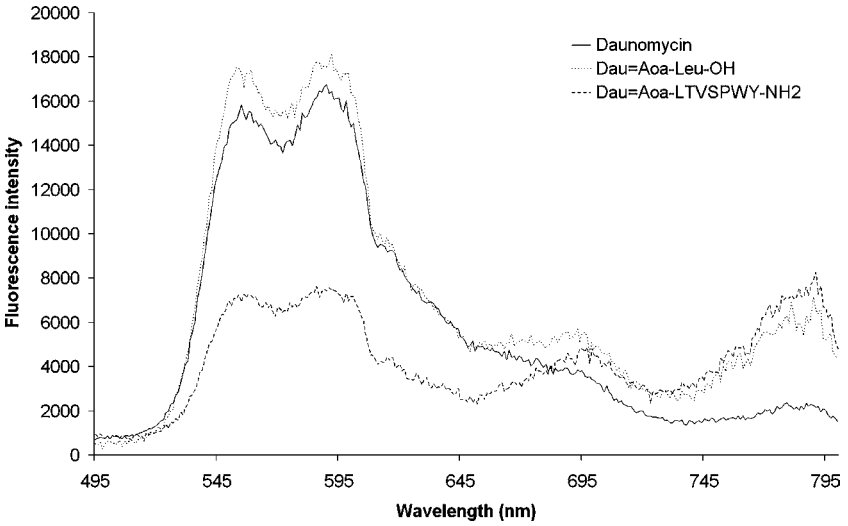

Figure 3. Emission spectra of Dau═Aoa-LTVSPWY-NH_2 and Dau═Aoa-Leu-OH conjugates as well as daunomycin using λ = 488 nm excitation and recorded at 10 μM concentration in Tris buffer (pH 7.4) containing 20 mM Tris-HCl and 50 mM NaCl.

wavelength under identical conditions. The emission spectra recorded between λ = 495 and 800 nm for daunomycin, Dau═Aoa-Leu-OH, and Dau═Aoa-LTVSPWY-NH_2 are shown in Figure 3. The comparative analysis of the shape of the curves indicates a high level of similarities. In each spectrum, two maximum points were identified (λ = 555 and 595 nm). The fluorescence intensity of the conjugate Dau═Aoa-LTVSPWY-NH_2 was lower compared to those of the other two compounds. One possible explanation of this phenomenon is the presence of the aromatic amino acids (Trp and Tyr) in the sequence of the peptide. Alston and co-workers studied the influence of peptide sequence and conformation on the fluorescence of tryptophan containing peptides and proteins. Large differences in the emission spectra of the peptides were detected, suggesting that the amino acid sequence influences the fluorescence intensity either directly through quenching by the side chains or, more likely, indirectly through an effect on the conformational ensembles of the peptides.[49]

Stability/Degradation of Dau═Aoa-LTVSPWY-NH_2 Conjugate. The stability of the conjugate under acidic and neutral conditions (aqueous buffer solutions; pH 2.5, 5.0, and 7.0) was determined for a period of 3−24 h by analytical RP-HPLC. The recorded chromatograms are shown in the Supporting Information (Figures S2−S4). It was found that, at all investigated pH values, the chromatogram of the Dau═Aoa-LTVSPWY-NH_2 conjugate did not markedly change even after 24 h. These results indicate that the conjugate is stable in the pH range studied at room temperature at least for 24 h. Furthermore, the stability of this compound was determined in 10% serum containing DMEM cell culture medium (pH 7.3). Similarly, aliquots were taken from the solution after 3 and 24 h and analyzed by RP-HPLC. The chromatograms (S5) clearly show that even after 24 h the Dau═Aoa-LTVSPWY-NH_2 conjugate is stable under the circumstances applied in the *in vitro* experiments.

Considering a potential pathway for compounds entering the cells, the degradation of the Dau═Aoa-LTVSPWY-NH_2 conjugate in the presence of rat lysosome homogenate was also investigated.

The stability/degradation of Dau═Aoa-LTVSPWY-NH_2 was determined up to 24 h, and the cleavage products were identified by LC-MS as shown in Figure 4 and the Supporting Information (Figure S6).

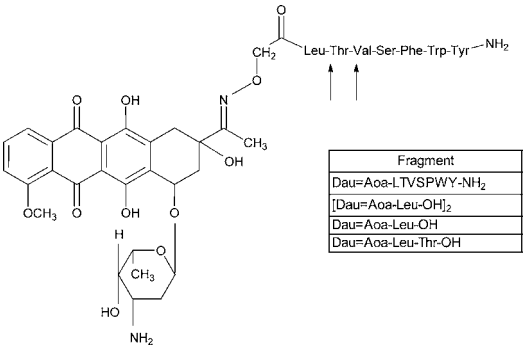

Fragment	$Mw_{calc.}$	$Mw_{exp.}$
Dau=Aoa-LTVSPWY-NH_2	1446.58	1446.40
$[Dau=Aoa-Leu-OH]_2$	1427.48	1427.30
Dau=Aoa-Leu-OH	713.74	713.90
Dau=Aoa-Leu-Thr-OH	814.84	815.00

Figure 4. Cleavage sites (black arrows) and the corresponding fragments identified by LC-MS after incubation of the Dau═Aoa-LTVSPWY-NH_2 conjugate in the presence of rat liver lysosomal homogenate.

After 5 min of incubation with the rat liver lysosomal homogenate, the cleavage of the -Thr-Val- peptide bond was detected by mass spectrometry (the Dau═Aoa-Leu-Thr-OH fragment was observed in the mass spectrum at m/z 816.0 (1+)). After 2 h, one more proteolytic fragment, Dau═Aoa-Leu-OH, was detected at m/z 714.9 (1+), indicating the cleavage of the -Leu-Thr- peptide bond. However, no cleavage of the oxime bond between Dau and aminooxy-acetyl-Leu was observed. After 6, 8, and 24 h, only the Dau═Aoa-Leu-OH proteolytic fragment could be detected. The formation of a noncovalent dimer of Dau═Aoa-Leu-OH was also determined by mass spectrometry (m/z 1428.3 (1+)). The LC-MS analysis of a conjugate solution incubated for 24 h at 37 °C in the absence of the lysosomal homogenate did not lead to the identification of any degradation product; only the intact conjugate was detected at m/z 1447.8 (1+) (Supporting Information, Figure S6). In conclusion, the conjugate was chemically stable under the conditions studied and specifically cleaved by the lysosomal enzymes, with the smallest drug containing metabolite being Dau═Aoa-Leu-OH.

dx.doi.org/10.1021/bc2004236|*Bioconjugate Chem.* 2011, 22, 2154−2165

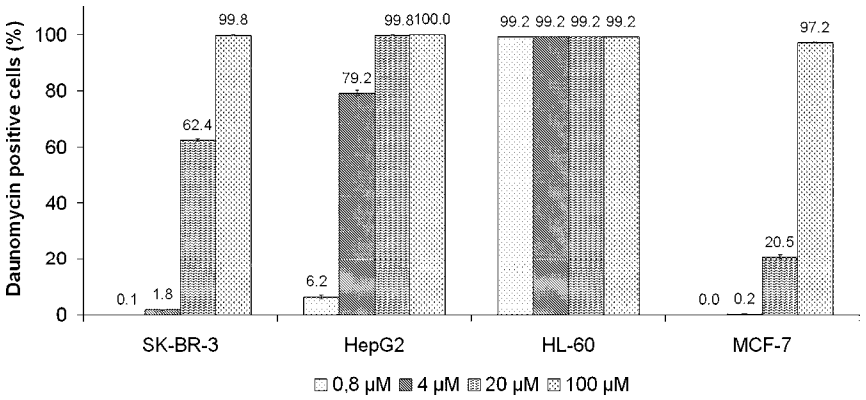

Figure 5. Ratio of daunomycin-positive cells after treatment with Dau═Aoa-LTVSPWY-NH_2 conjugate in the 0.8−100 μM concentration range for 90 min.

Table 1. Cytotoxicity Expressed as IC_{50} ± SD Values (in μM) of Dau═Aoa-LTVSPWY-NH_2 Conjugate and Free Daunomycin as a Function of Time on HL-60 Cells

	time (h)			
compd	3	24	48	72
Dau	8.03 ± 3.25	0.02 ± 0.01	0.001 ± 0.000	$<2.56 \times 10^{-4}$
Dau═Aoa-LTVSPWY-NH_2	>100	10.21 ± 0.27	2.75 ± 1.04	2.02 ± 0.94

DNA-Binding Ability of Dau═Aoa-Leu-OH and Dau═Aoa-LTVSPWY-NH_2 Conjugates. The apparent binding constant (K), proportional to the DNA-binding ability of the compounds, was determined by using the neighbor exclusion model[46] for conjugate Dau═Aoa-LTVSPWY-NH_2, for conjugate Dau═Aoa-Leu-OH (considered as the smallest drug containing metabolite of Dau═Aoa-LTVSPWY-NH_2), and for free daunomycin as a control. We found that all the compounds were able to bind to DNA. However, the binding efficacies were different. The following order could be established: K ($\times 10^5$) (M^{-1}) = 11.70 for Dau > K ($\times 10^5$) (M^{-1}) = 3.23 for Dau═Aoa-Leu-OH > K ($\times 10^5$) (M^{-1}) = 2.75 for Dau═Aoa-LTVSPWY-NH_2. These data indicate that the interaction between Dau and DNA is more pronounced than the interaction with the conjugates. It is interesting to note that no marked difference was observed in the DNA-binding capacity between Dau═Aoa-LTVSPWY-NH_2 with seven amino acid residues in the chain and Dau═Aoa-Leu-OH possessing only a single amino acid attached to daunomycin. This means that not only the intact conjugate, Dau═Aoa-LTVSPWY-NH_2 but also its degradation product can efficiently bind to the DNA.

***In Vitro* Cytostatic Effect of the Dau═Aoa-LTVSPWY-NH_2 Conjugate.** The *in vitro* cytostatic effect of the Dau═Aoa-LTVSPWY-NH_2 conjugate and free daunomycin was determined and expressed as IC_{50} values on four human cancer cell lines: HL-60 human leukemia, HepG2 human hepatoma, MCF-7 human breast adenocarcinoma, and SK-BR-3 human breast cancer cell lines. We found that the conjugate and also the free daunomycin exerted the highest cytostatic effect on HL-60 cells. Concerning the *in vitro* cytostatic effect of the conjugate, the following order could be established: HL-60 (IC_{50} = 0.53 ± 0.12 μM) > HepG2 (IC_{50} = 3.07 ± 0.02 μM) > MCF-7 (IC_{50} = 7.42 ± 0.49 μM) > SK-BR-3 (IC_{50} = 37.90 ± 2.83 μM). These data clearly indicate that the conjugate was less effective on SK-BR-3 cells, while on HepG2 and MCF-7 cells it had a higher cytostatic effect. We expected a higher cytostatic effect on SK-BR-3 cells, because the ErbB-2 receptor is overexpressed on these cells,[42] while MCF-7 has a normal ErbB-2 expression level. The comparison of the cytostatic effect of free daunomycin results in a slightly different order: HL-60 (IC_{50} = 0.05 ± 0.03 μM) > MCF-7 (IC_{50} = 0.18 ± 0.09 μM) > HepG2 (IC_{50} = 0.66 ± 0.21 μM) > SK-BR-3 (IC_{50} = 3.64 ± 0.52 μM). However, the IC_{50} values for MCF-7 and HepG2 differ only marginally. In the case of HepG2, the IC_{50} value of the conjugate was 4.5 times higher than that of daunomycin. The ratio between the IC_{50} for the conjugate per IC_{50} for the free drug was 10.6, 41.2, and 10.4 in the cases of the HL-60, MCF-7, and SK-BR-3 cells, respectively, indicating that on MCF-7 cells the relative effectivity of this conjugate was not as high as it was on HL-60, SK-BR-3, and HepG2 cells.

Cellular Uptake of Dau═Aoa-LTVSPWY-NH_2 Conjugate. Cellular uptake of compounds (Dau═Aoa-LTVSPWY-NH_2 conjugate and Dau) was studied by flow cytometry, and the percentage of daunomycin positive cells was determined. Data are shown in Figure 5. We observed concentration dependent cellular uptake in the cases of SK-BR-3, HepG2, and MCF-7 cells but not in the case of HL-60 cells. The percentage of the daunomycin-positive cells was almost 100% after treating HL-60 cells with any concentration of the conjugate. Daunomycin was taken up the most efficiently by HL-60 and MCF-7 cells at a concentration of 0.8 μM (data not shown), while cellular uptake of the conjugate was observed only at 20 μM concentration for MCF-7 cells, and also at this concentration, the ratio of daunomycin-positive cells was only 20.5%. Cellular uptake of the conjugate was higher in the case of HepG2 and SK-BR-3 cells compared to that of MCF-7.

Optimization of Treatment Conditions for Proteomic Studies. On the basis of *in vitro* cytostasis and cellular uptake data obtained after the treatment with the Dau═Aoa-LTVSPWY-NH_2 conjugate, HL-60 cells were selected for further studies. We were interested in determining the alterations in the protein expression profile of treated HL-60 cells by proteomic methods. Therefore, first the optimal

dx.doi.org/10.1021/bc2004236 | *Bioconjugate Chem.* 2011, 22, 2154−2165

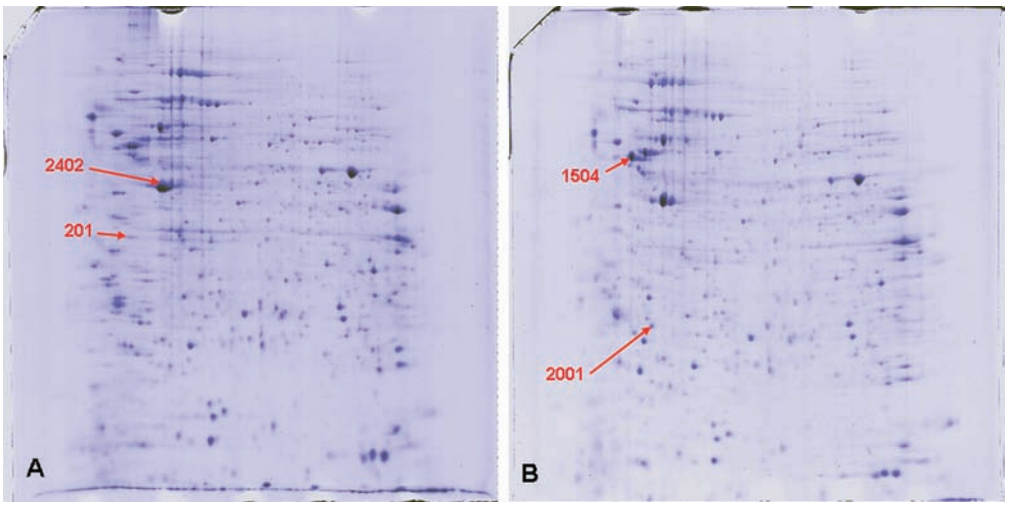

Figure 6. Protein expression profile of nontreated (A) and daunomycin-treated HL-60 cells (B). Arrows and spot numbers show the significantly different spots on the gel where the expression level was higher.

Table 2. Identified Proteins with Altered Expression Due to the Treatment with Daunomycin[a]

identified protein	spot number	average level in control sample	average level in Dau-treated sample	fold-change	Mascot score	M_r (Da)	p*I*
proliferating cell nuclear antigen (PCNA) (Cyclin)—*Homo sapiens* (Human)—[PCNA_HUMAN]	201	1440.7	171.5	0.12	2111	28768.78	4.57
tubulin β chain (tubulin β-5 chain)—*Homo sapiens* (human)—[TBB5_HUMAN]	1504	1337.6	9713.9	7.26	11510	49670.82	4.78
Ran-specific GTPase-activating protein (Ran-binding protein 1) (RanBP1)—*Homo sapiens* (Human)—[RANG_HUMAN]	2001	789.7	1648.5	2.09	560	23310.12	5.19
actin, cytoplasmic 1 (Beta-actin)—*Homo sapiens* (Human)—[ACTB_HUMAN]	2402	11178.5	1615.8	0.14	17877	41736.73	5.29

[a]Spot number is for the identification of the spots on the gel. Average levels of the proteins in different samples are calculated by PDQuest 8.0 software. Fold change is the ratio of the average protein expression level in the daunomycin-treated and control samples. M_r is the theoretical molecular weight, while p*I* is the theoretical isoelectric point of the identified protein.

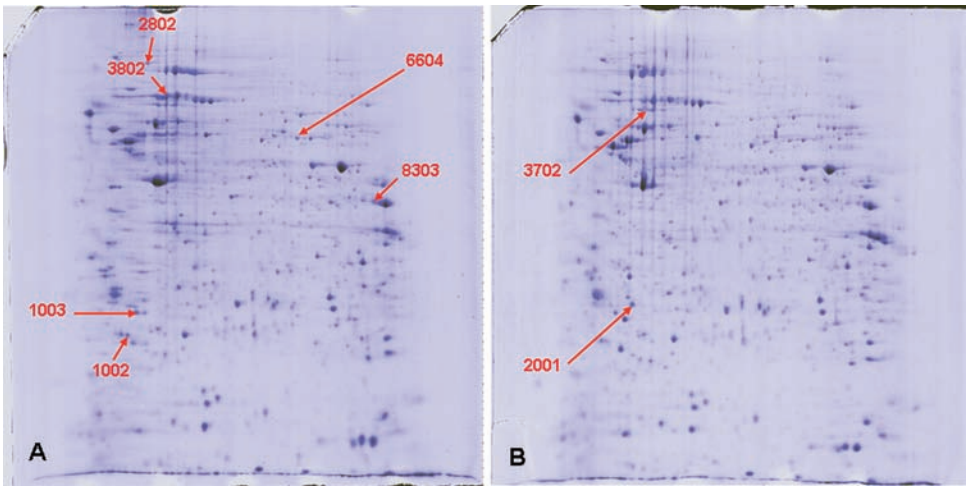

Figure 7. Protein expression profile of nontreated (A) and Dau=Aoa-LTVSPWY-NH_2 conjugate-treated HL-60 cells (B). Arrows and spot numbers show the significantly different spots on the gel where the expression level was higher.

treatment conditions (time and concentration) had to be established. For this purpose, the *in vitro* cytotoxicity of Dau=Aoa-LTVSPWY-NH_2 and daunomycin was determined on HL-60 human leukemia cells after 3, 24, 48, and 72 h of treatment. The calculated IC_{50} values of the compounds are shown in Table 1. After 3 h, the conjugate was not cytotoxic in the concentration range applied [(2.6×10^{-4})–10^2 μM]. The IC_{50} values of the Dau=Aoa-LTVSPWY-NH_2 conjugate decreased with time to IC_{50} = 10.21 ± 0.27 μM (24 h) and IC_{50} = 2.75 ± 1.04 μM (48 h). In the case of treatment with daunomycin for 72 h, the cells died almost completely; therefore, this treatment time could not be used to compare the effects of daunomycin

dx.doi.org/10.1021/bc2004236|*Bioconjugate Chem.* 2011, 22, 2154–2165

Table 3. Identified Proteins with Altered Expression Due to the Treatment with the Dau=Aoa-LTVSPWY-NH_2 Conjugate[a]

identified protein	spot number	average level in: control sample	average level in: Dau=Aoa-LTVSPWY-NH_2 treated sample	fold-change	Mascot score	M_r(Da)	p*I*
translationally controlled tumor protein (TCTP) (p23) (histamine-releasing factor) (HRF) (fortilin)—*Homo sapiens* (Human)—[TCTP_HUMAN]	1002	1406.2	5.6	0.004	3665	19595.34	4.84
Rho GDP-dissociation inhibitor 2 (Rho GDI 2) (Rho-GDI beta) (Ly-GDI)—*Homo sapiens* (human)—[GDIS_HUMAN]	1003	2253.9	5.6	0.002	3288	22988.01	5.10
Ran-specific GTPase-activating protein (Ran-binding protein 1) (RanBP1)—*Homo sapiens* (human)—[RANG_HUMAN]	2001	789.7	1805.0	2.29	560	23310.12	5.19
transitional endoplasmic reticulum ATPase (TER ATPase) (15S Mg(2+)-ATPase p97 subunit) (valosin-containing protein) (VCP)—*Homo sapiens* (human)—[TERA_HUMAN]	2802	994.4	271.7	0.27	2657	89321.80	5.14
plastin-2 (L-plastin) (lymphocyte cytosolic protein 1) (LCP-1) (LC64P)—*Homo sapiens* (human)—[PLSL_HUMAN]	3702	482.3	1065.6	2.21	4924	70288.39	5.29
heat shock cognate 71 kDa protein (heat shock 70 kDa protein 8)—*Homo sapiens* (human)—[HSP7C_HUMAN]	3802	6507.8	5.6	0.001	10972	70898.09	5.37
D-3-phosphoglycerate dehydrogenase (EC 1.1.1.95) (3-PGDH)—*Homo sapiens* (Human)—[SERA_HUMAN]	6604	1067.9	526.0	0.49	4131	56650.5	6.29
fructose-bisphosphate aldolase A (EC 4.1.2.13) (muscle-type aldolase) (lung cancer antigen NY-LU-1)—*Homo sapiens* (Human)—[ALDOA_HUMAN]	8303	2105.1	999.3	0.47	1143	39420.02	8.30

[a]Spot number is for the identification of the spots on the gel. Average levels of the proteins in different samples are calculated by PDQuest 8.0 software. Fold change is the ratio of the average protein expression level in the conjugate-treated and control samples. M_r is the theoretical molecular weight, while p*I* is the theoretical isoelectric point of the identified protein.

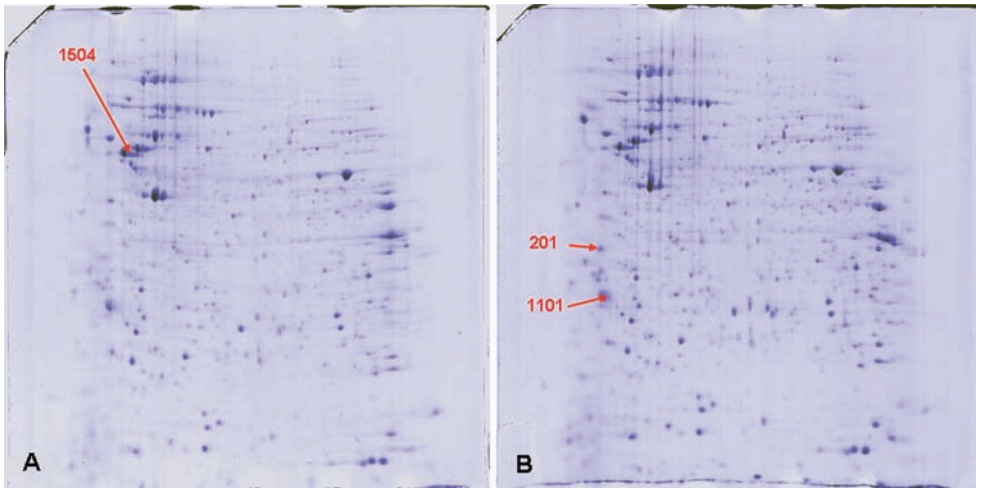

Figure 8. Protein expression profile of daunomycin-treated (A) and Dau=Aoa-LTVSPWY-NH_2 conjugate-treated HL-60 cells (B). Arrows and spot numbers show the significantly different spots on the gel where the expression level was higher.

and the conjugate. In the case of 24 and 48 h treatment times, both daunomycin and the conjugate had a cytotoxic effect on HL-60 cells; however, the free daunomycin was more cytotoxic.

On the basis of these data the following conditions were selected for the proteomic studies: c = 9 μM for Dau=Aoa-LTVSPWY-NH_2 conjugate, c = 0.024 μM for daunomycin, and 24 h treatment time.

Protein Expression Profile of Treated and Nontreated HL-60 Cells. After optimizing the treatment conditions, HL-60 human leukemia cells were treated for 24 h with Dau=Aoa-LTVSPWY-NH_2 conjugate or with daunomycin. Proteins were isolated from treated as well as from nontreated control cells and separated by two-dimensional gel electrophoresis. Gel patterns after staining were compared using the PDQuest software. Comparisons of representative gels are shown in Figures 6–8. The spots with higher optical density are denoted with an arrow and are shown only on the gel where higher expression is observed. In the sample from cells treated with daunomycin, four differently expressed proteins could be observed compared to the nontreated control cells (Figure 6, Table 2). Two proteins (tubulin β chain and Ran-specific GTPase-activating protein) showed higher (7.26-fold and 2.09-fold, respectively) and two proteins (proliferating cell nuclear antigen and β-actin) showed lower (0.12-fold and 0.14-fold, respectively) expression levels in daunomycin-treated samples compared to nontreated sample.

In the case of a Dau=Aoa-LTVSPWY-NH_2-treated sample, eight significantly different spots were identified (Figure 7, Table 3) in comparison with the nontreated control sample. Two spots could be indicative of a higher (2.29-fold and 2.21-fold) level of protein expression. These are Ran-specific GTPase-activating protein, which is involved in the regulation of cell cycle, and an actin-binding protein, Plastin-2, respectively. However, the expression of six proteins decreased

Table 4. Identified Proteins with Different Expressions in the Daunomycin-Treated or Dau=Aoa-LTVSPWY-NH_2 Treated Samples[a]

identified protein	spot number	average level in Dau-treated sample	average level in Dau=Aoa-LTVSPWY-NH_2 treated sample	fold-change	Mascot score	M_r (Da)	p*I*
proliferating cell nuclear antigen (PCNA) (cyclin)—*Homo sapiens* (human)—[PCNA_HUMAN]	201	171.5	2165.8	12.63	2111	28768.78	4.57
14−3−3 protein γ (protein kinase C inhibitor protein 1) (KCIP-1)—*Homo sapiens* (human)—[1433G_HUMAN]	1101	157.7	1814.0	11.50	3116	28302.59	4.80
tubulin β chain (tubulin β-5 chain)—*Homo sapiens* (human)—[TBB5_HUMAN]	1504	9713.9	1981.3	0.20	11510	49670.82	4.78

[a]Spot number is for the identification of the spots on the gel. Average levels of the proteins in different samples are calculated by PDQuest 8.0 software. Fold change is the ratio of the average protein expression level in the conjugate and daunomycin-treated samples. M_r is the theoretical molecular weight, while p*I* is the theoretical isoelectric point of the identified protein.

after the treatment with the conjugate. The expression level of a heat-shock protein and two proteins involved in signaling decreased compared to the nontreated control cells.

The intensity of two additional spots corresponding to proteins involved in metabolic pathways (D-3-phosphoglycerate dehydrogenase and fructose-bisphosphate aldolase A) was weaker. This observation might suggest that the expression of these proteins could occur also at a lower level, but the drop is less marked (by 0.49-fold and 0.47-fold, respectively). It is important to point out that increased expression of the Ran-specific GTPase-activating protein was observed in both daunomycin- and Dau=Aoa-LTVSPWY-NH_2 conjugate-administered cells at a similar level (2.09-fold in Dau-treated and 2.29-fold in conjugate-treated samples, respectively).

Protein expression profiles of cells treated with daunomycin or with conjugate were also compared. The results are summarized in Figure 8 and Table 4. Three significantly different protein spots were detected. These changes suggest that one protein, the tubulin β chain, was expressed at a lower level (by 0.20-fold) in Dau=Aoa-LTVSPWY-NH_2 conjugate-treated cells. In contrast, the administration of HL-60 cells with the conjugated drug for 24 h resulted in markedly higher expression of two proteins: the proliferating cell nuclear antigen (by 12.63-fold) and the 14−3−3 protein γ (by 11.50-fold) compared to that of free daunomycin-treated cells.

DISCUSSION

Here, we report on the synthesis, characterization, and *in vitro* cytostatic effect of a new oxime bond containing the daunomycin conjugate Dau=Aoa-LTVSPWY-NH_2. The stability of this compound was investigated under different conditions, and it was found that even after 24 h the Dau=Aoa-LTVSPWY-NH_2 conjugate was not degraded either in 10% serum containing medium or in sodium acetate/acetic acid buffers in the pH range studied (pH 2.5−7.0). The conjugate in the presence of rat liver lysosomal homogenate was cleaved enzymatically, resulting in Dau=Aoa-Leu-OH as the smallest drug containing metabolite of the conjugate. This metabolite, as well as the Dau=Aoa-LTVSPWY-NH_2 conjugate, could bind efficiently to DNA; therefore, DNA synthesis might be inhibited by this compound in the cells.

The *in vitro* cytostatic and cytotoxic effect and cellular uptake of the conjugate indicated that the cellular uptake mechanism could be different in the case of the studied cell lines. The cellular uptake of the Dau=Aoa-LTVSPWY-NH_2 conjugate was limited in the case of MCF-7 cells, which express ErbB-2 in normal or low levels.[42] In contrast, SK-BR-3 cells, which are ErbB-2 overexpressing cells, could take up the conjugate more effectively. The IC_{50} value of Dau=Aoa-LTVSPWY-NH_2 on SK-BR-3 cells was higher compared to other investigated cell lines. Interestingly, free daunomycin was not as effective on this cell line as on the others (in this case the IC_{50} value of the conjugate was only 10.4 times higher than that of free daunomycin). This finding, e.g. the cells with the highest amount of targeted receptors showed the lowest cytostatic effect, needs to be studied further. Experiments are in progress to analyze the uptake mechanism. Efficient cellular uptake and a remarkable *in vitro* cytostatic effect of the Dau=Aoa-LTVSPWY-NH_2 conjugate were observed on HepG2 cells, which moderately express the ErbB-2 receptor.[43] The difference in the cellular uptake properties and the *in vitro* cytostatic effect of the Dau=Aoa-LTVSPWY-NH_2 conjugate on different cell lines could be explained by different cellular uptake mechanisms and/or the different intracellular fates of the compound. Also, the mode of action might be different for the Dau-conjugate compared to Dau itself. The conjugate had the highest cytostatic effect on HL-60 cells and the cellular uptake was also the most effective in the case of this cell line. On HL-60 cells, Trinks and co-workers could not detect ErbB receptors by Western blot analysis, while mRNA expression was observed.[50] These data suggest that in the case of HL-60 cells the conjugate could be taken up efficiently by one or more different mechanisms.

For a better understanding of the effect of the Dau=Aoa-LTVSPWY-NH_2 conjugate on HL-60 cells, we have initiated a comparative analysis of the protein expression profile of treated and nontreated cells and also of conjugate vs free daunomycin treated cells. We observed that the expression level of several proteins altered due to the treatment with the conjugate or with the free drug (Dau) in comparison with proteins from untreated cells. Most interestingly, three proteins were identified, whose expression was lower (tubulin β chain) or markedly higher (proliferating cell nuclear antigen and protein kinase C inhibitor protein 1) after administration of HL-60 cells with Dau−peptide conjugate vs free drug. The results of proteomic analysis performed and described in this paper could be adaptable for systematic analysis of the mechanism of action of bioconjugates with preferential properties vs the properties of the covalently attached free cargo (e.g., drug). On the basis of findings summarized in this paper, further studies are in progress to identify the potential role of proteins, whose expression level was dependent on the compounds (free vs conjugated drug) used for treatment and could be considered as relevant for target validation.

■ ASSOCIATED CONTENT

Supporting Information

Analytical RP-HPLC chromatogram of the purified conjugate, recorded chromatograms, and LC-MS analysis of a conjugate solution. This material is available free of charge via the Internet at http://pubs.acs.org.

■ AUTHOR INFORMATION

Corresponding Author

*Fax: 36 1 372 2620. Telephone: 36 1 372 2828. E-mail: fhudecz@elte.hu.

■ ACKNOWLEDGMENTS

This work was supported by Medichem2 (1A005/04), Hungarian Research Fund (OTKA K68285, TS44742), Ministry of Health (ETT 044-03/2009), GVOP-3.2.1-2004-04-0352/3.0, and University of Konstanz (Zukunftskolleg, Project 879/08).

■ REFERENCES

(1) Wiernik, P. H., and Dutcher, J. P. (1992) Clinical importance of anthracyclines in the treatment of acute myeloid leukemia. *Leukemia 6 Suppl 1*, 67−9.

(2) Takimoto, C. H., and Calvo, E. (2008) Principles of Oncologic Pharmacotherapy. In *Cancer Management: A Multidisciplinary Approach*, 11th ed., Chapter 3.

(3) Von Hoff, D. D., Rozencweig, M., Layard, M., Slavik, M., and Muggia, F. M. (1977) Daunomycin-induced cardiotoxicity in children and adults. A review of 110 cases. *Am. J. Med. 62*, 200−8.

(4) Riehm, H., and Biedler, J. L. (1971) Cellular resistance to daunomycin in Chinese hamster cells in vitro. *Cancer Res. 31*, 409−12.

(5) Shen, S. H., Gu, L. J., Liu, P. Q., Ye, X., Chang, W. S., and Li, B. S. (2008) Comparative proteomic analysis of differentially expressed proteins between K562 and K562/ADM cells. *Chin. Med. J. (Engl.) 121*, 463−8.

(6) Keenan, J., Murphy, L., Henry, M., Meleady, P., and Clynes, M. (2009) Proteomic analysis of multidrug-resistance mechanisms in adriamycin-resistant variants of DLKP, a squamous lung cancer cell line. *Proteomics 9*, 1556−66.

(7) Yang, Y. X., Hu, H. D., Zhang, D. Z., and Ren, H. (2007) Identification of proteins responsible for the development of adriamycin resistance in human gastric cancer cells using comparative proteomics analysis. *J. Biochem. Mol. Biol. 40*, 853−60.

(8) Jiang, Y. J., Sun, Q., Fang, X. S., and Wang, X. (2009) Comparative mitochondrial proteomic analysis of Rji cells exposed to adriamycin. *Mol. Med. 15*, 173−82.

(9) Chen, Y., Daosukho, C., Opii, W. O., Turner, D. M., Pierce, W. M., Klein, J. B., Vore, M., Butterfield, D. A., and St Clair, D. K. (2006) Redox proteomic identification of oxidized cardiac proteins in adriamycin-treated mice. *Free Radical Biol. Med. 41*, 1470−7.

(10) Li, X., Pan, W., Qiu, F., and Qiu, Z. Y. (2006) Proteomic approach to the effect of epirubicin on hepatoma cells at subcellular level. *Fen Zi Xi Bao Sheng Wu Xue Bao 39*, 407−13.

(11) Möller, A., Malerczyk, C., Völker, U., Stöppler, H., and Maser, E. (2002) Monitoring daunorubicin-induced alterations in protein expression in pancreas carcinoma cells by two-dimensional gel electrophoresis. *Proteomics 2*, 697−705.

(12) Hammer, E., Bien, S., Salazar, M. G., Steil, L., Scharf, C., Hildebrandt, P., Schroeder, H. W., Kroemer, H. K., Völker, U., and Ritter, C. A. (2010) Proteomic analysis of doxorubicin-induced changes in the proteome of HepG2cells combining 2-D DIGE and LC-MS/MS approaches. *Proteomics 10*, 99−114.

(13) Gaal, D., and Hudecz, F. (1998) Low toxicity and high antitumour activity of daunomycin by conjugation to an immunopotential amphoteric branched polypeptide. *Eur. J. Cancer 34*, 155−161.

(14) Szabó, R., Bánóczi, Z., Mezo, G., Láng, O., Kohidai, L., and Hudecz, F. (2010) Daunomycin-polypeptide conjugates with antitumor activity. *Biochim. Biophys. Acta 1798*, 2209−16.

(15) Baurain, R., Masquelier, M., Deprezde, C. D., and Trouet, A. (1983) Targeting of daunorubicin by covalent and reversible linkage to carrier proteins-lysosomal hydrolysis and antitumoral activity of conjugates prepared with peptidic spacer arms. *Drugs Exp. Clin. Res. 9*, 303−311.

(16) Nogusa, H., Yano, T., Kashima, N., Yamamoto, K., Okuno, S., and Hamana, H. (2000) Structure-activity relationships of carboxymethylpullulan-peptide-doxorubicin conjugates—systematic modification of peptide spacers. *Bioorg. Med. Chem. Lett. 10*, 227−30.

(17) Shiah, J. G., Sun, Y. G., Peterson, C. M., Straight, R. C., and Kopecek, J. (2000) Antitumor activity of N-(2-hydroxypropyl)-methacrylamide copolymer-mesochlorin e(6) and adriamycin conjugates in combination treatments. *Clin. Cancer Res. 6*, 1008−1015.

(18) Kamada, H., Tsutsumi, Y., Yoshioka, Y., Yamamoto, Y., Kodaira, H., Tsunoda, S., Okamoto, T., Mukai, Y., Shibata, H., Nakagawa, S., and Mayumi, T. (2004) Design of a pH-sensitive polymeric carrier for drug release and its application in cancer therapy. *Clin. Cancer Res. 10*, 2545−2550.

(19) Hurwitz, E. (1983) Specific and nonspecific macromolecule drug conjugates for the improvement of cancer-chemotherapy. *Biopolymers 22*, 557−567.

(20) Zunino, F., Dimarco, A., and Velcich, A. (1977) Steric influence of orientation of primary amino group at position 3 of sugar moiety of anthracycline antibiotics in DNA binding properties. *Cancer Lett. 3*, 271−275.

(21) Langer, M., Kratz, F., Rothen-Rutishauser, B., Wunderli-Allenspach, H., and Beck-Sickinger, A. G. (2001) Novel peptide conjugates for tumor-specific chemotherapy. *J. Med. Chem. 44*, 1341−1348.

(22) Rodrigues, P. C. A., Roth, T., Fiebig, H. H., Unger, C., Mulhaupt, R., and Kratz, F. (2006) Correlation of the acid-sensitivity of polyethylene glycol daunorubicin conjugates with their in vitro antiproliferative activity. *Bioorg. Med. Chem. 14*, 4110−4117.

(23) Yamamoto, K., Acton, E., and Henry, D. (1972) Antitumor activity of some derivatives of daunorubicin at the amino and methyl ketone functions. *J. Med. Chem. 15*, 872−5.

(24) Patel, L. N., Zaro, J. L., and Shen, W. C. (2007) Cell penetrating peptides: Intracellular pathways and pharmaceutical perspectives. *Pharm. Res. 24*, 1977−1992.

(25) Ingallinella, P., Di Marco, A., Taliani, M., Fattori, D., and Pessi, A. (2001) A new method for chemoselective conjugation of unprotected peptides to dauno- and doxorubicin. *Bioorg. Med. Chem. Lett. 11*, 1343−1346.

(26) Capobianco, M. L., De Champdoré, M., Arcamone, F., Garbesi, A., Guianvarc'h, D., and B Arimondo, P. (2005) Improved synthesis of daunomycin conjugates with triplex-forming oligonucleotides. The polypurine tract of HIV-1 as a target. *Bioorg. Med. Chem. 13*, 3209−18.

(27) Meyer-Losic, F., Quinonero, J., Dubois, V., Alluis, B., Dechambre, M., Michel, M., Cailler, F., Fernandez, A. M., Trouet, A., and Kearsey, J. (2006) Improved therapeutic efficacy of doxorubicin through conjugation with a novel peptide drug delivery technology (Vectocell). *J. Med. Chem. 49*, 6908−6916.

(28) Banoczi, Z., Peregi, B., Orban, E., Szabo, R., and Hudecz, F. (2008) Synthesis of daunomycin-oligoarginine conjugates and their effect on human leukemia cells (HL-60). *ARKIVOC*, 140−153.

(29) Wong, B. K., Defeo-Jones, D., Jones, R. E., Garsky, V. M., Feng, D. M., Oliff, A., Chiba, M., Ellis, J. D., and Lin, J. H. (2001) PSA-specific and non-PSA-specific conversion of a PSA-targeted peptide conjugate of doxorubicin to its active metabolites. *Drug Metab. Dispos. 29*, 313−318.

(30) Rousselle, C., Clair, P., Lefauconnier, J. M., Kaczorek, M., Scherrmann, J. M., and Temsamani, J. (2000) New advances in the transport of doxorubicin through the blood-brain barrier by a peptide vector-mediated strategy. *Mol. Pharmacol. 57*, 679−686.

(31) Mezo, G., Manea, M., Szabo, I., Vincze, B., and Kovacs, M. (2008) New Derivatives of GnRH as Potential Anticancer Therapeutic Agents. *Curr. Med. Chem. 15*, 2366−2379.
(32) Miklán, Z., Orbán, E., Csík, G., Schlosser, G., Magyar, A., and Hudecz, F. (2009) New daunomycin−oligoarginine conjugates: Synthesis, characterization and effect on human leukemia and human hepatoma cells. *Biopolymers 6*, 489−501.
(33) Iivanainen, E., and Elenius, K. (2010) ErbB targeted drugs and angiogenesis. *Curr. Vasc. Pharmacol. 8*, 421−31.
(34) Hynes, N. E., and MacDonald, G. (2009) ErbB receptors and signaling pathways in cancer. *Curr. Opin. Cell Biol. 21*, 177−84.
(35) Shadidi, M., and Sioud, M. (2003) Selective targeting of cancer cells using synthetic peptides. *Drug Resist. Updates 6*, 363−71.
(36) Hung, M. C., Hortobagyi, G. N., and Ueno, N. T. (2000) Development of clinical trial of E1A gene therapy targeting HER-2/neu-overexpressing breast and ovarian cancer. *Adv. Exp. Med. Biol. 465*, 171−80.
(37) Alaoui-Jamali, M. A., and Qiang, H. (2003) The interface between ErbB and non-ErbB receptors in tumor invasion: clinical implications and opportunities for target discovery. *Drug Resist. Updates 6*, 95−107.
(38) Klapper, L. N., Kirschbaum, M. H., Sela, M., and Yarden, Y. (2000) Biochemical and clinical implications of the ErbB/HER signaling network of growth factor receptors. *Adv. Cancer Res. 77*, 25−79.
(39) Shadidi, M., and Sioud, M. (2003) Identification of novel carrier peptides for the specific delivery of therapeutics into cancer cells. *FASEB J. 17*, 256−8.
(40) Wang, X. F., Birringer, M., Dong, L. F., Veprek, P., Low, P., Swettenham, E., Stantic, M., Yuan, L. H., Zobalova, R., Wu, K., Ledvina, M., Ralph, S. J., and Neuzil, J. (2007) A peptide conjugate of vitamin E succinate targets breast cancer cells with high ErbB2 expression. *Cancer Res. 67*, 3337−44.
(41) Lochmann, D., Jauk, E., and Zimmer, A. (2004) Drug delivery of oligonucleotides by peptides. *Eur. J. Pharm. Biopharm. 58*, 237−51.
(42) Seoane, S., Montero, J. C., Ocaña, A., and Pandiella, A. (2010) Effect of multikinase inhibitors on caspase-independent cell death and DNA damage in HER2-overexpressing breast cancer cells. *J. Natl. Cancer Inst. 102*, 1432−46.
(43) Liu, J., Ahiekpor, A., Li, L., Li, X., Arbuthnot, P., Kew, M., and Feitelson, M. A. (2009) Increased expression of ErbB-2 in liver is associated with hepatitis B x antigen and shorter survival in patients with liver cancer. *Int. J. Cancer 125*, 1894−901.
(44) Orbán, E., Mező, G., Schlage, P., Csík, G., Kulić, Z., Ansorge, P., Fellinger, E., Möller, H. M., and Manea, M. (2010) In vitro degradation and antitumor activity of oxime bond-linked daunorubicin-GnRH-III bioconjugates and DNA-binding properties of daunorubicin−amino acid metabolites. *Amino Acids 2*, 469−483.
(45) Chaires, J. B., Dattagupta, N., and Crothers, D. M. (1982) Studies on interaction of anthracycline antibiotics and deoxyribonucleic acid: equilibrium binding studies on interaction of daunomycin with deoxyribonucleic acid. *Biochemistry 21*, 3933−40.
(46) McGhee, J. D., and von Hippel, P. H. (1974) Theoretical aspects of DNA−protein interactions: co-operative and non-co-operative binding of large ligands to a one-dimensional homogeneous lattice. *J. Mol. Biol. 86*, 469−89.
(47) Collins, S. J., Gallo, R. C., and Gallagher, R. E. (1977) Continuous growth and differentation of human myeloid leukemic-cells in suspension culture. *Nature 270*, 347−349.
(48) Slater, T. F., Sawyer, B., and Strauli, U. (1963) Studies on succinate-tetrazoliumreductase systems. III. Points of coupling of four different tetrazolium salts. *Biochim. Biophys. Acta 77*, 383−393.
(49) Alston, R. W., Lasagna, M., Grimsley, G. R., Scholtz, J. M., Reinhart, G. D., and Pace, C. N. (2008) Peptide sequence and conformation strongly influence tryptophan fluorescence. *Biophys. J. 94*, 2280−7.
(50) Trinks, C., Djerf, E. A., Hallbeck, A. L., Jönsson, J. I., and Walz, T. M. (2010) The pan-ErbB receptor tyrosine kinase inhibitor canertinib induces ErbB-independent apoptosis in human leukemia (HL-60 and U-937) cells. *Biochem. Biophys. Res. Commun. 393*, 6−10.

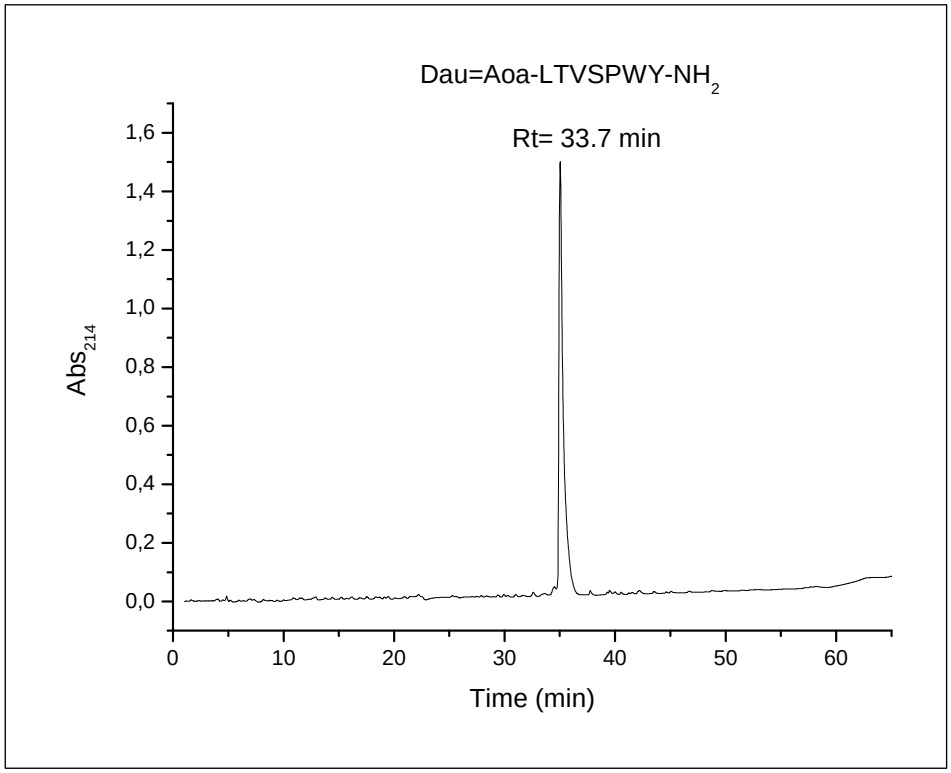

S1: Analytical RP-HPLC chromatogram of Dau=Aoa-LTVSPWY-NH_2 conjugate

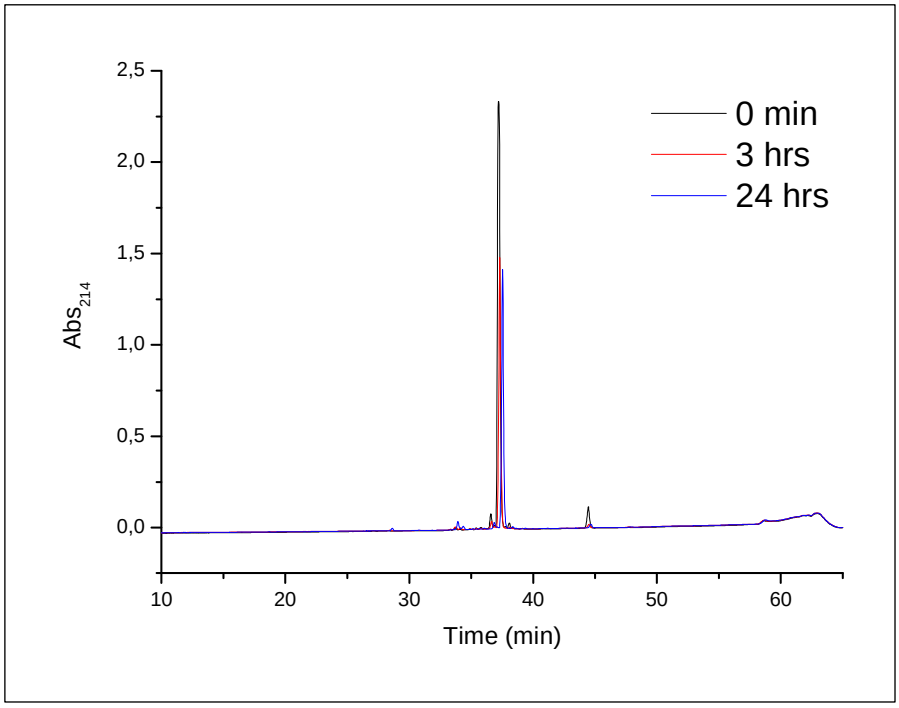

S2: Stability Dau=Aoa-LTVSPWY-NH_2 conjugate as documented by the RP-HPLC analytical chromatograms recorded in 0.1 M sodium citrate/citric acid buffer at pH 2.5 after 3 and 24 hrs (for details see Materials and methods)

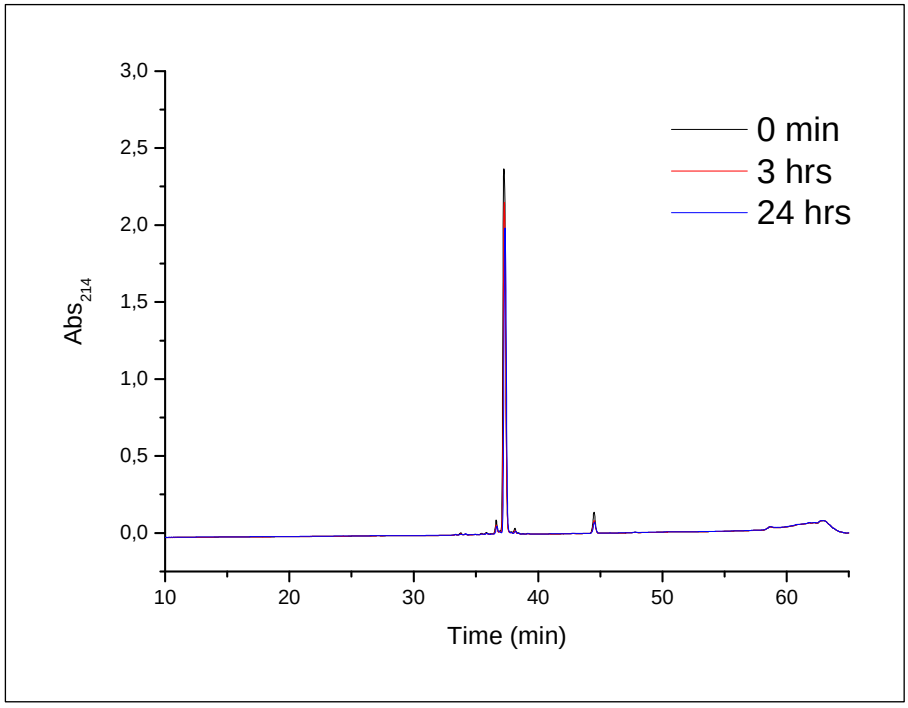

S3: Stability of Dau=Aoa-LTVSPWY-NH_2 conjugate as documented by the RP-HPLC analytical chromatograms recorded in 0.1 M sodium citrate/citric acid buffer at pH 5.0 after 3 and 24 hrs (for details see Materials and methods)

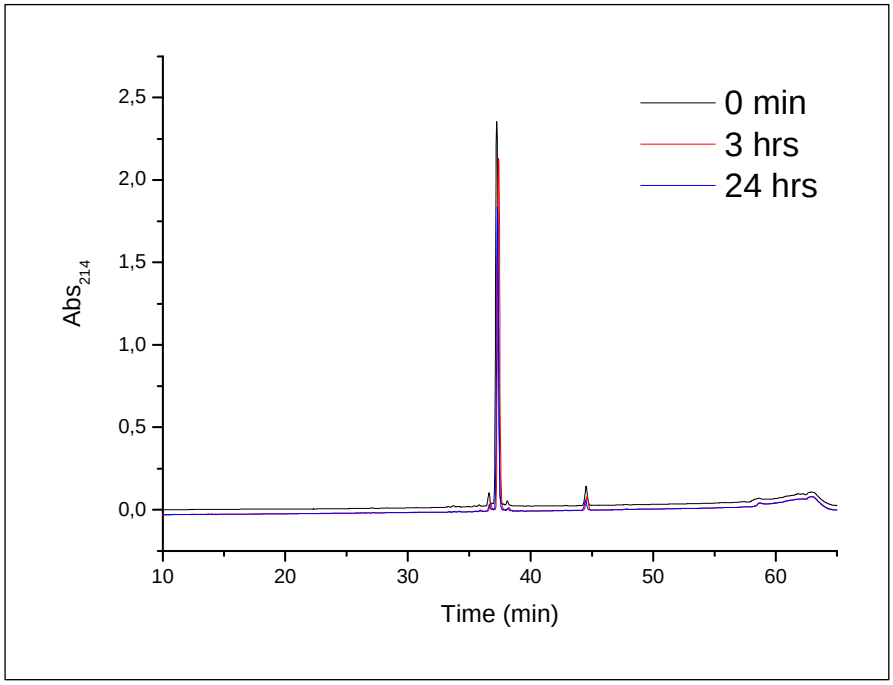

S4: Stability of Dau=Aoa-LTVSPWY-NH_2 conjugate as documented by the RP-HPLC analytical chromatograms recorded in 0.1 M sodium citrate/citric acid buffer at pH 7.0 after 3 and 24 hrs (for details see Materials and methods)

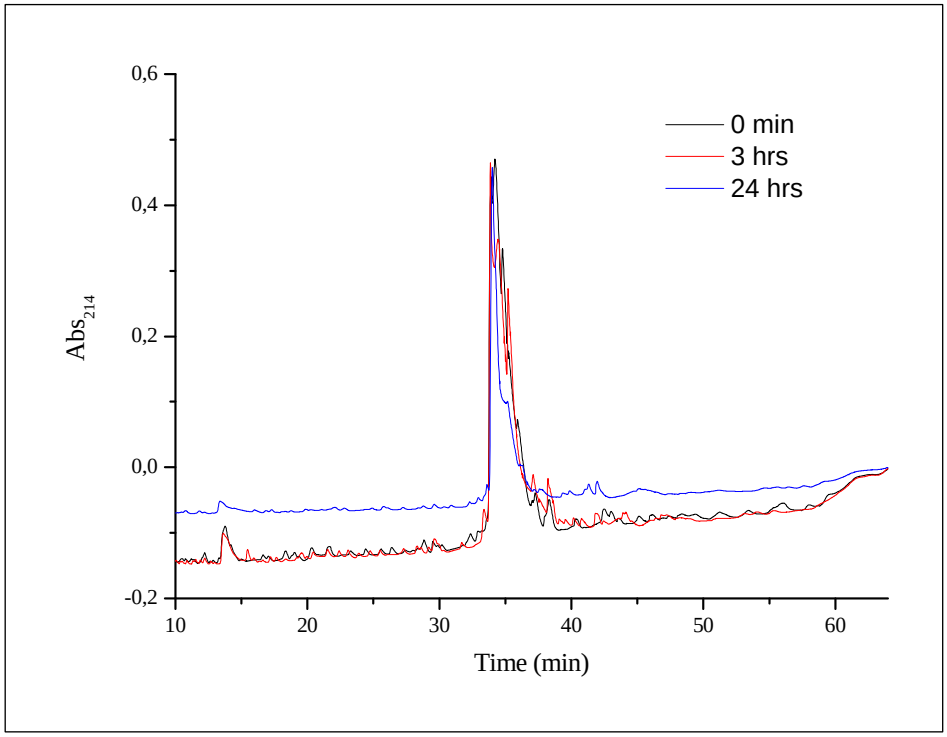

S5: Stability of Dau=Aoa-LTVSPWY-NH_2 conjugate in 10% FCS containing cell culture medium as documented by the RP-HPLC analytical chromatograms recorded after 3 and 24 hrs (for details see Materials and methods)

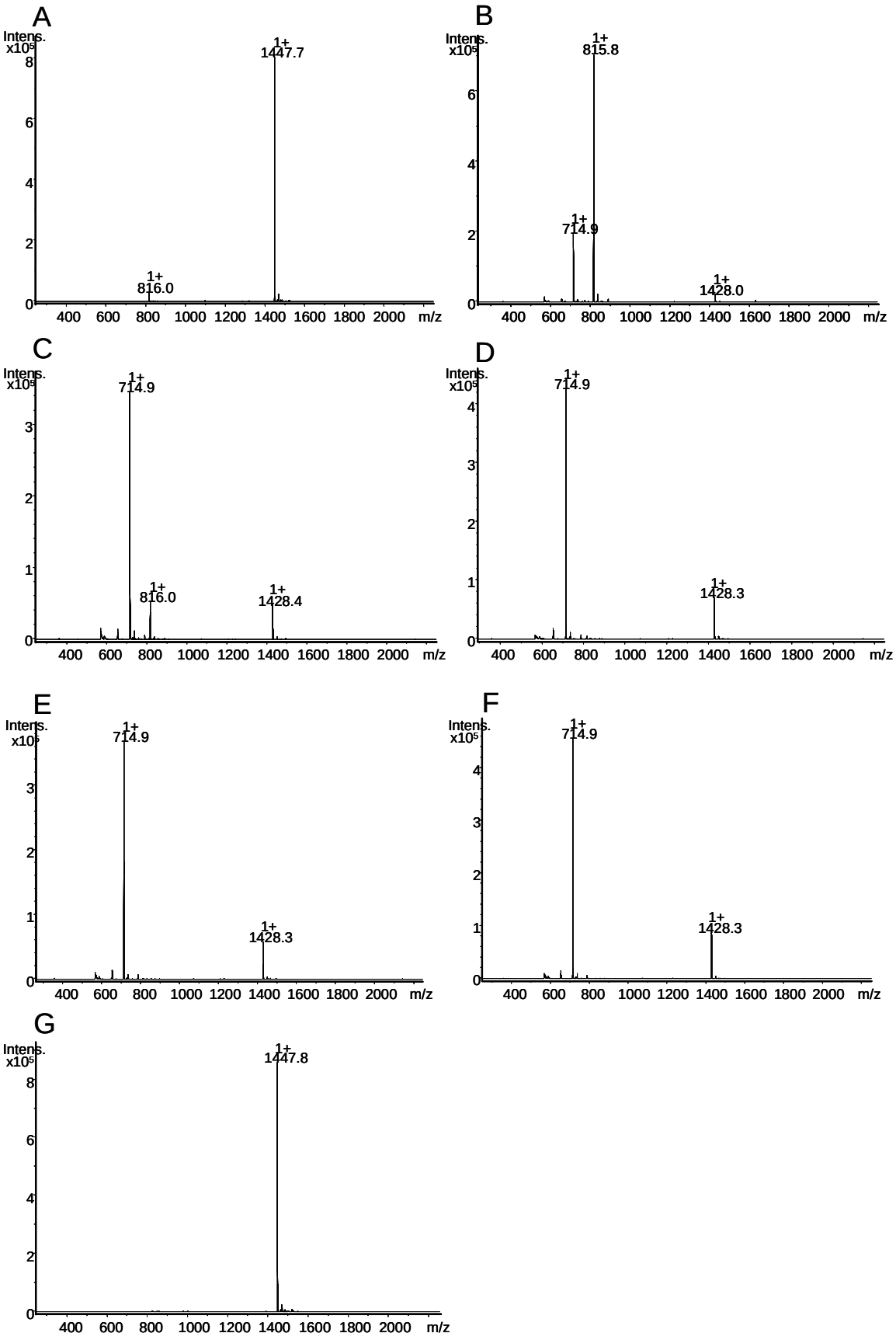
A
Intens.
x10⁵
1+
1447.7
1+
816.0
B
Intens.
x10⁵
1+
815.8
1+
714.9
1+
1428.0
C
Intens.
x10⁵
1+
714.9
1+
816.0
1+
1428.4
D
Intens.
x10⁵
1+
714.9
1+
1428.3
E
Intens.
x10⁵
1+
714.9
1+
1428.3
F
Intens.
x10⁵
1+
714.9
1+
1428.3
G
Intens.
x10⁵
1+
1447.8
400 600 800 1000 1200 1400 1600 1800 2000 m/z

S6: Degradation of Dau=Aoa-LTVSPWY-NH_2 conjugate in the presence of rat liver lysosomal homogenate as documented by the LC-MS spectra recorded after 5 min (A), 2 hrs (B), 4 hrs (C), 6 hrs (D), 8 hrs (E), or 24 hrs (F) incubation. As control conjugate sample dissolved in 0.2 M sodium acetate buffer, pH = 5.0 was incubated at 37°C for 24 hrs in the absence of lysosomal homogenate and analyzed by LC-MS (G). Mass spectra averaged over the chromatographic window where the compounds eluted are shown. (For details see Materials and methods.)

Bioconjugate Chemistry

ARTICLE

pubs.acs.org/bc

Conjugation of Type I Antifreeze Protein to Polyallylamine Increases Thermal Hysteresis Activity

Özge Can[†] and Nolan B. Holland*

Department of Chemical & Biomedical Engineering, Cleveland State University, 2121 Euclid Avenue, Cleveland, Ohio 44115, United States

ABSTRACT: Antifreeze proteins (AFPs) are ice binding proteins found in some plants, insects, and Antarctic fish allowing them to survive at subzero temperatures by inhibiting ice crystal growth. The interaction of AFPs with ice crystals results in a difference between the freezing and melting temperatures, termed thermal hysteresis, which is the most common measure of AFP activity. Creating antifreeze protein constructs that reduce the concentration of protein needed to observe thermal hysteresis activities would be beneficial for diverse applications including cold storage of cells or tissues, ice slurries used in refrigeration systems, and food storage. We demonstrate that conjugating multiple type I AFPs to a polyallylamine chain increases thermal hysteresis activity compared to the original protein. The reaction product is approximately twice as active when compared to the same concentration of free proteins, yielding 0.5 °C thermal hysteresis activity at 0.3 mM protein concentration. More impressively, the amount of protein required to achieve a thermal hysteresis of 0.3 °C is about 100 times lower when conjugated to the polymer (3 μM) compared to free protein (300 μM). Ice crystal morphologies observed in the presence of the reaction product are comparable to those of the protein used in the conjugation reaction.

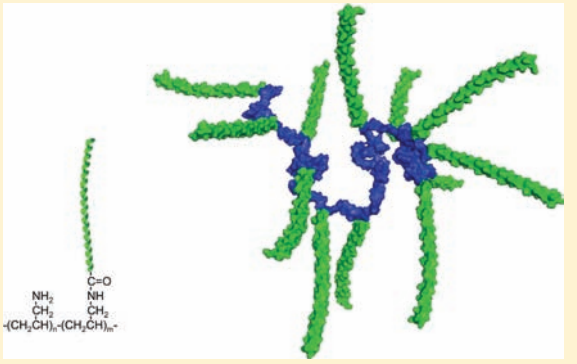

INTRODUCTION

Antifreeze proteins (AFPs) help organisms to survive at subzero temperatures or at temperatures lower than the freezing point of their body fluids by inhibiting ice crystal growth. Interest in this phenomenon has given rise to many studies in order to gain more information as to how they prevent the ice crystal growth.[1] It is generally accepted that AFPs bind to specific planes of the ice surface, which stops subsequent crystal growth at temperatures below the colligative melting point. This interaction of AFPs with ice crystals results in thermal hysteresis, which is the difference between the freezing and melting temperatures. AFPs also prevent the redistribution of the water between ice crystals and the solution referred to as ice recrystallization.[2] These properties have use in potential applications such as cold storage of cells or tissues, ice slurries used for refrigeration systems, and food storage.[3−8] To minimize the amount of protein needed for a given application, antifreeze proteins with thermal hysteresis activity at low concentrations are desirable.

Among AFPs, there is a considerable variance in thermal hysteresis activity, even among proteins with similar structures. The most extensively characterized type I fish AFP is the winter flounder HPLC6 protein, which has three repeats of 11 amino acid residues.[9,10] A longer type I AFP is AFP9 from winter flounder, which has four repeat sequences.[11] This longer protein is more active than its shorter isoform, illustrating the general effect of increased size on the thermal hysteresis activity. More recently, a much larger type I AFP was discovered in American plaice with a molecular weight of approximately 17 kDa. This protein is five times larger than the AFP9 and exhibited significant thermal hysteresis activity even at low concentrations.[12,13]

Differences in thermal hysteresis activity have also been observed in other types of AFPs. For example, the activity of β-helical insect AFPs is affected by the addition or deletion of coils from the structure of the protein. It has been shown that enhanced activity in longer insect AFPs results from the larger ice surface binding area of the proteins, as long as the repeating sequences continue to match the ice crystal lattice structure.[14,15]

For the globular type III antifreeze proteins, a different mechanism for increased activity has been reported. Miura et al. observed enhanced activity in a natural protein consisting of two type III AFP domains connected by a nine residue linker.[16] They compared the activity of this protein with its single domain counterpart and reported that the two-domain protein is more active than the single domain protein. This enhancement is most pronounced at low concentrations, yielding thermal hysteresis activities as much as 6 times greater than the monomer. This effect was explained by the assumption that the average distance between the two domains of the protein adsorbed on the surface is smaller than that of the adsorbed monomers. Hence, in order to saturate the ice surface and stop the ice growth, a smaller amount of dimer would be needed as compared to the monomer.

A more detailed investigation of the increased activity of the type III dimers showed that a recombinant two-domain type III AFP from Antarctic eel pout is twice as active as its monomer.[17] However, when they inactivated one of the domains, its activity was reduced to only 1.2 times greater than that of the monomer.

Received: August 9, 2011
Revised: September 10, 2011
Published: September 12, 2011

ACS Publications © 2011 American Chemical Society

When two monomers were linked through a disulfide bond such that two domains could not bind to the ice surface simultaneously, the dimer was again only 1.2 times as active as its monomer, indicating that the two domains need to be both active and able to simultaneously bind to the ice surface to achieve maximum activity.

Expanding on this principle, thermal hysteresis activity of type III was further increased by adding domains by tandem repetition to create three and four domain proteins.[18] However, diminishing return above three domains was observed. On the basis of the reported flexibility of the linker,[19,20] this likely is the result of limited freedom of the domains in the multimer, particularly the central domains that are confined at both termini.

To overcome the limited mobility of tandem repeats, we present here a different strategy for increasing the number of domains per molecule. Type I AFPs are conjugated to a polymer chain through their carboxy-terminal end. This results in multiple binding domains per chain, while still retaining individual domain mobility. Type I AFP, as opposed to a more active AFP, was chosen for two reasons. First of all, it consists of a single α helix with no disulfide bonds or post-translational modification, so large quantities of active protein (~100 mg/L of culture) can be expressed in *E. coli* and purified using relatively simple procedures.[21] Second, it could be modified to remove acidic residues that would compete with the carboxy-terminus in the conjugation reaction. The goal of the work is to reduce the amount of protein necessary to observe significant thermal hysteresis activity, so the low overall thermal hysteresis of the Type I AFP is not a primary issue.

MATERIALS AND METHODS

Synthesis and Cloning of the Genes for the Proteins. *E. coli* strain BL21*(DE3) (Invitrogen) was used as the cloning and the expression host strain using the pET20b vector (Novagen). The procedure for obtaining the gene for producing the type I AFP genes was previously described by Solomon and Appels.[21] We used a slightly modified version of their technique to obtain the sequence for rAFP (Table 1). Briefly, four primers were used, two of which included the major portion of the sequence that was extended using the two other shorter primers according to the overlap extension technique. It is noteworthy that rAFP was designed based on 11 amino acid repeat sequences found in the native winter flounder proteins, but differs in that the repeat sequences have less variability than the native proteins and it contains five 11 residue repeats instead of the three or four repeats naturally found.

In order to conjugate this protein to a polyallylamine (PAA) specifically through its carboxy terminus, we produced a variant of the protein with the two aspartic acid residues replaced by asparagines, which have a similar side group size but without the carboxylic acid group (Table 1). This modified protein, rAFP-N, was prepared with the same procedure to create the gene for producing rAFP except using a slightly modified forward extension primer to replace the aspartic acid residues with asparagines.

PCR amplifications were carried out using a thermal cycler (Thermo Electron Corp.) in a 50 μL reaction containing 0.01 μM template primers, 1.25 μM short primers, nuclease free water, and PCR master mix (Promega). Purified DNA and the pET20b expression vector were each 10-fold over digested with NdeI and *Bam*HI restriction endonucleases. Digestion products were prepared for ligation by purification with agarose gel electrophoresis.

Table 1. Amino Acid Sequence and Thermal Hysteresis Activity of Reported AFP Constructs

protein	sequence/structure	activity at 0.3 mM (°C)
rAFP	MD TASDAAAAAAL (TAANAAAAAAL)$_4$ TAR	0.28
rAFP-N	MN TASNAAAAAAL (TAANAAAAAAL)$_4$ TAR	0.23
rAFP-N/PAA	Polyallylamine-*graft*-rAFP-N	0.50

Quick Ligase Buffer (New England Biolabs) was used in 5 min ligation reaction including approximately 50 ng of the vector DNA and a 10-fold molar excess of the insert DNA followed by plating. After overnight growth, colonies were selected and plasmid DNA was purified using a miniprep kit (Qiagen). DNA sequencing (Cleveland State University Genomics Laboratory) was used to verify that the gene was ligated into the plasmid properly.

Protein Expression and Purification. Overnight cultures of transformed bacteria in 5 mL of ampicillin containing LB medium was used to inoculate 1 L cultures having 100 mg ampicillin. Samples were induced with isopropyl-β-D-thiogalactopyranoside (IPTG) (Thermo Fisher Scientific) after cultures reached an optical density of 0.6 at 600 nm. Induced samples were shaken in an incubator at 37 °C for 6 h.

Samples were purified (>95% as measured by polyacrylamide gel electrophoresis and reverse-phase HPLC) using ethanolic extraction according to the protocol reported by Solomon and Appels.[21] The purified protein was dialyzed against 100 mM ammonium bicarbonate using 1000 Da cutoff membrane followed by lyophilization.

Molecular weights of the proteins were determined by mass spectrometry as 5108.6 and 5105.6 Da for rAFP and rAFP-N, respectively. These results were in accordance with the weights calculated from the primary sequences. Concentration of a master solution was determined by amino acid analysis (University of Oklahoma Molecular Biology Proteomics Facility).

Conjugation Reactions. In a round-bottom flask, 5 μL polyallylamine (Sigma-Aldrich) (M_w ~17 000, 20 wt % in water) was mixed with 24 μL EDC (1-Ethyl-3-[3-dimethylaminopropyl]carbodiimide hydrochloride) (Sigma-Aldrich) and 10.9 μL sulfo-NHS (*n*-hydroxysulfosuccinimide) (Sigma-Aldrich) in 300 μL 0.4% acetic acid, 30 mM ammonium bicarbonate.[22] Approximately 13 times molar excess of the rAFP-N (0.3 mM) was added to the reaction mixture, which was stirred for 2 h at room temperature. Unreacted impurities were removed by dialysis using 3500 MW cutoff Spectra/Por dialysis membrane.

Size Exclusion HPLC. A 500 μL aliquot of the reaction mixture was loaded on the 20 mL bioscale size exclusion column (Bio-Rad Laboratories) filled with Toyopearl HW-55F resin (Tosoh). Reaction buffer solution was pumped through the column in the down-flow mode at a flow rate of 1 mL/min. UV absorbance at 230 and 280 nm were used to monitor the eluted sample.

Thermal Hysteresis Experiments. The concentration dependence of the thermal hysteresis activity of the AFPs was measured as the difference between the melting and the freezing temperatures of protein solutions. The melting and freezing points were measured as previously described using a homebuilt nanoliter osmometer attached to an optical microscope (Olympus).[23] Briefly, a single drop of protein solution was suspended in oil.

The droplet was flash frozen at around −30 °C and, upon increasing the temperature to the melting point, was thawed slowly until a single ice crystal was obtained. The temperature was subsequently decreased (0.01 °C/min) until reaching the freezing temperature, where rapid crystal growth was observed.

RESULTS

We successfully expressed and purified two different recombinant type I antifreeze proteins, rAFP and rAFP-N (Table 1), as verified by DNA sequencing of the gene, mass spectrometry, and amino acid analysis. The rAFP protein was first designed and expressed by Solomon and Appels,[21] based on the HPLC6 winter flounder type I AFP. It consists of initial HPLC6 residues, including the first 11-residue repeat sequence, followed by four of the terminal HPLC6 11-residue repeats. The five 11-residue repeats is greater than the three commonly found in nature. The rAFP-N protein is the same as rAFP except that mutations were introduced to substitute the two aspartic acid residues with asparagine residues. This eliminates the acidic side groups that could compete with the protein carboxy terminus in the conjugation reaction with the amine groups of the polyallylamine.

The conjugation reaction product of rAFP-N (5.1 kD) with PAA (17 kD) was passed through a size exclusion chromatography column (Figure 1) and fractionated to determine which peaks contained active antifreeze protein, as determined by thermal hysteresis measurements and ice crystal morphologies. The 280 nm absorbance is attributed to the PAA, whereas both the protein and PAA absorb at 230 nm. The first (high molecular weight) peak contains active antifreeze protein and corresponds to the reaction product. The second peak also exhibits activity, and is attributed to unreacted protein. None of the other peaks contained active protein.

All three protein constructs (rAFP, rAFP-N, and rAFP-N/PAA) exhibit thermal hysteresis activity (Figure 2). Although rAFP and rAFP-N have comparable activities up to 0.2 mM, the activity for rAFP-N was lower than that for rAFP at higher concentrations. We speculate that the lower thermal hysteresis activity of rAFP-N may be the result of reduced solubility since the charged aspartic acid residues were removed to facilitate the specific conjugation reactions, but it could also be caused by structural differences induced by the point mutations. When compared to reported thermal hysteresis values of its shorter isoform HPLC-6,[24] rAFP is more active at all concentrations measured, i.e., up to 2 mM.

The activity of the rAFP-N/PAA is measured using the reaction mixture, which includes both the rAFP-N conjugated to the PAA and any unreacted protein. For comparison to the unconjugated protein, the thermal hysteresis is plotted against the protein domain concentration, which includes both protein domains conjugated to the polymer and free unreacted domains. This domain concentration is based on the known amount of protein added in the reaction. At concentrations below 0.3 mM of rAFP-N, the rAFP-N/PAA reaction product is at least twice as active compared to rAFP or rAFP-N. It would have been preferable to compare the conjugation product purified from unreacted protein by chromatography. However, quantification of the protein domain concentration in the fractionated samples was not successful. We attempted using NMR, but the signal from the acetic acid in the sample buffer, which was necessary to solubilize the product, overwhelmed the NMR spectra of the sample. Amino acid analysis of the product also did not produce reliable results presumably because of the interference of the polymer backbone.

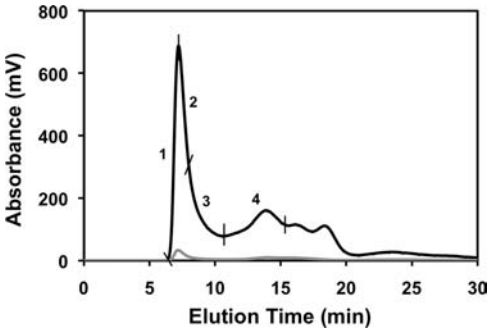

Figure 1. Size exclusion chromatograph of the conjugation reaction mixture. The sample was fractionated at several intervals to identify the peaks that contained active antifreeze proteins. The sample is detected by UV absorbance (black line: 230 nm, gray line: 280 nm).

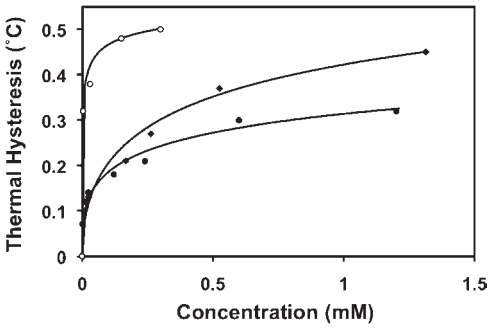

Figure 2. Concentration dependence of thermal hysteresis. Thermal hysteresis measurements of the pure proteins, rAFP (diamonds) and rAFP-N (solid circles), and the reaction product, rAFP-N/PAA (open circles), were measured at a cooling rate of 0.01 °C/min. The concentrations for rAFP-N/PAA indicate the molar concentration of the rAFP-N protein molecules used in the reaction mixture.

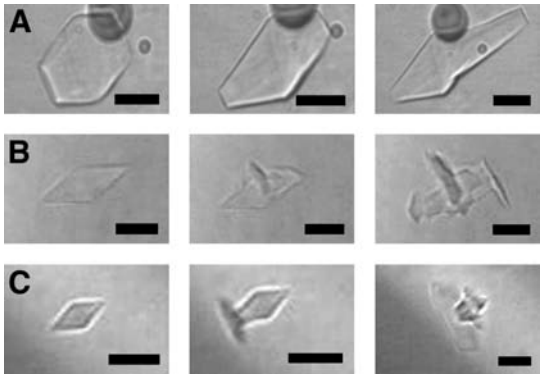

Figure 3. Ice crystal morphologies in the presence of antifreeze protein constructs: A, rAFP (530 μM); B, rAFP-N (600 μM); C, rAFP-N/PAA (32 μM of rAFP-N). For all samples, the *c*-axis is parallel to the paper plane. Scale bars are 10 μm.

Ice crystal morphologies were observed in the presence of the AFP. At all concentrations, the ice crystal morphologies in the presence of rAFP were similar, with ice crystals between 10 and 15 μm at low concentrations and slightly larger at 0.53 mM (Figure 3A). Truncated bipyramidal ice crystals are initially

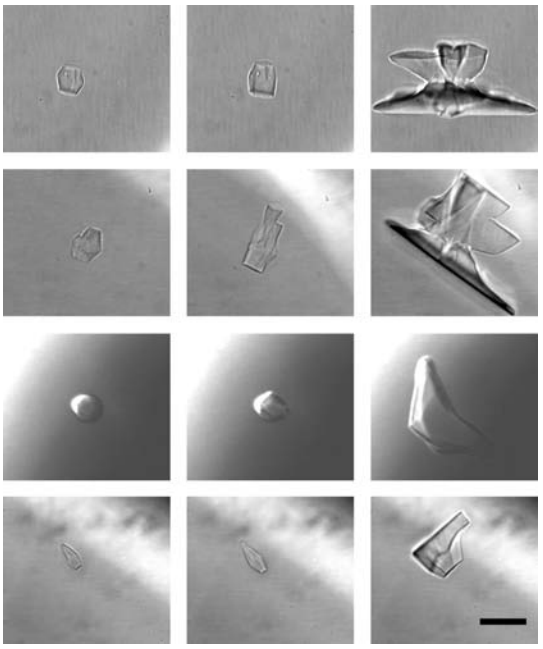

Figure 4. Ice crystal morphologies in the presence of the HPLC purified rAFP-N/PAA. The *c*-axis is parallel to the paper plane except for the third row, in which it is perpendicular to the paper plane. From left to right: Initial single ice crystal, ice crystal just before and after the burst point, respectively. First row is the left arm of the first peak in Figure 1, while the remaining rows represent the top-right of the first peak, bottom-right of the first peak, and the second peak in Figure 1, respectively. No ice crystal morphology change was detected for the remainder of the peaks. Scale bar is 10 μm.

formed, followed by more complete bipyramid formation over time. Similar hexagonal bipyramidal ice crystal morphologies have been reported in the presence of the shorter isoform of rAFP.[25] At the burst point, the ice crystals fail at the bipyramid tip growing in the direction of the *c*-axis. The rAFP-N also produced bipyramidal structures, which were frequently truncated at lower concentrations. Surprisingly, the rAFP-N burst point morphology was substantially different than rAFP. Ice crystals failed at the edge and center of the crystal with ice crystal growth always along the *a*-axis (Figure 3B). Ice crystal morphologies of the rAFP-N/PAA reaction product revealed similar behavior as rAFP-N except that much smaller ice crystals were obtained at all concentrations (Figure 3C). Again, failure occurred at the tip and at the center of the ice crystal growing along the *a*-axis, similar to rAFP-N.

The first and second peaks of the rAFP-N/PAA reaction product purified by size exclusion chromatography (Figure 1) were fractionated and ice crystal morphologies were observed (Figure 4). The concentration for these samples is unknown due to the inability to quantify the conjugated protein adequately. Thermal hysteresis activities of the samples from first row to the fourth row are 0.25, 0.28, 0.20, and 0.11 °C, respectively. No ice crystal morphology change was detected for the remainder of the peaks indicating that the first two peaks constitute the majority of the reacted and unreacted protein.

DISCUSSION

Activity of antifreeze proteins is primarily measured through the concentration-dependent thermal hysteresis, which is the difference between the melting and freezing points of ice crystals in AFP solutions. Thermal hysteresis results from the noncolligative depression of the freezing point through AFP interaction with the ice crystal surface. Several factors have been reported to affect the thermal hysteresis activity of a given protein, including the size of the protein (steric effect), the surface area and lattice matching of the ice binding face (affinity), and the ability of the multiple protein domains to bind with the ice surface simultaneously (avidity).[14,15,17,20] The widely accepted mechanism for thermal hysteresis is described by a model based on the Kelvin effect.[26] Once proteins bind to the ice surface, the spacing between the adsorbed protein molecules determines the level of thermal hysteresis activity. This model relies on the pinning of the ice crystal by the proteins leading to curvature of the growing ice surface between the protein molecules resulting in an increased energy barrier for the addition of water molecules. This can stop the growth of the ice crystal, effectively lowering the freezing point. Since the growth of the ice crystals has been observed to be completely stopped, the proteins must be irreversibly adsorbed to the ice.

Irreversible adsorption conflicts with the observed concentration dependence of thermal hysteresis, which suggests that there is an equilibrium process occurring. To reconcile these observations, Kristiansen and Zachariassen[27] presented a convincing model with a two-step process: protein equilibrium (reversible) binding occurs at the colligative freezing temperature as the ice begins to form, but as the crystals mature, the proteins become trapped in the surface (irreversible) to result in thermal hysteresis. The concentration dependence of thermal hysteresis is a result of different protein concentrations present at the interface due to the reversible binding step.

On the basis of the above model, for a given antifreeze protein that binds to a specific plane of the ice surface, increasing the concentration at the interface during the reversible adsorption step will tend to increase the thermal hysteresis. Adsorption/desorption equilibrium should therefore be considered when designing an antifreeze protein molecule. The most common approach used to increase surface concentrations has been to increase the affinity of protein binding to the ice, by increasing the area of the protein binding face for helical AFPs.[11,12] The increase in affinity reduces the rate of desorption leading to an increased equilibrium protein concentration at the surface. Increasing the affinity is to some extent limited in that the quality of lattice matching diminishes with the addition of helical repeats.

Increased avidity also can result in increased thermal hysteresis, particularly at low protein concentrations, as has been reported with the naturally occurring two-domain type III AFP.[20] Using a modified Langmuir adsorption model, we illustrated that this can be explained by an increased surface concentration during reversible adsorption.[28] This insight inspired the design of the high-avidity AFP construct produced by the conjugation of multiple AFPs to a polymer chain (Figure 5). The high avidity results in an increased concentration of the surface-bound proteins and activity of the product. Hence, a smaller concentration of protein is required to obtain the same activity compared to free AFP.

The proposed mechanism of action is for the increase in activity of the rAFP-N/PAA is the increased avidity. During the reversible step of the AFP interaction with ice crystals, multiple proteins attached to a single polymer chain can adsorb to the ice surface. Even if there was a relatively weak interaction of

Figure 5. Schematic representations of rAFP-N/PAA reaction product. The rAFP-N models were created by extending the length of winter flounder AFP (PDB ID 1WFA[37]) while maintaining the α-helical structure, using *DeepView/Swiss-PdbViewer* software program.[38] PAA (17 kDa) was produced using *PyMOL* version 0.99.

the individual proteins, resulting in significant probability of exchange of the molecules, desorption of one or more of the protein molecules would not be enough to disengage the whole construct from the surface. All proteins would need to desorb simultaneously, leading to near-zero probability of complete desorption. This will lead to high surface coverage even at low solution concentrations. It is noteworthy that, using a similar approach, the conjugation of hydrophobic side chains to polymers has been used to produce stable adsorbed layers on hydrophobic surfaces.[29]

As expected, in the reaction product containing the AFP conjugated to the PAA we observed an increase in thermal hysteresis compared to equivalent concentrations of pure protein, particularly at low concentrations. We expect that using reaction mixture containing both the conjugate and unreacted protein underestimates the actual thermal hysteresis values of conjugation product with no free AFP. The degree of this underestimation may be relatively small in light of the reported conferring of full activity to a defective AFP by the addition of a small fraction of an active AFP.[30] Even with the potential underestimation of the effectiveness, it is impressive that the conjugated product was able to achieve a thermal hysteresis of 0.3 °C with about 1% of the total protein concentration needed for the free AFP (3 μM of the protein domain compared to 300 μM, respectively). This drastically lowers the total amount of protein necessary to achieve the same activity.

If the high avidity of the rAFP-N/PAA leads to high surface coverage particularly at low concentrations, one may question why a greater increase in thermal hysteresis is not observed. Although there is significant thermal hysteresis activity improvement within the concentration range studied, these values fall below the thermal hysteresis values reported for the hyperactive type I AFP.[13] A likely answer is that the distribution of the protein along the polymer both in distance and in frequency may not be optimal for maximizing surface coverage. This could lead to incorrect alignment of the protein molecules on the ice lattice. The reaction product obtained in this study has multiple protein molecules attached to a polyamine carrying multiple ice binding sites. It is likely that misalignment of the ice binding faces during the reversible exchange is more pronounced for this bigger molecule compared to individual protein molecules and hence there might be a limit to the number of protein molecules on the polymer chain that can simultaneously align with the ice surface. By changing the ratio of protein to polymer, an optimal number of proteins for the maximizing thermal hysteresis activity could be obtained. If greater thermal hysteresis is desired, another approach could be to use more active antifreeze proteins such as insect antifreeze proteins.

Different types of AFPs produce different ice crystal morphologies, which is attributed to their structural differences.[31] For example, type I AFPs bind to the bipyramidal (201) plane of ice.[26] Molecular modeling studies revealed that the main source of this interaction was the steric compatibility between the ice plane and the AFP.[32] Type III AFPs comparably bind to the prism (100) plane of the ice crystal.[33] Similarly, steric contributions and hydrophobic interactions were found to play an important role in ice binding of these AFPs by using molecular dynamics simulations, ice docking, and energy minimization studies.[26,34−36] The ice crystal morphology observed for both rAFP-N and the conjugation product rAFP-N/PAA is initially a truncated bipyramid that may grow with time to form a more complete bipyramid, more often at higher concentrations. The similar behavior suggests that the conjugation does not alter the manner in which the proteins bind to the ice surface. It is unknown why the morphology of the ice crystal growth is different between the rAFP and the rAFP-N. The conversion of the two aspartic acids to asparagines are outside of the binding region of the protein and are not expected to alter the simple α-helical fold of the protein. For some unknown reason, the loss of the charged residues leads to the greater prevalence of truncated bipyramidal crystals, as well as burst growth along the *a*-axis instead of the *c*-axis.

Creating superior AFP constructs that have thermal hysteresis activity at low concentrations would make it more feasible economically to use them as additives for cryopreservation and refrigeration systems. We have successfully demonstrated a potential route toward this goal. Through the use of higher-activity AFP domains, such as insect AFPs, and optimizing the density of conjugation, even greater improvements in activity might be obtained.

AUTHOR INFORMATION

Corresponding Author

*E-mail: n.holland1@csuohio.edu.

Present Addresses

[†]Department of Medical Biochemistry, School of Medicine, Acibadem University, Istanbul, Turkey.

ACKNOWLEDGMENT

We thank A. H. Heuer and A. McIlwain (Case Western Reserve University) for use of and assistance with the nanoliter osmometer and M. A. Ruegsegger (The Ohio State University) for helpful advice with the bioconjugation procedure. This research is supported by awards from the American Heart Association (Scientist Development Grant, 0635084N) and the Cleveland State University Doctoral Dissertation Research Expense Award Program.

ABBREVIATIONS

AFP, antifreeze protein; PAA, polyallylamine; rAFP, recombinant type I fish AFP; rAFP-N, rAFP with aspartic acid residues replaced by asparagine; rAFP-N/PAA, polyallylamine-*graft*-rAFP-N

REFERENCES

(1) Venketesh, S., and Dayananda, C. (2008) Properties, potentials, and prospects of antifreeze proteins. *Crit. Rev. Biotechnol. 28*, 57–82.

(2) Knight, C. A., Wen, D. Y., and Laursen, R. A. (1995) Nonequilibrium antifreeze peptides and the recrystallization of ice. *Cryobiology 32*, 23–34.

(3) Amir, G., Horowitz, L., Rubinsky, B., Yousif, B. S., Lavee, J., and Smolinsky, A. K. (2004) Subzero nonfreezing cryopreservation of rat hearts using antifreeze protein I and antifreeze protein III. *Cryobiology 48*, 273–282.

(4) Soltys, K. A., Batta, A. K., and Koneru, B. (2001) Successful nonfreezing, subzero preservation of rat liver with 2,3-butanediol and type I antifreeze protein. *J. Surg. Res. 96*, 30–34.

(5) Chao, H. M., Davies, P. L., and Carpenter, J. F. (1996) Effects of antifreeze proteins on red blood cell survival during cryopreservation. *J. Exp. Biol. 199*, 2071–2076.

(6) Inada, T., and Modak, P. R. (2006) Growth control of ice crystals by poly(vinyl alcohol) and antifreeze protein in ice slurries. *Chem. Eng. Sci. 61*, 3149–3158.

(7) Egolf, P. W., and Kauffeld, M. (2005) From physical properties of ice slurries to industrial ice slurry applications. *Int. J. Refrig. 28*, 4–12.

(8) Griffith, M., and Ewart, K. V. (1995) Antifreeze proteins and their potential use in frozen foods. *Biotechnol. Adv. 13*, 375–402.

(9) Yang, D. S. C., Sax, M., Chakrabartty, A., and Hew, C. L. (1988) Crystal-structure of an antifreeze polypeptide and its mechanistic implications. *Nature 333*, 232–237.

(10) Patel, S. N., and Graether, S. P. (2010) Structures and ice-binding faces of the alanine-rich type I antifreeze proteins. *Biochem. Cell Biol. 88*, 223–229.

(11) Chao, H., Hodges, R. S., Kay, C. M., Gauthier, S. Y., and Davies, P. L. (1996) A natural variant of type I antifreeze protein with four ice-binding repeats is a particularly potent antifreeze. *Protein Sci. 5*, 1150–1156.

(12) Gauthier, S. Y., Marshall, C. B., Fletcher, G. L., and Davies, P. L. (2005) Hyperactive antifreeze protein in flounder species. *FEBS J. 272*, 4439–4449.

(13) Marshall, C. B., Chakrabartty, A., and Davies, P. L. (2005) Hyperactive antifreeze protein from winter flounder is a very long rod-like dimer of alpha-helices. *J. Biol. Chem. 280*, 17920–17929.

(14) Leinala, E. K., Davies, P. L., Doucet, D., Tyshenko, M. G., Walker, V. K., and Jia, Z. C. (2002) A beta-helical antifreeze protein isoform with increased activity - Structural and functional insights. *J. Biol. Chem. 277*, 33349–33352.

(15) Marshall, C. B., Daley, M. E., Sykes, B. D., and Davies, P. L. (2004) Enhancing the activity of a beta-helical antifreeze protein by the engineered addition of coils. *Biochemistry 43*, 11637–11646.

(16) Miura, K., Ohgiya, S., Hoshino, T., Nemoto, N., Suetake, T., Miura, A., Spyracopoulos, L., Kondo, H., and Tsuda, S. (2001) NMR analysis of type III antifreeze protein intramolecular dimer - Structural basis for enhanced activity. *J. Biol. Chem. 276*, 1304–1310.

(17) Baardsnes, J., Kuiper, M. J., and Davies, P. L. (2003) Antifreeze protein dimer - When two ice-binding faces are better than one. *J. Biol. Chem. 278*, 38942–38947.

(18) Nishimiya, Y., Ohgiya, S., and Tsuda, S. (2003) Artificial multimers of the type III antifreeze protein - Effects on thermal hysteresis and ice crystal morphology. *J. Biol. Chem. 278*, 32307–32312.

(19) Holland, N. B., Nishimiya, Y., Tsuda, S., and Sönnichsen, F. D. (2007) Activity of a two-domain antifreeze protein is not dependent on linker sequence. *Biophys. J. 92*, 541–546.

(20) Holland, N. B., Nishimiya, Y., Tsuda, S., and Sönnichsen, F. D. (2008) Two domains of RD3 antifreeze protein diffuse independently. *Biochemistry 47*, 5935–5941.

(21) Solomon, R. G., and Appels, R. (1999) Stable, high-level expression of a type antifreeze protein in *Escherichia coli*. *Protein Express. Purif. 16*, 53–62.

(22) Hermanson, G. T. (2008) *Bioconjugate Techniques*, 2nd ed., Academic Press, Burlington, MA.

(23) Miller, N. E. (2003) "Burst-Point" Morphologies of Ice Crystals in the Presence of Antifreeze Proteins, Masters Thesis, Department of Materials Science and Engineering, Case Western Reserve University, Cleveland, OH.

(24) Baardsnes, J., Kondejewski, L. H., Hodges, R. S., Chao, H., Kay, C., and Davies, P. L. (1999) New ice-binding face for type I antifreeze protein. *FEBS Lett. 463*, 87–91.

(25) Evans, R. P., and Fletcher, G. L. (2001) Isolation and characterization of type I antifreeze proteins from Atlantic snailfish (*Liparis atlanticus*) and dusky snailfish (*Liparis gibbus*). *Biochim. Biophys. Acta 1547*, 235–244.

(26) Knight, C. A., Cheng, C. C., and Devries, A. L. (1991) Adsorption of alpha-helical antifreeze peptides on specific ice crystal-surface planes. *Biophys. J. 59*, 409–418.

(27) Kristiansen, E., and Zachariassen, K. E. (2005) The mechanism by which fish antifreeze proteins cause thermal hysteresis. *Cryobiology 51*, 262–280.

(28) Can, O., and Holland, N. B. (2009) Modified Langmuir isotherm for a two-domain adsorbate: Derivation and application to antifreeze proteins. *J. Colloid Interface Sci. 329*, 24–30.

(29) Holland, N. B., Qiu, Y. X., Ruegsegger, M., and Marchant, R. E. (1998) Biomimetic engineering of non-adhesive glycocalyx-like surfaces using oligosaccharide surfactant polymers. *Nature 392*, 799–801.

(30) Takamichi, M., Nishimiya, Y., Miura, A., and Tsuda, S. (2009) Fully active QAE isoform confers thermal hysteresis activity on a defective SP isoform of type III antifreeze protein. *FEBS J. 276*, 1471–1479.

(31) Chao, H., Deluca, C. I., and Davies, P. L. (1995) Mixing antifreeze protein types changes ice crystal morphology without affecting antifreeze activity. *FEBS Lett. 357*, 183–186.

(32) Lal, M., Clark, A. H., Lips, A., Ruddock, J. N., and White, D. N. J. (1993) Inhibition of ice crystal-growth by preferential peptide adsorption: A molecular modeling study. *Faraday Discuss. 95*, 299–306.

(33) Madura, J. D., Baran, K., and Wierzbicki, A. (2000) Molecular recognition and binding of thermal hysteresis proteins to ice. *J. Molec. Recog. 13*, 101–113.

(34) Haymet, A. D. J., Ward, L. G., and Harding, M. M. (1999) Winter flounder "antifreeze" proteins: Synthesis and ice growth inhibition of analogues that probe the relative importance of hydrophobic and hydrogen-bonding interactions. *J. Am. Chem. Soc. 121*, 941–948.

(35) Loewen, M. C., Chao, H. M., Houston, M. E., Baardsnes, J., Hodges, R. S., Kay, C. M., Sykes, B. D., Sönnichsen, F. D., and Davies, P. L. (1999) Alternative roles for putative ice-binding residues in type I antifreeze protein. *Biochemistry 38*, 4743–4749.

(36) Sönnichsen, F. D., DeLuca, C. I., Davies, P. L., and Sykes, B. D. (1996) Refined solution structure of type III antifreeze protein: Hydrophobic groups may be involved in the energetics of the protein-ice interaction. *Structure 4*, 1325–1337.

(37) Sicheri, F., and Yang, D. S. C. (1995) Ice-binding structure and mechanism of an antifreeze protein from winter flounder. *Nature 375*, 427–431.

(38) Guex, N., and Peitsch, M. C. (1997) SWISS-MODEL and the Swiss-PdbViewer: An environment for comparative protein modeling. *Electrophor. 18*, 2714–2723.

Bioconjugate Chemistry

TECHNICAL NOTE

pubs.acs.org/bc

Trivalent PEGylated Platform for the Conjugation of Bioactive Compounds

Ángela Torres,[‡,†] Carlos Mas-Moruno,[§,†] Enrique Pérez-Payá,[∥,⊥] Fernando Albericio,[*,§,#] and Miriam Royo[*,‡,#]

[‡]Combinatorial Chemistry Unit, Barcelona Science Park, University of Barcelona, Baldiri Reixac 10, 08028-Barcelona, Spain

[§]Institute for Research in Biomedicine, Barcelona Science Park, Baldiri Reixac 10, 08028-Barcelona, Spain

[∥]Department of Medicinal Chemistry, Príncipe Felipe Research Centre, 46013-Valencia, Spain

[⊥]IBV-CSIC, 46010-Valencia, Spain

[#]CIBER-BBN, Networking Centre on Bioengineering Biomaterials and Nanomedicine, 08028-Barcelona, Spain

Supporting Information

ABSTRACT:

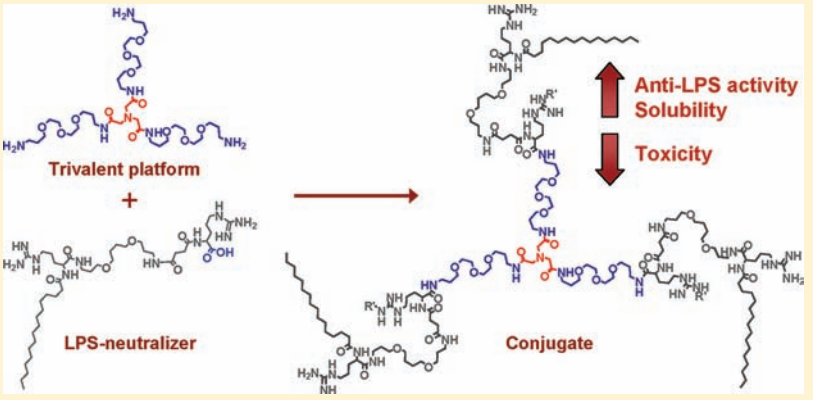

PEGylated multivalent structures are a new class of platform for biological applications due to their biocompatibility properties. Here, we present the synthesis of a trivalent structure **1** based on poly(ethylene glycol) units (PEG) as potential synthetic multifunctional carrier molecule. To evaluate whether this PEGylated platform could be useful for the conjugation of bioactive compounds, a well-known lipopolysaccharide (LPS) inhibitor **2**, developed in our laboratory, was selected to be conjugated to **1**. The LPS-neutralizing activity of the resulted conjugates and precursors was established using the chromogenic *Limulus* amebocyte lysate (LAL) assay. The trivalent structure **1** did not show LPS-binding activity, nonconjugate LPS inhibitor **2** showed high LPS-neutralizing activity, and the trivalent conjugate **4** displayed increased LPS-neutralizing activity and a reduced toxicity profile. These results prove the efficacy of this trivalent platform as a multivalent ligand scaffold for biological applications.

INTRODUCTION

The conjugation of bioactive compounds to oligo- and polymeric materials constitutes a useful strategy of outstanding interest in the field of medicinal chemistry.[1,2] These materials can be used either as carrier systems for drug delivery or as bioactive multivalent platforms for the presentation of several copies of a pharmacological agent with a specific topology. Overall, these systems should enable the administration of much lower doses of the drug with higher efficiency, thereby minimizing unwanted side effects. Additionally, for substances with poor water solubility, these systems afford the possibility to increase this property and hence the effectiveness of the drug.

Dendrimer structures have emerged as a new class of biopolymers with structural properties[3−5] and biological applications of interest.[6−10] These compounds are highly branched polymers with a well-defined chemical composition and structure. In this regard, PEGylated dendrimers, in which a multifunctional dendritic core is attached to polyethylene glycol (PEG) chains, are a subclass of dendrimers that maintain the special features of the dendrimers and amplify the properties of PEG.[11,12] PEG is a highly flexible, water-soluble, nontoxic, and non-immunogenic polymer. Drug or protein conjugation to PEG increases its solubility in water, protects against degrading enzymes, and prevents immunogenicity, preserving the original biological functions of the conjugated bioactive molecules.[13] In addition, the presence of PEG reduces kidney ultrafiltration, improves bioavailability,

Received: September 22, 2010
Revised: July 18, 2011
Published: August 25, 2011

ACS Publications © 2011 American Chemical Society

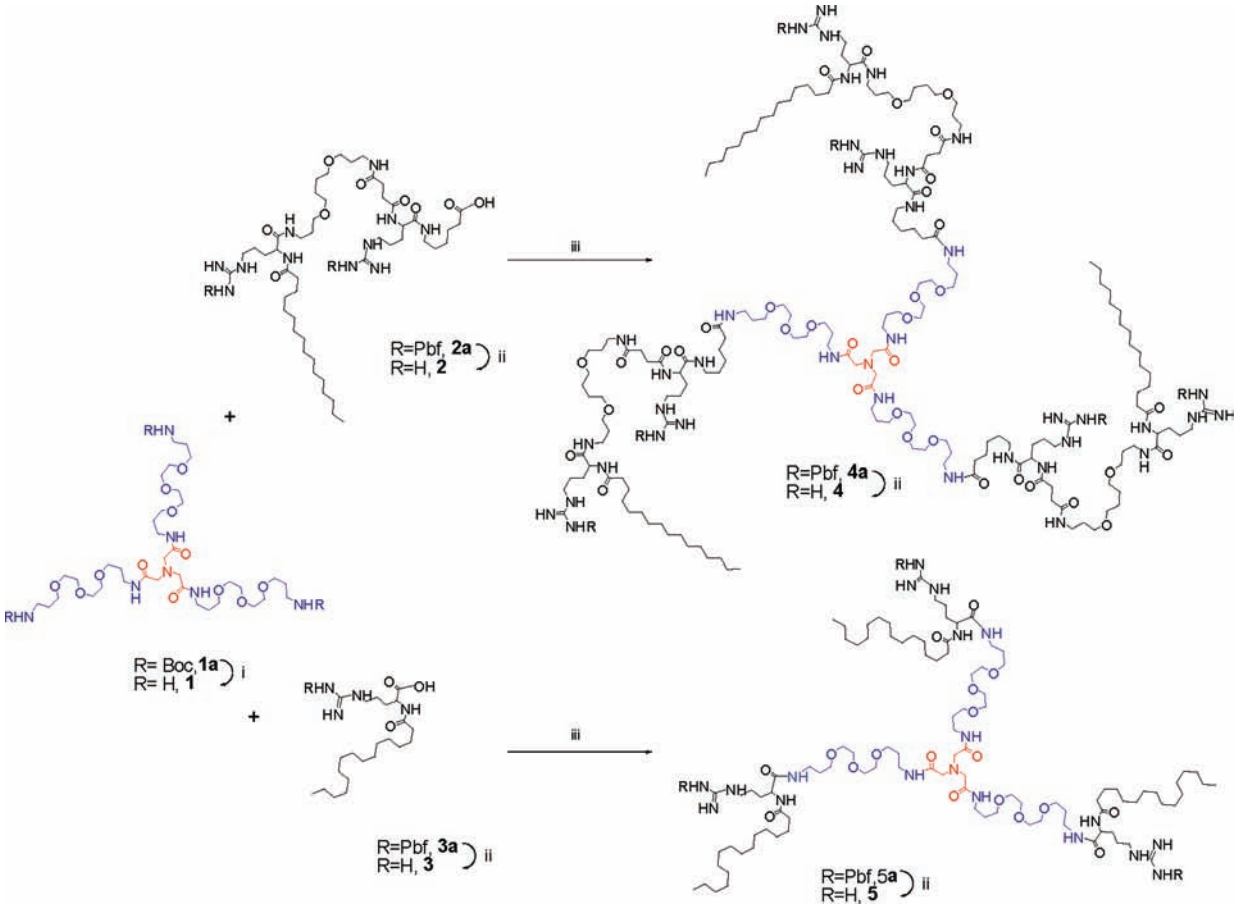

Figure 1. Synthesis of conjugates **4** and **5**. Trivalent platform **1** is depicted drawing multifunctional core NTA in red and the PEG chains in blue. The potent LPS-neutralizing agent **2** and the amphipathic monomer **3** are also shown. (i) TFA-DCM (1:1); (ii) TFA-H_2O-TIS (95:2.5:2.5); (iii) PyBOP, HOBt, DIEA.

increasing drug half-life, and, in general, facilitates its administration.[14,15] In fact, various PEGylated dendrimers have been described and showed lower toxicity, fewer hemolytic properties, long blood circulation times, low organ accumulation, and high accumulation in tumor tissue.[16−18]

Nevertheless, the synthesis of highly branched dendritic structures is often tedious and challenging and involves considerable synthetic effort, generally resulting in low yields of final dendrimers.[19] Simple, easy-to-synthesize multivalent platforms (i.e., generation 0 dendrimers) that are able to maintain some of these unique dendrimer properties are the optimal scaffolds to construct new multivalent ligands. Multivalence is a phenomenon whereby multiple, simultaneous, energetically coupled target/ligand interactions enhance the overall activity and selectivity compared to the corresponding monomeric interaction.

Here, we describe the synthesis of a very promising class of trivalent PEG-based platform **1**, which consists of three copies of monodisperse PEG units attached to nitrilotriacetic acid (NTA) as trivalent ligand scaffold (Figure 1). In addition to the conjugation of multiple copies of bioactive compounds, such platforms may also increase water solubility and reduce toxicity of the conjugated molecules caused by the presence of PEG moieties.

To evaluate whether this PEGylated platform could be useful in the conjugation of bioactive compounds, a LPS inhibitor developed in our laboratory, compound **2**,[20] was selected to be conjugated to **1** (Figure 1). LPS is a bacterial endotoxin present in the outer leaflet of Gram-negative bacteria that plays a major role in Gram-negative sepsis.[21] Sepsis is a serious systemic response to infection that represents the foremost cause of death in intensive care units (ICUs),[22] accounting for 750 000 hospitalizations in the U.S. annually.[23,24] To date, only one example of dendrimers with LPS-neutralizing activity has been reported.[25,26] In these studies, David and co-workers examined a variety of amine-terminated poly(amidoamine) (PAMAM) dendrimers.[27] The authors derivatized the surface amines of these dendrimers with lipopolyamines and obtained a multibranched dendritic structure that neutralized LPS-induced inflammatory responses *in vitro* and afforded protection against endotoxic shock in a murine model.[26] No reports concerning other types of dendritic-like multivalent structures have been found in the literature.

The selected LPS-inhibitor, compound **2**, was successfully conjugated to the trivalent platform **1**, thereby rendering a new construct **4** with an improved endotoxin-neutralizing activity and toxicity profile, confirming the utility of this new PEGylated platform as a multivalent scaffold.

EXPERIMENTAL PROCEDURES

General Materials and Methods. All chemicals and solvents were purchased from Calbiochem-Novabiochem AG, Iris Biotech GmbH, Fluka Chemika, Albatross Chem, GL Biochem, Sigma-Aldrich, Panreac, KaliChemie, Merck KGaA, or Scharlau and

were used as received without further purification. Distilled and deionized water was used for the preparation and rinsing of all solutions. Endotoxin-free water, LPS from *E. coli* 055:B5 and Polymyxin B were purchased from Sigma. The LAL reagent and the chromogenic substrate were obtained from Cambrex. Analytical RP-HPLC was performed using an Alliance 2695 Waters chromatography system with a RP Symmetry column and a Waters 996 photodiode array detector, using different linear gradients (see SI). Semipreparative HPLC was carried out on a Waters chromatography system equipped with a Waters 2487 dual absorbance detector and ESI-MS Waters Micromass ZQ), performed on a Symmetry column with linear gradients of B, MeCN (with 0.1% TFA), in A, H_2O (with 0.1% TFA), at a flow rate of 20 mL/min, using different linear gradients (see SI). Flash RP-LC was performed on a Combi Flash system from Isco Teledyne using RediSep C_{18} cartridges (4 g) with linear gradients of B, MeCN (with 0.1% TFA), in A, H_2O (with 0.1% TFA), at a flow rate of 20 mL/min (see SI for elution conditions). HPLC-MS was performed on Waters Alliance 2695 chromatography system equipped with Waters 995 photodiode array detector and ESI-MS Waters Micromass ZQ), on a Symmetry column with linear gradients of B, MeCN (with 0.1% FA), in A, H_2O (with 0.1% FA), at a flow rate of 20 mL/min (see SI for elution conditions). Mass spectra were recorded on a Voyager MALDI-TOF spectrometer using either ACH or SA matrices dissolved in H_2O/MeCN/FA (1:1:0.1). ^{1}H NMR spectra were recorded on a Varian Mercury 400 spectrometer at 400 MHz in DO_2. Peptide solid-phase synthesis was carried out following standard methods[28] described in Supporting Information section.

Synthesis of (TOTA)$_3$NTA (1). NTA (12.0 mg, 0.063 mmol), was preactivated for 15 min with DIC (29.4 μL, 0.19 mmol) and HOBt (28.3 mg, 0.19 mmol) in 10 mL of DCM−DMF (7:3). Then, Boc-TOTA (73.6 mg, 0.23 mmol) and TEA (52.74 μL, 0.38 mmol) dissolved in 10 mL of DCM−DMF (7:3) were added to the preactivated NTA. The reaction was stirred for 48 h under N_2 atmosphere at room and checked by RP-HPLC (conditions A). The solvent mixture was evaporated under vacuum, and the residue was dissolved in DCM; washed with saturated $NaHCO_3$ and brine; dried over $MgSO_4$ and evaporated to dryness under vacuum to obtain **1a** as yellow oil (76.2 mg, 95% yield, 67% purity). The crude mixture **1a** was purified using a flash chromatography system with a RP C_{18} column (condition G in SI) to afford **1a** (83% of recovery yield). **1a**: RP-HPLC (t_R = 23.1 min, purity 97%, condition A in SI); MALDI-TOF (m/z calcd. for $C_{51}H_{99}N_7O_{18}$ 1097.74, found 1098.6 [M+H]+). ^{1}H NMR (400 MHz, D_2O): δ ppm 1.43 (s, 27H), 1.71−1.84 (m, 12H), 3.21 (m, 6H), 3.26 (bs, 6H), 3.36 (dd, J = 6.8, 12.4 Hz, 6H), 3.53 (t, J = 6.02, 6.02 Hz, 12H), 3.56−3.66 (m, 24H), 5.12 (bs, 3H), 7.73 (bs, 3H). ^{13}C NMR (400 MHz, MeOD): δ ppm 28.37, 29.15, 29.60, 37.23, 38.34, 50.49, 59.79, 69.34, 69.37, 70.08, 70.42, 76.68, 77.00, 77.32, 77.32, 156.06, 170.33. Then, compound **1a** was treated with 15 mL of TFA−DCM (1:1) for 30 min. TFA was removed by evaporation to dryness yielding **1** (41.1 mg, 96% yield). **1**: RP-HPLC (t_R = 8.1 min, purity 88%, condition A in SI), MALDI-TOF (m/z calcd. for $C_{36}H_{75}N_7O_{12}$ 797.55, found 798.6 $[M+H]^+$).

Synthesis of 2a. Fmoc-6-aminohexanoic acid (1 equiv) and DIEA (10 equiv) were sequentially added to 2-chlorotrityl chloride resin (300 mg, 1.00 mmol/g) and the resin was stirred for 1 h. The incorporation was followed by a 10 min capping step with MeOH (240 μL). After Fmoc removal, Fmoc-Arg(Pbf)−OH (4 equiv) was incorporated into the resin using 2 × 45 min consecutive coupling treatments with HATU (4 equiv) in DMF as coupling reagent in the presence of DIEA (8 equiv). Next, the Fmoc group was removed and Fmoc-protected N1-(Fmoc)-1,12-diamino-4,9-dioxadodecan-succinamic acid (4 equiv) was coupled overnight using HOAt (4 equiv), PyBOP (4 equiv), and DIEA (12 equiv). Then, the Fmoc group was removed and Fmoc-Arg(Pbf)-OH was incorporated using the conditions explained above. Finally, palmitic acid (5 equiv) was added overnight with HOAt (5 equiv), PyBOP (5 equiv), and DIEA (15 equiv). The compound was then cleaved using TFA−DCM (1:99) (5 × 0.5 min). Solvents were evaporated and the residue was dissolved in H_2O−MeCN (1:1) and lyophilized to afford **2a** (139.1 mg, 32% yield). The crude product was purified by semipreparative RP-HPLC (condition F in SI) to yield **2a** with optimal purity. **2a** RP-HPLC (t_R = 14.9 min, purity 97%, condition D in SI), ES+MS (m/z calcd. for $C_{74}H_{125}N_{11}O_{15}S_2$ 1471.9, found 738 [M+H]+/2).

Synthesis of 2. The synthesis of **2** has been described elsewhere.[20] Fmoc-6-aminohexanoic acid (4 equiv) was coupled to Rink Amide MBHA resin with DIC (4 equiv) and HOAt (4 equiv) in DMF for 6 h. Subsequent steps in solid phase were carried out as explained for the synthesis of **2a**. Finally, the cleavage of the compound from the solid support and deprotection of side-chain groups was carried out with TFA−H_2O−TIS (95:2.5:2.5) for 2 h. TFA was then removed by evaporation with nitrogen and the crude compound was precipitated with cold anhydrous TBME, dissolved in H_2O−MeCN (1:1) and lyophilized. Then, it was purified by semipreparative RP-HPLC (condition E in SI) to yield the desired **2** with excellent purity. **2** RP-HPLC (t_R = 10.4 min, purity 98%, condition C in SI), MALDI-TOF (m/z calcd. for $C_{48}H_{94}N_{12}O_8$ 966.73, found 967.81 $[M+H]^+$).

Synthesis of 3. Fmoc-Arg(Pbf)-OH (1 equiv) in DCM and DIEA (10 equiv) were sequentially added to CTC resin (218 mg, 1.00 mmol/g), and the resin was stirred for 1 h. At the end of the coupling, a treatment with MeOH (175 μL) for 10 min was carried out to cap the free chloride groups of the resin. The Fmoc group was removed and palmitic acid (5 equiv) was added overnight with HOAt (5 equiv), PyBOP (5 equiv), and DIEA (15 equiv) as coupling reagents. Cleavage of the final compound from the resin was afforded by mild acidic treatments with TFA−DCM (1:99; 5 × 0.5 min). The solvents were evaporated, the compound dissolved in H_2O−MeCN (1:1), and lyophilized to obtain **3a** (102.7 mg, 71% yield), which was used without purification. **3a** HPLC (t_R = 16.8 min, purity 95%, condition D in SI). Then, **3a** was treated with TFA−H_2O−TIS (95:2.5:2.5) for 1 h. TFA was evaporated and the residue was dissolved in MeOH, precipitated with cold TBME, dissolved in H_2O−MeCN (1:1), and lyophilized to obtain 4.2 mg of **3** with 86% of yield. **3** RP-HPLC (t_R = 19.5 min, purity 89%, condition B in SI), MALDI-TOF (m/z calcd. for $C_{22}H_{44}N_4O_3$ 412.34, found 413.01 $[M+H]^+$).

Synthesis of Compound (2-TOTA)$_3$NTA (4). Compound **2a** (20.0 mg, 0.0136 mmol) dissolved in 10 mL of DCM−DMF (7:3) was preactivated for 15 min by adding PyBOP (7.1 mg, 0.0136 mmol) and HOBt (2.0 mg, 0.0136). Then, **1** (3.30 mg, 0.0041) and DIEA (4.6 μL, 0.0272 mmol) dissolved in 10 mL of DCM−DMF (7:3) were added. The mixture was stirred under N_2 atmosphere at room temperature for 72 h; the reaction was controlled by RP-HPLC (condition B in SI). The solvent was evaporated under vacuum and the residue dissolved in DCM; washed with saturated $NaHCO_3$, 10% HCl, and brine; dried over $MgSO_4$; and evaporated to dryness. The crude product was dissolved in MeOH and precipitated with cold TBME to obtain **4a** (18.8 mg, 70% yield). **4a**: RP-HPLC (t_R = 26.3 min, purity

80%, condition B in SI); MALDI-TOF (m/z calcd. for $C_{258}H_{444}N_{40}O_{54}S_6$ 5162.91, found 5180.02 $[M+18]^+$). Then, **4a** (18.8 mg) was treated with TFA−H_2O−TIS (95:2.5:2.5) for 3 h and TFA was evaporated. The residue was dissolved in MeOH and precipitated with cold TBME. After centrifugation−decantation, the compound was dissolved in H_2O−MeCN (1:1) and lyophilized to afford **4** as a white solid (6.1 mg, 86% yield). **4**: RP-HPLC (t_R = 17.2 min, purity 83%, condition B in SI); MALDI-TOF (m/z calcd. for $C_{180}H_{348}N_{40}O_{36}$ 3648.94, found 3649.93 $[M+H]^+$).

Synthesis of (3-TOTA)$_3$NTA (5). **3a** (20.0 mg, 0.030 mmol) was preactivated for 15 min with PyBOP (15.7 mg, 0.030 mmol) and HOBt (4.5 mg, 0.030 mmol) in 10 mL of DCM−DMF (7:3). Compound **1** (7.26 mg, 0.0091 mmol) and DIEA (10.2 μL, 0.060 mmol) were dissolved in 10 mL of DCM−DMF (7:3) and after stirring for 10 min were added to the preactivated compound **3a**. The mixture reaction was stirred under N_2 atmosphere at room temperature for 72 h and controlled by RP-HPLC (condition B). Then, the solvent was evaporated under vacuum and the residue was dissolved in DCM; washed with saturated $NaHCO_3$, 10% HCl, and brine; dried over $MgSO_4$; filtered; and evaporated to dryness to obtain **5a**. This compound was dissolved in MeOH and precipitated by the slow addition of cold MeCN (20.2 mg, 81% yield). **5a**: RP-HPLC (t_R = 26.6 min, purity 84%, condition B in SI); MALDI-TOF (m/z calcd. for $C_{141}H_{249}N_{19}O_{27}S_3$ 2738.79, found 2762.01 $[M+Na]^+$). The protected **5a** (20.2 mg, 0.0073 mmol) was treated with TFA, as previously explained for compound **4**. Workup yielded **5** as a white solid (8.6 mg, 88% yield). **5** RP-HPLC (t_R = 14.9 min, purity 92%, condition B in SI); MALDI-TOF (m/z calcd. for $C_{102}H_{201}N_{19}O_{18}$ 1981.8, found 1981.78 $[M+H]^+$).

LPS Neutralizing Activity. All solutions used in the LPS-neutralizing activity assay were tested to ensure they were endotoxin-free, and the material was sterilized by heating for 3 h at 180 °C. LPS-neutralizing activity was measured using the chromogenic *Limulus* Amebocyte Lysate (LAL) test, following the manufacturer's instructions (Cambrex). The LAL reagent contains a clottable protein that is activated in the presence of non-neutralized LPS, being an extremely sensitive indicator of the presence of endotoxin. When activated, this enzyme catalyzes the release of *p*-nitroaniline (pNA) from the colorless chromogenic substrate Ac-Ile-Glu-Ala-Arg-pNA. The released pNA can be measured photometrically at 405 nm. Compounds were initially dissolved in sterile phosphate buffered saline, PBS (137 mM NaCl, 2.7 mM KCl, 4.3 mM Na_2HPO_4, 1.4 mM KH_2PO_4, pH 7.0) at a concentration of 100 μM and preincubated with LPS (100 pg/mL in sterile, endotoxin-free water) in a 96-well microplate for 60 min at 37 °C. Polymyxin B (10 μg/mL in sterile PBS) was used as a positive control. The colorimetric reaction was started by adding 12.5 μL of LAL reagent (reconstituted by adding 1.4 mL of LAL reagent water) for an incubation period of 10 min at 37 °C. After this time, non-neutralized LPS was detected by the addition of 25 μL of the chromogenic substrate (reconstituted with 6.5 mL of LAL reagent water) for 5 to 8 min at 37 °C. Acetic acid (25% v/v final concentration) was added to stop the reaction, and the absorbance was monitored at 405 nm in a Multiskan Ascent microplate plate reader (ThermoLabsystems). At this concentration, compounds that showed an LPS neutralization above 75% were tested to determine their IC_{50} (the concentration required to neutralize 50% of LPS *in vitro*). IC_{50} values were determined by a serial dilution assay using 100 pg/mL of LPS and a range of compound concentrations (50 to 0.001 μM). All assays were run in triplicate, and the curves were automatically adjusted by nonlinear regression using *Prism 4* (GraphPad) software.

Cell Culture. Mouse macrophages (RAW 264.7) were obtained from ATCC (American Type Culture Collection, USA). The cells were grown in Dulbecco's Modified Eagle's Medium (DMEM, Gibco BRI) supplemented with 10% fetal bovine serum (FBS−Gibco BRI) and 1% L-glutamine. The cultures were incubated at 37 °C in a humidified atmosphere of 5% CO_2−95% air. Subcultures of macrophages were prepared every 2−3 days by scraping cells into fresh medium.

MTT Cell Viability Assays. Cell viability was evaluated by a MTT (3-(4,5-dimethyl-2-thiazolyl)-2,5-diphenyl-2*H*-tetrazolium bromide) assay. RAW 264.7 cells were seeded in sterile 96-well microtiter plates at a seeding density of 6×10^4 cells/mL in DMEM supplemented with 10% FBS and allowed to settle for 24 h. Compounds were added at a 10 μM concentration to the plates and the cells were further incubated for 24 h. After removal of the medium, the precipitated formazan crystals were dissolved in optical grade DMSO (100 μL), and the plates were read at 570 nm using a Wallac 1420 Workstation.

RESULTS AND DISCUSSION

Design of Drug Conjugates with LPS-Neutralizing Activity. The trivalent PEGylated platform (compound **1**, Figure 1) was obtained by convergent synthesis from the condensation of a commercially available propylene glycol (TOTA) and a trifunctional core (NTA). This and other types of polycarboxylic acids have been used *in vivo* as chelating agents for metals and their complexes as contrast agents for magnetic resonance imaging (MRI).[29,30] Since their physiological removal was confirmed in studies,[31] they have been considered excellent cores for the design of further biological applications.

As a first step and in order to evaluate whether our trivalent platform would be useful for the conjugation of biologically active compounds, we conjugated **2** to the trivalent structure **1** (Figure 1). In an ongoing research program currently underway in our laboratory, compound **2** has recently been reported to show high LPS-neutralizing activity.[20] This compound displays unique chemical features for optimal LPS binding: two Arg residues conveniently separated by a PEG linker and a fatty acid linked at the *N*-terminus. In fact, the cationic residues interact with the negative phosphate groups of lipid A[32] which is the endotoxic moiety of the LPS,[33,34] while the palmitic acid promotes hydrophobic interactions with the lipophilic part of the endotoxin[35] and confers amphipathicity to the whole molecule, a prerequisite for LPS neutralization.[36] Moreover, the presence of a PEG spacer is of interest in terms of improved water solubility and pharmacokinetic profiles.[14] In addition, the palmitoyl Arg monomer **3** was included in the design to further evaluate the relevance of the topology of positive charges in terms of LPS interaction (Figure 1).

Synthesis of Trivalent PEGylated Platforms. The synthesis of the trivalent platform **1** was achieved after conjugation of conveniently monoprotected TOTA into the NTA core (see Scheme 1 in Supporting Information). From diverse reaction conditions evaluated, the use of DIC in the presence of HOBt and TEA in DMF−DCM (7:3) for 48 h gave the best results. To ensure an optimal yield, an excess of base was required to avoid amine proton capture. The use of Fmoc as the protecting group of TOTA was precluded in this design because of partial Fmoc elimination during the coupling reaction. Hence, Boc-TOTA was

coupled to NTA under the conditions described above to yield the Boc-protected compound **1a** (95% yield, 67% purity). The protected compound was then purified using an automated flash chromatography system with a reverse-phase C_{18} column under acid conditions. It is essential to purify the compound while it is being protected to separate it efficiently from other byproduct. Finally, the Boc group was removed by treatment with TFA 50% in DCM for 30 min to obtain **1**.

Conjugation of Bioactive Compounds to the Trivalent Platform. To achieve proper conjugation, the carboxamide group of compound **2** was replaced by a free carboxylic acid and Arg side chains were kept protected with the Pbf group (see Scheme 2 in Supporting Information). The synthesis of **2** has been reported in detail elsewhere.[20] CTC resin was used as solid support in order to obtain the free carboxylic acid compound **2** required for amide bond conjugation. After the addition of Fmoc-6-aminohexanoic acid (Fmoc-Ahx-OH) using DIEA as a base, Fmoc-Arg(Pbf)-OH was coupled with two consecutive treatments with the reactive aminium salt HATU.[37] Next, N1-(Fmoc)-1, 12-diamino-4,9-dioxadodecan-succinamic acid was coupled overnight using PyBOP instead of HATU to prevent *N*-terminus guanidylation.[38] After the second Arg coupling, palmitic acid was added overnight. The compound was finally cleaved from the solid support with mild acid treatments to yield **2a**. In turn, **3a** was easily obtained on solid phase after incorporation of Fmoc-Arg(Pbf)-OH into CTC, and subsequent Fmoc removal and palmitic acid coupling.

Thus, **2a** and **3a** were conjugated to **1** with the coupling reagent PyBOP in the presence of HOBt and DIEA under anhydrous conditions (Figure 1). The reactions were monitored by HPLC (see Supporting Information). The conjugation HPLC traces of **2a** with **1** showed that the conjugated compound **4a** polarity did not diminish drastically compared with its precursor **2a**, even though **4a** contained three palmitoyl residues and six protected side chain arginines (Arg(Pbf)). The same effect was observed for the conjugate **5a** (data not shown). This behavior illustrates how PEG-containing platforms are useful molecules to solubilize hydrophobic compounds. After completion of the conjugation, a series of workup methods were evaluated, and we found that simple extraction and precipitation procedures were useful to obtain the protected conjugates with optimal purities, thus avoiding tedious and both compound and time-consuming RP-HPLC purifications. Finally, the protected conjugates were treated with TFA to yield the desired conjugates **4** and **5** with purities higher than 80% without any purification steps.

LPS-Neutralizing Activity. The LPS-neutralizing activity of the conjugated constructs **4** and **5** was assayed using the chromogenic *Limulus* amebocyte lysate (LAL) assay.[39] The activity of these compounds was compared against the activity of unconjugated **2** and **3** to study the effect of the conjugation. Finally, trivalent platform **1** was also included to determine whether this structure displayed on its own anti-LPS activity. All compounds were tested at 100 μM, and the assay was performed as described in the Experimental Procedures. The anti-LPS peptide polymyxin B (PMB)[40] was used as a positive control in this assay (Figure 2).

The trivalent structure **1** did not display LPS-binding activity. This result correlates well with other studies that describe how, although necessary, the presence of positive charges is not enough for effective LPS binding and neutralization.[35] Moreover, the inability of this platform to neutralize LPS is relevant, since it ensures that these structures will not interfere with the biological activity of bioactive conjugated molecules and will only act as

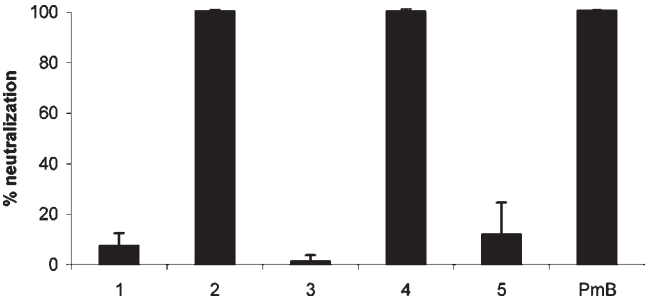

Figure 2. Inhibitory activity of the compounds was determined using the chromogenic LAL assay. PMB was included as a positive control. Compounds were tested at a 100 μM concentration in the presence of 100 pg/mL of LPS. The LPS-binding assay was performed in three independent assays as described in the Experimental Procedures. Data are represented with ± standard deviation (SD).

Table 1. LPS Neutralization Activity (IC_{50}) and Cell Viability of Compounds 2 and 4

compound	IC_{50} (μM)[a]	% of cell viability[b]
2	18 ± 1	109 ± 18
4	9 ± 1	110 ± 14

[a] Inhibition of the compounds was determined using the chromogenic LAL assay. The inhibitory activity is represented as IC_{50}. Standard deviations (SD) are also included. The assay was performed as described in the Experimental Procedures. [b] Cell viability was evaluated using RAW 264.7 cells, after 24 h of incubation in the presence of 10 μM concentration of compounds by MTT assay. The assay is described in the Experimental Procedures.

multivalent scaffolds. At the evaluated concentration, **2** showed high LPS-neutralizing activity, which is consistent with published data.[20] In contrast, monomeric compound **3** was inactive, thereby suggesting that two positively charged residues were required to interact with lipid A, regardless of amphipathicity. Finally, conjugates **4** and **5** showed interesting behaviors. Construct **4** retained the neutralizing activity of inhibitor **2** and totally neutralized LPS at 100 μM. In contrast, compound **5** had poor activity, even though three copies of the acyl-Arg monomer were exposed to LPS. Hence, as previously observed with other LPS-binders, even though these compounds are usually cationic their LPS neutralizing properties lie on the appropriate geometrical distribution of the positive charges on the binder chemical structure rather than on their number.[35,41] To further analyze the effect of conjugation and multivalency, compounds **2** and **4** were subjected to serial dilutions, and their IC_{50} values (i.e., the concentration required to neutralize 50% of LPS *in vitro*) were calculated (Table 1).

The experimental IC_{50} values obtained revealed that the conjugation of **2** to the PEGylated trivalent structure involved a twofold enhancement of its LPS-neutralizing activity. Such improvement correlates with the presence of three equal copies of bioactive compound **2** in construct **4**, suggesting an almost full exposure of **2** in the multivalent construct.

The trivalent structures proposed herein are cationic in nature, and it is known that some amphipathic cationic compounds could present basal toxicity associated to cell membrane activity.[42,43] Thus, we examined the toxicity, if any, of these conjugates in cells. In order to choose an appropriate cell model, we selected RAW 264.7 murine macrophages. These cells are a powerful model to

study LPS-induced cell signaling as well as the efficacy of LPS inhibitors, given that they are critical members of the innate immune system and play a major role in the pathogenesis of sepsis.[21] In fact, the inhibition of inflammatory mediators such as tumor necrosis factor-α (TNF-α) from LPS-challenged macrophages[44] is usually measured to determine the efficacy of LPS-neutralizers.[33,45] However, cationic dendrimers have recently been described to induce apoptosis in this cell model.[46] Thus, in a first attempt to determine whether these multivalent platforms are viable agents for future *in vitro* and *in vivo* studies, the cytotoxicity of compounds **2** and **4** was evaluated using MTT assays. These compounds were tested at a concentration close to their IC_{50} values, or 10 μM. At this concentration, both compounds were nontoxic (Table 1). It has already been reported that these cells can tolerate **2** at 10 μM, although it becomes moderately toxic at higher concentrations.[20] Interestingly, **4** was devoid of any toxic effect even though it contained three copies of **2**. These findings are consistent and support the notion that both PEGylation and the conjugation of molecules to cationic dendrimers is a viable strategy to reduce or even remove their intrinsic toxicity while maintaining the bioactive properties of the drug.[16]

CONCLUSIONS

Here, we have presented the synthesis of a novel trivalent PEGylated structure. This platform was obtained by convergent synthesis from the condensation of a commercially available propylene glycol (TOTA) and NTA as the multifunctional core. The value of this PEGylated platform for the conjugation of bioactive compounds was assayed with compound **2,** a previously described LPS-neutralizer. As a proof of concept, compound **2** was conjugated to the trivalent structure **1** to render construct **4**. The conjugated compound displayed improved LPS-neutralizing activity and a reduced toxicity profile over the parent compound, thus proving the efficacy of this platform as a multivalent ligand scaffold for biological applications.

ASSOCIATED CONTENT

Supporting Information. Detailed chromatographic elution methods used for characterization and purification, peptide solid-phase synthesis method used, scheme of synthesis of trivalent platform **1**, compounds **2a** and **3a**, analytical HPLC traces of the conjugate **4a** synthesis, ^{1}H and ^{13}C NMR of compound **1a**, and HPLC traces and MS spectra of compounds **4** and **5**. This material is available free of charge via the Internet at http://pubs.acs.org.

AUTHOR INFORMATION

Corresponding Author

*F.A. E-mail: albericio@irbbarcelona.org. M.R. Phone: 0034 934037122. Fax: 0034 934037126. E-mail: mroyo@pcb.ub.es

Author Contributions

†These authors contributed equally to the present study.

ACKNOWLEDGMENT

This work was partially supported by the "Fundació La Marató de TV3" (TV3 telethon), the Spanish Ministry of Science and Innovation (MICINN) (CTQ2005-00315, CTQ2008-00177, BIO2007-60666, and CSD2008-00005) and the CICYT (CTQ2006-03794/BQU), the "Generalitat de Catalunya" (2005SGR 00662), the Institute for Research in Biomedicine, and the Barcelona Science Park. A.T. and C.M.M. are IRB and FPU (MEC) fellows, respectively.

ABBREVIATIONS

ACH, cyano-4-hydroxycinnamic acid; Boc-TOTA, 1-(*t*-butyloxycarbonyl-amino)-4,7,10-trioxa-13-tridecanamine; CTC, 2-chlorotrityl chloride resin; D_2O, deuterated water; DCM, dichloromethane; DIC, *N,N′*-diisopropylcarbodiimide; DIPEA, *N,N*-diisopropylethylamine; DMF, *N,N*-dimethylformamide; FA, formic acid; HATU, *O*-(7-azabenzotriazole-1-yl)-1,1,3,3-tetramethyluroniumhexafluorophosphate; HOAt, 1-hydroxy-7-azabenzotriazole; HOBt, 1-hydroxybenzotriazole; MALDI-TOF, matrix-assisted laser-desorption—time-of-flight; MeCN, acetonitrile; MeOH, methanol; NTA, nitrilotriacetic acid; SA, sinapinic acid; PyBOP, benzotriazole-1-yl-oxy-tris(pyrrolidino)phosphonium hexafluorophosphate; TBME, *t*-butylmethyl ether; TEA, triethylamine; TFA, trifluoroacetic acid; TIS, triisopropylsilane

REFERENCES

(1) Lutz, J. F., and Börner, H. G. (2008) Modern trends in polymer bioconjugate design. *Prog. Polym. Sci. 33*, 1–39.

(2) Khandare, J., and Minko, T. (2006) Polymer-drug conjugates: Progress in polymeric prodrugs. *Prog. Polym. Sci. 31*, 359–397.

(3) Crespo, L., Sanclimens, G., Pons, M., Giralt, E., Royo, M., and Albericio, F. (2005) Peptide and amide bond-containing dendrimers. *Chem. Rev. 105*, 1663–1681.

(4) Seiler, M. (2002) Dendritic polymers-interdisciplinary research and emerging applications for unique structural properties. *Chem. Eng. Technol. 25*, 237–253.

(5) Fréchet, J. M. J. (2002) Supramolecular chemistry and self-assembly special feature: dendrimers and supremolecular chemistry. *Proc. Natl. Acad. Sci. U.S.A. 99*, 4782–4787.

(6) Svenson, S., and Tomalia, D. A. (2005) Dendrimers in biomedical applications-reflections on the field. *Adv. Drug Delivery Rev. 57*, 2106–2129.

(7) Boas, U., and Heegaard, M. H. (2004) Dendrimers in drug research. *Chem. Soc. Rev. 33*, 43–63.

(8) Lee, C. C., Mackay, J. A., Fréchet, J. M. J., and Szoka, F. C. (2005) Designing dendrimers for biological applications. *Nat. Biotechnol. 23*, 1517–1526.

(9) Niederhafner, P., Sebestik, J., and Jezek, J. (2005) Peptide dendrimers. *J. Pept. Sci. 11*, 757–788.

(10) Sanclimens, G., Shen, H., Giralt, E., Albericio, F., Saltzman, M. W., and Royo, M. (2005) Synthesis and screening of a small library of proline-based biodendrimers for use as delivery agents. *Biopolymers 80*, 800–814.

(11) Gajbhiye, V., Kumar, P. V., Tekade, R. K., and Jain, N. K. (2007) Pharmaceutical and biomedical potential of PEGylated dendrimers. *Curr. Pharm. Des. 13*, 415–429.

(12) Guillaudeu, S. J., Fox, M. E., Haidar, Y. M., Dy, E. E., Szoka, F. C., and Fréchet, J. M. J. (2008) PEGylated dendrimers with core functionality for biological applications. *Bioconjugate Chem. 19*, 461–469.

(13) Zhao, H., Rubio, B., Sapra, P., Wu, D., Reddy, P., Sai, P., Martinez, A., Gao, Y., Lozanguiez, Y., Longley, C., Greenberger, L. M., and Horak, I. (2008) Novel prodrugs of SN38 using multiarm poly(ethylenglycol) linker. *Bioconjugate Chem. 19*, 849–859.

(14) Greenwald, R. B., and Zhao, H. (2007) Poly (ethylene glycol) prodrugs: altered pharmacokinetics and pharmacodynamics. *Prodrugs: Challenges and Rewards. Part 1* (Stella, V. J., Borchardt, R. T., Hageman, M. J., Oliyai, R., Maag, H., and Tilley, J. W., Eds.) pp 283—338, Chapter 2.3.1, Springer, Boston.

(15) Greenwald, R. B., Choe, Y. H., McGuire, J., and Conover, C. D. (2003) Effective drug delivery by PEGylated conjugates. *Adv. Drug Delivery Rev. 55*, 217–250.

(16) Chen, H. T., Neerman, M. F., Parrish, A. R., and Simanek, E. E. (2004) Cytotoxicity, hemolysis and acute *in vivo* toxicity of dendrimers based on melamine, candidate vehicles for drug delivery. *J. Am. Chem. Soc. 126*, 10044–10048.

(17) Okuda, T., Kawakami, S., Akimoto, N., Niidome, T., Yamashita, F., and Hashida, M. (2006) PEGylated lysine dendrimers for tumor-selective targeting after intravenous injection in tumor-bearing mice. *J. Controlled Release 116*, 330–335.

(18) Okuda, T., Kawakami, S., Maeie, T., Niidome, T., Yamashita, F., and Hashida, M. (2006) Biodistribution characteristics of amino acid dendrimers and their PEGylated derivatives after intravenous administration. *J. Controlled Release 114*, 69–77.

(19) Sanclimens, G., Crespo, L., Giralt, E., Royo, M., and Albericio, F. (2004) Solid-phase synthesis of second-generation polyproline dendrimers. *Biopolymers 76*, 283–297.

(20) Mas-Moruno, C., Cascales, L., Mora, P., Cruz, L. J., Pérez-Payá, E., and Albericio, F. (2009) Design and facile solid-phase synthesis of peptide-based LPS-inhibitors containing PEG-like functionalities. *Biopolymers 92*, 508–517.

(21) Cohen, J. (2002) The immunopathogenesis of sepsis. *Nature 420*, 885–891.

(22) Riedemann, N. C., Guo, R. F., and Ward, P. A. (2003) Novel strategies for the treatment of sepsis. *Nat. Med. 9*, 517–525.

(23) O'Brien, J. M., Naeem, A. A., Aberegg, S. K., and Abraham, E. (2007) Sepsis. *Am. J. Med. 120*, 1012–1022.

(24) Angus, D. C., Linde-Zwirble, W. T., Lidicker, J., Clemont, G., Carcillo, J., and Pinsky, M. R. (2001) Epidemiology of severe sepsis in the United States: Analysis of the incidence, outcome, and associate cost of care. *Crit. Care Med. 29*, 1303–1310.

(25) Wood, S. J., Miller, K. A., and David, S. A. (2004) Anti-endotoxin agents. 2. Pilot high-throughput screening for novel lipopolysaccharide-recognizing motifs in small molecules. *Comb. Chem. High Throughput Screen. 7*, 733–743.

(26) Cromer, J. R., Wood, S. J., Miller, K. A., Nguyen, T., and David, S. A. (2005) Functionalized dendrimers as endotoxin sponges. *Bioorg. Med. Chem. Lett. 15*, 1295–1298.

(27) Tomalia, D. A., Baker, H., Dewald, J., Hall, M., Kallos, G., Martin, S., Roeck, J., Ryder, J., and Smith, P. (1985) A new class of polymers: starburst-dendritic macromolecules. *Polym. J. 17*, 117–132.

(28) Vazquez, J., Qushair, G., and Albericio, F. (2003) Qualitative Colorimetric Tests for Solid Phase Synthesis. *Methods Enzymol. Part B 369*, 21–35.

(29) Knopp, M. V., von Tengg-Kobligk, H., and Choyke, P. L. (2003) Functional magnetic resonance imaging in oncology for diagnosis and therapy monitoring. *Mol. Cancer Ther. 2*, 419–426.

(30) Baba, Y., Yamashita, Y., and Onomichi, M. (2002) Dynamic MR imaging and radiotherapy. *Magn. Reson. Med. Sci. 1*, 32–37.

(31) Krestin, G. P., Schuhmann-Giampieri, G., Haustein, J., Friedman, G., Neufang, K. R. R., Clauß, W., and Stöckl, B. (1992) Functional dynamic MRI, pharmacokinetics and safety of Gd-DTPA in patients with impaired renal function. *Eur. Radiol. 2*, 16–23.

(32) Mora, P., Mas-Moruno, C., Tamborero, S., Cruz, L. J., Pérez-Payá, E., and Albericio, F. (2006) Design of a minimized cyclic tetrapeptide that neutralizes bacterial endotoxins. *J. Pept. Sci. 12*, 491–496.

(33) Seydel, U., Schromm, A. B., Blunck, R., and Brandenburg, K. (2000) Chemical structure, molecular conformation, and bioactivity of endotoxins. *Chem. Immunol. 74*, 5–24.

(34) Brandenburg, K., Seydel, U., Schromm, A. B., Loppnow, H., Koch, M. H., and Rietschel, E. T. (1996) Conformation of lipid A, the endotoxic center of bacterial lipopolysaccharide. *J. Endotoxin Res. 3*, 173–178.

(35) Mas-Moruno, C., Cascales, L., Cruz, L. J., Mora, P., Pérez-Payá, E., and Albericio, F. (2008) Nanostructure formation enhances the activity of LPS-neutralizing peptides. *ChemMedChem 3*, 1748–1755.

(36) David, S. A. (2001) Towards a rational development of anti-endotoxin agents: novel approaches to sequestration of bacterial endotoxins with small molecules. *J. Mol. Recognit. 14*, 370–387.

(37) Carpino, L. A., El-Faham, A., Minor, C. A., and Albericio, F. (1994) Advantageous applications of azabenzotriazole (triazolopyridine)-based coupling reagents to solid-phase peptide synthesis. *J. Chem. Soc., Chem. Commun.* 201–203.

(38) Albericio, F., Bofill, J. M., El-Faham, A., and Kates, S. A. (1998) Use of onium salt-based coupling reagents in peptide synthesis. *J. Org. Chem. 63*, 9678–9683.

(39) *Guideline on validation of the limulus amebocyte lysate test as an end-product endotoxin test for human and animal parental drugs, biological products and medical services* (1987) U.S. Department of health and human services, P.H.S., Food and Drug administration.

(40) Tsubery, H., Ofek, I., Cohen, S., and Fridkin, M. (2000) Structure-function studies of polymyxine B nonapeptide: Implications to sensitization of gram-negative bacteria. *J. Med. Chem. 43*, 3085–3092.

(41) Burns, M. R., Jenkins, S. A., Wood, S. J., Miller, K., and David, S. A. (2006) Structure-activity relationships in lipopolysaccharide neutralizers: design, synthesis, and biological evaluation of a 540-Membered amphipathic bisamide library. *J. Comb. Chem. 8*, 32–43.

(42) Rittner, K., Benavente, A., Bompard, S., Heitz, F., Divita, G., Brasseur, R., and Jacobs, E. (2002) New basic membrane-destabilizing peptides for plasmid-based gene delivery in vitro and in vivo. *Mol. Ther. 5*, 104–114.

(43) Malik, N., Wiwattanapatapee, R., Klopsch, R., Lorenz, K., Frey, H., Weener, J. W., Meijer, E. W., Paulus, W., and Duncan, R. (2000) Dendrimers: relationship between structure and biocompatibility in vitro, and preliminary studies on the biodistribution of ^{125}I-labelled polyamidoamine dendrimers *in vivo*. *J. Controlled Release 65*, 133–148.

(44) Alexander, C., and Rietschel, E. T. (2001) Bacterial lipopolysaccharides and innate immunity. *J. Endotoxin Res. 7*, 167–202.

(45) Cascales, L., Mas-Moruno, C., Tamborero, S., Aceña, J. L., Sanz-Cervera, J. F., Fustero, S., Cruz, L. J., Mora, P., Albericio, F., and Pérez-Payá, E. (2008) Tiratricol neutralizes bacterial endotoxins and reduces lipopolysaccharide-induced TNF-a production in the cell. *Chem. Biol. Drug Des. 72*, 320–328.

(46) Kuo, J. H. S., Jan, M. S., and Chiu, H. W. (2005) Mechanism of cell death induced by cationic dendrimers in RAW 264.7 murine macrophage-like cells. *J. Pharm. Pharmacol. 57*, 489–495.

A trivalent PEGylated platform for the conjugation of bioactive compounds

Ángela Torres,[‡a] Carlos Mas-Moruno,[§a] Enrique Pérez-Payá,[¢,¥] Fernando Albericio*[§,∞] and Miriam Royo*[‡,∞]

[‡] ***Combinatorial Chemistry Unit, Barcelona Science Park, University of Barcelona, Baldiri Reixac 10, 08028 Barcelona, Spain; E-mail: mroyo@pcb.ub.es***

[§] ***Institute for Research in Biomedicine, Barcelona Science Park, Baldiri Reixac 10 , 08028-Barcelona, Spain; E-mail: albericio@irbbarcelona.org***

[¢] ***Department of Medicinal Chemistry, Príncipe Felipe Research Centre, 46013-Valencia, Spain***

[¥] ***IBV-CSIC, 46010-Valencia, Spain***

[∞] ***CIBER-BBN, Networking Centre on Bioengineering Biomaterials and Nanomedicine, 08028-Barcelona, Spain***

[a] These authors contributed equally to the present study

[*] To whom correspondence should be addressed: M. Royo: Phone: 0034 934037122. Fax: 0034 934037126. E-mail: mroyo@pcb.ub.es

Table of Contents

Chromatographic elution methods used for characterization and purification

Analytical RP-HPLC elution conditions:

A: C_4 (3.5 x 250 mm) column, gradient 0 to 65% of B in A in 30min.b
B: C_4 (3.5 x 250 mm) column, gradient 0 to 100% of B in A in 30 min.
C: C_{18} (4.6 x 150 mm) column, gradient 0-100% of B in A in 15 min.
D: C_{18} (4.6 x 150 mm) column, gradient 50 to100% of B in A in 15 min

Semi-preparative HPLC-MS elution conditions:

E: C_{18} (30 x 150 mm) column, gradient 0 to 100% of B in A in 30 min.
F: C_{18} (30 x 150 mm) column, gradient 50-100% of B in A in 30min.

Flash RP-LC elution conditions:

G: C_{18} RediSep of 4g column, gradient 0-100% of B in A in 20 min.

Analytical HPLC-MS eluton conditions

H: C_{18} (3.9 x 150 mm) column, gradient 50-100% of B in A in 15 min.

Peptide solid-phase synthesis method

Solid phase syntesis was carried out manually using the Fmoc strategy in polypropylene syringes fitted with polyethylene porous disks. Solvents and soluble reagents were removed by suction. Washings between deprotection and couplings steps were carried out with DMF and DCM using 10 mL of solvent/g of resin each time. When syntheses were performed on 2-chlorotrityl chloride resin (CTC); DCM was previously treated with basic alumina. The Fmoc group was removed by treatment with piperidine–DMF (1:4, v/v). All synthesis process was performed at 25 ºC. Couplings were monitored using standard colorimetric tests for solid-phase synthesis.[28]

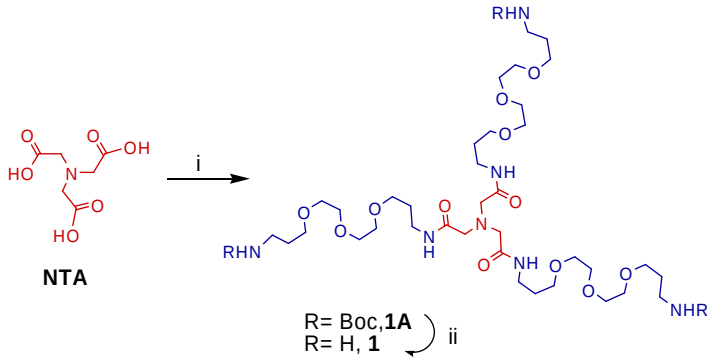

Scheme 1. Scheme 1. Synthesis of trivalent platform **1,** containing the multifunctional core NTA **(**in red), and the PEG chains (in blue) are shown. (i) Boc-TOTA, HOBt, TEA; (ii) TFA-DCM (1:1)

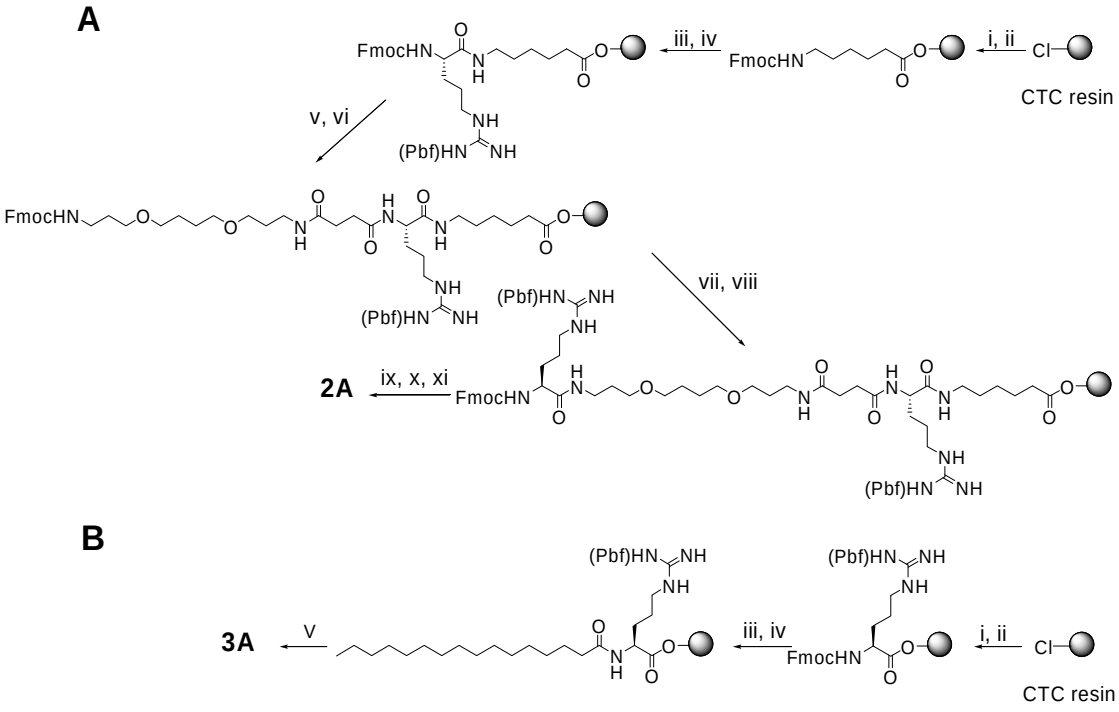

Scheme 2. Solid-phase synthesis of compounds **2a** (A) and **3a** (B). **A**: (i) Fmoc-Ahx-OH, DIEA, DCM; (ii) MeOH; (iii)piperidine, DMF; (iv) Fmoc-Arg(Pbf)-OH, HATU, DIEA, DMF; (v) piperidine, DMF; (vi) PEG-linker, HOAt, PyBOP, DIEA, DMF; (vii) piperidine, DMF; (viii) Fmoc-Arg(Pbf)-OH, HATU, DIEA, DMF; (ix) piperidine, DMF; (x) palmitic acid, HOAt, PyBOP, DIEA, DMF; (xi) TFA-DCM (1:99). **B**: (i) Fmoc-Arg(Pbf)-OH, DIEA, DCM; (ii) MeOH; (iii) piperidine, DMF; (iv) palmitic acid, HOAt, PyBOP, DIEA, DMF; (v) TFA-DCM (1:99).

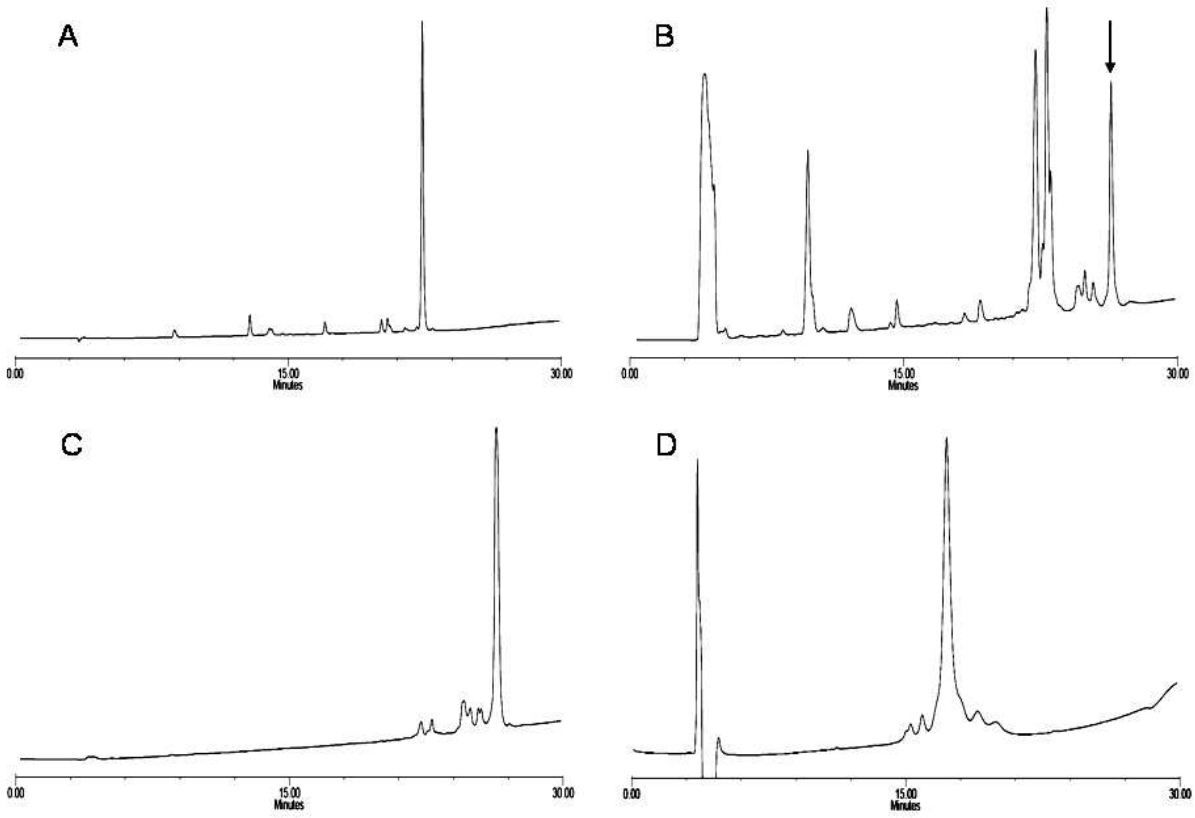

Analytical HPLC traces corresponding to different stages of the conjugate **4a** synthesis. **A**: Compound **2a**. **B**: Crude product of the synthesis at 72 h. The peak corresponding to the starting material is due to the excess equivalents used. Final compound **4a** is indicated by an arrow. **C**: Conjugate **4a** after work-up treatment. **D**: Conjugate **4** (**4a** deprotected).

(Boc-TOTA)$_3$NTA (1a)

RMN 1H

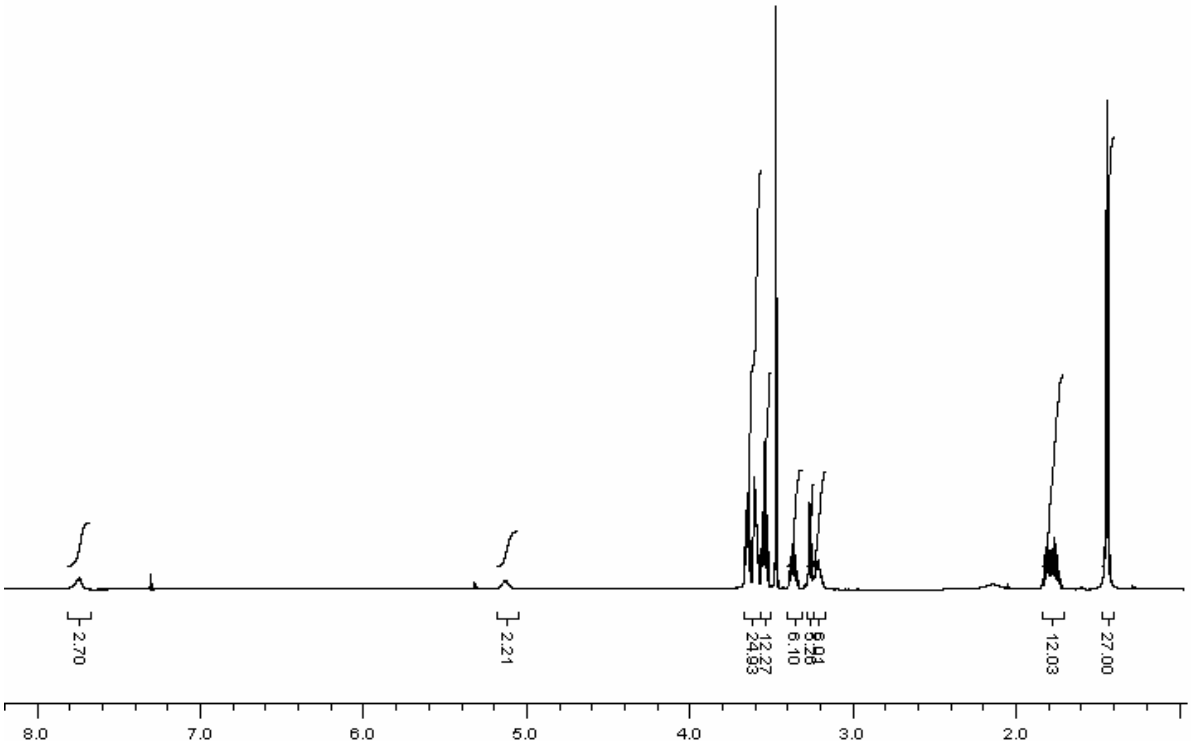

RMN 13C

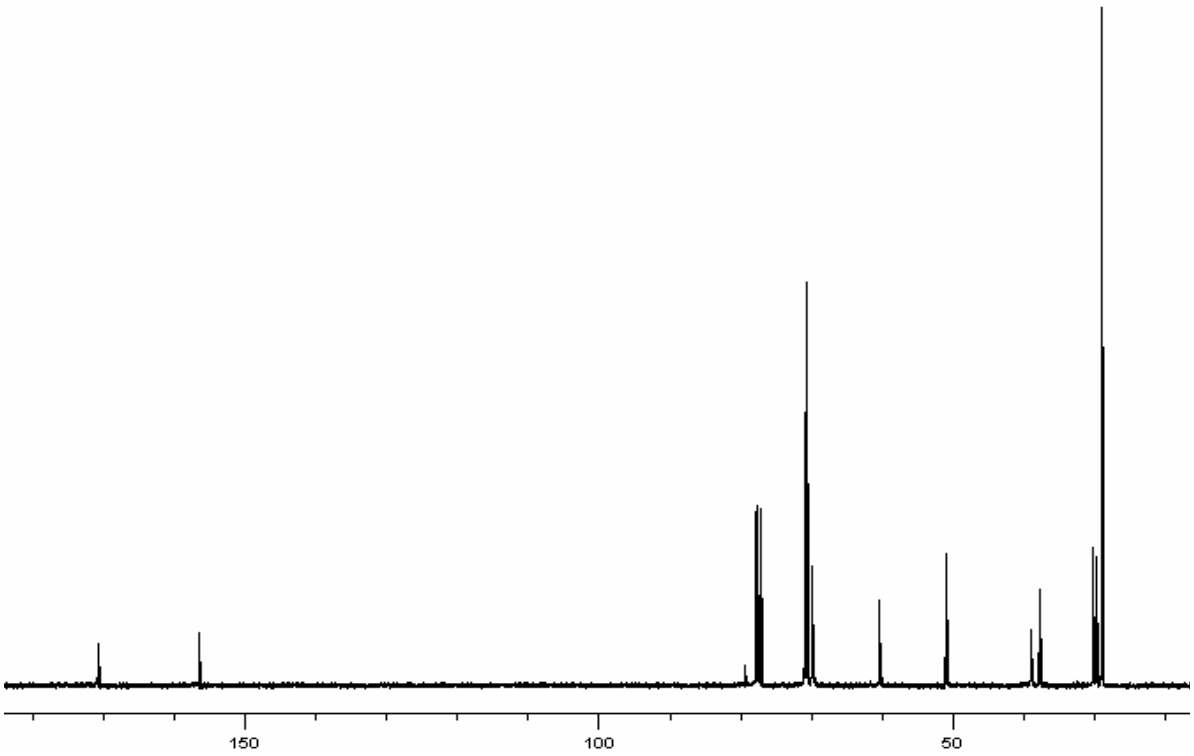

Compound (2-TOTA)$_3$NTA (4)

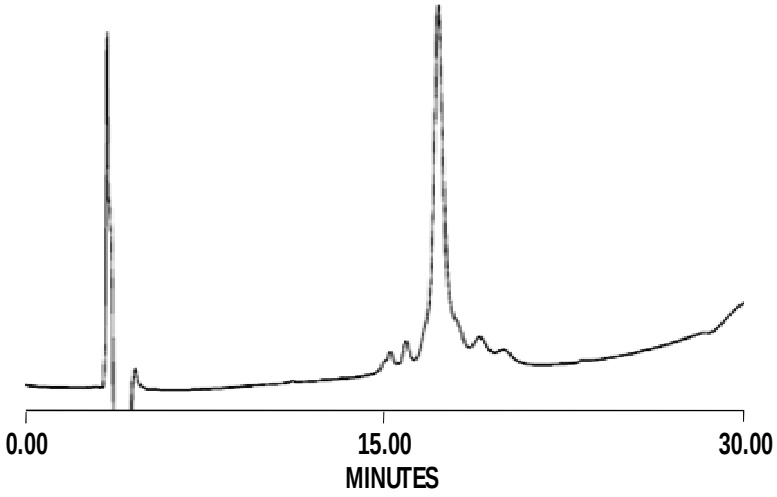

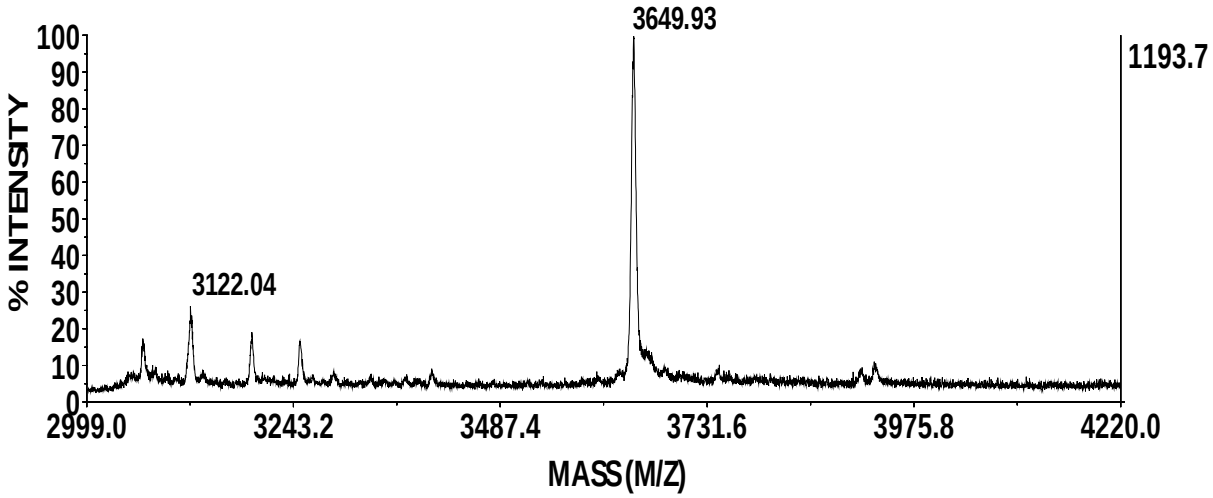

Compound (3-TOTA)$_3$NTA (5)

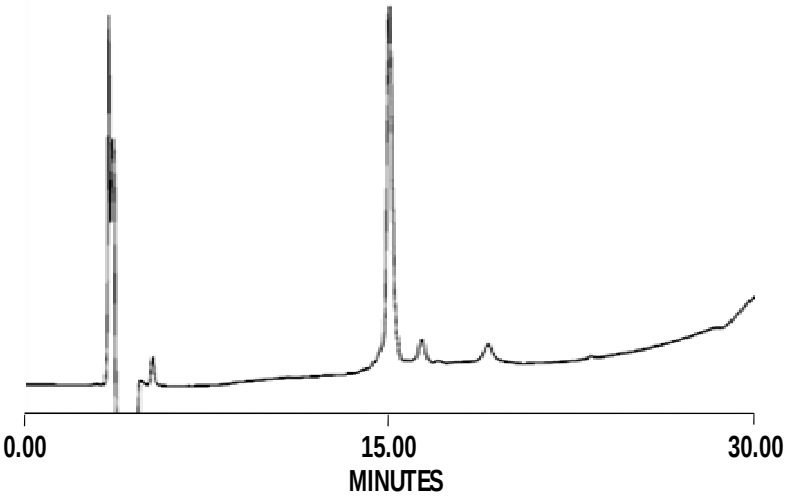

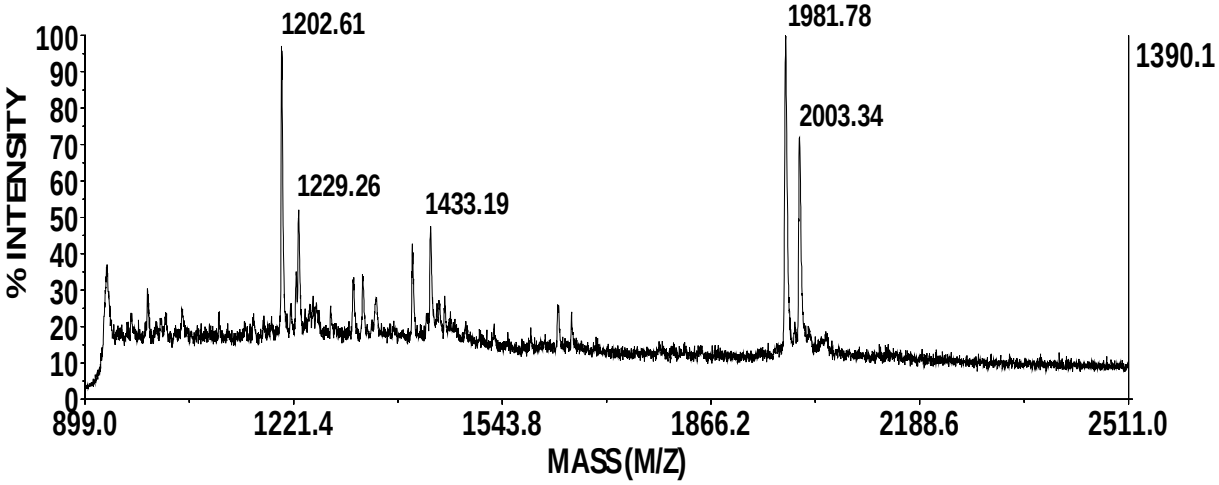

Bioconjugate Chemistry

TECHNICAL NOTE

pubs.acs.org/bc

Simple, Direct Conjugation of Bacterial O-SP—Core Antigens to Proteins: Development of Cholera Conjugate Vaccines

Peng Xu,[†] Mohammad Murshid Alam,[‡,§] Anuj Kalsy,[‡] Richelle C. Charles,[‡] Stephen B. Calderwood,[‡,∥] Firdausi Qadri,[§] Edward T. Ryan,[*,‡,∥,⊥] and Pavol Kováč[*,†]

[†]NIDDK, LBC, National Institutes of Health, 8 Center Drive, Bethesda, Maryland 20892-0815, United States

[‡]Division of Infectious Diseases, Massachusetts General Hospital, 55 Fruit Street, Boston, Massachusetts 02114, United States

[§]International Centre for Diarrhoeal Disease Research, Dhaka, Bangladesh (ICDDR,B), Mohakhali, 1212, Dhaka, Bangladesh

[∥]Harvard Medical School, 25 Shattuck Street, Boston, Massachusetts 02115, United States

[⊥]Department of Immunology and Infectious Diseases, Harvard School of Public Health, 677 Huntington Avenue, Boston, Massachusetts 02115, United States

ABSTRACT: Bacterial O-SP—core antigens can be conjugated to proteins in the same, simple way as synthetic, linker-equipped carbohydrates by applying squaric acid chemistry. Introduction of spacers (linkers) to either O-SP—core antigens or protein carriers, which is involved in commonly applied protocols, is not required. The newly developed method described here consists of preparation of a squaric acid monoester derivative of O-SP—core antigen, utilizing the amino group inherent in the core, and reaction of the monoester with the carrier protein. The intermediate monoester can be easily purified; its conjugation can be monitored by SELDI-TOF mass spectrometry and, thus, readily controlled, since the conjugation can be terminated when the desired carbohydrate—protein ratio is reached. Here, we describe production of conjugates containing the O-SP—core antigen of *Vibrio cholerae* O1, the major cause of cholera, a severe dehydrating diarrheal disease of humans. The resultant products are recognized by convalescent phase sera from patients recovering from cholera in Bangladesh, and anti-O-SP-core-protein responses correlate with plasma antilipopolysaccharide and vibriocidal responses, which are the primary markers of protection from cholera. The results suggest that such conjugates have potential as vaccines for cholera and other bacterial diseases.

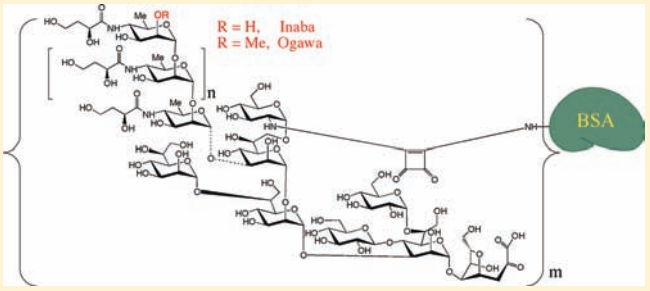

INTRODUCTION

Lipopolysaccharides (LPS) are carbohydrate polymers characteristic of Gram-negative bacteria. They consist of Lipid A, the toxic part through which the LPS is anchored into the bacterial cell wall, the intermediate core oligosaccharide, and the O-specific polysaccharide (O-antigen, O-SP), which extends into the bacterial environment, and is a virulence factor and the major protective antigen of *V. cholerae* and many other bacterial pathogens.[1−3] Because of their toxicity, complete LPS molecules are normally not used as components of vaccines, especially parenteral vaccines, although oral whole-organism killed vaccines contain a large component of LPS. Lipopolysaccharides can be detoxified in many ways, one of which is mild hydrolysis with dilute acetic acid, which separates the O-SP—core antigen from the Lipid A. Many methods for conjugation of carbohydrates, synthetic or bacterial, to proteins are available,[4−6] but most of them rely on significant chemical modification of the carbohydrate antigen to make it amenable to conjugation. Such approaches have the potential disadvantage that many epitopes in the antigen important for eliciting protective immunity may be changed by the treatment. This problem can be overcome by using for conjugation a functional group intrinsic to the polysaccharide, such as a carboxyl group in acidic polysaccharides or the free amino group in glucosamine that is present in the O-SP—core. A number of groups have produced conjugate vaccines targeting the O-SP of *Vibrio cholerae*, a Gram-negative bacterium and the cause of cholera, a severe dehydrating diarrheal illness of humans with epidemic potential.[7] Globally, almost all cholera is caused by organisms of two serotypes (Inaba and Ogawa) of the *V. cholerae* O1 serogroup. Protection against cholera is serogroup specific, and the vibriocidal response and anti-LPS antibodies are currently among the best markers of protection against cholera.[8] The vibriocidal response itself is largely directed against *V. cholerae* LPS.[9,10]

The first to attempt conjugation of an acid-detoxified *V. cholerae* LPS to proteins utilizing the amino group in the core were Gupta and co-workers.[11] They derivatized the O-SP—core antigen of *V. cholerae* O1 (serotype Inaba, Figure 1), as well as the carrier protein, with *N*-succinimidyl 3-(2-pyridyldithio) propionate, and effected single-point attachment between the two molecular

Received: April 19, 2011
Revised: August 31, 2011
Published: September 08, 2011

ACS Publications © 2011 American Chemical Society

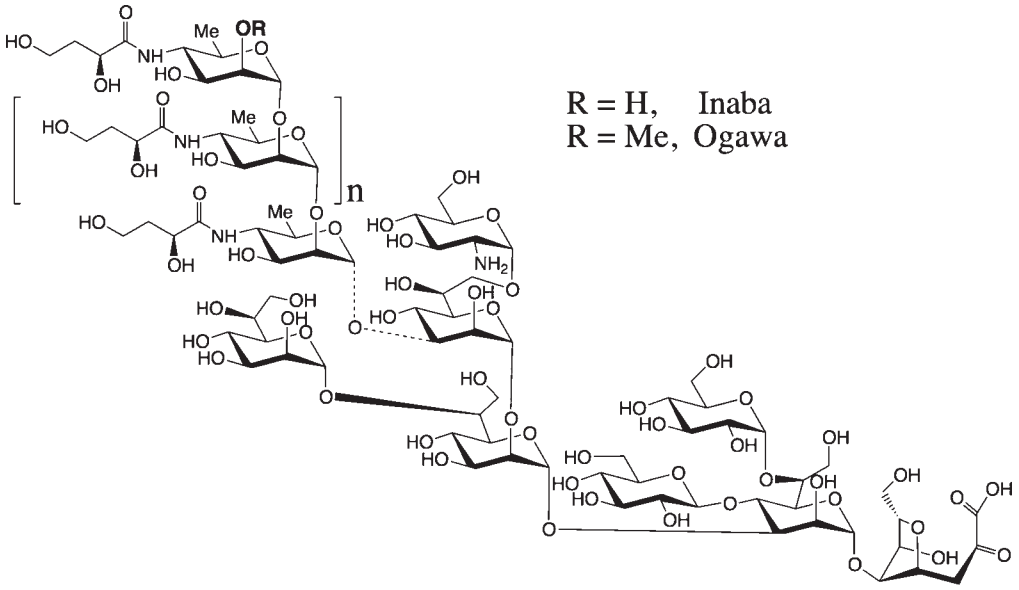

Figure 1. Structure of bacterial O-SP−core antigen of *Vibrio cholerae* O1, serotype Inaba and Ogawa. The dotted bond indicates that the linkage of the O-SP to core has not been established.

species. A similar approach, but using different chemistry, was taken by Mulard and co-workers[12] in their more recent, very carefully executed work. When the latter authors[12] revisited the approach by Gupta,[11] which involved derivatization of both carrier and antigen, they argued that introduction of linker was necessary to overcome the decreased reactivity of the amino group in the glucosamine, due to steric hindrance.

The squaric acid chemistry of conjugation of two amine species discovered by Tietze[13] has been shown to be a useful means for preparation of neoglycoconjugates from synthetic oligosaccharides.[14] The method is quite efficient,[6] but reservations have been expressed concerning its potential utility in conjugate vaccine development.[15] For instance, in limited animal studies, oligosaccharides linked to proteins via squaric acid chemistry induced lower antioligosaccharide antibody responses compared to responses induced by an oligosaccharide−protein conjugate linked via adipic acid chemistry, although both vaccines induced very prominent antioligosaccharide responses.[16] We have previously developed prototype cholera vaccines using short synthetic oligosaccharides involving the terminal sugar of *V. cholerae* O1 O-SP and squaric acid chemistry, and found these constructs to be immunogenic and protective in the standard cholera animal model,[17] calling into question the assumption that conjugation by squaric acid chemistry may not be of utility. We have examined a number of variables that affect the rate of conjugation by the squaric acid method.[18] On the basis of our more recent detailed study,[19] we have revised the original protocol and have now applied it to the full bacterial O-SP−core antigens of *V. cholerae* O1 Ogawa and Inaba, not just small oligosaccharide fragments, and a model protein BSA directly, without prior introduction of a linker to either O-SP−core antigen or protein carrier. Here, we report that such conjugation is not only possible, but equally simple as with synthetic, linker-equipped oligosaccharides and, as with synthetic oligosaccharides,[14] can be done with a very small amount of material. The method in the present form[19] is simple to perform, gives reproducible results, allows preparation of carbohydrate−protein constructs in a predictable way, and appears to be superior to protocols developed earlier.

EXPERIMENTAL PROCEDURES

General. V Vials equipped with Spin Vanes (Wheaton Science) were used as reaction vessels. Conjugation of carbohydrates was monitored by the BioRad Protein Chip SELDI system using NP-20 chip arrays. 3,5-Dimethoxy-4-hydroxycinnamic acid (sinapinic acid) was used as matrix. ^{13}C NMR spectra (150 MHz) of O-SP−core antigens were taken at ambient temperature for solutions in D_2O with a Bruker Avance 600 spectrometer equipped with a cryoprobe. Assignments of NMR signals could be confidently made by comparison with spectra of synthetic[20] α-glycosides of hexasaccharide fragments of the respective O-SPs, since spectra of the O-SP−core and the hexasaccharides showed close similarity of chemical shifts of equivalent carbon atoms of the internal residues and of the terminal upstream[21] residues. Bovine serum albumin (BSA) was purchased from Sigma (cat. no. A-4503), and used as supplied. Squaric acid dimethyl ester was purchased from Aldrich Chemical Co. and recrystallized from MeOH.

Isolation of the Lipopolysaccharides of *Vibrio cholerae* O1, Serotypes Inaba and Ogawa, and Preparation of the O-SP−core Antigens. LPS was obtained from *V. cholerae* O1, Ogawa (strain X-25049) or Inaba (strain 19479), by hot phenol/water extraction[22] followed by enzymatic treatment (DNase, RNase and protease), and ultracentrifugation (100 000 × *g* for 3 h). The pellet containing LPS was dialyzed against distilled water and freeze−dried. The LPS (10 mg/mL in 1% (v/v) aqueous acetic acid) was heated at 105 °C for 3 h.[23] Each hydrolysate was separated into chloroform-soluble and water-soluble fractions by thorough mixing with an equal volume of chloroform, followed by low-speed centrifugation. The water-soluble fraction containing the degraded polysaccharide moiety was separated, washed three or more times with chloroform, and then freeze−dried. The degraded polysaccharide was further fractionated by size exclusion chromatography (Sephacryl S-200) using water as eluant, giving two major peaks. The first peak corresponding to the O-SP−core[23,24] was isolated and freeze−dried. The crude O-SP−core products were further purified by ultrafiltration using centrifugal filter devices (3K Amicon Ultra, Millipore)

and dialyzed against 10 mM aqueous ammonium carbonate (centrifugation at 4 °C, 14 000 × *g*, 8 times, ~35 min each time) to remove the low molecular mass material. The retentate was lyophilized to afford the O-SP—core antigens as white solids.

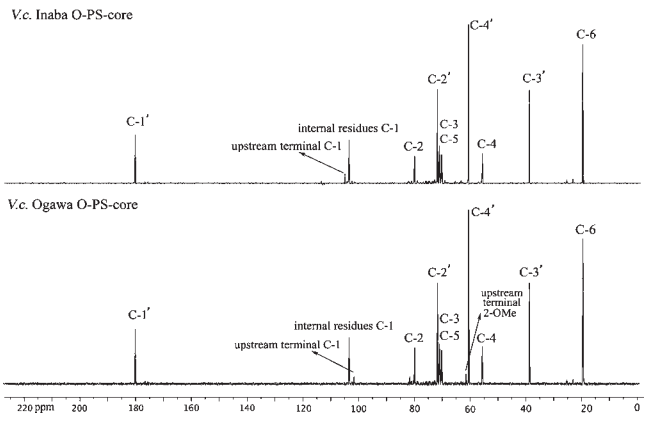

Figure 2. ^{13}C NMR spectra of the crude O-SP—core antigens of *V. cholerae*, serotype Inaba and Ogawa in D_2O.

The ^{13}C NMR spectra are in Figure 2. The SELDI-TOF mass spectral analysis indicated that the average molecular mass of the Inaba and Ogawa O-SP—core antigens were ~5100 and 5900 Da, respectively.

Preparation of Squarate Derivatives of the O-SP—core Antigens. 3,4-Dimethoxy-3-cyclobutene-1,2-dione (~0.5 mg) was added to a solution of O-SP—core antigen (0.80 mg and 0.92 mg for Inaba and Ogawa, respectively) in pH 7 phosphate buffer (0.05 M, 50 μL) contained in a 1 mL V-shaped reaction vessel, and the mixture was gently stirred at room temperature for 48 h. The resulting solution was transferred into an Amicon Ultra (0.5 mL, 3K cutoff) centrifuge tube and dialyzed against pure water (centrifugation at 4 °C, 14 000 × *g*, 8 times, ~35 min each time). The retentate was lyophilized to afford the O-SP—core squarate monomethyl ester as white solid [0.75 mg (94%) and 0.86 mg (93%)] for Inaba and Ogawa, respectively.

Conjugation of the O-SP—core Antigens to BSA. *Conjugation of the Inaba O-SP—core Antigen.* BSA (0.9 mg) and the methyl squarate derivative of the Inaba O-SP—core antigen described above (0.75 mg) were weighed into a 1 mL V-shaped reaction vessel and 60 μL of 0.5 M pH 9 borate buffer was added (to form ~2.5 mM solution with respect to the antigen; antigen/carrier = 10.8:1). A clear

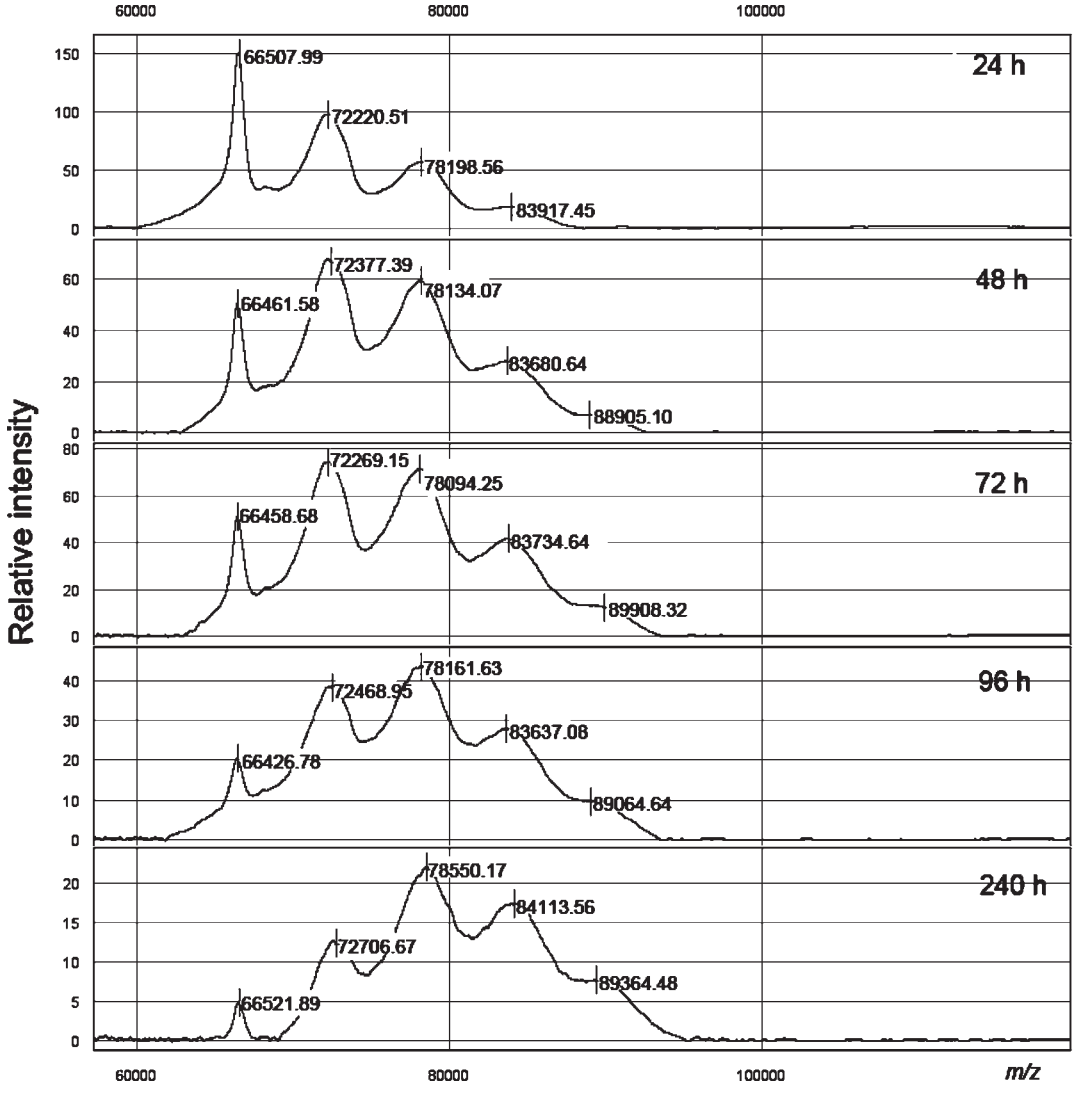

Figure 3. Monitoring of the conjugation of Inaba O-SP—core antigens to BSA.

dx.doi.org/10.1021/bc2001984 |*Bioconjugate Chem.* 2011, 22, 2179–2185

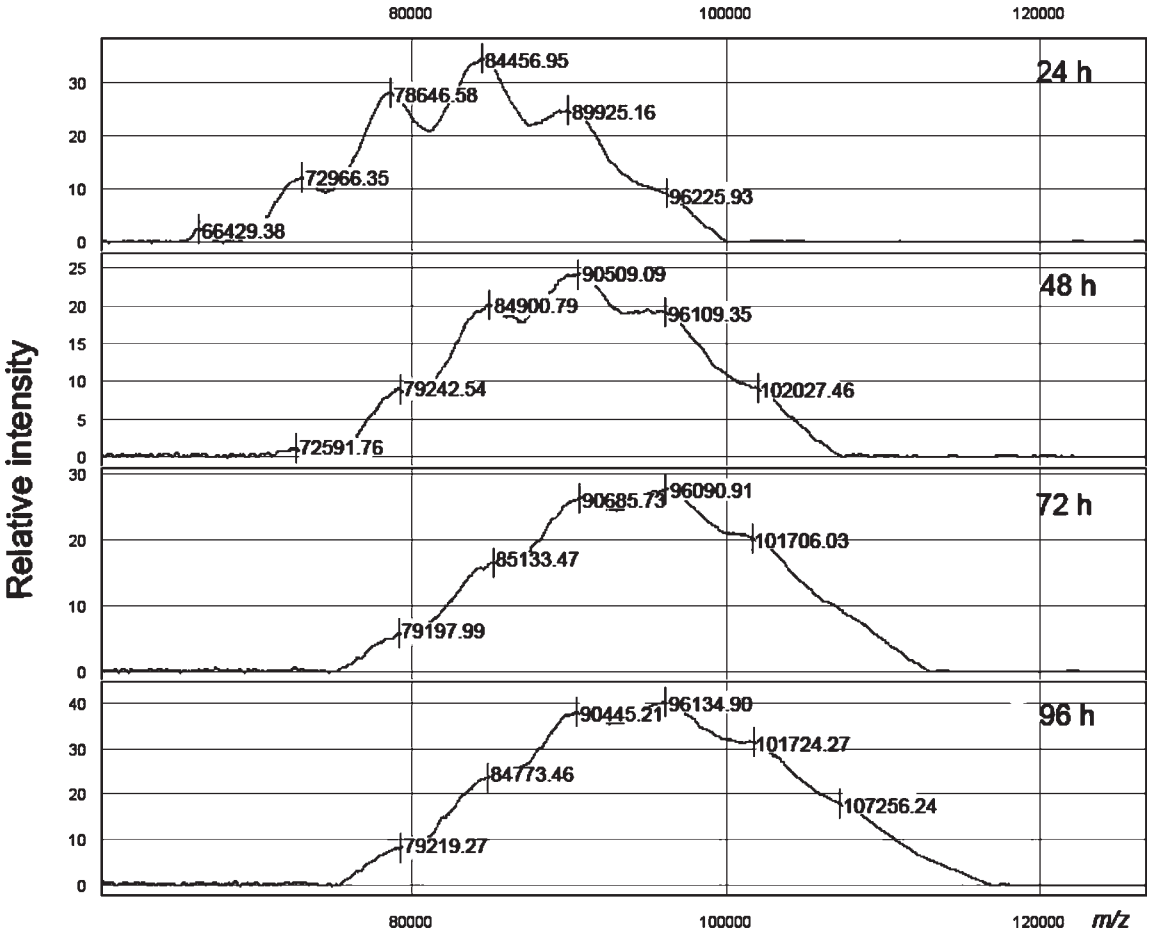

Figure 4. Monitoring of the conjugation of Ogawa O-SP−core antigens to BSA.

solution was formed. The mixture was stirred at room temperature and the reaction was monitored by SELDI-TOF MS at 24, 48, 72, 96, and 240 h (Figure 3), when the reaction was terminated by addition of 300 μL of pH 7 phosphate buffer. The solution was transferred into an Amicon Ultra (0.5 mL, 30 K cutoff) centrifuge tube and dialyzed (centrifugation at 4 °C, 10 000 × *g*, 8 times, 12 min) against 10 mM aqueous ammonium carbonate. After lyophilization, 0.80 mg (73%, based on BSA) of conjugate was obtained as a white solid. On the basis of the average MW of the hapten, the ratio hapten/BSA was 2.8:1 (conjugation efficiency, 26%).

Conjugation of the Ogawa O-SP−core Antigen. The protocol described above was followed with 0.86 mg of the methyl squarate derivative of the Ogawa antigen described above, 0.45 mg of BSA (antigen/carrier = 21.5: 1) and 30 μL of pH 9 borate buffer (~4.9 mM solution with respect to hapten). Monitoring of the progress of the conjugation is shown in Figure 4. After freeze−drying, 0.54 mg (84%, based on BSA) of conjugate was obtained as a white solid. On the basis of the average MW of the hapten, the ratio hapten/BSA was 4.8:1 (conjugation efficiency, 23%).

Evaluation of Immunoreactivity of Conjugates. *Assessing Lipopolysaccharide (LPS), O-SP−core-BSA, and BSA-Specific Antibody Responses in Plasma of Patients with Cholera, as Well as Vibriocidal Responses.* Acute and convalescent phase blood was obtained through fully Institutional Review Board-approved protocols from twenty individuals with *V. cholerae* O1 stool-culture-confirmed cholera (Ogawa = 10; Inaba = 10) admitted to the hospital of the International Centre for Diarrheal Diseases Research, in Dhaka Bangladesh (ICDDR, B). For this study, we used blood samples obtained on days 2 and 7 after onset of illness for antigen-specific and vibriocidal assays. We measured the vibriocidal antibody titer and antigen-specific IgG antibody responses using the homologous serotype of *V. cholerae* O1 LPS, or O-SP−core-BSA, Ogawa or Inaba.

We quantified anti-LPS, O-SP−core-BSA, and BSA IgG responses in plasma using standard enzyme-linked immunosorbent assay (ELISA) protocols.[25,26] To assess anti-LPS IgG responses, we coated ELISA plates with the homologous serotype of *V. cholerae* O1 LPS (2.5 μg/mL)[27] in PBS. To assess anti-O-SP−core-BSA or anti-BSA IgG responses, we coated ELISA plates with O-SP−core/BSA (1 μg/mL) or BSA (5 μg/mL) in carbonate buffer pH 9.6, respectively. To each well, we added 100 μL/well of plasma (diluted 1:50 in 0.1% BSA in phosphate-buffered saline−Tween) and detected the presence of antigen-specific antibodies using horseradish peroxidase-conjugated anti-human IgG antibody. After 1.5 h incubation at 37 °C, we developed the plates with a 0.55 mg/mL solution of 2,2′-azino-bis(3-ethylbenzthiazoline-6-sulfonic acid (ABTS; Sigma) with 0.03% H_2O_2 (Sigma), and determined the optical density at 405 nm with a Vmax microplate kinetic reader (Molecular Devices Corp. Sunnyvale, CA). Plates were read for 5 min at 14 s intervals, and the maximum slope for an optical density change of 0.2 U was reported as millioptical density units per minute (mOD/min). We normalized ELISA units by calculating the ratio of the optical density of the test sample to that of a standard of pooled convalescent-phase plasma from patients

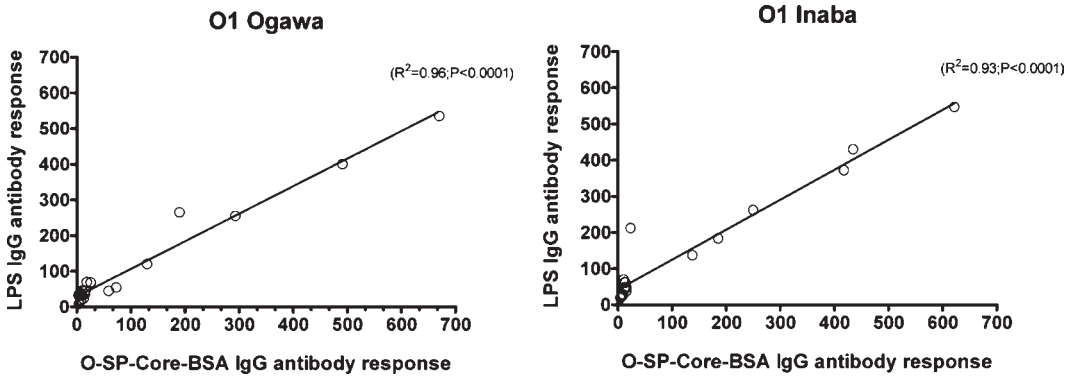

Figure 5. Correlation between anti-*V. cholerae* O1 LPS IgG antibody responses and corresponding O-SP−core-BSA IgG antibody responses. Lines designate the linear correlations between the responses. Antibody responses were assessed for 10 patients with Ogawa (left panel) and 10 with Inaba (right panel) during the acute and convalescent phases of infection.

recovered from cholera. We assessed vibriocidal responses as previously described, using guinea pig complement and the homologous serotype of *V. cholerae* O1 Ogawa (X-25049) or Inaba (19479) as the target organism.[25] The vibriocidal titer was defined as the reciprocal of the highest serum dilution resulting in >50% reduction of the optical density associated with *V. cholerae* growth compared to that of the positive control wells without plasma.[26] We compared the magnitude of acute to convalescent phase responses, and tested for significance using Wilcoxon Signed Rank test, and used linear regression for correlation analysis between vibriocidal antibody and antigen-specific antibody responses. All reported P values were two-tailed, with a cutoff of $P < 0.05$ considered a threshold for statistical significance.

■ RESULTS AND DISCUSSION

Conjugations were performed with O-SP−core antigens of *Vibrio cholerae* O1, serotypes Inaba and Ogawa, and the increasing molecular mass of the conjugate was monitored as described.[28] The structures of O-SPs of the two strains are very similar; they consist of a chain of (1→2)-α-linked moieties of 4-amino-4,6-dideoxy-α-D-mannopyranose (perosamine), the amino groups of which are acylated with 3-deoxy-L-*glycero*-tetronic acid. The O-SPs of the two strains differ in that the terminal, upstream perosamine moiety in the Ogawa strain carries a methoxy group at C-2 (Figure 1). The ^{13}C NMR spectra (Figure 2) of the antigens, where the signals of the O-SPs largely predominate, show all structurally significant peaks present in the spectra of the related, synthetic hexasaccharides.[20]

To ascertain whether simple, direct conjugation of O-PS−core antigens is feasible, the antigens were treated with an excess of squaric acid dimethyl ester at pH 7 for 2 days, when the product was isolated by dialysis followed by freeze−drying. The material thus obtained showed only moderate UV absorption at the wavelength characteristic of squaric acid, but successful formation of the corresponding monomethyl ester manifested itself when the material was treated with BSA at pH 9 resulting in smooth conjugate formation (Figures 3 and 4).

Knowing that the reaction rate of conjugation decreases with the size of oligosaccharides, and considering the actual reaction rates for a disaccharide, tetrasaccharide, and hexasaccharide,[19] the conjugation was carried out at initial Inaba O-SP−core/BSA ratio 1:1.2 (w/w), which corresponded to an approximate molar Inaba O-SP−core/BSA ratio of 10.8/1. The conjugation was performed at an O-SP−core concentration of ∼2.5 mM. When the conjugation process was terminated after 10 d, SELDI analysis of the purified conjugate after freeze−drying showed that the average molecular mass of the conjugate obtained was 81 000 Da (molar ratio O-SP−core/BSA = ∼2.8). The conjugate still contained some (∼5%) of the unchanged BSA (shown also in Figure 3, 240 h).

To ensure that no BSA used at the onset of the conjugation would be left unconjugated, the reaction of the Ogawa O-SP−core antigen was set up at a higher initial O-SP−core/BSA ratio [∼2:1 (w/w), which corresponded to an approximate initial molar Ogawa O-SP−core/BSA ratio of 21.5:1]. As shown in Figure 4, only a negligible amount of unchanged BSA was present in the conjugation mixture after 24 h of the reaction time. After 96 h, when the conjugation was terminated, the conjugate was isolated, and MS analysis by SELDI showed the average molecular mass of the conjugate obtained to be ∼95 000 Da (molar ratio O-SP−core/BSA = ∼4.8).

To assess the immunoreactivity of the conjugates and their potential use as cholera vaccines, we measured anti-O-SP−core-BSA antibody levels in the blood of patients with cholera in Bangladesh, and compared these responses to anti-LPS and vibriocidal responses, the latter two being among the primary predictors of protection against cholera.[8,29−31] There was excellent correlation of the immunoreactivity of the O-SP−core-BSA conjugates and the homologous anti-LPS responses in convalescent phase blood of humans recovering from cholera in Bangladesh (Ogawa, $R^2 = 0.96$, $P < 0.001$; Inaba, $R^2 = 0.93$, $P < 0.001$; Figure 5). There was also significant and antigen-specific increases in anti-O-SP−core-BSA responses in convalescent compared to acute phase blood for both the Ogawa and Inaba constructs ($P < 0.05$; Figure 6). Responses correlated with the vibriocidal response for Ogawa, and less well for Inaba (Ogawa, $R^2 = 0.74$, $P < 0.001$; Inaba, $R^2 = 0.2$, $P < 0.04$; Figure 7); importantly these correlation curves mirrored those of the LPS IgG to vibriocidal relationship.

As pointed out above, previous researchers have proposed that conjugate vaccines using squaric acid chemistry may not permit the development of maximal immune responses targeting sugar moieties. Here, we show that O-SP−core-protein conjugates produced by this simplified protocol are recognized by convalescent phase sera from patients recovering from cholera in Bangladesh, and anti-O-SP-core-protein responses correlate with plasma anti-LPS and vibriocidal responses. These results suggest that such conjugates might have utility as vaccines, although this can only be addressed by direct immunization studies and immunologic analysis. Currently available cholera vaccines use

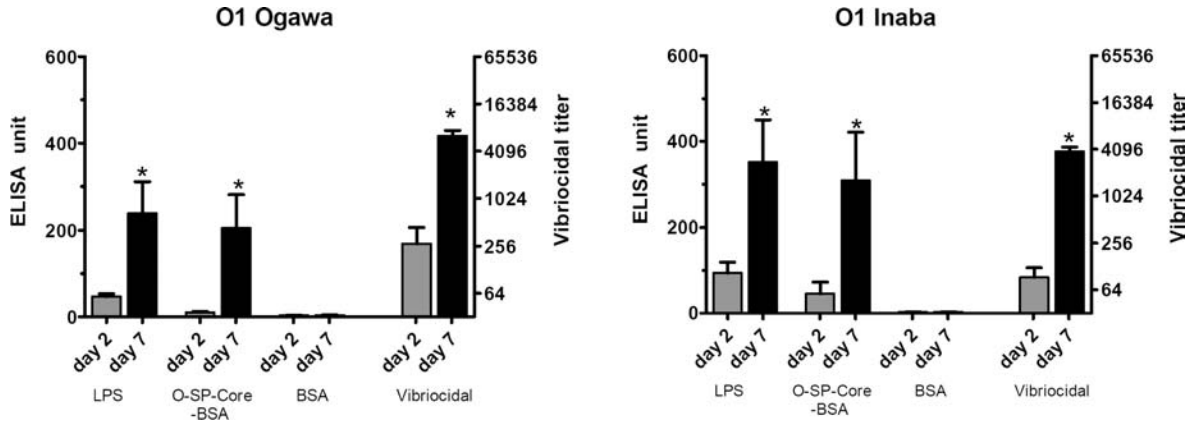

Figure 6. Mean normalized antigen-specific IgG and vibriocidal antibody responses in plasma (with standard errors of the means [SEM]). Plasma IgG and vibriocidal responses are shown on the left and right (log 2) axes, respectively. An asterisk denotes a statistically significant difference ($P < 0.05$) from the baseline (day 2) titer.

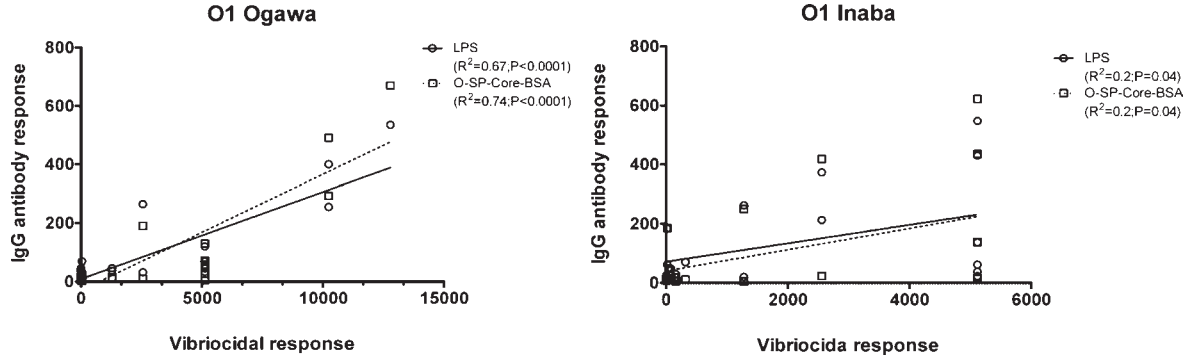

Figure 7. Correlation between vibriocidal antibody responses and the corresponding LPS or O-SP−core-BSA IgG antibody responses. Lines designate the linear correlations between the responses. Ogawa and Inaba refer to serotype of *V. cholerae* used in vibriocidal assay.

the oral route of immunization with killed whole cell preparations, require repetitive dosing, and provide protection that lasts for 6 to 36 months.[32] Infection with natural cholera results in protection that lasts for years or decades.[33−35] Development of inexpensive and simple-to-produce cholera vaccines that provide durable protective immunity would be significant. Whether a conjugate vaccine administered parenterally, transcutaneously, singly, or as a booster would fulfill these parameters is currently unclear and will be the objective of our future investigations.

CONCLUSIONS

We have shown that, when a sufficiently powerful method of conjugation is applied, coupling of bacterial O-SP−core antigens to proteins is a simple, high yielding process, and derivatization aimed at introducing linkers to either O-SP−core antigens or carrier proteins prior to conjugation is not necessary. This could eliminate lengthy and often costly operations involved in industrial conjugate production. Squaric acid chemistry of conjugation of amine-containing substances[13,19] is a useful tool for conjugation of carbohydrate antigens, synthetic or bacterial, to amine containing carriers. As can be expected from reaction rates determined for various oligosaccharides by this method,[19] high molecular mass substances, such as the fragments of LPS used in this work, conjugate at a proportionally diminished, but acceptable, rate and efficiency. Conjugation of O-SP−core antigens to protein carriers by this method utilizes the free amino group that is inherent in the LPS core and, thus, yields neoglycoconjugates with single-point attachment of ligands to carriers. From this point of view, the method is analogous to those involving chemical attachment of spacers to the synthons involved prior to conjugation.[11,12] Compared to the latter approaches, the conjugation described herein is much simpler and less laborious, and affords conjugates in higher yields with comparable overall conjugation efficiency. It produces conjugates that are fully and specifically recognized by immune responses in humans recovering from infection. Such features are particularly attractive for development of conjugate vaccines such as cholera, targeting infections of the world's most impoverished.

AUTHOR INFORMATION

Corresponding Author

*Tel 301-496-3569, Fax 301-480-5703, E-mail kpn@helix.nih.gov (P.K.); Tel 617-726-6175, Fax 617 726 7416, E-mail etryan@partners.org (E.T.R.).

ACKNOWLEDGMENT

This research was supported by the Intramural Research Program of the NIH, NIDDK, as well the International Centre for Diarrhoeal Disease Research, Dhaka, Bangladesh (ICDDR, B),

and NIAID AI077883 (ETR), AI058935 (SBC, FQ), AI089721 (RCC), and the Fogarty International Center (FIC) TW05572 (MMA, FQ).

REFERENCES

(1) Manning, P. A., Stroeher, U. H., and Morona, R. (1994) Molecular basis for O-antigen biosynthesis in *Vibrio cholerae* O:1 Ogawa-Inaba switching, in *Vibrio cholerae and Cholera: Molecular to Global Perspectives* (Wachsmuth, I. K., Blake, P. A., Olsvik, O., Eds.) pp 77−94, Chapter 6, American Society for Microbiology, Washington, DC.

(2) Passwell, J. H., Harlev, E., Ashkenazi, S., Chu, C., Miron, D., Ramon, R., Farzan, N., Shiloach, J., Bryla, D. A., Majadly, F., Roberson, R., Robbins, J. B., and Schneerson, R. (2001) Safety and immunogenicity of improved Shigella O-specific polysaccharide-protein conjugate vaccines in adults in Israel. *Infect. Immunol. 69*, 1351–1357.

(3) Robbins, J. B., Schneerson, R., Szu, S. C., and Pozsgay, V. (1999) Bacterial polysaccharide-protein conjugate vaccines. *Pure Appl. Chem. 71*, 745–754.

(4) Hermanson, G. T. (1996) *Bioconjugate Techniques*, Academic Press, New York.

(5) Dick, W. E., Jr., and Beurret, M. (1989) Glycoconjugates of bacterial carbohydrate antigens, in *Conjugate Vaccines* (Cruse, J. M., and Lewis, R. E., Jr., Eds.) pp 48−114, Krager, Basel.

(6) Bundle, D. R. (2011) New Frontiers in the Chemistry of Glycoconjugate Vaccines, in *Vaccine Design: Innovative Approaches and Novel Strategies* (Bagnoli, R. R. a. F., Ed.) Caister Academic Press.

(7) Ryan, E. T. (2011) The cholera pandemic, still with us after half a century: time to rethink. *PLoS Negl. Trop. Dis. 5*, e1003.

(8) Ramamurthy, T., Garg, S., Sharma, R., Bhattacharya, S. K., Nair, G. B., Shimada, T., Takeda, T., Kurazano, H., and Pal, A. (1993) Emergence of novel strain of *Vibrio cholerae* with epidemic potential in southern and eastern India. *Lancet 341*, 703–704.

(9) Majumdar, A. S., Dutta, P., Dutta, D., and Ghose, A. C. (1981) Antibacterial and antitoxin responses in the serum and milk of cholera patients. *Infect. Immun. 32*, 1–8.

(10) Svennerholm, A. M. (1975) Experimental studies on cholera immunization. 4. The antibody response to formalinized *Vibrio cholerae* and purified endotoxin with special reference to protective capacity. *Int. Arch. Allergy Appl. Immunol. 49*, 434–452.

(11) Gupta, R. K., Szu, S. C., Finkelstein, R. A., and Robbins, J. B. (1992) Synthesis, Characterization and some immunochemical properties of conjugates composed of the detoxified lipopolysaccharide of *Vibrio cholerae* O1 serotype Inaba bound to cholera toxin. *Infect. Immun. 60*, 3201–3208.

(12) Grandjean, C., Boutonnier, A., Dassy, B., Fournier, J.-M., and Mulard, L. A. (2009) Investigation towards bivalent chemically defined glycoconjugateimmunogens prepared from acid-detoxified lipopolysaccharide of *Vibrio cholerae* O1, serotype Inaba. *Glycoconjugate J. 26*, 41–55.

(13) Tietze, L. F., Schröter, C., Gabius, S., Brinck, U., Goerlach-Graw, A., and Gabius, H.-J. (1991) Conjugation of p-aminophenyl glycosides with squaric acid diester to a carrier protein and the use of neoglycoprotein in the histochemical detection of lectins. *Bioconjugate Chem. 2*, 148–153.

(14) Kamath, V. P., Diedrich, P., and Hindsgaul, O. (1996) Use of diethyl squarate for the coupling of oligosaccharide amines to carrier proteins and characterization of the resulting neoglycoproteins by MALDI-TOF mass spectrometry. *Glycoconjugate J. 13*, 315–319.

(15) Wu, X., Ling, C.-C., and Bundle, D. R. (2004) A new homobifunctional p-nitro phenyl ester coupling reagent for the preparation of neoglycoproteins. *Org. Lett. 6*, 4407–4410.

(16) Mawas, F., Niggemann, J., Jones, C., Corbel, M. J., Kamerling, J. P., and Vliegenthart, J. F. G. (2002) Immunogenicity in a mouse model of a conjugate vaccine made with a synthetic single repeating unit of type 14 pneumococcal polysaccharide coupled to CRM197. *Infect. Immun.* 5107–5114.

(17) Chernyak, A., Kondo, S., Wade, T. K., Meeks, M. D., Alzari, P. M., Fournier, J.-M., Taylor, R. K., Kováč, P., and Wade, W. F. (2002) Induction of protective immunity by synthetic *Vibrio cholerae* Hexasaccharide derived from *Vibrio cholerae* O:1 Ogawa lipopolysaccharide bound to a protein carrier. *J. Infect. Dis. 185*, 950–962.

(18) Zhang, J., Yergey, A., Kowalak, J., and Kováč, P. (1998) Studies towards neoglycoconjugates from the monosaccharide determinant of *Vibrio cholerae* O:1, serotype Ogawa using the diethyl squarate reagent. *Carbohydr. Res. 313*, 15–20.

(19) Hou, S.-j., Saksena, R., and Kováč, P. (2008) Preparation of glycoconjugates by dialkyl squarate chemistry revisited. *Carbohydr. Res. 343*, 196–210.

(20) Zhang, J., and Kováč, P. (1997) Synthesis of ligands related to the *Vibrio cholerae* specific antigen. Part 14. Synthesis of methyl a-glycosides of some higher oligosacchairde fragments of *Vibrio cholerae* O1, serotype Inaba and Ogawa. *Carbohydr. Res. 300*, 329–339.

(21) McNaught, A. D. (1997) Nomenclature of carbohydrates. *Carbohydr. Res. 297*, 1–92.

(22) Westfal, G., and Jann, K. (1965) Bacterial lipopolysaccharide. Extraction with phenol-water and further applications of the procedure. *Methods Carbohydr. Chem. 5*, 83–91.

(23) Raziuddin, S. (1980) Immunochemical studies of the lipopolysaccharides of *Vibrio cholerae*: constitution of O-specific side chain and core polysaccharide. *Infect. Immun. 27*, 211–215.

(24) Gustafsson, B., and T., H. (1985) Immunological characterization of *Vibrio cholerae* O:1 lipopolysaccharide, O-side chain, and core with monoclonal antibodies. *Infect. Immun. 49*, 275–280.

(25) Qadri, F., Wenneras, C., Albert, M. J., Hossain, J., Mannoor, K., Begum, Y. A., Mohi, G., Salam, M. A., Sack, R. B., and Svennerholm, A. M. (1997) Comparison of immune responses in patients infected with *Vibrio cholerae* O139 and O1. *Infect. Immun. 65*, 3571–3576.

(26) Qadri, F., Mohi, G., Hossain, J., Azim, T., Khan, A. M., Salam, M. A., Sack, R. B., Albert, M. J., and Svennerholm, A. M. (1995) Comparison of the vibriocidal antibody response in cholera due to *Vibrio cholerae* O139 Bengal with the response in cholera due to *Vibrio cholerae* O1. *Clin. Diagn. Lab. Immunol. 2*, 685–688.

(27) Qadri, F., Ahmed, F., Karim, M. M., Wenneras, C., Begum, Y. A., Abdus Salam, M., Albert, M. J., and McGhee, J. R. (1999) Lipopolysaccharide- and cholera toxin-specific subclass distribution of B-cell responses in cholera. *Clin. Diagn. Lab. Immunol. 6*, 812–818.

(28) Chernyak, A., Karavanov, A., Ogawa, Y., and Kováč, P. (2001) Conjugating Oligosaccharides to proteins by squaric acid diester chemistry; rapid monitoring of the progress of conjugation, and recovery of the unused ligand. *Carbohydr. Res. 330*, 479–486.

(29) Mosley, W. H., Ahmad, S., Benenson, A. S., and Ahmed, A. (1968) The relationship of vibriocidal antibody titre to susceptibility to cholera in family contacts of cholera patients. *Bull. World Health Organ. 38*, 777–785.

(30) Glass, R. I., Svennerholm, A. M., Khan, M. R., Huda, S., Huq, M. I., and Holmgren, J. (2008) Seroepidemiological studies of El Tor cholera in Bangladesh: association of serum antibody levels with protection. *J. Infect. Dis. 151*, 236–242.

(31) Harris, J. B., LaRocque, R. C., Chowdhury, F., Khan, A. I., Logvinenko, T., Faruque, A. S. G., Ryan, E. T., Qadri, F., and Calderwood, S. B. (2008) Susceptibility to *Vibrio cholerae* infection in a cohort of household contacts of patients with cholera in Bangladesh. *PLoS Negl. Trop. Dis. 2*, e221.

(32) Cholera vaccines: WHO position paper. *Wkly. Epidemiol. Rec.* 2010, *85*, 117−1278.

(33) Koelle, K., Rodo, X., Pascual, M., Yunus, M., and Mostafa, G. (1974) Refractory periods and climate forcing in cholera dynamics. *Nature 436*, 696–700.

(34) Cash, R. A., Music, S. I., Libonati, J. P., Craig, J. P., Pierce, N. F., and Hornick, R. B. (1974) Response of man to infection with *Vibrio cholerae*. II. Protection from illness afforded by previous disease and vaccine. *J. Infect. Dis. 130*, 325–333.

(35) Cash, R. A., Music, S. I., Libonati, J. P., Snyder, M. J., Wenzel, R. P., and Hornick, R. B. (1974) Response of man to infection with *Vibrio cholerae*. I. Clinical, serologic, and bacteriologic responses to a known inoculum. *J. Infect. Dis. 129*, 45–52.

Bioconjugate Chemistry

TECHNICAL NOTE

pubs.acs.org/bc

Evaluation of the Synthesis of Sialic Acid-PAMAM Glycodendrimers without the Use of Sugar Protecting Groups, and the Anti-HIV-1 Properties of These Compounds

Russell Clayton,[†] Janee' Hardman,[†] Celia C. LaBranche,[‡] and Katherine D. McReynolds*[,†]

[†]Department of Chemistry, California State University, Sacramento, 6000 J Street Sacramento, California 95819-6057, United States

[‡]Division of Surgical Sciences, Duke University, Durham, North Carolina 27710, United States

Supporting Information

ABSTRACT: A study was undertaken to evaluate the feasibility of synthesizing six sialic acid-PAMAM glycodendrimers using unprotected sialic acid in as few as 1−4 steps using two different reaction pathways, and to assess the sulfated derivatives for anti-HIV activity. The syntheses were accomplished through either the direct attachment of the sialic acid carboxyl group to amine-terminated PAMAM (a divergent-like approach) using BOP coupling, or by first reacting sialic acid with a polar bifunctional spacer molecule, attaching the sugar-linker to carboxy-terminated PAMAM (a convergent-like approach), and again using BOP-mediated coupling reactions. It was hypothesized that the latter approach would be the most successful method, as any steric congestion between the sialic acid and the PAMAM would be minimized using an intervening polar linker. However, the divergent-like synthesis proved to be the superior method, resulting in 11.4%, 14%, and 28% of the fully substituted generations 0, 1, and 2 sialic acid-PAMAM conjugates, respectively, as compared to 6.4% of only the generation −0.5 sialic acid-linker-PAMAM conjugate for the convergent-like method. Upon sulfation of the four glycodendrimers, binding capabilities to the recombinant HIV protein, gp120, were assessed using an ELISA assay. Compounds that showed promising binding characteristics were then further assessed for inhibition of HIV-1 infection using a well-characterized luciferase reporter gene neutralization assay. The generation 2 sulfated sialic acid-PAMAM glycodendrimer, **sulfo-6**, bearing 16 sialic acids with 11 sulfate groups incorporated at 4.03% sulfur content by weight, was found to inhibit all four HIV-1 strains tested in the low micromolar range.

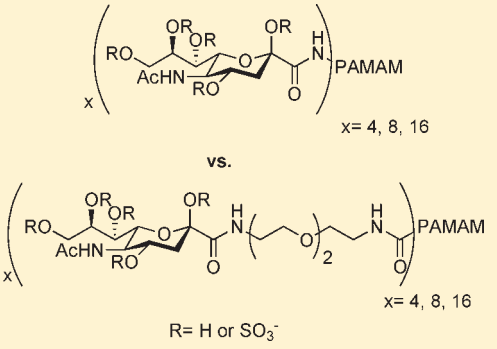

INTRODUCTION

By the close of 2009, there were an estimated 33.3 million people worldwide infected with HIV. This included 2.6 million newly infected, and 1.8 million deaths.[1] This is a 3-fold increase compared to 1990.[2] HAART (highly active antiretroviral therapy) slows the progression of HIV to AIDS, and lengthens and improves the quality of life for those infected. There are now 4 million people worldwide on HAART, with 73% of those in Africa. However, three times as many people need treatment in resource-limited nations that are not receiving it.[3,4]

In addition to millions still needing HAART treatment, the utility of antiretroviral drugs is further limited by viral resistance and toxicity issues.[5,6] Moreover, there still exists no safe, effective vaccine or prophylactic drug approved for preventing the acquisition of HIV. The introduction of potent and cost-effective therapies able to not only treat HIV, but also prevent the transmission of the virus is of the utmost importance. This is particularly critical in regions of the world such as sub-Saharan Africa, where 67% of the world's HIV infected individuals reside.[2,7] Here, an estimated 80% of people infected are not aware of their own HIV status, and 90% of individuals do not know their partner's status.[3]

Sulfated polysaccharides have long been recognized as having potent anti-HIV activity. Several naturally occurring sulfated polysaccharides, such as heparin sulfate (HS) and dextran sulfate (DS), inhibit the binding of HIV to CD4 positive cells *in vitro* in the μg/mL or μM range (Figure 1).[8−10] The inhibition of HIV by polyanionic polysaccharides has been actively studied. There are regions in the HIV surface glycoprotein gp120 containing multiple basic amino acids, namely, the principle neutralizing domain (V3 loop, amino acids 303−338), the C-terminal region (amino acids 495−516), and a conserved region involved in chemokine coreceptor binding (discontinuous amino acids in regions 117−123, 207, 419−444).[11−14] These regions have been shown to interact with polyanions such as HS and DS, which prevent binding to complementary antibodies.[13,15] Surface plasmon resonance (SPR) studies revealed strong polyanion-gp120 binding with immobilized HS and monomeric gp120, yielding an affinity constant of 220 nM. These studies also determined that an average of 4.4 gp120 molecules bind each

Received: June 23, 2011
Revised: August 10, 2011
Published: August 22, 2011

 © 2011 American Chemical Society

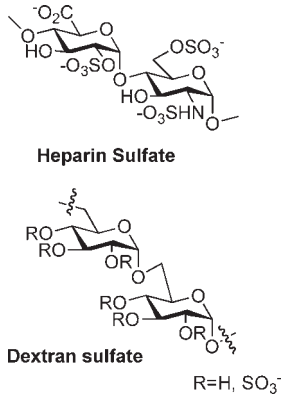

Figure 1. Structures of polyanionic polysaccharides possessing anti-HIV activity.

chain of heparin, indicating that higher avidity binding would be possible in a multivalent sense.[15−17] Mechanistically, it has been proposed that HIV binds to cell surfaces electrostatically between the polybasic V3 loop and host cell surface heparan sulfate proteoglycans (HSPG).[18] Another group suggested that a sequential process occurs, whereby first HSPG binds through a high-affinity, selective interaction with the V3 loop on gp120, followed by a second, lower-affinity interaction between such polyanions and the conserved chemokine coreceptor region.[15] It has also been noted that the binding between gp120 and polyanions occurs without disrupting the gp120-CD4 interaction, further strengthening the argument that the polybasic regions of gp120 bind to the chemokine coreceptors.[11,15,18]

HS and DS, while having strong affinity to the basic regions of gp120, are also anticoagulants, making it difficult to achieve therapeutic anti-HIV levels of the drugs without compromising blood clotting time.[19] Additionally, in phase I/II clinical trials, DS was found to be poorly absorbed orally, and when given intravenously, resulted in toxic side effects such as reversible thrombocytopenia and alopecia and did not yield a therapeutic effect based on HIV marker levels such as p24.[20,21] However, a later study of DS found good oral absorption of DS into the bloodstream indicating that DS has therapeutic potential and merits further study.[22]

A wide variety of other polysaccharides isolated from native sources, and either naturally or synthetically sulfated, have been found to have *in vitro* anti-HIV activity. Included are polysaccharides isolated from bacteria such as *E. coli* K5, marine plants such as algae, marine invertebrate animals such as tunicates and sponges, and land plants such as lichen.[23] These sulfated homo- and heteropolysaccharides contain numerous simple monosaccharide building blocks such as glucuronic acid, *N*-acetylglucosamine, galactose, mannuronic acid, and L-fucose, to name a few. Most of these polysaccharides have anti-HIV activities in the μg/mL range, all suffer from polydispersity of structure, and some have toxicity issues similar to DS and HS.[23]

Sulfated polysaccharides, while potent *in vitro* inhibitors of HIV, have not yet proven to be effective drug candidates for HIV due to their inherent polydispersity, as well as toxicity issues. We hypothesize that, if several shorter chains of the sulfated sugars are anchored to a carrier molecule, anti-HIV activity can be maintained, while toxicity and polydispersity of structure can be decreased or eliminated. A carrier molecule that can be utilized in this fashion is a dendrimer.

Dendrimers are a unique class of multivalent polymers, first reported by Tomalia and co-workers in 1985.[24] They are globular in shape and consist of a wide variety of architectures, with diverse sizes and chemical composition. Dendrimers are built in series with varying numbers of branches, which gives rise to a group of related molecules known as generations (G). With each branching reaction comes an increase in the number of branches, and subsequently, the next highest generation. Dendrimers can be synthesized in one of two ways, either divergently or convergently. Divergent synthesis involves building the dendrimer from the core outward, while a convergent strategy entails first building blocks of the molecule separately, then attaching them to a minimal core structure in the final step. Dendrimers have been used in many medical applications ranging from drug delivery to uses as immunodiagnostic reagents, MRI contrast reagents, gene delivery vectors, immunostimulation agents/adjuvants, or drug delivery vehicles.[25−30] Dendrimer research is important due to the diversity of structures that can be devised and their utility in numerous biological applications. It is important to understand the toxicity, solubility, and other properties of dendrimers, to ensure that they can be safely used in the development of new therapeutics. PAMAM (poly(amido amine))-based dendrimers have been well-evaluated both *in vitro* and *in vivo*. In the *in vivo* studies in mice and rats, it has been found that PAMAM is cytotoxic in a size-dependent fashion, with larger generations being more toxic.[31] Other properties affecting toxicity are charge (anionic PAMAM is less toxic than cationic) and surface modification with other groups, such as PEG (polyethylene glycol) or sugars.[32] PEGylation/glycosylation of PAMAM yields dendrimers with much lower toxicity profiles.[31]

When dendrimers are glycosylated, they are known as glycodendrimers, a class of compounds first reported by Roy in 1993.[33] Glycodendrimers built on a variety of dendrimer scaffolds such as PAMAM have found numerous uses in medicine due to the multivalent effect. Monovalent carbohydrates typically have weak millimolar binding constants in protein−carbohydrate recognition.[34] However, binding affinities achieved by the multivalent effect are orders of magnitude improved over a one molecule−one receptor binding event.[35,36] In nature, the multivalent effect is observed in many interactions, for example, in the viral infection by influenza where the viral trimeric hemagglutinin protein recognizes multiple copies of the carbohydrate sialic acid on the host cell.[37] A variety of sialic acid glycodendrimers were formulated as multivalent inhibitors of the binding between hemagglutinin and the host cell. The degree of inhibition achieved by these glycodendrimers was 32−50 000-fold higher than from monovalent sialic acid.[37] Glycodendrimers, therefore, present an alluring prospect for other medical applications because they increase the valency of a biologically active carbohydrate and improve the binding constants between the carbohydrate and the target protein.[38,39]

Scientists have begun to explore glycodendrimers as anti-HIV agents. Many of these are glycosphingolipid (GSL) mimics, as it is known that GSLs can be utilized by HIV-1 as alternate host cell receptors in the infection process.[40] The first account by Schengrund reported the synthesis of sulfated galactosyl ceramide (SGalCer)-coated polypropyleneimine (PPI) dendrimers, directed at preventing infection in CD4-negative cells.[41,42] In their studies, they determined that gp120 bound to their glycodendrimers in the nM range, as compared to the known polysaccharide HIV inhibitor DS, which bound in the pM range. Cytotoxicity of the glycodendrimers at up to 3 mg/mL was not

observed. Since this initial report, there have been a few more examples of potential anti-HIV glycodendrimers. Two other GalCer-based dendrimers were reported by Castillon and co-workers and Blanzat, Turrin, and co-workers.[43,44] One had a polyglycerol (PG) dendrimer core, and had lower activity than the Schengrund glycodendrimers.[42,43] The other GalCer glycodendrimers were based on a phosphonic acid core, and determined to have sub-μM IC_{50}s in a cell-based HIV assay (IC_{50} is the concentration that reduces HIV infection by 50%). However, these suffered from high cytotoxicities.[44,45] Another report was of a polylysine-sulfated cellobiose system.[46,47] This glycodendrimer was found to have an EC_{50} (effective concentration for 50% effect) of 3.2 μg/mL, comparable to the NRTI (nucleoside reverse transcriptase inhibitor) ddC (2′-3′-dideoxycytidine), and was also determined to have low cytotoxicity. Additionally, a mannose-based PG glycodendrimer was reported that targeted the dendritic cell lectin DC-SIGN.[48] The IC_{50} activity of this glycodendrimer was μM, similar to the others. Finally, Schengrund and co-workers recently reported two types of glycodendrimers based on the PPI core, terminating in either of the glycosphingolipid derived sugar headgroups, 3′-sialyllactose (GM_3) or globotriose (Gb_3).[40] The GM_3 and Gb_3 glycodendrimers were assessed for anti-HIV-1 activity in T-cells and primary peripheral blood mononuclear cells (PMBCs), and yielded IC_{50} values ranging from 0.1 to 7.4 μg/mL.[40]

While the above results are encouraging, the search for easy to make, cost-effective, and potent new anti-HIV therapeutics remains a significant goal for the scientific/medical community in light of the high rate of infection continuing to this day, the longer life spans of infected individuals, and the therapeutic failures occurring due to drug toxicity and resistance. All of these factors contribute to fewer therapeutic strategies available to a patient the longer they have been infected. Additionally, if new anti-HIV therapeutics can be designed in such a way that they are simple and cost-effective to produce, it will be easier to implement therapy in resource-limited regions of the world, where the bulk of HIV infections are occurring.

Along these lines, we endeavored to create an initial trial set of 6 compounds based on the commercially available dendrimer core, PAMAM (G = −0.5, 0, 0.5, 1, 1.5, and 2), and the unprotected sugar, sialic acid (**10**, Scheme 2). This could be accomplished by one of two pathways, a one-step divergent-like pathway (Scheme 4), whereby sialic acid was directly coupled to PAMAM, or a four-step convergent-like approach, where an intermediary linker (**8**, Scheme 1) was first reacted with sialic acid, then the sugar−linker conjugate coupled to PAMAM Scheme 3). The first approach was anticipated to be the most difficult as the sialic acid carboxyl group is sterically congested and might not be accessible enough to the also sterically crowded multiple reaction centers in PAMAM. These potential pitfalls led us to develop the second pathway, where a long linear hydrophilic linker was first attached to sialic acid, followed by reaction of the sugar−linker to PAMAM. This was thought to be the best approach, as the steric consequences suffered by both reaction partners would be greatly minimized in the presence of the hydrophilic linker. Whichever pathway produced the desired glycodendrimer conjugates with the best yields would then be utilized in further syntheses.

As for the individual sugar and dendrimer choices, there were many factors to consider. PAMAM was chosen primarily because of its availability and also because there was an abundance of data available on the cellular toxicities of PAMAM-based molecules

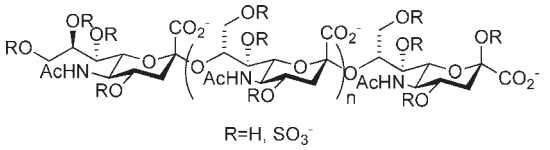

Figure 2. Sulfated colominic acid.

(*vide supra*). Sialic acid was chosen for a few key reasons as well. First, it contains a carboxyl group attached to the anomeric carbon, making it easy to append it to either an amino-bearing linker or to an amino-terminated PAMAM using standard solution-phase peptide coupling methodologies, all without having the sugar protected. Second, some preliminary anti-HIV data have been reported for a sialic acid-based polysaccharide, colominic acid, in the sulfated form. Colominic acid is an α-2→8-linked polymer of sialic acid (Figure 2). Yang and co-workers found EC_{50} values as low as 0.06 μg/mL for the larger molecular weight, more highly sulfated derivatives of colominic acid (MW ranging from 8 to 16 kDa, sulfation 8−12%) in MT-4 and C8166 cell lines infected with HIV in the presence of these molecules.[19] Their assay control, DS, yielded EC_{50} values of 0.5 and 2.51 μg/mL in the same cell lines, respectively. Finally, by using the base sugar from a polymer with known anti-HIV activity, we would be able to quickly ascertain if utilizing PAMAM as a scaffold for the multivalent presentation of sulfated sugars to the target protein, gp120, was as/more effective in binding to gp120/inhibiting HIV infection than the known sulfated linear polysaccharide standard, DS.

Once synthesized, all of the sulfated sialic acid-PAMAM glycodendrimers could be assessed for anti-HIV-1 activity by two separate, yet complementary assays. The first assay, a fast ELISA (enzyme-linked immunosorbent assay) developed in our lab, could be used to screen for the presence of gp120 binding. If activity was found, a second, more sensitive luciferase reporter gene assay could then be utilized to determine how well the sulfoglycodendrimers were able to inhibit HIV-1 infection of TZM-bl cells.

EXPERIMENTAL PROCEDURES

General Materials and Methods. All nuclear magnetic resonance (NMR) spectroscopy was performed on a Bruker Avance III 500 MHz NMR spectrometer with either D_2O or $CDCl_3$ solvents purchased from Acros. To simplify the analysis of the ^1H NMR spectra for compounds **1**−**6**, the integrations were normalized for 1/4 of total protons, the equivalent of 1 branch of the full glycodendrimer. For ^{13}C analysis, 3-(trimethylsilyl) tetradeutero sodium propionate (TSP) from Wilmad was used as a zero point reference, and all spectra were proton decoupled. MALDI mass spectral analysis was conducted on a Kratos/Shimadzu Axima-CFR MALDI-TOF (University of the Pacific) and a Bruker Reflex III MALDI-TOF (The Ohio State University). High-resolution ESI mass spectral analysis was conducted on an IonSpec Fourier transform mass spectrometer (University of Arizona). Flash chromatography was performed using flash silica gel (32−63 μM) from Dynamic Adsorbents Inc. Dialysis purification was performed using Spectra/por Biotech Cellulose Ester dialysis membrane from Spectrum Laboratories Inc. Reverse-phase high-pressure liquid chromatography (RP-HPLC) was conducted on a Hewlett-Packard TI-series 1050 using a Grace Prevail C-18 5 μ 250 × 10 mm column. Fast-paced liquid chromatography (FPLC) was performed with a Pharmacia pump P-500 with a LC Controller LCC-500 Plus.

The column used in conjunction with the FPLC was a Bio-Gel P-10 2.5 cm × 120 cm column.

The reagents used came from a variety of sources and were used without further purification: All poly(amidoamine) (PAMAM) dendrimers were purchased from Aldrich. Benzotriazol-1-yloxytris-(dimethylamino)phosphonium hexafluorophosphate (BOP) was from Nova Biochem. *N,N*-Diethylisopropyl amine (DIPEA) was purchased from Alfa Aesar. Trifluoroacetic acid (TFA), triethylamine (TEA), ammonium bicarbonate, and *N,N*-dimethylformamide (DMF) were from EMD. Di-*tert*-butyl dicarbonate ($(Boc)_2O$) was purchased from Acros. 1,8-Diaminotriethyleneglycol was obtained from Huntsman. *N*-Acetylneuraminic acid (sialic acid) was purchased from Nacalai Tesque. 500 kDa dextran sulfate was purchased from Sigma-Aldrich.

Note on Characterization. All labels on protons in the ^1H NMR data correspond to assignments given on the spectra. The spectra can be found in the Supporting Information section.

Nomenclature Note. All glycodendrimers are named as follows: The number of end points, tetramer, octamer, or 16-mer, followed by glyco-. If a linker is present between PAMAM and sialic acid, the abbreviation DATEG (1,8-diaminotriethyleneglycol) appears. The name terminates in PAMAM dendrimer.

{2-[2-(2-Amino-ethoxy)-ethoxy]-ethyl}-carbamic Acid *tert*-Butyl Ester (8). 1,8-Diaminotriethyleneglycol **7** (5.0 g, 33.8 mmol) was weighed into a flame-dried 500 mL round-bottomed flask. Methanol (135 mL) was added, followed by TEA (340 mg, 3.4 mmol), then $(Boc)_2O$ (7.38 g, 33.8 mmol). The reaction was heated to 35 °C and stirred overnight. The solvents were evaporated under reduced pressure and the crude residue was purified by flash chromatography using 1:1 methanol/chloroform, giving **8** as a viscous golden oil (4.25 g, 17.1 mmol, 51% yield). ^1H NMR (D_2O): δ 1.41 (s, 9H, H_T), 2.79 (t, 2H, J = 5.4 Hz, H_S), 3.25 (t, 2H, J = 5.4 Hz, H_P), 3.57 (q, 4H, J = 5.0 Hz, 9.7 Hz, H_Q), 3.66 (s, 4H, H_R). ^{13}C NMR (D_2O, TSP internal std): δ 30.4, 42.6, 72.1, 72.2, 74.9, 161.

***N*-Acetylneuraminic Acid {2-[2-(2-Amino-ethoxy)-ethoxy]-ethyl}-amide (11).** Sialic acid (**10**, 100 mg, 0.32 mmol) was weighed into a flame-dried 25 mL round-bottomed flask, dissolved into DMF (2 mL) and placed under nitrogen. BOP (210 mg, 0.48 mmol) was added to the solution as a solid. In a separate flask, the linker **8** (87 mg, 0.35 mmol) was dissolved in DMF (1 mL). DIPEA (170 mg, 1.28 mmol) was then added. This mixture was next added to the sialic acid solution. The reaction was heated to 35 °C and stirred for 24 h. The solvent was evaporated under reduced pressure. The crude was dissolved in 1:2 dichloromethane/TFA (12 mL) and stirred for 2 h before the solvents were evaporated under reduced pressure. The crude material was purified with RP-HPLC using a gradient of deionized water/0.1% trifluoroacetic acid and acetonitrile/0.1% trifluoroacetic acid giving **11**, as a gummy white solid (155 mg, 0.35 mmol, 88% yield). ^1H NMR (D_2O): δ 1.67 (t, 1H, J = 12.2 Hz, H_B), 2.03 (s, 3H, H_C), 2.31 (dd, 1H, J = 4.7 Hz, 13 Hz, H_A), 3.19 (t, 3H, J = 4.8 Hz, H_P), 3.43 (m, 2H, H_S), 3.55−3.73 (M, 11H, $H_{G,H,J,Q,R}$), 3.82 (dd, 1H, J = 2.6 Hz, 11.9 Hz, H_E), 3.89 (t, 1H, J = 10.3 Hz, H_I), 4.05 (m, 2H, $H_{D,F}$). ^{13}C NMR (D_2O, TSP internal std): δ 22.3, 39.0, 39.3, 39.8, 52.4, 63.4, 66.6, 67.0, 68.4, 68.9, 69.7, 69.8, 70.4, 70.7, 96.0, 173, 175. High-resolution electrospray mass spectrometry (HR-ESI+: $[M + H]^+$ ($C_{17}H_{34}N_3O_{10}$) calcd m/z = 440.2239. Found m/z = 440.2238.

General Procedure for the Synthesis of Glyco-DATEG-PAMAM Dendrimers. PAMAM G = −0.5, 0.5, and 1.5 (1 equiv) were transferred to a 10 mL round-bottomed flask, G = −0.5 as a solid, and 0.5 and 1.5 as a 20% wt solution in methanol. The methanol was evaporated from G = 0.5 and 1.5 *in vacuo*. Next, DIPEA (2.5 equiv/arm) was added, and flushed with nitrogen. DIPEA (2.5 equiv/arm) was added, followed by BOP (1.2 equiv/arm). The sugar linker **11** (1.1 equiv/arm) was placed into a second 10 mL round-bottomed flask and dissolved in DMF (1 mL). The two solutions were mixed together, heated to 35 °C, and stirred under nitrogen for 1, 7, and 14 days, respectively. The solvents were evaporated under reduced pressure and the crude product was dialyzed with 500 MWCO tubing in a 1 L flask against nanopure water. The water was changed once every hour for four hours, and allowed to stir overnight at 4 °C . The remaining crude material was then lyophilized. The dialyzed crude material was then purified using RP-HPLC with a linear gradient between water/0.1% trifluoroacetic acid and acetonitrile/0.1% trifluoroacetic acid. Fractions containing the product were collected, grouped, and further purified using a 2.5 × 120 cm Bio-Gel P-10 in 0.03 M ammonium bicarbonate. A 6.4% yield of only compound **1** was achieved by this method.

General Procedure for the Synthesis of GlycoPAMAM Dendrimers. Sialic acid (**10**, 1.1 equiv/arm) was weighed into a flame-dried 10 mL round-bottomed flask, flushed with nitrogen, then dissolved into DMF (4 mL). BOP (1.5 equiv/arm) was then added as a solid. PAMAM G = 0, 1, or 2 (20% wt in methanol) (1 equiv) was next weighed into a separate 10 mL round-bottomed flask and the methanol was evaporated under reduced pressure. DMF (1.5−2.0 mL) and DIPEA (2.5 equiv/arm) were added to the flask with PAMAM. The PAMAM solution was then added to the sialic acid solution, heated to 35 °C, and the reaction was stirred for 1, 7, or 14 days, respectively, under nitrogen. The crude reaction product was dialyzed with 500 MWCO tubing against nanopure water. The water was changed once an hour for four hours, then left stirring overnight at 4 °C. The crude material was then purified using RP-HPLC with a linear gradient between water/0.1% trifluoroacetic acid and acetonitrile/0.1% trifluoroacetic acid providing compounds **2**, **4**, and **6** in 11.4%, 14%, and 28% yields, respectively.

General Sulfation Procedure. Nonselective sulfation of the glycodendrimers was carried out according to the procedure of Kunou et al.[49] Briefly, the glycodendrimers were sulfated under a nitrogen atmosphere at 0 °C, using a 3:1 ratio of SO_3−pyridine complex to hydroxyl groups per sugar unit. 10 mg of each glycodendrimer and the appropriate mass of SO_3−pyrindine complex were each dissolved in 1.25 mL of dry DMF under N_2. The sulfating solution was added dropwise into the glycodendrimer solutions and the reaction mixtures were stirred for 1 h at 0 °C under N_2. The reactions were terminated by the addition of 0.5 mL ice−cold water and the pH values of the reaction mixtures were adjusted to above 9 with 2 M NaOH. The reaction mixtures were next added dropwise to 50 mL of ice−cold acetone and left to precipitate at −20 °C for 24 h. The precipitates were collected by centrifugation, then decantation of the acetone. The precipitates were dissolved in small volumes of water and purified via dialysis (either 500 or 1000 MWCO tubing was used, Spectra/Por) against purified DI water at 4 °C. The sulfated glycodendrimers were then obtained as fine white solids by lypohilization. Finally, the sulfated glycodendrimers were evaluated by Columbia Analytics in Tucson, AZ, to determine the % sulfur for each. From this information, the approximate number of sulfate groups incorporated into each glycodendrimer was determined. For **sulfo-1**, **2**, **4**, and **6**, the %S

incorporated into each glycodendrimer was 11.22%, 15.32%, 2.02%, and 4.03%, respectively.

General procedure for the competitive ELISA with biotinylated recombinant gp120. A competitive ELISA was developed to determine the inhibitive binding properties of the sulfated glycodendrimers against the HIV-1 monoclonal antibody peroxidase-labeled murine mAb1101-P gp120 HIV-1 (Immunodiagnostics), to biotin-labeled rgp120 HIV-1 IIIB (b-rgp120, Immunodiagnostics). Dextran sulfate (500 kDa) was used as a positive assay control, and buffer was used as a negative assay control. Competition between the b-rgp120 and the mAb was evidenced by a decrease in the overall absorbance at 450 nm. To run the assay, a 1:5000 dilution of b-rgp120 was prepared in PBS and 100 μL of this dilution was transferred to the wells of Reacti-Bind NeutrAvidin-coated strip plates (Thermo Scientific). The plates were incubated for 1 h at 25 °C while shaking at medium speed in a Jitterbug Plate Incubator Shaker (Boekel). The plates were washed three times with PBS containing 0.05% (v/v) Tween 20. 200 μL of PBS containing 1% (w/v) BSA was added to each well to block nonspecific binding sites and the plates were incubated for 1 h at 25 °C while shaking at medium speed. While blocking, a 1:1000 dilution of the mAb 1101-P, and 0.2−400 μg/mL dilutions of the sulfated glycodendrimers were prepared in PBS-Tween 20 containing 0.1% (w/v) BSA. The plates were washed three times, and then the wells were treated in duplicate with 50 μL of the sulfated glycodendrimer dilutions plus 50 μL of the mAb1101-P dilution and incubated for 1 h at 25 °C while shaking at medium speed. The plates were washed three times. The wells were treated with 100 μL of SureBlue peroxidase substrate (KPL) and the kinetic reaction absorbances were read for 10 min at 655 nm on a BioRad model 550 plate reader. The kinetic reaction was stopped by the addition of 100 μL of 1 M HCl to each well. The end point absorbances were read at 450 nm. The duplicate end point readings were averaged and plotted against the log of the concentration (g/L) in a nonlinear regression analysis using GraphPad *Prism 4* software. From this, IC_{50} (inhibitory concentration to achieve 50% of the effect, in this case 50% less binding between b-rgp120 and the mAb) values in μg/mL and R^2 values were determined. A minimum of two assays were completed for each glycodendrimer or standard.

HIV Neutralization Luciferase Reporter Gene Assay. Inhibition of HIV infectivity by the sulfated glycodendrimers was assessed in a formally optimized, validated, and GCLP (good clinical laboratory practice)-compliant infectivity reduction assay according to the method of Montefiori *et al.* and conducted at Duke University in the GCLP-certified Primate Central Immunology Laboratory.[50,51] The solid glycodendrimer samples and dextran sulfate were prepared for analysis as follows: They were first dissolved in PBS and sterile-filtered to give 1 mg/mL concentrations. The 1 mg/mL stock solutions were serially diluted 1:3 in concentrations ranging from 50 to 0.02 μg/mL. The HIV-1 strains utilized in the assay included Q23.17 (Clade A), MN.3 (Clade B), MW965.26 (Clade C), and TV1.21 (Clade C). The cells assayed for infection were TZM-bl cells expressing CXCR4, and engineered to express the human cell receptors CD4 and CCR5, in addition to the enzymes, firefly luciferase and *Escherichia coli* β-galactosidase. An additional positive control, HIVIG-C, a purified IgG pooled from HIV^+ donors from South Africa, was prepared from a stock 12.5 mg/mL solution and used in the assays in 1:3 dilutions ranging from 625 to 0.29 μg/mL.

RESULTS AND DISCUSSION

The purpose of this work was to examine the ease of synthesizing glycodendrimers of various generations using both convergent-like and divergent-like synthetic strategies, and to perform some preliminary assessments for potential HIV-1 activity. With the sole exception of the preparation of compound **8**, no protecting group chemistry was used in this study. Because protecting group strategies require two additional steps per group, and result in lower overall yields, eliminating these steps saves time, and precludes the need for numerous purification steps. To achieve this, a synthetic route was devised where the reactions were conducted in a polar solvent to ease solubility issues, the reagents would not target the unprotected hydroxyls, and the chemistry utilized was efficient enough to allow for the desired conversion to the fully substituted products could be readily achieved. Whichever strategy proved superior would then allow for the creation of a variety of glycodendrimers of various sizes and sugar compositions more quickly. To test the convergent-like strategy for the synthesis of dendrimers, sialic acid was coupled to a hydrophilic linker, **8**, which was then attached to PAMAM, both utilizing amide linkages. As linker **8** was amine terminated, the half generations of carboxylic acid-terminated PAMAM ($G = -0.5$, 0.5, and 1.5) were employed in these cases. For the divergent-like strategy, the carboxyl group of sialic acid was coupled directly to the terminal amine of PAMAM $G = 0$, 1, and 2.

Glycodendrimer Synthesis. Generations −0.5, 0.5, and 1.5 were coupled to the sugar−linker complex through a convergent synthetic method. To achieve this, the linker (1,8-diaminotriethyleneglycol, **7**) was singly protected with di-*tert*-butyldicarbonate ($(Boc)_2O$). As both ends of the linker are chemically equivalent, this reaction afforded three products: unreacted starting material (**7**), the monoprotected linker (**8**), and the diprotected linker (**9**). Monoprotected linker (**8**) was isolated by normal phase flash chromatography using 1:1 chloroform and methanol, giving the desired product (**8**) in a 51% yield (Scheme 1).

The monoprotected linker (**8**) was next coupled to sialic acid (**10**) using benzotriazol-1-yloxytris(dimethylamino)phosphonium hexafluorophosphate (BOP) coupling conditions. After overnight reaction at 35 °C, the Boc protecting group was removed in 1:2 dichloromethane/trifluoroacetic acid (TFA) (Scheme 2).

Compound **11** was purified by reverse-phase high-pressure liquid chromatography (RP-HPLC), giving the desired product in 88% overall yield for two steps. Next, the sugar−linker (**11**) was attached to PAMAM generations −0.5, 0.5, or 1.5 via an amide coupling using BOP and DIPEA (*N*,*N*-diisopropylethylamine) in DMF at 35 °C, under nitrogen for 1, 7, or 14 days, respectively, producing glycodendrimers **1** and **3** (Scheme 3).[52] Glycodendrimer **5**, unfortunately, was not isolated.

To make compounds **2**, **4**, and **6** using a divergent-like approach, sialic acid (**10**) was mixed with the appropriate PAMAM and allowed to react using BOP coupling conditions at 35 °C under nitrogen gas for 1, 7, or 14 days. This produced glycodendrimers **2**, **4**, and **6** (Scheme 4).

Glycodendrimer Characterization. One of the primary goals of the research presented herein was to develop an efficient synthetic strategy to evaluate convergent and divergent-like synthetic methods to determine which method was simpler/more efficient for the synthesis of sialic acid-coupled glycodendrimers as that could serve as effective and potent anti-HIV-1 agents. An additional goal involved the minimization/elimination of the polydispersity inherent to the

Scheme 1. Monoprotection of Diaminotriethylene Glycol (8)

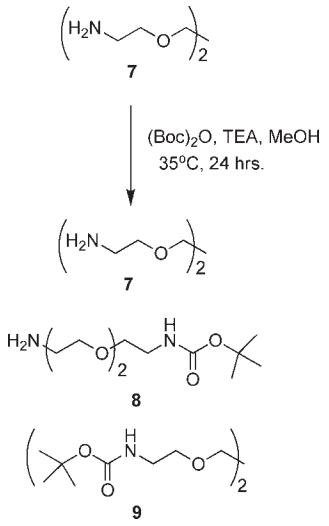

Scheme 2. Amide Coupling of Sialic Acid to Linker, Followed by Deprotection

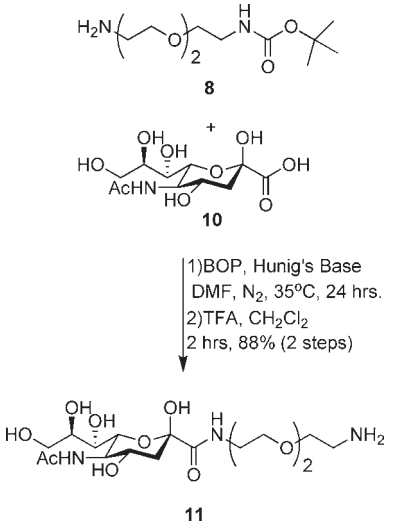

Scheme 3. Amide Coupling of Sugar−Linker PAMAM Generations −0.5, 0.5, and 1.5

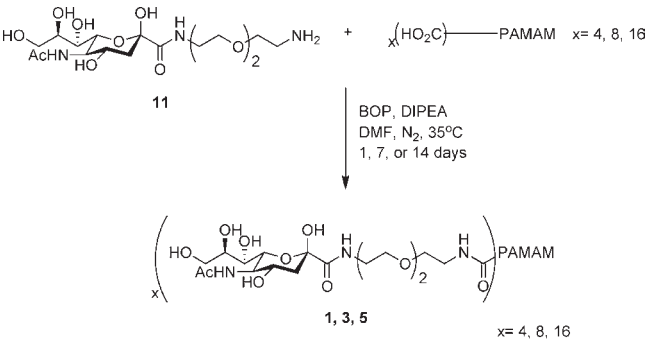

Scheme 4. Amide Coupling of Sialic Acid (10) to PAMAM Generations 0, 1, and 2

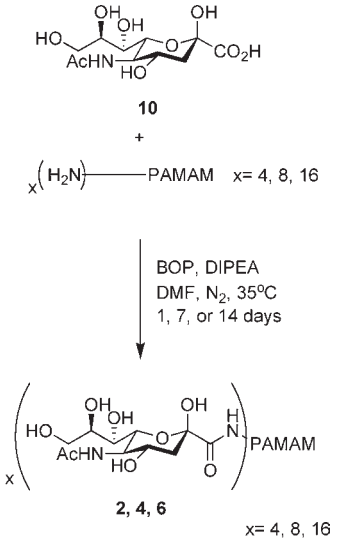

polysaccharides known to have anti-HIV activity. If successful, this would result in structurally well-defined glycodendrimers, and allow for a greater understanding of which features are the most critical for anti-HIV-1 activity. This was viewed as an important aspect of the study as many of the previous reports yielded incompletely substituted glycodendrimers (*vide supra*).[40,41,43,46,47] In the current study, the divergent-like approach consisted of only a single step between sialic acid and the appropriate amine-terminated PAMAM via a BOP coupling (Scheme 4). This synthesis was anticipated to be difficult, as the carboxyl group on sialic acid is sterically hindered. That, along with a large, bulky dendrimer, and the simultaneous occurrence of multiple reactions in the coupling step, was expected to present a great synthetic challenge and result in understandably low yields. The convergent-like synthesis, on the other hand, was expected to be much more facile as an intermediary polar primary amine-terminated linker was first attached to sialic acid in a 1:1 reaction, which was then coupled to carboxy-terminated PAMAM dendrimers (Scheme 3). This strategy was expected to be advantageous, as the steric issues between sialic acid and PAMAM would be minimized by the presence of a long polar spacer molecule. It was thus anticipated that the coupling between the sialic acid-linker (**11**) and various PAMAM cores would result in greater yields than the divergent-like approach.

It was therefore a surprise to find that the divergent-like synthetic method, where sialic acid was directly coupled to PAMAM, produced the desired fully substituted products in higher yields than the convergent-like approach. For the divergent-like reactions, compounds **2**, **4**, and **6** were all isolated and completely characterized via ^{1}H NMR, ^{13}C NMR, and MALDI-MS in modest yields of 11.4%, 14%, and 28%, respectively. The yields were likely low due to the steric issues previously mentioned.

For the convergent-like method, however, the addition of the diaminotriethylene glycol linker was expected to aid the reactions by reducing steric hindrance, yet resulted in minimal/no product isolation. Compound **1** was only isolated/characterized in 6.4% yield. For compound **3**, the impurity of the sample and the low quantities produced precluded the ability to obtain confirmatory ^{1}H or ^{13}C data; only MALDI MS analysis was possible. The calculated molecular weight for **3** is 4462 Da; however, MALDI MS showed small peaks for (M+H) m/z = 4467, (M−H_2O)

dx.doi.org/10.1021/bc200331v |*Bioconjugate Chem.* 2011, 22, 2186–2197

Scheme 5. Nonselective Sulfation of Glycodendrimer Products

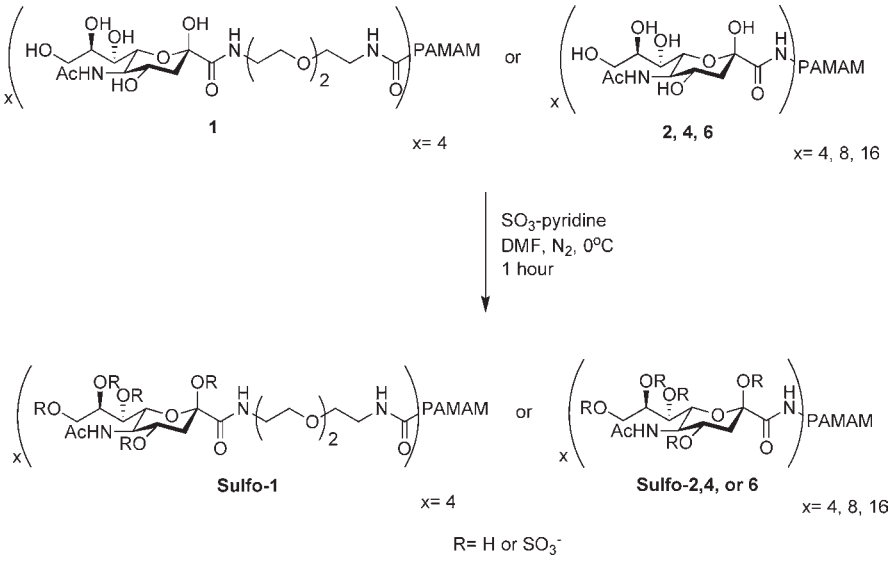

m/z = 4448, and (M−2H_2O) m/z = 4428, along with impurity peaks (M-compd **11**-H_2O) m/z = 4027 and (M-2 compd **11**) m/z = 3619. Compound **3** has more than 180 carbon atoms, so it is likely there are at least two ^{13}C atoms adding weight beyond the calculated molecular mass. Compound **5** was neither isolated nor confirmed, even after multiple attempts at synthesizing and purifying this molecule. We hypothesize that the linker may have been too conformationally flexible, allowing the linker to fold back on itself and participate in intramolecular hydrogen bonding with the polar face of the sialic acid. It is believed that this would result in reduced/absent reactivity of the sugar−linker to PAMAM.

These results clearly indicate that, for our system, the divergent-like synthesis was the superior method as fully substituted sialic acid glycodendrimers resulted. Yield improvements for the divergent-like approach are currently being sought in the laboratory through substitution of the solvent and/or coupling reagent. It is thought that a better combination can be found for this system that will behave more favorably with the polarity/solubility issues of the reactants, and result in improved yields, all while maintaining the ability to use unprotected sugars.

Assessment of anti-HIV Activity. The second major goal of the work presented herein involved the evaluation of sulfated derivatives of the glycodendrimers for possible anti-HIV activity. Once all of the glycodendrimers (**1**, **2**, **4**, and **6**) were successfully isolated and characterized, they were sulfated and purified according to the method of Kunou et al. (Scheme 5).[49] As this method is not selective as to the location or number of sulfates incorporated on the sugar hydroxyl groups, and the molecules had been completely characterized after their initial synthesis, further NMR and mass spectral analysis was not conducted. Instead, elemental analysis for % sulfur (%S) was completed. Using the %S for each glycodendrimer, the average number of sulfate groups incorporated into each glycodendrimer was calculated. The %S for sulfated compounds **sulfo-1**, **2**, **4**, and **6** were 11.22%, 15.32%, 2.02%, and 4.03%, respectively, which translated to an average number of sulfate groups incorporated of 10, 13, 2−3, and 11, respectively. The nonregiospecific sulfation method was utilized, rather than a more selective method, as these require additional protection/deprotection steps to incorporate the sulfate group on a specific hydroxyl group. As this was a preliminary study to elucidate a synthetic path that would yield glycodendrimers with anti-HIV-1 activity in the fewest possible steps, it was decided that achieving a completely monomolecular compound at this stage of the project in terms of both the number of sugars and sulfate groups incorporated was of lesser importance than achieving a fully substituted glycodendrimer product. This will, however, continue to be a goal in future work.

To evaluate whether or not the sulfated glycodendrimers had the capability of binding to the target HIV-1 protein, gp120, a simple in-house competitive binding ELISA assay was developed. This assay was utilized as an initial screen to quickly assess whether or not the sulfated glycodendrimers had the ability to bind to b-rgp120 (biotinylated recombinant gp120) and thereby inhibit the binding between b-rgp120 and an HRP (horseradish peroxidase)-labeled monoclonal antibody specific to the V3 loop of gp120. Briefly, b-rgp120 was incubated with NeutrAvidin-coated plates. NeutrAvidin is a proprietary biotin-binding protein capable of binding with high avidity to biotin-containing molecules and adhering them more/less permanently to the surface of the plate. This was done to ensure that gp120, with a high carbohydrate composition (∼50% by weight), did not wash off of the plate. After blocking the open sites with bovine serum albumin (BSA), the competitive binding step was initiated where both the HRP-labeled monoclonal antibody specific to the V3-loop of gp120 and either the serially diluted sulfated glycodendrimer or assay controls were incubated with the anchored gp120. After the prescribed incubation period and rinsing, the HRP substrate was added, and the reaction was monitored for 10 min at 655 nm, to observe linearity of the kinetics. The reaction was then stopped with the addition of HCl and the plate read again at 450 nm to ascertain the end point absorbances.

All of the sulfated glycodendrimers (**sulfo-1**, **2**, **4**, **6**) were initially evaluated by the ELISA. Each compound was assayed in duplicate wells a minimum of two times, and all results were compared to the positive assay control, 500 kDa dextran sulfate (Figure 1), containing 17% sulfur (2.3 sulfates/sugar).[53] Dextran

Table 1. Summary of Pertinent Structural and HIV Assay Data for Sulfated Glycodendrimers and Positive Assay Controls, Dextran Sulfate, and Antibody HIVIG-C

compound	approxx MW (g/mol)	% sulfur	avg # sulfates	ELISA IC_{50}[d]	Q23.17 (Clade A) IC_{50}[e]	MN.3 (Clade B) IC_{50}[e]	MW965.26 (Clade C) IC_{50}[e]	TV1.21 (Clade C) IC_{50}[e]
Sulfo-1	2821	11.22	10 (2.5/sugar)	>71 μM	NA[a]	NA[a]	NA[a]	NA[a]
Sulfo-2	2707	15.32	13 (3.25/sugar)	>74 μM	NA[a]	NA[a]	NA[a]	NA[a]
Sulfo-4	3992	2.02	2 to 3 (0.25−0.38/sugar)	>50 μM	>12.5 μM[c]	>12.5 μM[c]	>12.5 μM[c]	>12.5 μM[c]
Sulfo-6	8777	4.03	11 (0.69/sugar)	>23 μM[b]	5.1 μM	2.4 μM	1.6 μM	4.0 μM
Dextran Sulfate	500 000	17	2.3/sugar	1.6 nM	8.2 nM	4.4 nM	2.8 nM	2.6 nM
HIVIG-C	150 000	NA[a]	NA[a]	NA[a]	98.7 nM	35.3 nM	8.7 nM	0.34 μM

[a] NA = Not applicable/no assay was conducted. [b] Reduction in the absorbance at 450 nm by **Sulfo-6** was only observed at the highest compound concentrations tested and did not reach the cutoff level of a 50% reduction in absorbance at 450 nm. [c] Reduction in the luciferase signal by **Sulfo-4** was only observed at the highest compound concentrations tested and did not reach the 50% neutralization cutoff. [d] Values are the sample concentration (μM) at which the absorbance at 450 nm was reduced by 50% compared to the control wells (no test sample). Sample concentrations ranged from 0.1 to 200 μg/mL in the assay wells. [e] Values are the sample concentration (μM) at which relative luminescence units (RLUs) were reduced 50% compared to virus control wells (no test sample). Sample concentrations ranged from 0.02 to 50 μg/mL for the sulfoglycodendrimers and DS, and 0.29−625 μg/mL for HIVIG-C.

sulfate consistently results in an average IC_{50} (inhibitory concentration for a 50% reduction in gp120 binding) of 1.6 nM with an R^2 value of 0.99 for the nonlinear regression fit for dose−response analysis (Table 1). **Sulfo-1**, **2**, and **4** did not fit nonlinear regression dose−response curves, evidenced by low R^2 values (data not shown). For **Sulfo-6**, higher concentrations of this molecule led to a noticeable decline in the absorbance at 450 nm, indicating that some binding to gp120 was achieved; however, a 50% inhibition of antibody binding to b-rgp120 was not achieved. It was hypothesized that lack of quantitative results by the ELISA may have had more to do with the lower sensitivity limits of the ELISA, rather than whether or not the compounds actually had anti-HIV activity, and we are in the process of optimizing the ELISA assay to improve its sensitivity. The decision was therefore made to evaluate the two higher-order sulfated glycodendrimers (**sulfo-4** and **6**) directly for anti-HIV activity using the luciferase reporter gene assay because it is a more sensitive assay. **Sulfo-1** and **sulfo-2** were not evaluated further, because we had recently determined that other sulfated glycodendrimers of similar size did not yield anti-HIV-1 activity in the luciferase assay (data not shown).

The luciferase reporter gene assay used in this analysis was first developed by Shaw and co-workers, then further optimized and validated by Montefiori and colleagues.[50,51,54] This assay evaluates a single round of infection of a modified TZM-bl cell line, derived from HeLa. TZM-bl cells express the HIV-1 coreceptor, CXCR4, and have been engineered to express coreceptor CCR5 and receptor CD4, in addition to the integrated reporter genes for firefly luciferase and the β-galactosidase gene from *Escherichia coli*. The pseudoviruses utilized (Q23.17 (Clade A), MN.3 (Clade B), MW965.26 (Clade C), and TV1.21 (Clade C)) are infectious, but are not able to replicate to yield viable virions and are thus limited to one round of infection. Upon infection of the TZM-bl cells, the *tat* gene carried by the pseudovirus is expressed and the resultant Tat protein trans-activates the luciferase reporter gene. Development of the assay involves quantifying the luminescence resulting from the enzyme activity of luciferase, which is directly proportional to the number of infection events by the pseudoviruses. Addition of an agent with anti-HIV activity results in a decrease in the luminescence signal. Both **sulfo-4** and **6** were analyzed in the TZM-bl luciferase reporter gene assay, in addition to the positive control, dextran sulfate. The IC_{50} values (Table 1) are the sample concentration at which the relative luminescence units were reduced by 50% compared to virus control wells (no test sample). HIV inhibitory activity was detected for **Sulfo-6**, with IC_{50} values for all viruses tested in the low micromolar range. Reduction in luciferase signal by **Sulfo-4** was only observed at the highest compound concentrations tested and did not reach the 50% neutralization cutoff. The positive controls, dextran sulfate and HIVIG-C, were both potent inhibitors as expected, yielding nM inhibition in all four HIV-1 strains, except TV1.21 for HIVIG-C, which was μM.

As with all *in vitro* assays, the results obtained are constrained by the system used. Experiments in other laboratories have shown that HIV neutralization assays in the TZM-bl cell system may be less sensitive than assays in other cells, such as T cell lines and PHA-stimulated PBMCs,[40] and that viruses produced in 293T cells are more sensitive to neutralizing antibodies than the same virus produced in PBMCs.[55] We have also observed that an assay based on the T cell line A3R5 can be 10- to 100-fold more sensitive in the detection of neutralizing antibodies than the TZM-bl assay, but only for viruses with a tier 2 (less-sensitive) neutralization phenotype (unpublished data).[56] The viruses assayed here for inhibition by **sulfo-4** and **sulfo-6** are all tier 1 (more neutralization sensitive) and are equally sensitive to neutralizing antibodies when assayed in TZM-bl and A3R5 cells. However, it is possible that neutralization by sulfated polysaccharides may behave differently in these two assay systems than neutralization by antibodies, and the results here may underestimate the potential of these two compounds to inhibit HIV in an optimal *in vitro* assay. Like Louder *et al.*, we have also found that a virus produced in 293T cells is more sensitive to neutralization by antibodies than the same virus grown in activated human PBMCs. The viruses used herein were pseudoviruses produced in 293T cells. In humans, the infecting HIV would likely have been produced by lymphoid or monocytoid cells. If HIV inhibition by sulfated polysaccharides follows the trend observed with neutralization by antibodies, the results here may overestimate the inhibition of HIV by **sulfo-4** and **sulfo-6** in an infected individual. Clearly, further studies are needed to understand the true utility of these and similar compounds in protection from HIV infection *in vivo*, but the results presented

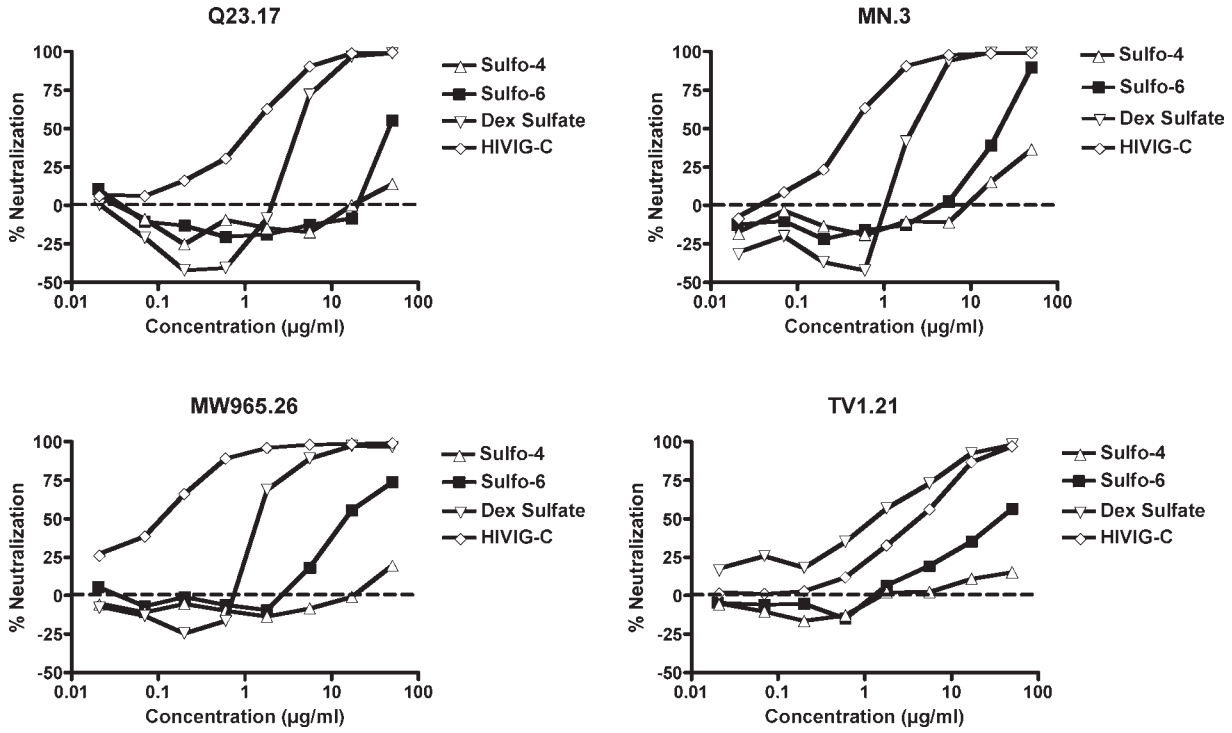

Figure 3. HIV-1 luciferase reporter gene assay results for % neutralization of four different HIV-1 strains (Q23.17, MN.3, MW965.26, and TV1.21) in TZM-bl cells by glycodendrimers **sulfo-4** and **sulfo-6** with positive controls, dextran sulfate and HIVIG-C.

here provide encouragement for continuing to evaluate this strategy (Figure 3).

The combined data from both the ELISA and luciferase reporter gene assay suggest a few conclusions regarding the potential of these molecules as anti-HIV molecules. First, the assays were found to be complementary to one another: the luciferase assay confirmed the anti-HIV activity of **sulfo-6** that was suggested by the ELISA result. This supports our strategy for screening glycodendrimer compounds: the ELISA serves as a simple screen for whether or not a sulfated glycodendrimer has the ability to bind the target gp120 protein, while the luciferase assay measures how well the sulfated glycodendrimers prevent the infection of the TZM-bl cells. Second, the activity of **sulfo-6** is superior to that of **sulfo-4**. **Sulfo-4** contains 2.02% sulfur, 8 sugar residues and a MW of approximately 4000 Da. It cannot be determined from the data gathered whether the poor activity observed for **sulfo-4** was due to the small size, the low % sulfur, or as a result of both factors. Further study of these effects is required. Therefore, all future sulfoglycodendrimers envisioned will need to be equal/larger than **sulfo-6**, and have a minimum of 4% sulfur (by wt). It is hypothesized that, as the sulfoglycodendrimers increase in size/sulfur content, both assays will be better able to quantitate the HIV-1 activity, as the sulfoglycodendrimers will be more adept at binding to gp120 multivalently, and potentially serve as effective anti-HIV-1 agents. This is supported by a report by Subramaniam and co-workers, where it was reported that the native trimeric spike of gp120 has a width of 15 nm.[57] Compared with the known diameters of unsubstituted PAMAM $G = 1$ and 2, which are 1.9 and 2.6 nm, respectively, it can be theorized that the glycodendrimers reported herein can interact with/bind to at least one gp120 monomer apiece.[58] It is also supported by reports in the literature illustrating a variety of (glyco)dendrimer-based molecules with anti-HIV activity (μM—nM), with molecular weights ranging from 12 400 to 24 581 Da.[41,43,47,59] As we have now reported a sulfoglycodendrimer (**sulfo-6**) with a MW of 8777 Da and 4.03% sulfur with μM activity across all HIV-1 strains evaluated, we are satisfied that the ELISA/luciferase assay combination will provide adequate sensitivity for future molecules evaluated, as these will all be larger in size and contain a minimum of 4% sulfate (by wt). Finally, in taking the sialic acid monosaccharide, presenting it multivalently on PAMAM, and sulfating it, we were able to observe modest μM activity (IC_{50} values ranging from 1.6 to 5.1 μM). These values compared well to the EC_{50} value of 0.4 μM for an 8000 Da sulfated colominic acid derivative containing 6% sulfur, as reported by Yang et al.[19] This indicates that the strategy of taking smaller pieces of a polysaccharide of known anti-HIV properties and presenting them in a multivalent sense on a dendrimer scaffold can yield structurally well-defined sulfoglycodendrimers with good anti-HIV activity. This approach may also result in derivatives with reduced or absent toxicity issues as compared to the sulfated polydisperse polysaccharides from which they are derived. This latter issue will be addressed in future studies.

CONCLUSIONS

In summary, an initial series of 6 sulfoglycodendrimers were sought, synthesized by either a divergent-like or convergent-like approach, as potential anti-HIV agents. The syntheses were planned with the fewest steps possible and no sugar protecting group chemistry, to find the fastest and most facile way to make sulfoglycodendrimers in the best yields possible. While it was initially believed that the four-step convergent-like approach would be the best reaction sequence, as the steric issues of both sialic acid and PAMAM were minimized through the addition of an intermediary hydrophilic linker, only **1** was produced, and in poor yield. This contrasts with the one-step divergent-like pathway, which at the outset was not expected to work well, given that

both the sialic acid and PAMAM structures were sterically congested. Surprisingly, this path led to the production of all three desired glycodendrimers, **2**, **4**, and **6**, in modest yields, and all in one step. Glycodendrimers **1**, **2**, **4**, and **6** were all fully substituted with respect to the number of sugars attached to the reactive groups terminating the various generations of PAMAM, thereby eliminating the polydispersity of structure found in the parent polysaccharide colominic acid. While the chemical sulfation process was not regioselective, it was viewed to be of lesser importance at the current time than finding the appropriate synthetic method and determining the general minimum structural requirements necessary for these molecules to have anti-HIV-1 activity. This was achieved in **sulfo-6**. The synthesis of a completely monomolecular product in terms of the number of both sugars and sulfates incorporated remains a future goal.

In addition to finding an appropriate synthesis for the glycodendrimers, a simple binding screen and well-characterized confirmatory functional assay were utilized to rapidly determine their potential anti-HIV activity. Upon evaluation of the sulfoglycodendrimers, **sulfo-1**, **2**, **4**, and **6**, the in-house ELISA screening assay suggested that only **sulfo-6** bound to b-rgp120. This was confirmed using the more sensitive luciferase reporter gene neutralization assay, which detected μM activity for **sulfo-6**. Thus, we have shown that a simple monosaccharide building block derived from a known anti-HIV sulfated polysaccharide can yield molecules possessing anti-HIV-1 activity when appended to a multivalent scaffold, even though they are smaller in size than the parent polysaccharide.

■ ASSOCIATED CONTENT

Supporting Information. Full synthetic and characterization details of the sialic acid-PAMAM glycodendrimers and NMR spectra are provided. This material is available free of charge via the Internet at http://pubs.acs.org.

■ AUTHOR INFORMATION

Corresponding Author

*Tel: 1-916-278-6551. Fax: 1-916-278-4986. E-mail: kdmcr@csus.edu.

■ ACKNOWLEDGMENT

The authors are indebted to Dr. David Montefiori from Duke University for providing the expertise and resources for acquiring the HIV luciferase reporter gene assay results (supported by NIH contract AI30034). We would additionally like to thank Drs. Shiu-Lok Hu and Yun Li at Washington State University for the extensive conversations, guidance, and initial HIV luciferase reporter gene assay results (with partial support provided by NIH P51 grant RR000166). The authors would finally like to thank Careena Cary for running the sulfation reactions, and Drs. Andreas Franz from the University of the Pacific and Dr. Arpad Somogyi from the University of Arizona, for their assistance with the mass spectral analysis. Financial support for this work from NIH-AREA (1R15AI068444-01), Research Corporation Cottrell College Science Award (CC6610), and an NSF-MRI grant to fund the 500 MHz NMR (CHE MRI-0922676) are gratefully acknowledged.

■ REFERENCES

(1) *UNAIDS* (2010) pp 364, UNAIDS.
(2) *UNAIDS* (2009) pp 100, UNAIDS.
(3) Granich, R., Crowley, S., Vitoria, M., Lo, Y.-R., Souteyrand, Y., Dye, C., Gilks, C., Guerma, T., De Cock, K. M., and Williams, B. (2010) Highly active antiretroviral treatment for the prevention of HIV transmission. *J. Int. AIDS Soc. 13*, 1–8.
(4) Broder, S. (2010) The development of antiretroviral therapy and its impact on the HIV-1/AIDS pandemic. *Antiviral Res. 85*, 1–18.
(5) Este, J. A., and Cihlar, T. (2010) Current status and challenges of antiretroviral research and therapy. *Antiviral Res. 85*, 25–33.
(6) Hawkins, T. (2010) Understanding and managing the adverse effects of antiretroviral therapy. *Antiviral Res. 85*, 201–209.
(7) Gupta, U., and Jain, N. K. (2010) Non-polymeric nano-carriers in HIV/AIDS drug delivery and targeting. *Adv. Drug. Delivery Rev. 62*, 478–490.
(8) Ito, M., Baba, M., Sato, A., Pauwels, R., De Clerq, E., and Shigeta, S. (1987) Inhibitory effect of dextran sulfate and heparin on the replication of human immunodeficiency virus (HIV) *in vitro*. *Antiviral Res. 7*, 361–367.
(9) Mitsuya, H., Looney, D. J., Kuno, S., Ueno, R., Wong-Staal, F., and Broder, S. (1988) Dextran sulfate suppression of viruses in the HIV family: inhibition of virion binding to CD4+ cells. *Science 240*, 646–649.
(10) Baba, M., Pauwels, R., Balzarini, J., Arnout, J., Desmyter, J., and De Clercq, E. (1988) Mechanism of inhibitory effect of dextran sulfate and heparin on replication of human immunodeficiency virus *in vitro*. *Proc. Natl. Acad. Sci. U.S.A. 85*, 6132–6136.
(11) Callahan, L. N., Phelan, M., Mallinson, M., and Norcross, M. A. (1991) Dextran sulfate blocks antibody binding to the principal neutralizing domain of human immunodeficiency virus type 1 without interfering with gp120-CD4 interactions. *J. Virol. 65*, 1543–1550.
(12) Batinic, D., and Robey, F. A. (1992) The V3 region of the envelope glycoprotein of human immunodeficiency virus type 1 binds sulfated polysaccharides and CD4-derived synthetic peptides. *J. Biol. Chem. 267*, 6664–6671.
(13) Meshcheryakova, D., Andreev, S., Taraswova, S., Sidorova, M., Vafina, M., Kornilaeva, G., Karamov, E., and Kaitov, R. (1993) CD4-derived peptide and sulfated polysaccharides have similar mechanisms of anti-HIV activity based on electrostatic interactions with positively charged gp120 fragments. *Mol. Immunol. 30*, 993–1001.
(14) Rizzuto, C. D., Wyatt, R., Hernandez-Ramos, N., Sun, Y., Kwong, P. D., Hendrickson, W. A., and Sodroski, J. (1998) A conserved HIV gp120 glycoprotein structure involved in chemokine receptor binding. *Science 280*, 1949–1953.
(15) Moulard, M., Lortat-Jacob, H., Mondor, I., Roca, G., Wyatt, R., Sodroski, J., Zhao, L., Olson, W., Kwong, P. D., and Sattentau, Q. J. (2000) Selective interactions of polyanions with basic surfaces on human immunodeficiency virus type 1 gp120. *J. Virol. 74*, 1948–1960.
(16) Bertozzi, C. R., and Kiessling, L. L. (2001) Chemical glycobiology. *Science 291*, 2357–2364.
(17) Kiessling, L. L., Gestwicki, J. E., and Strong, L. E. (2000) Synthetic multivalent ligands in the exploration of cell-surface interactions. *Curr. Opin. Chem. Biol. 4*, 696–703.
(18) Roderiquez, G., Oravecz, T., Yanagishita, M., Bou-Habib, D. C., Mostowski, H., and Norcross, M. A. (1995) Mediation of human immunodeficiency virus type 1 binding by interaction of cell surface heparan sulfate proteoglycans with the V3 region of envelope gp120-gp41. *J. Virol. 69*, 2233–2239.
(19) Yang, D.-W., Ohta, Y., Yamaguchi, S., Tsukada, Y., Haraguchi, Y., Hoshino, H., Amagai, H., and Kobayashi, I. (1996) Sulfated colominic acid: an antiviral agent that inhibits the human immunodeficiency virus type I *in vitro*. *Antiviral Res. 31*, 95–104.
(20) Lorentson, K. J., Hendrix, C. W., Collins, J. M., Kornhauser, D. M., Petty, B. G., Klecker, R. W., Flexner, C., Eckel, R. H., and Lietman, P. S. (1989) Dextran sulfate is poorly absorbed after oral administration. *Ann. Intern. Med. 111*, 561–566.

(21) Flexner, C., Barditch-Crovo, P. A., Kornhauser, D. M., Farzadegan, H., Nerhood, L. J., Chaisson, R. E., Bell, K. M., Lorentsen, K. J., Hendrix, C. W., Petty, B. G., and Lietman, P. S. (1991) Pharmacokinetics, Toxicity, and Activity of Intravenous Dextran Sulfate in Human Immunodeficiency Virus Infection. *Antimicrob. Agents Chemother. 35*, 2544–2550.

(22) Hiebert, L. M., Wice, S. M., Jaques, L. B., Williams, K. E., and Conly, J. M. (1999) Orally administered dextran sulfate is absorbed in HIV-positive individuals. *J. Lab. Clin. Med. 133*, 161–170.

(23) McReynolds, K. D., and Gervay-Hague, J. (2007) Chemotherapeutic interventions targeting HIV interactions with host-associated carbohydrates. *Chem. Rev. 107*, 1533–1552.

(24) Tomalia, D. A., Baker, H., Dewald, J. R., Hall, M., Kallos, G., Martin, S., Roeck, J., Ryder, J., and Smith, P. (1985) A new class of polymers: starburst-dendritic macromolecules. *Polymer J. (Tokyo) 17*, 117–132.

(25) Kono, K., Kojima, C., Hayashi, N., Nishisaka, E., Kiura, K., Watarai, S., and Harada, A. (2008) Preparation and cytotoxic activity of poly(ethylene glycol)-modified poly(amidoamine) dendrimers bearing adriamycin. *Biomaterials 29*, 1664–1675.

(26) Fant, K., Esbjorner, E. K., Jenkins, A., Grossel, M. C., Lincoln, P., and Norden, B. (2010) Effects of PEGylation and acetylation of PAMAM dendrimers on DNA binding, cytotoxicity, and in vitro transfection efficiency. *Mol. Pharmaceutics 17*, 1734–1746.

(27) Medina, S. H., and El-Sayed, M. E. H. (2009) Dendrimers as carriers for delivery of chemotherapeutic agents. *Chem. Rev. 109*, 3141–3157.

(28) Rolland, O., Turrin, C.-O., Caminade, A.-M., and Majoral, J.-P. (2009) Dendrimers and nanomedicine: multivalency in action. *New J. Chem. 33*, 1809–1824.

(29) Heegaard, P. M. H., Boas, U., and Sorensen, N. S. (2010) Dendrimers for vaccine and immunostimulatory uses. A review. *Bioconjugate Chem. 21*, 405–418.

(30) Tekade, R. K., Kumar, P. V., and Jain, N. K. (2009) Dendrimers in oncology: an expanding horizon. *Chem. Rev. 109*, 49–87.

(31) Labieniec, M., and Watala, C. (2009) PAMAM dendrimers-diverse biomedical applications. Facts and unresolved questions. *Cent. Eur. J. Biol. 4*, 434–451.

(32) Jevprasesphant, R., Penny, J., Jalal, R., Attwood, D., McKeown, N. B., and D'Emanuele, A. (2003) The influence of surface modification on the cytotoxicity of PAMAM dendrimers. *Int. J. Pharm. 252*, 263–266.

(33) Roy, R., Zanini, D., Meunier, S. J., and Romanowska, A. (1993) Solid-phase synthesis of dendritic sialoside inhibitors of influenza A virus haemagglutinin. *J. Chem. Soc., Chem. Commun.* 1869–1872.

(34) Dimick, S. M., Powell, S. C., McMahon, S. A., Moothoo, D. N., Naismith, J. H., and Toone, E. J. (1999) On the meaning of affinity: cluster glycoside effects and concanavalin A. *J. Am. Chem. Soc. 121*, 10286–10296.

(35) Pohl, N. L., and Kiessling, L. L. (1999) Scope of multivalent ligand function. Lactose-bearing neoglycopolymers by ring-opening metathesis polymerization. *Synthesis Special Issue* 1515–1519.

(36) Wang, J.-Q., Chen, X., Zacharek, S., Chen, Y., and Wang, P. G. (1999) Enhanced inhibition of human anti-gal antibody binding to mammalian cells by synthetic α-gal epitope polymers. *J. Am. Chem. Soc. 121*, 8174–8181.

(37) Reuter, J. D., Myc, A., Hayes, M. M., Gan, Z., Roy, R., Qin, D., Yin, R., Piehler, L. T., Esfand, R., Tomalia, D. A., and Baker, J. R. (1999) Inhibition of viral adhesion and infection by sialic-acid-conjugated dendritic polymers. *Bioconjugate Chem. 10*, 271–278.

(38) Woller, E. K., and Cloninger, M. J. (2001) The lectin-binding properties of six generations of mannose-functionalized dendrimers. *Org. Lett. 4*, 7–10.

(39) Ashton, P. R., Hounsell, E. F., Jayaraman, N., Nilsen, T. M., Spencer, N., Stoddart, J. F., and Young, M. (1998) Synthesis and biological evaluation of α-D-mannopyranoside-containing dendrimers. *J. Org. Chem. 63*, 3429–3437.

(40) Borges, A. R., Wieczorek, L., Johnson, B., Benesi, A. J., Brown, B. K., Kensinger, R. D., Krebs, F. C., Wigdahl, B., Blumenthal, R., Puri, A., McCutchan, F. E., Birx, D. L., Polonis, V. R., and Schengrund, C.-L. (2010) Multivalent dendrimeric compounds containing carbohydrates expressed on immune cells inhibit infection by primary isolates of HIV-1. *Virology 408*, 80–88.

(41) Kensinger, R. D., Yowler, B. C., Benesi, A. J., and Schengrund, C.-L. (2004) Synthesis of novel, multivalent glycodendrimers as ligands for HIV-1 gp120. *Bioconjugate Chem. 15*, 349–358.

(42) Kensinger, R. D., Catalone, B. J., Krebs, F. C., Wigdahl, B., and Schengrund, C.-L. (2004) Novel polysulfated galactose-derivatized dendrimers as binding antagonists of human immunodeficiency virus type 1 infection. *Antimicrob. Agents Chemother. 48*, 1614–1623.

(43) Morales-Serna, J. A., Boutureira, O., Serra, A., Matheu, M. I., Diaz, Y., and Castillon, S. (2010) Synthesis of hyperbranched β-galceramide-containing dendritic polymers that bind HIV-1 rgp120. *Eur. J. Org. Chem.* 2657–2660.

(44) Perez-Anes, A., Stefaniu, C., Moog, C., Majoral, J.-P., Blanzat, M., Turrin, C.-O., Caminade, A.-M., and Rico-Lattes, I. (2010) Multivalent catanionic galcer analogs derived from first generation dendrimeric phosphonic acids. *Bioorg. Med. Chem. 18*, 242–248.

(45) Blanzat, M., Turrin, C.-O., Aubertin, A.-M., Couturier-Vida, C., Caminade, A.-M., Majoral, J.-P., Rico-Lattes, I., and Lattes, A. (2005) Dendritic catanionic assemblies: in vitro anti-HIV activity of phosphorous-containing dendrimers bearing Galβ1Cer analogs. *ChemBioChem 6*, 2207–2213.

(46) Han, S., Baigude, H., Hattori, K., Yoshida, T., and Uryu, T. (2007) Synthesis of new spherical and hemispherical oligosaccharides with polylysine core scaffold. *Carbohydr. Poly. 68*, 26–34.

(47) Han, S., Yoshida, D., Kanamoto, T., Nakashima, H., Uryu, T., and Yoshida, T. (2010) Sulfated oligosaccharide cluster with polylysine core scaffold as a new anti-HIV dendrimer. *Carbohydr. Poly. 80*, 1111–1115.

(48) Tabarani, G., Reina, J. J., Ebel, C., Vives, C., Lortat-Jacobs, H., Rojo, J., and Fieschi, F. (2006) Mannose hyperbranched dendritic polymers interact with clustered organization of DC-SIGN and inhibit gp120 binding. *FEBS Lett. 580*, 2402–2408.

(49) Konou, M., Koizumi, M., Shimizu, K., Kawase, M., and Hatanaka, K. (2000) Synthesis of sulfated colominic acids and their interaction with fibroblast growth factors. *Biomacromolecules 1*, 451–458.

(50) Li, M., Gao, F., Mascola, J. R., Stamatatos, L., Polonis, V. R., Koutsoukos, M., Voss, G., Goepfert, P., Gilbert, P., Greene, K. M., Bilska, M., Kothe, D. L., Salazar-Gonzalez, J. F., Wei, X., Decker, J. M., Hahn, B. H., and Montefiori, D. C. (2005) Human immunodeficiency virus type 1 env clones from acute and early subtype B infections for standardized assessments of vaccine-elicited neutralizing antibodies. *J. Virol. 79*, 10108–10125.

(51) Montefiori, D. C. (2009) Measuring HIV neutralization in a luciferase reporter gene assay, in HIV protocols, 2nd ed. (Prasad, V. R., and Kalpana, G. V., Eds.) pp 395−404, Humana Press, New York.

(52) Suhara, Y., Kurihara, M., Kittaka, A., and Ichikawa, Y. (2006) Efficient synthesis of carbopeptoid oligomers: insight into mimicry of beta-peptide. *Tetrahedron 62*, 8207–8217.

(53) Sigma-Aldrich Product Information Sheet, Dextran Sulfate, D8906. http://www.sigmaaldrich.com/catalog/Lookup.do?D7=0&N17=2&N16=AND(CONTEXT:1,OR(LOCATION:US,LOCATION:0))&N3=mode%20matchpartialmax&N5=All&N4=dextran%20sulfate&N1=S_ID&ST=RS&QS=ON&N25=0&F=TD (accessed 08/30/11).

(54) Wei, X., Decker, J. M., Wang, S., Hui, H., Kappes, J. C., Wu, X., Salazar-Gonzalez, J. F., Salazar, M. G., Kilby, J. M., Saag, M. S., Komarova, N. L., Nowak, M. A., Hahn, B. H., Kwong, P. D., and Shaw, G. M. (2003) Antibody neutralization and escape by HIV-1. *Nature 422*, 307–312.

(55) Louder, M. K., Sambor, A., Chertova, E., Hunte, T., Barrett, S., Ojong, F., Sanders-Buell, E., Zolla-Pazner, S., McCutchan, F. E., Roser, J. D., Gabuzda, D., Lifson, J. D., and Mascola, J. R. (2005) HIV-1 envelope pseudotyped viral vectors and infectious molecular clones expressing the same envelope glycoprotein have a similar neutralization phenotype, but culture in peripheral blood mononuclear cells is associated with decreased neutralization sensitivity. *Virology 339*, 226–238.

(56) Seaman, M. S., Janes, H., Hawkins, N., Grandpre, L. E., Devoy, C., Giri, A., Coffey, R. T., Harris, L., Wood, B., Daniels, M. G., Bhattacharya, T., Lapedes, A., Polonis, V. R., McCutchan, F. E., Gilbert, P. B., Self, S. G., Korber, B. T., Montefiori, D. C., and Mascola, J. R. (2010) Tiered categorization of a diverse panel of HIV-1 Env pseudoviruses for assessment of neutralizing antibodies. *J. Virol. 84*, 1439–1452.

(57) Liu, J., Bartesaghi, A., Borgnia, M. J., Sapiro, G., and Subramaniam, S. (2008) Molecular architecture of native HIV-1 gp120 trimers. *Nature 455*, 109–113.

(58) Devarakonda, B., Hill, R. A., and de Villiers, M. M. (2004) The effect of PAMAM dendrimer generation size and surface functional group on the aqueous solubility of nifedipine. *Int. J. Pharm. 284*, 133–140.

(59) McCarthy, T. D., Karellas, P., Henderson, S. A., Giannis, M., O'Keefe, D. F., Heery, G., Paull, J. R. A., Matthews, B. R., and Holan, G. (2005) Dendrimers as drugs: discovery and preclinical and clinical development of dendrimer-based microbicides for HIV and STI prevention. *Mol. Pharmaceutics 2*, 312–318.

Supporting Information

Experimental Procedures:

Tetrameric glyco-DATEG-PAMAM dendrimer (**1)**: PAMAM G = -0.5 (24 mg, 0.055 mmol) was weighed into a flame-dried 10 mL round-bottomed flask and dissolved in DMF (1 mL), and flushed with nitrogen. DIPEA (71 mg, 0.55 mmol) was added, followed by BOP (120 mg, 0.27 mmol). The sugar linker **11** (100 mg, 0.23 mmol) was placed into a second 10 mL round-bottomed flask and dissolved in DMF (1 mL). The two solutions were mixed together, heated to 35˚C, and stirred under nitrogen for 24 hours. The solvents were evaporated under reduced pressure and the crude product was dialyzed with 500 MWCO tubing in a 1L flask against nanopure D.I. water. The water was changed once every hour for four hours, and allowed to stir overnight at 4˚C. The remaining crude material was then lyophilized. The dialyzed crude material was then purified using RP-HPLC with a linear gradient between water/0.1% trifluoroacetic acid and acetonitrile/0.1% trifluoroacetic acid. Fractions containing the product were collected, grouped, and purified through size exclusion chromatography with 0.03 M ammonium bicarbonate as the mobile phase. This provided compound **1**, as a fluffy white solid (3 mg, 0.0017 mmol, 6.4% yield). ^{1}H NMR (D_2O): δ 1.73 (m, 1H, H_B), 2.09 (s, 3H, H_C), 2.36 (dd, 1H, *J*= 5.0Hz, 16.4Hz, H_A), 2.49 (t, 2H, J=7.2Hz, H_M), 2.68 (s, 1H, H_K), 2.87 (t, 2H, *J*=7.1Hz, H_L), 3.43 (t, 3H, J=5.4Hz, H_P), 3.49 (m, 3H, H_S), 3.67 (m, 17H, $H_{G,J,Q,R}$), 3.78 (m, 1H, H_H), 3.88 (dd, 1H, *J*=2.6Hz, 11.8Hz, H_E), 3.95 (t, 1H, *J*=9.7Hz, H_I), 4.11 (m, 2H, $H_{D,F}$). ^{13}C NMR (D_2O, TSP internal): δ 24.9, 35.2, 41.6, 41.7, 42.4, 51.90, 51.92, 54.9, 66.0, 69.5, 71.0, 71.4, 71.6, 71.6, 72.2, 72.3, 72.9, 73.2, 98.3, 98.3, 98.4, 175.6, 177.6, 177.7. MALDI-TOF: $[M + Na]^+$ ($C_{82}H_{148}N_{14}O_{44}Na$) calcd m/z = 2055.9671, Found m/z = 2058.4.

Tetrameric glycoPAMAM dendrimer (**2)**: Sialic acid (cmpd **10**, 200 mg, 0.66 mmol) was weighed into a flame-dried 10 mL round-bottomed flask, flushed with nitrogen, then dissolved into DMF (4 mL). BOP (400 mg, 0.9 mmol) was then added as a solid. PAMAM G=0 (20% by wt. in methanol) (75 mg, 0.15 mmol) was next weighed into a separate 10 mL round-bottomed flask and the methanol was evaporated under reduced pressure. DMF (1.5 mL) and DIPEA (190 mg, 1.5 mmol) were added to the flask with PAMAM. The PAMAM solution was then added to the sialic acid solution, heated to 35˚C, and the reaction was stirred for four days under nitrogen. The crude reaction product was dialyzed with 500 MWCO tubing against nanopure water. The

water was changed once an hour for three hours then left stirring overnight at 4˚C. The crude material was then purified using RP-HPLC with a linear gradient between water/0.1% trifluoroacetic acid and acetonitrile/0.1% trifluoroacetic acid providing compound **2**, as a fluffy white solid (29.4 mg, 0.017 mmol, 11.4% yield). ^{1}H NMR (D_2O): δ 1.69 (t, 1H, *J*=12.3Hz, H_B), 2.08 (s, 3H, H_C), 2.34 (dd, 1H, *J*=4.9Hz,13Hz, H_A) , 2.76 (m, 2H, H_M), 3.40 (m, 7H, $H_{K,L,N,O}$), 3.61 (d, 1H, *J*=9.3Hz, H_G), 3.66 (dd, 1H, *J*=6.3Hz, 11.8Hz, H_J), 3.77 (m, 1H, H_H), 3.87 (dd, 1H, *J*= 2.4Hz, 11.8Hz, H_E), 3.94 (t, 1H, *J*=10.3Hz, H_I), 4.09 (m, 2H, $H_{D,F}$). ^{13}C NMR (D_2O, TSP internal std): δ 25.1, 32.7, 41.56, 41.6, 42.7, 51.6, 52.5, 55.2, 66.2, 69.7, 71.3, 73.2, 73.5, 98.6, 118.2, 120.5, 165.8, 166.1, 175.6, 175.9, 177.9. MALDI-TOF: $[M + Na]^+$ ($C_{66}H_{116}N_{14}O_{36}Na$) calcd m/z = 1703.7574, Found m/z =1703.8.

Octameric glyco-DATEG-PAMAM dendrimer (**3**): Sugar linker **11** (53 mg, 0.12 mmol) was weighed into a flame-dried 10 mL round-bottomed flask, flushed with nitrogen, then dissolved into DMF (1 mL). BOP (58 mg, 0.13 mmol) was added as a solid. PAMAM G=0.5 (20% by wt. in methanol) (16 mg, 0.013 mmol) was weighed into a separate 10 mL round-bottomed flask and the methanol was removed *in vacuo*. Next, DMF (1 mL), then DIPEA (34 mg, 0.26 mmol), were added to the PAMAM. The PAMAM mixture was added to the sugar linker. The reaction was heated to 35˚C for seven days. The solvents were evaporated *in vacuo* and the crude was freeze-dried. The crude was dialyzed with 500 MWCO tubing against nanopure water. The water was changed every hour for four hours, then stirred overnight at 4˚C. The crude material was next purified using RP-HPLC with a linear gradient between water/0.1% trifluoroacetic acid and acetonitrile/0.1% trifluoroacetic acid. This was followed by size exclusion chromatography in 0.03 M ammonium bicarbonate buffer. ^{1}H and ^{13}C NMR showed the PAMAM was not fully substituted. For compound **3**, the calculated molecular weight for $C_{182}H_{328}N_{34}O_{92}$ $[M+H]^+$ was 4462.2031. MALDI MS showed small peaks for $[M+H]^+$ m/z=4467.033, $[M-H_2O]$ m/z=4447.926, and $[M-2H_2O]$ m/z=4428.818, but also found was [M-cmpd **11**-H_2O] m/z=4027.557. While MALDI MS shows evidence that **3** was synthesized, it was not present in a large enough quantity to get clear ^{1}H or ^{13}C data.

Octameric glycoPAMAM dendrimer (**4)**: Sialic acid (**10,** 190 mg, 0.62 mmol) was weighed into a flame-dried 10 mL round-bottomed flask, flushed with nitrogen, then dissolved in DMF (4 mL). BOP (310 mg, 0.7 mmol) was added as a solid. PAMAM G=1 (20% by wt. in methanol)

(100 mg, 0.07 mmol) was weighed into a separate 10 mL round-bottomed flask and the methanol was evaporated off under reduced pressure. DMF (2 mL) and DIPEA (180 mg, 1.4 mmol) were added to the PAMAM. The two solutions were mixed and the reaction was stirred under nitrogen for seven days. The solvents were then evaporated *in vacuo* and the crude was freeze-dried. The crude solid was next dialyzed with 500 MWCO tubing against nanopure D.I. water. The water was changed every hour for four hours then stirred overnight at 4˚C. The crude material was next purified using RP-HPLC with a linear gradient between water/0.1% trifluoroacetic acid and acetonitrile/0.1% trifluoroacetic acid. This was followed by size exclusion chromatography using Biogel P-10 gel in 0.03 M ammonium bicarbonate buffer producing compound **4**, as a fluffy white solid (28 mg, 0.0101 mmol, 14% yield). ^{1}H NMR (D_2O): δ 1.68 (t, 2H, *J*=12.3Hz, H_B), 2.07 (s, 6H, H_C), 2.33 (dd, 2H, *J*= 5.0Hz, 13.1Hz, H_A), 2.43 (m, 6H, H_M), 2.63 (m, 1H, H_K), 2.83 (m, 6H, H_L), 3.33 (m, 12H, $H_{N,O}$), 3.60 (d, 2H, *J*=9.6Hz, H_G), 3.66 (dd, 2H, *J*=6.2Hz, 11.8Hz, H_J), 3.77 (m, 2H, H_H), 3.86 (dd, 2H, *J*=2.4Hz, 11.8Hz, H_E), 3.93 (t, 2H, *J*=10.2Hz, H_I), 4.07 (m, 4H, $H_{D,F}$). ^{13}C NMR (D_2O, TSP internal std.): δ 25.0, 35.3, 35.5, 39.6, 41.3, 41.7, 42.5, 51.8, 52.8, 54.0, 55.0, 66.0, 69.5, 69.54, 71.1, 72.9, 73.2, 98.4, 175.7, 177.6, 177.9. MALDI-TOF: $[M + H]^+$ ($C_{150}H_{264}N_{34}O_{76}$) calcd m/z = 3757.7837, Found m/z =3759.3.

16-mer glyco-DATEG-PAMAM dendrimer (**5)**: Sugar linker **11** (75 mg, 0.17 mmol) was weighed into a flame-dried 10 mL round-bottomed flask, flushed with nitrogen, then dissolved into DMF (1 mL). BOP (93 mg, 0.21 mmol) was added as a solid. PAMAM G=1.5 (20% by wt. in methanol) (25 mg, 0.0085 mmol) was weighed into a separate round-bottomed flask and the methanol was evaporated off *in vacuo*. Next, DMF (1 mL), then DIPEA (44 mg, 0.34 mmol) were added to PAMAM. The PAMAM mixture was added to the sugar-linker. The reaction was heated to 35˚C and run for 14 days. The solvents were then evaporated *in vacuo*, and the crude was freeze-dried. The crude solid was next dialyzed with 500 MWCO tubing against nanopure water. The water was changed every hour for four hours, then stirred overnight at 4˚C. The crude material was then purified using RP-HPLC with a linear gradient between water/0.1% trifluoroacetic acid and acetonitrile/0.1% trifluoroacetic acid. This was followed by size exclusion chromatography using Biogel P-10 gel in 0.03 M ammonium bicarbonate buffer. ^{1}H NMR showed that no fractions contained the fully substituted product. Compound **5** was not isolated. No clear ^{1}H NMR was collected that indicated the presence of compound **5**, therefore, no samples were sent out for MALDI-MS analysis.

16-mer glycoPAMAM dendrimer (**6)**: Sialic acid (**10**, 46 mg, 0.15 mmol) was weighed into a flame-dried 10 mL round-bottomed flask, flushed with nitrogen, then dissolved in DMF (1 mL). BOP (84 mg, 0.19 mmol) was added as a solid. PAMAM G=2 (20% by wt. in methanol) (25 mg, 0.0077 mmol) was weighed into a separate round-bottomed flask and the methanol was evaporated under reduced pressure. DMF (1 mL) and DIPEA (40 mg, 0.31 mmol) were added to the PAMAM. The two solutions were mixed, heated to 35˚C, and reaction was stirred under nitrogen for 14 days. The solvents were then evaporated under reduced pressure and the crude sample was freeze-dried. The crude solid was then dialyzed with 500 MWCO tubing. The water was changed once an hour for four hours, then stirred overnight at 4˚C. Initial purification was conducted using RP-HPLC with a linear gradient between water/0.1% trifluoroacetic acid and acetonitrile/0.1% trifluoroacetic acid. This was followed by size exclusion chromatography using Biogel P-10 gel in 0.03 M ammonium bicarbonate buffer providing compound **6**, as a fluffy white solid (17 mg, 0.00215 mmol, 28% yield). ^{1}H NMR (D_2O): δ 1.70 (m, 4H, H_B), 2.10 (s, 12H, H_C), 2.35 (dd, 4H, *J*=4.9Hz, 13.1Hz, H_A), 2.46 (m, 14H, H_M), 2.68 (m, 1H, H_K), 2.86 (m, 14H, H_L), 3.36 (m, 24H, $H_{N,O}$), 3.63 (d, 4H, *J*=9.5 Hz, H_G), 3.69 (dd, 4H, *J*= 6.2 Hz, 11.8Hz, H_J), 3.79 (m, 4H, H_H), 3.89 (dd, 4H, *J*= 2.4 Hz, 11.8Hz, H_E), 3.96 (t, 4H, *J*=10.2 Hz, H_I), 4.10 (d, 8H, *J*=10.8 Hz, $H_{D,F}$). ^{13}C NMR (D_2O, TSP internal std): δ 25.0, 35.5, 39.6, 41.3, 41.7, 51.9, 54.1, 55.0, 66.0, 69.45, 69.5, 71.1, 73.0, 73.3, 98.32, 98.34, 98.36, 98.38, 175.7, 177.7, 177.9, 166.6 MALDI-TOF: $[M + Na]^+$ ($C_{318}H_{560}N_{74}O_{156}Na$) calcd m/z = 7934.8056, Found m/z =7937.166.

[1]H Nuclear Magnetic Resonance Spectra at 500 MHz

{2-[2-(2-Amino-ethoxy)-ethoxy]-ethyl}-carbamic acid tert-butyl ester (compound **8**) [1]H NMR in D_2O

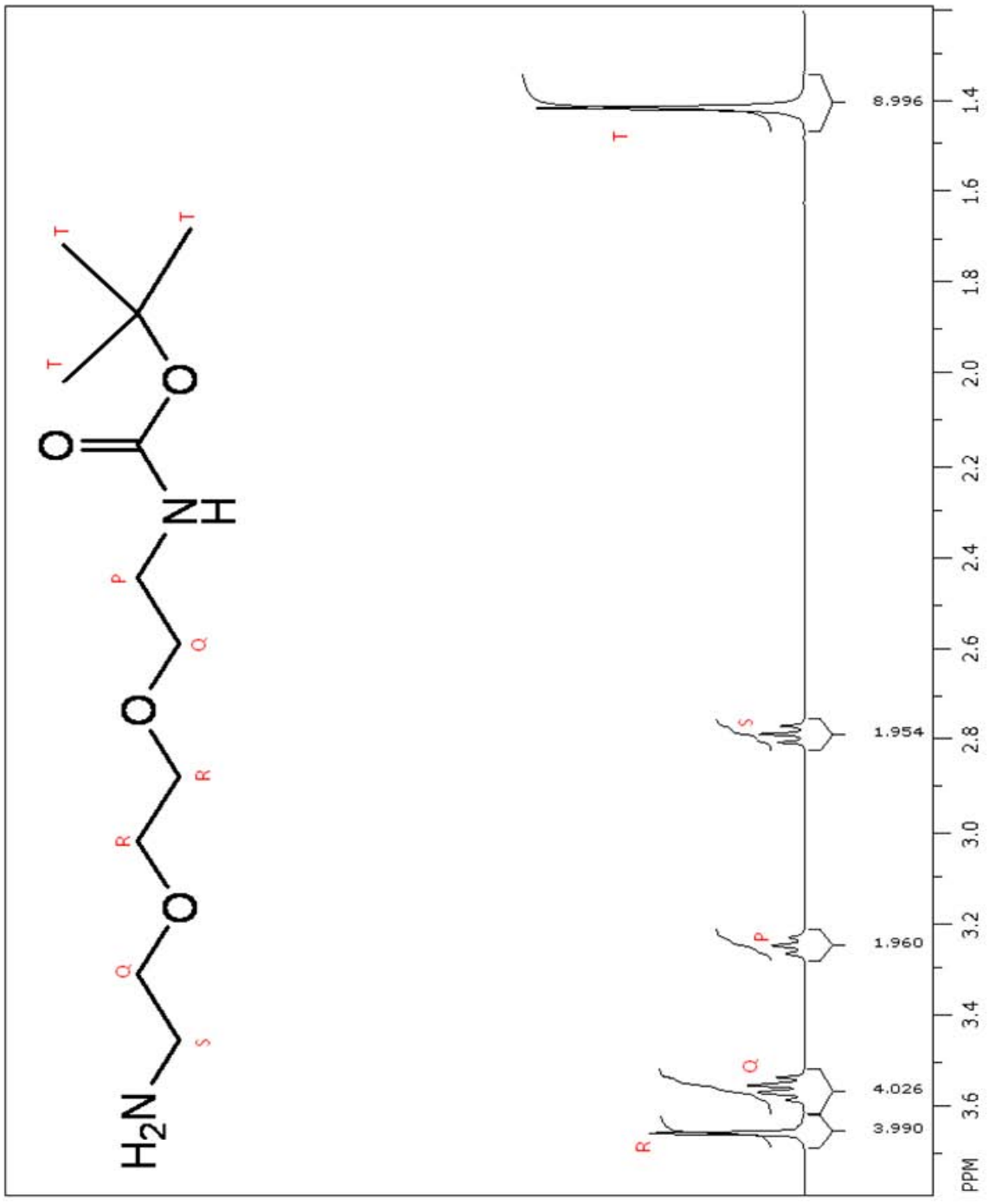

N-Acetylneuraminic acid {2-[2-(2-amino-ethoxy)-ethoxy]-ethyl}-amide (compound **11**) ^{1}H NMR in D_2O

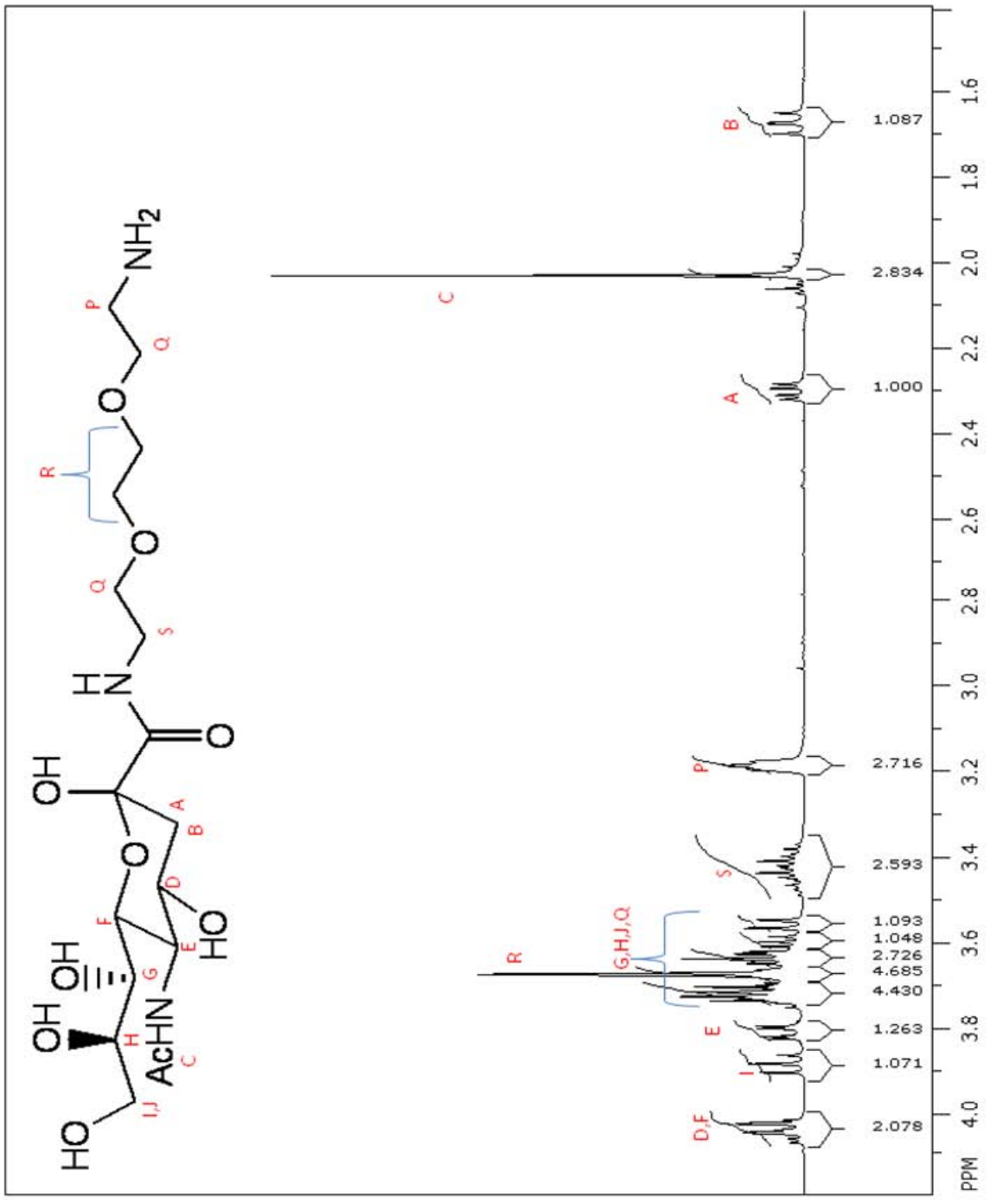

Tetrameric glyco-DATEG-PAMAM dendrimer (compound **1**) ^{1}H NMR in D_2O

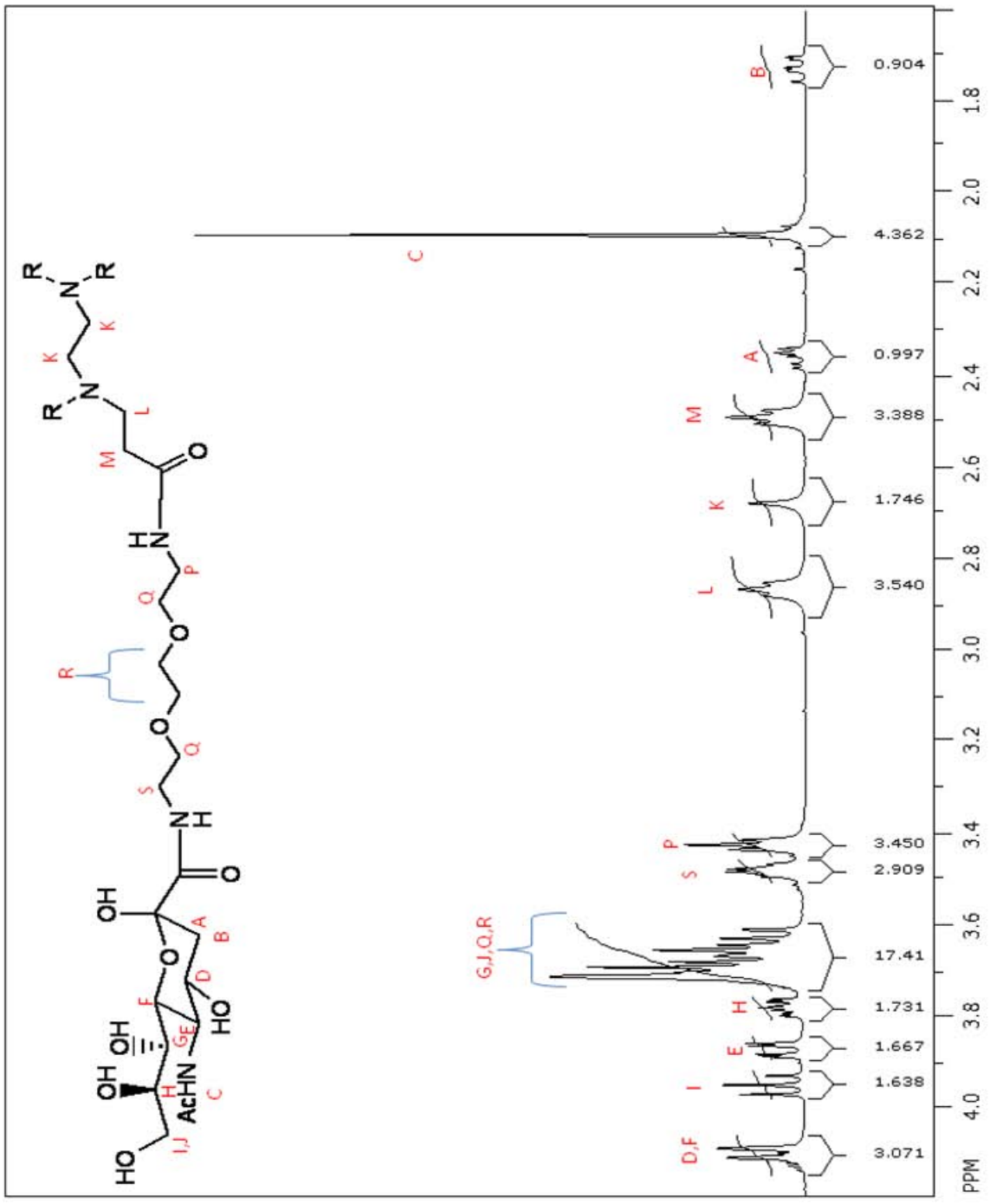

Tetrameric glycoPAMAM dendrimer (compound **2**) ^{1}H NMR in D_2O

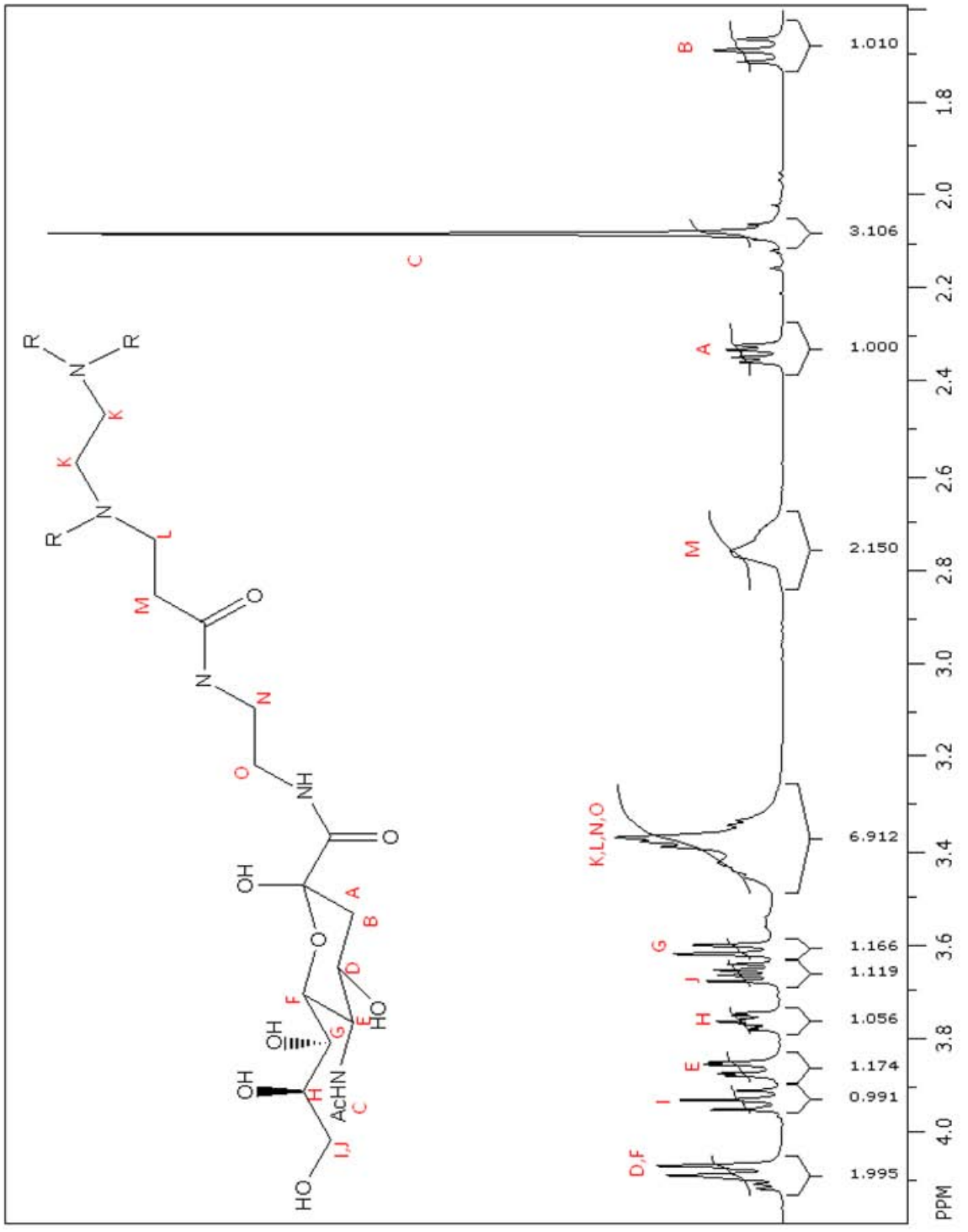

Octomeric glycoPAMAM dendrimer (compound **4**) ^{1}H NMR in D_2O

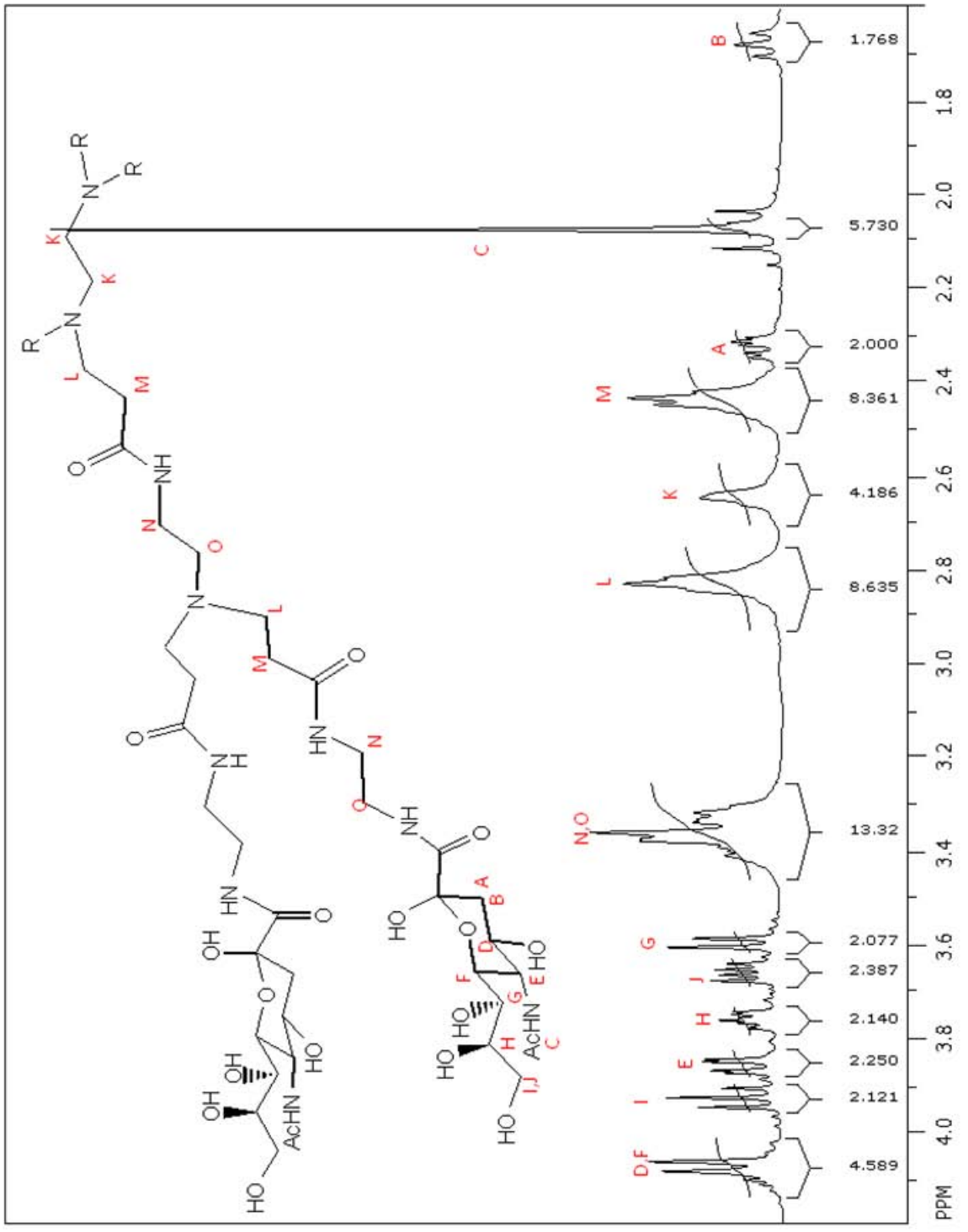

16-mer glycoPAMAM dendrimer (compound **6**) ^{1}H NMR in D_2O

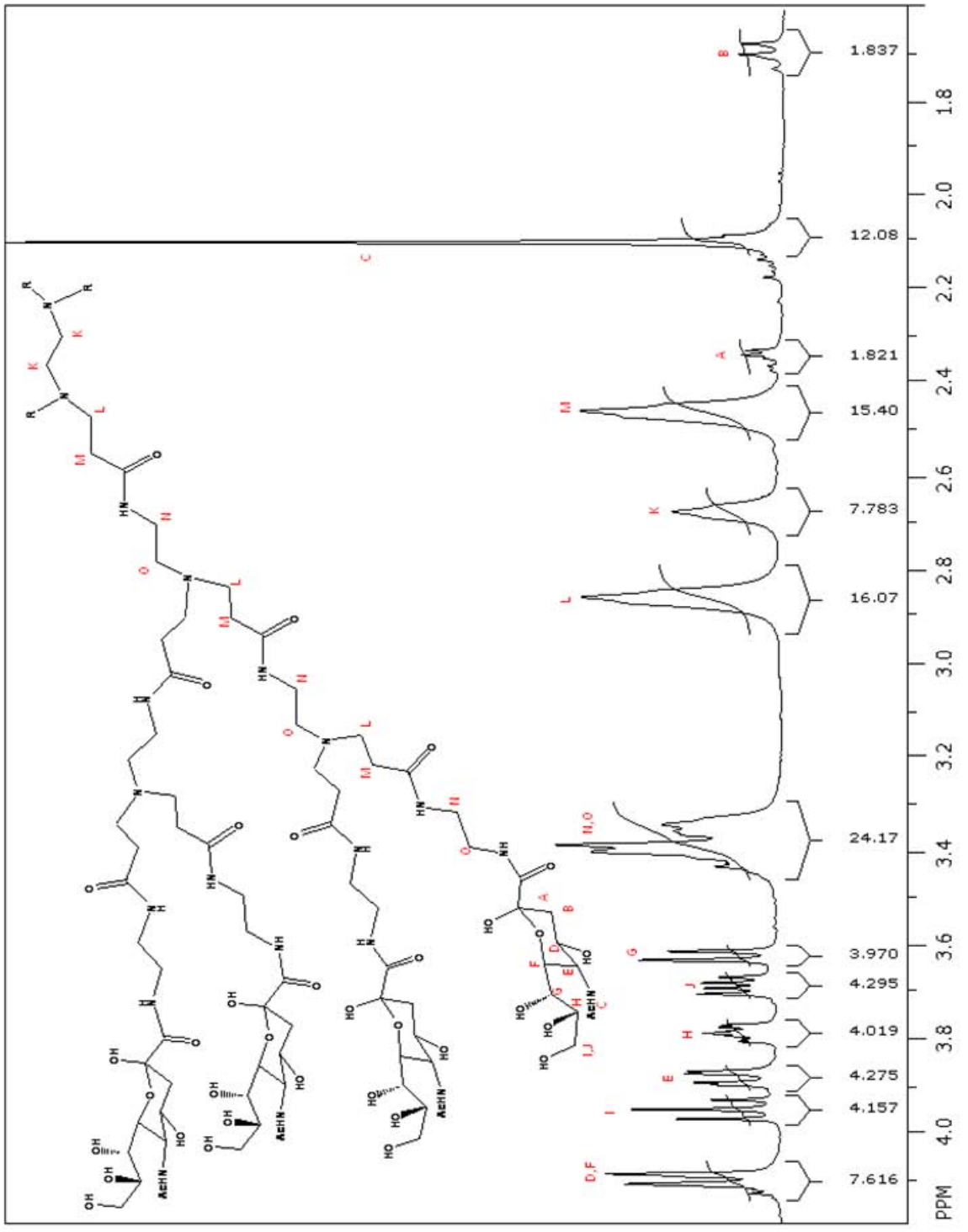

^{13}C Nuclear Magnetic Resonance Spectra at 125 MHz

{2-[2-(2-Amino-ethoxy)-ethoxy]-ethyl}-carbamic acid tert-butyl ester (compound **8**) ^{13}C NMR in D_2O

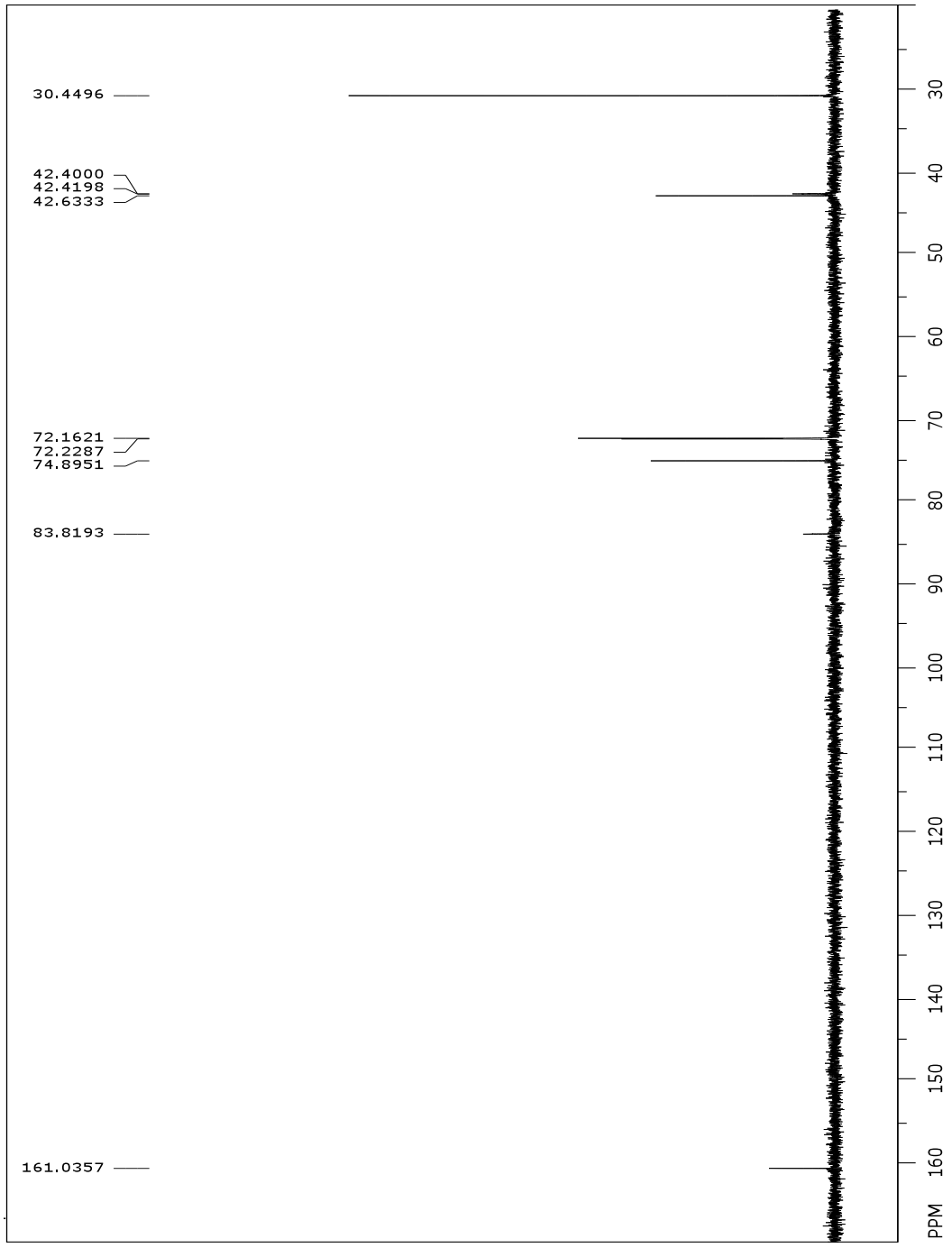

N-Acetylneuraminic acid {2-[2-(2-amino-ethoxy)-ethoxy]-ethyl}-amide (compound **11**) ^{13}C NMR in D_2O

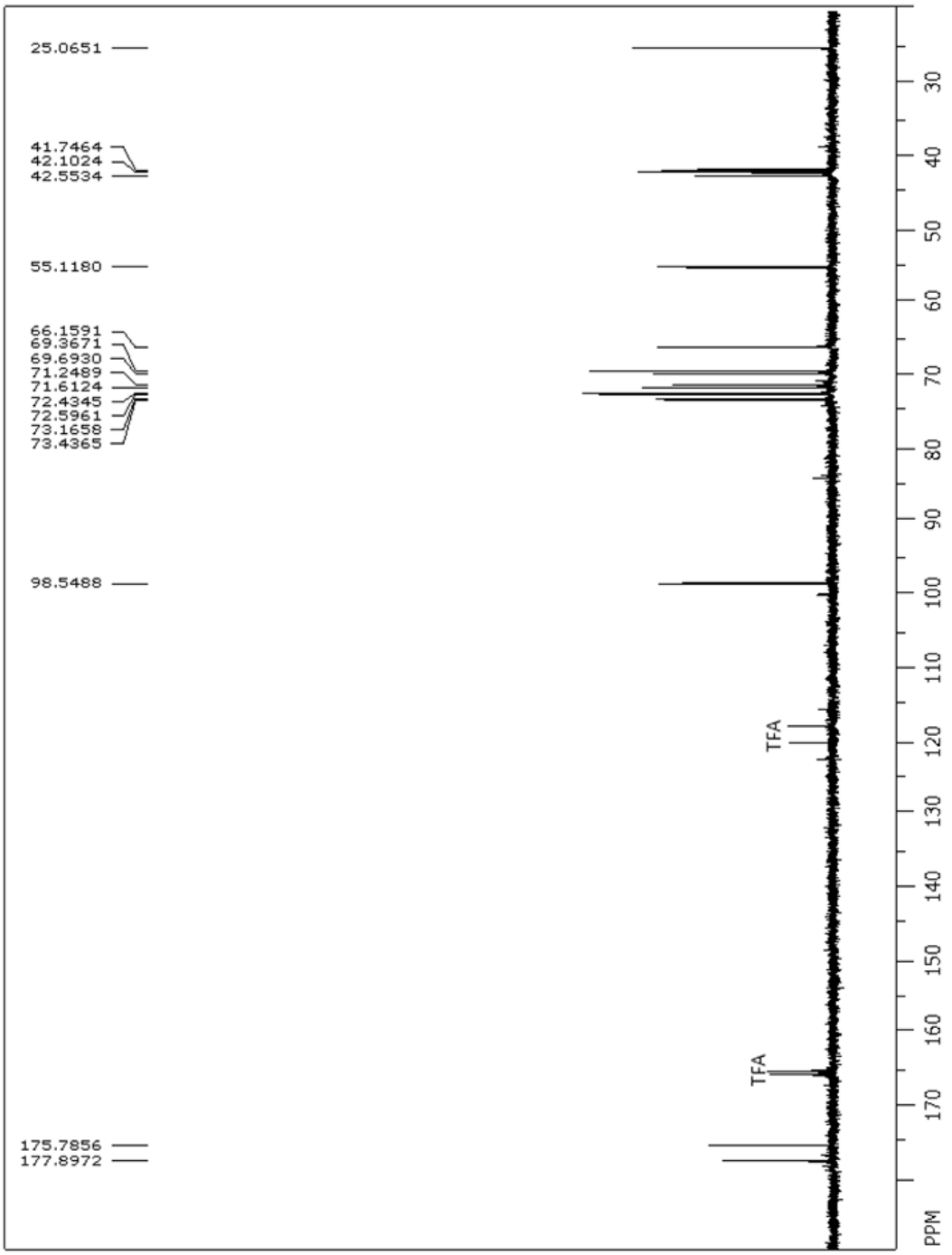

Tetrameric glyco-DATEG-PAMAM dendrimer (compound **1)** ^{13}C NMR in D_2O

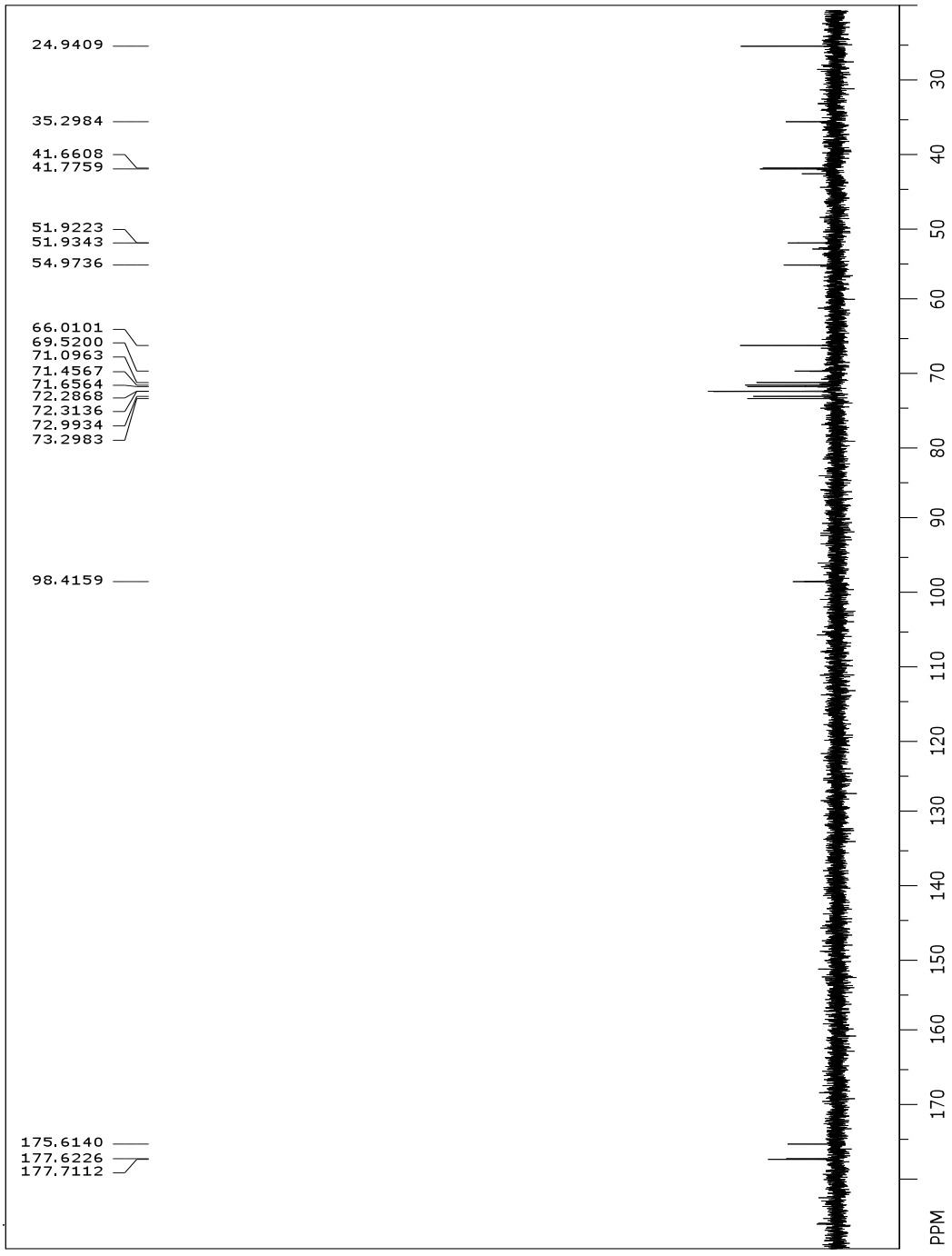

Tetrameric glycoPAMAM dendrimer (compound **2**) ^{13}C NMR in D_2O

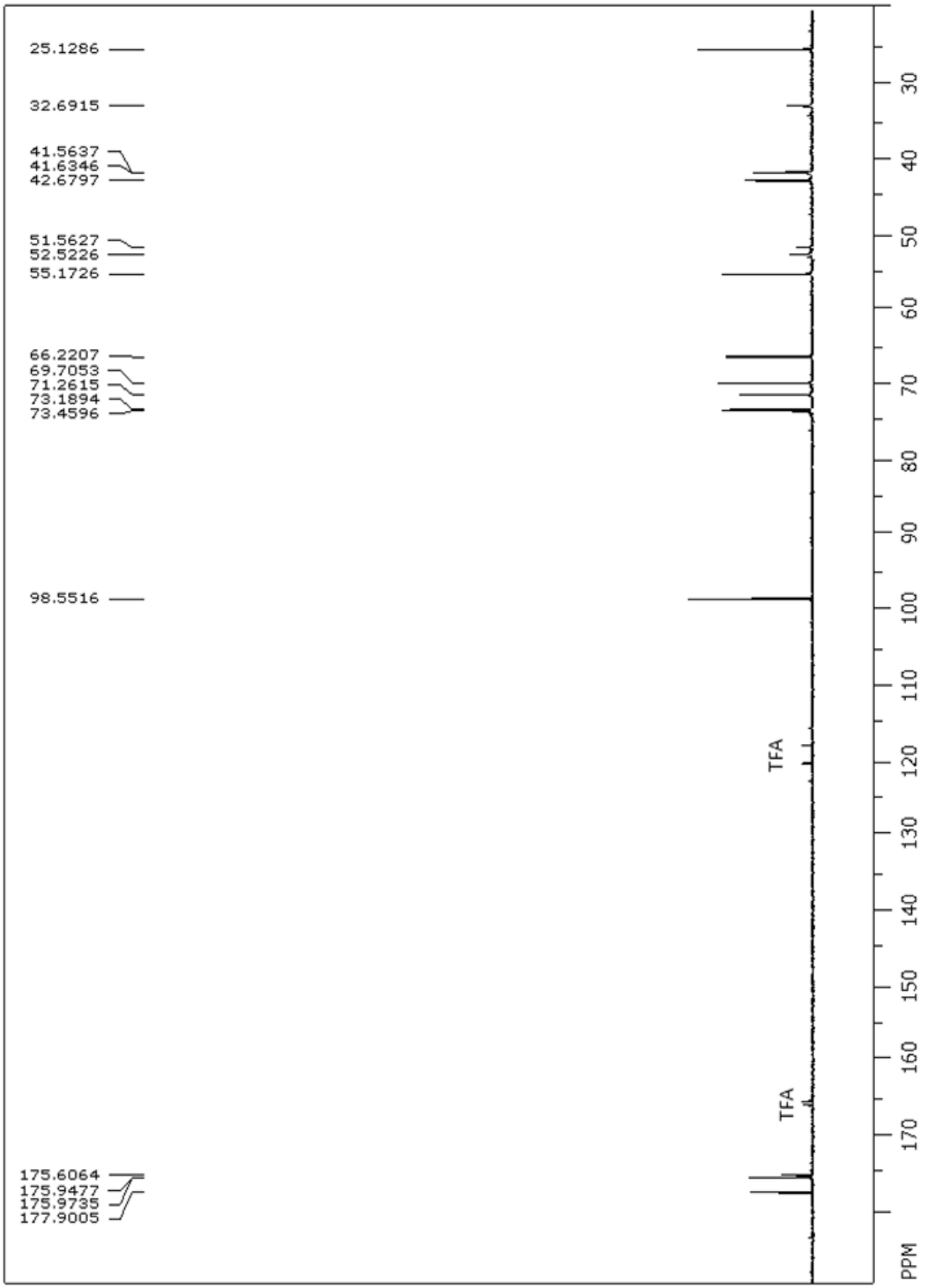

Octameric glycoPAMAM dendrimer (compound **4)** ^{13}C NMR in D_2O

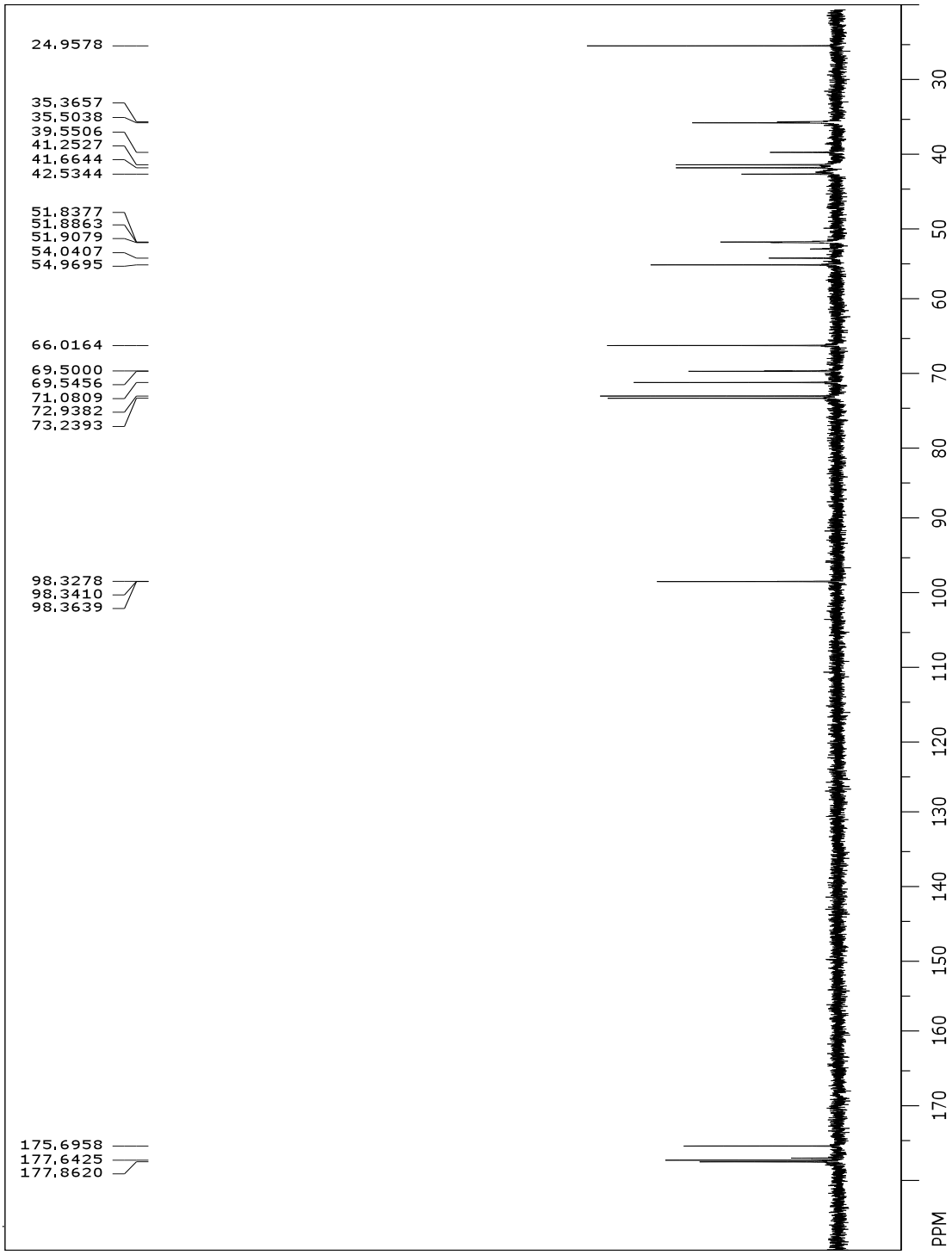

16-mer glycoPAMAM dendrimer (compound **6)** ^{13}C NMR in D_2O

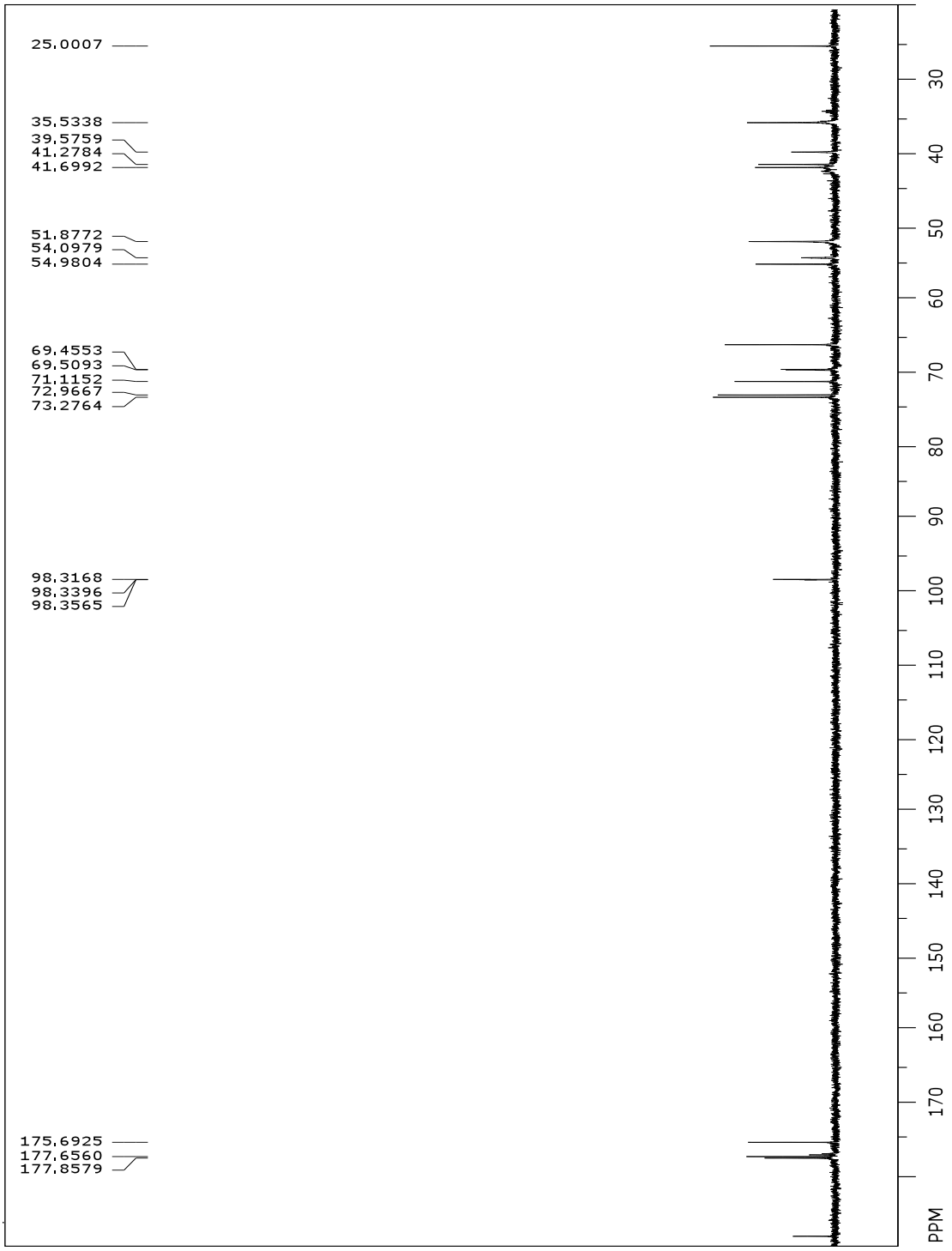

Bioconjugate Chemistry

CORRECTION

pubs.acs.org/bc

Facile Synthesis of Symmetric, Monofunctional Cyanine Dyes for Imaging Applications

Lai-Qiang Ying,* and Bruce P. Branchaud

Bioconjugate Chemistry **2011**, *22*, 865–869 DOI: 10.1021/bc2001006

RETRACTION

Facile Synthesis of Symmetric, Monofunctional Cyanine Dyes for Imaging Applications, by Lai-Qiang Ying and Bruce P. Branchaud, *Bioconjugate Chem.*, **2011**, *22* (5), pp 865−869, DOI: 10.1021/bc2001006, has been retracted at the request of the authors and Life Technologies. The article was submitted for publication without the approval of Life Technologies.

Published: September 16, 2011

Bioconjugate Chemistry

Review

pubs.acs.org/bc

Regenerative Biomaterials that "Click": Simple, Aqueous-Based Protocols for Hydrogel Synthesis, Surface Immobilization, and 3D Patterning

Chelsea M. Nimmo[†,‡] and Molly S. Shoichet*[,†,‡,§,∥]

[†]The Donnelly Centre for Cellular and Biomolecular Research, [‡]Department of Chemistry, [§]Department of Chemical Engineering and Applied Chemistry, and [∥]Institute of Biomaterials and Biomedical Engineering, University of Toronto, Toronto, Ontario, Canada

ABSTRACT: The click chemistry era has generated a library of versatile "spring-loaded" reactions that offer high yields, regio- and stereospecificity, and outstanding functional group tolerance. These powerful transformations are particularly advantageous for the design of sophisticated biomaterials that require high levels of precision and control, namely, materials that promote tissue regeneration such as hydrogels, 2D functionalized substrates, and 3D biomimetic scaffolds. In this review, the synthesis and application of regenerative biomaterials via click chemistry are summarized. Particular emphasis is placed on the copper(I)-catalyzed alkyne−azide cycloaddition, Diels−Alder cycloadditions, and thiol−click coupling.

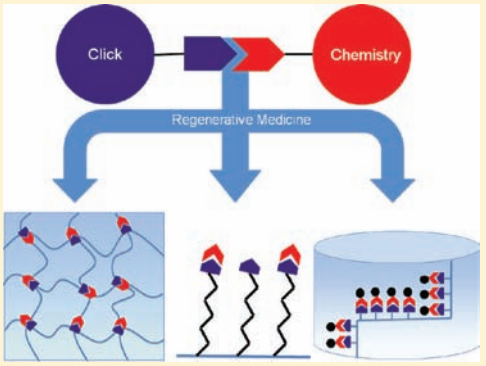

INTRODUCTION

In the simplest terms, tissue engineering has been defined as the delivery of biomolecules, cells, and supporting structures to the body to promote self-healing.[1] To accomplish this, biocompatible materials are required to serve as either structural supports for tissue regeneration or delivery vehicles for cell and drug transplantation. Biomaterials can also represent investigative tools to elucidate mechanisms vital to regeneration. Common materials employed within regenerative medicine strategies include both two-dimensional (2D) substrates and three-dimensional (3D) biomaterials. 2D substrates are most often used as exploratory tools to study the presentation of specific bioactive factors on cell fate. 3D biomaterials are similarly exploited, but can also be manipulated to serve as a space filling agent, a delivery vehicle, or a tissue engineering scaffold.[2] These strategies require well-defined structural materials and surfaces that impose sophisticated function in order to advance the field of regenerative medicine. This has created a trend toward the convergence of synthetic organic techniques within regenerative biomaterials.

The exponential growth of click chemistry research within the past decade has greatly facilitated the development of chemoselective chemistries applicable within regenerative medicine. In 2001, Sharpless and co-workers introduced the term "click chemistry" to define a set of nearly perfect reactions that resemble natural biochemical ligations.[3] These "spring-loaded" reactions are orthogonal, regioselective, and highly efficient. Moreover, click reactions can be performed in aqueous solutions at room or physiological temperature, and display outstanding functional group tolerance, making them compelling reactions within the bioengineering toolkit for polymer synthesis and bioconjugation.[4]

Given that there has been a number of outstanding reviews written on polymer synthesis via click chemistry for biomedical applications,[4−7] this review will focus on the emerging trend of click chemistry within the field of regenerative medicine. A prime example is click cross-linked hydrogels. Click reactions have also gained popularity as bioconjugation techniques for decorating 2D cell substrates, and as elegant patterning chemistries for immobilizing bioactive factors within 3D scaffolds (Figure 1). The review begins with a brief overview of three common click reactions employed within regenerative biomaterials, and further highlights their use in tissue engineering and regenerative medicine.

COMMON CLICK REACTIONS IN REGENERATIVE BIOMATERIALS

The term click chemistry often refers to the common copper(I)-catalyzed alkyne−azide cycloaddition (CuAAC) (Scheme 1A). This reaction is very similar to the classic Huisgen cycloaddition[8] where an organic azide reacts with an alkyne to form a triazole ring. Through the addition of a Cu(I) catalyst, Meldal[9] and Sharpless[10] demonstrated that the Huisgen cycloaddition reaction can proceed at low temperatures with high rates, efficiency, and regiospecificity. Moreover, near-perfect conversion is obtainable in both aqueous and organic

Received: June 1, 2011
Revised: September 16, 2011
Published: October 13, 2011

ACS Publications © 2011 American Chemical Society

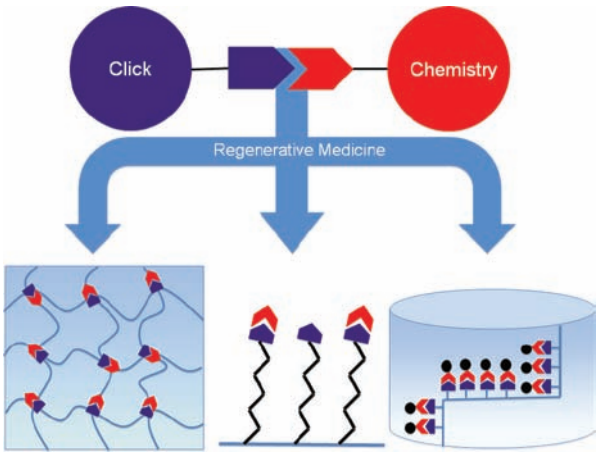

Figure 1. Schematic representation of click chemistry applied to regenerative biomaterials. Click chemistry has been employed as a cross-linking chemistry for hydrogel synthesis, and as bioconjugation techniques for decorating 2D cell culture.

Scheme 1. Common Click Reactions for Regenerative Biomatenals[a]

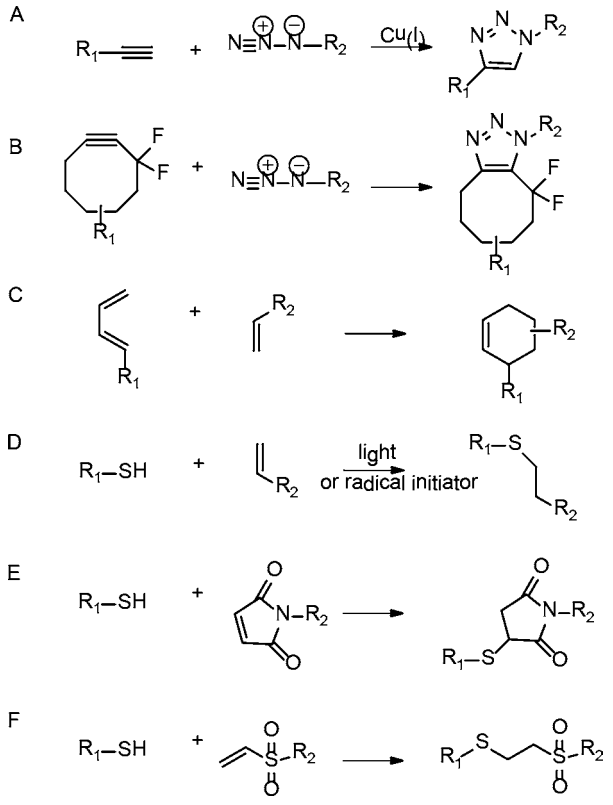

[a](A) Copper(I)-catalyzed alkyne–azide cycloaddition (CuAAC), (B) azide–alkyne coupling (SPAAC), (C) Diels–Alder (DA) cycloaddition, (D) Radical- mediated thiol–ene coupling, (E) Thiol-Michael addition between maleimides, and (F) between thiols and vinyl sulfones.

solvents. CuAAC has proved to be particularly advantageous within biomedical applications considering that the starting materials, azides and terminal alkynes, are remarkably stable within biological systems, enabling facile introduction of these reactive groups into a wide range of biomolecules. Moreover, alkynes and azides are not found in nature, thereby limiting side products from forming.

However, the term click chemistry is not limited to the CuAAC reaction, but embodies a synthetic philosophy of many reactions with distinct mechanisms and conditions. A comparison of click chemistries for regenerative biomaterials is summarized in Table 1. According to Sharpless, a reaction can achieve click status if it consists of readily available orthogonal reactants that combine under mild conditions to produce a single stereospecific product, with little or no isolation.[3] Within the past decade, there has been increasing investigation into reactions that meet this definition, yet do not require a metal catalyst.[11] The Bertozzi lab has developed a reaction of azides with cyclooctyne derivatives[12] referred to as strain-promoted azide–alkyne coupling (SPAAC) (Scheme 1B). These cyclooctyne derivatives greatly increase reactivity of azide–alkyne cycloadditions in the absence of copper, particularly when difluorinated.[13] Baskin et al. exploited this phenomenon to conjugate fluorophores to biological molecules by incorporating a *gem*-difluoro group next to a strained alkyne.[14] Reported reaction rates were 30–60 times faster compared to those with nonfluorinated cyclooctynes.

Another click cycloaddition is exemplified by the Diels–Alder (DA) reaction; a highly selective [4 + 2] cycloaddition between an electron-rich diene and an electron-poor dienophile (Scheme 1C). This reaction was first reported by Otto Diels and Kurt Alder in 1928,[15] making the DA cylocaddition the oldest known click reaction. DA chemistries offer high yields and minimal sides reactions, and require very little energy. Contrary to other click reactions, which commonly result in carbon–heteroatom bonds, carbon–carbon bonds are formed in DA cycloadditions. These bonds are thermally reversible at elevated temperatures. Water has been shown to accelerate DA reactions,[16,17] making the DA reaction particularly desirable for biomedical applications.

Beyond cycloadditions, other highly efficient reactions, such as nucleophilic substitutions, radical additions, and Michael additions, are also considered click reactions. In particular, thiol-click chemistries have recently gained merit within the field of regenerative biomaterials. Schlaad and co-workers were the first to identify the radical-mediated thiol–ene reaction as a click reaction.[80] In the mechanism, a radical abstracts a hydrogel from the thiol to form an active thiyl radical, allowing for an addition reaction between the thiyl radical and the carbon–carbon double bond or "ene". While both heat and light can be used to generate radicals to initiate the thiol–ene mechanism (Scheme 1D), photoinitiation of the radical addition reaction between thiols and alkenes allows for spatial and temporal control. Using light, the reaction can be easily manipulated by controlling the light intensity, the dose, or the duration.[79] This thiol-click reaction has found specific applications for biofunctionalization and surface modification.[18]

Thiol-Michael addition reactions represent another principle variation among the thiol–click chemistries applicable to regenerative biomaterials (Scheme 1E, F). The Michael addition of thiols to electron-deficient "enes" has been investigated since at least the 1940s,[81] and to this day, it continues to be a versatile tool within the field of bioconjugate chemistry. Thiol–click Michael additions typically involve α,β-unsaturated carbonyl compounds, and depend upon the nucleophilicity of the thiol component.[79] Thiol–maleimide click coupling (Scheme 1E) is a particularly relevant example for this review, as it is frequently exploited for protein conjugation.[71,72,75,76] The vinyl sulfone–thiol click reaction (Scheme 1F) has served as an important cross-linking mechanism for the synthesis of enzyme-degradable hydrogels.[44]

Table 1. Comparison of Common Click Reactions for Regenerative Biomaterials

click reaction	pH	reaction time	reactivity	specific advantages	specific disadvantages	biomaterial application
CuAAC	3–12	<1 h	increases at lower pH, or increased Cu(I)	azides/alkynes not found in nature	unstable and toxic copper catalyst required	hydrogel synthesis,[21−29] 2D protein immobilization[57−62]
SPAAC	7.4	<1 h	Increases with difluorination of cyclooctyne	no copper requirement	difficult synthesis of difluorinated cyclooctynes	PEG hydrogel synthesis[30,31]
DA	5.5–6.5	<8 h	accelerated by water	no catalyst required	longer reaction time	HA hydrogel synthesis,[42] 2D protein immobilization[63,64]
Thiol–ene	6–8	<2 h	radical-mediated	spatial/temporal control	cross-reactivity with thiols, photoinitiator often required	hydrogel synthesis,[48,49] 2D protein immobilization,[65,66] hydrogel patterning[30,31,74]
Thiol–Michael	6–8	<1 h	Depends on the nucleophilicity of the thiol component	facile introduction of proteins	cross-reactivity with thiols	hydrogel synthesis,[43,44,46,47] hydrogel patterning[71,72,75,76]

CLICK CROSS-LINKED HYDROGELS FOR TISSUE ENGINEERING AND DRUG DELIVERY

Hydrogels are water-swollen, cross-linked polymer networks capable of imitating the mechanical and architectural nature of the cellular microenvironement of soft tissue.[19] Due to their high water content, hydrogels permit facile transport of oxygen, nutrients, soluble factors, and waste. Moreover, many hydrogels are biocompatible, biodegradable, and can be synthesized and processed under relatively mild conditions. Accordingly, hydrogels represent an optimal platform for many regenerative medicine strategies. Often, hydrogel matrices are used to provide a blank canvas in which biomolecules are immobilized, thereby providing a defined chemical environment to guide cell fate. Synthetic poly(ethylene glycol) (PEG) and naturally derived agarose are two common examples of such hydrogels.[73,75]

The mechanical characteristics of hydrogels are dictated by the number of cross-links formed between the polymer chains via covalent bonds or noncovalent interactions. In the past, popular hydrogel cross-linking methodologies have included radical polymerization and high-energy irradiation.[20] The majority of these reactions require cytotoxic cross-linking agents or initiators, which can reduce biocompatibility of the material. Within the past decade, click chemistry has emerged as a viable alternative for both chemically cross-linked hydrogels and their biofunctionalization. While copper is also known to be cytotoxic, the strained reactions described above overcome this deficit of CuAAC chemistry.

Alkyne–Azide Click Cross-Linked Hydrogels. Ossipov et al. were the first to recognize the CuAAC reaction as an efficient chemoselective cross-linking method for hydrogel synthesis.[21] Poly(vinyl alcohol) (PVA) was functionalized with either acetylene or azide groups, and cross-linked by mixing their aqueous solutions together with copper sulfate ($CuSO_4$) and sodium ascorbate as the cycloaddition catalyst. In another example, alkyne-modified PVA was cross-linked with bifunctional PEG-diazide cross-linkers. Hydrogels prepared with polyfunctional PVA formed higher-modulus gels with reduced swelling compared to those synthesized with the bifunctional PEG cross-linker.

Hawker and co-workers[22] applied the CuAAC click cross-linking reaction to the synthesis of pure PEG hydrogels. In their approach, diacetylene- and tetraazide-functionalized PEG were reacted in a 2:1 ratio at room temperature under aqueous conditions in the presence of $CuSO_4$ and sodium ascorbate. By manipulating both the polymer and catalyst concentration, they were able to tune the cross-linking efficiency. Following hydrogel formation, both acetylene and azide functionalized chromophores were swollen into the hydrogel to visualize any unreacted azide/acetylene functional groups. This revealed less than 0.2% unreacted functional groups, confirming the efficient nature of the CuAAC reaction. The degree of swelling and stress/extension properties of the hydrogels were also examined by varying the length of the diacetylene PEG chain.

To illustrate the utility of the CuAAC cross-linked PEG hydrogels as tissue engineering and drug delivery scaffolds, various researchers have incorporated peptides and degradable linkers within their click cross-linked networks. In particular, inclusion of the fibronectin tripeptide sequence, arginine-glycine-aspartate (RGD), has been shown to be an essential additive in almost all "blank slate" hydrogel formulations for tissue culture. RGD is a prime cell adhesion site that is

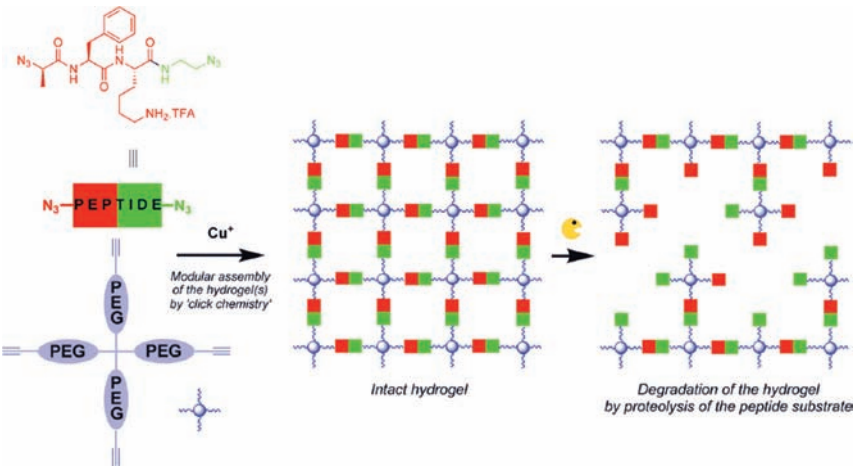

Figure 2. Schematic representation of the synthesis of CuAAC cross-linked PEG hydrogels.[25] Incorporation of enzymatically degradable peptides renders hydrogels susceptible to degradation by trypsin proteases. (Copyright American Chemical Society, reproduced with permission from ref 25.)

recognized by many integrin receptors;[23] therefore, incorporation of this peptide facilitates cell-matrix interactions. Liu et al. synthesized diazide-functionalized RGD peptides to cross-link tetraacetylene PEG under aqueous conditions with $CuSO_4$ and sodium ascorbate.[24] By varying the temperature, catalyst, and precursor concentrations, the gelation time was altered from 2 to 30 min. An increase in temperature or $CuSO_4$ resulted in a decreased gelation time. The storage modulus was also tailored by changing the azide linker length. These RGD peptide hydrogels were tested for fibroblast delivery to promote tissue repair. By increasing the concentration of RGD peptide, fibroblast adhesion and proliferation also increased.

In a similar approach, van Dijk et al. incorporated a protease-sensitive peptide within a CuAAC cross-linked PEG hydrogel (Figure 2).[25] Alkyne-functionalized star-shaped PEG molecules (either 4- or 8-armed with a MW of 10 and 20 kDa, respectively) were cross-linked with the protease-sensitive bis-azido peptide in aqueous solution in the presence of $CuSO_4$ and sodium ascorbate. Incubation of the hydrogels in trypsin leads to complete degradation of hydrogels after 40−80 h, depending on the cross-link density.

The CuAAC reaction has also been employed as a cross-linking method for natural polymers. While hydrogels formed from synthetic materials, such as PEG, offer a blank canvas permissive to cell function, materials native to the extracellular matrix (ECM) can promote cell function.[19] A prime example of a native material commonly employed in regenerative strategies is hyaluronic acid (HA)—a ubiquitous nonsulfated glycosaminoglycan, which impacts embryonic development, tissue organization, wound healing, and angiogenesis.[26] Crescenzi et al. used the CuAAC click reaction to cross-link HA.[27] Hyaluronic acid (HA) was modified with either azide or alkyne groups and cross-linked in water with Cu(I) at room temperature. Their hydrogel revealed intriguing characteristics for both drug release and tissue engineering applications. As a model for drug delivery, benzidamine and doxorubicin were encapsulated within the click hydrogels, which displayed release profiles ranging from hours to several weeks, depending on the cross-link density. To confirm the possibility that these hydrogels could serve as tissue engineering scaffolds, yeast cells were imbedded within the hydrogels, following removal of the copper catalyst through dialysis. Cells exhibited 80% proliferating activity after 24 h in culture. In a follow-up study, the influence of the dialkyne structure on the properties of these HA click cross-linked hydrogels was examined.[28] HA azido-derivatives cross-linked with shorter dialkynes experienced weaker storage moduli, corresponding to predicted cross-linking densities as determined by ^{1}H NMR.

Gao and co-workers also employed the CuAAC reaction to cross-link natural biopolymers.[29] Both HA and chondroitin sulfate (CS) were modified to contain azide functionalities, and cross-linked with gelatin that had been modified with an alkyne functionality. They argue that this triple copolymer system better mimics the natural components of ECM by incorporating proteoglycans, such as CS, and denatured collagen products, such as gelatin, to promote cell surface adhesion. Aqueous solutions of the polymers were combined and catalyzed by Cu(I) to form a hydrogel with the time to gelation varying as a function of catalyst concentration. Chondrocytes were cultured *in vitro* to assess the cytotoxicity of the click hydrogels. After 3 days in culture, a confluent layer of cells had formed, confirming the benefit of this click cross-linked hydrogel for chondrocyte adhesion and proliferation.

Anseth and co-workers have gone beyond traditional CuAAC cross-linking chemistry and synthesized PEG hydrogels via SPAAC, to bestow copper-free, physiological conditions within their networks.[30] In their approach, a four-arm PEG tetra-azide was reacted with difunctionalized difluorinated cyclooctyne polypeptide sequence, to incorporate enzymatically degradable cross-linker sequences throughout the material. Gelation occurred in less than 5 min, and both rheological and ^{1}H NMR data support the ideality of the network, similar to previous click-based networks.[22] This click strategy tolerates cell encapsulation with high viabilities (>90% at 24 h). As an extension of this study, De Forest et al. enabled control over cross-link density and shear moduli of these SPAAC cross-linked PEG hydrogels.[31] By altering either the azide to cyclooctyne ratio or the molecular weight of PEG, hydrogels were synthesized with tunable moduli ranging 1000−6000 Pa. These SPAAC cross-linked PEG hydrogels have also served as patterning platforms for the immobilization of biological functionalities using thiol−ene click photocoupling[30,31] (see Click Patterning of 3D Scaffolds section).

A drawback of CuAAC cross-linking is the lack of temporal and spatial control due to the generation of the catalytic Cu(I) species.[32] Spatial and temporal control of network formation is paramount in many tissue engineering applications. To overcome

this, Adzima et al. sought to catalyze the CuAAC cross-linking reaction via the photochemical reduction of Cu(II) to Cu(I).[32] Generating Cu(I) photochemically is analogous to the initiation of a radical or carbocation species in traditional photopolymerization processes, resulting in total spatial and temporal control of the CuAAC reaction. The authors developed this photoinducible azide–alkyne cycloaddtion (pCuAAC) reaction to synthesize hydrogels by irradiating multifunctional alkyne and azide functionalized PEG monomers in the presence of $CuSO_4$ and Irgacure 2959 photoinitiator. To extend this system to biological systems, the authors suggest modifications to mimic reverse-ATRP polymerizations that require significantly lower copper levels.[33]

Diels–Alder Click Cross-linked Hydrogels. Although the DA click reaction has long served as an exceptional cross-linking method for the synthesis of complex polymer networks,[34−37] the preparation of cross-linked hydrogels via DA chemistry remains largely unexplored. A few DA hydrogels have been synthesized with synthetic polymers;[38−41] however, these studies have mainly examined the effect of temperature on both gelation time and retro-DA reaction. Recently, Shoichet and co-workers reported a DA cross-linked hydrogel with a specific tissue engineering application in mind.[42] Furan-modified HA was synthesized and cross-linked via dimaleimide-PEG to form a stable hydrogel by mixing the two aqueous solutions at room temperature (Scheme 2). By controlling the furan to maleimide molar ratio, the mechanical and degradation properties of the DA hydrogels could be altered. The reported shear modulus of the hydrogels ranged from 275 to 680 Pa, similar to that of central nervous system tissue. After 14 days of culture *in vitro*, endothelial cells displayed high levels of cell survival (>98%), and appeared to interact with the HA matrix. The minimal swelling, complete degradation, and cell-interactive properties of these DA hydrogels make them promising materials for soft tissue engineering.

Scheme 2. Formation of Diels-Alder Hyaluronic Acid Click Hydrogels[42]

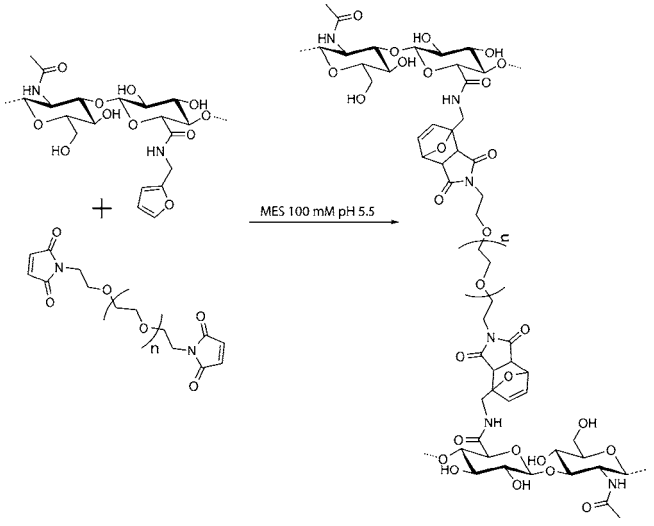

Thiol–Click Cross-Linked Hydrogels. Qiu et al. were the first to harness the thiol-Michael click reaction for hydrogel formation.[43] PEG-based copolymers containing multiple thiol functionalities were cross-linked via divinylsulfone-PEG in neutral phosphate buffer. This system proved to be bioorthogonal, as protein additives did not interfere with the click cross-linking reaction; however, these proteins did not contain any exposed thiols that could interfere with the reaction. A thiol-click cross-linked hydrogel may be inappropriate for protein delivery if any free thiol groups are present on the proteins. Notwithstanding this limitation, when proteins were incorporated into these gels, their release was sustained for 2–4 weeks.

Hubbell and co-workers took advantage of this Michael-type addition click reaction to synthesize hydrogels with characteristics similar to that of native ECM.[44] Their approach was to incorporate integrin-binding sites for cell adhesion and enzyme-degradable sites into the matrix such that cell-secreted matrix metalloproteinases (MMPs) would enable cell migration into and remodeling of the biomimetic ECM.[45] To achieve this, they cross-linked bis-cysteine MMP substrate peptides with vinyl sulfone-functionalized multiarm PEG. The resulting click hydrogel networks displayed a defined molecular architecture, and allowed for invasion by primary human fibroblasts. Cellular invasion was shown to be dependent on the proteolytic activity of the incorporated peptide. The hydrogels were also employed as a drug delivery vehicle for the recombinant human bone morphogenetic protein (BMP2) to rat cranium defects. Correlating with their work *in vitro*, bone regeneration *in vivo* depended on the enzymatic sensitivity of the incorporated substrate.

Chawla et al. recently developed a 3D cell culture platform for mesenchymal stem cells (MSCs) by cross-linking a saccharide-peptide copolymer via Michael-type conjugation addition between cysteine (Cys) and vinyl sulfone (VS).[46] By altering the pH of the cross-linking reaction, or the VS to Cys ratio, they were able to tune both the degradation and mechanical properties of the gel. Hydrogels that were cross-linked with an equimolar ratio of VS to Cys maintained their mechanically stability for longer than 21 days *in vitro*, similar to dextran hydrogels cross-linked by Michael addition.[47] These hydrogels also exhibited a rapid gelation time, suggesting utility for in situ surgical procedures, and displayed a microporous network when visualized under environmental scanning electron microscopy. Cell encapsulation was facilitated by the cross-linking reaction occurring in culture medium. MSCs remained viable after 14 days (>90%) in culture.

The radical-mediated thiol–ene click reaction has also been employed as a hydrogel cross-linking method. Anseth and co-workers developed a platform for hydrogel synthesis by a step-growth reaction mechanism via thiol and norbornene functionalities.[48] Not always achievable with simple Michael addition, thiol–ene photopolymerization offers spatial and temporal control of network formation. Hydrogels were synthesized by mixing norbornene-functionalized PEG with either chymotrypsin- or MMP-degradable linkers in a 1:1 stoichiometric ratio in PBS. The networks maintained high cell viability following encapsulation (>95% following 24 h). Anderson et al. utilized these thiol–ene photopolymerized PEG hydrogels to examine MSC behavior in response to network properties.[49] Both MMP cleavable peptide linkers and nondegradable PEG-dithiol linkers were incorporated into the hydrogel to monitor how MSC degradation of the matrix affects their differentiation behavior. Their findings suggest that directed chondrogenic and adipogenic differentiation of MSCs are facilitated by increased cell-mediated hydrogel degradation.

CLICK IMMOBILIZATION OF PEPTIDES ON 2D SURFACES

Well-defined chemically modified substrates, such as self-assembled monolayers (SAMs), serve as investigative tools to explore fundamental interactions applicable to regenerative strategies. Surface functionalization is particularly advantageous when engineering substrates for cell culture to harness control over cell-matrix interactions. Many have employed this strategy to immobilize ECM-derived biomolecules for ultimate characterization of their effects on cell adhesion.[50−53] Popular immobilization strategies in the past have been based on adsorption or covalent modification of a protein's functional group(s) to a chemically activated surface.[54,55] These methods can result in side reactions and are difficult to characterize both physically and in terms of cellular response. Accordingly, there has been a paradigm shift in the existing approaches for surface functionalization from unspecific and nonselective reactions toward highly specific orthogonal reactions that ensure bioactivity and facilitate characterization of engineered surfaces.[56]

CuAAC Click Immobilization. CuAAC is chemoselective against common functionalities in biomolecules, and thus, stable reactive species can be introduced within biomolecules with ease. Accordingly, CuAAC serves as an effective click reaction to chemoselectively immobilize peptides to otherwise bioinert SAMs. Becker and co-workers developed a universal technology for surface conjugation of any biomolecule containing accessible azide groups.[57] SAMs were subjected to oxidation by UV exposure, creating a monotonically increasing carboxyl density gradient. A bifunctional propargyl-functionalized linker was then attached to the carboxylic moieties of the gradient to yield an alkyne gradient, making it susceptible to modification with any azido-derivatized species via CuAAC chemistry. The authors tested their methodology by conjugating the RGD tripeptide sequence in a density gradient ranging from 0 to 140 pmol cm^{-2}. Smooth muscle cells cultured on the RGD gradient surfaces revealed enhanced cell attachment with increased RGD concentration. Alkyne-modified KGRGDS has also been successfully coupled by CuAAC chemistry to self-assembled polymeric micelles with azide-functional groups, thereby yielding RGD-functionalized polymeric nanoparticles that specifically bind to corneal epithelial cells.[58]

Becker and co-workers later exploited their CuAAC technology to couple osteogenic growth peptide (OGP) to SAMs in order to explore the effects of OGP density on preosteoblast cell adhesion, morphology, and proliferation.[59] OGP has been recognized as a promising agent for bone tissue engineering applications because it stimulates tissue regeneration of bone defects.[60] To create the peptide gradient, the carboxylic acid functionalities on the SAM layer were reacted with the amine terminal of a bifunctional amine-poly(ethylene oxide)-alkyne linker, resulting in an alkyne gradient. Azide-terminated OGP peptides were then conjugated to the alkyne gradient by immersing substrates in a solution of $CuSO_4$, sodium ascorbate, and peptide for 24 h at 40 °C. Preosteoblast cells were cultured on the OGP functionalized gradient surfaces in serum-free conditions for 7 days. Cell adhesion was highest at low OGP peptide concentrations. At day 3, cells experienced faster doubling rates compared to cells cultured on control surfaces, but this effect subsided by day 7. This is indicative of the natural transition made by osteoblasts from proliferative to maturation phases. Gene expression experiments also verified this phenomena with a 10-fold increase in collagen I expression between days 3 and 7, coinciding with the initial stages of bone mineralization.

Hudalla and Murphy fabricated SAMs expressing a variation of the adhesive RGD peptide, RGDSP, as a means to study stem cell adhesion.[50] This was achieved via CuAAC. SAMs were first prepared by immersing a gold substrate in an ethanolic solution of 80 mol % tri(ethylene glycol) alkanethiolate ($HS\text{-}EG_3$) and 20 mol % azide-terminated hexa(ethylene glycol) alkanethiolate ($HS\text{-}EG_6\text{-}N_3$). The resulting mixed SAMs contained approximately 10% $HS\text{-}EG_6\text{-}N_3$ and 90% $HS\text{-}EG_3$ (Figure 3A); however, this result could be

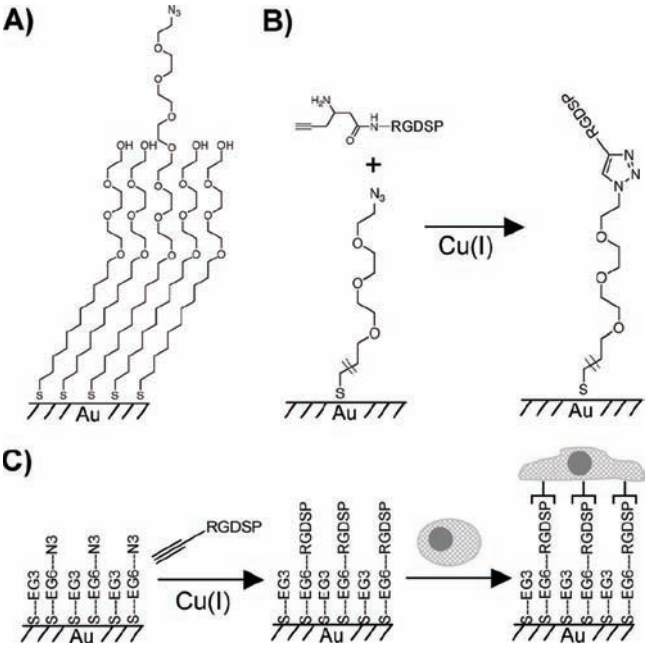

Figure 3. CuAAC click immobilization of peptides to SAM substrates to study stem cell adhesion.[50] (A) Mixed SAMs bearing azide groups; (B) reaction between azide-functionalized SAMs with acetylene-bearing RGDSP; (C) the surface density of RGDSP immobilized via CuAAC affects mesenchymal stem cell adhesion and spreading. (Copyright American Chemical Society, reproduced with permission[50].)

tailored by varying the ratio of $HS\text{-}EG_6\text{-}N_3$ and $HS\text{-}EG_3$. The SAMs were classified as bioinert, as they displayed minimal nonspecific protein adsorption. Acetylene-bearing RGDSP (Hex-RGDSP) was then conjugated to the SAMs via $HS\text{-}EG_6\text{-}N_3$ in the presence of a Cu(I) catalyst (Figure 3B). The CuAAC reaction efficiency illustrated near-quantitative conjugation upon the addition of a tertiary amine, which has been a proven method utilized by others to enhance CuAAC efficiency by binding the Cu(I) catalyst.[61] MSCs were cultured on top of the RGDSP-presenting SAMs. RDGSP surface density and intermolecular spacing regulated MSC morphology and attachment (Figure 3C).

In a followup study, Hudalla and Murphy demonstrated that CuAAC conjugation of biomolecules to SAM substrates can be conducted in parallel with other chemistries, namely, carbodiimide condensation.[62] Incorporation of carboxylate-terminated hexaethylene glycol alkanethiolate ($HS\text{-}EG_6\text{-}COOH$) with the original mixed SAM allowed for conjugation of two distinct peptides, RGDSP and TYRSRKY, a

proteoglycan-binding peptide. These experiments revealed that these distinct extracellular factors work synergistically to regulate MSC adhesion on 2D substrates. They also demonstrated that soluble biomolecules, such as heparin, can disrupt specific cell-material interactions, and in turn direct MSC adhesion.

Diels–Alder Click Immobilization. Yousaf and Mrksich were the first to exploit the DA reaction for protein immobilization on 2D surfaces.[63] In their approach, SAMs were modified with a hydroquinonequinone group, which upon oxidation provides a quinone, enabling a cycloaddition between the quinone and a cyclopentadiene (cp). To demonstrate this DA approach, they immobilized a biotin-cp conjugate, and tested the affinity of the immobilized biotin for streptavidin. This work demonstrated that the DA click reaction is an attractive bioconjugation technique for a wide variety of applications, which could be extended to regenerative therapies. The authors also state that this method would allow for controlled, sequential immobilization of several biomolecules.

Sun et al. demonstrated the use of sequential click reactions for protein immobilization on solid surfaces.[64] First, the DA click reaction was used to immobilize a heterobifunctional PEG linker carrying alkyne and cyclodiene terminal groups onto an N-(E-maleimidocaproyl)-functionalized glass slide. This resulted in an exposed alkyne-terminated PEGylated surface, vulnerable to conjugation with azide-containing biomolecules via CuAAC click chemistry. Again, biotin was chosen as a model protein for immobilization. Biotin-PEG-azide was added to a glass vial containing the alkyne-PEGylated glass slide, $CuSO_4$, and a tertiary amine ligand. The reaction was left at 4 °C for 12 h. Biotinylated glass slides were then immersed in a solution of dilute FITC-conjugated streptavidin at 4 °C for 2 h. Confocal fluorescence images verified the fidelity of the click protein immobilization. This technique is applicable to a wide range of functionally complex biomolecules for the design of biomimetic surfaces.

Thiol–Ene Click Immobilization. Waldmann and co-workers reported the use of the thiol–ene reaction to photochemically pattern proteins and other biomolecules onto solid surfaces.[65] Polyamidoamine dendrimers, containing an aminocaproic acid spacer, were covalently attached to a silicon oxide wafer surface. Cystamine was then conjugated to the spacer, which upon disulfide reduction, exposed free thiols on the surface. A solution of terminal-olefin-functionalized biomolecules were spread onto the surfaces, and covered with a photomask. Following irradiation at 365–405 nm, a covalently attached pattern of thioethers was obtained. As a test application, biotin was photochemically patterned onto a thiolated wafer, and subsequently incubated in a solution of Cy5-labeled streptavidin to render a fluorescent pattern surface. Immobilization was shown to be dependent on irradiation time and concentration of immobilized peptide. They further exemplified the broad applicability of their patterning method by immobilizing alkaline phosphatase, Ras, and phosphopeptide, all of which retained their bioactivity and binding affinities.

In an extension of this work, Waldmann and co-workers demonstrated fast, oriented covalent immobilization of proteins directly from lysates, eliminating any additional protein chemical modifications.[66] The authors took advantage of the fact that, in cells, many proteins are post-translationally S-farnesylated at a C-terminal "CAAX-box" by protein farnesyltransferase (FTase).[67] By genetically coding for the CAAX tag, the authors enabled farnesylation *in vitro* or *in vivo* with FTase, creating a facile method for "ene" incorporation into a protein of interest. Once farnesylated, these proteins were immobilized via the thiol–ene photochemical click reaction to surface-exposed thiols.

■ CLICK PATTERNING OF 3D SCAFFOLDS

Throughout the past decade, several scaffolds have emerged aiming to mimic the cellular microenvironment and ultimately control cell fate and guide tissue regeneration. These scaffolds can be fine-tuned to study a specific parameter of the microenvironment. Notably, the effect of peptide presentation on the cell has been examined by spatially immobilizing proteins and adhesion peptides in 3D patterns within scaffolds. Growth factors localized in 3D scaffolds remain bioactive[68−70] and have been shown to orient axonal growth,[71,72] guide cellular migration,[73] and cause morphological changes.[30] The stringent spatial resolution and controlled biochemical heterogeneity required for 3D patterning make simple bioorthogonal chemistries paramount. The use of click reactions for 3D patterning of scaffolds allows significant spatial control when combined with multiphoton processing.[75,76] Additionally, many of these hydrogel scaffolds are click cross-linked, and sequentially click patterned.[30,31,74]

Alkyne–Azide Click Patterning. Recently, Bowman and co-workers demonstrated 3D patterning of hydrogels via pCuAAC.[32] The transient generation of Cu(I) facilitates spatial and temporal control of the CuAAC reaction. PEG hydrogels were first synthesized by a thiol-yne reaction, ensuring a stoichiometric excess of alkynes. Postgelation, a solution of photoinitiator (Irgacure 2959), copper sulfate, and an azide-labeled fluorophore was swollen into the gel. Upon irradiation with a photomask, Cu(I) is generated within the irradiated areas, catalyzing the pCuAAC reaction between the azide-fluorophore and the pendant alkynes in the polymer network, ultimately producing a spatially defined fluorescent pattern within the hydrogel. The authors note that future work is required to translate this system to biological systems.

Thiol–Ene Click Patterned Scaffolds. Immobilization of bioactive growth factors via thiol conjugation has become increasingly popular given the ease of cysteine incorporation within a peptide, making the thiol–ene click reaction particularly relevant for 3D patterning. Anseth and co-workers developed a sequential click protocol relevant to both hydrogel synthesis and postgelation modification.[30,31,74] Click cross-linked PEG hydrogels were first formed via CuAAC, as an extension of the method taken by Malkock et al.[22] To enable photopatterning of their PEG hydrogels, multifunctional photoreactive polypeptide sequences were included within the network structure by incorporating the non-natural amino acid, Fmoc-Lys(alloc)-OH.[74] The allyloxycarbonyl (alloc) protecting group contains a vinyl functional group capable of reacting with any thiol-containing compound, such as cysteine. Upon exposure to UV light, thiyl radicals are generated via the photocleavage of a hydrogen-abstracting initiator, thereby using light to achieve spatial and temporal control of thiol–ene functionalization within the network. To illustrate this technique, a fluorescently labeled cysteine containing peptide was patterned within PEG hydrogels via transparency-based photolithographic patterning techniques.

This thiol−ene photopatterning method was later employed to immobilize peptides and proteins within PEG hydrogels cross-linked via SPAAC (Figure 4).[30] Spatial and temporal

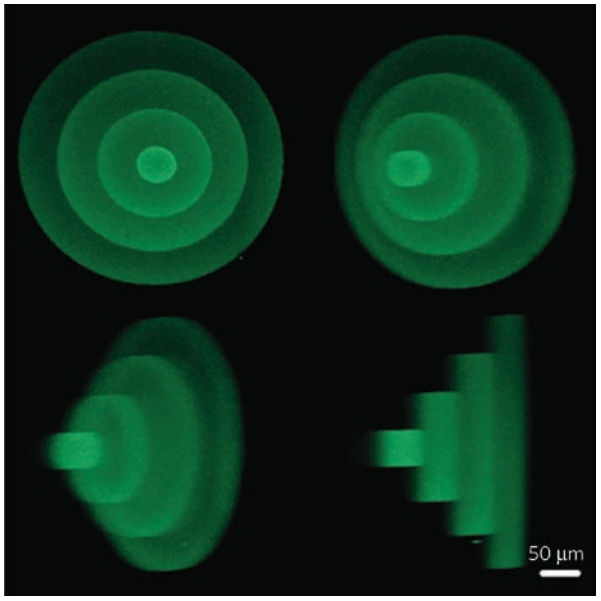

Figure 4. 3D biochemical patterning of PEG hydrogels via thiol−ene photocoupling.[30] Fluorescently tagged peptides were patterned within SPAAC cross-linked networks. (Copyright Macmillan Publishers Limited, reproduced with permission.[30])

control was validated by selectively exposing certain locations within the hydrogel matrix to light, and by controlling light intensity and exposure time. Furthermore, the thiol−ene reaction was confirmed to be cytocompatible, as 3T3 cells encapsulated within the hydrogel maintained high viability throughout patterning (>90% at 24 h post encapsulation), and thiol−ene immobilization of RGD within the network was shown to influence cell morphology. In a follow-up study, DeForest et al. verified that patterning concentration within the hydrogel is directly proportional to the dosage of light, as well as the photoinitiator concentration.[31] Using this system, they were able to construct well-defined 3D biochemical gradients of multiple peptides, offering potential promise to elucidate fundamental biological processes essential to regenerative medicine such as induced cell migration.

Thiol−Maleimide Click Patterning. The thiol−maleimide reaction exemplifies a variation of the thiol-Michael click reaction. Shoichet and co-workers have exploited this click reaction for 3D patterning of agarose hydrogels.[68,72,75,76] Covalent modification of agarose with S-2-nitrobenzyl-cysteine (S-NBC) renders a photolabile matrix, which upon UV irradiation releases free thiols capable of reacting with any thiol-reactive biomolecule through Michael addition. Thiol channels were created on exposure to a focused laser beam, and reacted with a maleimide-terminated RGD peptide. This immobilized RGD channel volume promoted neurite extension and cell migration.[72] This system was also applied to study the effect of immobilized platelet derived growth factor AA (PDGF-AA) on neural stem/progenitor cell (NSPC) differentiation.[68] Hydrogels with immobilized RGD and PDGF-AA supported NSPC adhesion and preferential differentiation to oligodendrocytes.

In order to advance this click technology toward more sophisticated architectures that better mimic the native extracellular matrix, agarose was later modified with a coumarin derivative, which upon exposure to a pulsed infrared laser yields free thiols.[75] The use of this photolabile group allows for intricate 3D control by way of multiphoton excitation. Aizawa et al. exploited this coumarin multiphoton patterning technique to immobilize a gradient of the angiogenic factor, VEGF165, within agarose hydrogels.[76] Primary endothelial cells responded to this immobilized gradient by displaying tip and stalk cell morphology, eventually forming tubule-like structures as they migrated in response to the VEGF gradient (Figure 5).

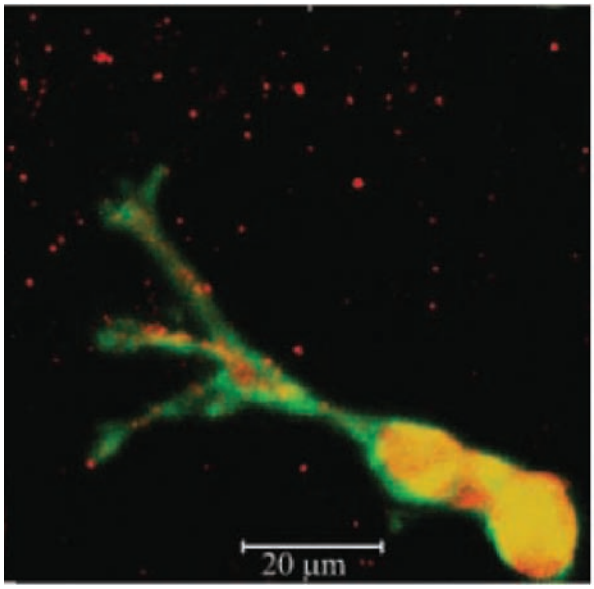

Figure 5. Primary endothelial cells guided in 3D patterned agarose hydrogel.[76] VEGF165 was immobilized in a concentration gradient within the scaffold using the thiol-maleimide click reaction. (Copyright Wiley-VCH Verlag GmbH & Co. KGaA; reproduced with permission.[76])

The "click" nature of thiol addition to a maleimide unit was also exercised by Kosif et al.[77] with the immobilization of proteins in PEG-methacrylate based hydrogels. Hydrogel synthesis was achieved using AIBN initiated thermal polymerization, by which they directly incorporated a furan-protected maleimide containing monomer. This furan-protected maleimide represents a DA adduct which is susceptible to thermal cycloreversion. Postgelation, a thermal cycloreversion step activated the maleimide group to its thiol-reactive form. To evaluate this system as a potential template for bioconjugation, thiolated-biotin was covalently attached to the hydrogels, and its affinity for streptavidin investigated. This system is particularly intriguing as it incorporates the retro-DA click reaction, which is not commonly applied in regenerative biomaterials.

■ CONCLUDING REMARKS

Click chemistry has long been recognized as a powerful tool within biotechnology applications, and has since begun to gain popularity for the preparation of functionalized materials applicable in regenerative medicine strategies. These elegant, versatile reactions represent attractive building blocks for engineered hydrogel networks, decorated 2D cell culture

surfaces, and patterned 3D biomimetic scaffolds. Click chemistry is particularly compelling for hydrogel formation and modification because it is water-based chemistry. Moreover, the click reaction provides impeccable control over the conformation of the protein or peptide immobilized, thereby maximizing its bioactivity. With the formation of stable covalent bonds, one can be confident of a well-defined system with which to study cellular response.

Each click reaction, however, has limitations that warrant consideration. The obvious shortcoming of CuAAC is the copper requirement. Copper has been shown to be cytotoxic, and increased copper intake has been linked to hepatitis, Alzheimer's disease, and other neurological disorders.[78] Another disadvantage of CuAAC is alkyne homocoupling. Although rare, alkynes may react with another alkyne instead of an azide.[9] The evolution of SPAAC has played a substantial role in catalyzing the development of click reactions beyond CuAAC; however, the difluorinated cyclooctynes can be difficult to synthesize[14] thereby complicating what would normally be a simple reaction. Collaboration between chemists and bioengineers, as well as increased commercial access to starting materials, will overcome some of these synthetic limitations.

The DA click cycloaddition is a "reagent-free" click reaction that does not require catalyst, photoinitiator, or radical initiation. Moreover, the DA reaction is accelerated in aqueous solutions, an ideal characteristic for biomaterial design. Despite these strengths, the DA click reaction has been much less explored relative to the CuAAC and thiol-click reactions, perhaps due to longer reaction times. Although it has not been specifically reported, the reaction time for the formation of HA hydrogels via Diels–Alder click chemistry is likely greater than 8 h since hydrogels are allowed to form overnight.[42] The rate of reaction can be accelerated with heat or photoinitiation if required. DA adducts can also undergo cycloreversion, but this is only relevant at higher temperatures, and thus should not pose a problem to biomaterials used *in vitro* or *in vivo*.

Recently, the thiol–click reaction has emerged as a prominent reaction within the field of regenerative biomaterials, particularly as a tool for protein conjugation, given the simplicity of immobilization via functional groups common to proteins. However, it is difficult to control protein immobilization via thiol-Michael addition due to cross-reactivity. In terms of 3D patterning, this can be avoided by spatially controlling where free thiols are exposed within a photolabile matrix using two-photon laser technology. The anionic chain process of thiol-Michael click reactions is thought to reduce its efficiency and rate. On the other hand, the photoinitiated thiol–ene click reaction occurs by free-radical addition, offering enhanced spatial and temporal control. However, this method often requires a photoinitiator, which can be cytotoxic and hence reduce the biocompatibility of the material. Finally, free thiols are susceptible to disulfide bond formation via oxidation, which further limits the efficiency of thiol–ene click reactions.

What other bioorthogonal reactions are likely to emerge within the field of regenerative medicine? Popik and co-workers have recently developed a photoinducible azide–alkyne cycloaddition reaction circumventing the copper catalyst requirement.[82] Generation of a dibenzocyclooctyne from a photoprotected cyclopropenone provides spatial and temporal control over the reaction under ambient conditions. While this chemistry has not been applied to biomaterials to date, use of this reaction would harness spatial and temporal control to the already bioorthongal reactants without the use of a copper catalyst. A highly effective click reaction for protein immobilization is the Staudinger ligation.[83] The simple nature of this chemistry makes it an excellent candidate for the synthesis of 2D substrates used to study stem cell proliferation/differentiation. While we have reviewed several examples of thiol–ene and thiol–Michael click reactions applied to regenerative biomaterials, the thiol–yne reaction not yet been tested in regenerative medicine. This reaction is capable of consecutive reaction with two thiol functional groups.[84] Application of this chemistry to hydrogel synthesis would provide scaffolds with high cross-link densities. Finally, while not traditionally defined as "click", the orthogonal chemistry of peptide binding pairs has recently been used to design hydrogels with 3D immobilized proteins.[85] Physical binding pairs, barnase–barstar and streptavidin–biotin, were exploited to simultaneously immobilize differentiation factors within an agarose hydrogel. Application of this technology in the future will avoid multistep protocols, while preserving protein bioactivity.

In a short period of time, the use of click chemistry within the field of regenerative medicine has exploded. The ability to synthesize biomaterials with pristine definition and architecture to ultimately control cell fate is unprecedented. To this day, click reactions continue to evolve with the identification of new orthogonal chemistries. Bioengineers will continue to translate these improved chemoselective methodologies to their regenerative materials. Already, we have seen a considerable increase in the use of click reactions for biochemically patterning 3D hydrogels, which we anticipate will increase further. Sequential click reactions will likely emerge as a key approach to design sophisticated biomaterials in a simplistic manner.

AUTHOR INFORMATION

Corresponding Author

*E-mail: molly.shoichet@utoronto.ca, Phone: 416.978.1460, Fax: 416.978.4317.

ACKNOWLEDGMENTS

We are grateful to financial support from NSERC Discovery Grant (M.S.S.) and Alexander Graham Bell Canada Graduate Scholarship (C.M.N.).

REFERENCES

(1) Langer, R., and Vacanti, J. P. (1993) Tissue engineering. *Science 260*, 920–926.

(2) Drury, J. L., and Mooney, D. J. (2003) Hydrogels for tissue engineering: scaffold design variables and applications. *Biomaterials 24*, 4337–4351.

(3) Kolb, H. C., Finn, M. G., and Sharpless, K. B. (2001) Click chemistry: diverse chemical function from a few good reactions. *Angew. Chem., Int. Ed. 40*, 2004–2021.

(4) van Dijk, M., Rijkers, D. T. S., Liskamp, R. M. J., van Nostrun, C. F., and Hennink, W. E. (2009) Synthesis and applications of biomedical and pharmaceutical polymers via click chemistry methodologies. *Bioconjugate Chem. 20*, 2001–2016.

(5) Golas, P. L., and Matyjaszewski, K. (2009) Marrying click chemistry with polymerization: expanding the scope of polymeric materials. *Chem. Soc. Rev. 39*, 1338–1354.

(6) Fournier, D., Hoogenboom, R., and Schubert, U. S. (2007) Clicking polymers: a straightforward approach to novel macromolecular architectures. *Chem. Soc. Rev. 36*, 1369–1380.

(7) Binder, W. H., and Sachsenhofer, R. (2007) 'Click' chemistry in polymer and materials science. *Macromol. Rapid Commun. 28*, 15−24.
(8) Huisgen, R. (1968) Cycloadditions − defintion, classification, and characterization. *Angew. Chem., Int. Ed. Engl. 7*, 321−328.
(9) Tornoe, C. W., Christensen, C., and Meldal, M. (2002) Peptidotriazoles on solid phase: [1,2,3]-triazoles by regiospecific copper(I)-catalyzed 1,3-dipolar cycloadditions of terminal alkynes to azides. *J. Org. Chem. 67*, 3057−3064.
(10) Rostovtsev, V. V., Green, L. G., Fokin, V. V., and Sharpless, K. B. (2002) A stepwise Huisgen cycloaddition process: Copper(I)-catalyzed regioselective "ligation" of azides and terminal alkynes. *Angew. Chem., Int. Ed. 41*, 2596−2599.
(11) Becer, C. R., Hoogenboom, R., and Schubert, U. S. (2009) Click chemistry beyond metal-catalyzed cycloaddition. *Angew. Chem., Int. Ed. 48*, 4900−4908.
(12) Agard, N. J., Prescher, J. A., and Bertozzi, C. R. (2004) A strain-promoted [3 + 2] azide-alkyne cycloaddition for covalent modification of biomolecules in living systems. *J. Am. Chem. Soc. 126*, 15046−15047.
(13) Codelli, J. A., Baskin, J. M., Agard, N. J., and Bertozzi, C. R. (2008) Second-generation difluorinated cyclooctynes for cooper-free click chemistry. *J. Am. Chem. Soc. 130*, 11486−11493.
(14) Baskin, J. M., Prescher, J. A., Laughlin, S. T., Agard, N. J., Chang, P. V., Miller, I. A., Lo, A., Codelli, J. A., and Bertozzi, C. R. (2007) Copper-free click chemistry for dynamic in vivo imaging. *Proc. Natl. Acad. Sci. U.S.A. 104*, 16793−16797.
(15) Diels, O., and Alder, K. (1928) Synthesen in der hydroaromatischen Reihe. *Justus Liebigs Ann. Chem. 460*, 98−122.
(16) Otto, S., and Engberts, J. B. (2003) Hydrophobic interactions and chemical reactivity. *Org. Biomol. Chem. 1*, 2809−2820.
(17) Rideout, D. C., and Breslow, R. J. (1980) Hydrophobic acceleration of Diels-Alder reactions. *J. Am. Chem. Soc. 102*, 7816−7817.
(18) Hoyle, C. E., and Bowman, C. N. (2010) Thiol-ene click chemistry. *Angew. Chem., Int. Ed. 49*, 1540−1573.
(19) Slaughter, B. V., Khurshid, S. S., Fisher, O. Z., Khademhosseini, A., and Peppas, N. A. (2009) Hydrogels in regenerative medicine. *Adv. Mater. 21*, 3307−3329.
(20) Hennink, W. E., and van Nostrum, C. F. (2002) Novel crosslinking methods to design hydrogels. *Adv. Drug Delivery Rev. 54*, 13−36.
(21) Ossipov, D. A., and Hilborn, J. (2006) Poly(vinyl alcohol)-based hydrogels formed by "click chemistry". *Macromolecules 39*, 1709−1718.
(22) Malkoch, M., Vestberg, R., Gupta, N., Mespouille, L., Dubois, P., Mason, A. F., Hedrick, J. L, Liao, Q., Frank, C. W., Kingsbury, K., and Hawker, C. J. (2006) Synthesis of well-defined hydrogel networks using Click chemistry. *Chem. Commun.*, 2774−2776.
(23) D'Souza, S. E., Ginsberg, M. H., and Plow, E. F. (1991) Arginyl-glycyl-aspartic acid (RGD): a cell adhesion motif. *Trends Biochem. Sci. 16*, 246−250.
(24) Liu, S. Q., Ee, P. L. R., Ke, C. Y., Hedrick, J. L., and Yang, Y. Y. (2009) Biodegradable poly(ethylene glycol)-peptide hydrogels with well-defined structure and properties for cell delivery. *Biomaterials 30*, 1453−1461.
(25) Van Dijk, M., van Nostrum, C. F., Hennink, W. E., Rijkers, D. T. S., and Liskamp, R. M. J. (2010) Synthesis and characterization of enzymatically biodegradable PEG and peptide-based hydrogels prepared by click chemistry. *Biomacromolecules 11*, 1608−1614.
(26) Allison, D. D., and Grande-Allen, K. J. (2006) Review. Hyaluronan: a powerful tissue engineering tool. *Tissue Eng. 12*, 2131−2140.
(27) Crescenzi, V., Cornelio, L., Di Meo, C., Nardecchia, S., and Lamanna, R. (2007) Novel hydrogels via click chemistry: synthesis and potential biomedical applications. *Biomacromolecules 8*, 1844−1850.
(28) Testa, G., Di Meo, C., Nardecchia, S., Capitani, D., Mannina, L., Lamanna, R., Barbetta, A., and Dentini, M. (2009) Influence of dialkyne structure on the properties of new click-gels based on hyaluronic acid. *Int. J. Pharm. 378*, 86−92.
(29) Hu, X., Li, D., Zhou, F., and Gao, C. (2011) Biological hydrogel synthesized from hyaluronic acid, gelatin and chondroitin sulfate by click chemistry. *Acta Biomater. 7*, 1618−1626.
(30) DeForest, C. A., Polizzotti, B. D., and Anseth, K. S. (2009) Sequential click reactions for synthesizing and patterning three-dimensional cell microenvironments. *Nat. Mater. 8*, 659−664.
(31) DeForest, C. A., Sims, E. A., and Anseth, K. S. (2010) Peptide-functionalized click hydrogels with independently tunable mechanics and chemical functionality for 3D cell culture. *Chem. Mater. 22*, 4783−4790.
(32) Adzima, B. J., Tao, Y., Kloxin, C. J., DeForest, C. A., Anseth, K. S., and Bowman, C. N. (2011) Spatial and temporal control of the alkyne-azide cycloaddition by photoinitiated Cu(II) reduction. *Nat. Chem. 3*, 258−261.
(33) Wang, J.-S., and Matyjaszewski, K. (1995) 'Living'/controlled radical polymerization. Transition-metal-catalyzed atom transfer radical polymerization in the presence of a conventional radical initiator. *Macromolecules 28*, 7572−7573.
(34) Gheneim, R., Perez-Berumen, C., and Gandini, A. (2002) Diels-Alder reactions with novel polymeric dienes and dienophiles: synthesis of reversibly crosslinked elastomers. *Macromolecules 35*, 7246−7253.
(35) Adzima, B. J., Aguirre, H. A., Kloxin, C. J., Scott, T. F., and Bowman, C. N. (2008) Rheological and chemical analysis of reverse gelation in a covalently crosslinked Diels-Alder polymer network. *Macromolecules 41*, 9112−9117.
(36) Chen, X., Dam, M. A., Ono, K., Mal, A., Shen, H., Nutt, S. R., Sheran, K., and Wudl, F. (2002) A thermally re-mendable crosslinked polymeric material. *Science 295*, 1698−1702.
(37) Costanzo, P. J., Demaree, J. D., and Beyer, F. L. (2006) Controlling dispersion and migration of particulate additives with block copolymers and Diels-Alder chemistry. *Langmuir 22*, 10251−10257.
(38) Chujo, Y., Sada, K., and Saegusa, T. (1990) Reversible gelation of polyoxazoline by means of Diels-Alder reaction. *Macromolecules 23*, 2636−2641.
(39) Wei, H.-L., Yang, Z., and Shen, Y.-M. (2009) Thermosensitive hydrogels synthesized by fast Diels-Alder reactions in water. *Polymer 50*, 2836−2840.
(40) Wei, H.-L., Yang, J., Chu, H.-J., Yang, Z., Ma, C.-C., and Yao, K. (2011) Diels-Alder reaction in water for straightforward preparation of thermoresponsive hydrogels. *J. Appl. Polym. Sci. 120*, 974−980.
(41) Wei, H.-L., Yang, Z., and Shen, Y.-M. (2009) Thermosensitive hydrogels synthesized by fast Diels-Alder reactions in water. *Polymer 50*, 2836−2840.
(42) Nimmo, C. M., Owen, S. C., and Shoichet, M. S. (2011) Diels-Alder click crosslinked hyaluronic acid hydrogels for tissue engineering. *Biomacromolecules 12*, 824−830.
(43) Qui, B., Stefanos, S., Ma, J., Lalloo, A., Perry, B. A., Leibowitz, M. J., Sinko, P. J., and Stein, S. (2003) A hydrogel prepared by in situ crosslinking of a thiol-containing poly(ethylene glycol)-based copolymer: a new biomaterial for protein drug delivery. *Biomaterials 24*, 11−18.
(44) Lutolf, M. P., Lauer-Fields, J. L., Schmoekel, H. G., Metters, A. T., Weber, F. E., Fields, G. B., and Hubbell, J. A. (2003) Synthetic matrix metalloproteinase-sensitive hydrogels for the conduction of tissue regeneration: Engineering cell-invasion characteristics. *Proc. Natl. Acad. Sci. U.S.A. 100*, 5413−5418.
(45) Sternlicht, M. D., and Werb, Z. (2001) How matrix metalloproteinase's regulate cell behavior. *Annu. Rev. Dev. Biol. 17*, 463−516.
(46) Chawla, K., Yu, T.-B., Liao, S. W., and Guan, Z. (2011) Biodegradable and biocompatible synthetic saccharide-peptide hydrogels for three-dimensional stem cell culture. *Biomacromolecules 12*, 560−567.
(47) Hiemstra, C., van der Aa, L. J., Zhang, Z., Dijkstra, P. J., and Feijen, J. (2007) Rapidly in situ-forming degradable hydrogels from dextran thiols through Michael addition. *Biomacromolecules 8*, 1548−1556.

(48) Fairbanks, B. D., Schwartz, M. P., Halevi, A. E., Nuttelman, C. R., Bowman, C. N., and Anseth, K. S. (2009) A versatile synthetic extracellular matrix mimic via thiol-norbornene photopolymerization. *Adv. Mater. 21*, 5005−5010.
(49) Anderson, S. B., Lin, C.-C., Kuntzler, D. V., and Anseth, K. S. (2011) The performance of human mesenchymal stem cells encapsulated in cell-degradable polymer-peptide hydrogels. *Biomaterials 32*, 3564−74.
(50) Hudalla, G. A., and Murphy, W. L. (2009) Using "click" chemistry to prepare SAM substrates to study stem cell adhesion. *Langmuir 25*, 5737−5746.
(51) Roberts, C., Chen, C. S., Mrksich, M., Martichonok, V., Ingber, D. E., and Whitesides, G. M. (1998) Using mixed self-assembled monolayers presenting RGD and (EG)3OH groups to characterize long-term attachement of bovine capillary endothelial cells to surfaces. *J. Am. Chem. Soc. 120*, 6548−6555.
(52) Arnold, M., Cavalcanti-Adam, E. A., Glass, R., Blummel, J., Eck, W., Kantlehner, M., Kessler, H., and Spatz, J. P. (2004) Activation of integrin function by nanopatterned adhesive interfaces. *ChemPhysChem 5*, 383−388.
(53) Koepsel, J. T., and Murphy, W. L. (2009) Patterning discrete stem cell culture environments via localized self-assembled monolayer replacement. *Langmuir 25*, 12825−12834.
(54) Lahiri, J., Isaacs, L., Tien, J., and Whitesides, G. M. (1999) A strategy for the generation of surfaces presenting ligands for studies of binding based on an active ester as a common reactive intermediate: a surface plasmon resonance study. *Anal. Chem. 71*, 777−790.
(55) Houseman, B. T., Gawalt, E. S., and Mrksich, M. (2003) Maleimide-functionalized self-assembled monolayers for the preparation of peptide and carbohydrate biochips. *Langmuir 19*, 1522−1531.
(56) Nebhani, L., and Barner-Kowollik, C. (2009) Orthogonal transformations on solid substrates: efficient avenues to surface modification. *Adv. Mater. 21*, 3442−3468.
(57) Gallant, N. D., Lavery, K. A., Amis, E. J., and Becker, M. L. (2007) Universal gradient substrates for "click" biofunctionalization. *Adv. Mater. 19*, 965−969.
(58) Lu, J., Shi, M., and Shoichet, M. S. (2009) Click chemistry functionalized polymeric nanoparticles target corneal epithelial cells through RGD-cell surface receptors. *Bioconjugate Chem. 20*, 87−94.
(59) Moore, N. M., Lin, N. J., Gallant, N. D., and Becker, M. L. (2010) The use of immobilized osteogenic growth peptide on gradient substrates synthesized via click chemistry to enhance MC3T3-E1 osteoblast proliferation. *Biomaterials 31*, 1604−1611.
(60) Gabet, Y., Muller, R., Regev, E., Sela, J., Shteyer, A., Salisbury, K., Chorev, M., and Bab, I. (2004) Osteogenic growth peptide modulates fracture callus structural and mechanical properties. *Bone 35*, 65−73.
(61) Chan, T. R., Hilgraf, R., Sharpless, K. B., and Fokin, V. V. (2004) Polytrizaoles as copper(I)-stabilizing ligands in catalysis. *Org. Lett. 6*, 2853−2855.
(62) Hudalla, G. A., and Murphy, W. L. (2010) Immobilization of peptides with distinct biological activities onto stem cell culture substrates using orthogonal chemistries. *Langmuir 26*, 6449−6456.
(63) Yousaf, M. N., and Mrksich, M. (1999) Diels-Alder reaction for the selective immobilization of protein to electroactive self-assembled monolayers. *J. Am. Chem. Soc. 121*, 4286−4287.
(64) Sun, X.-L., Stabler, C. L., Cazalis, C. S., and Chaikof, E. L. (2006) Carbohydrate and protein immobilization onto solid surfaces by sequential Diels-Alder and azide-alkyne cycloadditions. *Bioconjugate Chem. 17*, 52−57.
(65) Jonkheijm, P., Weinrich, D., Kohn, M., Engelkamp, H., Christianen, P. C. M., Kuhlmann, J., Mann, J. C., Nusse, D., Schroeder, H., Wacher, R., Breinbauer, R., Niemeyer, C. M., and Waldmann, H. (2008) Photochemical surface patterning by the thiol-ene reaction. *Angew. Chem. 120*, 4493−4496.
(66) Weinrich, D., Lin, P.-C., Jonkheijm, P., Nguyen, U. T. T., Schroder, H., Niemeyer, C. M., Alexandrov, K., Goody, R., and Waldmann, H. (2010) Oriented immobilization of farnesylated proteins by the thiol-ene reaction. *Angew. Chem., Int. Ed. 49*, 1252−1257.
(67) Hightower, K. E., and Fierk, C. A. (1999) Zing-catalyzed sulfur alkylation: insights from protein farnesyltransferase. *Curr. Opin. Chem. Biol. 3*, 176−181.
(68) Aizawa, Y., Leipzig, N., Zahir, T., and Shoichet, M. (2008) The effect of immobilized platelet derived growth factor AA on neural stem/progenitor cell differentiation on cell-adhesive hydrogels. *Biomaterials 29*, 4676−4683.
(69) Rahman, N., Purpura, K. A., Wylie, R. G., Zandstra, P. W., and Shoichet, M. S. (2010) The use of vascular endothelial growth factor functionalized agarose to guide pluripotent stem cell aggregates toward blood progenitor cells. *Biomaterials 31*, 8262−8270.
(70) Leipzig, N. D., Xu, C., Zahir, T., and Shoichet, M. S. (2010) Functional immobilization of interferon-gamma induces neuronal differentiation of neural stem cells. *J. Biomed. Mater. Res., Part A 93*, 625−633.
(71) Musoke-Zawedde, P., and Shoichet, M. S. (2006) Anisotropic three-dimensional peptide channels guide neurite outgrowth within a biodegradable hydrogel matrix. *Biomed. Mater. 1*, 162−169.
(72) Luo, Y., and Shoichet, M. S. (2004) A photolabile hydrogel for guided three-dimensional cell growth and migration. *Nat. Mater. 3*, 249−253.
(73) Lee, S. H., Moon, J. J., and West, J. L. (2008) Three-dimensional micropatterning of bioactive hydrogels via two-photo laser scanning photolithography for guided 3D cell migration. *Biomaterials 29*, 2962−2968.
(74) Polizzotti, B. D., Fairbanks, B. D., and Anseth, K. S. (2008) Three-dimensional biochemical patterning of click-based composite hydrogels via thiolene photopolymerization. *Biomacromolecules 9*, 1084−1087.
(75) Wosnick, J. H., and Shoichet, M. S. (2008) Three-dimensional chemical patterning of transparent hydrogels. *Chem. Mater. 20*, 55−60.
(76) Aizawa, Y., Wylie, R., and Shoichet, M. (2010) Endothelial cell guidance in 3D patterned scaffolds. *Adv. Mater. 22*, 4831−4835.
(77) Kosif, I., Park, Eun-Ju, P., Sanyal, R., and Sanyal, A. (2010) Fabrication of maleimide containing thiol reactive hydrogels via Diels-Alder/Retro-Diels-Alder strategy. *Macromolecules 43*, 4140−4148.
(78) Wang, T., and Guo, Z. J. (2006) Copper in medicine: homeostasis, chelation therapy and antitumor drug design. *Curr. Med. Chem. 13*, 525−537.
(79) Hoyle, C. E., Lowe, A. B., and Bowman, C. N. (2010) Thiol-click chemistry: a multifaceted toolbox for small molecule and polymer synthesis. *Chem. Soc. Rev. 39*, 1355−1387.
(80) Gress, A., Volkel, A., and Schlaad, H. (2007) Thio-click modification of poly[2-(3-butenyl)-2-oxazoline]. *Macromolecules 40*, 7928−7933.
(81) Hurd, C. D., and Gershbein, L. L. (1947) Reactions of mercaptans with acrylic and methacrylic derivatives. *J. Am. Chem. Soc. 69*, 2328−2335.
(82) Poloukhtine, A. A., Mbua, N. E., Wolfert, M. A., Boons, G.-J., and Popik, V. V. (2009) Selective labeling of living cells by a photo-triggered click reaction. *J. Am. Chem. Soc. 131*, 15769−15776.
(83) Soellner, M. B., Dickson, K. A., Nillson, B. L., and Raines, R. T. (2003) Site-specific protein immobilization by Staudinger ligation. *J. Am. Chem. Soc. 125*, 11790−11791.
(84) Fairbanks, B. D., Scott, T. F., Kloxin, C. J., Anseth, K. S., and Bowman, C. N. (2008) Thiol-yne photopolymerizations: novel mechanism, kinetics, and step-growth formation of highly cross-linked networks. *Macrimolecules 42*, 211−217.
(85) Wylie, R. G., Ahsan, S., Aizawa, Y., Maxwell, K. L., Morshead, C. M., and Shoichet, M. S. (2011) Three-dimensional, spatially-controlled simultaneous patterning of multiple growth factors in hydrogels. *Nat. Mater.*, accepted.

Bioconjugate Chemistry

Communication

pubs.acs.org/bc

A Molecular Umbrella Approach to the Intracellular Delivery of Small Interfering RNA

Lauren L. Cline,[†] Vaclav Janout,[†] Michael Fisher,[‡] Rudolph L. Juliano,[‡] and Steven L. Regen*[,†]

[†]Department of Chemistry, Lehigh University, Bethlehem, Pennsylvania 18015, United States

[‡]Division of Pharmaceutics, Eshelman School of Pharmacy, University of North Carolina, Chapel Hill, North Carolina 27599, United States

Supporting Information

ABSTRACT: A series of diwalled and tetrawalled molecular umbrellas have been synthesized using cholic acid, spermidine, and lysine as starting materials. Coupling of these molecular umbrellas to an octaarginine peptide afforded agents that were capable of promoting the transport of small interfering RNA to HeLa cells, as judged by the knockdown of enhanced green fluorescent protein expression. The efficiency of this knockdown was found to increase with an increasing number of facially amphiphilic walls present, and also when a cleavable disulfide linker was replaced with a noncleavable, maleimido moiety; i.e., a group that is not susceptible to thiolate-disulfide interchange. The knockdown efficiency that was observed for one tetrawalled molecular umbrella–octaargine conjugate was comparable to that observed with a commercially available transfection agent, Lipofectamine 2000, but the conjugate showed less cytotoxicity.

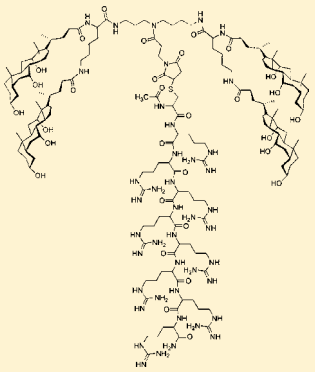

The ability of small interfering RNA (siRNA) to silence gene expression has generated considerable interest in recent years because of its potential as a chemotherapeutic agent and a biological tool.[1−4] One of the major goals in this area has been to improve the delivery of siRNA directly to the cytosol to allow for more efficient incorporation into the RNA-induced silencing complex (RISC), a key step in the silencing process.[2] To date, most approaches that have been used to deliver siRNA appear to rely on endocytotic pathways. Because endosomal release is known to be inefficient, a more direct means of delivery would be highly desirable. In particular, if siRNA could be transported into the cytosol via passive diffusion, significant improvement in their efficacy should be possible. With this ultimate goal in mind, we have begun to explore molecular umbrellas as delivery agents for siRNA.[5] Here, we report our results with first-generation molecular umbrellas bearing a pendant octaarginine peptide moiety for binding to siRNA.

As discussed elsewhere, molecular umbrellas are conjugates composed of two or more facial amphiphiles (i.e., "walls") that are attached to a central scaffold.[5] When immersed in a hydrophilic environment, these molecules create a hydrophilic exterior. Conversely, when immersed in a hydrophobic environment, they create a hydrophobic exterior. Recently, we have shown that the transport properties of molecular umbrellas in model membranes do not follow the classic size/lipophilicity rule.[6] Specifically, bilayer transport rates were found to increase with increasing numbers of umbrella walls and increasing facial hydrophilicity. This is exactly the opposite of what is expected on the basis of existing drug transport theory.[7] In addition, we and other researchers have shown that molecular umbrellas can readily enter live HeLa cells and that passive transport may play a significant role in this entry.[8,9] On the basis of these features, molecular umbrellas offer an opportunity for promoting the passive transport of biologically active agents across cell membranes in ways that have not previously been possible.

As a first step in exploring molecular umbrellas for siRNA delivery, we examined a series of molecular umbrella–octaarginine conjugates for their ability to reduce (i.e., "knock down") gene expression of enhanced green fluorescent protein (eGFP) in HeLa cells. Octaarginine was chosen because of its contiguous array of positive charges for binding to siRNA through electrostatic interactions and hydrogen bonding. Our working hypothesis was that such conjugates would create a "slide" within a plasma membrane for the passage of siRNA and/or a "sheath" that shields the siRNA as it crosses the bilayer (Figure 1). A related mechanism that can also be envisioned is one in which the conjugates act like "ferries" to shuttle the cargo across the membranes (not shown). In this study, our primary aim was fourfold: (i) to determine whether molecular umbrella–octaarginine conjugates can promote siRNA-induced knockdown of eGFP expression beyond that of octaarginine itself, (ii) to test whether knockdown efficiency

Received: July 5, 2011
Revised: September 13, 2011
Published: October 11, 2011

ACS Publications © 2011 American Chemical Society

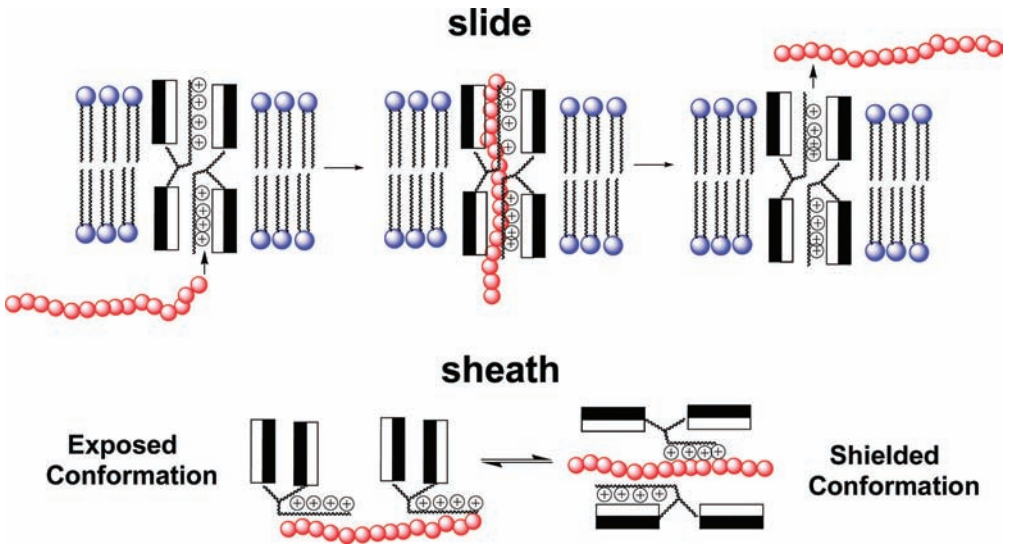

Figure 1. Hypothetical slide created by two diwalled molecular umbrella–oligoarginine conjugates inserting into a plasma membrane (top) vs a sheath (bottom), affording an exposed or shielded conformation. The black and white rectangles represent lipophilic and hydrophilic faces of the umbrella, respectively, and the red spheres represent individual units of the siRNA.

is dependent on the size of the umbrella that is used, (iii) to determine whether the introduction of a cleavable linker into a molecular umbrella–octaarginine conjugate can improve knockdown efficiency, and (iv) to judge the potential importance of a slide versus a sheath mechanism of delivery.[2]

With this purpose in mind, five agents were chosen as synthetic targets for this work, that is, conjugates **1**–**5** (Figure 2). Thus, comparison of **1** with **2** and comparison of **3** with **4** address the question of how umbrella size may influence siRNA delivery. Comparison of **1** with **3** and comparison of **2** with **4**, bearing a cleavable disulfide or a noncleavable maleimido moiety for conjugation, address the question of conjugate lability on knockdown efficiency. As a control for investigating the role that only the peptide portions of these conjugates play in siRNA delivery, we synthesized an octaarginine analogue (**5**), which contains a 2-mercaptoethanol moiety instead of a molecular umbrella. To place the knockdown efficiencies of these agents in perspective, we have compared them with that found using Lipofectamine 2000, a proprietary formulation that is widely used as a "gold standard" for transfection.

The synthetic method that was used to prepare conjugate **1** is shown in Scheme 1. In brief, Boc protection of the terminal amino groups of spermidine with 2-(Boc-oxyimino)-2-phenylacetonitrile (Boc-ON) to give **6**, followed by acylation with *N*-[*O*-1,2,3-benzotriazin-4(3*H*)onyl]-3-(2-pyridyldithio)-propionate (BPDP), afforded **7**.[10] Subsequent deprotection to give **8** followed by acylation with the *N*-hydroxysuccinimide ester of cholic acid (Ch-NHS) afforded **9**, which was then reacted with the free thiol form of **5** (designated as Pep-SH) to give **1**. The synthesis of **2** was conducted in a similar manner (Scheme 2). In this case, lysine dicholamide was first activated with *N*,*N*,*N*′,*N*′-tetramethyl-*O*-(*N*-succinimidyl)uronium tetrafluoroborate (TSU) and then used to acylate **8** to give **10**.[11] Conjugate **4** was synthesized by first acylating both terminal amino groups of spermidine with lysine dicholamide, followed by acylation of its secondary amine with 3-maleimidopropanoic acid and conjugated addition of Pep-SH (Scheme 3). The analogous diwalled conjugate, **3**, was synthesized by a similar route (note shown). Finally, the control peptide, **5**, was obtained by reacting Pep-SH with 2-(2-pyridyldithio)ethanol (not shown).

Using procedures described in the Supporting Information and 50 nM eGFP siRNA, knockdown efficiencies were determined with concentrations of **1**–**5** that varied from 100 to 2000 nM. In control experiments, in which HeLa cells were treated with only eGFP siRNA or with eGFP siRNA and **5**, no significant knockdown was observed (Figure 3). Because a primary aim of this work was to compare the efficacy of **5** with those of corresponding molecular umbrella conjugates under similar experimental conditions, no effort was made to find other conditions under which **5** shows significant activity, e.g., by using higher concentrations of **5**. In contrast, when the siRNA was first incubated with **1**, the extent of knockdown increased on going from 100 to 1000 nM; however, at a concentration of 2000 nM, the extent of knockdown was found to decrease. This corresponds to the concentration at which cytotoxicity began to occur. Similar results were observed with **2** except that the knockdown efficiency was found to be significantly greater (Figure 3). Thus, an increase in the number of umbrella walls resulted in a significant increase in transport activity.[6] Compared with that of Lipofectamine 2000, however, the ability of **2** to induce eGFP knockdown was significantly weaker. Also reported in Figure 3 are the corresponding cytotoxicities of these delivery agents, as determined by a standard MTS assay. None of the conjugates displayed any decrease in cell viability until a concentration of 1000 nM was reached. This can be compared to the case of Lipofectamine 2000, which shows 76.8% cell viability using optimal conditions described by the manufacturer.

To judge the consequences that a cleavable linker has on molecular umbrella-assisted transport of siRNA, we examined the relative activities of **3** and **4** (Figure 4). Similar to **1**, the diwalled analogue **3** showed very low activity. However, for the tetrawalled conjugate that contained the maleimido linkage (i.e., **4**), its activity was significantly greater than that of its cleavable counterpart, **2**, and it compared favorably to that of Lipofectamine 2000. Control experiments conducted with **4**, alone, showed no knockdown and no cytotoxicity at 500 nM.

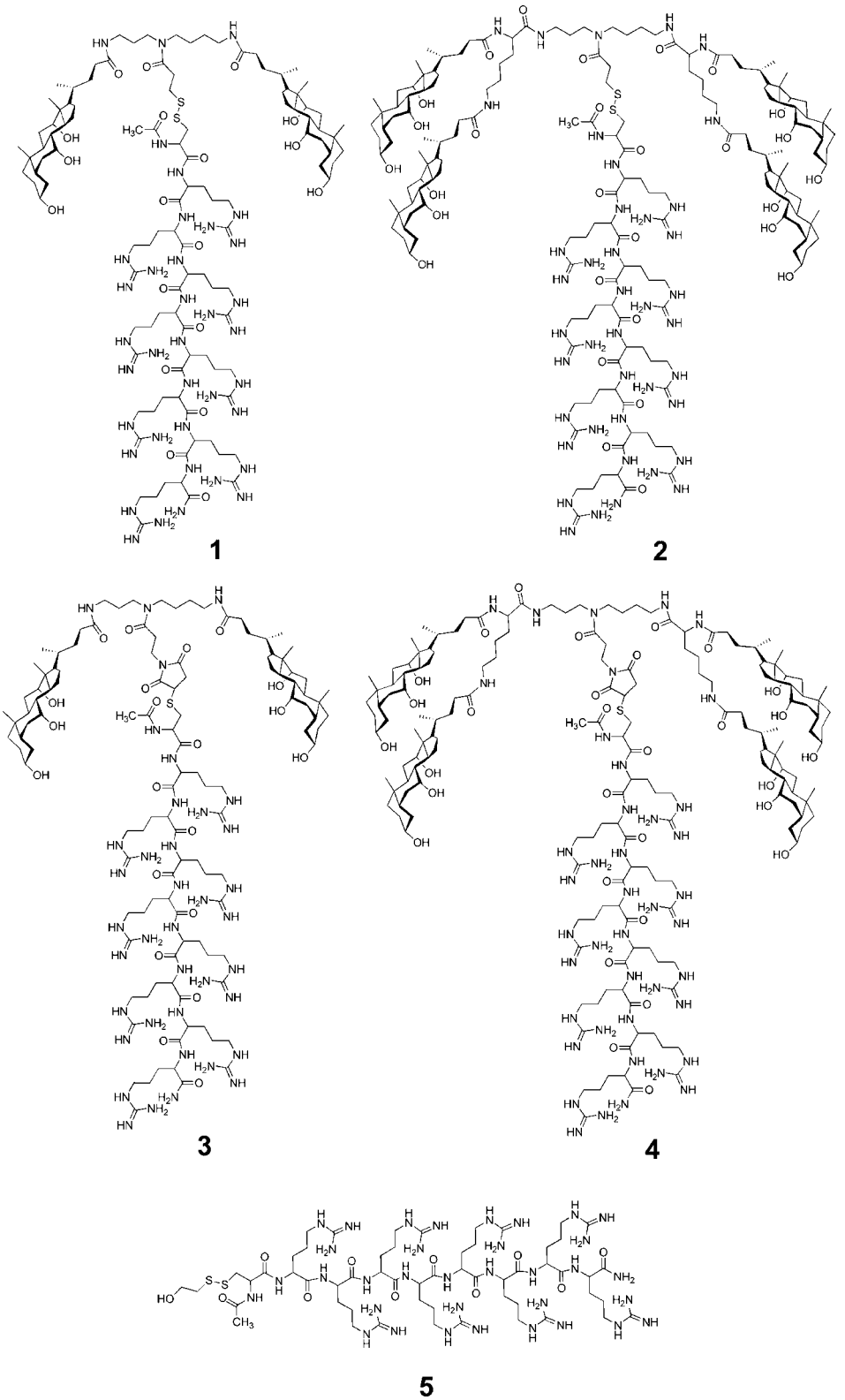

Figure 2. Molecular structures of umbrella−octaarginine conjugates **1**−**4** and control peptide **5**.

Although we hypothesized that the cleavable analogues might exhibit greater activity because of a greater ability to release siRNA into the cytoplasm, the exact opposite was observed. We presently suspect that cleavage on the outer surface of the HeLa cells via neighboring cysteine groups of membrane proteins may be responsible for this difference. It is also noteworthy that under optimized conditions (i.e., using 500 nM molecular umbrella conjugate), **4** exhibited no significant decrease in cell viability, whereas the use of Lipofectamine 2000 resulted in a moderate decrease in cell viability.

In an effort to judge the potential importance of a slide versus a sheath mechanism of transport, we conducted

dx.doi.org/10.1021/bc200347x | *Bioconjugate Chem.* 2011, 22, 2210−2216

Scheme 1. Synthesis of 1

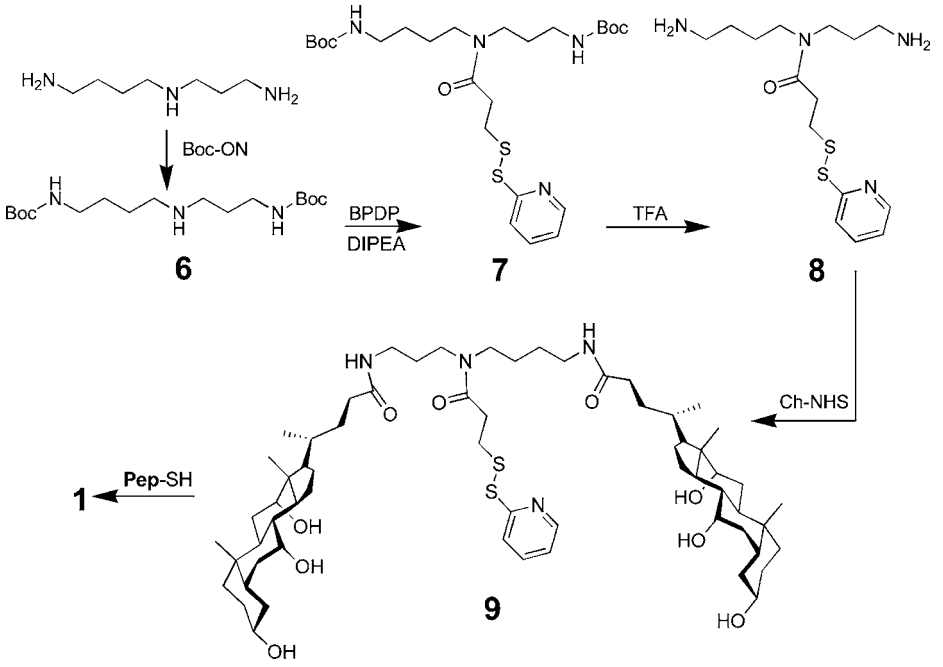

Scheme 2. Synthesis of 2

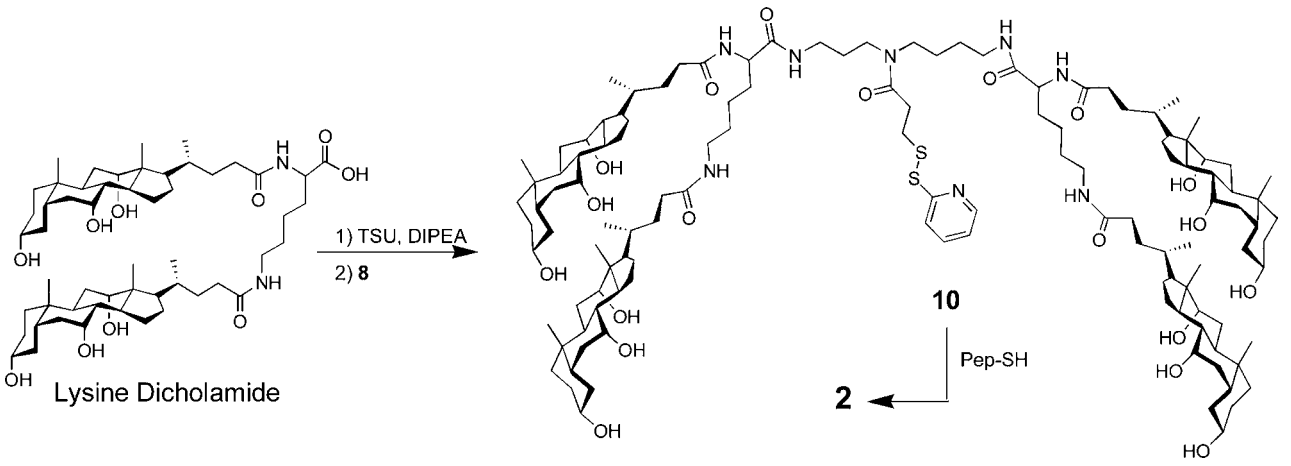

knockdown experiments with **4** in two different ways: (i) by incubating HeLa cells with the conjugate prior to the addition of siRNA and (ii) by incubating **4** with the siRNA followed by incubation with the HeLa cells. As shown in Figure 5, the latter (where the umbrella conjugate is premixed with the eGFP siRNA) clearly results in a greater knockdown efficiency. These results suggest that contributions from a sheath mechanism of delivery are likely to be more important than those from a slide mechanism (Figure 5).

To judge the consequences that a cleavable linker has on molecular umbrella-assisted transport of siRNA, we examined the relative activities of **3** and **4** (Figure 4). Similar to **1**, the diwalled analogue **3** showed very low activity. However, for the tetrawalled conjugate that contained the maleimido linkage (i.e., **4**), its activity was significantly greater than that of its cleavable counterpart, **2**, and it compared favorably to that of Lipofectamine 2000. Control experiments conducted with **4**, alone, showed no knockdown and no cytotoxicity at 500 nM.

These findings demonstrate the feasibility of applying molecular umbrella chemistry to siRNA transport. They also show that significant improvements are possible in the case of molecular umbrella–octaargine conjugates by increasing the number of umbrella walls and increasing the stability of the linker used to connect both components. The fact that the knockdown efficiency of **4** is at a level that is comparable to that of Lipofectamine 2000 while **4** exhibits reduced cytotoxicity provides considerable incentive for exploring molecular umbrellas more broadly in this context. It should be noted, in this regard, that this comparison is based on experiments in which HeLa cells were transfected for 4 h with the siRNA complexes in serum-free media prior to changing to serum-containing media. When serum was present throughout the entire course of the transfection, the activity of **4** was reduced by ~50% (Supporting Information). In contrast, serum had a negligible effect on the activity of Lipofectamine 2000. Whether further changes in the composition and structure of such molecular umbrella conjugates can minimize such reduction in activity remains to be established.

Efforts currently in progress are focused on (i) the synthesis of related conjugates in which the sense strand of a double-

dx.doi.org/10.1021/bc200347x | *Bioconjugate Chem.* 2011, 22, 2210–2216

Scheme 3. Synthesis of 4

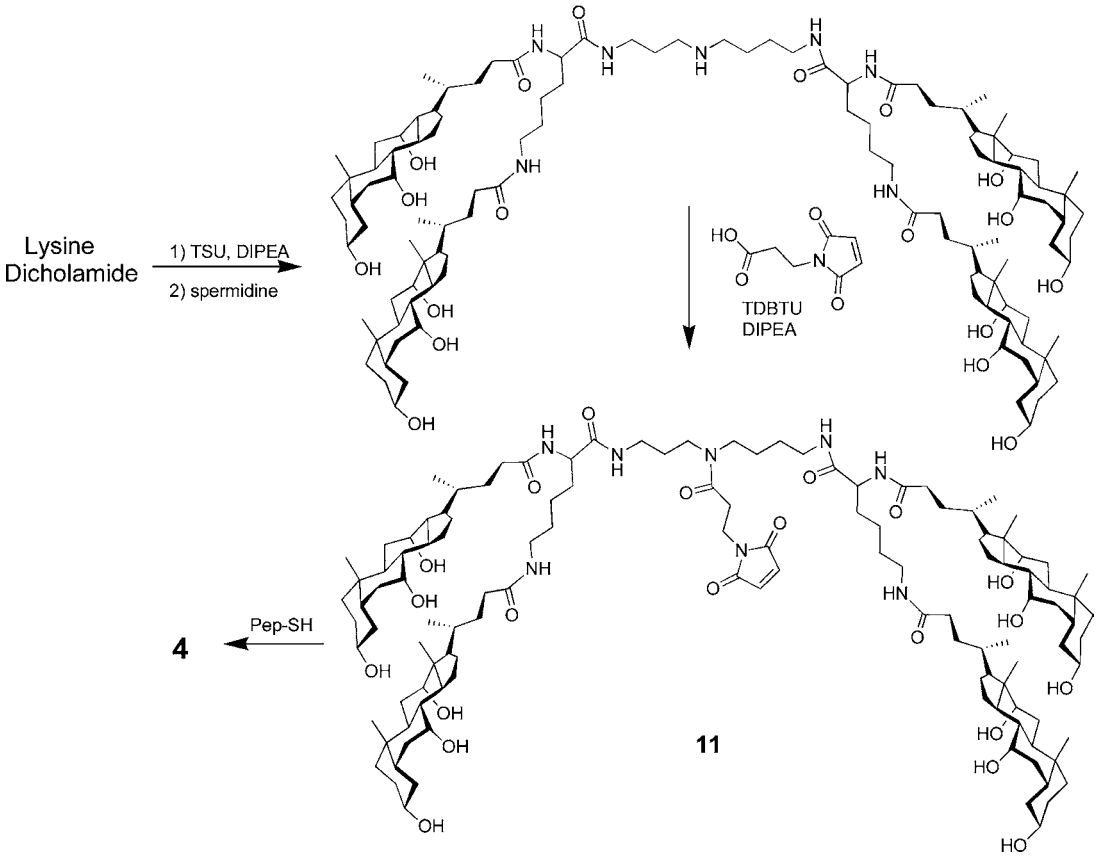

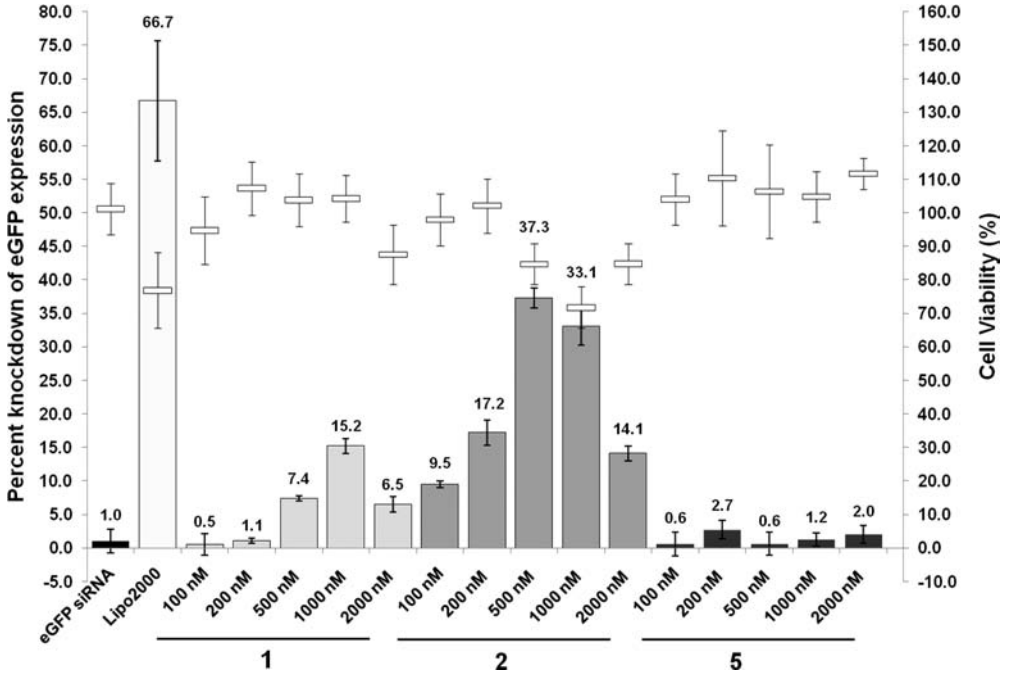

Figure 3. Percentage of eGFP knockdown (bar graph) and cell viability (empty rectangles) using varying concentrations of **1** (DW-S-S-Pep), **2** (TW-S-S-Pep), and **5** (OH-S-S-Pep) as compared to those of cells that were untreated. Lipofectamine 2000 was used as described by the manufacturer. Values for percent knockdown of eGFP expression are given above each column and represent the average of a typical experiment conducted in triplicate. Error bars represent the standard deviation of these values.

stranded siRNA has been covalently attached to the handle of a molecular umbrella, thereby circumventing the need for a pendant octaarginine moiety, and (ii) gaining insight into the probable contributions made from passive transport and endocytotic pathways for cellular entry. The results of these studies will be reported in due course.

dx.doi.org/10.1021/bc200347x | *Bioconjugate Chem.* 2011, 22, 2210–2216

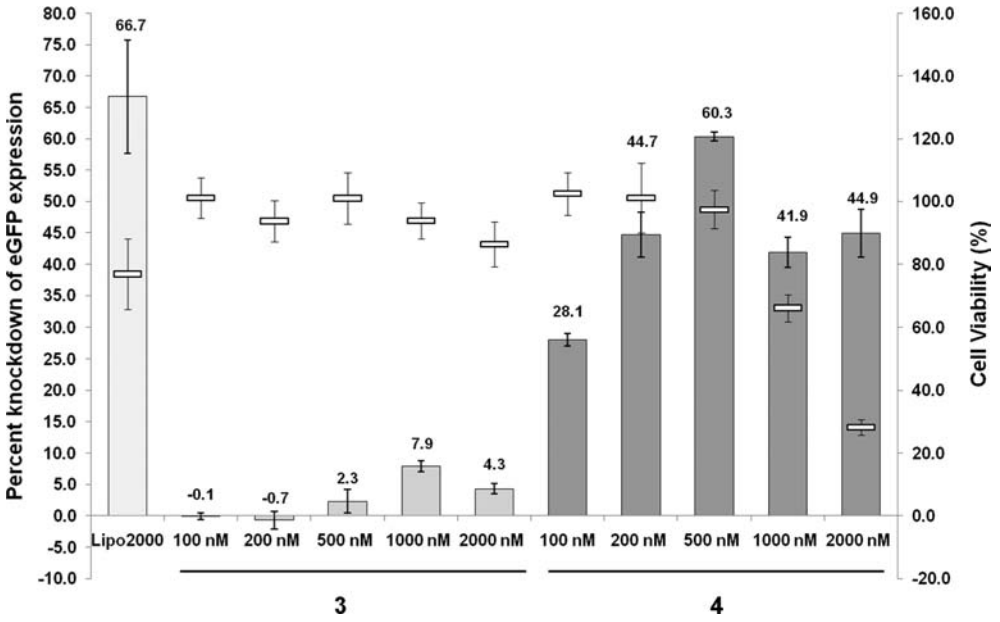

Figure 4. Percentage of eGFP knockdown (bar graph) and cell viability (empty rectangles) using varying concentrations of **3** (DW-mal-Pep) and **4** (TW-mal-Pep) as compared to those of cells that were untreated. Lipofectamine 2000 was used as described by the manufacturer. Values for percent knockdown of eGFP expression are given above each column and represent the average of a typical experiment conducted in triplicate. Error bars represent the standard deviation of these values.

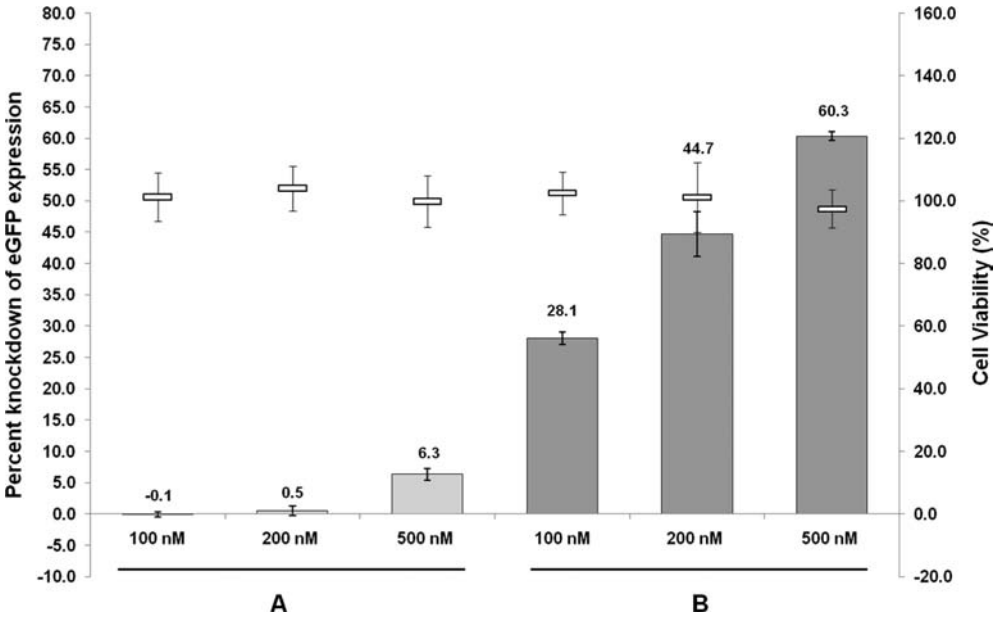

Figure 5. Percentage of eGFP knockdown (bar graph) and cell viability (empty rectangles) for **4** when the molecular umbrella–octaarginine conjugate was (A) first incubated with the HeLa cells prior to addition of the eGFP siRNA or (B) premixed with the eGFP siRNA, followed by incubation with the HeLa cells. Values for percent knockdown of eGFP expression are given above each column and represent the average of a typical experiment conducted in triplicate. Error bars represent the standard deviation of these values.

■ ASSOCIATED CONTENT

Supporting Information

Experimental procedures and supplementary data. This material is available free of charge via the Internet at http://pubs.acs.org.

■ AUTHOR INFORMATION

Corresponding Author

*E-mail: slr0@lehigh.edu.

■ ACKNOWLEDGMENTS

We are grateful to our colleague, Prof. Lynne Cassimeris, for the generous use of her cell culture facilities and for valuable technical advice. This work was funded by the National Institutes of Health (PHS GM51814).

■ REFERENCES

(1) Stanton, M. G., and Colletti, S. L. (2010) Medicinal chemistry of siRNA delivery. *J. Med. Chem.* *53*, 7887–7901.

(2) Juliano, R., Alam, R. M., Dixit, V., and Kang, H. (2008) Mechanisms and strategies for effective delivery of antisense and siRNA oligonucleotides. *Nucleic Acids Res. 36*, 4158−4171.
(3) Wolfrum, C., Shi, S., Jayaprakash, K. N., Jayaraman, M., Wang, G., Pandey, R. K., Rajeev, K. G., Nakayama, T., Charrise, K., Ndungo, E. M., Zimmermann, T., Koteliansky, V., Manoharan, M., and Stoffel, M. (2007) Mechanisms and optimization of in vivo delivery of lipophilic siRNAs. *Nat. Biotechnol. 25*, 1149−1157.
(4) Mahon, K. P., Love, K. T., Whitehead, K. A., Qin, J., Akinc, A., Leshchiner, E., Leshchiner, I., Langer, R., and Anderson, D. G. (2010) Combinatorial approach to determine functional group effects on lipidoid-mediated siRNA delivery. *Bioconjugate Chem. 21*, 1448−1454.
(5) Janout, V., and Regen, S. L. (2009) Bioconjugate-based molecular umbrellas. *Bioconjugate Chem. 20*, 183−192.
(6) Mehiri, M., Chen, W.-H., Janout, V., and Regen, S. L. (2009) Molecular umbrella transport: Exceptions to the classic size/lipophilicity rule. *J. Am. Chem. Soc. 131*, 1338−1339.
(7) Pidgeon, C., Ong, S., Liu, H., Qiu, X., Pidgeon, M., Dantzig, A. H., Munroe, J., Homback, W. J., Kasher, J. S., Glunz, L., and Szczerba, T. (1995) IAM chromatography: An in vitro screen for predicting drug permeability. *J. Med. Chem. 38*, 590−594.
(8) Mehiri, M., Jing, B., Ringhoff, D., Janout, V., Cassimeris, L., and Regen, S. L. (2008) Cellular entry and nuclear targeting by a highly anionic molecular umbrella. *Bioconjugate Chem. 19*, 1510−1513.
(9) Ge, D., Wu, D., Wang, Z., Shi, W., Wu, T., Zhang, A., Hong, S., Wang, J., Zhang, Y., and Ren, L. (2009) Cellular uptake mechanism of molecular umbrella. *Bioconjugate Chem. 20*, 2311−2316.
(10) Janout, V., Lanier, M., and Regen, S. L. (1999) *N*-[O-1,2,3-Benzotriazin-4(3H)one-yl]-3,(2-pyridyldithio)propionate: A more reactive alternative to SPDP. *Tetrahedron Lett. 40*, 1107−1108.
(11) Chen, W. H., Shao, X. B., and Regen, S. L. (2005) Poly(choloyl)-based amphiphiles as pore-forming agents: Transport-active monomers by design. *J. Am. Chem. Soc. 127*, 12727−12735.

A Molecular Umbrella Approach to the Intracellular Delivery of siRNA

Lauren L. Cline,[†] Vaclav Janout,[†] Michael Fisher,[≠] Rudolph L. Juliano,[≠] Steven L. Regen[†]

Department of Chemistry, Lehigh University,[†] Bethlehem, Pennsylvania 18015, and Division of Pharmaceutics, Eshelman School of Pharmacy, University of North Carolina at Chapel Hill,[≠] North Carolina 27599

Supporting Information

Methods and Materials. ^{1}H NMR spectra were recorded in either CD_3OD or $CDCl_3$ using a Bruker 500 spectrometer and the solvent as a reference. Silica gel 60 (Fluka, particle size 0.035~0.070 mm, 220-440 mesh) was used for all column chromatographic purifications. Thin-layer chromatography (TLC) was performed on a glass plate precoated with silica gel and a fluorescence indicator (EMD). Detection on TLC was made by use of sulfuric acid 10% in water, iodine or UV (254 or 365 nm). All reagents and chemicals were obtained from commercial sources and used upon as received unless otherwise stated. All molecular umbrella-octaarginine conjugates were purified by preparative reverse phase (RP)-HPLC and characterized by ^{1}H NMR and high resolution mass spectrometry (HRMS).

High glucose containing Dulbecco's modified Eagle's medium (DMEM-H), DEPC-treated water, trypsin-EDTA solution, G 418 disulfate salt, and antibiotic antimycotic solution were purchased from Sigma Aldrich (St. Louis, MO). Lipofectamine™ 2000, fetal bovine serum (FBS), and OPTI-MEM reduced serum media were obtained from Invitrogen (Carlsbad, CA). **Pep**-SH (i.e., Ac-CRRRRRRRR-NH_2) was custom-

synthesized by GenScript USA, Inc. (Piscataway, N.J). Duplexed and desalted siRNA was purchased from ThermoScientific Dharmacon siRNA Technologies (Lafayette, CO) with the sense and antisense sequences 5'-GACGUAAACGGCCACAAGUdTdT and 5'-ACUUGUGGCCGUUUACGUCdTdT, respectively. HeLa cells that stably expressed enhanced green fluorescent protein (HeLa eGFP cells) were obtained from Professor Juliano's laboratory (University of North Carolina, Chapel Hill, NC). The cells were maintained in normal growth medium containing DMEM-H with 10% FBS, 400 µg/mL G 418, and 1% antibiotic antimycotic solution and grown at 37°C and 5% CO_2. A Cell Titer 96 Aqueous non-radioactive cell proliferation assay (MTS assay) was purchased from Promega (Madison, WI).

Boc-protected Spermidine (6). To a solution that was prepared from 0.26 g (1.79 mmol) of spermidine, 15 mL of CH_3OH and 0.545 g (5.38 mmol) of triethylamine was added 0.974 g (3.96 mmol) of 2-(Boc-oxyimino)-2-phenylacetonitirile) ("Boc-ON"). After stirring the resulting solution at room temperature for 24 h, the solvent was then removed under reduced pressure. Subsequent purification of the residue by column chromatography [silica gel, using a gradient starting from $CHCl_3/CH_3OH$ (10/1, v/v) and ending in $CHCl_3/CH_3OH/NH_4OH$ (75/20/3, v/v/v)] afforded 310 mg (50 %) of **5** having ^{1}H NMR (500 MHz, CD_3OD, 298K): 3.19(m,2H); 3.11(t,2H); 2.66(m,2H); 2.60(m,2H); 1.64(m,2H); 1.52(m,4H); 1.44(bs,18H).

Conjugate 7. To a solution that was made from 155 mg (0.45 mmol) of **6**, 2 mL of DMF and 156 µL (0.9 mmol) of N,N-diisopropyl-N-ethylamine (DIPEA) was added 162 mg

(0.9 mmol) of *N*-[O-1,2,3-benzotriazin-4(3H) one-yl]-3,(2-pyridyldithio)propionate (BPDP), directly as solid. For the synthesis of BPDP, see: Sarinya Shawaphun, S.; Janout; V.; Regen; S. L. (1999) Transbilayer movement of molecular umbrellas. *J. Amer. Chem. Soc. 121,* 5860-5865.

After stirring this solution for 18 h at room temperature, the solvent was removed under reduced pressure. Subsequent trituration with aqueous $NaHCO_3$ followed by water, and purification by column chromatography [silica gel, $CHCl_3/CH_3OH/NH_4OH$ (300/10/1, v/v/v) afforded 123 mg (50 %) of **7** having ^{1}H NMR (500 MHz, CD_3OD, 298 K): 8.40 (d, 1H); 7.81(m,2H); 7.22(d, 1H); 3.35(t, 2H); 3.25(t, 2H); 3.05(m, 6H); 2.79(t, 2H); 1.68(m, 2H); 1.54(m, 4H); 1.42(d,18H).

Deprotection of 7 to give 8. Deprotection was carried out by dissolving 122 mg (2.25 mmol) of **7** in a solution made from 4.5 mL of $CHCl_3$ plus 1.5 mL of CF_3CO_2H (TFA), followed by stirring for 2.5 h at room temperature. Removal of the solvents under reduced pressure, followed by drying (16 h, 23°C, 1 mm Hg) afforded 76.8 mg (100%) of **8** having ^{1}H NMR (500 MHz, CD_3OD, 298 K): 8.45 (d, 1H); 7.88(m, 2H); 7.28(d, 1H); 3.47(t, 2H); 3.30(m, 2H); 3.09(t, 2H); 2.87(m, 6H); 1.90(m, 2H); 1.63(m, 4H).

Umbrella Conjugate 9. To a solution derived from cholic acid 200 mg (0.489 mmol), 3 mL of DMF and 65.7 mg (0.509 mmol) of DIPEA was added 156 mg (498 µmol) of N_1,N_1,N_2,N_2-tetramethyl-N-[O-succinimidyl]-uronium tetrafluoroborate TSU. After stirring the mixture for 2 h at room temperature, a solution of 83.3 mg (0.244 mmol) of **8** in 1.0 mL DMF and 0.4 mL (2.3 mmol) DIPEA was added and resulting solution stirred

for an additional 18 h at room temperature. Removal of solvents under reduced pressure at 50°C gave a crude product that was washed, sequentially, with 5% $NaHCO_3$ and water. The crude product was then dissolved in 5 mL of CH_3OH and this solution then added to 1% $NaHCO_3$ to precipitate a crude product. After centrifuging washing with water, and freeze drying, the product was purified by preparative thin layer chromatography [silica gel, $CHCl_3$/CH_3OH/water/NH_4OH (70/20/1, v/v/v/v) to give 199 mg (74%) of **9** having ^{1}H NMR (500 MHz, CD_3OD, 298K): 8.40 (d, 2H); 7.84(m, 2H); 7.23(d, 1H); 3.93(s, 4H); 3.78(d, 4H); 3.36(m, 8H); 3.18(m, 8H); 3.06(m, 2H); 2.78(m, 2H); 0.71-2.35(m, 138H); 0.70(s, 12H). This ^{1}H NMR spectrum was identical to that previously reported: Sarinya Shawaphun, S.; Janout; V.; Regen; S. L. (1999) Transbilayer movement of molecular umbrellas. *J. Amer. Chem. Soc. 121,* 5860-5865.

Umbrella-Peptide Conjugate 1. To a solution that was made from 6.5 mg (5.9 μmol) of **9** in 500 μL of CH_3OH was added solution of 9.10 mg (6.4 μmol) of **Pep**-SH in 500 uL of CH_3OH. After stirring at room temperature under an argon atmosphere for 48 h the mixture was subjected, directly, to purification by reverse phase HPLC [C18 column, 0.06% TFA in water/CH_3CN/$(CH_3)_2CHOH$] using a gradient that started with 80/10/35, v/v/v and ended with 5/10/85, v/v/v. Concentration under reduced pressure at 45°C, followed by freeze drying for 48 h afforded 12.0 mg (81%) of **1** having ^{1}H NMR (500 MHz, D_2O, 298 K) δ: 4.70 (t, 1H); 4.40 (m, 8H), 3.92(bs, 2H); 3.72(bs, 2H), 3.36 (m, 2H); 3.27(m, 4H), 3.12(bs, 16H), 3.08(m, 4H); 2.90 (m, 2H); 2.75 (m, 2H); 0.79-2.20 (m, 100H); 1.98 (s, 9H); 0.58(s, 6H); MALDI-TOF MS m/z (MH+) Calcd. for $C_{111}H_{204}N_{37}O_{19}S_2$: 2423.5570. Found: 2423.5488.

Synthesis of Conjugate 10. To a solution derived from lysine dicholamide 219 mg (0.236 mmol) and 3 mL of DMF was added 87.3 mg (250 µmol) O-3,4-dihydro-4-oxo-1,2,3-benzotriazin-3-yl-N,N,N',N'-tetramethyl-uronium tetrafluoro borate (DBTU) and 37.5 mg (0.290 mmol) of DIPEA. After stirring the mixture for 3 h at room temperature, a solution of 36.9 mg (0.108 mmol) of **8** in 1.5 mL of DMF and 0.2 mL (1.15 mmol) of DIPEA was added and resulting solution stirred for an additional 18 h at room temperature. Removal of solvents under reduced pressure at 50°C gave a crude product that was washed, sequentially, with 5% $NaHCO_3$ and water. The crude product was then dissolved in 5 mL of CH_3OH and this solution then added to 1% $NaHCO_3$ to precipitate crude product. After centrifuging, washing with water, and freeze drying, the product was purified by preparative thin layer chromatography [silica gel, $CHCl_3$/CH_3OH/water/NH_4OH (85/25/2/1, v/v/v/v) to give 126 mg (54%) of **10** having ^1H NMR (500 MHz, CD_3OD, 298K): 8.39 (d,2H); 7.80(m,2H); 7.21(d,1H); 4.26(m,2H); 3.93(s,4H); 3.78(d,4H); 3.36(m,8H); 3.18(m,8H); 3.06(m,2H); 2.78(m,2H); 0.71-2.35(m, 138H); 0.70(s,12H). HRMS: for $C_{133}H_{202}N_8O_{19}S_2Na$ calc.: 2182.4420 ; found: 2182.4408

Umbrella-Peptide Conjugate 2. To a solution that was made from 15.0 mg (7.0 µmol) of **10** in 1mL of CH_3OH was added solution of 9.2 mg (6.51µmol) of **Pep**-SH in 500 µL of CH_3OH. After stirring at room temperature under and argon atmosphere for 48 h the mixture was subjected, directly, to purification by reverse phase HPLC [C18 column, 0.06% TFA in water/CH_3CN/iso-propylalcohol, using a gradient that started with

40/5/35, v/v/v and ended with 5/10/95, v/v/v. Concentration under reduced pressure at 45°C, followed by freeze drying for 48 h afforded 11.80 mg (33%) of **2** having ^{1}H NMR (500 MHz, D_2O, 298 K) δ: 4.70 (t, 1H); 4.40 (m, 8H), 3.92(bs, 2H); 3.72(bs, 2H), 3.36 (m, 2H); 3.27(m, 4H), 3.12(bs, 16H), 3.08(m, 4H); 2.90 (m, 2H); 2.75 (m, 2H); 0.79-2.20 (m, 100H); 1.98 (s, 9H); 0.58(s,6H); MALDI-TOF MS m/z (MH+) Calcd. for $C_{171}H_{304}N_{41}O_{29}S_2$: 3460.2010. Found: 3460.3106 .

Synthesis of Conjugate 11. To a solution that was made from 200 mg (0.215 mmol) of lysine dicholamide, 1.4 mL of DMF and 42 µL of DIPEA was added 82.0 mg (0.235 mmol) of N,N,N',N'-tetramethyl-O-(3,4-dihydro-4-oxo-1,2,3-benzotriazin-3-yl) uranium tetrafluoroborate (DBTU). After stirring for 18 h at room temperature, a solution made from 15.7 mg of spermidine (0.108 mmol) plus 400 µL of DMF and 100 µL of DIPEA was then added. Further stirring for 18 h at room temperature in closed flask, followed by concentration under reduced pressure, afforded a crude product that was purified by column chromatography [silica gel, $CHCl_3/CH_3OH/NH_4OH$ (80/35/7, vol/vol/vol) to give 46 mg (22%) of the N_1,N_3-bisconjugate of spermidine and lysine dicholeamide having ^{1}H NMR (CD_3OD, δ): 4.21(m, 2H); 3.94(s, 4H); 3.79(s, 4H); 3.40(m, 6H); 3.16(m, 8H); 2.64(m, 4H); 0.9-2.30(m, 138H); 0.69(s, 12H).

To a solution that was made from 6.0 mg (35.4 µmol) of 3-maleimido-propanoic acid, 0.3 mL of DMF and 6.3 µL of DIPEA (0.0353mmol) was added 13.0 mg (0.0373 µmol) of DBTU. After stirring for 3 h at room temperature, a solution that was made from 0.5 mL of DMF, 30 µL DIPEA (0.168 mmol) of 58.0 mg (29.5 µmol) of the N_1,N_3-bisconjugate of spermidine and lysine dicholeamide and 20 µL DIPEA was added. The

resulting mixture was stirred for an additional 18 h at room temperature. The product mixture was then concentrated under reduced pressure and the crude oily produce was washed with 5% $NaHCO_3$, followed by freeze drying. The crude product was then purified by RP HPLC [C18 column, using solvents A: EtOH/CH_3CN/water (10/5/90, v/v/v), B: EtOH/CH_3CN/water (96/8/4, v/v/v) starting at A/B=30/70, ending A/B=0/100) to give 42.2 mg (68%) of **11** having ^{1}H NMR (500 MHz, CD_3OD, 298 K): 6.28(s,2H); 4.28 (m,2H);3.94(s,4H);3.79(m, 6H);3.37(m, 6H)'3.15(m, 10H); 2.60(m, 2H);, 0.8-2.35(m,138H);,0.70(s,12H).

Umbrella-Peptide Conjugate 4. To a solution that was made from 9.8 mg (4.64 µmol) of **11** in 500 µL of CH_3OH was added solution of 8.71 mg (6.17 µmol) of **Pep**-SH in 1.2mL of MeOH at room temperature. After stirring under an argon atmosphere for 48 h, the mixture was subjected, directly, to purification by reverse phase HPLC [C18 column, 0.06% TFA in water/CH_3CN/$(CH_3)_2CHOH$ (using a gradient that started with 80/10/35, v/v/v and ended with 5/10/85, v/v/v. Concentration under reduced pressure at 45°C, followed by freeze drying for 48 h afforded 12.42 mg (76%) of **4** as a white solid, which was dissolved in pure water and dialyzed against pure water using a 100 Dalton cut-off. The resulting product exhibited ^{1}H NMR (500 MHz, CD_3OD, 298 K) δ: 4.70 (m, 1H); 4.34(m,8H); 4.22 (m, 2H); 3.95(s, 4H); 3.72(m, 6H); 3.36(m, 8H); 3.20(m,27H); 2.502.73(m,4H);0.85-2.35(m, 170H); 2.05(s, 3H); 0.69(s, 12H). MALDI-TOF MS m/z (MH+) Calcd. for $C_{176}H_{308}N_{41}O_{29}S_2$: 3524.3323. Found: 3524.3135.

2-Mercaptoethanol-Peptide Conjugate 5. To a solution of 15.0 mg (0.0761 mmol) of 2-[2-hydroxyethyldithio]-pyridine in 500 µL of CH_3OH was added 5.01mg (3.5 µmol) of **Pep**-SH. After stirring under an argon atmosphere for 48 h, the mixture was diluted by adding 10 mL H_2O and subjected to dialysis using MWCO 500 Da. Concentration under reduced pressure at 45°C, followed by freeze drying for 48 h afforded 4.85 mg (93%) of **5** having ^{1}H NMR (500 MHz, D_2O, 298 K) δ: 4.70 (t, 1H); 4.37(m,8H); 3.82(t,2H); 3.19(m, 16H); 3.00(m,2 H);, 2.86(t,2H); 2.03(s,3H); 1.60(m,32H). MALDI-TOF MS m/z. $C_{58}H_{11}N_{34}O_{11}S_2$ MH+ calc.: 1487.8608; found: 1487.8572

siRNA Transfection. HeLa eGFP cells were seeded into a 24-well plate at a density of 20,000 cells/well and grown for 24 h in DMEM-H medium with 10% FBS added. Cells were grown without antibiotics or G 418 present for at least one cell passage prior to transfection. Molecular umbrella-oligoarginine conjugates **1** and **2** were dissolved in DEPC-treated water and these stock solutions (250 µM) then stored at 5°C; conjugates **3** and **4** were stored as solids at -80°C and were dissolved immediately prior to use. The duplexed siRNA was also dissolved in DEPC-treated water (75 µM) and stored in 50 µL aliquots at -80º C. The concentration of siRNA was determined using UV absorption at 260 nm. Prior to transfection, molecular umbrella-oligoarginine stocks were diluted with OPTI-MEM buffer (4, 8, 20, 40, and 80 µM) and the siRNA diluted with OPTI-MEM buffer (2 µM). The resulting two solutions were then combined (1/1, vol/vol) and incubated at room temperature for 30 min. Growth medium was removed and the cells then rinsed with warm OPTI-MEM. To each well was added 950 µL of fresh OPTI-MEM medium and 50 µL of molecular umbrella-siRNA complex mixture. The cells

were incubated at 37°C and 5% CO_2 for 4 h. Medium was then removed and replaced with DMEM-H with 1.5% FBS added and the cells incubated at 37°C and 5% CO_2 for 72 h. The cells were rinsed with PBS and incubated for 5 min with 1x trypsin-EDTA solution (0.3 mL). OPTI-MEM containing 10% FBS (1 mL) was added to each well, and the solution was vigorously pipetted to remove cells from the bottom of the plate. The cells were pelleted by centrifugation for 5 min at 750 rpm. The pellet was then resuspended in 0.5 mL PBS and analyzed for eGFP fluorescence using a BD FACS CANTOII flow cytometer. Lipofectamine™ 2000 was used as a reference, following optimum procedures as described by the manufacturer. The percent knockdown of eGFP expression was determined using the BD FACSDiva software and correcting for eGFP fluorescence in untreated cells.

Cell Viability Measurements. The cell viability of the eGFP-expressing HeLa cells after treatment with the molecular umbrella-siRNA complexes was determined using the MTS assay (CellTiter 96® AQ_{ueous} Non-Radioactive Cell Proliferation Assay provided by Promega). Cell viability was determined at the conclusion of the transfection experiment (72 h after exposure to the complexes). In brief, cells were treated with trypsin-EDTA solution (0.3 mL) for 5 min after which OPTI-MEM media containing 10% FBS (1 mL) was added. The cell suspension was vigorously mixed to remove all cells from the bottom of the plate, and a 130 µL aliquot was transferred to a 96-well plate. At this time, 25 µL of the MTS/PMS solution was added to each well and the plate incubated at 5% CO_2 for 2 h (37°C). The UV-VIS absorbance of each sample (total volume of 155 µL) was analyzed at 492 nm using a Labsystems Multiskan Ascent microplate reader. Cell viability was expressed by the following equation: cell viability (%) = ($Abs_{sample}/Abs_{control}$)

x 100%, where Abs_{sample} was the absorbance of the cell solution when treated with molecular umbrella-siRNA complexes and $Abs_{control}$ was the absorbance of untreated cells. All absorbance values were corrected for background signal of the solution with no cells present.

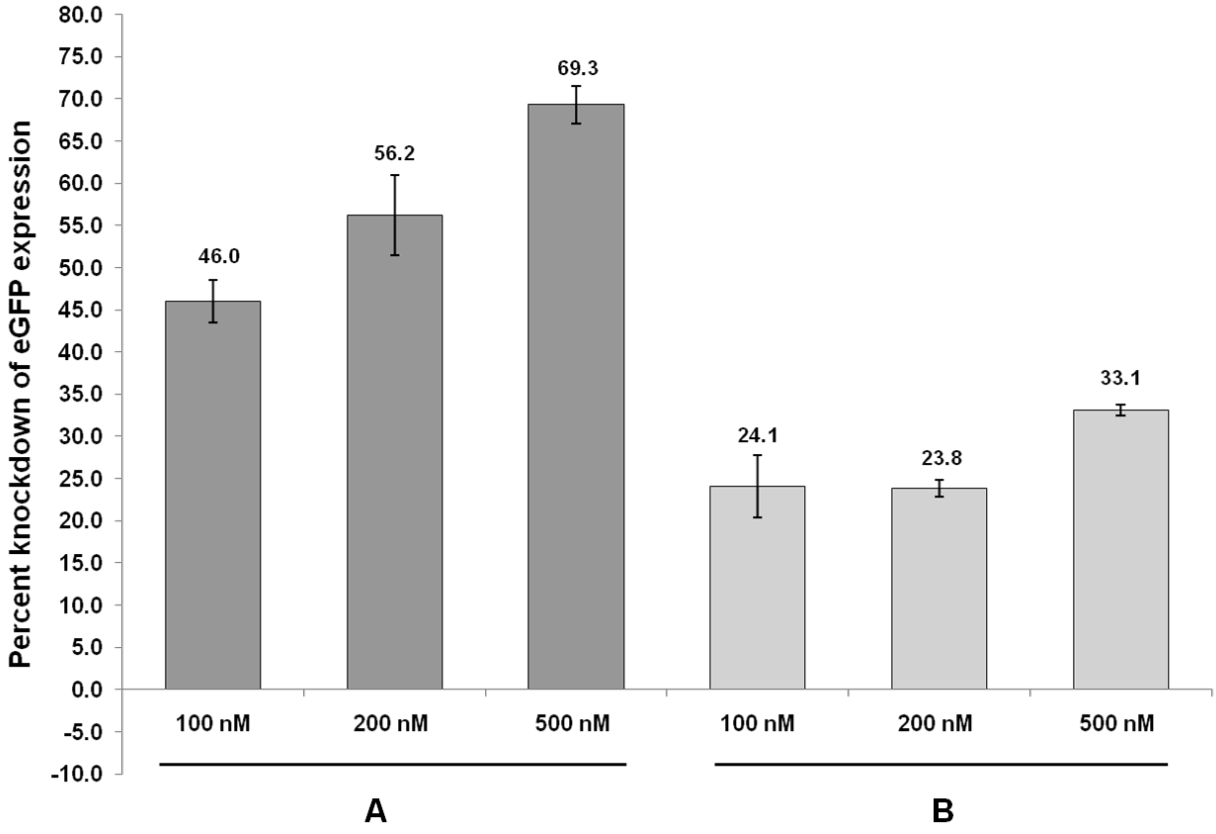

Figure S1. Percentage of eGFP knockdown for 4 when the 4 h siRNA transfection asssay was (A) done without fetal bovine serum (FBS) present in the OPTI-MEM buffer, or (B) done with 10% FBS added to the OPTI-MEM buffer. Values for percent

knockdown of eGFP expression are given above each column and represent the average of a typical experiment done in triplicate. Error bars represent the standard deviation of these values.

Bioconjugate Chemistry

Communication

pubs.acs.org/bc

Novel Conjugation of Norvancomycin–Fluorescein for Photodynamic Inactivation of *Bacillus subtilis*

Hui-Zhou Gao,[†] Ke-Wu Yang,*[,†] Xiang-Long Wu,[†] Jia-Yun Liu,[‡] Lei Feng,[†] Jian-Min Xiao,[†] Li-Sheng Zhou,[†] Chao Jia,[†] and Zhen Shi[†]

[†]Key Laboratory of Synthetic and Natural Functional Molecule Chemistry of Ministry of Education; College of Chemistry and Materials Science, Northwest University, Xi'an 710069, P. R. China

[‡]Clinical Laboratory, Xijing Hospital, The Fourth Military Medical University of Chinese PLA, Xi'an 710032, P. R. China

Supporting Information

ABSTRACT: A simple and unique conjugation of norvancomycin–fluorescein (VanF) has been achieved. It was characterized by UV–vis and fluorescence spectra and confirmed by MALDI-TOF mass spectrum. The photodynamic assay indicated that VanF effectively inactivated the Gram-positive *Bacillus subtilis* (ATCC 6633) from clinic with inactivation rate of 30–70% within 1–7.5 μM. In vitro, VanF showed low antimicrobial activity with value of >128 μg/mL, binding affinity with value of 180 nM per 10^8 cells/mL against the bacteria strains. The fluorescence imaging showed that VanF could label the *B. subtilis strain*, but not the *Escherichia coli* (ATCC 25922), *Enterococcus faecalis* (ATCC 51299, VanD), and VRE strains from clinic.

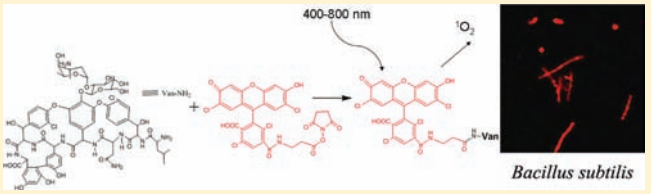

Glycopeptide antibiotics, such as vancomycin and norvancomycin, were used to combat infection of the Gram-positive bacteria by inhibiting the bacterial cell wall synthesis.[1] However, the overuse of glycopeptide antibiotics in the clinical setting has resulted in the vancomycin-resistant *Enterococcus* (VRE), which is typically due to the mutation of peptidoglycan sequence from *N*-acyl-D-Ala-D-Ala to *N*-acyl-D-Ala-D-Lac, resulting in the substantial decrease of binding affinity to vancomycin.[2,3] There are no useful antibiotics for treatment of vancomycin-resistant bacteria,[4] but photodynamic therapy (PDT) may have such potential. PDT is a photochemistry-based emerging technology that relies on the wavelength-specific light activation of certain nontoxic photosensitizers (PSs) to produce active molecular species that are toxic to surrounding logical targets.[5,6] PSs have been conjugated to antibodies or peptide for treatment of the area of bacteria infection, but the molecules of these targets are so big and labeling PS to antibodies or peptide is relatively complicated.[7] So, developing easier and smaller targets is very necessary. Xing and co-workers reported a simple and specific conjugation of vancomycin–porphyrins to use for fluorescent imaging and antibacterial studies of VRE.[2]

Eosin has been employed as PS to treat basal cell carcinoma.[8] The chlorinated fluoresceins, synthesized by us earlier,[9–11] has the same parent structure as eosin (Figure 1). The similarity suggests that the new compound could be linked to antibiotic to construct an efficient conjugation of drug–fluorescein that may apply to a biological target. On the basis of this idea, we constructed a novel compound norvancomycin-chlorinated fluorescein (VanF), and explored photodynamic inactivation experiments, as well as antimicrobial activity, binding affinity, and fluorescence imaging against *B. subtilis*.

VanF was prepared according to Scheme 1. Norvancomycin hydrochloride (32 mg) and chlorinated fluorescein[11] (18 mg) were dissolved in 2 mL 0.1 M phosphate-buffered saline (PBS) buffer (pH 8.5). The pH of the resulting mixture was adjusted to 9.5 and stirred for 20 h at 4 °C; the reaction mixture was loaded onto a silica gel column, eluted with methanol, collected, and the fractions containing the target compound (monitored by UV–vis) pooled, concentrated, and loaded onto a Sephadex G-25 column to offer the purified VanF with yield 54%.

VanF was characterized by UV–vis and fluorescence spectra and confirmed by MALDI-TOF (matrix-assisted laser desorption ionization, time-of-flight) mass spectrum, the peak at m/z 2023.15 $[M+Na-2H]^-$ corresponding to VanF was clearly observed (Figure 2). The spectroscopic characterization showed that VanF had a nearly 4-fold decrease in fluorescence emission and a nearly 40% decrease in absorbance compared to chlorinated fluorescein (Figure 3).

The photodynamic inactivation of VanF against the Gram-positive bacteria *B. subtilis* was assayed as previously described.[12] Briefly, the *B. subtilis* culture was washed with PBS buffer, incubated with the tested compounds in the dark at 37 °C for 20 min with shaking, and illuminated by light with wavelength of 400–800 nm (350 mW), which was produced by Xenon lamp and isolated by means of the optical filters, for 5 min to offer the phototreated samples. The assays showed that the phototreated VanF effectively inactivates *B. subtilis*; with the increase of VanF concentration, the bacterial lethality increased (Figure 4a). When the concentration of VanF was 7.5 μM, the bacterial lethality

Received: July 18, 2011
Revised: October 16, 2011
Published: October 17, 2011

ACS Publications © 2011 American Chemical Society

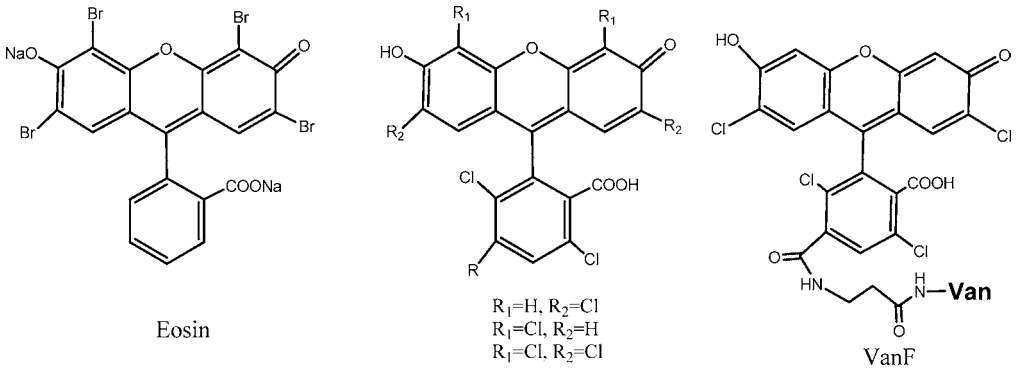

Figure 1. Structure of eosin, the chlorinated fluoresceins, and VanF.

Scheme 1. Conjugation of Chlorinated Fluorescein and Norvancomycin

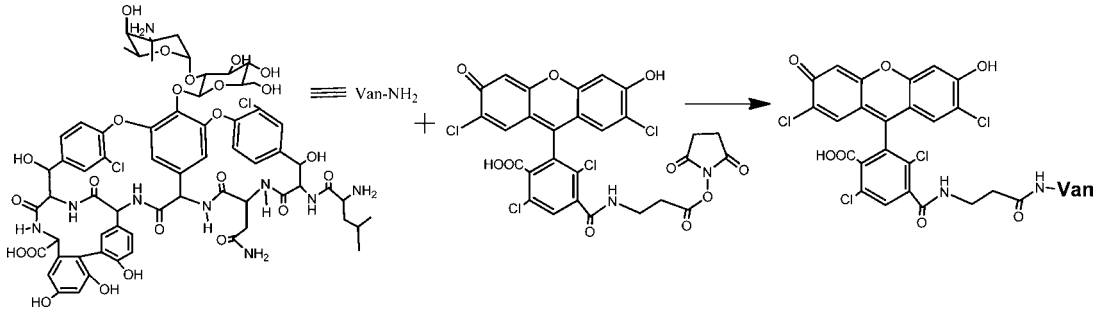

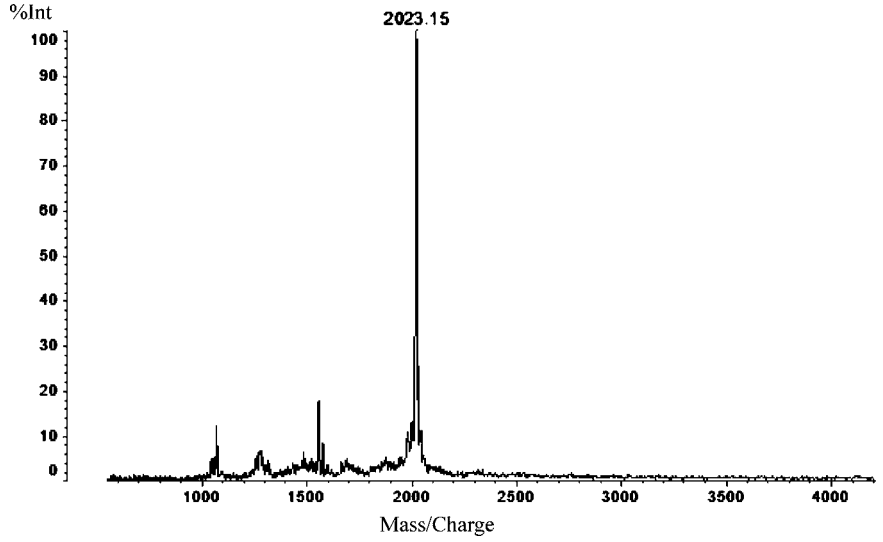

Figure 2. MALDI-TOF mass spectrum of VanF.

reached to 70%. Also, the bacterial lethality was dependent on the irradiation time; with the increase in irradiation time, the bacterial lethality increased (Figure 4b), and it reached 68% after 5 min irradiation with concentration of 5 μM VanF. Eosin and fluoresceins could successfully produce the singlet oxygen ($^1O_2$) to inactivate the living cells;[13] this suggests that the photodynamic inactivity of VanF against *B. subtilis* is due to the effect of the singlet oxygen species.[14,15]

Furthermore, we tested VanF with the Gram-negative bacteria *Escherichia coli*, which contained the antibiotic-resistant plasmid; it was induced with IPTG to produce the metallo-β-lactamase CcrA (B1 subgroup),[16] ImiS (B2 subgroup),[17] and L1 (B3 subgroup),[18] respectively. The results showed that VanF had no obvious photodynamic inactivation toward the tested bacteria. This may be ascribed to the large fluorescence group, which blocked VanF from attaching to the bacteria, or the outer membrane of Gram-negative bacteria, which blocked PS from entering the bacteria.[15]

In vitro antimicrobial activities of VanF were evaluated by determination of MIC according to the Clinical and Laboratory Standards Institute (CLSI) macrodilution (tube) method.[19] The MIC value of VanF against *B. subtilis* (ATCC 6633) was larger than that of norvancomycin (Table 1), indicating that the antimicrobial efficacy of VanF decreased. The decreased activity of VanF implied that chlorinated fluorescein conjugated to norvancomycin (Figure 1), in which the large fluorescence group blocked VanF to bind to the peptidoglycan sequence

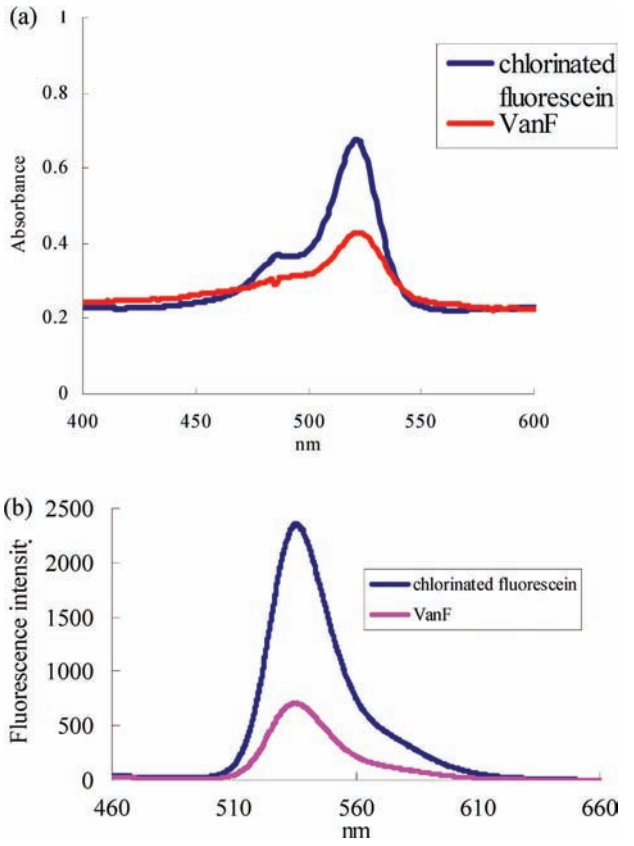

Figure 3. UV−vis (a) and fluorescence (b) spectra of VanF and chlorinated fluorescein. The concentrations of the tested compounds were 8 μM (for UV−vis spectra) and 3.75 μM (for fluorescence spectra) in 10 mM PBS buffer at pH 7.5 (λ_{ex} = 400 nm).

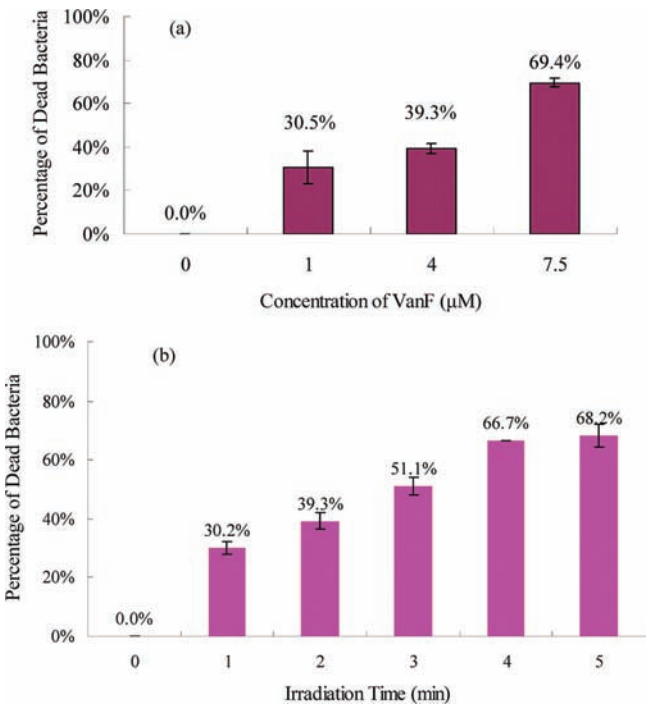

Figure 4. (a) Photodynamic inactivation of *B. subtilis* strains with different concentrations of VanF. (b) Time-dependent bacterial lethality with incubation of 5 μM VanF.

Table 1. MIC Values of VanF and Norvancomycin

compounds	*B. subtilis*
norvancomycin	4 μg/mL
VanF	>128 μg/mL

N-acyl-D-Ala-D-Ala. Further, the binding affinity of VanF to *B. subtilis* was quantified. The results showed that both VanF (7.5 μM, saturation concentration) and chlorinated fluorescein (3.75 μM, saturation concentration) weakly bond to the bacteria (Figure 5) with values of 180 and 46 nM per 10^8 cells/mL,

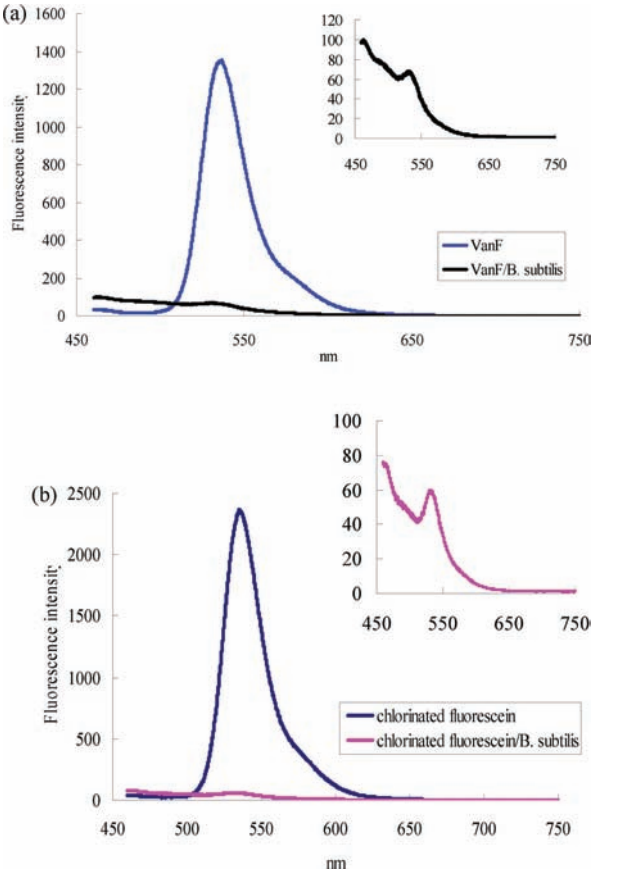

Figure 5. Binding abilities of VanF (a) and chlorinated fluorescein (b) to *B. subtilis*. The concentration of VanF was 7.5 μM in 10 mM PBS buffer at pH 7.5 and the concentration of chlorinated fluorescein was 3.75 μM in 10 mM PBS buffer at pH 7.5. Both the concentrations of VanF and chlorinated fluorescein are saturation concentration.

respectively, while VanF had 4-fold stronger binding ability than the chlorinated fluorescein. In this investigation, the low antimicrobial activity and low binding affinity of VanF are consistent.

Imaging was conducted using VanF (Figure 6). Both VanF and chlorinated fluorescein showed obvious fluorescent imaging of *B. subtilis*, indicating that both of them could be used as fluorescent probes. Meanwhile, VanF was also tested to label the *Escherichia coli* (ATCC 25922), *Enterococcus faecalis* (ATCC 51299, VanD), and VRE from clinic, but the results indicated that it could label neither Gram-negative bacteria nor vancomycin-resistant bacteria.

In conclusion, we successfully constructed a novel fluorescence antibiotic VanF by conjugation of the chlorinated

dx.doi.org/10.1021/bc200382d | *Bioconjugate Chem.* 2011, 22, 2217−2221

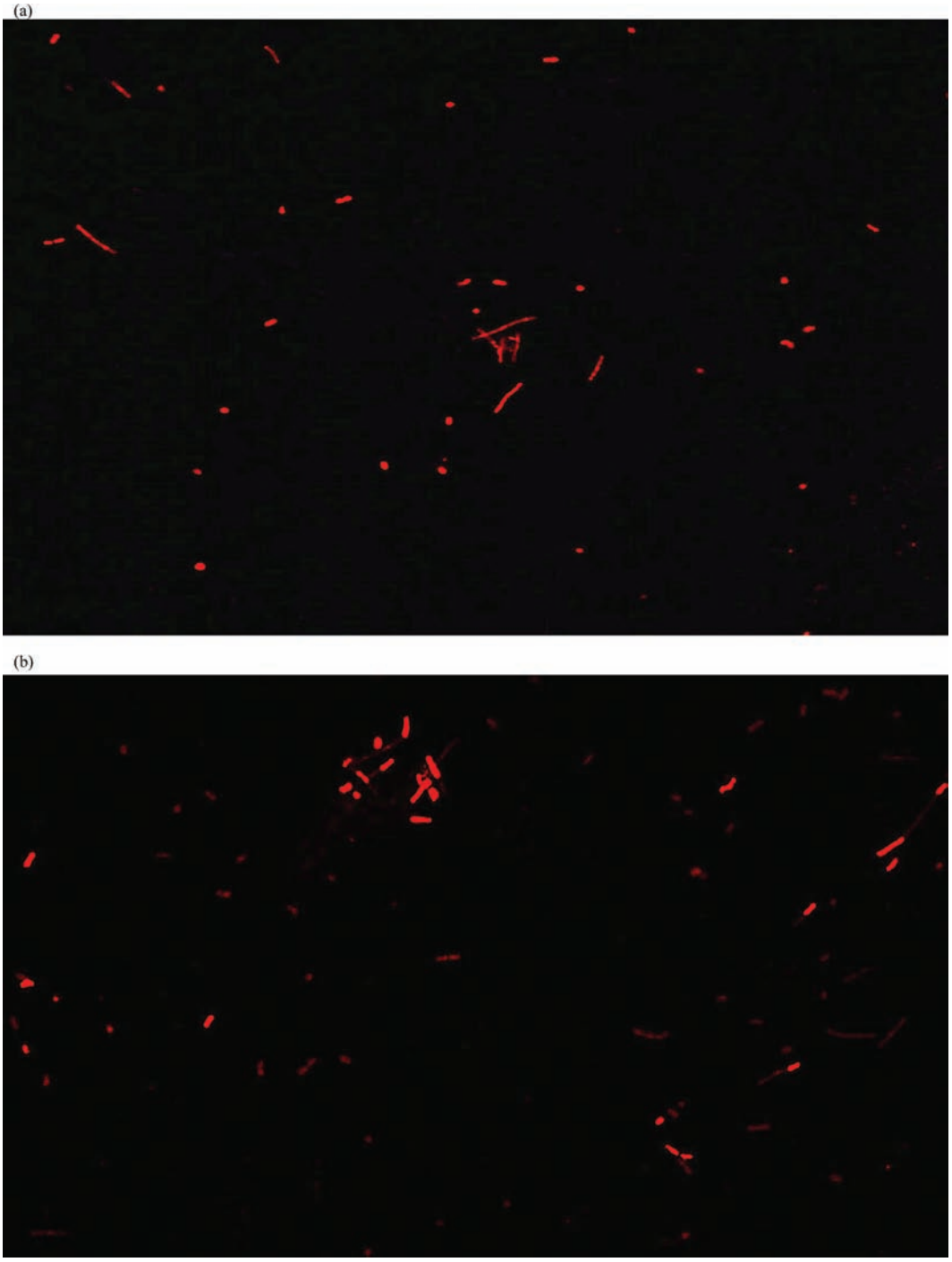

Figure 6. Fluorescent imaging of *B. subtilis* labeled with VanF (a) and chlorinated fluorescein (b). The concentrations of the tested compounds were 10 μM in 10 mM PBS buffer at pH 7.5.

fluorescein and norvancomycin. VanF was characterized by UV−vis and fluorescence spectra and confirmed by MALDI-TOF mass spectrum. The biological assay showed that VanF had effective photodynamic inactivation against *B. subtilis*, low antimicrobial activity with value of >128 μg/mL and binding affinity with value of 180 nM per 10^8 cells/mL to the tested bacteria. The fluorescence imaging showed that VanF could label the *B. subtilis strain*, but not the *Escherichia coli* (ATCC 25922), *Enterococcus faecalis* (ATCC 51299, VanD), and VRE strains from clinic.

■ ASSOCIATED CONTENT

Ⓢ Supporting Information

Materials and instruments, methods and experimental procedures. This material is available free of charge via the Internet at http://pubs.acs.org.

■ AUTHOR INFORMATION

Corresponding Author

*Tel/Fax: +8629-8830-2429; E-mail: kwyang@nwu.edu.cn (K. W. Yang).

■ ACKNOWLEDGMENTS

We are grateful for assistance in the photodynamic studies from Dr. Dan Sun at the Laboratory of Photonics and Photon Technique in Northwest University. We thank Dr. Michael Crowder at Miami University for the plasmids containing metallo-β-lactamase genes. This work was supported by grants (to K. W. Y.) from National Natural Science Fund of China (20972127), Doctoral Fund of China (200806970005), Natural Science Fund of Shaanxi Province (2009JM2002), and Key Fund for International Cooperation of Shaanxi Province (2010KW-16).

■ REFERENCES

(1) Jovetic, S., Zhu, Y., Marcone, G. L., Marinelli, F., and Tramper, J. (2010) β-Lactam and glycopeptide antibiotics: first and last line of defense? *Trends Biotechnol. 28*, 596−604.

(2) Xing, B., Jiang, T., Bi, W., Yang, Y., Li, L., Ma, M., Chang, C.-K., Xu, B., and Yeow, E. K. L. (2011) Multifunctional divalent vancomycin: the fluorescent imaging and photodynamic antimicrobial properties for drug resistant bacteria. *Chem. Commun. 47*, 1601−1603.

(3) Crowder, M. W. (2006) Combating vancomycin resistance in bacteria: targeting the *D*-ala-*D*-ala dipeptidase VanX. *Infect. Disord. Drug Targets 6*, 147−158.

(4) Taubes, G. (2008) The Bacteria Fight Back. *Science 321*, 356−361.

(5) Lovell, J. F., Liu, T. W. B., Chen, J., and Zheng, G. (2010) Activatable photosensitizers for imaging and therapy. *Chem. Rev. 110*, 2839−2857.

(6) Zheng, X., Sallum, U. W., Verma, S., Athar, H., Evans, C. L., and Hasan, T. (2009) Exploiting a bacterial drug-resistance mechanism: a light-activated construct for the destruction of MRSA. *Angew. Chem., Int. Ed. 48*, 2148−2151.

(7) Celli, J. P., Spring, B. Q., Rizvi, I., Evans, C. L., Samkoe, K. S., Verma, S., Pogue, B. W., and Hasan, T. (2010) Imaging and photodynamic therapy: mechanisms, monitoring, and optimization. *Chem. Rev. 110*, 2795−2838.

(8) Detty, M. R., Gibson, S. L., and Wagner, S. J. (2004) Current clinical and preclinical photosensitizers for use in photodynamic therapy. *J. Med. Chem. 47*, 3897−3915.

(9) Wu, X. L., Tian, M., He, H. Z., Sun, W., Li, J. L., and Shi, Z. (2009) Synthesis and biological applications of two novel fluorescent proteins-labeling probes. *Bioorg. Med. Chem. Lett. 19*, 2957−2959.

(10) Tian, M., Wu, X. L., Zhang, B., Li, J. L., and Shi, Z. (2008) Synthesis of chlorinated fluoresceins for labeling proteins. *Bioorg. Med. Chem. Lett. 18*, 1977−1979.

(11) Wu, X. L. (2010) Synthesis of novel fluorescent probes for monoclonal antibody and pH probes and application in immuno-fluorescene histochemistry. Ph.D. thesis, College of Chemistry and Materials Science, Northwest University.

(12) Xing, C., Xu, Q., Tang, H., Liu, L., and Wang, S. (2009) Conjugated polymer/porphyrin complexes for efficient energy transfer and improving light-activated antibacterial activity. *J. Am. Chem. Soc. 131*, 13117−13124.

(13) Takemoto, K., Matsuda, T., McDougall, M. G., Klaubert, D. H., Hasegawa, A., Los, G. V., Wood, K., Miyawaki, A., and Nagai, T. (2011) Chromophore-assisted light inactivation of HaloTag fusion proteins labeled with eosin in living cells. *ACS Chem. Biol. 6*, 401−406.

(14) Ragàs, X., Agut, M., and Nonell, S. (2010) Singlet oxygen in Escherichia coli: New insights for antimicrobial photodynamic therapy. *Free Radic. Biol. Med. 49*, 770−776.

(15) Spesia, M. B., Caminos, D. A., Pons, P., and Durantini, E. N. (2009) Mechanistic insight of the photodynamic inactivation of Escherichia coli by a tetracationic zinc (II) phthalocyanine derivative. *Photodiagn. Photodyn. Ther. 6*, 52−61.

(16) Wang, Z., and Benkovic, S. J. (1998) Purification, characterization, and kinetic studies of a soluble Bacteroides fragilis metallo-β-lactamase that provides multiple antibiotic resistance. *J. Biol. Chem. 273*, 22402−22408.

(17) Crawford, P. A., Sharma, N., Chandrasekar, S., Sigdel, T., Walsh, T. R., Spencer, J., and Crowder, M. W. (2004) Over-expression, purification, and characterization of metallo-β-lactamase ImiS from *Aeromonas veronii* bv. sobria. *Protein Expr. Purif. 36*, 272−279.

(18) Crowder, M. W., Walsh, T. R., Banovic, L., Pettit, M., and Spencer, J. (1998) Overexpression, purification, and characterization of the cloned metallo-β-lactamase L1 from Stenotrophomonas maltophilia. *Antimicrob. Agents Chemother. 42*, 921−926.

(19) CLSI. (2009) Methods for dilution antimicrobial susceptibility tests for bacteria that grow aerobically: approved standard-8th ed., CLSI M07-A8, Clinical and Laboratory Standards Institute, Wayne, PA.

Supporting Information

A Novel Conjugation of Norvancomycin-fluorescein for Photodynamic Inactivation of *Bacillus subtilis*

General: Muller-Hinton Broth was obtained form Beijing Aoboxing Biotech. Company Ltd. Norvancomycin hydrochloride was obtained from North China Pharmaceutical Company, LTD. Other chemical reagents were purchased from commercial supplies. UV-vis spectra were recorded on Agilent 8453 UV-Vis spectrometer. The fluorescence emission spectra were recorded on HITACHI F-4500 Fluorescence spectrophotometer. Fluorescence imaging studies were carried out on Olympus FluoView FV1000 Confocal Microscope. MALDI-TOF-MS were acquired on an AXIMA-CFR time-of-flight (TOF) mass spectrometer.

MIC test:

Norvancomycin hydrochloride was dissolved in dd H_2O to obtain 1280 μg/ml stock solution and VanF was dissolved in 0.01M PBS buffer (pH 7.5) to obtain the same 1280 μg/ml stock solution. The chosen bacteria were ***Bacillus subtilis*** (ATCC 6633). The MICs were determined by the Clinical and Laboratory Standards Institute (CLSI) macrodilution (tube) broth method.[1]

Bacterial strain and preparation of cultures:

Single colony of ***B. subtilis*** (ATCC 6633) on solid Luria-Bertani (LB) plates were transferred to 10 ml of LB culture medium and were grown at 37 ˚C overnight. The bacteria were harvested by centrifuging (4˚C, 4000 rpm for 10 min) and washed with 0.01M PBS buffer (pH 7.5) three times. The supernatant was discarded and the remaining bacteria were re-suspended in the same PBS buffer and adjusted to O. D. 600 of 0.5-0.6.

Evaluation of photodynamic inactivation of bacterial strains:

Photodynamic experiments were performed according to the methods previously described.[2] Exactly, bacterial cells suspension were incubated with different concentrations of VanF in the dark for 20 min at 37 □ in a shaker. All samples were illuminated with white light (400-800 nm, 350 mW) isolated from the emission of a Xemon lamp for 5 minutes. Bacterial suspensions were centrifuged (4000 rpm for 10 min, at 4 ˚C). The supernatant was removed directly, the bacterial pellet was suspended and serially diluted (5×10^4)-fold in 0.01M PBS buffer (pH 7.5). A 75 μL portion of the diluted bacterial cells was spread on the advance prepared solid LB agar plate and incubated overnight at 37 ˚C. The single colonies formed were counted. The percentage of dead bacteria was evaluated by dividing the number of colony-forming units between the samples incubated with photosensitizers with light illumination and the controls without light illumination.

Binding affinity experiments

Suspensions of ***B. subtilis*** (ATCC 6633) in PBS were incubated with VanF (7.5 μM) or chlorinated

fluorescein (3.75 μM) at 37 °C for 40 min in the dark in a shaker. Then, the cultures were centrifuged (4000 rpm for 10 min) and the supernatant was removed directly. The bacterial pellet was suspended in 1.5 mL of 2% SDS, incubated overnight at 4 °C, and then sonicated for 30 min. The concentration of chlorinated fluorescein and VanF was determined by fluorescence intensity. Emission spectra of chlorinated fluorescein and VanF without ***B. subtilis*** were taken as controls. The fluorescence values of samples were referred to the samples labeling ***B. subtilis***.

Imaging test:

Imagining test was performed according to the methods previously described.[3] Equivalent 10 μM of VanF or chlorinated fluorescein and the bacterial cells suspensions were mixed together and then incubated in the dark for 1 hour at 37 ˚C in a shaker. After three times 0.01M PBS buffer (pH 7.5) washing, the bacterial cells were spotted on glass slides, immobilized by the coverslips, and the cell imaging tests were conducted with a Olympus FluoView FV1000 Confocal Microscope.

References

(1) CLSI. (2009) Methods for dilution antimicrobial susceptibility tests for bacteria that grow aerobically: approved standard-Eighth Edition, CLSI M07-A8, Clinical and Laboratory Standards Institute, Wayne, PA.

(2) Xing, C., Xu, Q., Tang, H., Liu, L., and Wang, S. (2009) Conjugated Polymer/Porphyrin Complexes for Efficient Energy Transfer and Improving Light-Activated Antibacterial Activity. ***J. Am. Chem. Soc. 131***, 13117-13124.

(3) Xing, B., Jiang, T., Bi, W., Yang, Y., Li, L., Ma, M., Chang, C.-K., Xu, B., and Yeow, E. K. L. (2011) Multifunctional divalent vancomycin: the fluorescent imaging and photodynamic antimicrobial properties for drug resistant bacteria. ***Chem. Commun. 47***, 1601-1603.

Bioconjugate Chemistry

Article

pubs.acs.org/bc

Photosensitizing Carrier Proteins for Photoinducible RNA Interference

Yuka Matsushita-Ishiodori, Rina Kuwabara, Hiroyuki Sakakoshi, Tamaki Endoh,[†] and Takashi Ohtsuki*

Department of Bioscience and Biotechnology, Okayama University, 3-1-1 Tsushimanaka, Okayama 700-8530, Japan

Supporting Information

ABSTRACT: RNA interference (RNAi) is being widely explored as a tool in functional genomics and tissue engineering, and in the therapy of intractable diseases, including cancer and neurodegenerative diseases. Recently, we developed a photoinducible RNAi method using photosensitizing carrier proteins, named CLIP-RNAi (CPP-linked RBP-mediated RNA internalization and photoinduced RNAi). Novel carrier proteins were designed for this study to establish a highly efficient delivery system for small interfering RNA (siRNA) or short hairpin RNA (shRNA) and to demonstrate light-dependent gene silencing. In addition, the results suggested that the dissociation of the siRNA (or shRNA) from carrier proteins in the cytoplasm is a critical event in CLIP-RNAi-mediated gene silencing.

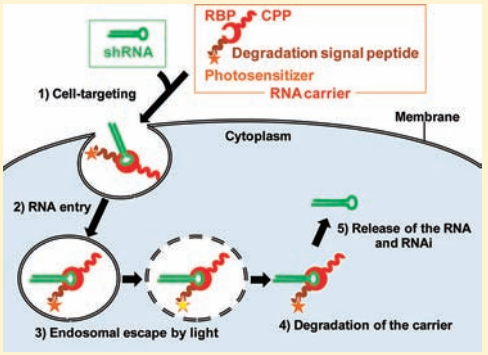

INTRODUCTION

RNA interference (RNAi)-mediated gene silencing is a valuable method for investigating gene function and for use in clinical applications.[1,2] To deliver small interfering RNAs (siRNAs) and short hairpin RNAs (shRNAs) efficiently into the cytosol, many RNA carriers, including lipids, nanoparticles, polymers, and viral vectors, have been developed.[3] However, there is much room for improvement with respect to target gene specificity and the ability to regulate gene expression.

In this regard, Shah et al. recently developed caged siRNAs, which enabled a spatially and temporally controlled RNAi.[4] In this method, the attachment of photolabile protecting groups (caging groups) to siRNA blocks gene silencing activity in the absence of light, while the removal of the caging groups from the siRNA with an external light trigger results in the induction of the RNAi. A great variety of photolytic compounds capable of attaching themselves to RNAs have been identified, although their widespread use is limited by the optical wavelength for deprotection, which must be around 350 nm.[5]

Previously, we reported that the utilization of a fluorescent dye attached to an RNA carrier protein enabled light-dependent gene silencing.[6−8] We designed a cell-permeable RNA-binding protein (TatU1A) labeled with a fluorescent dye (TatU1A-dye) as an RNA carrier. TatU1A is a fusion protein between a TAT-derived cell-penetrating peptide (CPP)[9] and the U1A RNA-binding protein (RBP).[10] The TatU1A-dye could undertake the specific delivery of an shRNA containing a U1A binding sequence in its loop region.[6,7] The complexes formed between the TatU1A-dye and shRNA (TatU1A-dye/shRNA) were internalized by cells via an endocytotic pathway. TatU1A-dye/shRNA complexes were entrapped in endosomes before photoirradiation, while after irradiation they were released into the cytosol where they mediated gene silencing. This delivery system was named "CLIP-RNAi (CPP-linked RBP-mediated RNA internalization and photoinduced RNAi)", and in this study, its use is demonstrated with newly designed carrier proteins (CPP-RBPs).

EXPERIMENTAL PROCEDURES

Plasmid Construction. Double-stranded DNA encoding the flock house virus (FHV) coat peptide (residues 35 to 49) (RRRRNRTRRNRRRVR) was prepared by primer extension using the following primers, 5′- CCGCCCATGGGCAGCA-GCCATCATCATCATCATCACAGCAGCGGCCGCCGTC-GCCGCAACCGCACCCGCCG-3′ (sense, *Nco*I site underlined) and 5′-CGCCGCTAGCGTAATCCGGAACATCG-TATGGGTAGCCGCGCACGCGACGGCGGTTGCGGCG-GGTGCGGTTGCG-3′ (antisense, *Nhe*I site underlined), and cloned into the *Nco*I-*Nhe*I site of the previously constructed pET-TatU1A-C plasmid,[6] yielding pET-FHVU1A-C. The DNA segment encoding the Tat peptide (YGRKKRRQRRR) of pET-TatU1A-C was converted to the cytoplasmic transduction peptide 512 (CTP512) (YGRARRRRRRR) using the QuikChange Site-Directed Mutagenesis Kit (Stratagene) with the following primers: 5′-GCAGCGGCTACGGCCGCGCGCGTCGCCG-CCGTCGCCGTCGCGGCTACCC-3′ (sense) and 5′-GGGTA-GCCGCGACGGCGACGGCGGCGACGCGCGCGGCCGTAG-CCGCTGC-3′ (antisense).

The coding sequence for the RNA-binding domain of *Drosophila* Sex lethal protein (*Sxl*), was amplified with the

Received: February 21, 2011
Revised: October 6, 2011
Published: October 11, 2011

ACS Publications © 2011 American Chemical Society

primers 5′-CCGCTCGAGTTAGGATCCCTTGCCATGCTCCTCAG-3′ (sense, *Xho*I site underlined) and 5′-CGCGCTAGCGGCGCAAGCAACACCAACCTG-3′ (antisense, *Nhe*I site underlined) from the *Drosophila Sxl* cDNA clone, EDM1133−6921617 (Open Biosystems). Double-stranded DNA encoding the bacteriophage λ N peptide (λN) was amplified using the following primers: 5′-CCGCTCGAGTTAGGATCCAGGGCGGTTAACTGGTTTTGCGCTTACCCCAACCAACAGGGGATTTGCTGCTTCCATTG-3′ (sense, *Xho*I site underlined) and 5′-CGCGCTAGCGGCCTGGATGCACAAACACGCCGCCGCGAACGTCGCGCAGAGAAACAGGCTCAATGGAAAGCAGCAAATCC-3′ (antisense, *Nhe*I site underlined). The coding sequences for *Sxl* or λN were cloned into the *Xho*I-*Nhe*I site of pET-TatU1A-C,[6] yielding pET-TatSxl-C, and pET-TatλN-C, respectively.

Double-stranded DNA encoding the degradation signal peptide CL1 (ACKNWFSSLSHFVIHL) was prepared by primer extension using the following primers: 5′-CCGCGGATCCGCTTGCAAGAACTGGTTCAGTAGCTTAAGCCACTTTGTGA-3′ (sense, *Bam*HI site underlined) and 5′-CGGCCTCGAGTTAGCAGCTGTTAAGGTGGATCACAAAGTGGCTTAAGCTA-3′ (antisense, *Xho*I site underlined), and cloned into the *Bam*HI-*Xho*I site of pET-TatU1A-C,[6] yielding pET-TatU1A-CL1-C. All of the constructs contained a C-terminal Cys residue for later modification with Alexa Fluor 546 (Alexa546) C5 maleimide (Molecular Probes). The coding sequences of the above-mentioned plasmid vectors were confirmed by sequencing analysis with an ABI PRISM 310 genetic analyzer.

Purification and Fluorescent Labeling of Proteins. The CPP-RBP plasmids described above were introduced into *Escherichia coli* BL21(DE3). Transformants were grown at 37 °C, and expression of CPP-RBPs was induced by the addition of isopropyl-β-D-thiogalactopyranoside (1 mM), followed by growth at 30 °C for 16 h. CPP-RBP proteins were purified as described previously,[6] except for the TatU1A-CL1 protein, which was purified from the insoluble fraction.

The carrier proteins were labeled with Alexa546 as previously described.[6,7] Protein concentration was determined using a Protein Assay Kit (Bio-Rad), and the labeling efficiencies were calculated by measuring the absorbance of Alexa546 with a NanoDrop 1000 Spectrophotometer (Thermo Scientific). In all experiments, the labeling efficiencies were adjusted to 30% using separately prepared unlabeled carrier proteins.

Preparation of siRNAs and shRNAs. The shRNA sequence used was as follows: 5′-GGCUACGUCCAGGAGCGCACAUUGCACUCCGUCGCGUCCUGGACGUAGCCUU-3′ (U1A binding sequences underlined).[6,7] This shRNA and the 3′-FAM-labeled shRNA were from JBioS (Japan).

To construct siRNA-type cargo RNAs, antisense and sense strands were dissolved in distilled water at final concentrations of 20 μM and were annealed by incubation at 90 °C for 1 min followed by a 60 min incubation at 37 °C. The target sequence in the enhanced green fluorescent protein (EGFP) mRNA was 5′-UGCGCUCCUGGACGUAGCCUU-3′. The sense strands contained 5′ short extensions, which bound to their respective RBPs, to make *U1A*-siRNA (5′-GGGCAUUGCACUCCGCCCUCUGGCUACGUCCAGGAGCGCAUU-3′), *Sxl*-siRNA (5′-GGUUGUUUUUUUUCUGGCUACGUCCAGGAGCGCAUU-3′), and *λN*-siRNA (5′-GGCCCUGAAAAAGGGCCUCUGGCUACGUCCAGGAGCGCAUU-3′). The RBP binding sequences are underlined. The 3′-FAM-labeled antisense strand was purchased from JBioS and annealed with the sense strands to make FAM-labeled siRNAs.

Cell Culture. Chinese hamster ovary (CHO) cells and destabilized EGFP stably expressing CHO (EGFP-CHO) cells[6] were cultured in Ham's F-12 medium (Sigma) supplemented with 10% fetal bovine serum (Biowest), 100 units/mL penicillin, and 100 μg/mL streptomycin (Gibco, Invitrogen, US).

Cellular RNA Delivery by Carrier Proteins. The FAM-labeled RNA (200 nM) and carrier protein (2 μM) were mixed in T buffer [20 mM HEPES-KOH (pH 7.4), 115 mM NaCl, 5.4 mM KCl, 1.8 mM $CaCl_2$, 0.8 mM $MgCl_2$, and 13.8 mM glucose] and incubated at 37 °C for 10 min. CHO cells were grown on a 96-well plate to 70% confluence and were treated for 2 h with the carrier/RNA complex mentioned above. After washing, the cells were visualized using a fluorescence microscope (Olympus, Japan). For endosomal escape of the carrier/RNA complex, cells were irradiated at 540 ± 10 nm for 11 s with a 100 W halogen lamp (Olympus USH-1030 L) passed through the 40× objective lens as described previously.[6,7]

Induction of RNAi-Mediated EGFP Gene Silencing and Analysis of EGFP Gene Expression. EGFP-CHO cells were grown on a 96-well plate to 70% confluence and treated for 2 h with the unlabeled RNA/carrier protein complex. The RNA was delivered to the cells by the carrier protein, and photoaccelerated endosomal escape was induced by irradiation at 540 ± 10 nm for 64 s with a 100 W halogen lamp passed through the 4× objective lens as described above. After 20 h of irradiation, cells were recovered from dishes and resuspended in PBS. The EGFP mean fluorescence intensities (MFIs) were analyzed by flow cytometry using FACSCalibur and *CellQuest* software (BD Biosciences). Data were acquired from 10 000 cells in all experiments.

RESULTS AND DISCUSSION

Design of Carrier Proteins (CPP-RBPs). We previously demonstrated CLIP-RNAi-mediated EGFP silencing using CPP-RBP protein (TatU1A) as an RNA carrier, and the silencing efficiency was 60−70%.[6,7] The insufficient RNAi efficacy may be due to insufficient RNA delivery efficiency that relates to the cell-targeting activity of the CPP moiety of CPP-RBP or the size and RNA binding efficiency of the RBP moiety, or may be due to inhibition of the activity of the RNA with tightly bound CPP-RBP. To establish a highly efficient siRNA or shRNA delivery system, a series of CPP-RBP proteins was constructed and purified (Figure 1).

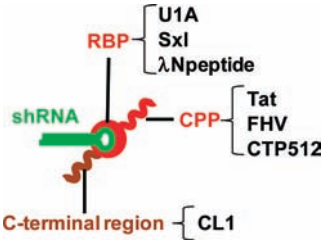

Figure 1. RNA carrier protein design. Schematic diagram of the RNA carrier proteins used in this study. CPP, cell-penetrating peptide; RBP, RNA-binding protein. The C-terminal cysteine was labeled with Alexa546 as a photosensitizer.

First, CPP-U1A variants were prepared to examine whether changing the CPP moiety of TatU1A significantly improved the RNA delivery efficiency. An FHV coat peptide and a CTP512 peptide were selected as the CPP moiety. Recently, it was reported that the cellular uptake of the FHV peptide was higher than that of the

dx.doi.org/10.1021/bc200095a | *Bioconjugate Chem.* 2011, 22, 2222−2226

Tat peptide.[11] The FHV peptide was internalized by various cell types about 15- to 21-fold more efficiently than the Tat peptide. Cytoplasmic transduction peptides (CTPs) were designed to ensure efficient cytoplasmic delivery using computer-based molecular modeling.[12] The CTP512 peptide was evaluated as the leading CTP as it possessed a transduction capacity approximately 5-fold that of the Tat peptide.

Next, Tat-RBP variants were prepared. A partial sequence of the *Drosophila* Sex lethal protein and the bacteriophage λ N protein were used for the RBP moiety. Sex-lethal protein has two RNA-binding domains (RBDs), which are required for specific RNA binding.[13−15] In this study, the protein region (173 amino acids), which included the two RBDs, was used and is hereafter referred to as Sxl. The dissociation constant (K_d) of the Sxl/RNA complex (~5 pM) is lower than that of the U1A/RNA complex (20 pM);[16,17] therefore, high RNAi efficiency due to increased RNA delivery efficiency might be expected from the Sxl/RNA interaction. In addition, the N-terminal region (36 amino acids) of the bacteriophage λ N protein, which included a relatively small RNA binding motif, was employed, and is hereafter referred to as λN. The high specificity and affinity of the complex between λN and the target RNA (K_d = 5 nM) have been demonstrated previously.[18,19] The small size of λN may offer advantages over the internalization of other carrier proteins.

Furthermore, to investigate whether the dissociation of the carrier protein from shRNA or siRNA in the cytoplasm accelerated RNAi-mediated gene silencing, a C-terminally extended TatU1A bearing the degradation signal peptide CL1 (TatU1A-CL1) was designed. The CL1 peptide is known to act as a degradation signal peptide via the ubiquitin−proteasome pathway,[20,21] and the degradation of carrier proteins is thought to promote the release of free shRNA or siRNA into the cytoplasm.

Effects of CPPs on RNAi Efficiency. To examine the effects of CPPs on RNAi efficiency, three CPP-U1A variants (TatU1A, FHVU1A, and CTP512U1A) were constructed and purified. The CPP-U1As were labeled with Alexa546 and were tested to determine whether they carried the shRNA into cells and whether the carrier/shRNA complexes were released from the endosome by photostimulation. FAM-labeled shRNAs were used to visualize RNA localization. As shown in Figure 2, in all cases, the Alexa546 and FAM fluorescence signals showed punctuate distributions before irradiation, indicating that the carrier/shRNA complexes were trapped in endosomes, as reported previously.[6,7] After irradiation at 540 ± 10 nm, the Alexa546 and FAM signals for all three variants were dispersed throughout the cytosol. Moreover, there was no significant difference in FAM fluorescence intensity between TatU1A and FHVU1A, suggesting that they had almost equal transfection efficiencies. Quantitative fluorescence image analysis of microscopic images in Figure 2 using *cellSens Dimension* software (Olympus) indicated that mean FAM intensity with CTP512U1A was about 45% lower than that with TatU1A.

Next, the RNAi efficiencies with the CPP-U1A carriers were examined by evaluating the knockdown of EGFP expression in EGFP-CHO cells. EGFP silencing at 20 h after photostimulation was assessed by flow cytometry. As is clearly shown in Figure 3A, a dramatic light-dependent reduction in EGFP MFI was observed with TatU1A-Alexa. The treatment of cells with the TatU1A-Alexa/shRNA(anti-EGFP) complex followed by photostimulation induced a 70% decrease in MFI when compared with the control cells treated with T-buffer only, while without irradiation, no decrease in MFI was observed in cells treated with the carrier/shRNA complex (Figure 3A). Similarly, treatment with the

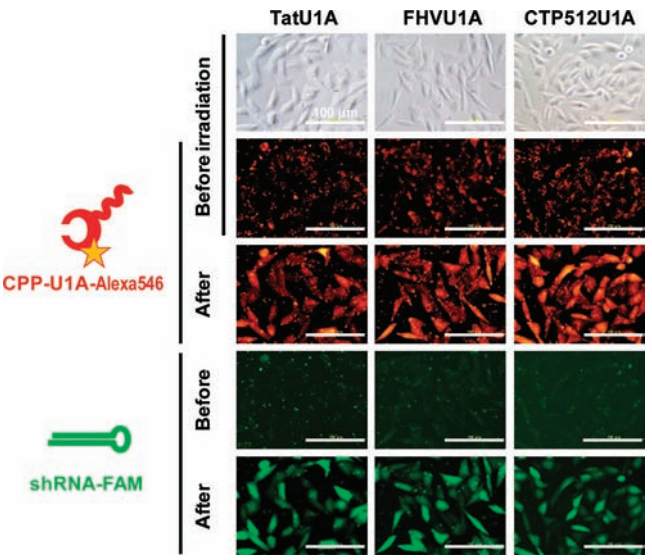

Figure 2. Translocation of the CPP-U1A/shRNA complexes via endocytosis. CHO cells were treated with CPP-U1A-Alexa546/shRNA-FAM complexes for 2 h at 37 °C and irradiated (540 ± 10 nm light passed through a 40× objective lens for 11s) as described in Experimental Procedures. Images were taken before and 2 min after irradiation.

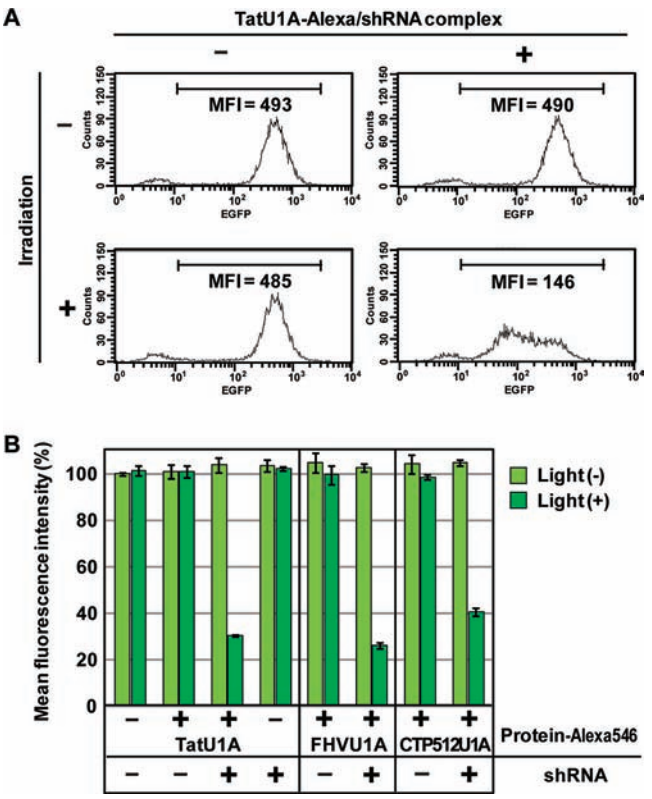

Figure 3. EGFP silencing by CPP-U1A-Alexa/shRNA complexes. The shRNA has an anti-GFP sequence and a U1A-binding sequence. (A) Flow cytometric analysis of EGFP-expressing cells treated with TatU1A-Alexa546/shRNA complexes and irradiated (540 ± 10 nm light passed through a 4× objective lens for 64 s). Cells were collected for flow cytometric analysis at 20 h after irradiation. The silencing effect was assessed by measuring EGFP mean fluorescence intensity (MFI). (B) Comparison of CPP-U1A proteins in EGFP silencing. EGFP MFIs of cells treated with different CPP-U1A-Alexa546/shRNA complexes are compared to control cells treated with T-buffer only.

dx.doi.org/10.1021/bc200095a | *Bioconjugate Chem.* 2011, 22, 2222−2226

FHVU1A-Alexa/shRNA or CTP512U1A-Alexa/shRNA complexes induced a 74% and 59% decrease in MFI, respectively (Figure 3B). These data indicate that the three CPP-U1A variants had a similar effect on EGFP silencing, although the RNAi efficiency of the CTP512U1A-Alexa/shRNA complex was slightly lower than the other two. We suggest that the low RNAi efficiency with CTP512U1A was due to the lower delivery efficiency of CTP512U1A compared to that of the other two variants.

Effects of RBPs on RNAi Efficiency. Next, the RNAi efficiencies of the Tat-RBP variants (TatU1A, TatSxl, and TatλN) were compared to investigate the effects of the RBPs. As shown in Figure 4A, the siRNAs carried by TatU1A-Alexa

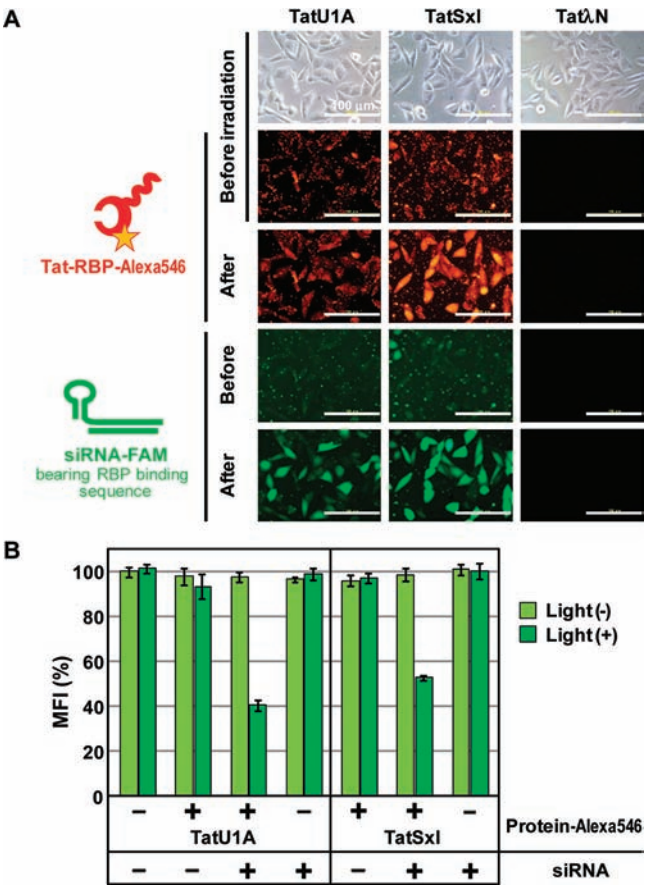

Figure 4. Comparison of Tat-RBP proteins with respect to cellular delivery and EGFP silencing. (A) Translocation of the Tat-RBP-Alexa546/siRNA. The sense strand of the siRNA contained 5′ short extensions for the binding to U1A, Sxl, or λN. Transfection and fluorescence microscopy were carried out as described in the legend to Figure 2. (B) Comparison of Tat-RBP proteins with respect to EGFP silencing. The silencing effects were calculated as described in the legend to Figure 3.

and TatSxl-Alexa diffused into the cytoplasm in a photo-dependent manner. However, in the case of TatλN, cellular uptake of the carrier protein and the siRNA was not observed, irrespective of irradiation. Hence, only the effects of the two carrier proteins, TatU1A-Alexa and TatSxl-Alexa, on RNAi efficiency were investigated. Unexpectedly, TatSxl-Alexa exhibited a lower RNAi efficiency (47% decrease in MFI compared to the control) than TatU1A-Alexa (59% decrease in MFI compared to the control) (Figure 4B), although quantitative fluorescence image analysis of microscopic images of Figure 4A indicated that the cellular uptake of siRNA with TatSxl-Alexa was higher than that with TatU1A (data not shown). Given that the dissociation constant of the Sxl/RNA complex is reportedly one order lower than that of the U1A/RNA complex,[16,17] these results suggested that the dissociation of carrier proteins from shRNA or siRNA in the cytoplasm might be important for RNAi efficiency.

Importance of RBP/RNA Dissociation on RNAi Efficiency. To investigate this possibility further, the influence of the CL1 peptide on the RNAi efficiency was examined using CHO cells. As shown in Figure 5 and Supporting Information

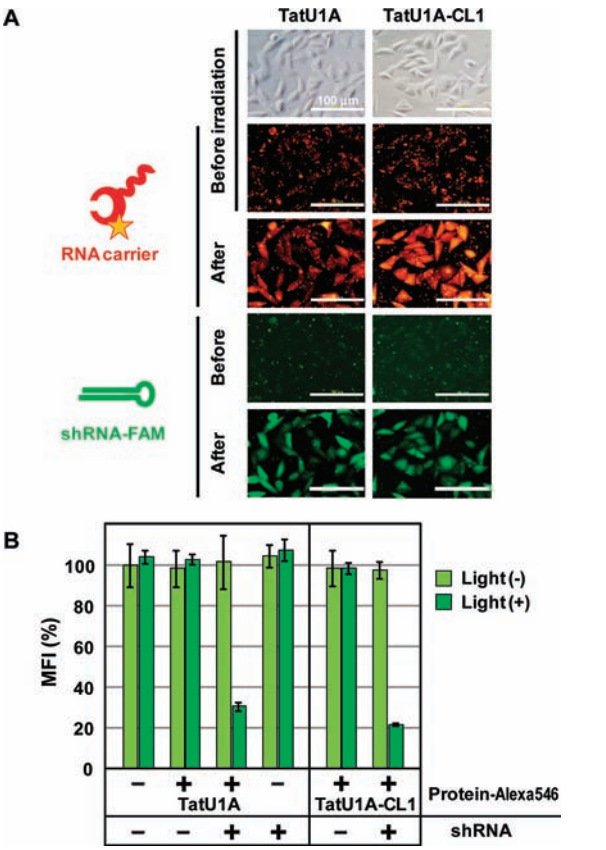

Figure 5. Influence of the CL1 peptide on cellular delivery and EGFP silencing. (A) Translocation of the TatU1A-CL1-Alexa546/shRNA. Transfection and fluorescence microscopy were carried out as described in the legend to Figure 2. (B) Comparison of TatU1A-CL1 with TatU1A in EGFP silencing. The silencing effects were calculated as described in the legend to Figure 3.

Figures S1 and S2, although the internalization efficiency and the light-dependent diffusion of TatU1A-CL1-Alexa with the shRNA to the cytoplasm was equivalent to that of TatU1A-Alexa, the use of TatU1A-CL1-Alexa increased the RNAi efficiency (78% decrease in MFI) compared to TatU1A-Alexa (69% decrease in MFI). This tendency was also confirmed in other cell types (Figure S3). EGFP-silencing using the TatU1A-CL1-Alexa/shRNA complex was also confirmed by analyzing the EGFP level on a SDS-PAGE gel (Figure S4A). The EGFP silencing level was dependent on the size of the area irradiated (Figure S4A and B), and the cells treated with the complex were not damaged by photostimulation (Figure S4C). These results suggest that the dissociation of the shRNA from the carrier protein in the cytoplasm is a critical event in CLIP-RNAi-mediated gene silencing.

dx.doi.org/10.1021/bc200095a | Bioconjugate Chem. 2011, 22, 2222–2226

CONCLUSION

The results presented here demonstrated that the three CPP-U1A variants, TatU1A, FHVU1A, and CTP512U1A, possessed similar carrier qualities and suggested that U1A was superior to Sxl as the RBD moiety of the Tat-RBP. Attachment of the degradation signal peptide, CL1, accelerated RNAi-mediated gene silencing, suggesting that the dissociation of the carrier protein and RNA due to the degradation of the carrier in the cytosol is important for mediating RNAi activity. TatU1A-CL1, which showed almost 80% RNAi efficiency, is an excellent candidate RNA carrier protein for the CLIP-RNAi method. CLIP-RNAi performed with the new carrier protein designed for this study would be available for clinical and cell-engineering applications.

ASSOCIATED CONTENT

Supporting Information

Additional information (Figures S1−S4) as described in the text. This material is available free of charge via the Internet at http://pubs.acs.org.

AUTHOR INFORMATION

Corresponding Author

*Tel: 81-86-251-8218; Fax: 81-86-251-8219; E-mail: ohtsuk@cc.okayama-u.ac.jp.

Present Address

[†]Frontier Institute for Biomolecular Engineering Research (FIBER), Konan University, 7−1−20 minatojimaminamimachi, Chuo-ku, Kobe 650−0047, Japan

ACKNOWLEDGMENTS

We thank Prof. H. Ohmori and Dr. M. Magari (Okayama University) for their introduction to flow cytometric analysis techniques. This work was supported by a Grant-in-Aid for Young Scientists (A) to T. O.

REFERENCES

(1) Fire, A., Xu, S., Montgomery, M. K., Kostas, S. A., Driver, S. E., and Mello, C. C. (1998) Potent and specific genetic interference by double-stranded RNA in *Caenorhabditis elegans*. *Nature 391*, 806−811.

(2) Pecot, C. V., Calin, G. A., Coleman, R. L., Lopez-Berestein, G., and Sood, A. K. (2011) RNA interference in the clinic: challenges and future directions. *Nat. Rev. Cancer 11*, 59−67.

(3) Monaghan, M., Pandit, A. (2011) RNA interference therapy via functionalized scaffolds. *Adv. Drug Delivery Rev.* in press [Epub ahead of print].

(4) Shah, S., Rangarajan, S., and Friedman, S. H. (2005) Light-activated RNA interference. *Angew. Chem., Int. Ed. 44*, 1328−1332.

(5) Casey, J. P., Blidner, R. A., and Monroe, W. T. (2009) Caged siRNAs for spatiotemporal control of gene silencing. *Mol. Pharmaceutics 6*, 669−685.

(6) Endoh, T., Sisido, M., and Ohtsuki, T. (2008) Cellular siRNA delivery mediated by a cell-permeant RNA-binding protein and photoinduced RNA interference. *Bioconjugate Chem. 19*, 1017−1024.

(7) Endoh, T., Sisido, M., and Ohtsuki, T. (2009) Spatial regulation of specific gene expression through photoactivation of RNAi. *J. Controlled Release 137*, 241−245.

(8) Endoh, T., and Ohtsuki, T. (2009) Cellular siRNA delivery using cell-penetrating peptides modified for endosomal escape. *Adv. Drug Delivery Rev. 61*, 704−709.

(9) Gump, J. M., and Dowdy, S. F. (2007) TAT transduction: the molecular mechanism and therapeutic prospects. *Trends Mol. Med. 13*, 443−448.

(10) Oubridge, C., Ito, N., Evans, P. R., Teo, C. H., and Nagai, K. (1994) Crystal structure at 1.92 A resolution of the RNA-binding domain of the U1A spliceosomal protein complexed with an RNA hairpin. *Nature 372*, 432−438.

(11) Nakase, I., Hirose, H., Tanaka, G., Tadokoro, A., Kobayashi, S., Takeuchi, T., and Futaki, S. (2009) Cell-surface accumulation of flock house virus-derived peptide leads to efficient internalization via macropinocytosis. *Mol. Ther. 17*, 1868−1876.

(12) Kim, D., Jeon, C., Kim, J. H., Kim, M. S., Yoon, C. H., Choi, I. S., Kim, S. H., and Bae, Y. S. (2006) Cytoplasmic transduction peptide (CTP): new approach for the delivery of biomolecules into cytoplasm in vitro and in vivo. *Exp. Cell Res. 312*, 1277−1288.

(13) Bell, L. R., Maine, E. M., Schedl, P., and Cline, T. W. (1988) Sex-lethal, a Drosophila sex determination switch gene, exhibits sex-specific RNA splicing and sequence similarity to RNA binding proteins. *Cell 55*, 1037−1046.

(14) Kanaar, R., Lee, A. L., Rudner, D. Z., Wemmer, D. E., and Rio, D. C. (1995) Interaction of the sex-lethal RNA binding domains with RNA. *EMBO J. 14*, 4530−4539.

(15) Handa, N., Nureki, O., Kurimoto, K., Kim, I., Sakamoto, H., Shimura, Y., Muto, Y., and Yokoyama, S. (1999) Structural basis for recognition of the *tra* mRNA precursor by the Sex-lethal protein. *Nature 398*, 579−585.

(16) Hall, K. B., and Stump, W. T. (1992) Interaction of N-terminal domain of U1A protein with an RNA stem/loop. *Nucleic Acids Res. 20*, 4283−4290.

(17) Lee, A. L., Volkman, B. F., Robertson, S. A., Rudner, D. Z., Barbash, D. A., Cline, T. W., Kanaar, R., Rio, D. C., and Wemmer, D. E. (1997) Chemical shift mapping of the RNA-binding interface of the multiple-RBD protein sex-lethal. *Biochemistry 36*, 14306−14317.

(18) Tan, R., and Frankel, A. D. (1995) Structural variety of arginine-rich RNA-binding peptides. *Proc. Natl. Acad. Sci. U. S. A. 92*, 5282−5286.

(19) Scharpf, M., Sticht, H., Schweimer, K., Boehm, M., Hoffmann, S., and Rosch, P. (2000) Antitermination in bacteriophage λ. The structure of the N36 peptide-*boxB* RNA complex. *Eur. J. Biochem. 267*, 2397−2408.

(20) Gilon, T., Chomsky, O., and Kulka, R. G. (1998) Degradation signals for ubiquitin system proteolysis in *Saccharomyces cerevisiae*. *EMBO J. 17*, 2759−2766.

(21) Bodner, R. A., Outeiro, T. F., Altmann, S., Maxwell, M. M., Cho, S. H., Hyman, B. T., McLean, P. J., Young, A. B., Housman, D. E., and Kazantsev, A. G. (2006) Pharmacological promotion of inclusion formation: a therapeutic approach for Huntington's and Parkinson's diseases. *Proc. Natl. Acad. Sci. U. S. A. 103*, 4246−4251.

Supporting Information

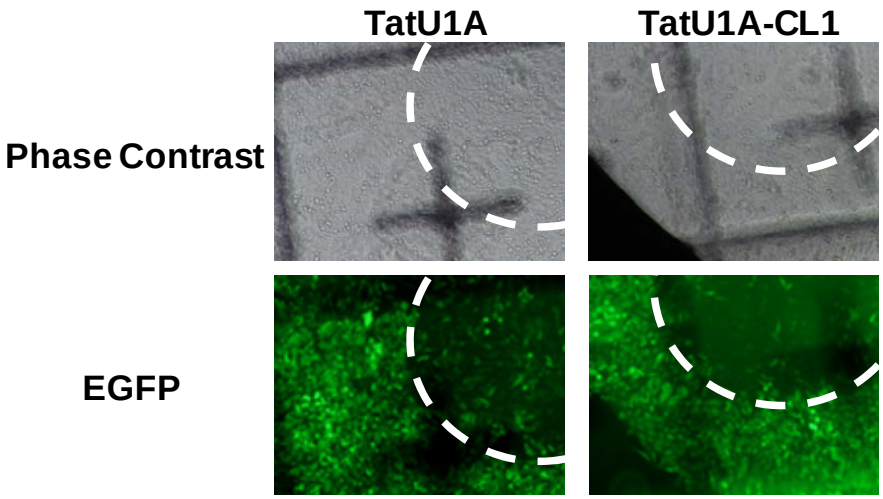

Fig. S1. EGFP silencing in EGFP-CHO cells. Anti-EGFP shRNA (200 nM) was mixed with TatU1A-Alexa546 or TatU1A-CL1-Alexa546 for complex formation, added to EGFP-CHO cells, and incubated at 37ºC for 2 h. After 20 h of irradiation (540 ± 10 nm light passed through a 4× objective lens for 64 s), fluorescent images were evaluated. The irradiated area is to the right of the dotted line.

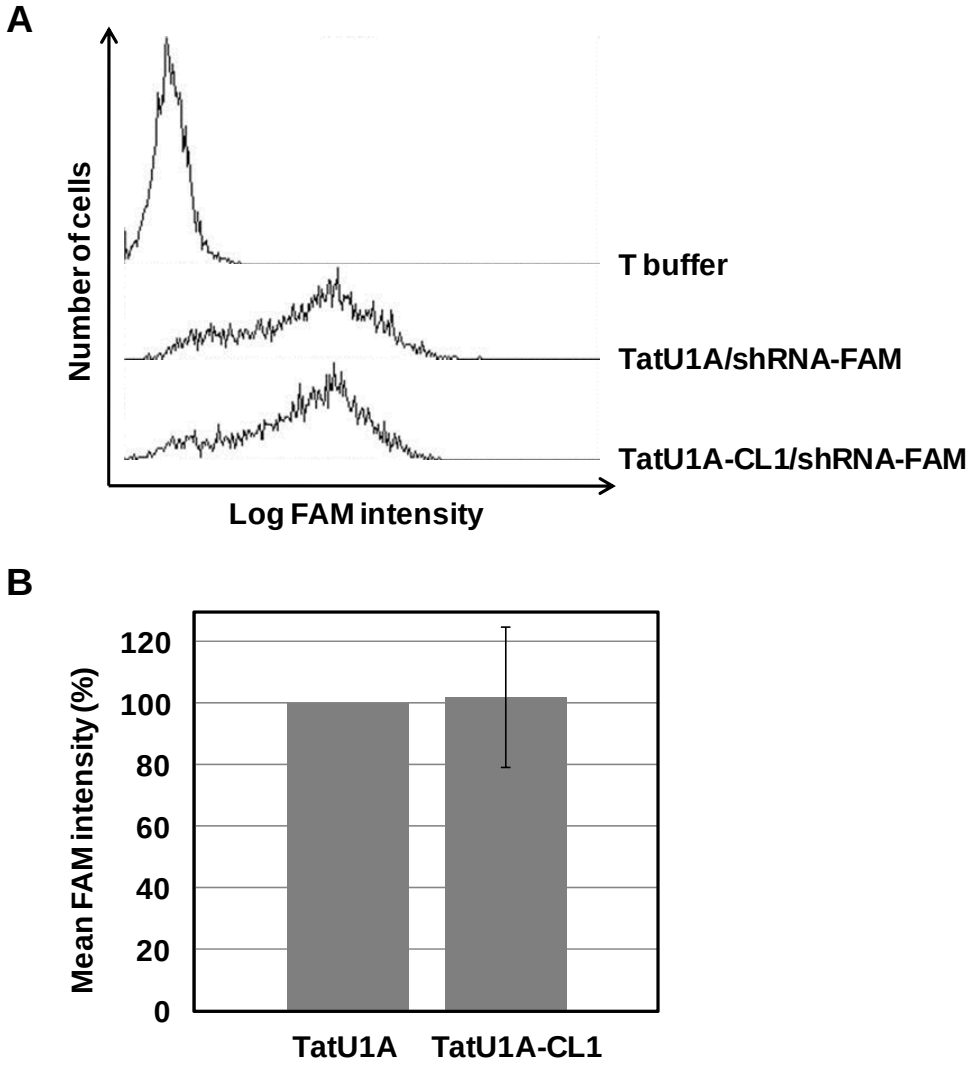

Fig. S2. Cellular FAM intensities after incubation of CHO cells with TatU1A-Alexa/shRNA-FAM or TatU1A-CL1-Alexa/shRNA-FAM. (**A**) The FAM intensities of the cells were evaluated by flow cytometry using FACSCalibur (BD Bioscience). (**B**) Mean FAM intensities with TatU1A and TatU1A-CL1 were analyzed using Cell Quest software (BD Bioscience).

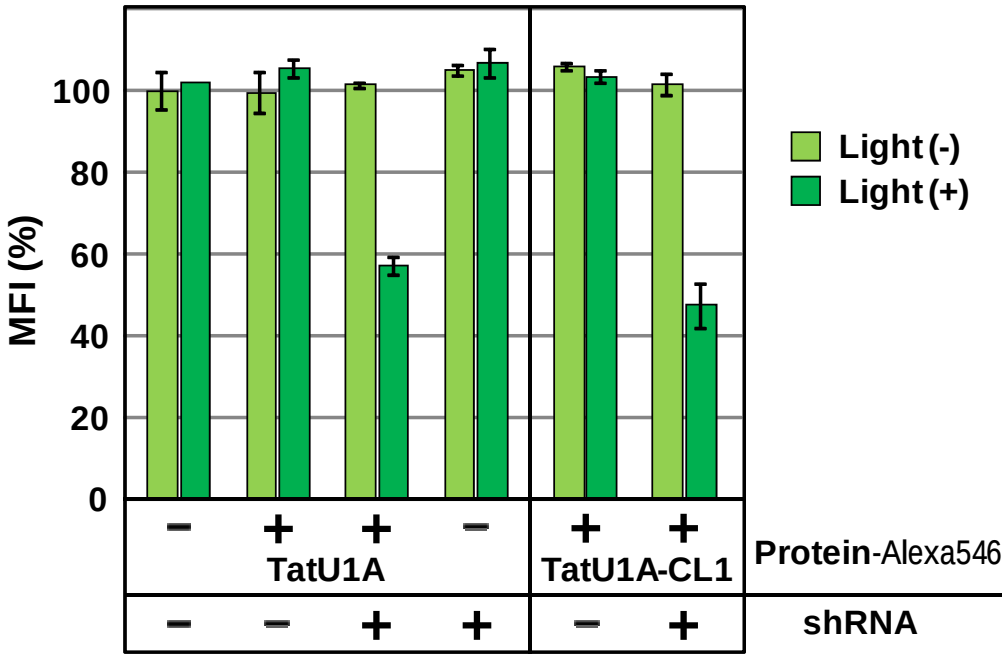

Fig. S3. Evaluation of the knockdown of EGFP expression in EGFP stably-expressing human malignant mesothelioma cells. Cells were treated with TatU1A-Alexa546/shRNA or TatU1A-CL1-Alexa546/shRNA complexes and irradiated (540 ± 10 nm light passed through a 4× objective lens for 64 s). Cells were collected for flow cytometric analysis at 20 h after irradiation. The silencing effect was assessed by measuring EGFP MFI.

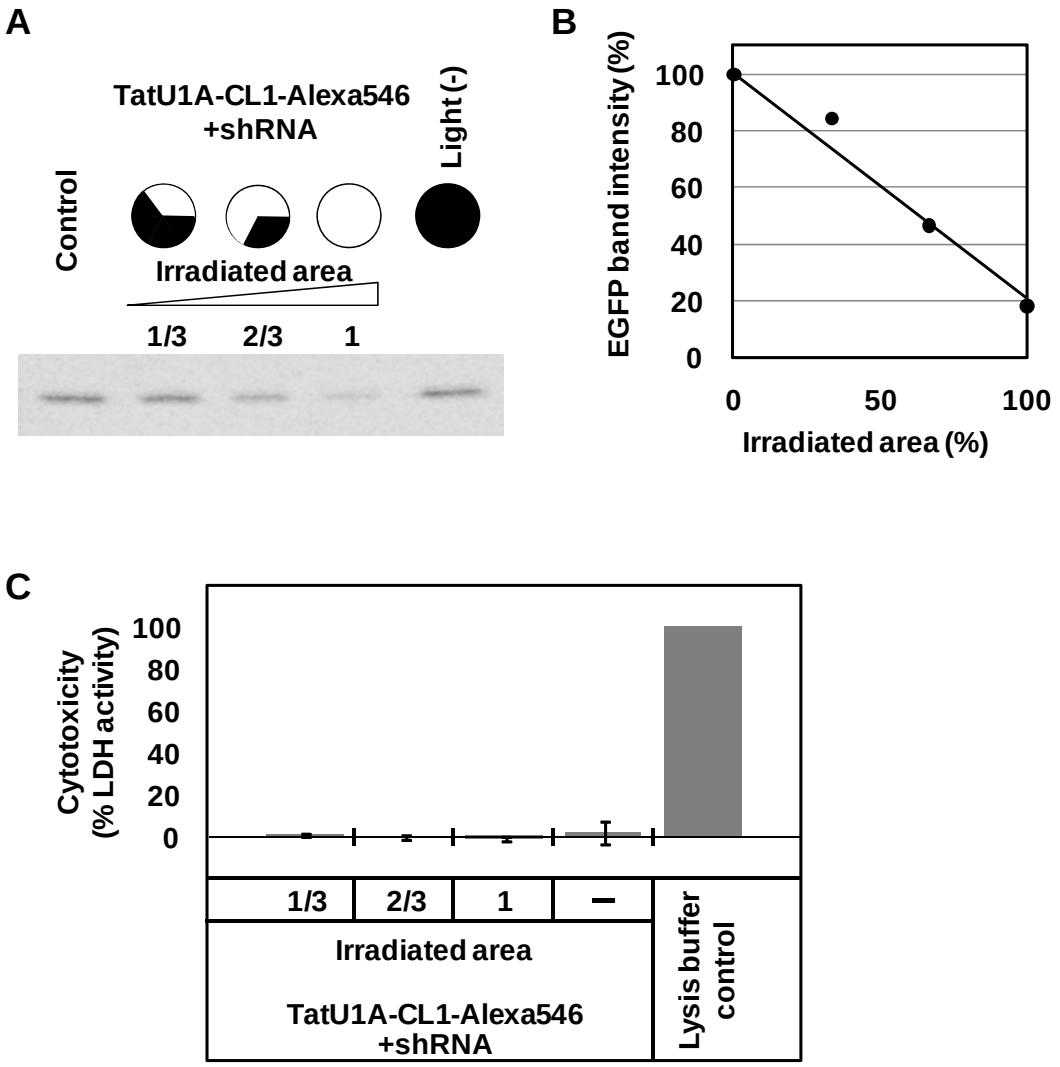

Fig. S4. Partial photoinduction of EGFP silencing. (**A**) Photomasking films were prepared to enable partial photostimulation of cells in the microwells of a 96-well plate, as described previously (Endoh *et al.* J. Controlled Release 137, 241-5, 2009). The photomasking film was attached to the bottom of the culture plate, and the cells were irradiated using a 4× objective lens. Cell lysates were obtained 20 h after photostimulation, and were applied to a 15 % SDS-polyacrylamide gel without boiling. Since EGFP maintains its fluorescence under this condition, EGFP was imaged by using a fluorescence image scanner (HITACHI FMBIO-SC01). (**B**) The EGFP intensity in the

partially irradiated wells. The EGFP intensity decreased depending on the size of the photostimulation area while the amount of total protein remained almost constant. As judged by the band intensity, the EGFP intensity decreased to 18% when the entire area was subjected to photostimulation. (**C**) Cytotoxicity after treatment with the TatU1A-CL1-Alexa546/shRNA complex and photostimulation. At 20 h after photostimulation, cytotoxicity was evaluated using the Cytotoxicity Detection Kit (LDH) (Roche, Switzerland), as described previously (Endoh *et al.* Bioconjug. Chem. 19, 1017-24, 2008).

Bioconjugate Chemistry

Article

pubs.acs.org/bc

Method for Enhancing Cell Penetration of Gd^{3+}-based MRI Contrast Agents by Conjugation with Hydrophobic Fluorescent Dyes

Takehiro Yamane,[†,‡] Kenjiro Hanaoka,[†,‡] Yasuaki Muramatsu,[†,‡] Keita Tamura,[§] Yusuke Adachi,[§] Yasushi Miyashita,[§] Yasunobu Hirata,[∥] and Tetsuo Nagano*[,†,‡]

[†]Graduate School of Pharmaceutical Sciences, The University of Tokyo, 7-3-1, Hongo, Bunkyo-ku, Tokyo 113-0033, Japan

[‡]CREST, Japan Science and Technology Agency, 5, Sanbancho, Chiyoda-ku, Tokyo, 102-0075, Japan

[§]Department of Physiology, The University of Tokyo School of Medicine, 7-3-1, Hongo, Bunkyo-ku, Tokyo 113-0033, Japan

[∥]Department of Cardiovascular Medicine, The University of Tokyo Hospital, 7-3-1, Hongo, Bunkyo-ku, Tokyo 113-0033, Japan

Supporting Information

ABSTRACT: Gadolinium ion (Gd^{3+}) complexes are commonly used as magnetic resonance imaging (MRI) contrast agents to enhance signals in T_1-weighted MR images. Recently, several methods to achieve cell-permeation of Gd^{3+} complexes have been reported, but more general and efficient methodology is needed. In this report, we describe a novel method to achieve cell permeation of Gd^{3+} complexes by using hydrophobic fluorescent dyes as a cell-permeability-enhancing unit. We synthesized Gd^{3+} complexes conjugated with boron dipyrromethene (**BDP-Gd**) and Cy7 dye (**Cy7-Gd**), and showed that these conjugates can be introduced efficiently into cells. To examine the relationship between cell permeability and dye structure, we further synthesized a series of **Cy7-Gd** derivatives. On the basis of MR imaging, flow cytometry, and ICP-MS analysis of cells loaded with **Cy7-Gd** derivatives, highly hydrophobic and nonanionic dyes were effective for enhancing cell permeation of Gd^{3+} complexes. Furthermore, the behavior of these **Cy7-Gd** derivatives was examined in mice. Thus, conjugation of hydrophobic fluorescent dyes appears to be an effective approach to improve the cell permeability of Gd^{3+} complexes, and should be applicable for further development of Gd^{3+}-based MRI contrast agents.

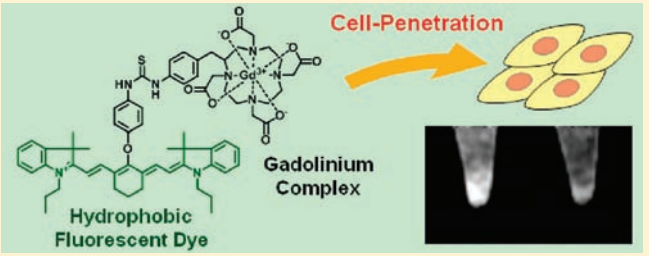

INTRODUCTION

Many imaging techniques, such as X-ray computed tomography (CT), ultrasonography (US), positron emission tomography (PET), and magnetic resonance imaging (MRI), are currently available for the diagnosis of diseases.[1] On the other hand, MRI is useful not only for clinical diagnosis, but also for in vivo imaging in basic research.[2] MRI is based on the NMR signals derived from protons of water molecules, and can provide three-dimensional images of internal body structures noninvasively with high resolution. Gadolinium ion (Gd^{3+}) complexes are commonly used as MRI contrast agents. Paramagnetic Gd^{3+} ions greatly shorten the longitudinal relaxation time (T_1) of water protons by interaction with nearby water molecules.[3] As a result, MR signals of tissues in which Gd^{3+} ions have accumulated show high intensities in T_1-weighted MR images. More recently, sensors based on Gd^{3+} complexes enable us to visualize lesions which are otherwise difficult to detect, as well as biological processes such as gene expression and enzymatic reaction inside the body.[4,5]

On the other hand, Gd^{3+} complexes are generally cell-impermeable, because of their high hydrophilicity, and are distributed only extracellularly. Recently, attempts have been made to develop cell-permeable Gd^{3+} complexes; for example, the attachment of cell-penetrating peptides (CPPs) such as polyarginines or HIV-1 tat peptides is a well-known method to internalize Gd^{3+} complexes or other molecules into cells.[6−9] CPPs consist of positively charged amino acids such as arginine or lysine, and it is reported that electrostatic interactions between the cationic CPPs and the anionic cell-membrane trigger cell-penetration of the CPPs.[10,11] The internalization pathways of CPPs are thought to be endocytosis and macropinocytosis, and its mechanism is highly dependent on incubation conditions or conjugated molecules.[12−14] However, in the case of MRI contrast agents, entrapment of CPPs in endosomes and/or lysosomes might lead to problems such as relaxivity quenching. On the other hands, there is a report that polyarginine-conjugated Gd^{3+} complexes easily leaked from cells;[6] therefore, the increased cell retention via disulfide bond incorporation was also reported.[15,16] Because of the relatively low sensitivity of MRI, it is often difficult to detect small amounts of the Gd^{3+} complexes by MRI; therefore, an efficient method to internalize and retain Gd^{3+} complexes inside cells is still needed in order to extend the applicability of MRI contrast agents.

Received: March 11, 2011
Revised: August 15, 2011
Published: October 11, 2011

ACS Publications © 2011 American Chemical Society

For this purpose, we focused on fluorescent dyes, because some fluorescent dyes can easily permeate the cell membrane, and the cell permeation property should be controllable by modification of their chemical structures. So, we anticipated that the conjugation of fluorescent dyes to cell-impermeable Gd^{3+} complexes would endow the complexes with cell membrane permeability. The chemical structures of a few fluorescent dye-Gd^{3+} complex conjugates (**dye-Gd**s) have been reported so far. One report described the cell permeation of the Cy5.5-Gd^{3+} complex conjugate in the presence of LDL, but the cell permeation ability was derived from the LDL.[17] Another report described a rhodamine-Gd^{3+} complex conjugate (**Gd(Rhoda-DOTA)**), but when **Gd(Rhoda-DOTA)** was introduced into cells by injection, no MRI contrast enhancement was obtained.[18] Furthermore, Parker et al. reported cell-permeable fluorescent lanthanide complexes, but they did not examine the utility of their Gd^{3+} complexes as MRI contrast agents.[19,20] On the other hand, Mishra et al. reported DO3A-ethylamine-derived contrast agents such as biotin-conjugated, maleimide-bearing, and FITC-coupling Gd^{3+} complexes, and the FITC-conjugated contrast agent was used for MRI and optical labeling of NIH-3T3 cells by the incubation for 18 h.[21]

Here, we report a novel approach to develop cell-permeable Gd^{3+} complexes by using hydrophobic fluorescent dyes as a cell-permeability-enhancing unit. We also examined the relaxivity of **dye-Gd**s, the relationship between cell permeability and dye structure, and the distribution of **dye-Gd**s inside cells. Furthermore, the behavior of cell-permeable and cell-impermeable **dye-Gd**s in mouse was also examined by MRI.

EXPERIMENTAL SECTION

Materials. *p*-NH_2-Bn-DOTA (DOTA = 1,4,7,10-tetraazacyclododecane-1,4,7,10-tetraacetate) and DOTA-mono[*N*-(2-aminoethyl)ethanamide]-tris(*t*-butyl ester) were purchased from Macrocyclics (Dallas, Texas, USA). All other reagents and solvents were purchased from Tokyo Chemical Industry Co. (Tokyo, Japan), Wako Pure Chemical Industries (Osaka, Japan), Dojindo Laboratories (Kumamoto, Japan), Invitrogen (Carlsbad, CA), or Aldrich Chemical Co. (St. Louis, MO) and were used without further purification. Silica gel column chromatography was performed by using Chromatorex-NH (Fuji Silysia Chemical, Kasugai, Japan) or Silica Gel 60 (Spherical) (Kanto Chemical Co., Tokyo, Japan).

Instruments. ^1H and ^{13}C NMR spectra were recorded by using a JEOL JNM-LA300 or JNM-LA400 spectrometer. Mass spectra (ESI) were measured by using a JEOL JMS-T100LC AccuTOF spectrometer. UV−visible spectra were obtained on a Shimadzu UV-1650 spectrophotometer. Fluorescence spectroscopic studies were performed on a Hitachi F-4500 spectrofluorometer. Longitudinal water proton relaxation time (T_1) was measured by using an NMR instrument operating at 20 MHz, 0.47 T (Minispec mq20, Bruker, Germany). HPLC analyses were performed on an Inertsil ODS-3 column (GL Sciences Inc.; 4.6 mm × 250 mm) using an HPLC system composed of a pump (PU-2080, JASCO) and a detector (MD-2015 or FP-2025, JASCO). HPLC purifications were performed on an Inertsil ODS-3 column (GL Sciences Inc.; 10.0 × 250 mm) using an HPLC system composed of a pump (PU-2080, JASCO) and a detector (MD-2015 or FP-2025, JASCO).

Fluorometric Analysis. Excitation slit width, emission slit width, and photomultiplier voltage were 10 nm, 10 nm, and 400 V for **Cy7-Gd** derivatives, and 2.5 nm, 2.5 nm, and 700 V for other **dye-Gd**s, respectively. The spectra of **dye-Gd**s were measured in an aqueous solution buffered to pH 7.4 (100 mM HEPES buffer) at room temperature. Relative fluorescence quantum efficiencies of **dye-Gd**s were determined by comparing the area under the emission spectrum of the sample (on an energy scale) with that of fluorescein in 0.1 M NaOH aqueous solution (Φ = 0.85, for **BDP-Gd** and **FL-Gd**), rhodamine B in ethanol (Φ = 0.97, for **Gd(Rhoda-DOTA)**) or indocyanine green (ICG) in DMSO (Φ = 0.13, for **Cy7-Gd** derivatives).

Relaxivity Measurements. The longitudinal water proton relaxation times (T_1) of aqueous solutions of **dye-Gd**s were measured in phosphate-buffered saline (PBS, Dulbecco's phosphate-buffered saline, pH 7.4) with or without 4% human serum albumin at 37 °C, 20 MHz, 0.47 T (Minispec mq20, Bruker). T_1 values were measured from 30 points generated by using the standard inversion−recovery procedure. The r_1 relaxivities (mM^{-1} s^{-1}) of **dye-Gd**s were determined from the slope of the plot of $1/T_1$ versus concentration of **dye-Gd**s (0.50, 0.20, 0.10, 0.05, and 0 mM) except **Cy7-Gd**. The r_1 relaxivity of **Cy7-Gd** was determined at different concentrations of **Cy7-Gd** (0.10, 0.075, 0.05, 0.025, and 0 mM), because of its low solubility.

Cell Culture. HeLa cells (human cervical cancer cells) and NIH-3T3 cells (mouse fibroblasts) were cultured in Dulbecco's modified Eagle's medium (DMEM) supplemented with 10% (v/v) fetal bovine serum, penicillin (100 units/mL), and streptomycin (100 units/mL) at 37 °C in a humidified incubator containing 5% CO_2 in air. SHIN3 cells (human ovarian cancer cells) were cultured in Roswell Park Memorial Institute (RPMI) 1640 medium supplemented with 10% (v/v) fetal bovine serum, penicillin (100 units/mL), and streptomycin (100 units/mL) at the same condition with HeLa cells or NIH-3T3 cells.

Fluorescence Microscopic Imaging of Cells. Cells were plated onto 35 mm poly(L-lysine)-coated glass-bottomed dishes (MatTek Corporation, Ashland, MA) and cultured for 2 days. The medium was removed, then **dye-Gd**s in medium (10 μM, containing 0.1% DMSO as a cosolvent) were added and incubation was continued for 2 h. The stained cells were washed twice with PBS, and fluorescence microscopic images were captured in PBS. We used an inverted microscope (IX 71, Olympus) with a 60× objective lens (PlanApo 60× /1.40 oil, Olympus) and *MetaFluor 6.1* software (Universal Imaging, Media PA). The fluorescence images were observed through a filter cube (NIBA for **BDP-Gd** and **FL-Gd**, WIG for **Gd(Rhoda-DOTA)**, and Cy7 for **Cy7-Gd**, Olympus).

MR Imaging of Cells. HeLa cells were plated onto 90 mm noncoated dishes (Fast Gene) and cultured for 3 days. The medium was removed, and then **dye-Gd**s in DMEM (100 μM, containing 0.1% DMSO as a cosolvent) were added and incubation was continued for 2 h. The stained cells were washed once with PBS buffer. The cells were harvested with trypsin-EDTA solution (GIBCO, 0.25% trypsin, 1 mM EDTA·Na), and DMEM was added. The cells were transferred to a 15 mL centrifuge tube, and centrifuged at 1000 rpm, 4 °C for 3 min. After removal of the supernatant, DMEM was added and the cells were transferred to a micro test tube, then centrifuged at 6200 rpm for 3 min. The tube was filled with DMEM, and MR imaging was performed using a 4.7 T MRI scanner (Biospec 47/40, Bruker) with 100 mT/m actively shielded gradient coils equipped with a transmit/receive birdcage coil (od/id: 255/197 nm, Bruker). T_1-weighted MRI

parameters were as follows: fast spin echo sequence, repetition time (TR), 323 ms; echo time (TE), 14 ms; matrix size, 384 × 384; field of view (FOV), 88 × 88 mm^2; slice thickness, 1.5 mm; in-plane resolution, 0.23 × 0.23 mm^2; number of signals averaged, 40; scan time, 15.5 min. Dunnett's test was used to assess differences in the MR signal intensities between sample and control cells. $p < 0.05$ was considered statistically significant.

ICP-MS Measurements. **Dye-Gd**-labeled HeLa cells used in MR imaging were resuspended and transferred to a 15 mL centrifuge tube, then 20% sodium dodecyl sulfate solution (SDS, 3 mL) was added, and the cells were incubated for 2 days. The solution was diluted to 10 mL with ultrapure water, and concentrations of Gd^{3+} ion in the diluted solutions were measured by ICP-MS. Tukey's test (Figure 3c) and Student's *t* test (Figure 6c) were used to assess the significance of differences in the concentrations of Gd^{3+} ion between different groups of cells.

Flow Cytometric (FCM) Analyses. HeLa cells were plated onto 35 mm poly(L-lysine)-coated glass-bottomed dishes (MatTek Corporation) and cultured for 3 days. After removal of the medium, **Cy7-Gd** derivatives in DMEM (10 μM, containing 0.1% DMSO as a cosolvent) were added and incubation was continued for 2 h. The stained cells were washed 3 times with PBS buffer, then incubated with trypsin-EDTA solution (GIBCO, 0.25% trypsin, 1 mM EDTA·Na), and DMEM was added to the dishes. The cells were transferred to a 15 mL centrifuge tube, and centrifuged at 1000 rpm for 3 min. The supernatant was removed. The cells were resuspended in 0.5 mL of PBS, and fluorescence analyses were performed using a BD LSR II Flow Cytometer (Beckman Coulter; 633 nm laser excitation and a 750−810 nm emission filter). Each analysis was performed with 10 000 cells.

Co-Staining with Organelle-Specific Fluorescent Dyes. HeLa cells were plated onto 35 mm poly(L-lysine)-coated glass-bottomed dishes (MatTek Corporation, Ashland, MA) and cultured for 2 days. (i) Dextran-Alexa488 conjugate, which accumulates in lysosomes, was prepared from Alexa Fluor488 5-SDP ester (Invitrogen) and dextran, and purified on a PD-10 column (GE Healthcare). Dextran-Alexa488 conjugate in PBS (1 mg/mL) was mixed with the same quantity of DMEM, and then added to the dish, after removal of the medium. After incubation for 4 h, the stained cells were washed three times with PBS. The medium was replaced with DMEM and incubation was continued for 20 h. After removal of the medium, **dye-Gd**s in DMEM (10 μM, containing 0.1% DMSO as a co-solvent) were added and incubation was continued for 2 h. The stained cells were washed twice with PBS, and confocal fluorescence microscopy images were captured in PBS. (ii) Mitotracker Red, which accumulates in mitochondria, and **dye-Gd**s in DMEM (100 nM and 10 μM, respectively, containing 0.1% DMSO as a co-solvent) were added after removal of the medium, and incubation was continued for 2 h. The stained cells were washed twice with PBS, and confocal fluorescence microscopy images were captured in PBS. (iii) BODIPY TR ceramide, which accumulates in Golgi apparatus, in DMEM (5 μM, containing 0.5% DMSO as a co-solvent) was added after removal of the medium, and incubation was continued for 30 min. The stained cells were washed three times with PBS. The medium was replaced with DMEM and incubation was continued for 30 min. After removal of the medium, **dye-Gd**s in DMEM (10 μM, containing 0.1% DMSO as a co-solvent) were added and incubation was continued for 2 h. The stained cells were washed twice with PBS and confocal fluorescence microscopy images were captured in PBS. We used a confocal imaging system (TCS-SP5, Leica) equipped with a white light laser, Leica Application Suite Advanced Fluorescence (LAS-AF), and a 40× objective lens (HSX PL APO 40×/1.25−0.75 oil CS, Leica). The excitation wavelength and the fluorescence emission wavelength were 495 nm and 505−530 nm for **BDP-Gd** and dextran−Alexa488 conjugate, 552 nm and 600−620 nm for **Gd(Rhoda-DOTA)**, 600 nm and 650−680 nm for BODIPY TR ceramide, and 670 nm and 750−800 nm for **Cy7-Gd** and **6**, respectively.

Fluorescence Imaging of Mice. All procedures were approved by the Animal Care and Use Committee of the University of Tokyo. BALB/cAJcl-*nu*/*nu* (male, 8-week-old) were purchased from CLEA Japan, Inc. Mice were anesthetized by intraperitoneal injection of pentobarbital (Nembutal, Dainippon Sumitomo Pharma Co., 50 mg/kg). A solution of **1** or **6** in saline (100 μM, 100 μL) was administered to the mice via the orbital vein, and fluorescence images were captured with a Maestro In-Vivo Imaging System (CRi Inc., Woburn, MA). The excitation wavelength was 670−710 nm, and fluorescence emission (780−900 nm) was obtained. After imaging at each time point, the mice were sacrificed with CO_2 gas, and blood was collected immediately from the heart. After incision of the femoral vein, PBS was injected from the heart to wash out residual blood, and organs were harvested. Fluorescence images of isolated organs and blood were captured.

MR Imaging of Mice. This experiment complied with the rules for animal experiments of The University of Tokyo. Mice were fixed on a custom-made cradle and anesthetized continuously with a mixture of oxygen and 1.5−2.0% isoflurane (Forane, Abbott Japan). MR imaging was performed before the injection of **dye-Gd**s. Then, compound **1**, **6**, or Gd-DTPA in saline (5 mM, 100 μL) was administered to the mice via the orbital vein, and MR imaging was performed from 10 min after the injection. For MRI experiments, we used a 4.7 T MRI scanner (Biospec 47/40, Bruker, Germany), 100 mT/m actively shielded gradient coils equipped with a transmitter birdcage coil (od/id: 255/197 nm, Bruker), and a receiver surface coil (35 mm, Takashima Seisakusho, Japan). T_1-weighted MR images were obtained with the following parameters: sequence, fast spin echo; repetition time (TR), 300 ms; echo time (TE), 9.8 ms; matrix size, 256 × 256; field of view (FOV), 64 × 64 mm^2; slice thickness, 1.0 mm; in-plane resolution, 0.25 × 0.25 mm^2; number of signals averaged, 3. T_1 maps were obtained with the following parameters: repetition time (TR), 7000, 2000, 1000, 600, 300, 200, 150, 100 ms; echo time (TE), 9.8 ms; matrix size, 128 × 128; field of view (FOV), 80 × 50 mm^2; slice thickness, 1.0 mm; in-plane resolution, 0.63 × 0.30 mm^2; number of signals averaged, 1; scan time, 12.1 min. Mice were kept warm at 37 °C with a heating pad during MR imaging. The experiments were carried out twice for each compound. T_1 values of mouse liver were measured within two regions of interest (ROI) in the left and right sides of the liver, respectively. (The T_1 values of the center of the liver were unclear because of the presence of the aorta.) Each ROI contained 102 voxels, and the T_1 values of the liver were calculated by averaging T_1 values of voxels in both the left and right ROIs. Student's *t* test was used to assess the significance of the differences in T_1 values of the liver between pre- and postinjection of **1**, **6**, or Gd-DTPA.

Fluorescence Microscopic Imaging of Liver Slices. This experiment complied with the rules for animal experiments of

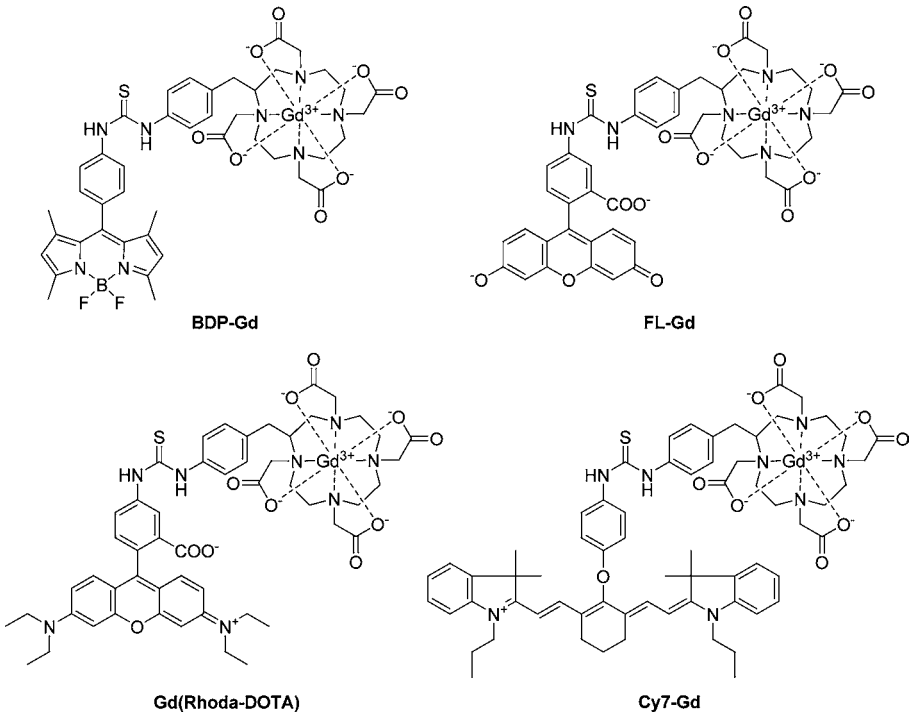

Figure 1. Structures of **dye-Gd**s and Gd-DTPA.

The University of Tokyo. Mice were anesthetized by intraperitoneal injection of pentobarbital (50 mg/kg), and a solution of **1** or **6** in saline (5 mM, 100 μL) was administered via the orbital vein. After 30 min, the mice were sacrificed with CO_2 gas. After incision of the femoral vein, PBS was injected from the heart to wash out the blood. Then, the liver was harvested, washed three times with PBS, embedded in OCT compound (Tissue-Tek), frozen on 2,2-dimethylbutane cooled with liquid N_2, and cut into 5-μm-thick frozen sections. Fluorescence images of the sections were captured on a confocal imaging system (TCS-SP5, Leica) equipped with a white light laser, Leica Application Suite Advanced Fluorescence (LAS-AF), and a 63× objective lens (HSX PL APO 63×/1.40−0.60 oil CS, Leica). The excitation wavelength and the fluorescence emission wavelength were 670 nm and 700−800 nm, respectively.

RESULTS AND DISCUSSION

First, we carried out screening to identify fluorescent dyes which can promote entry of Gd^{3+}-DOTA complexes into cells. We chose boron dipyrromethene (BODIPY), fluorescein, rhodamine B, and Cy7 dye, which have different chemical properties such as hydrophilicity, positive or negative charge, molecular weight, and so forth. The chemical structures of prepared **dye-Gd**s are shown in Figure 1. These **dye-Gd**s were synthesized by conjugation of fluorescent dye isothiocyanates to *p*-NH_2-Bn-DOTA, and the conjugates were subsequently coordinated to Gd^{3+} ion. Fluorescein isothiocyanate and rhodamine B isothiocyanate were commercial products, while BODIPY isothiocyanate and Cy7 isothiocyanate were synthesized by the reaction of the aniline compounds and thiophosgene. **Gd(Rhoda-DOTA)** was previously reported in ref 18 where it was stated not to show contrast enhancement in MR imaging of *Xenopus* embryos.

The fluorescence properties and r_1 relaxivities of **dye-Gd**s are summarized in Table 1. In particular, the r_1 relaxivities of

Table 1. Chemical Properties of dye-Gds

	r_1 (mM^{-1} s^{-1})[a]				
	PBS	4% albumin	λ_{abs} (nm)[b]	λ_{em} (nm)[b]	Φ_{fl}[b,c]
BDP-Gd	22	24	497	509	0.16
FL-Gd	4.1	5.9	493	518	0.63
Gd(Rhoda-DOTA)	6.3	17	557	582	0.28
Cy7-Gd	32	32	768	786	0.063

[a]Data were measured at 20 MHz in PBS. [b]Data were measured in 0.1 M HEPES buffer (pH 7.4). [c]Φ_{fl} is the relative fluorescence quantum yield determined by using fluorescein in 0.1 M NaOH aqueous solution (0.85, for **BDP-Gd**, **FL-Gd**), rhodamine B in EtOH (0.65, for **Gd(Rhoda-DOTA)**), or indocyanine green in DMSO (0.13, for **Cy7-Gd**) as a fluorescence standard.

BDP-Gd and **Cy7-Gd** in PBS were about 5 and 8 times larger than that of Gd-DTPA (DTPA: diethylenetriamine-*N,N,N′,N″,N″*-pentaacetic acid; the r_1 relaxivity of Gd-DTPA was 4.1 mM^{-1} s^{-1} under the same conditions), which is a widely used Gd^{3+} complex.[22] We think that these high relaxivities are derived from the high hydrophobicity of BODIPY and Cy7 dye. **BDP-Gd** and **Cy7-Gd** seem to exhibit stacking in aqueous solution, based on the low fluorescence quantum yields and their spectra, and the resulting increment of apparent molecular weight may lead to enhancement of the r_1 relaxivity because of the slow molecular rotation of the Gd^{3+} complex.[22,23] However, additional effect of albumin was hardly observed about **BDP-Gd** and **Cy7-Gd**. Only **Gd(Rhoda-DOTA)** showed a large increment of the r_1 relaxivity in 4% albumin solution, and this may be due to the interaction with albumin molecules.

Next, we examined the cell permeability of **dye-Gd**s. HeLa cells were incubated with 10 μM **dye-Gd**s for 2 h, then fluorescence images of the cells were captured. No toxicity was observed under these conditions. Fluorescence microscopic

dx.doi.org/10.1021/bc200127t | *Bioconjugate Chem.* 2011, 22, 2227−2236

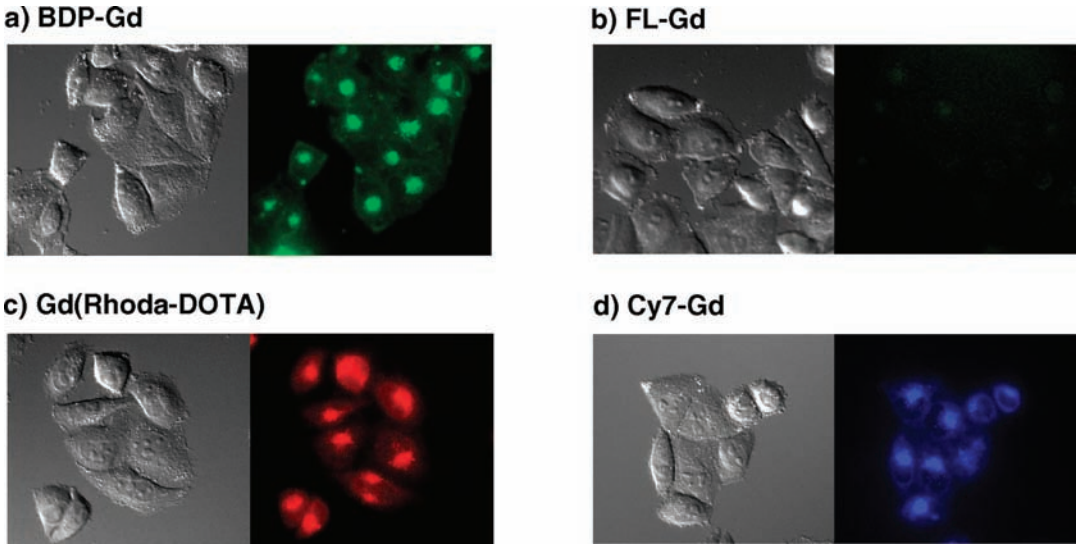

Figure 2. Fluorescence images of HeLa cells incubated with **dye-Gd**s (10 μM). The left and right panels show differential interference contrast (DIC) and fluorescence micrographs of HeLa cells, respectively. (a) **BDP-Gd**, (b) **FL-Gd**, (c) **Gd(Rhoda-DOTA)**, (d) **Cy7-Gd**.

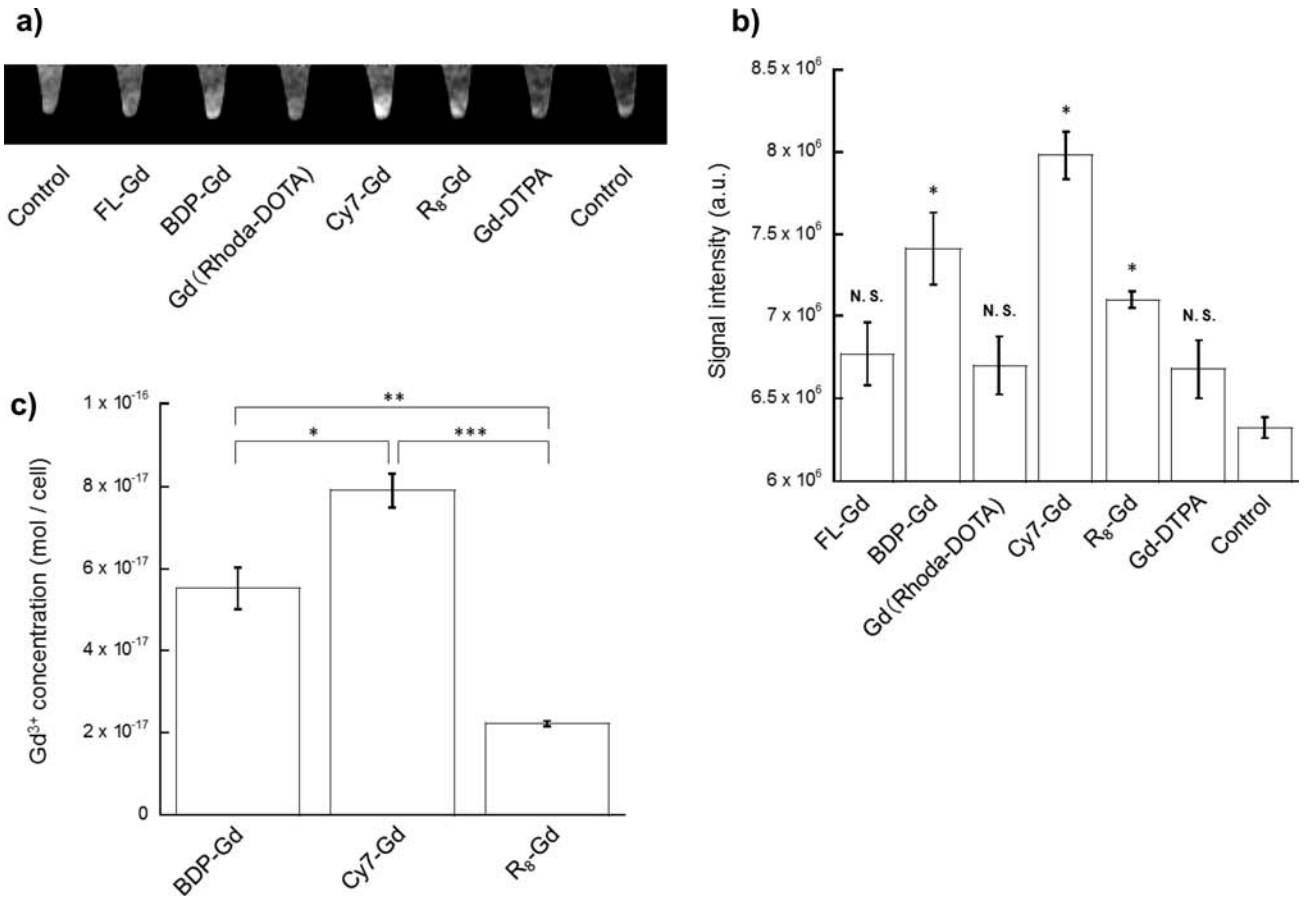

Figure 3. (a) T_1-weighted MR image of HeLa cells incubated with **dye-Gd**s, **R_8-Gd**, and Gd-DTPA (100 μM) for 2 h. (b) MR signal intensities in T_1-weighted MR image of HeLa cells incubated with **dye-Gd**s (n = 3). *p < 0.05. N.S., not significant. (c) Concentrations of Gd^{3+} ion in HeLa cells measured by ICP-MS (n = 3). In the cases of **FL-Gd**, **Gd(Rhoda-DOTA)**, and Gd-DTPA, the concentrations of Gd^{3+} ion could not be measured because the apparent values were too small. *p < 0.05, **p < 0.01, and ***p < 0.001. Error bars show standard error.

analysis demonstrated efficient cell permeation of **BDP-Gd**, **Gd(Rhoda-DOTA)**, and **Cy7-Gd**, whereas **FL-Gd** was not taken into the cells at all (Figure 2). Fluorescein is anionic and relatively hydrophilic compared with the other dyes. According to the results of costaining with organelle-specific fluorescent dyes, each **dye-Gd** showed a different distribution inside cells (Supporting Information Figure S1). **BDP-Gd** showed good overlap with BODIPY TR ceramide, which specifically accumulates in Golgi apparatus, and **Cy7-Gd** was accumulated in lysosomes and mitochondria. In addition, we examined the

dx.doi.org/10.1021/bc200127t | *Bioconjugate Chem.* 2011, 22, 2227–2236

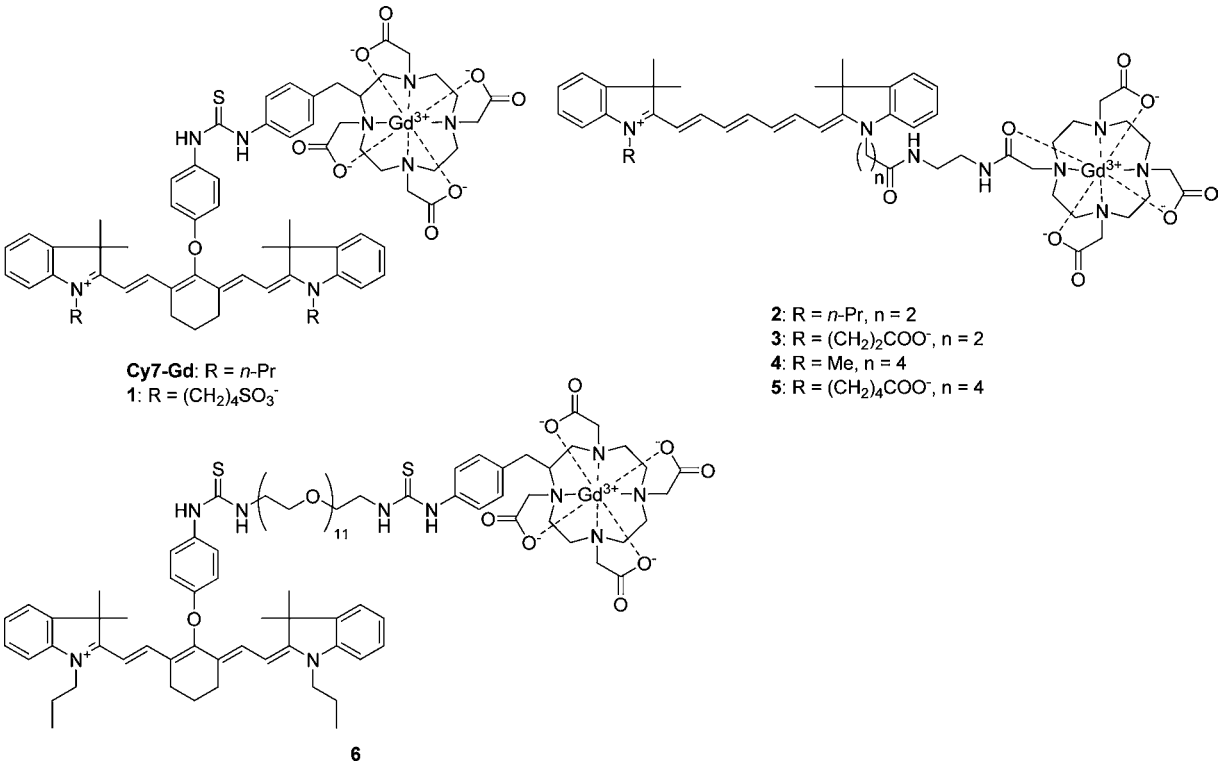

Figure 4. Structures of **Cy7-Gd**s.

contrast effect of **dye-Gd**s by MR imaging of live cells (Figure 3a,b). In the T_1-weighted MR images, **BDP-Gd**, **Cy7-Gd**, and $\mathbf{R_8}$**-Gd**, a cell-permeable octaarginine-conjugated Gd^{3+} complex[6] exhibited significant enhancement of the MR signal of HeLa cells. On the other hand, significant enhancement was not observed with cell-impermeable **FL-Gd** or Gd-DTPA. Moreover, **Gd(Rhoda-DOTA)** also did not produce a significant change of the MR signal, although its fluorescence was observed in fluorescence microscopy. When we compared the efficiency of cell permeation of **dye-Gd**s by using ICP-MS, **BDP-Gd** and **Cy7-Gd** showed higher cell permeation than $\mathbf{R_8}$**-Gd**, while the quantity of **Gd(Rhoda-DOTA)** in the cells was much lower than those of the other cell-permeable **dye-Gd**s (Figure 3c). Thus, **BDP-Gd** and **Cy7-Gd** showed good cell permeability and acted as MRI contrast agents. Furthermore, we examined the cell permeability of **BDP-Gd** and **Cy7-Gd** using other cell lines (Supporting Information Figure S2). **BDP-Gd** and **Cy7-Gd** were taken into both NIH/3T3 cells and SHIN3 cells, and the fluorescence intensities of the cells were equivalent to that in the case of HeLa cells.

To further examine the relationship between the chemical structure of Gd^{3+} complexes and the cell permeability, we synthesized various **Cy7-Gd** derivatives (**Cy7-Gd**s) (Figure 4). We chose **Cy7-Gd**s as a basic scaffold because structural elaboration is easier than in the case of **BDP-Gd**. Compound **1** has two anionic sulfo groups, and **2**, **3**, **4**, and **5** have asymmetric structures. Compound **6** has a poly(ethylene glycol) (PEG) chain between the Cy7 dye and Gd^{3+} complex. All of compounds **1**−**6** showed higher solubility in water than did **Cy7-Gd**. The fluorescence properties and r_1 relaxivities of these **Cy7-Gd**s are summarized in Table 2. Compounds **1** and **6** showed high r_1 relaxivities, whereas compounds **2**−**5** showed low r_1 relaxivities, almost the same as that of Gd-DTPA. It is considered that these differences arise from differences in the degree of stacking of these compounds on the basis of the low fluorescence quantum yields. Alternatively, hydrophobicity and/or flexibility of linker of **1** and **6** such as thiourea-phenyl moiety might change the local rotational dynamics of the Gd^{3+} complex and the r_1 relaxivities. Moreover, additional effect of albumin was hardly observed about **1** and **6**, while compounds **2**−**5** showed the high r_1 relaxivities in 4% albumin solution by their interactions with albumin molecules.

Table 2. Chemical Properties of Cy7-Gds

	r_1 (mM^{-1} s^{-1})[a]				
	PBS	4% albumin	λ_{abs} (nm)[b]	λ_{em} (nm)[b]	Φ_{fl}[b,c]
Cy7-Gd	32	32	768	786	0.063
1	20	25	769	785	0.072
2	4.0	12	743	762	0.14
3	4.9	11	743	763	0.12
4	4.6	13	741	761	0.14
5	5.0	12	745	765	0.14
6	18	20	771	786	0.078

[a]Data were measured at 20 MHz in PBS. [b]Data were measured in 0.1 M HEPES buffer (pH 7.4). [c]Φ_{fl} was determined by using indocyanine green in DMSO (0.13) as a fluorescence standard.

Cell permeation of **Cy7-Gd**s was examined by means of fluorescence microscopy and FCM analysis (Figure 5). When cells were incubated with **1** bearing sulfo groups, no fluorescence was observed in the cells by fluorescence microscopy (Figure 5b). On the other hand, **6** showed stronger fluorescence intensity than that of **Cy7-Gd** (Figure 5c). In FCM analysis, compounds **2**−**5** were less well taken into the cells than **Cy7-Gd**, and cell permeation of **3** and **5**, bearing a carboxy group in the Cy7 scaffold was lower than that of **2** and **4**, which have no carboxy group. Thus, as was expected, these results showed that anionic compounds were less effective for

dx.doi.org/10.1021/bc200127t | *Bioconjugate Chem.* 2011, 22, 2227−2236

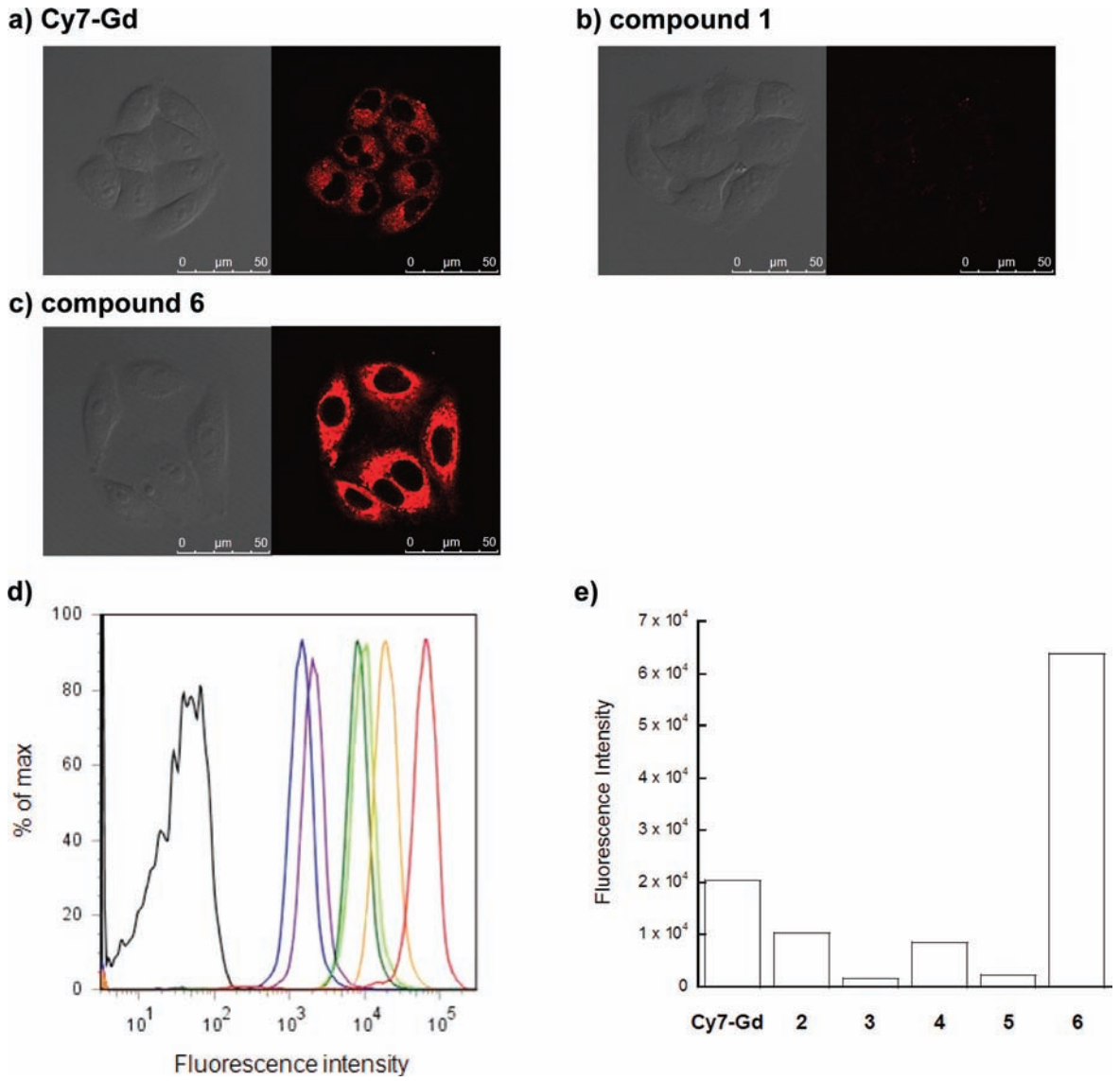

Figure 5. Confocal fluorescence microscopic images of HeLa cells incubated with (a) **Cy7-Gd**, (b) **1**, and (c) **6**. Left and right panels show DIC and fluorescence images, respectively. (d,e) FCM analysis of HeLa cells incubated with **Cy7-Gd** derivatives (10 μM). Each analysis was performed with 10 000 cells. Yellow, **Cy7-Gd**; light green, **2**; blue, **3**; deep green, **4**; purple, **5**; red, **6**; black, control.

cell permeation.[24] Compound **6** showed the highest fluorescence intensity among the **Cy7-Gd**s examined in FCM analysis, and was accumulated in mitochondria on the basis of the confocal fluorescence images (Supporting Information Figure S3). Furthermore, we examined the contrast effects of cell-permeable **6** and cell-impermeable **1** in MR imaging of live cells. Compound **6** showed a significant signal enhancement of live cells in MR imaging, whereas no significant enhancement was observed in the case of **1** (Figure 6a,b). In addition, a higher Gd^{3+} concentration of **6** was also observed in the cells on ICP-MS measurement (Figure 6c). From these results, PEG chains are thought to improve both cell permeation and water solubility,[25] and **6** was the best cell-permeable contrast agent among the **Cy7-Gd**s synthesized here.

We next examined the behaviors of cell-permeable **6** and cell-impermeable **1** in in vivo MR imaging of mice. These two compounds showed sufficient water solubility for MR imaging and had high r_1 relaxivities. First, compound **1** or **6** dissolved in saline (100 μM, 100 μL) was administered intravenously to nude mice, and then, the accumulation in various organs was observed by means of fluorescence imaging. Each compound accumulated mostly in the liver (Supporting Information Figure S4). The reason **1** and **6** accumulate in the liver is considered to be as follows. Indocyanine green (ICG), which is a tricarbocyanine dye, is accumulated specifically in the liver when it is administered, because it binds to serum protein such as albumin and lipoprotein, and is carried to the liver.[26] Therefore, ICG is used as a diagnostic agent to evaluate hepatic function (Diagnogreen Daiichi Sankyo). ICG is taken into hepatocytes via Na^+-independent basolateral membrane transport systems, such as organic anion transporting polypeptide 1 (OATP1) and organic anion transporter LST-1.[27,28] Compounds **1** and **6** also have tricarbocyanine structures, and therefore might be taken into the liver via the same pathways as ICG.

We also evaluated the MRI contrast effect of **1** and **6** in vivo. Cell-impermeable **1** or cell-permeable **6** in saline (5 mM, 100 μL) was administered intravenously to mice, and T_1-weighted MR images and T_1 maps of the body were measured (Figure 7). After the injection of **6**, MR signals of the liver were enhanced

dx.doi.org/10.1021/bc200127t | *Bioconjugate Chem.* 2011, 22, 2227–2236

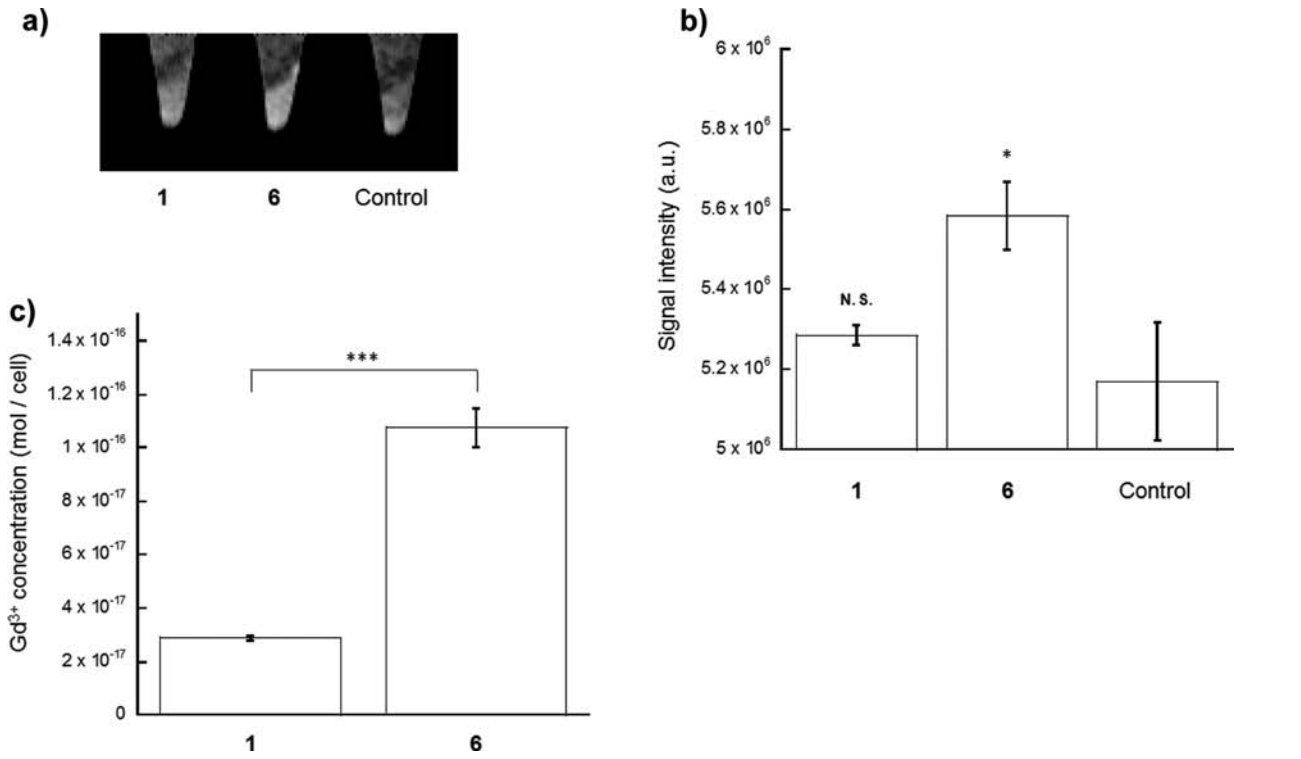

Figure 6. (a) T_1-weighted MR image of HeLa cells incubated with **Cy7-Gd**s (100 μM). (b) MR signal intensities in T_1-weighted MR image of HeLa cells (n = 3). *p < 0.05. N.S., not significant. (c) Concentrations of Gd^{3+} in HeLa cells (n = 3). ***p < 0.001. Error bars show standard error.

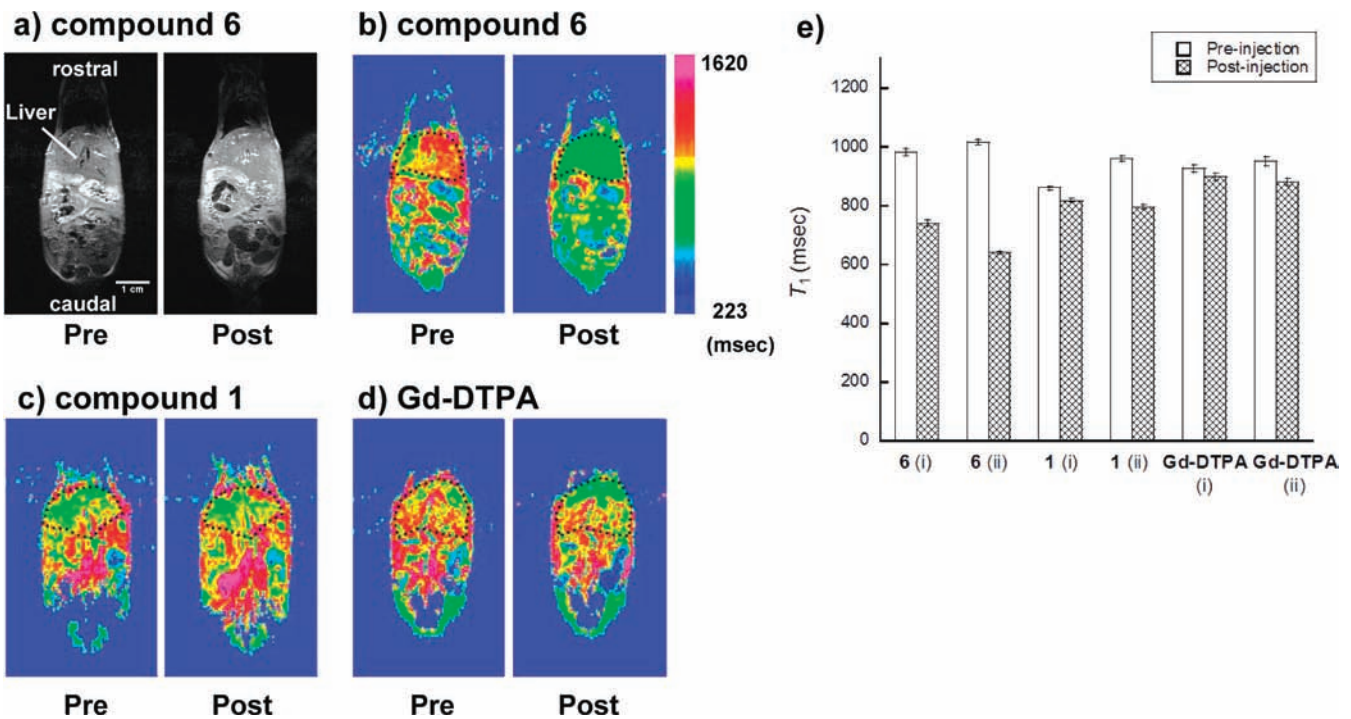

Figure 7. T_1-weighted MR images and T_1 maps of mice before (left) and after (right) the injection of **1**, **6**, or Gd-DTPA (5 mM, 100 μL). (a) T_1-weighted MR image of mouse injected with **6**. (b,c,d) T_1 maps of mice injected with (b) **6**, (c) **1**, and (d) Gd-DTPA. Dotted frames show the position of the liver. (e) The T_1 values in mouse liver in each experiment. Error bars show standard error (204 voxels). All changes of the T_1 values in each experiment were statistically significant (p < 0.001).

in T_1-weighted MR images, and the T_1 value of the liver decreased. Larger changes of the T_1 value in the liver were observed in the experiments with **6** (ΔT_1 = 241 and 353 ms) than in those with **1** (ΔT_1 = 70 and 151 ms), although accumulation of both compounds in the liver was observed in the fluorescence images (Supporting Information Figure S4). The changes of the T_1 values in the liver were small when Gd-DTPA was administered (ΔT_1 = 38 and 99 ms), and it was

dx.doi.org/10.1021/bc200127t | *Bioconjugate Chem.* 2011, 22, 2227–2236

considered that Gd-DTPA is nonspecifically distributed all over the body and rapidly eliminated through the kidney.

To clarify the reason **6** showed a higher MR signal in the liver than **1**, we observed the fluorescence images of mouse liver slices by means of confocal fluorescence microscopy. At 30 min after injection of **1** or **6** (5 mM, 100 μL, the same dose used in MRI), mice were sacrificed, and the livers were harvested. Frozen sections were prepared, and fluorescence microscopic images were obtained. Interestingly, the fluorescence intensity of hepatocytes of the mouse injected with **6** was much higher than that in the case of **1** (Figure 8), although

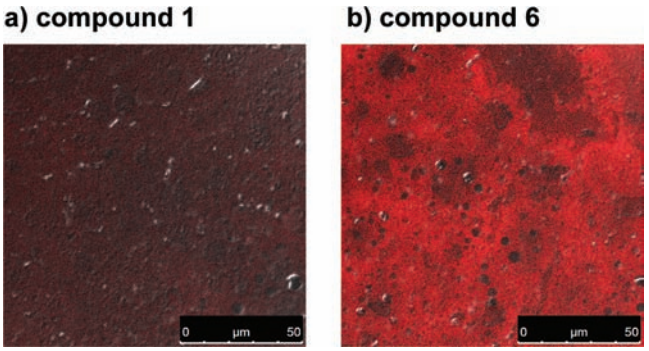

Figure 8. Fluorescence images of liver slices from mice injected with (a) **1** and (b) **6** (5 mM, 100 μL). Ex: 670 nm, Em: 700−800 nm.

the fluorescence intensities of the liver were almost the same after injection of the two compounds at low dose (100 μM, 100 μL, Supporting Information Figure S4). These results indicated that cell-permeable **6** is accumulated in hepatocytes more efficiently than cell-impermeable **1** at high dose (5 mM, 100 μL), and the difference of the MR signal would reflect the difference in the amount of **1** or **6** in the liver due to their biodistribution/excretion pathways.

CONCLUSION

In conclusion, we have developed a novel method for enhancing the cell permeation of Gd^{3+} complexes by using hydrophobic fluorescent dyes as a cell-permeation-promoting unit. We designed and synthesized various fluorescence dye−Gd^{3+} complex conjugates, and found that the Gd^{3+} complexes conjugated with BODIPY and Cy7 dye were efficiently accumulated into cells. We further examined the relationship between cell permeability and chemical structure in a series of **Cy7-Gd**s, and the results showed that a hydrophobic and nonanionic scaffold is favorable for the development of cell-permeable Gd^{3+} complexes. Among the synthesized **Cy7-Gd**s, compound **6** was the best cell-permeable MRI contrast agent. In addition, the behavior of **Cy7-Gd** derivatives in mice was also examined. Our method has the further advantage of enabling easy and detailed observation of the distribution of Gd^{3+} complexes inside cells or tissues by means of fluorescence imaging. This design strategy should be useful for further development of various MRI contrast agents.

ASSOCIATED CONTENT

Supporting Information

Synthetic procedures of **dye-Gd**s and additional fluorescence images. This material is available free of charge via the Internet at http://pubs.acs.org.

AUTHOR INFORMATION

Corresponding Author

*E-mail: tlong@mol.f.u-tokyo.ac.jp.

ACKNOWLEDGMENTS

This research was supported in parts by a Grant-in-Aid for JSPS Fellows (to T.Y.), by the Ministry of Education, Culture, Sports, Science and Technology of Japan (Specially Promoted Research 22000006 to T. N., 20689001, 19890047, and 21659024 to K. H.). K. H. was also supported by Sankyo Foundation of Life Science, the Research Foundation for Pharmaceutical Sciences, Inoue Foundation for Science, The Asahi Glass Foundation and Konica Minolta Science and Technology Foundation. We are grateful to Dr. Michiaki Kumagai for his help with ICP-MS analysis.

REFERENCES

(1) Weissleder, R., and Pittet, M. J. (2008) Imaging in the era of molecular oncology. *Nature 452*, 580−589.

(2) Nakahara, K., Adachi, Y., Osada, T., and Miyashita, Y. (2007) Exploring the neural basis of cognition: multi-modal links between human fMRI and macaque neurophysiology. *Trends Cogn. Sci. 11*, 84−92.

(3) Aime, S., Botta, M., Fasano, M., and Terreno, E. (1999) Prototropic and water-exchange processes in aqueous solutions of Gd(III) chelates. *Acc. Chem. Res. 32*, 941−949.

(4) Louie, A. Y., Huber, M. M., Ahrens, E. T., Rothbacher, U., Moats, R., Jacobs, R. E., Fraser, S. E., and Meade, T. J. (2000) In vivo visualization of gene expression using magnetic resonance imaging. *Nat. Biotechnol. 18*, 321−325.

(5) Hanaoka, K., Kikuchi, K., Urano, Y., and Nagano, T. (2001) Selective sensing of zinc ions with a novel magnetic resonance imaging contrast agent. *J. Chem. Soc., Perkins Trans. 2*, 1840−1843.

(6) Allen, M. J., MacRenaris, K. W., Venkatasubramanian, P. N., and Meade, T. J. (2004) Cellular delivery of MRI contrast agents. *Chem. Biol. 11*, 301−307.

(7) Lewin, M., Carlesso, N., Tung, C. H., Tang, X. W., Cory, D., Scadden, D. T., and Weissleder, R. (2000) Tat peptide-derivatized magnetic nanoparticles allow in vivo tracking and recovery of progenitor cells. *Nat. Biotechnol. 18*, 410−414.

(8) Mishra, R., Su, W., Pohmann, R., Pfeuffer, J., Sauer, M. G., Ugurbil, K., and Engelmann, J. (2009) Cell-penetrating peptides and peptide nucleic acid-coupled MRI contrast agents: evaluation of cellular delivery and target binding. *Bioconjugate Chem. 20*, 1860−1868.

(9) Olson, E. S., Jiang, T., Aguilera, T. A., Nguyen, Q. T., Ellies, L. G., Scadeng, M., and Tsien, R. Y. (2010) Activatable cell penetrating peptides linked to nanoparticles as dual probes for in vivo fluorescence and MR imaging of proteases. *Proc. Natl. Acad. Sci. U. S. A. 107*, 4311−4316.

(10) Frankel, A. D., and Pabo, C. O. (1988) Cellular uptake of the tat protein from human immunodeficiency virus. *Cell 55*, 1189−1193.

(11) Herce, H. D., and Garcia, A. E. (2007) Molecular dynamics simulations suggest a mechanism for translocation of the HIV-1 TAT peptide across lipid membranes. *Proc. Natl. Acad. Sci. U. S. A. 104*, 20805−20810.

(12) Juliano, R. L., Alam, R., Dixit, V., and Kang, H. M. (2009) Cell-targeting and cell-penetrating peptides for delivery of therapeutic and imaging agents. *Wiley Interdiscip. Rev. Nanomed. Nanobiotechnol. 1*, 324−335.

(13) Verdurmen, W. P., and Brock, R. (2011) Biological responses towards cationic peptides and drug carriers. *Trends Pharmacol. Sci. 32*, 116−124.

(14) Futaki, S., Nakase, I., Tadokoro, A., Takeuchi, T., and Jones, A. T. (2007) Arginine-rich peptides and their internalization mechanisms. *Biochem. Soc. Trans. 35*, 784−787.

(15) Endres, P. J., MacRenaris, K. W., Vogt, S., and Meade, T. J. (2008) Cell-permeable MR contrast agents with increased intracellular retention. *Bioconjugate Chem. 19*, 2049−2059.
(16) Digilio, G., Menchise, V., Gianolio, E., Catanzaro, V., Carrera, C., Napolitano, R., Fedeli, F., and Aime, S. (2010) Exofacial protein thiols as a route for the internalization of Gd(III)-based complexes for magnetic resonance imaging cell labeling. *J. Med. Chem. 53*, 4877−4890.
(17) Li, H., Gray, B. D., Corbin, I., Lebherz, C., Choi, H., Lund-Katz, S., Wilson, J. M., Glickson, J. D., and Zhou, R. (2004) MR and fluorescent imaging of low-density lipoprotein receptors. *Acad. Radiol. 11*, 1251−1259.
(18) Huber, M. M., Staubli, A. B., Kustedjo, K., Gray, M. H., Shih, J., Fraser, S. E., Jacobs, R. E., and Meade, T. J. (1998) Fluorescently detectable magnetic resonance imaging agents. *Bioconjugate Chem. 9*, 242−249.
(19) Montgomery, C. P., Murray, B. S., New, E. J., Pal, R., and Parker, D. (2009) Cell-penetrating metal complex optical probes: targeted and responsive systems based on lanthanide luminescence. *Acc. Chem. Res. 42*, 925−937.
(20) New, E. J., Congreve, A., and Parker, D. (2010) Definition of the uptake mechanism and sub-cellular localisation profile of emissive lanthanide complexes as cellular optical probes. *Chem. Sci. 1*, 111−118.
(21) Mishra, A., Pfeuffer, J., Mishra, R., Engelmann, J., Mishra, A. K., Ugurbil, K., and Logothetis, N. K. (2006) A new class of Gd-based DO3A-ethylamine-derived targeted contrast agents for MR and optical imaging. *Bioconjugate Chem. 17*, 773−780.
(22) Caravan, P., Ellison, J. J., McMurry, T. J., and Lauffer, R. B. (1999) Gadolinium(III) chelates as MRI contrast agents: Structure, dynamics, and applications. *Chem. Rev. 99*, 2293−2352.
(23) Lauffer, R. B., Parmelee, D. J., Dunham, S. U., Ouellet, H. S., Dolan, R. P., Witte, S., McMurry, T. J., and Walovitch, R. C. (1998) MS-325: Albumin-targeted contrast agent for MR angiography. *Radiology 207*, 529−538.
(24) Kawabata, E., Kikuchi, K., Urano, Y., Kojima, H., Odani, A., and Nagano, T. (2005) Design and synthesis of zinc-selective chelators for extracellular applications. *J. Am. Chem. Soc. 127*, 818−819.
(25) Sibrian-Vazquez, M., Ortiz, J., Nesterova, I. V., Fernandez-Lazaro, F., Sastre-Santos, A., Soper, S. A., and Vicente, M. G. (2007) Synthesis and properties of cell-targeted Zn(II)-phthalocyanine-peptide conjugates. *Bioconjugate Chem. 18*, 410−420.
(26) Olmedilla, L., Perez-Pena, J. M., Ripoll, C., Garutti, I., de Diego, R., Salcedo, M., Jimenez, C., and Banares, R. (2009) Early noninvasive measurement of the indocyanine green plasma disappearance rate accurately predicts early graft dysfunction and mortality after deceased donor liver transplantation. *Liver Transpl. 15*, 1247−1253.
(27) Abe, T., Kakyo, M., Tokui, T., Nakagomi, R., Nishio, T., Nakai, D., Nomura, H., Unno, M., Suzuki, M., Naitoh, T., Matsuno, S., and Yawo, H. (1999) Identification of a novel gene family encoding human liver-specific organic anion transporter LST-1. *J. Biol. Chem. 274*, 17159−17163.
(28) Yamada, T., Yoshikawa, M., Kanda, S., Kato, Y., Nakajima, Y., Ishizaka, S., and Tsunoda, Y. (2002) In vitro differentiation of embryonic stem cells into hepatocyte-like cells identified by cellular uptake of indocyanine green. *Stem Cells 20*, 146−154.

Supporting Information

"A Method for Enhancing Cell-penetration of Gd^{3+}-based MRI Contrast Agents by Conjugation with Hydrophobic Fluorescent Dyes" (Bioconjugate Chemistry)

Takehiro Yamane,[†,‡] Kenjiro Hanaoka,[†,‡] Yasuaki Muramatsu,[†,‡] Keita Tamura,[§] Yusuke Adachi,[§] Yasushi Miyashita,[§] Yasunobu Hirata,[#] and Tetsuo Nagano[†,‡,*]

[†]Graduate School of Pharmaceutical Sciences, The University of Tokyo, 7-3-1 Hongo, Bunkyo-ku, Tokyo 113-0033, Japan, [‡]CREST, Japan Science and Technology Agency, 5, Sanbancho, Chiyoda-ku, Tokyo 102-0075, Japan, [§]Department of Physiology, The University of Tokyo School of Medicine, 7-3-1 Hongo, Bunkyo-ku, Tokyo 113-0033, Japan, and [#]Department of Cardiovascular Medicine, The University of Tokyo Hospital, 7-3-1, Hongo, Bunkyo-ku, Tokyo 113-0033, Japan.

E-mail: tlong@mol.f.u-tokyo.ac.jp

Experimental Procedures and Characterization of Compounds

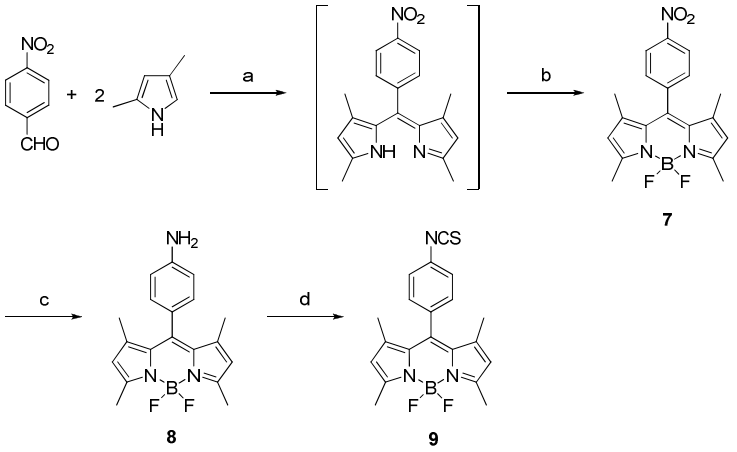

Scheme S1. Synthesis of BODIPY isothiocyanate. (a) (1) TFA, CH_2Cl_2, r.t., (2) chloranil, r.t.; (b) $BF_3 \cdot Et_2O$, TEA, toluene, r.t.; (c) Pd/C, CH_2Cl_2/MeOH, r.t., under H_2; (d) thiophosgene, Na_2CO_3, DMF, 0 ºC to r.t.

Synthesis of compounds 7 and 8: see reference S1.

Synthesis of compound 9: Compound **8** (101 mg, 0.30 mmol) and Na_2CO_3 (151 mg, 1.4 mmol) were dissolved in 25 mL of DMF. The resulting mixture was cooled at 0 ºC, and thiophosgene (100 μL, 1.3 mmol) was added dropwise under an argon atmosphere. The reaction mixture was warmed to room temperature and stirred for 2 h. The solvent was removed by evaporation, and the residue was purified by column chromatography (silica gel 60, CH_2Cl_2/hexane, 1:2) to afford compound **9** as an orange solid (113 mg, 99%). ^{1}H NMR (400 MHz, $CDCl_3$): δ 1.40 (s, 6H); 2.56 (s, 6H); 6.00 (s, 2H); 7.30 (d, 2H, ***J*** = 8.8 Hz); 7.37 (d, 2H, ***J*** = 8.8 Hz); ^{13}C NMR (100 MHz, $CDCl_3$): δ 14.6, 14.7, 121.5, 126.5, 129.6, 131.1, 132.3, 134.0, 137.1, 139.8, 142.8, 156.0; HRMS (ESI^+): Calcd for $[M+H]^+$, 382.1361; Found, 382.1326.

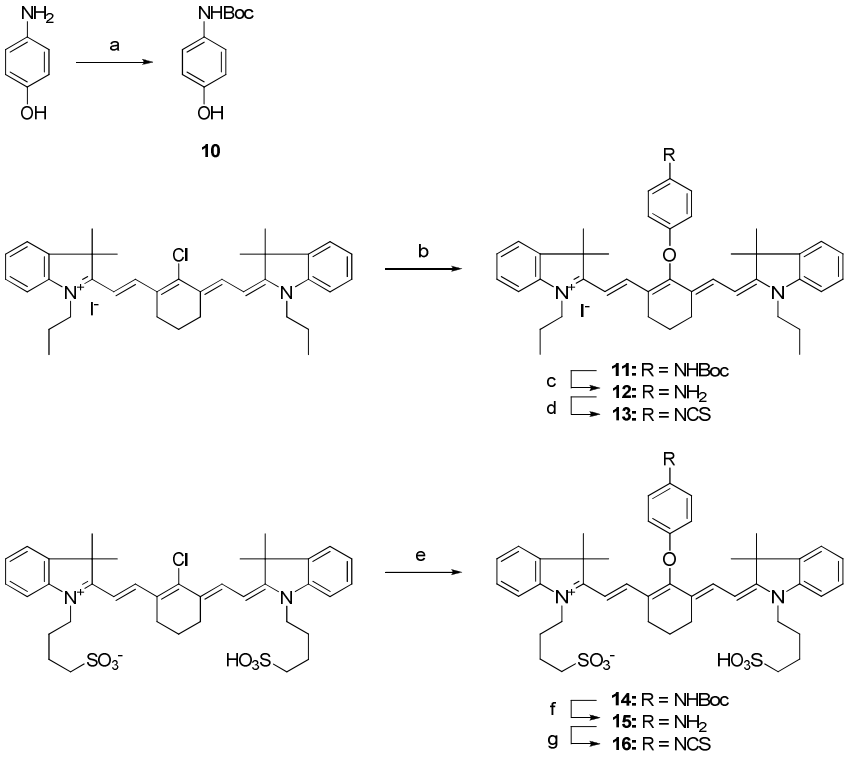

Scheme S2. Synthesis of Cy7 isothiocyanate. (a) Boc_2O, TEA, MeOH, r.t.; (b) **10**, NaH, DMF, r.t.; (c) TFA, CH_2Cl_2 / MeOH, r.t.; (d) thiophosgene, Na_2CO_3, DMF, 0 ºC to r.t.; (e) **10**, NaH, DMF, r.t.; (f) TFA, r.t.; (g) thiophosgene, Na_2CO_3, DMF, 0 ºC to r.t.

Synthesis of compound 10: 4-Aminophenol (327 mg, 3.0 mmol) and triethylamine (TEA, 630 μL, 4.5 mmol) were dissolved in 15 mL of MeOH. Boc_2O (786 mg, 3.6 mmol) was added, and the mixture was stirred for 4 h at room temperature. The solvent was removed by evaporation, and the residue was purified by column chromatography (silica gel 60, CH_2Cl_2/MeOH, 19:1) to afford compound **10** as a colorless solid (615 mg, 98%). ^{1}H NMR (300 MHz, $CDCl_3$): δ 1.51 (s, 9H), 5.54 (s, 1H), 6.36 (br s, 1H), 6.75 (d, ***J*** = 8.8 Hz, 2H), 7.18 (d, ***J*** = 8.8 Hz, 2H); ^{13}C NMR (75 MHz, CD_3OD): δ 28.7, 80.5, 116.2, 122.2, 132.3, 154.4, 155.9; HRMS (ESI$^-$): Calcd for [M-I]$^-$, 208.0974; Found, 208.0982.

Synthesis of compound 11: Compound **10** (126 mg, 0.60 mmol) was dissolved in 15 mL of DMF. Sodium hydride (60% in oil, 24 mg, 0.60 mmol) was added, and the mixture was stirred for 10 min at room temperature under an argon atmosphere. IR-780 iodide (Aldrich, 200 mg, 0.30 mmol) was added to the mixture, and stirring was continued overnight. The solvent was removed by evaporation, and the residue was purified by column chromatography (NH silica, CH_2Cl_2/MeOH, 19:1) to afford **11** as a purple solid (184 mg, 73%). ^{1}H NMR (300 MHz, $CDCl_3$): δ 1.05 (t, ***J*** = 7.4 Hz, 6H), 1.36 (s, 12H), 1.50 (s, 9H), 1.87 (sex, ***J*** = 7.4 Hz, 4H), 2.05 (t, ***J*** = 5.5 Hz, 2H), 2.72 (t, ***J*** = 5.5 Hz, 4H), 4.05 (t, ***J*** = 7.4 Hz, 4H), 6.05 (d, ***J*** = 14.3 Hz, 2H), 6.80 (br s, 1H), 6.99 (d, ***J*** = 9.0 Hz, 2H), 7.09 (d, ***J*** = 7.7 Hz, 2H), 7.20 (d, ***J*** = 7.7 Hz, 2H), 7.27 (d, ***J*** = 6.8 Hz, 2H), 7.34 (d, ***J*** = 6.8 Hz, 2H), 7.47 (d, ***J*** = 9.0 Hz, 2H), 7.91 (d, ***J*** = 14.3 Hz, 2H); ^{13}C NMR (75 MHz, $CDCl_3$): δ 11.6, 20.8, 21.1, 24.6, 27.9, 28.3, 46.1, 49.0, 80.4, 100.0, 110.5, 114.8, 120.6, 122.2, 122.5, 125.0, 128.6, 133.4, 141.0, 142.1, 153.0, 155.5, 164.5, 172.0; HRMS (ESI$^+$): Calcd for [M−I]$^+$, 712.4478; Found, 712.4478.

Synthesis of compound 12: Compound **11** (118 mg, 0.14 mmol) was dissolved in 2.5 mL of CH_2Cl_2, then 0.5 mL of trifluoroacetic acid (TFA) was added, and the mixture was stirred for 2 h at room temperature. The solvent was removed by evaporation. The residue was purified by column chromatography (NH silica, CH_2Cl_2/MeOH, 9:1) to afford **12** as a purple solid (99 mg, 95%). ^{1}H NMR (300 MHz, $CDCl_3$): δ 1.03 (t, ***J*** = 7.4 Hz, 6H), 1.38 (s, 12H), 1.86 (sex, ***J*** = 7.4 Hz, 4H), 2.02 (t, ***J*** = 5.8 Hz, 2H), 2.67 (t, ***J*** = 5.8 Hz, 4H), 4.00 (t, ***J*** = 7.4 Hz, 4H), 6.01 (d, ***J*** = 14.3 Hz, 2H), 6.70 (d, ***J*** = 8.8 Hz, 2H), 6.85 (d, ***J*** = 8.8 Hz, 2H), 7.06 (d, ***J*** = 7.6 Hz, 2H), 7.19 (d, ***J*** = 7.6 Hz, 2H), 7.27 (d, ***J*** =

6.4 Hz, 2H), 7.34 (td, ***J*** = 7.6, 1.2 Hz, 2H), 7.96 (d, ***J*** = 14.3 Hz, 2H); ^{13}C NMR (75 MHz, $CDCl_3$): δ 11.6, 20.7, 21.1, 24.4, 27.9, 45.9, 49.0, 99.7, 110.5, 115.0, 116.7, 122.1, 122.6, 124.9, 128.5, 141.0, 141.7, 142.2, 142.4, 153.2, 165.3, 171.9; HRMS (ESI^+): Calcd for $[M-I]^+$, 612.3954; Found, 612.3963.

Synthesis of compound 13: Synthetic procedure was the same as for **9**. Purification of the reaction mixture was carried out by column chromatography (silica gel 60, CH_2Cl_2/MeOH, 9:1) to afford **13** as a purple solid (34 mg, 75%). ^{1}H NMR (300 MHz, $CDCl_3$): δ 1.04 (t, ***J*** = 7.4 Hz, 6H), 1.35 (s, 12H), 1.86 (sex, ***J*** = 7.4 Hz, 4H), 2.04 (t, ***J*** = 5.8 Hz, 2H), 2.72 (t, ***J*** = 5.8 Hz, 4H), 4.07 (t, ***J*** = 7.4 Hz, 4H), 6.13 (d, ***J*** = 14.3 Hz, 2H), 7.06 (d, ***J*** = 8.8 Hz, 2H), 7.09 (d, ***J*** = 8.8 Hz, 2H), 7.17-7.28 (m, 6H), 7.36 (t, ***J*** = 7.6 Hz, 2H), 7.79 (d, ***J*** = 14.3 Hz, 2H); ^{13}C NMR (100 MHz, DMSO-$\boldsymbol{d}_6$): δ 11.1, 20.4, 20.6, 23.7, 27.2, 44.9, 48.6, 100.5, 111.4, 115.9, 121.1, 122.5, 123.9, 124.9, 128.3, 128.5, 132.6, 140.3, 140.9, 142.1, 158.4, 161.5, 171.8; HRMS (ESI^+): Calcd for $[M-I]^+$, 654.3518; Found, 654.3503.

Synthesis of compound 14: Synthetic procedure was the same as for **11**. Purification of the reaction mixture was carried out by column chromatography (Silica gel 60, CH_2Cl_2/MeOH, 2:1) to afford **14** as a purple solid (176 mg, 89%). ^{1}H NMR (300 MHz, CD_3OD): δ 1.26 (s, 12H), 1.39 (s, 9H), 1.83 (br s, 8H), 1.93 (br s, 2H), 2.65 (br s, 4H), 2.78 (t, ***J*** = 6.8 Hz, 4H), 4.03 (br s, 4H), 6.08 (d, ***J*** = 14.3 Hz, 2H), 6.93 (d, ***J*** = 9.2 Hz, 2H), 7.09 (t, ***J*** = 7.3 Hz, 2H), 7.18 (d, ***J*** = 7.7 Hz, 2H), 7.24-7.33 (m, 6H), 7.90 (d, ***J*** = 14.3 Hz, 2H), 8.79 (s, 1H); ^{13}C NMR (75 MHz, CD_3OD): δ 22.5, 23.6, 25.2, 27.2, 28.2, 28.7, 44.8, 50.2, 51.8, 80.7, 101.1, 112.0, 115.9, 121.7, 123.3, 123.6, 126.1, 129.7, 135.4, 142.5, 143.5, 143.6, 155.3, 157.0, 165.6, 173.6; HRMS (ESI^+): Calcd for $[M+Na]^+$, 944.3566; Found, 944.3530.

Synthesis of compound 15: Compound **14** (176 mg, 0.19 mmol) was dissolved in 2.5 mL of TFA, and the solution was stirred for 30 min at room temperature. TFA was removed by evaporation, and the residue was purified by column chromatography (silica gel 60, CH_2Cl_2/MeOH, 7:3) to afford **15** as a purple solid (168 mg, quant.). ^{1}H NMR (300 MHz, CD_3OD): δ 1.27 (s, 12H), 1.82 (br s, 8H), 1.92 (t, ***J*** = 5.3 Hz, 2H), 2.63 (t, ***J*** = 5.3 Hz, 4H), 2.76 (t, ***J*** = 6.8 Hz, 4H), 4.02 (t, ***J*** = 6.8 Hz, 4H), 6.08 (d, ***J*** =

14.3 Hz, 2H), 6.89 (d, ***J*** = 9.2 Hz, 2H), 6.93 (d, ***J*** = 9.2 Hz, 2H), 7.09 (t, ***J*** = 7.5 Hz, 2H), 7.19 (d, ***J*** = 7.5 Hz, 2H), 7.25 (d, ***J*** = 7.5 Hz, 2H), 7.27 (d, ***J*** = 7.5 Hz, 2H), 7.89 (d, ***J*** = 14.3 Hz, 2H); ^{13}C NMR (100 MHz, CD_3OD): δ 22.5, 23.6, 25.3, 27.2, 28.2, 44.9, 50.3, 51.8, 101.1, 112.1, 116.8, 121.6, 123.3, 123.6, 126.1, 129.8, 136.5, 142.4, 143.4, 143.7, 157.4, 165.6, 173.6; HRMS (ESI$^+$): Calcd for $[M+Na]^+$, 844.3042; Found, 844.3006.

Synthesis of compound 16: Synthetic procedure was the same as for **13**. Purification of the reaction mixture was carried out by column chromatography (Silica gel 60, CH_2Cl_2/MeOH, 2:1) to afford **16** as a purple solid (114 mg, >99%). ^{1}H NMR (300 MHz, DMSO-***d*$_6$**): δ 1.22 (s, 12H), 1.67 (br s, 8H), 1.88 (br s, 2H), 2.44 (br s, 4H), 2.67 (br s, 4H), 4.08 (br s, 4H), 6.19 (d, ***J*** = 14.3 Hz, 2H), 7.14 (t, ***J*** = 7.0 Hz, 2H), 7.20 (d, ***J*** = 8.4 Hz, 2H), 7.31 (t, ***J*** = 7.5 Hz, 2H), 7.35 (d, ***J*** = 8.4 Hz, 2H), 7.45 (d, ***J*** = 7.5 Hz, 4H), 7.67 (d, ***J*** = 14.3 Hz, 2H); ^{13}C NMR (100 MHz, CD_3OD): δ 22.4, 23.6, 25.2, 27.2, 28.2, 44.9, 50.3, 51.8, 101.4, 112.2, 117.3, 123.1, 123.4, 126.2, 126.8, 128.9, 129.8, 136.7, 142.5, 142.9, 143.6, 160.0, 164.3, 173.7; HRMS (ESI$^+$): Calcd for $[M+Na]^+$, 886.2606; Found, 886.2579.

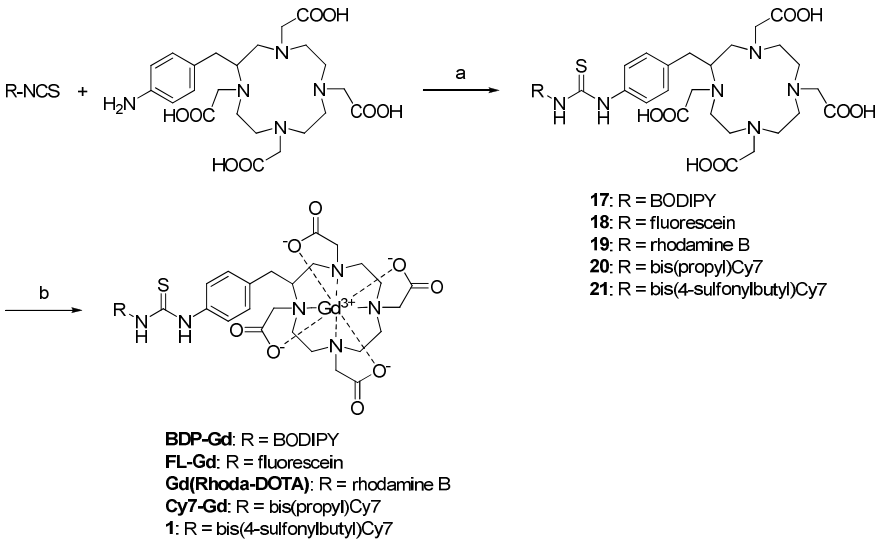

Scheme S3. Synthesis of **dye-Gd**s. (a) DIEA or TEA, MeOH or DMF, r.t.; (b) $GdCl_3$, 1.0 M HEPES buffer (pH 7.4), r.t.

Synthesis of compound 17: Compound **9** (101 mg, 0.27 mmol) and ***N*,*N***-diisopropylethylamine (DIEA, 92 μL, 0.53 mmol) were dissolved in 30 mL of

DMF. A solution of ***p***-NH_2-Bn-DOTA (160 mg, 0.32 mmol) in 10 mL of DMF was added, and the mixture was stirred for 24 h at room temperature. The solvent was removed by evaporation, and the residue was purified by preparative HPLC (gradient, A/B = 50/50 to 0/100, 20 min, solvent A: H_2O with 0.1% TFA; solvent B: CH_3CN/H_2O = 80/20 with 0.1% TFA) to afford **17** as an orange solid (222 mg, 94%). ^{1}H NMR (400 MHz, CD_3OD): δ 1.49 (s, 6H); 2.48 (s, 6H); 2.54-4.91 (m, 25H); 6.06 (s, 2H); 7.28 (d, 2H, ***J*** = 8.8 Hz); 7.32 (d, 2H, ***J*** = 8.3 Hz); 7.49 (d, 2H, ***J*** = 8.8 Hz); 7.72 (d, 2H, ***J*** = 8.3 Hz); ^{13}C NMR (100 MHz, CD_3OD): δ 14.6, 15.0, 32.8, 49.7, 49.8, 50.1, 51.3, 52.8, 53.8, 55.0, 57.1, 57.3, 57.5, 57.7, 116.6, 119.5, 122.2, 122.5, 125.8, 126.2, 129.6, 129.7, 130.7, 132.6, 132.8, 139.5, 141.8, 143.3, 144.7, 156.7, 182.2; HRMS (ESI^+): Calcd for $[M+H]^+$, 891.3846; Found, 891.3889.

Synthesis of compound 18: Fluorescein isothiocyanate (40 mg, 0.10 mmol), ***p***-NH_2-Bn-DOTA (55 mg, 1.1 mmol) and TEA (142 μL, 1.0 mmol) were dissolved in 4 mL of MeOH, and the mixture was stirred for 24 h at room temperature. The solvent was removed by evaporation, and the residue was purified by preparative HPLC (gradient, A/B = 80/20 to 0/100, 30 min) to afford **18** as a yellow solid (62 mg, 65%). ^{1}H NMR (400 MHz, CD_3OD): δ 2.58-4.32 (m, 25H), 6.57 (dd, ***J*** = 8.8, 2.4 Hz, 2H), 6.67(d, ***J*** = 8.8 Hz, 2H), 6.68 (d, ***J*** = 2.4 Hz, 2H), 7.19 (d, ***J*** = 8.4 Hz, 1H), 7.33 (d, ***J*** = 8.3 Hz, 2H), 7.50 (d, ***J*** = 8.3 Hz, 2H), 7.83 (dd, ***J*** = 8.3, 2.0 Hz, 1H), 8.21 (d, ***J*** = 2.0 Hz, 1H); ^{13}C NMR (100 MHz, CD_3OD): δ 103,5, 111.6, 113.9, 120.8, 125.8, 126.4, 129.0, 130.4, 130.7, 132.4, 142.6, 154.4, 161.8, 171.0; HRMS (ESI^+): Calcd for $[M+H]^+$, 899.2922; Found, 899.2919.

Synthesis of compound 19: Rhodamine B isothiocyanate (mixture of isomers, 59 mg, 0.11 mmol), ***p***-NH_2-Bn-DOTA (51 mg, 0.10 mmol) and TEA (138 μL, 1.0 mmol) were dissolved in 8 mL of MeOH, and the mixture was stirred for 24 h at room temperature. The solvent was removed by evaporation, and the residue was purified by preparative HPLC (gradient, A/B = 70/30 to 0/100, 30 min). The desired isomer was eluted after another isomer (elution time: 11.0 min and 12.2 min). Compound **19** was obtained as a red solid (29 mg, 59%). ^{1}H NMR (300 MHz, CD_3OD): δ 1.30 (t, ***J*** = 7.0 Hz, 12H), 2.58-4.32 (m, 25H), 3.67 (q, ***J*** = 7.0 Hz, 8H), 6.97(d, ***J*** = 2.4 Hz, 2H), 7.04 (dd, ***J*** = 9.6, 2.4 Hz, 2H), 7.25 (d, ***J*** = 9.6 Hz, 2H), 7.35 (d, ***J*** = 6.8 Hz, 2H), 7.36 (d, ***J*** = 8.3 Hz, 1H),

7.54 (d, ***J*** = 6.8 Hz, 2H), 8.07 (dd, ***J*** = 8.3, 2.4 Hz, 1H), 8.18 (d, ***J*** = 2.4 Hz, 1H); ^{13}C NMR (100 MHz, CD_3OD): δ 12.8, 46.8, 97.2, 115.0, 115.3, 119.6, 122.8, 126.3, 130.7, 131.7, 132.5, 132.6, 132.8, 157.1, 159.3, 161.0, 162.6, 162.9, 167.8, 182.3; HRMS (ESI^+): Calcd for $[M-CF_3COO^-]^+$, 1009.4494; Found, 1009.4471.

Synthesis of compound 20: Synthetic procedure was the same as for **18**. Purification of the reaction mixture was carried out by preparative HPLC (gradient, A/B = 60/40 to 0/100, 30 min) to afford **20** as a green solid (42 mg, 62%). ^{1}H NMR (300 MHz, $CDCl_3$): δ 1.01 (t, ***J*** = 7.4 Hz, 6H), 1.39 (s, 12H), 1.83 (sex, ***J*** = 7.4 Hz, 4H), 2.05 (t, ***J*** = 5.8 Hz, 2H), 2.60-4.30 (m, 25H), 2.74 (t, ***J*** = 5.8 Hz, 4H), 4.07 (t, ***J*** = 7.4 Hz, 4H), 6.16 (d, ***J*** = 14.3 Hz, 2H), 7.12 (d, ***J*** = 8.8 Hz, 2H), 7.20 (t, ***J*** = 7.6 Hz, 2H), 7.24-7.49 (m, 12H), 8.01 (d, ***J*** = 14.3 Hz, 2H); ^{13}C NMR (100 MHz, CD_3OD): δ 11.6, 21.8, 22.4, 25.2, 28.5, 46.4, 50.4, 101.1, 112.1, 115.8, 123.1, 123.3, 126.2, 126.3, 128.7, 129.7, 130.7, 135.3, 142.5, 143.3, 143.7, 159.0, 173.9, 182.7; ; HRMS (ESI^+): Calcd for $[M+H]^+$, 1163.6004; Found, 1163.5995.

Synthesis of compound 21: Synthetic procedure was the same as for **18**. Purification of the reaction mixture was carried out by preparative HPLC (gradient, A/B = 60/40 to 0/100, 30 min) to afford **21** as a green solid (20 mg, 46%). ^{1}H NMR (300 MHz, DMSO-***d*$_6$**): δ 1.31 (s, 12H), 1.69 (br s, 8H), 1.93 (br s, 2H), 2.43-4.37 (m, 37H), 6.22 (d, ***J*** = 14.3 Hz, 2H), 7.11-7.25 (m, 6H), 7.32-7.49 (m, 10H), 7.82 (d, ***J*** = 14.3 Hz, 2H), 7.45 (d, ***J*** = 7.5 Hz, 4H), 9.75 (s, 1H), 9.77 (s, 1H); ^{13}C NMR (100 MHz, DMSO-***d*$_6$**): δ 20.8, 22.5, 23.8, 26.0, 27.3, 27.5, 43.6, 48.6, 50.8, 100.3, 111.4, 114.1, 121.6, 122.3, 123.4, 124.7, 126.2, 128.5, 129.2, 134.0, 138.1, 140.8, 141.0, 142.1, 156.4, 162.7, 171.5, 179.6; HRMS (ESI⁻): Calcd for $[M-H]^-$, 1349.5297; found, 1349.5247.

General synthetic procedure of dye-Gds: The conjugate of fluorescent dye and DOTA was dissolved in 1.0 M HEPES buffer (pH 7.4). $GdCl_3 \cdot 6H_2O$ (1.5−2.0 eq.) was added to the solution, and the mixture was stirred at room temperature overnight. The reaction mixture was purified by preparative HPLC.

BDP-Gd: Orange solid (27 mg, 12%). HRMS (ESI^-): Calcd for $[M-H]^-$, 1044.2696; Found, 1044.2738; HPLC analysis: retention time, 14.7 min; purity, 99.7% integrated

intensity (eluent: A/B = 80/20 to 0/100, 20 min; flow rate = 1.0 mL/min; detection wavelength, 500 nm).

FL-Gd: Yellow solid (9.9 mg, 87%). HRMS (ESI^-): Calcd for $[M-H]^-$, 1052.1772; Found, 1052.1819; HPLC analysis: retention time, 9.2 min; purity, 99.9% integrated intensity (eluent: A/B = 80/20 to 0/100, 20 min; flow rate = 1.0 mL/min; detection wavelength, 450 nm).

Gd(Rhoda-DOTA): Red solid (10.0 mg, 40%). HRMS (ESI^-): Calcd for $[M-H]^-$, 1162.3343; Found, 1162.3362; HPLC analysis: retention time, 12.2 min; purity, 99.6% integrated intensity (eluent: A/B = 80/20 to 0/100, 20 min; flow rate = 1.0 mL/min; detection wavelength, 550 nm).

Cy7-Gd: Green solid (7.0 mg, 62%). HRMS (ESI^-): Calcd for $[M+CF_3COO^-]^-$, 1430.4782; found, 1430.4831; HPLC analysis: retention time, 15.1 min; purity, 99.8% integrated intensity (eluent: A/B = 50/50 to 0/100, 20 min; flow rate = 1.0 mL/min; detection wavelength, 780 nm).

Compound 1: Green solid (8.9 mg, 46%). HRMS (ESI^-): Calcd for $[M-H]^-$, 1504.4303; found, 1504.4348; HPLC analysis: retention time, 11.4 min; purity, 99.7% integrated intensity (eluent: A/B = 80/20 to 0/100, 20 min; flow rate = 1.0 mL/min; detection wavelength, 780 nm).

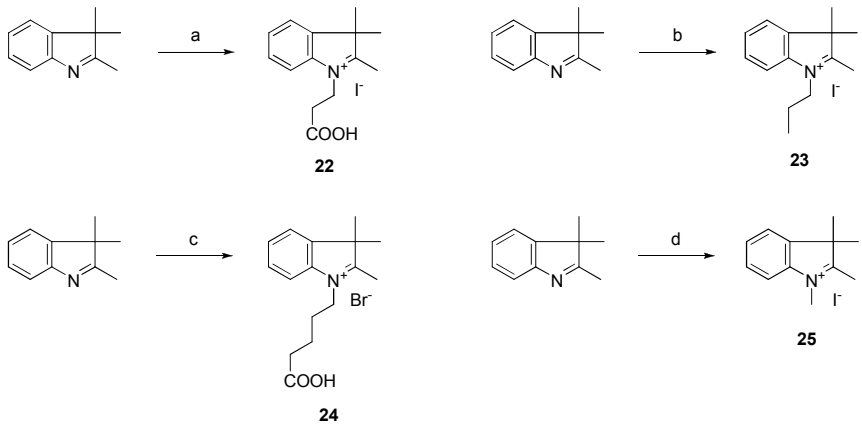

Scheme S4. Synthesis of indolenium salts. (a) 3-iodopropanoic acid, neat, 95 ºC; (b) 1-iodopropane, $CHCl_3$, reflux; (c) 5-bromovaleric acid, neat, 100 ºC; (d) iodomethane, $CHCl_3$, reflux.

Synthesis of compound 22: Neat 2,3,3-trimethylindolenine (3.22 mL, 20 mmol) and 3-iodopropanoic acid (4.0 g, 20 mmol) were stirred for 5 h at 95 ºC. The reaction mixture was cooled to room temperature, and the product was reprecipitated from acetone and diethyl ether to afford **22** as pale yellow plates (5.8 g, 80%). ^{1}H NMR (300 MHz, DMSO-***d*$_6$**): δ 1.53 (s, 6H), 2.87 (s, 3H), 2.98 (t, ***J*** = 7.0 Hz, 2H), 4.65 (t, ***J*** = 7.0 Hz, 2H), 7.62 (dd, ***J*** = 5.9, 2.9 Hz, 2H), 7.85 (dd, ***J*** = 5.9, 2.9 Hz, 1H), 8.00 (dd, ***J*** = 5.9, 2.9 Hz, 2H), 12.75 (br s, 1H); ^{13}C NMR (75 MHz, DMSO-***d*$_6$**): δ 14.4, 21.9, 31.1, 43.5, 54.3, 115.6, 123.5, 128.9, 129.3, 140.8, 141.7, 171.6, 197.9; HRMS (ESI$^+$): Calcd for $[M-I]^+$, 232.1338; found, 232.1374.

Synthesis of compound 23: 2,3,3-Trimethylindolenine (3.22 mL, 20 mmol) and 1-iodopropane (1.94 mL, 20 mmol) were dissolved in 6 mL of $CHCl_3$, and the mixture was heated to reflux in the dark under an argon atmosphere. The reaction mixture was stirred overnight, then cooled to room temperature, and the solvent was removed by evaporation. The residue was reprecipitated from acetone and diethyl ether to afford **23** as pale yellow needles (4.8 g, 73%). ^{1}H NMR (300 MHz, DMSO-***d*$_6$**): δ 1.00 (t, ***J*** = 7.3 Hz, 3H), 1.55 (s, 6H), 1.89 (sex, ***J*** = 7.3 Hz, 2H), 2.87 (s, 3H), 4.46 (t, ***J*** = 7.3 Hz, 2H), 7.62-7.65 (m, 2H), 7.85-7.87 (m, 1H), 7.99-8.03 (m, 1H); ^{13}C NMR (75 MHz, DMSO-***d*$_6$**): δ 10.7, 14.0, 20.7, 22.0, 48.8, 54.1, 115.5, 123.5, 128.9, 129.4, 141.0, 141.8, 196.5; HRMS (ESI$^+$): Calcd for $[2M+I]^+$, 531.2236; found, 531.2221.

Synthesis of compound 24: Neat 2,3,3-trimethylindolenine (3.22 mL, 20 mmol) and 3-iodovaleric acid (3.6 g, 20 mmol) were stirred overnight at 100 ºC. The reaction mixture was cooled to room temperature, and the product was recrystallized from CH_3CN to afford **24** as a pale red solid (2.1 g, 31%). ^{1}H NMR (300 MHz, DMSO-***d*$_6$**): δ 1.54 (s, 6H), 1.65 (quin, ***J*** = 7.3 Hz, 2H), 1.86 (quin, ***J*** = 7.3 Hz, 2H), 2.31 (t, ***J*** = 7.3 Hz, 2H), 2.85 (s, 3H), 4.49 (t, ***J*** = 7.3 Hz, 2H), 7.60-7.66 (m, 2H), 7.82-7.89 (m, 1H), 7.97-8.02 (m, 1H); ^{13}C NMR (75 MHz, DMSO-***d*$_6$**): δ 14.0, 21.4, 22.0, 26.6, 33.0, 47.2, 54.1, 115.4, 123.5, 128.9, 129.4, 141.1, 141.9, 174.0, 196.6; HRMS (ESI^+): Calcd for $[M-I]^+$, 260.1651; found, 260.1634.

Synthesis of compound 25: 2,3,3-Trimethylindolenine (3.22 mL, 20 mmol) and iodomethane (1.25 mL, 20 mmol) were dissolved in 6 mL of $CHCl_3$, and the mixture was heated to reflux in the dark under an argon atmosphere. The reaction mixture was stirred for 4 h, then cooled to room temperature, and the solvent was removed by evaporation. The residue was washed with acetone to afford **25** as a pale red solid (4.1 g, 69%). ^{1}H NMR (300 MHz, DMSO-***d*$_6$**): δ 1.54 (s, 6H), 2.78 (s, 3H), 3.98 (s, 3H), 7.59-7.66 (m, 2H), 7.82-7.85 (m, 1H), 7.90-7.93 (m, 1H); ^{13}C NMR (75 MHz, DMSO-***d*$_6$**): δ 14.1, 21.6, 34.7, 53.9, 115.1, 123.2, 128.7, 129.2, 141.5, 142.0, 195.9; HRMS (ESI^+): Calcd for $[2M+I]^+$, 475.1610; found, 475.1590.

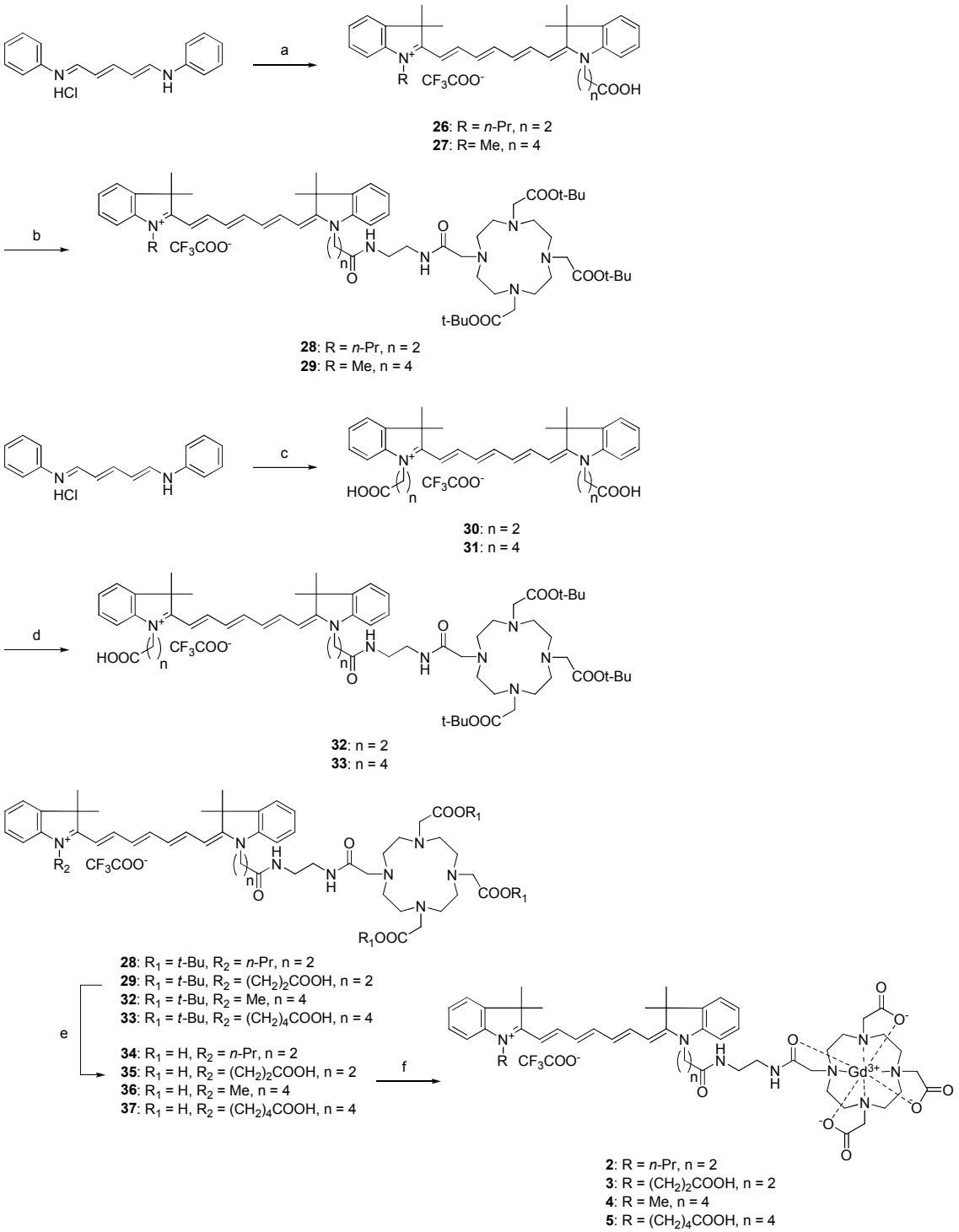

Scheme S5. Synthesis of Cy7-DO3A conjugates. (a) (1) **22** or **24**, AcOH, Ac_2O, reflux, (2) **23** or **25**, AcOK, Ac_2O, r.t.; (b) (1) DCC, NHS, DMF, r.t., (2) 2-aminoethyl-mono-amide-DOTA-tris(***t***-Bu ester), r.t.; (c) **23** or **25**, AcOK, Ac_2O, r.t.; (d) 2-aminoethyl-mono-amide-DOTA-tris(***t***-Bu ester), DCC, HOBt, DIEA, DMF, r.t.; (e) TFA, r.t.; (f) $GdCl_3$, 1.0 M HEPES buffer (pH 7.4), r.t.

Synthesis of compound 26: Glutaconaldehyde dianil monohydrochloride (1.79 g, 6.3 mmol) was dissolved in 20 mL of AcOH and 20 mL of Ac_2O. Compound **22** (2.2 g, 6 mmol) was added to the mixture, and whole was heated to reflux under an argon atmosphere. The reaction mixture was stirred for 30 min, then cooled to room temperature, and the solvent was removed by evaporation. The residue was dissolved in 25 mL of Ac_2O, and **23** (2.17 g, 6.6 mmol) and potassium acetate (2.0 g, 20 mmol) were added. The mixture was stirred overnight at room temperature. The solvent was removed by evaporation, and the residue was purified by column chromatography (NH silica, gradient, CH_2Cl_2 to CH_2Cl_2/MeOH, 19:1) and preparative HPLC (gradient, A/B, 50/50 to 0/100, 30 min) to afford **26** as a red solid (943 mg, 32%). ^{1}H NMR (400 MHz, DMSO-***d*$_6$**): δ 0.95 (t, ***J*** = 7.3 Hz, 3H), 1.61 (s, 6H), 1.63 (s, 6H), 1.73 (sex, ***J*** = 7.3 Hz, 2H), 2.67 (t, ***J*** = 7.3 Hz, 2H), 4.08 (t, ***J*** = 7.3 Hz, 2H), 4.24 (t, ***J*** = 7.3 Hz, 2H), 6.30 (d, ***J*** = 13.7 Hz, 1H), 6.47 (d, ***J*** = 13.2 Hz, 1H), 6.51 (t, ***J*** = 13.2 Hz, 1H), 6.56 (t, ***J*** = 13.2 Hz, 1H), 7.17 (t, ***J*** = 7.3 Hz, 1H), 7.26 (t, ***J*** = 7.3 Hz, 1H), 7.31 (d, ***J*** = 7.3, 1H), 7.35 (t, ***J*** = 7.3 Hz, 1H), 7.40 (t, ***J*** = 7.3 Hz, 1H), 7.44 (d, ***J*** = 7.3, 1H), 7.53 (d, ***J*** = 7.3, 1H), 7.60 (d, ***J*** = 7.3, 1H), 7.75 (t, ***J*** = 13.2 Hz, 1H), 7.82 (t, ***J*** = 13.2 Hz, 1H), 7.92 (t, ***J*** = 13.2 Hz, 1H), 12.54 (br s, 1H); ^{13}C NMR (100 MHz, DMSO): δ 11.0, 20.6, 27.1, 27.3, 31.4, 45.0, 48.3, 49.0, 103.1, 104.7, 104.8, 110.6, 111.5, 122.3, 122.5, 124.1, 125.1, 125.4, 125.6, 128.3, 128.5, 140.6, 141.3, 142.0, 142.1, 150.3, 152.1, 170.0, 172.0, 172.6; HRMS (ESI^+): Calcd for $[M+H]^+$, 495.3012; Found, 495.3016 .

Synthesis of compound 27: Glutaconaldehyde dianil monohydrochloride (900 mg, 3.2 mmol) was dissolved in 10 mL of AcOH and 10 mL of Ac_2O. Compound **24** (1.2 g, 3.0 mmol) was added to the mixture, and the whole was heated to reflux under an argon atmosphere. The reaction mixture was stirred for 30 min, then cooled to room temperature, and the solvent was removed by evaporation. The residue was dissolved in 15 mL of Ac_2O, and **25** (900 mg, 3.0 mmol) and potassium acetate (1.2 g, 12 mmol) were added. The mixture was stirred overnight at room temperature. The solvent was removed by evaporation, and the residue was dissolved in CH_2Cl_2. This solution was washed with water and brine, dried over Na_2SO_4, filtered through paper filter and evaporated. The residue was purified by column chromatography (NH silica, gradient, CH_2Cl_2 to CH_2Cl_2/MeOH, 4:1) and preparative HPLC (gradient, A/B, 50/50 to 0/100, 30 min) to afford **27** as a red solid (231 mg, 16%). ^{1}H NMR (300 MHz, CD_3OD): δ 1.69

(s, 12H), 1.71-1.90 (m, 4H), 2.40 (t, ***J*** = 7.0 Hz, 2H), 3.60 (s, 3H), 4.09 (t, ***J*** = 7.0 Hz, 2H), 6.27 (d, ***J*** = 13.9 Hz, 1H), 6.28 (d, ***J*** = 13.6 Hz, 1H), 6.55 (t, ***J*** = 12.7 Hz, 2H), 7.20-7.28 (m, 4H), 7.39 (t, ***J*** = 7.7 Hz, 1H), 7.40 (t, ***J*** = 7.7, 1H), 7.47 (d, ***J*** = 7.3 Hz, 2H), 7.59 (t, ***J*** = 12.7 Hz, 1H), 7.92 (t, ***J*** = 12.8 Hz, 1H), 7.94 (t, ***J*** = 13.2 Hz, 1H); ^{13}C NMR (100 MHz, CD_3OD): δ 9.2, 23.2, 27.8, 27.9, 28.0, 31.4, 34.2, 44.6, 50.2, 104.6, 111.66, 111.75, 116.4, 119.3, 123.3, 123.4, 125.9, 126.1, 127.0, 129.7, 142.37, 142.40, 143.7, 144.4, 152.9, 153.1, 157.7, 162.0, 162.4, 172.9, 173.9, 176.9; HRMS (ESI^+): Calcd for $[M-CF_3COO^-]^+$, 495.3012; Found, 495.3014.

Synthesis of compound 28: Compound **26** (50 mg, 0.10 mmol), dicyclohexyl carbodiimide (DCC, 41 mg, 0.20 mmol), and ***N***-hydroxysuccinimide (23 mg, 0.20 mmol) were dissolved in 5 mL of DMF, and the mixture was stirred overnight at room temperature. 2-Aminoethyl-mono-amide-DOTA-tris(***t***-Bu ester) (74 mg, 0.12 mmol) was added to the mixture, and stirring was continued for 2 days. The solvent was removed by evaporation, and the residue was purified by preparative HPLC (gradient, A/B = 60/40 to 0/100, 30 min) to afford **28** as a green solid (33 mg, 30%). ^{1}H NMR (400 MHz, CD_3OD): δ 1.05 (t, ***J*** = 7.3 Hz, 3H), 1.45 (s, 18H), 1.54 (s, 9H), 1.68 (s, 6H), 1.71 (s, 6H), 1.86 (sex, ***J*** = 7.3 Hz, 2H), 2.67 (t, ***J*** = 6.8 Hz, 2H), 2.97-4.20 (m, 26H), 4.31 (t, ***J*** = 6.8 Hz, 2H), 6.22 (d, ***J*** = 13.2 Hz, 1H), 6.41 (d, ***J*** = 13.2 Hz, 1H), 6.52 (t, ***J*** = 13.2 Hz, 1H), 6.59 (t, ***J*** = 12.7 Hz, 1H), 7.19 (t, ***J*** = 7.3 Hz, 1H), 7.23 (d, ***J*** = 7.8 Hz, 1H), 7.30 (t, ***J*** = 7.3 Hz, 1H), 7.35 (d, ***J*** = 7.8 Hz, 1H), 7.36 (t, ***J*** = 7.8 Hz, 1H), 7.43 d, ***J*** = 7.3 Hz, 1H), 7.43 (t, ***J*** = 7.3 Hz, 1H), 7.52 (d, ***J*** = 7.8 Hz, 1H), 7.60 (t, ***J*** = 12.7 Hz, 1H), 7.88 (t, ***J*** = 13.2 Hz, 1H), 8.00 (t, ***J*** = 13.2 Hz, 1H); ^{13}C NMR (100 MHz, DMSO): δ 11.5, 22.0, 27.9, 28.2, 28.5, 34.6, 39.8, 40.3, 41.3, 46.6, 49.7, 49.8, 50.8, 52.9, 54.9, 56.1, 83.1, 85.9, 103.8, 106.1, 111.3, 112.5, 123.3, 123.5, 125.4, 126.8, 127.0, 127.4, 129.6, 129.9, 142.0, 142.8, 143.5, 143.6, 151.7, 154.3, 157.8, 166.7, 171.3, 172.2, 172.4, 172.7, 175.0; HRMS (ESI^+): Calcd for $[M-CF_3COO^-]^+$, 1091.7273; found, 1091.7292.

Synthesis of compound 29: Synthetic procedure was the same as for **28**. Compound **29** was obtained as a green solid (60 mg, 55 %). ^{1}H NMR (400 MHz, CD_3OD): δ 1.44 (s, 18H), 1.52 (s, 9H), 1.677 (s, 6H), 1.682 (s, 6H), 1.71-1.83 (m, 4H), 2.29 (t, ***J*** = 6.8 Hz, 2H), 2.94-4.18 (m, 28H), 6.24 (d, ***J*** = 14.4 Hz, 1H), 6.28 (d, ***J*** = 14.4 Hz, 1H), 6.54 (t, ***J*** = 12.4 Hz, 1H), 6.55 (t, ***J*** = 12.4 Hz, 1H), 7.20-7.29 (m, 4H), 7.38 (t, ***J*** = 7.6 Hz, 1H),

7.40 (t, ***J*** = 7.6 Hz, 1H), 7.46 (t, ***J*** = 6.6 Hz, 2H), 7.58 (t, ***J*** = 12.4 Hz, 1H), 7.91 (t, ***J*** = 14.4 Hz, 1H), 7.94 (t, ***J*** = 14.4 Hz, 1H); ^{13}C NMR (100 MHz, CD_3OD): δ 24.0, 27.8, 28.0, 28.1, 28.5, 31.5, 36.5, 39.6, 40.4, 44.5, 50.1, 50.3, 53.0, 54.9, 56.2, 82.9, 85.9, 104.1, 105.1, 111.6, 111.8, 123.3, 123.4, 125.8, 126.2, 126.9, 127.0, 129.7, 129.8, 142.35, 142.41, 143.8, 144.3, 152.6, 153.3, 157.7, 166.7, 172.2, 172.6, 174.3, 175.8; HRMS (ESI$^+$): Calcd for $[M-CF_3COO^-]^+$, 1091.7273; Found, 1091.7263.

Synthesis of compound 30: Compound **22** (1.44 g, 4.0 mmol), glutaconaldehyde dianil monohydrochloride (570 mg, 2.0 mmol) and potassium acetate (785 mg, 8.0 mmol) were dissolved in 40 mL of Ac_2O, and the mixture was stirred under an argon atmosphere overnight. The solvent was removed by evaporation, and the residue was purified by column chromatography (Silica gel, gradient, CH_2Cl_2 to CH_2Cl_2/MeOH, 1:1) and preparative HPLC (gradient, A/B, 60/40 to 0/100, 30 min) to afford **30** as a green solid (346 mg, 33%). ^{1}H NMR (300 MHz, CD_3OD): δ 1.60 (s, 12H), 2.79 (t, ***J*** = 7.0 Hz, 4H), 4.37 (t, ***J*** = 7.0 Hz, 4H), 6.34 (d, ***J*** = 13.2 Hz, 2H), 6.58 (t, ***J*** = 13.7 Hz, 2H), 7.24 (t, ***J*** = 7.5 Hz, 2H), 7.31 (d, ***J*** = 7.5 Hz, 2H), 7.40 (t, ***J*** = 7.3, 2H), 7.47 (d, ***J*** = 7.3 Hz, 2H), 7.61 (t, ***J*** = 12.7 Hz, 1H), 7.95 (t, ***J*** = 13.2 Hz, 2H); ^{13}C NMR (100 MHz, CD_3OD): δ 29.0, 32.6, 40.9, 50.3, 105.1, 111.9, 123.4, 126.1, 127.5, 129.7, 142.4, 143.3, 153.3, 158.1, 173.3, 173.9; HRMS (ESI$^+$): Calcd for $[M-CF_3COO^-]^+$, 525.2753; Found, 525.2786.

Synthesis of compound 31: Compound **24** (1.21 g, 3.0 mmol), glutaconaldehyde dianil monohydrochloride (427 mg, 1.5 mmol) and potassium acetate (589 mg, 6.0 mmol) were dissolved in 30 mL of Ac_2O, and the mixture was stirred under an argon atmosphere overnight. The solvent was removed by evaporation, and the residue was purified by column chromatography (Silica gel, gradient, CH_2Cl_2 to CH_2Cl_2/MeOH, 1:1) and preparative HPLC (gradient, A/B, 50/50 to 0/100, 30 min) to afford **31** as a green solid (955 mg, >99%). ^{1}H NMR (300 MHz, CD_3OD): δ 1.69 (s, 12H), 1.71-1.90 (m, 8H), 2.39 (t, ***J*** = 7.0 Hz, 4H), 4.10 (t, ***J*** = 7.0 Hz, 4H), 6.29 (d, ***J*** = 13.6 Hz, 2H), 6.56 (t, ***J*** = 12.7 Hz, 2H), 7.24 (t, ***J*** = 7.5 Hz, 2H), 7.27 (d, ***J*** = 7.5 Hz, 2H), 7.39 (t, ***J*** = 7.5 Hz, 2H), 7.47 (d, ***J*** = 7.5 Hz, 2H), 7.60 (t, ***J*** = 12.1 Hz, 1H), 7.93 (t, ***J*** = 13.0 Hz, 2H); ^{13}C NMR (100 MHz, CD_3OD): δ 23.2, 27.8, 28.0, 34.2, 44.6, 50.3, 111.8, 123.4, 126.0, 127.1, 129.8, 142.4, 143.7, 153.1, 157.9, 162.5, 173.2, 176.9; HRMS (ESI$^+$):

Calcd for $[M-CF_3COO^-]^+$, 581.3379; found, 581.3378.

Synthesis of compound 32: Compound **30** (52.5 mg, 0.10 mmol), DCC (31 mg, 0.15 mmol), HOBt·H_2O (15 mg, 0.10 mmol), 2-aminoethyl-mono-amide-DOTA-tris(t-Bu ester) (74 mg, 0.12 mmol), and DIEA (35 μL, 0.20 mmol) were dissolved in 5 mL of DMF, and the mixture was stirred overnight at room temperature. The reaction mixture was purified by preparative HPLC (gradient, A/B, 50/50 to 0/100, 30 min) to afford **27** as a green solid (23 mg, 20%). ^{1}H NMR (400 MHz, CD_3OD): δ 1.45 (s, 18H), 1.54 (s, 9H), 1.69 (s, 6H), 1.69 (s, 6H), 2.68 (t, ***J*** = 6.8 Hz, 2H), 2.80 (t, ***J*** = 7.3 Hz, 2H), 2.92-4.20 (m, 28H), 4.35 (t, ***J*** = 6.8 Hz, 2H), 4.39 (t, ***J*** = 7.3 Hz, 2H), 6.31 (d, ***J*** = 13.7 Hz, 1H), 6.37 (d, ***J*** = 13.2 Hz, 1H), 6.56 (t, ***J*** = 12.4 Hz, 1H), 6.58 (t, ***J*** = 12.4 Hz, 1H), 7.22-7.29 (m, 3H), 7.32-7.49 (m, 5H), 7.62 (t, ***J*** = 12.4 Hz, 1H), 7.94 (t, ***J*** = 12.7 Hz, 1H), 7.97 (t, ***J*** = 12.7 Hz, 1H); ^{13}C NMR (100 MHz, CD_3OD): δ 28.0, 28.1, 28.5, 32.7, 34.6, 39.8, 40.3, 41.0, 41.6, 50.29, 50.33, 52.9, 54.9, 56.0, 83.3, 85.6, 104.8, 111.90, 111.94, 123.4, 126.08, 126.12, 127.4, 129.7, 142.4, 143.30, 143.35, 153.1, 153.2, 157.9, 172.47, 172.52, 173.2, 173.4, 173.9; HRMS (ESI^+): Calcd for $[M]^+$, 1121.7015; found, 1121.6976.

Synthesis of compound 33: Synthetic procedure was the same as for **32**. Compound **33** was obtained as a green solid (47 mg, 40%). ^{1}H NMR (400 MHz, CD_3OD): δ 1.45 (s, 18H), 1.53 (s, 9H), 1.69 (s, 6H), 1.70 (s, 6H), 1.72-1.84 (m, 8H), 2.29 (t, ***J*** = 7.1 Hz, 2H), 2.39 (t, ***J*** = 7.1 Hz, 2H), 2.88-4.25 (m, 28H), 4.06-4.14 (m, 4H), 6.25 (d, ***J*** = 13.6 Hz, 1H), 6.32 (d, ***J*** = 13.2 Hz, 1H), 6.51-6.60 (m, 2H), 7.21-7.31 (m, 4H), 7.36-7.49 (m, 4H), 7.60 (t, ***J*** = 12.9 Hz, 1H), 7.92 (t, ***J*** = 13.2 Hz, 1H), 7.96 (t, ***J*** = 13.2 Hz, 1H); ^{13}C NMR (100 MHz, DMSO-$\boldsymbol{d}_6$): δ 21.7, 22.3, 26.5, 26.6, 27.2, 27.7, 31.3, 33.3, 34.8, 37.8, 43.2, 47.7, 48.2, 48.6, 48.7, 50.9, 53.1, 54.4, 54.6, 81.2, 83.5, 110.9, 111.1, 112.2, 115.1, 118.1, 122.5, 124.6, 124.7, 128.5, 141.0, 141.0, 142.17, 142.20, 169.7, 169.74, 169.85, 171.5, 172.1, 174.3; HRMS (ESI^+): Calcd for $[M-CF_3COO^-]^+$, 1177.7641; found, 1177.7591.

General synthetic procedure of Cy7-DO3A: TFA (2 mL) was added to the conjugate of Cy7 dye and DO3A ***t***-Bu ester (18-57 μmol), and the mixture was stirred for 2 h at room temperature. TFA was removed by evaporation, and the residue was purified by

preparative HPLC.

Compound 34: Blue solid (14 mg, 55%). ^{1}H NMR (400 MHz, CD_3OD): δ 1.05 (t, ***J*** = 7.3 Hz, 3H), 1.68 (s, 6H), 1.70 (s, 6H), 1.86 (sex, ***J*** = 7.3 Hz, 2H), 2.69 (t, ***J*** = 6.8 Hz, 2H), 3.18-4.12 (m, 30H), 4.32 (t, ***J*** = 7.3 Hz, 2H), 6.27 (d, ***J*** = 13.7 Hz, 1H), 6.37 (d, ***J*** = 13.7 Hz, 1H), 6.55 (t, ***J*** = 13.7 Hz, 1H), 6.58 (t, ***J*** = 13.7 Hz, 1H), 7.19 (t, ***J*** = 7.6 Hz, 1H), 7.25-7.44 (m, 6H), 7.51 (d, ***J*** = 7.6 Hz, 1H), 7.59 (t, ***J*** = 12.9 Hz, 1H), 7.89 (t, ***J*** = 12.9 Hz, 1H), 7.98 (t, ***J*** = 12.9 Hz, 1H); ^{13}C NMR (100 MHz, CD_3OD): δ 11.5, 22.0, 27.9, 28.1, 34.6, 39.9, 40.2, 41.4, 46.5, 49.9, 50.6, 51.2, 51.7, 54.8, 55.6, 111.5, 112.4, 123.3, 123.4, 125.5, 126.5, 127.0, 127.2, 129.6, 129.8, 142.1, 142.7, 143.6, 152.0, 152.1, 153.9, 154.0, 157.7, 171.9, 172.9, 174.5; HRMS (ESI^+): Calcd for $[M-CF_3COO^-]^+$, 923.5395; found, 923.5421.

Compound 35: Blue solid (13 mg, 78%). ^{1}H NMR (400 MHz, CD_3OD): δ 1.68 (s, 6H), 1.69 (s, 6H), 2.72 (t, ***J*** = 6.8 Hz, 2H), 2.78 (t, ***J*** = 6.8 Hz, 2H), 3.24-3.88 (m, 28H), 4.34-4.39 (m, 2H), 6.31 (d, ***J*** = 13.7 Hz, 1H), 6.37 (d, ***J*** = 13.7 Hz, 1H), 6.56 (t, ***J*** = 12.4 Hz, 1H), 6.57 (t, ***J*** = 12.4 Hz, 1H), 7.21-7.47 (m, 8H), 7.60 (t, ***J*** = 12.4 Hz, 1H), 7.90-7.98 (m, 2H); ^{13}C NMR (100 MHz, CD_3OD): δ 28.0, 32.6, 34.7, 39.9, 40.2, 40.9, 41.6, 50.2, 50.4, 51.8, 54.5, 55.7, 104.9, 111.6, 111.8, 123.4, 126.0, 126.2, 127.4, 129.7, 142.3, 142.4, 143.3, 153.0, 153.4, 158.0, 172.7, 172.9, 173.5, 174.0; HRMS (ESI^+): Calcd for $[M-CF_3COO^-]^+$, 953.5137; found, 923.5132.

Compound 36: Blue solid (36 mg, 73%). ^{1}H NMR (300 MHz, CD_3OD): δ 1.69 (s, 12H), 1.69-1.86 (m, 4H), 2.30 (t, ***J*** = 6.6 Hz, 2H), 3.45-4.05 (m, 28H), 3.61 (s, 3H), 4.07 (t, ***J*** = 6.6 Hz, 2H), 6.25 (d, ***J*** = 13.6 Hz, 1H), 6.28 (d, ***J*** = 13.6 Hz, 1H), 6.54 (t, ***J*** = 12.7 Hz, 1H), 6.55 (t, ***J*** = 12.7 Hz, 1H), 7.20-7.29 (m, 4H), 7.36-7.49 (m, 4H), 7.59 (t, ***J*** = 12.7 Hz, 1H), 7.87-7.99 (m, 2H); ^{13}C NMR (100 MHz, (CD_3OD): δ 24.0, 27.8, 27.99, 28.03, 31.5, 36.4, 39.7, 40.4, 44.6, 50.2, 50.3, 51.3, 54.8, 55.6, 104.3, 111.7, 123.3, 123.4, 125.9, 126.2, 126.90, 129.7, 142.4, 143.8, 144.3, 152.7, 153.2, 157.6, 172.8, 174.1, 176.0; HRMS (ESI^+): Calcd for $[M-CF_3COO^-]^+$, 923.5395; found, 923.5406.

Compound 37: Blue solid (20 mg, 89%). ^{1}H NMR (400 MHz, CD_3OD): δ 1.68 (s, 12H), 1.71-1.84 (m, 8H), 2.32 (t, ***J*** = 6.8 Hz, 2H), 2.39 (t, ***J*** = 7.1 Hz, 2H), 3.23-3.89 (m,

28H), 4.06-4.12 (m, 4H), 6.27 (d, ***J*** = 13.2 Hz, 1H), 6.29 (d, ***J*** = 12.7 Hz, 1H), 6.51-6.58 (m, 2H), 7.21-7.29 (m, 4H), 7.36-7.48 (m, 4H), 7.58 (t, ***J*** = 12.7 Hz, 1H), 7.90-7.96 (m, 2H); ^{13}C NMR (100 MHz, CD_3OD): δ 23.2, 24.0, 27.8, 27.98, 28.01, 34.3, 36.4, 39.6, 40.3, 44.6, 44.7, 50.28, 50.33, 51.3, 54.6, 55.3, 55.6, 104.8, 111.9, 123.4, 126.0, 126.1, 127.0, 129.8, 142.5, 143.7, 152.9, 153.1, 157.8, 173.1, 173.3, 176.0, 176.9; HRMS (ESI^+): Calcd for $[M-CF_3COO^-]^+$, 1009.5763; found, 1009.5742.

Synthesis of Cy7-Gd derivatives: Synthetic procedure was the same as for **dye-Gd**s.

Compound 2: Blue solid (8.7 mg, 54%). HRMS (ESI^+): Calcd for $[M-CF_3COO^-]^+$, 1078.4401; found, 1078.4356; HPLC analysis: retention time, 12.7 min (eluent: A/B = 50/50 to 0/100, 20 min; flow rate = 1.0 mL/min; detection wavelength, 750 nm).

Compound 3: Blue solid (9.4 mg, 62%). HRMS (ESI^+): Calcd for $[M-CF_3COO^-]^+$, 1108.4143; found, 1108.4110; HPLC analysis: retention time, 11.3 min (eluent: A/B = 50/50 to 0/100, 20 min; flow rate = 1.0 mL/min; detection wavelength, 750 nm).

Compound 4: Blue solid (26 mg, 63%). HRMS (ESI^+): Calcd for $[M-CF_3COO^-]^+$, 1078.4401; found, 1078.4376; HPLC analysis: retention time, 12.5 min (eluent: A/B = 50/50 to 0/100, 20 min; flow rate = 1.0 mL/min; detection wavelength, 750 nm).

Compound 5: Blue solid (16 mg, 72%). HRMS (ESI^+): Calcd for $[M-CF_3COO^-]^+$, 1164.4769; found, 1164.4720; HPLC analysis: retention time, 12.3 min (eluent: A/B = 50/50 to 0/100, 20 min; flow rate = 1.0 mL/min; detection wavelength, 750 nm).

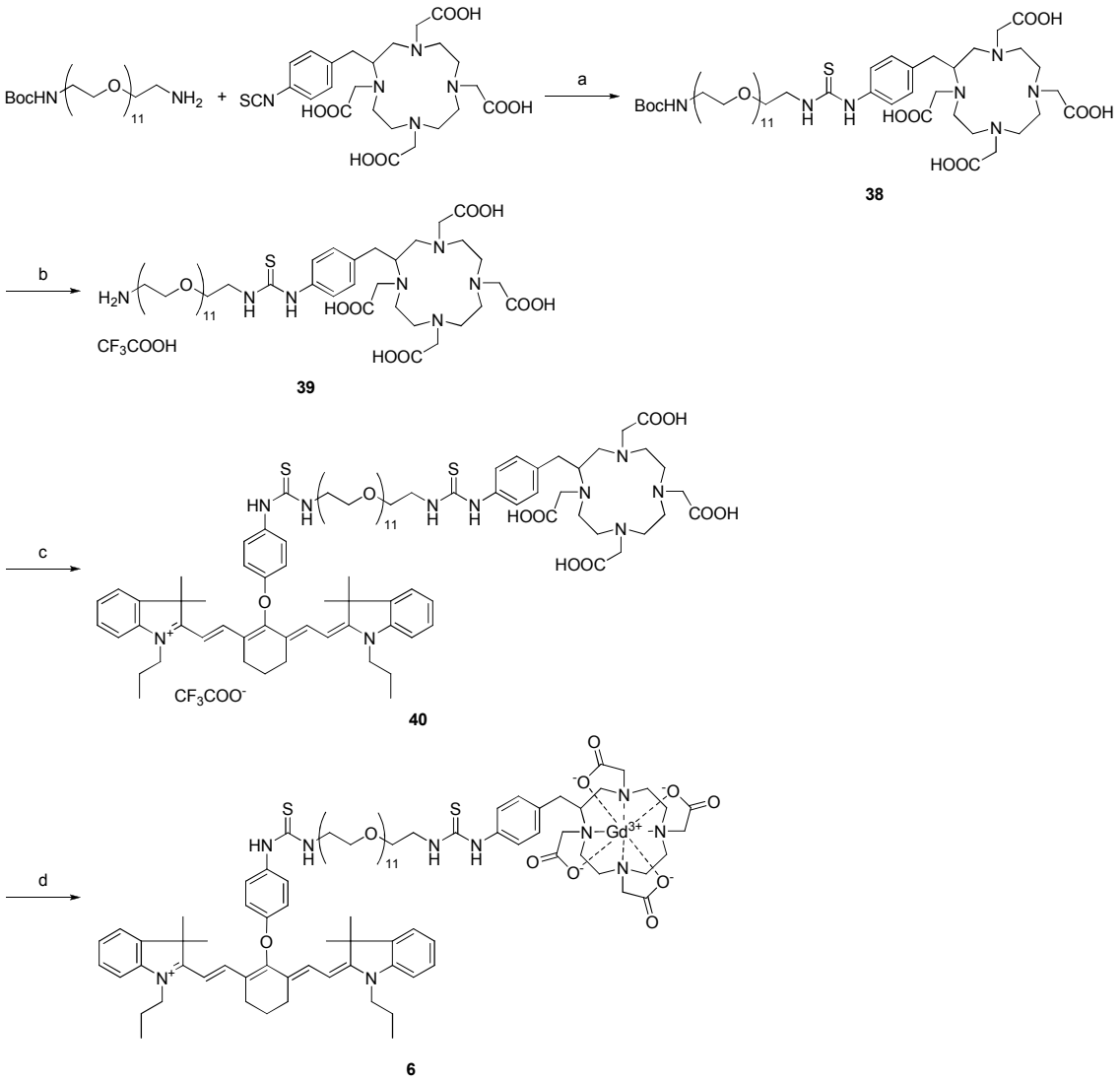

Scheme S6. Synthesis of compound **6**. (a) DIEA, DMF, r.t.; (b) TFA, CH_2Cl_2, r.t.; (c) **13**, DIEA, DMF, r.t.; (d) $GdCl_3$, 1.0 M HEPES buffer (pH 7.4), r.t.

Synthesis of compound 38: ***O***-(2-Aminoethyl)-***O′***-[2-(Boc-amino)ethyl]decaethylene glycol (Aldrich, 161 mg, 0.25 mmol) and DIEA (435 μL, 2.5 mmol) were dissolved in 2 mL of DMF. A solution of ***p***-SCN-Bn-DOTA (Macrocyclics, 154 mg, 0.28 mmol) in 2.5 mL of DMF was added, and the mixture was stirred for 2 days at room temperature. The solvent was removed by evaporation, and the residue was purified by preparative HPLC (gradient, A/B, 99/1 to 0/100, 30 min) to afford **38** as a colorless solid (281 mg, 94%). ^{1}H NMR (400 MHz, $CDCl_3$): δ 1.44 (s, 9H), 2.01-4.66 (m, 73H), 7.22-7.31 (m, 4H); ^{13}C NMR (100 MHz, $CDCl_3$): δ 28.8, 32.7, 41.3, 45.4, 49.6, 49.9, 50.2, 51.3, 52.8, 53.8, 55.0, 55.8, 57.1, 67.9, 70.3, 70.7, 70.95, 71.02, 71.1, 71.2, 71.3, 71.5, 80.1, 125.7, 130.8,

134.7, 139.4, 158.4, 169.0, 182.7; HRMS (ESI^+): Calcd for $[M+H]^+$, 1196.6224; found, 1196.6234.

Synthesis of compound 39: Compound **38** was dissolved in 8 mL of CH_2Cl_2, and 5 mL of TFA was added to the solution. The mixture was stirred for 2 h at room temperature. The solvent was removed by evaporation, and the residue was purified by preparative HPLC (gradient, A/B, 99/1 to 0/100, 30 min) to afford **39** as a colorless solid (227 mg, 89%). ^1H NMR (400 MHz, CD_3OD): δ 2.04-4.96 (m, 73H), 7.30 (d, ***J*** = 8.3 Hz, 2H), 7.41 (d, ***J*** = 8.3 Hz, 2H); ^{13}C NMR (100 MHz, CD_3OD): δ 32.7, 40.6, 45.3, 50.0, 51.2, 52.8, 53.7, 54.8, 55.6, 57.1, 57.5, 67.9, 70.3, 70.7, 70.9, 71.1, 71.16, 71.23, 71.29, 71.33, 71.42, 71.43, 125.7, 130.8, 134.7, 182.7; HRMS (ESI^+): Calcd for $[M-CF_3COO^-]^+$, 1096.5699; found, 1096.5696.

Synthesis of compound 40: Compound **13** (69 mg, 105 μmol) and DIEA (174 μL, 1.00 mmol) were dissolved in 4 mL of DMF. A solution of compound **39** (110 mg, 100 μmol) in 4 mL of DMF was added, and the mixture was stirred overnight at room temperature. The solvent was removed by evaporation, and the residue was purified by preparative HPLC (gradient, A/B, 60/40 to 0/100, 30 min) to afford **40** as a green solid (53.8 mg, 31%). ^1H NMR (300 MHz, $CDCl_3$): δ 0.92 (t, ***J*** = 7.5 Hz, 6H), 1.30 (s, 12H), 1.74 (sex, ***J*** = 7.5 Hz, 4H), 1.95 (s, 2H), 2.51-4.19 (m, 6H), 6.07 (d, ***J*** = 13.9 Hz, 2H), 7.03 (d, ***J*** = 9.2 Hz, 2H), 7.12 (t, ***J*** = 7.5 Hz, 2H), 7.18 (t, ***J*** = 7.7 Hz, 4H), 7.26-7.35 (m, 8H), 7.91 (d, ***J*** = 13.9 Hz, 4H); ^{13}C NMR (100 MHz, DMSO): δ 11.1, 20.4, 23.7, 27.4, 43.5, 44.9, 48.6, 68.6, 69.6, 69.8, 100.3, 111.3, 114.2, 115.2, 118.1, 121.5, 122.4, 124.8, 128.5, 129.3, 140.8, 141.0, 142.2, 157.9, 158.3, 162.8, 164.0, 171.7, 181.0; HRMS (ESI^+): Calcd for $[M-CF_3COO^-]^+$, 1749.9139; found, 1749.9185.

Synthesis of 6: Synthetic procedure was the same as for **Cy7-Gd** derivatives. Compound **6** was obtained as a green solid (17 mg, 86%). HRMS (ESI^-): Calcd for $[M+H]^+$, 1904.8145; found, 1904.8111; HPLC analysis: retention time, 15.6 min; purity, 99.7% integrated intensity (eluent: A/B = 50/50 to 0/100, 20 min; flow rate = 1.0 mL/min; detection wavelength, 780 nm).

Synthesis of R_8-Gd: See reference S2.

Supporting Figure

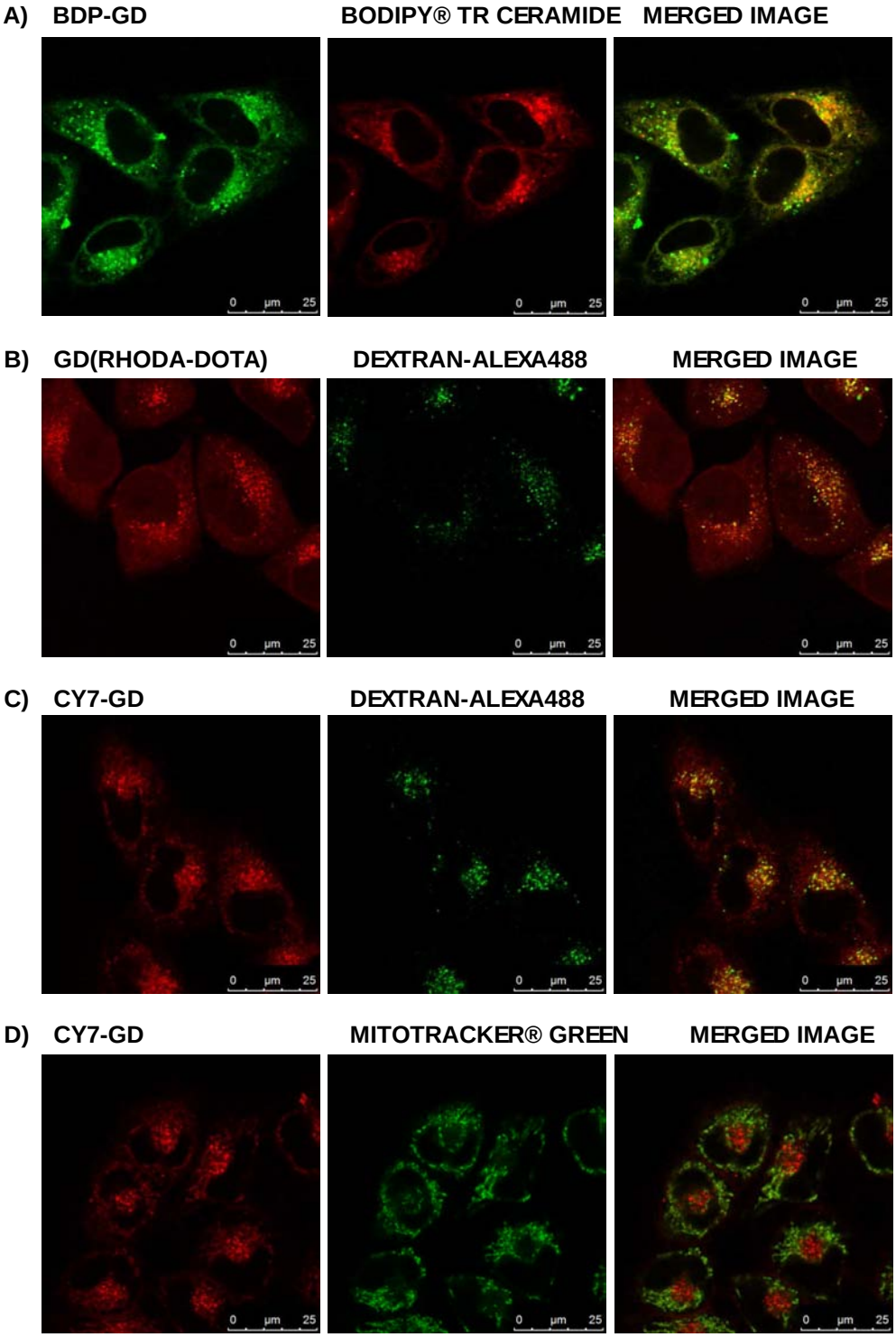

Figure S1. Confocal fluorescence microscopic images of HeLa cells incubated with **dye-Gd**s and organelle-specific probes. Left, center and right panels show **dye-Gd**s, organelle-specific probes and merged images, respectively.

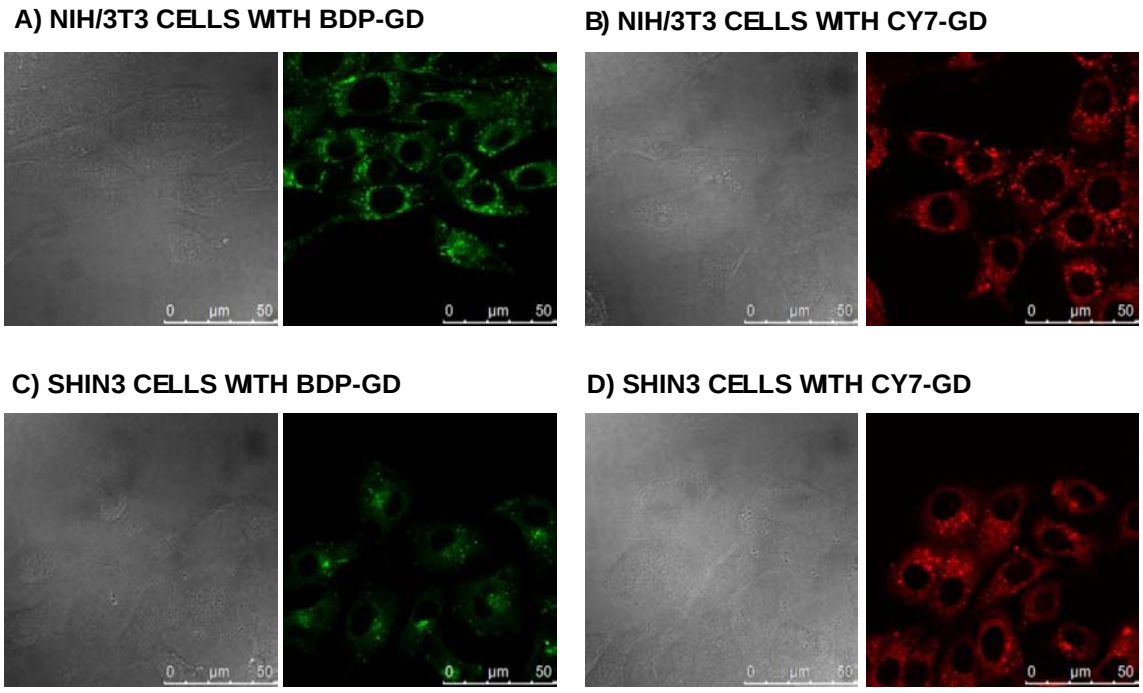

Figure S2. Fluorescence microscopic images of NIH/3T3 cells and SHIN3 cells incubated with **BDP-Gd** or **Cy7-Gd** (10 μM). The left and right panels show the differential interference contrast (DIC) and the fluorescence micrographs of cells, respectively.

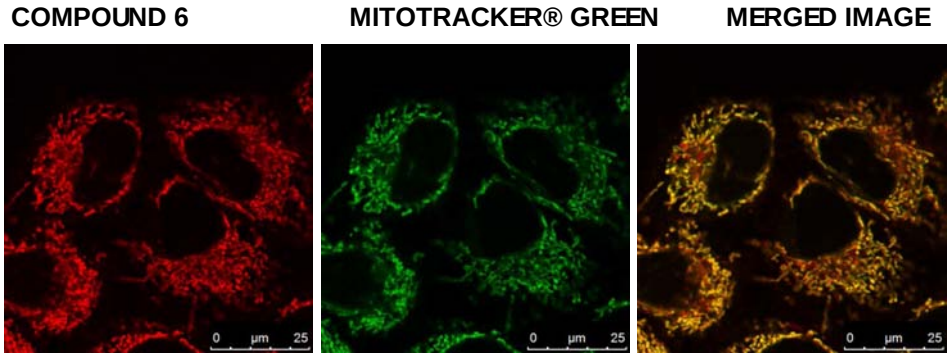

Figure S3. Confocal fluorescence microscopic images of HeLa cells incubated with **6** and Mitotracker® green. Left, center and right panels show **6**, Mitotracker® green and the merged image, respectively.

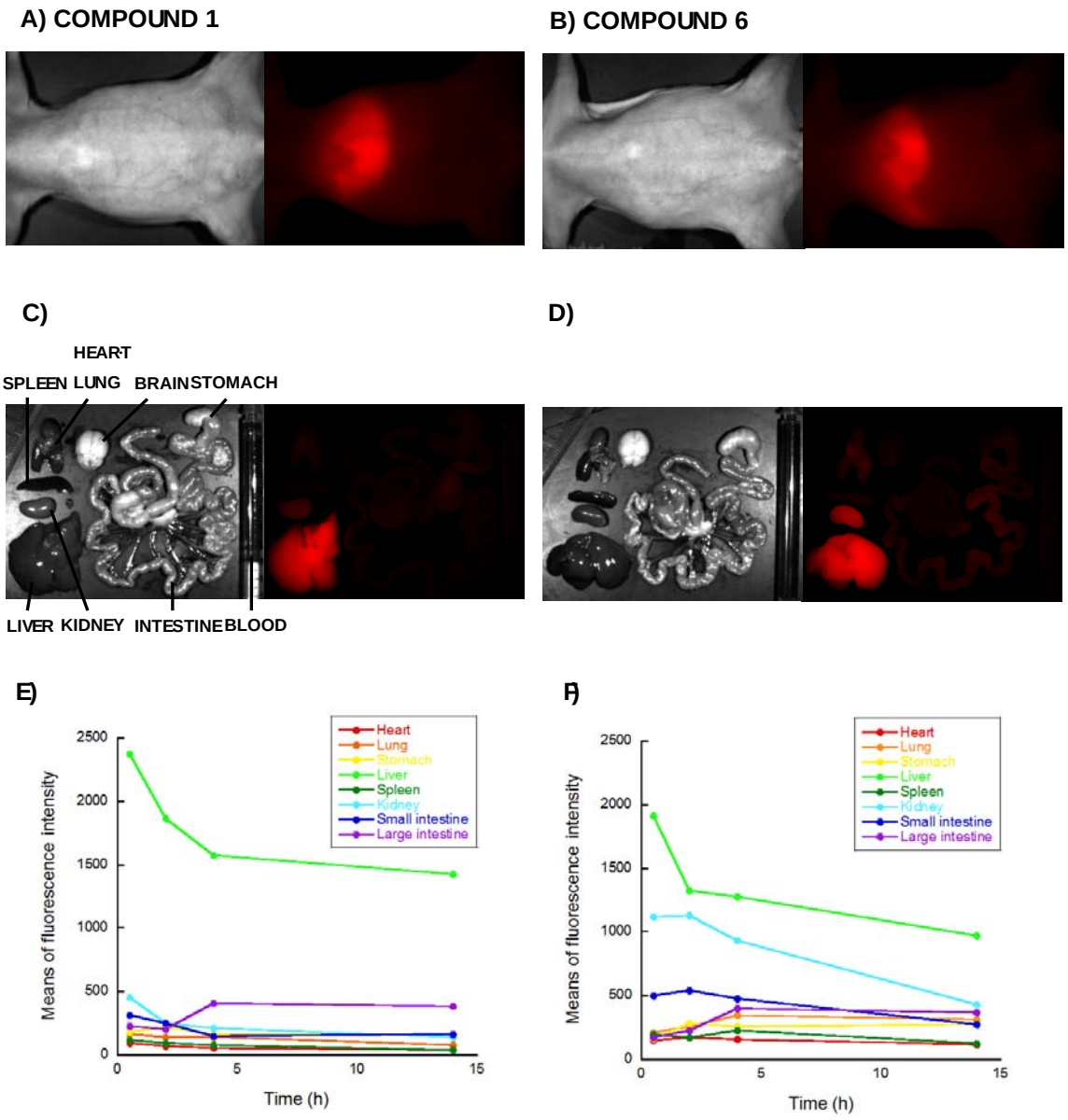

Figure S4. Fluorescence images of nude mouse injected with **1** (a,c,e) or **6** (b,d,f) (100 μM, 100 μL). The white light and the fluorescence images of (a,b) mouse body (5 min after injection) and (c,d) isolated organs (1 h after injection). (e,f) Time courses of the fluorescence intensities of organs ex. vivo.

References

(S1) Matsumoto, T.; Urano, Y.; Shoda, T.; Kojima, H.; Nagano, T. ***Org Lett*** **2007**, ***9***, 3375.

(S2) Allen, M. J.; MacRenaris, K. W.; Venkatasubramanian, P. N.; Meade, T. J. ***Chem Biol*** **2004**, ***11***, 301.

Bioconjugate Chemistry

Article

pubs.acs.org/bc

Polyamidoamine-Grafted Multiwalled Carbon Nanotubes for Gene Delivery: Synthesis, Transfection and Intracellular Trafficking

Min Liu,[†] Biao Chen,[†] Yanan Xue,[‡] Jie Huang,[†] Liming Zhang,[†] Shiwen Huang,[‡] Qingwen Li,[†] and Zhijun Zhang*[,†]

[†]Division of Nanobiomedicine, and Division of Nano-Devices and Materials, Suzhou Institute of Nano-tech and Nano-bionics, Chinese Academy of Sciences, Suzhou, 215123, P. R. China

[‡]Key Laboratory of Biomedical Polymers of Ministry of Education, Department of Chemistry, Wuhan University, Wuhan 430072, P. R. China

Supporting Information

ABSTRACT: Functionalized multiwalled carbon nanotubes (*f*-MWNTs) are of great interest and designed as a novel gene delivery system. In this paper, we presented synthesis of polyamidoamine-functionalized multiwalled carbon nanotubes (PAA-*g*-MWNTs) and their application as a novel gene delivery system. The PAA-*g*-MWNTs, obtained from amide formation between PAA and chemically oxidized MWNTs, were stable in aqueous solution and much less toxic to cells than PAA and PEI 25KDa. More importantly, PAA-*g*-MWNTs showed comparable or even higher transfection efficiency than PAA and PEI at optimal w/w ratio. Intracellular trafficking of Cy3-labeled pGL-3 indicated that a large number of Cy3-labeled pGL-3 were attached to nucleus membrane, the majority of which was localized in nucleus after incubation with cells for 24 h. We have demonstrated that PAA modification of MWNTs facilitate higher DNA uptake and gene expression *in vitro*. All these facts suggest potential application of PAA-*g*-MWNTs as a novel gene vector with high transfection efficiency and low cytotoxicity.

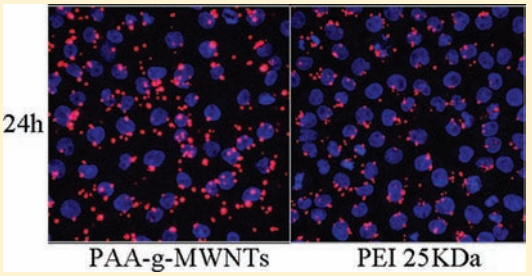

INTRODUCTION

Since application of viral vectors was restricted by their drawbacks such as high immunogenicity, high toxicity, low gene loading rate, and so on, researchers in this field have developed many types of nonviral gene vectors.[1−4] Recently, multiwalled carbon nanotubes (MWNTs) have been explored as an efficient novel gene delivery system due to their unique structure and properties. However, the as-prepared carbon nanotubes are water-insoluble, chemical modification of MWNTs is desired for their application in gene delivery.[5−12]

Dendrimer-grafted MWNTs have been developed as gene delivery vectors.[13−15] Dendrimers containing large numbers of surface primary amine groups can effectively improve water solubility of MWNTs; meanwhile, the surface primary amines can condense DNA via electrostatic interaction and then deliver foreign DNA into cells. Yao group[16,17] designed and synthesized several kinds of dendrimer-functionalized MWNTs, the obtained PAMAM-MWCNT possessed much lower cytotoxicity and higher transfection efficiency. However, the properties of dendrimers are mainly dependent on the number of their generations and the synthesis is usually complicated.[18]

Recently, linear polyamidoamine (PAA), which can be easily synthesized via one-step polyaddition of primary monoamines or bis(secondary amine) to bisacrylamines, has attracted much attention from researchers.[19] In a previous work, secondary and tertiary amines were introduced to the side chains to improve water solubility and transfection efficiency.[20] However, polymers with primary amino groups often show higher stability in saline solution and better transfection activity.[21] To date, there are few reports on PAA with pendant primary amine groups for gene delivery.[22]

Herein, we report a novel gene delivery system based on MWNTs grafted with PAA. In our strategy, PAA with pendant primary amine groups was synthesized via Michael polyaddition of N-Boc-protected diamine to *N,N*-methylenebis(acrylamide). Next, PAA was conjugated to MWNTs (PAA-*g*-MWNTs) through EDC chemistry. The composition, morphology, surface properties, and cytotoxicity of PAA-*g*-MWNTs were characterized by FT-IR spectroscopy, thermogravimetric analysis (TGA), scanning electron microscopy (SEM), zeta potential, and WST measurement. Finally, using pGL-3 as a reporter gene, we investigated the ability of PAA-*g*-MWNTs to deliver foreign luciferase gene, including transfection efficiency and intracellular trafficking.

EXPERIMENTAL PROCEDURES

Materials. MWNTs and EDAC were obtained from domestic suppliers. PAA (M_w = 1.8 × 10^4) was synthesized as described previously.[22] Branched PEI 25KDa was purchased from Sigma-Aldrich and used as received. *N*-Hydroxysuccinimide

Received: April 13, 2011
Revised: September 14, 2011
Published: October 13, 2011

ACS Publications © 2011 American Chemical Society

(NHS) was purchased from Alfa Aesar. Dulbecco's Modified Eagle's Medium (DMEM), fetal bovine serum (FBS), 0.25% Trypsin-EDTA, Opti-MEM, and Hoechst 33258 were purchased from Gibco BRL (Grand Island, NY). Label IT Cy3 Nucleic Acid Labeling Kit was obtained from Mirus Bio Corporation. Luciferase assay system was obtained from Promega Corporation. COS-7 and HeLa cell lines were purchased from China Center for Type Culture Collection (CCTCC) (Wuhan University) and cultured in DMEM supplemented with 10% FBS at 37 °C in a humidified air atmosphere containing 5% CO_2.

Amplification and Purification of Plasmid DNA. pGL-3 was used as the luciferase reporter gene and transformed in *E. coli* JM109. pEGFP-N1 was used as the green fluorescent protein gene and transformed in *E. coli* DH5R. Both plasmids were amplified in LB at 37 °C for 12−16 h at 250 rpm, and purified by QIAfilter plasmid Giga kit according to the manufacturer's protocol. The quantity and quality of plasmid DNA was analyzed by spectrophotometric analysis at 260 and 280 nm and by electrophoresis in 0.7% (w/v) agarose gel. The purified plasmid was dissolved in TE buffer and stored at −20 °C.

Synthesis and Characterization of PAA-*g*-MWNTs. Carboxylic acid groups were introduced onto MWNTs by acid treatment following a previous protocol.[23] Next, 10 mg of MWNTs-COOH obtained from the above step was dispersed into 10 mL of aqueous solution (pH = 6) of EDC (9.6 mg) and NHS (5.7 mg) via sonication. After sonication for 3 h, 40 mg of PAA was added to the above solution and changed the solution pH to 9. The mixture was then sonicated for further 4 h and stirred at room temperature overnight. Finally, the solution was dialyzed against distilled water (MWCO = 50 000) to remove the unreacted PAA. Next, the solution was centrifuged at 12 000 rpm for 30 min, the supernatant was sterile-filtered (Millipore 220 nm) and stored as a stock solution.

The structure and composition of the purified PAA-*g*-MWNTs were characterized by FTIR and TGA. TGA was performed by scanning from 100 to 800 °C under nitrogen at a heating rate of 20 °C min^{-1} by using TG/DTA 6200.

Morphology of the PAA-g-MWNTs/pEGFP-N1 complexes was characterized by SEM (FEI Quanta 400). The complexes at optimal w/w ratio of 15 were prepared as described above, followed by vortexing for 5 s and incubating for 30 min at room temperature. Afterward, a drop of the solution was deposited onto a glass slide and stored in a desiccator overnight.

Cytotoxicity Assay. The cytotoxicity of PAA-*g*-MWNTs to HeLa and COS-7 cells was evaluated by WST assay, in which PAA was also tested as a control. HeLa and COS-7 cells were seeded into 96 well plate at a density of 6000 and 5000 cells/well in 100 μL complete DMEM. When cells achieved about 50% confluence after incubation for 24 h, 100 μL aliquots of PAA-*g*-MWNT solutions in DMEM at different concentrations were added to a 96 well plate and incubated for another 24 h. Then, the DMEM was replaced with 100 μL fresh DMEM, and 10 μL of WST solution was added to each well except for the background wells and incubated for further 2 h. The absorbance at 450 nm was measured using a microplate reader (Perkin-Elmer Victor X4). The percent relative viability in reference to control wells containing complete DMEM without the added PAA-*g*-MWNTs was calculated by the following equation:

$$\text{relative cell viability (\%)} = 100 \times (A_{\text{test}} - A_0)/(A_{\text{control}} - A_0)$$

where A is absorbance at 450 nm, A_0 represents absorbance of the solution containing cells and complete DMEM without WST and PAA-*g*-MWNTs.

Preparation of PAA-*g*-MWNTs/DNA Complexes and Agarose Gel Retardation Assay. PAA-*g*-MWNTs/DNA complexes were freshly prepared in 150 mmol L^{-1} NaCl by mixing PAA-*g*-MWNTs with pEGFP-N1 at desired w/w ratios, followed by vortexing for 5 s and incubation for 30 min at room temperature.

The complexes for agarose gel retardation assay were prepared at w/w ratios of 1.5:1, 3:1, 4.5:1, 6:1, 9:1, 12:1, and 15:1 as described above. Gel electrophoresis was carried out in TAE buffer in 0.7% (w/v) agarose gel at 80 V for 80 min. The gel was visualized with a Fujifilm LAS-4000 image analyzer.

Zeta Potential Measurement. The zeta potential of samples was measured with Zetasizer Nano-ZS (Malvern Instruments) at 25 °C. The PAA-*g*-MWNTs/pEGFP-N1 complexes at various w/w ratios were freshly prepared as described above. After incubating for 30 min, the solution was diluted to 1 mL with pure water for zeta potential measurement.

In Vitro Transfection. In vitro transfection efficiency of complexes was evaluated on HeLa and COS-7 cells, pGL-3 was used as the report gene. Branched PEI 25KDa and PAA were used as a control. HeLa and COS-7 cells were separately seeded into 24 well plates at an appropriate density (6×10^4 for HeLa cells, and 5×10^4 for COS-7 cells) with 1 mL of complete DMEM. When the cells were incubated to 50−60% confluence in the 24 well plate, the medium was replaced with 400 μL of Opti MEM, and then, 100 μL aliquots of PAA-*g*-MWNT/DNA complexes at various w/w ratios were added to each well. After incubation for 4 h at 37 °C, the culture media was then replaced with 1 mL of complete DMEM, and the cells were incubated for further 48 h. All of the transfections were performed in duplicate. For luciferase expression, after 48 h of incubation, the medium was replaced with 200 μL of cell lysis buffer and freeze−thawed twice. The lysate was centrifuged at 12 000 rpm for 3 min, 20 μL of supernatant was mixed with 100 μL of the luciferase assay substrate (Promega), and light emission was measured with a Lumat 9507 luminometer (Berthold Germany) for 10 s. The relative light units (RLU/mg protein) were normalized against the total protein concentration in the cell extracts, which was determined using a BCA assay kit (Pierce).

To evaluate the effect of serum on gene delivery, we used Opti MEM containing 10% FBS for transfection of cells with PAA-*g*-MWNTs/DNA complexes. For transfection in the presence of serum, when the cells achieved 50−60% confluence, the medium was replaced with fresh Opti MEM containing 10% FBS, and then, complexes at various w/w ratios were added to each well. The other procedure was the same as that described above.

Intracellular Trafficking. pGL-3 was labeled by Label IT Cy3 Nucleic Acid Labeling Kit according to the manufacturer's protocol. Then, PAA-*g*-MWNTs at optimal w/w ratio (w/w ratio = 15) was screened through the evaluation by luciferase expression. PEI 25KDa at optimal w/w ratio (w/w = 1.3) was used as a control.

COS-7 cells were seeded onto a coverslip in a 24 well plate at a density of 4×10^4. After incubation for 24 h, the cells achieved 40−50% confluence, the medium was replaced with 400 μL of Opti MEM, and then PAA-*g*-MWNTs with labeled pGL-3 at w/w ratio of 15 were added to each well. After incubating for 4 h, the medium was replaced with 1 mL

Scheme 1. Synthesis Route of PAA-Functionlized MWNTs

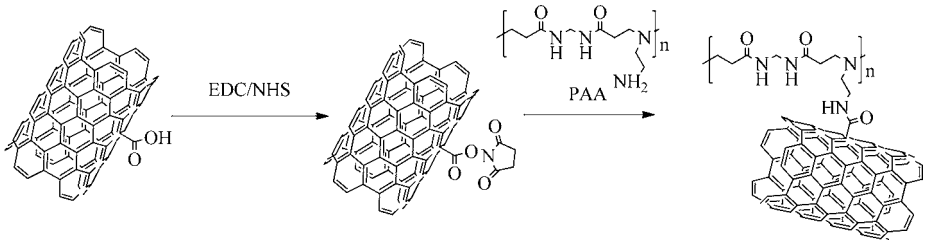

complete DMEM. At the end of each incubation period (4 h and 24 h), the medium was removed, and the coverslip was taken out and fixed with 4% formalin for 10 min. Then, the cells were rinsed with PBS twice, and 100 μL of Hoechst 33258 (5 μg/mL) was added onto the coverslip and incubated for 10 min. Finally, the coverslip was washed with PBS and mounted on a microscopic slide. Intracellular localization of Cy3-labeled DNA was visualized by Nikon confocal system with excitation at 405 and 543 nm for Hoechst and Cy3, respectively. Image analysis was used to determine whether Cy3-labeled DNA was localized inside or over the nucleus, 5−10 of *Z*-series images at 1 μm interval containing blue fluorescence (nucleus) were selected. DNA nucleus localization was confirmed by evidence of the colocalization of blue and red fluorescence.

RESULTS

Synthesis and Characterization of PAA-g-MWNTs. PAA was conjugated to the carboxyl groups on the surface of MWNTs, which is shown in Scheme 1. After purification, the obtained PAA-*g*-MWNTs were then characterized by FT-IR. For comparison purpose, IR spectra of PAA, MWNTs-COOH, and PAA-*g*-MWNTs are shown in Figure S1 (see Supporting Information). The CONH group formed between PAA and MWNTs-COOH shows IR bands at about 3400, 1650, and 1535 cm^{-1}, suggesting successful formation of PAA-*g*-MWNTs complexes.

The relative amount of PAA grafted onto the surface of MWNTs was evaluated by thermogravimetric analysis (TGA). As shown in Figure 1, MWNT-COOH was thermally stable up to 600 °C, while PAA and PAA-*g*-MWNTs began to degrade at about 300 °C. At 500 °C, PAA and PAA-*g*-MWNTs showed about 75.4% and 72.2% weight losses, respectively; thus, PAA-*g*-MWNTs contained about 95.7% PAA.

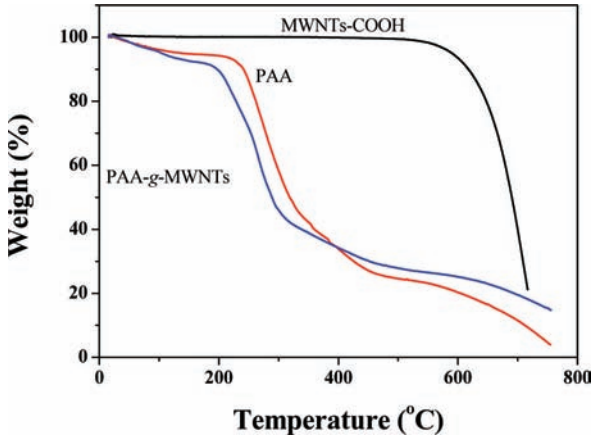

Figure 1. TGA curves of MWNTs, PAA, and PAA-g-MWNTs.

Cell Viability Assay. The relative cellular viabilities of PAA-*g*-MWNTs and PAA are presented in Figure 2. The cytotoxicity of PAA-*g*-MWNTs was found to be concentration dependent, which meant that the cell viability decreased with increasing concentration of PAA-*g*-MWNTs. Figure 2A shows the cytotoxicity of PAA-*g*-MWNTs against COS-7 cells; the viability of COS-7 cells incubated with the solution of PAA was about 40% at a concentration of 80 μg/mL, while the viability of COS-7 with PAA-*g*-MWNTs was about 80% at the same concentration, suggesting much lower cytotoxicity of PAA-*g*-MWNTs than that of PAA. Figure 2B gives the cytotoxicity of PAA-*g*-MWNTs against HeLa cells. The viability of HeLa cells against PAA-*g*-MWNTs and PAA at a concentration of 80 μg/mL was about 50% and 20%, respectively. The result is similar to that observed for COS-7 cells.

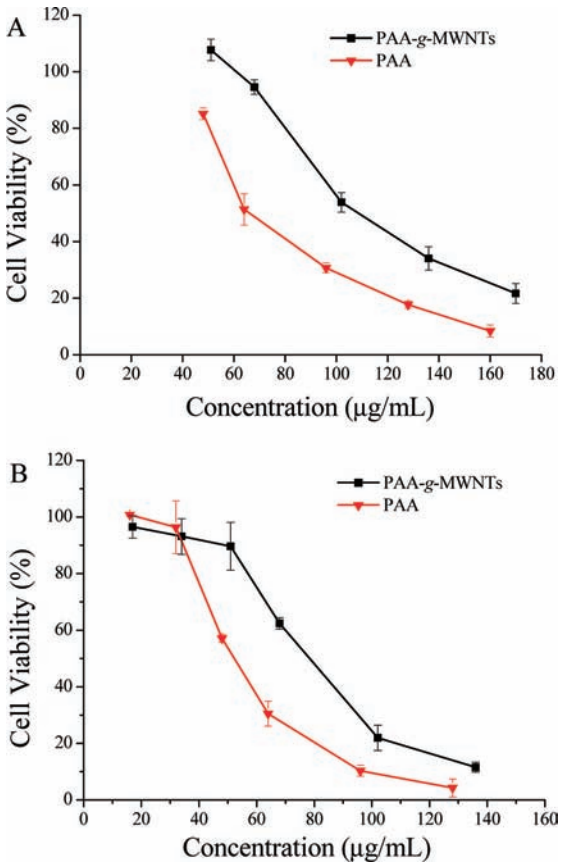

Figure 2. In vitro cytotoxicity of PAA-*g*-MWCNTs in COS-7 (A) and HeLa (B) cells. PAA was used as a control.

Agarose Gel Retardation. Agarose gel retardation assays were performed to study the condensation ability of PAA-*g*-MWCNTs. As shown in Figure 3, DNA was entirely retained in

dx.doi.org/10.1021/bc200189f | *Bioconjugate Chem.* 2011, 22, 2237−2243

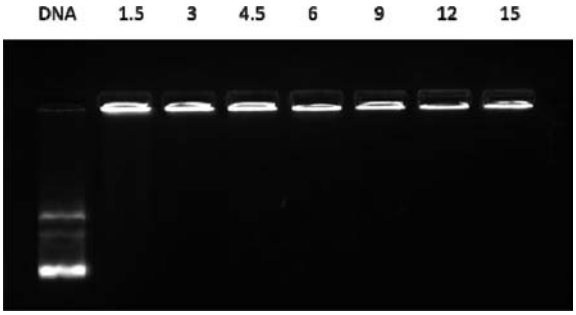

Figure 3. Agarose gel electrophoresis retardation assay of PAA-*g*-MWNTs/DNA complexes at various w/w ratios. Lane 1, naked DNA; lanes 2−8, w/w ratios of 1.5:1, 3:1, 4.5:1, 6:1, 9:1, 12:1, and 15:1, respectively.

the wells at w/w ratio above 1.5, suggesting high DNA binding ability at low w/w ratios.

Zeta Potential Measurement. It is well-known that positive surface charge of polymer/DNA complexes can facilitate the nonspecific attachment of complex nanoparticles to the negatively charged cellular membranes and the uptake of polycation/DNA complexes by cells. The zeta potential of PAA-*g*-MWNTs/DNA complexes was measured to assess their surface charge. As shown in Figure 4, at w/w ratios below 3, the

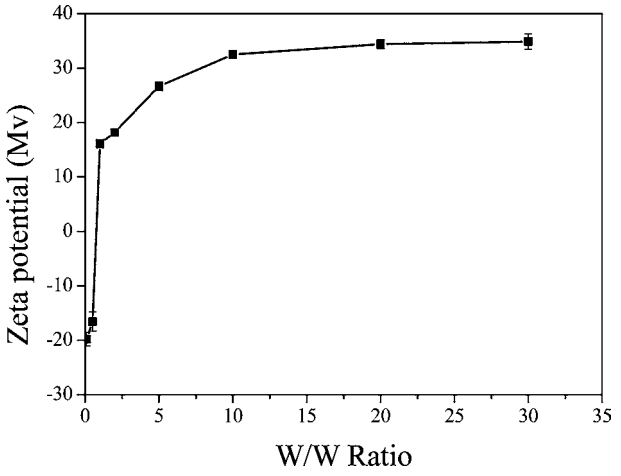

Figure 4. Zeta potentials of PAA-*g*-MWNT/DNA complexes at w/w ratios ranging from 0.5 to 30 in 10 mmol L^{-1} NaCl aqueous solution.

zeta potential of the complexes is negative, indicating incomplete complexation. With increase of the w/w ratio, the zeta potential increased rapidly and reached a plateau of about 35 mV.

In Vitro Transfection. In vitro transfection was conducted on COS-7 and HeLa cells to evaluate the ability of the PAA-*g*-MWNTs to deliver foreign DNA into cells. PAA and branched PEI 25KDa at the optimal w/w ratio were used as positive controls, and pGL-3 was used as the report gene.

The transfection results in Figure 5A reveal that PAA-*g*-MWNTs showed excellent transfection efficiency in COS-7 cells at w/w ratios from 2 to 30, which is comparable or higher than that of branched PEI 25KDa. Luciferase expression (RLU/mg protein) was related to the w/w ratio, with the w/w ratio increasing, the luciferase expression increased obviously. Optimized luciferase expression (RLU/mg protein) in COS-7 cells with PAA-*g*-MWNTs/pGL-3 complexes was a little higher than that with PEI/pGL-3 complexes. The high transfection

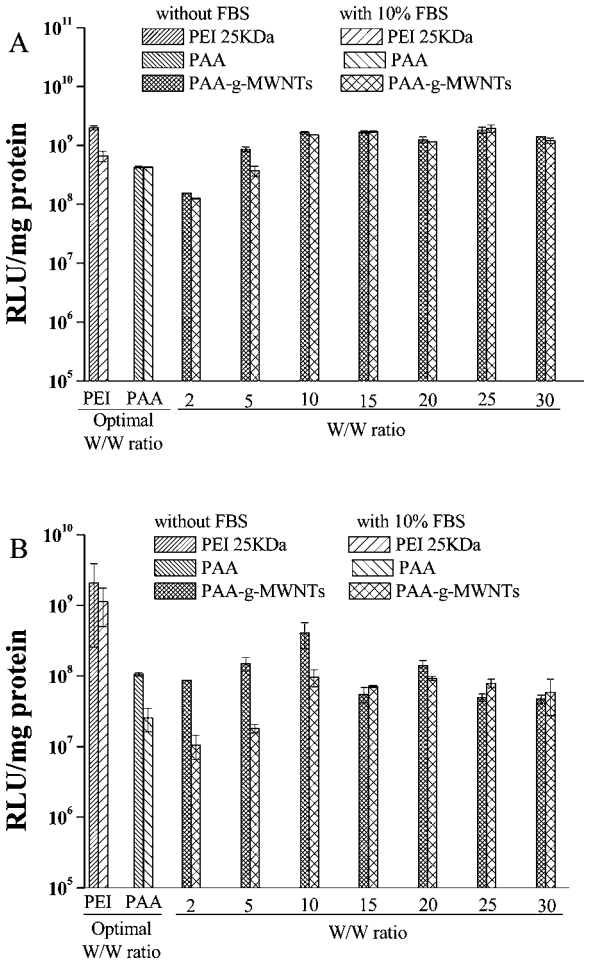

Figure 5. Transfection efficiencies of PAA-*g*-MWNTs/pGL-3 complexes in COS-7 (A) and HeLa (B) cells. PAA and branched PEI 25KDa were used as positive control.

efficiencies of PAA-*g*-MWNTs should be related to the combinational factors including low cytotoxicity, strong DNA binding ability and small particle size.

Similarly, the transfection results (Figure 5B) indicate that PAA-*g*-MWNTs still express high transfection efficiencies in HeLa cells, and the luciferase expression at optimal w/w ratio was comparable to that of PEI/pGL-3 complexes.

Serum protein can hinder cellular uptake and promote aggregation, often leading to reduction of the transfection efficiency. To understand the effect of serum on the DNA transfection, a transfection experiment was then performed with COS-7 cells in the presence of 10% FBS. As shown in Figure 5A, 10% of serum inhibited luciferase expression in COS-7 cells with each polycation tested in this work including PEI and PAA-*g*-MWNTs. The results illustrated that luciferase expression in COS-7 cells only slightly decreased at low w/w ratios; specifically, with the w/w ratio increasing, the luciferase expression could not be effectively prohibited by serum, indicating that the PAA-*g*-MWCNTs/DNA complexes were less serum-sensitive for in vitro transfection. Similar results were obtained in the case of HeLa cells.

Intracellular Trafficking of Cy3-Labeled pGL-3. Intracellular trafficking of Cy3-labeled pGL-3 was analyzed by CLSM and the result is shown in Figure 6. The optimal w/w ratio for PAA-*g*-MWNTs and PEI 25KDa was determined to be 15 and 1.3, respectively. In order to distinguish the nucleus and

dx.doi.org/10.1021/bc200189f | *Bioconjugate Chem.* 2011, 22, 2237−2243

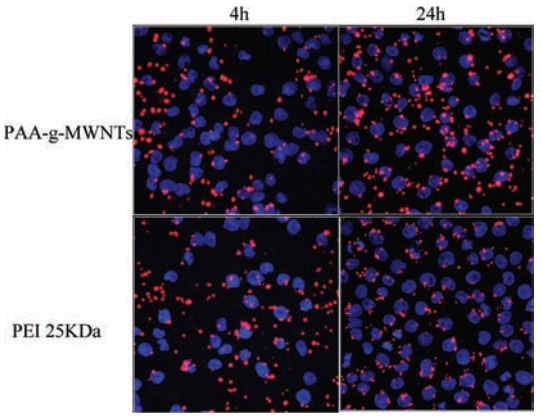

Figure 6. Intracellular trafficking of Cy3-labeled pGL-3 (red) when combined with PAA-*g*-MWNTs and PEI 25KDa at optimal w/w ratio. The localization of fluorescent particles in COS-7 cells was visualized at 4 and 24 h post-transfection. Nucleus (blue) was stained with Hoechst 33258.

DNA, Hoechst 33258 was used to stain the nucleus, which appeared to be blue fluorescence; meanwhile, the Cy3-labeled pGL-3 appeared to be red fluorescence.

As shown in Figure 6, after transfection for 4 h, Cy3-labeled pGL-3 was clearly visible. For PAA-*g*-MWNTs and PEI, a large amount of Cy3-labeled pGL-3 was dispersed in the cytoplasm and only a few red fluorescence particles were found interacting with the nucleus membrane. Meanwhile, very little Cy3-labeled pGL-3 was observed in the nucleus. After 24 h of transfection, significant differences appeared within each group: most of the red fluorescence particles were found aggregating in the nucleus. For PAA-*g*-MWNTs, lots of red fluorescence particles around the nucleus were observed, and almost all of the cells in the field of view showed DNA nucleus localization. Similar results were observed for PEI: there was no obvious difference with distribution of Cy3-labeled pGL-3 between PAA-*g*-MWNTs and PEI, except that cells transfected by PEI showed relatively lower fluorescence density in nuclear localization.

DISCUSSION

In our experiment, the carboxyl groups on the surface of MWNTs were first converted to succinimide-terminated (Scheme 1); after the carboxyl groups were activated, the cationic PAA was then added to the solution above, thus leading to the formation of PAA-*g*-MWNTs. Similar procedures were also reported previously.[24] The obtained aqueous solution of PAA-*g*-MWNTs was stable at room temperature without any precipitation for up to 6 months, as shown in Figure S2 (see Supporting Information); however, the aqueous solution of MWNTs-COOH precipitated rapidly, usually within a few hours.

The size and morphology of MWNTs-COOH, PAA-*g*-MWNTs, and PAA-*g*-MWNTs/DNA were characterized by SEM. Figure 7A,B shows the image of raw MWNTs-COOH and PAA-*g*-MWNTs. Obviously, after grafting with PAA, the morphology of MWNTs did not change significantly. Figure 7C presents the image of PAA-*g*-MWNTs/DNA. The SEM analysis did not reveal significant differences in size among the MWNTs-COOH, PAA-*g*-MWNTs, and PAA-*g*-MWNTs/DNA. A similar result was also reported by Gao and colleagues.[30]

Cytotoxicity of carriers is a very important factor in gene delivery. Previous work[25,26] demonstrated that polycations first combined with cell membrane via electrostatic interaction between positively charged polycations and negatively charged sites on the cells, which induced polycations to aggregate on the cell membrane and lead to cell death. Functionalization of carbon nanotubes has proven to be very useful for reducing their cytotoxicity.[27−29] Our results indicated that PAA-*g*-MWNTs showed no significant cytotoxicity to COS-7 cells at low concentration. However, with the concentration increasing, the cytotoxicity increased slowly. The IC_{50} values of PAA-*g*-MWNTs and PAA in COS-7 cells were estimated to be 108 and 66 μg/mL, respectively, much lower than that of PEI (IC_{50} = 10 μg/mL).[22] The IC_{50} values of PAA-*g*-MWNTs and PAA to HeLa cells are 78 and 52 μg/mL, respectively, which is similar to the case of COS-7 cells. Since PAA contains primary and tertiary amine groups, PAA-*g*-MWNTs may behave as a polycation molecule, and thus cause certain cytotoxicity.

The ability of vectors to condense DNA into small-sized particles is another important factor in gene delivery. To facilitate efficient gene expression, cationic polymers should strongly condense DNA to protect the DNA against digestion by enzymes, and thus improve transfection efficiency. The interaction of PAA-*g*-MWNTs with the pEGFP-N1 plasmid was investigated by gel retardation assay, zeta potential measurement, and SEM.

Gel retardation assay was performed to explore whether PAA-*g*-MWNTs could effectively bind DNA. The result in Figure 3 reveals that PAA-*g*-MWNTs could efficiently condense DNA, and entirely retain DNA at w/w ratio above 1.5. The zeta potential reached a plateau of about 35 mV, while the PAA/DNA complexes reached a plateau of about 20 mV,[22] which was much lower than that of PAA-*g*-MWNTs/DNA complexes. PAA-*g*-MWNTs with high zeta potential would facilitate electrostatic interaction between cationic PAA-*g*-MWNTs and polyanionic DNA.

Transfection efficiency is the most important factor in gene delivery. In our work, PAA-*g*-MWNTs could deliver foreign DNA into COS-7 and HeLa cells, with the transfection

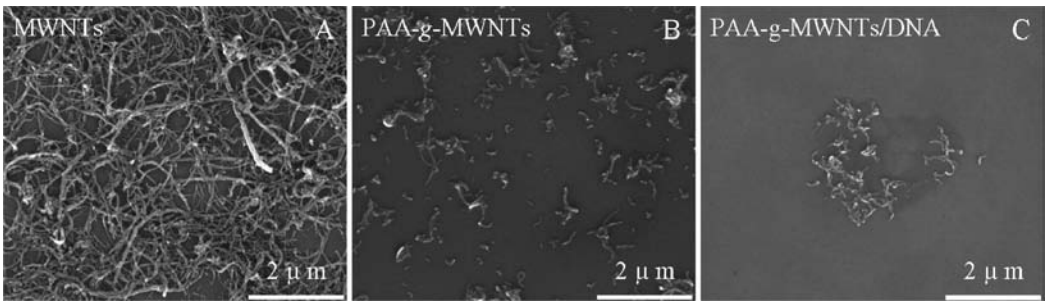

Figure 7. SEM images of MWNTs-COOH, PAA-*g*-MWNTs, and PAA-*g*-MWNTs/DNA.

dx.doi.org/10.1021/bc200189f | *Bioconjugate Chem.* 2011, 22, 2237−2243

efficiencies comparable or even higher than that of PEI 25KDa at optimal w/w ratio. Many factors are considered to affect transfection efficiencies, among which w/w ratio is the most important factor. With increasing of w/w ratio, the transfection efficiency rosed up steeply, then reached a plateau, and finally decreased. With the w/w ratio increasing, the cytotoxicity increased, leading to decrease in the cell viability and transfection efficiency. In addition, changing the w/w ratios would also alter the surface charge of PAA-*g*-MWNTs/DNA complexes, which could influence the DNA binding ability, and in turn, the transfection efficiency. Previous work has demonstrated that complexes with positive charge and small size are beneficial for cellular uptake and intracellular trafficking. In our study, PAA-*g*-MWNTs/DNA complexes possess high positive charge (35 mV), the average length is about 300 nm, and the diameter about 30−40 nm.

Cellular uptake and nuclei localization of PAA-*g*-MWNTs were studied by delivery of Cy3-labeled pGL-3 to cells. Besides the extracellular and cellular obstacles which reduced gene expression, nuclear envelope is recognized as one of the most important intracellular barriers. CLSM results in Figure 6 indicate that, for PAA-*g*-MWNTs and PEI, a majority of red fluorescence particles were attached to nucleus membrane within 4 h incubation, and some of them had already localized in the perinuclear region and localized in nucleus after 24 h incubation. On the basis of the results, intracellular trafficking and cellular uptake of Cy3-labeled pGL3 displayed that PAA-*g*-MWNTs showed superior DNA delivery ability to COS-7 nucleus than others.

CONCLUSIONS

In summary, PAA-grafted multiwalled carbon nanotubes were successfully prepared to deliver foreign DNA to cells. In comparison to PAA and PEI 25 KDa, PAA-*g*-MWNTs showed significantly low cytotoxicity and strong ability to condense DNA. Transfection efficiency results revealed that PAA-*g*-MWNTs possessed comparable or even higher luciferase expression than PAA and PEI at optimal w/w ratio. Intracellular trafficking of Cy3-labeled pGL-3 also displayed that PAA-*g*-MWNTs showed superior ability to deliver foreign DNA into cell nucleus. The current study may provide useful insight into design of novel nanovectors for efficient and nontoxic gene delivery.

ASSOCIATED CONTENT

Supporting Information

Additional figures as described in the text. This material is available free of charge via the Internet at http://pubs.acs.org.

AUTHOR INFORMATION

Corresponding Author

*Telephone: 86-0512-62872556; Fax: 86-0512-62603079; E-mail: zjzhang2007@sinano.ac.cn.

ACKNOWLEDGMENTS

The financial support of this research from NSFC (No. 20873090, 21073224) and Innovation Project of CAS (KJCX2.YW.M12) is gratefully acknowledged. We thank Characterization and Test Platform at SINANO for assistance with instrumentation.

REFERENCES

(1) Anderson, W. F. (1998) Human gene therapy. *Nature 392*, 25−30.
(2) Li, S., and Huang, L. (2000) Nonviral gene therapy: promises and challenges. *Gene Ther. 7*, 31−34.
(3) Wong, S. Y., Pelet, J. M., and Putnam, D. (2007) Polymer systems for gene delivery-past, present, and future. *Prog. Polym. Sci. 32*, 799−837.
(4) Mintzer, M. A., and Simanek, E. E. (2009) Nonviral vectors for gene delivery. *Chem. Rev. 109*, 259−302.
(5) Richard, C., Mignet, N., Largeau, C., Escriou, V., Bessodes, M., and Scherman, D. (2009) Functionalization of single- and multi-walled carbon nanotubes with cationic amphiphiles for plasmid DNA complexation and transfection. *Nano Res. 2*, 638−647.
(6) Liu, Y., Wu, D. C., Zhang, W. D., Jiang, X., He, C. B., Chung, T. S., Goh, S. H., and Leong, K. W. (2005) Polyethylenimine-grafted multiwalled carbon nanotubes for secure noncovalent immobilization and efficient delivery of DNA. *Angew. Chem., Int. Ed. 44*, 4782−4785.
(7) Pantarotto, D., Singh, R., McCarthy, D., Erhardt, M., Briand, J. P., Prato, M., Kostarelos, K., and Bianco, A. (2004) Functionalized carbon nanotubes for plasmid DNA gene delivery. *Angew. Chem., Int. Ed. 43*, 5242−5246.
(8) Herrero, M. A., Toma, F. M., Al-Jamal, K. T., Kostarelos, K., Bianco, A., Ros, T. D., Bano, F., Casalis, L., Scoles, G., and Prato, M. (2009) Synthesis and characterization of a carbon nanotube-dendron series for efficient siRNA delivery. *J. Am. Chem. Soc. 131*, 9843−9848.
(9) Feng, L. Z., Zhang, S., and Liu, Z. (2011) Graphene based gene transfection. *Nanoscale 3*, 1252−1257.
(10) Zhang, L. M., Lu, Z. X., Zhao, Q. H., Huang, J., Shen, H., and Zhang, Z. J. (2011) Enhanced chemotherapy efficacy by sequential delivery of siRNA and anticancer drugs using PEI-grafted graphene oxide. *Small 7*, 460−464.
(11) Liu, Z., Winters, M., Holodniy, M., and Dai, H. J. (2007) siRNA delivery into human T cells and primary cells with carbon-nanotube transporters. *Angew. Chem., Int. Ed. 46*, 2023−2027.
(12) Bartholomeusz, G., Cherukuri, P., Kingston, J., Cognet, L., Lemos, R., Leeuw, T. K., Gumbiner-Russo, L., Weisman, R. B., and Powis, G. (2009) In vivo therapeutic silencing of hypoxia-inducible factor 1 alpha (HIF-1α) using single-walled carbon nanotubes noncovalently coated with siRNA. *Nano Res. 2*, 279−291.
(13) Shi, X. Y., Wang, S. H., Shen, M. W., Antwerp, M. E., Chen, X. S., Li, C., Petersen, E. J., Huang, Q. G., Weber, W. J., and Baker, J. R. (2009) Multifunctional dendrimer-modified multiwalled carbon nanotubes: synthesis, characterization, and in *vitro* cancer cell targeting and imaging. *Biomacromolecules 10*, 1744−1750.
(14) Pan, B. F., Cui, D. X., Xu, P., Ozkan, C., Feng, G., Ozkan, M., Huang, T., Chu, B. F., Li, Q., He, R., and Hu, G. H. (2009) Synthesis and characterization of polyamidoamine dendrimer-coated multi-walled carbon nanotubes and their application in gene delivery systems. *Nanotechnology 20*, 125101.
(15) McCarroll, J., Baigude, H., Yang, C. S., and Rana, T. M. (2010) Nanotubes functionalized with lipids and natural amino acid dendrimers: a new strategy to create nanomaterials for delivering systemic RNAi. *Bioconjugate Chem. 21*, 56−63.
(16) Qin, W. L., Yang, K. Q., Tang, H., Tan, L., Xie, Q. J., Ma, M., Zhang, Y. Y., and Yao, S. Z. (2011) Improved GFP gene transfection mediated by polyamidoamine dendrimer-functionalized multi-walled carbon nanotubes with high biocompatibility. *Colloids Surf., B: Biointerfaces 84*, 206−213.
(17) Zhang, B. L., Chen, Q., Tang, H., Xie, Q. J., Ma, M., Tan, L., Zhang, Y. Y., and Yao, S. Z. (2011) Characterization of and biomolecule immobilization on the biocompatible multi-walled carbon nanotubes generated by functionalization with polyamidoamine dendrimers. *Colloids Surf., B: Biointerfaces 80*, 18−25.
(18) Dufes, C., Uchegbu, I. F., and Schatzlein, A. G. (2005) Dendrimers in gene delivery. *Adv. Drug Delivery Rev. 57*, 2177.
(19) Danusso, F., and Ferruti, P. (1970) Synthesis of tertiary amine polymers. *Polymer 11*, 88−113.

(20) Lin, C., Blaauboer, C. J., Timoneda, M. M., Lok, M. C., Steenbergen, M. V., Hennink, W. E., Zhong, Z. Y., Feijen, J., and Engbersen, J. F. J. (2008) Bioreducible poly(amido amine)s with oligoamine side chains: Synthesis, characterization, and structural effects on gene delivery. *J. Controlled Release 126*, 166−174.
(21) Reschel, T., Konak, C., Oupicky, D., Seymour, L. W., and Ulbrich, K. (2002) Physical properties and in *vitro* transfection efficiency of gene delivery vectors based on complexes of DNA with synthetic polycations. *J. Controlled Release 81*, 201−217.
(22) Liu, M., Chen, J., Cheng, Y. P., Xue, Y. N., Zhuo, R. X., and Huang, S. W. (2010) Novel poly(amidoamine)s with pendant primary amines as highly efficient gene delivery vectors. *Macromol. Biosci. 10*, 384−392.
(23) Liu, J., Rinzler, A. G., Dai, H. J., Hafner, J. H., Bradley, R. K., Boul, P. J., Lu, A., Iverson, T., Shelimov, K., Huffman, C. B., Rodriguez-Macias, F., Shon, Y. S., Lee, T. R., Colbert, D. T., and Smalley, R. E. (1998) Fullerene pipes. *Science 280*, 1253−1255.
(24) Ahmed, M., Jiang, X. Z., Deng, Z. C., and Narain, R. (2009) Cationic glycol-functionalized single-walled carbon nanotubes as efficient gene delivery vehicles. *Bioconjugate Chem. 20*, 2017−2022.
(25) Kunath, K., Harpe, A. V., Fischer, D., Petersen, H., Bickel, U., Voigt, K., and Thomas, K. (2003) Low-molecular-weight polyethylenimine as a non-viral vector for DNA delivery: comparison of physicochemical properties, transfection efficiency and in vivo distribution with high-molecular-weight polyethylenimine. *J. Controlled Release 89*, 113−125.
(26) Choksakulnimitr, S., Masuda, S., Tokuda, H., Takakura, Y., and Hashida, M. (1995) In *vitro* cytotoxicity of macromolecules in different cell culture systems. *J. Controlled Release 34*, 233−241.
(27) Lacerda, L., Ali-Boucetta, H., Herrero, M. A., Pastorin, G., Bianco, L., Prato, M., and Kostarelos, K. (2008) Tissue histology and physiology following intravenous administration of different types of functionalized multiwalled carbon nanotubes. *Nanomedicine 3*, 149−161.
(28) Dumortier, H., Lacotte, S., Pastorin, G., Marega, R., Wu, W., Bonifazi, D., Briand, J. P., Prato, M., Muller, S., and Bianco, A. (2006) Functionalized carbon nanotubes are non-cytotoxic and preserve the functionality of primary immune cells. *Nano Lett. 6*, 1522−1528.
(29) Singh, R., Pantarotto, D., Lacerda, L., Pastorin, G., Klumpp, C., Prato, M., Bianco, A., and Kostarelos, K. (2006) Tissue biodistribution and blood clearance rates of intravenously administered carbon nanotube radiotracers. *Proc. Natl. Acad. Sci. 103*, 3357−3362.
(30) Gao, L. Z., Nie, L., Wang, T. H., Qin, Y. J., Guo, Z. X., Yang, D. L., and Yan, X. Y. (2006) Carbon nanotube delivery of the GFP gene into mammalian cells. *ChemBioChem 7*, 239−242.

Supporting Information

Polyamidoamine-Grafted Multiwalled Carbon Nanotubes for Gene Delivery: Synthesis, Transfection and Intracellular Trafficking

Min Liu,[†] Biao Chen,[†] Yanan Xue,[‡] Jie Huang,[†] Liming Zhang,[†] Shiwen Huang,[‡] Qingwen Li,[†] and Zhijun Zhang[*,†]

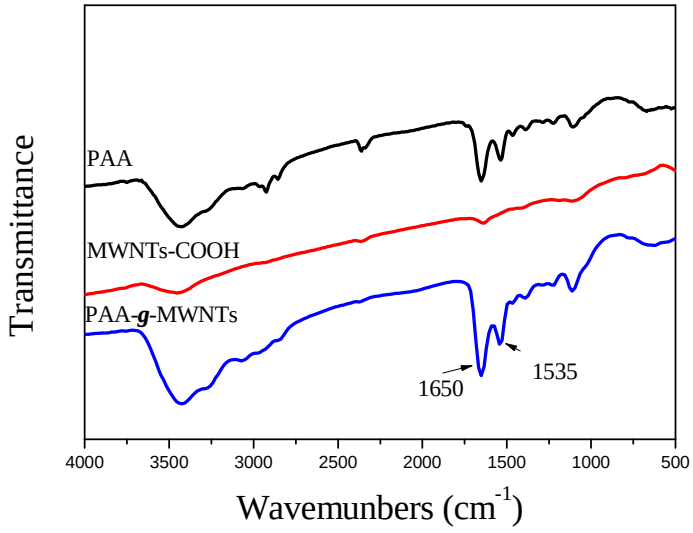

Figure S1. IR spectra of PAA, MWNTs-COOH, and PAA-***g***-MWNTs.

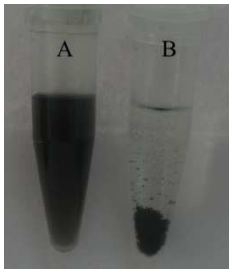

Figure S2. Photograph of (A) aqueous solution of PAA-***g***-MWNTs, which was still stable at ambient condition for up to 6 months, and (B) MWNTs dispersed in water, which was precipitated in several hours after preparation.

Bioconjugate Chemistry

Article

pubs.acs.org/bc

Synthesis and Transfection Efficiency of Cationic Oligopeptide Lipids: Role of Linker

Vijaya Gopal,[†] Jennifer Xavier,[†] Md. Zahid Kamal,[†] Srinath Govindarajan,[†] Makoto Takafuji,[‡] Shuta Soga,[‡] Takayuki Ueno,[‡] Hirotaka Ihara,[‡] and Nalam M. Rao*[,†]

[†]Centre for Cellular and Molecular Biology (Council of Scientific and Industrial Research), Uppal Road, Hyderabad, India 500007

[‡]Department of Applied Chemistry and Biochemistry, Kumamoto University, Kumamoto, Japan

Supporting Information

ABSTRACT: In the design of new cationic lipids for gene transfection, the chemistry of linkers is widely investigated from the viewpoint of biodegradation and less from their contribution to the biophysical properties. We synthesized two dodecyl lipids with glutamide as the backbone and two lysines to provide the cationic headgroup. Lipid 1 differs from Lipid 2 by the presence of an amide linkage instead of an ester linkage that characterizes Lipid 2. The transfection efficiency of lipoplexes with cholesterol as colipid was found to be very high with Lipid 1 on Chinese Hamster Ovary (CHO) and HepG2 cell lines, whereas Lipid 2 has shown partial transfection efficiency on HepG2 cells. Lipid 1 was found to be stable in the presence of serum when tested in HepG2 and CHO cells albeit with lower activity. Fluorescence-based dye-binding and agarose gel-based assays indicated that Lipid 1 binds to DNA more efficiently than Lipid 2 at charge ratios of >1:1. The uptake of oligonucleotides with Lipid 1 was higher than Lipid 2 as revealed by confocal microscopy. Transmission electron microscopy (TEM) images reveal distinct formation of liposomes and lipoplexes with Lipid 1 but fragmented and unordered structures with Lipid 2. Fusion of Lipids 1 and 2 with anionic vesicles, with composition similar to plasma membrane, suggests that fusion of Lipid 2 was very rapid and unlike a fusion event, whereas the fusion kinetics of Lipid 1 vesicles was more defined. Differential scanning calorimetry (DSC) revealed a high T_m for Lipid 1 (65.4 °C) while Lipid 2 had a T_m of 23.5 °C. Surface area–pressure isotherms of Lipid 1 was less compressible compared to Lipid 2. However, microviscosity measured using 1,6-diphenyl-1,3,5-hexatriene (DPH) revealed identical values for vesicles made with either of the lipids. The presence of amide linker apparently resulted in stable vesicle formation, higher melting temperature, and low compressibility, while retaining the membrane fluid properties suggesting that the intermolecular hydrogen bonds of Lipid 1 yielded stable lipoplexes of high transfection efficiency.

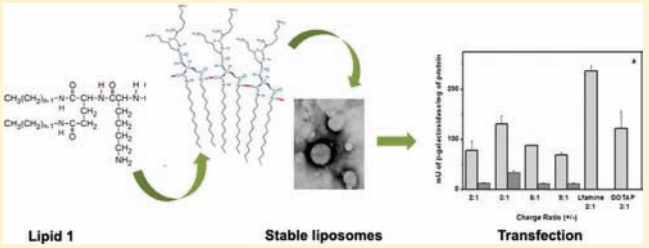

INTRODUCTION

Cationic lipid-based formulations offer attractive solutions for *in vitro* delivery of nucleic acids.[1−4] Liposomes containing cationic lipids electrostatically bind with the polyanionic nucleic acids resulting in a lipoplex that protects nucleic acids from degradation and facilitates endosomal uptake.[5,6] Structurally, cationic lipids are amphiphilic with a hydrophilic cationic headgroup connected with a linker to hydrophobic tails, usually alkyl chains.[7−9] Extensive investigations on chemistry and transfection efficiency of cationic lipids suggest that a wide variety of molecules are suitable when appropriate amphiphilicity is maintained.[5,6] Alkyl chains [8,10] and steroid molecules[11] are a few examples that were found suitable as hydrophobic groups, while a large variety of cationic groups such as primary or tertiary amines together with polyamine and quarternary ammonium,[12,13] guanidino groups,[14] and amino acids[15] were found to enhance transfection efficiency. The enhancement in transfection efficiency in the presence of a neutral lipid or a colipid such as phosphatidylethanolamine or cholesterol was the prime motivation to successfully test a large number of cationic lipids with colipids.

Transfection efficiency by cationic lipids is strongly dependent on the cell type and inclusion of colipids in formulations.[16−18] To obtain insight into the relationship between transfection efficiency and the properties such as size, charge, stability, and interaction with the biological membranes, cationic lipids have been extensively investigated.[15] These studies indicated that compact, fluid, and positively charged lipoplexes overcome serum destabilization, enhanced cellular associations, and eventual escape from the endosomes by fusion.[19] Amino acids or short peptides have been used, especially as headgroup moieties, in the design of cationic lipids.[15] Cationic amino acids lysine and arginine have been extensively used to provide the cationic headgroup[15] to facilitate complexation with the nucleic acids. The pK_a properties of amino acid histidine have been used successfully[20] to cause endosomolysis after uptake of lipoplex. However, use of amino acids as backbone for the cationic lipid has not been investigated. Earlier, we reported

Received: June 3, 2011
Revised: September 19, 2011
Published: October 11, 2011

ACS Publications © 2011 American Chemical Society

dx.doi.org/10.1021/bc2002874 | *Bioconjugate Chem.* 2011, 22, 2244–2254

synthesis and transfection efficiencies of pyridinium-based cationic lipids with glutamide as the backbone.[21] In the design of cationic lipids, linkers are used to connect the headgroup or the hydrophobic portion to the backbone, for example, glycerol.[22−24] This is to provide biodegradability and thereby safety due to decreased toxicities. Ester linkages are preferred over ether linkers[25] primarily for their biodegradability. In some reports, the linkers are designed to enhance the release of the nucleic acid from the lipoplex in response to a change in conditions inside the cell. For example, low pH labile bonds are used to dissociate the headgroup from the lipid in the endosomal compartment and release the plasmid DNA.[13] Reduction of linkers with disulfide bonds in the cytoplasmic milieu destabilizes the complex[26] thereby separating the nucleic acid from the liposomes. Recently, in an otherwise chemically similar lipid, the linker orientation was shown to have dramatic effect on the transfection properties of the lipid.[24] We report in this study two lysinated-glutamide lipids which differ from each other only in their linker chemistry, i.e., either amide or an ester designated as Lipid 1 and Lipid 2, respectively. Lipid 1 with an amide linker melts at a higher temperature and has higher transfection efficiency than the low melting counterpart Lipid 2 with the ester linker. This striking structural difference between the two lipids motivated further investigations to address whether the linker has any role in determining the transfection efficiency.

EXPERIMENTAL PROCEDURES

Materials. In this work, all chemicals and solvents were purchased and used without further purification. The chemical structures of the lipids were identified by melting point, FTIR, ^{1}H NMR, and elemental analysis. Melting points were determined on a micro melting point apparatus. FTIR spectra were performed on a JASCO FT/IR-4000 spectrometer. ^{1}H NMR spectra were recorded by a JEOL JNM-EX400 spectrometer using tetramethylsilane as an internal standard. Elemental analyses were performed with a Yanaco CHN Corder MT-3. ESI-HRMS was performed on a QSTAR XL hybrid MS/MS system (Applied Biosystems/MDS sciex), equipped with an ESI source.

1,6-diphenyl-1,3,5-hexatriene, ethidium bromide, NBD-DHPE, and Rhodamine −DHPE were purchased from Molecular Probes (USA). 1,2-Dioleoyl-*sn*-glycero-3-phosphoethanolamine (DOPE), cholesterol, L-α-phosphatidylglycerol (PG), and 1,2-dioleoyl-*sn*-glycero-3-phosphocholine (DOPC) were purchased from Avanti Polar Lipids (USA). Fluorescein (FAM) Labeling Kits were sourced from Ambion. 3-(4,5-Dimethylthiazol-2-yl)-2,5-diphenyltetrazolium bromide (MTT) and other reagents were purchased from Sigma Co.

Synthesis of Z-Lys(Z)-Lys(Z)-OH. *(A). Z-Lys(Z)-Lys(Z)-OMe.* Z-Lys(Z)-OH (3.42 g, 9.06 mmol), H-Lys(Z)-OMe·HCl (3.0 g, 9.06 mmol), and triethylamine (2.76 g, 27.1 mmol) were dissolved in chloroform. The solution was cooled to 0 °C, and DEPC (1.97 g, 1.09 mmol) was added to the solution and stirred for 30 min at this temperature. After stirring for 1 day at room temperature, the solution was concentrated *in vacuo*, and the residue was dissolved in chloroform. The solution was washed with 0.2 N HCl, 5 wt % $NaHCO_3$, and water. The solution was dried over Na_2SO_4, concentrated, and finally added to diethyl ether, which gave a white solid powder: yield 4.56 g (73%, 6.5 mmol); mp 103−105 °C; FT-IR (KBr) 3316, 2942, 1741, 1690, 1650, and 1542 cm^{-1}; ^{1}H NMR ($CDCl_3$) δ 1.37 (m, 4H, C*HCH$_2$CH_2), 1.49 (m, 4H, CH_2CH_2NH), 1.62 (m, 2H, CHCH_2(CH$_2$)$_3$NH), 1.83 (q, 2H, $CH_3OC(=O)C^*HCH_2$), 3.08−3.18 (m, 4H, C*H-(CH$_2$)$_3$CH_2NHC(=O)), 3.68 (s, 3H, CH_3), 4.18 (s, 1H, $CH_3OC(=O)C^*H$), 4.53 (s, 1H, NHC(=O)C*HNHC(=O)), 5.07 (m, 6H, C*H_2Ph), 7.35 (d, 15H, C_6H_5). Anal. Found: H, 6.77%; C, 63.4%; N, 7.97%. Calcd. for $C_{37}H_{46}N_4O_9$: H, 6.71%; C, 64.3%; N, 8.11%.

(B). Z-Lys(Z)-Lys(Z)-OH. Z-Lys(Z)-Lys(Z)-OMe (4.6 g, 6.60 mmol) and 1 N NaOH 19 mL (19 mmol) were dissolved in 100 mL methanol, stirred for 1 h at room temperature, and pH was adjusted to 2 by 1 N HCl. After removing methanol from the solution *in vacuo*, the residue was added to ethanol. The obtained white precipitate was removed by filtration, and the solution was concentrated and added to *n*-hexane to give a white precipitate. The precipitate was collected by filtration and dried *in vacuo*: yield 4.30 g (95% 6.35 mmol) mp 145−147 °C; FT-IR (KBr) 3322, 2941, 2863, 1692, 1652, and 1541 cm^{-1}; ^{1}H NMR ($CDCl_3$) δ 1.35 (m, 4H, C*HCH$_2$CH_2), 1.47 (m, 4H, CH_2CH_2NH), 1.63−1.86 (br, 4H, C*HCH_2), 3.10 (d, 4H, C*H(CH$_2$)$_3$CH_2NHC(=O)), 4.26 (s, 1H, HOC(=O)C*H), 4.50 (s, 1H, NHC(=O)C*HNHC(=O)), 5.06 (m, 6H, CH_2Ph), 7.29 (d, 15H, C_6H_5). Anal. Found: H, 6.86%; C, 63.44%; N, 8.08%. Calcd. for $C_{36}H_{44}N_4O_9$: H, 6.55%; C, 63.9%; N, 8.28%.

Synthesis of Lipid 1 (2C$_{12}$-Gln-Lys-Lys). *(A). Synthesis of 2C$_{12}$-Gln.* Synthesis of 2C$_{12}$-Gln was described earlier (*Bioconjugate Chem.* **2006**, *17*, 1530).

(B). 2C$_{12}$-Gln-Lys(Z)-Lys(Z)-Z. 2C$_{12}$-Gln (0.93 g, 1.93 mmol), Z-Lys(Z)-Lys(Z)-OH (1.30 g, 1.92 mmol), and triethylamine (0.37 g, 3.84 mmol) were dissolved in dry THF (100 mL). The solution was cooled to 0 °C, and DEPC (0.52 g, 2.88 mmol) was added to the solution and stirred for 1 day at room temperature. After stirring, the solution was concentrated *in vacuo*, and the lipid was recrystallized from ethanol, which gave a white solid powder: yield 1.07 g (50%, 0.94 mmol); mp 184−187 °C; FT-IR (KBr) 3295, 2925, 2853, 1693, 1637, and 1543 cm^{-1}; ^{1}H NMR ($CDCl_3$) δ 0.86−0.89 (t, 6H, CH_3), 1.25 (m, 36H, CH$_3$(CH_2)$_9$), 1.33 (s, 4H, CH_2CH$_2$NHC(=O)), 1.48 (br, 6H, C*H(CH_2)NHC(=O)), 1.58−2.40 (s, 8H, C*HCH$_2$CH_2CH$_2$, C*HCH$_2$CH$_2$CH_2), 2.44 (m, 2H, C*HCH$_2$CH_2C(=O)), 3.16−3.23 (br, 8H, CH_2NHC(=O), CH_2NHC(=O)O), 4.11 (s, 1H, C*HNHC(=O)), 4.35 (s, 1H, C*HNHC(=O)), 4.51 (s, 1H, C*HNHC(=O)), 4.92−5.15 (br, 6H, CH_2Ph) 7.28−7.34 (m, 15H, C_6H_5). Anal. Found: H, 8.94%; C, 68.3%; N, 8.56%; Calcd. for $C_{65}H_{101}N_7O_{10}$: H, 8.93%; C, 68.5%; N, 8.60%.

(C). 2C$_{12}$-Gln-Lys-Lys. 2C$_{12}$-Gln-Lys(Z)-Lys(Z)-Z (0.93 g, 0.82 mmol) was dissolved in 100 mL ethanol with heating, and Pd/carbon (0.5 g) was added to the solution. H_2 gas was bubbled slowly into the solution for 14 h at 70 °C. Pd/carbon was removed by filtration, and the solution was dried *in vacuo* to give a solid powder: yield 0.34 g (52%, 0.43 mmol, as a trihydrate); mp 104−107 °C; FT-IR (KBr) 3289, 2920, 2851, 1639, and 1557 cm^{-1}; ^{1}H NMR ($CDCl_3$) δ 0.87−0.90 (t, 6H, CH_3), 1.28 (m, 36H, CH$_3$(CH_2)$_9$), 1.52−2.17 (br, 20H, CH_2CHNHC(=O), CH_2C*H, CH_2CH$_2$C*H, CH_2(CH$_2$)$_2$C*H), 3.12−3.35 (br, 8H, CH_2-NHC(=O), CH_2NHC(C=O)O), 4.31−4.56 (br, 3H, C*HNHC(=O)). Anal. Found: H, 10.9%; C, 64.9%; N, 11.4%. Calcd. for $C_{41}H_{89}N_7O_7$: H, 11.3%; C, 62.2%; N, 12.4%. ESI-HRMS: m/z = +738.6569 (calcd value for $C_{41}H_{84}N_7O_4$ = 738.6584).

Synthesis of Lipid 2 (2C$_{12}$Glu-Lys-Lys). *(A). Didodecyl-L-Glutamate Toluene-p-Sulfonate (2C$_{12}$L-Glu TosOH).* L-Glutamic acid (6.0 g, 40.0 mmol), *p*-toluenesulfonic acid

(6.82 g, 48.0 mmol), and 1-dodecanol (17.8 g, 96.0 mmol) were dissolved in toluene (250 mL), and refluxed for 5 h by use of Dean−Stark apparatus. The solution was concentrated in vacuo, and the residue was dissolved in 200 mL of diethyl ether, and refrigerated to 4 °C for 1 day, which gave a white solid powder: yield 13.1 g (49%), mp 65−66 °C. Anal. Found: H, 9.93; C, 65.4; N, 2.40; Calcd. for $C_{36}H_{65}NO_7S$: H, 9.99; C, 65.9; N, 2.14. FT-IR (KBr) 2921 cm^{-1} (ν_{C-H}), 2850 cm^{-1} (ν_{C-H}), 1743 cm^{-1} (ν_{ester}), 1533 cm^{-1} (δ_{NH}), 1182 cm^{-1} (ν_{C-O}). ^1H NMR ($CDCl_3$, internal reference: tetramethylsilane) δ 0.86−0.90 (m, 6H, CH_3) δ 1.26 (m, 36H, CH_3-$(CH_2)_9$), δ 1.55 (m, 4H, $CH_2CH_2OC(=O)$), δ 2.15−2.25 (m, 2H, $C^*HCH_2CH_2C(=O)$), δ 2.34 (s, 1H,CH_3Ph), δ 2.43−2.58 (m, 2H, $C^*HCH_2CH_2C(=O)$), δ 3.95−4.11 (m, 4H, $CH_2CH_2OC(=O)$), δ 7.12−7.14 (d, 2H, C_6H_5), δ 7.72−7.74 (d, 2H, C_6H_5).

(B). $2C_{12}$Glu-Lys(Z)-Lys(Z)-Z. $2C_{12}$Glu-Lys(Z)-Lys(Z)-Z was synthesized by similar method with $2C_{12}$Gln-Lys(Z)-Lys(Z)-Z: yield 1.20 g (51%); mp 130−131.5 °C; FT-IR (KBr) 3307 cm^{-1} 2924 cm^{-1} (ν_{C-H}), 2853 cm^{-1} (ν_{C-H}), 1732 cm^{-1} ($\nu_{C=O(ester)}$), 1688 cm^{-1} ($\nu_{C=O(urethan)}$), 1640 cm^{-1} ($\nu_{C=O(amide)}$), 1543 cm^{-1} (δ_{N-H}), ^1H NMR ($CDCl_3$) δ 0.86−0.90 (m, 6H, CH_3), δ 1.26 (m, 40H, CH_3-$(CH_2)_9$, $C^*HCH_2CH_2CH_2$), δ 1.49 (m, 4H, $CH_2CH_2NHC(=O)$), δ 1.56 (m, 4H, $CH_2CH_2OC(=O)$), δ 1.68−1.88 (br, 4H, $CH_2C^*HNHC(=O)$), δ 1.94−2.01(m, 1H, $C^*HCH_2CH_2C(=O)$), δ 2.11−2.16 (m, 1H, $C^*HCH_2CH_2C(=O)$), δ 2.36 (m, 2H, $C^*HCH_2CH_2C(=O)$), δ 3.16 (m, 4H, $CH_2CH_2NHC(=O)$), δ 4.03 (m, 4H, $CH_2CH_2OC(=O)$), δ 4.15 (m, 1H, $CH_2OC(=O)C^*HNH$ $C(=O)$), δ4.38 (q, 1H, $NHC(=O)C^*HNH$ $C(=O)$), δ 4.53 (q, 1H, $NHC(=O)C^*HNH$ $C(=O)OCH_2Ph$), δ 5.07 (m, 6H, $PhCH_2OC(=O)$), δ 7.31 (d, 15H, C_6H_5). Anal. Found: H, 8.69; C, 67.8; N, 6.20; Calcd. For $C_{65}H_{99}N_5O_{12}$: H, 8.73; C, 68.3; N, 6.13.

(C). $2C_{12}$-Glu-LysLys. $2C_{12}$Glu-LysLys was synthesized by similar method with $2C_{12}$Gln-LysLys: yield 0.40 g (49%, 0.47 mmol, as a hexahydrate); FT-IR (KBr) 3307 cm^{-1} and 2925 cm^{-1} (ν_{C-H}), 2854 cm^{-1} (ν_{C-H}), 1737 cm^{-1} ($\nu_{C=O(ester)}$), 1654 cm^{-1} ($\nu_{C=O(amide)}$), 1557 cm^{-1} (δ_{N-H}), ^1H NMR ($CDCl_3$) δ 0.86−0.90 (m, 6H, CH_3), δ 1.27 (m, 36H, $CH_3(CH_2)_9$), δ 1.50−2.27 (br, 18H, CH_2), δ 2.51 (m, 2H, $C^*HCH_2CH_2C(=O)$), δ 3.15 (m, 4H, CH_2-NH_2), δ 4.14−4.20 (m, 4H, $CH_2CH_2OC(=O)$), δ 4.30−4.57 (br, 3H, $C^*HNHC(=O)$). Anal. Found: H, 9.4; C, 58.1; N, 8.00. Calcd. for $C_{41}H_{93}N_5O_{12}$: H, 11.1; C, 58.1; N, 8.26. ESI-HRMS: m/z = +740.6245 (calcd value for $C_{41}H_{82}N_5O_6$ = 740.6265).

Preparation of Liposomes. Cationic amphiphiles Lipid **1**, **2**, and the colipid cholesterol were dissolved in chloroform and mixed in glass vials at 1:1 mol ratio. Chloroform was then removed with a thin flow of nitrogen and the dried lipid film was kept under vacuum for 4−5 h. Subsequently, deionized water was added to the dried lipid film for overnight rehydration. The vial was vortexed thoroughly at RT to produce multilamellar vesicles (MLVs). MLVs were sonicated until clarity to obtain small unilamellar vesicles (SUV).

DNA-Binding Assay. *Agarose Gel Electrophoresis.* Plasmid $pGFPN_3$ was complexed with cationic lipids at charge ratios varying from 0.3:1 to 3:1 (lipid/DNA) to measure the DNA binding ability. In a typical binding assay, 0.6 nmol of DNA, corresponding to 200 ng of plasmid DNA, was complexed with the lipids, at indicated charge ratios, in 10 mM phosphate buffer (pH 7.5), deionized water or 0.5× PBS in a volume of 20 μL and incubated at room temperature for 30 min. After addition of the tracking dye bromophenol blue, samples were directly loaded on a 1% agarose gel with TAE buffer and electrophoresed at 80 V for approximately 2 h. The gel was stained with ethidium bromide (EtBr), post electrophoresis, and visualized under a transilluminator. DNA binding was also carried out by EtBr fluorescence titrations as described.[27]

Ethidium Bromide (EtBr) Fluorescence Quenching. The binding of DNA with Lipid **1** and **2** was studied using EtBr as the fluorescent probe. The lipids were reconstituted with colipids DOPE or cholesterol in deionized water using standard protocols. Bound EtBr was expelled from the DNA−EtBr complexes by the lipid. This displacement of EtBr is reflected as a drop in the fluorescence signal, since unbound EtBr does not fluoresce. All fluorescence measurements were carried out using a Hitachi F-4500 fluorescence spectrophotometer. The excitation wavelength, λ_{ex}, was 516 nm and the emission wavelength was kept at 598 nm (slit width 5 × 5 nm^2). Briefly, 2.3 μg of pCMV-β-gal plasmid DNA was added to 500 μL of 20 mM Tris−HCl buffer (pH 7.4) in a fluorescence cuvette. EtBr 0.23 μg, from a diluted stock solution, was added to DNA and the baseline fluorescence was determined. The fluorescence intensity obtained upon each addition of lipid was normalized relative to the fluorescence signal of DNA−EtBr complex, in the absence of the lipid, which was taken as 100%. The binding of DNA by the lipid was recorded after each addition at time intervals of 5 min.

Transfection. CHO, HepG2, cells were plated at a density of 10 000 cells per well in a 96-well plate on the previous day. Plasmid DNA pCMVβ-gal was purified by using the Qiagen Kit (endotoxin free) using the manufacturer's protocol and also by CsCl−EtBr density gradient ultracentrifugation using standard protocols. Plasmid (0.9 μg corresponding to 2.72 nmol) was complexed with varying amounts of Lipid **1** and **2**, formulated with cholesterol at 1:1 mol ratio, to obtain charge ratios varying from 1:1 to 9:1, DNA/Lipid, in DMEM without serum and incubated at RT for 30 min. Complexes were added to cells after appropriate dilution with DMEM to achieve 0.3 μg per well, and incubated for 3 h. The medium was then replaced with complete medium containing 10% serum.

Serum stability experiments were performed as described[21] in CHO and HepG2 cells. Briefly, transient transfections, *in vitro*, were done in the presence of fetal calf serum. Lipid/DNA complexes were prepared in the absence of serum and incubated for a period of 30 min at room temperature. Serum was then added to the complex to obtain the 10% final concentration and then added to the cells, seeded on a 96-well plate and the charge ratios varied from 2:1 to 12:1 Lipid/DNA. Data is represented as β-gal activity/well (20 000 cells). Reporter gene assay was carried out 48 h post transfection and efficiency depicted as relative β-gal activity. In these assays, cells were washed with PBS and lysed in 50 μL of lysis buffer (0.25 M Tris.HCl, pH 8.0, and 0.5% NP40). β-Gal activity was estimated by adding 50 μL of 2× substrate (1.33 mg/mL ONPG, 0.2 M sodium phosphate, pH 7.15, and 2 mM magnesium chloride) to an equal volume of the lysate in a fresh 96-well plate and incubated at 37 °C. Absorption at 405 nm was converted to β-gal units by using a standard curve generated with pure commercial enzyme.

Differential Scanning Calorimetry. Thermal transitions in Lipids **1** and **2** were performed using VP-DSC MicroCal calorimeter (VP-ITC model). The calorimetry was performed using Lipids **1** and **2** (8.8 mg/mL) vesicles prepared in deionized water as described above except the sonication step. All samples (250 μL) were degassed before acquiring the scans

which were performed between 10 °C and 95 ° C at a scan rate of 60 deg/h. Water or buffer baselines were obtained and subtracted from lipid scans.

Fluorescence Anisotropy Measurements. These measurements were carried out using Fluorolog 3−22 Fluorescence Spectrophotometer (Jobin Yvon,USA). Lipids **1** and **2** were prepared from chloroform stocks by the appropriate addition of the fluorescent probe DPH (1,6-diphenyl-1,3,5-hexatriene) at 300:1 mol ratio of Lipid/DPH, to obtain 2 mM stock of the lipid. This mixture was then dried under nitrogen gas. The residual chloroform was then removed in a vacuum for 4 h. Lipid films were then hydrated in 1 mL of buffer (Tris. HCl, pH 7.4, 100 mM) overnight, vortexed, and sonicated prior to the scans between 15 and 90 °C with 2.5 °C increments. Fluorescence anisotropy was measured by recording the DPH fluorescence values (excitation at 354 nm and emission at 427 nm) in parallel and perpendicular polarizer positions. Anisotropy values were calculated by instrument software.

Membrane Fusion. Membrane fusion between cationic lipid vesicles and anionic vesicles was monitored by Förster resonance energy transfer (FRET) between NBD-PE and Rhodamine DHPE. The liposomes containing the fluorophores were prepared with the following composition: DOPC:DOPE:egg PG:NBD-PE:Rh-PE at a mole ratio of 75:20:5:0.8:0.8. Cationic liposomes were prepared with Lipid **1** and **2** along with cholesterol in a mole ratio of 50:50. The fusion was initiated by mixing 50 nmol of cationic lipid vesicles with 10 nmol of fluorescent lipids in phosphate buffered saline (10 mM sodium phosphate buffer, pH 7.4, with 150 mM of sodium chloride) at 25 °C in stirring conditions. The increase in fluorescence was monitored in a Hitachi F4300 spectrofluorimeter by exciting the sample at 460 nm and collecting the emission at 530 nm. The total fluorescence was measured by adding Triton X-100 at a final concentration of 0.15%. The small but measurable quenching due to Triton X-100 was corrected. Anionic vesicles were also prepared using phophatidic acid instead of PG at the same mole ratio, and we obtained similar results.

Surface Area−Pressure Isotherms. The measurements were made on a Langmuir trough manufactured by Nima (model 622D) using high-purity water as subphase. Lipids **1** and **2** were prepared as stocks in chloroform and spread at the air−water interface in less than 5 μL. The pressure−area isotherms were obtained at compression rates of 50 cm^2 per minute. Since the surface area available with the trough does not allow us to monitor the collapse point of the monolayer, only the rate of change of the surface pressure for change in molecular area was used in the study.

Transmission Electron Microscopy. SUVs of Lipids **1** and **2** (2 mM) were prepared as described earlier. The vesicle solution was cast on the poly(vinyl acetate)-coated copper grid and stained with 1.0 wt % uranyl acetate aqueous solution. The TEM images were recorded by JEM-2000EX/FX (JEOL, Co. Ltd.) with 80 kV accelerating voltage.

Live Uptake of DNA by Confocal Microscopy. Chambered cover glass was plated with 20 000 cells (CHO) and incubated with lipoplexes (with 6:1 lipid/DNA charge ratio) prepared with Lipids **1** and **2** in 300 μL of DMEM containing Oregon Green-labeled plasmid pCMVβ-gal plasmid DNA prepared as described. After the incubation period of 3 h, DMEM was removed, and the cells were washed with PBS twice before obtaining images (Leica TCS S52). The cells containing labeled DNA (ChromaTide Oregon Green 488−5′dUTP): RhDHPE-labeled lipid complexes were visualized using the 488 nm excitation of argon laser, 405 nm excitation of diode while Rhodamine was detected using HeNe excitation wavelength of 543 nm. The emission collection wavelengths were 500−540 nm for Oregon Green, 415−485 nm for Hoechst 33258, and 560−615 nm for Rhodamine. In each panel, 5 slices of 0.5 μm were combined. Last panel indicates overlaid images depicting nuclear staining with Hoechst 33258.

Toxicity Assay. Cytotoxicity of the Lipids **1** and **2** were assessed in CHO cells using 3-(4,5-dimethylthiazol-2-yl)-2,5-diphenyltetrazolium bromide (MTT). Complexes prepared with lipid, were evaluated for their toxicity to cells by performing the MTT assay as described[27] in 96-well plates at charge ratios used in the transfection experiments. Cells were incubated with transfection complexes for 3 h at 37 °C in serum-free DMEM. Soon after transfection, cells were washed with PBS and replaced with 100 μL DMEM+25 μL MTT (2 mg/mL in PBS) for 3 h. The medium was removed and replaced with 100 μL DMSO/methanol 1:1 (v/v) and mixed to dissolve the formazan crystals. Absorbance was then measured at 540 nm with untreated cells serving as controls. Results were expressed as percent viability. [A540 (treated cells) − background/A540 (untreated cells) − background] × 100.

Small Angle X-ray Diffraction of the Lipid Vesicles. Vesicles of Lipids **1** and **2** with cholesterol were prepared as described above. The lipid concentration for SAXS studies was 5 mM and vesicles were used without sonication. Diffraction data were collected on a S3-MICROpix attached to a Dectris 100K Platus detector (Hecus Xray Systems, Graz, Austria) located 300 mm from the sample. Detector was precalibrated with silver behenate. Samples were filled in 1 mm thin-walled quartz-glass capillaries in tight thermal contact with a programmable Peltier unit. Samples were equilibrated for 10 min at each temperature before measurement. The data were fitted using *Fit2d* software.[28]

RESULTS

Synthesis of the Lipids. To investigate the role of the amide and ester linker in a cationic lipid on transfection properties, $2C_{12}$Glu and $2C_{12}$-Gln were synthesized and later coupled to Z-Lys (Z)-Lys(Z)-OH. The schemes for the synthesis of Lipid **1** (amide lipid) and Lipid **2** (ester lipid) is given in Scheme 1A,B. The purity was assessed by HPLC and chemical nature of the compounds was confirmed by FTIR, ^{1}H-NMR, and elemental analysis.

DNA Binding Properties of Lipid 1 and 2. *Agarose Gel Retardation Assay.* We initially investigated the DNA-binding ability of Lipid **1** and **2** by a gel-based assay. Both lipids formulated with cholesterol bind to plasmid DNA, pEGFPN$_3$ (Figure 1A). Formation of a complex and its retardation was observed with Lipids **1** and **2** with cholesterol as the colipid at 0.3:1 charge ratio. At charge ratios greater than 2:1, the complexes were either retained in the well or not amenable to EtBr binding after electrophoresis. The binding of lipids with the plasmid was found to be ratio-dependent. The binding of Lipid **1** was more avid compared to Lipid **2** when formulated with DOPE (data not shown). Therefore, only formulations with cholesterol were taken up for further biophysical investigations and cell biological activity *in vitro*.

Fluorescence Quenching. Binding strengths of cationic lipids with DNA are important to correlate the transfection properties of lipids to its chemical structure. Exclusion of EtBr

Scheme 1. A. Synthesis Scheme and Structure of Glutamide Lipid 1 (n = 12) with the Amide Linker. B. Synthesis Scheme and Structure of Lipid 2 (n = 12) with Ester Linker

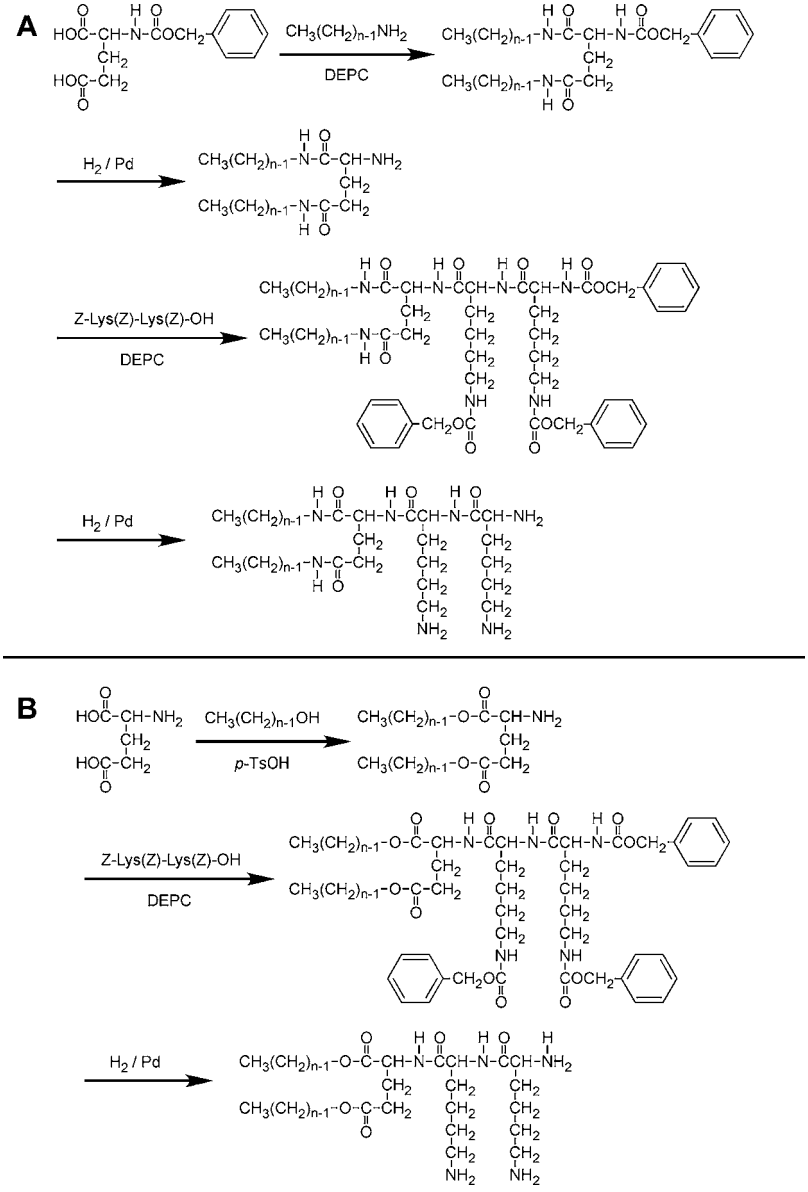

from DNA upon the addition of cationic lipid, and consequent enhancement of fluorescence, provides a sensitive and quantitative measurement for DNA binding. Figure 1B shows the DNA binding pattern of Lipid **1** in comparison to Lipid **2**, which was similar at lower charge ratios. However, at charge ratios above 1:1, Lipid **1** shows a slightly stronger binding with ~25% drop in the fluorescence intensity when compared to ~17% decrease with Lipid **2**.

Uptake of Lipoplexes in CHO Cells. We examined the cellular uptake of lipoplexes prepared with Lipid **1** and Lipid **2** formulated with cholesterol in CHO cells. An Oregon-Green labeled plasmid probe (green) was mixed with an equal proportion of unlabeled DNA to prepare lipoplexes labeled with 0.5 mol % of fluorescent lipid (RhDHPE), at the charge ratios indicated and added to CHO cells followed by incubation at 37 °C for 3 h. After thorough washes with DMEM, live cells were viewed by confocal microscopy. The upper panel, i.e., Lipid **1** (Figure 2), exhibited particulate bright red fluorescence originating from the Rhodamine-labeled lipid that colocalized with the labeled-plasmid DNA. Uptake of Lipid **2** was comparatively less (see merged panel of this figure). Quantitative analysis of the confocal image was done by measuring mean fluorescence intensity (MFI) per cell using *LAS AF* software. When compared with Lipid **2**, we observed a 3-fold increase in the MFI measured either by OG-labeled DNA or Rhodamine-labeled liposomes in the uptake of lipoplexes prepared with Lipid **1**/Chol.

Biophysical Characterization of the Lipids. *Determination of the Melting Temperature of the Lipids.* Hydrated lipid samples with and without the colipid, cholesterol, were subjected to thermal transitions in a differential scanning calorimeter (DSC). The heat capacity changes in the lipid phase as a function of temperature were plotted in Figure 3. The transition midpoints were found to be 65.4 and 23.5 °C for Lipid **1** and **2**, respectively. Similar transition midpoints was also found for these lipids in the presence of cholesterol. The transition midpoint for lipids is known to be determined by the chain length of the alkyl group. Since both lipids have identical chain length (C12) and identical head groups, the higher

dx.doi.org/10.1021/bc2002874 | *Bioconjugate Chem.* 2011, 22, 2244–2254

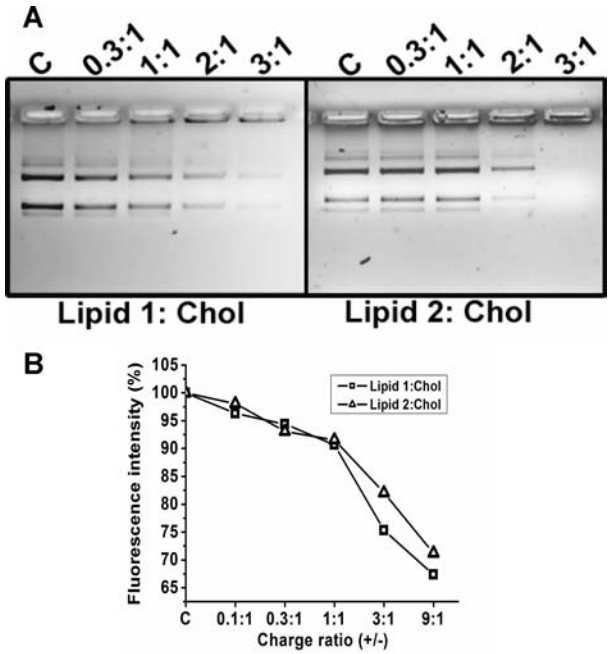

Figure 1. Binding of DNA with Lipids **1** and **2** in the presence of the colipid cholesterol: (A) 1% Agarose gel electrophoresis of plasmid pCMVβ-gal complexed with Lipids **1** and **2** at charge ratios varying from 0.3:1 to 3:1 Lipid/DNA, indicated above each well. Samples were electrophoresed using TAE buffer (pH 8.0) and visualized post-electrophoresis by staining with EtBr. Control in each panel denoted as "C" pertains to naked plasmid DNA. (B) Fluorescence quenching by EtBr exclusion assay of Lipids **1** and **2** formulated with colipid cholesterol. Fluorescence titration curves depict quenching of fluorescence due to release of EtBr from pCMVβ-gal plasmid DNA upon lipid binding in a buffer containing 20 mM Tris·HCl (pH 7.4).

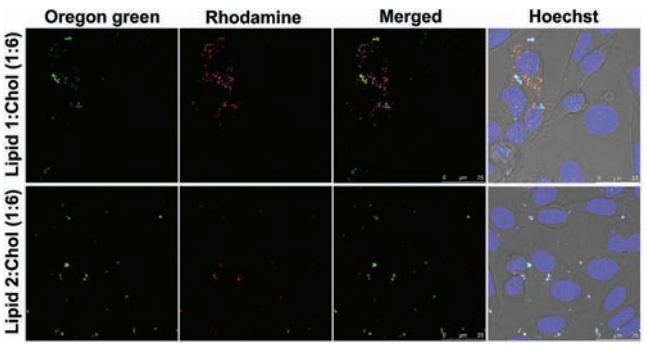

Figure 2. Uptake of lipoplexes and analysis by confocal microscopy: Transfection complexes with the corresponding lipid were added to cells in the absence of serum and incubated for 3 h. Lipid **1**/Chol at 6:1 DNA/Lipid (top) and Lipid **2**/Chol at 6:1 DNA/Lipid (bottom). DNA was labeled with Oregon-Green while liposomes were labeled with Rhodamine DHPE at 0.5 mol %. The merged panel indicate colocalization of the fluorophores. Cell nuclei were stained with Hoechst (blue). Panels on the extreme right depict images merged with the transmission channel. Five optical sections in the middle region, each of 0.5 μm thickness, were combined to generate the images.

melting temperature of Lipid **1** may have been due to additional interactions in Lipid **1**. To confirm the phase transitions, we used identical preparations of Lipid **1** and **2** with a fluorescent probe diphenyl hexatriene (DPH) at 300:1 ratio (lipid/DPH, mol/mol). Anisotropy of DPH is sensitive to the microviscosity of its location. DPH resides at the center of the bilayer and its

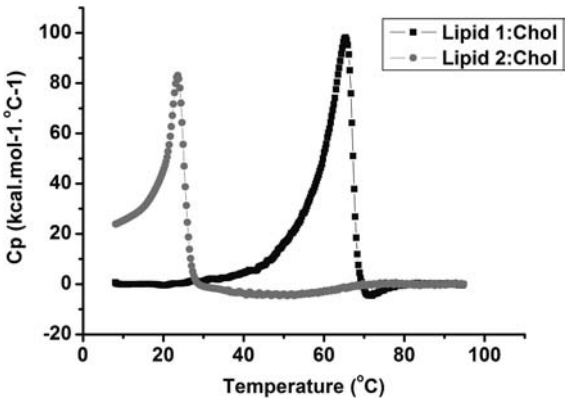

Figure 3. Differential scanning calorimetric scans of lipid vesicles: Thermograms of Lipid **1** and Lipid **2** formulated with equimolar amounts of cholesterol. Vesicles were prepared as described in methods.

anisotropy has been extensively used to estimate the phase transition temperatures of lipid assemblies. Lipid **1** exhibited a sharp phase transition around 67 °C, whereas Lipid **2** had a shallow transition at lower temperatures (Supporting Information Figure 1S). Thus, a higher melting temperature of Lipid **1** was confirmed by two independent methods.

Transmission Electron Microscopy (TEM). Having determined the melting temperature of liposomes of Lipids **1** and **2**, we sought to examine the structural features of these liposomes by transmission electron microscopy (TEM). The images obtained with Lipid **1** vesicles prepared with cholesterol or DOPE as the colipid at charge ratio 3:1 revealed the formation of very well-defined spherical structures with a clear inside–outside demarcation. The average size of the vesicles was between 100 and 200 nm in diameter. In contrast, liposomes prepared with Lipid **2** with either of the colipids resulted in supramolecular assemblies that were fragmented and poorly defined (Figure 4). The liposomal preparation with Lipid **2** resulted in structures with long continuous layers that were not discrete. Liposomes of Lipid **1** had unaltered morphology when the particles were prepared either in water or in the presence of PBS (ionic strength = 0.154) (data not shown).

To confirm our observations further, we subjected both the liposomal samples to small angle X-ray scattering (SAXS). SAXS provides information on characteristics of long-range-ordered structures and has been extensively used in identifying the phase properties of the lipids in membranes. The SAXS pattern of Lipids **1** and **2** as shown in Figure 5 indicated defined scatter peaks for Lipid **1** with ordered assembly, and the simulation fitted the scatter to ordered lamellar structures. The scatter profile of liposomes prepared with Lipid **2** resulted in a broad scatter peak indicative of an amorphous material. The peak distances in the scattergram were used to calculate the d_1 (thickness of the membrane). We obtained 3.58 nm for the thickness of the Lipid **1**. We obtained similar distance for Lipid **2** though the peak peak intensities were significantly smaller in case of this lipid. The thickness saturated phosphatidylcholine of 12-carbon chains gives a thickness of 3.0 nm, which is comparable with Lipid **1**. The results of SAXS confirm the absence of organized structure in the liposomes of Lipid **2**.

Compressibility of Lipid Monolayers. With a view to investigate the higher melting temperature of Lipid **1**, we spread both lipids on water subphase and monitored the changes in surface pressure as a function of area occupied by the molecule

dx.doi.org/10.1021/bc2002874 | *Bioconjugate Chem.* 2011, 22, 2244–2254

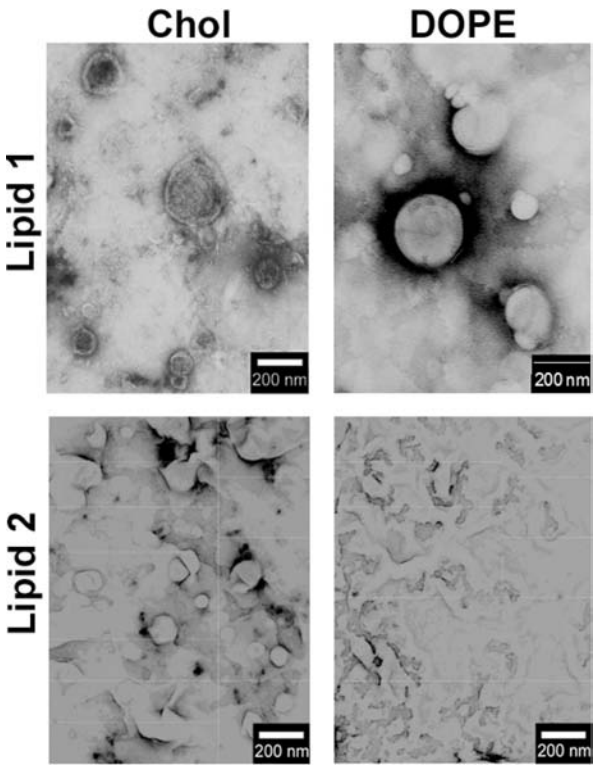

Figure 4. Transmission electron micrographs of Lipids **1** and **2**: Lipids formulated with DOPE or cholesterol were complexed with plasmid pCMVβ-gal DNA in 1× PBS buffer at Lipid/DNA 6:1 charge ratio. Lipoplexes were stained with uranyl acetate as described.

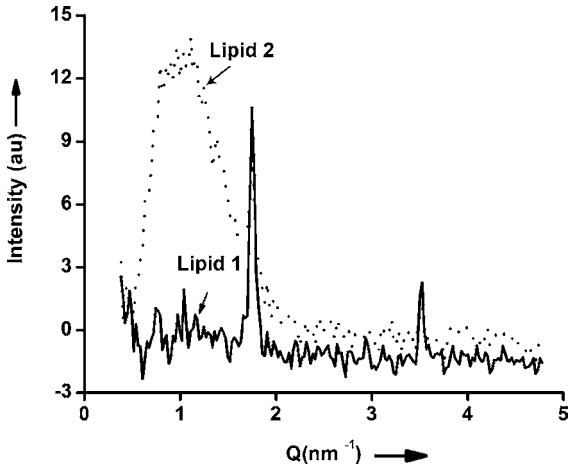

Figure 5. Small-angle X-ray diffraction of lipid vesicles: Vesicles of Lipids **1** and **2** formulated with cholesterol were prepared. The lipid concentration was kept at 5 mM and used without sonication. Diffraction data were collected and fitted using *Fit2d* software.

(Figure 6). Surface pressure vs area isotherms of monolayers of lipids provides information on the surface areas and intermolecular interactions. The slow compressibility of Lipid **1** compared to that of Lipid **2** suggested that the Lipid **1** monolayer experiences additional resistance to compression compared to Lipid **2**. This resistance may possibly be attributed to additional interactions between molecules.

Fusion Properties with Anionic Liposomes. Fusion of the membrane components of the lipoplex membrane with the

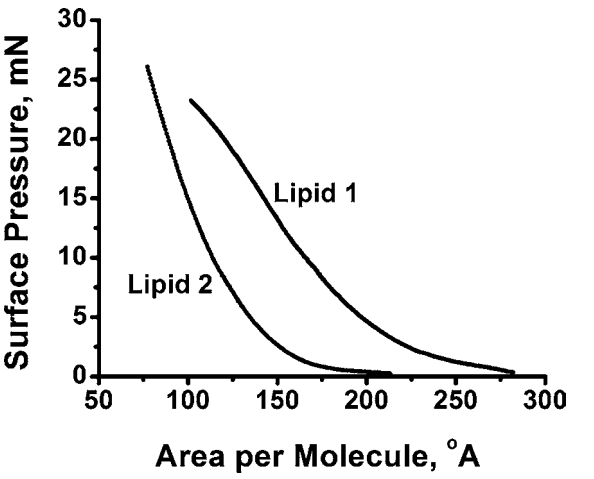

Figure 6. Surface pressure isotherms of Lipids **1** and **2** were generated in the presence of high-purity water as the subphase. Isotherms are representative of four independent measurements with very good reproducibility between the isotherms.

cellular membrane is critical for release of DNA. We monitored the fusion between cationic liposomes of both lipids along with the anionic vesicles prepared with a composition similar to the plasma membrane. The fusion kinetics was monitored using FRET between the donor, NBD-PE, and the acceptor, Rh-PE. Lipid **2** as seen in Figure 7 showed rapid increase in fluorescence

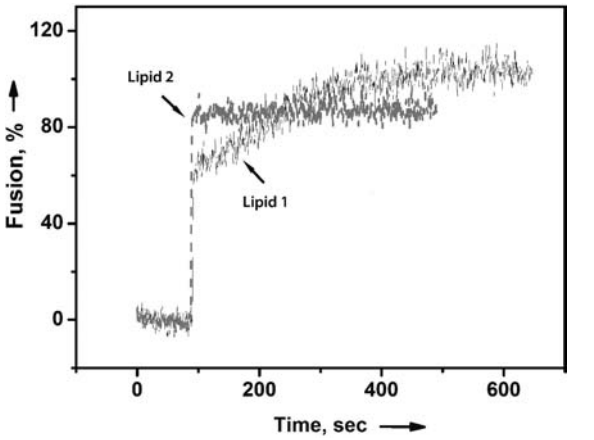

Figure 7. Membrane fusion kinetics: Membrane fusion between anionic vesicles with Lipid **1** or Lipid **2** was monitored by fluorescence resonance energy transfer between NBD-PE and Rhodamine PE, as described.

signal and reached a value representative of complete mixing, i.e., in the presence of Triton X-100, within 1 min. Many variations employed in the experimental design such as the ratio of labeled and unlabeled vesicle and composition of the labeled vesicles did not change the kinetics. Since Lipid **2** has poorly defined vesicles as seen in TEM, it is possible that these vesicles were unstable, hence show very rapid increase in fluorescence that was not typical of a fusion process. On the other hand, Lipid **1** shows comparatively slower kinetics of fusion with labeled vesicles. The fusion kinetics was similar when the labeled vesicles were prepared with phosphatidic acid instead of phosphatidylserine (data not reported).

dx.doi.org/10.1021/bc2002874 | *Bioconjugate Chem.* 2011, 22, 2244–2254

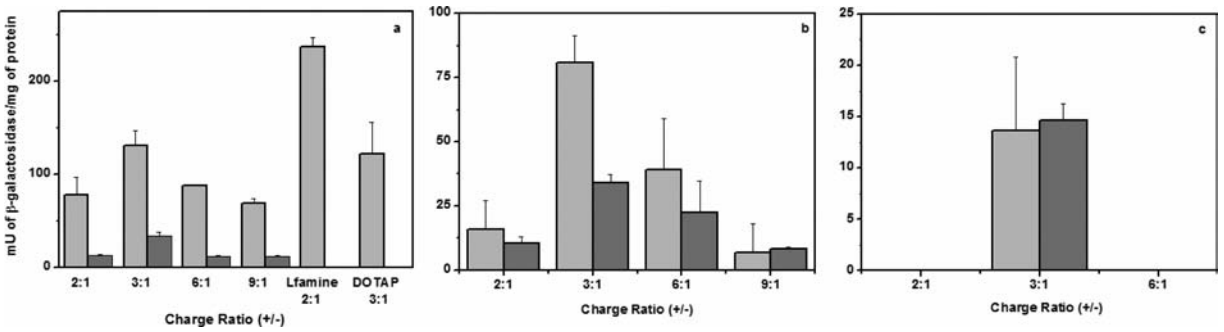

Figure 8. Transient transfection *in vitro*: (a) Transfection of CHO cells with Lipid **1** formulated with equimolar amounts of the colipid, cholesterol, at charge ratios varying from 2:1 to 9:1 Lipid/DNA in the absence (light gray) and presence of serum (dark gray) and normalized to milligrams protein. Graph depicts reporter gene activity at various charge ratios. Standards such as Lipofectamine (Lfamine) and DOTAP at 2:1 and 3:1 charge ratio, respectively, were included for comparison. Lipid **2** did not show any detectable reporter gene activity on CHO cells and was not plotted. (b) Transfection in HepG2 cells with Lipid **1**/Chol at the indicated charge ratios in the absence (light gray) and presence of serum (dark gray). (c) Transfection in HepG2 cells with Lipid **2**/Chol at the indicated charge ratio in the absence (light gray) and presence of serum (dark gray).

Biological Activity and Stability in Serum. *Transient Transfection in CHO and HepG2 Cells.* The lipids initially characterized for their DNA-binding properties were then tested for transfection efficiency in four cell lines, namely, CHO, HepG2, MCF-7, and HeLa. Both the lipids were formulated with DOPE or cholesterol as colipid and tested for transfection efficiency. Formulations with DOPE as colipid were consistently lower than formulations with cholesterol as colipid (data not shown), when tested in CHO cells. Hence, in all further studies only cholesterol-containing liposomes were used. Transient transfections of the two lipids at varying charge ratios from 2:1 to 9:1 Lipid/DNA, using pCMVβ-gal as the reporter gene, were performed as described in CHO cells (Figure 8a) and HepG2 cells (Figure 8b and c). When compared with the cationic lipid standards, i.e., DOTAP/DOPE and polycationic lipid, Lipofectamine, we observed slightly better transfection than DOTAP, and the efficiency was 50% of the transfection observed with Lipofectamine. We also tested the 14- and 16-carbon analogues of Lipid **1**, which is 12-carbon, and found that Lipid **1** has shown higher transfection than the 14- and 16-carbon analogues, >3-fold, Supporting Information Figure 2S. As in the case of HepG2, Lipid **1** (Figure 8b) exhibited much higher activity than Lipid **2** (Figure 8c). Lipid **2** was inefficient in all cell lines tested. The biological activity of Lipid **1** with the amide linkage was consistently higher than that of Lipid **2** that is ester-based in both HeLa cells Supporting Information Figure 3S and MCF-7 (data not reported). In all cell lines, maximal activity was observed at 3:1 Lipid/DNA with Lipid **1** formulated with cholesterol.

Although lipids bind DNA by charge−charge interaction, these may not protect DNA sufficiently from degradation by nucleases. Stability in serum is an important property when developing protocols for *in vivo* gene transfer. To assess the serum stability of Lipid **1**, serum was included in the medium, to a final concentration of 10%, at the time of incubation of cells with the complexes. As evident from Figure 8a−c, compared to the controls, i.e., in the absence of serum, Lipid **1** retained approximately 25% of its transfection efficiency in the presence of serum at 10% final concentration in CHO and 40−57% in the case of HepG2 cells at all charge ratios. Transfection decreased further in the presence of serum concentrations greater than 10%. Lipid **2** has observable but low transfection in HepG2 cells at 3:1 charge ratio and good stability in the presence of serum (Figure 8c). Overall, the transfection efficiency in the presence and absence of serum has a similar bell-shaped curve as a function of charge ratio.

Toxicity. Toxicity is an important issue to be dealt with while generating formulations useful for gene delivery protocols. We performed MTT-based cell viability assays at various charge ratios, i.e., 1:1 to 9:1 in CHO cells. Percent cell viabilities upon treatment with Lipid **1** at charge ratios 3:1 is ∼70% (Figure 9).

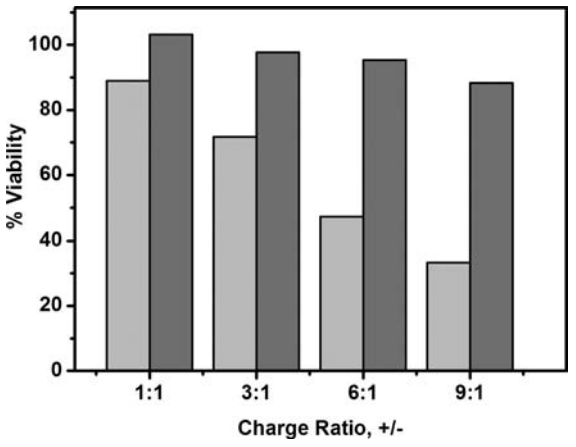

Figure 9. Determination of cell viability in CHO cells. Lipid **1** and **2**: DNA:Lipid complexes of Lipids **1** and **2** formulated with cholesterol was evaluated for cytotoxicity at the indicated charge ratios varying from 1:1 to 9:1 N/P. Following 3 h incubation, the MTT assay was performed. Percent cell viability represents experiments performed in triplicate as described in Materials and Methods. The absorption values obtained using reduced formazan, in the absence of lipids, were taken to be 100.

In contrast, Lipid **2** is inefficient at this charge ratio, although nontoxic. The utility of Lipid **1**/cholesterol offsets the observed toxicity making it effective *in vitro*.

DISCUSSION

Two glutamic acid-based lipids that have identical head groups and acyl chains were synthesized. These lipids differ from each other with respect to the chemistry of the linker connecting the acyl chains to glutamide. Lipid **1** with the amide linker exhibited high transfection efficiency in four different cell lines,

dx.doi.org/10.1021/bc2002874 | *Bioconjugate Chem.* 2011, 22, 2244−2254

when compared to Lipid **2** with an ester linker. Among the popular colipids such as DOPE and cholesterol, both lipids exhibited higher transfection efficiency with cholesterol compared to DOPE. The binding of lipids to DNA in EtBr exclusion assay showed identical profiles, however, at charge ratios >1:1, Lipid **1** shows stronger displacement of EtBr. Similar charge ratio dependency was also observed in gel retardation assay with these lipids. Electron microscopy images of the lipoplexes prepared using Lipids **1** and **2** along with the colipids cholesterol and DOPE showed clearly that Lipid **1** lipoplexes have a defined morphology, whereas Lipid **2** aggregates were irregular and amorphous. Lack of defined liposomal structure of Lipid **2** vesicles was also confirmed by broad scattering profile in SAXS. It is apparent that the stronger binding and formation of defined stable complexes are important in the interaction of Lipid **1** with cells and eventually in their uptake. The higher uptake of the lipoplexes with Lipid **1**, as seen from confocal microscopy may consequently be responsible for observed higher transfection efficiency. Lipid **1** has also demonstrated efficient transfection in the presence of serum when tested in both CHO and HepG2 cells. The benefits of serum in transfection protocols have been reported.[29,30] Stability in serum suggests the potential of these lipids for DNA delivery *in vivo*.

Biophysical Basis for Higher Transfection Efficiency with Lipid 1. DNA binding being a prerequisite for achieving good transfection efficiency, it must be condensed prior to cell uptake. Cationic lipids bind electrostatically to the DNA.[3,30] This process results in condensation and protection of the DNA and leads to the formation of complexes that are particulate in nature.[3,31] DNA present in a particle is more efficiently taken up by the cell and endocytosed than free DNA. Characterization of lipoplexes at varying charge ratios revealed that transfection efficiency sharply increases with DNA condensation, change in zeta potential from negative to positive value, and observations of ordered lipoplexes in electron micrographs.[32] Although DNA was found to be condensed below optimal charge ratios, DNA was accessible to nucleases leading to decrease in transfection. Stability of the lipoplex is critical for protecting the DNA during transfection and also enhancing the uptake of the lipoplex by the cells.[32] Though binding of Lipid **2** with the DNA was comparable to Lipid **1**, the packing of the DNA into lipoplexes may be inefficient leading to particles that may be large and variable in size. Thus, Lipid **2**, a 12-carbon lipid, does not provide sufficient stability for the formation of liposomes; hence, its uptake by cells and subsequent transfection is poor. Though Lipid **1** has same chain length and headgroup as Lipid **2**, its melting temperature was nearly 40 °C higher. Melting temperature of lipids depends strongly on the length of the acyl chains and increases with the increase in chain lengths. Since Lipids **1** and **2** have identical chain lengths, the higher melting temperature may be due to additional interactions between the molecules. The stabilizing effect of the intermolecular hydrogen bond was observed between the headgroups in phosphatidylethanolamines (PE), which increases the melting temperature of PEs by nearly 20 °C compared to phosphatidylcholines of similar alkyl chain length.[33] Such intermolecular hydrogen bonding was observed in Gemini quaternary ammonium surfactants that contain an amide linker but not in ester-containing surfactants.[34] In addition, the data on polarization of DPH, an indicator of microviscosity of the membrane, suggests that both lipids possess similar microviscosity values, corroborating the observations that the higher melting temperature of Lipid **1** does not originate from the hydrophobic portion of the molecule. The addition of the slow compression rate of Lipid **1** monolayers compared to Lipid **2** also points to the fact that Lipid **1** monolayers experience additional intermolecular interactions. Since the head groups of both lipids are identical, the altered isotherm may originate intermolecular interactions. The amine linkers of Lipid **1** possibly form a hydrogen bond with carbonyl group of the adjacent lipid in a liposome, thus providing additional stability necessary for a stable lipoplex (Figure 10). In our opinion, this is the first report

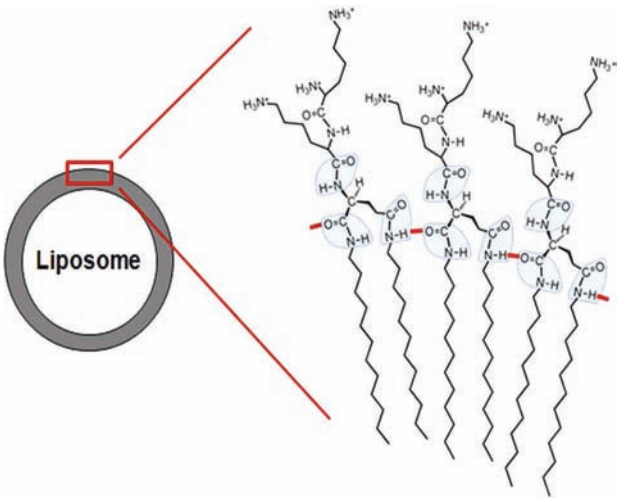

Figure 10. Intermolecular interactions of Lipid **1**. Model depicting stabilization of Lipid **1** through intermolecular interactions generated through hydrogen bonding.

of an approach to increase the stability and transfection of cationic liposomes by designing features favoring intermolecular hydrogen bonding.

Unsaturated lipids, predominantly oleic acid, containing cationic lipid formulations showed higher transfection efficiency than formulations with saturated lipids. Investigation of transfection efficiency with a given cationic lipid (DOTAP) along with phosphatidylethanolamine lipids with various acyl chains with different lengths indicated that unsaturated PEs are essential compared to saturated PEs for efficient transfection.[35] Hydrophobic moiety of cationic lipids strongly modulates their transfection activity. A study on the chain length variants of DOTAP suggests that DLTAP (*N*-[1-(2,3-dilauroyloxy)-propyl]-*N*,*N*,*N*-trimethylammonium methylsulfate) was least efficient in transfection.[36] In this context, the observation of higher transfection efficiency of Lipid **1**, despite having higher melting temperature, is interesting. It is observed that higher melting points of long acyl chain containing lipids do not mix with other membranes easily. Fusion between vesicles occurs readily above the phase transition temperature of the lipids. Below the phase transition temperature, the lipids are in crystalline phase and have restricted fluidity, essential for mixing of the membrane contents.[37] Within a cell, transfection processes involve membrane−membrane interactions between lipoplex and endosomal membrane and fusion.[38] Fusion is essential for dissociation of the cationic lipids from the DNA and release the DNA into the cytoplasm. Though Lipid **1** has higher melting temperature, its microviscocity as measured by DPH, is still in the range of 12-carbon lipids.

dx.doi.org/10.1021/bc2002874 | *Bioconjugate Chem.* 2011, 22, 2244−2254

Hence, the miscibility of Lipid **1** may not restrict fusion with other membranes. Amide linkers have been used in the design of cationic lipids and were found to be biodegradable and stable.[39] DOGS is a popular amide linker containing cationic lipid, where the amide linker is between the backbone and the headgroup.[40] A series of cationic lipids with amide and ester linkers to a pyridinium headgroup were synthesized. Amide linker containing lipids were found to be superior in transfection compared to the ester containing pyridinium lipids.[41] However, the amide containing lipids melt at slightly lower temperatures than the ester lipids. In another study, a series of detergents were synthesized with amide or ester linkers to amino acid head groups. The amide detergents bound to the oligonucleotides more efficiently than the ester containing detergents.[42] In Lipid **1**, the amide linker provides stability to the liposome and the lipoplex by forming an intermolecular hydrogen bond which did not seem to influence the membrane interactions crucial for transfection. Incorporating intermolecular interactions, such as hydrogen or ionic bonds, in cationic lipids offers yet another strategy to design efficient cationic lipids.

CONCLUSIONS

Stability of a lipoplex is important for achieving good transfection efficiencies. This is dependent on the nature of the cationic headgroup and DNA interactions and the hydrophobic volume of the lipid. The overview of lipid/DNA interactions and lipid properties of the two lipids, different in their linker chemistry, suggests that stable formation of liposomes with Lipid **1** was critical for superior transfection properties compared to Lipid **2**. Formulations made with Lipid **1** were stable in serum, thereby implying its utility for in vivo experimentation. Since the two lipids are identical in all aspects except for the linker, the stability of amide linker containing Lipid **1** is due to the presence of intermolecular hydrogen bonds leading to stable vesicles. This observation is supported by higher transition temperatures, TEM, SAXS, and monolayer studies. Incorporation of intermolecular interactions may be yet another way to increase the stability of the liposomes and thereby transfection.

ASSOCIATED CONTENT

Supporting Information

[Graphs depict thermal transitions of Lipids 1 and 2 using DPH, transfection efficiencies of Lipid analogues in comparison to Lipid 1 in CHO cells and transfection efficiency of Lipid 1 and 2 in HeLa cells. This material is available free of charge via the Internet at http://pubs.acs.org.

AUTHOR INFORMATION

Corresponding Author

*WP +91-40-27192514, Fax # +91-40-27160311, www.ccmb.res.in, E-mail: madhu@ccmb.res.in.

ACKNOWLEDGMENTS

This work was supported by JSPS-DST Bilateral Joint Project (# DST/INT/JSPS/Proj-38/2007) and a CSIR Network project (NWP0035). Advice of Drs. R. Nagaraj and B. Raman is gratefully acknowledged. We thank Nandini Rangaraj and Dr. Shoeb Ahmad for help with confocal microscopy and fluorescence anisotropy measurements, respectively. We thank Prasada Raju of Indian Institute of Chemical Technology, Hyderabad, for HR-ESI-MS analysis.

REFERENCES

(1) Chesnoy, S., and Huang, L. (2000) Structure and function of lipid-DNA complexes for gene delivery. *Annu. Rev. Biophys. Biomol. Struct. 29*, 27−47.

(2) Li, W., and Szoka, F. C. Jr. (2007) Lipid-based nanoparticles for nucleic acid delivery. *Pharm. Res. 24*, 438−49.

(3) Rao, N. M. (2010) Cationic lipid-mediated nucleic acid delivery: beyond being cationic. *Chem. Phy. Lipids 163*, 245−52.

(4) Nicolazzi, C., Garinot, M., Mignet, N., Scherman, D., and Bessodes, M. (2003) Cationic lipids for transfection. *Curr. Med. Chem. 10*, 1263−77.

(5) Audouy, S., and Hoekstra, D. (2001) Cationic lipid-mediated transfection in vitro and in vivo. *Mol. Membr. Biol. 18*, 129−43.

(6) Koynova, R., Wang., L., Tarahovsky, Y., and MacDonald, R. C. (2005) Lipid phase control of DNA delivery. *Bioconjugate Chem. 16*, 1335−9.

(7) Niculescu-Duvaz, D., Heyes, J., and Springer, C. J. (2003) Structure-activity relationship in cationic lipid mediated gene transfection. *Curr. Med. Chem. 10*, 1233−61.

(8) Barteau, B., Chèvre, R., Letrou-Bonneval, E., Labas, R., Lambert, O., and Pitard, B. (2008) Physicochemical parameters of non-viral vectors that govern transfection efficiency. *Curr. Gene Ther. 8*, 313−23.

(9) Montier, T., Benvegnu, T., Jaffrès, P. A., Yaouanc, J. J., and Lehn, P. (2008) Progress in cationic lipid-mediated gene transfection: a series of bio-inspired lipids as an example. *Curr. Gene Ther. 8*, 296−312.

(10) Tranchant, I., Thompson, B., Nicolazzi, C., Mignet, N., and Scherman, D. (2004) Physicochemical optimization of plasmid delivery by cationic lipids. *J. Gene Med. 6* (Suppl 1), S24−35.

(11) Gao, X., and Huang, L. (1991) A novel cationic liposome reagent for efficient transfection of mammalian cells. *Biochem. Biophys. Res. Commun. 179*, 280−5.

(12) Ren, T., Zhang, G., Liu, F., and Liu., D. (2000) Synthesis and evaluation of vitamin D-based cationic lipids for gene delivery in vitro. *Bioorg. Med. Chem. Lett. 10*, 891−4.

(13) Fichert, T., Regelin, A., and Massing, U. (2000) Synthesis and transfection properties of novel non-toxic monocationic lipids: Variation of lipid anchor, spacer and head group structure. *Bioorg. Med. Chem. Lett. 10*, 787−91.

(14) Floch, V., Loisel, S., Guenin, E., Hervé, A. C., Clement, J. C., Yaouanc, J. J., des Abbayes, H., and Férec, C. (2000) Cation substitution in cationic phosphonolipids: a new concept to improve transfection activity and decrease cellular toxicity. *J. Med. Chem. 43*, 4617−28.

(15) Heyes, J. A., Niculescu-Duvaz, D., Cooper, R. G., and Springer, C. J. (2002) Synthesis of novel cationic lipids: effect of structural modification on the efficiency of gene transfer. *J. Med. Chem. 45*, 99−114.

(16) Prasad, T, K., Rangaraj, N., and Rao, N, M. (2005) Quantitative aspects of endocytic activity in lipid-mediated transfections. *FEBS Lett. 579*, 2635−42.

(17) Hui, S. W., Langner, M., Zhao, Y. L., Ross, P., Hurley, E., and Chan, K. (1996) The role of helper lipids in cationic liposome-mediated gene transfer. *Biophys. J. 71*, 590−9.

(18) Simões, S., Slepushkin, V., Gaspar, R., de Lima, M. C., and Düzgüneş, N. (1998) Gene delivery by negatively charged ternary complexes of DNA, cationic liposomes and transferrin or fusigenic peptides. *Gene Ther. 5*, 955−64.

(19) Zuhorn, I. S., and Hoekstra, D. (2002) On the mechanism of cationic amphiphile-mediated transfection. To fuse or not to fuse: is that the question? *J. Membr. Biol. 189*, 167−79.

(20) Kumar, V. V., Pichon, C., Refregiers, M., Guerin, B., Midoux, P., and Chaudhuri, A. (2003) Single histidine residue in head-group region is sufficient to impart remarkable gene transfection properties to cationic lipids: evidence for histidine-mediated membrane fusion at acidic pH. *Gene Ther. 10*, 1206−15.

(21) Gopal, V., Prasad, T. K., Rao, N. M., Takafuji, M., Rahman, M. M., and Ihara, H. (2006) Synthesis and in vitro evaluation of glutamide-containing cationic lipids for gene delivery. *Bioconjugate Chem. 17*, 1530−6.

(22) Banerjee, R., Das, P. K., Srilakshmi, G. V., Chaudhuri, A., and Rao, N. M. (1999) Novel series of non-glycerol-based cationic transfection lipids for use in liposomal gene delivery. *J. Med. Chem. 42*, 4292−9.
(23) Kumar, V. V., Singh, R. S., and Chaudhuri, A. (2003) Cationic transfection lipids in gene therapy: successes, set-backs, challenges and promises. *Curr. Med. Chem. 10*, 1297−306.
(24) Rajesh, M., Sen, J., Srujan, M., Mukherjee, K., Sreedhar, B., and Chaudhuri, A. (2007) Dramatic influence of the orientation of linker between hydrophilic and hydrophobic lipid moiety in liposomal gene delivery. *J. Am. Chem. Soc. 129*, 11408−20.
(25) Ghosh, Y. K, Visweswariah, S. S., and Bhattacharya, S. (2002) Advantage of the ether linkage between the positive charge and the cholesteryl skeleton in cholesterol-based amphiphiles as vectors for gene delivery. *Bioconjugate Chem. 13*, 378−84.
(26) Legendre, J. Y., Trzeciak, A., Bohrmann, B., Deuschle, U., Kitas, E., and Supersaxo, A. (1997) Dioleoylmelittin as a novel serum-insensitive reagent for efficient transfection of mammalian cells. *Bioconjugate Chem. 8*, 57−63.
(27) Xavier, J., Singh, S, Dean, D. A., Rao, N. M., and Gopal, V. (2009) Designed multi-domain protein as a carrier of nucleic acids into cells. *J. Controlled Release 133*, 154−60.
(28) Hammersley, A. P., Svensson, S. O., Hanfland, M., Fitch, A. N., and Häusermann, D. (1996) Two-dimensional detector software: from real detector to idealised image or two-theta scan. *High Pressure Research 14*, 235−248.
(29) Simoes, S., Slepushkin, V., Pires, P., Gaspar, R., Pedroso de Lima, M. C., and Duzgunes, N. (2000) Human serum albumin enhances DNA transfection by lipoplexes and confers resistance to inhibition by serum. *Biochim. Biophys. Acta 1463*, 459−469.
(30) Tros de Ilarduya, C., Arangoa, M. A., and Duzgunes, N. (2003) Transferrin-lipoplexes with protamine condensed DNA for serum-resistant gene delivery. *Methods Enzymol. 373*, 342−356.
(31) Rao, N. M., and Gopal, V. (2006) Cell biological and biophysical aspects of lipid-mediated gene delivery. *Biosci. Rep. 26*, 301−24.
(32) Miller, A. D. The problem with cationic liposome/micelle-based non-viral vector systems for gene therapy. *Curr. Med. Chem. 10*, 1195-1211.
(33) Blume, A. (1983) Apparent molar heat capacities of phospholipids in aqueous dispersions: Effects of chain length and head group structure. *Biochemistry 22*, 5436−5442.
(34) Pisárčik, M., Polakovičová, M., Pupák, M., Devínsky, F., and Lacko, I. (2009) Biodegradable gemini surfactants. Correlation of area per surfactant molecule with surfactant structure. *J. Colloid Interface Sci. 329*, 153−159.
(35) Koynova, R., Tenchov, B., Wnag, L., and MacDonald, R. C. (2009) Hydrophobic moiety of cationic lipids strongly modulates their transfection activity. *Mol. Pharmaceutics 6*, 951−958.
(36) Regelin, A. E., Fankhaenel, S., Gürtesch, L., Prinz, C., von Kiedrowski, G., and Massing, U. (2000) Biophysical and lipofection studies of DOTAP analogs. *Biochim. Biophys. Acta 1464*, 151−164.
(37) Ma, B., Zhang, S., Jiang, H., Zhao, B., and Lv, H. (2007) Lipoplex morphologies and their influences on transfection efficiency in gene delivery. *J. Controlled Release 123*, 184−94.
(38) Friend, D. S., Papahadjopoulos, D., and Debs, R. J. (1996) Endocytosis and intracellular processing accompanying transfection mediated by cationic liposomes. *Biochim. Biophys. Acta 1278*, 41−50.
(39) Niculescu-Duvaz, D., Heyes, J., and Springer, C. J. (2003) Structure-activity relationship in cationic lipid mediated gene transfection. *Curr. Med. Chem. 10*, 1233−61.
(40) Behr, J. P., Demeneix, B., Loeffler, J. P., and Perez-Mutul, J. (1989) Efficient gene transfer into mammalian primary endocrine cells with lipopolyamine-coated DNA. *Proc. Natl. Acad. Sci. U. S. A. 86*, 6982−6.
(41) Zhu, L., Lu, Y., Miller, D. D., and Mahato, R. I. (2008) Structural and formulation factors influencing pyridinium lipid-based gene transfer. *Bioconjugate Chem. 19*, 2499−2512.
(42) Santhiya, D., Dias, R. S., Shome, A., Das, P. K., Miguel, M. G., Lindman, B, and Maiti, S. (2009) Role of linker groups between hydrophilic and hydrophobic moieties of cationic surfactants on oligonucleotide-surfactant interactions. *Langmuir 25*, 13770−13775.

Supporting information

Synthesis and transfection efficiency of cationic oligopeptide lipids: Role of linker

Vijaya Gopal[a], Jennifer Xavier[a], Mohammad Zahid Kamal[a], Srinath Govindarajan[a], Makoto Takafuji[b], Shuta Soga[b], Takayuki Ueno[b], Hirotaka Ihara[b], and Nalam M. Rao[a]*

Contents:

Figure 1S: Thermal transitions of liposomes made with Lipid 1 and 2 using DPH anisotropy. Liposomes prepared with lipid 1 and 2 and cholesterol as colipid were loaded with DPH (300:1mole ratio of lipid to DPH) and were subjected to linear temperature ramp and the anisotropy values were taken after equilibration at each temperature. The transition from high to low anisotropy with an increase in temperature is indicative of melting and where the midpoint of transition gives the melting temperature.

Figure 2S: Transfection efficiencies of chain length analogs of Lipid 1 on CHO cells. Lipsomes prepared with Lipid 1 and its 14- and 16- carbon analogs were complexed with plasmid pCMVβ-gal DNA. The transfection efficiency of the three lipoplexes, depicted in the bar diagram, represent β-activity of Lipid 1 C12-gray, C14-black and C16-white, in CHO cells.

Figure 3S: Transfection of HeLa cells with Lipid 1 and 2 formulated with equimolar amounts of the co-lipid cholesterol at charge ratios varying from 1:1, 3:1 and 6:1 Lipid/DNA. Graph depicts relative β-gal activity as described in the experimental section.

Figure 1S

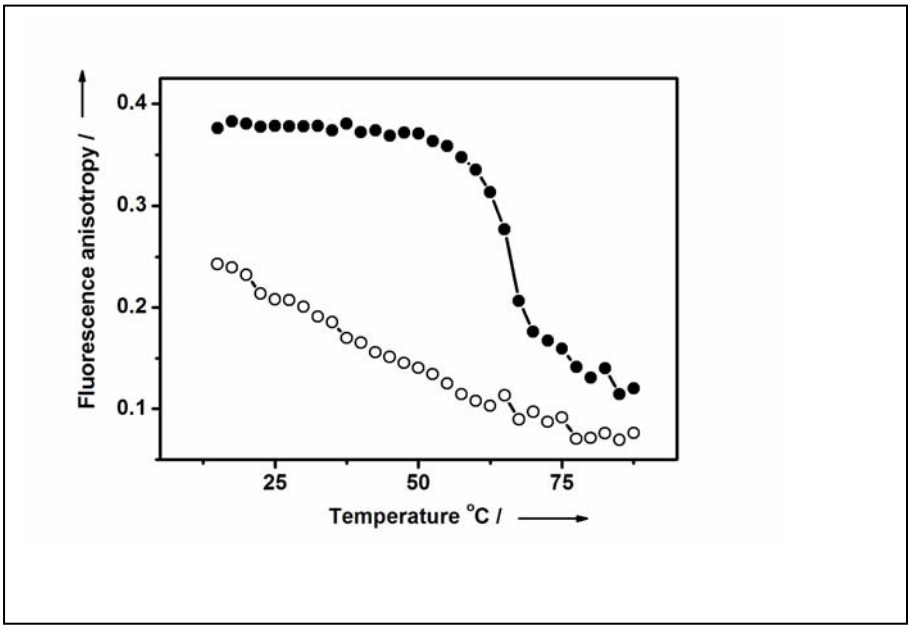

Figure 1S. Thermal transitions of liposomes made with Lipid 1 and 2 using DPH anisotropy. Liposomes prepared with lipid 1 and 2 and cholesterol as colipid were loaded with DPH (300:1mole ratio of lipid to DPH) and were subjected to linear temperature ramp. Anisotropy values were taken after equilibration at each temperature.

Figure. 2S

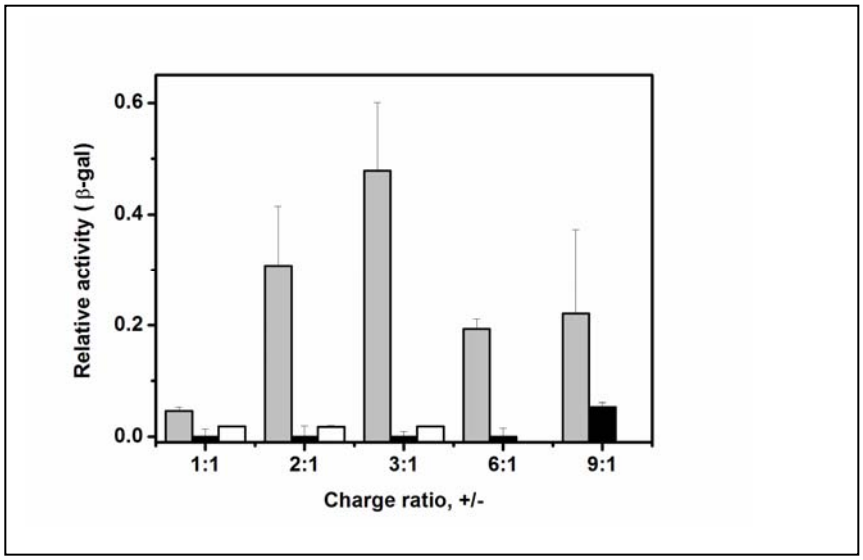

Figure 2S: Transfection efficiencies of chain length analogs of Lipid 1 on CHO cells. Lipsomes prepared with Lipid 1 and its 14- and 16- carbon analogs were complexed with plasmid pCMVβ-gal DNA. The transfection efficiency of the three lipoplexes, depicted in the bar diagram, represent β-activity of Lipid 1 C12-gray, C14-black and C16-white, in CHO cells .

Figure 3S

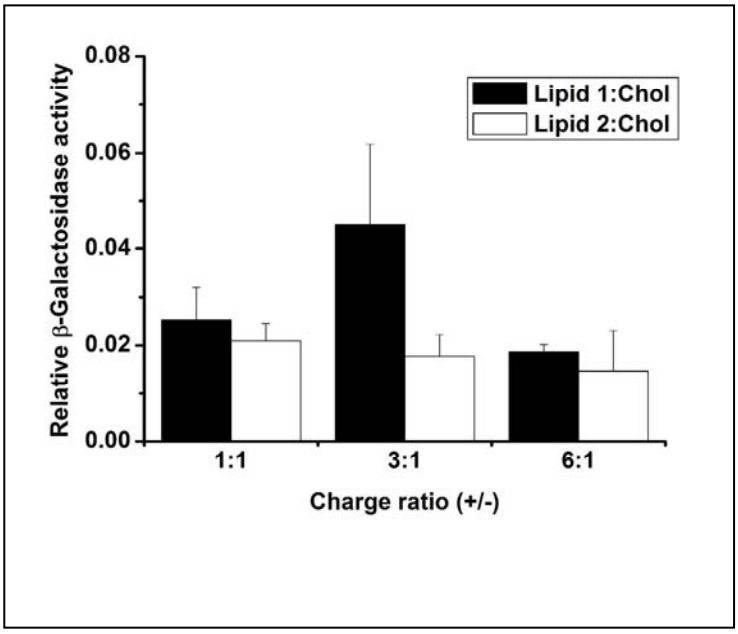

Figure 3S: Transfection of HeLa cells with Lipid 1 and 2 formulated with equimolar amounts of the co-lipid cholesterol at charge ratios varying from 1:1, 3:1 and 6:1 Lipid/DNA. Graph depicts relaltive β-gal activity as described in the experimental section.

Bioconjugate Chemistry

Article

pubs.acs.org/bc

Cell-Penetrating Peptides, PepFects, Show No Evidence of Toxicity and Immunogenicity *In Vitro* and *In Vivo*

Julia Suhorutsenko,[*,§,†] Nikita Oskolkov,[§] Piret Arukuusk,[§] Kaido Kurrikoff,[§] Elo Eriste,[§] Dana-Maria Copolovici,[§] and Ülo Langel[§,†]

[§]Institute of Technology, Tartu University, 50411 Tartu, Estonia

[†]Department of Neurochemistry, Stockholm University, 10692 Stockholm, Sweden

Supporting Information

ABSTRACT: Cell-penetrating peptide based vehicles have been developed for the delivery of different payloads into the cells in culture and in animals. However, several biological features, among which is the tendency to trigger innate immune response, limit the development of highly efficient peptide-based drug delivery vectors. This study aims to evaluate the influence of transportan 10 (TP10) and its chemically modified derivatives, PepFects (PFs), on the innate immune response of the host system. PFs have shown high efficiency in nucleic acid delivery *in vitro* and *in vivo*; hence, the estimation of their possible toxic side effects would be of particular interest. In this study, we analyzed cytotoxic and immunogenic response of PF3, PF4, and PF6 peptides in monocytic leukemia and peripheral blood mononuclear cell lines. In comparison with amphipathic PFs, TP10, TAT, stearyl-$(RxR)_4$ peptides, and the most widely used transfection reagents Lipofectamine 2000 and Lipofectamine RNAiMAX were also analyzed in this study. IL-1β, IL-18, and TNF-α cytokine release was detected using highly sensitive enzyme-linked immunosorbent assay (ELISA). Cell viability was detected by measuring the activity of cellular enzymes that reduce water-soluble tetrazolium salts to formazan dyes and apoptosis was evaluated by measuring the levels of caspase-1 and caspase-3/7 over untreated cells. All peptides were found to be nontoxic and nonimmunogenic *in vitro* at the concentrations of 10 μM and 5 μM, respectively, and at a dose of 5 mg/kg *in vivo*, suggesting that these CPPs exhibit a promising potential in the delivery of therapeutic molecules into the cell without risks of toxicity and inflammatory reactions.

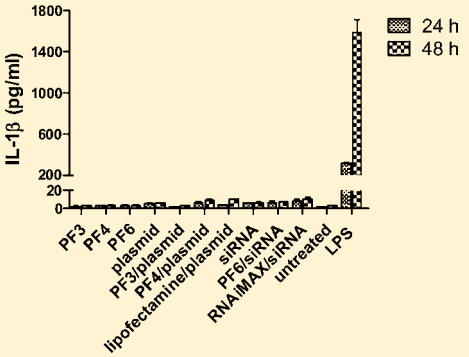

INTRODUCTION

Efficient internalization of therapeutic agents into target cells is very important to gain the desired therapeutic effect. However, since the plasma membrane limits the internalization of high molecular weight molecules into the cell, therapeutic applications of nucleic acids and proteins have been restricted.[1] Several techniques have been used to promote efficient drug delivery, for instance, electroporation, encapsulation in polymers or liposomes, viral delivery systems, and so forth. However, these approaches have several serious drawbacks, including complex manipulation, limited efficiencies in *in vitro* and *in vivo* systems, cytotoxicity, and undesired immunogenic effects.[2,3]

Cell-penetrating peptides (CPPs) have proven their ability to deliver various drug molecules, DNA, RNA, and proteins in cultured cells.[4] Synthetic CPPs were designed with predetermined structures and they maintain the parent peptide's functions. This enables different chemical modifications of the CPPs as well as expression with specific proteins or application together with other delivery vectors, which gives an advantage for the construction of novel, more efficient therapeutic agents.[5] Several modifications of CPPs have been investigated in order to improve gene delivery. In particular, stearic acid modification of different membrane-permeable relatively short peptides, such as TAT,[6] transportan,[7,8] octa-arginine (R_8),[9] and $(RxR)_4$, was shown to substantially increase their transfection efficiency.[6,8,10] It has been shown that stearic acid modification enhances CPP-mediated plasmid DNA delivery, promoting more efficient endosomal escape,[10] enhanced cellular association, as well as higher nuclear delivery.[9] Lysosomotropic agents such as chloroquine and methylamine are also capable of improving the release of therapeutic molecules from acidic endosomal compartments, raising the pH, and performing proteolytic cleavage;[11,12] however, their application *in vivo* for therapeutic use is limited, due to their toxicity.[13,14]

Although therapeutic protein agents and peptides used in clinical settings are generally considered nontoxic, antitherapeutic protein antibodies can develop during the treatment. Antitherapeutic protein antibodies or antidrug antibodies might neutralize or otherwise compromise the clinical effect of therapeutics and can also be associated with serious adverse events related to cross-reactivity with autologous proteins of the host organism.[15] Immune response to therapeutic proteins is categorized by activation of the immune system by foreign

Received: June 6, 2011
Revised: September 12, 2011
Published: October 5, 2011

ACS Publications © 2011 American Chemical Society

proteins, resembling immune response against pathogens or vaccines, involving T-cells, B-cells, and the innate immune system.[15]

The size, surface charge, surface hydrophilicity, surface morphology, and the amino acid sequence of the peptides can significantly affect the immunogenicity of the peptide/nucleic acid complexes and their clearance by the macrophages.[16] Additionally, undesired toxicity can be mediated through interactions of the oligonucleotides with the proteins. These effects can be sequence-dependent, such as interaction with Toll-like receptors (TLRs), or sequence-independent.[17] For example, RNA molecules can also affect TLRs 3, 7, and 8, eliciting undesired immune stimulation that manifests as hyperplasia in lymphoid organs and mononuclear cell infiltrates in nonlymphoid organs.[18,19] Therefore, development of suitable delivery system will depend not only on the efficiency of delivery vectors to transport therapeutic agents through the biological barriers, but also on their risks of producing side effects: toxicity and undesired immunogenicity.[20−22]

In the previous study, stearyl and chloroquine modifications introduced in the TP10 structure were successfully used to overcome the problem of endosomal entrapment of therapeutic agents.[5,23] The introduction of the stearyl moiety at different positions led to PF3 and PF4 peptides (Table 1), which enabled luciferase plasmid (pGL3) delivery at the concentration of 2 μM (Table 2).[23] Covalently bound chloroquine analogue[24] and stearyl moiety in different positions improved the activity of TP10 in serum,[8] generating the PepFect 6 (PF6) peptide, which promoted an efficient siRNA-delivery *in vitro* using only 50 nM siRNA and 2 μM PF6 peptide (Table 2).

Table 1. Peptide Sequences Used in This Study[a]

CPP	amino acid sequences	refs
TP10	AGYLLGKINLKALAALAKKIL-amide	40
PF3 (stearyl-TP10)	stearyl-AGYLLGKINLKALAALAKKIL-amide	8
PF4	AGYLLGK(stearyl)INLKALAALAKKIL-amide	41
PF6	stearyl-AGYLLGK[b]INLKALAALAKKIL-amide	5
TAT (48−60)	GRKKRRQRRRG-amide	42
stearyl-$(RxR)_4$	stearyl-$(RxR)_4$-amide	10

[a]Stearyl − *N*-terminal stearic acid moiety. [b]Trifluoromethylquinoline based derivative conjugated to succinylated lysine tree × - 6-aminohexanoic acid.

In this study, we tested PepFect peptides and PepFect/nucleic acid complexes for the undesired toxicity and immunogenicity both *in vitro* and *in vivo* using the concentrations and similar complex formation conditions, which have been previously reported and indicated to gain the best therapeutic effect. Possible toxic and immunogenic effects of TP10, PF3, PF4, and PF6 peptides were compared with the immunogenic activities of unmodified TP10, well-studied cationic peptides TAT and stearyl-$(RxR)_4$,[25] and the most widely used Lipofectamine transfection reagents. Our results show that PF peptides are efficient nontoxic and nonimmunogenic peptide-based vectors for nucleic acid delivery both *in vitro* and *in vivo,* suggesting promising perspectives for their future therapeutic applications without any risks of inflammation.

EXPERIMENTAL PROCEDURES

Synthesis of Cell-Penetrating Peptides. The peptides were synthesized in a stepwise manner at a 0.1 mmol scale on an automated peptide synthesizer (Applied Biosystemsmodel 433A) using *N*-Fmoc (*N*-fluorenylmethyloxycarbonyl) solid-phase peptide synthesis strategy. All the solvents and reagents used for the peptide synthesis were purchased from Sigma-Aldrich, Germany. Stearyl-modified peptides were prepared according to previously reported protocol,[8] and chloroquine modification from PF6 peptide was performed as described by El Andaloussi et al.[5] (Table 1). Peptides were purified by preparative reversed-phase HPLC (Agilent 1200) using C4 column (Phenomenex Jupiter C4, 5 μm, 300 Å, 250 × 10 mm) using a gradient of 5−100% acetonitrile/water containing 0.1% TFA. Molecular weights of the peptides were analyzed by MALDI-TOF mass-spectroscopy (The Voyager-DE PRO Biospectrometry System). The mass spectra were acquired in positive ion reflector mode using α-cyano-4-hydroxycinnamic acid as a matrix (Sigma−Aldrich), and purity was about 95% as determined by analytical HPLC. The molar concentrations of the peptide solutions were determined based on dilutions of accurately weighed substances.

HPRT1 siRNA. HPRT1 (hypoxanthine phosphoribosyltransferase 1) siRNA was provided by Peter Guterstam.[26] 500 μM stock solutions of siRNA were stored at −20 °C. Sequences of HPRT1 siRNA are as follows: sense 5′-GCCAGACUUU-GUUGGAUUUGAAATT and antisense 5′-AAUUUCAAAUC-CAACAAAGUCUGGCUU.

Plasmid pEGFP-C1. Plasmid pEGFP-C1 (Clontech Laboratories, Inc., USA), 4.7 kb, encodes a red-shifted variant of wild-type green fluorescent protein, GFP, which has been optimized for brighter fluorescence and higher expression in mammalian cells (excitation maximum at 488 nm and emission maximum at 507 nm). Plasmid was propagated and purified using Qiagen plasmid DNA purification kit (QIAGEN Group, USA), according to manufacturer's protocol.

Cell Cultures. THP-1, human acute monocytic leukemia cells (CLS, Germany), and PBMC, human peripheral blood mononuclear cells, isolated from healthy donor by standard density gradient centrifugation and washed in PBS to remove platelets were kindly provided by Dr. Alar Aints, were grown at 37 °C, 5% CO_2 in RPMI 1640 medium with glutamax supplement, 0.1 mM nonessential amino acids, 1.0 mM sodium

Table 2. Transfection Efficiencies of the PF Peptides

CPP	biological effect	cell line	peptide effective concentration	transfection efficiencies	refs
PF3 (stearyl-TP10)	plasmid delivery (pGL3)	CHO, U87	2.25 μM (CR 1:3)	10^8−10^9 RLU/mg	23
PF4	oligonucleotide (2̀OMe RNA) delivery	HeLa pLuc 705	1.4 μM (CR 1:7)	Up to 100-fold increase in splice correction over untreated	41
PF6	siRNA delivery	HEK, MEF, ES, Jurkat	2 μM (MR 40, 50 nM siRNA)	>80% of down regulation	5

dx.doi.org/10.1021/bc200293d | *Bioconjugate Chem.* 2011, 22, 2255−2262

pyruvate, 10% fetal bovine serum, 100 U/mL penicillin, and 100 mg/mL streptomycin (PAA Laboratories GmbH, Germany) further named as complete medium.

PF3/pEGFP-C1 and PF4/pEGFP-C1 Complex Formation. Complexes of peptides with plasmid DNA (pEGFP-C1) were prepared as described previously.[5] Briefly, 0.5 μg of green fluorescent protein expressing pEGFP-C1 plasmid was mixed with PF3 or PF4 at different plasmid/peptide charge ratios (CRs) 1:1 and 1:5 in MQ water in 1/10th of the final treatment volume (i.e., 30 μL). CRs were calculated theoretically, taking into account the positive charges of the peptide and negative charges of the plasmid. Final concentration of PF3 or PF4 was 0.75 μM at CR 1:1 and 3.75 μM at CR 1:5 (Table 3). Complexes were incubated for 1 h at room temperature.

Table 3. Layout of the Peptide/Nucleic Acid Complexes

CPP	pEGFP-C1 plasmid		HPRT1 siRNA	
PF3	CR 1:1	CR 1:5		
PF4	CR 1:1	CR 1:5		
PF6			MR 30, 100 nM siRNA	MR 40, 50 nM siRNA

PF6/siRNA Complex Formation. PF6 (100 μM stock solution) was mixed with HPRT1 siRNA (10 μM stock solution) in MQ water in 1/10th of final treatment volume (i.e., 30 μL), using peptide/siRNA molar ratios (MRs) 40 and 30, siRNA 50 nM and 100 nM, respectively, and were formed as described previously.[5] Complexes were incubated for 1 h at room temperature. In the case of Lipofectamine 2000 and Lipofectamine RNAiMAX (Invitrogen, Sweden), complexes were formed according to the manufacturer's protocol.

Formation and stability of all the peptide/nucleic acid complexes in the presence or absence of serum was confirmed by agarose gel (2%) stained with EtBr (0.5 μg/mL).

MTS Proliferation Assay. Long-term toxicity was evaluated using MTS proliferation assay (Promega, Sweden), which measures the activity of mitochondrial dehydrogenases to convert tetrazolium salts into formazan. 2×10^4 THP-1 cells were seeded into 96-well plate and treated with PF3, PF4, and PF6 peptides at the following concentrations: 1, 5, and 10 μM and peptide/nucleic acid complexes (PF3 or PF4 and pEGFP-C1 complexes at CR 1:1 and CR 1:5; PF6 and siRNA complexes at MR 40, 50 nM siRNA and at MR 30, 100 nM siRNA) for 24 h in complete medium. Thereafter, MTS proliferation assay was performed according to the manufacturer's protocol. Untreated cells were defined as 100% viable. The results are the means of three independent experiment performed in duplicate.

Cytokine Detection from Cell Culture Supernatants and Mouse Serum. THP-1 or PBMC cells were stimulated with 15 ng/mL of PMA (Phorbol 12-myristate 13-acetate (Sigma)) one day before experiment and then 1×10^6 cells were seeded into 24-well plates. Thereafter, the cells were incubated for 24 and 48 h with PF3, PF4, and PF6 at the concentration of 5 μM. In parallel, the cells were treated with plasmid/PF3 or plasmid/PF4 at CR 1:1 and 1:5 and HPRT1 siRNA/PF6 complexes at MR 40, 50 nM siRNA for 4 h in serum-free medium followed by addition of 1 mL complete medium. LPS (10 μg/mL) and poly (i:c) (0.1 μg/mL) were used as positive controls. Supernatants were collected after 24 and 48 h and applied on IL-1β, IL-18, and TNF-α ELISA kits according to manufacturer's protocol (Quantikine kit, R&D Systems, Inc., Minneapolis, MN, USA). The remaining cells were used for the preparation of the extracts, which were applied to the caspase-1 and caspase-3/7 activity assays. Optical density of supernatants from each well was determined using a Tecan Sunrise absorbance plate reader at wavelength of 450 nm with correction at 540 nm. Obtained absorbance values were directly proportional to cytokine concentration in each well. The results are the means of three independent experiment performed in duplicate.

Caspase Activity Assay. Extracts from 1×10^6 THP-1 or PBMC cells were prepared by lysing the cells with Lysis Buffer (R&D Systems, Inc., Minneapolis, MN, USA) for 40 min on ice, followed by incubation with caspase fluorogenic substrates (WEHED-AFC or Z-DEVD-R110 substrate for caspase-1 or caspase-3/7 activity detection, respectively) for 2 h at 37 °C. Measured fluorescence signals are proportional to enzyme activity and monitored over time using a fluorescence plate reader, set for excitation at 400 nm and emission at 505 nm according to manufacturer's protocol. Results are normalized by the cell count in each well and expressed as fold increase in caspase activity of apoptotic cells over untreated cells. The

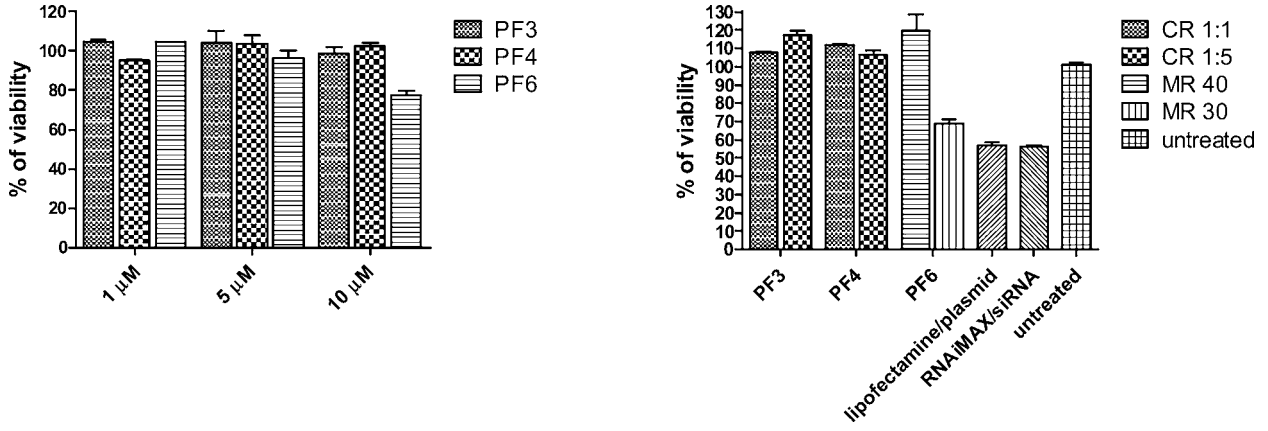

Figure 1. Cell proliferation test. THP-1 cells were incubated with PF3, PF4, and PF6 peptides for 24 h at concentrations of 1, 5, and 10 μM (a). Cells were treated with peptide/nucleic acid complexes: pEGFP-C1/PF3, pEGFP-C1/PF4, at CR 1:2 and 1:3 and HPRT siRNA/PF6, at MR 40, 50 nM siRNA and at MR 30, 100 nM siRNA for 24 h (b). All incubations were performed in complete medium. The values represent the mean of at least three independent experiments performed in duplicate (mean ± SEM).

dx.doi.org/10.1021/bc200293d | Bioconjugate Chem. 2011, 22, 2255–2262

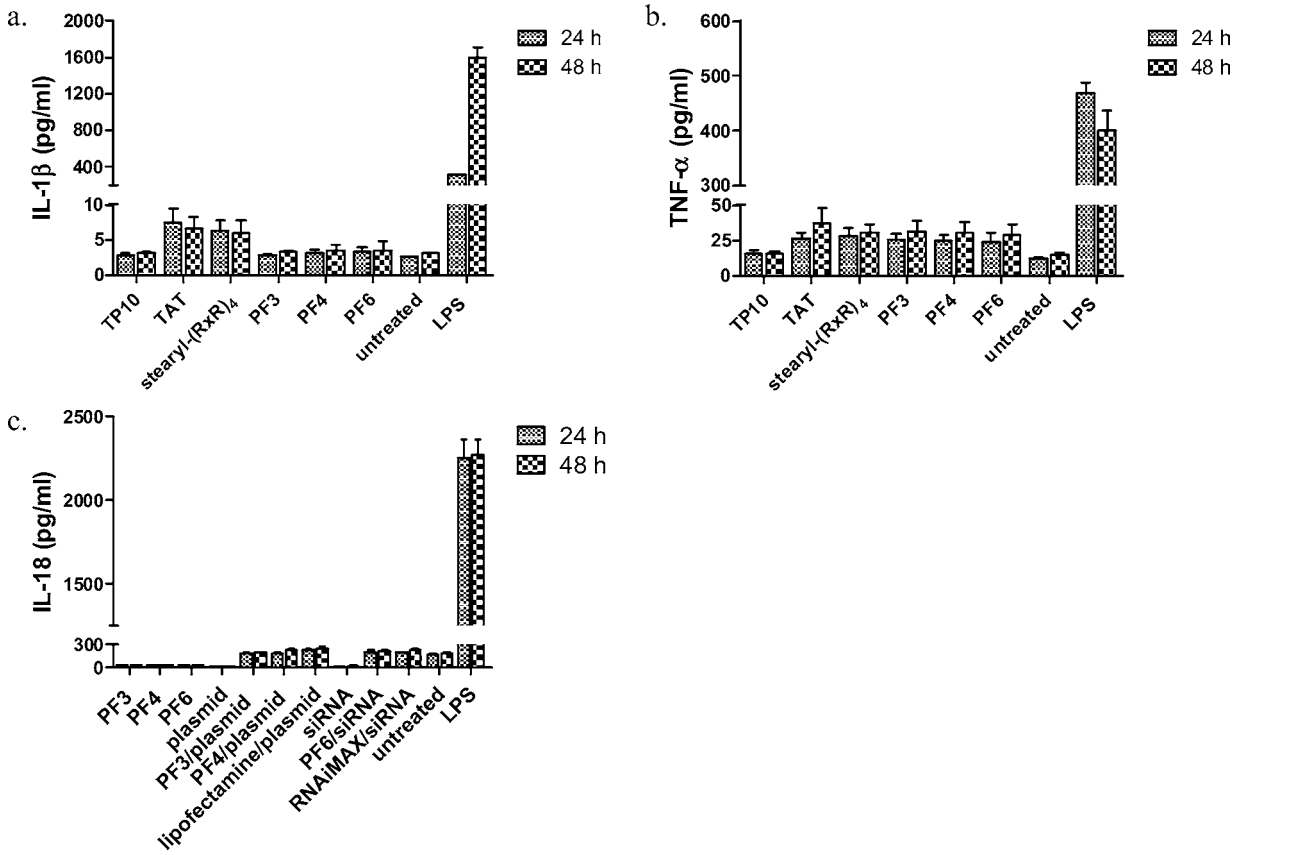

Figure 2. Cytokine release (pg/mL) in THP-1 cell culture supernatants were measured by ELISA assay. IL-1β (a) and TNF-α (b) release in cell culture supernatants were measured after 24 and 48 h of incubation with TP10, TAT, stearyl-$(RxR)_4$, PF3, PF4, and PF6 peptides. IL-18 (c) release was measured after incubation with PF3, PF4, and PF6 peptides, pEGFP-C1/PF3, pEGFP-C1/PF4, HPRT1 siRNA/PF6 and Lipofectamine 2000/pEGFP-C1 and Lipofectamine RNAiMAX/siRNA complexes. LPS (10 μg/mL) was used as a positive control. The values represent the mean of at least three independent experiments performed in duplicate (mean ± SEM).

results are the means of three independent experiment performed in duplicate.

***In Vivo* Toxicology.** C57BL/6 male and female animals (8−10 weeks old at the beginning of the experiments) were used for toxicity and immunogenicity assessments. Cytokine levels in serum were analyzed at 24 and 48 h after i.v. injections of 1 and 5 mg/kg of TAT (48−60) and their equimolar doses of 0.01 and 0.06 μmol per animal of TP10, stearyl-$(RxR)_4$, PF3, PF4, and PF6, respectively. Some animals received LPS (10 μg i.p.). Blood samples were collected via heart puncture, and serum was separated using serum gel-separation tubes (Terumo). Ketamine (75 mg/kg (Vetoquinol, Bioketan)) and dexmedetomidine (1.0 mg/kg (Laboratorios SYVA S.A.U., Dorbene)) in saline solution were applied via i.p. injection and used for anesthesia. Liver, kidney, lung, and spleen were dissected immediately after blood sample collection and rapidly frozen in 2-methylbutan at −60 °C. The cryosected slices were fixed in formalin and stained with hematoxylin and eosin. Slices were analyzed for pathological deviation. Two mice were used per group in three independent experiments.

Statistical Analysis. Values in all experiments are represented as mean ± SEM of three independent experiments done in duplicate. In toxicity measurements, decrease in viability was considered significant at $p < 0.001$ using ANOVA Dunnett's multiple comparison test.

RESULTS

***In Vitro* Toxicity and Immunogenicity.** Aiming to estimate possible toxic and immunogenic effects of PF3, PF4, and PF6 peptides we measured activity levels of caspases-1, 3, and 7 and interleukin IL-1β, IL-18, and TNF-α cytokine production by THP-1 and PBMC cells after 24 and 48 h of treatment. *In vitro* cell viability test showed no toxic effects in THP-1 cells treated with the peptides PF3, PF4, and PF6 at concentrations of 1, 5, and 10 μM and incubated for 24 h in complete medium (Figure 1a). Moreover, treatment with plasmid/peptide complexes at CR 1:1 and 1:5 or with peptide/siRNA complexes at MR 40, 50 nM siRNA also did not show any toxic effects. At the same time, treatment with peptide/siRNA complexes at MR 30, 100 nM siRNA reduced cell viability up to 30%. Therefore, only CPP/siRNA complexes at MR 40, 50 nM siRNA were preferred for the further *in vitro* experiments. Toxic effects were observed during the treatment with the lipofectamine/nucleic acid complexes, whereas only 55% of the cells remained viable after 24 h of incubation (Figure 1b). Estimation of the cytokine levels showed no enhanced interleukine release induced by PF3, PF4, and PF6 peptides in THP-1 or in PBMC cell lines (Figure 2a,b,c; Supporting Information Figure S1a). In parallel, we measured and analyzed the immunogenic influence of cationic peptides: TAT, stearyl-$(RxR)_4$, and chimeric amphipathic TP10. We found no influence of these peptides on THP-1 and PBMC cells (Figure 2 a,b; Figure S2) and the results were similar to

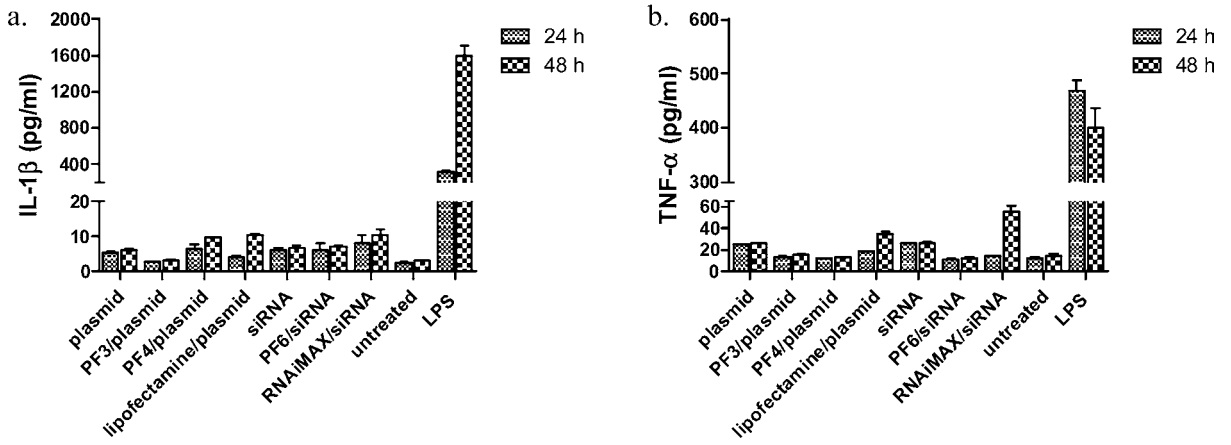

Figure 3. Cytokine release (pg/mL) in THP-1 cells treated with PF peptides/nucleic acid complexes. IL-1β (a) and TNF-α (b) measured by ELISA assay after 24 and 48 h of incubation with pEGFP-C1 plasmid (0.5 μg), siRNA (50 nM), pEGFP-C1/PF3, pEGFP-C1/PF4, HPRT1 siRNA/PF6, and Lipofectamine 2000/pEGFP-C1 and Lipofectamine RNAiMAX/siRNA complexes. LPS (10 μg/mL) was used as a positive control. The values represent the mean of at least three independent experiments performed in duplicate (mean ± SEM).

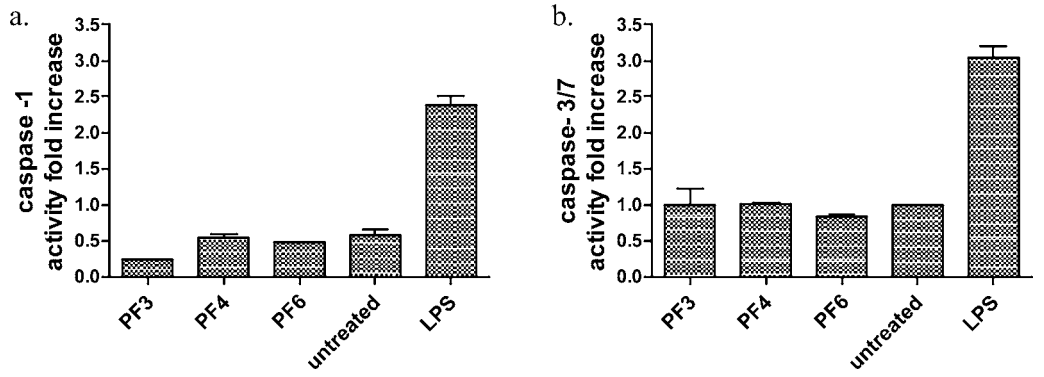

Figure 4. Caspase activity measured in THP-1 cell line. Caspase-1 (a) and caspase-3/7 (b) activity were measured in cells incubated with PF3, PF4, and PF6 peptides for 48 h as described previously. The results are expressed as fold increase in caspase activity of apoptotic cells over noninduced cells. The values represent the mean of at least three independent experiments performed in duplicate (mean ± SEM).

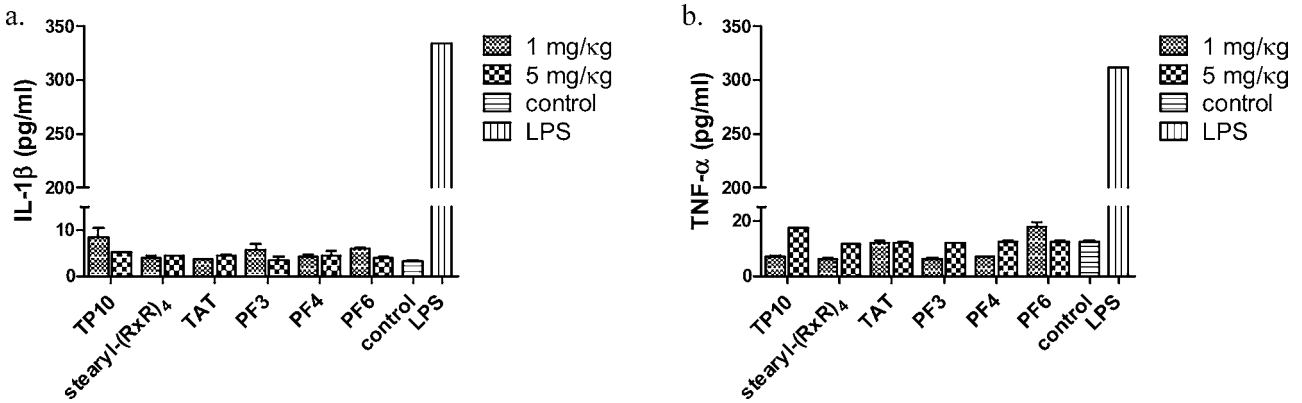

Figure 5. IL-1β and TNF-α cytokines level detection *in vivo*. Immunocompetent mice were treated with TP10, TAT, stearyl-$(RxR)_4$, PF3, PF4, and PF6 peptides at the dose of 0.01 or 0.06 μmol per animal (corresponding to 1 mg/kg and 5 mg/kg, respectively). Serum samples were collected 24 h after i.v. injections and applied to the ELISA assay. IL-1β (a) and TNF-α (b) levels were measured by a TECAN absorbance plate reader. The values represent the mean of at least three independent experiments performed in duplicate (mean ± SEM).

the effects exhibited by PF peptides. Modest increase in cytokine activity triggered by TAT and stearyl-$(RxR)_4$ was considered not statistically significant. Indicated influence on the release of IL-1β, TNF-α, and IL-18 was insignificant if compared to lipopolysaccharide (LPS) or poly (i:c) (used in this study as positive control for PBMC cells) after 24 and 48 h of incubation. Next, we analyzed whether the peptide/nucleic acid complexes formed at different charge ratios are able to trigger the cytokine release. No evidence of increased cytokine level was noticed in both THP-1 and PBMC cell lines in response to treatment with plasmid/peptide and siRNA/peptide complexes (Figure 3a,b; Figure S1b,c) at CR 1:5 for

dx.doi.org/10.1021/bc200293d | *Bioconjugate Chem.* 2011, 22, 2255–2262

plasmid and for siRNA at 50 nM concentration, which is the highest effective dose of siRNA used in the previous studies.[5] Thereafter, we estimated the caspase-1 and caspase-3/7 activity in the cells treated with 5 μM PF peptides and peptide/nucleic acid complexes measuring the rate of hydrolysis of a fluorogenic substrate in the cell lysates. Caspase activity rates 2-fold over those of noninduced cells or higher were considered to be significant caspase activity of apoptotic cells in these studies. Measured caspase-1 and caspase-3/7 activity was similarly compared with the caspase activity of the untreated cells (Figure 4a,b). The results showed that the peptides used in the current study lack apoptotic activity *in vitro*.

***In Vivo* Immunogenicity.** In order to confirm the *in vitro* data, the peptides were administrated to immunocompetent mice via i.v. injection followed by collection of the blood samples after 24 and 48 h. Mice that received 10 μg LPS were used in this study as a positive control. Similarly to the results obtained from *in vitro* studies, ELISA analyses of the separated serum samples also showed no evidence of enhanced IL-1β or TNF-α cytokine production after 24 or 48 h of treatment with PF3, PF4, PF6, TP10, TAT, and stearyl-$(RxR)_4$ peptides at doses of 0.01 and 0.06 μmol per animal (corresponding to 1 mg/kg and 5 mg/kg, respectively, as it is shown in Figure 5a,b). Indicated release of IL-1β and TNF-α cytokines was insignificant if compared to lipopolysaccharide (LPS). Additionally, no pathological deviations were observed in liver, kidney, lung, and spleen dissected from animals, which received 1 mg/kg and 5 mg/kg of PFs, TP10, TAT, and stearyl-$(RxR)_4$ peptides (data not shown).

DISCUSSION

Application of CPPs has evolved as an attractive tool to solve the problems of drug delivery.[27] However, successful usage of the drug carriers in clinics has been mostly limited by their possible undesired side effects, namely, immunogenicity and *in vivo* toxicity. The main goal of the current study was to evaluate the influence of the PepFect delivery agents on the immune activity *in vitro* and *in vivo*, which is a novel aspect of the PF peptide-based delivery system investigation. Despite the fact that CPPs contain fewer than 30 amino acids[28] and contain no evidence for oncogene activation,[27] the research on biological side effects of cationic and amphipathic peptides has still been receiving great attention.[20] Several independent experiments on cell viability, membrane integrity, as well as toxicity analyses suggested that amphipathic peptides such as TP10 affect cellular metabolism at the concentrations ranging from 5 to 10 μM, whereas the cationic CPPs penetratin, TAT, and nonaarginine showed no toxic effect at similar concentration range.[29] As PF peptide design is based on the TP10 peptide sequence with minor chemical modifications, we could not eliminate the possibility that they could induce undesired toxic and inflammatory effects *in vitro* and *in vivo*. It has been shown that TAT peptide induces no cytotoxicity *in vitro* even at the concentration up to 400 μM. In the same work, toxicity was evaluated *in vivo* by applying peptides to the rabbit's cornea 4 times daily for 7 days. At doses 1000 times the IC_{50} values, penetratin peptide showed no toxicity *in vivo* and TAT caused some mild eyelid swelling.[30] Similarly, polyarginine peptides also did not induce any cellular toxicity at siRNA/peptide ratio of negative/positive charges of 40.[30−32] These studies indicate that the use of TAT peptide for anticancer therapy, for instance, does not induce a measurable immune response, although long-term toxicity studies have not been performed yet.[3]

Chloroquine has been used for a long time in the treatment or prevention of malaria. Due to its immunosuppressive activity, chloroquine is applied for treatment of autoimmune disorders, such as rheumatoid arthritis and lupus erythematosus.[33] Recently, chloroquine was used to overcome the problems of endosomal escape of the entrapped and deactivated therapeutic molecules *in vitro*. The coaddition of chloroquine in solution enhances endosomal release of peptide-based delivery vehicles.[8] In order to promote endosomal escape and increase the transfection efficiency the chloroquine moieties were introduced in the PF6 structure.[5] At the same time, chloroquine has been associated with several toxicity cases, including retinal injury and skin irritations particularly when provided at high doses for a long time range.[34,35] Toxic side effects and the ability of chloroquine to influence immune system limit therapeutic application of this lysosomotropic agent *in vivo*.

In the current study, we investigated possible toxic and immunogenic activity of the PF peptides and compared them with the widely used cationic CPPs such as TAT, stearyl-$(RxR)_4$, and amphipathic TP10, trying to bring out the differences or possible enhanced influence of PF peptides on the activation of the immune system. During the analyses, the greatest attention received the peptide/nucleic acid complexes with the highest charge and molar ratios that proved to be stable in serum and showed a particular effectiveness in case of different cell line transfections.[5] Our results demonstrated the lack of viability reduction in THP-1 cell line, as well as no indication of primary inflammatory effects after 24 or 48 h of incubation with PF peptides. Peptides showed no toxic influences on THP-1 cell viability even at concentration of 10 μM, although this was observed mainly in serum containing complete medium (Figure 1 a,b). Moreover, lipofectamine agents exhibited strong cytotoxic effect, reducing cells viability up to 55%. None from the measured IL-1β, IL-18, and TNF-α cytokines were overexpressed in the THP-1 cells in response to TP10, TAT, stearyl-$(RxR)_4$, or PF peptide treatment (Figure 2 a,b,c).

Similarly, no evidence of enhanced *in vitro* IL-1β production was observed also in noncancer PBMC cell line (Figure S1a, Figure S2). The peptides were applied at the concentration of 5 μM dose, which corresponds to the peptide amount used for complex formation. As expected, the cells treated with the peptide/nucleic acid complexes similarly showed no increase in cytokine release if compared with the peptide-treated or untreated cells (Figure 3a,b; Figure S1b,c). None of the lipofectamine reagents induced the increased cytokine production at the recommended manufacturer̀s dose *in vitro* (Figure 2c; Figure 3a,b; Figure S1b,c). At the same time, cells incubated with LPS demonstrated increased cytokine level in growth medium, more then 100 times higher than in the untreated cells (Figure 2 a,b,c; Figure 3a,b; Figure S1 a,b,c).

Thereafter, we estimated if PF peptides could possibly trigger apoptotic events in immune cells. We performed total caspase-1 and caspase-3/7 activity measurements *in vitro*. Caspases are crucial mediators of programmed cell death (apoptosis).[36] Among them, caspase-3 is a frequently activated death protease, catalyzing the specific cleavage of many key cellular proteins, initiating apoptosis.[37] Caspase-1 or ICE (interleukin-1β converting enzyme) is an essential regulator of inflammatory responses through its capacity to process and activate proIL-1β, proIL-18, and proIL-33.[38,39] Therefore, caspase-1 is considered "inflammatory" caspase. We measured caspase-1 and caspase-3/

7 activity in the immune cells treated with PF3, PF4, and PF6 peptides. No activation of the measured caspases was detected in the cells, compared to LPS, suggesting that these peptides lack caspase-dependent apoptotic activity (Figure 4a,b).

In summary, we found that PFs peptides are not toxic or immunogenic at tested concentrations *in vitro*, and we proceeded with testing PF3, PF4, and PF6 peptides *in vivo*. Similar to the results from *in vitro* studies, none of the peptides induced an increase of the cytokine levels in blood serum (Figure 5a,b) or caused pathological deviations in liver, kidney, lung, and spleen of the treated animals (data not shown). PF peptides, which were obtained by chemically modifying the TP10 peptide sequence, exhibited similar effects with TP10, and also with TAT and stearyl-$(RxR)_4$ peptides, showing no influence on the host system. The peptide dose used for i.v. injections in current *in vivo* immunogenicity study, 5 mg/kg, was much higher than the dose used for *in vivo* nucleic acid delivery in the previous study.[5] Having evaluated the data obtained with TP10, TAT, stearyl-$(RxR)_4$ peptides and compared then with the results of PF peptides, we conclude that the peptides have no evidence of inflammatory effects *in vivo*. PF peptides resemble the effects shown by TP10, suggesting that introduced stearyl and chloroquine groups in TP10 sequence do not interfere with cellular immunogenicity.

Although the novel TP10 analogues used in this study were found not to be toxic and immunogenic *in vitro* and *in vivo*, long-term toxicity studies have not been performed yet to confirm the data. The current study confirms that PF3, PF4, and PF6 peptides have indeed a promising potential in plasmid and siRNA delivery without evidence of undesired toxicity and inflammation.

■ ASSOCIATED CONTENT

Ⓢ Supporting Information

Figure S1: IL-1β cytokine release measured by ELISA assay in PBMC cells incubated with PF peptides and peptide/nucleic acid complexes. Figure S2: IL-1β cytokine release measured by ELISA assay in PBMC cells incubated with TP10, TAT, and stearyl-$(RxR)_4$ peptides. This material is available free of charge via the Internet at http://pubs.acs.org.

■ AUTHOR INFORMATION

Corresponding Author

*Laboratory of Molecular Biotechnology, Institute of Technology, University of Tartu, Nooruse 1, 50411 Tartu, Estonia. Phone: +372-7-37-4866; Fax:+372-7-37-4900; e-mail: julia.suhorutsenko@ut.ee.

■ ACKNOWLEDGMENTS

This work was supported by EU through the European Regional Development Fund through the Center of Excellence in Chemical Biology, Estonia, by the targeted financing SF0180027s08 from the Estonian Government, by European Social Fund's Doctoral Studies and Internalisation Programme DoRa. Dana M. Copolovici was supported by a postdoctoral fellowship of the Estonian Science Foundation-Mobilitas-MJD64. We thank Dr. Alar Aints for providing and culturing PBMC cells, Peter Guterstam for providing HPRT1 siRNA and Samir El Andaloussi for providing a fruitful discussion.

■ ABBREVIATIONS

CPP, cell-penetrating peptide; CR, charge ratio; MR, molar ratio; PBMC, peripheral blood mononuclear cell line; THP-1, human acute monocytic leukemia cell line; poly (i:c), polyinosinic polycytidylic acid; LPS, lipopolysaccharide; TLR, toll-like receptors; ELISA, enzyme-linked immunosorbent assay; TP10, transportan 10; PF, PepFects; IL-1β, interleukin-1β; IL-18, interleukin-18; TNF-α, tumor necrosis factor-α; TLRs, Toll-like receptors; *N*-Fmoc, *N*-fluorenylmethyloxycarbonyl; HPLC, high-performance liquid chromatography; MALDI-TOF, matrix-assisted laser desorption/ionization, time-of-flight; HPRT1, hypoxanthine phosphoribosyltransferase 1; PMA, phorbol 12-myristate 13-acetate; poly (i:c), polyinosinic:polycytidylic acid; EtBr, ethidium bromide; LPS, lipopolysaccharide; MTS, 3-(4,5-dimethylthiazol-2-yl)-5-(3-carboxymethoxyphenyl)-2-(4-sulfophenyl)-2*H*-tetrazolium; ICE, interleukin-1β converting enzyme

■ REFERENCES

(1) Harada, H., Kizaka-Kondoh, S., and Hiraoka, M. (2006) Antitumor protein therapy; application of the protein transduction domain to the development of a protein drug for cancer treatment. *Breast Cancer 13*, 16−26.

(2) Rennert, R., Neundorf, I., and Beck-Sickinger, A. G. (2008) Calcitonin-derived peptide carriers: mechanisms and application. *Adv. Drug Delivery Rev. 60*, 485−98.

(3) Bitler, B. G., and Schroeder, J. A. (2010) Anti-cancer therapies that utilize cell penetrating peptides. *Recent Pat. Anticancer Drug Discovery 5*, 99−108.

(4) Lindberg, S., Copolovici, D. M., and Langel, Ü. (2011) Therapeutic delivery opportunities, obstacles and applications for cell-penetrating peptides. *Therapeutic Delivery 2*, 71−82.

(5) El Andaloussi, S., Lehto, T., Mäger, I., Rosenthal-Aizman, K., Oprea, I. I., Simonson, O. E., Sork, H., Ezzat, K., Copolovici, D. M., Kurrikoff, K., Viola, J. R., Zaghloul, E. M., Sillard, R., Johansson, H. J., Said Hassane, F., Guterstam, P., Suhorutsenko, J., Moreno, P. M., Oskolkov, N., Halldin, J., Tedebark, U., Metspalu, A., Lebleu, B., Lehtio, J., Smith, C. I., and Langel, Ü. (2011) Design of a peptide-based vector, PepFect6, for efficient delivery of siRNA in cell culture and systemically in vivo. *Nucleic Acids Res. 39*, 3972−3987.

(6) Futaki, S., Ohashi, W., Suzuki, T., Niwa, M., Tanaka, S., Ueda, K., Harashima, H., and Sugiura, Y. (2001) Stearylated arginine-rich peptides: a new class of transfection systems. *Bioconjugate Chem. 12*, 1005−11.

(7) Lundin, P., Johansson, H., Guterstam, P., Holm, T., Hansen, M., Langel, Ü., and El Andeloussi, S. (2008) Distinct uptake routes of cell-penetrating peptide conjugates. *Bioconjugate Chem. 19*, 2535−42.

(8) Mäe, M., El Andaloussi, S., Lundin, P., Oskolkov, N., Johansson, H. J., Guterstam, P., and Langel, Ü. (2009) A stearylated CPP for delivery of splice correcting oligonucleotides using a non-covalent co-incubation strategy. *J. Controlled Release 134*, 221−7.

(9) Akita, H., Ito, R., Khalil, I. A., Futaki, S., and Harashima, H. (2004) Quantitative three-dimensional analysis of the intracellular trafficking of plasmid DNA transfected by a nonviral gene delivery system using confocal laser scanning microscopy. *Mol. Ther. 9*, 443−51.

(10) Lehto, T., Abes, R., Oskolkov, N., Suhorutsenko, J., Copolovici, D. M., Mager, I., Viola, J. R., Simonson, O. E., Ezzat, K., Guterstam, P., Eriste, E., Smith, C. I., Lebleu, B., Samir El, A., and Langel, U. (2010) Delivery of nucleic acids with a stearylated (RxR)4 peptide using a non-covalent co-incubation strategy. *J. Controlled Release 141*, 42−51.

(11) Seglen, P. O., Grinde, B., and Solheim, A. E. (1979) Inhibition of the lysosomal pathway of protein degradation in isolated rat hepatocytes by ammonia, methylamine, chloroquine and leupeptin. *Eur. J. Biochem. 95*, 215−25.

(12) Lammers, G., and Jamieson, J. C. (1989) Studies on the effect of lysosomotropic agents on the release of Gal beta 1−4GlcNAc alpha-

2,6-sialytransferase from rat liver slices during the acute-phase response. *Biochem. J. 261*, 389−93.
(13) Ciftci, K., and Levy, R. J. (2001) Enhanced plasmid DNA transfection with lysosomotropic agents in cultured fibroblasts. *Int. J. Pharm. 218*, 81−92.
(14) Cann, H. M., and Verhulst, H. L. (1961) Fatal acute chloroquine poisoning in children. *Pediatrics 27*, 95−102.
(15) De Groot, A. S., and Scott, D. W. (2007) Immunogenicity of protein therapeutics. *Trends Immunol. 28*, 482−90.
(16) Jabbari, E. (2009) Targeted delivery with peptidomimetic conjugated self-assembled nanoparticles. *Pharm. Res. 26*, 612−30.
(17) Bennett, C. F., and Swayze, E. E. RNA targeting therapeutics: molecular mechanisms of antisense oligonucleotides as a therapeutic platform. *Annu. Rev. Pharmacol. Toxicol. 50*, 259-93.
(18) Henry, S. P., Giclas, P. C., Leeds, J., Pangburn, M., Auletta, C., Levin, A. A., and Kornbrust, D. J. (1997) Activation of the alternative pathway of complement by a phosphorothioate oligonucleotide: potential mechanism of action. *J. Pharmacol. Exp. Ther. 281*, 810−6.
(19) Bouchard, P. R., Hutabarat, R. M., and Thompson, K. M. (2009) Discovery and development of therapeutic aptamers. *Annu. Rev. Pharmacol. Toxicol. 50*, 237−57.
(20) Verdurmen, W. P., and Brock, R. (2011) Biological responses towards cationic peptides and drug carriers. *Trends Pharmacol. Sci.*
(21) Temsamani, J., and Vidal, P. (2004) The use of cell-penetrating peptides for drug delivery. *Drug Discovery Today 9*, 1012−9.
(22) Järver, P., Mäger, I., and Langel, Ü. (2010) In vivo biodistribution and efficacy of peptide mediated delivery. *Trends Pharmacol. Sci. 31*, 528−35.
(23) Lehto, T., Simonson, O. E., Mäger, I., Ezzat, K., Sork, H., Copolovici, D. M., Viola, J. R., Zaghloul, E. M., Lundin, P., Moreno, P. M., Mäe, M., Oskolkov, N., Suhorutsenko, J., Smith, C. E., and Andaloussi, S. E. (2011) A peptide-based vector for efficient gene transfer in vitro and in vivo. *Mol. Ther.*, doi:10.1038/mt.2011.10.
(24) Cheng, J., Zeidan, R., Mishra, S., Liu, A., Pun, S. H., Kulkarni, R. P., Jensen, G. S., Bellocq, N. C., and Davis, M. E. (2006) Structure-function correlation of chloroquine and analogues as transgene expression enhancers in nonviral gene delivery. *J. Med. Chem. 49*, 6522−31.
(25) Duchardt, F., Fotin-Mleczek, M., Schwarz, H., Fischer, R., and Brock, R. (2007) A comprehensive model for the cellular uptake of cationic cell-penetrating peptides. *Traffic 8*, 848−66.
(26) Guterstam, P., Lindgren, M., Johansson, H., Tedebark, U., Wengel, J., El Andaloussi, S., and Langel, Ü. (2008) Splice-switching efficiency and specificity for oligonucleotides with locked nucleic acid monomers. *Biochem. J. 412*, 307−13.
(27) Snyder, E. L., and Dowdy, S. F. (2004) Cell penetrating peptides in drug delivery. *Pharm. Res. 21*, 389−93.
(28) Drin, G., Cottin, S., Blanc, E., Rees, A. R., and Temsamani, J. (2003) Studies on the internalization mechanism of cationic cell-penetrating peptides. *J. Biol. Chem. 278*, 31192−201.
(29) Kilk, K., Mahlapuu, R., Soomets, U., and Langel, Ü. (2009) Analysis of in vitro toxicity of five cell-penetrating peptides by metabolic profiling. *Toxicology 265*, 87−95.
(30) Akkarawongsa, R., Cullinan, A. E., Zinkel, A., Clarin, J., and Brandt, C. R. (2006) Corneal toxicity of cell-penetrating peptides that inhibit Herpes simplex virus entry. *J. Ocul. Pharmacol. Ther. 22*, 279−89.
(31) Vives, E., Schmidt, J., and Pelegrin, A. (2008) Cell-penetrating and cell-targeting peptides in drug delivery. *Biochim. Biophys. Acta 1786*, 126−38.
(32) Kim, W. J., Christensen, L. V., Jo, S., Yockman, J. W., Jeong, J. H., Kim, Y. H., and Kim, S. W. (2006) Cholesteryl oligoarginine delivering vascular endothelial growth factor siRNA effectively inhibits tumor growth in colon adenocarcinoma. *Mol. Ther. 14*, 343−50.
(33) Savarino, A., Boelaert, J. R., Cassone, A., Majori, G., and Cauda, R. (2003) Effects of chloroquine on viral infections: an old drug against today's diseases? *Lancet Infect. Dis. 3*, 722−7.
(34) Gaynes, B. I., Torczynski, E., Varro, Z., Grostern, R., and Perlman, J. (2008) Retinal toxicity of chloroquine hydrochloride administered by intraperitoneal injection. *J. Appl. Toxicol. 28*, 895−900.
(35) Aghahowa, S. E., Obianwu, H. O., Isah, A. O., and Arhewoh, I. M. (2010) Chloroquine-induced Pruritus. *Indian J. Pharm. Sci. 72*, 283−9.
(36) Danial, N. N., and Korsmeyer, S. J. (2004) Cell death: critical control points. *Cell 116*, 205−19.
(37) Porter, A. G., and Janicke, R. U. (1999) Emerging roles of caspase-3 in apoptosis. *Cell Death Differ. 6*, 99−104.
(38) Dinarello, C. A. (2002) The IL-1 family and inflammatory diseases. *Clin. Exp. Rheumatol. 20*, S1−13.
(39) Ogura, Y., Sutterwala, F. S., and Flavell, R. A. (2006) The inflammasome: first line of the immune response to cell stress. *Cell 126*, 659−62.
(40) Soomets, U., Lindgren, M., Gallet, X., Hallbrink, M., Elmquist, A., Balaspiri, L., Zorko, M., Pooga, M., Brasseur, R., and Langel, Ü. (2000) Deletion analogues of transportan. *Biochim. Biophys. Acta 1467*, 165−76.
(41) El Andaloussi, S., Lehto, T., Lundin, P., and Langel, Ü. (2011) Application of PepFect peptides for the delivery of splice-correcting oligonucleotides. *Methods Mol. Biol. 683*, 361−73.
(42) Futaki, S., Suzuki, T., Ohashi, W., Yagami, T., Tanaka, S., Ueda, K., and Sugiura, Y. (2001) Arginine-rich peptides. An abundant source of membrane-permeable peptides having potential as carriers for intracellular protein delivery. *J. Biol. Chem. 276*, 5836−40.

SUPPORTING INFORMATION

Cell-Penetrating Peptides, PepFects Show No Evidence of Toxicity and Immunogenicity *In Vitro* and *In Vivo*

Julia Suhorutsenko[*,§,†], Nikita Oskolkov[§], Piret Arukuusk[§], Kaido Kurrikoff[§], Elo Eriste[§], Dana-Maria Copolovici[§] and Ülo Langel[§,†]

[§]Tartu University, Institute of Technology, 50411 Tartu, Estonia

[†]Stockholm University, Department of Neurochemistry, 10692 Stockholm, Sweden

*To whom correspondence should be addressed: JS, Laboratory of Molecular Biotechnology, Institute of Technology, University of Tartu, Nooruse 1, 50411 Tartu, Estonia. Phone: +372-7-37-4866; Fax:+372-7-37-4900; e-mail: julia.suhorutsenko@ut.ee

SUPPORTING FIGURES

(a)

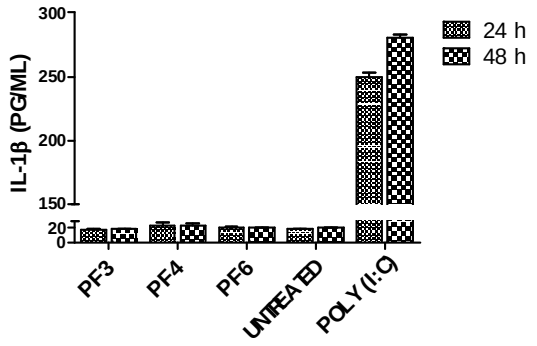

(b)

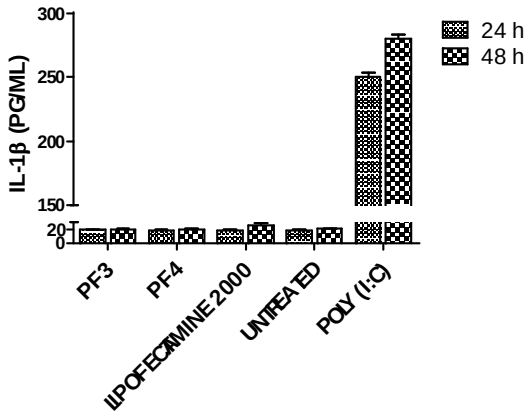

(c)

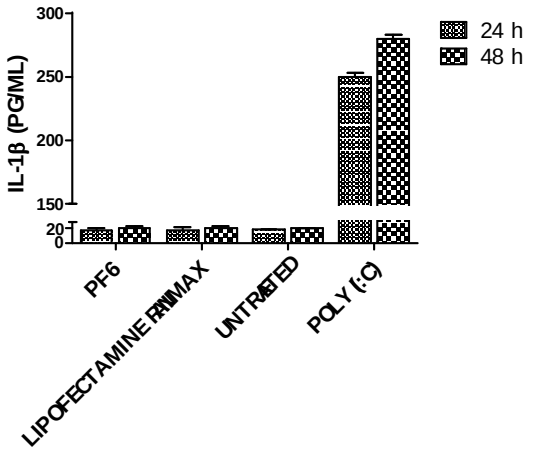

Figure S1. IL-1β cytokine release measured by ELISA assay in PBMC cells incubated with PF peptides and peptide/nucleic acid complexes. IL-1β release in cell culture supernatants after 24 and 48 h of incubation with PF3, PF4 and PF6 (a), with plasmid/CPP complexes: pEGFP-C1/PF3, pEGFP-C1/PF4 and Lipofectamine™ 2000 (b) and with HPRT1 siRNA/PF6 complexes and Lipofectamine™ RNAiMAX (c). Poly (i:c) (0.1 μg/ml) was used as a positive control. The values represent the mean of at least three independent experiments performed in duplicate (mean ± SEM).

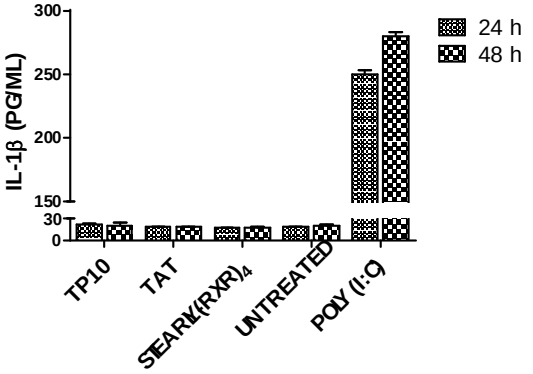

Figure S2. IL-1β cytokine release measured by ELISA assay in PBMC cells incubated with TP10, TAT and stearyl-$(RxR)_4$ peptides. IL-1β measured by ELISA assay after 24 and 48 h of incubation with the peptides. Poly (i:c) (0.1 μg/ml) was used as a positive control. The values represent the mean of at least three independent experiments performed in duplicate (mean ± SEM).

Bioconjugate Chemistry

Article

pubs.acs.org/bc

Synthesis and Evaluation of a Series of 1,2,4,5-Tetrazines for Bioorthogonal Conjugation

Mark R. Karver, Ralph Weissleder, and Scott A. Hilderbrand*

Center for Systems Biology, Massachusetts General Hospital and Harvard Medical School, 185 Cambridge Street Suite 5.210, Boston, Massachusetts 02114, United States

Supporting Information

ABSTRACT: 1,2,4,5-Tetrazines have been established as effective dienes for inverse electron demand [4 + 2] Diels–Alder cycloaddition reactions with strained alkenes for over 50 years. Recently, this reaction pair combination has been applied to bioorthogonal labeling and cell detection applications; however, to date, there has been no detailed examination and optimization of tetrazines for use in biological experiments. Here, we report the synthesis and characterization of 12 conjugatable tetrazines. The tetrazines were all synthesized in a similar fashion and were screened in parallel to identify candidates most ideally suited for biological studies. In depth follow-up studies revealed compounds with varying degrees of stability and reactivity that could each be useful in different bioorthogonal applications. One promising, highly stable, and water-soluble derivative was used in pretargeted cancer cell labeling studies, confirming its utility as a bioorthogonal moiety.

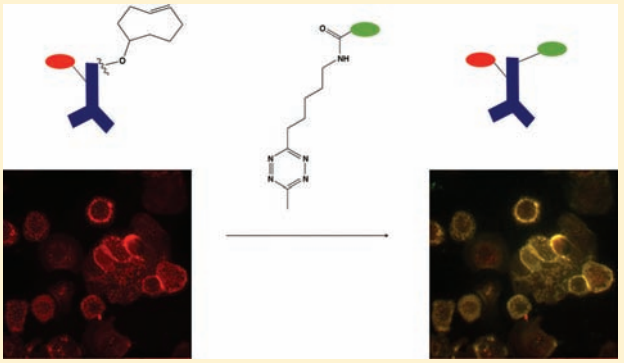

INTRODUCTION

Bioorthogonal 'click' chemistry reactions are a powerful tool for exploring different aspects of biological systems. The ability to perform these chemical reactions in cellular environments (*in cellulo* chemistry) and host organisms (*in vivo* chemistry) without interference from biological components allows for selective 'tagging' of cellular targets and provides a means to image or track biochemical components and interactions. The most widely used and well-known bioorthogonal reaction is the azide and alkyne [3 + 2] cycloaddition.[1] The use of ring strain to promote this reaction was a major development in the field allowing for the [3 + 2] cycloaddition to proceed at room temperature without the need for catalysts.[2] Notable accomplishments utilizing this chemistry have involved the labeling of cell surface glycoconjugates,[3] cell membrane lipids,[4] and glycans in living organisms,[5,6] among others.[7,8] Another bioorthogonal reaction using a similar concept, but employing 1,2,4,5-tetrazines and strained alkenes for [4 + 2] inverse electron demand cycloadditions, has emerged more recently.[9−11] This reaction has gained popularity due to the potential for extremely fast cycloaddition kinetics with *trans*-cyclooctene (TCO) as the dienophile. Applications have included fluorescent cancer cell labeling,[12,13] *in vivo* cancer imaging with ^{111}In,[14] ^{18}F radiolabeling,[15−17] as well as cancer cell detection applications.[18,19]

The effectiveness of the strained alkene–tetrazine reaction is clear, but there has been little detailed investigation on optimizing the reactant properties for bioorthogonal use. However, there is a wealth of reactivity data in nonaqueous media, beginning with the observation in the late 1950s that tetrazines can react with unsaturated compounds.[20] Following this publication, much progress was made in synthesizing different tetrazines for reactions with various dienophiles[21,22] including kinetic analysis of this cycloaddition reaction with different dienophiles by Sauer.[23−25] Sauer reported a range of [4 + 2] cycloaddition reactivity based on the nature of the dienophile that spans 9 orders of magnitude with 1,2,4,5-tetrazines including the first use of norbornene and TCO, which have been the primary dienophiles used in recent bioorthogonal literature.[25,26] TCO has proven to be a much faster reactant than norbornene for bioorthogonal applications,[9,10] but the latter is more stable and commercially available. No reported attempts at improving the dienophile reactivity for bioorthogonal use with tetrazines were published until a recent article emerged describing a new derivative of TCO.[27] The large cycloaddition rate differences seen by changing the chemical nature of the dienophile are equaled by changing the substituents in the 3 and 6 positions of 1,2,4,5-tetrazines.[28] However, only a few tetrazines have been employed in biological environments for bioorthogonal labeling. The primary tetrazines used for this application found in recent literature are the 3,6-monoaryl as well as the diaryl-*s*-tetrazines shown in Figure 1. Tetrazine **A** and carboxylic acid modified versions of this compound shown in Figure 1 have

Received: June 8, 2011
Revised: September 1, 2011
Published: September 28, 2011

ACS Publications © 2011 American Chemical Society

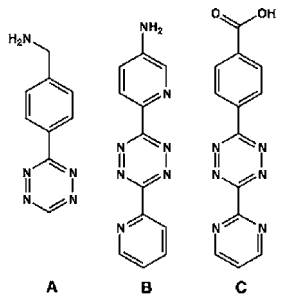

Figure 1. Chemical structures of tetrazines used in reported bioorthogonal applications. (A) (4-(1,2,4,5-tetrazin-3-yl)phenyl)-methanamine, (B) 6-(6-(pyridin-2-yl)-1,2,4,5-tetrazin-3-yl)pyridin-3-amine, (C) 4-(6-(pyrimidin-2-yl)-1,2,4,5-tetrazin-3-yl)benzoic acid.

been employed for many applications by our lab,[12,13,15,17−19] whereas tetrazines **B** and **C** have been reported elsewhere and were used for various purposes including the postsynthetic modification of DNA as well as for the synthesis of a 'BioShuttle' that effectively assists in transporting cargo into cells.[9,11,14,29−31] These tetrazines fall within the mid-range of reported cycloaddition reactivity with dienophiles mainly because some of the tetrazines with the fastest kinetics are not stable in water.[32] With such a large range of reactivity, many substituents are likely to be suitable for bioorthogonal use and could have a significant impact on the kinetics of the reaction. In dealing with bioorthogonal reactions, another parameter besides the rate constant that should be considered is aqueous solution stability. Here, we report the design, synthesis, and characterization of a series of 12 conjugatable tetrazines with varying functional groups. We demonstrate a variety of solution stabilities and reaction rates and validate the bioorthogonal use of a new highly stable and water-soluble tetrazine.

EXPERIMENTAL PROCEDURES

General Considerations. All chemicals and reagents were purchased from commercial sources and used without further purification. (*E*)-Cyclooct-4-en-1-yl (2,5-dioxopyrrolidin-1-yl) carbonate (TCO−carbonate) was synthesized as previously described.[13] NMR spectra were collected on a Varian 500 MHz spectrometer. ^{1}H and ^{13}C NMR spectra were referenced to residual solvent peaks or TMS (0.00 ppm). All phosphate buffered saline (PBS) solutions used were composed of 0.01 M phosphate buffer, 0.0027 M potassium chloride, and 0.137 M sodium chloride, pH 7.4. HyClone DBPS/Modified was used for DPBS. HyClone USDA tested fetal bovine serum was used in FBS stability studies. Herceptin (trastuzumab) was purchased from Genentech. Analytical high-performance liquid chromatography (HPLC) and liquid chromatography−mass spectrometry (LCMS) were performed on a Waters 2695 HPLC equipped with a 2996 diode array detector, a Micromass ZQ4000 ESI-MS module, and a Varian 100 × 2.0 mm RPC$_{18}$ column at a flow rate of 0.3 mL/min. Preparative HPLC was performed on a Varian ProStar model 210 instrument equipped with a model 335 diode array detector, a model 701 fraction collector, and a Varian 250 × 21.2 mm RPC$_{18}$ column at a flow rate of 21 mL/min. HPLC buffers contained: buffer A (0.1% trifluoroacetic acid (TFA) in H_2O) and buffer B (acetonitrile with 10% H_2O and 0.1% TFA). Three to five milligram portions of all compounds were weighed 3× on a Mettler Toledo AB265-S/Fact balance with an accuracy of 0.03 mg in the preparation of stock solutions. Mass spectrometry measurements for exact mass were performed by the Department of Chemistry Instrumentation Facility at the Massachusetts Institute of Technology using a Bruker Daltonics 4.7 T Fourier Transform Ion Cyclotron Mass Spectrometer (FTMS).

Synthesis. *General Tetrazine Synthesis Procedure.* Compounds **1**−**12** were synthesized by mixing 2 mmol of 4-(aminomethyl)benzonitrile, ethyl 6-aminohexanimidate dihydrochloride, or 4-cyanobenzoic acid with 10 mmol of formamidine acetate, acetamidine hydrochloride, 2-cyanopyridine, or pyrimidine-2-carbonitrile under N_2. Anhydrous hydrazine (2 mL) was then added slowly to the solid mixture with stirring (Note: This procedure should be carried out in a well-ventilated fume hood due to the formation of ammonia gas). Reactions were then stirred at room temperature or with heat for 30 min to 2 h. Sodium nitrite (10 mmol) in water was added to the reaction mixture followed by dropwise addition of 2% aqueous HCl until the solution reached approximately pH 3. The solution turned red and stopped bubbling indicating that the dihydrotetrazines were oxidized to the tetrazines (Note: This procedure should be carried out in a well-ventilated fume hood due to the formation of nitrogen oxide gases). The crude aqueous mixtures were then subjected to one of two general workups.

Workup A (compounds **1**−**8**): The oxidized acidic solutions were extracted with dichloromethane (DCM) until the organic layer was colorless. The organic fractions were discarded and the aqueous layer was then saturated with NaCl and basified by addition of solid $NaHCO_3$ (compounds **1**−**4**) or Na_2CO_3 (compounds **5**−**8**) and immediately extracted with DCM. The organic layers were then dried with $MgSO_4$, filtered, and the solvent was removed by rotary evaporation (alternatively, approximately 300 μL of TFA was added prior to rotary evaporation) to yield a crude product mixture.

Workup B (compounds **9**−**12**): The oxidized acidic solutions yielded a pink/red precipitate, which was filtered or separated by centrifugation and washed with 2% aqueous HCl to afford a crude product mixture.

The crude mixtures of all compounds (**1**−**12**) were then purified by HPLC, using the appropriate gradient of buffer A and buffer B, and lyophilized (Note: in some cases, especially with the pyridyl and pyrimidyl substituted compounds, multiple rounds of HPLC purification were necessary due to poor resolution of the product peak). The resulting TFA salts of amine containing compounds **1**−**8** were then dissolved in 0.1% HCl, loaded onto Waters Sep-Pak Vac 10 g C_{18} cartridges and flushed with approximately 10 column volumes of 0.1% HCl. The hydrochloride salts of purified compounds **1**−**8** were then eluted with a mixture of 0.1% HCl and MeCN and either dried in vacuo or lyophilized to dryness.

Synthesis of Ethyl 6-Aminohexanimidate Dihydrochloride. 6-Aminohexanenitrile (50 mmol) was dissolved in anhydrous EtOH (30 mL). Excess HCl gas was bubbled into the solution on an ice bath with stirring for 1 h. The ice bath was removed and HCl bubbling was continued for 24 h. The solvent was then removed by rotary evaporation giving a crystalline solid that was then stirred in cold *i*PrOH (30 mL), filtered, and washed with cold *i*PrOH (2 × 10 mL). After drying in vacuo, pure ethyl 6-aminohexanimidate dihydrochloride salt (9.05 g, 78%) was obtained as a white solid. ^{1}H NMR (500 MHz, DMSO-d_6) δ 1.35 (5H, pentet, J = 15.5 Hz), 1.54−1.66 (4H, m), 2.63 (2H, t, J = 7 Hz), 2.72−2.78 (2H, m), 4.42 (2H, quartet, J = 21 Hz), 8.11 (3H, s, N−H); ^{13}C NMR (125 MHz, DMSO-d_6) δ 179.37, 69.33, 38.75, 32.55, 26.76,

25.32, 24.72, 13.84 ppm. HRMS−ESI $[M + H]^+$ m/z calcd for $[C_8H_{19}N_2O]^+$ 159.1492, found 159.1489.

*(4-(1,2,4,5-Tetrazin-3-yl)phenyl)methanamine Hydrochloride (**1**).* The reaction time was 30 min at 80 °C. The title compound as the TFA salt was purified by HPLC using a 0−50% buffer B gradient. A red crystalline solid was obtained after anion exchange to the hydrochloride salt (17% yield, 76 mg). ^{1}H NMR (500 MHz, D_2O) δ 4.37 (2H, s), 7.75 (2H, d, J = 8.0 Hz), 8.54 (2H, d, J = 8.0 Hz), 10.43 (1H, s); ^{13}C NMR (125 MHz, D_2O) δ 169.11, 160.39, 140.49, 134.95, 132.62, 131.84, 45.60 ppm. HRMS−ESI $[M + H]^+$ m/z calcd for $[C_9H_{10}N_5]^+$ 188.0931, found 188.0934.

*(4-(6-Methyl-1,2,4,5-tetrazin-3-yl)phenyl)methanamine Hydrochloride (**2**).* The reaction time was 30 min at 80 °C. The title compound as the TFA salt was purified by HPLC using a 0−50% buffer B gradient. A red/purple crystalline solid was obtained after anion exchange to the hydrochloride salt (17% yield, 81 mg). ^{1}H NMR (500 MHz, D_2O) δ 3.11 (3H, s), 4.36 (2H, s), 7.74 (2H, d, J = 8.5 Hz), 8.48 (2H, d, J = 8.0 Hz); ^{13}C NMR (125 MHz, D_2O) δ 170.36, 166.71, 140.06, 134.89, 132.61, 131.44, 45.59, 23.00 ppm. HRMS−ESI $[M + H]^+$ m/z calcd for $[C_{10}H_{12}N_5]^+$ 202.1087, found 202.1090.

*(4-(6-(Pyridin-2-yl)-1,2,4,5-tetrazin-3-yl)phenyl)-methanamine Hydrochloride (**3**).* The reaction time was 2 h at 80 °C. The cooled reaction mixture was suspended in a mixture of 25 mL of MeCN, 10 mL of MeOH, and 4 mL of TFA giving a clear yellow-orange solution. Solid $NaNO_2$ (10 mmol) was then added and the reaction was allowed to stir for 15 min. After removing the solvent by rotary evaporation, the residue was washed with DCM and the organics were discarded, leaving an oil. The oil was then dissolved in water (50 mL), saturated with solid $NaHCO_3$, and extracted with DCM. The combined DCM fractions were concentrated and the title compound as the TFA salt was purified by HPLC using a 0−25% buffer B gradient. A red crystalline solid was obtained after anion exchange to the hydrochloride salt (22% yield, 132 mg). ^{1}H NMR (500 MHz, DMSO-d_6) δ 4.19 (2H, s), 7.53 (1H, t, J = 5 Hz), 7.83 (2H, d, J = 8 Hz), 8.19 (1H, t, J = 8 Hz), 8.56−8.64 (3H, m), 8.95 (1H, d, J = 5 Hz); ^{13}C NMR (125 MHz, DMSO-d_6) δ 163.17, 163.03, 150.33, 149.87, 138.85, 137.99, 131.55, 129.85, 127.89, 126.57, 124.01, 41.73 ppm. HRMS−ESI $[M + H]^+$ m/z calcd for $[C_{14}H_{13}N_6]^+$ 265.1196, found 265.1190.

*(4-(6-(Pyrimidin-2-yl)-1,2,4,5-tetrazin-3-yl)phenyl)-methanamine Hydrochloride (**4**).* The reaction time was 2 h at 80 °C. The cooled reaction mixture was treated as in **3**. The title compound as the TFA salt was purified by HPLC using a 0−25% buffer B gradient. A red crystalline solid was obtained after anion exchange to the hydrochloride salt (17% yield, 102 mg). ^{1}H NMR (500 MHz, D_2O) δ 4.35 (2H, s), 7.74 (2H, d, J = 8.5 Hz), 7.86 (1H, t, J = 5 Hz), 8.58 (2H, d, J = 8.0 Hz), 9.13 (2H, d, J = 5.5 Hz); ^{13}C NMR (125 MHz, D_2O) δ 167.32, 164.79, 161.60, 160.45, 141.00, 134.30, 132.78, 132.14, 126.75, 45.60 ppm. HRMS−ESI $[M + H]^+$ m/z calcd for $[C_{13}H_{12}N_7]^+$ 266.1149, found 266.1140.

*5-(1,2,4,5-Tetrazin-3-yl)pentan-1-amine Hydrochloride (**5**).* The reaction time was 2 h at room temperature. The title compound as the TFA salt was purified by HPLC using a 0−25% buffer B gradient. A pink crystalline solid was obtained after anion exchange to the hydrochloride salt (6% yield, 24 mg). ^{1}H NMR (500 MHz, D_2O) δ 1.53 (2H, pentet, J = 15.5 Hz) 1.75 (2H, pentet, J = 15.5 Hz), 1.99 (2H, pentet, J = 15.5 Hz) 3.02 (2H, t, J = 7.5 Hz), 3.39 (2H, t, J = 7.5 Hz), 10.36 (1H, s); ^{13}C NMR (125 MHz, D_2O) δ 175.63, 160.63, 42.25, 37.13, 29.71, 29.35, 27.99 ppm. HRMS−ESI $[M + H]^+$ m/z calcd for $[C_7H_{14}N_5]^+$ 168.1244, found 168.1241.

*5-(6-Methyl-1,2,4,5-tetrazin-3-yl)pentan-1-amine Hydrochloride (**6**).* The reaction time was 2 h at room temperature. The title compound as the TFA salt was purified by HPLC using a 0−100% buffer B gradient. A purple crystalline solid was obtained after anion exchange to the hydrochloride salt (21% yield, 92 mg). ^{1}H NMR (500 MHz, D_2O) δ 1.51 (2H, pentet, J = 15.5 Hz) 1.73 (2H, pentet, J = 15 Hz), 1.95 (2H, pentet, J = 15 Hz) 3.02 (2H, t, J = 7.5 Hz), 3.34 (2H, t, J = 7.5 Hz), 4.77 (3H, s); ^{13}C NMR (125 MHz, D_2O) δ 172.49, 170.45, 42.21, 36.42, 29.78, 29.29, 27.91, 22.97 ppm. HRMS−ESI $[M + H]^+$ m/z calcd for $[C_8H_{16}N_5]^+$ 182.1400, found 182.1405.

*5-(6-(Pyridin-2-yl)-1,2,4,5-tetrazin-3-yl)pentan-1-amine Hydrochloride (**7**).* The reaction time was 30 min at 80 °C. The title compound as the TFA salt was purified by HPLC using a 0−50% buffer B gradient. An orange/red crystalline solid was obtained after anion exchange to the hydrochloride salt (10% yield, 55 mg). ^{1}H NMR (500 MHz, DMSO-d_6) δ 1.48 (2H, pentet, J = 15 Hz), 1.66 (2H, pentet, J = 15.5 Hz), 1.96 (2H, pentet, J = 15 Hz), 2.72−2.82 (2H, m), 3.35 (2H, t, J = 7), 7.70−7.76 (1H, m), 8.16 (1H, t, J = 7.5 Hz), 8.53 (1H, d, J = 7.5 Hz), 8.91 (1H, d, J = 5 Hz); ^{13}C NMR (125 MHz, DMSO-d_6) δ 169.78, 163.19, 150.23, 150.00, 137.98, 126.46, 123.83, 38.39, 33.82, 26.60, 26.54, 25.11 ppm. HRMS−ESI $[M + H]^+$ m/z calcd for $[C_{12}H_{17}N_6]^+$ 245.1509, found 245.1503.

*5-(6-(Pyrimidin-2-yl)-1,2,4,5-tetrazin-3-yl)pentan-1-amine Hydrochloride (**8**).* The reaction time was 30 min at 80 °C. The title compound as the TFA salt was purified by HPLC using a 0−50% buffer B gradient. A red crystalline solid was obtained after anion exchange to the hydrochloride salt (2% yield, 12 mg). ^{1}H NMR (500 MHz, D_2O) δ 1.59 (2H, pentet, J = 15 Hz) 1.80 (2H, pentet, J = 15.5 Hz), 2.08 (2H, pentet, J = 15.5 Hz) 3.05 (2H, t, J = 8 Hz), 3.52 (2H, t, J = 8 Hz), 7.86 (1H, t, J = 5.5 Hz), 9.14 (2H, d, J = 5.5 Hz); ^{13}C NMR (125 MHz, D_2O) δ 174.31, 165.18, 161.60, 160.45, 126.71, 42.19, 36.87, 29.68, 29.30, 27.99 ppm. HRMS−ESI $[M + H]^+$ m/z calcd for $[C_{11}H_{16}N_7]^+$ 246.1462, found 246.1465.

*4-(1,2,4,5-Tetrazin-3-yl)benzoic Acid (**9**).* The reaction time was 30 min at 80 °C. The title compound was purified as a pink solid by HPLC using a 0−100% buffer B gradient (18% yield, 73 mg). ^{1}H NMR (500 MHz, DMSO-d_6) δ 8.22 (2H, d, J = 8.0 Hz), 8.62 (2H, d, J = 8.5 Hz), 10.66 (1H, s); ^{13}C NMR (125 MHz, DMSO-d_6) δ 166.58, 164.98, 158.16, 135.62, 134.22, 130.11, 127.88 ppm. HRMS−ESI $[M - H]^-$ m/z calcd for $[C_9H_5N_4O_2]^-$ 201.0418, found 201.0416.

*4-(6-Methyl-1,2,4,5-tetrazin-3-yl)benzoic Acid (**10**).* The reaction time was 30 min at 80 °C. The title compound was purified as a purple solid by HPLC using a 0−100% buffer B gradient (11% yield, 48 mg). ^{1}H NMR (500 MHz, DMSO-d_6) δ 3.03 (3H, s), 8.20 (2H, d, J = 9.0 Hz), 8.58 (2H, d, J = 8 Hz); ^{13}C NMR (125 MHz, DMSO-d_6) δ 167.84, 167.17, 163.30, 136.18, 134.43, 130.67, 128.06, 21.36 ppm. HRMS−ESI $[M - H]^-$ m/z calcd for $[C_{10}H_7N_4O_2]^-$ 215.0574, found 215.0574.

*4-(6-(Pyridin-2-yl)-1,2,4,5-tetrazin-3-yl)benzoic Acid (**11**).* The reaction time was 90 min at 80 °C. The title compound was purified as a purple solid by HPLC using a 0−100% buffer B gradient (3% yield, 17 mg). ^{1}H NMR (500 MHz, DMSO-d_6) δ 7.74 (1H, t, J = 6.5 Hz), 8.17 (1H, d, J = 7.5 Hz), 8.24 (2H, d, J = 9.0 Hz), 8.62 (1H, d, J = 8.0 Hz), 8.69 (2H, d, J = 8.5 Hz), 8.95 (1H, d, J = 3.5); ^{13}C NMR (125 MHz, DMSO-d_6) δ

165.57, 162.02, 161.99, 149.46, 148.89, 136.78, 134.39, 133.16, 129.14, 126.92, 125.57, 123.09 ppm. HRMS–ESI $[M + H]^+$ m/z calcd for $[C_{14}H_{10}N_5O_2]^+$ 280.0829, found 280.0827.

*4-(6-(Pyrimidin-2-yl)-1,2,4,5-tetrazin-3-yl)benzoic Acid (**12**).* The reaction time was 90 min at 80 °C. The title compound was purified as a red solid by HPLC using a 0–100% buffer B gradient (2% yield, 12 mg). ^{1}H NMR (500 MHz, DMSO-d_6) δ 7.78 (1H, t, J = 5.0 Hz), 8.19 (2H, d, J = 8.5 Hz), 8.64 (2H, d, J = 8.5 Hz), 9.14 (2H, d, J = 5.0 Hz); ^{13}C NMR (125 MHz, DMSO-d_6) δ 167.15, 163.64, 163.36, 159.48, 159.00, 135.82, 134.94, 130.73, 128.83, 123.51 ppm. HRMS–ESI $[M + H]^+$ m/z calcd for $[C_{13}H_9N_6O_2]^+$ 281.0781, found 281.0784.

*Synthesis of AF750–Tetrazine Conjugate (AF750–**6**).* The succinimidyl ester of AlexaFluor-750 (AF750, Invitrogen, 2.5 mg) was dissolved in 10 mM phosphate buffer, pH 8.3. Excess (approximately 10-fold molar excess, 4 mg) tetrazine **6** was then added immediately and the solution was allowed to stir at room temperature in the dark for 5 h. The product was identified by LCMS and purified by HPLC using a 0–100% buffer B gradient. The resulting fractions containing the desired compound were neutralized with NaOH, desalted by flushing with deionized water after loading on Waters Sep-Pak Vac 10 g C_{18} cartridges, eluted with a mixture of water/MeCN, frozen, and lyophilized to yield purified product as determined by analytical HPLC (see Supporting Information Figure S1).

Kinetics. *Tetrazine Kinetics with Norbornene.* Cycloaddition kinetics were monitored using a Tecan Safire2 microplate reader in clear flat-bottomed 96-well plates. Norbornene carboxylic acid ((1*S*,2*S*,4*S*)-bicyclo[2.2.1]hept-5-en-2-ylacetic acid) (NB) was used in excess as the dienophile at 1, 2, 3, 4, and 5 mM concentrations with each of the 12 tetrazines (100 μM) in triplicate. Stock solutions of reactants in DMSO were diluted in PBS pH 7.4 to a final concentration of 5% DMSO. The decrease of the tetrazine absorbance measured at 515 nm was monitored at 37 °C (NB PBS solutions were allowed to pre-equilibrate at 37 °C in the instrument for 10 min before addition of the tetrazine). The k_{obs} (s^{-1}) values were then calculated using the Prism software package, averaged, and plotted against the concentration of NB to yield the second order rate constants (k_2, M^{-1} s^{-1}) from the slope of the line. Trials for each tetrazine were done in duplicate. The relative (to tetrazine **1**) rate constants for each of the 12 tetrazines can be seen in Supporting Information Figure S2.

Tetrazine Kinetics with TCO. Kinetics were performed with the major isomer of (*E*)-cyclooct-4-enol (TCO) and selected tetrazines using an Applied Photophysics Stopped-Flow spectrophotometer. Stock solutions of reactants in DMSO were diluted in PBS pH 7.4 to a final concentration of 1% DMSO. Solutions of TCO and tetrazine were loaded into the individual chambers of the spectrophotometer and equilibrated to 37 °C for 10 min. Samples were then mixed by the instrument in a 1:1 (v/v) ratio and the decrease of the tetrazine absorbance measured at 515 nm was monitored at regular intervals. Final concentrations of reactants were 1.0, 1.5, 2.0, and 2.5 mM for TCO and 50 mM for the tetrazines. Baseline corrected k_{obs} (s^{-1}) values were calculated using Prism and the results of 4 runs were averaged for each concentration of TCO using the standard deviation as the error. The average k_{obs} values were then plotted against the concentration of TCO to yield the second order rate constants (k_2, M^{-1} s^{-1}) from the slope of the line and the error from the standard deviation in the slope calculated in Prism.

Tetrazine Stability Studies. *Stability in Phosphate Buffered Saline.* The stability of tetrazines **1**–**12** in PBS was measured using a Tecan Safire2 microplate reader in clear flat-bottomed 96-well plates. DMSO stocks of tetrazines were diluted in PBS pH 7.4 to 0.2 mM and a final DMSO concentration of 1%. The decrease of the tetrazine absorbance measured at 515 nm was monitored for 14 h at 37 °C. Three independent trials (containing three wells for each tetrazine) were conducted and the average of the three wells for each tetrazine was calculated for each trial. The PBS corrected averages from each of the three trials were themselves averaged and the relative (to tetrazine **1**) percent tetrazine remaining can be seen in Supporting Information Figure S3 where the error is the standard deviation of the three trials.

Stability in Serum (FBS). The stabilities of selected tetrazines in 100% fetal bovine serum were measured using an Agilent 8453 UV–visible spectrophotometer. The compounds were added to pre-equilibrated serum at 37 °C in a capped quartz cuvette at a final concentration of 1 mM and 1% DMSO. A higher concentration of tetrazine was used as compared to the PBS stability measurements due to a small but significant baseline drift over time from the FBS resulting in absorbance that overlaps with the tetrazine absorbance at 515 nm. The decrease of the tetrazine absorbance measured at 515 nm was monitored for 10 h at 37 °C. This procedure was repeated three times and the serum only corrected percent decreases were averaged and the standard deviation was used as the error.

Antibody Labeling. Herceptin (5 mg) was dissolved in 10 mM $NaHCO_3$ pH 8.4 buffer before adding approximately 3 mol equiv (0.25 mg) AlexaFluor-568 succinimidyl ester (AF568, Invitrogen). The reaction was allowed to shake at room temperature overnight in the dark. HerceptinAF568 was then purified from unconjugated fluorophore using an Amicon centrifugal filter (3K MWCO, Millipore) and determined to have approximately 1–2 fluorophores/antibody by absorbance using 91 300 M^{-1} cm^{-1} as the extinction coefficient for AF568. Fluorophore labeled Herceptin was further labeled with excess TCO–succinimidyl carbonate as described previously.[19]

Cell Studies. *Flow Cytometry.* Confluent SKBR-3 cells were suspended using 0.05% Trypsin/0.53 mM EDTA, washed by centrifugation with DPBS, and placed in microcentrifuge tubes. HerceptinAF568 only (control) or HerceptinAF568–TCO were then added separately to individual tubes to a final concentration of 10 μg/mL in 100 μL total volume of DBPS. After incubating for 30 min at room temperature, cells were washed by centrifugation with DPBS (3 × 1 mL). AF750–**6** in DMSO was then added to give a final concentration of 10 μM in 100 μL of DBPS and was allowed to incubate for 30 min at room temperature (the final DMSO concentration was 1%). Cells were then washed by centrifugation with DBPS (4 × 1 mL) before resuspension in DPBS containing 5% FBS. AF568 and AF750 fluorescence was then assessed with a Becton Dickinson LSRII flow cytometer using the PE and APC-Cy7 channels, respectively. Data collected was analyzed using the FlowJo software package.

Microscopy. SKBR-3 Human breast cancer cells were cultured in breakaway glass chamber slides. HerceptinAF568–TCO labeled antibody (HerceptinAF568 only for controls) was incubated with the cells at a final concentration of approximately 10 μg/mL for 30 min in growth media (McCoy's 5A containing 10% FBS 1% L-Glutaimine 1% Penstrep and 2% $NaHCO_3$). Cells were then washed 4× with media before

Scheme 1. Synthesis of Tetrazines 1−12

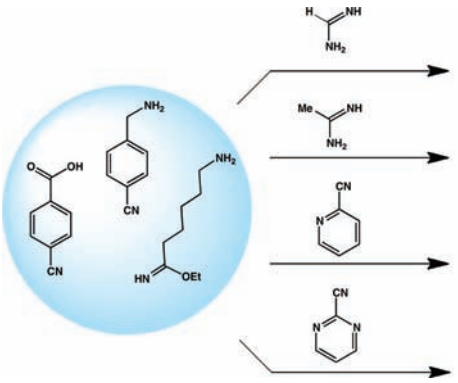

Tetrazine	R_1	R_2
1	-($BzNH_2$)	H
2	-($BzNH_2$)	Me
3	-($BzNH_2$)	2-Pyridyl
4	-($BzNH_2$)	2,6-Pyrimidyl
5	-$(CH_2)_5NH_2$	H
6	-$(CH_2)_5NH_2$	Me
7	-$(CH_2)_5NH_2$	2-Pyridyl
8	-$(CH_2)_5NH_2$	2,6-Pyrimidyl
9	4-(carboxy)phenyl-	H
10	4-(carboxy)phenyl-	Me
11	4-(carboxy)phenyl-	2-Pyridyl
12	4-(carboxy)phenyl-	2,6-Pyrimidyl

incubating with 10 μM AF750−**6** for 30 min in growth media. The cells were then washed 4× with DPBS and fixed by incubating with Cytofix fixation buffer (BD Biosciences) for 20 min. After washing 4× with DPBS, the chambers were removed and the cells were preserved with ProLong Gold (Invitrogen). Images were taken using a Nikon Eclipse 80i fluorescence microscope and imaged in the Y-2E/C and INDO CY GR channels for AF568 and AF750, respectively. Identical image acquisition settings were used for both the control and experimental data sets. Images were analyzed using ImageJ applying identical leveling adjustments to control and experimental data across the individual channels.

RESULTS AND DISCUSSION

Synthesis of Tetrazines. A series of 1,2,4,5-tetrazines was synthesized with the goal of testing the effects different substituents have on the solution stability and cycloaddition kinetic properties of these compounds. A total of 12 tetrazines were synthesized based on three conjugatable scaffolds and four different substituent groups. The substituents used varied in both size and electronic properties. Tetrazines **1**−**12** were all synthesized in a similar manner as shown in Scheme 1. After the appropriate carbonitrile/imidate ester/amidine pair was allowed to react in hydrazine, the crude reaction mixtures containing the dihydrotetrazine intermediates were oxidized with $NaNO_2$ in water and 2% aqueous HCl. The crude tetrazine mixtures were then purified and characterized by NMR (^{1}H and ^{13}C) and HRMS in yields ranging from 2 to 22%. Several of the pyrimidyl and pyridyl substituted tetrazines proved difficult to purify resulting in lower reported yields. It was often the case that material of approximately 80−85% purity could be obtained in much higher yields, but subsequent and often multiple rounds of chromatography to obtain ≥95% purity substantially lowered the overall yield of several of these compounds.

Tetrazine Kinetics with Norbornene and PBS Stability. With the goal of narrowing down the number of tetrazines used for in depth follow-up studies, the synthesized compounds **1**−**12** were screened initially in parallel. In 96-well plates, tetrazines **1**−**12** were incubated with norbornene carboxylic acid ((1*S*,2*S*,4*S*)-bicyclo[2.2.1]hept-5-en-2-ylacetic acid) (NB) to determine their relative inverse electron demand [4 + 2] cycloaddition kinetics (Supporting Information Scheme S1 depicts the generic reaction). NB was used in these initial screens due to its previous bioorthogonal utility in this reaction,[10,33] as well as its commercial availability. In all cases, NB was used in excess (at least 10-fold) and the disappearance of the visible absorption band of the tetrazine ring was monitored spectrophotometrically to obtain the pseudo-first-order rate constants (k_{obs} s^{-1}). Reactions had varying half-lives ranging from 1.5 to 60 min and were monitored until completion of the cycloaddition at 37 °C. The k_{obs} values at each concentration of NB were then used to calculate the relative second-order rate constants for all tetrazines. In general, tetrazines with stronger electron withdrawing groups (**4** and **8**) attached to the tetrazine ring showed faster kinetics, whereas electron donating groups (**2**, **6**, and **10**) resulted in slower cycloaddition reactions when compared to hydrogen substituted tetrazine **1** (see Supporting Information Figure S2). This is consistent with the general [4 + 2] inverse electron demand reaction in that more electron deficient dienes result in faster cycloadditions.[28] However, it is also important to note that hydrogen substituted tetrazines resulted in faster kinetics than would be predicted based on their 'neutral' character suggesting other parameters such as sterics may play an important role in the rate of this reaction.

The solution stability of the tetrazines in PBS pH 7.4 at 37 °C was investigated. This screen was done in parallel in which the compounds were incubated in 96-well plates and the absorbance of the tetrazine at 515 nm was used to determine the percent tetrazine remaining after 14 h. The relative stabilities compared to tetrazine **1** can be seen in Supporting Information Figure S3. In general, compounds with stronger electron withdrawing groups showed lower stability than hydrogen substituted tetrazines and the electron donating alkyl substituted tetrazines exhibited the highest stability.

In addition to these observed trends in kinetics and stability, other factors such as aqueous solubility and ease of synthesis/purification were also considered before selecting tetrazines for more in depth follow-up studies. Overall, 3,6-diaryl tetrazines demonstrate lower aqueous solubility than those with methyl or hydrogen substituents. For example, 3,6-diphenyl tetrazine is not soluble to any measurable amount in 100% water and **12** is not soluble above 0.2 mM, whereas **6** readily dissolves at concentrations above 500 mM. Taking all these data into account, tetrazines **1**−**9** were chosen for further evaluation.

Tetrazine Kinetics with TCO and Serum Stability. The selected tetrazines were tested for their cycloaddition kinetics against the highly reactive dienophile TCO. A stopped-flow spectrophotometer was used to follow the decrease of the absorption at 515 nm of each tetrazine when mixed with excess TCO at 37 °C in PBS pH 7.4. Reactions had varying half-lives ranging from 9 to 3000 ms and were monitored until completion of the cycloaddition at 37 °C. As with NB,

dx.doi.org/10.1021/bc200295y | *Bioconjugate Chem.* 2011, 22, 2263−2270

second-order rate constants were calculated for cycloaddition reactions of the tetrazines with TCO (Table 1). These data

Table 1. Second Order [4 + 2] Cycloaddition Rate Constants of Selected Tetrazines with TCO in PBS at 37°C[a]

tetrazine	k_2 ($M^{-1}s^{-1}$)	error
1	26000[a]	500
2	820	70
3	5300	400
4	22000	2000
5	4900	100
6	210	20
7	2300	300
8	4400	300
9	30000	3000

[a]Discrepancies between the rate constant reported here for **1** and TCO of 26 000 M^{-1} s^{-1} and a previous report from our lab[13] of 6000 M^{-1} s^{-1} may be explained by the methods used. The current method herein evaluated the kinetics of the free molecules in solution directly by absorbance of the tetrazine, whereas the previous study was conducted using TCO modified antibody physically absorbed to a surface and fluorescence readout after incubation with a tetrazine–fluorophore conjugate.

again show that hydrogen substituted tetrazines demonstrate exceptionally fast kinetics up to 30 000 M^{-1} s^{-1} for **9**. Interestingly, tetrazine **4**, which displayed faster kinetics than **1** and **9** with NB, while still relatively fast, was slightly slower than the reaction of these two tetrazines with TCO as the dienophile. This is perhaps due to steric interference between the 3,6-diaryl **4** and TCO that was not encountered with monosubstituted **1** and **9**. Even the slowest measured tetrazine **6** at 210 M^{-1} s^{-1} is still much faster than any of the reactions with NB, which was previously shown to be sufficient for pretargeted cell labeling studies.[10] Together with the NB kinetics, these data suggest a rate advantage for hydrogen substituted tetrazines over more bulky aryl substituents. To test the effect pH has on the reaction kinetics, another physiologically relevant pH was chosen, pH 5.0, approximating what is expected to occur within lysosomes. At this pH, representative compounds **1** and **3** showed no significant change in second-order rate constant compared to the reaction at pH 7.4.

As tetrazines continue to become increasingly important moieties in biological labeling/detection studies, a more physiologically relevant stability experiment was conducted with the selected compounds. Tetrazines were incubated in pure fetal bovine serum (FBS) at 37 °C and the decrease in absorbance at 515 nm was measured. The average percent remaining over 10 h can be seen in Figure 2. The most stable tetrazine was **6**, with greater than 96% remaining after 10 h, followed by the other alkyl substituted tetrazines and ending with the least stable electron withdrawing group containing tetrazine **4**. These results mimic the data observed in the previous PBS stability studies in that tetrazines with electron donating groups were the most stable. Depending on the individual application, any one of the tetrazines analyzed in this manuscript could be of importance. For example, if the tetrazine is to be employed where rapid reaction kinetics are desired, a faster compound that also has a good balance of chemical stability such as **1** or **9** would be a logical choice. Many applications of **1** have already been demonstrated (vide

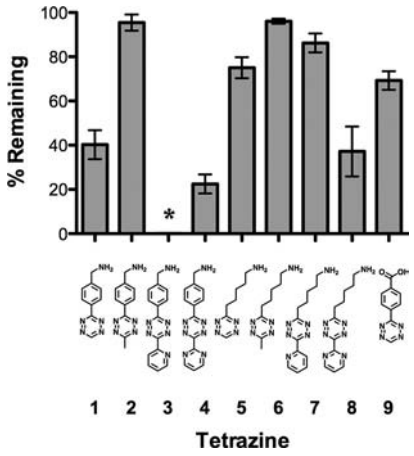

Figure 2. Stability of selected tetrazines in FBS at 37 °C after 10 h. *It was not possible to measure the serum stability of tetrazine **3** due to formation of a precipitate after incubation in FBS for approximately 1.5–2 h.

supra) including conjugation to proteins and nanoparticles.[19,33] However, in applications where rapid cycloaddition kinetics may not be as critical and improved chemical stability would be more beneficial, a tetrazine able to withstand more harsh chemical environments or endure long-term solution storage such as **2** or **6** may be of more value.

Cancer Cell Labeling. To confirm the biological utility of the new tetrazine derivatives, **6** was chosen as a representative compound for validation in pretargeted labeling studies with live SKBR-3 human breast cancer cells. Since we have already used the much faster tetrazine **1** in a similar experiment,[13] we wanted to demonstrate that the slowest tetrazine from this study was still a practical cycloaddition partner with TCO for bioorthogonal use. Despite showing the slowest reaction kinetics, tetrazine **6** demonstrated the best serum stability, was extremely water-soluble, and was synthesized/purified in relatively high yield. SKBR3 cells overexpress HER2/neu receptors and have been shown previously to be useful in pretargeted cell labeling assays with a tetrazine–norbornene system.[10] The HER2/neu antibody, Herceptin, was labeled with AF568 and TCO through sequential incubations with the dye succinimidyl ester and then TCO–succinimidyl carbonate. The fluorescent labeling allows tracking of the antibody, and in order to follow the cycloaddition reaction, the free amine of tetrazine **6** was reacted with the succinimidyl ester of AF750 to afford AF750–**6**. For confirmation of cycloaddition reactivity in a biological environment, SKBR3 cells were incubated with labeled antibodies HerceptinAF568–TCO or HerceptinAF568 (control). After washing, antibody labeled cells were then incubated with AF750–**6**, washed again, and analyzed by flow cytometry. Histograms showing the antibody labeling of cells incubated with both the control and TCO labeled Herceptin can be seen in Figure 3A. This figure indicates that the TCO loaded antibody shows identical affinity for the cells as the AF568 only loaded Herceptin. Figure 3B demonstrates that cells labeled with HerceptinAF568–TCO react with AF750–**6** through the significant shift in near-infrared fluorescence of these cells compared to the HerceptinAF568 labeled control cells. This study confirms the effectiveness of our selected tetrazine for bioorthogonal labeling.

To corroborate the flow cytometry data, we looked at the same HerceptinAF568–TCO reaction but using AF750–**6**

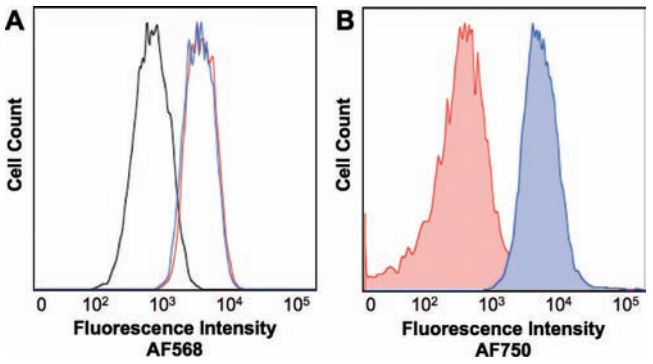

Figure 3. Flow cytometry histograms of SKBR3 cells. (A) AF568 fluorescence of cells only (black), cells incubated with HerceptinAF568 (red), or HerceptinAF568–TCO (blue) followed by AF750–**6**. (B) AF750 fluorescence of cells incubated with HerceptinAF568 (red) or HerceptinAF568–TCO (blue) followed by AF750–**6**.

under fluorescence microscopy. The antibodies from the flow cytometry experiment were used along with AF750–**6** as the cycloaddition partner (see Scheme 2). SKBR3 cells were

Scheme 2. Cell Labeling Experiment

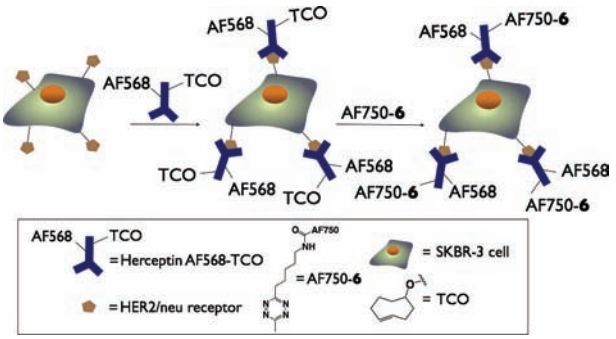

incubated individually with the labeled antibodies, followed by washing, subsequent incubation with AF750–**6**, and imaging (Figure 4). As can be seen in this figure, cells labeled with

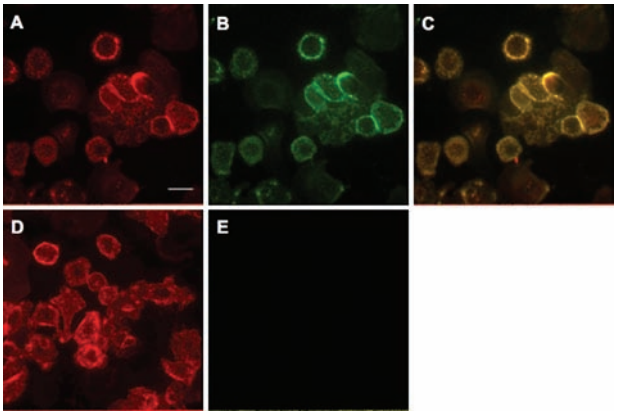

Figure 4. Fluorescent microscopy images of SKBR3 cells. Cells were treated with HerceptinAF568–TCO (A–C) or control HerceptinAF568 (D and E) followed by AF750–**6** for 30 min. Displayed is fluorescence from (A) AF568, (B) AF750, (C) AF568/AF750 merge, (D) AF568, (E) AF750. Scale bar (top left): 50 μm.

HerceptinAF568–TCO are also labeled with AF750–**6**, but cells incubated with control HerceptinAF568 showed no fluorescence in the 750 nm channel. This study further demonstrates that our selected tetrazine is useful in bioorthogonal labeling on par with previously reported compounds.

CONCLUSIONS

The series of 12 1,2,4,5-tetrazines was synthesized with a combination of four substituent groups and three conjugatable handles. Upon initial screening for reactivity and solution stability of these compounds, several were chosen for more in depth follow-up studies. These studies revealed a considerable range of serum stabilities and cycloaddition reactivities with TCO. Overall, tetrazines substituted with electron donating groups tended to be more stable, but had slower cycloaddition kinetics, and hydrogen substituted tetrazines, such as **1** and **9**, demonstrated a good balance of solution stability and fast reaction kinetics compared to compounds that would electronically be more favorable suggesting these tetrazines may react faster due to less steric interference with the dienophile. On the basis of these data along with ease of synthesis/purification, a tetrazine (**6**) was selected with exceptional chemical stability for biological evaluation. This selected tetrazine, despite demonstrating relatively slow kinetics, was then shown to be suitable for bioorthogonal use based on pretargeted cancer cell labeling studies using flow cytometry and fluorescence microscopy. The presented tetrazines add more compounds to the inverse electron demand [4 + 2] cycloaddition arsenal that can be chosen from for different bioorthogonal labeling applications depending on the desired chemical properties.

ASSOCIATED CONTENT

Supporting Information

Analytical HPLC trace of AF750–**6** and initial tetrazine screens. This material is available free of charge via the Internet at http://pubs.acs.org.

AUTHOR INFORMATION

Corresponding Author

*Mailing address: Center for Systems Biology, Massachusetts General Hospital and Harvard Medical School, 185 Cambridge St. Suite 5.210, Boston, MA 02114. Phone: (617) 643-5679. Fax: (617) 726-5799. E-mail: scott_hilderbrand@hms.harvard.edu.

ACKNOWLEDGMENTS

The authors would like to thank Dr. Jack Szostak at MGH for the use of the Stopped-Flow spectrophotometer. The authors would also like to thank Alex Chudnovskiy and Elizabeth Tiglao of CSB for technical assistance with cell culture and flow cytometry and Neal K. Devaraj for helpful discussions. This research is supported in part by NIH grants RO1EB010011 and P50CA86355.

REFERENCES

(1) Moses, J. E., and Moorhouse, A. D. (2007) The Growing Applications of Click Chemistry. *Chem. Soc. Rev. 36*, 1249–1262.

(2) Agard, N. J., Prescher, J. A., and Bertozzi, C. R. (2004) A Strain-Promoted [3 + 2] Azid–Alkyne Cycloaddition for Covalent Modification of Biomolecules in Living Systems. *J. Am. Chem. Soc. 126*, 15046–15047.

(3) Ning, X., Guo, J., Wolfert, M. A., and Boons, G.-J. (2008) Visualizing Metabolically Labeled Glycoconjugates of Living Cells by

Copper-Free and Fast Huisgen Cycloadditions. *Angew. Chem., Int. Ed. 47*, 2253−2255.
(4) Neef, A. B., and Schultz, C. (2009) Selective Fluorescence Labeling of Lipids in Living Cells. *Angew. Chem., Int. Ed. 48*, 1498−1500.
(5) Chang, P. V., Prescher, J. A., Sletten, E. M., Baskin, J. M., Miller, I. A., Agard, N. J., Lo, A., and Bertozzi, C. R. (2010) Copper-free Click Chemistry in Living Animals. *Proc. Natl. Acad. Sci. U.S.A. 107*, 1821−1826.
(6) Laughlin, S. T., Baskin, J. M., Amacher, S. L., and Bertozzi, C. R. (2008) In Vivo Imaging of Membrane-Associated Glycans in Developing Zebrafish. *Science 320*, 664−667.
(7) Jewett, J. C., and Bertozzi, C. R. (2010) Cu-free Click Cycloaddition Reactions in Chemical Biology. *Chem. Soc. Rev. 39*, 1272−1279.
(8) Sletten, E. M., and Bertozzi, C. R. (2009) Bioorthogonal Chemistry: Fishing for Selectivity in a Sea of Functionality. *Angew. Chem., Int. Ed. 48*, 6974−6998.
(9) Blackman, M. L., Royzen, M., and Fox, J. M. (2008) Tetrazine Ligation: Fast Bioconjugation Based on Inverse-Electron-Demand Diels−Alder Reactivity. *J. Am. Chem. Soc. 130*, 13518−13519.
(10) Devaraj, N. K., Weissleder, R., and Hilderbrand, S. A. (2008) Tetrazine-Based Cycloadditions: Application to Pretargeted Live Cell Imaging. *Bioconjugate Chem. 19*, 2297−2299.
(11) Waldeck, W., Wiessler, M., Ehemann, V., Pipkorn, R., Spring, H., Debus, J., Didinger, B., Mueller, G., Langowski, J., and Braun, K. (2008) TMZ-BioShuttle—A Reformulated Temozolomide. *Int. J. Med. Sci. 5*, 273−284.
(12) Devaraj, N. K., Hilderbrand, S., Upadhyay, R., Mazitschek, R., and Weissleder, R. (2010) Bioorthogonal Turn-On Probes for Imaging Small Molecules Inside Living Cells. *Angew. Chem., Int. Ed. 49*, 2869−2872.
(13) Devaraj, N. K., Upadhyay, R., Haun, J. B., Hilderbrand, S. A., and Weissleder, R. (2009) Fast and Sensitive Pretargeted Labeling of Cancer Cells through a Tetrazine/trans-Cyclooctene Cycloaddition. *Angew. Chem., Int. Ed. 48*, 7013−7016.
(14) Rossin, R., Verkerk, P. R., Bosch, S. M. v. d., Vulders, R. C. M., Verel, I., Lub, J., and Robillard, M. S. (2010) In Vivo Chemistry for Pretargeted Tumor Imaging in Live Mice. *Angew. Chem., Int. Ed. 122*, 3447−3450.
(15) Keliher, E. J., Reiner, T., Turetsky, A., Hilderbrand, S. A., and Weissleder, R. (2011) High-yielding, Two-step ^{18}F Labeling Strategy for 18F-PARP1 Inhibitors. *ChemMedChem 6*, 424−427.
(16) Li, Z., Cai, H., Hassink, M., Blackman, M. L., Brown, R. C. D., Conti, P. S., and Fox, J. M. (2010) Tetrazine−trans-Cyclooctene Ligation for the Rapid Construction of ^{18}F Labeled Probes. *Chem. Commun. 46*, 8043−8045.
(17) Reiner, T., Keliher, E. J., Earley, S., Marinelli, B., and Weissleder, R. (2011) Synthesis and In Vivo Imaging of a ^{18}F-Labeled PARP1 Inhibitor Using a Chemically Orthogonal Scavenger-assisted High-performance Method. *Angew. Chem., Int. Ed. 50*, 1922−1925.
(18) Haun, J. B., Castro, C. M., Wang, R., Peterson, V. M., Marinelli, B. S., Lee, H., and Weissleder, R. (2011) Micro-NMR for Rapid Molecular Analysis of Human Tumor Samples. *Sci. Transl. Med. 3*, 71ra16.
(19) Haun, J. B., Devaraj, N. K., Hilderbrand, S. A., Lee, H., and Weissleder, R. (2010) Bioorthogonal Chemistry Amplifies Nanoparticle Binding and Enhances the Sensitivity of Cell Detection. *Nat. Nanotechol. 5*, 660−665.
(20) Carboni, R. A., and Lindsey, R. V. Jr. (1959) Reactions of Tetrazines with Unsaturated Compounds. A New Synthesis of Pyridazines. *J. Am. Chem. Soc. 81*, 4342−4346.
(21) Boger, D. L., and Sakya, S. M. (1988) Inverse Electron Demand Diels-Alder Reactions of 3,6-Bis(methylthio)-1,2,4,5-tetrazine: 1,2-Diazine Introduction and Direct Implementation of a Divergent 1,2,4,5-Tetrazine → 1,2-Diazine → Benzene (Indoline/Indole) Diels−Alder Strategy. *J. Org. Chem. 53*, 1415−1423.
(22) Soenen, D. R., Zimpleman, J. M., and Boger, D. L. (2003) Synthesis and Inverse Electron Demand Diels−Alder Reactions of 3,6-Bis(3,4-dimethoxybenzoyl)-1,2,4,5-tetrazine. *J. Org. Chem. 68*, 3593−3598.
(23) Sauer, J., and Lang, D. (1964) Diels-Alder-Reaktionen der 1.2.4.5-Tetrazine. *Angew. Chem. 76*, 603.
(24) Sauer, J., Lang, D., and Mielert, A. (1962) Reaktivitaetsfolge von Dienen gegenueber Maleinsaeureanhydrid bei der Diels-Alder-Reaktion. *Angew. Chem. 74*, 352−353.
(25) Sauer, J., and Wiest, H. (1962) Diels-Alder-additionen mit "inversem" Elektronenbedarf. *Angew. Chem. 74*, 353.
(26) Thalhammer, F., Wallfahrer, U., and Sauer, J. (1990) Reaktivitaet Einfacher Offenkettiger und Cyclischer Dienophile bei Diels-Alder-Reaktionen mit Inversem Elektronenbedarf. *Tetrahedron Lett. 31*, 6851−6854.
(27) Taylor, M. T., Blackman, M. L., Dmitrenko, O., and Fox, J. M. (2011) Design and Synthesis of Highly Reactive Dienophiles for the Tetrazine-trans-Cyclooctene Ligation. *J. Am. Chem. Soc. 133*, 9646−9649.
(28) Sauer, J. (1995) Structure-reactivity Problem in Cycloaddition Reactions to Form Heterocyclic Compounds. *Chem. Heterocycl. Compd. 31*, 1140−1154.
(29) Pipkorn, R., Waldeck, W., Didinger, B., Koch, M., Mueller, G., Wiessler, M., and Braun, K. (2009) Inverse-electron-demand Diels-Alder Reaction as a Highly Efficient Chemoselective Ligation Procedure: Synthesis and Function of a BioShuttle for Temozolomide Transport into Prostate Cancer Cells. *J. Pept. Sci. 15*, 235−241.
(30) Schoch, J., Wiessler, M., and Jaeschke, A. (2010) Post-synthetic Modification of DNA by Inverse-electron-demand Diels−Alder Reaction. *J. Am. Chem. Soc. 132*, 8846−8847.
(31) Wiessler, M., Waldeck, W., Kliem, C., Pipkorn, R., and Braun, K. (2010) The Diels-Alder-Reaction with Inverse-Electron-Demand, a Very Efficient Versatile Click-Reaction Concept for Proper Ligation of Variable Molecular Partners. *Int. J. Med. Sci. 7*, 19−28.
(32) Kaempchen, T., Massa, W., Overheu, W., Schmidt, R., and Seitz, G. (1982) Zur Kenntnis von Reaktionen des 1,2,4,5-Tetrazin-3,6-dicarbonsaeure-dimethylesters mit Nucleophilen. *Chem. Ber. 115*, 683−694.
(33) Han, H.-S., Devaraj, N. K., Lee, J., Hilderbrand, S. A., Weissleder, R., and Bawendi, M. G. (2010) Development of a Bioorthogonal and Highly Efficient Conjugation Method for Quantum Dots Using Tetrazine-norbornene Cycloaddition. *J. Am. Chem. Soc. 132*, 7838−7839.

Supplementary Information for:

Synthesis and Evaluation of a Series of Conjugatable 1,2,4,5-Tetrazines for Bioorthogonal Conjugation

Mark R. Karver, Ralph Weissleder and Scott A. Hilderbrand*

[*] To whom correspondence should be addressed

List of Contents:

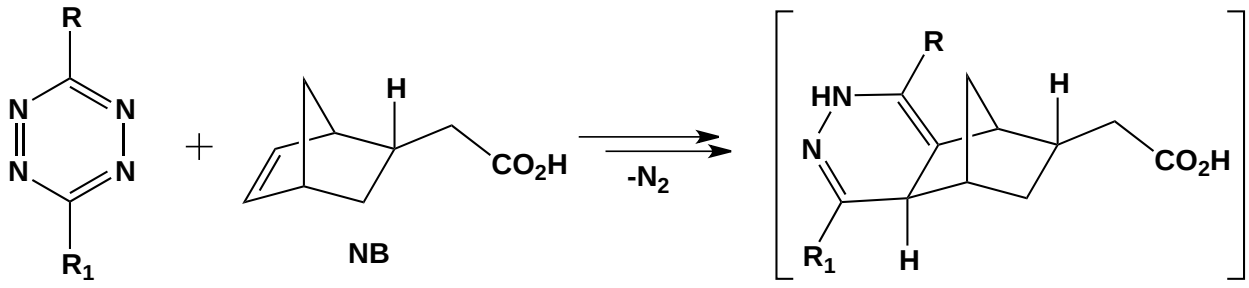

Scheme S1. General cycloaddition reaction of (1S,2S,4S)-bicyclo[2.2.1]hept-5-en-2-ylacetic acid (Norbornene, NB) with a generic 1,2,4,5-tetrazine showing one representative reaction product isomer.

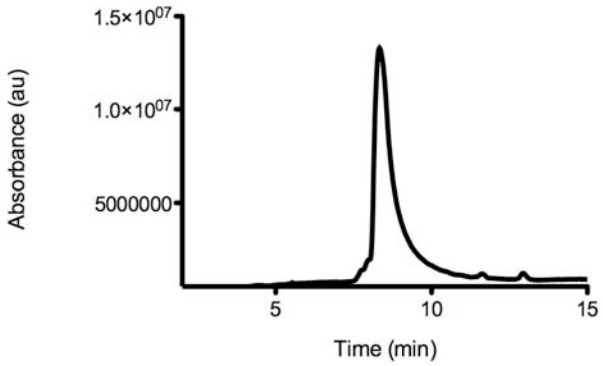

Figure S1. HPLC trace of purified AF750-**6** using a 0-100% buffer B gradient over 15 min.

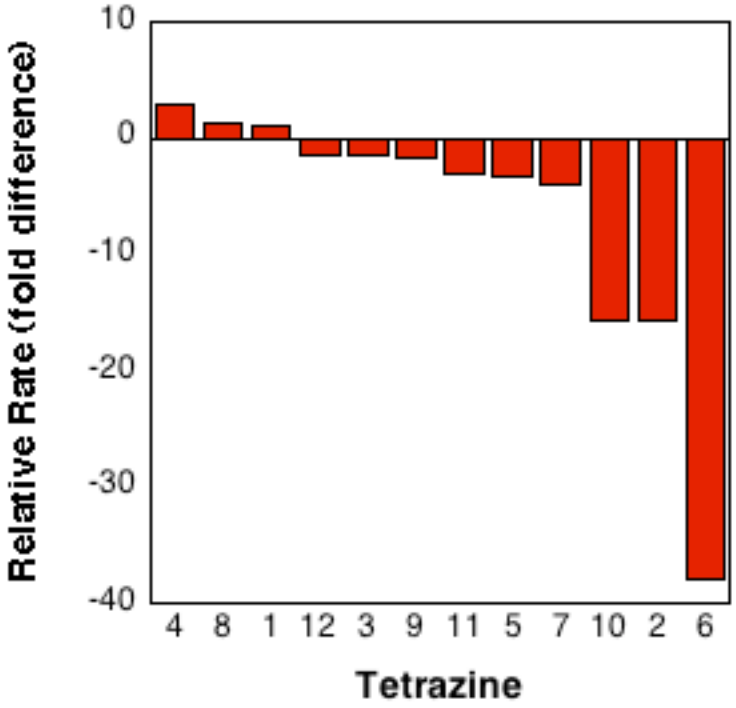

Figure S2. Relative second order [4+2] cycloaddition rate constants to **1** (4-(1,2,4,5-tetrazin-3-yl)phenyl)methanamine (k_2 = 1) of tetrazines **1-12** with NB in PBS at 37℃.

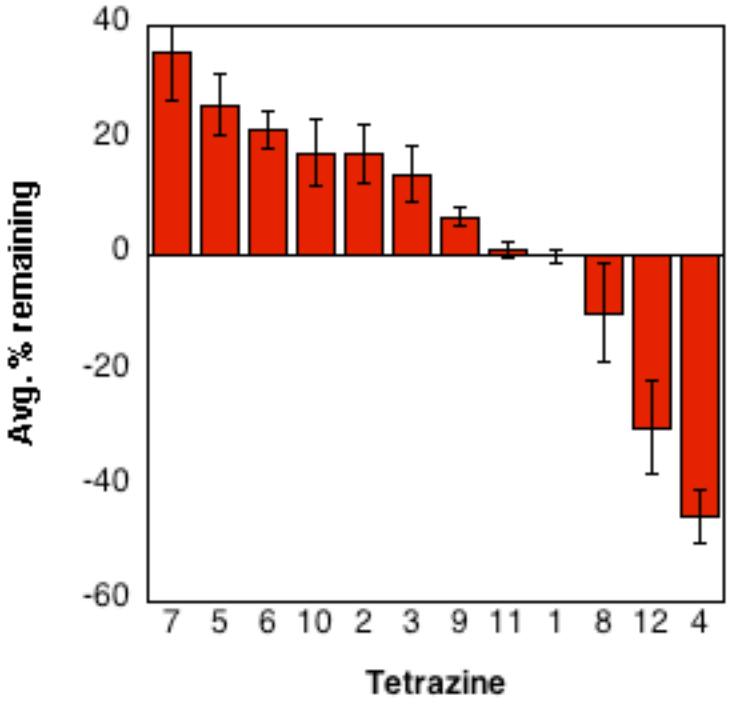

Figure S3. Relative tetrazine stability in relation to **1** in PBS after 14 h at 37℃.

Bioconjugate Chemistry

ARTICLE

pubs.acs.org/bc

Screening and Optimization of Ligand Conjugates for Lysosomal Targeting

Igor Meerovich, Alexander Koshkaryev, Ritesh Thekkedath, and Vladimir P. Torchilin*

Center for Pharmaceutical Biotechnology & Nanomedicine, Northeastern University, 312 Mugar Hall, 360 Huntington Avenue, Boston, Massachusetts 02115, United States

ABSTRACT:

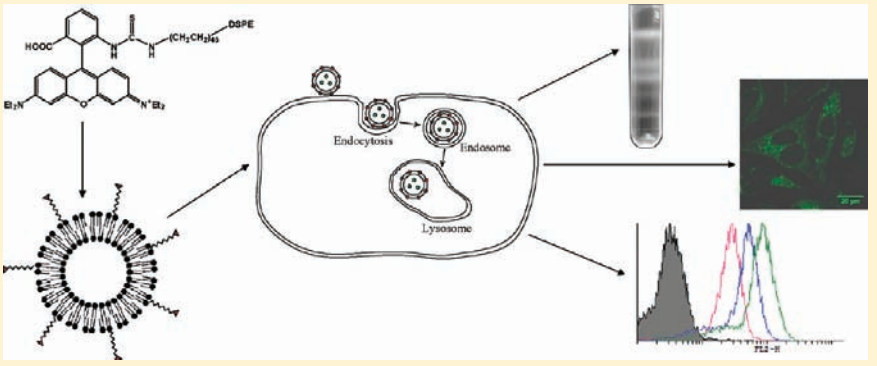

The use of lysosome-targeted liposomes may significantly improve the delivery of therapeutic enzymes and chaperones into lysosomes for the treatment of lysosomal storage disorders. The aim of this research was to synthesize new potentially lysosomotropic ligands on a base of Neutral Red and rhodamine B and to study their ability to enhance specific lysosomal delivery of surface-modified liposomes loaded with a model compound, fluorescein isothiocyanate-dextran (FD). The delivery of these liposomes and their content to lysosomes in HeLa cells was investigated by confocal immunofluorescent microscopy, subcellular fractionation, and flow cytometry. Confocal microscopy demonstrated that liposomes modified with derivatives of rhodamine B provide a good rate of colocalization with the specific lysosomal markers. The comparison of fluorescence of FD in lysosomes isolated by subcellular fractionation also showed that the efficiency of lysosomal delivery of the liposomal load by liposomes modified with some of synthesized ligands was significantly higher compared to that with plain liposomes. These results were additionally confirmed by flow cytometry of the intact cells treated with liposomes loaded with 5-dodecanoylaminofluorescein di-β-D-galactopyranoside, a specific substrate for the intralysosomal β-galactosidase, using a number of cell lines, including macrophages with induced phenotype of lysosomal enzyme deficiency; two of the synthesized ligands—rhodamine B DSPE-PEG_{2k}-amide and 6-(3-(DSPE-PEG_{2k})-thioureido) rhodamine B—demonstrated enhanced lysosomal delivery, in some cases, higher than that for commercially available rhodamine B octadecyl ester, with the best results (the enhancement of the lysosomal delivery up to 75% greater in comparison to plain liposomes) shown for the cells with induced lysosomal enzyme deficiency phenotype. Use of liposomes modified with rhodamine B derivatives may be advantageous for the development of drug delivery systems for the treatment of lysosome-associated disorders.

INTRODUCTION

Many pharmaceutical agents, including various large (enzymes, antibodies, other polypeptides) and small molecules, must be delivered specifically to particular cell organelles in order to efficiently exert their therapeutic action. Such delivery is still mainly an unresolved problem,[1] although some attempts have been made to target mitochondria and nuclei using liposomes modified with mitochondriotropic[2] or nucleotropic agents.[3]

Lysosomes represent one of the important intracellular targets. In a number of inherited human metabolic disorders, the lysosomal storage disorders (LSDs), defects in the lysosomal enzymes, lead to a progressive accumulation of unmetabolized substrates.[4] LSD symptoms may vary widely depending on the particular mutations inherited and the specific metabolic pathways affected; LSD clinical manifestations typically include deterioration of neurological function (50% of LSDs are associated with central nervous system (CNS) disorders), as well as pulmonary, hepatic, splenic, cardiovascular, and renal dysfunction. Other tissues and functions also often affected in LSDs include the immune system, bone, connective tissue, skeletal and cardiac muscle, dermis, and ocular function.[5,6] The clinical course and the severity of individual LSDs usually correlate with levels of residual enzyme activity.

The most extensively used strategy for treatment of LSDs is enzyme replacement therapy (ERT), based on the exogenous

Received: June 27, 2011
Revised: August 24, 2011
Published: September 13, 2011

ACS Publications © 2011 American Chemical Society

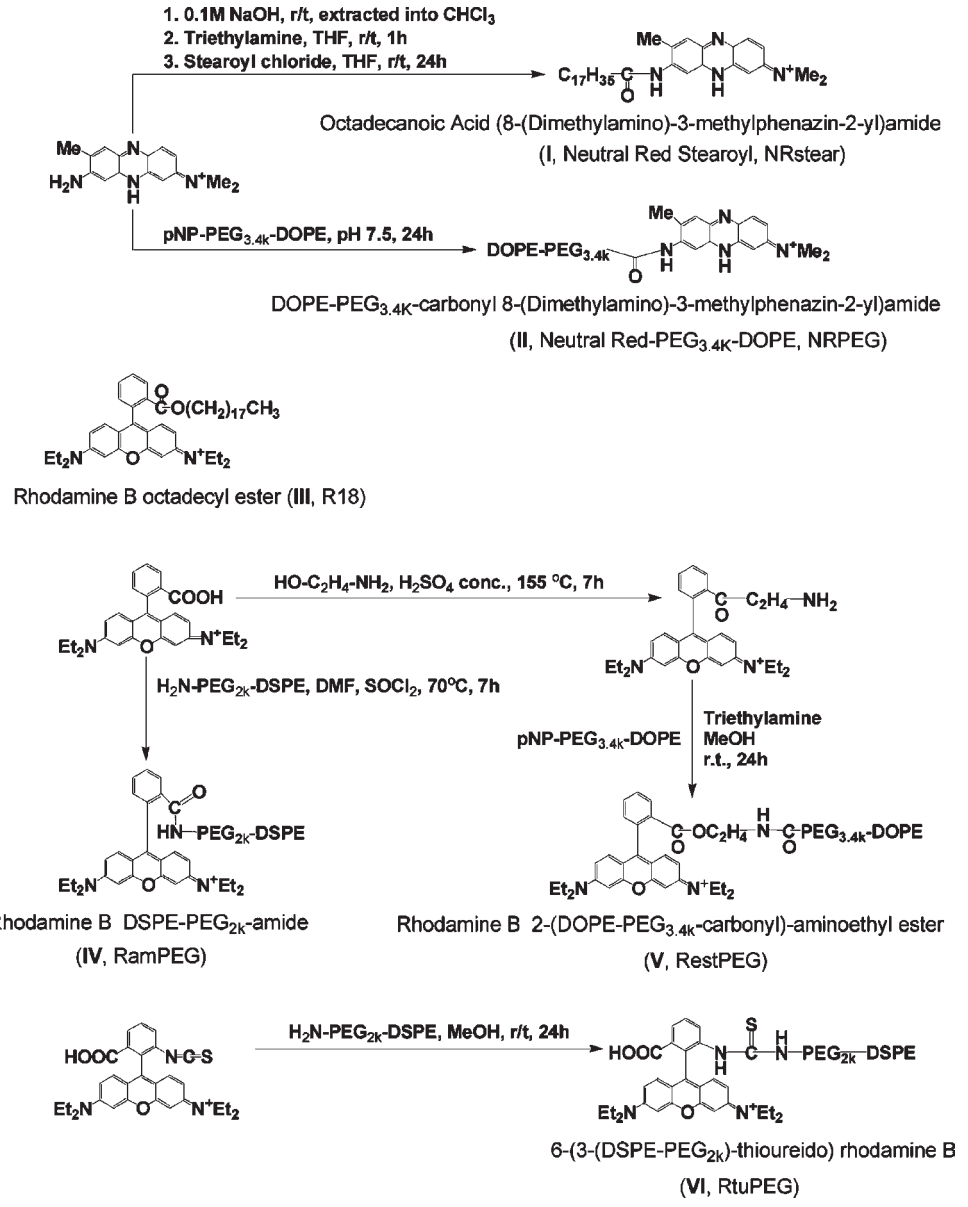

Figure 1. Synthesis of derivatives of Neutral Red and rhodamine B.

administration of active enzymes.[7] Also, among the potential advances in LSD treatment is the so-called "chaperone therapy", also called "enzyme enhancement therapy", aimed at the improperly folded mutant proteins, that are stabilized by the exogenously administered small molecules, resulting in an increase in the levels of functional enzyme. It was shown to be a promising treatment strategy for several LSDs including Gaucher disease, the GM1 and GM2 gangliosidoses, and Fabry disease.[8] However, this procedure remains limited and expensive because of the instability, poor delivery, and rapid degradation of the administered enzymes.

The use of liposome-immobilized enzymes introduced more than 30 years ago new opportunities for enzyme therapy, especially in the treatment of diseases localized to liver cells which are natural targets for liposomes.[9] Still, these liposome-based preparations are not in general clinical use for ERT, and a clear need to sharply increase the efficiency of the delivery of the liposomal enzymes to lysosomes inside cells still exists. Improvement in liposome-based enzyme delivery can be achieved by using liposomes specifically targeted to lysosomes.

Another important aspect related to the lysosomal targeting for drug delivery is the involvement of lysosomes in the treatment of cancer via the activation of the lysosome-dependent cell death pathway.[10] It has been proven that the moderate permeabilization of lysosomal membranes can result in cell apoptosis. On the other hand, secreted lysosomal cathepsins degrade protein components of the extracellular matrix and thus contribute actively to tumor angiogenesis.[11] Thus, it may be useful to develop a delivery system with specific lysosomal targeting that can provide inhibition of lysosomal enzymatic activity in cancer cells or deliver lysosome-destabilizing agents that will cause cancer cell apoptosis.

A large variety of small molecules have been identified which specifically target and accumulate in lysosomes. Among them, Neutral Red and rhodamine B are routinely used for the visualization of lysosomes and other acidic organelles in live

dx.doi.org/10.1021/bc200336j |*Bioconjugate Chem.* 2011, 22, 2271–2282

cells.[12,13] The commercially available rhodamine B octadecyl ester is used widely to monitor membrane fusion[14] and for the study of lysosomal metabolism.[15] As shown by Vult von Steyern et al.,[16] rhodamine B accumulates specifically in the lysosomes of denervated skeletal muscle. Huth et al. have shown a preferential build-up of the liposomes within lysosomes, when the liposomal membrane was labeled with rhodamine B-phosphoethanolamine.[17] With this in mind, we originally proved the general concept of the possibility to prepare the lysosome-targeted liposomes based on the use of commercially available Rhodamine B octadecyl ester.[18]

The aim of the current work was to synthesize different ligands based on Neutral Red (NR) and rhodamine B (RhB) with short and long poly(ethylene glycol) spacers suitable for introduction into the lipid bilayer and compare their ability to enhance the lysosomal delivery of these ligand-modified liposomes loaded with the model compound FITC-dextran.

MATERIALS AND METHODS

Materials. Egg phosphatidylcholine (ePC), cholesterol (Chol), 1,2-distearoyl-*sn*-glycero-3-phosphoethanolamine-*N*-[amino(polyethylene glycol)-2000] (DSPE-PEG_{2k}-amine) and 1,2-dioleoyl-*sn*-glycero-3-phosphoethanolamine (DOPE) were purchased from Avanti Polar Lipids (Alabaster AL, USA). Fluorescein isothiocyanate-dextran (FD) with molecular weight (MW) of 4400, Neutral Red (NR), rhodamine B (RhB), rhodamine B octadecyl ester (R18), rhodamine B isothiocyanate (RhB-ITC), polyoxyethylene(MW 3400)-bis(*p*-nitrophenyl carbonate) ($PEG_{3.4k}$-$(pNP)_2$), triethylamine (TEA), β-galactosidase (product number G0413), protease inhibitor cocktail (PIC), phorbol myristate acetate (PMA), and conduritol B epoxide (CBE) were purchased from Sigma-Aldrich (St. Louis MO, USA). *p*-Nitrophenylcarbonyl-(polyethylene glycol-3400)-dioleylphosphatidylethanolamine (pNP-$PEG_{3.4k}$-DOPE) was prepared and purified according to the method in ref 19. Bio-Gel A-1.5 m sorbent was purchased from Bio-Rad (Hercules CA, USA). Lysosome Enrichment Kit, Coomassie-based protein assay kit, and DyLight 350-conjugated goat antimouse IgG were obtained from Pierce Biotechnology (Rockford IL, USA). Fluorescein di-β-D-galactopyranoside (FDG), dodecanoylamino fluorescein di-β-D-galactopyranoside (C_{12}FDG), and 5-(pentafluorobenzoylamino) fluorescein di-β-D-glucopyranoside (PFB-FDGlu) were purchased from Invitrogen/Molecular Probes, Inc. (Eugene OR, USA). Mouse monoclonal (H4B4) anti-lysosome-associated membrane protein antibody (anti-Lamp2) was purchased from Abcam (Cambridge MA, USA). Fluoromount-G mounting medium was purchased from SouthernBiotech (Birmingham AL, USA). Cell cultures of human epithelial cervical cancer CCL-2 (HeLa), mouse melanoma CRL-6475 (B16(F10)), mouse Lewis lung carcinoma CRL-1642 (LLC), mouse embryo fibroblasts CRL-1658 (NIH/3T3), rat myocardium myoblasts CRL-1446 (H9c2), and human monocytes (U-937[20]) were purchased from the American Type Culture Collection (ATCC, Manassas VA, USA). Cell culture media and supplements were from CellGro (Kansas City MO, USA). All other chemicals and buffer components were analytical-grade preparations. Distilled and deionized water was used in all experiments.

Conjugates of Neutral Red and Rhodamine B. The studied cnojugates and paths of their synthesis are shown in Figure 1. Substances were synthesized from commercially available Neutral Red, rhodamine B, and rhodamine B isothiocyanate, except for rhodamine B octadecyl ester (R18, as ligand **III**), which also was commercially available.

Synthetic Procedures. *Synthesis of Octadecanoic Acid (8-(Dimethylamino)-3-methylphenazin-2-yl)amide (**I**, NRstear).* **I** was made starting with the Neutral Red acid−base indicator (NR), according to procedure developed by Suzuki et al.[21] Neutral Red (120 mg) was dissolved in distilled water, and 0.1 M aqueous NaOH was added. The desalted Neutral Red was extracted with chloroform. The organic fraction was dried over Na_2SO_4 and evaporated, resulting in 68.6 mg of free-base form of Neutral Red. The intermediate product and 75 mg of triethylamine (TEA, 7.4 mmol) were dissolved together in 22.5 mL of tetrahydrofuran (THF) and the mixture was stirred for 1 h at room temperature. Stearoyl chloride (128 mg, 0.42 μmol) of was dissolved with 0.75 mL of THF and added to the reaction mixture, which was stirred for 24 h at room temperature. The THF was evaporated and the residue obtained was dissolved in 20 mL of chloroform. The chloroform phase was washed twice with 20 mL of 1 N HCl and 1 N NaOH, and once with the same deionized water, dried over Na_2SO_4, and evaporated. The residue was purified by silica gel column chromatography with *n*-hexane−ethyl acetate (1:3, R_f = 0.83) as the eluent to yield the final product (18.4 mg of purified product, yield 13%). ^{1}H NMR ($CDCl_3$, 400 MHz) δ 0.83−0.91 (m, 3H, −CH_3), 1.22−1.43 (m, 30H, −CH_2−), 1.53−1.61 (m, 2H, −CH_2CH_2CO−), 1.75−1.84 (m, 3H, Ar−CH_3), 2.17 (s, 1H, Ar−N*H*−Ar), 3.19 (s, 6H, Ar═$N^+(CH_3)_2$), 3.96−4.00 (m, 1H, Ar−*H*), 4.19−4.24 (t, *J* = 6.05 Hz), 4.64 (s, 1H, Ar-*H*), 4.72 (s, 1H, Ar−*H*), 5.04 (s, 1H, Ar−*H*), 7.06 (d, *J* = 7.06 Hz, 1H, Ar−*H*), 7.39 (s, 1H, Ar−*H*), 7.53 (dd, *J* = 9.64 Hz, 1H, Ar−*H*), 7.70, 7.90 (s, 1H, Ar−*H*), 7.98 (d, *J* = 9.61 Hz, 1H, Ar−*H*).

*Synthesis of DOPE-$PEG_{3.4K}$-carbonyl 8-(Dimethylamino)-3-methylphenazin-2-yl)amide (**II**, NRPEG).* **II** was made from NR by reaction with *p*-nitrophenylcarbonyl-(polyethylene glycol-3400)-dioleylphosphatidylethanolamine (pNP-$PEG_{3.4k}$-DOPE), according to ref 19 using less basic conditions (pH 7.5) to avoid precipitation of NR that occurs at pH above 8.0. pNP-$PEG_{3.4k}$-DOPE (6 mg, 1.37 μmol) of was dissolved in 2 mL of phosphate buffered saline with pH adjusted to 7.5 containing a 3-fold excess of NR (1.2 mg; 4.15 μmol). After fully dissolving the pNP-$PEG_{3.4k}$-DOPE, the resultant mixture was sparged with nitrogen and stirred for 24 h at room temperature. The excess of NR was separated by dialysis against deionized water using Spectra/Por cellulose ester dialysis membranes (Spectrum Laboratories, Rancho Domingues, CA, USA) with a molecular weight cutoff size of 2000 Da. Product was purified from the nonconjugated DOPE-$PEG_{3.4k}$-COOH by silica gel column chromatography with chloroform−methanol (4:1, R_f = 0.65) as the eluent to yield the final product (yield of purified product 2.3 mg, 38%). ^{1}H NMR ($CDCl_3$, 400 MHz): δ 0.87−0.89 (m, 6H, −CH_3 of fatty acid chains), 1.00−1.50 (m, 44H, −CH_2− of fatty acid chains), 1.5−1.8 (s, 4H, −COO−CH_2−CH_2−), 1.90−2.14 (m, 8H, −CH_2−CH_2−CH═), 2.20−2.50 (m, 4H, CH_2−CH_2−COO− of fatty acid chains), 3.18 (s, 6H, Ar═$N^+(CH_3)_2$), 3.20−3.50 (m, 2H, −CH_2−CH_2−NH_2CO), 3.53−3.78 (m, PEG chains), 3.78−3.85 (m, 2H, CH_2−CH_2−O−), 4.20−4.48 (m, 2H, −O−CH_2−CH−(CH_2−/O−), 5.07−5.18 (m, 1H, −O−C*H*(CH_2−)$_2$), 5.19−5.41 (m, 4H, −CH═C*H*−), 6.90−8.00 (m, 5H, Ar−*H*), 8.06−8.32 (m, 1H, Ar−N*H*−CO).

*Synthesis of Rhodamine B DSPE-PEG_{2k}-amide (**IV**, RamPEG).* **IV** was made from rhodamine B by amidification with

dx.doi.org/10.1021/bc200336j |*Bioconjugate Chem.* 2011, 22, 2271–2282

DSPE-PEG_{2k}-amide. Rhodamine B (7.7 mg, 16.1 μmol) was dissolved in 2 mL of dimethylformamide (DMF). Thionylchloride (2.0 mg, 16.2 μmol; used as catalyst) was added to the rhodamine B and the mixture was stirred at 55 °C for 40 min. DSPE-PEG_{2k}-amine (15 mg, 5.37 μmol) was added dropwise to the stirred solution of activated rhodamine B, and the resulting mixture was stirred for additional 7 h at 70 °C under a reverse condenser. The resulting mixture was diluted with deionized water 1:5, and the nonreacted rhodamine B was separated by dialysis against deionized water using Spectra/Por cellulose ester dialysis membranes with cutoff size of 2000 Da. Product was purified from the nonconjugated DSPE-PEG_{2k}-amine by silica gel column chromatography with chloroform−methanol (4:1, R_f = 0.62) as the eluent to yield the final product (yield of purified product 2.0 mg, 11%). ^{1}H NMR ($CDCl_3$, 400 MHz): δ 0.87−0.89 (t, 6H, $-CH_3$ of fatty acid chains), 1.15−1.70 (m, 60H, $-CH_2-$ of fatty acid chains, + 6H, Ar−N-$(CH_2CH_3)_2$), 2.22−2.44 (q, 4H, CH_2-CH_2-COO- of fatty acid chains), 3.18−3.42 (m, 2H, $OPO_3-CH_2-CH_2-NH_2CO-Ar{=}N^+(CH_3)_2$), 3.20−3.50 (m, 2H, $-CH_2-CH_2-NH_2CO-$), 3.43−4.50 (m, $-CH_2-CH_2-O-$ of PEG chains), 5.07−5.18 (m, 1H, $-O-CH(CH_2-)_2$), 6.78 (m, 2H, Ar−*H*), 7.00 (m, 2H, $Ar-CONH_2-CH_2$), 7.53 (td, 1H, Ar−*H*), 8.02 (m, 1H, Ar−*H*).

*Synthesis of Rhodamine B 2-(DOPE-$PEG_{3.4k}$-carbonyl)-aminoethyl Ester (**V**, RestPEG).* **V** was synthesized starting with the rhodamine B 2-aminoethyl ester, synthesized from rhodamine B as described by Derkacheva et al.[22] and generously provided by the authors. Rhodamine B 2-aminoethyl ester (2.6 mg, 4.6 μmol) was dissolved in 0.5 mL of methanol and activated by adding 0.47 mg (4.6 μmol) of TEA. pNP-$PEG_{3.4k}$-DOPE (6 mg, 1.37 μmol) was dissolved in an activated rhodamine B 2-aminoethyl ester solution. The resultant mixture was sparged with nitrogen and stirred for 24 h at room temperature. The excess of rhodamine B 2-aminoethyl ester was separated by dialysis against deionized water using Spectra/Por cellulose ester dialysis membranes with a cutoff size of 2000 Da. Product was purified from the nonconjugated DOPE-$PEG_{3.4k}$-COOH by silica gel column chromatography with chloroform−methanol (4:1, R_f = 0.52) as the eluent to yield the final product (yield of purified product 4.0 mg, 62%). ^{1}H NMR ($CDCl_3$, 400 MHz) δ 0.84−0.91 (m, 6H, $-CH_3$ of fatty acids), 1.09−1.20 (m, 6H, Ar−$N(CH_2CH_3)_2$), 1.23−1.37 (m, 32H, $-CH_2-$ of fatty acids), 1.40−1.43 (m, 6H, $Ar{=}N^+(CH_2CH_3)_2$), 1.54−1.62, 1.66−1.84 (m, 4H, $-CH_2-CH_2-COO-$), 1.97−2.04 (m, 8H, $-CH_2-CH{=}CH-$), 2.24−2.31 (m, 6H, $-CH_2-CO-$), 3.30−3.38 (m, 2H, $-CH_2-NH-COO-$), 3.44−3.48 (m, 4H, Ar−$N(CH_2-CH_3)_2$), 3.54 (s, 2H, $-CH_2-NH-CO-$), 3.58−3.84 (m, PEG chains), 3.92−4.00, 4.10−4.17 (m, 4H, $-PO_4-CH_2-$), 4.18−4.22 (m, 2H, $-CH_2-O-CO-$), 4.36−4.42 (m, 4H, $-O-CH(CH_2-O-)_2$), 5.18−5.23 (m, 2H, Ar−*H* and $-O-CH(CH_2-O-)_2$), 5.29−5.38 (m, 4H, $-CH{=}CH-$ of fatty acids), 5.84−5.90 (s, 1H, Ar−*H*), 6.80−6.93 (m, 1H, Ar−*H*), 7.04−7.20 (m, 2H, Ar−*H*), 7.27−7.34 (m, 1H, Ar−*H*), 8.33 (dd, *J* = 27.89 Hz, 1H, Ar−*H*).

*Synthesis of 6-(3-(DSPE-PEG_{2k})-thioureido) Rhodamine B (**VI**, RtuPEG).* **VI** was made starting with a rhodamine B isothiocyanate (mix of isomers, from Sigma). Rhodamine B isothiocyanate (7.7 mg, 16.1 μmol) was dissolved in 1 mL of methanol, and the solution was used to dissolve 15 mg (5.38 μmol) of DSPE-PEG_{2k}-amine; the resultant mixture was sparged with nitrogen and stirred for 48 h at room temperature. After the reaction, the excess of Rhodamine B isothiocyanate was separated by dialysis against deionized water using Spectra/Por cellulose ester dialysis membranes with a cutoff size of 2000 Da. Product was purified from the nonconjugated DSPE-PEG_{2k}-amine by silica gel column chromatography with chloroform−methanol (4:1, R_f = 0.56) as the eluent to yield the final product (yield of purified product 5.8 mg, 33%). ^{1}H NMR ($CDCl_3$, 400 MHz): δ 0.77−0.99 (m, 6H, $-CH_3$ of fatty acids), 1.03−1.51 (m, 6H, Ar−$N(CH_2CH_3)_2$), 1.57−1.72 (m, 4H, $-CH_2COO-$ of fatty acids), 2.01, 2.28−2.39 (m, 4H, $-CH_2COO-$ of fatty acids), 3.21−3.35 (m, 2H, $-CH_2-CH_2-NHCOO-$) 3.41−3.45 (m, 4H, Ar−$N(CH_2CH_3)_2$), 3.50−4.25 (m, PEG chains), 5.00−5.18 (m,1H, Ar−*H*), 6.23−6.26 (dd, *J* = 6.26 Hz, 1H, Ar−*H*), 6.60, 6.80−6.94 (m, 1H, Ar−*H*), 7.26 (m, 1H, Ar−*H*), 7.51−7.56 (s, 1H, $-CH_2-NH-CS-NH-$), 7.69−7.74 (m, 1H, Ar−*H*), 7.81−7.87 (d, *J* = 7.83 Hz, 1H, Ar−*H*).

Preparation of Liposomal Formulations. Plain and ligand-modified FD-loaded liposomes were obtained from lipid films prepared by evaporating the solvent from mixtures of chloroform solutions of egg phosphatidylcholine (ePC) and cholesterol (7:3 molar ratio) in chloroform,[19] optionally supplemented with respective ligands (1 mol %) in ethanol or chloroform. After removing the solvent on a rotary evaporator followed by freeze−drying on a Freeze-Dry System Freezone 4.5 (Labconco, Kansas City, MO), films were redissolved in chloroform and re-dried. The films were hydrated by vigorous vortexing with phosphate-buffered saline (PBS: 137 mM NaCl, 8 mM Na_2HPO_4, 2.7 mM KCl, 1.5 mM KH_2PO_4, pH 7.4) or PBS supplemented with FD (molecular weight 4400, 45 mg/mL) to produce a total lipid content of 10 mg/mL. The hydrated lipid films were extruded 21 times through Nuclepore polycarbonate membranes with 200 nm pore size (Whatman, Clifton, NJ) using an Avanti Mini-Extruder device (Avanti Polar Lipids, Alabaster, AL). Liposomes were separated from non-incorporated FD by gel-filtration on a BioGel 1.5 M column (0.7 × 24 cm). Final lipid content in the liposomal fraction was calculated from the ratio of volumes of loaded formulation and the eluted fraction. Effective inclusion of FD into liposomes was evaluated using the BioTek Synergy HT microplate reader (BioTek, Winooski, VT) by measuring fluorescence (ex/em: 485/528 nm) of liposomes diluted 1/100 with PBS (pH 7.4) supplied with 0.2% Triton X-100 (to avoid a possible FRET effect), and calculating FD concentration according to a preliminary calibration made under the same conditions, with subsequent normalization to total lipid content.

Alternatively, for the evaluation of lysosomal uptake of the liposomal load by flow cytometry, both plain and ligand-modified liposomes were produced with a load of C_{12}FDG, a 12-carbon lipophilic variant of fluorescein di-β-D-galactopyranoside (FDG).[23] C_{12}FDG solubilized in DMSO was added to a mixture of ePC, Chol, and ligand dissolved in chloroform, at 1.5% molar to total lipids. After evaporation of the solvents, the lipid film was redissolved in chloroform. After a second chloroform evaporation and freeze−drying of the film, C_{12}FDG-loaded liposomes were prepared by hydration of the lipid film in PBS with subsequent extrusion and separation from non-incorporated ligands and C_{12}FDG as described above. To estimate C_{12}FDG loading, C_{12}FDG-liposomes were resuspended in PBS at 150 μg/mL and incubated with or without recombinant β-galactosidase (0.635 μg/mL) for 24 h at 37 °C. After the liposome dissolution with 0.2% Triton X-100 (to avoid a possible FRET effect), the fluorescent intensity of the C_{12}-fluorescein produced by enzymatic hydrolysis of C_{12}FDG was measured on a BioTek Synergy HT microplate reader (ex/em: 485/528 nm) and normalized for lipid content.

Characterization of Liposomes. Liposome size distribution was determined by dynamic light scattering using a Coulter N4MD Submicrometer Particle Size Analyzer (Beckman-Coulter, Fullerton, CA). Zeta-potential of liposomal preparations was measured at 25 °C in 0.1 mM KCl solution (diluted to a lipid content of 0.2−0.3 μg/mL) using the Zeta-Plus Instrument (Brookhaven Instruments, Holtsville, NY).

Cell Cultures. The fluorescent microscopy and subcellular fractionation studies were done on HeLa cells, used for experiments up to passage 16. For the cell experiments, HeLa cells were grown at 37 °C at 5% CO_2 and 95% humidity in Dulbecco Modified Eagle's medium (DMEM) supplemented with 10% fetal bovine serum (FBS), 100 U/mL penicillin, 100 μg/mL streptomycin, and 2 mM glutamine. To reseed the cell cultures or harvest them for subcellular fractionation or flow cytometry studies, cells were detached by trypsinization with 0.5% trypsin in PBS containing 0.025% EDTA. B16(F10), LLC, NIH/3T3, and H9c2 cells were grown and treated according to the same general protocol.

The U-937 monocytes, that were used for modeling the phenotype of lysosomal enzyme deficiency disorder, were grown in flasks suspended in RPMI-1640 medium supplemented with 10% FBS, 100 U/mL penicillin, 100 μg/mL streptomycin, and 2 mM glutamine. To induce the needed phenotype, the cells were first seeded in 6-well plates 5×10^6 cells per well in complete RPMI-1640 and cultured for 48 h in the presence of 10nM phorbol myristate acetate (PMA; Sigma-Aldrich).[24] The mature attached macrophages were washed twice with the sterile PBS and cultured for an additional 72 h in complete RPMI-1640, supplied with 200 μM of conduritol B epoxide (CBE; Sigma-Aldrich).[25,26] To harvest the macrophages for flow cytometry studies after the incubation with liposomes, the cells were detached using 4 mg/mL lidocaine in PBS containing 0.025% EDTA.

Lysosomal β-Glucocerebrosidase Enzymatic Activity Assay. The efficiency and stability of the induction of the lysosomal enzyme deficiency phenotype in U-937 cells were evaluated by the residual enzymatic activity of the lysosomal β-glucocrebrosidase after the treatment of the cells with PMA and CBE immediately, as well as after different recovery times after the removal of the CBE-containing medium replaced by the fresh complete RPMI-1640 medium. For this evaluation, the cells were seeded and subsequently treated with PMA and CBE as described above. At specific time points after removal of the CBE, the cells were detached using lidocaine and EDTA, dispersed in 300 μL of PBS (pH 7.4), supplemented with 50 μM of specific β-glucocerebrosidase substrate, 5-(pentafluorobenzoylamino) fluorescein di-β-D-glucopyranoside (PFB-FDGlu), and incubated for 1 h at 37 °C. Residual enzymatic activity, resulting in the formation of the fluorescent fluorescein derivative, was evaluated from the intensity of the green fluorescence determined at the emission wavelength of 520 nm (channel FL-1) by flow cytometry, with macrophages not treated with the CBE as a control.

Interaction of Liposomes with Cells *in Vitro*. Cells grown to the needed extent of confluence were incubated with liposomes added at amounts calculated to provide the same FD or C_{12}FDG load to cells for every liposomal formulation, in their respective serum-free media for 4 h, then washed twice with medium to remove nonbound liposomes and used for studies. When required, cells treated with liposomes for 4 h were washed twice with fresh medium to remove nonbound liposomes and incubated for an additional chase period of 20 h at 37 °C in 5% CO_2 in complete liposome-free medium (denoted further in the text as 4 + 20 h incubation).

Immunofluorescence Microscopy. Intracellular trafficking and localization of FD-loaded ligand-modified liposomes were preliminarily tested using a fluorescent microscope Nikon Eclipse E400 (Japan) equipped with a 6 V-20W halogen lamp, filter blocks for blue (EX/DM/BA 330−380/400/435 nm), green (465−495/505/515−565), and red (528−553/565/600−600) spectral channels and 100× oil-immersion objective. After the initial evaluation, the samples obtained by incubation of cells with liposomes that provided better colocalization with lysosomes were re-evaluated using a Zeiss LSM 700 upright confocal microscope (Thornwood, NY) equipped with a 63×, 1.4-numerical aperture plan-apochromat oil-immersion objective. HeLa cells were grown on microscope coverslips in 6-well plates seeded in complete DMEM medium at 10^4 cells per well. When cells reached 40−50% confluence, plain and ligand-modified liposomes were added to cells in amounts providing an equal FD load for all formulations with an average concentration of total lipids 50 μg/mL and incubated as described. After incubation, cells were washed with PBS and fixed with 4% paraformaldehyde in PBS (pH 7.4) for 15 min at room temperature (RT), followed by a PBS wash, quenching with $NaBH_4$ in PBS for 5 min, and another PBS wash. The cells were then permeabilized by incubation with 0.2% saponin and 1% BSA in PBS for 10 min at RT, washed three times with a blocking solution (1% BSA in PBS, pH 7.4), and kept for 30 min in the same buffer. The cells were stained with the mouse antihuman Lamp2 mAb diluted with blocking solution (1:50) for 60 min at RT, and washed five times with the blocking solution. Visualization was achieved by cell incubation with DyLight 350-conjugated goat antimouse IgG (1:100 dilution) for 60 min at RT followed with five washes with the blocking solution. Individual coverslips were mounted cell-side down onto fresh glass slides with fluorescence-free glycerol-based mounting medium (Fluoromount-G; Southern Biotechnology Associates, Inc.) and studied under bright light and under epifluorescence with UV, Rhodamine/TRITC, and Fluorescein/FITC filters. Co-localization of liposomes and lysosomal markers was characterized for individual cells (N = 8 to 20 for different liposomal formulations) by Pearson's correlation coefficient (PCC) and Manders' overlap coefficient (MOC),[27] calculated using *ImageJ* 1.42 software (National Institutes of Health, Bethesda, MD) with MBF bundle of plug-ins (McMaster University, Hamilton, ON, Canada).

Evaluation of Lysosomal Delivery by Subcellular Fractionation. Hela cells were grown to 90% confluence under the above-described conditions and incubated with liposomes added at amounts calculated to provide the same FD load on cells for all formulations in complete DMEM for 4 + 20 h.

In order to isolate the lysosome-enriched fractions, the cells ($(\sim 0.7-1.0) \times 10^8$ cells per sample) were collected by trypsinization and washed with ice-cold PBS. The cell pellet was resuspended in 1 mL of the reagent A of the Lysosome Enrichment Kit (Pierce Biotechnology, Rockford IL, USA) complemented with 1% (v/v) of a protease inhibitor cocktail. After 2 min incubation on ice, the cells were lysed by sonication (20 bursts, 3 s each, at 6 W). The cell lysate was treated with 1 mL of the reagent B of the same kit. The mixture was gently shaken several times and centrifuged at 500 g for 10 min at 4 °C to pellet nuclei and any remaining intact cells. The postnuclear supernatant was then adjusted with OptiPrep gradient medium

Table 1. Composition and Properties of Plain and Ligand-Modified Liposomal Formulations

	composition (mol %)							
liposomal formulation	ePC	Chol	ligand	C_{12}FDG	size ± SD (nm)	zeta ± SD (mV)	FD/lipids (mg/mg)	C_{12}FDG loading (% to Lip-C_{12}FDG)
Lip-FD	70	30	—	—	200 ± 70	−13.7 ± 6.5	0.31 ± 0.16	—
Lip-C12FDG	70	30	—	1.5	205 ± 85	−10.1 ± 1.2	—	100
Lip-NRstear-FD	70	30	1	—	210 ± 72	−8.1 ± 4.9	0.06 ± 0.01	—
Lip-NRPEG-FD	70	30	1	—	169 ± 47	−20.1 ± 4.6	0.17 ± 0.01	—
Lip-RestPEG-FD	70	30	1	—	153 ± 27	−31.0 ± 8.2	0.25 ± 0.02	—
Lip-R18	70	30	1	—	232 ± 51	11.5 ± 2.5	—	—
Lip-R18-FD	70	30	1	—	240 ± 75	−6.4 ± 4.6	0.28 ± 0.15	—
Lip-R18-C12FDG	70	30	1	1.5	201 ± 40	−10.2 ± 1.0	—	112 ± 30
Lip-RamPEG	70	30	1	—	208 ± 30	−0.6 ± 3.1	—	—
Lip-RamPEG-FD	70	30	1	—	179 ± 68	−5.2 ± 0.5	0.39 ± 0.12	—
Lip-RamPEG-C12FDG	70	30	1	1.5	180 ± 49	−33.3 ± 4.4	—	145 ± 37
Lip-RtuPEG	70	30	1	—	198 ± 42	−0.3 ± 1.3	—	—
Lip-RtuPEG-FD	70	30	1	—	179 ± 44	−11.4 ± 7.3	0.26 ± 0.07	—
Lip-RtuPEG-C12FDG	70	30	1	1.5	184 ± 65	−28.1 ± 3.5	—	119 ± 29

(Pierce Biotechnology; 60% v/v solution of Iodixanol) to 15% of Iodixanol, loaded onto the top of discontinuous density gradient with the following steps from top to bottom: 17%, 20%, 23%, 27%, and 30% of Iodixanol (by respective dilutions of OptiPrep), and subjected to ultracentrifugation at 145 000 *g* for 2 h at 4 °C using Beckman Coulter Optima XL ultracentrifuge equipped with SW41Ti swinging bucket rotor (Beckman Coulter, Krefeld, Germany). A total of 5 resultant fractions were collected from the top of the tube, diluted with PBS to the equal total volume of 6 mL, pelleted at 30 000 *g* for 30 min at 4 °C using Beckman Coulter Optima TLX Tabletop equipped with TLA-100.3 fixed angle rotor (Beckman Coulter, Krefeld, Germany), and then resuspended in equal volumes of cold PBS. All collected fractions were evaluated for lysosomal β-galactosidase activity and analyzed for protein, FD, and ligand content.

Protein concentration in each fraction was determined using a Coomassie protein assay in triplicate by measuring absorption at 595 nm using BioTek Synergy HT microplate reader (BioTek Instruments, Winooski, VT, USA). FD and ligand content in fractions were determined by measuring the fluorescence intensity of equal volumes of each fraction in triplicate, using the same microplate reader at 485/528 nm and 530−590 nm (ex/em), respectively. The quantity of FD in each subcellular fraction was calculated using a calibration by standard FD solutions in PBS.

The lysosomal β-galactosidase activity was evaluated by dispersing 50 μL of each fraction in 150 μL of PBS supplemented with 15 μM of fluorescein di-β-D-galactopyranoside (FDG) and incubating the mix for 18 h at 37 °C. The intensity of fluorescence of the resultant product was measured using a microplate reader at 485/528 nm.

Measured and calculated values for each ligand, FD, and relative β-galactosidase activity were normalized to the protein content, and their fractional distribution was calculated as a percent of the normalized value in each fraction to the total sum of all fractions.

Flow Cytometry Analysis. The binding of plain and rhodamine-based ligand-modified liposomes to cultured cells was evaluated by flow cytometry. Control (untreated) HeLa cells or cells treated with liposomes were washed twice with DMEM and trypsinized. The harvested cells were washed twice with PBS, resuspended in 1 mL of ice-cold PBS, and their fluorescence determined using a fluorescence-activated cell sorter (FACS). Data acquisition was performed on a Becton Dickinson FACScan (Becton Dickinson, San Jose, CA), and the data were analyzed using *CellQuest* software (Becton Dickinson). The green and red fluorescence were determined respectively at the emission wavelengths of 520 and 580 nm (channels FL-1 and FL-2). To eliminate possible overlap of rhodamine fluorescence with channel FL-1, the compensation between FL-1 and FL-2 channels was applied using the cells incubated with nonloaded ligand-modified liposomes as an additional control.

The data were tested for statistical significance using the Student's paired *t* test. *P*-values were considered significant at $p \leq 0.05$.

RESULTS

All liposomal formulations were characterized for size, zeta-potential, and FD or relative C_{12}FDG content (see Table 1).

In all cellular studies *in vitro*, liposomes were added for incubation with cells at dilutions providing the same FD or C_{12}FDG load to cells for all liposomal formulations.

Intracellular Localization of Ligand-Modified Liposomes. The lysosomotropic ability of ligands was initially tested by fluorescent microscopy of HeLa cells incubated with plain or ligand-modified FD-loaded liposomes, fixed and treated as described in Methods.

Both derivatives of Neutral Red showed low or no colocalization of liposomal FD with antibody-marked lysosomes (PCC/MOC for Lip-NRstear-FD and Lip-NRPEG-FD liposomes were, respectively, −0.032/0.007 and 0.403/0.567) and were excluded from further study, while samples of cells incubated with rhodamine B derivatives showed elevated colocalization of liposomal load in comparison to plain Lip-FD liposomes under the same conditions and were reanalyzed using the more accurate method of confocal microscopy.

Figures 2 and 3 show representative confocal fluorescence micrographs of HeLa cells incubated with plain or ligand-modified

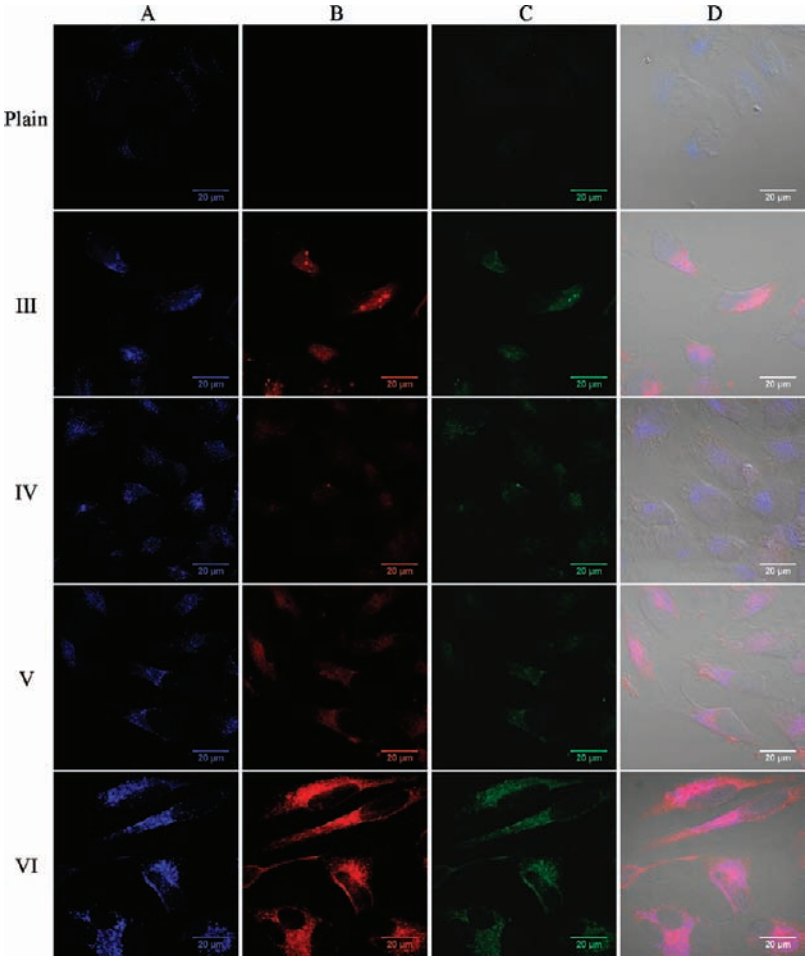

Figure 2. Confocal microscopy images of the intracellular distribution of FD-loaded liposomes modified with rhodamine B derivatives (incubation 4 h). Rows: "Plain" — cells incubated with plain Lip-FD liposomes (as control), rows III to VI — cells incubated, respectively, with Lip-R18-FD, Lip-RamPEG-FD, Lip-RestPEG-FD, and Lip-RtuPEG-FD liposomes. Columns: A (blue channel) — fluorescence of anti-Lamp2 antibody-stained lysosomes; B (red channel) — fluorescence of RhB-derivative modified liposomes; cells incubated with plain liposomes were not observed under this regime, respective position Plain-B is filled with a blank panel; C (green channel) — fluorescence of FITC-dextran; D — Overlay of A, B, and C images with their respective DIC image. Scale bar = 20 μm.

FD-loaded liposomes for 4 h, without and with an additional chase period of 20 h.

Estimation of colocalization of ligand-modified liposomes with lysosome-specific marker (Table 2) after 4 h of incubation showed that liposomes with rhodamine B derivatives provided a much higher rate of lysosomal localization in comparison to such for plain FD-loaded liposomes (MOP = 0.410; PCC = 0.619).

An additional chase period of 20 h after the 4 h incubation of cells with liposomes generally decreased the colocalization of FITC-dextran with anti-Lamp2 mAb-labeled lysosomes for both plain and ligand-modified liposomes. However, lysosomal colocalization of FD delivered by rhodamine-conjugated liposomes remained significantly higher than for plain Lip-FD liposomes (Figure 3, Table 2).

Evaluation of Intracellular Distribution of FD-Loaded Ligand-Modified Liposomes Incubated with Cultured HeLa Cells, by Subcellular Fractionation. To study the organelle distribution of ligand-modified liposomes and their FD load by subcellular fractionation, the cultured HeLa cells were incubated for 4 + 20 h with liposomes diluted to provide the same FD load on cells, originally chosen to keep the average liposomal lipid load of 50 μg/mL and then kept at the same level (9.8 μg/mL).

As shown by β-galactosidase activity assay, about 60% of the lysosomal β-galactosidase was concentrated in fraction 1 with a minor part (about 20%) in fraction 2 and negligible amounts in other fractions.

The fractional distribution of each ligand was calculated as a percent of the fluorescence measured at 530/590 nm (ex/em) for each fraction and normalized to the protein content to the total sum of normalized fluorescent intensities of fractions 1 to 5. Results shown in Figure 4A demonstrate that most of all rhodamine B-based liposome-attached ligands accumulated in the lysosome-enriched fractions (about 50% in fraction 1 or 60−70% in fractions 1 + 2).

The fractional distribution of absolute protein-normalized content of FD is demonstrated in Figure 4B. The absolute accumulation of FD in the first fraction compared with the value for the same fraction from fractionation of cells incubated with plain FD-loaded liposomes showed statistical significant difference for Lip-R18-FD (p = 0.05) and Lip-RtuPEG-FD (p = 0.005), with more moderate enhancement for Lip-RamPEG-FD

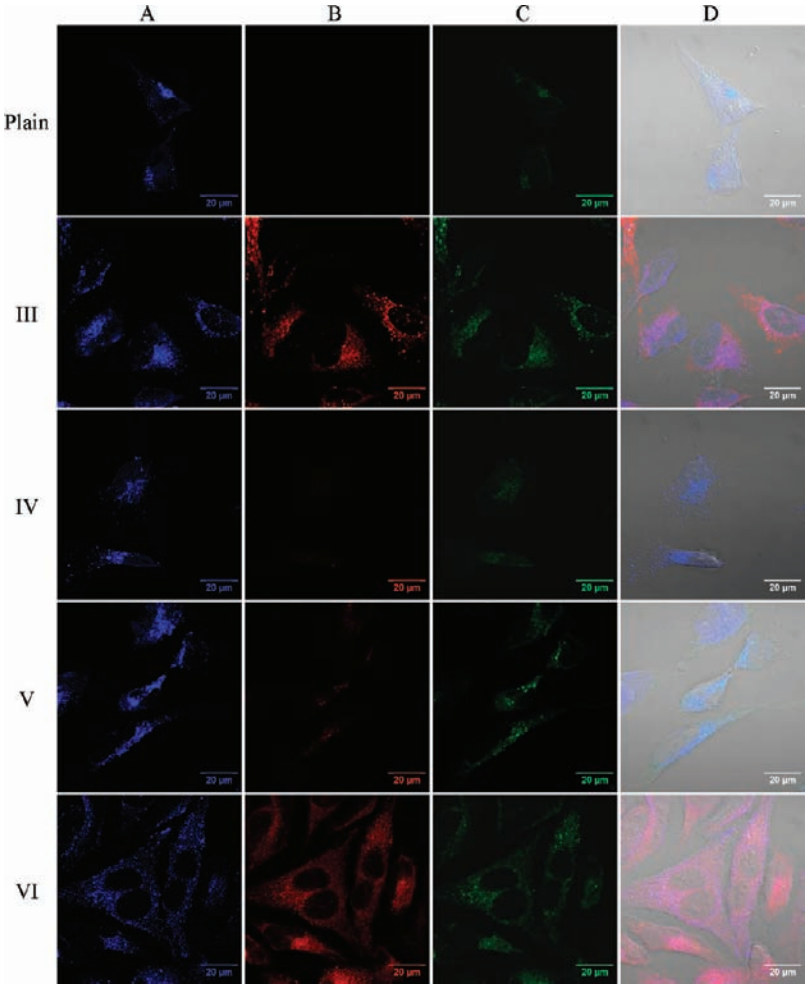

Figure 3. Confocal microscopy images of the intracellular distribution of FD-loaded liposomes modified with rhodamine B derivatives (incubation 4 + 20 h). Rows: "Plain" — cells incubated with plain Lip-FD liposomes (as control), rows III to VI — cells incubated respectively with Lip-R18-FD, Lip-RamPEG-FD, Lip-RestPEG-FD, and Lip-RtuPEG-FD liposomes. Columns: A (blue channel) — fluorescence of anti-Lamp2 antibody-stained lysosomes; B (red channel) — fluorescence of RhB-derivative modified liposomes; cells incubated with plain liposomes were not observed under this regime, respective position Plain-B is filled with blank panel; C (green channel) — fluorescence of FITC-dextran; D — Overlay of A, B, and C images with their respective DIC image. Scale bar = 20 μm.

Table 2. Averaged Coefficients of Colocalization of Ligand-Modified Liposomes and Liposomal FD Load with Anti-Lamp2 mAb Labeled Lysosomes, Determined from Micrographs Obtained by Confocal Immunofluorescent Microscopy[a]

	incubation 4 h				incubation 4 + 20 h			
	Ligand to anti-Lamp2 mAb		FD to anti-Lamp2 mAb		Ligand to anti-Lamp2 mAb		FD to anti-Lamp2 mAb	
liposomal formulation	PCC	MOC	PCC	MOC	PCC	MOC	PCC	MOC
Lip-FD (Plain)	—	—	0.410	0.619	—	—	0.363	0.508
Lip-R18-FD (III)	0.769	0.864	0.756***	0.857***	0.708	0.791	0.726**	0.808**
Lip-RamPEG-FD (IV)	0.637	0.790	0.656**	0.769**	0.523	0.693	0.588*	0.735**
Lip-RestPEG-FD (V)	0.726	0.816	0.604**	0.745**	0.544	0.711	0.613**	0.760**
Lip-RtuPEG-FD (VI)	0.816	0.877	0.862***	0.902***	0.695	0.805	0.632**	0.767**

[a] PCC — Pearson's correlation coefficient, MOC — Mander's overlap coefficient. Values are presented as mean for N cells (N = 8 to 20 for different liposomal formulations). $^{*}p < 0.05$. $^{**}p < 0.01$. $^{***}p < 0.001$.

and absence of FD delivery enhancement for Lip-RestPEG-FD liposomes (Table 3). The observed increase of FD fluorescence was not determined by a possible overlap of RhB and FITC spectral channels as was shown previously for liposomes modified with rhodamine B octadecyl ester[18] by comparing the green channel fluorescence of fractions obtained from nontreated cells

or cells incubated with ligand-modified liposomes without a FD load.

Thus, liposomes modified with R18, RtuPEG, and RamPEG which demonstrated enhancement of lysosomal delivery of their FD load were chosen for further studies.

Flow Cytometric Evaluation of General Uptake of Ligand-Modified Liposomes by Cell. The general interaction of cells with FD-loaded liposomes modified with rhodamine-based ligands (R18, RtuPEG, and RamPEG) was evaluated with tumor (HeLa and B16(F10)) and normal (NIH/3T3 and H9c2) cell lines using the flow cytometry method.

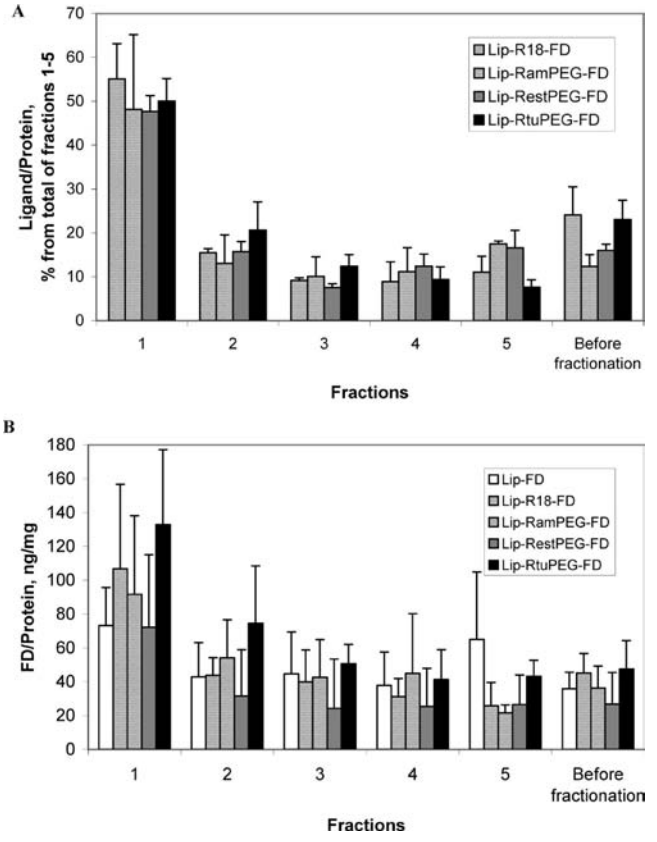

Figure 4. Relative fractional distribution of protein-normalized fluorescence of rhodamine B derivatives (A) and fractional distribution of protein-normalized FD content (B) in fractionated HeLa cells incubated with different ligand-modified liposomes for 4 + 20 h (number of experiments $n = 6$).

Liposomes were added to cells in amounts calculated to provide the same total FD content in cell medium (originally chosen to have average lipid load on cells 100 μg/mL, then kept the same) of 36.44 μg/mL. After incubation with liposomes for 4 h, cells were harvested as described in Methods and used for measurements. Since used cell lines had different autofluorescence, results were presented as relative FL-1 fluorescence values normalized to the value of FL1 for nontreated cells.

Results are shown in Table 4. In most cases, cells incubated with FD-loaded liposomes surface-modified with rhodamine B derivative ligands showed a significant increase of FL-1 channel fluorescence in comparison to plain FD-loaded liposomes.

Evaluation of Lysosomal Targeting by Flow Cytometry Using Liposomes Loaded with C_{12}FDG. To additionally confirm and compare the ability of liposomes modified with rhodamine B derivatives to specifically target lysosomes, we evaluated their specific lysosomal targeting by flow cytometric analysis of live cells using liposomes loaded with C_{12}FDG, a lipophilic substrate for the lysosomal β-galactosidase, as was proposed in ref 18, assuming FL1 fluorescence will be emitted only by product of its hydrolysis by lysosomal β-galactosidase (C_{12}-fluorescein).

The plain and ligand-modified liposomal formulations were prepared, loaded with C_{12}FDG and characterized as described in Methods. Despite the introduction of C_{12}FDG into the lipid bilayer of the liposomes, its effective load (evaluated by β-galactosidase cleavage of C_{12}FDG localized on the surface of the intact liposomes) varied between plain and ligand-modified liposomes. Because of this, we studied the lysosomal uptake of ligand-modified liposomes with intact cultured cells, adding the liposomal formulations to cells in amounts that provided the same total load of C_{12}FDG as plain C_{12}FDG-loaded liposomes at concentration of 200 μg/mL by total lipids.

The lysosomal uptake was evaluated on a number of cultured tumor and normal cell lines including HeLa, B16(F10) melanoma, LLC carcinoma, NIH/3T3 fibroblasts, and H9c2 myoblasts.

Considering the general purpose of the study, the enhancement of the lysosomal load was also specially evaluated on U-937 monocytes matured to macrophages with induced phenotype of lysosomal enzymatic deficiency disorder.[24−26] The acquisition of the lysosomal enzyme deficiency phenotype by the cells was confirmed by evaluation of the residual lysosomal β-glucocerebrosidase enzymatic activity (see Methods) immediately as well as 24, 48, and 72 h after the removal of the CBE-containing medium. It was observed that, immediately after the removal of the CBE, the cells retained about 35% of the β-glucocrebrosidase activity of the control (macrophages without CBE treatment).

Table 3. Characterization or Intracellular Distribution of Liposomal FD Delivered by Different Ligand-Modified Liposomes

liposomal formulation	relative content of FD in fraction 1 (% from total sum of fractions 1 to 5)	content of FD in fraction 1 (ng/mg proteins)	content of FD in loaded lysate, (ng/mg proteins)	paired t test of FD content in fraction 1 against the fraction 1 of sample incubated with plain FD-loaded liposomes (P-value)	ratio of FD contents in fraction 1 and loaded nuclei-free lysate
Lip-FD	27.8 ± 8.5	73.2 ± 22.5	35.9 ± 9.7	—	2.04
Lip-R18-FD	43.1 ± 20.2	106.7 ± 50.0	45.2 ± 11.5	0.05	2.36
Lip-RamPEG-FD	35.9 ± 18.3	91.6 ± 46.5	36.3 ± 12.9	0.19	2.52
Lip-RestPEG-FD	40.1 ± 23.8	72.3 ± 42.8	26.8 ± 18.7	0.94	2.70
Lip-RtuPEG-FD	38.7 ± 12.9	132.8 ± 44.3	47.6 ± 16.8	0.005	2.79

dx.doi.org/10.1021/bc200336j |*Bioconjugate Chem.* 2011, 22, 2271–2282

Table 4. General FD Delivery to Cells by Ligand-Modified Liposomes

liposomal formulation	cell line			
	HeLa	B16(F10)	NIH/3T3	H9c2
Ratios of Averaged Normalized General Uptake of FD by Different Cells (By Values of Fluorescence Intensity in FL-1 Channel) Provided by Ligand-Modified Liposomes to the Value for Plain Liposomes[a]				
Lip-R18-FD	1.73	1.55	1.25	1.40
Lip-RamPEG-FD	1.65	1.38	0.90	1.24
Lip-RtuPEG-FD	1.67	1.97	1.16	1.43
Paired *t* test of Averaged Normalized General Uptake of FD Provided by Ligand-Modified Liposomes in Comparison with the Value for Plain Liposomes (*P*-value)				
Lip-R18-FD	0.0001	0.013	0.036	0.03
Lip-RamPEG-FD	0.0001	0.002	0.237	0.02
Lip-RtuPEG-FD	0.0003	0.002	0.006	0.05

[a] Due to different autofluorscence of cell lines, values of FL-1 fluorescence of cells incubated with liposomes were used normalized to the respective values for nontreated cells. Number of experiments n = 3 to 6.

Table 5. Lysosomal Uptake of C_{12}FDG Delivered to Cells by Ligand-Modified Liposomes

liposomal formulation	cell line					
	HeLa	B16(F10)	LLC	NIH/3T3	H9c2	U-937
	Ratios of Averaged Normalized Lysosomal Uptake of C_{12}FDG by Different Cells (By Values of Fluorescence Intensity in FL-1 Channel) Provided by Ligand-Modified Liposomes to the Value for Plain Liposomes [a]					
Lip-R18-C_{12}FDG	1.17	1.09	1.47	1.04	1.15	1.35
Lip-RamPEG-C_{12}FDG	1.27	1.02	1.15	1.22	1.12	1.75
Lip-RtuPEG-C_{12}FDG	1.12	1.26	1.29	1.13	1.16	1.55
	Paired *t* test of Averaged Normalized Lysosomal Uptake of C_{12}FDG Provided by Ligand-Modified Liposomes in Comparison with the Value for Plain Liposomes (*P*-value)					
Lip-R18-C_{12}FDG	0.013	0.024	0.00002	0.073	0.014	0.149
Lip-RamPEG-C_{12}FDG	0.017	0.38	0.001	0.001	0.020	0.0074
Lip-RtuPEG-C_{12}FDG	0.035	0.003	0.021	0.005	0.007	0.0004

[a] Due to different autofluorscence of cell lines, values of FL1 fluorescence of cells incubated with liposomes were used normalized to the respective values for nontreated cells. Number of experiments n = 3 to 6.

The enzymatic activity recovered to 47−49% of control by 24−48 h post-CBE removal and to 62% after 72 h. All experiments with flow cytometric evaluation of the lysosomal delivery of liposomal load with activated U-937 cells were performed within a short time range after induction of the lysosomal deficiency by adding the liposome-containing medium immediately after removal of CBE.

The results presented in Table 5 show that, for all tested cell lines, the cells incubated with C_{12}FDG-loaded liposomes modified with rhodamine B derivatives used demonstrated significantly increased C_{12}FITC fluorescence compared to the cells treated with the plain liposomes, for at least two out of three ligands. The extent of the enhancement of the lysosomal targeting of the model substance (and the ligand providing the best enhancement) differed among cell lines, achieving the maximum values for cells with the induced phenotype of lysosomal disorder.

DISCUSSION

In our earlier paper,[18] we demonstrated that liposomes modified with rhodamine B octadecyl ester acquire the ability to specifically target lysosomes and allow for an increased delivery of a liposome-entrapped model substance (FITC-dextran with a relatively high molecular mass of 4400 Da) to these organelles.

In the current study, we attempted to develop and study other potential lysotropic ligands based on commercially available rhodamine B and Neutral Red, routinely used for the visualization of lysosomes in live cells.[12,13] A number of liposomal formulations with a ligand-modified surface were prepared using synthesized RhB and NR derivatives and loaded with FD. Their interaction with cultured cells and the ability to deliver FD to lysosomes were investigated using fluorescent microscopy, subcellular fractionation, and flow cytometry in comparison to plain FD-loaded liposomes and previously studied liposomes modified with rhodamine B octadecyl ester.

The fluorescent microscopy studies have demonstrated that liposomes modified with RhB derivatives generally show an elevated colocalization of both the liposome-attached ligand and loaded FD with a specific lysosomal marker Lamp2 (visualized using anti-Lamp2 monoclonal antibodies), while liposomes modified with derivatives of NR show much less effect. Additional study by subcellular fractionation of cells incubated with FD-loaded liposomes modified with rhodamine B derivatives and comparison of the fluorescence of lysosome-enriched fractions

with those for the cells treated with control nonmodified liposomes confirmed the lysosome-targeting ability of three rhodamine B derivatives.

Since methods such as cell staining for microscopy or subcellular fractionation of cell lysates are considered disruptive, this tendency was checked on intact live cells of several cell lines by flow cytometry, proving both an increased general accumulation of rhodamine-modified liposomes by cells and their increased delivery into the lysosomes, thus confirming the data obtained by microscopy and subcellular fractionation methods.

The evaluation of the specific lysosomal delivery of a model drug substance by liposomes modified with rhodamine B derivatives showed the best results for the cells with an induced phenotype of a lysosomal enzyme deficiency disorder (the enhancement of the lysosomal uptake of C_{12}FDG by different rhodamine B-based conjugates in the range 35−75% in comparison to nonmodified liposomes). Still, it should be noted that the development of drug delivery systems for specific LSDs, such as Gaucher disease, GM1 and GM2 gangliosidoses, and Fabry disease, requires evaluation of the efficiency of lysosomal delivery by those systems using the respective specific cell lines and animal models.

CONCLUSION

The study has demonstrated that modification of the liposomal surface with Rhodamine B-based ligands increases the delivery of liposomal FITC-dextran to lysosomes. Liposomes modified with two of the synthesized ligands—rhodamine B DSPE-PEG_{2k}-amide and 6-(3-(DSPE-PEG_{2k})-thioureido) rhodamine B—enhance lysosomal delivery of model drug load *in vitro*, in some cases, higher than commercially available rhodamine B octadecyl ester and can be used for further investigation and potentially for development of drug forms for the treatment of the lysosomal storage disorders. The choice of the optimal rhodamine B-based ligand and the extent of the lysosomal delivery enhancement *in vitro* depend on the cell line. Still, the best results (the enhancement of the lysosomal delivery up to 75% greater in comparison to plain liposomes) has been shown for the cells with induced lysosomal enzyme deficiency phenotype.

AUTHOR INFORMATION

Corresponding Author

*Vladimir P. Torchilin, Ph.D., D.Sc., Professor and Director, Center for Pharmaceutical Biotechnology and Nanomedicine, Northeastern University, 312 Mugar Hall, 360 Huntington Ave., Boston, MA 02115. E-mail: v.torchilin@neu.edu. Phone: 617-373-3206. Fax: 617-373-4201.

ACKNOWLEDGMENT

The research was funded by NIH grant RO1 CA 128486 to Vladimir P. Torchilin.

ABBREVIATIONS

ePC, egg phosphatidylcholine; Chol, cholesterol; DSPE-PEG_{2k}-amine, 1,2-distearoyl-*sn*-glycero-3-phosphoethanolamine-*N*-[amino-(polyethylene glycol)-2000]; DOPE, 1,2-dioleoyl-*sn*-glycero-3-phosphoethanolamine; FD, fluorescein isothiocyanate-dextran; NR, Neutral Red; RhB, rhodamine B; R18, rhodamine B octadecyl ester; RhB-ITC, rhodamine B isothiocyanate; $PEG_{3.4k}$-$(pNP)_2$, polyoxyethylene(MW 3400)-bis(p-nitrophenyl carbonate; TEA, triethylamine; PIC, protease inhibitor cocktail; PMA, phorbol myristate acetate; CBE, conduritol B epoxide; pNP-$PEG_{3.4k}$-DOPE, p-nitrophenylcarbonyl-(polyethylene glycol-3400)-dioleylphosphatidylethanolamine; mAb, monoclonal antibody; IgG, immunoglobulin G; FDG, fluorescein di-β-D-galactopyranoside; C_{12}FDG, dodecanoylamino fluorescein di-β-D-galactopyranoside; PFB-FDGlu, 5-(pentafluorobenzoylamino) fluorescein di-β-D-glucopyranoside; anti-Lamp2, mouse monoclonal (H4B4) antilysosome-associated membrane protein antibody; THF, tetrahydrofuran; NRstear, octadecanoic acid (8-(dimethylamino)-3-methylphenazin-2-yl)amide; NRPEG, DOPE-$PEG_{3.4k}$-carbonyl 8-(dimethylamino)-3-methylphenazin-2-yl)amide; RamPEG, rhodamine B DSPE-PEG_{2k}-amide; RestPEG, rhodamine B 2-(DOPE-$PEG_{3.4k}$-carbonyl)-aminoethyl ester; RtuPEG, 6-(3-(DSPE-PEG_{2k})-thioureido) rhodamine B; FBS, fetal bovine serum; PBS, phosphate buffered saline; RT, room temperature; BSA, bovine serum albumin; DIC, differential interference contrast; PCC, Pearson's correlation coefficient; MOC, Mander's overlap coefficient; FACS, fluorescence-activated cell sorter; Lip, liposomes; EDTA, ethylenediamintetraacetic acid; SD, standard deviation

REFERENCES

(1) Torchilin, V. P. (2006) Recent approaches to intracellular delivery of drugs and DNA and organelle targeting. *Annu. Rev. Biomed. Eng. 8*, 343–75.

(2) Boddapati, S. V., D'Souza, G. G., Erdogan, S., Torchilin, V. P., and Weissig, V. (2008) Organelle-targeted nanocarriers: specific delivery of liposomal ceramide to mitochondria enhances its cytotoxicity in vitro and in vivo. *Nano Lett. 8*, 2559–63.

(3) Ko, Y. T., Kale, A., Hartner, W. C., Papahadjopoulos-Sternberg, B., and Torchilin, V. P. (2009) Self-assembling micelle-like nanoparticles based on phospholipid-polyethyleneimine conjugates for systemic gene delivery. *J. Controlled Release 133*, 132–8.

(4) Raas-Rothschild, A., Pankova-Kholmyansky, I., Kacher, Y., and Futerman, A. H. (2004) Glycosphingolipidoses: beyond the enzymatic defect. *Glycoconj. J. 21*, 295–304.

(5) Scriver, C. R., Sly, W. S., Childs, B., Beaudet, A. L., Valle, D., Kinzler, K. W., and Vogelstein, B. (2000) *The Metabolic and Molecular Bases of Inherited Disease*, 8 ed., McGraw-Hill Professional, New York.

(6) Muro, S. (2010) New biotechnological and nanomedicine strategies for treatment of lysosomal storage diseases. *Wiley Interdiscip. Rev. Nanomed. Nanobiotechnol. 2*, 189–204.

(7) Grabowsky, G. A., and Desnick, R. J. (1981) Enzyme replacement in genetic diseases, *Enzymes as Drugs* (Holcenberg, J. S., and Roberts, J., Eds.) Wiley, New York.

(8) Butters, T. D. (2007) Pharmacotherapeutic strategies using small molecules for the treatment of glycolipid lysosomal storage disorders. *Expert Opin. Pharmacother. 8*, 427–35.

(9) Gregoriadis, G. (1978) Liposomes in the therapy of lysosomal storage diseases. *Nature 275*, 695–6.

(10) Kirkegaard, T., and Jaattela, M. (2009) Lysosomal involvement in cell death and cancer. *Biochim. Biophys. Acta 1793*, 746–54.

(11) Boya, P., Andreau, K., Poncet, D., Zamzami, N., Perfettini, J. L., Metivier, D., Ojcius, D. M., Jäättelä, M., and Kroemer, G. (2003) Lysosomal membrane permeabilization induces cell death in a mitochondriondependent fashion. *J. Exp. Med. 197*, 1323–1334.

(12) Horobin, R. W. (2002) Xanthenes. *Conn's Biological Stains: A Handbook of Dyes, Stains and Fluorochromes for Use in Biology and Medicine* (Horobin, R. W., Kiernan, J. A., and Conn, H. J., Eds.) p 237, Chapter 16, BIOS Scientific Publishers, Oxford, U.K.

(13) Minier, C., and Moore, M. N. (1996) *Mar. Ecol.: Prog. Ser. 142*, 165–173.

(14) Hoekstra, D., de Boer, T., Klappe, K., and Wilschut, J. (1984) Fluorescence method for measuring the kinetics of fusion between biological membranes. *Biochemistry 23*, 5675–5681.

(15) Kuwana, T., Mullock, B. M., and Luzio, J. P. (1995) Identification of a lysosomal protein causing lipid transfer, using a fluorescence assay designed to monitor membrane fusion between rat liver endosomes and lysosomes. *Biochem. J. 308*, 937–946.

(16) Vult von Steyern, F., Josefsson, J. O., and Tagerud, S. (1996) Rhodamine B, a fluorescent probe for acidic organelles in denervated skeletal muscle. *J. Histochem. Cytochem. 44*, 267–74.

(17) Huth, U., Wieschollek, A., Garini, Y., Schubert, R., and Peschka-Suss, R. (2004) Fourier transformed spectral bio-imaging for studying the intracellular fate of liposomes. *Cytometry A 57*, 10–21.

(18) Koshkaryev, A., Thekkedath, R., Pagano, C., Meerovich, I., and Torchilin, V. P. (2011) Targeting of lysosomes by liposomes modified with octadecyl-rhodamine B. *J. Drug Targeting*, Epub ahead of print (DOI: 10.3109/1061186X.2010.550921).

(19) Torchilin, V. P., Levchenko, T. S., Lukyanov, A. N., Khaw, B. A., Klibanov, A. L., Rammohan, R., Samokhin, G. P., and Whiteman, K. R. (2001) p-Nitrophenylcarbonyl-PEG-PE-liposomes: fast and simple attachment of specific ligands, including monoclonal antibodies, to distal ends of PEG chains via p-nitrophenylcarbonyl groups. *Biochim. Biophys. Acta 1511*, 397–411.

(20) Sundstrom, C., and Nilsson, K. (1976) Establishment and characterization of a human histiocytic lymphoma cell line (U-937). *Int. J. Cancer 17*, 565–77.

(21) Suzuki, K., Hirayama, E., Sugiyama, T., Yasuda, K., Okabe, H., and Citterio, D. (2002) Ionophore-based lithium ion film optode realizing multiple color variations utilizing digital color analysis. *Anal. Chem. 74*, 5766–5773.

(22) Derkacheva, V. M., Mikhalenko, S. A., Solov'eva, L. I., Alekseeva, V. I., Marinina, L. E., Savina, L. P., Butenin, A. V., and Luk'yanets, E. A. (2007) Phthalocyanines and related compounds: XLIV. Synthesis of conjugates of phthalocyanines with rhodamines. *Russian Journal of General Chemistry 77*, 1117–1125.

(23) Plovins, A., Alvarez, A. M., Ibanez, M., Molina, M., and Nombela, C. (1994) Use of fluorescein-di-beta-D-galactopyranoside (FDG) and C12-FDG as substrates for beta-galactosidase detection by flow cytometry in animal, bacterial, and yeast cells. *Appl. Environ. Microbiol. 60*, 4638–41.

(24) Baek, Y. S., Haas, S., Hackstein, H., Bein, G., Hernandez-Santana, M., Lehrach, H., Sauer, S., and Seitz, H. (2009) Identification of novel transcriptional regulators involved in macrophage differentiation and activation in U937 cells. *BMC Immunol. 10*, 18.

(25) Newburg, D. S., Shea, T. B., Yatziv, S., Raghavan, S. S., and McCluer, R. H. (1988) Macrophages exposed in vitro to conduritol B epoxide resemble Gaucher cells. *Exp. Mol. Pathol. 48*, 317–23.

(26) Yatziv, S., Newburg, D. S., Livni, N., Barfi, G., and Kolodny, E. H. (1988) Gaucher-like changes in human blood-derived macrophages induced by beta-glucocerebrosidase inhibition. *J. Lab. Clin. Med. 111*, 416–20.

(27) Manders, E. M. M., Verbeek, F. J., and Aten, J. A. (1993) Measurement of co-localisation of objects in dual-colour confocal images. *J. Microsc. 169*, 375–382.

Bioconjugate Chemistry

Article

pubs.acs.org/bc

Synthesis, Photophysical, Electrochemical, Tumor-Imaging, and Phototherapeutic Properties of Purpurinimide-*N*-substituted Cyanine Dyes Joined with Variable Lengths of Linkers

Michael P. A. Williams,[†] Manivannan Ethirajan,[†] Kei Ohkubo,[§] Ping Chen,[∥] Paula Pera,[†] Janet Morgan,[‡] William H. White, III,[†] Masayuki Shibata,*[,⊥] Shunichi Fukuzumi,*[,§,#] Karl M. Kadish,*[,∥] and Ravindra K. Pandey*[,†]

[†]PDT Center, Department of Cell Stress Biology, Roswell Park Cancer Institute, Buffalo New York 14263, United States

[‡]Department of Dermatology, Roswell Park Cancer Institute, Buffalo New York 14263, United States

[§]Department of Material and Life Sciences, Graduate School of Engineering, Osaka University, ALCA, Japan Science and Technology Agency (JST), Osaka, Japan

[∥]Department of Chemistry, University of Houston, Houston, Texas 77204-5003, United States

[⊥]Department of Health Informatics, University of Medicine & Dentistry of New Jersey−SHRP, Newark, New Jersey 07107, United States

[#]Department of Bioinspired Science, Ewha Womans University, Seoul 120-750, Korea

Supporting Information

ABSTRACT: Purpurinimide methyl esters, bearing variable lengths of N-substitutions, were conjugated individually to a cyanine dye with a carboxylic acid functionality. The results obtained from *in vitro* and *in vivo* studies showed a significant impact of the linkers joining the phototherapeutic and fluorescence imaging moieties. The photosensitizer−fluorophore conjugate with a PEG linker showed the highest uptake in the liver, whereas the conjugate linked with two carbon units showed excellent tumor-imaging and PDT efficacy at 24 h postinjection. Whole body imaging and biodistribution studies at variable time points portrayed enhanced fluorescent uptake of the conjugates in the tumor compared to that in the skin. Interestingly, the conjugate with the shortest linker and the one joining with two carbon units showed faster clearance from normal organs, e.g., the liver, kidney, spleen, and lung, compared to that in tumors. Both imaging and PDT efficacy of the conjugates were performed in BALB/c mice bearing Colon26 tumors. Compared to the others, the short linker conjugate showed poor tumor fluorescent properties and as a corollary does not exhibit the dual functionality of the photosensitizer−fluorophore conjugate. For this reason, it was not evaluated for *in vivo* PDT efficacy. However, in Colon26 tumor cells (*in vitro*), the short linker was highly effective. Among the conjugates with variable linkers, the rate of energy transfer from the purpurinimide moiety to the cyanine moiety increased with deceasing linker length, as examined by femtosecond laser flash photolysis measurements. No electron transfer from the purpurinimide moiety to the singlet excited state of the cyanine moiety or from the singlet excited state of the cyanine moiety to the purpurinimide moiety occurred as indicated by a comparison of transient absorption spectra with spectra of the one-electron oxidized and one-electron reduced species of the conjugate obtained by spectroelectrochemical measurements.

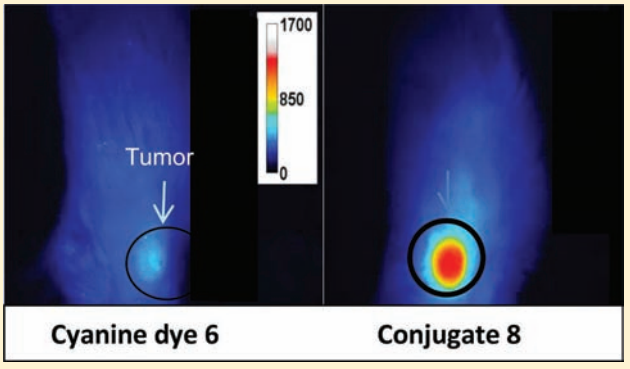

1. INTRODUCTION

Current treatment modalities for patients afflicted by cancer include surgery, radiation therapy, chemotherapy, and a relatively novel option called photodynamic therapy (PDT).[1−5] Surgery is used to excise abnormal growths and surrounding tissue, but the procedure is invasive and may be complicated by relapse of the cancer if not all of the tumor cells are removed. Chemotherapy employs different cytotoxic chemicals to attack or block specific cellular and molecular mechanisms that aid tumor growth. Unfortunately, patients on chemotherapeutics suffer from side effects due to adverse drug toxicities. Radiation uses ionizing energy to attack neoplastic cells, but it is nonspecific and may cause damage to surrounding healthy tissue, which can lead to the occurrence of secondary cancers. PDT uses a drug known as a photosensitizer, light, and oxygen to destroy tumors and their surrounding vasculature.

Received: June 30, 2011
Revised: September 14, 2011
Published: October 11, 2011

ACS Publications © 2011 American Chemical Society

Scheme 1. Synthesis of Purpurinimide–Cyanine Dye Conjugates Joined with Variable Lengths of Linkers[a]

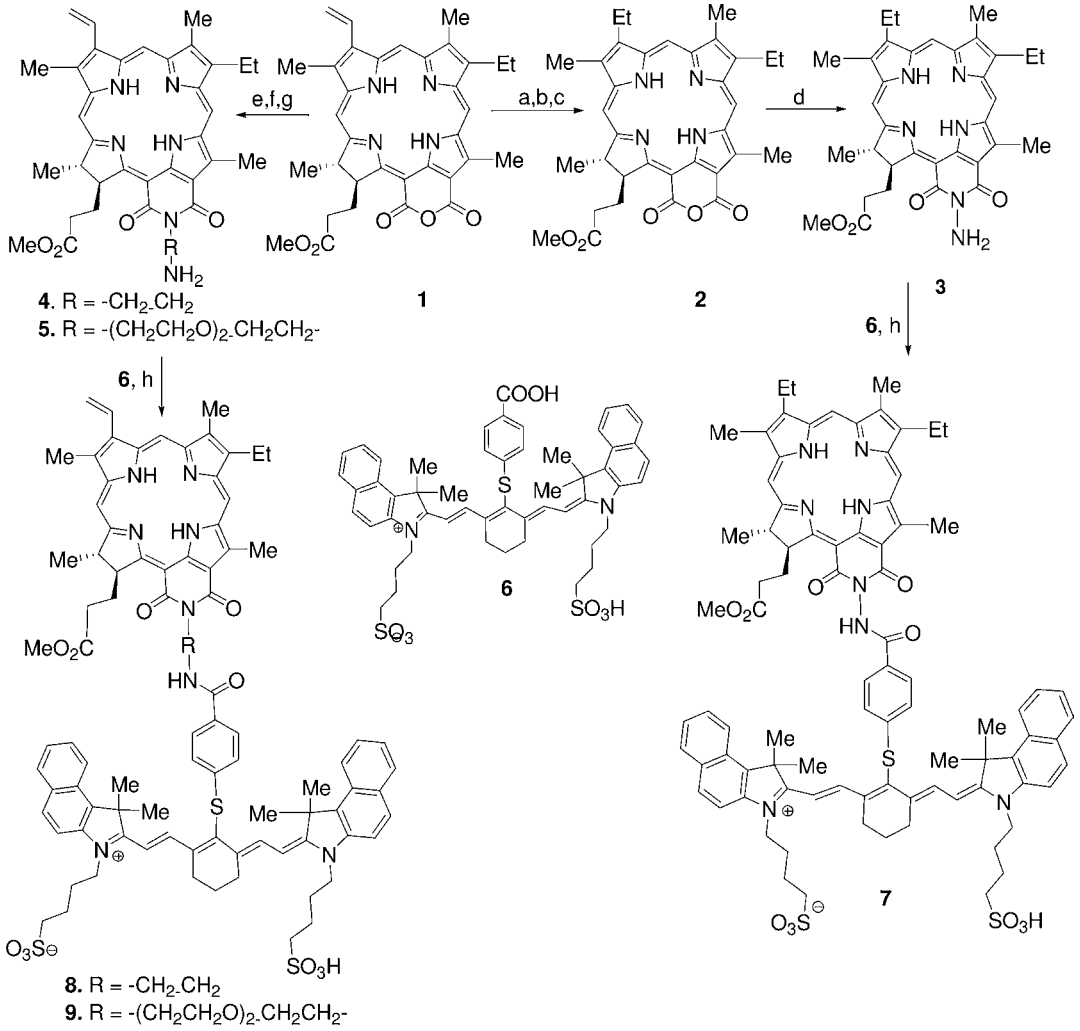

[a]Reagents and conditions: (a) $Zn(OAc)_2$, reflux in MeOH, 2 h; (b) Pd/carbon, H_2 THF, 12 h; (c) TFA, 2 h, RT; (d) NH_2–NH_2(anhydrous), pyridine DCM/HCL, RT; (e) R_1=$(CH_2)_2$, DCM, CH_2N_2, KOH/MeOH; (f) R_2=$(C_2H_4O)_2C_2H_4$, CH_2N_2, KOH/MeOH; (g) DCM/TFA (1:4), 2 h; (h) DMTMM, DMF, 12 h.

Scheme 2. Preparation of a Cyanine Dye with Carboxylic Acid Functionality

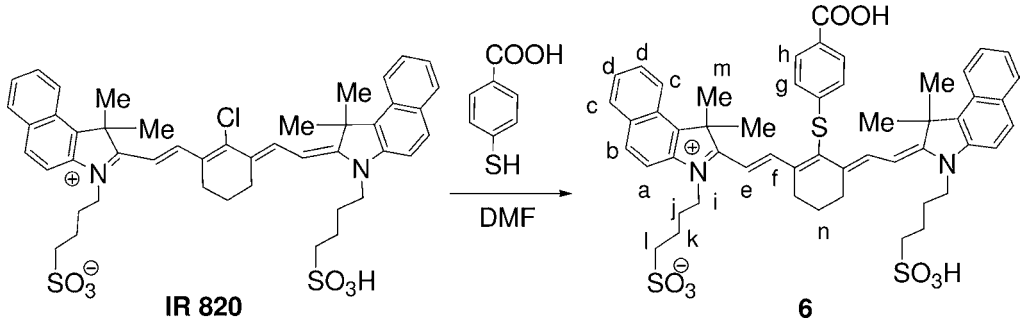

PDT has several advantages in that (i) there is no systemic, organ, or tissue toxicity, (ii) it is noninvasive, and (iii) it can be used repeatedly as a primary or adjuvant treatment.[6–9] With the current advent of imaging technologies to monitor tumor responses to treatment, we have shown that the utilization of a certain photosensitizer–cyanine dye conjugate which contains the tumor-avid photosensitizer 3-(1′-hexyloxyethyl)-pyropheophorbide-a (HPPH) for treatment and a fluorophore cyanine dye for optical imaging could be highly advantageous to treat deeply seated tumors and monitor the treatment response.[10] The ability to image real time events using fluorescence has made optical imaging an attractive modality to study cellular and molecular events[11] and to visualize events *in vivo*, especially in tumors.[12] Noninvasive in nature, optical imaging instruments are simpler and less expensive to operate and can allow precise assessment of the location and size of a tumor, providing

dx.doi.org/10.1021/bc200345p | *Bioconjugate Chem.* 2011, 22, 2283–2295

information on its invasiveness in adjacent tissue.[13,14] The work discussed herein describes the synthesis, molecular modeling, photophysical, electrochemical, tumor-imaging, and the photodynamic therapeutic potential of a series of longer wavelength photosensitizer (purpurinimides, 700 nm) joined to a cyanine dye with variable lengths of linkers. Among the near-infrared (NIR) dyes, cyanine dyes in general have shown enormous potential for optical imaging.[15−19]

2. RESULTS AND DISCUSSION

2.1. Chemistry. For the synthesis of purpurinimide-*N*-substituted cyanine dye conjugates, purpurin-18 methyl ester **1** was synthesized from chlorophyll-a by following the literature procedure, which was converted into mesopurpurin-18 methyl ester **2** by following the standard methodology.[20] Reaction of **2** with hydrazine hydrate gave N-amino mesopurpurin-18 methyl ester **3** in 50% yield.[21] By following a similar approach, **1** was individually reacted with diethyl diamine and carbamic acid to produce the corresponding N-substituted analogues **4** and **5** both with 89% yield. Reaction of these N-substituted purpurin-18 methyl esters with a cyanine dye **6** containing a carboxylic acid functionality (obtained in 80% yield by reacting commercially available IR820 with *p*-thiol-benzoic acid) gave purpurinimide−cyanine dye conjugates **7**−**9** in which two chromophores (photosensitizer and fluorophore) are joined at variable linker lengths with yields ranging from 32 to 37%. The reaction sequences for the preparation of the conjugates and the cyanine dyes are shown in Schemes 1 and 2.

Structures of the intermediates and the final products were confirmed by ^{1}H NMR and CHN/mass spectrometry (including HRMS) analysis. The purity of the final conjugates (compounds **7**−**9**) was determined by HPLC analysis.

2.2. Molecular Modeling. In order to examine the effects of linker lengths joining the two chromophores (conjugates **7**, **8**, and **9**) in photophysical, electrochemical, tumor-imaging and photodynamic efficacy, a molecular modeling study was performed. The three-dimensional model of the conjugates were built with the molecular modeling software SYBYL (Tripos Inc., St. Louis, MO) followed by the energy minimization with the PM3 semiempirical molecular orbital theory using the Spartan 02 software package (Wave function Inc., Irvine, CA). Figure 1 shows the resulting structures of the conjugates **7**, **8**, and **9** (Scheme 1) in extended conformation. The distances between the nitrogen atom in the purpurinimide ring system and the sulfur atom adjacent to the cyanine dye of the conjugates were calculated and are displayed in Figure 1. As expected, the smaller the linker length, the shorter the observed distance between two chromophores.

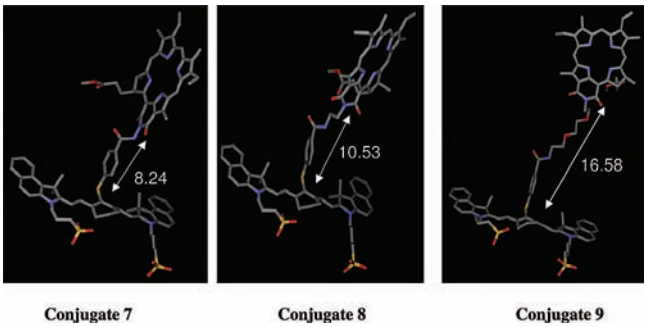

Figure 1. Three-dimensional representation of the conjugates with different lengths between the cyanine dye and the purpurinimide in extended conformation obtained from molecular modeling and energy optimization with PM3.

Since the above structures are appropriate for single molecules in gas phase, they may not be relevant to the structures of the conjugates in solution, in cells, or *in vivo* environments where physical properties and biological activities of these conjugates are examined. In order to gain some insights, the conformational flexibility of these conjugates were examined with the stochastic search module of MOE software using the MMFFs force field and charges (Chemical Computing Group, Montreal, Quebec, Canada). Again, the distance between two chromophores was measured for some of the resulting low energy conformers as shown in Figure 2.

As can be seen from the Figure 2 caption, the distances between the two chromophores remain more or less constant for conjugates **7** and **8**, while it shows a large variation for conjugate **9**. It is reasonable considering the length of the linker for these conjugates. Although the mean distances are similar between conjugates **7** and **8**, closer inspections reveal the significant difference between these conjugates. First, the standard deviation is much smaller for conjugate **7** than for **8**, reflecting the limited flexibility of **7**. Second, this limited flexibility is also the source of the limited range in the relative orientation of two chromophores for conjugate **7** as shown in Figure 2a where various low energy conformers of conjugate **7** are superimposed using the purpurinimide ring as a reference. It clearly shows that the cyanine dye and the linker can assume many different conformations but that they cannot assume a conformation that brings two chromophores close together. Thus, the purpurinimide ring remains exposed to its surroundings for this conjugate. Compared to conjugate **7**, some part of the purpurinimide ring is covered by the cyanine dye or thiophenol group in conjugate **8**, as shown in Figure 2b. Although there are a large variety of conformers for conjugate **9**, there are some conformers where a large portion of the purpurinimide ring is covered by the cyanine dye and/or thiophenol group as shown in Figure 2c. Photophysical experiments clearly indicated that intramolecular energy transfer occurred from the singlet excited state of the purpurinimide moiety to the cyanine moiety with the rate of transfer increasing with decreasing linker distance. This is an opposite trend from the linker length dependence on the *in vitro* PDT efficacy. The photophysical results are consistent with the distance dependence of energy transfer, while the conformational flexibility may explain the excellent *in vitro* PDT efficacy of conjugate **7** and the decrease of efficacy with increasing linker length. If the purpurinimide rings are not exposed to the environment, the compound may not be able to produce singlet oxygen because it cannot interact with water molecules. Alternatively, even if singlet oxygen is produced, it may not reach to the cellular target because the singlet oxygen produced may interact with the closely seated cyanine dye before it reaches the target site(s).

2.3. Photodynamics. In order to examine the photodynamics of purpurinimide, cyanine, and the conjugates, time-resolved transient absorption spectra were recorded by femtosecond laser flash photolysis in deaerated DMSO solutions as shown in Figure 3. Transient absorption bands of purpurinimide **4** observed at 500 and 530 nm taken at 2 ps after femtosecond laser excitation (Figure 3a) are assigned as the singlet excited state of **4** (^{1}**4***). The transient absorption of ^{1}**4*** decreased as the absorption band of the triplet excited state

Figure 2. (a) Various conformers for conjugate **7** with limited flexibility in the linker are superimposed using the purpurinimide ring as reference. Standard color for each atom type is used. The purpurinimide ring (shown in the left portion of this figure) is exposed to surroundings. (b) Examples of the low energy conformer for conjugate **8**. The purpurinimide moiety is shown in orange and the cyanine dye−thiophenol moiety in cyan, and the linker regions are based on standard atom type based color. There are some overlaps between the purpurinimide ring and the cyanine dye ring. (c) Example of the low energy conformer for conjugate **9**. The same color scheme as that in panel b is used. Because of the flexibility of the long linker, diverse conformations are possible, and some of the low energy conformers show an extensive interaction between the purpurinimide ring and the cyanine dye−thiophenol moiety. Mean distance between the two moieties in panel a (conjugate **7**) = 8.18 Å (SD 0.10); in panel b (conjugate **8**) = 8.55 Å (SD 0.51); and in panel c (conjugate **9**) = 9.85 Å (SD 2.27).

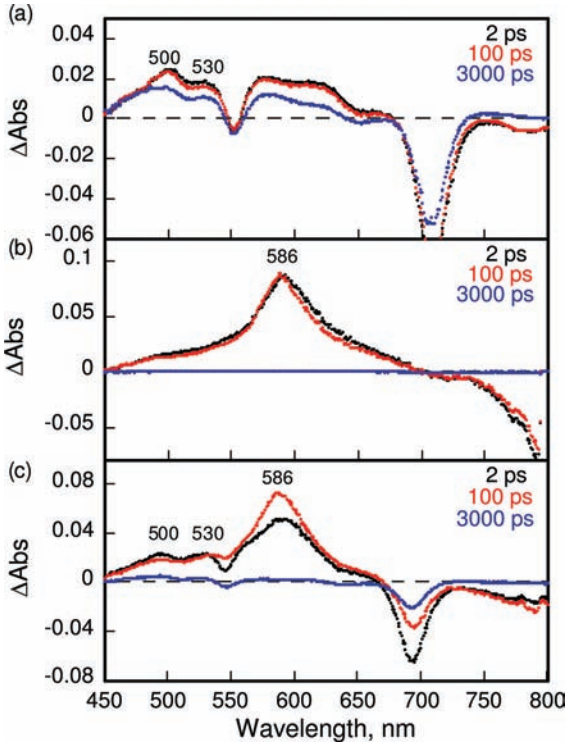

Figure 3. Transient absorption spectra of purpurinimide **4**, cyanine **6**, and conjugate **7** in deaerated DMSO taken at 2, 100, and 3000 ps after femtosecond laser flash excitation at 410 nm.

of **4** appeared. The transient absorption band of the singlet excited state of cyanine **6** is observed at 586 nm as shown in Figure 3b. The lifetimes of the singlet excited state of **4** and **6** were determined from decays of the absorption at >3 ns and 500 ps, respectively. In the case of conjugate **7** shown in Figure 3c, the transient absorption bands due to both singlet excited states of purpurinimide and cyanine were observed at 500, 530, and 586 nm at 2 ps because both moieties were excited by laser flash excitation at 410 nm. The absorption bands at 500 and 530 nm due to the singlet excited state of the purpurinimide moiety decreased, accompanied by an increase in the absorption band at 586 nm due to the singlet excited state of the cyanine moiety. This indicates that energy transfer from the singlet excited state of purpurinimide to the cyanine moiety occurs efficiently to afford the singlet excited state of cyanine. The energy transfer dynamics in **7** were determined from the rise of the absorption band at 586 nm as shown in the left panel of Figure 4a. The energy transfer rate constant was determined to be 6.7×10^{11} s^{-1}. Similarly, the energy transfer rate constants of conjugates **8** and **9** were also determined from the rise of the absorption band at 586 nm in Figure 4b and c to be 1.4×10^{11} and 1.3×10^{11} s^{-1}, respectively. The energy transfer rate constant increases with decreasing distance between the energy donor and acceptor estimated from the theoretical calculations (*vide supra*). The decay time profiles at 586 nm are shown on the right side of Figure 4. The decay rate constants of **7**−**9** agree well with the value of the cyanine reference **6** due to intersystem crossing to the triplet excited state. An energy transfer from the singlet excited state of the purpurinimide moiety to the cyanine moiety is feasible because the singlet energy of the purpurinimide (1.76 eV) is higher than that of the cyanine (1.41 eV), which were obtained from the absorption and fluorescence maxima, λ_{abs} = 689 nm and λ_{fl} = 720 nm for **4**, and λ_{abs} = 849 nm and λ_{fl} = 915 nm for **6**, respectively. Thus, in the purpurinimide−cyanine systems, intramolecular energy transfer at the singlet excited state occurs efficiently from the purpurinimide moiety to the cyanine moiety, followed by intersystem crossing to the triplet excited state of the cyanine moiety. No electron transfer from the purpurinimide moiety to the cyanine moiety was observed as expected from the disfavored energetics as indicated by the redox potentials of the conjugates (*vide infra*).

2.4. Electrochemical Properties. Cyclic voltamograms of **7**−**9** are illustrated in Figure 5, which also includes the reference compounds **4** and **6**. The first one-electron oxidation potentials of **7**−**9** (E_{ox}) are all located at $E_{1/2}$ = 0.52 V vs SCE, which is similar to the E_{ox} value of compound **6** (0.56 V vs SCE). The first one-electron reduction potentials of **7**−**9** (E_{red1}) are also identical at $E_{1/2}$ = −0.55 V vs SCE, which agrees with the E_{red1} value of cyanine **6** (−0.56 V vs SCE). The second one-electron reduction potentials of **7**−**9** (E_{red2}) are also nearly the same and range from −0.64 to −0.69 V vs SCE, which agree with the E_{red1} value of compound **4** (−0.69 V vs SCE). Thus, there seems to be little or no interaction between the purpurinimide and cyanine moieties in the conjugates **7**−**9**, irrespective of the difference in the distance between them.

The second one-electron oxidation of the purpurinimide moiety of the conjugates **8** and **9** is irreversible, and the peak potential ranges from 0.89 to 0.92 V vs SCE, which is similar to that of **4** (0.94 V). The energy of the charge-separated state of **7**−**9** to be produced by electron transfer from the purpurinimide moiety to the singlet excited state of the cyanine

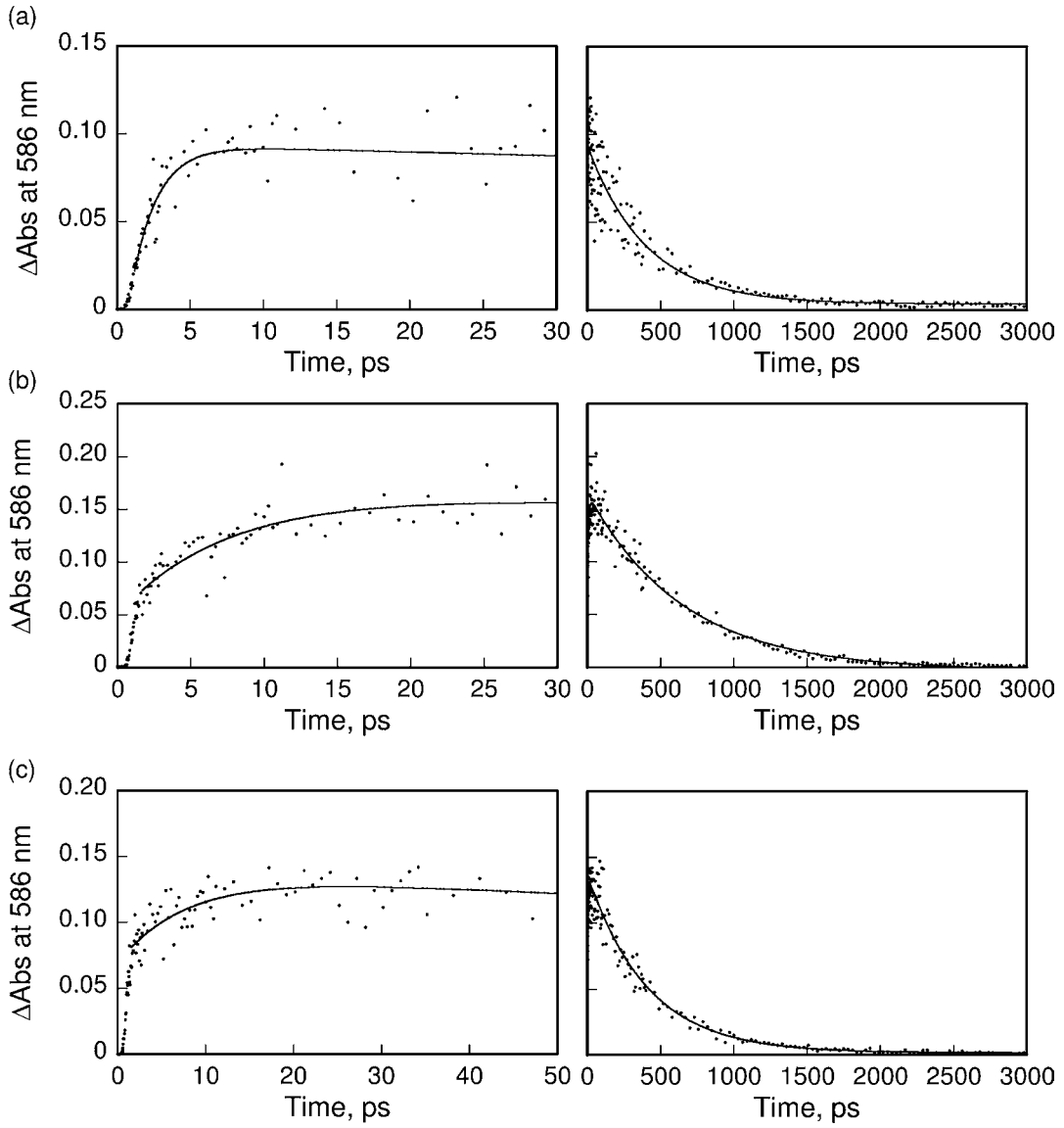

Figure 4. Rise and decay time profiles of the absorbance at 586 nm of (a) **7**, (b) **8**, and (c) **9** in deaerated DMSO after femtosecond laser excitation at 410 nm. Left panels: short time range. Right panels: long time range.

moiety is roughly estimated to be 1.6 eV, which is higher than the energy of the singlet excited state of cyanine (1.41 eV). The energy of the charge-separated state of **7**−**9** in the reverse direction from the singlet excited state of the cyanine moiety to the purpurinimide moiety is also estimated to be 1.74 eV, which is higher than the energy of the singlet excited state of cyanine (1.41 eV). Thus, electron transfer from the singlet excited state of the cyanine moiety to the purpurinimide moiety is energetically feasible. However, no electron transfer occurred from the purpurinimide moiety to the singlet excited state of the cyanine moiety as shown in Figure 3. This indicates that the intersystem crossing from the singlet excited state of the cyanine moiety to the triplet excited state is much faster than the electron transfer.

The absence of a charge-separated state of **7**−**9** was further confirmed by measuring the purpurinimide radical cation and the cyanine radical anion by use of a spectroelectrochemistry (*vide infra*). Figure 6a shows the spectral changes (in blue) which occurred during the one-electron reduction of cyanine **6** at an applied potential of −0.70 V. A new absorption maximum at 531 nm, which is assigned to the cyanine radical anion, appears, and this was accompanied by a disappearance of absorption bands at 773 and 849 nm due to cyanine. A clean isosbestic point is seen in this transfer. The radical anion can be further reduced to the dianion at an applied potential of −1.60 V vs SCE. A similar spectral change is observed for the first one-electron reduction of conjugate **7** (Figure 6b), where the radial anion of the cyanine moiety has an absorption band at 533 nm. Figure 6c shows the spectral changes upon the one-electron reduction of purpurinimide **4** at an applied potential of −0.90 V, in which the Soret band at 417 nm and the visible band at 689 nm are decreased in intensity, while an obvious radical band appears at 593 nm. These spectral changes shown in red are quite similar to the second reduction of conjugate **7** at −0.80 V also shown in red (see Figure 6b). A comparison of the spectral change for **6**, **7**, and **4** during each reduction illustrates the similarity between conjugates **7**, cyanine **6**, and purpurinimide **4**, also suggesting that the purpurinimide and cyanine moieties in **7** are almost independent of each other during electron transfer processes.

dx.doi.org/10.1021/bc200345p | *Bioconjugate Chem.* 2011, 22, 2283−2295

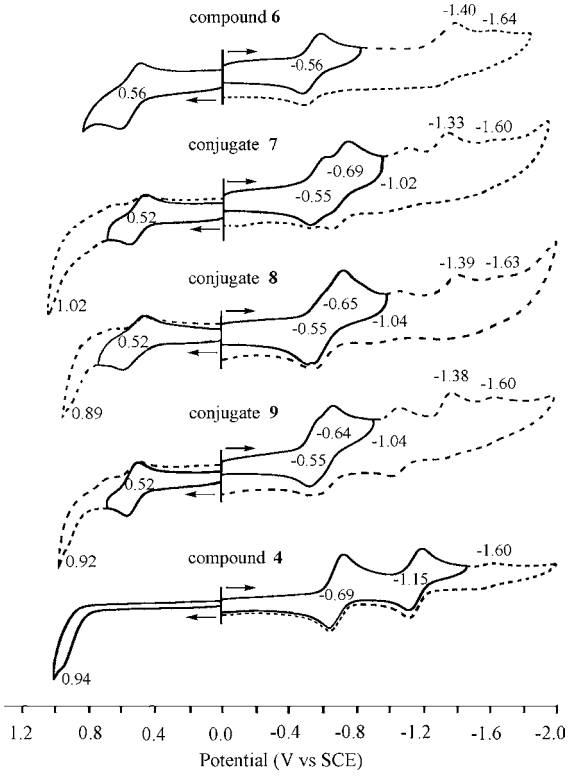

Figure 5. Cyclic voltammograms of compounds **4** and **6**–**9** in DMSO containing 0.1 M TBAP at a scan rate of 0.1 V/s.

Figure 7a shows the spectral changes which occur upon the one-electron oxidation of cyanine **6** at an applied potential of 0.70 V. A new absorption maximum appears at 650 nm, which is assigned as due to the cyanine radical cation. The absorption band due to the cyanine radical cation in conjugate **7** is slightly blue-shifted to 637 nm (Figure 7b). The purpurinimide radical cation could not be observed by spectroelectrochemistry because of irreversible oxidation, as shown in Figure 7c, where the absorption band due to **4** only disappears at an applied potential of 1.0 V vs SCE. The absence of an absorption band at 533 nm due to the radical anion of cyanine (Figure 6b) or the absorption band at 637 nm due to the radical cation of the cyanine (Figure 7b) confirms that there is no electron transfer from the purpurinimide moiety to the singlet excited state of the cyanine moiety or from the singlet excited state of the cyanine moiety to the purpurinimide moiety in the conjugate.

2.5. Biological Studies. *2.5.1. In Vitro PDT Efficacy.* Because of the insoluble nature of conjugates **7**–**9**, various formulations were used to dissolve the compounds in appropriate concentrations. Among all the formulations, reasonable solubility was obtained in both 1% Tween 80 in 5% dextrose–water solution.[22] The *in vitro* PDT efficacy of conjugates **7**–**9** was determined in Colon26 cells by following the standard MTT assay[23] (for details, see the Experimental Procedures). In brief, the cells were incubated for 24 h with **7**, **8**, and **9** at variable concentrations and then exposed to laser light (1.0 J/cm^2) at 695, 713, and 710 nm (the longest absorption wavelengths corresponding to the purpurinimide portion for the respective conjugates). The PDT efficacy (cell

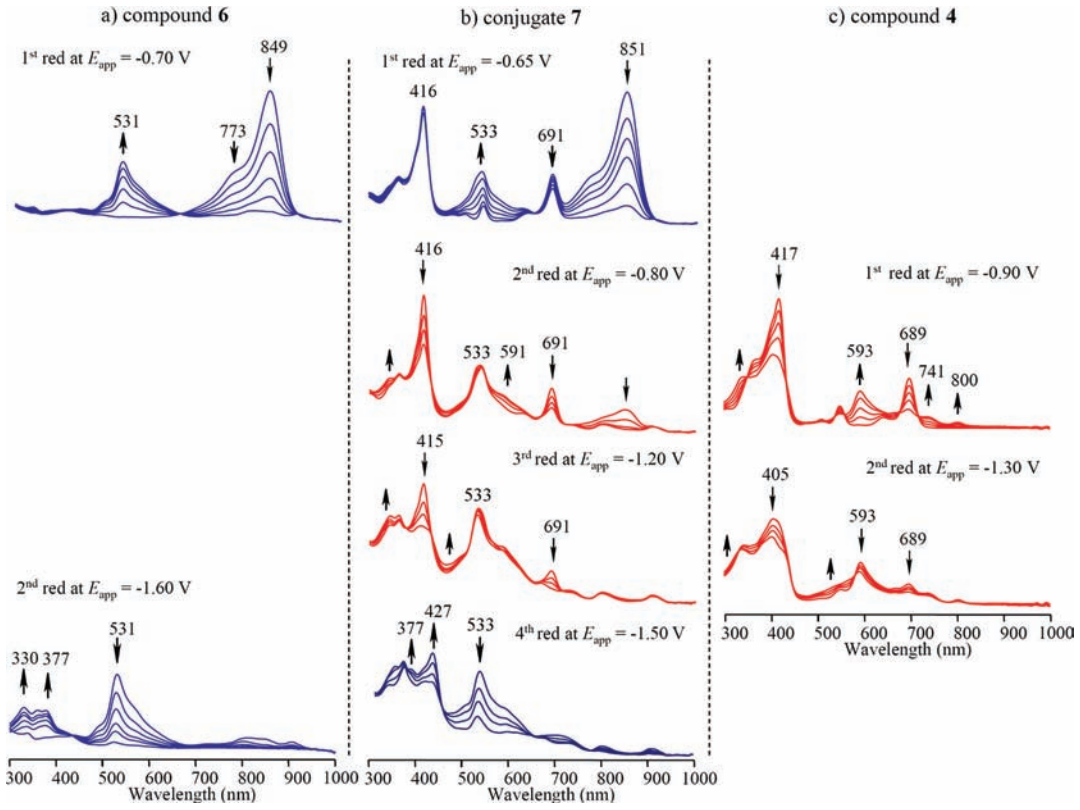

Figure 6. Thin-layer UV–visible spectra of (a) **6**, (b) **7**, and (c) **4** upon the controlled reducing potentials in DMSO containing 0.1 M TBAP. The blue spectral changes in conjugate **7** correspond to a reduction on the cyanine dye moiety. The red spectral changes are assigned at the reduction at the purpurinimide unit of the conjugate.

dx.doi.org/10.1021/bc200345p | *Bioconjugate Chem.* 2011, 22, 2283–2295

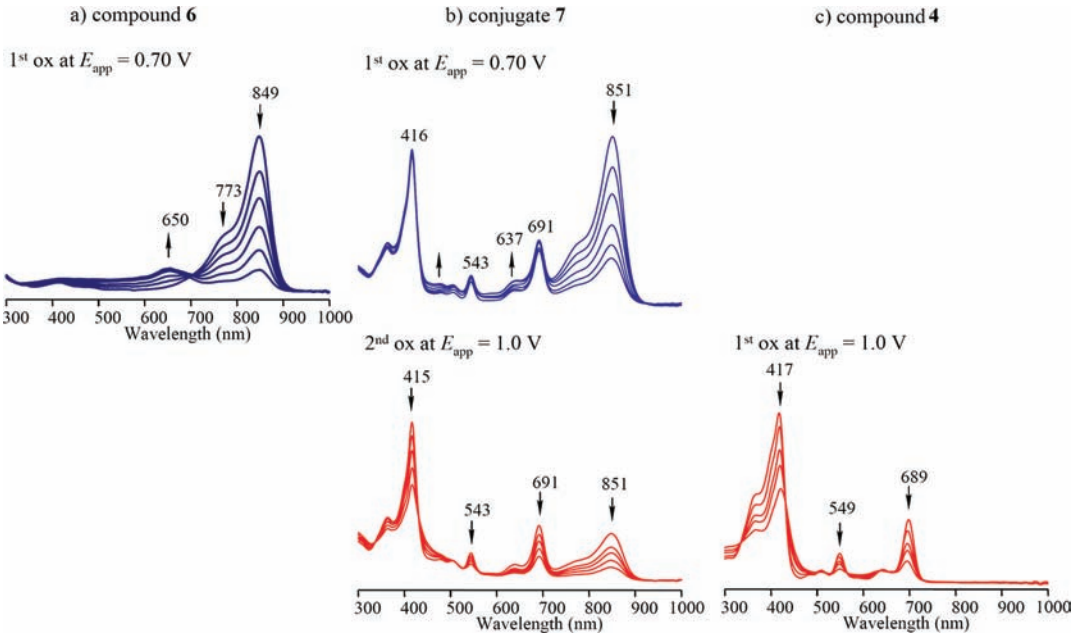

Figure 7. Thin-layer UV–visible spectra of (a) **6**, (b) **7**, and (c) **3** upon the controlled reducing potentials in DMSO containing 0.1 M TBAP.

kill) was calculated from 4 replicate wells in 3 separate experiments, and each standard error is representative of 3 separate experiments. The results, summarized in Figure 8 and

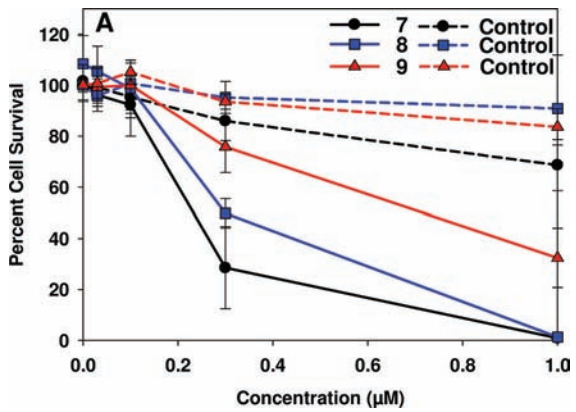

Figure 8. MTT plotted assay of **7**, **8**, and **9** incubated for 24 h at various concentrations with Colon26 cells followed by a light dose of 1.0 J/cm^2 at a dose rate of 3.2 mW/cm^2.

Table 1. IC_{50} (50% Cell Kill) Concentrations of Conjugates 7, 8, and 9[a]

conjugate	IC_{50} (μM)	distance (Å) between the two moieties
7 (short linker)	0.22	8.18
8 (medium linker)	0.32	8.55
9 (long linker)	0.69	9.85

[a]Average distance of various conformers is shown in the caption to Figure 2.

Table 1, show that increasing the distance between the photosensitizer and cyanine dye decreases the *in vitro* PDT efficacy. The LD_{50}s of the conjugates were determined by the best fit curves (plotted in Sigmaplot) to the dose–response data. The IC_{50} values confirmed a decreased *in vitro* PDT efficacy in this series of conjugates by increasing the linker length between the purpurinimide and the cyanine dye.

2.5.2. In Vivo Fluorescence Imaging. Cyanine dye **6** has the required photophysical properties (long wavelength absorption with significant Stokes shift), for fluorescence imaging but was not tumor-avid.[24] To investigate the use of tumor-avid purpurinimides as vehicles to deliver the nontumor-avid cyanine dye to the tumor, we used fluorescence imaging as a tool to investigate the effect of the linker *in vivo*.[25] Compared to the therapeutic dose, the imaging dose was quite low, and therefore, we were able to evaluate the imaging potential of the three conjugates **7**–**9**. Each conjugate was injected i.v. via the tail vein at a dose of 0.03 μmol/kg into BALB/c mice (9 mice/group) bearing Colon26 tumors on the shoulder.

Figure 9 represents fluorescent images of the tumors at 24, 48, and 72 h postinjection of conjugates **7**, **8**, and **9** (3 mice/time point) after each drug was injected. The color scale represents fluorescence intensity, where blue is the lowest intensity, and red/white is the highest. After imaging, the mice at each time point were sacrificed, and the organs were removed and imaged *ex vivo* to demonstrate the distribution and clearance rates of the conjugates. Conjugate **8** exhibited the highest fluorescent intensity in the tumors of all the compounds at 24 h and was gradually clear from the tumor by 72 h. Conjugate **9** showed a moderate but lower fluorescence intensity than compound **8**, which cleared from the tumor at a much faster rate. Interestingly, conjugate **7** gave low, barely noticeable fluorescence intensity in the tumor, which could either indicate poor fluorescence quantum yield for the cyanine dye portion of this compound or low tumor selectivity.

The *ex vivo* fluorescence intensities of various organs (ear, heart, kidney, liver, lung, muscle, small intestine, spleen, stomach, and tumors) are shown in Figure 10. As expected, conjugate **9** in which the photosensitizer is joined with the cyanine dye via a PEG linker exhibited highest fluorescence (high uptake) in the liver compared to **7** and **8**. The high affinity for this compound to the liver could be due to the more

dx.doi.org/10.1021/bc200345p | *Bioconjugate Chem.* 2011, 22, 2283–2295

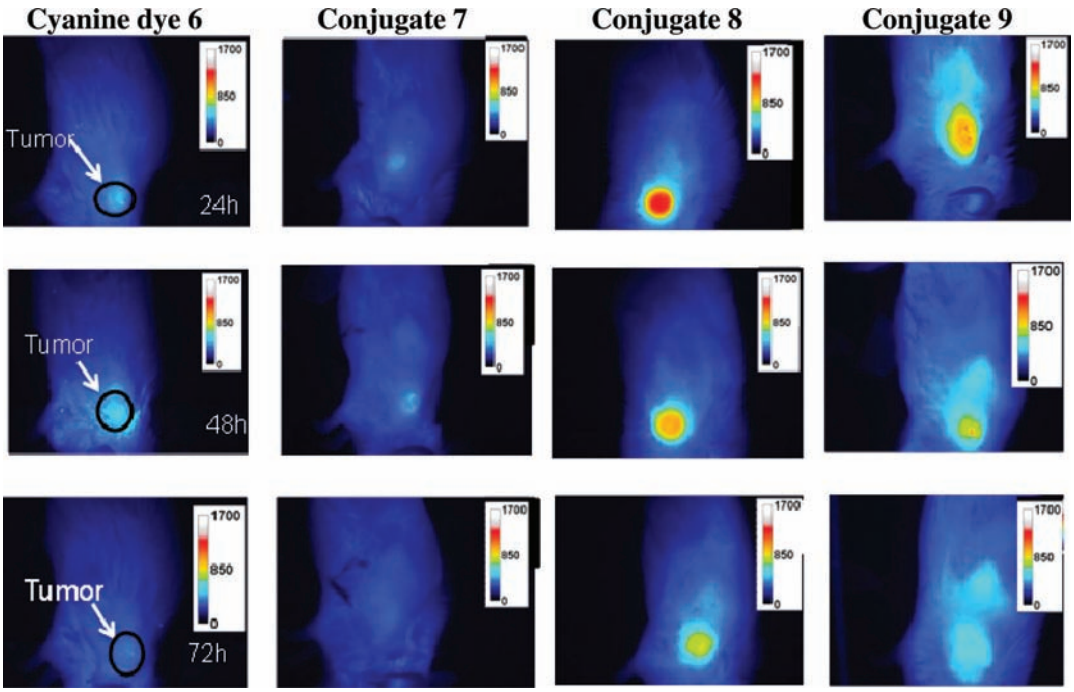

Figure 9. Comparative whole body images of conjugates **7**–**9** along with cyanine dye **6** (dose: 0.03 μmol/kg) in BALB/c mice bearing Colon26 tumors. Images were taken at 24, 48, and 72 h postinjection using a 12 bit Nuance camera (CRI, Worburn, MA) with a 782 continuous wave laser for excitation and a 800 and 830 nm long pass filter to collect fluorescence. Images were then analyzed using Image J software.

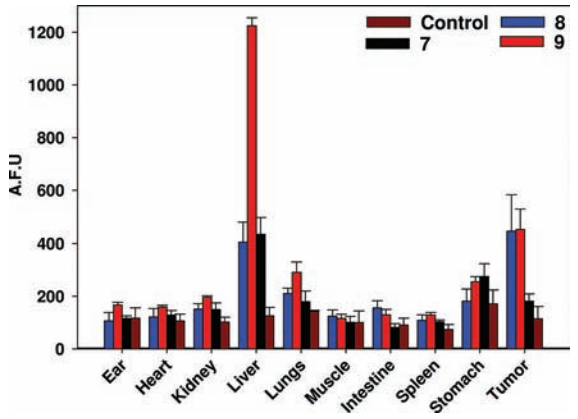

Figure 10. Fluorescence biodistribution of conjugates **7**–**9** and various organs [3 mice (BALB/c bearing Colon26 tumors]. Organs from the mice were removed and then imaged/analyzed at 24 h postinjection (dose: 0.03 μmol/kg). The fluorescence intensity of each organ was analyzed by Image J software.

lipophilic nature of the linker connecting the purpurinimide and cyanine dye. Interestingly, the PEG linker also showed comparable tumor avidity. Since the purpose of this study is to create a molecule that can act as both a fluorescent imaging and a therapeutic agent *in vivo*, conjugate **7** was not examined any further due to its weak uptake in tumors compared to that of the other two conjugates, determined by fluorescence imaging. However, further studies at lower time points may produce improved efficacy, and these studies with this and other agents are currently in progress.

2.5.3. Comparative In Vivo Tumor Uptake of the Conjugates. *In vivo* reflectance spectroscopy was used to determine the maximum uptake of the conjugates at various time points.[26] Mice were injected through the orbital venous plexus, the reflectance in tumors was measured at 24 and 48 h, and the drug concentrations were determined (see Figure 11). This approach was extremely useful in providing the knowledge of the pharmacokinetic characteristics (especially the clearance from the tumor) of the conjugates and also the shift in their *in vivo* absorption. Under a similar dose of the drug (2.5 μmol/kg), conjugate **8** showed maximum tumor uptake (BALB/c mice bearing Colon26 tumors) at 24 h postinjection, which decreased over the next 24 h. Conjugate **9** showed a small increase in uptake at 48 h compared to that at 24 h.

Comparatively, conjugate **8** showed a higher tumor uptake than **9** at both 24 and 48 h. Since our objective has been to develop a candidate with both imaging and therapy capabilities and conjugate **7** showed limited PDT efficacy, it was decided not to explore its imaging potential.

2.5.4. In Vivo Photosensitizing Efficacy. Preliminary *in vivo* PDT efficacy of conjugates **8** and **9** was measured by tail vein injection into BALB/c mice (5 mice/group) bearing Colon26 tumors (average tumor volume 27 mm^3) at a dose of 2.5 μmol/kg (which gave approximately 50% tumor cure with the HPPH–cyanine dye conjugate, our lead compound).[10] The tumors were illuminated with light (135 J/cm^2, 74 mW/cm^2) at 24 h postinjection, with the best time point for the maximum photosensitizer uptake in the tumor determined by fluorescence imaging and *in vivo* reflectance spectroscopy. From the preliminary results summarized in Figure 12A, it can be seen that compared to **8**, the conjugate **9** exhibited limited long-term efficacy and that all mice showed tumor regrowth at 10–12 days post-treatment. Under similar treatment parameters, conjugate **8** showed 100% tumor cure, and no tumor growth was observed at day 60. We further investigated the efficacy of conjugate **8** at variable doses (1.5, 2.0, and 2.5 μmol/kg), and the light dose was kept the same (135 J/cm^2, 75mW/cm^2). From the results summarized in Figure 12B, it can be seen that at the lowest dose of 1.5 μmol/kg, conjugate **8** showed limited efficacy, but at higher doses, a significant PDT response was

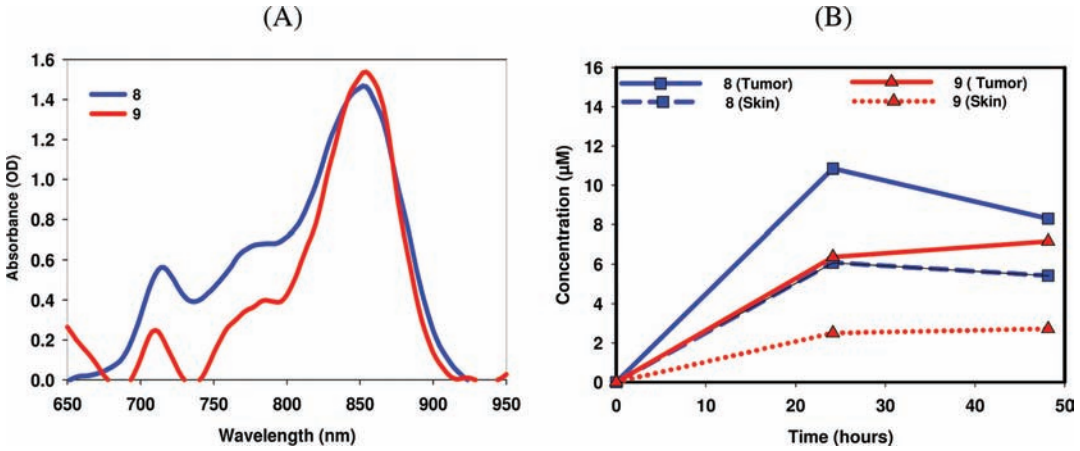

Figure 11. (A) *In vivo* absorption spectra of conjugates **7** and **8** determined by *in vivo* reflectance spectroscopy in a Colon26 tumor implanted in BALB/c mice at 24 h postinjection. (B) Tumor vs skin uptake of the conjugates at 24 and 48 h postinjection (drug dose: 2.5 μmol/kg).

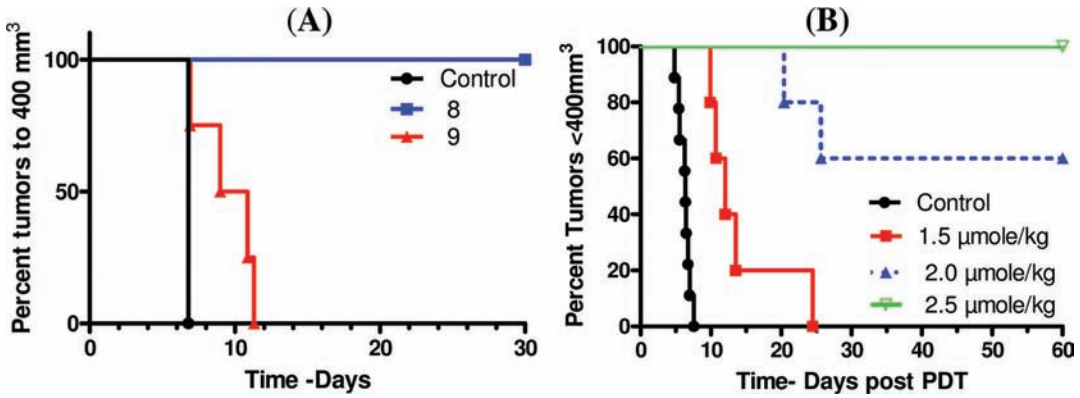

Figure 12. (A) Comparative *in vivo* photosensitizing efficacy of conjugates **8** and **9** in BALB/c mice (5 mice/group) bearing Colon26 tumors at a dose of 2.5 μmol/kg, and (B) *in vivo* efficacy of **8** at variable drug doses. The tumors were exposed to light (135 J/cm^2 and 75mW/cm^2) at their longest wavelength absorption at 24 h postinjection (i.v.) of the photosensitizers. The tumor growth was measured daily. Under the treatment parameters used, the mice treated with conjugate **8** at a dose of 2.5 μmol/kg did not show any tumor regrowth, and the tumors were flat on day 60 post-treatment.

observed (2.0 μmol/kg, 3/5 mice, and at 2.5 μmol/kg, 5/5 mice, were tumor free on day 60).

3. CONCLUSIONS

An efficient synthetic pathway was developed to create purpurinimide−cyanine dye dual functional agents. *In vitro* results suggested that increasing the carbon chain length from a short linker to a long linker decreases the PDT efficacy of the compounds. Fluorescence imaging showed that **7** (short linker) had poor imaging capabilities compared to that of **8** (medium linker) and **9** (long linker) and was not studied further. Conjugate **9** exhibited the highest liver fluorescent values. This may be due to the more lipophilic nature of the linker connecting the two molecules, which shows higher affinity to the liver. *In vivo* reflectance spectroscopy showed that conjugate **8** exhibited higher tumor uptake than **9** and should therefore produce *in vivo* PDT efficacy. The comparative *in vivo* PDT confirmed the higher efficacy of conjugate **8** over **9** and produced 100% tumor response (5/5 BALB/c mice bearing Colon26 tumors were tumor free after day 60 post-treatment), whereas **9**, under similar treatment parameters showed limited PDT activity. This study with a small number of conjugates indicates that conjugate **8** with a medium length of linker shows potential for both tumor imaging and therapy. However, further studies with a larger group of compounds should help in selecting the best candidates, and the synthesis of the related analogues is underway. The low PDT and imaging capabilities of conjugate **7** could be due to its faster *in vivo* clearance. Therefore, further studies with conjugate **7** at shorter time intervals between the injection of the drug and light treatment are also in progress.

4. EXPERIMENTAL PROCEDURES

All chemicals were of reagent grade and used as such. All reagents were purchased from Aldrich chemical company and were used as received. All photophysical experiments were carried out using spectroscopic grade solvents. Solvents were dried using standard methods unless stated otherwise. Reactions were carried out under nitrogen atmosphere and were monitored by precoated (0.20 cm) silica TLC plastic sheet (20 cm × 20 cm) strips (POLYGRAM SIL N-HR) and or/UV−visible spectroscopy. UV−visible spectra were recorded on a Varian Cary 50 Bio UV−visible spectrophotometer using dichloromethane/methanol as solvent unless otherwise specified. ^{1}H NMR spectra were recorded on Varian 400 spectrometers at 303 K in $CDCl_3$ or ∼10% of CD_3OD in $CDCl_3$ or DMSO-d_6. Proton chemical shifts (δ) are reported in parts per million (ppm) relative to $CDCl_3$ (7.26 ppm), CD_3OD

dx.doi.org/10.1021/bc200345p | *Bioconjugate Chem.* 2011, 22, 2283−2295

(3.34 ppm) or TMS (0.00 ppm). Coupling constants (J) are reported in Hertz (Hz), and s, d, t, q, p, m, and br refer to singlet, doublet, triplet, quartet, pentet, multiplet, and broad, respectively. Mass spectral data (Electro Spray Ionization, ESI, by fusion) were obtained from Biopolymer Facility, Roswell Park Cancer Institute, Buffalo, NY, and HRMS data were obtained from the Mass Spectrometry Facility, Michigan State University, East Lansing, MI. Elemental analysis were done at Midwest Microlab LLC., Indianapolis, IN.

4.1. *N*-Amino Purpurinimide Methyl Ester (3). Mesopurpurin-18 methyl ester (**2**) (0.138 mmol, 80 mg) was dissolved in 15 mL of anhydrous pyridine and stirred under argon. Hydrazine anhydrate (1.3 mmol, 42 mg, 42 μL) was added to 2 mL of anhydrous pyridine, which was then added slowly to the stirring mixture. The completion of the reaction was checked by UV−vis in regular intervals until the wavelength intensity at λ_{max} of 701 nm was maximal. After 4 h, 1 N HCl (25 mL) and dichloromethane (20 mL) were added, and the stirring was continued for another 1.5 h. The reaction mixture was then transferred into a separation funnel. Additional dichloromethane (200 mL) was added, the organic layer was washed with water (200 mL × 3). The dichloromethane (DCM) layer was separated, dried over anhydrous sodium sulfate, and filtered.. The crude reaction product obtained after evaporating DCM was purified on an alumina column by eluting with a 1% MeOH/DCM solvent system to afford a purple/magenta crystal of **3**[21] (42.4 mg, 50% yield). UV−vis λ_{max} (in CH_2Cl_2): 359 nm (ε = 5.8 × 10^4), 416 (ε = 10.0 × 10^5), 548 (ε = 1.9 × 10^5), 643 (ε = 8.60 × 10^3), 700 (ε = 4.94 × 10^4) . ^{1}H NMR (400 MHz, 3 mg/1 mL $CDCl_3$, δ ppm) 9.07, 8.95, and 8.42 (each s, 1H for 5H, 10H and 20H), 5.72 (broad s, N−NH_2), 5.29 (m, 1H, for 17H), 4.33 (m, 1H for 18H), 3.63 (q, 2H for 8^1CH_2) 3.62 (s, 3H for $12CH_3$), 3.61 (s, 3H for $17^2CO_2CH_3$), 3.33 (m, 2H for 3^1CH_2) 3.18 (s, 3H for $2CH_3$), 3.00 (s, 3H for $7CH_3$), 2.78 and 1.978 (m, 2H for 17^1 CH_2), 2.46 (m, 2H for 17^2 CH_2) 1.76 (d J = 7.2 Hz, 3H for $18CH_3$), 1.66 (t, J = 7.2 Hz, 3H for 8^2CH_3), 1.50 (m, 3H for 3^2CH_3). EIMS (m/z): 595 (M + H). Elemental Anal. Calcd. for $C_{34}H_{38}N_6O_4$: C, 68.67; H, 6.44; N, 14.13. Found: C, 68.70; H, 6.43; N, 14.01.

4.2. *N*-Boc Diethlyene Purpurinimide Methyl ester (4a). Purpurin-18 methyl ester (50 mg, 0.0865 mmol) (**1**) was added to a dry 100 mL round bottomed flask and put under house vacuum for 20 min. N-Boc ethylenediamine (48.50 mg, 0.30275 mmol) was placed under nitrogen for 10 min and then added to the flask containing Purpurin-18 using a long needle. Under a nitrogen atmosphere, 5−10 mL of anhydrous DCM was added to the reaction mixture, which was stirred for 39 h, monitoring with UV−vis. A wavelength of 665 nm indicated the opening of the six-membered anhydride ring system. It was then treated with diazomethane, the intermediate amide, as methyl ester was not isolated, and immediately treated with a catalytic amount of KOH/MeOH. The base catalyzed intramolecular cyclization afforded the desired analogue exhibiting the long wavelength absorption at 707 nm. The reaction mixture was purified by preparative plates using a 5% MeOH/DCM solvent system, and the desired band was scratched off and resuspended in 5% methanol/dichloromethane. The silica was removed by filtration. Solvents were evaporated, and the residue **4a** was precipitated with DCM/*n*-hexane (60 mg, 86% yield). UV−vis λ_{max} (in CH_2Cl_2): 365 nm, 418 nm, 550 nm, 707 nm. ^{1}H NMR (400 MHz, 3 mg/1 mL $CDCl_3$, δ ppm) 9.40, 9.20, and 8.56 (each s, 1H for 5H, 10H and 20H); 7.83 (dd, J = 11.6, 5.2 Hz 1H, $3^1CH{=}CH_2$); 6.24 (d, J = 16.4 Hz, 1H, trans $3^2CH{=}CH_2$), 6.12, (d, J = 8.4 Hz, 1H cis $3^2CH{=}CH_2$); 5.46 (br s, 1H, N-*H*-CH_2−CH_2−N-Boc); 5.37 (d, J = 4 Hz, 1H for 17H), 4.62 (m, 2H, NH−C*H*$_2$−CH_2−N-Boc); 4.37 (q, 1H for 18H); 3.59 (s, 3H, $17^2CO_2CH_3$); 3.49 (q, 2H for NH−CH_2−C*H*$_2$-N-Boc); 3.79 (d, J = 5.2 Hz, 1H for 8^1CH_2); 3.73 (s, 3H for $12CH_3$) ; 3.33 (s, 3H for $2CH_3$); 3.04 (s, 3H for 7 CH_3); 2.72, 2.46, 2.44, and 2.06 (each m, 1H for 2 × 17^1H and 2 × 17^2H); 1.79 (d, J = 8 Hz, 3H for 18^1 CH_3); 1.60 (t, J = 7.6 Hz 3H for 8^2 CH_3); −0.128 and −0.215 (br s, 1H for 2NH). EIMS (m/z): 721 (M + H).

4.3. Diethlyene Amino Purpurinimide Methyl Ester (4). *N*-Boc diethlyene purpurinimide methyl ester (**4a**) was treated with a 4:1 ratio of TFA/dry DCM and stirred for 2 h. The TFA was removed by high vacuum for 5 h, and the remainder was purified on an alumina column with 5% MeOH/DCM as the solvent system. The resulting compound was isolated as a dark purple liquid, compound **4**, which was concentrated by evaporating the liquid under vacuum to afford dark purple crystals (54 mg, 89% yield) UV−vis λ_{max} (in CH_2Cl_2): 365 nm (ε = 4.5 × 10^4), 419 nm (ε = 1.18 × 10^5), 551 nm (ε = 4.6 × 10^4), 706 nm (ε = 4.2 × 10^4). ^{1}H NMR (400 MHz, 3 mg/1 mL $CDCl_3$, δ ppm) 9.65, 9.44, 8.78 (each s, 1H for 5 H, 10H and 20H); 8.03 (dd, J = 17.6, 11.6 Hz, 1H, $3^1CH{=}CH_2$), 6.45 (d, J = 18.0, 1H, *trans* $3^2CH{=}CH_2$), 6.34 (d, J = 11.6, 1H *cis* $3^2CH{=}CH_2$), 5.58 (d, J = 8.4 Hz, 1H for 17H); 4.81 (t, J = 6.8 Hz, 2H for N−C*H*$_2$-CH_2−N), 4.58 (q, J = 7.2 Hz, 1H for 18H), 3.95 (s, 3H, $12CH_3$), 3.81 (s, 3H, $17^2CO_2CH_3$), 3.80 (q, J = 7.6 Hz, 2H, 8^1CH_2), 3.54−3.59 (m, 5H, $2CH_3$ and N−CH_2-C*H*$_2$-N), 3.27 (s, 3H, $7CH_3$), 2.96, 2.67, 2.62, and 2.22 (each m, 1H, 2 × 17^1H and 2 × 17^2H), 2.00 (d, J = 7.2 Hz, 3H, $18CH_3$), 1.82 (t, J = 7.6 Hz, 3H, 8^2CH_3) 0.08 and 0.00 (each br s, 1H, 2NH). EIMS (m/z): 621.1 (M + H). Elemental Anal. Calcd. for $C_{40}H_{48}N_6O_6$: C, 69.66; H, 6.50; N, 13.54. Found: C, 68.63; H, 6.51; N, 12.88.

4.4. *N*-Boc Glycol Purpurinimide Methyl Ester (5a). *N*-Boc-2,2′-(ethylene-1,2-dioxy) bisethylamine was prepared by following the literature procedure.[10] It (50 mg, 0.2015 mmol) was dissolved in 5 mL of dry DCM. This was added to a stirring mixture of purpurin-18 methyl ester (50 mg, 0.0865 mmol) in 10 mL of dry DCM. The reaction was stirred for 39 h under a nitrogen atmosphere with UV−vis monitoring (a shift from 700 nm to 665 nm). The reaction was then treated with diazomethane/KOH/MeOH until a red shift to 707 nm indicated the reaction was complete. A preparation scale TLC separation was done with a 5% MeOH/DCM solvent system, and the desired band was scratched off, and the desired product was isolated by following the method as discussed above to yield compound **5a** (60 mg, 86% yield). UV−vis λ_{max} (in CH_2Cl_2): 365.1 nm, 419 nm, 549 nm, 707 nm. ^{1}H NMR (400 MHz, 3 mg/1 mL $CDCl_3$, δ ppm) 9.58, 9.32, and 8.56 (each s, 1H for 5 H, 10H and 20H), 7.88 (dd, J = 8.0, 10.4 Hz 1H, $3^1CH{=}CH_2$); 6.24 (d, J = 16.0 Hz, 1H, trans $3^2CH{=}CH_2$); 6.14 (d, J = 11.6, 1H cis $3^2CH{=}CH_2$);5.32 (m, 1H for 17H); 5.10 (br s, 1H for N−CH_2-CH_2−(O−CH_2)$_2$-N*H*Boc); 4.73 (t, J = 8.0 Hz, 2H for N−C*H*$_2$-CH_2−(O−CH_2)$_2$-NHBoc); 4.34 (q, 1H for 18H); 2.70, 2.40, 2.35, and 1.98 (each m 1H, 2 × 17^1H and 2 × 17^2H); −0.05 and −0.15 (br s, 1H for 2NH). EIMS (m/z): 809 (M + H).

4.5. *N*-Glycol Purpurinimide Methyl Ester (5). Purpurin-18-*N*-Boc-glycol-imide (**5a**) was treated with a 4:1 ratio of TFA/Dry DCM and stirred for 2 h. The reaction was concentrated by evaporating under vacuum. The crude mixture

was purified on an alumina column with 5% MeOH/DCM as the solvent system. The resultant compound after the standard workup afforded dark purple crystals of **5** (54 mg, 89% yield). UV−vis λ_{max} (in CH_2Cl_2): 365 nm ($\varepsilon = 4.5 \times 10^4$), 419 nm ($\varepsilon = 1.18 \times 10^5$), 551 nm ($\varepsilon = 2.1 \times 10^5$), 707 nm ($\varepsilon = 4.30 \times 10^4$). ^{1}H NMR (400 MHz, 3 mg/1 mL $CDCl_3$, δ ppm) 9.58, 9.34, and 8.56 (each s, 1H for 5H, 10H and 20H); 7.90 (dd, J = 11.6, 11.6 Hz, 1H for 3^1CH═CH_2); 6.30 (d, J = 16.4 Hz, 1H for *trans*-3^2CH═CH_2); 6.15(d, J = 10.4 Hz, 1H for *trans*-3^2CH═CH_2); 5.33 (m, 1H for 17H); 4.73 (t, J = 1.6 Hz, 2H for N−CH_2-CH_2−(O−CH_2)$_2$-NH_2); 4.63 (q, 1H for18H); 4.07 (m, 2H for N−CH_2-CH_2-(O−CH_2)$_2$-NH_2); 3.85 (m, 2H for N-(O−CH_2)$_2$-CH_2-CH_2−NH_2); 3.79(s, 3H for 12CH_3); 3.70 (t, J = 36 Hz, N-(CH_2)$_2$−O-CH_2-CH_2−O-(CH_2)$_2NH_2$); 3.62 (q, 2H for 8^1CH_2); 3.56 (s, 3H for $17^2CO_2CH_3$) ; 3.51 (m, 2H for N-(CH_2)$_2$−O-CH_2-CH_2−O-(CH_2)$_2NH_2$); 3.34 (s, 3H for 18 CH_3); 3.14 (s, 3H for 7CH_3); 2.80, 2.70, 2.40, and 1.99 (each m 1H, 2 × 17^1H and 2 × 17^2H); 1.95 (m, 2H for N-(O−CH_2)$_2$-CH_2−CH_2-NH_2); 1.86 (broad s, 2H for NH_2); 1.74 (d, J = 7.2 Hz, 3H for 18CH_3); 1.65 (t, J = 7.6 Hz, 3H for 8^2 CH_3); 0.059 and −0.146 (broad s, 1H for 2NH). EIMS (m/z): 709 (M + H). Elemental Anal. Calcd. for $C_{40}H_{48}N_6O_6$: C, 67.78; H, 6.83; N, 11.86. Found: C, 67.59; H, 6.60; N, 10.90.

4.6. Cyanine Dye (6). To a dry round bottomed flask containing IR-820 (342 mg, 0.402 mmol) stirring in anhydrous DMF was added 4-carboxythiophenol (186.2 mg, 1.20 mmol), and the mixture was stirred overnight under a nitrogen atmosphere. The crude reaction product obtained after the standard workup was purified over a silica column using a 5−25% DCM/MeOH solvent system, and a green liquid was collected. The liquid was concentrated by evaporation under vacuum and scratched to afford dark green crystals of **6** yield (270 mg, 80%). UV−vis λ_{max} (in MeOH) 835 nm ($\varepsilon = 1.96 \times 10^5$); ^{1}H NMR (400 MHz, 3 mg/1 mL MeOH, δ ppm) 8.87 (d, 2H, J = 14 Hz), 8.15 (d, 2H, J = 14 Hz), 8.79−7.99(m, 6H), 7.57−7.63 (m,4H), 7.44 (t, 2H, J = 7.2 Hz), 7.36 (d, 2H, J = 8.4 Hz), 6.40 (d, 2H, J = 14 Hz), 4.27 (t, 4H, J = 7.6 Hz), 2.85−2.92(m, 8H), 1.93−2.10 (m, 10 H), 1.77 (s, 12H). EIMS (m/z): 989.4 (M^+ + 2Na). HRMS: Calcd. for $C_{53}H_{56}N_2O_8S_3Na$: 967.3097. Found: 967.3127.

4.7. Conjugate 7. In a dry round bottomed flask containing cyanine dye **6** (121.62 mg, 0.1289 mmol), DMTMM (39.25 mg, 1.1 equiv) was stirred in 5 mL of anhydrous DMF under a nitrogen atmosphere for 2 h. *N*-Amino purpurinimide methyl ester **3** (80 mg, 0.1289 mg) was stirred in 5 mL of anhydrous DMF in a separate round bottomed flask and was added to the flask containing the cyanine dye after 2 h. The reaction was stirred overnight and was purified by a preparative silica TLC plate using a 20% MeOH/DCM solvent system. The desired band was collected and resuspended in 5% methanol dichloromethane. It was then filtered, and the solvents were concentrated. The residue was crystallized/precipitated as dark purple crystals; yield (40 mg, 32%). UV−vis λ_{max} (in MeOH): 361 nm ($\varepsilon = 3.9 \times 10^4$), 412 ($\varepsilon = 9.6 \times 10^4$), 544 ($\varepsilon = 1.7 \times 10^4$), 693 ($\varepsilon = 4.5 \times 10^4$), 837 ($\varepsilon = 1.5 \times 10^5$). ^{1}H NMR (400 MHz, 3 mg/1 mL MeOH, δ ppm) 9.72, 9.37, 8.81 (each s, 1H, for 5H, 10H and 20H); 8.78 (d, J = 2.4 Hz, 2H, cyanine dye F); 8.29 (d, J = 8 Hz, 2H, cyanine dye B); 8.09 (m, 6H, cyanine dye H and D); 7.81 (d, J = 8.8 Hz, 2H, cyanine dye G); 7.64 (t, J = 12 Hz, 4H, cyanine dye C); 7.51(t, J = 8 Hz, 2H, cyanine dye A); 6.50 (d, J = 16 Hz, 3H, cyanine dye E); 5.01 (m, 2H cyanine dye SO_3H), 4.91 (m, 1H for 17H); 4.35 (m, 4H for cyanine dye H and 1H for 18H); 3.80(br doublet, 4H, 2H for 3^1 CH_2 and 2H for 8^1CH_2); 3.75 (d, 7H, 4H for $17^2CO_2CH_3$ and 3H); 3.35 (H_2O peak and hidden 3H for 12CH_3 singlet peak); 3.335 and 3.225 (s, 4H, 3 for 7CH_3 and 1H); 2.90 (m, 5H for cyanine dye K and L); 2.50 (m, 2H, 17^2CH_3 within DMSO peak); 2.32 (m, 2H for 17^1CH_2); 2.06−1.52 (many multiplets, 41H, 12H for cyanine dye J and N, 3H for cyanine dye M, 9H for 3^2CH_3, 18^1CH_3 and 8^2CH_3, and 17 H). EIMS (m/z): 1520 (M − H). HRMS: Calcd. for $C_{87}H_{92}N_8O_{11}S_3$: 1520.6048. Found: 1520.6048.

4.8. Conjugate 8. In a dry round bottomed flask, cyanine dye **6** (92.4 mg, 0.098 mmol) and DMTMM (30 mg, 0.1078 mmol) were stirred in 5 mL of anhydrous DMF in a nitrogen atmosphere for 2 h. Diethlyeneaminopurpurinimide methyl ester **4** (70 mg, 0.098 mmol) was stirred in 5 mL of anhydrous DMF in a separate round bottomed flask and was added into the flask containing the cyanine dye after 2 h. The reaction was stirred overnight and was purified on a preparation scale TLC plate using a 20% MeOH/DCM solvent system. The desired fraction was collected, and the residue obtained after evaporating the solvent was crystallized/precipitated with DCM/hexane as dark purple crystals; yield (35 mg, 37%). UV−vis λ_{max} (in MeOH): 365 nm ($\varepsilon = 3.8 \times 10^4$), 418 nm ($\varepsilon = 8.2 \times 10^4$), 549 nm ($\varepsilon = 1.6 \times 10^4$), 707 nm ($\varepsilon = 4.6 \times 10^4$), 842 nm ($\varepsilon = 1.6 \times 10^5$). ^{1}H NMR (400 MHz, 3 mg/1 mL MeOH, δ 9.59, 9.42, and 8.86 (each s, 1H for 5H, 10H and 20H); 8.61 (d, 2H for cyanine dye f, J=14 Hz); 8.16 (dd, J = 8 Hz,40 Hz, 1H, 3^1CH═CH_2); 8.06 (d, 2H for cyanine dye B, J=8.4 Hz); 7.98−7.95 (m, 4H for cyanine dye H and D); 7.73−7.67(m, 4H for cyanine dye G and C); 7.47 (t, 2H for cyanine dye A, J = 7.2 Hz); 7.34 (d, 2H for cyanine dye E, J = 8.4 Hz); 6.38 (t, 3H, 2H for cyanine dye E, 1H for trans 3^2CH═CH_2, J = 14 Hz); 6.20 (d, 1H for cis 3^2CH═CH_2, J = 11.6); 5.12 (d, 1H for 17H, J = 1.2 Hz); 4.53−4.40(m, 3H, 1H for 18H and 2H for N−CH_2-CH_2−N); 4.24 (broad s, 3H for cyanine dye I); 3.81 (s, 3H for 12 CH_3); 3.69 (m, 1H for NH); 3.60 (s, 3H for $17^2CO_2CH_3$); 3.39−3.31 (m, 2H for 8^1CH_2, 3H for 2CH_3 and 2H for N−CH_2-CH_2-N, 8H for cyanine dye K and L); 3.13(s, 3H for 7 CH_3); 2.33−2.20 (each m, 1H for, 2 × 17^1H and 2 × 17^2H); 2.10−2.08 (each m, 8H for cyanine dye J and N); 1.925 (m, 3H for 18 CH_3); 1.74−1.52 (m, 15 H, 3H for 8^2CH_3 and 12 H for cyanine dye M); −0.35 and −0.41 (each br s, 1H for 2NH). EIMS (m/z): 1546 (M − H). HRMS Calcd. for $C_{89}H_{94}N_8O_{11}S_3$: 1546.6204. Found: 1546.6244.

4.9. Conjugate 9. In a dry round bottomed flask, cyanine dye **6** (142.7 mg, 0.151 mmol) and DMTMM (45.96 mg, 0.1661 mmol) were stirred in 5 mL of anhydrous DMF in a nitrogen atmosphere for 2 h. *N*-Glycolpurpurinimide methyl ester **5** (90 mg, 0.151 mmol) stirred in 5 mL of anhydrous DMF in a separate round bottomed flask was added to the flask containing the cyanine dye after 2 h. The reaction was stirred overnight and was purified on a preparation scale TLC plate using a 20% MeOH/DCM solvent system as discussed for the foregoing compound. The desired fraction was collected and concentrated, crystalized with DCM/hexane to afford dark purple crystals; yield (40 mg, 32%). UV−vis λ_{max} (in MeOH): 366 nm ($\varepsilon = 4.5 \times 10^4$), 416 nm ($\varepsilon = 1.0 \times 10^5$), 549 nm ($\varepsilon = 2.7 \times 10^4$), 707 nm ($\varepsilon = 5.8 \times 10^4$), 842 nm ($\varepsilon = 2.1 \times 10^5$). ^{1}H NMR (400 MHz, 3 mg/1 mL MeOH): δ 9.67,9.46 and 8.88 (each s, 1 H for 5H, 10H and 20H); 8.62 (d, 2H for cyanine dye f, J = 14 Hz); 8.10 (d, 4H, cyanine dye j, J = 11.6 Hz);7.85 (m, 4H, cyanine dye M); 7.79 (d, 2H for cyanine dye a, J = 7.2 Hz); 7.40 (d, 2H for cyanine dye b, J = 7.2 Hz); 6.39 (m, 3H, 1H for 3^1CH═CH_2 and 2H for cyanine dye e); 6.19 (d, 1 H

for $3^2CH{=}CH_2$, J = 7.6 Hz); 5.18 (m, 1H for *cis*-$3^2CH{=}CH_2$); 4.4 (m, 1H for 18H); 4.2 (m,1H for 17H); 3.75 (s,3H for 12 CH_3);3.51 (s, 3H for 2 CH_3); 3.30(s, 3H for $17^2CO_2CH_3$);3.15 (s, 3H for 7 CH_3); 2.80 (m, 8H for cyanine dye i and j); 2.60, 2.55, 2.40, and 2.36 (each m, 1H for, 2 × 17^1H and 2 × 17^2H); 1.90 (m, 5H for cyanine dye c and h); 1.63(s, 3H for 18 CH_3); 1.50 (t, 3H for 8^2CH_3, J=7.2 Hz); −0.35 and −0.41 (each br s, 1H for 2NH). EIMS (m/z): 1634 (M − H); HRMS Calcd. for $C_{93}H_{103}N_8O_{13}S_3$: 1634.6746. Found: 1634.6729.

4.10. *In Vivo* Fluorescence Imaging. Fluorescence imaging was performed using approved protocols in accordance with the Guide for the Use of Laboratory Animals. A 12 bit Nuance camera (CRI, Worburn, MA) was used to image the conjugates *in vivo* using a 782 continuous wave laser for an excitation source. The fluorescence was collected after filtering through two 600 nm long pass filters in series and 800 and 830 nm long pass filters. Prior to imaging, BALB/c mice bearing Colon26 tumors on the shoulder with an average diameter of 4−5 mm were shaved and depilated with Nair cream to remove the hair over the tumor and the surrounding skin. Conjugates **7**, **8**, and **9** were injected via the tail vein at 0.03 μmol/kg. At 24, 48, and 72 h postinjection, mice were anesthetized with ketamine/xylene (100/10 mg/kg), placed in the light box, and imaged. The localization and biodistribuition of the conjugates were determined by sacrificing 3 mice/time points and imaging the organs. The images were processed using an image calculator.[27]

4.11. *In Vivo* Photosensitizing Efficacy. BALB/c mice (5 mice/group) were implanted subcutaneously in the right shoulder with 1 × 10^6 Colon26 cells per 50 μL of RPMI-1640 medium. When tumors grew to 4−5 mm diameter, mice were injected with 2.5 μmol/kg of **8** and **9** via tail vein injection. Twenty-four hours postinjection, the mice were restrained within Plexiglas holders, and exposed tumors were treated with laser light for 135 J/cm^2 at 75mW/cm^2. Following treatment, tumor growth was monitored daily and measured with calipers along the length and width of the tumors. Tumor volumes were calculated by using the formula $V = LXW^2/2$. Mice were considered cured if no palpable tumor grew within 30 days of being treated, or they were euthanized when the tumor volume reached 400 mm^3.

4.12. Molecular Modeling. *4.12.1. Conjugate Structures.* The three-dimensional structures of purpurinimide−cyanine dye conjugates (**7**−**9**) were built with SYBYL molecular modeling software, version 8.0 (Tripos Inc., St. Louis, MO). The purpurinimide moiety was taken from previous studies[28] utilizing appropriate crystal structure. The cyanine dye moiety was built from a SYBYL fragment library and standard geometry using the extended conformation. Both moieties were fully energy optimized with a semiempirical molecular orbital method, PM3, using the Spartan 02 software (Wave function Inc., Irvine, CA). Finally, energy optimized moieties were joined with specific linkers with standard geometry using SYBYL software. Each conjugate as a whole was again energy optimized with PM3 using Spartan software.

4.12.2. Conjugate Conformations. The PM3 energy optimized structure for each conjugate was used as the initial conformation for limited conformational search to explore the conformational flexibility of these conjugates. Because of the size of molecules, molecular mechanics instead of the molecular orbital method was used for this study. The stochastic conformational search was performed using Molecular Operating Environment (MOE) software, version 2010.10, from Chemical Computing Group (Montreal, Quebec, Canada). Standard MMFFs force field and charges were used for the stochastic conformational search where the dihedral angles were randomly modified, followed by energy minimization in dihedral angles first, then energy minimization in Cartesian space. During the conformational search, the chiral centers were maintained as the original structure. No attempt was made to perform an exhaustive conformational search due to uncertainty in the environment of the conjugate in the cell or in an *in vivo* situation.

4.13. Photophysical Properties. Femtosecond transient absorption spectroscopy experiments were conducted using an ultrafast source, Integra-C (Quantronix Corp.), an optical parametric amplifier, TOPAS (Light Conversion Ltd.), and a commercially available optical detection system, Helios, provided by Ultrafast Systems, LLC. The source for the pump and probe pulses were derived from the fundamental output of Integra-C (780 nm, 2 mJ/pulse and fwhm = 130 fs) at a repetition rate of 1 kHz. Seventy-five percent of the fundamental output of the laser was introduced into TOPAS, which has optical frequency mixers resulting in a tunable range from 285 to 1660 nm, while the rest of the output was used for white light generation. Prior to generating the probe continuum, a variable neutral density filter was inserted in the path in order to generate a stable continuum, then the laser pulse was fed to a delay line that provides an experimental time window of 3.2 ns with a maximum step resolution of 7 fs. In our experiments, a wavelength between 350 to 450 nm of TOPAS output, which is the fourth harmonic of signal or idler pulses, was chosen as the pump beam. As this TOPAS output consists of not only desirable wavelength but also unnecessary wavelengths, the latter were deviated using a wedge prism with a wedge angle of 18°. The desirable beam was irradiated at the sample cell with a spot size of 1 mm diameter where it was merged with the white probe pulse in a close angle (<10°). The probe beam after passing through the 2 mm sample cell was focused on a fiber optic cable, which was connected to a CCD spectrograph for recording the time-resolved spectra (410−1600 nm). Typically, 2500 excitation pulses were averaged for 5 s to obtain the transient spectrum at a set delay time. Kinetic traces at appropriate wavelengths were assembled from the time-resolved spectral data. All measurements were conducted at room temperature, 295 K.

The fluorescence measurements were carried out with an absolute PL quantum yield measurement system (Hamamatsu photonics Co., Ltd., C9920-02) with excitation at 680 nm.

4.14. Electrochemical Measurements. Cyclic voltammetry was carried out with an EG&G Model 173 potentiostat/galvanostat. A homemade three-electrode cell was used and consisted of a glassy carbon working electrode, a platinum wire counter electrode, and a saturated calomel reference electrode (SCE). The SCE was separated from the bulk of the solution by a fritted-glass bridge of low porosity which contained the solvent/supporting electrolyte mixture. All potentials are referenced to the SCE.

UV−visible spectroelectrochemical experiments were performed with an optically transparent platinum thin-layer electrode of the type described in the literature.[29] Potentials were applied with an EG&G Model 173 potentiostat/galvanostat. Time-resolved UV−visible spectra were recorded with a Hewlett-Packard Model 8453 diode array rapid scanning spectrophotometer.

Tetra-*n*-butylammonium perchlorate (TBAP, ≥ 99%) was recrystallized from ethyl alcohol and dried under vacuum at 40 °C for at least one week prior to use. Dimethylsulfoxide (DMSO, ≥ 99.9%) were obtained from Sigma-Aldrich Chemical Co. and used without further purification.

■ ASSOCIATED CONTENT

Ⓢ Supporting Information

The NMR/Mass spectra of compounds **3**−**9**, the HPLC profiles of conjugates **7**−**9**, and the experimental details of MTT assay and in vivo reflectance spectroscopy. This material is available free of charge via the Internet at http://pubs.acs.org.

■ AUTHOR INFORMATION

Corresponding Author

*E-mail: ravindra.pandey@roswellpark.org.

■ ACKNOWLEDGMENTS

This research was supported by Grants-in-Aid (Nos. 20108010 and 23750014) and the Global COE program "Global Education and Research Center for Bio-Environmental Chemistry" of Osaka University from the Ministry of Education, Culture, Sports, Science and Technology, Japan and KOSEF/MEST through WCU project (R31-2008-000-10010-0) from Korea to S.F. and The Robert Welch Foundation (Grant E-680) to K.M.K. and CA 127369 (NIH) to R.K.P.

■ REFERENCES

(1) Dougherty, T. J. (1996) A brief history of clinical photodynamic therapy development at Roswell Park Cancer Institute. *J. Clin. Laser Med. Surg. 14*, 219−221.

(2) Pandey, R. K., Goswami, L. N., Chen, Y., Gryshuk, A., Missert, J. R., Oseroff, A, and Dougherty, T. J. (2006) Nature: A rich source for developing multifunctional agents. Tumor-imaging and photodynamic therapy. *Lasers Surg. Med. 38*, 445−467.

(3) Celli, J. P., Bryan, Q., Spring, B. Q., Rizvi, I., Evans, C. L., Samkoe, K. S., Verma, S., Pogue, B. W, and Hasan, T. (2010) Imaging and photodynamic therapy: mechanisms, monitoring, and optimization. *Chem. Rev. 110*, 2795−2838.

(4) Ethirajan, M., Saenz, C., Dobhal, M., and Pandey, R. K. (2008) The Role of Porphyrin Chemistry in Tumor Imaging and Photodynamic Therapy, in *Advances in Photodynamic Therapy* (Hamblin, M. R., and Mroz, P., Eds.) Artech House, Boston, MA.

(5) Ethirajan, M., Chen, Y., Joshi, P, and Pandey, R. K. (2011) The role of porphyrin chemistry in tumor imaging and photodynamic therapy. *Chem. Soc. Rev. 40*, 340−362.

(6) Dougherty, T. J., Gomer, C. J., Henderson, B. W., Jori, G., Kessel, D., Korbelik, M., Moan, J, and Peng, Q. (1998) Photodynamic therapy. *J. Natl. Cancer Inst. 90*, 889−905.

(7) Henderson, B. W., and Dougherty, T. J. (1992) How does photodynamic therapy work? *Photochem. Photobiol. 55*, 145−157.

(8) Macdonald, I., and Dougherty, T. J. (2001) Basic principles of photodynamic therapy. *J. Porphyrins Phthalocyanines 5* (105), 2001−2011.

(9) Gryshuk, A., Chen, Y., Goswami, L, N., Pandey, S., Missert, J. R., Ohulchanskyy, T., Potter, W., Prasad, P. N., Oseroff, A, and Pandey, R. K. (2007) Structure-Activity relationship among purpurinimides and bacteriopurpurinimides: Trifluoromethyl substituent enhanced the photosensitizing efficacy. *J. Med. Chem. 50*, 1754−1767.

(10) Chen, Y., Gryshuk, A., Achilefu, S., Ohulchansky, T., Potter, W., Zhong, T., Morgan, J., Chance, B., Prasad, P. N., Henderson, B. W., Oseroff, A, and Pandey, R. K. (2005) A novel approach to a bifunctional photosensitizer for tumor imaging and phototherapy. *Bioconjugate Chem. 16*, 1264−1274.

(11) Massound, T. F, and Gambhir, S. S. (2003) Molecular imaging in living subjects: seeing fundamental biological process in a new light. *Genes Dev. 17*, 545−580.

(12) Brindle, K. (2008) New approaches for imaging tumor responses to treatment. *Nat. Rev. Cancer 8*, 94−107.

(13) Pandey, R. K., James, N., Chen, Y, and Dobhal, M, P. (2008) Cyanine dye based compounds for tumor imaging with and without photodynamic therapy. *Top. Heterocycl. Chem. 14*, 41−74.

(14) Jager, H. R., Taylor, M. N., Theodossy, T, and Hopper, C. (2005) MR imaging-guided interstitial photodynamic laser therapy for advanced head and neck tumors. *Am. J. Neuroradiol. 26*, 1193−1200.

(15) Mishra, A., Behera, R. K., Behera, P. K., Mishra, B. K, and Behera, G. B. (2000) Cyanines during the 1990s: A review. *Chem. Rev. 100*, 1973−2012.

(16) Ornelas, C., Lodescar, R., Durandin, A., Canary, J. W., Pennell, R., Liebes, L. F, and Weck, M. (2011) Combining aminocyanine dyes with polyamide dendrons: A promising strategy for imaging in the near-infrared Region. *Chem.—Eur. J. 17*, 3619−3629.

(17) Narayanan, N, and Patonay, G. (1995) A new method for the synthesis of Heptamethine cyanine dyes: Synthesis of a new near-infrared fluorescent labels. *J. Org. Chem. 60*, 2391−2395.

(18) Majumdar, S. R, Majumdar, R. B., Grant, C. M, and Waggoner, A. S (1996) Cyanine-labeling reagents: sulfobenzindocyanine succinimidyl esters. *Bioconjugate Chem. 7*, 356−362.

(19) Strekowksi, L., Mason, C. J., Lee, H., Gupta, R., Sowell, J, and Patonay, G. (2003) Synthesis of water-soluble near infrared cyanine dyes functionalized with 9 succiniimdioxyl- carbonyl group. *J. Heterocycl. Chem. 40*, 913−916.

(20) Zheng, G., Potter, R. W., Camacho, S. H., Missert, J. R., Wang, G., Bellnier, D. A., Henderson, B. W., Rodgers, M. A., Dougherty, T. J, and Pandey, R. K. (2001) Synthesis, photophysical properties, tumor uptake, and preliminary in vivo photosensitizing efficacy of a homologous series of 3-(1′-Alkyloxy)ethyl-3-devinylpurpurin-18-N-alkylimides with variable lipophilicity. *J. Med. Chem. 44*, 1540−1559.

(21) Mironov, A. F., Grin, M. A., Tsiprovskiy, A. G., Kachala, V. V., Karmakova, T. A., Pltyutinskaya, A. D, and Yakubovskaya, R. I. (2003) New bacteriochlorin derivatives with a fused N-aminoimide ring. *J. Porphyrins Phthalocyanines 7*, 725−730.

(22) Pandey, S. K., Gryshuk, A. L., Sajjad, M., Zheng, X., Chen, Y., Abuzeid, M. M., Morgan, J., Charamisinau, I., Nabi, H. A., Oseroff, A, and Pandey, R. K. (2005) Multimodality agents for tumor imaging and PDT: A possible see and treat approach. *J. Med. Chem. 48*, 6286−6295.

(23) Kawada, K., Yonei, T., Ueoka, H., Kiura, K., Tabata, M., Takigawa, N., Harada, M, and Tanimoto, M. (2002) Comparison of chemosensitivity tests. Clonogeneic assay versus MTT assay. *Acta Med. Okayama 56 3*, 129−134.

(24) Patterson, M. S., Schwartz, E., and Wilson, B. C. (1989) Quantitative reflectance spectrophotometry for the noninvasive measurement of photosensitizer concentration in tissue during photodynamic therapy. *SPIE 1065*, 115−122.

(25) Potter, W. R., Bellnier, D. A., Pandey, R., Parsons, J. R., and Dougherty, T. J. Sensitizer pharmacokinetics by in vivo reflection spectroscopy, unpublished results.

(26) Zeng, G., Chen, Y., Intes, X., Chance, B, and Glickson, J. D. (2004) Contrast-enhanced near IR optical imaging for subsurface cancer detection. *J. Porphyrins Pthalocyanines 8*, 1106−1117.

(27) http://rsb.info.nih.gov/ij/

(28) Pandey, S. K., Zheng, X., Morgan, J., Missert, J. R., Liu, T. H., Shibata, M, Bellnier, D. A., Oseroff, A. R., Henderson, B. W., Dougherty, T. J, and Pandey, R. K. (2007) Purpurinimide carbohydrate conjugates: effect of the position of the carbohydrate moiety in photosensitizing efficacy. *Mol. Pharm. 4*, 448−64.

(29) Lin, X. Q, and Kadish, K. M. (1985) Vacuum-tight thin-layer spectroelectrochemical cell with a doublet platinum gauze working electrode. *Anal. Chem. 57*, 1498−1501.

Supporting Information

Synthesis, Photophysical, Electrochemical, Tumor-Imaging and Phototherapeutic Properties of Purpurinimide-N-substituted Cyanine Dyes Joined with Variable Length of Linkers

Michael P.A. Williams[1], Manivannan Ethirajan[1], Kei Ohkubo[3], Ping Chen[4], Paula Pera[1], Janet Morgan[2], William H. White III[1], Masayuki Shibata[5,*], Shunichi Fukuzumi[3,6*], Karl M. Kadish[4,*] and Ravindra K. Pandey[1,*]

[1]PDT Center, Department of Cell Stress Biology, Roswell Park Cancer Institute, Buffalo NY, 14263, [2] Department of Dermatology, Roswell Park Cancer Institute, Buffalo NY 14263, [3]Department of Material and Life Sciences, Graduate School of Engineering, Osaka University, ALCA, Japan Science and Technology Agency (JST), Osaka, Japan, [4]Department of Chemistry, University of Houston, Houston, TX 77204-5003, [5]Department of Health Informatics, University of Medicine & Dentistry of New Jersey –SHRP, Newark, NJ 07107, [6]Department of Bioinspired Science, Ewha Womans University, Seoul 120-750, Korea

Contents

***In Vitro* Phototoxicity Assay (MTT Assay):** To determine the *in vitro* efficacy of the compounds the following procedure was performed. Colon-26 cells were grown in RPMI 1640 with 10% FCS, 2mM L-Glutamine, 50 IU penicillin/50 µg/ml streptomycin. Cells were maintained in 5 % CO_2 and 95% air at 100% humidity. For phototoxicity studies, Colon-26 cells were plated in 96 well plates at a density of 3500 cells/well in complete medium. 4 h later, compounds were added at concentrations ranging from 0.003 to 1 µM. After 24 h incubation in the dark at 37 °C, the cells were irradiated with laser light from an argon pumped dye laser using fluences of 0-2 J/cm^2 at a dose rate of 3.2 mW/cm^2 with light adjusted to the specific maximum wavelength of each drug. The light treatment is shown in Figure 13. After irradiation, the cells were incubated for 48h. After 48 h, 15 µL/well of 4 mg/ml 3-(4,5-dimethylthiazol-2-yl)-2,5-diphenyltetrazolium bromide MTT in PBS was added, and cells were incubated for a further 4 h. MTT is a yellow water soluble tetrazolium salt that is taken up by cells, reduced to water insoluble purple formazan crystals by metabolically active (viable) cells. The MTT-containing media was removed, and 100µl DMSO was added to solubilize the formazan crystals. The absorbance of the wells was read on a microtiter plate reader at a wavelength of 560 nm. The results were plotted as percent growth of control (untreated) cells *vs.* concentration range for each individual drug.

***In Vivo* Reflectance Spectroscopy:** *In vivo* reflectance spectroscopy is a non-invasive method of following the pharmacokinetics and measuring the concentration of a photosensitizer in an experimental animal. By measuring the light diffusely reflected from tissue containing the dye, the time at which the concentration is at its maximum can be determined and the light treatment can be delivered at the optimal tumor to normal tissue ratio, for the greatest selectivity. As described in reference 9, monochromatic light was delivered through a quartz fiber which was placed perpendicular to and touching the tissue. At a measured distance (3-5 mm) from the delivery fiber, a pick up fiber is also placed in contact with the tissue. Light is delivered at optical power levels of about 1µW to avoid any potential PDT effects during measurement. Light

$$C = \frac{1}{2 * \varepsilon}\left\{\left\{-\sqrt{{\mu_s}^2 + \frac{4}{3}{\alpha_0}^2} + \sqrt{{\mu_s}^2 + \frac{4}{3}\left(\frac{OD}{r} + {\alpha_0}^2\right)^2}\right\}\right. \qquad \text{Equation 1}$$

that enters the pickup fiber was conducted to a silicon photodiode detector that measured the photocurrent linear in power over 7-8 orders of magnitude. The wavelength was varied from 650-1000 nm and a spectrum of diffusely scattered photons was recorded. The concentration *C* was calculated using the formula in equation 1. Where ε is the molar extinction coefficient, α0 is the intrinsic tissue coefficient, OD is diffuse optical density, μ_3 is the reduced scattering coefficient, r is the distance from the detector to the pickup fiber. Molar extinction coefficient (ε) is measured using the Beer- Lambert law (A= ε lc).

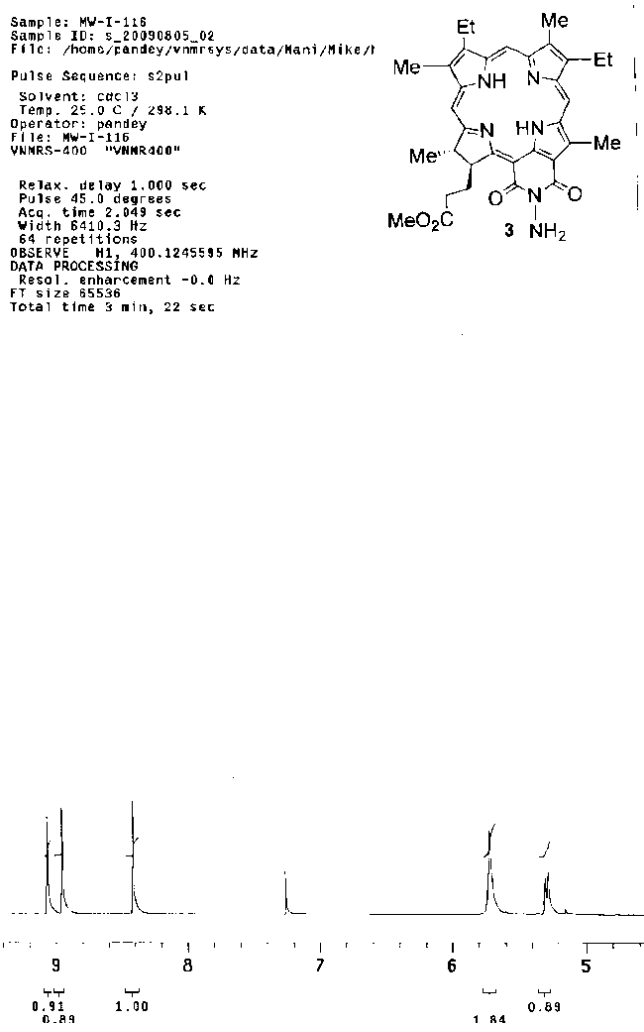
Sample: MW-I-116
Sample ID: s_20090805_02
File: /home/pandey/vnmrsys/data/Mani/Mike/1
Pulse Sequence: s2pul
Solvent: cdcl3
Temp. 25.0 C / 298.1 K
Operator: pandey
File: MW-I-116
VNMRS-400 "VNMR400"
Relax. delay 1.000 sec
Pulse 45.0 degrees
Acq. time 2.049 sec
Width 6410.3 Hz
64 repetitions
OBSERVE H1, 400.1245595 MHz
DATA PROCESSING
Resol. enhancement -0.6 Hz
FT size 65536
Total time 3 min, 22 sec
Et
Me
Me
Et
NH
N
N
HN
Me
Me
O
N
O
MeO2C
3
NH2
9
8
7
6
5
4
3
2
1
-0
ppm
0.91
1.00
0.89
1.84
0.89
0.95
5.27
2.65
3.22
2.15
3.64
4.61
2.12

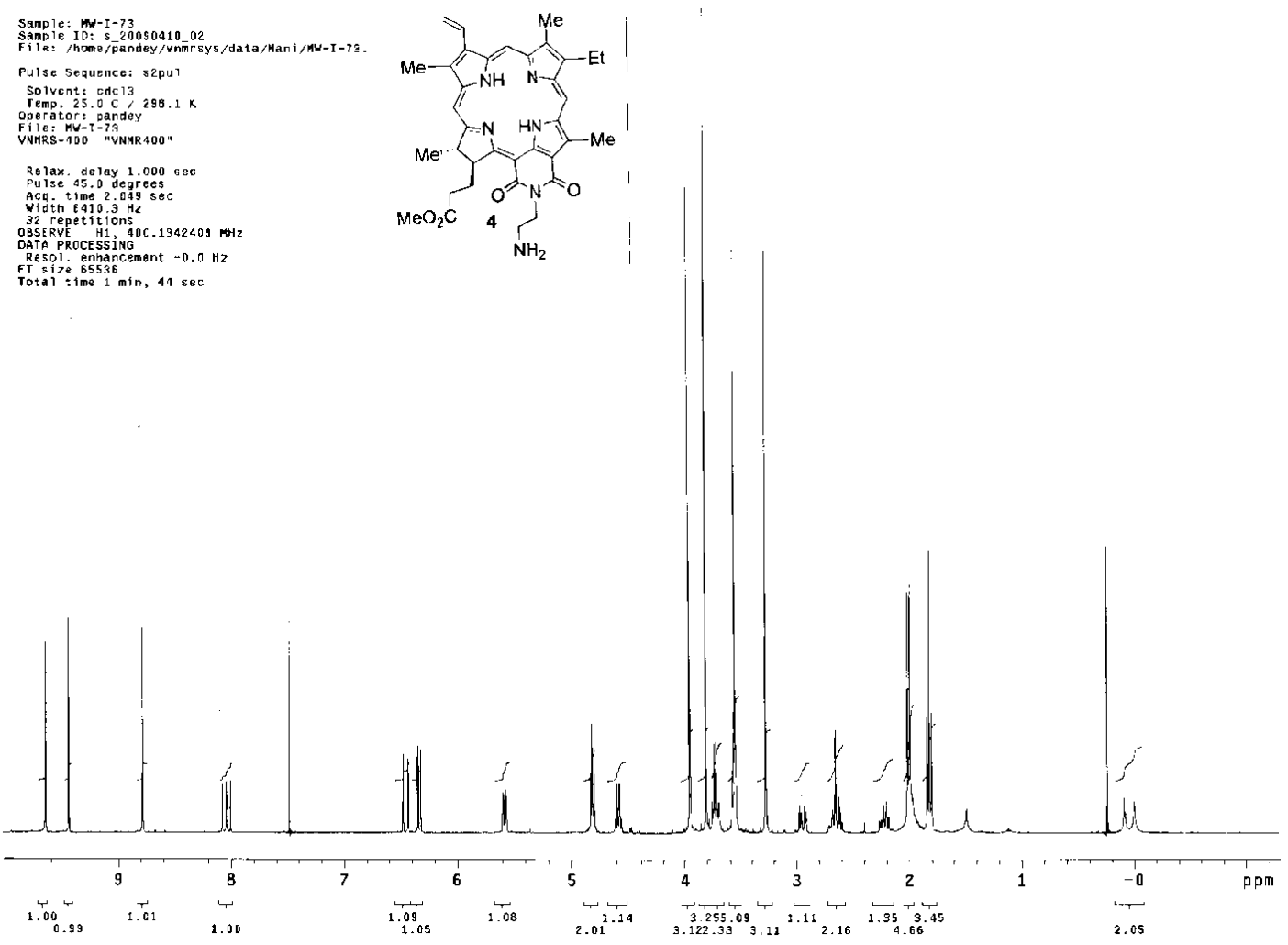
Sample: MW-I-73
Sample ID: s_20080410_02
File: /home/pandey/vnmrsys/data/Mani/MW-I-73.
Pulse Sequence: s2pul
Solvent: cdcl3
Temp. 25.0 C / 298.1 K
Operator: pandey
File: MW-I-73
VNMRS-400 "VNMR400"
Relax. delay 1.000 sec
Pulse 45.0 degrees
Acq. time 2.049 sec
Width 8410.3 Hz
32 repetitions
OBSERVE H1, 400.1942409 MHz
DATA PROCESSING
Resol. enhancement -0.0 Hz
FT size 65536
Total time 1 min, 44 sec
Me
Et
Me
NH
N
N
HN
Me
Me
O
O
N
MeO2C
4
NH2
9
8
7
6
5
4
3
2
1
-0
ppm
1.00
0.99
1.01
1.00
1.09
1.05
1.08
1.14
2.01
3.25
5.09
3.12
2.33
3.11
1.11
2.16
1.35
3.45
4.66
2.05

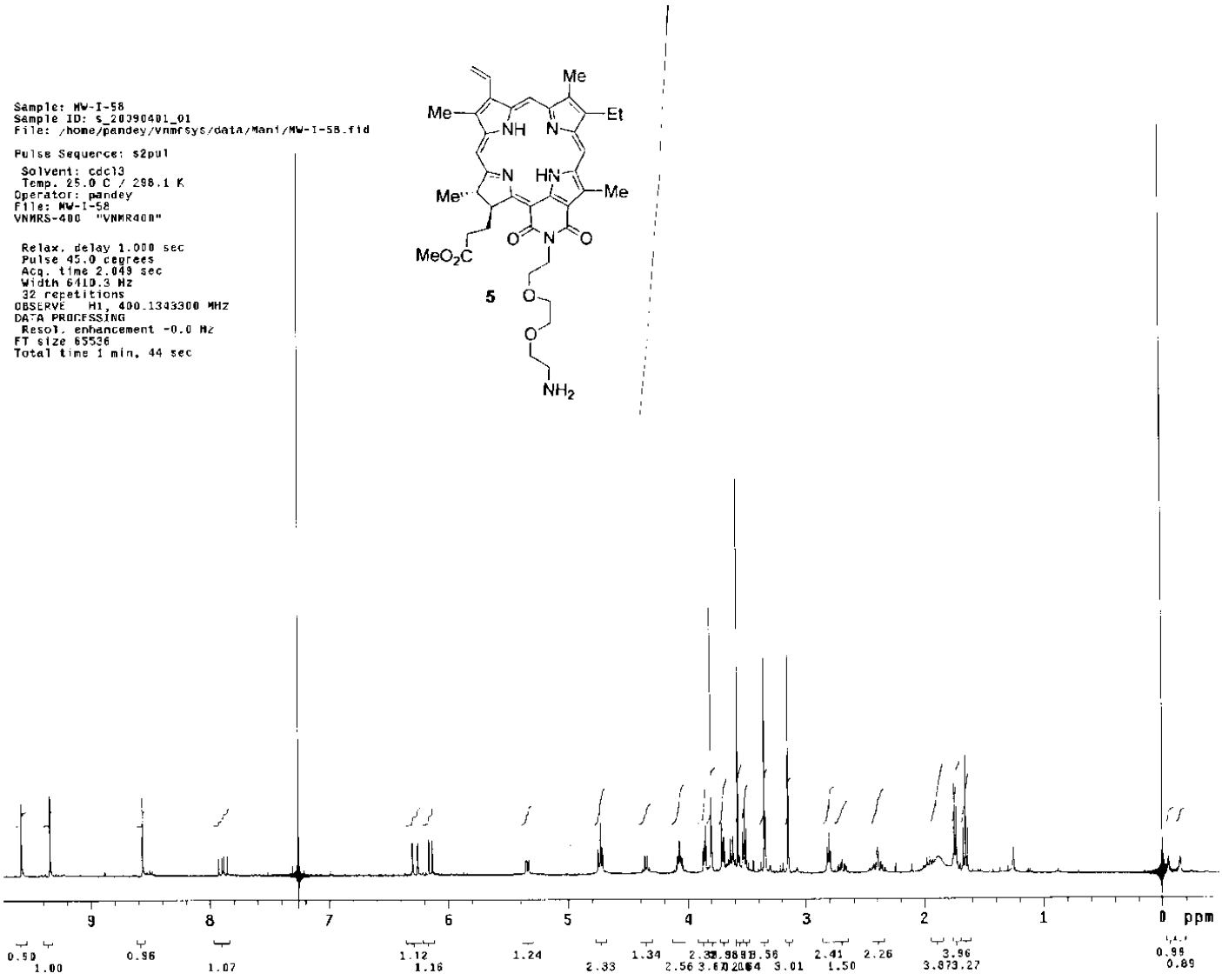
Sample: MW-I-58
Sample ID: s_20090401_01
File: /home/pandey/Vnmrsys/data/Mani/MW-I-58.fid
Pulse Sequence: s2pul
Solvent: cdcl3
Temp. 25.0 C / 298.1 K
Operator: pandey
File: MW-I-58
VNMRS-400 "VNMR400"
Relax. delay 1.000 sec
Pulse 45.0 degrees
Acq. time 2.049 sec
Width 6410.3 Hz
32 repetitions
OBSERVE H1, 400.1343300 MHz
DATA PROCESSING
Resol. enhancement -0.0 Hz
FT size 65536
Total time 1 min, 44 sec
Me
Et
NH
N
HN
Me
Me
MeO2C
O
N
O
5
O
O
NH2
9
8
7
6
5
4
3
2
1
0 ppm
0.50
1.00
0.96
1.07
1.12
1.16
1.24
2.33
1.34
2.56
3.01
2.41
1.50
2.26
3.96
3.87
3.27
0.99
0.89

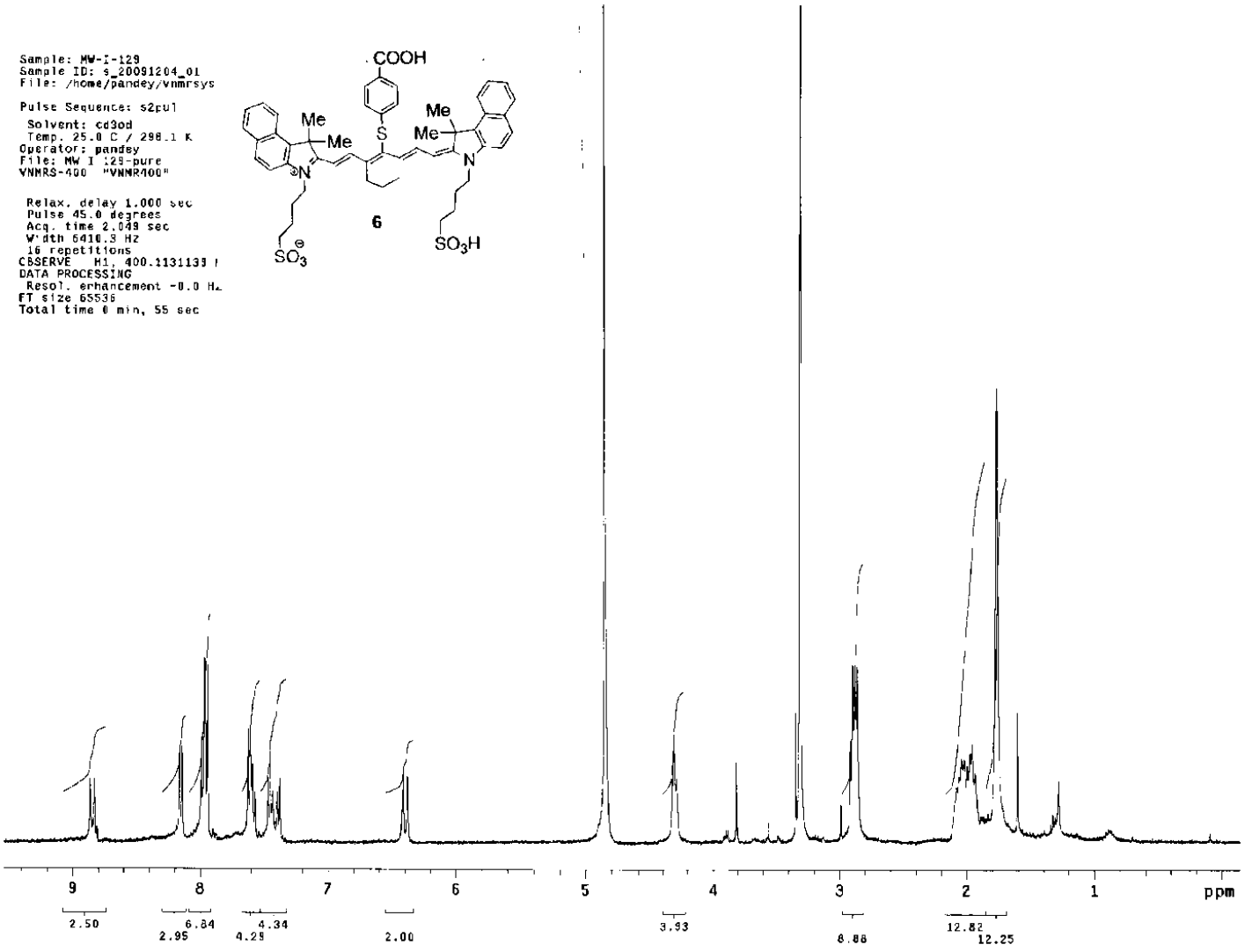
Sample: MW-I-129
Sample ID: s_20091204_01
File: /home/pandey/vnmrsys
Pulse Sequence: s2pul
Solvent: cd3od
Temp. 25.0 C / 298.1 K
Operator: pandey
File: MW I 129-pure
VNMRS-400 "VNMR400"
Relax. delay 1.000 sec
Pulse 45.0 degrees
Acq. time 2.049 sec
Width 5410.3 Hz
16 repetitions
OBSERVE H1, 400.1131133 I
DATA PROCESSING
Resol. enhancement -0.0 Hz
FT size 65536
Total time 0 min, 55 sec
COOH
Me
Me
S
Me
Me
N
N
SO3
SO3H
6
9
8
7
6
5
4
3
2
1
ppm
2.50
2.95
6.84
4.29
4.34
2.00
3.93
8.88
12.82
12.25

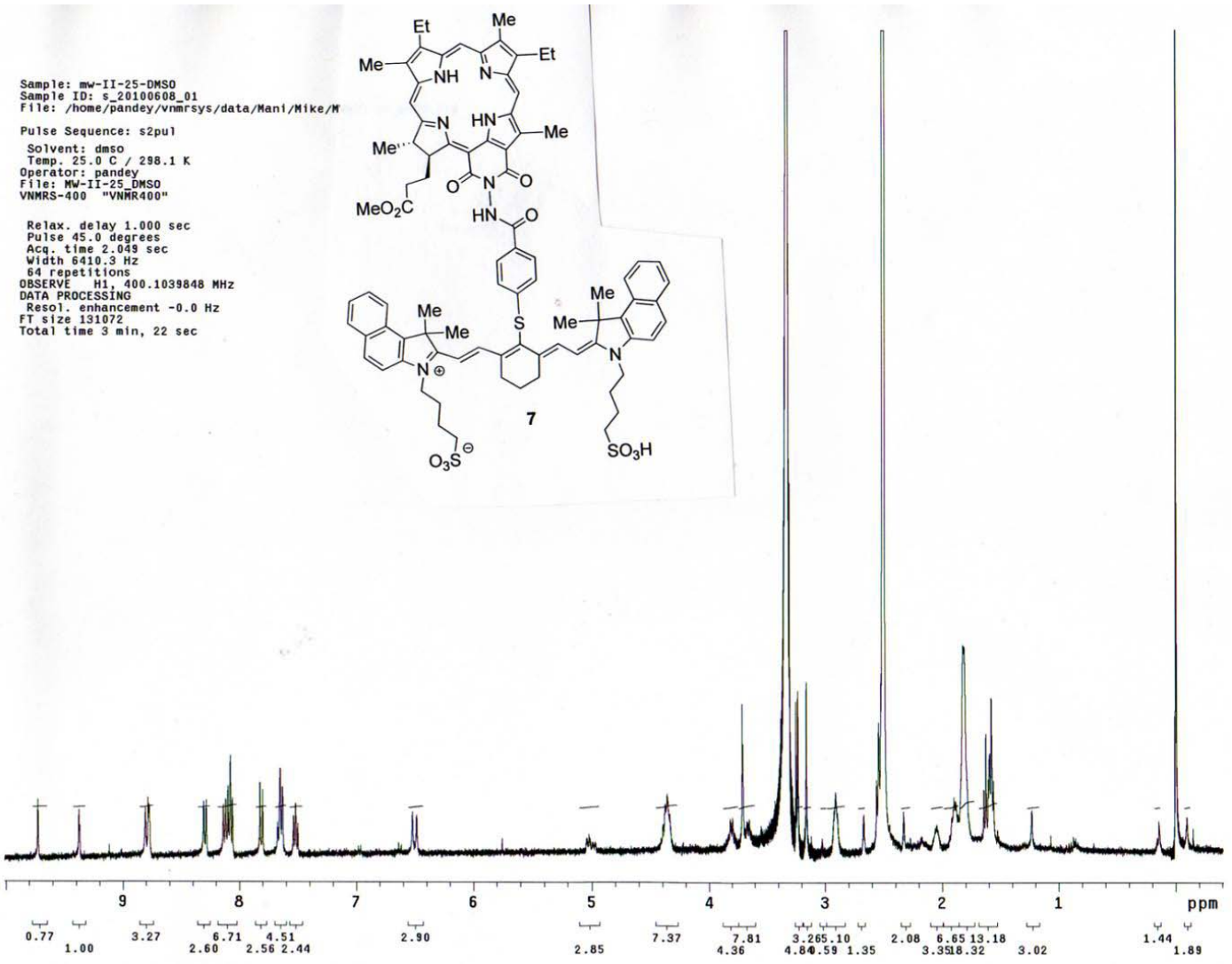
Sample: mw-II-25-DMSO
Sample ID: s_20100608_01
File: /home/pandey/vnmrsys/data/Mani/Mike/M
Pulse Sequence: s2pul
Solvent: dmso
Temp. 25.0 C / 298.1 K
Operator: pandey
File: MW-II-25_DMSO
VNMRS-400 "VNMR400"
Relax. delay 1.000 sec
Pulse 45.0 degrees
Acq. time 2.049 sec
Width 6410.3 Hz
64 repetitions
OBSERVE H1, 400.1039848 MHz
DATA PROCESSING
Resol. enhancement -0.0 Hz
FT size 131072
Total time 3 min, 22 sec
7
ppm
0.77
1.00
3.27
2.60
6.71
2.56
4.51
2.44
2.90
2.85
7.37
4.36
7.81
4.84
3.26
0.59
5.10
1.35
2.08
3.35
6.65
18.32
13.18
3.02
1.44
1.89

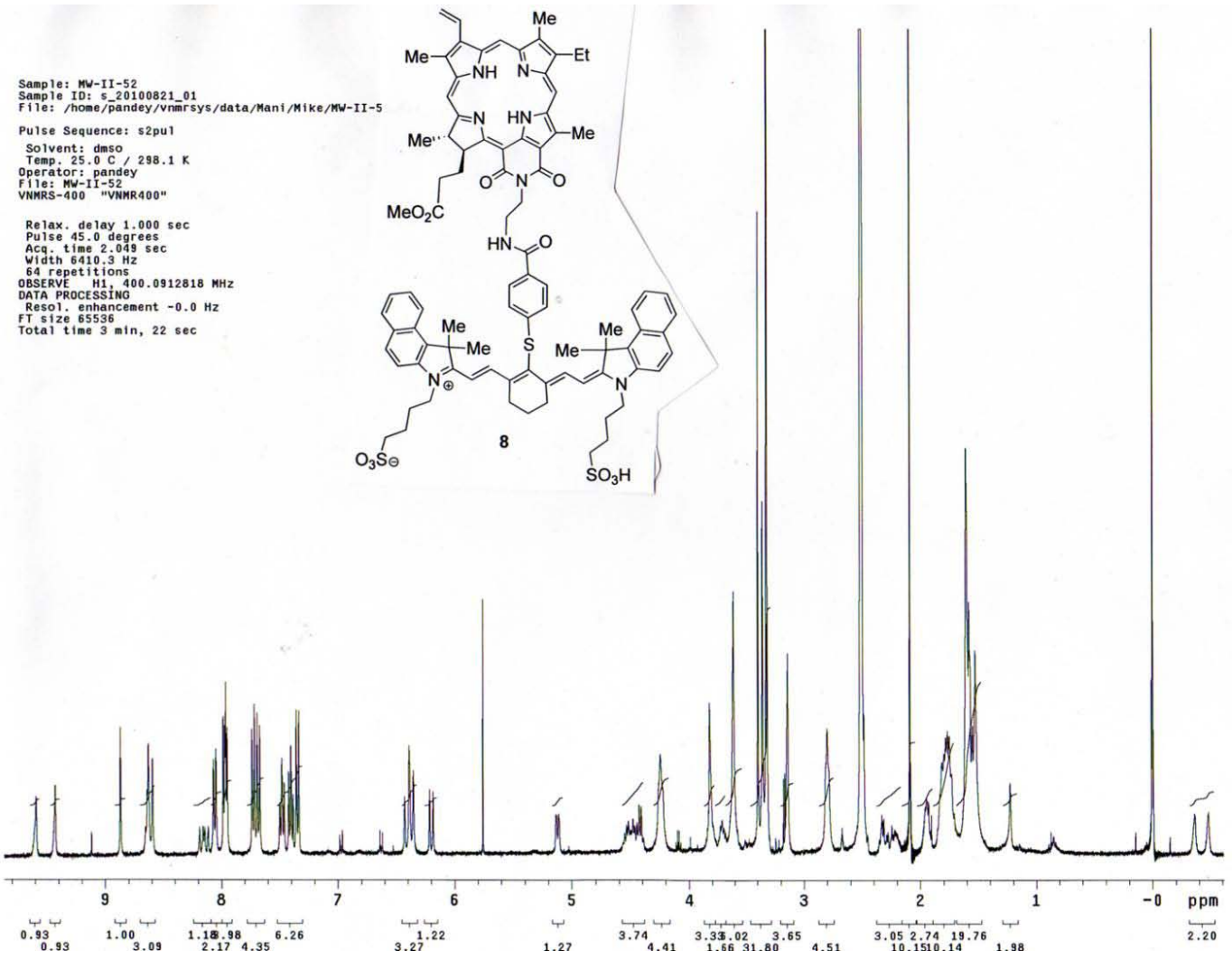
Sample: MW-II-52
Sample ID: s_20100821_01
File: /home/pandey/vnmrsys/data/Mani/Mike/MW-II-5
Pulse Sequence: s2pul
Solvent: dmso
Temp. 25.0 C / 298.1 K
Operator: pandey
File: MW-II-52
VNMRS-400 "VNMR400"
Relax. delay 1.000 sec
Pulse 45.0 degrees
Acq. time 2.049 sec
Width 6410.3 Hz
64 repetitions
OBSERVE H1, 400.0912818 MHz
DATA PROCESSING
Resol. enhancement -0.0 Hz
FT size 65536
Total time 3 min, 22 sec
8
ppm

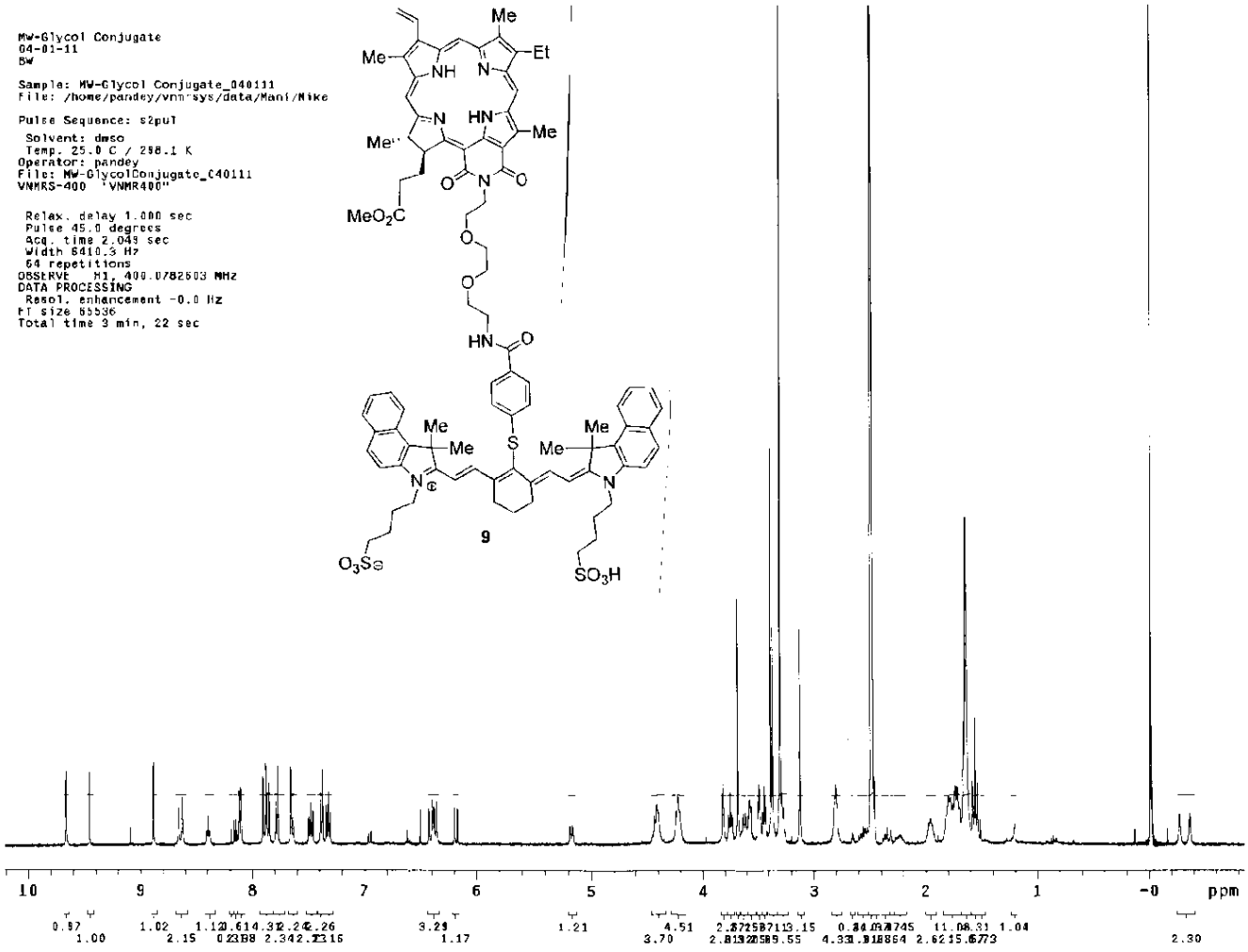
MW-Glycol Conjugate
04-01-11
SW
Sample: MW-Glycol Conjugate_040111
File: /home/pandey/vnmrsys/data/Mani/Mike
Pulse Sequence: s2pul
Solvent: dmso
Temp. 25.0 C / 298.1 K
Operator: pandey
File: MW-GlycolConjugate_C40111
VNMRS-400 "VNMR400"
Relax. delay 1.000 sec
Pulse 45.0 degrees
Acq. time 2.049 sec
Width 5410.3 Hz
64 repetitions
OBSERVE H1, 400.0782603 MHz
DATA PROCESSING
Resol. enhancement -0.0 Hz
FT size 65536
Total time 3 min, 22 sec
9
10
9
8
7
6
5
4
3
2
1
-0
ppm

HPLC Analysis

Method: HPLC analysis of conjugates # **7**, # **8**, and # **9** was carried out using a Waters Delta 600 System consisting of the 600 Controller, 600 Fluid Handling Unit and 996 Photodiode Array Detector equipped with a Waters Symmetry C18 column, 5 micron, with dimensions 4.6 x150mm. The mobile phase flow program was as follows: flow rate of 1.0 ml / min; mobile phase composition - 75% Methanol/ 25% water from 0 to 20 minutes , then a linear gradient to 100% Methanol from 20 minutes to 30 minutes, maintained at 100% Methanol from 30 minutes on.. Data collected and spectrally monitored from 300 nm to 799 nm. Percent purity of compounds based on 416 nm channel.

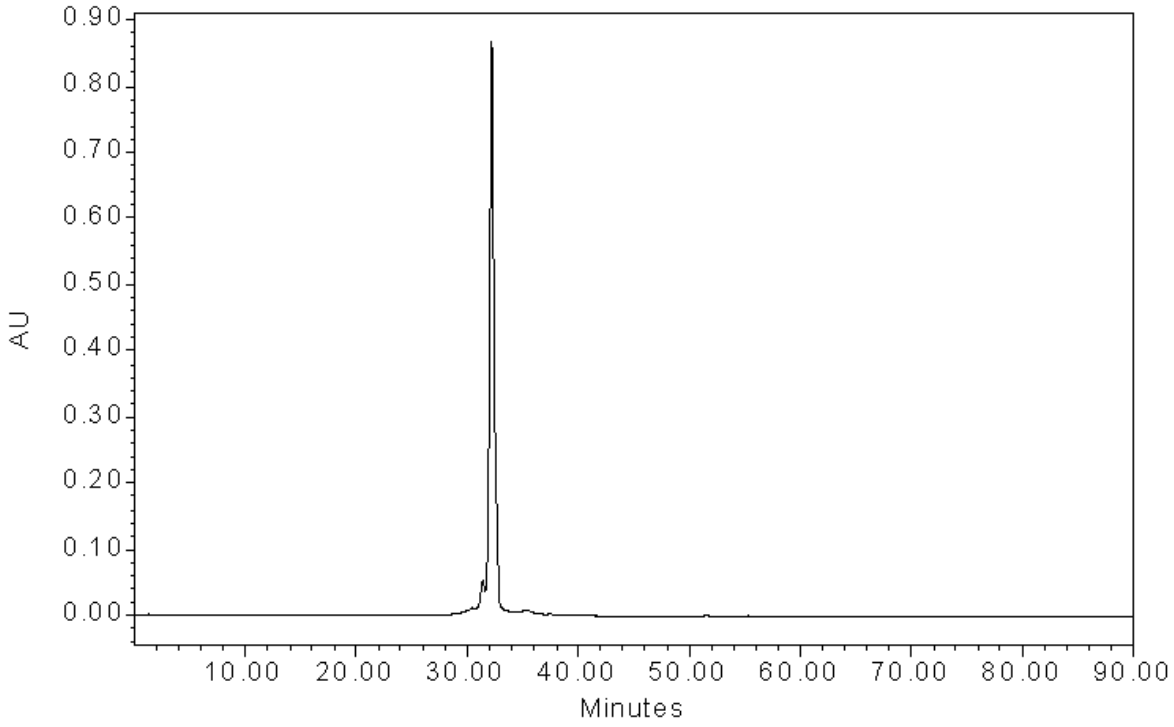

Figure S1: HPLC Chromatogram of Conjugate # **7**

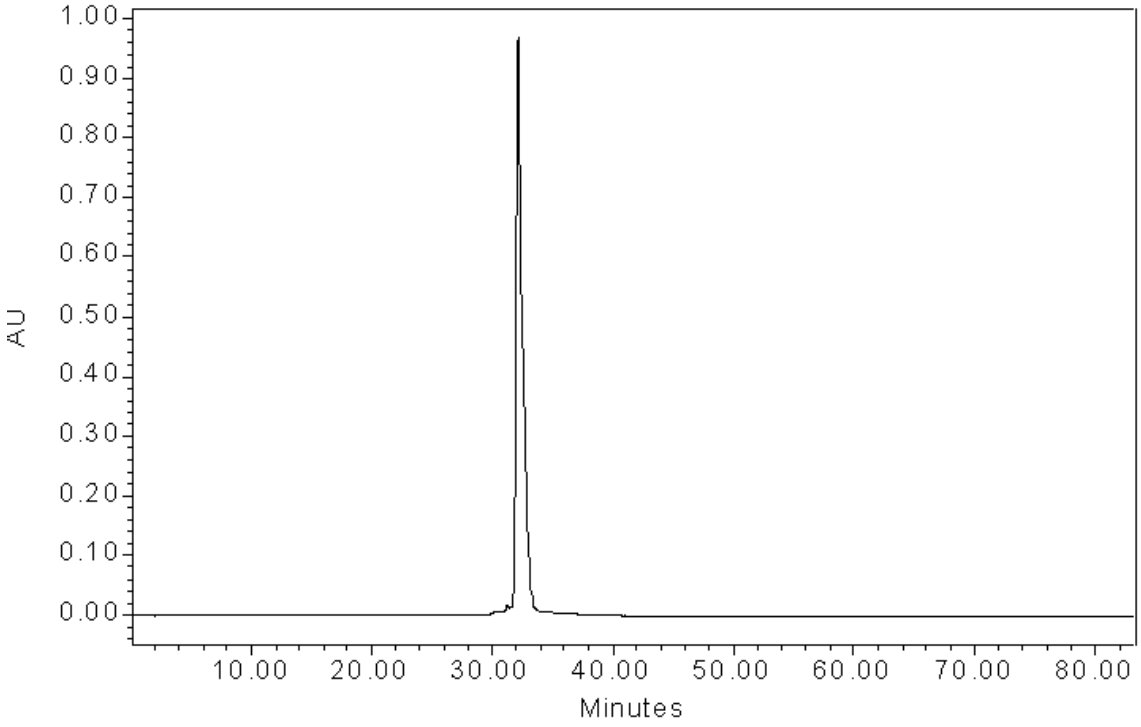

Figure S2: HPLC Chromatogram of Conjugate # **8**

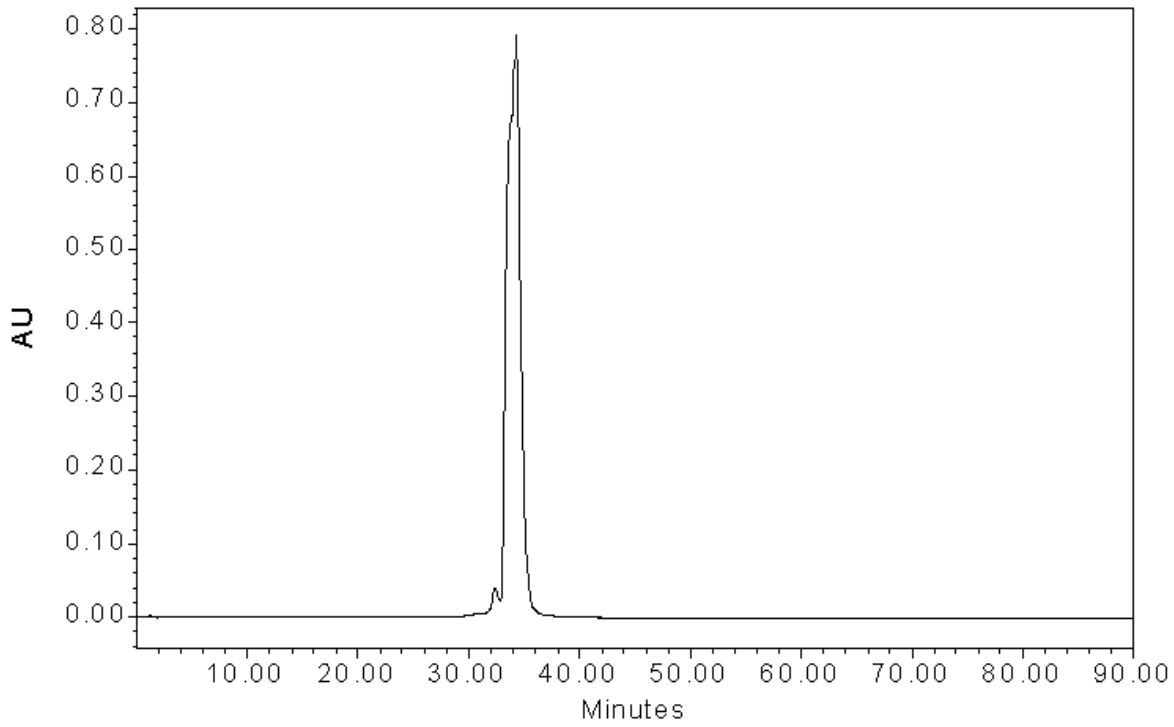

Figure S3: HPLC Chromatogram of Conjugate # **9**

Bioconjugate Chemistry

Article

pubs.acs.org/bc

Multiple Presentation of Scfv800E6 on Silica Nanospheres Enhances Targeting Efficiency Toward HER-2 Receptor in Breast Cancer Cells

Serena Mazzucchelli,[‡,§,†] Paolo Verderio,[§,†] Silvia Sommaruga,[‡,§] Miriam Colombo,[‡,§] Agnese Salvadè,[‡] Fabio Corsi,[‡] Patrizia Galeffi,[∥] Paolo Tortora,[§] and Davide Prosperi*[,§,⊥]

[‡]Dipartimento di Scienze Cliniche "Luigi Sacco", Università di Milano, Ospedale L. Sacco, Via G.B. Grassi 74, 20157 Milano, Italy

[§]Dipartimento di Biotecnologie e Bioscienze, Università di Milano-Bicocca, Piazza della Scienza 2, 20126 Milano, Italy

[∥]UTAGRI-GEN, ENEA, R. C. Casaccia, Via Anguillarese 301, 00123 Roma, Italy

[⊥]Istituto di Scienze e Tecnologie Molecolari, CNR, via Fantoli 16/15, 20138 Milano, Italy

Supporting Information

ABSTRACT: Spherical silica nanoparticles (SNP) have been synthesized and functionalized with anti-HER-2 scFv800E6 antibody by both localized histidine-tag recognition, leading to an oriented protein ligation, and glutaraldehyde cross-linking, exploiting a statistical reactivity of lysine amine groups in the primary sequence of the molecule. The targeting efficiency of nanocomplexes in comparison with free scFv was evaluated by flow cytometry using a HER-2 antigen-positive MCF-7 breast cancer cell line, exhibiting a 4-fold increase in scFv binding efficacy, close to the affinity of intact anti-HER-2 monoclonal antibody, which suggests the effectiveness of presenting multiple scFv molecules on nanoparticles in improving antigen recognition. Unexpectedly, the conjugation method did not affect the binding efficacy of scFv, suggesting a structural role of lysines in the scFv molecule. Confocal laser scanning microscopy confirmed the binding of nanocomplexes to HER-2 and also provided evidence of their localization at the cell surface.

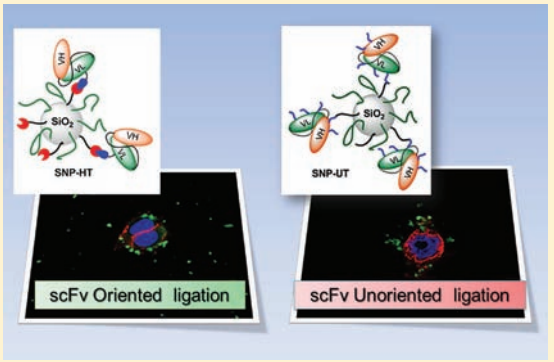

INTRODUCTION

Monoclonal antibodies (mAbs) are versatile and unique molecules that have found applications in the investigation, diagnosis, and treatment of many diseases, including cancer.[1] Although mAbs display high affinity and selectivity for the target, antibody-based therapies are often less effective toward solid tumors, because only a small amount of mAbs can indeed accumulate at the tumor tissue, due to their high immunogenicity and low penetration. Moreover, mAbs remain circulating for an extended time because their large size prevents excretion by renal clearance.[2] Recently, recombinant antibodies with modified properties have been designed in order to improve tissue penetration and biodistribution.[3] Among them, small antibody fragments consisting of the variable V_H and V_L regions connected through a synthetic loop, called single-chain fragment variable recombinant antibodies (scFv), hold great promise.[4] Target-specific scFvs are usually obtained through genetic engineering by phage display technology.[5] ScFv display has improved biodistribution compared to intact IgGs due to small size (typically in the 20−30 kDa range) and absence of a highly immunogenic stem. However, a poor retention time and a decreased affinity and specificity caused by their monovalent binding strongly limit their application in cancer immunotherapy. Hence, while immunogenicity is remarkably reduced and scFv clearance is accelerated, the binding efficacy is often reduced compared to their parent mAb resulting in a remarkably lower affinity for the receptor.

Multimerization has been recently envisaged as a strategy to enhance the functional affinity (avidity) of scFv increasing the k_a by 2−3 orders relative to the monovalent fragment.[6−8] Different multimerization strategies have been proposed to couple monovalent domains to produce multivalent antibodies, by chemical manipulation or using protein engineering approaches, including formation of diabodies, tribodies, tetrabodies, and minibodies.[9,10] Multimerized scFvs combine features from mAb and scFv that improve tumor penetration, as low immunogenicity and high affinity toward their receptor, and increase circulation time due to their large size, which prevents renal excretion.[10] So far, the conjugation of antibody fragments to nanoparticles has been seldom exploited. It has been observed that scFv having low affinity toward the epidermal growth factor receptor, when present in multiple copies on a liposome, allowed for tight receptor binding, thus filling the affinity gap between scFv and a high-affinity mutant obtained by molecular evolution.[11] However, functionalization

Received: July 4, 2011
Revised: October 14, 2011
Published: October 20, 2011

ACS Publications © 2011 American Chemical Society

of immunoliposomes does not offer a suitable control of number and orientation of the scFv ligand displayed on their surface. Such control of scFv presentation could be better optimized by using inorganic nanoparticles.[12−14] Here, we present a strategy to enhance scFv target binding efficacy that makes use of silica nanoparticles as a multimerization scaffold. As proof of concept, we chose scFv800E6 produced in *Pichia pastoris*, that recognizes the breast cancer membrane marker HER-2.[15] Among the numerous examples of inorganic nanoparticles available so far, silica nanoparticles have been extensively studied, due to their broad application and the ease of synthesis and stable functionalization with organic ligands.[16,17] In this work, we have explored synthesis and surface functionalization of silica nanoparticles (SNP) in order to immobilize scFv800E6 by two different approaches (Scheme 1): (1) the first method exploits a localized histidine tag recognition leading to an oriented ligation of scFv; (2) the second involves a reductive amination strategy *via* glutaraldehyde cross-linking on the nanoparticle exploiting a statistical reactivity of lysine amine groups on the primary sequence of the scFv molecule.

Scheme 1. Mechanism of "Oriented" and "Unoriented" Immobilization of scFv800E6 on Functionalized Silica Nanospheres[a]

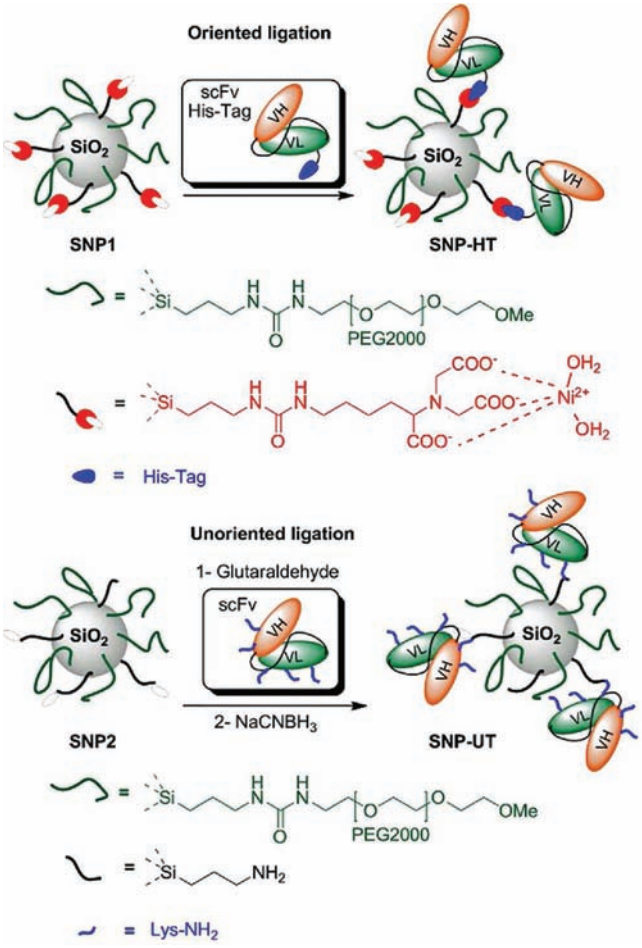

[a]Method 1: SNP1 functionalized with Ni-NTA groups tightly and specifically interact with scFv histidine tag leading to an oriented protein immobilization (SNP-HT). Method 2: the available amino groups of lysine residues of scFv bind to SNP2 via the aldehydic groups, which have been generated on the surface of nanoparticles by glutaraldehyde addition, resulting in a random ligation (SNP-UT).

EXPERIMENTAL PROCEDURES

Materials and Methods. All reagents and solvents were purchased from Sigma-Aldrich (St. Louis, MO), Fluka (St. Gallen, Switzerland), and Riedel-de Haën (Seelze, Germany) and used as received without further purification. Water was deionized and ultrafiltered by a Milli-Q apparatus (Millipore Corporation, Billerica, MA). Ultrasounds were generated by S15H Elmasonic Apparatus (Elma, Singen, Germany). TEM images of nanoparticles were obtained by a Zeiss EM-109 microscope (Oberkhochen, Germany) operating at 80 kV. Dynamic light scattering (DLS) measurements were performed at 90° with a 90 Plus Particle Size Analyzer from Brookhaven Instrument Corporation (Holtsville, NY) working at 15 mW of a solid-state laser (λ = 661 nm). Zeta-potential measurements were elaborated on the same instrument equipped with AQ-809 electrode and data were processed by *ZetaPlus* software. UV−vis spectra were recorded by using a Nanodrop 2000C spectrophotometer (Thermo Fisher Scientific, Wilmington, Germany) in a range of wavelengths from 190 to 600 nm.

Synthesis of SNP. Monodisperse silica nanospheres were obtained as described in previous work.[18] Briefly, a 25% NH_4OH solution in water (12.5 mL) and ethanol (250 mL) were mixed under magnetic stirring at 300 rpm. To the above solution was added a mixture of TEOS (6.25 mL, 28 mmol) dissolved in ethanol (7 mL) at a rate of 1 mL min^{-1} through a dropping funnel. The reaction was stirred for 20 h at room temperature (RT). At the end of the reaction, the solution became milky and the product was collected from the suspension by centrifugation at 8300 × *g* for 30 min. The white particulate was washed several times with ethanol (4 × 100 mL). Next, SNP (1.5 g) was dried under vacuum. SNP (100 mg) was redispersed in ethanol at a concentration of 4 mg mL^{-1} for further experiments.

Synthesis of Fully PEG-Coated SNP (SPEG). In a dried round-bottom flask, *O*-(2-aminoethyl)-*O*′-methylpolyethylene glycol 2000 (100 mg, 50 μmol) was dissolved in anhydrous CH_2Cl_2 (1 mL); subsequently, Et_3N (8 μL, 55 μmol) and (3-isocyanatopropyl)triethoxysilane (15 μL, 60 μmol) were added and the reaction run overnight at RT with magnetic stirring under argon atmosphere. When the reaction was completed, the solution was filtered and the clear filtrate was evaporated under reduced pressure. The resultant yellow pale oil was redissolved in a minimum amount of CH_2Cl_2 (300 μL), and cold Et_2O (10 mL) was added to precipitate the product as a white solid. The product was washed twice with Et_2O (10 mL) and finally dried under vacuum. APTS-PEG2000 (98 mg) was used immediately without further purification. The conjugation reaction was performed as follows.[18,19] A suspension of SNP in EtOH (20 mL, 1 mg mL^{-1}) was warmed at 60 °C; next, 25% NH_4OH (50 μL) and APTS-PEG2000 (20 mg, 10 μmol) were added and the resultant mixture was subjected to vigorous magnetic stirring at 60 °C overnight. The particulate was collected by centrifugation at 8300 × *g* for 15 min and washed with EtOH (2 × 10 mL) and water (10 mL). The resultant SPEG were redispersed in water (10 mL) for analyses.

Synthesis of SNP1. N^{α},N^{α}-Bis(carboxymethyl)-L-lysine (NTA) was synthesized according a previous work.[20] NTA (100 mg, 380 μmol) was suspended in anhydrous CH_2Cl_2 (8 mL) and THF (3 mL). Subsequently, Et_3N (211 μL, 1.52 mmol) and (3-isocyanatopropyl)triethoxysilane (113 μL, 456

dx.doi.org/10.1021/bc200352x | *Bioconjugate Chem.* 2011, 22, 2296−2303

μmol) were added and the reaction run overnight at RT with magnetic stirring under argon atmosphere. The resulting suspension was filtered, and the clear filtrate was evaporated under reduced pressure. The pale yellow oil was redissolved in a minimum amount of MeOH (500 mL) and cold Et_2O (10 mL) was added to precipitate the product as a white solid. The product was washed twice with Et_2O (10 mL) and finally dried under vacuum. APTS-NTA (132 mg) was used immediately without further purification.

For the conjugation reaction,[18,19] a suspension of SNP in EtOH/H_2O 1:1 (20 mL, 1 mg mL^{-1}) was warmed at 60 °C; 25% NH_4OH (50 μL), APTS-NTA (10 mg, 20 μmol), and APTS-PEG2000 (10 mg, 5 μmol) were added, and the mixture was left under vigorous stirring at 60 °C overnight. Next, the particulate was collected by centrifugation at 8300 × *g* for 15 min and washed with EtOH (2 × 10 mL) and water (10 mL). Nanoparticles were resuspended in water (20 mL) for further chelation with nickel ions. A green solution of 0.1 M $NiCl_2 \cdot 6H_2O$ in deionized water (2 mL) was added to the above suspension of nanoparticles; the pH was adjusted to pH 8.0 with 0.1 N NaOH, and the resultant mixture were kept under magnetic stirring for 30 min at RT. Then, particles were collected by centrifugation and the pale blue supernatant was discarded. The pale green particulate was washed thrice with water (10 mL) and, finally, SNP1 were resuspended in water (5 mL) and stored for further conjugation with His-tagged scFv800E6.

Synthesis of SNP2. The conjugation reaction[18,19] was performed as follows. A suspension of SNP in EtOH (20 mL, 1 mg mL^{-1}) was warmed at 60 °C; then, 25% NH_4OH (50 μL), APTS (5 μL, 20 μmol), and APTS-PEG2000 (10 mg, 5 μmol) were added and the resultant mixture was kept under vigorous magnetic stirring at 60 °C overnight. The particulate was collected by centrifugation at 8300 × *g* for 15 min and washed with EtOH (2 × 10 mL) and water (10 mL). The resultant SNP2 were stored in water (10 mL) for further conjugation with scFv.

Determination of Amine Groups on SNP2. Following a method described in the literature,[21] an aqueous mixture containing 1 M picrylsulfonic acid TNBS (10 μL) and 0.05 M $Na_2B_4O_7$ (1.5 mL) was added to a sample of aminated SNP2 (6 mg). The suspension was sonicated for 1 min and then heated at 70 °C for 10 min. At the end of reaction, the mixture was allowed to cool to RT; SNP2 was then separated from the supernatant by centrifugation at 11 200 × *g* and washed with water (1 mL), 50% acetone in water (1 mL), 100% acetone (1 mL), and water (2 × 1 mL). SNP2 was then suspended in NaOH 1 M (5 mL) and heated to 70 °C under vigorous stirring for 10 min. The suspension was cooled to RT and SNP2 were separated by centrifugation. An aliquot of the particle-free supernatant (1 mL) was then withdrawn and its absorbance read at 410 nm. Each particle contained silica (d = 2.2×10^6 g m^{-3}) with an average radius of 40 nm = 4.0×10^{-8} m. The average volume and mass of SiO_2 nanoparticles were 2.68×10^{-22} m^3 and 5.90×10^{-16} g, respectively. Hence, 1 mg of SiO_2 contained 1.02×10^{14} particles. By determination of residual absorbance due to picric acid released from reaction (Supporting Information Scheme S4), we established that 0.012 μmol of ligand APTS were immobilized on the particle surface corresponding to about 708 NH_2 groups/particle.

Dynamic Light Scattering and ζ-Potential Measurements. Viscosity and refractive index of deionized water were used to characterize the solvent. Nanoparticles were dispersed in water under sonication for several minutes before analyses; sporadically, to avoid the formation of large aggregates, the suspension was filtered through a 0.45 μm cellulose acetate filter. The final sample concentration used for measurements was typically 0.025 mg mL^{-1} (Figure S1). The same procedure was followed for hydrodynamic size distribution behavior of nanoparticles in deionized water by different Na^+ concentrations (1 mM to 20 mM) (Figure S2).

Strains and Plasmids. *P. pastoris* KM71H (*arg4; aox1::ARG4*) (Invitrogen) was used as host for expressing scFv800E6 gene. Plasmid pPICZαA (Invitrogen) was used for constructing plasmid vector, as previously described.[15]

Purification of scFv800E6. The clone KM71H-pPICZαA-scFv800E6-4 was grown in 10 mL YPD medium (1% yeast extract, 2% peptone, 2% dextrose) at 30 °C overnight with shaking at 250 rpm. The cultures were centrifuged at 1500 × *g* for 4 min, and then, the pellets were resuspended in 200 mL of BMMY (1% yeast extract, 2% peptone, 100 mM potassium phosphate pH 6.0, 1.34% YNB, 0.00004% biotin, 0.5% methanol) with 0.8% glycerol yielding an initial OD 600 value of 10. The culture was induced by daily addition of methanol to a final concentration of 0.5%. After 48 h of methanol treatment, the culture supernatant was filtered through 0.22 μm filters and dialyzed overnight in 50 mM sodium phosphate pH 8.0, 300 mM NaCl. The dialyzed medium was loaded at a flow rate of 0.5 mL/min onto a Ni-NTA Agarose (Qiagen) column (bed volume 0.5 mL) pre-equilibrated with 50 mM sodium phosphate pH 8.0, 300 mM NaCl, and 10 mM imidazole. The column was washed with 50 mM sodium phosphate pH 8.0, 300 mM NaCl, 20 mM imidazole, and the protein eluted with a stepwise imidazole gradient, 100 mM to 200 mM, in the same buffer. Fractions were collected and analyzed by SDS-PAGE. SDS-PAGE was performed according to Laemmli,[22] using 12% (v/v) polyacrylamide gels. The proteins were detected by Coomassie Brilliant Blue R-250 staining. Protein content was determined both by measuring absorbance at 280 nm and by using the Coomassie Plus Protein Assay Reagent (Termo Fisher Scientific) and bovine plasma immunoglobulin G as the standard protein.

Conjugation of His-tag scFv800E6 (SNP-HT). In a plastic tube, SNP1 (1 mg) were incubated with purified scFv800E6 (50 μg) in phosphate-buffered saline (PBS; EuroClone) in a final volume of 1000 μL and the mixture was stirred on an orbital shaker for 10 min at RT. SNP-HT were isolated from unreacted scFv800E6 by centrifugation at 11 200 × *g* for 5 min and the supernatant was discarded. Nanoparticles were washed three times with PBS (500 μL) and stored in PBS at 4 °C for further experiments. By measuring the absorbance at 280 nm, we determined an amount of scFv800E6 immobilized on nanoparticles of 26 μg per mg of SNP-HT.

Unoriented Conjugation of scFv800E6 (SNP-UT). Particle-glutaraldehyde cross-linking,[23] followed by imine reduction[24] with $NaCNBH_3$ were performed as follows. In a plastic tube, amino SNP2 (1 mg) was dispersed in borate buffer pH 7.6 (600 μL). A 5 mM glutaraldehyde solution in the same buffer (400 μL, 20 μmol) was added under stirring at RT. After 2 h, particles were isolated by centrifugation and washed once with borate buffer pH 7.6 (1 mL) and twice with PBS pH 7.4 (1 mL). At the end of the washing, nanoparticles were resuspended at a concentration of 1 mg mL^{-1} in the same buffer (1 mL) and the suspension cooled at 4 °C with an ice bath. scFv800E6 (50 μg in PBS) was added to the suspension

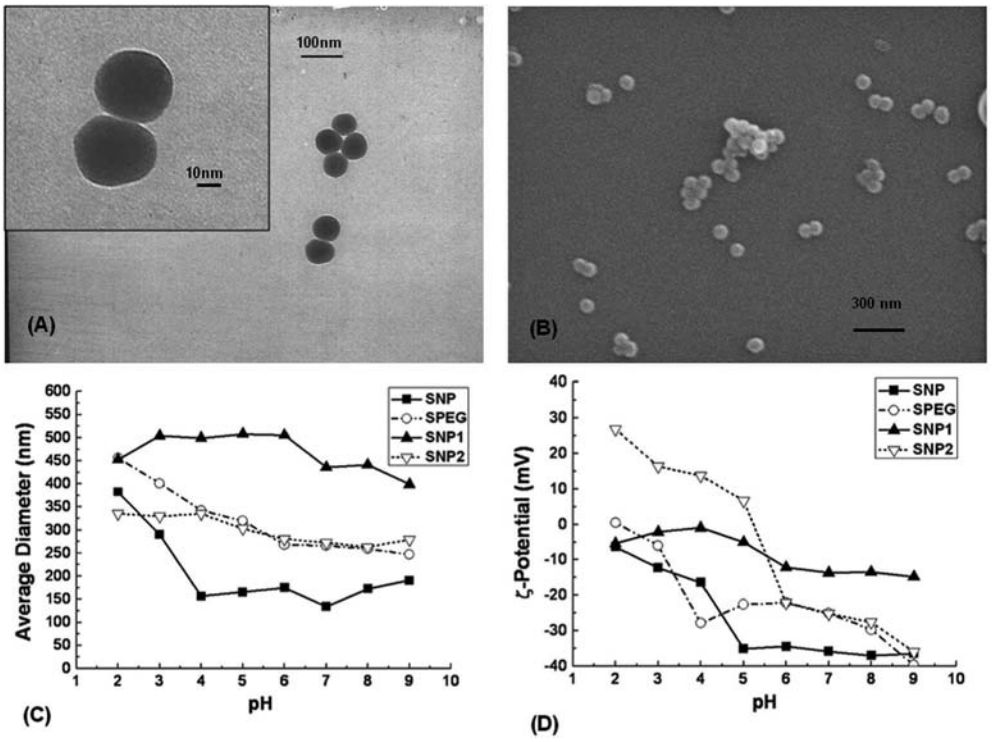

Figure 1. Characterization of modified silica nanoparticles: (A) TEM (Inset: magnification) and (B) SEM images of as-synthesized SNP. (C) DLS and (D) ζ-potential measurements of SNP, SPEG, SNP1, and SNP2 as a function of pH in aqueous solution.

and the resultant mixture was stirred on the orbital shaker for 3 h at 4 °C. ScFv-functionalized nanoparticles were recovered after centrifugation and washed twice with PBS (1 mL). Subsequently, a $NaBH_3CN$ solution (10 μL, 1 mg mL^{-1}) in PBS buffer pH 7.4 was added to the nanoparticle suspension in the same medium (1 mL) and incubated for 3 h at 4 °C. After centrifuging, SNP-UT were washed several times with PBS (3 × 1 mL) and finally were stored in the same buffer at 4 °C for further experiments. By measuring the absorbance at 280 nm, we determined an amount of scFv800E6 of 43 μg per mg of SNP-UT.

Dot Blot Assay. Dot blot was performed by filtering proteins and/or nanoparticles onto PVDF membranes, utilizing a Manifold I dot blot apparatus (GE Healthcare), and incubating in blocking solution (5% skim milk in PBS, Tween 0.05%) for 1 h at RT. The membrane was then probed for 1 h at RT in blocking solution using rabbit anti-Myc-HRP antibody (Invitrogen) at a 1:5000 dilution. Membranes were rinsed thrice in 0.05% Tween in PBS for 10 min. Immunoreactive spots were revealed using ECL Western blotting reagent (GE Healthcare).

Cell Cultures. MCF-7 and MDA cell lines were used as HER-2 positive and HER-2 negative targets, respectively. Cells were cultured in 50% Dulbecco's Modified Eagle's Medium (DMEM) and 50% F12, supplemented with 10% fetal bovine serum, L-glutamine (2 mM), penicillin (50 UI mL^{-1}), and streptomycin (50 mg mL^{-1}) at 37 °C and 5% CO_2 in a humidified atmosphere and subcultured prior to confluence using trypsin/EDTA. Cells culture medium and chemicals were purchased from EuroClone.

Flow Cytometry. Cells were cultured on a multiwell dish until subconfluence. Then, equal aliquots were incubated 15 min at 37 °C in the presence of one of the following: (i) 5 μg mL^{-1} scFv, (ii) 25.6 μg mL^{-1} TZ, (iii) SNP-HT, and (iv) SNP-UT. For each sample, 0.171 nmole of antibody, either free or immobilized on nanoparticles, was used. After incubation time, cells were washed twice with PBS and treated with typsin for 3 min. Digestion with trypsin was stopped with culture medium, cells were transferred in FACS tubes and washed twice with PBS. Then, cells were incubated for 30 min at 4 °C in blocking solution (PBS, 2% Bovine Serum Albumin) and immunodecorated with 1 μL of FITC-conjugated antibody to whole murine IgG (MP Biomedicals) for 30 min at 4 °C. The excess secondary antibody was removed by washing cells six times with PBS. Labeled cells were resuspended with 0.5 mL of PBS and analyzed on a FACS Calibur flow cytometer (Becton Dickinson). Ten thousand events were acquired for each analysis, after gating on viable cells, and isotype-control antibodies were used to set the appropriate gates.

Stability Assay of scFv Conjugation on SNP-HT. Five micrograms of scFv immobilized on SNP-HT was incubated at 37 °C with 0.1 mL of culture medium. After incubation time, SNP-HT was centrifuged 15 min at 15 000 × *g* at 4 °C, and supernatants (S1, S4, S24, and S48) were filtered onto a PVDF membrane utilizing a Manifold I dot blot apparatus (GE Healthcare). The membrane was incubated in blocking solution (5% skim milk in PBS, Tween 0.05%) for 1 h at RT, then probed 1 h at RT in blocking solution using rabbit anti-Myc-HRP antibody (Invitrogen) at a 1:5000 dilution. Membranes were rinsed thrice in 0.05% Tween in PBS for 10 min. Immunoreactive spots were revealed using ECL Western blotting reagent (GE Healthcare). Five micrograms of scFv immobilized on SNP-HT and 0.1 mL of culture medium were used, respectively, as positive and negative control.

Confocal Laser Scanning Microscopy. Cells were cultured on collagen (Sigma) precoated coverglass slides until subconfluence. Cells were incubated 1 h at 37 °C with 20 μg/mL of free-scFv800E6, and with equal amounts of scFv800E6

immobilized on SNP-HT and SNP-UT. Then, cells were washed with PBS, fixed for 10 min with 4% paraformaldehyde (Sigma), and treated for 10 min with 0.1 M glycine (Sigma) in PBS. A blocking step was performed for 1 h at RT with a solution containing 2% bovine serum albumin (Sigma) and 2% goat serum in PBS. ScFv was revealed by a FITC-conjugated antibody to whole murine IgG (MP Biomedicals) at a 1:300 dilution by incubating for 2 h at RT. Nuclei were stained with DAPI (4′,6-diamidino-2-phenylindole, Invitrogen) at 0.2 μg mL^{-1} in PBS with 0.1% Saponin (Sigma) for 20 min at RT. Membranes were stained with DiD oil (Invitrogen) at a 1:300 dilution by incubating 30 min at 37 °C. Microscopy analysis was performed with a Leica SP2 AOBs microscope confocal system. Images were acquired with 63× magnification oil immersion lenses at 1024 × 1024 pixel resolution.

RESULTS AND DISCUSSION

Uniform 60 nm spherical SNPs were synthesized by hydrolysis and condensation of tetraethyl orthosilicate (TEOS) in a 25% NH_4OH ethanolic solution.[18] In method 1, previously prepared APTS-PEG2000-OMe[25] and APTS-NTA in a 1:1 molar ratio were co-condensed on SNP in alkaline ethanol resulting in NTA-functionalized SNP1 (Schemes S1,2 in SI).[19] According to previous reports,[26] PEG chains enhanced the nanoconjugate solubility in buffered media and prevented nonspecific adsorption of proteins. ScFv800E6 protein containing a 6 × His-affinity tag was produced in *P. pastoris*, secreted in culture medium, and purified through affinity chromatography, as previously described.[15] Subsequent Ni^{2+} chelation by nitriloacetic acid groups of SNP1 promoted the active Ni^{2+}-NTA affinity-oriented immobilization of His-tagged scFv (SNP-HT) by incubation at room temperature. In method 2, APTS-PEG2000-OMe and APTS in a 1:1 molar ratio were co-condensed on SNP (Scheme S3 in SI).[23] Next, the covalent attachment of scFv was performed via glutaraldehyde cross-linking resulting in functional SNP2, stabilized by reduction of the diimine intermediate with $NaCNBH_3$,[27] to give SNP-UT. In Figure 1, TEM (A) and SEM (B) images show that the core size of SNP was 60 ± 5 nm indicating a homogeneous formulation of silica nanospheres. The hydrodynamic diameter of SNP in ethanol was 78.3 ± 2.2 nm, as determined by dynamic light scattering (DLS, Figure S1 in SI). The pH-dependent behavior of SNP, SNP1, SNP2, and fully PEG-coated nanosilica (SPEG) was investigated by DLS in the 2−9 pH range (Figure 1C). All the nanosilica tested did not exhibit the formation of critical aggregates between pH 4 and 9. Zeta potential (ζ) of SNP, SPEG, SNP1, and SNP2 in water in the 2−9 pH range was also investigated (Figure 1D). From pH 5 to 9, SNP were strongly negatively charged (−35.85 ± 0.64 mV), whereas at pH 4 and lower, the charge approached neutrality (−6.40 ± 1.77 mV). Similar behavior was also observed for SPEG, although they were only −25.01 ± 0.38 mV at pH 7 because of the charge-shielding effect of the PEG layer on the nanoparticle surface. In contrast, SNP1 exhibited a remarkably low surface charge at pH 7 (−13.64 ± 0.74 mV), in accordance with the presence of the Ni^{2+} chelates on the external carboxylic groups of NTA. This charge did not appreciably change in the pH range tested. SNP2 were negatively charged (−25.23 ± 1.03 mV) at pH 7−9. However, below pH 5, a gradual shift of the charge to positive values (+16.39 ± 1.35 mV at pH 3) was observed, in line with the presence of protonated amino groups of APTS in acidic conditions.

After conjugation, the amount of scFv800E6 on SNP-HT and SNP-UT was quantified by protein assay of supernatants at 280 nm using a calculated $\varepsilon_{280\ nm}$ of 55 600 M^{-1}. The immobilization of scFv on SNP-HT was also confirmed by dot-blot assay (Figure 2). SNP-HT (5 μg) and free scFv (0.5, 0.2, 0.1, and 0.05 μg) were filtered onto a polyvinylidene fluoride (PVDF) membrane and then probed with an anti-Myc-HRP antibody. Intensities of immunoreactive spots of SNP-HT and 0.1 μg of free scFv were comparable. This reasonably fits with the amount of bound scFv that we inferred from the determination of unbound protein, i.e., 0.125 μg.

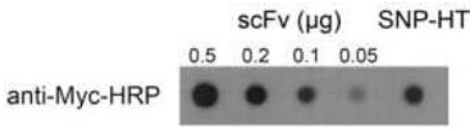

Figure 2. Dot-blot assay of SNP-HT conjugated with scFv. Different amounts of scFv800E6 (0.5, 0.2, 0.1, and 0.05 μg) and an aliquot of SNP-HT were filtered on a PVDF membrane, then probed with anti-Myc-HRP antibody and revealed with an ECL substrate.

To assess the effect of multivalent presentation of scFv on silica nanoparticles, SNP-HT and SNP-UT binding toward HER-2 receptor in breast cancer cells was evaluated by flow cytometry. Free scFv, the commercial anti-HER-2 mAb (trastuzumab, TZ), SNP-HT, and SNP-UT, containing equal amounts of conjugated scFv, were incubated 15 min with HER-2-positive MCF-7 cells.[28] Flow cytometry evidenced a right-shift of fluorescence signal accounting for an increase in scFv binding efficacy upon multimerization due to SNP conjugation (Figure 3). Values reported in Figure 3B show a 3-fold increase in mean fluorescence intensity of SNP-UT sample in comparison with free scFv at the same scFv concentration. Moreover, scFv multimerized on SNP *via* glutaraldehyde cross-linking (SNP-UT) exhibited a mean fluorescence intensity value very close to that of intact TZ, indicating that there was a significant improvement in receptor binding capability, which can be attributed to avidity effect. However, the conjugation strategy exploited for scFv multimerization on SNP surfaces (method 1 vs method 2) did not prove to be crucial in enhancing scFv binding efficiency. Indeed, SNP-HT and SNP-UT exhibited similar fluorescence intensities when assessed by flow cytometry. To account for this unexpected result, we inspected the localization of lysines in scFv sequence. Multiple sequence alignment of scFv800E6 with other scFv sequences available in the NCBI database revealed that all lysine residues are highly conserved. This clearly indicates that these residues are not directly involved in HER-2 binding. Instead, quite likely they only play a structural role. Therefore, an involvement of this residue in glutaraldehyde cross-linking is not expected to interfere significantly with HER-2 binding.

Moreover, to exclude the release of scFv from SNP-HT and assess the stability of this conjugation method, we have incubated SNP-HT for 1, 4, 24, and 48 h at 37 °C and 5% CO_2 atmosphere. Supernatants of incubation were then filtered on PVDF membrane and probed with an anti-Myc-HRP antibody. Release of scFv800E6 in cell culture medium was not observed under the conditions tested, confirming that scFv conjugation on SNP-HT was stable within 48 h of incubation at 37 °C (Figure 4).

To validate flow cytometry data, the specificity of binding between SNP-HT or SNP-UT and HER-2 was assessed by

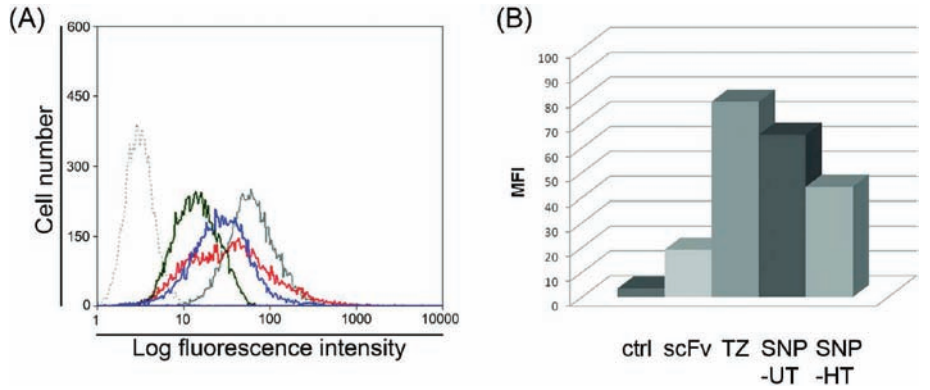

Figure 3. Multivalent presentation of scFv800E6 onto SNP-HT and SNP-UT enhances binding avidity toward HER-2 receptor. (A) MCF-7 cells were incubated with scFv (black), SNP-HT (blue), SNP-UT (red), or trastuzumab (TZ; gray continuous) and processed by flow cytometry. ScFv incubation with HER-2 cells as negative control (gray dashed line). (B) Mean fluorescence intensity (MFI).

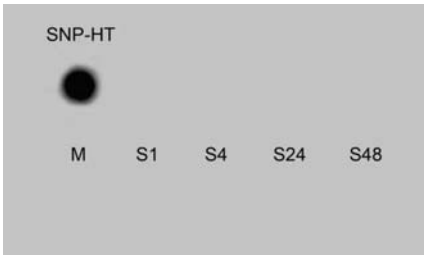

Figure 4. Stability assay of scFv conjugation on SNP-HT. 5 μg of scFv immobilized on SNP-HT was incubated at 37 °C with 0.1 mL of culture medium. After incubation time, SNP-HT were centrifuged 15 min at 15 000 × *g* at 4 °C and supernatants (S1, S4, S24, and S48) were filtered on a PVDF membrane. Membranes were then probed with anti-Myc-HRP antibody and revealed with an ECL substrate. 5 μg of scFv immobilized on SNP-HT was used as a positive control. 0.1 mL of culture medium (M) was used as negative control.

confocal laser scanning microscopy (Figure 5). As HER-2 is a transmembrane receptor, we expected an accumulation of SNP-HT and SNP-UT at the level of the cell membrane of HER-2-positive cells only, which would confirm that nanoparticle capture occurs via specific membrane receptor-mediated internalization. HER-2 positive MCF-7 cells (Figure 5) were treated with scFv to assess HER-2 expression and cellular surface distribution. SNP-HT and SNP-UT were incubated in parallel with both MCF-7 and MDA cells (Figure 6) at a scFv concentration of 25 μg mL^{-1} of culture medium for 1 h at 37 °C. In order to discriminate between specific binding to the membrane receptor and a possible nonspecific adsorption of SNP, we revealed scFv, SNP-HT, and SNP-UT with FITC-labeled antiwhole mouse secondary antibodies (green), instead of exploiting intrinsically fluorescent silica nanospheres (Figures 5A,6A). Nuclei were stained with DAPI (Figures 5B,6B) while membranes were stained with DiD oil (Figures 5C,6C). As expected, both SNP-HT and SNP-UT (Figure 5A) were observed on HER-2-positive MCF-7 cell surface but not on HER-2-negative MDA cells (Figure 6A), which demonstrates that they are actually capable of specifically targeting their transmembrane receptor. Merged images in Figure 5D also show that SNP-UT and SNP-HT were mostly localized on cell membrane after 1 h incubation, although a small amount of nanoparticles were already internalized.

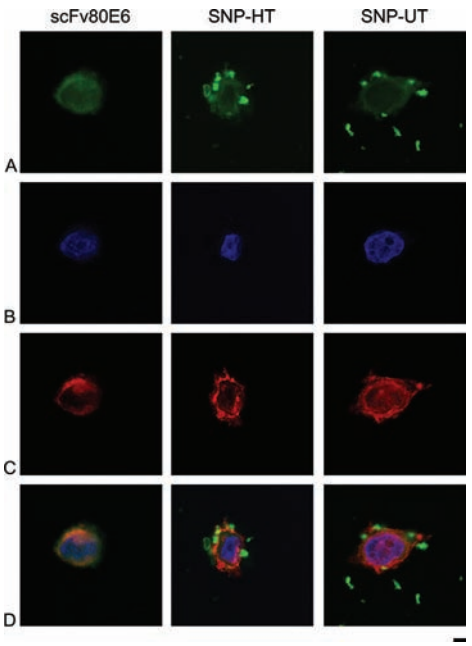

Figure 5. Assessment of HER-2 target efficacy of SNP-HT and SNP-UT on HER-2 positive cells. SNP-HT and SNP-UT were incubated with MCF-7 cells at a scFv concentration of 25 μg mL^{-1}. Free scFv was used as a positive control. ScFv, SNP-HT, and SNP-UT were revealed with FITC-labeled antiwhole mouse secondary antibodies (green, A). Nuclei were stained with DAPI (B), membranes (MB) with DiD oil (C). Merge images are shown in D. Scale bar: 10 μm.

CONCLUSION

In summary, we present a nanoparticle-based multimerization strategy aimed at enhancing the functional affinity of scFv toward cancer cell receptors. So far, the increase in binding efficiency of an antibody fragment has been primarily obtained by either chemically linking the individual scFv units or constructing multivalent variants by connecting antibody fragment with oligomerization domains. Our strategy lead to the facile and reliable development of nanoparticles allowing for multiple presentation of scFv molecules on a rigid nanosized spherical surface, which proved very effective and selective in binding the specific transmembrane receptor in living cells, as assessed by flow cytometry and confocal microscopy. These results suggest that the use of size- and shape-controlled inorganic nanoparticles as a multimerization scaffold is capable

dx.doi.org/10.1021/bc200352x | *Bioconjugate Chem.* 2011, 22, 2296–2303

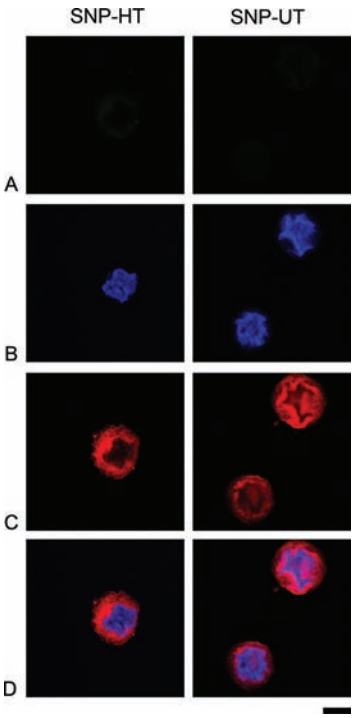

Figure 6. Assessment of HER-2 target efficacy of SNP-HT and SNP-UT on HER-2 negative cells. SNP-HT and SNP-UT were incubated with MDA cells at a scFv concentration of 25 μg mL^{-1}. ScFv on SNP-HT and SNP-UT was revealed with FITC-labeled antiwhole mouse secondary antibodies (green, A). Nuclei were stained with DAPI (B), membranes (MB) with DiD oil (C). Merge images are shown in D. Scale bar: 10 μm.

to improve scFv target binding efficacy, reaching an affinity value very close to that of native TZ, the mAb currently utilized in clinical practice.

■ ASSOCIATED CONTENT

Ⓢ Supporting Information

Experimental details for fully PEG-coated SNP (SPEG), SNP1 and SNP2, scheme of conjugation of SNP-HT and SNP-UT, determination of amine groups on SNP2, Dynamic Light Scattering and ζ-potential measurements. This material is available free of charge via the Internet at http://pubs.acs.org.

■ AUTHOR INFORMATION

Corresponding Author

*E-mail: davide.prosperi@unimib.it; Phone: (+39) 0264483302; Fax: (+39)0264483565.

Author Contributions

†These authors contributed equally to the research.

■ ACKNOWLEDGMENTS

We thank R. Allevi for TEM images, S. Citterio for helpful discussion of cell cytometry result. This work was partly supported by "Assessorato alla Sanità", Regione Lombardia, and Sacco Hospital (NanoMeDia Project), "Fondazione Romeo ed Enrica Invernizzi" and "Centro di Microscopia Elettronica per lo sviluppo delle Nanotecnologie applicate alla medicina" (CMENA, Univ. of Milan). M.C. and S.M. acknowledge "Centro di Microscopia Elettronica per lo sviluppo delle Nanotecnologie applicate alla medicina" (CMENA, University of Milan) for doctoral and postdoctoral fellowships, respectively.

■ REFERENCES

(1) Sanz, L., Cuesta, A. M., Compte, M., and Alvarez-Vallina, L. (2005) Antibody engineering: facing new challenges in cancer therapy. *Acta Pharmacol. Sin. 26*, 641−648.

(2) Holliger, P., and Hudson, P. J. (2005) Engineered antibody fragments and the rise of single domains. *Nat. Biotechnol. 9*, 1126−1136.

(3) Goel, A., Augustine, S., Baranowska-Kortylewicz, J., Colcher, D., Booth, B. J. M., Pavlinkova, G., Tempero, M., and Batra, S. K. (2001) Single-dose versus fractionated radioimmunotherapy of human colon carcinoma xenografts using 131I-labelled multivalent CC49 single chain fvs. *Clin. Cancer Res. 7*, 175−184.

(4) Sanz, L., Blanco, B., and Alvarez-Vallina, L. (2004) Antibodies and gene therapy: teaching old "magic bullets" new tricks. *Trends Immunol. 25*, 85−91.

(5) Bayly, A. M., Kortt, A. A., Hudson, P. J., and Power, B. E. (2002) Large-scale bacterial fermentation and isolation of scFv multimers using a heat-inducible bacterial expression vector. *J. Immunol. Methods 262*, 217−227.

(6) Wittel, U. A., Jain, M., Goel, A., Chauhan, S. C., Colcherand, D., and Batra, S. K. (2005) The in vivo characteristics of genetically engineered divalent and tetravalent single-chain antibody constructs. *Nucl. Med. Biol. 32*, 157−164.

(7) Gall, L. F., Kipriyanov, S. M., Moldenhauer, G., and Little, M. (1999) Di-, tri- and tetrameric single chain Fv antibody fragments against human CD19: effect of valency on cell binding. *FEBS Lett. 453*, 164−168.

(8) Ravn, P., Danielczyk, A., Jensen, K. B., Kristensen, P., Christensen, P. A., Larsen, M., Karsten, U., and Goletz, S. (2004) Multivalent scFv display of phagemid repertoires for the selection of carbohydrate-specific antibodies and its application to the Thomsen−Friedenreich antigen. *J. Mol. Biol. 343*, 985−996.

(9) Natarajan, A., Du, W., Xiong, C-Y, DeNardo, G. L., DeNardo, S. J., and Gervay-Hague, J. (2007) Construction of di-scFv through a trivalent alkyne−azide 1,3-dipolar Cycloaddition. *Chem. Commun. 695*, 685−697.

(10) Devey, S. M., and Lebedenko, E. N. (2008) Multivalency: the hallmark of antibodies used for optimization of tumor targeting by design. *BioEssays 30*, 904−918.

(11) Zhou, Y., Drummond, D. C., Zou, H., Hayes, M. E., Adams, G. P., Kirpotin, D. B., and Marks, J. D. (2007) Impact of single-chain Fv antibody fragment affinity on nanoparticle targeting of epidermal growth factor receptor-expressing tumor cells. *J. Mol. Biol. 371*, 934−947.

(12) Ackerson, C. J., Jadzinsky, P. D., Jensen, G. J., and Kornberg, R. D. (2006) Rigid, specific, and discrete gold nanoparticle/antibody conjugates. *J. Am. Chem. Soc. 128*, 2635−2640.

(13) Yang, L., Mao, H., Wang, A., Cao, Z., Peng, X., Wang, X., Duan, H., Ni, C., Yuan, Q., Adams, G., Smith, M. Q., Wood, W. C., Gao, X., and Nie, S. (2009) Single chain epidermal growth factor receptor antibody conjugated nanoparticles for in vivo tumor targeting and imaging. *Small 5*, 235−243.

(14) Huang, X., Peng, X., Wang, Y., Wang, Y., Shin, D. M., El-Sayed, M. A., and Nie, S. (2010) A reexamination of active and passive tumor targeting by using rod-shaped gold nanocrystal and covalently conjugated peptide ligands. *ACSNano 4*, 5887−5896.

(15) Sommaruga, S., Lombardi, A., Salvadè, A., Mazzucchelli, S., Corsi, F., Galeffi, P., Tortora, P., and Prosperi, D. (2011) Highly efficient production of anti-HER2 scFv antibody targeting for tumor targeting breast cancer cells. *Appl. Microbiol. Biotechnol. 91*, 613−621.

(16) Burns, A., Ow, H., and Weisner, U. (2006) Fluorescent core-shell silica nanoparticles: towards "lab on a particle" architectures for nanobiotechnology. *Chem. Soc. Rev. 35*, 1028−1042.

(17) Rossi, M. L., Shi, L., Rosenzweig, N., and Rosenzweig, Z. (2006) Fluorescent silica nanosphere for digital counting assay of the breast cancer marker HER2/neu. *Biosens. Bioelectron. 21*, 1900−1906.

(18) Wu, T., Zhang, Y., Wang, X., and Liu, S. (2008) Fabrication of hybrid silica nanoparticles densely grafted with thermoresponsive poly(N-isopropylacrylamide) brushes of controlled thickness via surface-initiated atom transfer radical polymerization. *Chem. Mater. 20*, 101−109.
(19) Kim, S. H., Jeyakumar, M., and Katznellenbogen, J. A. (2007) Dual-mode fluorophore-doped nickel nitriloacetic acid-modified silica nanoparticles combine histidine-tagged protein purification with site-specific fluorophore labeling. *J. Am. Chem. Soc. 129*, 13254−13264.
(20) Scmitt, L., Dietrich, C., and Tampè, R. (1994) Synthesis and characterization of chelator-lipids for reversible immobilization of engineered proteins at self-assembled lipid interfaces. *J. Am. Chem. Soc. 116*, 8485−8491.
(21) Halling, P. J., and Dunnill, P. (1979) Improved nonporous magnetic supports for immobilized enzymes. *Biotechnol. Bioeng. 21*, 393−416.
(22) Laemmli, U. K. (1970) Cleavage of structural proteins during the assembly of the head of bacteriophage T4. *Nature 227*, 680−85.
(23) Corsi, F., De Palma, C., Colombo, M., Allevi, R., Nebuloni, M., Ronchi, S., Rizzi, G., Tosoni, A., Trabucchi, E., Clementi, E., and Prosperi, D. (2009) Towards ideal magnetofluorescent nanoparticles for bimodal detection of breast-cancer cells. *Small 5*, 2555−2564.
(24) Han, H. J., Kannan, R. M.., Wang, S., Mao, G., Kusanovic, J. P., and Romero, R. (2010) Multifunctional dendrimer template antibody presentation on biosensor surfaces for improved biomarker detection. *Adv. Funct. Mater. 20*, 409−421.
(25) Kohler, N., Fryxell, G. E., and Zhang, M. (2004) A bifunctional poly(ethylene glycol) silane immobilized on metallic oxide-based nanoparticles for conjugation with cell targeting agents. *J. Am. Chem. Soc. 126*, 7206−7211.
(26) Lin, W., Garnett, M. C., Schacht, E., Davis, S. S., and Illum, L. (1999) Preparation and in vitro characterization of HSA-mPEG nanoparticles. *Int. J. Pharm. 189*, 161−170.
(27) Hu, F., Wei, L., Zhou, Z., Ran, Y., Li, Z., and Gao, M. (2006) Preparation of biocompatibile magnetite nanocrystals for in vivo magnetic resonance detection of cancer. *Adv. Mater. 18*, 2553−2556.
(28) Mazzucchelli, S., Colombo, M., De Palma, C., Salvadè, A., Verderio, P., Coghi, M. D., Clementi, E., Tortora, P., Corsi, F., and Prosperi, D. (2010) Single-domain protein A-engineered magnetic nanoparticles: a step towards a universal strategy to site-specific labeling of antibodies for targeted detection of tumor cells. *ACS Nano 10*, 5693−5702.

Supporting Information

Multiple Presentation of Scfv800E6 on Silica Nanospheres Enhances Targeting Efficiency Towards Breast Cancer Cells

Serena Mazzucchelli,[1] Paolo Verderio,[1] Silvia Sommaruga,[2] Miriam Colombo,[1,2] Agnese Salvadè,[2] Fabio Corsi,[2] Patrizia Galeffi,[3] Paolo Tortora,[1] Davide Prosperi[1,4,*]

[1]Dipartimento di Biotecnologie e Bioscienze, Università di Milano-Bicocca, Piazza della Scienza 2, 20126 Milano, Italy. [2]Dipartimento di Scienze Cliniche "Luigi Sacco", Università di Milano, Ospedale L. Sacco, Via G.B. Grassi 74, 20157 Milano, Italy. [3]UTAGRI-GEN, ENEA, R. C.Casaccia, Via Anguillarese 301, 00123 Roma, Italy. [4]Istituto di Scienze e Tecnologie Molecolari, CNR, via Fantoli 16/15, 20138 Milano, Italy.

E-mail: davide.prosperi@unimib.it

LIST OF CONTENTS

I. Scheme of synthesis of fully PEG-coated SNP (SPEG).

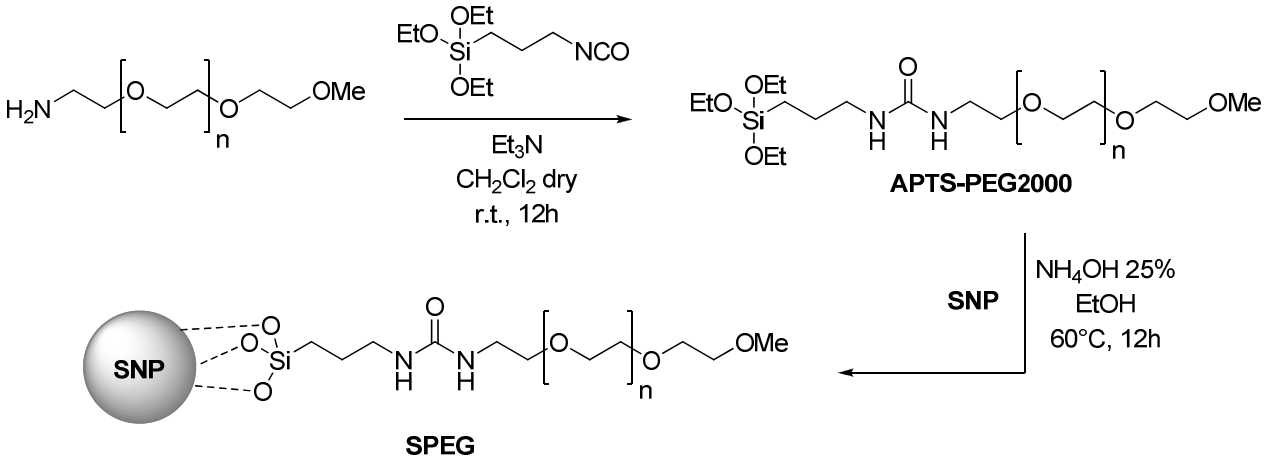

Scheme S1: Synthetic strategy to SPEG

II. Scheme of synthesis of SNP1.

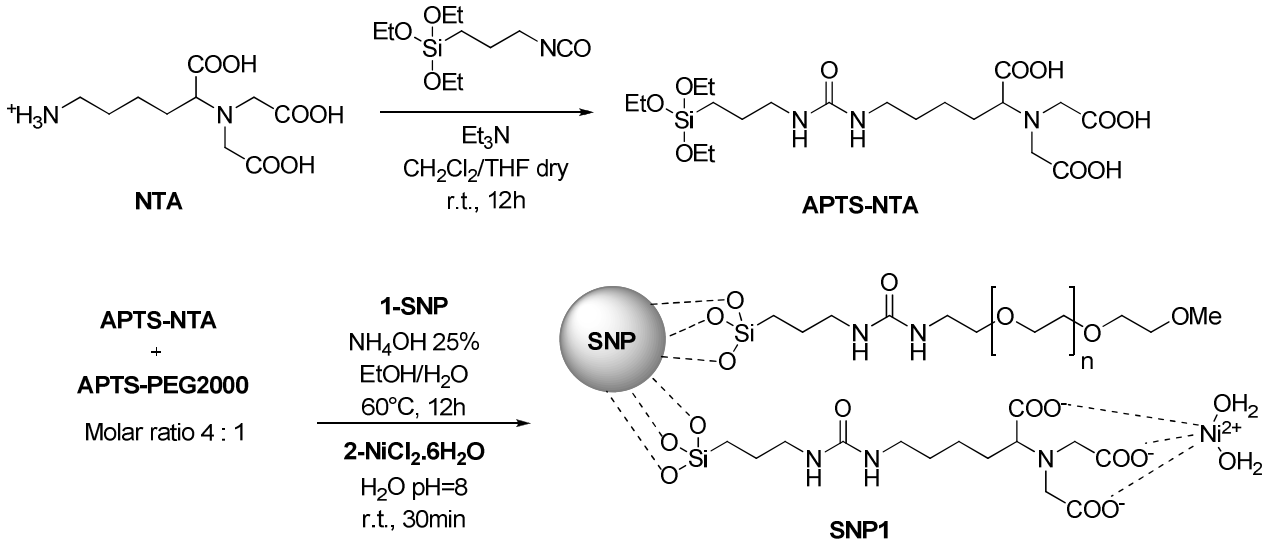

Scheme S2: Synthetic strategy to SNP1

III. Scheme of synthesis of SNP2.

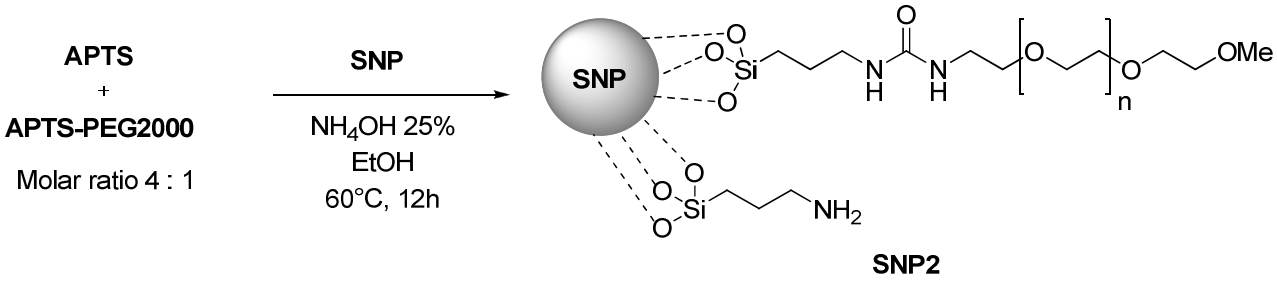

Scheme S3: Synthetic strategy to SNP2

IV. Determination of amine groups on SNP2.

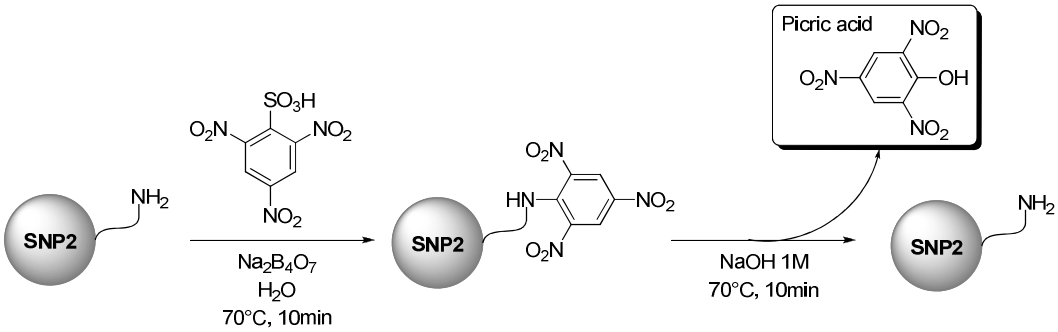

Scheme S4: Quantification of amine reactive groups: TBNS assay.

V. Scheme of conjugation of His-tag scFv800E6 (SNP-HT).

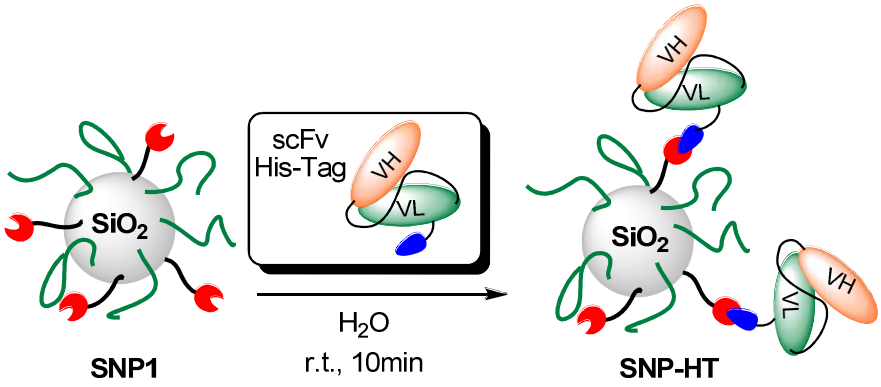

Scheme S5: Synthetic strategy to SNP-HT.

VI. Scheme of the unoriented conjugation of scFv800E6 (SNP-UT).

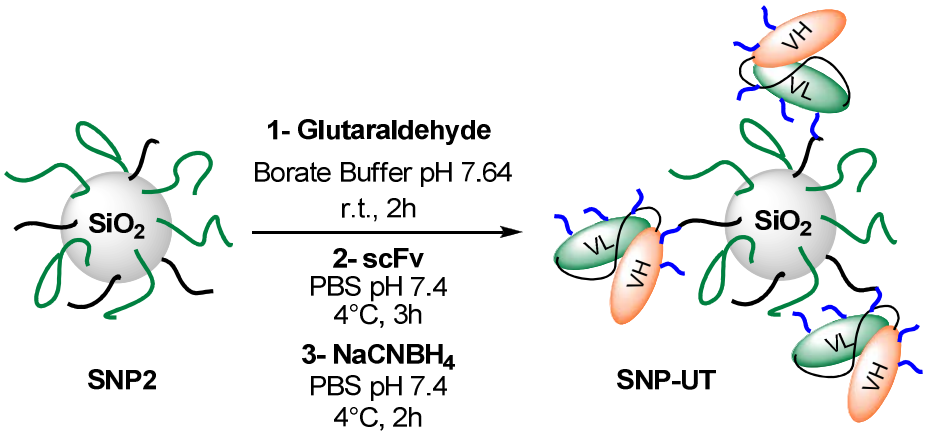

Scheme S6: Synthetic strategy to SNP-UT.

VII. Dynamic Light Scattering and ζ-Potential measurements.

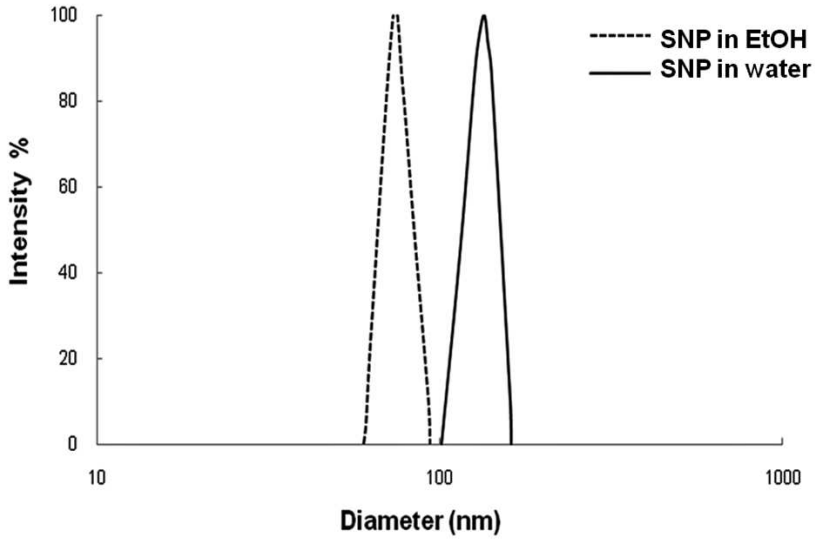

Figure S1. Hydrodynamic size distribution histogram of SNP in ethanol (73.3 nm, polydispersity 0.132; dashed line) and in deionized water (133.8 nm, polydispersity 0.232; continous line). The horizontal scale is semi-logarithmic. SNP ζ-Potential in deionized water was -35.86 mV (± 0.64).

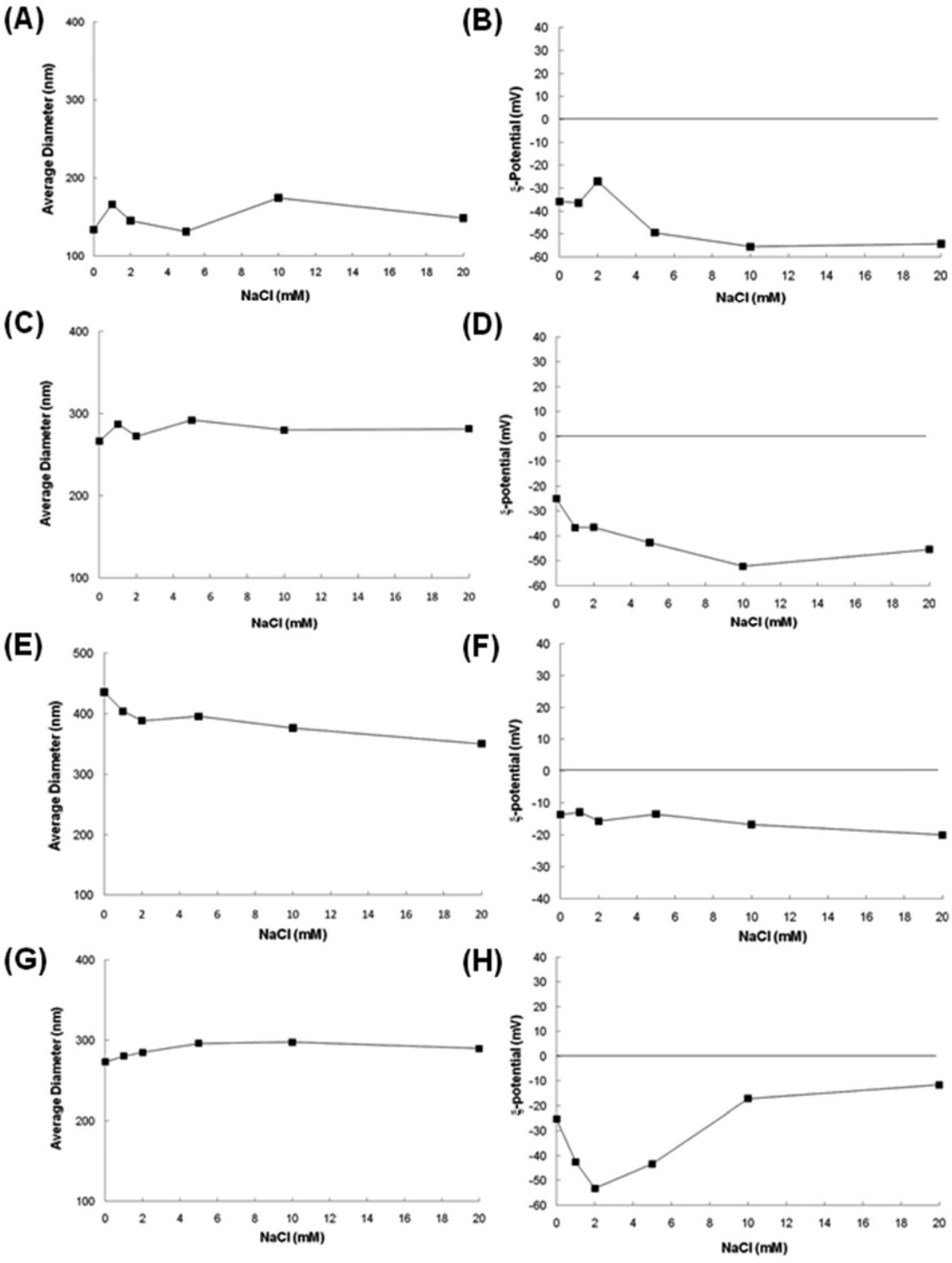

Figure S2. (A) Hydrodynamic size distribution behavior of SNP in deionized water at different Na^+ concentrations. SNP hydrodynamic radius was unaltered by the salts concentration. (B) ζ-Potential profiles of SNP in deionized water at increasing of Na^+ concentrations: as expected, Na^+ was adsorbed in the liquid hydration sphere of nanoparticles in order to increase solubility of silica in aqueous medium. The charge became strongly negative at higher concentration of salts (NaCl 10 mM , –55.50 mV ± 0.54) which implied an enhanced stability of colloidal suspension. (C)

Hydrodynamic radius of SPEG at pH 7.0 in deionized water (266.2 nm, polydispersity 0.322) was unaltered by different Na^+ concentrations (1 mM to 20 mM). (D) ζ-Potential profiles of SPEG at increasing of Na^+ concentrations (1 mM to 20 mM): as expected, Na^+ was adsorbed in the liquid hydration sphere of nanoparticles in order to increase solubility of silica in aqueous medium. The charge became strongly negative at higher concentration of salts (NaCl 10 mM, -52.19 mV ± 1.13) which implied an enhanced stability of colloidal suspension. (E) Hydrodynamic radius of SNP1 at pH 7.0 in deionized water (435.8 nm, polydispersity 0.325) decreased with increasing Na^+ concentrations; at pH 7.0 with 20 mM NaCl SNP1 hydrodynamic radius was 350.2 nm, polydispersity 0.199. (F) ζ-Potential profiles of SNP1 at increasing of Na^+ concentrations. In this case the charge was similar even at higher concentration of salts (20 mM NaCl, -20.02 mV ± 1.78). (G) Hydrodynamic radius of SNP2 at pH 7.0 in water (272.8 nm, polydispersity 0.298) was unaltered by different Na^+ concentrations; at pH 7.0 and 20 mM NaCl, SNP2 hydrodynamic radius was 289.3 nm, polydispersity 0.303. (H) ζ-Potential profiles of SNP2 at increasing of Na^+ concentrations. In this case, the charge was strongly negative at low salt concentrations (2 mM NaCl, -53.24 mV ± 0.70), but at higher concentrations (20 mM NaCl) the charge decreased to -11.62 mV ± 1.10.

REFERENCES

[1] Wu, T., Zhang, Y., Wang, X., and Liu, S. (2008) Fabrication of hybrid silica nanoparticles densely grafted with thermoresponsive poly(***N***-isopropylacrylamide) brushes of controlled thickness via surface-initiated atom transfer radical polymerization. ***Chem. Mater. 20***, 101-109.

[2] Kim, S. H., Jeyakumar, M., and Katznellenbogen, J. A. (2007) Dual-mode fluorophore –doped Nickel nitriloacetic acid-modified silica nanoparticles combine Histidine-tagged protein purification with site-specific fluorophore labeling. ***J. Am. Chem. Soc. 129***, 13254-13264.

[3] Scmitt, L., Dietrich, C., and Tampè, R. (1994) Synthesis and characterization of chelator-lipids for reversible immobilization of engineered proteins at self-assembled lipid interfaces. ***J. Am. Chem. Soc. 116***, 8485-8491.

[4] Halling, P. J., and Dunnill, P. (1979) Improved nonporous magnetic supports for immobilized enzymes. ***Biotechnol. Bioeng. 21***, 393-416.

[5] Sommaruga, S., Lombardi, A., Salvadè, A., Mazzucchelli, S., Corsi, F., Galeffi, P., Tortora, P., and Prosperi, D. (2011) Highly efficient production of anti-HER2 scFv antibody targeting for tumor targeting breast cancer cells. ***Appl. Microbiol. Biotechnol.*** DOI: 10.1007/s00253-011-3306-3

[6] Laemmli, U. K. (1970) Cleavage of structural proteins during the assembly of the head of bacteriophage T4. ***Nature 227***, 680-85.

[7] Corsi, F., De Palma, C., Colombo, M., Allevi, R., Nebuloni, M., Ronchi, S., Rizzi, G., Tosoni, A., Trabucchi, E., Clementi, E., and Prosperi, D. (2009), Towards ideal magnetofluorescent nanoparticles for bimodal detection of breast-cancer cells. ***Small***. ***5***, 2555-2564.

[8] Han, H. J., Kannan, R. M.., Wang, S., Mao, G., Kusanovic, J. P., and Romero, R. (2010), Multifunctional dendrimer template antibody presentation on biosensor surfaces for improved biomarker detection. ***Adv***. ***Funct***. ***Mat***. ***20***, 409-421.

Bioconjugate Chemistry

ARTICLE

pubs.acs.org/bc

Synthesis and Biological Evaluation of Water-Soluble Progesterone-Conjugated Probes for Magnetic Resonance Imaging of Hormone Related Cancers

Preeti A. Sukerkar,[†] Keith W. MacRenaris,[†] Taryn R. Townsend,[†] Roshan A. Ahmed,[‡] Joanna E. Burdette,*[,‡] and Thomas J. Meade*[,†]

[†]Department of Chemistry, Department of Molecular Biosciences, Department of Neurobiology and Physiology, and Department of Radiology, Northwestern University, Evanston, Illinois 60208, United States

[‡]Department of Medicinal Chemistry and Pharmacognosy, University of Illinois at Chicago, Chicago, Illinois 60607, United States

Supporting Information

ABSTRACT: Progesterone receptor (PR) is strongly associated with disease prognosis and therapeutic efficacy in hormone-related diseases such as endometriosis and breast, ovarian, and uterine cancers. Receptor status is currently determined by immunohistochemistry assays. However, noninvasive PR imaging agents could improve disease detection and help elucidate pathological molecular pathways, leading to new therapies and animal disease models. A series of water-soluble PR-targeted magnetic resonance imaging (MRI) probes were synthesized using Cu(I)-catalyzed click chemistry and evaluated *in vitro* and *in vivo*. These agents demonstrated activation of PR *in vitro* and preferential accumulation in PR(+) compared to PR(-) human breast cancer cells with low toxicity. In xenograft tumor models, the agents demonstrated enhanced signal intensity in PR(+) tumors compared to PR(-) tumors. The results suggest that these agents may be promising MRI probes for PR(+) diseases.

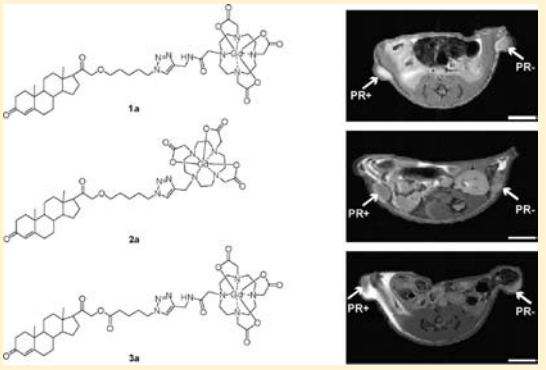

INTRODUCTION

Biomedical imaging has traditionally focused on detecting abnormalities in gross anatomical structures.[1] However, there has been a recent increase in the interest of developing targeted agents that noninvasively provide information about physiological and pathological processes on a molecular level.[1−4] In this regard, steroid receptors have emerged as particularly attractive targets for molecular imaging due to their role in promoting the growth of breast, ovarian, uterine, and prostate cancers.[5]

Previous attempts to image steroid receptors have focused on positron emission tomography (PET).[1,6] PET imaging of estrogen receptor (ER) in breast cancer and androgen receptor (AR) in prostate cancer has been successful.[7−10] However, imaging of progesterone receptor (PR) has been limited in humans due to rapid metabolism of the tracers by 20-hydroxysteroid dehydrogenase.[11−13] In addition, PET suffers from the disadvantages of low spatiotemporal resolution and requirements of a nearby cyclotron and radiochemistry facilities.[2]

Magnetic resonance imaging (MRI) offers excellent spatiotemporal resolution without exposure to harmful radiation or the need for specialized radiochemistry equipment.[2] Although the sensitivity of PET imaging agents far surpasses that of any other modality, MRI contrast agents can be optimized to enhance the otherwise low sensitivity of these probes.[2,14,15] Therefore, MRI is an excellent alternative to PET for detecting steroid receptors and, in particular, PR.

Several PR-targeted MRI contrast agents have been previously developed.[16−18] One of these agents, referred to as ProGlo, preferentially accumulated and enhanced MR signal in tissues and tumors with high PR expression.[19] In contrast to the PR-targeted PET imaging agent, ProGlo may be less rapidly metabolized due to the steric hindrance from the Gd(III) chelate preventing binding to 20-hydroxysteroid dehydrogenase.[20]

Due to the low solubility of ProGlo in aqueous media, *in vivo* delivery of this agent was limited to subcutaneous or intraperitoneal injection routes rather than intravenous injections.[19] Furthermore, the effect of hydrophobicity on nonspecific interactions with biomolecules and the correlation between hydrophobicity and toxicity have been well-documented in numerous drugs.[21−23] The association of ProGlo with toxicity when intraperitoneally injected into athymic nude mice was, therefore, not surprising, and is likely a consequence of its hydrophobic properties and nonspecific interactions, necessitating the development of water-soluble contrast agents. Minimizing lipophilicity in

Received: July 5, 2011
Revised: August 16, 2011
Published: October 05, 2011

ACS Publications © 2011 American Chemical Society

imaging agents has been reported to decrease background signal by reducing nonspecific interactions in tissues.[1] In addition, imaging breast cancers, as opposed to tumors that form in the peritoneal space, should be significantly improved by intravenous imaging agent delivery, which can take advantage of leaky vasculature to accumulate and remain inside those tumors specifically expressing PR.

The current work describes the synthesis of a novel series of water-soluble PR-targeted MR probes. These new agents demonstrated activation of PR *in vitro* with lower cytotoxicity than ProGlo. Higher cellular Gd(III) accumulation was observed in comparison to a nontargeted agent, particularly in PR(+) cells. Finally, these agents preferentially enhanced signal intensity in PR(+) tumors compared to PR(-) tumors and were not associated with toxicity in preliminary *in vivo* studies.

EXPERIMENTAL SECTION

General Methods. Unless noted, materials and solvents were purchased from Sigma-Aldrich Chemical Co. (St. Louis, MO) and used without further purification. $GdCl_3 \cdot 6H_2O$ and 1,4,7,10-tetraazacyclododecane (cyclen) were purchased from Strem Chemicals (Newburyport, MA) and used without further purification. Unless noted, all reactions were performed under a nitrogen or argon atmosphere. DMSO, *N*,*N*-dimethylformamide, and methanol were purified using a Glass Contour Solvent system. Deionized water was obtained from a Millipore Q-Guard System equipped with a quantum Ex cartridge (Billerica, MA). Thin-layer chromatography (TLC) was performed on EMD 60F 254 silica gel plates. Visualization of the developed chromatogram was performed by CAM stain and platinum stain. Standard grade 60 Å 230−400 mesh silca gel (Sorbent Technologies) was used for flash column chromatography. ^{1}H and ^{13}C NMR spectra were obtained on a Bruker 500 MHz Avance III NMR Spectrometer with deuterated solvent as noted. Electrospray ionization mass spectrometry (ESI-MS) spectra were taken on a Varian 1200 L single-quadrupole mass spectrometer. High-resolution mass spectrometry data were acquired on an Agilent 6210 LC-TOF (ESI, APCI, APPI). Analytical reverse-phase HPLC-MS was performed on a Varian Prostar 500 system with a Waters Atlantis C18 column (4.6 × 250, 5 μm). This system is equipped with a Varian 380 LC ELSD system, a Varian 363 fluorescence detector, a Varian 335 UV−vis detector, and a Varian 1200 L Quadrupole MS detector. Preparative runs were performed on a Waters Atlantis C18 column (19 × 250, 10 μm). Mobile phase consisted of water (solvent A) and HPLC-grade acetonitrile (solvent B).

Synthesis. *{1,4,7-Tris(carboxymethyl)-10-[10-(6-(2-((10R,13S,17S)-10,13-dimethyl-3-oxo-2,3,6,7,8,9,10,11,12,13,14,15,16,17-tetradecahydro-1H-cyclopenta[a]phenanthren-17-yl)-2-oxoethoxy)hexyl]-1,4,7,10-tetraazacyclododecanato}Gd(III) (ProGlo).* The synthesis and purification of ProGlo were performed as previously described.[17]

*2-(10,13-Dimethyl-3-oxo-2,3,6,7,8,9,10,11,12,13,14,15,16,17-tetradecahydro-1H-cyclopenta[a]phenanthren-17-yl)-2-oxoethyl 5-bromopentanoate (**8**).* A solution of 21-hydroxyprogesterone (300 mg, 1.36 mmol), 5-bromovaleric acid (111 mg, 0.613 mmol), diisopropyl carbodiimide (DIC) (122 μL, 0.786 mmol), and 4-(dimethylamino)pyridinium-4-toluenesulfonate (DPTS) (207 mg, 0.666 mmol) in anhydrous dichloromethane (1.1 mL) was stirred for 16 h at room temperature. The reaction mixture was diluted in dichloromethane and washed with water three times. The organic layer was dried over sodium sulfate and concentrated by rotary evaporation. The crude residue was purified by flash chromatography with hexanes/ethyl acetate (1:1) as the eluent to afford **8** as a white solid (348 mg, 75%). ^{1}H NMR (500 MHz, $CDCl_3$) δ 5.65 (1H, s, 4-H), 4.68 (1H, d, J = 17, $COCH_2O$), 4.45 (1H, d, J = 17, $COCH_2O$) 3.36 (2H, t, J = 6.5, CH_2Br), 2.47−0.80 (complex, 26H), 1.12 (3H, s, CH_3), 0.63 (3H, s, CH_3); ^{13}C NMR (125 MHz, $CDCl_3$) δ 203.77, 199.80, 172.71, 171.17, 124.18, 69.34, 59.31, 56.41, 53.79, 51.04, 44.91, 38.81, 38.56, 35.94, 35.77, 34.16, 33.39, 32.98, 32.1, 32.2, 24.71, 23.62, 23.07, 21.22, 17.59, 13.43; ESI-MS m/z $[M + H]^+$ observed: 494.8, calculated: 495.2.

*2-(10,13-Dimethyl-3-oxo-2,3,6,7,8,9,10,11,12,13,14,15,16,17-tetradecahydro-1H-cyclopenta[a]phenanthren-17-yl)-2-oxoethyl 5-azidopentanoate (**10**).* To a solution of **8** (325 mg, 0.639 mmol) in anhydrous *N*,*N*-dimethylformamide (7 mL) was added sodium azide (415 mg, 6.39 mmol). The reaction mixture was heated to 65 °C and stirred overnight. Excess sodium azide was filtered off and the solvent was removed by rotary evaporation. The crude residue was dissolved in ethyl acetate and washed with water three times. The organic layer was dried over sodium sulfate and concentrated followed by flash chromatography in hexanes/ethyl acetate (4:3) to give **10** (206 mg, 71%). ^{1}H NMR (500 MHz, CD_3CN) δ 5.62 (1H, s, 4-H), 4.72 (1H, d, J = 17, $COCH_2O$), 4.53 (1H, d, J = 17, $COCH_2O$), 3.31 (2H, t, J = 6.5, CH_2N_3), 2.55−0.99 (complex, 26H), 1.17 (3H, s, CH_3), 0.64 (3H, s, CH_3); ^{13}C NMR (125 MHz, CD_3CN) δ 204.49, 199.18, 173.04, 171.81, 123.86, 69.81, 59.25, 56.55, 54.21, 51.43, 44.95, 39.12, 38.60, 36.20, 35.94, 34.28, 33.36, 32.96, 32.52, 28.46, 24.79, 23.62, 23.07, 21.46, 17.35, 13.20. ESI-MS m/z $[M + Na]^+$ observed: 478.3, calculated: 478.3.

*17-(2-((5-Bromopentyl)oxy)acetyl)-10,13-dimethyl-6,7,8,9,10,11,12,13,14,15,16,17-dodecahydro-1H-cyclopenta[a]phenanthren-3(2H)-one (**7**).* A mixture of 21-hydroxyprogesterone (200 mg, 0.605 mmol), 1,5-dibromopentane (1.65 mL, 12.1 mmol), 40% KOH (300 μL), and tetrabutylammonium hydroxide (60 μL) was stirred for 16 h at room temperature. The reaction mixture was diluted in dichloromethane and washed with water three times. The organic layer was dried over sodium sulfate and concentrated by rotary evaporation. The crude residue was purified by flash chromatography with hexanes/ethyl acetate (2:1) as the eluent to afford **7** as a colorless oil (125 mg, 43%). ^{1}H NMR (500 MHz, $CDCl_3$) δ 5.67 (s, 1H), 3.96 (q, J = 17.2 Hz, 2H), 3.41 (t, J = 6.4 Hz, 2H), 3.38−3.31 (m, 2H), 2.56 (t, J = 9.1 Hz, 1H), 2.40−2.09 (m, 6H), 1.96 (m, 1H), 1.90−1.74 (m, 5H), 1.72−1.16 (m, 14H), 1.12 (s, 3H), 1.05−0.86 (m, 2H), 0.65−0.58 (m, 3H). ^{13}C NMR (125 MHz, $CDCl_3$) δ 207.55, 198.50, 169.94, 122.92, 75.79, 70.34, 61.56, 57.43, 55.12, 52.51, 43.53, 37.54, 34.61, 32.85, 31.74, 31.47, 30.82, 28.69, 27.74, 23.77, 23.47, 21.81, 19.97, 16.34, 12.55. ESI-MS m/z $[M + H]^+$ observed: 481.1, calculated: 481.2.

*17-(2-((5-Azidopentyl)oxy)acetyl)-10,13-dimethyl-6,7,8,9,10,11,12,13,14,15,16,17-dodecahydro-1H-cyclopenta[a]phenanthren-3(2H)-one (**9**).* To a solution of **7** (125 mg, 0.261 mmol) in anhydrous *N*,*N*-dimethylformamide (7 mL) was added sodium azide (169 mg, 2.61 mmol). The reaction mixture was heated to 65 °C and stirred overnight. Excess sodium azide was filtered off and the solvent was removed by rotary evaporation. The crude residue was dissolved in ethyl acetate and washed with water three times. The organic layer was dried over sodium sulfate and concentrated followed by flash chromatography in hexanes/ethyl acetate (2:1) to give **9** (78 mg, 68%). ^{1}H NMR (500 MHz, CD_3OD) δ 5.61 (d, J = 4.9 Hz, 1H), 3.39 (t, J = 6.4 Hz, 2H), 3.25−3.17 (m, 4H), 2.60 (t, J = 9.1 Hz, 1H), 2.45−2.33 (m, 2H), 2.25−2.15 (m, 2H), 2.12−2.03 (m, 1H), 1.99 (m, 1H), 1.89−1.76 (m, 2H), 1.70−1.29 (m, 15H), 1.29−1.15 (m, 2H),

1.13 (d, J = 11.0 Hz, 4H), 1.04−0.87 (m, 2H), 0.60 (s, 3H). ^{13}C NMR (125 MHz, CD_3OD) δ 210.81, 202.29, 174.92, 124.24, 78.00, 72.34, 62.71, 59.71, 57.39, 55.16, 52.43, 45.67, 39.99, 39.72, 36.81, 34.72, 33.90, 33.20, 30.15, 29.75, 25.52, 24.46, 24.17, 23.76, 22.15, 17.67, 13.96. ESI-MS m/z $[M + Na]^+$ observed: 464.2, calculated: 464.3.

General Procedure for Click Chemistry. All click chemistry reactions were run in 1:1 methanol/water or 1:1 DMSO/water solutions. The steroid derivative (1 equiv) and Gd(III) or Eu(III) chelate (1.1 equiv) were dissolved and N_2 gas was bubbled through the solution to remove oxygen. Sodium ascorbate (1 equiv), $CuSO_4$ (0.167 equiv), and [(1-benzyl-1*H*-1,2,3-triazol-4-yl)methyl]amine (TBTA) (0.02 equiv) were added and the reaction mixture was stirred at 60 °C for 24 h. The crude residue was purified by reverse-phase preparative HPLC using a ramp from 0% to 100% B over 20 min. Analytical HPLC traces of the purified complexes are given in the Supporting Information.

*{2,2′,2″-(10-(2-(((1-(5-(2-(10,13-Dimethyl-3-oxo-2,3,6,7,8,9,10,11,12,13,14,15,16,17-tetradecahydro-1H-cyclopenta[a]phenanthren-17-yl)-2-oxoethoxy)pentyl)-1H-1,2,3-triazol-4-yl)methyl)amino)-2-oxoethyl)-1,4,7,10-tetraazacyclododecane-1,4,7-triyl)triacetate}gadolinium (**1a**).* HRMS (ESI) m/z $[M + H]^+$ observed: 1034.4231, calculated: 1034.4267 for $C_{45}H_{68}GdN_8O_{10}$.

*{2,2′,2″-(10-((1-(5-(2-(10,13-Dimethyl-3-oxo-2,3,6,7,8,9,10,11,12,13,14,15,16,17-tetradecahydro-1H-cyclopenta[a]phenanthren-17-yl)-2-oxoethoxy)pentyl)-1H-1,2,3-triazol-4-yl)methyl)-1,4,7,10-tetraazacyclododecane-1,4,7-triyl)triacetate}gadolinium (**2a**).* HRMS (ESI) m/z $[M + H]^+$ observed: 977.4066, calculated: 977.40524 for $C_{43}H_{65}GdN_7O_9$.

*{2,2′,2″-(10-(2-(((1-(5-(2-(10,13-Dimethyl-3-oxo-2,3,6,7,8,9,10,11,12,13,14,15,16,17-tetradecahydro-1H-cyclopenta[a]phenanthren-17-yl)-2-oxoethoxy)-5-oxopentyl)-1H-1,2,3-triazol-4-yl)methyl)amino)-2-oxoethyl)-1,4,7,10-tetraazacyclododecane-1,4,7-triyl)triacetate}gadolinium (**3a**).* HRMS (ESI) m/z $[M + H]^+$ observed: 1049.4078, calculated: 1049.40775 for $C_{45}H_{66}GdN_8O_{11}$.

*{2,2′,2″-(10-(2-(((1-(5-(2-(10,13-Dimethyl-3-oxo-2,3,6,7,8,9,10,11,12,13,14,15,16,17-tetradecahydro-1H-cyclopenta[a]phenanthren-17-yl)-2-oxoethoxy)pentyl)-1H-1,2,3-triazol-4-yl)methyl)amino)-2-oxoethyl)-1,4,7,10-tetraazacyclododecane-1,4,7-triyl)triacetate}europium (**1b**).* HRMS (ESI) m/z $[M + H]^+$ observed: 1031.4252, calculated: 1031.4256 for $C_{45}H_{68}EuN_8O_{10}$.

*{2,2′,2″-(10-((1-(5-(2-(10,13-Dimethyl-3-oxo-2,3,6,7,8,9,10,11,12,13,14,15,16,17-tetradecahydro-1H-cyclopenta[a]phenanthren-17-yl)-2-oxoethoxy)pentyl)-1H-1,2,3-triazol-4-yl)methyl)-1,4,7,10-tetraazacyclododecane-1,4,7-triyl)triacetate}europium (**2b**).* HRMS (ESI) m/z $[M + H]^+$ observed: 974.4058, calculated: 974.40416 for $C_{43}H_{65}EuN_7O_9$.

*{2,2′,2″-(10-(2-(((1-(5-(2-(10,13-Dimethyl-3-oxo-2,3,6,7,8,9,10,11,12,13,14,15,16,17-tetradecahydro-1H-cyclopenta[a]phenanthren-17-yl)-2-oxoethoxy)-5-oxopentyl)-1H-1,2,3-triazol-4-yl)methyl)-amino)-2-oxoethyl)-1,4,7,10-tetraazacyclododecane-1,4,7-triyl)-triacetate}europium (**3b**).* HRMS (ESI) m/z $[M + H]^+$ observed: 1045.4074, calculated: 1045.40487 for $C_{45}H_{66}EuN_8O_{11}$.

Relaxivity. Solutions of **1a**, **2a**, **3a**, **4a**, **5a**, and **6a** were prepared in 500 μL of Millipore water for T_1 and T_2 acquisition. T_1 and T_2 relaxation times were measured on a Bruker mq60 NMR analyzer equipped with *Minispec v 2.51* rev. 00/NT software (Billerica, MA, USA) operating at 1.41 T (60 MHz) and 37 °C. T_1 relaxation times were measured using an inversion recovery pulse sequence using the following parameters: 4 scans per point, 10 data points for fitting, monoexponential curve fitting, phase cycling, 10 ms first pulse separation, and a recycle delay and final pulse separation of $\geq 5T_1$. The Gd(III) concentration of each solution was determined using ICP-MS. The inverse of the relaxation time ($1/T_1$, s^{-1}) was plotted against Gd(III) concentration (mM) and fitted to a straight line with $R^2 > 0.99$. The slope of the fitted line was recorded as the relaxivity, r_1.

Octanol−Water Partition Coefficients. Approximately 1 mg of each compound was dissolved in 1 mL of a 1:1 mixture of water/1-octanol. After shaking the sample tube vigorously for 30 s, the tube was placed on a rotator for gentle mixing over 4 h. The tube was then removed from the rotator and allowed to sit for 10 h to ensure complete separation of the aqueous and organic phases. 50 μL was removed from each layer and subjected to ICP-MS to determine the Gd concentration in each layer. The partition coefficient was calculated from the following equation: $\log_{10} P = \log_{10}(C_o/C_w)$, where $\log_{10} P$ is the logarithm of the partition coefficient, C_o is the concentration of Gd in the 1-octanol layer, and C_w is the concentration of Gd in the water layer.

Determination of *q*. The Eu(III) complexes were dissolved in D_2O and H_2O. The emission was monitored at 614 nm with excitation at 395 nm on a Hitachi F4500 fluorescence spectrophotometer operating in phosphorescence lifetime mode. Twenty-five scans were averaged and fit to a monoexponential decay ($R^2 > 0.98$) to give the phosphorescent lifetimes which were entered into this equation (corrected for one amide oscillator): $q = 1.0\ (k_{H2O} - k_{D2O} - 0.25 - 0.075)$.[24,25]

Receptor Binding to nPR. The progesterone receptor A ligand binding domain (amino acids 675−933) fused to GST (PR-LBD-GST; 80 nM), a fluorescently tagged PR ligand (fluoromone green PL; 4 nM), and progesterone, ProGlo, **1a**, or **3a** (several concentrations) were incubated in PR screening buffer with 4 mM dithiothreitol (DTT) in a total volume of 100 μL for 4 h at room temperature according to the manufacturer's protocol (Invitrogen, Carlsbad, CA, USA). Each sample was measured using the Beacon 2000 fluorescence polarization analyzer (Invitrogen, Carlsbad, CA) located in the Northwestern University Keck Facility. The machine was used in static mode, batch blank, no delay, with an average of 1 read per cycle, at 22 °C. A sample containing only buffer and PR-LBD-GST with no fluorescent PL was used as the blank to eliminate background signal from the protein or buffer. A sample with no competitor was used to determine 100% binding capacity of the PR-LBD-GST for the PL ligand. Curve fitting and error calculation was performed using *Prism* software from GraphPad Software, Inc. (La Jolla, CA).

General Cell Culture. Dulbecco's modified phosphate buffered saline (DPBS), media, sera, and dissociation reagents were purchased from Invitrogen (Carlsbad, CA). Cell culture consumables (flasks, plates, etc.) were purchased from VWR (Radnor, PA). Charcoal dextran stripped FBS was purchased from Atlanta Biologicals (Lawrenceville, GA). MDA-MB-231 cells were cultured using phenol red free α-MEM (modified to contain 20 ng/mL insulin) supplemented with 10% FBS (characterized) or with 10% charcoal dextran stripped FBS. T47D cells were cultured using phenol red free RPMI 1640 (modified to contain 1.0 mM sodium pyruvate, 1.0 mM HEPES, and 4.5 g/L glucose) supplemented with 10% FBS or 10% charcoal dextran stripped FBS. Prior to all experiments, cells were plated in the appropriate medium containing noncharcoal dextran stripped FBS. After plating, this medium was replaced with medium containing the stripped FBS and allowed to sit for 24 h, at which point the medium was replaced with fresh stripped medium and the cells were allowed to sit for another 24 h prior to

beginning the experiment. MDA-MB-231 and T47D cells were harvested by incubation with 0.25% TrypLE for 10 min at 37 °C in a 5.0% CO_2 incubator. All incubations were carried out at 37 °C in a 5.0% CO_2 incubator unless otherwise specified.

Cell Counting and Percent Cell Viability Determination Using Guava EasyCyte Mini Personal Cell Analyzer (PCA) System. After cell harvesting, an aliquot (15 or 30 μL) of the cell suspensions were mixed with Guava ViaCount reagent (final sample volume of 150 μL) and allowed to stain at room temperature for at least 5.0 min (no longer than 20 min). Stained samples were then vortexed for 10 s, after which cells were counted and percent cell viability determined via manual analysis using a Guava EasyCyte Mini Personal Cell Analyzer (PCA) and ViaCount software module. For each sample, 1000 events were acquired with dilution factors that were determined based upon optimum machine performance (~25−70 cells/μL). Instrument reproducibility was assessed daily using GuavaCheck Beads and following the manufacturer's suggested protocol using the Daily Check software module.

Cellular Uptake Studies. Contrast agents were dissolved in the appropriate medium (containing stripped FBS) for each cell line (T47D and MDA-MB-231) at concentrations of 2, 1, 0.5, 0.25, and 0.125 mM of contrast agent. For concentration-dependent cellular uptake, cells were incubated with 2, 1, 0.5, and 0.25 mM of each contrast agent for 4 h. For the time dependent cellular uptake, cells were incubated with 0.125 mM contrast agent for 1, 4, 10, and 24 h. After incubation, the media was removed, and the cells were rinsed twice with PBS and trypsinized. An aliquot was used for cell counting and the remaining portion was analyzed for Gd(III) content by ICP-MS. Each condition was done in triplicate.

Fractionation of Nuclear, Cytoplasmic, and Membrane Components. T47D and MDA-MB-231 cells were incubated with 0.250 mM of contrast agent (in the appropriate medium containing stripped FBS) for 10 h. After incubation, the cells were rinsed twice with PBS, trypsinized, pelleted (500*g* for 5 min), and resuspended in PBS. A portion was removed for cell counting, and the rest was pelleted (500*g* for 5 min) and the PBS removed. Cytoplasmic and nuclear fractions were extracted using a NE-PER Nuclear and Cytoplasmic Extraction Kit according to manufacturer protocol (Pierce, Rockford, IL). The remaining pellet after cytoplasmic and nuclear extraction was assumed to consist mainly of membrane. Each fraction was analyzed for Gd(III) content by ICP-MS.

Cytotoxicity. The CellTiter 96 AQ_{ueous} Non-Radioactive Cell Proliferation Assay (Promega, Madison, WI) was used to measure cell viability. Cells were plated at 5000 cells/well in 96 well plates and maintained in medium containing stripped serum for 48 h before beginning the experiment. ProGlo, progesterone, **1a**, **2a**, **3a**, and **4a** were dissolved in varying concentrations in media. After 24 h of incubation, the assay was run according to manufacturer protocol. Absorbance was measuring using a Biotek Synergy4 microplate reader in the High Throughput Analysis Facility at Northwestern University.

Luciferase Assay for nPR Activation. T47D cells were grown in phenol-free medium, and cells were trypsinized and plated in 24-well plate (50 000 cells/well). Incubation of cells with the pPRE-luciferase plasmid (100 ng/well, construct provided by Dr. Ken Korach, NIEHS, NIH), RSV-β-galactosidase (100 ng/well, provided by Dr. William T. Beck, University of Illinois at Chicago), and Lipofectamine 2000 (1 μL per well, Invitrogen, Carlsbad, CA) in Opti-MEM was performed overnight at 37 °C inside a humidified incubator. The cells were treated with **1a**, **2a**, **3a**, and **4a** for an additional 24 h.

To measure luciferase production, cells were lysed in 100 μL GME buffer (25 mM glycylglycine at pH 7.8, 15 mM $MgSO_4$, 4 mM EGTA, 1 mM dithiothreitol, and 1% Triton X-100) and lysates were added to assay buffer (GME buffer, 16.5 mM KPO_4, 2.2 mM ATP, and 1.1 mM dithiothreitol). Luciferase substrate was injected followed by a 30 s read by a FLUOstar OPTIMA (BMG Lab Tech, Offenburg, Germany). LacZ activity (50 μL lysate) was measured from cleavage of ONPG. The sample results were normalized to β-galactosidase to account for transfection efficiency by dividing the sum of the luciferase activity by the sum of the β-galactosidase activity. Fold change was calculated by taking the luciferase value, dividing by the β-galactosidase activity, and then dividing by the solvent control, which was set equal to one.

RT-PCR. Total RNA was isolated using Qiagen RNA easy columns with on column DNase added according to the manufacture (Qiagen, Valencia, CA). RNA samples (2 μg) were then primed with random hexamers and reverse transcribed with M-MLV Reverse Transcriptase (Promega, Madison, WI) according to manufacturer's instructions. From the original RT reaction, 1 μL was subjected to PCR amplification in a 25 μL volume with Taqman Universal PCR SYBR Green Master Mix (Applied Biosystems, Foster City, CA) under the following conditions: 50 °C hold 2 min, 95 °C hold for 10 min, the 40 cycles of 95 °C for 15 s, 65 °C for 30 s, and 72 °C for 1 min. The primers used were designed using Integrated DNA technologies primer quest for ZBTB16 forward 5′TGTTTGAGATCCTCTTCCACCG-CA3′ and reverse 5′ TCTCCAGCATCTTCAGGCACTGTT3′ and normalized to GAPDH forward 5′ ATGGGGAAGGTGAA-GGTCG3′ and reverse 5′GGGGTCATTGATGGCAACAATA3′.

ICP-MS Sample Preparation and Instrument Parameters. For octanol−water partition coefficients, relaxivity, and cell studies, ACS reagent grade nitric acid (70%) was added to solutions of the agent in water or 1-octanol, cell suspensions, and media (for a 1.0:1.0 v/v sample/nitric acid) in 15 mL conical tubes and placed at 65 °C for at least 4.0 h to allow for complete sample digestion. For samples in 1-octanol, tubes were vented every 30 min due to buildup of pressure. Nanopure H_2O and internal standard (either indium or multielement) were added to produce a final solution of 3.0% nitric acid (v/v) and 5.0 ng/mL internal standard. Gd(III) standards were prepared at 0.10, 0.25, 0.50, 1.0, 5.0, 10, 25, and 50 ng/mL concentrations with 3.0% nitric acid (v/v) and internal standard final concentrations.

ICP-MS was performed on a computer-controlled Thermo (Waltham, MA) X Series II inductively coupled plasma mass spectrometer equipped with a CETAC 260 autosampler. Each sample was acquired using 1 survey run and 3 main (peak jumping) runs. The isotopes selected were ^{156,157}Gd, as well as ^{115}In and ^{165}Ho (as internal standards for data interpolation and machine stability).

Animal Experiments. Female Balb/C athymic nude mice were acquired from Harlan (Indianapolis, IN) and housed under pathogen free conditions. All animal studies were conducted at Northwestern University in accordance with the National Institutes of Health Guide for the Care and Use of Laboratory Animals and established institutional animal use and care protocols. Due to low circulating estradiol levels in nude mice, a 17β-estradiol pellet (Innovative Research of America, Sarasota, FA, 70-day release, 0.72 mg/pellet) was implanted subcutaneously in the nape of the neck to ensure growth of estrogen-dependent

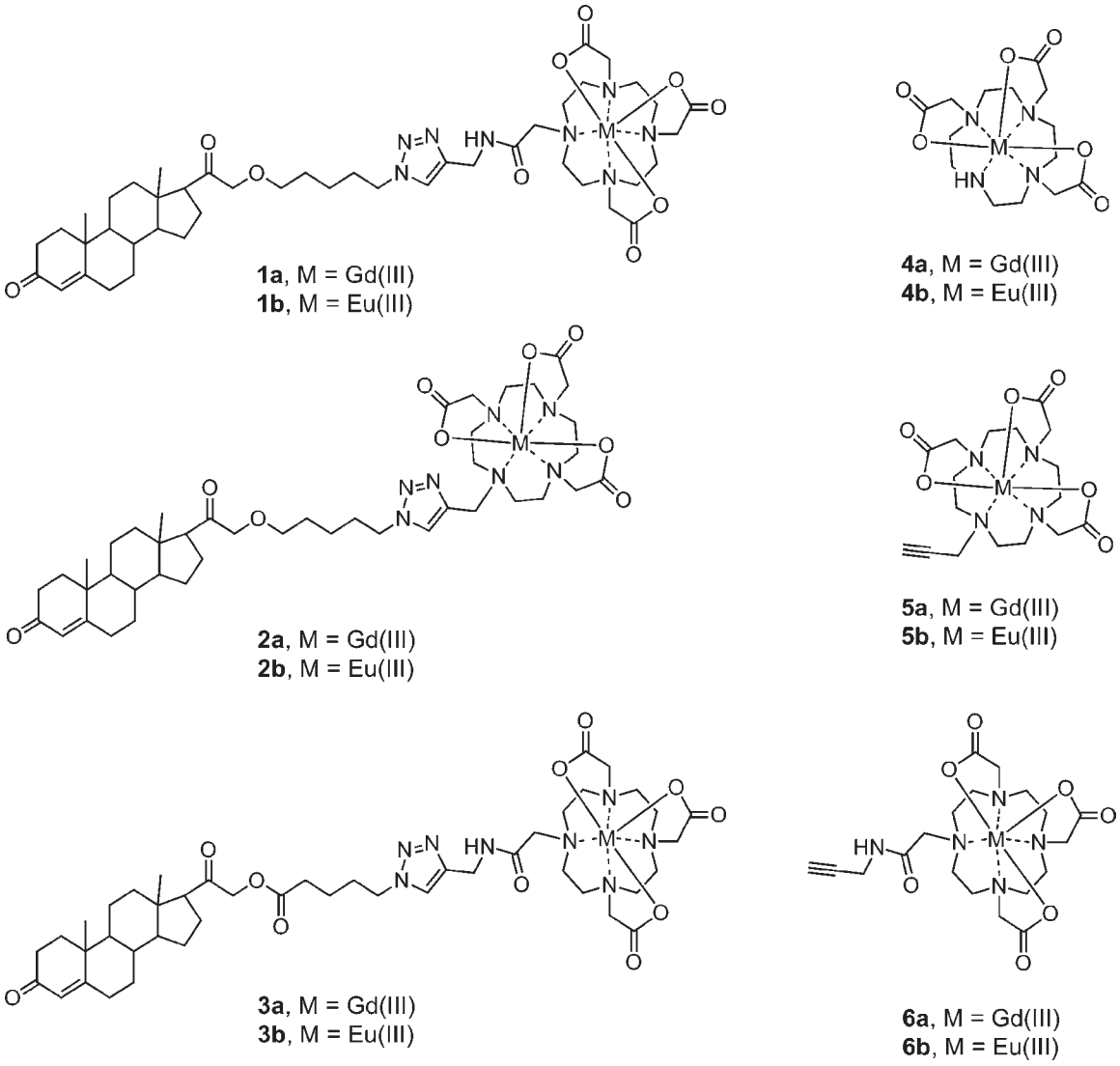

Figure 1. Chemical structures of the PR-targeted agents (**1**−**3**) and the nontargeted control agents (**4**−**6**) used in this study.

T47D cells. Two to seven days later, T47D and MDA-MB-231 ($(1-2) \times 10^6$) cells were suspended in Matrigel (1:1 volume) and injected subcutaneously into the rear flank (T47D cells on the right side and MDA-MB-231 cells on the left). Mice were monitored for tumor growth every two to three days after injection of cells. Mice were imaged two to three weeks after xenografting when tumors were palpable with a minimum weight of 20 mg (determined after tumor removal postimaging).

***In Vivo* MR Imaging.** Xenografted nude mice were injected intraperitoneally (n = 1 per compound) with each agent (0.15 mmGd/kg) dissolved in 50 μL DMSO. During imaging, mice were maintained under anesthesia (1−3% isoflurane) but were allowed to wake up and recover between imaging time points. Tubing containing heated water was positioned under the mouse to keep a constant body temperature. All MR imaging was performed on a 89 mm bore size PharmaScan 7.05 T MR imager fitted with shielded gradient coils (Bruker BioSpin, Billerica, MA, USA) using a RF RES 300 1H 089/038 quadrature transmit receive volume coil (Bruker BioSpin, Billerica, MA, USA).

Standard T_1-weighted multislice multiecho (MSME) scans with fat suppression were used for imaging the uterus, ovaries, and xenografts: TR = 700 ms, TE = 10.635 ms, FOV = 35 × 35 mm, matrix size = 256 × 256, slice thickness = 1.0 mm, contiguous slices. Images were analyzed using *ImageJ*. Contrast-to-noise ratio (CNR) was calculated using the equation $CNR = (SI_{Tissue} - SI_{Muscle})/\sigma_{noise}$ where SI_{Tumor} is the signal intensity in the tumor, SI_{Muscle} is the signal intensity in the muscle, and σ_{noise} is the standard deviation of the noise. CNRs were averaged over two to three axial slices in which the tumors were clearly demarcated.

RESULTS

Click Chemistry Synthesis of Water-Soluble PR-Targeted MRI Contrast Agents. ProGlo was proven to be a successful PR-targeting MRI contrast agent *in vitro* and *in vivo*.[17,19] However, its insolubility in aqueous media resulted in a degree of toxicity and limited *in vivo* delivery.[19] In order to increase the solubility of ProGlo while attempting to retain its biological properties, the core structure of the targeting steroid and the Gd(III) chelate were maintained while the linker was modified. The structures of the new PR-targeted agents and nontargeted control agents used in this study are presented in Figure 1.

Scheme 1. Synthesis of the Azide Derivatives of Progesterone (9 and 10)[a]

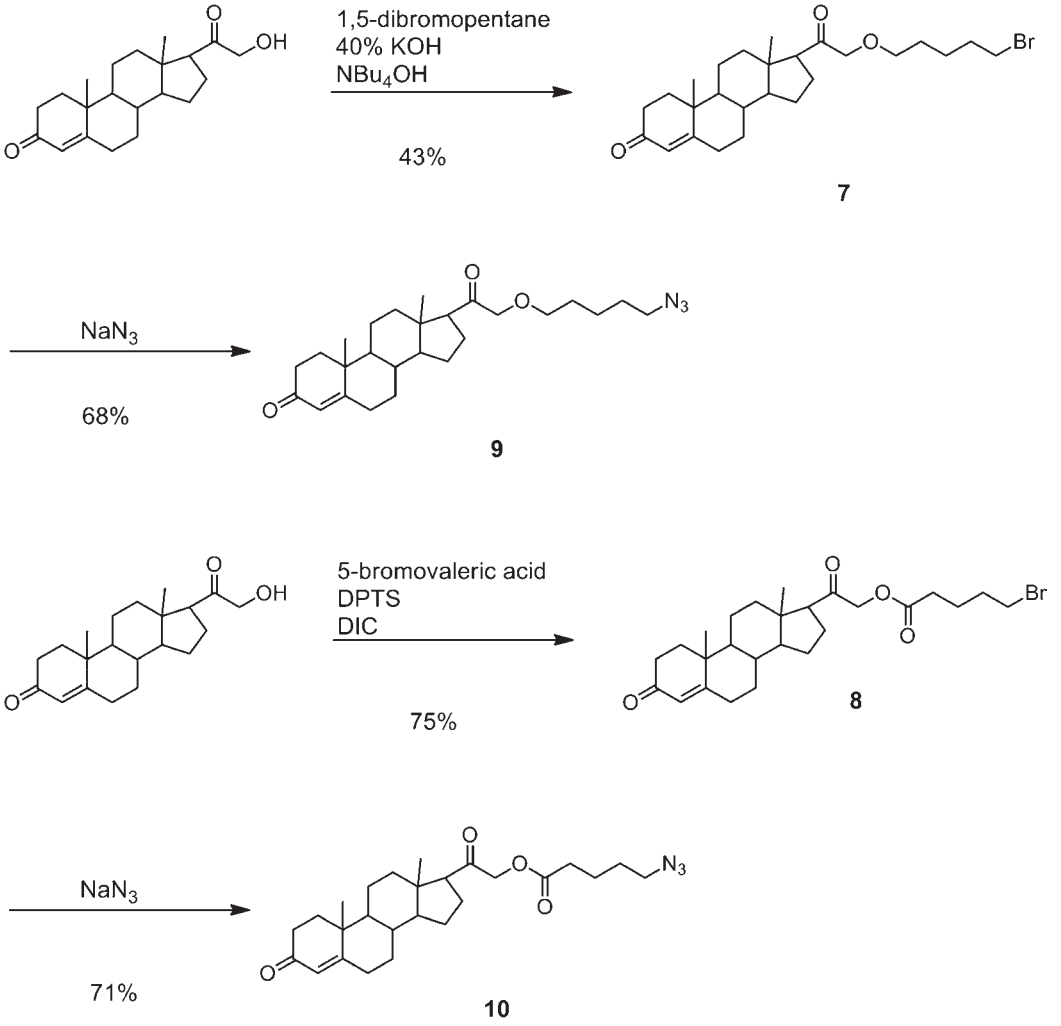

[a] These were synthesized and coupled to the alkyne-functionalized Gd(III) or Eu(III) chelates via Cu(I)-catalyzed click chemistry.

The synthesis of each water-soluble PR-targeted agent began with the coupling of 1,5-dibromopentane or 5-bromovaleric acid to 21-hydroxyprogesterone off the 21-hydroxyl group because PR is known to accommodate bulky substituents on the D ring of the progesterone.[17,26,27] Reaction with sodium azide yielded the azido derivative of these steroids (Scheme 1). Using copper-catalyzed click chemistry (Scheme 2),[28,29] these steroid derivatives were attached to alkyne-functionalized Gd(III) chelates, **5a** and **6a**, which were synthesized using modifications of previously reported procedures.[19,30−34]

Relaxivities, Hydration Numbers, and Octanol−Water Partition Coefficients of Progesterone-Conjugated MRI Probes. The longitudinal relaxivities of the PR-targeted agents and **4a** are similar to those reported for clinically used contrast agents, about 4−5 mM^{-1} s^{-1} (Table 1).[35,36] Like most clinically used contrast agents, each of the PR-targeted agents has approximately one water molecule bound to the Gd(III), as determined by analysis of hydration number (q) on the Eu(III) analogues of these agents (Table 1). For complex **2b**, the coordination of one water molecule, rather than two, indicates that the triazole ring from the click reaction coordinates to the Gd(III), an effect that was previously reported.[33] For **3b** and **1b**, the q of one is due to the coordination of the amide group back to the metal.

Octanol−water partition coefficients (log P) were measured to determine the hydrophobicity of these agents, which correlates to the cellular permeability and tissue distribution (Table 1).[21,37] The negative log P value for **4a** was characteristic of its high water solubility. The log P values of these water-soluble PR-targeted agents are between the values for ProGlo and **4a**, indicating an intermediate hydrophobicity.

High Receptor Binding Affinity is Maintained by Progesterone-Modified Gd(III) Chelates. The new water-soluble agents were expected to have receptor binding affinities similar to that of ProGlo because the chemical modification occurred at the same position on the steroid. Compounds **1a** and **3a** were chosen to compare the effect of the ether to an ester linker in terms of PR binding (**2a** was not tested because this molecule has the same linker as **1a**). The relative binding affinities (RBAs) of these agents and of ProGlo were measured (Table 1). Both **1a** and **3a** have RBAs similar to that of ProGlo and about 100-fold less than that of progesterone. These results are consistent with previously published data that demonstrated approximately 100-fold lower binding affinity of ProGlo compared to unmodified progesterone.[17] Although **3a**

dx.doi.org/10.1021/bc2003555 |*Bioconjugate Chem.* 2011, 22, 2304–2316

Scheme 2. Synthesis of the Water-Soluble Progesterone-Conjugated MRI Contrast Agents via Copper-Catalyzed Click Chemistry

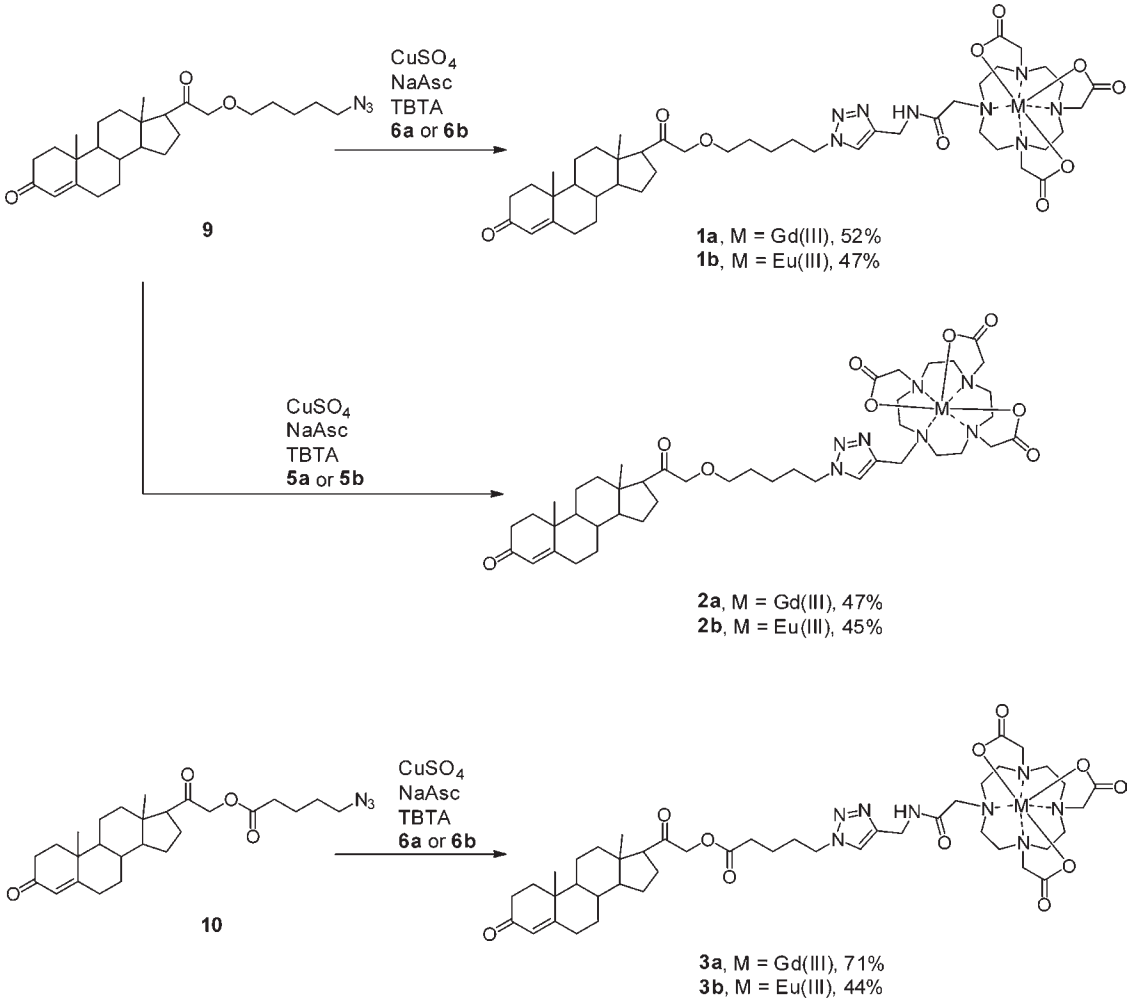

Table 1. Characterization of the Water-Soluble PR-Targeted Agents and Nontargeted Control Agents

agent[a]	r_1 (mM^{-1} s^{-1})[b]	r_2 (mM^{-1} s^{-1})[b]	q	log P	RBA
1	4.16 ± 0.05	4.78 ± 0.26	0.75	−0.37 ± 0.09	0.40%
2	4.16 ± 0.50	4.48 ± 0.33	1.03	−0.59 ± 0.04	n.d.[c]
3	4.26 ± 0.13	4.90 ± 0.14	1.24	−0.27 ± 0.08	0.29%
ProGlo	5.35 ± 0.74	6.14 ± 0.81	n.d.	1.40 ± 0.08	0.45%
4	4.05 ± 0.018	4.75 ± 0.35	2.13	−2.96 ± 0.35	n.d.
5	4.98 ± 0.069	5.64 ± 0.24	2.16	n.d.	n.d.
6	3.36 ± 0.11	3.89 ± 0.20	1.21	n.d.	n.d.

[a] Gd(III) complexes (**1a**−**6a**) were used for measuring relaxivities, log P, and RBA; Eu(III) complexes (**1b**−**6b**) were used for measuring q. [b] 1.41 T, 37 °C. [c] n.d. = not determined.

demonstrated a minimal decrease in binding affinity (likely due to the presence of the additional carbonyl), the RBAs of these agents indicate that the modifications made to the linker did not significantly affect their ability to bind PR as compared to ProGlo.

Progesterone-Conjugated MRI Probes Demonstrate Enhanced Cellular Association. To determine the cell permeability of the compounds, PR(+) (T47D) and PR(-) (MDA-MB-231) human breast cancer cells were incubated with **1a**, **2a**, **3a**, and **4a**. Time- and concentration-dependent experiments were performed to identify the optimal dose and incubation times of the agents (Figure 2). Each agent demonstrated increased cellular Gd(III) accumulation with increased incubation concentrations in both cell lines. However, time-dependent accumulation was observed only for **2a** in the PR(+) cells. The uptake of **1a** in the PR(+) cells increased slightly after 1 h and then stabilized, while the Gd(III) levels in PR(+) cells incubated with **3a** had decreased by 24 h in comparison to earlier time points. No time dependence in uptake was seen in PR(-) cells as the Gd(III) levels

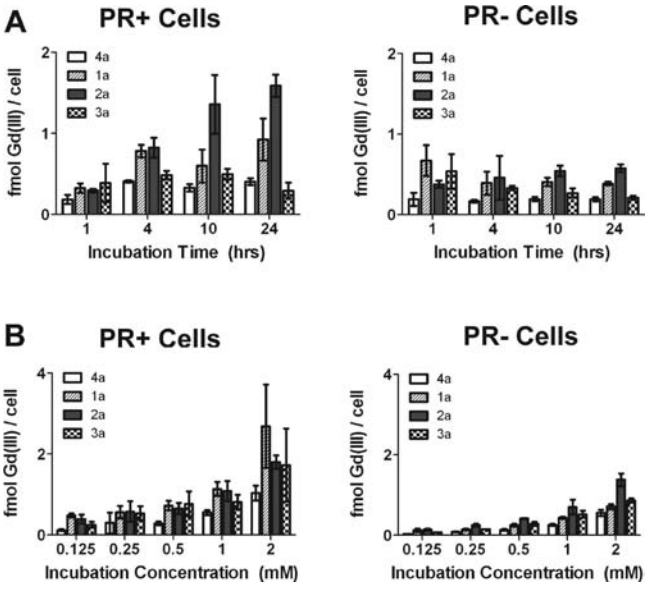

Figure 2. Cellular uptake of PR-targeted agents and nontargeted control. (A) Time-dependent cellular uptake of Gd(III) in PR(+) versus PR(-) cells after incubation with **4a**, **1a**, **2a**, and **3a**. (B) Concentration-dependent cellular uptake of Gd(III) in PR(+) versus PR(-) cells after incubation with **4a**, **1a**, **2a**, and **3a**. Error bars represent mean ± standard deviation.

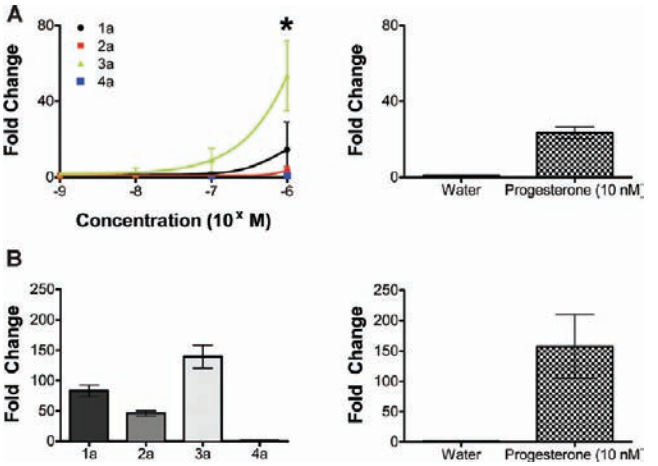

Figure 3. Progesterone Gd(III) chelates initiate gene transcription. (A) Incubation with **3a** resulted in the greatest transcriptional activation of luciferase reporter gene, while incubation with **4a** resulted in no transcriptional activation (left). The asterisk denotes a significant difference in activation after incubation with **3a** compared to **1a** (at the highest incubation concentration, $p < 0.05$, Student's t test). Activation with water or 10 nM progesterone is shown as a control (right). (B) Endogenous gene transcription is consistent with the luciferase assay. Induction of ZBTB16 was normalized to GAPDH. Error bars represent mean ± standard deviation.

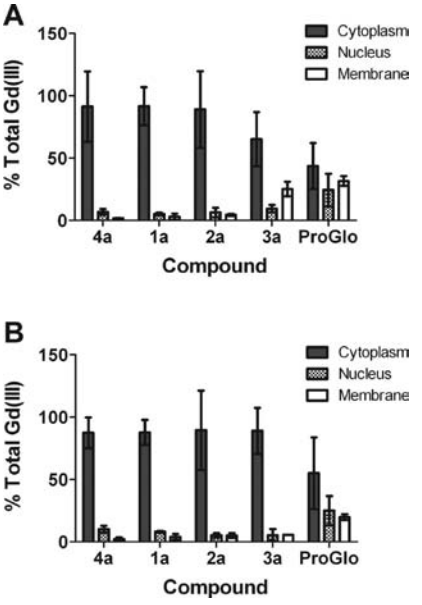

Figure 4. Subcellular localization of the water-soluble PR-targeted agents, ProGlo, and nontargeted **4a**. (A) Subcellular localization in PR(+) T47D cells. (B) Subcellular localization in PR(-) MDA-MB-231 cells. Error bars represent mean ± standard deviation. The water-soluble agents predominantly localized to the cytoplasm, whereas ProGlo was distributed in significant levels in the nucleus and membrane.

remained constant at all time points or even decreased (for **3a**). The uptake of the steroid-conjugated agents was higher than that of **4a** at all time points and cell lines, except for **3a**, which showed equal or lower Gd(III) than **4a** at the 24 h time point in both cell lines. These results indicate that the presence of the steroid moiety encourages cellular uptake of the targeted contrast agents when compared to the nonfunctionalized Gd(III) chelate.

Importantly, the Gd(III) accumulation of the PR-targeted agents was significantly higher in PR(+) than in PR(-) cells. While the uptake of **4a** was higher in PR(+) cells than in PR(-) cells, the difference in uptake was lower than for the progesterone-conjugated agents (particularly **1a** and **2a**). These data indicate that conjugation with progesterone increases the ability of Gd(III) contrast agents to associate with cells. In addition, the increased Gd(III) accumulation in PR(+) cells compared to PR(-) cells suggests that PR likely plays a role in the accumulation and retention of these progesterone-conjugated agents.

Water-Soluble PR-Targeted Agents Cross the Cell Membrane and Activate PR. Progesterone receptors bind to a region of DNA referred to as the progesterone response element (PRE).[17] This DNA element was ligated to the luciferase gene and used to verify the ability of the compounds to cross the cell membrane and interact with PR to form a functional transcription complex. The change in luciferase activity at increasing incubation concentrations of each PR-targeted contrast agent is shown in Figure 3a (left graph). The graph on the right in Figure 3 shows the change in luciferase activity when cells were incubated with either water or 10 nM progesterone as a positive control. As expected, the control compound **4a** did not induce PRE-mediated transcription to any significant extent. However, incubation with each of the progesterone derivatives resulted in luciferase activity, indicating that these compounds entered the cells and bound to PR as agonistic ligands. Interestingly, **3a** was the most effective agent despite its low cell uptake and lower relative binding affinity for PR *in vitro* compared to **1a** and **2a**. Compound **2a** demonstrated the lowest efficacy of the three progesterone-conjugated agents.

To further investigate the ability of the contrast agents to activate transcription, PR-regulation of the gene ZBTB16 was examined based on previous reports of its induction in T47D

cells (Figure 3b). The increase in ZBTB16 transcription in response to **1a**−**4a** and progesterone was measured and normalized to GAPDH. Each progesterone-conjugated agent activated transcription after incubation at 10 nM, providing further evidence that these agents cross the cell membrane and bind to PR. Furthermore, the transcriptional activation demonstrated the same relative potency as the luciferase assays in that **3a** demonstrated the highest activation of endogenous gene transcription. As expected, control agent **4a** did not result in transcription of endogenous ZBTB16.

Water-Soluble MRI Contrast Agents Localize to the Cytoplasm. To examine the cellular distribution of the water-soluble PR-targeted agents as compared to **4a** and ProGlo, PR(+) and PR(-) cells incubated with each agent were subjected to a nuclear cytoplasmic fractionation kit (Figure 4). The pellet remaining after isolation of the nuclear and cytoplasmic fractions was assumed to contain material that was primarily associated with cell membrane proteins.

As expected, the majority of each agent was found in the cytoplasm of each cell type. However, the fraction of agent in the cytoplasm was lowest for ProGlo in both PR(+) and PR(-) cells. For **4a** and the water-soluble PR-targeted agents, the fraction of agent in the cytoplasm was around 80−90% in both cell lines except for **3a**, which showed a lower fraction in the cytoplasm of the PR(+) cells. The fraction of Gd(III) in the nucleus and membrane was similar for **4a** and the water-soluble agents in both cell lines, although **3a** had a higher presence in the pellet fraction in the PR(+) cells. ProGlo was found in high levels (relative to **1a**−**4a**) in the pellet and in the nucleus in both cell lines.

The majority of PR resides in the cytoplasm, but it was expected that incubation with the targeted contrast agents would result in translocation of a fraction of the total cytoplasmic receptor to the nucleus, leading to higher levels of Gd(III) in the nucleus after incubation with the targeted agents compared to **4a**. While the luciferase assays and real-time PCR indicated that PR was activated, the difference in levels of progesterone-conjugated agents versus **4a** that translocated to the nucleus was likely too low to detect using ICP-MS. However, the cell fractionation data indicate that in cells incubated with the water-soluble contrast agents, the majority of the Gd(III) associated with these cells is intracellular and not interacting within the membrane. While this was true for cells incubated with ProGlo, 20−30% of the total ProGlo was detected in the remaining membrane pellet fraction. The hydrophobicity of ProGlo likely increased nonspecific interaction with nontargeted biomolecules and could explain high levels of the agent in the membrane, as well as the higher levels in the nucleus compared to fractions from cells incubated with the water-soluble agents.

Water-Soluble Agents Demonstrate Lower Cytotoxicity than ProGlo. To determine the toxicity profile of the agents, a MTS assay of cell viability was conducted after incubating T47D or MDA-MB-231 cells with varying concentrations of each agent for a 24 h period. The toxicities of the water-soluble agents were compared to that of progesterone, ProGlo, and the nontargeted **4a**, and the data are presented in Figure 5.

As expected, in PR(+) T47D cells, the water-soluble PR-targeted agents were less toxic than ProGlo at all concentrations except for the lowest concentration tested. In addition, progesterone was more toxic than the water-soluble agents at the highest concentration tested (2.5 mM), but reached similar levels at 1.25 mM and lower. Control agent **4a** was nontoxic at all concentrations tested. In PR(-) MDA-MB-231 cells, all agents had similar toxicity profiles, including **4a**. While the effect on cell viability in both cell types was similar for ProGlo and progesterone, **4a** and the water-soluble PR-targeted agents were surprisingly more toxic in the MDA-MB-231 cells than in the T47D cells. **3a** was the most toxic of the water-soluble agents in both cell lines.

Water-Soluble Progesterone-Conjugated MRI Contrast Agents Specifically Enhance Contrast in PR(+) Preliminary Xenograft Images. To determine whether the water-soluble progesterone-conjugated agents would increase the contrast-to-noise ratio (CNR) of PR(+) tumors relative to PR(-) tumors *in vivo*, athymic nude mice with PR(+) and PR(-) xenografted tumors were injected intraperitoneally with **1a**, **2a**, or **3a** dissolved in DMSO and imaged at 2 and 6 h postinjection. Intraperitoneal injection was chosen over subcutaneous injection because it yielded more consistent results in previous studies, and the parent compound, ProGlo, has been more extensively studied for its biodistribution after intraperitoneal injection.[19] In addition, while these agents are water-soluble, they were dissolved in DMSO to compare back to previous *in vivo* imaging with the insoluble ProGlo and the control agent **4a**.[19]

After injection of each of the PR-targeted agents, the PR(+) tumor exhibited significantly higher CNR than the PR(-) tumor at 6 h postinjection with **2a**, 2 and 6 h postinjection with **1a**, and 2 h postinjection with **3a** (Figure 6A, top graphs). At all other time points, the CNRs in the PR(+) and PR(-) were not significantly different. This is in contrast to the CNRs after injection with nontargeted **4a**, in which the CNRs of the PR(+) and PR(-) tumors were not significantly different at any time point.[19] The uptake of these agents in the different tumor types can be partially attributed to PR-independent mechanisms, which would explain the presence of contrast agent in the PR(-) tumors. However, the increased CNR in the PR(+) compared to the PR(-) tumor is seen only with the progesterone-functionalized agents, indicating that the agents used here are targeting PR *in vivo*. Most likely, the higher accumulation in the PR(+) tumors is a result of accumulation and retention due to interaction with PR as previously reported[17] rather than PR-driven uptake of the agents.

Analysis of the xenograft images revealed that the PR-targeted agents each increased the CNR in both tumors over the preinjection CNR levels, particularly after injection of **1a** and **3a** (Figure 6A, bottom graphs). Injection with ProGlo was previously reported to similarly increase CNR several-fold in both tumors, while injection with Gd-DO3A resulted in only minimal increases in CNR over time. Furthermore, the fold changes in CNR (compared to the preinjection CNR) in the PR(+) tumors after injection with **1a** and **3a** were 16% and 34% higher, respectively, at the 2 h time point than with ProGlo.[19] Injection with **3a** resulted in the highest overall increase in CNR of the three agents, but **1a** demonstrated a several-fold increase in CNR along with higher CNR in the PR(+) tumor than the PR(-) tumor at both the 2 and 6 h time points. These data provide evidence that the water-soluble PR-targeted probes function better as tumor imaging agents compared to nonfunctionalized **4a**, and they preferentially target PR(+) cancer cells over PR(-) cancer cells (in similar fashion to ProGlo). Of the three water-soluble agents tested, **1a** provided an optimal balance between tumor uptake and specificity for PR(+) cells compared to PR(-) cells. Representative images of the xenografts at each time point are shown in Figure 6B.

Importantly, there was no observed toxicity associated with mice that were intraperitoneally injected with these water-soluble

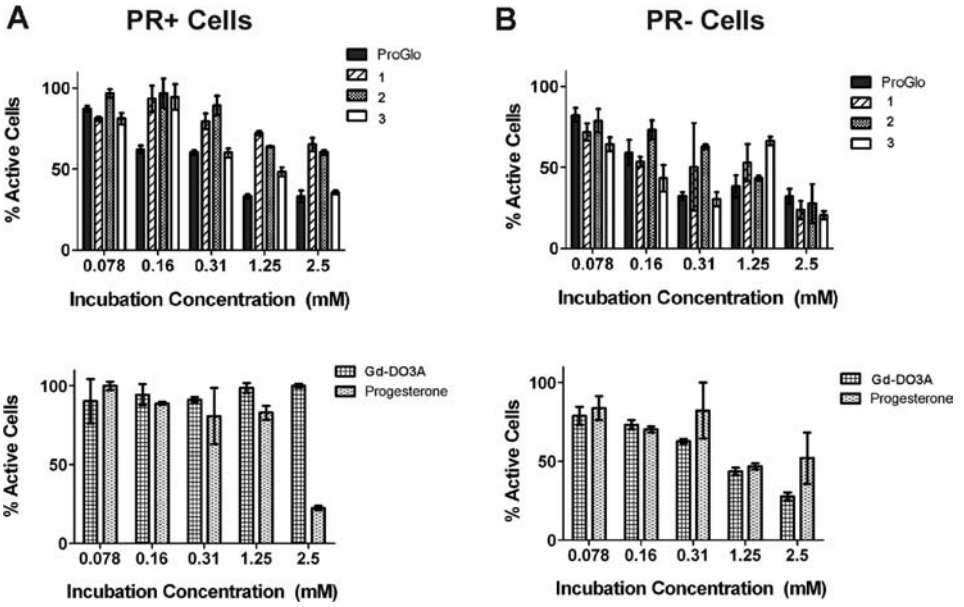

Figure 5. Cytotoxicity of the PR-targeted agents (top graphs) compared to progesterone and nontargeted **4a** (bottom graphs). (A) Cell viability in PR(+) T47D cells. (B) Cell viability in PR(-) MDAMB-231 cells. The water-soluble PR-targeted agents are associated with lower toxicity than ProGlo in both cell lines.

PR-targeted agents. Intraperitoneal injection with ProGlo had previously been associated with toxicity (xenografted mice injected with ProGlo in this manner became lethargic after the 6 h time point and did not survive to 24 h).[19] The mice injected with the water-soluble agents, however, remained active and survived to 24 h after injection with no changes in behavior.

DISCUSSION

Steroid receptors such as PR correlate with disease prognosis and therapeutic efficacy in breast cancer.[5,38] Receptor status is currently determined by immunohistochemistry assays of tumor biopsy samples, but noninvasive PR imaging agents would allow for improved molecular characterization, treatment decisions, and repeat analyses.[12] The hydrophobic PR-targeted ProGlo previously described demonstrated accumulation in, and consequent enhancement of, CNRs in PR-rich organs and tumors *in vivo*.[19] Here, we have described the synthesis and biological testing of several new water-soluble ProGlo derivatives. These agents were associated with lower toxicity than ProGlo, but retained the ability to target PR *in vitro* and in preliminary *in vivo* experiments.

ProGlo is preferentially taken up by and retained in PR(+) cells and enhances the signal intensity of PR-rich tissues *in vitro* and *in vivo*. However, this agent was associated with toxicity both *in vitro* and *in vivo*[19] due to its hydrophobic nature.[21−23] To decrease toxicity while maintaining PR targeting and biological activity, the structure of ProGlo was modified by using click chemistry to introduce a 1,2,3-triazole ring into the linker between progesterone and the Gd(III) chelate, which resulted in increased solubility. 1,4-Disubstituted 1,2,3-triazole are known to possess a large dipole moment, and the nitrogen atoms act as hydrogen bond acceptors, which improves the solubility in water.[39] In addition, this triazole is spaced several carbons away from the steroid and did not interfere with receptor binding, as evidenced by the similar RBAs for these novel agents as compared to ProGlo.

The induction of luciferase and endogenous progesterone-regulated ZBTB16 by each PR-targeted agent indicates that these agents crossed the cell membrane and bound to PR at biologically significant amounts. While **3a** was not taken up well by cells, the ester may have hydrolyzed (due to the presence of esterases or via other mechanisms) to release 21-hydroxyprogesterone. This cleavage product would bind more strongly to PR and could explain the higher transcriptional activity observed after incubation with **3a**.

The water-soluble progesterone-conjugated agents were less toxic than ProGlo due to their hydrophilic nature. The reduced toxicity is partially explained by decreased nonspecific interactions with these water-soluble agents as compared to ProGlo, as demonstrated by the cell fractionation experiments. ProGlo was distributed almost evenly across all the compartments analyzed, while the water-soluble agents were primarily located in the cytoplasm, indicating more nonspecific interaction between Proglo and off-target biomolecules. Incubation with **3a** resulted in Gd(III) accumulation in the membrane of the PR(+) cells, possibly due to ester hydrolysis and subsequent production of a Gd(III) chelate with a pentanoic acid tail that could insert in cell membranes. This ester cleavage might explain the high signal intensity surrounding the PR(+) tumor in the *in vivo* images taken 2 h after injection with **3a**, as well. In addition, ester hydrolysis would release 21-hydroxyprogesterone, which would enter the cells at high levels and could explain the higher cytotoxicity observed after incubation with this agent.

Studies in tumor xenografts demonstrated that **1a**, **2a**, and **3a** preferentially enhanced CNR in PR(+) tumors as compared to PR(-) tumors at 2 and/or 6 h after injection. Injection of control agent **4a**, by contrast, resulted in minimal changes in CNR at 2 and 6 h postinjection and no difference between the PR(+) and PR(-) tumors. Of these PR-targeted agents, **1a** was the most promising in that it resulted in higher CNR in the PR(+) tumor than the PR(-) tumors at both 2 and 6 h postinjection. In addition, the fold change in CNR compared to preinjection levels

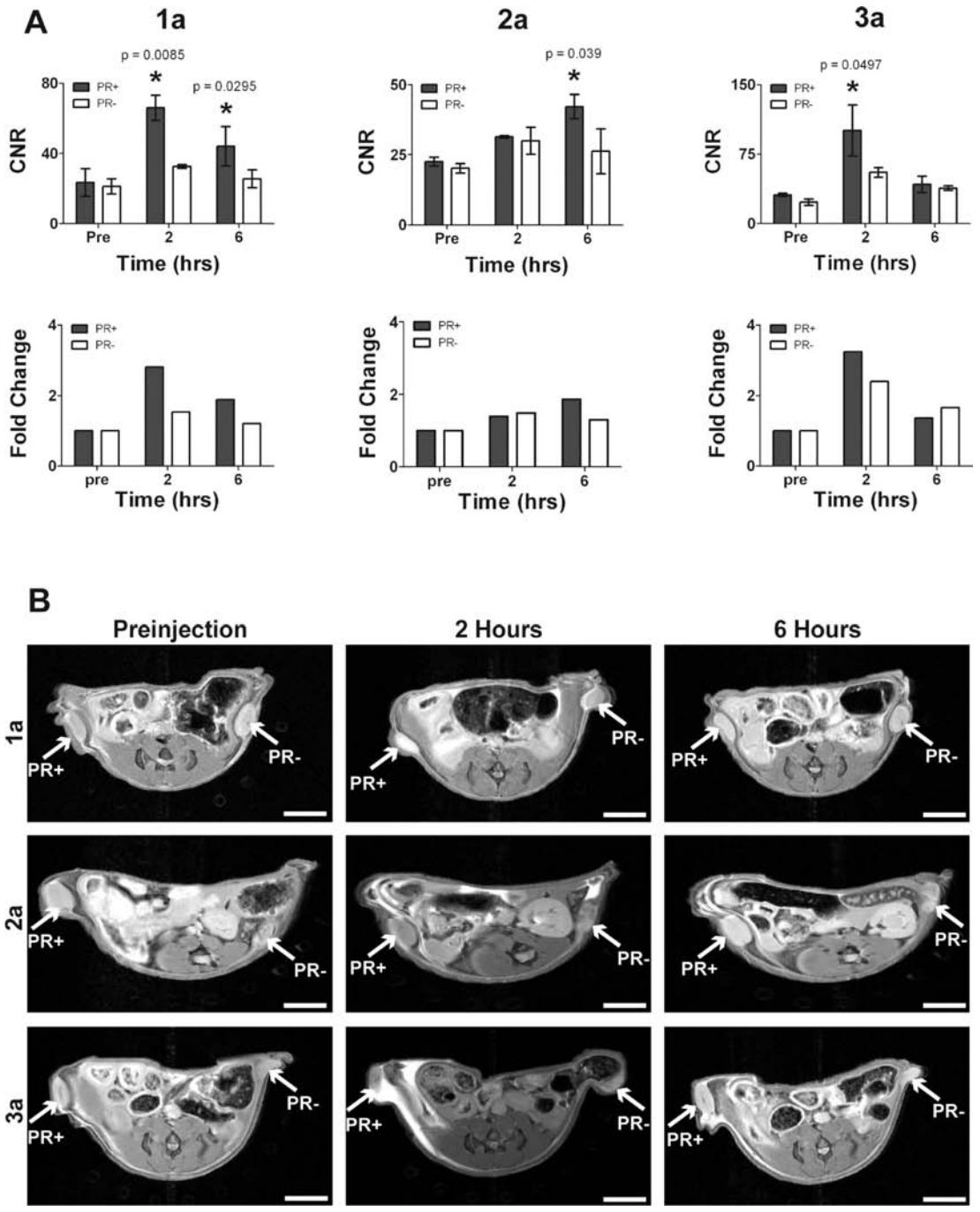

Figure 6. Xenograft images before and after injection of water-soluble agents. (A) Changes in contrast-to-noise ratio (CNR) in individual mice after intraperitoneal injection of **1a**, **2a**, or **3a** (top graphs) and fold change in CNRs compared to preinjection CNR levels (bottom graphs). The water-soluble progesterone-conjugated agents preferentially enhanced CNR in the PR(+) tumors compared to the PR(-) tumors (asterisks, Student's *t* test $p < 0.05$). Error bars represent ± standard deviation of the mean. (B) Representative images of xenografted mice injected subcutaneously with **1a** (top panels), **2a** (middle panels), or **3a** (bottom panels). White scale bars represent 5 mm.

was higher in the PR(+) tumor than the PR(-) tumor at both time points after injection. The accumulation of Gd(III) in these tumors may have been time-dependent. Injection with **1a** and **3a** increased CNR by 2 h, but CNR had decreased by 6 h. Injection with **2a**, however, resulted in a slow increase in CNR over time. Interestingly, this pattern corresponded to the cellular accumulation in cells where **2a** was the only agent tested that demonstrated time-dependent accumulation in PR(+) cells. Studies are ongoing to determine the optimal postinjection imaging time points for each of these agents.

The changes in CNR in the PR(+) tumor after injection of the water-soluble PR-targeted agents were comparable to or greater than the changes seen after injection of ProGlo previously demonstrated.[19] The difference between CNRs of the PR(+) and PR(-) tumors was greater after injection of these water-soluble agents than after intraperitoneal injection of ProGlo,

indicating that these agents possibly have more bioavailability due to their enhanced solubility. Finally, these water-soluble agents were associated with less *in vivo* toxicity than ProGlo. The enhanced solubility and bioavailability combined with the decreased toxicity might both be attributed to the less hydrophobic nature of these agents. Further *in vivo* investigations are being conducted to determine biodistribution of these agents and the optimal mode of injection.

Recent reports have asserted that, although there has been a focus on developing drugs that accumulate in cancer cells, this accumulation might actually prevent drugs from penetrating deep within tumors and decrease their efficacy.[40−42] Drugs that accumulate quickly within cells tend not to penetrate deeper areas of tumors, while less cell-permeable drugs travel further within the tumor and are more effective.[42] This indicates that decreasing lipophilicity of the agent would reduce cellular accumulation and allow for improved tumor penetration. The ability to inject water-soluble agents intravenously would also increase tumor penetration, as the angiogenic vasculature of the tumor would likely leak the agent allowing for accumulation. For imaging agents, this property of tumor penetration would be essential in terms of measuring receptor levels in a tumor with heterogeneous receptor distribution.[43] The PR-targeted agents described here would likely penetrate tumors better than ProGlo and increase signal intensity of the entire tumor rather than the surface especially since it can only be administered intraperitoneally or subcutaneously. Thus, in future work, the water-soluble PR-targeted agents might prove to be excellent tumor targeted contrast agents *in vivo*.

In conclusion, a series of water-soluble PR-targeted MRI contrast agents were designed and synthesized. These agents crossed cell membranes PR(+) T47D cells and activated PR at biologically relevant levels but exhibited lower *in vitro* and *in vivo* toxicity than the more hydrophobic ProGlo. Finally, these progesterone-conjugated agents enhanced CNR in PR(+) tumors as compared to PR(-) tumors in preliminary imaging studies in xenografts, warranting further *in vivo* investigations to prepare PR-targeted MR agents for noninvasive diagnosis of hormone related cancers and for elucidating the molecular pathways involved in these diseases.

■ ASSOCIATED CONTENT

Supporting Information. Synthetic procedures, analytical HPLC traces of purified complexes, and Table S1. This material is available free of charge via the Internet at http://pubs.acs.org.

■ AUTHOR INFORMATION

Corresponding Author

*Thomas J. Meade, PhD, Department of Chemistry, Molecular Biosciences, Neurobiology and Physiology, and Radiology, Northwestern University, 2145 Sheridan Road, Evanston, IL 60208, E-mail: tmeade@northwestern.edu. Joanna E. Burdette, PhD, College of Pharmacy, Department of Medicinal Chemistry and Pharmacognosy, University of Illinois at Chicago, 900 South Ashland, Chicago, IL 60607, E-mail: joannab@uic.edu.

■ ACKNOWLEDGMENT

We thank Dr. Teresa Woodruff for helpful advice. This work was supported by NIH grants R01EB005866 and R21CA143331. P.A.S. acknowledges support from the CDMRP Breast Cancer Research Program (BC093977) and is an ARCS (Achievement Rewards for College Scientists) Foundation Scholar. A portion of this work was completed at the Northwestern University Integrated Molecular Structure Education and Research Center. A description of the facility and full funding disclosure can be found at http://pyrite.chem.northwestern.edu/analyticalserviceslab/asl.htm. Imaging was performed at the Northwestern University Center for Advanced Molecular Imaging generously supported by NCI CCSG P30 CA060553 awarded to the Robert H Lurie Comprehensive Cancer Center. MRI was performed on the 7T Bruker Pharmascan system purchased with the support of NCRR 1S10RR025624-01. Metal analysis was performed at the Northwestern University Quantitative Bioelemental Imaging Center generously supported by NASA Ames Research Center NNA04CC36G.

■ REFERENCES

(1) Gambhir, S. S. (2002) Molecular imaging of cancer with positron emission tomography. *Nat. Rev. Cancer 2*, 683–693.

(2) Weissleder, R. (2002) Scaling down imaging: molecular mapping of cancer in mice. *Nat. Rev. Cancer 2*, 11–18.

(3) Weissleder, R. (2006) Molecular imaging in cancer. *Science 312*, 1168–1171.

(4) Pysz, M. A., Gambhir, S. S., and Willmann, J. K. (2010) Molecular imaging: current status and emerging strategies. *Clin. Radiol. 65*, 500–516.

(5) Ahmad, N., and Kumar, R. (2011) Steroid hormone receptors in cancer development: a target for cancer therapeutics. *Cancer Lett. 300*, 1–9.

(6) Benard, F., and Turcotte, E. (2005) Imaging in breast cancer: Single-photon computed tomography and positron-emission tomography. *Breast Cancer Res. 7*, 153–162.

(7) Linden, H. M., Stekhova, S. A., Link, J. M., Gralow, J. R., Livingston, R. B., Ellis, G. K., Petra, P. H., Peterson, L. M., Schubert, E. K., Dunnwald, L. K., Krohn, K. A., and Mankoff, D. A. (2006) Quantitative fluoroestradiol positron emission tomography imaging predicts response to endocrine treatment in breast cancer. *J Clin. Oncol. 24*, 2793–2799.

(8) Yoshida, Y., Kurokawa, T., Sawamura, Y., Shinagawa, A., Okazawa, H., Fujibayashi, Y., and Kotsuji, F. (2007) The positron emission tomography with F18 17beta-estradiol has the potential to benefit diagnosis and treatment of endometrial cancer. *Gynecol. Oncol. 104*, 764–766.

(9) Dehdashti, F., Picus, J., Michalski, J. M., Dence, C. S., Siegel, B. A., Katzenellenbogen, J. A., and Welch, M. J. (2005) Positron tomographic assessment of androgen receptors in prostatic carcinoma. *Eur. J. Nucl. Med. Mol. Imaging 32*, 344–350.

(10) Roy, F.-N., Croteau, E., Ouellet, R., Bujold, R., Forget, A., Dufresne, J., van Lier, J., and Benard, F. (2010) Predictive value of (16 alpha[18-F]-fluoroestradiol) FES-PET in recurrent estrogen receptor positive (ER+) breast cancer. *J. Nucl. Med. Meeting Abstr. 51*, 56.

(11) Katzenellenbogen, J. A., Zhou, H. B., Lee, J. H., Mayne, C. G., and Carlson, K. E. (2010) Imaging progesterone receptor in breast tumors: synthesis and receptor binding affinity of fluoroalkyl-substituted analogues of Tanaproget. *J. Med. Chem. 53*, 3349–3360.

(12) Lee, J. H., Zhou, H. B., Dence, C. S., Carlson, K. E., Welch, M. J., and Katzenellenbogen, J. A. (2010) Development of [F-18]fluorine-substituted Tanaproget as a progesterone receptor imaging agent for positron emission tomography. *Bioconjugate Chem. 21*, 1096–1104.

(13) Verhagen, A., Studeny, M., Luurtsema, G., Visser, G. M., De Goeij, C. C., Sluyser, M., Nieweg, O. E., Van der Ploeg, E., Go, K. G., and Vaalburg, W. (1994) Metabolism of a [18F]fluorine labeled progestin (21-[18F]fluoro-16 alpha-ethyl-19-norprogesterone) in humans: a clue for future investigations. *Nucl. Med. Biol. 21*, 941–52.

(14) Frullano, L., and Meade, T. J. (2007) Multimodal MRI contrast agents. *J. Biol. Inorg. Chem. 12*, 939–949.

(15) Major, J. L., and Meade, T. J. (2009) Bioresponsive, cell-penetrating, and multimeric MR contrast agents. *Acc. Chem. Res. 42*, 893–903.
(16) Lee, J., Zylka, M. J., Anderson, D. J., Burdette, J. E., Woodruff, T. K., and Meade, T. J. (2005) A steroid-conjugated contrast agent for magnetic resonance imaging of cell signaling. *J. Am. Chem. Soc. 127*, 13164–13166.
(17) Lee, J., Burdette, J. E., MacRenaris, K. W., Mustafi, D., Woodruff, T. K., and Meade, T. J. (2007) Rational design, synthesis, and biological evaluation of progesterone-modified MRI contrast agents. *Chem. Biol. 14*, 824–834.
(18) Saha, P., Hodl, C., Strauss, W. S. L., Steiner, R., Goessler, W., Kunert, O., Leitner, A., Haslinger, E., and Schramm, H. W. (2010) Synthesis, in vitro progesterone receptors affinity of gadolinium containing mifepristone conjugates and estimation of binding sites in human breast cancer cells. *Bioorg. Med. Chem. 18*, 1891–1898.
(19) Sukerkar, P. A., Macrenaris, K. W., Meade, T. J., and Burdette, J. E. (2011) A steroid-conjugated magnetic resonance probe enhances contrast in progesterone receptor expressing organs and tumors in vivo. *Mol. Pharmaceutics 8*, 1390–1400.
(20) Couture, J. F., Legrand, P., Cantin, L., Luu-The, V., Labrie, F., and Breton, R. (2003) Human 20alpha-hydroxysteroid dehydrogenase: crystallographic and site-directed mutagenesis studies lead to the identification of an alternative binding site for C21-steroids. *J. Mol. Biol. 331*, 593–604.
(21) Leo, A., Hansch, C., and Elkins, D. (1971) Partition coefficients and their uses. *Chem. Rev. 71*, 525–616.
(22) Leo, A. J. (1987) Some advantages of calculating octanol-water partition coefficients. *J. Pharm. Sci. 76*, 166–168.
(23) Price, D. A., Blagg, J., Jones, L., Greene, N., and Wager, T. (2009) Physicochemical drug properties associated with in vivo toxicological outcomes: a review. *Expert Opin. Drug Metab. Toxicol. 5*, 921–931.
(24) Beeby, A., Clarkson, I. M., Dickins, R. S., Faulkner, S., Parker, D., Royle, L., de Sousa, A. S., Williams, J. A. G., and Woods, M. (1999) Non-radiative deactivation of the excited states of europium, terbium and ytterbium complexes by proximate energy-matched OH, NH and CH oscillators: an improved luminescence method for establishing solution hydration states. *J. Chem. Soc., Perkin Trans. 2* 493–504.
(25) Quici, S., Cavazzini, M., Marzanni, G., Accorsi, G., Armaroli, N., Ventura, B., and Barigelletti, F. (2005) Visible and near-infrared intense luminescence from water-soluble lanthanide [Tb(III), Eu(III), Sm(III), Dy(III), Pr(III), Ho(III), Yb(III), Nd(III), Er(III)] complexes. *Inorg. Chem. 44*, 529–537.
(26) Williams, S. P., and Sigler, P. B. (1998) Atomic structure of progesterone complexed with its receptor. *Nature 393*, 392–396.
(27) Madauss, K. P., Deng, S. J., Austin, R. J., Lambert, M. H., McLay, I., Pritchard, J., Short, S. A., Stewart, E. L., Uings, I. J., and Williams, S. P. (2004) Progesterone receptor ligand binding pocket flexibility: crystal structures of the norethindrone and Mometasone furoate complexes. *J. Med. Chem. 47*, 3381–3387.
(28) Kolb, H. C., Finn, M. G., and Sharpless, K. B. (2001) Click chemistry: diverse chemical function from a few good reactions. *Angew. Chem., Int. Ed. Engl. 40*, 2004–2021.
(29) Tornoe, C. W., Christensen, C., and Meldal, M. (2002) Peptidotriazoles on solid phase: [1,2,3]-triazoles by regiospecific copper(i)-catalyzed 1,3-dipolar cycloadditions of terminal alkynes to azides. *J. Org. Chem. 67*, 3057–3064.
(30) Song, Y., Kohlmeir, E. K., and Meade, T. J. (2008) Synthesis of multimeric MR contrast agents for cellular imaging. *J. Am. Chem. Soc. 130*, 6662–6663.
(31) Viguier, R. F., and Hulme, A. N. (2006) A sensitized europium complex generated by micromolar concentrations of copper(I): toward the detection of copper(I) in biology. *J. Am. Chem. Soc. 128*, 11370–11371.
(32) Prasuhn, D. E., Jr., Yeh, R. M., Obenaus, A., Manchester, M., and Finn, M. G. (2007) Viral MRI contrast agents: coordination of Gd by native virions and attachment of Gd complexes by azide-alkyne cycloaddition. *Chem. Commun. (Camb.)* 1269–1271.
(33) Stasiuk, G. J., and Lowe, M. P. (2009) Click chemistry with lanthanide complexes: a word of caution. *Dalton Trans.* 9725–9727.
(34) Lebedev, A. Y., Holland, J. P., and Lewis, J. S. (2010) Clickable bifunctional radiometal chelates for peptide labeling. *Chem. Commun. (Camb.) 46*, 1706–1708.
(35) Caravan, P., Ellison, J. J., McMurry, T. J., and Lauffer, R. B. (1999) Gadolinium(III) chelates as MRI contrast agents: structure, dynamics, and applications. *Chem. Rev. 99*, 2293–2352.
(36) Meade, T. J., Taylor, A. K., and Bull, S. R. (2003) New magnetic resonance contrast agents as biochemical reporters. *Curr. Opin. Neurobiol. 13*, 597–602.
(37) Leeson, P. D., and Springthorpe, B. (2007) The influence of drug-like concepts on decision-making in medicinal chemistry. *Nat. Rev. Drug Discovery 6*, 881–890.
(38) Orlando, L., Schiavone, P., Fedele, P., Calvani, N., Nacci, A., Rizzo, P., Marino, A., D'Amico, M., Sponziello, F., Mazzoni, E., Cinefra, M., Fazio, N., Maiello, E., Silvestris, N., Colucci, G., and Cinieri, S. (2010) Molecularly targeted endocrine therapies for breast cancer. *Cancer Treat. Rev. 36* (Suppl 3), S67–S71.
(39) Marik, J., and Sutcliffe, J. L. (2006) Click for PET: rapid preparation of [18F]fluoropeptides using CuI catalyzed 1,3-dipolar cycloaddition. *Tetrahedron Lett. 47*, 6681–6684.
(40) Tunggal, J. K., Cowan, D. S., Shaikh, H., and Tannock, I. F. (1999) Penetration of anticancer drugs through solid tissue: a factor that limits the effectiveness of chemotherapy for solid tumors. *Clin. Cancer Res. 5*, 1583–1586.
(41) Minchinton, A. I., and Tannock, I. F. (2006) Drug penetration in solid tumours. *Nat. Rev. Cancer 6*, 583–592.
(42) Bryce, N. S., Zhang, J. Z., Whan, R. M., Yamamoto, N., and Hambley, T. W. (2009) Accumulation of an anthraquinone and its platinum complexes in cancer cell spheroids: the effect of charge on drug distribution in solid tumour models. *Chem. Commun. (Camb.)* 2673–2675.
(43) Mankoff, D. A., Link, J. M., Linden, H. M., Sundararajan, L., and Krohn, K. A. (2008) Tumor receptor imaging. *J. Nucl. Med. 49* (Suppl 2), 149S–163S.

Synthesis and Biological Evaluation of Water-soluble Progesterone-Conjugated Probes for Magnetic Resonance Imaging of Hormone Related Cancers

Preeti A. Sukerkar[1], Keith W. MacRenaris[1], Taryn R. Townsend[1], Roshan A. Ahmed[2], Joanna E. Burdette[2*], Thomas J. Meade[1*]

Synthesis and Characterization:

Synthesis and characterization of compound **4a** was previously described,[1] and compound **4b** was synthesized similarly. Compounds **4b**, **5a**, **5b**, **6a**, and **6b** were synthesized using modified literature procedures.[1-6]

General Procedure for Click Chemistry

All click chemistry reactions were run in 1:1 methanol:water or 1:1 DMSO:water solutions. The steroid derivative (1 eq) and Gd(III) or Eu(III) chelate (1.1 eq) were dissolved and N_2 gas was bubbled through the solution to remove oxygen. Sodium ascorbate (1 eq), $CuSO_4$ (0.167 eq), and [(1-benzyl-1H-1,2,3-triazol-4-yl)methyl]amine (TBTA) (0.02 eq) were added and the reaction mixture was stirred at 60^o C for 24 hours. The crude residue was purified by reverse phase preparative HPLC using a ramp from 0 to 100% B over 20 minutes.

{2,2',2''-(1,4,7,10-tetraazacyclododecane-1,4,7-triyl)triacetate}europium (4b). HRMS (ESI) ***m/z*** $[M + H]^+$ observed: 495.0895, calculated: 495.08939 for $C_{14}H_{24}N_4O_6Eu$. Analytical HPLC trace of the purified compound is shown below.

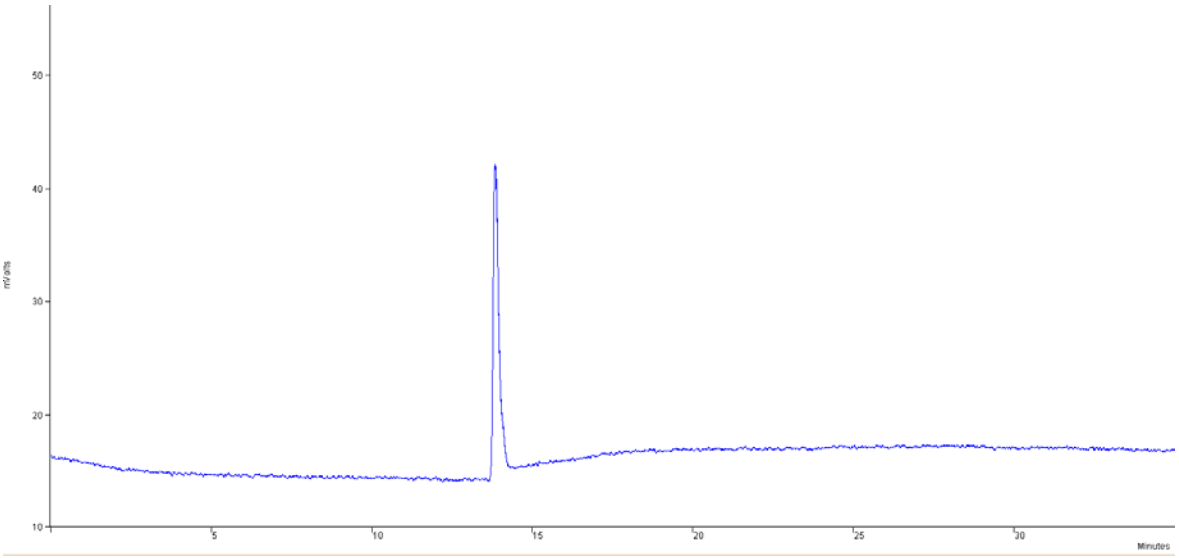

{2,2',2''-(10-(prop-2-yn-1-yl)-1,4,7,10-tetraazacyclododecane-1,4,7-triyl)triacetate}gadolinium (5a). HRMS (ESI) ***m/z*** $[M + H]^+$ observed: 536.1070, calculated: 536.10607 for $C_{17}H_{26}GdN_4O_6$. Analytical HPLC trace of the purified compound is shown below.

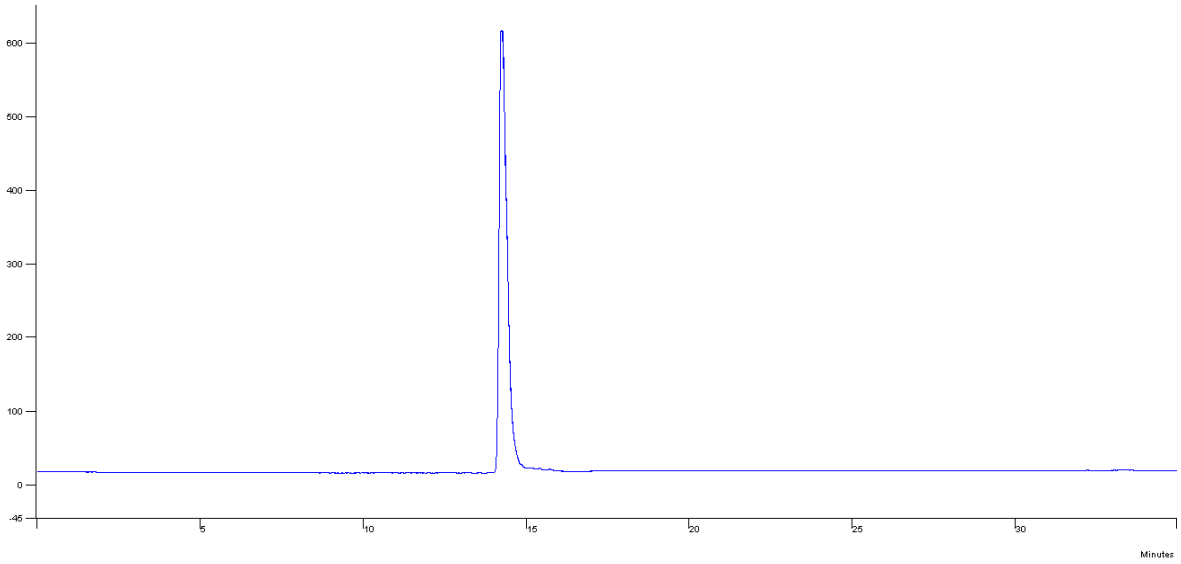

{2,2',2''-(10-(prop-2-yn-1-yl)-1,4,7,10-tetraazacyclododecane-1,4,7-triyl)triacetate}europium (5b). HRMS (ESI) ***m/z*** $[M + H]^+$ observed: 533.1050, calculated: 533.10503 for $C_{17}H_{26}EuN_4O_6$. Analytical HPLC trace of the purified compound is shown below.

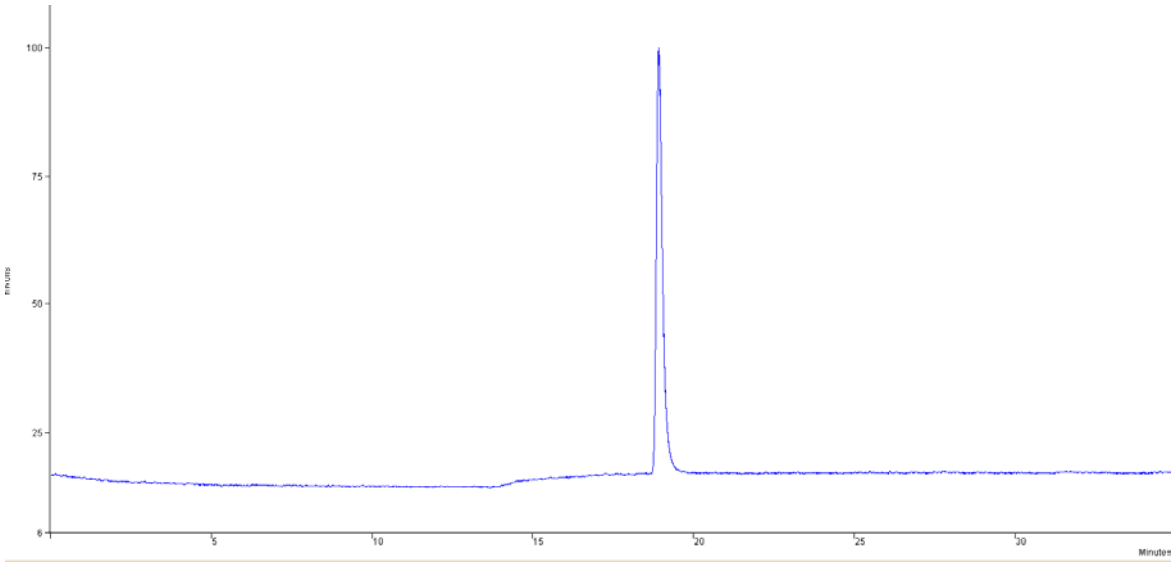

{2,2',2''-(10-(2-oxo-2-(prop-2-yn-1-ylamino)ethyl)-1,4,7,10-tetraazacyclododecane-1,4,7-triyl)triacetate}gadolinium (6a). HRMS (ESI) ***m/z*** $[M + H]^+$ observed: 593.1301, calculated: 593.12753 for $C_{19}H_{29}GdN_5O_7$. Analytical HPLC trace of the purified compound is shown below.

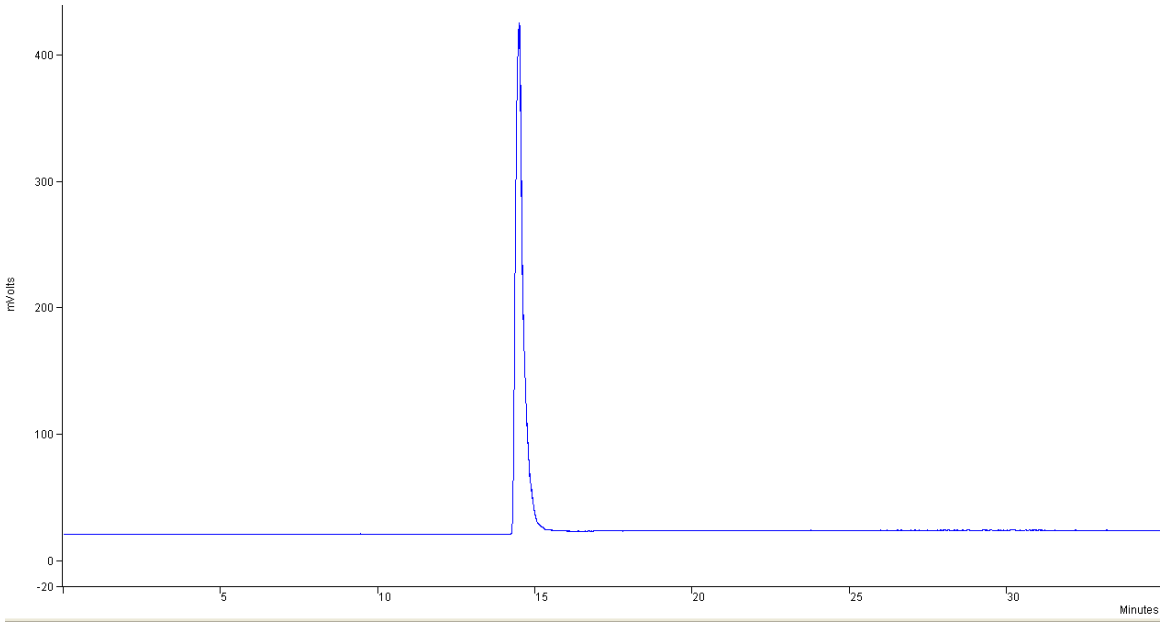

{2,2',2''-(10-(2-oxo-2-(prop-2-yn-1-ylamino)ethyl)-1,4,7,10-tetraazacyclododecane-1,4,7-triyl)triacetate}europium (6b). HRMS (ESI) ***m/z*** $[M + H]^+$ observed: 590.1259, calculated: 590.12649 for $C_{19}H_{29}EuN_5O_7$. Analytical HPLC trace of the purified compound is shown below.

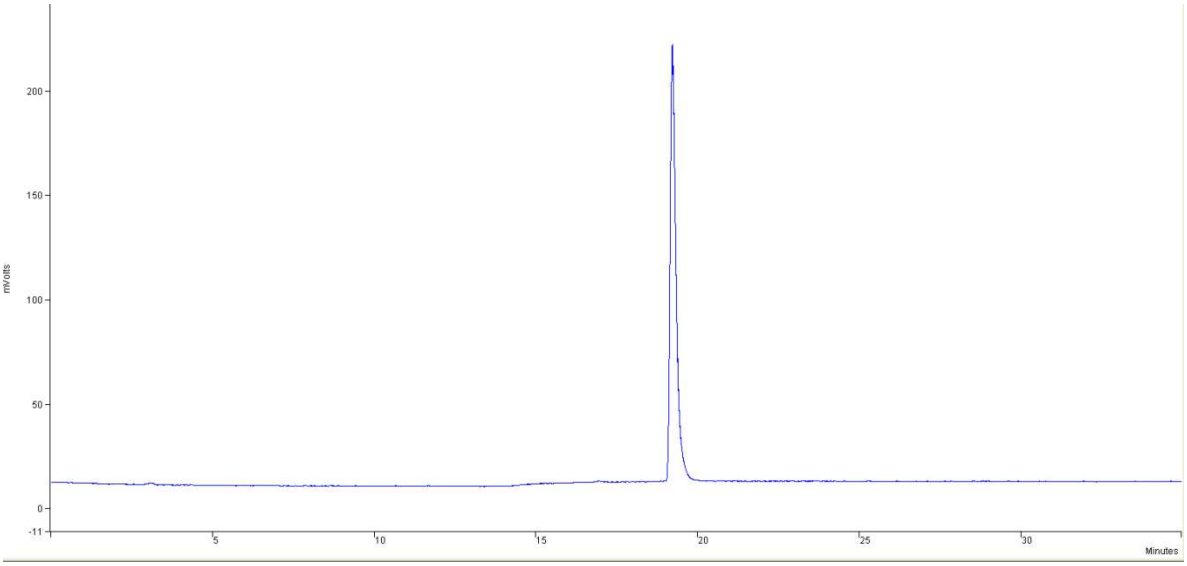

{2,2',2''-(10-(2-(((1-(5-(2-(10,13-dimethyl-3-oxo-2,3,6,7,8,9,10,11,12,13,14,15,16,17-tetradecahydro-1H-cyclopenta[a]phenanthren-17-yl)-2-oxoethoxy)pentyl)-1H-1,2,3-triazol-4-yl)methyl)amino)-2-oxoethyl)-1,4,7,10-tetraazacyclododecane-1,4,7-triyl)triacetate}gadolinium (1a) Analytical HPLC trace of the purified compound is shown below.

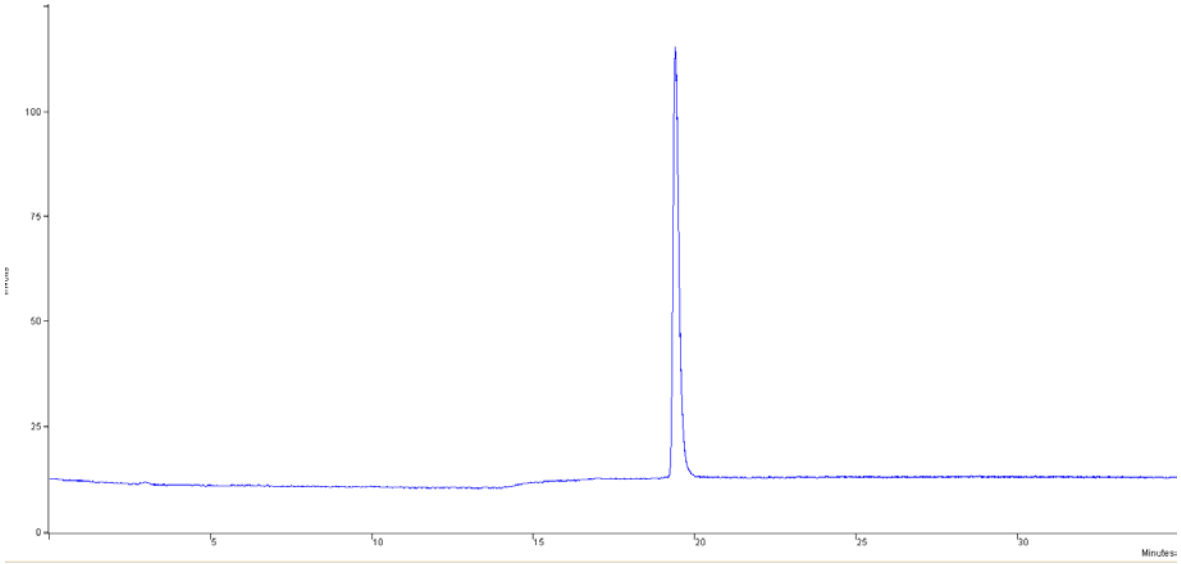

{2,2',2''-(10-((1-(5-(2-(10,13-dimethyl-3-oxo-2,3,6,7,8,9,10,11,12,13,14,15,16,17-tetradecahydro-1H-cyclopenta[a]phenanthren-17-yl)-2-oxoethoxy)pentyl)-1H-1,2,3-triazol-4-yl)methyl)-1,4,7,10-tetraazacyclododecane-1,4,7-triyl)triacetate}gadolinium (2a)

Analytical HPLC trace of the purified compound is shown below.

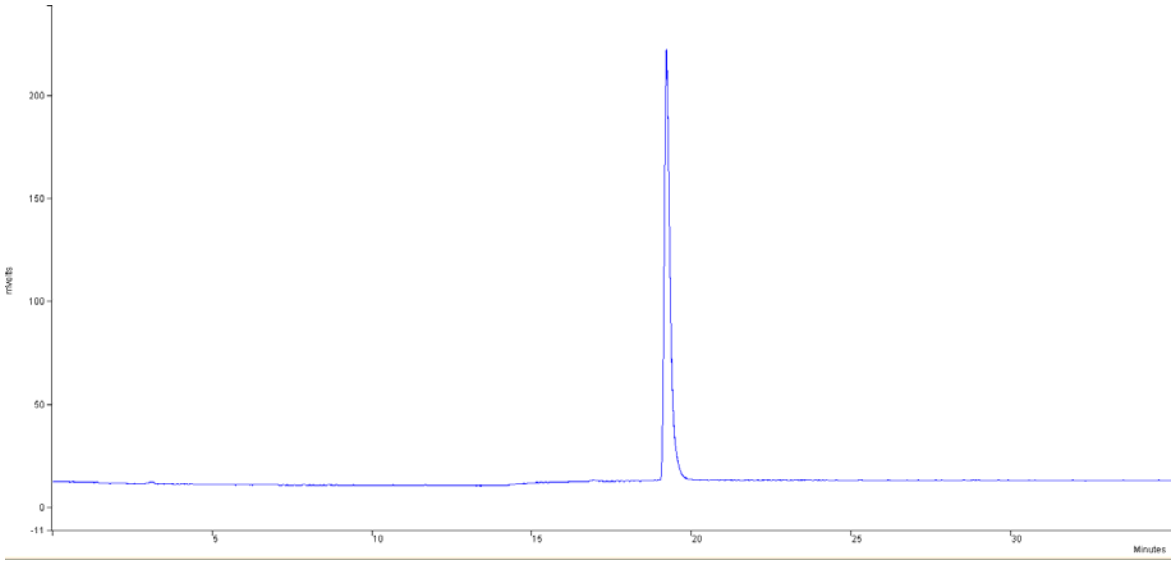

{2,2',2''-(10-(2-(((1-(5-(2-(10,13-dimethyl-3-oxo-2,3,6,7,8,9,10,11,12,13,14,15,16,17-tetradecahydro-1H-cyclopenta[a]phenanthren-17-yl)-2-oxoethoxy)-5-oxopentyl)-1H-1,2,3-triazol-4-yl)methyl)amino)-2-oxoethyl)-1,4,7,10-tetraazacyclododecane-1,4,7-triyl)triacetate}gadolinium (3a) Analytical HPLC trace of the purified compound is shown below.

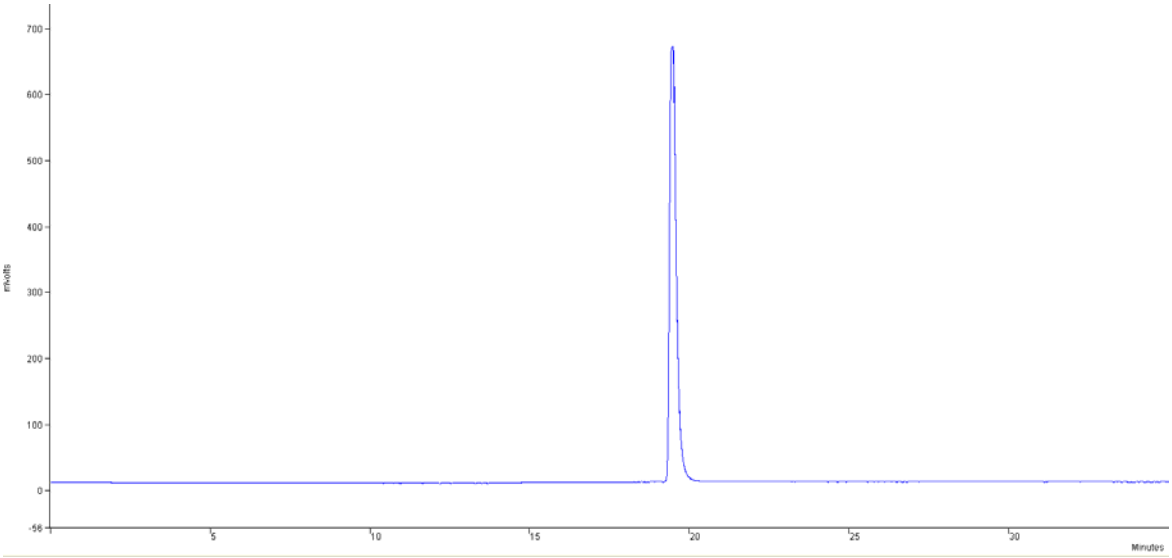

{2,2',2''-(10-(2-(((1-(5-(2-(10,13-dimethyl-3-oxo-2,3,6,7,8,9,10,11,12,13,14,15,16,17-tetradecahydro-1H-cyclopenta[a]phenanthren-17-yl)-2-oxoethoxy)pentyl)-1H-1,2,3-triazol-4-yl)methyl)amino)-2-oxoethyl)-1,4,7,10-tetraazacyclododecane-1,4,7-triyl)triacetate}europium (1b) Analytical HPLC trace of the purified compound is shown below.

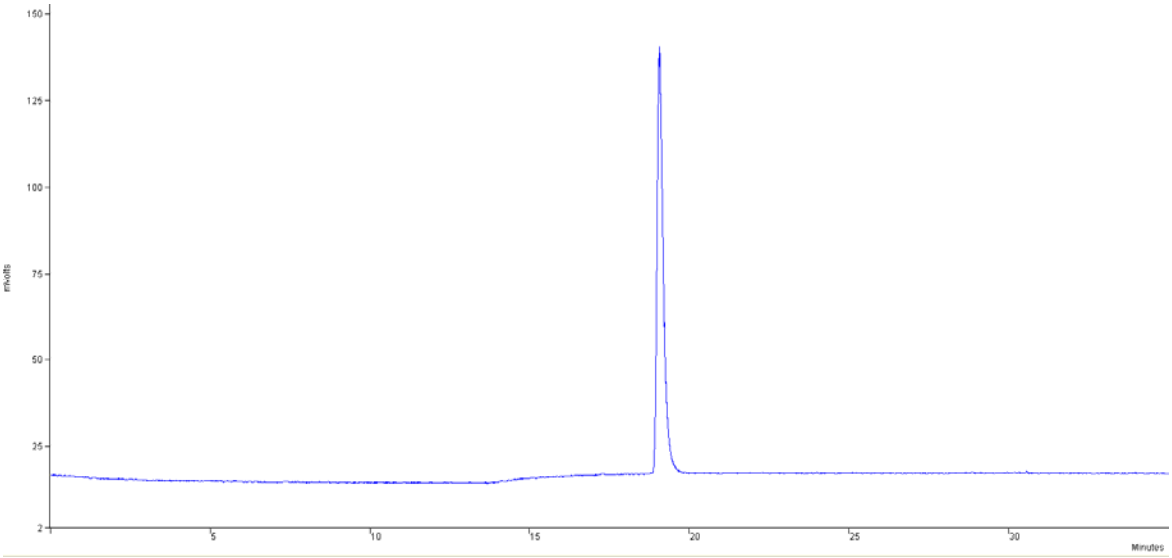

{2,2',2''-(10-((1-(5-(2-(10,13-dimethyl-3-oxo-2,3,6,7,8,9,10,11,12,13,14,15,16,17-tetradecahydro-1H-cyclopenta[a]phenanthren-17-yl)-2-oxoethoxy)pentyl)-1H-1,2,3-triazol-4-yl)methyl)-1,4,7,10-tetraazacyclododecane-1,4,7-triyl)triacetate}europium (2b) Analytical HPLC trace of the purified compound is shown below.

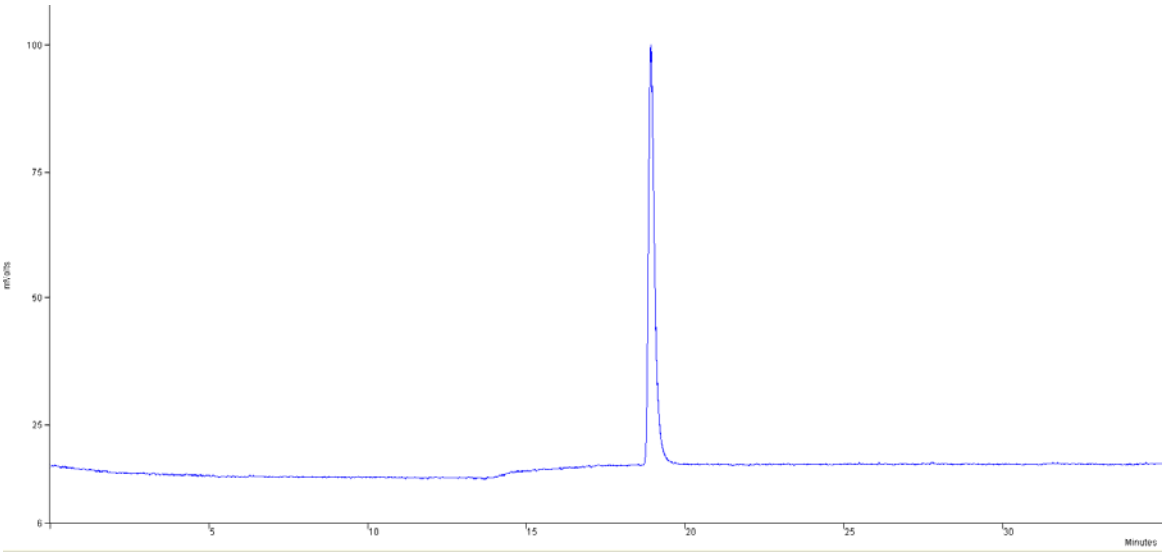

{2,2',2''-(10-(2-(((1-(5-(2-(10,13-dimethyl-3-oxo-2,3,6,7,8,9,10,11,12,13,14,15,16,17-tetradecahydro-1H-cyclopenta[a]phenanthren-17-yl)-2-oxoethoxy)-5-oxopentyl)-1H-1,2,3-triazol-4-yl)methyl)amino)-2-oxoethyl)-1,4,7,10-tetraazacyclododecane-1,4,7-triyl)triacetate}europium (3b) Analytical HPLC trace of the purified compound is shown below.

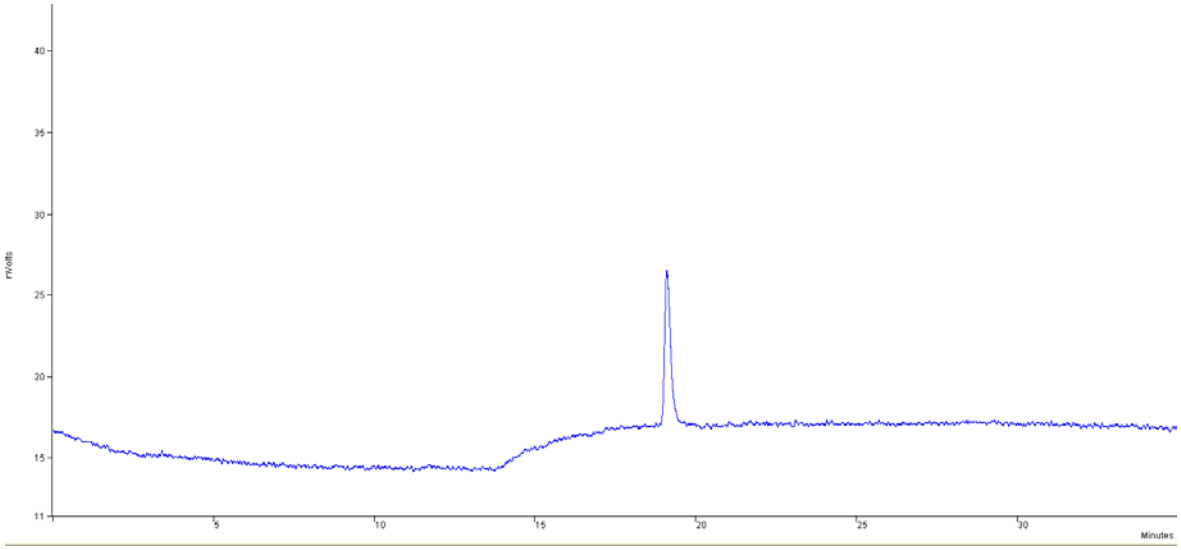

Table S1. $Log_{10}IC_{50}$ and Standard Errors for PR Binding

Agent[a]	$log_{10}IC_{50}$	Standard Error
1	3.43	0.14
2	n.d.	n.d.
3	3.65	0.25
ProGlo	3.37	0.86
Progesterone	1.03	0.09

References

(1) Sukerkar, P. A., Macrenaris, K. W., Meade, T. J., and Burdette, J. E. (2011) A Steroid-Conjugated Magnetic Resonance Probe Enhances Contrast in Progesterone Receptor Expressing Organs and Tumors in Vivo. ***Mol Pharmaceutics, 8***, 1390-1400.

(2) Song, Y., Kohlmeir, E. K., and Meade, T. J. (2008) Synthesis of multimeric MR contrast agents for cellular imaging. ***J Am Chem Soc 130***, 6662-6663.

(3) Viguier, R. F., and Hulme, A. N. (2006) A sensitized europium complex generated by micromolar concentrations of copper(I): toward the detection of copper(I) in biology. ***J Am Chem Soc 128***, 11370-11371.

(4) Prasuhn, D. E., Jr., Yeh, R. M., Obenaus, A., Manchester, M., and Finn, M. G. (2007) Viral MRI contrast agents: coordination of Gd by native virions and attachment of Gd complexes by azide-alkyne cycloaddition. ***Chem Commun (Camb)***, 1269-1271.

(5) Stasiuk, G. J., and Lowe, M. P. (2009) Click chemistry with lanthanide complexes: a word of caution. ***Dalton Trans***, 9725-9727.

(6) Lebedev, A. Y., Holland, J. P., and Lewis, J. S. (2010) Clickable bifunctional radiometal chelates for peptide labeling. ***Chem Commun (Camb) 46***, 1706-1708.

Bioconjugate Chemistry

Article

pubs.acs.org/bc

The Conformation of the Poly(ethylene glycol) Chain in Mono-PEGylated Lysozyme and Mono-PEGylated Human Growth Hormone

Sheetal S. Pai,[†] Boualem Hammouda,[§] Kunlun Hong,[∥] Danilo C. Pozzo,[⊥] Todd M. Przybycien,*[,†,‡] and Robert D. Tilton*[,†,‡]

[†]Center for Complex Fluids Engineering, Department of Chemical Engineering, and [‡]Department of Biomedical Engineering, Carnegie Mellon University, Pittsburgh, Pennsylvania 15213, United States

[§]NIST Center for Neutron Research, National Institute of Standards and Technology, Gaithersburg, Maryland 20899, United States

[∥]Center for Nanophase Materials Sciences and Chemical Science Division, Oak Ridge National Laboratory, Oak Ridge, Tennessee 37831, United States

[⊥]Department of Chemical Engineering, University of Washington, Seattle, Washington 98195, United States

Supporting Information

ABSTRACT: Covalent conjugation of poly(ethylene glycol) or "PEGylation" has proven an effective strategy to improve pharmaceutical protein efficacy by hindering recognition by proteases, inhibitors, and antibodies and by retarding renal clearance. Because it determines the strength and range of intermolecular steric forces and the hydrodynamic properties of the conjugates, the configuration of protein-conjugated PEG chains is the key factor determining how PEGylation alters protein in vivo circulation time. Mono-PEGylated proteins are typically described as having a protective PEG shroud wrapped around the protein, but recent dynamic light scattering studies suggested that conjugates adopt a dumbbell configuration, with a relatively unperturbed PEG random coil adjacent to the globular protein. We used small-angle neutron scattering (SANS) to distinguish between the dumbbell model and the shroud model for chicken-egg lysozyme and human growth hormone covalently conjugated to a single 20 kDa PEG chain. The SANS contrast variation technique was used to isolate the PEG portion of the conjugate. Scattering intensity profiles were well described by the dumbbell model and inconsistent with the shroud model.

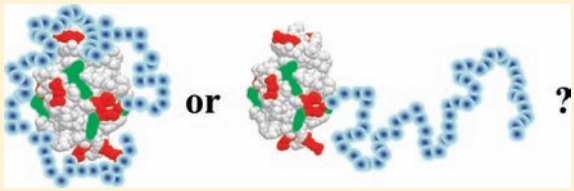

INTRODUCTION

Covalent conjugation of poly(ethylene glycol) (PEG) to proteins, PEGylation, has proven to be an effective strategy to increase in vivo circulation times of protein therapeutics, with consequent improvements in pharmaceutical efficacy.[1] The benefits derive from decreased renal clearance rates, decreased proteolytic degradation, and decreased immune response.[1−4] Decreased renal clearance is attributed to the larger hydrodynamic radius of the conjugates that hinders glomerular filtration. Protective effects are attributed to steric and hydration repulsions between PEGylated proteins and other activity-degrading proteins, [5] including immunoproteins, proteases, or inhibitors. These protective effects can accrue without loss of protein biological activity, depending on the number, molecular weight, and location of the attached PEG chains on the protein. PEGylation may also enhance protein thermal stability, making some conjugates more resistant to unfolding than their unmodified counterparts.[6] Examples of PEGylated proteins that have been approved for therapeutic use by the U.S. Food and Drug Administration include PEGasys (interferon α-2a; Genentech USA, Inc.), PEG-Intron (interferon α-2b; Merck & Co., Inc.), Neulasta (granulocyte colony-stimulating factor; Amgen), Adagen (adenosine deaminase; Sigma-Tau Pharmaceuticals, Inc.), Oncaspar (L-asparaginase; Sigma-Tau Pharmaceuticals, Inc.), and Somavert (growth hormone; Pfizer).[7] Recent work in this laboratory and others[8−11] indicates that PEG conjugation may also significantly improve the preservation of protein native structure and bioactivity during sustained release from biodegradable depots, in part by modifying the damaging interactions between the conjugates and the interfaces that they encounter during encapsulation and release.

Understanding the configuration of PEG chains when conjugated to proteins is necessary to interpret the steric protective effect and hindered renal clearance for circulating proteins in vivo and conjugate adsorption and associated denaturation in sustained-release delivery devices. Additionally, this information is important for interpreting filtration behavior[12] and chromatographic behavior[13,14] of PEGylated proteins during purification operations.

The commonly presumed structure of mono-PEGylated proteins is the shroud model, according to which an attached

Received: July 7, 2011
Revised: September 22, 2011
Published: September 28, 2011

ACS Publications © 2011 American Chemical Society

PEG chain wraps around the protein to create a shielding effect.[5,7,13−21] Lacking direct probes of the grafted PEG conjugate structure, investigators have relied on the shroud model to interpret hydrodynamic or thermodynamic measurements. For example, Fee and Van Alstine analyzed the size exclusion chromatographic behavior of PEG-conjugated proteins in terms of the protein shroud model.[13] Using three proteins (α-lactalbumin, β-lactoglobulin dimer, and bovine serum albumin), each conjugated with one or more PEG chains having one of three different molecular masses (2.4, 5.6, or 22.5 kDa), the authors concluded that the protein and conjugated PEG interacted to create a spheroid complex in which the PEG formed a layer surrounding the protein; this morphological model and corresponding geometrically based predictions did represent size exclusion chromatography retention times well for both mono-PEGylated and poly-PEGylated conjugates.[13] García-Arellano et al. used the shroud model to interpret data on the thermal stability of horse heart cytochrome *c* singly or multiply modified with 0.35, 0.75, or 2 kDa PEG;[15] the authors presumed that the PEG acts as a cage and coils around the protein surface.[15] Manjula et al. used molecular dynamics simulations to predict the configuration of 5, 10, and 20 kDa PEG chains attached to hemoglobin; they concluded that instead of passively extending from the surface of the protein, the PEG chain folds upon itself in a separate domain on the surface of the protein.[14] While the shroud model may be appropriate for multiple PEG chains attached to a protein, we investigate the conformation of one PEG chain attached to a protein as motivated by the current pharmaceutical relevance of mono-PEGylated species. Early development of PEGylated protein therapeutics was based on grafting several low molecular weight PEG chains (5 kDa); however, the trend is toward grafting a smaller number of larger PEG chains, such as 20 kDa linear PEG or 40 kDa branched PEG grafts that provide improved performance relative to the multiply conjugated proteins.[5,19] The current work is motivated by a competing model for the configuration of protein-conjugated PEG chains in mono-PEGylated species: the dumbbell model wherein the PEG conjugate exists as a relatively unperturbed random coil adjacent to, but not surrounding, the protein.

The configuration of a random coil polymer chain in solution is dictated by polymer segment excluded volume interactions and the configurational entropy of the chain. We contend that the entropic cost of wrapping a PEG chain around a globular protein that has a radius of gyration that is comparable to that of the PEG would be prohibitive. It should be noted that absent a large externally applied pressure, PEG chains do not adsorb to proteins, so there is little or no enthalpic driving force to wrap the PEG around the protein. Using dynamic light scattering (DLS), we determined that the hydrodynamic diameter of a monoPEG−lysozyme conjugate was comparable to the sum of the individual diameters of a single lysozyme plus a single 20 kDa PEG. The diffusion coefficient determined by DLS could be interpreted in terms of a cylinder having a length equal to the sum of the unperturbed PEG and lysozyme hydrodynamic diameters.[9] The same trend was observed previously in our group for ribonuclease A (RNase A) and monoPEG−RNase A.[8] Because the protein and polymer have similar dimensions in solution, it is unlikely that a single 20 kDa PEG chain would be able to wrap around these proteins. The DLS data for the monoPEG−protein conjugates support a dumbbell model. Similarly, in a study of partition coefficients obtained from size exclusion chromatography data for PEG, proteins, and the corresponding PEGylated proteins, Molek and Zydney determined that the effective spherical volume of PEGylated proteins could be estimated as the sum of the volumes of the protein and free PEG. The sieving coefficients were consistent with the conjugated PEG chains behaving as a random coil.[12] Fee later showed that these estimates hold true for systems where the PEG chain is substantially larger than the protein itself.[22] He et al. compared small-angle X-ray scattering (SAXS) and small-angle neutron scattering (SANS) data in order to draw conclusions about the shape of di-PEGylated human galectin; their findings support the dumbbell model.[23] The authors found a slight compression of the random coils with increased solution concentration of the PEGylated protein.[23] Finally, Svergun et al. used SAXS to study PEG-conjugated hemoglobin and reported that the major part of the PEG chain protrudes away from hemoglobin.[24] The authors also stated that a portion of the PEG chain interacts with the protein.[24]

The distinction between the shroud and the dumbbell models remains unresolved, because the effective conjugate sizes that would be predicted by the two models fall within the margin of error for the conventional macromolecular sizing techniques available. Thus, purely size-based methods, which are inherently indirect methods of characterizing polymer configuration, are incapable of adequately discriminating between the two prevailing conjugate models.

We used SANS as a direct method to discriminate between the dumbbell and the shroud models. This approach takes particular advantage of the unique ability to contrast match the aqueous medium with individual portions of the conjugate to exclusively probe the conformation of the remainder of the conjugate. This is not possible with X-ray or light scattering in aqueous systems. Here, we report the configuration of a single 20 kDa PEG chain grafted to either 14 kDa chicken-egg lysozyme or 22 kDa human growth hormone (HGH), grafted predominantly at the N terminus. Using mixtures of D_2O and H_2O to isolate the scattering from the PEG portion of the conjugate, we conclude that a single conjugated PEG chain exists as a random coil with dimensions similar to those of the free PEG chains in solution. The contrast-matched SANS data were well described by the random coil form factor, confirming the suitability of the dumbbell model for these conjugates. This conclusion was further supported by the inability to fit SANS data to a core−shell form factor model that would capture a polymer shell wrapped around a protein core, without resorting to unphysical model parameters. Because of its relevance to protein therapeutics, we also investigated the configuration of the PEG conjugate in a plasmalike, high oncotic pressure environment, finding similar configurations for the PEG conjugates in dilute solution and in the model plasmalike environment.

EXPERIMENTAL PROCEDURES

Materials. Chicken-egg lysozyme (Sigma-Aldrich Co., catalog no. L-6876) and deuterium oxide (Cambridge Isotopes, D > 99%) were used without further purification. HGH was donated by Genentech Inc. Methoxy-PEG−propionaldehyde (mPEG−PA), 20.7 kDa, was donated by Dr. Reddy's Laboratories (Cambridge, United Kingdom) and used without further purification. A sample of 22.2 kDa perdeuterated mPEG−PA (*d*mPEG−PA) was synthesized by the Center for Structural Molecular Biology (CSMB) Bio-Deuteration Laboratory at Oak Ridge National Laboratory and used without further purification. The molecular weights of the hydrogenated and deuterated mPEG−PA samples were determined by matrix-assisted laser desorption/ionization (MALDI) mass

spectrometry (PerSeptive Voyager STR MS, Applied Biosystems). The average degrees of polymerization for the hydrogenated mPEG−PA and the deuterated mPEG−PA were 470 and 461, respectively. Conjugation reaction and conjugate purification buffers were prepared from sodium phosphate monobasic and dibasic anhydrous salts (Fisher Scientific, 99% pure) and sodium chloride (Sigma-Aldrich Co., 99% pure). Sodium cyanoborohydride (Sigma-Aldrich Co., 95% pure) and 4-(2-hydroxyethyl)-1-piperazineethanesulfonic acid (HEPES, Sigma-Aldrich Co., ≥ 95% pure) were used as received. All water was purified by reverse osmosis followed by treatment to 18 MΩ/cm resistivity using a Barnstead NANOpure Diamond system. Synthesis of *d*mPEG−PA is described in the Supporting Information, S1.

Protein PEGylation and Conjugate Characterization. We reacted lysozyme with either the ∼20 kDa hydrogenated mPEG−PA (*h*mPEG−PA) or the deuterated mPEG−PA (*d*mPEG−PA) (1:6 mol ratio) in a pH 5.1, 100 mM sodium phosphate buffer containing 20 mM sodium cyanoborohydride, conditions established to strongly favor N-terminal PEGylation of the protein, [25] and fractionated the product into monoPEGylated and diPEGylated samples by size exclusion chromatography as described in detail previously.[9] We used MALDI mass spectrometry to determine the number of PEG molecules attached to lysozyme in each collected fraction, as described previously.[9] The location of the PEG modification was determined previously to be primarily the N-terminal lysine, with slight modification at lysine residues 33 and 97.[9] To obtain an appropriate concentration, we pooled together the purified monoPEG−lysozyme fractions from eight separate PEGylations, for both the *h*mPEG−PA and the *d*mPEG−PA. The pooled monoPEG−lysozyme samples then underwent several rounds of buffer exchange into 10 mM HEPES, pH 7.4, using a diafiltration technique with 3000 MWCO centrifugal filter units (Millipore, catalog no. UFC900324). HGH was reacted with *d*mPEG−PA (1:6 mol ratio), separated, and buffer exchanged in the same manner described above for lysozyme.

The secondary structures of the lysozyme conjugates were characterized to determine if PEGylation resulted in structural perturbations using circular dichroism (CD) spectroscopy (J-810 Spectropolarimeter, Jasco, Inc.). Far UV CD spectra of unmodified lysozyme and hydrogenated monoPEG−lysozyme and deuterated monoPEG−lysozyme indicate that the secondary structure of lysozyme was not significantly altered upon PEGylation (Figure S1 in the Supporting Information, S2). The CD spectra were further analyzed using CD Pro software[26] to provide quantitative estimates of secondary structure contents (Table S1 in the Supporting Information, S2). Results indicate that conjugate secondary structure estimates were consistent with those of the unmodified protein. Finally, all samples, in pH 7.4 10 mM HEPES buffer, were dried on a lyophilizer (Unitrap II, VirTis) before transporting them with ice packs to be reconstituted for SANS experiments. Lyophilization did not significantly impact the secondary structure of the lysozyme conjugates, as determined by CD (data not shown).

SANS. SANS experiments were performed at the National Institute of Standards and Technology (NIST) Center for Neutron Research (NCNR) using the 30 m SANS instrument NG3[27] and at Oak Ridge National Laboratory (ORNL) using the 30 m Bio-SANS instrument at the High Flux Isotope Reactor (HFIR). Each lyophilized sample was suspended in the appropriate medium (H_2O, D_2O, or H_2O−D_2O mixture) at room temperature and immediately loaded into quartz cells with a 1 mm path length. At NIST, a neutron wavelength of 6 Å was used at three detector distances (1.3, 4, and 13 m) to gather scattering profiles. At ORNL, two detector distances, 0.3 and 6 m, were used to gather scattering profiles. The SANS data were fully reduced by referencing an open beam neutron flux and subtracting the background incoherent scattering. All scattering profiles were analyzed using IGOR Pro macros developed at NIST.[28]

The H_2O−D_2O composition points of minimum scattering intensity for lysozyme and HGH were first determined using contrast variation on pure lysozyme and pure HGH samples in solutions containing various hydrogen isotope ratios (D/H). The ratio at which the scattering length densities of lysozyme and buffer were matched and therefore lysozyme did not contribute to the scattering signal was determined as 46% D_2O, which agreed well with the reported value in the literature for lysozyme.[29] The ratio for HGH was determined as 48% D_2O. These ratios were used for all subsequent contrast-matched samples to mask the lysozyme or HGH and probe only the PEG portion of the PEG−protein conjugates. Lysozyme, HGH, and mPEG−PA were measured in 100% D_2O at dilute concentrations. Hydrogenated and deuterated monoPEG−lysozyme samples were measured in 100% D_2O and 46% D_2O, respectively. Deuterated monoPEG−HGH was measured in 48% D_2O. All samples that were originally lyophilized in pH 7.4 10 mM HEPES were resuspended into a volume of the appropriate water solvent to recover a pH 7.4 10 mM HEPES solution.

RESULTS AND DISCUSSION

SANS data are analyzed first in terms of a pair-distance distribution function (PDDF), which has the advantage of being model-independent, followed by the Guinier analysis that yields a more quantitative description of the distribution of mass in the scattering particle, followed by data fits to form factor models that discriminate between candidate structures.

PDDF. A first order classification of the shape of a scattering particle is obtained directly from $P(r)$, the PDDF.[30] $P(r)$ is related to the frequency of interatomic vector lengths, r, within the particle.[31] $P(r)$ functions were calculated for all samples from the entire scattering curve [$(I(q)$, to be shown below] using model-free inverse Fourier transformation.[30] Figure 1 displays the $P(r)$ analysis for lysozyme, unconjugated *h*mPEG−PA (hydrogenated mPEG propionaldehyde), and mono-*h*mPEG−lysozyme in 100% D_2O. The distance at which $P(r)$ falls to zero indicates the largest distance spanned by the scattering particle. This maximum dimension for mono-*h*mPEG−lysozyme, 21.20 ± 0.08 nm, is larger than the sum of the maximum dimension of lysozyme, 3.44 ± 0.06 nm, plus that of unconjugated *h*mPEG−PA, 13.33 ± 0.06 nm, where the latter dimensions are taken from the corresponding $P(r)$ functions. The statistical error bars correspond to 95% confidence limits.

Guinier Analysis. The Guinier approximation provides the radius of gyration, R_G, of the scattering particle. For low values of the scattering vector q, R_G can be extracted from the slope of ln I versus q^2, as $\ln I(q) = \ln I(0) - [(R_G^2)/3]q^2$ provided the approximation is applied in the limit of $qR_G \ll 1$. The scattering vector q is defined as $(4\pi/\lambda)\sin(\theta)$ where λ is the wavelength of the incident neutrons and 2θ denotes the scattering angle.[32,33] Values for R_G thus determined are listed in Table 1. Values for R_G for lysozyme and *h*mPEG−PA in 100% D_2O are comparable to those reported previously.[9,34] As was the case with $P(r)$, R_G for mono-*h*mPEG−lysozyme,

dx.doi.org/10.1021/bc2003583 | Bioconjugate Chem. 2011, 22, 2317−2323

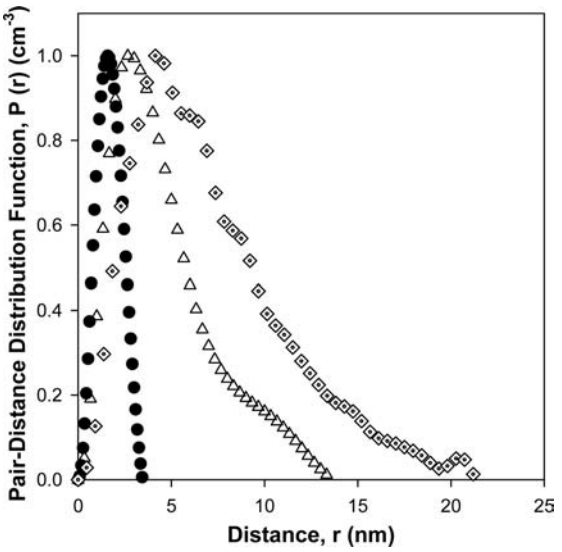

Figure 1. PDDFs, $P(r)$, for lysozyme (closed circles), hydrogenated mPEG−PA (open triangles), and hydrogenated monoPEG−lysozyme (dotted diamonds) in 100% D_2O containing 10 mM HEPES. The $P(r)$ maximum for each species is scaled to unity. The maximum extension of each particle is the point at which the function crosses the abscissa. The maximum extension of lysozyme, 3.44 ± 0.02 nm, plus the maximum extension of mPEG−PA, 13.33 ± 0.06 nm, is comparable to the maximum extension of monoPEG−lysozyme, 21.20 ± 0.08 nm. The statistical error bounding values correspond to 95% confidence limits.

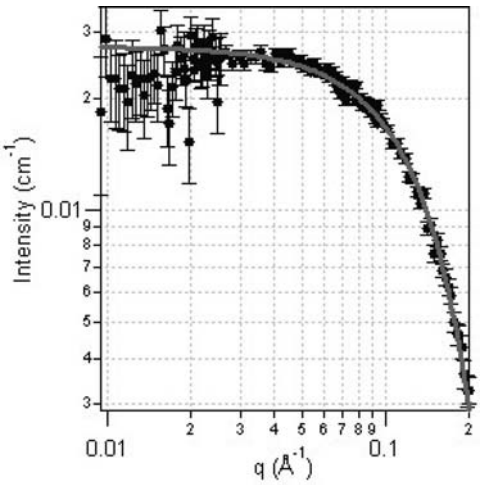

Figure 2. Comparison of the experimental scattering curve of lysozyme in 100% D_2O (filled circles), containing 10 mM HEPES, with the theoretical smeared curve of the sphere model for a monodisperse spherical particle with uniform scattering length density (solid line). Error bars represent the standard deviation of the intensity at each q value. For the fit, the scattering length density of the sphere was fixed at 2.56×10^{-6} Å $^{-2}$, and the scattering length density of the solvent was fixed at 6.33×10^{-6} Å $^{-2}$. The best fit generated a radius of 1.549 ± 0.001 nm. The statistical error bounding values correspond to 95% confidence limits.

6.8 ± 0.5 nm, is larger than the sum of R_G for lysozyme, 1.4 ± 0.2 nm, plus R_G for *h*mPEG−PA, 3.4 ± 0.3 nm. The statistical error bounding values correspond to 95% confidence limits.

Data Reduction and Form Factor Analysis. Using macros developed at NIST, all data were reduced and analyzed as $I(q)$ versus q using IGOR Pro software (WaveMetrics, Inc.).[28] Figures 2 and 3 permit comparison of the experimental scattering intensity profiles of lysozyme in 100% D_2O, containing 10 mM HEPES, and perdeuterated homopolymer mPEG−PA (*d*mPEG−PA) in 46% D_2O, containing 10 mM HEPES, with the theoretical smeared model curves for monodisperse spheres (sphere model[33]) and linear random coil polymer chains (Debye model[32]), respectively. A *d*mPEG−PA sample was used to increase the signal-to-noise ratio when employing the contrast variation technique to measure the scattering profile of deuterated monoPEG−lysozyme (mono-*d*mPEG−lysozyme) in 46% D_2O, containing 10 mM HEPES. This is the ratio of D_2O necessary to contrast match the lysozyme, determined experimentally, allowing only the PEG portion of the conjugate to be probed. Lysozyme was well described by the sphere model with radius R = 1.549 ± 0.001 nm (Figure 2), and the unconjugated *d*mPEG−PA was well described by the random coil Debye model with R_G = 3.718 ± 0.003 nm (Figure 3). The statistical error bounding values correspond to 95% confidence limits. The

Table 1. Dimensions Generated for All Species for All Data Analysis Methods[a]

species[b]	solvent with 10 mM HEPES (% D_2O)	data analysis method			
		DLS R_H (nm)[cd]	PDDF (nm)[ef]	Guinier R_G (nm)[gh]	model fitting (nm)[ij]
unmodified lysozyme	100	2.0 ± 0.9	max. ext. = 3.44 ± 0.02	1.4 ± 0.2	1.549 ± 0.001 (sphere, R_H)
*h*mPEG−PA	100	3.5 ± 1.4	max. ext. = 13.33 ± 0.06	3.4 ± 0.3	3.591 ± 0.001 (Debye, R_G)
mono-*h*mPEG− lysozyme	100	5.8 ± 2.6	max. ext. = 21.20 ± 0.08	6.8 ± 0.5	N/A
*d*mPEG−PA	46	N/A	N/A	N/A	3.718 ± 0.003 (Debye, R_G)
mono-*d*mPEG−lysozyme[k]	46	N/A	N/A	N/A	5.135 ± 0.006 (Debye, R_G)
mono-*d*mPEG−lysozyme[k]	46; plus 15 mg/mL lysozyme[l]	N/A	N/A	N/A	3.239 ± 0.002 (Debye, R_G)
mono-*d*mPEG−HGH[m]	48	N/A	N/A	N/A	5.012 ± 0.008 (Debye, R_G)

[a]Dimensions from DLS are also shown. [b]Abbreviations: *h*mPEG−PA, hydrogenated methoxy-PEG−propionaldhyde; *d*mPEG−PA, deuterated methoxy-PEG−propionaldehyde; hmono-*h*mPEG−lysozyme, hydrogenated monoPEG−lysozyme; mono-*d*mPEG−lysozyme, deuterated monoPEG−lysozyme; mono-*d*mPEG−HGH, deuterated monoPEG−HGH. [c]R_H is the hydrodynamic radius of an equivalent sphere determined by DLS, based on the intensity-weighted average distribution. [d]Error values correspond to the half width at half max of the light scattering peak. [e]The distance at which the PDDF falls to zero is an indication of the largest distance spanning the scattering particle, that is, the maximum extension (max. ext.) of the particle.[30,31] [f]The statistical error bounding values correspond to 95% confidence limits. [g]According to the Guinier approximation, the intensity at small q depends on the radius of gyration R_G of the scattering particle . [h]Error values correspond to 95% confidence limits. [i]Experimental scattering profiles were compared to theoretical smeared curves for monodisperse spheres (sphere model) and linear polymer chains (Debye model). [j]The statistical error bounding values correspond 95% confidence limits. [k]Lysozyme portion of conjugate is contrast-matched for SANS. [l]Conditions necessary to achieve an oncotic pressure similar to that of typical mammalian blood plasma. [m]HGH portion of conjugate is contrast-matched for SANS.

dx.doi.org/10.1021/bc2003583 | *Bioconjugate Chem.* 2011, 22, 2317−2323

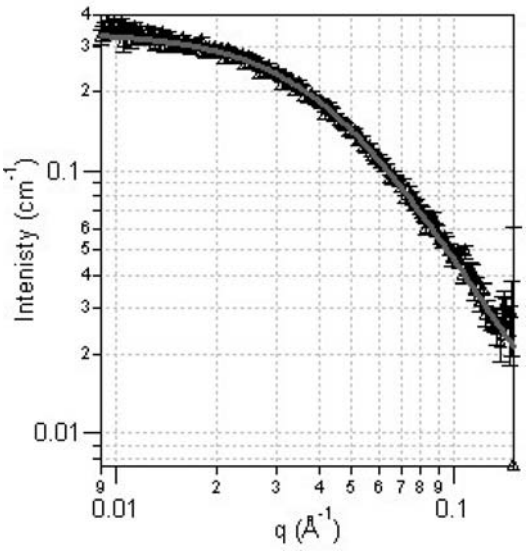

Figure 3. Comparison of the experimental scattering curve of deuterated mPEG–PA in 46% D_2O (open triangles), containing 10 mM HEPES, with the theoretical smeared curve of the Debye model for a random coil (solid line). Error bars represent the standard deviation of the intensity at each q value. The best fit generated a radius of gyration, R_G, of 3.718 ± 0.003 nm. The statistical error bounding values correspond to 95% confidence limits.

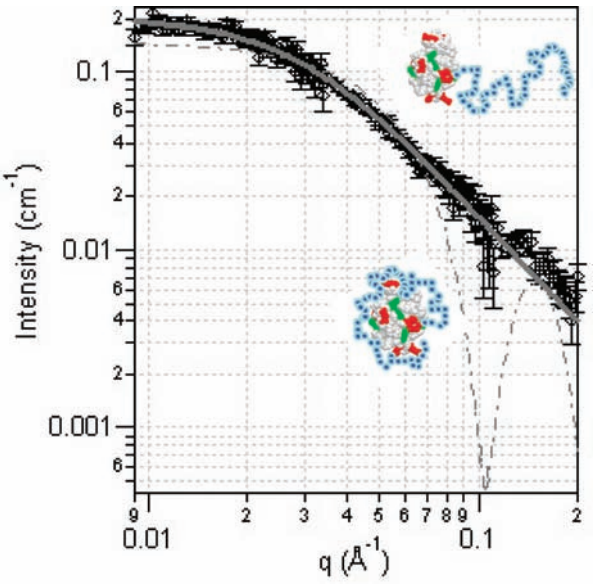

Figure 4. Comparison of the experimental scattering curve for deuterated monoPEG–lysozyme in 46% D_2O (dotted diamonds), containing 10 mM HEPES, with the theoretical smeared curve of the Debye model for a random coil (solid line) and the theoretical smeared core–shell model for a spherical particle of uniform scattering length density, surrounded by a shell having a different scattering length density (dashed line). Error bars represent the standard deviation of the intensity at each q value. The best fit generated a radius of gyration, R_G, of 5.135 ± 0.006 nm. The statistical error bounding values correspond to 95% confidence limits. Schematics qualitatively illustrate the dumbbell configuration (upper right) if the PEG chain followed the Debye model and the shroud configuration (lower left) if the PEG chain followed the core–shell model. Because of the contrast matching conditions, the protein is "invisible" to the neutrons in these measurements.

fitted radius of gyration for *d*mPEG–PA is somewhat smaller than the 6.7 nm *z*-average root-mean-square radius of gyration predicted by a light scattering correlation for PEG at 25 °C where $\langle R_G^2 \rangle = 4.08 \times 10^{-18} M_w^{1.16}$ cm^2.

To first test the suitability of the dumbbell model, the experimental scattering profile $I(q)$ of mono-*d*mPEG–lysozyme in 46% D_2O was compared to the theoretical smeared curve for a linear random coil polymer chain (Debye model). The quality of the random coil fit of the contrast-matched data in Figure 4 indicates that the conjugated PEG chain behaves as a random coil adjacent to the protein, supporting the dumbbell model.

As a counter-argument, the experimental scattering profile of mono-*d*mPEG–lysozyme in 46% D_2O, containing 10 mM HEPES, was then also compared to the theoretical smeared core–shell model for a spherical core of uniform scattering length density, surrounded by a shell having a different scattering length density; a successful fit to such a model would be consistent with the shroud model. The core–shell fit was applied in two different manners to attempt to achieve a satisfactory fit. In both cases, the scattering length densities of the core and solvent were set to be equal since the protein core was contrast-matched. In case 1, no other fitting constraints were applied, and the model fit generated a core radius of 2.98 ± 0.15 nm, a shell thickness of 0.08 ± 0.3 nm, and a shell scattering length density of $\rho_{shell} = 1.59 \times 10^{-6}$ Å^{-2}; this scattering length density falls outside the range of the solvent ($\rho_{solvent} = 2.56\times 10^{-6}$ Å^{-2}) and pure *d*PEG ($\rho_{dPEG} = 5.73 \times 10^{-6}$ Å^{-2}) and is therefore nonphysical for a mixture of *d*PEG and solvent. In case 2, the core radius was set to 1.55 nm, as previously determined by applying the sphere model to lysozyme SANS. The model then generated a shell thickness of 2.236 ± 0.002 nm, and the fitted scattering length density of the shell, $\rho_{shell} = 2.32 \times 10^{-6}$ Å^{-2}, was again nonphysical. The fringes predicted by the fit to the smeared core–shell model were absent in the experimental data. The statistical error bars correspond to 95% confidence limits.

On the basis of the agreement of contrast-matched SANS data for mono-*d*mPEG–LYZ with the random coil (Debye) model and not the core–shell model, we conclude that the conjugate adopts a dumbbell configuration (Figure 4) with the PEG chain forming an independent random coil domain rather than a shroud "wrapped" around the protein. As seen in Table 1, R_G for the lysozyme-conjugated *d*mPEG–PA chain is approximately 30% larger than that measured for free *d*mPEG–PA in 100% D_2O, containing 10 mM HEPES. This is expected because this PEG is end-anchored to the protein surface. As an isolated, nonadsorbing but end-grafted chain, configurational entropy dictates that it would be elongated relative to the unconjugated chain.[35]

Extension to Additional Proteins. The measurements described in the previous section were extended to include a protein of pharmaceutical interest, HGH, covalently conjugated to a single ~20 kDa *d*mPEG–PA chain. The contrast variation technique was again employed to measure the scattering profile of mono-*d*mPEG–HGH in 48% D_2O, containing 10 mM HEPES, the experimentally determined D_2O content to contrast match HGH in buffer. The excellent agreement of the experimental scattering profile of mono-*d*PEG–HGH with the Debye model (Figure S2 in the Supporting Information, S3) again is consistent with the grafted PEG chain existing as a random coil adjacent to the protein, that is, adopting the dumbbell configuration.

dx.doi.org/10.1021/bc2003583 | *Bioconjugate Chem.* 2011, 22, 2317–2323

Determining the Configuration of the PEG Chain in Plasmalike Environments. All measurements described thus far were in dilute solution, but blood has a large oncotic pressure that may influence the PEG conformation in a PEGylated therapeutic protein. To determine the behavior of the conjugated PEG chain as it might exist in blood, we mimicked the oncotic pressure of plasma by dissolving the mono-*d*mPEG−lysozyme (20 kDa *d*mPEG−PA) in a 15 mg/mL solution of unconjugated lysozyme, the concentration of lysozyme necessary to create an oncotic pressure typical of mammalian plasma, ∼2500 Pa, in 46% D_2O, containing 10 mM HEPES, to contrast-match lysozyme. The data are again well described by the random coil model, consistent with the dumbbell configuration, but now, R_G for the PEG conjugate, 3.238 ± 0.002 nm, is about 15% smaller than that for an unconjugated *d*mPEG−PA chain in 46% D_2O, containing 10 mM HEPES, 3.718 ± 0.003 nm (Figure S3 in the Supporting Information, S4). The statistical error bounding values correspond to 95% confidence limits. Evidently, competition for water in the plasmalike environment causes a small decrease of the excluded volume of the conjugated PEG chain but does not alter the tendency to adopt a random coil configuration. This is consistent with the effect of high conjugate concentration noted by He et al. [23]

Implications. It is well established that the covalent attachment of PEG increases in vivo blood circulation times for protein therapeutics. The implications of the dumbbell configuration for the steric protection of a conjugated protein can now be considered. In the case of a single grafted PEG chain per protein, the dumbbell configuration leaves part of the protein unprotected, but it does provide a locally strong steric repulsion force to protect the conjugated part of the molecule. In contrast, the shroud configuration, if it occurred, would have spread its protective effect over a larger fraction of the protein surface. Yet, by spreading a limited polymer mass over a large area, the local segmental density in any one region would be rather low and would afford only a weak and short-range steric repulsion, since the range of steric forces imparted by grafted polymer chains is dictated by the normal extension of the chain away from the surface and the magnitude scales with the local segment density. The random coil dumbbell configuration offers strong but more highly localized protection of the protein. For example, the nearer the site of PEGylation is to a binding epitope, the more effective its protection would be. Similar considerations come into play concerning the degree to which a conjugated PEG chain could disrupt access to a protein active site.

CONCLUSION

SANS was employed with a contrast variation technique to probe only the PEG portion of the PEG−protein conjugate to directly determine the configuration of a single ∼20 kDa PEG chain covalently attached to lysozyme or HGH. Analyses of the scattering data in terms of the pairwise distance distribution function, the Guinier analysis of conjugate radius of gyration, and model fitting to the Debye random coil polymer scattering form factor are consistent with a dumbbell model in which the PEG chain behaves as a random coil adjacent to the protein and directly challenge the more commonly presumed shroud configuration in which the PEG chain wraps around the protein, creating a shielding effect.

ASSOCIATED CONTENT

Supporting Information

Characterization of the PEGylated conjugates and synthesis of the perdeuterated methoxy-PEG−propionaldehyde, SANS data, and model fits for lysozyme in the plasmalike environment and for HGH. This material is available free of charge via the Internet at http://pubs.acs.org.

AUTHOR INFORMATION

Corresponding Author

*Tel: 412-268-3857. E-mail: todd@andrew.cmu.edu (T.M.P.). Tel: 412-268-1159. E-mail: tilton@andrew.cmu.edu (R.D.T.).

ACKNOWLEDGMENTS

The identification of commercial products does not imply endorsement by the National Institute of Standards and Technology nor does it imply that these are the best for the purpose. This material is based on work supported by the National Science Foundation under Grant CBET 0755284 and utilized facilities supported in part by the National Science Foundation under Agreement No. DMR-0454672. We thank Dr. Reddy's Laboratories, LLC, and Genentech, Inc., for their generous donation of mPEG−propionaldehyde and HGH, respectively. A portion of this research was conducted at the Center for Nanophase Materials Sciences (CNMS), which is sponsored at Oak Ridge National Laboratory (ORNL) by the Office of Basic Energy Sciences, U.S. Department of Energy, through the CNMS user program (user proposal number: CNMS2009-212). A portion of this research at ORNL's High Flux Isotope Reactor was sponsored by the Scientific User Facilities Division, Office of Basic Energy Sciences, U.S. Department of Energy. This work benefited from DANSE software developed under NSF award DMR-0520547.

REFERENCES

(1) Pai, S. S., Przybycien, T. M., and Tilton, R. D. (2009) Poly(ethylene glycol)-Modified Proteins: Implications for Poly-(lactide-co-glycolide)-Based Microsphere Delivery. *AAPS J. 11*, 88−98.

(2) Freitas, D. d. S., and Abrahao-Neto, J. (2010) Biochemical and biophysical characterization of lysozyme modified by PEGylation. *Int. J. Pharm. 392*, 111−117.

(3) Michaelis, M., Cinatl, J., Cinatl, J., Pouckova, P., Langer, K., Kreuter, J., and Matousek, J. (2002) Coupling of the antitumoral enzyme bovine seminal ribonuclease to polyethylene glycol chains increases its systemic efficacy in mice. *Anti-Cancer Drugs 13*, 149−154.

(4) Harris, J. M., Martin, N. E., and Modi, M. (2001) Pegylation—A novel process for modifying pharmacokinetics. *Clin. Pharmacokinet. 40*, 539−551.

(5) Greenwald, R. B., Choe, Y. H., McGuire, J., and Conover, C. D. (2003) Effective drug delivery by PEGylated drug conjugates. *Adv. Drug Delivery Rev. 55*, 217−250.

(6) Shu, J. Y., Tan, C., DeGrado, E. D., and Xu, T. (2008) New design of helix bundle peptide-polymer conjugates. *Biomacromolecules 9*, 2111−2117.

(7) Morar, S., Schrimsher, J. L., and Chavez, M. D. (2006) PEGylation of Proteins: A Structural Approach: Structural properties of PEGylated proteins could play an increasingly important role in developing optimal therapeutic protein drugs. *Biopharm. Int. 19*, 34−44.

(8) Daly, S. M., Przybycien, T. M., and Tilton, R. D. (2005) Adsorption of Poly(ethylene glycol)-Modified Ribonuclease A to a Poly(lactide-co-glycolide) Surface. *Biotechnol. Bioeng. 90*, 856−868.

(9) Daly, S. M., Przybycien, T. M., and Tilton, R. D. (2005) Adsorption of Poly(ethylene glycol)-Modified Lysozyme to Silica. *Langmuir 21*, 1328−1337.

(10) Diwan, M., and Park, T. G. (2003) Stabilization of recombinant interferon-α by pegylation for encapsulation in PLGA microspheres. *Int. J. Pharm. 252*, 111−122.

(11) Diwan, M., and Park, T. G. (2001) Pegylation enhances protein stability during encapsulation in PLGA microspheres. *J. Controlled Release 73*, 233−244.

(12) Molek, J. R., and Zydney, A. L. (2006) Ultrafiltration Characteristics of Pegylated Proteins. *Biotechnol. Bioeng. 95*, 474−482.
(13) Fee, C. J., and Alstine, J. M. V. (2004) Prediction of the Viscosity Radius and the Size Exclusion Chromatography Behavior of PEGylated Proteins. *Bioconjugate Chem. 15*, 1304−1313.
(14) Manjula, B. N., Tsai, A., Upadhya, R., Perumalsamy, K., Smith, P. K., Malavalli, A., Vandegriff, K., Winslow, R. M., Intaglietta, M., Prabhakaran, M., Friedman, J. M., and Acharya, A. S. (2003) Site-Specific PEGylation of Hemoglobin at Cys-93(β): Correlation between the Colligative Properties of the PEGylated Protein and the Length of the Conjugated PEG Chain. *Bioconjugate Chem. 14*, 464−472.
(15) Garcia-Arellano, H., Valderrama, B., Saab-Rincon, G., and Vazquez-Duhalt, R. (2002) High Temperature Biocatalysis by Chemically Modified Cytochrome c. *Bioconjugate Chem. 13*, 1336−1344.
(16) Kozlowski, A., Charles, S. A., and Harris, J. M. (2001) Development of Pegylated Interferons for the Treatment of Chronic Hepatitis C. *BioDrugs 15*, 419−429.
(17) Roberts, M. J., Bentley, M. D., and Harris, J. M. (2002) Chemistry for peptide and protein PEGylation. *Adv. Drug Delivery Rev. 54*, 459−476.
(18) Schmidt, P. G., Campbell, K. M., Hinds, K. D., and Cook, G. P. (2007) PEGylated bioactive molecules in biodegradable polymer microparticles. *Expert Opin. Biol. Ther. 7*, 1427−1436.
(19) Harris, J. M., and Chess, R. B. (2003) Effect of PEGylation on pharmaceuticals. *Nature Rev. Drug Discovery 2*, 214−221.
(20) Abuchowski, A., Es, T. V., Palczuk, N. C., and Davis, F. F. (1977) Alteration of Immunological Properties of Bovine Serum Albumin by Covalent Attachment of Polyethylene Glycol. *J. Biol. Chem. 252*, 3578−3581.
(21) Li, D., Manjula, B. N., and Acharya, A. S. (2006) Extension Arm Facilitated PEGylation of Hemoglobin: Correlation of the Properties with the Extent of PEGylation. *Protein J. 25*, 263−274.
(22) Fee, C. J. (2007) Size comparison between proteins PEGylated with branched and linear poly(ethylene glycol) molecules. *Biotechnol. Bioeng. 98*, 725−731.
(23) He, L., Wang, H., Garamus, V. M., Hanley, T., Lensch, M., Gabius, H.-J., Fee, C. J., and Middelberg, A. (2010) Analysis of MonoPEGylated Human Galectin-2 by Small-Angle X-ray and Neutron Scattering: Concentration Dependence of PEG Conformation in the Conjugate. *Biomacromolecules 11*, 3504−3510.
(24) Svergun, D. I., Ekström, F., Vandegriff, K. D., Malavalli, A., Baker, D. A., Nilsson, C., and Winslow, R. M. (2008) Solution Structure of Poly(ethylene) Glycol-Conjugated Hemoglobin Revealed by Small-Angle X-Ray Scattering: Implications for a New Oxygen Therapeutic. *Biophys. J. 94*, 173−181.
(25) Kinstler, O. B., Gabriel, N. E., Farrar, C. E., and DePrince, R. B. (1998) N-Terminally chemically modified protein compositions and methods. U.S. Patent.
(26) Sreerama, N., and Woody, R. W. (2000) Estimation of protein secondary structure from CD spectra: Comparison of CONTIN, SELCON and CDSSTR methods with an expanded reference set. *Anal. Biochem. 287*, 252−260.
(27) Glinka, C. J., Barker, J. G., Hammouda, B., Krueger, S., Moyer, J. J., and Orts, W. J. (1998) The 30 m Small-Angle Neutron Scattering Instruments at the National Institute of Standards and Technology. *J. Appl. Crystallogr. 31*, 430−445.
(28) Kline, S. R. (2006) Reduction and analysis of SANS and USANS data using IGOR Pro. *J. Appl. Crystallogr. 39*, 895−900.
(29) Stuhrmann, H. B., and Fuess, H. (1976) A Neutron Small-Angle Scattering Study of Hen Egg-White Lysozyme. *Acta Crystallogr., Sect. A, Cryst. Phys., Diffr., Theor. Gen. Crystallogr. A32*, 67−74.
(30) Glatter, O., and Kratky, O., Eds. (1982) *Small Angle X-ray Scattering*, Vol. *515*, Academic Press Inc., New York, NY.
(31) Hong, X., and Hao, Q. (2009) High resolution pair-distance distribution function P(r) or protein solutions. *Appl. Phys. Lett. 94*, 1−3.
(32) Svergun, D. I., and Koch, M. H. J. (2003) Small-angle scattering studies of biological macromolecules in solution. *Rep. Prog. Phys. 66*, 1735−1782.
(33) Roe, R.-J. (2000) *Methods of X-Ray and Neutron Scattering in Polymer Science*, pp 1−331, Oxford University Press, Inc., New York.
(34) Pai, S. S., Przybycien, T. M., and Tilton, R. D. (2010) Protein PEGylation Attenuates Adsorption and Aggregation on a Negatively Charged and Moderately Hydrophobic Polymer Surface. *Langmuir 26*, 18231−18238.
(35) Fleer, G. J., Stuart, M. A. C., Scheutjens, J. M. H. M., Cosgrove, T., and Vincent, B. (1993) *Polymers at Interfaces*, pp 1−502, Chapman & Hall, London.

Supporting Information

The Conformation of the Poly(ethylene glycol) Chain in Mono-PEGylated Lysozyme and Mono-PEGylated Human Growth Hormone

Sheetal S. Pai[1], Boualem Hammouda[3], Kunlun Hong[4], Danilo C. Pozzo[5], Todd M. Przybycien[1,2*], Robert D. Tilton[1,2*]

[1]Center for Complex Fluids Engineering, [1]Department of Chemical Engineering, [2]Department of Biomedical Engineering, Carnegie Mellon University, Pittsburgh, PA 15213, USA;

[3]NIST Center for Neutron Research, National Institute of Standards and Technology, Gaithersburg, MD 20899, USA; [4]Center for Nanophase Materials Sciences and Chemical Science Division, Oak Ridge National Laboratory, Oak Ridge, TN 37831, USA; [5]Department of Chemical Engineering, University of Washington, Seattle, WA 98195, USA

*To whom correspondence should be addressed (e-mail: tilton@andrew.cmu.edu, phone: 412-268-1159; e-mail: todd@andrew.cmu.edu, phone: 412-268-3857)

Contents

Supporting Information S1: Synthesis of Deuterated Methoxy-PEG-propionaldehyde

The synthesis of protected aldehyde-functionalized deuterated PEO (Scheme 1) was achieved using custom-made glass reactors with constrictions and breakseal techniques.[1] All reagents were purchased from Aldrich and purified by standard procedures for high vacuum anionic polymerizations. In a typical polymerizing reaction, 0.3 mmol of 3,3-diethoxy-1-propanol were reacted with 0.3 mmol of potassium triphenylmethane ($(C_6H_5)_3CK$) in THF for 30 min. at room temperature. Then 6.2 grams of EO-d4 was added to the reactor and then the mixture was allowed to react for 2 days at 45°C. The polymerization was terminated by introducing degassed acidic methanol. After precipitating into hexanes and filtering, PEO-d4 polymer was obtained and then dried under vacuum to constant weight.

Scheme S1. Synthesis aldehyde-functionalized deuterated PEO.

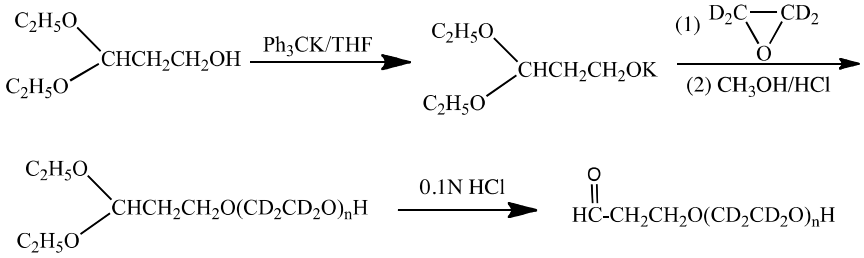

Transformation of the acetal group at the polymer end to the desired aldehyde group was carried out by stirring 3.13 grams of the as-synthesized PEO-d4 in 60 mL deionized water containing 15 mL of 0.1 N HC1 for overnight. Then the solution was dialyzed against deionized water for 2 days and the polymer was recovered using freezing drying.

Size exclusion chromatography (SEC) and nuclear magnetic resonance (^{13}C-NMR) were used to determine the molecular weights, polydispersities of the polymers. SEC determinations were performed on a Waters system equipped with a Waters 2695 pump, a Waters 2414 differential refractive index and Wyatt MiniDawn light scattering detectors, and 3 Polymer Lab Mixed-B columns with effective molecular weight range from 1,000 to 1,000,000 g/mol. THF was used as the eluent, and the flow rate was 1.0 mL/min at 30 °C. The system was calibrated using monodispersed linear polystyrene standards. ^{13}C-NMR spectra were obtained on a Varian Vnmr 500 spectrometer in $CDCl_3$. The molecular weight was estimated from the intensities of 3,3-diethoxy-1-propyl and EO-d4. The aldehyde functionality was confirmed by the ^{13}C-NMR peak appeared at 201.1ppm from the deprotected PEO-d4 sample.n

Supporting Information S2: Protein PEGylation and Conjugate Characterization

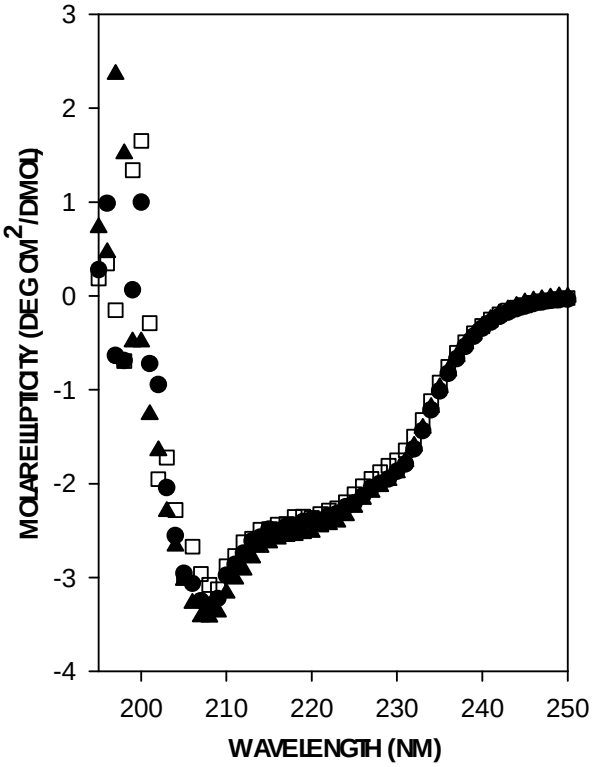

Figure S1. Circular dichroism spectra of unmodified lysozyme (filled circles), hydrogentated monoPEG-lysozyme (filled triangles) and deuterated monoPEG-lysozyme (open squares) in pH 7.4 10 mM HEPES buffer.

Table S1. Secondary structure fractions of unmodified lysozyme and monoPEG-lysozyme with both hydrogenated and deuterated mPEG-PA.

Species	**Secondary Structure Fractions**[a]					
	α-helix		**β-sheet**			
	regular	**distorted**	**regular**	**distorted**	**Turns**	**Unordered**
Unmodified Lysozyme	0.17 ± 0.04	0.15 ± 0.03	0.13 ± 0.01	0.062 ± 0.001	0.21 ± 0.04	0.27 ± 0.02
Hydrogenated monoPEG-Lysozyme	0.15 ± 0.04	0.18 ± 0.04	0.09 ± 0.03	0.07 ± 0.02	0.23 ± 0.02	0.27 ± 0.03
Deuterated monoPEG-Lysozyme	0.15 ± 0.06	0.15 ± 0.05	0.15 ± 0.03	0.08 ± 0.02	0.19 ± 0.03	0.28 ± 0.04

[a]Error values are the standard deviations of fraction values determined by three regression algorithms (SELCON3, CDSSTR, and CONTIN/LL) used to quantify secondary structure in CDPro[2].

Supporting Information S3: Contrast-Matched SANS Analysis of PEGylated Human Growth Hormone

The measurements described in the main paper for PEGylated lysozyme were extended to include an additional protein, human growth hormone (HGH), covalently conjugated to a single 20 kDa ***d***mPEG-PA chain. The contrast variation technique was once again employed to measure the scattering profile of deuterated monoPEG-hGH in 48% D_2O containing 10 mM HEPES buffer, the experimentally determined D_2O content to contrast match HGH. Figure S2 displays the experimental scattering profile of the ***d***monoPEG-hGH in 48% D_2O, with the Debye model fit. The excellent agreement of the experimental scattering profile of ***d***monoPEG-HGH with the Debye model (Figure S2) again confirms that the grafted PEG chain exists as a random coil adjacent to the protein and leading the conjugate to adopt a dumbbell configuration.

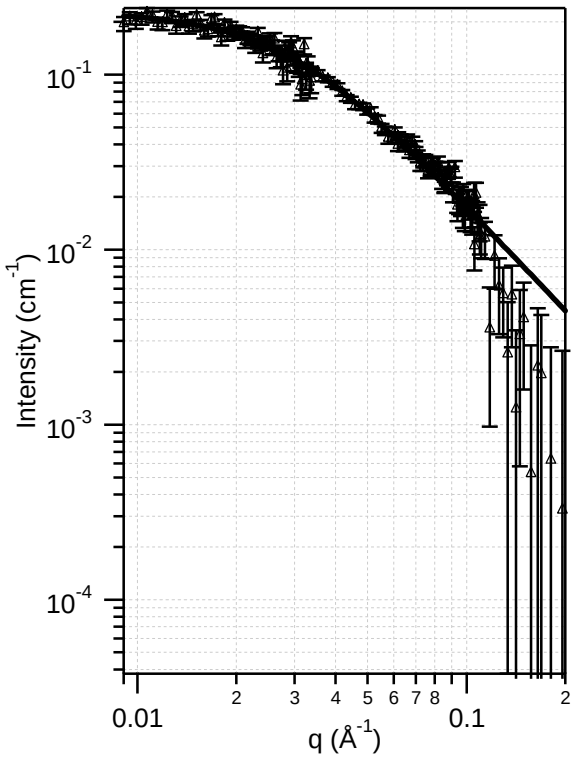

Figure S2. Comparison of the experimental scattering curve for deuterated monoPEG-HGH in 48% D_2O (open triangles), containing 10 mM HEPES, with the theoretical smeared curve of the Debye model for a random coil (solid line). Error bars represent the standard deviation of the intensity at each q value. The best fit generated a radius of gyration, R_G, of 5.012 ± 0.008 nm. The statistical error bars correspond to 95% confidence limits. A lack of fringes in the data over this ***q*** range indicates inconsistency with the core-shell model.

Supporting Information S4: Determining the Configuration of the Conjugated PEG Chain in Plasma-Like Environments

In order to predict the behavior of the conjugated PEG chain in blood, we mimicked the oncotic pressure of blood plasma by dissolving the mono-***d***PEG-lysozyme (20 kDa ***d***mPEG-PA) in a 15 mg/ml solution of unconjugated lysozyme to achieve an oncotic pressure similar to that of typical mammalian blood plasma , ~2500 Pa . This was dissolved in 46% D_2O, containing 10 mM HEPES, to contrast match lysozyme. Figure S3 displays the experimental contrast matched SANS ***I(q)*** for the conjugated ***d***PEG chains on mono-***d***PEG-lysozyme in these plasma-like conditions, along with the Debye model fit . The data were again well described by the random coil model, consistent with the dumbbell configuration. Here, $\boldsymbol{R_G}$ for the PEG conjugate, 3.239 ± 0.002 nm, was somewhat smaller than that for an unconjugated ***d***mPEG-PA chain in pure 46% D_2O, 3.718 ± 0.003 nm.

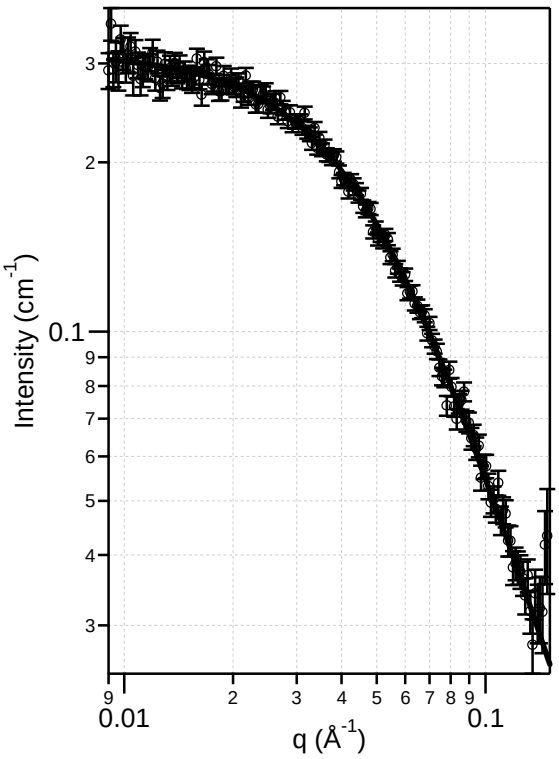

Figure S3. Comparison of the experimental scattering curve for deuterated monoPEG-lysozyme in a solution of 46% D_2O, with 10 mM HEPES, containing 15 mg/ml lysozyme (open circles) with the theoretical smeared curve of the Debye model for a random coil (solid line). Error bars represent the standard deviation of the intensity at each $\boldsymbol{q}$ value. The best fit generated a radius of gyration, $\boldsymbol{R_G}$, of 3.239 ± 0.002 nm. The statistical error bars correspond to 95% confidence limits. A lack of fringes in the data over this $\boldsymbol{q}$ range indicates inconsistency with the core-shell model.

References

(1) Uhrig, D., and Mays, J. W. (2005) Experimental techniques in high-vacuum anionic polymerization. ***Journal of Polymer Science Part A: Polymer Chemistry***. 43, 6179-6222.

(2) Sreerama, N., and Woody, R. W. (2000) Estimation of protein secondary structure from CD spectra: Comparison of CONTIN, SELCON and CDSSTR methods with an expanded reference set. ***Analytical Biochemistry***. 287, 252-260.

Bioconjugate Chemistry

Article

pubs.acs.org/bc

Nuclear Targeted Silver Nanospheres Perturb the Cancer Cell Cycle Differently than Those of Nanogold

Lauren A. Austin, Bin Kang,‡ Chun-Wan Yen, and Mostafa A. El-Sayed*

Laser Dynamics Laboratory, School of Chemistry and Biochemistry, Georgia Institute of Technology, Atlanta, Georgia 30332-0400, United States

Supporting Information

ABSTRACT: Plasmonic nanoparticle research has become increasingly active due to potential uses in biomedical applications. However, little is known about the intracellular effects these nanoparticles have on mammalian cells. The aim of this work is to investigate whether silver nanoparticles (AgNPs) conjugated with nuclear and cytoplasmic targeting peptides exhibit the same intracellular effects on cancer cells as peptide-conjugated gold nanoparticles (AuNPs). Nuclear and cytoplasmic targeting spherical AgNPs with a diameter of 35 nm were incubated in a cancer (HSC-3) and healthy (HaCat) cell line. By utilizing flow cytometry, confocal microscopy, and real-time dark field imaging, we were able to analyze how targeting AgNPs affect the cell cycle and cell division. These experiments demonstrated that nuclear-targeting AgNPs cause DNA double-strand breaks and a subsequent increase in the sub G1 (apoptotic) population in our cancer cell model at much lower concentrations than previously reported for nuclear targeting AuNPs. Unlike the M phase accumulation seen in cancer cells treated with AuNPs, an accumulation in the G2 phase of the cell cycle was observed in both cell models when treated with AgNPs. Additionally, real-time dark field imaging showed that cancer cells treated with nuclear targeting AgNPs did not undergo cell division and ultimately underwent programmed cell death. A possible explanation of the observed results is discussed in terms of the chemical properties of the nanoparticles.

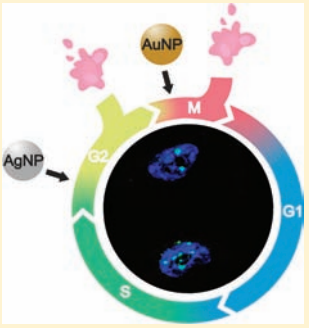

INTRODUCTION

Plasmonic nanoparticles (NPs) have been heavily studied due to their small size and unique optical and photothermal properties.[1,2] Their nanometer size allows NPs to permeate the cellular membrane and interact with biomolecules inside the cell, which can lead to disruption of cellular functions.[3−6] Cancer cells, which overexpress a certain ligand receptor, have the ability to be selectively targeted by NPs that have undergone surface conjugations to the respective receptor's complementary ligand.[7−9] Conjugated NPs also have the ability to intracellularly target specific organelles and/or locations within the cell.[8,10−14] A heavily targeted organelle within the cell is the nucleus. The nucleus houses the cell's genetic material and is responsible for maintaining proper cellular activities.[15] Any alteration to the nucleus and its genetic material could result in improper regulation of the cell cycle and cell death. The nucleus is most commonly targeted through the conjugation of a nuclear localizing signal (NLS) to the surface of the NPs.[8,12−14] This signal is known to interact with cytosolic factors forming stable complexes that are docked at the nuclear pore complex (NPC) in the nuclear membrane.[8] Our group's recent work has provided evidence that nuclear targeting of gold nanoparticles (AuNPs) in cancer (HSC-3) cells results in DNA damage, cytokinesis (M phase) arrest, and ultimately cell death.[14] Although this work demonstrates the alteration of the cell cycle in the presence of nuclear targeting AuNPs, it is still unknown if different nuclear targeting metallic nanoparticles, such as silver nanoparticles (AgNPs), will exhibit the same effect.

AgNPs have been extensively used in antimicrobial applications,[16,17] but little is known about the behavior and resulting cellular response when they are targeted to different organelles of mammalian cells. AgNPs are known for their active generation of reactive oxygen species (ROS).[18,19] ROS are a major source of oxidative stress within a cell and can cause damage to several cellular components. Disruption to DNA replication and ribosomal subunit protein expression after introduction of AgNPs into cells has been reported.[18] This disruption was attributed to the Ag^+ release from the surface oxidation of the AgNPs after they have been introduced into culture media and internalized in the cells. The resulting induction of DNA damage and subsequent cell death has potential applications in cancer and disease therapeutics.

In the present work, we systematically studied the cell cycle and cell division of cancer and healthy human cells in the presence of 35 nm pegylated and peptide-conjugated AgNPs. The results suggest that AgNPs localized at the nucleus cause DNA double-strand breaks and an increase in the sub G1 (apoptotic) population in the cancer cell model. G2 accumulation was also seen in both cancer and healthy cell

Received: July 18, 2011
Revised: October 13, 2011
Published: October 20, 2011

ACS Publications © 2011 American Chemical Society

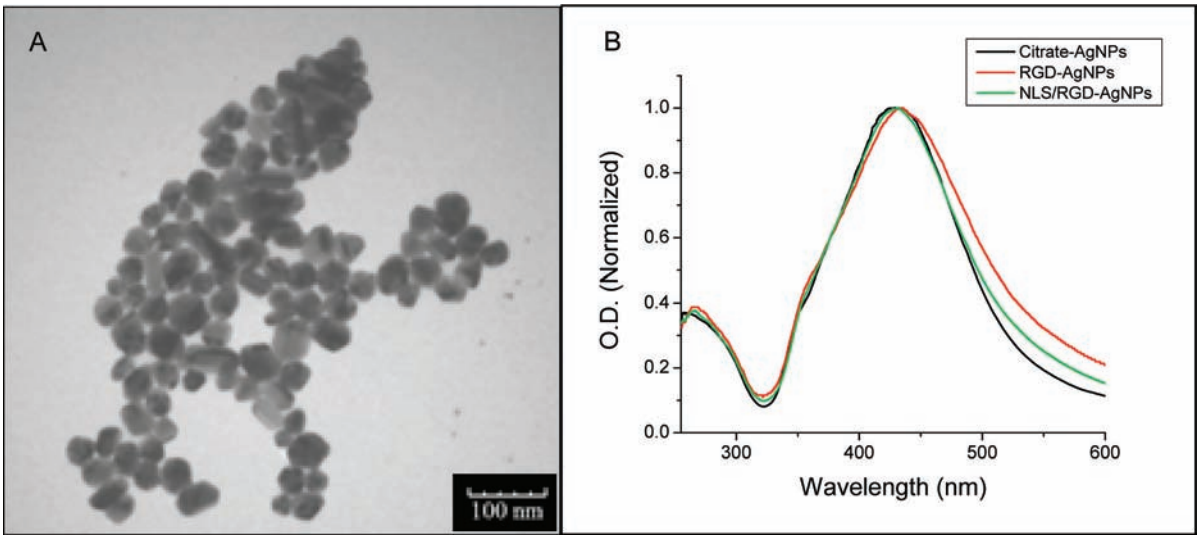

Figure 1. (A) TEM image of the AgNPs used in this study and (B) UV−vis spectra of citrate-capped AgNPs conjugated with RGD (red) and NLS/RGD (green) peptides showing the characteristic shift and peak broadening of the AgNP surface plasmon.

lines. The ROS generation from AgNPs is considered the main cause of the cell cycle alteration.

EXPERIMENTAL SECTION

AgNP Synthesis. Citrate-stabilized AgNPs with an average diameter of 35 nm were synthesized by the reduction of silver ions ($AgNO_3$) with sodium citrate.[20] Briefly, a 100 mL solution of 0.2 mM $AgNO_3$ and 0.3 mM trisodium citrate was brought to a boil under continuous stirring. After 30 min, boiling and stirring were discontinued and the solution was cooled to room temperature. TEM and DLS analysis showed an average particle diameter of 35 nm (Figure 1 and Table 1). The surface plasmon resonance band showed a peak absorbance at 430 nm (Figure 1). TEM images were taken on a JEOL 100CX-2 transmission electron microscope and the average diameter was determined using *ImageJ*.

Table 1. Hydrodynamic Diameters and Zeta Potentials of AgNPs

sample	hydrodynamic diameter (nm)	zeta potential (mV)
Citrate-AgNPs	35	−41
PEG-AgNPs	55	−18
NLS/RGD-AgNPs	57	14
RGD-AgNPs	56	16

AgNP Peptide Conjugation. The citrate-stabilized AgNPs were then pegylated to inhibit aggregation before peptide conjugation. A 1.0 mM solution of mPEG-SH 5000 (Laysan Bio, Inc.) diluted with DI water was added to a AgNP solution to achieve a 10^3 times greater concentration of mPEG-SH 5000 than AgNPs. The PEG-AgNP solution was allowed to incubate at room temperature overnight, and excess PEG was removed by centrifugation (13 500 rpm, 8 min). The PEG-AgNPs were redispersed in PBS. The pegylated particles were further conjugated with peptides following a previously established method.[13] For RGD peptide (RGDRGDRGDRGDPGC) and PEG-AgNP conjugation, a 1.0 mM RGD solution diluted in DI water was added to the PEG-AgNP solution to attain 10^3 molar excess of the RGD peptide than PEG-AgNPs. For NLS peptide (CGGGPKKKRKVGG) and PEG-AgNP conjugation, a 5 mM NLS peptide solution was added to a PEG-AgNP solution, so the NLS peptide was in 10^4 times molar excess. Last, conjugation of PEG-AgNPs with both RGD and NLS peptides was achieved by adding the peptides in 10^3 and 10^4 times molar excess, respectively, compared to the PEG-AgNPs. All peptide−particle solutions were allowed to shake overnight at room temperature and excess peptides were removed by centrifugation (13 500 rpm, 8 min). Particles were redispersed in PBS. The conjugation with PEG and the peptides was characterized by UV−vis spectroscopy and DLS analysis (Figure 1 and Table 1). To achieve the desired final concentrations (0.1 nM and 0.4 nM), the peptide-conjugated AgNPs were further diluted with DMEM cell culture medium.

Cell Culture. HSC-3 (human oral squamous cell carcinoma), a malignant epithelial cell line, and HaCat (human karatinocytes), a nonmalignant epithelial cell line, were cultured in Dulbecco's Modified Eagle's Medium (DMEM) (Mediatech) supplemented with 4.5 g/L glucose and sodium pyruvate, 10% v/v fetal bovine serum (FBS) (Mediatech), and 1% antimycotic solution (Mediatech). Cell cultures were kept at 37 °C in a 5% CO_2 humidified incubator.

Dark Field Imaging Overlays. Cells were cultured on collagen-coated 18-mm-diameter glass coverslips for 24 h and incubated for 24 h with 0.1 nM peptide−AgNP solutions diluted in DMEM. The coverslips were then washed with DPBS buffer and fixed with 4% paraformaldehyde. Images were obtained with an inverted Olympus IX70 microscope with a dark field condenser (U-DCW). A 100×/1.35 oil Iris objective (UPLANAPO) was used to collect the scattered light from the AgNP-treated samples.

AgNP Uptake Assay. HSC-3 and HaCat cells were cultured for 24 h in DMEM and then incubated for another 24 h with 0.1 nM peptide−AgNP solutions diluted in DMEM. Particle solutions were removed and the solution's OD values at 430 nm were taken using a microplate reader (SpectraMax Plus). Cells were counted using an inverted Olympus IX70 microscope with a 10× objective. Particle uptake values were normalized to the number of cells and are reported as a relative percent uptake. Statistical significance was determined from the

dx.doi.org/10.1021/bc200386m | *Bioconjugate Chem.* 2011, 22, 2324−2331

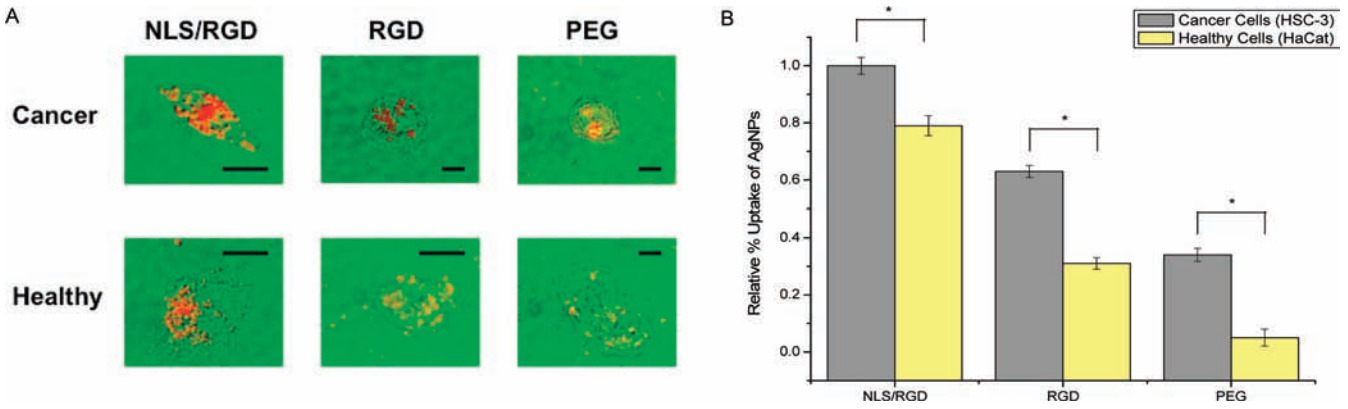

Figure 2. (A) Dark field images overlays of single cells showing where the strong scattering AgNPs reside in the cell. Dark field images show that NLS/RGD-AgNPs are highly localized at the nucleus while RGD and PEG conjugated AgNPs are dispersed throughout the cytoplasm. Scale bar: 10 μm. (B) The relative percent uptake of the conjguated AgNPs incubated in cancer (gray) and healthy (yellow) cells for 24 h. Cancer cells show a higher relative uptake of conjugated AgNPs when compared to healthy cells. All values were normalized to the number of cells present in the sample. Asterisks (*) indicate a P value of <0.05.

comparison of cancer (HSC-3) treated cells and healthy (HaCat) treated cells.

Cell Cycle Analysis with Flow Cytometry. Cells were grown for 24 h in culture medium (DMEM) and then incubated with AgNPs in culture medium (DMEM) for 24 h. After AgNP incubation, cells were fixed with −20 °C cold ethanol (70%) until analysis. To prepare for flow cytometry analysis, fixed cell suspensions were centrifuged at 1250 rpm for 12 min, and the cell pellet was redispersed in PBS. Cells were treated with 200 μg/mL RNase (Sigma) for 30 min at 37 °C. Following RNase treatment, DNA staining with 100 μg/mL of propidium iodine (Sigma) was conducted at room temperature for 15 min. A BD LSR II (BD Biosciences) with a 488 nm excitation laser and fluorescence detection in the PE channel was used to run flow cytometry. The obtained cell cycle data was analyzed using *FloJo* (Tree Star Inc.), a flow cytometry analyzing software.

Cell Synchronization. Nocodozale, a mitoic inhibitor, was used to synchronize HSC-3 and HaCat cells in the prometaphase (M phase). Cells were grown for 14 h in the presence of 80 ng/mL nocodazole, and mitoic cells were collected by shake-off. The motoic cells were released in fresh culture medium (DMEM) and collected at the indicated time points. Cells were then washed three times with PBS and fixed with −20 °C cold ethanol (70%) for further analysis by flow cytometry.

Confocal Microscopy and DNA Damage Test. HSC-3 and HaCat cells were grown on 18-mm-diameter glass coverslips and treated with their respective peptide−AgNP concentration. Cell fixation was conducted with 2% paraformaldehyde for 15 min, and cells were washed in PBS for 3 × 10 min. Cells were then permeabilized for 5 min on ice in 0.2% Triton X-100 and blocked in PBS with 1% BSA for 3 × 10 min at room temperature. Blocked cells were incubated with anti-γ-H2AX antibody (Bethyl Laboratories, Inc.) for one hour, washed in PBS with 1% BSA for 3 × 10 min at room temperature, and then incubated for 1 h at room temperature with FITC-conjugated goat antirabbit secondary antibody (Bethyl Laboratories, Inc.). Last, cells were washed in PBS with 1% BSA for 3 × 10 min at room temperature and stained with 4,6-diamidino-2-phenylindole (DAPI) for 5 min. Confocal images were taken using a Zeiss LSM 510 NLO META multiphoton excitation confocal microscope.

Real-Time Dark Field Imaging. A homemade setup was based on the modification of an inverted Olympus IX70 microscope.[21] The samples were grown in 35 mm culture plates for 24 h and then incubated with peptide-conjugated AgNPs in culture medium (DMEM) for 24 h. Samples were placed inside a mini cell chamber that was mounted on the stage of the microscope. The mini cell chamber allowed the sample to maintain a temperature of 37 °C and a carbon dioxide concentration of 5% CO_2. The scattered light from the sample was collected using a long working distance 40× objective. A Nikon D200 digital camera was used to capture the dark field pictures every two minutes.

Statistical Analysis. Statistical analysis of experimental values are conveyed as mean ± standard deviaion of at least three independent experiments. The data were analyzed using the *t test calculator* (GraphPad Software, GraphPad Software, Inc.), and statistical significance was determined from untreated (control) to treated (AgNPs incubation) samples unless otherwise noted. Data were considered statistically significant if the P value was <0.05.

RESULTS AND DISCUSSION

Synthesis and Conjugation of AgNPs. The silver nanoparticles (AgNPs) used in this work were synthesized by the reduction of silver nitrate with trisodium citrate.[20] The relatively monodispersed AgNPs had an average diameter of 35 nm, as shown by TEM (Figure 1). UV−vis spectroscopy further confirmed the synthesis of 35 nm silver particles, as the spectra showed the characteristic surface plasmon resonance (SPR) peak at 430 nm (Figure 1). Table 1 shows measurements of the hydrodynamic diameter (HD) and the zeta potential of the synthesized AgNPs.

The citrate-capped AgNPs were then conjugated with poly(ethylene glycol) (PEG) in order to increase their stability in the culture medium and prevent nonspecific binding of proteins to the surface of the particles.[22] The PEG-stabilized AgNPs were further conjugated with arginine-glycine-aspartic acid (RGD) and nuclear localization signal (NLS) peptides. RGD is known to target $\alpha v\beta 6$ as well as other αv integrins on the cell surface and assists in receptor-mediated endocytosis in cancer cells.[23−25] NLS has a characteristic lysine-lysine-lysine-arginine-lysine (KKKRK) sequence. Biomolecules labeled with this nuclear tag are known to bind to importin α and β in the

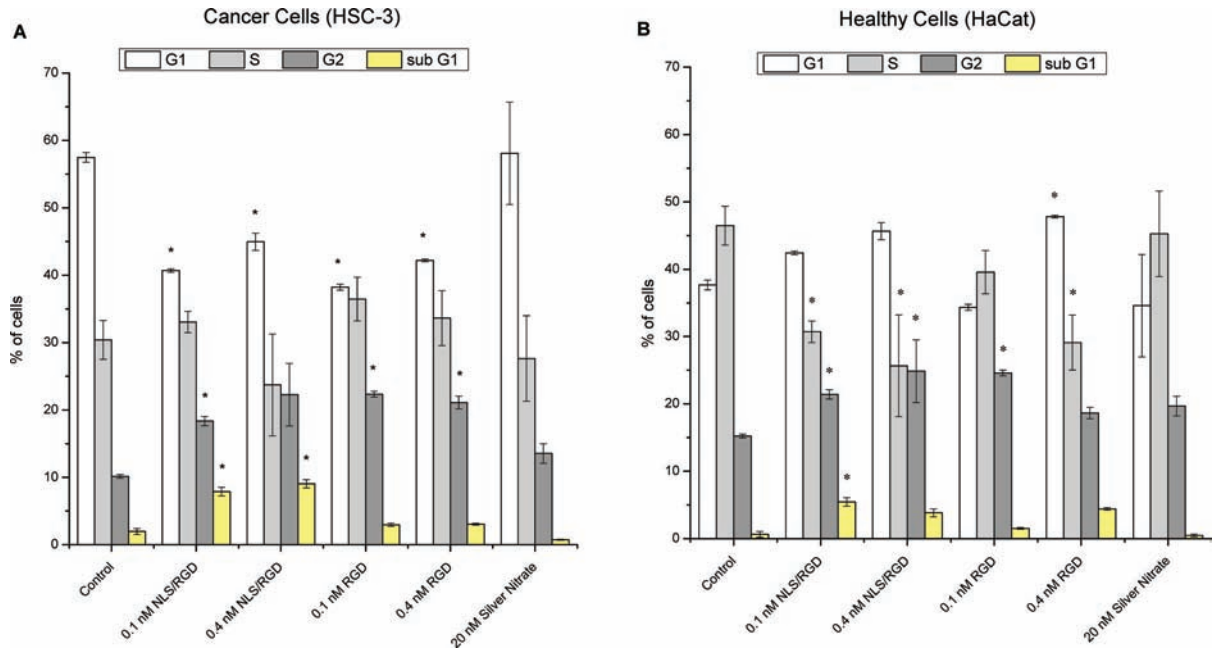

Figure 3. Complete cell cycle analysis of cancer and healthy cells by using flow cytometry. Cancer cells show a significant increase in the sub G1 (DNA deficient) population after treatment with NLS/RGD-AgNPs when compared to the control (A). G2 accumulation is seen in both cell models when treated with peptide-conjugated AgNPs. Asterisks (*) indicate a P value of <0.05.

cytoplasm and be actively transported into the nucleus through the nuclear pore complex (NPC).[26] The bioconjugation with the NLS and RGD peptides was confirmed through UV−vis spectroscopy and dynamic light scattering (DLS) measurements. The UV−vis spectra in Figure 1 show a slight red shift in the particles after conjugation with the peptides. The red shift was attributed to the change in the dielectric constant of the surrounding environment of the AgNPs. The DLS measurements, reported in Table 1, show the HD of AgNPs increased 20 nm after conjugation with the surface ligands. A change in the zeta potential of the particles was also observed after conjugation.

Additionally, the stability of the peptide-conjugated particles was investigated after 24 h of incubation in culture medium. The UV−vis spectra of the incubated AgNPs did not show a significant alteration in the SPR indicating that nanoparticle aggregation did not occur and the particles were stable in the biological environment (data not shown).

Localization and Relative Uptake of AgNPs in Cells. A major advantage of using silver nanoparticles in biomedical applications is their enhanced light scattering, which allows their localization and distribution to be imaged in different biological environments.[1] In this experiment, we wanted to determine the localization and relative uptake of the pegylated and peptide-conjugated AgNPs in two different cell lines. The cell lines used were human oral squamous cells carcinoma (HSC-3) and human keratinocytes (HaCat) cells, which modeled cancer and healthy cells, respectively. HSC-3 cells have been reported to express αv integrins (i.e., $\alpha v\beta 3$ and $\alpha v\beta 5$) and overexpress $\alpha v\beta 6$ integrins, an RGD receptor, on their cell surface.[27,28] We hypothesized that RGD conjugation would enhance the uptake of AgNPs by cancer cells since our healthy cell line has not been shown to overexpress $\alpha v\beta 6$ integrins unless induced by transforming growth factor-$\beta 1$ (TGF$\beta 1$).[29] To investigate the uptake and localization of NLS/RGD-AgNPs, RGD-AgNP and PEG-AgNP dark field imaging was utilized. The dark field image overlays seen in Figure 2A show that AgNPs conjugated with the nuclear targeting signal (NLS) are localized at the nucleus of both cell models, while RGD-AgNPs and PEG-AgNPs were dispersed within the cytoplasm. Figure 2A images also reveal that cancer cells show an apparent overall increase in AgNP uptake when compared to healthy cells.

To quantify the uptake of the different AgNPs in the cancer and healthy cell lines, the relative percent uptake of particles was determined. AgNP uptake, as reported in Figure 2B, was calculated through the normalization of the data to the number of cells present in each sample well. Cancer cells showed a statistically significant ($P < 0.05$) higher relative percent uptake of all conjugated AgNPs when compared to heatlhy cells. Furthermore, NLS/RGD-AgNPs exhibited the greatest relative percent uptake in both cell lines. The increased uptake in cancer cell lines is thought to be due to the overexpression of $\alpha v\beta 6$ integrins on their cellular membrane;[27] however, other αv integrins on the cell surface could have also contributed to the trend seen.[24,25] The cause for the differences between RGD and NLS/RGD particle uptake in both cell lines is still unclear; however, the overall surface charge of the particles could enhance/hinder the particle's ability to undergo receptor-mediated endocytosis.

Cell Cycle Analysis and Cell Synchronization of AgNP Treated Cells. After it was shown that NLS/RGD-AgNPs did localize at the nucleus, we investigated whether this localization caused cell cycle disruption in both cell models. To determine the effects of the peptide-conjugated AgNPs on cancer and healthy cells, complete cell cycle analysis was performed using flow cytometry. The complete cell cycle analysis of cancer and healthy cells treated with 0.1 nM and 0.4 nM conjugated AgNPs for 24 h, as to allow successful uptake of the particles, is shown in Figure 3. Cancer cells treated with 0.1 nM and 0.4 nM NLS/RGD-AgNP showed a statistically significant ($p < 0.05$) increase in the sub G1 (DNA deficient[30]) population (Figure

dx.doi.org/10.1021/bc200386m | Bioconjugate Chem. 2011, 22, 2324−2331

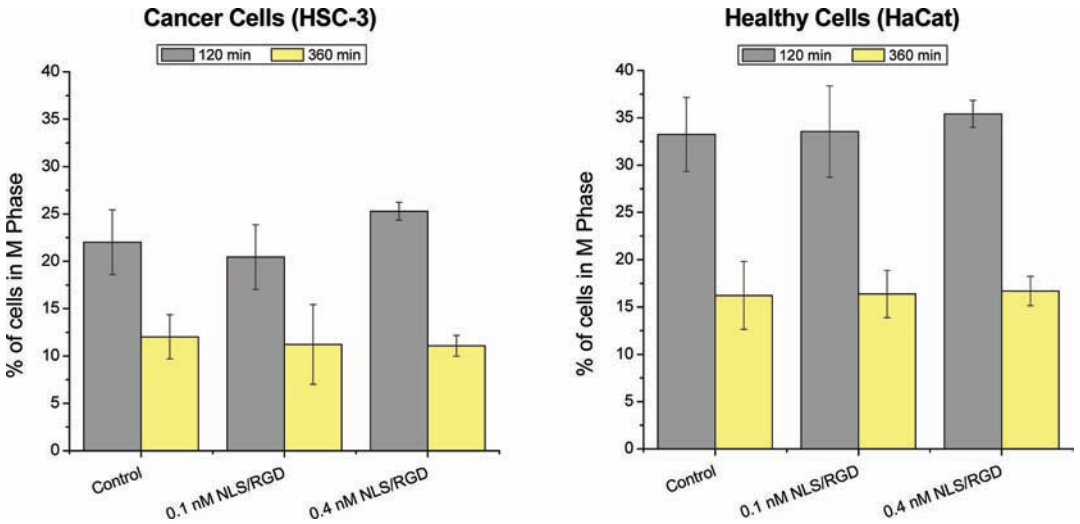

Figure 4. Cell synchronization of NLS/RGD-AgNPs treated cells. Significant M phase accumulation was not seen between control and NLS/RGD-AgNP treated cells in both cancer (A) and healthy (B) cells. Cells were synchronized with nocodazole in the prometaphase (M phase), and cell cycle analysis was conducted at 120 and 360 min. Statistical significance was determined from a P value of <0.05.

3A). The sub G1 population resulting from incubation with 0.1 nM nuclear-targeting AgNPs suggested that there was an increased toxicity of AgNPs in our cancer cell model when compared to AuNPs.[14] The sub G1 population also appears to increase as the concentration of nuclear-targeting AgNPs introduced into the cancer cells increases from 0.1 nM (~8.0%) to 0.4 nM (~9.0%). Additionally, cancer cells treated with NLS/RGD-AgNPs showed an accumulation in the G2/M phase of the cell cycle indicating the presence of nuclear targeting AgNPs disrupted the transition of G2/M or M/G1.

Contrary to the results seen with nuclear-targeting AuNPs, a significant sub G1 population was also seen in healthy cells when treated with NLS/RGD-AgNPs for 24 h (Figure 3B). It is believed that the lack of overexpression of $\alpha v\beta 6$ integrins[29] on their cell surface and reduced uptake of nuclear-targeting AgNPs contributes to the reduced sub G1 population in healthy cells when compared to our cancer cell model. Nevertheless, the presence of the DNA deficient population in healthy cells provides further evidence of the harmful, toxic effects AgNPs have when compared to AuNPs. Moreover, healthy cells show G2/M accumulation upon treatment with NLS/RGD-AgNPs indicating that the presence of nuclear-targeting AgNPs prevents normal transitions between the different phases of the cell cycle.

To ensure that the NLS peptide was necessary to induce significant sub G1 populations in cancer and healthy cells, we examined the effect that RGD and PEG conjguated AgNPs had on the cell cycle. Cancer and healthy cells treated with RGD-AgNPs did not show a significant increase in the sub G1 population when compared to their controls but did show G2/M accumulation. The G2/M accumulation seen in our work is consistent with work reported from AshaRani et al., as they observed similar G2 accumulation in human glioblastoma cells (U251) and normal human lung fibroblast cells (IMR-90) when treated with starch-coated AgNPs.[31] However, their starch-coated particles did not produce DNA-deficient populations. This suggests that alteration of the cell cycle occurs in the presence of AgNPs, but the observed increase in apoptotic populations is only induced when AgNPs are localized at the nucleus. Moreover, cell cycle analysis of cancer and healthy cells treated with 0.1 nM and 0.4 nM PEG-AgNP showed no significant increase in the sub G1 or apoptotic population when compared to untreated cells (SI Figure S2).

The two main reported causes for the appearance of an apoptotic population upon treatment with AgNPs are the leaching of Ag^+ ions from the AgNPs and the generation of reactive oxygen species (ROS) from nano metal oxide materials (AgNPs can oxidize easily to form Ag_2O).[31,32] To determine if the alteration in the cell cycle was due to free Ag^+ ions alone, cancer and healthy cells were incubated for 24 h with 20 nM $AgNO_3$ and their cell cycles were analyzed. Neither cell model showed significant ($P < 0.05$) cell cycle alteration (Figure 3) when compared to their controls. This result suggested that the apoptotic population is not solely due to the leaching of Ag^+ ions and could be partly due to the generation of ROS from the silver metal oxide inside the cancer cells.[33] ROS species are known to cause oxidative stress and DNA damage inside cells, which is a leading cause of apoptosis.[34−37] Additionally, it has been reported that upregulation of p53, a protein that is overexpressed when DNA damage occurs and causes cell cycle arrest and apoptosis, was seen after cells were incubated with unconjugated AgNPs.[38] It is possible that incubation with NLS/RGD-AgNPs also causes upregulation of p53 and signals for programmed cell death in our cancer cell model.

To further investigate alterations to the cell cycle, cell synchronization experiments were conducted to determine whether M phase arrest was seen after incubation with NLS/RGD-AgNPs. Nocodozale, a mitotic inhibitor, was used to synchronize cancer and healthy cells in the prometaphase (M phase).[39,40] On the basis of our group's previous work with nuclear-targeting AuNPs,[14] which showed abscission of two daughter cells occurring in ~2 h for untreated cells and ~4 h for particle treated cells, we chose 120 and 360 min for points of analysis. As seen in Figure 4, there was no significant M phase accumulation in the cancer or healthy cells after treatment with NLS/RGD-AgNPs. These results differ from NLS/RGD-AuNPs, as M phase accumulation in cancer cells was seen.[14] Since complete cell cycle analysis revealed an increase in the G2/M population, and the cell cycle synchronization experiment did not show M phase accumulation, it is proposed that the arrest has taken place in the G2 phase. This suggests that cancer cells treated with NLS/RGD-

AgNPs were unable to pass through the G2 checkpoint of the cell cycle, the cell's last opportunity to evaluate its genetic material before entering mitosis,[41] and resulted in apoptosis if their DNA was unable to be repaired. Furthermore, these experiments indicate that irreversible DNA damage occurs at different phases in the cell cycle when different plasmonic nanoparticles are used (Figure 5).

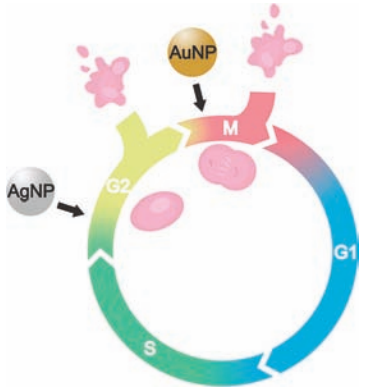

Figure 5. Summary of the difference in the effect of spherical nuclear-targeting AgNPs and AuNPs on the cell cycle. Cell cycle accumulation was seen in the G2 phase when cancer and healthy cells were treated with peptide-conjugated AgNPs. It has been reported[13] that nuclear-targeting AuNPs show cell cycle accumulation in the M phase of the cell cycle.

Confocal Microscopy and DNA Damage Test. DNA damage, in cancer and healthy cells treated with nuclear targeting AgNPs, was suggested from the sub G1 population and G2 accumulation in the flow cytometry experiments. To further investigate whether DNA damage was a result of incubation with nuclear-targeting AgNPs, treated cells were tested for double-strand breaks (DSBs) in DNA by confocal microscopy. Confocal images of untreated and treated cancer cells are shown in Figure 6. The nuclei have been stained blue with DAPI and DSBs as indicated by bright green FITC fluorescence foci. DNA DSBs are seen in cancer cells treated with 0.1 nM and 0.4 nM NLS/RGD-AgNPs (Figure 6B,C). When cancer cells were treated with 0.1 nM and 0.4 nM NLS/RGD-AuNPs, DNA DSBs were only seen after incubation with the 0.4 nM concentration.[14] This provides supplementary evidence that AgNPs exhibit more harmful effects on cancer cells than AuNPs. Confocal images of healthy cells treated with the highest concentration of NLS/RGD-AgNPs showed no DSBs (SI Figure S3). The absence of DSBs is due to the lower nanoparticle concentration at the nucleus in healthy cells compared to cancer cells. We attributed the decreased nanoparticle concentration at the nucleus to the reported lack of overexpression of $\alpha v\beta 6$ integrins, an RGD receptor, in our healthy cell line when compared to our cancer cell line.[27,29] These images confirm that NLS/RGD-AgNPs induce irreversible DNA damage in cancer cells, leading to an increased sub G1 (apoptotic) population. The confocal images further suggested that the selective targeting facilitated by the RGD peptide conjugation caused an increased vulnerability to DNA damage in cancer cells compared to healthy cells.

Real-Time Dark Field Imaging of AgNP Treated Cancer Cells. We also wanted to investigate in real time whether the presence of nuclear targeting AgNPs in our cancer cell model interferes with proper cellular division. The dynamics of cell division were monitored by long-term live-cell plasmonic scattering imaging.[21] Figure 7 displays representative real-time dark field images of cell division in our cancer cell model. Untreated cancer cells underwent proper division and showed no cell death. However, when cancer cells were incubated with varying concentrations of NLS/RGD-AgNPs normal cell division was not observed (Figure 7) and cell death resulted. These images differs from our group's previous work when using NLS/RGD-AuNPs, which showed cytokinesis (M phase) arrest in cancer cells after incubation with nuclear-targeted AuNPs.[14] The inability of cells treated with NLS/RGD-AgNPs to reach cytokinesis (M phase) provides further evidence that cells have arrested and accumulated in the G2 phase of the cell cycle due to the increased cytotoxicity of AgNPs compared to AuNPs.

CONCLUSIONS

The cell cycle and cell division of cancer (HSC-3) and healthy (HaCat) cells in the presence of conjugated AgNPs were systematically studied. DNA damage and apoptosis were seen in cancer cells that were treated with nuclear-targeting AgNPs. Real-time dark field imaging suggested that cancer cells treated with NLS/RGD-AgNPs are unable to successfully divide and ultimately undergo cell death. Complete cell cycle analysis showed a significant increase in the sub G1 population of

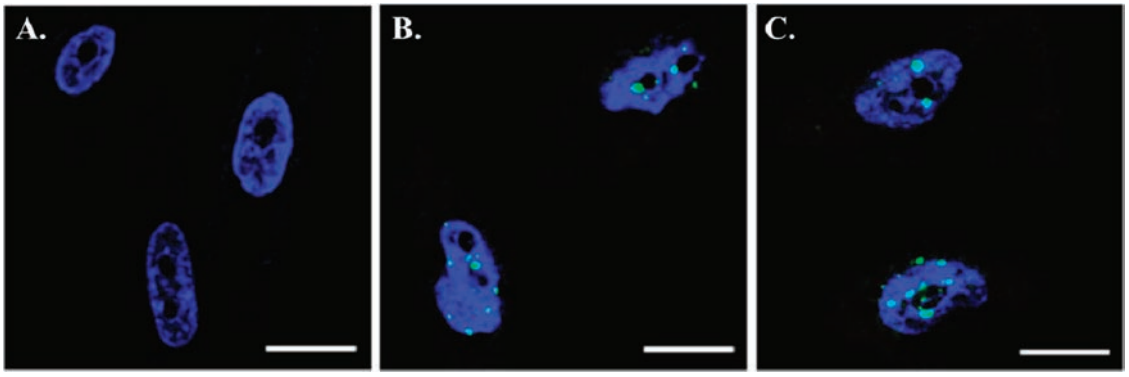

Figure 6. Confocal images of DNA damage in cancer cells resulting from incubation with NLS/RGD-AgNPs. The cells' nuclei were stained with DAPI (blue), and DNA double-strand breaks (DSBs) were stained with FITC (green). No DNA damage was seen in untreated cancer cells (A). DNA double-strand breaks (green foci) were seen in cells treated with (B) 0.1 nM and (C) 0.4 nM NLS/RGD-AgNPs. Cells were incubated with nuclear-targeting AgNPs for 24 h. Scale bar: 10 μm.

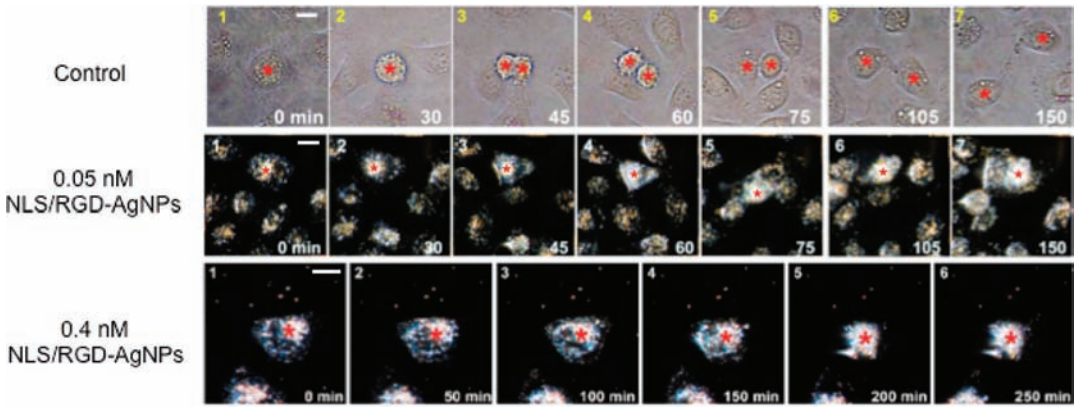

Figure 7. Real-time dark field images of cancer cells. Untreated cells (top) showed proper cell division while cells treated with 0.05 nM (middle) and 0.4 nM (bottom) nuclear-targeting AgNPs were unable to successfully divide and resulted in programmed cell death. The red stars indicate the cells of interest. Scale bar: 10 μm.

cancer cells after treatment with nuclear-targeting AgNPs. G2 accumulation was also seen in cancer and healthy cells during cell cycle analysis. The resulting G2 accumulation in cells treated with varying concentrations of AgNPs differed from the M phase accumulation in cells treated with 0.4 nM NLS/RGD-AuNPs. In cancer cells, the G2 accumulation accompanied by the increase in the sub G1 population suggests cells were unable to pass through the G2 checkpoint and the G2-M transition has been affected. The cause of the altered cell cycle was attributed to DNA damage, as seen with confocal microscopy. The basis for the observed DNA damage could potentially be a result of ROS generation from the AgNPs, as we eliminated leaching Ag^+ ions as the sole reason. These results demonstrate the importance of systematically studying the intracellular effects of each surface ligand and plasmonic nanoparticle combination to ensure the desired biomedical function and cytotoxicity are achieved.

■ ASSOCIATED CONTENT

Ⓢ Supporting Information

Additional figures and images as described in the text. This material is available free of charge via the Internet at http://pubs.acs.org.

■ AUTHOR INFORMATION

Corresponding Author

*E-mail: melsayed@gatech.edu. Phone: 404.894.0292. Fax: 404.894.0294.

Present Address

‡College of Material Science and Technology, Nanjing University of Aeronautics and Astronautics, Nanjing 210016, P.R. China.

■ ACKNOWLEDGMENTS

M.A.E. would like to thank Julius Brown Chair Funding (3306559GT) and the NIH-NCI support (U01CA151802-01). L.A. would like to thank the GT GAANN Fellowship (3306FT8). B.K. thanks the China Scholar Council (2008683010) and the Doctor Innovation Funds of China NUAA (BCXJ08-09). The authors would like to thank Brian Snyder for taking TEM micrographs of the synthesized silver nanoparticles.

■ REFERENCES

(1) Kelly, K. L., Coronado, E., Zhao, L. L., and Schatz, G. C. (2002) The optical properties of metal nanoparticles: the influence of size, shape, and dielectric environment. *J. Phys. Chem. B 107*, 668−677.

(2) Huang, X., El-Sayed, I. H., Qian, W., and El-Sayed, M. A. (2006) Cancer cell imaging and photothermal therapy in the near-infrared region by using gold nanorods. *J. Am. Chem. Soc. 128*, 2115−2120.

(3) Braydich-Stolle, L., Hussain, S., Schlager, J. J., and Hofmann, M.-C. (2005) In vitro cytotoxicity of nanoparticles in mammalian germline stem cells. *Toxicol. Sci. 88*, 412−419.

(4) Hussain, S. M., Hess, K. L., Gearhart, J. M., Geiss, K. T., and Schlager, J. J. (2005) In vitro toxicity of nanoparticles in BRL 3A rat liver cells. *Toxicol. in Vitro 19*, 975−983.

(5) Ahamed, M., Karns, M., Goodson, M., Rowe, J., Hussain, S. M., Schlager, J. J., and Hong, Y. (2008) DNA damage response to different surface chemistry of silver nanoparticles in mammalian cells. *Toxicol. Appl. Pharmacol. 233*, 404−410.

(6) Arora, S., Jain, J., Rajwade, J. M., and Paknikar, K. M. (2008) Cellular responses induced by silver nanoparticles: In vitro studies. *Toxicol. Lett. 179*, 93−100.

(7) Chung, L. W. K., Isaacs, W. R., and Simons, J. W. (2001) *Prostate Cancer: Biology, Genetics & the New Therapeutics*, Humana Press Inc., Totowa, NJ.

(8) Panyam, J., and Labhasestwar, V. (2004) Targeting Intracellular Targets. *Curr. Drug Delivery 1*, 235−247.

(9) Kumar, C. S. S. R. (2007) *Nanomaterials for Cancer Diagnosis*, Wiley-VCH Verlag GmbH & Co, Weinheim.

(10) Murphy, M. P. (1997) Selective targeting of bioactive compounds to mitochondria. *Trends Biotechnol. 15*, 326−330.

(11) Murphy, M. P., and Smith, R. A. J. (2000) Drug delivery to mitochondria: the key to mitochondrial medicine. *Adv. Drug Delivery Rev. 41*, 235−250.

(12) Tkachenko, A. G., Xie, H., Coleman, D., Glomm, W., Ryan, J., Anderson, M. F., Franzen, S., and Feldheim, D. L. (2003) Multifunctional gold nanoparticle-peptide complexes for nuclear targeting. *J. Am. Chem. Soc. 125*, 4700−4701.

(13) Oyelere, A. K., Chen, P. C., Huang, X., El-Sayed, I. H., and El-Sayed, M. A. (2007) Peptide-conjugated gold nanorods for nuclear targeting. *Bioconjugate Chem. 18*, 1490−1497.

(14) Kang, B., Mackey, M. A., and El-Sayed, M. A. (2010) Nuclear targeting of gold nanoparticles in cancer cells induces DNA damage, causing cytokinesis arrest and apoptosis. *J. Am. Chem. Soc. 132*, 1517−1519.

(15) Rastogi, S. C. (2007) *Cell Biology*, New Age International Publishers.

(16) Yoon, K.-Y., Hoon Byeon, J., Park, J.-H., and Hwang, J. (2007) Susceptibility constants of Escherichia coli and Bacillus subtilis to silver and copper nanoparticles. *Sci. Total Environ. 373*, 572−575.

(17) Lok, C.-N., Ho, C.-M., Chen, R., He, Q.-Y., Yu, W.-Y., Sun, H., Tam, P.K.-H., Chiu, J.-F., and Che, C.-M. (2006) Proteomic analysis of the mode of antibacterial action of silver nanoparticles. *J. Proteome Res. 5*, 916−924.
(18) Foldbjerg, R., Olesen, P., Hougaard, M., Dang, D. A., Hoffmann, H. J., and Autrup, H. (2009) PVP-coated silver nanoparticles and silver ions induce reactive oxygen species, apoptosis and necrosis in THP-1 monocytes. *Toxicol. Lett. 190*, 156−162.
(19) Carlson, C., Hussain, S. M., Schrand, A. M., K. Braydich-Stolle, L., Hess, K. L., Jones, R. L., and Schlager, J. J. (2008) Unique cellular interaction of silver nanoparticles: size-dependent generation of reactive oxygen species. *J. Phys. Chem. B 112*, 13608−13619.
(20) Freund, P. L., and Spiro, M. (1985) Colloidal catalysis: the effect of sol size and concentration. *J. Phys. Chem. 89*, 1074−1077.
(21) Qian, W., Huang, X., Kang, B., and El-Sayed, M. A. (2010) Dark-field light scattering imaging of living cancer cell component from birth through division using bioconjugated gold nanoprobes. *J. Biomed. Opt. 15*, 046025.
(22) Wuelfing, W. P., Gross, S. M., Miles, D. T., and Murray, R. W. (1998) Nanometer gold clusters protected by surface-bound monolayers of thiolated poly(ethylene glycol) polymer electrolyte. *J. Am. Chem. Soc. 120*, 12696−12697.
(23) Busk, M., Pytela, R., and Sheppard, D. (1992) Characterization of the integrin alpha v beta 6 as a fibronectin-binding protein. *J. Biol. Chem. 267*, 5790−5796.
(24) Takayama, S., Hatori, M., Kurihara, Y., Shirota, T., and Shintani, S. (2009) Inhibition of TGF-β1 suppresses motility and invasiveness of oral squamous cell carcinoma cell lines via modulation of integrins and down-regulation of matrix-metalloproteinases. *Oncol. Rep. 21*, 205−210.
(25) Dehari, H., Ito, Y., Nakamura, T., Kobune, M., Sasaki, K., Yonekura, N., Kohama, G., and Hamada, H. (2003) Enhanced antitumor effect of RGD fiber-modified adenovirus for gene therapy of oral cancer. *Cancer Gene Ther. 10*, 75−85.
(26) Dingwall, C., and Laskey, R. A. (1991) Nuclear targeting sequences -- a consensus? *Trends Biochem. Sci. 16*, 478−481.
(27) Xue, H., Atakilit, A., Zhu, W., Li, X., Ramos, D. M., and Pytela, R. (2001) Role of the [alpha]v[beta]6 integrin in human oral squamous cell carcinoma growth in vivo and in vitro. *Biochem. Biophys. Res. Commun. 288*, 610−618.
(28) Jones, J., Watt, F. M., and Speight, P. M. (1997) Changes in the expression of αv integrins in oral squamous cell carcinomas. *J. Oral Pathol. Med. 26*, 63−68.
(29) Koivisto, L., Larjava, K., Häkkinen, L., Uitto, V., Heino, J., and Larjava, H. (1999) Different integrins mediate cell spreading, haptotaxis and lateral migration of HaCaT keratinocytes on fibronectin. *Cell Adhes. Commun. 7*, 245−257.
(30) Cooke, M. S., Evans, M. D., Dizdaroglu, M., and Lunec, J. (2003) Oxidative DNA damage: mechanisms, mutation, and disease. *FASEB 17*, 1195−1214.
(31) AshaRani, P. V., Low Kah Mun, G., Hande, M. P., and Valiyaveettil, S. (2008) Cytotoxicity and genotoxicity of silver nanoparticles in human cells. *ACS Nano 3*, 279−290.
(32) Hossain, Z., and Huq, F. (2002) Studies on the interaction between Ag+ and DNA. *J. Inorg. Biochem. 91*, 398−404.
(33) Kawata, K., Osawa, M., and Okabe, S. (2009) In vitro toxicity of silver nanoparticles at noncytotoxic doses to HepG2 human hepatoma cells. *Environ. Sci. Technol. 43*, 6046−6051.
(34) Moustafa, M. H., Sharma, R. K., Thornton, J., Mascha, E., Abdel-Hafez, M. A., Thomas, A. J., and Agarwal, A. (2004) Relationship between ROS production, apoptosis and DNA denaturation in spermatozoa from patients examined for infertility. *Hum. Reprod. 19*, 129−138.
(35) Rowe, L. A., Degtyareva, N., and Doetsch, P. W. (2008) DNA damage-induced reactive oxygen species (ROS) stress response in Saccharomyces cerevisiae. *Free Radical Biol. Med. 45*, 1167−1177.
(36) Simon, H. U., Haj-Yehia, A., and Levi-Schaffer, F. (2000) Role of reactive oxygen species (ROS) in apoptosis induction. *Apoptosis 5*, 415−418.
(37) Wiseman, H., and Halliwell, B. (1996) Damage to DNA by reactive oxygen and nitrogen species: role in inflammatory disease and progression to cancer. *Biochem. J. 313*, 17−29.
(38) Hsin, Y.-H., Chen, C.-F., Huang, S., Shih, T.-S., Lai, P.-S., and Chueh, P. J. (2008) The apoptotic effect of nanosilver is mediated by a ROS- and JNK-dependent mechanism involving the mitochondrial pathway in NIH3T3 cells. *Toxicol. Lett. 179*, 130−139.
(39) Samson, F., Donoso, J. A., Heller-Bettinger, I., Watson, D., and Himes, R. H. (1979) Nocodazole action on tubulin assembly, axonal ultrastructure and fast axoplasmic transport. *J. Pharmacol. Exp. Ther. 208*, 411−417.
(40) Poxleitner, M. K., Dawson, S. C., and Cande, W. Z. (2008) Cell cycle synchrony in Giardia intestinalis cultures achieved by using nocodazole and aphidicolin. *Eukaryotic Cell 7*, 569−574.
(41) Schönthal, A. H., Ed. (2004) *Checkpoint Controls and Cancer*, Humana Press, Totowa, NJ.

Supporting Information

Nuclear Targeted Silver Nanospheres Perturb the Cancer Cell Cycle Differently from those of Nanogold

Lauren A. Austin[†] , Bin Kang[†, ‡], Chun-Wan Yen[†], Mostafa A. El-Sayed [†,*]

[†]Laser Dynamics Laboratory, School of Chemistry and Biochemistry, Georgia Institute of Technology, Atlanta, GA 30332-0400

[‡]Permanent address: College of Material Science and Technology, Nanjing University of Aeronautics and Astronautics, Nanjing 210016, P.R. China

[*]Corresponding Author Email: melsayed@gatech.edu

	CANCER (HSC-3)	HEALTHY (HACAT)
CONTROL	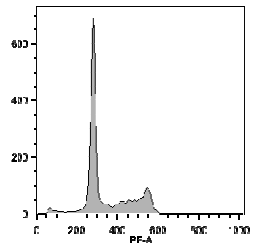	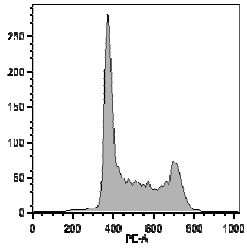
0.1 NM NLS/RGD	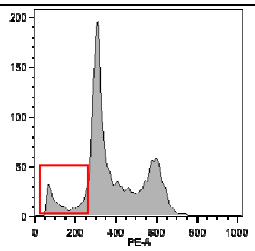	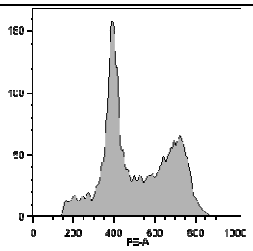
0.4 NM NLS/RGD	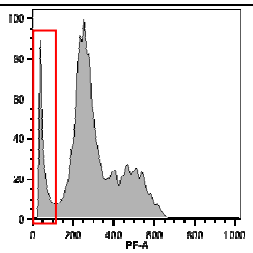	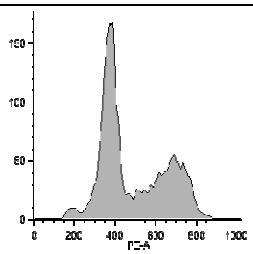
0.1 NM RGD	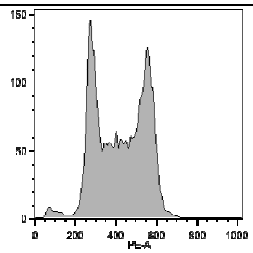	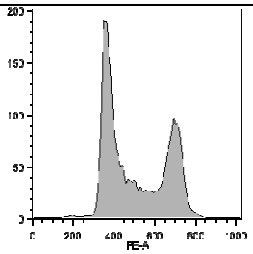
0.4 NM RGD	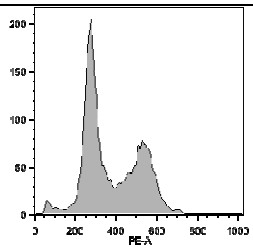	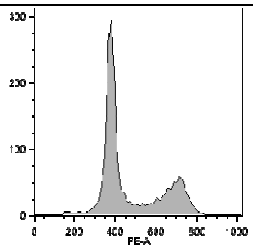
20 NM $AgNO_3$	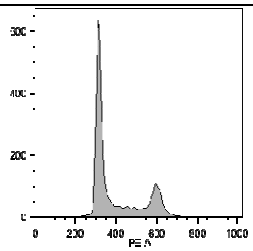	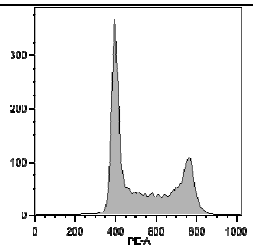

Figure S1. DNA histograms of cancer and healthy cells treated with conjugated AgNPs. Nuclear targeting (NLS/RGD) AgNPs caused the increase in the sub G1 population of cancer cells (red box) and G2 accumulation in both cancer and healthy cells.

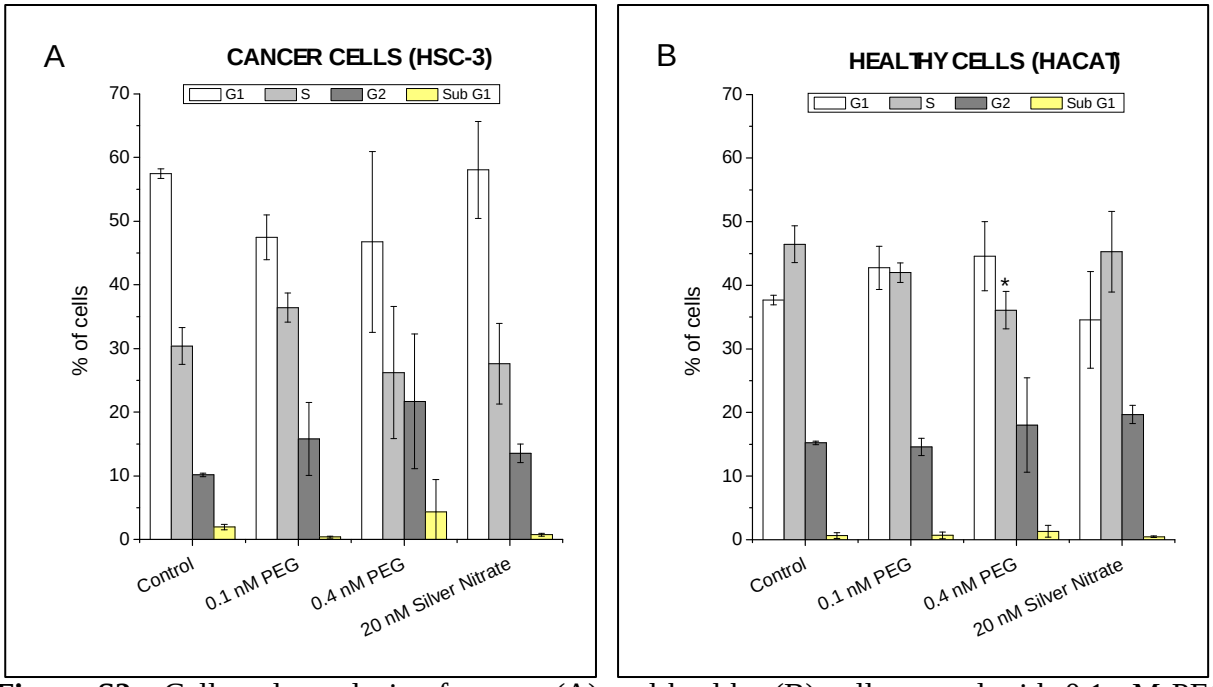

Figure S2. Cell cycle analysis of cancer (A) and healthy (B) cells treated with 0.1 nM PEG-AgNPs and 0.4 nM PEG-AgNPs. There was no significant alteration in the cell cycle in both cell models when compared to their controls.

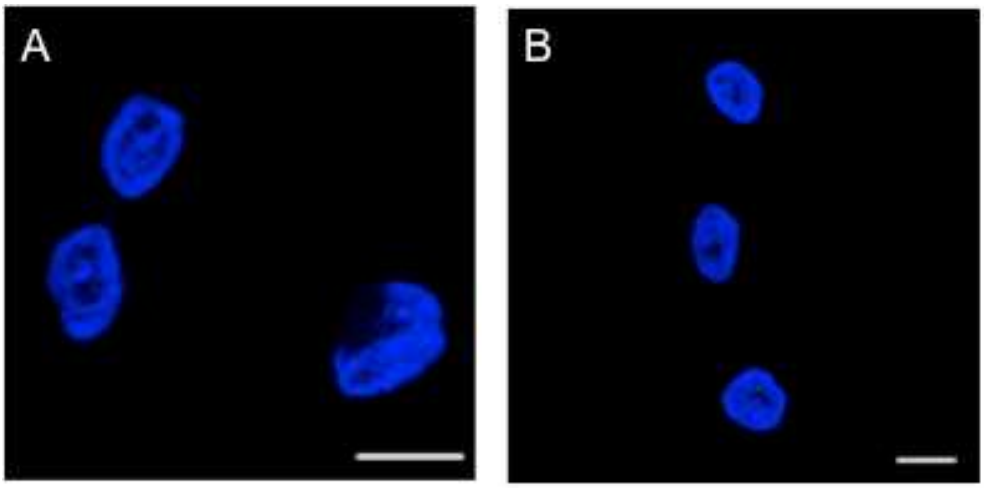

Figure S3. Confocal images of healthy (HaCat) cells after treatment with NLS/RGD-AgNPs. DNA double strand breaks, detected by the green fluorescence foci, were not seen in either untreated (A) or 0.4 nM NLS/RGD-AgNPs treated (B) healthy cells. Cells were incubated with nuclear targeting AgNPs for 24 hours. Scale bar: 10 μm.

Bioconjugate Chemistry

Article

pubs.acs.org/bc

Protein Heteroconjugation by the Peroxidase-Catalyzed Tyrosine Coupling Reaction

Kosuke Minamihata,[†] Masahiro Goto,[†,§] and Noriho Kamiya*[,†,§]

[†]Department of Applied Chemistry, Graduate School of Engineering, and [§]Center for Future Chemistry, Kyushu University

Supporting Information

ABSTRACT: Combining different proteins can integrate the functions of each protein to produce novel protein conjugates with wider ranges of applications. We have previously introduced a peptide containing tyrosine residues (Y-tag) at the C-terminus of *Escherichia coli* alkaline phosphatase (BAP). The tyrosine residues in the Y-tag were efficiently recognized by horseradish peroxidase (HRP) and were site-specifically cross-linked with each other to yield BAP homoconjugates. In this study, the HRP-catalyzed tyrosine coupling reaction was used for protein heteroconjugation. Streptavidin (SA) was selected as the conjugation partner for BAP. The Y-tag (GGGGY) was genetically introduced to the C-terminus of SA. Prior to heteroconjugation, the reactivity of the Y-tagged SA was examined. The Y-tagged SA cross-linked to form an SA homoconjugate upon HRP treatment, whereas wild-type SA remained essentially intact. In the heteroconjugation reaction of BAP and SA, the Y-tagged BAP and SA were efficiently cross-linked with each other upon HRP treatment. The functions of the BAP-SA conjugates were evaluated by measuring the BAP enzymatic activity on a biotin-coated plate. The BAP-SA conjugate tethered to the plate showed BAP enzymatic activity, indicating that both BAP and SA retained their functions following heteroconjugation. The BAP-SA conjugate prepared from both Y-tagged BAP and SA showed the highest enzymatic activity on the biotin-coated plates. This result illustrates the advantage of the protein conjugation reaction in which multiple numbers of proteins can be conjugated at the same time.

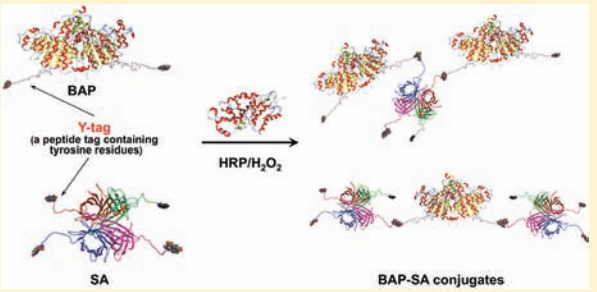

INTRODUCTION

There is significant interest in the heteroconjugation reaction of different proteins because this reaction combines distinct protein functionalities, thereby increasing the integrative functions of conjugated proteins and providing an alternative use of proteins in many fields.[1−4] Many approaches to achieve protein heteroconjugation have been proposed. The most straightforward approach is to genetically fuse two proteins, producing so-called fusion or chimeric proteins.[5−7] This technique enables the production of homogeneous protein conjugates by controlling sophisticated protein expression systems of living organisms. Protein expression systems have been extensively used for the purpose of protein production and purification[5,6] and in *in vivo* imaging.[7] By using this method, it is possible to theoretically conjugate any set of proteins; however, there is the risk of protein misfolding which results in the loss of protein function or the formation of insoluble inclusion bodies.

Post-translational protein modification (PTM) has general versatility to produce protein heteroconjugates, because PTM works with mature proteins thereby avoiding the problems associated with the expression of fusion proteins. Heterobifunctional linkers, which cross-link primary amino groups including an N-terminal amino acid and the side-chain of lysine, and/or the thiol group of cysteine, have been widely used to produce antibody-based heteroconjugates because antibodies possess cysteine residues available for this purpose.[8−10] Although the reaction is simple and easy to apply, the hereroconjugation reaction using heterobifunctional linkers is limited between two proteins, because one protein must have an available cysteine and the other protein should contain no cysteines. Moreover, the cross-linking reaction must be conducted in two steps, including the reduction of disulfide bonds and purification. Self-labeling proteins, such as the SNAP-tag and Halo-tag, have become powerful protein modification tools to introduce small molecules site-specifically to proteins.[11,12] These techniques should offer the potential to produce protein−protein heteroconjugates; however, negligible effort has been made using this method, probably because the introduction of small chemical substrates to target proteins is required.[11] Intein-mediated protein ligation is also applicable to protein heteroconjugation, but problems associated with the misfolding of the intein-fusion protein can arise.[5,13]

Enzymatic post-translational modifications represent the most promising way to produce protein−protein heteroconjugates.[3,14−17] Transglutaminase (TGase) has been studied and used in site-specific protein modifications including protein heteroconjugation, because the cross-linking of different pairs of natural amino acids, glutamine, and lysine residues is

Received: July 31, 2011
Revised: October 16, 2011
Published: October 17, 2011

 © 2011 American Chemical Society

possible.[3,15] The transpeptidase from *Staphylococcus aureus*, Sortase A (SrtA), is another enzyme that has been employed for site-specific protein−protein conjugations.[14,16,17] SrtA catalyzes the heteroconjugation reaction of two proteins. In this reaction, one protein possesses the C-terminal LPXTG sequence and the other protein has an N-terminal oligoglycine sequence. SrtA cleaves the peptide bond between the threonine and glycine residues of the LPXTG sequence and forms a peptide bond between the C-terminal end of the threonine residue and the N-terminal end of the oligoglycine.[14] Protein conjugations mediated by these enzymes require only the addition of short peptide tags, which are composed of natural amino acids. The problems associated with using these enzymes are that TGase has relative broad substrate recognition of amino substrates and the reaction efficiency of SrtA-catalyzed transpeptidation is not high because of competitive hydrolytic cleavage reactions.

Besides these well-studied enzymes, various oxidoreductases, including tyrosinase, laccase, and peroxidase, have also been employed for the purpose of protein modifications.[18−22] These enzymes catalyze the oxidation reaction of tyrosine and form *o*-quinone and phenoxy radicals in the side-chains. These activated tyrosine species are subsequently conjugated with primary amino groups[20,21] or other tyrosine residues.[18,19,22] Tyrosine residues can be found in modified forms, including dityrosine and trityrosine, in various kinds of structural proteins in nature,[23−26] suggesting the potential use of tyrosine as a target for PTM. As a target for protein modification, tyrosine residues have several advantages over common targets such as primary amino groups, carboxylic acid groups, or the thiol group. Tyrosine is a hydrophobic amino acid, and hence, the number of tyrosine residues exposed on a protein surface is generally lower than the hydrophilic amino acids, implying higher site-specificity in targeting tyrosine compared with other amino acids. Tyrosine is rather stable in physiological conditions, and therefore, it is not readily involved in common nucleophilic reactions such as amine coupling, indicating that selective modification of tyrosine residues is orthogonal to other common protein modification strategies.

We have recently reported site-specific protein cross-linking using the horseradish peroxidase (HRP) mediated oxidative tyrosine-coupling reaction.[27] In this previous report, peptide tags containing tyrosine residues (Y-tags) were genetically introduced at the C-terminus of *Escherichia coli* alkaline phosphatase (BAP). We demonstrated that as a proof-of-concept study the Y-tagged BAP became reactive to the enzymatic reaction of horseradish peroxidase (HRP), which resulted in the formation of site-specifically cross-linked BAP via the Y-tag.

Here, we explored the protein heteroconjugation of a Y-tagged BAP with a functional protein by the HRP-mediated tyrosine coupling reaction. Streptavidin (SA) derived from *Streptomyces avidinii* was selected as a promising conjugation partner. SA is a tetrameric protein, and each subunit binds to one water-soluble vitamin, biotin, with extraordinarily strong affinity.[28] SA has been extensively used in multiple fields such as biochemical, pharmaceutical, and biophysical applications.[29,30] The heteroconjugate of SA and alkaline phosphatase (AP) is applicable to the enzyme-linked immunosorbent assay (ELISA), staining of cells and tissues, and Western blotting. SA-AP conjugates are thus commercially available from several chemical companies. Unlike other enzyme-mediated protein conjugation reactions, the HRP catalyzed tyrosine-coupling reaction can cross-link a multiple number of SA and BAPs in one step, which results in the formation of $(BAP)_n$-$(SA)_m$ conjugates. In this report, the Y-tag was genetically introduced to the C-terminus of SA and BAP and the heteroconjugation of BAP and SA was demonstrated to prepare BAP-SA conjugates by the HRP-catalyzed tyrosine coupling reaction.

EXPERIMENTAL PROCEDURES

Materials and Instruments. Wild-type BAP (WT-BAP) and Y-tagged BAP (CY1-BAP) bearing the thrombin cleavage sequence (LVPRGS) and Y-tag (GGGGY) at the C-terminus were prepared according to our previous report.[27] The plasmid coding the core streptavidin (127 a.a.) was synthesized by the Codon Device (Cambridge, MA, USA). HRP-type VI (250−330 units/mg solid using pyrogallol) was purchased from Sigma Aldrich Co. H_2O_2 (30 wt %) was purchased from Wako Pure Chemical Industries, Ltd. (Osaka, Japan). All other reagents were purchased and used as received. A cation exchange column (HiTrap SP HP 1 mL) and a desalting column (PD-10) were purchased from GE Healthcare Bio-Sciences. A size-exclusion chromatography column (TSKgel G4000SW) was purchased from Tosoh Co. All chromatography experiments for the purification of SAs were conducted on a BioLogic DuoFlow Chromatography System (Bio-Rad Laboratories, Inc.).

Gene Construction of SA. The gene coding the core SA was amplified by PCR to introduce the Y-tag (GGGGY) to the 3′ terminal end, and the restriction enzyme sequences of *Nde*I and *Hind*III were also appended to the 5′ and 3′ termini, respectively. The PCR products were digested with *Nde*I and *Hind*III and cloned into the *Nde*I and *Hind*III sites of the pET22b + plasmid followed by transformation into *E. coli* JM109 to yield an expression plasmid coding for Y-tagged SA (abbreviated as CY1-SA). Wild-type SA (abbreviated as WT-SA) was also prepared in the same manner as the Y-tagged SA, but without the addition of the Y-tag sequence at the C-terminus.

Expression and Purification of the Recombinant SAs. The general purification process of SAs was carried out as previously described.[31,32] The expression of SA was carried out in *E. coli* BL21(DE3). After transformation, single colonies were selected from the agar plates containing 100 μg/mL of ampicillin and inoculated into 5 mL of LB medium containing 100 μg/mL of ampicillin. The medium was precultured overnight at 37 °C. The precultured medium was then poured into 500 mL of LB medium containing 100 μg/mL ampicillin and grown until the OD_{600} reached ∼0.9. Isopropyl β-D-thiogalactoside (IPTG) was added to the medium to a final concentration of 100 mg/L to induce the expression of the target SA. All protein expressions were performed for 4 h at 37 °C. The cells were then collected by centrifugation at 5000 *g* for 20 min at 4 °C. The cell pellets were washed with the pellet wash buffer (10 mM Tris-HCl, 1 mM EDTA, and 100 mM NaCl, pH 8.0) twice and subsequently resuspended in 30 mL of the inclusion body wash buffer (30 mM Tris-HCl, 2 mM EDTA, 0.1% Triton-X100, pH 8.0). The cell suspensions were frozen with liquid nitrogen and stored at −80 °C until purification. For the purification of SAs, the frozen cell suspensions were completely thawed on ice and 10 mg of lysozyme, 100 μL of 1 mg/mL DNase I and RNase A, and 120 μL of 1 M $MgCl_2$ were added. The suspensions were then incubated on ice for 30 min and then sonicated for 3 min to lyse cells. The supernatant and the insoluble materials containing inclusion bodies of SAs were separated by centrifugation at 5800 *g* for 10 min at 4 °C. The insoluble materials were thoroughly resuspended in 30 mL of the inclusion body wash buffer by pipetting and the inclusion bodies were collected at 5800 *g* and 4 °C.

This washing process was repeated until the inclusion bodies became white in color. This involved repeating the wash steps at least four times. The obtained inclusion bodies were further washed three times in the same manner using the pellet wash butter to remove the surfactant, Triton-X100. The inclusion bodies were then dissolved into 750 μL of a 6 M guanidinium hydrochloride solution (pH 1.5) and centrifuged at 20,800 *g* for 15 min at 4 °C. The supernatant containing the unfolded SA was dropped into vigorously stirred 50 mL of TBS (25 mM Tris-HCl, 137 mM NaCl, 2.68 mM KCl, pH 7.4) at 4 °C and then stirred gently overnight to refold SAs. The following day, 12.58 g of well-ground ammonium sulfate was gradually added to the TBS solution and stirring was continued for a further three hours. The generated settlings in the solution were removed using No. 2 filter paper. The SA in the solution was precipitated by adding a further 11.8 g of ammonium sulfate and stirring was continued at 4 °C overnight. The precipitated SA was collected by centrifugation at 20 800 *g* for 10 min and dissolved into 2.5 mL of TBS. The SA solution was filtrated using a 0.2 μm membrane filter and the buffer was exchanged to the cation chromatography binding buffer (100 mM succinic acid, 10 mM EDTA, pH 4.2) using PD 10 Sepharose columns. The SA solution was applied to a cation exchange column that was pre-equilibrated with the binding buffer. The column was washed with five column bed volumes of the binding buffer. SAs were eluted by a salt gradient of the elution buffer (100 mM succinic acid, 10 mM EDTA, 1 M NaCl, pH 4.4) from 0% to 35% with five column bed volumes, and 0.5 mL fractions were collected. A small portion of each fraction was taken and mixed with a HABA (2-(4′-hydroxyazobenzene)-benzoic acid) solution to determine the presence of SAs. The fractions containing SA were gathered and concentrated into a volume of ~0.9 mL using an ultrafiltration membrane (MWCO 10 kDa). The SA solution was next purified using a SEC column equilibrated with the SEC mobile phase (20 mM Tris-Acetate pH 7.2). All of the BAP solutions were applied to the SEC column using a 1 mL sample loop, and size-exclusion chromatography was carried out at flow rate of 0.5 mL/min. Fractions containing SA were collected and finally desalted into 10 mM Tris-HCl (pH 8.0) on PD 10 Sepharose columns. The concentrations of the obtained SA solutions were measured using the BCA assay and bovine serum albumin (BSA) as the standard. The purities of the SA samples were determined by SDS-PAGE analysis. The purification procedure was used for the production of all SA constructs.

Heteroconjugation Reaction of BAP and SA. BAP, SA, and HRP were dissolved in 10 mM Tris-HCl (pH 8.0) at final concentrations of 0.2 mg/mL, 0.2 mg/mL, and 0.1 mg/mL, respectively. The sample solutions were incubated at 37 °C, and the heteroconjugation reaction of BAP and SA was conducted by adding 1 μL of a 500 μM H_2O_2 solution five times every 10 min to a final concentration of 50 μM. After overnight incubation, the sample solutions were analyzed by SDS-PAGE and native-PAGE analyses. Prior to native-PAGE analyses, biotin-4-fluorescein was added to the sample solutions at a final concentration of 50 μM and incubated for 1 h at 4 °C.

Thrombin Treatment of CY1-BAP-SA Conjugates. CY1-BAP bears a thrombin cleavage site between BAP and the Y-tag; however, the CY1-SA construct does not have this protease site. Therefore, it is possible to cleave the Y-tag of CY1-BAP selectively. For the purpose of analyzing how CY1-BAP and SAs are conjugated to each other, (CY1-BAP)-SA conjugates were subjected to thrombin cleavage. After the heteroconjugation reaction of CY1-BAP and SAs, thrombin was added to the solutions at a final concentration of 20 U/mL. The solutions were analyzed in the same manner by SDS-PAGE and native-PAGE analyses.

Immobilization of BAP-SA Conjugates to a Biotin-Coated Plate. To standardize the experimental conditions, the BAP enzymatic activities of the BAP-SA conjugates were first measured in the solution state. After the heteroconjugation reaction, 10 μL of each BAP-SA conjugate sample was taken and added to 990 μL of 1 mM *p*-nitrophenylphosphate (*p*-NPP)/1 M Tris-HCl (pH 8.0) in a UV quotes cell. The absorbance increase derived from the generated *p*-nitrophenol (*p*-NP) at 410 nm was monitored for 3 min at 25 °C. One unit of BAP enzymatic activity was defined as an activity that catalyzes the dephosphorization reaction of 1 μmol of *p*-NPP in 1 min, and the *p*-NP absorbance coefficient of 16 900 M^{-1} cm^{-1} was employed to calculate the unit value. All the sample solutions were then diluted using 10 mM Tris-HCl (pH 8.0) to a concentration of 0.5 unit/mL and 125 mM of NaCl was added. To immobilize the BAP-SA conjugates, 100 μL of each BAP-SA conjugate solution was added to a well of biotin-coated plates (Pierce Biotin Coated Clear 8-Well Strip Plates) preliminarily washed with TBS three times and then incubated at 25 °C for 30 min. The wells were washed with TBS three times to remove unbounded proteins. Lastly, BAP enzymatic activities were measured in each well by adding 200 μL of 1 mM *p*-NPP/1 M Tris-HCl (pH 8.0) to each well and the increase in the absorbance at 410 nm was monitored for 10 min at 37 °C.

RESULTS AND DISCUSSION

Homoconjugation Reaction of SA. Prior to heteroconjugation, SAs were treated with HRP in the absence of BAP and the reactivity of SAs against HRP treatment was evaluated. The results of SDS-PAGE analyses of HRP-treated SA samples are shown in Figure 1. The band representing monomeric

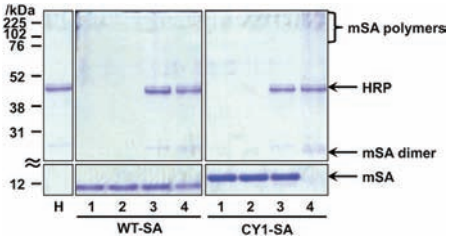

Figure 1. SDS-PAGE analyses of HRP-treated SAs. Lane H: HRP; Lane 1: SA; Lane 2: SA with the addition of H_2O_2; Lane 3: SA with the addition of HRP; Lane 4: SA with the addition of HRP and H_2O_2.

WT-SA at ~12 kDa remained after HRP treatment (Lane 4 for WT-SA), with a slight decrease in intensity. Additionally, a new band corresponding to the mSA dimer, close to a band arising from a contaminating protein in the HRP sample (<32 kDa), can be observed, yet the intensity is very weak. These results suggest that the intrinsic tyrosine residues of SA can be partly recognized by HRP. In contrast, the band of monomeric CY1-SA completely disappeared after HRP treatment and new bands corresponding to the mSA dimer and polymers emerged (Lane 4 for CY1-SA). This observation indicates that the tyrosine residues in the appended Y-tag were efficiently recognized by HRP and polymerized, since dityrosine, a coupling product of tyrosyl radicals, can be reactivated by HRP and form branched

cross-linkage. Figure 2 shows the molecular image of a subunit of SA showing its intrinsic tyrosine residues as CPK models. As

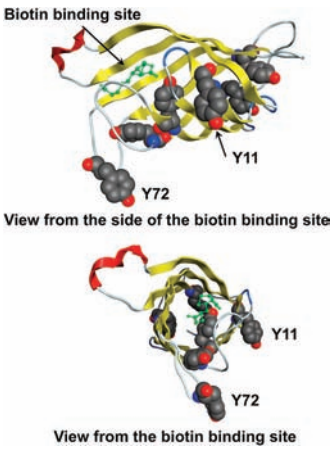

Figure 2. Molecular images of a subunit of WT-SA showing its intrinsic tyrosine residues as CPK models (PDB ID: 1MK5). The numbering of the amino acids began from the initiation codon of the methionine.

seen in Figure 2, Y11 and Y72 of SA are exposed on the surface of the protein. In particular, Y72 is located on a loop and is likely to be relatively flexible. We hypothesized that these two tyrosine residues are responsible for the homoconjugation of WT-SA upon HRP treatment and evaluated the reactivities of these two tyrosine residues by introducing the mutations Y11F and Y72F to WT-SA (see Supporting Information). The formation of dityrosine, one of the products of the tyrosine coupling reaction, was monitored by measuring the fluorescence intensity at 400 nm. The Y72F mutation significantly reduced the formation of the dityrosine upon HRP treatment, whereas the Y11F mutation had negligible effect. Therefore, Y72 is likely to be the primary tyrosine residue that is recognized by HRP and facilitates homoconjugation of WT-SA. This result also shows that, to be recognized by HRP, a tyrosine residue must not only be exposed on the protein surface but also needs to be in a flexible region, as the Y11 of WT-SA appears to be not recognized by HRP. The crystallographic data of five amino acid residues at the C-terminus of SA were not obtained (PDB ID: 1MK5), indicating high flexibility of the C-terminal region. Thus, the introduction of a flexible tyrosine residue as a Y-tag at the flexible SA C-terminus drastically increased the reactivity against HRP treatment, suggesting that the cross-linking of CY1-SA predominantly occurred through the Y-tag. The results obtained here demonstrate that the peroxidase-catalyzed tyrosine-coupling reaction is generally applicable to recombinant Y-tagged proteins.

Heteroconjugation Reaction of BAP and SA. BAP and SA were treated with HRP for the heteroconjugation reaction. The results of the SDS-PAGE and native-PAGE analyses of BAP-SA conjugation samples are shown in Figure 3. When WT-BAP and WT-SA were treated with HRP, both proteins exhibited virtually no reactivity, resulting in the presence of no new bands, and no observed change around 52 and 12 kDa, corresponding to mBAP and mSA, respectively (Figure 3A, Lane 1 for WT-BAP). The presence of a cross-linked WT-SA species was observed in the fluorescence image of the native-PAGE; however, this band was extremely weak.

In the case of either BAP or SA possessing a Y-tag, the heteroconjugation reaction between BAP and SA occurred only

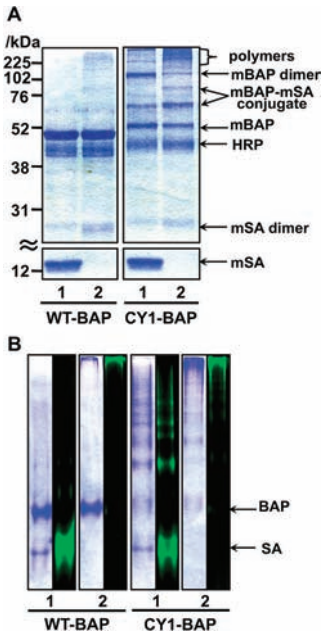

Figure 3. SDS-PAGE (A) and native-PAGE (B) analyses of the heteroconjugation reaction of BAP and SA. Lane 1: BAP with the addition of WT-SA, HRP, and H_2O_2; Lane 2: BAP with the addition of CY1-SA, HRP, and H_2O_2. In the native-PAGE analysis, SA was visualized by biotin-4-fluorescein (right of each picture).

when the Y-tag was appended to BAP. In the SDS-PAGE analysis, new bands emerged at ~60 kDa and above the mBAP dimer bands (around 102 kDa) with a ladder distribution (Figure 3A, Lane 1 for CY1-BAP). The new band at ~60 kDa corresponds to the mBAP-mSA conjugate based on the molecular weight, and the higher molecular weight bands are presumably conjugates in which mSA is attached to mBAP oligomers and polymers. In the native-PAGE analysis, most of the bands of the conjugates exhibited fluorescence from biotin-4-fluorescein indicating the presence of SA (Figure 3B, Lane 1 for CY1-BAP). This result shows that, when CY1-BAPs are cross-linked with each other, WT-SA was partly involved in protein conjugation. In contrast, WT-BAP was not cross-linked with CY1-SA even though CY1-SA was highly self-cross-linked in the same solution. These results can be explained as follows. As explained earlier, WT-SA has two largely exposed intrinsic tyrosine residues, Y11 and Y72, and Y72 can be recognized by HRP. However, although Y72 of WT-SA can be recognized by HRP and also the radical exchange reaction from the Y-tag of CY1-BAP can help to activate the exposed tyrosine residues of WT-SA, a large portion of WT-SA remained unreacted. Therefore, the heteroconjugation efficiency between CY1-BAP and WT-SA was not high. On the other hand, WT-BAP possesses no intrinsic tyrosine residues that are fully exposed on the surface of BAP, resulting in no heteroconjugation reaction between CY1-SA.

In the case of the heteroconjugation reaction of CY1-BAP and CY1-SA, in the SDS-PAGE analyses, the mSA band completely disappeared and multiple bands corresponding to BAP-SA conjugates emerged (Figure 3A, Lane 2 for CY1-BAP). The emergence of a new band at ~80 kDa corresponds to the mBAP-$(mSA)_2$ conjugate. The mBAP-$(mSA)_2$ conjugate was considered to be a form of a branched conjugate cross-linked through the Y-tag of each protein or a form where one Y72 of an mSA dimer, which is formed by intramolecular cross-linking

dx.doi.org/10.1021/bc200420v | Bioconjugate Chem. 2011, 22, 2332–2338

via the Y-tags, is involved in the cross-coupling with the Y-tag of mBAP. It is interesting that such conjugates were not observed in the case of the heteroconjugation reaction between CY1-BAP and WT-SA. In the solution of CY1-BAP and WT-SA, the homoconjugation reaction of WT-SA through its exposed tyrosine residue Y72 may compete with the heteroconjugation reaction with CY1-BAP. Thus, the cross-linking of WT-SAs was not observed and no further reaction of such species with CY1-BAP was observed. As a result, it can be assumed that the mBAP-$(mSA)_2$ conjugate was solely observed in the co-cross-linking of CY1-BAP and CY1-SA. In the native-PAGE analysis of the (CY1-BAP)-(CY1-SA) conjugate, the molecular weight of the conjugates dramatically increased when compared with the (CY1-BAP)-(WT-SA) conjugate, indicating efficient conjugation between BAP and SA through the Y-tag (Figure 3B, lane 2 for CY1-BAP). No precipitate was observed in the solution after the heteroconjugation reaction of CY1-BAP and CY1-SA, despite the extremely high molecular weight of the (CY1-BAP)-(CY1-SA) conjugate that barely enters the running gel of the native-PAGE.

Thrombin Treatment of CY1-BAP-SA Conjugates. To evaluate the cross-linking morphologies of the BAP-SA conjugate, the Y-tag of CY1-BAP was cleaved by thrombin treatment. Ideally, the efficiency of the heteroconjugation reaction is equivalent to the efficiency of the homoconjugation reaction of BAP and SA. Assuming that CY1-BAP and SA consistently cross-link with each other, the Y-tag cleavage from CY1-BAP after the heteroconjugation reaction should yield a substantial amount of free SA. The results of the SDS-PAGE and native-PAGE analyses of (CY1-BAP)-SA conjugate samples after thrombin treatment are shown in Figure 4. The conjugate

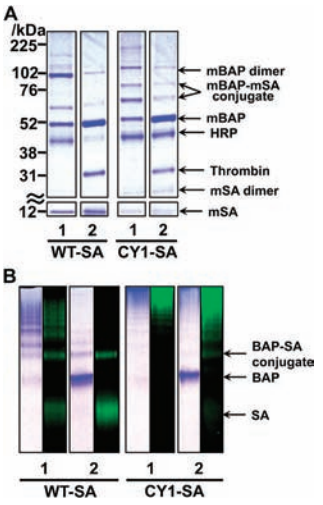

Figure 4. SDS-PAGE (A) and native-PAGE (B) analyses of thrombin-treated CY1-BAP-SA conjugates. Lane 1: SA with the addition of CY1-BAP, HRP, and H_2O_2; Lane 2: thrombin was added to the samples of lane 1 and incubated for 12 h at 37 °C. In the native-PAGE analysis, SA was visualized by biotin-4-fluorescein (right of each picture).

of WT-SA and CY1-SA was almost completely digested by thrombin, and resulted in the presence of SA monomers and BAP monomers in the SDS- and native-PAGE analyses (Lane 2 for WT-SA). The results indicate that the (CY1-BAP)-(WT-SA) conjugate was cross-linked site-specifically through the Y-tag of CY1-BAP. In the case of the (CY1-BAP)-(CY1-SA) conjugate, thrombin treatment should also digest the conjugates to yield BAP monomers. However, from the result of the native-PAGE analysis, it is clear that most of the CY1-SA remained in the highly cross-linked form even after thrombin treatment (Figure 4B, lane 2 for CY1-SA). The molecular weight of the (CY1-BAP)-(CY1-SA) conjugate decreased upon thrombin treatment; therefore, CY1-BAP and CY1-SA are clearly conjugated to each other. However, it is clear that the majority of CY1-SA has self-conjugated. SA is a tetramer protein, and hence, CY1-SA possesses four flexible Y-tags in a molecule, indicating the high probability of intramolecular cross-linking of the Y-tag upon HRP treatment. Additionally, the intrinsic tyrosine residues of SA contribute to the homoconjugation of CY1-SA. In addition, the molar concentration of SA was much higher than that of BAP in the reaction mixture (0.2 mg/mL of each protein). For these reasons, CY1-SA was found to be highly self-cross-linked, even in the presence of the reactive CY1-BAP protein.

Immobilization of BAP-SA Conjugates to a Biotin-Coated Plate. The protein functions of both BAP and SA were examined by immobilizing BAP-SA conjugates onto biotin-coated plates. In this study, the resultant BAP-SA conjugates were conjugates of BAP and SA in the ratio of *n* to *m*. As a result, when the BAP-SA conjugate was cast onto the biotin-coated plates, if one SA binds to one biotin, multiple numbers of BAP will be immobilized. After immobilization of the BAP-SA conjugate on the biotin-coated plates, the BAP enzymatic activities were measured and the results are shown in Figure 5. Enzymatic activity of BAP was detected on the

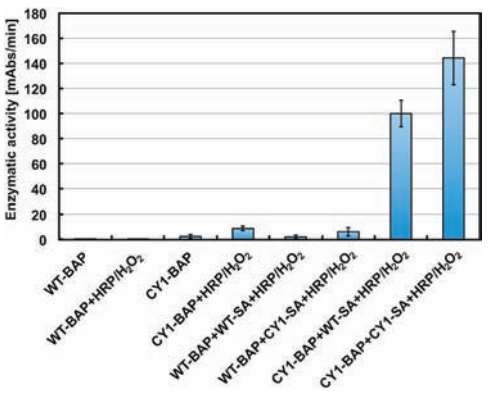

Figure 5. Enzymatic activity of BAP-SA conjugates on a biotin-coated plate.

biotin-coated plates; therefore, both BAP and SA retained their functions after the heteroconjugation reactions. BAP-SA conjugates prepared from CY1-BAP exhibited higher enzymatic activity than the others. This is because of the successful heteroconjugation of CY1-BAP with SA (Figure 3). When both SA and BAP possess the Y-tag, the tyrosine coupling efficiency was much higher than the other conditions examined, and hence, the (CY1-BAP)-(CY1-SA) conjugate showed the highest enzymatic activity on the biotin-coated plates. In addition, the (CY1-BAP)-(WT-SA) conjugate showed considerably higher enzymatic activity despite the absence of the Y-tag on SA. Under the reaction conditions for the CY1-BAP/WT-SA conjugation, CY1-BAP occasionally cross-linked with WT-SA and also self-cross-linked to yield CY1-BAP oligomers and polymers. Therefore, the conjugation ratio of BAP and SA in (CY1-BAP)-(WT-SA) conjugates is ideal for exhibiting high BAP enzymatic activity on the biotin-coated plates, to which

dx.doi.org/10.1021/bc200420v | *Bioconjugate Chem.* 2011, 22, 2332–2338

polymeric CY1-BAP with a small fraction of conjugated WT-SA was captured. However, since the heteroconjugation efficiency between CY1-BAP and WT-SA was not high, the overall enzymatic activity of the (CY1-BAP)-(WT-SA) conjugate was not as high as that of the (CY1-BAP)-(CY1-SA) conjugate.

The ratio of BAP and SA appears to be important in achieving high BAP enzymatic activity on the plates. Thus, (CY1-BAP)-(CY1-SA) conjugates were prepared by differing the ratio of SA/BAP. Here, the BAP concentration was fixed at 0.2 mg/mL and evaluated in the same manner. The results are shown in Figure 6. We expected that the (CY1-BAP)-(CY1-SA) conjugate prepared at a low ratio of SA/BAP should exhibit high enzymatic activity of BAP on the biotin-coated plate, because a large number of CY1-BAP could be attached to a small number of SA molecules. Contrary to our expectation, as the ratio of SA/BAP decreased, the conjugates exhibited lower enzymatic activity. Additionally, at SA/BAP ratios over 1/1, there was no significant difference in the BAP enzymatic activity on the biotin-coated plate. This can be explained as follows. As we discussed earlier, the CY1-SA preferentially self-cross-linked even in the presence of CY1-BAP. Therefore, in the solutions of the (CY1-BAP)-(CY1-SA) conjugate prepared at low ratios of SA/BAP, a large amount of CY1-BAP was not cross-linked with SA and most of the CY1-SA was self-cross-linked intramolecularly because of the low concentration used. As the ratio of SA/BAP increased, the efficiency of the co-cross-linking between BAP and SA increased, resulting in the immobilization of more BAP molecules on the biotin-coated plate. However, at the same time, the amount of SA conjugates, which were not co-cross-linked with BAP, also increased. Those SA conjugates would cover the surface of the biotin-coated plate, resulting in the immobilization of fewer BAP proteins on the plate. With these two processes taking place, the BAP enzymatic activity on the surface saturated at the SA/BAP ratio over 1/1. The results indicate that, to obtain high BAP enzymatic activity on the biotin-coated plate, at least equivalent amounts of SA against BAP are required.

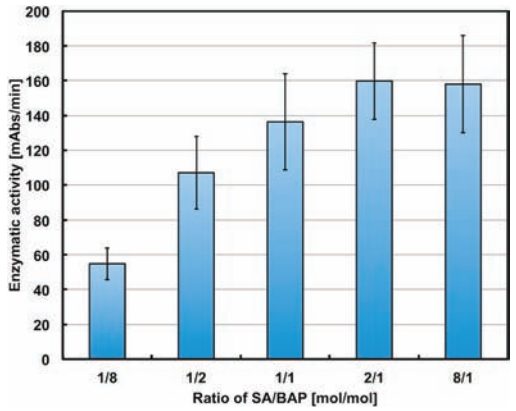

Figure 6. Enzymatic activity of (CY1-BAP)-(CY1-SA) conjugates prepared at various ratios of SA/BAP. The CY1-BAP concentration was fixed at 0.2 mg/mL (approximately 4 μM of mBAP). The ratio of SA/BAP was calculated from molar amounts of monomeric SA and BAP.

CONCLUSION

In this report, we demonstrated the heteroconjugation of BAP and SA by the HRP-catalyzed tyrosine cross-linking reaction. WT-SA exhibited very low reactivity against HRP treatment: the main reaction site of WT-SA upon HRP treatment was Y72. However, introduction of a Y-tag drastically increased the reactivity of SA against HRP treatment, which resulted in the homoconjugation of CY1-SA. The BAP-SA conjugate was efficiently obtained by HRP treatment when Y-tags were introduced to both SA and BAP. CY1-BAP and WT-SA were also cross-linked; however, WT-BAP did not cross-link with CY1-SA because of the presence of the exposed tyrosine residues on SA and the absence of exposed tyrosine residues on the surface of BAP. Thrombin treatment of the BAP-SA conjugate revealed that the (CY1-BAP)-(WT-SA) conjugate had site-specifically cross-linked with each other through the Y-tag of CY1-BAP. Thrombin treatment of the (CY1-BAP)-(CY1-SA) conjugate yielded BAP monomers, but most of the CY1-SA remained in high molecular weight forms, suggesting that CY1-SA was highly self-cross-linked even in the presence of CY1-BAP. The BAP-SA conjugate prepared from CY1-BAP and CY1-SA showed the highest enzymatic activity when immobilized on a biotin-coated plate because of the higher heteroconjugation efficiency.

ASSOCIATED CONTENT

Supporting Information

The dityrosine fluorescence measurements on WT-SA and its mutants for the evaluation of the cross-linking site of the WT-SA conjugate upon HRP treatment. This material is available free of charge via the Internet at http://pubs.acs.org.

AUTHOR INFORMATION

Corresponding Author

*Phone: +81-92-802-2806. FAX: +81-92-802-2810. E-mail: nori_kamiya@mail.cstm.kyushu-u.ac.jp.

ACKNOWLEDGMENTS

This work was supported in part by a Grant-in-Aid for the Global COE program, "Science for Future Molecular Systems" from the Ministry of Education, Culture, Sports, Science and Technology of Japan. K.M. was supported by Research Fellowships of the Japan Society for the Promotion of Science (JSPS) for Young Scientists.

ABBREVIATIONS

Abs, absorbance; AP, alkaline phosphatase; BAP, bacterial alkaline phosphatase; BCA, bicinchoninic acid; BSA, bovine serum albumin; EDTA, ethylenediaminetetraacetic acid; ELISA, enzyme-linked immunosorbent assay; HRP, horseradish peroxidase; HABA, 2-(4′-hydroxyazobenzene) benzoic acid; IPTG, isopropyl β-D-thiogalactoside; LB medium, Lysogeny Broth medium; mBAP, monomeric bacterial alkaline phosphatase; mSA, monomeric streptavidin; MWCO, molecular weight cut off; OD, optical density; PAGE, polyacrylamide gel electrophoresis; PCR, polymerase chain reaction; *p*-NP, *p*-nitrophenol; *p*-NPP, *p*-nitrophenylphosphate; PTM, post-translational protein modification; SA, streptavidin; SDS, sodium dodecyl sulfate; SEC, size exclusion chromatography; TBS, Tris-buffered saline; Tris, tris(hydroxymethyl)aminomethane; WT, wild-type

REFERENCES

(1) Shah, D., and Shen, W.-C. (1996) Transcellular delivery of an insulin-transferrin conjugate in enterocyte-like caco-2 cells. *J. Pharm. Sci. 85*, 1306−1311.

(2) Giepmans, B. N. G., Adams, S. R., Ellisman, M. H., and Tsien, R. Y. (2006) The Fluorescent toolbox for assessing protein location and function. *Science 312*, 217−224.

(3) Hirakawa, H., Kamiya, N., Tanaka, T., and Nagamune, T. (2007) Intramolecular electron transfer in a cytochrome P450cam system with a site-specific branched structure. *Protein Eng. Des. Sel. 20*, 453−459.

(4) Hirakawa, H., and Nagamune, T. (2010) Molecular assembly of P450 with ferredoxin and ferredoxin reductase by fusion to PCNA. *ChemBioChem 11*, 1517−1520.

(5) Guo, C., Li, Z., Shi, Y., Xu, M., Wise, J. G., Trommer, W. E., and Yuan, J. (2004) Intein-mediated fusion expression, high efficient refolding, and one-step purification of gelonin toxin. *Protein Expr. Purif. 37*, 361−367.

(6) Waugh, D. S. (2005) Making the most of affinity tags. *Trends Biotechnol. 23*, 316−320.

(7) Newman, R. H., Fosbrink, M. D., and Zhang, J. (2011) Genetically encodable fluorescent biosensors for tracking signaling dynamics in living cells. *Chem. Rev. 111*, 3614−3666.

(8) Yoshitake, S., Imagawa, M., Ishikawa, E., Niitsu, Y., Urushizaki, I., Nishiura, M., Kanazawa, R., Kurosaki, H., Tachibana, S., Nakazawa, N., and Ogawa, H. (1982) Mild and efficient conjugation of rabbit Fab' and horseradish peroxidase using a maleimide compound and its use for enzyme immunoassay. *J. Biochem. 92*, 1413−1424.

(9) Bieniarz, C., Husain, M., Barnes, G., King, C. A., and Welch, C. J. (1996) Extended length heterobifunctional coupling agents for protein conjugations. *Bioconjugate Chem. 7*, 88−95.

(10) Hylarides, M. D., Mallett, R. W., and Meyer, D. L. (2001) A robust method for the preparation and purification of antibody/streptavidin conjugates. *Bioconjugate Chem. 12*, 421−427.

(11) Chidley, C., Mosiewicz, K., and Johnsson, K. (2008) A Designed protein for the specific and covalent heteroconjugation of biomolecules. *Bioconjugate Chem. 19*, 1753−1756.

(12) Hinner, M. J., and Johnsson, K. (2010) How to obtain labeled proteins and what to do with them. *Curr. Opin. Biotechnol. 21*, 766−776.

(13) Hackenberger, C. P. R., Chen, M. M., and Imperiali, B. (2006) Expression of N-terminal Cys-protein fragments using an intein refolding strategy. *Bioorg. Med. Chem. 14*, 5043−5048.

(14) Mao, H., Hart, S. A., Schink, A., and Pollok, B. A. (2004) Sortase-mediated protein ligation: A new method for protein engineering. *J. Am. Chem. Soc. 126*, 2670−2671.

(15) Tanaka, T., Kamiya, N., and Nagamune, T. (2004) Peptidyl linkers for protein heterodimerization catalyzed by microbial transglutaminase. *Bioconjugate Chem. 15*, 491−497.

(16) Yamamoto, T., and Nagamune, T. (2009) Expansion of the sortase-mediated labeling method for site-specific N-terminal labeling of cell surface proteins on living cells. *Chem. Commun.*, 1022−1024.

(17) Sakamoto, T., Sawamoto, S., Tanaka, T., Fukuda, H., and Kondo, A. (2010) Enzyme-mediated site-specific antibody-protein modification using a ZZ domain as a linker. *Bioconjugate Chem. 21*, 2227−2233.

(18) Matheis, G., and Whitaker, J. R. (1984) Peroxidase-catalyzed cross linking of proteins. *J. Protein Chem. 3*, 35−48.

(19) Malencik, D. A., and Anderson, S. R. (1996) Dityrosine formation in calmodulin: cross-linking and polymerization catalyzed by *Arthromyces* peroxidase. *Biochemistry 35*, 4375−4386.

(20) Thalmann, C. R., and Lötzbeyer, T. (2002) Enzymatic cross-linking of proteins with tyrosinase. *Eur. Food Res. Technol. 214*, 276−281.

(21) Lewandowski, A. T., Small, D. A., Chen, T., Payne, G. F., and Bentley, W. E. (2006) Tyrosine-based "Activatable Pro-Tag": Enzyme-catalyzed protein capture and release. *Biotechnol. Bioeng. 93*, 1207−1215.

(22) Mattinen, M.-L., Hellman, M., Permi, P., Autio, K., Kalkkinen, N., and Buchert, J. (2006) Effect of protein structure on laccase-catalyzed protein oligomerization. *J. Agric. Food Chem. 54*, 8883−8890.

(23) Andersen, S. O. (1964) The cross-links in resilin identified as dityrosine and trityrosine. *Biochim. Biophys. Acta 93*, 213−215.

(24) LaBella, F., Keeley, F., Vivian, S., and Thornhill, D. (1967) Evidence for dityrosine in elastin. *Biochem. Biophys. Res. Commun. 26*, 748−753.

(25) Raven, D. J., Earland, C., and Little, M. (1971) Occurrence of dityrosine in tussah silk fibroin and keratin. *Biochim. Biophys. Acta 251*, 96−99.

(26) Waykole, P., and Heidemann, E. (1976) Dityrosine in collagen. *Connect. Tissue Res. 4*, 219−222.

(27) Minamihata, K., Goto, M., and Kamiya, N. (2011) Site-specific protein cross-linking by peroxidase-catalyzed activation of a tyrosine-containing peptide tag. *Bioconjugate Chem. 22*, 74−81.

(28) Green, N. M. (1990) Avidin and streptavidin. *Methods Enzymol. 184*, 51−67.

(29) Wilchek, M., and Bayer, E. A. (1988) The avidin-biotin complex in bioanalytical applications. *Anal. Biochem. 171*, 1−32.

(30) Wilchek, M., and Bayer, E. A. (1990) Introduction to avidin-biotin technology. *Anal. Biochem. 184*, 5−133.

(31) Sano, T., and Cantor, C. R. (1990) Expression of a cloned streptavidin gene in *Escherichia coli*. *Proc. Natl. Acad. Sci. U.S.A. 87*, 142−146.

(32) Howarth, M., and Ting, A. Y. (2008) Imaging proteins in live mammalian cells with biotin ligase and monovalent streptavidin. *Nat. Protoc. 3*, 534−544.

Supporting Information

Protein heteroconjugation by the peroxidase-catalyzed tyrosine coupling reaction

Kosuke Minamihata,[†] Masahiro Goto,[†,§] and Noriho Kamiya[†,§,*]

[†]Department of Applied Chemistry, Graduate School of Engineering, Kyushu University

[§]Center for Future Chemistry, Kyushu University

[*]Corresponding author:

Professor Noriho Kamiya

Phone: +81-92-802-2806

FAX: +81-92-802-2810

E-mail: nori_kamiya@mail.cstm.kyushu-u.ac.jp

CONTENTS

1. Measurement of fluorescence emission from dityrosine.

To evaluate of which intrinsic tyrosine residues are responsible for homoconjugation of WT-SA upon HRP treatment, the formation of dityrosine was monitored by measuring the fluorescence emission from dityrosine at ~400 nm with an excitation light of ~320 nm. The suspected intrinsic tyrosine residues of WT-SA, Y11 and Y72, were substituted by phenylalanine (in single letter form: F). We prepared three types of WT-SA mutants, WT-SA(Y11F), WT-SA(Y72F), and WT-SA(Y11F/Y72F) by the site-directed mutagenesis technique using KOD-Plus-Mutagenesis Kit (TOYOBO Co., Ltd., Osaka, Japan). The fluorescence from dityrosine of WT-SA, WT-SA mutants, and CY1-SA was measured using a fluorescence spectrophotometer (PerkinElmer LS55) before and after the 3 min HRP treatment. The HRP treatment condition was same as the homoconjugation reaction of SAs in the manuscript except that the reaction was conducted with a volume of 400 µL. The fluorescence spectra from 360 to 600 nm were obtained with an excitation wavelength of 315 nm and a sharp cut-off filter set at 350 nm. The excitation spectra were measured from 280 to 350 nm while monitoring the fluorescent intensity at 400 nm with a sharp cut-off filter at 390 nm. Also, the increase in the fluorescence intensity at 420 nm (excitation light of 315 nm with a sharp cut-off filter at 350 nm) was measured by using time-driven measurement mode. The reaction condition was same as mentioned above, but the reaction was conducted in a quarts cell (cell volume of 400 µL) for fluorescence measurement. After H_2O_2 was pipetted to the reaction mixture in a quarts cell all at once, the measurement was immediately started and monitored for 3 min. The results are shown in **Figure S1**.

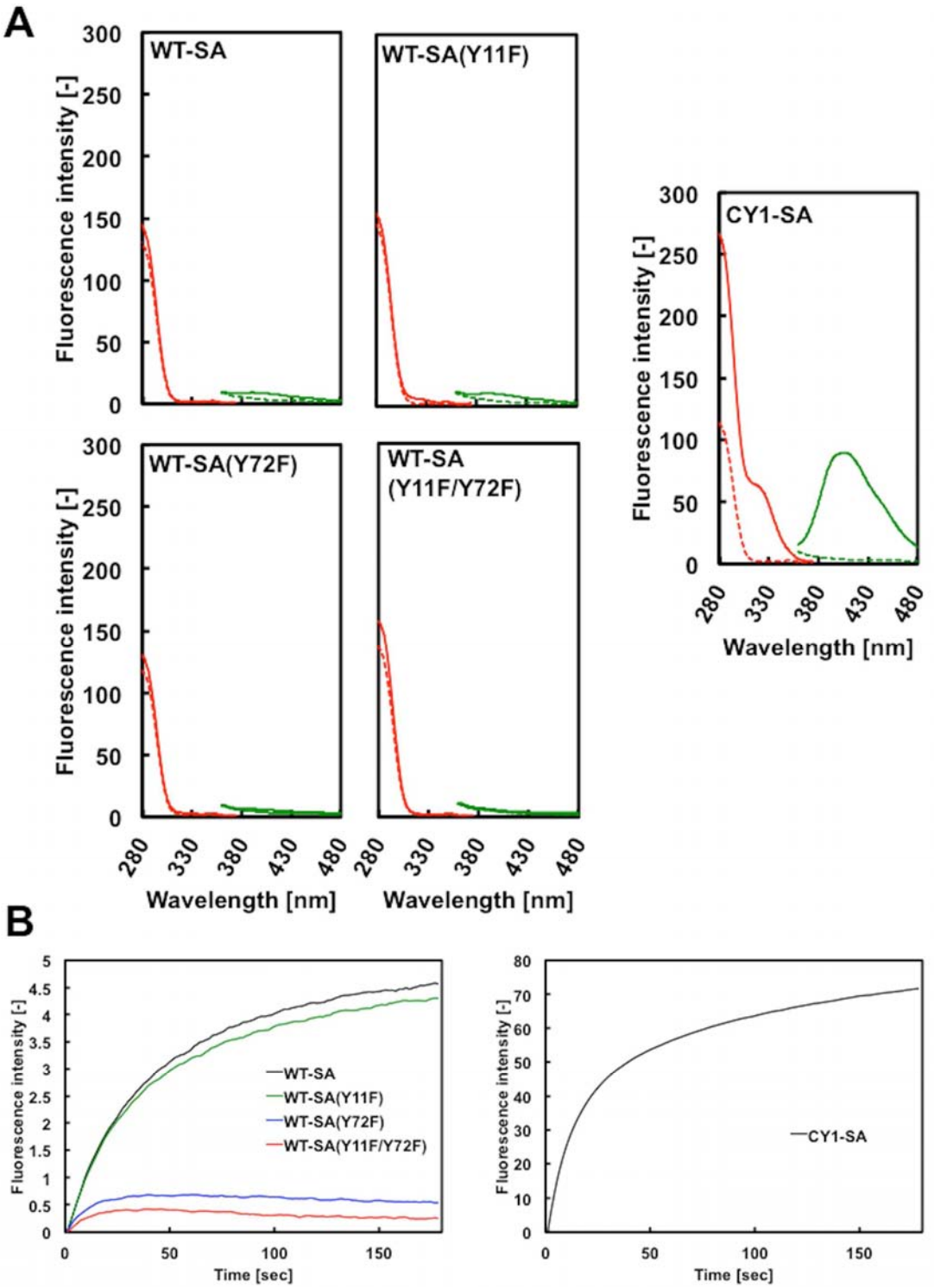

Figure S1. Measurements of fluorescence from dityrosine on WT-SA, WT-SA mutants and CY1-SA. A: Excitation and fluorescence spectra of WT-SA, WT-SA mutants and CY1-SA; red lines, excitation spectra; green lines, fluorescence spectra; dotted lines, before HRP treatment; solid lines, after HRP treatment. ; B: time-driven measurements of fluorescence intensity at 420 nm on WT-SA, WT-SA mutants and CY1-SA.

Bioconjugate Chemistry

Article

pubs.acs.org/bc

Efficient Cellular Delivery of β-Galactosidase Mediated by NrTPs, a New Family of Cell-Penetrating Peptides

Margarida Rodrigues,[†] Beatriz G. de la Torre,[‡] Gandhi Rádis-Baptista,[§] Nuno C. Santos,*[,†] and David Andreu*[,‡]

[†]Instituto de Medicina Molecular, Faculdade de Medicina da Universidade de Lisboa, Lisbon, Portugal

[‡]Department of Experimental and Health Sciences, Pompeu Fabra University, Barcelona Biomedical Research Park, Barcelona, Spain

[§]Laboratório de Bioquímica e Biotecnologia, Instituto de Ciências do Mar, Universidade Federal do Ceará, Fortaleza, Brazil

ABSTRACT: Nucleolar targeting peptides (NrTPs), a recently developed family of cell-penetrating peptides, have been shown to be very efficient in entering cells and accumulating in their nucleoli. In this work, we have used conjugates of NrTP6 (YKQSHKKGGKKGSG) covalently linked to β-galactosidase in order to demonstrate the capacity of NrTP for intracellular delivery of large molecules. NrTP6/β-galactosidase conjugates, prepared by maleimide-based chemistry, were stable and enzymatically active on the standard 4-methylumbelliferyl β-D-galactopyranoside substrate. Their translocation into HeLa cells, monitored by β-galactosidase activity as a readout of the uptake, showed efficient cellular entry and thus demonstrated the potential of NrTPs for intracellular delivery of large-size cargos with preservation of biological activity.

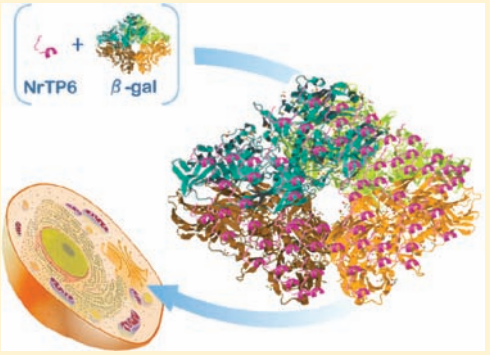

INTRODUCTION

Cell-penetrating peptides (CPPs) are short cationic sequences that, without disrupting membranes, can enter cells and carry over various types of cargo molecules.[1−3] Interest in these peptides started two decades ago with the observation that the HIV-1 accessory protein Tat is able to translocate into cells.[1] Since that time, CPPs have been shown capable of transporting biologically active cargos to the cell interior, both *in vivo* and *in vitro*.[4−6] Additionally, considerable effort has been invested in understanding the ability of CPPs to internalize various cargos [e.g., proteins, nucleic acids, fluorophores, radiolabels, magnetic resonance imaging (MRI) contrast agents, quantum dots, and so forth[7−10]], with the aim of developing CPPs into molecular tools with potential applications in basic research, diagnostics, or therapeutics. Relevant examples are pep-1 (Chariot), currently used as a commercial transfection reagent,[6,11,12] and KAI-9803, a selective δ-protein kinase C inhibitor conjugated to Tat that reduces injury associated with ischemia and reperfusion in animal models, presently undergoing phase IIb clinical trials.[13]

In principle, for any cargo intended to be ferried into a cell, a conjugate with a CPP can be envisaged. For instance, CPPs conjugated to either nucleic acids or proteins have been successfully used for transfection or antibody delivery.[14−16] Their eventual application in the therapeutic delivery of different drugs remains a challenging yet promising area of CPP research.[4,7,13] Studies of Tat-mediated protein translocation opened the way to CPP-facilitated delivery of proteins of different types and sizes, among which GFP (30 kDa), IgG (120−150 kDa), or β-galactosidase (465 kDa) have already been successfully tested.[2,4−7] β-Galactosidase (β-gal), in particular, is a frequent [2,6] and convenient cargo for CPP-mediated protein delivery, given its large size and its well-characterized enzymatic activity, for which different assays are available.[17−19] As to the conjugation of CPPs to the cargo of interest, whether a protein, a nucleic acid, or a nanoparticle, a number of approaches involving chemical conjugation, simple electrostatic interaction, or molecular fusion have been described.[2,4,6,20−22]

Nucleolar targeting peptides (NrTPs) were first described in 2008 as the result of structural minimization of the sequence of crotamine,[23] a 42-residue toxin that is one of the main components of the venom of the South American rattlesnake (*Crotalus durissus terrificus*).[24] The representative NrTP1 sequence (YKQCHKKGGKKGSG)[23] has been shown to possess remarkable translocating properties, namely, fast internalization (<15 min) and preferential nucleolar localization. For the purpose of this study, the original Cys at position 4 of NrTP1 has been mutated to Ser, and an extra Cys added to the C-terminal to facilitate conjugation. The resulting analogue, NrTP6 (YKQSHKKGGKKGSG), shows no detriment in CPP properties in the free form (unpublished), and we hereby demonstrate its ability to translocate large biomolecules into cells with full preservation of activity, a necessary condition

Received: August 1, 2011
Revised: September 23, 2011
Published: October 5, 2011

ACS Publications © 2011 American Chemical Society

for NrTP-mediated delivery of therapeutically relevant cargos into cells and tissues. Our positive results offer obvious opportunities for NrTP application, given that the nucleolus has a key role in ribosome biogenesis and the control of the cell cycle and, more recently, has been reported to take part in the control of stress and viral infection.[25−27]

EXPERIMENTAL PROCEDURES

Chemicals. Fmoc-protected amino acids, 2-(1*H*-benzotriazol-1-yl)-1,1,3,3-tetramethyluronium hexafluorophosphate (HBTU) and Fmoc-Rink-amide (MBHA) resin were obtained from Iris Biotech GmbH (Marktredwitz, Germany). HPLC-grade acetonitrile, and peptide synthesis-grade *N*,*N*-dimethylformamide (DMF), dichloromethane (DCM), *N*,*N*-diisopropylethylamine (DIEA), and trifluoroacetic acid (TFA) were from Carlo Erba-SDS (Peypin, France). 4-Methylumbelliferyl *β*-D-galactopyranoside (MUG), Triton X-100, *β*-galactosidase (EC 3.2.1.23) from *Escherichia coli* (grade VI), and 3-maleimidobenzoic acid *N*-hydroxysuccinimide ester (MBS) were obtained from Sigma (Madrid, Spain). DMEM, trypsin 0.05%, phosphate buffer saline (PBS), fetal bovine serum (FBS), penicillin, and streptomycin were from Invitrogen (Spain). All other chemicals were from Aldrich (Madrid, Spain)

Peptide Synthesis. The NrTP6 (YKQSHKKGGKKGSG) sequence was synthesized with an extra Cys residue at either the C- (i.e., NrTP6-C) or the N-terminus (C-NrTP6). Solid-phase peptide synthesis was done by Fmoc-based chemistry on Fmoc-Rink-amide (MBHA) resin (0.1 mmol) in a model 433 peptide synthesizer (Applied Biosystems, Foster City, CA) running FastMoc protocols. Couplings used 8-fold molar excess of both Fmoc L-amino acid and HBTU, and 16-fold molar excess of DIEA. Side chain protecting groups were *tert*-butyl (Ser, Tyr), *tert*-butyloxycarbonyl (Lys), and trityl (Cys, Gln, His). After chain assembly, full deprotection and cleavage of the N-deblocked resin were carried out with trifluoroacetic acid (TFA)-water-ethanedithiol-triisopropylsilane (94:2.5:2.5:1 v/v, 90 min, rt). Finally, peptides were precipitated by addition of chilled diethyl ether, taken up in H_2O, and lyophilized. Analytical reversed-phase HPLC was performed on a Luna C_{18} column (4.6 mm × 50 mm, 3 μm, Phenomenex). Linear gradients of solvent B (0.036% TFA in acetonitrile) into A (0.045% TFA in H_2O) were used for elution at a flow rate of 1 mL/min, with UV detection at 220 nm. Preparative HPLC runs were performed on a Luna C_{18} column (21.2 mm × 250 mm, 10 μm; Phenomenex), using linear gradients of solvent B (0.1% in acetonitrile) into A (0.1% TFA in H_2O), as required, with a flow rate of 25 mL/min. Matrix-assisted time-of-flight mass spectra were recorded in the reflector mode in a Voyager DE-STR workstation (Applied Biosystems, Foster City, CA) using α-hydroxycinnamic acid as matrix. Fractions of adequate HPLC homogeneity and with the expected mass were combined, lyophilized, and used in the cell uptake experiments.

Conjugation. The protocol for conjugation of NrTP6 to *β*-gal was adapted from Leteef et al.[28] Briefly, 1 mg of *β*-gal was dissolved in 2.1 mL of cold PBS and 4 mg of MBS were dissolved in 400 μL of DMF (1 μM and 32 mM *β*-gal and MBS concentrations, respectively). 160 μL of the MBS solution was then added to the *β*-gal solution under constant stirring and allowed to react for 30 min at 4 °C, to convert the protein Lys residues into maleimide units. The reaction mixture was then loaded to a Sephadex G-25 PD-10 desalting column (GE Healthcare) pre-equilibrated with 50 mM phosphate buffer, pH 6. 1 mL fractions were collected at 4 °C, and the three with highest absorbance at 290 nm were pooled and mixed with 1 mg (0.6 mmol) of either NrTP6-C or C-NrTP6, to assess the effect of the conjugation position on cargo internalization and preservation of bioactivity. The pH was adjusted to 7.5, and the mixture was incubated for 3 h and then dialyzed against 6 changes (30 min each) of 10 mM phosphate buffer pH 7.4, at 4 °C. The total protein concentration in the conjugates was determined by the Bradford method.[29] Conjugates with 100-fold lower concentrations of MBS (0.32 mM instead of 32 mM) were prepared likewise.

***β*-Gal Enzyme Assay.** The colorless 4-methylumbelliferyl-*β*-D-galactopyranoside (MUG) substrate is hydrolyzed by *β*-gal into 4-methylumbelliferone (4-MU), whose formation was monitored by its bright blue fluorescence (λ_{exc} = 360 nm, λ_{exc} = 440 nm, pH 7.4). Briefly, MUG was dissolved at 0.5 mM concentration in PBS containing 5 mM $MgCl_2$ and the enzyme reaction was started with the addition of either free *β*-gal (0−6 μg/mL) or conjugate (0−10 μg/mL), following a procedure adapted from previous reports.[6,30] The kinetics of 4-MU production was monitored by fluorescence intensity measurements, for 90 min, on a TECAN Infinite 200 Multimode microplate reader (Männedorf, Switzerland).

Uptake of NrTP6-C/*β*-gal (or C-NrTP6) Conjugate. Having established the activity of the NrTP6/*β*-gal conjugates in cell-free conditions, their internalization by human adenocarcinoma epithelial (HeLa) cells (gently supplied by Dr. Xavier Mayol, Cancer Cell Line Repository, Municipal Institute of Medical Research, Barcelona) was next studied. Cells were cultured in Dulbecco's Modified Eagle's Medium (DMEM), supplemented with 10% (v/v) of heat inactivated fetal bovine serum (FBS), 10 U/mL penicillin, and 100 μg/mL streptomycin, at 37 °C in a 5% CO_2 atmosphere. Cells were used for internalization experiments when they reached ca. 80% confluence. Experiments were performed either in Petri dishes (35 mm × 10 mm) or in 4-well plates. Briefly, conjugate (0−12 μg/mL) was incubated with cells for 60 min at 37 °C and 5% CO_2 atmosphere. Trypsin was added after incubation to detach cells and hydrolyze extracellular nonincorporated (membrane and nonmembrane bound) conjugate. Next, cells were harvested, centrifuged twice at 500 *g* for 5 min (with an intervening PBS wash), and permeabilized with 0.1% (v/v) Triton X-100 for 15 min at 25 °C. A last centrifugation step was done also at 500 *g* for 5 min and supernatant was assayed for enzymatic activity by fluorescence spectroscopy accordingly with the procedure described above. For these samples, 4-MU end point concentrations were also precisely quantified by UV absorbance after stopping the reaction by alkalinization with 50 mM NaOH to pH 9. UV absorbance measurements (ε_{360} = 1.9 × 10^4 M^{-1} cm^{-1}) were also done on a TECAN Infinite 200 Multimode microplate reader. The efficiency of internalization was studied either with a fixed cell density (2 × 10^5 cells/mL) at different conjugate concentrations or, alternatively, with a fixed amount of conjugate (7 μg/mL) and variable cell densities, in the (2−12) × 10^5 cells/mL range. Cell viability was controlled throughout the 60 min incubation both by the trypan blue exclusion assay and by differential interference contrast microscopy (DIC) in a Leica TSC-SP2 microscope (Wetzlar, Germany). Controls using nonconjugated enzyme and peptide, either combined or separately, were also performed. Moreover, an extensive study of *β*-gal residual activity was done, testing the enzyme in the 0−170 μg/mL concentration range.

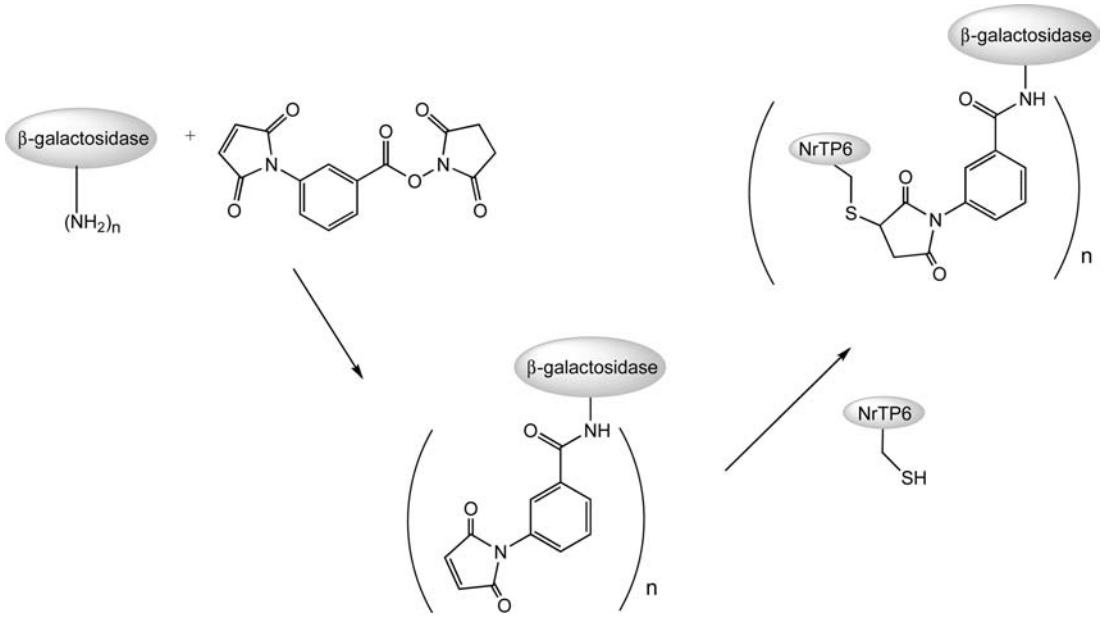

Figure 1. Maleimide-mediated conjugation of NrTP6-C and C-NrTP6 to *β*-galactosidase. The Cys residue was either on the C- or on the N-terminus of the peptide (NrTP6-C or C-NrTP6, respectively).

RESULTS AND DISCUSSION

Chemical conjugation, either protein (or peptide)-protein[13,16,28] or protein (or peptide)-nucleic acid,[20,31,32] is a well-established procedure for covalent attachment of two molecules. Figure 1 illustrates the conjugation between NrTP6 and *β*-gal, the latter chosen as a model to test CPP-mediated uptake of large cargos.[1,2,6] *β*-Gal activity was used as a readout of the uptake, with the fair assumption that activity and internalization are directly related. *β*-Gal is a large homotetramer, with 1023 amino acid residues per subunit, often used as a reporter of product transcription. The enzyme catalyzes the hydrolysis of lactose and other *β*-D-galactosides into monosaccharides. Although very specific for the galactose moiety, it is rather promiscuous regarding the rest of the substrate, which has allowed the development of different colorimetric assays for measuring activity.[33] For our study, we chose as probe 4-methylumbelliferyl-*β*-D-galactoside (MUG), hydrolyzed by *β*-gal to fluorescent 4-methylumbelliferone (4-MU).[6,30] *β*-Gal activity was measured by means of progression curves of fluorescent product formation (Figure 2). The enzymatic assay was conducted under substrate excess conditions, ensuring quasi-steady-state enzyme activity. In this way, initial rates can be assumed as V_{max} and, hence, k_{cat} is defined by the slope of the v_0 vs conjugate concentration variation (Figure 2). Fluorescence data were normalized by dividing by the fluorescence intensity of a 1 μg/mL solution of free *β*-gal after 90 min. Prior to cell uptake experiments, the enzymatic activity of various NrTP6/*β*-gal conjugates was confirmed (Figure 3A), a linear relationship being found between v_0 and conjugate concentration up to 2.5 μg/mL. The enzymatic activity was also compared with that of free *β*-gal at different stages of the protocol to ensure that no loss of activity was occurring. Results revealed a linear relationship between enzymatic activity and concentration from 0 to 5 μg/mL of free *β*-gal, with a k_{cat} of 26.3×10^{-3} μg^{-1} mL min^{-1} and r^2 = 0.995.

Next, HeLa cells were incubated with the conjugate and activity was measured in the cell-free extract upon addition of

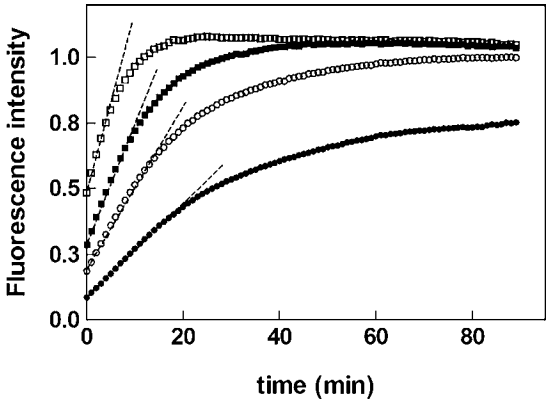

Figure 2. Time-course of *β*-galactosidase enzymatic activity. Fluorescence intensity, proportional to the 4-MU product concentration, was recorded at 440 nm (excitation at 360 nm) over 90 min after addition of enzyme to MUG substrate. The above kinetic curves correspond to 0.5 μg/mL (●), 1 μg/mL (○), 1.5 μg/mL (■), and 2.5 μg/mL (□) free *β*-gal concentrations, respectively. Fluorescence intensity values were normalized to the intensity for 1 μg/mL of *β*-gal at 90 min. Initial rates, v_0, were determined from the initial slope of the curves. The same procedure was used for *β*-gal conjugate samples (alone or after cell incubation).

MUG. Figure 3B shows a clear dependence of product formation on conjugate concentration, hence supporting the efficient delivery of NrTP6-conjugated *β*-gal into HeLa cells. Incubation with nonconjugated *β*-gal (Figure 3B) resulted in no product formation, in further support of the inability of *β*-gal to enter cells unless conjugated to an efficient CPP. The fact that the tetrameric form of *β*-gal is required for enzymatic activity clearly demonstrates that the conjugate not only enters cells, but does so while preserving its proper folding and oligomerization, i.e., with minimal interference, if any, from NrTP on the cargo structure. A control experiment with a mixture of nonconjugated NrTP6 and *β*-gal gave negative results that ruled out the possibility of NrTP6 electrostatic binding to *β*-gal, forming conjugates with translocating activity.

dx.doi.org/10.1021/bc200421z | *Bioconjugate Chem.* 2011, 22, 2339–2344

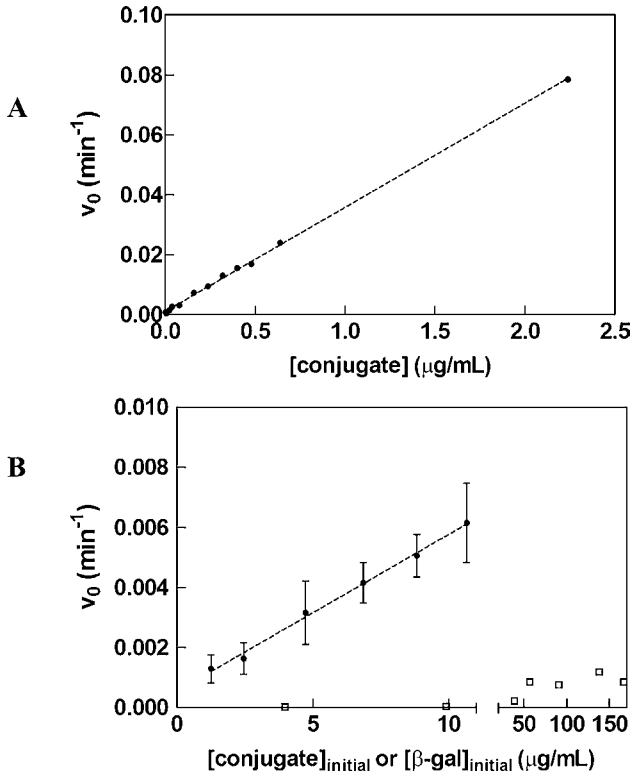

Figure 3. Enzymatic activity of the NrTP6-C/β-gal conjugate. (A) Standard activity in the absence of cells. (B) Activities of conjugate (circles) and β-gal (open squares) incubated with a cell-free extract (initially 2×10^5 HeLa cells/mL) for 60 min. Initial rates, v_0, were determined as indicated in Figure 2. k_{cat} values of 34.7×10^{-3} and 0.52×10^{-3} μg^{-1}.mL.min^{-1}, for conjugate alone and for the cell-free extract, respectively, were obtained. Results are from duplicates of a representative experiment.

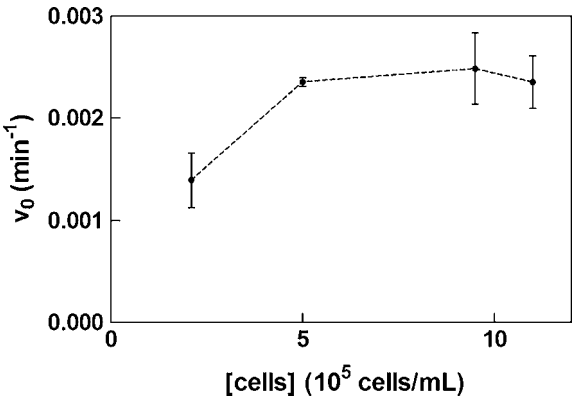

Figure 4. Effect of cell number on the enzymatic activity of the NrTP6-C/β-gal conjugate. Conjugate (7 μg/mL) was incubated with various cell densities for 60 min, at 37 °C. Initial rates, v_0, were determined as indicated in Figure 2. Results are from duplicates of a representative experiment.

The apparent decrease in the k_{cat} of β-gal from 34.7×10^{-3} to 0.52×10^{-3} μg^{-1} mL min^{-1} upon HeLa cell internalization (Figure 3 B) may be explained by several factors: The first, and possibly most relevant, is the fact that not all the conjugate is internalized. This is supported by Figure 4, where the fraction of internalized conjugate is shown to increase until a threshold level is reached. Another important factor for the apparent lower activity of the conjugate in the cell-free extract is competition for β-gal between MUG and endogenous substrates, mainly membrane components such as ganglioside GM1, lactosylceramides, glycoproteins, and keratin sulfate.[34,35] On the other hand, no significant competition for MUG appears to exist between endogenous and conjugated β-gal, as observed by the nonsignificant amounts of 4-MU detected in control experiments using nonconjugated NrTP (data not shown). In the above scenarios, CPP-to-cell ratio, rather than absolute CPP concentration, would appear to be influential in the uptake (or delivery) capacity of NrTP6, with the possibility of improving the delivery by increasing the volume of incubating peptide.[36]

Assuming no change in the intrinsic activity of NrTP6-delivered β-gal upon entering the cell, given that the apparent decrease in activity is essentially due to the equilibrium between the conjugate inside and outside the cell, the fraction of conjugate that penetrates the cell can be calculated from the above k_{cat} data to be 1.51%. Even if that value is underestimated, it is within the range reported for the uptake of other conjugates (0.07% to 5%).[37−39] Cargo size, even if CPP-mediated, is known to affect the efficiency of translocation, as observed, e.g., for the best-studied Tat.[40] Indeed, the highest reported uptake efficiency (5%) corresponds to a oligodeoxynucleotide−doxorubicin conjugate,[37] much smaller than the present NrTP6/β-gal conjugates (6.5 kDa vs 465 kDa). Our results reveal an intracellular conjugate concentration in the 3−57 μg/mL range, depending on the initial conjugate concentration and assuming a volume of 2.6 pL for a HeLa cell.[41] Assuming 116 NrTP6 copies bound to each β-gal tetramer (one per Lys residue), and from the respective molecular weights of β-gal and NrTP6 (465 and 1.6 kDa), it follows that approximately 72% and 28% of conjugate weight correspond to β-gal and NrTP, respectively. From this, the concentration of internalized β-gal can be estimated to be in the 2−41 μg/mL range. This rather high local concentration, entirely due to CPP-mediated internalization, clearly envisages relevant results with other more application-driven cargos.

Additional aspects explored in the present study included cell viability, as well as the influence of the position (N- or C-terminal) and extent of conjugation upon NrTP6/β-gal uptake. With regard to cell viability, both trypan blue exclusion and DIC live imaging after 60 min incubation with either type of conjugate (NrTP6-C or C-NrTP6-derived) revealed over 98% viability and no detectable signs of morphological changes or cellular stress over that period. Further comparison between both types of conjugates also showed similar uptake levels, either in cell-free assays (Figure 5) or upon incubation with HeLa cells (Figure 6), suggesting that positioning of the Cys residue at either the N- and C-terminal end has similar impact on both the conjugation and translocation efficiencies. Finally, results in Figure 6 also show that no significant differences exist between conjugates made with amounts of the bifunctional MBS reagent differing by a factor of 100.

The experimental results of the present report offer a necessary proof-of-concept for the intracellular delivery of large molecules mediated by NrTPs. It is worth noting that, two decades after introduction of the CPP concept, studies on delivery of drugs and other cargos by the most extensively studied CPPs (e.g., Tat, Ant, pep-1, and oligo-arginines) are still ongoing and, for the more recently discovered CPPs, insights on their translocation abilities and the underlying mechanisms are still scarce. In this regard, the present results are a valuable contribution to establishing the role of NrTPs as

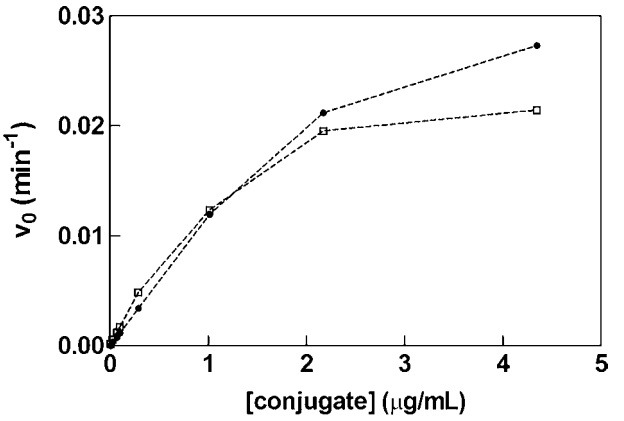

Figure 5. Effect of N- vs C-terminal conjugation on enzymatic activity. NrTP6-C (open squares) and C-NrTP6 (circles) derived β-gal conjugates assayed in the absence of cell extract. Initial rates, v_0, were determined as indicated in Figure 2.

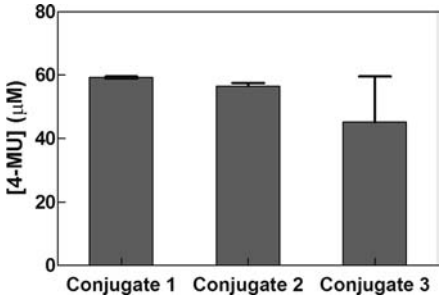

Figure 6. Effect of conjugation position and NrTP6/β-gal density on uptake efficiency. Conjugates **1**−**3** are, respectively, NrTP6-C/β-gal, C-NrTP6/β-gal, and NrTP6-C/β-gal prepared with 100-fold less MBS. [4-MU] was determined spectrophotometrically ($\varepsilon_{360\ nm}$ = 1.9 × 10^4 M^{-1} cm^{-1} at pH 9), after incubation with HeLa cells for 60 min, at 37 °C, and 90 min reaction in the cell-free extract, stopped with NaOH 50 mM. Results are duplicates from a representative experience. Scale bars represent the range of variation.

useful biotools. β-Gal is a rather large protein (size estimated as 17.4 × 13.0 × 7.5 nm^3 from Protein Data Bank (entry 1DP0) data, using the UCSF Chimera software, http://plato.cgl.ucsf.edu/chimera/), far exceeding the thickness of cell membranes. The fact that it is also well above the size of many therapeutically relevant cargos (e.g., antibodies are ∼150 kDa), in conjunction with the preferential nucleolar localization of NrTPs, allows to envisage promising applications for NrTPs in areas such as immunotherapy or cell cycle regulation.

AUTHOR INFORMATION

Corresponding Author

*Nuno C. Santos, Instituto de Medicina Molecular, Faculdade de Medicina da Universidade de Lisboa, Av. Prof. Egas Moniz, 1649-028 Lisbon, Portugal. Tel.: +351 217999480; Fax: +351 217999477; E-mail: nsantos@fm.ul.pt. David Andreu, Department of Experimental and Health Sciences, Pompeu Fabra University, Barcelona Biomedical Research Park, Dr Aiguader 88, 08003 barcelona, Spain. Tel.: +34-933160868; Fax: +34-933160901; E-mail: david.andreu@upf.edu.

ACKNOWLEDGMENTS

This work was funded by the Portuguese Ministry of Science, Technology and Higher Education (Fundação para a Ciência e a Tecnologia, FCT-MCTES; including M.R. PhD grant SFRH/BD/37432/2007), the Spanish Ministry of Science and Innovation (MICINN, grant BIO2008-04487-CO3 to D.A.), the European Union 7th Framework Program (IRSES project MEMPEPACROSS) and the European Biophysical Societies Association (EBSA).

REFERENCES

(1) Frankel, A. D., and Pabo, C. O. (1988) Cellular uptake of the tat protein from human immunodeficiency virus. *Cell 55*, 1189−1193.

(2) Schwarze, S. R., Ho, A., Vocero-Akbani, A., and Dowdy, S. F. (1999) In vivo protein transduction: delivery of a biologically active protein into the mouse. *Science 285*, 1569−1572.

(3) Zorko, M., and Langel, U. (2005) Cell-penetrating peptides: mechanism and kinetics of cargo delivery. *Adv. Drug Delivery Rev. 57*, 529−545.

(4) Kameyama, S., Horie, M., Kikuchi, T., Omura, T., Takeuchi, T., Nakase, I., Sugiura, Y., and Futaki, S. (2006) Effects of cell-permeating peptide binding on the distribution of ^{125}I-labeled Fab fragment in rats. *Bioconjugate Chem. 17*, 597−602.

(5) Fawell, S., Seery, J., Daikh, Y., Moore, C., Chen, L. L., Pepinsky, B., and Barsoum, J. (1994) Tat-mediated delivery of heterologous proteins into cells. *Proc. Natl. Acad. Sci. U. S. A. 91*, 664−668.

(6) Henriques, S. T., Costa, J., and Castanho, M. A. (2005) Translocation of beta-galactosidase mediated by the cell-penetrating peptide pep-1 into lipid vesicles and human HeLa cells is driven by membrane electrostatic potential. *Biochemistry 44*, 10189−10198.

(7) Stewart, K. M., Horton, K. L., and Kelley, S. O. (2008) Cell-penetrating peptides as delivery vehicles for biology and medicine. *Org. Biomol. Chem. 6*, 2242−2255.

(8) Bhorade, R., Weissleder, R., Nakakoshi, T., Moore, A., and Tung, C. H. (2000) Macrocyclic chelators with paramagnetic cations are internalized into mammalian cells via a HIV-tat derived membrane translocation peptide. *Bioconjugate Chem. 11*, 301−305.

(9) Bullok, K. E., Dyszlewski, M., Prior, J. L., Pica, C. M., Sharma, V., and Piwnica-Worms, D. (2002) Characterization of novel histidine-tagged Tat-peptide complexes dual-labeled with (99m)Tc-tricarbonyl and fluorescein for scintigraphy and fluorescence microscopy. *Bioconjugate Chem. 13*, 1226−1237.

(10) Kaufman, C. L., Williams, M., Ryle, L. M., Smith, T. L., Tanner, M., and Ho, C. (2003) Superparamagnetic iron oxide particles transactivator protein-fluorescein isothiocyanate particle labeling for in vivo magnetic resonance imaging detection of cell migration: uptake and durability. *Transplantation 76*, 1043−1046.

(11) Morris, M. C., Depollier, J., Mery, J., Heitz, F., and Divita, G. (2001) A peptide carrier for the delivery of biologically active proteins into mammalian cells. *Nat. Biotechnol. 19*, 1173−1176.

(12) Chariot. simple efficient protein deliver system. http://www.activemotif.com/catalog/37/chariot-protein-delivery-reagent (accessed July 2011).

(13) Johnson, R. M., Harrison, S. D., and Maclean, D. (2011) Therapeutic applications of cell-penetrating peptides. *Cell-Penetrating Peptides:Methods and Protocols* (Langel, Ü., Ed.) pp 535−551, Springer, New York.

(14) Moy, P., Daikh, Y., Pepinsky, B., Thomas, D., Fawell, S., and Barsoum, J. (1996) Tat-mediated protein delivery can facilitate MHC class I presentation of antigens. *Mol. Biotechnol. 6*, 105−113.

(15) Kim, D. T., Mitchell, D. J., Brockstedt, D. G., Fong, L., Nolan, G. P., Fathman, C. G., Engleman, E. G., and Rothbard, J. B. (1997) Introduction of soluble proteins into the MHC class I pathway by conjugation to an HIV tat peptide. *J. Immunol. 159*, 1666−1668.

(16) Eguchi, A., Akuta, T., Okuyama, H., Senda, T., Yokoi, H., Inokuchi, H., Fujita, S., Hayakawa, T., Takeda, K., Hasegawa, M., and Nakanishi, M. (2001) Protein transduction domain of HIV-1 Tat protein promotes efficient delivery of DNA into mammalian cells. *J. Biol. Chem. 276*, 26204−26210.

(17) Gee, K. R., Sun, W. C., Bhalgat, M. K., Upson, R. H., Klaubert, D. H., Latham, K. A., and Haugland, R. P. (1999) Fluorogenic

substrates based on fluorinated umbelliferones for continuous assays of phosphatases and beta-galactosidases. *Anal. Biochem. 273*, 41−48.
(18) Buelow, P. (1964) The ONPG test in diagnostic bacteriology. methodological investigations. *Acta Pathol. Microbiol. Scand. 60*, 376−386.
(19) Boezi, J. A., and Cowie, D. B. (1961) Kinetic studies of beta-galactosidase induction. *Biophys. J. 1*, 639−647.
(20) Muratovska, A., and Eccles, M. R. (2004) Conjugate for efficient delivery of short interfering RNA (siRNA) into mammalian cells. *FEBS Lett. 558*, 63−68.
(21) Caron, N. J., Torrente, Y., Camirand, G., Bujold, M., Chapdelaine, P., Leriche, K., Bresolin, N., and Tremblay, J. P. (2001) Intracellular delivery of a Tat-eGFP fusion protein into muscle cells. *Mol. Ther. 3*, 310−318.
(22) Chiu, Y. L., Ali, A., Chu, C. Y., Cao, H., and Rana, T. M. (2004) Visualizing a correlation between siRNA localization, cellular uptake, and RNAi in living cells. *Chem. Biol. 11*, 1165−1175.
(23) Radis-Baptista, G., de la Torre, B. G., and Andreu, D. (2008) A novel cell-penetrating peptide sequence derived by structural minimization of a snake toxin exhibits preferential nucleolar localization. *J. Med. Chem. 51*, 7041−7044.
(24) Nicastro, G., Franzoni, L., de Chiara, C., Mancin, A. C., Giglio, J. R., and Spisni, A. (2003) Solution structure of crotamine, a Na^+ channel affecting toxin from Crotalus durissus terrificus venom. *Eur. J. Biochem. 270*, 1969−1979.
(25) Carmo-Fonseca, M., Mendes-Soares, L., and Campos, I. (2000) To be or not to be in the nucleolus. *Nat. Cell Biol. 2*, E107−112.
(26) Boisvert, F. M., van Koningsbruggen, S., Navascues, J., and Lamond, A. I. (2007) The multifunctional nucleolus. *Nat. Rev. Mol. Cell Biol. 8*, 574−585.
(27) Emmott, E., and Hiscox, J. A. (2009) Nucleolar targeting: the hub of the matter. *EMBO Rep. 10*, 231−238.
(28) Lateef, S. S., Gupta, S., Jayathilaka, L. P., Krishnanchettiar, S., Huang, J. S., and Lee, B. S. (2007) An improved protocol for coupling synthetic peptides to carrier proteins for antibody production using DMF to solubilize peptides. *J. Biomol. Technol. 18*, 173−176.
(29) Bradford, M. M. (1976) A rapid and sensitive method for the quantitation of microgram quantities of protein utilizing the principle of protein-dye binding. *Anal. Biochem. 72*, 248−254.
(30) McGuire, J. B., James, T. J., Imber, C. J., St Peter, S. D., Friend, P. J., and Taylor, R. P. (2002) Optimisation of an enzymatic method for beta-galactosidase. *Clin. Chim. Acta 326*, 123−129.
(31) Lapiene, V., Kukolka, F., Kiko, K., Arndt, A., and Niemeyer, C. M. (2010) Conjugation of fluorescent proteins with DNA oligonucleotides. *Bioconjugate Chem. 21*, 921−927.
(32) Shiraishi, T., and Nielsen, P. E. (2006) Enhanced delivery of cell-penetrating peptide-peptide nucleic acid conjugates by endosomal disruption. *Nat. Protoc. 1*, 633−636.
(33) Juers, D. H., Jacobson, R. H., Wigley, D., Zhang, X. J., Huber, R. E., Tronrud, D. E., and Matthews, B. W. (2000) High resolution refinement of beta-galactosidase in a new crystal form reveals multiple metal-binding sites and provides a structural basis for alpha-complementation. *Protein Sci. 9*, 1685−1699.
(34) Tanaka, H., Meisler, M., and Suzuki, K. (1975) Activity of human hepatic beta-galactosidase toward natural glycosphingolipid substrates. *Biochim. Biophys. Acta 398*, 452−463.
(35) Tanaka, H., and Suzuki, K. (1977) Substrate specificities of the two genetically distinct human brain beta-galactosidases. *Brain Res. 122*, 325−335.
(36) Hallbrink, M., Oehlke, J., Papsdorf, G., and Bienert, M. (2004) Uptake of cell-penetrating peptides is dependent on peptide-to-cell ratio rather than on peptide concentration. *Biochim. Biophys. Acta 1667*, 222−228.
(37) Ren, Y., and Wei, D. (2004) Quantification intracellular levels of oligodeoxynucleotide-doxorubicin conjugate in human carcinoma cells in situ. *J. Pharm. Biomed. Anal. 36*, 387−391.
(38) Balayssac, S., Burlina, F., Convert, O., Bolbach, G., Chassaing, G., and Lequin, O. (2006) Comparison of penetratin and other homeodomain-derived cell-penetrating peptides: interaction in a membrane-mimicking environment and cellular uptake efficiency. *Biochemistry 45*, 1408−1420.
(39) Rothbard, J. B., and Jones, L. R. (2011) Quantitation of cellular and topical uptake of luciferin-oligoarginine conjugates. *Methods Mol. Biol. 683*, 487−504.
(40) Tunnemann, G., Martin, R. M., Haupt, S., Patsch, C., Edenhofer, F., and Cardoso, M. C. (2006) Cargo-dependent mode of uptake and bioavailability of TAT-containing proteins and peptides in living cells. *FASEB J. 20*, 1775−1784.
(41) Zhao, L., Kroenke, C. D., Song, J., Piwnica-Worms, D., Ackerman, J. J., and Neil, J. J. (2008) Intracellular water-specific MR of microbead-adherent cells: the HeLa cell intracellular water exchange lifetime. *NMR Biomed. 21*, 159−164.

Bioconjugate Chemistry

Article

pubs.acs.org/bc

Multi-Path Quenchers: Efficient Quenching of Common Fluorophores

Pete Crisalli and Eric T. Kool*

Department of Chemistry, Stanford University, Stanford, California 94305-5080, United States

Supporting Information

ABSTRACT: Fluorescence quenching groups are widely employed in biological detection, sensing, and imaging. To date, a relatively small number of such groups are in common use. Perhaps the most commonly used quencher, dabcyl, has limited efficiency with a broad range of fluorophores. Here, we describe a molecular approach to improve the efficiency of quenchers by increasing their electronic complexity. Multi-Path Quenchers (MPQ) are designed to have multiple donor or acceptor groups in their structure, allowing for a multiplicity of conjugation pathways of varied length. This has the effect of broadening the absorption spectrum, which in turn can increase quenching efficiency and versatility. Six such MPQ derivatives are synthesized and tested for quenching efficiency in a DNA hybridization context. Duplexes placing quenchers and fluorophores within contact distance or beyond this distance are used to measure quenching via contact or FRET mechanisms. Results show that several of the quenchers are considerably more efficient than dabcyl at quenching a wider range of common fluorophores, and two quench fluorescein and TAMRA as well as or better than a Black Hole Quencher.

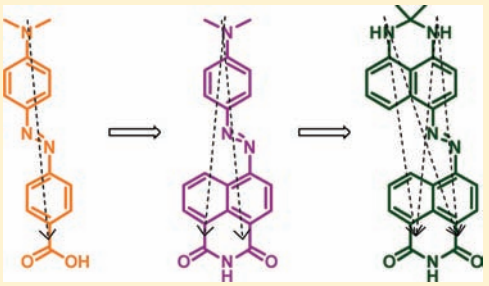

INTRODUCTION

Fluorescence quenchers are employed in a wide variety of fluorometric assays, particularly for detection of nucleic acids, reporting on enzymatic activity, and detecting other molecules of interest with turn-on responses.[1−11] However, for optimal performance, delicate matching of fluorophore and quencher is often needed, imposing limits on molecular designs and complicating applications.[12−14] For example, in order to cover the emission spectrum from violet to near-infrared, multiple different quenchers are needed, which can be an obstacle in assays designed to detect multiple analytes in one sample.[14,15] 4-(Dimethylamino)-azobenzene-4′-carboxylic acid (Dabcyl), perhaps the most commonly used fluorescence quencher, is generally limited to quenching of fluorophores that emit in the violet to green region of the visible spectrum (approximately 390 to 520 nm).[11,16] To cover fluorophores that emit further to the red, a variety of other quenchers have been developed, such as the Black Hole Quenchers (BHQ)[16] and QSY quenchers;[17] however, coverage of a broad spectrum still requires the use of multiple quenchers. In the BHQ series, for example, a total of four different compounds are necessary to provide for quenching of all commonly used wavelengths in fluorescence assays.[13] QSY quenchers are even more limited in quenching ability as a result of their narrow absorbance spectra.[12,14] Recently, some nonfluorescent cyanine-based quenchers have been reported that do have broadened spectral properties and provide for efficient quenching in caspase assays.[8] However, these quenchers display strong spectral overlap only with near-IR emitting fluorophores and may not quench other fluorophores as effectively.

Most commonly, quenching of fluorophores occurs by one of two mechanisms: contact quenching and FRET quenching.[12−14,18,19] In contact quenching, the fluorophore and quencher are in sufficiently close proximity to allow for direct electronic interaction of the excited state of the fluorophore with the quencher molecule.[18−21] Consequently, absorbed light at the excitation wavelength will primarily be nonradiatively transferred as heat to the surrounding environment, with only a limited amount of energy released as fluorescence. When the distance between the fluorophore and the quencher is increased, generally to the range 20−100 Å, the alternative mechanism of FRET quenching is observed.[12,14,18] In this mechanism, quenching efficiency is dependent upon the orientation of the fluorophore and quencher, the distance between them, and the overlap of the emission spectrum of the fluorophore and the absorption spectrum of the quencher.[12,14] To take advantage of these mechanisms, it is desirable to design quenchers with broadened absorbance spectra to allow for a greater range of fluorophore emissions that can be quenched by the FRET mechanism, while maintaining strong contact quenching.[12,14]

To address this issue, we have designed a novel set of quenchers that have multiple electronic conjugation pathways. By altering the existing scaffolds of common quenchers to increase the number of electron donor and acceptor groups, a series of Multi-Path Quenchers (MPQs) has been designed that provides for broader absorbance properties, in turn allowing for fluorescence quenching of a considerably wider range of fluorophores for each given quencher (Figure 1). Five new quenchers based on modifications to the dabcyl structure as well as one based upon modification of a Black Hole Quencher scaffold have been prepared and tested in a DNA context for

Received: August 1, 2011
Revised: October 14, 2011
Published: October 28, 2011

 © 2011 American Chemical Society

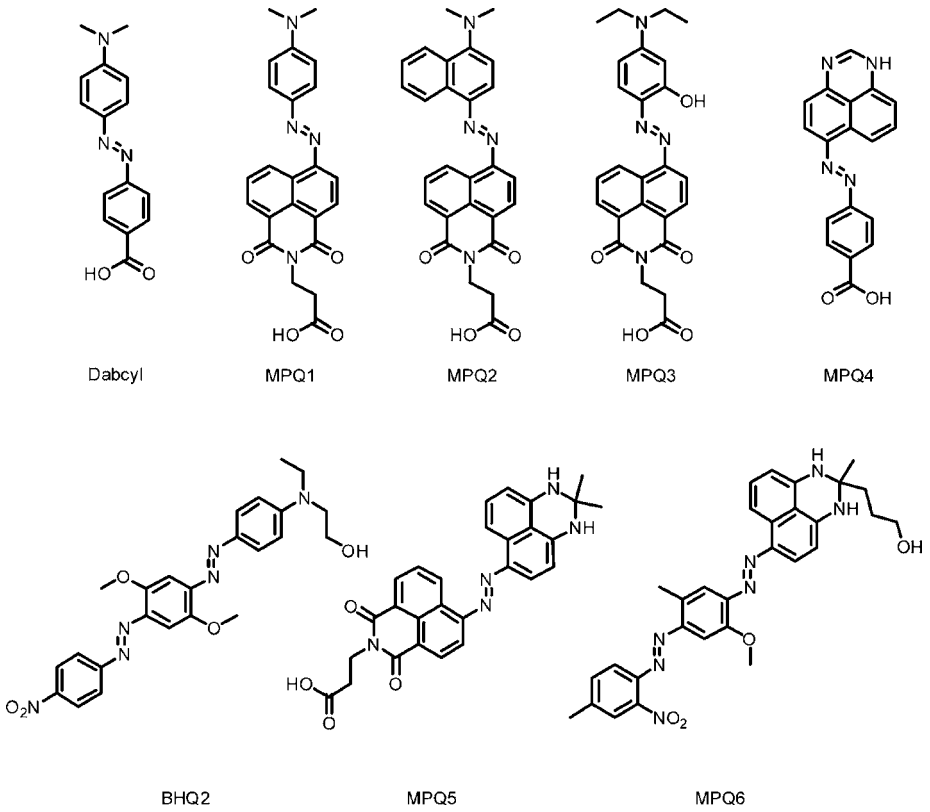

Figure 1. Structures of Multi-Path Quenchers (MPQs) and commercially available quenchers used in this study.

quenching efficiency, for comparison with previous studies.[3] We find that this strategy yields broadened absorption spectra and enhances efficiency over a wider range of wavelengths as compared with a common quencher such as dabcyl.

EXPERIMENTAL PROCEDURES

Chemicals and Reagents. Chemicals were purchased from Sigma-Aldrich and used without further purification. Solvents were purchased from Acros Organics and used as received. UltraMild DNA phosphoramidites and solid supports were purchased from Glen Research. BHQ2 phosphoramidite and 3′-Quasar 670 CPG were purchased from Biosearch Technologies. AlexaFluor 350 succinimidyl ester was purchased from Invitrogen. 5′-Fluorophore-modified oligonucleotides were purchased from Biosearch Technologies (FAM, TAMRA, Quasar 670) or Stanford University Protein and Nucleic Acid Facility (Cy3) and purified by HPLC.

Instrumentation. ^{1}H and ^{13}C NMR spectra were recorded on a Varian 400 MHz NMR or a Varian 500 MHz NMR spectrometer and internally referenced to the residual solvent signal; J values are reported in Hz. Oligonucleotides sequences were synthesized on an ABI 394 DNA synthesizer using UltraMild reagents and phosphoramidites. ESI-MS analysis was performed by the Stanford University Mass Spectroscopy Facility. Analytical and semipreparative high-performance liquid chromatography was performed on a LC-CAD Shimadzu liquid chromatograph, equipped with a SPD-M10A VD diode array detector and a SCL 10A VP system controller using reverse-phase C18 columns (Grace ProSphere C18−300 10 μ). DNA concentrations were determined on a Cary 100 Bio UV−vis spectrophotometer at 90 °C. Fluorescence measurements were performed on a Fluorolog 3 Jobin Yvon fluorophotospectrometer equipped with an external temperature controller. Oligonucleotide masses were determined by the Stanford University Protein and Nucleic Acid Facility using a Perspective Voyager-DE RP Biospectrometry MALDI-TOF mass-spectrometry instrument using a 3-hydroxypicolinic acid/diammonium hydrogen citrate matrix.

Synthetic Procedures. *Methyl 3-(6-Amino-1,3-dioxo-1H-benzo[de]isoquinolin-2(3H)-yl)propanoate (1).* 0.196 g (0.81 mmol) of 4-nitronaphthalic anhydride[23,24] and 0.107 g (1.5 eq, 1.21 mmol) of β-alanine were refluxed in 4 mL ethanol for 3 h. The resulting orange suspension was cooled to room temperature, diluted with water, and filtered to provide 0.185 g (73%) of the nitro intermediate. The intermediate was suspended in 3 mL methanol, and 0.7 mL concentrated HCl and 0.569 g (5.1 equiv, 3 mmol) tin(II) chloride dihydrate was added and the solution was heated to reflux for 2 h. Cooling to room temperature and dilution with water followed by filtration provided 0.125 g (71%) of a bright yellow−brown solid. ^{1}H NMR (DMSO-d_6, 400 MHz): 8.61 (1H, d, J = 8.4), 8.41 (1H, d, J = 7.6), 8.18 (1H, d, J = 8.4), 7.64 (1H, dd, J = 7.6), 7.46 (2H, brs, N*H*), 6.83 (1H, d, J = 8.4), 4.24 (2H, t, J = 7.2), 3.57 (3H, s), 2.61 (2H, t, J = 7.2). ^{13}C NMR (DMSO-d_6, 100 MHz): 32.3, 35.3, 51.5, 107.3, 108.2, 119.3, 121.6, 124.0, 129.4, 129.7, 131.0, 134.0, 152.8, 162.7, 163.7, 171.4. ESI MS: M + H$^+$ = 299.58 (Calc 299.10).

General Procedure for MPQ Methyl Ester Synthesis.[25] 1.5 mL concentrated H_2SO_4 was cooled to 0 °C in an ice−water bath. 0.249 g (1.05 equiv, 3.6 mmol) sodium nitrite was slowly added. The viscous suspension was heated to 65 °C until complete dissolution occurred, and then cooled to 0 °C. 1.02 g (3.04 mmol) of **1** was added in portions over 30 min. Two milliliters acetic acid was added to aid in solubility. After stirring at room temperature for 3 h, a solution of 3.4 mmol coupling partner in 0.65 mL acetic acid was added dropwise at 0 °C. The

dx.doi.org/10.1021/bc200424r | *Bioconjugate Chem.* 2011, 22, 2345−2354

resulting suspension was stirred for 1 h, then diluted with saturated sodium acetate and stirred at 0−10 °C for 3 h. The resulting solution was filtered, washed with warm water, and crystallized in ethanol to afford the azo dye methyl ester **2**.

*MPQ1 Methyl Ester (**2a**).* (50% yield) ^{1}H NMR ($CDCl_3$, 400 MHz): 9.25 (1H, d, J = 7.2), 8.63−8.67 (2H, m), 8.04 (2H, d, J = 7.6), 7.96 (1H, d, J = 8.4), 7.83 (1H, dd, J = 7.2), 6.80 (2H, d, J = 7.6), 4.52 (2H, t, J = 7.4), 3.71 (3H, s), 3.17 (6H, s), 2.80 (2H, t, J = 7.4). ^{13}C NMR ($CDCl_3$, 100 MHz): 32.7, 36.2, 40.4, 51.9, 111.6, 112.3, 121.8, 122.3, 126.5, 126.8, 131.0, 131.6, 132.1, 144.7, 152.2, 153.5, 164.0, 164.4, 171.9. ESI MS: M + H$^+$ = 431.42 (Calc 431.17).

*MPQ2 Methyl Ester (**2b**).* (62% yield) ^{1}H NMR ($CDCl_3$, 400 MHz): 9.34 (1H, d, J = 8.8), 9.11 (1H, d, J = 8.0), 8.67−8.70 (2H, m), 8.22 (1H, d, J = 8.4), 8.10−8.14 (2H, m), 7.89 (1H, dd, J = 8.0), 7.69 (1H, dd, J = 8.0), 7.59 (1H, dd, J = 7.6), 7.11 (1H, d, J = 8.4), 4.54 (2H, t, J = 7.4), 3.71 (3H, s), 3.11 (6H, s), 2.81 (2H, t, J = 7.4). ^{13}C NMR ($CDCl_3$, 100 MHz): 32.7, 36.3, 44.8, 52.0, 112.8, 112.9, 114.0, 122.6, 123.8, 125.0, 125.6, 127.2. 127.6, 131.0, 131.7, 132.0, 143.3, 152.0, 156.4, 163.9, 164.3, 167.7, 171.9. ESI MS: M + H$^+$ = 481.92 (Calc 481.19).

*MPQ3 Methyl Ester (**2c**).* (52% yield) ^{1}H NMR ($CDCl_3$, 400 MHz): 8.59−8.63 (3H, m), 8.09 (1H, d, J = 8.4), 7.78 (1H, dd, J = 7.8), 7.38 (1H, d, J = 9.6), 6.53 (1H, dd, J = 9.6, 2.6), 5.97 (1H, d, J = 2.6), 4.50 (2H, t, J = 7.4), 3.70 (3H, s), 3.51 (4H, q, J = 7.2), 2.78 (2H, t, J = 7.4), 1.30 (6H, t, J = 7.2). ^{13}C NMR ($CDCl_3$, 100 MHz): 13.1, 32.7, 36.2, 45.6, 51.9, 98.1, 110.8, 111.6, 122.7, 126.9, 128.6, 131.6, 132.6, 154.9, 163.8, 171.9. ESI MS: M + H$^+$ = 475.42 (Calc 475.20).

*MPQ5 Methyl Ester (**2d**).* (20% yield) ^{1}H NMR ($CDCl_3$, 400 MHz): 9.34 (1H, d, J = 8.4), 8.66−8.68 (2H, m), 8.40 (d, 1H, J = 8.4), 8.19 (d, 1H, J = 8.4), 8.09 (d, 1H, J = 8.0), 7.84 (dd, 1H, J = 7.6), 7.50 (dd, 1H, J = 7.6), 6.62 (d, 1H, J = 7.2), 6.55 (d, 1H, J = 8.4), 4.53 (t, 2H, J = 7.2), 3.71 (s, 3H), 2.81 (t, 2H, J = 7.2), 1.61 (s, 6H). ^{13}C NMR: (spectrum could not be obtained due to poor solubility). ESI MS: M + H$^+$ = 508.42 (Calc 508.20).

General Procedure for Methyl Ester Hydrolysis. 500 mg MPQ methyl ester was dissolved in anhydrous THF (at a concentration of 0.085 M). To this solution, 2.02 equiv potassium trimethylsilanolate was added, and the resulting solution stirred overnight at room temperature, at which point TLC indicated consumption of starting material. The solvent was removed *in vacuo* and the resulting solid dissolved in a minimal amount of water. Hydrochloric acid (1 M) was added to precipitate the free carboxylic acid, which was filtered, washed with water, and dried. The product **3** was used for DNA conjugation without further purification. All free acids were found to be poorly soluble in common deuterated solvents.

*MPQ1 (**3a**).* (80% yield) ^{1}H NMR ($CDCl_3$, 500 MHz): 9.26−9.35 (1H, m), 8.64−8.96 (2H, m), 7.96−8.05 (3H, m), 7.84−7.91 (1H, m), 6.80 (2H, d, J = 9.0), 4.54 (2H, t, J = 7.0), 3.18 (s, 6H), 2.87 (2H, t, J = 7.0). NMR indicates some degradation to naphthalic anhydride during prolonged storage. ^{13}C NMR: (spectrum could not be obtained due to poor solubility). ESI MS: M + H$^+$ = 417.33 (Calc 417.16).

*MPQ2 (**3b**).* (36% yield) ^{1}H NMR ($CDCl_3$, 500 MHz): 9.45 (1H, d, J = 8.5), 9.12 (1H, d, J = 7.5), 8.71−8.75 (2H, m), 8.24 (1H, d, J = 8.0), 8.14−8.18 (2H, m), 7.96 (1H, dd, J = 8.0), 7.73 (1H, dd, J = 7.0, 1.5), 7.63 (1H, dd, J = 7.0, 1.5), 7.14 (1H, dd, J = 8.5), 4.59 (2H, t, J = 7.0), 3.17 (6H, s), 2.91 (2H, t, J = 7.0). ^{13}C NMR: (spectrum could not be obtained due to poor solubility). NMR and ESI-MS indicate that this compound degrades to the naphthalic anhydride during prolonged storage. ESI MS: M + H$^+$ = 467.50 (Calc 467.17).

*MPQ3 (**3c**).* (80% yield) ^{1}H NMR ($CDCl_3$, 500 MHz): 8.62−8.66 (3H, m), 8.12 (1H, dd, J = 8.5, 2.5), 7.80 (1H, dd, J = 7.0), 7.41 (1H, d, J = 9.5), 6.55 (1H, dd, J = 9.5, 2.5), 5.99 (1H, d, J = 2.5), 4.51 (2H, t, J = 7), 3.52 (4H, q, J = 7), 2.79 (2H, t, J = 7), 1.31 (6H, t, J = 7). ^{13}C NMR (spectrum could not be obtained due to poor solubility). ESI MS: M + H$^+$ = 461.33 (Calc 461.18).

*MPQ5 (**3d**).* (87% yield) ^{1}H and ^{13}C NMR data could not be obtained as a result of very poor solubility in common NMR solvents. ESI MS: M + H$^+$ = 494.42 (Calc 494.18).

*MPQ4 (**3e**).* A solution of 0.270 g (1.05 equiv, 3.90 mmol) $NaNO_2$ in 2 mL H_2O was added dropwise to a mixture of 0.510 g (1.0 equiv, 3.72 mmol) 4-aminobenzoic acid in 12 mL 1 M HCl at 0 °C. After 30 min, a solution of 0.657 g (1.05 equiv, 3.90 mmol) of 1-H-perimidine in 9 mL 1 M HCl was added, and the resulting suspension stirred at 0 °C for 2 h. The suspension was diluted with a solution of 2.15 g NaOAc in 15 mL H_2O, stirred at room temperature for 2 h, then filtered and washed with warm water to give a dark purple solid. Crystallization from ethanol afforded 0.916 g (78%). A complex ^{1}H NMR spectrum results from tautomerization in the perimidine scaffold (see Supporting Information). ^{13}C NMR data could not be obtained as a result of poor solubility in common NMR solvents. ESI MS: M + H$^+$ = 317.25 (Calc 317.10).

*3-(2-Methyl-2,3-dihydro-1H-perimidin-2-yl)propan-1-ol (**4**).* 6.19 g (39 mmol) 1,8-diaminonaphthalene was added to a solution of 4.35 mL (1.1 equiv, 43 mmol) 5-hydroxy-2-pentanone and 0.089 g (0.01 equiv, 0.4 mmol) *p*-toluenesulfonic acid monohydrate in 15 mL ethanol. The solution was stirred at 60 °C for 90 min, whereupon the solution had solidified. The resulting solid was cooled to room temperature, filtered, washed with ethanol, and crystallized from aqueous ethanol to yield a pale gray solid (4.11 g, 43%). ^{1}H (DMSO-d_6, 400 MHz): 7.07 (2H, dd, J = 7.8), 6.83 (2H, d, J = 8.4), 6.34 (2H, d, J = 7.2), 6.29 (2H, brs, N*H*), 4.37 (1H, t, O*H*), 3.30 (2H, m), 1.53−1.62 (4H, m), 1.29 (3H, s). ^{13}C NMR (DMSO-d_6, 100 MHz): 26.5, 27.1, 36.9, 61.2, 65.5, 103.6, 111.5, 114.0, 127.0, 134.2, 141.8. ESI MS: M + H$^+$ = 243.50 (Calc 243.15).

*MPQ6 (**5**).* 0.291 g (1.20 mmol) of **4** was dissolved in a solution of 20 mL 1:1 THF/acetone stirred at 0 °C. 0.600 g (1.2 equiv, 1.44 mmol) Fast Corinth V was added in portions to give a dark blue solution, which was stirred at 0 °C for 1 h. The reaction was diluted with water and extracted 3 times with CH_2Cl_2. The combined organic extracts were washed once with water, once with brine, dried ($MgSO_4$), filtered, and the solvent removed *in vacuo*. Column chromatography (5% MeOH in CH_2Cl_2 containing 0.5% Et_3N) afforded 0.094 g (14%) of a dark purple solid. ^{1}H NMR ($CDCl_3$, 400 MHz): 8.19 (1H, d, J = 8.0), 7.84 (1H, d, J = 8.8), 7.66−7.69 (3H, m), 7.40−7.47 (3H, m), 6.53−6.56 (2H, m), 4.02 (3H, s), 3.66 (2H, t, J = 6.0), 2.74 (3H, s), 2.50 (3H, s), 1.88−1.92 (2H, m), 1.75−1.80 (2H, m), 1.52 (3H, s). ^{13}C NMR ($CDCl_3$, 100 MHz): 17.0, 21.3, 27.2, 27.6, 29.8, 38.6, 56.3, 62.7, 99.0, 112.8, 119.2, 124.4, 133.6, 141.3, 143.6, 147.4. ESI MS: M + H$^+$ = 554.42 (Calc 554.25).

*MPQ6 Phosphoramidite (**6**).* 0.164 g (0.296 mmol) MPQ6 was dissolved in 2.5 mL anhydrous acetonitrile, 0.15 mL (3 equiv, 0.861 mmol) *N,N*-diisopropylethylamine was added and

Scheme 1. Synthesis of Multi-Path Quenchers[a]

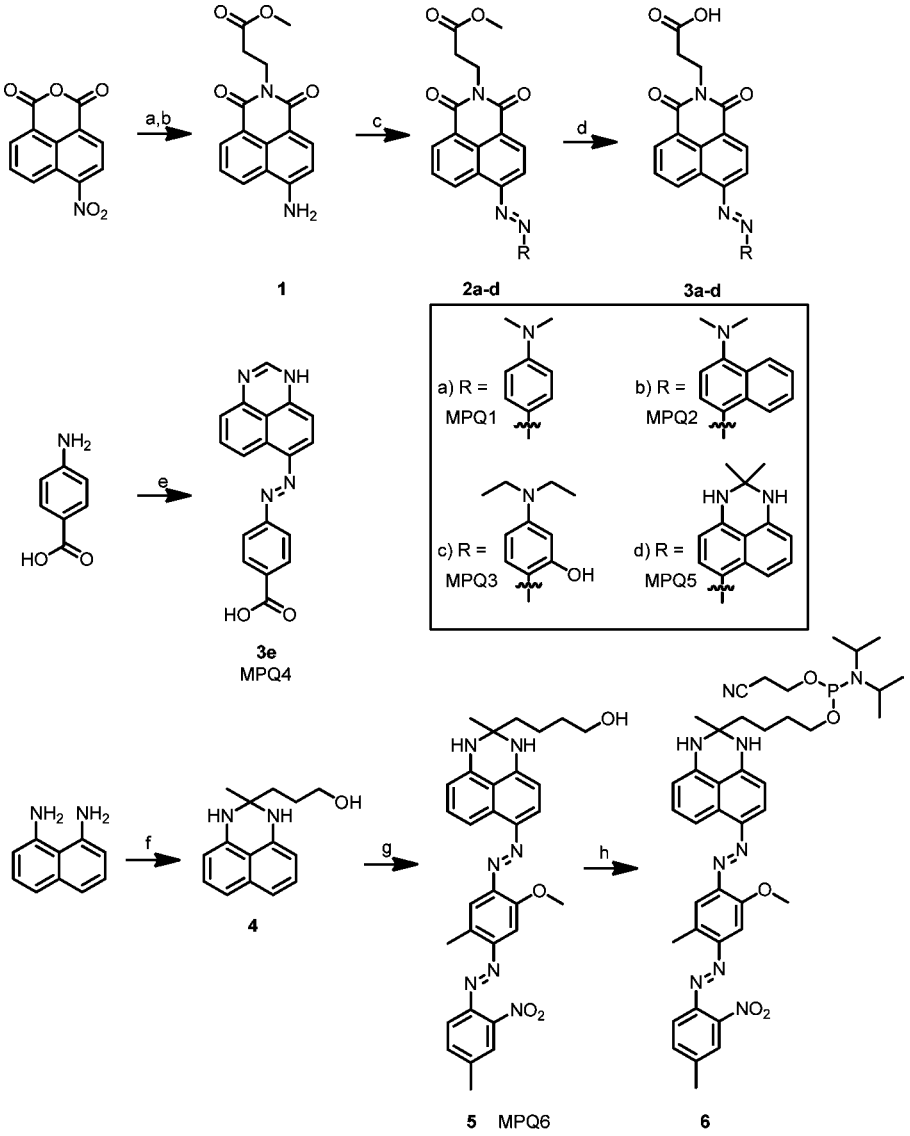

[a](a) β-alanine, EtOH, (73%). (b) $SnCl_2$, MeOH, HCl, (71%). (c) (i) $NaNO_2$, H_2SO_4; (ii) aniline derivative; (iii) NaOAc (20−62%). (d) KOTMS, THF (36−87%). (e) (i) $NaNO_2$, HCl; (ii) 1*H*-perimidine, NaOAc. (f) 5-Hydroxy-2-pentanone, pTsOH (43%). (g) Fast Corinth V, 1:1 THF/acetone, 0 °C (14%). (h) 2-Cyanoethyl *N,N*-diisopropylchlorophosphoramidite, DIPEA.

the solution was stirred at room temperature under argon. 0.10 mL (1.5 equiv, 0.448 mmol) 2-cyanoethyl *N,N*-diisopropylchlorophosphoramidite was added and the resulting solution was stirred at room temperature under argon for 2 h. The solution was concentrated and purified by column chromatography (2:3 EtOAc/Hexanes → 2:1 EtOAc/Hexanes, containing 0.5% Et_3N) to yield 0.036 g product (13%). ^{31}P NMR displayed two peaks at 148.61 ppm and 148.55 ppm, and the product was used for DNA synthesis without further characterization.

DNA Conjugation. TAMRA-, Fluorescein-, and Quasar 670-conjugated DNA sequences were synthesized using their respective 3′ CPGs, cleaved, and purified by HPLC using a gradient elution of 0.05 M TEAA and acetonitrile. AlexaFluor 350 succinimidyl ester and ATTO 590 succinimidyl ester were reacted with 3′-amino modified DNA. Cy3-modified DNA was synthesized using Cy3 Phosphoramidite (Glen Research) with 5′ to 3′ synthesis. Quencher-labeled oligonucleotides were synthesized with a 5′-amino-modifier **5** appended to the 5′-terminus. The monomethoxy-trityl protecting group was removed on the synthesizer using alternating 10 s cycles of deprotection reagent (3% trichloroacetic acid in DCM) and DCM washes for 3 min. The solid support was added to a suspension containing 35 mM quencher-COOH, 35 mM 1-hydroxy-7-azabenzotriazole (HOAt), 35 mM 2-(7-Aza-1*H*-benzotriazole-1-yl)-1,1,3,3-tetramethyluronium hexafluorophosphate (HATU), and 150 mM diisopropylethylamine (DIPEA) in 750 μL anhydrous DMF. Solutions were shaken at room temperature and protected from light for 16 h, then rinsed with 4 × 500 μL DMF and 4 × 500 μL AcCN. The labeled DNA was cleaved from the solid support using UltraMild conditions (0.05 M K_2CO_3 in MeOH) at room temperature for 4 h, filtered to remove CPG, diluted with water, and purified by reverse-phase HPLC.

Fluorescence Experiments. A solution of 30 nM of fluorescently labeled 20mer was created in a total volume of

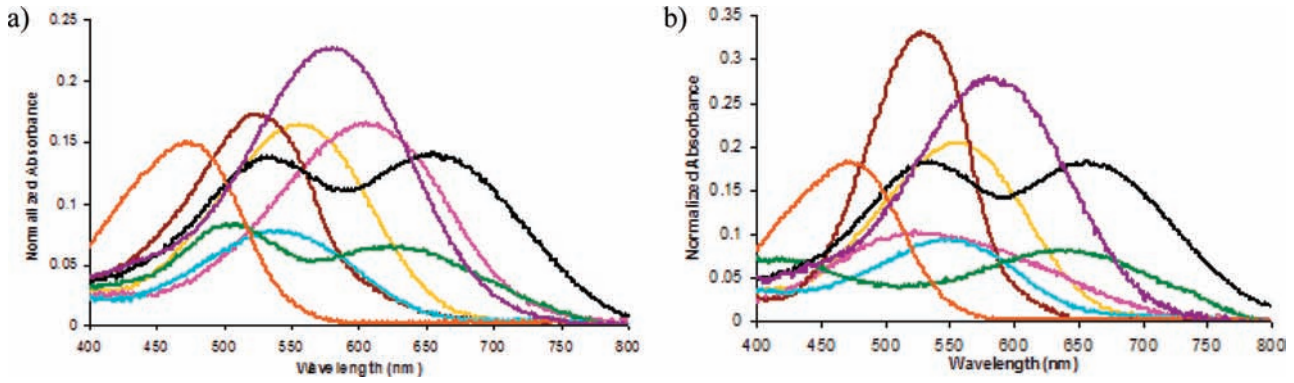

Figure 2. Absorption spectra (normalized to absorbance at 260 nm) of quenchers on (a) 20mer and (b) 15mer oligonucleotide sequences. MPQ1 (yellow), MPQ2 (magenta), MPQ3 (brown), MPQ4 (cyan), MPQ5 (green), MPQ6 (black), Dabcyl (orange), BHQ2 (purple).

Table 1. Spectral Properties of Quenchers Conjugated at the 5′-Terminus of 20mer and 15mer Oligonucleotides

	20mer		15mer	
quencher	λ_{max}	$\Delta\lambda_{(half\ max)}$	λ_{max}	$\Delta\lambda_{(half\ max)}$
MPQ1	557 nm	481–618 (137 nm)	560 nm	481–619 (138 nm)
MPQ2	614 nm	522–676 (154 nm)	524 nm	446–640 (194 nm)
MPQ3	521 nm	461–574 (113 nm)	529 nm	478–571 (93 nm)
MPQ4	539 nm	467–606 (139 nm)	551 nm	469–611 (142 nm)
MPQ5	503 nm, 623 nm	447–689 (242 nm)	646 nm	524–723 (199 nm)
MPQ6	536 nm, 656 nm	463–731 (268 nm)	537 nm, 657 nm	463–736 (273 nm)
Dabcyl	472 nm	405–520 (115 nm)	472 nm	405–519 (114 nm)
BHQ2	580 nm	503–649 (146 nm)	581 nm	507–652 (145 nm)

800 μL hybridization buffer (10 mM $MgCl_2$, 70 mM Tris·borate, pH 7.55) at 37 °C. The fluorescence of the solution was taken in triplicate (using published excitation and emission values with excitation and emission slits of 2 and 5 nm, respectively) and averaged. A concentrated solution of quencher labeled DNA was added to bring the final volume to 150 nM. The oligonucleotides were allowed to hybridize until the fluorescence emission remained constant, then the fluorescence spectrum was taken in triplicate and averaged. Quenching efficiency was calculated at the emission maxima by dividing the quenched fluorescence by the initial fluorescence, multiplying by 100, then subtracting from 100.[14] All experiments were performed in triplicate and averaged.

RESULTS

Quencher Design. The new quencher structures are given in Figure 1. These were designed with the standard diazo dye framework analogous to the common dabcyl quencher, but with larger conjugated multifunctional donors or acceptors. The purpose of the design was to provide multiple conjugated pathways from donor to acceptor groups, thus potentially broadening the absorption spectra of the dyes. The first five (MPQ1–5) were built on the standard azobenzene framework, while the sixth (MPQ6) was designed as a multipathway variant of the bis-azobenzene framework common to BHQ quenchers.

Synthesis. As shown in Scheme 1, reaction of β-alanine with 4-nitronaphthalic anhydride and subsequent reduction of the nitro group easily afforded **1** which could be diazotized to allow for formation of MPQs by reaction with a variety of anilines. Similar derivatives of these compounds were reported earlier for use as disperse dyes, and the properties of the compounds synthesized are consistent with those previously reported.[25,26] Hydrolysis of the methyl ester afforded a carboxylic acid moiety that could easily be attached to amino-modified DNA by HATU/HOAt coupling. DNA synthesis utilized UltraMild protecting groups to avoid hydrolysis of the naphthalimide core under regular ammonia or ammonia/methylamine cleavage/deprotection. MPQ6 was prepared by the addition of dihydroperimidine **4** to Fast Corinth V salt in a cold solution of 1:1 THF/atone, and readily converted to a phosphoramidite for DNA coupling, again with UltraMild conditions. DNA sequences were selected to maintain consistency with previous oligonucleotide-based experiments for comparing fluorescence quenchers.[14] For comparison with the new quenchers, we prepared analogous DNA conjugates of dabcyl and of BHQ2, possibly the two most widely used quenchers. BHQ2 was selected instead of BHQ1 based upon the better performance of BHQ2 against a variety of fluorophores in previous studies.[14] For testing the quenchers, we prepared DNA conjugates of common fluorescent dyes with varied emission properties, emitting from the blue to the far red (442 to 662 nm).

Spectral Properties. Absorption data for the six MPQs conjugated to DNAs are given in Figure 2 and Table 1. The data reveal that, as designed, the MPQ dyes have considerably broadened absorbance spectra compared to their parent quencher molecules (dabcyl and BHQ). Save for MPQ3, all other quenchers containing the naphthalimide core show significantly increased $\Delta\lambda_{1/2\ max}$ values when compared to dabcyl, validating the design strategy. This is particularly the case for MPQ2 and MPQ5, whose $\Delta\lambda_{1/2\ max}$ values are considerably greater and even further red-shifted than the other dyes.

For the naphthalimide derivatives, where the electron acceptor has been altered to incorporate a second conjugation pathway, we noted some differences in spectral properties

dx.doi.org/10.1021/bc200424r | Bioconjugate Chem. 2011, 22, 2345–2354

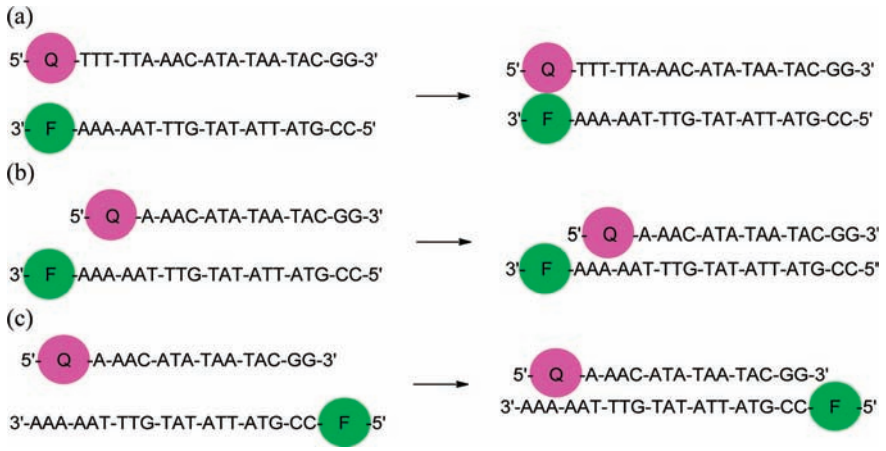

Figure 3. DNA hybridization formats used for determining (a) contact quenching (b) mixed mechanism quenching and (c) FRET quenching efficiencies of MP quenchers.

Table 2. Contact Quenching Efficiencies of Fluorophore/Quencher Pairs[a]

	Alexa 350	FAM	Cy 3	TAMRA	Atto 590	Quasar 670
quencher	λ_{em} = 442 nm	λ_{em} = 517 nm	λ_{em} = 563 nm	λ_{em} = 580 nm	λ_{em} = 624 nm	λ_{em} = 662 nm
MPQ1	73.6 ± 0.7%	95.4 ± 0.2%	98.0 ± 0.4%	86.0 ± 0.7%	96.3 ± 0.2%	96.1 ± 0.3%
MPQ2	72.4 ± 0.1%	94.9 ± 0.4%	97.6 ± 0.2%	87.8 ± 0.4%	96.1 ± 0.1%	97.0 ± 0.2%
MPQ3	74.7 ± 0.9%	96.5 ± 0.2%	97.3 ± 0.2%	86.8 ± 0.5%	96.6 ± 0.2%	93.3 ± 0.4%
MPQ4	72.1 ± 1.2%	96.0 ± 0.2%	97.6 ± 0.3%	88.8 ± 1.0%	96.2 ± 0.7%	94.7 ± 0.2%
MPQ5	69.7 ± 3.5%	93.7 ± 0.1%	96.8 ± 0.4%	85.7 ± 0.4%	95.1 ± 0.2%	95.4 ± 0.3%
MPQ6	71.6 ± 1.8%	95.2 ± 0.2%	98.2 ± 0.6%	87.2 ± 0.2%	96.4 ± 0.2%	95.6 ± 0.8%
Dabcyl	75.7 ± 0.7%	96.0 ± 0.2%	97.4 ± 0.1%	87.3 ± 0.6%	95.7 ± 0.3%	83.9 ± 0.4%
BHQ2	77.0 ± 0.7%	96.5 ± 0.2%	98.9 ± 0.3%	87.8 ± 0.2%	97.4 ± 0.3%	98.2 ± 0.2%

[a]Results are provided as the average of three experiments with standard deviation shown. See Figure 3a for structural context.

between the 20mer and 15mer quencher−oligonucleotide conjugates. As anticipated, the parent quencher dabcyl shows negligible change in spectral properties, maintaining an absorbance maxima of 472 nm and a $\Delta\lambda_{1/2\ max}$ of 115 nm in both sequences. Both MPQ1 and MPQ3, however, display slight red-shifts upon moving from the 20mer oligonucleotide to a different 15mer sequence context. MPQ2, in contrast, shows a considerable blue shift and significant broadening on going from the 20mer to the 15mer DNA.

Altering the electron donating group also provides for some interesting and broadened spectral properties. As seen with MPQ4, a considerable red shift is observed in the absorbance maximum, while an almost 35 nm increase in $\Delta\lambda_{1/2\ max}$ is observed compared to dabcyl. Much like MPQ1−3, this quencher also shows a change when moved from the 20mer to a 15mer, with the $\Delta\lambda_{1/2\ max}$ increasing and the absorbance maximum again shifting to the red.

MPQ5 and MPQ6, incorporating the dihydroperimidine moiety, displayed the most distinct spectral properties. Whereas all other quenchers possess a single broadened absorbance maximum, MPQ5 and MPQ6 display two maxima. MPQ5, like the other quenchers, exhibits a slightly altered absorbance spectrum as the sequence of the oligonucleotide changes, while MPQ6, like BHQ2, maintains approximately the same spectrum on the two DNAs. For these last two quenchers, the formation of a red-shifted absorbance maximum comes with a moderate cost to the extinction coefficient. When compared to MPQ1, MPQ5 clearly displays a lower extinction coefficient at the λ_{max}, both on DNA and in ethanol (see Supporting Information). Comparison of BHQ2 and MPQ6 yields the same result, indicating that the addition of the new conjugation pathway may reduce the extinction coefficient of each individual peak.

The most obvious benefit of the added conjugation is observed in a comparison of MPQ6 with its parent BHQ1. While BHQ1 displays an absorption maximum at 534 nm and generally quenches fluorophores that emit in the range from 480 to 580 nm,[16] MPQ6 displays considerably broadened properties. MPQ6 shares one conjugation pathway with BHQ1, giving rise to an absorbance maximum at 537 nm, but the alternative conjugation pathway inherent to the dihydroperimidine scaffold adds an absorption at 656 nm as well, extending the range of quenching available to the dye greatly (vide infra). Thus, MPQ6 has a $\Delta\lambda_{1/2\ max}$ ranging from 465 to 735 nm (270 nm total), considerably greater than BHQ2 (146 nm) and in fact greater than the quenching ranges of BHQ1 and BHQ2 combined.

Fluorescence experiments confirmed that these quenchers are completely nonemissive, as excitation of solutions containing the DNA-labeled quenchers at 100 nM concentration showed no measurable emission above that of buffer (see Supporting Information). Extinction coefficients were determined at the absorbance maximum of each compound in ethanol and can be found in the Supporting Information; note that they differ slightly from the absorbance maxima found when the quenchers are placed on DNA in Figure 2 and Table 1.

Quenching Efficiency. Quenching efficiency was determined by the use of DNA hybridization as a means of controlling fluorophore−quencher distance (Figure 3).[14] As

Table 3. Mixed Mechanism Quenching Efficiencies of Fluorophore/Quencher Pairs[a]

	Alexa 350	FAM	Cy 3	TAMRA	Atto 590	Quasar 670
quencher	λ_{em} = 442 nm	λ_{em} = 517 nm	λ_{em} = 563 nm	λ_{em} = 580 nm	λ_{em} = 624 nm	λ_{em} = 662 nm
MPQ1	66.4 ± 0.9%	90.7 ± 0.4%	85.6 ± 0.4%	79.7 ± 0.7%	93.6 ± 1.0%	90.2 ± 0.5%
MPQ2	66.6 ± 3.1%	89.1 ± 0.3%	84.0 ± 0.7%	79.6 ± 0.2%	91.3 ± 0.8%	91.1 ± 0.3%
MPQ3	66.0 ± 0.1%	89.1 ± 0.4%	83.5 ± 1.0%	77.9 ± 0.3%	89.5 ± 1.1%	78.7 ± 0.5%
MPQ4	62.2 ± 2.5%	84.1 ± 0.2%	85.1 ± 0.6%	79.1 ± 0.9%	92.6 ± 0.6%	82.8 ± 1.3%
MPQ5	58.7 ± 1.2%	77.4 ± 1.8%	80.2 ± 0.3%	75.5 ± 0.6%	90.0 ± 1.1%	85.9 ± 0.7%
MPQ6	64.8 ± 0.8%	87.8 ± 0.8%	92.9 ± 0.4%	80.6 ± 0.3%	95.2 ± 0.4%	93.5 ± 0.3%
Dabcyl	70.4 ± 3.2%	87.1 ± 0.3%	77.8 ± 0.9%	64.3 ± 0.7%	80.7 ± 1.7%	66.5 ± 3.7%
BHQ2	71.6 ± 0.8%	91.9 ± 1.1%	90.8 ± 0.6%	81.2 ± 0.3%	95.4 ± 0.5%	94.6 ± 0.1%

[a]Results are provided as the average of three experiments with standard deviation shown. See Figure 3b for structural context.

Table 4. FRET Quenching Efficiences of Fluorophore/Quencher Pairs[a]

	FAM	Cy 3	TAMRA	Atto 590	Quasar 670
quencher	λ_{em} = 517 nm	λ_{em} = 563 nm	λ_{em} = 580 nm	λ_{em} = 624 nm	λ_{em} = 662 nm
MPQ1	53.1 ± 1.4%	62.4 ± 0.7%	77.1 ± 0.5%	45.6 ± 1.5%	28.9 ± 0.8%
MPQ2	50.3 ± 0.2%	60.7 ± 2.2%	74.9 ± 1.4%	43.9 ± 0.8%	33.5 ± 1.2%
MPQ3	60.2 ± 1.3%	59.6 ± 0.9%	74.1 ± 0.4%	29.1 ± 0.9%	22.2 ± 0.5%
MPQ4	47.3 ± 1.4%	56.9 ± 1.9%	73.7 ± 0.6%	33.4 ± 2.1%	25.6 ± 2.9%
MPQ6	50.4 ± 0.9%	64.4 ± 1.2%	78.6 ± 0.4%	57.6 ± 0.6%	43.0 ± 0.5%
Dabcyl	41.3 ± 0.9%	52.1 ± 2.8%	71.1 ± 0.8%	26.8 ± 1.9%	22.5 ± 3.1%
BHQ2	54.3 ± 1.0%	63.5 ± 1.8%	80.4 ± 1.2%	60.0 ± 1.3%	40.4 ± 2.8%
No Quencher	29.2 ± 0.7%	53.2 ± 1.2%	71.4 ± 1.1%	23.3 ± 1.4%	23.9 ± 1.5%

[a]Results are provided as the average of three experiments with standard deviation shown. See Figure 3c for structural context.

such, fluorophores were attached to the 3′ end of the sequence 5′-CCG-TAT-TAT-ATG-TTT-AAA-AA-3′ and quenchers were attached to the 5′ end of complementary 15mer or 20mer sequences. Use of a 20mer context (placing dye and quencher immediately adjacent to one another at the duplex terminus) allowed for analysis of contact quenching. The selected 15mer sequence had been previously reported to allow for examination of FRET quenching,[14] but the observation of ground state complex formation between quencher-labeled 15mers and fluorophore containing 20mers indicates a strong degree of contact quenching as well, consistent with other quencher studies and indicating a mixed mechanism of quenching for the sequences shown in Figure 3b (see Supporting Information).[27] To allow for analysis of quenching entirely by FRET, 5′ fluorophore labeled sequenches were used (see Figure 3c), separating the quencher and fluorophore by 15 bp of duplex structure. Contact quenching data would be most relevant for molecular applications where dye and quencher are in very close proximity, whereas FRET data may be most predictive of applications in which the two are held at some distance. Since FRET efficiency depends on spectral overlap, one expects that FRET quenching performance would be more strongly dependent on absorption characteristics than contact quenching, providing a better means of examining the newly created quenchers.

Quenching efficiencies were measured as fraction (percent) loss of emission intensity upon hybridization to the fluorophore of interest, as displayed in Table 2 (contact quenching), Table 3 (mixed mechanism quenching), and Table 4 (FRET quenching). We also compared the fluorescence ratios (fluorescence in the unquenched state divided by fluorescence in the quenched state) of the quenchers against each fluorophore (Figure 3), which better illustrates the differences among the dyes, and which is often the most important factor in a fluorometric assay.

Contact and Mixed Mechanism Quenching. As anticipated, quenching of AlexaFluor 350 (λ_{em} = 442 nm) is poor for the MPQ series (Figure 3a), with dabcyl having a greater quenching efficiency (75.7% contact, 70.4% FRET) than those prepared and tested. This is consistent with the fact that dabcyl is the most blue-shifted quencher of those assayed and has the greatest spectral overlap with AlexaFluor 350. However, the quenchers of the MPQ series (particularly MPQ3) nearly equal dabcyl in contact quenching of this dye. BHQ2 is slightly superior to either of these quenchers in performance with this blue coumarin fluorophore.

The data show enhanced performance of the red-shifted MPQ quenchers as the emission wavelength of the fluorophore increases. For fluorescein (λ_{em} = 517 nm, Figure 4b), it is readily observed that MPQ3 is as efficient as even BHQ2 in contact quenching, while four of the novel quenchers (MPQ1, MPQ2, MPQ3, and MPQ6) all display superior quenching abilities in a mixed mechanism context. At the emission of Cy3 (λ_{em} = 563 nm), only MPQ5 performs less efficiently than dabcyl in terms of contact quenching, with all others displaying superior performance to the common quencher. These results begin to show the red-shifted properties of the new quenchers created, as the parent dabcyl is no longer able to efficiently quench Cy3 emission, while the new dyes display considerably better quenching properties. Moreover, MPQ6 is particularly intriguing, as it is equals (contact quenching) or even surpasses (mixed mechanism quenching) BHQ2 in quenching of Cy3 emission.

As emission shifts further red to TAMRA (λ_{em} = 580 nm), all MPQ quenchers display markedly greater quenching efficiency than dabcyl (Figure 4d). We note that TAMRA (unique among the fluorophores tested here, as it is poorly quenched in general[14]) is relatively poorly quenched by all quenchers including dabcyl and BHQ2, an effect observed previously. Moreover, MPQ4 is as good at contact quenching of TAMRA

dx.doi.org/10.1021/bc200424r | Bioconjugate Chem. 2011, 22, 2345–2354

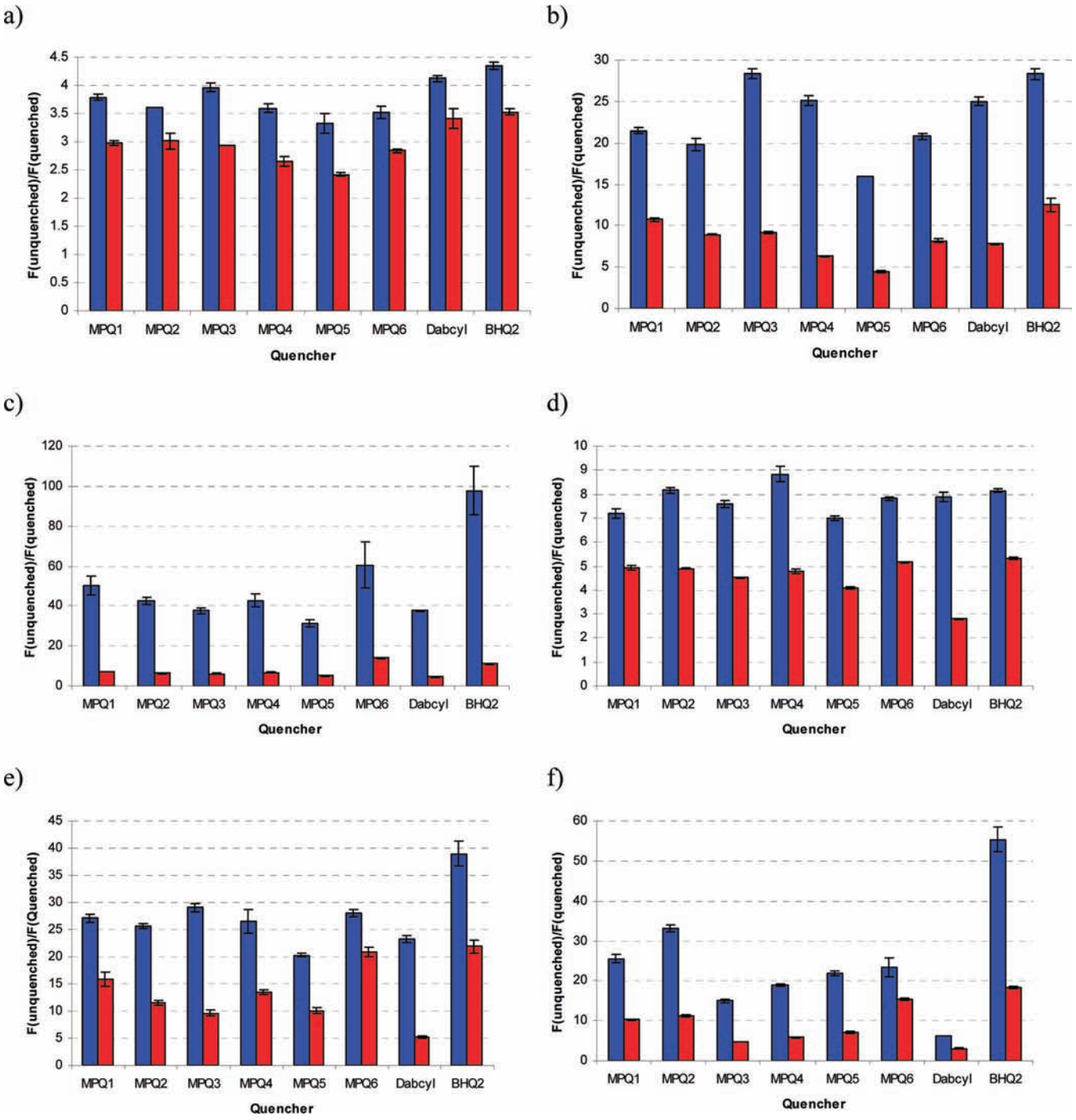

Figure 4. Fluorescence quenching ratios for contact (blue) and mixed mechanism (red) quenching with (a) AlexaFluor 350, (b) Fluorescein, (c) Cy 3, (d) TAMRA, (e) ATTO 590, and (f) Quasar 670.

as even BHQ2, while all but MPQ3 and MPQ5 are approximately as efficient in mixed mechanism quenching as BHQ2. Again, MPQ6 offers promising results, as it displays comparable quenching properties to BHQ2. At the emission of Atto 590 (λ_{em} = 624 nm), all quenchers still perform markedly better than the parent dabcyl (Figure 4e), with MPQ5 again serving as the single exception. Although not operating by an entirely FRET mechanism, the advantages of the red-shifted absorbance properties become clearer as the relatively small five-base increase in length between quencher and fluorophore greatly affects the quenching ability of dabcyl with considerably smaller effect on the ability of the MPQs to quench the emission of Atto 590. Quasar 670 (a Cy5 variant, λ_{em} = 662 nm) was the furthest-red emitting fluorophore tested. At this wavelength, the limits of certain MPQs begin to become evident, although contact quenching overall remains highly efficient (up to 97%; see Tables 2 and 3 and Figure 4f).

FRET Quenching. To properly assess quenching based entirely on a FRET mechanism, hybridization of 5′-quencher labeled sequenches to 5′-fluorophore labeled sequences was carried out (Figure 3c).[27] As a result of the poor spectral overlap of all new quenchers with the emission of the short-

wavelength AlexaFluor 350 (λ_{em} = 442 nm), FRET quenching of this fluorophore was not examined. Similarly, with the poor quenching efficiency of MPQ5, particularly in mixed mechanism quenching studies (Table 2) and the low extinction coefficient of this compound relative to the others synthesized, the quencher was not used in FRET quenching studies.

FRET quenching studies were complicated by the inherent nucleobase quenching by the 3′-dG on the quencher-containing strand. To account for this, an oligonucleotide sequence lacking a 5′ quencher was synthesized and served as a control for quenching due only to the 3′-dG (Table 4). Although such quenching was negligible for fluorescein, Atto 590, and Quasar 670, the 3′-dG was found to strongly quench both Cy3 and TAMRA emission (Table 4). Quenching of TAMRA by guanosine is well-known and unsurprising,[28,29] but quenching of Cy3 in this context was unexpected, as previous studies had indicated an activation of Cy3 fluorescence by guanine.[14,28]

In general terms, the FRET results (Table 4) confirm the expanded quenching properties of the new dyes, with all new quenchers performing better than dabcyl for all fluorophores tested. MPQ1 and MPQ2 were even capable of quenching Atto 590 to a moderate degree, while the parent dabcyl showed, as expected, negligible quenching of the red-emitting dye, indicating the ability to red-shift the absorbance properties and quenching abilities. MPQ6 again provides superior results, as it was able to quench all fluorophores as well as or even better than BHQ2 in an entirely FRET context. Whereas BHQ1 (the parent compound of MPQ6) is a poor FRET quencher of red-emitting fluorophores such as Quasar 670 and Atto 590 as a result of negligible spectral overlap,[27] incorporation of the dihydroperimidine subunit in MPQ6 gives rise to a greatly broadened absorbance spectrum and results in a compound with FRET quenching efficiency better than BHQ2, as in the case of Quasar 670.

DISCUSSION

Overall, the data show that several MPQ dyes outperform their parent dye (dabcyl) in performance in a contact quenching format with all of the fluorophores tested except the most blue-shifted fluorophore (Alexa 350). As for quenching by the FRET mechanism, which is most relevant to the present electronic design concept, all of the MPQ quenchers perform better than dabcyl with all of the fluorophores. This confirms that broadening of the absorbance spectrum of the quencher can confer superior performance. While most of the new dyes do not exceed the quenching ability of the advanced BHQ2 compound, a number of MPQ quenchers equal this quencher's performance with specific fluorescent labels, and thus could be considered as serious alternatives to this molecule.

The chief intent of the molecular design of MPQs was to broaden the efficient quenching range of the parent quenchers. The data show that this approach is successful: several of the MPQs give >95% contact quenching and excellent FRET quenching of fluorophores as far to the blue as fluorescein and as far red as Quasar 670, while the parent dabcyl compound quenches none of the five fluorophores significantly in the FRET mode and only one better than 95% in the contact mode. Thus, we conclude that incorporation of the naphthalimide core does result in the desired increase in generality and a greater range of fluorescence quenching beyond that of dabcyl. Moreover, incorporation of the dihydroperimidine moiety into the BHQ1 scaffold affords a new quencher (MPQ6) that also displays quenching efficiency over a wide wavelength range.

All five quenchers derived from the dabcyl structure (MPQs 1−5) display significantly enhanced quenching of all fluorophores emitting beyond fluorescein, in both contact and FRET quenching. As such, they should be considered as excellent alternatives to dabcyl in any assay that relies on quenching of a fluorophore emitting above approximately 520 nm and even as far as 624 nm, as shown by the ability of MPQ1 and MPQ2 to effectively quench the emission of Atto 590 in the FRET mode. MPQ3 appears to be an excellent quencher specifically for fluorescein, as it performed better than other quenchers for this fluorophore in both contact and FRET quenching. Further, MPQ6 uniquely serves as a competitive alternative to BHQ2 for both contact and FRET quenching of all fluorophores used in this study, particularly those emitting between approximately 560 and 670 nm. As the FRET quenching of this compound is approximately equal to or greater than BHQ2 for Fluorescein, Cy3, TAMRA, Atto 590, and Quasar 670, it may have its greatest utility in FRET-based fluorescence assays.

To our knowledge, the only previous similar approach in quencher design (i.e., taking advantage of increased electronic complexity) employed an azulene dimer, but was limited to quenching only in the near-IR region with limited efficiency.[30] An alternative design utilizing an azaphthalocyanine structure displayed a broadened absorbance spectrum, but has only been fully assayed to date in quenching of FAM and Cy5.[27] Experiments further displayed the ability of the azophthalocyanine dye to quench a larger set of fluorophores (ranging in emission from 517 nm to 703 nm), but only in a contact quenching setting, without exploration of FRET quenching of the expanded set of fluorophores.[31] The use of the perimidine scaffold has been shown before to proffer a red-shift to fluorescent dyes,[32] but the current work is the first case of the use of perimidine for altering the properties of fluorescence quenchers.

One interesting aspect of the spectral properties of some the new Multi-Path Quenchers is their environmental sensitivity. MPQs 1−5 undergo moderate to significant changes upon a change in nearly DNA sequence. For all but MPQ4, this is likely the result of the incorporation of the naphthalimide core, which is well-known to be environmentally sensitive itself.[22,33] In addition, the 4-aminonaphthalimide core has been employed in DNA sensors due to its inherent environmental sensitivity, providing a further explanation for the changes observed here.[34] As use of the 4-aminonaphthalimide core has shown environmental dependence in different DNA settings, it is likely that such is the same explanation for the derived quenchers, but a further exploration is necessary to allow for an accurate conclusion of the mechanism creating the different absorbance spectra for MPQs 1−5. It seems possible, however, that one might in the future take advantage of this property in the design of "smart quenchers", where the environment of the quencher could be part of the design, either blue-shifting or red-shifting the absorbance spectrum in response to structure or changes in environment. Further investigation is needed to explore this possibility.

ASSOCIATED CONTENT

Supporting Information

NMR spectra of quencher dyes and intermediates, HPLC purity and MALDI-TOF of quencher and fluorophore

substituted DNAs, and additional spectral data. This material is available free of charge via the Internet at http://pubs.acs.org.

AUTHOR INFORMATION

Corresponding Author

*E-mail: kool@stanford.edu. Tel.: 650-724-4741. Fax: 650-725-0295.

ACKNOWLEDGMENTS

This work was supported by the National Institutes of Health (GM068122 and GM067201).

REFERENCES

(1) Franzini, R. M., and Kool, E. T. (2009) Efficient nucleic acid detection by templated reductive quencher release. *J. Am. Chem. Soc. 131* (44), 16021−16023.

(2) Franzini, R. M., and Kool, E. T. (2011) Two successive reactions on a DNA template: a strategy for improving background fluorescence and specificity in nucleic acid detection. *Chem.—Eur. J. 17* (7), 2168−2175.

(3) Tyagi, S., and Kramer, F. R. (1996) Molecular beacons: probes that fluoresce upon hybridization. *Nat. Biotechnol. 14* (3), 303−308.

(4) Nakayama, S., Yan, L., and Sintim, H .O. (2008) Junction probes − sequence specific detection of nucleic acids via template enhanced hybridization processes. *J. Am. Chem. Soc. 130* (38), 12560−12561.

(5) Li, J., Wang, F., Mamon, H., Kulke, M. H., Harris, L., Maher, E., Wang., L., and Makrigiorgos, G. M. (2006) Antiprimer quenching-based real-time PCR and its application to the analysis of clinical cancer samples. *Clin. Chem. 52* (4), 624−633.

(6) Dai, N., Guo, J., Teo, Y. N., and Kool, E. T. (2011) Protease probes built from DNA: multispectral fluorescent DNA-peptide conjugates as caspase chemosensors. *Angew. Chem., Int. Ed. 50* (22), 5105−5109.

(7) Dai, N., Teo, Y. N., and Kool, E. T. (2010) DNA-polyfluorophore excimers as sensitive reporters for esterases and lipases. *Chem. Commun. 46* (8), 1221−1223.

(8) Peng, X., Chen, H., Draney, D. R., Volcheck, W., Schutz-Geschwender, A., and Olive, D. M. (2009) A nonfluorescent, broad-range quencher dye for Förster resonance energy transfer assays. *Anal. Biochem. 388*, 220−228.

(9) Matayoshi, E. D., Wang, G. T., Kraft, G. A., and Erickson, J. (1990) Novel fluorogenic substrates for assaying retroviral proteases by resonance energy transfer. *Science 247*, 954−958.

(10) Blum, G., Mullins, S. R., Keren, K., Fonovic, M., Jedeszko, C., Rice, M. J., Sloane, B. F., and Bogyo, M. (2005) Dynamic imaging of protease activity with fluorescently quenched activity-based probes. *Nat. Chem. Biol. 1* (4), 203−209.

(11) Tung, C. (2004) Fluorescent peptide probes for in vivo diagnostic imaging. *Pept. Sci. 76* (5), 391−403.

(12) Marras, S. E. (2006) Selection of fluorophore and quencher pairs for fluorescent nucleic acid hybridization probes. In *Fluorescent Energy Transfer Nucleic Acid Probes: Designs and Protocols* (Didenko, V. V., Ed.) Methods in Molecular Biology, Vol *335*, Humana Press Inc., Totowa, NJ.

(13) Johansson, M. K. (2006) Choosing reporter-quencher pairs for efficient quenching through formation of intramolecular dimers. In *Fluorescent Energy Transfer Nucleic Acid Probes: Designs and Protocols* (Didenko, V. V., Ed.) Methods in Molecular Biology, Vol *335*, Humana Press Inc., Totowa, NJ.

(14) Marras, S. A. E., Kramer, F. R., and Tyagi, S. (2002) Efficiencies of fluorescence resonance energy transfer and contact-mediated quenching in oligonucleotide probes. *Nucleic Acids Res. 30*, e122.

(15) Vicens, M. C., Sen, A., Vanderlaan, A., Drake, T. J., and Tan, W. (2005) Investigation of molecular beacon aptamer-based bioassay for platelet-derived growth factor detection. *ChemBioChem 6* (5), 900−907.

(16) Cook, R. M., Lyttle, M., and Dick, D. Dark quenchers for donor-acceptor energy transfer. U.S. Patent 7,019,129, March 28, 2006.

(17) Haugland, R. P., Singer, V. L., Yue, S. L. Xanthene dyes and their application as luminescence quenching compounds. U.S. Patent 6,399,392, March 4, 2002.

(18) Tyagi, S., Bratu, D. P., and Kramer, F. R. (1998) Multicolor molecular beacons for allele discrimination. *Nat. Biotechnol. 16*, 49−53.

(19) Johansson, M. K., Fidder, H., Dick, D., and Cook, R. M. (2002) Intramolecular dimers: a new strategy to fluorescence quenching in dual-labeled oligonucleotide probes. *J. Am. Chem. Soc. 124* (24), 6950−6956.

(20) Lakowicz, J. R. (1999) *Principles of Fluorescence Spectroscopy*, Kluwer Academic/Plenum Publishers, New York.

(21) Bernacchi, S., and Mely, Y. (2001) Exciton interaction in molecular beacons: a sensitive sensor for short range modifications of the nucleic acid structure. *Nucleic Acids Res. 29*, e62.

(22) Yuan, D., Brown, R. G., Hepworth, J. D., Alexiou, M. S., and Tyman, J. H. P. (2008) The synthesis and fluorescence of novel *N*-substituted-1,8-naphthylimides. *J. Heterocyclic Chem. 45* (2), 397−404.

(23) Cava, M. P., Merkel, K. E., and Schlessinger, R. H. (1965) Pleiadene systems − II: on the mechanism of acepleiadylene formation − a vinylogous elimination in the acenaphthene series. *Tetrahedron 21* (11), 3059−3064.

(24) Jones, L. A., Joyner, C. T., Kim, H. K., and Kyff, R. A. (1970) Acenaphthane I. The preparation of derivatives of 4,5-diamino naphthalic anhydride. *Can. J. Chem. 48* (20), 3132−3135.

(25) Gharanjing, K., Arami, M., Rouhani, S., Bahrami, H., Movassagh, B., and Mahmoodi, N. M. (2007) Synthesis and characterization of novel monazo N-ester-1,8-naphthalimide disperse dyestuffs. *J. Chin. Chem. Soc. 54* (10), 1021−1028.

(26) Wojciechowski, K. (1990) Spectral properties of disperse dyes, derivatives of *N*-methylnaphthalimidoazobenzene. *Dyes Pigm. 12*, 273−286.

(27) Kopecky, K., Novakova, V., Miletin, M., Kučera, R., and Zimcik, P. (2010) Solid-phase synthesis of azaphthalocyanine-oligonucleotide conjugates and their evaluation as new dark quenchers of fluorescence. *Bioconjugate Chem. 21*, 1872−1879.

(28) Torimura, M., Kurata, S., Yamada, K., Yokomaku, T., Kamagata, Y., Kanagawa, T., and Kurane, R. (2001) Fluorescence-quenching phenomenon by photoinduced electron transfer between a fluorescent dye and a nucleotide base. *Anal. Sci. 17*, 155−160.

(29) Xiao, S. J., Hu, P. P., Li, Y. F., Huang, C. Z., Huang., Huang, T., and Xiao, G. F. (2009) Aptamer-mediated turn-on fluorescence assay for prion protein based on guanine quenched fluophor. *Talanta 79* (5), 1283−1286.

(30) Pham, W., Weissleder, R., and Tung., C. H. (2002) An azulene dimer as a near-infrared quencher. *Angew. Chem., Int. Ed. Engl. 41* (19), 3659−3662.

(31) Kopecky, K., Novakova, V., Miletin, M., Kučera, R., and Zimcik, P. (2011) Synthesis of new azaphthalocyanine dark quencher and evaluation of its quenching efficiency with different fluorophores. *Tetrahedron 67*, 5956−5963.

(32) Bello, K. A., Corns, S. N., and Griffiths, J. (1993) Near-infrared-absorbing squaraine dyes containing 2,3-dihydroperimidine terminal groups. *J. Chem. Soc., Chem. Commun. 5*, 452−454.

(33) Loving, G., and Imperiali, B. (2008) A versatile amino acid analogue of the solvatochromic fluorophore 4-*N*,*N*-dimethylamino-1,8-naphthalimide: a powerful tool for the study of dynamic protein interactions. *J. Am. Chem. Soc. 130* (41), 13630−13638.

(34) Lu, E., Peng, X., Song, F., and Fan, J. (2005) A novel fluorescent sensor for triplex DNA. *Bioorg. Med. Chem. Lett. 15* (2), 255−257.

SUPPORTING INFORMATION

Multi-Path Quenchers: Efficient Quenching of Common Fluorophores

Pete Crisalli, Eric T. Kool*

Department of Chemistry, Stanford University
Stanford, CA 94305-5080 (USA)

e-mail: kool@stanford.edu

Table of Contents

Strand	Mass Calc	Mass Observed	Purity (HPLC)
Alexa350 20mer	6543.110	6544.614	98.86%
FAM 20mer	6678.201	6678.831	99.55%
Cy3 20mer	6618.312	6617.014	99.86%
TAMRA 20mer	6734.274	6734.328	99.30%
ATTO590 20mer	6821.371	6822.563	98.02%
Quasar670 20mer	6743.396	6742.522	99.94%
MPQ1 15mer	5156.014	5156.707	98.54%
MPQ1 20mer	6676.244	6675.056	99.52%
MPQ2 15mer	5206.029	5205.537	97.74%
MPQ2 20mer	6726.259	6713.450	98.53%
MPQ3 15mer	5200.040	5200.674	99.70%
MPQ3 20mer	6720.270	6720.037	99.03%
MPQ4 15mer	5053.971	5052.607	87.30%
MPQ4 20mer	6576.191	6576.154	99.13%
MPQ5 15mer	5233.040	5233.804	N/A*
MPQ5 20mer	6753.270	6754.076	96.04%
MPQ6 15mer	5206.041	5205.809	99.29%
MPQ6 20mer	6726.271	6724.371	99.15%
DABCYL 15mer	5021.018	5021.461	98.55%
DABCYL 20mer	6541.248	6541.436	98.19%
BHQ2 15mer	5130.993	5129.682	98.55%
BHQ2 20mer	6651.223	6650.192	99.18%

Table S1: MALDI-TOF calculated and observed masses of DNA sequences used.
*An insufficient amount of labelled DNA was prepared to obtain an analytical HPLC

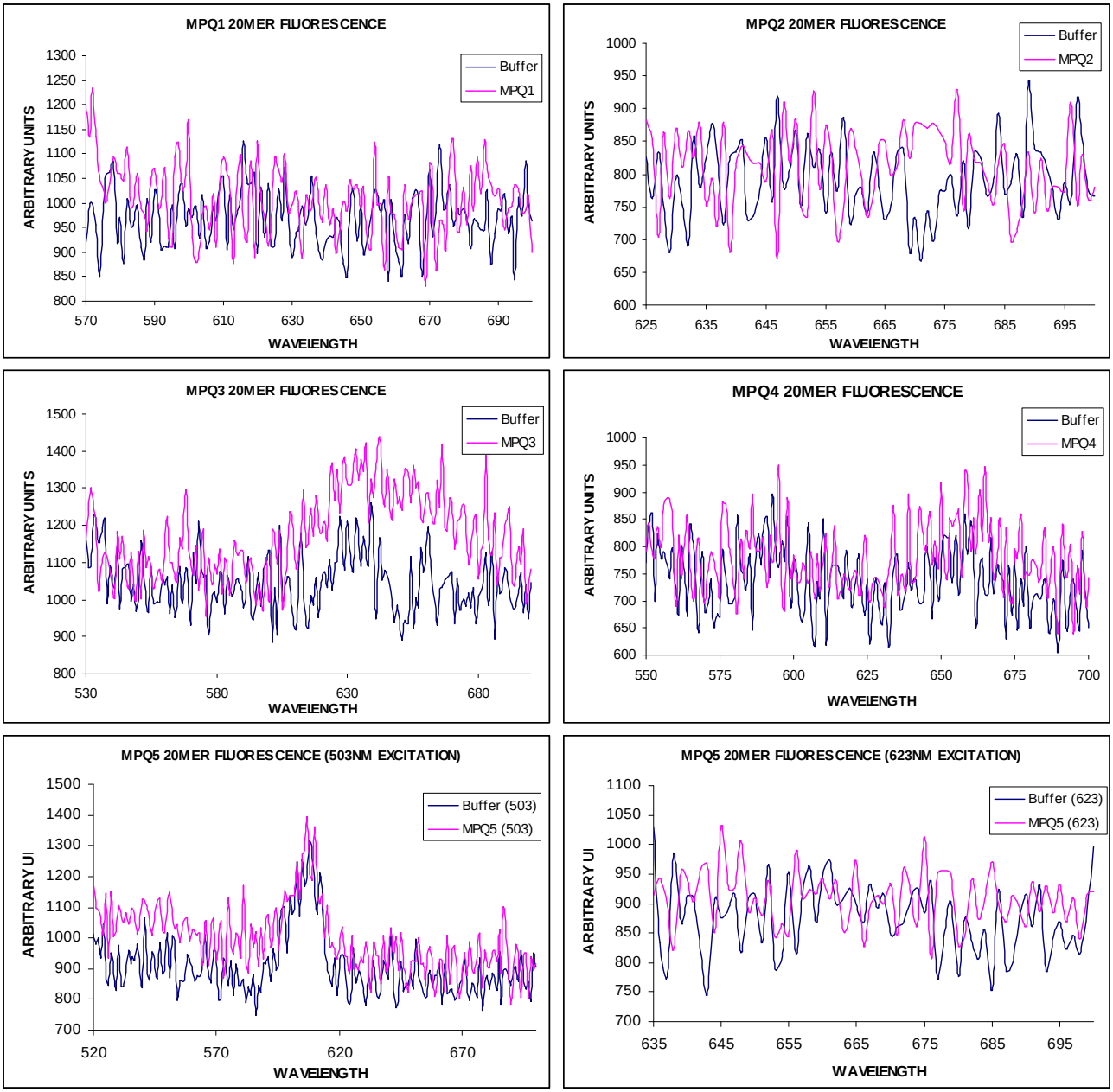

Figure S1: Fluorescence spectra of quencher 20mers (---) compared to buffer alone (---). Samples (100nM) were excited at the λ_{max} values indicated in Table XXXX.

Quencher	λ_{max}	ε_{max}	ε_{260}
MPQ1	512	36400	25100
MPQ2	516	19200	10300
MPQ3	517	50800	15000
MPQ4	522	22600	10800
MPQ5	617	8700	18200
MPQ6	620	28700	N.D.*

Table S2: Absorbance maxima and extinction coefficients (in L M^{-1} cm^{-1}) for multiple pathway quenchers in ethanol. ε_{260} values are provided for quenchers in 9:1 PBS:DMF

* Value could not be determined as a result of aggregation. A value of 8000 L M^{-1} cm^{-1} was used in DNA concentration calculations (the value of BHQ1 at 260 nm).

Figure S2: Ground state complex formation between MPQ 20mers and 3'-Fluorescein 20mer. Duplexes were formed by annealing a solution 1 μM of each strand in hybridization buffer at 70 °C for 5 minutes then allowing to cool to room temperature over 30 minutes. The simple sum was created by adding solutions containing only 1 μM of either quencher or fluorophore labelled strand.

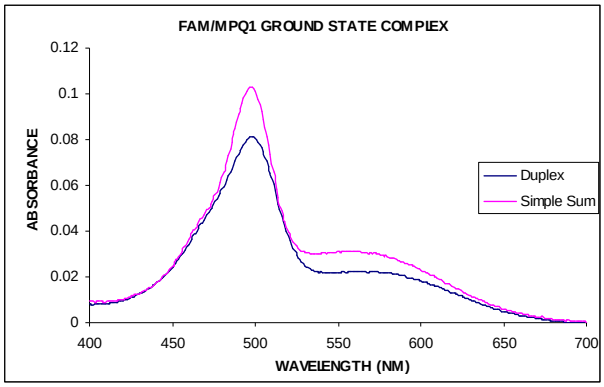

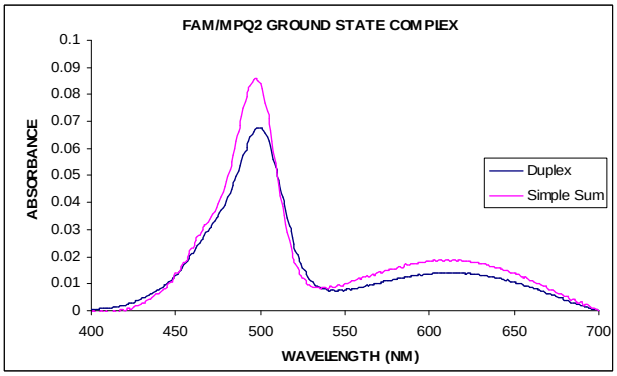

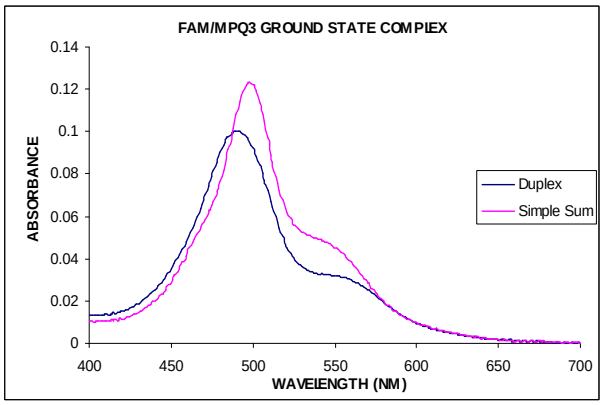

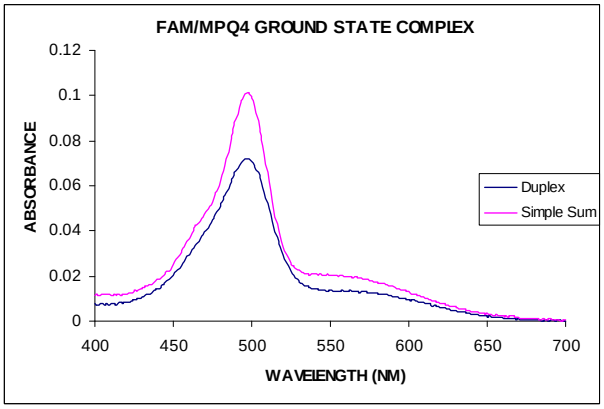

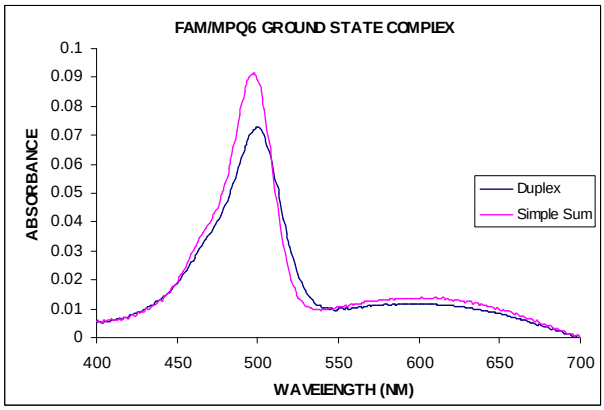

Figure S2: Ground state complex formation between 5'-Dabcyl or 5'-BHQ2 15mers and 3' Fluorophore labelled 20mers. Duplexes were formed by annealing a solution 1 μM of each strand in hybridization buffer at 70 °C for 5 minutes then allowing to cool to room temperature over 30 minutes. The simple sum was created by adding solutions containing only 1 μM of either quencher or fluorophore labelled strand.

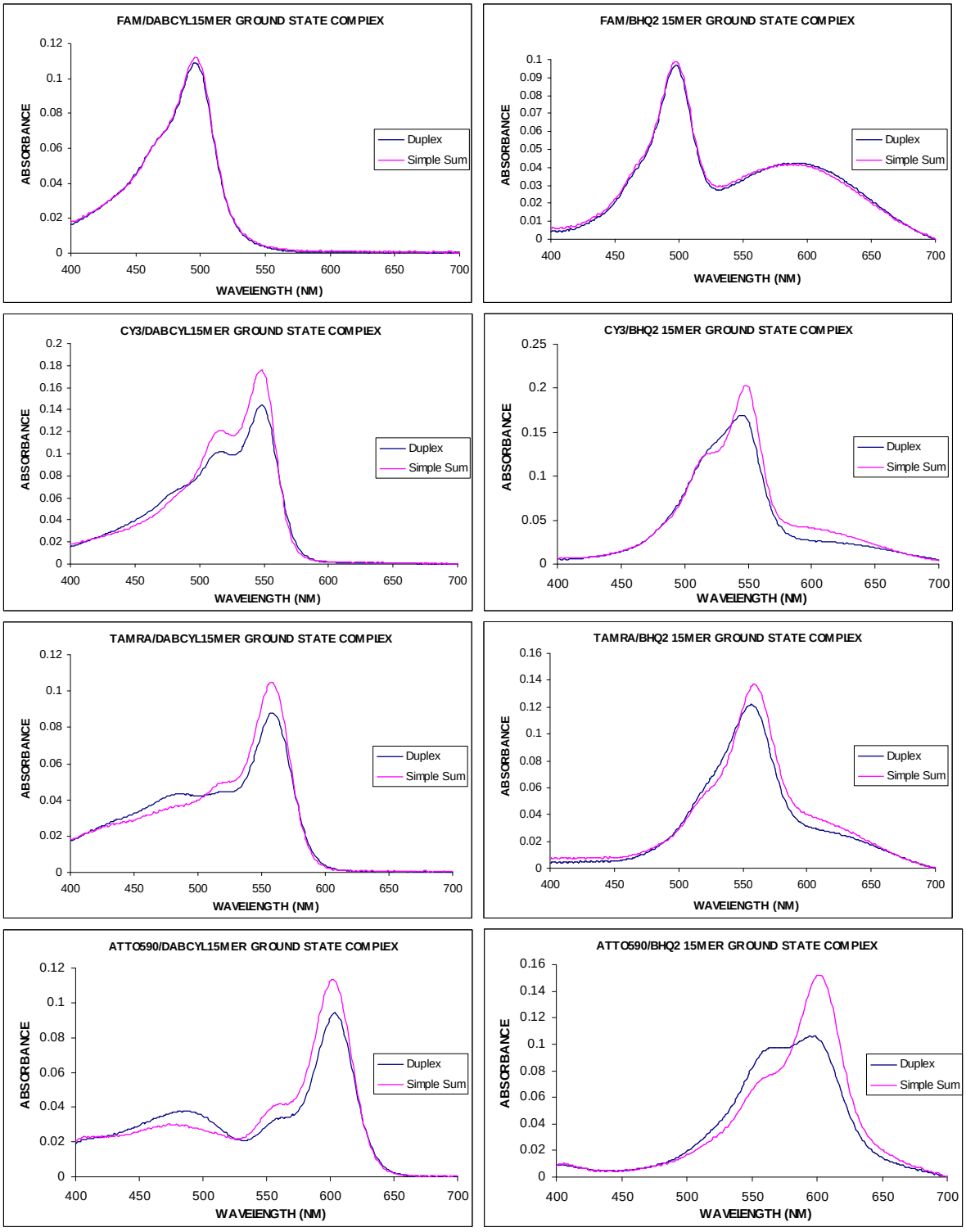

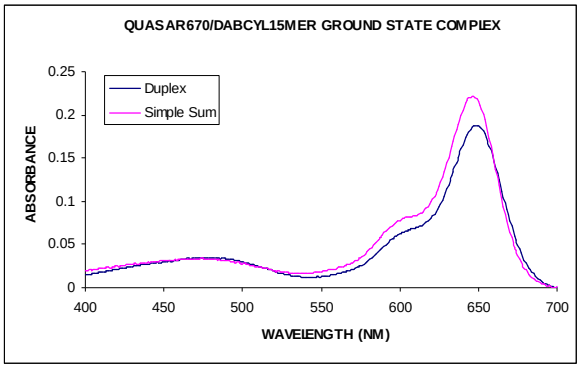
QUASAR670/DABCYL15MER GROUND STATE COMPLEX
Duplex
Simple Sum
ABSORBANCE
0.25
0.2
0.15
0.1
0.05
0
400
450
500
550
600
650
700
WAVELENGTH (NM)

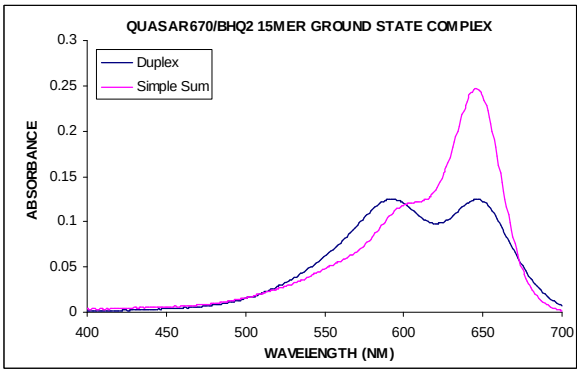
QUASAR670/BHQ2 15MER GROUND STATE COMPLEX
Duplex
Simple Sum
ABSORBANCE
0.3
0.25
0.2
0.15
0.1
0.05
0
400
450
500
550
600
650
700
WAVELENGTH (NM)

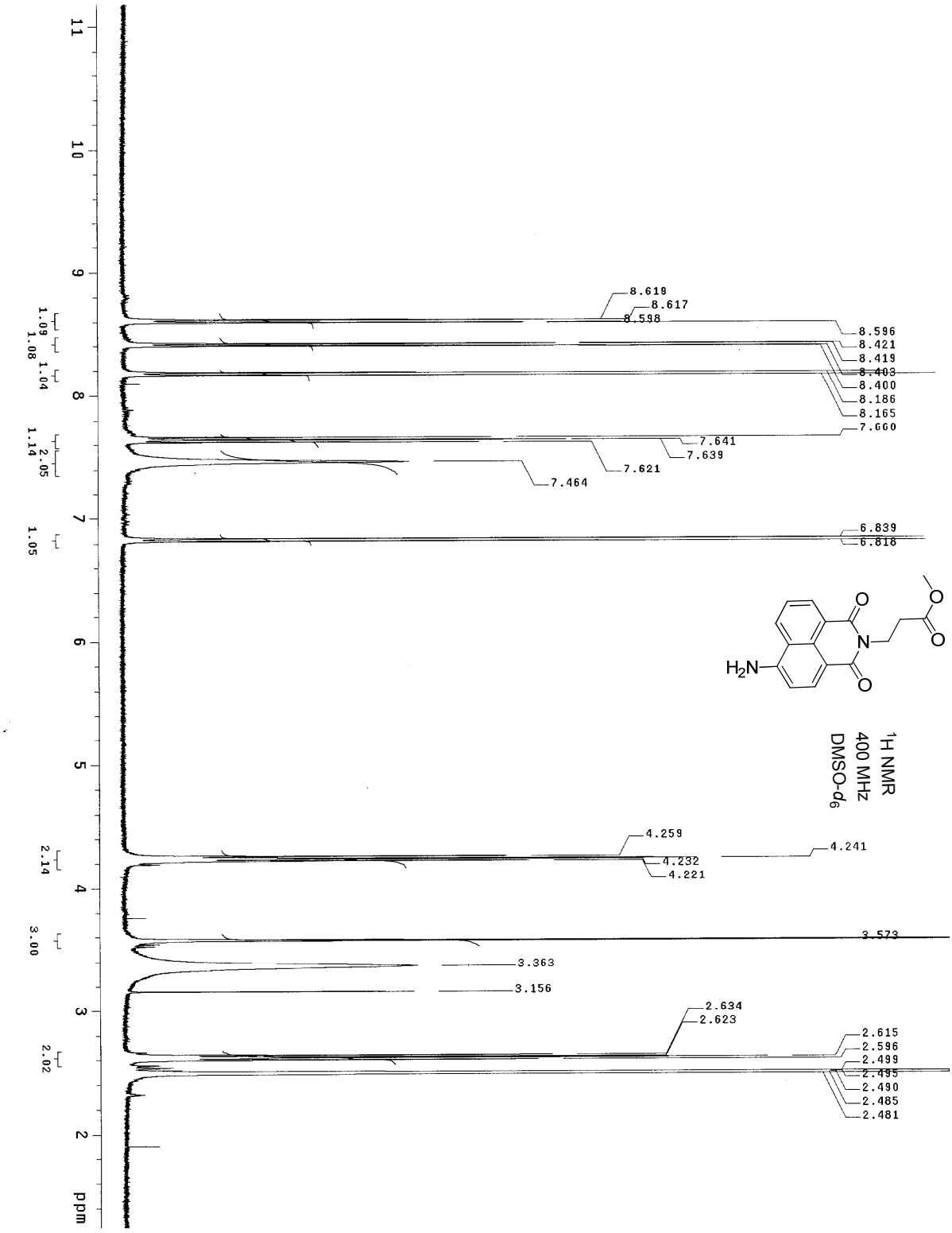
8.619
8.617
8.598
8.596
8.421
8.419
8.403
8.400
8.186
8.165
7.660
7.641
7.639
7.621
7.464
6.839
6.818
4.259
4.241
4.232
4.221
3.573
3.363
3.156
2.634
2.623
2.615
2.596
2.499
2.495
2.490
2.485
2.481
1.09
1.08
1.04
1.14
2.05
1.05
2.14
3.00
2.02
ppm
^{1}H NMR
400 MHz
DMSO-d_6

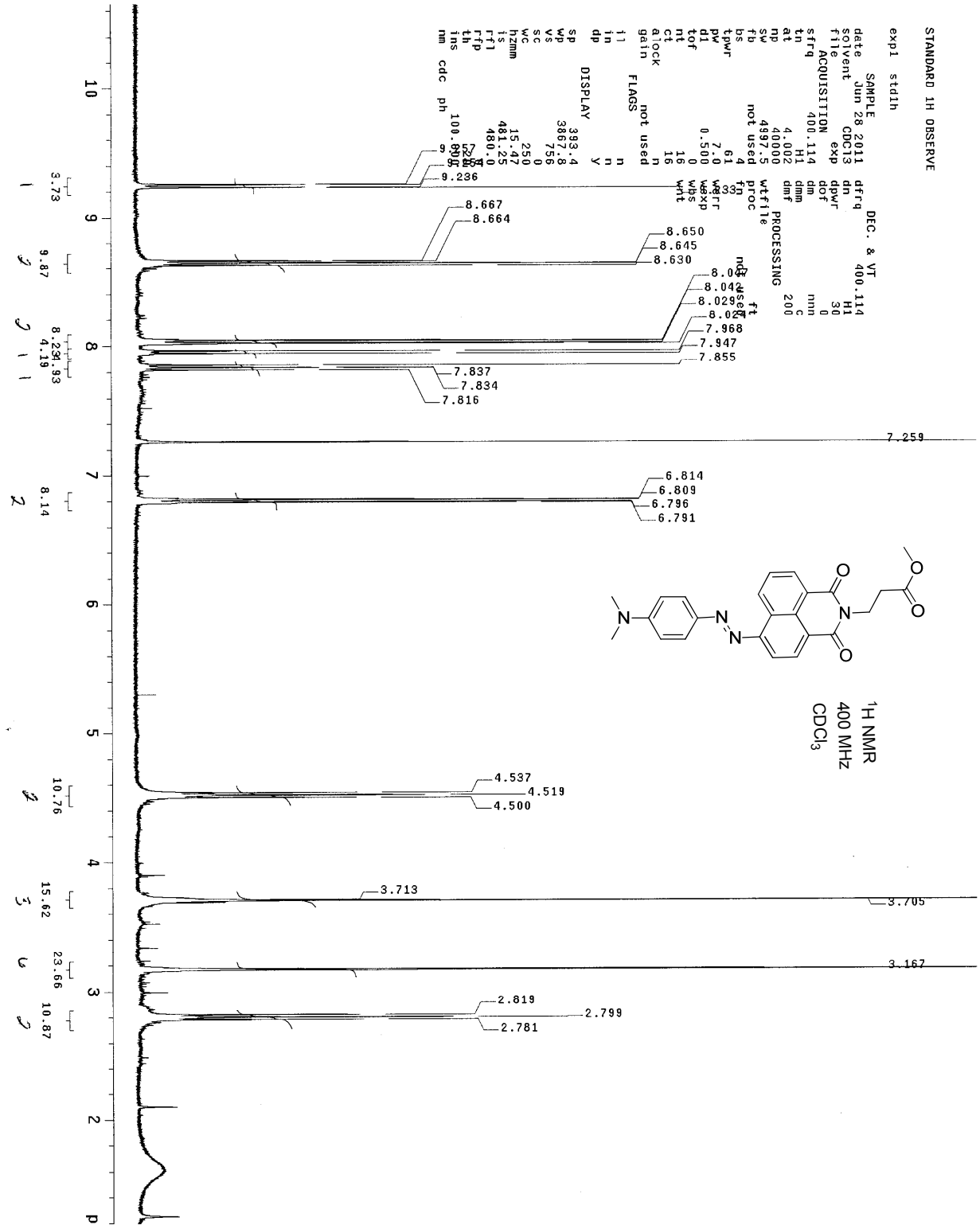
STANDARD 1H OBSERVE
exp1 stdih
SAMPLE
date Jun 28 2011
solvent CDCl3
file exp
ACQUISITION
sfrq 400.114
tn H1
at 4.002
np 40000
sw 4997.5
fb 61
bs 4
tpwr 61
pw 7.0
d1 0.500
tof 0
nt 16
ct 16
alock n
gain n
FLAGS
il n
in n
dp y
DISPLAY
sp 393.4
wp 3867.8
vs 756
sc 0
wc 250
hzmm 15.47
is 481.25
rfl 480.0
rfp
th
ins
nm
cdc ph
100.00
9.254
9.236
8.667
8.664
8.650
8.645
8.630
8.042
8.029
8.025
7.968
7.947
7.855
7.837
7.834
7.816
7.259
6.814
6.809
6.796
6.791
4.537
4.519
4.500
3.713
3.705
3.167
2.819
2.799
2.781
DEC. & VT
dfrq 400.114
dn H1
dpwr 30
dof 0
dm nnn
dmm c
dmf 200
PROCESSING
wtfile
proc ft
not used
not used
FLAGS
not used
gain
alock
ct
nt
wt
tof
d1
pw
tpwr
bs
fb
sw
np
at
tn
sfrq
file
solvent
date
exp1 stdih
STANDARD 1H OBSERVE
1H NMR
400 MHz
CDCl3
3.73
9.87
8.23
4.19
1.93
8.14
10.76
15.62
23.66
10.87

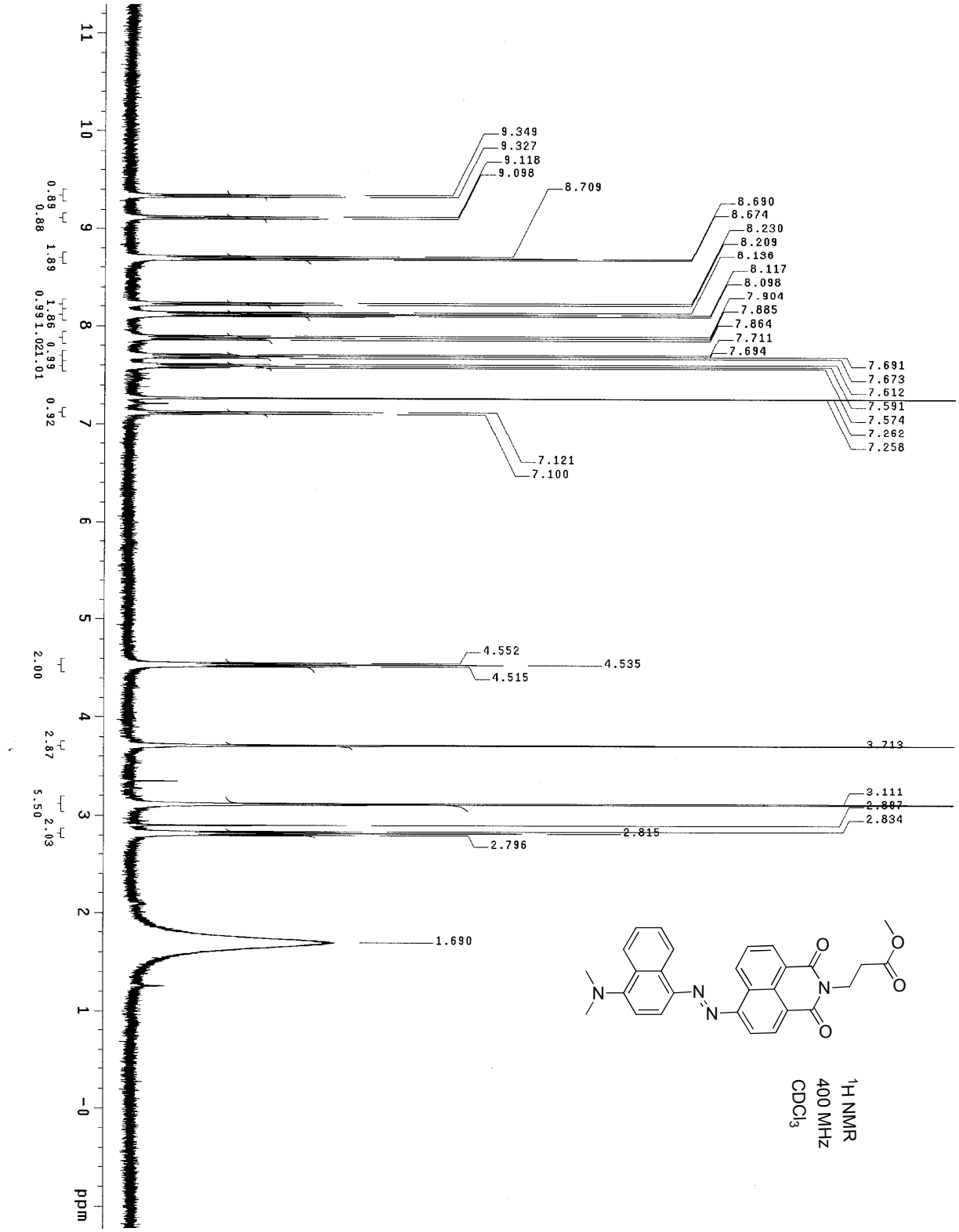
9.349
9.327
9.118
9.098
8.709
8.690
8.674
8.230
8.209
8.136
8.117
8.098
7.904
7.885
7.864
7.711
7.694
7.691
7.673
7.612
7.591
7.574
7.262
7.258
7.121
7.100
4.552
4.535
4.515
3.713
3.111
2.887
2.834
2.815
2.796
1.690
0.89
0.88
1.89
1.86
0.99
1.02
1.01
0.92
2.00
2.87
5.50
2.03
ppm
1H NMR
400 MHz
CDCl3

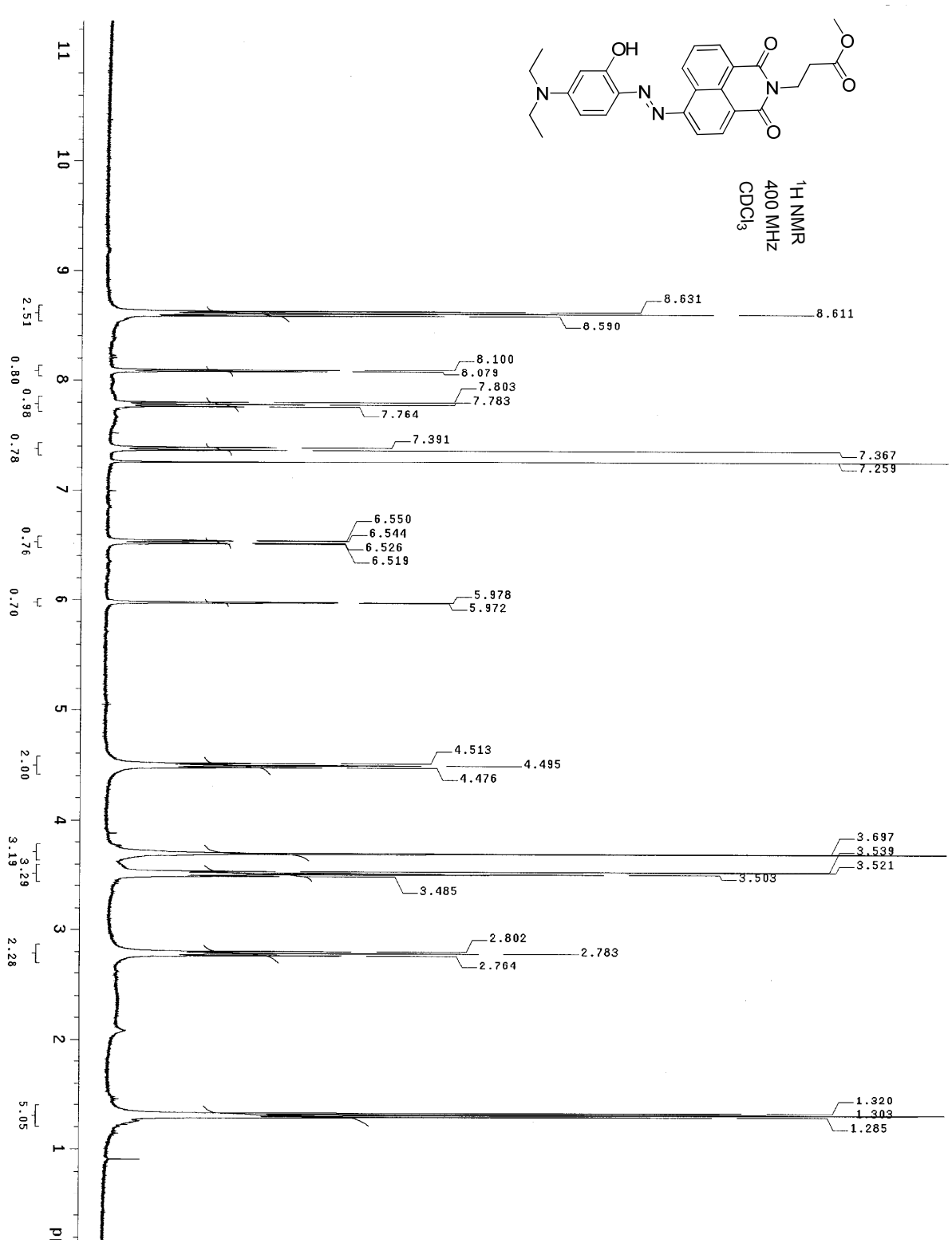
OH
N
N
N
O
N
O
O
O
^{1}H NMR
400 MHz
$CDCl_3$
8.631
8.611
8.590
8.100
8.079
7.803
7.783
7.764
7.391
7.367
7.259
6.550
6.544
6.526
6.519
5.978
5.972
4.513
4.495
4.476
3.697
3.539
3.521
3.503
3.485
2.802
2.783
2.764
1.320
1.303
1.285
2.51
0.80
0.98
0.78
0.76
0.70
2.00
3.19
3.29
2.28
5.05

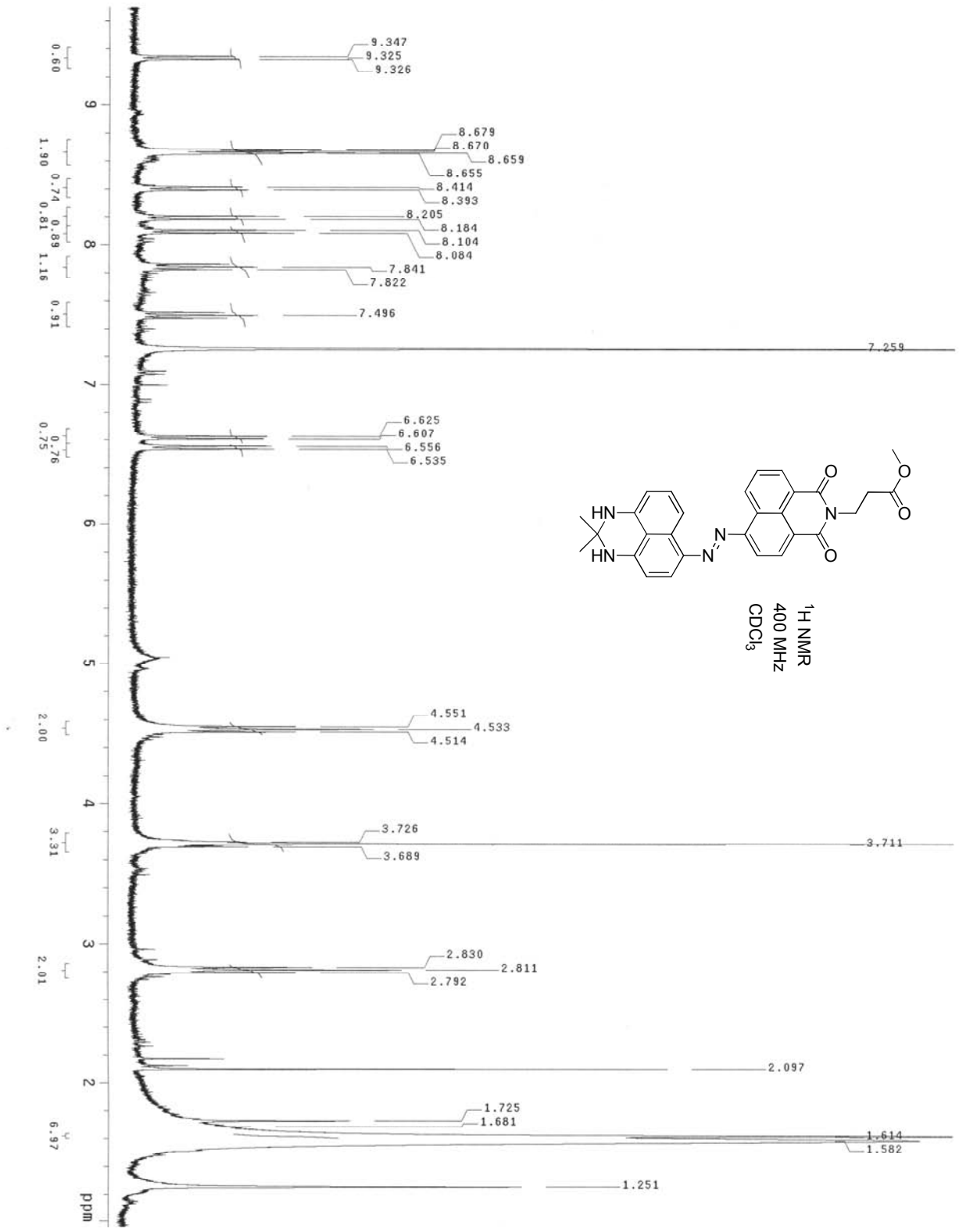
9.347
9.325
9.326
8.679
8.670
8.659
8.655
8.414
8.393
8.205
8.184
8.104
8.084
7.841
7.822
7.496
7.259
6.625
6.607
6.556
6.535
4.551
4.533
4.514
3.726
3.711
3.689
2.830
2.811
2.792
2.097
1.725
1.681
1.614
1.582
1.251
ppm
HN
HN
N
N
O
O
N
O
O
^{1}H NMR
400 MHz
$CDCl_3$

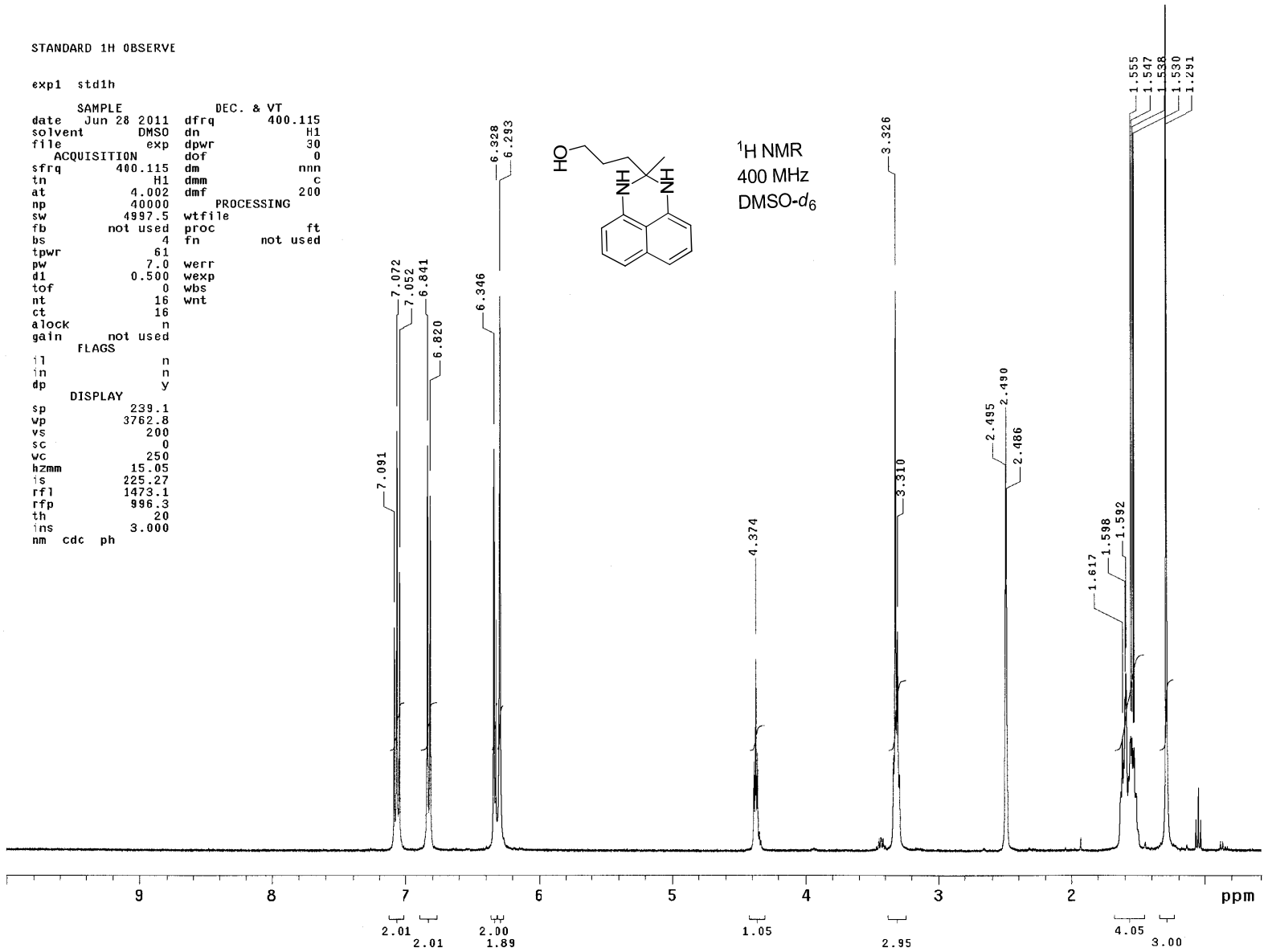
STANDARD 1H OBSERVE
exp1 std1h
SAMPLE
date Jun 28 2011
solvent DMSO
file exp
ACQUISITION
sfrq 400.115
tn H1
at 4.002
np 40000
sw 4997.5
fb not used
bs 4
tpwr 61
pw 7.0
d1 0.500
tof 0
nt 16
ct 16
alock n
gain not used
FLAGS
il n
in n
dp y
DISPLAY
sp 239.1
wp 3762.8
vs 200
sc 0
wc 250
hzmm 15.05
is 225.27
rfl 1473.1
rfp 996.3
th 20
ins 3.000
nm cdc ph
DEC. & VT
dfrq 400.115
dn H1
dpwr 30
dof 0
dm nnn
dmm c
dmf 200
PROCESSING
wtfile
proc ft
fn not used
werr
wexp
wbs
wnt
HO
NH
NH
1H NMR
400 MHz
DMSO-d6
7.091
7.072
7.052
6.841
6.820
6.346
6.328
6.293
4.374
3.326
3.310
2.495
2.490
2.486
1.617
1.598
1.592
1.555
1.547
1.538
1.530
1.291
9
8
7
6
5
4
3
2
ppm
2.01
2.01
2.00
1.89
1.05
2.95
4.05
3.00

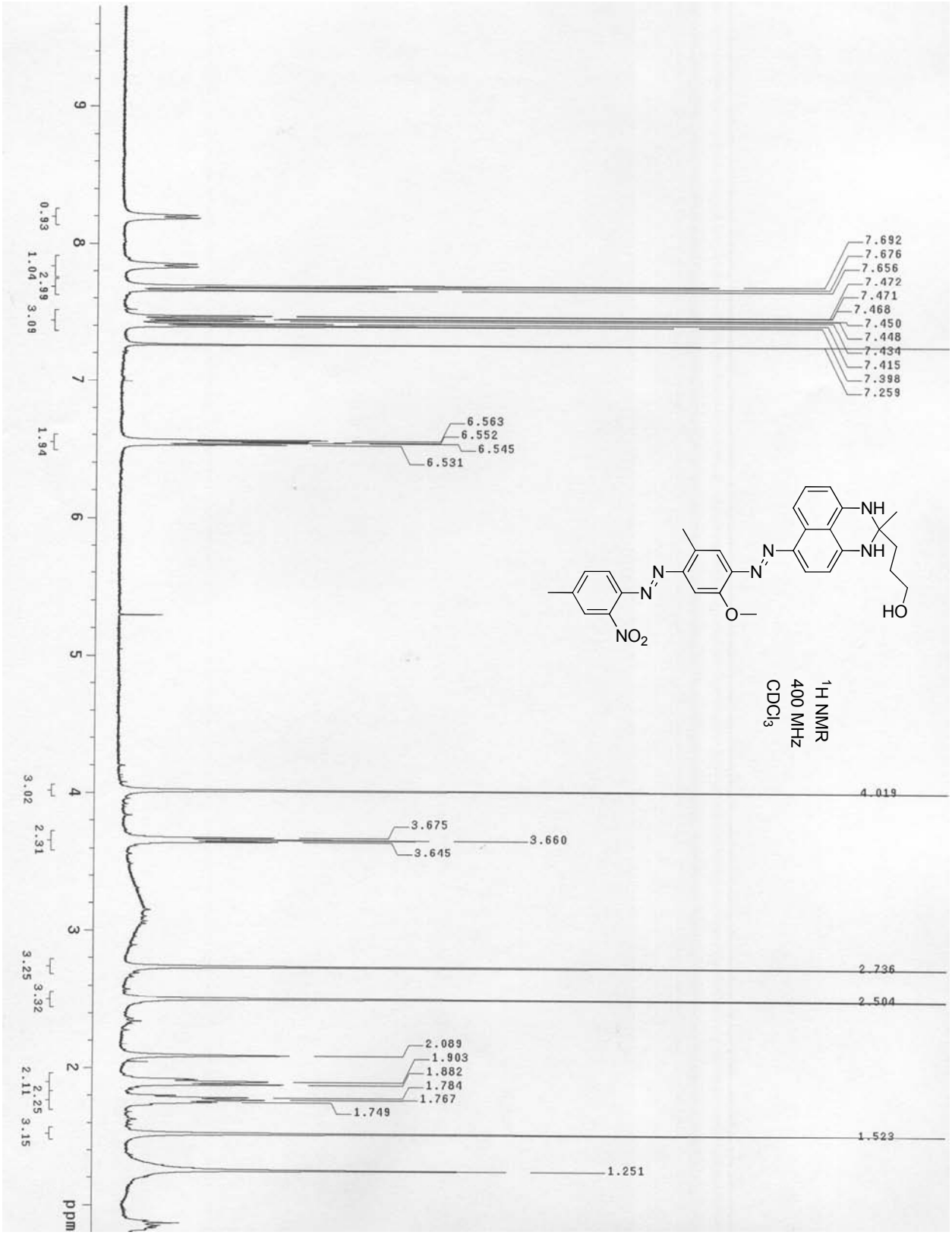
7.692
7.676
7.656
7.472
7.471
7.468
7.450
7.448
7.434
7.415
7.398
7.259
6.563
6.552
6.545
6.531
4.019
3.675
3.660
3.645
2.736
2.504
2.089
1.903
1.882
1.784
1.767
1.749
1.523
1.251
0.93
1.04
2.99
3.09
1.94
3.02
2.31
3.25
3.32
2.11
2.25
3.15
ppm
NH
NH
N
N
N
N
O
HO
NO2
1H NMR
400 MHz
CDCl3

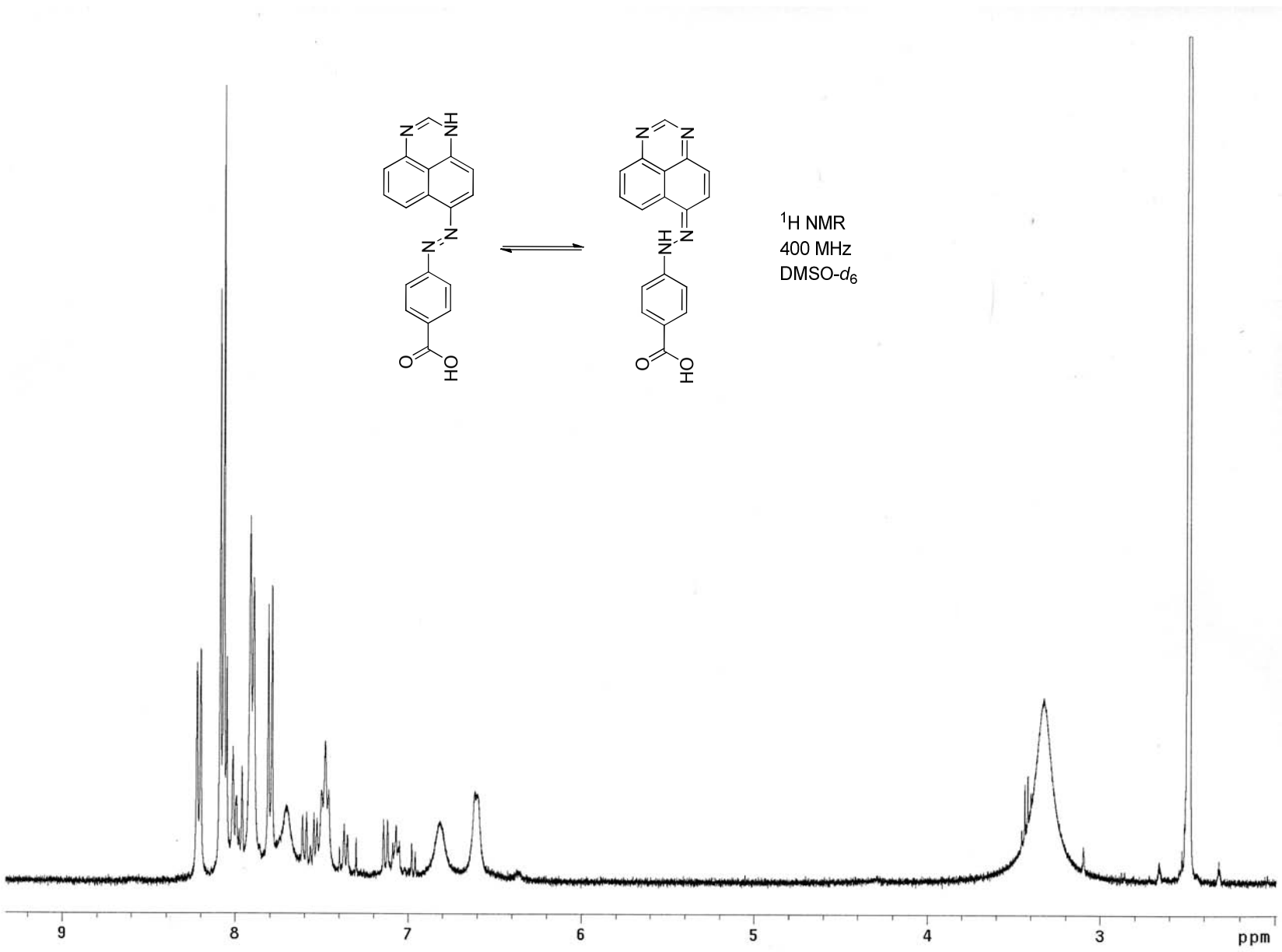
^{1}H NMR
400 MHz
DMSO-d_6
9
8
7
6
5
4
3
ppm

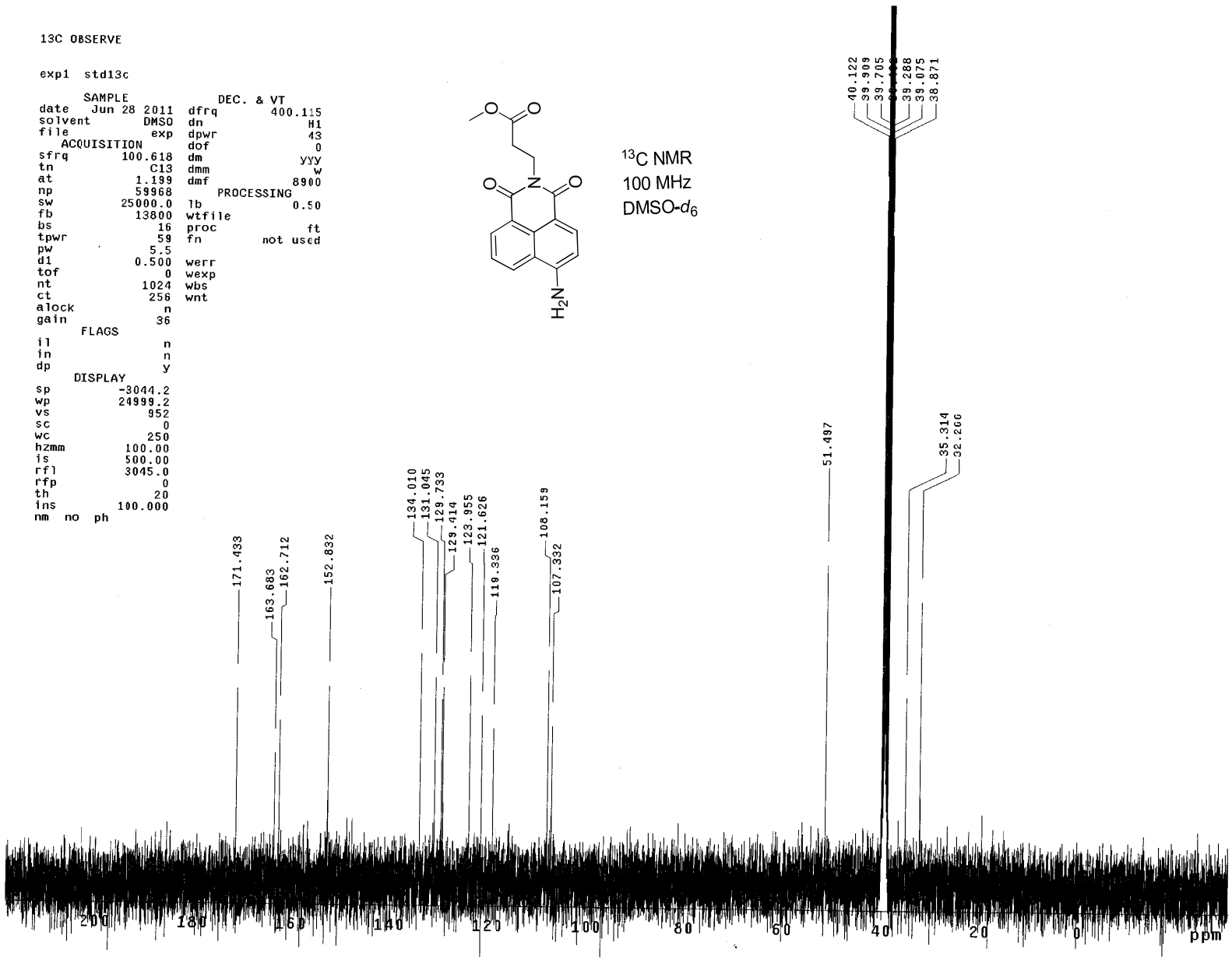
13C OBSERVE
exp1 std13c
SAMPLE
date Jun 28 2011
solvent DMSO
file exp
ACQUISITION
sfrq 100.618
tn C13
at 1.199
np 59968
sw 25000.0
fb 13800
bs 16
tpwr 59
pw 5.5
d1 0.500
tof 0
nt 1024
ct 256
alock n
gain 36
FLAGS
il n
in n
dp y
DISPLAY
sp -3044.2
wp 24999.2
vs 952
sc 0
wc 250
hzmm 100.00
is 500.00
rfl 3045.0
rfp 0
th 20
ins 100.000
nm no ph
DEC. & VT
dfrq 400.115
dn H1
dpwr 43
dof 0
dm yyy
dmm w
dmf 8900
PROCESSING
lb 0.50
wtfile
proc ft
fn not used
werr
wexp
wbs
wnt
^{13}C NMR
100 MHz
DMSO-d_6
40.122
39.909
39.705
39.288
39.075
38.871
171.433
163.683
162.712
152.832
134.010
131.045
129.733
129.414
123.955
121.626
119.336
108.159
107.332
51.497
35.314
32.266
200
180
160
140
120
100
80
60
40
20
0
ppm

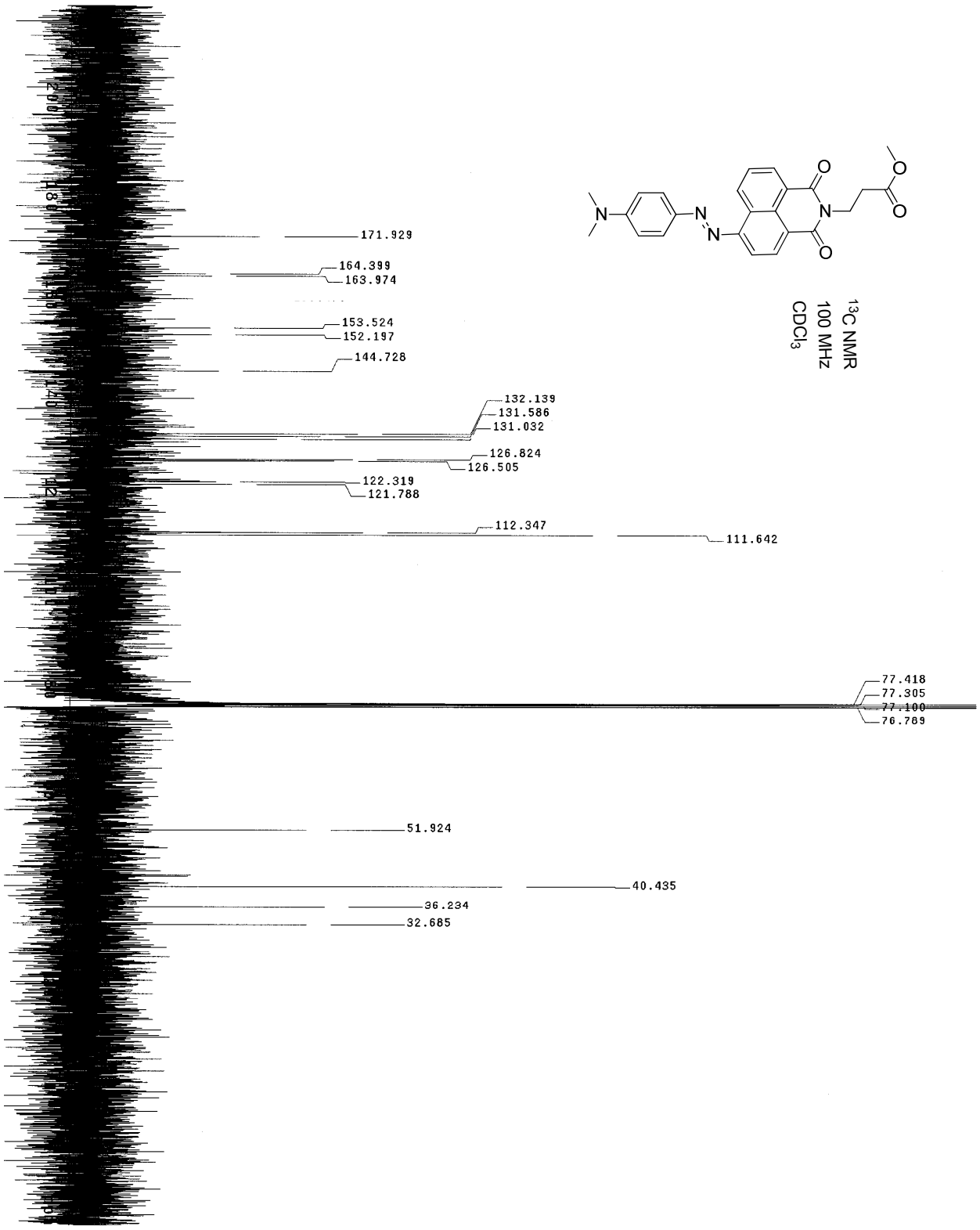
171.929
164.399
163.974
153.524
152.197
144.728
132.139
131.586
131.032
126.824
126.505
122.319
121.788
112.347
111.642
77.418
77.305
77.100
76.789
51.924
40.435
36.234
32.685
^{13}C NMR
100 MHz
$CDCl_3$

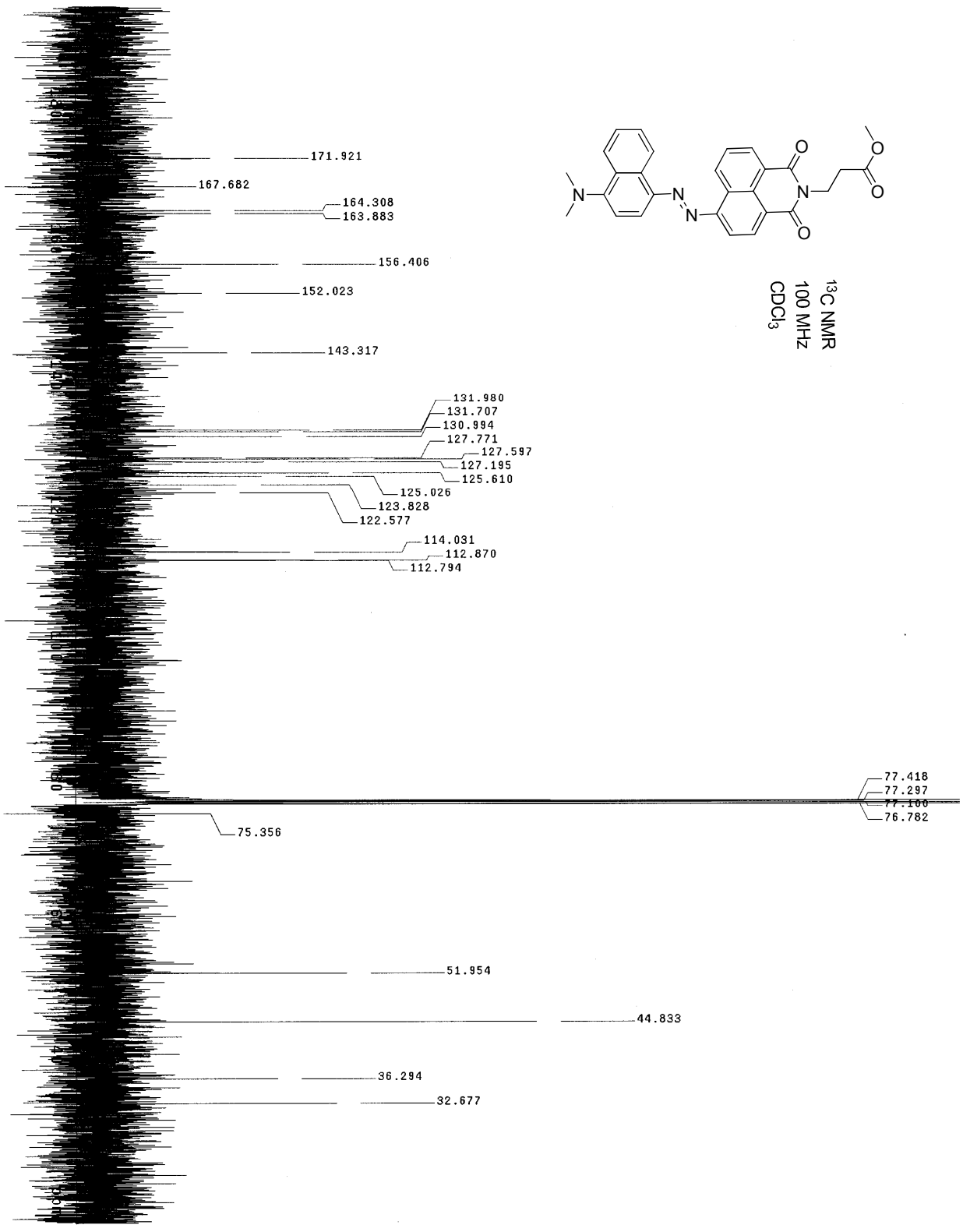
171.921
167.682
164.308
163.883
156.406
152.023
143.317
131.980
131.707
130.994
127.771
127.597
127.195
125.610
125.026
123.828
122.577
114.031
112.870
112.794
77.418
77.297
77.100
76.782
75.356
51.954
44.833
36.294
32.677
O
N
N
N
O
O
O
O
^{13}C NMR
100 MHz
$CDCl_3$

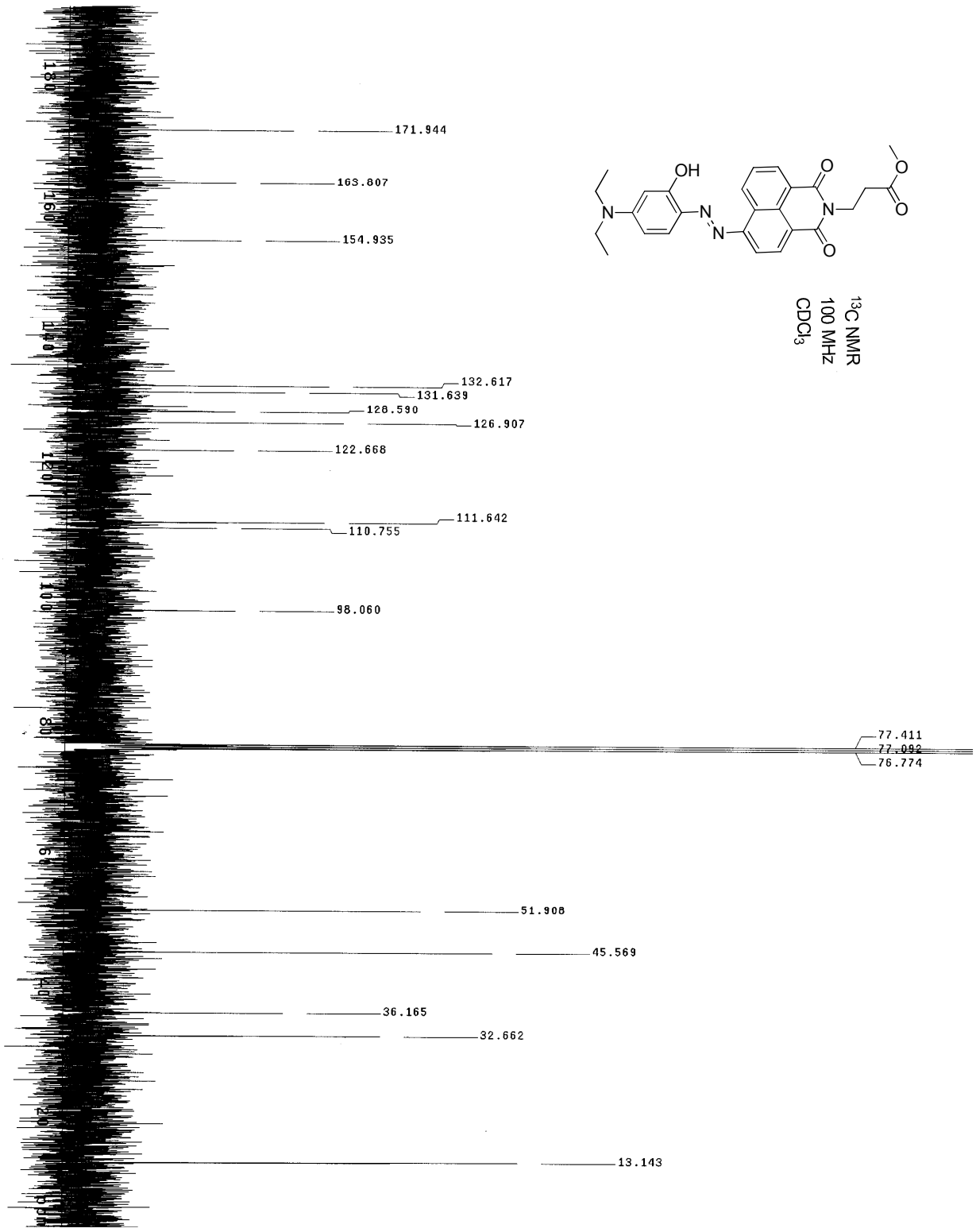
171.944
163.807
154.935
132.617
131.639
128.590
126.907
122.668
111.642
110.755
98.060
77.411
77.092
76.774
51.908
45.569
36.165
32.662
13.143
OH
N
N
N
O
O
O
O
^{13}C NMR
100 MHz
$CDCl_3$

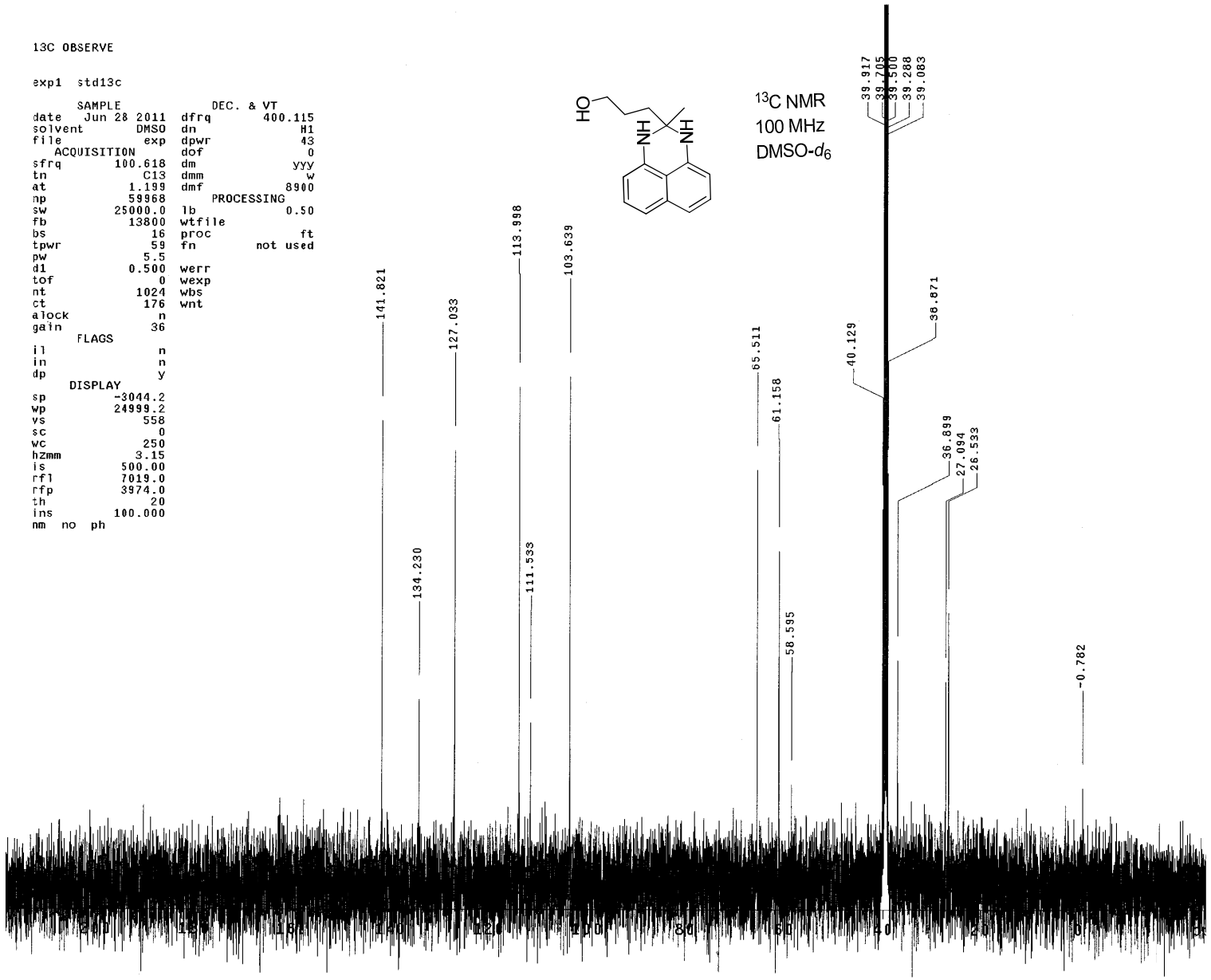
13C OBSERVE
exp1 std13c
SAMPLE
date Jun 28 2011
solvent DMSO
file exp
ACQUISITION
sfrq 100.618
tn C13
at 1.199
np 59968
sw 25000.0
fb 13800
bs 16
tpwr 59
pw 5.5
d1 0.500
tof 0
nt 1024
ct 176
alock n
gain 36
FLAGS
il n
in n
dp y
DISPLAY
sp -3044.2
wp 24999.2
vs 558
sc 0
wc 250
hzmm 3.15
is 500.00
rfl 7019.0
rfp 3974.0
th 20
ins 100.000
nm no ph
DEC. & VT
dfrq 400.115
dn H1
dpwr 43
dof 0
dm yyy
dmm w
dmf 8900
PROCESSING
lb 0.50
wtfile
proc ft
fn not used
werr
wexp
wbs
wnt
HO
NH
NH
13C NMR
100 MHz
DMSO-d6
141.821
134.230
127.033
113.998
111.533
103.639
65.511
61.158
58.595
40.129
39.917
39.705
39.500
39.288
39.083
38.871
36.899
27.094
26.533
-0.782

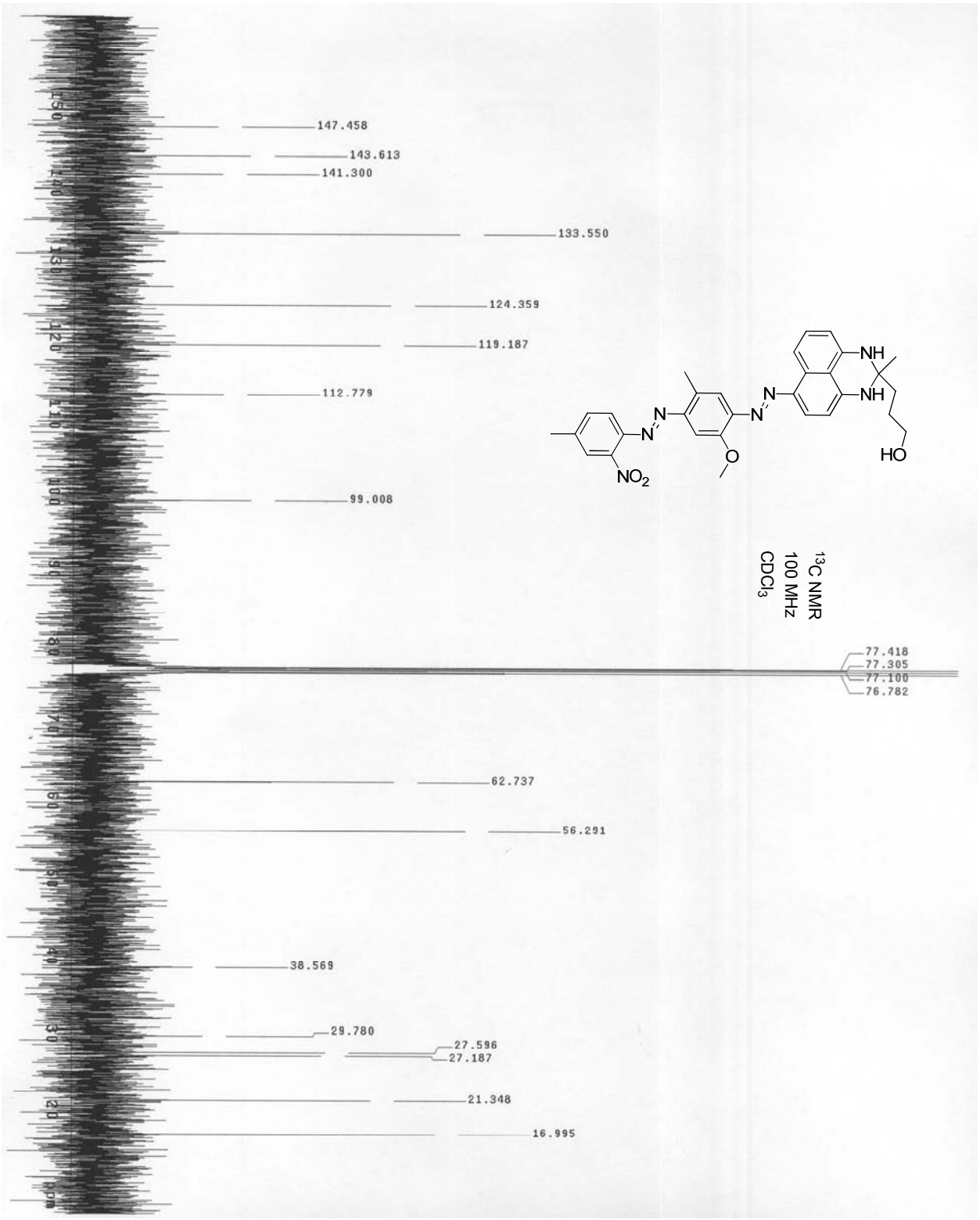
147.458
143.613
141.300
133.550
124.359
119.187
112.779
99.008
77.418
77.305
77.100
76.782
62.737
56.291
38.569
29.780
27.596
27.187
21.348
16.995
NH
NH
N
N
N
N
O
HO
NO2
13C NMR
100 MHz
CDCl3

Bioconjugate Chemistry

Review

pubs.acs.org/bc

Interaction of G-Quadruplexes with Nonintercalating Duplex-DNA Minor Groove Binding Ligands

Akash K. Jain[‡] and Santanu Bhattacharya*[,‡,†]

[‡]Department of Organic Chemistry, Indian Institute of Science, Bangalore 560 012, India

[†]Chemical Biology Unit, Jawaharlal Nehru Centre for Advanced Scientific Research, Bangalore 560 012, India

ABSTRACT: The enzyme telomerase synthesizes the G-rich DNA strands of the telomere and its activity is often associated with cancer. The telomerase may be therefore responsible for the ability of a cancer cell to escape apoptosis. The G-rich DNA sequences often adopt tetra-stranded structure, known as the G-quadruplex DNA (G4-DNA). The stabilization of the telomeric DNA into the G4-DNA structures by small molecules has been the focus of many researchers for the design and development of new anticancer agents. The compounds which stabilize the G-quadruplex in the telomere inhibit the telomerase activity. Besides telomeres, the G4-DNA forming sequences are present in the genomic regions of biological significance including the transcriptional regulatory and promoter regions of several oncogenes. Inducing a G-quadruplex structure within the G-rich promoter sequences is a potential way of achieving selective gene regulation. Several G-quadruplex stabilizing ligands are known. Minor groove binding ligands (MGBLs) interact with the double-helical DNA through the minor grooves sequence-specifically and interfere with several DNA associated processes. These MGBLs when suitably modified switch their preference sometimes from the duplex DNA to G4-DNA and stabilize the G4-DNA as well. Herein, we focus on the recent advances in understanding the G-quadruplex structures, particularly made by the human telomeric ends, and review the results of various investigations of the interaction of designed organic ligands with the G-quadruplex DNA while highlighting the importance of MGBL-G-quadruplex interactions.

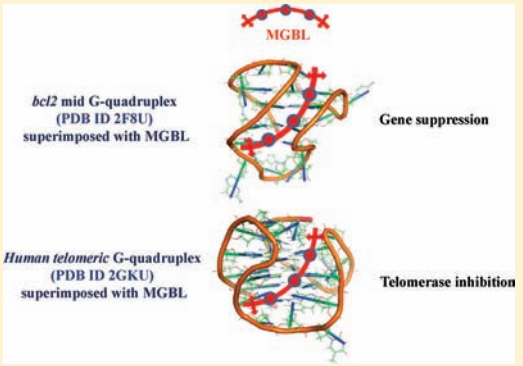

INTRODUCTION

At the ends of the chromosomes, i.e., the telomeres, DNA does not consist of a complex protein-coding sequence. Instead, these are made of a simple sequence such as TTGGGG in the ciliate *Tetrahymena*[1] or TTAGGG in humans,[2] which are repeated a few hundred times in humans and fewer times in ciliates. The bulk of telomeric DNA adopts a double-helical conformation keeping the GT-rich sequence paired with its CA-rich complement. However, the 3′-end of such DNA protrudes as a single-stranded overhang in all the eukaryotes studied.[2−5] This DNA sequence binds to specific proteins, which cap the chromosome ends either directly or by inducing a particular DNA structure.[5]

DNA in the cell nucleus is copied and transcribed by enzymes such as DNA and RNA polymerases. DNA synthesis is catalyzed by DNA polymerase, an enzyme which has crucial role in the DNA replication. A DNA polymerase elongates the new DNA strand from 5′ to 3′ direction, by adding a free nucleotide onto the growing 3′-end of the new strand. It never begins the synthesis of a new chain, and therefore, it needs a primer to add the first nucleotide at the 3′-OH group of the primer. The first two bases of the primer are always the RNA bases, while other bases may be either DNA or RNA. Primers are synthesized by an enzyme, primase. Conversion of the duplex DNA into a single-stranded DNA, with the help of an enzyme, called helicase, facilitates the replication of each strand. Complete replication of the overhanging end of the chromosome cannot be accomplished by conventional DNA polymerases.[4] In almost all eukaryotes, the chromosomal end-replication problem is solved by the enzyme telomerase, a ribonucleoprotein.[5] A portion of the RNA subunit of telomerase provides the nucleic acid template that the DNA cannot provide for itself.[6,7] The enzyme telomerase is upregulated in nearly 80−90% of the cancer cells, leading to an abnormal growth of cells.[7] Telomerase inhibition therefore comprises a key strategy for the development of anticancer agents. This is because studies so far have shown that the telomerase inhibitors can stop the proliferation of the cancer cells or cause apoptosis of the cancer cells, while they have no effect on most of the normal cells.[8]

The telomere cap is composed of telomerase (having the components *hTERT*, *hTERC*, *Hsp90*, *Tp1*, and so forth), telomere-associated proteins (like *TRF1*, *TRF2*, Tankyrase, *TIN2*, *POT1*, Dykserin, and so forth), and telomeric DNA repair proteins (for instance, *MRE11*, *RAD50*, *KU70*, *XRCC5*/*KU80*, and *H2AX*, etc.). This machinery maintains the length of

Received: May 30, 2011
Revised: September 14, 2011
Published: November 10, 2011

ACS Publications © 2011 American Chemical Society

the telomere.[9] A G-quadruplex selective ligand triggers the folding of the G-rich repeats of DNA into a G4-DNA structure. In turn, this inhibits the binding of telomerase and its associated proteins with telomere, thereby stopping the telomere elongation process.[9] Since G4-DNAs do not serve as substrates for the telomerase, these structures have been the focus of much research in medicinal and biological chemistry as attractive targets for the anticancer drug design.[7,9,10] All G4-DNAs contain a basic repeating and stacking motif, the G-quartet structure, which is formed by four guanine bases and held in a plane by the Hoogsteen mode of hydrogen bonds (Figure 1A).[7−11] DNA is a potential target for several

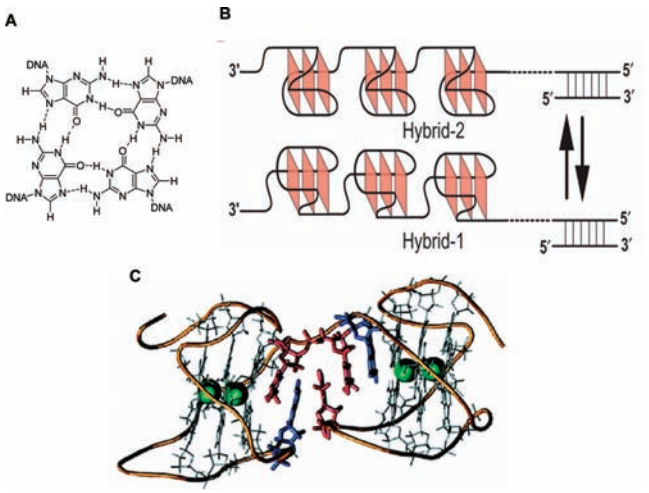

Figure 1. (A) Structure of a G-quartet is shown, in which the hydrogen bonding patterns are also indicated. (B) Schematic model of the DNA secondary structure in human telomeres. The hybrid-type telomeric G-quadruplex structures can be readily folded and stacked end to end to form compact-stacking structures for multimers in the elongated telomeric DNA. Figure adapted from ref 23, with permission of the Oxford University Press. (C) Average structure from molecular dynamics simulation of the Hybrid-12 model; dT and dA residues, in the junction region between the quadruplex units, are shown in red and blue, respectively. Figure adapted from the ref 28, with permission of the American Chemical Society.

anticancer drugs and there are many possible mechanisms of action.[12] G-quadruplex interactive compounds inhibit telomerase by stabilizing the single-stranded 3′-telomere ends as G4-DNA.[7,11]

Besides telomeres, the G4-DNA forming sequences occur in biologically relevant regions of the genome including the immunoglobulin switch regions,[13] the transcriptional regulatory regions of a number of genes such as the insulin gene,[14] and also the promoter regions of several oncogenes such as *c-kit*, *c-myc*, *c-myb*, *K-RAS*, *bcl-2*, and many others.[15−18] Formation of G-quadruplex structures from these G-rich promoter sequences induced by a small molecular ligand provides a means of achieving selective gene regulation and thereby target a protein, the product of gene expression. This has been demonstrated for the *c-myc* oncogene at the nuclease hypersensitivity element (NHE) III_1 which is responsible for up to 90% of *c-myc* transcription.[15,19]

Topology of these G-quadruplex structures depends on the DNA sequence, number of telomeric repeats, oligodeoxynucleotide (ODN) concentration, and an appropriate stabilizing cation.[20] A 27-mer G4-DNA forming sequence in *c-myc* forms a dynamic mixture of four intramolecular quadruplexes which differ in their loop arrangements.[15,19] Similarly, a 22-mer G4-DNA forming sequence, *c-kit87up*, in the promoter region of *c-kit* forms a unique intramolecular quadruplex in K^+ solution.[21] Presently, much of the research effort involving G-quadruplex DNA is directed toward the study of G4-DNA formed by human telomeric repeats $d[T_2AG_3]_n$, particularly a 21-mer sequence $d[T_2AG_3]_3G_3$ and a 22-mer $d[AG_3(T_2AG_3)_3]$. Altering the TTAGGG to TTAGAG in any one of the repeats of T_2AG_3 converts an intramolecular to an intermolecular G-quadruplex with varying degrees of parallel and antiparallel-stranded character, depending on the length of the incubation time, the concentration of the ion present in solution (Li^+, Na^+, or K^+), and the exact DNA sequence.[22] A human telomeric DNA repeat sequence can form two related types of the G4-DNA structures, known as hybrid-1 or hybrid-2 structures (Figure 1B), depending on the flanking segments, out of which the hybrid-2 type is predicted to be the major structural component in the human telomeric DNA.[23−26] These solution structures are different from the K^+-stabilized crystal structure of the G4-DNA derived from 22-mer sequence $d(AG_3[T_2AG_3]_3)$.[26] Other possible G4-DNA conformations adopted by short human telomeric sequences and quadruplex-forming sequences in other genes were already reviewed.[27] Recently, a dimeric structure for the eight-repeat human telomeric sequence containing 2-folded quadruplex units was reported on the basis of high-resolution G4-DNA structure obtained for the four-repeat sequence (Figure 1C).[28] Different topologies of the G4-DNA (in telomeric and genomic regions) having some unusual intermediates as shown by NMR experiments were reviewed recently.[29]

Drug−DNA complex formation may be divided into two broad areas via (i) covalent and (ii) noncovalent interactions.[30] Covalent interactions are generally irreversible. DNA alkylating agents like nitrogen mustards fall under this category. Also *cis*-platin cross-links to DNA, specifically through the N-7 atom of purines of DNA base pairs impeding their hydrogen bond forming capacity with cDNA bases. Such compounds inhibit transcription, translation, and replication of DNA and have long been used as anticancer drugs.[30−32]

Intercalative and nonintercalative drugs represent the major classes of noncovalently interacting compounds.[33] Intercalators generally insert between the layers of nucleic acid base pairs and disrupt the shape of the double-helix significantly, thereby preventing replication and transcription often by untwisting the DNA.[30,31,33] Nonintercalative molecules interact with the duplex DNA through its major and minor grooves. These grooves differ in their electrostatic potential, hydrogen bonding characteristics, steric requirements, hydrophobicity, hydration, and microenvironmental polarity.[30,31,33−39] Most of the DNA binding proteins associate through the major groove of the duplex DNA, while small molecular mass ligands bind via both the major and minor grooves of DNA.[33] DNA minor groove binding ligands (MGBLs) are generally "crescent-shaped" molecules which recognize the minor grooves in a sequence-specific manner. Oligopeptides (netropsin, distamycin-A),[34,40] benzimidazoles (Hoechst 33258, Hoechst 33342),[37] DAPI,[33] berenil,[33] bis-quaternary cations (SN 6999, SN 7167, SN 18071),[31] cyanine dyes (DTDC, DODC),[31] and so forth are some of the well-known MGBLs of low molecular mass. These molecules typically recognize 3−5 base pairs, and some of their analogues including dimers recognize even longer stretches of DNA.[34−42]

MGBLs bind with the non *B*-DNA and multistranded DNA structures too. There are reports on the studies of the complexes of MGBLs involving *ps*-DNA[31] and triplex[31,43] and G-quadruplex DNA.[44] Herein, we provide an overview of the nature of interaction of G-quadruplex DNA with low molecular mass organic ligands with a special emphasis on MGBLs. Since G-quadruplexes are involved in several important cellular functions, the studies of these complexes should be useful in the design and discovery of some effective chemotherapeutic agents.

G-QUADRUPLEXES AND ORGANIC LIGANDS

G-quadruplex DNA structures have affinity for small, positively charged organic ligands. G4-DNAs have several sites of interaction with an organic ligand, mainly through the G-tetrads and the grooves. G-quadruplex stabilizing molecules (particularly the end-stacking ones) often have the following features, e.g., a central symmetrical and a planar core, an extended delocalized π-electron system, tertiary amines which become positively charged due to the protonation under physiological conditions of pH, and the side chains that are able to form hydrogen bonds with the DNA bases and with the phosphate backbone of the loops.[45] Many end-stacking ligands fit this description, although this is not always a general rule. Thus, the compounds that bind with the G4-DNA grooves may have entirely different molecular features. In 1997, a crystal structure of G4-DNA formed by hexanucleotide TG_4T in Na^+ solution was elucidated. This showed several distinct structural features different from that of the duplex DNA.[46] This includes notably the possession of four quasi-equivalent grooves along with a pronounced channel of negative electrostatic potential running through the center of the planes of the G-quartets, allowing the metal ions to be coordinated between the planes in a bipyramidal antiprismatic manner. Structural properties of the G4-DNA grooves vary according to molecularity and type (strand orientation) of the G-quadruplex.[47] Four-stranded intermolecular G4-DNA has four identical grooves that are of about the same size as the minor groove of *B*-DNA.[48] In contrast to the parallel-stranded G-quadruplexes, the four grooves in an antiparallel quadruplex are not identical, e.g., fold-over monomeric G4-DNAs with diagonal loops have one wide groove, two medium-sized grooves, and one narrow groove.[49] Taking these features into account, many compounds were synthesized to target the G4-DNA formed by the human telomeric DNA sequence.[50] Structures of some small organic cation-G4-DNA complexes have been recently reviewed[27] and are supposed to be helpful in finding out new structure-based leads for the design of anticancer drugs. The intramolecular G4-DNA made by the sequence $d[AG_3(T_2AG_3)_3]$ has seven major binding sites available for a drug, made up of two G-tetrads for end-stacking (parallel-loop and diagonal-loop), one wide groove, two medium-sized grooves, one narrow groove, and top parallel loop binding sites (Figure 2). Thus, the geometries and functional groups of the G-quadruplexes are different from that of the duplex DNA. A drug can bind to multiple sites suggested by its skeleton and functional groups present in it. Thus, although 3,6-bis(1-methyl-4-vinylpyridinium iodine) carbazole (BMVC, **1**) exerts a strong interaction with all the sites, its binding with the end-stacked G-quartets is the most favorable.[51]

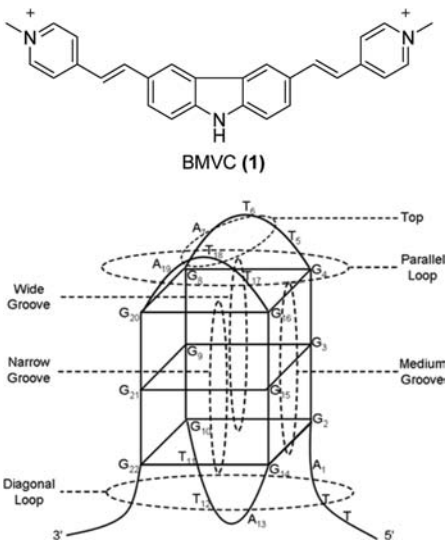

Figure 2. Molecular structure of 3,6-Bis(1-methyl-4-vinylpyridinium iodine) carbazole (BMVC, top) and a sketch of the G4-DNA structure made by human 22-mer telomeric DNA showing its binding sites for a drug (bottom). Figure adapted from ref 51, with permission of the American Chemical Society.

G-QUADRUPLEXES IN NON-TELOMERIC REGIONS

As mentioned earlier, G4-DNA forming motifs have been identified and characterized in functional regions (e.g., promoters and enhancers) of many oncogenes such as *c-kit*, *c-myc*, *c-myb*, *K-RAS*, *bcl-2*, and other cell growth-related genes.[13−21,29,52] Most of these G4-DNA motifs in the gene promoter regions have physical chemical properties and structural characteristics that might make them interact strongly with putative drugs.[18] Further, they have such diverse structures that a high degree of selectivity might be possible.[18,21,29] The initial report on genome-wide analyses highlighting multiple regulatory roles of G4-DNA structure appeared in 2006,[53] followed by a number of recent reports.[17,54−56] G4-DNA formation in genes may affect the cellular function in different possible ways. G4-DNA formation in the insulin-linked polymorphic region upstream of the insulin gene enhanced its transcription, where single/double mutations that disrupted the G4-DNA structure afforded reduced promoter activity.[14] On the other hand, G4-DNA also acts as a "silencer element" for certain oncogenes.[15,18,57] Several proteins from different organisms that interact with the G4-DNA have been reported.[58−60] They play an important role in transcription of certain genes and can be classified by function into five major groups. These are those that (i) increase the stability of G4-DNA, (ii) destabilize G4-DNA in a noncatalytic way, (iii) unwind catalytically G4-DNA in an ATP-dependent fashion, (iv) promote the formation of G4-DNA, or (v) specifically cleave DNA at or adjacent to a quadruplex forming domain. G4-DNA structures in the promoter regions have generally been targeted by end-stacking ligands, which have been already reviewed.[18]

GROOVE BINDING LIGANDS FOR G-QUADRUPLEX DNA

As discussed above, the bulk of the research concerning the G4-DNA binding ligands has focused heavily on the ligands having aromatic rings that could potentially stack on the terminal G4-planes on both ends of the G4-DNA. Other potential binding

dx.doi.org/10.1021/bc200268a | *Bioconjugate Chem.* 2011, 22, 2355−2368

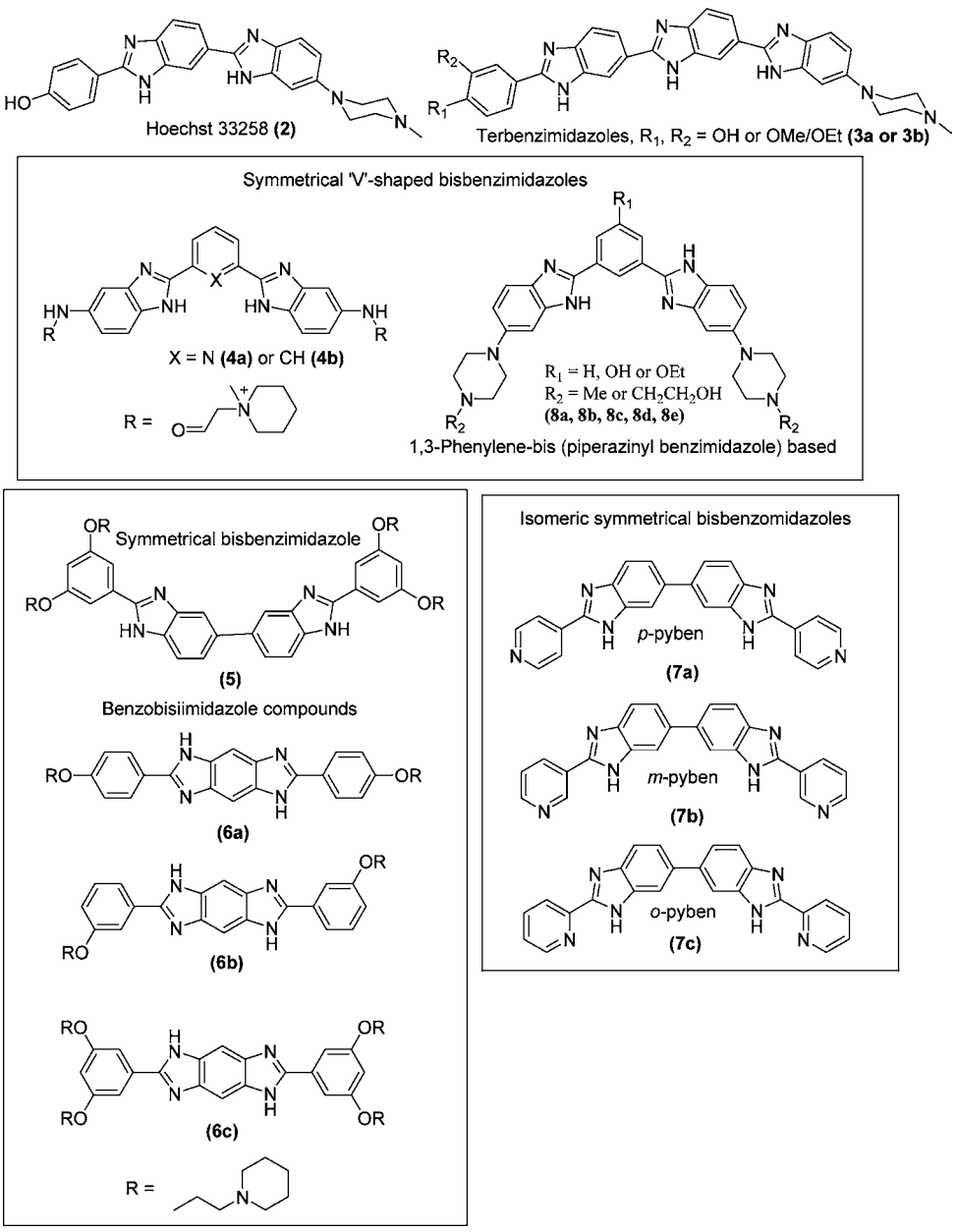

Figure 3. Molecular structures of benzimidazole-based ligands: Hoechst 33258, terbenzimidazoles, 'V'-shaped bisbenzimidazoles,[67] benzobisimidazoles,[68] symmetrical isomeric bisbenzimidazoles used to study tunable binding with the duplex DNA in presence of metal ion,[63] symmetrical 'V'-shaped bisbenzimidazoles based on 1,3-phenylene-bis(piperazinyl benzimidazole) [R_1 = H, R_2 = CH_2CH_2OH;[69] R_1 = OH or OEt, R_2 = Me or CH_2CH_2OH],[70] benzobisimidazoles,[68] symmetrical isomeric bisbenzimidazoles used to study tunable binding with the duplex DNA in presence of metal ion.[63]

sites include the four grooves of the G4-DNA. The width, depth, and accessibility of these four grooves depend on the strand alignment and the topologies of the connecting loops. The structural differences between the duplex and the G4-DNA grooves offer an alternative yet important strategy for the design and synthesis of new ligands for differentiation between the two nucleic acid structures. The grooves are protected by the double-chain-reversal loops, but edgewise and diagonal loops do not have such restrictions. The G4-plane is made by the Watson–Crick base pairing scheme, and the major groove edges of guanines and minor groove edges are still available for further recognition. It was shown that an adenine can align with the minor groove edge of a G4-plane guanine, to form a sheared G.A noncanonical pair, leading to the creation of a A(G.G.G.G) pentad.[61] The structure-based design of ligands and their consequent synthesis to achieve significant binding with individual grooves of defined G4-DNAs is still an ongoing challenge in the field. Since the dimensions of the G4-DNA grooves differ with the type of the G4-DNA, donor–acceptor patterns of the H-bonding sites also vary.[62] Thus, successful implementation of the groove binding is an important strategy to selectively target a particular G4-DNA structure.

FEATURES OF THE GROOVE BINDING LIGANDS

Benzimidazole Based Scaffolds. The benzimidazole moiety is structurally related to the purine bases and is found in several biologically relevant natural compounds. Bisbenzimidazole-based Hoechst 33258 generally binds with 4–5

dx.doi.org/10.1021/bc200268a | Bioconjugate Chem. 2011, 22, 2355–2368

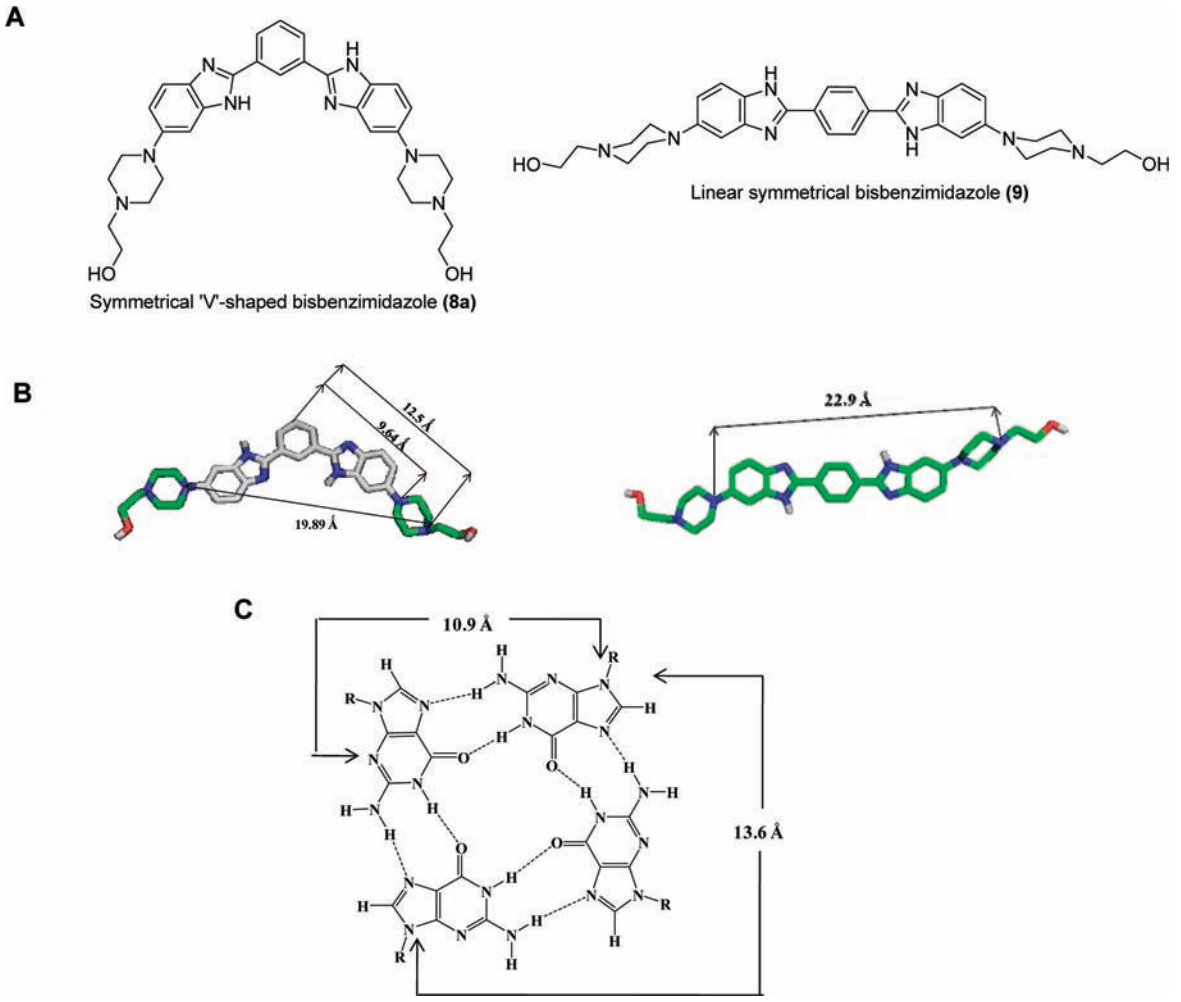

Figure 4. (A) Chemical structures of symmetrical 'V'-shaped bisbenzimidazole (**8a**) and its linear isomer (**9**).[69] (B) Optimized structures at the B3LYP/6-31G* level of theory of **8a** and **9** (adapted from the ref 69, with permission of the American Chemical Society). (C) Structures of the G-tetrad along with interatomic distances.

contiguous AT base pairs of the duplex DNA (**2**, Figure 3). In contrast, the terbenzimidazoles bind with extended sequences of DNA (**3**, Figure 3).[37−39] Other benzimidazole derivatives were also studied to modulate their binding affinity toward duplex and other higher-order DNA structures.[30,31,37,43] Interestingly, three symmetrical isomeric bisbenzimidazole compounds show very different binding affinity toward AT-rich duplex DNA (Figure 3).[63] Hoechst 33258 binds with the G4-DNA formed by the DNA sequence derived from human *c-myc* promoter region, d($G_4AG_3TG_4AG_3TG_4A_2G_2TG_4$). Using UV, fluorescence spectroscopic, and SPR techniques, a binding constant of the order of 10^6 M^{-1} was estimated.[64] Anisotropy measurements and higher lifetime obtained from time-resolved decay experiments reveal that Hoechst 33258 bound to G4-DNA is rotationally restricted in a less polar environment than in the bulk buffered medium. As Hoechst 33258 is known to bind specifically to A−T-rich regions of the duplex DNA, the likelihood of Hoechst 33258 interacting with the AAGGT loop of the G4-DNA was proposed.[64] Later on, the binding was examined by NMR data too.[65] Upon addition of Hoechst 33258 to the solution of a G4-DNA made from a 24-mer sequence d[$TGAG_3TG_4$ $AG_3TG_4A_2G_2$] (pu24), the imino protons of the top G4-plane's residues are found to be most perturbed (shifted toward upfield and broadened).[65] This is an observation which is consistent with the stacking of these ligands on the top G-tetrad. Further, imino proton of G13, which is involved in the terminal G-quartet formation, is greatly broadened, suggesting multiple stacking configurations of Hoechst 33258 over G13. Recently, Hoechst 33258 was shown to stabilize the G4-DNA, a sequence derived from the human telomeric repeats in solution having Na^+ ions, but not K^+.[66] However, in the molecular crowding conditions mimicked by the addition of polyethylene glycol (PEG), it lost its G-quadruplex binding affinity and consequent telomerase inhibition activity.[66] The negative effect of the molecular crowding could be attributed to the reduced affinity between the ligands and the G4-DNA, possibly as a consequence of decreased water activity and enhanced viscosity of the medium.

Two symmetrical V-shaped bisbenzimidazole derivatives were prepared and one of them was shown to induce the G4-DNA formation and stabilize it.[67] The benzimidazole constructs that are more effective have pyridine as the central aromatic core and substitutions on benzimidazoles at 3- and 6-positions (**4a**), making a planar and relatively nonflexible conformation because of the intramolecular H-bonding between the imidazole hydrogen and the nitrogen of pyridine. This compound (**4a**) also showed effective nuclease resistance activity.[67] Other molecules having benzene as the central ring

dx.doi.org/10.1021/bc200268a | *Bioconjugate Chem.* 2011, 22, 2355−2368

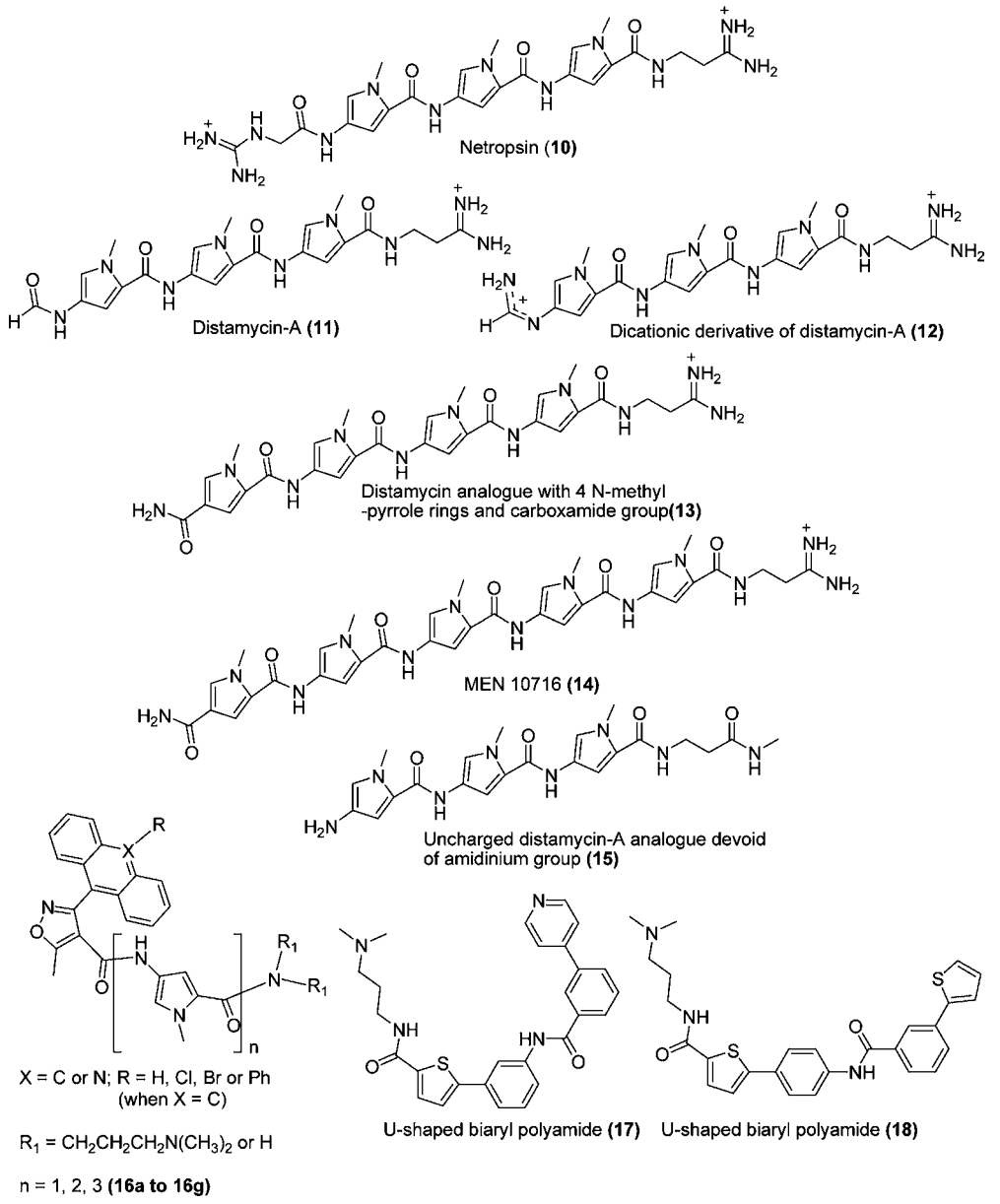

Figure 5. Chemical structures of netropsin, distamycin-A, and carbamoyl analogues of distamycin having 4 and 5 *N*-methyl-pyrrole rings and dicationic derivative[76] of distamycin-A (distamycin-A analogue having 5 rings is called MEN 10716),[82] uncharged distamycin-A analogue devoid of amidinium group,[83] anthracenylioxazole lexitropsin conjugates,[84] and planar U-shaped byaryl polyamides.[85]

and substitutions at 1- and 2-positions, however, show much less affinity toward the G4-DNA. Recently, a symmetrical, linear bisbenzimidazole (**5**) and some benzobisimidazole compounds (**6a**–**6c**, Figure 3) were tested against the duplex and the G4-DNA.[68] Linear bisbenzimidazole (**5**) was found to bind with the double-helical DNA, while the benzobisimidazole compounds were found to stabilize the G4-DNA preferentially over the duplex DNA. Side chains have an important role in the G-quadruplex binding and telomerase inhibition. These benzobisimidazole derivatives have a conjugated aromatic surface, which probably aids their binding with a G-quadruplex DNA via π–π stacking.[68]

The shape of a G-quadruplex ligand has an important role toward the affinity and stabilization of the G4-DNA. G4-DNA interactions with two isomeric bisbenzimidazole-based compounds with different shapes ('V'-shaped, angular vs linear; Figure 3) were investigated.[69] While the linear isomer (**9**) shows little affinity for the monomolecular G4-DNA structure generated in the presence of Na^+, the 'V'-shaped angular isomer (**8a**, R_1 = H, R_2 = CH_2CH_2OH), expected to cover three guanines of the G-quartet, induces a significant structural change of the intramolecular G4-DNA, above a threshold concentration. The structural change was evident from the pronounced changes observed both in the CD spectra and from the electrophoretic experiments using the G4-DNA. Notably, this V-shaped isomer also induces the G4-DNA formation without any added cation. The ligand-G4-DNA complexes were also investigated by computational methods, which provide additional information on the structure–activity relationships (Figure 4). Dimensions of the angular isomer match with those of the G-quartet, and it should cover three guanines of the G-quartet. The linear isomer, which should cover two guanines of the G-quartet, caused less structural change and provided little stabilization to the G4-DNA. In agreement with these

observations, TRAP assay results with the telomerase extracted from A549 cells show that the angular isomer is a significantly more effective inhibitor of the telomerase activity.[69]

A series of symmetrical 'V'-shaped bisbenzimidazoles based on 1,3-phenylene-bis (piperazinyl benzimidazole) compounds was synthesized (**8b**−**8d**, Figure 3). These compounds induce G4-DNA formation even without any added cation with the ODN sequence $d(T_2G_4)_4$ relevant to *Tetrahymena*.[70] Binding affinity of these molecules toward the G-quadruplex increases upon introduction of an electron-donating ethoxy group on the central phenyl ring. The dimensions of these compounds match with those of the G-tetrad plane as per calculations, suggesting that end-stacking as the possible mode of the G-quadruplex stabilization. Appearance of an induced circular dichoric (ICD) signal at a higher drug: DNA ratio, however, indicates the groove binding as well.[70]

Oligopeptides and Related Lexitropsins. Some reports are available regarding the interaction of netropsin (Nt, **10**), distamycin-A (Dist-A, **11**), and their other oligopeptide analogues with the G4-DNA (Figure 5). This class of molecules acts as the minor-groove binders (MGB) for the duplex DNA.[34,35,42] Binding properties of these *N*-methyl pyrrole containing cresent-shaped oligopeptides with the duplex DNA depend on the number of pyrrole rings and the presence or absence of a leading amide (in Dist-A).[34] Longer analogues (beyond four/five consecutive rings) tend to lose their selectivity toward certain AT-rich DNA sequences. This is because the curvature of such long ligands often fails to match with the pitch of the DNA double-helix, disrupting the H-bonding and van der Waals interactions necessary for the specific sequence recognition.[31,34,36] Dist-A and Nt were also investigated with the three G-quadruplexes characterized by different groove widths: $[d(TG_4T)]_4$ (Q1), $[d(G_4T_4G_4)]_2$ (Q2), and $d(G_4T_2G_4TGTG_4T_2G_4)$ (Q3) using homonuclear NMR.[71] Below 2:1 ligand/G-quadruplex stoichiometry, Dist-A, in a dimeric form, binds with each groove of the tetraplex to form short-lived complexes on an NMR time scale. At higher drug/DNA ratios, a second Dist-A dimer specifically binds with the tetraplex, to give a 4:1 complex, in slow exchange with the 2:1 complex. Nt was found to be in a fast chemical exchange with all three kinds of G-quadruplexes, whereas Dist-A interacted tightly with Q1 and, to a less extent, with Q2. Both molecules possess higher affinity toward the duplex DNA than the G4-DNA. Two opposite models were proposed for the Dist-A complexed, parallel G4-DNA containing ODNs of different sequences in K^+ buffers. The first one suggests that Dist-A molecules bind as dimers in the two opposite grooves of the G4-DNA $[d(TG_4T)]_4$;[72,73] while the second one suggests that two Dist-A molecules stack on the terminal G-tetrad planes of the G4-DNAs made up of each of $[d(TAG_3T_2A)]_4$, $[d(TAG_4T_2)]_4$, and $[d(TAG_5T)]_4$ on the basis of NMR studies.[74] Below 2:1 ligand−tetraplex stoichiometry, Dist-A, in a dimeric form, binds to each groove of the tetraplex to form short-lived complexes on the NMR time scale. Therefore, only one set of signals for the four strands was observed. The fast exchange behavior of the lower complex (2:1 Dist-A-G4-DNA) could be changed only to an intermediate regime by decreasing the temperature of the system. As the temperature was reduced from 300 to 280 K, there was a general broadening of the resonances, with peaks belonging to Dist-A broadening more than the other peaks, probably due to the slower reorientation of the Dist-A dimer. At higher drug/DNA ratios, a second Dist-A dimer specifically binds with the G4-DNA, to give a 4:1 complex, in slow exchange with the 2:1 complex, as evidenced from the appearance of separate proton resonances for the two species. This behavior may be explained assuming that the binding of the second drug pair is more favorable than the binding of the first one.[72] Nt is involved in fast exchange on the NMR time scale with its binding sites on the tetraplex.[72]

A new modified oligonucleotide, namely, $d(TGG^{Me}GGT)$, having G^{Me} (8-methyl-2′-deoxyguanosine), able to fold into a quadruplex, was used to study its interactions with Dist-A.[73] Thus, the 8-methyl group of the four dG^{Me} of the quadruplex $[d(TGG^{Me}GGT)]_4$ faces right into the very central region of the grooves, pointing outward from the G4-DNAs. As a result, if Dist-A interacts with the groove of the G-quadruplex, the presence of these bulky groups in the very central region of the four grooves should prevent (or at least should limit) the insertion of Dist-A molecules. Consequently, the formation of a stable complex would be impeded. In the case of $[d(TG_4T)]_4$, Dist-A displayed a high affinity toward the G4-DNA as evidenced from the appearance of a new set of signals during the NMR titration. Furthermore, Dist-A caused a loss of the original fourfold symmetry of the free G4-DNA. During the entire titration process of the G-quadruplex $[d(TGG^{Me}GGT)]_4$, the four strands remain magnetically equivalent and only a general change in the chemical shift resonances are observed. Thus, the presence of the methyl groups in the central region of the grooves does affect the binding of Dist-A to the quadruplex, and hence, Dist-A interacts with the grooves of the quadruplex. The affinity between Dist-A and $[d(TG_4T)]_4$ is enhanced (∼10-fold) when the ratio of Dist-A and the quadruplex is increased.[73]

Dist-A was reported to stack on the terminal G4-planes having the flanking bases of the G4-DNA.[74] This allowed detection of 2:1, 4:1, and 8:1 Dist-A/G4-DNA complexes. Dist-A also inhibits the interaction of BLM helicase (an enzyme which unwinds the G4-DNA) with the G4-DNA. Dist-A inhibited binding of the G-quadruplex by nucleoilin (Nuc)-RGG_9. However, Dist-A exerts no effect on the interaction of G4-DNA with either a full-length murine nucleolin (Nucleolin) or a recombinant nucleolin possessing amino acid residues 281−709 that is devoid of the acidic N-terminus (Nuc-1,2,3,4-RGG_9) or recombinant nucleolin having only four RBD domains (RNA binding domains, Nuc-1,2,3,4).[74] These results show that Dist-A may be used to probe the interactions of G4-DNAs with certain proteins. These also indicate that at least two independent modes of protein−G4-DNA interactions may be studied by the sensitivity to Dist-A.

In another report, interactions of Dist-A, tel01, and DTC with the G4-DNA were studied using ESI-MS.[75] When two different ligand−G4-DNA complexes were subjected to a mass spectral analysis, distinct fragmentation patterns were observed. Tel01-G4-DNA complexes underwent a facile loss of the drug and produced single-strand ODN, while Dist-A-G4-DNA complexes produced single-strand ODN ions bound with the Dist-A. DTC-G4-DNA complexes had similar fragmentation patterns.[75] Thus, it may be concluded that DTC and Dist-A bind with $[d(T_2G_5T)]_4$ through the grooves. Different binding behavior observed with such drug molecules suggests that a sequence-dependent interaction prevails in the G4-DNA recognition events.

Recently, Nt and a dicationic derivative of Dist-A (**12**, Figure 5) were studied with $[d(TG_4T)]_4$ G4-DNA using NMR titrations and isothermal titration calorimetry (ITC).[76] Dicationic derivatives form 2:1 complex with the G4-DNA.

Interactions in both cases (Nt and the dicationic Dist-A) are entropically driven with a small favorable enthalpic contribution. The stoichiometry and thermodynamic properties of interactions of Dist-A/its analogues with G4-DNA are affected by the presence of different cations in solution. Dist-A and its two carbamoyl derivatives (**13**, **14**; having 4 and 5 *N*-methyl-pyrrole rings, respectively, Figure 5) were reported to behave differently from the target $[d(TG_4T)]_4$ and $d[AG_3(T_2AG_3)_3]$ G4-DNAs in K^+ and Na^+ solutions.[77] Out of these carbamoyl derivatives, one having 5 *N*-methyl-pyrrole rings (**14**) is also called MEN 10716. Dist-A and its 4 *N*-methyl-pyrrole derivative bind with the parallel quadruplex structure $[d(TG_4T)]_4$ in 1:1 stoichiometry in solution containing Na^+.[78] Dist-A and the 4 *N*-methyl-pyrrole derivative bind with the investigated G4-DNA in both solution conditions; conversely, the 5 *N*-methyl-pyrrole derivative seems to have a lower G4-DNA affinity in any case as evidenced from the ITC and ^1H NMR studies.[77] The 4 *N*-methyl-pyrrole derivative, however, showed a 10-fold higher G4-DNA affinity than the duplex DNA.[78]

A number of amide-linked oligo *N*-methyl-pyrroles based on Dist-A molecules, having 2 to 6 pyrrole rings and substitutions at different positions (2,4-substitution vs 2,5-substitution), were also synthesized. These interact with a human intramolecular G4-DNA $d[G_3(T_2AG_3)_3]$.[79] Several of these molecules show an enhanced ratio of binding constants toward the G4-DNA vs the duplex DNA compared to that of Dist-A itself or its analogue with a 2,5-disubstituted pyrrole system. The G-quadruplex binding affinity increases with the number of *N*-methyl-pyrrole units of this class of ligands, suggesting that such an interaction is consistent with a mixed groove/G-quartet stacking mode of binding. A qualitative molecular model of a six-repeat pyrrole polyamide molecule docked onto the crystal structure of a human 22-mer G-quadruplex structure is shown (Figure 6),

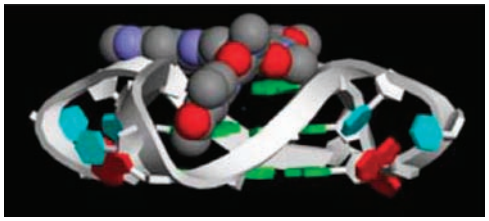

Figure 6. Qualitative molecular model of a six-repeat pyrrole polyamide molecule docked onto the crystal structure of the human 22-mer G-quadruplex structure. Figure adapted from the ref 79, with permission of the Royal Society of Chemistry.

where the two repeats of the polyamides located in a G4-DNA groove and the others stack on a terminal G-quartet surface.[79]

Oligoamides having up to 3 *N*-methyl-pyrrole (Py) or -imidazole (Im) units were shown to have less effect on the G-quadruplex stability than other known end-stacking G4-DNA ligands like Tel 01, porphyrin, DAPER, PIPER, and so forth.[80,81] In contrast, oligoamides having 4 or more rings induce stabilization of the G-quadruplexes.

Dist-A derivative MEN 10716 (**14**, Figure 5) inhibits the human telomerase enzyme in a dose-dependent manner.[82] Exposure of human melanoma *JR8* cell extracts and *U2-OS* human steogenic sarcoma cell line extracts to MEN 10716 induced a dose-dependent inhibition of the telomerase activity, with an IC_{50} value of 24 ± 3 mM. A chronic exposure of the *H460* nonsmall cell lung cancer cells to the above drug (100 mM every other day for 50 days) induced a consistent inhibition (>85%) of the telomerase activity.[82] Inhibition of the telomerase by Dist-A and its 2,5-disubstituted derivative was also determined using a modified PCR based TRAP assay.[79] These two compounds were examined in this experiment up to a concentration of 100 μM, and concomitant controls were carried out to ensure that there was no interference with the correct functioning of *Taq* polymerase at these concentrations. Dist-A exhibited a $^{tel}EC_{50}$ value of ~25 μM, whereas its 2,5-disubstituted derivative showed no telomerase inhibitory activity even at 100 μM. However, both compounds show significant PCR inhibition, suggesting that the positive result obtained in the TRAP assay is not necessarily due to the telomerase inhibition and other mechanisms are possible.[79] Dist-A also inhibits protein interactions with the G4-DNA. The utility of Dist-A as a probe of the G4-DNA−protein interactions was thus demonstrated and two separate modes of the protein−G4-DNA interactions, which may be analyzed by the sensitivity to Dist-A, were proposed.[74]

An uncharged Dist-A analogue, where the major change in its structure involved the replacement of the amidinium group by an uncharged *N*-methyl amide moiety (**15**, Figure 5), was used to probe the importance of the unique Coulombic interactions in the Dist-A/$[d(TG_4T)]_4$ complex formation.[83] Removal of the positively charged terminal group results in an exceptional ligand−G4-DNA complex formation in which the grooves as well as the 3′-end of the telomeric DNA are occupied. Furthermore, a lack of charge in the ligand molecule does not affect the relative orientation of two molecules of the analogue forming a dimer. The positively charged amidinium moiety of the Dist-A interacts with the phosphate groups of the G-quadruplex, providing a favorable (although small) enthalpic contribution, while the analogue, where the amidinium group is replaced by the uncharged *N*-methyl amide moiety, cannot interact with electrostatic complementarity.[83] The binding affinity of the uncharged analogue with the G4-DNA as

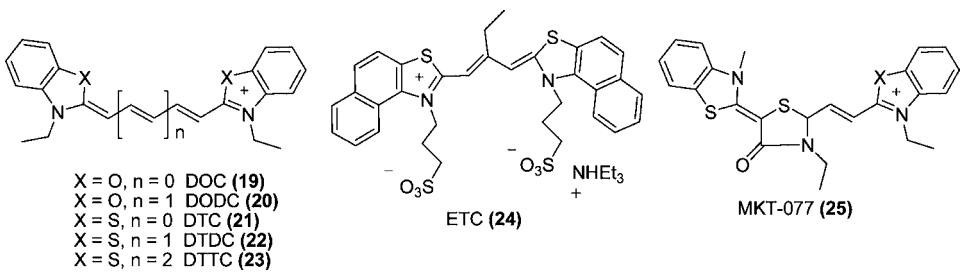

Figure 7. Chemical structures of common carbocyanine dyes (**19**−**23**), dyes ETC (**24**), and MKT-077 (**25**) synthesized based on cyanine dyes.

measured from ITC is 9×10^5 M^{-1} at 25 °C. However, no comparison of binding affinity with Dist-A was given.

Some anthracenyl isoxazole lexitropsin conjugates (**16**, **17**; Figure 5) were developed recently. Plausible binding modes of these compounds after energy minimization have suggested that one of them binds with the G4-DNA via intercalation, by displacing a guanine. Other compounds bind via a stacking mode with the G-tetrad.[84] G4-DNA formed by the sequence d[5′-CATGGTGGT$_3$(G_3TTA)$_4$CCAC-3′] quench the fluorescence of ligands suggesting a $\pi-\pi$ stacking interaction of the ligand with the G-tetrad. Some planar U-shaped biaryl polyamides (**17**, **18**) possessing high selectivity toward the G-quadruplex over the duplex DNA were also developed.[85] Compound **17** shows high selectivity for the human telomeric G4-DNA, while compound **18** is selective for two *c-kit* G4-DNAs.

Cyanine Based Ligands. Carbocyanine dyes (**19**−**23**, Figure 7) represent another class of MGBLs which are often studied with the G4-DNA. These compounds form complexes with the minor grooves of the duplex DNA, and show pronounced exciton splitting in their ICD spectra.[30,86] Stacked species are important for the recognition of G4-DNA. Studies with the duplex DNAs demonstrate that ligands that bind DNA as stacked dimers have enhanced binding affinity/selectivity over similar ligands which bind as monomers.[86] Similar stacking in the G4-DNA grooves seems to be a favorable way to selectively recognize different G4-DNA structures. Such a mode of interaction probably optimizes through an induced fit component, between the stacked ligands and the G-bases of the G-quadruplexes. On the basis of different spectroscopic studies, 3,3′-diethyloxa-dicarbocyanine (**20**, DODC) was shown to bind with the grooves of a dimeric hairpin G-DNA.[87] DODC−G4-DNA interaction resulted in some unique spectral signatures, e.g., a new absorbance peak (534 nm), an ICD signal (534−626 nm), a quenching of the fluorescence intensity of the ligand on excitation with the visible light, and a strong energy transfer from DNA.[87] In the electrophoresis experiments, only the G4-DNA bound to DODC were detectable above the background. However, neither the duplex DNA bound to DODC nor the free G4-DNA was observable. G4-DNA was detectable even in the presence of a high concentration of the duplex DNA. This demonstrates the ability to detect a small amount of dimeric hairpin quadruplex in the presence of a large amount of the duplex DNA. The concentration ratio was limited by the capacity of the gel.[87] Satellite hole spectroscopy studies also supported the groove-binding model for DODC with the G4-DNA.[88]

A different study using competition dialysis assay suggests that DODC has a preference for the triplex DNA compared to the G4-DNA. Although no structural information is available on this molecule in the DNA-bound form, it is possible that due to the geometric features, DODC could be binding to a G-quadruplex groove rather than stacking on a G-quartet. If this is indeed true, then its affinity should be highly sensitive to the groove dimensions, which vary along with the type of the G4-DNA.[62] Electrospray ionization mass spectrometric patterns also support the diethylthiocarbocyanine iodide (**21**, DTC) binding with the G4-DNA grooves.[75,89,90] Dissociation patterns of the DTC/G4-DNA complexes resemble those of Dist-A. Therefore, it is predicted that DTC interacts with the parallel G4-DNA [d(T_2G_5T)$_4$] through groove-binding.[75] Tel01 was found to interact via end-stacking with the G4-planes of the G4-DNA.[75] However, binding to G4-DNA and telomerase inhibition by only DTC among all the carbocyanines tested appears to be a result which is ambiguous.[90]

SPR studies indicate that Dist-A binds very weakly to the telomeric DNA sequence attached on a support.[72] The binding of Dist-A is likely to be seen in the experimental methods such as NMR, which employs high concentrations of the ligand.[72] Screening experiments with other MGB polyamides also did not reveal any significant G4-DNA interactions. These results are contrary to other reports, where Dist-A and its analogues have been studied with the G4-DNA using NMR and ESI-MS.[71−73,75] DODC was shown to have higher affinity toward the G-quadruplex grooves via stacking, as suggested by the negative ICD spectra, and is presented as a more promising G4-DNA groove-binding model system.[91] Dist-A did not show any induced signal. A new fluorescence-based study of the G4-DNA ligands was reported using DODC and DTDC as reporter molecules along with other G-quadruplex ligands.[92] *N*-Methyl mesoporphyrin IX (NMM), DODC, and DTDC (**22**) allow the monitoring of several structural features of G4-DNA, as these molecules detect G4-DNA structure specifically. These three molecules were used as reporter molecules to screen six G4-DNA ligands. The fluorescence intensity of the reporter increases when it binds to the G4-DNA. Addition of ligands can either enhance or diminish the fluorescence due to the reporter molecule. DODC and DTDC also exhibit ICD upon binding to the most of the G4-DNAs indicating groove binding. NMM competes with DODC and DTDC in binding with d($G_2T_2G_2TGTG_2T_2G_2$). NMM also competes with DODC in binding with d(T_2AG_3)$_4$.[92] Recently, binding of a novel cyanine dye 3,3′-di(3-sulfopropyl)-4,5,4′,5′-dibenzo-9-ethylthiacarbocyanine triethylammonium salt (ETC, **24**, Figure 7) was studied with unimolecular human telomeric G-quadruplex, owing to its common properties with the G4-DNA ligands.[93] ETC also has specific interactions with an intramolecular telomeric G4-DNA via end stacking.[94] ETC stacks on one specific end of the hybrid, some selective parallel and antiparallel G-quadruplexes, or on both ends of the normal parallel G4-DNA. Nearby loop structures also play an important role in the binding. Some specific lateral or unusual propeller loops "snatch" part of ETC molecule and facilitate stacking on the end G-quartet, while the diagonal or special lateral snap-back loops block the access of ETC molecule to the G4-DNA frame.

Several *in vitro* G4-DNA related biological activities of MGBLs were also reported. G-quadruplex ligands, e.g., TMPyP4, NMM, coraylene, Dist-A, DODC, and DTC, along with perylene diimides (PDI) were investigated as inhibitors of the G-quadruplex and the duplex DNA helicase activities of the T-antigen (T-ag).[95] G-quadruplex helicase activity was found to be strong and similar to that of duplex DNA helicase activity of the T-ag. Analysis of the SV40 genome demonstrates the presence of sequences that may form intramolecular G-quadruplexes, which are presumed to be natural substrates for the G4-DNA helicase activity involving the T-ag. Dist-A, which does not inhibit the G-quadruplex unwinding activity of bloom syndrome homologue (BLM) gene, was found to be a weak inhibitor of the G4-DNA unwinding activity of the T-ag. DODC weakly inhibits the G′2 (bimolecular G-quadruplex) unwinding activity of the T-ag. A number of other G4-DNA ligands including Hoechst 33258 and DTC were found to be, however, not as effective inhibitors of the G4-DNA unwinding activity of the T-ag. PDIs were found to be potent and selective inhibitors of the T-ag associated G4-DNA helicase activity.[95] The effect of DODC on telomerase activity was also explored.

It reduced telomerase activity in pheochromocytoma PC-12 cells in a dose-dependent manner (10−100 mM) after 12 h of treatment.[96]

In another study, DODC inhibited telomerase in nasopharyngeal carcinoma NPC-Tax (a control NPC cell line), but not in NPC-TW01 cells, when studied with the extracts from cells, which were treated with 0.7 mM of DODC for 1−3 days. On direct addition of DODC to the study media, inhibition was observed at 10 mM for the NPC-Tax and 500 mM for the NPC-TW01 nasopharyngeal carcinoma cells, respectively.[97] DODC itself was able to induce apoptotic cell death, although it did not reduce the telomerase activity in the NPC-TW01 cells. Instead, DODC induced the cell apoptosis via a mitochondrion-mediated mechanism. DODC inhibited the uptake of another mitochondrial probe 3,3′-dihexyloxacarbocyanine iodide. By proteomic comparative analysis, it was apparent that DODC induced the increase of prohibition level in the mitochondria, indicating an occurrence of the mitochondrial perturbation. Moreover, DODC increases the levels of p53 and an 18 kDa truncated Bax on mitochondria, which in turn potentiates the release of cytochrome *c* for the activation of caspases.[97] In a different study, at the tested concentrations, DODC had little effects on the hydrolysis of the substrates under question in presence of either K^+ or Li^+ ions, or on the stability of the $d[T_{24}(G_3TTA)_3G_3]$ G4-DNA and on the electrophoretic mobilities of either $d[T_{24}(G_3T_2A)_3G_3]$ or $d[T_{24}GTGTGAGTG_2AG_2TGTGAG_2T]$.[98] DODC did neither inhibit the exonuclease hydrolysis nor the telomerase activity.[97] It also destabilized the G4-DNA under experimental conditions. The synergistic effects between low-dose arsenic trioxide and DODC on the apoptosis of HT1080 cells were also investigated.[99] Results reveal that low-dose arsenic could block cell cycle arrest at the G2/M phase and induce apoptosis, whereas DODC could block cell cycle arrest at the G0/G1 phase but does not induce apoptosis. However, cells pretreated with DODC showed greater sensitivity to arsenic than untreated cells. DODC alone could induce the hairpin G-quadruplex formation and inhibit the telomerase activity in a dose-dependent manner. It has been predicted that DODC can synergistically enhance the apoptosis induced by arsenic, suggesting that increased cell senescence in response to arsenic is induced by an altered telomere state rather than by a loss of telomerase.[99] Rhodacyanine dye MKT-077 (**25**, Figure 7) has also been reported to have telomerase inhibition activity.[100] Due to its structural similarity with DODC, an interaction with the G4-DNA may be possible for the activity.[62]

The binding mode of DODC with the G4-DNA is a matter of considerable interest. One can imagine four possible modes of noncovalent association: (a) intercalation between the G-quartets, (b) binding through the grooves, (c) interaction with the thymine loops, and (d) outside binding. The possibility of outside binding can be easily eliminated on the basis of the fluorescence collisional quenching data and the ICD spectra. On the basis of the ICD spectra obtained for DODC complexed with two different G-quadruplexes $[d(G_4T_4G_4)]_2$ and $[d(G_3T_4G_3)]_2$, which have similar loops, binding only to the loops is overruled. Furthermore, the dye does not bind specifically to the unimolecular hairpin Watson−Crick duplex containing a T_4 loop. Thus, groove binding and intercalation remain as the two plausible modes of specific binding.[87] On the basis of preliminary NMR data, DODC is suggested to bind within the loops of the G4-DNA.[92] CD and fluorescence competition studies with these ligands also suggest binding with the loops of the G4-DNA. Atomic resolution data are, however, needed to unambiguously determine the structures of the G4-DNA-cyanine dye complexes.[92] However, for the cyanine dye−duplex DNA complexes, the appearance of ICD spectra is due to the groove binding. Other classical MGBLs (berenil, DAPI, SN-18071, etc.) have still not been examined for their interaction with the G4-DNAs.

CONCLUDING REMARKS AND PERSPECTIVES

Telomeres, *r*DNA, and promoter regions have been identified as potential targets, and there are over 350 000 predicted sequences in the genome that can fold into G-quadruplex structures, raising the daunting task of determining selective targets for these drugs.[17,101] G-quadruplex ligands acting on both telomeric and nontelomeric quadruplexes have significant biological importance and quite a few of them are in clinical trials.[18,29,102,103] Few examples include G4-DNA binding ligands, RHPS4,[104] telomestatin,[105] derivative of telomestatin HXDV,[106] BRACO-19,[107] porphyrin TMPyP4,[15] quarfloxin (CX-3543),[108] 307A,[109] triazines,[110] and so forth. Quarfloxacin was originally developed to bind to the c-myc promoter. Instead, it appears to bind ribosomal quadruplexes, interfering with the binding of the protein nucleolin, which normally binds to the G-quadruplex structures, leading to cell death in cancerous cells. Quarfloxin is in the phase II clinical trials for the treatment of carcinoid/neuroendocrine tumors.[108,111] However, it is still a long way off to get G4-DNA binding ligands as successful anticancer agents.

As discussed earlier, the ligands which bind to the G-quadruplex grooves also exert stabilizing effects. The grooves of the G4-DNA structures have different characteristics than the grooves of the duplex DNA, and thus, the ligands that bind only with the grooves of the G4-quadruplex selectively should be able to recognize DNA in a structure-specific manner with high affinity. DNA minor groove binding ligands are known to be able to distinguish the variable groove widths engendered by a specific sequence.[112] G4-DNA structures give many variations within the generic theme of a G-quadruplex forming motif. Therefore, ligand design and development in the future would necessitate dealing with more complex issues of structural variations. Thus, this should not be limited to duplex versus G4-DNA distinction only. Availability of alternating groove widths in the G-quadruplexes in this regard may provide a platform toward selective targeting of specific topological and conformational forms of the G4-DNA. Ligands capable of spanning two or more grooves in the G-quadruplex may be able to distinguish one form from another based upon the appropriate groove dimensions and their specific orientations. Furthermore, "designed" MGBLs should be capable of selective targeting as well. To find new quadruplex groove binding agents, the molecular nature of the G-quadruplex grooves must therefore be considered judiciously. Interestingly, all known grooves of the G-quadruplex structures that have been characterized are chemically and conformationally quite different from the minor grooves of the duplex DNA. Thus, the recognition of the grooves of these nucleic acid structures is supposed to give a higher degree of selectivity over other types of DNA structural motifs, which may not be possible in the case of most of the existing end-stacking G-quadruplex ligands. Therefore, to understand the structural and conformational requirements for the recognition of the grooves of G4-DNA,

many of the existing MGBLs should be chemically modified logically.

Toward the success of the G-quadruplex binding ligands at the genetic level, the hypothesis proposed by Huppert is relevant,[111] in that the fusion of the G4-DNA recognition molecules with systems that bind to specific sequences of the duplex DNA are feasible. Tethering MGBLs that are able to recognize six or more contiguous DNA base pairs (e.g., terbenzimidazoles)[37−39,43] or longer "designed" Py/Im polyamides[33−36,39] might provide an increase in the specificity and binding affinity depending on the nature, length, and/or flexibility of the linkers used.

Some of the MGBLs discussed so far bind with the non-natural or model G-quadruplexes like $[d(TG_4T)]_4$ and also those made from the modified nucleotides.[71−78] These MGBLs may not be of much use in developing a drug. However, MGBLs that bind with the natural G-quadruplexes may be of significant medicinal importance. These include cyanine dyes,[81−88] oligopeptide-based on distamycin analogues, in particular, the longer oligopeptides,[69−73] and certain benzimidazoles.[64−70] Longer oligopeptides lose helical phase matching with the grooves of the duplex-DNA and thus prefer to bind with the non *B*-DNA structures. Carbon skeleton of benzimidazoles,[69,70] oligopeptides,[85] and cyanine dyes may be suitably crafted to make them G-quadruplex DNA-specific. Thus, MKT-077, a compound structurally similar to DODC, is already being used in clinical trials as an anticancer agent.[113] It shows selective cytotoxity toward cancer cells,[114] which may be due to its ability to localize specifically on the mitochondria of the cancer cells.[113] Examples of G-quadruplex binding MGBLs discussed in this review should therefore serve as a useful source for the design of a whole new class of highly selective groove-binding ligands with attractive biological properties.

AUTHOR INFORMATION

Corresponding Author

*E-mail: sb@orgchem.iisc.ernet.in. Phone: (91)-80-22932664. Fax: (91)-80-23600529.

ACKNOWLEDGMENTS

This work was supported by a grant from the Department of Science and Technology (DST), New Delhi, India, as J. C. Bose Fellowship to S.B. A.K.J. is thankful to DST, New Delhi, for a Fast Track Grant for young scientists.

REFERENCES

(1) Blackburn, E. H., and Gall, J. G. (1978) A tandemly repeated sequence at the termini of the extrachromosomal ribosomal RNA genes in Tetrahymena. *J. Mol. Biol. 120*, 33−53.

(2) Morin, G. B. (1989) The human telomere terminal transferase enzyme is a ribonucleoprotein that synthesizes TTAGGG repeats. *Cell 59*, 521−529.

(3) Griffith, J. D., Comeau, L., Rosenfield, S., Stansel, R. L., Bianchi, A., Moss, H., and Lange, Tde. (1999) Mammalian telomeres end in a large duplex loop. *Cell 97*, 503−514.

(4) Lingner, J., Cooper, J. P., and Cech, T. R. (1995) Telomerase and DNA end replication: no longer a lagging strand problem? *Science 269*, 1533−1534.

(5) Greider, C. W., and Blackburn, E. H. (1985) Identification of a specific telomere terminal transferase activity in tetrahymena extracts. *Cell 43*, 405−413.

(6) Yu, G. L., Bradley, J. D., Attardi, L. D., and Blackburn, E. H. (1990) In vivo alteration of telomere sequences and senescence caused by mutated tetrahymena telomerase RNAs. *Nature 344*, 126−132.

(7) Cech, T. R. (2000) Life at the end of the chromosome: Telomeres and telomerase. *Angew. Chem., Int. Ed. 39*, 34−43.

(8) Chen, H., Li, Y., and Tollefsbol, T. O. (2009) Strategies targeting telomerase inhibition. *Mol. Biotechnol. 41*, 194−199.

(9) Phatak, P., and Burger, A. M. (2007) Telomerase and its potential for therapeutic intervention. *Br. J. Pharmacol. 152*, 1003−1011.

(10) Balasubramanian., S., and Neidle, S. (2009) G-quadruplex nucleic acids as therapeutic targets. *Curr. Opin. Chem. Biol. 13*, 345−353.

(11) McEachern, M. J., Krauskopf, A., and Blackburn, E. H. (2000) Telomeres and their control. *Annu. Rev. Genet. 34*, 331−358.

(12) Hurley, L. H. (2002) DNA and its associated processes as targets for cancer therapy. *Nat. Rev. Cancer 2*, 188−200.

(13) Sen, D., and Gilbert, W. (1988) Formation of parallel four-stranded complexes by guanine-rich motifs in DNA and its implications for meiosis. *Nature 334*, 364−366.

(14) Catasti, P., Chen, X., Moyzis, R. K., Bradbury, E. M., and Gupta, G. (1996) Structure−function correlations of the insulin-linked polymorphic region. *J. Mol. Biol. 264*, 534−545.

(15) Siddiqui-Jain, A., Grand, C. L., Bearss, D. J., and Hurley, L. H. (2002) Direct evidence for a G-quadruplex in a promoter region and its targeting with a small molecule to repress *c-myc* transcription. *Proc. Natl. Acad. Sci. U.S.A. 99*, 11593−11598.

(16) Todd, A. K., Haider, S. M., Parkinson, G. N., and Neidle, S. (2007) Sequence occurrence and structural uniqueness of a G-quadruplex in the human *c-kit* promoter. *Nucleic Acids Res. 35*, 5799−5808.

(17) Huppert, J. L., and Balasubramanian, S. (2007) G-quadruplexes in promoters throughout the human genome. *Nucleic Acids Res. 35*, 406−413.

(18) Balasubramanian, S., Hurley, L. H., and Neidle, S. (2011) Targrtting G-quadruplexes in gene promoters: a novel anticancer strategy. *Nat. Rev. Drug Discovery 10*, 261−275.

(19) Ou, T.-M., Lu, Y.-J., Zhang, C., Huang, Z.-S., Wang, X.-D., Tan, J.-H., Chen, Y., Ma, D.-L., Wong, K.-Y., Tang, J. C-O., Chan, A. S-C., and Gu, L.-Q. (2007) Stabilization of G-quadruplex DNA and down-regulation of oncogene *c-myc* by quindoline derivatives. *J. Med. Chem. 50*, 1465−1474.

(20) Davis, J. T. (2004) G-Quartets 40 Years Later: From 5′-GMP to molecular biology and supramolecular chemistry. *Angew. Chem., Int. Ed. 43*, 668−669.

(21) Phan, A. T., Kuryavyi, V., Burge, S., Neidle, S., and Patel, D. J. (2007) Structure of an unprecedented G-quadruplex scaffold in the human c-kit promoter. *J. Am. Chem. Soc. 129*, 4386−4392.

(22) Pedroso, I. M., Duarte, L. F., Yanez, G., Burkewitz, K., and Fletcher., T. M. (2007) Sequence specificity of inter- and intra-molecular G-quadruplex formation by human telomeric DNA. *Biopolymers 87*, 74−84.

(23) Jixun, D., Megan, C., Chandanamali, P., Roger, A. J., and Danzhou, Y. (2007) Structure of the hybrid-2 type intramolecular human telomeric G-quadruplex in K^+ solution: insights into structure polymorphism of the human telomeric sequence. *Nucleic Acids Res. 35*, 4927−4940.

(24) Phan, A. T., Luu, K. N., and Patel, D. J. (2006) Different loop arrangements of intramolecular human telomeric (3 + 1) G-quadruplexes in K^+ solution. *Nucleic Acids Res. 34*, 5715−5719.

(25) Dai, J., Carver, M., and Yang, D. (2008) Polymorphism of human telomeric quadruplex structures. *Biochimie 90*, 1172−1183.

(26) Parkinson, G. N., Lee, M. P., and Neidle, S. (2002) Crystal structure of parallel quadruplex from human telomeric DNA. *Nature 417*, 876−880.

(27) Phan, A. T., Kuryavyi, V., and Patel, D. J. (2006) DNA architecture: from G to Z. *Curr. Opin. Struct. Biol. 16*, 288−298.

(28) Petraccone, L., Trent, J. O., and Chaires, J. B. (2008) The tail of the telomere. *J. Am. Chem. Soc. 130*, 16530−16532.

(29) Yang, D., and Okamoto, K. (2010) Structural insights into G-quadruplexes: towards new anticancer drugs. *Future Med. Chem. 2*, 619−646.

(30) Bhattacharya, S., and Chaudhuri, P. (2008) Medical implications of benzimidazole derivatives as drugs designed for targeting DNA and DNA associated processes. *Curr. Med. Chem. 15*, 1762−1777.
(31) Jain, A. K., and Bhattacharya, S. (2010) Groove binding ligands for interaction with non B-DNA duplex and triplex DNA. *Bioconjugate Chem. 21*, 1389−1403.
(32) Fuertes, M. A., Castilla, J., Alonso, C., and Perez, J. M. (2002) Novel concepts in the development of platinum antitumor drugs. *Curr. Med. Chem. - Anti-Cancer Agents 2*, 539−551.
(33) Neidle, S. (1981) The molecular bases for the action of some DNA-binding drugs. *Prog. Med. Chem. 16*, 151−221.
(34) Thomas, M., Varshney, U., and Bhattacharya, S. (2002) Distamycin analogs without leading amide at the N-terminus: Comparative binding properties to AT and GC rich DNA sequences. *Eur. J. Org. Chem.*, 3604−3615.
(35) Bhattacharya, S., and Thomas, M. (2000) Facile synthesis of oligopeptide distamycin analogs devoid of hydrogen bond donors or acceptors at the N-terminus: Sequence-specific duplex DNA binding as a function of peptide chain length. *Tetrahedron Lett. 41*, 5571−5575.
(36) Bhattacharya, S., and Thomas, M. (2001) DNA recognition by the first *tail-to-tail* linked distamycin-like oligopeptide dimers. *Chem. Commun.*, 1464−1465.
(37) Tawar, U., Jain, A. K., Dwarakanath, B. S., Chandra, R., Singh, Y., Chaudhury, N. K., Khaitan, D., and Tandon, V. (2003) Influence on phenyl ring disubstitution on bisbenzimidazole and terbenzimidazole cytotoxicity: Synthesis and biological evaluation as radioprotectors. *J. Med. Chem. 46*, 3785−3792.
(38) Tawar, U., Jain, A. K., Chandra, R., Singh, Y., Dwarakanath, B. S., Chaudhury, N. K., Good, L., and Tandon, V. (2003) Minor groove binding DNA ligands with expanded A/T sequence length recognition, selective binding to bent DNA regions and enhanced fluorescent properties. *Biochemistry 42*, 13339−13346.
(39) Jain, A. K., Gupta, S. K., and Tandon, V. (2009) Evaluation of electronic effect of phenyl ring substituents on the DNA minor groove binding properties of novel bis and terbenzimidazoles: Synthesis and spectroscopic studies of ligand-DNA interaction. *Oligonucleotides 19*, 329−340.
(40) Ghosh, S., Usharani, D., Paul, A., De, S., Jemmis, E. D., and Bhattacharya, S. (2008) Design, synthesis, and DNA binding properties of photoisomerizable azobenzene-distamycin conjugates: An experimental and computational study. *Bioconjugate Chem. 19*, 2332−2345.
(41) Ghosh, S., Defrancq, E., Lhomme, J. H., Dumy, P., and Bhattacharya, S. (2004) Efficient conjugation and characterization of distamycin based peptides with selected oligonucleotide stretches. *Bioconjugate Chem. 15*, 520−529.
(42) Bhattacharya, S., and Thomas, M. (2000) DNA binding properties of novel distamycin analogs that lack the leading amide unit at the N-terminus. *Biochem. Biophys. Res. Commun. 267*, 139−144.
(43) Jain, A. K., Awasthi, S. K., and Tandon, V. (2006) Triple helix stabilization by covalently linked DNA−bisbenzimidazole conjugate synthesized by maleimide−thiol coupling chemistry. *Bioorg. Med. Chem. 14*, 6444−6452.
(44) Jain, A. K., and Bhattacharya, S. (2011) Recent developments in the chemistry and biology of G-quadruplexes with reference to the DNA groove binders. *Curr. Pharm. Des.*, in press.
(45) Arora, A., Balasubramanian, C., Kumar, N., Agrawal, S., Ojha, R. P., and Maiti, S. (2008) Binding of berberine to human telomeric quadruplex − spectroscopic, calorimetric and molecular modeling studies. *FEBS J. 275*, 3971−3983.
(46) Phillips, K., Dauter, Z., Murchie, A. I. H., Lilley, D. M. J., and Luisi, B. (1997) The crystal structure of a parallel-stranded guanine tetraplex at 0.95Å resolution. *J. Mol. Biol. 273*, 171−182.
(47) Han, H., Langley, D. R., Rangan, A., and Hurley, L. H. (2001) Selective interactions of cationic porphyrins with G-quadruplex structures. *J. Am. Chem. Soc. 123*, 8902−8913.
(48) Wang, Y., and Patel, D. J. (1992) Guanine residues in d(T_2AG_3) and d(T_2G_4) form parallel-stranded potassium cation stabilized G-quadruplexes with anti glycosidic torsion angles in solution. *Biochemistry 31*, 8112−8119.
(49) Wang, Y., and Patel, D. J. (1993) Solution structure of a parallel-stranded G-quadruplex DNA. *J. Mol. Biol. 234*, 1171−1183.
(50) Read, M. A., Harrison, R. J., Romagnoli, B., Tanious, F. A., Gowan, S. H., Reszka, A. P., Wilson, W. D., Kelland, L. R., and Neidle, S. (2001) Structure-based design of selective and potent G quadruplex-mediated telomerase inhibitors. *Proc. Natl. Acad. Sci. U.S.A. 98*, 4844−4849.
(51) Yang, D.-Y., Chang, T.-C., and Sheu, S.-Y. (2007) Interaction between human telomere and a carbazole derivative: A molecular dynamics simulation of a quadruplex stabilizer and telomerase inhibitor. *J. Phys. Chem. A 111*, 9224−9232.
(52) Nambiar, M., Goldsmith, G., Moorthy, B. T., Lieber, M. R., Joshi, M. V., Choudhary, B., Hosur, R. V., and Raghavan, S. C. (2011) Formation of a G-quadruplex at the BCL2 major breakpoint region of the t(14;18) translocation in follicular lymphoma. 936−948. *Nucleic Acids Res. 39*, 936−948.
(53) Rawal, P., Kummarasetti, V. B. R., Ravindran, J., Kumar, N., Halder, K., Sharma, R., Mukerji, M., Das, S. K., and Chowdhury, S. (2006) Genome-wide prediction of G4 DNA as regulatory motifs: Role in *Escherichia coli* global regulation. *Genome Res. 16*, 644−655.
(54) Du, Z., Zhao, Y., and Li, N. (2009) Genome-wide colonization of gene regulatory elements by G4 DNA motifs. *Nucleic Acids Res. 37*, 6784−6798.
(55) Verma, A., Yadav, V. K., Basundra, R., Kumar, A., and Chowdhury, S. (2009) Evidence of genome-wide G4 DNA-mediated gene expression in human cancer cells. 4194−4204. *Nucleic Acids Res. 37*, 4194−4204.
(56) Du, Z., Zhao, Y., and Li, N. (2008) Genome-wide analysis reveals regulatory role of G4 DNA in gene transcription. *Genome Res. 18*, 233−241.
(57) Cogoi, S., Paramasivam, M., Filichev, V., Geci, I., Pedersen, E. B., and Xodo, L. E. (2009) Identification of a new G-quadruplex motif in the *KRAS* promoter and design of pyrene-modified G4-decoys with antiproliferative activity in pancreatic cancer cells. *J. Med. Chem. 52*, 564−568.
(58) Fry, M. (2007) Tetraplex DNA and its interacting proteins. *Front. Biosci. 12*, 4336−4351.
(59) Paramasivam, M., Membrino, A., Cogoi, S., Fukuda, H., Nakagama, H., and Xodo, L. E. (2009) Protein hnRNP A1 and its derivative Up1 unfold quadruplex DNA in the human KRAS promoter: implications for transcription. *Nucleic Acids Res. 37*, 2841−2853.
(60) Thakur, R. K., Kumar, P., Halder, K., Verma, A., Kar, A., Parent, J.-L., Basundra, R., Kumar, A., and Chowdhury, S. (2009) Metastases suppressor NM23-H2 interaction with G-quadruplex DNA within c-MYC promoter nuclease hypersensitive element induces c-MYC expression. *Nucleic Acids Res. 37*, 172−183.
(61) Phan, A. T., Kuryavyi, V., Ma, J. B., Faure, A., Andreola, M. L., and Patel, D. J. (2005) An interlocked dimeric parallel-stranded DNA quadruplex: a potent inhibitor of HIV-1 integrase. *Proc. Natl. Acad. Sci. U.S.A. 102*, 634−639.
(62) Kerwin, S. M. (2000) G-quadruplex DNA as a target for drug design. *Curr. Pharm. Des. 6*, 441−478.
(63) Chaudhuri, P., Ganguly, B., and Bhattacharya, S. (2007) An experimental and computational analysis on the differential role of the positional isomers of symmetric bis-2-(pyridyl)-1*H*-benzimidazoles as DNA binding agents. *J. Org. Chem. 72*, 1912−1923.
(64) Maiti, S., Chaudhury, N. K., and Chowdhury, S. (2003) Hoechst 33258 binds to G-quadruplex in the promoter region of human c-myc. *Biochem. Biophys. Res. Commun. 310*, 505−512.
(65) Phan, A. T., Kuryavyi, V., Gaw, H. Y., and Patel, D. J. (2005) Small-molecule interaction with a five-guanine-tract G-quadruplex structure from the human MYC promoter. *Nat. Chem. Biol. 1*, 167−163.
(66) Chen, Z., Zheng, K-w., Hao, Y-h., and Tan, Z. (2009) Reduced or diminished stabilization of the telomere G-quadruplex and

inhibition of telomerase by small chemical ligands under molecular crowding condition. *J. Am. Chem. Soc. 131*, 10430−10438.
(67) Li, G., Huang, J., Zhang, M., Zhou, Y., Zhang, D., Wu, Z., Wang, S., Weng, X., Zhou, X., and Yang, G. (2008) Bis(benzimidazole)-pyridine derivative as a new class of G-quadruplex inducing and stabilizing ligand. *Chem. Commun.*, 4564−4566.
(68) Huang, J., Li, G., Wu, Z., Song, Z., Zhou, Y., Shuai, L., Weng, X., Zhou, X., and Yang, G. (2009) Bisbenzimidazole to benzobisimidazole: from binding B-form duplex DNA to recognizing different modes of telomere G-quadruplex. *Chem. Commun.*, 902−904.
(69) Bhattacharya, S., Chaudhuri, P., Jain, A. K., and Paul, A. (2010) Symmetrical bisbenzimidazoles with benzenediyl spacer: The role of the shape of the ligand on the stabilization and structural alterations in telomeric G-quadruplex DNA and telomerase inhibition. *Bioconjugate Chem. 21*, 1148−1159.
(70) Jain, A. K., Reddy, V. V., Paul, A., Muniyappa, K., and Bhattacharya, S. (2009) The synthesis and evaluation of a novel class of G-quadruplex stabilizing small molecules based on 1, 3-Phenylene-bis (piperazinyl benzimidazole) system. *Biochemistry 48*, 10693−10704.
(71) Randazzo, A., Galeone, A., Esposito, V., Varra, M., and Mayol, L. (2002) Interaction of distamycin A and netropsin with quadruplex and duplex structures: a comparative 1H-NMR study. *Nucleosides, Nucleotides, Nucleic Acids 21*, 535−545.
(72) Randazzo, A., Galeone, A., and Mayol, L. (2001) ^{1}H-NMR study of the interaction of distamycin A and netropsin with the parallel stranded tetraplex $[d(TGGGGT)]_4$. *Chem. Commun. 11*, 1030−1031.
(73) Martino, L., Virno, A., Pagano, B., Virgilio, A., Di Micco, S., Galeone, A., Giancola, C., Bifulco, G., Mayol, L., and Randazzo, A. (2007) Structural and thermodynamic studies of the interaction of distamycin A with the parallel quadruplex structure $[d(TGGGGT)]_4$. *J. Am. Chem. Soc. 129*, 16048−16056.
(74) Cocco, M. J., Hanakahi, L. A., Huber, M. D., and Maizels, N. (2003) Specific interactions of distamycin with G-quadruplex DNA. *Nucleic Acids Res. 31*, 2944−2951.
(75) David, W. M., Brodbelt, J., Kerwin, S. M, and Thomas, P. W. (2002) Investigation of quadruplex oligonucleotide-Drug interactions by electrospray ionization mass spectrometry. *Anal. Chem. 74*, 2029−2033.
(76) Pagano, B., Fotticchia, I., Tito, S., De Mattia, C. A., Mayol, L., Novellino, E., Randazzo, A., and Giancola, C. (2010) Selective binding of distamycin A derivative to G-quadruplex structure [d(TGGGGT)]-4. *J. Nucleic. Acids*, doi:10.4061/2010/247137.
(77) Pagano, B., Virno, A., Mattia, C. A., Mayol, L., Randazzo, A., and Giancola, C. (2008) Targeting DNA quadruplexes with distamycin A and its derivatives: An ITC and NMR study. *Biochimie 90*, 1224−1232.
(78) Pagano, B., Mattia, C. A., Virno, A., Randazzo, A., Mayol, L., and Giancola, C. (2007) Thermodynamic analysis of quadruplex DNA-drug interaction. *Nucleosides, Nucleotides, Nucleic Acids 26*, 761−765.
(79) Moore, M. J. B., Cuenca, F., Searcey, M., and Neidle, S. (2006) Synthesis of distamycin A polyamides targeting G-quadruplex DNA. *Org. Biomol. Chem. 4*, 3479−3488.
(80) Zhou, J., Yuan, G., Liu, J., and Zhan, C.-G. (2007) Formation and stability of G-quadruplexes self-assembled from guanine-rich strands. *Chem.—Eur. J. 13*, 945−949.
(81) Li, H., Liu, Y., Lin, S., and Yuan, G. (2009) Spectroscopy probing of the formation, recognition, and conversion of a G-quadruplex in the promoter region of the bcl-2 oncogene. *Chem.—Eur. J. 15*, 2445−2452.
(82) Zaffaroni, N., Lualdi, S., Villa, R., Bellarosa, D., Cermele, C., Felicetti, P., Rossi, C., Orlandi, L., and Daidone, M. G. (2002) Inhibition of telomerase activity by a distamycin derivative: effects on cell proliferation and induction of apoptosis in human cancer cells. *Eur. J. Cancer 38*, 1792−1801.
(83) Cosconati, S., Marinelli, L., Trotta, R., Virno, A., Tito, S. D., Romagnoli, R., Pagano, B., Limongelli, V., Giancola, C., Baraldi, P. G., Mayol, L., Novellino, E., and Randazzo, A. (2010) Structural and conformational requisites in DNA quadruplex groove binding: Another piece to the puzzle. *J. Am. Chem. Soc. 132*, 6425−6433.
(84) Han, X., Li, C., Mosher, M. D., Rider, K. C., Zhou, P., Crawford, R. L., Fusco, W., Paszczynski, A., and Natale, N. R. (2009) Design, synthesis and biological evaluation of a novel class of anticancer agents: Anthracenylisoxazole lexitropsin conjugates. *Bioorg. Med. Chem. 17*, 1671−1680.
(85) Rahman, K. M., Reszka, A. P., Gunaratnam, M., Haider, S. M., Howard, P. W., Fox, K. R., Neidle, S., and Thurston, D. E. (2009) Biaryl polyamides as a new class of DNA quadruplex-binding ligands. *Chem. Commun.*, 4097−4099.
(86) Garoff, R. A., Litzinger, E. A., Connor, R. E., Fishman, I., and Armitage, B. A. (2002) Helical aggregation of cyanine dyes on DNA templates: effect of dye structure on formation of homo- and heteroaggregates. *Langmuir 18*, 6330−6337.
(87) Chen, Q., Kuntz, I. D., and Shafer, R. H. (1996) Spectroscopic recognition of guanine dimeric hairpin quadruplexes by a carbocyanine dye. *Proc. Natl. Acad. Sci. U.S.A. 93*, 2635−2639.
(88) Cheng, J.-Y., Lin, S.-H., and Chang, T.-C. (1998) Vibrational investigation of DODC cation for recognition of guanine dimeric hairpin quadruplex studied by satellite holes. *J. Phys. Chem. B 102*, 5542−5546.
(89) Chiang, C.-C., Cheng, J.-Y., and Chang, T.-C. (1999) Satellite hole spectral method and its applications to dye−DNA complexes. *Proc. Natl. Sci. Counc. Repub. China, Part A 23*, 679−694.
(90) Kerwin, S. M., Sun, D., Kern., J. T., Rangan, A., and Thomas, P. W. (2001) G-quadruplex DNA binding by a series of carbocyanine dyes. *Bioorg. Med. Chem. Lett. 11*, 2411−2414.
(91) White, E. W., Tanious, F., Ismail, M. A., Reszka, A. P., Neidle, S., Boykin, D. W., and Wilson, W. D. (2007) Structure-specific recognition of quadruplex DNA by organic cations: influence of shape, substituents and charge. *Biophys. Chem. 126*, 140−153.
(92) Paramasivan, S., and Bolton, P. H. (2008) Mix and measure fluorescence screening for selective quadruplex binders. *Nucleic Acids Res. 36*, e106.
(93) Yang, Q., Xiang, J., Yang, S., Zhou, Q., Li, Q., Tang, Y., and Xu, G. (2009) Verification of specific G-quadruplex structure by using a novel cyanine dye supramolecular assembly: I. recognizing mixed G-quadruplex in human telomeres. *Chem. Commun.*, 1103−1105.
(94) Yang, Q., Xiang, J., Yang, S., Li, Q., Zhou, Q., Guan, A., Zhang, X., Zhang, H., Tang, Y., and Xu, G. (2010) Verification of specific G-quadruplex structure by using a novel cyanine dye supramolecular assembly: II. The binding characterization with specific intramolecular G-quadruplex and the recognizing mechanism. *Nucleic Acids Res. 38*, 1022−1033.
(95) Tuesuwan, B., Kern, J. T, Thomas, P. W., Rodriguez, M., Li., J., David, W. M., and Kerwin, S. M. (2008) Simian virus 40 large T-antigen G-quadruplex DNA helicase inhibition by G-quadruplex DNA-interactive agents. *Biochemistry 47*, 1896−1909.
(96) Fu, W., Begley, J. G., Killen, M. W., and Mattson, M. P. (1999) Anti-apoptotic role of telomerase in pheochromocytoma cells. *J. Biol. Chem. 274*, 7264−7271.
(97) Li, C. P., Huang, J. H, Chang, A. C., Hung, Y. M., Lin, C. H., Chao, Y., Lee, S. D., Whang-Peng, J., and Huang, T. S. (2004) A G-quadruplex ligand 3, 30-diethyloxadicarbocyanine iodide induces mitochondrionmediated apoptosis but not decrease of telomerase activity in nasopharyngeal carcinoma NPC-TW01 cells. *Pharm. Res. 21*, 93−100.
(98) Yao, Y., Wang, Q., Hao, Yu-h., and Tan, Z. (2007) An exonuclease I hydrolysis assay for evaluating G-quadruplex stabilization by small molecules. *Nucleic Acids Res. 35*, e68.
(99) Zhang, Y., Cao, E.-H., Liang, X.-Q., and Qin, J.-F. (2003) Increasing sensitivity to arsenic trioxide-induced apoptosis by altered telomere state. *Eur. J. Pharmacol. 474*, 141−147.
(100) Naasani, I., Seimiya, H., Yamori, T., and Tsuruo, T. (1998) Screening for antitelomerase agents with the aid of COMPARE analysis. *Proc. Am. Assoc. Cancer Res. 39*, 3854.
(101) Huppert, J. L., and Balasubramanian, S. (2005) Prevalence of quadruplexes in the human genome. *Nucleic Acids Res. 33*, 2908−2916.

(102) Millar, K. M., and Rodriguez, R. (2011) G-quadruplexes: selective DNA targeting for cancer therapeutics? *Expert Rev. Clin. Pharmacol. 4*, 139−142.
(103) Folini, M., Venturini, L., Cimino-Reale, G., and Zaffaroni, N. (2011) Telomeres as targets for anticancer therapies. *Expert Opin. Ther. Targets 15*, 579−593.
(104) Leonetti, C., Scarsella, M., Riggio, G., Rizzo, A., Salvati, E., DIncalci, M., Staszewsky, L., Frapolli, R., Stevens, M. F., Stoppacciaro, A., Mottolese, M., Antoniani, B., Gilson, E., Zupi, G., and Biroccio, A. (2008) G-Quadruplex ligand RHPS4 potentiates the antitumoractivity of camptothecins in preclinical models of solid tumors. *Clin. Cancer Res. 14*, 7284−7291.
(105) Gomez, D., Wenner, T., Brassart, B., Douarre, C., O'Donohue, M.-F., El Khoury, V., Shin-ya, K., Morjani, H., Trentesaux, C., and Riou, J.-F. (2006) Telomestatin-induced telomere uncapping is modulated by POT1 through G-overhang extension in HT1080 human tumor cells. *J. Biol. Chem. 281*, 38721−38729.
(106) Tsai, Y-C, Qi, H, Lin, C-P, Lin, C.-P., Lin, R.-K., Kerrigan, J. E., Rzuczek, S. G., Edmond J. LaVoie, E. J., Rice, J. E., Pilch, D. S., Lyu, Y. L., and Liu, L. F. (2009) A G-quadruplex stabilizer induces M-phase cell cycle arrest. *J. Biol. Chem. 284*, 22535−22543.
(107) Burger, A. M., Dai, F., Schultes, C. M., Reszka, A. P., Moore, M. J., Double, J. A., and Neidle, S. (2005) The G-quadruplex-interactive molecule BRACO-19 inhibits tumor growth, consistent with telomere targeting and interference with telomerase function. *Cancer Res. 65*, 1489−1496.
(108) Drygin, D., Siddiqui-Jain, A., O'Brien, S., Schwaebe, M., Lin, A., Bliesath, J., Ho, C. B., Proffitt, C., Trent, K., Whitten, J. P., Lim, J. K. C., Von Hoff, D., Anderes, K., and Rice, W. G. (2009) Anticancer activity of CX-3543: a direct inhibitor of rRNA biogenesis. *Cancer Res. 69*, 7653−7661.
(109) Pennarun, G., Granotier, C., Gauthier, L. R., Gomez, D., and Boussin, F. D. (2005) Apoptosis related to telomere instability and cell cycle alterations in human glioma cells treated by new highly selective G-quadruplex ligands. *Oncogene 24*, 2917−2928.
(110) Riou, J. F., Guittat, L., Mailliet, P., Laoui, A., Renou, E., Petitgenet, O., Megnin-Chanet, F., Helene, C., and J. L. Mergny, J. L. (2002) Cell senescence and telomere shortening induced by a new series of specific G-quadruplex DNA ligands. *Proc. Natl. Acad. Sci. U.S.A. 99*, 2672−2677.
(111) Huppert, J. L. (2007) Four-stranded DNA: cancer, gene regulation and drug development. *Philos. Trans. R. Soc. A 365*, 2969−2984.
(112) Franklin, S. A., and Barton, J. K. (1998) Differential DNA recognition by the enantiomers of 1-Rh $(MGP)_2$phi: A combination of shape selection and direct readout. *Biochemistry 37*, 16093−16105.
(113) Koya, K., Li, Y., Wang, H., Ukai, T., Tatsuta, N., Kawakami, M., Shishido, T., and Chen, L. B. (1996) MKT-077, a novel rhodacyanine dye in clinical trials, exhibits anticarcinoma activity in preclinical studies based on selective mitochondrial accumulation. *Cancer Res. 56*, 538−543.
(114) Kawakami, M., Koya, K., Ukai, T., Tatsuta, N., Ikegawa, A., Ogawa, K., Shishido, T., and Chen, L. B. (1998) Structure−activity of novel rhodacyanine dyes as antitumor agents. *J. Med. Chem. 41*, 130−142.

Bioconjugate Chemistry

Communication

pubs.acs.org/bc

DNA-Encoded Signal Conversion for Sensitive Microgravimetric Detection of Small Molecule–Protein Interaction

Yue-Hua Fei,[†] Dengyou Liu,[‡] Zai-Sheng Wu,*[,†] Guo-Li Shen,*[,†] and Ru-Qin Yu[†]

[†]State Key Laboratory of Chemo/Biosensing and Chemometrics, Chemistry and Chemical Engineering College, Hunan University, Changsha 410082, P R China

[‡]Science College of Hunan Agricultural University, Changsha 410128, PR China

Supporting Information

ABSTRACT: Identification and quantification of small organic molecules capable of binding to a protein of interest with reasonable affinity and specificity is a central problem. Via developing DNA-encoded recognizing probe, we validate a proof-of-principle for constructing of small target-to-DNA conversion that screens the small molecule–protein interaction. Successful identification of β-indole acetic acid, abscisic acid, or 2,4-dichlorophenoxyacetic acid/corresponding antibody binding implies its fascinating potential for interrogating small molecule/protein interaction.

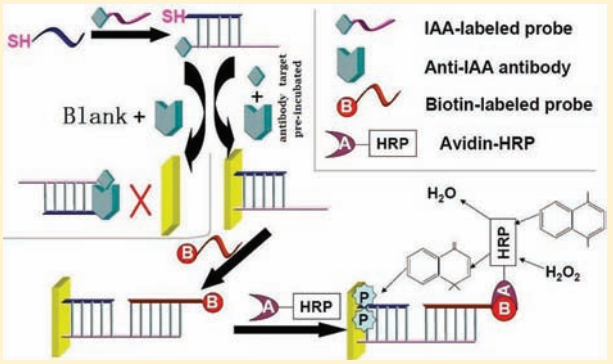

The identification and quantification of small organic molecules capable of binding to a protein of interest with reasonable affinity and specificity is a central problem in chemistry, biology, and medicine. Although spectroscopic and chromatographic measurements for the exploration of small-molecule/protein interaction and detection of small molecules have achieved impressive results,[1−5] these traditional techniques generally require expensive instrument, specific signal reporters, or cumbersome assay procedures. Thus, the development of a universal protocol for the convenient, cost-effective, sensitive, and selective detection of small molecules remains a compelling need. Considering the enormous capabilities[6−11] of oligonucleotides in site-specific labeling, sequence-specific biobarcoding, versatile amplification, and isolation, the DNA-encoded oligonucleotide probe has emerged as an appealing tool for the construction and screening of large chemical libraries.[12] However, for the existing aptameric screening systems, the ability of aptamer probes to convert the probes/target molecule binding into a measurable signal is highly dependent on their conformational change originating from the formation of the target binding pockets.[5,13−17] Moreover, aptamers are the greatly appreciated binding molecules against the corresponding targets. To meet the requirements of many technological applications, it would be desirable to introduce a universal signaling scheme for detecting some organic ligands with low molecular weight (e.g., oligonucleotides and non-nucleic acid biomolecules).[18] Inspired by the biological behavior change (for example, susceptibility to enzymatic cleavage[6,19] or polymerization[20]) of original or modified oligonucleotide probes upon binding to specific target molecules, utilizing microgravimetric quartz-crystal-microbalance, we proposed a novel signaling scheme for investigating the interaction of small molecule with specific protein. This screening scheme is based on the design of a target molecule-linked DNA hybrid that is responsible for the transduction of common immunoreaction into the specific oligonucleotide detection. The present "signal-on" microgravimetric biosensor can not only screen the small target molecule, but also provide quantitative analysis with desirable analytical features (e.g., low detection limit, high sensitivity, and selectivity, as well as a wide dynamic range and cost-effectiveness).

Phytohormone screening is considerably significant to agriculture, horticulture, and other related fields. Considering the pressing needs for the precise and sensitive measurements, β-indole acetic acid (IAA), a small plant hormone molecule regulating the plant growth was used as the model target molecule for testing proposed analytical technique. It is well-known that the characteristics of sensing platform are highly dependent on the signaling format. Namely, the "signal-on" reporting mechanism is superior to the "signal-off" one in terms of the detection sensitivity and working range. Although the sandwich immunoassay format is promising for sensitively detecting the target antigen, small molecules cannot simultaneously interact with two antibodies, precluding their inter-

Received: February 16, 2011
Revised: September 9, 2011
Published: October 13, 2011

ACS Publications © 2011 American Chemical Society

rogation by "signal-on" two-site immunoassay including the powerful "immuno-PCR" amplification technique.[21] In the present communication, the change in the self-assembly behavior of thiolated small molecule-tethered DNA hybrid, which is closely related with the presence of target analyte in sample, was employed to translate the interaction of antibody with small molecules into microgravimetric sigal. The DNA sequences involved in the encoding oligonucleotide-based sensing are detailed in Table 1. The screening principle of

Table 1. Oligonucleotides Designed in This Study[a]

Oligonucleotide name	Sequence (5'-3')
Assembling probe	GGCAGGATCGGACAGC-SH
Steric hindrance-related probe (recognition probe being attached to IAA)	NH_2-GCTGTCCGATCCTGCCACTCTGACGAGCT ACTGACC
Signaling probe	Biotin-TTTGGTCAGTAGCTCGTCAG

[a]The assembling probe is modified with thiol group at the 3′ end to self-assemble onto the surface of quartz-crystal-microbalance (QCM). The steric hindrance-related probe is functionalized with amino groups at the 5′ end in order to prepare recognition probes by being covalently attached to IAA molecule containing a COOH moiety; the signaling probe is biotinylated at the 5′ end to capture the avidin-HRP conjugate. Because two underlined segments are complementary to each other as the shaded parts behave, the three sequences are designed to form the sandwich hybrid complex via hybridization reaction.

the microgravimetric assay platform that converts the presence of target small molecules into the appearance of DNA probes (defined as small target-to-DNA conversion), as well as the signaling procedure, is illustrated in Scheme 1. The proposed

Scheme 1. Schematic Diagram of the Amplified Detection of IAA

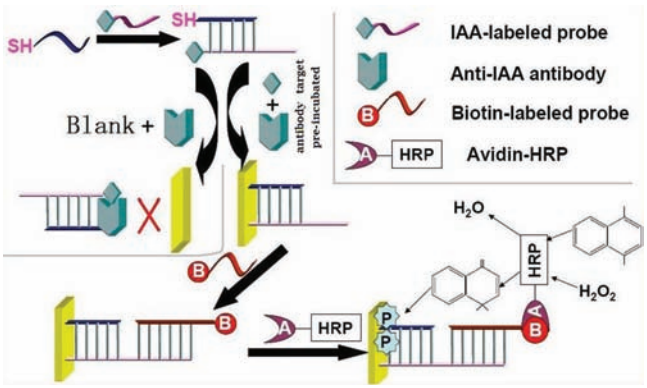

scheme is essentially a competitive assay between the labeled and free small molecule, which compete for binding the antibody protein. When adding target molecule sample, the free IAA can bind to the anti-IAA antibody protein by preincubating in a solution, inhibiting the formation of antibody/IAA-labeled probe (also called recognition probe)/assembling probe complex in the subsequence step. Namely, the IAA attached to recognition probe/assembling probe hybrid cannot interact with antibody because the binding site of antibody is occupied by free IAA. In this case, the thiol of assembling probe can randomly run into the quartz-crystal-microbalance (QCM) surface, resulting in the s-Au bond. Thus, the recognition probe is easily captured on the surface. It is well-known that the rigid DNA duplex is easier to immobilize onto the gold substrate in a spatially ordered manner than a flexible single-stranded DNA molecule. Naturally, during this step, not only is the intrinsic self-assembly behavior of the thiolated probe maintained, but hybridization of this probe with the recognition probe can also improve the capability to self-assembly on the QCM surface. Subsequently, the biotin-labeled probe can be immobilized on the resulting surface of QCM (also used as an electrode when performing the electrochemical measurements to characterize the sensing interfaces at different stages of target detection) via specific hybridization to the fragment close to the 3′ end. As a result, the avidin-HRP is capable of being adsorbed onto the resultant QCM via the biotin−avidin bridge. In the presence of H_2O_2, the HRP-biocatalyzed oxidation of 4-chloro-1-naphthol occurs and the precipitation of the insoluble product is produced on the support surfaces, generating an enhanced mass or electrochemical signal (this process is called the signal amplification step, only involved during evaluation of the features of the proposed microgravimetric sensing platform). In contrast, in the absence of IAA in the sample, the assembling probe/recognition probe conjugate can interact with antibody protein, forming the triplex. Because the thiol group is designed to be in close proximity to the terminal IAA of recognition probe, binding of the recognition probe to the antibody protein, a large biomolecule, can cause steric hindrance serving as the barrier to the self-assembly of a thoil-labeled assembling probe/recognition probe hybrid. As a result, encoding DNA is not adsorbed onto the QCM surface. This is capable of inhibiting the subsequent transducing reaction and amplification process. In this case, no signal is observed. Apparently, via encoding the information on the IAA/antibody interaction and decoding the appearance of DNA recognition probe, a versatile amplification route for exploring small molecule/protein interaction in a "signal-on" manner is developed. The developed small target-to-DNA conversion scheme is described in detail in the text; the characterization of the resulting microgravimetric transducer is represented; the screening ability is validated and primary application is evaluated to afford convincing evidence for the reliability and practicality of the proposed fluorescence assay.

The rationality of the proposed design for screening the small molecule/protein interaction is validated by the impedance data. As shown in Figure 1, even if the biomolecules confined on the electrode surfaces are different from each other, each attachment of the molecules involved can consistently induce a considerable increase in the electrochemical impedance, indicating the expected attachment and bioactivity of surface-confined biomolecules. Considering the intrinsic feature of biomolecules and binding affinity at different stages, it is reasonable that a different change in impedance is observed. For example, compared with the difference between lines a and b, line c does not exhibit a significant increase. This should be attributed to the fact that the signaling probe has no large moiety (e.g., HRP) and is immobilized via hybridizing to the surface-confined recognition probe rather than self-assembling directly onto the electrode surface as the thiolated probe/recognition probe hybrid does. Moreover, due to the shorter base sequence, the amount of its negative charge is smaller than the overall value of assembling probe/recognition probe conjugate, generating the comparatively weak electrostatic repulsion between dissolved ferricyanide and resultant electrode. In contrast, substantial increase in impedance is observed for line e compared with all other lines. This is

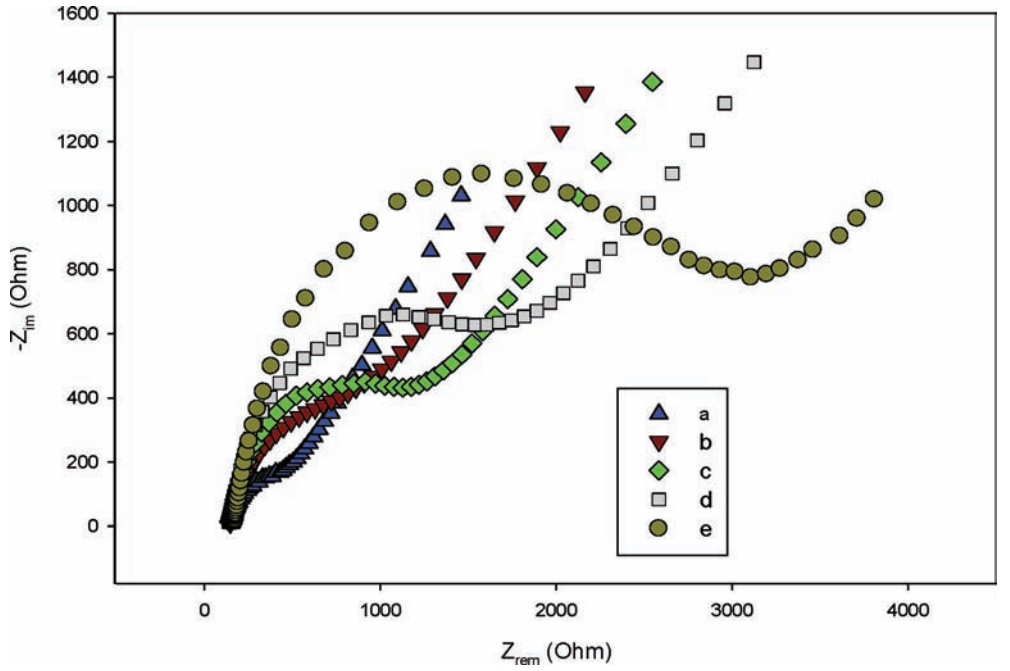

Figure 1. Nyquist diagram of Faradic impedance measurements collected for the same QCM with different modified surfaces corresponding to the following: (a) the bare QCM; (b) the self-assembly of the mixture of tube 1 and tube 2 onto the QCM (see the experimental section for the details); (c) hybridization of the surface b with signaling probe; (d) exposure of interface c to HRP-avidin; (e) the same as interface d but with the biocatalyzed deposition in the presence of 1×10^{-3} M 4-chloro-1-naphthol and 1.5×10^{-4} M H_2O_2. The IAA concentration of 20 μM is involved in this section.

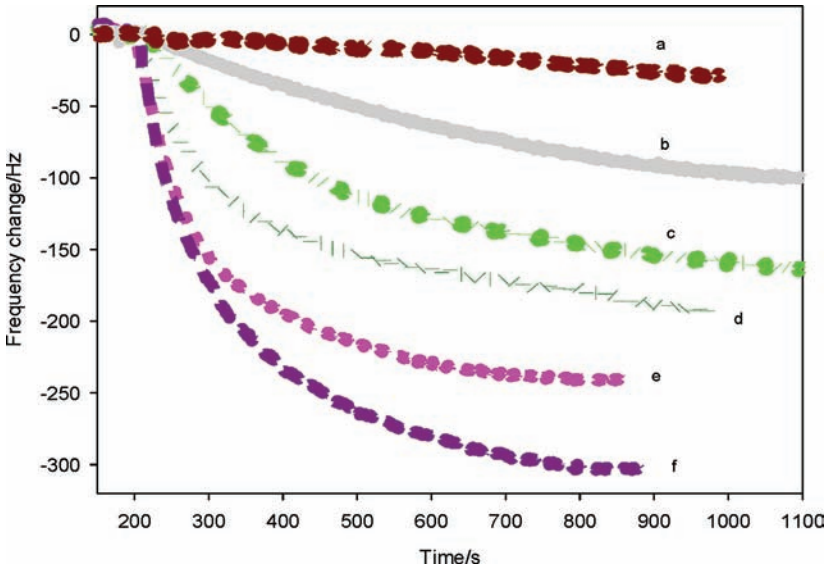

Figure 2. Capability of microgravimetric quartz-crystal-microbalance transducer. The lines indicate typical characteristics of frequency responses in the absence (a,b) and presence of 0.2 μM IAA (c), 0.4 μM IAA (d), 2 μM IAA (e), and 20 μM IAA (f) under given conditions. Note that line a corresponding to the blank sample has no HRP-avidin compared with line b.

because the biocatalyzed precipitation of the insoluble product can directly electrically insulate the electrode surface. As an effective technique to probe the interface properties of functionalized electrodes, the measured data by impedance spectroscopy provide the strong evidence that the proposed screening strategy can efficiently work.

To confirm the feasibility of the DNA encoding-based sensing scheme, the interactions between the IAA at the different concentrations and the constant concentration of antibody protein are monitored in a real-time manner. The measured data are shown in Figure 2. The frequency change directly reflects the amount of biocatalyzed insoluble precipitation by avidin-HRP, which is associated with the content of surface-confined assembling probe/recognition probe hybrid that is highly dependent on the number of target in solution. Thus, the frequency shift is employed to evaluate the small molecule/protein interaction. The experimental data clearly shows that the presence of IAA can rapidly induce the frequency shift especially in the first period of time (e.g., line c), and the higher concentration of IAA results in the larger

dx.doi.org/10.1021/bc200086c | *Bioconjugate Chem.* 2011, 22, 2369–2376

frequency change (e.g., line e), indicating a success in screening the interaction of small molecules with protein. Assuming there is a dynamic equilibration between IAA/antibody complex and free IAA and antibody, increasing the concentration of IAA in the sample can promote the formation of antibody/IAA complex. Naturally, this decreases the amount of antibody that can bind to the IAA-labeled assembling probe/recognition probe hybrid. Consequently, more recognition probes can be immobilized onto the substrate surfaces, finally generating a larger frequency shift. Although the blank sample produces a slight frequency shift (line b), it can be easily distinguished from target samples even at the low concentration (line c). The unwanted frequency change should be attributed to the nonspecific adsorption avidin-HRP onto the QCM surface and/or other factors. Frequency shift upon the blank is expected to be alleviated (see the following section for the further discussion). Taking into account the observation that frequency shift corresponding to target samples especially at the high concentration (e.g., line f) tends to stabilize after 800 s, this incubation time is selected in the subsequent experiments (this data-processing method is called the steady-state measurement) though the blank sample (line b) can make the crystal frequency further rise after this response point.

To exactly evaluate the utility of the small target-to-DNA conversion-based sensing protocol for the quantification of small molecule, the IAA at various concentrations were detected under identical conditions and a dose−response curve was constructed. The results are described in Figure 3.

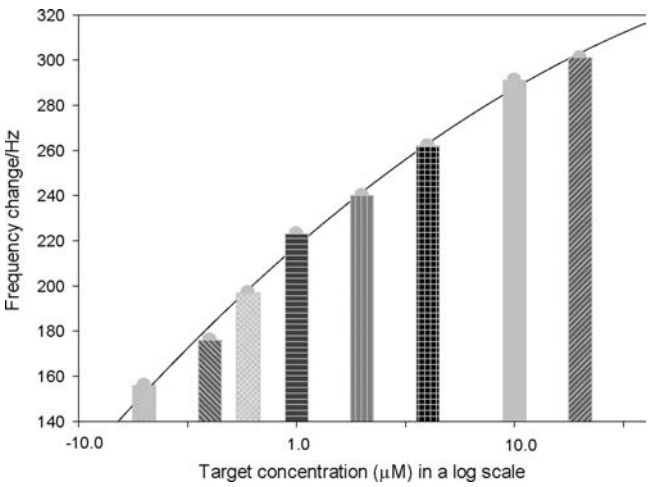

Figure 3. Calibration curve describing the relationship between the frequency responses and the concentration of IAA under given conditions. The curves are expressed as the frequency decreases against the logarithm of IAA concentration. The regression equation is $Y = 217.6 + 83.57X - 13.71X^2$ with a correlation coefficient of 0.9947, where Y represents the difference between recorded frequency values after and before injecting biocatalytic deposition solution, while X is the logarithm of IAA concentration, respectively. The largest relative standard deviation of three measurements performed for samples is not more than 7.5%. The detection limit is 0.1 μM, which is defined as three times the standard deviation corresponding to the blank sample measurement.

The detection limit is 0.1 μM, indicating a value improved by 9 times to 2 orders of magnitude compared with the previously reported biosensors on the basis of both optical[22] and electrochemical[23] measurements for the detection of the same target molecule. The dynamic response range for IAA is observed to be from 0.1 to 20 μM, suggesting a substantially improved screening capability. The more detailed comparison with two or more other literature works in terms of other assay features is shown in Table S1 of Supprting Information. It is noteworthy that those measurements were carried out under randomly given conditions. The further improved analytical characteristics are expected to be achieved after optimizing the parameters influencing the response signal.

The assay selectivity against several other molecules is depicted in Supporting Information Figure S1. The frequency shift corresponding to nontarget molecules is less than 8.0% assuming that the IAA-triggered signal (the difference between the frequencies of blank and IAA) is 100%. The recovery results provide the immediate evidence that the newly developed piezoelectric transducer shows good quality in accuracy and stability (shown in Supporting Information Table S2).

To validate the universality of the proposed screening strategy, utilizing the same DNA probes, the interactions of the other two small molecules, abscisic acid (ABA) and 2,4-dichlorophenoxyacetic acid (2,4-D), with their respective antibodies were investigated according to the procedure similar to that for IAA assay. The results are shown in Figure 4. Regardless of target species, the frequency change of QCM increases with increasing target concentration (Figure 4A and B). The rise of the frequency shift originates from the fact that more and more assembling probe/recognition probe hybrids are freed. Taking into account the competition between free targets and labeled targets for antibodies, this reflects that the increasing number of target molecules interact with the antibody proteins. The measured results also indicate that the different concentrations of target species in samples can be detected via the developed strategy. Namely, quantification of ABA and 2,4-D can be implemented via the DNA-encoded signal conversion strategy. Strikingly, although no substantial difference (not more than 5%) between the frequency changes at high concentration (e.g., 20 μM) of IAA (Figure 3), ABA (Figure 4A), and 2,4-D (Figure 4B) is observed, the low concentration of ABA or 2,4-D more easily induces the frequency change of QCM. ABA (Figure 4A Inset) and 2,4-D (Figure 4B Inset) at concentration of 0.4 μM can cause the signal intensities of 38% and 35%, respectively, while IAA at the same concentration only leads to the signal intensity of 24% (Figure 4C). From this, one can infer that more desirable analytical characteristics could be achieved when the DNA-encoded signal conversion strategy is employed to detect ABA and 2,4-D. These experimental results, as well as comparative data, validate to a great extent the universality and intriguing assay capability of the developed screening strategy.

In the present work, a successful "signal-on" sensing strategy possessing the desirable signal amplification capability is proposed for screening the interaction of anti-IAA antibody with IAA and quantitative detection of IAA. Along this line, a proof of concept is for the first time presented for other small molecules of interest including chemical and biological species via utilizing steric hindrance-mediated behavior change (e.g., self-assembly and intermolecular binding) of DNA oligonucleotides. Oligonucleotides serve as the information-encoded molecules during the small target-to-DNA conversion. Decoding the oligonucleotides involved can unambiguously screen the small target/protein interaction. This not only achieves a "signal-on" response mechanism, but also circumvents the drawbacks usually encountered by the conventional small molecule assays, facilitating the design of a sensing

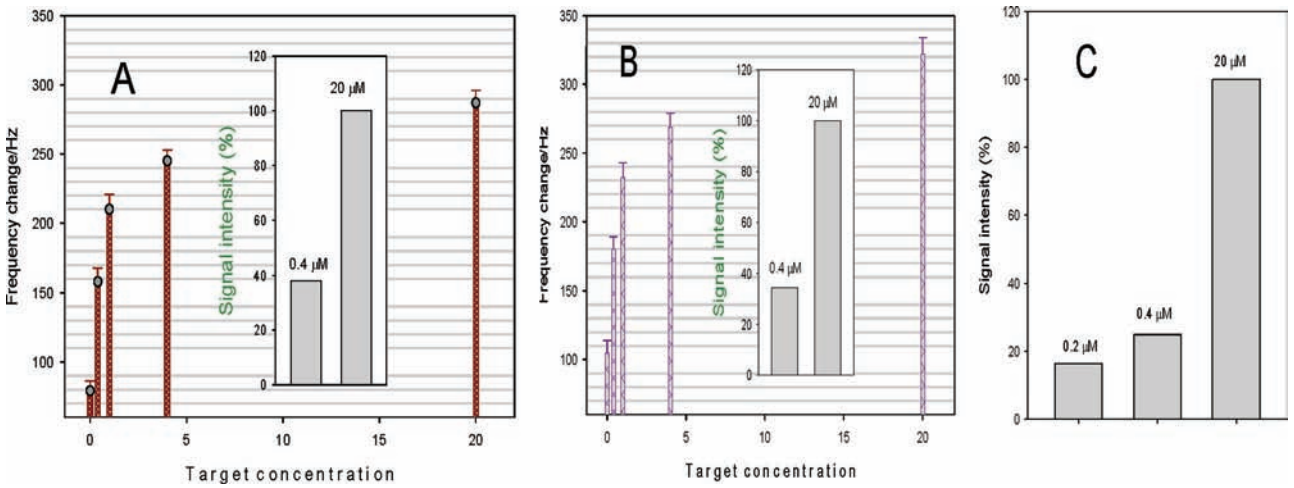

Figure 4. DNA-encoded signal conversion for screening the interaction between ABA (A), 2,4-D (B), and their respective antibody protein. The signaling procedure similar to that for IAA assay was employed. The error bars represent standard deviations of three measurements performed for each sample. To evaluate the capability of the sensing strategy to investigate the different small molecules, the largest frequency shift induced by the highest concentration of targets was assigned as 100%. On the basis of this assumption, the frequency changes corresponding to the low concentration of targets were accurately calculated. Utilizing this method, the data obtained from the ABA, 2,4-D, and IAA assays are depicted in A Inset, B Inset, and C, respectively. The data in C are estimated from Figure 3.

scheme and a screening procedure. For example, a considerable amount of immunosensing systems for the detection of small molecules rely usually on anti-immune complex antibodies. Not only are those antibodies difficult to produce, but the systems also exhibit high cross-reactivity with the unliganded primary antibody.[24] Additionally, aptamer probes are attracting increasing attention from analysts and biochemists, and substantial research efforts have been focused on devising aptameric systems to obtain the information on a wide variety of target species including small molecules. However, even if the sandwich-type assay is not considered that requires each target analyte to be simultaneously bound by two antibodies, the oligonucleotides responsible for recognizing small molecules must have the unique features so that the structure-switching upon the addition of analytes is ensured to occur[5,25−27] or the binding activity can be maintained even after being split into two half-sites.[17,28] In contrast, because the oligonucleotides used in the proposed signaling protocol are the common strands, the encoding DNAs require nothing about the base sequence or second structure. This indicates a general and desired tool holding the appreciated potential for targeting applications. As an attractive sensing strategy for transducing the small molecule/protein interaction into a detectable signal, the small target-to-DNA conversion scheme exhibits other several distinct advantages as listed below.

Because the small molecule/protein interaction is independent of the oligonucleotide sequences as indicated in Scheme 1, the assay systems for different targets could be cost-effectively designed by sharing the DNA probes except for substituting other species for IAA when preparing the recognition probes. The detection of ABA and 2,4-D has preliminarily proven this intrinsic advantage. Moreover, oligonucleotide is suitable for the construction of various recognition probes for specific targets due to its outstanding features, such as huge diversity of unique sequences, sufficient biostability, easy synthesis, and modification. Additionally, different DNA sequences can be used to prepare recognition probes for recognizing target molecules in a one-to-one manner. In this case, employing other measurement techniques, for example, fluorescence spectroscopy, simultaneous detection of different small molecules is expected to be readily achieved after designing a proper signaling scheme (e.g., labeling DNA probes with different fluorescent dyes as described in the following section).

Moreover, after converting the interaction of small molecules with proteins into the emergence of DNA sequences, extracting the information on small molecules can be accomplished via screening the DNA sequences. This signaling strategy represents an appealing avenue for screening the small molecules through various preexisting toolkits available for DNA manipulation. Besides the methods to manipulate DNAs, this makes the seeming impossible measurement techniques for small molecule assays, as well as signal amplification methods, possible. For example, microgravimetric transducer for the detection of molecules with small molecular weight could not be achieved unless anti-immune complex antibodies were devised.[29] However, the detection of IAA based on microgravimetric measurement can be achieved via the developed sensing scheme even without any anti-immune complex antibodies, demonstrating the promising signaling strategy for small molecules of interest. Note that other techniques (e.g., electrochemical and fluorescent measurements) are also capable of executing such a small target-to-DNA conversion and could possibly offer other advantages (for example, assay convenience and high sensitivity). For example, compared with the microgravimetric transducer that only records the frequency change during the signal amplification step, the electrochemical measurement can obtain the overall signal intensity value corresponding to several steps (difference between line a and line e of Figure 1 in which each of the impedance changes from line b to line e are closely associated with the content of IAA in the sample). In this case, the signal-to-noise ratio can increase from 3.6 to 7.0. This intrinsic, attractive feature endows the current sensing scheme with additional advantages, making it a potentially robust tool suitable for screening small molecules.

Polymerase chain reaction (PCR) and rolling circle amplification (RCA) activated by DNA polymerase can dramatically replicate the linear and circularized oligonucleotide strands under specific conditions, respectively, affording

powerful tools for the sensitive immuoassay. Immuno-PCR[30−33] and immuno-RCA[34,35] based immunosensing systems exhibited impressive assay performances (allowing detection of protein analytes with zeptomole[36] or subzeptomole[35] sensitivity), indicating a dominant direction for developing ultrasensitive immunoassays. However, both amplification techniques require cumbersome antibody−DNA conjugation processes to convert the antigen−antibody immunoreaction events into DNA strand detection. To circumvent the aforementioned limitations, although aptamer sequences able to directly recognize their target proteins with high affinity and specificity have recently been used to implement the binding event conversion,[37−39] the formation of sandwich structure is yet the prerequisite for designing the detection schemes. The small target-to-DNA conversion strategy described in the present work facilitates the applications of DNA-based signal amplification biotechnologies (e.g., PCR and RCA) in the small molecule recognition.

Additionally, the small target-to-DNA conversion is based on the change of self-assembly behavior of thiolated assembling probe/recognition probe hybrid due to the increase in steric hindrance between terminal thiol group and the QCM surface upon the IAA/antibody interaction. However, the increase in steric hindrance could essentially inhibit the binding of recognition probe-labeled small species to specific receptors (for instance, interaction between recognition probe-labeled biotin and avidin or enzyme-conjugated avidin), offering the excellent opportunity to develop a variety of optical or electrochemical signaling schemes for sensitively investigating the small molecule/protein interaction. As a conceptual model system for screening the interaction between small molecules and proteins in a homogeneous manner, the small target-to-DNA conversion-based fluorescent assay scheme is described in Supporting Information Scheme S1. Small molecules in sample can compete with the recognition probe-labeled ones for antibody protein, freeing the DNA hybrid. This promotes the binding of biotin conjugated to assembling probe to the QD surface-confined avidin, generating the FRET from QDs to fluorescent dyes. In the absence of target, antibody protein may easily bind to the recognition probe-conjugated small molecule, leading to the increase of steric hindrance that prohibits the interaction between surface-confined avidin and biotin of assembling probe. In this case, the distance between fluorescent dye and QD is great. Thus, FRET does not occur and no optical signal is observed. If encoding DNA sequences modified with different fluorescent dyes are involved in this system, the simultaneous detection of different small molecules could be implemented.

Nevertheless, addition efforts should be made to further improve the analytical capability of the proposed system. As shown in Figure 2, the blank sample can make the crystal frequency continuously decrease even if slowly. The failure to suppress the blank-induced frequency change could be attributed to two possible causes. First, the HRP−avidin conjugates could be adsorbed onto the QCM surface presumably via replacing the preadsorbed glycin molecules rather than the specific avidin/biotin binding reaction. Second, the small amount of assembling probe/recognition probe hybrid could not bind to the antibody protein event in the absence of target under given conditions. This results in the unwanted immobilization of assembling probe/recognition probe hybrid that, in turn, causes the adsorption of HRP−avidin conjugates during the subsequent assay step. Regardless of the anchoring nature, residual HRP−avidin conjugates can slowly catalyze the oxidation of 4-chloro-1-naphthol in the presence of H_2O_2, generating a continuous decrease of crystal frequency. Presumably, the former should be cured via optimizing the incubation time for the interaction between HRP−avidin and biotin of the signaling probe on the QCM surface or via substituting other stronger blockers for glycin molecules, and the latter should be capable of being inhibited via increasing the concentration of antibody protein involved. Another efficient method to suppress the effect of the blank frequency change on the sensing performance is to pursue the maximum reaction rate-based data. Namely, the optimal time response dot (OPD), which is defined as the datum point corresponding to the maximum slope in the real-time measurement curve, is employed for quantitative detection of target molecule. To confirm the rationality of this alternative, the frequency values corresponding to the 250 s response dot, at which the frequency value in line b approaches that in line a, are used to characterize the sensing platform. The calculated data show that the signal-to-noise ration is increased from 3.6 to 15.5, exhibiting superior properties over the steady-state measurement technique. Clearly, it is natural that the screening capability of the small target-to-DNA conversion-based microgravimetric transducer can be further improved if additional efforts are made along the aforementioned directions.

Additionally, the essential requirement for the DNA-encoded signal conversion is that the binding of labeled small molecules to antibody proteins can successfully proceed. Presumably, attachment of oligonucleotides, especially double-stranded oligonucleotides, to the small molecules, could more or less inhibit the immunoreaction between small molecules and antibodies, compromising the capability to transfer the recognition event into the detectable signal. Thus, although three small molecules (IAA, ABA, and 2,4-D) were sensitively detected, the developed signaling strategy could not possibly be applied to analyze any small molecules.

In summary, DNA oligonucleotides are used to mediate the transition of interaction between IAA and specific antibody into the detectable signal, elegantly developing a microgravimetric biosensor for the small molecule detection. Utilizing the transducer, not only can the efficient investigation of IAA/antibody interaction and sensitive quantification of IAA be accomplished compared with the conventional assays, but also the analytical capability is expected to be further improved. More importantly, via encoding and decoding with the aid of the DNA probes, a novel small target-to-DNA conversion concept is represented, paving the way to develop the various sensing platforms for the expansion of IAA detection methods to other small targets and analytes. It seems plausible that the success in developing DNA-encoded microgravimetric transducer for IAA assay provides the proof-of-principle evidence that validates the DNA strand-encoded small molecule/protein recognition process and promotes the application of versatile oligonucleotide-based signaling schemes and relative signal amplification biotechnologies in basic and applied research besides in the genomics.

■ ASSOCIATED CONTENT

Ⓢ Supporting Information

Additional information as described in the text. This material is available free of charge via the Internet at http://pubs.acs.org.

AUTHOR INFORMATION

Corresponding Author

*Phone: 86-731-88821916; Fax: (+86) 731-88821916; E-mail address: wuzaisheng@163.com (Z.S. Wu); glshen@hnu.cn (G.L. Shen).

ACKNOWLEDGMENTS

Financial assistance is gratefully acknowledged from the National Natural Science Foundation of China (Grants No. 90817101, 20905022, 20775023, and 20865006) and "973" National Basic Research Program of China (No. 2007CB310500).

REFERENCES

(1) Tagliaro, F., Antonioli, C., De Battisti, Z., Ghielmi, S., and Marigo, M. (1994) Reversed-phase high-performance liquid chromatographic determination of cocaine in plasma and human hair with direct fluorimetric detection. *J. Chromatogr, A. 674* (1−2), 207−215.

(2) Trachta, G., Schwarze, B., Saegmuller, B., Brehm, G., and Schneider, S. (2004) Combination of high-performance liquid chromatography and SERS detection applied to the analysis of drugs in human blood and urine. *J. Mol. Struct. 693* (1−3), 175−185.

(3) Buryakov, I. A. (2004) Express analysis of explosives, chemical warfare agents and drugs with multicapillary column gas chromatography and ion mobility increment spectrometry. *J. Chromatogr., B 800* (1−2), 75−82.

(4) Strano-Rossi, S., Molaioni, F., Rossi, F., and Botre, F. (2005) Rapid screening of drugs of abuse and their metabolites by gas chromatography/mass spectrometry: application to urinalysis. *Rapid Commun. Mass Spectrom. 19* (11), 1529−1535.

(5) Baker, B. R., Lai, R. Y., Wood, M. S., Doctor, E. H., Heeger, A. J., and Plaxco, K. W. (2006) An electronic, aptamer-based small-molecule sensor for the rapid, label-free detection of cocaine in adulterated samples and biological fluids. *J. Am. Chem. Soc. 128*, 3138−3139.

(6) Wu, Z., Zhen, Z., Jiang, J.-H., Shen, G.-L., and Yu, R.-Q. (2009) Terminal protection of small-molecule-linked DNA for sensitive electrochemical detection of protein binding via selective carbon nanotube assembly. *J. Am. Chem. Soc. 131*, 12325−12332.

(7) Huh, Y. S., Lowe, A. J., Strickland, A. D., Batt, C. A., and Erickson, D. (2009) Surface-enhanced raman scattering based ligase detection reaction. *J. Am. Chem. Soc. 131*, 2208−2213.

(8) Hill, H. D., and Mirkin, C. A. (2006) The bio-barcode assay for the detection of protein and nucleic acid targets using DTT-induced ligand exchange. *Nat. Protoc. 1*, 324−336.

(9) Huang, Y., Zhang, Y. L., Xu, X. M., Jiang, J. H., Shen, G. L., and Yu, R. Q. (2009) Highly specific and sensitive electrochemical genotyping via gap ligation reaction and surface hybridization detection. *J. Am. Chem. Soc. 131*, 2478−2480.

(10) Schweitzer, B., and Kingsmore, S. (2001) Combining nucleic acid amplification and detection. *Curr. Opin. Biotechnol. 12*, 21−27.

(11) Xu, X. Y., Georganopoulou, D. G., Hill, H. D., and Mirkin, C. A. (2007) Homogeneous detection of nucleic acids based upon the light scattering properties of silver-coated nanoparticle probes. *Anal. Chem. 79*, 6650−6654.

(12) Mannocci, L., Zhang, Y., Scheuermann, J., Leimbacher, M., De Bellis, G., Rizzi, E., Dumelin, C., Melkko, S., and Neri, D. (2008) High-throughput sequencing allows the identification of binding molecules isolated from DNA-encoded chemical libraries. *Proc. Natl. Acad. Sci. U.S.A. 105* (46), 17670−17675.

(13) Stojanovic, M. N., Prada, P., and Landry, D. W. (2001) Aptamer-based folding fluorescent sensor for cocaine. *J. Am. Chem. Soc. 123*, 4928−4931.

(14) Stojanovic, M. N., Prada, P., and Landry, D. W. (2000) Fluorescent sensors based on aptamer self-assembly. *J. Am. Chem. Soc. 122*, 11547−11548.

(15) He, J. L., Wu, Z. S., Zhou, H., Wang, H. Q., Jiang, J. H., Shen, G. L., and Yu, R. Q. (2010) Fluorescence aptameric sensor for strand displacement amplification detection of cocaine. *Anal. Chem. 82*, 1358−1364.

(16) Wu, Z. S., Guo, M. M., Zhang, S. B., Chen, C. R., Jiang, J. H., Shen, G. L., and Yu, R. Q. (2007) Reusable electrochemical sensing platform for highly sensitive detection of small molecules based on structure-switching signaling aptamers. *Anal. Chem. 79*, 2933−2939.

(17) Zuo, X., Xiao, Y., and Plaxco, K. W. (2009) High specificity, electrochemical sandwich assays based on single aptamer sequences and suitable for the direct detection of small-molecule targets in blood and other complex matrices. *J. Am. Chem. Soc. 131*, 6944−6945.

(18) Melkko, S., Scheuermann, J., Dumelin, C. E., and Neri, D. (2004) Encoded self-assembling chemical libraries. *Nat. Biotechnol. 22*, 568−574.

(19) Zhang, S., Metelev, V., Tabatadze, D., Zamecnik, P. C., and Bogdanov, A. Jr. (2008) Fluorescence resonance energy transfer in near-infrared fluorescent oligonucleotide probes for detecting protein−DNA interactions. *Proc. Natl. Acad. Sci. U.S.A. 105*, 4156−4161.

(20) Zhu, C. F., Wen, Y. Q., Li, D., Wang, L. H., Song, S. P., Fan, C. H., and Willner, I. (2009) Inhibition of the in vitro replication of DNA by an aptamer−protein complex in an autonomous DNA machine. *Chem.—Eur. J. 15*, 11898−11903.

(21) Kobayashi, N., Iwakami, K., Kotoshiba, S., Niwa, T., Kato, Y., Mano, N., and Goto, J. (2006) Immunoenzymometric assay for a small molecule,11-deoxycortisol, with attomole-range sensitivity employing an scFv−enzyme fusion protein and anti-idiotype antibodies. *Anal. Chem. 78*, 2244−2253.

(22) Jiao, C. X., Niu, C. G., Chen, L. X., Shen, G. L., and Yu, R. Q. (2003) 4-Allyloxy-7-aminocoumarin as a fluorescent carrier for optical sensor preparation and indole-3-acetic acid assay. *Sens. Actuators, B 94*, 176−183.

(23) Li, J., Xiao, L. T., Zeng, G. M., Huang, G. H., Shen, G. L., and Yu, R. Q. (2003) A renewable amperometric immunosensor for phytohormone β-indole acetic acid assay. *Anal. Chim. Acta 494*, 177−185.

(24) González-Techera, A., Vanrell, L., Last, J. A., Hammock, B. D., and González-Sapienza, G. (2007) Phage anti-immune complex assay: general strategy for noncompetitive immunodetection of small molecules. *Anal. Chem. 79*, 7799−7806.

(25) Nutiu, R., and Li, Y. (2003) Structure-switching signaling aptamers. *J. Am. Chem. Soc. 125*, 4771−4778.

(26) Zuo, X., Song, S., Zhang, J., Pan, D., Wang, L., and Fan, C. (2007) A target-responsive electrochemical aptamer switch (TREAS) for reagentless detection of nanomolar ATP. *J. Am. Chem. Soc. 129*, 1042−1043.

(27) Zhang, S. B., Hu, R., Hu, P., Wu, Z. S., Shen, G. L., and Yu, R. Q. (2010) Blank peak current-suppressed electrochemical aptameric sensing platform for highly sensitive signal-on detection of small molecule. *Nucleic Acids Res. 38*, e185.

(28) Fahlman, R. P., and Sen, D. (2002) DNA conformational switches as sensitive electronic sensors of analytes. *J. Am. Chem. Soc. 124*, 4610−4616.

(29) Jin, X. F., Jin, X. Y., Liu, X. P., Chen, L. G., Jiang, J. H., Shen, G. L., and Yu, R. Q. (2009) Biocatalyzed deposition amplification for detection of aflatoxin B1 based on quartz crystal microbalance. *Anal. Chim. Acta 645*, 92−97.

(30) Sano, T., Smith, C. L., and Cantor, C. R. (1992) Immuno-PCR: very sensitive antigen detection by means of specific antibody-DNA conjugates. *Science 258*, 120−122.

(31) Ruzicka, V., Marz, W., Russ, A., and Gross, W. (1993) Immuno-PCR with a commercially available avidin system. *Science 260*, 698−699.

(32) Javaherian, S., Musheev, M. U., Kanoatov, M., Berezovski, M. V., and Krylov, S. N. (2009) Selection of aptamers for a protein target in cell lysate and their application to protein purification. *Nucleic Acids Res. 37*, e62.

(33) Gullberg, M., Gú stafsdó ttir, S. M., Schallmeiner, E., Jarvius, J., Bjarnegård, M., Betsholtz, C., Landegren, U., and Fredriksson, S.

(2004) Cytokine detection by antibody-based proximity ligation. *Proc. Natl. Acad. Sci. U.S.A. 101*, 8420−8424.

(34) Schweitzer, B., Wiltshire, S., Lambert, J., O'Malley, S., Kukanskis, K., Zhu, Z., Kingsmore, S. F., Lizardi, P. M., and Ward, D. C. (2000) Immunoassays with rolling circle DNA amplification: a versatile platform for ultrasensitive antigen detection. *Proc. Natl. Acad. Sci. U.S.A. 97*, 10113−10119.

(35) Schweitzer, B., Roberts, S., Grimwade, B., Shao, W., Wang, M., Fu, Q., Shu, Q., Laroche, I., Zhou, Z., Tchernev, V. T., Christiansen, J., Velleca, M., and Kingsmore, S. F. (2002) Multiplexed protein profiling on microarrays by rolling-circle amplification. *Nat. Biotechnol. 20*, 359−365.

(36) Nam, J. M., Thaxton, C. S., and Mirkin, C. A. (2003) Nanoparticle-based bio-bar codes for the ultrasensitive detection of proteins. *Science 301*, 1884−1886.

(37) Fredriksson, S., Gullberg, M., Jarvius, J., Olsson, C., Pietras, K., Gú stafsdó ttir, S. M., östman, A., and Landegren, U. (2002) Protein detection using proximity-dependent DNA ligation assays. *Nat. Biotechnol. 20*, 473−477.

(38) Di Giusto, D. A., Wlassoff, W. A., Gooding, J. J., Messerle, B. A., and King, G. C. (2005) Proximity extension of circular DNA aptamers with real-time protein detection. *Nucleic Acids Res. 33*, e64.

(39) Zhou, L., Ou, L. J., Chu, X., Shen, G. L., and Yu, R. Q. (2007) Aptamer-based rolling circle amplification: a platform for electrochemical detection of protein. *Anal. Chem. 79*, 7492−7500.

Bioconjugate Chemistry

Communication

pubs.acs.org/bc

Top-down Synthesis of Versatile Polyaspartamide Linkers for Single-Step Protein Conjugation to Materials

Chaenyung Cha,[†] Jae Hyun Jeong,[‡] Xin Tang,[§] Andrew T. Zill,[†] Y. S. Prakash,[∥] Steven C. Zimmerman,[†] Taher A. Saif,[§] and Hyunjoon Kong*[,‡]

[†]Department of Chemistry, [‡]Department of Chemical and Biomolecular Engineering, University of Illinois, 600 South Mathews Avenue, Urbana, Illinois 61801, United States

[§]Department of Mechanical Science and Engineering, University of Illinois, 1206 West Green Street, Urbana, Illinois 61801, United States

[∥]Department of Anesthesiology, Mayo Clinic, 200 SW First Street, Rochester, Minnesota 55905, United States

Supporting Information

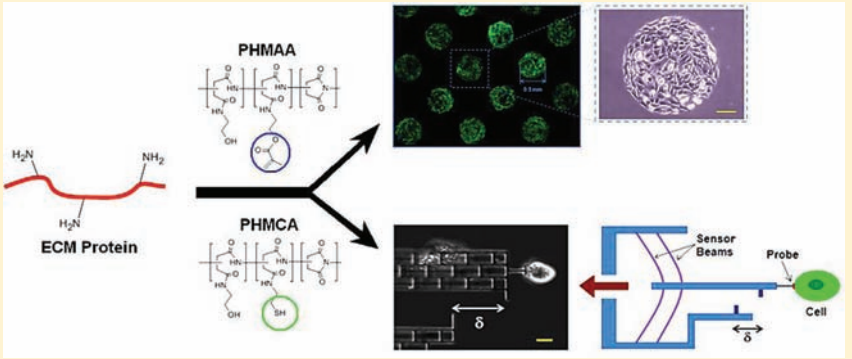

ABSTRACT: Materials used in various biological applications are often modified with proteins to regulate biomolecular and cellular adhesion. Conventional strategies of protein conjugation accompany monovalent bifunctional protein linkers, which present several limitations in molecular synthesis and protein conjugation. Herein, we present a new strategy of preparing multivalent polyaspartamide linkers in a simple top-down manner, and also demonstrate that the resulting polymer linkers allow us to readily conjugate proteins to both organic and inorganic materials. The top-down synthesis of polyaspartamide linkers was performed by partially opening succinimidyl ring moieties of polysuccinimide (PSI) with the controlled number of nucleophiles reactive to photo-cross-linked hydrogel or gold-coated inorganic materials: (1) Poly(2-hydroxyethyl-*co*-2-methacryloxyethyl aspartamide) (PHMAA) presenting methacrylate was used to micropattern fibronectin or collagen on a hydrogel in order to regulate cell adhesion and growth area on a micrometer scale. (2) Poly(2-hydroxyethyl-*co*-2-mercaptoethyl aspartamide) (PHMCA) presenting thiol functional groups was used to link fibronectin to a gold-coated silicon microelectromechanical probe designed to measure cell traction force. Overall, these multivalent polyaspartamide protein linkers will greatly assist efforts to analyze and regulate the cellular adhesion to and phenotypic activities of a wide array of substrates and devices.

A variety of organic and inorganic materials are widely used in the assembly of in vitro cell culture platforms, biomedical implants, and biomicroelectromechanical systems (bio-MEMS) devices.[1−5] These materials are usually chemically linked with a series of proteins, such as fibronectin, collagen, and antibodies, in order to control cellular adhesion to the materials.[6,7] The number and spacing of these proteins act as insoluble signals to regulate cellular phenotypes.[8−10] Various forms of bifunctional linkers are increasingly used for stable protein conjugation.[11−14] These linkers largely contain two monovalent functional groups: one reactive to a protein and the other reactive to a material. These linkers require multiple modification and purification steps during molecular synthesis and protein conjugation to target substrates, thus necessitating extensive labor. In addition, the number of monovalent linkers should increase in tandem with the amount of protein conjugated to the materials due to their monovalency, which raises concerns over increased cytotoxicity and inadvertent changes in material properties.

To resolve these challenges encountered with the use of monovalent linkers, this study presents a simple top-down synthetic strategy to prepare a polyaspartamide linker with controlled multivalencies of reactive groups to both proteins and materials. In addition, this study demonstrates that the polymeric linkers allow us to conjugate cell adhesion proteins with a single step. Polysuccinimide (PSI) with the average

Received: June 27, 2011
Revised: October 26, 2011
Published: November 5, 2011

 © 2011 American Chemical Society

Scheme 1. Synthesis of PHMAA and Its Reaction with Fibronetin (Fn) to form Fn-PHMAA[a]

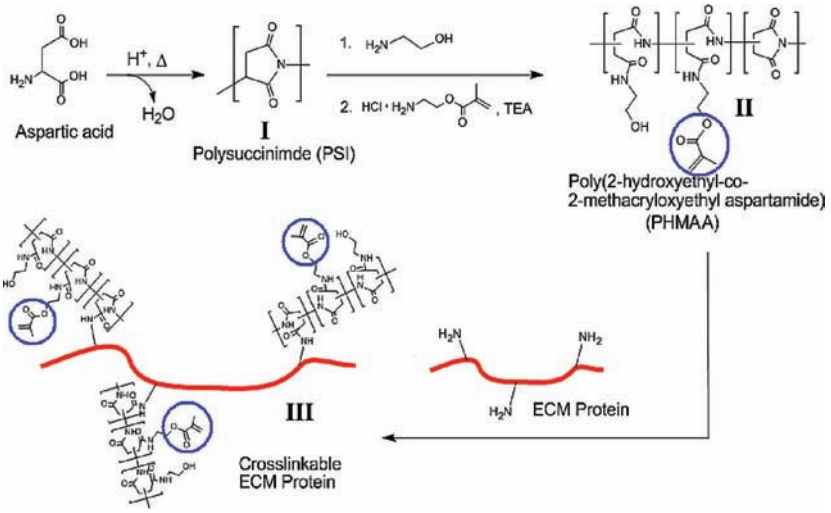

[a]Chemically reactive methacrylic groups are marked with blue circles.

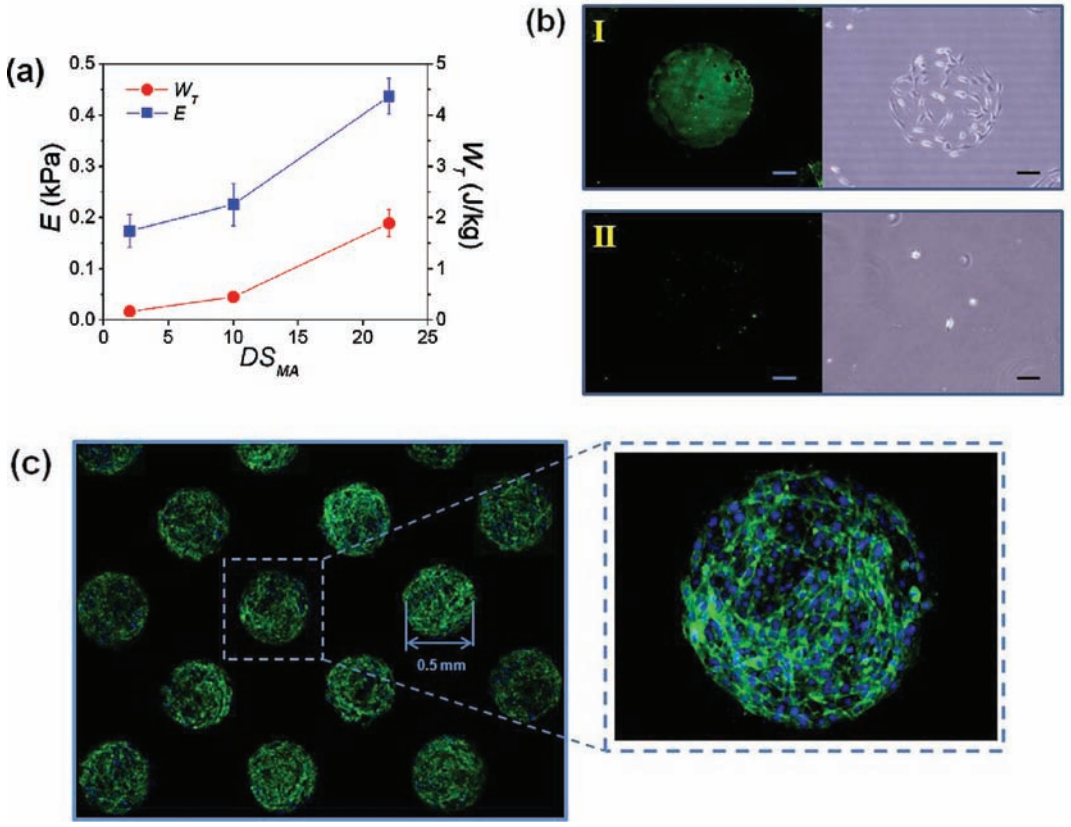

Figure 1. (a) Elastic modulus (E) and tensile energy (W_T) of polyacrylamide hydrogel cross-linked with PHMAA with varying degree of methacrlyate substitution (DS_{MA}). (b) Circular pattern of Fn-PHMAA (**I**, left) or pure Fn (**II**, left) on polyacrylamide hydrogel visualized with immunoflurescent labeling. Fibroblast adhesion was more active on the Fn-PHMAA pattern (**I**, right), compared with pure Fn pattern (**II**, right) (Scale bar: 100 μm.) (c) Proliferation of fibroblasts within the circular pattern of Fn-PHMAA visualized with fluorescein-phalloidin (green) and DAPI (blue), respectively (a magnified image of a circular pattern shown on the right).

molecular weight of 22 000 g mol^{-1} was synthesized by acid-catalyzed polycondensation of aspartic acid and used as a starting molecule (Scheme 1 (**I**) and Figure S1a in Supporting Information).[15] PSI consists of a series of succinimidyl units which allow ring-opening nucleophilic addition.[16,17] In this study, we partially opened the succinimidyl rings of PSI with a controlled amount of amine-based nucleophiles that are reactive to a target material, in order to create a polyaspartamide linker in a top-down manner. The protein of interest, which also contains amine groups, would be conjugated to the intact succinimidyl groups of polyaspartamide in the same fashion as the amine-based nucleophilic substituents. This synthetic strategy allows the linker to present a variety of functional groups needed for conjugation to specific

dx.doi.org/10.1021/bc200339s | Bioconjugate Chem. 2011, 22, 2377–2382

Scheme 2. Synthesis of PHMCA and Its Reaction with Fibronetin (Fn) to Form Fn-PHMCA[a]

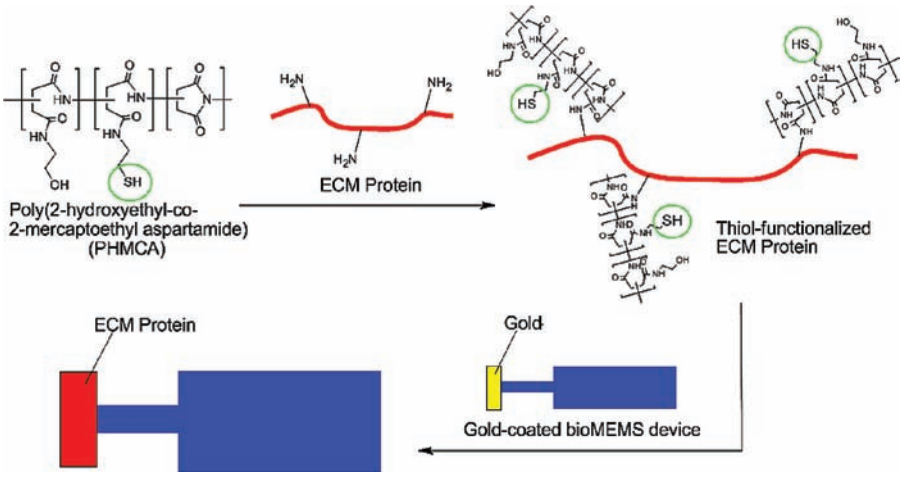

[a]Chemically reactive thiol groups are marked with green circles. Fn-PHMCA was used to conjugate Fn to gold-coated bio-MEMS device.

materials simply by using nucleophiles containing different functional groups. Here, we demonstrate the function and versatility of this polyaspartaminde linker with two applications: (1) protein conjugation to a hydrogel using a polyaspartamide linker containing methacrylic groups, and (2) protein conjugation to a gold-coated bio-MEMS device using a polyaspartamide linker containing thiol groups.

First, we synthesized a polyaspartamide linker that can conjugate cell adhesion proteins to a hydrogel that is conventionally used for in vitro cell culture. For this purpose, designated amounts of ethanolamine and 2-aminoethyl methacrylate were added sequentially to PSI to prepare poly(2-hydroxyethyl-co-2-methacryloxyethyl aspartamide) (PHMAA) (Scheme 1 (**II**) and Figure S1b in Supporting Information). The addition of 2-aminoethyl methacrylate to PSI presented the linker with methacrylic groups needed for radical polymerization. The ethanolamine allowed us to control the number of unreacted succinimidyl groups independent of the number of methacrylic groups, and also to render the linker water-soluble by presenting hydroxyl groups.

These hydroxyl groups were not reactive toward unreacted succinimidyl groups of the PHMAA, as confirmed with minimal changes in the peak integrals corresponding to unreacted succinimidyl groups in the ^{1}H NMR spectrum (Figure S1b in Supporting Information). Separately, PSI was mixed with ethylene glycol to further determine whether hydroxyl groups are reactive toward succinimidyl groups. The ^{1}H NMR spectrum of the resulting product was identical to that of original PSI (Figure S1d in Supporting Information), without showing any changes in peaks corresponding to unreacted succnimidyl groups. On the other hand, PSI mixed with ethylenediamine resulted in immediate polymeric precipitation.

The ability of PHMAA to copolymerize with gel-forming monomers was evaluated by examining whether the PHMAA can cross-link acrylamide monomers to form a hydrogel and to further control hydrogel properties. PHMAA was able to cross-link acrylamide to form a hydrogel via in situ free radical polymerization (Figure S2 in Supporting Information). Furthermore, the PHMAA could increase the elastic modulus and resistance to fracture of the hydrogel with the degree of methacrylic substitution (DS_{MA}), the percentage of succinimidyl groups conjugated with methacrylic groups (Figure 1a). We suggest that mechanical properties of the hydrogel should be further tuned by increasing concentrations of acrylamide and PHMAA. In addition, mechanical properties of hydrogels were not significantly changed during incubation in neutral media, which addresses the lack of significant hydrolysis of unreacted succinimidyl units of PHMAA.

PHMAA was then reacted with fibronectin (Fn), a cell adhesion protein, to prepare Fn reactive to a hydrogel (Fn-PHMAA) (Scheme 1, **III**). The DS_{MA} of PHMAA used to conjugate Fn was kept constant at 10%. The reaction between PHMAA and Fn was confirmed by monitoring the decrease of free amine groups quantified with TNBS (trinitrobenzenesulfonic acid) assay (Table S1 and Figure S3 in Supporting Information).[18] Increasing the amount of Fn while keeping PHMAA constant led to a more rapid decrease of amine groups in the TNBS assay. Furthermore, ^{1}H NMR analysis of PHMAA reacted with varying amounts of glycine, as a model amino acid, showed that the degree of substitution of glycine (DS_{Gly}), analyzed with peak integral ratio of the reacted glycine to the total succinimidyl groups, could be varied from 3.6% to 11.9%. These results show that the multivalency of unreacted succinimidyl groups in PHMAA facilitated reactions with multiple amine groups in protein.

The resulting Fn-PHMAA was used to control the size and spacing of cell adhesion domains on a polyacrylamide hydrogel, combined with a microcontact printing technique (Figure S4 in Supporting Information).[19] Briefly, a circular array of Fn-PHMAA was placed on a glass surface using a microcontact stamp onto which the Fn-PHMAA was physically adsorbed. Both the diameter and spacing of the circles were kept constant at 500 μm. The subsequent in situ cross-linking reaction between acrylamide and *N*,*N*,*N*′,*N*′-methylene bisacrylamide on top of the micropatterened Fn-PHMAA resulted in a polyacrylamide hydrogel which presented circular arrays of fibronectin with regular size and spacing on its surface, as confirmed with immunofluorescent labeling (Figure 1b). The fibronectin mass per circular pattern, determined from a colorimetric immunoassay, was kept constant at 5 μg cm^{-2}. In contrast, the same polyacrylamide hydrogel fabrication on top of pure Fn without PHMAA, a negative control, resulted in limited conjugation of Fn to the surface.

The circular patterns of Fn on the polyacrylamide hydrogel were recognized by cells plated on the gel. Fibroblasts seeded on the hydrogel surface with circularly patterned Fn-PHMAA

dx.doi.org/10.1021/bc200339s | *Bioconjugate Chem.* 2011, 22, 2377–2382

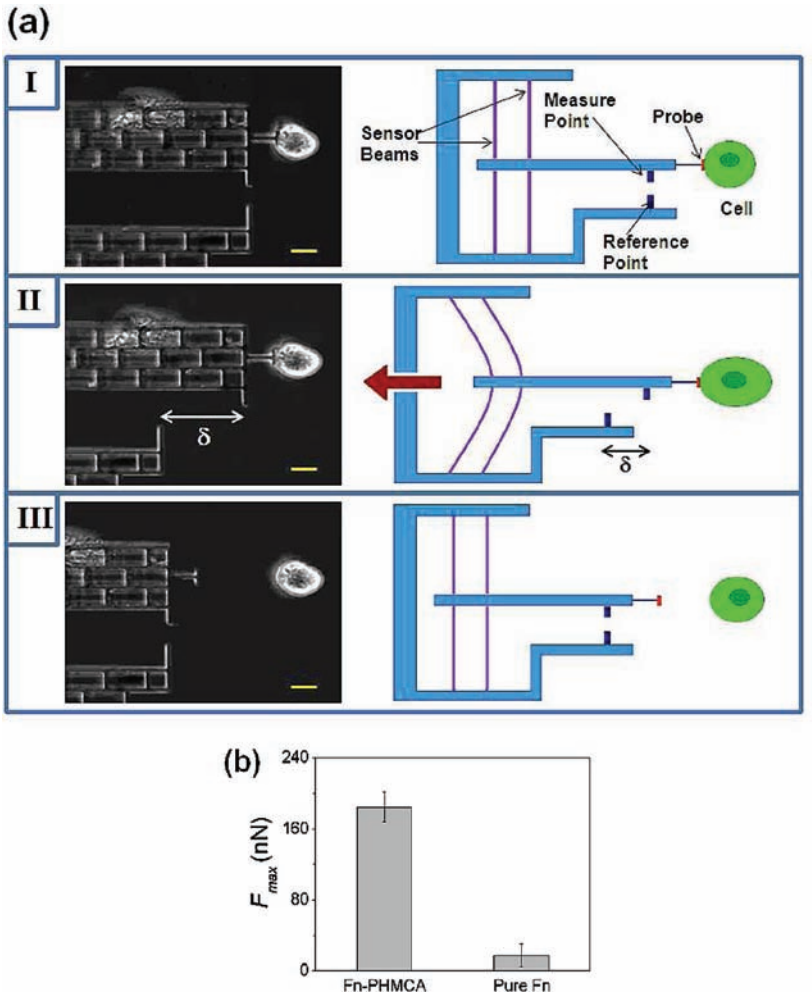

Figure 2. (a) Schematic description of measurement of cell force response using a bio-MEMS device. First, the probe conjugated with Fn is placed in contact with cell (**I**). After incubation, the device is moved away from the cell laterally (red arrow) at a constant rate (**II**). The probe is connected to sensor beams. Due to the cell's adhesion to the probe, it is displaced from the original position, as indicated by the difference between the measurement point and reference point. The probe is continuously pulled until it is finally detached from the cell (**III**). (Scale bar: 15 μm.) (b) The maximum applied force (F_{max}) was significantly larger when the probe was conjugated with Fn-PHMCA than with pure Fn.

adhered exclusively on the patterned area (Figure 1b-**I**). Furthermore, the cells adhered to the circular pattern proliferated over time, while remaining confined to the patterned area (Figure 1c and Figure S5 in Supporting Information). In contrast, the hydrogel patterned with pure Fn displayed limited cell adhesion (Figure 1b-**II**).

The same results were also observed when type I collagen and human airway smooth muscle cells (haSMCs) were used instead of Fn and fibroblasts (Figure S6 in Supporting Information). For this study, collagen linked with PHMAA (DS_{MA} = 10%) was used to pattern the polyacrylamide hydrogel surface with a circular array of collagen at a density of 10 μg cm^{-2}, following the same procedure as described in SI Figure S4. haSMCs exclusively adhered and proliferated within this circularly patterned hydrogel area. This result verifies that PHMAA can chemically link a variety of cell adhesion proteins to the hydrogel and control spatial organization of a wide array of anchorage-dependent cells.

Next, we synthesized a polyaspartamide linker modified with a controlled number of thiol groups for its use in protein conjugation to gold-coated inorganic substrates (Scheme 2). Gold has been extensively used in biosensors such as bio-MEMS and surface plasmon resonance (SPR), due to its inertness, robust structural integrity, and excellent conductivity.[20,21] These gold-coated devices are commonly modified with cell adhesion proteins or antibodies using a thiol-substituted bifunctional monovalent linker, which is typically synthesized via multiple substitution and purification steps. Here, we synthesized poly(2-hydroxyethyl-2-mercaptoethyl aspartamide) (PHMCA) with the controlled number of thiol groups. The same synthetic procedure to create PHMAA in Scheme 1 was used, except that cysteamine was used as a nucleophile to present thiol groups (Scheme 2 and Figure S1c in Supporting Information). The number of thiol groups in PHMCA, which are available to react with gold, was determined to be 10 per molecules, according to a colorimetric assay using Ellman's reagent.[22] The percentage of cysteamine that side-reacted to form thioester linkages was 24% (see Supporting Information). PHMCA was then mixed with Fn to prepare the Fn-PHMCA, and the reaction between PHMCA and Fn was confirmed with TNBS assay, as conducted for Fn-PHMAA (data not shown).

The resulting Fn-PHMCA was used to chemically modify the surface of the gold-coated probe of a bio-MEMS device which is designed to measure force exerted by cells under local uniaxial stretching.[23,24] The bio-MEMS device is made from a single crystal silicon wafer, and the surface of its probe was

dx.doi.org/10.1021/bc200339s | *Bioconjugate Chem.* 2011, 22, 2377–2382

coated with gold to prevent nonspecific interaction with cells (Figure S7 in Supporting Information). Then, the probe was immersed in a solution of Fn-PHMCA to chemically link Fn to the probe (Scheme 2). Separately, another device was also immersed in a solution of pure Fn as a negative control.

The probe modified with Fn-PHMCA or pure Fn was allowed to contact a fibroblast to form specific bonds between Fn and cellular integrins. The device was then pulled from the cell at a rate of 1 μm s^{-1}, and its maximum stretching force (F_{max}) before the cell detachment from the probe was calculated by the equation $F_{max} = k\delta$, where k is the spring constant of the sensor beams to which the probe is attached, and δ is the displacement of the probe from its original position (Figure 2a). The probe coated by the pure Fn was readily detached from the cell with only a small displacement (average $\delta \approx 6$ μm, $F_{max} \approx 20$ nN), indicating poor linkage between Fn and the probe. In contrast, the cell contacted by a Fn-PHMCA modified probe exerted a significant force resulting in an average δ of 55 μm ($F_{max} \approx 185$ nN) (Figure 2b). Furthermore, the F_{max} values were minimally changed during repeated use of the same probe, demonstrating that the chemical linkage of Fn-PHMCA to the gold-coated probe was well retained.

In summary, this study presents a novel strategy of synthesizing versatile polyaspartamide linkers that allow convenient conjugation of proteins to a variety of materials. The synthetic strategy of introducing functional groups by nucleophilic addition to PSI in a top-down manner allowed us to independently control the number of units reactive to proteins and those to materials in a highly efficient manner. In addition, these linkers allow a convenient one-step conjugation of various proteins to organic and inorganic materials. However, the chemical reaction between the linker and protein may cause a small portion of proteins to be denatured, the extent of which should be more carefully examined in future studies. These mutivalent linkers therefore present several attributes superior to conventional monovalent linkers. Furthermore, we expect that the versatility of the polyaspatamide linkers, due to their synthetic strategy of presenting functional groups in a simple top-down manner, will make it possible to further utilize a wide array of conjugation chemistries necessary for tailormade materials.

■ ASSOCIATED CONTENT

Supporting Information

Detailed experimental methods and supporting figures. This material is available free of charge via the Internet at http://pubs.acs.org.

■ AUTHOR INFORMATION

Corresponding Author

*E-mail: hjkong06@illinois.edu.

■ ACKNOWLEDGMENTS

This work was supported by grants from the National Science Foundation (Career DMR-0847253, ECCS-1002165, and STC-EBICS Grant CBET-0939511).

■ REFERENCES

(1) Dario, P., Carrozza, M. C., Benvenuto, A., and A., M. (2000) Micro-systems in biomedical applications. *J. Micromech. Microeng. 10*, 235−244.

(2) Drury, J. L., and Mooney, D. J. (2003) Hydrogels for tissue engineering: scaffold design variables and applications. *Biomaterials 24*, 4337−4351.

(3) Grayson, A. C. R., Shawgo, R. S., Johnson, A. M., Flynn, N. T., Yawen, L. I., Cima, M. J., and Langer, R. (2004) A BioMEMS review: MEMS technology for physiologically integrated devices. *Proc. IEEE 92*, 6−21.

(4) Schmidt, J. J., Rowley, J., and Kong, H. J. (2008) Hydrogels used for cell-based drug delivery. *J. Biomed. Mater. Res., Part A 87A*, 1113−1122.

(5) Shin, H., Jo, S., and Mikos, A. G. (2003) Biomimetic materials for tissue engineering. *Biomaterials 24*, 4353−4364.

(6) Hubbell, J. A. (1999) Bioactive biomaterials. *Curr. Opin. Biotechnol. 10*, 123−129.

(7) Sakiyama-Elbert, S., and Hubbell, J. (2001) Functional Biomaterials: Design of novel biomaterials. *Ann. Rev. Mater. Res. 31*, 183−201.

(8) Geiger, B., Spatz, J. P., and Bershadsky, A. D. (2009) Environmental sensing through focal adhesions. *Nat. Rev. Mol. Cell Biol. 10*, 21−33.

(9) Bae, M.-S., Park, Y. J., Mooney, D. J., and Lee, K. Y. (2007) RGD island spacing controls phenotype of primary human fibroblasts adhered to ligand-organized hydrogels. *Macromol. Res. 15*, 469−472.

(10) Brandl, F., Sommer, F., and Goepferich, A. (2007) Rational design of hydrogels for tissue engineering: Impact of physical factors on cell behavior. *Biomaterials 28*, 134−146.

(11) Pelham, R. J., and Wang, Y.-l. (1997) Cell locomotion and focal adhesions are regulated by substrate flexibility. *Proc. Nat. Acad. Sci. U.S.A. 94*, 13661−13665.

(12) Lee, H. J., Lee, J.-S., Chansakul, T., Yu, C., Elisseeff, J. H., and Yu, S. M. (2006) Collagen mimetic peptide-conjugated photopolymerizable PEG hydrogel. *Biomaterials 27*, 5268−5276.

(13) Madison, L. D., Rosenzweig, S. A., and Jamieson, J. D. (1984) Use of the heterobifunctional cross-linker m-maleimidobenzoyl N-hydroxysuccinimide ester to affinity label cholecystokinin binding proteins on rat pancreatic plasma membranes. *J. Biol. Chem. 259*, 14818−14823.

(14) Jin, L., Horgan, A., and Levicky, R. (2003) Preparation of end-tethered DNA monolayers on siliceous surfaces using heterobifunctional cross-linkers. *Langmuir 19*, 6968−6975.

(15) Tomida, M., Nakato, T., Matsunami, S., and Kakuchi, T. (1997) Convenient synthesis of high molecular weight poly(succinimide) by acid-catalysed polycondensation of l-aspartic acid. *Polymer 38*, 4733−4736.

(16) Kang, H. S., Yang, S. R., Kim, J.-D., Han, S.-H., and Chang, I.-S. (2001) Effects of grafted alkyl groups on aggregation behavior of amphiphilic poly(aspartic acid). *Langmuir 17*, 7501−7506.

(17) Craparo, E. F., Cavallaro, G., Bondi, M. L., Mandracchia, D., and Giammona, G. (2006) PEGylated nanoparticles based on a polyaspartamide. Preparation, physico-chemical characterization, and intracellular uptake. *Biomacromolecules 7*, 3083−3092.

(18) Habeeb, A. F. S. A. (1966) Determination of free amino groups in proteins by 'trinitrobenzenesulfonic acid. *Anal. Biochem. 14*, 328−336.

(19) Inerowicz, H. D., Howell, S., Regnier, F. E., and Reifenberger, R. (2002) Multiprotein immunoassay arrays fabricated by microcontact printing. *Langmuir 18*, 5263−5268.

(20) Gooding, J. J., Mearns, F., Yang, W., and Liu, J. (2003) Self-assembled monolayers into the 21st century: Recent advances and applications. *J. Electroanal. 15*, 81−96.

(21) Green, R. J., Frazier, R. A., Shakesheff, K. M., Davies, M. C., Roberts, C. J., and Tendler, S. J. B. (2000) Surface plasmon resonance analysis of dynamic biological interactions with biomaterials. *Biomaterials 21*, 1823−1835.

(22) Ellman, G. L. (1959) Tissue sulfhydryl groups. *Arch. Biochem. Biophys. 82*, 70−77.

(23) Yang, S., and Saif, T. (2005) Micromachined force sensors for the study of cell mechanics. *Rev. Sci. Instrum. 76*, 044301−8.

(24) Yang, S., and Saif, T. (2005) Reversible and repeatable linear local cell force response under large stretches. *Exp. Cell Res. 305*, 42–50.

Bioconjugate Chemistry

Communication

pubs.acs.org/bc

^{89}Zr-Labeled Dextran Nanoparticles Allow in Vivo Macrophage Imaging

Edmund J. Keliher,[†] Jeongsoo Yoo,[†,∥] Matthias Nahrendorf,[†] Jason S. Lewis,[‡] Brett Marinelli,[†] Andita Newton,[†] Mikael J. Pittet,[†] and Ralph Weissleder*[,†,§]

[†]Center for Systems Biology, Massachusetts General Hospital, 185 Cambridge Street, CPZN 5206, Boston, Massachusetts 02114, United States

[‡]Program in Molecular Pharmacology and Chemistry and Department of Radiology, Memorial Sloan-Kettering Cancer Center, New York, New York 10065, United States

[§]Department of Systems Biology, Harvard Medical School, 200 Longwood Avenue, Boston, Massachusetts 02115, United States

[∥]Department of Molecular Medicine, Kyungpook National University School of Medicine, Daegu, South Korea

Supporting Information

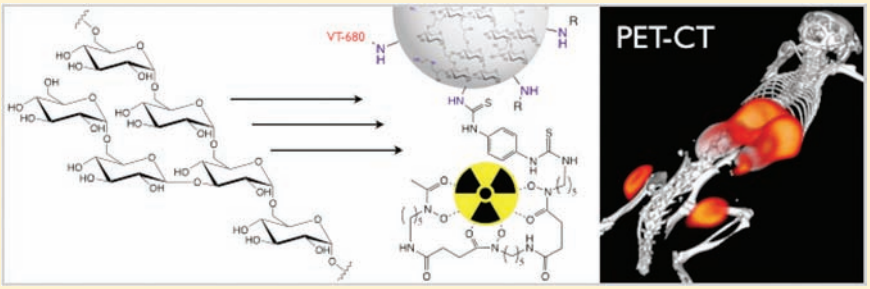

ABSTRACT: Tissue macrophages play a critical role both in normal physiology and in disease states. However, because of a lack of specific imaging agents, we continue to have a poor understanding of their absolute numbers, flux rates, and functional states in different tissues. Here, we describe a new macrophage specific positron emission tomography imaging agent, labeled with zirconium-89 (^{89}Zr), that was based on a cross-linked, short chain dextran nanoparticle (13 nm). Following systemic administration, the particle demonstrated a vascular half-life of 3.9 h and was found to be located primarily in tissue resident macrophages rather than other white blood cells. Subsequent imaging of the probe using a xenograft mouse model of cancer allowed for quantitation of tumor-associated macrophage numbers, which are of major interest in emerging molecular targeting strategies. It is likely that the material described, which allows the visualization of macrophage biology in vivo, will likewise be useful for a multitude of human applications.

INTRODUCTION

Macrophages are white blood cells that are produced by the differentiation of monocytes after their entry into tissues. While their primary role is to phagocytose pathogens and cellular debris, in response to tissue insults they can also act to stimulate the recruitment of lymphocytes and other immune cells. However, despite their known importance and widespread distribution throughout the body, little quantitative information exists regarding their total mass, relative numbers at different sites, distribution profiles across different diseases, or their mobilization and flux rates under both disease and normal physiologic conditions. Early landmark papers[1] used macrophage specific antibodies (F4/80 in mice) to estimate macrophage numbers under resting conditions or have attempted macrophage quantitation using other molecular markers (e.g., Mac-3,[2] CD68,[3] or PG-M1[4]).

In previous work, our laboratory developed dextran-coated nanomaterials that, upon systemic administration, were readily engulfed by mononuclear phagocytic cells. They could thus be used as imaging probes for examining the function of these cells in humans.[5,6] Importantly, we now not only have shown that dextran-coated iron oxide nanoparticles have high macrophage avidity but also have used them for magnetic resonance imaging (MRI)[5,6] and optical[7] as well as positron emission tomography (PET) imaging.[8,9] While these multimodal nanoparticles were originally developed for MRI, using MRI to quantify exact nanoparticle numbers in vivo in different organs is often complicated, particularly in bone marrow and lung tissue. Radiolabeled nanomaterials have only recently been synthesized but have already shown potentially interesting clinical applications.[8−13] In general, it is possible to administer radiolabeled nanomaterials at much lower concentrations than their magnetic (and fluorescent) counterparts. Furthermore, their pharmacokinetics can also be titrated by size and surface

Received: July 26, 2011
Revised: October 27, 2011
Published: October 31, 2011

ACS Publications © 2011 American Chemical Society

optimization and can be matched with PET isotopes with the appropriate decay rate (e.g., ^{18}F, ^{64}Cu, ^{68}Ga, and ^{89}Zr).

Given the absence of optimized macrophage specific nanoparticulate imaging agents, our goal was to systematically develop such materials through an iterative synthesis and screening procedure.[14] Here, we describe the characteristics and in vivo behavior of one lead compound identified from an initial larger screen. This nanoparticle is composed of several short (10 kDa) dextran strands cross-linked into a 13 nm diameter nanoparticle. Because our aim is to ultimately use these materials clinically, we avoided the use of longer chain length linear dextrans as synthetic building blocks, because of their associated hypersensitivities.[15] Rather, given their long clinical history,[16] we chose to incorporate shorter dextrans into the nanoparticles. We subsequently showed that the described preparation is readily labeled with ^{89}Zr ($t_{1/2}$ = 78.4 h; β^+ = 22.3%) via desferrioxamine and can be used with PET to quantitate macrophages in vivo. Finally, in view of the recent interest regarding the role of tumor-associated macrophages (TAMs) in cancer,[17,18] we validated the agent by quantitating tumoral macrophages in a mouse model of cancer.

RESULTS

Nanoparticle Characterization. Cross-linked dextran nanoparticles (DNPs) were synthesized and aminiated following a modified literature procedure that uses epichlorohydrin as a cross-linking agent.[14] Following workup, dialysis for several days provided highly pure DNPs. The size of the particles could then be reproducibly controlled as a function of the duration of the cross-linking reaction. Varying the duration of the reaction allowed synthesis of three preparations (mean diameters of 5, 6, and 13 nm), as measured by dynamic laser light scattering (DLS). The size distribution by volume data for these preparations is presented in Figure 1B and Figure SI.1 of the Supporting Information. The dextran concentration of these three preparations was determined by employing a sugar-reducing quantitative colorimetric method in the presence of phenol and sulfuric acid.[19] The amine concentrations relative to the dextran concentration were 1.09, 0.93, and 1.17 μmol/mg of dextran, respectively, for the three different DNPs.[20] Characterization of the 13 nm DNPs by matrix-assisted laser desorption ionization (MALDI) mass spectrometry demonstrated a mean molecular mass of 80 kDa for these particles. Dextran's weight contribution to the particles was determined to be 53, 54, and 43% for the 5, 6, and 13 nm DNPs, respectively. The mean number of amine groups per 13 nm DNP particle was measured to be 40.

Particle size and morphology were further verified by transmission electron microscopy (TEM). TEM images (Figure 1) not only demonstrated the nanoparticles' spherical shape and homogeneous appearance but also showed mean (narrow) diameters and overall sizes consistent with the DLS measurements. In negative controls, no globular-shaped nanoparticles were observed.

Modification of the particle surface for in vivo use was based on the relative modification of amines. The particles were first labeled with one or two fluorochromes [VT-680 (Perkin-Elmer)] per nanoparticle to allow intravital microscopy, flow-assisted cytometry, and immunofluorescence histology. Second, ~20% of amines were capped with the zirconium chelator desferrioxamine, an FDA-approved drug. Finally, to investigate the effects of pharmacokinetic modulation, all remaining amines were either left free or capped by reaction with an

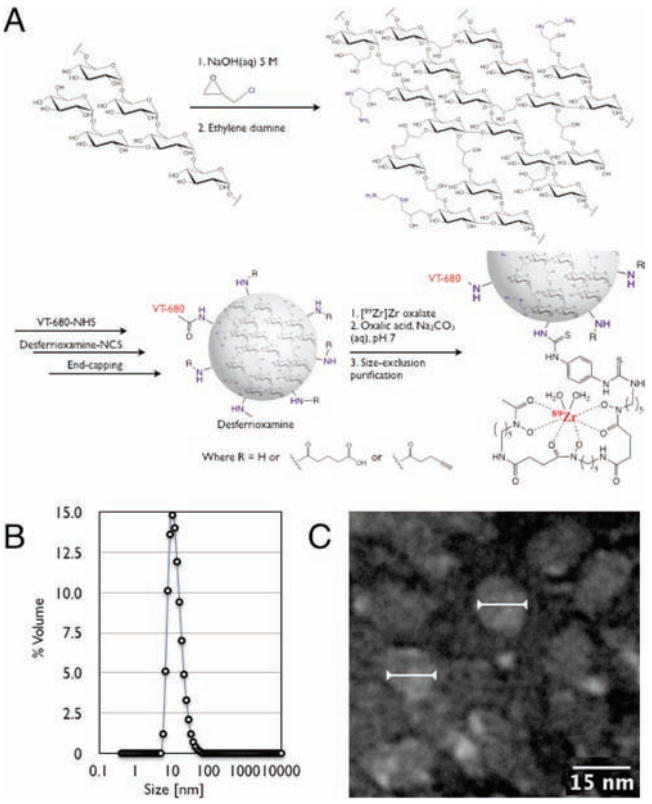

Figure 1. (A) General synthesis and radiolabeling of dextran nanoparticles (DNPs). (B) Dynamic laser light scattering data for the 13 nm DNP preparation. (C) Transmission electron microscopy image of several individual DNPs measuring 13 nm in diameter on average (arrows).

excess amount of succinic anhydride or pentynoyl-NHS ester. Following each modification step, DNPs were purified either by size exclusion chromatography or by size exclusion membrane filtration. As expected, when DNP-NH_2 was fully capped with succinic anhydride, a dramatic shift in ζ potential was observed from 30.0 to -30.1 ± 1.0, indicating a change in the surface charge from positive to negative.

The desferrioxamine-conjugated DNPs were labeled with [^{89}Zr]Zr oxalate in quantitative yield within 1 h, following a previously described procedure.[21] Within 25 min at 25 °C, the radiochemical yield of DNPs with ^{89}Zr was higher than 99.5%. The trace amount of free ^{89}Zr ions was then removed by centrifugal membrane filtration. The radiochemical purity was 100%, and no remaining free ^{89}Zr ions were detected on the high-performance liquid chromatography (HPLC) chromatogram after purification. The ^{89}Zr-labeled DNPs did not show any sign of degradation, determined by ITLC, at 36 °C in phosphate-buffered saline (PBS), for up to 5 days. While ^{18}F is the most common PET tracer used in the clinical setting, the longer-lived ^{89}Zr was chosen for this work in anticipation that nanoparticles would require longer circulation times for uptake into macrophages.

In Vivo Testing. To understand the effects of size and capping on pharmacokinetics, we performed blood half-life measurements. For the pentynoyl-capped 5, 6, and 13 nm DNPs (Figure 2A), the blood half-life data fit a two-phase exponential decay model, with values of 0.2, 0.9, and 6.1 h, respectively. The 5 and 6 nm preparations showed considerable renal excretion and much lower levels of macrophage

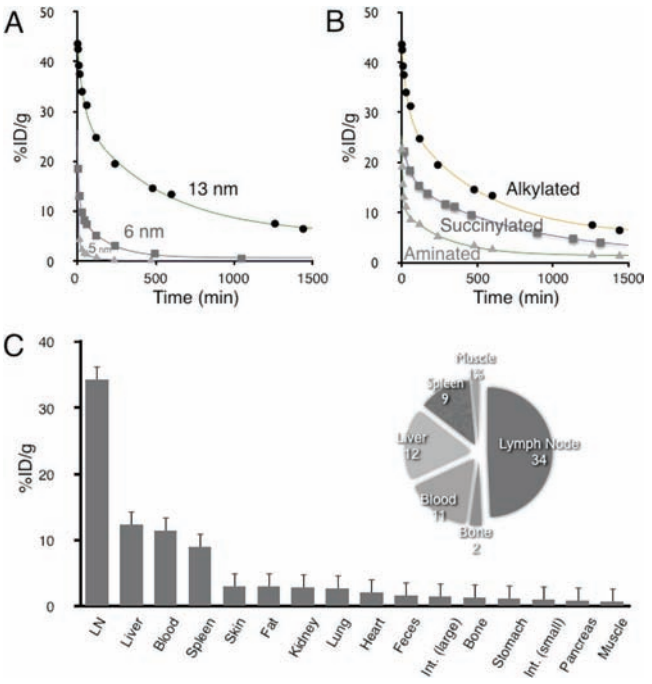

Figure 2. Pharmacokinetics of different DNPs. (A) Effect of size on blood half-life. (B) Effect of surface modification on blood half-life. (C) Biodistribution plotted as tissue concentration 24 h after intravenous administration of succinylated 13 nm DNPs. The inset shows the distribution in major organs.

accumulation, and thus, subsequent efforts focused solely on the 13 nm DNPs. To further determine the effects of surface modification on blood half-life, we compared desferrioxamine-labeled DNP with free amines, succinic anhydride, or pentynoyl-NHS ester capping (Figure 2B). The two-phase blood half-lives were 1.3 h for the aminated, 3.9 h for the succinylated, and 6.1 h for the pentynoylated preparations. These results demonstrate that blood half-life can be modulated on the basis of particle size as well as surface modification chemistry. Reasoning that the succinylated 13 nm DNP had ideal pharmacokinetics for ^{89}Zr, we chose it for biodistribution experiments. Figure 2C summarizes the organ distribution 24 h after injection of 100 μCi showing primary accumulation in lymph nodes [34 ± 16% of the injected dose/g of tissue (% IDGT)], liver (12 ± 2% IDGT), blood [11 ± 1% IDGT, located primarily in circulating leukocytes (see below)], and spleen (9 ± 1% IDGT), with much lower levels of accumulation in most other tissues, including bone, kidneys, and intestines. If we adjust for excretion (19.2 ± 0.8% of the injected dose over 24 h) and the body mass of the main organs, the overall activity of the succinylated 13 nm DNP was 22 ± 3% in liver, 19 ± 2% in circulating cells, and 2 ± 0.1% in spleen, with the remainder distributed in other organs.

In Vivo Imaging. We next performed PET-CT imaging using the same ^{89}Zr-labeled DNP described above in a cancer mouse model. We used a syngeneic colon carcinoma (CT26) mouse model because it had been used extensively for investigations of tumor infiltrating host cells,[22] vaccines,[23] and other studies.[24,25] Figure 3 shows representative images from different mice bearing the xenografts. The extent of tumoral uptake was surprisingly high (20 ± 5% IDGT), surpassing concentrations of other reticuloendothelial system RES organs in some animals. To determine whether tumoral accumulation was due to cellular uptake or extraversion and interstitial accumulation, we performed extensive correlative histology and flow cytometry studies.

Harvested tumors were sliced into ~1 mm sections and imaged by autoradiography to juxtapose sections to Mac-3 (a macrophage specific stain) histological stain. Overall, there was good agreement between "hot spots" and Mac3 positivity through the sections (Figure 4). Histology showed distinct uptake of fluorescent DNPs in Mac3 positive cells and a general lack of uptake in Mac3 negative cells (Figure 4).

To further investigate the pharmacokinetics and cellular uptake of the DNP, we performed confocal intravital microscopy studies. H2B-RFP-expressing HT1080 tumor cells were implanted in dorsal skinfold window chambers, and after the tumors had grown for 8 days, animals received CLIO-FITC, a commonly used macrophage imaging agent.[6] The following day, fluorescent DNP nanoparticles were administered systemically, and animals were imaged over time. Figure 5A shows representative imaging 3 h postinjection demonstrating DNP (red) primarily in the vasculature with little cellular uptake or even interstitial accumulation. Tumor cells (blue) and tumor-associated macrophages (TAMs, green) were clearly identified. Twenty-four hours postinjection, most of the DNPs had localized exclusively to TAMs with little compound remaining in the vasculature or tumor cells. The Pearson's colocalization

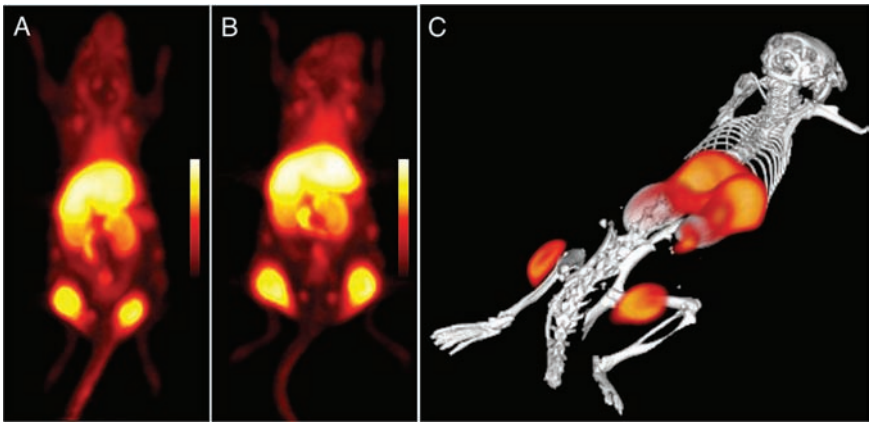

Figure 3. PET imaging of ^{89}Zr-labeled DNPs in mice bearing bilateral flank tumors (24 h after administration). (A and B) Two different animals showing similar distributions in all four tumors (coronal stacks). (C) Three-dimensional rendering of the animal pictured in panel A.

dx.doi.org/10.1021/bc200405d | *Bioconjugate Chem.* 2011, 22, 2383–2389

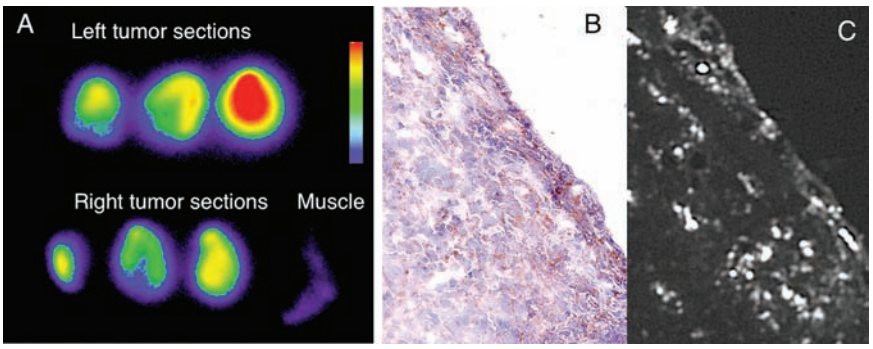

Figure 4. Autoradiography and histology of the distribution of DNPs. (A) Autoradiography of 1 mm tumor and other tissue sections showing predominant accumulations in tumors. (B) Representative Mac3 immunohistology section. (C) Distribution of fluorescent DNPs in Mac3 positive cells, adjacent sections to that shown in B.

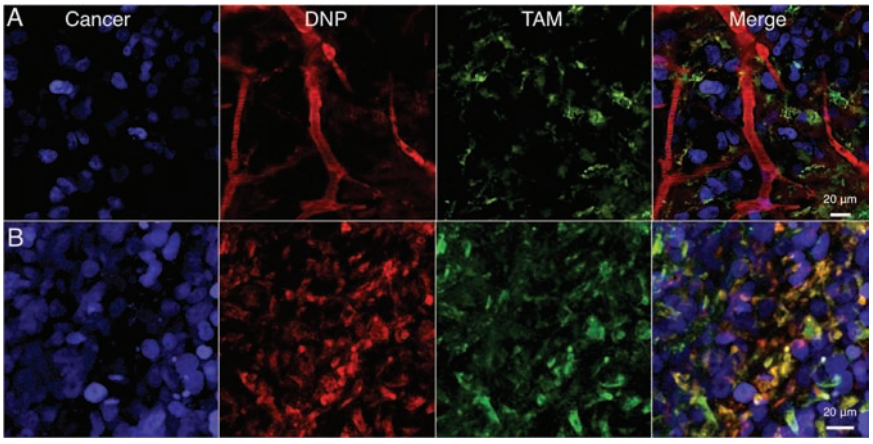

Figure 5. Microscopy of the distribution of DNPs in the tumor microenvironment in a live mouse (A) 3 h after injection and (B) 24 h after injection. Initially, the DNP is primarily seen in the vasculature, whereas it is almost exclusively colocalized (yellow) with TAMs after 24 h.

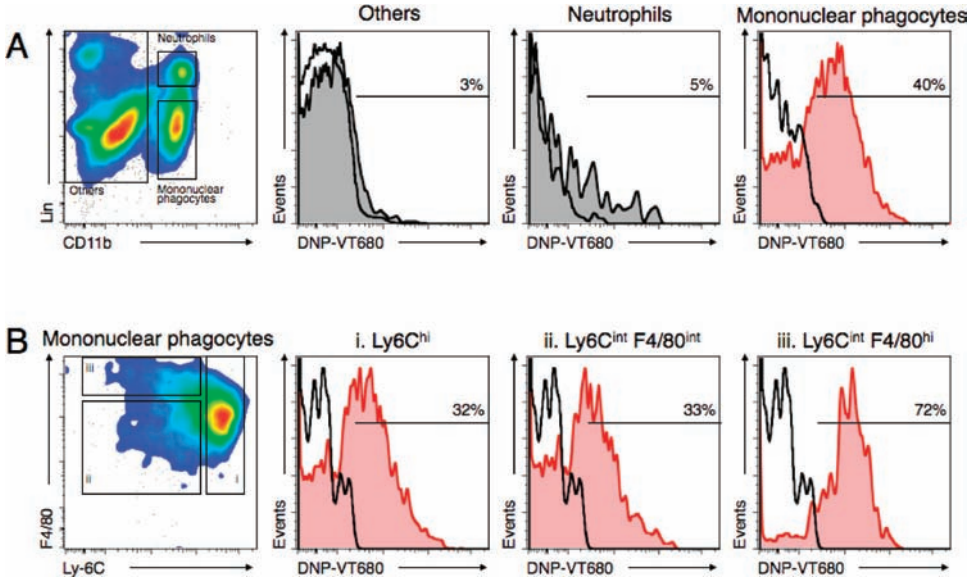

Figure 6. (A) Flow cytometric identification of mononuclear phagocytes ($CD11b^+$ Lin^{low}), neutrophils [$CD11b^+$ Lin^{high} ($Ly\text{-}6G^+$)], and other cells ($CD11b^-$) in the tumor stroma (left). The three histograms at the right show the percent of each population with detectable DNP-680 particles. Nearly all fluorescent DNP (DNP-680) is associated with mononuclear phagocytes. (B) Flow cytometric identification of mononuclear phagocyte subsets. $CD11b^+$ Lin^{low} cells were further divided into $Ly6C^{hi}$ (i) and $Ly6C^{int}$ $F4/80^{int}$ (ii) monocyte-like cells and $Ly\text{-}6C^{int}$ $F4/80^{hi}$ macrophages (left). The three histograms at the right show the percent of each population with detectable DNP-680 particles. DNP is associated with both monocyte subsets ($Ly6C^{hi}$ and $Ly6C^{lo}$) as well as with macrophages ($F4/80^{hi}$).

dx.doi.org/10.1021/bc200405d | *Bioconjugate Chem.* 2011, 22, 2383–2389

coefficient between DNP (red) and TAM (green) was 0.82 ± 0.07 (n = 5).

To augment the results of the IVM imaging, we performed flow cytometry on harvested tissues 24 h after administration of fluorescently labeled DNP. Presented in Figure 6, these data indicate that 40% of TAMs were positive for DNPs while only 5% of neutrophils and 3% of other lymphocytes were positive for DNPs. Figure SI.3 of the Supporting Information includes FACS data analysis of the uptake of DNPs in liver and kidney tissues. Here, 35 and 40% of macrophages are positive for DNP in the liver and kidney, respectively, and 7 and 9% of all other lymphocytes in these organs are positive for DNP. Together, these data and the IVM indicate strong specificity of DNPs for macrophages.

DISCUSSION

We have synthesized a 13 nm nanoparticle comprised of short, cross-linked dextrans that were modified with desferrioxamine to chelate ^{89}Zr for imaging of macrophages by PET. The nanoparticle was stable and biocompatible and accumulated specifically in tissue resident macrophages upon systemic administration. We show that cellular accumulation is complete within 24 h of administration (vascular $t_{1/2}$ of 3.9 h), showing faster kinetics compared to those of larger dextran nanoparticles in clinical use (vascular $t_{1/2}$ of ~24−48 h).[6] We did not observe any adverse effects at the doses used, and this is consistent with observations from dextran preparations in clinical use.[26] It should be pointed out that the PET dose was <5% of the MR comparable dose of iron oxide nanoparticles[9] and could be further reduced with higher specific activity. Imaging and corroborative experiments in xenograft tumor models showed extensive accumulation in TAMs, and this should be particularly useful for prognostication of cancers[27,28] or therapy assessment.[29,30]

Previously used dextran nanoparticles were primarily designed to have magnetic iron oxide cores and were naturally larger (20−200 nm). To determine the ideal size of dextran nanoparticles for PET applications, we initially performed a size optimization study leading up to the current preparation. Specifically, we synthesized analogous dextran nanoparticles 5, 6, and 13 nm in diameter [chosen from a larger size range (2−30 nm) study performed previously] and determined their pharmacokinetics, renal clearance rates, and macrophage uptake in vivo. Perhaps as expected, the 5 nm nanoparticle showed considerable renal clearance whereas the 13 nm nanoparticle had the highest level of macrophage uptake and was thus chosen for subsequent experiments. Prior to this study, we also compared the biological behavior of linear and cross-linked dextrans and found the latter to be better tolerated. While the current preparation indeed shows ideal imaging characteristics and clean macrophage uptake, on the basis of the intravital microscopy and flow cytometry result, we anticipate a few changes for future clinical preparations. For one, we would anticipate using a ^{68}Ga tracer to minimize radiation exposure and perhaps modulate the anticipated longer human blood half-life through modification of residual amines with alternative capping agents.[14]

A number of prior studies have used alternative PET agents for imaging macrophages, including ^{18}FDG,[31,32] ligands for the peripheral benzodiazepine receptor ligands (e.g., PK11195),[33,34] or magneto-optical nanoparticles.[8,9] Although commonly used, FDG is not macrophage specific as many nonphagocytic cells will also internalize glucose, particularly cancer, neuronal, and muscle cells as well as other leukocytes.[35,36] Peripheral benzodiazepine receptor ligands have been primarily used for neuroinflammation studies, and few validation studies of peripheral macrophages are available. The receptor is now known to be the translocator protein (TSPO), an 18 kDa protein that has many functions and is found in diverse tissues, including heart, liver, adrenal, testis, brain, and lymphatic tissue, in addition to leukocytes and macrophages.[37] Therefore, any imaging agent targeting this receptor would not be specific for macrophages.

We anticipate that the developed macrophage selective imaging agents will be useful for a number of applications in which quantitation of macrophages and inflammation levels are important. One of the most obvious applications is in cancer therapy where inflammation has been associated with inverse prognosis[27] and where antimacrophage strategies are now being employed to enhance therapeutic effects.[30] Another application is quantitation of inflammation in atherosclerosis and myocardial infarction in patients undergoing statin treatments. Macrophage imaging could be used as a surrogate of lesion activity. Finally, there are numerous other medical applications where foci of infection or inflammation require localization (e.g., neuroinflammation, Crohn's disease, and arthritis) or quantitation (e.g., macrophage activity in fat tissue of obese patients). We hope that the described material and future clinical derivatives fulfill the requirements of specificity and may be uniquely suited for clinical imaging.

ASSOCIATED CONTENT

Supporting Information

Experimental data regarding nanoparticle size distribution, intravital microscopy, and flow cytometry analysis and complete materials and methods. This material is available free of charge via the Internet at http://pubs.acs.org.

AUTHOR INFORMATION

Corresponding Author

*Center for Systems Biology, Massachusetts General Hospital, 185 Cambridge St., CPZN 5206, Boston, MA 02114. Phone: (617) 726-8226. E-mail: rweissleder@mgh.harvard.edu.

Author Contributions

E.J.K. and J.Y. contributed equally to this work.

ACKNOWLEDGMENTS

We acknowledge the help of Dr. Rainer Kohler for help with intravital microscopy, Dr. Yvonne Fisher-Jeffes for review of the manuscript, and Yoshiko Iwamoto for performing histology. We also thank Nicholas Ramos (Memorial Sloan-Kettering Cancer Center) for ^{89}Zr production. This work was funded in part by National Institutes of Health Grants P50 CA86355, U54 CA126515, U54 CA151884, HHSN268201000044C, and U24 CA092782.

REFERENCES

(1) Lee, S. H., Starkey, P. M., and Gordon, S. (1985) Quantitative analysis of total macrophage content in adult mouse tissues. Immunochemical studies with monoclonal antibody F4/80. *J. Exp. Med. 161*, 475−489.

(2) Ho, M. K., and Springer, T. A. (1983) Tissue distribution, structural characterization, and biosynthesis of Mac-3, a macrophage surface glycoprotein exhibiting molecular weight heterogeneity. *J. Biol. Chem. 258*, 636−642.

(3) Di Gregorio, G. B., Yao-Borengasser, A., Rasouli, N., Varma, V., Lu, T., Miles, L. M., Ranganathan, G., Peterson, C. A., McGehee, R. E., and Kern, P. A. (2005) Expression of CD68 and macrophage chemoattractant protein-1 genes in human adipose and muscle tissues: Association with cytokine expression, insulin resistance, and reduction by pioglitazone. *Diabetes 54*, 2305−2313.

(4) Thiele, J., Braeckel, C., Wagner, S., Falini, B., Dienemann, D., Stein, H., and Fischer, R. (1992) Macrophages in normal human bone marrow and in chronic myeloproliferative disorders: An immunohistochemical and morphometric study by a new monoclonal antibody (PG-M1) on trephine biopsies. *Virchows Arch. A: Pathol. Anat. Histopathol. 421*, 33−39.

(5) Gaglia, J. L., Guimaraes, A. R., Harisinghani, M., Turvey, S. E., Jackson, R., Benoist, C., Mathis, D., and Weissleder, R. (2011) Noninvasive imaging of pancreatic islet inflammation in type 1A diabetes patients. *J. Clin. Invest. 121*, 442−445.

(6) Harisinghani, M. G., Barentsz, J., Hahn, P. F., Deserno, W. M., Tabatabaei, S., van de Kaa, C. H., de la Rosette, J., and Weissleder, R. (2003) Noninvasive detection of clinically occult lymph-node metastases in prostate cancer. *N. Engl. J. Med. 348*, 2491−2499.

(7) Leimgruber, A., Berger, C., Cortez-Retamozo, V., Etzrodt, M., Newton, A. P., Waterman, P., Figueiredo, J. L., Kohler, R. H., Elpek, N., Mempel, T. R., Swirski, F. K., Nahrendorf, M., Weissleder, R., and Pittet, M. J. (2009) Behavior of endogenous tumor-associated macrophages assessed in vivo using a functionalized nanoparticle. *Neoplasia 11*, 459−468.

(8) Nahrendorf, M., Keliher, E., Marinelli, B., Leuschner, F., Robbins, C. S., Gerszten, R. E., Pittet, M. J., Swirski, F. K., and Weissleder, R. (2011) Detection of macrophages in aortic aneurysms by nanoparticle positron emission tomography-computed tomography. *Arterioscler., Thromb., Vasc. Biol. 31*, 750−757.

(9) Nahrendorf, M., Zhang, H., Hembrador, S., Panizzi, P., Sosnovik, D. E., Aikawa, E., Libby, P., Swirski, F. K., and Weissleder, R. (2008) Nanoparticle PET-CT imaging of macrophages in inflammatory atherosclerosis. *Circulation 117*, 379−387.

(10) Pressly, E. D., Rossin, R., Hagooly, A., Fukukawa, K., Messmore, B. W., Welch, M. J., Wooley, K. L., Lamm, M. S., Hule, R. A., Pochan, D. J., and Hawker, C. J. (2007) Structural effects on the biodistribution and positron emission tomography (PET) imaging of well-defined ^{64}Cu-labeled nanoparticles comprised of amphiphilic block graft copolymers. *Biomacromolecules 8*, 3126−3134.

(11) Schipper, M. L., Cheng, Z., Lee, S. W., Bentolila, L. A., Iyer, G., Rao, J., Chen, X., Wu, A. M., Weiss, S., and Gambhir, S. S. (2007) microPET-based biodistribution of quantum dots in living mice. *J. Nucl. Med. 48*, 1511−1518.

(12) Almutairi, A., Rossin, R., Shokeen, M., Hagooly, A., Ananth, A., Capoccia, B., Guillaudeu, S., Abendschein, D., Anderson, C. J., Welch, M. J., and Frechet, J. M. (2009) Biodegradable dendritic positron-emitting nanoprobes for the noninvasive imaging of angiogenesis. *Proc. Natl. Acad. Sci. U.S.A. 106*, 685−690.

(13) Nahrendorf, M., Keliher, E., Marinelli, B., Waterman, P., Feruglio, P. F., Fexon, L., Pivovarov, M., Swirski, F. K., Pittet, M. J., Vinegoni, C., and Weissleder, R. (2010) Hybrid PET-optical imaging using targeted probes. *Proc. Natl. Acad. Sci. U.S.A. 107*, 7910−7915.

(14) Weissleder, R., Kelly, K., Sun, E. Y., Shtatland, T., and Josephson, L. (2005) Cell-specific targeting of nanoparticles by multivalent attachment of small molecules. *Nat. Biotechnol. 23*, 1418−1423.

(15) Zinderman, C. E., Landow, L., and Wise, R. P. (2006) Anaphylactoid reactions to Dextran 40 and 70: Reports to the United States Food and Drug Administration, 1969 to 2004. *J. Vasc. Surg. 43*, 1004−1009.

(16) Macdougall, I. C. (2009) Evolution of iv iron compounds over the last century. *Journal of Renal Care 35* (Suppl. 2), 8−13.

(17) Pittet, M. J. (2009) Behavior of immune players in the tumor microenvironment. *Curr. Opin. Oncol. 21*, 53−59.

(18) Coussens, L. M., and Pollard, J. W. (2011) Leukocytes in mammary development and cancer. *Cold Spring Harbor Perspect. Biol.*, DOI: doi: 10.1101/cshperspect.a003285.

(19) Dubois, M., Gilles, K. A., Hamilton, J. K., Rebers, P. A., and Smith, F. (1956) Colorimetric Method for Determination of Sugars and Related Substances. *Anal. Chem. 28*, 350−356.

(20) Snyder, S. L., and Sobocinski, P. Z. (1975) An improved 2,4,6-trinitrobenzenesulfonic acid method for the determination of amines. *Anal. Biochem. 64*, 284−288.

(21) Holland, J. P., Divilov, V., Bander, N. H., Smith-Jones, P. M., Larson, S. M., and Lewis, J. S. (2010) ^{89}Zr-DFO-J591 for immunoPET of prostate-specific membrane antigen expression in vivo. *J. Nucl. Med. 51*, 1293−1300.

(22) Mempel, T. R., Pittet, M. J., Khazaie, K., Weninger, W., Weissleder, R., von Boehmer, H., and von and Andrian, U. H. (2006) Regulatory T cells reversibly suppress cytotoxic T cell function independent of effector differentiation. *Immunity 25*, 129−141.

(23) Pedersen, A. E., Buus, S., and Claesson, M. H. (2006) Treatment of transplanted CT26 tumour with dendritic cell vaccine in combination with blockade of vascular endothelial growth factor receptor 2 and CTLA-4. *Cancer Lett. 235*, 229−238.

(24) Yang, X. D., Ai, W., Asfaha, S., Bhagat, G., Friedman, R. A., Jin, G., Park, H., Shykind, B., Diacovo, T. G., Falus, A., and Wang, T. C. (2011) Histamine deficiency promotes inflammation-associated carcinogenesis through reduced myeloid maturation and accumulation of CD11b+Ly6G+ immature myeloid cells. *Nat. Med. 17*, 87−95.

(25) Stangl, S., Gehrmann, M., Riegger, J., Kuhs, K., Riederer, I., Sievert, W., Hube, K., Mocikat, R., Dressel, R., Kremmer, E., Pockley, A. G., Friedrich, L., Vigh, L., Skerra, A., and Multhoff, G. (2011) Targeting membrane heat-shock protein 70 (Hsp70) on tumors by cmHsp70.1 antibody. *Proc. Natl. Acad. Sci. U.S.A. 108*, 733−738.

(26) Singh, A., Patel, T., Hertel, J., Bernardo, M., Kausz, A., and Brenner, L. (2008) Safety of ferumoxytol in patients with anemia and CKD. *Am. J. Kidney Dis. 52*, 907−915.

(27) Steidl, C., Lee, T., Shah, S. P., Farinha, P., Han, G., Nayar, T., Delaney, A., Jones, S. J., Iqbal, J., Weisenburger, D. D., Bast, M. A., Rosenwald, A., Muller-Hermelink, H. K., Rimsza, L. M., Campo, E., Delabie, J., Braziel, R. M., Cook, J. R., Tubbs, R. R., Jaffe, E. S., Lenz, G., Connors, J. M., Staudt, L. M., Chan, W. C., and Gascoyne, R. D. (2010) Tumor-associated macrophages and survival in classic Hodgkin's lymphoma. *N. Engl. J. Med. 362*, 875−885.

(28) Mantovani, A., Allavena, P., Sica, A., and Balkwill, F. (2008) Cancer-related inflammation. *Nature 454*, 436−444.

(29) De Palma, M., and Lewis, C. E. (2011) Cancer: Macrophages limit chemotherapy. *Nature 472*, 303−304.

(30) DeNardo, D. G., Brennan, D. J., Rexhepaj, E., Ruffell, B., Shiao, S. L., Madden, S F., Gallagher, W. M., Wadhwani, N., Keil, S. D., Junaid, S. A., Rugo, H. S., Hwang, E. S., Jirström, K., West, B. L., and Coussens, L. M. (2011) Leukocyte Complexity Predicts Breast Cancer Survival and Functionally Regulates Response to Chemotherapy. *Cancer Discovery 1*, 52−64.

(31) Rogers, I. S., and Tawakol, A. (2011) Imaging of coronary inflammation with FDG-PET: Feasibility and clinical hurdles. *Curr. Cardiol. Rep. 13*, 138−144.

(32) Galban, C. J., Bhojani, M. S., Lee, K. C., Meyer, C. R., Van Dort, M. E., Kuszpit, K. K., Koeppe, R. A., Ranga, R., Moffat, B. A., Johnson, T. D., Chenevert, T. L., Rehemtulla, A., and Ross, B. D. (2010) Evaluation of treatment-associated inflammatory response on diffusion-weighted magnetic resonance imaging and 2-[^{18}F]-fluoro-2-deoxy-D-glucose-positron emission tomography imaging biomarkers. *Clin. Cancer Res. 16*, 1542−1552.

(33) Schweitzer, P. J., Fallon, B. A., Mann, J. J., and Kumar, J. S. (2010) PET tracers for the peripheral benzodiazepine receptor and uses thereof. *Drug Discovery Today 15*, 933−942.

(34) Chauveau, F., Boutin, H., Van Camp, N., Dolle, F., and Tavitian, B. (2008) Nuclear imaging of neuroinflammation: A comprehensive review of [^{11}C]PK11195 challengers. *Eur. J. Nucl. Med. Mol. Imaging 35*, 2304−2319.

(35) Locasale, J. W., Vander Heiden, M. G., and Cantley, L. C. (2010) Rewiring of glycolysis in cancer cell metabolism. *Cell Cycle 9*, 4253.

(36) Vander Heiden, M. G., Locasale, J. W., Swanson, K. D., Sharfi, H., Heffron, G. J., Amador-Noguez, D., Christofk, H. R., Wagner, G., Rabinowitz, J. D., Asara, J. M., and Cantley, L. C. (2010) Evidence for an alternative glycolytic pathway in rapidly proliferating cells. *Science 329*, 1492−1499.

(37) Papadopoulos, V., Baraldi, M., Guilarte, T. R., Knudsen, T. B., Lacapere, J. J., Lindemann, P., Norenberg, M. D., Nutt, D., Weizman, A., Zhang, M. R., and Gavish, M. (2006) Translocator protein (18 kDa): New nomenclature for the peripheral-type benzodiazepine receptor based on its structure and molecular function. *Trends Pharmacol. Sci. 27*, 402−409.

Bioconjugate Chemistry

Communication

pubs.acs.org/bc

Specific Pathogen Detection Using Bioorthogonal Chemistry and Diagnostic Magnetic Resonance

Monty Liong,[†,∥] Marta Fernandez-Suarez,[‡,§,∥] David Issadore,[†] Changwook Min,[†] Carlos Tassa,[†] Thomas Reiner,[†] Sarah M. Fortune,[‡] Mehmet Toner,[§] Hakho Lee,*[,†] and Ralph Weissleder*[,†]

[†]Center for Systems Biology and [§]BioMEMS Resource Center, Massachusetts General Hospital/Harvard Medical School, Boston, Massachusetts, United States

[‡]Department of Immunology and Infectious Diseases, Harvard School of Public Health, Boston, Massachusetts, United States

Supporting Information

ABSTRACT: The development of faster and more sensitive detection methods capable of identifying specific bacterial species and strains has remained a longstanding clinical challenge. Thus to date, the diagnosis of bacterial infections continues to rely on the performance of time-consuming microbiological cultures. Here, we demonstrate the use of bioorthogonal chemistry for magnetically labeling specific pathogens to enable their subsequent detection by nuclear magnetic resonance. Antibodies against a bacterial target of interest were first modified with *trans*-cyclooctene and then coupled to tetrazine-modified magnetic nanoprobes, directly on the bacteria. This labeling method was verified by surface plasmon resonance as well as by highly specific detection of *Staphylococcus aureus* using a miniaturized diagnostic magnetic resonance system. Compared to other copper-free bioorthogonal chemistries, the cycloaddition reaction reported here displayed faster kinetics and yielded higher labeling efficiency. Considering the short assay times and the portability of the necessary instrumentation, it is feasible that this approach could be adapted for clinical use in resource-limited settings.

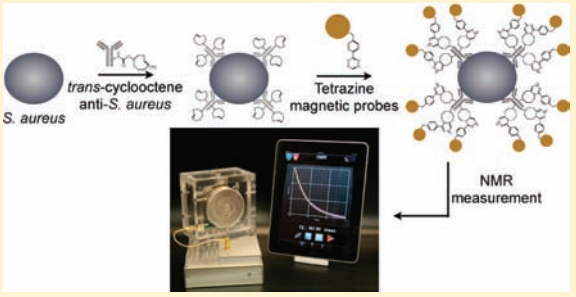

Faster assays, combined with detection of multiple bacterial species and strains, would not only improve global health but effectively lower healthcare costs.[1,2] Examples of these detection methods include fluorescence imaging using sugar molecules (e.g. maltohexaose and trehalose) for highly specific labeling of targeted bacteria,[3,4] and colorimetric assay based on enzyme−gold nanoparticle system.[5] In an effort to develop a simple diagnostic test that could be routinely used for the detection of bacterial pathogens in resource-limited clinical settings, we extended a bioorthogonal binding method to the identification of bacterial pathogens. The method is based on a two-step strategy in which antibodies are first modified to bind specific targets and are then coupled to multiple magnetic probes. Signals from these probes can subsequently be detected by nuclear magnetic resonance (NMR). Furthermore, in cases where target concentrations are low, this method has the added advantage of being able to amplify target signals.[6,7] A major challenge to developing diagnostic tests for bacteria has been achieving accurate detection of target pathogens from complex specimens, which may contain multiple bacterial strains. We have now overcome this hurdle by employing the cycloaddition bioorthogonal reaction of *trans*-cyclooctene (TCO)-modified antibodies to robustly and efficiently label bacteria with tetrazine (Tz)-modified magnetic nanoprobes (MNPs).[8] The labeled pathogens were then detected using a newly developed diagnostic magnetic resonance (DMR) system. Here, the clinical potential of this method is demonstrated by the accurate and rapid (<30 min) detection of *Staphylococcus aureus* (*S. aureus*) in human sputa.

It is often the case that the use of large affinity ligands results in low conjugation efficiency to nanoprobes and thus ineffective binding of the conjugates to targeted cells.[6] As a result, each new preparation of immunoconjugates for cellular labeling requires an optimization process to maximize its binding to targeted samples. As an alternative strategy, the use of bioorthogonal covalent reactions has become of increasing interest as a novel platform for biological labeling. Such reactions not only are highly selective toward their binding partners, but also have fast reactivity in biological solutions and at ambient temperatures.[9−11] The approach is also modular and generalizable. Namely, a vast array of affinity ligands for cellular targeting can be prepared using bioorthogonal components, and generic probes can be used for labeling.[12] Tz/TCO cycloaddition in particular has demonstrated great potential: it is catalyst-free, shows good stability in biological media, displays much faster reaction kinetics compared to other bioorthogonal reactions, and is capable of significantly amplifying probe-loading onto targets.[13,14] Indeed, recently, this reaction was successfully adapted to the molecular profiling of cancer cells[6,7,15] as well as to *in vivo* imaging.[16]

Received: September 8, 2011
Revised: November 1, 2011
Published: November 2, 2011

ACS Publications © 2011 American Chemical Society

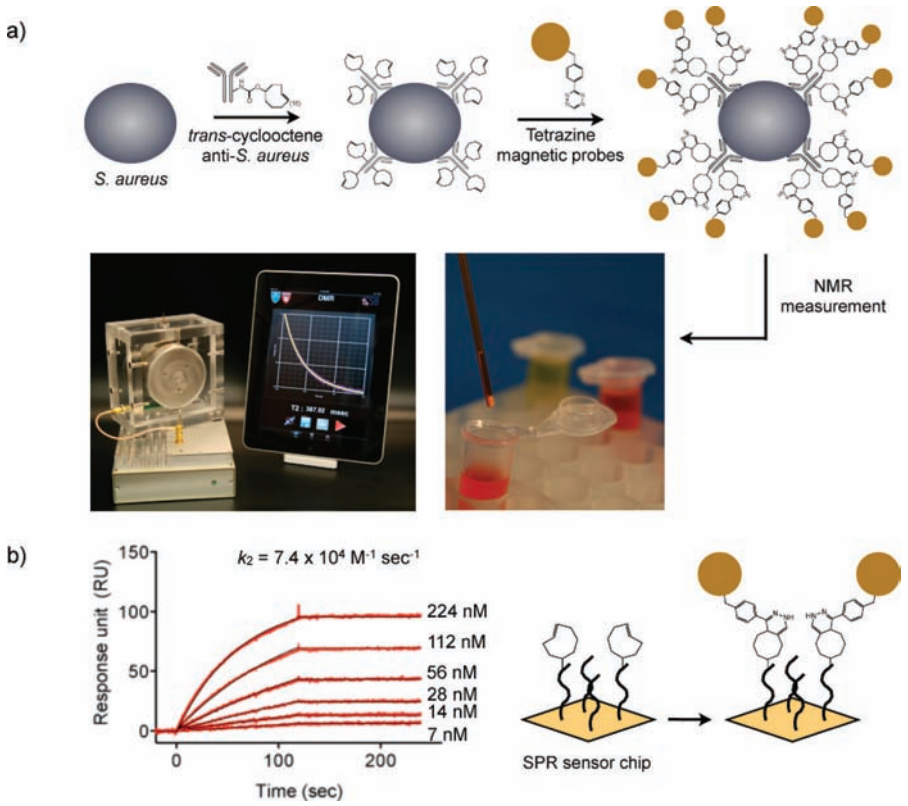

Figure 1. (a) Schematic of the two-step magnetic labeling method involving the cycloaddition of *trans*-cyclooctene (TCO) to tetrazine (Tz). *Staphylococcus aureus* (*S. aureus*) cells were first targeted with TCO-modified antibodies and then coupled to Tz-modified magnetic nanoprobes. Given that each antibody is bound by ~15 TCO molecules, multiple probes can be attached to each marker. The labeled cells were subsequently loaded into a disposable tube for detection using a diagnostic magnetic resonance device. (b) Surface plasmon resonance (SPR) measurements (left) and a schematic of the binding kinetics between Tz-modified probes and surface-immobilized TCO (right). The fast second-order rate constant (k_2 = 7.4 × 10^4 M^{-1} s^{-1}), determined by flowing the probes at different concentrations, is largely due to the multivalent binding of Tz-MNPs.

The cycloaddition reaction of Tz and TCO offers a modular platform for effectively coupling magnetic probes to the surface of a particular target using a generalized labeling strategy. Figure 1a describes the developed two-step approach for bacterial detection based on the Tz/TCO reaction. We initially coupled amine-reactive Tz to the amine groups present on the MNPs; MNPs were composed of an iron oxide core and a dextran coating.[17] Likewise, affinity ligands were modified with amine-reactive TCO. Samples were first incubated with TCO-conjugated antibodies to specifically target the bacteria before coupling with Tz-modified MNPs (Tz-MNPs). This labeling method rendered the bacteria superparamagnetic, and thus enhanced the transverse relaxation of the samples, as determined by NMR. After loading the samples into disposable tubes, their relaxation rates (R_2) were measured using a miniaturized DMR system.[18]

The binding kinetics of the probes to TCO molecules were characterized using surface plasmon resonance (SPR).[19] To determine the association constant of the Tz-modified probes to TCO, sequentially increasing concentrations of Tz-MNPs were flowed over the SPR sensor surface, which was functionalized with TCO molecules. With a measured second-order rate constant of $k_2 \approx 7.4 \times 10^4$ M^{-1} s^{-1} at room temperature, the reaction of Tz-MNPs with TCO proved fast and highly stable under the continuous flow stream of the SPR (Figure 1b). The capacity of the MNPs for multivalent binding and the fast kinetics of Tz/TCO thus indicated its suitability for rapid magnetic labeling of targeted bacteria.

S. aureus was selected as the specific target for pathogen detection, for which a highly selective antibody against the bacteria (anti-SA) was used as the affinity ligand. The antibodies were subsequently modified with TCO; an average of ~15 TCO molecules were conjugated to each antibody, as determined by matrix-assisted laser desorption/ionization-time-of-flight (MALDI-TOF) mass spectrometry (SI Figure S1). Each MNP was functionalized with approximately ~8 fluorescent moieties and ~56 Tz molecules, as measured by the SPDP assay.[20] The bacteria were first tagged with TCO-anti-SA before being sequentially coupled to Tz-MNPs. Fluorescence microscopy (Figure 2a) showed that bacterial labeling using the bioorthogonal approach was both efficient and consistent. In contrast, control samples showed only punctate traces of green fluorescence, thus confirming the minimal nonspecific binding of the Tz-probes (Figure 2b).

The specificity of the Tz/TCO labeling method was further investigated by applying the assay to other relevant pathogens. About 10^5 CFU of the target bacteria (*S. aureus*), an acid-fast species (*Mycobacterium smegmatis*), as well as Gram-negative (*Haemophilus influenzae, Escherichia coli, Pseudomonas aeruginosa*), and Gram-positive bacteria (*Streptococcus pneumoniae*) were each mixed with TCO-anti-SA and then incubated with Tz-MNPs in a 300 μL volume. Each sample was then concentrated by centrifugation and transferred to the sample chamber of the DMR device for analysis (~10^4 CFU in 2 μL volume). The measured ΔR_2 value for each sample was then converted to cellular relaxivity Δr_2 (ΔR_2 divided by cell

dx.doi.org/10.1021/bc200490r | *Bioconjugate Chem.* 2011, 22, 2390–2394

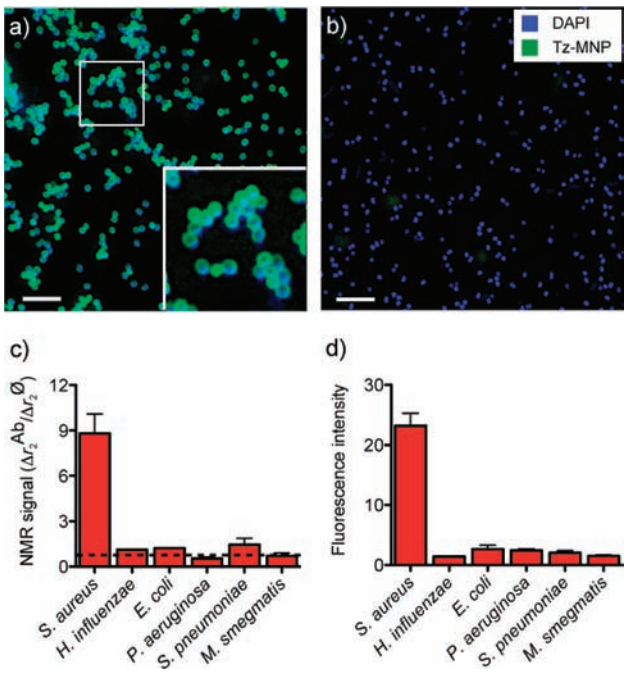

Figure 2. Selective bacterial labeling using bioorthogonal chemistry. (a) DAPI stained *S. aureus* (blue) were targeted with TCO-anti-SA and labeled with fluorescent Tz-modified probes (green). Labeling of the bacterial membrane can be clearly seen in the enlarged inset image (bottom right; higher magnification of boxed region). Scale bar, 5 μm. (b) Minimal fluorescence from the probes was observed on the control nontargeted bacterial samples. (c) Detection of *S. aureus* using the diagnostic magnetic resonance (DMR) device (~10^4 CFU in 2 μL volume). A panel of bacterial strains was incubated first with TCO-antibodies (specific for *S. aureus*) and then with Tz-MNPs, before undergoing measurement with DMR. The displayed nuclear magnetic resonance (NMR) signals were determined by calculating the ratio of cellular relaxivities between the targeted (Δr_2^{Ab}) and control ($\Delta r_2^{\varnothing}$) samples. Bioorthogonal labeling yielded accurate and elevated NMR signals for the targeted *S. aureus*, but not for other bacteria. (d) Fluorescence measurements of the bacterial samples, as determined by flow cytometry. The mean fluorescence intensity was normalized by calculating the ratio between each bacterial sample and the nontargeted control. *S. aureus* showed considerably higher normalized fluorescence intensity than other bacteria. Overall, the fluorescence measurements obtained by flow cytometry showed an excellent correlation with measurements obtained by DMR.

concentration), a value which is proportional to the number of MNPs per bacterium.[21] For *S. aureus*, the Δr_2 was ~9-fold higher than the background, whereas the Δr_2 for other pathogens showed a small or no increase over the baseline (Figure 2c). Corresponding fluorescence measurements by flow cytometry also correlated well with the DMR results (Figure 2d), thus demonstrating the reliable dual-labeling capability of the method for both optical and magnetic detection. Since the DMR device requires only small sample volumes (~2 μL), it could be useful as a complementary diagnostic technique in cases where only scant samples are available.

We next evaluated the efficacy of this bioorthogonal labeling method using clinically relevant samples (Figure 3). Expectorated samples were prepared by spiking *S. aureus* (~10^5 CFU) into human sputa (1 mL volume). Reagents for three different bioorthogonal groups were synthesized to compare their labeling efficiency in clinical samples, namely, Tz/TCO, Tz-norbornene (Tz/Norb), and dibenzylcyclooctyne-azide

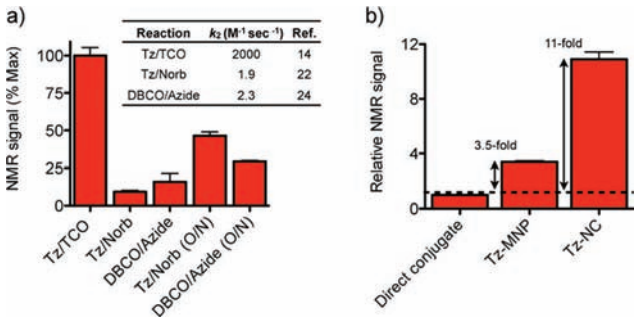

Figure 3. Comparison of the effectiveness of different bioorthogonal labeling strategies. (a) After liquefying human sputa containing *S. aureus* (~10^5 in 1 mL sputa), the bacteria were targeted and labeled using three different reactions. The inset table summarizes previously reported k_2 second-order rate constants for the different bioorthogonal chemistries. The Tz/TCO system was more effective in labeling bacteria than either of the alternative catalyst-free bioorthogonal chemistries, even with overnight (O/N) incubation (8 h). (b) The two-step labeling approach proved better at labeling bacteria than direct immunoconjugation. By using materials with higher magnetization (nanocrystals/NC versus magnetic nanoprobes/MNP), the NMR signal and detection sensitivity could be enhanced further.

(DBCO/Azide). For the Tz/Norb method, antibodies were tagged with norbornene and Tz-MNPs were used as the binding probes;[22,23] for the strain-promoted DBCO/Azide method, azide-modified antibodies and DBCO-MNPs were used (SI Figure S2).[24] Following sputum liquefaction, all samples were labeled with antibodies conjugated to the above-listed small molecules and their corresponding probes. The labeled samples were then divided for subsequent bacterial counts and DMR measurement. At the optimal probe concentration (50 μg/mL) and incubation time (15 min), the Tz/TCO labeling method yielded considerably higher DMR signals, outperforming Tz/Norb and DBCO/Azide methods even after longer overnight (O/N) incubation times (8 h) (Figure 3a). This result is consistent with previous reports which have shown that the Tz/TCO system has kinetics that are several orders of magnitude faster than other bioorthogonal reactions (Figure 3a inset).[14,22,24]

The modular Tz/TCO approach provided a facile method for enhancing the specificity and sensitivity of bacterial detection. In addition, by enabling the attachment of multiple MNPs per target, the Tz/TCO system resulted in a far higher DMR signal (>350%) to that of direct antibody–MNP conjugates (Figure 3b). The detection threshold for *S. aureus*, using the Tz/TCO MNPs was determined to be ~200 CFU with cutoff ΔR_2 value of 5% (SI Figure S3). The detection sensitivity can be further enhanced by increasing the r_2 relaxivity of the magnetic particles, which is achieved by using materials with strong magnetization and by increasing the size of the magnetic nanocrystals. Indeed, by replacing the MNPs with doped iron oxide nanocrystals (NCs) with higher transverse relaxivity (r_2 = 380 mM^{-1} s^{-1}, SI Figure S4),[25] the DMR sensitivity could be further improved (>300%). While the cross-linked iron oxide MNPs (transverse relaxivity r_2 = 70 mM^{-1} s^{-1}) are sufficient for initial labeling and detection experiments, the highly magnetic NCs would be useful for detection of pathogens in scant samples. The Tz/TCO method could also be extended to antibodies against other target pathogens for labeling and detection (SI Figure S5). Since DMR detection requires small volumes of samples, a parent

dx.doi.org/10.1021/bc200490r | *Bioconjugate Chem.* 2011, 22, 2390–2394

specimen can be divided into smaller aliquots, and each sample can be profiled for different pathogens via modular Tz/TCO approach. Such a capacity would be particularly useful in cases of infection where specific bacterial species are suspected or need to be ruled out in complex biological samples. The recent outbreak of enterohemorrhagic *Escherichia coli* (EHEC) strain O104:H4 exemplifies such needs. We are currently investigating this approach for the detection of *Mycobacterium tuberculosis* in clinical sputum samples.

In summary, we have developed a magnetic labeling assay capable of rapid pathogen detection using bioorthogonal conjugation chemistry. The cycloaddition between TCO-labeled *S. aureus* and Tz-modified MNPs enables specific bacteria to be labeled and subsequently detected. The magnetic labeling approach is efficient, chemoselective for the targeted pathogen (determined by the antibody used), and applicable to sputum samples. By using this magnetic labeling technique together with the miniaturized detection device (DMR), the strategy could serve as a promising diagnostic platform for pathogen detection within a point-of-care clinical setting.

■ ASSOCIATED CONTENT

Supporting Information

Experimental procedure and supplementary figures. This material is available free of charge via the Internet at http://pubs.acs.org.

■ AUTHOR INFORMATION

Corresponding Author

*Prof. Hakho Lee E-mail: hlee@mgh.harvard.edu. Prof. Ralph Weissleder E-mail: rweissleder@mgh.harvard.edu. Center for Systems Biology, Simches Research Center, 185 Cambridge St., Boston, MA 02114. Phone: 617-726-8226, Fax: 617-643-6133.

Author Contributions

‖These authors contributed equally to this work.

■ ACKNOWLEDGMENTS

We thank B. Akerley, M. Lipsitch, S. Lory, and C. Thompson for providing the laboratory reference bacterial strains; S. Agasti, H. J. Chung, R. Gorbatov, J. B. Haun, M. Karver, and N. Sergeyev for assistance with experiments; Y. Fisher-Jeffes for reviewing the manuscript. This work was supported in part by NIBIB grants R01-EB010011 (R.W.), R01-EB00462605A1 (R.W.), P41 EB002503 (M.T.), NHLBI contract HHSN268201000044C (R.W.), NIH grant T32CA79443 (R.W.), United States Army Medical Research Acquisition Activity Grant W81XWH-10-2-0161 (S.M.F.), and the Massachusetts General Hospital Executive Committee on Research fellowship (M.F.S.).

■ REFERENCES

(1) Urdea, M., Penny, L. A., Olmsted, S. S., Giovanni, M. Y., Kaspar, P., Shepherd, A., Wilson, P., Dahl, C. A., Buchsbaum, S., Moeller, G., and Burgess, D. C. H. (2006) Requirements for high impact diagnostics in the developing world. *Nature 444*, 73−79.

(2) Chin, C. D., Linder, V., and Sia, S. K. (2007) Lab-on-a-chip devices for global health: Past studies and future opportunities. *Lab Chip 7*, 41−57.

(3) Backus, K. M., Boshoff, H. I., Barry, C. S., Boutureira, O., Patel, M. K., D'Hooge, F., Lee, S. S., Via, L. E., Tahlan, K., Barry, C. E., and Davis, B. G. (2011) Uptake of unnatural trehalose analogs as a reporter for *Mycobacterium tuberculosis*. *Nat. Chem. Biol. 7*, 228−235.

(4) Ning, X., Lee, S., Wang, Z., Kim, D., Stubblefield, B., Gilbert, E., and Murthy, N. (2011) Maltodextrin-based imaging probes detect bacteria *in vivo* with high sensitivity and specificity. *Nat. Mater. 10*, 602−607.

(5) Miranda, O. R., Li, X., Garcia-Gonzalez, L., Zhu, Z.-J., Yan, B., Bunz, U. H. F., and Rotello, V. M. (2011) Colorimetric bacteria sensing using a supramolecular enzyme-nanoparticle biosensor. *J. Am. Chem. Soc. 133*, 9650−9653.

(6) Haun, J. B., Devaraj, N. K., Hilderbrand, S. A., Lee, H., and Weissleder, R. (2010) Bioorthogonal chemistry amplifies nanoparticle binding and enhances the sensitivity of cell detection. *Nat. Nanotechnol. 5*, 660−665.

(7) Haun, J. B., Castro, C. M., Wang, R., Peterson, V. M., Marinelli, B. S., Lee, H., and Weissleder, R. (2011) Micro-NMR for rapid molecular analysis of human tumor samples. *Sci. Transl. Med. 3*, 71ra16.

(8) Blackman, M. L., Royzen, M., and Fox, J. M. (2008) Tetrazine ligation: Fast bioconjugation based on inverse-electron-demand Diels-Alder reactivity. *J. Am. Chem. Soc. 130*, 13518−13519.

(9) Baskin, J. M., Prescher, J. A., Laughlin, S. T., Agard, N. J., Chang, P. V., Miller, I. A., Lo, A., Codelli, J. A., and Bertozzi, C. R. (2007) Copper-free click chemistry for dynamic *in vivo* imaging. *Proc. Natl. Acad. Sci. U.S.A. 104*, 16793−16797.

(10) Debets, M. F., van Berkel, S. S., Dommerholt, J., Dirks, A. J., Rutjes, F. P. J. T., and van Delft, F. L. (2011) Bioconjugation with strained alkenes and alkynes. *Acc. Chem. Res.*, DOI: 10.1021/ar200059z.

(11) Lim, R. K. V., and Lin, Q. (2010) Bioorthogonal chemistry: Recent progress and future directions. *Chem. Commun. 46*, 1589−1600.

(12) Sletten, E. M., and Bertozzi, C. R. (2009) Bioorthogonal chemistry: Fishing for selectivity in a sea of functionality. *Angew. Chem., Int. Ed. 48*, 6974−6998.

(13) Devaraj, N. K., and Weissleder, R. (2011) Biomedical applications of tetrazine cycloadditions. *Acc. Chem. Res.*, DOI: 10.1021/ar200037t.

(14) Taylor, M. T., Blackman, M. L., Dmitrenko, O., and Fox, J. M. (2011) Design and synthesis of highly reactive dienophiles for the tetrazine-*trans*-cyclooctene ligation. *J. Am. Chem. Soc. 133*, 9646−9649.

(15) Devaraj, N. K., Upadhyay, R., Haun, J. B., Hilderbrand, S. A., and Weissleder, R. (2009) Fast and sensitive pretargeted labeling of cancer cells through a tetrazine/*trans*-cyclooctene cycloaddition. *Angew. Chem., Int. Ed. 48*, 7013−7016.

(16) Rossin, R., Verkerk, P. R., van den Bosch, S., M., Vulders, R. C. M., Verel, I., Lub, J., and Robillard, M. S. (2010) *In vivo* chemistry for pretargeted tumor imaging in live mice. *Angew. Chem., Int. Ed. 49*, 3375−3378.

(17) Pittet, M. J., Swirski, F. K., Reynolds, F., Josephson, L., and Weissleder, R. (2006) Labeling of immune cells for *in vivo* imaging using magnetofluorescent nanoparticles. *Nat. Protocols 1*, 73−79.

(18) Issadore, D., Min, C., Liong, M., Chung, J., Weissleder, R., and Lee, H. (2011) Miniature magnetic resonance system for point-of-care diagnostics. *Lab Chip 11*, 2282−2287.

(19) Tassa, C., Duffner, J. L., Lewis, T. A., Weissleder, R., Schreiber, S. L., Koehler, A. N., and Shaw, S. Y. (2009) Binding affinity and kinetic analysis of targeted small molecule-modified nanoparticles. *Bioconjugate Chem. 21*, 14−19.

(20) Josephson, L., Tung, C.-H., Moore, A., and Weissleder, R. (1999) High-efficiency intracellular magnetic labeling with novel superparamagnetic-Tat peptide conjugates. *Bioconjugate Chem. 10*, 186−191.

(21) Lee, H., Yoon, T.-J., Figueiredo, J.-L., Swirski, F. K., and Weissleder, R. (2009) Rapid detection and profiling of cancer cells in fine-needle aspirates. *Proc. Natl. Acad. Sci. U. S. A. 106*, 12459−12464.

(22) Devaraj, N. K., Weissleder, R., and Hilderbrand, S. A. (2008) Tetrazine-based cycloadditions: Application to pretargeted live cell imaging. *Bioconjugate Chem. 19*, 2297−2299.

(23) Han, H.-S., Devaraj, N. K., Lee, J., Hilderbrand, S. A., Weissleder, R., and Bawendi, M. G. (2010) Development of a

bioorthogonal and highly efficient conjugation method for quantum dots using tetrazine-norbornene cycloaddition. *J. Am. Chem. Soc. 132*, 7838−7839.

(24) Ning, X., Guo, J., Wolfert, M. A., and Boons, G.-J. (2008) Visualizing metabolically labeled glycoconjugates of living cells by copper-free and fast Huisgen cycloadditions. *Angew. Chem., Int. Ed. 47*, 2253−2255.

(25) Liong, M., Shao, H., Haun, J. B., Lee, H., and Weissleder, R. (2010) Carboxymethylated polyvinyl alcohol stabilizes doped ferrofluids for biological applications. *Adv. Mater. 22*, 5168−5172.

Bioconjugate Chemistry

Article

pubs.acs.org/bc

Covalent Immunoglobulin Labeling through a Photoactivable Synthetic Z Domain

Anna Konrad,[†] Amelie Eriksson Karlström,[‡] and Sophia Hober*,[†]

[†]Division of Proteomics, AlbaNova University Center, [‡]Division of Molecular Biotechnology, School of Biotechnology, Royal Institute of Technology (KTH), SE-106 91 Stockholm, Sweden

ABSTRACT: Traditionally, labeling of antibodies has been performed by covalent conjugation to amine or carboxyl groups. These methods are efficient but suffer from nonspecificity, since all free and available amine/carboxyl groups have the possibility to react. This drawback may lead to uncontrolled levels and locations of the labeling. Hence, the labeled molecules might behave differently and, possibly, the binding site of the antibody will also be affected. In this project, we have developed a highly stringent method for labeling of antibodies by utilizing an immunoglobulin-binding domain from protein A, the Z domain. Domain Z has been synthesized with an amino acid analogue, benzoylphenylalanine, capable of forming covalent attachment to other amino acids upon UV-exposure. This feature has been used for directed labeling of immunoglobulins and subsequent use of these in different assays.

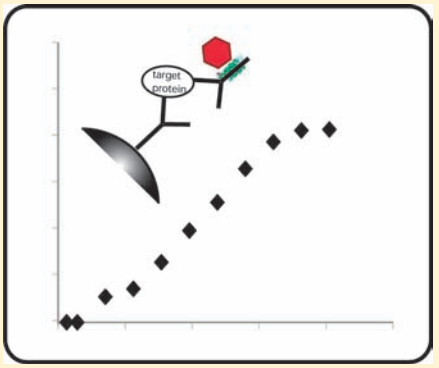

INTRODUCTION

Immunoglobulins, or antibodies, are a group of molecules that are extensively used as affinity reagents in many applications in research, clinical diagnostics, and therapy. With the ability to bind their ligands with high affinity and in a selective manner, they are of great importance, and are, by far, the most commonly used affinity reagents.[1] As when employing any affinity reagent, the method used for detection needs to be considered. The antibodies' excellent capacities to bind their ligands need to be combined with high selectivity in order to be of great use. As a consequence, techniques for labeling of antibodies necessarily need to be of high quality. To make detection of the antibody and its binding events possible, a reporter group is normally attached to the antibody. Methods most commonly used when conjugating reporter groups to the antibody are based on the exploration of amine or carboxyl groups in the protein for coupling.[2] Another application that ordinarily takes advantage of the surface-exposed functional groups in the protein is the immobilization to a solid support. When applying amine- or carboxyl-based chemistry, normally a high degree of labeling or immobilization is obtained, but unfortunately, the binding site might be compromised, since the control of level and location of the labeling/coupling is limited. This means that optimization of the protocol is needed for every antibody and every conjugation/immobilization. Hence, a method for labeling, where specific and controlled conjugation can be achieved, would be a great advantage. To obtain specific conjugation, molecules that have a natural, specific, and defined binding to antibodies could be employed. Moreover, to be able to conjugate the antibodies in a complex environment, with other proteins in the conjugation mixture, is desirable due to stabilizing molecules often being added to the antibody mixture for stabilizing purposes.

Several Ig-binding molecules have been reported in literature.[3−5] Among these, staphylococcal protein A (SpA), binding to VH and Fc, is one of the best characterized. Staphylococcal protein A is frequently used in many different applications, such as affinity chromatography, where its ability to bind antibodies is utilized. The protein is used both for purification of IgG molecules[6] and as affinity tag for protein purification.[7] The five homologous domains, EDABC, that constitute protein A, each consists of approximately 58 aa, and share the Ig-binding feature.[8] NMR analysis of the structure of the B domain shows a three-helix bundle with the helices ordered in an antiparallel fashion. The domains of protein A exhibit binding to both the Fc and Fab regions of immunoglobulins. By X-ray crystallography, the structure of the B domain in complex with the Fc region of IgG has been solved, and it revealed an interaction that mostly involved amino acids of hydrophobic character.[9] Binding seems to occur in the interface between CH_2 and CH_3 of IgG, where 11 residues from helix 1 and helix 2 of the B domain are suggested to participate.[9,10] Also, the structure of the interaction between protein A and the Fab region has been solved. The crystal structure of the D domain binding the Fab region of human IgM disclosed the involvement of 11 residues of helices 2 and 3 from the D domain and an interaction of a polar character with the variable heavy chain.[11] By altering two positions in the B-domain of protein A, an engineered variant called the Z

Received: January 26, 2011
Revised: October 12, 2011
Published: October 26, 2011

ACS Publications © 2011 American Chemical Society

dx.doi.org/10.1021/bc200052h | *Bioconjugate Chem.* 2011, 22, 2395−2403

Table 1. Amino Acid Sequences of Z5BPA and Z18BPA[a]

ZF5BPA (denoted Z5BPA) VENKXNKEQQNAFYEILHLPNLNEEQRNAFIQSLKDDPSQSANLLAEAKKLNDAQAPK^{Mtt}
ZH18BPA (denoted Z18BPA) VENKFNKEQQNAFYEILXLPNLNEEQRNAFIQSLKDDPSQSANLLAEAKKLNDAQAPK^{Mtt}

[a]Underlined amino acids were coupled twice during synthesis. X = benzoylphenylalanine.

domain has been made. In the N-terminal of the Z domain, an alanine residue was replaced by valine. A glycine-to-alanine substitution was made for the removal of a hydroxylamine cleavage site,[12] which also resulted in loss of binding to the Fab region.[11,13] The Z domain is small (6.7 kDa), easy to produce, and has a stable three-dimensional structure and also the capacity to refold.[14] It was previously proven to be suitable for chemical peptide synthesis, thereby making the introduction of synthetic active groups possible, extending the usability of the domain.[15]

Benzoylphenylalanine (BPA) is a synthetic amino acid that can be incorporated in a peptide during synthesis. Benzophenone (BP), which is part of BPA, is a photoreactive group that forms covalent bonds to other amino acids upon UV-exposure. BPA is considered to be efficient, stable, and also easy to handle,[16] and it is primarily used when mapping protein−ligand interactions. When mapping interactions, the strategy is to produce variants of a protein with BPA incorporated at different positions, and then allow the protein to bind its interaction partner.[17] When subjecting the complex to UV light, BPA forms a diradical, which renders the generation of a covalent bond between the protein and its interaction partner possible.

The utilization of an antibody-binding protein domain with an incorporated photoreactive group for attachment to antibodies has previously been reported by Jung et al. By using a modified C2 domain from streptococcal Protein G and covalently attaching BP at positions 21 and 29 via two incorporated cysteines, a photoreactive procedure could be used for modification of the antibodies. It was demonstrated that this approach could be used for directed antibody immobilization onto a surface. The strategy included recombinant production of the domain and by site-directed mutagenesis two cysteines were incorporated. The cysteines were labeled by maleimide chemistry for attachment of the photoreactive group, BP, into the domain.[18]

In this study, we report the development of a stringent and effective method for specific covalent labeling of immunoglobulins. By the use of a synthetic Z domain with the photoreactive probe BPA incorporated in the amino acid sequence, covalent conjugation to the antibody has been achieved. In this report, SPPS has been used as a means for production, and in this manner, we are able to incorporate the BPA as an unnatural amino acid specifically in the peptide backbone. Thereby, production and modification could be made in a single manufacturing process. Moreover, a detection-handle, biotin, could be incorporated in a specific position into the protein. By combining the inherent affinity of the Z domain and the Fc-fragment with the ability of BPA to create a covalent bond, specifically labeled antibodies were successfully achieved, characterized, and tested in different platforms.

MATERIAL AND METHODS

General. In this study, recombinantly produced Zwt was used as a reference.[12] The protein domain was randomly biotinylated resulting in an average of four biotin moieties/domain, as measured by MALDI-MS (data not shown).

Several antibodies used were kind gifts; FITC-BSA-specific antibody (human IgG1 and mouse IgG2a, BioInvent International AB) and antibody specific for His_6-ABP (polyclonal, Atlas Antibodies AB).

Production of Peptides. The two variants ZF5BPA (Z5BPA) and ZH18BPA (Z18BPA) were produced by solid-phase peptide synthesis using Fmoc/*t*Bu protection strategy. The syntheses were performed on a 433 A Peptide synthesizer (Applied Biosystems) using an acid-labile Fmoc-amide resin (substitution 0.67 mmol g^{-1}, Applied Biosystems). Cleavage of the Fmoc group was performed using 20% (v/v) piperidine in NMP. The coupling reactions were performed with a 10-fold molar excess of amino acid activated with 2-(1*H*-benzotriazole-1-yl)-1,1,3,3-tetramethyluronium hexafluorophosphate (HBTU) and 1-hydroxybenzotriazole (HOBt) (both from Iris Biotech GmbH) and DIEA in NMP. Apart from the amino acids underlined in Table 1, single couplings were carried out. Unreacted amino groups were capped with acetic anhydride. Standard side-chain protecting groups were used except in position 58, where Fmoc-Lys(Mtt)-OH (NovaBiochem) was introduced. The photactivable probe Fmoc-BPA-OH (Peptech Corporation) was incorporated in position 5 in Z5BPA and in position 18 in Z18BPA.

Incorporation of biotin in Z5BPA and Z18BPA was performed with the peptides still bound to the resin. The peptide-resin was treated with TFA/TIS/DCM (1:5:94) for the removal of the 4-methyltrityl (Mtt) group protecting the ε-amine of Lys58. Biotin was coupled with 5 equiv of D-biotin (Sigma), activated with HBTU/HOBt/DIEA in NMP for 2 × 1 h, with the reactions monitored using Kaiser test.[19]

The removal of protecting groups and release from the resin were achieved by treatment with TFA/TIS/H_2O (95:2.5:2.5) for 2 h at room temperature. The peptides were extracted in H_2O/*tert*-butyl methyl ether (1:1) and lyophilized.

HPLC and MS. The products from the syntheses of Z5BPA and Z18BPA were analyzed and purified by RP-HPLC, using a Silica-C18 column with 3.5 μm particle size and 4.6 × 150 mm length (Agilent Technologies). A flow rate of 0.9 mL min^{-1} and a gradient of solvent B (0.1% TFA/CH_3CN, vol/vol) in solvent A (0.1% TFA/H_2O, vol/vol) were used. Fractions obtained from RP-HPLC were analyzed by MS, and the correct products were pooled and lyophilized. The protein concentration of the samples was determined by amino acid analysis (Aminosyraanalyscentralen).

Mass spectrometry was used to verify that correct products were obtained. The products from the syntheses of Z5BPA and Z18BPA were analyzed by ESI-MS, performed on a Q-TOF II (Waters Corporation, Micromass MS Technologies). For Z5BPA-bio and Z18BPA-bio, the fractions collected in RP-HPLC were analyzed using a MALDI-MS Biflex IV (BRUKER Daltonics). As reference and for external calibration myoglobin, carbonic anhydrase II (CA II) and insulin (all obtained from Sigma-Aldrich) were used.

General Procedure for Photoconjugation. 100 nM antibodies and 1 μM Z5BPA-bio or Z18BPA-bio in PBS were incubated in 20 °C for 1 h. Cross-linking was achieved by exposure to light, 365 nm (Spectronics Corporation) for

45 min, or 1 h on ice. For the analysis of conjugated antibodies by Biacore and Western Blot, Fc and Fab fragments as well as full-length IgG were used. 1.3 μM of the antibody/antibody fragment was mixed with 26 μM Z5BPA-biotin in PBST and incubated at room temperature for 1 h. The antibody solutions were exposed to light at 365 nm for 2 h on ice.

For buffer exchange spin concentrators with a 10 kDa cutoff (Vivaspin, Sartorius Stedim Biotech) were used, centrifugation at 15 000 rcf for 10 min. Buffers used were 0.2 M HAc (VWR), pH 3.2, for lowering the pH and PBST for restoring the pH to 7. The protein content was analyzed by measuring absorbance at 280 nm (280 nm, ε = 210 00 M^{-1} cm^{-1}).

Luminex. *Bead Coupling.* Proteins and antibodies were coupled to beads according to the manufacturer's recommendation (COOH Microspheres, Luminex Corporation). 1.6 μg antibody to FITC-BSA was used for coupling to approximately 5×10^5 beads. Protein FITC-BSA (BioInvent International AB) and His_6-ABP (Atlas Antibodies AB) were coupled using 2 μg for approximately 2.5×10^5 beads and 10 μg for 1×10^6 beads, respectively. Coupled beads were kept at 4 °C in a storage buffer (Blocking Reagent for ELISA, Roche Applied Science).

Analysis of Photoconjugated Antibodies. Antibodies subjected to photoconjugation were diluted with PBST to a concentration of 100 nM. Filter plates (0.45 μm MSHVN45 MultiScreen HTS, Millipore) were used for incubation of 45 μL diluted antibody with 5 μL bead solution (200 beads/μL) at 23 °C with mixing for 1 h. Washing with 3 × 50 μL PBST was performed before PhycoLink Streptavidin-R-Phycoerythrin (2.2 μg mL^{-1}) (Prozyme) was supplied. After incubation (23 °C for 20 min) and washing (3 × 50 μL PBST), the fluorescence was measured with Luminex Lx200. When performing the sandwich assay, the first incubation with beads was made with target protein at 23 °C for 1 h; thereafter, a wash step (3 × 50 μL PBST) was introduced, followed by the procedure described above.

SPR-Analysis. Analysis of the binding kinetics of Z5BPA and Z18BPA to different IgG molecules was performed by the use of SPR technology (BIAcore 2000 instrument, Biacore). Antibodies and human serum albumin (HSA) were immobilized onto a CM5 sensor chip resulting in approximately 2000 response units (RU) for the antibodies, and 700 RU for HSA. A flow rate of 30 μL min^{-1} at 25 °C was used during the analysis. HBS-EP (HEPES 100 mM, NaCl 1.5 M, EDTA 34 mM (Merck) and 0.05% (v/v) surfactant p20 (VWR)) was used as a running buffer, and for regeneration of surfaces 10 mM HCl. The proteins were analyzed in concentrations ranging from 1.6 nM to 203.5 nM for Z5BPA-bio, 11.9 nM to 1560 nM for Z18BPA-bio, and 5.0 nM to 635 nM for Zwt. All samples were run in duplicate. The software *BIAevaluation 3.2* (BIAcore AB) was employed to determine the dissociation constants based on the Langmuir 1:1 model.

The antigen His_6-ABP was immobilized onto a CM5 sensor chip resulting in 280 response units (RU). Polyclonal rabbit IgG targeting the HisABP-construct was subjected to the photolabeling procedure either with photoreactive Z5BPA-biotin or without the reagent, both performed in duplicate. The samples were diluted to a concentration of 100 nM and flown over the Biacore surface with the antigen for analysis of the ability of the antibody to bind the antigen. The resulting Biacore curves were referenced against a blank chip surface. To obtain K_D values for the photolabeled and unlabeled antibodies, *GraphPad Prism* was used for nonlinear regression analysis of binding data from the Biacore. The curve fits were calculated from an average curve of duplicate samples, conjugated and unconjugated antibodies, respectively, flown over the chip surface.

Western Blot. Protein or antibodies (2−3 μg) were separated on SDS-PAGE gradient gels (NuPAGE 4−12% Bis-Tris SDS-PAGE, NuPAGE 3−8% Tris-Acetate (Invitrogen) or Criterion 10−20% Tris-HCl (Bio-Rad) under reducing conditions, followed by transfer to PVDF membranes (Invitrogen or Bio-Rad) according to the manufacturer's recommendations. Membranes were soaked in methanol and blocked (0.5% casein in 1×PBST vol/vol) for 1 h at 20 °C. To directly detect biotinylated proteins, the membrane was incubated with peroxidase-conjugated streptavidin (diluted 1:70 000, DakoCytomation). For detection of specific proteins, the membranes were first incubated with antibodies (of rabbit, goat species, respectively) specific for HisABP or human albumin for 1 h, followed by washing (1×PBST). Detection was made possible by either peroxidase-conjugated streptavidin (diluted 1:5000, DakoCytomation) or peroxidase-conjugated IgG directed to goat antibodies (diluted 1:100 000, Sigma-Aldrich). Detection was carried out with Immobilion Western Chemiluminescent HRP substrate (Millipore) according to the manufacturer.

RESULTS

Design and Synthesis of Z-Variants. The procedure of labeling and covalent attachment of reporter groups to antibodies is traditionally done through the chemistry of amine or carboxyl groups in the antibody. This is an efficient method, but since the labeling occurs randomly, many different groups in the protein have the possibility to react and the conjugated group might influence the binding of the antibody to its antigen. Hence, an optimization of the labeling conditions is a necessity for every antibody, and therefore, an alternative method for specific and directed labeling would be beneficial for many applications. Directed labeling would also be beneficial for antibodies in complex environment, where other proteins surround the antibody. Here, we report a novel method that enables a specific labeling of antibodies where a photoactivable probe together with a specific binding event is utilized to achieve covalent and specific attachment to immunoglobulins. To achieve a specific and reliable covalent labeling, the IgG-binding domain Z was utilized.

After studying the structural data available on Protein A (domain B) and its interaction surface with IgG, the positions Phe5 and His18 were chosen to be exchanged for BPA. Phenylalanine 5 is positioned in the N-terminal part of the domain, close to the first helix, and it is also claimed to participate in the binding between the B-domain and IgG (Deisenhofer 1981). The other position, histidine 18, is the last amino acid in the first helix, and it is not suggested to be part of the binding to IgG, but is situated in close proximity to the binding surface. Hence, two variants of the Z domain were produced, Z5BPA and Z18BPA. To achieve specific incorporation of the photoreactive probe, the two molecules were produced using solid-phase peptide synthesis. In Table 1, the sequences of the synthesized molecules are shown, where underlined amino acids were coupled twice during synthesis to ensure a high yield of the product. In both Z5BPA and Z18BPA, a D2E substitution was made to avoid aspartimide formation during synthesis. This substitution had previously been shown not to interfere with the structural or functional behavior of the Z domain.[15]

The synthesis products, Z5BPA and Z18BPA, were purified using RP-HPLC, and the purified correct products were verified using MS (data not shown). To enable easy and flexible detection and to be able to analyze the efficiency of the conjugation, the two variants were specifically biotinylated in at the C-terminus of the protein domain. This was made by applying an orthogonal strategy, through the incorporation of a lysine protected with a 4-methyltrityl (Mtt) group in the last position in the sequence of the domains. Also, these protein products were successfully purified to homogeneity and analyzed by MS (Figure 1a and b).

Analysis of the Binding Characteristics of the Z-Variants. The ability of the Z domain to refold after synthesis has been shown previously,[15] and therefore, retained binding to IgG was expected. However, with the introduction of BPA in different positions in the proximity of, or in the binding surface, there is a potential risk of influencing the ability to bind IgG. Therefore, an analysis of the binding kinetics of the two Z variants using surface plasmon resonance (SPR) was made. The ability of the two novel Z variants to bind to different IgG molecules was analyzed and compared to the parental Z domain. The analysis revealed an affinity of Z5BPA-bio/to IgG complex comparable to the parental Z/IgG. However, a considerably lower affinity was detected when analyzing the binding of Z18BPA-bio to IgG (Table 2).

Evaluation of Covalent Coupling of Z-Variants to Immunoglobulins. For the evaluation of covalent coupling of the two modified Z domains to IgG, two approaches were employed. In the first approach, polyclonal rabbit IgG was coupled to Luminex beads and then incubated with the synthetic Z domains, followed by light-induced activation of the covalent coupling (Figure 2A, setup 1). Thereafter, the beads were washed with a low-pH buffer in order to break all noncovalent interactions. By comparing the biotinylation of beads washed with low pH, with beads washed with neutral buffer, we were able to show that Z5BPA-bio could be covalently attached to IgG. Different concentration of the participating molecules and also different times for the UV light activation was used, and it was concluded that the most effective ratio between IgG and Z was 1:10 (IgG:Z). Moreover, the time for illumination of the reaction vessel was set to 1 h. Also, data show that the variant Z18BPA-bio was not covalently linked to IgG by this treatment (Figure 2B). To ensure that this behavior was not concentration-dependent, a higher concentration of Z18BPA-bio was used (1:500, IgG:Z), but still no covalent coupling was obtained (data not shown).

The successful conjugation of Z5BPA-bio to IgG was further confirmed in the second approach, where cross-linking was performed in solution and the photoconjugated antibodies were evaluated in the Luminex system. In this experiment, Z5BPA-bio and IgG were incubated in solution and subjected to UV light for cross-linking. To remove excess unbound Z molecules, a spin filter column (10 kDa cutoff) was used. This also allows for buffer exchange and lowering of pH, which enable release of noncovalently bound Z molecules from IgG. Hence, the bound and cross-linked Z domains will stay attached to the IgG molecules, while noncovalently bound Z domains will be released and washed away. In order to investigate the efficiency of covalent coupling of the bound Z5BPA-bio to the antibody, a sample of the photoconjugated antibodies was taken out before lowering the pH. Also, as negative control recombinantly produced and biotinylated Z was used. For evaluation of the covalent conjugation, antigens were linked to Luminex beads

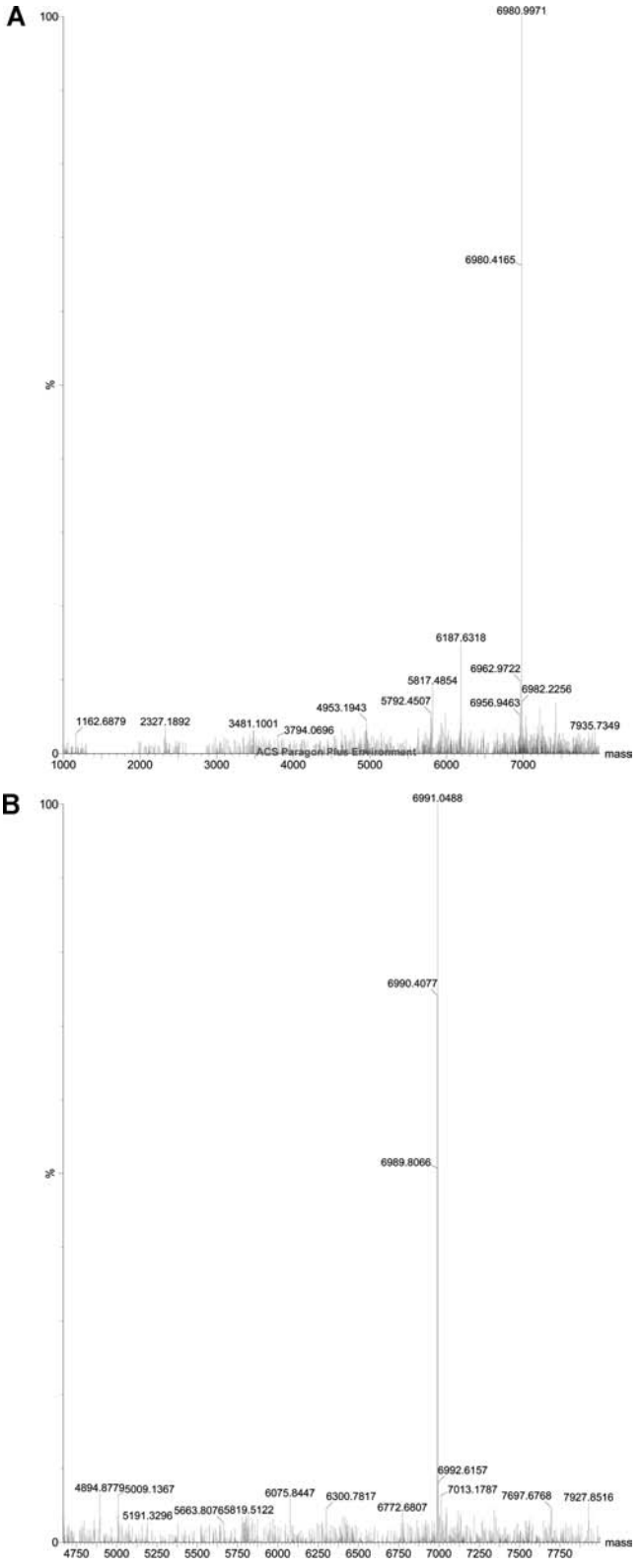

Figure 1. Mass spectrometry analysis of the synthetic Z domains. (A) The mass spectrum of Z5BPA-bio showing a molecular weight of 6981 Da (theoretical molecular weight: 6984 Da). (B) The mass spectrum of Z18BPA-bio showing a molecular weight of 6991 Da (theoretical molecular weight: 6994 Da).

and subsequently incubated with corresponding IgG molecules from the conjugation experiment (Figure 2A, setup 2). In the negative control, biotinylated Z, the signal diminishes when

Table 2. K_D values for Z5BPA-bio, Zwt, and Z18BPA-bio Binding to Human IgG1 and Mouse IgG2a

	Z5BPA-bio	Z18BPA-bio	Zwt
Human IgG1	10 nM	60 μM	20 nM
Mouse IgG2a	650 nM	-	550 nM
Rabbit IgG poly	30 nM	-	60 nM

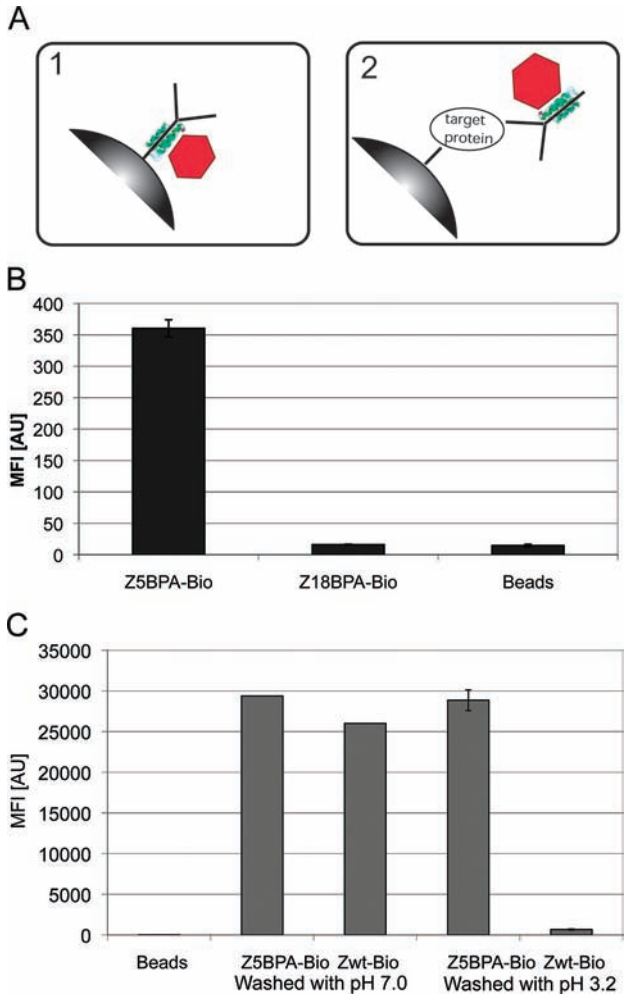

Figure 2. Covalent conjugation of the Z-variants was evaluated by using the Luminex platform. (A) The two different strategies used for analysis of covalent coupling are shown. In strategy 1, the antibodies were covalently coupled to Luminex beads. Thereafter, the beads were incubated together with the different Z variants and illuminated with UV-light. After washing, the biotinylation was detected by fluorescently labeled streptavidin. In strategy 2, the IgG and Z-variants were mixed and illuminated in solution. After illumination, the protein mixtures were washed, with a buffer with pH 3.2 or 7.0. To enable this, spin concentrators were used. After further washing and increasing the pH to neutral, the antibody solution was mixed with Luminex beads with already covalently attached antigens. Also, here the biotinylation was detected by fluorescently labeled streptavidin. (B) The cross-linking of Z5BPA-bio and Z18BPA-bio to polyclonal rabbit IgG. As negative control, uncoupled beads were used. Strategy 1 in (A) was used. Mean value of two different experiments is shown.

lowering the pH; hence. the noncovalent interaction between Z and IgG is possible to break with low pH (Figure 2C). Moreover, Z5BPA-bio is efficiently linked to the IgG molecules since the IgG molecules after treatment with low pH still give a strong signal. Also, the ability to bind the antigen indicates that the paratope of the antibody is intact. Evaluation of the conjugation efficacy was made by comparing the achieved signal before and after treatment with low pH. Therefore, the conclusion that more than 80% of the bound Z-molecules were efficiently cross-linked to the immunoglobulins could be drawn (Figure 2C).

Specificity of Labeling. Since many manufactured antibodies are stabilized by the addition of other proteins, commonly albumin, it is important to be able to perform the conjugation in complex solutions. To investigate the selectivity of the labeling, a solution containing eight times more HSA than specific monoclonal antibodies was prepared. The efficiency of the conjugation was analyzed and compared with conjugation without HSA (assay number 1 in Figure 3A). The efficiency of the labeling is not affected by the presence of HSA (Figure 3B). To assess any unwanted biotinylation of HSA, a Western blot experiment was performed. In the first experiment, all biotinylated proteins were detected (Figure 3C, left panel), and in the second setup, the present HSA molecules were detected (Figure 3C, right panel). This experiment indicates that no covalent coupling of the biotinylated Z-domains to HSA has occurred. However, since the migration of HSA in SDS-PAGE is rather similar to the heavy chain of IgG in complex with the Z domain, another experiment was performed. This time, the biotinylation was assessed using Luminex analysis. An HSA-binding protein was covalently attached to Luminex beads. Thereafter, the UV-exposed IgG-Z5BPA-bio or HSA-Z5BPA-bio mixture was mixed with the beads. Now, HSA or IgG is able to bind to the beads, by using either the covalent coupled protein's inherent ability to bind HSA or the conjugated antibody's ability to bind to the antigen. Thereafter, biotinylation was assessed through fluorescently labeled streptavidin. By utilizing the ability of the antibodies to selectively bind to the antigen-conjugated beads (assay number 1 in Figure 3A), high signals from the antigen binding IgG-molecules could be detected. Since similar signal intensity was detected both before and after washing with low pH, we could conclude that the conjugation of Z5BPA-bio to the antibodies was very effective. Furthermore, the conclusion that no biotinylation of HSA was obtained could be drawn since no signal was detected from the HSA-binding beads mixed with fluorescently labeled streptavidin (assay number 2 in Figure 3A). However, the ability of HSA to bind to the beads was confirmed by HSA-recognizing antibodies conjugated with biotin (setup 3 in Figure 3A,D). These results also show that the covalent attachment of Z to IgG is specific since no biotinylation of HSA could be detected.

To investigate the influence of labeling on the antigen binding capacity of the antibody an SPR-analysis of conjugated and unconjugated antibodies, binding was performed. As can be seen in Figure 4A–C, conjugated and unconjugated antibodies show the same affinity to its antigen, which confirms that the antigen-binding site is preserved after complete conjugation (Figure 4). The similar K_D values obtained for conjugated and unconjugated, 6.0 nM and 6.4 nM, respectively, clearly show that the antigen site of the antibody remains unaffected after being subjected to the conjugation process (Figure 4B,C).

To further show the specificity of the conjugation, Z5BPA-biotin was allowed to react with full-length antibodies, Fc fragments, and Fab fragments. The obtained conjugations were analyzed by Western blot. Figure 5 shows that conjugation occurs at the Fc part of the antibody, since no biotinylation could be detected on the Fab fragments. However, biotinylation

dx.doi.org/10.1021/bc200052h | Bioconjugate Chem. 2011, 22, 2395–2403

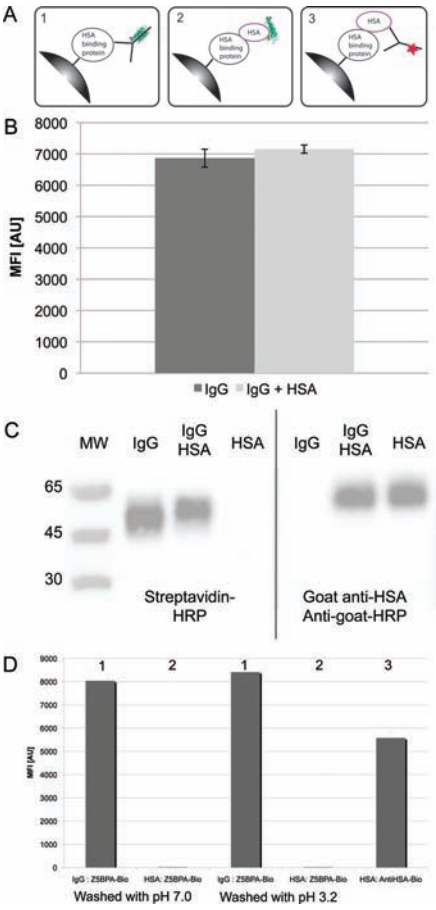

Figure 3. Degree of covalently linked Z5BPA-bio domain in a complex sample was analyzed. Samples of antibodies to be photoconjugated with Z5BPA-biotin were supplemented with 800 nM HSA (Albumina Kabi). (A) Three different strategies used for analysis of covalent coupling are shown. An HSA-binding protein was covalently attached to the Luminex beads. These beads could be used in three different ways. According to strategy 1, the attached protein is used as an antigen, since the labeled antibody is directed to this protein. In strategy 2, the protein is used to bind to HSA. In these two experiments, streptavidin-R-phycoerythrin is used to detect any biotinylation. In strategy 3, antibodies with biotin are used to detect the bound HSA. (B) Degree of cross-linking was analyzed both with and without HSA in the sample. Covalent linking of Z5BPA-bio was unaffected by the HSA present in the sample. Setup according to strategy 1 in Figure (A) was used. (C) To assess if Z5BPA-bio was able to covalently bind to the HSA molecule, a Western blot was performed. In the left panel, the amount of covalently linked Z5BPA-bio in three different samples was analyzed using streptavidin-HPR. No attachment to the HSA molecule could be detected. In the right panel, the presence of HSA in the samples was analyzed by using goat antibodies targeting HSA, visualized with HRP-conjugated antigoat antibodies. (D) To confirm the conclusion from the previous experiment, a Luminex experiment was made where both the amount of biotinylated IgG molecules and HSA molecules were analyzed using strategy 1 in (A). The number of biotinylated IgG molecules was shown to be high, both after and before treatment with low pH. This indicates a high degree of covalent coupling by Z5BPA-bio. The amount of biotinylated HSA-molecules was analyzed using strategy 2 in (A). No biotinylation could be detected before or after treatment with low pH. To ensure the presence of HSA, a third strategy was used (number 3 in (A)); hence, detecting HSA with an HSA-binding antibody and thereby the presence of HSA was confirmed.

was detected on both the full-length antibodies and the Fc fragments (Figure 4D).

Use of Conjugated Antibodies. The photoconjugated antibodies were used in a sandwich assay setup where capture antibodies were coupled to beads and incubated with target protein in various concentrations (Figure 5A). After thorough washing, target-specific photoconjugated antibodies were added. The beads were washed, and the fluorescence from streptavidin-R-phycoerythrin was detected by using the Luminex platform. Analyses using both human monoclonal antibodies and mouse monoclonal antibodies recognizing FITC-BSA were successfully performed, and the antigen could be detected down to a concentration of 0.1 ng/mL within a concentration window spanning 4 orders of magnitude (Figure 5).

Also, the conjugated antibodies were used for detection in a Western blot assay. By conjugation of the antibodies with Z5BPA-bio, the protein targeted by the antibodies could be detected by streptavidin-HRP. In Figure 5C, two Western blot membranes are shown. On the rightmost membrane, proteins are detected with covalently conjugated antibodies, and on the left membranes, as a negative control, the same antibodies were used, but in the conjugation step, Z-Bio, lacking the BPA group, was used. The molecular weights of the protein bands detected are as expected; hence, the system works both in a sandwich setup with the antigen in solution and in detection of proteins bound to a membrane.

DISCUSSION

To be able to covalently attach the Z domain to immunoglobulins, the structural information on the binding site was thoroughly studied. Two amino acids in close proximity to the binding surface were exchanged for the photoactivable probe, BPA. Both suggested Z variants were successfully synthesized with high yield and the C-terminal biotinylation was efficiently and specifically made through an orthogonal protection strategy (Figure 1). The interaction between IgG and the two synthesized Z variants was analyzed revealing a retained affinity for the Z5BPA-bio molecule, while Z18BPA-bio showed very low affinity (~100 μM, Table 2). For the Z5BPA-bio molecule, both the on- and off-rates are in the same range as for the parental Z domain (data not shown). The retained affinity of the Z5BPA-bio variant could be explained by steric similarity of phenylalanine and BPA making the inherent structure of Z intact. The addition of the extra benzoyl group seems to fit well between the two molecules upon binding. On the other hand, replacement of histidine 18 for BPA is deleterious and destroys the interaction with IgG. This could be due to the change of charge in the position of amino acid 18. Also, the larger side chain of the unnatural amino acid could sterically inhibit the ability to bind IgG. This photoactivable molecule has previously been used to covalently label antibodies through incorporation in an antibody binding molecule from protein G,[18] but a different strategy for production of the binding domain was used. In this publication, they have recombinantly produced the IgG-binding domain and after purification covalently attached a BPA-group via a cysteine. Moreover, the area of application in the referred study was to covalently attach the antibodies onto a solid support in an oriented way. In this project, we have focused on labeling of the antibodies for detection purposes.

A very important characteristic of a molecule used for selective labeling is the efficiency of the covalent linking. Hence, a thorough characterization of this was performed. Different IgG molecules were used for this analysis, and in

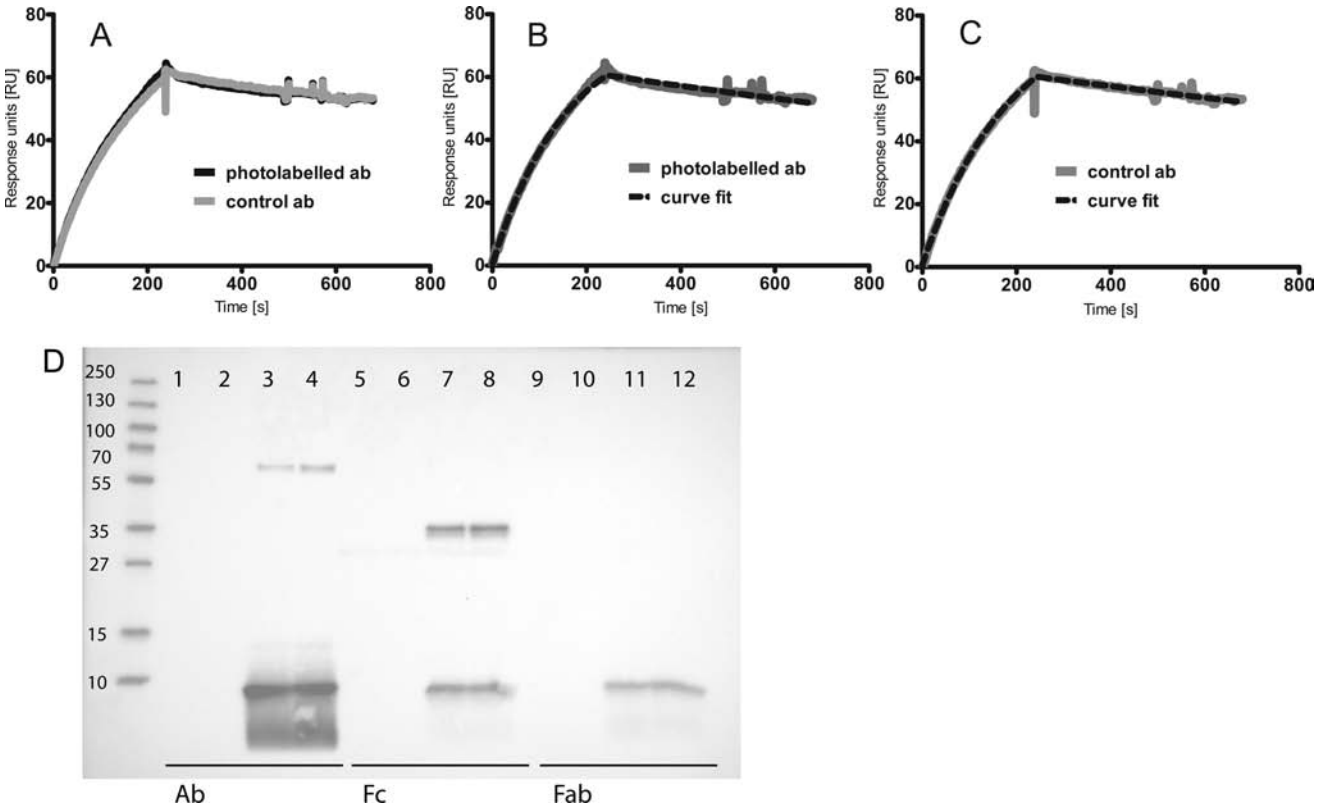

Figure 4. Investigation into the performance of an antibody was made by analyzing the affinity constant for antigen binding before and after conjugation. Moreover, specificity of the conjugation was assessed by Western blot analysis. (A) SPR analysis of antibodies targeting their antigen was performed, before and after conjugation. Antigen was immobilized on the chip and the antibodies were flowed over the surface. Average of duplicate samples is shown. Nonlinear regression analysis were made of the binding curve of (B) photolabeled antibodies giving a K_D value of 6.0 nM and (C) control antibodies giving a K_D value of 6.4 nM. Hence, the labeling procedure does not influence the performance of the antibody. (D) Western Blot analysis of duplicate samples of conjugated and unconjugated full-length antibodies (lanes 1−4), Fc fragments (lanes 5−8), and Fab fragments (lanes 9−12). Z5BPA conjugates specifically to the Fc part of the antibodies.

the experiment, the amount of covalently attached Z-domains were compared with the amount of Z-domains able to bind to the IgG molecules. All immunoglobulins with affinity for Z were successfully covalently labeled, with an efficiency of more than 80% when the ratio 1:10 (IgG:Z) was used (Figure 2).

When using the coupling strategy in complex solution, we could conclude that no unwanted covalent labeling could be detected, despite high concentration of both HSA and Z5BPA-bio (Figure 3). This is of utmost importance and shows that the benzophenone (BP) group needs to be in very close proximity to create a covalent link, thereby ensuring specific and directed covalent attachment. Hence, specific and stable interaction as well as UV light of correct wavelength is needed. The necessity of UV light makes this photoactivable probe convenient and easy to handle since no light protection is needed during the synthesis, purification, or other experimental steps where no conjugation is desired. Moreover, if a covalent bond not is created, the probe relaxes to the ground state after excitation and thereby the uncoupled Z molecules are possible to use in a next round of labeling (data not shown).

To assess the functionality of the covalently linked antibodies, three different methods were used. A sandwich assay was successfully designed by taking advantage of capturing antibodies covalently linked to Luminex beads. The prepared beads were incubated with different concentrations of antigen (Figure 5A). Hence detection could be made by streptavidin using conjugated antibodies from both mouse and human. Also, an ordinary Western blot was made showing that here also the conjugated antibodies successfully detect the anticipated proteins on the membrane. These data show that the covalent linkage between IgG and Z5BPA-bio is stable and usable in different well-known assays. When performing the sandwich assay, antigen concentrations down to 0.1 ng/mL could be detected. The conjugated antibodies in this study could possibly have one or two biotin on each antibody since only one biotin is incorporated in each Z domain. Hence, by introducing more than one biotin or even by directly introducing a number of fluorescent probes in the Z domain the detection level will likely be improved. The comparison of the ability of conjugated and unconjugated antibodies to bind their antigen by SPR analysis shows that the procedure allows the antibody to retain its binding to the antigen and that the covalently attached photoreactive Z5BPA-biotin does not influence the reactivity of the antibody (Figure 4). The specificity of the labeling is further demonstrated by the Western blot experiment where biotin is detected only if the antibody or antibody fragment is covalently conjugated. The data clearly show that conjugation is achieved on the full-length antibody and also on Fc fragment. However, no conjugation could be detected on the Fab fragment (Figure 4D).

Here, we have presented a stringent and effective method for labeling of antibodies by utilizing an IgG-binding protein domain, Z. By introducing a photoactivable group in the

dx.doi.org/10.1021/bc200052h | *Bioconjugate Chem.* 2011, 22, 2395−2403

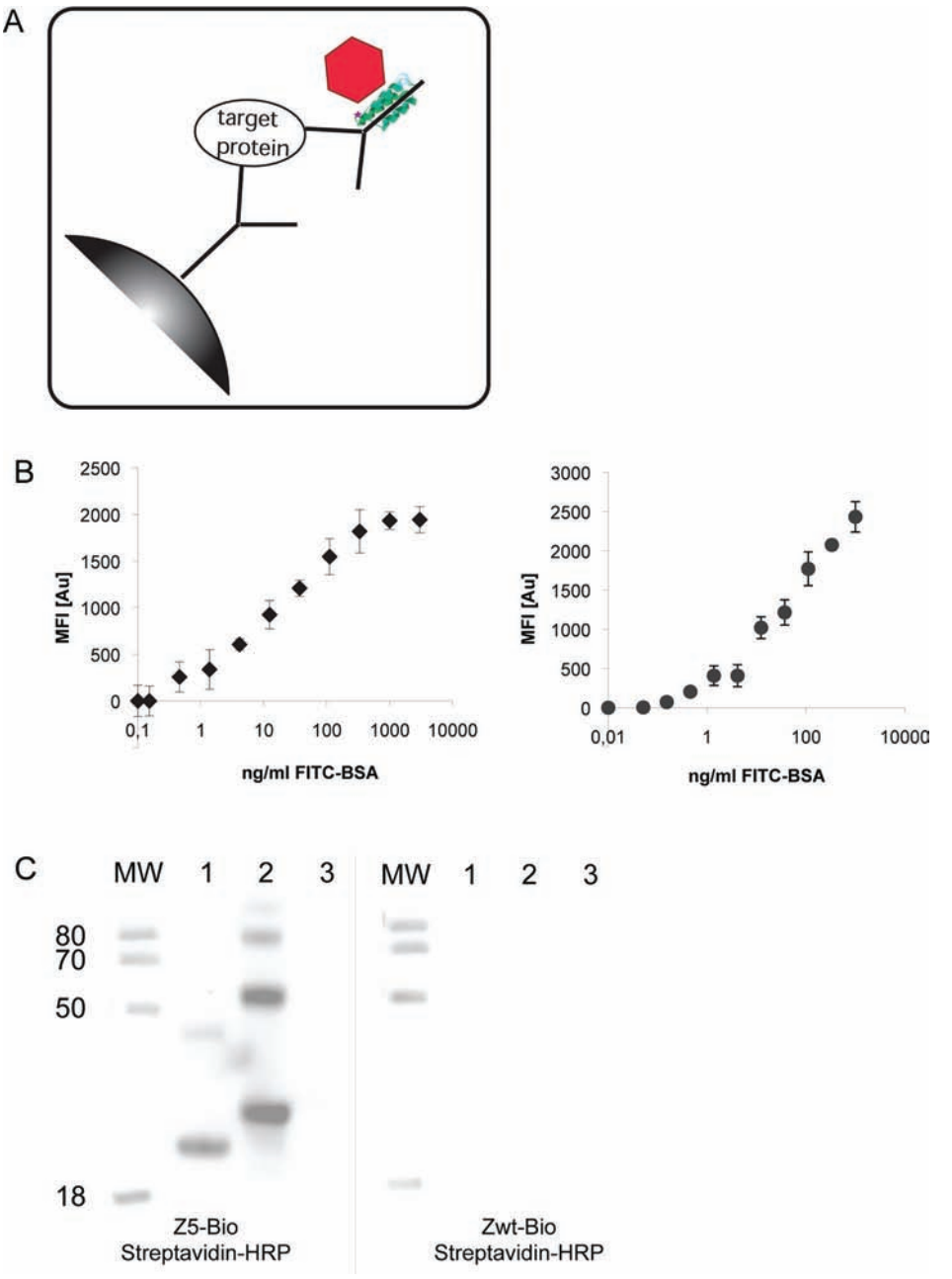

Figure 5. Covalently cross-linked antibodies were used in two common assays. (A) Sandwich analysis where the capturing antibodies were attached to Luminex beads. (B) Incubation of beads with different concentrations of antigen and subsequent washing. The amount of captured antigen was analyzed by using detection antibodies covalently linked to Z5BPA-bio in combination with streptavidin-R-phycoerythrin. The diagram to the left shows human monoclonal IgG1 targeting FITC-BSA, and in the right diagram, mouse monoclonal IgG2a is used; the mean values of three experiments are shown. (C) Covalently cross-linked antibodies were used in a Western blot analysis. In the left panel, detection was made by using an antibody covalently linked to Z5BPA-bio, and in the right panel, the same antibody but with Zwt-bio was used as control. Protein samples on the gel are as follows: MW, a molecular weight marker; lane 1, His6ABP (19 kDa); lane 2, His6ABP-PrEST (25.5 kDa).

protein scaffold during synthesis, a covalent linkage between IgG and the synthesized protein domain can be created with very high efficacy. This linkage has been shown to be efficiently formed and stable under different conditions. Here, we have been using biotin as the reporting group, but a large variety of different groups could be introduced in the protein domain to tailor-make the antibodies for a certain purpose. The new approach for labeling of antibodies presented here is both flexible and reliable and would be suitable for a wide range of applications where antibodies are used in the capture or detection step.

AUTHOR INFORMATION

Corresponding Author

*Tele: +46 5537 8330. Fax: +46 5537 8481. E-mail: sophia.hober@biotech.kth.se.

ACKNOWLEDGMENTS

The authors would like to thank P-Å. Nygren and J. Schwenk for fruitful discussions. G. Sundqvist is acknowledged for assistance with the MS analyses. The ProNova VINN Excellence Centre for Protein Technology financially supported

this work with Atlas Antibodies AB, BioInvent International AB, GE Healthcare Bio-Sciences AB, Gyros AB, Mabtech AB and Olink AB as active partners in the project.

REFERENCES

(1) Borrebaeck, C. A. (2000) Antibodies in diagnostics - from immunoassays to protein chips. *Immunol. Today 21*, 379−82.
(2) Brinkley, M. (1992) A brief survey of methods for preparing protein conjugates with dyes, haptens, and cross-linking reagents. *Bioconjugate Chem. 3*, 2−13.
(3) Bjorck, L. (1988) Protein L. A novel bacterial cell wall protein with affinity for Ig L chains. *J. Immunol. 140*, 1194−7.
(4) Bjorck, L., and Kronvall, G. (1984) Purification and some properties of streptococcal protein G, a novel IgG-binding reagent. *J. Immunol. 133*, 969−74.
(5) Forsgren, A., and Sjoquist, J. (1966) "Protein A" from S. aureus. I. Pseudo-immune reaction with human gamma-globulin. *J. Immunol. 97*, 822−7.
(6) Langone, J. J. (1982) Applications of immobilized protein A in immunochemical techniques. *J. Immunol. Methods 55*, 277−96.
(7) Ståhl, S., Nilsson, J., Hober, S., Uhlén, M., and Nygren, P.-Å. (1999) in *The Encyclopedia of Bioprocess Technology: Fermentation, Biocatalysis and Bioseparation* (Fleckinger, M. C., and Drew, S. W., Eds.) pp 8−22, John Wiley and Sons Inc., New York.
(8) Uhlén, M., Guss, B., Nilsson, B., Gatenbeck, S., Philipson, L., and Lindberg, M. (1984) Complete sequence of the staphylococcal gene encoding protein A. *J. Biol. Chem. 259*, 1695−1702.
(9) Deisenhofer, J. (1981) Crystallographic refinement and atomic models of a human Fc fragment and its complex with fragment B of protein A from Staphylococcus aureus at 2.9- and 2.8-A resolution. *Biochemistry 20*, 2361−70.
(10) Gouda, H., Shiraishi, M., Takahashi, H., Kato, K., Torigoe, H., Arata, Y., and Shimada, I. (1998) NMR study of the interaction between the B domain of staphylococcal protein A and the Fc portion of immunoglobulin G. *Biochemistry 37*, 129−36.
(11) Graille, M., Stura, E. A., Corper, A. L., Sutton, B. J., Taussig, M. J., Charbonnier, J.-B., and Silverman, G. J. (2000) Crystal stucture of a Staphylococcus aureus protein A domain complexed with the Fab fragment of a human IgM antibody: Structural basis for recognition of B-cell receptors and superantigen activity. *Proc. Natl. Acad. Sci. 97*, 5399−5404.
(12) Nilsson, B., Moks, T., Jansson, B., Abrahmsen, L., Elmblad, A., Holmgren, E., Henrichson, C., Jones, T. A., and Uhlen, M. (1987) A synthetic IgG-binding domain based on staphylococcal protein A. *Protein Eng. 1*, 107−13.
(13) Jansson, B., Uhlén, M., and Nygren, P.-Å. (1998) All individual domains of staphylococcal protein A show Fab binding. *FEMS Immunol. Med. Microbiol. 20*, 69−78.
(14) Ståhl, S., and Nygren, P. A. (1997) The use of gene fusions to protein A and protein G in immunology and biotechnology. *Pathol. Biol. (Paris) 45*, 66−76.
(15) Engfeldt, T., Renberg, B., Brumer, H., Nygren, P. A., and Karlstrom, A. E. (2005) Chemical synthesis of triple-labelled three-helix bundle binding proteins for specific fluorescent detection of unlabelled protein. *ChemBioChem 6*, 1043−50.
(16) Dorman, G., and Prestwich, G. D. (2000) Using photolabile ligands in drug discovery and development. *Trends Biotechnol. 18*, 64−77.
(17) Kawamura, A., Hindi, S., Mihai, D. M., James, L., and Aminova, O. (2008) Binding is not enough: flexibility is needed for photocrosslinking of Lck kinase by benzophenone photoligands. *Bioorg. Med. Chem. 16*, 8824−9.
(18) Jung, Y., Lee, J. M., Kim, J. W., Yoon, J., Cho, H., and Chung, B. H. (2009) Photoactivable antibody binding protein: site-selective and covalent coupling of antibody. *Anal. Chem. 81*, 936−42.
(19) Kaiser, E., Colescott, R. L., Bossinger, C. D., and Cook, P. I. (1970) Color test for detection of free terminal amino groups in the solid-phase synthesis of peptides. *Anal. Biochem. 34*, 595−8.

Bioconjugate Chemistry

Article

pubs.acs.org/bc

Supramolecular Assemblies of Histidinylated α-Cyclodextrin in the Presence of DNA Scaffold during CDplexes Formation

Véronique Bennevault-Celton,[#,‡] Allan Urbach,[#,§] Olivier Martin,[§] Chantal Pichon,[†] Philippe Guégan,[‡] and Patrick Midoux*[,†]

[†]Centre de Biophysique Moléculaire CNRS UPR 4301, University of Orléans and Inserm, Rue Charles Sadron, F-45071 Orléans Cedex 2, France

[‡]Laboratoire Analyse et Modélisation pour la Biologie et l'Environnement, CNRS UMR8587, University of Evry Val d'Essonne, Rue du Père Jarlan, 91025 Evry Cedex, France

[§]Institut de Chimie Organique et Analytique, UMR CNRS 6005, University of Orléans, 45067 Orléans cedex 2, France

Supporting Information

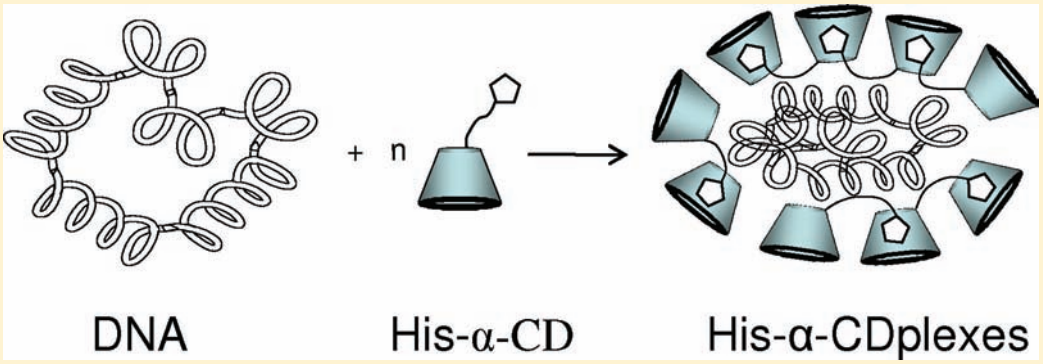

ABSTRACT: α-Cyclodextrin was transformed in a cationic unit after *per* substitution with histidine (His-α-CD) and lysine (Lys-α-CD) molecules on the primary face. His-α-CD and Lys-α-CD were used to form electrostatic complexes (CDplexes) with a plasmid DNA encoding luciferase gene, and the ability of CDplexes to transfect mammalian cells was examined using HEK293-T7 cells. The luciferase activity in cells transfected with His-α-CDplexes was 8-fold higher than that obtained Lys-α-CDplexes. When the transfection was carried out in the presence of chloroquine, the luciferase activity with His-α-CDplexes and Lys-α-CDplexes increased 6 and 25 times, respectively. The lower enhancement with His-α-CDplexes confirmed that histidine induced a proton sponge effect inside endosomes upon imidazole protonation, favoring DNA delivery in the cytosol. At the same time, we found that the condensation of DNA with His-α-CD was unexpectedly stronger than that obtained with the lysyl-α-CD counterpart. Moreover, it was as strong as that observed with high molecular weight polylysine. NMR (ROESY and DOSY) investigations in the absence of DNA showed that an inclusion complex is formed between the imidazole ring of histidine and the hydrophobic cavity of CD but no His-α-CD polymers can be formed by intermolecular interactions. These results suggest that intermolecular interactions between imidazole and His-α-CD cavity could be involved to form supramolecular assemblies in the presence of a DNA scaffold leading to DNA condensation into low diameter particles.

INTRODUCTION

Cyclodextrins are natural biocompatible cyclic oligosaccharides composed of 6, 7, or 8 D(+)-glucose units linked by α-1,4-linkages and named α-, β-, or γ-cyclodextrin, respectively. Recently, various cyclodextrin-based gene delivery systems have been developed.[1] For instance, cyclodextrin can be transformed in a cationic unit after *per* substitution with small cationic molecules. These derivatives can condense a plasmid DNA (pDNA) to form CDplexes that can be used for the transfection of mammalian cells. For example, α- and β-cyclodextrins have been *per* substituted with oligoethylenimine repeat units (from 1 to 14).[2,3] The transfection efficiency of HEK293 and COS-7 cells increased as the length of the oligoethylenimine moiety increased from diethylenetriamine to pentaethylenehexamine residues. β-Cyclodextrin was used also as a scaffold to prepare a homogeneous sevenfold symmetric polyaminothiourea amphiphiles for gene transfer.[4−6] Cationic cyclodextrins have been derivatived in cationic polyrotaxanes either with a poly(ethylene oxide)-poly(propylene oxide)-poly(ethylene oxide) triblock copolymer, a PEI-b-PEG-b-PEI copolymer or α,ω-dimethacrylate poly(ethylene glycol).[7−9] For certain CD derivatives, the transfection efficiency was comparable to that obtained with JetPEI, the gold standard cationic polymer. One of the major barriers for gene transfer is

Received: March 31, 2011
Revised: October 17, 2011
Published: October 21, 2011

 © 2011 American Chemical Society

Scheme 1. Synthetic Scheme of α-Cyclodextrin Derivatives: (1) NH_2-α-CD; (2) His-α-CD; (3) Lys-α-CD

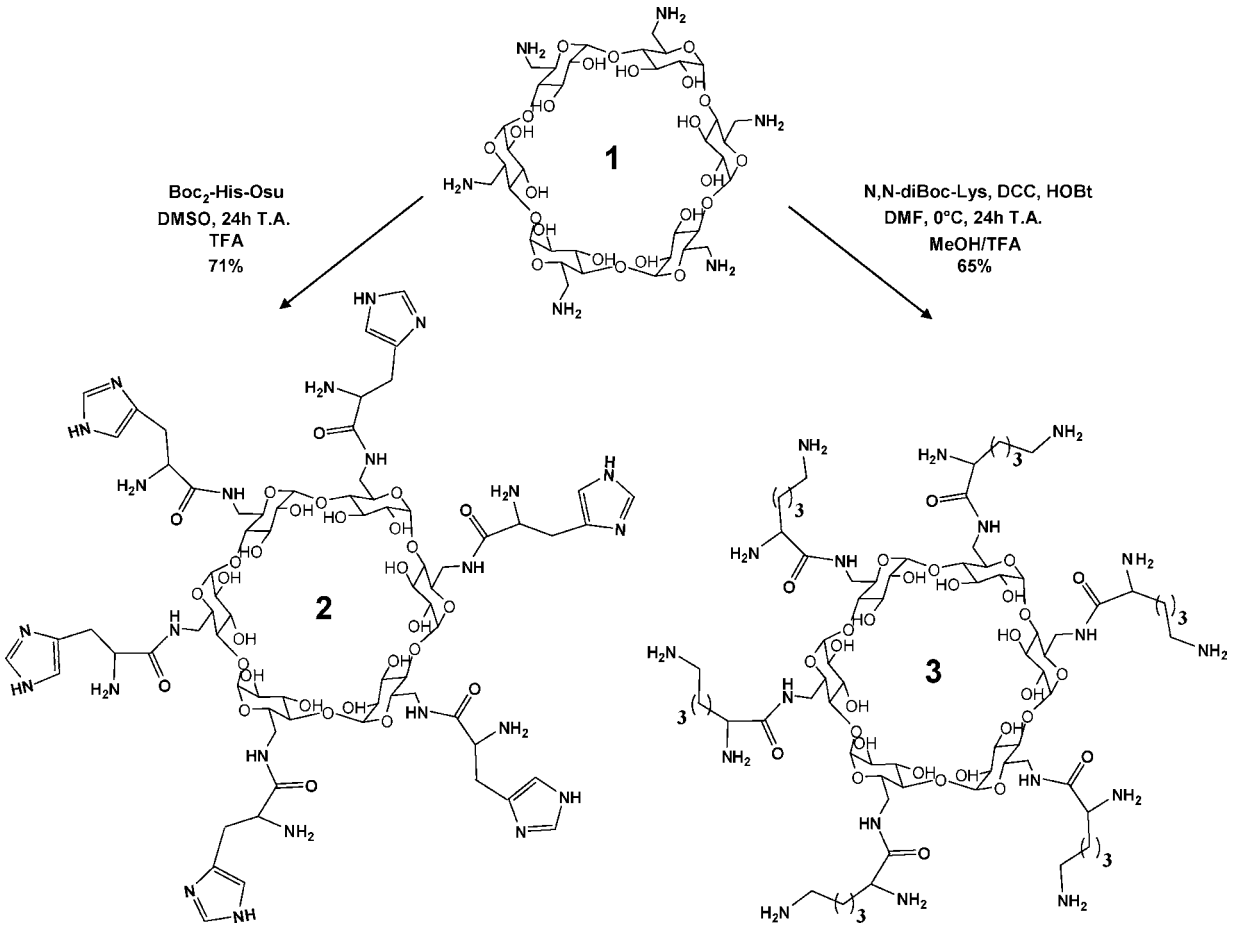

the endosome escape allowing the delivery of the plasmid DNA in the cytosol. For this purpose, histidine can be used. The imidazole ring of histidine is a weak base that has the ability to acquire a cationic charge when the pH of the environment drops below 6. As has been demonstrated for poly(histidine), this phenomenon can induce membrane fusion and/or membrane permeation in an acidic medium.[10,11] Moreover, the accumulation of protonated histidine residues inside acidic vesicles can induce a proton sponge effect, which increases their osmolarity and their swelling. The proof of concept has been shown with polylysine partially substituted with histidine residues that has caused a tremendous increase by 3−4.5 orders of magnitude of the transfection efficiency of DNA/polylysine polyplexes.[12] Then, several histidine-rich polymers and peptides as well as lipids with imidazole polar heads have been reported to be efficient carriers to deliver nucleic acids including DNA and RNA *in vitro* and *in vivo*.[13] More remarkable, histidylated carriers are often weakly cytotoxic, making them promising chemical vectors for nucleic acid delivery.

Here, we have used α-CD as a scaffold to prepare histidylated CD as DNA carrier. α-CD was chosen because of its lower propensity to form an inclusion complex with cholesterol than β-CD.[14−16] Indeed, β-CD has been shown to extract cholesterol from cell membranes. We have synthesized the hexakis(6-deoxy-6-histidinyl)cyclomaltohexaose (His-α-CD) (**2**) (Scheme 1). This derivative had six α-amino groups usable for pDNA interaction and six imidazole rings for acid-mediated membrane destabilization after CDplex uptake by the cells into endosomes. The polyamino α-CD counterparts, the hexakis(6-deoxy-6-amino)cyclomaltohexaose (NH_2-α-CD) (**1**) and the hexakis(6-deoxy-6-lysinyl)cyclomaltohexaose (Lys-α-CD) (**3**), were also synthesized (Scheme 1). The former had six amino groups as His-α-CD and the latter twelve. The capacity of these cationic α-CD derivatives to condense pDNA was determined and the transfection efficiency of CDplexes was evaluated in HEK293-T7 cells using the luciferase gene as read-out. Unexpectedly, a strong condensation of pDNA by His-α-CD was evidenced. Furthermore, we showed by NMR investigations the involvement of an inclusion complex between the imidazole ring of histidine and the hydrophobic cavity of CD. These results suggest that supramolecular assemblies of His-α-CD in the presence of a DNA scaffold could occur during the formation of His-α-CDplexes.

EXPERIMENTAL PROCEDURES

All reagents were purchased from Sigma (St. Quentin Fallavier, France) unless otherwise stated.

The synthesis of hexakis(6-deoxy-6-iodo)cyclomaltohexaose has been adapted from ref 17, and hexakis(6-deoxy-6-azido)cyclomaltohexaose from ref 3 and hexakis(6-deoxy-6-amino)cyclomaltohexaose from ref 18. The detailed experimental protocols and the characterizations are reported in the Supporting Information (S1).

Hexakis(6-deoxy-6-histidinyl)cyclomaltohexaose (His-α-CD). Boc_2-His-OSu (0.59 g, 1.30 mmol) was added to a stirring solution of hexakis(6-deoxy-6-amino)-cyclomaltohexaose (0.20 g, 0.207 mmol) in DMSO (5 mL),

dx.doi.org/10.1021/bc200167p | *Bioconjugate Chem.* 2011, 22, 2404−2414

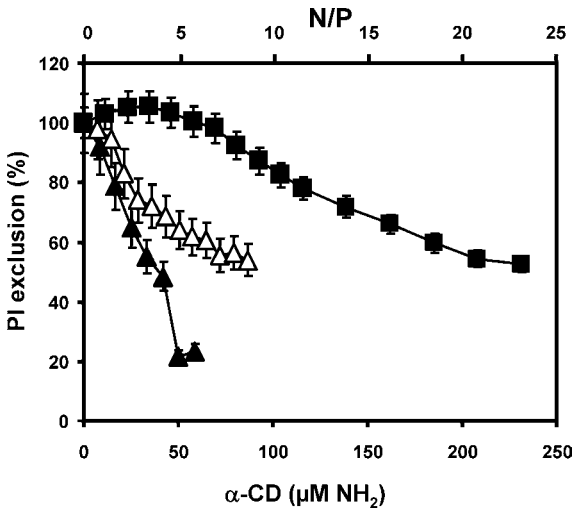

Figure 1. Interaction of polyamino-α-CD derivatives with DNA. Aliquots of solution containing polyamino-α-CD derivatives were sequentially added to pDNA (2.5 μg) in 650 μL of 10 mM Hepes buffer, pH 7.4, in the presence of ethidium bromide (2 μM). The fluorescence intensity was measured (λ_{ex} = 530 nm; λ_{em} = 580 nm) after each addition of samples, and the fraction of dye exclusion was calculated from the fluorescence intensity measured in the absence and in the presence of polyamino-α-CD derivatives. N/P corresponds to the ratio between the number of positive charges of polyamino-α-CD derivatives and that of the negative charges of the pDNA phosphate. His-α-CD (▲); Lys-α-CD (△); NH_2-α-CD (■).

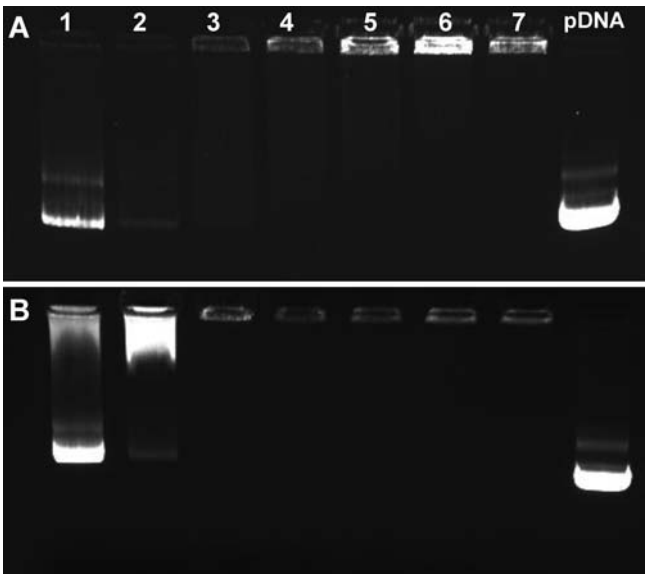

Figure 2. Agarose gel electrophoresis shift assay of pDNA in the presence of various quantities of His-α-CD (A) and Lys-α-CD (B). Lanes 1, 2, 3, 4, 5, 6, 7, and 8 correspond to pDNA/CD weight ratios (μg/μg) of 1/0.5, 1/1, 1/2, 1/3, 1/4, 1/6, and 1/8, respectively. pDNA line correspond to migration of pDNA in the absence of any polyamino α-CD derivatives. Electrophoresis was conducted for 1 h under 80 V/cm through a 0.6% agarose gel containing ethidium bromide (1 μg/mL) in 95 mM Tris, 89 mM boric acid, and 2.5 mM EDTA (pH 8.6). An ultraviolet lightbox was used to visualize ethidium bromide-stained DNA in gels.

and the reaction was carried out at room temperature for 24 h. Then, 2 mL of trifluoroacetic acid (TFA) was added and the medium was stirred for 12 h. After removal of TFA under reduced pressure, the product was recovered by precipitation in ethyl acetate (AcOEt) with 71% yield (0.45 g). ^{1}H NMR (D_2O, 300 MHz): δ ppm 7.7 (H10), 6.9 (H9), 4.5 (H1), 4.0 (H7), 3.8 (H3), 3.6 (H5), 3.5 (H6), 3.3 (H2), 3.0 (H8), 2.8 (H4). ^{13}C NMR (D_2O, 100 MHz): δ ppm 171.7 (C═O, amide), 163.3 (q, C═O, TFA), 136.8 (C-10 arom. imidazole), 132.9 (C quat. arom. imidazole), 116.7 (C-9 arom. imidazole), 117.0 (CF_3, TFA), 101.9 (C-1), 82.6 (C-4), 72.8, 72.1, 69.7 (C-2, C-3, C-5), 53.8 (C-7; $CHNH_3$), 39.6 (C-6), 30.2 (C-8). For $C_{72}H_{108}N_{24}O_{30}$, MS (MALDI-TOF/TOF): 1795.8 uma $[M + Li]^+$, 1827.8 uma $[M + K]^+$.

Hexakis(6-deoxy-6-lysinyl)cyclomaltohexaose (Lys-α-CD). *N*,*N*-diBoc-lysine (0.432 g, 1.24 mmol) was dissolved in dry DMF (10 mL). 1-Hydroxybenzotriazole (HOBt) (0.176 g, 1.30 mmol) was added, and the solution was cooled to 0 °C in an ice bath. *N*,*N*′-Dicyclohexylcarbodiimide (DCC) (0.261 g, 1.27 mmol) was then added, and the temperature was maintained at 0 °C for a further 60 min. The reaction mixture was then allowed to warm to room temperature during which time dicyclohexylurea precipitated out. After stirring for a further 60 min at room temperature, a suspension of hexakis(6-deoxy-6-amino)cyclomaltohexaose (0.200 g, 0.207 mmol) and methyl morpholine (0.14 mL) in dry DMF (5 mL) was added to the reaction medium and the solution was stirred at room temperature for 24 h. The dicyclohexylurea precipitate was filtered off, and the filtrate was concentrated under reduced pressure at 50 °C as oil. Then, saturated $NaHCO_3$ (100 mL) was added to the oil to give a suspension which was stirred for 1 h and filtered. The precipitate was washed with H_2O and dried under high vacuum. The crude product underwent subsequent Boc deprotection in a MeOH/TFA (10:2; v/v) solution at room temperature, and the solvent was evaporated and replaced by AcOEt (5 mL). The precipitate was filtered and the expected product was recovered in 65% yield (0.418 g). ^{1}H NMR (D_2O, 500 MHz): δ ppm 4.95 (d, 6 H), 3.40−4.08 (m, 36 H), 3.31 (m, 6 H), 3.02 (m, 12 H), 1.96 (m, 12 H), 1.74 (m, 12 H), 1.49 (m, 12 H). ^{13}C NMR (D_2O, 125 MHz): δ ppm 170.1 (C═O, amide), 162.6−163.4 (C═O, TFA), 113.1−120.1 (CF_3), 102.1 (C-1), 82.9 (C-4), 72.7, 72.3 (C-2, C3), 70.0 (C-5), 53.3 (C-7; $CHNH_3$), 39.5 (C-6), 39.2 (C-11; CH_2NH_3), 30.9, 26.6, 21.8 (C-8, C-9, C-10; CH_2). For $C_{72}H_{138}N_{18}O_{30}$ (M_w = 1735), MS (MALDI-TOF/TOF): 1736.0 uma $[M + H^+]$.

Polymers. PLK_6 and PLK_{190}—poly(L-lysine) with degree of polymerization of 6 and 190, respectively—were purchased from Sigma Aldrich and Bachem (Bubendorf, Switzerland), respectively. $K_{20}H_{20}$ was a poly(L-lysine) with degree of polymerization of 20 (NeoMPS SA, Strasbourg, France) in which all the ε-amino functions of the lysyl residues were substituted with histidine residues as described.[19]

Cells and Cell Culture. Human embryonic kidney 293T7 cells were grown at 37 °C in a humidified atmosphere containing 5% CO_2 in MEM medium containing 10% heat inactivated fetal bovine serum (PAA Laboratories, Les Mureaux, France), 2 mM L-glutamine (Fischer Bioblock, Illkirch, France), 100 U/mL penicillin (Fischer Bioblock), 100 U/mL streptomycin (Fischer Bioblock), and Geneticin (400 μg/mL).[20] Cells were mycoplasma-free as evidenced by MycoAlert Mycoplasma Detection Kit (Lonza, Levallois Perret, France).

Plasmids. pTG11033 (pCMV-Luc; 9514 bp) (kindly given by Transgene S.A., Strasbourg, France) was a plasmid DNA encoding the *firefly* luciferase gene under the control of the

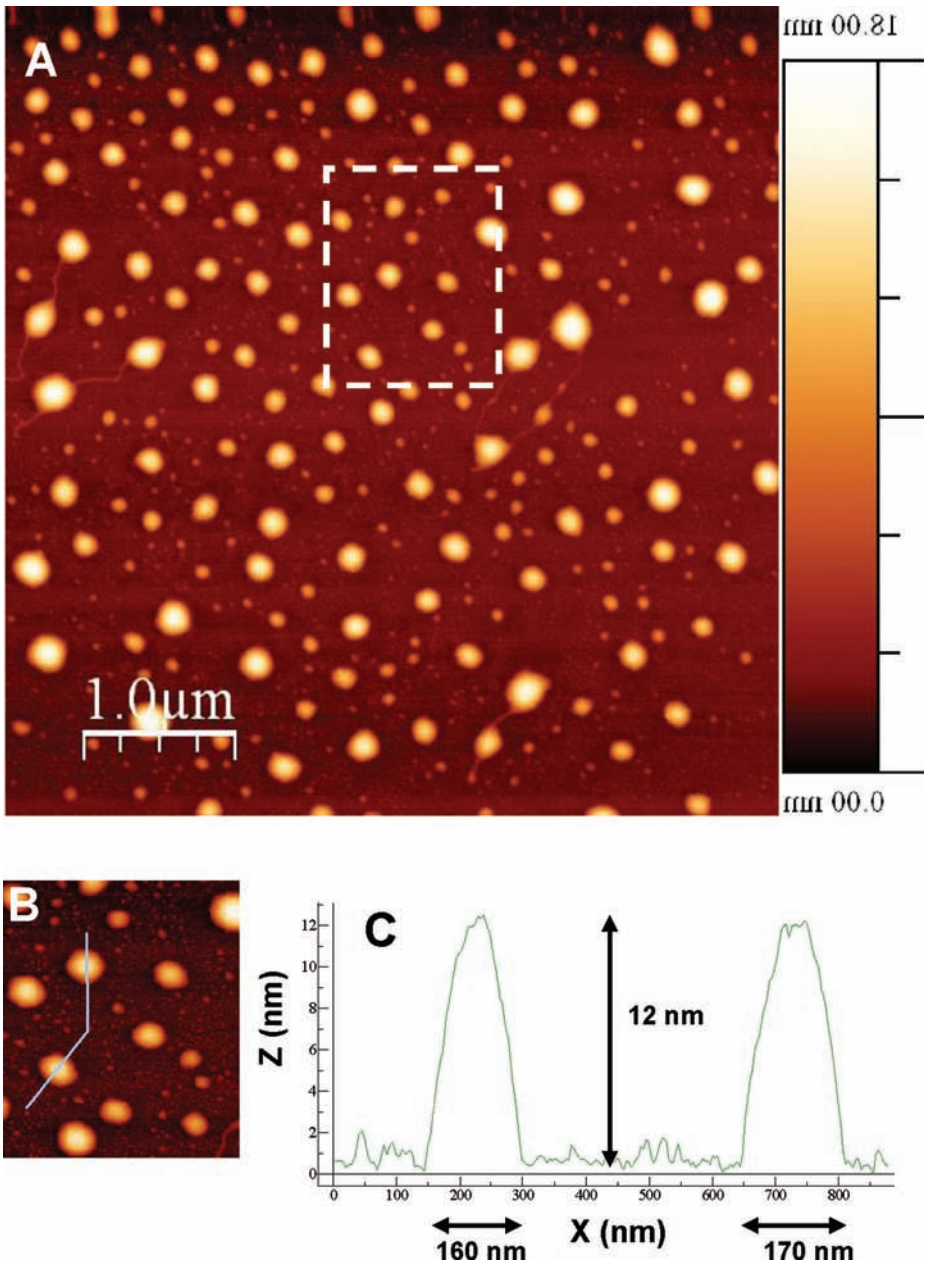

Figure 3. AFM morphology of His-α-CD/pDNA complexes (N/P of 4.2). (A) 2D topography: tapping mode in air; scan size: 5 μm, scan rate: 0.603 Hz, I. Gain: 0.4, P. Gain: 0.5, Amp. Set.: 1.1 V (−0.067 V/ASAE), Drive Amp.: 25 mV, Z Limit: 850 nm. Scale intensity. Bar next to images represents the Z scale in nm. (B) image in the square. (C) AFM profile of His-α-CD/pDNA complexes along the line in image in (B) where Z is the height and X the diameter.

human cytomegalovirus promoter. Supercoiled plasmid DNA was isolated by a standard alkaline lysis method, and purification was carried out with the QIAGEN Mega Kit (QIAGEN, Courtaboeuf, France).

Dye Exclusion Experiments. Aliquots of solution containing cationic derivatives were sequentially added to pDNA (2.5 μg) in 650 μL of 10 mM Hepes buffer, pH 7.4, in the presence of ethidium bromide (2 μM). The fluorescence intensity was measured (λ_{ex} = 530 nm; λ_{em} = 580 nm) after each addition of samples and the fraction of dye exclusion was calculated from the fluorescence intensity measured in the absence and in the presence of cationic derivatives.

Measurements of Size and ζ Potentials. CDplexes were prepared by adding 40 μg of His-α-CD or Lys-α-CD in 60 μL of 10 mM Hepes buffer, pH 7.4, to 10 μg pDNA in 140 μL of 10 mM Hepes buffer, pH 7.4. The solution was mixed by up−down pipetting, vortexed for 4 s, and allowed to stand for 30 min at 20 °C. Then, CDplexes were diluted to 1.4 mL in 10 mM Hepes buffer, pH 7.4. Their size and their ζ potential were measured with ZetaSizer 3000 (Malvern Instruments, Orsay, France). The size was measured by quasi-elastic laser light scattering (QELS) with a sample refractive index of 1.59 and a viscosity of 0.89. The system was calibrated with the 200 ± 5 nm polystyrene polymers (Duke Scientific Corps, Palo Alto, CA). The diameter of CDplexes was calculated in the automatic mode. Their ζ potential was measured by electrophoretic mobility. The following parameters were set up: viscosity, 0.891 cP; dielectric constant, 79; temperature, 25 °C;

dx.doi.org/10.1021/bc200167p | *Bioconjugate Chem.* 2011, 22, 2404−2414

F(Ka), 1.50 (Smoluchowsky); maximum voltage of the current, 15 V. The system was calibrated with DTS 5050 standard from Malvern. Measurements were done ten times with the zero-field correction. The ζ potential was calculated with the Smoluchowsky approximation.

Atomic Force Microscopy. Two microliter aliquots of His-α-CD/pDNA complexes at a mass ratio of 4:1 prepared in 10 mM hepes buffer were adsorbed for 5 min on freshly cleaved muscovite mica. The surface was rinsed thoroughly with ultrapure water and dried for 2 h under vacuum-drying. AFM imaging was performed in tapping mode with Tap300A1-G tip (Budget Sensors, Combo, US) at a scanning speed of 0.603 Hz with an AFM Veeco Dimension 3100 (Veeco, Santa Barbara, CA) using high frequency (300 kHz) and Tap300Al-G silicon probe with tip radius <10 nm (Budget Sensors). Images were treated using the *WSxM 5.0* software.[21]

Transfections. Two days prior to transfection, cells were seeded at 1×10^5 cells per 2 cm^2 in culture medium (1 mL) in a 24-well plate. At the time of the experiment, cell cultures were 80% confluent. CDplexes were prepared by adding 30 μg of His-α-CD or Lys-α-CD in 45 μL of 10 mM Hepes buffer, pH 7.4, to 7.5 μg pDNA in 105 μL of 10 mM Hepes buffer, pH 7.4. The solution was mixed by up−down pipetting, vortexed for 4 s, and allowed to stand for 30 min at 20 °C. It was adjusted to 1.5 mL with culture medium supplemented with 10% FBS before transfection. The medium was removed, the CDplex solution (0.5 mL, 2.5 μg pDNA) was added in each well, and cells were incubated for 4 h at 37 °C. Then, the medium was removed, and cells were cultured 48 h at 37 °C in complete culture medium. Luciferase activity was measured using a Lumat LB9507 luminometer (Lumat LB9507, Berthold, Wildbach, Germany), and the luciferase activity (Relative Light units, RLU) was normalized to RLU per milligram extracted protein.[22]

NMR Experiments. NMR experiments were carried out in D_2O using an Avance 300 MHz Bruker instrument, except for the rotating frame Overhauser effect spectroscopy (ROESY) and heteronuclear 2D experiments which were realized using an Avance 600 MHz Bruker instrument. The temperature calibration of the 300 MHz spectrometer was performed with a sample of 100% CH_3OH in the temperature range between 298 and 313 K.

For the diffusion-ordered spectroscopy (DOSY) experiments, the maximum field gradient strength was calibrated using a homemade Plexiglas phantom (8 mm ±0.01 length and a width equal to the inner diameter of the NMR tube) inserted in a H_2O-filled NMR tube and using the pulse program *calibgp*.[23] Some "negative" projection images of the phantom as a function of applied field gradient strength is given (Supporting Information Figure S2). The linear plot of the obtained gradient strengths against the gradient strength setting (GPZ1) used gave a maximum field gradient strength equal to 56.8 G/cm. The accuracy of the calibrations was checked by measuring the self-diffusion coefficient of a mixture H_2O/D_2O (10%/90% in moles) at 25 °C.[24] The DOSY experiments were carried out using the stegp1s pulse sequence with a linear gradient of 16 steps between 2% and 95%. Before each diffusion experiment, the proton relaxation times were determined in order to correctly set the D1 parameter of the DOSY sequence, and the length of the gradient δ and the diffusion time Δ were optimized for each analyzed product.

RESULTS AND DISCUSSION

Synthesis of α-CD Derivatives. Hexakis(6-deoxy-6-amino)cyclomaltohexaose was synthesized according to previous reported procedures. Then, the coupling between protected amino acid and hexakis(6-deoxy-6-amino)-cyclomaltohexaose were conducted following two synthetic pathways in order to reach a good yield of each product (Scheme 1). Deprotection of the amine functions of the grafted amino groups were then performed to obtain the expected products. ^{1}H NMR (SI Figures S3 and S4) and ^{13}C NMR (SI Figure S5 and S6) spectra show that His-α-CD and Lys-α-CD were synthesized with good purity. MS (MALDI-TOF/TOF) spectrum of the histidinylated conjugate show peaks at 1795.8 and 1827.8 uma (respectively, Li^+ and K^+ adducts) confirming the presence of α-CD substituted by 6 histidyl residues (SI Figures S7). MS (MALDI-TOF/TOF) spectrum of the lysylate conjugate indicated a molecular weight of 1736 uma corresponding to α-CD substituted with 6 lysyl residues (SI Figures S8). Undersubstitution of the CD was detected by mass spectroscopy as witnessed by the presence of a peak at 1608.9 uma, which corresponds to modified cyclodextrin with one glucopyranose unit having an hydroxyl function at the 6 position (SI Figure S8). This compound was found to form a complex with HOBt-TFA salt, demonstrated by a peak at 1880.1 uma, at a concentration not detectable by NMR.

Interaction of Polyamino α-CD Derivatives with DNA. The ability of each polyamino α-CD to condense a plasmid DNA was evaluated by fluorescence dye exclusion using ethidium bromide. This nonfluorescent molecule becomes fluorescent once intercalated between the base pairs of the plasmid DNA. Conversely, the fluorescence intensity drops due to dye exclusion when DNA condensation occurs in the presence of polycationic molecules. As shown in Figure 1, the dye exclusion depended on the polyamino α-CD types. The fluorescence intensity decreased rapidly when the amount of His-α-CD increased, indicating a strong condensation of the plasmid DNA. The maximum of the dye exclusion reached 80% in the presence of 7.5 μg (4.2 nmol) His-α-CD corresponding to a N/P charge ratio of 4.2. N/P was the charge ratio between the number of positive charges of the polyamino α-CD derivatives and the negative charges of the pDNA phosphate. All the pDNA phosphate functions are negatively charged and the 12 amino groups of Lys-α-CD are positively charged at pH 7.4. On the basis of our previous results on histidylated polylysine, we have hypothesized that His-α-CD contained 8 positive charges at pH 7.4. We have indeed reported that the protonation of the imidazole groups in histidylated polylysine occurs at a 1.1 pH unit higher (6.9) than that of histidine, meaning that 2 of the 6 imidazole rings are protonated at pH 7.4.[25] Surprisingly, no significant dye exclusion and no DNA condensation were observed in the presence of NH_2-α-CD. The fluorescence intensity decreased much more in the presence of Lys-α-CD than in the presence of NH_2-α-CD. The maximum of the dye exclusion reached 50% in the presence of 17 μg (120 nmol) Lys-α-CD at N/P of 15. While Lys-α-CD contained more positive charges than His-α-CD, DNA condensation with Lys-α-CD was lower than with His-α-CD. The formation of DNA complexes with the polyamino α-CD derivatives was monitored by agarose gel electrophoresis (Figure 2). The gel retardation experiments indicated that no migration of 1 μg pDNA was observed from 1 μg His-α-CD and 2 μg Lys-α-CD. Compared to pDNA/Lys-α-CD, the lower

level of BET staining of pDNA with His-α-CD from a 1/1 weight ratio evidenced a better DNA condensation that was in line with dye exclusion experiments. In these weight ratios, the migration of pDNA was observed with α-CD-NH_2 confirming the absence of pDNA condensation (not shown).

Physicochemical Parameters of DNA/Polyamino α-CD Derivatives Complexes (CDplexes). The size and the ζ potential of CDplexes were measured at their optimal DNA/CD ratio. Dynamic light scattering measurements of His-α-CDplexes at N/P of 4.2 indicated that their diameter was close to 225 ± 45 nm with a polydispersity index (PDI) of 0.31 indicative of a relative homogeneity of the size distribution. These CDplexes were slightly positive (ζ potential = 7 ± 5 mV). In contrast, the size of Lys-α-CDplexes at same N/P was close to 640 ± 90 nm (PDI of 0.64) and the ζ potential was −1 ± 3 mV. This result confirmed the higher DNA condensation capacity of His-α-CD. The lower DNA condensation capacity of Lys-α-CD formed larger and less homogeneous CDplexes. His-α-CDplexes were cast on mica and observed by AFM. All the pDNA was complexed with His-α-CD and formed globular particles (Figure 3A,B). On the basis of the AFM profiles, His-α-CDplexes demonstrated the average diameter and height of 170 and 12 nm, respectively (Figure 3C). Compared to DLS, the CDplexes dimension was slightly smaller with AFM because AFM provides measurement of a single particle, while DLS gives the mean value for the non-monodispersed solution of particles.[26]

Transfection Efficiency. The ability of these CDplexes to transfect mammalian cells was examined using HEK293-T7 cells and pCMVLuc, a plasmid encoding the luciferase gene. The cells were incubated for 4 h with CDplexes containing 2.5 μg pDNA. Figure 4 shows that the luciferase activity in cells

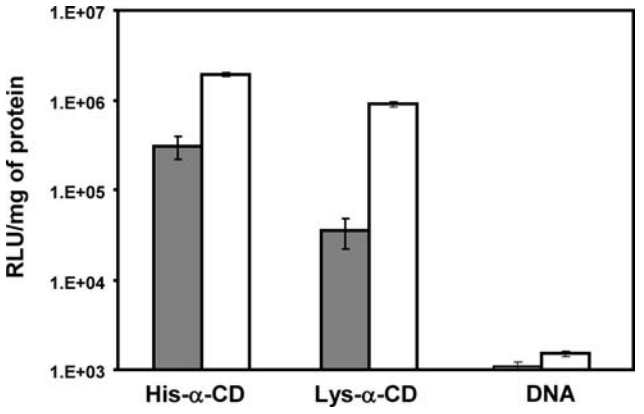

Figure 4. Transfection of HEK293-T7 cells with CDplexes. Cells were transfected with pCMVLuc (2.5 μg) free or complexed with His-α-CD or Lys-α-CD at N/P of 5.3 and 8.5, respectively. Transfection was carried out in the absence (gray bars) or the presence (white bars) of 100 μM chloroquine. The luciferase activity expressed as relative light units per mg protein (RLU/mg of protein) was measured upon 48 h of culture. The values shown are averages of three independent experiments.

transfected with His-α-CDplexes (3×10^5 RLU/mg of protein) was 8-fold higher than that obtained Lys-α-CDplexes. When the transfection was carried out in the presence of chloroquine—a lysosomotropic reagent that favors destabilization of acid vesicles [27]—the luciferase activity of His-α-CDplexes and Lys-α-CDplexes increased 6 and 25 times, respectively. The enhancement was lower with His-α-CD compared to Lys-α-CD, because His-α-CD contains acid-protonable imidazole groups that induce a proton sponge effect inside endosomes which favors the delivery of pDNA into the cytosol in the absence of chloroquine. Here, the protonation behavior of the imidazole groups in His-α-CDplexes is expected to be as in polyplexes made with histidylated polylysine (His-pLK). We have indeed reported that the ζ potential of His-pLK polyplexes increased 8 times when the pH decreased from 7.5 to 5.0 indicating that the protonation of the imidazole groups in His-pLK occurs in polyplexes.[25] The transfection efficiency of His-α-CD was about 3 orders of magnitude lower than that of lPEI (6×10^8 RLU/mg proteins), the gold standard cationic polymer. Nevertheless, the transfection efficiency of His-α-CD was as high as that of HeLa and H9c2 cells with pDNA complexed with a β-cyclodextrin substituted with seven tetraethylenpentamine residues.[28] It was close to the transfection of HEK293 cells with pCMV-Luc complexed with a *per* ethylenimine α-CD (2×10^6 RLU/mg of protein) that contained also protonable amines.[2] Of note, DNA complexed with *per* oligoethylenimine α-CD became very efficient (1×10^9 RLU/mg proteins) when the number of ethylenimine repeat units reached 4.[8]

Comparative DNA Condensation Capacity of His-α-CD and Poly(L-lysines). The unexpected DNA condensation capacity of His-α-CD prompted us to compare this ability with that of other cationic polymers such as poly(L-lysine) by using fluorescence dye exclusion. Surprisingly, DNA condensation with His-α-CD (8 NH_2 functions per CD molecule) was close to that observed with PLK_{190} (190 NH_2 functions per polymer molecule) (Figure 5). The maximum of the dye exclusion

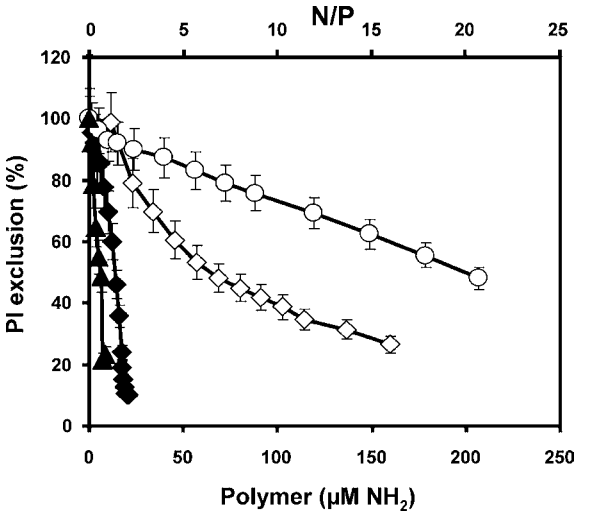

Figure 5. Interaction of polymers with DNA. Aliquots of solution containing polymers were sequentially added to pDNA (2.5 μg) in 650 μL of 10 mM Hepes buffer, pH 7.4, in the presence of ethidium bromide (2 μM). The fluorescence intensity was measured (λ_{ex} = 530 nm; λ_{em} = 580 nm) after each addition of sample and the fraction of dye exclusion was calculated from the fluorescence intensity measured in the absence and in the presence of polymers. N/P corresponds to the ratio between the number of positive charges of polymers and that of the negative charges of the pDNA phosphate. His-α-CD (▲); PLK_{190} (◆); PLK_6 (◇); $K_{20}H_{20}$ (○).

reached 90% in the presence of 0.11 μM (i.e., 21 μM NH_2) PLK_{190} at N/P of 2. The DNA condensation capacity of His-α-CD was higher than with PLK_6 containing 6 NH_2 functions per

dx.doi.org/10.1021/bc200167p | Bioconjugate Chem. 2011, 22, 2404–2414

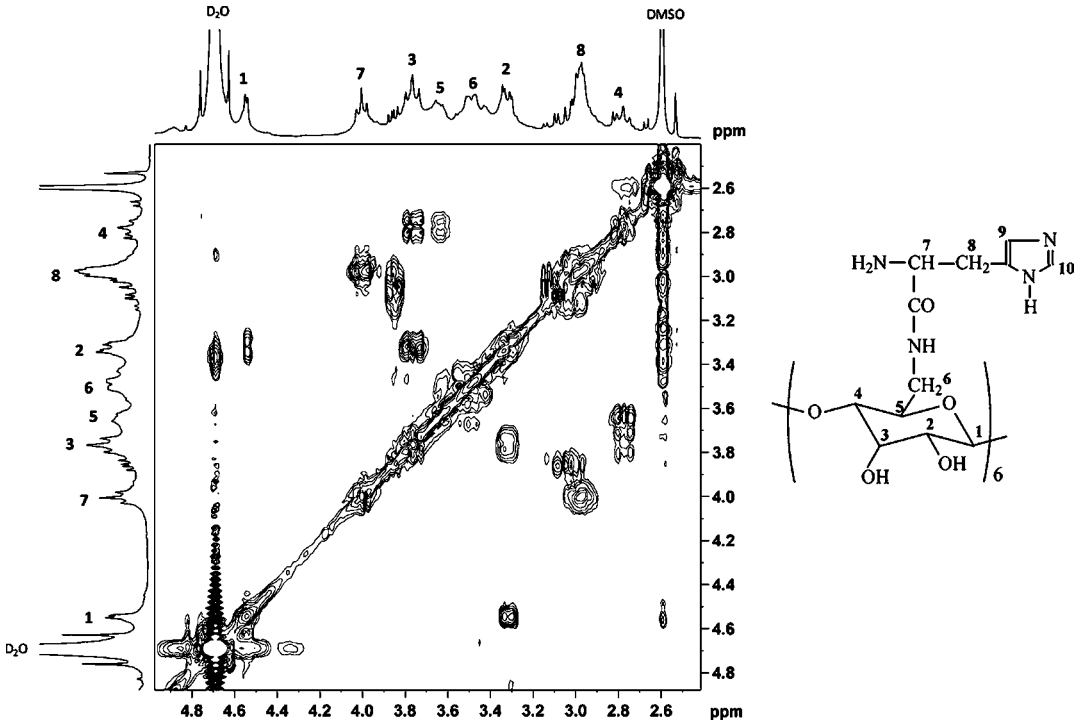

Figure 6. COSY NMR experiment of His-α-CD.

polymer molecule (Figure 5). Surprisingly, the DNA condensation was much higher with His-α-CD than with $K_{20}H_{20}$ (Figure 5). This latter polymer was a poly(L-lysine) of 20 lysyl residues that were substituted with a histidine residue linked on their ε-amino group. On the basis of the number of positive charges, one would be expected that DNA condensation will be stronger with $K_{20}H_{20}$ than with His-α-CD. Note that the DNA condensation with $K_{20}H_{20}$ was also lower than with PLK_6. Therefore, the DNA condensation capacity of His-α-CD did not involve only interaction of the positive charges of the α-CD derivative with the phosphate groups of the nucleic acid, but suggested the formation of a supramolecular structure allowing cooperative interaction with DNA involving CD and histidine. Indeed, it is known that the imidazole group can form an inclusion complex with the hydrophobic cavity of cyclodextrin.[29] Binding constants of imidazole to α-cyclodextrin are approximately 6 times higher than those for β-cyclodextrin as measured by microcalorimetric technique. Therefore, we have examined by NMR investigation the possible formation of supramolecular structures from His-α-CD molecules which could explain the strong interaction with pDNA.

Characterization of Supramolecular Association by NMR. *CD Derivatives ROESY NMR Experiments.* First, 1D and 2D NMR of His-α-CD were performed to confirm the structure of the product. On the basis of the ^{1}H NMR spectra of the initial reactants and on the correlation spectroscopy (COSY) NMR spectrum, all the peaks of the His-α-CD ^{1}H spectrum were assigned (Figure 6). It was observed that integration of the peak at 7.75 ppm of the proton borne by the carbon between the two nitrogen atoms decreased with time until complete exchange with deuterium. This fact was also observed for each imidazole derivative. The heteronuclear single quantum correlation (HSQC) experiment of His-α-CD was used to identify each carbon of the product (SI Figure S9).

To examine the possible formation of supramolecular structures from His-α-CD molecules, a 2D ROESY NMR experiment was carried out to determine which protons were close to each other in space even if they were not bonded. The spectrum in Figure 7 shows that the CD proton H5, which is located inside the CD cavity, is correlated to the proton H9 of the imidazole group *via* an intense negative cross-peak, whereas there is no cross-peak between the proton H5 and the proton H10 belonging to the imidazole group. In the same way, we observe a negative cross-peak between the protons H3 and H10 and no correlation between H3 and H9. This result demonstrates that an inclusion complex occurs through the CD primary side. Discrimination between intra- (Figure 8b) and intermolecular (Figure 8c) interaction between the CD cavity and the imidazole moieties requires more investigation. When the same experiments were performed with Lys-α-CD, the 2D ROESY NMR spectrum showed no negative cross-peak between the proton H5 of the CD and the methylene groups of the lysine (peaks 8, 9, and 10), indicating the absence of inclusion between lysyl residue and the hydrophobic cavity of CD (SI Figure S10, Figure 9).

CD Derivatives DOSY NMR Experiments. Diffusion-ordered spectroscopy (DOSY) experiments were attempted to determine whether His-α-CD allowed supramolecular assemblies or not. DOSY NMR which is based on a pulse-field gradient spin−echo NMR experiment, in which components experience diffusion, provides relevant information for the study of mixtures or for the structure characterization of polymers (see Supporting Information).[30,31] On the basis of the scheme in Figure 8c, His-α-CD supramolecular species would be dimers or higher molecular weight species. Thus, a decrease of the diffusion coefficients would be correlated to the increase of the molecular weight of the molecules. First, the diffusion coefficients of D_2O, L-histidine, and α-CD in an equimolar mixture of α-CD and L-histidine were, respectively, found equal

dx.doi.org/10.1021/bc200167p | *Bioconjugate Chem.* 2011, 22, 2404−2414

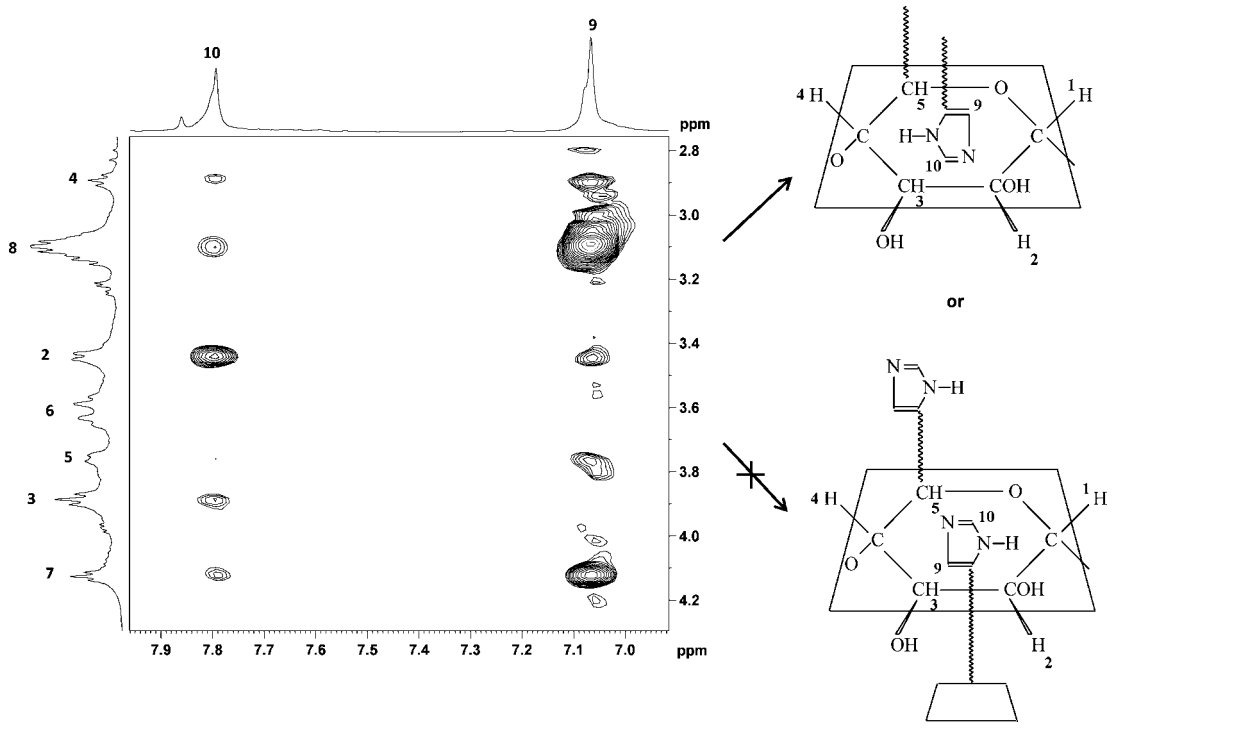

Figure 7. Zoomed ROESY NMR experiment of His-α-CD in D_2O.

to 1.86×10^{-9} $m^2.s^{-1}$, 5.92×10^{-10} $m^2.s^{-1}$, and 2.82×10^{-10} $m^2.s^{-1}$ (SI Figures S11 and S12; Table 1). Then, the diffusion coefficient of α-CD alone (2.78×10^{-10} $m^2.s^{-1}$) or in an equimolar mixture with methyl-L-histidine (2.83×10^{-10} $m^2.s^{-1}$) were determined (Table 1). The DOSY treatment of His-α-CD alone gave a diffusion coefficient of 1.93×10^{-10} $m^2.s^{-1}$ from the peak at ~7.0 ppm or 2.21×10^{-10} $m^2.s^{-1}$ taking into account the broad peak located between 2.8 ppm and 4.3 ppm (protons from the CD and histidine group) (SI Figure S13; Table 1). These close values confirm that the imidazole group was linked to α-cyclodextrin. The DOSY treatment of Lys-α-CD gave 1.85×10^{-10} $m^2.s^{-1}$ from the anomeric peak, 1.83×10^{-10} $m^2.s^{-1}$ from the broad peak between 4.2 and 3.1 ppm, 1.75×10^{-10} $m^2.s^{-1}$ from the peak at 2.9 ppm, 1.87×10^{-10} $m^2.s^{-1}$ from the peak at 1.9 ppm, 1.78×10^{-10} $m^2.s^{-1}$ from the peak at 1.6 ppm, and 1.86×10^{-10} $m^2.s^{-1}$ from the peak at 1.35 ppm (SI Figure S14). These values were very close, giving an average diffusion coefficient of 1.83×10^{-10} $m^2.s^{-1}$ (Table 1).

Overall, these experiments show that the diffusion rates of the solvent molecules are almost the same whatever the considered DOSY and corresponds to the highest values compared to the investigated molecules. When α-CD is substituted with α-amino acids, the diffusion coefficient is lower than the initial α-CD in agreement with its higher hydrodynamic volume. The comparison of the two grafted α-CD (having a similar molar mass) shows that the diffusion coefficient of His-α-CD is slightly higher than that of Lys-α-CD, explained by the higher hydrodynamic volume of the protonated Lys-α-CD compared to that of His-α-CD. The diffusion coefficient measurements of His-α-CD were confirmed by increasing the attenuation, i.e., the values of Δ and δ (run 5, Table 1). The signal-to-noise ratio decrease was compensated by a higher number of scans (run 6, Table 1), and no variation of the diffusion coefficient was noticed (runs 4, 5 and 6, Table 1). Taking in account the ROESY experiment showing the interaction between the imidazole ring and the hydrophobic cavity of the α-CD, and the diffusion values, it appears that only intramolecular interactions occur between His-α-CD molecules under NMR conditions. Compared with transfection experiments, NMR experiments with His-α-CD were performed at a much higher CD concentration (~100 times higher), and no large diffusive species was detected, suggesting that the supramolecular association of His-α-CD was not favored under any NMR conditions, i.e., without plasmid added to the CD derivatives. During His-α-CDplex formation, interaction between amino groups of His-α-CD and DNA phosphate moieties might provide a scaffold for a template association of His-α-CD via inclusion complexes between CD and the histidine moieties (Figure 8c). This effect can be compared to the spontaneous polymerization by disulfide bond when sulfhydryl cross-linking peptides or polymers were bound to pDNA leading to stable DNA condensates.[32−34]

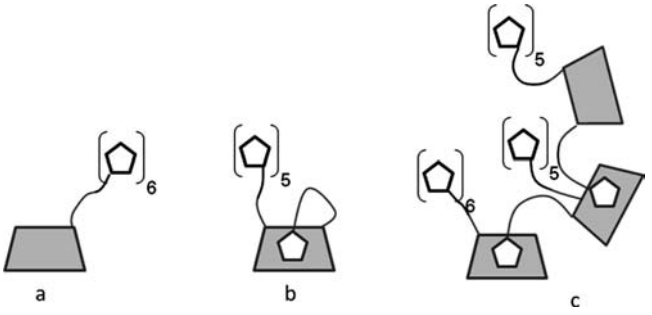

Figure 8. Schematic representation of the various forms of CD derivatives.

dx.doi.org/10.1021/bc200167p | *Bioconjugate Chem.* 2011, 22, 2404−2414

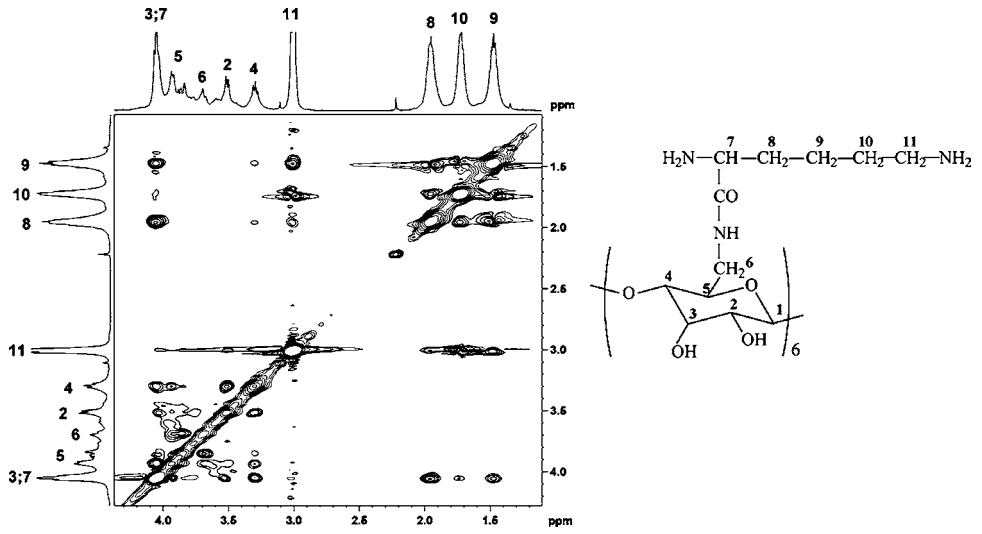

Figure 9. ROESY NMR experiment of Lys-α-CD in D_2O.

Table 1. DOSY NMR Experiments: Determination of the Diffusion Coefficients (D) of Different Samples[a]

		D ($m^2.s^{-1}$)		
run	signal used for the D determination	peak at 7 ppm	H_1	CD broad
1	α-CD		2.78×10^{-10}	2.70×10^{-10}
2	mixture (1/1) α-CD/histidine	5.92×10^{-10}	2.82×10^{-10}	
3	mixture (1/1) α-CD/Me-Lhistidine	5.32×10^{-10}	2.83×10^{-10}	
4	His-α-CD	1.93×10^{-10}		2.21×10^{-10}
5	His-α-CD	2.00×10^{-10}		2.11×10^{-10}
6	His-α-CD	2.05×10^{-10}		2.10×10^{-10}
7	Lys-α-CD		1.85×10^{-10}	1.83×10^{-10}

[a] $M_{\alpha CD}$ = 972 g/mol; $M_{histidine}$ = 155 g/mol; $M_{Me\text{-}Lhistidine}$ = 169 g/mol; $M_{His\text{-}\alpha\text{-}CD}$ = 1789 g/mol; $M_{Lys\text{-}\alpha\text{-}CD}$ = 1735 g/mol. Runs 1,2,34: Δ = 200 ms and δ = 4.5 ms; runs 5 and 6: Δ = 300 ms and δ = 6 ms. Note that no calculation was conducted from the peak at 7.7 ppm because it disappeared with time, and from the anomeric CD proton which overlapped with the solvent peak for His-α-CD.

CONCLUSION

In the present work, we demonstrated that His-α-CD can condense a plasmid DNA allowing the formation of CDplexes that transfect cells. At the same time, we found that the DNA condensation capacity of His-α-CD is unexpectedly higher than that obtained with the lysyl-α-CD counterpart. NMR studies demonstrated that the formation of an inclusion complex between histidine and the hydrophobic cavity of CD occurs and only intramolecular interaction occurs between His-α-CD molecules in the absence of DNA. These results suggest that intermolecular interactions between imidazole and His-α-CD cavity can take place to form supramolecular assemblies in the presence of a DNA scaffold increasing the DNA condensation.

ASSOCIATED CONTENT

Supporting Information

Experimental protocol. His-α-CD DOSY NMR experiments. Images projection of the phantom with increasing gradient strength (only images obtained with 5% to 50% of the maximum gradient strength are shown; a residual signal is observed due to water in the inside screw thread for ease of phantom handling). ^1H NMR of hexakis(6-deoxy-6-histidinyl)cyclomaltohexaose (His-α-CD). ^1H NMR of hexakis(6-deoxy-6-lysinyl)-cyclomaltohexaose (Lys-α-CD). ^{13}C NMR of hexakis(6-deoxy-6-histidinyl)cyclomaltohexaose (His-α-CD). ^{13}C NMR of hexakis(6-deoxy-6-lysinyl)cyclomaltohexaose (Lys-α-CD). MS (MALDI-TOF/TOF) spectrum of hexakis(6-deoxy-6-histidinyl)-cyclomaltohexaose (His-α-CD). MS (MALDI-TOF/TOF) spectrum of hexakis(6-deoxy-6-lysinyl)cyclomaltohexaose (Lys-α-CD). HSQC experiment of His-α-CD in D_2O (experiment with water suppression, which explains the reason the D_2O and anomeric proton signals did not appear). COSY experiment of Lys-α-CD in D_2O at 25.2 °C; [Lys-α-CD] = 9.3×10^{-3} mol/L. ^1H spectrum of a mixture (1/1) of αCD and L-histidine in D_2O at 25.2 °C; [αCD] = [L-histidine] = 21.6×10^{-3} mol/L. ln I versus $\gamma^2g^2\delta^2(\Delta-\delta/3)$ plot considering the anomeric proton at 4.97 ppm; [α-CD] = [L-histidine] = 21.6×10^{-3} mol/L in D_2O; 25.2 °C. ln I versus $\gamma^2g^2\delta^2(\Delta-\delta/3)$ plot considering the peaks resonated between 4.3 and 2.8 ppm. [His-α-CD] = 9.0×10^{-3} mol/L in D_2O; 25.2 °C; Δ = 200 ms; δ = 4.5 ms. ln I versus $\gamma^2g^2\delta^2(\Delta-\delta/3)$ plot considering the peaks resonated between 4.2 and 3.1 ppm; [Lys-α-CD] = 9.3×10^{-3} mol/L in D_2O; 25.2 °C. This material is available free of charge via the Internet at http://pubs.acs.org.

AUTHOR INFORMATION

Corresponding Author

*Phone: +33 2 38 25 55 65; E-mail: patrick.midoux@cnrs-orleans.fr.

Author Contributions

[#]Both investigators contributed equally and should be considered as senior authors.

■ ACKNOWLEDGMENTS

We warmly thank Cristine Gonçalves, Loic Lebègue, and Marie-Jeanne Clement for their excellent technical assistance. We are grateful to Fréderic Foucher for AFM analyses. We thank Guillaume Gaban and the Mass Spectroscopy platform of CBM for mass spectroscopy analyses. This work was supported by grants from Association Française contre les Myopathies (AFM) and Vaincre La Mucoviscidose (VLM).

■ REFERENCES

(1) Ortiz Mellet, C., Garcia Fernandez, J. M., and Benito, J. M. (2010) Cyclodextrin-based gene delivery systems. *Chem. Soc. Rev. 40*, 1586−1608.

(2) Yang, C., Li, H., Goh, S. H., and Li, J. (2007) Cationic star polymers consisting of alpha-cyclodextrin core and oligoethylenimine arms as nonviral gene delivery vectors. *Biomaterials 28*, 3245−3254.

(3) Srinivasachari, S., Fichter, K. M., and Reineke, T. M. (2008) Polycationic beta-cyclodextrin "click clusters": monodisperse and versatile scaffolds for nucleic acid delivery. *J. Am. Chem. Soc. 130*, 4618−4627.

(4) Diaz-Moscoso, A., Balbuena, P., Gomez-Garcia, M., Ortiz Mellet, C., Benito, J. M., Le Gourrierec, L., Di Giorgio, C., Vierling, P., Mazzaglia, A., Micali, N., Defaye, J., and Garcia Fernandez, J. M. (2008) Rational design of cationic cyclooligosaccharides as efficient gene delivery systems. *Chem. Commun. (Camb.)*, 2001−2003.

(5) Diaz-Moscoso, A., Le Gourrierec, L., Gomez-Garcia, M., Benito, J. M., Balbuena, P., Ortega-Caballero, F., Guilloteau, N., Di Giorgio, C., Vierling, P., Defaye, J., Ortiz Mellet, C., and Garcia Fernandez, J. M. (2009) Polycationic amphiphilic cyclodextrins for gene delivery: synthesis and effect of structural modifications on plasmid DNA complex stability, cytotoxicity, and gene expression. *Chemistry 15*, 12871−12888.

(6) Ortega-Caballero, F., Mellet, C. O., Le Gourrierec, L., Guilloteau, N., Di Giorgio, C., Vierling, P., Defaye, J., and Garcia Fernandez, J. M. (2008) Tailoring beta-cyclodextrin for DNA complexation and delivery by homogeneous functionalization at the secondary face. *Org. Lett. 10*, 5143−5146.

(7) Peres, B., Richardeau, N., Jarroux, N., Guegan, P., and Auvray, L. (2008) Two independent ways of preparing hypercharged hydrolyzable polyaminorotaxane. *Biomacromolecules 9*, 2007−2013.

(8) Yang, C., Wang, X., Li, H., Goh, S. H., and Li, J. (2007) Synthesis and characterization of polyrotaxanes consisting of cationic alpha-cyclodextrins threaded on poly[(ethylene oxide)-ran-(propylene oxide)] as gene carriers. *Biomacromolecules 8*, 3365−3374.

(9) Choi, H. S., Ooya, T., and Yui, N. (2006) One-pot synthesis of a polyrotaxane via selective threading of a PEI-b-PEG-b-PEI copolymer. *Macromol. Biosci. 6*, 420−424.

(10) Wang, C. Y., and Huang, L. (1984) Polyhistidine mediates an acid-dependent fusion of negatively charged liposomes. *Biochemistry 23*, 4409−4416.

(11) Uster, P. S., and Deamer, D. W. (1985) pH-dependent fusion of liposomes using titratable polycations. *Biochemistry 24*, 1−8.

(12) Midoux, P., and Monsigny, M. (1999) Efficient gene transfer by histidylated polylysine/pDNA complexes. *Bioconjug. Chem. 10*, 406−411.

(13) Midoux, P., Pichon, C., Yaouanc, J. J., and Jaffres, P. A. (2009) Chemical vectors for gene delivery: a current review on polymers, peptides and lipids containing histidine or imidazole as nucleic acids carriers. *Br. J. Pharmacol. 157*, 166−178.

(14) Rodal, S. K., Skretting, G., Garred, O., Vilhardt, F., van Deurs, B., and Sandvig, K. (1999) Extraction of cholesterol with methyl-beta-cyclodextrin perturbs formation of clathrin-coated endocytic vesicles. *Mol. Biol. Cell 10*, 961−974.

(15) Kilsdonk, E. P., Yancey, P. G., Stoudt, G. W., Bangerter, F. W., Johnson, W. J., Phillips, M. C., and Rothblat, G. H. (1995) Cellular cholesterol efflux mediated by cyclodextrins. *J. Biol. Chem. 270*, 17250−17256.

(16) Ohtani, Y., Irie, T., Uekama, K., Fukunaga, K., and Pitha, J. (1989) Differential effects of alpha-, beta- and gamma-cyclodextrins on human erythrocytes. *Eur. J. Biochem. 186*, 17−22.

(17) Benkhaled, A., Cheradame, H., Fichet, O., Teyssié, D., and Guégan, P. (2008) Synthesis and characterization of amphiphilic per-(6-thio-2,3-trimethylsilyl) cyclodextrin: application to langmuir film formation. *Polym. Carbohydr. 73*, 482−489.

(18) Guillo, F., Hamelin, B., Julien, L., Canceill, J., Lehn, J.-M., De Robertis, L., and Driguez, H. (1995) Synthesis of symmetrical cyclodextrin derivatives bearing multiple charges. *Bull. Soc. Chim. Fr. 132*, 857−866.

(19) Pichon, C., Roufai, M. B., Monsigny, M., and Midoux, P. (2000) Histidylated oligolysines increase the transmembrane passage and the biological activity of antisense oligonucleotides. *Nucleic Acids Res. 28*, 504−512.

(20) Brisson, M., He, Y., Li, S., Yang, J. P., and Huang, L. (1999) A novel T7 RNA polymerase autogene for efficient cytoplasmic expression of target genes. *Gene Ther. 6*, 263−270.

(21) Horcas, I., Fernandez, R., Gomez-Rodriguez, J. M., Colchero, J., Gomez-Herrero, J., and Baro, A. M. (2007) WSXM: a software for scanning probe microscopy and a tool for nanotechnology. *Rev. Sci. Instrum. 78*, 013705.

(22) Midoux, P., Mendes, C., Legrand, A., Raimond, J., Mayer, R., Monsigny, M., and Roche, A. C. (1993) Specific gene transfer mediated by lactosylated poly-L-lysine into hepatoma cells. *Nucleic Acids Res. 21*, 871−888.

(23) Seedhouse, S. J., and Hoffman, M. M. (2008) Magnetic field gradient calibration as an experiment to illustrate magnetic resonance imaging. *J. Chem. Educ. 85*, 836−838.

(24) Holz, M., and Weingärtner, H. (1991) Calibration in accurate spin-echo self-diffusion measurements using 1H and less-common nuclei. *J. Magn. Reson. 92*, 115−125.

(25) Bello Roufaï, M., and Midoux, P. (2001) Histidylated polylysine as DNA vector: Elevation of the imidazole protonation and reduced cellular uptake without change in the polyfection efficiency of serum stabilized negative polyplexes. *Bioconjugate Chem. 12*, 92−99.

(26) Hoo, C. M., Starostin, N., West, P., and Mecartney, M. L. (2008) A comparison of atomic force microscopy (AFM) and dynamic light scattering (DLS) methods to characterize nanoparticle size distributions. *J. Nanoparticle Res 10*, 89−96.

(27) Erbacher, P., Roche, A. C., Monsigny, M., and Midoux, P. (1996) Putative role of chloroquine in gene transfer into a human hepatoma cell line by DNA/lactosylated polylysine complexes. *Exp. Cell Res. 225*, 186−94.

(28) Srinivasachari, S., and Reineke, T. M. (2009) Versatile supramolecular pDNA vehicles via "click polymerization" of beta-cyclodextrin with oligoethyleneamines. *Biomaterials 30*, 928−938.

(29) Rekharsky, M. V., Nemykina, E. V., Eliseev, A. V., and Yatsimirsky, A. K. (1992) Thermodynamics of molecular recognition of nitrogen heterocycles: Part 1. Interation of imidazole and imidazolium cation with alpha cyclodextrin and beta cyclodextrin. *Thermochim. Acta 202*, 25−33.

(30) Williamson, R. T., Chapin, E. L., Carr, A. W., Gilbert, J. R., Graupner, P. R., Lewer, P., McKamey, P., Carney, J. R., and Gerwick, W. H. (2000) New diffusion-edited NMR experiments to expedite the duplication of known compounds from natural product mixtures. *Org. Lett. 2*, 289−292.

(31) Stessman, C. C., Ebel, R., Corvino, A. J., and Crews, P. (2002) Employing dereplication and gradient 1D NMR methods to rapidly characterize sponge-derived sesterterpenes. *J. Nat. Prod. 65*, 1183−1186.

(32) Park, Y., Kwok, K. Y., Boukarim, C., and Rice, K. G. (2002) Synthesis of sulfhydryl cross-linking poly(ethylene glycol)-peptides and glycopeptides as carriers for gene delivery. *Bioconjugate Chem. 13*, 232−239.

(33) Kwok, K. Y., Park, Y., Yang, Y., McKenzie, D. L., Liu, Y., and Rice, K. G. (2003) In vivo gene transfer using sulfhydryl cross-linked PEG-peptide/glycopeptide DNA co-condensates. *J. Pharm. Sci. 92*, 1174−1185.

(34) McKenzie, D. L., Smiley, E., Kwok, K. Y., and Rice, K. G. (2000) Low molecular weight disulfide cross-linking peptides as nonviral gene delivery carriers. *Bioconjugate Chem. 11*, 901−909.

Bioconjugate Chemistry

Article

pubs.acs.org/bc

Comparison Study of [^{18}F]FAl-NOTA-PRGD2, [^{18}F]FPPRGD2, and [^{68}Ga]Ga-NOTA-PRGD2 for PET Imaging of U87MG Tumors in Mice

Lixin Lang,[†,#] Weihua Li,[†,‡,#] Ning Guo,[†] Ying Ma,[†] Lei Zhu,[†] Dale O. Kiesewetter,[†] Baozhong Shen,[‡] Gang Niu,[†,§] and Xiaoyuan Chen*[,†]

[†]Laboratory of Molecular Imaging and Nanomedicine (LOMIN), [§]Imaging Sciences Training Program, Radiology and Imaging Sciences, Clinical Center, National Institute of Biomedical Imaging and Bioengineering (NIBIB), National Institutes of Health (NIH), Bethesda, Maryland 20892, United States

[‡]Department of Medical Imaging and Nuclear Medicine, the Fourth Affiliated Hospital, Harbin Medical University, Harbin 150001, China

ABSTRACT: [^{18}F]FPPRGD2, an F-18 labeled dimeric cyclic RGDyK peptide, has favorable properties for PET imaging of angiogenesis by targeting the $\alpha_v\beta_3$ integrin receptor. This radiotracer has been approved by the FDA for use in clinical trials. However, the time-consuming multiple-step synthetic procedure required for its preparation may hinder the widespread usage of this tracer. The recent development of a method using an F-18 fluoride-aluminum complex to radiolabel peptides provides a strategy for simplifying the labeling procedure. On the other hand, the easy-to-prepare [^{68}Ga]-labeled NOTA-RGD derivatives have also been reported to have promising properties for imaging $\alpha_v\beta_3$ integrin receptors. The purpose of this study was to prepare [^{18}F]FPPRDG2, [^{18}F]FAl-NOTA-PRGD2, and [^{68}Ga]Ga-NOTA-PRGD2 and to compare their pharmacokinetics and tumor imaging properties using small animal PET. All three compounds showed rapid and high tracer uptake in U87MG tumors with high target-to-background ratios. The uptake in the liver, kidneys, and muscle were similar for all three tracers, and they all showed predominant renal clearance. In conclusion, [^{18}F]FAl-NOTA-PRGD2 and [^{68}Ga]Ga-NOTA-PRGD2 have imaging properties and pharmacokinetics comparable to those of [^{18}F]FPPRGD2. Considering their ease of preparation and good imaging qualities, [^{18}F]FAl-NOTA-PRGD2 and [^{68}Ga]NOTA-PRGD2 are promising alternatives to [^{18}F]FPPRGD2 for PET imaging of tumor $\alpha_v\beta_3$ integrin expression.

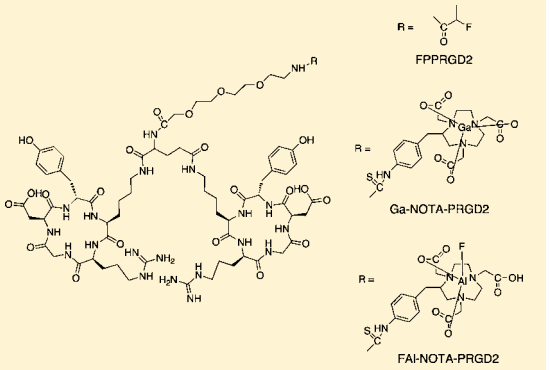

INTRODUCTION

Tumor angiogenesis is the process of new blood vessel formation necessary for tumor growth and metastasis,[1] and the integrin $\alpha_v\beta_3$ receptor plays an important role in promoting, sustaining, and regulating the angiogenesis.[2,3] In recent years, major efforts and progress have been made in the development of radiolabeled Arg-Gly-Asp (RGD) containing peptides to image tumor angiogenesis by targeting integrin $\alpha_v\beta_3$ receptors in various types of tumors.[4,5] It is widely accepted that imaging tumor angiogenesis can be used not only for early detection of cancers, but also for monitoring treatment outcomes.[4,6−9] Cyclic RGD peptides with various modifications have been labeled with ^{99m}Tc[10] and ^{111}In[11] for SPECT imaging and labeled with ^{18}F,[12] ^{64}Cu,[13] ^{68}Ga,[14,15] and ^{89}Zr[16] for PET imaging. The peptide modifications have included dimerization and polymerization of up to 8 cyclic RGD peptide units to increase binding affinity, and the attachment of polar functional groups—such as sugar and poly(ethylene glycol) (PEG)—to increase renal excretion.[17,18] [^{18}F]FPPRGD2, an F-18 labeled dimeric cyclic RGDyK peptide with mini-PEGylation, has favorable properties for PET imaging of tumor angiogenesis, and it has been approved by the FDA for use in clinical trials[18,19]

F-18 is the most widely used positron emitting radioisotope for PET imaging, and its physical properties are ideally suited for RGD peptide-based PET imaging probes. The majority of methods used in labeling RGD peptides with ^{18}F use a prosthetic group, such as *N*-succinimidyl 4-[^{18}F]fluorobenzoate ([^{18}F]SFB)[20] or 4-nitrophenyl 2-[^{18}F]fluoropropionate ([^{18}F]-NPFP),[7] and the time-consuming multiple-step synthetic procedure required for preparation may hinder the widespread use of these ^{18}F-labeled RGD tracers. The preparation of [^{18}F]FPPRGD2 also faces these challenges. Efforts have been made with some success to simplify the labeling procedure by direct labeling of RGD peptides with a preattached functional group with a proper leaving group for fluoride displacement.[21] On the other hand, labeling radioactive metal ions through a preattached chelator on RGD peptides has been blessed with a much simpler procedure. One advantage of using coordination chemistry is that only very small amounts of chelators are required to reach high labeling yield, which allows the radiotracer to be prepared without the need of HPLC

Received: April 18, 2011
Revised: September 16, 2011
Published: October 24, 2011

ACS Publications © 2011 American Chemical Society

purification, while maintaining reasonable specific activity levels. The easy preparations of ^{68}Ga-labeled NOTA-RGD derivatives are examples that have been reported to have promising properties for tumor imaging.[14,15,22]

Application of chelation chemistry has led to recent discovery and development of ^{18}F fluoride−aluminum complexes to radiolabel peptides that provide a strategy to simplify the labeling procedure.[23,24] The goal of this study was to prepare [^{18}F]FPPRDG2, [^{18}F]FAl-NOTA-PRGD2, and [^{68}Ga]Ga-NOTA-PRGD2 from the same pegylated dimeric RGD peptide PEG3-E[c(RGDyK)]$_2$ (denoted as PRGD2) and to compare their pharmacokinetics and imaging properties in a U87MG glioblastoma xenograft model using microPET.

MATERIALS AND METHODS

The p-SCN-Bn-NOTA was purchased from Macrocyclics (Dallas, TX) and PRGD2 was obtained from Peptides International (Louisville, KY). All of the other chemicals were purchased from Sigma-Aldrich. A Waters 600 high-performance liquid chromatography (HPLC) system with a Waters 996 photodiode array detector (PDA) using a preparative C_{18} HPLC column (PROTO 300 C_{18} 5 μm, 250 × 20 mm, Higgins Analytical, Inc.) was used for peptide purification. A Varian BOND ELUT C_{18} column (100 mg) was used for solid-phase extraction. Another Waters 600 HPLC pump with a Waters 996 PDA and an online radioactivity detector (Beckman) using a semiprep C_{18} HPLC column (Vydac C_{18} peptide and protein 5 μm, 250 × 10 mm, Grace Davison) was used for purification of radiolabeled compounds. A Perkin-Elmer 200 series HPLC pump with a Waters 2487 UV detector and a Bioscan Flow-Count detector using an analytical C_{18} HPLC column (Vydac C_{18} peptide and protein 5 μm, 250 × 4.6 mm, Grace Davison) was used for analysis or purification of labeled compounds. Mass spectra were obtained with a Waters LC-MS system (Waters, Milford, MA) that included an Acquity UPLC system coupled to a Waters Q-Tof Premier high-resolution mass spectrometer. The ^{68}Ge/^{68}Ga generator was purchased from Ithemba Laboratories (South Africa) and ^{18}F-fluoride was obtained from the NIH cyclotron facility.

Preparation of NOTA-PRGD2. NOTA-PRGD2 was synthesized following our previously reported procedure with modifications.[15] Briefly, 7.0 mg (15.5 μmol) of *p*-SCN-Bn-NOTA in 50 μL of dimethyl sulfoxide (DMSO) was added to a 4 mL glass vial containing 21.0 mg (14 μmol) of PRGD2 and 20 μL of diisopropylethylamine in 0.3 mL *N*,*N*-dimethylformamide (DMF). After 1 h, the reaction was quenched with 20 μL of acetic acid in 1 mL water. The reaction mixture was purified with a preparative HPLC running a linear gradient starting from 6% A (0.1% TFA in acetonitrile) and 94% B (0.1% TFA in water) for 5 min and increasing to 65% A at 35 min with a flow rate of 12 mL/min. The fractions containing the desired product (55%) were collected and lyophilized to give 15.0 mg of white powder. The purity of the product was >95% by analytical HPLC (t_R = 16.4 min). LC-MS: $[MH]^+$ = 1989.69 (m/z), calc: 1988.91 ($C_{87}H_{128}N_{24}O_{28}S$).

Preparation of Al-NOTA-PRGD2. To a 1 mL V-vial containing 1.1 mg of NOTA-PRGD2 in 0.2 mL of deionized water was add 0.21 mg of aluminum chloride in 20 μL 0.5 M pH 4.0 sodium acetate buffer. The vial was sealed and the mixture was heated at 105 °C for 10 min and then injected onto a preparative RP HPLC C_{18} column with a linear gradient starting from 6% A (0.1% TFA in acetonitrile) and 94% B (0.1% in water) for 5 min and increasing to 65% A at 35 min at the flow rate of 12 mL/min. A single peak at the retention time of 19.7 min was collected and analyzed with LC-MS. The peak had the $[MH]^+$ = 2013.6660 (m/z) which matched the calculated mass for Al-NOTA-PRGD2 ($C_{87}H_{125}AlN_{24}O_{28}S$: 2012.8631). The sample was lyophilized overnight to give 1.1 mg of white powder (99%). The purity of the product was >97% by analytical HPLC (Dionex, 4.6 × 150 mm) with a retention time of 15.5 min with a baseline separation from the NOTA-PRGD2 (16.4 min).

Preparation of FAl-NOTA-PRGD2. To a 1 mL V-vial containing 0.2 mL of deionized water were added 10 μL of 2 mM aluminum chloride in 0.1 M pH 4.0 sodium acetate buffer and 7 μL of 3.0 mM sodium fluoride in 0.1 M pH 4.0 sodium acetate buffer. The mixture was heated at 100 °C for 10 min, and 5 μL of 2.5 mM NOTA-PRGD2 in 0.1 M pH 4.0 sodium acetate buffer was added to the reaction mixture, which was then heated at 100 °C for another 10 min. The solution was cooled and injected onto an analytical RP C_{18} column (Vydac C_{18}) running a linear gradient starting from 5% A (0.1% TFA in acetonitrile) and 95% B (0.1% TFA in water) for 2 min and increasing to 65% A at 32 min at 1 mL/min. The peaks at 15.5 min and 15.7 were collected as a single fraction. The LC-MS analysis showed two mass components in this fraction with $[MH]^+$ = 2013.67 (m/z) corresponding to the mass of Al-NOTA-PRGD2 (R_t = 15.5 min) and $[MH]^+$ = 2033.65 (m/z) corresponding to FAl-NOTA-PRGD2 (calculated for $C_{87}H_{126}AlFN_{24}O_{28}S$: 2032.87).

Preparation of Ga-NOTA-PRGD2. To a 1 mL V-vial containing 2.6 mg of NOTA-PRGD2 in 0.3 mL of deionized water was add 0.5 mg of gallium chloride in 0.1 mL of 0.1 M pH 4.0 sodium acetate buffer. The mixture was heated at 80 °C for 10 min and then injected onto a preparative RP HPLC C_{18} column running the same gradient as described above. A single peak at the retention time of 19.5 min was collected and lyophilized overnight to give 2.6 mg of white powder (99%). LC-MS: $[MH]^+$ = 2056.0730 (m/z) corresponding to Ga-NOTA-PRGD2 (calculated for $C_{87}H_{125}GaN_{24}O_{28}S$: 2054.8072).

Preparation of 4-Nitrophenyl 2-[^{18}F]-fluoropropionate. The 4-nitrophenyl [^{18}F]-2-fluoropropionate was prepared on a GE TRACERLab FXN according to a published procedure[19] with some modifications. For a typical run, [^{18}F]fluoride was trapped on an ^{18}F Separation Cartridge (CHROMAFIX, 30-PS-HCO_3) from a source vial containing the aqueous [^{18}F]fluoride (3.7 GBq, 0.2 mL) by pulling the vacuum line. The activity was eluted to a glassy-carbon reaction vessel with 1 mL 90% acetonitrile containing 15.0 mg of K222 and 3.5 mg of potassium carbonate. The liquid in the reaction vessel was removed with vacuum to produce anhydrous [^{18}F]fluoride. After cooling, 5 mg of ethyl 2-bromopropionate in 0.5 mL of acetonitrile was added to the reaction vessel and heated at 100 °C for 10 min to form ethyl 2-[^{18}F]-fluoropropionate. At the end the of the reaction, 125 μL of 0.2 N potassium hydroxide in 375 μL of acetonitrile was added to the reaction vessel, which was then heated at 100 °C for another 10 min to produce the potassium salt of 2-[^{18}F]fluoropropionic acid. The solution was diluted with 1 mL of acetonitrile and the liquid was removed with vacuum, and 20 mg of bis-4-nitropenyl carbonate in 1 mL of acetonitrile was added to react with potassium 2-[^{18}F]fluoropropionate to form 4-nitrophenyl 2-[^{18}F]fluoropropionate at 100 °C for 10 min. After cooling, the reaction mixture was diluted with 1 mL of 25% acetonitrile/water with 5% acetic acid and loaded onto a

semiprep Phenomenex Luna C_{18} column running at 5 mL/min with 40% acetonitrile/water containing 0.1% TFA as the mobile phase. The product was collected at the retention time of 21 min into a flask containing 30 mL of water with 0.1% acetic acid. The solution containing the desired product was passed through a Waters Sep-Pak Plus C_{18} cartridge and the activity trapped on the cartridge was washed with 1 mL of water.

Preparation of [^{18}F]FPPRGD2. The activity trapped on the C_{18} cartridge as described above was eluted manually with 1 mL of methylene chloride into a 1 mL polypropylene tube and the water layer on top of the methylene chloride was removed by using a syringe. The methylene chloride in the tube was evaporated under argon flow at room temperature, and 1 mg of PRGD2 in 0.1 mL of DMSO containing 20 μL of diisopropylethylamine was added to the tube and heated at 80 °C for 10 min. At the end of the reaction, the reaction mixture was cooled and diluted with 0.7 mL of water containing 25 μL of acetic acid and loaded onto a semiprep HPLC column (Vydac C_{18}) running a linear gradient starting from 5% A (0.1% TFA in acetonitrile) and 95% B (0.1% TFA in water) for 2 min and increasing to 65% A at 32 min at 5 mL/min. The desired product was collected at a retention time of 14 min and diluted with 10 mL water and trapped on a Varian Bond Elut C_{18} column (100 mg). The radioactivity trapped on the C_{18} column was eluted with 0.3 mL of 1 mM HCl−ethanol solution, and the ethanol was removed with argon flow, and the final product was then dissolved in PBS.

[^{18}F]FAl-NOTA-PRGD2. Three microliters of 2 mM aluminum chloride in 0.2 M pH 4 sodium acetate buffer was added to a 1 mL V-vial containing 0.1 mL of aqueous [^{18}F]fluoride (0.37 GBq), which was then heated at 100 °C for 10 min to form the aluminum−fluoride complex. The vial was cooled, 6 μL of 2 mM NOTA-PRGD2 in 0.2 M pH 4 sodium acetate buffer was added, and then the vial was heated at 100 °C for another 10 min. At the end of the reaction, the mixture was injected onto an analytical HPLC column (Vydac C_{18}) running a linear gradient starting from 5% A (0.1% TFA in acetonitrile) and 95% B (0.1% TFA in water) for 2 min and increasing to 65% A at 32 min at 1 mL/min. The radioactive peak containing the desired product was collected at a retention time of 16 min and diluted with 15 mL of water and trapped on a Varian Bond Elut C_{18} column (100 mg). The radioactivity trapped on the C_{18} column was eluted with 0.3 mL of 80% ethanol/water with 2% acetic acid, the ethanol solution was evaporated with argon flow, and the final product was then dissolved in PBS. A separate procedure was performed without HPLC purification and the reaction mixture was directly loaded onto the C_{18} cartridge.

[^{68}Ga]Ga-NOTA-PRGD2. The fresh ^{68}Ga activity was eluted from the ^{68}Ge/^{68}Ga generator with 0.6 M HCl at 0.5 mL per fraction into the 1.5 mL polypropylene tubes. The fraction containing the most radioactivity (~0.15 GBq) was added to 0.45 mL of 1 M HEPES buffer and 15 μg of NOTA-PRGD2 in 5 μL of 0.2 M pH 4 sodium acetate buffer. The mixture was heated at 80 °C for 10 min. At the end of the reaction, the activity was loaded onto an analytical HPLC column (Vydac C_{18}) running a linear gradient starting from 5% A (0.1% TFA in acetonitrile) and 95% B (0.1% TFA in water) for 2 min and increasing to 65% A at 32 min at 1 mL/min. The desired product was collected at 16 min, diluted with 15 mL of water, and trapped onto a 100 mg Varian Bond Elut C18 column. The radioactivity trapped on the C_{18} column was eluted with 0.3 mL of 80% ethanol/water with 2% acetic acid, the ethanol solution was removed with argon flow, and the final product was redissolved in PBS. A separate procedure was performed without HPLC purification, and the reaction mixture was directly loaded onto the C_{18} cartridge. The reactions were done at room temperature and at 80 °C. The crude mixture and purified product were also analyzed with analytical HPLC for their radiochemical purities.

Cell Binding Assay. The $\alpha_v\beta_3$ receptor binding assay was performed to determine binding affinities of E[c(RGDyK)]$_2$ analogues. Briefly, U87MG cell line was cultured in DMEM medium (GIBCO) containing 10% (v/v) fetal bovine serum (GIBCO) supplemented with penicillin (100 μg/mL), streptomycin (100 μg/mL), nonessential amino acids (100 μM), and sodium pyruvate (1 mM) at 37 °C with 5% CO_2. When grown up to 80% confluence, cells were scraped off and suspended with binding buffer [25 mM 2-amino-2-(hydroxymethyl)-1,3-propanediol, hydrochloride (Tris-HCl), pH 7.4, 150 mM NaCl, 1 mM $CaCl_2$, 0.5 mM $MgCl_2$ and 1 mM $MnCl_2$, 0.1% bovine serum albumin (BSA)] at a final concentration of 2×10^6 cells/mL. In a 96-well plate, 1×10^5 U87 MG cells/well were incubated with ^{125}I-Echistatin (0.74 kBq/well, PerkinElmer, Inc.) in binding buffer in the presence of different concentrations of E[c(RGDyK)]$_2$ analogues at room temperature for 1 h. After incubation, the plate was washed three times with phosphate buffered saline (PBS) containing 0.1% BSA, and the radioactivity was measured by γ-counting. The EC_{50} values were calculated by nonlinear regression analysis using the *GraphPad Prism* computer-fitting program (GraphPad Software, Inc., San Diego, CA). Each data point is a result of the average of triplicate wells.

Preparation of Animal Tumor Models. All animal studies were conducted in accordance with the principles and procedures outlined in the Guide for the Care and Use of Laboratory Animals and were approved by the Institutional Animal Care and Use Committee of the Clinical Center, NIH. The human glioblastoma cell line U87MG was grown in DMEM medium supplemented with 10% fetal bovine serum (FBS), 100 IU/mL penicillin, and 100 μg/mL streptomycin (Invitrogen), and in a humidified atmosphere containing 5% CO_2 at 37 °C. The cells were harvested by trypsinization with trypsin/EDTA. The U87MG tumor model was developed in 5 to 6-week-old female athymic nude mice (Harlan Laboratories) by injection of 5×10^6 cells in their right shoulders. Tumor growth was monitored using caliper measurements of perpendicular axes of the tumor. The mice underwent small-animal PET studies when the tumor volume reached 100−300 mm^3 (3−4 weeks after inoculation).

MicroPET Imaging and Analysis. PET scans and image analysis were performed using an Inveon microPET scanner (Siemens Medical Solutions). About 3.7 MBq of ^{18}F or ^{68}Ga labeled tracer was administered via tail vein injection under isoflurane anesthesia. For blocking study, about 300 μg of unlabeled dimeric RGD peptide E[c(RGDyK)]$_2$ was injected 30 min before the [^{18}F]FAl-NOTA-PRGD2. Five-minute static PET images were acquired at 30 min, 1 h, and 2 h postinjection (n = 3−5 per group). The images were reconstructed using a two-dimensional ordered-subset expectation maximum (2D OSEM) algorithm, and no correction was applied for attenuation or scatter. For each scan, regions of interest (ROIs) were drawn using vendor software (*ASI Pro* 5.2.4.0) on decay-corrected whole-body coronal images. The radioactivity concentrations (accumulation) within the tumors, muscle, liver, and kidneys were obtained from mean pixel values within the

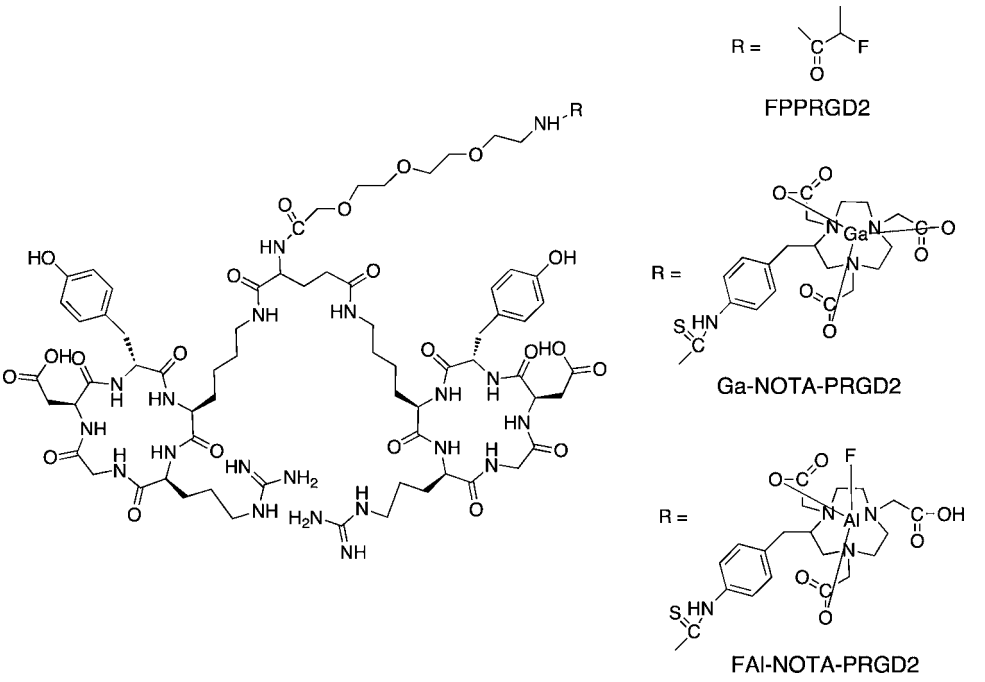

Figure 1. Chemical structures of dimeric RGD peptides.

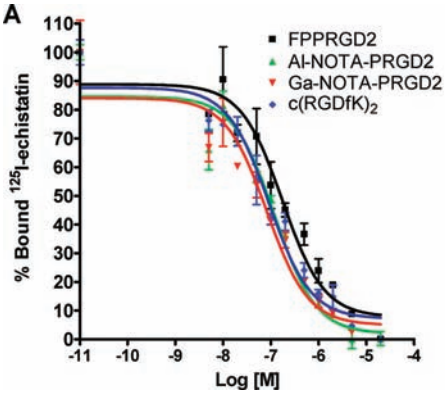

B

Compound	IC_{50} (nM)
FPPRGD2	175.4
Al-NOTA-PRGD2	119.2
Ga-NOTA-PRGD2	82.7
$c(RGDfK)_2$	91.4

Figure 2. (A) Cell binding assay of RGD peptides in U87MG cells; (B) IC_{50} of each RGD compound (n = 3).

multiple ROI volume and then converted to MBq per milliliter. These values were then divided by the administered activity to obtain (assuming a tissue density of 1 g/mL) an image-ROI-derived percent injected dose per gram (%ID/g).

Biodistribution Study of [^{18}F]FAl-NOTA-PRGD2. Immediately after PET imaging, the tumor-bearing mice with or without blocking dose were sacrificed and dissected. Blood, tumor, major organs, and tissues were collected and wet-weighed. The radioactivity in the wet whole tissue was measured with a γ-counter (Perkin- Elmer). The results were expressed as percentage of injected dose per gram of tissue (% ID/g). Values were expressed as mean ± SD (n = 4 per group).

In Vitro Stability of [^{18}F]FAl-NOTA-PRGD2. About 5.6 MBq of [^{18}F]FAl-NOTA-PRGD2 in 50 μL of PBS was added to 400 μL of mouse serum and incubated at 37 °C. About 60 μL of this serum sample was taken out at 1, 30, 60, and 120 min and put into a plastic tube. An equal volume of acetonitrile was added to each tube and centrifuged at 6000 rpm for 8 min. The supernatant was separated from the pellet, and both the supernatant and pellet were measured for their radioactivity. The supernatant was diluted with 300 μL of PBS and injected on to an analytical HPLC. The tube was measured for its radioactivity before and after HPLC injection. The radioactivity coming out of HPLC column was also collected and measured.

RESULTS

Chemistry. The structures of PEGylated dimeric RGD peptides are shown in Figure 1. The 2-fluoropropanoyl labeled PRGD2 is designated as FPPRGD2. *S*-2-(4-Isothiocyanatobenzyl)-1,4,7-triazacyclononane-1,4,7-triacetic acid is designated as p-SCN-Bn-NOTA. The p-SCN-Bn-NOTA labeled PRGD2 is designated as NOTA-PRGD2. The aluminum NOTA-PRGD2 complex is designated as Al-NOTA-PRGD2, and the aluminum fluoride complex of NOTA-PRGD2 is designated as FAl-NOTA-PRGD2. Gallium NOTA-PRGD2 complex is designated as Ga-NOTA-PRGD2.

NOTA-PRGD2, Al-NOTA-PRGD2, and Ga-NOTA-PRGD2 were prepared at mg scale that can be lyophilized and weighed for further use. The yield of Al-NOTA-PRGD2 and Ga-NOTA-PRGD2 was almost quantitative. Chemical purities of these compounds were >97% determined by analytical HPLC analysis. FAl-NOTA-PRGD2 was prepared in small-scale

reaction, collected from HPLC and used directly as the reference compound. The identities of nonradioactive compounds were determined by LC-MS, which observed m/z ions that matched their calculated molecular weights. Preparation of FAl-NOTA-PRGD2 yielded a mixture of FAl-NOTA-PRGD2 and Al-NOTA-PRGD2 that were not separable by HPLC.

In order to confirm that adding metal NOTA complex to the PRGD2 does not affect the binding affinity of the peptides to integrin receptors, we performed competitive cell binding assays with ^{125}I-echistatin as the radioligand in integrin $\alpha_v\beta_3$ positive U87MG cells. Results of the cell-binding assays were plotted and fitted to sigmoid curves for the displacement of ^{125}I-echistatin from U87MG cells (Figure 2A). The IC_{50} values are listed in Figure 2B. The results indicated that the adding metal NOTA complex to PRGD2 had up to 2-fold increase on the binding affinity of the peptides compared to that of FPPRGD2.

Radiochemisty. The radiolabeling of the three compounds is summarized in Table 1. The radiochemical yield for 4-nitrophenyl 2-[^{18}F]fluoropropionate prepared from Tracer FX-FN system was around 20−25%, and the yield for coupling of 4-nitrophenyl 2-[^{18}F]fluoropropionate with PRGD2 was over 75%. The overall yield was 10−15% (uncorrected) with a total synthesis time of around 3 h and the measured specific activity was 114 ± 72 GBq/μmol (EOB). The labeling efficiency for [^{18}F]FAL-NOTA-PRGD2 varied between 5% and 25%, depending on the reaction volumes. When the reaction volume was between 50 and 100 μL, the yield was consistently between 20% and 25% (uncorrected). The total synthesis time was about 40 min with HPLC purification and about 25 min without HPLC purification. The radiochemical purity was over 97%. The radiochemical yield for [^{68}Ga]Ga-NOTA-PRGD was about 70% (uncorrected) with HPLC in a total synthesis time of 30 min.

Table 1. Comparison of Reaction Condition and Yield of [^{18}F]FAl-NOTA-PRGD2, [^{18}F]FPPRDG2, and [^{68}Ga]Ga-NOTA-PRGD2

tracer name	total time (min)	HPLC	reaction temperature	labeling yield (n = 5)
[^{18}F] FPPRDG2	180	yes	80 °C	10−15%
[^{68}Ga]NOTA-PRGD2	30	yes	80 °C	75%
	15	no	RT	40%
[^{18}F]FAl-NOTA-PRGD2	40	yes	100 °C	5−25%
	25	no	100 °C	5−25%

Purification of Radiolabeled Products by Solid-Phase Extraction. To further simplify the labeling procedure, the solid-phase extraction method was used to prepare both [^{18}F]FAl-NOTA-PRGD2 and [^{68}Ga]Ga-NOTA-PRGD2. The tracer could be prepared in about 15 min. Without the HPLC purification, the specific activity was determined by the amount of peptide used, assuming the complete recovery of peptide and the amount of radioactivity used. In our preparation of these two tracers, 12 nmol of PRDGD2 was used to make [^{18}F]FAl-NOTA-PRGD2, and 8 nmol of peptide was used to make [^{68}Ga]Ga-NOTA-PRGD2. In this study, ^{18}F activity was limited to 0.37−1.5 GBq, and ^{68}Ga activity limited to 0.15−0.20 GBq . For a 37 MBq of product, at the end of synthesis the specific activity was 6.14 GBq/μmol for [^{18}F]FAl-NOTA-PRGD2 and 9.25 GBq/μmol for [^{68}Ga]Ga-NOTA-PRGD2. For a 0.37 GBq of product, the specific activities were 30.71 GBq/μmol and 46.25 GBq/μmol, respectively, for [^{18}F]FAl-NOTA-PRGD2 and [^{68}Ga]Ga-NOTA-PRGD2. For [^{68}Ga]Ga-NOTA-PRGD2, when only solid-phase extraction was used the radiochemical yield was 40% at room temperature and reached over 90% at 80 °C. The radiochemical purity was also >97% for room temperature reaction with a slight decrease of radiochemical purity (95%) at 80 °C.

***in Vitro* Stability of the Radiotracers.** Both [^{68}Ga]Ga-NOTA-PRGD2 and [^{18}F]FAl-NOTA-PRGD2 were stable in PBS at room temperature. After 4 h, the radiochemical purities were >95% with HPLC analysis. We also tested the stability of [^{18}F]FAl-NOTA-PRGD2 in mouse serum up to 2 h at 37 °C. After treating the serum samples with acetonitrile and centrifugation, 85% of radioactivity was in solution. The recovery of radioactivity from HPLC was >96% without any detectable F-18 fluoride. The parent compound at 1, 30, 60, and 120 min constituted 96.8%, 96.6%, 95.1%, and 95.0% of recovered radioactivity, respectively.

MicroPET Imaging. After radiolabeling, we applied the three imaging probes to *in vivo* PET imaging with U87MG tumor bearing mice. The representative decay-corrected coronal images at different time points after injection of the radiotracers are shown in Figures 3−5. The U87MG tumors were clearly visualized with good tumor-to-background contrast with all of the tracers as early as 30 min postinjection (p.i.). The quantitative tracer uptake of tumors and major organs is summarized in Table 2, expressed as % ID/g. At 60 min p.i., the tumor uptake of [^{18}F]FPPRGD2 was 2.56 ± 0.48% ID/g (n = 5), which was consistent with a previous report.[18] As for [^{68}Ga]Ga-NOTA-PRGD, the tumor uptake was 2.98 ± 0.53% ID/g (n = 3). The tumor uptake of [^{18}F]FAl-NOTA-PRGD2 was 3.92 ± 0.18%ID/g (n = 4), which was significantly higher than that of the other two tracers (p < 0.05). Besides tumor

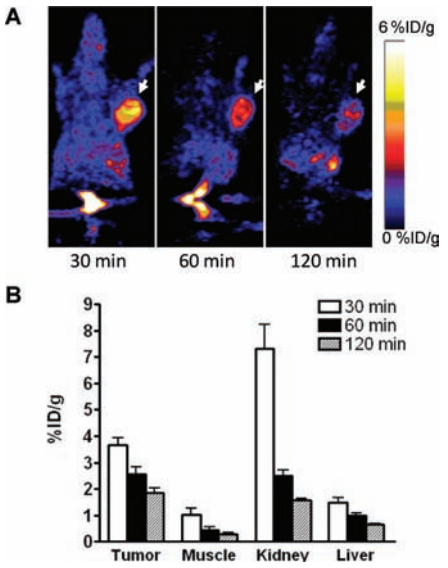

Figure 3. *In vivo* PET imaging of U87MG xenografted mice by [^{18}F]FPPRGD2. (A) Decay-corrected whole-body coronal microPET images of U87MG tumor-bearing mice at 30, 60, and 120 min after injection of 3.7 MBq of [^{18}F]FPPRGD2. Tumors are indicated by arrows. (B) Quantification of [^{18}F]FPPRGD2 in U87MG tumor, liver, kidneys, and muscle. ROIs are shown as mean %ID/g ± SD.

dx.doi.org/10.1021/bc200197h | *Bioconjugate Chem.* 2011, 22, 2415−2422

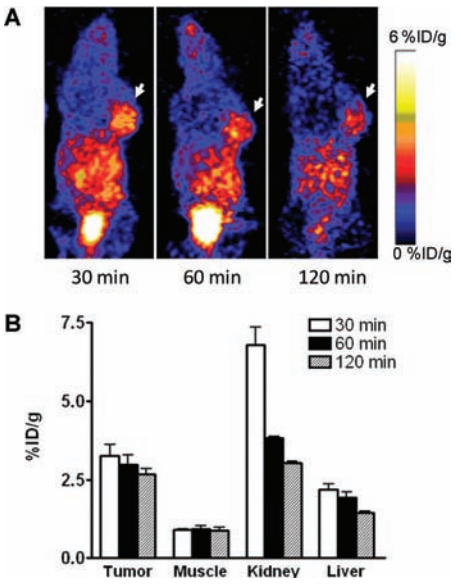

Figure 4. *In vivo* PET imaging of U87MG xenografted mice by [^{68}Ga]Ga-NOTA-PRGD2. (A) Decay-corrected whole-body coronal microPET images of U87MG tumor-bearing mice at 30, 60, and 120 min after injection of 3.7 MBq of [^{68}Ga]Ga-NOTA-PRGD2. Tumors are indicated by arrows. (B) Quantification of [^{68}Ga]Ga-NOTA-PRGD2 in U87MG tumor, liver, kidneys, and muscle. ROIs are shown as mean %ID/g ± SD.

uptake, all tracers showed relatively high kidney accumulation, especially at the early time point (30 min p.i.), then dropped significantly afterward, indicating rapid renal clearance. All three tracers showed relatively low liver uptake. Compared with the other two tracers, [^{18}F]FPPRGD2 showed faster clearance from tumors. We believe this may be a consequence of the lower binding affinity of FPPRGD2 as determined by vitro cell binding affinity study.

Biodistribution Studies. In order to further confirm the PET imaging quantification, the biodistribution of [^{18}F]FAl-NOTA-PRGD2 with and without blocking dose was evaluated in U87MG tumor-bearing athymic nude mice immediately after PET imaging (Figure 6). Consistent with PET imaging data, the tumor uptake measured by direct tissue sampling and gamma-counting was 1.45 ± 0.47%ID/g at the 2 h time point. The tracer accumulations in the kidneys and liver were 4.88 ± 0.82 and 1.47 ± 0.50%ID/g, respectively, at 2 h p.i. In the blocking experiment, U87MG tumor showed significantly decreased accumulation of [^{18}F]FAl-NOTA-PRGD2 with an uptake value of 0.15 ± 0.04%ID/g ($p < 0.001$).

DISCUSSION

Labeling peptides and proteins with ^{18}F is usually achieved using prosthetic groups. The required multistep procedure for preparation of the prosthetic group, its purification, subsequent protein coupling step, and final purification results in relatively low overall radiochemical yield. In addition, multistep syntheses are more difficult to automate.[25] F-18 click chemistry has been used in several studies to label peptides.[26] However, it requires the preparation of azide or alkyne functional group modified peptides and two radiochemical synthesis steps, and in some cases, it involves volatile [^{18}F]-azide synthon. Alternatively, several groups including our lab have developed direct labeling methods of peptides with ^{18}F.[21,27,28]

We have applied [^{18}F]FPPRDG2 to monitor the treatment effect of various anticancer drugs longitudinally on mouse tumor models.[7−9] The routine preparation of [^{18}F]FPPRDG2, which is a 3 h procedure, is quite challenging. Currently, there is no commercially available automated synthesizer that is capable of producing [^{18}F]FPPRDG2 without major modifications. McBride and Laverman et al.[23,24,29] reported the method of using the [^{18}F]fluoride-aluminum-NOTA complex for labeling peptides. Although the radiolabeling conditions required heating, the inherent thermal stability of RGD peptides suggested that they would be good substrates for this radiolabeling method. The precursor for making [^{18}F]-

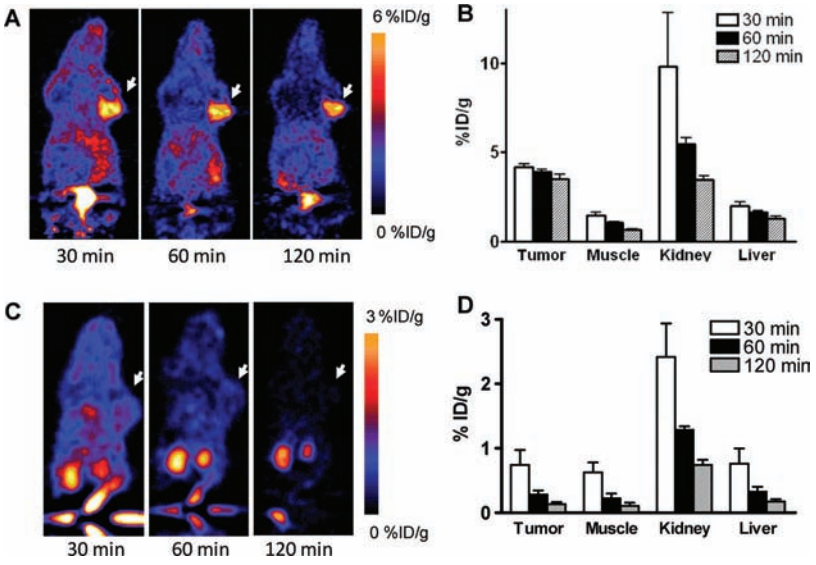

Figure 5. *In vivo* PET imaging of U87MG xenografted mice with [^{18}F]FAl-NOTA-PRGD2. Decay-corrected whole-body coronal microPET images of U87MG tumor-bearing mice at 30, 60, and 120 min after injection of 3.7 MBq of [^{18}F]FAl-NOTA-PRGD2 without (A) and with (C) blocking dose. Tumors are indicated by arrows. Quantification of [^{18}F]FAl-NOTA-PRGD2 in U87MG tumor, liver, kidneys, and muscle without (B) and with (D) blocking dose. ROIs are shown as mean %ID/g ± SD.

dx.doi.org/10.1021/bc200197h | *Bioconjugate Chem.* 2011, 22, 2415−2422

Table 2. Biodistribution of Dimeric RGD Peptide Tracers in U87MG Tumor-Bearing Mice, Determined by PET Imaging (% ID/g ± SD)

	[^{18}F]FPPRDG2			[^{68}Ga]NOTA-PRGD2			[^{18}F]FAl-NOTA-PRGD2		
	30 min	60 min	120 min	30 min	60 min	120 min	30 min	60 min	120 min
tumor	3.65 ± 0.51	2.56 ± 0.48	1.85 ± 0.30	3.25 ± 0.62	2.98 ± 0.53	2.66 ± 0.32	4.20 ± 0.23	3.92 ± 0.18	3.53 ± 0.45
muscle	1.03 ± 0.42	0.44 ± 0.22	0.28 ± 0.09	0.91 ± 0.02	0.92 ± 0.18	0.87 ± 0.18	1.49 ± 0.25	1.07 ± 0.06	0.68 ± 0.06
kidney	7.31 ± 1.61	2.49 ± 0.36	1.57 ± 0.09	6.80 ± 0.97	3.81 ± 0.08	3.02 ± 0.11	9.80 ± 5.21	5.45 ± 0.61	3.46 ± 0.44
liver	1.48 ± 0.33	1.00 ± 0.11	0.64 ± 0.05	2.18 ± 0.30	1.92 ± 0.34	1.44 ± 0.08	2.02 ± 0.32	1.66 ± 0.13	1.28 ± 0.28

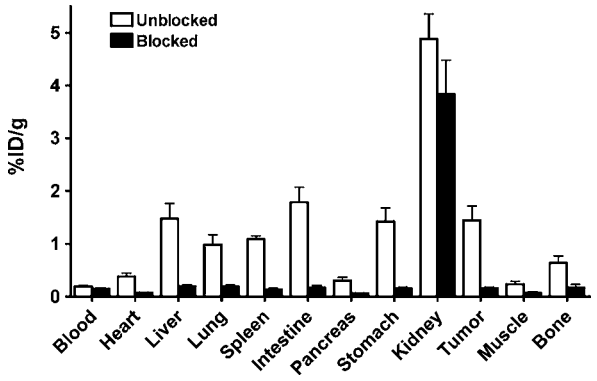

Figure 6. *Ex vivo* biodistribution of [^{18}F]FAl-NOTA-PRGD2 (3.7 MBq per mouse) in U87MG tumor bearing nude mice at 2 h time points after microPET scans with or without unlabeled RGD peptide as blocking agent. Columns, mean %ID/g (n = 4 per group); bars, SD.

FPPRDG2 was chosen as building block for direct comparison studies.

The dimeric PRGD2 peptide was selected for this comparison study for three major reasons. Dimeric PRGD2 showed higher affinity for $\alpha_v\beta_3$ integrin receptor than its monomeric counterpart. PEGylation improved the properties by reducing the renal retention of this class of compounds. Finally, the terminal amine of the PEG moiety served as an attachment point of the radiolabel.[18] Attachment of an NOTA functional group to this terminal amine of PRGD2 provided a chelate that can be effectively utilized for both [^{18}F]fluoride-aluminum and ^{68}Ga. In this study, we successfully prepared [^{18}F]FAl-NOTA-PRGD2 and compared its imaging quality with that of [^{18}F]FPPRDG2 and [^{68}Ga]Ga-NOTA-PRGD2 as an integrin $\alpha_v\beta_3$ imaging agent in U87MG mouse tumor model. The results were very encouraging, and further studies are needed to determine if [^{18}F]FAl-NOTA-PRGD2 is suitable for clinical use.

We applied HPLC columns to purify labeled NOTA complexes. The [^{18}F]FAl-NOTA-PRGD2 was eluted as a single radioactive peak. It overlapped with Al-NOTA-PRGD2 complex and had a baseline separation from NOTA-PRGD2. It has been reported that, when NOTA was used as the chelator, two interchangeable radioactive peaks were formed.[29] This was explained as the formation of two isomers of the complex. However, in our preparation only a single radioactive peak was observed. Since [^{18}F]FAl-NOTA-PRGD2 was not separated from Al-NOTA-PRGD2 in our case, the specific activity was determined by the amount of aluminum chloride used. Our labeling yield was lower than reported by Laverman et al.,[29] but the amount of peptide used in our reaction was also less. In order to allow radiolabeling without HPLC purification, we limited the use of peptide to a 2:1 ratio with aluminum chloride. Although others have used a QMA column to purify and concentrate ^{18}F-fluoride,[23] in our hands aqueous ^{18}F activity was used directly from the target, and the QMA treatment did not change the labeling yield. Generator-produced ^{68}Ga with its 68 min half-life is an attractive alternative for institutions without a cyclotron. In this study, the same peptide was used for labeling Ga-68 for a direct comparison. Labeling yield for forming Ga-68 complex was higher than for forming F-18 FAl complex, and the amount of peptide needed was also less.

When the solid-phase extraction was used for the preparation of both [^{18}F]FAl-NOTA-PRGD2 and [^{68}Ga]Ga-NOTA-PRGD2, the tracer could be prepared in about 15 to 25 min. Compared with that of [^{18}F]FPPRDG2, this procedure is tremendously time-saving. Moreover, with a scale-up preparation for a 0.37 GBq of product, the specific activity went up to 30.7 GBq/μmol and 46.2 GBq/μmol, respectively, for [^{18}F]FAl-NOTA-PRGD2 and [^{68}Ga]Ga-NOTA-PRGD2. These specific activity levels should meet the requirement for clinical studies. For Ga-68 labeling, specific activity can be further increased by using less peptide. Another important aspect of using solid-phase extraction is that the standard kit can be formulated and distributed. This is especially important for multiple-center studies, since the amount of peptide used can be predetermined precisely.

After applying the tracers to *in vivo* PET imaging, we found that FPPRGD2 showed tumor uptake and major organ distribution that were similar to those in one of our previous studies.[18] However, the tumor uptake of [^{68}Ga]Ga-NOTA-PRGD2 was somewhat lower than that in another study.[22] The reason for this is unclear, and we will investigate the *in vivo* behavior of this tracer further for potential clinical translation. Another issue is that both [^{18}F]FAl-NOTA-PRGD2 and [^{68}Ga]Ga-NOTA-PRGD2 showed longer tumor retention than that of [^{18}F]-FPPRDG2 in U87MG tumors. Although we do not have a definitive explanation for this, we cannot exclude the possibility of transchelation of the metal ions within the tumor region.

CONCLUSION

Both [^{18}F]FAl-NOTA-PRGD2 and [^{68}Ga]Ga-NOTA-PRGD2 can be prepared with or without HPLC purification in a much simpler fashion than [^{18}F]FPPRGD2. Moreover, these two new radiotracers have imaging properties and pharmacokinetics that are comparable to, or superior than, those of [^{18}F]FPPRGD2. Considering the ease of preparation and imaging quality, [^{18}F]FAl-NOTA-PRGD2 and [^{68}Ga]Ga-NOTA-PRGD2 are promising alternatives to [^{18}F]FPPRGD2 for PET imaging of tumor $\alpha_v\beta_3$.

AUTHOR INFORMATION

Corresponding Author

*Tel: 301-451-4246. Fax: 301-480-0679. E-mail: shawn.chen@nih.gov.

Author Contributions

[#]These two authors contributed equally.

■ ACKNOWLEDGMENTS

This project was supported by the Intramural Research Program of the National Institute of Biomedical Imaging and Bioengineering (NIBIB), National Institutes of Health (NIH) and the International Cooperative Program of the National Science Foundation of China (NSFC) (81028009). We thank Dr. Henry S. Eden for proof-reading the manuscript.

■ REFERENCES

(1) Folkman, J. (1971) Tumor angiogenesis: therapeutic implications. *N. Engl. J. Med. 285*, 1182−6.

(2) Stupack, D. G., and Cheresh, D. A. (2004) Integrins and angiogenesis. *Curr. Top. Dev. Biol. 64*, 207−38.

(3) Niu, G., and Chen, X. (2011) Why integrin as a primary target for imaging and therapy. *Theranostics 1*, 30−47.

(4) Beer, A. J., Kessler, H., Wester, H.-J., and Schwaiger, M. (2011) PET imaging of integrin $\alpha v\beta 3$ expression. *Theranostics 1*, 48−57.

(5) Zhou, Y., Chakraborty, S., and Liu, S. (2011) Radiolabeled cyclic RGD peptides as radiotracers for imaging tumors and thrombosis by SPECT. *Theranostics 1*, 58−82.

(6) Morrison, M., and Cuthbertson, A. (2011) Integrin imaging to evaluate treatment response. *Theranostics 1*, 149−153.

(7) Sun, X., Yan, Y., Liu, S., Cao, Q., Yang, M., Neamati, N., Shen, B., Niu, G., and Chen, X. (2011) ^{18}F-FPPRGD2 and ^{18}F-FDG PET of response to Abraxane therapy. *J. Nucl. Med. 52*, 140−6.

(8) Yang, M., Gao, H., Sun, X., Yan, Y., Quan, Q., Zhang, W., K, A. M., Rosenblum, M. G., Niu, G., and Chen, X. (2011) Multiplexed PET probes for imaging breast cancer early response to $VEGF_{121}$/rGel treatment. *Mol. Pharm. 8*, 621−628.

(9) Yang, M., Gao, H., Yan, Y., Sun, X., Chen, K., Quan, Q., Lang, L., Kiesewetter, D., Niu, G., and Chen, X. (2011) PET imaging of early response to the tyrosine kinase inhibitor ZD4190. *Eur. J. Nucl. Med. Mol. Imaging 38*, 1237−1247.

(10) Noiri, E., Goligorsky, M. S., Wang, G. J., Wang, J., Cabahug, C. J., Sharma, S., Rhodes, B. A., and Som, P. (1996) Biodistribution and clearance of ^{99m}Tc-labeled Arg-Gly-Asp (RGD) peptide in rats with ischemic acute renal failure. *J. Am. Soc. Nephrol. 7*, 2682−8.

(11) Ahmadi, M., Sancey, L., Briat, A., Riou, L., Boturyn, D., Dumy, P., Fagret, D., Ghezzi, C., and Vuillez, J. P. (2008) Chemical and biological evaluations of an ^{111}In-labeled RGD-peptide targeting integrin $\alpha v\beta 3$ in a preclinical tumor model. *Cancer Biother. Radiopharm. 23*, 691−700.

(12) Chen, X., Park, R., Shahinian, A. H., Tohme, M., Khankaldyyan, V., Bozorgzadeh, M. H., Bading, J. R., Moats, R., Laug, W. E., and Conti, P. S. (2004) ^{18}F-labeled RGD peptide: initial evaluation for imaging brain tumor angiogenesis. *Nucl. Med. Biol. 31*, 179−89.

(13) Chen, X., Liu, S., Hou, Y., Tohme, M., Park, R., Bading, J. R., and Conti, P. S. (2004) MicroPET imaging of breast cancer alphav-integrin expression with ^{64}Cu-labeled dimeric RGD peptides. *Mol. Imaging Biol. 6*, 350−9.

(14) Jeong, J. M., Hong, M. K., Chang, Y. S., Lee, Y. S., Kim, Y. J., Cheon, G. J., Lee, D. S., Chung, J. K., and Lee, M. C. (2008) Preparation of a promising angiogenesis PET imaging agent: ^{68}Ga-labeled c(RGDyK)-isothiocyanatobenzyl-1,4,7-triazacyclononane-1,4,7-triacetic acid and feasibility studies in mice. *J. Nucl. Med. 49*, 830−6.

(15) Li, Z. B., Chen, K., and Chen, X. (2008) ^{68}Ga-labeled multimeric RGD peptides for microPET imaging of integrin $\alpha v\beta 3$ expression. *Eur. J. Nucl. Med. Mol. Imaging 35*, 1100−8.

(16) Jacobson, O., Zhu, L., Niu, G., Weiss, I. D., Szajek, L. P., Ma, Y., Sun, X., Yan, Y., Kiesewetter, D. O., Liu, S., and Chen, X. (2010) MicroPET imaging of integrin $\alpha v\beta 3$ expressing tumors using ^{89}Zr-RGD Peptides. *Mol. Imaging Biol.*, Dec 16. [Epub ahead of print]

(17) Dijkgraaf, I., Liu, S., Kruijtzer, J. A., Soede, A. C., Oyen, W. J., Liskamp, R. M., Corstens, F. H., and Boerman, O. C. (2007) Effects of linker variation on the in vitro and in vivo characteristics of an ^{111}In-labeled RGD peptide. *Nucl. Med. Biol. 34*, 29−35.

(18) Liu, S., Liu, Z., Chen, K., Yan, Y., Watzlowik, P., Wester, H. J., Chin, F. T., and Chen, X. (2010) ^{18}F-labeled galacto and PEGylated RGD dimers for PET imaging of $\alpha v\beta 3$ integrin expression. *Mol. Imaging Biol. 12*, 530−8.

(19) Chin, F. T., Shen, B., Liu, S., Berganos, R. A., Chang, E., Mittra, E., Chen, X., and Gambhir, S. S. (2011) First Experience with clinical-grade [^{18}F]FPPRGD2: An automated multi-step radiosynthesis for clinical PET studies. *Mol. Imaging Biol.*, Mar 12. [Epub ahead of print]

(20) Zhang, X., Xiong, Z., Wu, Y., Cai, W., Tseng, J. R., Gambhir, S. S., and Chen, X. (2006) Quantitative PET imaging of tumor integrin $\alpha v\beta 3$ expression with ^{18}F-FRGD2. *J. Nucl. Med. 47*, 113−21.

(21) Jacobson, O., Zhu, L., Ma, Y., Weiss, I. D., Sun, X., Niu, G., Kiesewetter, D. O., and Chen, X. (2011) Rapid and simple one-step F-18 labeling of peptides. *Bioconjugate Chem. 22*, 422−8.

(22) Liu, Z., Niu, G., Shi, J., Liu, S., Wang, F., and Chen, X. (2009) ^{68}Ga-labeled cyclic RGD dimers with Gly3 and PEG4 linkers: promising agents for tumor integrin $\alpha v\beta 3$ PET imaging. *Eur. J. Nucl. Med. Mol. Imaging 36*, 947−57.

(23) McBride, W. J., D'Souza, C. A., Sharkey, R. M., Karacay, H., Rossi, E. A., Chang, C. H., and Goldenberg, D. M. (2010) Improved ^{18}F labeling of peptides with a fluoride-aluminum-chelate complex. *Bioconjugate Chem. 21*, 1331−40.

(24) McBride, W. J., Sharkey, R. M., Karacay, H., D'Souza, C. A., Rossi, E. A., Laverman, P., Chang, C. H., Boerman, O. C., and Goldenberg, D. M. (2009) A novel method of ^{18}F radiolabeling for PET. *J. Nucl. Med. 50*, 991−8.

(25) Jacobson, O., and Chen, X. (2010) PET designated flouride-18 production and chemistry. *Curr. Top. Med. Chem. 10*, 1048−59.

(26) Thonon, D., Kech, C., Paris, J., Lemaire, C., and Luxen, A. (2009) New strategy for the preparation of clickable peptides and labeling with 1-(azidomethyl)-4-[^{18}F]-fluorobenzene for PET. *Bioconjugate Chem. 20*, 817−23.

(27) Hohne, A., Mu, L., Honer, M., Schubiger, P. A., Ametamey, S. M., Graham, K., Stellfeld, T., Borkowski, S., Berndorff, D., Klar, U., Voigtmann, U., Cyr, J. E., Friebe, M., Dinkelborg, L., and Srinivasan, A. (2008) Synthesis, ^{18}F-labeling, and in vitro and in vivo studies of bombesin peptides modified with silicon-based building blocks. *Bioconjugate Chem. 19*, 1871−9.

(28) Mu, L., Hohne, A., Schubiger, P. A., Ametamey, S. M., Graham, K., Cyr, J. E., Dinkelborg, L., Stellfeld, T., Srinivasan, A., Voigtmann, U., and Klar, U. (2008) Silicon-based building blocks for one-step ^{18}F-radiolabeling of peptides for PET imaging. *Angew. Chem., Int. Ed. Engl. 47*, 4922−5.

(29) Laverman, P., McBride, W. J., Sharkey, R. M., Eek, A., Joosten, L., Oyen, W. J., Goldenberg, D. M., and Boerman, O. C. (2010) A novel facile method of labeling octreotide with ^{18}F-fluorine. *J. Nucl. Med. 51*, 454−61.

Bioconjugate Chemistry

Article

pubs.acs.org/bc

Engineering Cell Surfaces via Liposome Fusion

Debjit Dutta,[†] Abigail Pulsipher,[†] Wei Luo,[†] Hugo Mak,[‡] and Muhammad N. Yousaf*[,†]

[†]Department of Chemistry and the Carolina Center for Genome Science, University of North Carolina at Chapel Hill, Chapel Hill, North Carolina 27599-3290, United States

[‡]Department of Chemistry, Centre for Research on Biomolecular Interactions, Life Sciences Research Building, York University, Toronto, Ontario, Canada M3J 1P3

ABSTRACT: In this study, we have rewired cell surfaces with ketone and oxyamine molecules based on liposome fusion for applications in cell-surface engineering. Lipid vesicles, functionalized with ketone and oxyamine molecules, display complementary chemistry and undergo recognition, docking, and subsequent fusion upon covalent oxime bond formation. Liposome fusion was characterized by several techniques including matrix-assisted laser-desorption/ionization mass spectrometry (MALDI-MS), light scattering, fluorescence resonance energy transfer (FRET), and transmission electron microscopy (TEM). When cultured with cells, ketone- and oxyamine-containing liposomes undergo spontaneous membrane fusion to present the respective molecules from cell surfaces. Ketone-functionalized cell surfaces serve as sites for chemoselective ligation with oxyamine-conjugated molecules. We tailored and fluorescently labeled cell surfaces with an oxyamine-conjugated rhodamine dye. As an application of this cell-surface engineering strategy, ketone- and oxyamine-functionalized cells were patterned on oxyamine- and ketone-presenting surfaces, respectively. Cells adhered, spread, and proliferated in the patterned regions via interfacial oxime linkage. The number of ketone molecules on the cell surface was also quantified by flow cytometry.

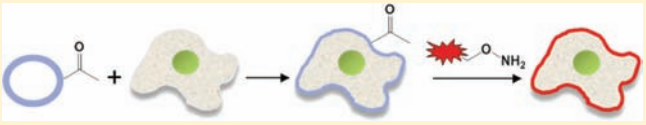

INTRODUCTION

Membrane fusion processes are ubiquitous in biology and span multicellular communication, extracellular signaling, reconstruction of damaged organelles, and integration of cells into complex tissues and organs.[1] As a result, there has been much interest in developing model systems to mimic biological membranes to investigate the mechanisms of fusion and for use in various biotechnological applications. For example, cells secrete and display proteins and lipids during vesicle trafficking events that either diffuse into the ECM or become components of the cell membrane after fusion.[2] Naturally, lipid vesicles provide an ideal platform for such studies and have been widely used to examine various membrane-related processes, including fusion.[3−5] In order for fusion to occur, the membranes must be brought into close proximity, followed by bilayer destabilization.[6] Fusion of such lipid vesicles or liposomes can be initiated by using divalent cations, polycations,[7] positively charged amino acids,[8] and membrane-disrupting peptides.[9,10] Historically, synthetic chemical agents have also been employed to fuse vesicle membranes[11−14] through nonspecific interactions. However, recent exciting efforts to improve selectivity and control over vesicle fusion have been achieved through the use of small, synthetic molecular recognition pairs.[15,16] Since vesicle fusion is a natural process and has been shown to influence the construction of cells into multicellular organisms, much research has focused on using liposomes to deliver cargo, reagents, nanomaterials, and therapeutic agents to cells. To our knowledge, there have been very few reports of employing liposome fusion to cell membranes as a method to deliver small chemical functional groups in order to tailor the cell membrane for subsequent bio-orthogonal and chemoselective ligation reactions.[17] This platform would find wide use in studying fundamental cell behavior and provide a range of new tools for tissue engineering and biomedical applications.

Cell-surface receptors that decorate the cell membrane influence a number of biological processes, such as cell adhesion, differentiation, intercellular communication, and tissue formation.[18] As such, methods that selectively engineer the cell surface by introducing chemoselective functional groups will have a significant role in directing and influencing many biological processes for applications in cell-based therapies, drug delivery, and tissue engineering.[19−23] Previous cell-surface modification strategies involve the introduction of chemoselective functional groups through metabolic and genetic engineering approaches.[24−26] However, such strategies may perturb cellular processes by altering cellular physiology.[27]

In this study, we present a method to tether chemoselective ketone and oxyamine groups from cell surfaces by liposome delivery toward the goal of rewiring the cell surface. Alkyl ketone and oxyamine molecules spontaneously insert into lipid vesicles upon synthesis. When mixed, chemical recognition occurs, producing stable oxime bonds under physiological conditions. The reaction is also bio-orthogonal and, thus, does not interfere with any other chemical moieties in its cellular surroundings.[28−31] The synthetic ketone and oxyamine molecules fused on the cell membrane serve as cell-surface receptors, providing tools for the attachment of other functional materials, biomolecules, and probes on the cell

Received: May 5, 2011
Revised: October 27, 2011
Published: November 5, 2011

 © 2011 American Chemical Society dx.doi.org/10.1021/bc200236m | *Bioconjugate Chem.* 2011, 22, 2423−2433

Scheme 1. List of Liposomes, Molecules, and Cells Used in This Study[a]

[a](1) Keto-LUV; (2) oxy-LUV; (3) keto-NBD-PE LUV; (4) oxy-rhod-PE LUV; (5) ketone-functionalized liposomes; (6) oxyamine-functionalized liposomes; (7) fluorescein-ketone; (8) rhod-oxyamine; (9) ketone-functionalized fbs; and (10) oxyamine-functionalized fbs.

surface. Liposome fusion was characterized by matrix-assisted laser-desorption/ionization mass spectrometry (MALDI-MS), dynamic light scattering (DLS), fluorescence resonance energy transfer (FRET), transmission electron microscopy (TEM), fluorescence-activated cell sorting (FACS), and fluorescence microscopy analyses.

MATERIALS AND METHODS

All chemical reagents were of analytical grade and used without further purification. Lipids egg palmitoyl-oleoyl phosphatidylcholine (POPC), egg 1-palmitoyl-2-oleoyl-phosphatidylglycerol (POPG), 1,2-dioleoyl-3-trimethylammonium-propane (DOTAP), egg 1,2-diphytanoyl-*sn*-glycero-3-phosphoethanolamine-*N*-(7-nitro-2-1,3-benzoxadiazol-4-yl) (ammonium salt) (NBD-PE), and egg 1,2-dipalmitoyl-*sn*-glycero-3-phosphoethanolamine-*N*-(lissamine rhodamine B sulfonyl) (ammonium salt) (Rhod-PE) were purchased from Avanti Polar Lipids (Alabaster, AL). Antibodies and fluorescent dyes were obtained from Invitrogen (Carlsbad, CA). FITC-labeled beads were purchased from Spherotech, Inc. (Forest Lake, IL) and all other chemicals were obtained from Sigma-Aldrich or Fisher. Swiss 3T3 albino mouse fibroblasts (fbs) were obtained from the Tissue Culture Facility at the University of North Carolina (UNC).

Transmission electron microscopy (TEM) images were acquired using a TF30He Polara G2 (FEI company) electron cryomicroscope, operating at 300 keV. Images were recorded using a Tietz single port model 415 4k × 4k CCD camera with a 15 μm pixel size. Fluorescence resonance energy transfer measurements (FRET) were performed using a SPEX Fluorolog-3 Research T-format Spectrofluorometer with an excitation wavelength of 471 nm. Dynamic light scattering was performed using a Nikomp model 200-laser particle sizer with a 5 mW HeNe laser at an excitation wavelength of 632.8 nm and using a Wyatt DynoPro plate reader. Flow cytometry was performed using a Dako CyAn ADP (Beckman-Coulter, Brea, CA), and the data was analyzed with *Summit 4.3* software. Phase contrast and fluorescent imaging was performed and processed using a Nikon TE2000-E inverted microscope and *Metamorph* software, respectively.

Syntheses. Tetra(ethylene glycol)-terminated alkanethiol (EG_4) was synthesized as previously reported.[32] Fluorescein-ketone (**7**; Scheme 1) was synthesized as previously reported.[33] The syntheses of *O*-dodceyloxyamine (**A**; Scheme 2) and rhod-oxyamine (**8**) are described below.

*2-(Dodecyloxy)isoindoline-1,3-dione (**B**).* To a solution of *N*-hydroxyphthalimide (1.96 g, 12.04 mmol, 1.5 equiv) and sodium bicarbonate (10.11 g, 12.04 mmol, 1.5 equiv) in DMF (20 mL) at 80 °C was added 1-bromododecane (1.93 mL, 8.02 mmol). The mixture was refluxed and stirred for 12 h. The reaction was diluted with DCM and washed with H_2O (6 × 50 mL), 1 M $NaHCO_3$ (3 × 50 mL), and H_2O (2 × 50 mL), dried over $MgSO_4$, and concentrated to afford a white solid, **B** (2.66 g, 87%). ^{1}H NMR (400 MHz, $CDCl_3$) δ 0.91 (m, 3H), 1.28 (bm, 16H), 1.47−1.49 (m, J = 9.2 Hz, 2H), 1.77−1.83 (m, J = 22.0 Hz, 2H), 4.20−4.23 (t, J = 13.6 Hz, 2H), 7.28−7.30, 7.75−7.77 (dm, J = 4.8, Hz, J = 5.6 Hz, 2H, 2H). (ESI) (m/z) [M + H$^+$]: 332.28.

Scheme 2. Synthesis of *O*-Dodecyloxyamine (A)[a]

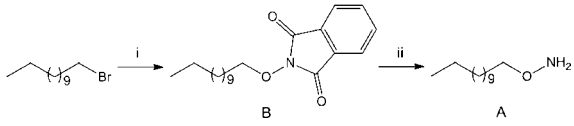

[a]Reagents and conditions. (i) *N*-hydroxyphthalimide (1.5 equiv), $NaHCO_3$ (1.5 equiv), DMF, reflux, 80 °C, 12 h; 87%; and (ii) hydrazine (6 equiv), dry DCM, N_2, 12 h; 74%.

*O-Dodecyloxyamine (**A**).* To a solution of **B** (2.65 g, 8.00 mmol) in dry DCM (30 mL) under inert atmosphere (Ar) was slowly added hydrazine (1.53 mL, 48.00 mmol, 6 equiv). Upon addition, a white precipitate immediately formed. The mixture was stirred for 12 h. The reaction was diluted with DCM and washed with H_2O (6 × 50 mL), dried over $MgSO_4$, and concentrated to afford a pale yellow oil, **A** (1.18 g, 74%). ^{1}H NMR (400 MHz, $CDCl_3$) δ 0.88−0.91 (t, J = 13.6 Hz, 3H), 1.28 (s, 18H), 1.57−1.60 (m, J = 14.0 Hz, 2H), 3.65−3.69 (t, J = 13.2 Hz, 2H). (ESI) (m/z) [M + H$^+$]: 201.22.

*(N-(4-(tert-Butoxycarbonylamino)butyl)sulfamoyl)-2-(6-(diethylamino)-3-(diethyliminio)-3H-xanthen-9-yl)-benzenesulfonate (**C**).* To a solution of rhodamine lissamine (0.880 g, 1.53 mmol) in chloroform ($CHCl_3$, 30 mL) at room temperature (RT) was added N-BOC-1,4-diaminobutane (0.431 g, 2.29 mmol, 1.5 equiv) and TEA (0.305 mL, 2.29, 1.5 equiv). The mixture was stirred for 8 h and then extracted with H_2O (6 × 25 mL). The organic layers were concentrated to afford a dark purple solid **C**. ^{1}H NMR was taken in $CDCl_3$ to confirm **C** (1.045 g, 95%). TLC conditions for entire synthesis: $CHCl_3$/MeOH (7.5:2.5). ^{1}H NMR (400 MHz, MeOD) δ 1.09−1.07 (t, J = 8.1 Hz, 6H), 1.36−1.33 (m, J = 12.3, 15H), 1.66−1.64 (m, J = 8.6 Hz, 4H), 3.47−3.44 (m, J = 12.1, 6H), 4.20−4.18 (q, J = 7.8 Hz, 4H), 5.66 (s, 1H), 5.77 (d, 1H), 6.01 (d, 1H), 6.34−6.30 (m, J = 16.1 Hz, 2H), 7.21 (d, 1H), 7.29 (d, 1H), 7.98 (d, 1H), 8.04 (d, 1H). (ESI) (m/z) [M + H$^+$]: 716.31.

*5-(N-(4-Aminobutyl)sulfamoyl)-2-(6-(diethylamino)-3-(diethyliminio)-3H-xanthen-9-yl)benzenesulfonate (**D**).* To **C** (0.600 g, 0.837 mmol) was added a solution of TFA, H_2O, and triisopropylsilane (TIPS) in a ratio of 95:2.5:2.5 (10 mL). The mixture was stirred at RT under N_2 for 3 h and was then extracted with $CHCl_3$ and H_2O (4 × 25 mL). The organic layers were dried and concentrated to afford a purple solid, **D** (0.45 g, 85%). ^{1}H NMR (400 MHz, MeOD) δ 1.11−1.09 (t, J = 8.7, 6H), 1.33−1.31 (m, J = 7.4 Hz, 6H), 1.70−1.67 (m, 4H, J = 12.5, 4H), 2.63−2.62 (m, J = 4.6 Hz, 2H), 3.51−3.49 (m, J = 8.7 Hz, 6H), 4.20−4.18 (q, J = 7.8 Hz, 4H), 5.64 (s, 1H), 5.71 (d, 1H; Ar−H), 6.02 (d, 1H), 6.32−6.30 (m, J = 8.3 Hz, 2H), 7.24 (d, 1H), 7.30 (d, 1H), 7.98 (d, 1H), 8.04 (d, 1H). (ESI) (m/z) [M + H$^+$]: 628.27.

dx.doi.org/10.1021/bc200236m | *Bioconjugate Chem.* 2011, 22, 2423−2433

Scheme 3. Synthesis of Rhod-Oxyamine (8)[a]

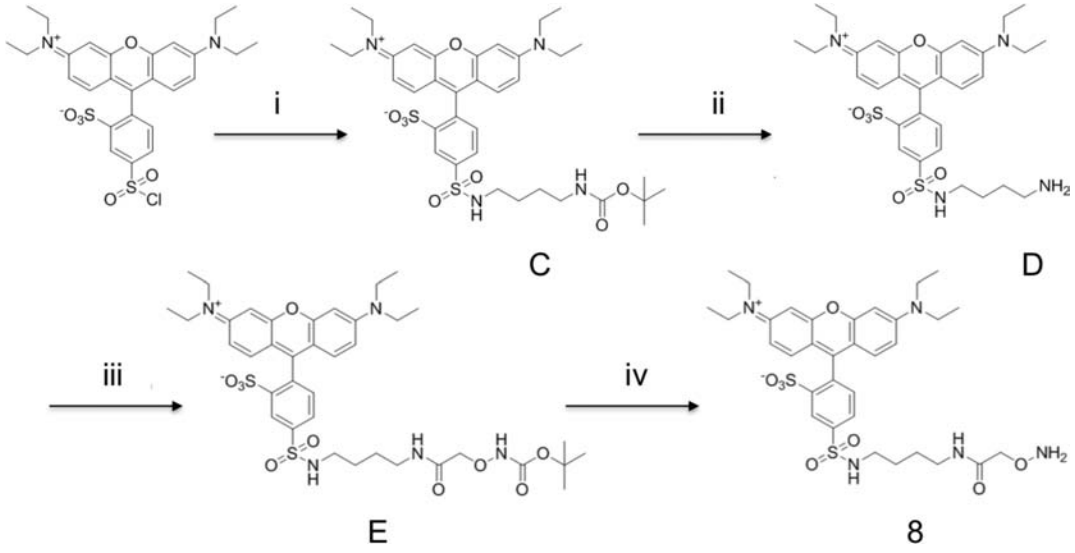

[a]Reagents and conditions. (i) N-BOC-1,4-diaminobutane (1.5 equiv), TEA (1.5 equiv), $CHCl_3$, N_2, 25 °C, 8 h; 95%, (ii) triisopropylsilane (TIPS)/H_2O/TFA (2.5:2.5:95), N_2, 25 °C, 3 h; 85%, (iii) *N*-hydroxysuccinimide (NHS, 2 equiv), *N,N′*-dicyclohexylcarbodiimide (DCC, 2 equiv), aminooxy acetic acid (2 equiv), TEA (excess), DMF, N_2, 25 °C, 4 h; 60%, and (iv) TIPS/H_2O/TFA (2.5:2.5:95), N_2, 25 °C, 3 h; 81%.

*2-(6-(Diethylamino)-3-(diethyliminio)-3H-xanthen-9-yl)-5-(N-(2,2-dimethyl-4,8-dioxo-3,6-dioxa-5,9-diazatridecan-13-yl)sulfamoyl)benzenesulfonate (**E**).* To a solution containing *N,N′*-dicyclohexylcarbodiimide (DCC, 0.394 g, 1.91 mmol, 2 equiv), *N*-hydroxysuccinimide (NHS, 0.220 g, 1.91 mmol 2 equiv), and aminooxy acetic acid (0.356 g, 1.91 mmol, 2 equiv) in DMF was stirred under N_2 for 0.5 h. **D** (0.43 g, 0.684 mmol) was then added in DMF (20 mL), followed by TEA (excess). The mixture was strirred for 4 h and then concentrated. Flash chromatography was performed using $CHCl_3$/MeOH (8:2) to elute, **E**. The product was concentrated to afford a purple solid **E** (0.32 g, 60%). ^{1}H NMR (400 MHz, MeOD) δ 1.10−1.08 (t, J = 8.8, 6H), 1.39−1.36 (m, J = 12.3 Hz, 15H), 1.65−1.63 (m, J = 7.9, 4H), 3.08−3.06 (m, J = 8.0, 2H), 3.48−3.46 (m, J = 8.3, 6H), 4.17−4.15 (q, J = 7.7, 4H), 4.38 (s, 2H), 5.61 (s, 1H), 5.73 (d, 1H), 6.02 (d, 1H), 6.31−6.30 (m, J = 4.4, 2H), 7.24 (d, 1H), 7.32 (d, 1H), 7.96 (d, 1H), 8.09 (d, 1H). (ESI) (m/z) [M + H$^+$]: 801.31.

*5-(N-(4-(2-(aminooxy)acetamido)butyl)sulfamoyl)-2-(6-(diethylamino)-3-(diethyliminio)-3H-xanthen-9-yl)-benzenesulfonate (rhod-oxyamine, **8**; Scheme 3).* To **E** (0.30 g, 0.374 mmol) was added a solution of TFA, H_2O, and triisopropylsilane (TIPS) in a ratio of 95:2.5:2.5 (10 mL). The mixture was stirred at RT under N_2 for 3 h and was then extracted with $CHCl_3$ and H_2O (4 × 25 mL). The organic layers were dried and concentrated to afford a purple solid, and flash chromatography was performed using $CHCl_3$/MeOH (8:2) to elute **8** (0.21 g, 81%). ^{1}H NMR (400 MHz, $CDCl_3$) δ 1.12−1.00 (t, J = 8.2, 6H), 1.42−1.40 (m, J = 7.9, 6H), 1.62−1.60 (m, J = 7.7, 4H), 3.07−3.05 (m, J = 8.0, 2H), 3.45−3.42 (m, J = 12.4, 6H), 4.11−4.09 (q, J = 8.4, 4H), 4.24 (s, 2H), 5.64 (s, 1H), 5.75 (d, 1H), 6.02 (d, 1H), 6.29−6.27 (m, J = 4; 2H), 7.28 (d, 1H), 7.31 (d, 1H), 7.92 (d, 1H), 8.05 (d, 1H). (ESI) (m/z) [M + H$^+$]: 701.28.

Formation of Lipid Vesicles. *Liposome Fusion Studies.* Dodecanone (55 μL, 10 mM in $CHCl_3$ at 5 mol %) was dissolved with egg palmitoyl-oleoyl phosphatidylcholine (POPC) (430 μL, 10 mg/mL in $CHCl_3$, at 95 mol %) and *O*-dodecyloxyamine (60 μL, 10 mM in $CHCl_3$ at 5 mol %) was mixed with POPC (410 μL, 10 mg/mL in $CHCl_3$ at 75 mol %), and egg 1-palmitoyl-2-oleoyl-phosphatidylglycerol (POPG) (92 μL, 10 mg/mL in $CHCl_3$ at 20 mol %). Both lipid sample mixtures were then concentrated under high vacuum for 4 h. The dried lipid samples were reconstituted and brought to a final volume of 3 mL in PBS buffer, pH 7.4. The contents of the vial were warmed to 50 °C and sonicated for 20 min, in a tip sonicator, until the solution became clear and large unilamellar vesicles (LUVs) containing ketone (keto-LUV, **1**; Scheme 1) or oxyamine (oxy-LUV, **2**) groups were formed.

FRET Fusion Studies. NBD-PE and rhod-PE were added to two separate vials at 2 mol %. The dried lipid samples were then reconstituted in 2.43 mL of PBS buffer, pH 7.4. The contents of the vial were warmed to 50 °C and sonicated for 20 min, in a tip sonicator, until the solution became clear, and LUVs containing ketone (keto-NBD-PE LUVs, **3**) or oxyamine (oxy-rhod-PE LUVs, **4**) groups were formed.

Liposome Fusion to Cells. To generate ketone- and oxyamine-containing liposomes for cell fusion studies, dodecanone (55 μL, 10 mM solution in $CHCl_3$ at 5 mol %) and *O*-dododecyloxyamine (60 μL, 10 mM solution in $CHCl_3$ at 5 mol %) were dissolved with egg-POPC (424 μL, 10 mg/mL in $CHCl_3$ at 93 mol %) and 1,2-dioleoyl-3-trimethylammonium-propane (DOTAP, 10 μL, 10 mg/mL in $CHCl_3$ at 2 mol %) in chloroform followed by concentration under high vacuum for 4 h. The dried lipid samples were then reconstituted and brought to a final volume of 3 mL in PBS buffer, pH 7.4. The contents of the vial were warmed to 50 °C and sonicated for 20 min, in a tip sonicator, until the solution became clear, and LUVs containing ketone (**5**) or oxyamine (**6**) groups were formed.

Matrix-Assisted Laser-Desorption/Ionization Mass Spectrometry (MALDI-MS). Preparation of Gold-Coated MALDI Sample Plates. Gold-coated MALDI sample plates (123 × 81 mm) (Applied Biosystems, Foster City, CA) were prepared by electron-beam deposition (Thermionics Laboratory Inc., Hayward, CA) of titanium (5 nm) and then gold (12 nm). In order to form self-assembled monolayers (SAM) of

alkanethiolates on the plates, the slides were immersed in a 1 mM solution of aminooxyundecanethiol in EtOH for approximately 1 min, rinsed with EtOH and dried, and then backfilled with a 1 mM solution of mercaptoundecanol in EtOH for 1 h. Once removed from solution, the surfaces were rinsed with EtOH and dried before use.

Liposome Preparation. Keto-LUVs (**1**) were generated as previously described and were then delivered and allowed to react with the oxyamine-terminated MALDI sample plate (90 min). The plates were then washed with water (3 × 3 mL) and EtOH (2 × 3 mL) and dried before use.

MALDI Analyses. MS analyses were carried out using an AB SCIEX TOF/TOF 5800 System (Applied Biosystems, Foster City, CA).

Dynamic Light Scattering (DLS). Keto- (**1**) and oxy- (**2**) LUVs were generated as previously described and tested by DLS for monodispersity and uniformity. Light scattering experiments were performed using a Nikomp model 200 laser particle sizer with a 5 mW helium−neon laser at an exciting wavelength of 632.8 nm. Standard deviation determinations were made using Gaussian analysis. A Wyatt DynoPro dynamic scattering plate reader was used to collect the light scattering data.

FRET Analyses. Keto- (**3**) and oxy- (**4**) LUVs containing NBD-PE and rhod-PE, respectively, were generated as previously described and tested by FRET. All fluorescence measurements were performed in a SPEX Fluorolog-3 Research T-format Spectrofluorometer. NBD fluorescence was measured at 471 nm (excitation) and 531 nm (emission), maintaining narrow excitation slits to reduce light scattering interference. To obtain FRET measurements, the NBD dye was excited at 471 nm, and the emission was scanned through 600 nm, and the emission signal for rhod-PE was observed at 578 nm. Fluorescence was followed immediately after mixing oxy-rhod-PE LUV (**4**, 3 mM in PBS, 100 μL) with keto-NBD-PE LUV (**3**, 3 mM in PBS, 100 μL) for approximately 2 h at 2 min intervals. The total lipid concentrations were adjusted to 0.2 mM, and the two LUV populations had a 1:1 molar ratio. A constant flow of water was passed through the cuvette holder for temperature control. The temperature was maintained at 25 °C.

TEM Analyses. Keto- (**1**) and oxy- (**2**) LUVs were made as previously described (0.2 mM in PBS, pH 7.4). The two vesicle solutions (1:1) were mixed at room temperature for 30 min. Four microliter aliquots of vesicles suspended in buffer applied to standard lacey carbon EM grids were prepared according to published methods. The specimens were blotted from behind and then submerged into aurenyl acetate solution for staining. The hydrated specimens were then placed in a TF30He Polara G2 (FEI company) electron cryomicroscope operating at 300 keV. Images were recorded using a Tietz single port model 415 4k × 4k CCD camera with a 15 μm pixel size on the chip. Pixel sizes at the specimen level were used to calculate accurate dimensions for the specimen.

Cell Adhesion Patterning. Self-assembled monolayers (SAMs) presenting aldehyde or oxyamine and tetra(ethylene glycol) (EG_4) groups were patterned using microfluidic oxidation and microfluidic lithography, respectively.[34,35] EG_4 has been shown to passivate substrates against cell and protein adsorption.[36] Therefore, the ratio of EG_4 and aldehyde or oxyamine groups was 90:10 to ensure that fibroblasts (fbs) were only adhering to the patterned surface regions that presented 10% oxyamine or aldehyde groups, driven via oxime conjugation. Fbs were separately cultured with keto- (**5**) or oxy- (**6**) LUVs as previously described and were then seeded ($\sim 10^2$ cells/mL, 2 h) to the patterned oxyamine or aldehyde surfaces, respectively. Media that 10% calf bovine serum (CBS) and 1% penicillin/streptomycin was then added, and the substrates were incubated at 37 °C in 5% CO_2 for 4 d. Cells cultured with liposomes, not containing the key functional groups, did not attach to the patterned surfaces. Substrates were then stained and imaged by fluorescence microscopy. Exposure times of 400 and 1200 ms were used to image nuclei and actin, respectively.

Fibroblast (Fb) Culture. Swiss 3T3 albino mouse fbs and Rat2 fbs were cultured in Dulbecco's Modified Eagle Medium (Gibco) containing 10% calf bovine serum (CBS) and 1% penicillin/streptomycin at 37 °C in 5% CO_2.

Delivery of Functionalized Liposomes to Cells. Cells were seeded onto a tissue culture plate and allowed to grow for 48 h at 37 °C in 5% CO_2 in CBS media.

Cell-Surface Engineering. Two cell-surface engineering methods were employed to fluorescently label fbs. In this first method, a solution of oxy-LUVs (**6**, 3 mM) was incubated with a ketone-functionalized fluorescein (**7**, 0.15 mM, 1 equiv, 2 h), forming fluorescently labeled liposomes. The liposomes were then added to fbs in culture for 2 h. After fusion, the cells were washed with PBS (3 × 2 mL), trypsinized (1 mL, 5 min, 37 °C, 5% CO_2), diluted with CBS-containing media ($\sim 10^2$/mL), and seeded to a glass substrate (1 × 1 cm^2, 2 h). The cells were then imaged under a fluorescence microscope with an exposure time of 1/1200 s. In the second method, a solution of keto-LUVs (**5**, 200 μL, 0.6 mM) was added to fbs in culture for 2 h, resulting in membrane fusion and subsequent display of ketones from the cell surface (**9**). Rhod-oxyamine (**8**, 100 μL, 0.7 mM in H_2O) was then added the cells for 2 h. After oxime formation, the fbs were washed with PBS (3 × 2 mL), trypsinized (1 mL, 5 min, 37 °C, 5% CO_2), diluted with CBS-containing media ($\sim 10^2$/mL), and seeded to a glass substrate (1 × 1 cm^2, 2 h). The cells were then imaged under a fluorescence microscope with an exposure time of 1/1200 s.

Flow Cytometry. Liposomes with varying oxyamine mol % (i.e., 0%, 1%, 5%, and 10%) were generated and cultured with separate populations of fbs (**6**, 3 mM, 4 h), resulting in membrane fusion and subsequent display of oxyamine groups from cell surfaces (**10**). Ketone-functionalized fluorescein (**7**, 0.15 mM 2 h) was then reacted with the fbs, generating fluorescently labeled cells. The control cells (i.e., not displaying oxyamine groups) were incubated with ketone−fluorescein for 2 h each, under the same conditions. The cells were then washed with PBS (3 × 5 mL), trypsinized (1 mL, 5 min, 37 °C, 5% CO_2), centrifuged (5 min, 1000 rpm), resuspended in RPM I (without phenol red), centrifuged (5 min, 1000 rpm), and resuspended in RPMI ($\sim 10^7$ cells/2 mL). Fluorescence-assisted cell sorting analyses (FACS) of the control and fbs with 1%, 5%, and 10% oxyamine were then performed (2 × 10^3 cells). Fluorescence measurements were calibrated using RCP-5-30 beads ($\sim 10^7$ beads/mL, 2 × 10^3 beads counted, Spherotech, Inc., Lake Forest, IL) of known fluorescein equivalent molecule density.[37] The RCP-5-30 beads contain a mixture of several similar size particles with different fluorescence intensities and a blank. Every particle contains a mixture of fluorophores that allows excitation at any wavelength from 365 to 650 nm. As a result, the RCP-30-5 beads have a twofold purpose: (1) calibrate the different channels in the flow cytometer being used and (2) cross-calibrate the relative number of fluorophores with cells or particles stained with known number

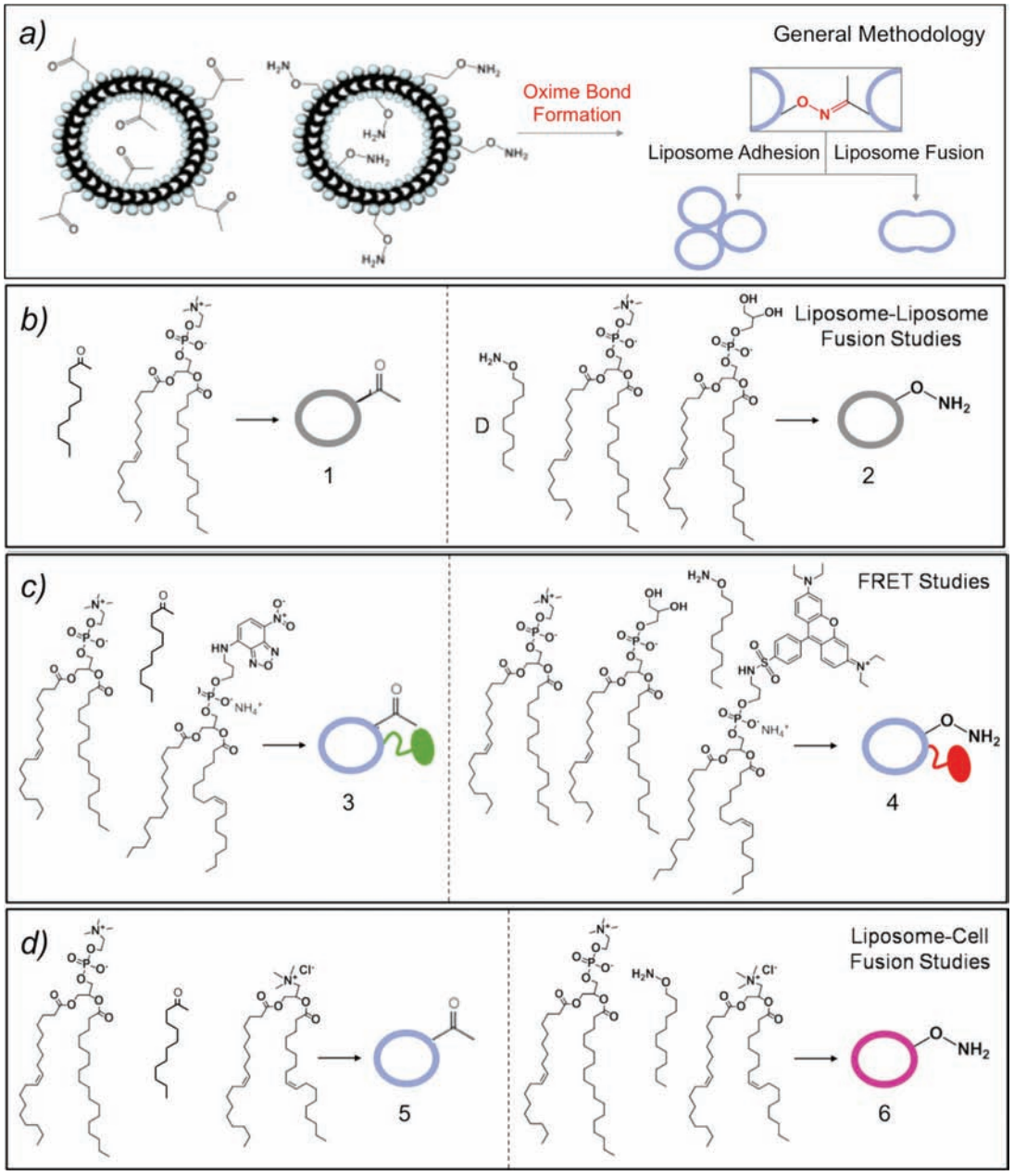

Figure 1. General schematic and corresponding lipid components for the formation of fused and adhered liposomes based on chemoselective oxime conjugation. (a) When mixed, ketone- and oxyamine-tethered liposomes react chemoselectively to form an interfacial, covalent oxime linkage, resulting in liposome docking and adhesion. Docked liposomes either fuse or form multiadherent structures. (b) Dodecanone molecules were incorporated into neutral, POPC at a ratio of 5:95 to form keto-LUVs (**1**), while *O*-dodecyloxyamine molecules were incorporated into POPC and negatively charged, POPG at a ratio of 5:75:20 to form oxy-LUVs (**2**). These liposomes were used for liposome−liposome fusion studies. (c) Dodecanone molecules were incorporated into POPC and fluorescence donor, NBD-PE at a ratio of 5:93:2 to form keto-NBD-PE LUVs (**3**). *O*-Dodecyloxyamine molecules were incorporated into POPC, POPG, and fluorescence acceptor, rhod-PE at a ratio of 5:73:20:2 to form oxy-rhod-PE LUVs (**4**). These liposomes were used for FRET studies. (d) Dodecanone molecules were incorporated into POPC and positively charged, DOTAP at a ratio of 5:97:2 to form ketone-presenting liposomes (**5**). *O*-Dodecyloxyamine molecules were incorporated into POPC and DOTAP at a ratio of 5:93:2 to form oxyamine-presenting liposomes (**6**). These liposomes were used for cell-liposome fusion studies.

of spectral matching fluorophores, such as FITC, to estimate the number of fluorophores on stained cells. No background is required to be subtracted because the different fluorophores are calibrated to the different flow cytometer channels. The raw data obtained in Figure 5b was cross-calibrated to the calibration curve that is generated with the RCP-30-5 beads to obtain the values seen in Figure 5c. The approximations of FITC molecules per cell in Figure 5c were determined by cross calibrating the 0% (control), 1%, 5%, and 10% oxyamine-containing liposomes to the standard curve (blank and 5 fluorophores) generated using the manufacturer's Excel spreadsheet and instructions (Spherotech, Inc., Lake Forest, IL). After generating a standard calibration curve with the RCP-30-5 beads, the mean fluorescence intensities obtained from the FITC channel were cross-calibrated with the curve using the manufacturer's spreadsheet to produce an approximation of the number of molecules per cell. The number of counted beads in each sample were the same.

dx.doi.org/10.1021/bc200236m | *Bioconjugate Chem.* 2011, 22, 2423−2433

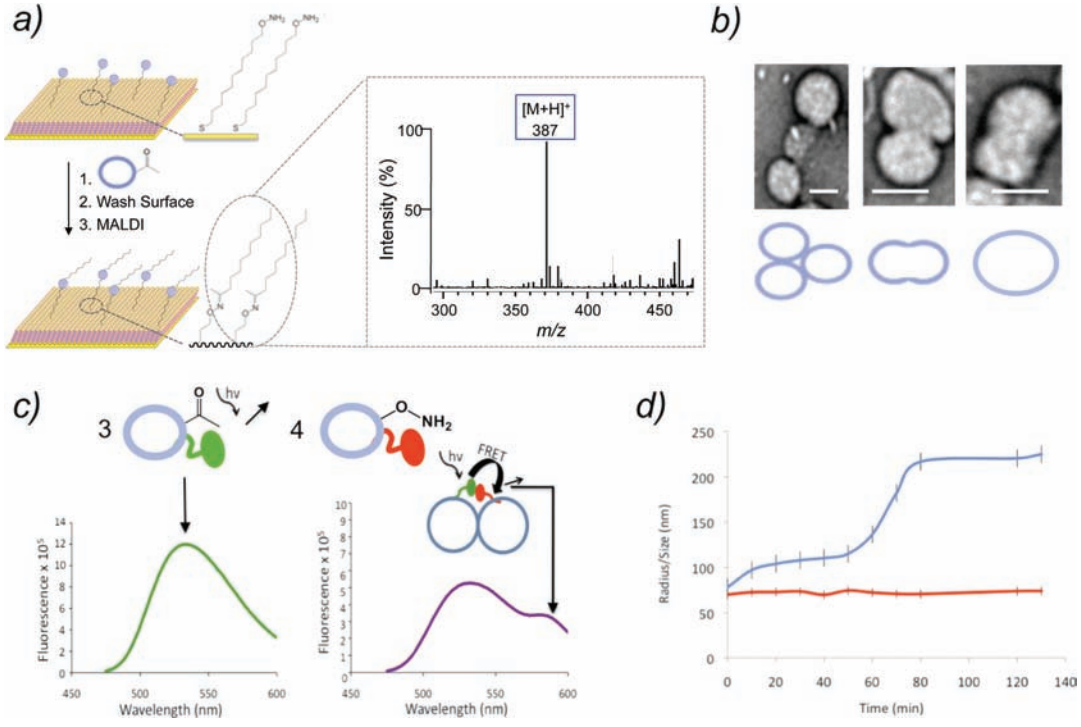

Figure 2. Characterization of the formation of fused and adhered liposomes based on chemoselective oxime conjugation. (a) Mass spectrometry (MS) data representing the oxime ligation of keto-LUVs to self-assembled monolayers (SAMs) of oxyamine-terminated alkanethiol on a gold surface is displayed. Matrix-assisted laser desorption/ionization (MALDI) was performed after keto-LUVs were delivered to the surface, and a mass of 387 units was detected, confirming oxime conjugation. (b) Structural analyses using transmission electron microscopy (TEM), representing the adhesion and fusion of keto- (**1**) and oxy- (**2**) LUVs over time. The following images are shown from left to right: multiadherent liposomes that are not fused; partially fused liposomes; and a single, large liposome after complete fusion. The scale bars represent 60 nm. (c) Fluorescence resonance energy transfer (FRET) analysis of liposome adhesion and fusion was monitored over 2 h. Fluorescence emission of keto-NBD-PE/PC LUVs (**3**), excited at 460 nm, was observed by scanning 475−600 nm (green trace). Fluorescence emission of keto-NBD-PE/PC LUVs (**3**) mixed with oxy-rhod-PE/PC/POPG LUVs (**4**) is represented (purple trace). A new FRET emission peak is observed at 578 nm showing mixed liposome adhesion. (d) Dynamic light scattering (DLS) was performed upon mixing liposomes (**1** and **2**) to monitor vesicle size change as a function of time. Increases in vesicle size were observed due to aggregation, adhesion, or fusion (blue trace). Liposome saturation was reached ~80 min after mixing. Without the presence of ketone and oxyamine functional groups, the LUV size remains constant (red trace).

Fluorescent intensities based on number of cells counted were compared to the standard bead and control cells lacking fluorescent molecule conjugation and approximate numbers of fluorescent compound bound to the surface was calculated. Flow cytometry was carried out using a Dako CyAn ADP (Beckman-Coulter, Brea, CA), and data was analyzed with *Summit 4.3* software.

■ RESULTS AND DISCUSSION

In previous studies, we demonstrated how chemoselective oxime chemistry can be used to present biospecific ligands from supported, model fluid lipid bilayer membranes for protein receptor recognition.[38] We also showed that the resultant oxime bond is extremely stable under physiological conditions.[33−35] In this report, we employ a similar oxime ligation strategy to generate a number of large unilamellar vesicles (LUVs) that present ketone or oxyamine functional groups. We first initiated liposome−liposome fusion events through molecular recognition and subsequent oxime bond formation and characterized the fusion using fluorescence resonance energy transfer (FRET), matrix-assisted laser-desorption/ionization mass spectrometry (MADLI-MS), dynamic light scattering (DLS), and transmission electron microscopy (TEM). Next, liposomes containing ketone and oxyamine groups were cultured with 3T3 Swiss albino fibroblasts, resulting in membrane fusion and display of oxyamines and ketones from the cell surface for further fluorescent probe conjugation. For the liposome−liposome fusion events studied by MALDI-MS (Figure 2a), DLS (Figure 2d), and TEM (Figure 2b), dodecanone and dodecyloxyamine molecules were incorporated, separately, into neutral, egg palmitoyl-oleoyl phosphatidylcholine (POPC) at a ratio of 5:95 to form keto-LUVs (**1**) and oxy-LUVs (**2**), respectively (Figure 1a,b). When observing liposome fusion via FRET analyses (Figure 2c), dodecanone molecules were mixed with POPC and fluorescence donor, egg 1,2-diphytanoyl-*sn*-glycero-3-phosphoethanolamine-*N*-(7-nitro-2-1,3-benzoxadiazol-4-yl) (NBD-PE) at a ratio of 5:93:2 to form keto-NBD-PE-LUVs (**3**), while dodecyloxyamine molecules were incorporated into POPC, negatively charged, egg 1-palmitoyl-2-oleoyl-phosphatidylglycerol (POPG), and fluorescence acceptor, egg 1,2-dipalmitoyl-*sn*-glycero-3-phosphoethanolamine-*N*-(lissamine rhodamine B sulfonyl) (rhod-PE) at a ratio of 5:73:20:2 to form oxy-rhod-PE-LUVs (**4**). Finally, liposomes that contained dodecanone, POPC, and cationic lipid, 1,2-dioleoyl-3-trimethylammonium-propane (DOTAP) (5:93:2, **5**) and liposomes that composed of dodecyloxyamine, POPC, and DOTAP (5:93:2, **6**) were generated to investigate liposome-cell fusion processes (Figure 1d). Cationic lipid, DOTAP, was incorporated to induce membrane fusion due to the electrostatic interactions with the negatively charged cell surface.[39,40]

dx.doi.org/10.1021/bc200236m | *Bioconjugate Chem.* 2011, 22, 2423−2433

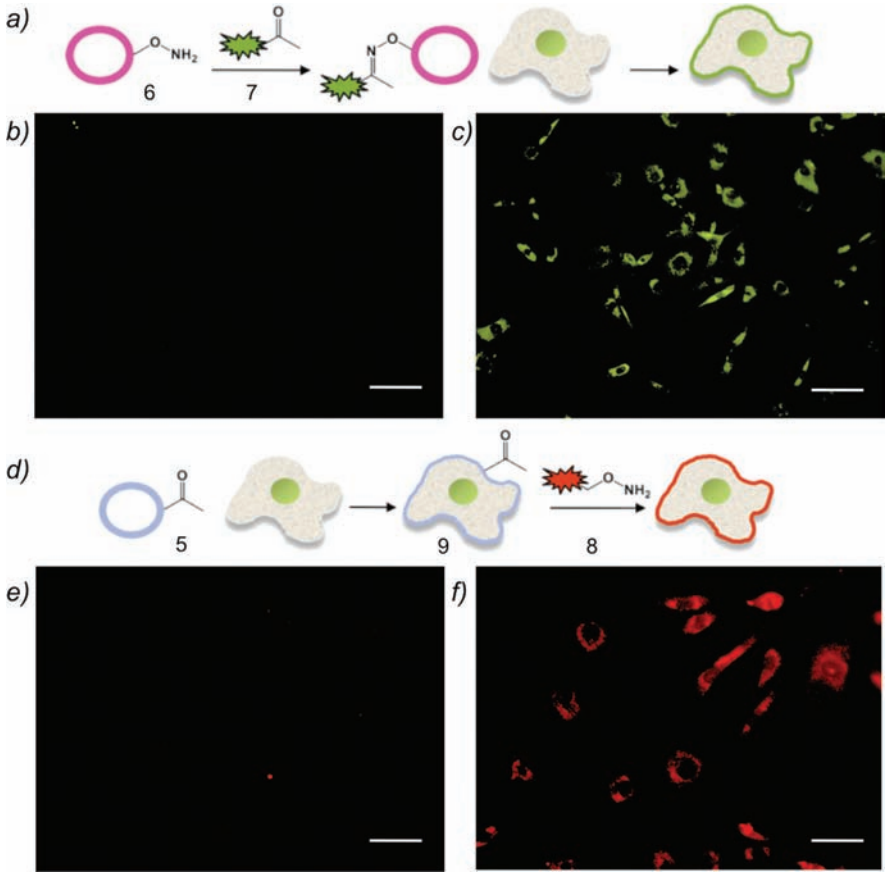

Figure 3. (Top) Schematic describing the delivery and subsequent fusion of fluorescent liposomes to cell surfaces with corresponding brightfield and fluorescent images. (a) Oxy-LUVs (**6**, 3 mM) were reacted with fluorescein−ketone (**7**, 0.15 mM, 2 h) to generate green fluorescent liposomes. The fluorescent liposomes were then added to fbs in culture, resulting in the fluorescent labeling of cells after liposome fusion to the cell membrane. Micrographs show (b) control cells where liposomes not containing oxyamine groups were incubated with fluorescein−ketone and added to fbs in culture for 2 h and (c) green fluorescently labeled cells after oxyamine-functionalized liposomes were incubated with fluorescein−ketone and delivered to fbs (2 h). (Bottom) General schematic and images for cell-surface tailoring using liposome fusion and chemoselective oxime chemistry. (d) Keto-LUVs (**5**, 3 mM) were added and fused with the cells to display these groups from the cell surface (**9**). Addition of rhod-oxyamine (**8**, 0.7 mM in H_2O, 2 min) resulted in chemoselective oxime formation and red fluorescent labeling of the cells. Images display (e) control fbs where liposomes not displaying ketones were fused to the membrane (2 h) and rhod-oxyamine was added and no fluorescence was observed, and (f) fluorescently labeled cells after ketone-functionalized liposomes were fused to fbs (2 h) and cells were incubated with rhod-oxyamine. Scale bars for b,c,d,e represent 50 and 30 μm, respectively.

Fusion Methodology and DLS Analyses. Our general fusion methodology is described in Figure 1a. Two liposome populations (**1** and **2**, **3** and **4**, or **5** and **6**) were mixed, resulting in liposome docking, adhesion, and finally fusion due to the formation of stable, interfacial oxime bonds. Depending on the application, liposomes fuse to each other, forming larger liposomal structures (Figure 2b) or to cell surfaces and then be further conjugated with the corresponding oxime component. DLS was performed upon mixing liposomes **1** and **2** over 2 h to monitor vesicle size change as a function of time. Increases in vesicle size were observed due to aggregation, adhesion, or fusion (blue trace, Figure 2d). Liposome saturation was reached ~80 min after mixing. We believe that, in some cases, liposomes **1** and **2** associate with each other through oxime chemistry and initiate docking/adhesion until enough liposomes have clustered to induce a sharp growth in size. We initially varied the ketone and oxyamine concentrations and found through our cell-surface engineering experiments and FACS analyses that higher ketone and oxyamine concentrations led to increases of these functional groups on the cell surface. However, increasing the concentration of functional groups led to faster fusion events but did not necessarily increase the liposome size after liposome−liposome fusion. We are studying the detailed relationship among the kinetics of liposome fusion, liposome size, and concentration of functional groups in the liposome. In control reactions, LUVs not presenting ketones were reacted with LUVs containing oxyamines (**1**) (red trace, Figure 2d). Likewise, LUVs containing ketone groups (**2**) were mixed with LUVs that did not display oxyamines. For both of these control experiments, no size change was observed over time. This result strongly supports that liposome adhesion and fusion are driven by chemoselective oxime bond formation between the ketone- and oxyamine-alkanes.

TEM. Structural insight into the formation of different adhered and fused liposomes was observed through TEM (Figure 2b).[41] Vesicles of different sizes and shapes result after 2 h of liposome mixing (keto-LUV, **1**, and oxy-LUV, **2**). The liposome size gradually increases with time and is consistent with the data collected from other sizing experiments (e.g., DLS). Upon reaction, the following three structures were observed: multiadherent liposomes that were not fused,

dx.doi.org/10.1021/bc200236m | *Bioconjugate Chem.* 2011, 22, 2423−2433

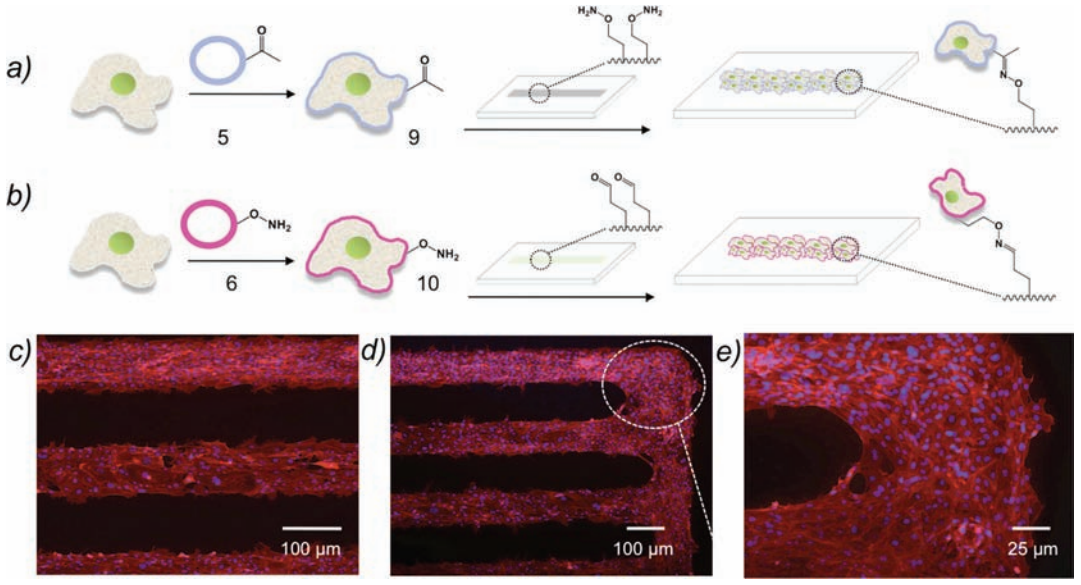

Figure 4. Schematics and fluorescent micrographs of rewired cells adhered to patterned self-assembled monolayers (SAMs) of alkanethiolates on gold substrates. (a,b) Keto- (**5**) and oxy-LUVs (**6**, 3 mM, 4 h) were cultured with separate fb populations, producing ketone- and oxyamine-presenting fbs (**9** and **10**, respectively). These cells were then seeded (~10^2 per mL, 2 h) to patterned, oxyamine- and aldehyde-terminated SAMs (10%), respectively, and allowed to adhere through stable oxime conjugation. The unpatterned surface regions present tetra(ethylene glycol), which resists cell and protein adsorption. The cells then grew and proliferated only filling out the oxyamine- and aldehyde-tethered surface regions, respectively. (c) Fluorescent micrograph of patterned ketone-fbs (**9**), adhered to an oxyamine-terminated SAM is shown. (d,e) Fluorescent micrographs of patterned oxyamine-fbs (**10**), adhered to an aldehyde-terminated SAM are demonstrated. Cells were stained with DAPI (blue, nucleus) and phalloidin (red, actin).

partially fused liposomes, and completely fused, large uni- and multilamellar liposomes (Figure 2b).

FRET. Figure 2c shows a liposome fusion assay involving FRET characterization. A lipid-bound FRET pair, NBD-PE (donor) and rhod-PE (acceptor), were incorporated at 2 mol % concentration during liposome generation to produce keto-NBD-PE LUVs (**3**) and oxy-rhod-PE LUVs (**4**), respectively. Hypothetically, fusion of these vesicles should result in a gradual decrease in the donor emission peak and an increase in acceptor emission peak[40] due to the close proximity of these dyes. As shown, vesicle mixing resulted in this FRET fusion signature. Fusion was observed immediately upon mixing **3** and **4**, slowing within 2 h to a stable population, which is similar to earlier sizing results. An emission peak was not observed for the acceptor rhodamine dye when performing control experiments that tested the energy transfer with an LUV that did not contain oxyamines. Similar results were observed when LUVs that did not contain ketones or oxyamines were mixed. This data further supports that liposome aggregation and fusion are based on chemoselective oxime bond formation.

MALDI-MS. Oxime conjugation, after keto-LUV (**1**) fusion, was confirmed by MALDI-MS analysis. Self-assembled monolayers (SAMs) of aminooxyundecanethiol were formed on a gold-coated, sample plate. A solution containing keto-LUVs (**1**) was then allowed to fuse and react with the surface for 90 min, followed by MALDI-MS examination. A mass of 387 units was detected, confirming successful oxime conjugation, resulting from liposome fusion on the surface (Figure 2a).

Cell-Surface Labeling. Chemical approaches to engineer cell surfaces have emerged as powerful tools for a variety of biomedical and biotechnological applications, including tissue engineering, drug delivery, and cell-based therapies.[24] Several metabolic and genetic approaches to display small molecular recognition pairs at cell surfaces for further covalent modification have been achieved through Click chemistry[42] and Staudinger ligation.[20] However, such strategies may alter cellular physiology and interfere with normal biochemical pathways.[28] In this report, we use oxime chemistry to tailor and fluorescently label cell surfaces via a novel liposome fusion strategy. As mentioned, cationic lipid, DOTAP, was incorporated within keto- and oxy-LUVs to initiate electrostatic destabilization and subsequent fusion to the cell membrane.[39] As such, the minimum DOTAP concentration required to facilitate liposome–cell fusion was determined to be 2% through fluorescence labeling optimization. Keto-LUVs were generated using DOTAP and POPC concentrations that ranged from 0.5% to 5% and 90% to 94.5%, respectively, while maintaining a 5% ketone concentration. These liposomes were incubated with fibroblasts (fbs) for 4 h, conjugated with an oxyamine-tethered rhodamine (rhod-oxyamine, **8**) (0.7 mM, 2 h), and the cell fluorescence intensities were then compared. From 2% to 5% DOTAP, the intensities were almost identical, indicating that 2% DOTAP is sufficient to initiate fusion. The liposomes for liposome–cell fusion events were approximately ~60 nm in diameter, similar to those used for the liposome–liposome fusion characterization.

Given this optimized lipid ratio (POPC/ketone or oxyamine/DOTAP at 93:5:2), two cell-surface engineering methods were employed to fluorescently label fbs. Similar to our optimization experiments, a solution of keto-LUVs (**5**, 200 μL, 0.6 mM) was added to fbs in culture for 2 h, resulting in membrane fusion and subsequent display of ketones from the cell surface (**9**) (Figure 3d). Rhod-oxyamine (**8**, 100 μL, 0.7 mM in H_2O) was then added the cells for 2 h. After oxime formation, the fbs were washed with PBS, trypsinized, diluted with CBS-containing media (~10^2/mL), seeded to a glass substrate, and imaged under a fluorescent microscope. As

dx.doi.org/10.1021/bc200236m | *Bioconjugate Chem.* 2011, 22, 2423–2433

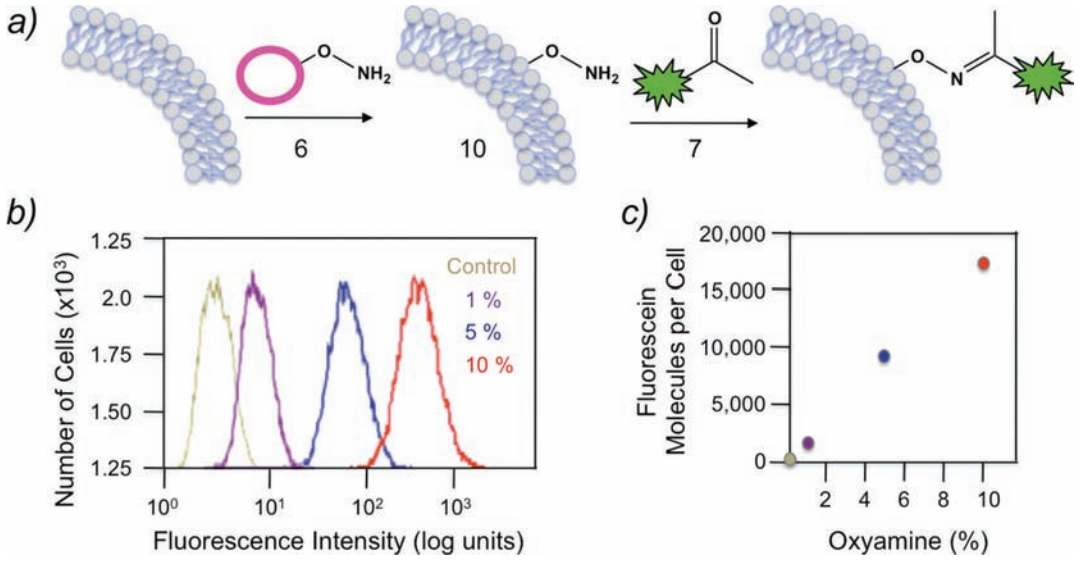

Figure 5. Cell surface molecule quantification using flow cytometry. (a) Oxy-LUVs (**6**, 3 mM) were added to fbs in culture (4 h), resulting in membrane fusion and subsequent display of oxyamine groups from cell surfaces (**10**). Ketone-functionalized fluorescein (**7**, 0.15 mM, 2 h) was then reacted with the fbs, generating fluorescently labeled cells. (b) Liposomes with varying oxyamine mol % (0%, 1%, 5%, and 10%) were generated and cultured with separate populations of fbs. After reacting with ketone−fluorescein, the cell populations were washed with PBS, trypsinized, centrifuged, resuspended in RPMI media, and tested using FACS analyses. As shown, the fluorescence intensity increased with increasing oxyamine concentration. (c) The number of molecules present at the cell surface with respect to oxyamine concentration was quantified using flow cytometry. A bead with a known FITC molecule density was employed as a standard comparison to calculate the number of oxyamines after oxy-LUVs (**6**) with 0%, 1%, 5%, and 10% oxyamine was cultured with cells. As the oxyamine concentration increased, the molecules per cell increased linearly (0%, 128; 1%, 1600; 5%, 9800; and 10%, 17 400). Twenty thousand cells were counted for each sampling.

observed in Figure 3f, the conjugation of rhod-oxyamine with ketone-presenting fbs resulted in the red fluorescence labeling of cells. When the control fbs (i.e., no ketone groups present) were reacted with rhod-oxyamine (**8**) and then imaged, no fluorescence was observed (Figure 3e). Demonstrating the flexibility of this liposome-based surface labeling strategy, we modified fb surfaces to present a ketone-functionalized fluorescein dye (**7**) after oxy-LUV-ketone-fluorescein conjugation and subsequent membrane fusion (Figure 3a). A solution of oxy-LUVs (**6**, 3 mM) was incubated with a ketone-functionalized fluorescein (**7**, 0.15 mM, 1 equiv, 2 h), generating fluorescently labeled liposomes. The liposomes were then added to fbs in culture for 2 h. After fusion, the cells were washed with PBS, trypsinized, diluted with CBS-containing media (~10^2/mL), seeded to a glass substrate, and imaged under a fluorescent microscope. Figure 3c presents green fluorescently labeled fbs after fusion with fluorescein-functionalized LUVs. Through fluorescent and confocal imaging, it appears that, after membrane fusion and/or endocytosis of cultured liposomes, fluorescence is also observed in several membrane organelles. This is an advantage of the system in that ketone or oxyamine groups are present at the cell surface and also decorate various internal membranes. It may be possible to label internal organelles with oxyamine chemistry for future targeting studies and applications. We assume that these lipids and fluorophores are packaged and trafficked to and from the cell surface and internal compartments. However, enough functional groups are present on the cell surface to provide handles for further oxime chemistry conjugation to tailor cell surfaces. When liposomes not containing oxyamine groups were incubated with fluorescein−ketone and added to fbs in culture for 2 h, no fluorescence was observed (Figure 3b). Thus, our control images indicated that reaction and labeling does not occur without the proper oxime recognition pair (Figure 3b and e). Furthermore, under these conditions, we observed no changes in cell behavior upon liposome fusion to cells, which is a very important feature for future *in vivo* applications. Thus, by combining liposome fusion and oxime chemistry, we were able to tailor the cell surface with either ketone groups or oxyamine groups, which may act as chemoselective cell-surface receptors for a range of small molecules, ligands, biomolecules, and nanoparticles.

Cell Patterning: Rewiring Adhesion. The ability to pattern and adhere cells to different materials, such as thin metal films, polymer scaffolds, and nanoparticles, with a simple and straightforward chemoselective and bio-orthogonal approach would be beneficial for cell biology, tissue engineering, and biotechnology. Thus, we employed liposome fusion-based toward cell-surface engineering to modify and rewire cell surface to adhere to patterned 2D substrates, directed through stable oxime bond conjugation. Figure 4a,b illustrates the strategy to rewire cell surfaces for the goal of cell adhesion to self-assembled monolayers (SAMs) of alkanethiolates on gold substrates. Employing microfluidic oxidation[34] and lithography,[35] aldehyde and oxyamine SAMs, respectively, were patterned at a ratio of 10%. The remaining 90% of the surface was backfilled with tetra(ethylene glycol) alkanethiol, which is known to pacify biomaterials against nonspecific protein adsorption and cell adhesion.[36] Meanwhile, fbs were cultured separately with keto- (**5**) and oxy-LUVs (**6**, 3 mM, 4 h), resulting in membrane fusion and subsequent display of ketones (**9**) and oxyamines (**10**) from cell surfaces. The resulting ketone- and oxyamine-presenting fbs were then seeded (~10^2 cells/mL, 2 h) to the patterned oxyamine and aldehyde substrates, respectively, and allowed to react and form stable oxime linkages in the patterned regions. The cells were cultured for 4 d on these substrates, growing and proliferating in the patterned regions. The results of patterned keto-fbs on

dx.doi.org/10.1021/bc200236m | *Bioconjugate Chem.* 2011, 22, 2423−2433

oxyamine SAMs are shown in Figure 4c; patterned oxy-fbs on aldehyde SAMs are displayed in Figure 4d,e. Furthermore, unmodified cells did not attach to the surface. Thus, this strategy allows for a bottom-up, bio-orthogonal synthetic approach to rewire how cells adhere to materials and does not require metabolic or genetic cell manipulations.

Flow Cytometry. Flow cytometry was performed to further verify the ability of tailoring small molecules to cell surfaces through covalent oxime bond formation. This method also enables the quantification of ketone and oxyamine molecules that are present at the cell surface after liposome delivery and subsequent membrane fusion. Liposomes that incorporated varying oxyamine concentrations of (i.e., 0, 1, 5, and 10 mol %) were generated (**6**, 3 mM), cultured with separate fb populations for 4 h, resulting in membrane fusion and oxyamine display (**10**, Figure 5a). A ketone-modified fluorescein dye (**7**, 0.15 mM, 2 h) was then conjugated to the cell surfaces in each population, producing green fluorescently labeled fbs. The FACS analyses results are demonstrated in Figure 5b. Twenty thousand cells were counted for all samples. As shown, the fluorescence intensity increases with increasing number of oxyamine molecules present for fluorescein conjugation. Additionally, the control cell population that was fused with unmodified liposomes and reacted with ketone–fluorescein (**7**) demonstrated the lowest intensity. Furthermore, a bead with known FITC molecule density was calibrated and used as a standard comparison to quantify the number of oxyamine molecules present at the cell surface after fusion.[37] Figure 5c displays the correlation between oxyamine mol % and oxyamine molecules per cell counted by FACS analyses. The calculated molecules per cell for the control fbs and oxyamine-presenting fbs that were fused with 1%, 5%, and 10% oxyamine were approximately 128, 1300, 9800, and 17 400, respectively. A linear trend was observed; as the molecule concentration increased, the fluorescence intensity and number of molecules at the cell surface increased. Thus, the density of molecules that decorate cell surfaces can be controlled and quantified using this liposome fusion-based methodology for cell-surface engineering.

CONCLUSION

In summary, we developed a chemoselective synthetic cell receptor system based on a liposome delivery and fusion strategy. Ketone and oxyamine groups were introduced to a liposomal system and chemoselective vesicle fusion was achieved using molecular recognition and interfacial oxime bond formation. Subsequent delivery of the decorated liposomes to cells lead to fusion and modification of a cell surface by bio-orthogonal reactive groups that serve as synthetic chemoselective cell receptors. Ketone and oxyamine modified cells were patterned on solid surfaces, displaying oxyamine and ketone groups, respectively. Thus, rewiring cell adhesion was achieved using chemoselective oxime bond formation and without using any cell adhesive ligands, such as Arg-Gly-Asp (RGD) and fibronectin. Since no biomolecules are used with this strategy, no long-term stability and degradation issues in complex cell culture media or *in vivo* will affect cell targeting or cell assembly. This methodology may have diverse applications in biomedical technologies including tissue engineering and regenerative medicine. Cells displaying ketone and oxyamine groups can react chemoselectively to form three-dimensional (3D) and tissue-like structures as directed through *in situ* oxime bond formation.[43] This method can be extended to generate 3D cell coculture systems and study cell–cell interactions. The ketone- and oxyamine-functionalized liposomes may have extensive applications in drug delivery and diagnostic applications, in which the interior of the liposome contains cargo while the exterior surface can be simultaneously functionalized with the tracking agent.

AUTHOR INFORMATION

Corresponding Author

*Tel: (416) 736-2100; Fax: (416) 736-77712; E-mail mnyousaf@yorku.ca.

ACKNOWLEDGMENTS

The authors thank Dr. Nancy Thompson and her lab group for use of equipment and expertise in liposome chemistry, Lisa Bixby for help with FACS analysis, and Brian Lamb for aid with MS data collection. This work was supported by the Carolina Center for Cancer Nanotechnology Excellence, the Burroughs Wellcome Foundation (Interface Career Award), the National Science Foundation, and York University.

REFERENCES

(1) Mayer, A. (2002) Membrane fusion in eukaryotic cells. *Annu. Rev. Cell. Develop. Biol. 18*, 289.

(2) Rowan, A. (2006) Clamping down on exocytosis. *Nat. Rev. Mol. Cell Biol. 7*, 555–561.

(3) Ellens, H., Bentz, J., and Szoka, F. C. (1985) Proton- and calcium- induced fusion and destabilization of liposomes. *Biochemistry 24*, 3099–3106.

(4) Dennison, S. M., Greenfield, N., Lenard, J., and Lentz, B. R. (2002) VSV Transmembrane domain (TMD) peptide promotes PEG-mediated fusion of liposomes in a conformationally sensitive fashion. *Biochemistry 41*, 14925–14934.

(5) Evans, K. O., and Lentz, B. R. (2002) Kinetics of lipid rearrangements during poly(ethylene glycol)-mediated fusion of highly curved unilamellar vesicles. *Biochemistry 41*, 1241–1249.

(6) Jahn, R., Lang, T., and Sudhof, T. C. (2003) Membrane fusion. *Cell 112*, 519–533.

(7) McNew, J. A., Weber, T., Parlati, F., Johnston, R. J., Melia, T. J., Sollner, T. H., and Rothman, J. E. (2000) Close is not enough: Snare-dependent membrane fusion requires an active mechanism that transduces force to membrane anchors. *J. Cell Biol. 150*, 105–117.

(8) Soolner, T. H. (2004) Intracellular and viral membrane fusion: An uniting mechanism. *Curr. Opin. Biol. 16*, 429–435.

(9) Parlati, F., Weber, T., McNew, J. A., Westermann, B., Sollner, T. H., and Rothman, J. E. (1999) Rapid and efficient fusion of phospholipid vesicles by the α-helical core of a SNARE complex in the absence of an N-terminal regulatory domain. *Proc. Natl. Acad. Sci. U.S.A. 96*, 12565–12570.

(10) Paumet, F., Rahimian, V., and Rothman, J. E. (2004) The specificity of SNARE-dependent fusion is encoded in the SNARE motif. *Proc. Natl. Acad. Sci. U.S.A. 101*, 3376–3380.

(11) Richard, A., Marchi-Artzner, V., Lalloz, M.-N., Brienne, M.-J., Artzner, F., Gulik-Krzywicki, T., Guedeau-Boudeville, M.-A., and Lehn, J.-M. (2004) Fusogenic supramolecular vesicle systems induced by metal ion binding to amphiphilic ligands. *Proc. Natl. Acad. Sci. U.S.A. 101*, 15279–15284.

(12) Marchi-Artzner, V., Gulik-Krzywicki, T., Guedeau-Boudeville, M.-A., Gosse, C., Sanderson, J. M., Dedieu, J.-C., and Lehn, J.-M. (2001) Selective adhesion, lipid exchange and membrane-fusion processes between vesicles of different sizes bearing complementary molecular recognition groups. *ChemPhysChem 2*, 367–376.

(13) Marchi-Artzner, V., Jullien, L., Gulik-Krzywicki, T., and Lehn, J.-M. (1997) Molecular recognition induced aggregation and fusion between vesicles containing lipids bearing complementary hydrogen bonding head groups. *Chem. Commun. 1*, 117–118.

(14) Paleos, C. M., and Tsiourvas, D. (2006) Interaction between complementary liposomes: A process leading to multicompartment sytems formation. *J. Mol. Recognition 19*, 60−67.
(15) Chan, Y.-H. M., Lengerich, B., and Boxer, S. G. (2009) Effects of linker sequences on vesicle fusion mediated by lipid-anchored DNA oligonucleotides. *Proc. Nat. Acad. Sci. U.S.A. 106*, 979−984.
(16) Gong, Y., Luo, Y., and Bong, D. (2006) Membrane activation: Selective vesicle fusion via small molecule recognition. *J. Am. Chem. Soc. 128*, 14430−14431.
(17) Sarkar, D., Vemula, P. K., Zhao, W., Gupta, A., Karnik, R., and Karp, J. M. (2010) Engineered mesenchymal stem cells with self-assembled vesicles for systemic cell targeting. *Biomaterials 31*, 5266−5274.
(18) Winans, K. A., and Bertozzi, C. R. (1995) Cracking the carbohydrate code for selectin recognition. *Chem. Biol. 5*, R313−R315.
(19) Kellam, B., De Bank, P. A., and Shakesheff, K. A. (2003) Chemical modification of mammalian cell surfaces. *Chem. Soc. Rev. 32*, 327−337.
(20) Saxon, E., and Bertozzi, C. R. (2000) Cell surface engineering by a modified Staudinger ligation. *Science 287*, 2007−2010.
(21) Lin, C. W., and Ting, A. Y. (2006) Transglutaminase-catalyzed site-specific conjugation of small-molecule probes to proteins in vitro and on the surface of living cells. *J. Am. Chem. Soc. 128*, 4542−4543.
(22) Liu, W., Brock, A., Chens, S., Chen, S., and Schultz, P. G. (2007) Genetic incorporation of unnatural amino acids into proteins in mammalian cells. *Nat. Methods 4*, 239−244.
(23) Wilson, J. T., Krishnamurthy, V. R., Cui, W., Qu, Z., and Chaikof, E. L. (2009) Noncovalent cell surface engineering with cationic graft copolymers. *J. Am. Chem. Soc. 131*, 18228−18229.
(24) Prescher, J. A., and Bertozzi, C. R. (2005) Chemistry in living systems. *Nat. Chem. Biol. 1*, 13−21.
(25) Chen, I., Howarth, M., Lin, W., and Ting, A. Y. (2005) Site-specific labeling of cell surface proteins with biophysical probes using biotin ligase. *Nat. Methods 2*, 99−104.
(26) Boonyarattanakalin, S., Martin, S. E., Sun, Q., and Peterson, B. R. (2006) A synthetic mimic of human Fc receptors: Defined chemical modification of cell surfaces enables efficient endocytotic uptake of human Immunoglobulin G. *J. Am. Chem. Soc. 128*, 11463−11470.
(27) Rabuka, D., Forstner, M. B., Groves, J. T., and Bertozzi, C. R. (2008) Noncovalent cell surface engineering: Incorporation of bioactive synthetic glycopolymers into cellular membranes. *J. Am. Chem. Soc. 130*, 5947−5953.
(28) Rose, K. (1994) Facile synthesis of homologous artificial proteins. *J. Am. Chem. Soc. 116*, 30−33.
(29) Rideout, D., Calogeropoulou, T., Jaworski, J., and McCarthy, M. (1990) Synergism through direct covalent bonding between agents: A strategy for rational design of chemotherapeutic combinations. *Biopolymers 29*, 247−262.
(30) Rideout, D. (1994) Self assembling drugs: A new approach to biochemical modulation in cancer chemotherapy. *Cancer. Invest. 12*, 189−202.
(31) Shao, J., and Sham, J. P. (1995) Unprotected peptides as building blocks for the synthesis of peptide dendrimers with oxime, hydrazone and thiazolidine linkages. *J. Am. Chem. Soc. 117*, 3893−3899.
(32) Pale-Grosdemange, C., Simons, E. E., Prime, K. L., and Whitesides, G. M. (1991) Formation of self-assembled monolayers by chemisorption of derivatives of oligo(ethylene glycol) of structure HS(CH2)11(OCH2CH2)mOH on gold. *J. Am. Chem. Soc. 113*, 12−20.
(33) Park, S., and Yousaf, M. N. (2008) *Langmuir 24*, 6201−6207.
(34) Westcott, N. P., Pulsipher, A., Lamb, B. M., and Yousaf, M. N. (2008) Expedient generation of patterned surface aldehydes by microfluidic oxidation for chemoselective immobilization of ligands and cells. *Langmuir 24*, 9237−9240.
(35) Lamb, B. M., Barrett, D. G., Westcott, N. P., and Yousaf, M. N. (2008) Microfluidic lithography of SAMs on gold to create dynamic surfaces for directed cell migration and contiguous cell cocultures. *Langmuir 24*, 8885−8889.
(36) Harder, P., Grunze, M., Dahint, R., Whitesides, G. M., and Laibinis, P. E. (1998) Molecular conformation in Oligo(ethylene glycol)-terminated self-assembled monolayers on gold and silver surfaces determines their ability to resist protein adsorption. *J. Phys. Chem. B 102*, 426−436.
(37) Hsiao, S. C., Shum, B. J., Onoe, H., Douglas, E. S., Gartner, Z., Mathies, R. A., Bertozzi, C. R., and Francis, M. B. (2009) Direct cell surface modification with DNA for the capture of primary cells and the investigation of myotube formation on defined patterns. *Langmuir 25*, 6985−6991.
(38) Dutta, D., Pulsipher, A., and Yousaf, M. N. (2010) Selective tethering of ligands and proteins to a microfluidically patterned electroactive fluid ipid bilayer. *Langmuir 26*, 9835−9841.
(39) Csiszar, A., Hersch, N., Dieluweit, S., Biehl, R., Merkel, R., and Hoffmann, B. (2010) Novel fusogenic liposomes for fluorescent cell labeling and membrane modification. *Bioconjugate Chem. 21*, 537−543.
(40) Beigel, M., Keren-Zur, M., Laster, Y., and Loyter, A. (1988) Poly(aspartic acid)-dependent fusion of liposomes bearing the quaternary ammonium detergent [[[(1,1,3,3-tetramethylbutyl)cresoxy]ethoxy]ethyl]dimethylbenzyl ammonium hydroxide. *Biochemistry 27*, 660−666.
(41) Beck, P., Liebi, M., Kohlbrecher, J., Ishikawa, T., Ruegger, H., Fischer, P., Walde, P., and Windhab, E. (2010) Novel type of bicellar discs from a mixture of DMPC and DMPE-DTPA with complexed lanthanides. *Langmuir 26*, 5382−5387.
(42) Chang, M., Prescher, J. A., Sletten, E. M., Baskin, J. M., Miller, I. A., Agard, N. J., Lo, A., and Bertozzi, C. R. (2010) Copper-free Click chemistry in living animals. *Proc. Natl. Acad. Sci. U.S.A. 107*, 1821−1826.
(43) Dutta, D., Pulsipher, A., Luo, W., and Yousaf, M. N. (2011) Synthetic chemoselective rewiring of cell surfaces: generation of 3-dimensional tissue structures. *J. Am. Chem. Soc. 133*, 8704−8713.

Bioconjugate Chemistry

Article

pubs.acs.org/bc

In Vivo Detection of Phospholipase C by Enzyme-Activated Near-Infrared Probes

Theresa M. Mawn, Anatoliy V. Popov, Nancy J. Beardsley, Klara Stefflova,[†] Matthew Milkevitch,[‡] Gang Zheng,[§] and E. James Delikatny*

Department of Radiology, University of Pennsylvania, Philadelphia, Pennsylvania 19104, United States

ABSTRACT: In this article, the characterization of the first near-infrared (NIR) phospholipase-activated molecular beacon is reported, and its utility for *in vivo* cancer imaging is demonstrated. The probe consists of three elements: a phospholipid (PL) backbone to which the NIR fluorophore, pyropheophorbide *a* (Pyro), and the NIR Black Hole Quencher 3 (BHQ) were conjugated. Because of the close proximity of BHQ to Pyro, the Pyro-PtdEtn-BHQ probe is self-quenched until enzyme hydrolysis releases the fluorophore. The Pyro-PtdEtn-BHQ probe is highly specific to one isoform of phospholipase C, phosphatidylcholine-specific phospholipase C (PC-PLC), responsible for catabolizing phosphatidylcholine directly to phosphocholine. Incubation of Pyro-PtdEtn-BHQ *in vitro* with PC-PLC demonstrated a 150-fold increase in fluorescence that could be inhibited by the specific PC-PLC inhibitor tricyclodecan-9-yl xanthogenate (D609) with an IC_{50} of 34 ± 8 μM. Since elevations in phosphocholine have been consistently observed by magnetic resonance spectroscopy in a wide array of cancer cells and solid tumors, we assessed the utility of Pyro-PtdEtn-BHQ as a probe for targeted tumor imaging. Injection of Pyro-PtdEtn-BHQ into mice bearing DU145 human prostate tumor xenografts followed by *in vivo* NIR imaging resulted in a 4-fold increase in tumor radiance over background and a 2 fold increase in the tumor/muscle ratio. Tumor fluorescence enhancement was inhibited with the administration of D609. The ability to image PC-PLC activity *in vivo* provides a unique and sensitive method of monitoring one of the critical phospholipase signaling pathways activated in cancer, as well as the phospholipase activities that are altered in response to cancer treatment.

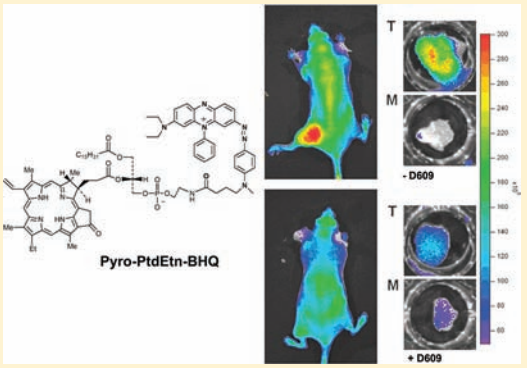

INTRODUCTION

Molecular imaging techniques offer the potential ability to detect cancer at a curable stage, to monitor and adjust patient treatments, and to improve the efficiency of cancer drug development.[1] Direct monitoring of a molecular target allows detailed elucidation of key metabolic pathways and specific cellular processes that become deregulated in cancer.[2−6] Lipids play an important role in the regulation of cellular responses and communication,[7] so it is not surprising that the lipid metabolic profile has been found to be altered in a variety of cancers. The development of probes for imaging lipid metabolism has been relatively unexplored but holds great promise for resolving and monitoring specific molecular targets for anticancer therapy.

Magnetic resonance spectroscopy (MRS) has been used extensively to study the biochemistry and physiology of cancer cells and solid tumors by observing changes in the lipid metabolites of phosphatidylcholine (PtdCho). Over the past two decades, ^{1}H- and ^{31}P-MRS have consistently revealed the presence of increased levels of phosphocholine (PC) in breast,[8−14] prostate,[13,15−18] and brain[8,13,16,19−21] cancer cells and solid tumors. Elevated levels of PC, in particular, have been correlated with the degree of malignancy,[22−24] and it has been shown that PC levels decrease in response to chemotherapeutic treatment.[25] Although elevations in PC have been attributed to up-regulation of choline transport and choline kinase activity,[22,25] there is also evidence that increased PtdCho catabolism may also play a role.[14,26,27] Phosphatidylcholine-specific phospholipase C (PC-PLC) hydrolyzes PtdCho to PC and diacylglycerol and has been implicated in contributing to the irregular choline metabolism in cancer.[26,28,29] It is of growing importance to resolve the source of PC as a potential marker for the malignant phenotype[10,30] and for assessing tumor response to therapy.[31,32]

In a previous paper, we reported the synthesis of a series of self-quenched near-infrared (NIR) fluorescent probes sensitive to the actions of phospholipases.[33] This follows from our studies in which the enzymatic activation of a protease-sensitive probe resulted in the separation of a fluorophore from a dark quencher leading to increased fluorescence.[34,35] In this article, we focus on one probe, Pyro-PtdEtn-BHQ (1-palmitoyl-2-pyropheophorbide-*sn*-glycero-3-phosphoethanolamine-BHQ-3), which is highly specific to PC-PLC, in order to directly examine the contribution of the catabolic pathway to increased levels of PC. The NIR fluorophore, pyropheophorbide *a* (Pyro; λ_{ex} = 410, 665 nm; λ_{em} = 670, 725 nm), is attached to the *sn*-2

Received: May 7, 2011
Revised: September 29, 2011
Published: October 31, 2011

ACS Publications © 2011 American Chemical Society

position, and the NIR Black Hole Quencher 3 (BHQ, absorbance range: 620−730 nm) is conjugated to the headgroup. The close proximity of the quencher to the fluorophore results in fluorescence quenching. Upon enzymatic cleavage by PC-PLC, the fluorescent moiety is separated from the phospholipid, and fluorescence is restored. Results from a positive control, a fluorescent unquenched lipid analogue, Pyro-PtdEtn (1-palmitoyl-2-pyropheophorbide-*sn*-glycero-3-phosphoethanolamine), are also reported.

It is demonstrated that Pyro-PtdEtn-BHQ exhibits a marked specificity for PC-PLC and that it can be activated in cultured DU145 human prostate tumor cells and tumor xenografts. Moreover, fluorescence can be attenuated using tricyclodecan-9-yl xanthogenate (D609), a specific inhibitor to PC-PLC, both in solution and *in vivo*. These data indicate that the catabolic pathway of PC formation via PC-PLC may be an important contributor to the alterations in choline metabolism seen in cancer progression and development.

MATERIALS AND METHODS

Synthesis of Pyro-PtdEtn-BHQ and Pyro-PtdEtn. The detailed synthesis and characterization of a series of phospholipase-sensitive fluorophores has been published elsewhere.[33] Pyropheophorbide *a* (λ_{abs} = 665 nm, λ_{em} = 725 nm) was prepared from *Spirulina Pacifica* algae (Cyanotech Corporation, Kailua-Kona, HI, USA) according to a previously published procedure.[36] *N-tert*-butoxycarbonyl-1-palmitoyl-*sn*-glycero-3-phosphoethanolamine (Lyso-PtdEtn-N-Boc, Avanti Polar Lipids, Inc., Alabaster, AL) was acylated with Pyro in the presence of *N*-(3-dimethylaminopropyl)-N′-ethyl carbodiimide hydrochloride (EDC), and 4-dimethylaminopyridine (DMAP). N-Boc deprotection with trifluoroacetic acid resulted in the permanently fluorescent phospholipid analogue, Pyro-PtdEtn, at 30% yield (50 mg). Further N-acylation of Pyro-PtdEtn with BHQ succinimidyl ester hexafluorophosphate (BHQ-3-$SU^+PF_6^-$, λ_{abs} = 620−730 nm, Biosearch Technologies, Novato, CA) in the presence of triethylamine (Et_3N) in CH_2Cl_2 gave rise to Pyro-PtdEtn-BHQ at 15% yield (20 mg).

Phospholipases. Phospholipases were obtained from Sigma (St. Louis, MO), dissolved in Tris buffer (50 mM Tris-HCl, pH 7.4) and stored in aliquots at −20 °C. Mammalian phospholipase isoforms were used whenever available: $sPLA_2$ (type IB, porcine pancreas and bovine pancreas), otherwise bacterial isoforms were employed: PC-PLC (*Bacillus cereus*), PI-PLC (*B. cereus*), SMase (*B. cereus*), and PC-PLD (*Streptomyces chromofuscus*).

Lipid Dispersions. Pyro-PtdEtn-BHQ or Pyro-PtdEtn (ε = 110,000 M^{-1} cm^{-1} at 410 nm) was combined with PtdCho (chicken egg, Avanti Polar Lipids, Inc., Alabaster, AL) in chloroform and dried under a stream of nitrogen. Lipid films were rehydrated with buffer (50 mM Tris-HCL, pH 7.4), and small unilamellar vesicles were formed by sonication until an optically clear dispersion was obtained. For TLC and MALDI-TOF experiments, a concentration of 200 μM Pyro-PtdEtn-BHQ was used at a mole fraction of 0.05 in egg PtdCho. For kinetic experiments, a concentration of 1 μM Pyro-PtdEtn-BHQ was used at mole fractions of 0.002−0.04 in egg PtdCho.

TLC Assay. Aliquots (200 μL) of the sonicated Pyro-PtdEtn-BHQ/egg-PtdCho (MF 0.05) lipid dispersion were incubated at 37 °C with 1 U of enzyme: PC-PLC, PI-PLC, SMase, PC-PLD, type IA $sPLA_2$, or type IB $sPLA_2$. After 24 h, a sample from each aliquot was separated on an UV Silica Gel TLC plate using the solvent chloroform/methanol (100:15). Fluorescent bands due to cleavage were detected using a 385 nm UV lamp. The *Rf* of each band was compared to a control Pyro-PtdEtn-BHQ/lipid dispersion that had not been exposed to enzyme.

HPLC and MALDI-TOF Mass Spectrometry. Products of the Pyro-PtdEtn-BHQ-phospholipase cleavage experiments were separated using reverse-phase HPLC. The HPLC system consisted of a Waters 600 controller with a quaternary pump equipped with a Waters 2996 diode array detector (Waters Corp, Milford, CT) and a Zorbax 300SB-C3 column (4.6 × 150 mm, Agilent Corp, Santa Clara, CA). The flow rate of the mobile phase was 1.5 mL/min. The mobile phase composition was (A) acetonitrile, (B) 0.1 M triethylamine + acetic acid, pH 7, and (C) methanol. Solvent composition began with 80% solvent A and 20% solvent B, which was increased to 90% A and 10% B over 10 min. Conditions were then changed to 90% A and 10% C for 10 min followed by 90% C and 10% A over 60 min. The identity of isolated fragments was subsequently confirmed with MALDI-TOF MS using an Applied Biosystems Voyager DE Mass Spectrometer with positive mode ionization. The matrix consisted of α-cyano-4-hydroxycinnamic acid or 2-(4-hydroxyphenylazo)benzoic acid.

Confocal Microscopy Studies. Cells (1×10^5 cells/mL) were grown on Nunc chambered culture slides for 24 h and incubated for 1 h at 37 °C with 10 μL of 5 μM Pyro PL or Pyro-PtdEtn-BHQ in saline or saline as a control. The cells were rinsed, mounted, and observed via confocal microscopy on a Zeiss LSM 510 META confocal microscope with λ_{ex} = 633 nm and λ_{em} = 665−718 nm. The intensity density was quantified from each image using ImageJ software and normalized to the area occupied by cells.

Kinetics Analysis by Fluorescence Spectroscopy. A Molecular Devices SpectraMax M5 microplate reader was used to measure the fluorescence from 100 μL samples containing 1 μM substrate dispersed in egg-PtdCho vesicles in buffer (50 mM Tris-HCl, pH 7.4). Following enzyme addition, the initial rate measured in relative fluorescence units per minute (RFU/min) was determined using SoftMax Pro Software (Molecular Devices, Sunnyvale, CA) with λ_{ex} = 410 nm and λ_{em} = 675 nm.

Cell Culture. The human prostate carcinoma cell line, DU145, was maintained in MEM Eagle culture medium supplemented with 10% (v/v) fetal calf serum, 2 mM L-glutamine, and 1% penicillin/streptomycin and buffered with 20 mM sodium bicarbonate. Cultures were grown in 150 cm^2 filter cap tissue culture flasks using standard culture conditions of 37 °C and 5% CO_2 in air.

***In Vivo* NIR Fluorescence Imaging.** DU145 cells (5×10^6) were injected subcutaneously above the left hind legs of 4−6 week old athymic nude mice (NCI, Fort Dietrich, MD). Tumors were grown for 4−6 weeks until they reached a volume of 200−400 mm^3. Mice were fed low-fluorescent pellets (Labdiet 5 V02, Animal Specialties and Provisions, LLC, PA) for 1−3 days prior to imaging. Mice were anesthetized with 100 μL of ketamine (50 mg/mL) /acepromazine (5 mg/mL). Prescan visible and fluorescent images were taken with a Xenogen IVIS system using Cy5.5 fluorescence filters (λ_{ex} = 615−667 nm, λ_{em} = 695−770 nm), and an exposure time of 1 s. Following the prescan image, the mice were injected i.v. with 80 nmol Pyro-PtdEtn or Pyro-PtdEtn-BHQ solubilized in 50 mM Tris-HCl, pH 7.4, and 0.1% Tween-80 (200 μL/mouse). In inhibition experiments, D609 (Sigma-Aldrich, St. Louis, MO) was administered intraperitoneally at a dose of 50 μg/g body weight 30 min prior to and 30, 60, and 120 min post-injection

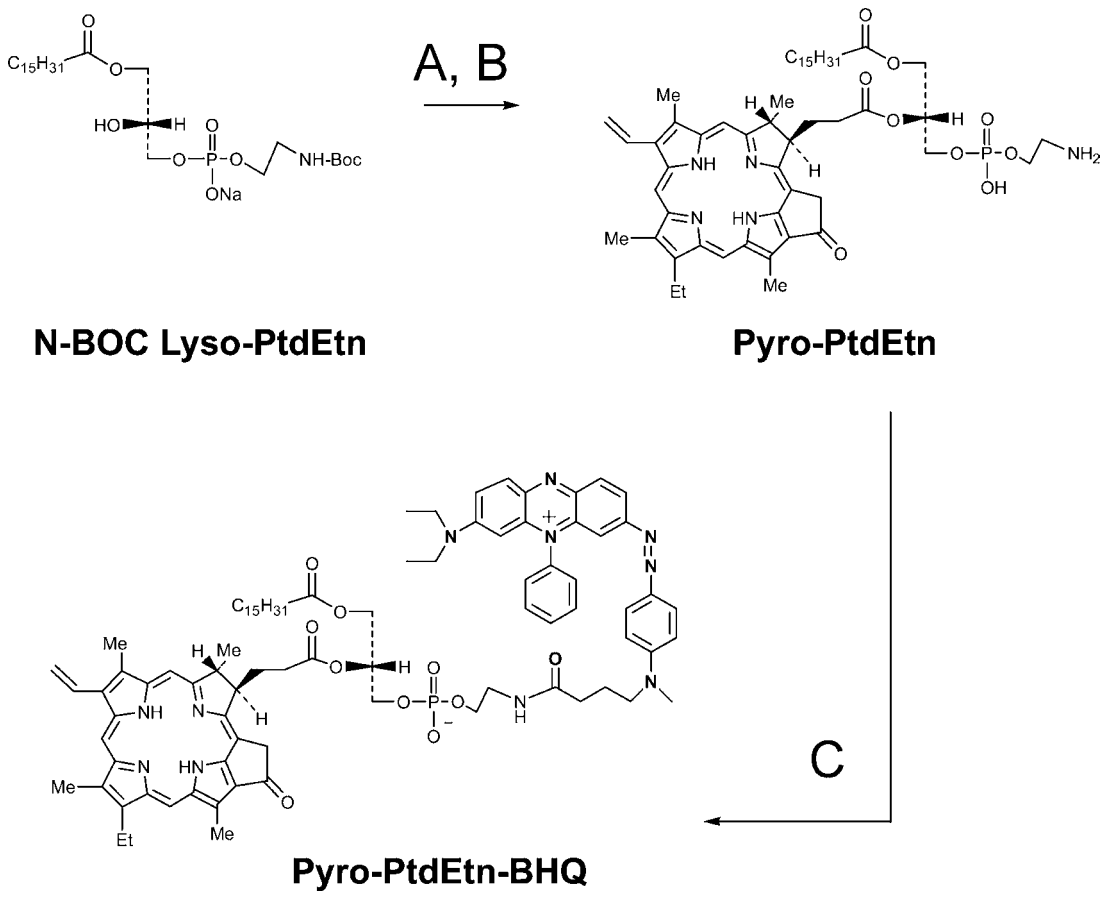

Figure 1. Synthesis of Pyro-PtdEtn and Pyro-PtdEtn-BHQ. (A) Pyro, EDC, DMAP, and CH_2Cl_2, at 25 °C, 72 h, argon (Ar); (B) TFA and CH_2Cl_2, at 0 °C, 4 h, Ar; (C) BHQ-3-$SU^+PF_6^-$, Et_3N, and CH_2Cl_2, at 25 °C, 12 h, Ar.

of Pyro-PtdEtn-BHQ.[37,38] Images were acquired every few minutes for the first 1.5 h, followed by every hour up to 6 h, and then again between 24 and 30 h. Background fluorescence was subtracted from all images. A region of interest was drawn around both the tumor and the contralateral muscle, and the average radiance was measured (photons/s/cm^2/sr). The tumor/muscle average radiance ratios were calculated at each time point.

Amplex Red Assay of PC-PLC Activity in Extracts of Tumor Xenografts. DU145 tumors were excised from euthanized mice and weighed (~90 mg). Tumors were sliced, minced, and transferred to 15 mL centrifuge tubes in 7 mL of cold PBS (without Ca^{2+} or Mg^{2+}). Samples were centrifuged at 7000 rpm for 8 min. PBS was removed, and pellets were lysed at 4 °C for 30 min with 0.5 mL of lysis buffer (50 mM Tris-HCl at pH 7.4, 1% Triton X-100, 1 Complete Mini protease inhibitor tablet, 1 mM EGTA, 2 mM EDTA, and 150 mM NaCl). The lysed suspensions were homogenized for 5 min and centrifuged at 13,500 rpm for 10 min, and the supernatant fraction was collected and stored at −80 °C. PC-PLC activity was determined by adding the thawed supernatant fraction to a reaction mixture containing 0.4 mM Amplex Red, 1 unit/mL horseradish peroxidase, 4 unit/mL alkaline phosphatase, 0.1 unit/mL choline oxidase, and 0.5 mM PtdCho in 1× Reaction Buffer (50 mM Tris-HCl, pH 7.4, 0.14 M NaCl, 10 mM dimethylglutarate, and 2 mM $CaCl_2$).[39] PC released from PtdCho by PC-PLC is converted to choline by alkaline phosphatase, which is further oxidized to form H_2O_2. In the presence of horseradish peroxidase, the H_2O_2 reacts with Amplex Red to generate the fluorophore, resorufin, which was detected using λ_{ex} = 560 nm and λ_{em} = 590 nm on the SpectraMax M5 plate reader.

Statistical Analysis. All data are presented as the mean ± SD. Statistical analysis of *in vivo* tumor/muscle average radiance was conducted using a Student's *t*-test. The test performed was two-tailed when testing Pyro-PtdEtn against Pyro-PtdEtn-BHQ (±D609) and one-tailed when testing Pyro-PtdEtn-BHQ against Pyro-PtdEtn-BHQ + D609. A p value ≤0.05 was considered to be significant.

RESULTS

Synthesis and Spectral Characteristics of Pyro-PtdEtn and Pyro-PtdEtn-BHQ. The synthesis of Pyro-PtdEtn and Pyro-PtdEtn-BHQ is presented in Figure 1. The close proximity of BHQ to Pyro, as well as the strong BHQ absorbance over the Pyro emission wavelength region, results in efficient contact and FRET quenching of this construct.

Specificity and Sensitivity. To determine probe specificity, Pyro-PtdEtn-BHQ was incubated for 24 h with a range of phospholipases: PC-PLC, phosphatidylinositol-specific PLC (PI-PLC), sphingomyelinase (SMase), phosphatidylcholine-specific phospholipase D (PC-PLD), type IA secretory phospholipase A_2 ($sPLA_2$), type IB $sPLA_2$ (porcine), and type IB $sPLA_2$ (bovine). TLC analysis showed that Pyro-PtdEtn-BHQ could be cleaved by PC-PLC, and to a lesser extent, SMase and PC-PLD (Figure 2) with the fluorescent Pyro moiety appearing under UV light as a red spot with a retention factor (Rf) of 0.9 (Columns 2 and 4). The sample

dx.doi.org/10.1021/bc200242v | *Bioconjugate Chem.* 2011, 22, 2434–2443

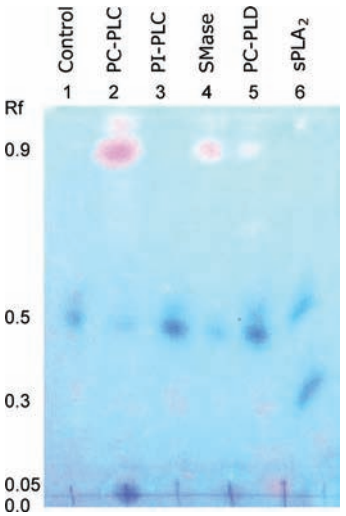

Figure 2. Specificity determined by TLC. Pyro-PtdEtn-BHQ/egg-PtdCho lipid dispersions were incubated with enzymes for 24 h and the products separated on a TLC plate using chloroform/methanol (100:15): 1, Control (no enzyme); 2, PC-PLC; 3, PI-PLC; 4, SMase; 5, PC-PLD; and 6, sPLA2 (IB, porcine). BHQ moieties were visible as blue spots, while fluorescent Pyro moieties were observed as red spots under UV excitation (385 nm). No enzyme activity was observed by PI-PLC, whereas sPLA2 (porcine type IB) cleavage showed 2 nonfluorescent spots. The observed cleaved products confirmed by HPLC followed by MALDI-TOF are as follows: *Rf* = 0.9, 1- acyl-2-pyropheophorbide glycerol (lanes 2, 4, and 5); *Rf* = 0.5, Pyro-PtdEtn-BHQ; *Rf* = 0.3, Lyso-Pyro- PtdEtn-BHQ (lane 6); *Rf* = 0.05 (red), 1-acyl-2-pyropheophorbide-3-phosphate (lane 5); *Rf* = 0.0 (blue), phospho-BHQ-3 (lanes 2, 4, and 5).

exposed to PC-PLD (Column 5) resulted in two fluorescent products, at *Rf* 0.9 and 0.05, while the uncleaved Pyro-PtdEtn-BHQ and the cleaved nonfluorescent product, phospho-BHQ-3, were visible as dark spots at *Rf* 0.5 and 0.0, respectively. No activity was observed with PI-PLC (Column 3). Type IB (porcine) $sPLA_2$ released one nonfluorescent product at *Rf* 0.3 (Column 6), whereas no cleavage was seen using either type IA $sPLA_2$ or type IB $sPLA_2$ (bovine).

To confirm these assignments, the TLC samples were analyzed by HPLC with UV−visible detection and MALDI-TOF MS (Figure 3). Figure 3A shows the HPLC chromatogram of Pyro-PtdEtn-BHQ, showing two closely separated peaks at retention times (RT) of 56.4 and 57.9 min. MALDI-TOF MS confirmed that the high RT peak corresponded to free Pyro-PtdEtn-BHQ (Table 1, calculated molecular weight (MW), 1497.8 Da; found, 1497.7 *m*/*z*), whereas the low RT peak (Figure 3D; found, 1498.2 *m*/*z*) also displayed a series of low MW ions from 500−800 *m*/*z* and may correspond to lipids from vesicle-encapsulated Pyro-PtdEtn-BHQ. Upon treatment with PC-PLC, we observed two cleavage products (Figure 3B). The corresponding UV−visible spectra (Figure 3C) showed that the first product (RT = 21.0 min) exhibited the absorbance spectrum of Pyro, whereas the second (RT = 53.4 min) exhibited the spectrum of BHQ. MALDI-TOF MS further validated that Pyro-PtdEtn-BHQ was cleaved by PC-PLC into two products that had MWs consistent with 1-palmitoyl-2-pyropheophorbide glycerol (calculated, 846.5 Da; found, 846.2 *m*/*z*) and phosphoethanolamine-BHQ-3 (calculated, 669.3 Da; found, 669.7 *m*/*z*), as shown in Figure 3E and F, respectively, and in Table 1. Incubation with SMase resulted in the same cleavage products (Table 1). MALDI-TOF MS also confirmed the existence of the two fluorescent products detected by HPLC in the sample treated with PC-PLD, the expected 1-palmitoyl-2-pyropheophorbide-*sn*-glycero-3-phosphate and 1-palmitoyl-2-pyropheophorbide glycerol, the same product released

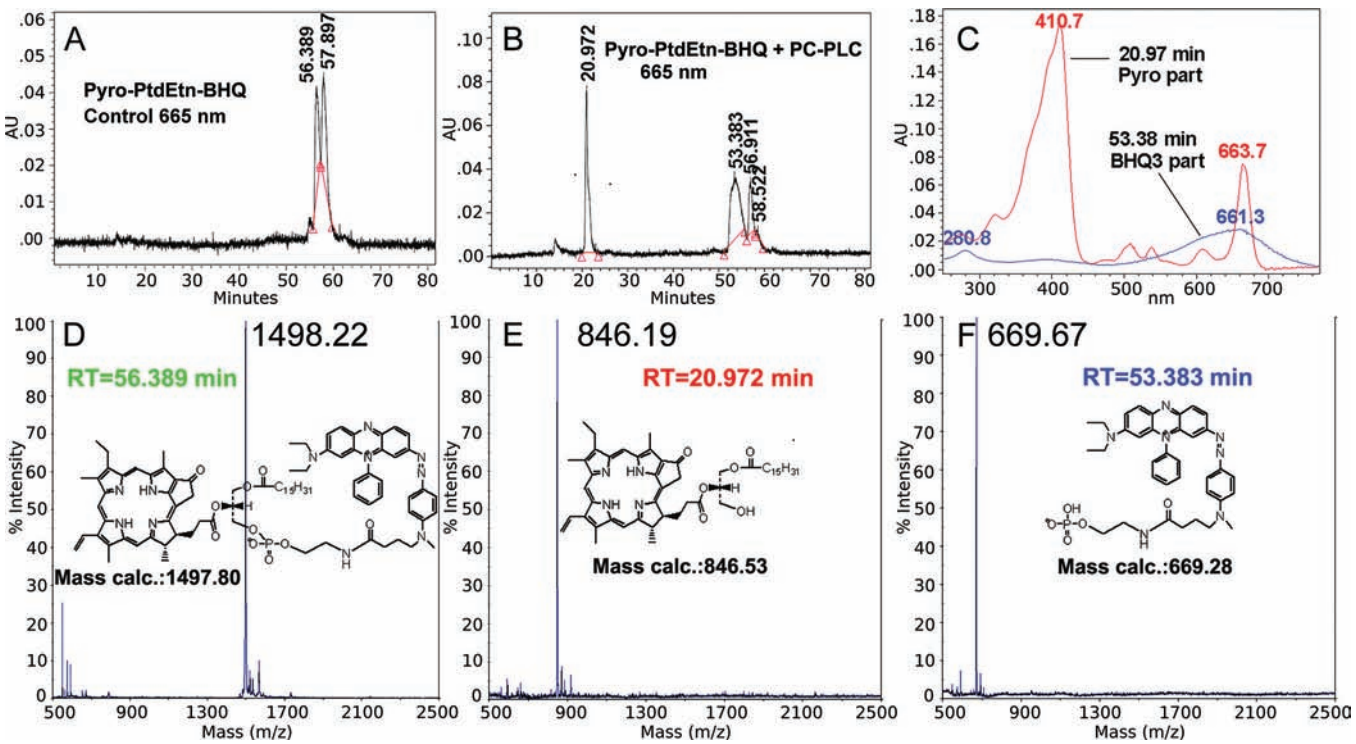

Figure 3. Validation of PC-PLC activation of Pyro-PtdEtn-BHQ. HPLC chromatogram of (A) Pyro-PtdEtn-BHQ and (B) cleavage products of Pyro-PtdEtn-BHQ from the actions of PC-PLC; (C) corresponding UV spectra of cleaved products; MALDI-TOF mass spectra and chemical structures of (D) Pyro-PtdEtn-BHQ and PC-PLC derived products: (E) 1-palmitoyl-2-pyropheophorbide glycerol and (F) phospho-BHQ-3.

dx.doi.org/10.1021/bc200242v | *Bioconjugate Chem.* 2011, 22, 2434−2443

Table 1. MALDI-TOF Parent Ion Peaks and Calculated Masses for Pyro-PtdEtn-BHQ and Enzymatic Cleavage Products

enzyme	product(s)	calculated exact mass (Da)	observed mass (m/z)
none	1-palmitoyl-2-pyropheophorbide-*sn*-glycero-3-phosphoethanolamine-BHQ-3 (pyro-PtdEtn-BHQ)	1497.8	1497.7
			1498.2
PC-PLC	1-palmitoyl-2-pyropheophorbide glycerol	846.5	846.2
	phosphoethanolamine-BHQ-3	669.3	669.7
SMase	1-palmitoyl-2-pyropheophorbide glycerol	846.5	846.2
	phosphoethanolamine-BHQ-3	669.3	669.7
PC-PLD	1-palmitoyl-2-pyropheophorbide 3-phosphate	926.5	926.4
	BHQ-3 ethanolamide	590.3	591.4
			590.4
	1-palmitoyl-2-pyropheophorbide glycerol	846.5	846.2
	phosphoethanolamine-BHQ-3	669.3	669.7
sPLA2 1B	2-pyropheophorbide-*sn*-glycero-3-BHQ-3	1259.6	1258.5
	palmitic acid	256.2	256.3
			257.3

by PC-PLC (Table 1), suggesting a cross-reactivity or a PC-PLC impurity. We found the nonfluorescent product released by $sPLA_2$ (type IB, porcine) to be the result of phospholipase A_1 activity having a molecular weight consistent with 2-pyropheophorbide-*sn*-glycero-3-BHQ-3 (Table 1), presumably also due to the lack of enzyme specificity or enzyme impurity.

Although PC-PLC, SMase, and PLD all demonstrated the ability to hydrolyze Pyro-PtdEtn-BHQ after incubation for 24 h, observation of these reactions by fluorescence spectroscopy revealed that the kinetics of these reactions were very different (Figure 4A).

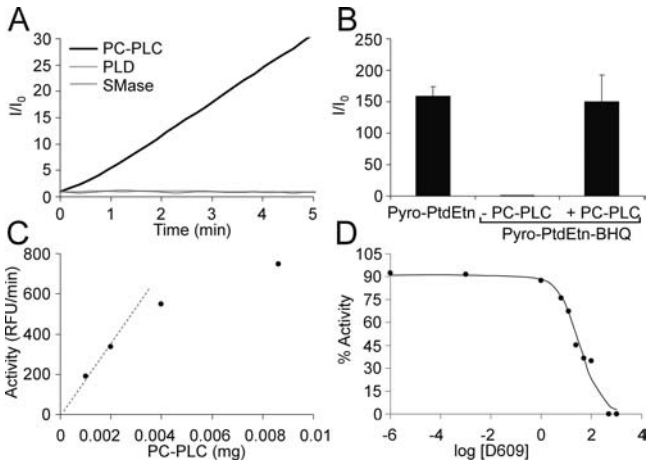

Figure 4. Characterization of Pyro-PtdEtn-BHQ kinetics. (A) Time-dependent increase in fluorescence of 1 μM Pyro-PtdEtn-BHQ incubated with 10 U each of PC-PLC, PLD, or SMase; (B) fold increase in fluorescence of 1 μM Pyro-PtdEtn-BHQ before and after complete activation by PC-PLC, as compared to that of Pyro-PtdEtn at equal concentrations (error bars represent s.d., n = 3); (C) dependence of fluorescence release from Pyro-PtdEtn-BHQ on PC-PLC concentration; (D) inhibition of PC-PLC activity toward 1 μM Pyro-PtdEtn-BHQ by D609 (IC_{50} = 34 ± 8 μM).

The addition of PC-PLC (10 U) to 1 μM Pyro-PtdEtn-BHQ dispersed in egg-PtdCho vesicles (MF 0.02) led to a 30-fold increase in fluorescence within 5 min. In contrast, the fluorescence released by PC-PLD and SMase was negligible even after 1 h, indicating a remarkable sensitivity of Pyro-PtdEtn-BHQ for PC-PLC. As shown in Figure 4B, the complete hydrolysis of Pyro-PtdEtn-BHQ by PC-PLC *in vitro* resulted in a ~150-fold fluorescence increase, equaling the fluorescence of Pyro-PtdEtn at equal concentrations.

We determined the dependence of activity on enzyme concentration by adding increasing amounts of PC-PLC to 1 μM Pyro-PtdEtn-BHQ in egg-PtdCho dispersions (MF 0.003). The activity of PC-PLC with Pyro-PtdEtn-BHQ (Figure 4C) increased with enzyme and was linear up to 0.002 mg (0.5 U) of enzyme.

The rate of Pyro-PtdEtn-BHQ hydrolysis could be inhibited by D609, a specific PC-PLC inhibitor.[40] Activity was measured as a function of D609 concentration after the addition of 0.5 U PC-PLC (Figure 4D). Complete inhibition was achieved with 500 μM D609 and an IC_{50} of 34 ± 8 μM was determined.

Probe Uptake in Cancer Cells. To confirm the cellular uptake of Pyro-PtdEtn-BHQ, confocal fluorescence microscopy studies were performed on DU145 human prostate cancer cells incubated with Pyro-PtdEtn, Pyro-PtdEtn-BHQ, or PBS as a control (Figure 5). Pyro-PtdEtn-treated DU145 cells exhibited

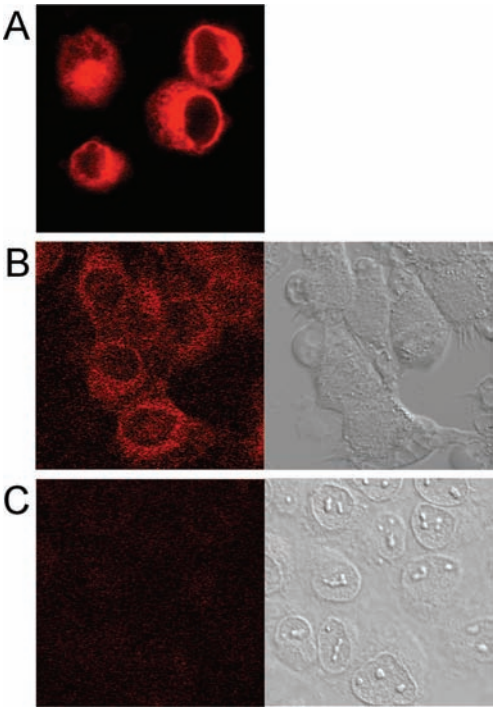

Figure 5. Confocal microscopy studies. Fluorescence (Left) and bright field (Right) micrographs of DU145 cells incubated for 1 h with (A) 5 μM Pyro-PtdEtn, (B) 5 μM Pyro-PtdEtn-BHQ, or (C) PBS as a control.

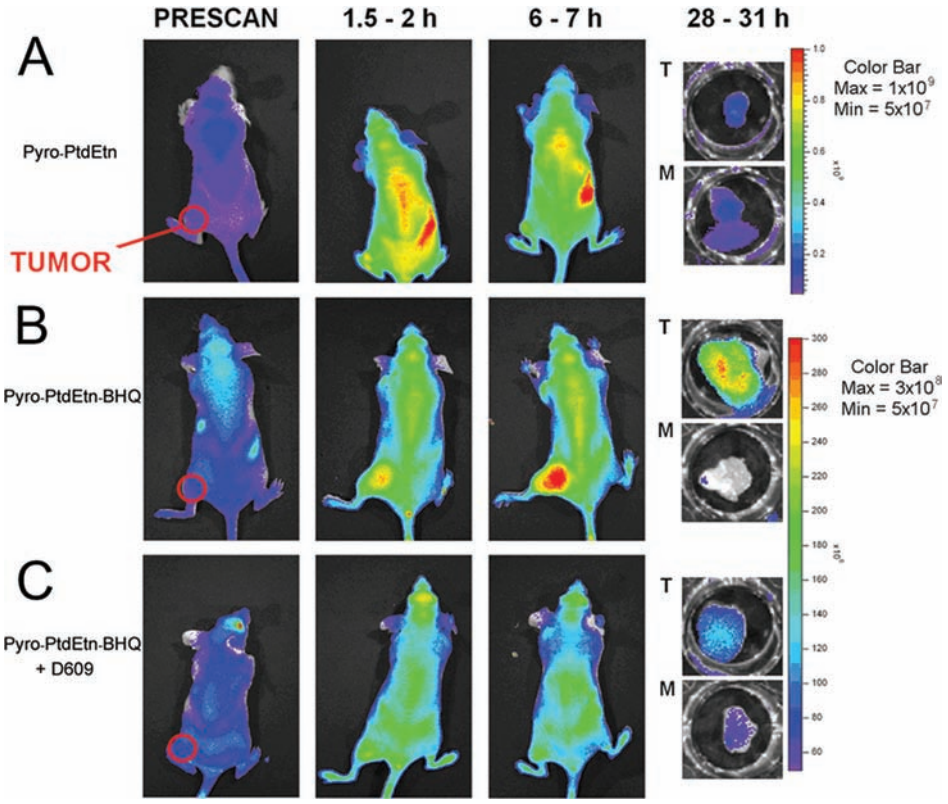

Figure 6. *In vivo* imaging of Pyro-PtdEtn, Pyro-PtdEtn-BHQ, and Pyro-PtdEtn-BHQ + D609 treatment. Nude mice bearing DU145 tumors on the left hind flank received 80 nmol i.v. of (A) Pyro-PtdEtn or (B and C) Pyro-PtdEtn-BHQ dispersed in 0.1 μM Tween-80. Mice in (C) received additional D609 injections (50 μg/g body weight, i.p.) at −30, 30, 60, and 120 min postinjection of Pyro-PtdEtn-BHQ. Images are shown at prescan, 1.5−2 h, and 6−7 h. The tumor (T) and muscle (M) tissues from each mouse were excised at 28−31 h.

a strong predominantly cytoplasmic fluorescent signal (Figure 5A). DU145 cells incubated with Pyro-PtdEtn-BHQ exhibited perinuclear and punctate cytoplasmic fluorescence that was approximately 8-fold less intense, due to differential cell uptake, incomplete intracellular activation, or quenching by BHQ (Figure 5B). Fluorescence in cells incubated with Pyro-PtdEtn-BHQ was approximately 10-fold more intense than DU145 cells incubated only with PBS (Figure 5C).

***In Vivo* Imaging of PC-PLC Activity.** We evaluated the efficacy of Pyro-PtdEtn-BHQ as a potential fluorescent imaging agent for detecting PC-PLC activity *in vivo*. Nude mice bearing DU145 human prostate tumor xenografts were injected with either Pyro-PtdEtn-BHQ or Pyro-PtdEtn as a positive control. Fluorescence images were acquired over the first 6 h and continued the next day between 24 and 30 h. Pyro-PtdEtn exhibited fast circulation throughout the body, accumulating primarily in the stomach, liver, and intestines (Figure 6A). By 6 h, the substrate was clearing through the digestive tract. By 28 h, very little radiance remained in the tumor or the contralateral muscle, as seen in the excised tissues in Figure 6 (T, tumor; M, muscle). Injection of Pyro-PtdEtn-BHQ, however, led to a gradual increase in tumor radiance within 1.5 h (Figure 6B) that was greatly increased at 6 h. At 30 h, we could still observe a high level of radiance in the excised tissue relative to the contralateral muscle tissue. Note that the Pyro-PtdEtn radiance detected *in vivo* is ∼3-fold higher than that of the cleaved Pyro-PtdEtn-BHQ radiance, which suggests that complete hydrolysis of Pyro-PtdEtn-BHQ is not being achieved.

In order to validate that the increase in tumor radiance after Pyro-PtdEtn-BHQ injection was due to PC-PLC activation, mice were injected with the PC-PLC inhibitor D609. As expected, D609 treatment inhibited *in vivo* activation of Pyro-PtdEtn-BHQ, resulting in reduced tumor radiance (Figure 6C). At 31 h, the excised tumor tissue exhibited half as much radiance as that found without D609 treatment.

Representative time dependence of the tumor and contralateral muscle radiance measurements for Pyro-PtdEtn, Pyro-PtdEtn-BHQ, and Pyro-PtdEtn-BHQ + D609 are shown in Figure 7. Administration of Pyro-PtdEtn led to a sharp increase in tumor and muscle radiance, reaching a maximum tumor radiance of ∼10-fold over baseline at 30 min, followed by an immediate drop as the probe begins to clear, and return to prescan level by 24 h post-injection (Figure 7A). In contrast, Pyro-PtdEtn-BHQ tumor radiance gradually increased ∼4-fold over baseline during the first 4 h and was maintained continually up to 24 h before beginning to clear from the tumor (Figure 7B). From 2−24 h, the tumor radiance increased to about 2.5-fold greater than that in the contralateral muscle and was significantly greater at 24 h ($p < 0.05$). Pre- and post-treatment with D609 caused an overall attenuation of tumor radiance as soon as 2 h after injection and continued to suppress probe activation until clearance at 28 h (Figure 7C). The average of the tumor/muscle radiance ratios for each condition are presented in Figure 7D. Here a 2-fold increase in tumor/muscle ratio was observed by 24 h in mice treated with Pyro-PtdEtn-BHQ. D609 treatment significantly inhibited the activation of Pyro-PtdEtn-BHQ at the 24 h time point ($p < 0.05$), decreasing the tumor/muscle ratio back to baseline.

At the end of the experiment (28−31 h post-injection), the organs were excised and imaged on the IVIS-100 in 24 well

dx.doi.org/10.1021/bc200242v | *Bioconjugate Chem.* 2011, 22, 2434−2443

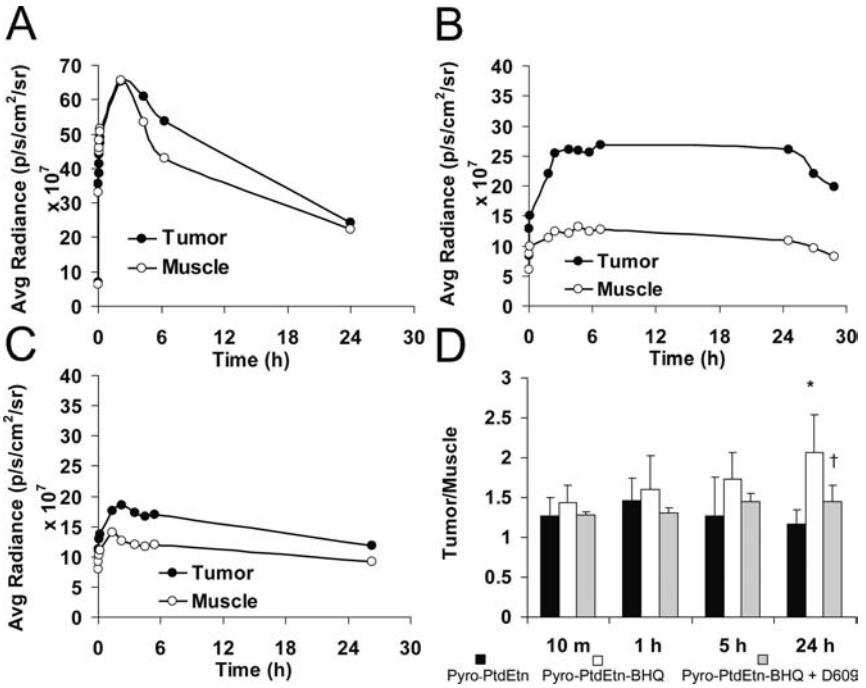

Figure 7. Representative time courses of measured tumor and muscle average radiances. The average radiance from the tumor and muscle tissue and was quantified in mice injected with (A) Pyro-PtdEtn, (B) Pyro-PtdEtn-BHQ, and (C) Pyro-PtdEtn-BHQ + D609. (D) Tumor/muscle average radiance. The average tumor radiance was normalized to muscle for Pyro-PtdEtn (n = 5), Pyro- PtdEtn-BHQ (n = 5), and Pyro-PtdEtn-BHQ + D609 treatment (n = 3). Error bars represent SD. * Significantly (p = 0.011) different from Pyro-PtdEtn. † Significantly (p = 0.024) different from Pyro- PtdEtn-BHQ without D609 treatment.

plates (Table 2). These data show major residual fluorescence in the stomach, intestine, and liver and indicate that these probes are excreted via the bile, liver, and stool as would be expected for a lipid soluble probe.

Validation of PC-PLC Activity in Extracts of DU145 Tumor Xenografts. To validate the presence of PC-PLC activity in DU145 tumor xenografts, the Amplex Red PC-PLC Assay Kit (Invitrogen, Eugene, OR) was used in excised tumor extracts. PC-PLC activity was shown to increase linearly as a function of total supernatant protein (Figure 8A) as detected by increases in resorufin fluorescence (Figure 8A). This activity was shown to decrease as a function of D609 concentration (Figure 8B).

■ DISCUSSION

In this article, we report a direct, sensitive, and feasible method for detecting PC-PLC activity employing a self-quenched phospholipid analogue that restores NIR fluorescence upon enzymatic hydrolysis. A high specificity was found for PC-PLC in solution studies, and enzyme activity was detected in cultured DU145 human prostate cells and *in vivo* using a DU145 tumor xenograft mouse model.

Although activatable fluorescent probes to detect phospholipase activity *in vitro* have been previously reported,[41−47] Pyro-PtdEtn-BHQ is unique in that it contains the NIR fluorochrome, pyropheophorbide *a*, which allows for increased photon penetration through biological tissue in a spectral region where tissue autofluorescence is markedly reduced.[48] This modification means that *in vivo* NIR optical detection of phospholipase activity has been made possible. Pyropheophorbide was chosen as the fluorophore for these studies because when conjugated, it is both neutral and hydrophobic, two properties necessary for the lipid-based probe to be incorporated into membranes. However, pyropheophorbide *a* is also a known photosensitizer, with a high singlet oxygen quantum yield, opening the possibility that this and other related probes could be used for photodynamic therapy to treat tumors *in vivo*.

This article shows that Pyro-PtdEtn-BHQ is highly specific to PC-PLC, when compared to several other phospholipase isoforms. As a phospholipid analogue, Pyro-PtdEtn-BHQ was also shown to be a substrate for PC-PLD and SMase, although with much less activity. Thus, it is possible that increases in activity could arise from activation by other enzymes, at a much slower rate. The inhibition studies with D609 would indicate that that is probably not the case. However, it is known that enzyme specificity and affinity for phospholipase-sensitive probes can be adjusted by altering the hydrophobicity and the length of the intervening fatty acyl chain at the *sn*-2 position.[33,49−51] We are currently in the process of synthesizing and testing a range of phospholipase probes of varying enzyme specificities and NIR fluorochromes, which will allow for multispectral detection of several phospholipases simultaneously.[33] This proposed molecular imaging strategy will lead to the development of probes specific to other important phospholipases and allow us to test these hypotheses in detail.

In this study, some bacterial isoforms of phospholipases were used for *in vitro* testing. This is due to the commercial unavailability of mammalian isoforms of these enzymes. A controversy also exists in the literature as to the origin of PC-PLC activity in mammals, as a mammalian isoform of this protein has never been cloned. However, isoforms have been isolated from mammalian sources.[52,53] There is also substantial evidence that the mammalian PC-PLC has functional similarity to the bacterial isoform. PC-PLC activity, as measured by D609-sensitive PC release from PtdCho, has been demonstrated in

Table 2. Fluorescence Intensity Observed in Excised Organs[a]

probe	organ/ adrenal glands	kidney	liver	spleen	heart	intestine	lung	muscle	stomach	tumor	pancreas
Pyro-PtdEtn (5)	$2.40\pm0.29\times10^9$	$6.09\pm2.47\times10^9$	$1.45\pm0.61\times10^{10}$	$4.67\pm1.50\times10^9$	$2.67\pm0.76\times10^9$	$1.85\pm1.03\times10^{10}$	$4.12\pm1.61\times10^9$	$2.48\pm1.20\times10^9$	$1.19\pm0.30\times10^{10}$	$3.71\pm1.96\times10^9$	$3.70\pm1.71\times10^9$
Pyro-PtdEtn-BHQ (5)	$1.70\pm0.62\times10^9$	$3.25\pm0.66\times10^9$	$8.96\pm2.16\times10^9$	$2.68\pm0.78\times10^9$	$1.78\pm0.64\times10^9$	$1.18\pm1.06\times10^{10}$	$2.00\pm0.56\times10^9$	$1.72\pm0.67\times10^9$	$1.56\pm0.46\times10^{10}$	$3.44\pm1.40\times10^9$	$2.54\pm0.91\times10^9$
Pyro-PtdEtn-BHQ + D609 (2)	$9.80\pm0.25\times10^8$	$2.55\pm0.54\times10^9$	$1.02\pm0.19\times10^{10}$	$1.90\pm0.46\times10^9$	$1.22\pm0.21\times10^9$	$2.09\pm0.74\times10^{10}$	$1.41\pm0.55\times10^9$	$1.27\pm0.34\times10^9$	$1.97\pm1.11\times10^{10}$	$1.68\pm0.02\times10^9$	$1.55\pm0.33\times10^9$

[a]Data are expressed as photon flux (photons/s). The numbers of animals for each condition are in parentheses. Organs were removed from mice 28−31 h after injection of the probe and imaged in 24-well plates using the IVIS-100 system. The data show that residual fluorescence remains predominantly in the liver, intestine, and stomach, indicating excretion via the liver and stool.

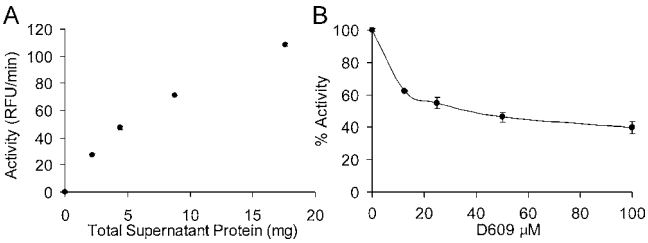

Figure 8. PC-PLC activity measured by Amplex Red. (A) Activity measured in relative fluorescence units per minute (RFU/min) as a function of protein (mg) from extracts of DU145 tumor xenografts. (B) Inhibition of PC-PLC activity in supernatants by D609.

cytoplasmic extracts of NIH-3T3 cells.[26] Polyclonal antibodies against *B. cereus* PC-PLC have been used to detect the translocation of a cross-reactive mammalian PC-PLC from the cytosol in control cells to the plasma membrane in oncogene-transformed cells.[26] An increased plasma membrane PC-PLC expression has also been shown to accompany tumor progression in ovarian cancer cell lines.[54] This PC-PLC activity could be measured with the Amplex Red assay and was sensitive to the action of D609. Our imaging results are consistent with these studies in that Pyro-PtdEtn-BHQ detected the presence of a D609-sensitive PC-PLC activity in DU145 tumors, which could be confirmed in extracts with the Amplex Red assay. We hope that the development of this probe will allow further investigation into the origins of PC-PLC activity and aid in the resolution of this controversy.

One of the added benefits of using enzyme-activated fluorescent imaging probes is the advantage of inherent signal amplification.[55,56] Our solution studies demonstrate an increase in fluorescence up to 150-fold greater than background. *In vivo*, although affected by the absorbance and scattering effects of biological tissue, an ∼4-fold increase in radiance was observed and a 2-fold increase in tumor to muscle fluorescence ratio. This signal increase over the background compares well with other recently reported enzyme-activated NIR probes used for imaging tumors *in vivo*, such as a cathepsin-sensitive probe[56] and a caspase 1 selective probe,[57] which display 3−4-fold and 1.7-fold tumor increases, respectively. These results establish Pyro-PtdEtn-BHQ as an excellent candidate for molecular imaging.

The *in vivo* results described in this work indicate that PC-PLC may be an important molecular marker for cancer. The additional coregistration of images obtained using phospholipase-activated NIR fluorescent probes with choline metabolite levels obtained from *in vivo* MRS could critically impact the field of cancer detection by offering a sensitive and specific method of examining the lipid catabolic pathways linked to the malignant phenotype.

AUTHOR INFORMATION

Corresponding Author

*Molecular Imaging Laboratory, Department of Radiology, University of Pennsylvania School of Medicine, Room 284, Chemistry Building 1958 Wing, 231 South 34th St., Philadelphia, PA 19104. Phone: (215) 898-3105. Fax: (215) 746-8764. E-mail: delikatn@mail.med.upenn.edu.

Present Addresses

[†]Cancer Research UK, Cambridge Research Institute, Cambridge, CB2 0RE, United Kingdom.

‡School of Science and Health, Philadelphia University, Philadelphia, PA 19144.
§Ontario Cancer Institute/University Health Network, MaRS Center, Toronto, ON, M5G 1L7, Canada.

■ ACKNOWLEDGMENTS

This work was supported by the National Cancer Institute (NCI) grants R01 CA114347 and R01 CA129176, National Institute of Biomedical Imaging and Bioengineering (NIBIB) grant R21 EB002537, the Small Animal Imaging Resource Program (SAIRP) grant R24 CA83105, the Metabolic Magnetic Resonance Research and Computing Center (MMRRCC) training grant T32-HL07614, and the NIH Research Resource grant P41 RR002305. Imaging was performed at the University of Pennsylvania Small Animal Imaging Facility (SAIF) Optical/Bioluminescence Core, supported by NIH grant CA105008, and we are grateful to Dr. Y. Yvette Liu for her technical assistance.

■ REFERENCES

(1) Weissleder, R. (2006) Molecular imaging in cancer. *Science 312*, 1168−11671.
(2) Stefflova, K., Chen, J., Li, H., and Zheng, G. (2006) Targeted photodynamic therapy agent with a built-in apoptosis sensor for in vivo near-infrared imaging of tumor apoptosis triggered by its photosensitization in situ. *Mol. Imaging 5*, 520−532.
(3) Blasberg, R. G. (2003) Molecular imaging and cancer. *Mol. Cancer Ther. 2*, 335−343.
(4) Mahmood, U., and Weissleder, R. (2003) Near-infrared optical imaging of proteases in cancer. *Mol. Cancer Ther. 2*, 489−496.
(5) Stefflova, K., Chen, J., and Zheng, G. (2007) Using molecular beacons for cancer imaging and treatment. *Front. Biosci. 12*, 4709−4721.
(6) Pham, W., Choi, Y., Weissleder, R., and Tung, C.-H. (2004) Developing a peptide-based near-infrared molecular probe for protease sensing. *Bioconjugate Chem. 15*, 1403−1407.
(7) Eyster, K. M. (2007) The membrane and lipids as integral participants in signal transduction: lipid signal transduction for the non-lipid biochemist. *Adv. Physiol. Educ. 31*, 5−16.
(8) Podo, F. (1999) Tumour phospholipid metabolism. *NMR Biomed. 12*, 413−439.
(9) Jacobs, M. A., Barker, P. B., Bottomley, P. A., Bhujwalla, Z., and Bluemke, D. A. (2004) Proton magnetic resonance spectroscopic imaging of human breast cancer: A preliminary study. *J. Magn. Reson. Imaging 19*, 68−75.
(10) Singer, S., Souza, K., and Thilly, W. G. (1995) Pyruvate utilization, phosphocholine and adenosine triphosphate (ATP) are markers of human breast tumor progression: a 31P- and 13C-nuclear magnetic resonance (NMR) spectroscopy study. *Cancer Res. 55*, 5140−5145.
(11) Katz-Brull, R., and Degani, H. (1996) Kinetics of choline transport and phosphorylation in human breast cancer cells; NMR application of the zero trans method. *Anticancer Res. 16*, 1375−1380.
(12) Gribbestad, I. S., Sitter, B., Lundgren, S., Krane, J., and Axelson, D. (1999) Metabolite composition in breast tumors examined by proton nuclear magnetic resonance spectroscopy. *Anticancer Res. 19*, 1737−1746.
(13) Negendank, W. (1992) Studies of human tumors by MRS: a review. *NMR Biomed. 5*, 303−324.
(14) Glunde, K., Jie, C., and Bhujwalla, Z. M. (2004) Molecular causes of the aberrant choline phospholipid metabolism in breast cancer. *Cancer Res. 64*, 4270−4276.
(15) Ackerstaff, E., Pflug, B. R., Nelson, J. B., and Bhujwalla, Z. M. (2001) Detection of increased choline compounds with proton nuclear magnetic resonance spectroscopy subsequent to malignant transformation of human prostatic epithelial cells. *Cancer Res. 61*, 3599−3603.
(16) Kurhanewicz, J., Vigneron, D. B., and Nelson, S. J. (2000) Three-dimensional magnetic resonance spectroscopic imaging of brain and prostate cancer. *Neoplasia 2*, 166−189.
(17) Swindle, P., McCredie, S., Russell, P., Himmelreich, U., Khadra, M., Lean, C., and Mountford, C. (2003) Pathologic characterization of human prostate tissue with proton MR spectroscopy. *Radiology 228*, 144−151.
(18) Milkevitch, M., Shim, H., Pilatus, U., Pickup, S., Wehrle, J. P., Samid, D., Poptani, H., Glickson, J. D., and Delikatny, E. J. (2005) Increases in NMR-visible lipid and glycerophosphocholine during phenylbutyrate-induced apoptosis in human prostate cancer cells. *Biochim. Biophys. Acta 1734*, 1−12.
(19) Bhakoo, K. K., Williams, S. R., Florian, C. L., Land, H., and Noble, M. D. (1996) Immortalization and transformation are associated with specific alterations in choline metabolism. *Cancer Res. 56*, 4630−4635.
(20) Li, X., Lu, Y., Pirzkall, A., McKnight, T., and Nelson, S. J. (2002) Analysis of the spatial characteristics of metabolic abnormalities in newly diagnosed glioma patients. *J. Magn. Reson. Imaging 16*, 229−237.
(21) Maris, J. M., Evans, A. E., McLaughlin, A. C., D'Angio, G. J., Bolinger, L., Manos, H., and Chance, B. (1985) 31P nuclear magnetic resonance spectroscopic investigation of human neuroblastoma in situ. *N. Engl. J. Med. 312*, 1500−1505.
(22) Eliyahu, G., Kreizman, T., and Degani, H. (2007) Phosphocholine as a biomarker of breast cancer: molecular and biochemical studies. *Int. J. Cancer 120*, 1721−1730.
(23) Katz-Brull, R., Seger, D., Rivenson-Segal, D., Rushkin, E., and Degani, H. (2002) Metabolic markers of breast cancer: enhanced choline metabolism and reduced choline-ether-phospholipid synthesis. *Cancer Res. 62*, 1966−1970.
(24) Aboagye, E. O., and Bhujwalla, Z. M. (1999) Malignant transformation alters membrane choline phospholipid metabolism of human mammary epithelial cells. *Cancer Res. 59*, 80−84.
(25) Al-Saffar, N. M., Troy, H., Ramirez de Molina, A., Jackson, L. E., Madhu, B., Griffiths, J. R., Leach, M. O., Workman, P., Lacal, J. C., Judson, I. R., and Chung, Y. L. (2006) Noninvasive magnetic resonance spectroscopic pharmacodynamic markers of the choline kinase inhibitor MN58b in human carcinoma models. *Cancer Res. 66*, 427−434.
(26) Podo, F., Ferretti, A., Knijn, A., Zhang, P., Ramoni, C., Barletta, B., Pini, C., Baccarini, S., and Pulciani, S. (1996) Detection of phosphatidylcholine-specific phospholipase C in NIH-3T3 fibroblasts and their H-ras transformants: NMR and immunochemical studies. *Anticancer Res. 16*, 1399−1412.
(27) Iorio, E., Ricci, A., Bagnoli, M., Pisanu, M. E., Castellano, G., Di Vito, M., Venturini, E., Glunde, K., Bhujwalla, Z. M., Mezzanzanica, D., Canevari, S., and Podo, F. (2010) Activation of phosphatidylcholine cycle enzymes in human epithelial ovarian cancer cells. *Cancer Res. 70*, 2126−2135.
(28) Ferretti, A., Podo, F., Carpinelli, G., Chen, L., Borghi, P., and Masella, R. (1993) Detection of neutral active phosphatidylcholine-specific phospholipase C in Friend leukemia cells before and after erythroid differentiation. *Anticancer Res. 13*, 2309−2317.
(29) Wu, X., Lu, H., Zhou, L., Huang, Y., and Chen, H. (1997) Changes of phosphatidylcholine-specific phospholipase C in hepatocarcinogenesis and in the proliferation and differentiation of rat liver cancer cells. *Cell Biol. Int. 21*, 375−381.
(30) Gelmon, K. A., Eisenhauer, E. A., Harris, A. L., Ratain, M. J., and Workman, P. (1999) Anticancer agents targeting signaling molecules and cancer cell environment: challenges for drug development? *J. Natl. Cancer Inst. 91*, 1281−1287.
(31) Beloueche-Babari, M., Chung, Y. L., Al-Saffar, N. M., Falck-Miniotis, M., and Leach, M. O. (2010) Metabolic assessment of the action of targeted cancer therapeutics using magnetic resonance spectroscopy. *Br. J. Cancer 102*, 1−7.
(32) Podo, F., Canevari, S., Canese, R., Pisanu, M. E., Ricci, A., and Iorio, E. (2011) MR evaluation of response to targeted treatment in cancer cells. *NMR Biomed. 24*, 648−672.

(33) Popov, A. V., Mawn, T. M., Kim, S., Zheng, G., and Delikatny, E. J. (2010) Design and synthesis of phospholipase C and A2-activatable near-infrared fluorescent smart probes. *Bioconjugate Chem. 21*, 1724−1727.
(34) Zheng, G., Chen, J., Stefflova, K., Jarvi, M., Li, H., and Wilson, B. C. (2007) Photodynamic molecular beacon as an activatable photosensitizer based on protease-controlled singlet oxygen quenching and activation. *Proc. Natl. Acad. Sci. U.S.A. 104*, 8989−8994.
(35) Stefflova, K., Chen, J., Marotta, D., Li, H., and Zheng, G. (2006) Photodynamic therapy agent with a built-in apoptosis sensor for evaluating its own therapeutic outcome in situ. *J. Med. Chem. 49*, 3850−3856.
(36) Zheng, G., Li, H., Zhang, M., Lund-Katz, S., Chance, B., and Glickson, J. D. (2002) Low-density lipoprotein reconstituted by pyropheophorbide cholesteryl oleate as target-specific photosensitizer. *Bioconjugate Chem. 13*, 392−396.
(37) Ansari, M. A., Joshi, G., Huang, Q., Opii, W. O., Abdul, H. M., Sultana, R., and Butterfield, D. A. (2006) In vivo administration of D609 leads to protection of subsequently isolated gerbil brain mitochondria subjected to in vitro oxidative stress induced by amyloid beta-peptide and other oxidative stressors: relevance to Alzheimer's disease and other oxidative stress-related neurodegenerative disorders. *Free Radical Biol. Med. 41*, 1694−1703.
(38) Goggel, R., Winoto-Morbach, S., Vielhaber, G., Imai, Y., Lindner, K., Brade, L., Brade, H., Ehlers, S., Slutsky, A. S., Schutze, S., Gulbins, E., and Uhlig, S. (2004) PAF-mediated pulmonary edema: a new role for acid sphingomyelinase and ceramide. *Nat. Med. 10*, 155−160.
(39) Zhou, M., Diwu, Z., Panchuk-Voloshina, N., and Haugland, R. P. (1997) A stable nonfluorescent derivative of resorufin for the fluorometric determination of trace hydrogen peroxide: applications in detecting the activity of phagocyte NADPH oxidase and other oxidases. *Anal. Biochem. 253*, 162−168.
(40) Amtmann, E. (1996) The antiviral, antitumoural xanthate D609 is a competitive inhibitor of phosphatidylcholine-specific phospholipase C. *Drugs Exp. Clin. Res. 22*, 287−294.
(41) Thuren, T., Virtanen, J. A., Somerharju, P. J., and Kinnunen, P. K. (1988) Phospholipase A2 assay using an intramolecularly quenched pyrene-labeled phospholipid analog as a substrate. *Anal. Biochem. 170*, 248−255.
(42) Hendrickson, H. S., Hendrickson, E. K., Johnson, I. D., and Farber, S. A. (1999) Intramolecularly quenched BODIPY-labeled phospholipid analogs in phospholipase A(2) and platelet-activating factor acetylhydrolase assays and in vivo fluorescence imaging. *Anal. Biochem. 276*, 27−35.
(43) Wichmann, O., Gelb, M. H., and Schultz, C. (2007) Probing phospholipase a(2) with fluorescent phospholipid substrates. *ChemBioChem 8*, 1555−1569.
(44) Farber, S. A., Olson, E. S., Clark, J. D., and Halpern, M. E. (1999) Characterization of Ca2+-dependent phospholipase A2 activity during zebrafish embryogenesis. *J. Biol. Chem. 274*, 19338−19346.
(45) Prestwich, G. D., Chen, R., Feng, L., Ozaki, S., Ferguson, C. G., Drees, B. E., Neklason, D. A., Mostert, M. J., Porter-Gill, P. A., Kang, V. H., Shope, J. C., Neilsen, P. O., and Dewald, D. B. (2002) In situ detection of phospholipid and phosphoinositide metabolism. *Adv. Enzyme Regul. 42*, 19−38.
(46) Manna, D., and Cho, W. (2007) In *Methods in Enzymology* (Brown, H. A., Ed.) pp 15−28, Academic Press, New York.
(47) Rose, T. M., and Prestwich, G. D. (2006) Synthesis and evaluation of fluorogenic substrates for phospholipase D and phospholipase C. *Org. Lett. 8*, 2575−2578.
(48) Frangioni, J. V. (2003) In vivo near-infrared fluorescence imaging. *Curr. Opin. Chem. Biol. 7*, 626−634.
(49) Caramelo, J. J., Florin-Christensen, J., Florin-Christensen, M., and Delfino, J. M. (2000) Mapping the catalytic pocket of phospholipases A2 and C using a novel set of phosphatidylcholines. *Biochem. J. 346* (Pt 3), 679−690.
(50) el-Sayed, M. Y., DeBose, C. D., Coury, L. A., and Roberts, M. F. (1985) Sensitivity of phospholipase C (*Bacillus cereus*) activity to phosphatidylcholine structural modifications. *Biochim. Biophys. Acta 837*, 325−335.
(51) Lewis, K. A., Bian, J. R., Sweeney, A., and Roberts, M. F. (1990) Asymmetric short-chain phosphatidylcholines: defining chain binding constraints in phospholipases. *Biochemistry 29*, 9962−9970.
(52) Wolf, R. A., and Gross, R. W. (1985) Identification of neutral active phospholipase C which hydrolyzes choline glycerophospholipids and plasmalogen selective phospholipase A2 in canine myocardium. *J. Biol. Chem. 260*, 7295−7303.
(53) Clark, M. A., Shorr, R. G., and Bomalaski, J. S. (1986) Antibodies prepared to *Bacillus cereus* phospholipase C crossreact with a phosphatidylcholine preferring phospholipase C in mammalian cells. *Biochem. Biophys. Res. Commun. 140*, 114−119.
(54) Spadaro, F., Ramoni, C., Mezzanzanica, D., Miotti, S., Alberti, P., Cecchetti, S., Iorio, E., Dolo, V., Canevari, S., and Podo, F. (2008) Phosphatidylcholine-specific phospholipase C activation in epithelial ovarian cancer cells. *Cancer Res. 68*, 6541−6549.
(55) Kircher, M. F., Josephson, L., and Weissleder, R. (2002) Ratio imaging of enzyme activity using dual wavelength optical reporters. *Mol. Imaging 1*, 89−95.
(56) Bogdanov, A. A. Jr., Lin, C. P., Simonova, M., Matuszewski, L., and Weissleder, R. (2002) Cellular activation of the self-quenched fluorescent reporter probe in tumor microenvironment. *Neoplasia 4*, 228−236.
(57) Messerli, S. M., Prabhakar, S., Tang, Y., Shah, K., Cortes, M. L., Murthy, V., Weissleder, R., Breakefield, X. O., and Tung, C. H. (2004) A novel method for imaging apoptosis using a caspase-1 near-infrared fluorescent probe. *Neoplasia 6*, 95−105.

Bioconjugate Chemistry

Article

pubs.acs.org/bc

Comparison of Pretargeted and Conventional CC49 Radioimmunotherapy Using ^{149}Pm, ^{166}Ho, and ^{177}Lu

Huma Mohsin,[†] Fang Jia,[‡] Jeffrey N. Bryan,[‡] Geethapriya Sivaguru,[‡] Cathy S. Cutler,[§] Alan R. Ketring,[§] William H. Miller,[∥] Jim Simón,[¶] R. Keith Frank,[¶] Louis J. Theodore,[#] Don B. Axworthy,[#] Silvia S. Jurisson,[†,§] and Michael R. Lewis*[,‡,⊥]

[†]Department of Chemistry, [‡]Department of Veterinary Medicine and Surgery, [§]University of Missouri Research Reactor, and [∥]Nuclear Science and Engineering Institute, University of Missouri-Columbia, Columbia, Missouri, United States

[⊥]Research Service, Harry S. Truman Memorial Veterans' Hospital, Columbia, Missouri, United States

[¶]IsoTherapeutics Group, LLC, Angleton, Texas, Unites States

[#]Aletheon Pharmaceuticals, Seattle, Washington, United States

ABSTRACT: The therapeutic efficacies of radiolabeled biotin, pretargeted by monoclonal antibody (mAb)−streptavidin fusion protein CC49 scFvSA, were compared to those of radiolabeled mAb CC49, using the three radiolanthanides in an animal model of human colon cancer. The purpose of the present study was to compare antibody pretargeting to conventional radioimmunotherapy using ^{149}Pm, ^{166}Ho, or ^{177}Lu. Nude mice bearing LS174T colon tumors were injected sequentially with CC49 scFvSA, the blood clearing agent biotin-GalNAc$_{16}$, and ^{149}Pm-, ^{166}Ho-, or ^{177}Lu-DOTA-biotin. Tumor-bearing mice were alternatively administered ^{149}Pm-, ^{166}Ho-, or ^{177}Lu-MeO-DOTA-CC49. Therapy with pretargeted ^{149}Pm-,^{166}Ho-, and ^{177}Lu-DOTA-biotin increased the median time of progression to a 1 g tumor to 50, 41, and 50 days post-treatment, respectively. Therapy with ^{149}Pm-,^{166}Ho-, and ^{177}Lu-MeO-DOTA-CC49 increased the median time to progression to 53, 24, and 67 days post-treatment, respectively. In contrast, saline controls showed a median time to progression of 13 days postinjection. Treatment with pretargeted ^{149}Pm-, ^{166}Ho-, and ^{177}Lu-biotin or ^{149}Pm-, ^{166}Ho-, and ^{177}Lu-CC49 increased tumor doubling time to 18−36 days, compared to 3 days for saline controls. Among treated mice, 23% survived >84 days post-therapy, and 11% survived 6 months, but controls survived <29 days. Long-term survivors showed tumor growth inhibition or partial regression, extensive necrosis in residual masses, and no evidence of nontarget tissue toxicity at necropsy. Both pretargeted and conventional RIT demonstrated considerable efficacy in an extremely aggressive animal model of cancer. Our results identified ^{177}Lu as an optimal radiolanthanide for future evaluation of these agents in toxicity and multiple-dose therapy studies.

INTRODUCTION

Radiolabeled monoclonal antibodies have been used extensively for radioimmunotherapy (RIT), most notably treatment of non-Hodgkin's lymphoma.[1] However, RIT is generally unsuccessful in solid tumor therapy due to insufficient tumor uptake without bone marrow toxicity. In addition, high tumor-to-background ratios generally cause radiolabeled mAbs to exhibit relatively poor imaging contrast.

The mAb CC49 is a pancarcinoma antibody[2] that targets the tumor-associated glycoprotein-72 (TAG-72).[3] Immunohistochemical studies demonstrated that its first-generation mAb, B72.3, binds to the majority of human epithelial malignancies,[4−9] including 82% of colon carcinomas,[10] while being essentially nonreactive with most normal human tissues.[11] The mAb CC49 has the same range of immunoreactivity as B72.3.[2,11] However, CC49 has a 6.4-fold higher binding affinity for TAG-72 than B72.3,[2] enabling it to react with a greater number of malignant cell types.[11]

Compared to B72.3, ^{131}I-labeled CC49 showed greater tumor xenograft targeting[12] and improved therapeutic efficacy[13] in nude mouse models. Clinical RIT trials of ^{131}I-CC49 demonstrated high tumor uptake, but did not produce any substantial responses.[14−16] Therefore, a single-chain (scFv) construct of CC49 was developed and shown to have promise for tumor therapy in tumor-bearing mouse models.[17] Additional improvements in RIT will likely require novel approaches, such as the use of different radionuclides, new antibody constructs, and novel delivery platforms.

First, the development of new therapeutic radionuclides, such as radiolanthanides, should be explored. The decay characteristics of three radiolanthanides for tumor therapy are compared to traditionally used ^{131}I and ^{90}Y in Table 1. All of these radiolanthanides have γ emissions suitable for tracking RIT

Received: May 19, 2011
Revised: November 2, 2011
Published: November 5, 2011

ACS Publications © 2011 American Chemical Society

dx.doi.org/10.1021/bc200258x | *Bioconjugate Chem.* 2011, 22, 2444−2452

Table 1. Decay Characteristics of Radionuclides for Tumor Therapy

radionuclide	$t_{1/2}$ (h)	β^- MeV (%)	γ keV (%)	range in tissue (mm)
^{149}Pm	53.1	0.78 (9)	286 (3.1)	5
		1.06 (90)		
^{166}Ho	26.9	1.76 (47)	81 (5.4)	9
		1.84 (52)		
^{177}Lu	159.6	0.497 (90)	208 (11)	2
^{131}I	192	0.606 (87)	364 (82)	3
^{90}Y	64.0	2.27 (100)	---	11

agents in living systems and estimating absorbed radiation doses to normal and malignant tissues. The radiolanthanides ^{149}Pm, ^{166}Ho, and ^{177}Lu have a range of half-lives and β^- energies for therapy. An advantage to using these radiolanthanides is that their chemistries are quite similar. DOTA, a macrocyclic chelating agent, complexes many radiometals, including lanthanides, with extremely high thermodynamic, kinetic, and *in vivo* stability.[18] DOTA can be used for stable attachment of ^{149}Pm, ^{166}Ho, or ^{177}Lu to RIT constructs.

Antibody pretargeting is a RIT approach in which an antibody conjugate or fusion protein is attached to an artificial "receptor". Such an agent is administered first and allowed to accumulate in tumors. Then, radionuclide therapy is given in the form of a small molecule that binds rapidly with high affinity to the mAb-receptor construct prelocalized to tumor cells. This process can cause immediate accumulation of therapeutic radiation in tumors, allowing for considerable improvements in tumor-to-background ratios, tumor absorbed dose, therapeutic efficacy, and normal organ toxicity.

Strategies for pretargeting include mAb/hapten,[19−25] biotin/avidin or streptavidin,[26−39] and oligonucleotide/antisense oligonucleotide analogue[40−43] approaches. The high-affinity binding of biotin to streptavidin ($\sim 10^{13}$ M^{-1}) makes this system especially attractive for pretargeted RIT. Both mAb−biotin and mAb−streptavidin conjugates have been investigated for pretargeting of radiolabeled streptavidin and biotin, respectively. However, radiolabeled streptavidin has been shown to result in high kidney uptake and high liver uptake resulting from cross-linking of circulating biotinylated mAb, compromising tumor targeting.[36] Clearance of biotinylated mAb with cold streptavidin or avidin have only slightly increased tumor-to-blood ratios.[44,45] Furthermore, radiolabeled streptavidin diffuses slowly into tumors over a 24 h period.[38] Thus, radiolabeled streptavidin can show considerable retardation in its tumor penetration. Pharmacokinetic modeling studies[46] indicated that a protocol involving radiolabeled biotin and mAb−streptavidin conjugates produces the highest tumor-to-blood ratio and residence time of radioactivity in tumors. Small, hydrophilic, and rapidly diffusible pretargeting agents undergoing rapid renal elimination, with minimal uptake in normal tissues, are ideal.[47]

A chemical streptavidin conjugate[48] of CC49 was labeled *ex vivo* with ^{111}In-DTPA-biocytin. This conjugate showed very similar tumor uptake and biodistribution as ^{111}In-DTPA-CC49. These studies suggested that streptavidin-CC49 constructs have potential for pretargeting applications.

As opposed to a whole antibody chemical conjugate, the use of a fusion protein based on the murine CC49 scFv construct and streptavidin (CC49 scFvSA)[49,50] was evaluated. CC49 scFvSA forms a 176 kDa tetramer with high immunoreactivity and high biotin binding efficiency and stability.[49,51] Evidence of *in vivo* stability of the fusion protein was suggested by specific tumor uptake, as well as intended uptake in the liver following administration of a synthetic clearing agent.[49] The biodistribution of CC49 scFvSA-pretargeted ^{111}In-DOTA-biotin in nude mice bearing LS174T human colon cancer xenografts demonstrated very similar tumor uptake as a chemical conjugate, but with an increase in tumor-to-blood ratio.[52]

CC49 scFvSA has also been used to pretarget ^{149}Pm-, ^{166}Ho-, and ^{177}Lu-DOTA-biotin to LS174T colorectal tumors in nude mice.[35] Maximum tumor uptakes of ^{149}Pm (22.9% ID/g), ^{166}Ho (30.2% ID/g), and ^{177}Lu (35.4% ID/g) were achieved at 1 to 4 h postinjection. Extremely rapid blood clearance was accompanied by urinary excretion of 59−66% ID within 1 h. In LS174T-bearing nude mice, the biodistributions of CC49 scFvSA-pretargeted ^{149}Pm-, ^{166}Ho-, and ^{177}Lu-DOTA-biotin were very similar. Most normal tissue uptakes were nearly identical for all three radiometals at all time points. Thus, this pretargeting system provided a highly uniform delivery platform for the evaluation of new therapeutic lanthanide radionuclides.

However, the three radiolanthanides showed some significant differences in maximum LS174T xenograft uptake and washout of radioactivity from the tumor with time. Areas under the time−activity curves showed that ^{177}Lu had the highest tumor-to-blood ratio, an indication that it might provide the best "therapeutic index" for pretargeted RIT. Yet, preliminary dosimetry estimates suggested that washout reduced the mouse tumor absorbed dose from ^{177}Lu by 4- to 5-fold, compared to ^{149}Pm and ^{166}Ho. Therefore, differences in tumor uptake and retention, physical half-lives, and β^- particle path lengths may play important roles in determining the effectiveness of pretargeted RIT with these radiolanthanides. In the present studies, the therapeutic efficacies of radiolabeled biotin, pretargeted by CC49 scFvSA, were compared to those of intact radiolabeled mAb CC49, using the three radiolanthanides, ^{149}Pm, ^{166}Ho, and ^{177}Lu, in nude mice bearing human colon cancer xenografts.

EXPERIMENTAL PROCEDURES

General. $^{149}PmCl_3$ (50 mCi in 25−50 μL of 0.05 M HCl), $^{166}HoCl_3$ (80 mCi in 50−80 μL of 0.05 M HCl), and $^{177}LuCl_3$ (25 mCi in 10−20 μL of 0.05 M HCl) were obtained from the University of Missouri (MU) Research Reactor (MURR; Columbia, MO). The mAb−streptavidin fusion protein CC49 scFvSA,[51] clearing agent biotin−$GalNAc_{16}$,[51] and DOTA−biotin were obtained from NeoRx Corporation (Seattle, WA). Methoxy-DOTA (MeO−DOTA)[53] was provided by the DOW Chemical Company (Freeport, TX). CC49 was produced from the hybridoma cell line provided by Dr. Jeffrey Schlom at the National Cancer Institute (Bethesda, MD). Reversed-phase thin-layer chromatography (TLC) was performed on Whatman (Clifton, NJ) $MKC_{18}F$ plates. The TLC plates were developed in 10% (w/v) ammonium acetate/methanol (1:1). Radio-TLC detection was accomplished using a Bioscan (Washington, DC) AR-2000 imaging scanner. The purity of the conventional radioimmunoconjugates was confirmed by gel filtration HPLC (GF-HPLC), using a Waters Delta 600 (Waters, Milford, MA) chromatograph equipped with a manual Rheodyne injector, a Waters 2487 dual-wavelength UV detector, a Packard 500TR Flow Scintillation Analyzer (Packard, Downers Grove, IL) with a LQ flow cell for ^{149}Pm, ^{166}Ho, and ^{177}Lu, a Waters busSAT/

IN analog−digital interface, and the Waters *Millennium 32* software package. A Superose 12 HR 10/30 (Amersham Pharmacia, Torrance, CA) column (300 × 10 mm), an isocratic mobile phase of 100 mM NaH_2PO_4/0.05% NaN_3, pH 6.8, and a flow rate of 0.50 mL/min were used. All solutions were prepared using ultrapure water (18 MΩ-cm resistivity). All other reagents were purchased Fischer Scientific (Pittsburgh, PA). Outbred female nu/nu mice (4−6 weeks of age) were obtained from Harlan Sprague−Dawley (Indianapolis, IN). Tumors were measured using Vernier calipers (Scienceware, D-2922/B/KWB).

Cell Line. The LS174T cell line was obtained from the American Type Culture Collection (Manassas, VA). Immediately prior to implantation into nude mice, the cells were tested for mycoplasma and screened for a panel of 13 murine pathogens by PCR. All test results were negative, and all sentinel mice in the facility housing the nude mice tested negative for these pathogens during the course of the studies.

Radiolabeling of Pretargeting RIT Conjugates. The labeling procedure used was previously described by Lewis et al.[35] Briefly, to 32.0 mCi of ^{149}Pm, 10.0 mCi of ^{166}Ho, or 25.0 mCi of ^{177}Lu in 80 μL of 0.20 M ammonium acetate, pH 5.0, containing approximately 1 mg/mL of gentisic acid, was added 32 μg of DOTA−biotin, 10 μg of DOTA−biotin, and 25 μg of DOTA−biotin, respectively. The reaction mixtures were incubated at 80 °C for 1 h, after which 1 mM DTPA, pH 6.0, was added. The reaction mixtures were incubated at room temperature for 10 min, after which radiochemical purity was assessed by reversed-phase radio-TLC. Typical labeling efficiencies were 99−100%.

Radiolabeling of Conventional RIT Conjugates. A modified method previously described by Mohsin et al. was used to label MeO-DOTA-CC49.[53] MeO−DOTA has been shown to bind ^{149}Pm, ^{166}Ho, and ^{177}Lu with high kinetic stability, as demonstrated by an *in vitro* hydroxyapatite assay.[53] An initial specific activity of 5 μCi/μg was used for ^{149}Pm-, ^{166}Ho-, and ^{177}Lu labeling reactions. In the labeling reactions, 320−365 μL of 1.0 M ammonium acetate, pH 4.5, was added to 6.5 mCi of $^{149}PmCl_3$ in 24.0 μL of 0.05 M HCl, 3.0 mCi of $^{166}HoCl_3$ in 2.0 μL of 0.05 M HCl, or 7.0 mCi of $^{177}LuCl_3$ in 3.0 μL of 0.05 M HCl, followed by 1.04−1.42 mg of MeO-DOTA-CC49 in 320−370 μL of 0.25 M ammonium acetate, pH 7.0. The reaction mixture was incubated at 43 °C for 1 h, and DTPA, pH 6.0, was added to a final concentration of 1 mM. The reaction mixture was allowed to stand for 15 min at room temperature and then purified using a Bio-Spin 6 column (Bio-Rad, Hercules, CA) equilibrated with 10 mM Na_2HPO_4/150 mM NaCl. Labeling efficiencies ranged from 65% to 80%. The specific activity was adjusted to 1 μCi/μg after purification, by dilution with unmodified CC49. Radiochemical purity was determined after purification by GF-HPLC.

Therapy Studies. All therapy studies were conducted in compliance with the guidelines established by the Animal Care and Use Committee of the University of Missouri-Columbia Animal Care Quality Assurance Office. Female athymic nude mice (20−25 g) were implanted subcutaneously (s.c.) in the hind flank with 2 × 10^6 LS174T human colon cancer cell suspensions (0.15 mL) in Hank's Balanced Salt Solution. The tumor xenografts grew to100−400 mg by day 15. All mice were fed a biotin-deficient diet (Purina Biotin Deficient Diet 5836, Purina Mills, Richmond, IN) for 6 days prior to radiopharmaceutical administration and up to 7 days postinjection.

For pretargeted RIT, groups of 8−10 mice were given a single injection of CC49 scFvSA (600 μg, 3.4 nmol), i.v. via the tail vein (t = 0). After 20−24 h, the synthetic clearing agent, biotin-$GalNAc_{16}$ (100 μg, 12.5 nmol), was given i.v. via the tail vein. Four hours after the clearing agent was administered, the mice received a tail vein injection of ^{149}Pm-, ^{166}Ho-, or ^{177}Lu-DOTA-biotin, at doses of 1.25 mCi/1.25 μg, 1.0 mCi/1.0 μg, and 1.5 mCi/1.5 μg, respectively. For conventional RIT, groups of 8−10 mice were given a single tail vein injection of ^{149}Pm-, ^{166}Ho-, or ^{177}Lu-MeO-DOTA-CC49, at doses of 250 μCi/250 μg, 200 μCi/200 μg, and 300 μCi/300 μg, respectively. Tumor growth was assessed by taking three-dimensional measurements of tumor volume using Vernier calipers. Tumor volume was calculated using the formula: V = (length × width × depth) × $\pi/6$.

Tumor Dosimetry. Mouse xenograft absorbed doses were calculated as described previously[54] using a modification of the method of Hui et al.[55] The model of Hui et al. is based on the dimensions and masses of organs in a nude mouse of approximately 25 g body weight. All organs were modeled as ellipsoids, with the exception of bone and bone marrow. Whole femur was selected to represent the bone and bone marrow, which were modeled as concentric cylinders. Radioactivity was assumed to be uniformly distributed within each of the organs, the carcass, and the tumor. Self-organ tumor absorbed radiation energy was determined as the amount of absorbed energy remaining in the tumor per radioactive decay. Cross-organ tumor absorbed radiation energy was determined using the approximation that the energy of β^- particles that escaped the source organ was deposited in adjacent organs.[55] The ratios of energy deposited in the tumor from adjacent organs were assumed to be approximately proportional to the ratios of the surface areas that overlapped with the tumor. To better simulate the geometry of a flank xenograft, it was assumed that the tumor was a sphere, with half the volume in contact with the remainder of body and half, covered with 0.5 mm of skin, protruding above the surface.

The Monte Carlo radiation transport code MCNP-4C[56] was used to obtain absorbed fractions for monoenergetic β^- particles. MCNP-4C was run in photon electron mode, in order to track both β^- particles and Bremsstrahlung radiation produced by the particles. For each monoenergetic β energy, 10^4 histories were run on a standard desktop personal computer, resulting in absorbed energy uncertainties on the order of 1%. When the absorbed fractions are averaged over the 25 to 50 energy bins representing a β spectrum, the final uncertainties are smaller than 1%. Standard energy cutoffs (0.001 MeV) and weight cutoffs for both β^- particles and photons were used. To calculate absorbed fractions for the polyenergetic β^- spectra of ^{149}Pm, ^{166}Ho, and ^{177}Lu, absorbed fractions were first determined at 51 energies from 0.025 to 2.5 MeV. β spectra were then calculated using the NUCDECAY code[57] and these monoenergetic responses were numerically integrated over the respective radiolanthanide spectra. An S-value was calculated for an average tumor weight of 200 mg, assuming radioactivity to be uniformly distributed within a sphere of unit density. This approach assumes that tumors of similar size in different animals have similar uptake characteristics, and the resulting absorbed dose is an average of that absorbed by each tumor.

Statistical Analysis. Response to therapy was assessed based on the number of days required for tumor volume to reach 1 g, using one-way analysis of variance (ANOVA) using

statistical software *SPSS 12.0.1* (Chicago, IL). The survival fraction of each treatment group was evaluated by Kaplan–Meier density analysis using *SPSS 12.0.1*, with a confidence interval of 95% ($p < 0.05$).

RESULTS AND DISCUSSION

An optimized pretargeting protocol,[49] based on the use of CC49 scFvSA, was employed for these studies. Injection of 600 μg (3.4 nmol) of CC49 scFvSA was sufficient to saturate tumors, as previously shown by the biodistribution of ^{125}I-labeled fusion protein.[49] After maximum tumor uptake at approximately 24 h, a molar excess of 100 μg (12.5 nmol) of the synthetic clearing agent biotin-GalNAc$_{16}$ was administered. This dose allowed for maximum clearance of circulating fusion protein to the liver for metabolic degradation, while having no effect on tumor retention.[51] After a sufficient time for clearance (4 h later), radiolanthanide-labeled DOTA–biotin was injected. DOTA–biotin was labeled to the same specific activity with all three radiometals, so different amounts of DOTA–biotin were administered using ^{149}Pm, ^{166}Ho, and ^{177}Lu. However, in each case the dose of fusion protein was in molar excess, allowing efficient binding of differing amounts of radiolabeled DOTA–biotin.

In the case of intact CC49,[53] we found that radiolanthanide labeling of the antibody at 5 μCi/μg, followed by dilution to 1 μCi/μg, gave superior radiolabeling and biodistribution results. Therefore, all CC49 doses were prepared according to this procedure.[53] While the amounts of radiolabeled CC49 administered differed among the three lanthanides, for each radiometal the tumor targeting would occur under conditions of antigen excess, allowing efficient uptake of the radiolabeled mAb.

The present studies compared directly, versus saline controls, the therapeutic efficacies of ^{149}Pm, ^{166}Ho, and ^{177}Lu for both pretargeted and conventional RIT in the same animal model of cancer. Initial single-dose therapy studies of CC49 scFvSA-pretargeted ^{149}Pm-, ^{166}Ho-, and ^{177}Lu-DOTA-biotin (Figure 1), as well as ^{149}Pm-, ^{166}Ho-, and ^{177}Lu-MeO-DOTA-CC49 (Figure 2), were performed in nude mice bearing LS174T human colon carcinoma xenografts. Animals were injected with radiopharmaceuticals or control vehicle on day 15 of tumor growth. After CC49 scFvSA pretargeting, mice were injected with 1.25 mCi of ^{149}Pm-DOTA-biotin, 1.0 mCi of ^{166}Ho-DOTA-biotin, or 1.5 mCi of ^{177}Lu-DOTA-biotin. For conventional RIT, mice received 0.25 mCi of ^{149}Pm-MeO-DOTA-CC49, 0.2 mCi of ^{166}Ho-MeO-DOTA-CC49, or 0.3 mCi of ^{177}Lu-MeO-DOTA-CC49.

Because these studies were not taken to toxicity, the relative injected doses of each of the radiopharmaceuticals had to be estimated from previously obtained biodistribution data.[35,53] A major consideration was blood uptake, which would result in whole body irradiation and potential toxicity. A second consideration was tumor uptake, taking into account the half-life of the radionuclide and the maximum time of tumor localization. Due to its slow blood clearance, these factors were especially important for the intact antibody. For example, ^{166}Ho has a half-life of 26.9 h and a maximum tumor uptake at 96 h, meaning that most radioactive decays will occur in the blood and result in whole body irradiation. Thus, blood-to-tumor ratios were used to estimate injected doses of radiolanthanide-labeled CC49. Using 0.2 mCi of ^{166}Ho-, 0.25 mCi of ^{149}Pm-, and 0.3 mCi of ^{177}Lu-MeO-DOTA-CC49, the area under the curve (AUC) blood-to-tumor ratios[53] were each approximately

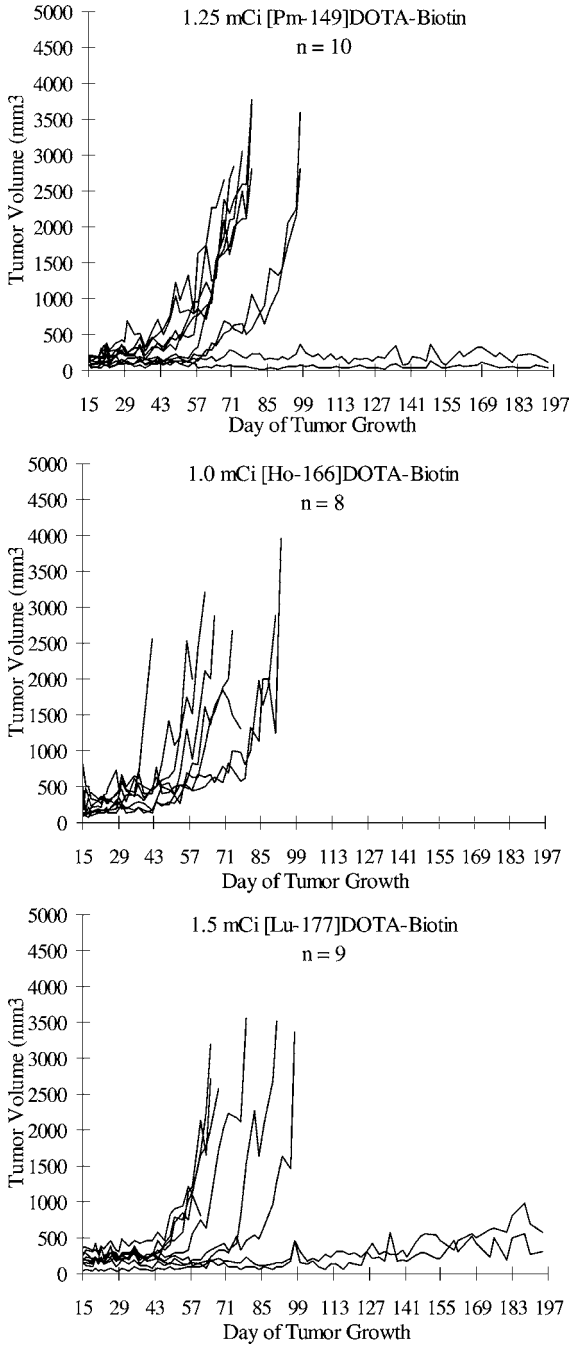

Figure 1. Tumor growth curves for LS174T-bearing nude mice treated with CC49 scFvSA-pretargeted ^{149}Pm-, ^{166}Ho-, and ^{177}Lu-DOTA-biotin.

0.1. The respective doses of ^{166}Ho-, ^{149}Pm-, and ^{177}Lu-DOTA-biotin were five times higher than those administered using the intact antibody, based on approximate whole body clearance of the pretargeting protocol. In the conventional and pretargeted RIT studies, no animals showed any signs of overt systemic toxicity, such as weight loss >20%, lethargy, or diarrhea.

We previously determined that the most statistically relevant end point criterion in this model is time to progression to a tumor burden of 1 g.[58] Figures 3 and 4 show the Kaplan–Meier plot of time to progression to a 1 g tumor for pretargeted and conventional RIT groups, respectively. Therapy with pretargeted ^{149}Pm-, ^{166}Ho-, and ^{177}Lu-DOTA-biotin increased the median time to progression to 50 ± 10, 41 ± 5, and 50 ± 10

dx.doi.org/10.1021/bc200258x | *Bioconjugate Chem.* 2011, 22, 2444–2452

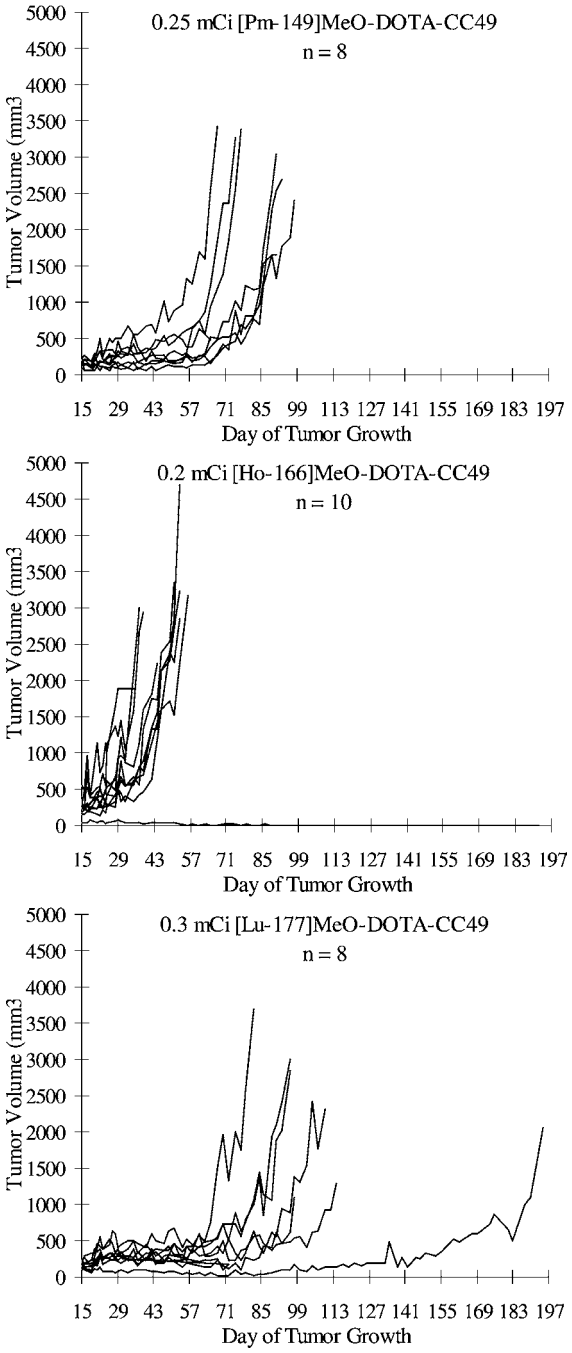

Figure 2. Tumor growth curves for LS174T-bearing nude mice treated with ^{149}Pm-, ^{166}Ho-, and ^{177}Lu-MeO-DOTA-CC49.

days post-treatment, respectively. Therapy with ^{149}Pm-, ^{166}Ho-, and ^{177}Lu-MeO-DOTA-CC49 increased the median time to progression to 53 ± 7, 24 ± 2, and 67 ± 9 days post-treatment, respectively. In contrast, saline controls showed a median time to progression of 13 ± 1 days postinjection and a mean tumor volume doubling time of only 3 days. Treatment with pretargeted ^{149}Pm-, ^{166}Ho-, and ^{177}Lu-biotin increased the average tumor volume doubling time to 27, 38, and 36 days, respectively. Therapy with ^{149}Pm-, ^{166}Ho-, and ^{177}Lu-CC49 increased mean tumor volume doubling time to 18, 10, and 36 days, respectively.

The mean times to progression to a 1 g tumor were lowest for ^{166}Ho pretargeted and conventional RIT, compared to the

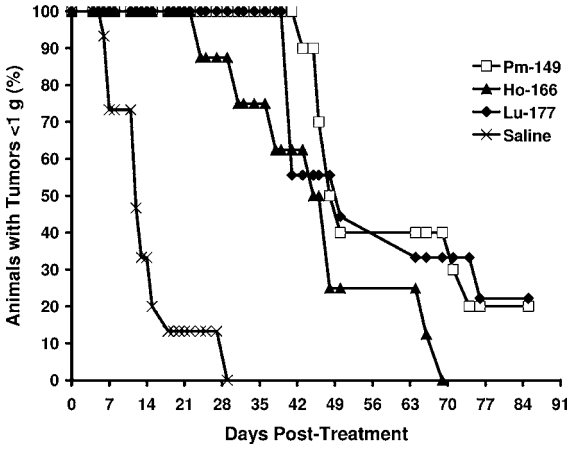

Figure 3. Time to progression to a tumor burden of 1 g in LS174T-bearing nude mice (n = 8−10 per group) treated with CC49 scFvSA-pretargeted ^{149}Pm-, ^{166}Ho-, and ^{177}Lu-DOTA-biotin, compared to saline controls.

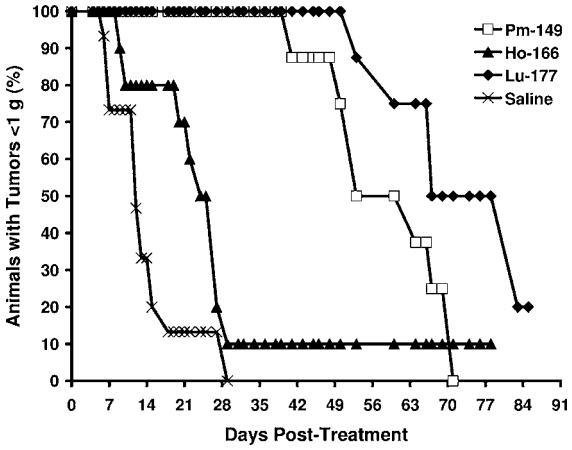

Figure 4. Time to progression to a tumor burden of 1 g in LS174T-bearing nude mice (n = 8−10 per group) treated with ^{149}Pm-, ^{166}Ho-, and ^{177}Lu-MeO-DOTA-CC49, compared to saline controls.

other two radiolanthanides. For conventional RIT, a possible explanation for this result could be that it takes 96 h to reach maximum tumor uptake, and the half-life of ^{166}Ho is only 26.9 h. Most of the ^{166}Ho decay would then occur in the blood and not at the tumor site. In the case of pretargeting, maximum tumor uptake occurs within 4 h.[35] However, the 1.76 and 1.84 MeV β^- particles of ^{166}Ho have a maximum range of approximately 9 mm in soft tissue, meaning that proportionally less radiative energy, compared to ^{149}Pm and ^{177}Lu, would be deposited in the LS174T xenograft.

For pretargeted RIT using ^{149}Pm and ^{177}Lu, the mean times to progression to a tumor burden of 1 g were statistically identical. However, a significant difference was observed between ^{149}Pm and ^{177}Lu in the case of conventional RIT, with ^{177}Lu-MeO-DOTA-CC49 showing superior tumor growth inhibition. With these two radiolanthanides, both pretargeted and conventional RIT effected highly durable therapeutic responses in an extremely aggressive animal model of human colon cancer. Because ^{177}Lu and ^{149}Pm were statistically equivalent for pretargeting, but ^{177}Lu was superior for conventional RIT, ^{177}Lu was selected as an optimal radiolanthanide for future evaluation of both delivery platforms in toxicity and multiple-dose therapy studies.

dx.doi.org/10.1021/bc200258x | Bioconjugate Chem. 2011, 22, 2444−2452

Among mice treated with CC49 scFvSA-pretargeted ^{149}Pm-, ^{166}Ho-, and ^{177}Lu-DOTA-biotin and ^{149}Pm-, ^{166}Ho-, and ^{177}Lu-MeO-DOTA-CC49, 23% survived >84 days post-therapy, and 11% survived 6 months, at which time the studies were terminated. All saline controls had to be sacrificed within 29 days of injection, with a median survival of only 18 days postinjection, demonstrating the highly aggressive nature of the LS174T model. Median survival in both the pretargeted ^{149}Pm and ^{177}Lu treatment groups was 82 days post-therapy, while in the conventional ^{149}Pm and ^{177}Lu RIT groups, median survival was 89 and 98 days, respectively. A summary of the therapy results is given in Table 2.

Table 2. Summary of Therapy Results

radiopharmaceutical	median survival (days)	survival at 84 days (%)	survival at 6 months (%)
^{149}Pm-DOTA-biotin	82	40	20
^{166}Ho-DOTA-biotin	70	25	0
^{177}Lu-DOTA-biotin	82	40	20
^{149}Pm-CC49	89	50	0
^{166}Ho-CC49	53	10[a]	10[a]
^{177}Lu-CC49	98	75	12.5

[a]Represents one animal with a 38 mg tumor that survived 6 months.

Some of the best previously reported outcomes of any therapeutic interventions in nude mice bearing established (>100 mg) LS174T xenografts have been a 63.2 day mean survival[59] following administration of ^{90}Y-labeled anti-CEA mAb ZCE025 and bone marrow transplantation and a 95.5 day median survival[60] after multiple bolus injections of ^{131}I-CC49, both of which were optimized treatment regimens. A more direct comparison of the CC49scFvSA pretargeting system can be found in an evaluation of the intraperitoneal model of LS174T colon cancer. Buchsbaum et al.[51] used the same CC49scFvSA protocol, injected intraperitoneally, to obtain very similar biodistributions of ^{177}Lu, compared to our intravenous administration of ^{149}Pm, ^{166}Ho, and ^{177}Lu in the flank xenograft model.[35] In pretargeted ^{177}Lu therapy studies, Buchsbaum and co-workers achieved 57 and 60 day median survivals, following single injections of 600 or 800 μCi, respectively. These results were superior to those obtained with ^{90}Y. The ^{177}Lu doses they used were also considerably lower than the dose employed in our experiments, and death was used as the end point for their studies. In contrast, we injected 1.5 mCi of pretargeted ^{177}Lu-DOTA-biotin and measured time to progression to a 1 g tumor, as frequent ulcerations complicated further evaluation of the flank xenograft model. Regardless of these differences, the results of our initial single-dose therapy studies of pretargeted and conventional RIT with radiolanthanides compare favorably with the best results in the literature. In addition to studies in tumor-bearing mice, a CC49scFvSA/^{90}Y-DOTA-biotin pretargeting protocol has also been evaluated in patients with metastatic colon cancer, demonstrating the potential clinical utility of pretargeting with this fusion protein.[61]

All 6-month survivors showed no macroscopic or microscopic evidence of nontarget tissue toxicity at necropsy. These animals experienced tumor growth inhibition, partial regression, and, in one instance, complete regression. However, the mouse microscopically free of disease after 6 months initially had a 38 mg tumor treated with ^{166}Ho-MeO-DOTA-CC49, which was an anomalous outcome. Histopathology of the residual masses from all other 6-month survivors (Figure 5) revealed extensive

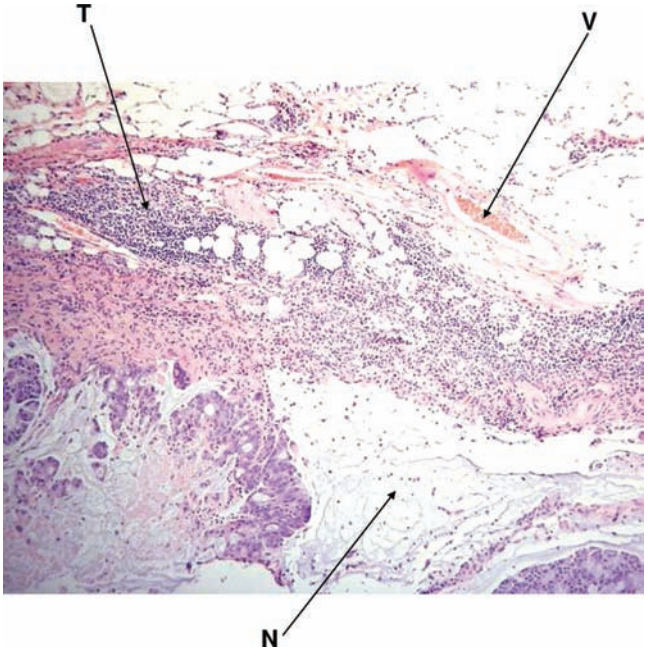

Figure 5. Hematoxylin- and eosin-stained section of the residual mass of a mouse 6 months after treatment with 1.5 mCi of CC49 scFvSA-pretargeted ^{177}Lu-DOTA-biotin, showing extensive necrosis (N), viable tumor tissue (T), and blood vessels (V).

(80−90%) tumor necrosis, with multifocal areas of pyogranulomatous inflammatory infiltrates. Conversely, 10−20% of each mass also consisted of viable and, with one exception, well-vascularized tumor cells exhibiting mitotic rates of 8−10 or 10−12 per 400 power field. However, these long-term survivors all had complete tumor growth inhibition or partial regression at 6 months post-therapy, suggesting that, in spite of the relatively high mitotic rates, the tumor cell-loss factor substantially outweighed the degree of proliferation.

■ CONCLUSIONS

These studies provide impetus to investigate why these experimental therapies demonstrate such considerable efficacy and how they can be improved further in an adjuvant setting. All animals with residual malignancy remained healthy with stable disease or in partial remission for a period corresponding to at least 25% of their life expectancy. This remarkable finding raises the possibility that radiolanthanide agents for pretargeted and conventional RIT may one day allow colorectal cancer patients to experience relatively normal longevity and quality of life. The future implementation of optimized radiolanthanide treatment regimens, such as multiple-dose therapy, has the potential to be even more efficacious for cancer treatment.

■ AUTHOR INFORMATION

Corresponding Author

*Phone: (573) 814-6000, ext. 53703. FAX: (573) 814-6551. E-mail: LewisMic@missouri.edu.

■ ACKNOWLEDGMENTS

This research, under Award Number DAMD 17-02-1-0103, was supported by the Department of Defense Prostate Cancer

Research Program, which is managed by the U.S. Army Medical Research and Materiel Command. This work was also funded by Grant URB-01-015 from the University of Missouri Research Board and a grant from the University of Missouri College of Veterinary Medicine Committee on Research. The authors would like to thank Dr. Jeffrey Schlom for providing the CC49 hybridoma cell line, as well as Dr. Christopher Johnson for assistance with statistical software *SPSS 12.0.1*. We also acknowledge the support of the U.S. Department of Veterans Affairs, for providing resources and the use of facilities at the Harry S. Truman Memorial Veterans' Hospital in Columbia, MO.

■ ABBREVIATIONS:

CC49, pancarcinoma monoclonal antibody; B72.3, pancarcinoma monoclonal antibody; scFv, single-chain antibody; SA, streptavidin; LS174T, human colon cancer cell line; $GalNAc_{16}$, *N*-acetyl galactosamine hexadecamer; DOTA, 1,4,7,10-tetraazacyclododecane-1,4,7,10-tetraacetic acid; MeO-DOTA, methoxy-DOTA; RIT, radioimmunotherapy; TAG-72, tumor-associated glycoprotein-72; DTPA, diethylenetriaminepentaacetic acid; % ID, percent injected dose; % ID/g, percent injected dose per gram of tissue; TLC, thin-layer chromatography; GF-HPLC, gel filtration high performance liquid chromatography; AUC, area under the curve

■ REFERENCES

(1) Eary, J. F. (1991) Radioimmunotherapy of B-cell lymphoma. *Ann. Oncol. 2* (Suppl. 2), 187−190.

(2) Muraro, R., Kuroki, M., Wunderlich, D., Poole, D. J., Colcher, D., Thor, A., Greiner, J. W., Simpson, J. F., Molinolo, A., Noguchi, P., and Schlom, J. (1988) Generation and characterization of B72.3 second generation monoclonal antibodies reactive with the tumor-associated glycoprotein 72 antigen. *Cancer Res. 48*, 4588−4596.

(3) Sheer, D. G., Schlom, J., and Cooper, H. L. (1988) Purification and composition of the human tumor-associated glycoprotein (TAG-72) defined by monoclonal antibodies CC49 and B72.3. *Cancer Res. 48*, 6811−6818.

(4) Johnston, W. W., Szpak, C. A., Thor, A., and Schlom, J. (1986) Phenotypic characterization of lung cancers in fine needle aspiration biopsies using monoclonal antibody B72.3. *Cancer Res. 46*, 6462−6470.

(5) Lyubsky, S., Madariaga, J., Lozowski, M., Mishriki, Y., Schuss, A., Chao, S., and Lundy, J. (1988) A tumor-associated antigen in carcinoma of the pancreas defined by monoclonal antibody B72.3. *Am. J. Clin. Pathol. 89*, 160−167.

(6) Nuti, M., Yoshio, A., Teramato, Y. A., Mariani-Costantini, R., Horan Hand, P., Colcher, D., and Schlom, J. (1982) A monoclonal antibody (B72.3) defines patterns of distribution of a novel tumor-associated antigen in human mammary carcinoma cell populations. *Int. J. Cancer 29*, 539−545.

(7) Ohuchi, N., Thor, A., Nose, M., Fujita, J., Kyogoku, M., and Schlom, J. (1986) Tumor-associated glycoprotein (TAG-72) detected in adenocarcinomas and benign lesions of the stomach. *Int. J. Cancer 38*, 643−650.

(8) Stramignoni, D., Bowen, R., Atkinson, B. F., and Schlom, J. (1983) Differential reactivity of monoclonal antibodies with human colon adenocarcinomas and adenomas. *Int. J. Cancer 31*, 543−552.

(9) Thor, A., Gorstein, F., Ohuchi, N., Szpak, C. A., Johnston, W. W., and Schlom, J. (1986) Tumor-associated glycoprotein (TAG-72) in ovarian carcinomas defined by monoclonal antibody B72.3. *J. Natl. Cancer Inst. 76*, 995−1003.

(10) Thor, A., Ohuchi, N., Szpak, C. A., Johnston, W. W., and Schlom, J. (1986) Distribution of oncofetal antigen tumor-associated glycoprotein-72 defined by monoclonal antibody B72.3. *Cancer Res. 46*, 3118−3124.

(11) Molinolo, A., Simpson, J. F., Thor, A., and Schlom, J. (1990) Enhanced tumor binding using immunohistochemical analyses by second generation anti-tumor-associated glycoprotein 72 monoclonal antibodies versus monoclonal antibody B72.3 in human tissue. *Cancer Res. 50*, 1291−1298.

(12) Colcher, D., Minelli, M. F., Roselli, M., Muraro, R., Simpson-Milenic, D., and Schlom, J. (1988) Radioimmunolocalization of human carcinoma xenografts with B72.3 second generation monoclonal antibodies. *Cancer Res. 48*, 4597−4603.

(13) Schlom, J., Eggensperger, D., Colcher, D., Molinolo, A., Houchens, D., Miller, L. S., Hinkle, G., and Siler, K. (1992) Therapeutic advantage of high-affinity anticarcinoma radioimmunoconjugates. *Cancer Res. 52*, 1067−1072.

(14) Divgi, C. R., Scott, A. M., Dantis, L., Capitelli, P., Siler, K., Hilton, S., Finn, R. D., Kemeny, N., Kelsen, D., Kostakoglu, L., Schlom, J., and Larson, S. M. (1995) Phase I radioimmunotherapy trial with iodine-131-CC49 in metastatic colon carcinoma. *J. Nucl. Med. 36*, 586−592.

(15) Murray, J. L., Macey, D. L., Kasi, L. P., Rieger, P., Cunningham, J., Bhadkamkar, V., Zhang, H. Z., Schlom, J., Rosenblum, M. G., and Podoloff, D. A. (1994) Phase II radioimmunotherapy trial with ^{131}I-CC49 in colorectal cancer. *Cancer 73*, 1057−1066.

(16) Tempero, M., Leichner, P., Dalrymple, G., Harrison, K., Augustine, S., Schlom, J., Anderson, J., Wisecarver, J., and Colcher, D. (1997) High-dose therapy with iodine-131-labeled monoclonal antibody CC49 in patients with gastrointestinal cancers: a phase I trial. *J. Clin. Oncol. 15*, 1518−1528.

(17) Pavlinkova, G., Booth, B. J. M., Batra, S. K., and Colcher, D. (1999) Radioimmunotherapy of human colon cancer xenografts using a dimeric single-chain Fv antibody construct. *Clin. Cancer Res. 5*, 2613−2619.

(18) Volkert, W. A., and Hoffman, T. J. (1999) Therapeutic radiopharmaceuticals. *Chem. Rev. 99*, 2269−2292.

(19) Barbet, J., Peltier, P., Bardet, S., Vuillez, J. P., Bachelot, I., Denet, S., Olivier, P., Leccia, F., Corcuff, B., Huglo, D., Proye, C., Rouvier, E., Meyer, P., and Chatal, J. F. (1998) Radioimmunodetection of medullary thyroid carcinoma using indium-111 bivalent hapten and anti-CEA × Anti-DTPA-indium bispecific antibody. *J. Nucl. Med. 39*, 1172−1178.

(20) Gautherot, E., Le Doussal, J.-M., Bouhou, J., Manetti, C., Martin, M., Rouvier, E., and Barbet, J. (1998) Delivery of therapeutic doses of radioiodine using bispecific antibody-targeted bivalent haptens. *J. Nucl. Med. 39*, 1937−1943.

(21) Goodwin, D. A., Meares, C. F., McCall, M. J., McTigue, M., and Chaovapong, W. (1988) Pretargeted immunoscintigraphy of murine tumors with indium-111-labeled bifunctional haptens. *J. Nucl. Med. 29*, 226−234.

(22) Goodwin, D. A., Meares, C. F., Watanabe, N., McTigue, M., Chaovapong, W., Ransome, C. M., Renn, O., Greiner, D. P., Kukis, D. L., and Kronenberger, S. I. (1994) Pharmacokinetics of pretargeted monoclonal antibody 2D12.5 and ^{88}Y-janus-2-(*p*-nitrobenzyl)-1,4,7,10-tetraazacyclododecanetetraacetic acid (DOTA) in BALB/c mice with KHJJ mouse adenocarcinoma: a model for ^{90}Y radioimmunotherapy. *Cancer Res. 54*, 5937−5946.

(23) Klivényi, G., Schuhmacher, J., Patzelt, E., Hauser, H., Matys, R., Moock, M., Regiert, T., and Maier-Borst, W. (1998) Gallium-68 chelate imaging of human colon carcinoma xenografts pretargeted with bispecific anti-$CD44_{V6}$/anti-gallium chelate antibodies. *J. Nucl. Med. 39*, 1769−1776.

(24) Kranenborg, M. H. G. C., Boerman, O. C., Griffiths, G. L., Oosterwijk, J. C., de Weijert, M. C. A., McBride, B., Hansen, H. J., Oosterwijk, E., and Corstens, F. H. M. (1998) Two-step targeting of RCC tumors in mice: improved tumor uptake and retention with a bivalent chelate. *J. Nucl. Med. 39*, 78P.

(25) Le Doussal, J.-M., Chetanneau, A., Gruaz-Guyon, A., Martin, M., Gautherot, E., Lehur, P.-A., Chatal, J.-F., Delaage, M., and Barbet, J. (1993) Bispecific monoclonal antibody-mediated targeting of an indium-111-labeled DTPA dimer to primary colorectal tumors:

pharmacokinetics, biodistribution, scintigraphy and immune response. *J. Nucl. Med. 34*, 1662−1671.
(26) Axworthy, D. B., Beaumier, P. L., Bottino, B. J., Goshorn, S., Mallett, R. W., Stone, D. M., Su, F.-M., Theodore, L. J., Yau, E. K., and Reno, J. M. (1996) Preclinical optimization of pretargeted radioimmunotherapy components: high efficiency, curative ^{90}Y delivery to mouse tumor xenografts. *Tumor Targeting 2*, 156−157.
(27) Axworthy, D. B., Reno, J. M., Hylarides, M. D., Mallett, R. W., Theodore, L. J., Gustavson, L. M., Su, F.-M., Hobson, L. J., Beaumier, P. L., and Fritzberg, A. R. (2000) Cure of human carcinoma xenografts by a single dose of pretargeted yttrium-90 with negligible toxicity. *Proc. Natl. Acad. Sci. U.S.A. 97*, 1802−1807.
(28) Cremonesi, M., Ferrari, M., Chinol, M., Stabin, M. G., Grana, C., Prisco, G., Robertson, C., Tosi, G., and Paganelli, G. (1999) Three-step radioimmunotherapy with yttrium-90 biotin: dosimetry and pharmacokinetics in cancer patients. *Eur. J. Nucl. Med. 26*, 110−120.
(29) Dosio, F., Magnani, P., Paganelli, G., Samuel, A., Chiesa, G., and Fazio, F. (1993) Three-step tumor pre-targeting in lung cancer immunoscintigraphy. *J. Nucl. Biol. Med. 37*, 228−232.
(30) Foulon, C. F., Alston, K. L., and Zalutsky, M. R. (1998) Astatine-211-labeled biotin conjugates resistant to biotinidase for use in pretargeted radioimmunotherapy. *Nucl. Med. Biol. 25*, 81−88.
(31) Foulon, C. F., Bigner, D. D., and Zalutsky, M. R. (1999) Preparation and characterization of anti-tenascin monoclonal antibody-streptavidin conjugates for pretargeting applications. *Bioconjugate Chem. 10*, 867−876.
(32) Kalofonos, H. P., Rusckowski, M., Siebecker, D. A., Sivolapenko, G. B., Snook, D., Lavender, J. P., Epenetos, A. A., and Hnatowich, D. J. (1990) Imaging of tumor in patients with indium-111-labeled biotin and streptavidin-conjugated antibodies: preliminary communication. *J. Nucl. Med. 31*, 1791−1796.
(33) Knox, S. J., Goris, M. L., Tempero, M., Weiden, P. L., Gentner, L., Breitz, H., Adams, G. P., Axworthy, D., Gaffigan, S., Bryan, K., Fisher, D. R., Colcher, D., Horak, I. D., and Weiner, L. M. (2000) Phase II trial of yttrium-90-DOTA-biotin pretargeted by NR-LU-10 antibody/streptavidin in patients with metastatic colon cancer. *Clin. Cancer Res. 6*, 406−414.
(34) Lewis, M. R., Wang, M., Axworthy, D. B., Theodore, L. J., Mallett, R. W., Fritzberg, A. R., Welch, M. J., and Anderson, C. J. (2003) In vivo evaluation of pretargeted ^{64}Cu for tumor imaging and therapy. *J. Nucl. Med. 44*, 1284−1292.
(35) Lewis, M. R., Zhang, J., Jia, F., Owen, N. K., Cutler, C. S., Embree, M. F., Schultz, J., Theodore, L. J., Ketring, A. R., Jurisson, S. S., and Axworthy, D. B. (2004) Biological comparison of ^{149}Pm-, ^{166}Ho-, and ^{177}Lu-DOTA-biotin pretargeted by CC49 scFv-streptavidin fusion protein in xenograft-bearing nude mice. *Nucl. Med. Biol. 31*, 213−223.
(36) Paganelli, G., Magnani, P., Zito, F., Villa, E., Sudati, F., Lopalco, L., Rossetti, C., Malcovati, M., Chiolerio, F., Seccamani, E., Siccardi, A. G., and Fazio, F. (1991) Three-step monoclonal antibody tumor targeting in carcinoembryonic antigen-positive patients. *Cancer Res. 51*, 5960−5966.
(37) Paganelli, G., Orecchia, R., Jereczek-Fossa, B., Grana, C., Cremonesi, M., De Braud, F., Tradati, N., and Chinol, M. (1998) Combined treatment of advanced oropharyngeal cancer with external radiotherapy and three-step radioimmunotherapy. *Eur. J. Nucl. Med. 25*, 1336−1339.
(38) Saga, T., Weinstein, J. N., Jeong, J. M., Heya, T., Lee, J. T., Le, N., Paik, C. H., Sung, C., and Neumann, R. D. (1994) Two-step targeting of experimental lung metastases with biotinylated antibody and radiolabeled streptavidin. *Cancer Res. 54*, 2160−2165.
(39) Weiden, P. L., Breitz, H. B., Press, O., Appelbaum, J. W., Bryan, J. K., Gaffigan, S., Stone, D., Axworthy, D., Fisher, D., and Reno, J. (2000) Pretargeted radioimmunotherapy (PRIT^{TM}) for treatment of non-Hodgkin's lymphoma (NHL): initial phase I/II study results. *Cancer Biother. Radiopharm. 15*, 15−29.
(40) Bos, E. S., Kuijpers, W. H. A., Meesters-Winters, M., Pham, D. T., de Haan, A. S., van Doornmalen, A. M., Kaspersen, F. M., van Boeckel, C. A. A., and Gougeon-Bertrand, F. (1994) *In vitro* evaluation of DNA-DNA hybridization as a two-step approach in radioimmunotherapy of cancer. *Cancer Res. 54*, 3479−3486.
(41) Kuijpers, W. H. A., Bos, E. S., Kaspersen, F. M., Veeneman, G. H., and van Boeckel, C. A. A. (1993) Specific recognition of antibody-oligonucleotide conjugates by radiolabeled antisense nucleotides: a novel approach for two-step radioimmunotherapy of cancer. *Bioconjugate Chem. 4*, 94−102.
(42) Liu, G., Mang'era, K., Liu, N., Gupta, S., Rusckowski, M., and Hnatowich, D. J. (2002) Tumor pretargeting in mice using ^{99m}Tc-labeled morpholino, a DNA analog. *J. Nucl. Med. 43*, 384−391.
(43) Wang, Y., Chang, F., Zhang, Y., Liu, N., Liu, G., Gupta, S., Rusckowski, M., and Hnatowich, D. J. (2001) Pretargeting with amplification using polymeric peptide nucleic acid. *Bioconjugate Chem. 12*, 807−816.
(44) Yao, Z., Zhang, M., Kobayashi, H., Sakahara, H., Nakada, H., Yamashina, I., and Konishi, J. (1995) Improved targeting of radiolabeled streptavidin in tumors pretargeted with biotinylated monoclonal antibodies through an avidin chase. *J. Nucl. Med. 36*, 837−841.
(45) Zhang, M., Sakahara, H., Yao, Z., Saga, T., Nakamoto, Y., Sato, N., Nakada, H., Yamashina, I., and Konishi, J. (1997) Intravenous avidin chase improved localization of radiolabeled streptavidin in intraperitoneal xenograft pretargeted with biotinylated antibody. *Nucl. Med. Biol. 24*, 61−64.
(46) Sung, C., and van Osdol, W. W. (1995) Pharmacokinetic comparison of direct antibody targeting with pretargeting protocols based on streptavidin-biotin binding. *J. Nucl. Med. 36*, 867−876.
(47) Goodwin, D. A. (1995) Tumor pretargeting: almost the bottom line. *J. Nucl. Med. 36*, 876−879.
(48) Ngai, W. M., Reilly, R. M., Polihronis, J., and Shpitz, B. (1995) *In vitro* and *in vivo* evaluation of streptavidin immunoconjugates of the second generation TAG-72 monoclonal antibody CC49. *Nucl. Med. Biol. 22*, 77−86.
(49) Graves, S. S., Dearstyne, E., Lin, Y., Zuo, Y., Sanderson, J., Schultz, J., Pantalias, A., Gray, D., Axworthy, D., Jones, H. M., and Auditore-Hargreaves, K. (2003) Combination therapy with pretarget CC49 radioimmunotherapy and gemcitabine prolongs tumor doubling time in a murine xenograft model of colon cancer more effectively than either monotherapy. *Clin. Cancer Res. 9*, 3712−3721.
(50) Schultz, J., Lin, Y., Sanderson, J., Zuo, Y., Stone, D., Mallett, R., Wilbert, S., and Axworthy, D. (2000) A tetravalent single-chain antibody-streptavidin fusion protein for pretargeted lymphoma therapy. *Cancer Res. 60*, 6663−6669.
(51) Buchsbaum, D. J., Khazaeli, M. B., Axworthy, D. B., Schultz, J., Chaudhuri, T. R., Zinn, K. R., Carpenter, M., and LoBuglio, A. F. (2005) Intraperitoneal pretarget radioimmunotherapy with CC49 fusion protein. *Clin. Cancer Res. 11*, 8180−8185.
(52) Buchsbaum, D. J., Khazaeli, M. B., LoBuglio, A. F., Meredith, R. F., Axworthy, D. B., Theodore, L., Schultz, J., Lin, Y.-K., Zuo, Y., Sanderson, J., and Zinn, K. R. (2000) Biodistribution and imaging of pretargeted ^{125}I-CC49sFV$_4$/SA fusion protein and ^{111}In-DOTA-biotin in an intraperitoneal tumor model. *Cancer Biother. Radiopharm. 15*, 395.
(53) Mohsin, H., Jia, F., Sivaguru, G., Hudson, M. J., Shelton, T. D., Hoffman, T. J., Cutler, C. S., Ketring, A. R., Athey, P. S., Simón, J., Frank, R. K., Jurisson, S. S., and Lewis, M. R. (2006) Radiolanthanide-labeled monoclonal antibody CC49 for radioimmunotherapy of cancer: biological comparison of DOTA conjugates and ^{149}Pm, ^{166}Ho, and ^{177}Lu. *Bioconjugate Chem. 17*, 485−492.
(54) Miller, W. H., Hartmann-Siantar, C., Fisher, D., Descalle, M.-A., Daly, T., Lehmann, J., Lewis, M. R., Hoffman, T., Smith, J., Situ, P. D., and Volkert, W. A. (2005) Evaluation of beta-absorbed fractions in a mouse model for ^{90}Y, ^{188}Re, ^{166}Ho, ^{149}Pm, ^{64}Cu, and ^{177}Lu radionuclides. *Cancer Biother. Radiopharm. 20*, 436−449.
(55) Hui, T. E., Fisher, D. R., Kuhn, J. A., Williams, L. E., Nourigat, C., Badger, C. C., Beatty, B. G., and Beatty, J. D. (1994) A mouse model for calculating cross-organ beta doses from yttrium-90-labeled immunoconjugates. *Cancer 73* (Suppl.), 951−957.

(56) Briesmeister, J. F., Ed. (2000) *MCNP - A General Monte Carlo N-Particle Transport Code*, Version 4C, Report LA-13709-M, Los Alamos National Laboratory, Los Alamos, NM.
(57) ORNL. (1995) *NUCDECAY: Nuclear decay data for radiation dosimetry calculations for ICRP and MIRD*. RSICC DATA LIBRARY DLC-172, Oak Ridge National Laboratories.
(58) Bryan, J. N., Jia, F., Mohsin, H., Sivaguru, G., Anderson, C. J., Miller, W. H., Henry, C. J., and Lewis, M. R. (2011) Monoclonal antibodies for copper-64 PET dosimetry and radioimmunotherapy. *Cancer Biol. Ther. 11*, 1001−1007.
(59) Morton, B. A., Beatty, B. G., Mison, A. P., Wanek, P. M., and Beatty, J. D. (1990) Role of bone marrow transplantation in ^{90}Y antibody therapy of colon cancer xenografts in nude mice. *Cancer Res. 50* (Suppl.), 1008s−1010s.
(60) Buchsbaum, D. J., Khazaeli, M. B., Mayo, M. S., and Roberson, P. L. (1999) Comparison of multiple bolus and continuous injections of ^{131}I-labeled CC49 for therapy in a colon cancer xenograft model. *Clin. Cancer Res. 5* (Suppl.), 3153s−3159s.
(61) Forero-Torres, A., Shen, S., Breitz, H., Sims, R. B., Axworthy, D. B., Khazaeli, M. B., Chen, K. H., Percent, I., Besh, S., LoBuglio, A. F., and Meredith, R. F. (2005) Pretargeted radioimmunotherapy (RIT) with a novel anti-TAG-72 fusion protein. *Cancer Biother. Radiopharm. 20*, 379−390.

Bioconjugate Chemistry

Article

pubs.acs.org/bc

Fluorescence Imaging with Multifunctional Polyglycerol Sulfates: Novel Polymeric near-IR Probes Targeting Inflammation

Kai Licha,*[,†] Pia Welker,[†] Marie Weinhart,[‡] Nicole Wegner,[†] Sylvia Kern,[†] Stefanie Reichert,[‡] Ines Gemeinhardt,[#] Carmen Weissbach,[§] Bernd Ebert,[§] Rainer Haag,[‡] and Michael Schirner[†]

[†]mivenion GmbH, Robert-Koch-Platz 4, 10115 Berlin, Germany

[‡]Institut für Chemie und Biochemie, Freie Universität Berlin, Takustr. 3, 14195 Berlin, Germany

[#]Institut für Radiologie, Charité-Universitätsmedizin, Charitéplatz 1, 10098 Berlin, Germany

[§]Physikalisch-Technische Bundesanstalt, Abbestr. 2-12, 10587 Berlin, Germany

Supporting Information

ABSTRACT: We present a highly selective approach for the targeting of inflammation with a multivalent polymeric probe. Dendritic polyglycerol was employed to synthesize a polyanionic macromolecular conjugate with a near-infrared fluorescent dye related to Indocyanine Green (ICG). On the basis of the dense assembly of sulfate groups which were generated from the polyol core, the resulting polyglycerol sulfate (molecular weight 12 kD with ~70 sulfate groups) targets factors of inflammation (IC_{50} of 3−6 nM for inhibition of L-selectin binding) and is specifically transported into inflammatory cells. The *in vivo* accumulation studied by near-IR fluorescence imaging in an animal model of rheumatoid arthritis demonstrated fast and selective uptake which enabled the differentiation of diseased joints (score 1−3) with a 3.5-fold higher fluorescence level and a signal maximum at 60 min post injection. Localization in tissues using fluorescence histology showed that the conjugates are deposited in the inflammatory infiltrate in the synovial membrane, whereas nonsulfated control was not detected in association with disease. Hence, this type of polymeric imaging probe is an alternative to current bioconjugates and provides future options for targeted imaging and drug delivery.

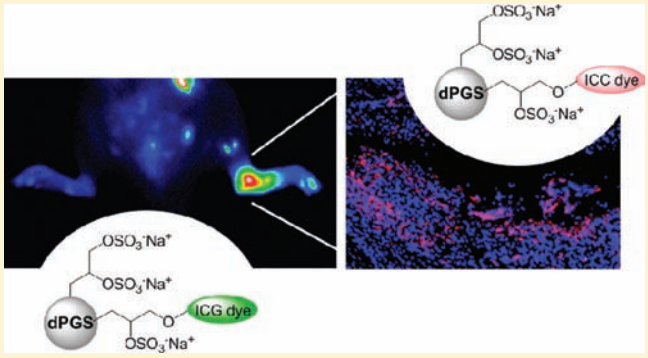

INTRODUCTION

Macromolecular conjugates are ideal entities for the delivery of drugs or diagnostics to diseased organs, tissues, and cells, as they can be effectively optimized for uptake, binding, release, and tolerability. Today, novel targeted macromolecules encompass mostly proteins and antibodies, which are recombinantly produced and either operate directly as therapeutics or are employed as carrier molecules for the delivery of conjugated effector molecules. A fundamental challenge with targeting molecules of biological origin is their inability in multipathway inhibition often leading to insufficient efficacy in the complex *in vivo* situation of disease treatment.[1]

An alternative to biological targeting molecules is provided by fully synthetic nanosized polymeric entities, which are accessible by comparably simple and economical chemical procedures. Many approaches using nanoparticles, dendrimers, and self-assembling systems as carriers for therapeutic drugs and diagnostic effectors are currently being followed.[2] Particularly, dendritic macromolecular polymers offer interesting applications for drug delivery and targeting. The multifunctional surface of dendritic structures is ideal to modify the physiological properties of the macromolecule by changing the surface properties, e.g., through conjugation with targeting structures or the assembly of charged moieties.[3,4] Most recently, we demonstrated that polyanionic, dendritic polyglycerol sulfates (dPGS) exert strong binding affinity to cellular targets involved in the inflammatory process, such as L- and P-selectins, which are bound with nanomolar affinity as demonstrated by a concentration-dependent SPR assay *in vitro*.[5,6] By inhibiting leucocyte infiltration *in vivo*, the substance exhibited efficient anti-inflammatory efficacy in a mouse dermatitis model.[5] Furthermore, dPGS binding to selectins was shown to increase with molecular weight and number of sulfate groups.[6] Polyanionic analogues employing polyglycerol sulfonates, carboxylates, or phosphates exert only weak binding to selectins (around μM), thereby revealing the particular specificity of dPGS.[7]

The underlying rationale of our studies described herein encompasses, on one hand, the evaluation of dPGS as carrier molecule for the targeting of diagnostic molecules to sites of

Received: May 30, 2011
Revised: November 5, 2011
Published: November 17, 2011

ACS Publications © 2011 American Chemical Society

inflammation and, on the other hand, to gain information on the *in vivo* distribution of such polymers. Thus, our aim was to generate a novel type of imaging probe involving near-IR dyes of the kind of Indocyanine Green (ICG). By visualizing the interaction of the polyanionic macromolecular conjugate within inflammatory processes, a novel molecular targeting mechanism is translated from the *in vitro* biological behavior to the performance as *in vivo* contrasting probe.

EXPERIMENTAL SECTION

Materials. All chemicals used were reagent grade, used as received, and purchased from Acros Organics (Belgium) or Sigma-Aldrich (Germany) unless stated otherwise. 11-Bromo-1-undecanol (>97%) was purchased from Fluka (Germany), and 4-(2-carboxyethyl)-phenylboronic acid from Alfa Aesar (Germany). Dendritic polyglycerol (dPG, compound **1**) with a molecular weight of 6000 g/mol and a PDI < 1.6 was synthesized according to literature via an anionic multi-branching ring-opening polymerization of glycidol and pentaerythritol as starter.[8,9] The ICC propargyl dye **5** was synthesized as published,[10] and is commercially available through IRIS Biotech, Germany. Dialysis was performed with regenerated cellulose tubings (MWCO 2000) purchased from Carl Roth. Reversed phase chromatographic purification was performed using RP-18 Redisep flash columns (ISCO CombiFlash Rf system). ^{1}H NMR and ^{13}C NMR spectra were recorded at 25 °C at concentrations of 100 g·L^{-1} on a JEOL ECX 400 spectrometer, operating at 400 and 101 MHz, respectively. NMR chemical shifts δ are reported in ppm and the deuterated solvent peak was used for calibration. Mass spectra were obtained from an ESI-Time-of-Flight LC/M mass spectrometer 6210 (Agilent Technologies) operating at a flow rate of 10 μL/min. Combustional analysis to determine degrees of sulfation was performed on a Vario EL III elemental analyzer. IC_{50} values were determined by SPR as published.[5]

Synthesis of Conjugates. *11-Azidoundecyl-polyglycerol (**2**).* dPG **1** (0.83 mmol, 5 g) was dissolved in dry DMF (40 mL) and statistically deprotonated with sodium hydride (60% in mineral oil, 2.08 mmol, 83 mg, 2.5 equiv) at 80 °C under Ar atmosphere for 30 min. 11-Azido-1-undecanyl-tosylate[11] (1.5 mmol, 0.54 g, 1.8 equiv) was added to the mixture and the reaction was kept for further 24 h at 80 °C. Subsequently, the solvent was removed under reduced pressure, the residue redissolved in aqua dest. (50 mL), and repeatedly extracted with DCM (3 × 50 mL). The aqueous phase was concentrated and further purified by dialysis in MeOH for 48 h, while the solvent was replaced three times. After concentration under reduced pressure and drying in high vacuum, 4.6 g (88%) of the title compound was obtained as a slightly yellow, viscous oil.

^{1}H (400 MHz, MeOH-d_4) δ 4.03−3.40 (m, dPG-backbone); 1.70−1.50 (m, alkyl-C$\underline{H}_2$CH$_2$O, alkyl-C$\underline{H}_2$CH$_2$N$_3$); 1.47−1.26 (m, 7×CH$_2$-alkyl). ^{13}C (101 MHz, MeOH-d_4) δ 81.5, 81.3, 79.7, 73.9, 72.8, 72.4, 72.2, 70.9, 70.6, 64.4, 63.0, 62.7 (PG-backbone), 52.4 (CH$_2$N$_3$), 31.7, 31.0, 30.6, 30.3, 29.9, 29.0, 28.6, 27.8, 27.0 (alkyl CH$_2$). IR (KBr) ν/cm^{-1} 3365 (s), 2927 (m), 2871 (m), 2071 (vs), 1122 (s), 1098 (s), 977 (m), 822 (m). Elemental analysis: calcd. C 49.065, H 8.250, N 0.680; found C 47.37, H 8.632, N 0.528.

*11-Azidoundecyl-polyglycerolsulfate (**3**).* Azidoundecyl-dPG **2** (0.63 mmol, 4.0 g) was dissolved in dry DMF (25 mL) and a solution of sulfurtrioxide pyridine complex (0.05 mol, 8.0 g, 80 equiv) in dry DMF (50 mL) was slowly added to the solution via a dropping funnel at 60 °C under Ar atmosphere and stirred for 5 h. Then, the reaction mixture was allowed to cool to room temperature and to react for further 24 h. The reaction was quenched by the addition of aqueous NaOH (1 M) until pH 8 was reached. The solvent was removed under reduced pressure and the crude product was dialyzed against water for 24 h while the solvent was replaced 3 times. After concentration under reduced pressure and drying in high vacuum, 8.1 g (92%) of the title compound was obtained as colorless solid. ^{1}H (400 MHz, D$_2$O) δ 4.58−4.17 (m, CH$_2$−OSO$_3$Na) 4.16−3.55 (m, dPG-backbone); 1.83−1.62 (m, alkyl-C$\underline{H}_2$CH$_2$O, alkyl-C$\underline{H}_2$CH$_2$N$_3$); 1.57−1.31 (m, 7×CH$_2$-alkyl). ^{13}C (101 MHz, D$_2$O) δ 79.1, 78.0, 76.6, 71.0, 70.3, 69.1, 68.4, 67.7 (PG-backbone), 52.1 (CH$_2$N$_3$), 29.5, 29.4, 29.3, 29.2, 29.0, 28.9, 29.8, 26.8, 26.1 (CH$_2$-alkyl). IR (KBr) ν/cm^{-1} 3481 (m), 2929 (m), 2871 (m), 2099 (m), 1653 (s), 1472 (m), 1255 (s), 1074 (s), 1048 (s), 939 (m), 779 (m). Elemental analysis: calcd. C 21.94, H 3.14, N 0.29, S 17.37; found C 19.48, H 3.204, N 0.238, S 17.20.

Meso-4-(2-carboxyethyl)phenyl NIR Dye from IR-820. A mixture of IR-820 (0.59 mmol, 0.5 g) and 4-(2-carboxyethyl)-phenylboronic acid (1.06 mmol, 0.21 g) in water (15 mL) was heated to 90 °C for 48 h in the presence of Pd(PPh$_3$)$_4$ (0.09 mol, 0.1 g). The reaction mixture was poured into diethyl ether and the resulting precipitate isolated by centrifugation. Purification was achieved by RP-18 chromatography (Combi-Flash) using water/methanol as eluent. Evaporation of methanol followed by lyophilization afforded 0.2 g (37%) of the product as green amorphous solid. ^{1}H (400 MHz, DMSO-d_6) δ 1.41 (s, 12H), 1.66−1.86 (m, 10H), 1.98 (t, 2H), 2.65−2.81(m, 8H), 3.10 (t, 2H), 4.24 (t, 4H), 6.28 (d, 2H), 7.23 (dd, 4H), 7.45 (t, 2H), 7.56 (dd, 4H), 7.71 (d, 2H), 8.01 (dd, 4H), 8.09 (d, 2H). MS (ESI-TOF) m/z calcd for $C_{55}H_{59}N_2NaO_8S_2$ $[M]^+$ 962.3611, found 962.3591; calcd $[M+Na]^+$ 985.3508, found 985.3491; calcd $[M-H+2Na]^+$ 1007.3328, found 1007.3308.

*Meso-propargyl NIR Dye (**4**).* To as solution of meso-4-(2-carboxyethyl)phenyl heptamethine dye (0.1 mmol, 100 mg) and 2-(1*H*-7-azabenzotriazol-1-yl)-1,1,3,3-tetramethyl uronium hexafluorophosphate (HATU; 0.18 mmol, 67 mg) in dry DMF (3 mL) was added diisopropylethylamine (0.2 mmol, 35 μL). After 30 min stirring at room temperature, a mixture of propargylamine (0.16 mmol, 10 μL) and diisopropylethylamine (0.3 mmol, 50 μL) was added and the reaction stirred at room temperature for 20 h. The product was precipitated with diethyl ether and isolated by centrifugation. Purification was achieved by RP-18 chromatography (CombiFlash) using water/methanol as eluent. Lyophilization afforded 55 mg (53%) of the product as green amorphous solid. ^{1}H (400 MHz, DMSO-d_6) δ 1.41 (s, 12H), 1.65−1.78 (m, 10H), 1.96 (t, 2H), 2.65−2.85 (m, 8H), 3.15 (t, 2H), 4.15−4.35 (m, 6H), 3.30 (t, 1H), 6.30 (d, 2H), 7.25 (dd, 4H), 7.45 (t, 2H), 7.58 (dd, 4H), 7.72 (d, 2H), 8.05 (dd, 4H), 8.10 (d, 2H). MS (ESI-TOF) m/z calcd for $C_{58}H_{61}N_3NaO_7S_2$ $[M]^+$ 999.2406, found 999.3692; calcd $[M+Na]^+$ 1022.2298, found 1022.3827; calcd $[M+K]^+$ 1038.3384, found 1038.3559.

*Polyglycerol Sulfate−NIR Dye Conjugate (**6**).* 11-Azidoundecanyl-polyglycerolsulfate **3** (7.0 μmol, 100 mg) and propargyl dye **4** (21 μmol, 21 mg) were dissolved in a 1:1 mixture of PBS/ethanol (1.2 mL). To this solution was added $CuSO_4 \cdot 5H_2O$ (3.0 μmol, 100 μL of a stock solution of 7.8 mg in 1 mL PBS), sodium ascorbate (6.0 mmol, 100 μL of a stock solution of 12.4 mg in 1 mL PBS) and another 200 μL of ethanol. The mixture was allowed to react at 40 °C for 72 h.

dx.doi.org/10.1021/bc2002727 | *Bioconjugate Chem.* 2011, 22, 2453−2460

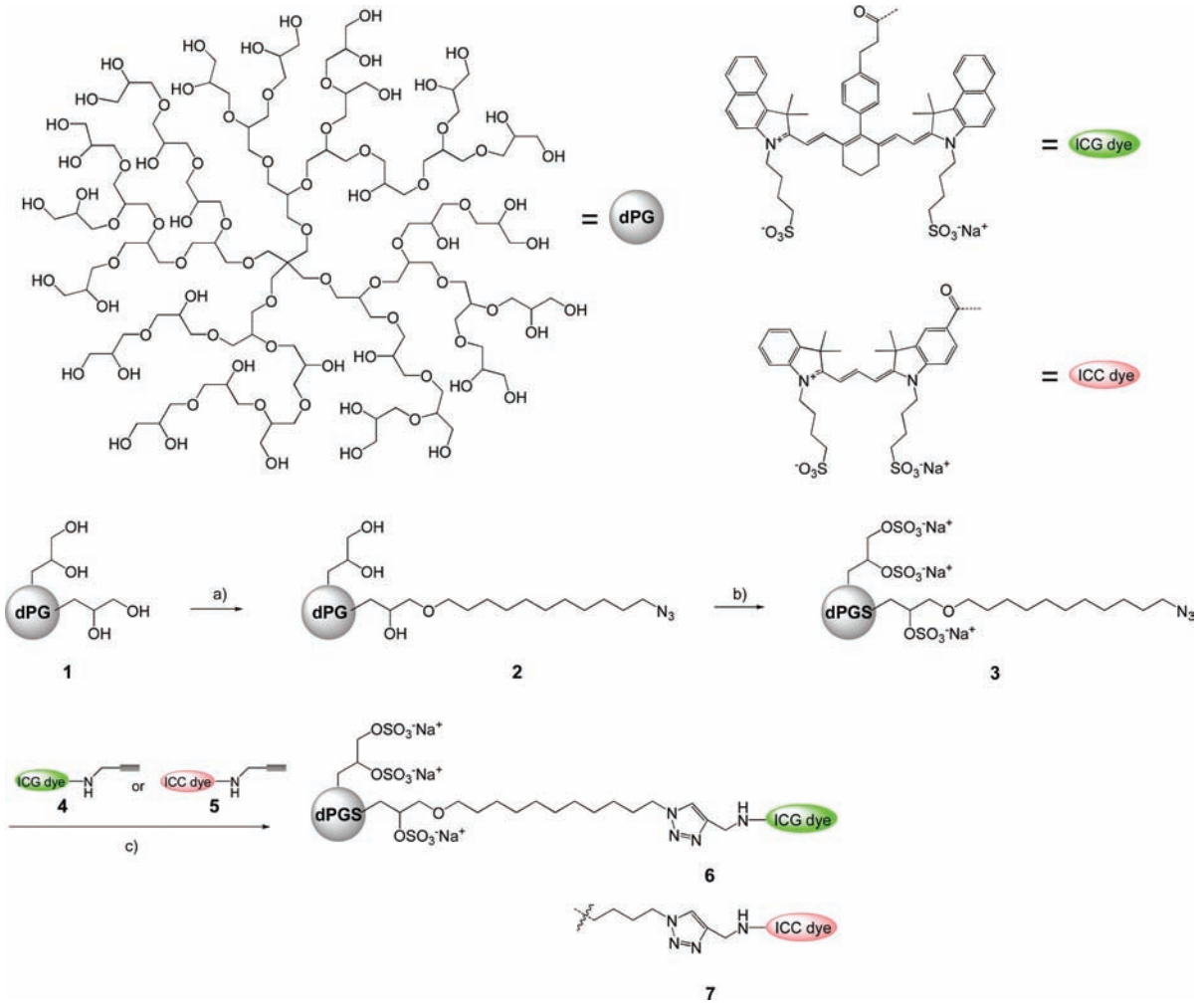

Figure 1. Chemical structures of conjugates and synthetic pathway: (a) NaH, 11-azido-1-undecanyltosylate, DMF, 80 °C, 24 h; (b) SO_3-pyridine, DMF, 60 °C, 5 h; (c) $CuSO_4$, Na-ascorbate, PBS/ethanol, 40 °C, 72 h.

After evaporation of ethanol, the residue was stirred in methanol/ethanol 1:1 and the supernatant decanted after precipitating the nonsoluble product by centrifugation. Finally, the product was isolated by RP-18 chromatography (Combi-Flash) eluting as first fraction with water as eluent. Lyophilization afforded 165 mg (77%) of **6** as green solid. ^{1}H (400 MHz, D_2O/DMSO-d_6 1:1) δ 8.40−6.20 (m, dye aromatic and polymethine groups, triazol group); 4.55−4.25 (m, CH_2−OSO_3Na); 4.20−3.60 (m, dPG-backbone); 2.20−1.80 (m, dye methylene groups); 1.65−1.20 (m, alkyl-$C\underline{H}_2CH_2O$, alkyl-$C\underline{H}_2CH_2N_3$, CH_2-alkyl linker, dye methyl groups). Elemental analysis: calcd. C 25.04, H 3.35, N 0.55, S 16.66; found C 22.41, H 2.412, N 0.539, S 17.93.

*Polyglycerol Sulfate−ICC Dye Conjugate (**7**).* 11-Azidoundecanyl-polyglycerolsulfate **3** (7.0 μmol, 100 mg) and propargyl ICC dye **5** (21 μmol, 15 mg) were reacted in a 1:1 mixture of PBS/ethanol (1.2 mL) and the product isolated as described for compound **6**. Lyophilization afforded 180 mg (85%) of **7** as red solid.

Photophysical Characterization. Absorption spectra were recorded on a Lambda 950 spectrophotometer (Perkin-Elmer), fluorescence spectra were measured with a JASCO FP-6500 spectrofluorometer (150 W xenon lamp, R928 Hamamatsu photomultiplier). Fluorescence quantum yields are calculated relative to the standard dye ICG in DMSO, which has a value of 13%.[12] Dye-to-polymer ratio was estimated from the UV−vis spectrum of a 5 μM conjugate solution prepared with the initial assumption of a dye-to-polymer molar ratio of 1 and a molecular weight of 13 000 g/mol.

Cell Culture. The epithelial human lung cancer cell line A549 was routinely propagated as follows: DMEM medium, with 10% fetal calf serum, 2% glutamine, and penicillin/streptomycin (all from PAN Biotech) added. Cells were seeded into medium at 1×10^5 cells/mL, cultured at 37 °C with 5% CO_2, and split 1:5 two times a week. Peripheral blood mononuclear cells (PBMC) were prepared from peripheral blood of different healthy donors by a sequence of differential centrifugation on Ficoll-Hypaque, adherence to polystyrene culture flasks for 2 h, and subsequent washing with RPMI containing 10% fetal calf serum (both from PAN Biotech) to remove nonadherent cells. The cells were stimulated with 100 ng/mL lipopolysaccharide (LPS; Sigma) for 24 h to prime proinflammatory processes.[13]

In Vivo Fluorescence Imaging. *Animal Model.* Animals in this study were maintained in accordance with the Guide for the Care and Use of Laboratory Animals published by the U.S. National Institute of Health (NIH publication no. 85−23, revised 1996). All experiments were approved by the local animal welfare committee. For arthritis studies, we used female Lewis rats with a body weight of (150 ± 10) g on arrival

dx.doi.org/10.1021/bc2002727 | *Bioconjugate Chem.* 2011, 22, 2453−2460

(Charles River) fed a normal diet. Collagen-induced arthritis (CIA) was induced as described before.[14−16] After fluorescence imaging, the animals were killed in deep anesthesia by intravenous injection of T61 ad us. vet. (Intervet) at a dose of 2 mL/animal.

Clinical Scoring. Clinical symptoms of the ankle joints after induction of arthritis are disposed in scores from 0 to 3. The ankle joints were scored in the following way: 0 − no clinical symptoms, 1 − low grade swelling, 2 − middle grade swelling and reddening, and 3 − high grade swelling, reddening, and mobility reduction.

Administration of Conjugates. The imaging probe **6** was dissolved in sterile PBS (PAN Biotech, Berlin, Germany) and administered i.v. via the tail vein at a dose of 4 mg/kg (corresponding to 0.15 μmol dye per kg). Animals included for later histology additionally received ICC conjugate **7** at a dose of 1 mg/kg.

Imaging Device and Image Processing. A camera-based fluorescence imaging system (Camera: EMCCD-Camera, IXON BV887, Andor) was used for imaging of animals. As excitation source, a light emitting diode (LED) array with λ_{max} of 750 nm illuminating an area of 20 cm × 20 cm and a short pass filter (λ = 750 nm, LCLL 750) were used. The following parameters were adjusted: exposure time, 100 ms; EM gain, 3000; delay, 18.8 ms; shift time, 0.9 ns/line; preamplifier, 4.6; detector temperature, −65 °C; binning, 2 pixel by 2 pixel; film, kinetic series with 3000 frames, kinetic cycle time, 200 ms, 1 accumulation; images, accumulation series with 100 frames, accumulation cycle time 200 ms. Two long pass filters ($\lambda_{50\%}$ = 800 nm, 5 OD, 800 LP, 800 ALP) were applied to suppress excitation light. The images were analyzed as published.[16] Briefly, regions of interest (ROI) were set and illumination intensities corrected for background. Images are normalized to the mean intensity from an ROI placed over the reference standard. Mean and 90th percentile values are determined in ROI for the right and left ankles, the area of the whiskers, and the eye.[16]

Cytochemistry. In the present study, cells were seeded at 5 × 10^4 cells/mL in a 24-well culture plate on glass coverslips (Sigma), and cultured for 24 h at 37 °C. Thereafter, cells were cultured with medium containing 10^{-6} M **6**, **7**, and 10^{-5} M polyglycerol-ICC (nonsulfated control)[17] for different times at 37 °C. Afterward, cells were fixed with cold acetone, rinsed, and covered with 4,6-diamidino-2-phenylindole (DAPI, Abcam, Cabridge, UK) for nuclear counterstain. Image acquisition was performed using a Leica DMRB microscope (Leica, Solms, Germany). Images were taken with a digital camera (Spot 32, Diagnostic Instruments).

Histochemistry. Histochemical staining was performed on paraffin sections (10 μm) of tissue of liver fixed with formalin or cryosections (5 μm) of tibiotarsal articulations. Tissues were removed 3 h post injection (p.i.) of dPGS-ICC or polyglycerol-ICC from control animals or rats with CIA. Tissue sections were deparaffinated and fixed with acetone. Non-decalcified tissues of tibiotarsal articulation were shock-frozen using liquid nitrogen. Microtome sections were removed from the block with cellotape and then transferred to slides, dried overnight, and fixed with acetone for 30 s.[18] DAPI was used for nuclear counterstain. Image acquisition was performed using a Leica DMRB microscope (Leica). Images were taken with a digital camera (Spot 32, Diagnostic Instruments).

RESULTS AND DISCUSSION

Synthesis of Polyglycerol Sulfate Conjugates with Cyanine Dyes. The synthetic path involves the derivatization of dendritic polyglycerol (dPG) with a reactive linker in a fashion in which approximately only one dye molecule on average is conjugated to the polymer. Dye conjugation via "Click" chemistry after sulfation of the majority of hydroxyl groups leads to the desired near-IR imaging conjugate. The synthesis is illustrated in Figure 1. The synthesis of dPG (compound **1** in Figure 1) was achieved by a one-step anionic multibranching ring-opening polymerization of glycidol started on the initiator pentaerythritol. After purification by dialysis, a highly viscous oil was obtained with a typical PDI of 1.4−1.6 and a number average molecular weight M_n of approximately 6000 g/mol.[8,9] Before the sulfation reaction to the desired polyglycerol sulfate, a small proportion of the hydroxyl groups was modified by reaction with 11-azidoundecanyl-1-tosylate forming an ether linkage between polymer and aliphatic chain. The appearance of the azide functionality in **2** was supported by IR (characteristic band at 2100 cm^{-1}). According to ^{1}H NMR signal integration (see Supporting Information), 60% of polymer carried a linker moiety on average. Subsequently, the material was sulfated with SO_3·pyridine complex[5,19] giving the azidoundecanyl-modified sulfated polyglycerol **3** in high yield. Elementary analysis revealed a high degree of sulfation of 92% (75 of theoretically 80 hydroxyl functions converted for M_n 6000 g/mol); thus, the M_n of the sulfated species is approximately 12 000 g/mol. Conjugation for near-infrared imaging in the spectral range of Indocyanine Green (ICG) was accomplished with the novel propargyl derivative **4**. We prepared this fluorescence label from the commercial dye IR-820 referring to a recently published procedure by Achilefu et al. who applied the Suzuki method of aryl-halide substitution to the central chloro function in the IR-820 structure.[20] In our approach, we used 4-(2-carboxyethyl)phenylboronic acid as reaction component, thereby introducing a carboxyethyl linker symmetrically into the chromophore. Amidation with propargylamine under standard conditions led to the desired derivative **4** for conjugation to the polyglycerolsulfate **3**. Coupling of **4** was achieved by copper-mediated 1,3-dipolar cycloaddition ("Click"-conjugation) between the azide group at the polymer and the propargyl residue at the dye. The resulting conjugate **6** was characterized by ^{1}H NMR and by photooptical methods. The conjugation reaction yielded a dye-to-polymer ratio of approximately 0.66 estimated from the absorption spectra (see below). We included furthermore a VIS fluorophore into our studies and synthesized an analogous conjugate (**7**) employing the indocarbocyanine (ICC) propargyl moiety **5** already published in other studies.[7,10] The influence of dye conjugation on target binding was determined by SPR (Biacore)[5,6] yielding inhibition (IC_{50}) values for L-selectin similar to nonconjugated dPGS of identical sulfation but without linker modification (conjugate **6**, IC_{50} 3 nM; conjugate **7**, IC_{50} 6 nM; nonconjugated dPGS, 4 nM). Hence, dye conjugation does not hamper target affinity of the resulting conjugate.

Photophysical Properties. In order to characterize the conjugate **6** with respect to its optical properties, we were interested in the dye-to-polymer ratio and in the resulting fluorescence quantum yield. The data for conjugate **6** in comparison with the free dye are summarized in Table 1. First, absorption measurements were conducted in phosphate-

Table 1. Photophysical Properties of Free Dye and Polyglycerolsulfate Conjugate 6

compound	solvent[a]	absorption max. (nm)[b]	fluorescence max. (nm)	FQ[c]
free dye	DMSO	806	836	0.052
	DMSO/PBS (1:1)	800	823	0.097
6	DMSO/PBS (1:1)	728, 804, –	823	0.027
	PBS	730, 792, 886	817	0.006
	serum	738, 806, 886	818	0.018
7	PBS	518, 553, –	568	n.d.
	serum	526, 559, –	572	n.d.

[a]Data for free dye in PBS and conjugate **6** in DMSO are not determined due to insolubility, and no reasonable spectra were obtainable. [b]Spectral data for **6** and **7** from left to right: dimer band, monomer band, J-band. [c]Fluorescence quantum yield relative to ICG in DMSO (0.13).[12]

buffered saline and in serum as most relevant physiological media. The spectra depicted in Figure 2 illustrate that the conjugate exhibits a pronounced tendency to form aggregates. For comparison, the theoretically optimal absorbance profile of the fluorophore is obtained by measuring the free dye in DMSO. Unfortunately, **6** is not soluble in DMSO or methanol due to the extremely high anionic charge, so we had to exclude this solvent. In PBS, strong aggregation is apparent from the collapsing extinction of the absorbance maximum of **6** at 792 nm and growth of the dimer shoulder at 730 nm, together with sign of a J-band at 886 nm. Also, the fluorescence yield is rather low at 0.6% (excitation 720 nm). This behavior has been studied intensively for protein and antibody conjugates with lipophilic fluorescent labels, mainly dyes of cyanine type.[21,22] In serum as the more physiologically relevant medium, we obtained a slightly restored main absorption band, accompanied by an increased fluorescence quantum yield of 1.8%. Despite insolubility in DMSO, a mixture of PBS/DMSO of 1:1 gave a similar spectrum and a quantum yield of 2.7%. Compared to other covalent conjugates of the ICG chromophore type[21,23] and also unmodified ICG in nanoformulations,[24] however, this level appears sufficient for further biological studies.

For the free dye, a very high extinction coefficient in DMSO was measured at 195 000 M^{-1} cm^{-1} representing the theoretically optimal condition to determine optical properties due to the absence of aggregation phenomena. Assuming an extinction coefficient of 150 000 M^{-1} cm^{-1} from the spectral shape in serum or PBS/DMSO (Figure 2) to estimate the dye-to-polymer ratio in **6**, a concentration of 3.3 μM, which corresponds to a dye loading of 66%, can be calculated. This is in approximate agreement with the maximal achievable loading based on 60% linker attachment (see above). The difficulty in accurately determining the ratio between a carrier unit and a dye is similar to observations with antibody conjugates with rather lipophilic heptamethine dyes, such as ICG.[21] In fact, as discussed by Villaraza et al., the clear analysis of dye loading as well as supposedly successfully achieved separation of covalently attached dye from aggregated nonattached impurities is difficult, as in size exclusion chromatography (SEC) both specimens may elute similarly. Furthermore, our polymer carriers do not exhibit UV absorption, thus lacking a method to quantify the polymer concentration by spectrophotometry.

Cellular Uptake. On the *in vitro* level, we have already demonstrated the ability of polyglycerol sulfates to inhibit L- and P-selectin binding with high specificity over other anionic groups, such as sulfonate and carboxylate.[7] Applying conjugates **6** and **7**, both of which exhibit high binding to L-selectin with conjugated fluorophore (see above) allows the translation to the cellular level. We found that the polymer clearly localizes within tumor cells, as well as in activated mononuclear cells, as shown in cell culture and tissue specimens.

Figure 3A illustrates that the NIR conjugate **6** appears comparably in A549 cells when setting up a microscope with excitation and detection technique capable of exciting and imaging the near-IR fluorophore permitting direct visualization of **6**. Compound **7**, employing ICC dye[7,10] with typical fluorescence properties fitting the Cy3-filter (550 nm/580 nm), allows the same subcellular localization with a sharper image

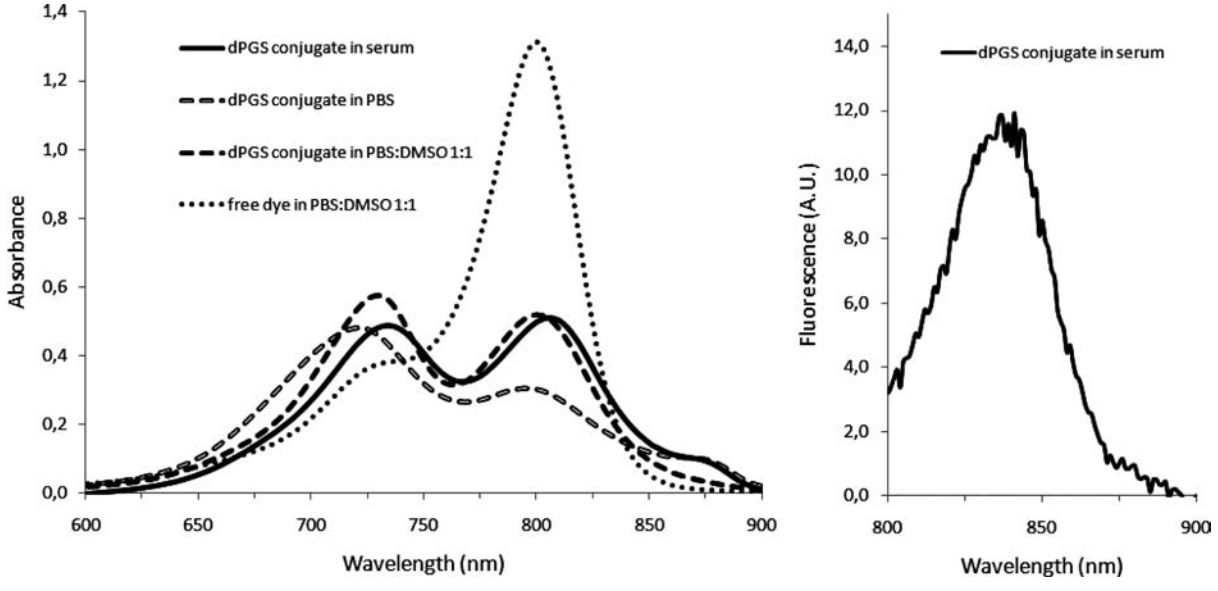

Figure 2. Absorbance spectra of conjugate **6** in different solvents compared to free dye in PBS/DMSO 1:1. Fluorescence emission spectrum of **6** in serum (excitation: 760 nm).

dx.doi.org/10.1021/bc2002727 | *Bioconjugate Chem.* 2011, 22, 2453–2460

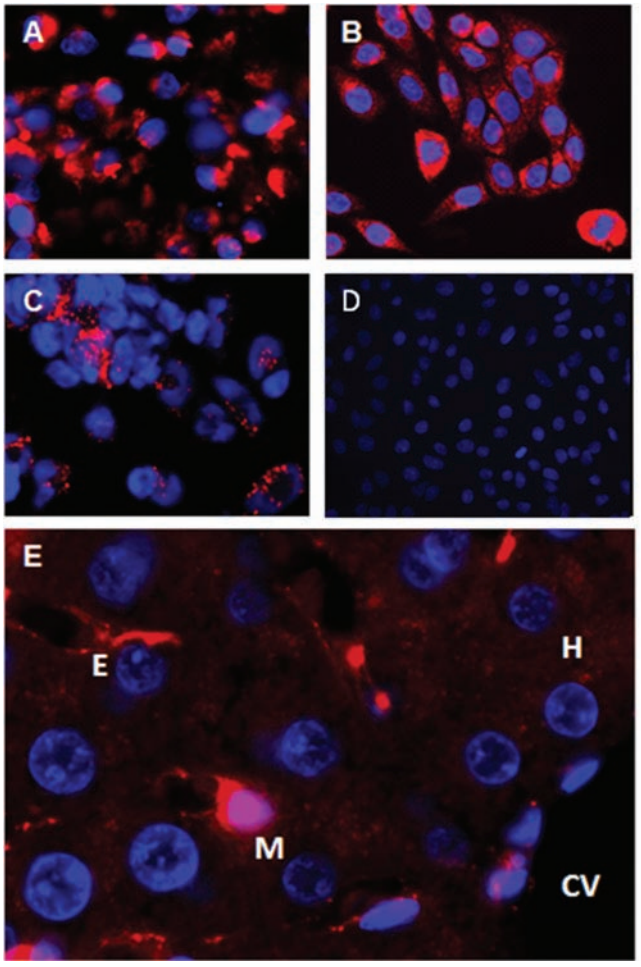

Figure 3. Uptake of dPGS conjugated with fluorescence dyes (red): A549 lung cancer cells cultured for 4 h with **6** (A) or **7** (B). (C) Monocytes isolated from human peripheral blood stimulated with 100 ng/mL LPS (24 h) and cultured for 4 h with **7**. (D) Control with polyglycerol-ICC on A549 lung cancer cells. (E) Paraffin-embedded tissue of rat 3 h p.i. of **7**. M − Liver macrophages (Kupffer cells), E −endothelial cells, H − hepatocyte, CV − central venule. Nuclear staining with DAPI (blue). Objective lens 40× (A−D), 100× (E).

impression (Figure 3B). As expected, no cellular signals after incubation with polyglycerol-ICC as control could be detected (Figure 3C). Due to the absence of technical routine solutions for microscopic imaging in the near-IR, we continued to employ compound **7** as standard probe for microscopic studies, hereby assured that **6** and **7** exhibit identical cellular uptake behavior as proven by the above-described bridging comparison. Accordingly, uptake of conjugate **7** could be demonstrated *in vitro* in human peripheral blood mononuclear cells stimulated with LPS to induce for inflammatory processes (Figure 3D). Moreover, intracellular localization after targeting to macrophages in the living organism was proven by studying liver tissue 3 h post i.v. injection of conjugate **7** into rats. As shown in Figure 3E, enrichment in rat liver macrophages (Kupffer cells) with a certain level of fluorescence signals also detectable in activated endothelial cells and hepatocytes can be followed *ex vivo* by fluorescence microscopy of liver tissue specimens.

In Vivo Imaging. Conjugate **6** was employed as imaging probe for *in vivo* studies using the well-established arthritis rat model in which joint inflammation is induced by the injection of bovine type II collagen.[15,16] After i.v. administration of the probe (dose: 4 mg/kg of polymer corresponding to 0.2 μmol/kg fluorophore), fluorescence images were generated up to 24 h post injection. Images from a time series of a control and two CIA animals are shown in Figure 4. The false colors allow easy identification of the diseased joints. As is typical in the disease progression of this animal model, a certain number of joints remains either unaffected or at a low disease score. In the fluorescence imaging setting, we were able to differentiate dye probe uptake depending on the acuteness of the inflammation within the same animal. In Figure 4, the middle row impressively shows that the absence of clinical signs (score 0) does not lead to pronounced fluorescence enhancement.

For further quantification, images were analyzed by applying appropriate regions of interest (ROIs) to the area of ankle joints, eyes, and a fluorescent reference cube. Accordingly, a total of 10 joints in control rats and 20 joints in arthritic animals were evaluated. The fluorescence intensity from the eyes is helpful as a basic signal indicating the pharmacokinetic behavior of the injected probe in the blood compartment.

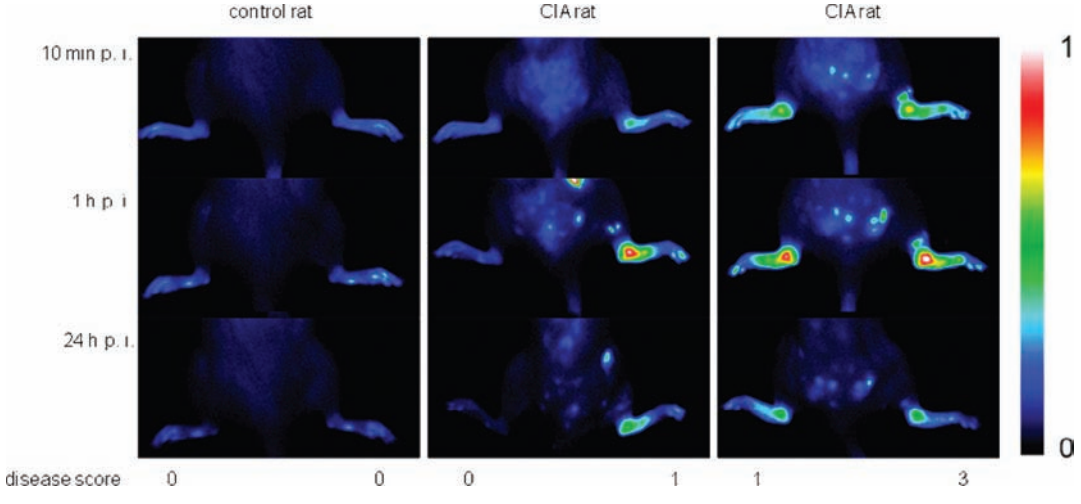

Figure 4. Comparison of fluorescence images in false colors (normalized to a fluorescence reference cube) of a control rat and rats with collagen-induced rheumatoid arthritis (different clinical scores are indicated) after 10 min, 1 h, and 24 h post injection of **6** (4 mg/kg b.w.). One representative example of at least $n = 5$.

dx.doi.org/10.1021/bc2002727 | *Bioconjugate Chem.* 2011, 22, 2453−2460

Figure 5 illustrates the resulting average signal kinetics of joints of healthy animals, and joints of treated animals, grouped into

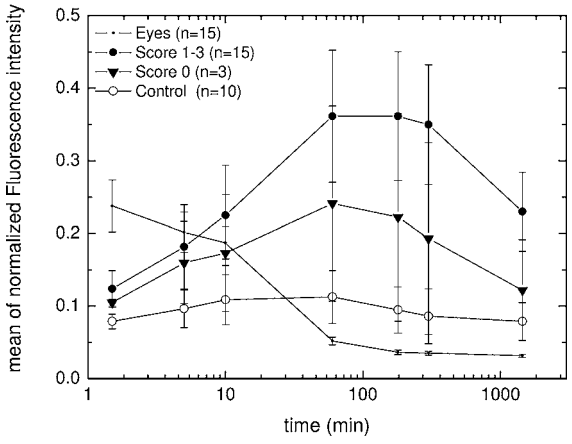

Figure 5. Temporal behavior of means of normalized fluorescence intensity derived from 90th percentiles of ROIs covering the ankle joints and the opened eye of the rats post injection of conjugate **6**. The error bars indicate the single standard deviation derived from the number of measured values *n* (individual joints as independent events).

score 0 and scores 1−3, as well as in the eye. The results show that conjugate **6** generates an almost 3.5-fold signal increase in the affected joint (score 1−3) at the time of maximal intensity at 60 min. Interestingly, for joints of the treated group with no clinical signs (score 0) a 2-fold signal enhancement in comparison to the healthy group can still be calculated (n = 3). Data of fluorescence intensity of ICG derived from ROIs over ankle joints at defined time intervals of each animal group were analyzed employing the Mann−Whitney test for independent samples. At 10 min after bolus injection, the significance of fluorescence intensity values between controls and diseased joints (score 1−3) was calculated (MedCalc, vers. 11.1.0.0) and the two tailored probability yielding $p < 0.0001$. The significance is even more pronounced at later time points, as can be seen from the difference of means in Figure 5. These findings indicate that the molecular targeting of the polyanionic macromolecule is effectively directed to early signs of the disease before clinical manifestation can be evidenced. In fact, the targeting of early signs in joint inflammation, involving the formation of autoantibodies activating macrophages, the release of proinflammatory cytokines, the activation of endothelial cells, and finally the infiltration of inflammatory cells in the articulation,[25] remains a challenge in diagnosis and treatment before clinical manifestation (edema, destruction of cartilage, and bone) occurs.[26]

The fluorescence signal measured over the eye, as a rough estimate for the change of dye concentration in the blood, reaches almost its minimal level at the time of maximal signal in the joints. This allows an explanation of the high and early contrast in the images. Typically, macromolecular targeting for diagnostic imaging purposes might be hampered by long-circulating probe fractions and resulting high signal background, so that the required target-to-blood signal ratios are not sufficiently developed. By employing the eye fluorescence as a provisional solution to monitor blood kinetics, a roughly estimated blood half-life is shorter than 1 h, fast enough for reasonable contrast enhancement.

Histological Examination of Tissues. To enable a postmortem histological recovery of the dPGS conjugate and confirm the *in vivo* imaging data, we analyzed tissues of the tibiotarsal articulation by fluorescence microscopy using the 550 nm channel (Cy3) to excite the ICC dye (Figure 6). No

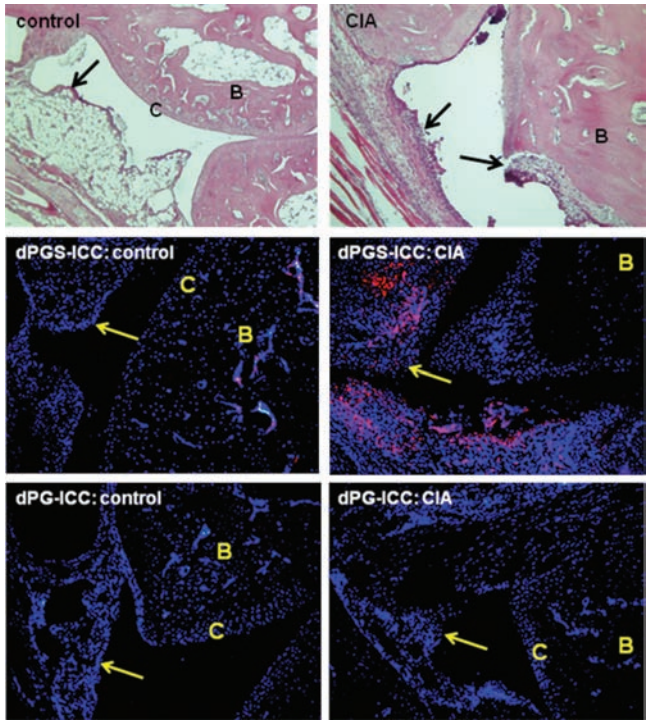

Figure 6. Conventional and fluorescence histology of tissues from tibiotarsal articulation of rats with collagen-induced rheumatoid arthritis (CIA) or healthy controls 3 hs post i.v. injection of dPGS-ICC (**7**) or nonsulfated PG-ICC.[17] Arrowhead: synovial membrane. B: bone. C: cartilage. Nuclear staining with DAPI (blue), compounds in red.

fluorescence signals were detectable in the articulations of healthy animals 3 h post i.v. administration of **7**. In the tissues of rats with CIA, conjugate **7** was enriched in the inflammatory infiltrate in the synovial membrane. The treatment of both control and CIA rats with nonsulfated polyglycerol−ICC conjugate[17] as control did not lead to uptake into the cells of the synovial membrane, thus further supporting the specific targeting behavior of dPGS observed with the near-IR fluorescent version **6** as *in vivo* imaging probe.

■ CONCLUSION

We have demonstrated that dendritic polyglycerol sulfate (dPGS) acts as a novel type of synthetic nanocarrier suited for inflammation-specific molecular imaging. The polymer was readily synthesized by a polymerization and sulfation procedure and conjugated with either a near-infrared dye or a VIS dye to facilitate *in vitro* and *in vivo* detection in disease models. Both conjugates behave similarly regarding its cellular uptake into epithelial cells and macrophages. The specific intracellular localization is yet to be further elucidated with respect to the mechanism involved. Our ongoing work involves studies on uptake possibly via transporter proteins and scavenger receptors into inflammatory cells, as well as the impact of the type of anionic group on cellular interaction.[7] Translation into the diagnostic application was accomplished by *in vivo*

dx.doi.org/10.1021/bc2002727 | *Bioconjugate Chem.* 2011, 22, 2453−2460

fluorescence imaging in a rat arthritis model, demonstrating fast and selective targeting of tissue inflammation and permitting the differentiation of early onset of disease progression. We conclude that dendritic macromolecules provide interesting opportunities beyond the usually employed drug delivery systems with nanoparticles and other high molecular weight systems based on passive targeting. Here, we utilized highly dense anionic charge to impart specific interaction with factors of inflammation, ultimately generating carrier systems for targeted diagnostics and therapeutics.

■ ASSOCIATED CONTENT

Ⓢ Supporting Information

Experimental procedures for the synthesis of 11-Azido-1-undecanol and 11-Azido-1-undecanyl-tosylate. ^{1}H NMR spectra for compounds **2**, **3**, and **6**. This material is available free of charge via the Internet at http://pubs.acs.org.

■ AUTHOR INFORMATION

Corresponding Author

*E-mail: licha@mivenion.com; tel.: +49-30-688379230; fax: +49-30-688379299.

■ ACKNOWLEDGMENTS

This work was supported by the European Regional Development Fund (EFRE) and by the Investitionsbank Berlin (IBB) code: 10138863.

■ REFERENCES

(1) Juliano, R. (2007) Challenges to macromolecular drug delivery. *Biochem. Soc. Trans. 35* (Pt 1), 41−3.

(2) Khandare, J., and Haag, R. (2010) Pharmaceutically used polymers: principles, structures, and applications of pharmaceutical delivery systems. *Handb. Exp. Pharmacol. 197*, 221−50.

(3) Svenson, S., and Tomalia, D. A. (2005) Dendrimers in biomedical applications—reflections on the field. *Adv. Drug Delivery Rev. 57*, 2106−29.

(4) Calderón, M., Quadir, M. A., Sharma, S. K., and Haag, R. (2010) Dendritic polyglycerols for biomedical applications. *Adv. Mater. 22*, 190−228.

(5) Dernedde, J., Rausch, A., Weinhart, M., Enders, S., Tauber, R., Licha, K., Schirner, M., Zügel, U., von Bonin, A., and Haag, R. (2010) Dendritic polyglycerol sulfates as multivalent inhibitors of inflammation. *Proc. Natl. Acad. Sci. U. S. A. 10*, 19679−84.

(6) Weinhart, M., Gröger, M., Enders, S., Riese, S. B., Dernedde, J., Kainthan, R. K., Brooks, D. E., and Haag, R. (2011) The role of dimension in multivalent binding events: structure-activity relationship of dendritic polyglycerol sulfate binding to L-selectin in correlation with size and surface charge density. *Macromol. Biosci. 11*, 1088−98.

(7) Weinhart., M., Gröger, D., Enders, S., Dernedde, J., and Haag, R. (2011) Synthesis of dendritic polyglycerol anions and their efficiency toward L-selectin inhibition. *Biomacromolecules 12*, 2502−11.

(8) Sunder, A., Hanselmann, R., Frey, H., and Mulhaupt, R. (1999) Controlled synthesis of hyperbranched polyglycerols by ring-opening multibranching polymerization. *Macromolecules 32*, 4240−46.

(9) Sunder, A., Mulhaupt, R., Haag, R., and Frey, H. (2000) Hyperbranched polyether polyols: a modular approach to complex polymer architectures. *Adv. Mater. 12*, 235−39.

(10) Sisson, A. L., Steinhilber, D., Rossow, T., Welker, P., Licha, K., and Haag, R. (2009) Biocompatible functionalized polyglycerol microgels with cell penetrating properties. *Angew. Chem., Int. Ed. Engl. 48*, 7540−5.

(11) Yang, J., Wang, Y., Rassat, A., Zhang, Y., and Sinaÿ, S. (2004) Synthesis of novel highly water-soluble 2:1 cyclodextrin/fullerene conjugates involving the secondary rim of *β*-cyclodextrin. *Tetrahedron 60*, 12163.

(12) Benson, R. C., and Kues, H. A. (1978) Fluorescence properties of indocyanine green as related to angiography. *Phys. Med. Biol. 23*, 159−163.

(13) Surette, M. E., Nadeau, M., Borgeat, P., and Gosselin, J. (1996) Priming of human peripheral blood mononuclear cells with lipopolysaccharides for enhanced arachidonic acid release and leukotriene synthesis. *Journal of Leukocyte Biology 59*, 709−715.

(14) Trentham, D. E., Townes, A. S., and Kang, A. H. (1977) Autoimmunity to type II collagen an experimental model of arthritis. *J. Exp. Med. 146*, 857−68.

(15) Fischer, T., Gemeinhardt, I., Wagner, S., Stieglitz, D. V., Schnorr, J., Hermann, K. G., Ebert, B., Petzelt, D., Macdonald, R., Licha, K., Schirner, M., Krenn, V., Kamradt, T., and Taupitz, M. (2006) Assessment of unspecific near-infrared dyes in laser-induced fluorescence imaging of experimental arthritis. *Acad. Radiol. 13*, 4−13.

(16) Vollmer, S., Vater, A., Licha, K., Gemeinhardt, I., Gemeinhardt, O., Voigt, J., Ebert, B., Schnorr, J., Taupitz, M., Macdonald, R., and Schirner, M. (2009) Extra Domain B fibronectin as a target for near-infrared fluorescence imaging of rheumatoid arthritis affected joints in vivo. *Mol. Imaging 8*, 330−340.

(17) Reichert, S., Welker, P., Calderón, M., Khandare, J., Mangoldt, D., Licha, K., Kainthan, R. K., Brooks, D. E., and Haag, R. (2011) Size-dependant cellular uptake of dendritic polyglycerol. *Small 7*, 820−9.

(18) Kuhne, M., Erben, U., Schulze-Tanzil, G., Köhler, D., Wu, P., Richter, F. J., John, T., Radbruch, A., Sieper, J., and Appel, H. (2009) HLA-B27-restricted antigen presentation by human chondrocytes to CD8+ T cells: potential contribution to local immunopathologic processes in ankylosing spondylitis. *Arthritis Rheum. 60*, 1635−46.

(19) Türk, H., Haag, R., and Alban, S. (2004) Dendritic polyglycerol sulfates as new heparin analogues and potent inhibitors of the complement system. *Bioconjugate Chem. 15*, 162−7.

(20) Lee, H., Mason, J. C., and Achilefu, S. (2008) Synthesis and spectral properties of near-infrared aminophenyl-, hydroxyphenyl-, and phenyl-substituted heptamethine cyanines. *J. Org. Chem. 73*, 723−5.

(21) Villaraza, A. J., Milenic, D. E., and Brechbiel, M. W. (2010) Improved speciation characteristics of PEGylated indocyanine green-labeled panitumumab: revisiting the solution and spectroscopic properties of a near-infrared emitting anti-HER1 Antibody for optical imaging of cancer. *Bioconjugate Chem. 21*, 2305−12.

(22) Pauli, J., Vag, T., Spieles, M., Wenzel, M., Kaiser, W. A., Resch-Genger, U., and Hilger, I. (2009) An in vitro characterization study of new near infrared dyes for molecular imaging. *Eur. J. Med. Chem. 44*, 3496−3503.

(23) Ogawa, M., Kosaka, N., Choyke, P. L., and Kobayashi, H. (2009) In vivo molecular imaging of cancer with a quenching near-infrared fluorescent probe using conjugates of monoclonal antibodies and indocyanine green. *Cancer Res. 69*, 1268−72.

(24) Yu, J., Javier, D., Yaseen, M. A., Nitin, N., Richards-Kortum, R., Anvari, B., and Wong, M. S. (2010) Self-assembly synthesis, tumor cell targeting, and photothermal capabilities of antibody-coated indocyanine green nanocapsules. *J. Am. Chem. Soc. 132*, 1929−38.

(25) Firestein, G. S. (2005) Immunologic mechanisms in the pathogenesis of rheumatoid arthritis. *J. Clin. Rheumatol. 11* (3 Suppl), S39−44.

(26) Brown, A. K. (2006) Remission in rheumatoid arthritis: time to reflect on methods of assessment. *Int. J. Adv. Rheumatol. 3*, 84−9.

Bioconjugate Chemistry

Article

pubs.acs.org/bc

Structurally Flexible Triethanolamine Core PAMAM Dendrimers Are Effective Nanovectors for DNA Transfection in Vitro and in Vivo to the Mouse Thymus

Xiaoxuan Liu,[⊥,†] Jiangyu Wu,[⊥,†] Miriam Yammine,[‡] Jiehua Zhou,[⊥] Paola Posocco,[□] Stephane Viel,[§] Cheng Liu,[⊥] Fabio Ziarelli,[¶] Maurizio Fermeglia,[□] Sabrina Pricl,[□] Genevieve Victorero,[‡] Catherine Nguyen,[‡] Patrick Erbacher,[▽] Jean-Paul Behr,[#] and Ling Peng*[,†]

[†]Aix-Marseille Université, Centre Interdisciplinaire de Nanoscience de Marseille, CNRS UPR 3118, Département de Chimie, 163 avenue de Luminy, 13288 Marseille cedex 09, France

[⊥]State Key Laboratory of Virology, College of Chemistry and Molecular Sciences, Wuhan University, Wuhan, 430072, P. R. China

[‡]INSERM U928, 163 avenue de Luminy, 13288 Marseille cedex 09, France

[§]Aix-Marseille Université, LCP UMR 6264, Campus de Saint Jérôme, av. Escadrille Normandie Niémen, case 512, 13013 Marseille, France

[¶]Aix-Marseille Université, Fédération des Sciences Chimiques, Spectropole, av. Escadrille Normandie Niémen, case 511, 13013 Marseille, France

[□]Molecular Simulation Engineering (MOSE) Laboratory, Department of Chemical Engineering, University of Trieste, Piazzale Europa 1, 34127 Trieste, Italy

[▽]Polyplus-transfection SA, Bioparc, Boulevard S. Brandt, BP90018, 67401 Illkirch, France

[#]Laboratoire de Chimie Génétique, Faculté de Pharmacie, CNRS UMR7514, 67401 Illkirch, France

Supporting Information

ABSTRACT: With the aim of developing dendrimer nanovectors with a precisely controlled architecture and flexible structure for DNA transfection, we designed PAMAM dendrimers bearing a triethanolamine (TEA) core, with branching units pointing away from the center to create void spaces, reduce steric congestion, and increase water accessibility for the benefit of DNA delivery. These dendrimers are shown to form stable nanoparticles with DNA, promote cell uptake mainly via macropinocytosis, and act as effective nanovectors for DNA transfection in vitro on epithelial and fibroblast cells and, most importantly, in vivo in the mouse thymus, an exceedingly challenging organ for immune gene therapy. Collectively, these results validate our rational design approach of structurally flexible dendrimers with a chemically defined structure as effective nanovectors for gene delivery, and demonstrate the potential of these dendrimers in intrathymus gene delivery for future applications in immune gene therapy.

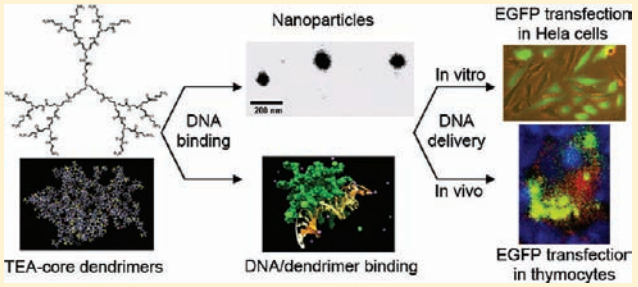

INTRODUCTION

DNA-based gene therapy and the recently developed small interfering RNA (siRNA)-based gene silencing show great promise as therapeutic approaches for treating and controlling inherited as well as acquired diseases. The main obstacle to successful gene therapy is the lack of safe and effective vectors for nucleic acid delivery. To date, the most efficient vectors are viral; however, these do have fatal drawbacks relating to immunogenicity and toxicity, in addition to practical problems concerning large-scale production and quality control. Therefore, developing safe and efficient nonviral vectors for nucleic acid delivery is urgently needed and of paramount importance for gene therapy.[1−4] Nonviral vectors are noninfectious and elicit only weak immune responses; thus, repeated injections can be used for the treatment of chronic diseases. Other important advantages include their convenient preparation and use, as well as their reasonable manufacturing cost. Their major disadvantage relates to a lower transfection efficiency compared to viral vectors. Therefore, improving the tranfection efficiency of nonviral vectors constitutes the ultimate aim and challenge.

Nonviral vectors are usually divided into two main classes—cationic lipids and polymers.[5] In both cases, the positive charges of the vectors interact with anionic nucleic acids and form stable complexes that protect the nucleic acid from

Received: June 2, 2011
Revised: October 27, 2011
Published: November 5, 2011

ACS Publications © 2011 American Chemical Society

dx.doi.org/10.1021/bc200275g | *Bioconjugate Chem.* 2011, 22, 2461−2473

degradation and promote cell uptake. Among the nonviral vectors, cationic dendrimers, characterized by a unique nanoscale spherical architecture, regular dendritic branching, and radial symmetry, are a special family of polymeric vectors.[6−8] The most extensively studied dendrimers for nucleic acid delivery are poly(amidoamine) (PAMAM) dendrimers,[9−13] which bear primary amines at the dendrimer surface and tertiary amines at the branching units inside.[14,15] Positively charged at physiological pH, these primary amines yield a high charge density at the dendrimer surface, which is responsible for ionic condensation with nucleic acids and binding to the cell surface. After entering the cells through endocytosis, the dendrimer delivery complexes are entrapped in endosomes where they are reported to release DNA into the cytosol via a "proton sponge" effect.[16,17] The released DNA molecules are eventually trapped in the nucleus where transcription can occur.

Paradoxically, DNA transfection with partially degraded and structurally fractured PAMAM dendrimers is 2 orders of magnitude higher than that of nondegraded ones.[13] This could be ascribed to the fact that partially degraded dendrimers are endowed with a more flexible and open structure compared to their intact counterparts, and are thus more accessible for interaction with DNA via both electrostatic interactions and mutual accommodation in space. In addition, the open and flexible structure allows water molecules to pervade the nanovector interior more easily, consequently increasing the availability of the inner tertiary amines for protonation. This, in turn, may result in an enhanced buffering capacity via a proton sponge effect, ultimately leading to more efficient DNA release and hence a better transfection efficiency.

Partially degraded and fractured PAMAM dendrimers are obtained either by thermal degradation or by alkaline hydrolysis of the intact dendrimers. However, these processes cannot offer precise control over structure. In addition, dendrimer synthesis is a time-consuming and painstaking process involving stepwise construction as well as tedious workup for separation and purification. Therefore, deliberately degrading a laboriously synthesized perfect dendrimer is neither satisfactory nor economical, and results in a waste of both manpower and energy. With this in mind, we wished to investigate whether rationally designed genuine (i.e., nondegraded) PAMAM dendrimers with flexible structures might behave similarly to their partially degraded rigid counterparts, thus enabling their use as efficient nanovectors for nucleic acid delivery.

We therefore conceived and synthesized structurally flexible PAMAM dendrimers starting with triethanolamine (TEA) as the dendrimer core (Figure 1A).[18−21] Our rationale for molecular design of structurally flexible dendrimers is rather straightforward: with TEA as the dendrimer core, the branching units start at a distance of 10 successive bonds away from the central amine, whereas the prototype NH_3-core PAMAM dendrimers branch out immediately at the central nitrogen of the NH_3 core.[14] Consequently, TEA-core dendrimers feature an extended core and are expected to be less congested in space, with their branching units and terminal end groups being less densely packed than those of NH_3-core dendrimers. We have previously reported these dendrimers for their efficient interaction with RNA molecules[18,19] and their effective delivery of small interfering RNA molecules.[20−23] However, their structural flexibility and their DNA delivery ability have not been investigated yet. Here, we report that these dendrimers have indeed flexible structure and are also effective nanovectors for DNA transfection in vitro and in vivo in the mouse thymus. It is worth mentioning here that the thymus is an attractive organ for immune gene therapy, as it is the primary site of production of functional T lymphocytes playing a crucial role in adaptive immune responses.[24] Owing to the potential use of an intrathymic gene transfer strategy for immune modulation, it is of primary importance to develop nanocarriers for effective DNA transduction in thymus.[25] Historically, gene transfer in the thymus has been a challenge with respect to efficiency and safety. Intrathymic transfection using viral[26−28] or nonviral[28] vectors or electroporation[29] was previously reported to be either inefficient or technically demanding. The results reported here provide the first experimental evidence that the structurally flexible PAPAM dendrimers are effective nanocarriers for DNA delivery and gene transfer in mouse thymus, which may introduce new perspectives to immune gene therapy via intrathymic dendrimer-mediated DNA delivery.

EXPERIMENTAL PROCEDURES

General. Plasmid DNA containing the luciferase gene was a gift from Prof. Barbara Demeneix (CNRS, Paris, France). EGFP plasmid pEGFP-N1 was purchased from Clontech (Clontech laboratories, Inc. CA, USA). Poly(lysine), ethidium bromide, endocytosis inhibitors (cytochalasin D, genistein, and chlorpromazine), paraformaldehyde, and bovine serum albumin (BSA) were supplied by Sigma (Sigma−Aldrich, Lyon, France). YOYO-1 iodide, endocytosis markers (Alexa-Fluor 647-labeled dextran, transferrin, and cholera toxin B), Alexa-Fluor 647-labeled Phalloidin, DAPI, and Hoechst 34580 were purchased from Invitrogen (Invitrogen Ltd., Paisley, UK). HeLa and $LMTK^-$ cells were grown in MEM with Earle's salt (Eurobio, Paris, France) and supplemented with 10% fetal bovine serum (FBS, Perbio, France), 2 mM Glutamax (Eurobio), 100 units/mL penicillin (Eurobio), and 100 μg/mL streptomycin (Eurobio). Cells were maintained at 37 °C in a 5% CO_2 humidified atmosphere.

NMR DOSY Experiments. DOSY experiments were performed at 300 K on a Bruker Avance spectrometer operating at 500 MHz for the ^{1}H Larmor frequency with a 5 mm triple-resonance inverse Bruker cryoprobe optimized for ^{1}H detection and equipped with an actively shielded *z*-gradient coil. D_2O solutions were prepared at 1 mg mL^{-1} by weighing the proper amount of dendrimer sample directly into the NMR sample tube and adding 0.6 mL of deuterated solvent. Note that the D_2O viscosity was taken as 1.05 cP. The NMR pulse sequence was based on a simulated echo and incorporated bipolar gradients and a longitudinal eddy current delay.[30] Typically, the diffusion time was kept constant at 700 ms and bipolar sine gradient pulses between 0.8 and 2.3 ms were employed. The gradient pulse recovery time and the longitudinal eddy current delay were set to 0.25 and 25 ms, respectively. To determine the weight average molecular weight of the dendrimers, the following procedure was followed. Because the lower generation TEA-core PAMAM dendrimers ($\mathbf{G_1}$−$\mathbf{G_3}$) have well-defined and fully characterized molecular weights, they were selected and used as references in order to obtain the corresponding scaling law (and hence the calibration curve) between the self-diffusion coefficients and the molecular weight of TEA-core dendrimers:

$$D = 5.958 \times 10^{-9} M_w^{-0.468} \quad (1)$$

By using eq 1, the molecular weight of all the TEA-core PAMAM dendrimers (G_1–G_7), including those used to build the calibration curve (G_1–G_3), were subsequently estimated (Figure 1B) from their self-diffusion coefficients D, and the

A

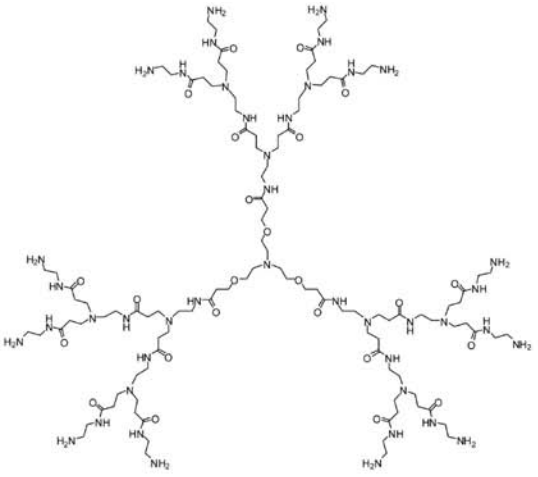

B

Dendrimer generation	Number of end groups	Diffusion coefficient [a] D ($\times 10^{-11}$ m^2 s^{-1})	Hydrodynamic Radius [a] Rh (nm)	Measured Mw		Calculated Mw
				DOSY [a]	GPC [b]	
G_1	6	22.0	0.95	1152	1177 [c]	1177
G_2	12	15.0	1.40	2610	2483	2547
G_3	24	10.9	1.92	5164	5143	5287
G_4	48	8.00	2.62	10001	11587	10767
G_5	96	5.43	3.85	22888	25320	21727
G_6	192	4.12	5.08	41288	55287	43648
G_7	384	2.84	7.37	91427	84011	87489

[a] From DOSY experiment (see text).
[b] From GPC measurement.[19]
[c] From ESI MS measurement.[18]

C

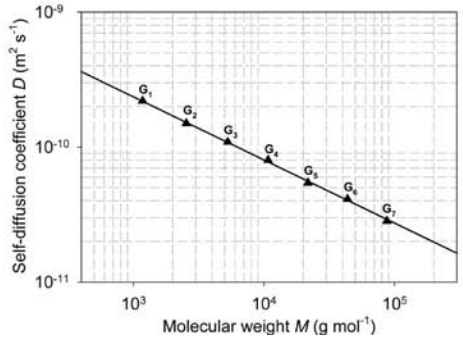

Figure 1. (A) TEA-core PAMAM dendrimer (G_2 was drawn for clarity). (B) General information of the synthesized TEA-core PAMAM dendrimers together with their self-diffusion coefficient D and hydrodynamic radius R_h obtained from DOSY NMR experiments. (C) DOSY-derived self-diffusion coefficient D as a function of the calculated molecular weight M for TEA-core PAMAM dendrimers G_1–G_7 (triangles). The best-fit was obtained as described in the Experimental Section.

results agreed very well (roughly ±5%) with those obtained previously by MS and GPC (Figure 1B).

Potentiometric pH Titration of Dendrimer. The G_5, G_6, or G_7 dendrimer was diluted to a concentration of primary amine of 1.25 mM. pH titration was carried out with 50 mM HCl using a Mettler Toledo 320-S pH meter.

Molecular Modeling. All MD simulations were performed using the *sander* and *pmemd* modules of the AMBER 9 suite of programs,[31] and the new version of the Dreiding force field recently developed by the Goddard group and specifically optimized for dendrimers in water solutions.[32,33] The free energy of binding between the dendrimers and the DNA was calculated according to a previously validated approach[34,35] based on the Molecular Mechanics–Poisson–Boltzmann methodology.[36] Calculations were carried out in parallel on 128 processors of IBM/BCX calculation cluster of the CINECA supercomputer facility, Bologna, Italy. The mesoscopic simulations were carried out with the DPD modulus of *Materials Studio* (v 4.4, Accelrys Inc., USA), according to a multiscale procedure developed by our group.[35]

Preparation of the Plasmid DNA/Dendrimer Complexes. The dendrimers were diluted to an appropriate concentration in 20 mM Tris-HCl buffer (pH 7.6) and 150 mM NaCl, with all solutions stored at 4 °C. The plasmid DNA was diluted to 20 ng/μL in 150 mM NaCl solution. Both solutions were mixed at various N/P (= [total end amines in dendrimer]/[phosphates in DNA]) and incubated at 37 °C for 30 min. The final concentration of plasmid DNA was adjusted to 10 ng/μL.

Gel Retardation Assays of the DNA/Dendrimer Complexes. Each complex (4 μL) containing 250 ng plasmid DNA and the corresponding dendrimer was kept at 37 °C in buffer solution for 30 min before loading on a 0.7% agarose gel in standard TAE buffer for electrophoresis. The DNA bands were stained by ethidium bromide and then detected by a Herolab EASY CCD camera (type 429K) (Herolab, Wiesloch, Germany).

Stability of DNA/Dendrimer Complex Against DNase. An aliquot of 1.8 μg of DNA and the indicated amounts of dendrimers was kept at 37 °C for 30 min. Then, the complexes were incubated in the presence of 1 unit DNase/μg DNA for 0, 5, 10, 20, 30, 45, 60, 75, and 90 min at 37 °C, and aliquots (4 μL) of the corresponding solution containing 200 ng of DNA were withdrawn, added to 0.44 μL 10% SDS solution on the ice, and then subjected to electrophoresis in 1.2% agarose gel in standard TAE buffer. The DNA bands were stained as described above.

Transmission Electron Microscope (TEM) Imaging. Studies were performed with a JEM-1230 electron transmission microscope. Ten microliters of a solution of plasmid DNA (5 ng/μL) were mixed with 10 μL of a solution of dendrimer in 50 mM Tris-HCl buffer (pH 7.4). After equilibration (30 min), 4 μL of this mixture were dropped on a standard carbon-coated copper TEM grid, and then allowed to evaporate (1 h at 30 °C, ambient pressure). The grid was then stained with uranyl acetate (2% in 50% alcoholic solution) for 3 min. Imaging was performed immediately after air–drying for 20 min.

Dynamic Light Scattering Measurement. The plasmid DNA solution was mixed with indicated amount of dendrimer solution at different N/P ratios. The final concentration of the plasmid DNA was 50 ng/μL. After incubating at 37 °C for 30 min, dynamic light scattering (DLS) measurements were performed using Zetasizer Nano-ZS (Malvern, Ltd., Malvern, UK) with a He–Ne ion laser of 633 nm.

dx.doi.org/10.1021/bc200275g | *Bioconjugate Chem.* 2011, 22, 2461–2473

Uptake of DNA/Dendrimer Complexes in HeLa Cells. To evaluate cellular uptake and subsequent intracellular routing of complexes, pCMVLuc was used and labeled with YOYO-1. Briefly, 20 μg of pCMVLuc was mixed with 5 μL of YOYO-1 (80 μM) and incubated at room temperature for 10 min in the dark. One day before use, HeLa cells were seeded at a density of 5×10^4 cells/chamber in 8-well glass chamber slides (Labtek, Nunc, USA). Preparation of the plasmid DNA/dendrimer complexes was performed as described before. Then, the complex containing YOYO-1-labeled plasmid DNA was added to the cells in Opti-MEM transfection medium.

Confocal Microscopy. After incubation for 1.5 h at 37 °C, the cells were washed with PBS and staining with Hoechst 34580. Zeiss LSM 510 Meta laser scanning confocal microscope equipped with inverted Zeiss Axiovert 200 M stand (Carl Zeiss GmbH, Jena, Germany) was used for visualization. Images were acquired using LSM 510 software (Carl Zeiss GmbH, Jena, Germany). For cell uptake in the presence of endocytosis markers, the Alexa-Fluor 647-labeled markers were added during the final 15 min incubation of DNA/dendrimer nanaoparticles prior to nuclear staining with Hoechst. For observation of actin rearrangement, after incubation for 15 min at 37 °C with DNA/dendrimer nanaoparticles, cells were fixed in 4% paraformaldehyde, permeabilized with 0.1% Triton, incubated with 1% bovine serum albumin (BSA), and stained with Alexa-Fluor 647 phalloidin to label actin fibers, then with DAPI to label the nuclei.

Flow Cytometry. The uptake mechanism of the DNA/dendrimer nanoparticles was examined by means of specific inhibitors of different endocytotic pathways. For inhibition experiments, the cells were seeded at a density of 5×10^5 cells in 3.5 cm dishes (Nunc, USA) one day before, then they were incubated with one of following inhibitors: cytochalasin D (to inhibit macropinocytosis), genistein (to inhibit caveolae-mediated endocytosis), or chlorpromazine (to inhibit clathrin-mediated endocytosis) for 1 h in completed medium before the DNA/dendrimer complexes were added. Inhibitors were used at concentrations in which they were not cytotoxic for HeLa cells. After incubation for 15 min at 37 °C with YOYO-1-labeled DNA/dendrimer complex, the cell uptake efficiency was measured using flow cytometry analysis (Beckman Coulter Epics Elite, Beckman Inc., Miami, FL). Each assay was performed in triplicate.

Luciferase Transfection in HeLa Cells. Transfection experiments were carried out using the protocol described previously.[37] Briefly, 24 h before transfection, 5×10^4 HeLa cells were seeded in 24-well tissue culture plates. The desired amount of dendrimer reagent or jetPEI (2 μL per μg of DNA) (Polyplus-Transfetion, Illkirch, France) and 1 μg of pCMVLuc were diluted separately in 50 μL of 150 mM NaCl solution. After 10 min, the transfection reagent solution was added to the DNA solution. The solution was homogenized and left 30 min. Before transfection, cells were incubated with 1 mL of MEM without serum. Then, 100 μL aliquots of pCMVLuc/dendrimer complex solution were added per well and the plates were incubated at 37 °C. After 4 h of incubation, 100 μL aliquots of FBS were added per well and the plates were further incubated at 37 °C for 24 h. Each experiment was done in triplicate.

Luciferase gene expression was measured using a commercial kit (Promega, France). After removing the complete medium, three washings with 1 mL of PBS solution were made. Then, 100 μL aliquots of 1× lysis buffer were added per well, and the plate was incubated at room temperature for 30 min. The lysates were collected and centrifuged at 14 000 *g* for 5 min. The luciferase assay was assessed with 5 μL of lysate after injection of 100 μL of luciferin solution. The luminescence (RLU) was monitored with an integration over 10 s with a luminometer (Berthold, France). Results are expressed as light units integrated over 10 s (RLU), per mg of cell protein using the BCA assay (Pierce, France).

EGFP Transfection in HeLa Cells. In vitro transfection efficiency was evaluated on HeLa cell line using a plasmid containing a reporter gene enhanced green fluorescence protein (EGFP). Cells were seeded into a 24-well plates at a density of 1×10^5 cells per well in 500 μL of complete medium 24 h prior to transfection. After the DNA/dendrimer complexes containing 1 μg of DNA were incubated with cells at 37 °C for 4 h, 50 μL FBS was added. After 48 h, cells were washed in PBS and immediately visualized by using an inverted fluorescence microscope Olympus IX70 equipped with an AxioCam HR digital camera from Carl Zeiss. Images were acquired using *AxioVision* software (Olympus Corp., NY, USA). For quantification, the cells were washed twice with PBS and collected. The fluorescent intensity of positive cells was measured with the flow cytometer (Beckman Coulter Epics Elite, Beckman Inc., Miami, FL).

Effect of Bafilomycin A1. The transfection experiments involving bafilomycin A1 were performed as described above except that the HeLa cells were preincubated with 200 nM bafilomycin A1 at 37 °C for 1 h.

EGFP Transfection in LMTK$^-$ Fibroblasts. Twenty-four hours before transfection, 1×10^4 LMTK$^-$ cells were seeded in 96-well tissue culture plates. The desired amount of dendrimers $\mathbf{G_5}-\mathbf{G_7}$ and DNA plasmid pEGFP-N1 (Clontech) were diluted separately in 50 μL of MEM media. Dendrimers were added to DNA and the solution was homogenized and left for 30 min. Then, 100 μL of pEGFP-N1/dendrimer complex solution was added per well and the plate was incubated at 37 °C. After 4 h, 10 μL of FBS was added per well and the plate was left for 48 h at 37 °C. Cells were visualized under fluorescence microscopy for the observation of EGFP positive cells and transfection efficiency was quantified by *Image-J* software. Cell viability was determined by MTT assay. Each experiment was carried out in triplicate.

EGFP Transfection in Mouse Thymus. C57/BL6 Wild Type (WT) mice (Charles River) were bred and maintained under specific-pathogen-free conditions. All experiments were done in agreement with the French and European ethical rules (authorization number: 13−27). Thymic in vivo gene transfer was performed at 5−6 weeks of age. Animals were anesthetized by intraperitoneal injection with a mixture of ketamine (100 mg/kg body weight; Imalgene 500; Rhone-Merieux) and xylazine (10 mg/kg body weight; Rompun 2%; Centravet). A 20 μL formulation containing 10 μg of pEGFP-N1 or pEGFP/dendrimer complexes prepared in 0.9% NaCl was slowly injected with an insulin syringe in each thymic lobe. Untreated mice were taken as negative control. Animals were kept warm until recovery. After 48 h, mice were sacrificed, and thymi were removed from anaesthetized animals and washed in PBS (1×), then analyzed for EGFP expression by confocal microscopy and flow cytometry.

Western Blot. Proteins were extracted by using the Nuclear Protein Extraction Kit (Panomics). Protein concentrations were measured using the Pierce BCA protein assay. Protein samples were run on SDS polyacrylamide gel (Invitrogen) and transferred to nitrocellulose membranes (BioRad). Incubation with the GFP antibody (1:1000, Roche) was performed

overnight at 4 °C. Mouse polyclonal anti-β-actin was used as loading control (Santa Cruz Biotechnology). Proteins were visualized using horseradish peroxidase-conjugated secondary antibody (1:1000; Amersham Pharmacia Biotech) and the enhanced chemiluminescence (ECL) detection system (Pierce).

Immunofluorescence. To identify the distribution and EGFP cell expression, 12 μm thymic sections were prepared by cryosectioning after embedding the organs in OCT (Sakura Finetech) and mounted on glass slides. Sliced samples were kept in a humidified chamber and were not allowed to dry during staining. Sections were fixed with 4% paraformaldehyde (Sigma Aldrich) in phosphate buffer for 1 h. Frozen sections were stained with anti-CD3 hybridomas (OKT3) (kindly provided by Dr. B. Malissen, CIML, Marseille, France). Alexa 546 goat anti-mouse IgG was used as secondary antibody. As negative control, untreated thymi were used in all experiments. Tissues were counterstained with 4′,6′-diamidino-2-phenylindole (DAPI) at 1 mg/mL and mounted with Mowiol fluorescent mounting medium (Calbiochem). Fluorescent images were acquired by a Zeiss LSM 510 confocal microscope with a 515−525 nm bandpass filter set to view EGFP, a 560 nm long-pass filter set to view Alexa-546, and a 420 nm long-pass filter set to view DAPI. All images were exposed using the same exposure time under the same magnification.

Flow Cytometry. Mice thymi were minced in FACS buffer (PBS 1×, 3% FCS, 0.02 sodium azide) to obtain thymocytes. Cell suspension was filtered through 200 μm nylon mesh and centrifuged at 1500 rpm for 5 min. Precipitated cells were resuspended in FACS buffer. One to two million thymocytes were first incubated with the 2.4G2 hybridoma supernatant to block nonspecific binding of labeled antibodies. Then, cells were stained with a mixture of PE-labeled CD4 and APC-labeled CD8 mAbs (BD Pharmingen). Viable and EGFP positive cells were examined using a FACScalibur flow cytometer and data analyzed with *FlowJo* software (Tree Star, Inc.).

Statistical Analysis. Statistical analysis was performed by a one-way ANOVA test followed by Fisher's protected least significant difference (PLSD) test (Statview 512, Brain Power Inc., Calabases, CA). $p \leq 0.05$ was considered significant (*); $p \leq 0.01$ (**); $p \leq 0.001$ (***).

RESULTS AND DISCUSSION

DOSY NMR Study of TEA-Core Dendrimers. The TEA-core PAMAM dendrimers of generation 1 to 7 ($\mathbf{G_1}$−$\mathbf{G_7}$) were synthesized and characterized in terms of structure and molecular weight as previously described (Figure 1).[18−22] In this work, we further studied their behavior in solution and their sizes and molecular weights using diffusion ordered NMR spectroscopy (DOSY).[38,39] DOSY is based on the pulsed gradient spin echo (PGSE) experiment,[40] which labels the spatial position of the nuclear spins using pulsed magnetic field gradients and allows us to infer the molecular self-diffusion coefficient from their translational displacement over a given time period. Specifically, DOSY[38] allows the self-diffusion coefficient D to be measured, which in turn is related at infinite dilution to the molecular size through the well-known Stokes−Einstein equation

$$D = \frac{kT}{6\pi\eta R_h} \quad (1)$$

where k is Boltzmann's constant, T is the absolute temperature, η is the solvent viscosity, and R_h is the hydrodynamic radius of the molecule (spherical approximation). In addition, DOSY data can be used to estimate the weight average molecular weight of macromolecules,[39] because calibration curves can be established to correlate the self-diffusion coefficient to the molecular weight of macromolecules under specific experimental conditions for a given set of compounds.

The self-diffusion coefficients D obtained for TEA-core dendrimers in D_2O solutions are reported in Figure 1B, together with the corresponding hydrodynamic radius R_h estimated for $\mathbf{G_1}$−$\mathbf{G_7}$ by using eq 1. As can be seen, the higher the dendrimer generation, the smaller the self-diffusion coefficient and the greater the hydrodynamic radius (Figure 1B). This is in line with the molecular construction of PAMAM dendrimers, higher-generation dendrimers displaying a greater weight and a larger size.

The hydrodynamic radii of TEA-core dendrimers as obtained by DOSY experiments were also compared to those reported in the literature for the NH_3-core dendrimers (Table S1 in Supporting Information).[41] Although both types of dendrimers exhibit similar chemical composition and molecular weights, these data showed that TEA-core dendrimers systematically had larger hydrodynamic radii—hence, larger molecular size—than the corresponding NH_3-core dendrimers.[39] Moreover, the difference in size between these two series of dendrimers increased significantly with increasing dendrimer generation, a clear indication that the TEA-core dendrimers assume a more extended conformation in solution. This can be explained by the larger core of the TEA-core dendrimers and by the branching units not directly connected to the focal point of the core, as opposed to NH_3-core dendrimers that exhibit highly compact structures due to the most closely and densely packed branching units. In other words, the molecular structure of TEA-core dendrimers in solution is much less compact than that of NH_3-core dendrimers, which in turn suggests that the former may comparatively possess higher structural flexibility.

We further studied the evolution of the measured self-diffusion coefficients as a function of their molecular weights for TEA-core PAMAM dendrimers. On a double-logarithmic $D = f(M_w)$ plot, all data are perfectly aligned (Figure 1C). Using the corresponding scaling law for TEA-core dendrimers (see Experimental section), we could estimate the molecular weights for dendrimers ($\mathbf{G_1}$−$\mathbf{G_7}$) from their corresponding self-diffusion coefficients D (Figure 1B). The molecular weights obtained in this way for the TEA-core dendrimers parallel the results previously determined by MS and are even closer to the calculated values than the GPC-derived values (Figure 1B).[19,20] This further confirms the quality of the TEA-core dendrimers synthesized in this work.

TEA-Core Dendrimers Have Flexible Structures Favoring Interaction with DNA. We next studied the structural flexibility of the TEA-core dendrimers and their complexes with DNA molecules by computer modeling using atomistic molecular dynamics (MD) and mesoscale simulation techniques. Due to the large size of dendrimers of generation 7 that would lead to extensive calculation and data processing, we performed MD simulations on isolated TEA-core dendrimers of generations 4, 5, and 6 ($\mathbf{G_4}$, $\mathbf{G_5}$, and $\mathbf{G_6}$), NH_3-core dendrimers of generations 4, 5, and 6 ($\mathbf{G_4}'$, $\mathbf{G_5}'$, and $\mathbf{G_6}'$) and their respective complexes with DNA. Here, we focus our comments only on the results obtained with dendrimers of generation 6.

Figure 2A,B shows two equilibrium MD snapshots of G_6 and G_6' respectively, and Figure 2C,D illustrates the superposition of different snapshots taken from their respective MD trajectories. The structural differences between these two dendrimers are blindingly obvious: while G_6 exhibits an open flexible conformation featuring void spaces within its interior (Figure 2A), G_6' is more rigid and compact, with uniformly distributed monomer units and no restricted void spaces in the entire molecule (Figure 2B). The enhanced flexibility of TEA-core dendrimers is well-testified by the wider conformational space visited by G_6 (Figure 2C) during the entire MD simulation with respect to the NH_3-core G_6' counterpart (Figure 2D). It is noted that the presence of hollow spaces in G_6 allows a significantly larger number of water molecules to penetrate into the dendrimer interior with respect to G_6'. This property makes the tertiary amine groups in the dendrimer interior more accessible to water molecules, and therefore more readily available for protonation and subsequent ammonium cation hydration in G_6. This, in turn, may lead to a higher buffering capacity, which was further confirmed by the results of potentiometric titration experiments, as the dendrimers G_5–G_7 displayed flat monotonic titration curves (see Figure 5D).

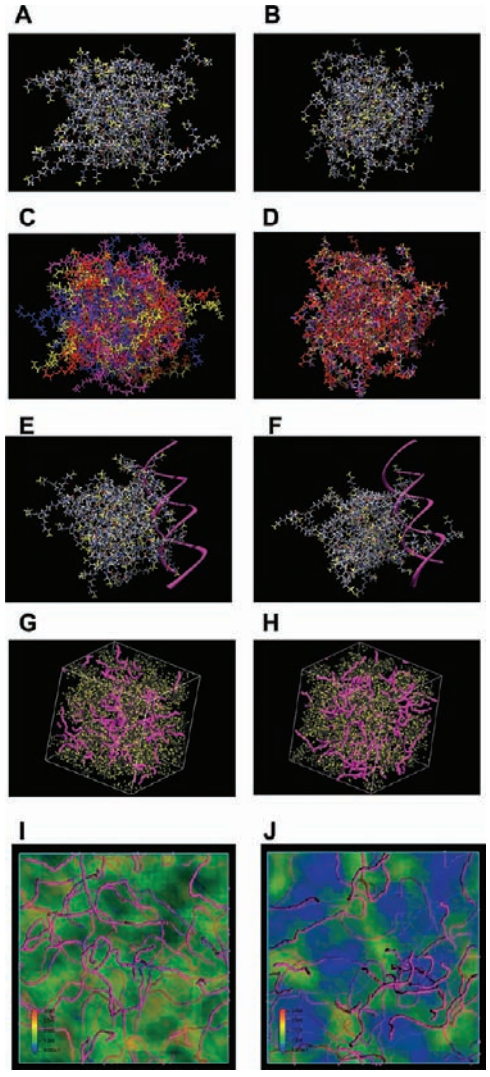

Figure 2. Equilibrium MD snapshots of (A) TEA-core dendrimer G_6 and (B) NH_3-core dendrimer G_6' (In the MD snapshots, dendrimer atoms are portrayed as colored sticks, except for the terminal units, which are portrayed as yellow sticks-and-balls. Atom color code: white, hydrogen; red, oxygen; blue, nitrogen; gray, carbon. Cl^- ions and water molecules have been omitted for clarity). Superposition of different conformations of TEA-core dendrimer G_6 (C) and NH_3-core dendrimer G_6' (D) taken as snapshot along the entire MD trajectory (The different dendrimer conformations are portrayed with different colors, while water and counterions are omitted for clarity). MD snapshots of (E) TEA-core dendrimer G_6 and (F) NH_3-core dendrimer G_6', in complex with a small fragment of double-helix DNA (Dendrimers are depicted as in panels (A) and (B), and DNA is highlighted as a magenta ribbon). Mesoscale morphologies of the self-assembled systems between TEA-core dendrimers G_6 and DNA (G), and NH_3-core G_6' and DNA (H) (The dendrimers are portrayed as gray beads except for the terminal units, which are painted in yellow. The DNA chains are represented as magenta sticks). Panels (I) and (J) highlight the different distribution of DNA and water within the self-assembled DNA/G_6 and DNA/G_6' nanoscopic systems (DNA is portrayed in magenta as in panels (G) and (H), while water is represented as colored density fields: according to the scale reported in the lower left corner of the panels, low density values are blue, while high density values are red).

Additional insightful structural information on DNA/dendrimer complexes was again obtained using atomistic molecular dynamics. The conformation of the TEA-core dendrimer G_6 is such that the outer branches can readily move toward the phosphate backbone of DNA during complex formation, and the surface amino groups can arrange themselves via "induced-fit" for optimal binding with DNA (Figure 2E). This observation is somehow reminiscent of histones undergoing an induced fit conformational change when binding to DNA to form the nucleosome. In contrast, the more rigid and compact structure of the NH_3-core dendrimer G_6' (Figure 2F) prevents this molecule from undergoing significant "induced-fit" conformational readjustment, and consequently, not all terminal amine groups are available to self-orient for optimal DNA binding.

Further evidence for the difference in structural flexibility between these two dendrimer series stem from the mesoscale simulations of their complexes with DNA molecules. A typical result of mesoscale simulation is the morphology and the structure of the matter at nanoscale level at the desired conditions of temperature and composition. Figure 2G,H compares the nanoscale morphology of the DNA/G_6 and DNA/G_6' systems, whereas Figure 2I,J highlights the different distribution of DNA and water within the self-assembled DNA/G_6 and DNA/G_6' nanoscopic systems. In the DNA/G_6 structure, the dendrimers are able to complex the DNA efficiently and homogeneously (Figure 2G,I). On the contrary, for G_6', some DNA chains are less well enwrapped in the system, and DNA bundles are still present (Figure 2H,J). The water density mapping at the mesoscale level also supports the hypothesis of a higher degree of hydration and a more uniform water molecule distribution in the DNA/G_6 system (Figure 2I) with respect to the DNA/G_6' one (Figure 2J). These results are in line with those obtained by MD, demonstrating the easy accessibility of water molecules to the interior of structurally flexible dendrimers.

TEA-Core Dendrimers Form Stable Nanoparticles with DNA and Protect DNA from Degradation. Knowledge of cationic dendrimers to self-assemble with anionic DNA via electrostatic interaction is well-established, and the formation of stable and nanoscale DNA/dendrimer complexes is a prerequisite for efficient cell uptake, intracellular delivery, and transgene expression.

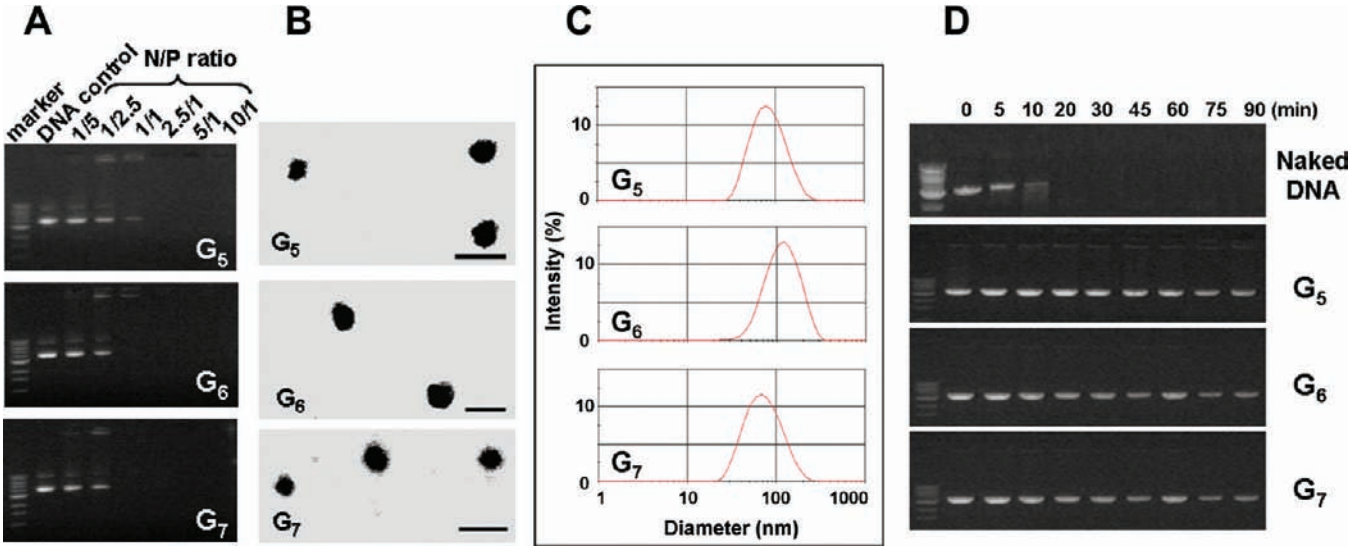

Figure 3. Formation of plasmid DNA/dendrimer complexes as revealed by agarose gel (A), transmission electron microscopy (B), dynamic light scattering (C), and the resulting complexes protect DNA from DNase degradation (D). (A) Migration of luciferase plasmid DNA (250 ng per well) in the presence of G_5−G_7 at charge ratios N/P 1/5−10/1 in 50 mM Tris-HCl buffer pH 7.4. (B) Transmission electron microscopic image of DNA/dendrimer complexes prepared in 50 mM Tris-HCl buffer pH 7.4 using 5 ng/μL plasmid DNA and G_5−G_7 at an N/P ratio of 10. Scale bars represent 200 nm. (C) Light scattering analysis of plasmid DNA/dendrimer complexes prepared using 50 ng/μL plasmid DNA and G_5−G_7 at an N/P ratio of 10. (D) Compared to the naked DNA (200 ng/well), which was degraded within 10 min in the presence of DNase, DNA complexed with G_5−G_7 at an N/P ratio of 2.5 was resistant to DNase and remained stable even after 90 min incubation.

We first studied the complex formation between plasmid DNA and TEA-core dendrimers using gel electrophoresis, a widely used technique for assessing complex formation with nucleic acids. Due to the cooperative electrostatic interactions, cationic dendrimers G_5−G_7 were able to fully condense negatively charged DNA at an N/P ratio above 2.5 (Figure 3A), totally preventing DNA from migration. This suggests the formation of positively charged and stable dendriplexes between dendrimers and plasmid DNA at an N/P ratio ≥2.5. In addition, the complex formation depended on the dendrimer generation: all DNA molecules were complexed with G_7 at N/P = 1,whereas free DNA was observed in trace and considerable amounts with G_6 and G_5, respectively (Figure 3A). This indicates that dendrimers of higher generations form more stable DNA/dendrimer complexes, presumably due to their greater cooperativity and tighter DNA binding domains.[42,43]

The size of the DNA/dendrimer complex is also critical for gene delivery. Due to their compatibility with both extracellular diffusion and endocytosis, small DNA/dendrimer nanoparticles would be an advantage for in vivo experiments. We examined the size and morphology of the DNA/dendrimer complexes using transmission electron microscopy (TEM). Compact, uniform, and nanoscale spherical particles were observed for the DNA/dendrimer complexes using dendrimers G_5−G_7 at N/P ratio of 10, with diameters around 100 nm (Figure 3B). This was further confirmed by dynamic light scattering (DLS), a technique which provides the size, size distribution, as well as surface potential (ζ-potential) of DNA/dendrimer complexes in solution. Results from DLS measurement showed that the DNA/dendrimer complexes have sizes around 100 nm using dendrimers G_5−G_7 at N/P ratios of 10 (Figure 3C). Moreover, ζ-potential measurement gave positive values around +30 mV for the DNA/dendrimer complexes. Taken together, these results demonstrate that the structurally flexible TEA-core PAMAM dendrimers readily condense plasmid DNA into compact and stable colloidal nanoparticles.

We then verified the ability of the DNA/dendrimer nanoparticles to protect DNA against enzymatic degradation. As shown in Figure 3D, naked DNA was completely digested by DNase within 10 min, whereas DNA complexed with dendrimer G_5−G_7 remained intact even after 90 min incubation with the DNase. This result demonstrates that the dendrimer nanoparticles effectively protect DNA from enzymatic degradation, which is a basic prerequisite for efficient DNA delivery.

Cell Uptake of DNA/Dendrimer Nanoparticles Mainly via Macropinocytosis. Cell uptake of DNA/dendrimer nanoparticles is one of the early events in gene delivery. We studied the internalization of DNA/dendrimer complexes in HeLa cells using live cell confocal microscopy with green fluorescent dye YOYO-1 labeled DNA. The green fluorescent DNA/G_6 nanoparticles were effectively internalized in the cells (Figure 4A), whereas no green particles could be observed in the absence of dendrimer under the same experimental conditions (data not shown). Consequently, the effective cell uptake of negatively charged DNA is unambiguously mediated by the cationic dendrimer which acts as nanocarrier.

It has been reported that several pathways can drive cell uptake of nanoparticles with sizes around 50−300 nm, such as macropinocytosis, clathrin-mediated endocytosis, and caveolae-mediated endocytosis.[44−49] We therefore used specific inhibitors and biomarkers of various endocytotic pathways to distinguish which pathway is taking DNA/dendrimer nanoparticles into cells. As illustrated in Figure 4B, cytochalasin D, a macropinocytosis inhibitor, reduced the cell uptake of DNA/G_6 in a dose-dependent manner. Genistein, an inhibitor specifically involved in caveolae-mediated endocytosis, had no notable inhibitory effect on cell uptake; whereas chlorpromazine, a specific inhibitor of clathrin-mediated endocytosis, led only to a slight uptake decrease. In addition, the YOYO-1 labeled DNA colocalized with a macropinocytosis marker dextran but not with transferrin or cholera toxin B (Figure 4C), markers of clathrin- and caveolae-mediated endocytosis, respectively.

dx.doi.org/10.1021/bc200275g | Bioconjugate Chem. 2011, 22, 2461−2473

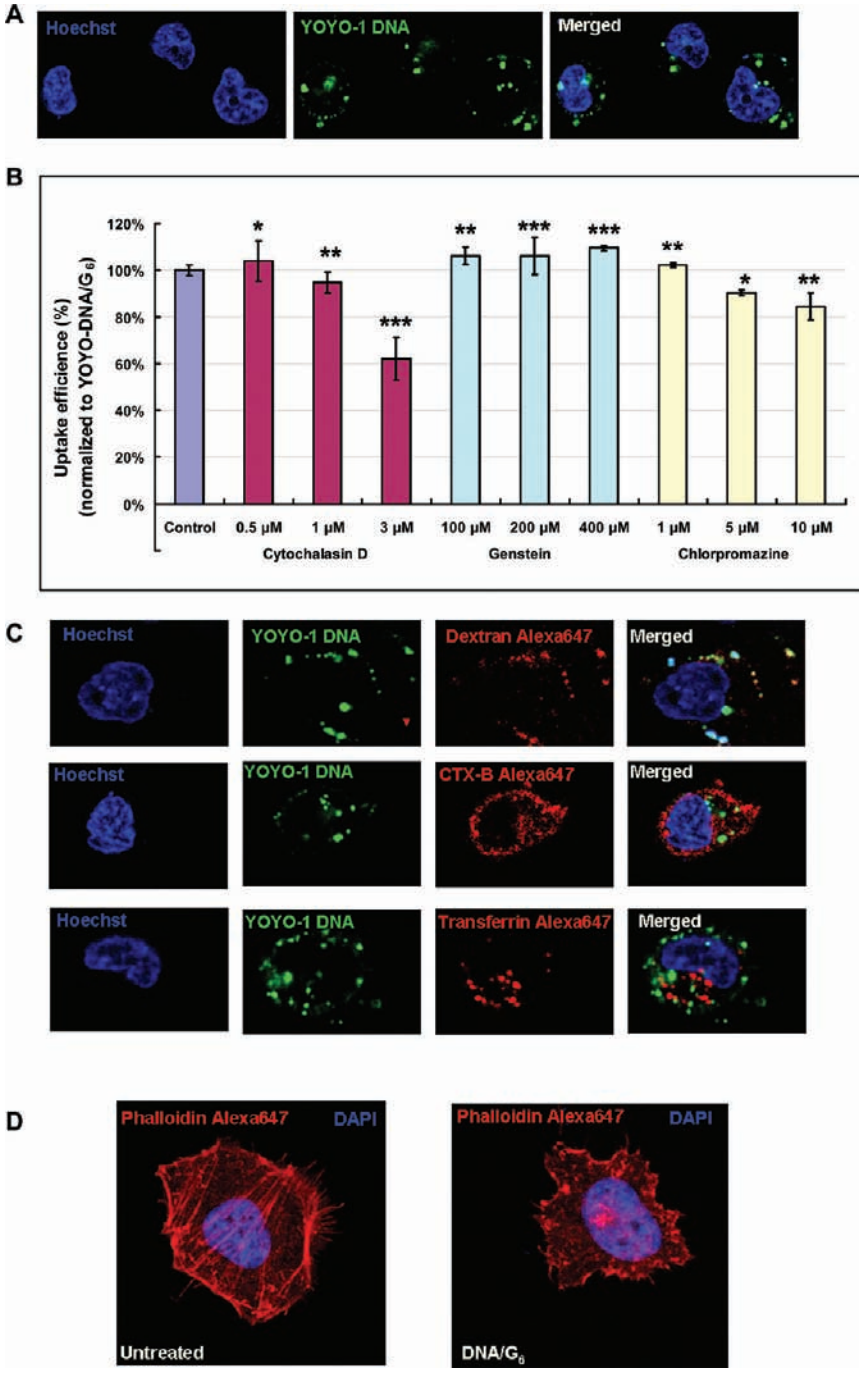

Figure 4. Uptake of YOYO-1-labeled DNA/$\mathbf{G_6}$ complexes in HeLa cells analyzed by live-cell-confocal microscopy (A), using specific inhibitors (B), and fluorescent endocytosis markers (C) of different uptake pathways and phalloidin probe for actin rearrangement (D). (A) Green channel image of the YOYO-1-labeled DNA/$\mathbf{G_6}$ nanoparticles, blue channel image of the nuclei of HeLa cells stained by Hoechst 34580, and merged image of both. (B) Effect of cytochalasin D (to inhibit macropinocytosis), genistein (to inhibit caveolae-mediated endocytosis), and chlorpromazine (to inhibit clathrin-mediated endocytosis) on the cell uptake of the YOYO-1-labeled DNA/$\mathbf{G_6}$ complexes on HeLa cells. (C) Cell uptake of YOYO-1-labeled DNA/$\mathbf{G_6}$ complexes in the presence of different endocytosis markers: dextran (marker of macropinocytosis), cholera toxin B (marker of caveolae-mediated endocytosis), and transferrin (marker of clathrin-mediated endocytosis). (D) Fluorescent labeling of actin fibers using phalloidin reveals actin depolymerization, a hallmark of macropinocytosis. *, ** and ***, differ from control ($p \leq 0.05$, $p \leq 0.01$ and $p \leq 0.001$ respectively) by Student's t test.

Furthermore, actin depolymerization, a hallmark of macropinocytosis, was observed after the application of the DNA/$\mathbf{G_6}$ particles using phalloidin marker (Figure 4D). Altogether, these results clearly demonstrate that macropinocytosis is the major uptake pathway.

Effective DNA Transfections in Vitro. For dendrimer-mediated DNA transfection in vitro, we first evaluated the luciferase gene expression in HeLa cells. Significant luciferase expression was obtained with dendrimers $\mathbf{G_5}$, $\mathbf{G_6}$, and $\mathbf{G_7}$ (Figure 5A), whereas the lower-generation dendrimers $\mathbf{G_1}$–$\mathbf{G_4}$ yielded dramatically reduced expression (data not shown). Moreover, DNA transfection was dependent on the N/P charge ratio. The most efficient gene transfection was observed with $\mathbf{G_6}$ at an N/P ratio of 10, with the efficiency being almost

dx.doi.org/10.1021/bc200275g | Bioconjugate Chem. 2011, 22, 2461–2473

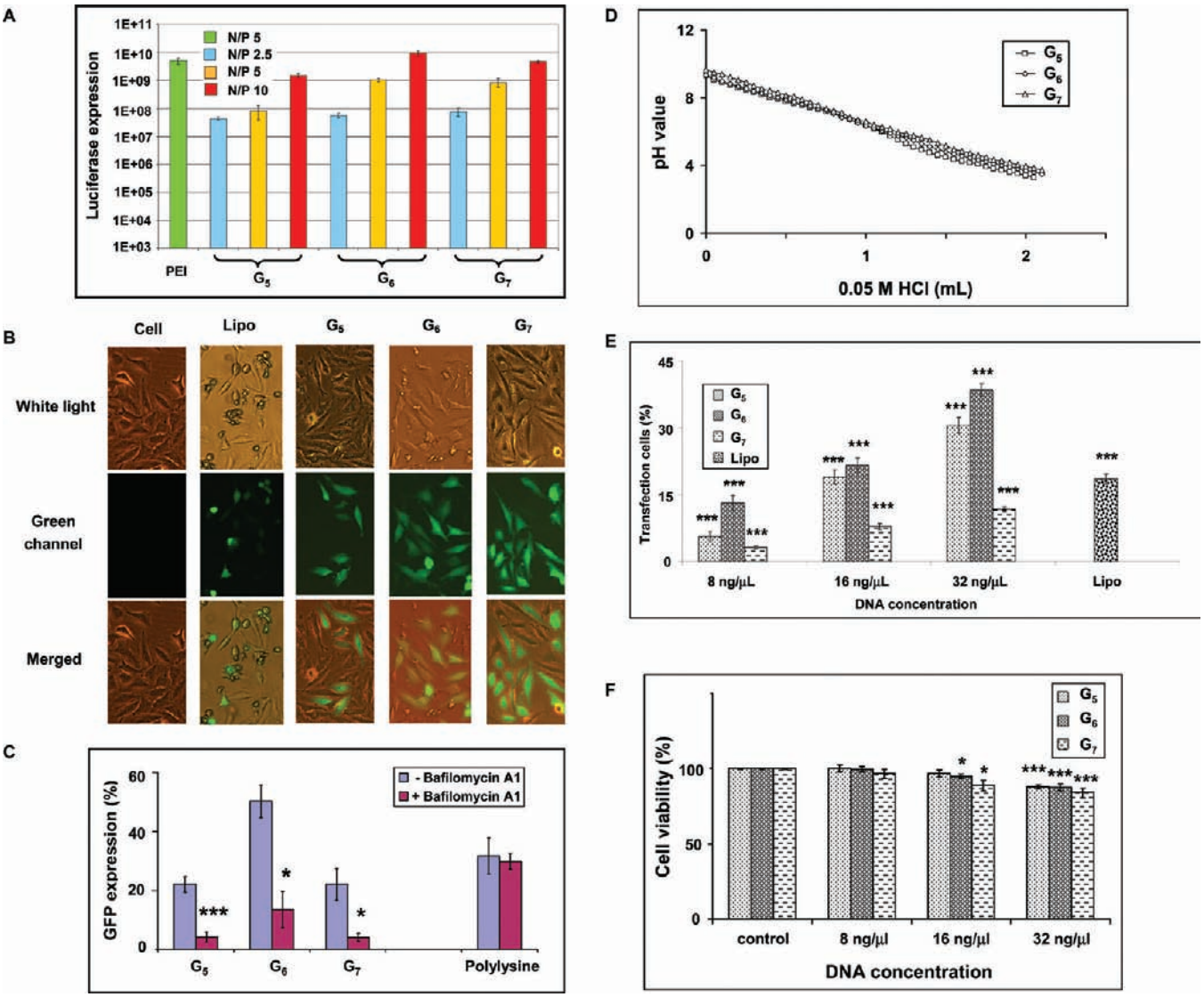

Figure 5. (A) Luciferase transfection in HeLa cells using TEA-core dendrimers G_5−G_7 as vectors (at various N/P ratios) and 1 μg of pCMVLuc plasmid. Luciferase activity was determined 24 h after transfection and expressed as RLU/mg protein of cell lysates. (B) Images of EGFP transfected HeLa cells using G_5−G_7 as vectors and 1 μg pEGFP-N1 plasmid at an N/P ratio of 10, compared to nontreatment control and cells treated with DNA/Lipofectamine complexes. (C) Effects of bafilomycin A1 on dendrimer-mediated and poly(lysine)-mediated transfection of EGFP in HeLa cells as measured by FACS flow cytometry. (D) pH titration curves of the dendrimers G_5−G_7. (E) EGFP transfection efficiencies of G_5−G_7 and Lipofectamine in mouse fibroblast LMTK$^-$ cells in the absence of serum. (F) MTT assay of the toxicity of DNA/dendrimer complexes in mouse fibroblast LMTK$^-$ cells. * and *** differ from control ($p \leq 0.05$ and $p \leq 0.001$, respectively) by Student's t test.

2-fold higher than that of poly(ethylene imine) (PEI), one of the most effective nonviral transfection reagents available to date.[16] It should be mentioned here that the thermally degraded fractured PAMAM dendrimers have a transfection activity similar to that of PEI.[9] We also compared the transfection efficiency of the TEA core dendrimer with the commercially available structurally rigid ethylenediamine (EDA) core dendrimer (Figure S1 in Supporting Information). Our results confirmed that TEA core dendrimer is more efficient for DNA transfection than the corresponding EDA-core dendrimer. With all the results presented here, we conclude that genuine (i.e., nondegraded), structurally flexible TEA-core dendrimers having precisely controlled structures are effective nanovectors for DNA transfection, with efficiencies similar or superior to PEI and hence to fractured PAMAM dendrimers.

In order to further assess the transfection efficacy in individual cells, we carried out assays for enhanced green fluorescent protein (EGFP) expression in HeLa cells using mock-transfected cells as negative control and Lipofectamine as a positive control (Figure 5B). Lipofectamine is one of the most commonly used lipid vectors, characterized also by its well-known cytotoxicity. Under our experimental conditions, most HeLa cells died after treatment with DNA/Lipofectamine; whereas G_5−G_7 dendrimers led to excellent EGFP expression, particularly G_6 being the most efficient vector, with a level of transfection up to 60%.

The above transfection results perfectly correlate with those previously obtained with fractured and degraded PAMAM dendrimers,[13] namely, that only higher-generation dendrimers mediate effective transfection. These higher-generation dendrimers contain larger DNA binding regions,[42,43] thus creating stronger interactions between DNA and dendrimer via

dx.doi.org/10.1021/bc200275g | Bioconjugate Chem. 2011, 22, 2461−2473

cooperative amplification. However, interactions that are too strong between DNA and dendrimer may prevent DNA release from complexes, thereby compromising transfection efficiency. This may explain why $\mathbf{G_6}$ has the best transfection efficiency compared to both the lower-generation dendrimer $\mathbf{G_5}$ and the higher-generation dendrimer $\mathbf{G_7}$.

We further examined whether the buffer-based endosomolytic activity plays an important role using bafilomycin A1. Bafilomycin A1 is a proton pump inhibitor and selectively inhibits vacuolar H^+-ATPase and prevents acidification of endosomes. Figure 5C shows a significant decrease of EGFP expression level in HeLa cells in the presence of bafilomycin A1 for dendrimer-mediated DNA delivery, suggesting that dendrimer-mediated DNA transfection was dependent on the endosomal acidification process. This is in line with the structural features of TEA-core PAMAM dendrimers, which harbor a large number of tertiary amines in the interior able to produce a robust buffer capacity and proton sponge effect for endosomal release. Additional support for this hypothesis comes from the result obtained from the pH titration experiment (Figre 5D) where indeed the dendrimers $\mathbf{G_5}$–$\mathbf{G_7}$ displayed flat titration curves, an indication of high buffer capacity. Since we had no NH_3-core PAMAM dendrimers available in our hands as a control, we then asked whether poly(lysine), which contains only primary amine groups and has been reported to be devoid of proton-sponge effect, could be used as a negative control. We therefore determined poly(lysine)-mediated EGFP expression in HeLa cells in the presence and absence of bafilomycin A1 (Figure 5C). As expected, there was no notable change of EGFP expression in the presence of bafilomycin A1, suggesting the absence of proton-sponge effect in poly(lysine)-mediated DNA transfection. These results demonstrate unambigously that the "proton-sponge" effect played an important role for our dendrimer mediated DNA transfection.

We next performed assays for EGFP expression in mouse fibroblast $LMTK^-$ cells. $LMTK^-$ fibroblasts are known to be difficult to transfect using nonviral vectors. Gratifyingly, our dendrimers $\mathbf{G_5}$–$\mathbf{G_7}$ led to effective EGFP expression (Figure 5E). The highest tranfection efficiency was achieved again using $\mathbf{G_6}$ at N/P = 10, with a transfection level of up to 40%, better than the commercial transfection reagent lipofectamine (Figure 5E). Under the serumless transfection conditions used, no significant toxicity was observed for $\mathbf{G_5}$–$\mathbf{G_7}$ (Figure 5F). The transfection efficiency was decreased in the presence of 10% serum in the transfection medium (Figure S2 in Supporting Information). This observation may limit their in vivo applications via systemic administration but much less by direct injection (vide infra).

Efficient DNA Transfection in Vivo via Intrathymic Injection. We further evaluated in vivo DNA transfection in the mouse thymus as a model. We used both $\mathbf{G_6}$ and $\mathbf{G_7}$ for the in vivo delivery of the EGFP plasmid as a proof-of-concept, since $\mathbf{G_6}$ showed the best DNA tranfection efficiency in vitro, whereas $\mathbf{G_7}$ was successfully used in siRNA delivery in various systems.[20−22] In addition, the DNA complexes with $\mathbf{G_6}$ and $\mathbf{G_7}$ were more stable and retained their size and surface potential values even at high salt concentration (Table S2 in Supporting Information). It should be mentioned that our dendrimers have reduced transfection efficiency in the presence of serum (Figure S2 in Supporting Information); we therefore sought to employ means that do not depend on blood circulation to reach the target organ. We thus chose direct intrathymic injection of DNA/dendrimer complexes.

In vivo DNA transfection experiments were carried out on C57/BL6 WT mice. Mice were first anesthetized, and a volume of 20 μL (containing 10 μg EGFP plasmid complexed with dendrimer at N/P ratio of 10) was then slowly injected into each thymic lobe. All mice survived well during and after the intervention; no signs of toxicity were observed. Strong EGFP expression in the thymi following injection of DNA/dendrimer complexes was revealed by Western blot analysis using an antibody against EGFP (Figure 6A), whereas only weak EGFP levels were detected following naked DNA injection. Therefore, the observed high expression of EGFP in mice thymi is a direct consequence of dendrimer-mediated DNA delivery.

We next examined the transfected thymi by confocal microscopy (Figure 6B). Untreated mice exhibited no EGFP signal (control in Figure 6B); mice with naked DNA injection showed a very weak EGFP signal, whereas EGFP expression mediated by $\mathbf{G_6}$ was significantly stronger (Figure 6B). In addition, costaining analysis with the CD3 thymocyte marker showed a colocalization with the green EGFP signal within these thymocytes (Figure 6B and enlarged in Figure 6C). Consequently, these results demonstrate an efficient and effective dendrimer-mediated DNA transfection in mouse thymus, specifically in thymocytes.

We further analyzed EGFP expression in the different subpopulations of thymocytes. It is known that thymocyte differentiation can be divided into three major stages defined by the expression of CD4 and CD8 markers. The most immature or double-negative stage is characterized by the lack of expression of CD4 and CD8 markers ($CD4^-CD8^-$, double-negative, DN). Double negative cells progress to a stage where there is expression of both CD4 and CD8 markers ($CD4^+CD8^+$, double-positive, DP) before lineage commitment to single-positive (SP) cells which express either CD4 (SP $CD4^+$) or CD8 (SP $CD8^+$) marker. We therefore immunophenotyped EGFP expression within the four main thymocyte subpopulations, namely, $CD4^-CD8^-$ double-negative (DN), $CD4^+CD8^+$ double-positive (DP), $CD4^+$ and $CD8^+$ single-positive (SP) (Figure 6D). We found high percentages of transfection (25.1% of DN, 1.59% of DP, 1.20% of SP $CD4^+$, and 6.96% of SP $CD8^+$ cells) in mice thymi treated with injection of DNA/dendrimer complexes. As expected, no signal was detected in untreated mice thymi, nor was any notable EGFP expression observed in mice thymi treated with naked DNA injection. This finding strongly confirms transgene expression to be a direct consequence of dendrimer-mediated DNA delivery. Finally, it is to be noted that the DN thymocytes were preferentially transfected. This is because immature DN thymocytes undergo rapid proliferation, and therefore lead to higher transfection with respect to the other three subpopulations. Additionally, notable transfection was also observed with more mature SP $CD8^+$ cells, which are considered relatively quiescent. Collectively, our results demonstrate that the structurally flexible TEA-core PAMAM dendrimers studied in this work are safe and effective nanovectors for intrathymic DNA delivery and gene expression. To our knowledge, this is the first experimental evidence that dendrimers could act as efficient nanovectors for DNA transfection in mouse thymus, opening new avenues for future applications of dendrimer-mediated gene therapy for both inherited and acquired immunodeficient diseases.

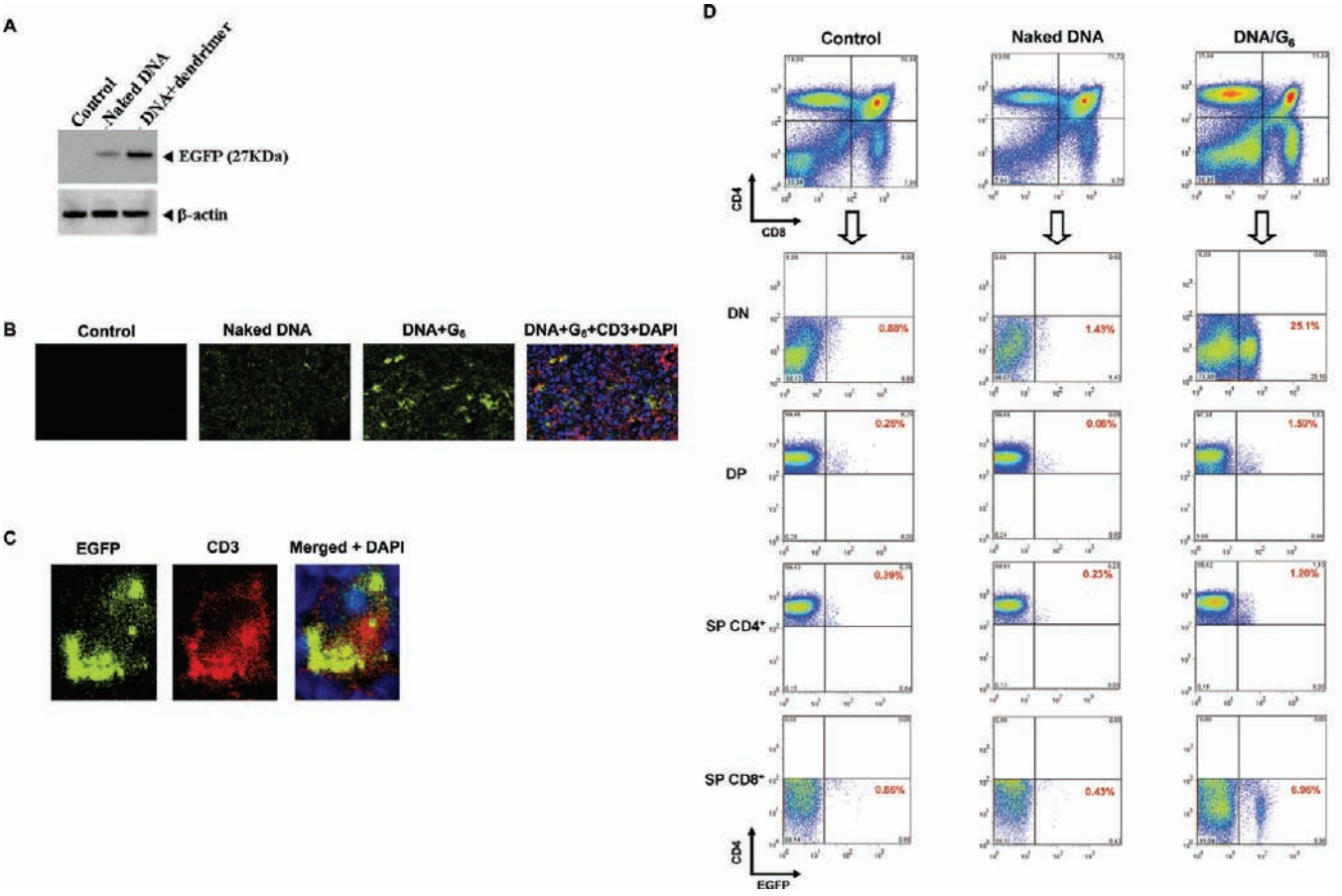

Figure 6. In vivo EGFP expression in thymi was assessed by Western blot (A), immunofluorescence (B and C) and flow cytometry (D). (A) Western blot analysis of EFGP protein expressed in mice thymi in the presence and absence of dendrimer compared to nontreated control. (B) The EGFP fluoresence was analyzed using confocal microscopy with thymi sections derived from mice that were nontreated (control), injected with naked DNA, or injected with DNA/dendrimer complexes: nuclei appear as blue (DAPI staining) and thymocytes as red (anti-CD3 antibody labeling). (C) Enlarged image showing EGFP transfected thymocytes costained with anti-CD3 antibody (red) and DAPI (blue for nuclei laebling). (D) Thymocyte profile stained with CD4 and CD8 monoclonal antibodies was analyzed by flow cytometry 48 h after injection. The percentage of each population of thymocytes is indicated within each quadrant. The different populations of thymocytes expressing EGFP protein were analyzed for thymi derived from mice that were nontreated (control), injected with naked DNA, and injected with DNA/$\mathbf{G_6}$ complexes, respectively. The percentage of EGFP transfected cells is indicated in red within the quadrant of each population. DN: $CD4^-CD8^-$ double-negative cells; DP: $CD4^+CD8^+$ double-positive cells; SP $CD4^+$: single-positive cells which express CD4 marker; SP $CD8^+$: single-positive cells which express CD8 marker.

CONCLUSION

We have developed triethanolamine (TEA) core PAMAM dendrimers as structurally flexible nanovectors for nucleic acid delivery. As shown in the present work, these dendrimers have greater structural flexibility and a more open conformation with void spaces in the interior. They self-assembled with DNA molecules into nanoparticles via an "induced fit" process, resembling histone/DNA interaction in nature. The resulting DNA/dendrimer nanoparticles could effectively protect DNA from degradation and facilitate cell entry mainly via macropinocytosis. Furthermore, due to their open and void structure, these dendrimers are well-adapted to act as 3D protons sponges per se with easier access of water molecules inside the dendrimer interior and leading to increased protonation of interior tertiary amines. This enhances the buffering capacity thus benefiting DNA endosome release. Fulfilling our expectations, these dendrimers were efficient nanovectors for gene delivery in vitro to transfection-resistant fibroblasts as well as in vivo to the mouse thymus, an extremely challenging organ for DNA transfection.

It has been previously reported that the thermally degraded fractured PAMAM dendrimers have an activity similar to PEI.[9] Our results demonstrate that genuine (i.e., nondegraded), structurally flexible dendrimers with precise structural features also are effective nanovectors for DNA transfection, with efficiencies similar or superior to PEI and hence to fractured PAMAM dendrimers. The experimental results presented here, coupled with computer-aided molecular simulations, provide evidence for the development of functional dendrimers for DNA transfection using rational design of structurally flexible dendrimers.[50−52] Compared to random thermal or alkaline degradation, a process which does not allow precise control over the structure, rational design based synthesis allows the development of dendrimer nanovectors with a defined yet flexible structure. Consequently, these dendrimers have a higher potential of becoming vectors for nucleic acid-based therapies in general.

It is important to note that these dendrimers are particularly effective in delivering and expressing a gene in the thymus. The thymus is an attractive organ for immune gene therapy, and yet,

dx.doi.org/10.1021/bc200275g | Bioconjugate Chem. 2011, 22, 2461−2473

gene transfer in the thymus is exceedingly challenging with respect to efficiency and safety. Previous work on intrathymic transfection using viral[26−28] and nonviral[28] vectors as well as electroporation[29] was either inefficient or technically demanding. We demonstrate here for the first time that the structurally flexible PAPAM dendrimers could effectively deliver DNA and reach a high level gene expression in the mouse thymus. Therefore, structurally flexible dendrimer-mediated gene transfer is a promising tool for further development of strategies aimed at immune gene therapy via intrathymic DNA delivery. In addition, as these dendrimers are also efficient nanovectors for siRNA delivery in vitro and in vivo,[20−22] they hold great potential for both in vitro (functional genomics) and in vivo (therapeutic) applications of nucleic acid delivery in general. Last but not least, structure-controlled, size-tailored dendrimers should provide useful tools for use in various applications in biotechnology such as targeted drug delivery systems and drugs based on mimicking the functions of certain natural biomacromolecules.[53]

■ ASSOCIATED CONTENT

Supporting Information

Figure S1, S2, Tables S1, S2 and related experimental details. This material is available free of charge via the Internet at http://pubs.acs.org.

■ AUTHOR INFORMATION

Corresponding Author

*Tel: (33) 4 91829154, Fax: (33) 4 91829301, e-mail: ling.peng@univmed.fr.

■ ACKNOWLEDGMENTS

This research was funded by Association Française contre les Myopathies (No. 13074, 10793), the international ERA-Net EURONANOMED European Research project DENANORNA, National Natural Science Foundation of China (No. 20572081), National Mega Project on Major Drug Development (No. 2009ZX0930-014), Wuhan University, CNRS, INSERM and under the auspice of European COST Action TD0802 "Dendrimers in Biomedical Applications". Liu Xiaoxuan is supported by China Scholarship Council. Miriam Yammine is supported by a grant from the INSERM.

■ REFERENCES

(1) Mintzer, M. A., and Simanek, E. E. (2009) Nonviral vectors for gene delivery. *Chem. Rev. 109*, 259−302.
(2) Mastrobattista, E., van der Aa, M. A., Hennink, W. E., and Crommelin, D. J. (2006) Artificial viruses: a nanotechnological approach to gene delivery. *Nat. Rev. Drug Discovery 5*, 115−121.
(3) Wolff, J. A. (2002) The "grand" problem of synthetic delivery. *Nat. Biotechnol. 20*, 768−769.
(4) Luo, D., and Saltzman, W. M. (2000) Synthetic DNA delivery systems. *Nat. Biotechnol. 18*, 33−37.
(5) Niidome, T., and Huang, L. (2002) Gene therapy progress and prospects: nonviral vectors. *Gene Ther. 9*, 1647−1652.
(6) Dutta, T., Jain, N. K., McMillan, N. A., and Parekh, H. S. (2010) Dendrimer nanocarriers as versatile vectors in gene delivery. *Nanomedicine 6*, 25−34.
(7) Guillot-Nieckowski, M., Eisler, S., and Diederich, F. (2007) Dendritic vectors for gene transfection. *New J. Chem. 31*, 1111−1127.
(8) Dufès, C., Uchegbu, I. F., and Schatzlein, A. G. (2005) Dendrimers in gene delivery. *Adv. Drug Delivery Rev. 57*, 2177−2202.
(9) Navarro, G., and Tros de Ilarduya, C. (2009) Activated and non-activated PAMAM dendrimers for gene delivery in vitro and in vivo. *Nanomedicine 5*, 287−297.
(10) Dennig, J., and Duncan, E. (2002) Gene transfer into eukaryotic cells using activated polyamidoamine dendrimers. *J. Biotechnol. 90*, 339−347.
(11) Haensler, J., and Szoka, F. C. Jr. (1993) Polyamidoamine cascade polymers mediate efficient transfection of cells in culture. *Bioconjugate Chem. 4*, 372−379.
(12) Kukowska-Latallo, J. F., Bielinska, A. U., Johnson, J., Spindler, R., Tomalia, D. A., and Baker, J. R. Jr. (1996) Efficient transfer of genetic material into mammalian cells using Starburst polyamidoamine dendrimers. *Proc. Natl. Acad. Sci. U. S. A. 93*, 4897−4902.
(13) Tang, M. X., Redemann, C. T., and Szoka, F. C. Jr. (1996) In vitro gene delivery by degraded polyamidoamine dendrimers. *Bioconjugate Chem. 7*, 703−714.
(14) Tomalia, D. A., Baker, H., Dewald, J., Hall, M., Kallos, G., Martin, S., Roeck, J., Ryder, J., and Smith, P. (1985) A new class of polymers: starburst-dendritic macromolecules. *Polym. J. 17*, 117−132.
(15) Tomalia, D. A., Naylor, A. M., and Goddard, W. A. III (1990) Starburst dendrimers: molecular-level control of size, shape, surface chemistry, topology, and flexibility from atoms to macroscopic matter. *Angew. Chem., Int. Ed. Engl. 29*, 138−175.
(16) Boussif, O., Lezoualc'h, F., Zanta, M. A., Mergny, M. D., Scherman, D., Demeneix, B., and Behr, J. P. (1995) A versatile vector for gene and oligonucleotide transfer into cells in culture and in vivo: polyethylenimine. *Proc. Natl. Acad. Sci. U. S. A. 92*, 7297−7301.
(17) Sonawane, N. D., Szoka, F. C. Jr., and Verkman, A. S. (2003) Chloride accumulation and swelling in endosomes enhances DNA transfer by polyamine-DNA polyplexes. *J. Biol. Chem. 278*, 44826−44831.
(18) Wu, J., Zhou, J., Qu, F., Bao, P., Zhang, Y., and Peng, L. (2005) Polycationic dendrimers interact with RNA molecules: polyamine dendrimers inhibit the catalytic activity of Candida ribozymes. *Chem. Commun. (Camb.)*, 313−315.
(19) Shen, X. C., Zhou, J., Liu, X., Wu, J., Qu, F., Zhang, Z. L., Pang, D. W., Quelever, G., Zhang, C. C., and Peng, L. (2007) Importance of size-to-charge ratio in construction of stable and uniform nanoscale RNA/dendrimer complexes. *Org. Biomol. Chem. 5*, 3674−3681.
(20) Zhou, J., Wu, J., Hafdi, N., Behr, J. P., Erbacher, P., and Peng, L. (2006) PAMAM dendrimers for efficient siRNA delivery and potent gene silencing. *Chem. Commun. (Camb.)*, 2362−2364.
(21) Liu, X. X., Rocchi, P., Qu, F. Q., Zheng, S. Q., Liang, Z. C., Gleave, M., Iovanna, J., and Peng, L. (2009) PAMAM dendrimers mediate siRNA delivery to target Hsp27 and produce potent antiproliferative effects on prostate cancer cells. *ChemMedChem 4*, 1302−1310.
(22) Zhou, J., Neff, C. P., Liu, X., Zhang, J., Li, H., Smith, D. D., Swiderski, P., Aboellail, T., Huang, Y., Du, Q., Liang, Z., Peng, L., Akkina, R., and Rossi, J. J. (2011) Systemic administration of combinatorial dsiRNAs via nanoparticles efficiently suppresses HIV-1 infection in humanized mice. *Mol. Ther.* doi:10.1038/mt.2011.1207.
(23) Liu, X. X., Rocchi, P., and Peng, L. (2012) Dendrimers as non-viral vectors for siRNA delivery. *New J. Chem.*, doi: 10.1039/C1031NJ20408D.
(24) Cournoyer, D., and Caskey, C. T. (1993) Gene therapy of the immune system. *Annu. Rev. Immunol. 11*, 297−329.
(25) Adjali, O., Montel-Hagen, A., Swainson, L., Marty, S., Vicente, R., Mongellaz, C., Jacquet, C., Zimmermann, V., and Taylor, N. (2009) In vivo and ex vivo gene transfer in thymocytes and thymocyte precursors. *Methods Mol. Biol. 506*, 171−190.
(26) Moreau, A., Vicente, R., Dubreil, L., Adjali, O., Podevin, G., Jacquet, C., Deschamps, J. Y., Klatzmann, D., Cherel, Y., Taylor, N., Moullier, P., and Zimmermann, V. S. (2009) Efficient intrathymic gene transfer following in situ administration of a rAAV serotype 8 vector in mice and nonhuman primates. *Mol. Ther. 17*, 472−479.
(27) Adjali, O., Marodon, G., Steinberg, M., Mongellaz, C., Thomas-Vaslin, V., Jacquet, C., Taylor, N., and Klatzmann, D. (2005) In vivo

correction of ZAP-70 immunodeficiency by intrathymic gene transfer. *J. Clin. Invest. 115*, 2287−2295.
(28) DeMatteo, R. P., Raper, S. E., Ahn, M., Fisher, K. J., Burke, C., Radu, A., Widera, G., Claytor, B. R., Barker, C. F., and Markmann, J. F. (1995) Gene transfer to the thymus. A means of abrogating the immune response to recombinant adenovirus. *Ann. Surg. 222*, 229-239; discussion 239−242.
(29) Irla, M., Saade, M., Kissenpfennig, A., Poulin, L. F., Leserman, L., Marche, P. N., Jouvin-Marche, E., Berger, F., and Nguyen, C. (2008) ZAP-70 restoration in mice by in vivo thymic electroporation. *PLoS One 3*, e2059.
(30) Wu, D., Chen, A., and Johnson, C. S. (1995) An improved diffusion-ordered spectroscopy experiment incorporating bipolar-gradient pulses. *J. Magn. Reson. Ser. A 115*, 260−264.
(31) Case, D. A., Darden, T. A., Cheatham, T. E., III, Simmerling, C. L., Wang, J., Duke, R. E., Luo, R., Merz, K. M., Pearlman, D. A., Crowley, M., Walker, R. C., Zhang, W., Wang, B., Hayik, S., Roitberg, A., Seabra, G., Wong, K. F., Paesani, F., Wu, X., Brozell, S., Tsui, V., Gohlke, H., Yang, L., Tan, C., Mongan, J., Hornak, V., Cui, G., Beroza, P., Mathews, D. H., Schafmeister, C., Ross, W. S., Kollman, P. A. (2006) *AMBER 9*, University of California, San Francisco, CA.
(32) Liu, Y., Bryantsev, V. S., Diallo, M. S., and Goddard, W. A. III. (2009) PAMAM dendrimers undergo pH responsive conformational changes without swelling. *J. Am. Chem. Soc. 131*, 2798−2799.
(33) Jorgensen, W. L., Chandrasekhar, J., Madura, J. D., Impey, R. W., and Klein, M. L. (1983) Comparison of simple potential functions for simulating liquid water. *J. Chem. Phys. 79*, 926−935.
(34) Pavan, G. M., Posocco, P., Tagliabue, A., Maly, M., Malek, A., Danani, A., Ragg, E., Catapano, C. V., and Pricl, S. (2010) PAMAM dendrimers for siRNA delivery: computational and experimental insights. *Chemistry 16*, 7781−7795.
(35) Posocco, P., Pricl, S., Jones, S., Barnard, A., and Smith, D. K. (2010) Less is more − multiscale modelling of self-assembling multivalency and its impact on DNA binding and gene delivery. *Chem. Sci. 1*, 393−404.
(36) Srinivasan, J., Cheatham, T. E., Cieplak, P., Kollman, P. A., and Case, D. A. (1998) Continuum Solvent Studies of the Stability of DNA, RNA, and phosphoramidate DNA helices. *J. Am. Chem. Soc. 120*, 9401−9409.
(37) Erbacher, P., Remy, J. S., and Behr, J. P. (1999) Gene transfer with synthetic virus-like particles via the integrin-mediated endocytosis pathway. *Gene Ther. 6*, 138−145.
(38) Peresada, S., Tonielli, A., Morici, R., and Johnson, C. S. (1999) Diffusion ordered nuclear magnetic resonance spectroscopy: principles and applications. *Prog. Nucl. Magn. Reson. Spectrosc. 34*, 203−256.
(39) Cohen, Y., Avram, L., and Frish, L. (2005) Diffusion NMR spectroscopy in supramolecular and combinatorial chemistry: an old parameter--new insights. *Angew. Chem., Int. Ed. Engl. 44*, 520−554.
(40) Stilbs, P. (1987) Fourier transform pulsed-gradient spin-echo studies of molecular diffusion. *Prog. Nucl. Magn. Reson. Spectrosc. 19*, 1−45.
(41) Mansfield, M. L., and Klusin, L. I. (1992) Intrinsic viscosity of model starburst dendrimers. *J. Phys. Chem. 96*, 3994−3998.
(42) Ottaviani, M. F., Sacchi, B., Turro, N. J., Chen, W., Jockusch, S., and Tomalia, D. A. (1999) An EPR Study of the Interactions between Starburst Dendrimers and Polynucleotides. *Macromolecules 32*, 2275−2282.
(43) Chen, W., Turro, N. J., and Tomalia, D. A. (2000) Using ethidium bromide to probe the interactions between DNA and dendrimers. *Langmuir 16*, 15−19.
(44) Huth, U. S., Schubert, R., and Peschka-Suss, R. (2006) Investigating the uptake and intracellular fate of pH-sensitive liposomes by flow cytometry and spectral bio-imaging. *J. Controlled Release 110*, 490−504.
(45) Manunta, M., Nichols, B. J., Tan, P. H., Sagoo, P., Harper, J., and George, A. J. (2006) Gene delivery by dendrimers operates via different pathways in different cells, but is enhanced by the presence of caveolin. *J. Immunol. Methods 314*, 134−146.
(46) Midoux, P., Breuzard, G., Gomez, J. P., and Pichon, C. (2008) Polymer-based gene delivery: a current review on the uptake and intracellular trafficking of polyplexes. *Curr. Gene Ther. 8*, 335−352.
(47) Seib, F. P., Jones, A. T., and Duncan, R. (2007) Comparison of the endocytic properties of linear and branched PEIs, and cationic PAMAM dendrimers in B16f10 melanoma cells. *J. Controlled Release 117*, 291−300.
(48) Perumal, O. P., Inapagolla, R., Kannan, S., and Kannan, R. M. (2008) The effect of surface functionality on cellular trafficking of dendrimers. *Biomaterials 29*, 3469−3476.
(49) Saovapakhiran, A., D'Emanuele, A., Attwood, D., and Penny, J. (2009) Surface modification of PAMAM dendrimers modulates the mechanism of cellular internalization. *Bioconjugate Chem. 20*, 693−701.
(50) Gorman, C. B., and Smith, J. C. (2000) Effect of repeat unit flexibility on dendrimer conformation as studied by atomistic molecular dynamics simulations. *Polymer 41*, 675−683.
(51) Merkel, O. M., Mintzer, M. A., Sitterberg, J., Bakowsky, U., Simanek, E. E., and Kissel, T. (2009) Triazine dendrimers as nonviral gene delivery systems: effects of molecular structure on biological activity. *Bioconjugate Chem. 20*, 1799−1806.
(52) Merkel, O. M., Mintzer, M. A., Librizzi, D., Samsonova, O., Dicke, T., Sproat, B., Garn, H., Barth, P. J., Simanek, E. E., and Kissel, T. (2010) Triazine dendrimers as nonviral vectors for in vitro and in vivo RNAi: the effects of peripheral groups and core structure on biological activity. *Mol. Pharm. 7*, 969−983.
(53) Lee, C. C., MacKay, J. A., Frechet, J. M., and Szoka, F. C. (2005) Designing dendrimers for biological applications. *Nat. Biotechnol. 23*, 1517−1526.

Bioconjugate Chemistry

Article

pubs.acs.org/bc

Synthetic Modification of Carboxymethylcellulose and Use Thereof to Prepare a Nanoparticle Forming Conjugate of Docetaxel for Enhanced Cytotoxicity against Cancer Cells

Mark J. Ernsting, Wei-Lun Tang, Noah MacCallum, and Shyh-Dar Li*

Drug Delivery and Formulation Group, Medicinal Chemistry Platform, Ontario Institute for Cancer Research, 101 College Street, Suite 800, Toronto, Ontario, M5G 0A3, Canada

ABSTRACT: A nanoparticle formulation of docetaxel (DTX) was designed to address the strengths and limitations of current taxane delivery systems: PEGylation, high drug conjugation efficiency (>30 wt %), a slow-release mechanism, and a well-defined and stable nanoparticle identity were identified as critical design parameters. The polymer conjugate was synthesized with carboxymethylcellulose (CMC), an established pharmaceutical excipient characterized by a high density of carboxylate groups permitting increased conjugation of a drug. CMC was chemically modified through acetylation to eliminate its gelling properties and to improve solvent solubility, enabling high yield and reproducible conjugation of DTX and poly(ethylene glycol) (PEG). The optimal conjugate formulation (Cellax) contained 37.1 ± 1.5 wt % DTX and 4.7 ± 0.8 wt % PEG, exhibited a low critical aggregation concentration of 0.6 μg/mL, and formed 118−134 nm spherical nanoparticles stable against dilution. Conjugate compositions with a DTX degree of substitution (DS) outside the 12.3−20.8 mol % range failed to form discrete nanoparticles, emphasizing the importance of hydrophobic and hydrophilic balance in molecular design. Cellax nanoparticles released DTX in serum with near zero order kinetics (100% in 3 weeks), was internalized in murine and human cancer cells, and induced significantly higher toxic effects against a panel of tumor cell lines (2- to 40-fold lower IC50 values) compared to free DTX.

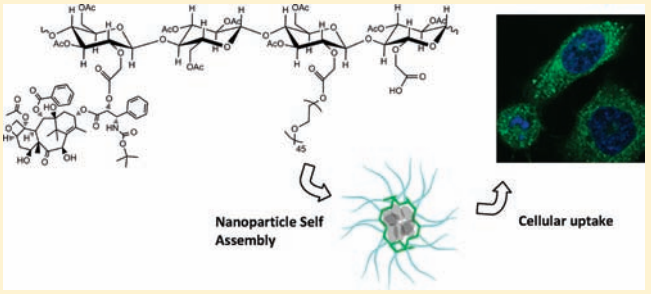

INTRODUCTION

The taxanes paclitaxel (PTX) and docetaxel (DTX) are common cancer therapy agents with a broad spectrum of antitumor activity, and are currently formulated with Cremophor EL/ethanol/saline[1] and Tween80/ethanol/saline, respectively, due to their water insolubility, each of which causes hypersensitivity reactions, requiring premedication regimes.[2,3] DTX is replacing PTX in clinical applications due to enhanced action,[4] and reports on polymeric formulations of DTX are indicating that the drug can be more effectively and safely delivered.[5−7] The use of polymers to improve solubility, pharmacokinetics (PK), pharmacodynamics (PD), bioavailability, efficacy, and toxicity profiles is commonly defined as polymeric therapeutics, and is a thriving field of study.[8−10] It has been demonstrated that soluble macromolecules with molecular weights (MW) above 40 kDa circulate longer than small molecule drugs in the bloodstream due to reduced renal clearance.[11,12] Further, Matsumura and Maeda observed that tumor vasculature is highly permeable, and that high MW polymers or nanoparticles can selectively accumulate in these tissues as a result.[13] Neovascular structures in malignant tissues tend to contain gaps through which <400 nm particles can extravasate,[14,15] and furthermore, lymphatic drainage in tumors is usually absent: particles can readily enter but not exit the tumor compartment.[16−18] The enhanced permeability and retention (EPR) effect provides significant motivation to develop polymer therapeutics, and has also given rise to nanomedicine, where structures comprising liposomes,[19−21] polymeric micelles,[22−24] polymersomes,[25−27] and dendrimers[28−30] can effectively deliver drug through this passive targeting effect.[31] However, polymers and particles can be readily opsonized and cleared in the reticulo-endothelial system (RES, bone marrow, liver, and spleen), reducing the effectiveness of these delivery systems.[19,32] PEGylation of a polymer or nanoparticle can reduce interaction of opsonins with the underlying chemistry through steric hindrance and reduction of hydrophobic and electrostatic interactions, minimizing clearance of the particle in the RES.[19,33−36]

Hydrophobic drugs such as PTX can be loaded non-covalently in nanoparticle formulations. Notable within this field are the PEG-PLA micelles (Genexol, now in phase II clinical trials)[37] and NK105, a PEG-aspartic acid formulation.[23] Both formulations improve upon administration of PTX through elimination of the Cremophor-based delivery vehicle, which causes hypersensitivity issues in human patients,[19] and by enabling treatment with an increased dose to improve efficacy. In comparison to Genexol and NK105, Opaxio (also known as Xyotax and Poliglumex) is a PTX−polyglutamate conjugate.

Received: June 6, 2011
Revised: October 20, 2011
Published: October 21, 2011

ACS Publications © 2011 American Chemical Society

The PK profiles of PTX (Taxol), NK105 (micelle), Genexol (micelle), and Opaxio (conjugate) have been compared, and half-lives were measured to be 13.3, 10.6, 11.4, and 120 h, respectively, in humans.[22,38] As hydrophobic drugs such as PTX and DTX rapidly partition from micelles to plasma proteins, depleting the nanoparticles of drug content,[39] conjugation of taxanes to the polymeric carrier to control release can be desirable.[40,41] The PK profiles of NK105 and Genexol were nearly identical to that of free PTX, whereas the Opaxio polymer conjugate was the only mode by which PK was substantially improved. Although the toxicity of PTX was substantially reduced with Opaxio in preclinical models, hypersensitivity is reported as one of the dose-limiting toxicities in clinical trials,[42] which might arise due to the polymer. Furthermore, Opaxio is not PEGylated, and 24 h postinjection was completely cleared from the blood circulation in mice.[43] The polyglutamate polymer chain is also hydrolytically labile, and is known to break down rapidly into lower MW fragments, leading to significant accumulation of PTX-containing identities in the kidney, heart, and lungs in addition to tumor and liver accumulation.[43] This nonspecific biodistribution may contribute to Opaxio's toxicity.

Developing a biocompatible polymer backbone with a good safety profile for drug delivery remains challenging. Polysaccharides have potential due to their known safety profiles and use as excipients in a variety of pharmaceutical products. Certain classes of polysaccharides are approved as excipients for oral, transcutaneous, and parenteral drug administration (FDA inactive ingredients database),[44] but when referenced against the synthetic polymer field, little work has been done with these biocompatible polysaccharides in the contemporary nanoparticle drug delivery field.[45−48] Cera et al. conjugated doxorubicin and daunomycin to carboxymethylcellulose (CMC) and hyaluronic acid (HA), and reported that these compounds were toxic to cells *in vitro*, but with lower potency compared to the free drug. In addition, the degree of CMC acid group substitution with doxorubicin was low (DS 9 mol %).[49] Uglea et al. conjugated benzocaine to CMC (DS >50 mol %) and oxidized CMC, and tested the effects of these polymers on s.c. sarcoma tumors in rat models, and reported moderate antitumor effect from a single i.p. injection.[50] Auzenne et al. conjugated PTX to HA (DS 10 mol %), and performed *in vitro* and *in vivo* efficacy assays.[51] Mice were implanted with ovarian carcinoma xenografts in the peritoneal cavity, and were treated with an intraperitoneal injection of 200 mg/kg PTX-HA, a treatment which effectively cured the mice and was well tolerated. Inoue et al. reported on a camptothecin analogue (DX-8591) conjugated to a carboxymethyldextran via a peptide spacer (DS 40 mol %), which demonstrated strong action against tumors in mice models and human patients.[52,53] Wang et al. conjugated PTX to heparin (20 wt %), but could only form nanostructures when coformulated with free PTX. [54] In short, polysaccharides appear to have potential as polymer therapeutics, with positive outcomes being reported for selected compositions. However, polysaccharides are generally water-soluble and are incompatible with organic solvents, limiting drug conjugation chemistry, resulting in low coupling yields for hydrophobic drugs (<20 wt %).[53,55] Low drug coupling appears to be linked with rapid drug release: the efficacy of polysaccharide conjugates may be improved through increased drug content. In addition, increasing drug content in the polymer conjugate may facilitate its assembly into stable nanoparticles that provide enhanced protection for the drug, improving PK and efficacy. In this work, we focus on using CMC as a polymer backbone for the delivery of DTX. There are several advantages to the use of CMC: (a) CMC finds widespread use in biomaterials (e.g., OP-1 putty), pharmaceutical formulation (FDA Inactive Ingredients Database), and food (FDA database of Select Committee on GRAS substances reviews); (b) CMC has been approved by FDA for parenteral use in products such as Vivitrol, Sandolog, and Sandostatin, and is known to be bioeliminable;[44] (c) there is no known biological activity compared to hyaluronan and heparin; and (d) CMC presents as an attractive candidate polymer due to a high carboxylate DS (0.8) compared to other polysaccharides (0.2−0.5), enabling the incorporation of high drug content and increased particle-forming properties. This report describes the synthesis and characterization of a nanoparticle forming PEGylated carboxymethylcellulose−DTX conjugate (Cellax), and provides in vitro evidence of an enhanced cytotoxicity against a panel of cancer cell lines.

MATERIALS AND METHODS

Sodium carboxymethylcellulose (CEKOL 30000, MW = 275K, degree of substitution (DS) = 0.82) was received from CPKelco (Atlanta, Georgia, USA), and is an FDA and EU foodgrade material. Glacial acetic acid, acetic anhydride, sulfuric acid, acetone, acetonitrile, poly(ethylene glycol) methyl ether (mPEG−OH, MW = 2000), 1-ethyl-3-(3-dimethylaminopropyl)-carbodiimide HCl (EDC HCl), *N*-hydroxysuccinimide (NHS), 4-dimethylaminopyridine (DMAP), and diethyl ether were purchased from Sigma Aldrich (Oakville, ON). DTX was purchased from LC Laboratories (Woburn, MA, USA). Slide-a-Lyzer dialysis cartridges were purchased from Pierce Biotechnology (Rockford, IL). Vivaspin 10 kDa MWCO ultracentrifugation filters were purchased from Fisher (Ottawa, ON, Canada). Cell culture materials (media and supplements) were purchased from Invitrogen (Burlington, ON, Canada). All other reagents were purchased from Sigma Aldrich (Oakville, ON).

^{1}H NMR Analysis. Samples were dissolved in deuterated chloroform ($CDCl_3$), deuterium oxide (D_2O), or *N,N*-dimethylsulfoxide (DMSO), and were analyzed on a Bruker 500 instrument. Spectra were processed using *TOPSpin* software.

HPLC, UPLC/MS, and GPC Analysis. DTX analysis was performed on an HPLC system consisting of a Waters e2696 Separation Module, 2414 RI and 2998 PDA detectors, and operated by *Empower Pro 2* software. The samples were injected onto an Agilent XDB-C18 column (1.8 μm, 4.6 × 50 mm) column with 0.35 mL/min 95/5 acetonitrile (MeCN)/water isocratic program. The method for analysis and detection of taxanes was derived from several published reports,[56−58] adapted for the instrumentation in the lab. For routine analysis, known taxane identities (docetaxel, paclitaxel, and 7-epidocetaxel) were identified by PDA detector with a selected wavelength of 274 nm. During method development, samples were analyzed by a Waters Acquity UPLC/MS system equipped with a PDA and SQ MS detector. In these analyses, samples were injected on an Acquity UPLC BEH C18 column (1.7 μm, 2.1 × 50 mm), at a flow rate of 0.4 mL/min, with a gradient program of 95/5 to 10/90 water/MeCN over 5 min. Detection of taxanes was in ES+ mode. Polymers were analyzed by a GPC system consisting of a Waters e2696 Separation Module, 2414 RI and 2998 PDA detectors, and operated by *Empower Pro 2* software. THF soluble samples were injected

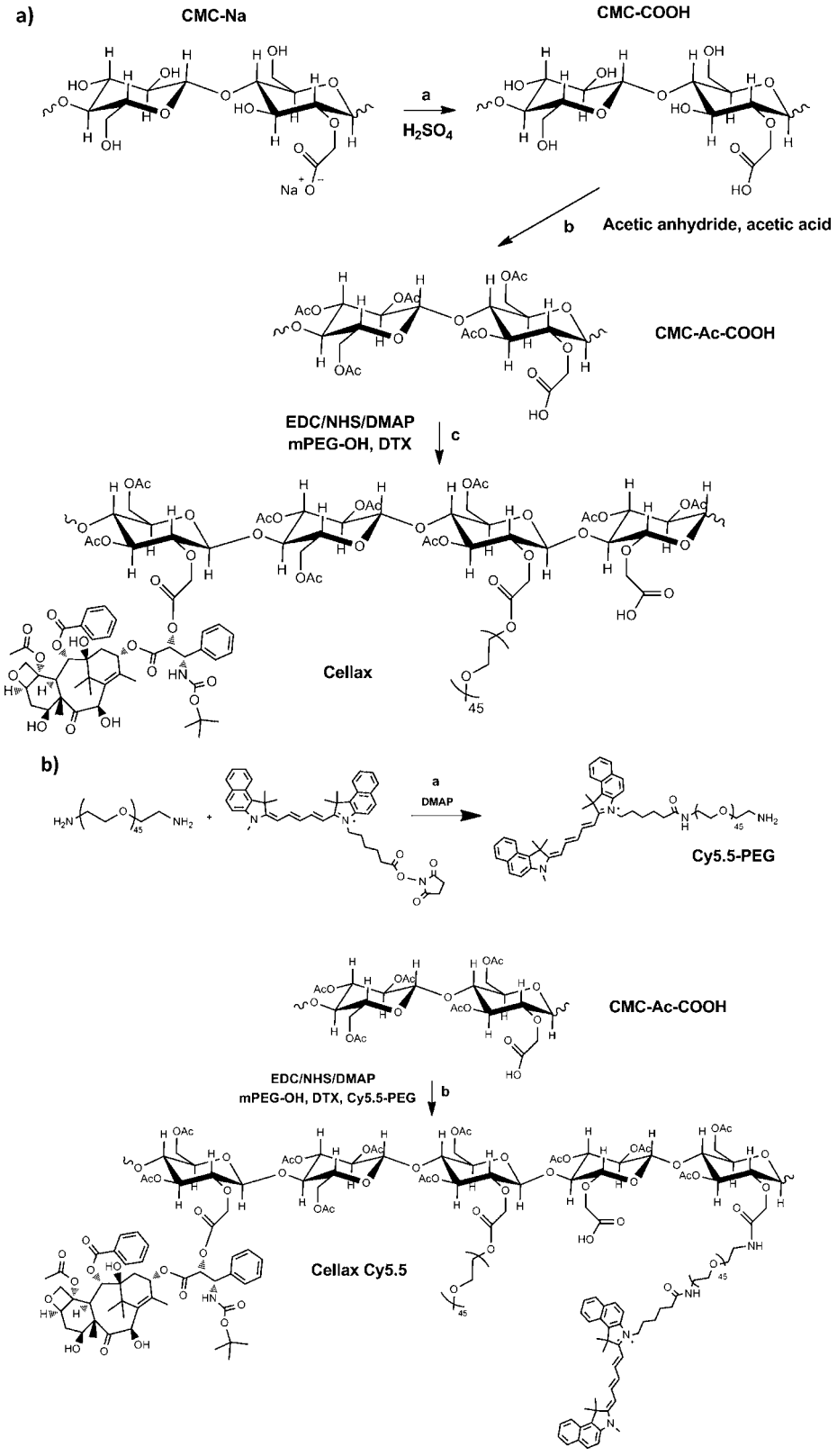

Figure 1. (a) Schematic of polymer modifications. Note that the distribution of anhydroglucose monomer substitutions is random: for ease of depiction, monomers are drawn in simplified form. Multiple carboxylic acid substitution per monomer is possible. a: Treatment of CMC-Na with H_2SO_4 followed by aqueous washes and acetic acid dehydration. b: Reaction of CMC−COOH with acetic anhydride in acetic acid solvent. c: Conjugation of docetaxel (DTX) and mPEG−OH (MW = 2000) with EDC/NHS/DMAP reagents to yield Cellax. (b) Preparation of a Cellax Cy5.5 conjugate. a: conjugation of PEG Bisamine to Cy5.5-NHS ester. b: Conjugation of DTX and PEG and Cy5.5 PEG with EDC/NHS/DMAP reagents to yield Cellax Cy5.5.

dx.doi.org/10.1021/bc200284b | *Bioconjugate Chem.* 2011, 22, 2474−2486

onto Waters Styragel HR5E and HR 3 columns (in series) with 0.35 mL/min THF flow rate. Water-soluble samples were analyzed using a Waters Ultrahydrogel 1000 column with a 1 mL/min flow rate of water. Detection of free DTX and PEG was by PDA (274 nm) and RI, respectively.

Calculation of Stoichiometry for the CMC Polymers. The CMC-Na polymer was modified with carboxymethyl groups, and was supplied by the manufacturer with an analyzed DS value of 0.82: each galactose monomer unit contained 0.82 mol carboxylic acid and 2.18 mol hydroxyl. The molecular weight of each monomer was approximated as 162 g/mol (galactose) + (59.01 g/mol (acid group) × 0.82) = 210 g/mol. These chemical composition values were used to calculate the stoichiometry of reactions performed on CMC polymers.

Acetylation of the CMC. The method for acetylation of CMC was adapted from a method reported by Namikoshi.[59] According to Figure 1, sodium carboxymethylcellulose (CMC-Na, 10 g) was weighed into a round-bottom flask, and was suspended in 20% sulfuric acid (200 mL) with vigorous stirring at room temperature for 2 h. The slurry of CMC−COOH was washed with water until the water tested neutral, and then washed with 3 × 30 mL glacial acetic acid volumes. The CMC−COOH was transferred to a round-bottom flask placed in an ice bath, and suspended in glacial acetic acid (50 mL). Acetic anhydride (30 mL) and sulfuric acid (1.2 mL) were added to the chilled slurry, the temperature was raised to 50 °C, and the solution was vigorously stirred for 3 h, or until the solution clarified. The reaction solution was concentrated by rotary evaporation (58 °C, 58 mbar) and was precipitated in deionized water. The water was extracted by centrifuging the suspension, the pellet was resuspended in water, and the process was repeated until reaching a neutral pH. The acetylated CMC (CMC-Ac) powder was dried under vacuum overnight, dissolved in minimal acetone, and precipitated through water. The polymer was centrifuged out of solution, dried by lyophilization, and analyzed by ^{1}H NMR in DMSO.

Synthesis of Cellax. The preparation of Cellax discussed throughout this report is described here (40 mol % DTX feed, 30 mol % PEG feed), followed by related reactions producing compositions across a range of DTX feeds. 40/30 Synthesis: acetylated carboxymethylcellulose (CMC-Ac, 300 mg, 1.2 mmol acid) was weighed into a 25 mL glass vial, and dissolved in MeCN (2 mL). EDC HCl (448 mg, 2.3 mmol) was dissolved in a mixture of MeCN (12 mL) and water (0.5 mL). NHS (269 mg, 2.3 mmol) and DMAP (29 mg, 0.23 mmol) were dissolved in MeCN (1 mL). mPEG−OH (702 mg, 0.35 mmol) was dissolved in MeCN (2 mL). DTX (378 mg, 0.47 mmol) was dissolved in a mixture of MeCN (12 mL) and DMF (1 mL). The EDC HCl, NHS, and DMAP reagents were added to the CMC-Ac solution, followed by addition of the mPEG−OH and the DTX (Figure 1a). The solution was stirred overnight at room temperature with protection from light. The solvent was removed by rotary evaporation (55 °C, 5 mbar), and the product (Cellax) was dissolved in MeCN (3 mL), and precipitated through 40 mL diethyl ether. The polymer was dried, redissolved in MeCN, and the precipitation was repeated twice. The solvent was removed by vacuum, and the fine powder was twice triturated with water (25 mL) and recovered by centrifugation. The product was analyzed by GPC for uncoupled PEG and DTX, and washing was repeated if residual reagent was detected. ^{1}H NMR analysis ($CDCl_3$) was conducted to confirm the presence of DTX and PEG, and to estimate molecular composition. ^{1}H NMR ($CDCl_3$) δ, 40 mol % DTX feed: 8.12 (d, 2H, C25 and C29), 7.61 (t, 1H, C27), 7.51 (t, 2H, C26 and C28), 7.41 (m, 4H, C31, C32, C34, C35), 7.34 (m, 1H, C33), 6.23 (m, 1H, C13), 5.71 (m, 1H, C2), 5.25 (m, 1H, C4′), 5.10 (br, 1H, C10), 4.98 (d, 1H, C5), 4.32 (m, 1H, C20-A), 4.25 (m, 1H, C7), 4.19 (br, 1H, C20−B), 3.64 (s, 4H, PEG), 3.38 (s, 3H, PEG), 3.0−5.5 (m, CMC polymer), 2.57 (m, 1H, C6-A), 2.38 (3H, C22), 2.02 (m, 3H, acetyl), 1.86 (m, 4H, C6 and C18), 1.75 (br, 3H, C19), 1.34 (s, 9H, C7′, C8′, C9′), 1.29 (s, 3H, C16), 1.14 (s, 3H, C17). In related syntheses, the feed ratio of DTX was varied (10, 20, 30, 50, and 90 mol %) to generate polymer compounds with differing levels of DTX content and constant PEG content. Synthesis and purification processes were identical to the 40 mol % feed described above. Compounds were dissolved in $CDCl_3$ for ^{1}H NMR analysis, and composition was estimated by integration of selected signals.

Synthesis of CMC-Ac-PEG (control polymer). A CMC-Ac-PEG control molecule was synthesized using the same conditions as described for Cellax. CMC-Ac (100 mg, 0.38 mmol acid) was reacted with mPEG−OH (230 mg, 0.12 mmol) in the presence of EDC HCl (147 mg, 0.77 mmol), NHS (88 mg, 0.77 mmol), and DMAP (9 mg, 0.08 mmol) in MeCN (6 mL). After overnight reaction, the solvent was removed by rotary evaporation (55 °C, 5 mbar), dissolved in water (5 mL), and dialyzed against multiple exchanges of water using 20 kDa MWCO Slide-a-lyzer dialysis cartridges. The purified product was recovered by lyophilization, and analyzed by aqueous-phase GPC to verify that unreacted PEG had been entirely extracted. Analysis of chemical composition was by ^{1}H NMR in D_2O.

Synthesis of Cy5.5 Labeled Cellax. Conjugation of Cy5.5 to Cellax was adapted from Wang at al. (Figure 1b).[54] PEG Bisamine$_{2000}$ (169 mg, 0.084 mmol) was dissolved in MeCN (2 mL), to which was added DMAP (1 mg, 0.008 mmol) and Cy5.5 NHS ester (50 mg, 0.084 mmol, 0.5 mL MeCN). The solution was stirred for 4 h at room temperature and protected from light. Acetylated carboxymethylcellulose (CMC-Ac, 100 mg, 0.39 mmol acid) was weighed into a 25 mL glass vial, and dissolved in MeCN (2 mL). EDC HCl (149 mg, 0.78 mmol) was dissolved in MeCN (4 mL) and water (0.15 mL). NHS (90 mg, 0.78 mmol) and DMAP (10 mg, 0.08 mmol) were dissolved in MeCN (0.5 mL). mPEG$_{2000}$−OH (156 mg, 0.08 mmol) was dissolved in MeCN (1 mL) with mild heating. DTX (157 mg, 0.19 mmol) was dissolved in MeCN (4 mL) and DMF (0.25 mL). The EDC HCl, NHS, and DMAP reagents were added to the CMC-Ac solution, followed by addition of the Cy5.5-PEG reaction solution and the mPEG$_{2000}$−OH and the DTX. The solution was stirred overnight at room temperature with protection from light. The product (Cy5.5 Cellax) was purified by the same procedure used to purify Cellax. ^{1}H NMR analysis ($CDCl_3$) was conducted to confirm the presence of DTX and PEG.

Cellax Particle Preparation. Cellax polymer conjugate (CMC-Ac-DTX-PEG) (2 mg) was dissolved in MeCN (0.2 mL), and added dropwise to a vortexing solution of 1.8 mL normal saline in a 15 mL conical tube. Vortexing was maintained for 1 min after solution addition. The resulting Cellax particle solutions were transferred to a Slide-a-lyzer 10 000 MWCO cartridge, and dialyzed against normal saline (100 mL) for 3 h, with two exchanges of dialysate. The particles were filtered through a 25 mm Millipore PVDF filter, and transferred to a Vivaspin centrifugal filter unit (10 000 MWCO), and spun at 3000 rpm to concentrate the particles. The size of the

particles was determined by dynamic light scattering with a particle analyzer (Zetasizer Nano-ZS, Malvern Instruments Ltd., Malvern, UK). DTX content of the Cellax nanoparticles was determined by diluting the sample 20× in 90/10 saline/DMSO, measuring UV absorbance at 274 nm (Nanodrop, ThermoScientific) and calculating DTX concentration using a DTX calibration curve.

Cellax-Cy5.5 particles were prepared with 95 wt % Cellax and 5 wt % Cellax-Cy5.5: Cellax (1.9 mg) and Cellax-Cy5.5 (0.1 mg) in MeCN (10 mg/mL) were added dropwise to a vortexing solution of 1.8 mL normal saline, and were purified and characterized for particle size and DTX content.

TEM Analysis. Cellax particles were diluted 100× in deionized water, and a 2 μL aliquot of solution was pipetted onto the surface of Formvar coated copper TEM grids (TedPella, Redding, CA) and allowed to air-dry. Analysis was performed on a Hitachi HD-2000 STEM at the Centre for Nanostructure Imaging (Department of Chemistry, University of Toronto), using a high angle annular dark field detector, with an activation voltage of 200 kV and a current of 10 mA.

Determination of Critical Aggregation Concentration. The fluorescence-based method for determination of the critical aggregation concentration (CAC) was adapted from Zhang.[6,60] 1,6-Diphenyl-1,3,5-hextriene (DPH, 1.175 mg) was dissolved in MeCN (10 mL) to form a stock solution. Cellax (10 mg) was dissolved in 1 mL of the DPH stock solution to form a 10 mg/mL solution, and was serially diluted with the DPH solution to form a series of 10 concentrations of Cellax in a constant concentration of DPH. One hundred microliter aliquots of each sample were precipitated dropwise in 900 μL normal saline on a vortexer at room temperature for 1 min. Fifty microliter aliquots of each particle solution were transferred to a black 96 well microplate, and fluorescence was measured (Ex 360, Em 460) on a Chameleon plate reader. Two distinct linear curves on a fluorescence vs log concentration plot converged, and the CAC was calculated by using linear algebraic solution for intersection of curves. To demonstrate the stability of Cellax nanoparticles on dilution, particles were diluted with normal saline to form a series of dilutions above and below the CAC, were incubated at 37 °C for 12 h, and particle size was analyzed (Zetasizer).

In Vitro Release of DTX from the Cellax Nanoparticles. Cellax particles were assayed for DTX content by UV assay and were spiked with PTX as an internal standard before mixing with an equal volume of fetal bovine serum (FBS) under aseptic conditions (final DTX and PTX contents were 100 μg/mL and 5 ug/mL, respectively, in 50% FBS).[55] Samples were incubated at 37 °C, and at selected time points (1, 2, 3, 4, 7, 14, and 21 days), 1 mL volumes were taken and combined with 3 mL ethyl acetate, the samples were mixed well for 30 min, and centrifuged at 4000 rpm for 5 min to separate the layers. The ethyl acetate layer was taken off, the solvent was evaporated off, and the residue resuspended in 0.5 mL MeCN and analyzed by HPLC. DTX and PTX peaks appeared at 7.8 and 8.1 min, respectively. A calibration curve for DTX was prepared by spiking a saline/FBS solution with DTX and the PTX internal standard, followed by the same extraction protocol, and this calibration was used to calculate the DTX content in the incubated samples. A new peak appeared in the analysis of incubated samples at 8.4 min, and by LC/MS analysis was determined to be an isomer of DTX (ES+ 878 mass). The isomer was quantified in a manner similar to DTX.

In Vitro Analysis of DTX Toxicity (IC50 Analysis). EMT-6 murine mammary carcinoma cells and LL/2 murine Lewis lung cell carcinoma cells were cultured in DMEM media supplemented with 10% FBS, penicillin (100 U/mL), and streptomycin (100 μg/mL). The mouse mammary carcinoma cell line EMT-6 was a generous gift from Dr. David Stojdl at the CHEO Research Institute and Dr. Douglas Mahoney at the University of Ottawa. All other cell lines were purchased from the NCI. The MDA-MB-231, PC3, and PAN02 lines were cultured in RPMI 1640 media supplemented with 10% FBS. For plating, cells were released from the culture flask with trypsin, resuspended at a concentration of 1×10^4 cell/mL, and 100 μL of cell suspension was added to the wells of 96 well polystyrene plates. A slight modification (5×10^4 cell/mL) was made for the MDA-MB-231 analysis, as these cells were slow-growing compared to the other cell lines. The cells were maintained for 24 h in culture (37 °C, 5% CO_2, humidified) before addition of particles. DTX solutions were made up in DMSO and diluted with media to form a 100 nM stock solution with 0.1% DMSO content (0.1% DMSO was determined to be nontoxic to the cell lines). These DTX samples were 2× serially diluted with 0.1% DMSO media. Cellax particles were assayed for DTX content, and 10× serially diluted with media. Polymer control (CMC(Ac)-PEG) solutions were prepared to match the mass concentration of the Cellax dilutions. The cultures were maintained for 3 days, at which time cell viability was assayed by the XTT assay. Briefly, a 1 mg/mL solution of XTT reagent and 1.53 mg/mL solution of phenazine methylsulfate in water were prepared, and 5 μL of phenazine methylsulfate was added to each mL of XTT solution. Fifteen microliter aliquots of the XTT solution were added to each well, the culture plates were incubated for 2 h at 37 °C, and absorbance of each well at 480 nm was then read. Wells treated with media (or 0.1% DMSO media) represent 100% viable cultures, and wells containing no cells represent background signal. In a parallel experiment, the DTX solutions added to the cultures were fractionated over two days, with addition of 1/4 the dose every 12 h for 2 days. The viability data were analyzed in GraphPad *Prism*, and the IC50 for each system was calculated.

In Vitro Analysis of Cellax Particle Uptake. EMT-6, LL/2, PAN02, PC3, and MDA-MB-231 cells were adjusted to 1×10^5 cell/mL, and 1 mL of cell suspension was added to 24 well plates containing sterile glass coverslips. After 24 h of incubation, media in each well was aspirated, and replaced with media containing Cellax-Cy5.5 (0.1 mg DTX/mL). Two parallel experiments were conducted with 10% FBS or 10% heat deactivated FBS containing media. The cell cultures were incubated for 12 h, after which the media was aspirated, and cells were fixed with 500 μL of methanol for 1 min. The methanol was aspirated, the wells were washed 2× with PBS, and 500 μL of 0.5 μg/mL DAPI solution was added. After 5 min, the DAPI solution was aspirated, and the slips were rinsed twice with PBS. The coverslips were mounted on glass slides with 95% glycerol/5% PBS, and imaged on an Olympus Fluoview confocal microscope (AOMF, Toronto, ON).

RESULTS AND DISCUSSION

Nanomedicine approaches to the detergent-free delivery of taxanes include polymeric micelles (NK105[23] and Genexol[37]), protein complexes such as Abraxane,[61] and polymer conjugates such as Opaxio.[40] While micelle-based PTX formulations such as NK105 increase the dose of PTX that can be safely

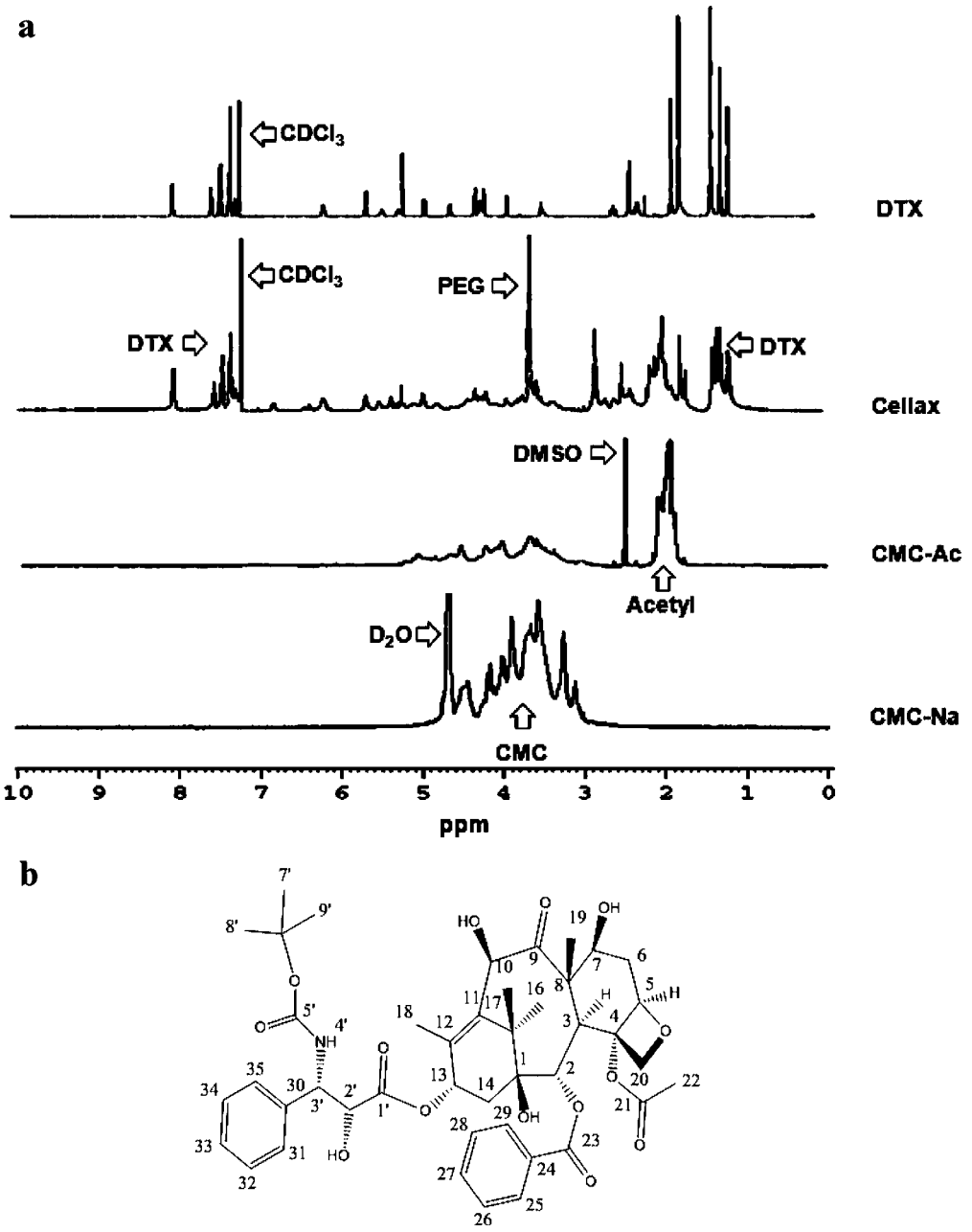

Figure 2. [1]H NMR of Cellax and Components. (a) Spectra of DTX, sodium carboxymethylcellulose (CMC-Na), acetylated CMC, and the Cellax product. (b) DTX with the carbon numbering scheme.

administered and improve antitumor efficacy and the PK profile in mouse models, the PK profile of the micelle formulated PTX in clinical trials is not improved over Taxol,[23,37] likely due to rapid plasma partitioning.[39] Similarly, Abraxane improves antitumor efficacy compared to Taxol by increasing the maximum tolerated dose, but the PK profile is not enhanced.[62] Conjugation of the drug to a polymeric carrier can control drug migration, and can enhance the PK and efficacy provided that the polymer is biocompatible and has low renal and RES clearance. Furthermore, the polymer should travel in blood in a state that enables permeation into malignant tissues by the EPR effect, exhibits a low volume of distribution, and contains a drug–polymer linker that is cleavable in tumor tissues. A clinically known example of this approach is a PTX–polyglutamic acid conjugate (Opaxio), which improves PK and has exhibited promise in phase I clinical trials.[42] However, a signal for needed improvement to the polymer therapeutic design is given by unpromising phase III clinical trial outcomes (www.celltherapeutics.com). The Opaxio polyglutamate backbone is labile, and the polymer is readily digested into low molecular weight fragments containing PTX, which widely distribute to normal organs including the kidneys, lungs, and heart:[43] if the polymer breaks down during transport to the tumor, the polymer therapeutic advantage is diminished.[43,63,64] Furthermore, Opaxio could not be detected 24 h postinjection in mice,[43] suggesting the need for improved PK, possibly via PEGylation. Prolonged blood circulation is a prerequisite for enhanced tumor uptake, the well-supported central hypothesis of the EPR effect.[32] Further, no published reports indicate that this polymer conjugate assembles into protective nanoparticles, and it is likely then that polymer amide linkages and the ester drug linkages are readily exposed to enzymatic degradation

dx.doi.org/10.1021/bc200284b | *Bioconjugate Chem.* 2011, 22, 2474–2486

during blood transport. Our objective in design of a polymer therapeutic was to prepare biocompatible cellulose-based nanoparticles to leverage the EPR effect and protect the drug from early release or alteration, to incorporate PEG to reduce RES clearance, and to release DTX in a controlled and slow release mechanism in the target tissue. CMC was selected based on its known safety profile as an excipient, and due to the reasonable stability of the backbone in human physiological conditions, ensuring maintenance of macromolecule integrity during circulation. In addition, CMC represents a viable backbone chemistry for conjugation due to its high DS (0.8). In our initial screening of known biocompatible polysaccharides, conjugation of DTX to carboxymethyl dextran (DS of 0.2) failed to yield particle forming identities, likely due to a low DS and corresponding low hydrophobic drug content. CMC presents with a minor limitation, however, as sodium CMC is water-soluble and gels in water, and is only sparingly soluble in organic solvents such as DMF or DMSO,[65] limiting synthesis options for non-water-soluble drugs. In the method development process, the sodium counterion on the carboxylic acid was exchanged with triethylamine (TEA) or tetrabutylammonium (TBA) in order to generate solvent-soluble polysaccharide as described by others.[34,66] However, the coupling efficiency of carboxylate groups to DTX and PEG esters using EDC/NHS chemistry was low (<10%), and particles formed using these materials were heterogeneous in size and prone to self-aggregation. Therefore, we first acetylated the hydroxyl groups of CMC using acetic anhydride with sulfuric acid catalysis to produce a solvent-soluble version of CMC.

Acetylation of CMC. The DS per anhydroglucose unit, as specified by the manufacturer, was 0.8 mol acid per mol anhydroglucose and, by inference, 2.2 mol hydroxyl per mol anhydroglucose. We calculated the theoretical moles of hydroxyl (converted to acetyl) groups and acid groups, and designed conjugation schemes accordingly. The reaction solution transitioned from a suspension to a clear yellow solution after 2 h of reaction, and by ^{1}H NMR analysis, conversion was quantitative and yields >90%. The resulting CMC-Ac polymer was a powdery white solid, readily soluble in DMF, THF, and MeCN, with no gelling properties. Figure 2A: ^{1}H NMR (DMSO) δ: 3.0−5.5 (m, CMC H), 2.02 (m, acetyl CH_3). ^{1}H NMR analysis confirmed the DS calculations: by integration of the ^{1}H NMR spectra, the ratio of anhydroglucose protons and acetyl protons was found to conform to prediction. Acetylation of the CMC polymer was quantitative provided that the CMC polymer was scrupulously washed in each stage of the protocol to remove residual sulfuric acid (to minimize discoloration) and residual water (inhibition of anhydride reaction).

Conjugation of DTX and PEG to CMC. CMC-Ac was soluble in DMF, but pilot DTX and PEG coupling reactions performed in DMF with EDC/NHS/DMAP did not exhibit good yields, and particles formed from these materials were unstable and nonuniform. In solvent screening, MeCN promoted higher conversions, and subsequently, all conjugation reactions were performed in MeCN. In addition, to minimize the dilution of reagents, 1.5 vol % water was added to dissolve EDC, and 3.0 vol % DMF was added to dissolve the DTX in the MeCN solvent. Purification of the polymer by dialysis was initially attempted, but as PEG, DTX, and the CMC reagents exhibit different solubility profiles, problems with precipitation and low purification efficiency occurred. Triturating finely ground Cellax product with water effectively extracted uncoupled PEG, and precipitation of MeCN solutions of Cellax through diethyl ether extracted uncoupled DTX. Complete extraction of the uncoupled PEG and DTX was confirmed by GPC analysis of the product. However, the Cellax polymer absorbed to the polystyrene columns, and GPC analysis was restricted to identification of impurities. The final product for all feed ratios was a fine white powder, readily soluble in acetonitrile, DMF, THF, and chloroform. Typical reactions yielded ~80 wt % of theoretical recovery. See Figure 2A for the NMR spectra of Na-CMC, CMC-Ac intermediate, DTX, and the final Cellax polymer, and Figure 2B for the DTX carbon numbering scheme. The relative mol % of each unit (CMC, PEG, and DTX) in the conjugate was estimated by integration of the spectra, and by back-calculation using the molecular weight of each component, mole and weight percentages were calculated. Polymer conjugates were prepared with a range of DTX mol % feeds (10, 20, 30, 40, 50, and 90 mol %). By ^{1}H NMR analysis, the peak assignments were identical in all polymer products, varying only in the integration of peaks assigned to PEG and DTX. As shown in Figure 3a, all

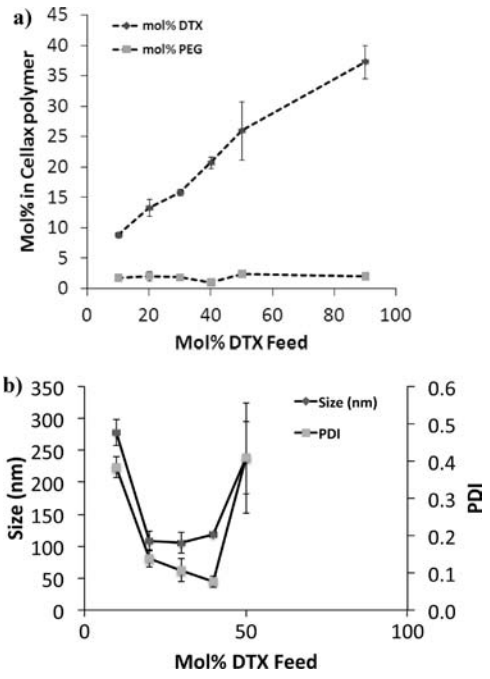

Figure 3. Optimization of Cellax formulation. (a) DTX was fed into the reactions at different ratios relative to the carboxylic acid content of the CMC(Ac) polymer, and PEG was maintained at a feed of 30 mol %. The resulting polymers were characterized for substitution with DTX and PEG. Good correlation between DTX feed and resulting Cellax composition was observed (R^2 = 0.94). (b) Cellax polymers formed nanoparticles when they contained a defined range of DTX content. Polymers with compositions outside this range formed larger less defined particles, or precipitated.

conjugates exhibited a similar DS for PEG (1.8 to 2.4 mol %, ~7% coupling conversion), and the DS for DTX varied in a linear relationship (R^2 = 0.98) with increasing molar feed. Docetaxel coupling conversion was ~50% of feed (Figure 3a). The MW of the Cellax polymer is estimated from NMR data to be 4.75 × 10^5 g/mol. The capability to perform the reaction in organic phase, the reproducible and high level of DTX coupling to the polymer, and the elimination of gelling properties confirmed the benefits of the CMC acetylation. All polymer

conjugates (10−90 mol % DTX feeds) were water-insoluble, and the formation of defined particles or disorganized precipitates depended on their specific composition. For the preferred composition (40 mol % DTX feed), the Cellax polymer contained 20.8 ± 1.6 mol % DTX (37.3 ± 1.5 wt %) and 1.1 ± 0.2 mol % PEG (4.7 ± 0.8 wt %). Polymers prepared across the 10−90 mol % feed range of composition were tested for particle forming characteristics (size and polydispersity index (PDI)): as seen in Figure 3b, polymers prepared with 20−40 mol % DTX feed (12.3−20.8 mol % DTX, 26.2−37.3 wt % DTX) yielded particles ranging 105−118 nm, with low PDI (<0.1). Outside this specific range of DTX composition, particle size exceeded 200 nm, particle PDI values were >0.3, and much of the polymer precipitated. Although PEG DS was low compared to DTX DS (1.8−2.4 mol %), increasing PEG content (either through >30 mol % feed or use of higher MW PEG5000) disrupted particle forming properties. For effective nanoparticle forming properties, the hydrophobic (DTX) and hydrophilic (PEG) elements of the Cellax macromolecule were balanced, so that when these amphiphilic structures contacted isotonic aqueous solution, they would assemble into stable nanoparticles and protect the drug cargo from direct exposure to serum enzymes.

Particle Formulation and Stability. Nanoparticles were prepared using the well-established nanoprecipitation method[67] by slow addition of a MeCN or THF solution of Cellax polymer conjugate into aqueous media (10× dilution), and desired particles were produced provided the concentration of Cellax in the organic solvent solution ranged between 10 and 25 mg/mL. It was observed that particles formed from 25 mg/mL solutions were approximately 150 nm in size, and particles formed from 10 mg/mL solutions were smaller (105−120 nm). For all subsequent work, the 10 mg/mL MeCN polymer solution and 10× dilution parameters (1 mg/mL polymer in particle solution) were set so as to provide for the smallest-sized population of nanoparticles. As described in Table 1,

Table 1. Cellax Particle Size Characteristics in Different Aqueous Systems (Zetasizer Measurements)

solution	size (nm)	PDI
PBS	134.0 ± 3.4	0.1 ± 0.08
Saline (0.9%)	118.2 ± 1.8	0.08 ± 0.02
Sucrose (10%)	128.5 ± 3.2	0.10 ± 0.04

Cellax nanoparticles could be formed in a variety of isotonic solutions with defined diameter (118−134 nm, PDI < 0.1). TEM analysis (Figure 4) of the particles in normal saline (104 ± 15 nm) supported the Zetasizer measurement (118 nm ±1.5 nm). The critical aggregation concentration (CAC), determined by the DPH assay, was 0.6 μg/mL. In comparison, hyaluronic−paclitaxel conjugates have a reported critical micelle concentration (cmc) of 7.8 μg/mL,[68] poly(glutamylglutamine-PTX) has a cmc of 25 μg/mL,[69] and PEG-polyesters typically have cmcs of the same order of magnitude (μg/mL levels) as Cellax.[70−72] Cellax particles were diluted serially to 0.5 μg/mL and examined for size stability: as dilution occurred, particle size exhibited only a minor increase when diluted to the limits of Zetasizer particle size detection, and did not disassemble (Figure 5). As Cellax was stable at the CAC, it is probable that these particles will remain stable at high dilution in biological systems. For example, in a 20 g mouse model treated at 40 mg DTX/kg, 200 μL of Cellax administered i.v. (10 mg Cellax/mL,

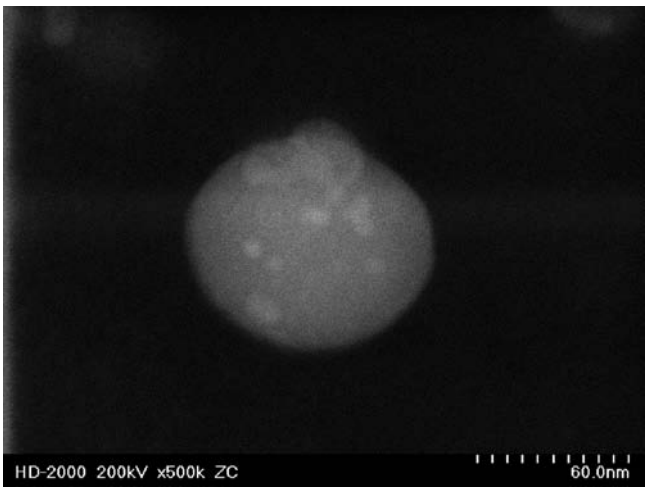

Figure 4. TEM analysis. Cellax particles were applied to Formvar coated copper grids, and analyzed by dark-field TEM (500 000× magnification). Six randomly picked particles were imaged, and the size was measured: particle diameter = 104 ± 15 nm.

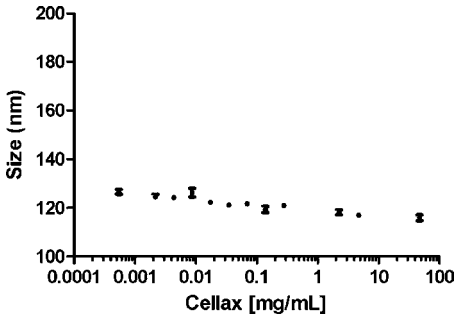

Figure 5. Dilution stability. Cellax particles were diluted from 47 mg/mL to 0.1 μg/mL (below the critical aggregation concentration and at the limits of particle size detection) and were stored for 24 h prior to analysis. Particle diameter increased slightly as the particles were diluted.

4 mg DTX/mL) would be diluted in ∼2 mL blood volume to 2 mg Cellax/mL. Considering the scenario when 90% of particles are out of circulation, the concentration of Cellax would be still well above CAC, and the DTX cargo would remain protected from serum esterases. In addition to stability against dilution, Cellax particles were stable in storage (>2 months, ongoing study) in saline, in contrast to reports on Abraxane and various PTX micelle formulations which exhibit limited stability in suspension.[73,74]

In Vitro DTX Release. The release of DTX from Cellax nanoparticles in serum was analyzed to affirm that hydrolysis of the ester bonds would occur. By LC/MS analysis, two identities with an ES^+ MS value of 808.8 m/z were detected, corresponding to DTX and a DTX isomer, 7-epidocetaxel: these peaks were analyzed to generate a total taxane release value.[57,75,76] The isomerization of Taxol (PTX) and Taxotere (DTX) in serum and the decreased activity are well-documented metabolic phenomena,[57,77,78] partly due to the unavoidable metabolism of taxanes in biological systems which supports the need to create a protective formulation for taxanes (i.e., nanoparticle encapsulated). As shown in Figure 6, the release of DTX over the course of 21 days (3.6%/day) was sustained, culminating in full release, with half of the total taxane released as active DTX. This data was contextualized

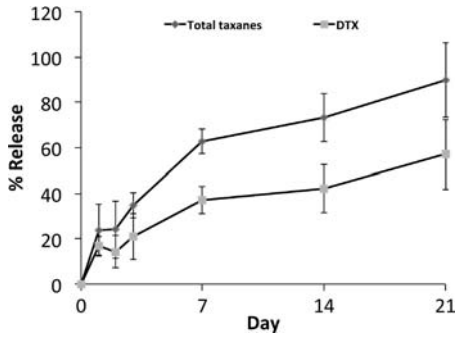

Figure 6. Release of DTX from Cellax particles in FBS containing saline (50 vol %). Particles were incubated at 37 °C in a 5% CO_2 atmosphere. At selected time points, samples were extracted and analyzed for taxanes by HPLC. Two peaks were detected: DTX and 7-epidocetaxol. Total taxanes refers to the combined release of DTX and the isomer, and indicates when full release had been reached.

with respect to published reports on taxane conjugates. For example, release of PTX from water-soluble carboxylmethyl dextran conjugates (5.5−6.5 wt % PTX) is rapid, with total release occurring within 3−4 days.[55] Release of DTX from water-soluble albumin conjugates (1.5 wt % DTX) is likewise rapid, with 40% release in 1 day.[7] Release of DTX from PEG conjugates (26 wt % DTX) is more controlled, with full release in 6 days.[6] Release of PTX from polyglutamic acid conjugates (35.8 wt % PTX) is slow and similar to Cellax, with 15−30% release recorded in 4−5 days.[43,79] It is posited that ready access of hydrolytic enzymes to the ester bonds linking the taxane to the macromolecule may drive the high rate of hydrolysis in low DS (<30 wt %) polymer conjugates. Conjugates with low drug content appear to exhibit rapid release profiles which might lead to reduced blood circulation time and efficacy. For Cellax, the high degree of substitution, the condensed state of the nanoparticle, and the addition of PEG shielding appears to effectively control the rate of hydrolysis, so that 3 weeks of sustained release were observed. Although the drug release rate

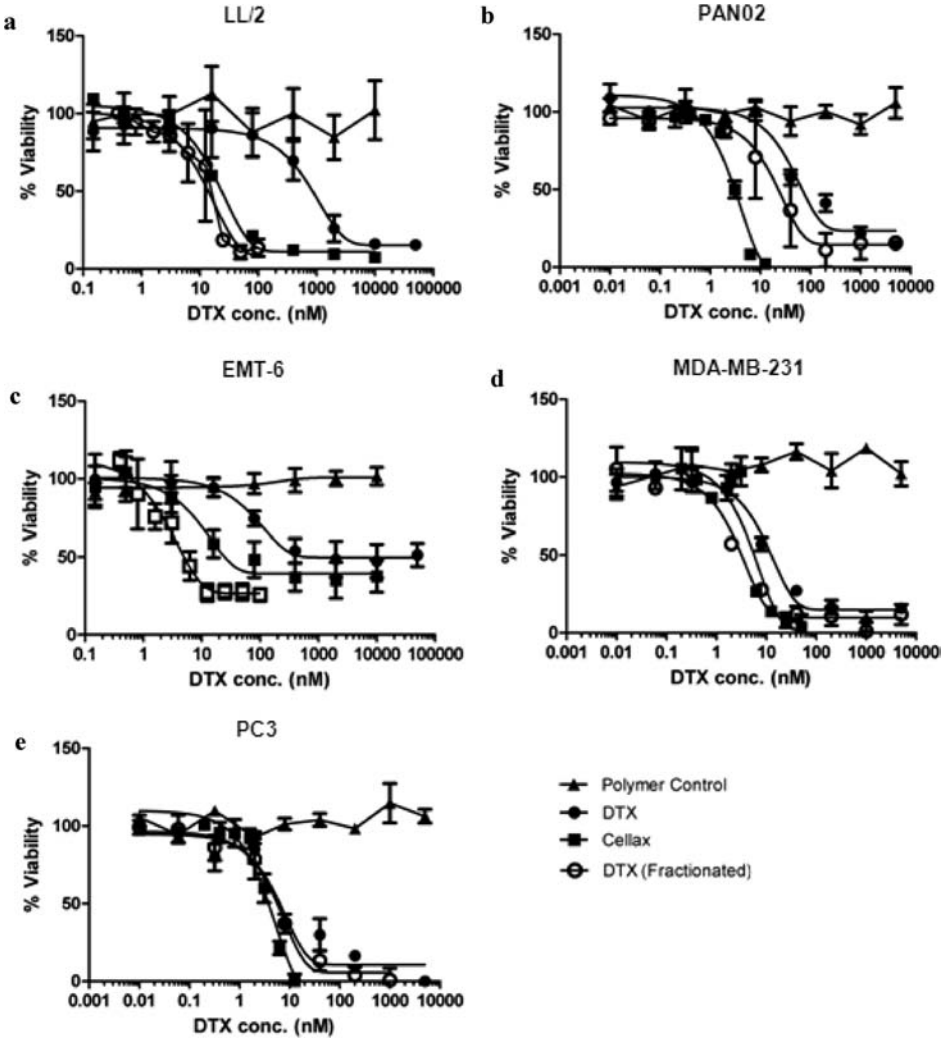

Figure 7. IC50 analysis of DTX toxicity. (a) LL/2. (b) PAN02. (c) EMT-6. (d) MDA-MB-231. (e) PC3. Cells were cultured on tissue culture polystyrene (1000 cell/well, 5000 cell/well for MDA-MB-231) for 1 day, followed by addition of media containing DTX, Cellax, or drug-free polymer controls. Polymer controls at each selected DTX concentration are matched to the Cellax sample by weight concentration (mg/mL). For fractionated treatment of free DTX, the dose was administered in four parts over two days, for a total dose matched to a bolus dose. Cultures were maintained for 3 days, until the no-treatment control wells approached confluence. Cell viability was determined by the XTT assay, with no-cell background signal being subtracted. IC50 curves were calculated in *GraphPad Pro*. Each group was $n = 9$, and error bars are ± standard deviation.

dx.doi.org/10.1021/bc200284b | *Bioconjugate Chem.* 2011, 22, 2474−2486

Table 2. In Vitro Cytotoxicity Analysis (IC50 Analysis)

cell line	IC50 DTX (nM) bolus dose	IC50 DTX (nM) fractionated dose	IC50 Cellax (nM)	fold increase in toxicity (Cellax vs bolus DTX)
LL/2 (murine, lung)	767 ± 10	12 ± 4	19 ± 3	40
PAN02 (murine, pancreatic)	71 ± 1	10 ± 8	3 ± 1	24
EMT-6 (murine, mammary)	80 ± 3	6 ± 3	9 ± 3	9
MD-MBA-231 (human, breast)	10 ± 4	3 ± 1	5 ± 1	2
PC3 (human, prostate)	6 ± 1	6 ± 1	3 ± 1	2

from Opaxio is well-controlled in vitro, the rapidly degradable backbone of the conjugate led to relatively short blood half-life in vivo (5.3 h)[40] and increased drug accumulation in normal tissues compared to conventional long-circulating nanoparticles.[32]

In Vitro Analysis (IC50 and uptake study). The cytotoxicity of different DTX formulations was measured by following cancer cell line viability. The concentration of control CMC(Ac)-PEG polymer in cell culture was matched to the concentrations of Cellax, and at no level were there any indications of cytotoxic effects on these cells (Figure 7). The cancer cell lines exhibited sensitivity to free DTX in conformity with published reports:[80,81] IC50 analysis confirmed an enhanced cytotoxic effect of Cellax against LL/2, PAN02, and EMT-6 lines, compared to free DTX, and a slightly superior effect against the PC3 and MDA-MB-231 lines (Table 2 and Figure 7). The Cellax treatment was 40× more toxic against LL/2, 24× more toxic against PAN02, 9× more toxic against EMT-6, and 2× more toxic against the MD-MBA-231 and PC3 lines. Increased Cellax toxicity was approximately related to the chemosensitivity of each cell line (a higher DTX IC50 correlated to a larger fold increase in toxicity when treated with Cellax). The same panel of cells exposed to fractionated matched doses of DTX over 2 days displayed IC50 values similar to the Cellax treated cells (Table 2). Cellax is a member of a small class of conjugates that are more effective than free drug *in vitro*,[82] as free drug tends to be more potent than conjugates or micelle formulations.[40,69] DTX is an anti-mitotic anti-neoplastic drug which binds to tubulin and impedes cell replication, ultimately inducing apoptosis and cell death.[83] Compared to a single bolus dose of DTX, the Cellax polymer released DTX continuously, and this sustained-release model represents a preferred dosing modality for this drug. A number of recent reports have emphasized the benefit of metronomic (fractionated) DTX exposure, as opposed to burst release. For example, De Souza et al. reported that a chitosan/laurinaldehyde/egg phosphatidylcholine/DTX gel (DTX-Po-Li_{gel}) slow-releasing DTX in the i.p. cavity exhibited significant activity against SKOV3-luc xenograft ovarian tumors compared to intermittent treatment with DTX.[84] In preclinical and clinical studies, the administration of lower and more frequent doses of chemotherapeutic has been observed to improve efficacy and reduce toxicity, with efficacy effects being attributed to increased cell death and anti-angiogenesis effects.[85,86] In this study, we confirmed a similar toxicity benefit with fractionated therapy against the chemo-insensitive cell lines (EMT-6, LL/2, and PAN02), with a smaller benefit observed for the chemosensitive PC3 and MDA-MB-231 lines. In addition to the benefits of slow release, internalization of the polymer-conjugate and enhanced release in lysosomes may further enhance the action of DTX. For example, Opaxio is reportedly internalized in the cytoplasm, and this process is understood to deliver more drug to the cell via accelerated hydrolysis of ester bonds (pH and enzyme mediated), enhancing the bioavailability of the taxane.[42] Similarly, the dendrimer conjugate of PTX developed by Khandare et al. also displayed significantly enhanced intracellular uptake leading to increased cytotoxicity compared to the free drug.[82] In our study, we found that Cy5.5-labeled Cellax nanoparticles were internalized in all five cell lines, both human and murine: the signal was punctate, suggesting uptake in vesicles, possibly through pinocytosis or phagocytosis (Figure 8). To control for the possibility that

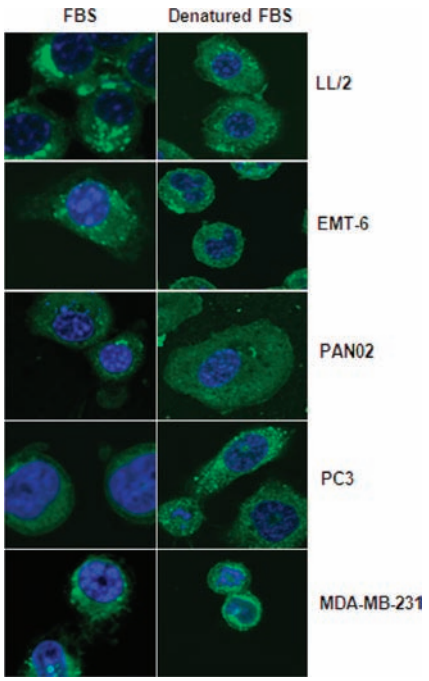

Figure 8. Cellular uptake of Cy5.5-labeled Cellax particles. Cells were cultured on glass coverslips in 12 well plates (1×10^4 cell/well), maintained for 24 h in FBS or denatured-FBS supplemented media, treated with Cellax particles (0.3 mg polymer/mL, 0.1 mg DTX/mL), and incubated for 24 h. Postincubation, cells were fixed, stained with DAPI, and visualized by confocal microscopy at 40× magnification.

Cy5.5 label was being cleaved extracellularly by FBS-sourced esterases and being internalized independent of the Cellax particle, we incubated the Cellax Cy5.5 particles in both active and heat-inactivated FBS-containing media: no difference in uptake was observed between the two groups. By NMR analysis of Cellax-Cy5.5 polymer, no significant deviations in composition compared to Cellax could be detected, but to minimize the influence of Cy5.5 chemistry on the biological behavior of Cellax particles, particles were prepared with a mixture of 95% Cellax and 5% Cellax-Cy5.5, yielding highly fluorescent particles with no alteration in physiochemical properties.

dx.doi.org/10.1021/bc200284b | *Bioconjugate Chem.* 2011, 22, 2474–2486

CONCLUSION

In summary, we have developed a new polymer conjugate of docetaxel with the following unique features: (A) the carboxymethylcellulose polymer backbone is biocompatible and reasonably stable with a proven safety profile, (B) the CMC was acetylated to facilitate high hydrophobic drug coupling (37 wt %) compared to other polysaccharide conjugates that have been reported, (C) the composition of the CMC polymer was optimized to form stable nanoparticles, and (D) the Cellax conjugate was PEGylated. The synthesis outcomes were low in variation with good control over composition and physical properties. Cellax released DTX at a slow and controlled rate of 3.8 wt % per day: in vitro, the cytotoxicity of Cellax was improved by 2−40-fold compared to free DTX, possibly arising due to the slow release mechanism and cellular internalization.

AUTHOR INFORMATION

Corresponding Author

*Tel: 647 260 7994; fax: 416 673 6664. E-mail address: sli@oicr.on.ca.

ACKNOWLEDGMENTS

We thank Ilya Gourevich at the Centre for Nanostructure Imaging (Department of Chemistry, University of Toronto) for his assistance with TEM imaging, and Dr. Ahmed Aman in the Medicinal Chemistry Platform at the Ontario Institute for Cancer Research for his assistance with analytical chemistry method development. Funding for this project was received from the Ontario Institute for Cancer Research.

REFERENCES

(1) Singla, A. K., Garg, A., and Aggarwal, D. (2002) Paclitaxel and its formulations. *Int. J. Pharm. 235*, 179−92.

(2) Shelley, W. B., Talanin, N., and Shelley, E. D. (1995) Polysorbate 80 hypersensitivity. *Lancet 345*, 1312−3.

(3) Gelderblom, H., Verweij, J., Nooter, K., and Sparreboom, A. (2001) Cremophor EL: the drawbacks and advantages of vehicle selection for drug formulation. *Eur. J. Cancer 37*, 1590−8.

(4) Jones, S. (2006) Head-to-head: Docetaxel challenges paclitaxel. *EJC Suppl. 4*, 4−8.

(5) Etrych, T., Sirova, M., Starovoytova, L., Rihova, B., and Ulbrich, K. (2010) HPMA copolymer conjugates of paclitaxel and docetaxel with pH-controlled drug release. *Mol. Pharm. 7*, 1015−26.

(6) Liu, J., Zahedi, P., Zeng, F., and Allen, C. (2008) Nano-sized assemblies of a PEG-docetaxel conjugate as a formulation strategy for docetaxel. *J. Pharm. Sci. 97*, 3274−90.

(7) Esmaeili, F., Dinarvand, R., Ghahremani, M. H., Amini, M., Rouhani, H., Sepehri, N., Ostad, S. N., and Atyabi, F. (2009) Docetaxel-albumin conjugates: preparation, in vitro evaluation and biodistribution studies. *J. Pharm. Sci. 98*, 2718−30.

(8) Li, C., and Wallace, S. (2008) Polymer-drug conjugates: recent development in clinical oncology. *Adv. Drug Delivery Rev. 60*, 886−98.

(9) Duncan, R. (2003) The dawning era of polymer therapeutics. *Nat. Rev. Drug Discovery 2*, 347−60.

(10) Ringsdorf, H. (1975) Structure and properties of pharmacologically active polymers. *J. Polym. Sci., Polym. Symp. 51*, 135−153.

(11) Yamaoka, T., Tabata, Y., and Ikada, Y. (1994) Distribution and tissue uptake of poly(ethylene glycol) with different molecular weights after intravenous administration to mice. *J. Pharm. Sci. 83*, 601−6.

(12) Seymour, L. W., Duncan, R., Strohalm, J., and Kopecek, J. (1987) Effect of molecular weight (Mw) of N-(2-hydroxypropyl)-methacrylamide copolymers on body distribution and rate of excretion after subcutaneous, intraperitoneal, and intravenous administration to rats. *J. Biomed. Mater. Res. 21*, 1341−58.

(13) Matsumura, Y., and Maeda, H. (1986) A new concept for macromolecular therapeutics in cancer chemotherapy: mechanisms of tumoritropic accumulation of proteins and the antitumor agent smancs. *Cancer Res. 46*, 6387−6392.

(14) Hashizume, H., Baluk, P., Morikawa, S., McLean, J. W., Thurston, G., Roberge, S., Jain, R. K., and McDonald, D. M. (2000) Openings between defective endothelial cells explain tumor vessel leakiness. *Am. J. Pathol. 156*, 1363−80.

(15) Hobbs, S. K., Monsky, W. L., Yuan, F., Roberts, W. G., Griffith, L., Torchilin, V. P., and Jain, R. K. (1998) Regulation of transport pathways in tumor vessels: role of tumor type and microenvironment. *Proc. Natl. Acad. Sci. U. S. A. 95*, 4607−12.

(16) Greish, K. (2010) Enhanced permeability and retention (EPR) effect for anticancer nanomedicine drug targeting. *Methods Mol. Biol. 624*, 25−37.

(17) Greish, K. (2007) Enhanced permeability and retention of macromolecular drugs in solid tumors: a royal gate for targeted anticancer nanomedicines. *J. Drug Targeting 15*, 457−64.

(18) Yuan, F., Dellian, M., Fukumura, D., Leunig, M., Berk, D. A., Torchilin, V. P., and Jain, R. K. (1995) Vascular permeability in a human tumor xenograft: molecular size dependence and cutoff size. *Cancer Res. 55*, 3752−6.

(19) Gabizon, A., Shmeeda, H., and Barenholz, Y. (2003) Pharmacokinetics of pegylated liposomal Doxorubicin: review of animal and human studies. *Clin. Pharmacokinet. 42*, 419−36.

(20) Drummond, D. C., Noble, C. O., Hayes, M. E., Park, J. W., and Kirpotin, D. B. (2008) Pharmacokinetics and in vivo drug release rates in liposomal nanocarrier development. *J. Pharm. Sci. 97*, 4696−740.

(21) Lindner, L. H., and Hossann, M. (2010) Factors affecting drug release from liposomes. *Curr. Opin. Drug Discovery Dev. 13*, 111−23.

(22) Hamaguchi, T., Kato, K., Yasui, H., Morizane, C., Ikeda, M., Ueno, H., Muro, K., Yamada, Y., Okusaka, T., Shirao, K., Shimada, Y., Nakahama, H., and Matsumura, Y. (2007) A phase I and pharmacokinetic study of NK105, a paclitaxel-incorporating micellar nanoparticle formulation. *Br. J. Cancer 97*, 170−6.

(23) Hamaguchi, T., Matsumura, Y., Suzuki, M., Shimizu, K., Goda, R., Nakamura, I., Nakatomi, I., Yokoyama, M., Kataoka, K., and Kakizoe, T. (2005) NK105, a paclitaxel-incorporating micellar nanoparticle formulation, can extend in vivo antitumour activity and reduce the neurotoxicity of paclitaxel. *Br. J. Cancer 92*, 1240−6.

(24) Lavasanifar, A., Samuel, J., and Kwon, G. S. (2002) Poly(ethylene oxide)-block-poly(L-amino acid) micelles for drug delivery. *Adv. Drug Delivery Rev. 54*, 169−90.

(25) Ahmed, F., Pakunlu, R. I., Brannan, A., Bates, F., Minko, T., and Discher, D. E. (2006) Biodegradable polymersomes loaded with both paclitaxel and doxorubicin permeate and shrink tumors, inducing apoptosis in proportion to accumulated drug. *J. Controlled Release 116*, 150−8.

(26) Discher, D. E., and Ahmed, F. (2006) Polymersomes. *Annu. Rev. Biomed. Eng. 8*, 323−41.

(27) Katz, J. S., Levine, D. H., Davis, K. P., Bates, F. S., Hammer, D. A., and Burdick, J. A. (2009) Membrane stabilization of biodegradable polymersomes. *Langmuir 25*, 4429−34.

(28) Svenson, S., and Tomalia, D. A. (2005) Dendrimers in biomedical applications--reflections on the field. *Adv. Drug Delivery Rev. 57*, 2106−29.

(29) Tekade, R. K., Kumar, P. V., and Jain, N. K. (2009) Dendrimers in oncology: an expanding horizon. *Chem. Rev. 109*, 49−87.

(30) Tomalia, D. A., Reyna, L. A., and Svenson, S. (2007) Dendrimers as multi-purpose nanodevices for oncology drug delivery and diagnostic imaging. *Biochem. Soc. Trans. 35*, 61−7.

(31) Misra, R., Acharya, S., and Sahoo, S. K. (2010) Cancer nanotechnology: application of nanotechnology in cancer therapy. *Drug Discovery Today 15*, 842−50.

(32) Li, S. D., and Huang, L. (2008) Pharmacokinetics and biodistribution of nanoparticles. *Mol. Pharmaceutics 5*, 496−504.

(33) Harris, J. M., Zalipsky, S., American Chemical Society, Division of Polymer Chemistry, and American Chemical Society, Meeting

(1997) *Poly(ethylene glycol): chemistry and biological applications*, American Chemical Society, Washington, DC.
(34) Immordino, M. L., Dosio, F., and Cattel, L. (2006) Stealth liposomes: review of the basic science, rationale, and clinical applications, existing and potential. *Int. J. Nanomed. 1*, 297−315.
(35) Owens, D. E. 3rd, and Peppas, N. A. (2006) Opsonization, biodistribution, and pharmacokinetics of polymeric nanoparticles. *Int. J. Pharm. 307*, 93−102.
(36) Harris, J. M., Martin, N. E., and Modi, M. (2001) Pegylation: a novel process for modifying pharmacokinetics. *Clin. Pharmacokinet. 40*, 539−51.
(37) Lim, W. T., Tan, E. H., Toh, C. K., Hee, S. W., Leong, S. S., Ang, P. C., Wong, N. S., and Chowbay, B. (2010) Phase I pharmacokinetic study of a weekly liposomal paclitaxel formulation (Genexol-PM) in patients with solid tumors. *Ann. Oncol. 21*, 382−8.
(38) Boddy, A. V., Plummer, E. R., Todd, R., Sludden, J., Griffin, M., Robson, L., Cassidy, J., Bissett, D., Bernareggi, A., Verrill, M. W., and Calvert, A. H. (2005) A phase I and pharmacokinetic study of paclitaxel poliglumex (XYOTAX), investigating both 3-weekly and 2-weekly schedules. *Clin. Cancer Res. 11*, 7834−40.
(39) Letchford, K., Liggins, R., Wasan, K. M., and Burt, H. (2009) In vitro human plasma distribution of nanoparticulate paclitaxel is dependent on the physicochemical properties of poly(ethylene glycol)-block-poly(caprolactone) nanoparticles. *Eur. J. Pharm. Biopharm. 71*, 196−206.
(40) Li, C., Yu, D. F., Newman, R. A., Cabral, F., Stephens, L. C., Hunter, N., Milas, L., and Wallace, S. (1998) Complete regression of well-established tumors using a novel water-soluble poly(L-glutamic acid)-paclitaxel conjugate. *Cancer Res. 58*, 2404−9.
(41) Duncan, R. (2006) Polymer conjugates as anticancer nanomedicines. *Nat. Rev. Cancer 6*, 688−701.
(42) Li, C. (2002) Poly(L-glutamic acid)--anticancer drug conjugates. *Adv. Drug Delivery Rev. 54*, 695−713.
(43) Li, C., Newman, R. A., Wu, Q. P., Ke, S., Chen, W., Hutto, T., Kan, Z., Brannan, M. D., Charnsangavej, C., and Wallace, S. (2000) Biodistribution of paclitaxel and poly(L-glutamic acid)-paclitaxel conjugate in mice with ovarian OCa-1 tumor. *Cancer Chemother. Pharmacol. 46*, 416−22.
(44) Turaev, A. S. (1995) Dependance of the biodegradability of carboxymethylcellulose on its supermolecular structure and molecular parameters. *Chem. Nat. Compd. 31*, 254−257.
(45) Liu, Z., Jiao, Y., Wang, Y., Zhou, C., and Zhang, Z. (2008) Polysaccharides-based nanoparticles as drug delivery systems. *Adv. Drug Delivery Rev. 60*, 1650−62.
(46) Janes, K. A., Calvo, P., and Alonso, M. J. (2001) Polysaccharide colloidal particles as delivery systems for macromolecules. *Adv. Drug Delivery Rev. 47*, 83−97.
(47) Prabaharan, M. (2008) Review paper: chitosan derivatives as promising materials for controlled drug delivery. *J. Biomater. Appl. 23*, 5−36.
(48) Prabaharan, M., and Mano, J. F. (2005) Chitosan-based particles as controlled drug delivery systems. *Drug Delivery 12*, 41−57.
(49) Cera, C., Palumbo, M., Stefanelli, S., Rassu, M., and Palu, G. (1992) Water-soluble polysaccharide-anthracycline conjugates: biological activity. *Anti-Cancer Drug Des. 7*, 143−51.
(50) Uglea, C. V., Parv, A., Corjan, M., Dumitriu, A. D., and Ottenbrite, R. M. (2005) Biodistribution and antitumor activity induced by carboxymethylcellulose conjugates. *J. Bioact. Compat. Polym. 20*, 571−583.
(51) Auzenne, E., Ghosh, S. C., Khodadadian, M., Rivera, B., Farquhar, D., Price, R. E., Ravoori, M., Kundra, V., Freedman, R. S., and Klostergaard, J. (2007) Hyaluronic acid-paclitaxel: antitumor efficacy against CD44(+) human ovarian carcinoma xenografts. *Neoplasia 9*, 479−86.
(52) Inoue, K., Kumazawa, E., Kuga, H., Susaki, H., Masubuchi, N., and Kajimura, T. (2003) CM-dextran-polyalcohol-camptothecin conjugate: DE-310 with a novel carrier system and its preclinical data. *Adv. Exp. Med. Biol. 519*, 145−53.
(53) Soepenberg, O., de Jonge, M. J., Sparreboom, A., de Bruin, P., Eskens, F. A., de Heus, G., Wanders, J., Cheverton, P., Ducharme, M. P., and Verweij, J. (2005) Phase I and pharmacokinetic study of DE-310 in patients with advanced solid tumors. *Clin. Cancer Res. 11*, 703−11.
(54) Wang, X., Li, J., Wang, Y., Cho, K. J., Kim, G., Gjyrezi, A., Koenig, L., Giannakakou, P., Shin, H. J., Tighiouart, M., Nie, S., Chen, Z. G., and Shin, D. M. (2009) HFT-T, a targeting nanoparticle, enhances specific delivery of paclitaxel to folate receptor-positive tumors. *ACS Nano 3*, 3165−74.
(55) Sugahara, S., Kajiki, M., Kuriyama, H., and Kobayashi, T. R. (2007) Complete regression of xenografted human carcinomas by a paclitaxel-carboxymethyl dextran conjugate (AZ10992). *J. Controlled Release 117*, 40−50.
(56) Hou, W., Watters, J. W., and McLeod, H. L. (2004) Simple and rapid docetaxel assay in plasma by protein precipitation and high-performance liquid chromatography-tandem mass spectrometry. *J. Chromatogr., B: Analyt. Technol. Biomed. Life Sci. 804*, 263−7.
(57) Kumar, D., Tomar, R. S., Deolia, S. K., Mitra, M., Mukherjee, R., and Burman, A. C. (2007) Isolation and characterization of degradation impurities in docetaxel drug substance and its formulation. *J. Pharm. Biomed. Anal. 43*, 1228−35.
(58) Kerns, E. H., Volk, K. J., Hill, S. E., and Lee, M. S. (1994) Profiling taxanes in Taxus extracts using lc/ms and lc/ms/ms techniques. *J. Nat. Prod. 57*, 1391−403.
(59) Namikoshi, H. (1985) Carboxyalkyl acetyl celluloses, their salts and a process for the preparation of them, U. S. Patent 4520192.
(60) Zhang, X., Jackson, J. K., and Burt, H. M. (1996) Determination of surfactant critical micelle concentration by a novel fluorescence depolarization technique. *J. Biochem. Biophys. Methods 31*, 145−50.
(61) Miele, E., Spinelli, G. P., Tomao, F., and Tomao, S. (2009) Albumin-bound formulation of paclitaxel (Abraxane ABI-007) in the treatment of breast cancer. *Int. J. Nanomed. 4*, 99−105.
(62) Sparreboom, A., Scripture, C. D., Trieu, V., Williams, P. J., De, T., Yang, A., Beals, B., Figg, W. D., Hawkins, M., and Desai, N. (2005) Comparative preclinical and clinical pharmacokinetics of a cremophor-free, nanoparticle albumin-bound paclitaxel (ABI-007) and paclitaxel formulated in Cremophor (Taxol). *Clin. Cancer Res. 11*, 4136−43.
(63) Duncan, R., and Vicent, M. J. (2010) Do HPMA copolymer conjugates have a future as clinically useful nanomedicines? A critical overview of current status and future opportunities. *Adv. Drug Delivery Rev. 62*, 272−82.
(64) Shaffer, S. A., Baker-Lee, C., Kennedy, J., Lai, M. S., de Vries, P., Buhler, K., and Singer, J. W. (2007) In vitro and in vivo metabolism of paclitaxel poliglumex: identification of metabolites and active proteases. *Cancer Chemother. Pharmacol. 59*, 537−48.
(65) Charpentier, D., Mocanu, G., Carpov, A., Chapelle, S., Merle, L., and Muller, G. (1997) New hydrophobically modified carboxymethylcellulose derivitives. *Carbohydr. Polym. 33*, 177−186.
(66) Facchini, A., and Segatti, F. (2005) N-methyl-amine derivitives of Carboxymethylcellulose, alginic acid N-methyl-amide or carboxymethyl starch, Eur. Patent EP 1 614 696 A1.
(67) Bilati, U., Allemann, E., and Doelker, E. (2005) Development of a nanoprecipitation method intended for the entrapment of hydrophilic drugs into nanoparticles. *Eur. J. Pharm. Sci. 24*, 67−75.
(68) Lee, H., Lee, K., and Park, T. G. (2008) Hyaluronic acid-paclitaxel conjugate micelles: synthesis, characterization, and antitumor activity. *Bioconjugate Chem. 19*, 1319−25.
(69) Van, S., Das, S. K., Wang, X., Feng, Z., Jin, Y., Hou, Z., Chen, F., Pham, A., Jiang, N., Howell, S. B., and Yu, L. (2010) Synthesis, characterization, and biological evaluation of poly(L-gamma-glutamyl-glutamine)- paclitaxel nanoconjugate. *Int. J. Nanomed. 5*, 825−37.
(70) Fairley, N., Hoang, B., and Allen, C. (2008) Morphological control of poly(ethylene glycol)-block-poly(epsilon-caprolactone) copolymer aggregates in aqueous solution. *Biomacromolecules 9*, 2283−91.
(71) Zhao, C. L., Winnik, M. A., Riess, G., and Croucher, M. D. (1990) Fluorescence probe technique used to study micelle formation in water soluble block copolymers. *Langmuir 6*, 514−516.

(72) Trivedi, R., and Kompella, U. B. (2010) Nanomicellar formulations for sustained drug delivery: strategies and underlying principles. *Nanomedicine (Lond.) 5*, 485−505.
(73) Liggins, R. T., and Burt, H. M. (2002) Polyether-polyester diblock copolymers for the preparation of paclitaxel loaded polymeric micelle formulations. *Adv. Drug Delivery Rev. 54*, 191−202.
(74) Luo, J., Xiao, K., Li, Y., Lee, J. S., Shi, L., Tan, Y. H., Xing, L., Holland Cheng, R., Liu, G. Y., and Lam, K. S. (2010) Well-defined, size-tunable, multifunctional micelles for efficient paclitaxel delivery for cancer treatment. *Bioconjugate Chem. 21*, 1216−24.
(75) Fanzioni, S., Hovda, K., Livi, V., KcKennon, M., Siviero, L., and Spoonemore, H. (2010) Method for determining the amount of conjugated taxane in polyglut acid - taxane conjugates, U. S. Patent 2010/0151582 A1.
(76) Kerns, E. H., Volk, K. J., and Hill, S. E. (1995) Profiling new taxanes using LC/MS and LC/MS/MS substructural analysis techniques. *Rapid Commun. Mass Spectrom. 9*, 1539−1545.
(77) Vuilhorgne, M., Gaillard, C., Sanderink, G., Royer, I., Monsarrat, B., Dubois, J., and Wright, M. (1994) *Metabolism of Taxoid Drugs*, ACS Symposium Series, Vol. *583*, American Chemical Society, Washington, DC.
(78) Bournique, B., and Lemarie, A. (2002) Docetaxel (Taxotere) is not metabolized by recombinant human CYP1B1 in vitro, but acts as an effector of this isozyme. *Drug Metab. Dispos. 30*, 1149−52.
(79) Wang, X., Zhao, G., Van, S., Jiang, N., Yu, L., Vera, D., and Howell, S. B. (2010) Pharmacokinetics and tissue distribution of PGG-paclitaxel, a novel macromolecular formulation of paclitaxel, in nu/nu mice bearing NCI-460 lung cancer xenografts. *Cancer Chemother. Pharmacol. 65*, 515−26.
(80) Liu, B., Yang, M., Li, R., Ding, Y., Qian, X., Yu, L., and Jiang, X. (2008) The antitumor effect of novel docetaxel-loaded thermosensitive micelles. *Eur. J. Pharm. Biopharm. 69*, 527−34.
(81) EU. (2010) European Medicines Agency - Assessment Report: Docefrez
(82) Khandare, J. J., Jayant, S., Singh, A., Chandna, P., Wang, Y., Vorsa, N., and Minko, T. (2006) Dendrimer versus linear conjugate: Influence of polymeric architecture on the delivery and anticancer effect of paclitaxel. *Bioconjugate Chem. 17*, 1464−72.
(83) Yvon, A. M., Wadsworth, P., and Jordan, M. A. (1999) Taxol suppresses dynamics of individual microtubules in living human tumor cells. *Mol. Biol. Cell 10*, 947−59.
(84) De Souza, R., Zahedi, P., Mariyama, C., H., Allen, C., Wilson, B. C., and Paquette-Miller, M. (2010) Continuous docetaxel chemotherapy improves therapeutic efficacy in murine models of ovarian cancer. *Mol. Cancer Therapeut. 9*, 1820−1830.
(85) Lord, R., Nair, S., Schache, A., Spicer, J., Somaihah, N., Khoo, V., and Pandha, H. (2007) Low dose metronomic oral cyclophosphamide for hormone resistant prostate cancer: a phase II study. *J. Urol. 177*, 2136−40.
(86) Kamat, A. A., Kim, T. J., Landen, C. N. Jr., Lu, C., Han, L. Y., Lin, Y. G., Merritt, W. M., Thaker, P. H., Gershenson, D. M., Bischoff, F. Z., Heymach, J. V., Jaffe, R. B., Coleman, R. L., and Sood, A. K. (2007) Metronomic chemotherapy enhances the efficacy of antivascular therapy in ovarian cancer. *Cancer Res. 67*, 281−8.

Bioconjugate Chemistry

Article

pubs.acs.org/bc

SNAP-Tag Technology Mediates Site Specific Conjugation of Antibody Fragments with a Photosensitizer and Improves Target Specific Phototoxicity in Tumor Cells

Ahmad Fawzi Hussain,[†] Florian Kampmeier,[†] Verena von Felbert,[‡] Hans-F. Merk,[‡] Mehmet Kemal Tur,*[,§,⊥] and Stefan Barth[†,∥,⊥]

[†]Department of Experimental Medicine and Immunotherapy, Institute of Applied Medical Engineering, Helmholtz-Institute for Biomedical Engineering

[‡]Department of Dermatology, University Hospital RWTH, Aachen, Germany

[§]Institute of Pathology, University Hospital Giessen and Marburg (UKGM), Giessen, Germany

[∥]Department of Pharmaceutical Product Development, Fraunhofer Institute for Molecular Biology and Applied Ecology, Aachen, Germany

ABSTRACT: Cancer cells can be killed by photosensitizing agents that induce toxic effects when exposed to nonhazardous light, but this also causes significant damage to surrounding healthy cells. The specificity of photodynamic therapy can be increased by conjugating photosensitizing agents to antibodies and antibody fragments that bind specifically to tumor cell antigens. However, standard conjugation reactions produce heterogeneous products whose targeting specificity and spectroscopic properties can be compromised. In this study, we used an antibody fragment (scFv-425) that binds to the epidermal growth factor receptor (EGFR) as a model to investigate the use of SNAP-tag fusions as an improved conjugation strategy. The scFv-425-SNAP-tag fusion protein allowed the specific conjugation of a chlorin e6 photosensitizer modified with *O*(6)-benzylguanine, generating a homogeneous product that was delivered specifically to EGFR$^+$ cancer cells and resulted in significant, tumor cell-specific cytotoxicity. The impact of our results on the development of photodynamic therapy is discussed.

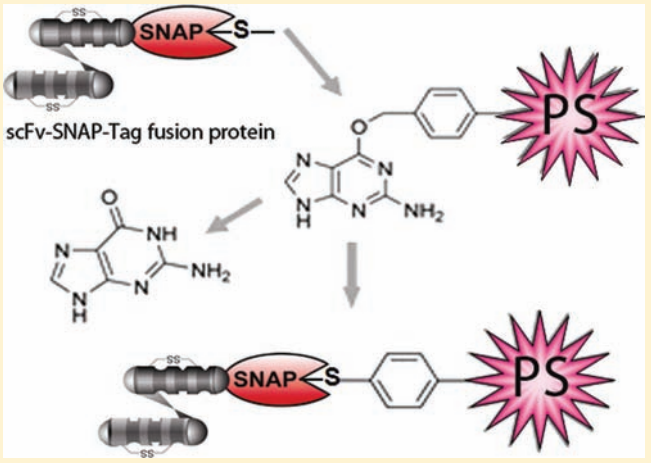

INTRODUCTION

Photodynamic therapy (PDT) is a promising and minimally invasive approach for the treatment of cancer. Following the introduction of improved photosensitizers and clinical application protocols, several FDA-approved PDT drugs have become available and others are in various stages of preclinical and clinical development.[1,2] The photosensitizing agent can exert its effect when activated by nonhazardous light directly, by becoming cytotoxic, or indirectly, by initiating the in situ production of toxic free radicals or reactive oxygen species (ROS). These processes cause damage to cells and ultimately induce cell death by apoptosis or necrosis.[3] The site of cellular damage depends on the photosensitizer type, the incubation period, and the mode of delivery.[4] In general, anionic photosensitizers localize in lysosomes, whereas cationic photosensitizers accumulate in mitochondria and cause damage there.[5]

One of the greatest challenges in PDT is the lack of specificity. Photosensitizers damage healthy tissue as well as tumor tissue after activation by light, and also can result in prolonged skin photosensitivity.[6] To increase the specificity of PDT, photosensitizers have been conjugated to tumor-specific monoclonal antibodies or single chain antibody fragments (scFv), resulting in so-called photoimmunoconjugates that deliver the photosensitizer directly to the tumor tissue, this approach is known as photoimmunotherapy (PIT).[7] Standard coupling reactions are unsuitable for the conjugation of photosensitizers and antibodies because there is no reliable way to ensure that antibody−photosensitizer conjugates are produced in the optimal stoichiometric ratio.[8,9] Furthermore, the chemical properties of the photosensitizer (e.g., hydrophobicity and the number and arrangement of charged groups) can alter the pharmacokinetic properties and biodistribution of the antibody, and may cause nonspecific binding and internalization behavior. Random conjugation can also cause the self-quenching of photosensitizer excited states, thus reducing photodynamic activity.[7] More controlled conjugation reactions are therefore required to overcome these limitations.

Received: June 10, 2011
Revised: September 14, 2011
Published: October 13, 2011

ACS Publications © 2011 American Chemical Society

The epidermal growth factor receptor (EGFR, erbB1, HER1), one of four members of the ErbB family of tyrosine kinase growth factor receptors, is overexpressed in approximately 30% of epithelial cancers and has thus become an attractive target for cancer immunotherapy.[10,11] The recombinant anti-EGFR antibody fragment scFv-425 binds to EGFR expressing cancer cells and internalized upon binding.[12] We used scFv-425 as a model for the development of a new conjugation strategy to improve the specificity and efficacy of PIT. To achieve these aims, we used scfv-425 as a targeting moiety fused to the SNAP-tag to enable site-specific conjugation with the photosensitizer chlorin e6. The SNAP-tag is a 20 kDa protein tag that binds covalently to substrates containing *O*(6)-benzylguanine (BG)[13,14] and has previously been used to modify scFv fusion proteins with fluorophores for optical imaging.[12,15] Chlorin e6 was modified with BG bridged by a (PEG-24) spacer to increase the distance between the photosensitizer and the protein. The target specific toxicity was analyzed in vitro with four tumor cell lines with varying amounts of EGFR expression.

EXPERIMENTAL PROCEDURES

Cell Culture. The human epidermal carcinoma cell line A431 (ATCC no.: CRL-259), human Hodgkin lymphoma cell line L540 (DSMZ no.: ACC 72), Chinese hamster ovary cell line CHO-K1 (ATCC: CCL-6), and human embryonic kidney cell line HEK-293T cells (ATCC: CRL-11268) were cultured in RPMI-1640 medium supplemented with 2 mM L-glutamine, 10% (v/v) fetal bovine serum (FBS), and 100 U/mL penicillin–streptomycin. The human breast carcinoma cell lines MDA-MB-468 (ATCC: HTB-132) and MDA-MB-231 (ATCC: HTB-26), and human cervical carcinoma cell line SiHa (ATCC: HTB-35) were cultured in DMEM with 10% (v/v) fetal bovine serum (FBS) and 100 U/mL penicillin–streptomycin. All cells were incubated at 37 °C in a 5% CO_2 atm. All media and additives were obtained from Invitrogen, Darmstadt, Germany.

Protein Expression and Purification. The sequence for each scFv was inserted into the SfiI and NotI-digested site of eukaryotic expression vector pMS-SNAP providing an N-terminal binding ligand (scFv-425 or scFv-Ki4) and a C-terminal SNAP-tag sequence. The TGA stop codon is generated immediately after His_6 tag sequence. His_6-tagged fusion proteins were purified from cell-free supernatants on an Äkta FLPC system with a 5 mL Ni-NTA Superflow cartridge (Qiagen, Hilden, Germany) after equilibration with 4× buffer (200 mM NaH_2PO_4, 1.2 M NaCl, 40 mM imidazole, pH 8). Bound His-tagged proteins were eluted with elution buffer (50 mM NaH_2PO_4, 300 mM NaCl, 250 mM imidazole, pH 8). After elution, proteins were dialyzed at 4 °C overnight against phosphate-buffered saline (PBS) containing 1 mM dithioerythritol (Carl Roth GmBH, Karlsruhe, Germany). Ectoine cryopreservative was added to a final concentration of 50 mM, and aliquots were stored at −20 °C.

Modification of Ce6 with Benzylguanine. The carboxyl groups of Ce6 (Porphyrin Products, Logan, UT) were modified with benzylguanine by mixing 2 mg Ce6 in dimethylformamide for 30 min at room temperature with 5-fold molar excess of EDC and sulfo-NHS (Sigma-Aldrich, St. Louis, MO). The activated mixture was then mixed with a 2-fold molar excess of the benzylguanine linker BG-PEG24-NH_2 (Covalys Biosciences AG, Witterswil, Switzerland) in the dark at room temperature overnight. The modified Ce6 was purified by HPLC using a Shimadzu Prominence HPLC system and a 2.5 μm (4.6 × 50 mm) Water XBridge $OSTC_{18}$ column (Waters, Milford, MA) at a flow rate of 1 mL/min. Separations were carried out using a 20 min gradient from 0.1 M TEAA to 100% acetonitrile, monitored at 280 and 410 nm. The masses of Ce6, BG-PEG24-NH2, and BG-PEG24-Ce6 were confirmed using a Micromass QTOFII mass spectrometer with an electrospray ion source Advion Nanomate (Advion, Ithaca, NY, USA) 7 μL sample volume, 1.4 kV. Accurate masses were derived from mass spectra in the range 300–2500 m/z using the MaxEnt3 algorithm (Micromass) in the range 400–2000 Da.

Protein Labeling. The purified SNAP-tag fusion proteins were conjugated with BG-modified dyes (Covalys Biosciences AG, Witterswil, Switzerland) or BG-modified Ce6 by incubation in the dark with a 1.5–3-fold molar excess of dye for 2 h at room temperature. Residual dye was removed by gel filtration chromatography using Zeba Spin Desalting Columns, 7K MWCO (Thermo Fisher Scientific, Rockford, IL). The theoretical extinction coefficient of the proteins and the extinction coefficients of the fluorescence dyes were used to determine the coupling efficiency photometrically.

Labeled proteins were visualized after separation by SDS-PAGE with either a UV transilluminator Gel Doc XR gel documentation (Bio-Rad Laboratories, München, Germany) or a CRi Maestro imaging system (CRi, Woburn, MA, USA) using the blue and yellow filter sets.

Flow Cytometry. The binding efficiency of the labeled and unlabeled fusion proteins was determined by flow cytometry using a FACSCalibur device and *CellQuest* software (Becton & Dickinson, Heidelberg, Germany). $EGFR^+$ cell lines A431, MDA-MB468, MDA-MB-231, and SiHa were used to test the binding efficiency of scFv-425-SNAP, and $EGFR^-$ cell lines L540 and CHO-K1 were used as negative controls. The control fusion protein scFv-Ki4-SNAP recognizes the antigen CD30 and should therefore bind to L540 cells but not to the other cell lines. Approximately 4×10^5 cells were incubated in 200 μL PBS containing 0.5 μg of labeled protein for 20 min on ice. The cells were then washed twice with 1.8 mL PBS in a conventional cell washer and analyzed by flow cytometry.

Confocal Microscopy. Cells were visualized with a TCS SP5 confocal microscope (LEICA Microsystem, Wetzlar, Germany). Cells were prepared as described above for flow cytometry. Binding efficiency was determined by incubating cells with the labeled fusion proteins for 30 min on ice. Internalization was monitored by incubating cells with the labeled fusion proteins for 30 min at 37 °C.

Phototoxicity of scFv-425-SNAP-Ce6. A431, MDA-MB468, MDA-MB-231, SiHa, and CHO-K1 cells (2×10^4) cultured in 96 well plates as described above were washed twice in PBS and then treated with increasing concentrations of either Ce6, scFv-425-SNAP-Ce6, or Ki4-scFv-SNAP-Ce6 followed by incubation for 3 h at 37 °C. Control cultures were incubated with 500 μg/mL zeocin instead of the photosensitizer. Cells were washed three times with PBS, then resuspended in 100 μL of fresh phenol red free culture medium. The cells were then irradiated with visible light (VIS) plus water-filtered infrared light A (wIRA) using the Hydrosun type 505 radiator with a water-containing cuvette and an orange filter OG590, with a spectrum in the range 580–1400 nm (Hydrosun Medizintechnik GmbH, Müllheim, Germany). The irradiation experiments were performed taking into account the physical and photobiological laws described by Piazena and Kelleher.[16] The cells were placed in a water-bath and temperature was controlled during irradiation (total irradiance: 112 mW/cm^2, dose: 25 J/cm^{2}a VIS, 76 J/cm2 wIRA, exposure time: 15 min). Thereafter, cells

were incubated for a further 24 h at 37 °C in a 5% CO_2 atmosphere.

Cell viability was determined using the XTT cell proliferation kit II (Roche, Mannheim Germany), 24 h after irradiation. Cells were incubated with 2,3-bis(2-methoxy-4-nitro-5-sulphonyl)-5[(phenyl-amino)carbonyl]-2*H*-tetrazolium hydroxide reagent (1 mg/mL), and incubated for 4 h at 37 °C. Reduction of XTT to formazan by viable tumor cells was monitored colorimetrically at an absorbance wavelength of 450 nm and a reference wavelength of 630 nm using an ELISA plate reader Elisareader ELx808 (Bio-TEK, Bad Friedrichsahll, Germany).

Caspase-3/7 activity in cell lysates was determined using the Apo-ONE Caspase-3/7 assay (Promega, Mannheim, Germany) 24 h after light activation. Briefly, 100 μL of Apo-ONE reagent was added to the cells, and they were incubated for 6 h before fluorescence readings were taken with an ELISA plate reader Elisareader ELx808 (Bio-TEK, Bad Friedrichschall, Germany) using an excitation wavelength of 485 nm and an emission wavelength of 535 nm. The concentration of ROS was determined by measuring the 485/535 nm fluorescence ratio of H2DCFDA (Invitrogen, Darmstadt, Germany). Briefly, 2×10^4 cells were incubated in the presence of 50 nM Ce6 or 200 nM scFv-425-SNAP-Ce6 and 10 μM H_2DCFDA for 30 min in PBS containing 1% FCS. The cells were washed twice with warm PBS containing 2.5% FCS, cultured for 2 h in RPMI-160 medium and illuminated as described above. Fluorescence readings were taken directly after illumination. A blank probe (cells and medium) reading was used as the background and subtracted from all the sample readings.

Data Analysis. Statistical analysis and curve fitting were performed with *GraphPad Prism* software (GraphPad, San Siego, CA). Data are presented as the mean ± MES. Student's *t* test and two-way analysis of variance were used to assess the significance of independent experiments. The criterion $p < 0.05$ was used to determine statistical significance.

RESULTS

Expression, Purification, and Functional Analysis of scFv-SNAP-Tag Fusion Proteins. The coding sequences for the EGFR-specific scFv-425 antibody fragment[12] and a control fragment (scFv-Ki4)[15] that binds to a different antigen (CD30) were transferred to the pMS-SNAP bicistronic vector to generate the complete scFv-425-SNAP and scFv-Ki4-SNAP cassettes, as shown in Figure 1A. The constructs were introduced into HEK-293T cells by transfection and stably transformed cells were identified by selection on zeocin and by monitoring green fluorescent protein (GFP) activity. The fusion proteins were isolated from the culture supernatant to a final purity of ~90% by affinity chromatography (using the C-terminal His_6 tag) and the final yield was 18 mg/L of protein in the supernatant (Figure 1B).

The activity of the SNAP-tag was confirmed in each of the fusion proteins by mixing the unprocessed culture supernatant, the flowthrough fraction, and the eluate from the chromatography step with BG-modified Vista Green (Figure 1C). The binding activity of the scFv-425-SNAP protein was confirmed by flow cytometry using one target cell line expressing EGFR (A431) and one control cell line lacking this antigen but expressing CD30 (L540). Binding was detected with a secondary anti-His_5 Alexa 488 antibody. Flow cytometry data confirmed the rapid and efficient binding of scFv-425-SNAP specifically to $EGFR^+$ target cells, whereas scFv-Ki4-SNAP bound only to the $CD30^+$ L540 cells (Figure 1D).

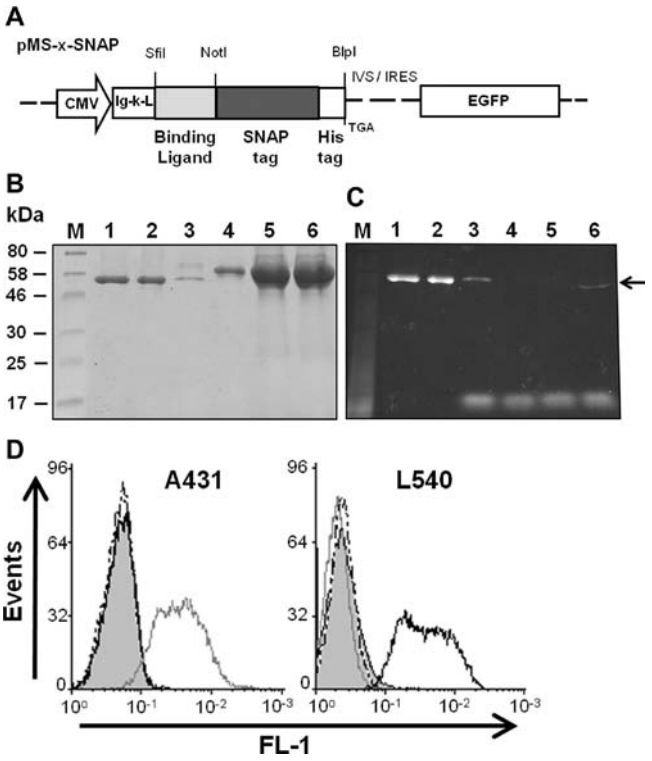

Figure 1. Construction, expression, and binding of the SNAP-tag fusion proteins. (A) Schematic diagram of the bicistronic eukaryotic expression cassettes for the recombinant SNAP-tag fusion proteins. Under the control of the cytomegalovirus (CMV) promoter, the pMS-scFv-425-SNAP vector encodes the antigen binding domain (scFv-425) joined in-frame to the SNAP-tag. The control vector is the same as described above, but the binding domain is replaced by scFv-Ki4. The fusion proteins are secreted by an immunoglobulin κ leader (Ig-κ-L) sequence, and a TGA stop codon is placed immediately after the C-terminal His_6-tag. The additionally transcribed internal ribosome entry site (IVS-IRES) mediates the cotranslational expression of enhanced fluorescent protein (EGFP). (B) Coomassie brilliant blue-stained SDS-PAGE of the purification fractions 1−4 (eluted with an imidazole concentration up to 250 nM) of scFv-425-SNAP protein and (C) corresponding BG-Vista Green-mediated in-gel UV visualization of the fusion protein (indicated by a black arrow). M, Prestained Protein Marker, Broad Range (7−175 kDa); 5, flowthrough; 6, supernatant of HEK-293T cells. (D) Flow cytometric binding analysis of scFv-425-SNAP and scFv-Ki4-SNAP control to $EGFR^+$ A431 and $EGFR^-$ L540 cells. Filled gray curves represent untreated cells. Cells were incubated with 0.5 μg/mL of the purified fusion protein scFv-425-SNAP (light gray curve) and scFv-Ki4-SNAP (black curve). Fluor 488-conjugated anti-Penta-His monoclonal antibody was used as the secondary antibody. To exclude nonspecific staining of the secondary antibody, omission of the His-tagged fusion protein served as control (dotted black curves).

Modification of the Photosensitizer Chlorin e6 with Benzylguanine. The photosensitizer chlorin e6 (Ce6) was modified successfully using *N*-(3-dimethylaminopropyl)-*N*′-ethylcarbodiimide hydrochloride (EDC), the sodium salt of hydroxysulfosuccinimide (sulfo-NHS), and a BG-PEG24-NH2 linker. Ce6 carboxyl groups were modified to BG groups, and the BG-modified Ce6 was purified using HPLC (data not shown). Ce6 modification with BG was confirmed by mass spectrometry. The accurate masses of Ce6 (597.215 Da), BG-PEG24-NH2 (1398.761 Da), and BG-PEG24-Ce6 (1979.004 Da) were detected on a Micromass QTOFII mass spectrometer, which confirmed that purified BG-PEG24-Ce6 had the same

dx.doi.org/10.1021/bc200304k | *Bioconjugate Chem.* 2011, 22, 2487−2495

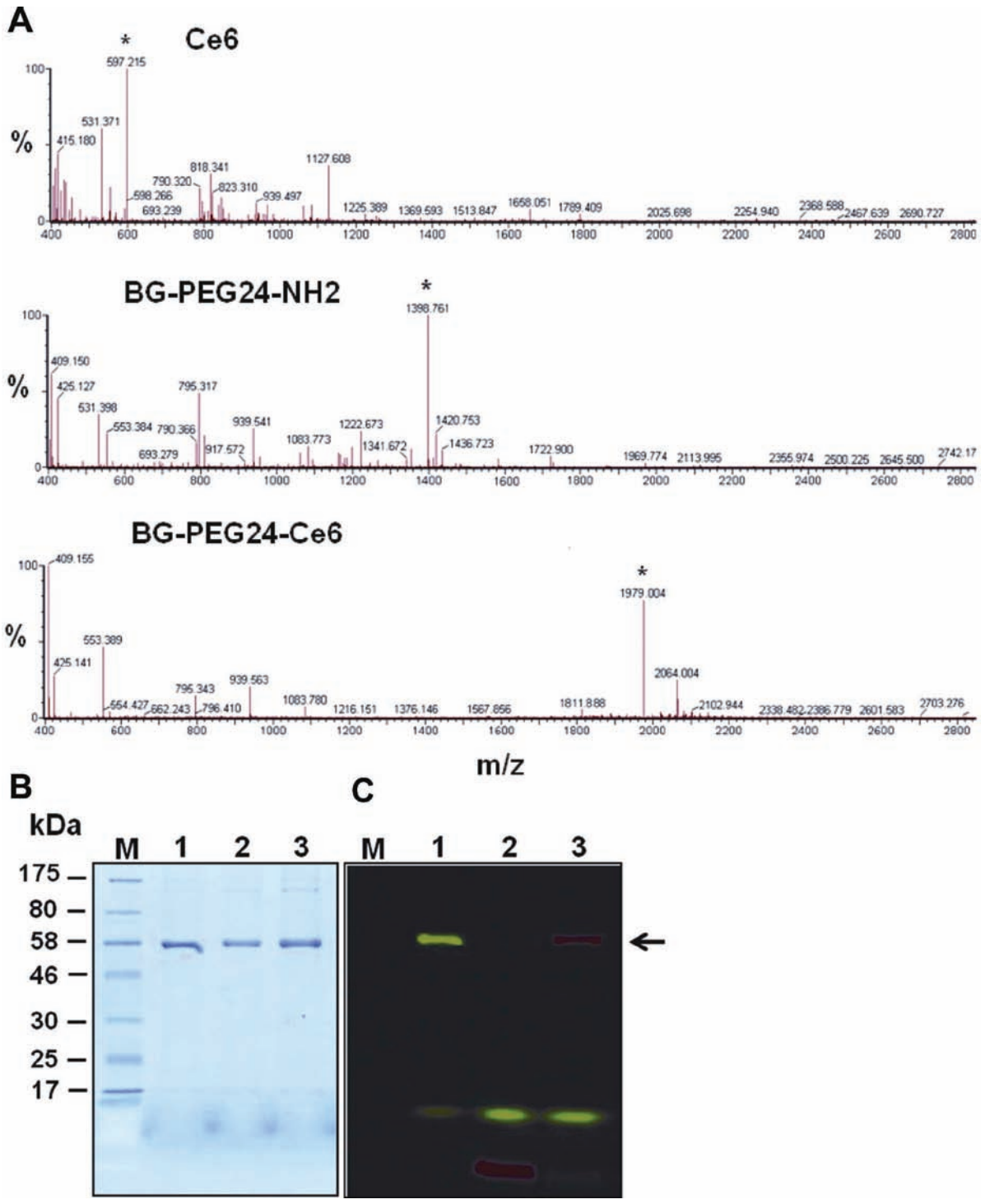

Figure 2. Analysis of Ce6 photosensitizer by mass spectrometry before and after modification with benzylguanine (BG). (A) ESI mass spectrum of Ce6, BG-PEG24-NH_2, and BG-PEG24-Ce6. The top panel represents Ce6 (597.215 Da), the middle panel represents BG-PEG24-NH_2 (1398.761 Da), and the bottom panel represents BG-PEG24-Ce6 (1979.004 Da), indicated by asterisks. The diagram presents the relative frequency (%) on the *y*-axis correlated to the mass-to-charge (m/z) ratio on the *x*-axis. (B) Coomassie brilliant blue-stained SDS-PAGE of coupling of BG-PEG24-Ce6 or BG-Vista Green to scFv-425-SNAP and (C) corresponding in-gel fluorescence visualization of the fusion proteins (indicated by a black arrow). The different dye spectra were unmixed based on their spectral patterns using CRi Maestro multispectral imaging system. M, Prestained Protein Marker, Broad Range (7−175 kDa); 1, scFv-425-SNAP incubated with a 1.5-fold molar excess of BG-Vista Green; 2, scFv-425-SNAP first blocked with bromothenylpteridine (BTP), then incubated with a 1.5-fold molar excess of BG-Ce6 for 2 h and then postincubated with a 1.5-fold molar excess of BG-VISTA Green; 3, scFv-425-SNAP first incubated with a 1.5-fold molar excess of BG-Ce6, and then incubated with a 1.5-fold molar excess of BG-Vista Green.

mass as the theoretical mass calculated for coupled Ce6 and BG-PEG24-NH2 (Figure 2A).

Protein Labeling with BG-Modified Fluorophores and Ce6. The functionality of the SNAP-tag was tested by coupling

dx.doi.org/10.1021/bc200304k | *Bioconjugate Chem.* 2011, 22, 2487−2495

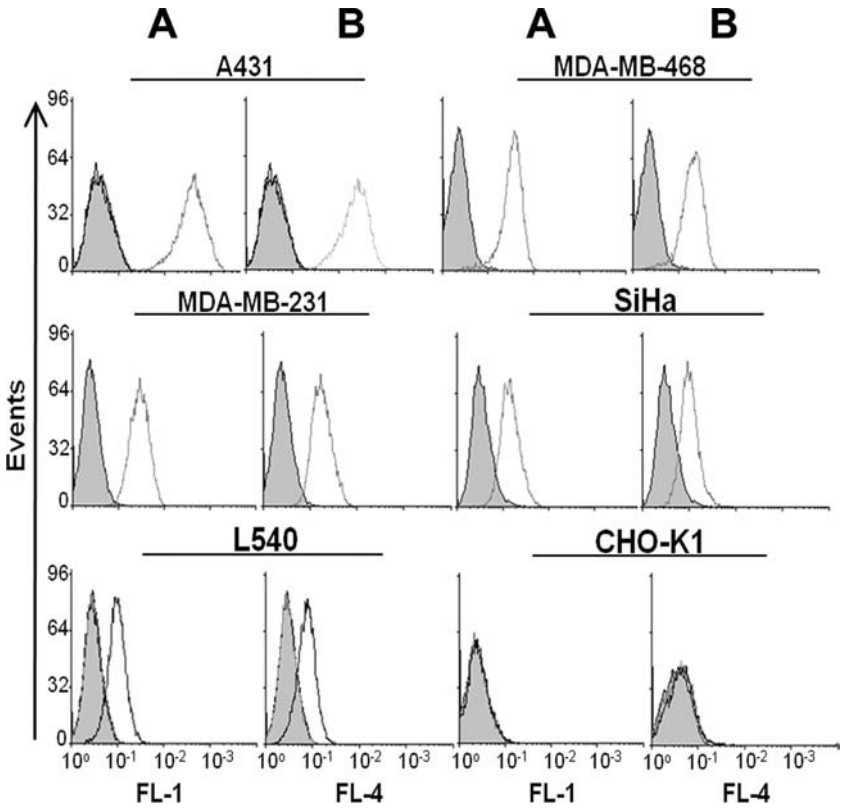

Figure 3. Binding activity of scFv-425-SNAP-Vista Green and scFv-425-SNAP-Ce6 to several EGFR$^+$ cell lines. Flow cytometry analysis was carried out after incubating 4×10^5 cells (filled gray curves) with each fusion protein for 20 min at 37 °C in PBS. Specific binding of (A) scFv-425-SNAP-Vista Green and (B) scFv-425-SNAP-Ce6 (light gray curves) to A431, MDA-MB-468, MDA-MB-231, SiHa, L540, and CHO-K1 cells were evaluated in parallel. As a control, scFv-Ki4-SNAP-Vista Green (black curves) was tested against L540 CHO-K1 and A431cells. Vista Green fluorescence (A) was analyzed in the FL-1 channel and Ce6 (B) in the FL-4 channel.

to BG-modified fluorescent dye, which revealed a labeling efficiency of 85−90% after a 2 h incubation at room temperature (data not shown). The reaction was repeated using BG-modified Ce6. The photosensitizer reacted solely with the active SNAP-tag in the fusion proteins and the reaction could be irreversibly blocked with bromothenylpteridine (BTP), as shown by postincubation with a 1.5-fold molar excess of BG-Vista Green. Analysis with the CRi Maestro imaging system showed no fluorescence associated with the previously blocked fusion protein and saturated SNAP binding to BG-Ce6 in nonblocked fusion proteins (Figure 2B, C).

Flow Cytometry and Confocal Microscopy. To determine the activity of labeled scFv-425-SNAP fusion proteins, flow cytometry analysis was carried out using proteins that had been labeled with either BG-Vista Green or BG-Ce6. All the labeled proteins showed a strong fluorescence signal on the corresponding target cell line (A431, MDA-MB-468, MDA-MB-231 and SiHa) but not on control cells (L540 and CHO-K1) after a 30 min incubation on ice (Figure 3). As expected, labeled scFv-Ki4-SNAP showed a strong fluorescence signal on L540 but not on A431 and CHO-K1 cells.

Confocal microscopy revealed strong, specific, and homogeneous membrane staining on A431, MDA-MB468, MDA-MB-231, and SiHa cells incubated with scFv-425-SNAP-Ce6 (Figure 4). The labeled fusion protein was specifically and efficiently taken up into EGFR$^+$ cell lines after a 30 min incubation at 37 °C but not at 4 °C. In contrast, no signal was detected when the EGFR$^-$ cell lines L540 and CHO-K1 were incubated with scFv-425-SNAP-Ce6 under the same conditions.

Photocytotoxicity of scFv-425-SNAP-Ce6. The cytotoxic effects of scFv-425-SNAP-Ce6 and unconjugated BG-Ce6 were evaluated using an XTT-based colorimetric cell proliferation assay with the four EGFR$^+$ cell lines and CHO-K1 as a negative controls. The viability of A431, MDA-MB-468, MDA-MB-231, and SiHa cells treated with scFv-425-SNAP-Ce6 was reduced significantly, in a concentration-dependent manner, after a 24 h incubation followed by light activation. The IC_{50} values were 48 nM (A431), 38 nM (MDA-MB-468), 200 nM (MDA-MB-231), and 218 nM (SiHa). CHO-K1 cells remained unaffected even when exposed to 800 nM of the conjugated fusion proteins, and the control construct scFv-Ki4-SNAP-Ce6 had a negligible effect in both A431 and CHO-K1 cells (Figure 5A). In contrast, unconjugated Ce6 was toxic toward all the cell lines, with IC_{50} values of 16 nM (A431), 22 nM (MDA-MB-468), 22 nM (MDA-MB-231), 26 nM (SiHa), and 18 nM (CHO-K1). These data are shown in Figure 5C.

Both the conjugated and unconjugated forms of Ce6 were toxic only after light activation, as confirmed by carrying out parallel experiments without the light activation step. No significant reduction in viability was observed in any of the cell lines (Figure 5B,D).

To determine whether scFv-425-SNAP-Ce6 selectively induced programmed cell death in target cells by triggering the apoptotic pathway, we analyzed the activity of caspase-3 and caspase-7 in A431, MDA-MB-231, MDA-MB468, SiHa, and CHO-K1 cells 24 h after light activation. Both scFv-425-SNAP-Ce6 (200 nM) and unconjugated Ce6 (50 nM) increased the levels of caspase-3 and caspase-7, whereas no

dx.doi.org/10.1021/bc200304k | *Bioconjugate Chem.* 2011, 22, 2487−2495

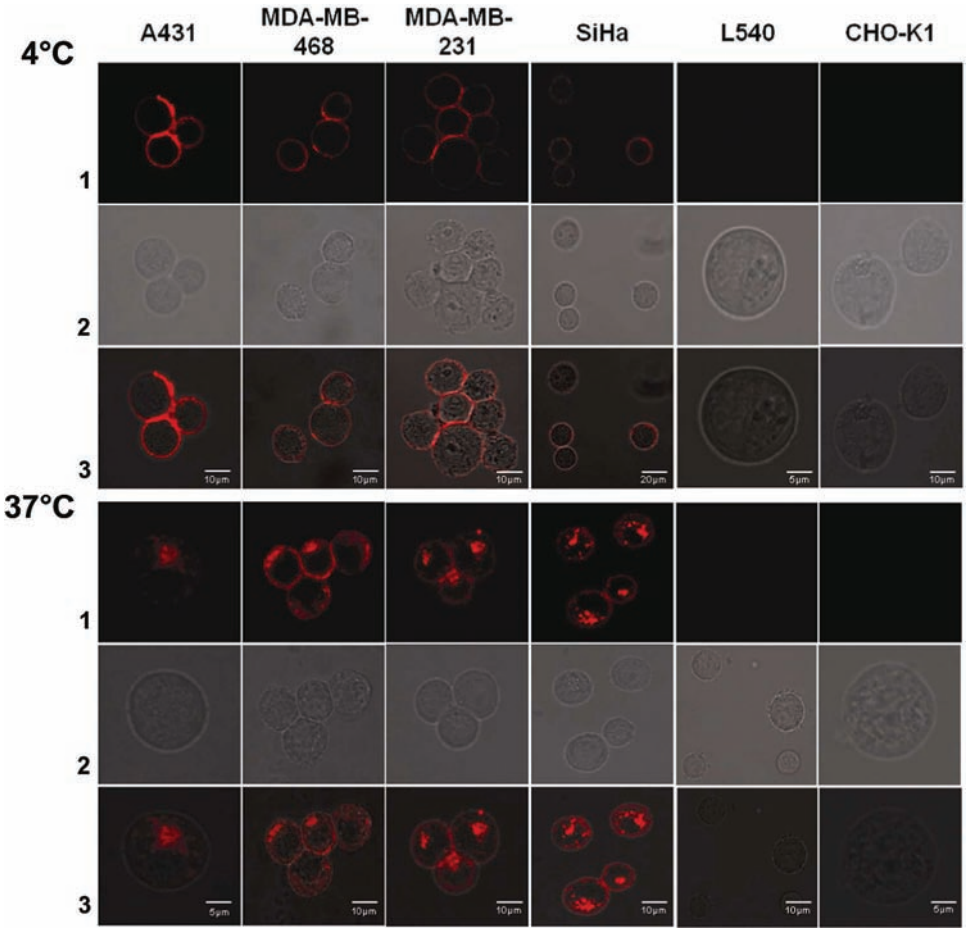

Figure 4. Binding and internalization of scFv-425-SNAP-Ce6 analyzed by confocal microscopy. Confocal images were obtained for the EGFR$^+$ cell lines A431, MDA-MB-468, MDA-MB-231, and SiHa, and for the EGFR$^-$ cell lines L540 and CHO-K1. All cells were incubated with 0.5 μg scFv-425-SNAP-Ce6 for 30 min at 4 °C (upper panel) or for 60 min at 37 °C (lower panel). (1) Ce6 fluorescence signal; (2) transmitted light; (3) overlay of fluorescence signal and transmitted light. Magnification is indicated by the white scale bars.

significant increase was observed in A431 cells treated with 200 nM scFv-Ki4-SNAP-Ce6 (Figure 5E).

The production of ROS in photoactivated A431 cells was investigated by measuring the 485/535 nm fluorescence of DCF, produced by the oxidation and deacetylation of 6-carboxy-2′,7′-dichlorodihydrofluoresceindiacetatedi(acetoxymethyl)ester (H_2DCFDA). We found that a burst of ROS synthesis follows light activation in the presence of 200 nM of the conjugated Ce6 and 50 nM of the unconjugated Ce6, but there was only a small increase in ROS levels in nonirradiated cells, barely above the background level observed in cells that were not treated with the photosensitizer (Figure 5F).

■ DISCUSSION

Photodynamic therapy (PDT) is a minimally invasive treatment that uses nontoxic photosensitizers and harmless visible light in combination with oxygen to produce cytotoxic reactive oxygen species that kill malignant cells by apoptosis and/or necrosis.[17] Many different photosensitizers have been developed, but we chose Ce6 as a model because it has been evaluated extensively in PDT studies and also has advantageous physical and chemical properties. Ce6 has an absorption maximum at 664 nm, which is a good compromise between photon efficacy and cell penetration,[18] and the presence of carboxyl groups allows further functionalization.[7]

One of the main drawbacks of PDT is the scattergun effect of activated photosensitizers, which tends to damage healthy as well as tumor cells. Targeted therapy using antibodies has revolutionized cancer treatment, and several antibodies that bind to tumor cell antigens have achieved blockbuster status. The efficacy of therapeutic antibodies can be improved by covalently linking them to additional effector molecules (e.g., radionuclides, drugs, or toxins),[19] as this achieves selective delivery and should reduce the systemic toxicity traditionally associated with small molecule drugs.[20] The same principle can be applied to photosensitizers, an approach known as photoimmunotherapy (PIT). Effector molecules are generally conjugated to antibodies using either the reduced sulfhydryl groups of cysteine residues or amino groups in lysine side chains. However, both methods yield heterogeneous products, comprising a mixture of conjugated antibodies with the effector attached at different sites and a variable number of effectors attached to each antibody resulting in a range of molar rations and very different pharmacokinetic, efficacy, and safety profiles.

Hamblett and colleagues[21] have studied the toxicity, pharmacokinetic properties, and therapeutic efficacy of heterogeneous antibody−drug conjugates by purifying three antibody fractions containing two, four, and eight conjugated molecules of monomethyl-auristatin E (MMAE). The fraction with eight MMAE groups was poorly tolerated and rapidly cleared compared to the other fractions and demonstrated the lowest

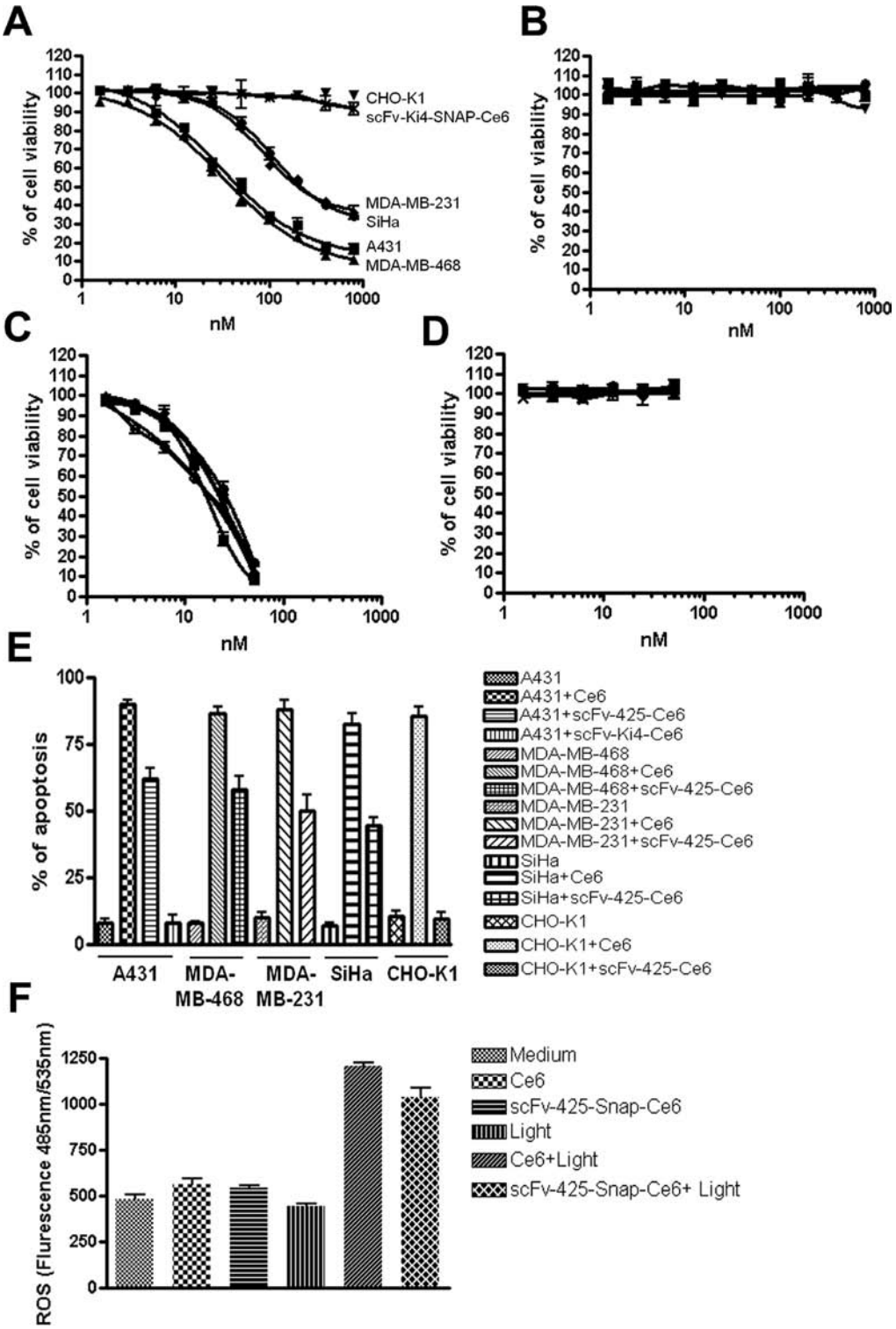

Figure 5. Evaluation of photodynamic therapeutic efficiency. Cell proliferation and apoptosis assays were carried out using the scFv-425-SNAP-Ce6. The cytotoxicity of scFv-425-Ce6 was determined against cell lines A431 (■), MDA-MB-468 (▲), MDA-MB-231 (♦), SiHa (●), and CHO-K1 (▼) using the XTT proliferation assay on (A) irradiated cells and (B) nonirradiated cells. The cytotoxicity of scFv-Ki4-SNAP-Ce6 against A431 cells (-X-) was tested as a control. The same cells were treated with different concentrations of unconjugated Ce6 and cell viability was analyzed (C) with and (D) without light activation. (E) Apoptosis was evaluated using the Apo-ONE Homogeneous Caspase-3/7 Assay, with 50 nM Ce6, 200 nM scFv-SNAP-Ce6, and 200 nM scFv-Ki4-SNAP-Ce6. (F) The generation of reactive oxygen species (ROS) due to illumination of photosensitized A431 cells was detected using the dichlorofluorescein derivative carboxy-H2DCFDA reagent.

efficacy. This suggests that the key design parameter for antibody−drug conjugates is the number of drug molecules attached to the antibody. However, even purifying antibodies that carry the same number of drug molecules still generates a complex mixture because of the many alternative attachment sites.[21] For example, there are approximately 40 lysine residues in a typical antibody, potentially resulting in more than one million different conjugated antibody species. Similarly, there

dx.doi.org/10.1021/bc200304k | *Bioconjugate Chem.* 2011, 22, 2487−2495

are between one and eight cysteine residues, typically generating approximately 100 conjugated variants. Each version of the antibody−drug conjugate typically displays a unique and unpredictable pharmacokinetic profile.[20]

To avoid the issues discussed above, we investigated the use of SNAP-tag technology to provide a unique conjugation site on the antibody, allowing the production of a homogeneous conjugate preparation. We engineered a construct in which the coding sequence of a scFv antibody that binds specifically to EGFR was genetically fused to the SNAP tag cassette, which endows the antibody with a SNAP-tag and therefore allows site-specific conjugation BG-modified substrates, in this case Ce6. This conjugation method can be applied to any antibody−photosensitizer combination as long as the antibody carries the SNAP-tag and the substrate is modified with a BG group. We therefore also prepared a control construct in which the scFv-Ki4, which binds to CD30 and is thus irrelevant for the treatment of $EGFR^+$ tumors, was also labeled with Ce6.

The conjugation reaction was successful, allowing the preparation of homogeneous samples of scFv-425-SNAP-Ce6 and scFv-Ki4-SNAP-Ce6. We then tested these preparations for their ability to kill tumor cells specifically. We found that scFv-425-SNAP-Ce6 selectively killed $EGFR^+$ cells in four human tumor-derived cell lines representing epidermal, breast, and cervical carcinomas (A431, MDA-MB-231, MDA-MB468, and SiHa) after exposure to light. The phototoxicity of scFv-425-SNAP-Ce6 was dependent on the presence of EGFR, receptor internalization and light, and toxicity was most potent in A431 and MDA-MB468 cells, which express the largest amount of the receptor [$(1-1.3) \times 10^6$ receptors/cell].[22,23] The other cells lines expressed less EGFR (1.3×10^5 receptors/cell for MDA-MB-231 and $(2 \times 10^4)-(2 \times 10^5)$ receptors/cell for SiHa),[23,24] and the toxicity of scFv-425-SNAP-Ce6 was concomitantly reduced, although not to the point where the fusion protein would be therapeutically ineffective. This means that scFv-425-SNAP-Ce6 can target a wide range of $EGFR^+$ cells, not only those with the highest expression levels. No toxicity was observed when $EGFR^-$ cells (CHO-K1) were exposed to scFv-425-SNAP-Ce6.

We have previously shown that scFv-425-SNAP accumulates directly in mouse kidneys after injection, and is subsequently detected in the bladder, indicating clearance by renal filtration. Despite the rapid clearance, the accumulation and retention of scFv-425-SNAP in tumor tissue was evidently sufficient to yield very high tumor to background ratio 10 h postinjection.[12]

In conclusion, we have demonstrated for the first time the conjugation of photosensitizers to a scFv antibody using SNAP-tag technology. This rapid and efficient method produces a homogeneous conjugate with define pharmacokinetic and therapeutic profiles. This provides proof of the principle that SNAP-tag technology can be used to produce targeted photoimmunotherapeutic agents for cancer therapy, avoiding the off-target effects that have thus far limited the development of PDT.

AUTHOR INFORMATION

Corresponding Author

*Dr. Mehmet Kemal Tur, Department of Experimental Pathology and Immunotherapy, Institute of Pathology, University Hospital Giessen and Marburg (UKGM), Langhans-Str. 10, 35392 Giessen, Germany, Tel: +49 (0) 641-985-41116, Fax: +49-641-985-41109, E-mail: mehmet.k.tur@patho.med.uni-giessen.de.

Author Contributions

[⊥]Contributed equally.

ACKNOWLEDGMENTS

The authors thank Dr. Richard Twyman for critical reading of the document.

REFERENCES

(1) Allison, R. R., and Sibata, C. H. (2010) Oncologic photodynamic therapy photosensitizers: A clinical review. *Photodiagnosis and Photodynamic Therapy 7*, 61−75.

(2) Huang, Z. (2005) A review of progress in clinical photodynamic therapy. *Technol. Cancer Res. Treat. 4*, 283−293.

(3) Palumbo, G. (2007) Photodynamic therapy and cancer: a brief sightseeing tour. *Expert Opin. Drug Delivery 4*, 131−148.

(4) Sibani, S. A., McCarron, P. A., Woolfson, A. D., and Donnelly, R. F. (2008) Photosensitiser delivery for photodynamic therapy. Part 2: systemic carrier platforms. Expert. *Opin. Drug Delivery 5*, 1241−1254.

(5) Woodburn, K. W., Vardaxis, N. J., Hill, S. J., Kaye, A. H., Reiss, J. A., and Phillips, D. R. (1992) Evaluation of porphyrin characteristic required for photodynamic therapy. *Photochem. Photobiol. 55*, 697−704.

(6) Olivo, M., Bhuvaneswari, R., Lucky, S. S., Dendukuri, N., and Thong, P. S. (2010) Targeted therapy of cancer using photodynamic therapy in combination with multi-faceted anti-tumor modalities. *Pharmaceuticals 3*, 1507−1529.

(7) Van Dongen, G. A. M. S., Visser, G. W. M., and Vrouenraets, M. B. (2004) Photosensitizer-antibody conjugates for detection and therapy of cancer. *Adv. Drug Delivery Rev. 56*, 31−52.

(8) Wang, L., Amphlett, G., Blattler, W. A., Lambert, J. M., and Zhang, W. (2005) Structural characterization of the maytansinoid-monoclonal antibody immunoconjugate, huN901−DM1, by mass spectrometry. *Protein Sci. 14*, 2436−2446.

(9) Jeger, S., Zimmermann, K., Blanc, A., Grünberg, J., Honer, M., Hunziker, P., Harriet, S., and Schibli, R. (2010) Site-specific and stoichiometric modification of antibodies by bacterial transglutaminase. *Angew. Chem., Int. Ed. 49*, 9995−9997.

(10) Hong, K., Kim, C. G., Lee, S. H., Chang, K. H., Shin, Y. W., Ryoo, K. H., Kim, S. H., and Kim, Y. S. (2010) A novel anti-EGFR monoclonal antibody inhibiting tumor cell growth by recognizing different epitopes from cetuximab. *J. Biotechnol. 145*, 84−91.

(11) Mendelsohn, J. (2002) Targeting the epidermal growth factor receptor for cancer therapy. *J. Clin. Oncol. 20*, 1−13.

(12) Kampmeier, F., Niesen, J., Koers, A., Ribbert, M., Brecht, A., Fischer, R., Kiessling, F., Barth, S., and Thepen, T. (2010) Rapid optical imaging of EGF receptor expression with a single-chain antibody SNAP-tag fusion protein. *Eur. J. Nucl. Med. Mol. Imaging 37*, 1926−1934.

(13) Gronemeyer, T., Chidley, C., Juillerat, A., Heinis, C., and Johnsson, K. (2006) Directed evolution of O6-alkylguanine-DNA alkyltransferase for applications in protein labeling. *PEDS 19*, 309−16.

(14) Juillerat, A., Juillerat, A., Gronemeyer, T., Keppler, A., Gendreizig, S., Pick, H., Vogel, H., and Johnsson, K. (2003) Directed evolution of O6-Alkylguanine-DNA alkyltransferase for efficient labeling of fusion proteins with small molecules in vivo. *Chem. Biol. 10*, 313−317.

(15) Kampmeier, F., Ribbert, M., Nachreiner, T., Dembski, S., Beaufils, F., Brecht, A., and Stefan, B. (2009) Site-specific, covalent labeling of recombinant antibody fragments via fusion to an engineered version of 6-Oalkylguanine DNA alkyltransferase. *Bioconjugate Chem. 20*, 1010−1015.

(16) Piazena, H., and Kelleher, D. K. (2010) Effects of infrared-A irradiation on skin: discrepancies in published data highlight the need for an exact consideration of physical and photobiological laws and appropriate experimental settings. *Photochem. Photobiol. 86*, 687−705.

(17) Bhatti, M., Yahioglu, G., Milgrom, L. R., Garcia-Maya, M., Chester, K. A., and Deonarain, M. P. (2008) Targeted photodynamic

therapy with multiply-loaded recombinant antibody fragments. *Int. J. Cancer 1 122*, 1155−63.

(18) Douillard, S., Olivier, D., and Patrice, T. (2009) In vitro and in vivo evaluation of Radachlorin® sensitizer for photodynamic therapy. *Photochem. Photobiol. Sci. 8*, 405−413.

(19) Adams, G. P., and Weiner, L. M. (2005) Monoclonal antibody therapy of cancer. *Nat. Biotechnol. 23*, 1147−1157.

(20) Junutula, J. R., Raab, H., Clark, S., Bhakta, S., Leipold, D. D., Weir, S., Chen, Y., Simpson, M., Tsai, S. P., Dennis, M. S., Lu, Y., Meng, Y. G., Ng, C., Yang, J., Lee, C. C., Duenas, E., Gorrell, J., Katta, V., Kim, A., McDorman, K., Flagella, K., Venook, K., Ross, S., Spencer, S. D., Wong, W. L., Lowman, H. B., Vandlen, R., Sliwkowski, M. X., Scheller, R. H., Polakis, P., and Mallet, W. (2008) Site-specific conjugation of a cytotoxic drug to an antibody improves the therapeutic index. *Nat. Biotechnol. 26*, 925−932.

(21) Hamblett, K. J., Senter, P. D., Chace, D. F., Sun, M. M. C., Lenox, J., Cerveny, C. C. G., Kissler, K., M., Bernhardt, S. X., Kopcha, A. K., Zabinski, R. F., Meyer, D. L., and Francisco, J. A. (2004) Effects of drug loading on the antitumor activity of a monoclonal antibody drug conjugate. *Clin. Cancer Res. 10*, 7063−7070.

(22) Gamou, S., Kim, Y. S., and Shimizu, N. (1986) Different responses to EGF in two human carcinoma cell lines, A431 and UCVA-1, possessing high numbers of EGF receptors. *Mol. Cell. Endocrinol. 37*, 205−213.

(23) Cai, K., Cai, Z., Chen, Z., Bailey, K. E., Scollard, D. A., Reilly, R. M., and Vallis, K. A. (2008) Relationship between induction of phosphorylated H2AX and survival in breast cancer cells exposed to ^{111}In-DTPA-hEGF. *J. Nucl. Med. 49*, 1353−1361.

(24) Nida, D. L., Rahman, M. S., Carlson, K. D., Richards-Kortum, R., and Follen, M. (2005) Fluorescent nanocrystals for use in early cervical cancer detection. *Gynecologic Oncol. 99*, 89−94.

Bioconjugate Chemistry

Article

pubs.acs.org/bc

Enhanced Affinity Bifunctional Bisphosphonates for Targeted Delivery of Therapeutic Agents to Bone

Jivan N. Yewle,[†] David A. Puleo,[‡] and Leonidas G. Bachas*[,§]

[†]Department of Chemistry, University of Kentucky, Lexington, Kentucky 40506-0055, United States

[‡]Center for Biomedical Engineering, University of Kentucky, Lexington, Kentucky 40506-0070, United States

[§]Department of Chemistry, University of Miami, 1301 Memorial Drive, Coral Gables, Florida 33146-0431, United States

ABSTRACT: Skeletal diseases have a major impact on the worldwide population and economy. Although several therapeutic agents and treatments are available for addressing bone diseases, they are not being fully utilized because of their uptake in nontargeted sites and related side effects. Active targeting with controlled delivery is an ideal approach for treatment of such diseases. Because bisphosphonates are known to have high affinity to bone and are being widely used in treatment of osteoporosis, they are well-suited for drug targeting to bone. In this study, a targeted delivery of therapeutic agent to resorption sites and wound healing sites of bone was explored. Toward this goal, bifunctional hydrazine-bisphosphonates (HBPs), with spacers of various lengths, were synthesized and studied for their enhanced affinity to bone. Crystal growth inhibition studies showed that these HBPs have high affinity to hydroxyapatite, and HBPs with shorter spacers bind more strongly than alendronate to hydroxyapatite. The HBPs did not affect proliferation of MC3T3-E1 preosteoblasts, did not induce apoptosis, and were not cytotoxic at the concentration range tested (10^{-6}–10^{-4} M). Furthermore, drugs can be linked to the HBPs through a hydrazone linkage that is cleavable at the low pH of bone resorption and wound healing sites, leading to release of the drug. This was demonstrated using hydroxyapatite as a model material of bone and 4-nitrobenzaldehyde as a model drug. This study suggests that these HBPs could be used for targeted delivery of therapeutic agents to bone.

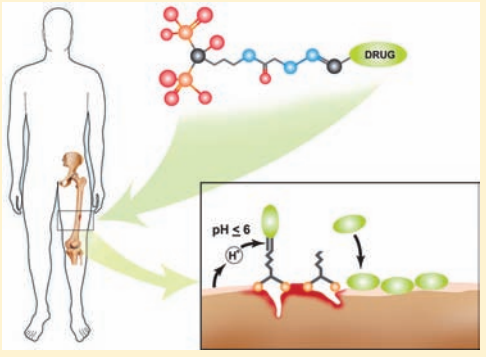

INTRODUCTION

Active targeting of therapeutic agents to bone reduces drug toxicity and improves drug bioavailability at the desired site.[1] Bone tissue is characterized by constant remodeling, whereby it continuously undergoes formation and resorption; perturbations in bone remodeling are associated with several metabolic bone diseases, such as osteoporosis.[2−4] Therefore, molecules that inhibit bone resorption or stimulate bone formation show drug activity against various skeletal disorders.[5] Although a range of therapeutic agents is available to treat skeletal disorders,[6] their clinical application is hampered by their uptake in nontargeted sites and the consequent undesired side effects.[7]

Several bisphosphonates (BPs) show antiresorptive properties and are being prescribed in the treatment of skeletal diseases.[6,8,9] BPs are stable analogues of naturally occurring pyrophosphate and have high affinity to bone and hydroxyapatite (HA).[10] Besides the two phosphonate groups, BPs have two other substituents (R^1 and R^2) on their geminal carbon. BPs with a hydroxyl or an amine group at R^1 facilitate tridentate binding to bone and HA, and show an increased affinity to these materials.[11,12] The overall nature of the R^2 substituent also contributes toward enhancing the bone-seeking ability and pharmacological properties of BPs.[10,13]

Recently, a number of drug targeting and drug delivery strategies have been reported using a range of delivery vehicles,

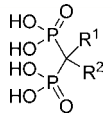

such as polymer scaffolds, liposomes, dendrimers, micelles, hydrogels, peptides, and antibodies.[14−21] However, drug targeting to bone sites requires molecules that have high affinity to bone. Besides BPs, other molecules, such as D-aspartic acid octapeptide,[20,21] polymalonic acid,[22] and tetracycline,[23,24] show affinity to bone. BPs have advantage over other molecules because their affinity can be tuned by changing their R^1 and R^2 substituents. Moreover, in addition to being prescribed as drugs, BPs are also being studied for drug targeting and drug delivery to bone,[25−30] including the administration of radiopharmaceuticals and imaging agents to bone for diagnostic applications.[31−35] For the purpose of drug targeting to bone, various strategies of BP-drug conjugation have been investigated by us and others.[29,35−38] Ideally, for targeted drug delivery to bone, BP-drug conjugates should have a stable linkage between the BP and drug molecule that can survive during systemic circulation of the conjugate following parenteral administration, and at the same time be labile at the

Received: June 15, 2011
Revised: November 10, 2011
Published: November 10, 2011

 © 2011 American Chemical Society dx.doi.org/10.1021/bc2003132 | *Bioconjugate Chem.* 2011, 22, 2496–2506

bone surface to release the drug locally. Most of the strategies mentioned above employ agents that are conjugated to BPs through stable, noncleavable linkages resulting in the administration of the complete conjugate to the treatment site.[25,29,31−33,35] Current approaches that employ cleavable linkages either are too labile to ensure delivery of the drug to the desired site[26,27] or show limited release providing inadequate availability of drug for action.[26] A strategy that involves labile conjugation to one of the phosphonate groups of BP could compromise the affinity of the corresponding BP-drug conjugate toward bone, because it is through the phosphonate groups that BPs bind to the mineral matrix.[27]

Herein, we report a novel strategy for targeted delivery of therapeutic agents to sites of low pH, such as bone resorption lacunae and areas of wound healing, through their conjugation to enhanced affinity bifunctional BPs with a pH-triggered cleavable linkage. In particular, we have synthesized seven novel hydrazine-bisphosphonates (HBPs) (**2**−**8**), which have a hydroxyl group as R^1, while R^2 contains a hydrazine functionality attached through spacers of various length and hydrophobicity (Table 1). Furthermore, experiments were performed to explore the binding affinity, cytotoxicity, drug conjugation, and pH triggered drug release of HBPs.

Table 1. Structure of Alendronate (1) and Hydrazine-Bisphosphonates (HBPs) (2−8)

Cpd	R^1	R^2
1	OH	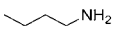
2	OH	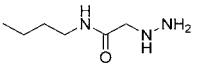
3	OH	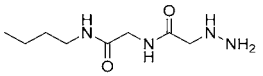
4	OH	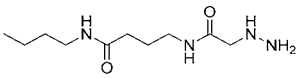
5	OH	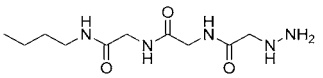
6	OH	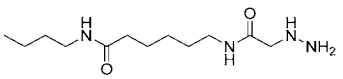
7	OH	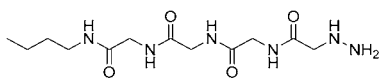
8	OH	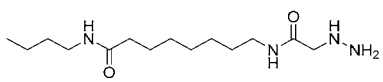

EXPERIMENTAL PROCEDURES

Materials. The osteoblastic cell line MC3T3-E1 was obtained from American Type Culture Collection (CRL-2593; ATCC, Rockville, MD). Alpha minimum essential medium (αMEM) and fetal bovine serum (FBS) were purchased from GIBCO-Invitrogen (Carlsbad, CA). The BCA protein assay kit was obtained from ThermoFisher Scientific (Rockford, IL). The cell proliferation reagent WST-1 was purchased from Roche (Mannheim, Germany). Ac-DEVD-AFC was obtained from Enzo Life Sciences (Plymouth Meeting, PA). 4-Aminobutanoic acid, 6-aminohexanoic acid, 8-aminooctanoic acid, glycine, glycylglycine, glycylglycylglycine, methanesulfonic acid, phosphorous acid, phosphorus trichloride, and 2,3,5,6-tetrafluorophenol (TFP) were purchased from Alfa Aesar (Ward Hill, MA). *N,N′*-Dicyclohexylcarbodiimide (DCC), triethylamine (TEA), tri-BOC-hydrazinoacetic acid (TBHA), reagent grade hydroxyapatite powder, potassium hydroxide, sodium acetate, sodium chloride, sodium hydroxide, etoposide, tris(hydroxymethyl)aminomethane hydrochloride (Tris-HCl), 4-(2-hydroxyethyl)piperazine-1-ethanesulfonic acid (HEPES), 3-[(3-cholamidopropyl)dimethylamino]-1-propanesulfonate (CHAPS), ethylenediaminetetraacetic acid disodium salt dihydrate (EDTA), sodium fluoride (NaF), sodium orthovanadate, leupeptin hemisulfate salt, aprotinin bovine, phenylmethylsulfonylfluoride, DL-dithiothreitol (DTT), glycerol, and Triton X-100 were purchased from Sigma-Aldrich (St. Louis, MO). Calcium chloride, hydrochloric acid, and potassium dihydrogen phosphate were obtained from EMD Chemicals (Gibbstown, NJ). Acetonitrile, chloroform, dichloromethane, diethyl ether, dimethyl sulfoxide (DMSO), hexane, and phosphoric acid were purchased from Mallinckrodt (Hazelwood, MO). The NMR solvents deuterium oxide and deuterated chloroform were purchased from Cambridge Isotope Laboratories (Andover, MA).

Apparatus. ^{1}H NMR, ^{31}P NMR, and ^{13}C NMR spectra were obtained on a Varian INOVA 400 MHz spectrometer (Palo Alto, CA). Electrospray ionization mass spectrometry was performed on a ThermoFinnigan LCQ mass spectrometer (Waltham, MA). HA crystal growth experiments were performed using an Isotemp Refrigerated Circulator and pH meter (Fisher Scientific, Pittsburgh, PA). UV−vis spectra were obtained with an Agilent 8453 UV−visible spectrophotometer (Agilent Technologies, Santa Clara, CA). Deionized water was produced using a Milli-Q water purification system (Millipore, Bedford, MA).

Scheme 1. Synthesis of Alendronate 1 and HBP 2

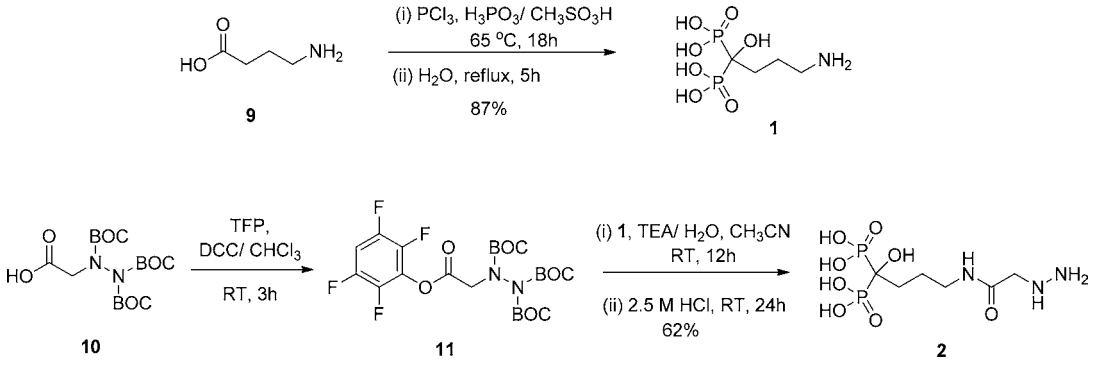

dx.doi.org/10.1021/bc2003132 | Bioconjugate Chem. 2011, 22, 2496−2506

Synthesis of (4-Amino-1-hydroxybutylidene)-bisphosphonic Acid Monosodium Salt (1). (4-Amino-1-hydroxybutylidene)bisphosphonic acid monosodium salt or monosodium alendronate (**1**) was synthesized in an inert atmosphere according to a previously reported procedure from 4-aminobutanoic acid (**9**)[39,40] as outlined in Scheme 1. A 25 mL flask was fitted with an addition funnel and a reflux condenser. Ice-cold water was circulated through the condenser. The system was flushed with nitrogen; and 4-aminobutyric acid (**9**) (4.0 g, 38.7 mmol), phosphorous acid (3.18 g, 38.7 mmol), and methanesulfonic acid (16 mL) were added to the flask. The mixture was heated for 5 min at 65 °C. PCl_3 (9.0 mL, 85.3 mmol) was added over 20 min, and the mixture was stirred for 18 h at 65 °C. The solution was cooled to 25 °C and quenched into 0−5 °C water (40 mL) with vigorous stirring. The reaction flask was rinsed with an additional 16 mL of water, and the combined solution was refluxed for 5 h at 110 °C. The solution was cooled to 23 °C, and the pH was adjusted to 4−4.5 with 50% (v/v) NaOH. The resulting mixture was allowed to react for 10−12 h at 0−5 °C. The white solid obtained was filtered and washed with cold water (20 mL) and 95% ethanol (20 mL). The solid was dried under vacuum at room temperature (RT) to obtain compound **1** as a white solid in 87.1% (9.22 g) yield. ^{1}H NMR (D_2O): δ 3.02 (t, 2H), δ 2.00 (m, 4H). ^{13}C NMR (MeCN/D_2O): δ 72.9 (t), δ 39.33 (s), δ 29.94 (s), δ 21.48 (t). ^{31}P NMR (H_3PO_4/D_2O): δ 18.53. MS (MALDI-TOFMS): 272 $[M+H+Na]^+$.

Synthesis of Tri-*tert*-butyl 2-(2-oxo-2-(2,3,5,6-tetrafluorophenoxy)ethyl)hydrazine-1,1,2-tricarboxylate (11). Tri-BOC-hydrazinoacetate (**10**) (90.0 mg, 0.231 mmol) and TFP (42.1 mg, 0.254 mmol) were dissolved in 5 mL chloroform. DCC (52.3 mg, 0.254 mmol) in 5 mL chloroform was added dropwise to the reaction mixture and stirred at RT. The progress of the reaction was followed by thin layer chromatography (TLC). After complete consumption of **10** (3 h), the 1,3-dicyclohexyl urea formed in the reaction mixture was removed by filtration, and the filtrate was evaporated *in vacuo*. The residue was then suspended in an adequate amount of hexane, the remaining 1,3-dicyclohexyl urea was removed by filtration, and the filtrate was evaporated *in vacuo* to obtain crude compound **11**. The crude material was purified by column chromatography (hexane/acetone 85/15 v/v) to obtain pure compound **11** as a pale yellow liquid in 97% (120.5 mg) yield. ^{1}H NMR (CD_3CN): δ 7.25 (m, 1H), δ 3.20 (s, 2H) δ 1.45 (m, 27H). ^{13}C NMR ($CDCl_3$): δ 168.01 (s), δ 154.35 (s), δ 153.75 (s), δ 150.54 (s), δ 148.70 (s), δ 147.10 (s), δ 146.40 (s), δ 102.10 (s), δ 84.22 (s), δ 83.27 (s), δ 82.21 (s), δ 54.33 (m), δ 28.20 (s).

Synthesis of (4-(2-Hydrazinylacetamido)-1-hydroxybutane-1,1-diyl)bisphosphonic Acid (2). Compound **1** (50.0 mg, 0.154 mmol) was suspended in 1 mL of deionized water, and TEA (93.2 mg, 0.923 mmol) was added to the suspension. After a few seconds of stirring at RT, the suspension became clear. The reaction was stirred at RT for 5 min. Compound **11** (124 mg, 0.231 mmol) was dissolved in 1.5 mL of acetonitrile and added to the reaction mixture. TEA (15.5 mg, 0.154 mmol) was added, and the reaction mixture was stirred at RT for 12 h. The reaction mixture was washed with diethyl ether (10 mL) and evaporated *in vacuo*. The obtained solid was treated with 2 mL of 2.5 M HCl, and the solution was stirred at RT for 24 h. The solvent was removed *in vacuo*, and the crude product was sonicated twice in ethanol at RT for 2 h and filtered to obtain a white solid of pure compound **2** in 62% (31 mg) yield. ^{1}H NMR (D_2O): δ 3.78 (s, 2H), δ 3.28 (t, 2H), δ 1.99 (m, 2H), δ 1.84 (m, 2H). ^{13}C NMR (MeCN/D_2O): δ 170.41 (s), δ 74.17 (t), δ 51.58 (s), δ 40.50 (s), δ 31.75 (s), δ 24.17 (s). ^{31}P NMR (H_3PO_4/D_2O): δ 19.08. MS (+ ESI): 322 $[M+H]^+$.

General Procedure for Synthesis of Compounds 13a−13f. Compound **12a−12f** (0.401 mmol, 1.2 equiv) was suspended in 1 mL of deionized water, and TEA (0.668 mmol, 2.0 equiv) was added to the suspension. After a few seconds of stirring at RT, the suspension became clear. The reaction was stirred at RT for 5 min. Compound **11** (0.334 mmol, 1.0 equiv) was dissolved in 1.5 mL of acetonitrile, and the solution was added to the reaction mixture. TEA (0.167 mmol, 0.5 equiv) was added, and the reaction mixture was stirred at RT for 12 h. The reaction mixture was washed with diethyl ether, and the solvent was evaporated *in vacuo* to obtain crude compound **13a−13f**. The crude product **13a−13f** was used in the next reaction without further purification.

*Compound **13a**.* Following the procedure shown for **13a−13f**, compound **13a** was obtained by amide coupling of compound **11** and glycine (**12a**) as a paste in 95% yield. ^{1}H NMR ($CDCl_3$): δ 4.10 (s, 2H), δ 3.98 (s, 2H), δ 1.45 (m, 27H). ^{13}C NMR ($CDCl_3$): δ 174.56 (s), δ 168.46 (s), δ 154.46 (s), δ 153.86 (s), δ 150.65 (s) δ 84.52 (s), δ 83.16 (s), δ 82.45 (s), δ 54.93 (m), δ 45.91 (m), δ 28.22 (s).

*Compound **13b**.* Following the procedure shown for **13a−13f**, compound **13b** was obtained by amide coupling of compound **11** and 4-aminobutenoic acid (**12b**) as a paste in 97% yield. ^{1}H NMR ($CDCl_3$): δ 4.10 (s, 2H), δ 3.60 (d, 2H), δ 2.35 (m, 2H), δ 1.30 (m, 2H), δ 1.45 (m, 27H). ^{13}C NMR ($CDCl_3$): δ 182.70 (s), δ 170.70 (s), δ 154.30 (s), δ 153.40 (s), δ 150.56 (s) δ 84.24 (s), δ 83.56 (s), δ 82.10 (s), δ 54.30 (m), δ 39.41 (m), δ 35.60 (m), δ 28.41 (s), δ 23.42 (m).

*Compound **13c**.* Following the procedure shown for **13a−13f**, compound **13c** was obtained by amide coupling of compound **11** and glycylglycine (**12c**) as a paste in 94% yield. ^{1}H NMR ($CDCl_3$): δ 4.02 (s, 2H), δ 3.99 (s, 2H), δ 3.80 (s, 2H), δ 1.45 (m, 27H). ^{13}C NMR ($CDCl_3$): δ 174.44 (s), δ 169.24 (s), δ 168.43 (s), δ 154.34 (s), δ 153.55 (s), δ 151.20 (s), δ 85.12 (s), δ 83.66 (s), δ 83.05 (s), δ 55.15 (m), δ 45.24 (m), δ 43.31 (m), δ 28.15 (s).

*Compound **13d**.* Following the procedure shown for **13a−13f**, compound **13d** was obtained by amide coupling of compound **11** and 6-aminohexanoic acid (**12d**) as a paste in 96% yield. ^{1}H NMR ($CDCl_3$): δ 4.03 (s, 2H), δ 3.33 (d, 2H), δ 2.21 (t, 2H), δ 1.61 (m, 2H), δ 1.45 (m, 27H), δ 1.28 (m, 2H). ^{13}C NMR ($CDCl_3$): δ 178.04 (s), δ 170.20 (s), δ 154.44 (s), δ 153.34 (s), δ 151.84 (s), δ 85.11 (s), δ 83.24 (s), δ 83.48 (s), δ 54.35 (m), δ 38.92 (m), δ 34.32 (m), δ 29.15 (s), δ 28.40 (s), δ 26.37 (s), δ 24.75 (s).

*Compound **13e**.* Following the procedure shown for **13a−13f**, compound **13e** was obtained by amide coupling of compound **11** and glycylglycylglycine (**12e**) as a paste in 93% yield. ^{1}H NMR ($CDCl_3$): δ 4.01 (s, 2H), δ 3.98 (d, 2H), δ 3.91 (d, 2H), δ 3.80 (d, 2H), δ 1.42 (m, 27H). ^{13}C NMR ($CDCl_3$): δ 174.45 (s), δ 169.75 (s), δ 169.51 (s), δ 168.01 (s), δ 154.55 (s), 151.40 (s), 151.14 (s), δ 85.40 (s), δ 85.29 (s), δ 83.51 (s), δ 55.49 (m), δ 45.30 (m), δ 43.77 (m), δ 43.34 (s), δ 28.19 (s).

*Compound **13f**.* Following the procedure shown for **13a−13f**, compound **13f** was obtained by amide coupling of compound **11** and 8-aminooctanoic acid (**12f**) as a paste in 95% yield. ^{1}H NMR ($CDCl_3$): δ 4.02 (s, 2H), δ 3.23 (m, 2H), δ 2.22 (t, 2H), δ 1.59 (m, 4H), δ 1.45 (m, 27H), δ 1.25 (m,

6H). ^{13}C NMR ($CDCl_3$): δ 178.40 (s), δ 170.05 (s), δ 154.14 (s), 151.25 (s), 151.19 (s), δ 85.17 (s), δ 85.39 (s), δ 83.89 (s), δ 38.90 (m), δ 34.00 (t), δ 30.10 (m), δ 29.12 (s), δ 29.65 (s), δ 26.58 (s), δ 24.54 (s).

General Procedure for Synthesis of Compounds 14a−14f. Compound **13a−13f** (0.386 mmol, 1.0 equiv) and TFP (0.425 mmol, 1.1 equiv) were dissolved in 15 mL chloroform. DCC (0.425 mmol, 1.1 equiv) in 10 mL chloroform was added dropwise to the reaction mixture and stirred at RT. The progress of the reaction was followed by TLC. After complete consumption of **13a−13f** (3 h), the 1,3-dicyclohexyl urea formed in the reaction mixture was removed by filtration, and the filtrate was evaporated *in vacuo*. The residue was then suspended in an adequate amount of hexane, the remaining 1,3-dicyclohexyl urea was removed by filtration, and the filtrate was evaporated *in vacuo* to obtain crude compound **14a−14f**. The crude product was purified by column chromatography (CH_2Cl_2/MeOH 90/10 v/v) to obtain the pure compound as a pale yellow liquid.

*Compound **14a***. Following the procedure shown for **14a−14f**, compound **14a** was obtained from **13a** by treatment of TFP and DCC as a sticky liquid. ^{1}H NMR ($CDCl_3$): δ 6.60 (s, 1H), δ 4.25 (s, 2H), δ 4.10 (s, 2H), δ 1.42 (m, 27H). ^{13}C NMR ($CDCl_3$): δ 174.02 (s), δ 168.32 (s), δ 154.21 (s), δ 153.14 (s), δ 150.78 (s), δ 148.72 (d), δ 146.89 (d), δ 146.10 (s), δ 101.80 (s), δ 84.12 (s), δ 83.85 (s), δ 82.64 (s), δ 54.41 (m), δ 45.00 (m), δ 28.44 (s).

*Compound **14b***. Following the procedure shown for **14a−14f**, compound **14b** was obtained from **13b** by treatment of TFP and DCC as a sticky liquid. ^{1}H NMR ($CDCl_3$): δ 6.60 (s, 1H), δ 4.05 (s, 2H), δ 3.20 (d, 2H), δ 2.67 (m, 2H), δ 1.97 (m, 2H), δ 1.42 (m, 27H). ^{13}C NMR ($CDCl_3$): δ 182.47 (s), δ 170.12 (s), δ 154.10 (s), δ 153.45 (s), δ 151.10 (s), δ 148.69 (d), δ 147.23 (d), δ 146.80 (s), δ 102.10 (s), δ 84.58 (s), δ 83.74 (s), δ 82.36 (s), δ 54.33 (m), δ 39.45 (m), δ 33.56 (m), δ 23.47 (s), δ 28.56 (s).

*Compound **14c***. Following the procedure shown for **14a−14f**, compound **14c** was obtained from **13c** by treatment of TFP and DCC as a sticky liquid. ^{1}H NMR ($CDCl_3$): δ 6.98 (s, 1H), δ 4.38 (s, 2H), δ 4.11 (s, 2H), δ 3.41 (s, 2H), δ 1.45 (m, 27H). ^{13}C NMR ($CDCl_3$): δ 170.28 (s), δ 169.52 (s), δ 167.00 (s), δ 156.00 (s), δ 151.12 (s), δ 150.02 (s), 148.23 (d), δ 147.45 (d), δ 146.69 (s), δ 102.47 (s), δ 85.67 (s), δ 85.00 (s), δ 83.90 (s), δ 55.87 (s), δ 45.65 (s), δ 43.06 (m), δ 28.14 (s).

*Compound **14d***. Following the procedure shown for **14a−14f**, compound **14d** was obtained from **13d** by treatment of TFP and DCC as a sticky liquid. ^{1}H NMR ($CDCl_3$): δ 6.97 (s, 1H), δ 4.05 (s, 2H), δ 3.95 (s, 2H), δ 2.31 (m, 2H), δ 2.62 (m, 4H), δ 1.80 (m, 2H), δ 1.45 (m, 27H). ^{13}C NMR ($CDCl_3$): δ 177.12 (s), δ 170.89 (s), δ 154.69 (s), δ 153.78 (s), δ 151.11 (s), 148.60 (d), δ 147.05 (d), δ 146.44 (s), δ 102.10 (s), δ 85.25 (s), δ 83.73 (s), δ 83.92 (s), δ 54.33 (m), δ 38.96 (m), δ 33.56 (m), δ 29.78 (s), δ 28.40 (s), δ 26.58 (s), δ 24.45 (s).

*Compound **14e***. Following the procedure shown for **14a−14f**, compound **14e** was obtained from **13e** by treatment of TFP and DCC as a sticky liquid. ^{1}H NMR ($CDCl_3$): δ 6.75 (s, 1H), δ 4.42 (d, 2H), δ 4.10 (m, 4H), δ 3.85 (d, 2H), δ 1.50 (m, 27H). ^{13}C NMR ($CDCl_3$): δ 170.81 (s), δ 170.10 (s), δ 170.05 (s), δ 165.87 (s), δ 156.00 (s), 154.80 (s), 151.20 (s), 148.48 (d), δ 147.23 (d), δ 146.10 (s), δ 103.76 (s), δ 85.79 (s), δ 85.51 (s), δ 84.07 (s), δ 55.96 (m), δ 49.46 (s), δ 43.61 (s), δ 40.82 (s), δ 28.11 (s).

*Compound **14f***. Following the procedure shown for **14a−14f**, compound **14f** was obtained from **13f** by treatment of TFP and DCC as a sticky liquid. ^{1}H NMR ($CDCl_3$): δ 6.98 (s, 1H), δ 4.05 (s, 2H), δ 3.95 (s, 2H), δ 2.40 (s, 2H), δ 1.65 (m, 4H), δ 1.38 (m, 6H), δ 1.45 (m, 27H). ^{13}C NMR ($CDCl_3$): δ 178.58 (s), δ 170.89 (s), δ 154.45 (s), 151.69 (s), 151.51 (s), 148.72 (d), δ 147.20 (d), δ 146.40 (s), δ 102.10 (s), δ 85.93 (s), δ 85.54 (s), δ 83.12 (s), δ 38.95 (m), δ 33.50 (t), δ 30.32 (m), δ 29.45 (s), δ 29.10 (s), δ 26.70 (s), δ 25.73 (s).

General Procedure for Synthesis of Compounds 3−8. Compound **1** (0.154 mmol, 1.0 equiv) was suspended in 1 mL of deionized water, and TEA (1.077 mmol, 7.0 equiv) was added to the suspension. After a few seconds of stirring at RT, the suspension became clear. The reaction was stirred at RT for 5 min. Crude compound **14a−14f** (0.231 mmol, 1.5 equiv) was dissolved in 1.5 mL of acetonitrile and added to the reaction mixture. TEA (0.154 mmol, 1.0 equiv) was added, and the reaction mixture was stirred at RT for 12 h. The reaction mixture was washed with diethyl ether (10 mL) and evaporated *in vacuo*. The obtained solid was treated with 2 mL of 2.5 M HCl, and the solution was stirred at RT for 24 h. The solvent was removed *in vacuo*; the crude product was sonicated twice in ethanol at RT for 2 h, and filtered to obtain pure compounds **3−8**.

*Compound **3***. Following the procedure shown for **3−8**, compound **1** was coupled to compound **14a** by amide linkage, followed by an acid treatment to obtain pure compound **3** as a white solid in 55% yield. ^{1}H NMR (D_2O): δ 3.95 (s, 2H), δ 3.84 (s, 2H), δ 3.26 (t, 2H), δ 1.98 (m, 2H), δ 1.84 (m, 2H). ^{13}C NMR (MeCN/D_2O): δ 172.10 (s), δ 171.74 (s), δ 74.15 (t), δ 51.40 (s), δ 47.62 (s) δ 40.60 (s), δ 31.70 (s), δ 24.09 (s). ^{31}P NMR (H_3PO_4/D_2O): δ 19.16. MS (+ ESI): 379 $[M+H]^+$.

*Compound **4***. Following the procedure shown for **3−8**, compound **1** was coupled to compound **14b** by amide linkage, followed by an acid treatment to obtain pure compound **4** as a white solid in 63% yield. ^{1}H NMR (D_2O): δ 3.73 (s, 2H), δ 3.22 (t, 4H), δ 2.25 (t, 2H), δ 1.95 (m, 2H), δ 1.80 (m, 4H). ^{13}C NMR (MeCN/D_2O): δ 176.87 (s), δ 170.46 (s), δ 74.16 (t), δ 51.54 (s), δ 40.66 (s), δ 39.52 (s), δ 34.04 (s), δ 31.84 (s), δ 25.66 (t), δ 24.16 (s). ^{31}P NMR (H_3PO_4/D_2O): δ 19.32. MS (+ ESI): 407 $[M+H]^+$.

*Compound **5***. Following the procedure shown for **3−8**, compound **1** was coupled to compound **14c** by amide linkage, followed by an acid treatment to obtain pure compound **5** as a white solid in 56% yield. ^{1}H NMR (D_2O): δ 4.04 (s, 2H), δ 3.92 (s, 2H), δ 3.86 (s, 2H), δ 3.25 (t, 2H), δ 1.96 (m, 2H), δ 1.84 (m, 2H). ^{13}C NMR (MeCN/D_2O): δ 171.55 (s), δ 170.79 (s), δ 170.62 (s), δ 72.82 (t), δ 50.04 (s), δ 42.15 (s) δ 41.88 (s), δ 39.26 (s), δ 30.06 (s), δ 22.71 (s). ^{31}P NMR (H_3PO_4/D_2O): δ 19.08. MS (+ ESI): 436 $[M+H]^+$.

*Compound **6***. Following the procedure shown for **3−8**, compound **1** was coupled to compound **14d** by amide linkage, followed by an acid treatment to obtain pure compound **6** as a white solid in 59% yield. ^{1}H NMR (D_2O): δ 3.73 (s, 2H), δ 3.22 (q, 4H), δ 2.25 (t, 2H), δ 1.98 (m, 2H), δ 1.82 (m, 2H), δ 1.59 (t, 2H), δ 1.52 (t, 2H), δ 1.30 (m, 2H). ^{13}C NMR (MeCN/D_2O): δ 177.70 (s), δ 169.94 (s), δ 73.95 (t), δ 51.36 (s), δ 40.43 (s) δ 39.86 (s), δ 36.37 (s), δ 31.64 (s), δ 28.62 (s), δ 26.15 (s), δ 25.68 (s), δ 23.99 (s). ^{31}P NMR (H_3PO_4/D_2O): δ 19.14. MS (+ ESI): 435 $[M+H]^+$.

*Compound **7***. Following the procedure shown for **3−8**, compound **1** was coupled to compound **14e** by amide linkage,

dx.doi.org/10.1021/bc2003132 | *Bioconjugate Chem.* 2011, 22, 2496−2506

followed by an acid treatment to obtain pure compound **7** as a white solid in 54% yield. ^{1}H NMR (D_2O): δ 3.73 (s, 2H), δ 3.22 (q, 4H), δ 2.25 (t, 2H), δ 2.00 (m, 2H), δ 1.82 (m, 2H), δ 1.55 (t, 2H), δ 1.45 (t, 2H), δ 1.30 (s, 6H). ^{13}C NMR (MeCN/D_2O): δ 178.82 (s), δ 170.70 (s), δ 74.58 (t), δ 52.25 (s), δ 49.01 (s), δ 41.25 (s), δ 40.95 (s), δ 37.36 (s), δ 32.54 (s), δ 29.73 (s), δ 29.57 (s), δ 27.41 (s), δ 26.88 (s), δ 24.81 (s). ^{31}P NMR (H_3PO_4/D_2O): δ 19.38. MS (+ ESI): 493 $[M+H]^+$.

Compound ***8***. Following the procedure shown for **3**−**8**, compound **1** was coupled to compound **14f** by amide linkage, followed by an acid treatment to obtain pure compound **8** as a white solid in 57% yield. ^{1}H NMR (D_2O): δ 4.06 (s, 2H), δ 4.0 (s, 2H), δ 3.92 (s, 2H), δ 3.86 (s, 2H), δ 3.25 (t, 2H), δ 1.98 (m, 2H), δ 1.84 (m, 2H). ^{13}C NMR (MeCN/D_2O): δ 173.19 (s), δ 172.01 (s), δ 172.17 (s), δ 171.92 (s), δ 74.15 (t), δ 51.45 (s) δ 43.73 (s), δ 43.49 (s), δ 43.15 (s), δ 40.60 (s), δ 31.67 (s), δ 24.15 (s). ^{31}P NMR (H_3PO_4/D_2O): δ 19.15. MS (+ ESI): 463 $[M+H]^+$.

Crystal Growth Inhibition Assay for Binding Affinity Study. As BPs target bone surfaces under active formation and resorption of HA,[41] a crystal growth inhibition assay was performed to measure the affinities of HBPs to HA. This method has commonly been used to examine BP binding affinity.[42,43] Kinetic experiments of HA crystal growth were performed in a nitrogen atmosphere in magnetically stirred (400 rpm) double-jacketed vessels at pH 7.4 and 37.0 ± 0.1 °C, as described in a previously reported procedure.[42,43] In brief, the reaction solution with final ionic strength of 0.15 M was prepared by mixing calcium chloride (2.0 mmol), potassium dihydrogen phosphate (2.0 mmol), and sodium chloride (132.0 mmol) followed by degassing and filtration. The titrant with final ionic strength of 0.15 M was prepared by mixing calcium chloride (2.0 mmol), potassium hydroxide (10.0 mmol), and sodium chloride (134.0 mmol) followed by degassing and filtration. The reaction was initiated by adding 5 mg seed mass of HA crystallites into 100 mL of reaction solution. The constant thermodynamic driving force for growth of HA crystals was maintained by keeping the pH constant at 7.4 with addition of titrant. The volume of titrant added was recorded as a measure of HA crystal growth. Crystal growth inhibition experiments were performed in presence of at least six different concentration of each of HBPs (**2**−**8**). For positive control, experiments were performed in presence of six different concentrations of alendronate (**1**), whereas for negative control, experiments were performed in the absence of any BP.

Cell Culture. The MC3T3-E1 cells were cultured in prewarmed αMEM medium that was supplemented with 10% FBS at 37 °C in a humidified atmosphere composed of 5% CO_2. The cells were seeded into 96-well plates at a density of 1×10^4 cells/well for *in vitro* quantification of intracellular protein and caspase activity. One day after seeding, the cultures were treated with various concentrations (1×10^{-6}, 1×10^{-5}, and 1×10^{-4} M) of HBPs. Cells without HBPs were used as a negative control, while cells treated with 10^{-6}, 10^{-5}, or 10^{-4} M of etoposide were used as positive controls. The plates were incubated again for 24, 48, and 72 h before use for further analysis. The experiments were conducted in triplicate and repeated at least three times to ascertain the reproducibility of the results.

Intracellular Protein Quantification. Intracellular protein was measured using a commercially available BCA assay kit. Briefly, the medium was removed, and the adherent cells were washed with PBS. The cultures were lysed by 10 min incubation in 50 μL of lysate buffer (20 mM Tris-HCl, pH 7.4, 150 mM NaCl, 1 mM EDTA, 10 mM NaF, 1 mM sodium orthovanadate, 5 μg/mL leupeptin, 0.14 U/mL aprotinin, 1 mM phenylmethylsulfonylfluoride, and 1% (v/v) Triton X-100), followed by 2 s of sonication. Volumes of 10 μL of the cell lysate samples and standards (solutions of known concentrations of bovine serum albumin) were added to the wells of a 96-well microtiter plate followed by addition of 200 μL of the working reagent; the well contents were mixed thoroughly by shaking the plate for 2 min. The plate was incubated at 37 °C for 30 min and then cooled to RT. The absorbance of the samples was measured at 562 nm on a plate reader. The amount of protein in the sample was calculated using a standard plot.

Cell Cytotoxicity Assay. The cytotoxicity of the HBPs was determined using a colorimetric WST-1 assay. The assay was conducted after 72 h of HBP treatment in accordance with the manufacturer's instructions. In brief, cultures in 96-well plates were incubated with 10 μL/well of cell proliferation reagent WST-1 at 37 °C for 60 min in a humidified atmosphere composed of 5% CO_2. The plate was cooled to RT, and the absorbance of the samples was measured at 450 nm on a plate reader.

Apoptosis Assay. Apoptosis was determined by measuring the intracellular caspase-3 activity. The cultures were lysed by 10 min of incubation in 50 μL of lysate buffer (20 mM Tris-HCl, pH 7.4, 150 mM NaCl, 1 mM EDTA, 10 mM NaF, 1 mM sodium orthovanadate, 5 μg/mL leupeptin, 0.14 U/mL aprotinin, 1 mM phenylmethylsulfonylfluoride, and 1% (v/v) Triton X-100), followed by 2 s of sonication. The cell lysate was treated with 50 μM Ac-DEVD-AFC in 50 mM HEPES buffer (pH 7.4, 100 mM NaCl, 0.1% CHAPS, 10 mM DTT, 1 mM EDTA, and 10% (v/v) glycerol) at RT for 60 min in the dark. The caspase-3 activity was determined by measuring the fluorescence at λ_{em} = 510 nm (λ_{ex} = 485).

Synthesis of Compound 16. Compound **2** (10.0 mg, 0.028 mmol) was suspended in 10 mL of deionized water. The reaction mixture was acidified with 10 μL of acetic acid. 4-Nitrobenzaldehyde (**15**) (8.4 mg, 0.056 mmol) was dissolved in DMSO and added to the above suspension. The reaction was stirred at RT for 48 h. The solvent was evaporated *in vacuo* to obtain crude product **16**. Compound **16** was dissolved in water and washed with ethyl acetate to remove excess reactant **15**. The water layer containing **16** was used in the next reaction without further purification.

Synthesis of Compound 19. 4-Nitrobenzoic acid (**18**) (100.0 mg, 0.598 mmol) and TFP (109.3 mg, 0.658 mmol) were dissolved in 5 mL acetone. DCC (135.8 mg, 0.658 mmol) in 5 mL acetone was added dropwise to the reaction mixture and stirred at RT. The progress of the reaction was followed by TLC. After complete consumption of **18** (3 h), the 1,3-dicyclohexyl urea formed in the reaction mixture was removed by filtration, and the filtrate was evaporated *in vacuo*. The residue was then suspended in an adequate amount of acetonitrile, the remaining 1,3-dicyclohexyl urea was removed by filtration, and the filtrate was evaporated *in vacuo* to obtain crude compound **19**. Compound **19** was used in the next reaction without further purification.

Synthesis of Compound 20. Compound **1** (60.0 mg, 0.185 mmol) was suspended in 1 mL of deionized water and TEA (111.9 mg, 1.108 mmol) was added to the suspension. After a few seconds of stirring at RT, the suspension became clear. The reaction was stirred at RT for 5 min. Crude

compound **19** (92.2 mg, 0.277 mmol) was dissolved in 1.5 mL of acetonitrile and added to the reaction mixture. TEA (18.7 mg, 0.185 mmol) was added, and the reaction mixture was stirred at RT for 12 h. The reaction mixture was washed with 10 mL diethyl ether several times, and the water layer was lyophilized to obtain a sticky solid. The reaction product was then sonicated twice in ethanol for 2 h at RT and filtered to obtain pure compound **20**. ^{1}H NMR (D_2O): δ 8.33 (d, 2H), δ 7.95 (d, 2H), δ 3.45 (t, 2H), δ 1.98 (m, 4H). ^{31}P NMR (H_3PO_4/D_2O): δ 18.23. MS (- ESI): 397 $[M-H]^-$.

***In Vitro* Studies of Drug Targeting and Drug Release.** Compound **16** is a HBP-drug conjugate, where a model drug (4-NBA) is conjugated to HBP **2** via hydrazone linkage. The conjugate was immobilized on HA surface and studied for its release at various pH solutions. In brief, compound **16** (1 mg) in water was equally distributed into three Eppendorf tubes and diluted to get 1.0 mL of total volume each. Excess of HA (50.0 mg) was added to each Eppendorf tube, and the tubes were stirred at RT for 0.5 h. After centrifugation at 1000 rpm for 5 min, the supernatant was discarded. The HA was washed twice with 1.0 mL water, followed by centrifugation, and the supernatant was discarded. A volume of 1.0 mL acetate solution (0.1 M sodium acetate, 0.05 M sodium chloride) of pH 5.0, 6.0, and 7.4 was added in three Eppendorf tubes, respectively. The Eppendorf tubes were incubated at 37 °C with continuous shaking. The suspensions were centrifuged at particular time points, and the absorbance of the supernatants was measured (λ = 265 nm, 1 cm cuvette) to calculate the amount of 4-NBA released from the immobilized conjugate.

For the control studies, the above experiment was repeated with compound **20**. Compound **20** is a BP-drug conjugate, where the model drug (4-NBA) is conjugated to alendronate via amide linkage. The conjugate was immobilized on the HA surface and studied for its release at various pH solutions. In brief, compound **20** (1 mg) in water was equally distributed into three Eppendorf tubes and diluted to get 1.0 mL of total volume each. Excess of HA (50.0 mg) was added to each Eppendorf tube, and the tubes were stirred at RT for 0.5 h. After centrifugation at 1000 rpm for 5 min, the supernatant was discarded. The HA was washed twice with 1 mL water, followed by centrifugation, and the supernatant was discarded. A volume of 1.0 mL acetate solution (0.1 M sodium acetate, 0.05 M sodium chloride) of pH 5.0, 6.0, and 7.4 was added in three Eppendorf tubes, respectively. The Eppendorf tubes were incubated at 37 °C with continuous shaking. The suspensions were centrifuged at particular time points, and the absorbance of the supernatants was measured (λ = 265 nm, 1 cm cuvette) to calculate the amount of 4-NBA released from the immobilized conjugate.

RESULTS AND DISCUSSION

BPs have high affinity toward bone and HA. After administration, BPs bind to bone surfaces where they can be internalized into osteoclasts and cause their apoptosis.[44−46] In other words, BPs control bone resorption through apoptosis of osteoclasts. However, this could be a drawback of the BP treatment because it disturbs the bone remodeling cycle. In general, bone remodeling is a lifelong process, whereby osteoblasts and osteoclasts work simultaneously for bone formation and bone resorption, respectively. Bone formation and bone resorption are interdependent processes, and therefore, osteoblastic function of bone formation also gets affected by controlling osteoclastic bone resorption. Along with controlling bone resorption, subsequent bone formation at resorption sites is crucial; this can be achieved by delivering therapeutic agents to bone resorption sites using bisphosphonates. Active drug targeting at sites of bone metastases and calcified neoplasms using polymeric carrier was reported previously. Alendronate and an antiangiogenic agent, TNP-470, were conjugated to *N*-(2-hydroxypropyl)methacrylamide (HPMA) through a cathepsin K sensitive tetrapeptide (Gly-Gly-Pro-Nle).[47,48] Because of alendronate conjugation, HPMA was found to be distributed to bone tumors and the endothelial compartments of bone metastases with a good antitumor efficacy. However, one could eliminate the polymeric carrier and make a simpler and smaller conjugate by coupling drugs directly to high affinity BPs via hydrolyzable bonds. Therefore, our overall goal is to make BPs capable of delivering drug molecules, including bone growth factors, at bone resorption sites. The first goal was to design novel BPs that demonstrate high binding affinity to HA and contain a functional group that could be used to conjugate therapeutic agents to BPs through an acid-labile linkage. Substituents (R^1 and R^2) at the germinal carbon of the BP contribute toward bone affinity; in particular, the presence of a hydroxyl at R^1 enhances bone affinity by enabling tridentate binding to HA.[10−12] In that regard, we chose 1-hydroxy-1,1-bisphosphonic acid as the basic backbone of bifunctional BPs.

The designed 1-hydroxy-1,1-bisphosphonic acid backbone has a hydroxyl at R^1, while the R^2 substituent was used to introduce a different functional group that could be subsequently used for attachment of therapeutic agents. The attachment of a therapeutic agent to BP is possible through several reversible and irreversible linkages such as amide, ester, imine, hydrazone, ether, and thioether coupling. However for drug delivery at wound healing sites and resorption sites, where the pH is acidic,[49,50] acid-labile linkages such as those provided by hydrazones and imines are more appropriate. Imine hydrolyses rapidly at pH $\leq$ 7.0,[51] while hydrazone is stable at physiological pH. Further, the rate of hydrolysis of the hydrazone linkage increases gradually with decrease in pH from 7.4.[52,53] Therefore, the hydrazone linkage presents advantages over the imine linkage when sustained drug release is desired at the bone surface. Hence, the hydrazine functionality was introduced in 1-hydroxy-1,1-bisphosphonic acid at R^2 to obtain bifunctional HBPs.

It is important that the HBP-drug conjugate should not only be stable during systemic circulation, but should also bind to the bone surface before releasing the drug at the desired site. The attached drug may sterically affect this interaction between the BP and the bone surface. Consequently, a spacer was introduced in the synthesized HBPs between the BPs and the terminal hydrazine. HBPs with several spacers of varying length and hydrophobicity were synthesized.

A straightforward synthesis was used to create the desired HBPs (**2**−**8**). Compound **2** has the shortest spacer attaching hydrazine to 1-hydroxy-1,1-bisphosphonic acid. To synthesize HBP **2**, monosodium alendronate was prepared first in an inert atmosphere according to a previously reported procedure from 4-aminobutanoic acid by reaction with phosphorous acid and phosphorus trichloride in methanesulfonic acid and subsequent hydrolysis.[39,40] The reactive ester of TBHA (**10**) was prepared by dropwise addition of DCC in chloroform to a mixture of TBHA and TFP in chloroform at RT. This reactive ester was then coupled with monosodium alendronate in basic condition at RT to obtain BOC-protected HBP **2**. The BOC-protection

dx.doi.org/10.1021/bc2003132 | *Bioconjugate Chem.* 2011, 22, 2496−2506

Scheme 2. Synthesis of HBPs 3−8

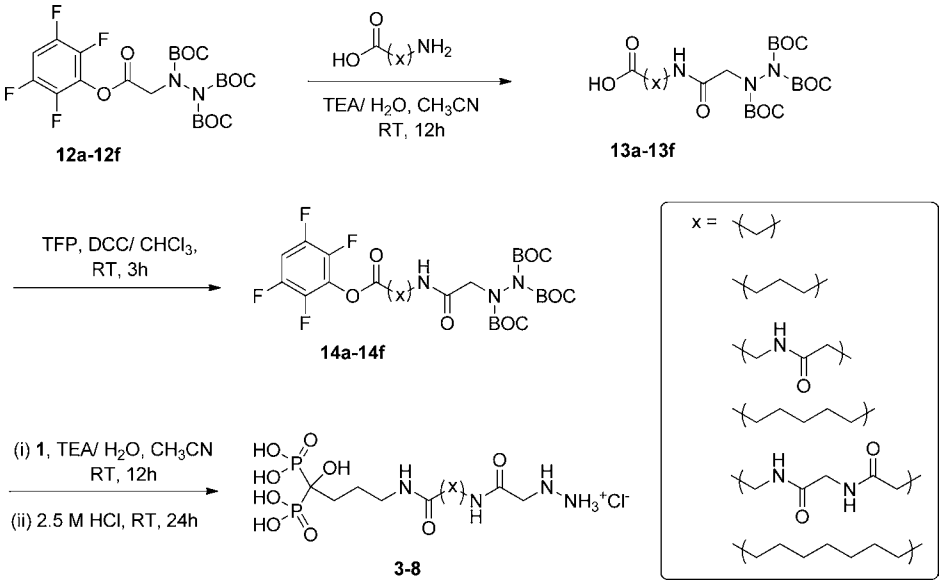

of the hydrazine group was removed with treatment of 2.5 M HCl to obtain HBP **2**. The crude product was sonicated twice in ethanol at RT for 2 h and filtered to obtain pure HBP **2** (Scheme 1).

Using a similar strategy, six other analogues of HBP **2** (**3**−**8**) with spacers of different length and hydrophobicity were synthesized by introducing various amino acids, such as glycine (**12a**), 4-aminobutanoic acid (**9**), glycylglycine (**12c**), 6-aminohexanoic acid (**12d**), glycylglycylglycine (**12e**), and 8-aminooctanoic acid (**12f**), respectively (Scheme 2). All seven HBPs were obtained and were characterized with ^{1}H NMR, ^{31}P NMR, ^{13}C NMR, and electrospray ionization mass spectrometry.

The binding affinities of the HBPs were measured and compared with alendronate, which is a commercially available BP having high affinity to HA. BPs are known to inhibit the crystal growth of HA and target bone surfaces under active formation and resorption of HA.[41] Therefore, a crystal growth inhibition assay, which is a widely used method for determination of binding affinity of BP,[42,43] was performed to measure the affinities of HBPs to HA. During the experiments, a favorable environment for crystal growth of HA was maintained. The crystal growth of HA was measured in the presence of various concentration HBPs. The pH was maintained at 7.4 by addition of titrant, and the volume of titrant added was recorded as a measure of HA crystal growth. A range of experiments were performed in presence of various concentrations (0, 1.0×10^{-7}, 2.5×10^{-7}, 5.0×10^{-7}, 7.5×10^{-7}, and 1.0×10^{-6} M) of HBPs and alendronate. For every experiment of HA crystal growth, a plot of the volume of titrant added vs time was generated. A typical set of plots is depicted in Figure 1. The growth rate (R) at any instant can be described by

$$R = \beta \frac{dV}{dt} \quad (1)$$

where dV/dt is the rate of titrant addition, and β is a constant whose value reflects the titrant concentration with respect to the surface area of HA during crystal formation; β was considered as constant for all experiments.

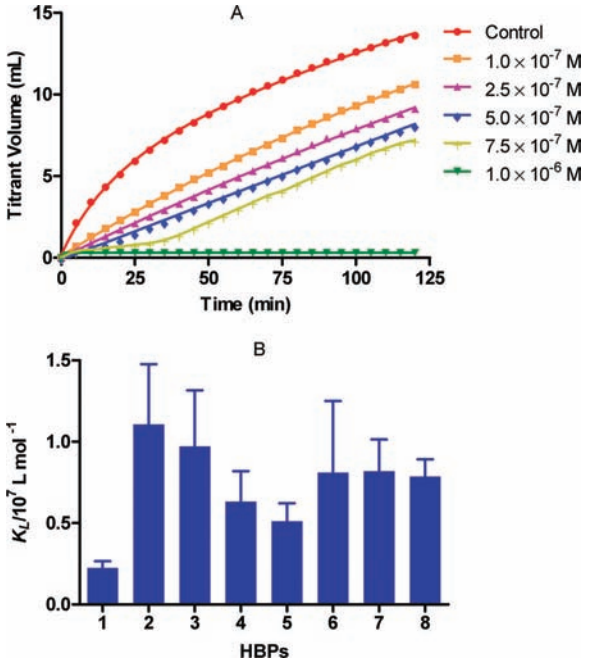

Figure 1. (A) Plot of HA crystal growth in the presence of varying concentrations of HBP **2** at pH 7.4 and 37 °C (seed mass = 5 mg). (B) Relative adsorption affinity constants (K_L) of alendronate (**1**) and HBPs **2**−**8** measured at varying concentrations of BPs ($C = 1.0 \times 10^{-7}$, 2.5×10^{-7}, 5.0×10^{-7}, and 7.5×10^{-7} M) at pH 7.4 and 37 °C. Data are the average ± one standard deviation ($n = 4$).

It can be noted from Figure 1 that the HA crystals appear to grow nonlinearly during the early stage of the experiment due to initial seeding of the HA crystals. The flat line parallel to the X-axis indicates the complete prevention of crystal growth. A pseudo-Langmuir adsorption isotherm can be used to describe the rates of HA crystal growth and can be expressed by

$$\frac{R_0}{R_0 - R_i} = 1 + \frac{1}{K_L C} \quad (2)$$

dx.doi.org/10.1021/bc2003132 | Bioconjugate Chem. 2011, 22, 2496−2506

where C is the concentration of BP added, and R_0 and R_i are the rates of HA crystal growth in the absence and presence of BP, respectively.

By rearranging eqs 1 and 2, the relative adsorption affinity constants (K_L) can be described by

$$K_L = \frac{\frac{dV_0}{dt} - \frac{dV_i}{dt}}{C\frac{dV_i}{dt}} \quad (3)$$

where dV_0/dt and dV_i/dt are the rates of titrant addition at early stage of the experiment in the absence and presence of BP, respectively.

The relative trend of binding affinities of alendronate (**1**) and HBPs (**2**–**8**) at various concentrations of BPs is shown in Figure 1. The shorter length HBPs (**2** and **3**) showed significantly higher binding affinities than alendronate ($p < 0.05$). Overall, all seven HBPs showed high binding affinities to HA, which makes them suitable for drug targeting.

Apart from its targeting ability, the ideal drug-carrier should not induce unnecessary toxic effects, especially against bone-forming cells (osteoblasts). HBPs could also have toxic affects toward other cells and tissues or affect cell differentiation, which could cause substantial morbidity.[54] The primary purpose of this study was to demonstrate the potential of HBPs for targeted delivery of the attached drugs at bone-resorption sites through *in vitro* experiments. Therefore, HBPs at various concentrations (10^{-6}–10^{-4} M) were evaluated for their possible cytotoxicity and apoptotic effect against preosteoblasts. The intracellular protein measured after 24, 48, and 72 h treatment of HBPs showed no abnormal changes in cell proliferation (Figure 2). The amount of protein in the HBP-treated cells was similar to the control over a period of 72 h. Cell viability studies were performed and metabolic activity was quantified using the commercially available WST-1 kit. MC3T3-E1 cells exposed to HBPs for 72 h showed activity similar to that of control (Figure 3). Although the metabolic activity of cells exposed to 10^{-4} M HBPs for 72 h showed 10% decrease in cell viability, the difference was not statistically significant.

Because caspases are required for cell apoptosis, the possibility of HBP-induced cell apoptosis was evaluated by measuring caspase-3 activity. Caspase-3 is a cysteine-aspartic acid protease and cleaves Ac-DEVD-AFC releasing the fluorogenic AFC, which can be quantified by fluorescence spectroscopy.[55] Apoptosis of MC3T3-E1 preosteoblasts was confirmed by treatment with 10^{-6}, 10^{-5}, or 10^{-4} M etoposide for 72 h, which resulted in 2–3-fold increase in caspase-3 activity (results not shown). As shown in Figure 4, however, HBPs did not induce apoptosis in MC3T3-E1 preosteoblasts after 72 h of exposure; all treatments resulted in statistically similar levels of caspase activity. Because HBPs showed no apoptotic and cytotoxic effects on preosteoblasts, HBPs could be utilized as a vehicle for drug delivery applications.

HBP **2** was used to demonstrate the targeted delivery of therapeutic agents to bone. In particular, in vitro drug targeting to HA and drug release from the HA surface was demonstrated using 4-NBA as a model drug. 4-NBA was conjugated with HBP **2** in DMSO/water, and then the conjugate was immobilized on HA by adding excess of HA particles to the reaction mixture at RT. HA with the attached conjugate was separated by centrifugation and washed thoroughly with water to remove unconjugated 4-NBA (Scheme 3). The triggered

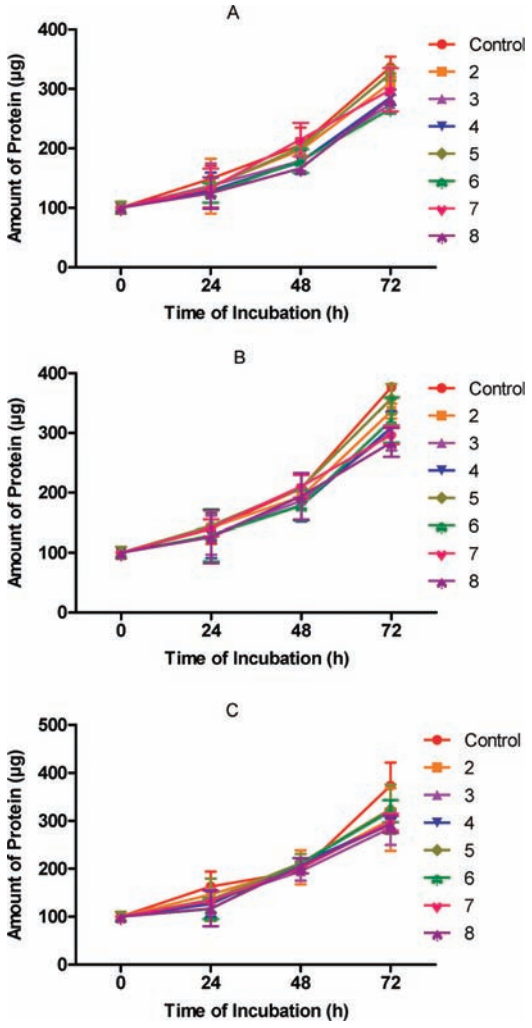

Figure 2. Intracellular protein contents showing MC3T3-E1 cell growth for 72 h after HBP treatment. Plots A, B, and C show results for exposure to HBPs at 1×10^{-6}, 1×10^{-5}, and 1×10^{-4} M, respectively. Error bars denote standard deviation.

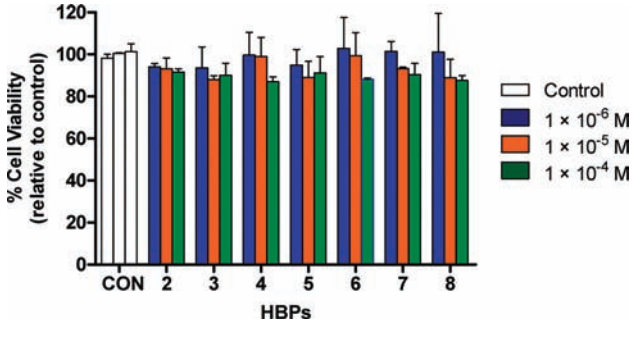

Figure 3. MC3T3-E1 cell viability measured after 72 h of incubation with no HBP (CON) and HBPs **2**–**8** at different concentrations (1×10^{-6}, 1×10^{-5}, and 1×10^{-4} M). The data are expressed as percentage of the control. The white, blue, orange, and green bars represent treatment of no HBP (control), 1×10^{-6}, 1×10^{-5}, and 1×10^{-4} M HBPs, respectively. Error bars denote standard deviations.

release of 4-NBA from the immobilized 4-NBA-HBP conjugate on HA was demonstrated at various pH as shown in Figure 5. HA with the attached conjugate was resuspended in 0.1 M sodium acetate (pH 5.0, 6.0, or 7.4) and incubated at 37 °C. The suspensions were centrifuged at particular time points, and

dx.doi.org/10.1021/bc2003132 | *Bioconjugate Chem.* 2011, 22, 2496–2506

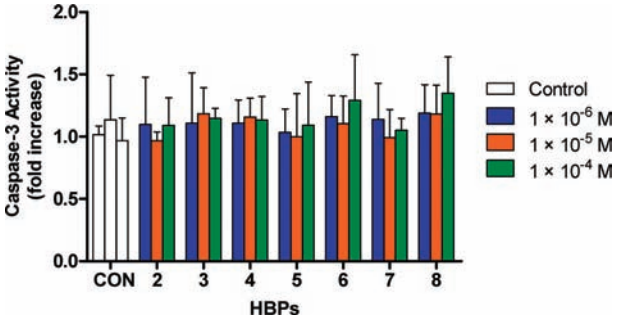

Figure 4. Apoptosis of MC3T3-E1 cells measured 72 h following addition of no HBP (CON) and HBPs **2**–**8** at three different concentrations (1×10^{-6}, 1×10^{-5}, and 1×10^{-4} M). The data are expressed as percentage of the control. The white, blue, orange, and green bars represent treatment of no HBP (control), 1×10^{-6}, 1×10^{-5}, and 1×10^{-4} M HBPs, respectively. Error bars denote standard deviations.

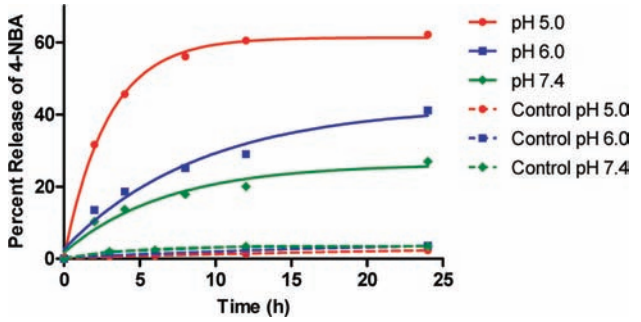

Figure 5. Percent release of 4-NBA (percentage of cleaved hydrazone bonds) from the immobilized conjugate on HA surface at 37 °C. Solid line and dotted line represent 4-NBA release from **17** and **21**, respectively.

the absorbance of the supernatants was measured at 265 nm using a UV–vis spectrophotometer to calculate the amount of released 4-NBA. It was observed that, in the first 12 h of incubation, there was approximately 60%, 30%, and 20% of 4-NBA released from the immobilized conjugate at pH 5.0, 6.0, and 7.4, respectively. Since HBPs have higher affinity for bone than does alendronate, they are expected to carry and deliver the attached drug at bone resorption sites as well as calcified bone tumors. Similar to this study, drug release at resorption sites was previously reported using a polymeric system with a spacer composed of a cathepsin K sensitive tetrapeptide (Gly-Gly-Pro-Nle).[56] Cathepsin K, which is expressed at higher level in osteoclasts, could cleave the polymer at the cathepsin K sensitive tetrapeptide and initiate drug release. However, cleavage of the polypeptide by cathepsin K could be affected by steric hindrance, which could change the rate of drug release. On the other hand, HBPs are not crowded molecules, and therefore, the rate of hydrolysis of the hydrazone and consequent drug release is expected to be affected less by steric effects.

To confirm that release of 4-NBA occurs via hydrazone cleavage rather than through desorption of the conjugate from the HA surface, 4-NBA was conjugated to alendronate (**1**) through formation of an amide bond. The conjugate was immobilized on HA surface by adding excess of HA particles, and then the particles were washed thoroughly with water to

Scheme 3. Synthesis, Immobilization of Model Drug–BP Conjugate, and Incubation at 37 °C in Acetate Solutions of Various pH[a]

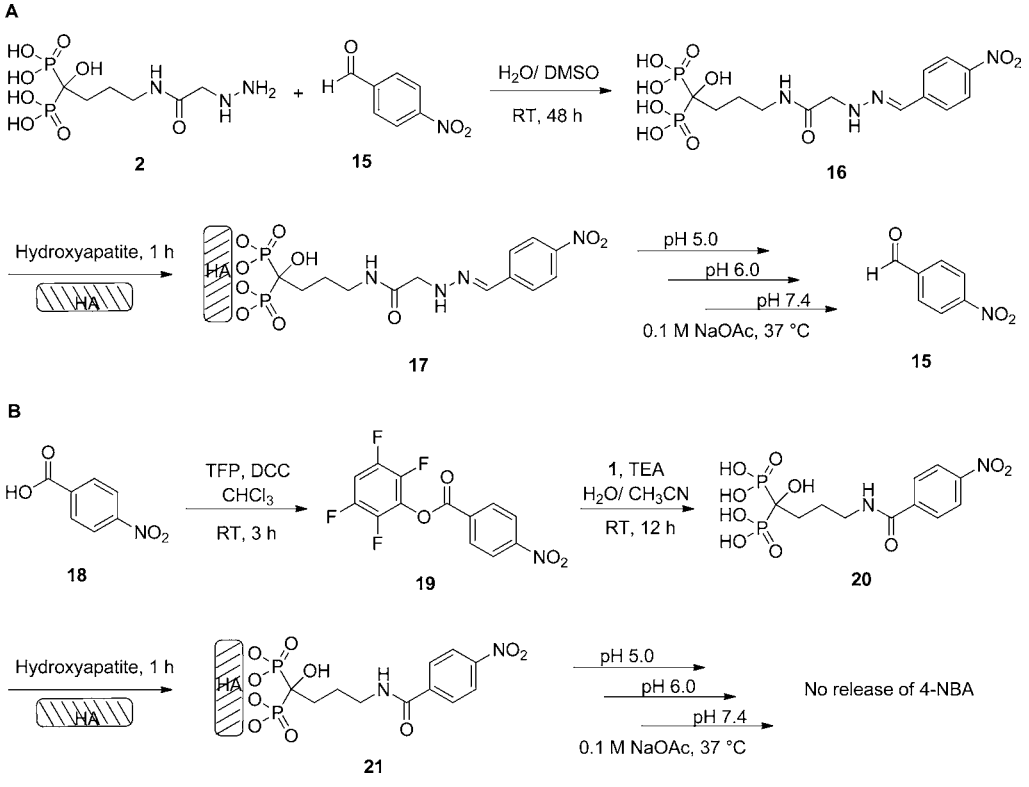

[a]Hatched area represents HA particles.

dx.doi.org/10.1021/bc2003132 | Bioconjugate Chem. 2011, 22, 2496–2506

remove unconjugated 4-NBA and nonspecifically adsorbed conjugate molecules. HA with the attached conjugate was treated similarly as described above, and the amount of released 4-NBA was measured by UV−vis spectroscopy (Scheme 3). From the control experiments, it was observed that there was no significant release of 4-NBA through desorption from the immobilized conjugate **21** (Figure 5).

CONCLUSION

In conclusion, we have reported the synthesis of novel, bifunctional HBPs (**2**−**8**), which show high binding affinities to HA. Through *in vitro* experiments, HBPs demonstrated no apoptotic and cytotoxic effects on MC3T3-E1, a preosteoblast cell. 4-NBA, a model drug, was bound to HA through a HBP, and its *in vitro* release at various pH was recorded. It was observed that hydrolysis of hydrazone bonds in the conjugate and subsequent release of 4-NBA was slow at physiological pH but much faster at pH lower than physiological, such as the pH in bone resorption sites and sites of wound healing.[49,50] Consequently, HBP−drug conjugates could be useful in local delivery of attached drugs to the resorptive microenvironment of bone tissue. Overall, this approach should improve the therapeutic index by boosting pharmacological efficacy and diminishing undesirable side effects.

AUTHOR INFORMATION

Corresponding Author

*Tel: 305-284-4021. Fax: 305-284-5637. E-mail: bachas@miami.edu.

ACKNOWLEDGMENTS

This research was supported by the US Army Medical Research and Materiel Command (W81XWH-09-1-0461) and the National Institutes of Health (AR048700). J.Y. thanks the University of Kentucky for a Research Challenge Trust Fund fellowship supporting this research. We thank Drs. M. Watson, A. Cammers, Y. Wei, E. Dikici, and E. Zahran for useful discussions.

REFERENCES

(1) Langer, R. (2001) Drug delivery: Drugs on target. *Science 293*, 58−59.
(2) Harada, S., and Rodan, G. A. (2003) Control of osteoblast function and regulation of bone mass. *Nature 423*, 349−355.
(3) Goltzman, D. (2002) Discoveries, drugs and skeletal disorders. *Nat. Rev. Drug Discovery 1*, 784−796.
(4) Salo, J., Lehenkari, P., Mulari, M., Metsikkö, K., and Väänänen, H. K. (1997) Removal of osteoclast bone resorption products by transcytosis. *Science 276*, 270−273.
(5) Deal, C. (2009) Future therapeutic targets in osteoporosis. *Curr. Opin. Rheumatol. 21*, 380−385.
(6) Vondracek, S. F., and Linnebur, S. A. (2009) Diagnosis and management of osteoporosis in the older senior. *Clin. Interventions Aging 4*, 121−136.
(7) Rodan, G. A., and Martin, T. J. (2000) Therapeutic approaches to bone diseases. *Science 289*, 1508−1514.
(8) Polascik, T. J. (2009) Bisphosphonates in oncology: Evidence for the prevention of skeletal events in patients with bone metastases. *Drug Des., Dev. Ther. 3*, 27−40.
(9) Lumachi, F., Brunello, A., Roma, A., and Basso, U. (2008) Medical treatment of malignancy-associated hypercalcemia. *Curr. Med. Chem. 15*, 415−421.
(10) Zhang, S., Gangal, G., and Uludağ, H. (2007) 'Magic bullets' for bone diseases: Progress in rational design of bone-seeking medicinal agents. *Chem. Soc. Rev. 36*, 507−531.
(11) van Beek, E. R., Lowik, C., Que, I., and Papapoulos, S. (1996) Dissociation of binding and antiresorptive properties of hydroxy bisphosphonates by substitition of the hydroxyl with an amino group. *J. Bone Miner. Res. 11*, 1492−1497.
(12) Sunberg, R. J., Ebetino, F. H., Mosher, C. T., and Roof, C. F. (1991) Designing drugs for stronger bones. *CHEMTECH 21*, 305−309.
(13) Chapurlat, R. D., and Delmas, P. D. (2006) Drug insight: Bisphosphonates for postmenopausal osteoporosis. *Nat. Clin. Pract. Endocrinol. Metab. 2*, 211−219.
(14) Peppas, N. A. (2004) Intelligent therapeutics: Biomimetic systems and nanotechnology in drug delivery. *Adv. Drug Delivery Rev. 56*, 1529−1531.
(15) Peppas, N. A. (2006) Vecteurs de médicaments innovants et ≪ intelligents ≫: leurs applications pharmaceutiques. *Ann. Pharm. Fr. 64*, 260−275.
(16) Langer, R., and Peppas, N. A. (2003) Advances in biomaterials, drug delivery, and bionanotechnology. *AIChE J. 49*, 2990−3006.
(17) Oh, Y.-K., Senter, P. D., and Song, S.-C. (2009) Intelligent drug delivery systems. *Bioconjugate Chem. 20*, 1813−1815.
(18) MacEwan, S. R., and Chilkoti, A. (2010) Elastin-like polypeptides: Biomedical applications of tunable biopolymers. *Pept. Sci. 94*, 60−77.
(19) Betre, H., Liu, W., Zalutsky, M. R., Chilkoti, A., Kraus, V. B., and Setton, L. A. (2006) A thermally responsive biopolymer for intra-articular drug delivery. *J. Controlled Release 115*, 175−182.
(20) Wang, D., Miller, S. C., Shlyakhtenko, L. S., Portillo, A. M., Liu, X.-M., Papangkorn, K., Kopečková, P., Lyubchenko, Y., Higuchi, W. I., and Kopeček, J. (2007) Osteotropic peptide that differentiates functional domains of the skeleton. *Bioconjugate Chem. 18*, 1375−1378.
(21) Wang, D., Sima, M., Mosley, R. L., Davda, J. P., Tietze, N., Miller, S. C., Gwilt, P. R., Kopečková, P., and Kopeček, J. (2006) Pharmacokinetic and biodistribution studies of a bone-targeting drug delivery system based on N-(2-Hydroxypropyl)methacrylamide copolymers. *Mol. Pharmaceutics 3*, 717−725.
(22) Thompson, W. J., Thompson, D. D., Anderson, P. S., Rodan, G. A. (1989) Polymalonic acids as boneaffinity agents, EP 0341961.
(23) Orme, M. W., and Labroo, V. M. (1994) Synthesis of [beta]-estradiol-3-benzoate-17-(succinyl-12A-tetracycline): A potential bone-seeking estrogen. *Bioorg. Med. Chem. Lett. 4*, 1375−1380.
(24) Zheng, H., Weng, L. (1997) Bone resorption inhibition/osteogenesis promotion pharmaceutical composition, U.S. Patent 5,698,542.
(25) Hirabayashi, H., Takahashi, T., Fujisaki, J., Masunaga, T., Sato, S., Hiroi, J., Tokunaga, Y., Kimura, S., and Hata, T. (2001) Bone-specific delivery and sustained release of diclofenac, a non-steroidal anti-inflammatory drug, via bisphosphonic prodrug based on the osteotropic drug delivery system (ODDS). *J. Controlled Release 70*, 183−191.
(26) Gil, L., Han, Y., Opas, E. E., Rodan, G. A., Ruel, R., Seedor, J. G., Tyler, P. C., and Young, R. N. (1999) Prostaglandin E2-bisphosphonate conjugates: Potential agents for treatment of osteoporosis. *Bioorg. Med. Chem. 7*, 901−919.
(27) Ora, M., Lönnberg, T., Florea-Wang, D., Zinnen, S., Karpeisky, A., and Lönnberg, H. (2008) Bisphosphonate derivatives of nucleoside antimetabolites: Hydrolytic stability and hydroxyapatite adsorption of 5′-β,γ-methylene and 5′-β,γ-(1-hydroxyethylidene) triphosphates of 5-fluorouridine and ara-cytidine. *J. Org. Chem. 73*, 4123−4130.
(28) El-Mabhouh, A., Angelov, C., McEwan, A., Jia, G., and Mercer, J. (2004) Preclinical investigations of drug and radionuclide conjugates of bisphosphonates for the treatment of metastatic bone cancer. *Cancer Biother. Radiopharm. 19*, 627−640.
(29) Herczegh, P., Buxton, T. B., McPherson, J. C. I., Kovács-Kulyassa, Á., Brewer, P. D., Sztaricskai, F., Stroebel, G. G., Plowman, K. M., Farcasiu, D., and Hartmann, J. F. (2002) Osteoadsorptive bisphosphonate derivatives of fluoroquinolone antibacterials. *J. Med. Chem. 45*, 2338−2341.

(30) Wang, J. B., Yang, C. H., Yan, X. M., Wu, X. H., and Xie, Y. Y. (2005) Novel bone-targeted agents for treatment of osteoporosis. *Chin. Chem. Lett. 16*, 859−862.
(31) Blower, P. (2006) Towards molecular imaging and treatment of disease with radionuclides: The role of inorganic chemistry. *Dalton Trans.*, 1705−1711.
(32) Ogawa, K., Mukai, T., Inoue, Y., Ono, M., and Saji, H. (2006) Development of a novel ^{99m}Tc-chelate-conjugated bisphosphonate with high affinity for bone as a bone scintigraphic agent. *J. Nucl. Med. 47*, 2042−2047.
(33) Martin, Torres, de Rosales, R., Finucane, C., Foster, J., Mather, S. J., and Blower, P. J. (2010) ^{188}Re(CO)$_3$-dipicolylamine-alendronate: A new bisphosphonate conjugate for the radiotherapy of bone metastases. *Bioconjugate Chem. 21*, 811−815.
(34) Zaheer, A., Lenkinski, R. E., Mahmood, A., Jones, A. G., Cantley, L. C., and Frangioni, J. V. (2001) In vivo near-infrared fluorescence imaging of osteoblastic activity. *Nat. Biotechnol. 19*, 1148−1154.
(35) Årstad, E., Hoff, P., Skattebøl, L., Skretting, A., and Breistøl, K. (2003) Studies on the synthesis and biological properties of non-carrier-added [^{125}I and ^{131}I]-labeled arylalkylidenebisphosphonates: Potent bone-seekers for diagnosis and therapy of malignant osseous lesions. *J. Med. Chem. 46*, 3021−3032.
(36) Ehrick, R. S., Capaccio, M., Puleo, D. A., and Bachas, L. G. (2007) Ligand-modified aminobisphosphonate for linking proteins to hydroxyapatite and bone surface. *Bioconjugate Chem. 19*, 315−321.
(37) Uludağ, H. (2002) Bisphosphonates as a foundation of drug delivery to bone. *Curr. Pharm. Des. 8*, 1929−1944.
(38) Doschak, M. R., Kucharski, C. M., Wright, J. E. I., Zernicke, R. F., and Uludağ, H. (2009) Improved bone delivery of osteoprotegerin by bisphosphonate conjugation in a rat model of osteoarthritis. *Mol. Pharmaceutics 6*, 634−640.
(39) Kieczykowski, G. R., Jobson, R. B., Melillo, D. G., Reinhold, D. F., Grenda, V. J., and Shinkai, I. (1995) Preparation of (4-amino-1-hydroxybutylidene)bisphosphonic acid sodium salt, MK-217 (alendronate sodium). An improved procedure for the preparation of 1-hydroxy-1,1-bisphosphonic acids. *J. Org. Chem. 60*, 8310−8312.
(40) Chebbi, I., Migianu-Griffoni, E., Sainte-Catherine, O., Lecouvey, M., and Seksek, O. (2010) In vitro assessment of liposomal neridronate on MDA-MB-231 human breast cancer cells. *Int. J. Pharm. 383*, 116−122.
(41) Rodan, G. A., and Fleisch, H. A. (1996) Bisphosphonates: Mechanisms of action. *J. Clin. Invest. 97*, 2692−2696.
(42) Koutsoukos, P., Amjad, Z., Tomson, M. B., and Nancollas, G. H. (1980) Crystallization of calcium phosphates. A constant composition study. *J. Am. Chem. Soc. 102*, 1553−1557.
(43) Nancollas, G. H., Tang, R., Phipps, R. J., Henneman, Z., Gulde, S., Wu, W., Mangood, A., Russell, R. G. G., and Ebetino, F. H. (2006) Novel insights into actions of bisphosphonates on bone: Differences in interactions with hydroxyapatite. *Bone 38*, 617−627.
(44) Fleisch, H. (1998) Bisphosphonates: mechanisms of action. *Endocr. Rev. 19*, 80−100.
(45) Rodan, G. A. (1998) Mechanisms of action of bisphosphonates. *Annu. Rev. Pharmacol. Toxicol. 38*, 375−388.
(46) Roelofs, A. J., Thompson, K., Gordon, S., and Rogers, M. J. (2006) Molecular mechanisms of action of bisphosphonates: Current status. *Clin. Cancer Res. 12*, 6222s−6230s.
(47) Segal, E., Pan, H., Ofek, P., Udagawa, T., Kopečková, P., Kopeček, J., and Satchi-Fainaro, R. (2009) Targeting angiogenesis-dependent calcified neoplasms using combined polymer therapeutics. *PloS ONE 4*, e5233.
(48) Segal, E., Pan, H., Benayoun, L., Kopečková, P., Shaked, Y., Kopeček, J., and Satchi-Fainaro, R. (2011) Enhanced anti-tumor activity and safety profile of targeted nano-scaled HPMA copolymer-alendronate-TNP-470 conjugate in the treatment of bone malignances. *Biomaterials 32*, 4450−4463.
(49) Schneider, L., Korber, A., Grabbe, S., and Dissemond, J. (2007) Influence of pH on wound-healing: A new perspective for wound-therapy? *Arch. Dermatol. Res. 298*, 413−420.
(50) Teitelbaum, S. L. (2000) Bone resorption by osteoclasts. *Science 289*, 1504−1508.
(51) Xu, S., Krämer, M., and Haag, R. (2006) pH-Responsive dendritic core-shell architectures as amphiphilic nanocarriers for polar drugs. *J. Drug Targeting 14*, 367−374.
(52) Kale, A. A., and Torchilin, V. P. (2007) Design, synthesis, and characterization of pH-sensitive PEG−PE conjugates for stimuli-sensitive pharmaceutical nanocarriers: The effect of substitutes at the hydrazone linkage on the pH stability of PEG−PE conjugates. *Bioconjugate Chem. 18*, 363−370.
(53) Sawant, R. M., Hurley, J. P., Salmaso, S., Kale, A., Tolcheva, E., Levchenko, T. S., and Torchilin, V. P. (2006) SMART" drug delivery systems: Double-targeted pH-responsive pharmaceutical nanocarriers. *Bioconjugate Chem. 17*, 943−949.
(54) Prommer, E. E. (2009) Toxicity of bisphosphonates. *J. Palliat. Med. 12*, 1661−1665.
(55) Lazebnik, Y. A., Kaufmann, S. H., Desnoyers, S., Poirier, G. G., and Earnshaw, W. C. (1994) Cleavage of poly(ADP-ribose) polymerase by a proteinase with properties like ICE. *Nature 371*, 346−347.
(56) Pan, H., Kopečková, P., Wang, D., Yang, J., Miller, S., and Kopeček, J. (2006) Water-soluble HPMA copolymer—prostaglandin E1 conjugates containing a cathepsin K sensitive spacer. *J. Drug Targeting 14*, 425−435.

Bioconjugate Chemistry

Article

pubs.acs.org/bc

Cell-Penetrating Conjugates of Coproporphyrins with Oligoarginine Peptides: Rational Design and Application for Sensing Intracellular O_2

Ruslan I. Dmitriev,[†] Honorata M. Ropiak,[†] Gelii V. Ponomarev,[‡] Dmitri V. Yashunsky,[‡] and Dmitri B. Papkovsky*,[†]

[†]Biochemistry Department, University College Cork, Cavanagh Pharmacy Building, Cork, Ireland

[‡]Institute of Biomedical Chemistry, Russian Academy of Medical Sciences, Pogodinskaia Ul. 10/2, 119992 Moscow, Russia

Supporting Information

ABSTRACT: A panel of phosphorescent oligoarginine conjugates of tetracarboxylic Pt(II)-coproporphyrin I dye (PtCP), monosubstituted with long peptides or tetra-substituted with short peptides and having different linkers and peripheral groups, is described. Their photophysical properties, cell loading efficiency, and mechanisms of transport into the cell were investigated and compared. The conjugates were seen to rely on endocytotic mechanisms of cell entry, which are different from that of the unconjugated oligoarginine peptide, and show diverse patterns of intracellular distribution. On the basis of this study, the tetra-substituted PtCP conjugate displaying whole cell distribution was selected for the sensing of intracellular O_2. This probe has been tested in biological experiments on a fluorescence plate reader, including the monitoring of *in situ* oxygenation of respiring cells and their responses to metabolic stimulation. Similar conjugates of the phosphorescent Pd(II)-coprorphyrin and fluorescent coproporphyrin-ketone were also synthesized and assessed for the sensing of low levels intracellular O_2 and ratiometric pH-sensing, respectively. The results produced and the structure–activity relationships determined can facilitate the rational design of new bioconjugates of porphyrin dyes tailored to specific applications.

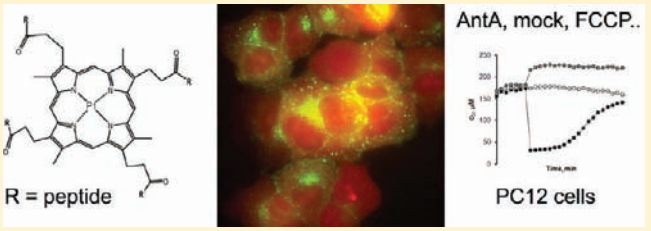

INTRODUCTION

Targeted delivery of molecules into the cell is required for many research (probes and effectors), diagnostic (imaging agents), and therapeutic (drugs) purposes. The main strategies to achieve this include direct (passive) translocation across the plasma membrane, facilitated transport through receptor or drug-mediated endocytosis, and the use of liposomes, delivery, and targeting vectors.[1−3] To date, significant progress has been achieved with nucleic acid and protein structures,[2] whereas the delivery of small molecules such as drugs, fluorophores, and other macrocyclic structures still require a better understanding of the mechanisms of intracellular transport and structure–activity relationships.[4−7]

Tetrapyrrols represented by numerous natural (porphyrins, heme, and vitamin B_{12}) and synthetic compounds are actively used as drugs (e.g., SOD mimetics[8]), photosensitizers in tumor photodynamic therapy (PDT),[9−11] oxygen-sensitive probes,[9,12] and labels.[13] For some of these applications, targeted delivery of the tetrapyrrol into the cell, tissue, or a particular subcellular compartment is an essential requirement. Thus, in PDT, the initial focus on the improvement of photophysical properties of drug candidates and distribution between normal and malignant tissue is now shifting toward more specific delivery of sensitizer molecules to a particular location within the cells (e.g., mitochondria rather than lysosomes[11,14]).

In quenched-phosphorescence sensing of molecular oxygen (O_2), where Pt(II)- and Pd(II)-porphyrins are commonly used,[15] there is a need to have both extracellular, cell-impermeable probes for imaging tissue and vasculature,[12,16] and intracellular probes targeted to subcellular compartments, particularly the mitochondria where most of the O_2 gets consumed.[17] However, hydrophobic tetrapyrrols show poor selectivity of intracellular accumulation and distribution, limited solubility in aqueous media, and high nonspecific binding to various biomolecular and cellular structures. Cationic porphyrins often possess cyto- and genotoxicity (via interaction with the DNA), and therefore, anionic dyes such as coproporphyrin and substituted tetraphenylporphyrin derivatives are more frequently used. However, these structures have low intrinsic ability to penetrate the plasma membrane of mammalian cells.[4,18]

Aiming to improve intracellular delivery and distribution of the porphyrins, several approaches have been proposed including functionalization with hydrophobic polyethyleneglycols[19] or sugars,[20] preparation of dendrimers and nanoparticles, or conjugation with other fluorophores such as rhod-

Received: June 21, 2011
Revised: October 24, 2011
Published: October 31, 2011

ACS Publications © 2011 American Chemical Society

Table 1. Description of Conjugates Prepared in This Study[a]

porphyrin dye	peptide sequence and conjugation site (underlined)	name of the conjugate	molecular weight	total number of R/ charge	RP-HPLC retention time (min)
PtCPTE-MI	CFRRRRRRRRR	PEPP1	2830	9/8	12
PtCPTE-PEG_{850}-MI	CFRRRRRRRRR	PEPP2	3700	9/8	12
PtCPTE-PEG_{850}-MI	MGRTVVVLGGGISGLAAGCGRRRRRRRRR	PEPP4	5200	10/9	15
PtCPTE-MI	MGRTVVVLGGGISGLAAGCGRRRRRRRRR	PEPP5	4350	10/9	16
PtCP(NH-$CH_2CH_2OH)_3$-PFP	NH_2-GRRRRRRRRR	PEPP6	2497	9/8	10.5
$PtCP(PFP)_4$	NH_2-RR-amide	PEPP3	2093	8/8	11
$PdCP(PFP)_4$	NH_2-RR-amide	PEPP3B	2004	8/8	N/D
$CPK(PFP)_4$	NH_2-RR-amide	PEPP3C	1916	8/8	N/D
$PtCP(PFP)_4$	NH_2-RRA-amide	T1	2378	8/8	N/D
$PtCP(PFP)_4$	NH_2-RRS-amide	T2	2442	8/8	N/D
$PtCP(PFP)_4$	NH_2-RGR-amide	T3	2322	8/8	N/D
$PtCP(PFP)_4$	NH_2-RRR	T4	2722	12/8	N/D
$PtCP(PFP)_4$	NH_2-Arg-OMe	T5	1529	4/4	11.5

[a]Structures of PtCP-conjugates are presented in Figure 1, and initial porphyrin dyes are shown in Supporting Information.

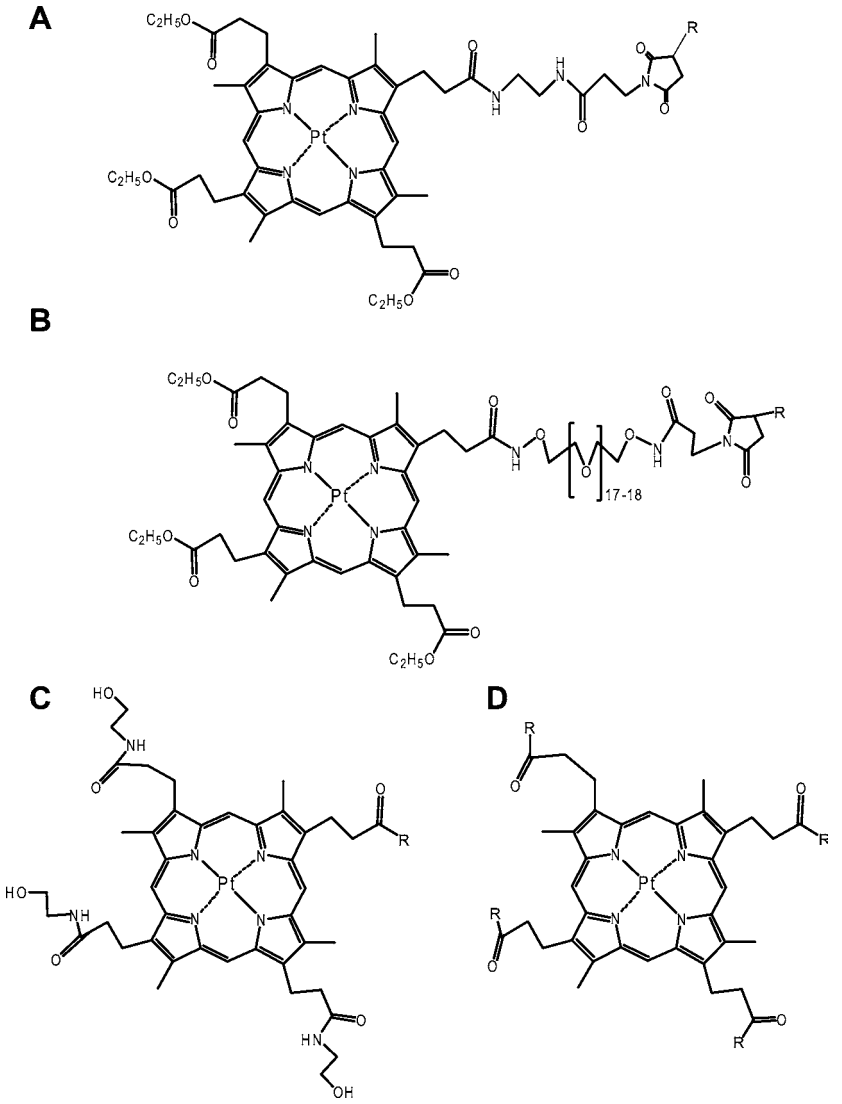

Figure 1. Structures of the PtCP conjugates. All conjugates have the same coproporphyrin core but different side groups. The position of conjugation with the peptide is designated by R. A, conjugates PEPP1 and PEPP5; B,: conjugates PEPP2 and PEPP4; C, conjugate PEPP6; and D, branched conjugates PEPP3 and T1-T5.

amine,[16,21−25] the use of escort peptide sequences (such as cyclic RGD),[26] or cell-penetrating peptides.[19,27] Thus, mono-substituted conjugates of porphyrins with Arg- and Pro-rich peptides have shown improved cell penetration, intracellular

dx.doi.org/10.1021/bc200324q | Bioconjugate Chem. 2011, 22, 2507−2518

accumulation, and retention of the key functionality in oxygen sensing applications or PDT.[28−31] However, this strategy requires a more detailed knowledge of structure−activity relationships.

Here, we describe a panel of new cell-penetrating conjugates of Pt-coproporphyrin I (PtCP) with oligoarginine peptides. Considering the cell penetrating behavior of oligoarginine peptide vectors[32] and the initial studies with monosubstituted PtCP conjugates with relatively long peptides (9−11 amino acids long),[28−31] we hypothesized that tetra-substituted (branched) PtCP conjugates with short Arg-rich peptides may also possess cell-penetrating ability. Therefore, we synthesized an extended panel of both mono- and tetra-substituted PtCP conjugates and evaluated them comparatively to establish structure−activity relationships. We demonstrate that depending on the substitution, linkers, peripheral groups, and hydrophilicity, the resulting conjugates can show different cell penetrating properties and intracellular distribution while retaining the important functional properties of the porphyrin moiety. These results provide the basis for the development of new porphyrin structures with controlled cell permeation and distribution for a range of biological applications.

EXPERIMENTAL PROCEDURES

Materials. The reactive derivatives of coproporphyrin I containing the amino (pentafluorophenyl, PFP)- and thiol-reactive (maleimido, MI) modifications (PtCPTE-MI, PtCP-$(PFP)_4$, PtCPTE-PEG_{850}-MI, PdCP$(PFP)_4$, CPK$(PFP)_4$, and PtCP$(NH\text{-}CH_2CH_2\text{-}OH)_3$-PFP) were synthesized in our lab. Their synthesis procedures and molecular structures are given in Supporting Information. Fluorescent probes MitoTracker Green, MitoTracker Red, LysoTracker Green, LysoTracker Red, and Alexa488-transferrin were from Invitrogen (USA), and phosphorescent probe MitoXpress was from Luxcel Biosciences (Cork, Ireland). Synthetic peptides (purity >85% by HPLC; structures confirmed by mass spectrometry) were from Genscript (Piscataway, NJ, USA). Luminescent cell viability kit CellTiter-Glo was from Promega (Madison, WI, USA), and $H_2NPEG_{850}NHBoc$ was from RAPP Polymere (Tubingen, Germany).

Standard cell culture 96 well plates from Sarstedt (Wexford, Ireland) were used for growing the cells and for time-resolved phosphorescence measurements. White 96 well plates from Greiner Bio-One (Frickenhausen, Germany) were used for the luminescent ATP assay. All other reagents were from Sigma-Aldrich Ltd. (Dublin, Ireland).

Preparation of Conjugates. The monosubstituted conjugates PEPP1−2, PEPP4−6 were prepared by mixing equimolar quantities (0.1−1.0 μmol scale) of the reactive porphyrin derivative and the corresponding peptide in DMSO (in the presence of triethylamine for amino-coupling), incubating for 24 h at room temperature, and purifying by RP-HPLC on a Discovery C18 column (1 × 25 cm, 5 μm, Sigma) using a gradient of CH_3CN in 0.1% TFA. The conjugate fractions were collected, vacuum-dried, reconstituted in DMSO, and stored in small aliquots at −18 °C. Typical yields were 30−90%.

The tetra-substituted conjugates PEPP3, PEPP3B, PEPP3C, and T1-T5 were prepared via amino-coupling in DMF in the presence of molar excess of triethylamine, using PtCP$(PFP)_4$ and peptide or L-Arg methyl ester at a 1:10 molar ratio, and incubating for 6−16 h at room temperature; 1−5 mg scale. Then, the mixture was diluted 1:10 with water, applied on the Discovery DSC-18 20 mL/5 g column (Supelco-Sigma), washed with MeOH/H_2O (1:1), and eluted with MeOH/H_2O/CH_3COOH (50:48:2). The conjugate fractions were vacuum-dried and reconstituted in water or DMSO. The yield was typically ∼90% with respect to the porphyrin. Purity of the conjugates was confirmed by RP-HPLC (see Supporting Information). The composition, chemical structure, and abbreviations of the conjugates are given in Table 1 and Figure 1.

Spectral Measurements. Absorption spectra were recorded on a 8453 UV−vis diode-array spectrophotometer (Agilent) and luminescence spectra on a LS50B luminescence spectrometer (PerkinElmer). Phosphorescence quantum yields were measured in PBS, containing 10% FBS (21% O_2) or with additional 5 mg/mL KH_2PO_4 and 5 mg/mL Na_2SO_3 (0% O_2) using PtCP as a reference.[33] Phosphorescence lifetimes of the conjugates were measured on a Cary Eclipse spectrometer (Varian-Agilent) using phosphorescence decay application and single-exponential fit. The pH-sensitive fluorescence of CPK and PEPP3C probes was measured at 0.25 μM concentration in a citrate−phosphate buffer system at pH 3−8 using 406 nm excitation wavelength with fluorescence emission collected at 600−700 nm. For measurement of the fluorescence of free base, the probes were dissolved in DMSO.

Cell Culture. Human colon carcinoma HCT116, rat pheochromocytoma PC12, human epithelial carcinoma HeLa, human neuroblastoma SH-SY5Y, human hepatocellular liver carcinoma HepG2, and murine embryonic fibroblasts MEF cells were from ATCC (Manassas, VA, USA). The cells were cultured in standard tissue culture flasks, collagen IV-coated 96-well microplates, 35 mm Petri dishes or collagen-poly-D-lysine-coated glass bottom dishes (MatTek, Ashland, MA), and 12-well chambers (Ibidi, Martinsried, Germany) using DMEM medium supplemented with 10% FBS (SH-SY5Y, HepG2, MEF, and HeLa cells) or McCoy 5A with 10% FBS (HCT116). PC12 cells were grown and differentiated as described previously.[29]

For the assessment of cellular uptake efficiency, cells were grown to a confluence 75−100%, incubated with 1 μM of the conjugate for 16 h, washed three times with medium, and measured on the TR-F plate reader. For the analysis by flow cytometry, cells were grown on 35 mm Petri dishes, similarly stained with conjugates, washed with PBS, trypsinized, and then analyzed.

Mechanisms of Cellular Uptake Studies. MEF and HCT116 cells were grown on glass-bottom dishes to a confluence 30−50% and incubated with the conjugates (5 μM PEPP3 or 2 μM PEPP4) for 6 h at 37 °C, then washed, and analyzed by fluorescence microscopy. Inhibitors of endocytosis were used as described previously[28] at concentrations 50 μM (EIPA, inhibits macropinocytosis), 5 mM (MBCD, inhibits lipid-raft dependent endocytosis), and 10 μg/mL (CPZ, inhibits clathrin-mediated endocytosis) with 30 min of preincubation. The influence of surface proteoglycans on cellular uptake was assessed by 1 h of preincubation and subsequent incubation with the conjugate in the presence of 50 μg/mL heparin sulfate (Sigma H6279). To see the effect of competition with unlabeled oligoarginine, cells were incubated with the probe in the presence of 10 μM GR_9 peptide. Temperature effect was studied by incubating the cells for 30 min at 4 °C and then with the conjugate for 6 h at 4 °C. ATP depletion was achieved by preincubating cells in glucose-free medium (DMEM/10% FBS/10 mM Galactose and 20 mM

HEPES, pH 7.2) for 1 h 45 min, followed by 15 min of incubation with 10 μM oligomycin, and then incubation with the conjugate for 6 h. To block the function of lysosomes, a 30 min preincubation with 0.25 μM concanamycin A was used.

In flow cytometry analysis, loaded cells were trypsinized, washed with Phenol Red-free DMEM with 10% FBS and 20 mM HEPES, pH 7.2, and measured on a Guava PCA-96 flow cytometer (Millipore, Billerica, MA, USA) under 532 nm laser and 675 nm emission filters, as recommended.[28]

Live cell microscopy was performed on a wide-field fluorescence microscope Axiovert 200 (Carl Zeiss, Goettingen, Germany) equipped with a 390 nm LED and filter cube (ex., 390/40 nm; em., 655/40 nm) for imaging of PtCP, PdCP, and CPK dyes. PEPP3B probe was imaged at decreased (2%) O_2. Staining with organelle-specific markers MitoTracker Green/Red (50 nM), LysoTracker Green/Red (100 nM), and transferrin-Alexa488 (0.5 μM) was performed for 30 min, followed by one washing.

Cell viability was assessed via total ATP levels using a CellTiter-Glo luminescent kit (Promega) and the manufacturer's protocol.

TR-F intensity and lifetime measurements were conducted on a Victor2 reader (Perkin-Elmer) as described previously[34] using D340 excitation and D642 emission filters, counting at two delay times, 30 μs (t_1) and 70 μs (t_2), gate time 100 μs, and integration time 1 s. For the PEPP3B probe, the D665 emission filter, t_1 = 400 μs and t_2 = 450 μs, gate time 1200 μs, and counting time 2 s were used. Lifetime was calculated as: $\tau = (t_2 - t_1)/\ln(F_1/F_2)$, where F_1 and F_2 correspond TR-F readings at delay times t_1 and t_2.

Conjugate uptake efficiency by dPC12, HCT116, HeLa, and MEF cells was assessed by comparing F_1 signals for the different probes and conditions.

Monitoring of Respiration and icO$_2$. Differentiated PC12 cells were stained with 2 μM PEPP3 (or PEPP3B) for 16 h in RPMI1640 supplemented with 1% HS and 100 ng/mL NGF and washed three times with the same medium then with Phenol Red-free DMEM containing 10 mM Glucose (or 10 mM Galactose instead), 1 mM Na-pyruvate, 20 mM HEPES, pH 7.2, and 100 ng/mL NGF. The cells were incubated for 2 h and then measured on a Victor2 plate reader. After baseline stabilization (~20−60 min depending on O_2), mitochondrial effectors were added to the cells (1/10 volume of 10× stock), and monitoring was resumed.

Calibration of PEPP3 phosphorescence lifetime was performed in the hypoxia chamber at 37 °C and different pO_2. Cells stained with the probe were treated with 10 μM AntA (to block respiration and local O_2 gradients) were monitored kinetically to determine steady-state τ values. These values were plotted against dissolved O_2 concentration (200 μM at 20.9% O_2, 37 °C[35]), from which, using Origin 6.0 (Microcal, USA) software, the following analytical function was obtained (r^2 = 0.9807): $[O_2] = 1551.73 - 57.55\cdot\tau + 0.5347\cdot\tau^2$.

Data Assessment. The microplate reader results are presented as the mean values with the standard deviation (error bars on the plots) obtained from at least 6 replicates. In cellular uptake experiments, the variability in each group was analyzed by one-tailed t test (significance level 0.05). The microscopy experiments were performed in triplicate. This ensures the consistency of the results.

RESULTS

Design and Synthesis of Cell-Penetrating PtCP Conjugates. Cell-penetrating ability of oligoarginine peptides and their conjugates mostly depends on the total number of Arg residues (7−9 are required for efficient transport), while their sequence and length are less important.[32] The conjugates of coproporphyrins demonstrate rather low cell-penetration for tricarboxylic PtCP and improved accumulation for the neutral derivatives (PtCPTE-CFR$_9$, PEPP1); however, the latter structures are quite hydrophobic and show a high degree of nonspecific binding and localization similar to those of lysosomes and endosomes.[29] Aiming to overcome these drawbacks, we prepared modified monosubstituted conjugates with (i) an additional hydrophilic PEG$_{850}$ moiety (PEPP2), (ii) mitochondrial targeting sequence[36] with (PEPP4), and (iii) without PEG$_{850}$ (PEPP5). In order to increase hydrophilicity and reduce nonspecific binding, three ester groups in PtCPTE were also replaced with ethanolamine (PEPP6) (Figure 1).

Four propionic acid residues allow simple tetra-substitution of the PtCP moiety. It was shown that branched oligoarginine sequences can also provide efficient intracellular delivery.[32,37] Therefore, we prepared tetra-substituted PtCP conjugates with eight (PEPP3), four (T5), and 12 (T4) Arg, and also with additional Ala (T1), Ser (T2), and Gly (T3) residues (Figure 1d).

The conjugations were performed by thiol or amino coupling using the reactive MI and PFP derivatives of PtCP, respectively, with purification by RP-HPLC[29] (Figure S1, Supporting Information). Some of the peptides were amidated at C-termini to eliminate zwitterionic structures and retain molecular charge at around +8 (except for T5, PEPP4, and PEPP5; see Table 1). The branched conjugates showed shorter retention times on the C18 column and higher hydrophilicity than the monosubstituted conjugates with a similar charge (e.g., PEPP5 and PEPP3). PEPP6 conjugate with ethanolamine modification was also quite hydrophilic (Table 1).

Photophysical Properties. All tetra-substituted conjugates displayed absorption spectra similar to those of free PtCP and its oligonucleotide conjugates.[38] For the monosubstituted conjugates, absorption maxima were slightly blue-shifted similar to those of protein conjugates,[13] which is indicative of J or H stacking interactions of the PtCP moiety [39] (Figure S2A-B, Supporting Information). Excitation and emission spectra remained unaffected for all the conjugates; however, the conjugation with peptides had a significant effect on the emission yield (Figure S2, Supporting Information). In 10% FBS (typical culturing conditions), quantum yields for the monosubstituted conjugates decreased at a higher length of the peptide (e.g., PEPP1 vs PEPP5) and the addition of the PEG spacer. For PEPP6 with three ethanolamine residues, the absorption spectra shift and internal quenching were much greater. Internal quenching, which was also high for tetra-substituted conjugates, can be largely reduced by the anionic surfactants (0.5 mM SDS), which solubilize the PtCP moiety (for PEPP3 in deoxygenated conditions, the quantum yield was 0.55; not shown). Similar interactions may occur with the conjugate inside the cells (see below). Despite the differences in quantum yields, all the PtCP conjugates displayed similar phosphorescence lifetimes: 20−23 μs in air-saturated and ~80 μs in deoxygenated media (DMEM with 10% FBS, Figure S2D, Supporting Information), i.e., similar to the other PtCP based probes.[34] The PEPP3 conjugate measured in DMEM at 0, 1,

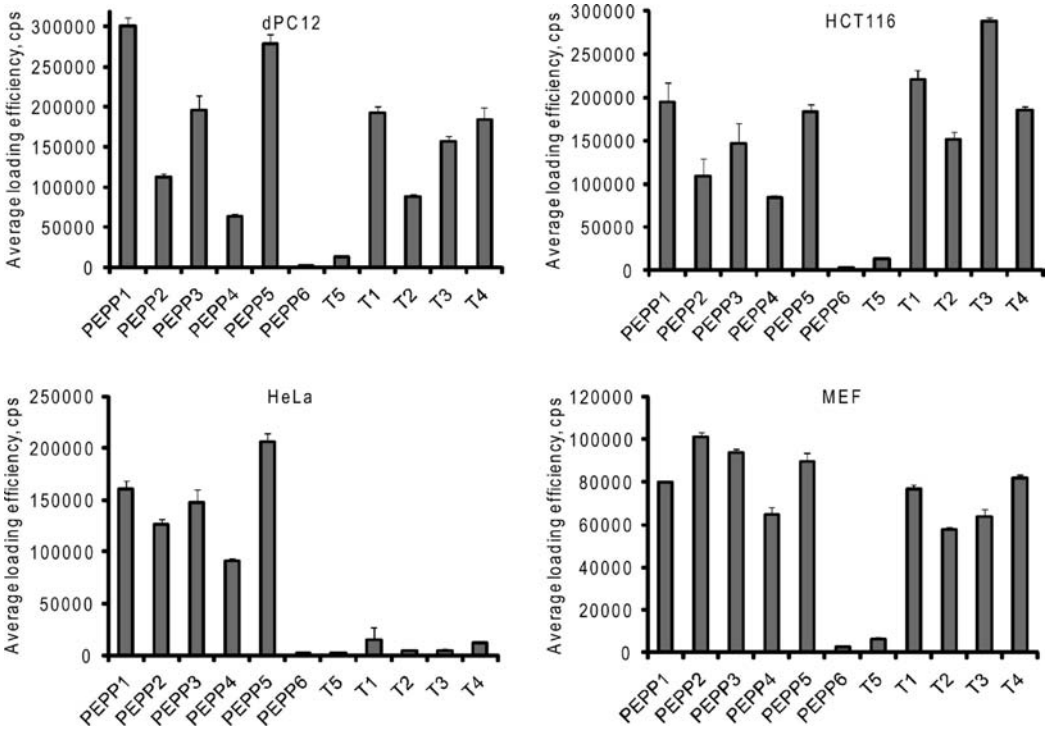

Figure 2. Uptake of conjugates by different mammalian cell lines. Cells were seeded onto collagen IV-coated 96 well plates, incubated with conjugates (1 μM) for 16 h, washed three times, and measured on a microplate reader.

10, 50, and 100% FBS showed no changes in phosphorescence emission lifetime (not shown).

Uptake of the Conjugates by Mammalian Cells. Cellular uptake of the conjugates was first analyzed in cell populations on the TR-F reader. Most of the conjugates showed efficient cell loading with MEF, HeLa, HCT116, and dPC12 cells at 1 μM and 16 h incubation (Figure 2). Linear and branched conjugates PEPP1 and PEPP3 produced high loading signals in all cell lines, whereas the PEG-modified PEPP2 showed a lower degree of loading. The more hydrophobic PEPP4 and PEPP5 with the mitochondrial targeting sequence displayed cell-specific penetration, while conjugates PEPP6 (ethanolamine-modified) and T5 (four Arg) showed poor accumulation in all cell lines tested. The tetra-substituted T1−T4 conjugates showed cell-specific loading: high for HCT116, moderate for dPC12, and poor for HeLa cells. The presence of additional amino acids in branched conjugates (Ala in T1 or Gly in T3) did not interfere with cell loading; however, the presence of Ser in T2 reduced it. As expected, the higher number of Arg in T4 did not improve loading. Therefore, we can conclude that 8−9 Arg ensure optimal cell penetration of coproporphyrin conjugates and that hydroxyl groups can decrease it (conjugates T2, PEPP6, and PEG-containing PEPP2 and PEPP4).

The above results on cell loading were verified by fluorescence microscopy and flow cytometry, which allow single cell analyses. Flow cytometry was not as sensitive as TR-F, and only highly loaded cells were detectable. For such samples, the whole population gave rather uniform fluorescent signals, and unloaded cells (scattering, but no fluorescence) were not seen. Fluorescence microscopy also confirmed the positive loading of HCT116 and MEF cells with the monosubstituted conjugates at 1 and 10 μM concentrations (Figures 3 and S3 (Supporting Information)), except for PEPP6, which was undetectable even at 10 μM and 16 h of incubation. Loading with T2 was marginally lower than that for T1, T3, or PEPP3 (Figure 4) confirming that hydroxyl groups interfere with cell penetrating ability. For T5, loading was detectable only at 10 μM, but with clear signs of toxicity and the appearance of a round cell shape.

Similar efficiency and loading patterns were observed with the other cell lines: rather weak for HeLa, moderate for PC12 and HCT116, and high for MEF, HepG2, and SH-SY5Y (data not shown). The differences can be explained by the different shape, size, membrane composition, and mechanisms of transport for these cells.

Intracellular Distribution of the Conjugates. Wide-field fluorescence microscopy imaging revealed that different conjugates show different intracellular distribution in HCT116, MEF, PC12, SH-SY5Y, and HepG2 cells (see representative data in Figures 3 and S3 (Supporting Information)). Compared to PEPP1, PEPP2 displayed a more diffused cytoplasmic distribution, while PEPP3 gave a more uniform distribution across the cell including the nucleus (Figure 4), with higher accumulation in the nucleus at 10 μM (Figures 3 and S3 (Supporting Information)). PEPP4 and PEPP5 harboring the mitochondrial targeting sequence (with or without PEG_{850} linker) displayed a better intracellular accumulation and brightness than PEPP1, but they did not localize in the mitochondria (Figure 4) and had localization similar to that of the endosomal marker transferrin (data not shown). All branched conjugates T1−T4 and PEPP3 showed very similar intracellular distribution, and the addition of Ala (T1), Gly (T3), or extra Arg (T4) had no visible effects (Figures 3, 4, and S3 (Supporting Information)). T2 with the Ser residue gave only a faint punctuated cytosolic pattern, and localization of T5 could not be assessed as the cells quickly died at high probe concentrations (not shown).

dx.doi.org/10.1021/bc200324q | *Bioconjugate Chem.* 2011, 22, 2507−2518

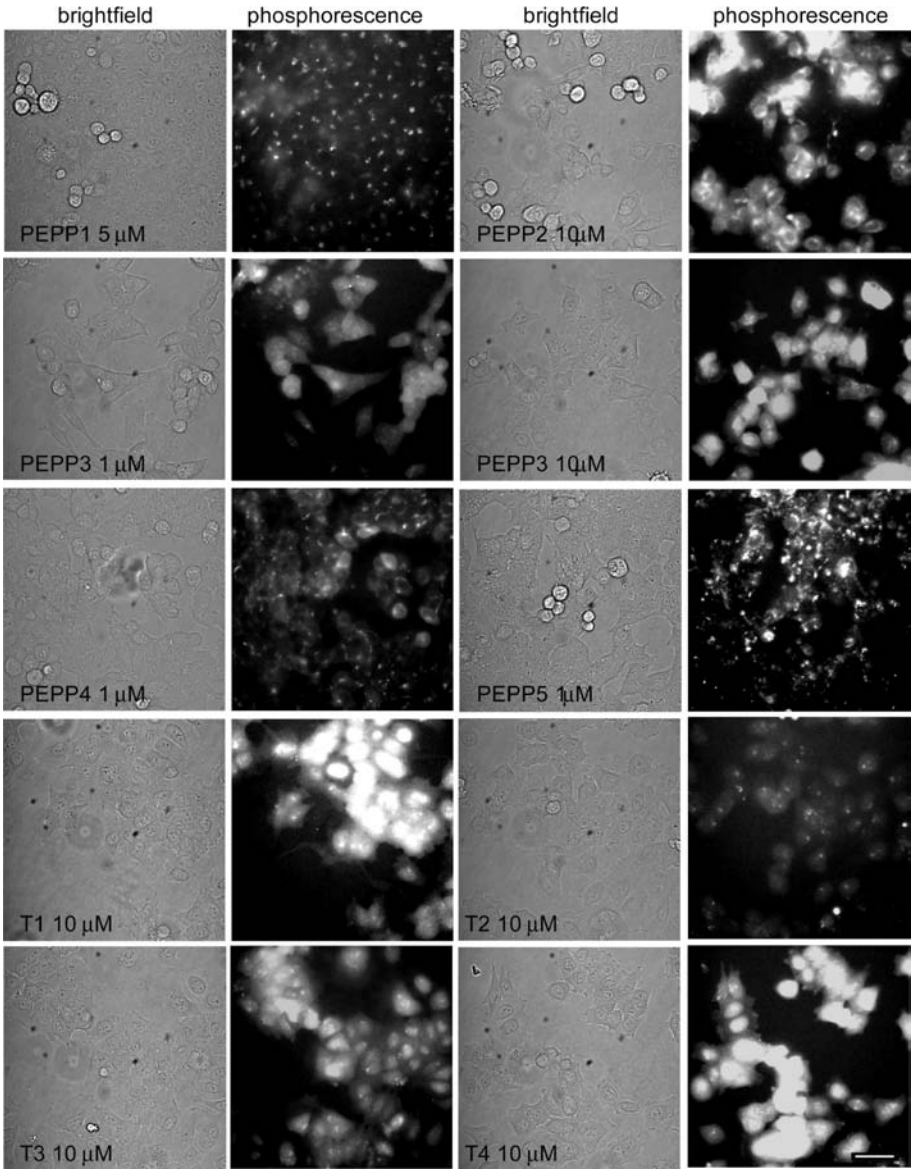

Figure 3. Fluorescence microscopy analysis of HCT116 cells stained with different PtCP conjugates. Cells were seeded onto collagen-poly-D-lysine coated glass bottom dishes at a concentration of 30,000/dish, incubated for 16−18 h with conjugates at specified concentrations, washed, and imaged. Brightfield and fluorescent (390 nm excitation/650 nm emission) images are shown. Scale bar = 50 μm.

Mechanisms of Cellular Uptake for Mono- and Tetra-Substituted Conjugates. Knowledge of the mechanisms of cellular uptake and cell entry pathways allows the regulation of transport of the cargo inside the cell. Such studies involve the inhibition of specific uptake pathways with drugs using the shortest treatment time to minimize the disruption of cellular function.[40,41] Since the flow cytometry method cannot distinguish between internalized and surface-bound probes, fluorescence microscopy which allows direct observation of the cell phenotype and the qualitative effect of inhibitors, was applied to study HCT116 and MEF cells. Two representative conjugates from each class were chosen for these experiments: PEPP3 (branched) and PEPP4 (linear). PtCP conjugates show rather slow rates of cellular uptake,[18,31,32,37,42] which were 4−6 h for PEPP3 and PEPP4 (Figure S4, Supporting Information). The unlabeled oligoarginine did not have a measurable effect on the loading of the conjugates (Figures 5 and S5 (Supporting Information)), thus indicating a different mechanism of uptake.

The main mechanisms of cell entry reported for oligoarginine, endocytosis and direct translocation,[37,40,43,44] can be assessed by analyzing the temperature and ATP dependence of the uptake. For PEPP3 and PEPP4, the loading at 4 °C was almost completely inhibited; however, weak staining of the cell surface for PEPP4 indicates that interaction with the cell membrane still occurs (Figures 5 and S5 (Supporting Information)). Uptake of PEPP3 and PEPP4 by the cells depleted in ATP (olygomycin and absence of glucose) was reduced significantly. We therefore concluded that both branched PEPP3 and linear PEPP4 rely on an endocytosis mechanism of cell entry.

Furthermore, inhibition of macropinocytosis by EIPA slightly reduced the uptake of branched conjugate PEPP3 by HCT116 and MEF cells, with the loss of nuclear localization (Figure 5). Inhibition of the clathrin-mediated pathway by CPZ reduced the uptake even more strongly, and inhibition of lipid-raft formation by MBCD had no effect. Noteworthy, 6 h of treatment with EIPA and CPZ still left a high percentage of

dx.doi.org/10.1021/bc200324q | *Bioconjugate Chem.* 2011, 22, 2507−2518

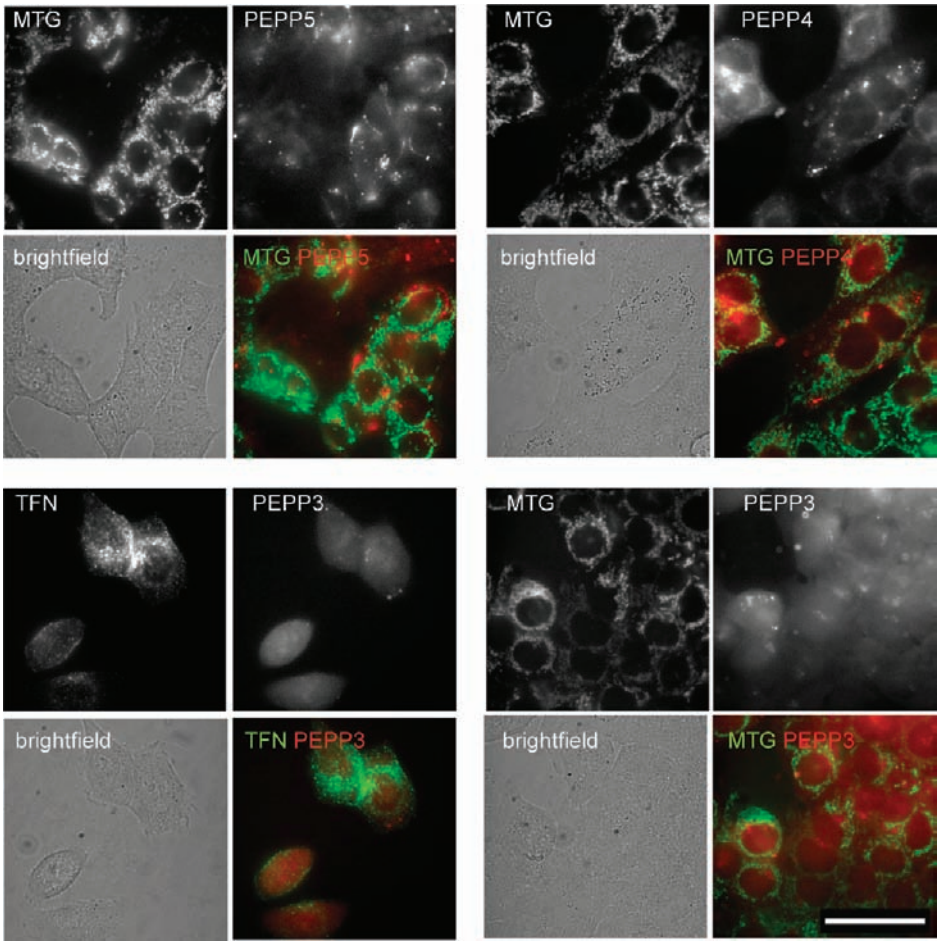

Figure 4. High resolution microscopy images of PEPP3–PEPP5 conjugates in HCT116 cells. Cells were loaded with PEPP4, PEPP5 (1 μM), and PEPP3 (5 μM) conjugates for 16 h, washed, and counter-stained with organelle-specific markers: MitoTracker Green (MTG, mitochondria) and transferrin-Alexa488 (TFN, pool of clathrin-dependent recycling endosomes). Scale = 50 μm.

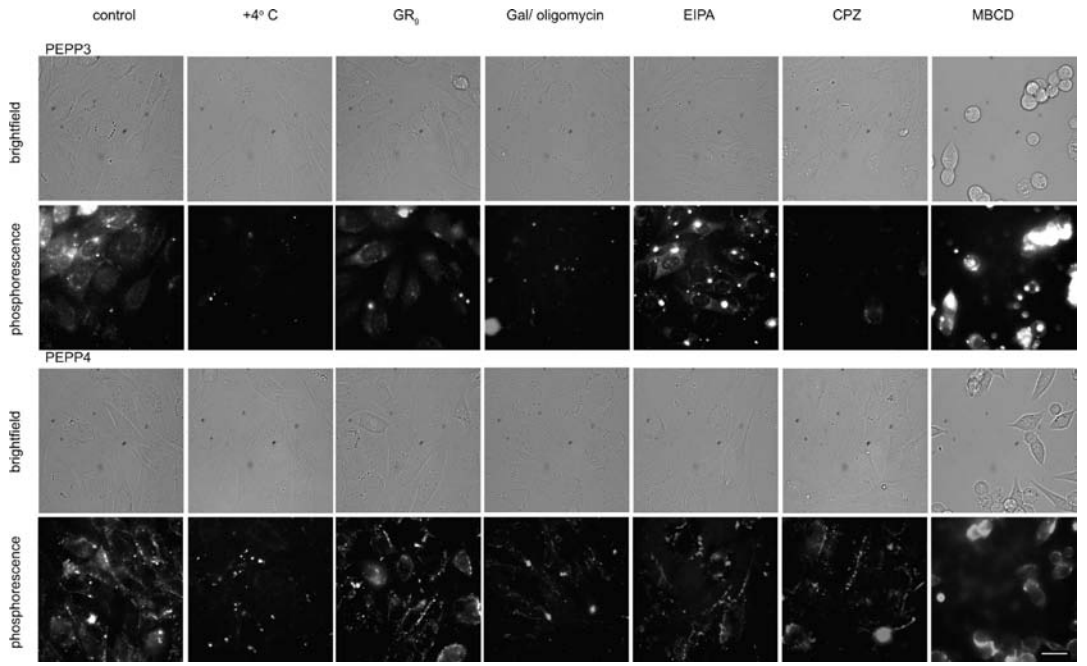

Figure 5. Effects of temperature, ATP depletion, the presence of unlabeled GR_9, and inhibitors of endocytosis on the cellular uptake of PEPP3 and PEPP4. MEF cells were incubated at 37 °C (or at 4 °C) with 5 μM PEPP3 or 2 μM PEPP4 for 6 h in the presence of GR_9 peptide and inhibitors or subjected to ATP depletion, then washed, and analyzed. Scale bar = 50 μm.

dx.doi.org/10.1021/bc200324q | *Bioconjugate Chem.* 2011, 22, 2507–2518

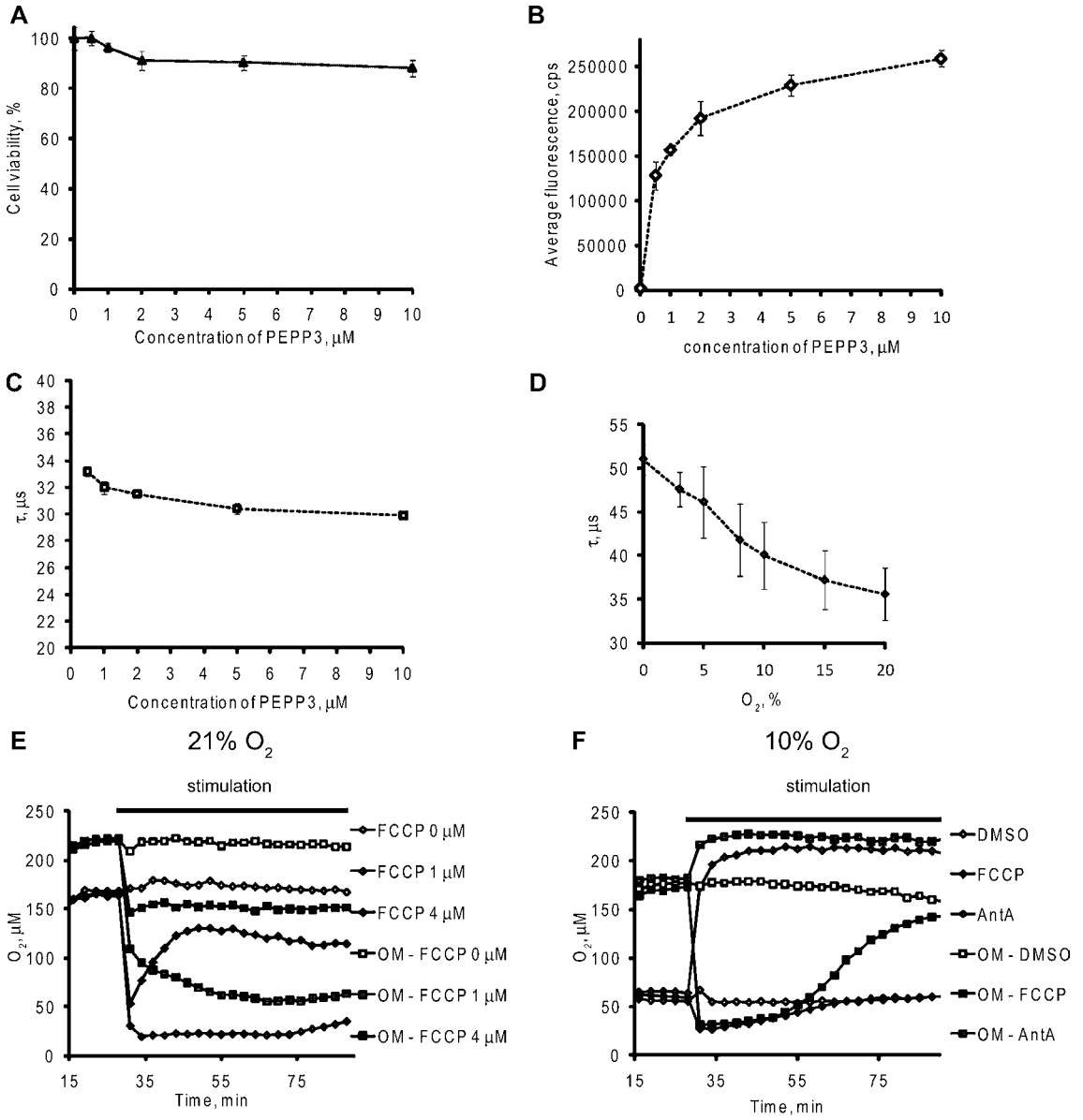

Figure 6. Monitoring of icO_2 with the PEPP3 probe in dPC12 cells. (A) Effect of PEPP3 (0−10 μM for 16 h, 37 °C) on the viability of dPC12 cells. (B) Kinetics of the loading of dPC12 cells with PEPP3 (0−10 μM for 16 h) measured by TR-F. (C) Average phosphorescence lifetimes for dPC12 cells loaded with PEPP3 (0−10 μM for 16 h). (D) Phosphorescence lifetime (τ) at different O_2 concentrations for dPC12 cells loaded with 2 μM PEPP3 for 16 h and treated with 10 μM antimycin A. (E and F) Metabolic responses (presented in O_2 scale) of PC12 cells loaded with PEPP3 and measured in glucose-free media. (E) Responses to FCCP addition for the cells pretreated with 10 μM oligomycin (OM) at 21% of external O_2. (F) The same as E but at 10% of external O_2.

viable cells, whereas treatment with MBCD changed cell morphology (round shape phenotype) and caused cell detachment. Similarly, treatment with EIPA and CPZ moderately decreased the uptake of monosubstituted PEPP4, and MBCD had no visible effect (Figure.5). Since the uptake of PEPP3 was significantly affected by CPZ, we performed a competition experiment with transferrin (marker of clathrin-mediated endocytosis[41]) and observed a partial (~30%) reduction of loading of the conjugate (Figure S5, Supporting Information).

These results indicate that PEPP3 and PEPP4 utilize both macropinocytosis and clathrin-mediated uptake pathways. This means that after internalization they should remain in recycling endosomes or undergo endosomal escape followed by migration to the cytoplasm and other compartments. Endosomal escape can be inhibited by agents that disturb the function of acidic compartments.[45−47] We treated MEF cells with concanamycin A (V-ATPase inhibitor) and observed that PEPP3 lost its nuclear localization, remaining only in the cytoplasm. This drug had no effect on PEPP4 (Figure S5, Supporting Information), thus suggesting that PEPP4 stays in recycling endosomes.

Furthermore, the presence of heparin sulfate caused a partial decrease of uptake and perinuclear localization of PEPP3, whereas for PEPP4, the uptake was completely abolished with the formation of visible aggregates (Figure S5, Supporting Information). This suggests that interactions cell surface sugars are important for the monosubstituted conjugates.

Monitoring of Intracellular O_2 with the PtCP Conjugates. The PEPP3 conjugate was among the best in terms

dx.doi.org/10.1021/bc200324q | *Bioconjugate Chem.* 2011, 22, 2507−2518

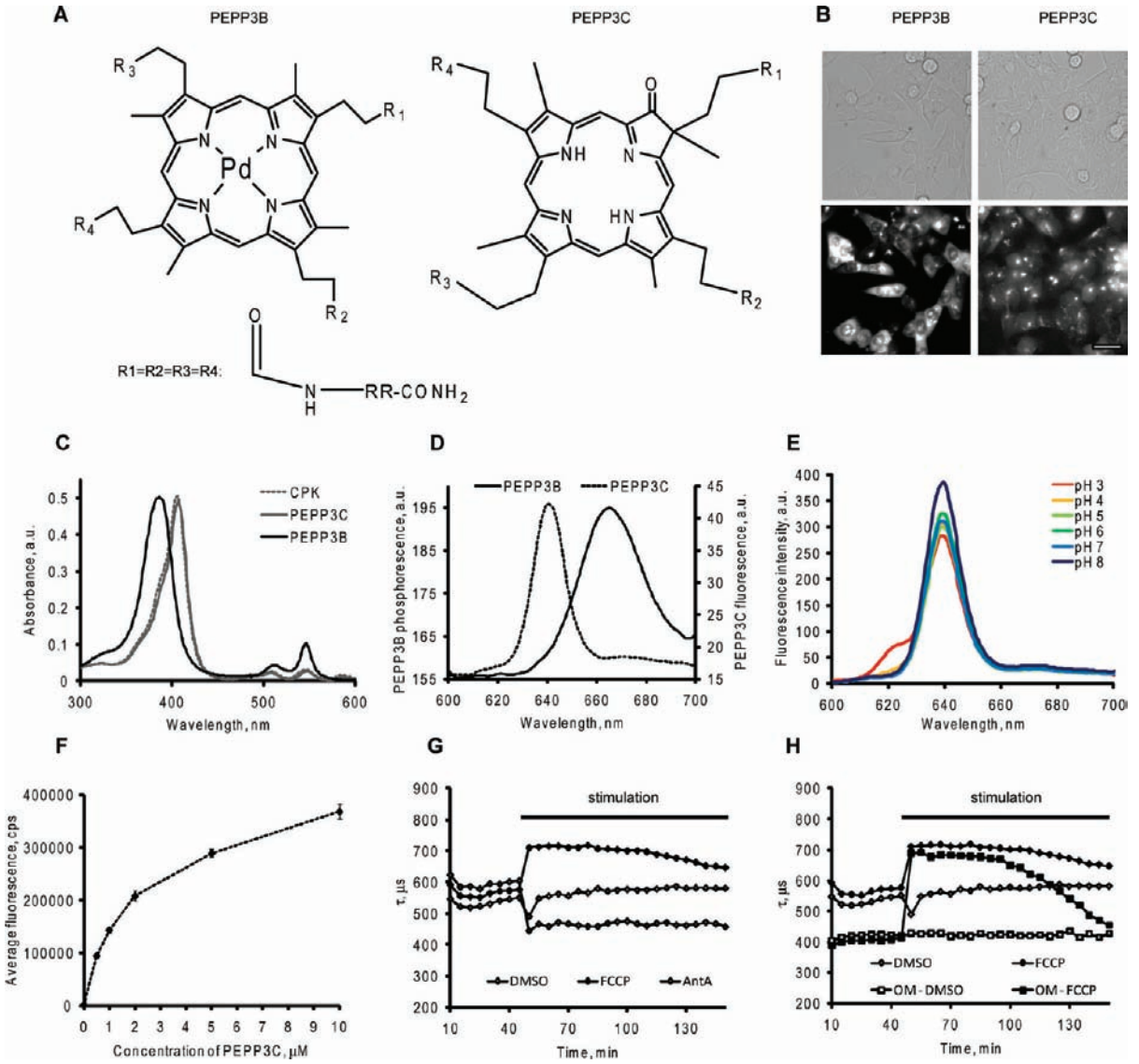

Figure 7. Properties of PEPP3B and PEPP3C conjugates. (A) Structures of the conjugates. (B) Fluorescence microscopy images of HCT116 cells stained with the conjugates (5 μM, 16 h). Scale bar = 50 μm. (C) UV−vis absorption spectra of CPK, PEPP3B, and PEPP3C. (D) Phosphorescence (PEPP3B) and fluorescence (PEPP3C) spectra. (E) Effect of pH on the fluorescence of PEPP3C measured at 0.25 μM in citrate−phosphate buffer. (F) Average fluorescence at 640 nm for dPC12 cells loaded with 0−10 μM PEPP3C for 16 h. (G−H) Metabolic responses (in phosphorescence lifetime scale) of PC12 cells loaded with PEPP3B in glucose-free media at 10% pO_2. (E) Responses to 1 μM FCCP and 10 μM AntA. (F) Responses to 1 μM FCCP for the cells pretreated with 10 μM OM.

of cellular uptake and distribution; therefore, we decided to test it as an O_2-sensing probe with dPC12 cells. Optimal loading was at around 2 μM producing minimal cell toxicity, high phosphorescence intensity signals, and stable lifetime values in resting cells (Figure 6a−c). To enable the determination of O_2 concentration, we calibrated PEPP3 in live nonrespiring dPC12 cells[35] by measuring its phosphorescence lifetime at different levels of atmospheric pO_2 and 37 °C. Calibration curve $O_2 = f(\tau)$ is shown in Figure 6d.

To test probe performance, the cells grown, differentiated, and loaded in standard microplates were treated with metabolic effectors: FCCP, oligomycin, and antimycin A (Figure 6e−f). Prior to stimulation, resting dPC12 cells demonstrated stable baseline signals, which reflect partial deoxygenation of the monolayer compared to the bulk medium. The addition of FCCP (mitochondrial uncoupler) induced a prominent response: a large decrease in cellular oxygen due to increased respiration (the cell layer is acting as a sink for dissolved O_2 and the medium layer as a diffusion barrier for atmospheric oxygen[35]). The response had a bell shape, decreasing at high concentration (4 μM) due to FCCP toxicity. Pretreatment of cells with 10 μM oligomycin (complex V inhibitor) decreased basal respiration (higher icO_2) and the magnitude of response (Figures 6e and S6, Supporting Information). Antimycin A (complex III inhibitor) increased icO_2 to ambient levels (Figures 6f and S6, Supporting Information). These results are in agreement with those of the other icO_2 probes.[28,29,34] They demonstrate that the PEPP3 conjugate works reliably as an icO_2 probe in the measurement of cell oxygenation and metabolic responses of cell populations producing good quality data in a simple format with high sample throughput.

Conjugates of the Other Coproporphyrin Dyes. Compared to PtCP, PdCP has a significantly longer unquenched phosphorescence lifetime (~1 ms) and therefore

dx.doi.org/10.1021/bc200324q | Bioconjugate Chem. 2011, 22, 2507−2518

is better suited for the sensing of physiological O_2 levels (0−50 μM[9]). In contrast to the phosphorescent dyes PtCP and PdCP, coproporphyrin-ketone (CPK) shows bright longwave fluorescence, structural and spectral similarity with chlorins, high photostability, and characteristic changes to pH. This makes CPK a promising candidate for use as a ratiometric pH probe[48] or a photosensitizer in PDT.[11] On the basis of PdCP and CPK dyes, we synthesized structural analogues of PEPP3 conjugate, PEPP3B and PEPP3C, respectively (Figure 7a), and investigated their properties.

PEPP3B and PEPP3C demonstrated absorption and emission spectra similar to those of unconjugated CPK and PdCP (Figure 7c−d). Thus, PEPP3B showed significantly longer lifetimes and higher sensitivity to O_2 than the PEPP3 probe, producing rather low phosphorescent signals at 21% O_2 due to strong quenching. PEPP3C exhibited bright fluorescence and pH-dependence, however, compared to those of free CPK, and spectral changes in fluorescence occurred at more acidic pH (pKa < 3), which did not match the cytosolic pH range (7.0−7.4) (Figures 7e and S7, Supporting Information). As expected, both PEPP3B and PEPP3C showed efficient uptake by HCT116 cells and intracellular distribution similar to that of PEPP3 (Figure 7b). In the case of PEPP3C, high fluorescent signals were observed (Figure 7f), suggesting its potential suitability for imaging and plate reader applications within the optimized range of working concentrations (2−10 μM, similar to PtCP-based branched conjugates). The behavior of the PEPP3B conjugate in the experiments with dPC12 cells on a microplate reader performed at 10% O_2 (Figure 7g,h) was seen to be similar to PEPP3. This conjugate produced similar signal patterns: basal respiration levels produced phosphorescence lifetimes of ∼500−600 μs, which dropped to ∼400 μs in oligomycin and antimycin treated cells and increased to ∼700 μs upon mitochondrial uncoupling with FCCP. This indicates that PEPP3B can be used for monitoring of icO_2 under hypoxia. Other conjugates of these two dyes with oligoarginine moieties can also be prepared.

DISCUSSION

A number of PtCP conjugates with long linear and short branched oligoarginine peptides, an additional mitochondria-targeting sequence, different side groups, and linkers were prepared and characterized. Testing these conjugates with several common cell lines allowed us to establish structure−activity relationships, which can aid in further rational design and application of such structures. For the monosubstituted conjugates with CFR_9 peptides, the hydrophilic PEG_{850} linker did not improve their cell loading and water solubility; however, this was achieved with tetra-substituted PtCP conjugates with the R_2-R_3 peptides. We also showed that the overall structure can affect the photophysical properties of PtCP moiety.

Analyzing the uptake of the conjugates by mammalian cells, we observed a large variation in its efficiency and subsequent intracellular distribution. The presence of hydroxyl groups (PEPP6 and T2) and the PEG_{850} linker (Figures 2−3 and S3 (Supporting Information)) slightly reduced the efficacy of cellular uptake. For the tetra-substituted conjugates, we found that a minimum 8 Arg residues is required for efficient internalization. Branched PtCP conjugates showed lower brightness (emission quantum yields) in aqueous solutions; however, TR-F signals in stained cells were comparable to the signals produced by the linear conjugates. This can be explained by the higher loading efficiency and/or elimination of internal quenching upon their internalization.

Compared to the previously reported PEPP1,[29] the new conjugates show better and more diverse intracellular distribution, ranging from endosomal to whole cell localization. The cytoplasmic accumulation was demonstrated for the linear oligoarginine conjugate with the PEG linker (PEPP2), while whole cell location with nuclear accumulation at higher concentrations was observed for branched (PEPP3, T1, T3, and T4) conjugates. Surprisingly, the targeting sequence in PEPP4 and PEPP5 did not lead to their mitochondrial accumulation. This can be explained by (i) special requirements for mitochondrial targeting of small molecules such as PtCP; (ii) limitations imposed by the endosomal cell entry (e.g., no escape from endosomes for PEPP4, Figure S5, Supporting Information); and (iii) functional inactivation of the targeting sequence within the supra-molecular structure (sterical factors).

Comparative analysis of branched (PEPP3) and linear (PEPP4) conjugates shows that both types use temperature- and ATP-dependent endocytosis mechanisms of cell entry. The latter is unaffected by MBCD and partially inhibited by EIPA and CPZ. This data points to the involvement of mixed uptake mechanisms. For the two different cell lines, MEF and HCT116, no significant differences were observed in cellular uptake, suggesting low cell-specificity. Cell penetration of the conjugates appears to be different from the unconjugated oligoarginine peptide, for which the uptake can vary in different cell lines.[2,43]

The structure−activity relationships established for the panel of PtCP conjugates can be exploited to design new cell-penetrating conjugates of porphyrin dyes with predetermined properties. This was illustrated by investigating icO_2 sensing properties of one chosen conjugate, PEPP3, and preparing its homologues from the PdCP and CPK dyes (PEPP3B and PEPP3C conjugates, respectively).

In the icO_2 sensing experiments, PEPP3 showed good analytical performance. It can be used at lower concentrations than the existing peptide-based probes,[28,29] with equal or shorter loading time (6−16 h) and without any significant effect on cell viability (Figure6). Furthermore, cell staining with PEPP3 did not interfere with the other cellular markers (LysoTracker Red, LysoTracker Green, Transferrin, MitoTracker Red, and MitoTracker Green; data not shown), thus indirectly confirming the minimal impact of the former on the function of these organelles. This probe was calibrated over physiological O_2 concentrations and tested in time-lapse respiration experiments with live cells on a TR-F reader, both under normoxic and hypoxic macro-environments. The profiles of cell oxygenation and responses to model drugs and metabolic stimulations measured with this conjugate were consistent with results obtained with the other probes.[28,34,49]

PEPP3B and PEPP3C conjugates based on the analogues of PtCP also demonstrated efficient accumulation in the cells and gave localization patterns similar to those of PEPP3. The PdCP based PEPP3B conjugate showed suitability for monitoring low O_2 under a hypoxic environment, while PEPP3C showed pH sensitivity, which was shifted toward the acidic range probably due to the multiple charges on R-residues. The latter should be kept in mind when designing the intracellular probes with pH-dependent properties. This study can also be used to develop new cell-permeable porphyrin based probes and drugs (e.g., PDT photosensitizers) targeted to different subcellular locations.

■ ASSOCIATED CONTENT

Ⓢ Supporting Information

Experimental procedures and the synthesis of initial dyes. This material is available free of charge via the Internet at http://pubs.acs.org.

■ AUTHOR INFORMATION

Corresponding Author

*Phone: +353-21-4901699. Fax: +353-21-4901698. E-mail: d.papkovsky@ucc.ie.

Notes

The authors declare no conflict of interest.

■ ACKNOWLEDGMENTS

This work was supported by the Science Foundation of Ireland, grant 07/IN.1/B1804, and by the Higher Education Authority (HEA) of Ireland.

■ ABBREVIATIONS

AntA, antimycin A; cps, counts per second; CPK, coproporphyrin ketone; CPZ, chlorpromazine; EIPA, 5-(*N*-ethyl-*N*-isopropyl)amiloride; FBS, fetal bovine serum; FCCP, carbonyl cyanide 4-(trifluoromethoxy) phenylhydrazone; HS, horse serum; icO_2, intracellular O_2; LED, light emitting diode; MI, maleimide; MBCD, methyl-*β*-D-cyclodextrin; OM, oligomycin; PBS, phosphate buffered saline; PdCP, Pd(II)-coproporphyrin I; PFP, pentafluorophenyl; PtCP, Pt(II)-coproporphyrin I; PtCPTE, triethyl ester of PtCP; RP-HPLC, reversed phase HPLC; TAT, trans-activator of transcription; TFA, trifluoroacetic acid; TR-F, time-resolved phosphorescence

■ REFERENCES

(1) Breunig, M., Bauer, S., and Goepferich, A. (2008) Polymers and nanoparticles: intelligent tools for intracellular targeting? *Eur. J. Pharm. Biopharm. 68*, 112−128.

(2) Gupta, B., Levchenko, T. S., and Torchilin, V. P. (2005) Intracellular delivery of large molecules and small particles by cell-penetrating proteins and peptides. *Adv. Drug Delivery Rev. 57*, 637−651.

(3) Fernandez-Moreira, V., Thorp-Greenwood, F. L., and Coogan, M. P. (2010) Application of d6 transition metal complexes in fluorescence cell imaging. *Chem. Commun. (Cambrideg, U. K.) 46*, 186−202.

(4) Rancan, F., Wiehe, A., Nobel, M., Senge, M. O., Omari, S. A., Bohm, F., John, M., and Roder, B. (2005) Influence of substitutions on asymmetric dihydroxychlorins with regard to intracellular uptake, subcellular localization and photosensitization of Jurkat cells. *J. Photochem. Photobiol., B 78*, 17−28.

(5) Endres, P. J., MacRenaris, K. W., Vogt, S., and Meade, T. J. (2008) Cell-permeable MR contrast agents with increased intracellular retention. *Bioconjugate Chem. 19*, 2049−2059.

(6) Medintz, I. L., Pons, T., Delehanty, J. B., Susumu, K., Brunel, F. M., Dawson, P. E., and Mattoussi, H. (2008) Intracellular delivery of quantum dot-protein cargos mediated by cell penetrating peptides. *Bioconjugate Chem. 19*, 1785−1795.

(7) Szeto, H. H., Schiller, P. W., Zhao, K., and Luo, G. (2005) Fluorescent dyes alter intracellular targeting and function of cell-penetrating tetrapeptides. *FASEB J. 19*, 118−120.

(8) Eckshtain, M., Zilbermann, I., Mahammed, A., Saltsman, I., Okun, Z., Maimon, E., Cohen, H., Meyerstein, D., and Gross, Z. (2009) Superoxide dismutase activity of corrole metal complexes. *Dalton Trans.*, 7879−7882.

(9) Papkovsky, D. B., and O'Riordan, T. C. (2005) Emerging applications of phosphorescent metalloporphyrins. *J. Fluoresc. 15*, 569−584.

(10) O'Connor, A. E., Gallagher, W. M., and Byrne, A. T. (2009) Porphyrin and nonporphyrin photosensitizers in oncology: preclinical and clinical advances in photodynamic therapy. *Photochem. Photobiol. 85*, 1053−1074.

(11) Kadish, S. K., and Guilard, R. (2010) *Handbook of Porphyrin Science: Phototherapy, Radioimmunotherapy and Imaging*, Vol. 4, World Scientific, Singapore.

(12) Dunphy, I., Vinogradov, S. A., and Wilson, D. F. (2002) Oxyphor R2 and G2: phosphors for measuring oxygen by oxygen-dependent quenching of phosphorescence. *Anal. Biochem. 310*, 191−198.

(13) O'Riordan, T. C., Soini, A. E., and Papkovsky, D. B. (2001) Monofunctional derivatives of coproporphyrins for phosphorescent labeling of proteins and binding assays. *Anal. Biochem. 290*, 366−375.

(14) Kessel, D., Luguya, R., and Vicente, M. G. H. (2003) Localization and Photodynamic Efficacy of Two Cationic Porphyrins Varying in Charge Distribution. *Photochem. Photobiol. 78*, 431−435.

(15) Papkovsky, D. B. (2004) Methods in optical oxygen sensing: protocols and critical analyses. *Methods Enzymol. 381*, 715−735.

(16) Lebedev, A. Y., Cheprakov, A. V., Sakadzic, S., Boas, D. A., Wilson, D. F., and Vinogradov, S. A. (2009) Dendritic phosphorescent probes for oxygen imaging in biological systems. *ACS Appl. Mater. Interfaces 1*, 1292−1304.

(17) Mik, E. G., Stap, J., Sinaasappel, M., Beek, J. F., Aten, J. A., van Leeuwen, T. G., and Ince, C. (2006) Mitochondrial PO2 measured by delayed fluorescence of endogenous protoporphyrin IX. *Nat. Methods 3*, 939−945.

(18) Fercher, A., Ponomarev, G. V., Yashunski, D., and Papkovsky, D. (2010) Evaluation of the derivates of phosphorescent Pt-coproporphyrin as intracellular oxygen-sensitive probes. *Anal. Bioanal. Chem. 396*, 1793−1803.

(19) Sibrian-Vazquez, M., Jensen, T. J., and Vicente, M. G. (2007) Synthesis and cellular studies of PEG-functionalized meso-tetraphenylporphyrins. *J. Photochem. Photobiol., B 86*, 9−21.

(20) Samaroo, D., Vinodu, M., Chen, X., and Drain, C. M. (2007) meso-Tetra(pentafluorophenyl)porphyrin as an efficient platform for combinatorial synthesis and the selection of new photodynamic therapeutics using a cancer cell line. *J. Comb. Chem. 9*, 998−1011.

(21) Koo, Y. E., Cao, Y., Kopelman, R., Koo, S. M., Brasuel, M., and Philbert, M. A. (2004) Real-time measurements of dissolved oxygen inside live cells by organically modified silicate fluorescent nanosensors. *Anal. Chem. 76*, 2498−2505.

(22) Buck, S. M., Koo, Y. E., Park, E., Xu, H., Philbert, M. A., Brasuel, M. A., and Kopelman, R. (2004) Optochemical nanosensor PEBBLEs: photonic explorers for bioanalysis with biologically localized embedding. *Curr. Opin. Chem. Biol. 8*, 540−546.

(23) Compagnin, C., Bau, L., Mognato, M., Celotti, L., Miotto, G., Arduini, M., Moret, F., Fede, C., Selvestrel, F., Rio Echevarria, I. M., Mancin, F., and Reddi, E. (2009) The cellular uptake of meta-tetra(hydroxyphenyl)chlorin entrapped in organically modified silica nanoparticles is mediated by serum proteins. *Nanotechnology 20*, 345101.

(24) Nishiyama, N., Nakagishi, Y., Morimoto, Y., Lai, P. S., Miyazaki, K., Urano, K., Horie, S., Kumagai, M., Fukushima, S., Cheng, Y., Jang, W. D., Kikuchi, M., and Kataoka, K. (2009) Enhanced photodynamic cancer treatment by supramolecular nanocarriers charged with dendrimer phthalocyanine. *J. Controlled Release 133*, 245−251.

(25) Ngen, E. J., Rajaputra, P., and You, Y. (2009) Evaluation of delocalized lipophilic cationic dyes as delivery vehicles for photosensitizers to mitochondria. *Bioorg. Med. Chem. 17*, 6631−6640.

(26) Conway, C. L., Walker, I., Bell, A., Roberts, D. J. H., Brown, S. B., and Vernon, D. I. (2008) In vivo and in vitro characterisation of a protoporphyrin IX-cyclic RGD peptide conjugate for use in photodynamic therapy. *Photochem. Photobiol. Sci. 7*, 290−298.

(27) Sibrian-Vazquez, M., Jensen, T. J., Hammer, R. P., and Vicente, M. G. (2006) Peptide-mediated cell transport of water soluble porphyrin conjugates. *J. Med. Chem. 49*, 1364−1372.

(28) Dmitriev, R. I., Ropiak, H. M., Yashunsky, D. V., Ponomarev, G. V., Zhdanov, A. V., and Papkovsky, D. B. (2010) Bactenecin 7 peptide

fragment as a tool for intracellular delivery of a phosphorescent oxygen sensor. *FEBS J. 277*, 4651−4661.
(29) Dmitriev, R. I., Zhdanov, A. V., Ponomarev, G. V., Yashunski, D. V., and Papkovsky, D. B. (2010) Intracellular oxygen-sensitive phosphorescent probes based on cell-penetrating peptides. *Anal. Biochem. 398*, 24−33.
(30) Sehgal, I., Sibrian-Vazquez, M., and Vicente, M. G. (2008) Photoinduced cytotoxicity and biodistribution of prostate cancer cell-targeted porphyrins. *J. Med. Chem. 51*, 6014−6020.
(31) Sibrian-Vazquez, M., Jensen, T. J., Fronczek, F. R., Hammer, R. P., and Vicente, M. G. (2005) Synthesis and characterization of positively charged porphyrin-peptide conjugates. *Bioconjugate Chem. 16*, 852−863.
(32) Futaki, S., Nakase, I., Suzuki, T., Youjun, Z., and Sugiura, Y. (2002) Translocation of branched-chain arginine peptides through cell membranes: flexibility in the spatial disposition of positive charges in membrane-permeable peptides. *Biochemistry 41*, 7925−7930.
(33) O'Riordan, T. C., Soini, A. E., Soini, J. T., and Papkovsky, D. B. (2002) Performance evaluation of the phosphorescent porphyrin label: solid-phase immunoassay of alpha-fetoprotein. *Anal. Chem. 74*, 5845−5850.
(34) O'Riordan, T. C., Zhdanov, A. V., Ponomarev, G. V., and Papkovsky, D. B. (2007) Analysis of intracellular oxygen and metabolic responses of mammalian cells by time-resolved fluorometry. *Anal. Chem. 79*, 9414−9419.
(35) Zhdanov, A. V., Ogurtsov, V. I., Taylor, C. T., and Papkovsky, D. B. (2010) Monitoring of cell oxygenation and responses to metabolic stimulation by intracellular oxygen sensing technique. *Integr. Biol. (Cambridge, U. K.) 2*, 443−451.
(36) Dailey, T. A., Woodruff, J. H., and Dailey, H. A. (2005) Examination of mitochondrial protein targeting of haem synthetic enzymes: in vivo identification of three functional haem-responsive motifs in 5-aminolaevulinate synthase. *Biochem. J. 386*, 381−386.
(37) Futaki, S., Nakase, I., Tadokoro, A., Takeuchi, T., and Jones, A. T. (2007) Arginine-rich peptides and their internalization mechanisms. *Biochem. Soc. Trans. 35*, 784−787.
(38) O'Sullivan, P. J., Burke, M., Soini, A. E., and Papkovsky, D. B. (2002) Synthesis and evaluation of phosphorescent oligonucleotide probes for hybridisation assays. *Nucleic Acids Res. 30*, e114.
(39) Drain, C. M., Batteas, J. D., Flynn, G. W., Milic, T., Chi, N., Yablon, D. G., and Sommers, H. (2002) Designing supramolecular porphyrin arrays that self-organize into nanoscale optical and magnetic materials. *Proc. Natl. Acad. Sci. U.S.A. 99*, 6498−6502.
(40) Duchardt, F., Fotin-Mleczek, M., Schwarz, H., Fischer, R., and Brock, R. (2007) A comprehensive model for the cellular uptake of cationic cell-penetrating peptides. *Traffic 8*, 848−866.
(41) Doherty, G. J., and McMahon, H. T. (2009) Mechanisms of endocytosis. *Annu. Rev. Biochem. 78*, 857−902.
(42) Kaplan, I. M., Wadia, J. S., and Dowdy, S. F. (2005) Cationic TAT peptide transduction domain enters cells by macropinocytosis. *J. Controlled Release 102*, 247−253.
(43) Nakase, I., Takeuchi, T., Tanaka, G., and Futaki, S. (2008) Methodological and cellular aspects that govern the internalization mechanisms of arginine-rich cell-penetrating peptides. *Adv. Drug Delivery Rev. 60*, 598−607.
(44) Ter-Avetisyan, G., Tunnemann, G., Nowak, D., Nitschke, M., Herrmann, A., Drab, M., and Cardoso, M. C. (2009) Cell entry of arginine-rich peptides is independent of endocytosis. *J. Biol. Chem. 284*, 3370−3378.
(45) Drose, S., and Altendorf, K. (1997) Bafilomycins and concanamycins as inhibitors of V-ATPases and P-ATPases. *J. Exp. Biol. 200*, 1−8.
(46) Poole, B., and Ohkuma, S. (1981) Effect of weak bases on the intralysosomal pH in mouse peritoneal macrophages. *J. Cell Biol. 90*, 665−669.
(47) Fischer, R., Kohler, K., Fotin-Mleczek, M., and Brock, R. (2004) A stepwise dissection of the intracellular fate of cationic cell-penetrating peptides. *J. Biol. Chem. 279*, 12625−12635.
(48) Papkovsky, D. B., and Ponomarev, G. V. (2001) Spectral-luminescent study of the porphyrin-diketones and their complexes. *Spectrochim. Acta, Part A 57*, 1897−905.
(49) Zhdanov, A. V., Dmitriev, R. I., and Papkovsky, D. B. (2010) Bafilomycin A1 activates respiration of neuronal cells via uncoupling associated with flickering depolarization of mitochondria. *Cell. Mol. Life Sci. 68*, 903−917.

Bioconjugate Chemistry

Article

pubs.acs.org/bc

Synthesis and Characterization of Biodegradable and Thermosensitive Polymeric Micelles with Covalently Bound Doxorubicin-Glucuronide Prodrug via Click Chemistry

M. Talelli,[†,⊥] K. Morita,[†,⊥] C. J. F. Rijcken,[†,∥] R. W. M. Aben,[‡] T. Lammers,[†,§] H. W. Scheeren,[‡] C. F. van Nostrum,[†] G. Storm,[†] and W. E. Hennink*[,†]

[†]Department of Pharmaceutics, Utrecht Institute for Pharmaceutical Sciences (UIPS), Utrecht University, Universiteitsweg 99, 3584 CG Utrecht, Netherlands

[‡]Radboud University Nijmegen, Institute for Molecules and Materials, Heyendaalseweg 135, 6525 AJ Nijmegen, Netherlands

[§]Department of Experimental Molecular Imaging, RWTH Aachen University, Pauwelsstrasse 30, 52074 Aachen, Germany

[∥]Crystal Delivery B.V., Padualaan 8, 3584 CH, Utrecht, Netherlands

Supporting Information

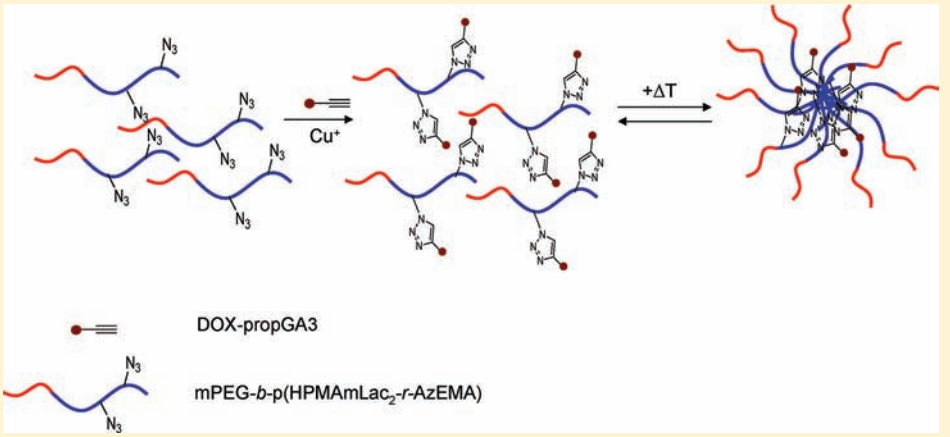

ABSTRACT: Doxorubicin is an anthracycline anticancer agent that is commonly used in the treatment of a variety of cancers, but its application is associated with severe side effects. Biodegradable and thermosensitive polymeric micelles based on poly(ethylene glycol)-*b*-poly[*N*-(2-hydroxypropyl) methacrylamide-lactate] (mPEG-*b*-p(HPMAmLac$_n$)) have been studied as drug delivery systems for therapeutic and imaging agents and have shown promising *in vitro* and *in vivo* results. The purpose of this study was to investigate the covalent coupling of a doxorubicin-glucuronide prodrug (DOX-propGA3) to the core of mPEG-*b*-p(HPMAmLac$_2$) micelles. This prodrug is specifically activated by human *β*-glucuronidase, an enzyme that is overexpressed in necrotic tumor areas. To this end, an azide modified block copolymer (mPEG$_{5000}$-*b*-p(HPMAmLac$_2$-*r*-AzEMA)) was synthesized and characterized, and DOX-propGA3 was coupled to the polymer via click chemistry with a high (95%) coupling efficiency. Micelles formed by this DOX containing polymer were small (50 nm) and monodisperse and released 40% of the drug payload after 5 days incubation at 37 °C in the presence of *β*-glucuronidase, but less than 5% in the absence of the enzyme. *In vitro* cytotoxicity experiments demonstrated that DOX micelles incubated with 14C cells showed the same cytotoxicity as free DOX only in the presence of *β*-glucuronidase, indicating full conversion of the polymer-bound DOX into the parent drug. Overall, this novel system is very promising for enzymatically responsive anticancer therapy.

INTRODUCTION

Doxorubicin (or adriamycin) is an anthracycline cytotoxic anticancer agent that is commonly used in the treatment of a variety of cancers.[1] Its activity is based on the killing of rapidly dividing cells, but is not selective to cancer cells.[2] Therefore, the clinical use of doxorubicin is associated with several side effects, the most important being cardiomyopathy, which can be life-threatening, and therefore severely limits the (cumulative) dose of the drug that can be administered.[3,4] Tumor-selective and efficient drug delivery systems are under investigation that ideally mask the side effects of doxorubicin and simultaneously increase its therapeutic efficacy.[5,6] Among the developed systems, liposomal doxorubicin (Doxil/Caelyx) has been the most successful and is presently used in the clinic,[7] while

Received: July 4, 2011
Revised: September 23, 2011
Published: October 21, 2011

ACS Publications © 2011 American Chemical Society

Scheme 1. Two-Step Synthesis of 2-Azidoethyl Methacrylate (AzEMA) by Conversion of 2-Bromoethanol to 2-Azidoethanol (A) and Subsequent Methacrylation Using Methacryloyl Chloride (B)

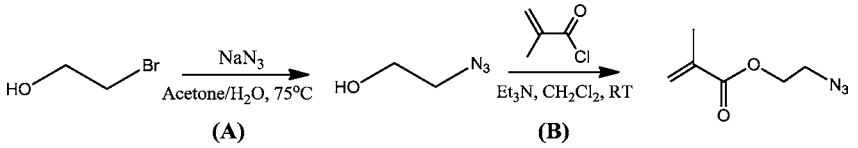

Scheme 2. Synthesis of mPEG$_{5000}$-*b*-p(HPMAmLac$_2$-*r*-AzEMA) Block Copolymer with Free Radical Polymerization Using mPEG$_2$ABCPA Macroinitiator and HPMAmLac$_2$ and AzEMA as Monomers

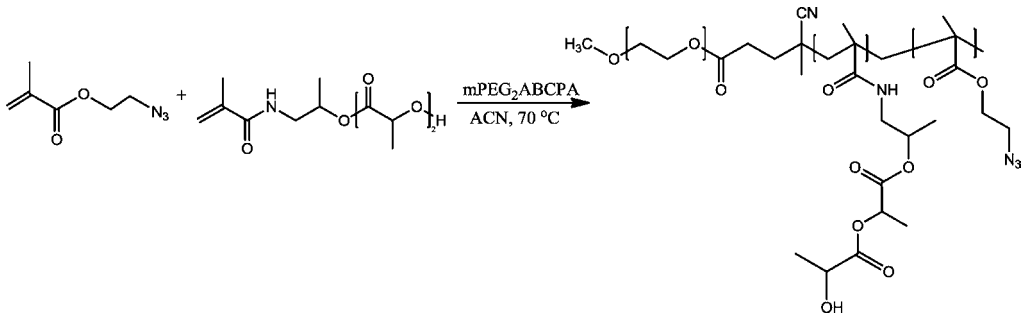

doxorubicin formulated in polymeric micelles has been investigated in clinical trials.[8] Besides particulate carriers, important work has also been done regarding drug−polymer conjugates, where doxorubicin is attached to water-soluble polymers through enzymatically or hydrolytically sensitive linkers.[9−13]

Alternatively, the therapeutic index of chemotherapeutics can also be improved by prodrugs.[14,15] A doxorubicin-glucuronide prodrug (DOX-GA3) has been studied by Haisma et al., and very promising *in vitro* and *in vivo* results have been obtained.[16−18] This prodrug is selectively activated in tumors by β-glucuronidase, an enzyme which is released in the necrotic tumor extracellular space.[19] When DOX-GA3 was intravenously injected into OVCAR-3 tumor bearing mice, a 60-fold higher maximum tolerated dose than free doxorubicin was observed. Importantly, increased therapeutic efficacy was found which was attributed to the decreased systemic toxicity of the prodrug and the increased drug concentrations found in tumor tissue after its administration, compared to mice treated with the parent drug.[18] However, DOX-GA3 displayed poor pharmacokinetics; it was completely eliminated from systemic circulation 4 h after i.v. injection.[17] Therefore, to improve its circulation kinetics, the same group investigated the more lipophilic methylester derivative DOX-mGA3. This derivative was shown to yield DOX-GA3 after hydrolysis of the methyl ester by esterases in blood, which was subsequently converted into DOX by activation by β-glucuronidase.[17] Importantly, this prodrug demonstrated an improved circulation half-life compared to DOX-GA3,[17] which was attributed to the slow release of DOX-GA3 in blood after administration of DOX-mGA3. Therefore, a better therapeutic efficacy was expected, which has not yet been studied to date. However, as was also concluded by de Graaf et al.,[17] it is expected that the DOX-mGA3 prodrug would be more therapeutically useful if its solubility was increased, which can be achieved by the use of suitable drug delivery systems. Therefore, by loading the prodrug in a suitable nanoparticulate carrier the circulation half-life can be substantially improved.

Biodegradable and thermosensitive diblock copolymers composed of poly(ethylene glycol)-*b*-poly[*N*-(2-hydroxypropyl)-methacrylamide-lactate] (mPEG-*b*-p(HPMAmLac$_n$)) have been studied as micelle-forming building blocks for the delivery of hydrophobic agents.[20,21] mPEG-*b*-p(HPMAmLac$_n$) consists of a permanently hydrophilic (mPEG) and a thermosensitive (p(HPMAmLac$_n$)) block, and forms polymeric micelles in aqueous solutions above its critical micelle temperature (CMT).[22] The ease of loading of these micelles and their tunable biodegradability, resulting from hydrolysis of the lactic acid side chains under physiological conditions causing micelle disintegration,[23,24] as well as their size (60−80 nm, suitable for passive targeting to tumors after i.v. administration through the EPR effect[25]), render them very attractive systems for drug delivery to tumors. In recent studies, mPEG-*b*-p(HPMAmLac$_n$) micelles have been successfully used to solubilize the cytostatic drug paclitaxel, the photosensitizer Si(sol)$_2$*Pc*, vitamin K, and an MRI contrast agent.[26−28] Importantly, core-cross-linking resulted in remarkably improved circulation kinetics and consequently in substantially enhanced EPR-mediated drug targeting to tumors.[29] In a recent study, we showed that when a doxorubicin derivative was coupled to the cross-linked core of mPEG-*b*-p(HPMAmLac$_n$) micelles through a pH-sensitive hydrolytically degradable linker and the formulation was intravenously injected into tumor bearing mice, an increased antitumor effect and prolonged survival of the animals as compared to free doxorubicin (with no side effects) was observed.[30] This increased efficacy was attributed to the hypothesis that, upon injection of micelles with covalently bound DOX, a higher amount of the anticancer agent reached the tumor, compared to i.v. injection of the free drug. Active targeting of mPEG-*b*-p(HPMAmLac$_n$) polymeric micelles has also recently been demonstrated, via the conjugation of an anti-EGFR nanobody on their surface, resulting in increased cellular binding and uptake.[31]

The purpose of this study was to investigate the covalent coupling of a doxorubicin-glucuronide prodrug to the core of mPEG-*b*-p(HPMAmLac$_2$) micelles. To this end, an azide modified block copolymer (mPEG$_{5000}$-*b*-p(HPMAmLac$_2$-*r*-AzEMA)) was synthesized (Schemes 1 and 2) and a propargyl derivative of DOX-mGA3 (DOX-propGA3) was coupled to it via click chemistry (Scheme 3), a synthetic methodology that has been receiving great attention in the pharmaceutical field

dx.doi.org/10.1021/bc2003499 | *Bioconjugate Chem.* 2011, 22, 2519−2530

Scheme 3. Click Reaction between mPEG$_{5000}$-*b*-p(HPMAmLac$_2$-*r*-AzEMA) Block Copolymer and DOX-propGA3

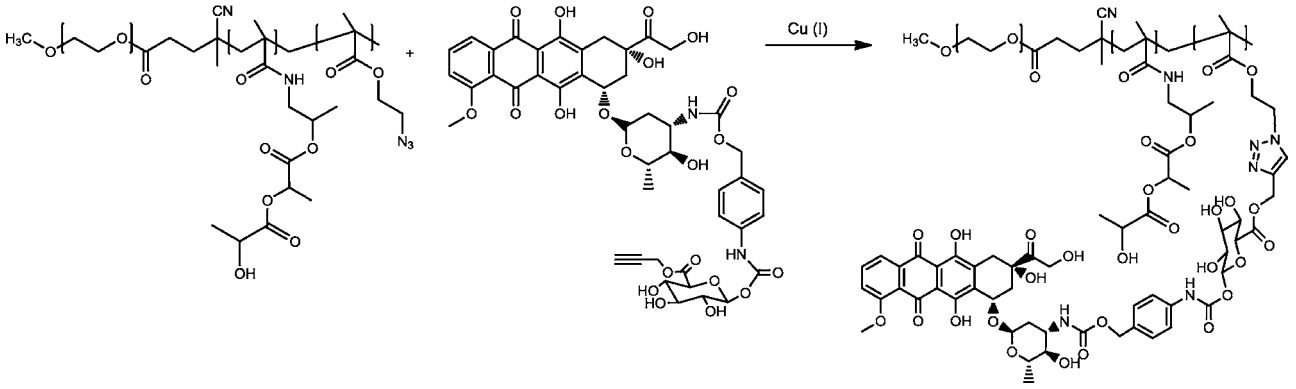

during the past years, due to its high efficiency and selectivity.[32−35] The obtained polymers were characterized for coupling efficiency and critical micelle concentration. It was demonstrated that DOX-propGA3 could be coupled in high yields (95%) and the polymers obtained were able to form micelles at low concentrations. Next, micelles of these block copolymers were formed, and characterized for size and release of doxorubicin in both the presence and absence of human *β*-glucoronidase. Last, the cytotoxicity of these micelles against UM-SCC-14C cells in the absence and presence of human *β*-glucoronidase was examined and compared to that of DOX-propGA3, DOX-GA3, and free DOX.

MATERIALS AND METHODS

General. Acetonitrile, dichloromethane, diethyl ether (Et_2O), and dimethylformamide (DMF) were purchased from Biosolve Ltd. (Valkenswaard, The Netherlands). HPMAmLac$_2$ was obtained from Syncom BV, Groningen, The Netherlands. The mPEG$_2$-ABCPA macroinitiator (4,4-azobis(4-cyanopentanoic acid)) was synthesized as reported previously.[21] 2-Bromoethanol, copper bromide (CuBr), copper sulfate ($CuSO_4$), hydroquinone monomethyl ether (MEHQ), methacryloyl chloride, sodium ascorbate, sodium azide, and triethylamine were purchased from Sigma-Aldrich Co. (Zwijndrecht, The Netherlands). *β*-Glucuronidace from bovine liver (type B-10, ∼10 000 units/mg solid) was purchased from Sigma-Aldrich Co. (Steinheim, Germany). ^{1}H NMR spectra were recorded using a Gemini 300 MHz spectrometer. FT-IR spectra of lyophilized samples were acquired using KBr pellets with a Bio-Rad FTS6000 (BIO-RAD, Cambridge, MA) system, by accumulating 512 scans per spectrum at a data point resolution of 2 cm^{-1}. GPC analysis was performed using a Waters 2695 controller equipped with a RI (for the detection of the polymer) and a UV (480 nm, for the detection of doxorubicin) detector. Separation was performed using a PLgel MIXED-D column (Polymer Laboratories) at 40 °C and DMF (with 10 mM LiCl) as the mobile phase, at a flow rate of 0.7 mL/min. The molecular weights of the polymers were determined using poly(ethylene glycol) standards and RI detection. DOX-propGA3 was synthesized essentially as described in ref 36 and DOX-GA3 as described in ref 37.

Synthesis of 2-Azidoethanol. Sodium azide (23.4 g, 360 mmol) and 2-bromoethanol (27.0 g, 216 mmol) were dissolved in a mixture of acetone (50 mL) and water (10 mL) and refluxed at 75 °C for 3 days. After removing acetone under vacuum, the product was 5 times extracted with 100 mL of ethyl acetate. The organic phase was dried using anhydrous $MgSO_4$ and the solvent was removed under vacuum, resulting in 10.4 g of 2-azidoethanol in the form of a slightly yellow oil (55% yield).

^{1}H NMR ($CDCl_3$) *δ* (ppm) 1.8 (O*H*, br), 3.4 (CH_2N$_3$, t), 3.8 (CH_2OH, t).

Synthesis of 2-Azidoethyl Methacrylate (AzEMA). 2-Azidoethanol (2.0 g, 23 mmol) and triethylamine (3.8 mL, 27 mmol) were dissolved in 40 mL dichloromethane and cooled in an ice bath. Next, methacryloyl chloride (2.6 g, 25 mmol) dissolved in 15 mL dichloromethane was slowly added for 20 min. The reaction was allowed to proceed for 2 h at room temperature. Next, 30 mL of a saturated $NaHCO_3$ aqueous solution was added and the mixture was stirred for 30 min in an ice bath to deactivate methacryloyl chloride. The organic phase was washed with 30 mL of a saturated NaCl solution once, dried using anhydrous $MgSO_4$, and concentrated under vacuum. The crude product was purified by flash silica gel chromatography (Acros silica gel 60 A, 0.030−0.075 mm, Geel, Belgium) with dichloromethane as an eluent, resulting in 2.59 g of 2-azidoethyl methacrylate (AzEMA) as a slightly yellow oil (73% yield). The monomer was stabilized by 400 ppm of hydroquinone monomethyl ether (MEHQ) to avoid premature polymerization and stored at −20 °C.

^{1}H NMR ($CDCl_3$) *δ* (ppm) 2.0 ($CH_2C(CH_3)CO$, s), 3.5 (CH_2N$_3$, t), 4.3 (CH_2CH$_2$N$_3$, t), 5.6 and 6.2 ($CH_2C(CH_3)CO$, t). IR ν_{max} 2106 cm^{-1} (N$_3$).

Synthesis of mPEG$_{5000}$-*b*-p(HPMAmLac$_2$-*r*-AzEMA). The synthesis of azide functionalized copolymers (mPEG$_{5000}$-*b*-p(HPMAmLac$_2$-*r*-AzEMA) (2−20% of AzEMA)) was performed by free radical polymerization using HPMAmLac$_2$ and AzEMA as monomers and (mPEG$_{5000}$)$_2$-ABCPA as radical macroinitiator (ratio of monomer/initiator was 150:1), according to a previously published procedure.[22] Briefly, the starting materials were dissolved in anhydrous acetonitrile in airtight glass vials at a total concentration of 300 mg/mL. After flushing with nitrogen for at least 10 min at room temperature, the solution was heated to 70 °C and stirred for 24 h at this temperature. Next, the formed polymers were precipitated by dropwise addition of the solution to an excess of diethyl ether. The supernatant was discarded and the precipitated polymers were dissolved in water, dialyzed (membrane cutoff 12−14 kDa) against water for at least 24 h, and finally recovered by freeze−drying.

^{1}H NMR ($CDCl_3$): *δ* (ppm) 6.5 (br, CONHCH$_2$), 5.0 (br, NHCH$_2$C*H*(CH$_3$)O and COC*H*(CH$_3$)OH), 4.4 (br, COC*H*(CH$_3$)OH), 4.1 (br, OCH_2 of AzEMA), 3.6 (br, PEG methylene protons), 3.5 (br, CH_2N$_3$ of AzEMA), 3.4 (br,

dx.doi.org/10.1021/bc2003499 | *Bioconjugate Chem.* 2011, 22, 2519−2530

$NHCH_2CH(CH_3)$), 2.0–0.6 (main chain protons of the $HPMAmLac_2$ block). The mole percentage of AzEMA (f_{AzEMA}) in the synthesized block copolymers was determined using ^1H NMR analysis using eq 1 and the number average molecular weight of the thermosensitive (core-forming) block (M_n) using eq 2

$$f_{AzEMA}(\%) = \frac{I_{4.1\,ppm}/2}{I_{4.4\,ppm} + I_{4.1\,ppm}/2} \times 100 \quad (1)$$

$$M_n = [(I_{4.1\,ppm}/2)\cdot M_w(AzEMA) + I_{4.4\,ppm} \cdot M_w(HPMAmLac_2)]/(I_{3.6\,ppm}/448) \quad (2)$$

$I_{4.1ppm}$, $I_{4.4ppm}$, and $I_{3.6ppm}$ are the integrals of the protons at 4.1, 4.4, and 3.6 ppm, respectively, and 448 the number of protons per PEG_{5000} chain. To calculate the M_n of the block copolymer, the above calculated value was added to the molecular weight of mPEG (5000).

Click Reaction of $mPEG_{5000}$-*b*-p(HPMAmLac$_2$-*r*-AzEMA) Block Copolymer with DOX-propGA3. $mPEG_{5000}$-p(95%$HPMAmLac_n$-*r*-5%AzEMA) (30 mg) and DOX-propGA3 (6.6 mg, 2 equiv to azide) were dissolved in 100 μL DMF. Then, CuBr (0.1–1 equiv to DOX-propGA3) dissolved in 300 μL DMF was added. After stirring at room temperature for 24 h under nitrogen, the polymer was precipitated in an excess of diethyl ether and collected by centrifugation and drying under nitrogen.

The above-described reaction was also performed in the presence of $CuSO_4$ and sodium ascorbate to yield Cu^+ *in situ*.[38] To this end, 5 mg of $mPEG_{5000}$-*b*-p($HPMAmLac_2$-*r*-5% AzEMA) and 1.1 mg of DOX-propGA3 (2 equiv to azide) were dissolved in 90 μL DMF. Then, $CuSO_4$ (0.1–1 equiv to DOX-propGA3) and sodium ascorbate (1 equiv to $CuSO_4$) dissolved in 10 μL water were added. After stirring at room temperature for 24 h under nitrogen, the polymer was precipitated by addition of the mixture to an excess of diethyl ether and collected by centrifugation and drying under nitrogen.

DOX-propGA3 was also coupled to the polymer in a ratio of 1 mol of DOX-propGA3 per mol of polymer. Briefly, 50 mg of $mPEG_{5000}$-p($HPMAmLac_n$-*r*-AzEMA) (with 10 or 20 mol % AzEMA relative to total monomers) and 2.5 mg DOX-propGA3 (1 equiv to mole of polymer, 5% w/w) were dissolved in 900 μL DMF. Next, $CuSO_4$ (1 equiv to DOX-propGA3) and sodium ascorbate (1 equiv to DOX-propGA3) dissolved in 100 μL H_2O were added, and the mixture was stirred for 48 h under a nitrogen atmosphere. Finally, the synthesized polymers were isolated by precipitation in diethyl ether, dissolved in water, and dialyzed (membrane cutoff 12–14 kDa) against water for at least 24 h, and finally recovered by freeze–drying.

Determination of the Critical Micelle Temperature (CMT). The CMT of the different polymers was determined by the change in turbidity of an aqueous solution of each polymer with temperature using a Shimadzu UV2450 UV/vis spectrometer, essentially as described previously.[39] The polymers were dissolved in 120 mM ammonium acetate buffer (pH 5.0) at 0 °C at a concentration of 2 mg/mL. The turbidity at 650 nm was measured every 0.2 °C during heating (1 °C/min). Onsets on the *X*-axis, obtained by extrapolation of the turbidity–temperature curves during heating to turbidity zero, were considered as the CMT.

Micelle Formation by the Rapid Heating Procedure. Micelles were formed via the "rapid heating" procedure as described previously.[40] In brief, the block copolymers were dissolved in 120 mM ammonium acetate buffer (pH 5.0) at a concentration of 5 mg/mL at 0 °C. Next, the solution (1 mL) was rapidly heated to 50 °C using a water bath under vigorously shaking to form micelles.

Determination of the Critical Micelle Concentration (CMC). The CMC of the azide containing block copolymers before and after conjugation of DOX-propGA3 was determined using pyrene as a fluorescent probe.[41] Micelles of the different block copolymers were formed as described in the Materials and Methods section. The micellar dispersions were cooled to room temperature and subsequently diluted with 120 mM ammonium acetate buffer (pH 5.0) yielding different polymer concentrations ranging from 10^{-5} to 2.5 mg/mL. Next, 5 μL of pyrene dissolved in acetone (concentration 0.18 mM) was added to 0.75 mL polymer solution. The samples were incubated overnight at room temperature in the dark to allow equilibration. Prior to the measurements, the solutions were incubated at 37 °C for at least 15 min.

Fluorescence excitation spectra of pyrene were obtained using a Horiba Fluorolog fluorometer (90° angle). The excitation spectra were recorded at 37 °C from 300 to 360 nm with the emission wavelength at 390 nm. The excitation and emission band slits were 4 and 2 nm, respectively. The intensity ratio of I_{338}/I_{333} was plotted against the polymer concentration to determine the CMC.[41] The excitation spectra of pyrene incorporated in empty mPEG-p$HPMAmLac_2$ micelles and in micelles with conjugated DOX-propGA3 were identical (data not shown), demonstrating that doxorubicin did not confound the CMC measurements.

Dynamic Light Scattering. DLS measurements were performed using a Malvern CGS-3 multiangle goniometer with a JDS Uniphase 22mW He–Ne laser operating at 632 nm, an optical fiber-based detector and a digital LV/LSE-5003 correlator. Autocorrelation functions were analyzed by the cumulants method (fitting a single exponential to the correlation function to obtain the mean size and the PDI) and the CONTIN routine (fitting a multiple exponential to the correlation function to obtain the distribution of particle sizes). All measurements were performed at a 90° angle.

Release of Doxorubicin from Polymeric Micelles. Micelles were formed as described in the Materials and Methods section, using $mPEG_{5000}$-*b*-p(90%$HPMAmLac_n$-*r*-10%AzEMA) containing 1 equiv of DOX-propGA3 per mol of total polymer. The release of DOX and DOX-GA3 from the micelles and also from free DOX-propGA3 (37 °C) was followed in time by diluting the samples with PBS pH 7.4 containing 0.1% (w/v) bovine serum albumin (final free DOX-propGA3 concentration 10 μg/mL, final polymer concentration in micelles 200 μg/mL corresponding to 10 μg/mL of DOX-propGA3) followed by addition of β-glucuronidase (final enzyme concentration was 20 μg/mL) and incubation at 37 °C. As a control, samples in the same buffer were also prepared, without the addition of the enzyme. Next, samples were taken at regular time points and analyzed with gradient HPLC chromatography, using a C18 Sunfire column and potassium phosphate buffer pH 3 (20 mM) with 5% acetonitrile as eluent A (75–60% in 12 min) and 100% acetonitrile as eluent B (25–40% in 12 min). The detection was performed using fluorescence at 480 nm excitation and 560 emission. The retention time of doxorubicin was 3 min, of

Table 1. Characteristics of mPEG$_{5000}$-*b*-p(HPMAmLac$_2$-*r*-AzEMA) with Various AzEMA Contents, as Well as Size Characteristics of the Micelles Formed by the Rapid Heating Procedure[40]

	mol % AzEMA (NMR)	M_n (NMR, kDa)	M_w(GPC, kDa)	M_n(GPC, kDa)	M_w/M_n (GPC)	CMT (°C)	Z_{ave} (nm)	PDI
mPEG-*b*-p(80%HPMAmLac$_2$-*r*-20%AzEMA)	9.7	15.2	27.5	13.1	2.1	1.8	51	0.11
mPEG-*b*-p(85%HPMAmLac$_2$-*r*-15%AzEMA)	6.5	16.6	27.8	13.9	2.0	3.0	51	0.11
mPEG-*b*-p(90%HPMAmLac$_2$-*r*-10%AzEMA)	4.6	18.4	26.4	14.9	1.8	3.6	53	0.07
mPEG-*b*-p(95%HPMAmLac$_2$-*r*-5%AzEMA)	2.9	20.1	24.3	12.0	2.0	4.7	54	0.10
mPEG-*b*-p(98%HPMAmLac$_2$-*r*-2%AzEMA)	-	21.1	25	13.7	1.8	5.2	63	0.05
mPEG-*b*-p(100%HPMAmLac$_2$-*r*-0%AzEMA)	-	22.4	27	15.9	1.7	5.3	61	0.04

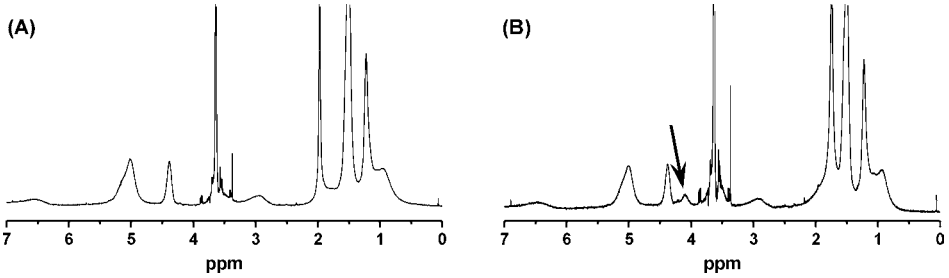

Figure 1. NMR spectra ($CDCl_3$) of (A) mPEG$_{5000}$-*b*-p(HPMAmLac$_2$) block copolymer and (B) mPEG$_{5000}$-*b*-p(80%HPMAmLac$_2$-*r*-20%AzEMA).

DOX-GA3 6.6 min, and of DOX-propGA3 10 min. Calibration was performed by injecting different volumes (0.3−50 μL) of a doxorubicin standard to result in a range of 0.016−2.76 nmol of DOX. The injection volume of the unknowns was 50 μL, and the concentrations (μmol/mL) of DOX and DOX-GA3 were calculated by comparing the area under the curve of the peak at 3 and 6.6 min, respectively, and comparing it to the doxorubicin calibration curve.

***In Vitro* Cytotoxicity.** Human head and neck squamous carcinoma (HNSCC) cells UM-SCC-14C (abbreviated as 14C, developed by Dr. T.E. Carey, Ann Arbor, MI, USA) were seeded into 96-well plates (4×10^3 cells/well) and cultured overnight in Dulbecco's Modified Eagle's medium (DMEM, Invitrogen, Breda, The Netherlands) containing L-glutamine (2 mM), 7.5% (v/v) fetal bovine serum, penicillin (100 IU/ml), streptomycin (100 μg/mL), at 37 °C in a humidified atmosphere containing 5% CO_2. Next, the medium was replaced with 100 μL of medium with or without β-glucuronidase (20 μg/mL). Dilutions of samples of DOX, DOX-GA3, and DOX-propGA3 and of mPEG-*b*-(90%pHPMAmLac$_2$-*r*-10% AzEMA) micelles with covalently bound DOX-propGA3 were prepared in HEPES buffer 5 mM, pH 7.4, to obtain final DOX concentrations 0.02−43.8 μM. Next, the dilutions were added in quadriplicates (50 μL), followed by incubation for 72 h. The viability of the adhered cells was determined using a WST-1 assay (Cell Proliferation Reagent WST-1, Roche Diagnostics GmbH, Roche Applied Science, 68298 Mannheim, Germany).

RESULTS AND DISCUSSION

Synthesis of 2-Azidoethyl Methacrylate (AzEMA). 2-Azidoethyl methacrylate (AzEMA) was synthesized as shown in Scheme 1, using a slightly modified previously published procedure.[42] In the first step, 2-bromoethanol was reacted with sodium azide and the formed compound, 2-azidoethanol, was obtained in a yield of 55% after extraction in ethyl acetate. The structure of 2-azidoethanol was confirmed by NMR analysis that showed a shift of the methylene proton peaks of the product compared to the starting material (2-bromoethanol) from 3.9 to 3.8 and from 3.5 to 3.4 (Figure S1, Supporting Information). Next, the alcohol moiety of 2-azidoethanol was reacted with methacryloyl chloride resulting in 2-azidoethyl methacrylate (AzEMA) which was obtained in a yield of 73%. After methacrylation and purification, the 3 additional peaks at 6.2, 5.6, and 2 ppm of the protons of the methacrylate group appeared. In addition, the peak at 3.8 ppm of the methyl proton adjacent to the alcohol was shifted to 4.3 ppm, indicating connection via esterification (Figure S2, Supporting Information). Lastly, IR analysis of AzEMA showed the characteristic peak of the azide at 2106 cm^{-1} [43,44] (Figure 2A).

Synthesis of mPEG$_{5000}$-*b*-p(HPMAmLac$_2$-*r*-AzEMA) Block Copolymer. mPEG$_{5000}$-*b*-p(HPMAmLac$_2$-*r*-AzEMA) with various amounts of AzEMA (2−20 mol % relative to total monomers) were synthesized by free radical polymerization using HPMAmLac$_2$ and AzEMA as monomers and mPEG$_2$ABCPA as radical macroinitiator (Scheme 2), using the same procedure as reported previously.[22] The characteristics of the synthesized polymers are summarized in Table 1. The different polymers were obtained in good yields (64−77%), and had M_n values (calculated using ^{1}H NMR analysis using eq 2) ranging from 15 to 22 kDa and M_w/M_n of around 2 (GPC analysis), which is a normal molecular weight distribution for polymers synthesized with this type of free radical polymerization.[22] Importantly, ^{1}H NMR analysis of block copolymers containing AzEMA revealed a unique resonance peak at 4.1 ppm (Figure 1B, arrow) which was not observed in the ^{1}NMR spectrum of the block copolymer without AzEMA (Figure 1A), and is assigned to the methyl protons at the β position to the azide group. The peaks of the methyl protons adjacent to the azide group at 3.5 ppm could not be clearly seen due to their overlap with the PEG peak. By integrating the peak at 4.1 ppm, the mol % AzEMA in the different copolymers was calculated using eq 1 and was found to be around 50% of the feed ratio (Table 1). IR analysis also showed a peak at 2100 cm^{-1} characteristic for the azide vibration,[43,45] the intensity of which also increased with increasing AzEMA content (Figure 2).

dx.doi.org/10.1021/bc2003499 | *Bioconjugate Chem.* 2011, 22, 2519−2530

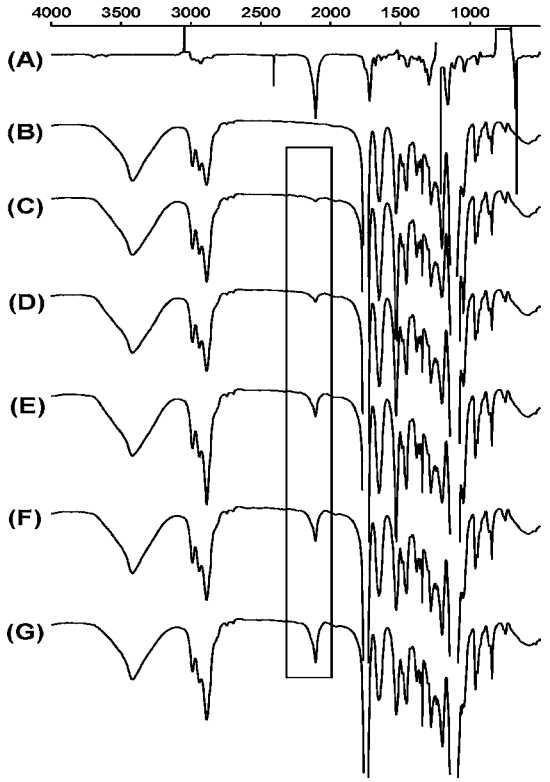

Figure 2. IR spectra of AzEMA monomer (A) and mPEG$_{5000}$-*b*-p(HPMAmLac$_2$-*r*-AzEMA) block copolymers containing 0% (B), 2% (C), 5% (D), 10% (E), 15% (F), and 20% (G) AzEMA.

The critical micelle temperature of the copolymer without azide was 5.3 °C (Table 1) which is in agreement with previous publications.[22] The CMT decreased with increasing AZEMA content, indicating that the incorporation of AzEMA increased the hydrophobicity of the copolymer, as expected from the incorporation of the more hydrophobic AzEMA (C log *P* of AzEMA was 2.31, versus −0.27 for HPMAmLac$_2$, as calculated by *ChemDraw Ultra 12.0* software).

Micelles of mPEG-*b*-p(HPMAmLac$_2$-*r*-AzEMA) copolymers were formed by a rapid heating procedure[40] and the particle size was measured by DLS (Table 1). The copolymers formed small micelles with average diameters 50−60 nm and a low PDI (~0.1).

Click-Coupling of DOX-propGA3 to mPEG$_{5000}$-*b*-p-(HPMAmLac$_2$-*r*-AzEMA). The conjugation of DOX-propGA3 to the polymer was carried out, as depicted in Scheme 3, using mPEG$_{5000}$-*b*-p(HPMAmLac$_2$-*r*-AzEMA) containing 5 mol % azide. CuBr as well as $CuSO_4$/sodium ascorbate were used as catalysts, and the reaction was performed for 24 h at room temperature in DMF. A ratio of 1:2 azide to alkyne was used. The reaction progress was monitored by IR (by the decrease of the azide vibration at 2100 cm^{-1}). When 0.1−1 equiv CuBr was used as a catalyst, no conjugation was observed, as evidenced from the observation that the intensity of the azide peak had not dropped (data not shown). Neither 0.1 nor 0.5 equiv of $CuSO_4$ in the presence of ascorbate was sufficient to accomplish the reaction (Figure 3B and C). The click reaction only occurred when the amount of $CuSO_4$ was increased to 1 equiv (relative to DOX-propGA3), as indicated by the complete disappearance of the azide peak (Figure 3D). This shows that, in the case of click reaction of the steric hindered doxorubicin molecule with the bulky polymer, *in situ* reduction

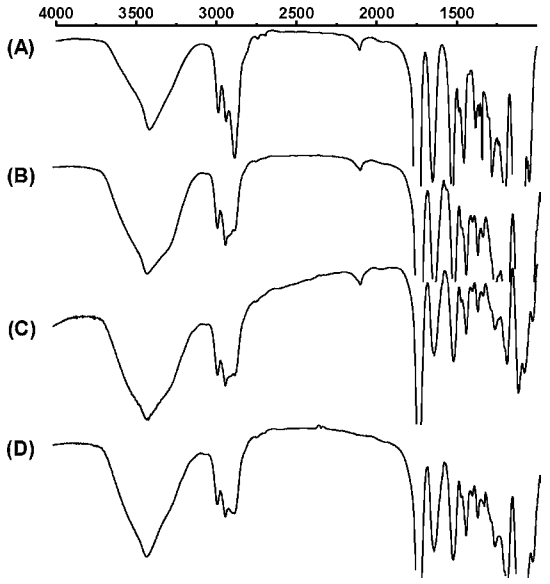

Figure 3. IR spectra of mPEG$_{5000}$-*b*-p(95%HPMAmLac$_2$-*r*-5%AzEMA) (A) and of conjugates of mPEG$_{5000}$-*b*-p(95%HPMAmLac$_2$-*r*-5% AzEMA) with DOX-propGA3 using a azide/alkyne ratio of 1:2 and 0.1 equiv (B), 0.5 equiv (C), and 1 equiv (D) of $CuSO_4$ (relative to DOX-propGA3) as a catalyst, in the presence of sodium ascorbate (1 equiv to $CuSO_4$).

of Cu^{2+} by ascorbate is required, as well as the presence of at least 1 equiv of $CuSO_4$.

The polymer−drug conjugate synthesized as described above, however, lost its thermosensitivity and was insoluble in water, most probably due to the high amount of hydrophobic DOX-propGA3 coupled, which makes it unsuitable to prepare micelles with the rapid-heating method (see Materials and Methods). Therefore, coupling reactions were carried out using diblock copolymers containing 20% and 10% AzEMA and 1 equiv of DOX-propGA3 per mol of polymer (corresponding to 5% w/w ratio of DOX-propGA3 to polymer), in the presence of 1 equiv $CuSO_4$ and ascorbate (relative to doxorubicin). IR analysis showed that the azide peak did not disappear completely, as expected from the excess of azide used (spectra not shown). The polymers obtained were freely soluble in water at 0 °C and had an CMT of ~1 °C (Table 3) which is slightly lower than the CMT of the azide polymer used for derivatization (CMT of 2−3 °C, Table 2). This decrease in CMT is probably due to the increased hydrophobicity of the polymer due to its conjugation with DOX-propGA3.

To prove convincingly that doxorubicin was covalently linked to the polymeric backbone, GPC analysis was performed using dual UV (480 nm, characteristic absorption for doxorubicin) and RI detection. The chromatograms of the polymers obtained by the conjugation using the polymer with 10% azide groups are shown in Figure 4. Figure 4A shows that mPEG$_{5000}$-*b*-p(90%HPMAmLac$_2$-*r*-10%AzEMA) eluted at 18 min (RI detection), while no signal was observed at 480 nm. On the other hand, DOX-propGA3 eluted at 22.3 min (both RI and UV (480 nm) detection) (Figure 4B). GPC analysis of the conjugate showed that the majority of DOX-propGA3 eluted at 16.6 min (UV detection, Figure 4C), which is close to the retention time of the polymer (17.8 min, Figure 4C; the slight shift in the signal peaks can be attributed to the GPC system, where the RI-detector was serially attached to the UV detector). A small peak was observed at the retention time of

Table 2. Results of Conjugation of mPEG$_{5000}$-*b*-p(HPMAmLac$_2$-*r*-AzEMA) to DOX-propGA3 (1 equiv DOX per mol of polymer) Using 1:1 $CuSO_4$/Sodium Ascorbate (1 equiv to DOX-propGA3) as Catalyst

polymer used	% conjugation	CMT (°C) (before/after DOX conjugation)	CMC (mg/mL) (before/after DOX conjugation)	Z_{ave} (nm)	PDI
mPEG-*b*-p(80%HPMAmLac$_2$-*r*-20%AzEMA)	95.8	1.8/0.9	0.06/0.08	48	0.06
mPEG-*b*-(90%pHPMAmLac$_2$-*r*-10%AzEMA)	94.1	3.6/0.4	0.04/0.08	51	0.07
mPEG-*b*-pHPMAmLac$_2$	-	5.3/-	0.03/-	61	0.04

free DOX-propGA3 (22.3 min, Figure 4C). From the area under the curve of the free and coupled DOX-propGA3 peaks, it was calculated that the coupling efficiency was 94%

Table 3. Concentration (μM) Required for 50% of Inhibition (EC_{50}) of Viability of 14C Cells Induced by Doxorubicin, DOX-GA3, DOX-propGA3, and Micelles with Covalently Bound DOX-propGA3 after Incubation for 72 h

	EC_{50} (μM DOX)	EC_{50} (μM DOX) with β-glucuronidase
DOX	0.10 ± 0.06	0.16 ± 0.02
DOX-GA3	21.3 ± 4.8	0.19 ± 0.04
DOX-propGA3	44.8 ± 3.2	0.63 ± 0.02
DOX-propGA3 micelles	47.3 ± 6.2	0.22 ± 0.01

(Table 2), indicating almost quantitative conjugation. Similar results were obtained when the polymer containing 20% azide was used (Table 2). When a physical mixture of polymer with DOX-propGA3 was analyzed using GPC (22% w/w DOX-propGA3 to polymer), the peaks of the polymer at 18 min (RI detection) and of DOX-propGA3 at 22.3 min (UV detection) were visible, but no shift of the DOX-propGA3 UV peak was observed (Figure 4D), indicating that the conjugation observed was due to the covalent coupling of DOX-propGA3 to the polymer.

To check whether the synthesized conjugates were still able to form micelles, the rapid heating procedure was applied and the critical micelle concentration was determined using pyrene as a fluorescent probe. The CMC was determined from the plot of the intensity ratio I_{338}/I_{333} as a function of polymer concentration (Figure 5). A red shift was observed with increasing polymer concentration, indicating the partitioning of pyrene in the hydrophobic environment of the micellar core.[41,46] Azide-containing polymers had a slightly higher CMC than the polymer without azide (Table 2). This is most probably because the azide containing polymers have slightly lower molecular weights (Table 1) and the CMC is known to increase with decreasing molecular weight of the core forming block.[47,48]

Conjugates of DOX with the azide block copolymers were shown to have a slightly higher CMC than the corresponding azide copolymers without DOX (Table 2). This was unexpected, as these conjugates possessed lower CMTs than the azide polymers, indicating that the thermosensitive block became more hydrophobic upon DOX conjugation. The log*P* of DOX-mGA3, which is structurally similar to DOX-propGA3, has been measured and it was found to be 1.27 (and 0.52 for DOX),[17] which demonstrates the lipophilic nature of the prodrug. It has been shown previously that the CMC decreases when a more hydrophobic block is used.[48] Therefore, we anticipated a lower CMC for these DOX-conjugated polymers. The fact that we did not observe a lower CMC for these conjugates might be due to the detection limit of the determination method used using pyrene partition.

Micelles formed by DOX-propGA3 conjugated polymers (10% or 20% azide content) above their CMC were characterized for size and polydispersity using DLS. Small (50 nm) monodisperse micelles were formed (Table 2) and DOX containing polymers had similar size characteristics as the corresponding polymers without DOX (Table 1), showing that the coupling of DOX-propGA3 to the polymer backbone did not affect the size of the micelles formed.

Release of Doxorubicin from mPEG$_{5000}$-*b*-p(HPMAmLac$_2$-*r*-AzEMA) Micelles with Conjugated DOX-propGA3. As has been shown previously, the methyl ester derivative of DOX-GA3 (DOX-mGA3) releases DOX in two steps: First, DOX-mGA3 is converted into DOX-GA3 via cleavage of the methyl ester group (by hydrolysis at pH 7.4 or by esterase activity), and next, DOX-GA3 is enzymatically converted into DOX by β-glucuronidase.[17] The first step is necessary, because DOX-mGA3 is a not good substrate for β-glucuronidase. As DOX-propGA3 differs from DOX-mGA3 only by the presence of a propargyl group instead of a methyl group, the same behavior was anticipated. The conversion of DOX-propGA3 to DOX was studied by incubating the prodrug in PBS/0.1% BSA buffer pH 7.4 with or without β-glucuronidase (20 μg/mL) and measurement using HPLC (Figure 6A). DOX-propGA3 showed a peak in the HPLC chromatogram at 10 min, while the retention time of doxorubicin was 3 min and that of DOX-GA3 6.6 min. Upon incubation of DOX-propGA3 for 24 h at pH 7.4 (37 °C), its peak at 10 min shifted to 6.6 min (Figure 6A), which demonstrates that DOX-propGA3 was quantitatively converted to the more hydrophilic DOX-GA3 derivative by hydrolysis of the propargyl ester. On the other hand, upon incubation for 24 h at pH 7.4 (37 °C) in the presence of β-glucuronidase, the DOX-propGA3 peak completely shifted to 3 min (Figure 6A), which shows that the prodrug was converted into DOX. The amount of DOX released was calculated from the peak area and compared with the DOX content of the prodrug, and it was demonstrated that after 24 h incubation at pH 7.4 (37 °C) in the presence of enzyme the conversion was almost quantitative (90%). Therefore, it is concluded that upon incubation in buffer pH 7.4 containing β-glucuronidase, DOX-propGA3 is converted into DOX-GA3 by hydrolysis of the propargyl ester, which is then subsequently converted into DOX by β-glucuronidase activity (Scheme 4).

HPLC analysis of the micelles with conjugated DOX-propGA3 before any incubation showed no peaks corresponding with DOX-propGA3, DOX-GA3, or DOX (Figure 6B), demonstrating again that no significant amount of unreacted DOX-propGA3 remained after conjugation and purification. Upon incubation for 24 h at pH 7.4 (37 °C), a peak at 6.6 min was observed corresponding with DOX-GA3, indicating that the conjugated DOX-propGA3 was converted to free DOX-GA3, most probably due to ester hydrolysis (Scheme 4). When the incubation was performed in the presence of β-glucuronidase, this peak shifted to 3 min indicating conversion into doxorubicin

dx.doi.org/10.1021/bc2003499 | *Bioconjugate Chem.* 2011, 22, 2519–2530

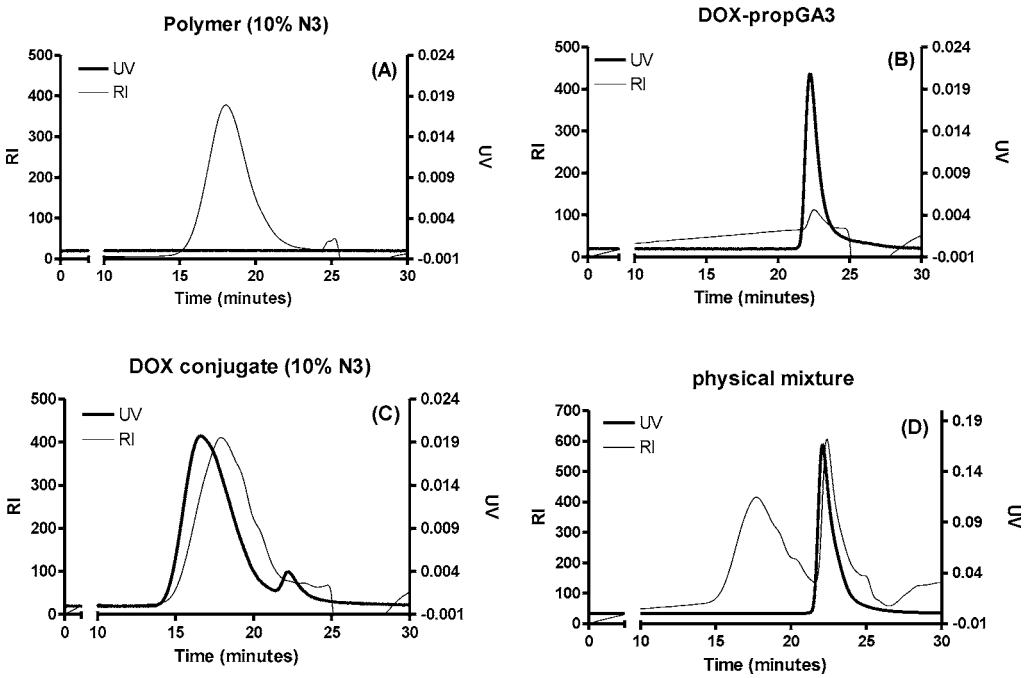

Figure 4. GPC analysis with dual RI and UV (480 nm) detection of (A) mPEG-*b*-p(90%HPMAm-*r*-10%AzEMA), (B) DOX-propGA3, (C) click conjugate of mPEG-*b*-p(90%HPMAm-*r*-10%AzEMA) with DOX-propGA3, and (D) physical mixture of mPEG-*b*-p(90%HPMAm-*r*-10%AzEMA) and DOX-propGA3.

by the enzyme (Figure 6B, Scheme 4). Determination of the amount of DOX released from the micelles demonstrated that after 5 days incubation in the presence of *β*-glucuronidase DOX was still being released from the micelles and had reached 35% of the total content, while less than 5% release was observed in the absence of *β*-glucuronidase (Figure 7A). Moreover, a 10-fold higher amount of enzyme gave no difference in release kinetics of DOX (results not shown). It has been shown in the past that the methyl ester of DOX-GA3 (DOX-mGA3) is not a good substrate for *β*-glucuronidase and that conversion into DOX only occurs after hydrolysis of the ester bond that yields DOX-GA3.[17] Consequently, since a 10-fold higher amount of enzyme did not accelerate the release, it is most likely that the conversion of polymer-bound DOX-propGA3 to DOX-GA3 via hydrolysis is the rate-limiting factor for the generation of DOX. To further clarify this, the release of DOX-GA3 from the micelles in the absence and presence of enzyme was also investigated. It was observed that in the absence of *β*-glucuronidase the area under the curve of DOX-GA3 peak (6.6 min) increased in time and reached 40% of the total content after 5 days (Figure 7B), demonstrating that DOX-GA3 was released from the micelles with no conversion to DOX. The rate of DOX-GA3 formation in

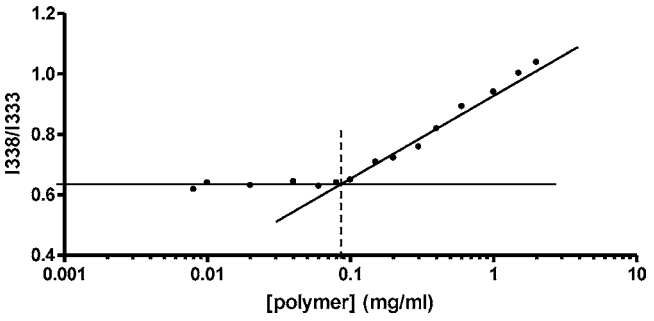

Figure 5. I_{338}/I_{333} for pyrene as a function of concentration of conjugate of DOX-propGA3 with mPEG-*b*-p(90%HPMAmLac$_2$-*r*-10% AzEMA). The CMC was calculated from the intersection of the horizontal line at low polymer concentrations with the tangent of the curve at high polymer concentrations.

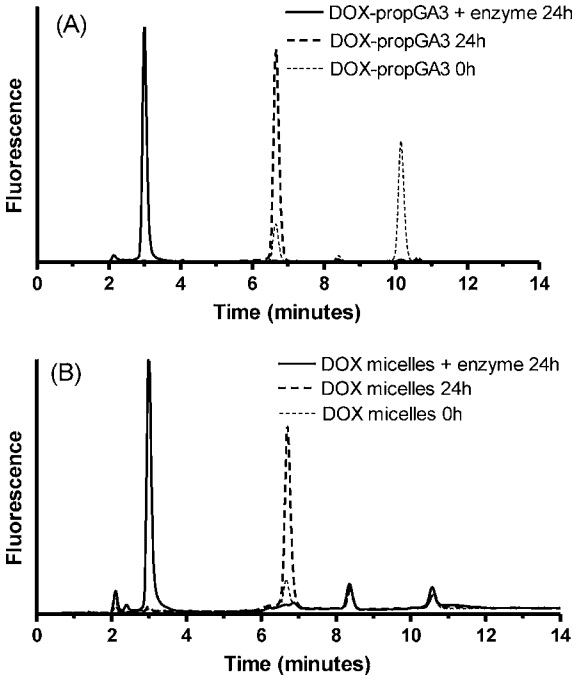

Figure 6. HPLC analysis of (A) DOX-propGA3 (10 *μ*g/mL) and of (B) micelles with covalently bound DOX-propGA3 (200 *μ*g/mL of polymer) before incubation (0 h), after 24 h incubation in a PBS/BSA 0.1% pH 7.4 buffer, and after 24 h incubation in a PBS/BSA 0.1% pH 7.4 buffer containing 20 *μ*g/mL *β*-glucuronidase. Doxorubicin had a retention time of 3 min, DOX-GA3 6.6 min, and DOX-propGA3 10 min.

dx.doi.org/10.1021/bc2003499 | *Bioconjugate Chem.* 2011, 22, 2519–2530

Scheme 4. Conversion of Free or Polymer-Bound DOX-propGA3 to DOX-GA3 by Chemical Hydrolysis and/or by Esterases and Subsequent Release of DOX by β-Glucuronidase

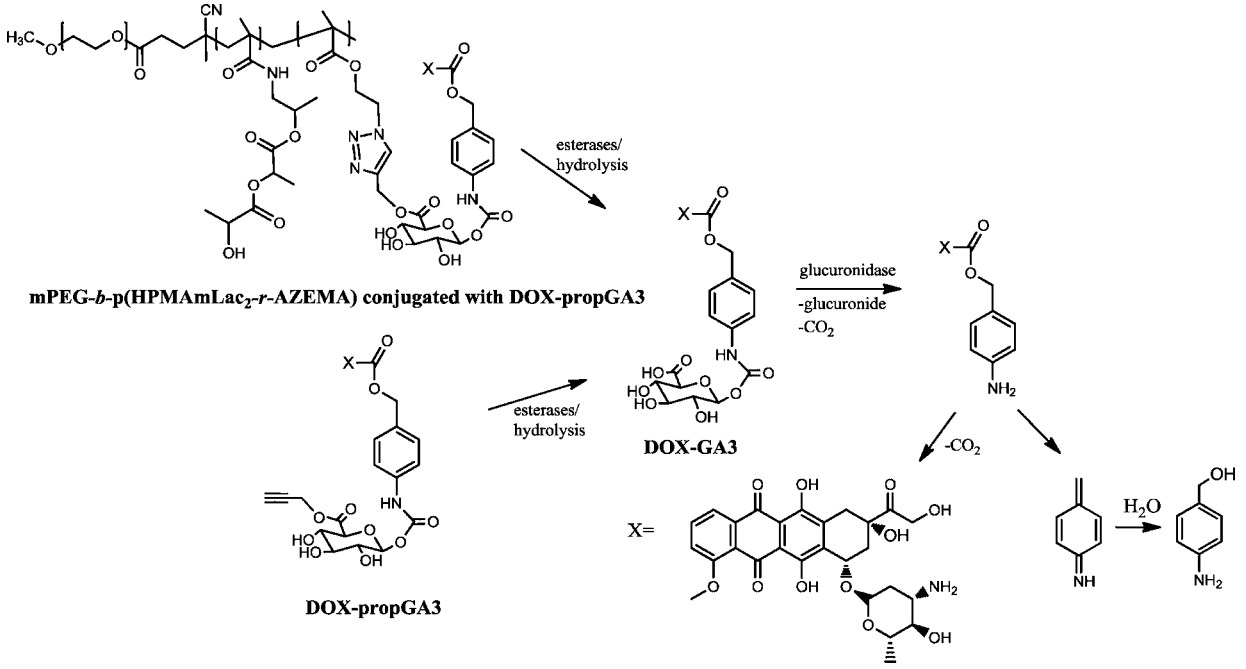

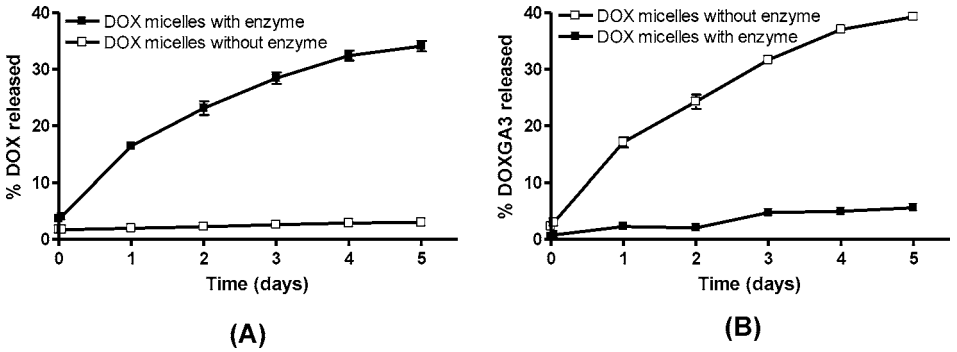

Figure 7. HPLC analysis of the release of DOX (A) and DOX-GA3 (B) from micelles (200 μg/mL polymer) with covalently bound DOX-propGA3 in the presence and absence of β-glucuronidase.

the absence of enzyme (Figure 7B) was similar to the rate of DOX formation in the presence of enzyme (Figure 7A) indicating that once DOX-GA3 was produced it was directly converted into DOX by the enzyme (also because in the presence of β-glucuronidase less than 10% DOX-GA3 was recovered). These observations confirm the hypothesis that the hydrolysis of the ester bond to convert polymer-bound DOX-propGA3 to free DOX-GA3 is the limiting factor for the DOX generation. Likely, the generation of DOX-GA3 from polymer-bound DOX-propGA3 is slower than from free DOX-propGA3 because the water activity in the hydrophobic core of the micelles is lower than in bulk, and therefore, the hydrolysis process slows down.[23] Besides, the hydrolysis of the ester bond might be slower due to the increased steric hindrance caused by its close proximity to the polymer backbone.

***In Vitro* Cytotoxicity.** The cytotoxicity of DOX, DOX-GA3, DOX-propGA3, and micelles with covalently bound DOX-propGA3 (prepared using mPEG-*b*-(90%pHPMAmLac$_2$-*r*-10%AzEMA)) against 14C cells was investigated both in the presence and in the absence of β-glucuronidase (Figure 8 and Table 3). Micelles without DOX showed no cytotoxicity (data not shown), which is in line with previous results.[27,30] As expected, DOX showed the highest cytotoxicity (EC_{50} of 0.10 μM; Table 3 and Figure 8A). In the presence of β-glucuronidase, approximately the same cytotoxicity was observed (Figure 8A; EC_{50} of 0.16 μM; Table 3), demonstrating that the enzyme did not affect the cytotoxic effect of free DOX. On the other hand, when cells were incubated with DOX-GA3 and DOX-propGA3 in the absence of enzyme, the observed cytotoxicity was about 200−300 times less compared to DOX (Table 3; EC_{50} 21.3 μM for DOX-GA3, 44.8 μM for DOX-propGA3). These results are in agreement with previous publications[17] and demonstrate that, in the culture medium, a minimum amount of DOX was formed from the prodrugs, which was also demonstrated in the previous section (Figure 7) after incubation in a pH 7.4 buffer. When DOX-GA3 and DOX-propGA3 were incubated with cells in medium containing β-glucuronidase, an increased cytotoxic effect was observed (Table 3, EC_{50} 0.19 μM for DOX-GA3, 0.63 μM for DOX-propGA3) which was in the same range as that of DOX. Similar results have been published for DOX-mGA3 and DOX-GA3.[17,18] It has been shown that DOX-mGA3 is not a good

dx.doi.org/10.1021/bc2003499 | *Bioconjugate Chem.* 2011, 22, 2519−2530

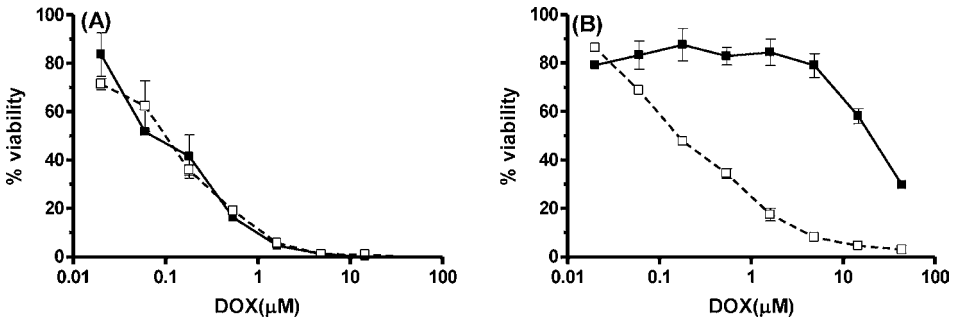

Figure 8. Viability of 14C cells in medium with (□) or without (■) β-glucuronidase (20 μg/mL), incubated for 72 h with (A) Doxorubicin and (B) mPEG-*b*-(90%pHPMAmLac$_2$-*r*-10%AzEMA) polymeric micelles with covalently bound DOX-propGA3.

substrate for β-glucuronidase and that conversion only occurs after hydrolysis of the ester bond,[17] so the same behavior is most likely also valid for DOX-propGA3. It can be assumed that, either due to chemical hydrolysis in the culture medium (as was observed in buffer; see previous section) or due to the presence of esterases, DOX-propGA3 was converted to DOX-GA3, which was then converted into DOX by β-glucuronidase.

Figure 8B shows the cytotoxicity results of 14C cells exposed to polymeric micelles with covalently bound DOX-propGA3 in the absence and presence of β-glucuronidase (Figure 8B). Without the addition of enzyme, a low cytotoxicity effect was observed (EC_{50} 47.3 μM), demonstrating again, as observed after incubation in a pH 7.4 buffer (Figure 7), that in the medium only a low amount of DOX was released. Importantly, in the presence of β-glucuronidase, the cytostatic activity became very similar to that of DOX (Figure 8B, EC_{50} 0.22 μM). This finding is rather interesting, as in the previous section it was demonstrated that the release of DOX from the micelles is incomplete even after 5 days incubation in the presence of β-glucuronidase at pH 7.4. This was attributed to the incomplete release of DOX-GA3 from the micellar core as compared to the release from free DOX-propGA3 (due to slow hydrolysis in the hydrophobic micellar core), which resulted in slow DOX release, because only DOX-GA3 is a good substrate for β-glucuronidase and not the polymer-bound drug. In previous studies, it has been demonstrated that conversion of DOX-mGA3 to DOX-GA3 is much faster in the presence of esterase than in buffer ($t_{1/2}$ was ~20 min in the presence of carboxylesterase and 10 h in buffer pH 7.4).[17] Therefore, most probably, esterases in the culture medium contributed to the complete conversion of polymer-bound DOX-propGA3 to DOX-GA3, which was then subsequently converted into DOX by the β-glucuronidase. This enzymatic conversion can occur by penetration of esterases into the core of the micelles or by cleavage of the produg form free polymer chains which are in dynamic equilibrium, a mechanism suggested for the enzymatic degradation of PEG-Oligo(ε-caprolactone) micelles by lipase.[49] As a result of both the chemical and enzymatic hydrolysis, micelles with covalently bound DOX-propGA3 released DOX-GA3 in the culture medium, which was then converted to DOX by the action of β-glucuronidase.

CONCLUSION

A novel, azide-modified block copolymer mPEG$_{5000}$-*b*-p-(HPMAmLac$_2$-*r*-AzEMA) was synthesized and a propargyl derivative of the DOX-GA3 prodrug (DOX-propGA3) was coupled to this copolymer via click chemistry with a very high (~90%) coupling efficiency. Micelles formed by this polymer were small (50 nm) and monodisperse. The glucuronide spacer of the prodrug used is known to be selectively cleaved by β-glucuronidase, an enzyme present in necrotic tumor areas. Indeed, it was shown that DOX micelles demonstrated the same cytotoxicity as free DOX when incubated with 14C cells in the presence of serum and β-glucuronidase. Therefore, improved *in vivo* antitumor efficacy is anticipated.

ASSOCIATED CONTENT

Supporting Information

Additional figures as described. This material is available free of charge via the Internet at http://pubs.acs.org.

AUTHOR INFORMATION

Corresponding Author

*Tel.: +31 30 253 6964; fax: +31 30 251 7839. E-mail: w.e.hennink@uu.nl.

Author Contributions

⊥Authors contributed equally.

ACKNOWLEDGMENTS

This project was funded by MEDITRANS, an Integrated Project funded by the European Commission under the "nanotechnologies and nano-sciences, knowledge-based multi-functional materials and new production processes and devices" (NMP), thematic priority of the Sixth Framework Program.

REFERENCES

(1) Momparler, R. L., Karon, M., Siegel, S. E., and Avila, F. (1976) Effect of adriamycin on DNA, RNA, and protein synthesis in cell free systems and intact cells. *Cancer Res. 36*, 2891−2895.

(2) Fornari, F. A., Randolph, J. K., Yalowich, J. C., Ritke, M. K., and Gewirtz, D. A. (1994) Interference by doxorubicin with DNA unwinding in MCF-7 breast tumor cells. *Mol. Pharmacol. 45*, 649−656.

(3) Hershman, D. L., McBride, R. B., Eisenberger, A., Wei, Y. T., Grann, V. R., and Jacobson, J. S. (2008) Doxorubicin, cardiac risk factors, and cardiac toxicity in elderly patients with diffuse B-cell non-Hodgkin's lymphoma. *J. Clin. Oncol. 26*, 3159−3165.

(4) Carvalho, C., Santos, R. X., Cardoso, S., Correia, S., Oliveira, P. J., Santos, M. S., and Moreira, P. I. (2009) Doxorubicin: The good, the bad and the ugly effect. *Curr. Med. Chem. 16*, 3267−3285.

(5) Patil, R. R., Guhagarkar, S. A., and Devarajan, P. V. (2008) Engineered nanocarriers of doxorubicin: A current update. *Crit. Rev. Ther. Drug 25*, 1−61.

(6) Torchilin, V. P. (2007) Targeted pharmaceutical nanocarriers for cancer therapy and imaging. *AAPS J. 9*, E128−E147.

(7) Drummond, D. C., Meyer, O., Hong, K., Kirpotin, D. B., and Papahadjopoulos, D. (1999) Optimizing liposomes for delivery of chemotherapeutic agents to solid tumors. *Pharmacol. Rev. 51*, 691−743.

(8) Matsumura, Y., and Kataoka, K. (2009) Preclinical and clinical studies of anticancer agent-incorporating polymer micelles. *Cancer Sci. 100*, 572−579.
(9) Kopecek, J., and Kopeckova, P. (2010) HPMA copolymers: Origins, early developments, present, and future. *Adv. Drug Delivery Rev. 62*, 122−149.
(10) Lammers, T. (2010) Improving the efficacy of combined modality anticancer therapy using HPMA copolymer-based nanomedicine formulations. *Adv. Drug Delivery Rev. 62*, 203−230.
(11) Sirova, M., Mrkvan, T., Etrych, T., Chytil, P., Rossmann, P., Ibrahimova, M., Kovar, L., Ulbrich, K., and Rihova, B. (2010) Preclinical evaluation of linear HPMA-doxorubicin conjugates with pH-sensitive drug release: Efficacy, safety, and immunomodulating activity in murine model. *Pharm. Res. 27*, 200−208.
(12) Duncan, R., Seymour, L. W., O'Hare, K. B., Flanagan, P. A., Wedge, S., Hume, I. C., Ulbrich, K., Strohalm, J., Subr, V., Spreafico, F., Grandi, M., Ripamonti, M., Farao, M., and Suarato, A. (1992) Preclinical evaluation of polymer-bound doxorubicin. *J. Controlled Release 19*, 331−346.
(13) Ulbrich, K., and Subr, V. (2010) Structural and chemical aspects of HPMA copolymers as drug carriers. *Adv. Drug Delivery Rev. 62*, 150−166.
(14) Kratz, F., Muller, I. A., Ryppa, C., and Warnecke, A. (2008) Prodrug strategies in anticancer chemotherapy. *ChemMedChem 3*, 20−53.
(15) Kratz, F., Ajaj, K. A., and Warnecke, A. (2007) Anticancer carrier-linked prodrugs in clinical trials. *Expert Opin. Invest. Drug 16*, 1037−1058.
(16) Houba, P. H. J., Leenders, R. G. G., Boven, E., Scheeren, J. W., Pinedo, H. M., and Haisma, H. J. (1996) Characterization of novel anthracycline prodrugs activated by human β-glucuronidase for use in antibody-directed enzyme prodrug therapy. *Biochem. Pharmacol. 52*, 455−463.
(17) Graaf, M. D., Nevalainen, T. J., Scheeren, H. W., Pinedo, H. M., Haisma, H. J., and Boven, E. (2004) A methylester of the glucuronide prodrug DOX-GA3 for improvement of tumor-selective chemotherapy. *Biochem. Pharmacol. 68*, 2273−2281.
(18) Houba, P. H. J., Boven, E., van Der Meulen-Muileman, I. H., Leenders, R. G. G., Scheeren, J. W., Pinedo, H. M., and Haisma, H. J. (2001) A novel doxorubicin-glucuronide prodrug DOX-GA3 for tumour-selective chemotherapy: Distribution and efficacy in experimental human ovarian cancer. *Br. J. Cancer 84*, 550−557.
(19) de Graaf, M., Boven, E., Scheeren, H. W., Haisma, H. J., and Pinedo, H. M. (2002) Beta-glucuronidase-mediated drug release. *Curr. Pharm. Design 8*, 1391−1403.
(20) Talelli, M., Rijcken, C. J. F., van Nostrum, C. F., Storm, G., and Hennink, W. E. (2010) Micelles based on HPMA copolymers. *Adv. Drug Delivery Rev. 62*, 231−239.
(21) van Nostrum, C. F., Neradovic, D., Soga, O., and Hennink, W. E. (2006) Polymeric micelles with transient stability: A novel delivery concept. *ACS Sympos. Ser. 923*, 40−54.
(22) Soga, O., van Nostrum, C. F., Ramzi, A., Visser, T., Soulimani, F., Frederik, P. M., Bomans, P. H. H., and Hennink, W. E. (2004) Physicochemical characterization of degradable thermosensitive polymeric micelles. *Langmuir 20*, 9388−9395.
(23) Neradovic, D., van Steenbergen, M. J., Vansteelant, L., Meijer, Y. J., van Nostrum, C. F., and Hennink, W. E. (2003) Degradation mechanism and kinetics of thermosensitive polyacrylamides containing lactic acid side chains. *Macromolecules 36*, 7491−7498.
(24) Rijcken, C. J. F., Soga, O., Hennink, W. E., and van Nostrum, C. F. (2007) Triggered destabilisation of polymeric micelles and vesicles by changing polymers polarity: An attractive tool for drug delivery. *J. Controlled Release 120*, 131−148.
(25) Maeda, H., Wu, J., Sawa, T., Matsumura, Y., and Hori, K. (2000) Tumor vascular permeability and the EPR effect in macromolecular therapeutics: A review. *J. Controlled Release 65*, 271−284.
(26) Rijcken, C. J. F., Hofman, J. W., van Zeeland, F., Hennink, W. E., and van Nostrum, C. F. (2007) Photosensitiser-loaded biodegradable polymeric micelles: Preparation, characterisation and in vitro PDT efficacy. *J. Controlled Release 124*, 144−153.
(27) Soga, O., Van Nostrum, C. F., Fens, M., Rijcken, C. J. F., Schiffelers, R. M., Storm, G., and Hennink, W. E. (2005) Thermosensitive and biodegradable polymeric micelles for paclitaxel delivery. *J. Controlled Release 103*, 341−353.
(28) Talelli, M., Rijcken, C. J. F., Lammers, T., Seevinck, P. R., Storm, G., Van Nostrum, C. F., and Hennink, W. E. (2009) Superparamagnetic iron oxide nanoparticles encapsulated in biodegradable thermosensitive polymeric micelles: Toward a targeted nanomedicine suitable for image-guided drug delivery. *Langmuir 25*, 2060−2067.
(29) Rijcken, C. J., Snel, C. J., Schiffelers, R. M., van Nostrum, C. F., and Hennink, W. E. (2007) Hydrolysable core-crosslinked thermosensitive polymeric micelles: Synthesis, characterisation and in vivo studies. *Biomaterials 28*, 5581−5593.
(30) Talelli, M., Iman, M., Varkouhi, A. K., Rijcken, C. J. F., Schiffelers, R. M., Etrych, T., Ulbrich, K., van Nostrum, C. F., Lammers, T., Storm, G., and Hennink, W. E. (2010) Core-crosslinked polymeric micelles with controlled release of covalently entrapped doxorubicin. *Biomaterials 31*, 7797−7804.
(31) Talelli, M., Rijcken, C. J. F., Oliveira, S., van der Meel, R., van Bergen en Henegouwen, P. M. P., Lammers, T., van Nostrum, C. F., Storm, G., and Hennink, W. E. (2011) Nanobody − shell functionalized thermosensitive core-crosslinked polymeric micelles for active drug targeting. *J. Controlled Release 151*, 183−192.
(32) Kolb, H. C., and Sharpless, K. B. (2003) The growing impact of click chemistry on drug discovery. *Drug Discovery Today 8*, 1128−1137.
(33) Kolb, H. C., Finn, M. G., and Sharpless, K. B. (2001) Click chemistry: diverse chemical function from a few good reactions. *Angew. Chem., Int. Ed. 40*, 2004−2021.
(34) Van Dijk, M., Rijkers, D. T. S., Liskamp, R. M. J., Van Nostrum, C. F., and Hennink, W. E. (2009) Synthesis and applications of biomedical and pharmaceutical polymers via click chemistry methodologies. *Bioconjugate Chem. 20*, 2001−2016.
(35) Golas, P. L., and Matyjaszewski, K. (2010) Marrying click chemistry with polymerization: Expanding the scope of polymeric materials. *Chem. Soc. Rev. 39*, 1338−1354.
(36) Aben, R. W. M., Scheeren, J. W., Lambertus, M. C., Johannes, J., de Vos, D., Haisma, H. J. (2009) Esters of glucuronide prodrugs of anthracyclines and method of preparation and use in tumor-selective chemotherapy U.S. Patent 20090227617
(37) Leenders, R. G. G., Damen, E. W. P., Bijsterveld, E. J. A., Scheeren, H. W., Houba, P. H. J., Van Der Meulen-Muileman, I. H., Boven, E., and Haisma, H. J. (1999) Novel anthracycline-spacer-β-glucuronide, -β-glucoside, and β-galactoside prodrugs for application in selective chemotherapy. *Bioorg. Med. Chem. 7*, 1597−1610.
(38) Meldal, M., and Tornoe, C. W. (2008) Cu-catalyzed azide-alkyne cycloaddition. *Chem. Rev. 108*, 2952−3015.
(39) Neradovic, D., Hinrichs, W. L. J., Kettenes-van Den Bosch, J. J., and Hennink, W. E. (1999) Poly(N-isopropylacrylamide) with hydrolyzable lactic acid ester side groups: A new type of thermosensitive polymer. *Macromol. Rapid Commun. 20*, 577−581.
(40) Neradovic, D., Soga, O., van Nostrum, C. F., and Hennink, W. E. (2004) The effect of the processing and formulation parameters on the size of nanoparticles based on block copolymers of poly(ethylene glycol) and poly(N-isopropylacrylamide) with and without hydrolytically sensitive groups. *Biomaterials 25*, 2409−2418.
(41) Wilhelm, M., Zhao, C. L., Wang, Y., Xu, R., Winnik, M. A., Mura, J. L., Riess, G., and Croucher, M. D. (1991) Poly(styrene-ethylene oxide) block copolymer micelle formation in water: A fluorescence probe study. *Macromolecules 24*, 1033−1040.
(42) Zhang, Y., He, H., Gao, C., and Wu, J. (2009) Covalent layer-by-layer functionalization of multiwalled carbon nanotubes by click chemistry. *Langmuir 25*, 5814−5824.
(43) Tsarevsky, N. V., Bencherif, S. A., and Matyjaszewski, K. (2007) Graft copolymers by a combination of ATRP and two different consecutive click reactions. *Macromolecules 40*, 4439−4445.

(44) Hideki, M., Ryohei, K., Chunhong, Z., Ryosuke, S., Toshifumi, S., and Toyoji, K. (2009) Synthesis of well-defined macrocyclic poly-(δ-valerolactone) by "Click Cyclization. *Macromolecules 42*, 5091−5096.
(45) Li, L. Y., He, W. D., Li, J., Zhang, B. Y., Pan, T. T., Sun, X. L., and Ding, Z. L. (2010) Shell-cross-linked micelles from PNIPAM-b -(PLL)2 Y-shaped miktoarm star copolymer as drug carriers. *Biomacromolecules 11*, 1882−1890.
(46) Kwon, G., Naito, M., Yokoyama, M., Okano, T., Sakurai, Y., and Kataoka, K. (1993) Micelles based on AB block copolymers of poly(ethylene oxide) and poly(β-benzyl L-aspartate). *Langmuir 9*, 945−949.
(47) Torchilin, V. P. (2007) Micellar nanocarriers: Pharmaceutical perspectives. *Pharm. Res. 24*, 1−16.
(48) Allen, C., Maysinger, D., and Eisenberg, A. (1999) Nano-engineering block copolymer aggregates for drug delivery. *Colloids Surf., B 16*, 3−27.
(49) Carstens, M. G., van Nostrum, C. F., Verrijk, R., de Leede, L. G. J., Crommelin, D. J. A., and Hennink, W. E. (2008) A mechanistic study on the chemical and enzymatic degradation of PEG-Oligo(ε-caprolactone) micelles. *J. Pharm. Sci. 97*, 506−518.

Bioconjugate Chemistry

Article

pubs.acs.org/bc

Activatable Optical Imaging with a Silica-Rhodamine Based Near Infrared (SiR700) Fluorophore: A comparison with cyanine based dyes

Thomas E. McCann,[†] Nobuyuki Kosaka,[†] Yuichiro Koide,[‡] Makoto Mitsunaga,[†] Peter L. Choyke,[†] Tetsuo Nagano,[‡] Yasuteru Urano,[§] and Hisataka Kobayashi*[,†]

[†]Molecular Imaging Program, Center for Cancer Research, National Cancer Institute, National Institutes of Health, 10 Center Drive, Bethesda, Maryland 20892-1088, United States

[‡]Graduate School of Pharmaceutical Sciences and [§]Medicine, The University of Tokyo, 7-3-1 Hongo, Bunkyo-ku, Tokyo 113-0033, Japan

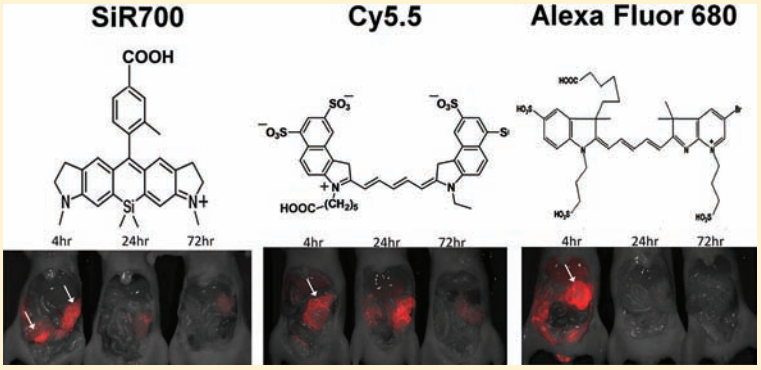

ABSTRACT: Optical imaging is emerging as an important tool to visualize tumors. However, there are many potential choices among the available fluorophores. Optical imaging probes that emit in the visible range can image superficial tumors with high quantum yields; however, if deeper imaging is needed then near-infrared (NIR) fluorophores are necessary. Most commercially available NIR fluorophores are cyanine based and are prone to nonspecific binding and relatively limited photostability. Silica-containing rhodamine (SiR) fluorophores represent a new class of NIR fluorophores, which permit photoactivation via H-dimer formation as well as demonstrate improved photostability. This permits higher tumor-to-background ratios (TBRs) to be achieved over longer periods of time. Here, we compared an avidin conjugated with SiR700 (Av-SiR700) to similar compounds based on cyanine dyes (Av-Cy5.5 and Av-Alexa Fluor 680) in a mouse tumor model of ovarian cancer metastasis. We found that the Av-SiR700 probe demonstrated superior quenching, enabling activation after binding-internalization to the target cell. As a result, Av-SiR700 had higher TBRs compared to Av-Cy5.5 and better biostability compared to Av-Alexa Fluor 680.

INTRODUCTION

Target-specific optical imaging probes are promising tools in the molecular imaging of cancer. Optical imaging probes offer high sensitivity, low cost, and portability, and do not entail exposure to ionizing radiation. However, optical imaging is limited by poor tissue penetration. The use of fluorophores that absorb and emit in the near-infrared (NIR) range have less absorption and scatter from tissue, permitting deeper tissue penetration than is possible with fluorophores based on visible light. Another critical feature of an optical imaging probe is that it has high tumor-to-background ratios (TBRs). One way to achieve this is to have extremely high binding affinities for the tumor and rapid excretion of the unbound compound. Another, more practical approach, is to activate the fluorescence only upon binding to the target tissue; thus, unbound conjugates yield a minimal signal while target-bound conjugates have a high signal leading to very high TBR. Optical imaging is unique in its ability to be activatable as opposed to radionuclide imaging that is "always on".[1,2] A number of quenching mechanisms have been implicated in fluorescence activation. One method is the formation of H-dimers using xanthene based fluorophores, such as rhodamine; H-dimer formation of these fluorophores leads to efficient quenching.[3]

An optical probe must also be able to withstand biodegradation after internalization since this affects the durability of the signal. Rhodamine core fluorophores generally demonstrate better photostability and biostability than cyanine-based dyes and have high fluorescence quantum yield.[4]

Thus, the optimal imaging probe is one that is highly activatable, yet photostable, and, absorbs and emits light in the NIR. While several cyanine based optical probes are commercially available, rhodamine based probes are not.

Received: July 10, 2011
Revised: October 10, 2011
Published: October 28, 2011

ACS Publications © 2011 American Chemical Society

dx.doi.org/10.1021/bc2003617 | *Bioconjugate Chem.* 2011, 22, 2531–2538

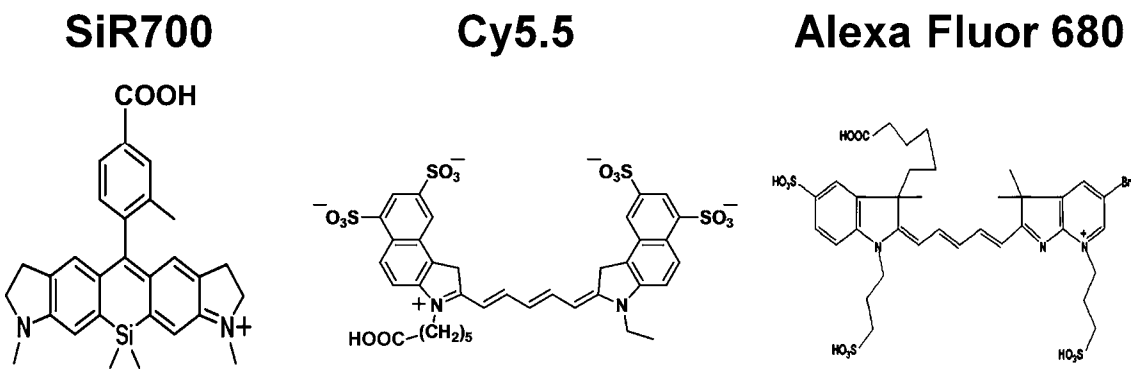

Figure 1. Chemical structures of NIR fluorophores compared in this study. SiR700 is a NIR fluorophore synthesized on a silica rhodamine core. We compared this to two commercially available NIR fluorophores synthesized using a cyanine core, Cy5.5, and Alexa Fluor 680. Carboxyl residues are modified to succinimidyl esters and used for functionalizing fluorophores.

Recently, Koide et al. described silica-containing rhodamine dyes (SiR), with excellent photophysical properties such as an emission peak at over 650 nm.[5] However, the ability of SiR dyes to quench via H-dimer formation *in vitro* and *in vivo*, while maintaining good *in vivo* photo- and biostability, has not been evaluated. Here, we compare conjugates of avidin SiR fluorophore (Av-SiR700) with two cyanine-based NIR fluorophores conjugates Av-Cy5.5 and Av-Alexa Fluor 680 (Av-Alexa680) in a mouse model of metastatic ovarian cancer during *in vivo* optical imaging.

EXPERIMENTAL PROCEDURES

Amino-Reactive NIR Fluorophores. Amino-reactive Cy5.5- and Alexa Fluor 680-succinimidyl esters were purchased from GE Healthcare (Piscataway, NJ) and Invitrogen Co. (Carlsbad, CA), respectively. The synthesis method of SiR700-succinimidyl esters has been published.[5,6] The chemical structures of all three NIR fluorophores are shown in (Figure 1).

Synthesis of Avidin-Conjugated NIR Fluorophores. Avidin (6 nmol), was purchased from Pierce Biochemical, Inc. (Milwaukee, WI), and was incubated with amino-reactive NIR fluorophores (Cy5.5 and SiR700; 60 nmol, Alexa680; 40 nmol) in 0.1 M phosphate buffer (pH 8.5) at room temperature for 15 min. Each mixture was purified with a Sephadex G25 column (PD-10; GE Healthcare, Piscataway, NJ). The protein concentration was determined by measuring the absorption at 280 nm with a UV−vis system (8453 UV−Visible Value System; Agilent Technologies, Santa Clara, CA). The concentration of NIR fluorophores was measured by absorption with the UV−vis system to confirm the number of fluorophore molecules conjugated to each avidin molecule.[7] The number of fluorophore molecules per all avidin conjugates was ~3.

H-Dimer Formation and Quenching Efficiency of Av-Cy5.5, Av-Alexa680, and SiR700 *in Vitro*. The quenching−dequenching characteristics of each avidin-conjugate were investigated by treating the conjugates with 5% SDS to disassociate any molecular interaction between fluorophores. The fluorescence signal intensity of each conjugate was measured with a fluorescence spectrometer before and after 5% SDS (Perkin-Elmer LS55, Perkin-Elmer, Shelton, CT). The absorption spectrum was measured with a UV−vis system (8453 UV−Visible Value System; Agilent Technologies).

Cell Culture. An established ovarian cancer cell line known to overexpress the β-D-galactose receptor, SHIN3, was used for *in vitro* fluorescence microscopy, flow cytometry, and *in vivo* optical imaging using a murine intraperitoneal disseminated ovarian cancer model. The cell lines were grown in RPMI 1640 medium (Gibco, Gaithersburg, MD) containing 10% fetal bovine serum (FBS) (Gibco), 0.03% L-glutamine at 37 °C, 100 units/mL penicillin, and 100 μg/mL streptomycin in 5% CO_2.

Fluorescence Microscopy. SHIN3 cells (1×10^4) were plated on a cover glass bottom culture well and incubated for 16 h. Then, Av-Cy5.5, Av-Alexa680, or Av-SiR700 was added to the medium (3 μg/mL), and the cells were incubated for 4 h. Cells were washed three times with phosphate-buffered saline (PBS), RPMI 1640 medium was added back to all samples not imaged immediately, and fluorescence microscopy was performed immediately (T0), 24, 48, or 72 h later using an Olympus BX61 microscope (Olympus America Inc., Melville, NY) equipped with the following filters: excitation wavelength, 590 to 650 nm; emission wavelength, 665 to 740 nm. Transmitted light differential interference contrast (DIC) images were also acquired.

Flow Cytometry. Flow cytometry was performed to detect the *in vitro* stability of Av-Cy5.5, Av-Alexa680, and Av-SiR700 in SHIN3 cancer cells. SHIN3 cells (1×10^4) were plated on a 6 well culture plate and incubated for 16 h. Av-Cy5.5, Av-Alexa680, or Av-SiR700 was added to the medium (3 μg/mL), and the cells were incubated for 8 h. Next, the cells were washed three times with PBS, RPMI 1640 medium was replaced, and cells were trypsinized either immediately, 24, 48, or 72 h later. Then, flow cytometry was performed. A 635 nm red diode laser was used for excitation, and fluorescence signal from cells was collected using a 661/16 nm band-pass filter. Cells were analyzed in a FACScan cytometer (Becton Dickinson, Franklin Lakes, NJ), and all data were analyzed using CellQuest software (Becton Dickinson). *In vitro* biostability of each NIR-probe was measured as the rate of change in mean fluorescence intensity (MFI) over time from 0 to 72 h.

Animal Model of Peritoneal Metastases. All procedures were carried out in compliance with the Guide for the Care and Use of Laboratory Animal Resources (1996), National Research Council, and approved by the institutional Animal Care and Use Committee. The tumor xenografts were established by intraperitoneal injection of 4×10^6 SHIN3 cells suspended in 200 μL of PBS in female nude mice (National Cancer Institute Animal Production Facility, Frederick, MD). Experiments with tumor-bearing mice were performed at 14−17 days after injection of the cells.

dx.doi.org/10.1021/bc2003617 | *Bioconjugate Chem.* 2011, 22, 2531−2538

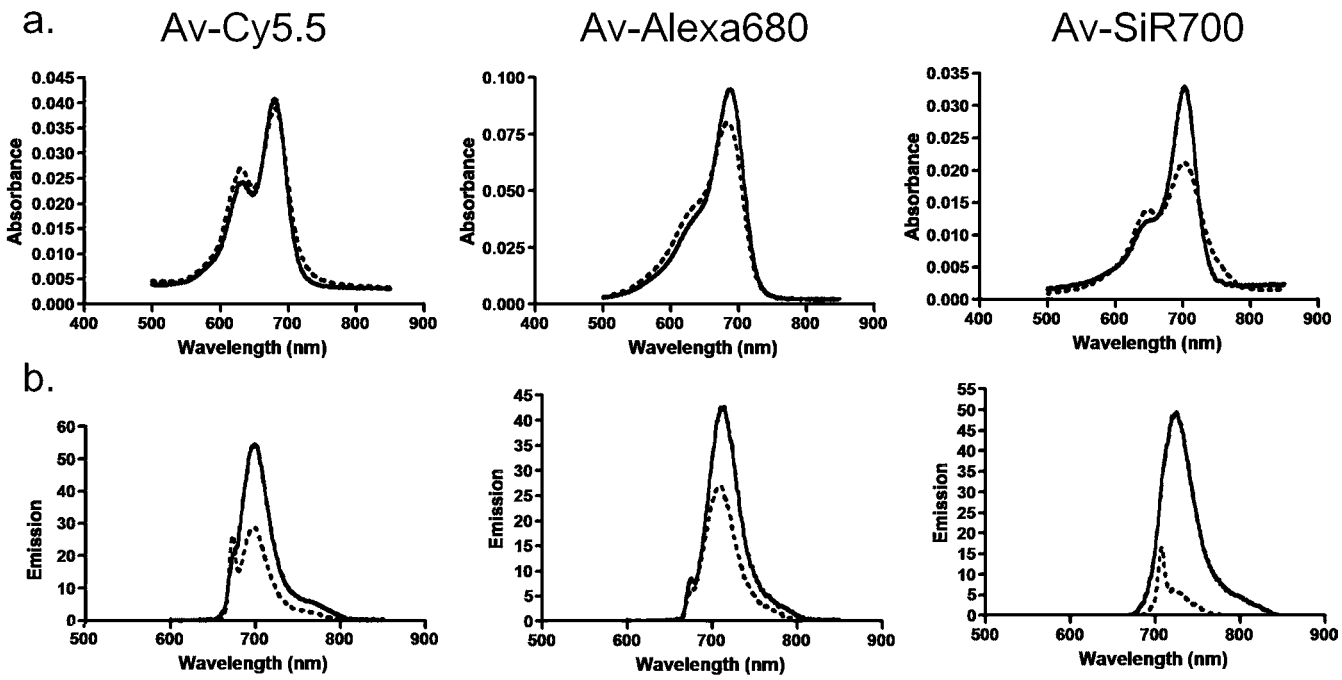

Figure 2. (a) Absorbance spectra of NIR imaging probes, consisting of a NIR fluorophore conjugated to avidin, without SDS (dashed line) and with SDS (solid line). The blue-shifted peak on the Av-Cy5.5 and Av-SiR700 curves without SDS represents H-dimer formation. Av-Alexa680 does not demonstrate H-dimer formation. Following SDS treatment, an increase in the Av-SiR700 monomer peak is characteristic of the dissociation of xanthene dimers forming excitons. (b) Emission spectra of NIR imaging probes without (dashed line) and with (solid line) SDS. Emission is increased following SDS treatment for all fluorophores; however, Av-SiR700 demonstrates the greatest increase in emission following SDS.

***In Vivo* Fluorescence Imaging.** Twenty-five micrograms each of Av-Cy5.5, Av-Alexa680, and Av-SiR700 was diluted in 300 μL of PBS and injected into the peritoneal cavities of tumor bearing mice. Then, 4, 24, or 72 h after intraperitoneal injection mice were euthanized with carbon dioxide inhalation. Immediately afterward, the abdominal cavities were exposed, and the 3 mice, each representing a different time point, were placed side by side on a nonfluorescent plate to compare fluorescence intensity for each NIR-probe over time. NIR fluorescence imaging was performed with the Pearl Imager (LI-COR Biosciences, Lincoln, NE). The instrument is a light-tight chamber equipped with a cooled charge-coupled device (CCD) camera. Illumination was provided by a 685 nm diode laser, and the peak emission band is at 720 nm. Images were acquired and processed using Pearl Cam Software v1.0 (LI-COR Biosciences).

Determination of TBRs for Each NIR Probe. NIR fluorescence images of the whole abdominal cavity were obtained as described above. The TBRs of each NIR probe were determined by placing a region of interest (ROI) over tumors labeled 4 h after injection of NIR probe and an ROI of equal size over surrounding normal abdominal tissue of the same animal. ROI total signal intensity for tumors was then compared with total signal intensity from the ROI of the surrounding tissue. Image processing was performed with Pearl Cam Software v1.0.

***Ex Vivo* Fluorescence Imaging For Quantitation.** Tumors were removed after *in vivo* imaging. Tumor explants were placed on a nonfluorescent plate, and NIR imaging was performed and processed.

Semi-Quantitative Analysis of *In Vivo* Stability of NIR-Probes. NIR fluorescence images of the tumor explants were obtained as described above. The *in vivo* stability of each NIR probe was compared using semiquantitative analysis. Briefly, ROIs were drawn around each tumor implant, and the average fluorescence intensity was used to quantify signal for each NIR probe at 4, 24, and 72 h after injection of the NIR probe. *In vivo* stability of each NIR probe over time was determined by comparing the percent decrease in the MFI relative to the MFI measured at the 4 h time point.

Statistical Analysis. Comparison of TBR between NIR probe and *in vivo* stability for each probe over time was done using one-way ANOVA with Tukey's multiple comparisons post-test. All statistical analysis was performed using GraphPad Prism, version 4.0c, for Macintosh (GraphPad Software, San Diego CA, www.graphpad.com).

RESULTS

Av-SiR700 Demonstrates H-Dimer Formation and Efficient Quenching *in Vitro*. The absorbance spectra of Av-Cy5.5, Av-Alexa680, and Av-SiR700 are displayed in Figure 2a. A blue-shifted absorbance peak representing H-dimer formation was observed for all three conjugates. The addition of SDS was used to dissociate the H-dimers. Following SDS addition, the absorption of Av-SiR700 demonstrated an increase in absorption of the monomer peak and a decrease in the blue-shifted H-dimer peak. Alternatively, Av-Cy5.5 and Av-Alexa680 demonstrated decreases in the H-dimer peak after the addition of SDS; however, there were small changes in the absorbance of the monomer peak. The amount of H-dimer formation was determined by the change in absorption of the H-dimer absorption peak relative to the monomer peak for all Av-Cy5.5, Av-Alexa680, and Av-SiR700 before and after the dissociation of H-dimers by the addition of SDS as described previously.[8] The H-dimer ratios for Av-Cy5.5, Av-Alexa680, and Av-SiR700 were 1.16, 1.29, and 2.13, respectively.

The amount of signal quenching from H-dimer formation can be appreciated by the amount of fluorescence activation

dx.doi.org/10.1021/bc2003617 | *Bioconjugate Chem.* 2011, 22, 2531–2538

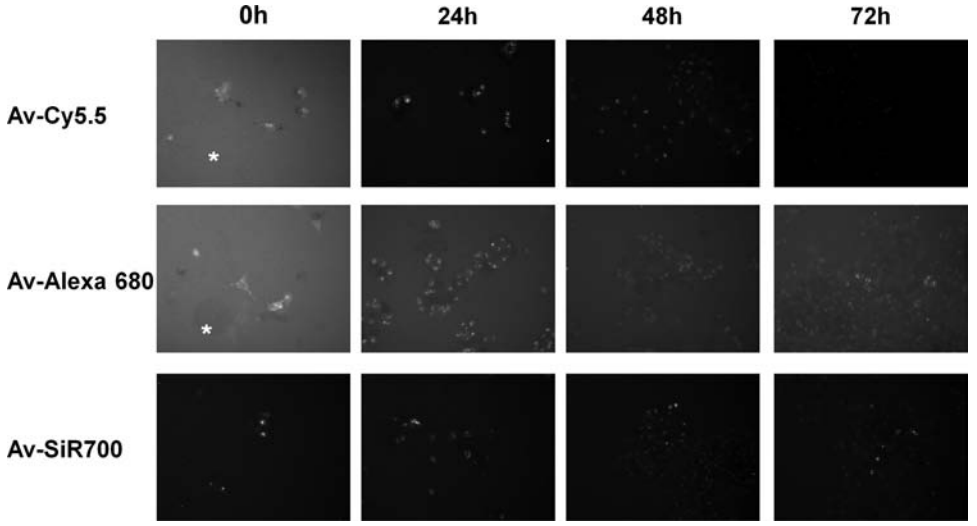

Figure 3. Serial fluorescence microscopy images of SHIN3 cells following incubation with NIR probes. SHIN3 cells were incubated with each NIR imaging probe for 4 h, and fluorescent microscopy was performed immediately (T0) and at 24, 48, and 72 h after thorough washing with PBS. At T0, SHIN3 cells could be identified after treatment with each probe, but Av-Cy5.5 and Av-Alexa680 demonstrated considerable background signal represented by fluorescence detected where there were no cells (asterisks). 24, 48, and 72 h demonstrate a gradual decrease in fluorescent signal for each NIR probe. Exposure time: Av-Cy5.5 and Av-SiR700 = 200 ms, and Av-Alexa680 = 500 ms.

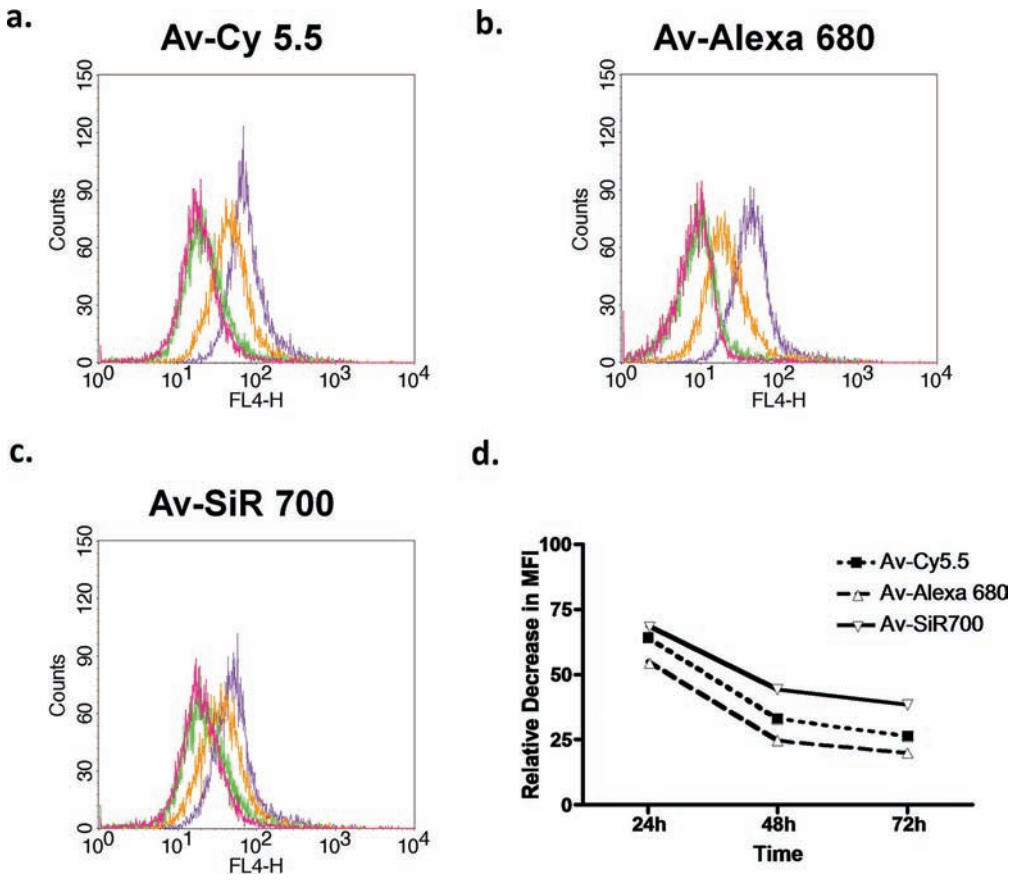

Figure 4. Flow cytometry analysis of SHIN3 cells immediately (purple), 24 h (orange), 48 h (green), and 72 h (magenta) after PBS wash and removal of (a) Av-Cy5.5, (b) Av-Alexa680, or (c) Av-SiR700, which demonstrates fluorescent signal degradation over time. Then, the amount of MFI degradation relative to T0 was compared (d). Av-SiR700 demonstrates less of a decrease in MFI from T0 than Av-Cy5.5 and Av-Alexa680 at all time points.

observed after the addition of SDS. Av-Cy5.5, Av-Alexa680, and Av-SiR700 all demonstrate an increase in fluorescence intensity after the addition of SDS (Figure 2b). The ratio of peak fluorescence intensity after SDS addition to peak fluorescence intensity before SDS addition for Av-Cy5.5, Av-Alexa680, and Av-SiR700 was 1.9, 1.58, and 8.35, respectively.

***In Vitro* Stability of NIR Probes.** *Fluorescence Microscopy.* After 4 h of incubation with 3 μg/mL of either Av-Cy5.5,

dx.doi.org/10.1021/bc2003617 | *Bioconjugate Chem.* 2011, 22, 2531–2538

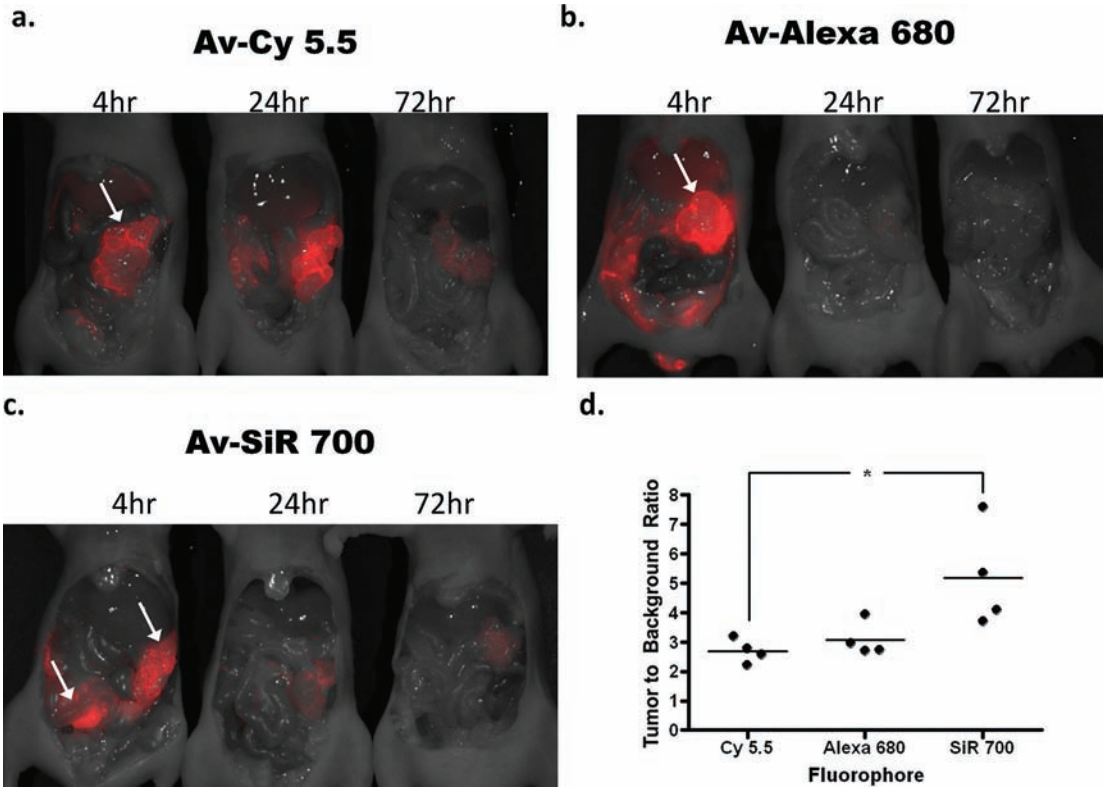

Figure 5. *In vivo* fluorescence images of tumor-bearing mice 4, 24, or 72 h after intraperitoneal injection of either (a) Av-Cy5.5, (b) Av-Alexa680, or (c) Av-SiR700. Images clearly identify SHIN3 tumors within the abdomen (arrows). Images clearly demonstrate the degradation of each NIR imaging probe over time. Interestingly, Av-Cy5.5 appears to demonstrate an increase in fluorescence intensity of the tumor from 4 to 24 h after Av-Cy5.5 injection. Whole body *in vivo* images were then used to calculate the TBR for each NIR imaging probe at 4 h after injection. ROIs were drawn around the tumors, and ROIs of the same size were drawn over the adjacent abdomen to determine the background signal. This is represented graphically (d), demonstrating that Av-SiR700 has a relatively higher TBR than Av-Alexa680 but that Av-SiR700 has a significantly greater TBR than Av-Cy5.5, ($p < 0.05$).

Av-Alexa680, or Av-SiR700, live cell imaging demonstrated intracellular uptake of each imaging probe documented by discrete intracellular punctuate signals representing probe uptake by lysosomes (Figure 3). At the initial time point (T0), images of SHIN3 cells using Av-Cy5.5 and Av-Alexa680 demonstrate high background signal due to nonspecific binding of Av-Cy5.5 and Av-Alexa680 to areas where there were no SHIN3 cells present (asterisks). Fluorescence microscopy of SHIN3 cells labeled with Av-SiR700 at T0 demonstrated specific labeling of SHIN3 cells with minimal nonspecific binding due to H-dimer formation and quenching. Serial imaging performed at 24, 48, and 72 h after washing with PBS demonstrated a progressive decrease in signal for all three NIR probes. However, Av-Cy5.5 and Av-SiR700 were brighter than Av-Alexa680 *in vitro*; therefore, live cell images were obtained at 200 ms for both Av-Cy5.5 and Av-SiR700, and images were obtained at 500 ms for Av-Alexa680.

Flow Cytometry. To evaluate the *in vitro* NIR imaging probe stability after target binding, we performed FACS on SHIN3 cells after 8 h of incubation with either Av-Cy5.5 or Av-Alexa680, or Av-SiR700. Then, we performed serial FACS analysis at 24, 48, and 72 h after the removal of each NIR imaging probe from the culture medium. The corresponding histograms are shown (Figure 4a–c). The MFI values for Av-Cy5.5, Av-Alexa680, and Av-SiR700 were used to determine the relative decrease in fluorescence signal (Figure 4d). Time course analysis was performed expressing MFI over time as a percentage of MFI at 0 h, and MFI values decreased for each NIR fluorophore by 35.8%, 44.9%, and 31%, respectively, at 24 h. At 48 h, the decrease in MFI from MFI at 0 h for Av-Cy5.5, Av-Alexa680, and Av-SiR700 was 67%, 75.3%, and 55.8%, respectively. After 72 h, the decrease in fluorescent intensity for each of the NIR probes from baseline was 73.7%, 80.1%, and 61.6%, respectively.

Assessment of NIR Probes *in Vivo*. To evaluate the *in vivo* characteristics of each NIR imaging probe, Av-Cy5.5, Av-Alexa680, or Av-SiR700 were injected into the peritoneal cavities of mice with disseminated peritoneal SHIN3 ovarian cancer implants, and side by side *in vivo* fluorescent images of the entire exposed abdomen were obtained at 4, 24, or 72 h after NIR imaging probe injection (Figure 5a–c). TBRs were determined by drawing an ROI over tumors and drawing an ROI of equal size over a nontumor-bearing area adjacent to the tumor within the abdominal cavity. The TBR for each NIR imaging probe is graphically represented (Figure 5d). The average TBRs of tumors targeted with Av-Cy5.5, Av-Alexa680, and Av-SiR700 at 4 h after the administration of each imaging probe was 2.7, 3.1, and 5.2, respectively. Av-SiR700 demonstrated the highest relative TBR of the NIR imaging probes we tested, but the TBR calculated for Av-SiR700 was only statistically significantly different compared to that of Av-Cy5.5 ($p < 0.05$).

To evaluate the *in vivo* stability of each NIR imaging probe, we removed tumors labeled with each NIR imaging probe and placed them on a nonfluorescent plate. Tumor explants for each NIR imaging probe were imaged side by side to compare

dx.doi.org/10.1021/bc2003617 | *Bioconjugate Chem.* 2011, 22, 2531–2538

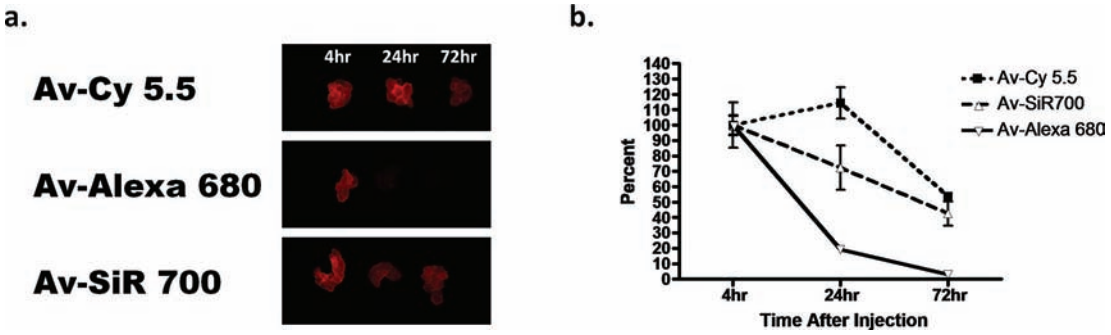

Figure 6. (a) Tumor explants following 4, 24, or 72 h after intraperitoneal injection of Av- Cy5.5, Av-Alexa680, or Av-SiR700 were used to semiquantitatively compare fluorescence intensity of each NIR imaging probe. ROIs were drawn around each tumor, and average fluorescence intensity was calculated. Then, values were calculated and graphed relative to the 4 h time point. The graph demonstrating the decrease in signal for each NIR imaging probe over time is shown (b). Av-Alexa680 demonstrates rapid decrease in fluorescence intensity with a significantly greater decrease in fluorescence intensity at 72 h than Av-Cy5.5 and Av-SiR700 with p values <0.001 and <0.01, respectively. Av-Cy5.5 demonstrates a relative increase in fluorescent intensity from 4 to 24 h but then shows a rapid decrease in fluorescence intensity. There was no significant difference in decrease in fluorescence intensity over time between Av-Cy5.5 and Av-SiR700.

Table 1. Calculated Extinction Coefficient Values of the Monomer and Dimer of Cy5.5, Alexa680, and SiR700 Conjugated with Avidin

reagents	Av-Cy5.5		Av-Alexa680		Av-SiR700	
forms	monomer	dimer	monomer	dimer	monomer	dimer
peak EC at long wavelength (nm)	250000/680	200000/680	180000/687	86000/687	100000/702	52000/702
peak EC at short wavelength (nm)	150000/629	210000/629	71000/631	110000/631	36000/647	47000/647
						(EC: cm/M)

the tumor signal at 4, 24, or 72 h after probe injection (Figure 6a). Then, an ROI was drawn around each tumor explant, and the average signal intensity was calculated and used to determine the decrease in signal over time for each NIR imaging probe. The time course showing the decrease of average intensity for each NIR imaging probe expressed as a percentage of fluorescence relative to the 4 h time point is illustrated in (Figure 6b). Change in average intensity relative to the 4 h time point at 24 h for Av-Cy5.5, Av-Alexa680, and Av-SiR700 was 114.5%, 19.3%, and 72.4%, respectively. At the 72 h time point, the decrease in average intensity for each NIR imaging probe as a percentage of the 4 h time point was 53.8%, 2.8%, and 42.6%, respectively. Av-Cy5.5 demonstrated less relative decrease in fluorescence when compared to those of Av-Alexa680 and Av-SiR700; however, the difference observed for Av-Cy5.5 was not statistically significant relative to that of Av-SiR700. Interestingly, *in vivo* average fluorescence of tumors labeled with Av-Cy5.5 demonstrated a relative increase in fluorescence between 4 and 24 h after injection. Av-Alexa680 demonstrated the lowest *in vivo* stability (compared with Av-Cy5.5 $p < 0.001$ and Av-SiR700 $p < 0.01$) at 72 h.

DISCUSSION

There are several key issues in optical probe design. The required tissue penetration of light needed for a specific clinical application is dependent on the wavelength of emitted light; NIR allows more depth of penetration than does visible light and results in lower autofluorescence. Another design parameter is the length of time that the fluorescence is required for an application, which is dependent on the biostability of the conjugate. Finally, the desired sensitivity of the agent is dependent on the TBR which can be improved by either increasing the binding affinity to the target or decreasing the background signal or both.[9−11] Advances in chemistry have led to the development of activateable optical imaging probes that have higher TBR when compared to "always on" fluorophores.[12−14] Several different mechanisms currently exist for the development of activateable optical imaging probes.

For instance, at high concentrations, xanthene derived fluorophores such as rhodamines form H-type and J-type homodimers that efficiently quench fluorescence.[15−17] H-type homodimers can also form at much lower concentrations after the fluorophore is covalently conjugated to proteins.[3] This homodimer formation induces short (H-dimer) or long (J-dimer) shifts of the fluorophore's absorbance spectra. The presence of a blue-shifted absorption peak in addition to the expected monomer absorption peak is indicative of H-dimer formation as shown in the Table 1. H-dimer absorption shifts may occur by several processes. Xanthene derived fluorophores are unique in that two identical molecules may come together to form H-homodimers with very short distances between the fluorophores. In this circumstance, the H-dimers may behave as a single quantum system that can delocalize excitation energy resulting in almost complete loss of fluorescence emission through excitation formation.[15] Once the conjugates are released from each other by changes in pH or by enzymatic processes, the fluorophores will again fluoresce. Another process by which fluorescence quenching may occur is when two fluorophores interact with each other such that they donate or accept partially excited photons from each other leading to the incoherent transfer of energy and resulting in fluorescence quenching.[16] This interaction, known as Forster resonance energy transfer (FRET), occurs at slightly larger distances up to 10 nm than H-dimer formation within 1 nm[15,16] and results in less effective quenching. Previously, activateable NIR optical imaging probes were based on cyanine core fluorophores.[18] Activateable NIR imaging probes using cyanine cores mostly

dx.doi.org/10.1021/bc2003617 | *Bioconjugate Chem.* 2011, 22, 2531−2538

utilized FRET as a means to quench fluorescence. However, with the development of SiR fluorophores, which have xanthene-based rhodamine cores, H-dimer formation readily occurs. SiR fluorophores are able to form H-dimers, as well as undergo FRET, and can be designed to utilize the photo-induced electron transfer (PeT) effect to create activatable probes.

One method of distinguishing quenching due to H-dimer formation from FRET quenching is by chemically dissociating the H-dimers and looking for a change in the absorbance characteristics.[17] The dissociation of quenched H-dimers results in a decrease in the H-dimer absorption peak and a subsequent increase in absorption of the monomer peak. However, molecules that are quenched primarily due to FRET demonstrate a minimal decrease in absorbance at the H-dimer peak; but they generally do not strongly influence the absorbance at the monomer peak. Thus, the absorbance of the monomer peak remains relatively unchanged even after dequenching, although the fluorescence signal can be activated regardless of either quenching mechanism.

In this study, SDS was used with the three agents, Av-SiR700, Av-Cy5.5, and Av-Alexa680, to detect changes in the absorbance characteristics of each imaging probe. Av-Cy5.5 initially demonstrated a blue-shifted peak in absorbance as well as the typical peak representing the monomer. However, upon addition of SDS, there was a slight increase in absorbance of the monomer peak that showed that only 32% of Cy5.5 molecules formed the H-type dimer. From this, it can be concluded that Av-Cy5.5 fluorescence quenching is mostly caused by FRET rather than the more effective H-dimer quenching. In contrast, upon addition of SDS to Av-SiR700, the decrease in the blue-shifted peak is accompanied by an increase in absorbance at the monomer peak suggesting that 80% of SiR700 molecules formed the H-type dimer resulted in the quenching of the SiR700, which is due to the formation of H-dimers, which effectively quenched fluorescence emission up to 88%.

It must be noted that different activation and quenching strategies may act independently of one another allowing the combination of multiple quenching methods. This was recently demonstrated by using H-dimer formation in combination with a pH dependent PeT quenching in the design of an activateable optical probe. This led to an optical imaging probe that demonstrated higher TBR for tumor nodules during endoscopy than an activateable probe that utilized H-dimer formation alone.[8]

Av-SiR700 demonstrated specific visualization of SHIN3 cells without nonspecific binding. However, both Av-Cy5.5 and Av-Alexa680 had nonspecific background signals observeable by fluorescence microscopy. FACS time course analysis was used to determine if Av-SiR700 was stable after endocytosis by target cells. At all time points analyzed, Av-SiR700 demonstrated less fluorophore degradation than Av-Cy5.5 and Av-Alexa680. Av-Alexa680 demonstrated the most rapid degradation of fluorescence emission of the three fluorophores tested.

The *in vivo* characteristics of Av-SiR700 were assessed by determining TBR and *in vivo* biostability by measuring degradation of fluorescence intensity over time. TBR analysis showed that Av-SiR700 demonstrated higher TBRs than either Av-Cy5.5 or Av-Alexa680. *In vivo* biostability of the fluorescence signal was determined by measuring the fluorescence intensity and graphing it as a ratio of fluorescence intensity at baseline. At 24 and 72 h after probe injection, Av-Cy5.5 had less deterioration of the fluorescence signal than either Av-Alexa680 or Av-SiR700. Av-Alexa680 had the most rapid *in vivo* degradation of fluorescence intensity. Interestingly, the tumor labeled with Av-Cy5.5 demonstrated higher fluorescence intensity at the 24 h time point than the 4 h time point. This may be explained by the nonspecific sequestration of Av-Cy5.5 in nontarget tissues with subsequent release of the imaging probe back into the circulation enabling Av-Cy5.5 continued access to the target tissue as reported with antibody-Cy5.5 conjugates in the previous study.[19] This nonspecific sequestration of Av-Cy5.5 in nontarget tissue may also be due to factors such as the probe's lipophilicity, charge, or pharmacokinetic profile.

Thus, the SiR700 demonstrates several desirable features. It is a NIR fluorophore, which utilizes a rhodamine core instead of the more typical cyanine core. Because SiR700 appears to use both H-dimer and FRET mechanisms for quenching, a more dramatic TBR could be achieved than with cyanine core fluorophores, Cy5.5, or Alexa680. Moreover, SiR700 demonstrates excellent biostability *in vivo*. Av-SiR700 was also found to have less nonspecific binding to the tissue than Av-Cy5.5, and Av-SiR700 demonstrated superior *in vivo* fluorescence stability when compared to that of Av-Alexa680. These findings suggest that SiR700, a member of a new class of NIR probes, exhibits desirable properties that could be useful for *in vivo* optical imaging.

AUTHOR INFORMATION

Corresponding Author

*Molecular Imaging Program, Center for Cancer Research, National Cancer Institute, NIH, Building 10, Room B3B69, MSC1088, Bethesda, MD 20892-1088. Phone: 301-451-4220. Fax: 301-402-3191. E-mail: kobayash@mail.nih.gov.

ACKNOWLEDGMENTS

This research was supported by the Intramural Research Program of the NIH, National Cancer Institute, Center for Cancer Research. The research year for T.M. was made possible through the Clinical Research Training Program, a public–private partnership supported jointly by the NIH and Pfizer Inc. (via a grant to the Foundation for NIH from Pfizer Inc.).

REFERENCES

(1) Urano, Y. (2008) Sensitive and selective tumor imaging with novel and highly activatable fluorescence probes. *Anal. Sci. 24*, 51–53.
(2) Weissleder, R., and Mahmood, U. (2001) Molecular imaging. *Radiology 219*, 316–333.
(3) Ogawa, M., Kosaka, N., Choyke, P. L., and Kobayashi, H. (2009) H-type dimer formation of fluorophores: a mechanism for activatable, in vivo optical molecular imaging. *ACS Chem. Biol. 4*, 535–546.
(4) Bremer, C., Ntziachristos, V., and Weissleder, R. (2003) Optical-based molecular imaging: contrast agents and potential medical applications. *Eur. Radiol. 13*, 231–243.
(5) Koide, Y., Urano, Y., Hanaoka, K., Terai, T., and Nagano, T. (2011) Development of an Si-rhodamine-based far-red to near-infrared fluorescence probe selective for hypochlorous acid and its applications for biological imaging. *J. Am. Chem. Soc. 133*, 5680–5682.
(6) Koide, Y., Urano, Y., Hanaoka, K., Piao, W., Kusakabe, M., Saito, N., Terai, T., Okabe, T., and Nagano, T. Development of NIR fluorescent dyes based on Si-rhodamine for in vivo imaging. *J. Am. Chem. Soc.*, submitted.
(7) Ogawa, M., Kosaka, N., Choyke, P. L., and Kobayashi, H. (2009) Tumor-specific detection of an optically targeted antibody combined with a quencher-conjugated neutravidin "quencher-chaser": a dual

"quench and chase" strategy to improve target to nontarget ratios for molecular imaging of cancer. *Bioconjugate Chem. 20*, 147−154.
(8) Ogawa, M., Kosaka, N., Regino, C. A., Mitsunaga, M., Choyke, P. L., and Kobayashi, H. (2010) High sensitivity detection of cancer in vivo using a dual-controlled activation fluorescent imaging probe based on H-dimer formation and pH activation. *Mol. Biosyst. 6*, 888−893.
(9) Hama, Y., Urano, Y., Koyama, Y., Bernardo, M., Choyke, P. L., and Kobayashi, H. (2006) A comparison of the emission efficiency of four common green fluorescence dyes after internalization into cancer cells. *Bioconjugate Chem. 17*, 1426−1431.
(10) Kosaka, N., Ogawa, M., Choyke, P. L., Karassina, N., Corona, C., McDougall, M., Lynch, D. T., Hoyt, C. C., Levenson, R. M., Los, G. V., and Kobayashi, H. (2009) In vivo stable tumor-specific painting in various colors using dehalogenase-based protein-tag fluorescent ligands. *Bioconjugate Chem. 20*, 1367−1374.
(11) Longmire, M., Kosaka, N., Ogawa, M., Choyke, P. L., and Kobayashi, H. (2009) Multicolor in vivo targeted imaging to guide real-time surgery of HER2-positive micrometastases in a two-tumor coincident model of ovarian cancer. *Cancer Sci. 100*, 1099−1104.
(12) Hama, Y., Urano, Y., Koyama, Y., Gunn, A. J., Choyke, P. L., and Kobayashi, H. (2007) A self-quenched galactosamine-serum albumin-rhodamineX conjugate: a "smart" fluorescent molecular imaging probe synthesized with clinically applicable material for detecting peritoneal ovarian cancer metastases. *Clin. Cancer Res. 13*, 6335−6343.
(13) Kobayashi, H., Ogawa, M., Alford, R., Choyke, P. L., and Urano, Y. (2010) New strategies for fluorescent probe design in medical diagnostic imaging. *Chem. Rev. 110*, 2620−2640.
(14) Ogawa, M., Kosaka, N., Longmire, M. R., Urano, Y., Choyke, P. L., and Kobayashi, H. (2009) Fluorophore-quencher based activatable targeted optical probes for detecting in vivo cancer metastases. *Mol. Pharmaceutics 6*, 386−395.
(15) Hernando, J., van der Schaaf, M., van Dijk, E. M. H. P., Sauer, M., García-Parajó, M. F., and van Hulst, N. F. (2003) Excitonic behavior of rhodamine dimers: a single-molecule study. *J. Phys. Chem. A 107*, 43−52.
(16) Lopez Arbeloa, I., and Ruiz Ojeda, P. (1982) Dimeric states of rhodamine B. *Chem. Phys. Lett. 87*, 556−560.
(17) Kemnitz, K., and Yoshihara, K. (1991) Entropy-driven dimerization of xanthene dyes in nonpolar solution and temperature-dependent fluorescence decay of dimers. *J. Phys. Chem. 95*, 6095−6104.
(18) Weissleder, R., Tung, C. H., Mahmood, U., and Bogdanov, A. Jr. (1999) In vivo imaging of tumors with protease-activated near-infrared fluorescent probes. *Nat. Biotechnol. 17*, 375−378.
(19) Ogawa, M., Regino, C. A., Choyke, P. L., and Kobayashi, H. (2009) In vivo target-specific activatable near-infrared optical labeling of humanized monoclonal antibodies. *Mol. Cancer Ther. 8*, 232−239.

Bioconjugate Chemistry

Article

pubs.acs.org/bc

^{90}Y labeled Phosphorodiamidate Morpholino Oligomer for Pretargeting Radiotherapy

Guozheng Liu,* Shuping Dou, Yuxia Liu, Yuzhen Wang, Mary Rusckowski, and Donald J. Hnatowich

Department of Radiology, University of Massachusetts Medical School, Worcester, Massachusetts 01655, United States

ABSTRACT: While ^{188}Re has been used successfully in mice for tumor radiotherapy by MORF/cMORF pretargeting, previous radiolabeling of the amine-derivatized cMORF with ^{90}Y, a longer physical half-life nuclide, was not very successful. After developing a method involving a prepurification heating step during conjugation that increases labeling efficiency and label stability, the biodistribution of ^{90}Y-DOTA-Bn-SCN-cMORF (^{90}Y-DOTA-cMORF) was measured in normal mice and in MORF-CC49 pretargeted mice that bear LS174T tumors. Absorbed radiation doses were then estimated and compared to those estimated for ^{188}Re. The pharmacokinetics of the ^{90}Y-DOTA-cMORF in normal mice and in the pretargeted nude mice was similar to that observed previously with ^{99m}Tc- and ^{188}Re-MAG$_3$-cMORFs. While the ^{90}Y-DOTA-cMORF cleared rapidly from normal tissues, tumor clearance was very slow and tumor radioactivity accumulation was constant for at least 7 days such that the tumor/blood (T/B) ratio increased linearly from 6 to 25 over this period. Therefore, by extrapolation, normal tissue toxicities following administration of therapeutic doses of ^{90}Y may be comparable to that observed for ^{188}Re in which the T/B increased from 5 to 20. In conclusion, radiolabeling of DOTA-cMORF with ^{90}Y was improved by introducing a prepurification heating step during conjugation. The ^{90}Y-DOTA-cMORF provided a similar T/B ratio and biodistribution to that of ^{188}Re-MAG$_3$-cMORF and was retained well in the tumor pretargeted with MORF-CC49. Because of the longer physical half-life, the T/NT absorbed radiation dose ratios were improved in most organs and especially in blood.

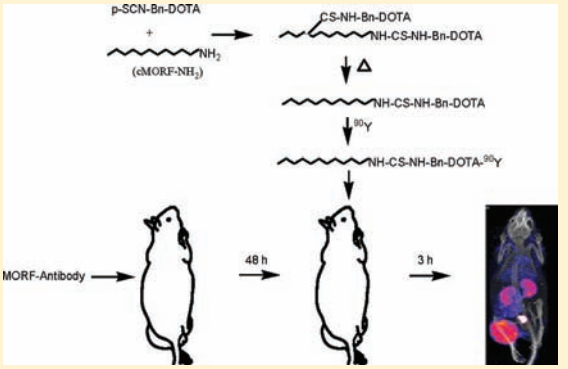

INTRODUCTION

Pretargeting using a pair of morpholino oligomers (MORF/cMORF) has been shown to be effective in preclinical studies.[1,2] A major advantage of the MORF/cMORF pretargeting approach is the ease with which the cMORF effector can be chemically modified, for example, to change chelators or linkers for different radionuclides, without affecting the cMORF/MORF affinity critical to the pretargeting approach. Thus far, this effector has been radiolabeled with ^{99m}Tc and ^{111}In for imaging and ^{188}Re for radiotherapy.[2−4] We now report on the radiolabeling of the cMORF with ^{90}Y, the biodistribution of ^{90}Y-cMORF, and the estimated absorbed radiation dose improvements using ^{90}Y-cMORF/MORF pretargeting compared to ^{188}Re-cMORF/MORF pretargeting. Although ^{90}Y and ^{188}Re have similar average beta energies (0.935 vs 0.716 MeV, respectively), under identical conditions (i.e., tumor retention and clearance from normal tissues) the longer physical half-life of ^{90}Y (64 h) compared to ^{188}Re (17 h) will provide higher tumor to organ absorbed radiation dose ratios because a larger portion of the ^{90}Y in circulation will be cleared without depositing its energy in the normal tissues.

Previous ^{90}Y labeling using *para*-isothiocyanate benzyl DOTA (i.e., p-SCN-Bn-DOTA) as a chelator was judged to be not very successful due to low labeling efficiencies.[5] A possible explanation for these marginal results may have been identified in a subsequent ^{111}In labeling of cMORF using p-SCN-Bn-DTPA as a chelator, in which heat-sensitive side conjugation products were observed.[6] Because introduction of a heating step after conjugation reaction and before purification, after subsequent labeling, was found to greatly improve label stability in that study, a similar approach was applied in this investigation using p-SCN-Bn-DOTA.

After successful ^{90}Y labeling, the biodistribution of cMORF was measured and the absorbed radiation doses to normal organs and tumor pretargeted with MORF-CC49 were estimated and compared with those previously reported for ^{188}Re-cMORF in the identical tumor model.[3,4] The dosages and timing determined to be optimal with ^{99m}Tc-cMORF[7] and used previously with ^{188}Re-cMORF[4] were again used in this study, because the antibody is the same and the blood clearance among ^{99m}Tc, ^{188}Re, and ^{90}Y labeled cMORFs was found to be similar. For the same reason and as explained below, the relationship between tumor accumulation of ^{90}Y-cMORF and tumor size was assumed and also confirmed to be the same as that for ^{188}Re-cMORF and ^{99m}Tc-cMORF.

MATERIALS AND METHODS

The MORF (5′-TCTTCTACTTCACAACTA) and cMORF (5′-TAGTTGTGAAGTAGAAGA) were obtained from Gene-Tools

Received: July 11, 2011
Revised: September 20, 2011
Published: October 11, 2011

ACS Publications © 2011 American Chemical Society

(Philomath, OR) with a primary amine attached to the 3′ equivalent terminal via a 3-carbon linker. The p-SCN-Bn-DTPA or -DOTA was from Macrocyclics (Dallas, TX). The P4 resin (Bio-Gel P-4 Gel, medium) was from Bio-Rad Laboratories (Hercules, CA). The $^{111}InCl_3$ and $^{90}YCl_3$ were from Perkin-Elmer Life Science Inc. (Boston, MA). The CC49 antibody that was produced from the CC49 hybridoma by Strategic Biosolutions (Ramona, CA) was conjugated with MORF as previously described.[7,8] All other chemicals were reagent grade and were used without purification.

The cMORF, MORF, and antibody concentrations were determined by UV spectrophotometry. All the cMORF preparations were analyzed by size exclusion HPLC. The HPLC system was equipped with a Superdex 75 HR10/30 column (optimal separation range: 3-70 kDa; Amersham Pharmacia Biotech, Piscataway, NJ) and with both UV and radioactivity in-line detectors. The eluant was 0.10 M pH 7.2 phosphate buffer at a flow rate of 0.60 mL/min. Radioactivity recovery was routinely measured and was always greater than 90%.

^{90}Y Measurements. Because ^{90}Y is a pure β emitter, accurate quantitation of radioactivity in organs can be difficult under certain circumstances.[9] In this investigation, we confirmed that radioactivity of liquid ^{90}Y samples may be accurately measured in a NaI(Tl) well detector by using standards,[9−11] provided that the volume was the same, the samples were in the same type of counting tube, and especially the radioactivity was homogeneously distributed. As such, tissue samples were digested in SOLVABLE solution (PerkinElmer, Waltham, MA) in 5 mL polystyrene tubes and the volume was adjusted to 2.5 mL before counting. The ^{90}Y radioactivity value provided by the manufacturer was considered to be accurate and was used to calibrate the NaI(Tl) well counter.

DOTA Conjugation and ^{90}Y Labeling of cMORF. In a previous study,[6] after conjugation with p-SCN-Bn-DTPA, the cMORF was radiolabeled efficiently with ^{111}In, but the radiolabel was shown to be unstable to heating. Suspecting that the conjugation procedure had produced both stable and unstable conjugates, heating the reaction mixture before purification in the conjugation process yielded a product that provided both a high radiolabeling efficiency and a stable ^{111}In label. The same approach was applied in this investigation to the conjugation of cMORF with p-SCN-Bn-DOTA. Thus, 2.5 mg of p-SCN-Bn-DOTA was dissolved in 0.25 mL of a 0.5 M Na_2CO_3−$NaHCO_3$ buffer at pH 9.8 and mixed with 2.3 mg of lyophilized 3′-amine-derivatized cMORF. After an overnight incubation at room temperature, 1 mL of 0.25 M NH_4OAc buffer at pH 5.2 was added and the conjugation solution was heated at 100 °C for about 3 h before loading onto a 1 × 50 cm open P4 column. The column was eluted with the 0.25 M NH_4OAc buffer and three peak fractions of about 0.6 mL were pooled. The radiolabeling was achieved by adding 1−3 μL of $^{90}YCl_3$ solution in 50 mM HCl to 10−30 μL of the purified DOTA-cMORF solution followed by heating at 100 °C for 10 min. All animal studies were performed with ^{90}Y-DOTA-Bn-SCN-cMORF prepared in this fashion (^{90}Y-cMORF).

In Vitro Stability of ^{90}Y-cMORF. The ^{90}Y-cMORF was tested for radiolabel stability in phosphate buffer, in saline, and in fresh mouse serum. Specifically, 60 μL of the ^{90}Y-cMORF solution was added to 250 μL of each medium before incubation either at room temperature (phosphate buffer and saline) or 37 °C (mouse serum). An aliquot was removed for HPLC analysis at different times over 48 h. In addition, the ^{90}Y-cMORF was radiolabeled at different specific activities up to 3.5 mCi/37 μg of cMORF in the final volume of 80 μL. The radiolabel stability was examined after 20 h at room temperature by HPLC for evidence of radiolysis.

Pharmacokinetics of ^{90}Y-cMORF. Optimization of a pretargeting protocol requires information on pharmacokinetics.[7,12−15] Accordingly, the in vivo behavior of the ^{90}Y labeled cMORF was again measured. Normal CD-1 mice (Charles River Laboratories, MA) in 5 groups (N = 4) each received 1 μg (45 μCi) of ^{90}Y-cMORF by a tail vein injection and were euthanized at 10 min, 0.5 h, 1 h, 3 h, or 6 h. Organs were harvested, digested, and counted as described above. The %ID and %ID/g were calculated against a standard of the injectate. All animal studies were performed with the approval of the UMMS Institutional Animal Care and Use Committee.

Subsequently, the dosage and timing parameters for pretargeting were selected following the guide lines described previously.[15] Any convenient dosage of the pretargeting antibody may be selected that does not saturate the accessible tumor antigens, and any pretargeting interval may be used that provides an acceptable antibody tumor/normal tissue ratio. Because the antibody and the mouse tumor model were the same, the antibody dosage and the pretargeting interval used in this study were identical to those previously used for ^{99m}Tc-cMORF and ^{188}Re-cMORF.[4,7] The optimal dosage of the cMORF effector is related to antibody dosage, pretargeting interval, and its own blood clearance curve. Because the blood clearance of ^{90}Y-cMORF was shown to be sufficiently similar to those of ^{99m}Tc-cMORF and ^{188}Re-cMORF, the optimal cMORF dosage determined previously was used again.

Twenty NIH Swiss Nude mice (Taconic Farms, Germantown, NY) each received 10^6 LS174T colon cancer cells in the left thigh. After 11 days, when the tumors were about 0.3 g, each mouse received via a tail vein 30 μg MORF-CC49 (MORFs per antibody = 0.68) and 48 h later 2.5 μg of ^{90}Y-MORF (50 μCi). Thus, the cMORF/MORF molar ratio was close to the optimal 3.1.[4,7] The biodistribution of the ^{90}Y-cMORF was followed for 7 days. The target thigh containing the tumor and the contralateral thigh were excised at the same anatomical position. The skin on both thighs was removed, and the tumor weight was calculated by subtracting the weight of the normal thigh from that of the tumored thigh. After the bone and as much of the muscle tissues as possible were removed, the tumor was cut into pieces of 0.3−0.4 g, digested, and the radioactivity was measured in a NaI(Tl) well counter along with other organs as described above. Because the dosages and timing in this study are assumed to be optimal based on the above discussion, the tumor accumulations of the effector may therefore be assumed to be at their MPTAs (Maximum Percent Tumor Accumulations, defined as the percent tumor accumulation under the condition when the MORFs in tumor are just saturated by the cMORF).[14,15]

Absorbed Radiation Dose Estimates. The estimated absorbed radiation doses to normal organs and to tumor by pretargeting with ^{90}Y-cMORF were compared with those by pretargeting with ^{188}Re-cMORF. The AUCs (Area Under the radioactivity−time Curve, also known as cumulated radioactivity concentration) were calculated from the best fits to the %ID/g data with decay corrections, to estimate the absorbed radiation doses for the normal organs of interest. Using the self-absorbed model [16,17] as in our previous ^{188}Re studies,[3,4] the absorbed radiation dose in Rads was calculated by the expression 2.143 × 0.935 (MeV) × AUC (μCi h/g), where 2.143 is a unit conversion factor and 0.935 MeV is the average energy of the ^{90}Y β particles.

Estimating the absorbed radiation dose to tumor is more complicated, since tumor accumulation is strongly related to tumor size[18−20] and the tumor size is an unpredictable variable among these studies. Therefore, a comparison of tumor dose for different effectors requires normalizing the tumor accumulation to a certain tumor size using its accumulation vs size relationship under optimal dosage and timing (i.e., at the MPTA). The relationship between ^{99m}Tc-cMORF accumulation and tumor size was previously measured accurately for a substantial number of animals over a range of tumor sizes.[18] Because the in vivo behavior of cMORF was found to be sufficiently independent of the radiolabels of ^{99m}Tc, ^{188}Re, and ^{90}Y, the MPTA-tumor size relationship for ^{99m}Tc-cMORF was assumed to be the same for ^{188}Re-cMORF and ^{90}Y-cMORF. This assumption was confirmed by comparing the predicted and observed tumor accumulations (see below). In the absorbed radiation dose comparison between ^{90}Y-cMORF and ^{188}Re-cMORF, a tumor size of 0.5 g was selected, since most tumors in this and our previous studies fall roughly in the range 0.25−1.0 g.

RESULTS

DOTA Conjugation and ^{90}Y Labeling of cMORF. Similar to the conjugation with p-SCN-Bn-DTPA,[6] conjugation of cMORF with p-SCN-Bn-DOTA without prepurification heating yields a conjugate that provides a high ^{111}In labeling efficiency (Figure 1A, a) but with label instability leading to partial decomposition after heating at 100 °C for 1 h (Figure 1A, b). The equivalent results with ^{90}Y are essentially identical (Figure 1A, c and d). However, if introducing a heating step after conjugation but before purification, the conjugation product can be radiolabeled with either ^{111}In or ^{90}Y at high efficiency and the label becomes stable against heating (Figure 1A, e and g, respectively). The hybridization ability of the cMORF after conjugation and radiolabeling with either ^{111}In or ^{90}Y is preserved, as shown by the shift to higher molecular weight of the labeled cMORF peaks upon the addition of its MORF complement (Figure 1A, f and h, respectively).

In Vitro Stability of ^{90}Y-cMORF. As shown in Figure 1B, b and c, after introducing the heating step into the conjugation procedure, the ^{90}Y radiolabel on cMORF is also stable in phosphate buffer, saline, and serum at least for 48 h (the small peak at 21 min in c is due to self-association of cMORF at room temperature). Figure 1 B, d−f, presents the radiochromatograms of ^{90}Y-cMORF after 20 h of incubation at room temperature in the 80 μL labeling solution at values of specific radioactivity of 63, 1430, and 3440 μCi/37 μg. The increasing decomposition products are most probably the result of radiolysis. To avoid complications due to radiolysis, samples of ^{90}Y-cMORF were used immediately after preparation.

Pharmacokinetics of ^{90}Y-cMORF. Table 1 presents the biodistributions at various times of ^{90}Y-cMORF (prepared by the modified conjugation that includes the prepurification heating) in normal mice and in tumored mice pretargeted with MORF-CC49. As shown by the data in normal mice, the

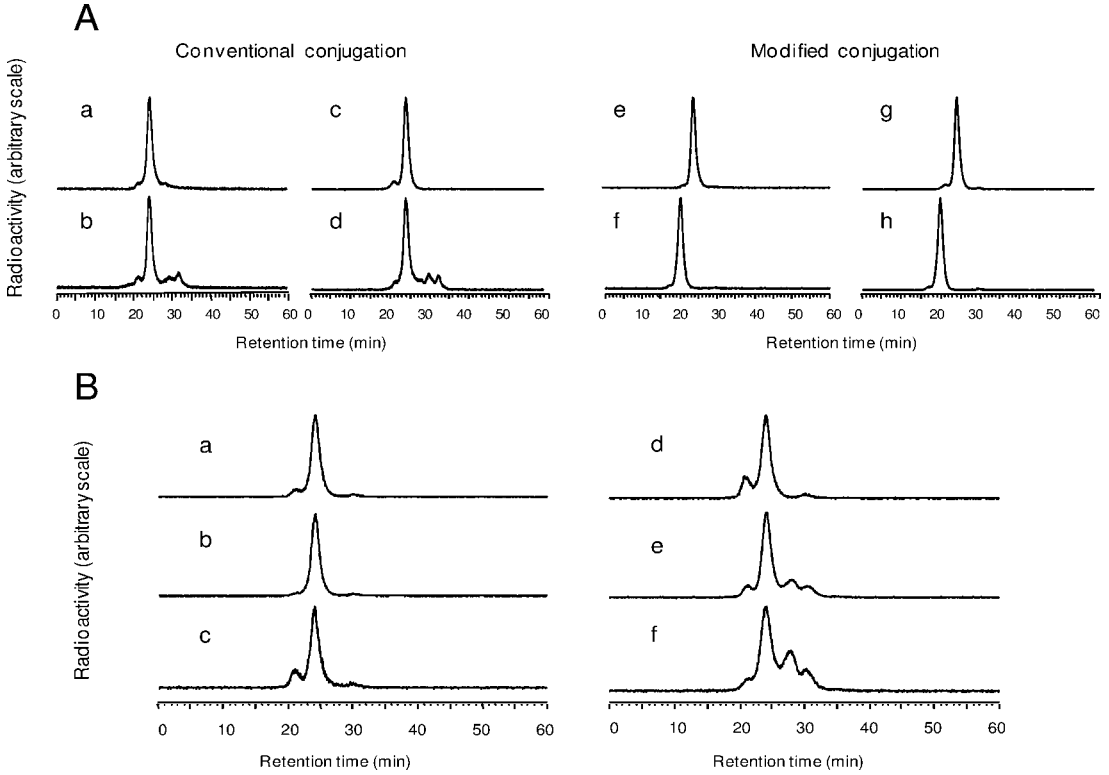

Figure 1. (A) HPLC radiochromatograms of ^{111}In and ^{90}Y labeled cMORFs after conjugating with p-SCN-Bn-DOTA without heating (i.e., conventional) and radiolabeling with mild heating (a and c, respectively) or heating at 100 °C for 1 h (b and d, respectively). Also presnted are the ^{111}In and ^{90}Y HPLC radiochromatograms of cMORF after conjugating with p-SCN-Bn-DOTA but after inclusion of the prepurification heating step during conjugation (i.e., modified) (e and g, respectively) as evidence of increased stability, and the corresponding radiochromatograms after addition of excess MORF (f and h, respectively) as evidence of preserved hybridization affinity. (B) HPLC radiochromatograms of ^{90}Y-cMORF (a) immediately before and (b) 48 h after incubation in serum at 37 °C and (c) 48 h after incubation in phosphate buffer at room temperature. Also presented are HPLC radiochromatgrams of ^{90}Y-cMORF after 20 h of incubation at room temperature in the 80 μL of labeling solution at specific radioactivities of 63, 1430, and 3440 μCi/37 μg cMORF (d−f), showing decomposition most probably due to radiolysis.

dx.doi.org/10.1021/bc200366t | Bioconjugate Chem. 2011, 22, 2539−2545

Table 1. Biodistribution (%ID/g and %ID/Organ) of ^{90}Y-cMORF in Normal CD-1 Mice (left) and in NIH Swiss Nude Mice Bearing LS174T Tumor Xenograft and Pretargeted with MORF-CC49 48 h Earlier (right)[a]

	Normal CD-1 mice					Pretargeted nude mice				
	10 min	30 min	1 h	3 h	6 h	3 h	26 h	71 h	119 h	166 h
					%ID/g					
Liver	0.92 ± 0.07	0.68 ± 0.14	0.58 ± 0.04	0.56 ± 0.10	0.58 ± 0.07	0.85 ± 0.05	0.98 ± 0.10	0.77 ± 0.02	1.03 ± 0.22	0.86 ± 0.14
Heart	1.12 ± 0.11	0.25 ± 0.05	0.16 ± 0.05	0.14 ± 0.07	0.07 ± 0.01	0.29 ± 0.06	0.19 ± 0.03	0.07 ± 0.01	0.09 ± 0.03	0.03 ± 0.03
Kidney	9.88 ± 1.59	4.38 ± 0.19	3.58 ± 0.40	3.56 ± 0.25	3.84 ± 0.37	4.49 ± 1.99	1.86 ± 0.40	0.89 ± 0.14	0.88 ± 0.13	0.57 ± 0.10
Lung	1.87 ± 0.49	0.94 ± 0.36	1.11 ± 0.98	0.89 ± 0.87	0.59 ± 0.21	0.60 ± 0.11	0.30 ± 0.06	0.19 ± 0.06	0.16 ± 0.06	0.09 ± 0.02
Spleen	0.57 ± 0.06	0.24 ± 0.02	0.18 ± 0.02	0.24 ± 0.07	0.19 ± 0.02	0.36 ± 0.03	0.40 ± 0.13	0.32 ± 0.05	0.58 ± 0.04	0.43 ± 0.10
Muscle	0.89 ± 0.10	0.19 ± 0.03	0.05 ± 0.01	0.04 ± 0.00	0.04 ± 0.01	0.20 ± 0.05	0.10 ± 0.01	0.04 ± 0.01	0.03 ± 0.01	0.02 ± 0.01
Pancreas	0.92 ± 0.22	0.31 ± 0.07	0.13 ± 0.01	0.09 ± 0.01	0.06 ± 0.01	0.25 ± 0.03	0.13 ± 0.02	0.07 ± 0.02	0.10 ± 0.05	0.05 ± 0.02
Salivary	1.09 ± 0.38	0.26 ± 0.04	0.12 ± 0.02	0.08 ± 0.01	0.10 ± 0.02	0.29 ± 0.04	0.18 ± 0.05	0.12 ± 0.03	0.16 ± 0.04	0.09 ± 0.04
Blood	4.27 ± 0.46	0.94 ± 0.13	0.41 ± 0.03	0.16 ± 0.01	0.10 ± 0.01	1.47 ± 0.28	0.79 ± 0.17	0.23 ± 0.02	0.21 ± 0.09	0.10 ± 0.03
Tumor	---	---	---	---	---	7.15 ± 2.19	5.21 ± 1.98	2.89 ± 1.07	3.95 ± 2.07	2.43 ± 1.08
					%ID/organ					
Stomach	0.29 ± 0.05	0.07 ± 0.01	0.04 ± 0.01	0.05 ± 0.05	0.02 ± 0.00	0.10 ± 0.05	0.11 ± 0.04	0.03 ± 0.01	0.03 ± 0.01	0.02 ± 0.00
Sm. Int	1.03 ± 0.10	0.51 ± 0.09	0.50 ± 0.04	0.15 ± 0.04	0.07 ± 0.00	0.64 ± 0.08	0.36 ± 0.11	0.33 ± 0.51	0.06 ± 0.01	0.05 ± 0.01
Lg. Int.	0.50 ± 0.06	0.11 ± 0.02	0.06 ± 0.00	0.40 ± 0.06	0.13 ± 0.03	0.19 ± 0.05	0.49 ± 0.10	0.07 ± 0.01	0.07 ± 0.02	0.04 ± 0.01
Tumor	---	---	---	---	---	2.77 ± 0.79	2.70 ± 0.40	2.78 ± 0.94	3.16 ± 0.49	2.67 ± 0.51
Tumor weight (g)	---	---	---	---	---	0.46 ± 0.30	0.56 ± 0.19	1.00 ± 0.26	1.01 ± 0.56	0.90 ± 0.34

[a]Mean ± SD.

^{90}Y-cMORF clears rapidly, similar to the ^{99m}Tc-cMORF and ^{188}Re-cMORF.[21,22] The blood and normal organ clearance is essentially completed by 3 h, although with slightly higher normal tissue levels.

Because of the longer half-life of ^{90}Y compared to ^{188}Re, tumor retention and normal organ clearance could be followed for longer periods. As shown in Table 1, the tumor accumulation in %ID is fairly constant with time, while the tumor accumulation in %ID/g is decreasing due to tumor growth. As for normal organs, except in kidney, the background radioactivity is much lower than that in tumor and clears rapidly, similar to our earlier results with ^{188}Re-cMORF.[3,4] Figure 2a–h reproduces the normal organ ^{90}Y levels from 3 h to 7 days from the table. The solid lines represent the best fits for the ^{90}Y-cMORF and the dotted lines represent those to the values for ^{188}Re-cMORF in our earlier study.[4]

The tumor accumulation vs size relationship for ^{99m}Tc-cMORF determined earlier in the identical animal model[18] was MPTA (%ID/g) = 4.51 × tumor weight (g)$^{-0.66}$. This relationship was assumed to hold true also for ^{90}Y-cMORF and ^{188}Re-cMORF, because the MPTA is proportional to the area under the blood clearance curve[13−15] and, as Table 2 presents, the blood clearance of the three effectors are sufficiently similar. This assumption is supported by the results presented in Table 1. From the table, the average tumor size at 3 h was 0.46 ± 0.30 g and, based on the above relationship, the MPTA for ^{90}Y-cMORF is calculated to be 7.53 %ID/g, therefore in close agreement with the measured 7.15 ± 2.19 %ID/g in Table 1. Previously, in the case of ^{188}Re-cMORF, the tumor accumulation was 8.66 ± 1.18 %ID/g for a tumor size of 0.36 g,[3] also in close agreement with the predicted value of 8.76 %ID/g. These agreements provide confidence in the following calculations of absorbed radiation doses in tumor using normalized tumor accumulation.

Absorbed Radiation Dose Estimate. The AUCs for organs were calculated from the best fits to the biodistribution data with decay correction. The AUC for tumor was based on a predicted tumor accumulation of 7.13 %ID/g for a 0.5 g LS174T tumor obtained from on the MPTA-tumor size relationship, assuming no tumor growth during the study. Both AUCs and the calculated absorbed radiation doses are listed in Table 3. Because of the higher accumulation and longer retention, the absorbed radiation dose to tumor by ^{90}Y pretargeting is at least 5-fold higher than those for other organs. The tumor dose would be even higher in a cohort of animals with smaller tumors than 0.5 g. For comparison, historical data for ^{188}Re pretargeting are also listed but again with the AUC and absorbed radiation dose for tumor size normalized to 0.5 g and calculated assuming no growth during therapy.

Figure 3 presents the T/NT AUC ratios (i.e., the absorbed radiation dose ratios or the therapeutic indexes[23]) for ^{90}Y pretargeting and two previous ^{188}Re pretargeting studies in the same mouse model.[3,4] Although the normal tissue backgrounds are slightly higher for ^{90}Y (Figure 2), the T/NT AUC ratios are not lower but higher due to its longer half-life.

DISCUSSION

Yttrium-90 is an attractive therapeutic radionuclide that has seen use in animal and patient studies while conjugated to antitumor antibodies. Of particular interest, ^{90}Y has been the radionuclide of choice in several pretargeting studies using avidin/biotin or the bispecific antibody/hapten recognition systems.[17,24−38] In the development of tumor radiotherapy approaches by MORF/cMORF pretargeting, we have previously employed ^{188}Re as the therapeutic radionuclide.[3,4] We now consider ^{90}Y as an alternative of longer physical half-life that can potentially improve radiotherapy effectiveness. Accordingly, in this investigation a method was developed to label this nuclide to the cMORF effector and to evaluate the

dx.doi.org/10.1021/bc200366t | Bioconjugate Chem. 2011, 22, 2539–2545

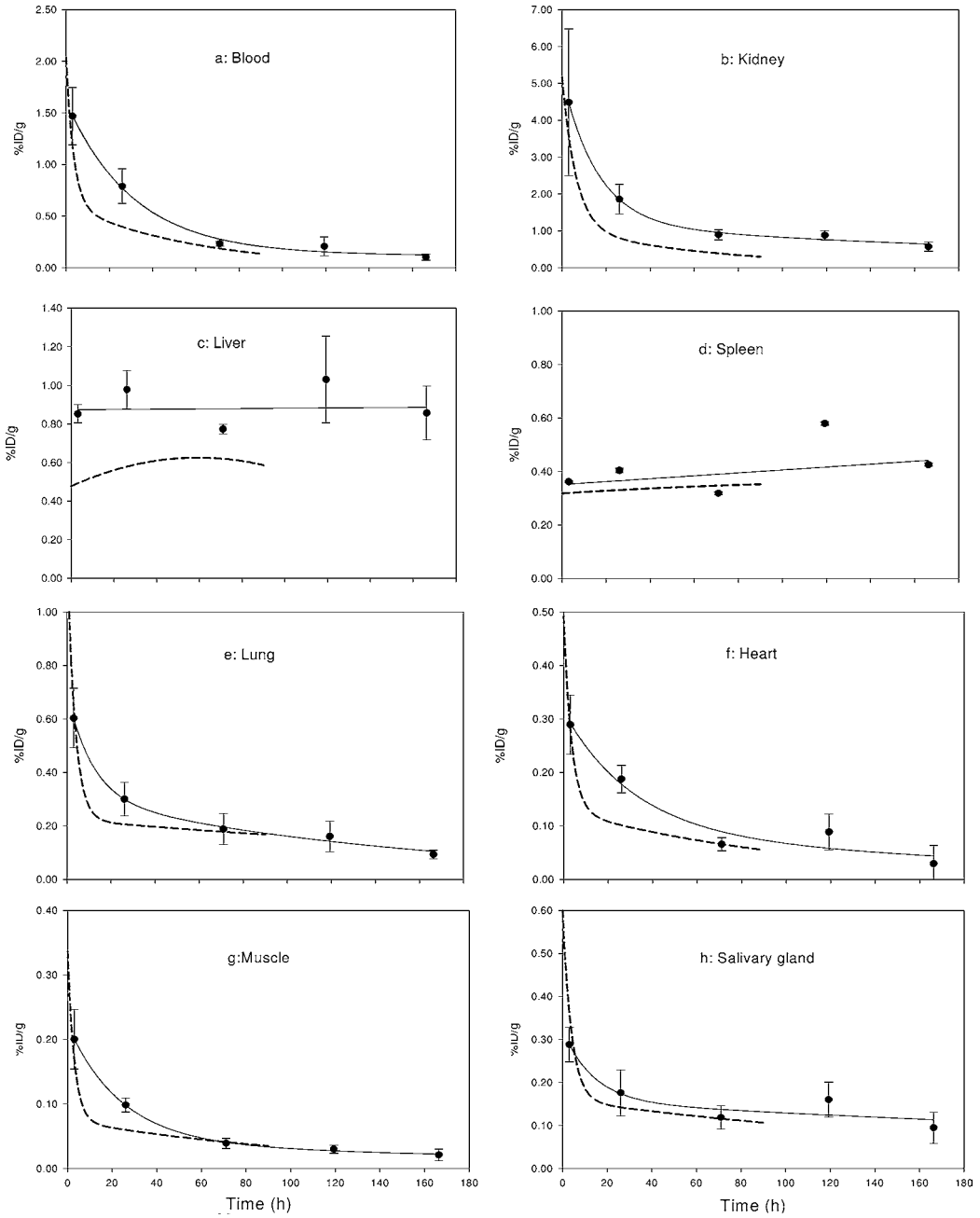

Figure 2. Pharmacokinetics of ^{90}Y-cMORF in normal organs (a–h) of tumored mice pretargeted with MORF-CC49. The solid lines represent the best fits and the dashed lines represent the clearance curves of ^{188}Re-cMORF from a previous pretargeting study (ref 4). Error bars represent 1 standard deviation.

properties of the ^{90}Y-cMORF in LS174T tumored NIH Swiss nude mice pretargeted with the MORF-CC49 antibody.

Although the radiolabeling of cMORF with ^{90}Y via p-SCN-Bn-DOTA was expected to present few difficulties, we observed instabilities of the ^{90}Y-cMORF, reminiscent of that observed previously when radiolabeling cMORF with ^{111}In via p-SCN-Bn-DTPA.[6] A search of the literature provided no mention of similar instabilities when these bifunctional chelators were used to label antibodies. In our earlier study of ^{111}In-cMORF, we were able to resolve the label instability by including a pre-purification heating step after conjugation. The same approach was applied in this investigation in connection with ^{90}Y-cMORF labeling and shown to be successful.

Changes in the effector or pretargeting antibody require the dosage and timing of the pretargeting protocol to be optimized. However, as we have now demonstrated, the pharmacokinetic and pretargeting behavior of cMORF is generally not influenced by the nature of the chelators and radiolabels at least among ^{99m}Tc-MAG$_3$-cMORF, ^{188}Re-MAG$_3$-cMORF, and ^{90}Y-DOTA-Bn-SCN-cMORF. Accordingly, optimization of the dosage and timing parameters for ^{90}Y pretargeting became unnecessary since the values for ^{99m}Tc had been previously determined[7] and can be used again with confidence. For the same reason, the tumor accumulation–size relationship useful for comparing potential therapeutic effects was assumed and confirmed to be the same as that for ^{99m}Tc established previously.

dx.doi.org/10.1021/bc200366t | *Bioconjugate Chem.* 2011, 22, 2539–2545

Table 2. Blood Levels (%ID/g) of ^{99m}Tc-cMORF, ^{188}Re-cMORF, and ^{90}Y-cMORF in Normal CD-1 Mice at Different Times Post Injection[a]

Time point	10 min	30 min	1 h	3 h
^{99m}Tc-cMORF	4.48[b]	1.89[b]	0.73[b]	0.06 ± 0.01[c]; 0.04 ± 0.01[d]
^{188}Re-cMORF	---	---	---	0.06 ± 0.01[d]
^{90}Y-cMORF	4.27 ± 0.46[e]	0.94 ± 0.13[e]	0.41 ± 0.03[e]	0.16 ± 0.01[e]

[a]Mean ± SD. [b]ref 13. [c]ref 21. [d]ref 22. [e]This study.

Table 3. AUCs (μCi h/g) and Absorbed Radiation Doses (rads) for the LS174T Tumor and Organs by cMORF/MORF Pretargeting for the Administration of 1 μCi of ^{90}Y- or ^{188}Re-cMORF

	tumor[a]	blood	kidney	liver	spleen	lung	heart	muscle	salivary gland	ref
					AUC (μCi h/g)					
^{90}Y	6.53	0.46	1.36	0.81	0.37	0.22	0.11	0.06	0.12	This study
^{188}Re	1.75	0.47	0.58	0.31	0.18	0.23	0.12	0.05	0.20	ref 3
^{188}Re	1.75	0.15	0.40	0.15	0.08	0.08	0.04	0.02	0.05	ref 4
					Dose (rad)					
^{90}Y	13.1	0.92	2.72	1.62	0.73	0.44	0.22	0.13	0.25	This study
^{188}Re	2.89	0.77	0.95	0.51	0.30	0.38	0.20	0.09	0.32	ref 3
^{188}Re	2.89	0.24	0.65	0.24	0.13	0.13	0.06	0.04	0.08	ref 4

[a]The AUC and absorbed radiation dose for tumor are calculated based on the predicted accumulation of 7.13 %ID/g for a tumor of 0.5 g under the assumption of no growth.

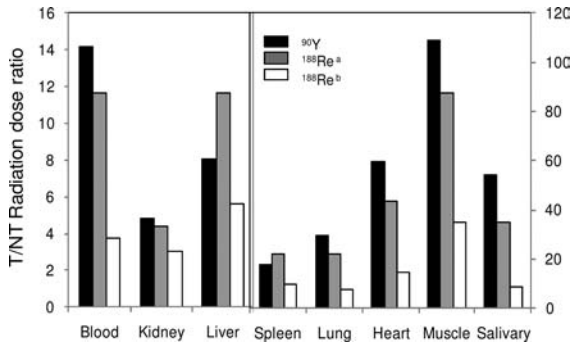

Figure 3. Histograms presenting the T/NT dose ratios (i.e., the tumor therapeutic indexes) for ^{90}Y and two previous ^{188}Re pretargeting studies in the same mouse model. (a) ref 4; (b) ref 3.

With the tracer level pretargeting data, potential therapeutic improvement of ^{90}Y as an alternative to ^{188}Re was evaluated. This evaluation was facilitated by using identical MORF and cMORF sequences, identical CC49 antibody and identical LS174T tumor model to that used previously.[7] Since the average β energies of ^{90}Y and ^{188}Re and the pharmacokinetics of the labeled cMORFs are similar, the T/NT dose ratio improvement is mainly due to the longer physical half-life.

CONCLUSION

Radiolabeling of DOTA-cMORF with ^{90}Y was improved by introducing a prepurification heating step into the conjugation process. The T/B ratio and biodistribution of ^{90}Y-DOTA-cMORF labeled in this fashion were found to be similar to that observed previously for ^{188}Re-MAG$_3$-cMORF. Nevertheless, because of the longer physical half-life of ^{90}Y, an improvement in therapeutic efficacy may be expected in future radiotherapy studies.

AUTHOR INFORMATION

Corresponding Author

*Guozheng Liu, Ph. D. Division of Nuclear Medicine, Department of Radiology, University of Massachusetts Medical School, 55 Lake Avenue North, Worcester, MA 01655-0243. Phone: 508-856-1958; Fax: 508-856-6363. E-mail: guozheng.liu@umassmed.edu.

ACKNOWLEDGMENTS

The authors are grateful to Dr. Schlom (Laboratory of Tumor Immunology and Biology, Center for Cancer Research, NCI, NIH, Bethesda, MD) for providing the CC49 hybridoma. Financial support was in part from the National Institute of Health (CA94994 and DK082894). No conflicts of interest are involved.

REFERENCES

(1) Liu, G., Mang'era, K., Liu, N., Gupta, S., Rusckowski, M., and Hnatowich, D. J. (2002) Tumor pretargeting in mice using ^{99m}Tc-labeled morpholino, a DNA analog. *J. Nucl. Med. 43*, 384−391.

(2) Liu, G., Cheng, D., Dou, S., Chen, X., Liang, M., Pretorius, P. H., Rusckowski, M., and Hnatowich, D. J. (2009) Replacing ^{99m}Tc with ^{111}In Improves MORF/cMORF pretargeting by reducing intestinal accumulation. *Mol. Imaging Biol. 11*, 303−307.

(3) Liu, G., Dou, S., Mardirossian, G., He, J., Zhang, S., Liu, X., Rusckowski, M., and Hnatowich, D. J. (2006) Successful radiotherapy of tumor in pretargeted mice by ^{188}Re-radiolabeled phosphorodiamidate morpholino oligomer, a synthetic DNA analogue. *Clin. Cancer Res. 12*, 4958−4964.

(4) Liu, G., Dou, S., Baker, S., Akalin, A., Cheng, D., Chen, L., Rusckowski, M., and Hnatowich, D. J. (2010) A preclinical ^{188}Re tumor therapeutic investigation using MORF/cMORF pretargeting and an antiTAG-72 antibody CC49. *Cancer Biol. Ther. 10*, 767−774.

(5) Liu, C. B., Liu, G. Z., Liu, N., Zhang, Y. M., He, J., Rusckowski, M., and Hnatowich, D. J. (2003) Radiolabeling morpholinos with ^{90}Y, ^{111}In, ^{188}Re, and ^{99m}Tc. *Nucl. Med. Biol. 30*, 207−214.

(6) Liu, G., Dou, S., Liu, Y., Liang, M., Chen, L., Cheng, D., Greiner, D., Rusckowski, M., and Hnatowich, D. J. (2011) Unexpected side products in the conjugation of an amine-derivatized morpholino oligomer with p-isothiocyanate benzyl DTPA and their removal. *Nucl. Med. Biol. 38*, 159−163.

(7) Liu, G., Dou, S., Pretorius, P. H., Liu, X., Chen, L., Rusckowski, M., and Hnatowich, D. J. (2010) Tumor pretargeting in mice using MORF conjugated CC49 antibody and radiolabeled complimentary cMORF effector. *Q. J. Nucl. Med. Mol. Imaging 54*, 333−340.

(8) He, J., Liu, G., Dou, S., Gupta, S., Rusckowski, M., and Hnatowich, D. J. (2007) An improved method for covalently conjugating morpholino oligomers to antitumor antibodies. *Bioconjugate Chem. 18*, 983−988.
(9) Hnatowich, D. J., Virzi, F., and Doherty, P. W. (1985) DTPA-coupled antibodies labeled with yttrium-90. *J. Nucl. Med. 26*, 503−509.
(10) Djokić, D., Janković, D., and Nikolić, N. (2009) Preparation and in vivo evaluation of ^{90}Y-meso-dimercaptosuccinic acid (^{90}Y-DMSA) for possible therapeutic use: comparison with ^{99m}Tc-DMSA. *Cancer Biother. Radiopharm. 24*, 129−136.
(11) Siegel, J. A., Zimmerman, B. E., Kodimer, K., Dell, M. A., and Simon, W. E. (2004) Accurate dose calibrator activity measurement of ^{90}Y-ibritumomab tiuxetan. *J. Nucl. Med. 45*, 450−454.
(12) Sharkey, R. M., Karacay, H., Richel, H., McBride, W. J., Rossi, E. A., Chang, K., Yeldell, D., Griffiths, G. L., Hansen, H. J., and Goldenberg, D. M. (2003) Optimizing bispecific antibody pretargeting for use in radioimmunotherapy. *Clin. Cancer Res. 9*, 3897S−913S.
(13) Liu, G., He, J., Dou, S., Gupta, S., Rusckowski, M., and Hnatowich, D. J. (2005) Further investigations of morpholino pretargeting in mice—establishing quantitative relations in tumor. *Eur. J. Nucl. Med. Mol. Imaging 32*, 1115−1123.
(14) Liu, G., Dou, S., He, J., Liu, X., Rusckowski, M., and Hnatowich, D. J. (2007) Predicting the biodistribution of radiolabeled cMORF effector in MORF-pretargeted mice. *Eur. J. Nucl. Med. Mol. Imaging 34*, 237−246.
(15) Liu, G., and Hnatowich, D. J. (2008) A semiempirical model of tumor pretargeting. *Bioconjugate Chem. 19*, 2095−2104.
(16) Gestin, J. F., Loussouarn, A., Bardies, M., Gautherot, E., Gruaz-Guyon, A., Saï-Maurel, C., Barbet, J., Curtet, C., Chatal, J. F., and Faivre-Chauvet, A. (2001) Two-step targeting of xenografted colon carcinoma using a bispecific antibody and 188Re-labeled bivalent hapten: biodistribution and dosimetry studies. *J. Nucl. Med. 42*, 146−153.
(17) Lubic, S. P., Goodwin, D. A., Meares, C. F., Song, C., Osen, M., and Hays, M. (2001) Biodistribution and dosimetry of pretargeted monoclonal antibody 2D12.5 and Y-Janus-DOTA in BALB/c mice with KHJJ mouse adenocarcinoma. *J. Nucl. Med. 42*, 670−678.
(18) Liu, G., Dou, S., Liang, M., Chen, X., Rusckowski, M., and Hnatowich, D. J. (2009) The ratio of maximum percent tumour accumulations of the pretargeting agent and the radiolabelled effector is independent of tumour size. *Eur. J. Cancer 45*, 3098−3103.
(19) Moshakis, V., McIlhinney, R. A. J, Raghaven, D., and Neville, A. M. (1981) Localization of human tumour xenografts after i.v. administration of radiolabelled monoclonal antibodies. *Br. J. Cancer 44*, 91−99.
(20) Siegel, J. A., Pawlyk, D. A., Lee, R. E., Sasso, N. L., Horowitz, J. A., Sharkey, R. M., and Goldenberg, D. M. (1990) Tumor, red marrow, and organ dosimetry for ^{131}I-labeled anti-carcinoembryonic antigen monoclonal antibody. *Cancer Res. 50*, 1039s−1042s.
(21) Liu, G., He, J., Dou, S., Gupta, S., Vanderheyden, J. L., Rusckowski, M., and Hnatowich, D. J. (2004) Pretargeting in tumored mice with radiolabeled morpholino oligomer showing low kidney uptake. *Eur. J. Nucl. Med. Mol. Imaging 31*, 417−424.
(22) Liu, G., Dou, S., He, J., Yin, D., Gupta, S., Zhang, S., Wang, Y., Rusckowski, M., and Hnatowich, D. J. (2006) Radiolabeling of MAG_3-morpholino oligomers with ^{188}Re at high labeling efficiency and specific radioactivity for tumor pretargeting. *Appl. Radiat. Isot. 64*, 971−978.
(23) DeNardo, S. J., Richman, C. M., Albrecht, H., Burke, P. A., Natarajan, A., Yuan, A., Gregg, J. P, O'Donnell, R. T., and DeNardo, G. L. (2005) Enhancement of the therapeutic index: from non-myeloablative and myeloablative toward pretargeted radioimmuno-therapy for metastatic prostate cancer. *Clin. Cancer Res. 11*, 7187s−7194s.
(24) Goodwin, D. A., Meares, C. F., Watanabe, N., McTigue, M., Chaovapong, W., Ransone, C. M, Renn, O., Greiner, D. P, Kukis, D. L., and Kronenberger, S. I. (1994) Pharmacokinetics of pretargeted monoclonal antibody 2D12.5 and ^{88}Y-Janus-2-(p-nitrobenzyl)-1,4,7,10-tetraazacyclododecanetetra-acetic acid (DOTA) in BALB/c mice with KHJJ mouse adenocarcinoma: a model for ^{90}Y radio-immunotherapy. *Cancer Res. 54*, 5937−5946.
(25) Chinol, M., Paganelli, G., Sudati, F., Meares, C., and Fazio, F. (1997) Biodistribution in tumour-bearing mice of two ^{90}Y-labelled biotins using three-step tumour targeting. *Nucl. Med. Commun. 18*, 176−182.
(26) Paganelli, G., Orecchia, R., Jereczek-Fossa, B., Grana, C., Cremonesi, M., De Braud, F., Tradati, N, and Chinol, M. (1998) Combined treatment of advanced oropharyngeal cancer with external radiotherapy and three-step radioimmunotherapy. *Eur, J, Nucl, Med. 25*, 1336−1339.
(27) Goodwin, D. A., Meares, C. F., and Osen, M. (1998) Biological properties of biotin-chelate conjugates for pretargeted diagnosis and therapy with the avidin/biotin system. *J. Nucl. Med. 39*, 1813−1818.
(28) DeNardo, S. J., DeNardo, G. L., Brush, J., and Carter, P. (1999) Phage library-derived human anti-TETA and anti-DOTA ScFv for pretargeting RIT. *Hybridoma 18*, 13−21.
(29) Cremonesi, M., Ferrari, M., Chinol, M., Stabin, M. G., Grana, C., Prisco, G., Robertson, C., Tosi, G., and Paganelli, G. (1999) Three-step radioimmunotherapy with yttrium-90 biotin: dosimetry and pharmacokinetics in cancer patients. *Eur. J. Nucl. Med. 26*, 110−120.
(30) Axworthy, D. B., Reno, J. M., Hylarides, M. D., Mallett, R. W., Theodore, L. J., Gustavson, L. M, Su, F., Hobson, L. J., Beaumier, P. L., and Fritzberg, A. R. (2000) Cure of human carcinoma xenografts by a single dose of pretargeted yttrium-90 with negligible toxicity. *Proc. Natl. Acad. Sci. U. S. A. 97*, 1802−1807.
(31) Breitz, H. B., Weiden, P. L., Beaumier, P. L., Axworthy, D. B., Seiler, C., Su, F. M., Graves, S., Bryan, K., and Reno, J. M. (2000) Clinical optimization of pretargeted radioimmunotherapy with anti-body-streptavidin conjugate and ^{90}Y-DOTA-biotin. *J. Nucl. Med. 41*, 131−140.
(32) Knox, S. J., Goris, M. L., Tempero, M., Weiden, P. L., Gentner, L., Breitz, H., Adams, G. P., Axworthy, D., Gaffigan, S., Bryan, K., Fisher, D. R., Colcher, D., Horak, I. D., and Weiner, L. M. (2000) Phase II trial of yttrium-90-DOTA-biotin pretargeted by NR-LU-10 antibody/streptavidin in patients with metastatic colon cancer. *Clin. Cancer Res. 6*, 406−414.
(33) Grana, C., Chinol, M., Robertson, C., Mazzetta, C., Bartolomei, M., De Cicco, C., Fiorenza, M., Gatti, M., Caliceti, P., and Paganelli, G. (2002) Pretargeted adjuvant radioimmunotherapy with yttrium-90-biotin in malignant glioma patients: a pilot study. *Br. J. Cancer 86*, 207−212.
(34) Pagel, J. M., Hedin, N., Subbiah, K., Meyer, D., Mallet, R., Axworthy, D., Theodore, L. J., Wilbur, D. S., Matthews, D. C., and Press, O. W. (2003) Comparison of anti-CD20 and anti-CD45 antibodies for conventional and pretargeted radioimmunotherapy of B-cell lymphomas. *Blood 101*, 2340−2348.
(35) Zhang, S., Xing, J., Zhang, Q., Song, F., Li, Y., Yang, X., and Chen, Z. (2006) Optimal design of Ig 5′ primers for construction of diverse phage antibody library established to select anti-HAb18GEF and anti-DOTA-Y Fabs for hepatoma pretargeting RIT. *Front. Biosci. 11*, 1733−1749.
(36) Urbano, N., Papi, S., Ginanneschi, M., De Santis, R., Pace, S., Lindstedt, R., Ferrari, L., Choi, S., Paganelli, G., and Chinol, M. (2007) Evaluation of a new biotin-DOTA conjugate for pretargeted antibody-guided radioimmunotherapy (PAGRIT). *Eur. J. Nucl. Med. Mol. Imaging 34*, 68−77.
(37) Karacay, H., Sharkey, R. M., Gold, D. V., Ragland, D. R., McBride, W. J., Rossi, E. A., Chang, C. H., and Goldenberg, D. M. (2009) Pretargeted radioimmunotherapy of pancreatic cancer xenografts: TF10-^{90}Y-IMP-288 alone and combined with gemcitabine. *J. Nucl. Med. 50*, 2008−2016.
(38) Sharkey, R. M., Karacay, H., Govindan, S. V., and Goldenberg, D. M. (2011) Combination radioimmunotherapy and chemo-immunotherapy involving different or the same targets improves therapy of human pancreatic carcinoma xenograft models. *Mol. Cancer Ther. 10*, 1072−1081.

Bioconjugate Chemistry

Article

pubs.acs.org/bc

Oxazine Dye-Conjugated DNA Oligonucleotides: Förster Resonance Energy Transfer in View of Molecular Dye−DNA Interactions

Annette Kupstat, Thomas Ritschel, and Michael U. Kumke*

Universität Potsdam, Institut für Chemie, Physikalische Chemie, Karl-Liebknecht-Straße 24-25, 14476 Potsdam-Golm, Germany

Supporting Information

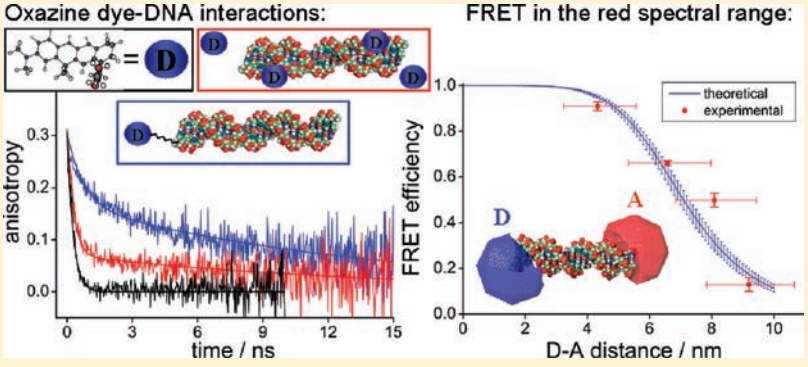

ABSTRACT: In this work, the photophysical properties of two oxazine dyes (ATTO 610 and ATTO 680) covalently attached via a C6-amino linker to the 5′-end of short single-stranded as well as double-stranded DNA (ssDNA and dsDNA, respectively) of different lengths were investigated. The two oxazine dyes were chosen because of the excellent spectral overlap, the high extinction coefficients, and the high fluorescence quantum yield of ATTO 610, making them an attractive Förster resonance energy transfer (FRET) pair for bioanalytical applications in the far-red spectral range. To identify possible molecular dye−DNA interactions that cause photophysical alterations, we performed a detailed spectroscopic study, including time-resolved fluorescence anisotropy and fluorescence correlation spectroscopy measurements. As an effect of the DNA conjugation, the absorption and fluorescence maxima of both dyes were bathochromically shifted and the fluorescence decay times were increased. Moreover, the absorption of conjugated ATTO 610 was spectrally broadened, and a dual fluorescence emission was observed. Steric interactions with ssDNA as well as dsDNA were found for both dyes. The dye−DNA interactions were strengthened from ssDNA to dsDNA conjugates, pointing toward interactions with specific dsDNA domains (such as the top of the double helix). Although these interactions partially blocked the dye-linker rotation, a free (unhindered) rotational mobility of at least one dye facilitated the appropriate alignment of the transition dipole moments in doubly labeled ATTO 610/ATTO 680−dsDNA conjugates for the performance of successful FRET. Considering the high linker flexibility for the determination of the donor−acceptor distances, good accordance between theoretical and experimental FRET parameters was obtained. The considerably large Förster distance of ∼7 nm recommends the application of this FRET pair not only for the detection of binding reactions between nucleic acids in living cells but also for monitoring interactions of larger biomolecules such as proteins.

INTRODUCTION

Dye-labeled oligonucleotides have many applications in life sciences.[1−3] These range from fundamental research in molecular and cell biology (e.g., the study of intracellular RNA distribution and dynamics[4,5] or the affinity and specificity of DNA-binding proteins[6,7]) to medical research [e.g., the characterization of potential RNA therapeutic agents (antisense oligonucleotides and ribozymes) for oligonucleotide therapy[8]]. In many cases, Förster resonance energy transfer (FRET)-based oligonucleotide probes are used. The FRET technique allows the detection of binding reactions between biomolecules without separation of excess probe material[8] and is therefore especially suited for in vivo applications such as live cell imaging.[1,5,9,10] Short terminally labeled nucleic acid FRET probes are preferably applied in RNAomics (RNA research). Here, different fundamental concepts such as competitive hybridization probes, side-by-side probes, and molecular beacons that contain short DNA (double-stranded, single-stranded, and hairpin-structured by intramolecular base pairing within one DNA single strand) are applied.[3,4]

Many dyes show specific molecular interactions with DNA; e.g., intercalation, groove binding, and a stacked conformation parallel to the terminal base pair of the DNA helix were described for cyanine dyes[11−16] and rhodamine dyes.[15−17] Such dye−DNA interactions may change the photophysical properties of the dyes, e.g., fluorescence enhancement,[18,19] alterations in fluorescence anisotropy,[13,17,20,21] or fluorescence quenching.[17,22−24]

Received: July 20, 2011
Revised: November 2, 2011
Published: November 10, 2011

ACS Publications © 2011 American Chemical Society

dx.doi.org/10.1021/bc200379y | *Bioconjugate Chem.* 2011, 22, 2546−2557

The demand for techniques that allow the visualization of RNA in living cells is increasing in RNAomics.[10] In particular, fluorescent probes that can be excited and detected in the visible red to near-infrared spectral range are very attractive for in vivo applications as their usage strongly reduces the level of photodamage of the living cells.[25,26] Further advantages are the elimination of the tissue background signal and an increase in tissue penetration depth due to the very low intrinsic absorption and fluorescence emission of the biological samples as well as reduced light scattering in this spectral range.[27−29] Moreover, rugged red diode lasers that are less expensive and more energy-efficient than gas lasers commonly applied in confocal laser scanning microscopes are available for excitation.[30−32] Thus, fluorescent probes containing red or near-infrared dyes are in demand for in vivo microscopy.[28] Cyanine and rhodamine dyes, e.g., Cy5 and TAMRA, are frequently used as FRET-based oligonucleotide probes[33,34] despite the strong dye−DNA interactions that have been revealed for those dyes (vide supra).

The FRET efficiency depends on the spectral overlap between the fluorescence emission of the donor (D) and the absorption of the acceptor (A) as an intrinsic property of the particular FRET pair and the actual distance between D and A, but also on the relative orientation of the respective transition dipoles between both dyes.[35] Consequently, a complete restricted mobility of the dyes due to strong molecular dye−DNA interactions may limit the applicability of a certain FRET pair for oligonucleotide probes.[36] In addition to dye−DNA interactions, the flexible molecular structure of cyanine dyes induces photoisomerization processes that compete with the fluorescence emission.[37−39]

Fluorescent dyes with absorption maxima between 600 and 750 nm that exhibit high extinction coefficients and decent quantum yields can be found among the ATTO dyes.[40] In contrast to the frequently used cyanine dyes, the chromophores of the ATTO dyes possess a more rigid molecular structure that is less prone to photophysical transformations such as isomerization.[40] However, until now, the photophysical properties of their bioconjugates and molecular dye−biomolecule interactions had been investigated in only a few studies.[41−47] To the best of our knowledge, only three studies have been published so far in which DNA conjugates of far-red ATTO dyes (ATTO 655, ATTO 647, and ATTO 647N) were used in FRET applications.[45−47]

In this study, two ATTO dyes were investigated with respect to their performance as a FRET pair for oligonucleotide probes. As the photophysics of the fluorescent probes provides the basis for the detection of the molecular event of interest (such as a binding interaction), the effects of the bioconjugation on the photophysical properties must be well characterized for each dye−biomolecule system on a case-to-case basis. An in-depth photophysical characterization of the oxazine derivatives ATTO 610 (D) and ATTO 680 (A) as well as of dye−DNA conjugates with different DNA lengths is presented. The two dyes were chosen because of the excellent spectral overlap, the high extinction coefficients, and the high fluorescence quantum yield of ATTO 610, making them an attractive novel FRET pair for bioanalytical applications in the far-red spectral range. Using tailor-made DNA strands, the FRET parameters and the experimental performance were determined and compared to theoretically obtained parameters. Moreover, the molecular interactions of the 5′-terminally attached dyes with ssDNA as well as dsDNA were investigated in detail using high-end fluorescence techniques such as time-resolved fluorescence anisotropy and fluorescence correlation spectroscopy.

EXPERIMENTAL PROCEDURES

Reagents and Chemicals. The carboxylated dyes ATTO 610 (A610-COOH) and ATTO 680 (A680-COOH) were purchased from ATTO-TEC GmbH (Siegen, Germany). Stock solutions of the carboxylated dyes were prepared in acetonitrile (analytical grade) at concentrations of 0.2−1 mM. Both dyes are oxazine derivatives. The structural formulas of A610-COOH[40] and A680-COOH[48] are shown in Figure 1 (left). The

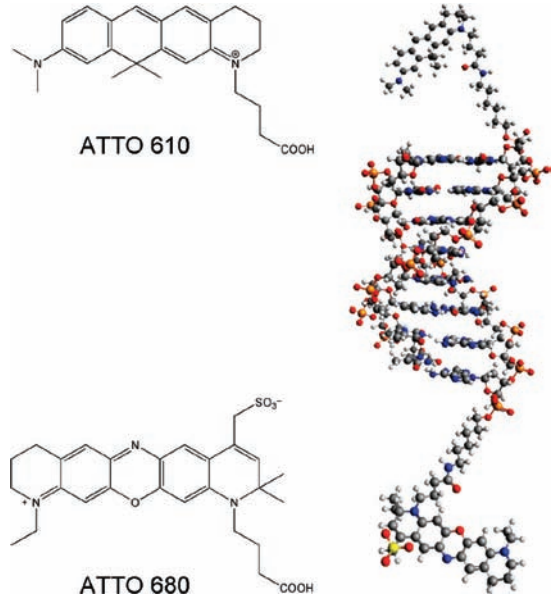

Figure 1. Structural formulas of ATTO 610 carboxylic acid (A610-COOH) and ATTO 680 carboxylic acid (A680-COOH) (left) and three-dimensional structure of the doubly labeled dye−dsDNA conjugates (right). The three-dimensional structure of the doubly labeled dye−dsDNA conjugates is shown for the 8 bp dsDNA conjugated at the opposite 5′-ends with the donor ATTO 610 (A610) and the acceptor ATTO 680 (A680) via a C6-amino linker.

molecular weights of the dyes, including counterions, are 491 g/mol for A610-COOH and 631 g/mol for A680-COOH.

A610 was conjugated via a linker of six carbon atoms (C6-amino linker) to the 5′-end of single-stranded DNA (ssDNA) of different lengths [8, 16, 20, and 24 bases (b)]. A680 was conjugated to the complementary ssDNA accordingly. The dye−ssDNA conjugates were custom-synthesized and purified (double HPLC grade) by IBA GmbH (Göttingen, Germany).[49] The sequences and molecular weights (M) of the oligonucleotides are summarized in Table 1. In addition, unlabeled complementary ssDNA was also purchased from IBA GmbH (double HPLC grade purification). The final concentration of each oligonucleotide sample was adjusted to 0.1 mM.

The spectroscopic characterization of the carboxylated dyes as well as the dye−ssDNA conjugates was conducted in doubly distilled water. For the fluorescence measurements, diluted solutions of the dyes and the dye−DNA conjugates were used (optical density at λ_{ex} < 0.1). For the investigation of FRET, double-stranded (ds) DNAs of 8, 16, 20, and 24 base pairs (bp) containing the donor (A610) on the one 5′-end and the acceptor (A680) on the opposite 5′-end were prepared by hybridization of the complementary dye−ssDNA conjugates

dx.doi.org/10.1021/bc200379y | Bioconjugate Chem. 2011, 22, 2546−2557

Table 1. Sequences and Molecular Weights (M) of the DNA Single Strands

identifier	DNA length [bases (b)]	DNA sequence (5′ → 3′)	M of the DNA (g/mol)
A610−8b ssDNA	8	AAGGCCTA	2418
A680−8b ssDNA	8	TAGGCCTT	2400
A610−16b ssDNA	16	ATCGAAGGCCTAGGTA	4926
A680−16b ssDNA	16	TACCTAGGCCTTCGAT	4830
A610−20b ssDNA	20	TATCCGAAGGCCTAGCGTAT	6113
A680−20b ssDNA	20	ATACGCTAGGCCTTCGGATA	6113
A610−24b ssDNA	24	ATATCGCGAAGGCCTAGCGGTATA	7396
A680−24b ssDNA	24	TATACCGCTAGGCCTTCGCGATAT	7300

(Figure 1, right). To obtain dsDNA conjugated with either A610 or A680, we hybridized the dye−ssDNA conjugates with the unlabeled complementary ssDNA. The dsDNA samples were studied in doubly distilled water containing 1 M NaCl (analytical grade).

Hybridization of the Dye−ssDNA Conjugates. Samples containing the two complementary DNA single strands, each at a final concentration of 0.03 mM in a 1 M NaCl solution, were prepared and placed in a polymerase chain reaction machine (Analytik Jena). Heating the samples to 363 K for 1 min abolished any intramolecular base pairing of the DNA single strands. The hybridization took place at 287 K (for the 8b DNA) and 318 K (for the 16b, 20b, and 24b DNA) for 15 h. A 1 M NaCl solution was used as the solvent to increase the melting temperature of the dsDNA (Table 2) and to shift the equilibrium in the direction of double-strand formation. In Table 2, the lengths and the melting temperatures of the dsDNA are listed. The DNA lengths were calculated using a length increment of 0.34 nm/bp, which is found in general for the B-type DNA double helix.

Table 2. Lengths and Melting Temperatures (T_m) of the DNA Double Strands

DNA length (bp)	DNA length (nm)	T_m (K) at 0.195 M monovalent cation	T_m (K) in a 1 M NaCl solution
8	2.72	297	309
16	5.44	316	328
20	6.80	325	337
24	8.16	330	342

Absorption and Fluorescence Spectroscopy. The absorption spectra were recorded in the spectral range of 230−750 nm using a Lambda 750 UV−vis spectrometer (Perkin-Elmer). The steady-state fluorescence measurements were performed using a Fluoromax-3 spectrofluorometer (Horiba Jobin Yvon) operated in the single-photon-counting mode. The time-resolved fluorescence measurements were taken using an FL920 spectrofluorometer (Edinburgh Instruments) equipped with a multichannel plate (Europhoton) and operated in a time-correlated single-photon-counting (TCSPC) mode. A SC450 supercontinuum source (Fianium) equipped with an acousto-optic tunable filter (AOTF) with a pulse width of 6 ps and 20 MHz repetition rate was used for excitation. A610 was excited (λ_{ex}) in the spectral range of 570−650 nm and A680 in the range of 615−688 nm. The fluorescence emission (λ_{em}) was recorded in the spectral range of 600−750 nm for A610 and 630−800 nm for A680. The exact excitation and emission wavelengths are given with the experimental results. The temperature was kept constant at 295 K. The single- and double-exponential fluorescence decays were analyzed according to eqs 1 and 2

$$I(t) = A \exp(-t/\tau) \quad (1)$$

$$I(t) = A_1 \exp(-t/\tau_1) + A_2 \exp(-t/\tau_2) \quad (2)$$

where I is the fluorescence intensity, A the pre-exponential factor, t the time, and τ the fluorescence decay time. The fractional contribution of component i to the total steady-state intensity (f_i) was defined according to eq 3. For the decay analysis, the commercial software package provided by Edinburgh Instruments (FAST software) was used.

$$f_i = \frac{A_i\tau_i}{\sum_{i=1}^{n} A_i\tau_i} \quad (3)$$

The fluorescence quantum yield (φ) of A610-COOH in 1 M NaCl solution was determined with a photoluminescence quantum yield measurement system (C9920, Hamamatsu Photonics). The data were analyzed with the commercial software package provided by Hamamatsu.

Fluorescence Anisotropy. Fundamental anisotropy as well as time-resolved fluorescence anisotropy was determined as described by Kupstat et al.[50] The fundamental anisotropy r_0 of the carboxylated dyes was measured at 277 K in glycerine. For the analysis of the anisotropy decays of the carboxylated dyes and the A610−dsDNA conjugates measured at a λ_{ex} of 650 nm and a λ_{em} of 675 nm, eq 4 was used

$$r(t) = r_0 \exp(-t/\theta) \quad (4)$$

where t is the time and θ the rotational correlation time. The double-exponential anisotropy decays of the dye−ssDNA and dye−dsDNA conjugates were analyzed using eq 5, which is an anisotropy model for the segmental mobility of a biopolymer-bound dye.[51]

$$r(t) = r_0\left[\alpha\exp\left(\frac{-t}{\theta_1}\right) + (1-\alpha)\exp\left(\frac{-t}{\theta_2}\right)\right] \quad (5)$$

where the parameter θ_1 refers to the rotational correlation time of the segmental motion and θ_2 refers to the rotational correlation time of the overall rotational motion of the macromolecule. The contribution of θ_1 to the overall anisotropy decay is given by the parameter α, and consequently, $(1-\alpha)$ represents the contribution of θ_2. The fundamental anisotropy that was separately determined under high-viscosity conditions (vide supra) to $r_0 = 0.3$ was fixed during the fitting of the anisotropy decays. For the dye−ssDNA conjugates, the parameter θ_2 was approximated assuming the rotational motion of a sphere

(calculated according to eq 6) and fixed during the fitting.

$$\theta = \frac{4\pi {R_h}^3 \eta}{3kT} \quad (6)$$

where R_h is the hydrodynamic radius of the dye−ssDNA conjugates in water determined from the FCS measurements (vide infra), η the solvent viscosity, k the Boltzmann constant, and T the temperature. For the evaluation of the experimental results, the rotational correlation times of the DNA double strands were calculated with HYDROPRO.[52]

Fluorescence Correlation Spectroscopy (FCS). The FCS measurements were performed on a single-molecule spectrometer system (MicroTime 200, Picoquant, and IX-71, Olympus) using a supercontinuum source with a pulse width of 6 ps and 20 MHz repetition rate (SC400-2 with AOTF, Fianium) for excitation. The power of the excitation light (λ_{ex} = 622 nm, and λ_{ex} = 630 nm) coupled to the microscope was in the range of 50−65 μW (measured without a lens). The excitation beam was focused into the sample by a microscope lens (Olympus PlanApo 100×, 1.40 oil objective). The fluorescent light was collected by the same lens and guided via a dichroic mirror, a long pass filter [RG-645 for A610 and RG-665 for A680 (Melles Griot)], a 50 μm pinhole, and a final 50:50 beam splitter onto two single-photon avalanche diodes (APDs) (Perkin-Elmer). The autocorrelation curves $G(t_{lag})$ were calculated by cross correlating photons from the two APDs using SymPhoTime version 5.1.31 (Picoquant). The dimensions of the focal volume (ω_0 and z_0) were determined using a calibration standard (ATTO 655-carboxylic acid in doubly distilled water).[53] The autocorrelation functions $G(t_{lag})$ were fitted according to eq 7

$$G(t_{lag}) = \frac{1}{N}\left(1 + \frac{t_{lag}}{t_{lat}}\right)^{-1}\left(1 + \frac{{\omega_0}^2}{{z_0}^2}\frac{t_{lag}}{t_{lat}}\right)^{-1/2} \quad (7)$$

where t_{lag} is the lag time, N the average molecule number in the focal volume, and t_{lat} the lateral diffusion time that a molecule needs to leave the focal volume.[54] Via t_{lat}, the diffusion coefficient D_{lat} can be calculated according to eq 8.

$$t_{lat} = \frac{{\omega_0}^2}{4D_{lat}} \quad (8)$$

The Stokes−Einstein equation (eq 9), where k is Boltzmann's constant, T the temperature, and η the solvent viscosity, relates D_{lat} with the hydrodynamic radius R_h of a (spherical) molecule in solution.

$$D_{lat} = \frac{kT}{6\pi\eta R_h} \quad (9)$$

Förster Resonance Energy Transfer (FRET). The Förster distance R_0 was calculated according to eq 10[55]

$$R_0 = \sqrt[6]{\frac{9\ln(10)\kappa^2\varphi_D J(\lambda)}{128\pi^5 N_A n^4}} \quad (10)$$

where κ^2 is an orientation factor for the transition dipole moments of donor (D) and acceptor (A), φ_D the quantum yield of D, $J(\lambda)$ the overlap integral, N_A Avogadro's number, and n the refractive index of the medium.

The average κ^2 is usually assumed to be $^2/_3$, which is appropriate in the case of complete rotational freedom of D and A (dynamic random averaging of the transition dipole moments of D and A).[35] Following the work of van der Meer,[56] κ^2 can be expressed in terms of the angle between the electric field of D and the absorption transition dipole moment of A (ω) and the angle between the emission transition dipole moment of D and the line connecting the centers of D and A (θ_D) according to eq 11.

$$\kappa^2 = \cos^2\omega(1 + 3\cos^2\theta_D) \quad (11)$$

Averaging over all possible ω values leads to eq 12, in which the average κ^2 can take values between $^1/_3$ and $^4/_3$ depending on θ_D (Figure 1S of the Supporting Information). An equivalent expression can be found for θ_A.

$$\overline{\kappa^2}(\theta_D) = \cos^2\theta_D + \frac{1}{3} \quad (12)$$

$J(\lambda)$ was determined as described by Kupstat et al.[50] using the fluorescence emission spectrum of A610-COOH and the absorption spectrum of A680-COOH. On the basis of R_0, the theoretical FRET efficiency (E_{theo}) can be calculated for different D−A distances (R) according to eq 13.

$$E_{theo} = \frac{{R_0}^6}{{R_0}^6 + R^6} \quad (13)$$

To take the high flexibility of the C6-amino linker into account when determining the actual R for the dye−dsDNA conjugates, we performed accessible volume (AV) simulations using FRETnps Tools.[57] The dsDNA structures were generated with the nucleic acid builder (NAB) that is part of AmberTools. The AVs of the dyes were simulated independently for each DNA end. For this simulation, the linker length was set to 1.6 nm (because of their flexibility, the C4 side chains of the dyes were considered as part of the linker), the linker diameter was set to 0.4 nm,[58] and dye diameters of 1.0 and 1.1 nm were used for A610 and A680, respectively. From the AV data, R distributions were obtained by numerical computation of the pair correlation function between the two one-particle densities. The peak maxima of the R distributions were used as the average distance between D and A in the dye−dsDNA conjugates with different DNA lengths.

The experimental FRET efficiency (E_{exp}) was determined from the fluorescence decays of D according to eq 14

$$E_{exp} = 1 - \frac{\tau_{DA}}{\tau_D} \quad (14)$$

where τ_{DA} is the fluorescence decay time of D in the presence and τ_D in the absence of A. To measure selectively D's fluorescence emission when A is present, we used an excitation wavelength (λ_{ex}) of 590 nm and an emission wavelength (λ_{em}) of 620 nm.

RESULTS

Effects of Bioconjugation on the Basic Photophysical Properties of the Dyes. The effects of DNA conjugation on the absorption and fluorescence properties of the dyes were investigated for the dye−ssDNA conjugates as well as for the singly labeled dye−dsDNA conjugates. The basic photophysical data of the free and conjugated dyes are summarized in Table 3.

The absorption spectra of the dye−ssDNA and dye−dsDNA conjugates basically comprise the absorption of the single moieties, namely, the absorption of the dye in the visible red

Table 3. Basic Photophysical Properties of the Free Dyes, the Dye−ssDNA Conjugates, and the Singly Labeled Dye−dsDNA Conjugates[a]

	absorption maximum (nm)	fluorescence excitation maximum (nm)	fluorescence emission maximum (nm)	fluorescence decay time τ (ns)
A610-COOH	616	616	634	3.3 ± 0.1
A610−ssDNA	623−629, shoulder at 650	623−625, shoulder at 650	640	4.0 ± 0.1 to 4.6 ± 0.1[b]
A610−dsDNA	629−647	625−629, shoulder at 650	636 and 665	4.2 ± 0.2
A680-COOH	680	680	697	1.7 ± 0.1
A680−ssDNA	688	688	703	2.1 ± 0.1 to 2.4 ± 0.1[b]
A680−dsDNA	688	688	702	2.4 ± 0.1

[a]The fluorescence emission and excitation spectra were measured with a λ_{ex} of 570 nm and a λ_{em} of 690 nm for A610 and a λ_{ex} of 615 nm and a λ_{em} of 730 nm for A680. The fluorescence decays were measured at a λ_{ex} of 615 nm and a λ_{em} of 635 nm for A610 and at a λ_{ex} of 688 nm and a λ_{em} of 703 nm for A680. The error of τ was determined from repeated measurements. [b]As the τ of the A610− and A680−ssDNA conjugates was slightly increased with an increase in DNA length, the range of τ is stated.

spectral range and the UV absorption band of the DNA with its maximum at ∼260 nm (Figure 2S of the Supporting Information). However, as a result of the DNA conjugation, the absorption maximum of A680 was bathochromically shifted by 8 nm compared to the absorption maximum of A680-COOH. For the A610−DNA conjugates, a larger effect was found. In addition to the 7−31 nm bathochromically shifted spectral position of the A610 absorption maximum, a significant spectral broadening compared to that of A610-COOH was found for the ssDNA- and dsDNA-conjugated dye (Figure 3S of the Supporting Information). These changes in the absorption of conjugated A610 were attributed to an additional absorption band formed at ∼650 nm that increased in intensity from ssDNA to dsDNA conjugates (for the ssDNA conjugates, this band was observed as a shoulder occurring at lower energies with regard to the regular absorption, whereas for the dsDNA conjugates, the band was distinctly increased in intensity resulting in a more red-shifted absorption maximum). This absorption band was differently pronounced for the dye−DNA conjugates with different DNA lengths (Figure 3S of the Supporting Information).

Trends similar to those found in the absorption spectra were observed in the fluorescence excitation spectra. The excitation spectra of both dyes showed the bathochromically shifted absorption upon conjugation to ssDNA and dsDNA (vide supra). As already found in the absorption spectra of conjugated A610 (vide supra), the additional band at ∼650 nm was more pronounced for the dye−dsDNA conjugates than for the dye−ssDNA conjugates (Figure 2, left, and Figure 4S of the Supporting Information). However, the band detected at ∼650 nm in the excitation spectra was less intense compared to that in the absorption spectra. Corresponding to the absorption measurements, the fluorescence emission maxima of the conjugated dyes were bathochromically shifted, as well (Table 3). However, no significant spectral broadening of the fluorescence emission was observed (Figure 2, right, and Figure 5S of the Supporting Information).

As a further consequence of DNA conjugation, the fluorescence decay times of the dyes were altered. Compared to that of A610-COOH, the decay time of the ssDNA-conjugated A610 (τ) was increased from 3.3 ± 0.1 ns to values between 4.0 ± 0.1 and 4.6 ± 0.1 ns depending on the DNA length (see Table 1S of the Supporting Information). The decay time of A680 was increased from 1.7 ± 0.1 ns for A680-COOH to values between 2.1 ± 0.1 and 2.4 ± 0.1 ns for the ssDNA-conjugated dye (see Table 1S of the Supporting Information). The fluorescence decay times of the dye−dsDNA conjugates were similar to those of the corresponding dye−ssDNA conjugates (Table 3). However, in contrast to those of the dye−ssDNA conjugates, the decay times of the dye−dsDNA conjugates showed, if any, only a minor dependence on DNA length.

In a further step, the A610−dsDNA conjugates were excited in the spectral range of the additional absorption band at a λ_{ex} of 650 nm (vide supra). An "anomalous" fluorescence emission band with a maximum λ_{em} at ∼665 nm that was not detected for A610-COOH was observed (Figure 2, right). The intensity of this emission band depended on temperature; with increasing temperature, the intensity decreased (Figure 6S of the Supporting Information, right). The same was observed in the fluorescence excitation spectra (Figure 6S of the Supporting Information, left). The corresponding fluorescence decays (λ_{ex} = 650 nm; λ_{em} = 675 nm; T = 295 K) were double-exponential containing a short component with a decay time τ_1 of 1.6 ± 0.1 ns (f_1 = 29−40%) and a long component with a τ_2 of 4.0 ± 0.2 ns (f_2 = 60−71%) (f_1 and f_2 differed slightly for the A610−dsDNA conjugates with different DNA lengths).

In a reference experiment, absorption and fluorescence spectra as well as the fluorescence decay time of A610-COOH in the presence of unlabeled 24 bp dsDNA were measured. Except for a small bathochromic shift of ∼3 nm in the absorption maximum, no further alterations in the absorption of A610-COOH were observed [no spectral broadening and no additional absorption band at 650 nm as observed for the DNA-conjugated dye (vide supra)]. The fluorescence spectra showed the regular excitation and emission bands of A610-COOH [no bathochromic shifts and no anomalous emission band at 665 nm as observed for the DNA-conjugated dye (vide supra)]. The fluorescence decay time of A610-COOH (λ_{ex} = 615 nm, and λ_{em} = 635 nm) was slightly increased from 3.3 ± 0.1 ns without DNA to 3.8 ± 0.1 ns in the presence of the dsDNA.

Interaction between Conjugated Dyes and ssDNA. To reveal molecular dye−ssDNA interactions, the mobility of the conjugated dyes was investigated using FCS and time-resolved fluorescence anisotropy measurements. Comparing the FCS curves of the free dyes and the dye−ssDNA conjugates in water, we found an increase of the lateral diffusion time t_{lat} (see Figure 3, left, for A610). The lateral diffusion time t_{lat} was increased with an increase in DNA length (see Figure 3, left, for A610). As t_{lat} was increased, the diffusion coefficient D_{lat} was decreased (according to eq 8). For both free dyes A610-COOH and A680-COOH, similar values of D_{lat} were obtained (Table 4). According to the similar molecular weight increase of the diffusing units when the dyes are conjugated to the ssDNA (see Table 1 for M values of the ssDNA), the D_{lat} values of both dyes were

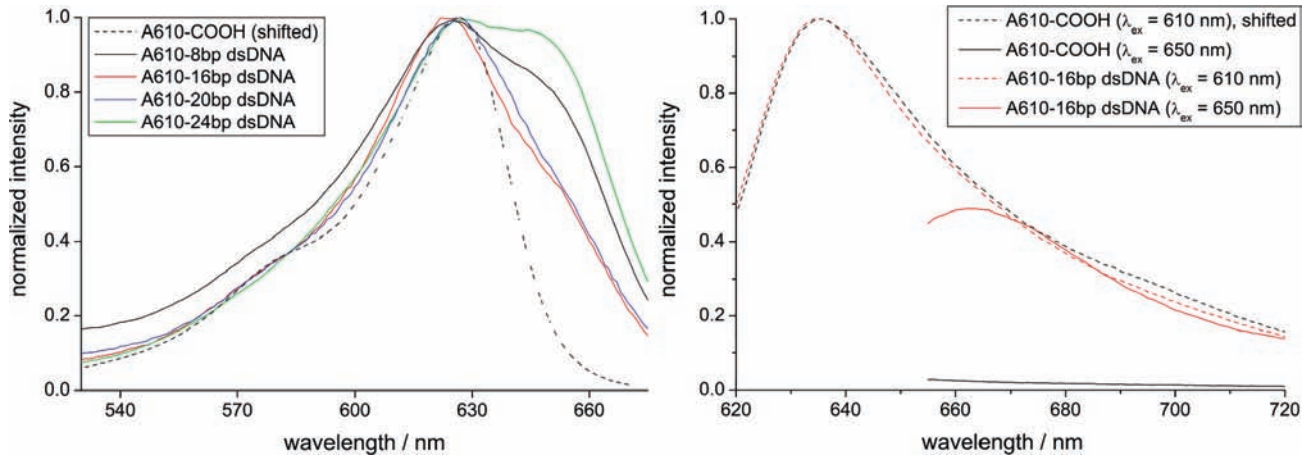

Figure 2. Fluorescence excitation (left) and emission (right) of the A610−dsDNA conjugates. The fluorescence excitation spectra were recorded at a λ_{em} of 690 nm and the emission spectra at λ_{ex} values of 610 and 650 nm. To provide a better comparison of the spectra, the A610-COOH excitation spectrum was bathochromically shifted by 11 nm and the emission spectrum (λ_{ex} = 610 nm) by 2 nm. The fluorescence emission spectra were normalized to the maximum of the regular fluorescence emission (at 634 and 636 nm, respectively).

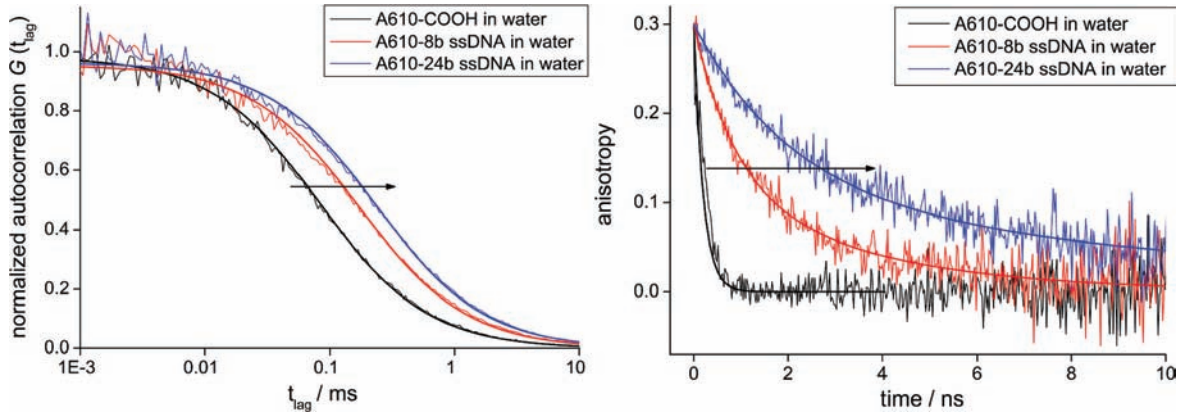

Figure 3. FCS curves (left) and time-resolved anisotropy decays (right) of the free dye A610-COOH and the A610−ssDNA conjugates. The FCS and the time-resolved anisotropy curves were measured at 295 K. For the FCS measurements, the samples were excited at a λ_{ex} of 622 nm and the emission was detected at a λ_{em} of >630 nm. The anisotropy decays were measured at a λ_{ex} of 615 nm and a λ_{em} of 635 nm.

decreased comparably with an increase in DNA length (Table 4). The hydrodynamic radii of the diffusing units (R_h) that were calculated via D_{lat} according to eq 9 are given in Table 4. As expected, an increase in R_h was found because of the ssDNA conjugation of the dyes, and a small R_h increase was observed with an increase in DNA length.

The rotational motion of the ssDNA-conjugated dyes was investigated with time-resolved fluorescence anisotropy measurements. For the free dyes in water, fast, single-exponential anisotropy decays were measured (see Figure 3, right, for A610-COOH). As expected from the comparable molecular weights of the dyes, similar rotational correlation times (θ) were determined for A610-COOH and A680-COOH (Table 5). These values are in good accordance with the rotational correlation times θ_{theo} (Table 5) that were calculated from the R_h values of the free dyes (Table 4) according to eq 6. Compared to those of the free dyes, the anisotropy decays of the ssDNA-conjugated dyes were slower (see Figure 3, right, for the ssDNA-conjugated A610). This effect was enhanced with an increase in DNA length. For the double-exponential anisotropy decays of the dye−ssDNA conjugates, the anisotropy model for the segmental mobility of a biopolymer-bound dye (eq 5) was successfully applied. In Table 5, the fit parameters provided by this

Table 4. Diffusion Coefficients (D_{lat}) and Hydrodynamic Radii (R_h) of the Free Dyes and the Dye−ssDNA Conjugates in Water at 295 K[a]

	D_{lat} (μm^2/ms) of A610	D_{lat} (μm^2/ms) of A680	R_h (nm) of A610	R_h (nm) of A680
COOH	0.31 ± 0.03	0.36 ± 0.04	0.7 ± 0.1	0.6 ± 0.1
8b ssDNA	0.15 ± 0.02	0.18 ± 0.02	1.5 ± 0.2	1.3 + 0.2/− 0.1
16b ssDNA	0.13 ± 0.01	0.16 ± 0.02	1.7 ± 0.1	1.4 ± 0.2
20b ssDNA	0.12 ± 0.01	0.14 ± 0.01	1.9 + 0.2/− 0.1	1.6 ± 0.1
24b ssDNA	0.10 ± 0.01	0.13 ± 0.01	2.3 + 0.3/− 0.2	1.7 ± 0.1

[a]The FCS measurements were performed using a λ_{ex} of 622 nm and a λ_{em} of >630 nm for A610 and a λ_{ex} of 630 nm and a λ_{em} of >640 nm for A680. The error in D_{lat} was determined from repeated measurements, and the error in R_h was calculated from the error in D_{lat}.

model [α (contribution of the fast rotational motion to the anisotropy decay), θ_1 (rotational correlation time of the fast motion), and θ_2 (rotational correlation times of the slow motion)] are summarized. θ_2 was calculated from R_h (Table 4) according to eq 6 and fixed during the fitting process. Comparable θ_2 values were obtained for the dye−ssDNA conjugates of equal DNA length because of their similar R_h values. As R_h was increased with an increase in DNA length, θ_2 was increased, as well (Table 5). The segmental motion of the dye−ssDNA

dx.doi.org/10.1021/bc200379y | Bioconjugate Chem. 2011, 22, 2546−2557

Table 5. Rotational Correlation Times (θ) of the Free Dyes, the Dye−ssDNA Conjugates, and the Singly Labeled Dye−dsDNA Conjugates at 295 K[a]

	θ (ns)	θ_{theo} (ns)
A610-COOH	0.3 ± 0.1	0.4 ± 0.1
A680-COOH	0.4 ± 0.1	0.2 ± 0.1

	α		θ_1 (ns)		θ_2 (ns)	
	ssDNA	dsDNA	ssDNA	dsDNA	ssDNA	dsDNA
A610−8b/bp	0.52 + 0.21/− 0.26	0.21 ± 0.05	0.7 + 0.3/− 0.4	0.6 ± 0.2	3.3 + 1.8/− 1.0	3.4 ± 0.2
A610−16b/bp	0.81 + 0.08/− 0.13	0.36 ± 0.03	1.7 + 0.1/− 0.2	1.1 ± 0.2	5.1 + 1.4/− 1.0	8.7 ± 0.5
A610−20b/bp	0.71 + 0.10/− 0.15	0.31 ± 0.03	1.8 + 0.2/− 0.3	1.2 ± 0.2	6.5 + 1.9/− 1.4	11.4 ± 0.7
A610−24b/bp	0.73 + 0.07/− 0.11	0.44 ± 0.02	2.3 + 0.2/− 0.3	1.1 ± 0.1	11.3 + 4.2/− 2.8	14.6 ± 1.0
A680−8b/bp	0.88 + 0.09/− 0.39	0.30 ± 0.13	1.0 + 0.1/− 0.2	0.8 ± 0.3	1.9 + 0.8/− 0.5	3.0 ± 0.3
A680−16b/bp	0.83 + 0.11/− 0.47	0.36 ± 0.07	1.4 + 0.1/− 0.4	1.3 ± 0.3	2.8 + 1.4/− 0.8	7.8 ± 1.0
A680−20b/bp	0.60 + 0.12/− 0.18	0.39 ± 0.07	1.3 + 0.2/− 0.3	1.3 ± 0.3	4.1 + 1.0/− 0.8	10.0 ± 1.6
A680−24b/bp	0.51 + 0.12/− 0.15	0.43 ± 0.09	1.1 + 0.2/− 0.3	1.6 ± 0.5	5.1 + 1.4/− 1.0	15.1 ± 3.3

[a]The dye−ssDNA conjugates were investigated in water and the dye−dsDNA conjugates in a 1 M NaCl solution. The corresponding anisotropy decays were measured at a λ_{ex} of 615 nm and a λ_{em} of 635 nm for A610 and a λ_{ex} of 688 nm and a λ_{em} of 703 nm for A680. θ_{theo} for the free dyes was calculated from R_h (Table 4). The error in θ_{theo} was determined from the error in R_h. The segmental rotational correlation time of the dye−DNA conjugates is θ_1. The contribution of the segmental motion to the anisotropy decay is given by α, and θ_2 refers to the overall rotational motion. θ_2 for the dye−ssDNA conjugates was calculated from R_h (Table 4) and fixed during the fitting process. The error in θ_2 was determined from the error in R_h. The error in θ_1 as well as α for the dye−ssDNA conjugates was determined from the error in θ_2. For the dye−dsDNA conjugates, the errors in α, θ_1, and θ_2 result from the error in the fit.

conjugates exhibited an increased rotational correlation time θ_1 compared to those of the free dyes (Table 5). For the A610−ssDNA conjugates, θ_1 was slightly increased with an increase in DNA length, whereas for the A680−ssDNA conjugates, a consistent θ_1 of ∼1 ns was obtained regardless of the DNA length (Table 5). For both dye−ssDNA conjugates, the segmental rotation contributed mostly to the depolarization process with an α of 60−90% (except for the A610−8b ssDNA and A680−24b ssDNA conjugate).

Interaction between Conjugated Dyes and dsDNA. The dye−dsDNA interactions were investigated on the singly labeled dye−dsDNA conjugates using time-resolved fluorescence anisotropy measurements. Similar to those of the dye−ssDNA conjugates (vide supra), double-exponential anisotropy decays that could be fitted very well with the model for the segmental mobility of a biopolymer-bound dye were measured (Figure 7S of the Supporting Information, blue line, and Figure 8S of the Supporting Information, blue and red line). However, compared to that of the dye−ssDNA conjugates, the contribution of segmental rotation to the anisotropy decay of the dye−dsDNA conjugates was decreased (Table 5). For both dyes, a similar rotational correlation time for the segmental motion (θ_1) of approximately 1 ns was determined (Table 5). As the molecular weight (M) is almost equal for the A610− and A680−dsDNA conjugates of the same length, the rotational correlation times for the overall rotation of the macromolecule (θ_2) are similar for the dye−dsDNA conjugates of equal length (Table 5). Assuming the M of the dyes (see Experimental Procedures) to be significantly smaller than the M of the DNA (Table 1), we approximated theoretical values for θ_2 by calculating the rotational correlation times of the DNA double helices with HYDROPRO.[52] Three rotational correlation times were obtained for each DNA double strand in the ranges of 3−4 ns for the 8 bp dsDNA, 6−13 ns for the 16 bp dsDNA, 8−21 ns for the 20 bp dsDNA, and 10−31 ns for the 24 bp dsDNA. The experimentally determined θ_2 values (Table 5) correspond well with the theoretical values.

In a further step, the fluorescence anisotropy of the A610−dsDNA conjugates at the anomalous fluorescence emission band [λ_{ex} = 650 nm, and λ_{em} = 675 nm (vide supra)] was investigated. Compared to the anisotropy decays measured at the regular fluorescence emission (λ_{ex} = 615 nm, and λ_{em} = 635 nm), significantly delayed anisotropy decays were found (Figure 7S of the Supporting Information). This delay can be attributed to a complete loss of segmental mobility. The anisotropy decays could be fitted single-exponentially providing a single rotational correlation time for each A610−dsDNA conjugate (Table 2S of the Supporting Information), which is in the range of the predicted rotational correlation times for the corresponding DNA double strand (vide supra).

To further investigate the dye−dsDNA interactions in a reference experiment, molecular interactions between the free dyes and unlabeled dsDNA were investigated. For A680-COOH in the absence and presence of unlabeled 24 bp dsDNA (λ_{ex} = 688 nm, and λ_{em} = 703 nm), no differences in the rotational correlation times (θ = 0.4 ± 0.1 ns for both samples) and the fluorescence decay time (τ = 1.8 ± 0.1 ns for both samples) were found. In contrast, the single-exponential fluorescence anisotropy decay of A610-COOH (λ_{ex} = 615 nm, and λ_{em} = 635 nm) in the absence of DNA (θ = 0.3 ± 0.1 ns) turned into a double-exponential decay in the presence of unlabeled 24 bp dsDNA (Figure 9S of the Supporting Information, red line). In the latter case, two rotational correlation times were obtained: θ_1 = 0.3 ns (this value was fixed to the rotational correlation time of free A610-COOH during the fit) with a contribution of 77 ± 1%, and θ_2 = 14.8 ± 1.7 ns with a contribution of 23 ± 1%. The obtained θ_2 is in excellent agreement with the θ_2 determined for the A610−24 bp dsDNA conjugate (Table 5).

Förster Resonance Energy Transfer (FRET). For the A610/A680 FRET pair, an overlap integral of 1.15×10^{16} nm^4 M^{-1} cm^{-1} was determined using the area-normalized fluorescence emission spectrum of A610-COOH and the absorption spectrum of A680-COOH measured in a 1 M NaCl solution. In the case of full rotational freedom of the D and A molecules, the average κ^2 is $^2/_3$, resulting in a Förster distance (R) of 7.1 ± 0.2 nm [calculated according to eq 10 using a φ_D of 0.6 and an n of 1.343 (for a 1 M NaCl solution)[59]]. The error in R_0 results from the experimental errors in the

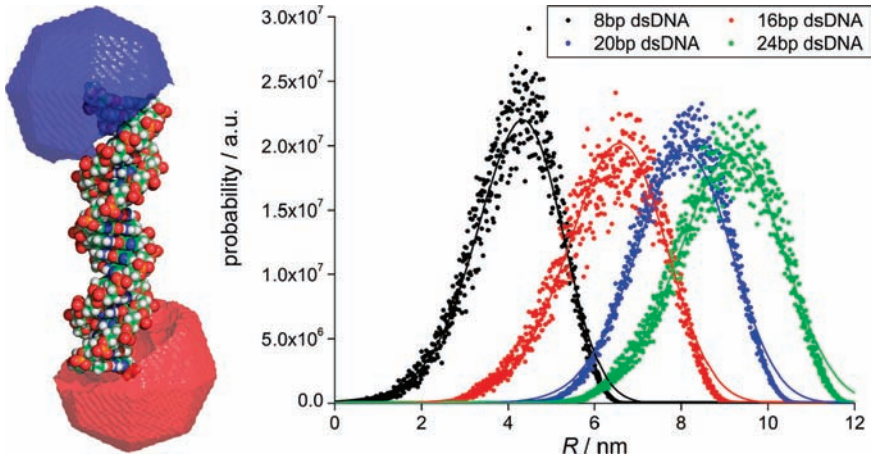

Figure 4. Accessible volumes (AV) for the dyes attached to the opposite 5′-ends of the DNA double helix (left) and D−A distance (R) distributions (right) calculated from the AV data. The accessible volumes of the dyes conjugated to the 20 bp dsDNA are colored blue for A610 and red for A680.

fluorescence quantum yield of A610 as well as in the extinction coefficient of A680. If one dye species (either the D or the A molecule) is fixed in a defined orientation and the other dye species is freely rotating, then the average values of κ^2 are found between $^1/_3$ (for a perpendicular orientation of the transition dipole moments to the line connecting the centers of D and A) and $^4/_3$ (for a parallel or antiparallel orientation of the transition dipole moments to the line connecting the centers of D and A) (according to eq 12; see also Figure 1S of the Supporting Information for a detailed analysis). In these cases, the corresponding limiting values for R_0 are 6.3 nm ($\kappa^2 = {}^1/_3$) and 8.0 nm ($\kappa^2 = {}^4/_3$). The experimental FRET efficiency was determined using the fluorescence decay time of A610 in the absence and presence of A680. For this purpose, the singly labeled A610−dsDNA and doubly labeled A610/A680−dsDNA conjugates were used. In the latter case, D and A are placed in defined proximity separated by the rigid dsDNA spacer. The volume that is accessible for the dyes because of the structural flexibility of the linker is illustrated in Figure 4 (left). The resulting D−A distance (R) distributions are shown in Figure 4 (right).

The fluorescence decays of the A610/A680−dsDNA conjugates were double-exponential (except for that of the A610/A680−24 bp dsDNA conjugate) containing a short component that depended on the length of the DNA spacer and a long component that was constant for all DNA lengths. The short component τ_{DA} ranging from 0.4 ± 0.05 to 3.7 ± 0.1 ns (Table 3S of the Supporting Information) was attributed to the fluorescence quenching of A610 due to FRET. The long component τ_2 ranging from 4.1 ± 0.1 to 4.3 ± 0.1 ns was similar to the τ determined for the A610−DNA conjugates in the absence of A (Table 3S of the Supporting Information). Consequently, τ_2 was attributed to those A610 molecules that did not participate in FRET because of an unfavorable and fixed orientation of the transition dipoles of both dyes ($\kappa^2 = 0$) as well as unpaired A610−ssDNA conjugates. The fluorescence decay of the A610/A680−24 bp dsDNA conjugates needed to be fitted single-exponentially, because τ_{DA} and τ_2 were not sufficiently differentiated to be resolved. The decay time of the A610−dsDNA conjugates (τ_D) is stated in Table 3S of the Supporting Information.

For a comparison of theoretically and experimentally obtained FRET parameters, the theoretical and the experimental FRET efficiency (E_{theo} and E_{exp}, respectively) were plotted versus the D−A distance (R) (Figure 5). E_{theo} was calculated for different R values via R_0 (for $\kappa^2 = {}^2/_3$) according to eq 13 (Figure 5, black

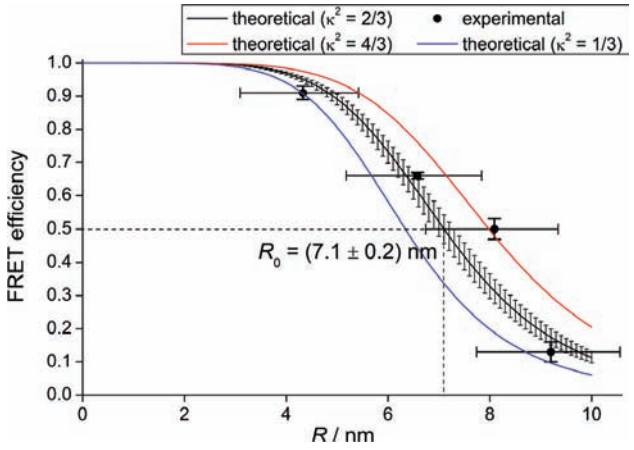

Figure 5. FRET efficiency of the A610/A680 FRET pair at different D−A distances (R). The error in E_{theo} (for $\kappa^2 = {}^2/_3$) was calculated from the error in R_0, which results from the experimental errors for the fluorescence quantum yield of A610 as well as the extinction coefficient of A680. The error in E_{exp} (vertical error bars, ΔE) was calculated from the errors in τ_{DA} and τ_D, which were determined from repeated measurements. The horizontal error bars (ΔR) indicate the distribution of E_{exp} that results from the full width at half-maximum of the R distributions (Figure 4, right). In addition, the interval of E_{theo}, which is defined by the minimal ($\kappa^2 = {}^1/_3$) and maximal ($\kappa^2 = {}^4/_3$) average κ^2 values, is shown (area between the blue line and the red line).

line). The error in E_{theo} was calculated from the error in R_0 (vide supra). E_{exp} was calculated according to eq 14 using τ_{DA} and τ_D (vide supra). The peak maxima of the R distributions (Figure 4, right) were used as the average distance between D and A, and E_{exp} was plotted versus these values (Figure 5, black dots). The error in E_{exp} was calculated from the errors in τ_{DA} and τ_D, which were determined from repeated measurements (Figure 5, ΔE, vertical error bars). The distribution of E_{exp} resulting from the full width at half-maximum of the R distributions (Figure 4, right) is indicated by the horizontal error bars (Figure 5, ΔR). In addition, E_{theo} was calculated for the minimal and maximal average κ^2 that can be achieved in the case of a complete rotational restriction of one dye species and rotational

dx.doi.org/10.1021/bc200379y | Bioconjugate Chem. 2011, 22, 2546−2557

freedom of the other (vide supra). The results are shown in Figure 5 (blue line for $\kappa^2 = {}^1/_3$ and red line for $\kappa^2 = {}^4/_3$). As one can see in Figure 5, E_{exp} fits very well in the range of the limiting E_{theo} for κ^2 values of ${}^1/_3$ and ${}^4/_3$.

DISCUSSION

As a general effect of DNA conjugation, the absorption and fluorescence maxima of both oxazine dyes were shifted to longer wavelengths and the fluorescence decay times were increased. Such changes in the basic photophysical properties upon bioconjugation have been observed previously for other dyes, including oxazine dyes.[23,37,46,60,61] For the conjugated A680, no influence of DNA length and sequence on absorption and fluorescence spectra was observed. However, the fluorescence decay times of both dyes were slightly increased with an increase in the length of the ssDNA; no such effect of chain length was seen in the case of conjugation to the dsDNA. Because of the structural flexibility of the ssDNA, small length-dependent changes in the microenvironment of the dyes may be induced, e.g., because of the rotational flexibility of the DNA−phosphate backbone or the formation of single intramolecular hydrogen bonds. Such a structural flexibility does not exist in the case of the dsDNA, and the accessible DNA microenvironment is now strictly defined (see Figure 4, left). Compared to A680, the conjugated A610 exhibited stronger alterations of its photophysics. In addition to the bathochromically shifted absorption maximum, an additional spectral broadening toward the red spectral range caused by a new absorption band was detected. The new absorption band was more intense for the dsDNA conjugates than for the ssDNA conjugates. The same was observed in the fluorescence excitation spectra, but the new band was less pronounced compared to the absorption spectra. The altered absorption points toward strong ground-state interactions between the electronic systems of A610 and DNA that require spatial proximity between them. In addition, a new red-shifted fluorescence emission band was detected upon excitation at the new absorption band. The new emission band along with the altered absorption might be an indication of a charge transfer process between the dye and DNA. Accordingly, at least two different species of A610 must be present, one species that shows the regular absorption/emission and one species causing the new absorption/emission band. The differences in the relative intensities (new to regular band) between absorption and excitation spectra may be attributed to differences in the fluorescence quantum yields of both species. In line with the results of the absorption measurements, the new emission band was much more intense for the dsDNA conjugates than for the ssDNA conjugates. The differences observed for the A610−ssDNA and −dsDNA conjugates concerning the relative intensity of the new absorption/emission band indicate that the three-dimensional DNA structure might play a role in mediating the charge transfer interaction. Although in the A610−dsDNA case the conjugates of different lengths possess the same three-dimensional DNA structure (B-type double helix), the new absorption band was differently pronounced (the same was observed for the A610−ssDNA conjugates). This suggests that the differences in the DNA sequence of the dye−DNA conjugates are responsible for the varying intensity of the new absorption band. The results of the anisotropy measurements and the AV simulations indicate that the terminal 5 bp are similar easily accessible for A610 in each DNA conjugate (vide infra). However, no clear dependence on the guanine-cytosine (GC) content (G is often involved in electron transfer processes and acts as a fluorescence quencher[41,46]) was found. To elucidate the influence of the terminal DNA sequence on the altered absorption/emission of conjugated A610, further investigations based on the systematic variation of the last base pairs are required.

To reveal steric dye−DNA interactions, we performed detailed time-resolved fluorescence anisotropy and fluorescence correlation spectroscopy (FCS) measurements. From the anisotropy and FCS results, it was concluded that the mobility of the dyes was altered because of the conjugation to ssDNA as well as to dsDNA. Comparable diffusion coefficients were determined for the A610− and A680−ssDNA conjugates of equal DNA length. Studies of the rotational mobility revealed steric interactions between dyes and DNA. The rotational motion of a dye that is covalently linked to a biomolecule can consist of several (coupled) rotational components (rotation of the dye, the linker, and the biomolecule around the different axes). In an anisotropy decay, the different rotations can only be resolved if they differ sufficiently in their corresponding rotational correlation times. The anisotropy model for the segmental mobility of a biopolymer-bound dye distinguishes between two rotational components, the fast segmental rotation of a part of the macromolecule including the dye (e.g., dye and linker) and the slow overall rotation of the whole macromolecule. This model was successfully applied in the analysis of the anisotropy decays of the dye−DNA conjugates. Because of DNA conjugation, the rotational correlation time of both dyes that is represented by the fast segmental motion (θ_1) was increased compared to that of the free dyes. This was due to the coupling of the rotational motions of the dye and C6-amino linker. For the dsDNA conjugates of both dyes as well as the A680−ssDNA conjugates, θ_1 was independent of DNA length whereas θ_1 for the A610−ssDNA conjugates was slightly increased with an increase in DNA length. In the case of the A610−ssDNA conjugates, this finding indicates a slightly hindered dye−linker rotation. The conjugated A610 might sterically interact with variable, length-dependent ssDNA structures that are formed due to the structural flexibility of the DNA single strands (e.g., by the formation of single intramolecular hydrogen bonds), resulting in a slightly delayed dye−linker rotation. On the other hand, the rigid DNA double helix provides a structurally similar microenvironment for the conjugated dyes that is independent of DNA length. Hence, the dye−linker rotation of the dsDNA conjugates of both dyes was independent of DNA length. The fast θ_1 of ∼1 ns that was determined for the segmental motion of the dye−dsDNA conjugates as well as the A680−ssDNA conjugates was consequently attributed to an unhindered dye−linker rotation. The contribution of the segmental rotation to the overall anisotropy decay (α) was decreased from the dye−ssDNA conjugates to the dye−dsDNA conjugates. For the ssDNA conjugates of both dyes, the segmental rotation dominated the anisotropy decay, whereas for the dye−dsDNA conjugates, the slow rotational motions of the whole macromolecules were dominant. These results indicate an increased level of coupling between the rotational motions of the conjugated dyes and the DNA molecules in the case of the dye−dsDNA conjugates. Such a rotational coupling of dye and DNA was also observed in a reference experiment, where the rotational mobility of free A610-COOH in the presence of unlabeled 24 bp dsDNA was investigated. In this case, two rotational correlation times were detected. One was equal to the rotational correlation time of the free dye in the absence of DNA, and the other corresponded to θ_2 for the slow

rotational motion of the dye−24 bp dsDNA conjugates. As the unlabeled DNA molecule by itself is not fluorescent under the applied excitation conditions, these results strongly point toward molecular dye−dsDNA interactions leading to an equilibrium between DNA-bound dye molecules whose fast rotation is completely hindered and unbound dye molecules that rotate freely. From these findings, we concluded that in the case of the dye−dsDNA conjugates two subpopulations of conjugated dyes exist, one that is able to perform a free fast dye−linker rotation and another subpopulation whose rotation was completely hindered because of strong molecular dye−dsDNA interactions. As the dye−DNA rotational coupling and, accordingly, the steric dye−DNA interactions were strengthened from ssDNA to dsDNA conjugates, we suppose that the dyes interact with specific domains of the DNA double helix or functional groups (e.g., hydroxyl groups) whose accessibility is promoted by the double-helix structure. For several prominent dyes, e.g., Cy3, Cy5, or tetramethylrhodamine, interactions with the major groove of the DNA double helix as well as stacked conformations on top of the dsDNA are described in the literature (for terminally attached dyes).[14−17] Such molecular interactions could lead to a hindrance of the dye rotation, resulting in a strong coupling of the dye mobility to the DNA rotation.[17,37] The AV simulations demonstrated that a region containing the terminal 5 bp of the DNA double helix is accessible for the conjugated dyes. Hence, interactions of dyes with specific dsDNA domains are sterically possible. These aspects support the assumption that molecular interactions with specific dsDNA domains are responsible for the complete rotational restriction that was observed for a fraction of dsDNA-conjugated dyes.

To shed more light upon the specific A610−dsDNA interactions causing the new absorption and anomalous fluorescence emission band (vide supra), we measured anisotropy decays using these specific excitation and emission wavelengths. In this case, the rotational mobility of the dye was completely coupled to the DNA rotation and a complete loss of the segmental mobility was observed. This result suggests that the electronic A610−DNA interactions observed in the absorption and emission spectra were accompanied by strong steric interactions between the dye and dsDNA. Although strong steric interactions were also observed between free A610-COOH and unlabeled dsDNA (vide supra), no alterations in absorption and fluorescence emission were found in this case (except for a minor bathochromic shift in the absorption maximum and a small decay time increase indicating a change in the microenvironment of the dye). This finding suggests that a specific steric dye−DNA arrangement is necessary to induce the altered absorption and dual fluorescence emission that is formed only when A610 is covalently attached to the end of the DNA double helix. Such a specific dye−DNA arrangement could be induced by hydrogen bonds between the dimethylamino group of A610 (see Figure 1, top left) and, e.g., the opposite 3′-OH end of the complementary strand of the DNA double helix. As we expect that such a dye−DNA interaction would be more and more disrupted with an increase in temperature, the influence of temperature on the intensity of the anomalous fluorescence band was investigated. In fact, the intensity of the anomalous fluorescence excitation and emission band was decreased with an increase in temperature. This result supports the assumption that specific interactions such as hydrogen bonds between a dye and DNA are responsible for the observed altered absorption and dual fluorescence emission of DNA-conjugated A610.

The results discussed above show that even structurally similar dyes (dyes of the same class) can be differently affected in their photophysics upon bioconjugation. For A610, strong alterations in the absorption and fluorescence properties were found that were not observed for A680 to the same extent. Although both dyes exhibited comparably pronounced steric interactions with the DNA in the case of the dye−dsDNA conjugates, A610 interacted with dsDNA even if it was not forced by covalent binding into the proximity of the DNA (in the case of no bioconjugation). The driving force for this interaction might be attributed to the increased hydrophobicity of A610 compared to that of A680 [which is more hydrophilic because of its sulfate group (see Figure 1, left)]. Both dyes possess nitrogen atoms that are able to form hydrogen bonds with functional groups of the DNA such as hydroxyl groups; however, the dimethylamino group of A610 is located in a more exposed position. Along with the higher hydrophobicity, this may result in a stronger dye−DNA interaction for A610 compared to A680.

For the investigation of FRET, doubly labeled dsDNA of different lengths was used in which the donor (D) A610 and the acceptor (A) A680 were attached to the opposite 5′-ends. The A610/A680−dsDNA conjugates showed a distance-dependent fluorescence quenching of A610 due to FRET. The rotational mobility of D and A influences the transition dipole orientation factor κ^2, which is an important parameter affecting the effective Förster distance and, thus, the FRET efficiency (according to eqs 10 and 13). In the anisotropy measurements of the singly labeled dsDNA conjugates, it was found that a subpopulation of the conjugated dyes was able to perform a free fast dye−linker rotation, whereas the rotational mobility of the other subpopulation was completely hindered (vide supra). As the dyes do not sterically interact, it was assumed that for the doubly labeled dsDNA conjugates all combinations of dye mobilities (D_{free}−A_{free}, D_{free}−A_{fixed}, D_{fixed}−A_{free}, and D_{fixed}−A_{fixed}) are equally probable. In the case of rotational freedom of both dye species (D_{free}−A_{free}), the average κ^2 is $^2/_3$ (according to eq 11 and averaging over the polar angle θ_D[56]). In the case of rotational freedom of one dye species (either D or A) and a complete rotational restriction of the other dye species (D_{free}−A_{fixed} and D_{fixed}−A_{free}), the minimal and maximal average κ^2 values are $^1/_3$ and $^4/_3$, respectively, depending on the angle between the transition dipole moments of the fixed dye species and the line connecting the centers between D and A (according to eq 12 and Figure 1S of the Supporting Information). Hence, assuming an average κ^2 between $^1/_3$ and $^4/_3$ is a good approximation in the majority of cases. The contribution of the fraction of doubly labeled dsDNA conjugates, in which the rotational mobility of both dyes was completely hindered (D_{fixed}−A_{fixed}), to FRET was assumed to be negligible because of unfavorable transition dipole orientations [the events, where no FRET occurs due to $\kappa^2 = 0$, can be realized in an infinite number of ways (whenever the electric field of D and the absorption transition dipole moment of A are perpendicular to each other; see eq 11)].[56] This assumption was supported by the occurrence of a second unquenched fluorescence decay time of A610 in the doubly labeled dsDNA conjugates. Consequently, the Förster distance and the resulting theoretical FRET efficiencies were calculated for both limiting cases of the average κ^2. Considering the high linker flexibility in the determination of the D−A distances, the experimental FRET efficiency calculated from the

fluorescence quenching of A610 (vide supra) was found to be exactly in the range of the theoretical FRET efficiencies for κ^2 values of $^1/_3$ and $^4/_3$. This excellent accordance strongly supports our assumption that at least one dye species (either D or A) facilitated the appropriate alignment of the transition dipoles in the doubly labeled dsDNA conjugates for FRET to be operative. A small experimental error must be taken into account for the experimental FRET efficiencies of the 20 and 24 bp dsDNA conjugates that was attributed to the inaccuracy of the resolution of two insufficiently differing fluorescence decay times (τ_{DA} was determined in the presence of τ_2), resulting in an increased E_{exp} for the 20 bp dsDNA conjugates and a slightly decreased E_{exp} for the 24 bp dsDNA conjugates.

In summary, we characterized a promising novel FRET pair for the far-red spectral range with regard to its applicability for oligonucleotide probes. In this process, we paid special attention to molecular dye−DNA interactions and the resulting alterations in the photophysics of the dyes. Our study underlines the necessity to conduct case-by-case studies for each fluorescence probe, even if the probes belong to the same class (e.g., like in our case to oxazine dyes), because of the possibility of dye-specific interactions, which may arise from small differences in the chemical structure. For the ATTO 610/ATTO 680 FRET pair, a considerably large Förster distance of approximately 7 nm was theoretically calculated and experimentally approved, recommending the application of this FRET pair not only for the detection of binding reactions between nucleic acids in living cells but also for the monitoring of interactions of larger biomolecules such as proteins.

■ ASSOCIATED CONTENT

Supporting Information

Average κ^2 as a function of θ_D; additional absorption, fluorescence excitation, and emission spectra of the free dyes and the dye−DNA conjugates; fluorescence decay times of the dye−ssDNA conjugates and the doubly labeled dsDNA conjugates; fluorescence anisotropy decays of the free dyes, the dye−dsDNA conjugates, and A610-COOH in the presence of unlabeled dsDNA; and rotational correlation times of the A610−dsDNA conjugates. This material is available free of charge via the Internet at http://pubs.acs.org.

■ AUTHOR INFORMATION

Corresponding Author

*Universität Potsdam, Institut für Chemie, Physikalische Chemie, Karl-Liebknecht-Straße 24-25, 14476 Potsdam-Golm, Germany. E-mail: kumke@uni-potsdam.de. Telephone: ++49/331/9775209. Fax: ++49/331/9775058.

■ REFERENCES

(1) Didenko, V. V. (2001) DNA probes using fluorescence resonance energy transfer (FRET): Designs and applications. *BioTechniques 31*, 1106−1121.

(2) Bao, G., Rhee, W. J., and Tsourkas, A. (2009) Fluorescent probes for live-cell RNA detection. *Annu. Rev. Biomed. Eng. 11*, 25−47.

(3) Cissell, K. A., Hunt, E. A., and Deo, S. K. (2008) Resonance energy transfer methods of RNA detection. *Anal. Bioanal. Chem. 393*, 125−135.

(4) Tyagi, S. (2009) Imaging intracellular RNA distribution and dynamics in living cells. *Nat. Methods 6*, 331−338.

(5) Tsuji, A., Koshimoto, H., Sato, Y., Hirano, M., Sei-lida, Y., Kondo, S., and Ishibashi, K. (2000) Direct observation of specific messenger RNA in a single living cell under a fluorescence microscope. *Biophys. J. 78*, 3260−3274.

(6) Anderson, B. J., Larkin, C., Guja, K., and Schildbach, J. F. (2008) Using fluorophore-labeled oligonucleotides to measure affinities of protein-DNA interactions. *Methods Enzymol. 450*, 253−272.

(7) Pagano, J. M., Clingman, C. C., and Ryder, S. P. (2011) Quantitative approaches to monitor protein-nucleic acid interactions using fluorescent probes. *RNA 17*, 14−20.

(8) Singh, Y., Pandey, A., Dubey, K. K., Watal, G., and Misra, K. (2000) Fluorescence resonance energy transfer: A diagnostic tool in oligonucleotide therapy. *Curr. Sci. 78*, 487−491.

(9) Schoen, I., Krammer, H., and Braun, D. (2009) Hybridization kinetics is different inside cells. *Proc. Natl. Acad. Sci. U.S.A. 106*, 21649−21654.

(10) Knemeyer, J.-P., Herten, D.-P., and Sauer, M. (2003) Detection and identification of single molecules in living cells using spectrally resolved fluorescence lifetime imaging microscopy. *Anal. Chem. 75*, 2147−2153.

(11) Losytskyy, M. Y., Volkova, K. D., Kovalska, V. B., Makovenko, I. E., Slominskii, Y. L., Tolmachev, O. I., and Yarmoluk, S. M. (2005) Fluorescent properties of pentamethine cyanine dyes with cyclopentene and cyclohexene group in presence of biological molecules. *J. Fluoresc. 15*, 849−857.

(12) Yarmoluk, S. M., Lukashov, S. S., OgulChansky, T. Y., Losytskyy, M. Y., and Kornyushyna, O. S. (2001) Interaction of cyanine dyes with nucleic acids. XXI. Arguments for half-intercalation model of interaction. *Biopolymers 62*, 219−227.

(13) Unruh, J. R., Gokulrangan, G., Lushington, G. H., Johnson, C. K., and Wilson, G. S. (2005) Orientational dynamics and dye-DNA interactions in a dye-labeled DNA aptamer. *Biophys. J. 88*, 3455−3465.

(14) Iqbal, A., Arslan, S., Okumus, B., Wilson, T. J., Giraud, G., Norman, D. G., Ha, T., and Lilley, D. M. J. (2008) Orientation dependence in fluorescent energy transfer between Cy3 and Cy5 terminally attached to double-stranded nucleic acids. *Proc. Natl. Acad. Sci. U.S.A. 105*, 11176−11181.

(15) Dolghih, E., Roitberg, A. E., and Krause, J. L. (2007) Fluorescence resonance energy transfer in dye-labeled DNA. *J. Photochem. Photobiol., A 190*, 321−327.

(16) Hillisch, A., Lorenz, M., and Diekmann, S. (2001) Recent advances in FRET: Distance determination in protein-DNA complexes. *Curr. Opin. Struct. Biol. 11*, 201−207.

(17) Dietrich, A., Buschmann, V., Müller, C., and Sauer, M. (2002) Fluorescence resonance energy transfer (FRET) and competing processes in donor-acceptor substituted DNA strands: A comparative study of ensemble and single-molecule data. *Rev. Mol. Biotechnol. 82*, 211−231.

(18) Anikovsky, M. Y., Tatikolov, A. S., and Kuzmin, V. A. (2002) Fluorescent properties of some thia- and oxacarbocyanine dyes in the presence of DNA. *Photochemistry 36*, 207−211.

(19) Larsson, A., Carlsson, C., Jonsson, M., and Albinsson, B. (1994) Characterization of the binding of the fluorescent dyes YO and YOYO to DNA by polarized light spectroscopy. *J. Am. Chem. Soc. 116*, 8459−8465.

(20) Sarkar, D., Das, P., Basak, S., and Chattopadhyay, N. (2008) Binding interaction of cationic phenazinium dyes with calf thymus DNA: A comparative study. *J. Phys. Chem. B 112*, 9243−9249.

(21) Norman, D. G., Grainger, R. J., Uhrín, D., and Lilley, D. M. J. (2000) Location of cyanine-3 on double-stranded DNA: Importance for fluorescence resonance energy transfer studies. *Biochemistry 39*, 6317−6324.

(22) Heinlein, T., Knemeyer, J.-P., Piestert, O., and Sauer, M. (2003) Photoinduced electron transfer between fluorescent dyes and guanosine residues in DNA-hairpins. *J. Phys. Chem. B 107*, 7957−7964.

(23) Neubauer, H., Gaiko, N., Berger, S., Schaffer, J., Eggeling, C., Tuma, J., Verdier, L., Seidel, C. A. M., Griesinger, C., and Volkmer, A. (2007) Orientational and dynamical heterogeneity of Rhodamine 6G terminally attached to a DNA helix revealed by NMR and single-molecule fluorescence spectroscopy. *J. Am. Chem. Soc. 129*, 12746−12755.

(24) Zozulya, V. (1999) Fluorescence properties of intercalating neutral chromophores in complexes with polynucleotides of various base compositions and secondary structures. *J. Fluoresc. 9*, 363−366.
(25) Piatkevich, K. D., Hulit, J., Subach, O. M., Wu, B., Abdulla, A., Segall, J. E., and Verkhusha, V. V. (2010) Monomeric red fluorescent proteins with a large Stokes shift. *Proc. Natl. Acad. Sci. U.S.A. 107*, 5369−5374.
(26) Keppler, A., Arrivoli, C., Sironi, L., and Ellenberg, J. (2006) Fluorophores for live cell imaging of AGT fusion proteins across the visibile spectrum. *BioTechniques 41*, 167−175.
(27) Kabelac, M., Zimandl, F., Fessl, T., Chval, Z., and Lankas, F. (2010) A comparative study of the binding of QSY 21 and Rhodamine 6G fluorescence probes to DNA: Structure and dynamics. *Phys. Chem. Chem. Phys. 12*, 9677−9684.
(28) Lin, Y., Weissleder, R., and Tung, C.-H. (2002) Novel near-infrared cyanine fluorochromes: Synthesis, properties, and bioconjugation. *Bioconjugate Chem. 13*, 605−610.
(29) Masotti, A., Vicennati, P., Boschi, F., Calderan, L., Sbarbati, A., and Ortaggi, G. (2008) A novel near-infrared indocyanine dye-polyethylenimine conjugate allows DNA delivery imaging in vivo. *Bioconjugate Chem. 19*, 983−987.
(30) Janossy, G., Jani, I. V., Kahan, M., Barnett, D., Mandy, F., and Shapiro, H. (2002) Precise CD4 T-cell counting using red diode laser excitation: For richer, for poorer. *Cytometry 50*, 78−85.
(31) Gui, M., Nagaraj, S., Rahavendran, S. V., and Karnes, H. T. (1997) Diode laser induced near infrared fluorescence detection for high-performance liquid chromatography analysis of indocyanine green in plasma. *Anal. Chim. Acta 342*, 145−149.
(32) Kupstat, A., Kumke, M. U., and Hildebrandt, N. (2011) Toward sensitive, quantitative point-of-care testing (POCT) of protein markers: Miniaturization of a homogeneous time-resolved fluoroimmunoassay for prostate-specific antigen detection. *Analyst 136*, 1029−1035.
(33) Martí, A. A., Li, X., Jockusch, S., Stevens, N., Li, Z., Raveendra, B., Kalachikov, S., Morozova, I., Russo, J. J., Akins, D. L., Ju, J., and Turro, N. J. (2007) Design and characterization of two-dye and three-dye binary fluorescent probes for mRNA detection. *Tetrahedron 63*, 3591−3600.
(34) Abe, H., and Kool, E. T. (2006) Flow cytometric detection of specific RNAs in native human cells with quenched autoligating FRET probes. *Proc. Natl. Acad. Sci. U.S.A. 103*, 263−268.
(35) Lakowicz, J. R. (2006) Energy transfer. *Principles of fluorescence spectroscopy*, 3rd ed., Chapter 13, pp 443−475, Springer, Berlin.
(36) Dos Remedios, C. G., and Moens, P. D. J. (1995) Fluorescence resonance energy transfer spectroscopy is a reliable "ruler" for measuring structural changes in proteins. *J. Struct. Biol. 115*, 175−185.
(37) Sanborn, M. E., Connolly, B. K., Gurunathan, K., and Levitus, M. (2007) Fluorescence properties and photophysics of the sulfoindocyanine Cy3 linked covalently to DNA. *J. Phys. Chem. B 111*, 11064−11074.
(38) Levitus, M., Negri, R. M., and Aramendía, P. F. (1995) Rotational relaxation of carbocyanines. Comparative study with the isomerization dynamics. *J. Phys. Chem. 99*, 14231−14239.
(39) Spiriti, J., Binder, J. K., Levitus, M., and van der Vaart, A. (2011) Cy3-DNA stacking interactions strongly depend on the identity of the terminal basepair. *Biophys. J. 100*, 1049−1057.
(40) Product catalogue 2011/2013 from ATTO-TEC, free download from https://www.atto-tec.com/index.php?id=70&L=1&language=en.
(41) Doose, S., Neuweiler, H., and Sauer, M. (2005) A close look at fluorescence quenching of organic dyes by tryptophan. *ChemPhysChem 6*, 2277−2285.
(42) Miller, A. E., Fischer, A. J., Laurence, T., Hollars, C. W., Saykally, R. J., Lagarias, J. C., and Huser, T. (2006) Single-molecule dynamics of phytochrome-bound fluorophores probed by fluorescence correlation spectroscopy. *Proc. Natl. Acad. Sci. U.S.A. 103*, 11136−11141.
(43) Marmé, N., Knemeyer, J.-P., Sauer, M., and Wolfrum, J. (2003) Inter- and intramolecular fluorescence quenching of organic dyes by tryptophan. *Bioconjugate Chem. 14*, 1133−1139.
(44) Polyakova, S. M., Belov, V. N., Yan, S. F., Eggeling, C., Ringemann, C., Schwarzmann, G., de Meijere, A., and Hell, S. W. (2009) New GM1 ganglioside derivatives for selective single and double labelling of the natural glycosphingolipid skeleton. *Eur. J. Org. Chem.*, 5162−5177.
(45) Kukolka, F., Schoeps, O., Woggon, U., and Niemeyer, C. M. (2007) DNA-directed assembly of supramolecular fluorescent protein energy transfer systems. *Bioconjugate Chem. 18*, 621−627.
(46) Vogelsang, J., Cordes, T., and Tinnefeld, P. (2009) Single-molecule photophysics of oxazines on DNA and its application in a FRET switch. *Photochem. Photobiol. Sci. 8*, 486−496.
(47) Schneider, U. V., Severinsen, J. K., Géci, I., Okkels, L. M., Johnk, N., Mikkelsen, N. D., Klinge, T., Pedersen, E. B., Westh, H., and Lisby, G. (2010) A novel FRET pair for detection of parallel DNA triplexes by the LightCycler. *BMC Biotechnol. 10*, 1−12.
(48) Strohbach, D. K. (2007) Modulation von Ribozymaktivität durch gezielte Kontrolle der Sekundärstruktur. Dissertation, p 41, free download from http://d-nb.info/985682604/34.
(49) Giusti, W. G., and Adriano, T. (1993) Synthesis and characterization of 5′-fluorescent-dye-labeled oligonucleotides. *Genome Res. 2*, 223−227.
(50) Kupstat, A., Knopp, D., Niessner, R., and Kumke, M. U. (2010) Novel intramolecular energy transfer probe for the detection of benzo-[a]pyrene metabolites in a homogeneous competitive fluorescence immunoassay. *J. Phys. Chem. B 114*, 1666−1673.
(51) Lakowicz, J. R. (2006) Segmental mobility of a biopolymer-bound fluorophore. *Principles of fluorescence spectroscopy*, 3rd ed., Chapter 11, pp 392−393, Springer, Berlin.
(52) Garcia de la Torre, J., Huertas, M. L., and Carrasco, B. (2000) Calculation of hydrodynamic properties of globular proteins from their atomic-level structure. *Biophys. J. 78*, 719−730.
(53) Dertinger, T., Pacheco, V., von der Hocht, I., Hartmann, R., Gregor, I., and Enderlein, J. (2007) Two-focus fluorescence correlation spectroscopy: A new tool for accurate and absolute diffusion measurements. *ChemPhysChem 8*, 433−443.
(54) Haustein, E., and Schwille, P. (2007) Fluorescence correlation spectroscopy: Novel variations of an established technique. *Annu. Rev. Biophys. Biomol. Struct. 36*, 151−169.
(55) Braslavsky, S. E., Fron, E., Rodriguez, H. B., Román, E. S., Scholes, G. D., Schweitzer, G., Valeur, B., and Wirz, J. (2008) Pitfalls and limitations in the practical use of Förster's theory of resonance energy transfer. *Photochem. Photobiol. Sci. 7*, 1444−1448.
(56) Van der Meer, B. W. (2002) Kappa-squared: From nuisance to new sense. *Rev. Mol. Biotechnol. 82*, 181−196.
(57) Muschielok, A., Andrecka, J., Jawhari, A., Brückner, F., Cramer, P., and Michaelis, J. (2008) A nano-positioning system for macromolecular structural analysis. *Nat. Methods 5*, 965−971.
(58) Sindbert, S., Kalinin, S., Nguyen, H., Kienzler, A., Clima, L., Bannwarth, W., Appel, B., Müller, S., and Seidel, C. A. M. (2011) Accurate distance determination of nucleic acids via Förster resonance energy transfer: Implications of dye linker length and rigidity. *J. Am. Chem. Soc. 133*, 2463−2480.
(59) Lin, J., and Brown, C. W. (1993) Simultaneous determination of physical and chemical properties of sodium chloride solutions by near infrared spectroscopy. *J. Near Infrared Spectrosc. 1*, 109−120.
(60) Brismar, H., Trepte, O., and Ulfhake, B. (1995) Spectra and fluorescence lifetimes of lissamine rhodamine, tetramethylrhodamine isothiocyanate, texas red, and cyanine 3.18 fluorophores: Influences of some environmental factors recorded with a confocal laser scanning microscope. *J. Histochem. Cytochem. 43*, 699−707.
(61) Sauer, M., Drexhage, K. H., Lieberwirth, U., Müller, R., Nord, S., and Zander, C. (1998) Dynamics of the electron transfer reaction between an oxazine dye and DNA oligonucleotides monitored on the single-molecule level. *Chem. Phys. Lett. 284*, 153−163.

Bioconjugate Chemistry

Article

pubs.acs.org/bc

Graphene Oxide–Polyethylenimine Nanoconstruct as a Gene Delivery Vector and Bioimaging Tool

Hyunwoo Kim,[†] Ran Namgung,[†] Kaushik Singha,[†] Il-Kwon Oh,[‡] and Won Jong Kim*[,†]

[†]Department of Chemistry, BK School of Molecular Science, Polymer Research Institute, Pohang University of Science and Technology, Pohang 790-784, Korea

[‡]Division of Ocean Systems Engineering, School of Mechanical, Aerospace and Systems Engineering, Korea Advanced Institute of Science and Technology, Daejeon 305-701, Korea

Supporting Information

ABSTRACT: Graphene oxide (GO) has attracted an increasing amount of interest because of its potential applications in biomedical fields such as biological imaging, molecular imaging, drug/gene delivery, and cancer therapy. Moreover, GO could be fabricated by modifying its functional groups to impart specific functional or structural attributes. This study demonstrated the development of a GO-based efficient gene delivery carrier through installation of polyethylenimine, a cationic polymer, which has been widely used as a nonviral gene delivery vector. It was revealed that a hybrid gene carrier fabricated by conjugation of low-molecular weight branched polyethylenimine (BPEI) to GO increased the effective molecular weight of BPEI and consequently improved DNA binding and condensation and transfection efficiency. Furthermore, this hybrid material facilitated sensing and bioimaging because of its tunable and intrinsic electrical and optical properties. Considering the extremely high transfection efficiency comparable to that of high-molecular weight BPEI, high cell viability, and its application as a bioimaging agent, the BPEI–GO hybrid material could be extended to siRNA delivery and photothermal therapy.

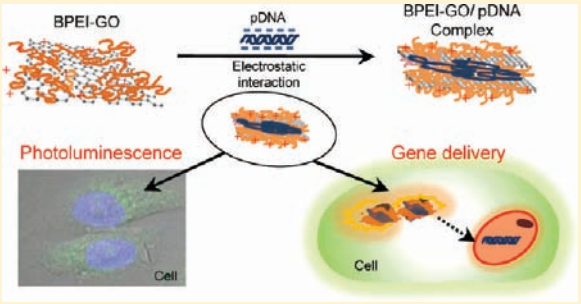

INTRODUCTION

Graphene, a single-atom-thick and two-dimensional sp^2 carbon networking material, has attracted great attention because of its remarkable electronic, mechanical, and thermal properties.[1−3] Graphene has also been used in biomedical fields, including biological sensing, molecular imaging, gene/drug delivery, and cancer therapy.[4−11] In particular, graphene oxide (GO), a precursor for graphene, is endowed with several favorable properties such as electronic, sp^2 $\pi-\pi$ interaction, and fluorescence quenching ability.[12−14] Moreover, GO possesses unique features such as facile synthesis, high water dispersibility, good colloidal stability, easily tunable surface functionalization, and good biocompatibility, which are highly conducive for bioapplications.[15] All these attributes make GO more potent than carbon nanotubes considering its in vitro and in vivo biological applications. Interestingly, sp^2 $\pi-\pi$ interaction between GO and a hydrophobic drug could facilitate the loading of the drug onto the GO surface, and this could be utilized in its facile application as a drug delivery carrier.[6,8] Similarly, the utility of GO could be extended to gene delivery and biological sensing considering the quenching properties of fluorescence-labeled DNA.[7] Strong $\pi-\pi$ stacking interaction between GO and single-stranded DNA (ssDNA) facilitates the loading of ssDNA onto GO and subsequently provides protection of DNA against enzymatic degradation.[16] However, no such interaction exists between GO and double-stranded DNA (dsDNA) as DNA bases are concealed within the double helix, preventing the generation of $\pi-\pi$ stacking interaction between dsDNA and GO.[17] Therefore, it is imperative to modify the GO to achieve effective loading of plasmid DNA (pDNA) and thereby efficient gene delivery. A feasible strategy for accomplishing such DNA complexation and transfection ability of GO could involve integration of cationic vectors.

Various viral and nonviral vector-mediated delivery strategies have been employed to achieve efficient gene transfection. The use of viral vectors, despite their high efficiency, has been impaired greatly because of the associated mutagenicity or oncogenesis, several host immune responses, and high cost of production.[18] Therefore, nonviral vectors, including cationic polymers, liposomes, dendrimers, and inorganic materials, attract significant attention in spite of their low efficacy.[19−21] There is a continuous effort to modify and refine these gene delivery systems either by adopting different strategies or by installing various functional attributes in the existing systems. Among cationic polymers such as polyethylenimine (PEI), chitosan, and Polyamidoamine (PAMAM), high molecular weight branched PEI (HMW BPEI) has been used widely as a gold standard for gene delivery vehicle. HMW BPEI showed high transfection efficiency because of enhanced cellular uptake and a high level of endosomal escape.[22,23] Nevertheless, the

Received: July 21, 2011
Revised: October 22, 2011
Published: October 31, 2011

 © 2011 American Chemical Society

associated cytotoxicity of HMW BPEI severely limited its use as an effective gene carrier. Interest has now shifted toward low-molecular weight (LMW) BPEI that exhibits relatively low cytotoxicity, but very poor transfection efficacy in comparison with HMW BPEI.[24,25] Furthermore, LMW BPEI exhibited enhanced cellular uptake and transfection efficiency with low cytotoxicity when it was conjugated to inorganic materials such as gold, silica, iron oxide, and carbon materials.[26−29] We presumed that hybrid gene carrier fabricated by conjugation of LMW BPEI to GO would increase the effective molecular weight of LMW BPEI and consequently improve DNA binding and condensation and transfection efficiency.

Recently, carbon-based fluorescent nanomaterials have garnered attention because of their considerably stable emissions and lower cytotoxicity, imposing less environmental concern. The photoluminescence (PL) of carbon-based nanomaterials generally emanated from isolated polyaromatic structures.[30,31] Interestingly though, GO itself contains an isolated polyaromatic structure; the PL properties of GO have not been explored much mainly because of its low emission efficiency.[32] The carboxylic and epoxy groups of GO are known to induce nonradiative recombination of localized electron−hole pairs and thereby confer the nonemissive property of GO. However, recent reports found that such nonradiative recombination of localized electron−hole pairs could be avoided by conjugating alkylamines to both the epoxy and carboxylic groups of GO through nucleophilic reaction. Consequently, the modification of nonradiative recombinative sites transforms GO into a highly efficient emitter.[33] One intention of this study has been to enhance the efficiency of PL intensity of GO by conjugating it with BPEI, and an elaborate investigation to gain further insight into the PL properties of the BPEI−GO nanoconstruct has been conducted.

We presumed that the newly designed BPEI−GO nanoconstruct may facilitate sensing and imaging because of its tunable and intrinsic electrical and optical properties. In this study, GO was modified with LMW BPEI, and their physiological properties (colloidal stability, DNA compaction ability, and transfection efficiency) and imaging properties were investigated.

EXPERIMENTAL PROCEDURES

Materials. The graphene oxide (GO) powder was obtained from Cheap-Tubes Inc. (Brattleboro, VT). Branched polyethylenimine (BPEI; molecular masses of 1.8 and 25 kDa) was purchased from Polyscience, Inc. (Warrington, PA). Triethylamine (TEA) was obtained from Samchun Chemicals. 1-Ethyl-3-[3-(dimethylamino)propyl]carbodiimide hydrochloride (EDC) was purchased from Sigma Chemical Co. (St. Louis, MO). *N*-Hydroxysuccinimide (NHS) was obtained from Fluka. The dialysis membrane (molecular mass cutoff of 3.5 kDa) was purchased from Spectrum Laboratories (Rancho Dominguez, CA). pDNA (pCMV-Luc) encoding luciferase was prepared from digestion and ligation using pGL3 (Promega, Madison, WI) and pcDNA3 (Invitrogen, Carlsbad, CA) vectors. Briefly, pGL3 was digested with XbaI and HindIII, and the following luc+ gene frame was purified by agarose gel electrophoresis and elution. Then, pCMV-Luc was constructed by insertion of the luc+ gene frame at the XbaI and HindIII restriction sites of pcDNA3 and amplified. pCMV-Luc was propagated in a chemically competent DH5α strain (GibcoBRL) and prepared from overnight bacterial cultures followed by alkaline lysis and column purification with a Qiagen plasmid Maxi kit (Qiagen, Valencia, CA). TOTO-3 iodide was purchased from Invitrogen (Eugene, OR), and mounting medium for fluorescence with DAPI was purchased from VECTOR (Burlingame, CA).

Synthesis of the BPEI−GO Conjugate. Prior to conjugation of BPEI to GO, the amount of carboxyl groups of GO was estimated by direct acid−base titration. To conjugate BPEI (M_w = 1.8 kDa) to the carboxyl groups of GO by EDC/NHS coupling, we dispersed the dried GOs in deionized water by sonication for 30 min, and EDC (54.3 mg, 0.4 mmol) and NHS (50.6 mg, 0.4 mmol) were added to the GO solution (0.5 mg/mL, 0.5 mg) in a vial. TEA (100 μL) was added to a BPEI solution (0.396 g) in deionized water. Subsequently, BPEI (M_w = 1.8 kDa) was added to the GO solution (1 mL, 0.5 mg/mL) and stirred for 1 day at room temperature. The resulting BPEI−GO solution was dialyzed against a 3500 Da molecular mass cutoff dialysis membrane in deionized water for 2 days to remove the unreacted BPEI.

Charaterization of GO and the BPEI−GO Conjugate. The concentration of BPEI in the BPEI−GO conjugate was determined by measuring the cuprammonium complex formed between BPEI and copper ion(II) at 630 nm using UV−vis spectrophotometry (UV 2550, Shimadzu), and the observed conjugation ratio of BPEI to GO was found to be 22, which is represented as BPEI−GO22. BPEI−GO5 and BPEI−GO8 were also synthesized by following the same procedure described above differing only in the amounts of BPEI1.8K used (0.04 g for BPEI−GO5 and 0.4 g for BPEI−GO8).

The size and morphology of GO and BPEI−GO were investigated with a tapping mode atomic force microscope (AFM, Nanoscope IIIa, Digital Instrument Inc.). A droplet of GO and BPEI−GO dispersion (~0.01 mg/mL) was cast onto a freshly prepared silicon oxide wafer (p-type), which was then dried at 80 °C. The chemical conjugation of BPEI to GO was confirmed by FT-IR spectroscopy (VERTEX70 FT-IR spectrophotometer, Bruker Optics) using a KBr pellet. The colloidal stability of GO, BPEI−GO, and the BPEI/GO mixture was checked by dispersing the samples in water, PBS, and DMEM medium containing 10% FBS for 30 min to 1 h at room temperature.

ζ Potential Measurements. The surface charge of GO, BPEI−GO, and BPEI−GO/pDNA complexes in DPBS buffer (pH 7.4) was confirmed by ζ potential measurements using a Zetasizer Nano Z (Malvern Instruments, Malvern, U.K.). BPEI−GO/DNA complexes were prepared at various N/P ratios [the ratio of concentrations of total nitrogen atoms (N) of BPEI to the phosphate groups (P) of pDNA] (2, 5, 10, and 20) by addition of the BPEI−GO suspension to the pDNA solution in DPBS buffer (pH 7.4). The final pDNA concentration was adjusted to 33 μg/mL. The mixtures were then incubated for 30 min prior to measurement of the ζ potential at room temperature.

Agarose Gel Retardation Assay. Complexes of pDNA with GO, BPEI1.8K, and BPEI−GO were prepared by addition of the sample suspension (10 μL) to the pDNA solution (10 μL) at various N/P ratios ranging from 0 to 50 in DPBS buffer and incubation for 30 min at room temperature. The complexes were then electrophoresed through a 1% (w/v) agarose gel containing ethidium bromide (EtBr, 0.5 μg/mL) in 0.5 TAE (Tris-acetate-EDTA) buffer at 100 V for 20 min. The gel was then analyzed on a UV illuminator (wiseUV WUV, DAIHAN Scientific, Seoul, Korea).

Cell Culture. A human cervical cancer cell line (HeLa) and a human prostate cancer cell line (PC-3) were cultured in a

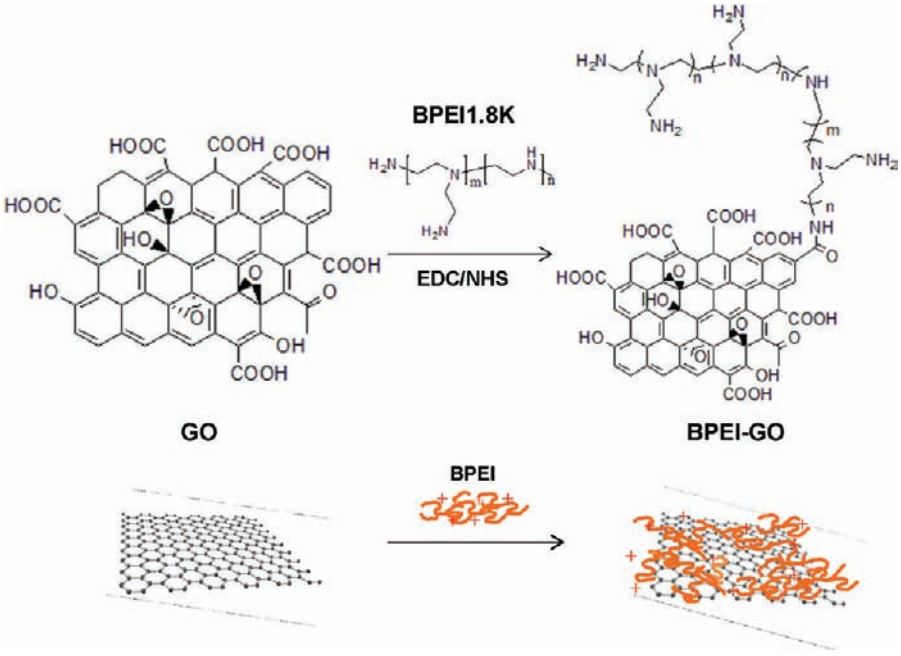

Figure 1. Synthetic scheme of BPEI−GO. BPEI (M_w = 1.8 kDa) was conjugated to the carboxyl groups of GO by EDC/NHS coupling. The dried GO was dispersed in deionized water by sonication for 30 min. EDC and NHS were added to the GO solution. TEA was added to a BPEI solution in deionized water. Subsequently, BPEI was added to the GO solution, and the mixture was stirred for 1 day at room temperature.

humidified atmosphere (5% CO_2) at 37 °C. Dulbecco's modified Eagle's medium (DMEM), Roswell Park Memorial Institute medium (RPMI-1640), penicillin/streptomycin, fetal bovine serum (FBS), and Dulbecco's phosphate-buffered saline (DPBS) were purchased from Invitrogen-Gibco (Carlsbad, CA). The luciferase assay kit and reporter lysis buffer were purchased from Promega, and the bicinchoninic acid (BCA) protein assay reagent kit was purchased from Pierce Chemical Co. (Rockford, IL). Cell viability was estimated by using 3-(4,5-dimethylthiazol-2-yl)-2,5-diphenyltetrazolium bromide (MTT) (Sigma-Aldrich).

Luciferase Reporter Gene Assay. HeLa and PC-3 cells were seeded on 24-well culture plates at an initial density of 7 × 10^4 cells/well and incubated for 24 h in 500 μL of DMEM or RPMI-1640 containing 10% FBS at 37 °C in a humidified atmosphere with 5% CO_2. Samples (10 μL) were complexed with 2 μg of pDNA (10 μL) at various N/P ratios and incubated for 30 min. The cells were incubated with the complexes (20 μL) in 250 μL of serum-free medium for 4 h and then incubated for 18 h in 500 μL of fresh medium containing 10% FBS. After the cells had been washed with DPBS, lysis buffer was then added to the well (200 μL/well) for lysis of cells. Luciferase reporter gene expression was evaluated using a microplate spectrofluorometer (VICTOR3 V Multilabel Counter, Perkin-Elmer, Wellesley, MA).

Cytotoxicity Assay. The cytotoxicity of complexes was evaluated by the MTT assay. Cells were seeded onto 96-well plates at a density of 1 × 10^4 cells/well and incubated for 24 h. pDNA (0.2 μg/μL) was complexed with the samples at various N/P ratios in DPBS buffer and incubated for 30 min. Complexes were incubated with the cells for 4 h in 100 μL of serum-free medium, followed by further incubation for 20 h in 200 μL of medium containing 10% FBS. Cell medium was replaced with 200 μL of fresh medium and 20 μL of an MTT solution (5 mg/mL) and incubated for an additional 4 h. The medium was then removed, and 150 μL of DMSO was added to the wells to dissolve the internalized purple formazan crystals. An aliquot (100 μL) was taken from each well and transferred to a fresh 96-well plate. The absorption was measured at 570 nm using a microplate spectrofluorometer. The relative percentage of the control cells (nontreated), which were not exposed to the transfection system, was used to represent 100% cell viability.

Photoluminescence Spectrum Study. The photoluminescence (PL) spectrum was recorded with a spectrofluorophotometer (RF-5301PC, SHIMADZU) to obtain the PL profile of BPEI−GO. The PL of BPEI−GO was scanned at various excitation wavelength ranging from 400 to 480 nm, and the λ_{max} excitation was found to be 480 nm. The λ_{max} excitation and λ_{max} emission of BPEI−GO were measured at 480 and 520 nm, respectively.

Confocal Fluorescence Microscopy Study. HeLa cells were seeded at a density of 1 × 10^4 cells/well in a 12-well plate over glass coverslips. Cells were incubated with BPEI−GO/pDNA complexes for a certain period of time at 37 °C. After the cellular uptake had been quenched via addition of cold DPBS, cells were washed twice with cold DPBS and fixed with 4% paraformaldehyde for 30 min at room temperature. Cells on a coverslip were mounted in Vectashield antifade mounting medium with DAPI (Vetor Laboratories), observed with a confocal laser scanning microscope (CLSM), and analyzed with Olympus Fluoview version 1.5.

■ RESULTS AND DISCUSSION

Synthesis and Characterization of BPEI−GO. To construct the GO-based gene delivery vector, LMW BPEI1.8K (M_w = 1.8 kDa) was covalently conjugated to the carboxyl group of GO using EDC/NHS chemistry (Figure 1). The amount of conjugated BPEI in BPEI−GO was analyzed by measuring the UV−vis absorbance of cuprammonium complexes of BPEI−GO at 630 nm, and the estimated conjugation ratios of BPEI to GO were found to be 5, 8, and 22 and were

dx.doi.org/10.1021/bc200397j | Bioconjugate Chem. 2011, 22, 2558−2567

denoted as BPEI−GO5, BPEI−GO8, and BPEI−GO22, respectively (Table 1). The successful conjugation of the carboxyl group of GO and amino group of BPEI was confirmed by FT-IR spectroscopy, which showed the characteristic peak of the amide bond at 1630−1695 cm^{-1}, confirming the reported value (Figure 2). The appearance of the vibration band around 1650 cm^{-1} due to the C═O stretching of the primary amide in BPEI−GO and the disappearance of the carboxylic group bands at 1733 cm^{-1} of pristine GO substantiated the formation of amide linkages. Furthermore, in the case of BPEI−GO, the absence of the band at 1050 cm^{-1} that was observed earlier in GO due to the presence of epoxide moieties clearly established the successful chemical conjugation. However, the band at 1626 cm^{-1} arising due to the C═C vibration of aromatic rings was observed in both GO and BPEI−GO and implied the preservation of the sp^2 character in BPEI−GO after the chemical conjugation.[34,35]

Table 1. Characteristics of the BPEI−GO Conjugate[a]

	reaction condition (equivalent to COOH of GO[b])			BPEI in BPEI−GO[c]		
BPEI−GO	BPEI (equiv)	EDC/NHS (equiv)	GO (mg)	mg	μmol	BPEI:GO conjugation ratio[d] (w/w)
BPEI−GO5	10	20		2.33	1.29	5
BPEI−GO8	10	200	0.5	3.94	2.18	8
BPEI−GO22	100	200		11.07	6.15	22

[a]The reaction was conducted in deionized water. [b]The amount of carboxyl groups of GO was estimated by direct acid−base titration. On the basis of the estimated carboxylic acid content, an excess molar ratio of EDC/NHS and BPEI were added to the GO for GO−BPEI synthesis. [c]The concentration of BPEI in BPEI−GO was determined by measuring the cuprammonium complex formed between PEI and copper(II) at 630 nm using UV−vis spectrophotometry. [d]Conjugation ratios were determined by calculating the weight of BPEI and GO in the BPEI−GO conjugate.

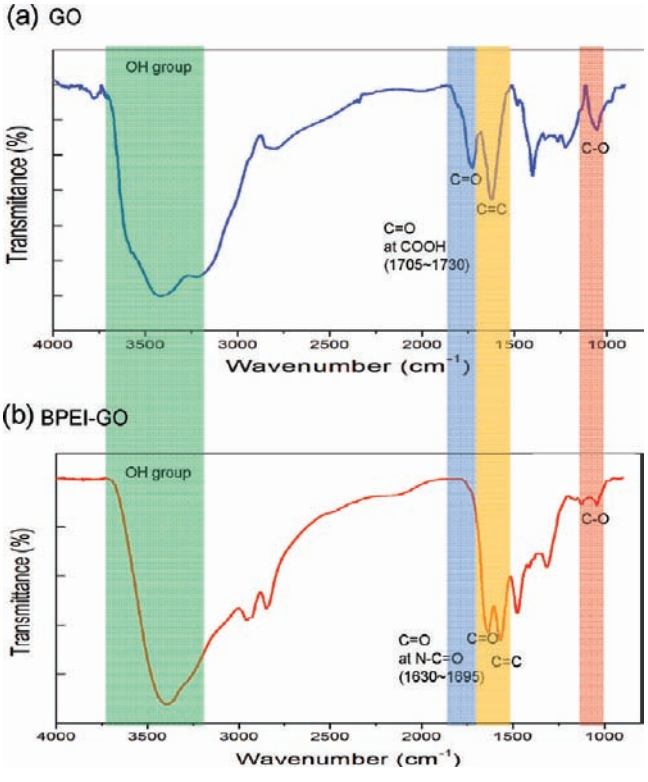

Figure 2. FT-IR spectra of GO (a) and BPEI−GO (b). Conjugation of the carboxyl group of GO and the amino group of BPEI was confirmed by FT-IR spectroscopy, which showed the characteristic peak of the amide bond at 1630−1695 cm^{-1}.

Colloidal property constitutes an important parameter in evaluating the viability of a biomaterial in a biological application. Accordingly, colloidal stability of GO, the BPEI/GO mixture, and the BPEI−GO conjugate was investigated in water, PBS, and 10% serum-containing medium (Figure 3).

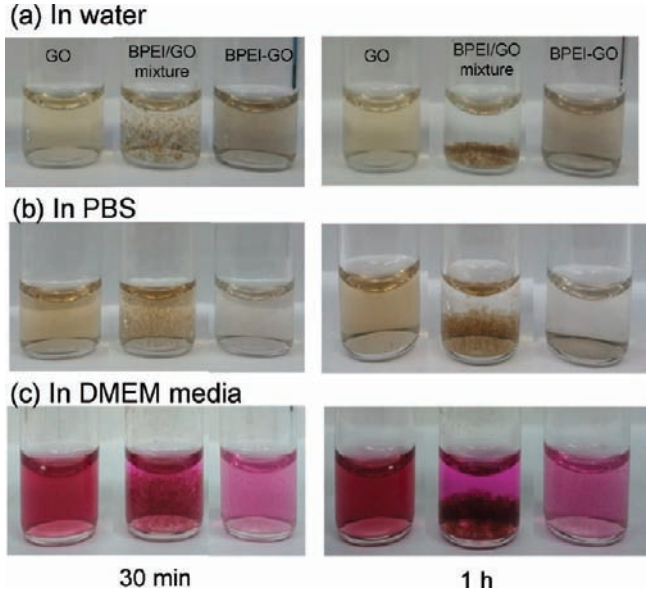

Figure 3. Colloidal stability of GO, the BPEI/GO mixture, and BPEI−GO22 in water (a), PBS (b), and DMEM medium containing 10% FBS (c).

Noticeable aggregation was observed for the BPEI/GO mixture, while no aggregation was observed for unmodified GO or the chemically modified BPEI−GO22 conjugate even after longer incubation times in all types of media under investigation. Such observations could easily be explained considering the charge repulsion phenomenon of colloids. In general, identical charges repel each other to provide colloidal stability. Therefore, negatively charged GO remains in good colloidal stability in solution because of the charge repulsion of GO particles (Figure S2 of the Supporting Information). Likewise, in the case of BPEI−GO, GO was evenly and completely coated with positively charged BPEI and showed excellent colloidal stability even under physiological conditions (10% serum-containing medium). However, colloidal stability was found to be very low for a simple BPEI/GO mixture that contained two oppositely charged molecules and allowed the charge interaction leading to aggregation. The effect of surface charges on colloidal stability was also be corroborated by ζ potential measurements as described later.

The size and morphology of GO and BPEI−GO with various degrees of conjugation was studied by AFM (Figure 4). The

dx.doi.org/10.1021/bc200397j | Bioconjugate Chem. 2011, 22, 2558−2567

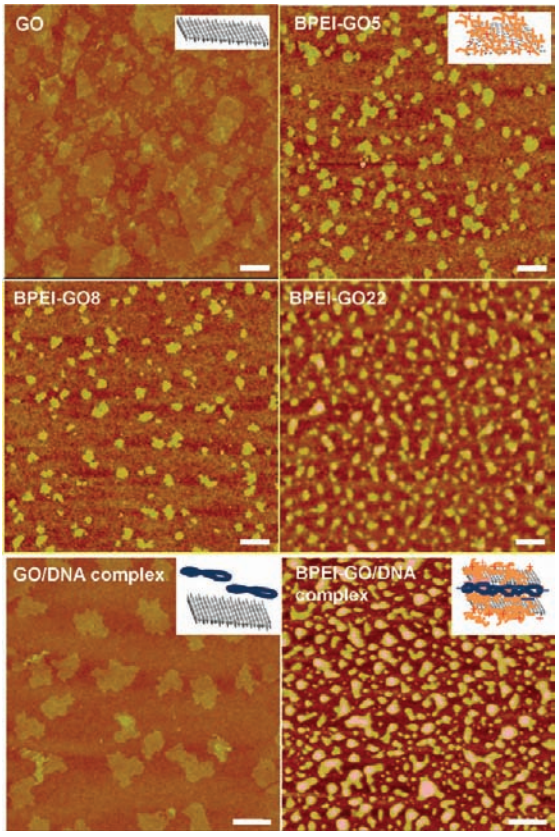

Figure 4. AFM images of GO, BPEI–GO, the GO/DNA complex, and the BPEI–GO/DNA complex. A droplet of GO and BPEI–GO dispersion was cast onto a freshly prepared silicon oxide wafer (p-type), followed by drying at 80 °C. The scale bar is 500 nm.

size of the unmodified GO was found to be 500–600 nm, and a thickness of 0.6–1.3 nm corresponds to one to two layers of GO. Interestingly, the BPEI–GO conjugate showed a reduced size of 100–200 nm and an increased thickness of 6–8 nm. However, the increase in the ratio of the degree of conjugation of BPEI to GO had little effect on the size and thickness of the BPEI–GO conjugates. Then, the effect of complexation with pDNA on the size and morphology of GO and BPEI–GO was investigated by AFM. As expected, complexation of GO with pDNA did not change the size and thickness of GO, which clearly demonstrated the absence of any significant interaction between GO and pDNA. In contrast, the size and thickness of BPEI–GO/pDNA complexes were increased to 300–400 and 16–18 nm, respectively, upon formation of the complex. The reduced size of BPEI–GO compared to that of GO could be attributed to the folding of the GO sheet. During EDC/NHS-mediated conjugation, the primary amine of BPEI not only formed an amide linkage with the carboxylic groups residing at the GO edges but also underwent a ring-opening reaction with the epoxy functionalities at the basal plane of the GO sheets.[36] It could be assumed that the free ends of the conjugated BPEI formed an amide linkage with the carboxylic groups present in the same or other GO sheet leading to the folding and cross-linking of the GO sheets, which resulted in the reduced size and increased thickness arising from the stacking of the GO sheets. The increase in the size and thickness of the BPEI–GO conjugate upon complexation with pDNA could be explained by considering the electrostatic interaction between the negatively charged pDNA and positively charged BPEI–GO conjugates. pDNA was thought to be sandwiched between two BPEI–GO stakes giving rise to the increased thickness. Such vertical stacking might lead to a multilayer structure. Similarly, complexation involving the laterally conjugated BPEI and pDNA might lead to lateral elongation and, hence, the increased size of the BPEI–GO/pDNA complex.

Formation of the Polyelectrolyte Complex and ζ Potential Measurements. It is necessary for an efficient gene carrier to interact with pDNA generally through electrostatic interaction and form a nanosized complex. As described above, unmodified GO does not interact with pDNA and, therefore, cannot form a complex with pDNA. However, GO modified with BPEI should acquire positive surface charge and is expected to interact with pDNA having a negatively charged phosphate backbone. Therefore, in this study, formation of a complex of the gene carrier with pDNA was investigated by agarose gel electrophoresis analysis. As expected, GO did not form a complex with pDNA even at higher N/P ratios of 50 because of its negative charge, while BPEI underwent complete complexation with pDNA at a low N/P ratio of 5 (Figure 5a). Although BPEI–GO5 having a lower conjugation ratio formed complexes with N/P ratios of

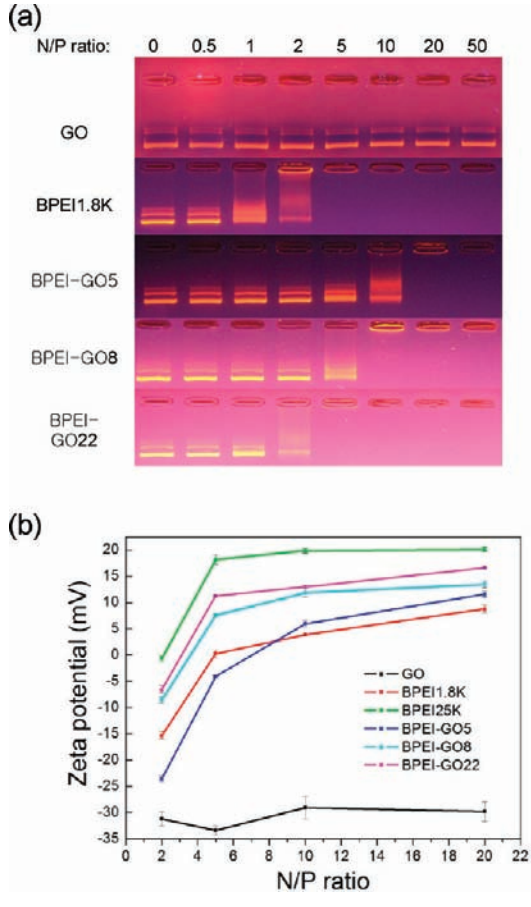

Figure 5. Agarose gel retardation study (a) and ζ potential measurements (b) of pDNA complexed with GO, BPEI1.8K, and BPEI–GO conjugates at various N/P ratios. (a) Complexes of pDNA with GO, BPEI1.8K, and BPEI–GO conjugates were electrophoresed through a 1% (w/v) agarose gel and then analyzed with a UV illuminator. (b) The final pDNA concentration for ζ potential measurement was adjusted to 33 μg/mL. The complexes were then incubated for 30 min prior to the measurement of ζ potential at room temperature.

dx.doi.org/10.1021/bc200397j | Bioconjugate Chem. 2011, 22, 2558–2567

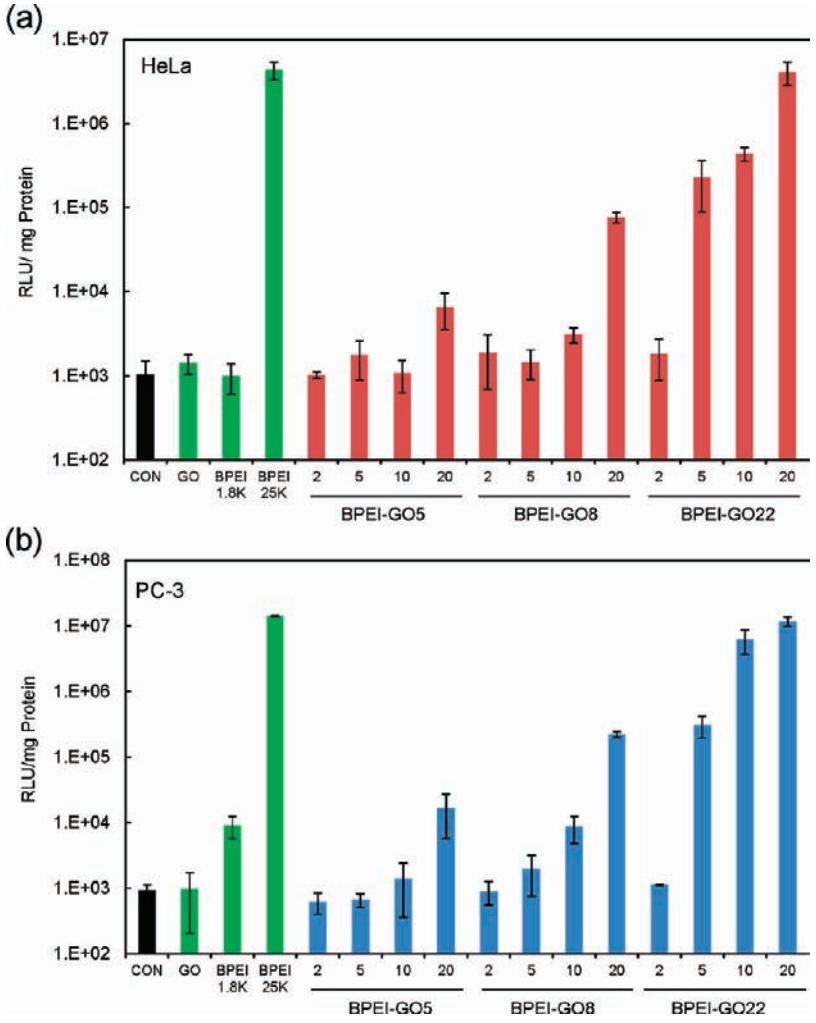

Figure 6. Transfection of GO, BPEI (1.8K and 25K), and BPEI−GO conjugates at predetermined N/P ratios in HeLa (a) and PC-3 (b) cell lines. Cells were seeded on 24-well culture plates at an initial density of 7×10^4 cells/well. The cells were incubated with the complexes in 250 μL of serum-free medium for 4 h and then incubated for 18 h in 500 μL of fresh medium containing 10% FBS. After the cells had been washed with DPBS, lysis buffer was then added in the well (200 μL/well) for lysis of cells. Luciferase reporter gene expression was evaluated using a microplate spectrofluorometer.

>10, the complexation ability of BPEI−GO5 was found to be weaker than that of unmodified BPEI, which might stem from the interfering effect of negatively charged GO through the disruption of the ionic interaction of BPEI and pDNA. The complexation ability of BPEI−GO conjugates with pDNA was enhanced with an increase in conjugation ratios because of the multivalent effect of BPEI−GO. Therefore, conjugation of positively charged BPEI to negatively charged GO ensured that BPEI−GO formed a nanosized complex with pDNA.

Along with complex formation ability, the surface charge of the nanocomplex governs the cellular uptake and transfection ability of the complex. Therefore, the surface charge of the nanocomplex was studied by ζ potential measurement (Figure 5b and Figure S2 of the Supporting Information). Over the entire range of N/P ratios, GO shows a negative ζ potential value, which clearly demonstrated its inability to form a complex with DNA. HMW BPEI25K forms a complex with pDNA at low N/P ratios and shows the highest positive value of ζ potential, while LMW BPEI1.8K has a lower ζ potential. BPEI−GO8 and BPEI−GO22 exhibited considerably higher positive ζ potentials than LMW BPEI1.8K. However, these complexes showed positive surface charges lower than that of HMW BPEI25K, and it was considered to be advantageous for BPEI−GO conjugates as the excessively high positive charge of HMW BPEI25K induced higher cytotoxicity. The positive surface charge and stable polyelectrolyte complex formation of BPEI−GO tend to interact favorably with the negatively charged cell surface, thereby facilitating efficient cellular uptake.

Gene Transfection Study. To investigate the immense potential of BPEI−GO as an efficient gene carrier, we performed the luciferase gene expression assays in HeLa and PC-3 cells. The transfection efficiency was evaluated for GO, BPEI25K, BPEI1.8K, and BPEI−GO complexes at various N/P ratios. Unmodified GO and LMW BPEI1.8K showed negligible gene transfection, but HMW BPEI25K showed stronger gene transfection ability, which is considered a gold standard in nonviral gene delivery carriers (Figure 6). Overall, the level of gene transfection was increased with an increase in the N/P ratio and conjugation ratio of BPEI to GO as shown in Figure 6. BPEI−GO22 showed considerable gene transfection even at an N/P ratio of 5. At N/P ratios of 10 and 20, transfection was comparable to that of BPEI25K in both types of cells (HeLa and PC-3). This observation of the strong gene transfection ability of BPEI−GO22 might be due to the multivalent effect of

dx.doi.org/10.1021/bc200397j | *Bioconjugate Chem.* 2011, 22, 2558−2567

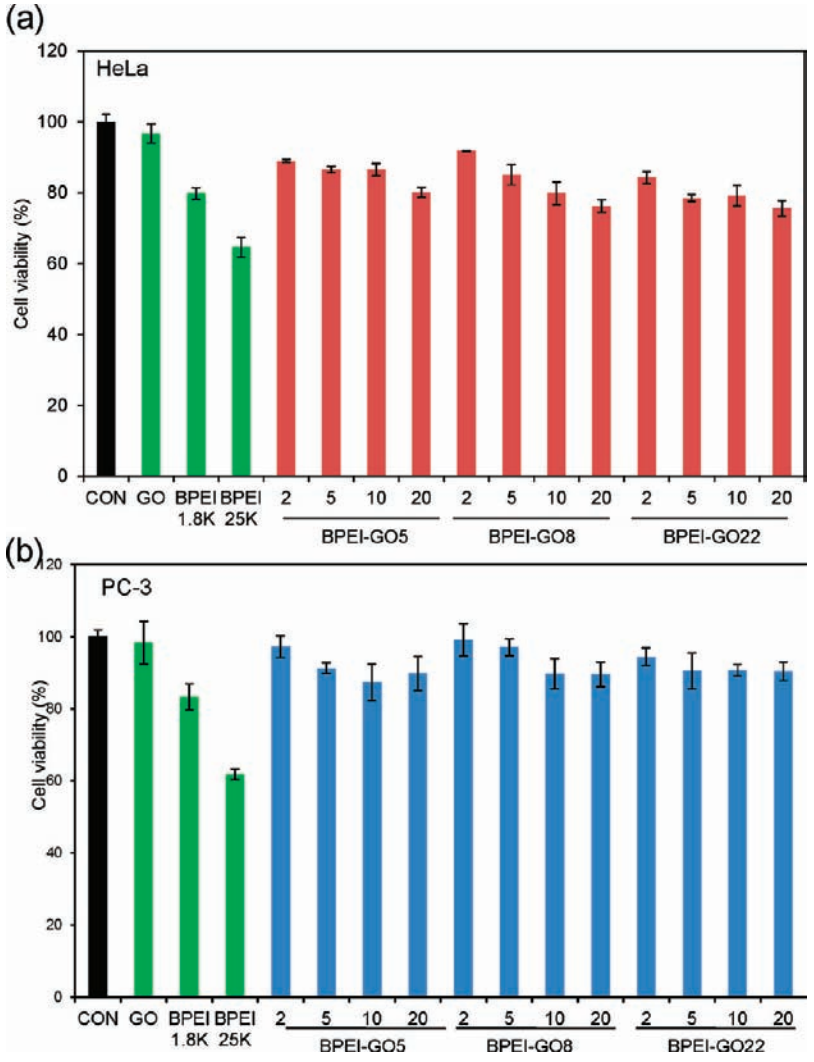

Figure 7. Cell viability profile of GO, BPEI (1.8K and 25K), and BPEI−GO conjugates at predetermined N/P ratios in HeLa (a) and PC-3 (b) cell lines. Cells were seeded onto 96-well plates at a density of 1×10^4 cells/well and incubated for 24 h. Complexes were incubated with the cells for 4 h in 100 μL of serum-free medium, followed by further incubation for 20 h in 200 μL of medium containing 10% FBS. Cell medium was replaced with 200 μL of fresh medium and 20 μL of an MTT solution (5 mg/mL) and incubated for an additional 4 h. The relative percentage of the control cells (nontreated), which were not exposed to the transfection system, was used to represent 100% cell viability.

LMW BPEI1.8K conjugated to the GO, which is favorable for formation of a stable polyelectrolyte complex with pDNA and highly positive surface charge. Though BPEI25K was considered as the gold standard in transfection, significant cytotoxicity of BPEI25K should be considered carefully before use. Therefore, the cell toxicity of all gene carriers was investigated with an MTT assay.

Cytotoxicity Assay. The cytotoxicity of GO, BPEI1.8K, BPEI25K, and BPEI−GO conjugates was studied by an MTT assay. As shown in Figure 7, GO did not show cell toxicity in HeLa cells. BPEI1.8K shows 80% cell viability; however, 40% of the cells were found to be dead in HMW BPEI25K-transfected cells. In the case of BPEI−GO, cell toxicity is increased slightly with an increase in N/P ratio, but BPEI−GO maintained >80% cell viability at all N/P ratios. Similar results were observed for PC-3 cells. Although HMW BPEI25K showed a high gene transfecion efficiency, its high cell toxicity rendered it less encouraging for practical application. However, BPEI−GO complexes demonstrated high transfection efficiency without inducing significant cytotoxicity. The low cytotoxicity of BPEI−GO can be attributed to the low cytotoxic character of LMW BPEI, which was retained in BPEI−GO even after conjugation with GO.[26−29] This implies the great potential of BPEI−GO as a nonviral gene delivery carrier with low toxicity.

Photoluminescence Study. The excellent optical property of GO makes it a very enticing agent in bioimaging and fluorescence-assisted cellular uptake tracking. In this study, we investigated the optical property of GO and BPEI−GO by UV−vis absorbance and PL spectroscopy. GO and BPEI−GO both exhibited UV−vis absorbance over a wide range of wavelengths, though the absorbance of BPEI−GO was found to be higher than that of GO (Figure 8a). The difference in absorbance could be rationalized on the basis of the accompanied surface modification during amidation and ring opening amination of epoxy moieties leading to the reduction of GO after conjugation of BPEI to GO, which is in good accordance with other reports.[37,38] The λ_{max} excitation and λ_{max} emission of BPEI-GO were found to be 480 and 520 nm, respectively (Figure 8b). Though the PL of GO and the BPEI/GO mixture was negligible, BPEI−GO displayed a significant increase in PL when excited at 480 nm; however, a further steep increase in PL intensity was observed when BPEI−GO

dx.doi.org/10.1021/bc200397j | Bioconjugate Chem. 2011, 22, 2558−2567

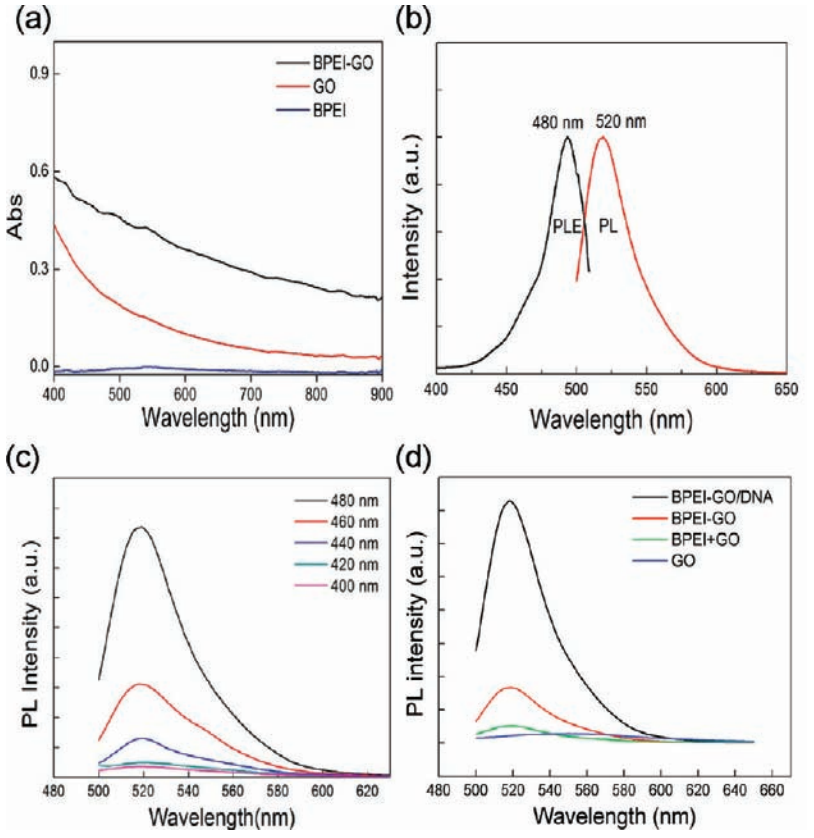

Figure 8. (a) UV−vis absorption spectrum of GO, BPEI, and BPEI−GO in water (0.01 mg/mL). (b) BPEI−GO photoluminescence excitation (PLE) spectrum with a detection wavelength of 480 nm and BPEI−GO PL spectrum excited at 480 nm. (c) BPEI−GO PL spectrum in water recorded for progressively longer excitation wavelengths from 400 to 480 nm in 20 nm increments. (d) PL spectrum of the BPEI−GO/DNA complex, BPEI−GO, the BPEI/GO mixture, and GO in water (0.01 mg/mL).

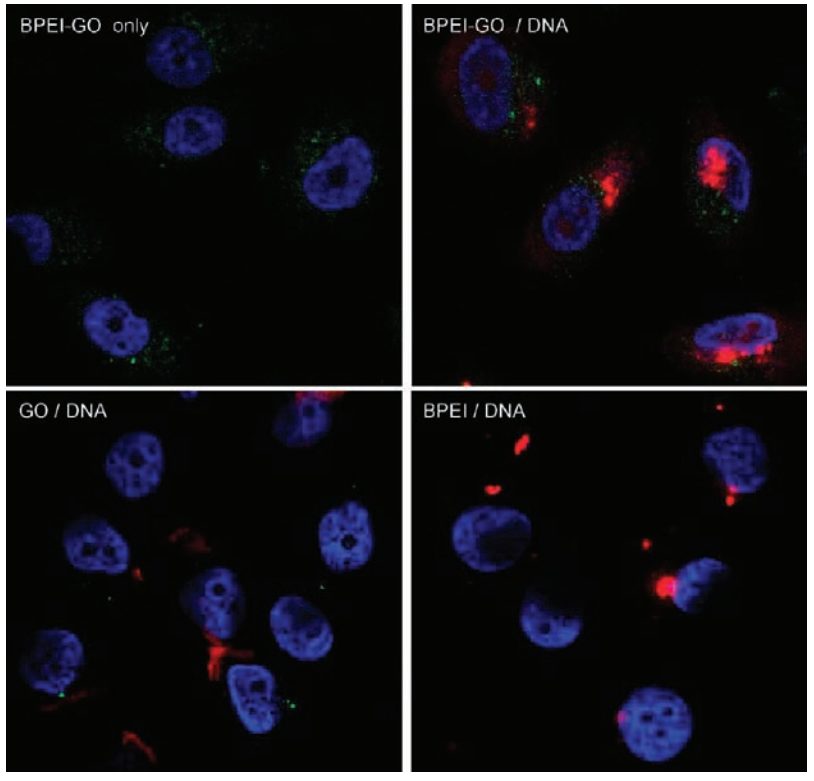

Figure 9. Confocal fluorescence microscopic images of a PC-3 cell line treated with BPEI−GO, DNA complexes with BPEI−GO, GO, and BPEI. pDNA was labeled with TOTO-3, and nuclei were stained with DAPI; a 488 nm laser was then applied to observe PL.

dx.doi.org/10.1021/bc200397j | *Bioconjugate Chem.* 2011, 22, 2558−2567

formed a complex with pDNA (Figure 8d). Both GO and BPEI−GO absorbed light over a wide range of wavelengths (Figure 8a), but GO displayed considerably low emission that could be attributed to the nonradiative emission of GO arising due to the presence of a carboxylic group and an epoxy group.[33] On the other hand, the conjugation of BPEI to GO effectively restored the conjugated aromatic clusters and suppressed the nonradiative emission of GO through nucleophilic binding of BPEI to the carboxylic group and the epoxy group of GO. At the same time, the ionic interaction between BPEI and GO adversely affected the PL; however, the combined effects gave rise to an overall increase in the PL intensity of BPEI−GO compared to that of GO. After incorporation of pDNA, BPEI preferentially formed a complex with pDNA and induced recovery of the PL intensity of BPEI−GO that was partially lost due to the ionic interaction between GO and BPEI.[39] The observed facts certainly prove the potential of BPEI-GO as a good emitter by reduction of nonradiative emission and induction of radiative emission.

Bioimaging Study. To evaluate the potential of BPEI−GO as a bioimaging reagent, we conducted the transfection studies of GO and BPEI−GO with or without pDNA complexation and tracked the movement of the complexes during the transfection using confocal microscopy (Figure 9 and Figure S3 of the Supporting Information). To visualize the movements of complexes, pDNA was labeled with TOTO-3 and nuclei were stained with DAPI, and then a 488 nm laser was applied to observe PL. No green PL was observed when GO and BPEI were employed alone, which was in accordance with a previous PL spectroscopy study. However, significant green fluorescence of BPEI−GO was observed after transfection into the cells, which confirmed the distribution of BPEI−GO in the cytosol. In addition, when the BPEI−GO/pDNA complex was transfected into cells, not only green fluorescence but also red fluorescence of pDNA was observed in cells, which demonstrated the efficacy of the developed dual-labeled complex in providing information regarding the location of BPEI−GO and pDNA. Therefore, these results clearly illustrate the potential of the BPEI−GO nanoconstruct as a bioimaging reagent.

CONCLUSION

In conclusion, to develop GO as an efficient gene carrier, it was imperative to conjugate a cationic gene carrier to GO as unlike ssDNA, dsDNA could not be loaded on GO through $\pi-\pi$ stacking interaction. Our work demonstrated the successful fabrication of GO through covalent linkage with LMW BPEI, which acted as a cationic gene carrier. It was confirmed that BPEI−GO possessed high gene delivery efficiency and exhibited high cell viability. Furthermore, the PL properties of GO were enhanced through conjugation of BPEI to GO, which advocated the immense potential of BPEI−GO as a fluorescence reagent. This highly efficient gene delivery and the excellent photoluminescence activities of the GO-based nanoconstruct will definitely merit further attention in the development of more sophisticated carrier systems that could serve both as a gene delivery vector and as a bioimaging tool. There are a few reports that demonstrated the fabrication of carbon nanotube-based nanomaterials and their enhanced efficiency in siRNA delivery[40] as well as in photothermal therapeutic applications.[41] Considering the extremely high transfection efficiency comparable to that of HMW BPEI and the high cell viability, its application could be extended to siRNA delivery, drug delivery, and photothermal therapy by installing further functional and structural attributes such as enhancing dispersibility through pegylation.

ASSOCIATED CONTENT

Supporting Information

Standard curve of BPEI quantification, ζ potentials of carriers, and confocal microscopic images of HeLa cells. This material is available free of charge via the Internet at http://pubs.acs.org.

AUTHOR INFORMATION

Corresponding Author

*Department of Chemistry, Pohang University of Science and Technology, Pohang 790-784, Korea. Phone: 82-54-279-2104. Fax: 82-54-279-3399. E-mail: wjkim@postech.ac.kr.

ACKNOWLEDGMENTS

This research was supported by the Converging Research Center Program (2011K000820) through the National Research Foundation of (NRF) funded by the Ministry of Education, Science and Technology, and a grant (K00060-283) from the Fundamental R&D Program for Core Technology of Materials funded by the Ministry of Knowledge Economy, Republic of Korea. We thank Prof. H. Choi for assistance in the AFM analysis.

REFERENCES

(1) Novoselov, K. S., Geim, A. K., Morozov, S. V., Jiang, D., Zhang, Y., Dubonos, S. V., Grigoreva, I. V., and Firsov, A. A. (2004) Electric field effect in atomically thin carbon films. *Science 306*, 666−669.

(2) Geim, A. K., and Novoselov, K. S. (2007) The rise of graphene. *Nat. Mater. 6*, 183−191.

(3) Li, X. L., Wang, X. R., Zhang, L., Lee, S. W., and Dai, H. J. (2008) Chemically derived, ultrasmooth graphene nanoribbon semiconductors. *Science 319*, 1229−1232.

(4) Yang, M., and Gong, S. (2010) Imumunosensor for the detection of cancer biomarker based on percolated graphene thin film. *Chem. Commun. 46*, 5796−5798.

(5) Hu, Y., Li, F., Bai, X., Li, D., Hua, S., Wang, K., and Niu, L. (2011) Label-free electrochemical impedance sensing DNA hybridization based on functionalized graphene sheets. *Chem. Commun. 47*, 1743−1745.

(6) Sun, X., Liu, Z., Welsher, K., Robinson, J. T., Goodwin, A., Zaric, S., and Dai, H. J. (2008) Nano-Graphene Oxide for Cellular Imaging and Drug Delivery. *Nano Res. 1*, 203−212.

(7) Peng, C., Hu, W., Zhou, W., Fan, C., and Huang, Q. (2010) Intracellular imaging with a graphene-based fluorescent probe. *Small 6*, 1686−1692.

(8) Liu, Z., Robinson, J. T., Sun, X. M., and Dai, H. J. (2008) PEGylated nanographene oxide for delivery of water-insoluble cancer drugs. *J. Am. Chem. Soc. 130*, 10876−10877.

(9) Chen, B., Liu, M., Zhang, L., Huang, J., Yao, J., and Zhang, Z. (2011) Polyethylenimine-functionalized graphene oxide as an efficient gene delivery vector. *J. Mater. Chem. 21*, 7736−7741.

(10) Yang, K., Zhang, S., Zhang, G., Sun, X., Lee, S. T., and Liu, Z. (2010) Graphene in mice: Ultrahigh in vivo tumor uptake and efficient photothermal therapy. *Nano Lett. 10*, 3318−3323.

(11) Markovic, Z. M., Harhaji-Trajkovic, L. M., Todorovic-Markovic, B. M., Kepic, D. P., Arsikin, K. M., Jovanovic, S. P., Pantovic, A. C., Dramicanin, M. D., and Trajkovic, V. S. (2011) In vitro comparison of the photothermal anticancer activity of graphene nanoparticles and carbon nanotubes. *Biomaterials 32*, 1121−1129.

(12) Zhang, Y., Tan, Y. W., Stormer, H. L., and Kim, P. (2005) Experimental observation of the quantum hall effect and Berry's phase in graphene. *Nature 438*, 201−204.

(13) Rochefort, A., and Wuest, J. D. (2009) Interaction of substituted aromatic compounds with graphene. *Langmuir 25*, 210−215.
(14) Lu, C. H., Yang, H. H., Zhu, C. L., Chen, X., and Chen, G. N. (2009) A Graphene Platform for Sensing Biomolecules. *Angew. Chem., Int. Ed. 48*, 4785−4787.
(15) Li, D., Mueller, M. B., Gilje, S., Kaner, R. B., and Wallace, G. G. (2008) Processable aqueous dispersions of graphene nanosheet. *Nat. Nanotechnol. 3*, 101−105.
(16) Lu, C. H., Zhu, C. L., Li, J., Liu, J. J., Chen, X., and Yang, H. H. (2010) Using graphene to protect DNA from cleavage during cellular delivery. *Chem Commun. 46*, 3116−3118.
(17) Tang, Z., Wu, H., Cort, J. R., Buchko, G. W., Zhang, Y., Shao, Y., Aksay, I. A., Liu, J., and Lin, Y. (2010) Constraint of DNA on functionalized graphene improves its biostability and specificity. *Small 6*, 1205−1209.
(18) Verma, I. M., and Somia, M. (1997) Gene therapy: Promises, problems and prospects. *Nature 389*, 239−242.
(19) Kim, W. J., and Kim, S. W. (2009) Efficient siRNA delivery with non-viral polymeric vehicles. *Pharm. Res. 26*, 657−666.
(20) Majeti, B. K., Karmali, P. P., Madhavendra, S. S., and Chaudhuri, A. (2005) Example of fatty acid-loaded lipoplex in enhancing in vitro gene transfer efficacies of cationic amphiphile. *Bioconjugate Chem. 16*, 676−684.
(21) Mintzer, M. A., and Simanek, E. E. (2009) Nonviral vectors for gene delivery. *Chem. Rev. 109*, 259−302.
(22) Boussif, O., Lezoualc'h, F., Zanta, M. A., Mergny, M. D., Scherman, D., Demeneix, B., and Behr, J. P. (1995) A versatile vector for gene and oligonucleotide transfer into cells in culture and in vivo: Polyethylenimine. *Proc. Natl. Acad. Sci. U.S.A. 92*, 7297−7301.
(23) Fischer, D., Bieber, T., Li, Y., Elsässer, H. P., and Kissel, T. (1999) A Novel Non-viral Vector for DNA Delivery Based on Low Molecular Weight, Branched Polyethylenimine: Effect of Molecular weight on Transfection Efficiency and Cytotoxicity. *Pharm. Res. 16*, 1273−1279.
(24) Bieber, T., and Elsässer, H. P. (2001) Preparation of a Low Molecular Weight polyethylenimine for Efficient Cell transfection. *BioTechniques 30*, 74−81.
(25) Gosselin, M. A., Guo, W., and Lee, R. J. (2001) Efficient Gene Transfer Using Reversibly Cross-Linked Low Molecular Weight Polyethylenimine. *Bioconjugate Chem. 12*, 989−994.
(26) Hu, C., Peng, Q., Chen, F., Zhong, Z., and Zhuo, R. (2010) Low Molecular Weight Polyethyleneimine Conjugated Gold Nanoparticles as Efficient Gene Vectors. *Bioconjugate Chem. 21*, 836−843.
(27) Namgung, R., Zhang, Y., Fang, Q. L., Singha, K., Lee, H. J., Kwon, I. K., Jeong, Y. Y., Park, I. K., Son, S. J., and Kim, W. J. (2010) Multifunctional silica nanotubes for dual-modality gene delivery and MR imaging. *Biomaterials 32*, 3042−3052.
(28) Namgung, R., Singha, K., Yu, M. K., Jon, S., Kim, Y. S., Ahn, Y., Park, I. K., and Kim, W. J. (2010) Hybrid superparamagnetic iron oxide nanoparticle-branched polyethylenimine magnetoplexes for gene transfection of vascular endothelial cells. *Biomaterials 31*, 4204−4213.
(29) Nunes, A., Amsharov, N., Guo, C., Van den Bossche, J., Santhosh, P., Karachalios, T. K., Nitodas, S. F., Burghard, M., Kostarelos, K., and Al-Jamal, K. T. (2010) Hybrid polymer-grafted multiwalled carbon nanotubes for in vitro gene delivery. *Small 6*, 2281−2291.
(30) Mochalin, V. N., and Gogotsi, Y. (2009) Wet chemistry route to hydrophobic blue fluorescent nanodiamond. *J. Am. Chem. Soc. 131*, 4594−4595.
(31) Liu, H., Ye, T., and Mao, C. (2007) Fluorescent carbon nanoparticles derived from candle soot. *Angew. Chem., Int. Ed. 46*, 6473−6475.
(32) Eda, G., Lin, Y. Y., Mattevi, C., Yamaguchi, H., Chen, H. A., Chen, I. S., Chen, C. W., and Chhowalla, M. (2010) Blue photoluminescence from chemically derived graphene oxide. *Adv. Mater. 22*, 505−509.
(33) Mei, Q., Zhang, K., Guan, G., Liu, B., Wang, S., and Zhang, Z. (2010) Highly efficient photoluminescent graphene oxide with tunable surface properties. *Chem. Commun. 46*, 7319−7321.
(34) Colthup, N. B., Daly, L., and Weberley, S. E. (1999) in *Introduction to Infrared and Raman Spectroscopy*, Academic Press, New York.
(35) Compton, O. C., Dikin, D. A., Putz, K. W., Brinson, L. C., and Nguyen, S. T. (2010) Electrically conductive "alkylated" graphene paper via chemical reduction of amine-functionalized graphene oxide paper. *Adv. Mater. 22*, 892−896.
(36) Dreyer, D. R., Park, S., Bielawski, C. W., and Ruoff, R. S. (2010) The chemistry of graphene oxide. *Chem. Soc. Rev. 39*, 228−240.
(37) Kim, Y. K., Kim, M. H., and Min, D. H. (2011) Biocompatible reduced graphene oxide prepared by using dextran as a multifunctional reducing agent. *Chem. Commun. 47*, 3195−3197.
(38) Zhang, Y., Chen, B., Zhang, L., Huang, J., Chen, F., Yang, Z., Yao, J., and Zhang, Z. (2011) Controlled assembly of Fe_3O_4 magnetic nanoparticles on graphene oxide. *Nanoscale 3*, 1446−1450.
(39) Nguyen, B. T., Gautrot, J. E., Ji, C., Brunner, P. L., Nguyen, M. T., and Zhu, Z. Z. (2006) Enhancing the photoluminescence intensity of conjugated polycationic polymers by using quantum dots as antiaggregation reagents. *Langmuir 22*, 4799−4803.
(40) Moon, H. K., Lee, S. H., and Choi, H. C. (2009) *In Vivo* Near-Infrared Mediated Tumor Destruction by Photothermal Effect of Carbon Nanotubes. *ACS Nano 3*, 3707−3713.
(41) Herrero, M. A., Toma, F. M., Al-Jamal, K. T., Kostarelos, K., Bianco, A., Ros, D. T., Bano, F., Casalis, L., Scoles, G., and Prato, M. (2009) Synthesis and Characterization of a Carbon Nanotube-Dendron Series for Efficient siRNA Delivery. *J. Am. Chem. Soc. 131*, 9843−9848.

Bioconjugate Chemistry

Article

pubs.acs.org/bc

In Vivo Specific Delivery of c-Met siRNA to Glioblastoma Using Cationic Solid Lipid Nanoparticles

Juyoun Jin,[#,†,‡] Ki Hyun Bae,[#,∥] Heekyoung Yang,[#,†,‡] Se Jeong Lee,[†,‡] Hyein Kim,[○] Yonghyun Kim,[†,‡] Kyeung Min Joo,[‡,§] Soo Won Seo,[⊥] Tae Gwan Park,*[,∥] and Do-Hyun Nam*[,†,‡]

[†]Department of Neurosurgery, Samsung Medical Center & Sungkyunkwan University School of Medicine, Seoul, South Korea

[‡]Cancer Stem Cell Research Center, Samsung Biomedical Research Institute, Seoul, South Korea

[§]Department of Anatomy, Seoul National University College of Medicine, Seoul, South Korea

[∥]Department of Biological Sciences, Korea Advanced Institute of Science and Technology, Daejeon, South Korea

[⊥]Department of Biomedical Engineering, Samsung Medical Center and Biomedical Research Institute, Sungkyunkwan University School of Medicine, Gangnam-gu, Seoul, South Korea

[○]Department of Biochemistry and Molecular Biology, Brain Korea 21 Project for Medical Science of Yonsei University, Yonsei University College of Medicine, Seoul, South Korea

ABSTRACT: RNA interference is a powerful strategy that inhibits gene expression through specific mRNA degradation. *In vivo*, however, the application of small interfering RNAs (siRNAs) is severely limited by their instability and their poor delivery into target cells and tissues. This is especially true with glioblastomas (GBMs), the most frequent and malignant form of brain tumor, that has limited treatment options due to the largely impenetrable blood-brain barrier. Here, cationic solid lipid nanoparticles (SLN), reconstituted from natural components of protein-free low-density lipoprotein, was conjugated to PEGylated c-Met siRNA. The c-Met siRNA-PEG/SLN complex efficiently down-regulated c-Met expression level, as well as decreased cell proliferation in U-87MG *in vitro*. In orthotopic U-87MG xenograft tumor model, intravenous administration of the complex significantly inhibited c-Met expression at the tumor tissue and suppressed tumor growth without showing any systemic toxicity in mice. Use of Cy5.5 conjugated SLN revealed enhanced accumulation of the siRNA-PEG/SLN complexes specifically in the brain tumor. Our data demonstrates the feasibility of using siRNA-PEG/SLN complexes as a potential carrier of therapeutic siRNAs for the systemic treatment of GBM in the clinic.

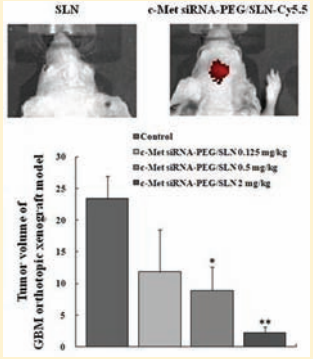

INTRODUCTION

Glioblastoma multiforme (GBM) is a very aggressive brain tumor, and the prognosis of patients with GBMs remains poor despite multidisciplinary treatment approaches, such as surgical resection, radiotherapy, and chemotherapy. Furthermore, GBM is particularly difficult to treat because the brain is endowed with a uniquely privileged immune environment by the blood-brain barrier (BBB). To date, the BBB remains largely impenetrable by the existing oncology drugs,[1] necessitating the development of novel delivery methods for treating GBM.

Toward this end, we previously developed a novel solid lipid nanoparticle (SLN) that can serve as a good carrier of cancer cell targeting moieties.[2] In particular, the SLNs were designed to carry small interfering RNAs (siRNAs). Use of siRNAs has been long-desired, because it can specifically silence oncogenes that control proliferation, apoptosis, angiogenesis, or migration of the tumor cells.[3] However, its application in the clinic has been limited due to its poor stability in biological fluids and nonspecific cellular uptake.[4−6] We overcame these issues by conjugating the siRNAs with poly(ethylene glycol) (PEG) and by mimicking naturally occurring low-density lipoprotein complexes that are common in bodily fluids[7] using poly-ethylenimine (PEI) to form nanoscale polyelectrolyte complex micelles *in vitro*.[2] This would now allow *in vivo* systemic administration of siRNA-based therapy possible, and the question remains whether the siRNA-PEG/SLN can also be effective in crossing the BBB.

Here, we report an orthotopic human brain tumor mouse model using the siRNA-PEG/SLN delivery system to evaluate its penetration across the BBB to the tumor site. Systemic intravenous administration of the SLN successfully and specifically delivered the siRNA to the tumor and lowered the tumor cell proliferation and tumorigenicity.

MATERIALS AND METHODS

Materials. Cholesterol hydrochloride (Chol), L-α-dioleoyl phosphatidylethanolamine (DOPE), and 3β-[*N*-(*N*′,*N*′-dimethylaminoethane)-carbamoyl]-cholesterol (DC-Chol) were obtained from Avanti Polar Lipids (Alabaster, AL). Cholesteryl oleate and glyceryl trioleate were purchased from Sigma-Aldrich (St. Louis, MO). All other chemicals were of analytical reagent grade.

Received: July 26, 2011
Revised: November 7, 2011
Published: November 9, 2011

ACS Publications © 2011 American Chemical Society

dx.doi.org/10.1021/bc200406n | *Bioconjugate Chem.* 2011, 22, 2568−2572

Synthesis of Cationic Solid Lipid Nanoparticles (SLN). Cationic solid lipid nanoparticles (SLNs) were produced by a modified emulsification-solvent evaporation method, as reported previously.[2] Briefly, cholesteryl oleate (22.5 mg), glyceryl trioleate (1.5 mg), DOPE (7 mg), Chol (5 mg), and DC-Chol (14 mg) were codissolved in 2 mL of chloroform/methanol mixture (2:1, v/v). After 10 mL of deionized water was added, the mixture was vortexed for 2 min and subsequently sonicated for 5 min using a Bronson Sonifier 450 equipped with a microtip (20 kHz, duty cycle = 35, output control = 3.5). The resulting emulsion was transferred to a round-bottom flask and then the solvent was rapidly evaporated at 60 °C at 20 mmHg using a rotary evaporator (EYELA, Japan). The produced SLNs were purified by extensive dialysis against deionized water (M_w cutoff of 100 kDa).

Formation of siRNA-PEG/SLN Complexes. An siRNA targeting human c-Met (sense; 5′-GUGCAGUAUCCUCUGA-CAGUU-(CH2)6 NH2−3′, antisense; 5′-CUG UCA GAG GAU ACU GCA CUU-3′) and a nontargeting (NT) siRNA (sense; 5′-GUUCAGCGUGUCCGGCGAGTT-(CH2)6-NH2−3′, antisense; 5′-CUCGCCGGACACGCUGCU-GAACTT-3′), both modified with 3′-hexylamine on the sense strand, were obtained from Samchunlly Inc. siRNA was conjugated with PEG through a disulfide bond as described previously.[8] SLN was incubated with siRNA-PEG conjugate at room temperature for 15 min in deionized water. To minimize interference from autofluorescence in *in vivo* imaging studies, siRNA-PEG/SLN complex was labeled with near-infrared Cy5.5. The diameter and surface zeta-potential were measured using a dynamic light scattering (DLS) instrument (Zeta-Plus, Brookhaven Instrument Co., NY) as described previously.[2] The SLN was observed by atomic force microscopy (AFM; PSIA XE-100, Park Systems, Santa Clara, CA) and transmission electron microscopy (TEM; Zeiss Omega 912, Carl Zeiss, Oberkochen, Germany).

Cell Culture and Transfection. U-87MG human GBM cells (ATCC) were grown in EMEM supplemented with 10% FBS, 2 mM L-glutamine, penicillin (100 units/mL), and streptomycin (100 μg/mL). For siRNA-PEG/SLN transfection, c-Met expressing U-87MG ells were plated on a 6-well plate at a density of 2.5×10^5 cells/well. After 24 h of incubation, the medium was replaced by fresh medium containing 0.5% FBS and 20 nM NT or 40 nM c-Met siRNA-PEG/SLN complexes were added to the cells. After 6 h incubation at 37 °C, the transfection medium was discarded and supplemented with medium containing 0.5% FBS. After an additional 24 h of incubation, the cells were harvested for Western blotting.

Western Blotting. Cell lysates were prepared from transiently transfected U-87MG cells by scraping 90% confluent 10 cm dishes into NP40 Cell Lysis Buffer (50 mM Tris, pH 7.4, 250 mM NaCl, 5 mM EDTA, 50 mM NaF, 1 mM Na_3VO_4, 1% NP40, 0.02% NaN_3) (Invitrogen Corporation, Camarillo, CA) containing protease inhibitor cocktail tablets (Roche, Laval, QC). The protein concentrations were determined using the Bradford protein assay (Bio-Rad Laboratories, Inc., Hercules, CA) according to the manufacturer's directions. Proteins were separated by SDS-PAGE, transferred onto PVDF membrane (GE Healthcare, Piscataway, NJ), and immunoblotted with primary antibodies overnight at 4 °C. A rabbit polyclonal antibody raised against a C-terminal cytoplasmic domain of human c-Met (1:200; Abcam, San Francisco, CA) was used. A mouse monoclonal antibody against β-actin (1:5000; Sigma, Saint Louis, MO) was used for the internal control. Bound antibodies were detected using horse radish peroxidase-conjugated goat antirabbit IgG (1:5000, Invitrogen) or goat antimouse IgG (1:5000, Zymed, San Francisco, CA) and were visualized via enhanced chemiluminescence (GE Healthcare).

In Vitro Proliferation Analysis. Cells were seeded at a density of 0.5×10^4 cells/well in 96-well plates and were transfected with NT or c-Met siRNA-PEG/SLN as described above. After transfection, cells were treated with 200 ng/mL of HGF for 24 h, 48 h, 72 h, or 96 h. Cell proliferation was quantified using Cell Counting Kit-8 (CCK-8) (Dojindo Molecular Technology, Gaithersburg, MD, USA), which assays cellular mitochondrial dehydrogenase activity as a measure of cell viability.

GBM Orthotopic Model and siRNA Treatment. Animal experiments were approved by the appropriate Institutional Review Boards of the Samsung Medical Center (Seoul, Korea) and conducted in accord with the "National Institute of Health Guide for the Care and Use of Laboratory Animals" (NIH publication no. 80−23, revised in 1996). For orthotopic GBM animal model, anesthetized 6-week-old male Balb/c-nu mice were secured in a rodent stereotactic frame, a hollow guide screw was implanted into a small drill hole made at 2 mm left and 1 mm anterior to the bregma, and 2×10^5 U-87MG cells in 5 μL HBSS were injected through this guide screw into the white matter at a depth of 2 mm [anterior/posterior (AP) +0.5 mm, medial/lateral (ML) +1.7 mm, dorsal/ventral (DV) −3.2 mm]. Two weeks after tumor cell implantation, mice were randomized into four groups (n = 7 for each group) and were given intravenous injection of SLN alone (control), 0.125 mg/kg, 0.5 mg/kg, or 2 mg/kg of c-Met siRNA-PEG/SLN complex intravenously three times once a week (Figure 3A). Brains were harvested and processed for paraffin embedding at six hours after the final injection.

For tumor mass volume quantification, standard H&E staining was performed in the paraffin sections and observed under optical microscope. The tumor volume was calculated by measuring the section with the largest tumor portion and applying the formula: $(\text{width})^2 \times \text{length} \times 0.5$. The c-Met expression in tumor was determined by immunohistological staining using mouse antihuman c-Met monoclonal antibody (Zymed). Peroxidase-conjugated secondary antibodies were used and visualized by incubating the slides with stable 3,3′-diaminobenzidine (DAB) for 10−20 min. The sections were rinsed with distilled water, counterstained with Gill's hematoxylin for 1 min, and mounted with Universal Mount (Research Genetics, Huntsville, AL).

In Vivo Quantification of c-Met siRNA-PEG/SLN Tumor-Tropism into the Brain. To evaluate tumor targeting of c-Met siRNA-PEG/SLN complex in U-87MG tumor-bearing mouse, siRNA-PEG/SLN complex conjugated with Cy5.5 was utilized. Three weeks after tumor cell implantation, mice were randomized into two groups (n = 3 for each group) and were given single intravenous injection of SLN alone (control) or 0.5 mg/kg c-Met siRNA-PEG/SLN-Cy5.5 complex (Figure 4A). Two days after injection, the mice were anesthetized with 2−3% isoflurane. The signal from Cy5.5 was detected in the region of the brain using a prototype Xenogen IVIS Spectrum *in vivo* imaging system (Caliper Life Science). Fluorescence intensity was analyzed as photons per second (p/s) by *Living Image 3.1* software (Caliper Life Science).

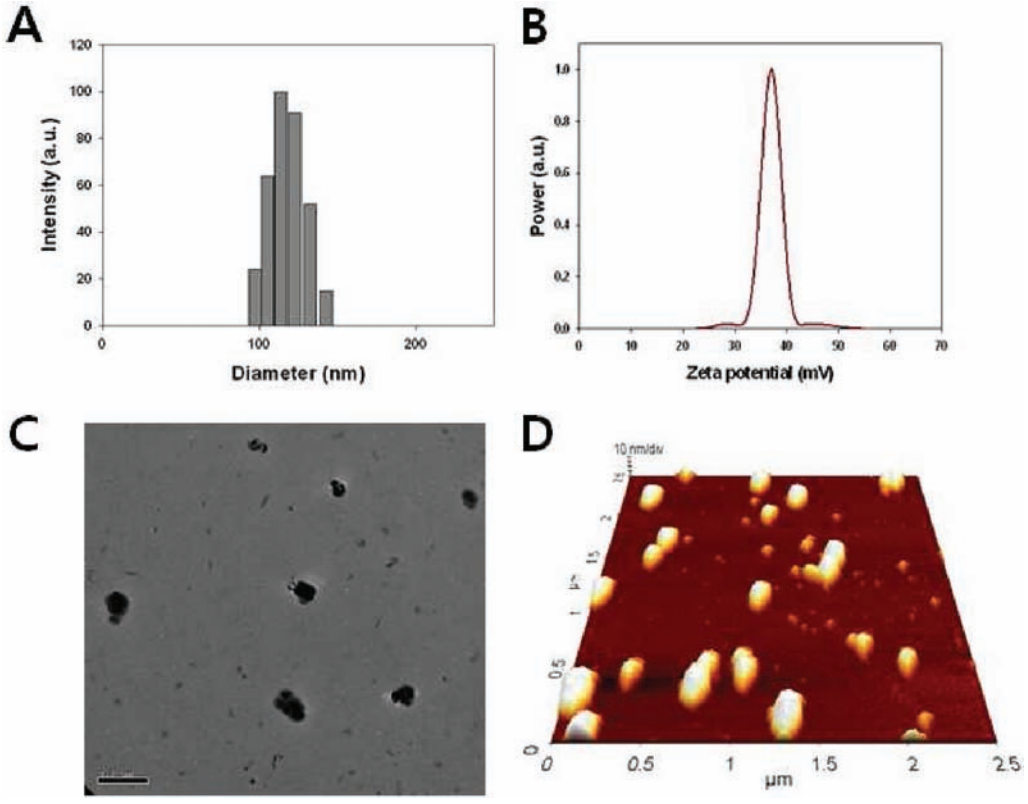

Figure 1. Characterization of solid lipid nanoparticle (SLN). (A) Size distribution of SLN and (B) zeta-potential value were measured by dynamic light scattering (DLS) and (C) TEM (scale bar = 500 nm) and (D) AFM images.

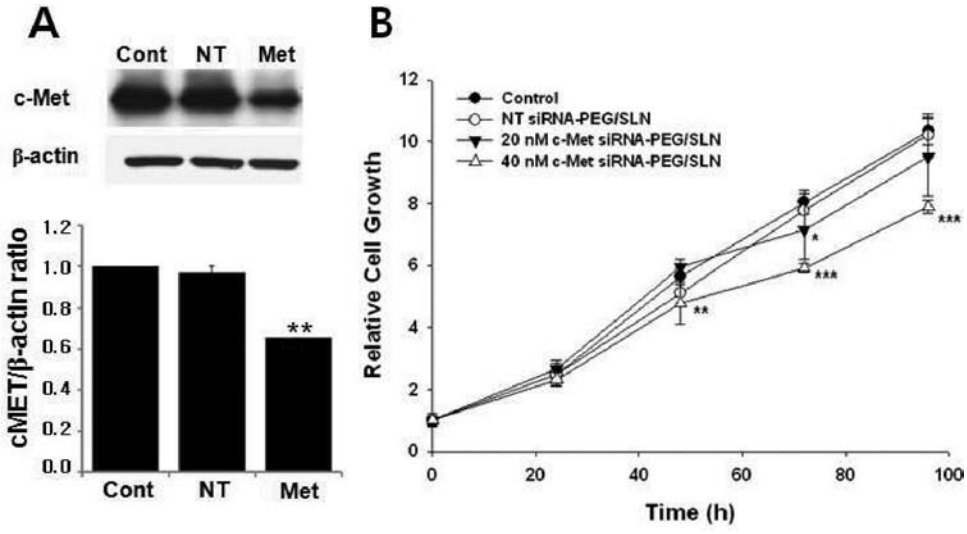

Figure 2. Effects of c-Met blockade in U87MG cell proliferation. (A) Western Blot analysis of U87MG transfected either with non-targeting (NT) siRNA-PEG/SLN complex or c-Met (Met) siRNA-PEG/SLN complex. c-Met siRNA-PEG/SLN complex efficiently reduced c-Met protein level. Endogenous human ß-actin was used as a control. (B) Inhibition of cell proliferation by transfection of c-Met siRNA-PEG/SLN complex. Values are mean ± SEM $*p < 0.05$, $**p < 0.01$, $***p < 0.001$ vs Control.

RESULTS AND DISCUSSION

Although siRNA is a promising nucleic acid drug in gene therapy, various intra- and extracellular barriers hamper therapeutic applications. Negatively charged siRNAs have extremely low cellular uptake and transfection efficiency, and undergo rapid chemical degradation when administered intravenously. To overcome the in vivo stability problem of siRNA, we report here a new delivery system for siRNAs that can readily cross the BBB for a targeted therapy of GBM. We chose to target c-Met, since its overexpression is associated with poor prognosis and invasiveness of tumors in GBM patients,[9] and we demonstrate that c-Met siRNA treatment can successfully attenuate GBM tumor growth in vivo.

Synthesis and Characterization of siRNA-PEG/SLN Complex. Our RNAi delivery system is based on the formation of SLN complex with PEGylated siRNA. PEGylated

dx.doi.org/10.1021/bc200406n | *Bioconjugate Chem.* 2011, 22, 2568–2572

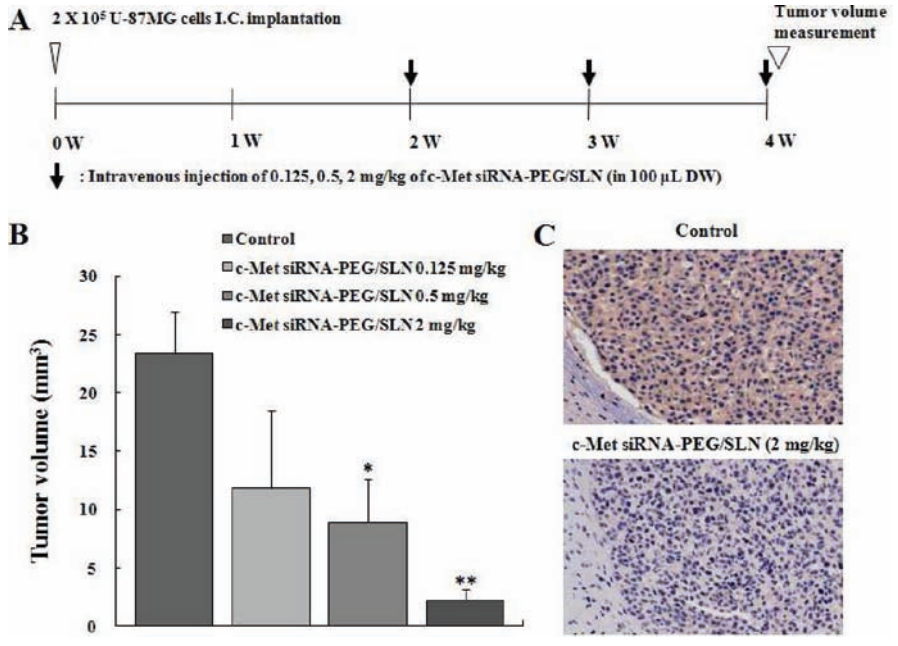

Figure 3. *In vivo* c-Met targeting in xenograft tumor. (A) The timeline for the assessment of in vivo antitumor activities of c-Met siRNA-PEG/SLN complex in an orthotopic xenograft model. (B) c-Met siRNA-PEG/SLN complex reduced U-87MG tumor volumes in a dose-dependent manner. Data are expressed as the mean ± SE. (C) Representative microphotographs of immunohistochemistry determining c-Met expression in the brains of control siRNA or c-Met siRNA treated mice. Immunopositive cells were visualized by brown DAB staining. Values are mean ± SEM $*p < 0.05$, $**p < 0.01$, vs Control.

c-Met siRNA or NT siRNA was conjugated with SLN at room temperature in deionized water. The mean diameter of SLN as measured by laser light scattering was 117.4 ± 11.7 nm (Figure 1A), and the zeta potential value of SLN was 37.3 ± 2.3 mV, indicating good stability of the complex (Figure 1B). The TEM (Figure 1C) and AFM (Figure 1D) observations confirmed the size and the spherical shape of the SLN. We demonstrated previously the ability to target the delivery of siRNA-PEG complex specifically to cancer cells in vitro.[2] Here, we show for the first time that these SLN could be utilized as nontoxic, serum-stable, and highly effective carriers for delivery of siRNA specifically to tumor site in vivo.

c-Met siRNA-PEG/SLN Complex Down-Regulates c-Met Protein and Tumor Cell Proliferation. To establish the efficacy and specificity of this targeting method, we used U-87MG glioblastoma cell lines positive for expression of c-Met. The c-Met siRNA-PEG/SLN complex exhibited profound inhibition extent of c-Met expression (32.5 ± 1.9% reduction, as compared to the no treatment control) than the NT siRNA-PEG/SLN complex (2.9 ± 3.0% reduction, as compared to the no-treatment control) ($P < 0.01$; Figure 2A). In the proliferation assay, treatment with the c-Met siRNA-PEG/SLN complex significantly reduced tumor cell proliferation in a dose dependent manner; 20 nM and 40 nM groups showed 13.1% and 23.4% tumor cell proliferation reduction, respectively, compared with NT siRNA-PEG/SLN complex group. No such reduction was observed with the NT siRNA-PEG/SLN complex compared to the control (Figure 2B). These results indicate that our c-Met siRNA-PEG/SLN complex specifically reduces proliferation of glioblastoma cells by controlling the expression of c-Met in vitro.

Antitumor Effects of c-Met siRNA-PEG/SLN Complex in a Glioma Xenograft Orthotopic Model. The antitumor effects of systemic administration of c-Met siRNA-PEG/SLN complex were evaluated by giving intravenous injection of the complex in U-87MG orthotopic models. Two weeks after tumor cell implantation, mice were randomized into four groups ($n = 7$ for each group) and were given intravenous injection of SLN alone (control), 0.125 mg/kg, 0.5 mg/kg, or 2 mg/kg of c-Met siRNA-PEG/SLN complex intravenously three times once a week (Figure 3A). The tumor volumes were determined at the day of last c-Met siRNA-PEG/SLN complex injection. Treatment with c-Met siRNA-PEG/SLN complex significantly inhibited U-87MG tumor growth in a dose-dependent manner; 0.125 mg/kg, 0.5 mg/kg, and 2 mg/kg groups showed 50%, 62%, and 91% tumor volume reduction, respectively, compared with the control group ($*P < 0.05$ and $**P < 0.01$ vs control, Figure 3B). Immunohistochemical staining of the tumor sections demonstrated that there was a down-regulation of c-Met with c-Met siRNA-PEG/SLN complex administration (Figure 3C). These results indicate that a SLN-based siRNA delivery system can overcome the current problems facing siRNA therapy. Here, we showed that GBM tumor volume reduction can be effectively achieved via RNAi-mediated down-regulation of c-Met. More importantly, we show that the SLN complex employed here allows for a systemic in vivo application of c-Met siRNAs in glioblastoma orthotopic models that can effectively control tumor growth. It should be noted that no significant difference in body weight changes was observed between mice with and without treatment of siRNA-PEG/SLN complex during the indicated experimental period (data not shown). This suggests that there was no apparent critical systemic toxicity caused by the formulations.

c-Met siRNA-PEG/SLN Complex Can Cross the Blood-Tumor Barrier and Specifically Target the Tumor Site. To investigate the in vivo BBB-permeability of the c-Met siRNA-PEG/SLN complex, we intravenously administered Cy5.5-labeled c-Met siRNA-PEG/SLN complex to mice bearing the U-87MG tumor (Figure 4A). At 48 h postinjection,

dx.doi.org/10.1021/bc200406n | *Bioconjugate Chem.* 2011, 22, 2568–2572

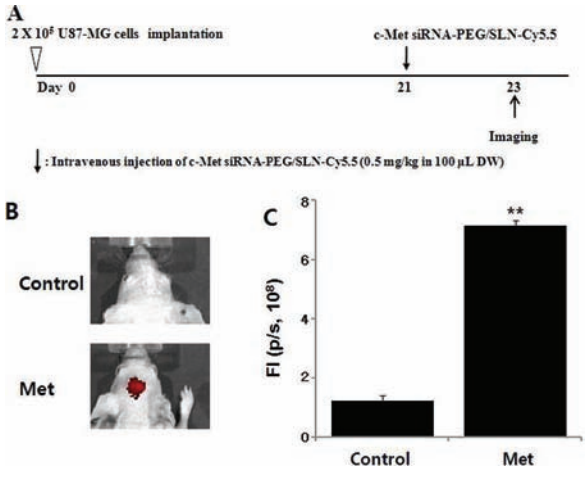

Figure 4. *In vivo* optical imaging of c-Met siRNA-PEG/SLN complex in tumor-bearing mice. (A) Detailed experimental schedules using the glioblastoma animal model are illustrated. (B) Distribution of Cy5.5-labed c-Met siRNA-PEG/SLN complex in brain bearing glioblastoma cells was visualized by *in vivo* fluorescent optical imaging. (C) Fluorescence intensity (FI) was analyzed. Values are mean ± SEM $^{**}p < 0.01$ vs Control.

Cy5.5-labeled c-Met siRNA-PEG/SLN complex showed higher fluorescence intensity in the brain compared to the no-treatment control (Figure 4 B,C). Grzelinski et al.[10] previously reported a similar delivery system of gene silencing but with local intratumor injection of siRNA/polyethlenimine complex in subcutaneous U-87MG model. Our work illustrates an improved delivery system that is effective even with systemic intravenous administration of the RNAi/nanoparticle complex in an orthotopic model. We speculate that siRNA-based therapy in orthotopic models may have been difficult to evaluate in the past due to the difficulty of delivery across the BBB. The system employed here showed that the siRNA-PEG/SLN can specifically cross the BBB to the tumor site (Figure 4) with no apparent systemic toxicity. This is highly significant since it provides proof-of-concept that in vivo diagnostics can also be a potential future application of the technology employed here. Caution should be taken by noting that the mice model used here lacks an intact immune system, so the innate immune response to RNAi will need to be addressed in future studies. Nevertheless, the tumor-tropic delivery of siRNAs across the BBB and the outstanding tumor volume reduction achieved by our system provide great promise for a clinical application in the near future.

CONCLUSIONS

Here, we present the SLN complexed with siRNAs as a viable platform for RNAi-based gene targeting, providing clinical rationale for the use of siRNAs against optimal targets of a given tumor. Specifically for GBM, we introduce SLN-complexed, c-Met-specific siRNAs as an efficient tool for attenuating tumor growth *in vitro* and *in vivo*. There was a successful tumor control via intravenous administration of the siRNA complex in the orthotopic GBM xenograft tumor model, along with specific tumor-tropic localization of the SLN per *in vivo* imaging. The model described here indicates that this approach is a highly feasible novel therapeutic option for GBM in the clinic.

AUTHOR INFORMATION

Corresponding Author

*Department of Neurosurgery, Samsung Medical Center, Sungkyunkwan University School of Medicine, 50 Irwon-dong Gangnam-gu, Seoul, South Korea 135-710. Tel: +82-2-3410-3497 Fax: +82-2-3410-0048 E-mail: nsnam@skku.edu.

Author Contributions

#Equal contribution.

ACKNOWLEDGMENTS

This work was supported by the National Research Foundation of KOREA (NRF) grant funded by the Korea government (MEST) (No.20090093731).

REFERENCES

(1) Rajadhyaksha, M., Boyden, T., Liras, J., El-Kattan, A., and Brodfuehrer, J. (2011) Current advances in delivery of biotherapeutics across the blood-brain barrier. *Curr. Drug Discovery Technol. 8*, 87–101.

(2) Kim, H. R., Kim, I. K., Bae, K. H., Lee, S. H., Lee, Y., and Park, T. G. (2008) Cationic solid lipid nanoparticles reconstituted from low density lipoprotein components for delivery of siRNA. *Mol. Pharm. 5*, 622–31.

(3) Hannon, G. J., and Rossi, J. J. (2004) Unlocking the potential of the human genome with RNA interference. *Nature 431*, 371–8.

(4) Oishi, M., Nagasaki, Y., Itaka, K., Nishiyama, N., and Kataoka, K. (2005) Lactosylated poly(ethylene glycol)-siRNA conjugate through acid-labile beta-thiopropionate linkage to construct pH-sensitive polyion complex micelles achieving enhanced gene silencing in hepatoma cells. *J. Am. Chem. Soc. 127*, 1624–5.

(5) Lu, P. Y., Xie, F., and Woodle, M. C. (2005) In vivo application of RNA interference: from functional genomics to therapeutics. *Adv. Genet. 54*, 117–42.

(6) Kim, S. H., Mok, H., Jeong, J. H., Kim, S. W., and Park, T. G. (2006) Comparative evaluation of target-specific GFP gene silencing efficiencies for antisense ODN, synthetic siRNA, and siRNA plasmid complexed with PEI-PEG-FOL conjugate. *Bioconjugate Chem. 17*, 241–4.

(7) Chung, N. S., and Wasan, K. M. (2004) Potential role of the low-density lipoprotein receptor family as mediators of cellular drug uptake. *Adv. Drug Delivery Rev. 56*, 1315–34.

(8) Kim, S. H., Jeong, J. H., Lee, S. H., Kim, S. W., and Park, T. G. (2006) PEG conjugated VEGF siRNA for anti-angiogenic gene therapy. *J. Controlled Release 116*, 123–9.

(9) Kong, D. S., Song, S. Y., Kim, D. H., Joo, K. M., Yoo, J. S., Koh, J. S., Dong, S. M., Suh, Y. L., Lee, J. I., Park, K., Kim, J. H., and Nam, D. H. (2009) Prognostic significance of c-Met expression in glioblastomas. *Cancer 115*, 140–8.

(10) Grzelinski, M., Urban-Klein, B., Martens, T., Lamszus, K., Bakowsky, U., Hobel, S., Czubayko, F., and Aigner, A. (2006) RNA interference-mediated gene silencing of pleiotrophin through polyethylenimine-complexed small interfering RNAs in vivo exerts antitumoral effects in glioblastoma xenografts. *Hum. Gene Ther. 17*, 751–66.

Bioconjugate Chemistry

Article

pubs.acs.org/bc

Oxygen Plasma Treated Interactive Polycarbonate DNA Microarraying Platform

Jesús Tamarit-López, Sergi Morais, Rosa Puchades, and Ángel Maquieira*

Departamento de Química, Instituto de Reconocimiento Molecular y Desarrollo Tecnológico, Universidad Politécnica de Valencia, Camino de Vera s/n, 46071 Valencia, Spain

Supporting Information

ABSTRACT: A novel DNA microarrying platform based on oxygen plasma activation of polycarbonate surface of compact disks (DVD) is presented. Carboxylic acid groups are generated in few seconds on polycarbonate in an efficient, fast, and clean way. Following this surface activation strategy, amino-modified oligonucleotide probes were covalently attached, reaching an immobilization density of 2 pmol cm^{-2}. Atomic force microscopy imaging revealed the nondestructive character of this treatment when applied for short times, allowing for disk scanning in standard DVD drives. DNA assays performed on oxygen plasma treated disks resulted very efficient with maximum hybridization yield of 93% and reaching a low limit of detection (200 pM) for perfect match synthetic oligonucleotide targets when reading the disk with a standard drive as detector. The approach was also evaluated by scoring single nucleotide polymorphisms with a discrimination ratio of 12.8. As proof of concept, the oxygen plasma treated interactive polycarbonate DNA microarraying platform was applied to the detection of PCR products of *Salmonella* spp., reaching a detection limit of 2 nM that corresponds to a DNA concentration of only 1 c.f.u./mL. The results confirm the suitability of the microarray platform for analysis of biological samples with high sensitivity.

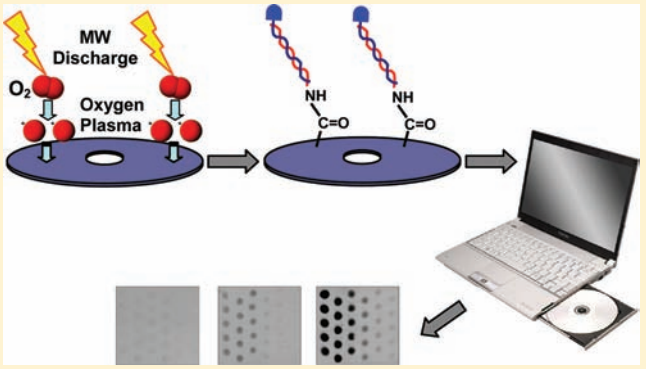

INTRODUCTION

DNA assays have been growing due to their broad applications in many fields (e.g., gene analysis, clinical diagnosis, or pathogen detection). Among the numerous assay types, oligonucleotide microarray technology allows for high-throughput, sensitive and selective DNA detection in a miniaturized format. For that, glass is the support commonly employed, but organic polymers also have high potential in microarray analysis due to their good mechanical and optical properties, mass production, and price.

Optical disks are attractive analytical supports, given the low cost of mass production and the countless surface chemistry strategies to attach probes for biosensing in different formats. Several approaches have been reported for bioanalytical applications in microarray format on optical disks.[1,2] Performances of drive as detector demonstrated that compact disk (CD) technology is very competitive. Ubiquity and the price of a disk reader provide huge advantages compared to the usual equipment, including fluorescence scanners and flow cytometers.

Electrostatic immobilization of DNA probes on positively charged surfaces, e.g., amino-silanized glass or charged-nylon membranes, is a common strategy to attach them in a random manner. However, covalent immobilization achieves probe directionality, reduces background noise, and develops a stable biomolecule layer.[3,4] Indeed, this strategy has been employed for the vast majority of commercial products because of its versatility, durability, and good functionality.[5,6]

Covalent linking of probes on optical disks requires functionalization of the surface since polycarbonate (PC), the main component of disks, lacks appropriated reactive chemical groups. A number of chemical and physical processes for covalent attachment of proteins and nucleic acid probes on PC surfaces are reported in the literature.[7−12] Most of these methods have limitations since they modify the opto-mechanical properties of the surface or use experimental setups that disable disk reading with disk drives. Also, classical chemical reactions must be carefully handled on disks as PC can be severely damaged. Our research group has developed chemical approaches, involving covalent attachment of probes on PC.[13−15] Several advantages were highlighted in DNA hybridization assays with limits of detection of 2.5 nM and scoring single nucleotide polymorphism (SNP), using covalently anchored aminated oligomers through a glutaraldehyde cross-linker.[14]

Received: August 3, 2011
Revised: October 31, 2011
Published: November 2, 2011

 © 2011 American Chemical Society dx.doi.org/10.1021/bc2004268 | *Bioconjugate Chem.* 2011, 22, 2573−2580

Table 1. Oligonucleotide Sequences of Probes and Targets[a]

name	sequence (5′−3′)	5′ end	3′ end
tracer	TTACGATCGATTAGTTAGCCC-$(T)_{15}$	Cy5	C_7-NH_2
probe 1	$(T)_{15}$-CCCGATTGATTAGCTAGCATT	C_7-NH_2	none
probe 2	$(T)_{10}$- TTTGATTACAGCCGGTGTACGACCCT	C_7-NH_2	none
target 1	AATGCTAGCTAATCAATCGGG	Cy5	none
target 2	AGGGTCGTACACCGGCTGTAATCAAA	digoxigenin	none
target 3	AGGGTCGTACA**T**CGGCTGTAATCAAA	digoxigenin	none
target 4	AGGGTCG**CG**CAC**TAT**CTGTAATCAAA	digoxigenin	none
target 5	A**CC**GTCG**CG**CAC**TAT**CTG**ATT**TCAAA	digoxigenin	none

[a]The nucleotide bases for polymorphism detection are marked in bold.

However, cleaner, easy-going, and more efficient methods are demanded. Thus, Li et al.[16] reported UV/O_3 treated compact disks, allowing the immobilization of biotin, oligonucletotides, and immunoglobulins by covalent linkage. Maintaining the disk structure, DNA hybridization events were detected with a sensitivity of 25 nM by analyzing errors of the disk reading in a standard CD drive. These figures should be improved to reach the sensitivity required in real applications.

Plasma methods have attracted much attention for surface modification of polymeric materials. It is generated by applying an electric discharge to a neutral gas, developing radicals highly reactive with any species or surface they reach. Plasma treatment is a fast, effective, and clean method to create chemical moieties with minimal waste products. Plasma methods to develop chemically reactive polymeric surfaces have been reviewed by Siow et al.[17] Surface modification of polymers by plasma has been widely physico-chemically characterized, including treated PC surfaces.[18] Oxygen plasma is reported to be more effective than others gases such as air, N_2, or Ar, for the treatment of PC, introducing oxygenated groups on the surface and providing a very low treatment depth and homogeneity on a molecular scale.[19] To the best of our knowledge, studies about the ability of these treated PC surfaces to covalently link DNA probes for bioassaying have not been published yet.

In this article, we describe an oxygen plasma activated PC surface of compact disks to covalently attach aminated oligonucleotide probes, developing a novel and general microarraying platform applicable to nucleic acid based methods. The optimal working conditions to maintain disk operations and surface activity were also approached despite the delicate structure of DVD (PC substrate covered with several layers of different materials) and the hard conditions inside the plasma reactor.

This novel microarray platform, compatible with disk reading, is created and applied, as a proof of concept, to score SNPs and detect polymerase chain reaction (PCR) products, achieving good performance.

EXPERIMENTAL PROCEDURES

Chemicals. The immobilization-printing buffer (HEPES: 50 mM 2-[4-(2-hydroxyethyl)piperazin-1-yl]ethanesulfonic acid buffer, containing 40% (v/v) glycerol, pH 7.0); hybridization buffer (3 × SSC: 45 mM sodium citrate buffer and 450 mM NaCl, pH 7.0); PBS-T (10 mM sodium phosphate buffer, 150 mM NaCl, and 0.05% (v/v) Tween 20, pH 7.2); and washing solutions were filtered through a 0.22 μm pore size nitrocellulose membrane from Whatman GmbH (Dassel, Germany), before use.

Oligonucleotides were from Sigma-Aldrich (Madrid, Spain), and the sequences are shown in Table 1. Digoxigenin labeled PCR products were 151 bp long and used to detect specifically *Salmonella* spp. Ten nanometer colloidal gold labeled antidigoxigenin immunoglobulin was from Aurion (Wageningen, The Netherlands). *N*-Hydroxysuccinimide (NHS), 1-ethyl-3-(3′-dimethylaminopropyl)carbodiimide (EDC), Crystal Violet, Tween 20, formamide, and silver enhancer solutions were supplied by Sigma-Aldrich (Madrid, Spain). Note: All the chemicals should be handled following the corresponding material safety data sheets.

Surface Activation and Characterization. DVD-R disks were purchased from MPO Ibérica (Madrid, Spain). The disks were first conditioned by gentle ethanol washing, water rinsing, and dried by centrifugation. For oxygen plasma activation, disks were introduced inside a microwave plasma reactor PVA Tepla 200 Plasma System (Feldkirchen, Germany) operating at 2.45 GHz and continuous 100 W power for 30 s. Oxygen pressure inside the reactor was 120 Pa. Disks were stored under vacuum and dry conditions until probe attachment.

Surface contact angle measurements were taken on OCA20 equipment and data analyzed using SCA20 software from Dataphysics Instruments GmbH (Filderstadt, Germany). The measurements were done in quintuplicate at room conditions with a volume drop of 10 μL.

X-ray photoelectron spectra were recorded with a Sage 150 spectrophotometer from SPECS Surface Nano Analysis GmbH (Berlin, Germany). Nonmonochromatic AlKa radiation (1486.6 eV) was used as the X-ray source operating at 30 eV constant pass energy for elemental specific energy binding analysis. Vacuum in the spectrometer chamber was 9×10^{-9} hPa and the sample area analyzed 1.0 mm^2. The surface topographies were examined with a Nanoscope IIIa atomic force microscope from Digital Instruments (Santa Barbara, CA, USA), operating in tapping mode in air at room temperature.

Crystal violet dye was employed to estimate the density of carboxylic acid groups generated on oxygen plasma treated PC surfaces, as previously described.[20] Raw polycarbonate surface from standard DVDs was used as the control.

Oligonucleotide Immobilization. Amino modified oligonucleotide probes were attached to oxygen plasma DVD by carbodiimide chemistry. To this end, the oligo probe was serially dissolved (concentration ranging from 0.05 to 5 μM) in printing buffer with EDC and NHS at 20 mM. Solutions were immediately microarrayed on the oxygen plasma activated surface as 50 nL drops with a noncontact dispenser (AD1500, Biodot Inc., Irvine, CA) in a 90% humidity environment. The disk layout consisted of eight segmented areas (45° separation) each one constituted of 30 spots of ∼500 μm diameter, spaced 1 mm and distributed in 6 columns and 5 rows. In this manner,

dx.doi.org/10.1021/bc2004268 | *Bioconjugate Chem.* 2011, 22, 2573−2580

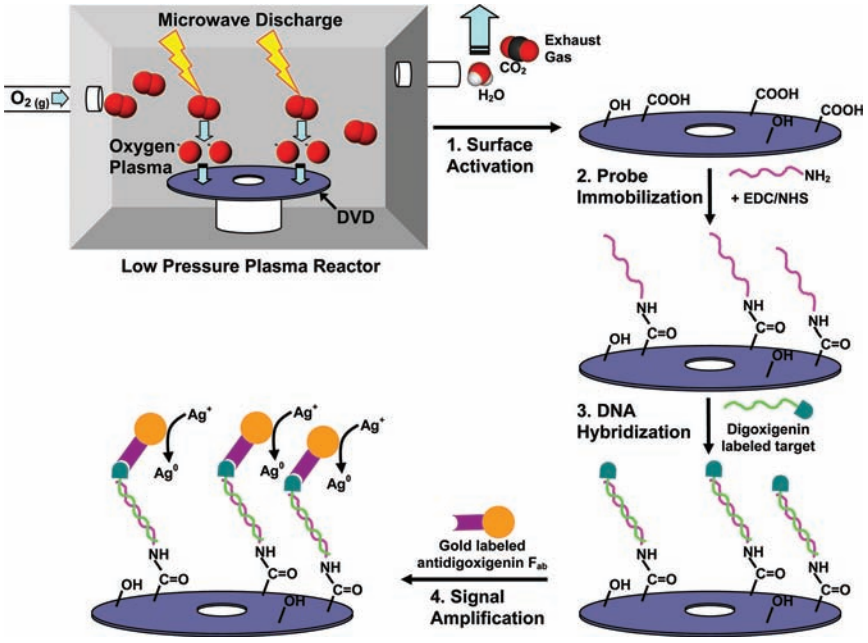

Figure 1. Scheme of oxygen plasma activation procedure of DVD PC surfaces, covalent attachment of oligonucleotides, DNA hybridization, and assay development.

eight samples can be simultaneously analyzed. The coupling reaction was carried out at 4 °C for 16 h under controlled humidity conditions. After that, the activated surface was washed with PBS-T for 1 min, rinsed with water, and dried by slight centrifugation.

DNA Hybridization Assays on DVD. For hybridization studies, both digoxigenin labeled oligomer target and PCR products were used. The latter, first, was denaturated into single DNA strands by high temperature treatment prior to their application to the disk. This method involves a 5 min incubation step at 95 °C followed by 1 min on ice. Target and PCR product solutions (100 μL) in hybridization buffer were evenly distributed on disk areas using 22 × 22 mm glass coverslips. After 1 h at 37 °C, the disk was washed with PBS-T, rinsed with deionized water, and dried by slight centrifugation. Next, 1 mL of gold labeled antidigoxigenin solution (1:100 in PBS-T) was dispensed onto the disk and covered with a 12 cm diameter dummy plastic surface. After 1 h at room temperature, the disk was washed, rinsed, and dried as before. To display the hybridization reaction, the disk was incubated with 1 mL of 1:1 (v/v) silver enhancer solution distributed as before and the reaction stopped by washing with water after 18 min at room temperature. The disk was dried as described above and read with a CD/DVD drive.

The CD/DVD drive was from LG Electronics (Englewood Cliffs, NJ, USA) and holds two lasers, 650 and 780 nm, which focus on the spiral data track of CD and DVD disks, respectively. During the disk reading, the laser hits the reaction product which modifies the optical properties of the disk surface, attenuating the signal captured by the photodiode. This signal is related with target concentration. A detailed description of the optical disk drive working as chemical detector is described elsewhere.[2] A scheme of surface activation, probe immobilization, and DNA hybridization assays is depicted in Figure 1.

Oligonucleotide Surface Density. The immobilization probe density was estimated by measuring the fluorescence of a Cy5-labeled oligonucleotide tracer (Table 1), and the hybridized target density was calculated through the fluorescence of the target-1 after hybridization with probe-1, immobilized on PC activated chips at different densities. The fluorescent intensity of the spots was determined by a homemade apparatus incorporating a charge couple device camera Retiga EXi from Qimaging Inc. (Burnaby, Canada) and light emitting diodes Toshiba TLOH157P as the fluorescence excitation source.[21]

After the corresponding immobilization and hybridization steps, the chips were washed, rinsed, and dried, the fluorescence signal of the spots was quantified, and the density of immobilized and hybridized DNA was extracted from the respective calibration curves (Figures S3 and S4, Supporting Information). For each experimental condition tested on the microarrays, 12 replicates spots of each solution were spotted on the treated polycarbonate DVD surface. The experiment was repeated three times. The immobilization and hybridization data presented are the average of these repetitions, and the error bars represent the standard deviation observed on this average. The yield of DNA hybridization was calculated as the ratio of the target to probe densities.

■ RESULTS AND DISCUSSION

Surface Characterization. Oxygen activated DVD surface was characterized by water contact angle measurements which give information about surface hydrophilicity that, in fact, is related to the presence of oxygenated functional groups. The contact angle in water decreased from 79° of raw hydrophobic PC surface to a constant value of 16° after 30 s plasma treatment (Figure 2A). The efficiency of oxygen plasma treatment was demonstrated considering that only 5 s of activation decreases the contact angle up to 30°, being in good agreement with that observed in raw polycarbonate after treatment with different plasma gases.[19,22] As is shown in Figure 2, uniformity of the oxidized surfaces was corroborated from the low dispersion of the contact angle measurements randomly taken on the disk surface.

dx.doi.org/10.1021/bc2004268 | Bioconjugate Chem. 2011, 22, 2573–2580

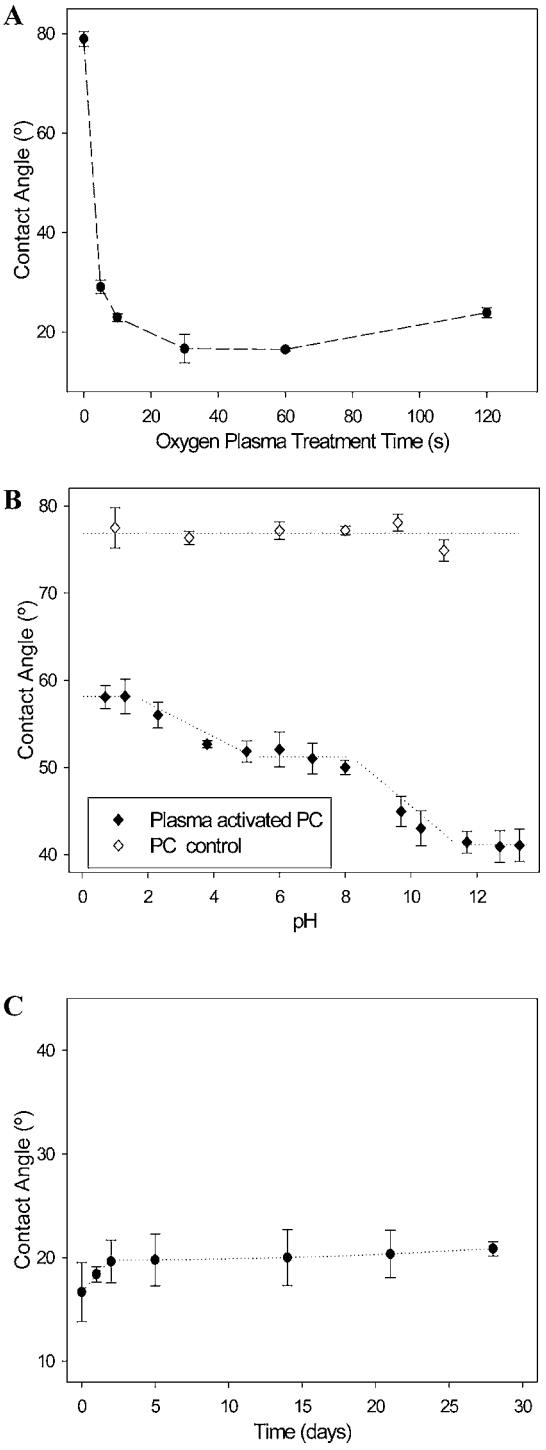

Figure 2. (A) Change of contact angle in water of DVD PC surfaces treated by oxygen plasma (100 W, 120 Pa) with the activation time. (B) Contact angle titration curves of untreated and oxygen plasma activated (100 W, 120 Pa, 30 s) DVD PC surfaces. The dotted lines are to facilitate reading only. (C) Variation of water contact angle of plasma treated DVD PC surfaces as a function of storage time in a vacuum desiccator.

Considering that the oxygen plasma treatment incorporates to the polycarbonate surface different oxygenated groups such as alcohols, carboxylic acids, and other carbonyl functions and that these groups are protonated or deprotonated depending on their pK_a and the pH of the medium, we found out their presence by means of a contact angle titration curve using buffered solutions. Thus, the contact angle was gradually decreased as the pH was raised, observing two smooth transitions from pH 1.0 to 5.0 and from 8.0 to 12.0 (Figure 2B). Contrarily, the contact angle remained constant on untreated disks within the pH range tested. This might suggest the presence of phenols and aromatic acids on the activated surface since the pK_a of benzoic acid and phenol is 4.2 and 9.9, respectively. Nevertheless, the smoothness of the titration leaps points to a mixture of several moieties and other functionalities, in different ratios, making it difficult to identify the nature of each chemical surface group. Although carboxylic acids are the only preferred groups for the subsequent covalent attachment of aminated probes, phenols would not interfere in the coupling efficiency of oligonucleotides through carbodiimide chemistry. Furthermore, phenols contribute to surface hydrophilicity, reducing the nonspecific adsorption of oligonucleotide targets and other assay reagents such as gold-labeled antidigoxigenin immunoglobulin.

The whole leap in the contact angle titration curve is about 20°, which is lower than that the obtained with other treatments.[23] However, the high density of the functional groups was determined by the crystal violet procedure. The differences in the signal obtained between activated and raw PC surfaces determine a density of ionizable groups (acids and phenols) of 1.2×10^{-9} mol cm^{-2}. This figure is higher than that reported for PC surfaces after 1 h of UV irradiation or 10 min of UV/ozone treatment (0.25 and 0.48×10^{-9} mol cm^{-2}, respectively).[24,25] Although the estimated density refers to functional ionizable groups, it can be considered that carboxylic acid moieties constitute approximately half of the total since the magnitudes of the two titration curve leaps were similar (Figure 2B). Even so, the density of carboxylic acid groups is much higher than 0.15×10^{-9} mol cm^{-2}, that is, the one calculated for close-packed ssDNA strands.[26]

The change of hydrophobicity of the treated surface was also studied by XPS. The C1s and O1s spectra of untreated and treated DVDs revealed a change in the atomic ratio O/C from 0.17 to 0.29 after oxygen plasma treatment for 30 s. Deconvolution of C1s spectra showed that new bonds of C–O are formed during the activation (Figure S1, Supporting Information). Thus, to the bands at 286.6 and 290.5 eV, due to single and quadruple bonds between C and O present in the chemical structure of PC, plasma activation adds new bands at 287.5 and 288.8 eV, corresponding to double and triple bonds, respectively.[18] This confirms the presence of new carbonyl and carboxylic groups on the treated surface. Also, a slight increase in the band height at 286.5 eV points the generation of new phenol or phenoxy functionalities. However, given the performances of the XPS technique, new spectra with higher resolution could be required to accurately corroborate these results.

Achieving an efficient functionalization of the surface is as important as keeping its physical properties in order to read the disks in a standard CD/DVD drive. AFM imaging of treated and untreated surfaces revealed that the topography of DVDs, in terms of root-mean-square roughness value (R_{rms}), does not change during the first minute of plasma treatment (Figure S2, Supporting Information). Contrarily, 5 min of activation resulted on disk imperfections (visible by naked eye) because the DVD is composed of several layers of materials whose adherence fails during prolonged plasma treatment. Nevertheless, shorter activation times produce only minimum etching

dx.doi.org/10.1021/bc2004268 | Bioconjugate Chem. 2011, 22, 2573–2580

of the surface, and PC chemical modification is the dominant process.

However, plasma treated polymer surfaces progressively lose their anchoring capacity during storage time: the aging effect. This phenomenon is detected through the increase of hydrophobicity (surface contact angle increasing). As is shown in Figure 2C, when plasma activated DVD PC surfaces were stored under vacuum and dry conditions, the water contact angle only increased from 16° to 21° after a month of storage. This means that the aging effect over the activated disks is minimum, and the surface continues being reactive for biomolecule immobilization after storage.

DNA Microarray Platform. A DVD derivatized surface with carboxylic acid moieties constitutes a potential platform to attach probes for biosensing purposes. The application of these modified surfaces by covalent immobilization of aminated oligonucleotide probes on 30 s plasma activated DVDs and further development of DNA hybridization-based assays was demonstrated for the first time.

A study to ascertain the best conditions for oligonucleotide immobilization on oxygen plasma treated PC surfaces was carried out. The pH is a paramount parameter that needs to be controlled when using carbodiimide chemistry; indeed, slightly acidic solutions (pH 5) are known to better stabilize active NHS esters, but alkaline conditions are needed to reach a good density of the nonprotonated amino group of modified oligonucleotides and for nucleophilic attack to occur at the activated surface (pK_a of conjugated acid of aliphatic amino is approximately 9.0). Thus, comparing different printing buffers, a maximum oligonucleotide immobilization density was reached at neutral medium (HEPES buffer pH 7.0).

The high hydrophilicity of the treated surfaces causes the spreading of the printed spots in a manner in which they overlapped each other. Also, this diffusion of the spotted solutions increased the evaporation speed, hindering reaction of probes with the disk surface. To control these issues, glycerol was added to the printing solution showing that 40% (v/v) was the optimal content to avoid the aforementioned problems.

Operating at the described conditions, the probe immobilization was studied over PC oxygen plasma treated surfaces at different times, using fluorescent dye marked oligonucleotide as the tracer (See Experimental Procedures).

Probe immobilization density increased with the surface treatment time, probably due to the higher carboxylic acid group density, but 1 min treatment or longer decreased the efficiency to attach oligonucleotides (Figure 3). Extended plasma treatments might also generate low molecular weight material on it, including a weak boundary layer, due to the etching of the surface.[18] This material, together with the immobilized probe, is removed from the surface after the washing step, and therefore, less amount of oligonucleotide is finally attached on the surface. However, the immobilization density increases with the concentration of oligonucleotide dispensed on the surface, reaching a plateau at concentrations between 5 and 10 μM.

An immobilization density of 2 pmol cm^{-2} was reached in the studied conditions. This density was similar to that reported by others authors working on activated plastics (5 and 10 pmol cm^{-2} for UV-Ozone activated PC and aminated PMMA, respectively)[25,27] or commercial reactive microarray glass slides (11 pmol cm^{-2}).[28] High immobilization densities do not necessarily imply an improvement in the hybridization yield, so

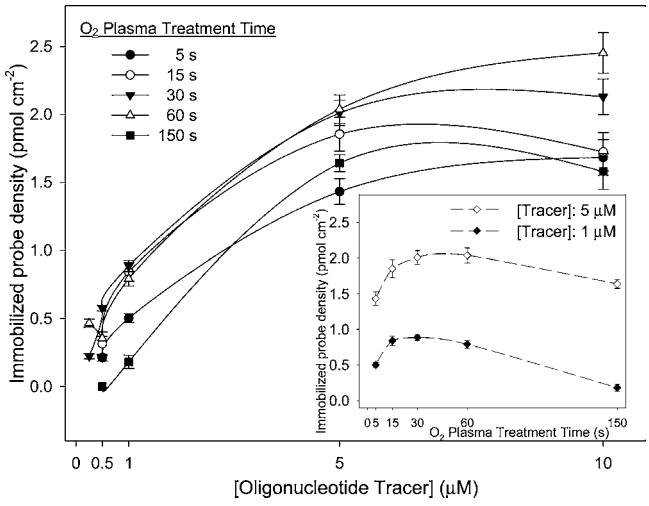

Figure 3. Oligonucleotide immobilization density on activated DVD PC surfaces by oxygen plasma (100 W, 120 Pa) at different times. Inlet, immobilized density dependence on the time of plasma activation for two concentrations of tracer. Density values were calculated from fluorescence intensity values of Cy5 labeled probes measured with a CCD camera.[21] EDC/NHS in printing buffer without probe oligonucleotide were employed as negative controls.

the obtained one is suitable to detect DNA with high sensitivity.

However, a negligible response (S/N < 3) was obtained from a nonspecific probe anchoring on a plasma treated polycarbonate surface when fluorescent labeled oligonucleotides without an amino group are used (Target 1) or when the amino modified oligonucleotides were used in the absence of EDC/NHS (negative controls). This confirmed that other reactive groups formed on the PC surface during the plasma treatment, such as epoxides or oxygen radicals, were not present in such an amount to react and produce significant nonspecific probe immobilization. Likewise, although some degree of $\pi-\pi$ or other hydrophobic interactions could be established between purine and pyrimidine bases and the aromatic moiety of the polycarbonate, no signal was observed, over nonactivated disks at the probe concentrations employed, supporting the suitability of the plasma treated surfaces for covalent attachment of aminated probes at low concentrations.

DNA Hybridization Assays. The performance of oxygen plasma activated DVDs to attach DNA probes was assessed through hybridization assays with oligonucleotides and PCR products, establishing its sensitivity and selectivity. Several considerations related with the design of the oligonucleotides sequence were taken into account before carrying out optimization studies. First, a poly T tail 10 to15 long was added at the 5′ end with the role of spacer to physically separate them from the surface, alleviating possible steric interferences.[29] Second, the length of probes and targets ranged 21 to 26 bp as a trade off between hybridization efficiency and specificity.[30]

The yield of hybridization was determined by comparison of the response obtained after the recognition event between Probe 1 and Target 1 to that achieved by the immobilization of tracer. As shown in Figure 4A, hybridized target density increased with target concentration, reaching a plateau at 200 nM for the tested probe concentrations (0.5−5 μM) and a maximum DNA target density of 0.93 pmol cm^{-2} (probe, 5 μM; target, 500 nM). This figure was similar to that achieved on other activated plastics[25,27] and corresponds to a hybrid-

dx.doi.org/10.1021/bc2004268 | Bioconjugate Chem. 2011, 22, 2573−2580

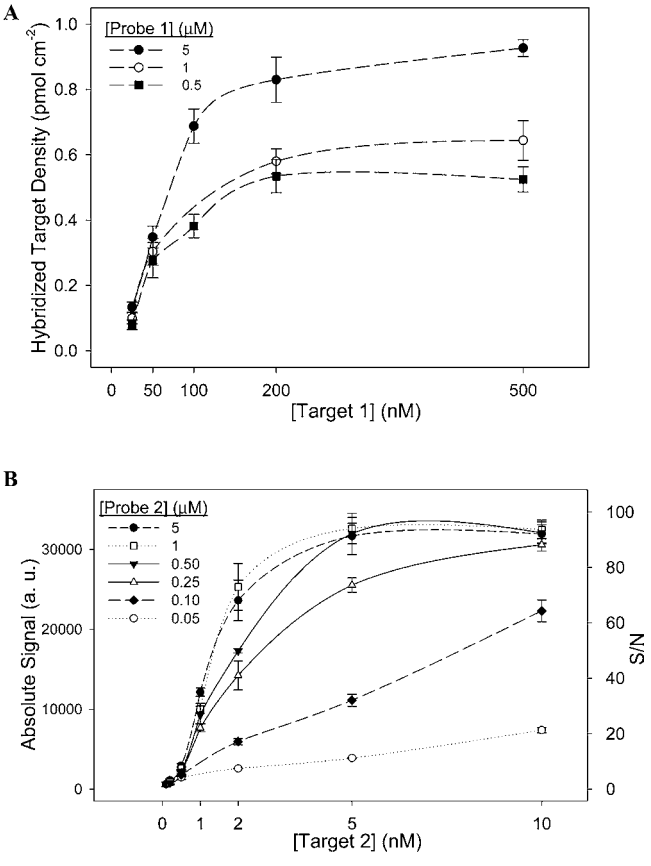

Figure 4. (A) Hybridized target density on oxygen plasma activated DVD PC surfaces (100 W, 120 Pa, 30 s), calculated from fluorescence intensity values of Cy5 labeled targets obtained with a CCD camera.[21] Hybridization buffer without target was employed as the negative control. (B) Absolute signal and S/N values (mean value ± standard deviation of 15 replicates) for DNA hybridization assays on plasma activated standard DVDs with different probe and target concentrations read with a standard DVD drive. Hybridization buffer without target was employed as the negative control.

ization yield of 46%. The efficiency is higher than that reached on other polymeric surfaces (between 6 and 18%), probably due to the superiority of this novel platform to immobilize probes at the optimal density. Indeed, it is well known that hybridization efficiency depends strongly on the amount of probe attached on the sensing surface in a manner that full hybridization is only achieved at lower probe densities because repulsive electrostatic and steric interactions are minimized.[31] Although recent approaches have reported to avoid it,[32] this "sweet spot" phenomenon has been confirmed multiple times by others authors over several DNA microarray supports.[33,34] Likewise, and in good agreement with these observations, the yield of hybridization on oxygen plasma activated PC was 93% at the lowest probe density tested (0.56 pmol cm^{-2}).

Detection of DNA target was performed on a DVD disk by using 5′-digoxigenin labeled oligonucleotides and gold labeled antidigoxigenin immunoglobulin and silver amplification to produce a solid reaction product. The hybridization assay performed with these reagents showed the highest S/N values compared to those of others using biotin labeled oligonucleotides and gold labeled streptavidin (Figure S5, Supporting Information). However, the modulation of the silver enhancement conditions is paramount to achieve an optimal contrast for detection.[35] Thus, shorter reactions do not develop enough reaction product for quantification whereas reactions that are too long increase the level and noise of the background, dropping the signal-to-noise ratio. In our case, 18 min was selected as the suitable amplification time to get the best contrast and S/R values. This time is longer than the optimal one found for assays over other PC disks, probably due to the different surface chemistry achieved with plasma treatment.[1,14] The linear dynamic range and limit of detection (LOD) related to the probe density and target concentration is shown in Figure 4B. Thus, a limit of detection of 200 pM, calculated as the concentration of target giving a signal equal to three times the standard deviation of the background signal, was reached when immobilizing the 5 μM probe. Likewise, the dynamic range for the hybridization assay can be improved by controlling the amount of immobilized probe and the reaction time of the silver enhancement step (e.g., shortening the reaction time to avoid saturation for higher target concentrations, Figure S6, Supporting Information).

At the conditions described here, the background signal was negligible (S/N < 3), saving the blocking step with BSA or ethanolamine and reducing assay time. In addition, such a background level is indicative of low nonspecific adsorption of gold-labeled antidigoxigenin immunoglobulin on this hydrophilic surface.

The relatively high yield of hybridized target achieved with our approach implies that very little amount of DNA probe is needed to obtain a detectable signal. Thus, dispensing 50 nL of 5 μM probe solution means that only 50 fmol of oligonucleotide per assay is used (considering a single spot as an individual assay), which is quite low compared to that in other protocols such as microfluidic arrays.

However, it is also important to keep the stability of the probe-coated surface with time. Thus, weekly hybridization assays demonstrated that the immobilized probes on plasma treated PC surfaces were active during, at least, two months after being printed on the disks without significant loss (12%) of the hybridization signal.

The selectivity of our approach was evaluated through hybridization assays using target oligonucleotides with mismatched bases with respect to the sequence of the immobilized probe. Negligible responses (S/N < 3) were obtained assaying 5 and 10 base-pair mismatch targets (Figure 5A) for a broad range of concentrations (from 0.1 to 500 nM). More interesting, due to its potential application in genotyping, is the ability of the sensing platform to discriminate single nucleotide polymorphisms (SNPs), predicting disease predispositions or drug responses in individuals.[36] Working with stringent conditions, such as a lower ionic strength hybridization buffer (1 × SSC) and the addition of formamide at 50% (v/v), maximum discrimination ratio of 12.8 was reached (Figure 5B), being in the range of those achieved with other approaches for oligonucleotides of similar length.[37]

Also, the potential of the new microarray disk surface for sensitive and selective detection of PCR amplified DNA products of pathogens was tested. The nucleotide sequence of the immobilized probe 2 was complementary to the central region of 151 bp amplicon specific to detect *Salmonella* spp. Although the high temperature pretreatment denatures PCR products (dsDNA) into ssDNA complementary strands, during its application on the disk, incubation time is an essential parameter to avoid amplicon reassociation and control the hybridization assay, as shown in Figure 5C. Thus, higher responses were obtained after 60 min. At the described

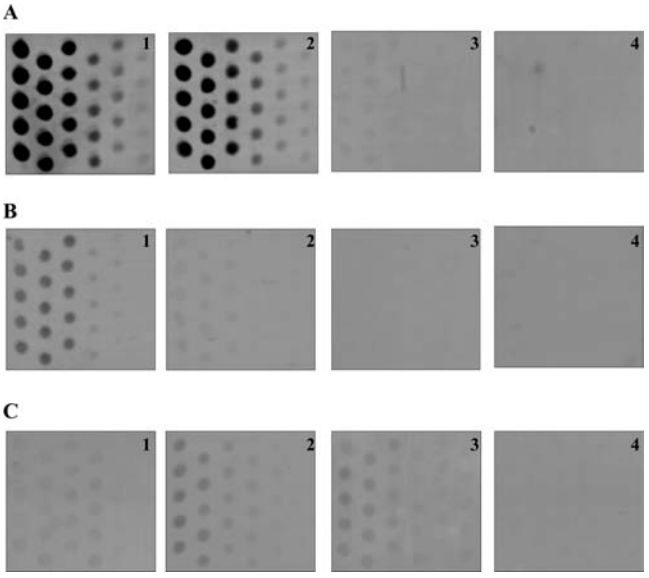

Figure 5. Optical density images of DNA hybridization assays performed on DVD-Rs and read with a standard DVD drive. Columns, from left to right, correspond to probe 2 at concentrations of 5, 1, 0.5, 0.25, 0.1, and 0.05 μM, respectively. (A) Hybridization with target at 5 nM in nonstringent conditions (3× SSC buffer without formamide). Panels 1−4 correspond to perfect match, single, 5, and 10 base mismatch oligonucleotides targets, respectively (targets 2, 3, 4, and 5, respectively). (B) Hybridization with target at 5 nM in stringent conditions (1× SSC buffer with formamide at 50% (v/v)). Panels 1−4 correspond to perfect match, single, 5, and 10 base mismatch targets, respectively (targets 2, 3, 4, and 5, respectively). (C) Panels 1−3 correspond to hybridization with *Salmonella* spp. PCR product at 2 nM for 15, 60, and 120 min, respectively. Panel 4 corresponds to hybridization with *Cronobacter* amplicon at 2 nM for 60 min used as the negative control. S/N values were 21.8, 17.0, 8.7, 5.5, 2.2, and 0.5 (panel 2) and 15.0, 11.4, 6.8, 3.8, 3.1, and 3.5 (panel 3) for 5, 1, 0.5, 0.25, 0.1, and 0.05 μM probe 2 concentration, respectively.

conditions, the new microarray was able to detect 2 nM of amplicon. This limit of detection is about 1 order of magnitude better than that reached with synthetic oligonucleotides, probably due to the lower diffusion coefficient of larger targets and the reassociation of the two amplicon strands during hybridization on the disk. However, negligible responses (S/N < 3) in the detection of negative PCR control products (*Cronobacter sakazakii*) confirmed the selectivity of our approach.

Considering the target solution volume used for hybridization assays (100 μL), and the number of spots printed per array (30), a limit of detection of 200 pM is equivalent to 700 amol of DNA molecules, which is 2 orders of magnitude lower than the reported one for DNA detection on UV/ozone treated compact disks.[16] However, differences in assay format (line array instead of spot microarray), type of disk (CD instead of DVD), and reading strategy (error reading detection instead of acquiring the attenuated analog signal) could be decisive for the differences found between the two approximations.[2,38] Indeed, at this stage, the approach presented here shows an important sensitivity enhancement on the state of the art (DNA microarrays on standard disk surfaces).[14,37] The detection limit of 2 nM of PCR product reached with our approach is equivalent to detect 150 μgL^{-1} of PCR amplified DNA. This result is very interesting because this amount of DNA comes from 1 colony-forming unit/mL. This achievement in sensitivity, together with the ultrafast and nonaggressive performance of surface modification protocol, reveal plasma treated DVDs as practical platforms for DNA microarray sensing. Moreover, the DVD disk and drive approach constitutes an analytical tool with high potential compared to other microarray detection platforms such as confocal fluorescent scanners or flow cytometers, with advantages such as low cost, portability, and high-throughput capability to analyze thousands of samples in field conditions.

CONCLUSIONS

Oxygen plasma treated DVD polycarbonate surface is a novel and superior DNA microarray support. The surface activation is fast and clean adding to the optical and mechanical properties of the disk's new capabilities, allowing scanning with standard disk drives. The treatment generates active and stable moieties on the polycarbonate surface, allowing for the covalent immobilization of amino modified probes with appropriate densities for developing sensitive DNA hybridization assays.

Mass production of functionalized disks could be carried out smartly and easily since only 30 s of treatment gives an appropriate surface density of functional moieties. At the same time, in this process, the chemical modification is independent of substrate geometry, making it possible to uniformly activate several disks during a single plasma treatment. This is a clean activation strategy because it requires tiny amounts of chemicals or solvents, avoiding the generation of classical synthesis waste byproducts, adding extra value as an environmentally friendly procedure.

However, polycarbonate could be derivatized with different functional groups by proper selection of the employed plasma gases (e.g., introduction of amines from ammonia plasma for attaching biomolecules containing carboxylic acids). Also, other immobilization strategies such as streptavidin−biotin or the use of monofunctional or bifunctional linkers are of direct and simple implementation.[39]

Detection of PCR amplified DNA products were also demonstrated, reaching high sensitivity and selectivity, with an inverse relationship between probe density and hybridization yield. The limits of detection are very low and comparable to those reported in the literature using fluorescent, enzymatic, or metal nanoparticle labels on plastic supports. The advantages shown by compact disk reading technology, such as ubiquity, low cost, portability, and high-throughput, give this approach scalability and great potential.

ASSOCIATED CONTENT

Supporting Information

XPS spectra and AFM images of treated and untreated disks; calibration curves for oligonucleotide surface density calculation; study of other oligonucleotide labels; signal amplification times; and hybridization conditions. This material is available free of charge via the Internet at http://pubs.acs.org.

AUTHOR INFORMATION

Corresponding Author

*Tel: +34-963877342; Fax: +34-963879349. E-mail: amaquieira@qim.upv.es.

ACKNOWLEDGMENTS

This research was funded through projects FEDER MICINN CTQ2010-15943 (CICYT, Spain) and by Generalitat Valenci-

ana (GV/2009/028 and PROMETEO/2010/008). The Spanish *Ministerio de Educación y Ciencia* provided J.T.-L. with a grant for his Ph.D. studies. We thank Juan Hurtado for his technical assistance with the plasma reactor.

REFERENCES

(1) Morais, S., Carrascosa, J., Mira, D., Puchades, R., and Maquieira, A. (2007) Microimmunoanalysis on standard compact discs to determine low abundant compounds. *Anal. Chem. 79*, 7628−7635.
(2) Morais, S., Tamarit-López, J., Carrascosa, J., Puchades, R., and Maquieira, A. (2008) Analytical prospect of compact disk technology in immunosensing. *Anal. Bioanal. Chem. 391*, 2837−2844.
(3) Du, Q., Larsson, O., Swerdlow, H., and Liang, Z. (2006) DNA immobilization: silanized nucleic acids and nanoprinting. *Top. Curr. Chem. 261*, 45−61.
(4) Ivanova, E. P., Wright, J. P., Pham, D. K., Brack, N., Pigram, P., Alekseeva, Y. V., Demyashev, G. M., and Nicolau, D. V. (2006) A comparative study between the adsorption and covalent binding of human immunoglobulin and lysozyme on surface-modified poly(tert-butyl methacrylate). *Biomed. Mater. 1*, 24−32.
(5) Di Giusto, D. A., and King, G. C. (2006) Special-Purpose modifications and immobilized functional nucleic acids for biomolecular interactions. *Top. Curr. Chem. 261*, 131−168.
(6) Sassolas, A., Leca-Bouvier, B. D., and Blum, L. J. (2008) DNA biosensors and microarrays. *Chem. Rev. 108*, 109−139.
(7) Bora, U., Sharma, P., Kumar, S., Kannan, K., and Nahar, P. (2006) Photochemical activation of a polycarbonate surface for covalent immobilization of a protein ligand. *Talanta 70*, 624−629.
(8) Witek, M. A., Llopis, S. D., Wheatley, A., McCarley, R. L., and Soper, S. A. (2006) Purification and preconcentration of genomic DNA from whole cell lysates using photoactivated polycarbonate (PPC) microfluidic chips. *Nucleic Acids Res. 34*, e74.
(9) Carion, O., Souplet, V., Olivier, C., Maillet, C., Medard, N., El-Mahdi, O., Durand, J.-O., and Melnyk, O. (2007) Chemical micropatterning of polycarbonate for site-specific peptide immobilization and biomolecular interactions. *ChemBioChem 8*, 315−322.
(10) Najmabadi, P., Ko, K.-S., La Clair, J. J., and Burkart, M. D. (2008) A method for fabrication of polycarbonate-based bioactive platforms. *JALA 13*, 284−288.
(11) Remacle, J., Alexandre, I., and Houbion, Y. (2002) US Patent 177144.
(12) La Clair, J. J., and Burkart, M. D. (2003) Molecular screening on a compact disc. *Org. Biomol. Chem. 1*, 3244−3249.
(13) Bañuls, M. J., González-Pedro, V., Puchades, R., and Maquieira, A. (2007) PMMA isocyanate-modified digital discs as a support for oligonucleotide-based assays. *Bioconjugate Chem. 18*, 1408−1414.
(14) Bañuls, M. J., García-Piñón, F., Puchades, R., and Maquieira, A. (2008) Chemical derivatization of compact disc polycarbonate surfaces for SNPs detection. *Bioconjugate Chem. 19*, 665−672.
(15) Tamarit-López, J., Morais, S., Puchades, R., and Maquieira, A. (2011) Direct hapten-linked multiplexed immunoassays on polycarbonate surface. *Biosens. Bioelectron. 26*, 2694−2698.
(16) Li, Y., Ou, L. M. L., and Yu, H.-Z. (2008) Digitized molecular diagnostics: reading disk-based bioassays with standard computer drives. *Anal. Chem. 80*, 8216−8223.
(17) Siow, K. S., Britcher, L., Kumar, S., and Griesser, H. J. (2006) Plasma methods for the generation of chemically reactive surfaces for biomolecule immobilization and cell colonization: a review. *Plasma Process. Polym. 3*, 392−418.
(18) Muir, B. W., Mc Arthur, S. L., Thissen, H., Simon, G. P., Griesser, H. J., and Castner, D. G. (2006) Effects of oxygen plasma treatment on the surface of bisphenol A polycarbonate: a study using SIMS, principal component analysis, ellipsometry, XPS and AFM nanoindentation. *Surf. Interface Anal. 38*, 1186−1197.
(19) Chen, T. N., Wuu, D. S., Wu, C. C., Chiang, C. C., Lin, H. B., Chen, Y. P., and Horng, R. H. (2006) Effects of plasma pretreatment on silicon nitride barrier films on polycarbonate substrates. *Thin Solid Films 514*, 188−192.
(20) Xu, F., Datta, P., Wang, H., Gurung, S., Hashimoto, M., Wei, S., Goettert, J., McCarley, R. L., and Soper, S. A. (2007) Polymer microfluidic chips with integrated waveguides for reading microarrays. *Anal. Chem. 79*, 9007−9013.
(21) Mira, D., Llorente, R., Morais, S., Puchades, R., Maquieira, A., and Martí, J. (2004) High throughput screening of surface-enhanced fluorescence on industrial standard digital recording media. *Proc. SPIE-Int. Soc. Opt. Eng. 5617*, 364−373.
(22) Sharma, R., Holcomb, E., Trigwell, S., and Mazumder, M. (2007) Stability of atmospheric-pressure plasma induced changes on polycarbonate surfaces. *J. Electrostatics 65*, 269−273.
(23) Wang, Z., and Li, R.-X. (2007) Fabrication of DNA micropatterns on the polycarbonate surface of compact discs. *Nanoscale Res. Lett. 2*, 69−74.
(24) McCarley, R. L., Vaidya, B., Wei, S., Smith, A. F., Patel, A. B., Feng, J., Murphy, M. C., and Soper, S. A. (2005) Resist-free patterning of surface architectures in polymer-based microanalytical devices. *J. Am. Chem. Soc. 127*, 842−843.
(25) Li, Y., Wang, Z., Ou, L. M. L., and Yu, H.-Z. (2007) DNA Detection on plastic: a mild and efficient surface activation protocol converts polycarbonate substrates to biochip platforms. *Anal. Chem. 79*, 426−433.
(26) Steel, A. B., Levicky, R. L., Herne, T. M., and Tarlov, M. J. (2000) Immobilization of nucleic acids at solid surfaces: effect of oligonucleotide length on layer assembly. *Biophys. J. 79*, 975−981.
(27) Fixe, F., Dufva, M., Telleman, P., and Christensen, C. B. V. (2004) Functionalization of poly(methyl methacrylate) (PMMA) as a substrate for DNA microarrays. *Nucleic Acids Res. 32*, e9.
(28) Gong, P., Harbers, G. M., and Grainger, D. W. (2006) Multi-technique comparison of immobilized and hybridized oligonucleotide surface density on commercial amine-reactive microarray slides. *Anal. Chem. 78*, 2342−2351.
(29) Shchepinov, M. S., Case-Green, S. C., and Southern, E. M. (1997) Steric factors influencing hybridisation of nucleic acids to oligonucleotides arrays. *Nucleic Acids Res. 25*, 1155−1161.
(30) Relógio, A., Schwager, C., Richter, A., Ansorge, W., and Valcárcel, J. (2002) Optimization of oigonucleotide-based DNA microarrays. *Nucleic Acids Res. 30*, e51.
(31) Vainrub, A., and Pettitt, B. M. (2002) Coulomb blockage of hybridization in two-dimensional DNA arrays. *Phys. Rev. E 66*, 041905.
(32) Song, K.-S., Nimse, S. B., Kim, J., Kim, J., Nguyen, V.-T., Ta, V.-T., and Kim, T. (2011) 9G DNA Chip: microarray based on the multiple interactions of 9 consecutive guanines. *Chem. Commun. 47*, 7101−7103.
(33) Peterson, A. W., Heaton, R. J., and Georgiadis, R. M. (2001) The effect of surface probe density on DNA hybridization. *Nucleic Acids Res. 29*, 5163−5168.
(34) Gong, P., and Levicky, R. (2008) DNA surface hybridization regimes. *Proc. Natl. Acad. Sci. U.S.A. 105*, 5301−5306.
(35) Taton, T. A., Mirkin, C. A., and Letsinger, R. L. (2000) Scanometric DNA array detection with nanoparticle probes. *Science 289*, 1757−1760.
(36) McCarthy, J. J., and Hilfiker, R. (2000) The use of single-nucleotide polymorphism maps in pharmacogenomics. *Nat. Biotechnol. 18*, 505−508.
(37) Morais, S., Marco-Molés, R., Puchades, R., and Maquieira, A. (2006) DNA microarraying on compact disc surfaces. Application to the analysis of single nucleotide polymorphisms in Plum pox virus. *Chem. Commun. 22*, 2368−2370.
(38) Morais, S., Tortajada-Genaro, L. A., Arnandis-Chover, T., Puchades, R., and Maquieira, A. (2009) Multiplexed microimmunoassays on a digital versatile disk. *Anal. Chem. 81*, 5646−5654.
(39) Hermanson, G. T. (2008) *Bioconjugate Techniques*, 2nd ed., Academic Press, San Diego, CA.

Bioconjugate Chemistry

Article

pubs.acs.org/bc

Influence of Minor Backbone Structural Variations in Modulating the in Vitro Gene Transfer Efficacies of α-Tocopherol Based Cationic Transfection Lipids

Bhavani Kedika and Srilakshmi V. Patri*

Department of Chemistry, National Institute of Technology, Warangal -506004, Andhra Pradesh, India

Supporting Information

ABSTRACT: Toward probing the influence of backbone structural variation in cationic lipid mediated gene delivery of α-tocopherol based lipids, two novel α-tocopherol based lipids **1** and **2** have been designed and synthesized. The only structural difference between the cationic amphiphiles **1** and **2** is the backbone structure, where lipid **1** has a non-glycerol backbone and lipid **2** has a glycerol backbone. The lipids **1** and **2** showed contrasting transfection efficiencies: lipid **1** showed high gene transfer efficacy in multiple cultured animals cell lines, whereas lipid **2** is transfection incompetent. In summary, the present findings demonstrate that in the case of α-tocopherol based lipids even minor structural variations like backbone can profoundly influence size, DNA binding characteristics, cellular uptake, and consequently gene delivery efficacies.

Structures of Lipids 1 and 2 containing the same hydrophobic region, same head group and linker group functionality but differ only in the backbone region.

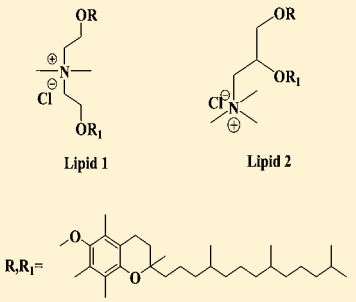

INTRODUCTION

To develop an efficient gene therapeutic approach, design of safe and efficient gene delivery reagents is a prerequisite. Cationic liposomes are one of the more promising nonviral systems for use in gene therapy.[1−18] Since the pioneering development of glycerol backbone-based cationic transfection lipid (*N*-[1-(2,3-dioleyloxy)propyl])-*N*,*N*,*N*-trimethylammonium chloride (DOTMA) in 1987,[19] design and syntheses of a plethora of more efficient cationic transfection lipids, including our own,[20] have been reported. The number of commercially available cationic lipid-based transfection kits are the fruits of such intense global efforts in developing safe and efficient cationic lipids for use in gene therapy. The molecular structures of most of these commercially available cationic transfection lipids contain glycerol as the backbone. With a view to address how important the presence of glycerol backbone in the molecular architectures of many commercially available cationic transfection lipids is, several groups have succeeded in developing a highly efficient series of non-glycerol-based novel transfection lipids.[21−29] The in vitro transfection efficiencies of some of these new cationic lipids developed are better than the most extensively used commercially available glycerol-based cationic amphiphiles used in transfecting cells.[21−29]

In our ongoing program on designing efficient novel cationic transfection lipids, we recently demonstrated the potential of novel α-tocopherol based monocationic lipids for use in liposomal gene delivery.[20] Understanding the structural parameters of cationic amphiphiles which can influence their gene transfer properties is important for designing efficient liposomal gene delivery reagents. Investigations into the role of various molecular-level modifications in different synthetic lipids on their membrane properties and further influence their gene transfer efficiencies are reported.[30−34] To our knowledge, the importance of structure of the backbone group linking the hydrophobic tail and hydrophilic head of cationic lipid is an unexplored area in cationic lipid gene delivery. To this end, with a view to understand the effect of structural variation in backbone on the transfection efficiencies of α-tocopherol based cationic amphiphiles, we have designed and synthesized two novel α-tocopherol based cationic lipids (**1** and **2**; Chart 1), wherein lipid **1** is with nonglycerol backbone and lipid **2** is with glycerol backbone. Findings from the transfection studies and DNA binding studies demonstrate that lipid **1** is more stable and highly transfecting when compared to lipid **2**. The fluorescence microscopic experiments reveal that lipid **1** has higher uptake by the cells and greater expression of reporter gene when compared to lipid **2**. Taken together, the present findings demonstrate that even minor structural variations like backbone in α-tocopherol based cationic amphiphiles can profoundly influence DNA binding, size, cellular uptake, and consequently gene delivery efficacies of cationic liposomes.

Received: August 11, 2011
Revised: October 7, 2011
Published: October 11, 2011

ACS Publications © 2011 American Chemical Society

Chart 1. Structure of Lipids 1 and 2

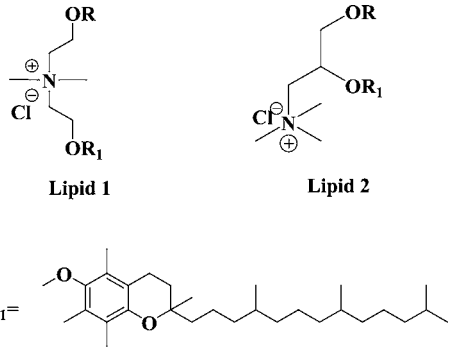

EXPERIMENTAL SECTION

General Procedures and Reagents. Mass spectral data were acquired by using a commercial LCQ ion trap mass spectrometer (ThermoFinnigan, SanJose, CA, USA) equipped with an ESI source. ^{1}H NMR spectra were recorded on a Varian FT 300 MHz NMR spectrometer. *N*-Methyl diethanol amine and *N*,*N*-dimethyl l,2,3-propane diol were purchased from Sigma Co. *p*-CMV-SPORT-*β*-gal plasmid, *α*5GFP plasmid, and Rhodamine-PE were generous gift from IICT (Indian Institute of Chemical Technology), Hyderabad. LipofectAmine-2000 was purchased from Invitrogen Life Technologies (USA). Cell culture media, fetal bovine serum, 3-(4,5-dimethylthiazol-2-yl)-2,5-diphenyltetrazolium bromide (MTT), poly(ethylene glycol) 8000, *o*-nitrophenyl-*β*-D-galactopyranoside were purchased from Sigma, St. Louis, USA. NP-40, antibiotics, and agarose were purchased from Hi-media, India. DOPC was purchased from Fluka (Switzerland). Unless otherwise stated, all the other reagents purchased from local commercial suppliers were of analytical grades and were used without further purification. The progress of the reaction was monitored by thin-layer chromatography using 0.25 mm silica gel plates. Column chromatography was performed with silica gel (Acme Synthetic Chemicals, India; finer than 200 and 60−120 mesh). Elemental analyses were performed by combustion procedure using Perkin-Elmer 2400 series II CHNS analyzer. Both the synthesized lipids **1** and **2** showed more than 95% purity.

Synthesis. Synthetic routes for preparing cationic lipids **1** and **2** are shown schematically in parts A and B, Scheme 1, respectively. Details of the synthetic procedures, purifications, and spectral characterizations of lipids **1** and **2**, as well as all their synthetic intermediates, shown in Scheme 1 are described below.

Synthesis of Lipid ***1*** *(Scheme 1 Part A). Synthesis of Tertiary Amine (Intermediate I Scheme 1 Part A).* A mixture of *N*-methyl diethanolamine (0.5 g, 4.19 mmol) and potassium hydroxide (∼4.0 g, 7.13 mmol) was taken in 10 mL of toluene in a two-necked round-bottomed flask fitted with a Dean−Stark apparatus. The reaction mixture is refluxed for two hours to remove the water as azeotropic mixture. To the reaction mixture, mesylated *α*-tocopherol (4.69 g, 9.22 mmol) (prepared as reported earlier[18]) is added and refluxed at 80 °C for 48 h. The solvent is evaporated and dried. The residue was taken in ethyl acetate (100 mL), washed with water (2 × 100 mL), dried over anhydrous magnesium sulfate, and filtered. The organic solvent is evaporated on a rotary evaporator. The column chromatographic purification of the resulting residue using 60−120 mesh size silica gel and eluting with 3−4% ethyl acetate (v/v) in hexane afforded 1.7 g, (42.92% yield, R_f = 0.8 in 10% ethyl acetate/hexane) of the intermediate tertiary amine.

^{1}H NMR (300 MHz, $CDCl_3$) δ ppm 0.75−0.95 [m, 24H, CH-C$\underline{H}_3$ tocopheryl], 1.55 [s, 6H, C$\underline{H}_3$-2 tocopheryl], 1.00−1.4 [m, 36H -(C$\underline{H}_2$)$_9$ tocopheryl], 1.8−1.9 [m, 4H, C$\underline{H}_2$-3 tocopheryl], 1.96−1.98 [s, 3H, N-C$\underline{H}_3$], 2.05 [s, 6H, C$\underline{H}_3$-5 tocopheryl], 2.15 [s, 6H, C$\underline{H}_3$-8 tocopheryl], 2.20 [s, 6H, C$\underline{H}_3$-7 tocopheryl], 2.55−2.6 [t, 4H, C$\underline{H}_2$-4 tocopheryl], 3.4−3.6[m,

Scheme 1. Synthesis of Lipids 1 and 2

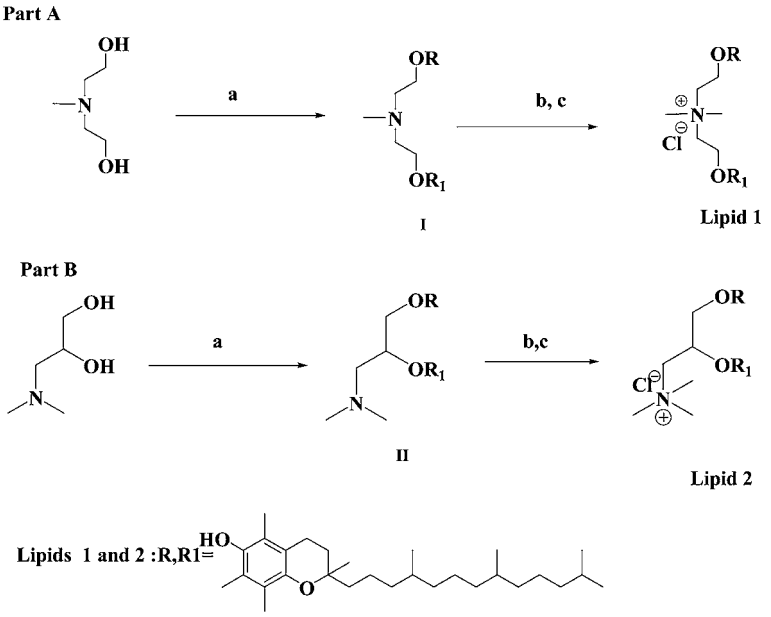

Reagents: a) Mesylated tocopherol, KOH, Toulene, 48 h b) Methyl Iodide, K_2CO_3, rt, 3 days c) Amberlyst anion exchange resin

dx.doi.org/10.1021/bc2004395 | *Bioconjugate Chem.* 2011, 22, 2581−2592

4H, N-C$\underline{H}_2$-CH$_2$-O-], 3.8−3.9 [m, 4H, N-CH$_2$-C$\underline{H}_2$-O-]. ESIMS: m/z 945 [M$^+$+1] for $C_{63}H_{109}NO_4^+$.

Synthesis of N,N-di[(O-α-deoxyα-tocopherol)-ethyl]-N,N-dimethylammonium chloride (lipid **1** *Scheme 1 Part A).* The intermediate tertiary amine obtained in step (a) of synthesis of lipid **1** (0.5 g, 0.52 mmol) was taken in a 25 mL round-bottomed flask and huge excess of methyl iodide (6 mL) was added to it. After stirring the reaction mixture at room temperature for 48 h, the solvent was removed on a rotary evaporator. The column chromatographic purification of the resulting residue using 60−120 mesh size silica and 2−3% (v/v) methanol in chloroform as eluent afforded the title compound as a quaternary iodide salt (0.4 g, 78.89% yield, R_f = 0.7, 10% methanol/chloroform). Finally, the pure title lipid **1** was obtained by subjecting the quaternized ammonium iodide salt to "repeated chloride ion exchange chromatography" using Amberlyst A-26 chloride anion exchange column and 60 mL of chloroform as eluent. ^{1}H NMR (300 MHz, CDCl$_3$) δ ppm 0.8−0.9 [m, 24H, CH-C$\underline{H}_3$ tocopheryl], 1.45 [s, 6H, C$\underline{H}_3$-2 tocopheryl], 1.00−1.4 [m, 36H -(C$\underline{H}_2$)$_9$ tocopheryl], 1.7−1.9 [m, 4H, C$\underline{H}_2$-3 tocopheryl], 2.05 [s, 6H, C$\underline{H}_3$-5 tocopheryl], 2.15 [s, 6H, C$\underline{H}_3$-8 tocopheryl], 2.20 [s, 6H, C$\underline{H}_3$-7 tocopheryl], 2.55−2.6 [t, 4H, C$\underline{H}_2$-4 tocopheryl], 3.7−3.8 [s, 6H, N-C$\underline{H}_3$], 4.1−4.2 [m, 4H, N-C$\underline{H}_2$-CH$_2$-O-], 4.35−4.45 [m, 4H, N-CH$_2$-C$\underline{H}_2$-O-]. ESIMS (lipid **1**): m/z 959 [M$^+$] for $C_{64}H_{112}NO_4^+$. Calculated: %N, 1.41; %C, 77.25; %H, 11.35. Observed: %N, 1.46; %C, 77.54; %H, 11.61.

Synthesis of Lipid **2** *(Scheme 1 Part B). Synthesis of Tertiary Amine (Intermediate II Scheme 1 Part B).* The intermediate tertiary amine is synthesized by taking a mixture of 3-(dimethylamino) propane-1,2-diol (0.5 g, 4.19 mmol), potassium hydroxide (∼4.0 g, 7.13 mmol), and mesylated α-tocopherol (4.69 g, 9.22 mmol) and following the same procedure as given in the synthesis of lipid **1**. The column chromatographic purification of the resulting residue using 60−120 mesh size silica gel and eluting with 4−5% ethyl acetate (v/v) in hexane afforded 2.0 g (50.50% yield R_f = 0.6, 10% ethyl acetate in hexane) of the intermediate tertiary amine. ^{1}H NMR (300 MHz, CDCl$_3$) δ ppm 0.8−0.9 [m, 24H, CH-C$\underline{H}_3$ tocopheryl], 1.55 [s, 6H, C$\underline{H}_3$-2 tocopheryl], 1.00−1.4 [m, 36H -(C$\underline{H}_2$)$_9$ tocopheryl], 1.7−1.9 [m, 4H, C$\underline{H}_2$-3 tocopheryl], 1.94−1.96 [s, 6H, N-C$\underline{H}_3$], 2.05 [s, 6H, C$\underline{H}_3$-5 tocopheryl], 2.15 [s, 6H, C$\underline{H}_3$-8 tocopheryl], 2.20 [s, 6H, C$\underline{H}_3$-7 tocopheryl], 2.55−2.6 [t, 4H, C$\underline{H}_2$-4 tocopheryl], 2.95−3.05 [m, 2H, CH$_2$-OR-CH-OR-C$\underline{H}_2$-N-(CH$_3$)$_2$], 4.0−4.1 [m, 1H, CH$_2$-OR-C$\underline{H}$-OR-CH$_2$-N-(CH$_3$)$_2$], 4.1−4.2 [m, 2H, C$\underline{H}_2$-OR-CH-OR-CH$_2$-N-(CH$_3$)$_2$]. ESIMS: m/z 944 [M$^+$] for $C_{63}H_{108}NO_4^+$.

Synthesis of N-([1-(2,3-dideoxyα-tocopherol)propyl])-N,N,N-trimethylammonium chloride (lipid **2** *Scheme 1 Part B).* The intermediate tertiary amine obtained in step a of synthesis of lipid **2** (0.5 g, 0.52 mmol) was quaternized using methyliodide. The quaternization is carried out following the procedure given in the synthesis of lipid **1** that yields the title compound as a quaternary iodide salt (0.43 g, 84.81% yield, R_f = 0.7, 10% methanol/chloroform). Finally, the pure title lipid **2** was obtained by subjecting the quaternized ammonium iodide salt to "repeated chloride ion exchange chromatography" using Amberlyst A-26 chloride ion exchange column and 60 mL of chloroform as eluent. ^{1}H NMR (300 MHz, CDCl$_3$) δ ppm 0.7−0.9 [m, 24H, CH-C$\underline{H}_3$ tocopheryl], 1.55 [m, 6H, C$\underline{H}_3$-2 tocopheryl], 1.00−1.4 [m, 36H -(C$\underline{H}_2$)$_9$ tocopheryl], 1.7−1.85 [m, 4H, C$\underline{H}_2$-3 tocopheryl], 2.05 [s, 6H, C$\underline{H}_3$-5 tocopheryl], 2.15 [s, 6H, C$\underline{H}_3$-8 tocopheryl], 2.20 [s, 6H, C$\underline{H}_3$-7 tocopheryl], 2.55−2.6 [t, 4H, C$\underline{H}_2$-4 tocopheryl], 3.8−3.9 [s, 9H, N-C$\underline{H}_3$], 4.15−4.25 [dd, 2H, CH$_2$-OR-CH-OR-C$\underline{H}_2$-N-(CH$_3$)$_3$], 4.3−4.45 [dd, 2H, C$\underline{H}_2$-OR-CH-OR-CH$_2$-N-(CH$_3$)$_3$], 4.7−4.8 [m, 1H, CH$_2$-OR-C$\underline{H}$-OR-CH$_2$-N-(CH$_3$)$_3$]. ESIMS (lipid **1**): m/z 959 [M$^+$] for $C_{64}H_{112}NO_4^+$. Calculated: %N, 1.41; %C, 77.25; %H, 11.35. Observed: %N, 1.74; %C, 77.05; %H, 11.05.

Cells and Cell Culture. B16F10, CHO, A-549, MCF-7, and HepG2 cell lines were procured from the National Centre for Cell Sciences (NCCS), Pune, India. Cells were cultured at 37 °C in Dulbecco's modified Eagle's medium (DMEM) with 10% fetal bovine serum, 50 μg/mL penicillin, 50 μg/mL streptomycin, and 20 μg/mL kanamycin in a humidified atmosphere containing 5% CO$_2$.

Preparation of Liposomes. The cationic lipid and the colipid (DOPC) in 1:2 mol ratio were dissolved in a mixture of chloroform and methanol (1:1) in a glass vial. The solvent was removed with a thin flow of moisture-free nitrogen gas and the dried lipid film was then kept under high vacuum for 8 h. One milliliter of sterile deionized water was added to the vacuum-dried lipid film and the mixture was allowed to swell overnight. Liposomes were vortexed for 1−2 min to remove any adhering lipid film and sonicated in a bath sonicator for 2−3 min at room temperature to produce multilamellar vesicles (MLV). MLVs were then sonicated in an ice bath until clarity using a Branson 450 sonifier at 100% duty cycle and 25 W output power for 1−2 min to give a clear, translucent solution. These resulting clear aqueous liposomes were used in forming lipoplexes.

Preparation of Plasmid DNA. *p*CMV-SPORT-β-gal plasmid was amplified in DH5α strain of *Escherichia coli*, isolated by the alkaline lysis procedure, and finally purified by PEG-8000 precipitation as described previously.[35] The purity of plasmid was checked by A_{260}/A_{280} ratio (around 1.9) and 1% agarose gel electrophoresis.

Transfection Biology. Cells were seeded at a density of 10 000 (for B16F10 and MCF-7) and 15 000 cells (for CHO, A-549, and HepG2) per well in a 96-well plate 18−24 h before the transfection. Then, 0.3 μg (0.91 nmol) of plasmid DNA was complexed with varying amounts of lipids in plain DMEM medium (total volume made up to 100 μL) for 30 min. The charge ratios were varied from 0.3:1 to 9:1 over these ranges of lipids. Just prior to transfection, cells plated in the 96-well plate were washed with PBS (2 × 100 μL) followed by the addition of lipoplexes. After 4 h of incubation, 100 μL of DMEM with 20% FBS was added to the cells. The medium was changed to 10% complete medium after 24 h, and the reporter gene activity was estimated after 48 h of incubation. The cells were washed twice with PBS (100 μL each) and lysed in 50 μL lysis buffer [0.25 M Tris-HCl (pH 8.0) and 0.5% NP40]. Care was taken to ensure complete lysis. The β-galactosidase activity per well was estimated by adding 50 μL of 2× substrate solution [1.33 mg/mL ONPG, 0.2 M sodium phosphate (pH 7.3), and 2 mM magnesium chloride] to the lysate in a 96-well plate. Absorbance of the product *ortho*-nitrophenol at 405 nm was converted to β-galactosidase units by using a calibration curve constructed using pure commercial β-galactosidase enzyme. Each transfection experiment was repeated 3 times on 3 different days. The transfection values reported were average values from three replicate transfection plates assayed on three different days. The values of β-galactosidase units in replicate plates assayed on the same day varied by less than 20%.

Transfection Biology in the Presence of Serum. Cells were seeded at a density of 10 000 (for B16F10 and MCF-7) and 15 000 cells (for CHO, A-549, and HepG2) per well in a 96-well plate 18−24 h before the transfection. Then, 0.3 μg (0.91 nmol) of plasmid DNA was complexed with lipids (**1** and **2**) in DMEM medium in the presence of increasing concentrations of added serum (10−50% v/v and total volume made up to 100 μL using plain DMEM medium) for 30 min. The lipid/DNA charge ratio of these lipoplexes was maintained at 9:1, at which both lipids showed their highest transfection ability in all five types of cells used for transfection (CHO, A-549, B16F10, HepG2, and MCF-7). The remaining experimental procedure and determination of β-galactosidase activity per well are similar to that reported for the in vitro transfection experiments.

Transfection Using α5GFP Plasmid. For α5GFP pDNA expression experiment, 25 000−30 000 cells per well were seeded in 24-well plates (Corning Inc., Corning, NY) for 12 h in 300 μL of growth medium such that the well became 30−50% confluent at the time of transfection. Liposomes of lipids **1** and **2** were complexed with α5GFP expressing *p*DNA (1 μg/well) at 9:1 lipid/DNA charge ratio in plain DMEM (total volume made up to 100 μL) for 30 min. The complexes were then diluted with 200 μL DMEM and added to the cells. After 4 h of incubation, DMEM was removed and cells were supplemented with complete medium. The cells were incubated for 24 h. Cells were washed with PBS (100 μL) and fixed with 3.8% paraformaldehyde in PBS at room temperature for 10 min. The green fluorescent cells expressing α5GFP were detected under an inverted fluorescence microscope (Nikon, Japan).

Cellular Uptake Studies by Inverted Fluorescence Microscopy. Cells were seeded at a density of 10 000 cells/well in a 96-well plate usually 18−24 h prior to the treatment in 200 μL of growth medium such that the well became 30−50% confluent at the time of transfection. *p*CMV-SPORT-β-gal DNA (0.3 μg of DNA diluted to 50 μL with serum-free DMEM media) was complexed with rhodamine-PE labeled cationic liposomes (diluted to 50 μL with DMEM) of lipids **1** and **2** using 9:1 lipid to DNA charge ratio. The cells were washed with PBS (1 × 200 μL), then treated with lipoplexes, and incubated at a humidified atmosphere containing 5% CO_2 at 37 °C. After 4 h of incubation, the cells were washed with PBS (3 × 200 μL) to remove the dye and fixed with 3.8% paraformaldehyde in PBS at room temperature for 10 min. The red fluorescent cells were detected under an inverted fluorescence microscope (Nikon, Japan).

Toxicity Assay. Cytotoxicity of lipids **1** and **2** was assessed by the 3-(4,5-dimethylthiazol-2-yl)-2,5-diphenyltetrazolium bromide (MTT) reduction assay as described earlier.[36] The cytotoxicity assay was performed in 96-well plates by maintaining the same ratio of number of cells to amount of cationic lipid, as used in the transfection experiments. MTT was added 24 h after the addition of cationic lipids to the cells followed by 3 h of incubation. Results were expressed as percentage viability = [A_{540} (treated cells) − background/A_{540} (untreated cells) − background] × 100.

DNA-Binding Assay. The DNA binding ability of cationic lipids **1**and **2** was assessed by conventional gel retardation assay on a 1% agarose gel (prestained with ethidium bromide) across the varying lipid/DNA charge ratios of 0.3:1 to 9:1. *p*CMV-SPORT-β-gal (0.30 μg) was complexed with varying amounts of cationic lipids in a total volume of 20 μL of DMEM and incubated at room temperature for 20−25 min. Four microliters of 6× loading buffer (0.25% bromophenol blue in 40% (w/v) sucrose in H_2O) was added to it, and 20 μL of the resultant solution was loaded in each well. The samples were electrophoresed at 80 V for 45 min and the DNA bands were visualized in the gel documentation unit.

DNase I Sensitivity Assay. Briefly, in a typical assay, pCMV-β-gal (0.6 μg) was complexed with varying amounts of the cationic lipids (using the indicated lipid/DNA charge ratios of 0.3:1 to 9:1) in a total volume of 20 μL in DMEM and incubated at room temperature for 30 min on a rotary shaker. Subsequently, the complexes were treated with 5 μL of DNase I (at a final concentration of 1 μg/mL) in the presence of 20 mM $MgCl_2$ in a final volume of 50 μL and incubated for 20 min at 37 °C. The reactions were then halted by adding EDTA (to a final concentration of 50 mM) and incubated at 60 °C for 10 min in a water bath. The aqueous layer was washed with 50 μL of phenol/chloroform mixture (1:1, v/v) and centrifuged at 10 000 rpm for 5 min. The aqueous supernatants were separated, loaded (15 μL) on a 1% agarose gel, and electrophoresed at 80 V for 2 h. The DNA bands were visualized with ethidium bromide staining.

Zeta Potential (ζ) and Size Measurements. The sizes and the surface charges (zeta potentials) of liposomes and lipoplexes were measured by photon correlation spectroscopy and electrophoretic mobility on a Zeta sizer $3000HS_A$ (Malvern, U.K.). The sizes were measured in Dulbecco's modified Eagle's medium (DMEM) with a sample refractive index of 1.59 and a viscosity of 0.89 cP. The system was calibrated by using the 200 nm ± 5 nm polystyrene polymer (Duke Scientific Corp., Palo Alto, CA). The diameters of liposomes and lipoplexes were calculated by using the automatic mode. The zeta potential was measured using the following parameters: viscosity, 0.89 cP; dielectric constant, 79; temperature, 25 °C; *F*(Ka), 1.50 (Smoluchowski); maximum voltage of the current, V. The system was calibrated by using DTS0050 standard from Malvern. Measurements were done 10 times with the zero-field correction. The potentials were calculated by using the Smoluchowski approximation.

RESULTS AND DISCUSSION

The present work illustrates the synthesis of lipids **1** and **2** and their physicochemical characteristics. The results of in vitro transfection experiments performed on five different types of cell lines to assess the transfection properties of lipoplexes of lipids **1** and **2** are reported. In addition, the inverted fluorescent microscope experiments in support of the results obtained in in vitro transfection studies are reported. A study of cytotoxicity in all the cell lines studied for transfection and serum compatibility of lipids **1** and **2** are also reported.

Chemistry. Toward probing the influence of the backbone structural variation in gene delivery efficacies of α-tocopherol based cationic amphiphiles, we designed and synthesized lipids **1** and **2** (Scheme 1) such that the two lipids architecturally differ only in the backbone functionality (non-glycerol and glycerol backbone). Lipid **1** was synthesized by reacting *N*-methyldiethanolamine with mesylated α-tocopherol to yield an intermediate followed by quarternization using methyl iodide and chloride ion exchange chromatography over Amberlyst anion exchange resin (Scheme 1, part A). To prepare lipid **2**, *N*,*N*-dimethyl-l,2,3-propanediol was reacted with mesylated α-tocopherol to yield tertiary amine as intermediate (Scheme 1, part B). The tertiary amine intermediate upon quarternization

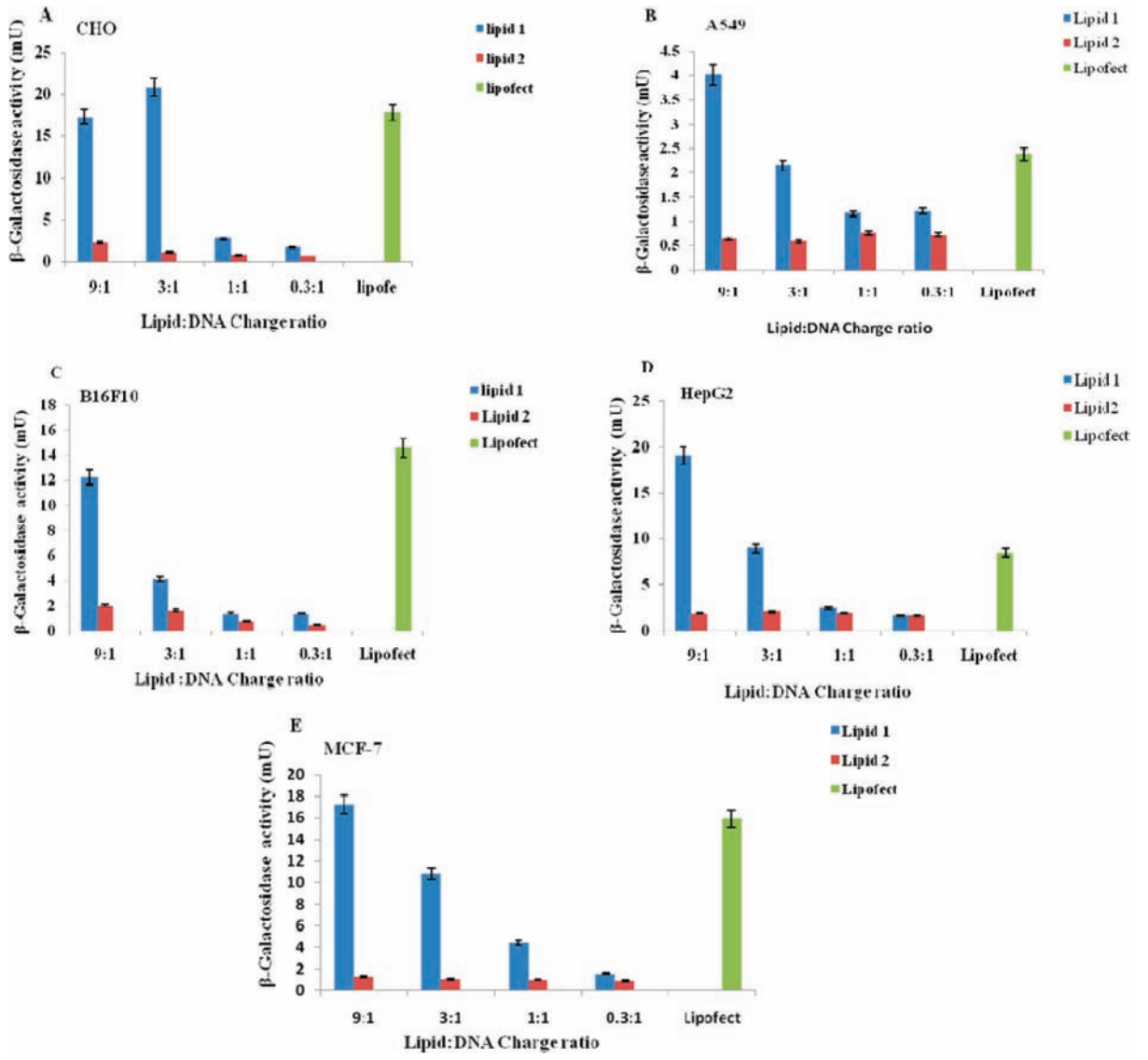

Figure 1. In vitro gene delivery efficiencies of lipids **1** and **2** in CHO (A), A549 (B), B16F10 (C), HepG2 (D), and MCF-7 (E) cell lines. Units of β-galactosidase activity were plotted against the varying lipid-to-DNA charge ratios (9:1−0.3:1). The transfection efficiencies of the lipids were compared to that of commercial formulation. Transfection experiments were performed as described in the text. Both lipids were tested on the same day, and the data presented are the average of three experiments performed on three different days.

with excess methyl iodide followed by chloride ion exchange over Amberlyst anion exchange resin afforded the target lipid **2** (Scheme 1, part B). The structures of all the intermediates (Scheme 1) and of the final target lipids **1** and **2** were confirmed by ^{1}H NMR and mass spectra. The purity of the final lipids were confirmed by elemental (C, H, N) analysis.

Transfection Biology. *In Vitro Transfection Studies.* Reporter gene expression assay was used in evaluating the in vitro gene delivery efficacies of lipids **1** and **2** in five cultured mammalian cells including A-549 (human lung carcinoma cells), B16F10 (murine melanoma cells), CHO (Chinese hamster ovary cells), HepG2 (human hepatocarcinoma), and MCF-7 (human breast adenocarcinoma cells) using *p*-CMV-SPORT-β-gal plasmid DNA as the reporter gene encoding the enzyme β-galactosidase across the lipid/DNA charge ratios of 9:1−0.3:1. Despite the presence of glycerol and nonglycerol backbone being the only structural differences between lipids **1** and **2**, only lipid **1** is competent in delivering reporter gene into all the five cell lines particularly at higher charge ratios, that is, at 3:1 and 9:1 (Figure 1, parts A−E).

Lipid **1** showed its higher gene delivery efficacies at lipid/DNA charge ratio of 9:1 in A-549, B16F10, HepG2, and MCF-7 cells (Figure 1, parts B−E, respectively) and at lipid/DNA charge ratio of 3:1 in CHO cells (Figure 1, part A). In contrast, lipid **2** turned out to be essentially incompetent in delivering genes into any of these five cells across the entire lipid/DNA charge ratios of 9:1−0.3:1 (Figure 1, parts A−E). Interestingly, lipid **1** is found to be comparable with or better than the commercially available formulation at specified lipid/DNA charge ratios in all cell lines except in B16 F10 type in which it is found to be less transfecting compared to commercial formulation. Lipid **1** is found to be one and half times better in transfecting A549 and nearly two and half times better in transfecting HepG2 type of cells compared to commercial formulation. Thus, the relative transfection profiles of lipids **1** and **2** summarized in parts A−E of Figure 1 demonstrate that the structural variation in the backbone region of α-tocopherol

dx.doi.org/10.1021/bc2004395 | *Bioconjugate Chem.* 2011, 22, 2581−2592

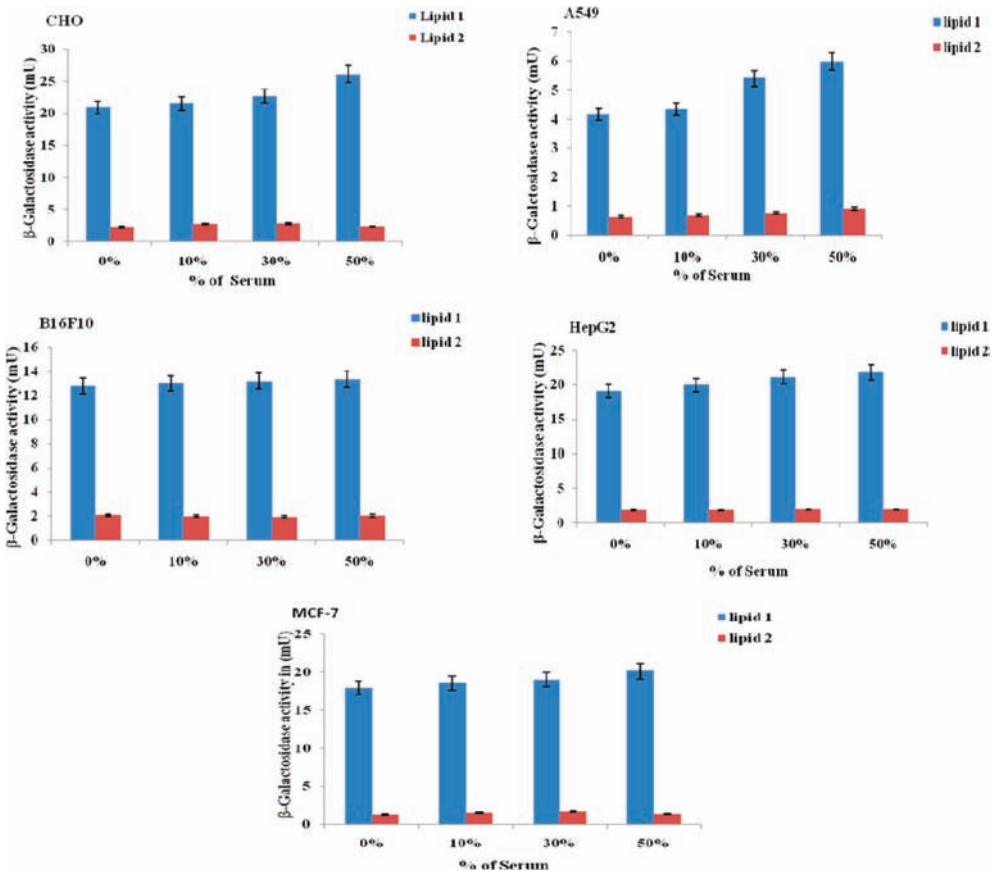

Figure 2. Transfection efficacies of the cationic lipids **1** and **2** in the presence of increasing concentrations of serum added. In vitro transfection efficiencies of lipid/DNA complexes prepared using *p*CMV-*β*-gal-SPORT reporter gene at lipid/DNA charge ratio of 9:1 were evaluated in the presence of increasing concentrations of serum added in CHO (A), A-549 (B), B16F10 (C), HepG2 (D), and MCF-7 (E) cell lines. Both the lipids were tested on the same day, and the data presented are the average of three experiments performed on three different days.

based cationic amphiphiles is a crucial parameter capable of profoundly influencing gene transfer efficacies of *α*-tocopherol based cationic amphiphiles.

Serum Compatibility. The gene transfer efficacies of cationic amphiphiles, in general, are evaluated either in complete absence of serum or in the presence of only 10% (v/v) added serum as disclosed in many prior reports.[23,29,37−41] However, the clinical success of cationic transfection lipids depends on their serum compatibility. The in vitro gene transfer efficacies of cationic amphiphiles usually get adversely affected in the presence of serum.[42−49] Such serum incompatibility of cationic transfection lipids is believed to begin via adsorption of negatively charged serum proteins onto the positively charged cationic liposome surfaces preventing their efficient interaction with cell surface and/or internalization.[50−52]

Toward probing the serum compatibility of the lipids **1** and **2**, in vitro gene transfer efficacies for the lipids **1** and **2** were evaluated across lipid/DNA charge ratio 9:1 at which both lipids showed their higher transfection ability in all five types of cell lines used for transfection (CHO, A-549, B16F10, MCF-7, and HepG2) in the presence of increasing concentrations of serum added (10−50%, v/v) (Figure 2). Interestingly, for reasons not clear at this stage of investigation, the in vitro gene transfer efficacy of lipid **1** is found to be increasing in the presence of up to 50% added serum while that of lipid **2** is found to be unaffected by concentration of serum added (Figure 2). Thus, the transfection efficiency of lipid **1** is found to be highly serum-compatible even at higher levels of added serum.

α5GFP Plasmid Transfection. The relative transfection efficacies of lipids **1** and **2** were also evaluated by the in vitro transfection studies using *α*5GFP (a plasmid DNA encoding green fluorescence protein) in representative HepG2 and A549 (Figure 3, I and II) cells using lipoplexes with 9:1 lipid/DNA charge ratio (the charge ratio where the lipid **1** shows higher transfection in both types of cell lines). After washing the cells with phosphate buffer saline, live HepG2 and A549 cells were viewed under an inverted fluorescence microscope. The numbers of fluorescently labeled cell lines are found to be more when the cells were treated with lipoplexes of lipid **1** than that of lipoplexes of lipid **2** (Figure 3).

Cellular Uptake Study. Results from in vitro transfection experiments demonstrate that lipid **1** is efficient in transfecting multiple cultured cell lines, whereas lipid **2** is incompetent in transfecting in any of these cell lines. Thus, in order to probe the role of cellular uptake behind the contrasting transfection profiles of lipids **1** and **2** the cellular uptake experiments were performed. The representative A549 and MCF-7 cell lines were treated with lipoplexes comprising *p*CMV-SPORT-*β*-gal plasmid DNA and rhodamine-PE labeled liposomes of lipids **1** and **2** with lipid/DNA charge ratio 9:1. The number of A549 and MCF-7 cell lines labeled red are found to be relatively more when treated with lipoplexes of lipid **1** against lipid **2** from the cellular uptake experiment (Figure 4). Thus, these results of cellular uptake experiments (Figures 4) support the

dx.doi.org/10.1021/bc2004395|*Bioconjugate Chem.* 2011, 22, 2581−2592

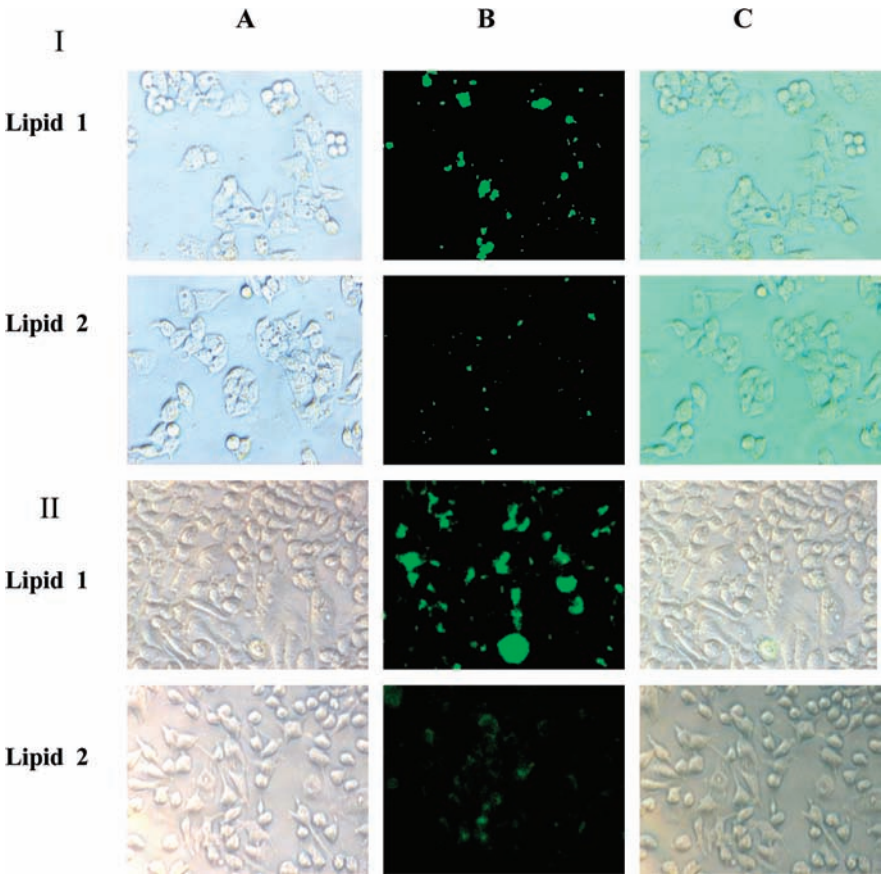

Figure 3. Inverted microscopic images of representative HepG2 (I) and A549 (II) cell lines transfected with lipoplexes of lipids (**1** and **2**) and α5GFP expressing plasmid DNA. Lipid/DNA charge ratios in all the lipoplexes were maintained at 9:1 (A) bright field images, (B) fluorescent images, and (C) overlay images. The details of inverted fluorescence microscopic experiments are described in the text.

notion that the varying transfection profiles of lipids **1** and **2** could be attributed to the cellular uptake variations of the respective lipids. This reemphasizes the supposition that the degree of cellular uptake plays an important role in contrasting transfection profiles of lipids **1** and **2**.

Lipid/DNA Binding Assay. The electrostatic binding interactions between the plasmid DNA and the cationic lipids **1** and **2** at varying lipid/DNA charge ratios were measured by conventional electrophoretic gel retardation assay and DNase I sensitivity assays (Figures 5 and 6). The corresponding electrophoretic gel patterns observed in the gel retardation assay for lipoplexes formed from lipids **1** and **2** are shown in (Figure 5). The gel patterns revealed striking contrasting DNA binding profiles of lipids **1** and **2**. Careful observation of the experimental results unveil that lipid **1** was capable of completely inhibiting electrophoretic mobility of plasmid DNA when lipoplexes were prepared at higher lipid/DNA charge ratios of 9:1 and 3:1 (Figure 5). In contrast, the lipid **2** was found to be completely inefficient in binding DNA even at this higher lipid/DNA charge ratios. At lower lipid/DNA charge ratios (1:1 and 0.3:1), the amount of free DNA associated with lipid **2** is found to be higher when compared to lipid **1** (Figure 5). The stability of lipoplexes formed by lipids **1** and **2** was further confirmed by monitoring the sensitivities of the lipoplexes upon treatment with DNase I. After the free DNA digestion by DNase I, the total DNA (both the digested and inaccessible DNA) was separated from lipid (by extracting with organic solvents) and loaded on a 1% agarose gel. Figure 6 summarizes the results of such DNase I protection experiments for lipoplexes prepared from the cationic lipids **1** and **2** across the entire lipid/DNA charge ratios of 9:1 to 0.3:1. The band intensities of inaccessible and therefore undigested DNA associated with transfection incompetent lipids **2** is found to be significantly less compared to those associated with transfection efficient lipid **1** across the lipid/DNA charge ratios of 9:1 to 0.3:1. Thus, the findings in the conventional gel mobility shift (Figure 5) and DNase I sensitivity assays (Figure 6) together are consistent with the supposition that strong lipid−DNA binding interactions in the lipoplexes perhaps play important role behind the higher transfection efficacies of lipid **1**.

The results of gel retardation assay and sensitivity of the lipoplexes upon treatment with DNase I in the presence of anionic lipid[53,54] (Supporting Information) reveal that the anionic lipid studied in this experiment can displace the ionic interaction between plasmid DNA and the cationic lipids **1** and **2**. It can be deduced from this result that the anionic molecules present in the cell can also displace the ionic interactions between plasmid DNA and the cationic lipids **1** and **2**, thereby releasing plasmid DNA into the cell cytoplasm.

Toxicity Studies. MTT-based cell viability assays were performed in all five types of cell lines used for transfection (CHO, A-549, B16F10, MCF-7, and HepG2) treating with lipoplexes of lipids **1** and **2** across the range of lipid/DNA charge ratios (9:1−0.3:1) used in the actual transfection experiments. Cell viabilities of both the lipids **1** and **2** in all five types of cell lines are found to be remarkably high (more than 85%) particularly up to the lipid/DNA charge ratios of 3:1

dx.doi.org/10.1021/bc2004395|*Bioconjugate Chem.* 2011, 22, 2581−2592

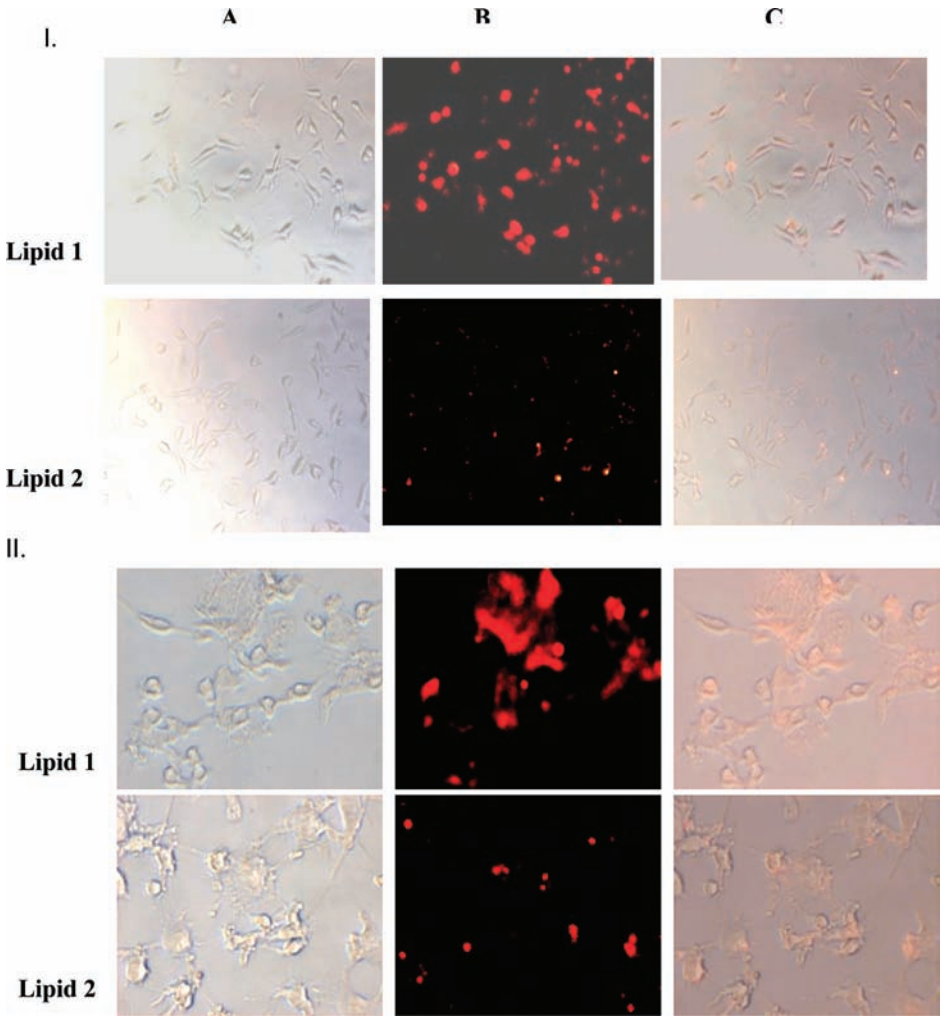

Figure 4. Cellular uptake of Rhodamine labeled lipoplexes. Inverted microscopic images of A549 (I) and MCF-7 (II) cell lines transfected with rhodamine labeled lipoplexes of lipids **1** and **2** prepared at higher in vitro transfection lipid/DNA charge ratios of 9:1 (A) bright field images, (B) fluorescent images, and (C) overlay images. The details of the experiments are described in the text.

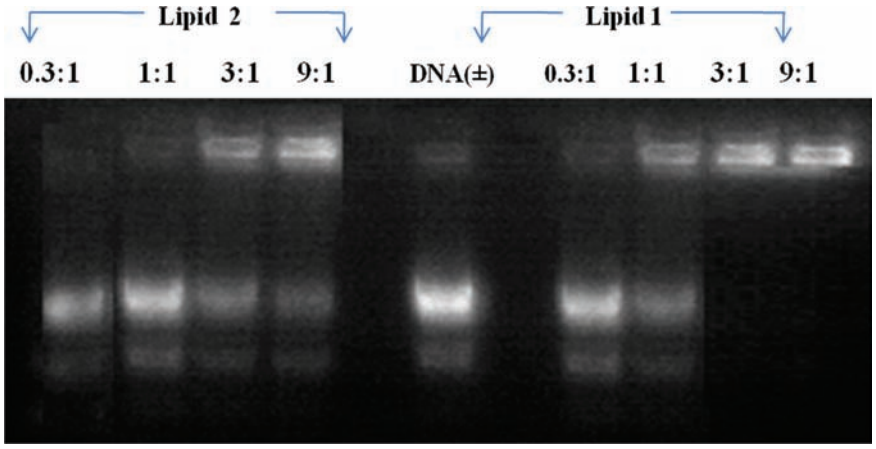

Figure 5. Electrophoretic gel patterns for lipoplex-associated DNA in gel retardation assay. The lipid/DNA charge ratios are indicated at the top of each lane. The details of the gel experiment are as described in the text.

(Figure 7). Except in CHO cell lines, in all the other cell lines the cell viabilities of both lipids **1** and **2** are found to be $\gtrsim$80% at higher charge ratio of 9:1. Thus, the contrasting in vitro gene transfer efficacies of the lipids **1** and **2** are unlikely to originate from varying cell cytotoxicities of the lipids.

Nanosizes and Global Surface Charges of the Lipoplexes. To gain insight into the liposomal physical properties, sizes, and surface potentials of the liposomes of lipids **1** and **2** (prepared in DI water) and their lipoplexes (prepared in DMEM) were measured using dynamic laser light scattering technique

dx.doi.org/10.1021/bc2004395 | *Bioconjugate Chem.* 2011, 22, 2581–2592

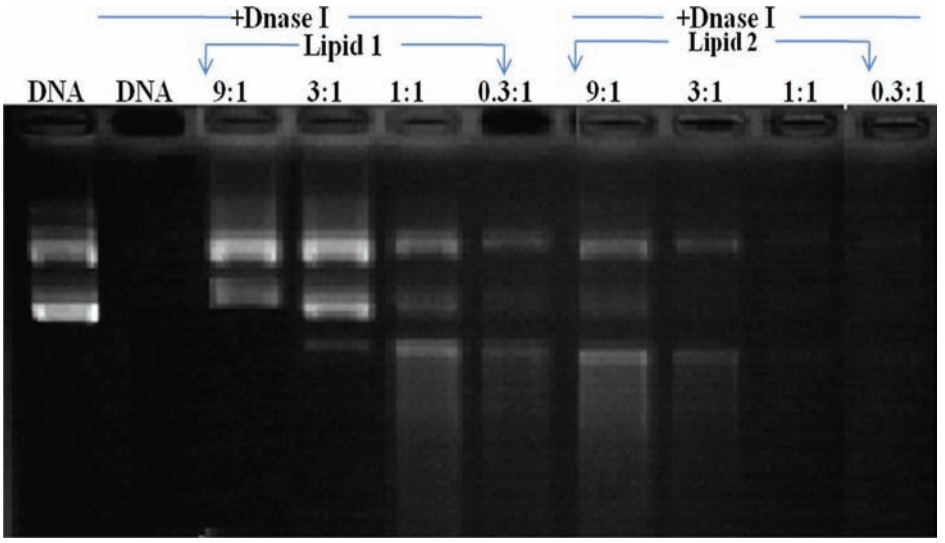

Figure 6. Electrophoretic gel patterns for lipoplex-associated DNA in DNase I sensitivity assay. The lipid/DNA charge ratios are indicated at the top of each lane. The details of the treatment are as described in the text.

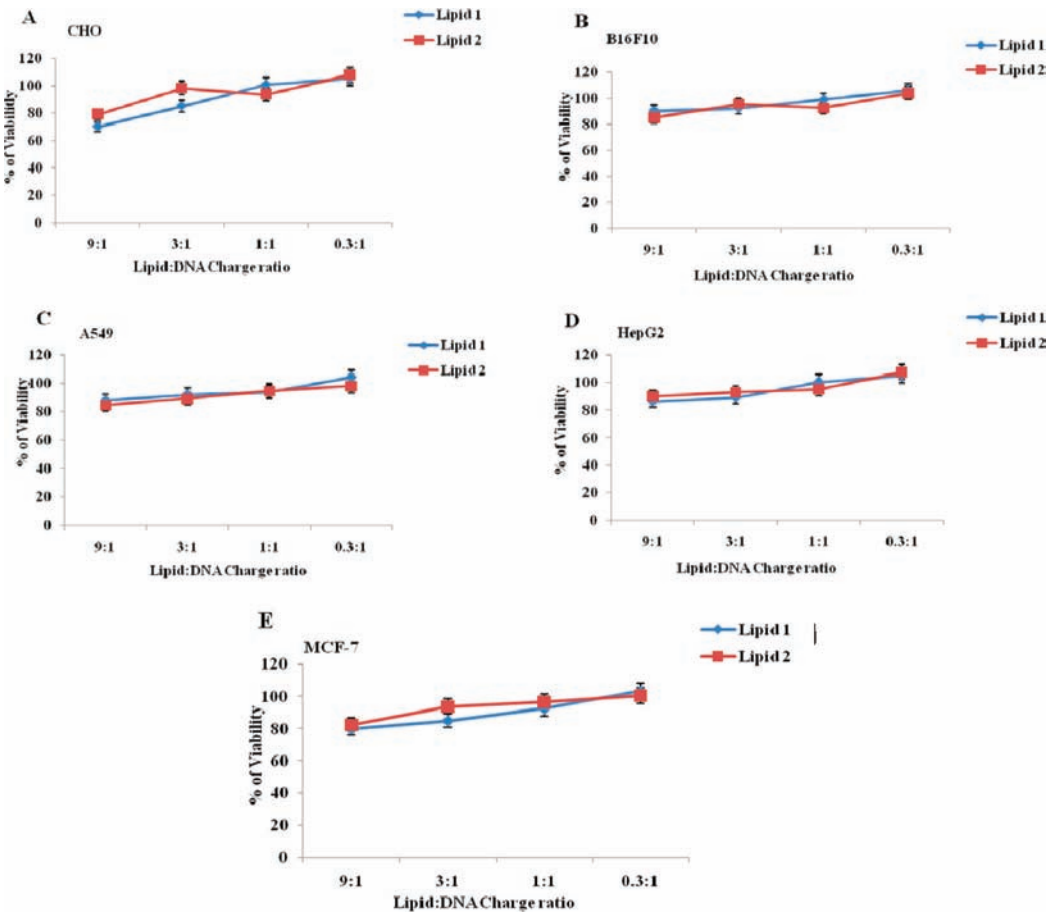

Figure 7. MTT-assay based percent cell viabilities of CHO (A), A-549 (B), B16F10 (C), HepG2 (D), and MCF-7 (E) cell lines treated with lipoplexes of lipids **1** and **2** with lipid/DNA charge ratios 9:1−0.3:1. The cell viability values shown are the average of triplicate experiments performed on same day. The details of the MTT-assay are as described in the text.

(Zetasizer 3000A, Malvern Instruments, U.K.). The sizes and surface potentials of these liposomes and lipoplexes were measured in the absence and in the presence of 10% serum.

Liposomes of lipid **1** were found to be smaller in size compared to liposomes of lipid **2** (Table 1). Lipoplexes of lipid **1** were found to increase from 350 to 800 nm in size as lipid/DNA charge ratios decreased from 9:1 to 0.3:1, whereas lipoplexes of lipid **2** showed steady increase from 600 to 750 nm (Table 1). Significant lipoplex size reduction at higher lipid/DNA charge ratios for lipid **1** can be attributed to the

dx.doi.org/10.1021/bc2004395|*Bioconjugate Chem.* 2011, 22, 2581−2592

Table 1. Hydrodynamic Diameters and Zeta Potentials (ζ) of Lipoplexes[a]

Lipid	Lipid/DNA (molar ratio)					
	1:0	0.3:1	1:1	3:1	9:1	
			Size (nm)			
1	175.4 ± 3.5 (149.2 ± 1.0)	781.7 ± 16.7 (626.1 ± 4.5)	740.3 ± 22.2 (592.7 ± 6.8)	570.6 ± 26.0 (383.9 ± 19.1)	352.6 ± 49.7 (256.3 ± 12.6)	
2	253.2 ± 5.3 (219.1 ± 4.4)	739.2 ± 24.1 (529.2 ± 27.1)	706.6.2 ± 9.5 (512.4 ± 11.5)	640.6 ± 18.5 (420.2 ± 1.5)	686.7 ± 2.8 (497.9 ± 10.6)	
			Zeta potentials (mV)			
1	22.2 ± 3.1 (18.7 ± 3.5)	−12.5 ± 1.8 (−8.2 ± 4.9)	4.7 ± 3.2 (1.2 ± 0.8)	5.9 ± 2.1 (3.4 ± 1.4)	17.6 ± 5 (13.8 ± 3.2)	
2	9.5 ± 6.5 (7.1 ± 2.0)	−14.9 ± 1.8 (−12.8 ± 3.5)	−1.5 ± 1.6 (−5.2 ± 1.5)	5.1 ± 5.0 (1.4 ± 2.1)	8.3 ± 1.0 (6.5 ± 4.0)	

[a]Sizes and ζ potentials of liposomes and lipoplexes of lipids **1** and **2** in the absence and in the presence of 10% serum (values within parentheses) were measured by laser light scattering technique using Zetasizer 3000A (Malvern Instruments, U.K). Values shown are the averages obtained from three (size) and ten (zeta potential) measurements.

pronounced DNA condensation efficacies of lipid **1** and hence the higher transfection efficacies of lipid **1** at higher lipid/DNA charge ratios when compared to lipid **2**. Interestingly, the global surface potentials of lipoplexes of lipid **1** were found to be somewhat more positive than those for lipoplexes of lipid **2** in the lipid/DNA charge ratio range 9:1−0.3:1 (Table 1). Results of size and zeta potentials of liposomes and lipoplexes of lipids **1** and **2** in the presence of serum are as shown in the parentheses of Table 1. Significant reduction in size of liposomes and lipoplexes of lipids **1** and **2** was observed. This reduction in size of lipoplexes in the presence of serum was reported earlier.[55] The observed size reduction of lipoplexes in the presence of serum may be the result of a number of factors, including viscosity, serum protein binding, refractive index, and the partial dissociation of the lipoplexes. These observations suggest that the serum-induced decrease in size may not be the primary cause of the higher transfection efficiency of lipid **1** in the presence of serum.

CONCLUSIONS

In summary, the findings described provide the first experimental evidence for the influence of backbone structural variation in liposomal gene delivery of α-tocopherol based cationic lipids. Two α-tocopherol based cationic amphiphiles **1** and **2** were designed and synthesized containing the same hydrophobic region, same headgroup and linker group functionality, but differ only in the backbone region. In vitro findings delineated that lipid **1** showed higher gene transfer efficacies than lipid **2** in multiple cultured mammalian cells including CHO, B16F10, HepG2, MCF-7, and A549. Findings in dynamic laser light scattering studies revealed that lipid **1** significantly condenses DNA compared with lipid **2**. Inverted fluorescence microscopic studies using lipoplexes of lipids **1** and **2** containing green fluorescent protein encoding plasmid DNA and Rhodamine-labeled lipoplexes of lipids **1** and **2** respectively demonstrated significantly higher expression of GFP and higher cellular uptake with lipoplexes of lipid **1**. To conclude, the findings described demonstrate the dramatic influence of backbone structural variation in liposomal gene delivery of α-tocopherol based cationic lipids.

ASSOCIATED CONTENT

Supporting Information

^{1}H NMR spectra of lipids **1** and **2** and intermediates. Mass Spectra of lipids **1** and **2** and intermediates. Elemental analysis data for lipids **1** and **2**. Results and experiment on efficiency of DNA release from the lipoplexes of lipids **1** and **2** in the presence of anionic lipid. Mechanism of the reaction between the mesylated tocopherol and N-methyl diethanolamine or 3-(dimethylamino) propane-1,2-diol. This material is available free of charge via the Internet at http://pubs.acs.org.

AUTHOR INFORMATION

Corresponding Author

*Phone No. 0091-870-2462672. Fax No. 0091-870-2459547. E-mail: pv_slakshmi@yahoo.com.

ACKNOWLEDGMENTS

Financial supports for this work from Department of Science and Technology, DST (to P.V. Srilakshmi), Government of India, New Delhi and from National Institute of Technology, Warangal (the doctoral research fellowship to K. Bhavani) are

gratefully acknowledged. We greatly acknowledge Dr. Arabinda Chaudhuri of Division of Lipid Science and Technology, Indian Institute of Chemical Technology, Hyderabad, India, and his group for extending the tissue culture lab facilities to us and also for their immense help in carrying out the transfection experiments.

■ ABBREVATIONS USED:

DOPC, 1,2-Dioleoyl-*sn*-glycero-3-phosphocholine; DMEM, Dulbecco's modified Eagle's medium; DMAP, 4-(dimethylamino)pyridine; FBS, fetal bovine serum; PBS, phosphate-buffered saline; ONPG, *o*-nitrophenyl-*β*-D-galacto-pyranoside.

■ REFERENCES

(1) Fabio, K., Gaucheron, J., Giorgio, C. D., and Vierling, P. (2003) Novel galactosylated polyamine bolaamphiphiles for gene delivery. *Bioconjugate Chem. 14*, 358−367.

(2) Heyes, J. A., Duvaz, D. N., Cooper, R. G., and Springer, C. J. (2002) Synthesis of novel cationic lipids: effect of structural modification on the efficiency of gene transfer. *J. Med. Chem. 45*, 99−114.

(3) McGregor, C., Perrin, C., Monck, M., Camilleri, P., and Kirby, A. J. (2001) Rational approaches to the design of cationic gemini surfactants for gene delivery. *J. Am. Chem. Soc. 123*, 6215−6220.

(4) Guenin, E., Herve, A. C., Floch, V., Loisel, S., Yaounac, J. J., lement, J. C., Ferec, C., and des Abbayas, H. (2000) Cationic phosphonolipids containing quaternary phosphonium and arsonium groups for DNA transfection with good efficiency and low cellular toxicity. *Angew. Chem., Int. Ed. 39*, 629−631.

(5) Floch, V., Loisel, S., Guenin, E., Herve, A. C., Clement, J. C., Yaouanc, J. J., des Abbayes, H., and Ferec, C. (2000) Cation substitution in cationic phosphono lipids: a new concept to improve transfection activity and decrease cellular toxicity. *J. Med. Chem. 43*, 4617−4628.

(6) Ghosh, Y. K., Visweswariah, S. S., and Bhattacharya, S. (2000) Nature of linkage between the cationic headgroup and cholesterol skeleton controls gene transfection efficiency. *FEBS Lett. 473*, 341−344.

(7) Fichert, T., Regelin, A., and Massing, U. (2000) Synthesis and transfection properties of novel nontoxic monocationic lipids: variations of lipid anchor, spacer and headgroup structure. *Bioorg. Med. Chem. Lett. 10*, 787−791.

(8) Kawakami, S., Sato, A., Nishikawa, M., Yamashita, F., and Hashida, M. (2000) Mannose receptor mediated gene tranfer into macrophases using novel mannosylated cationic liposomes. *Gene Ther. 7*, 292−299.

(9) Choi, J. S., Lee, E. J., Jang, H. S., and Sang, J. P. (2000) New cationic liposomes for gene transfer into mammalian cells with high efficiency and low toxicity. *Bioconjugate Chem. 12*, 108−113.

(10) Byk, G., Wetzer, B., Frederic, M., Dubertret, C., Pitard, B., Jaslin, G., and Scherman, D. (2000) Reduction-sensitive lipopolyamines as a novel nonviral gene delivery system for modulated release of DNA with improved transgene expression. *J. Med. Chem. 43*, 4377−4387.

(11) Miller, A. D. (1998) Cationic Liposomes in Gene Therapy. *Angew. Chem., Int. Ed. 37*, 1768−1785, and references therein.

(12) Wang, J., Guo, X., Xu, Y., Barron, L., and Szoka, F. C. Jr. (1998) Synthesis and characterization of long chain alkyl acyl carnitine esters. potentially biodegradable cationic lipids for use in gene delivery. *J. Med. Chem. 41*, 2207−2215.

(13) Byk, G., Dubertret, C., Escriou, V., Frederic, M., Jaslin, G., Rangara, R., Pitard, B., Crouzet, J., Wils, P., Schwartz, B., and Scherman, D. (1998) Synthesis, activity, and structure-activity relationship studies of novel cationic lipids for DNA transfer. *J. Med. Chem. 41*, 224−235.

(14) Kawakami, S., Nishikawa, M., Yamashita, F., Takakura, Y., and Hashida, M. (1998) Asialo glycoprotein receptor-mediated gene transfer using novel galactosylated cationic liposomes. *Biochem. Biophys. Res. Commun. 252*, 78−83.

(15) Eastman, S. J., Siegel, C., Tousignant, J., Smith, A. E., Cheng, S. H., and Scheule, R. K. (1997) Biophysical characterisation of cationic lipid:DNA complexes. *Biochim. Biophys. Acta 1325*, 41−62.

(16) Felgner, J. H., Kumar, R., Sridhar, C. N., Wheeler, C. J., Tsai, Y. J., Border, R., Ramsey, P., Martin, M., and Felgner, P. L. (1994) Enhanced gene delivery and mechanism studies with a novel series of cationic lipid formulations. *J. Biol. Chem. 269*, 2550−2561.

(17) Karmali, P. P., and Chaudhuri, A. (2007) Carriers of gene medicines: resolved issues, open questions, and future promises. *Med. Res. Rev. 27*, 696−722.

(18) Bhattacharya, S., and Bajaj, A. (2009) Advances in gene delivery through molecular design of cationic lipids. *Chem. Commun.*, 4632−4656.

(19) Felgner, P. L., Gadek, T. R., Holm, M., Roman, R., Chan, H. W., Wenz, M., Northrop, J. P., Ringold, G. M., and Danielsen, M. (1987) Lipofection: a highly efficient lipid mediated DNA transfection procedure. *Proc. Natl. Acad. Sci. U.S.A. 84*, 7413−7417.

(20) Bhavani, K., and Srilakshmi, P. V. (2011) Design, synthesis and in vitro transfection biology of novel *α*-tocopherol based monocationic lipids: a structure activity investigation. *J. Med. Chem. 54* (2), 548−561.

(21) Karmali, P. P., Kumar, V. V., and Chaudhuri, A. (2004) Design, syntheses and in vitro gene delivery efficacies of novel mono-, di-, and tri-lysinated cationic lipids: a structure activity investigation. *J. Med. Chem. 47*, 2123−2132.

(22) Majeti, B. K., Singh, R. S., Yadav, S. K., Reddy, B. S., Ramakrishna, S., Diwan, P. V., Madhavendra, S. S., and Chaudhuri, A. (2004) First examples of enhanced intravenous transgene expression in mouse lung using cyclic-head cationic lipids. *Chem. Biol. 11*, 427−437.

(23) Singh, R. S., and Chaudhuri, A. (2004) Single additional methylene group in the head-group region imparts high gene transfer efficacy to a transfection-incompetent cationic lipid. *FEBS Lett. 556*, 86−90.

(24) Kumar, V. V., Pichon, C., Refregiers, M., Guerin, B., Midoux, P., and Chaudhuri, A. (2003) Single histidine residue in head-group region is sufficient to impart remarkable gene transfection properties to cationic lipids: evidence for histidine-mediated membrane fusion at acidic pH. *Gene Ther. 10*, 1206−1215.

(25) Kumar, V. V., Singh, R. S., and Chaudhuri, A. (2003) Cationic transfection lipids in gene therapy: successes, set-backs, challenges and promises. *Curr. Med. Chem. 10*, 1297−1306, and references therein.

(26) Singh, R. S., Mukherjee, K., Banerjee, R., Chaudhuri, A., Hait, S. K., Moulik, S., Ramadas, Y., Vijayalakshmi, A., and Rao, N. M. (2002) Anchor-dependency for non-glycerol based cationic lipofectins: mixed bag of regular and anomalous transfection profiles. *Chem.—Eur. J. 8*, 900−909.

(27) Srilakshmi, G. V., Sen, J., Chaudhuri, A., Ramdas, Y., and Rao, N. M. (2002) Anchor-dependent lipofection with non-glycerol based cytofectins containing single 2-hydroxyethyl head groups. *Biochim. Biophys. Acta 1559*, 87−95.

(28) Banerjee, R., Mahidhar, Y. V., Chaudhuri, A., Gopal, V., and Rao, N. M. (2001) Design, synthesis and transfection biology of novel cationic glycolipids for use in liposomal gene delivery. *J. Med. Chem. 44*, 4176−4185.

(29) Banerjee, R., Das, P. K., Srilakshmi, G. V., Chaudhuri, A., and Rao, N. M. (1999) A novel series of non-glycerol based cationic transfection lipids for use in liposomal gene delivery. *J. Med. Chem. 42*, 4292−4299.

(30) Bhattacharya, S., and Haldar, S. (1995) Synthesis, thermotropic behavior, and permeability properties of vesicular membranes composed of cationic mixed-chain surfactants. *Langmuir 11*, 4748−4757.

(31) Bajaj, A., Kondaiah, P., and Bhattacharya, S. (2007) Synthesis and gene transfer activities of novel serum compatible cholesterol-based gemini lipids possessing oxyethylene-type spacers. *Bioconjugate Chem. 18*, 1537−1546.

(32) Bhattacharya, S., and Dileep, P. V. (2004) Cationic oxyethylene lipids. Synthesis, aggregation, and transfection properties. *Bioconjugate Chem. 15*, 508−519.
(33) Bajaj, A., Kondaiah, P., and Bhattacharya, S. (2008) Effect of the nature of the spacer on gene transfer efficacies of novel thiocholesterol derived gemini lipids in different cell lines: a structure−activity investigation. *J. Med. Chem. 51*, 2533−2540.
(34) Rajesh, M., Sen, J., Srujan, M., Mukherjee, K., Sreedhar, B., and Chaudhuri, A. (2007) Dramatic influence of the orientation of linker betweenhydrophilic and hydrophobic lipid moiety in liposomal gene delivery. *J. Am. Chem. Soc. 129*, 11408−11420.
(35) Sambrook, J., Fritsch, E. F., and Maniatis, T. (1989) Molecular Cloning A Laboratory Manual, 2nd ed.; Cold Spring Harbor Laboratory. Press: Cold Spring Harbor, NY.
(36) Hansen, M.-B., Neilson, S. E., and Berg, K. (1989) Re-examination and further development of a precise and rapid dye method for measuring cell growth/ cell kill. *J. Immunol. Methods. 119*, 203−210.
(37) McGregor, C., Perrin, C., Monck, M., Camilleri, P., and Kirby, A. J. (2001) Rational approaches to the design of cationic gemini surfactants for gene delivery. *J. Am. Chem. Soc. 123*, 6215−6220.
(38) Prata, C. A. H., Zhao, Y., Barthelemy, P., Li, Y., Luo, D., McIntosh, T. J., Lee, S. J., and Grinstaff, M. W. (2004) Charge-reversal amphiphiles for gene delivery. *J. Am. Chem. Soc. 126*, 12196−12197.
(39) Bell, P. C., Bergsma, M., Dolbnya, I. P., Bras, W., Stuart, M. C. A., Rowan, A. E., Feiters, M. C., and Engberts, J. B. F. N. (2003) Transfection mediated by gemini surfactants: engineered escape from the endosomal compartment. *J. Am. Chem. Soc. 125*, 1551−1558.
(40) Guenin, E., Herve, A. C., and Floch, V. (2000) Cationic phosphonolipids containing quaternary phosphonium and arsonium groups for DNA transfection with good efficiency and low cellular toxicity. *Angew. Chem., Int. Ed. Engl. 39*, 629−631.
(41) Heyes, J. A., Duvaz, D. N., Cooper, R. G., and Springer, C. J. (2002) Synthesis of novel cationic lipids: effect of structural modification on the efficiency of gene transfer. *J. Med. Chem. 45*, 99−114.
(42) Scriou, V., Ciolina, C., Lacroix, F., Byk, G., Scherman, D., and Wils, P. (1998) Cationic lipid-mediated gene transfer: effect of serum on cellular uptake and intracellular fate of lipopolyamine/DNA complexes. *Biochim. Biophys. Acta 1368*, 276−288.
(43) Vitiello, L., Bockhold, K., Joshi, P. B., and Worton, R. G. (1998) Transfection of cultured myoblasts in high serum concentration with DODAC:DOPE liposomes. *Gene Ther. 5*, 1306−1313.
(44) Turek, J., Dubertret, C., Jaslin, G., Antonakis, K., Scherman, D., and Pitard, B. (2000) Formulations which increase the size of lipoplexes prevent serum-associated inhibition of transfection. *J Gene Med. 2*, 32−40.
(45) Thierry, A, R., Rabinovich, P., Peng, B., Mahan, L. C., Bryant, J. L., and Gallo, R. C. (1997) Characterization of liposome-mediated gene delivery: expression, stability and pharmacokinetics of plasmid DNA. *Gene Ther. 4*, 226−237.
(46) Zelphati, O., Uyechi, L. S., Barron, L. G., and Szoka, F. C. Jr. (1998) Effect of serum components on the physico-chemical properties of cationic lipid/oligonucleotide complexes and on their interactions with cells. *Biochim. Biophys. Acta 1390*, 119−133.
(47) Yang, J. P., and Huang, L. (1998) Time-dependent maturation of cationic liposome−DNA complex for serum resistance. *Gene Ther. 5*, 380−387.
(48) Yang, J. P., and Huang, L. (1997) Overcoming the inhibitory effect of serum on lipofection by increasing the charge ratio of cationic liposome to DNA. *Gene Ther. 4*, 950−960.
(49) Li, S., Tseng, W. C., Stolz, D. B., Wu, S. P., Watkins, S. C., and Huang, L. (1999) Dynamic changes in the characteristics of cationic lipidic vectors after exposure to mouse serum: implications for intravenous lipofection. *Gene Ther. 6*, 585−594.
(50) Li, S., Rizzo, M. A., Bhattacharya, S., and Huang, L. (1998) Characterization of cationic lipid−protamine−DNA (LPD) complexes for intravenous gene delivery. *Gene Ther. 5*, 930−937.
(51) Crook, K., Stevenson, B. J., Dubouchet, M., and Porteous, D. J. (1998) Inclusion of cholesterol in DOTAP transfection complexes increases the delivery of DNA to cells in vitro in the presence of serum. *Gene Ther. 5*, 137−143.
(52) Lewis, J. G., Lin, K. Y., Kothavale, A., Flanagan, W. M., Matteucci, M. D., De Prince, R. B., Mook, R. A. Jr., Hendren, R. W., and Wagner, R. W. (1996) A serum-resistant cytofectin for cellular delivery of antisense oligodeoxynucleotides and plasmid DNA. *Proc. Natl. Acad. Sci. U. S. A. 93*, 3176−3181.
(53) Xu, Y., and Szoka, F. C. Jr. (1996) Mechanism of DNA release from cationic liposome/DNA complexes used in cell transfection. *Biochemistry 35*, 5616−5623.
(54) Bhattacharya, S., and Mandal, S. S. (1998) Evidence of interlipidic ionpairing in anion-induced DNA release from cationic amphiphile- DNA complexes. Mechanistic implications in transfection. *Biochemistry 37*, 7764−7777.
(55) Konopka, K., Overlid, N., Nagaraj, C. A., and Düzgüneş, N. (2006) Serum decreases the size of metafectene- and genejammer-dna complexes but does not affect significantly their transfection activity in SCCVII murine squamous cell carcinoma cells. *Cell. Mol. Biol. Lett. 11*, 171−190.

Bioconjugate Chemistry

Article

pubs.acs.org/bc

Functional Fluorescently Labeled Bithiazole ΔF508-CFTR Corrector Imaged in Whole Body Slices in Mice

Holly R. Davison,[†] Stephanie Taylor,[‡] Chris Drake,[‡] Puay-Wah Phuan,[§] Nico Derichs,[§] Chenjuan Yao,[§] Ella F. Jones,[‡] Julie Sutcliffe,[∥] A. S. Verkman,[§] and Mark J. Kurth*,[†]

[†]Department of Chemistry, University of California, Davis, One Shields Avenue, Davis, California 95616, United States

[‡]Department of Radiology and Biomedical Engineering, University of California, San Francisco, 185 Berry Street, San Francisco California 94107, United States

[§]Departments of Medicine & Physiology, Cardiovascular Research Institute, University of California, San Francisco, Health Science East Tower, Room 1246, 505 Parnassus Avenue, San Francisco, California 94143, United States

[∥]Department of Biomedical Engineering, Division of Hematology/Oncology, Department of Internal Medicine, and Center for Molecular and Genomic Imaging, University of California, Davis, Genome and Biomedical Sciences Facility, 451 Health Sciences Drive, Davis, California 95616, United States

Supporting Information

ABSTRACT: We previously reported the identification and structure–activity analysis of bithiazole-based correctors of defective cellular processing of the cystic fibrosis-causing CFTR mutant, ΔF508-CFTR. Here, we report the synthesis and uptake of a functional, fluorescently labeled bithiazole corrector. Following synthesis and functional analysis of four bithiazole–fluorophore conjugates, we found that **5**, a bithazole-based BODIPY conjugate, had low micromolar potency for correction of defective ΔF508-CFTR cellular misprocessing, with comparable efficacy to benchmark corrector corr-**4a**. Intravenous administration of **5** to mice established its stability in extrahepatic tissues for tens of minutes. By fluorescence imaging of whole-body frozen slices, fluorescent corrector **5** was visualized strongly in gastrointestinal organs, with less in lung and liver. Our results provide proof-of-concept for mapping the biodistribution of a ΔF508-CFTR corrector by fluorophore labeling and fluorescence imaging of whole-body slices.

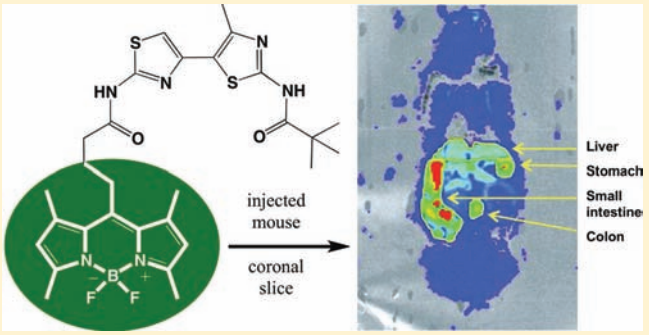

INTRODUCTION

The genetic disease cystic fibrosis (CF) is caused by mutations in the gene encoding the cystic fibrosis transmembrane conductance regulator (CFTR) protein, a cAMP-regulated chloride channel expressed in epithelial cells in lung, pancreas, testis, intestine, and other organs.[1,2] The most common CF-causing CFTR mutation is deletion of phenylalanine at residue 508 (ΔF508), which produces a misfolded protein that is retained at the endoplasmic reticulum (ER) and rapidly degraded.[3−6] A major focus in CF research is the identification and development of compounds, termed correctors, that normalize defective ΔF508-CFTR cellular processing to promote its plasma membrane targeting.[7−10]

By high-throughput screening, we previously reported the identification of bithiazole-based ΔF508-CFTR correctors such as corr-**4a**.[11] Corr-**4a** improved ΔF508-CFTR trafficking, resulting in partial restoration of cell chloride permeability. Following structure–activity relationship (SAR) studies conducted on 148 methylbithiazole analogues revealed that the substitution of the phenyl amide at position X (**2**; Figure 1) for a pivoyl amide improved potency,[12] and the addition of a dimethylamino-substituted phenyl moiety at position Y improved water solubility while retaining corrector activity.[13]

These findings have led us to further assess the utility of functional bithiazole derivatives at positions X and Y as ΔF508-CFTR correctors. With the intent to monitor the *in vitro* and *in vivo* efficacies of these compounds, we have incorporated photostable fluorescent dyes onto the bithiazole core (**3**–**6**; Figure 1). Herein, we report the synthesis and characterization of four fluorescently labeled bithiazole-based compounds, along with their corrector activity, as a proof-of-concept demonstration of the use of fluorescent CF correctors to probe uptake. While these derivatives are not development candidates, the work here demonstrates the possibility of synthesizing a functional fluorescent corrector whose uptake can be studied using imaging methodology.

Received: August 17, 2011
Revised: October 18, 2011
Published: October 31, 2011

ACS Publications © 2011 American Chemical Society

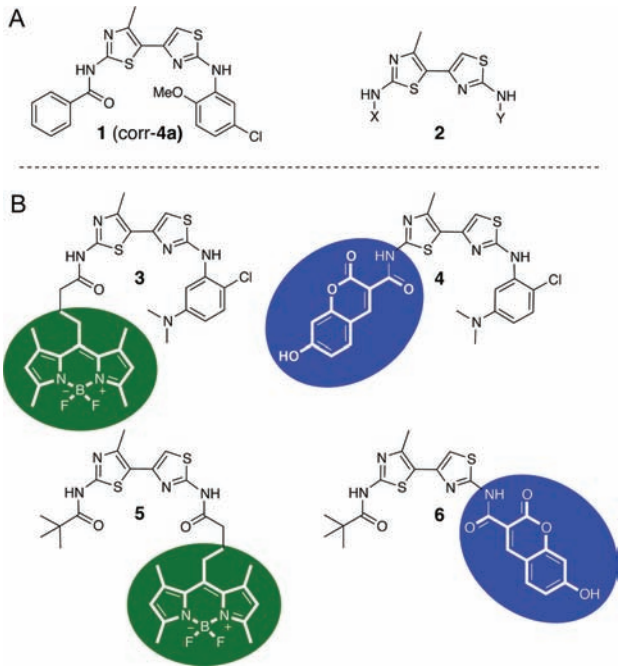

Figure 1. (A) Bithiazole-based ΔF508-CFTR correctors. (B) **3**–**6**: fluorescent dye analogues of corr-**4a**.

EXPERIMENTAL PROCEDURES

General Methods and Materials. All chemicals were purchased from commercial suppliers and used without further purification unless otherwise noted. Analytical thin layer chromatography was carried out on precoated glass plates (silica gel 60 F_{254}, 250 μm thickness) and visualized with UV light at 245 nm. Flash chromatography was performed with 60 Å, 32–63 μm silica gel (Scientific Absorbents). Synthesized products were concentrated by rotary evaporation under reduced pressure. ^{1}H NMR spectra were recorded at 400 or 600 MHz at ambient temperature with DMSO-d_6, $CDCl_3$, or CD_3OD as solvent. ^{13}C NMR spectra were recorded at 100 or 150 MHz at ambient temperature with DMSO-d_6, $CDCl_3$, or CD_3OD as solvent. Chemical shifts are reported in parts per million relative to $CHCl_3$ (^{1}H, δ 7.26, ^{13}C, 77.16), DMSO-d_5 (^{1}H, δ 2.50, ^{13}C, 39.52), or CHD_2OD (^{1}H, δ 3.31, ^{13}C, 49.00). Infrared spectra were recorded on an ATI-FTIR spectrometer (Mattson Genesis II). The specifications of the LC-MS are as follows: electrospray (+) ionization, mass range 150–1500 Da, 20 V cone voltage, and Xterra MS C_{18} column (2.1 mm × 50 mm × 3.5 μm). Dye precursors 4-(4,4-difluoro-1,3,5,7-tetramethyl-4-bora-3*a*-diaza-s-indacene-8-yl)-butyric acid (**7**)[14] and 7-hydroxycoumarin-3-carboxylic acid (**8**)[15,16] were synthesized and characterized according to literature methods. Bithiazole intermediates 1-(2-amino-4-methylthiazol-5-yl)-ethanone HCl (**9**),[17] 1-(2-amino-4-methylthiazol-5-yl)-2-bromoethanone (**10**), 1-(2-chloro-5-(dimethylaminophenyl)-thiourea (**11**), and *N*-(5-acytyl-4-methylthiazol-2-yl)pivalamide (**13**)[18] were synthesized as previously described.

***N*^{2}-(2-Chloro-5-(dimethylamino)phenyl)-4′-methyl-4,5′-bithiazole-2,2′-diamine (12).** Bromothiazole **10** (3.14 g, 11.56 mmol) and thiourea **11** (2.28 g, 9.92 mmol) were dissolved in ethanol (27 mL), and the mixture was heated to reflux for 2 h. After cooling to room temperature, the solid was collected by filtration and rinsed with cold ethanol to afford aminobithiazole **12** (3.68 g, 79%) as a pale pink solid. IR (neat) ν_{max} 3388, 3210, 3035, 1628, 1609, 1586, 1544, 1514, 1474, 1450, 1406, 1068, 1048, 879, 870, 807 cm^{-1}; ^{1}H NMR (400 MHz, DMSO-d_6) δ 2.40 (s, 3H), 3.08 (s, 6H), 7.00 (d, J = 8.8 Hz, 1H), 7.15 (s, 1H), 7.46 (d, J = 8.8 Hz, 1H), 8.24 (s, 1H), 9.47 (br s, 2H), 10.01 (s, 1H); ^{13}C NMR (150 MHz, DMSO-d_6) δ 17.05, 40.32, 101.12, 104.46, 107.57, 108.99, 114.41, 129.34, 137.41, 143.05, 143.88, 149.84, 162.79, 165.73; MS (ESI) m/z calcd. 365.05, found 366.04 $[M + H]^+$.

General Procedure for Preparation of Fluorescent Bithazole Probes 3–6 via CDI-Mediated Amide Formation. Fluorophore **7** (or **8**; 1.5 equiv) was dissolved in DMF (2.21 mL/mmol fluorophore) followed by the addition of carbonyldiimidazole (CDI; 1.5 equiv). The mixture was stirred for 30 min at room temperature, and aminobithiazole **12** (or **15**; 1 equiv) was added in one portion. The reaction was warmed to 80 °C and stirred for 48 h. After cooling to room temperature, the mixture was poured into water to precipitate the product. The solid was collected by filtration, rinsed with water, and dried under vacuum to yield **3**–**6**, each as a crude solid.

10-(4-(2-(2-Chloro-5-(dimethylamino)phenylamino)-4′-methyl-4,5′-bithiazol-2′-ylamino)-4-oxobutyl)-5,5-difluoro-1,3,7,9-tetramethyl-5*H*-dipyrrolo[1,2-*c*:1′,2′-*f*]-[1,3,2]diazaborinin-4-ium-5-uide (3). According to the general procedure for amide formation, **7** (138 mg, 0.41 mmol), DMF (0.91 mL), CDI (66 mg, 0.41 mmol), and **12** (100 mg, 0.27 mmol) gave crude solid, which was purified by flash column chromatography (1.25:1 hexane/EtOAc) to produce **3** (36 mg, 19%) as a red solid; IR (neat) ν_{max} 2916, 1686, 1600, 1581, 1535, 1513, 1431, 1017, 843 cm^{-1}; ^{1}H NMR (400 MHz, $CDCl_3$) δ 2.04 (m, 2H), 2.35 (s, 6H), 2.49 (s, 6H), 2.54 (s, 3H), 2.58 (m, 2H), 3.01 (m, 2H), 3.05 (s, 6H), 6.01 (s, 2H), 6.35 (dd, J = 2.8, 8.9 Hz, 1H), 6.62 (s, 1H), 7.20 (d, J = 8.9 Hz, 1H), 7.62 (br s, 1H), 7.88 (d, J = 2.8 Hz); ^{13}C NMR (100 MHz, $CDCl_3$) δ 14.61, 16.49, 17.28, 26.97, 27.45, 36.06, 40.92, 102.68, 102.82, 107.32, 108.77, 122.02, 122.32, 129.37, 131.54, 136.82, 140.49, 142.40, 144.62, 150.44, 154.42, 155.90, 162.92, 169.28; MS (ESI) m/z calcd. 681.21, found 682.19 $[M + H]^+$.

***N*-(2-(2-Chloro-5-(dimethylamino)phenylamino)-4′-methyl-4,5′-bithiazol-2′-yl)-7-hydroxy-2-oxo-2*H*-chromene-3-carboxamide (4).** According to the general procedure for amide formation, **8** (154 mg, 0.75 mmol), DMF (1.65 mL), CDI (121 mg, 0.75 mmol), and **12** (200 mg, 0.50 mmol) gave crude solid, which was purified by recrystallization in EtOH to yield **4** (108 mg, 20%) as an orange solid; IR (neat) ν_{max} 3276, 2208, 2164,1695, 1679, 1529, 1509, 1373, 1264, 1195, 1134, 834 cm^{-1}; ^{1}H NMR (400 MHz, DMSO-d_6) δ 3.02 (s, 6H), 6.44 (dd, J = 2.9, 8.9 Hz, 1H), 6.86 (d, J = 1.9, 1H), 6.94 (dd, J = 2.1, 8.6 Hz, 1H), 7.01 (s, 1H), 7.22 (d, J = 8.9 Hz, 1H), 7.91 (d, J = 8.7 Hz, 1H), 8.07 (d, J = 2.8 Hz, 1H), 8.96 (s, 1H), 9.63 (s, 1H), 11.33 (br s, 1H), 11.85 (s, 1H); ^{13}C NMR (100 MHz, DMSO-d_6) δ 17.09, 40.54, 102.02, 103.96, 104.44, 108.94, 111.26, 111.84, 114.85, 121.90, 129.41, 132.63, 137.43, 141.87, 142.91, 149.33, 149.76, 153.72, 156.66, 159.71, 161.31, 163.24, 164.63; MS (ESI) m/z calcd. 553.06, found 554.11 $[M + H]^+$.

***N*-(5-(2-Bromoacetyl)-4-methylthiazol-2-yl)pivalamide (14).** A solution of **13** (6.5 g, 27.1 mmol) in 30% HBr in AcOH (40 mL) was treated with $PryH^+Br_3^-$ (11.25 g, 35.17 mmol) and stirred at room temperature for 48 h. Water was added and the aqueous layer was extracted with CH_2Cl_2. The combined organic extracts were washed with saturated

dx.doi.org/10.1021/bc2004457 | *Bioconjugate Chem.* 2011, 22, 2593–2599

$NaHCO_3$ and brine. The organic layer was dried over sodium sulfate, filtered, and evaporated under reduced pressure. The residue was purified by flash column chromatography (20−40% EtOAc/hexane) to yield 4.23 g (49%) of the title compound **14** as a white solid; IR (neat) ν_{max} 3260, 2970, 2928, 1687, 1660, 1530, 1493, 1370, 1318, 1280, 1220, 1196, 1136, 975, 819 cm^{-1}; ^1H NMR (600 MHz, $CDCl_3$) δ 1.28 (s, 9H), 2.52 (s, 3H), 4.17 (s, 2H); ^{13}C NMR (150 MHz, $CDCl_3$) δ 17.85, 26.82, 33.58, 39.37, 121.19, 157.27, 160.69, 177.27, 184.34; MS (ESI) m/z calcd. 318.00, found 318.97 $[M + H]^+$.

***N*-(2-Amino-4′-methyl-4,5′-bithiazol-2′-yl)pivalamide (15).** To a solution of **14** (2.38 g, 7.46 mmol) in EtOH (15 mL) was added thiourea (568 mg, 7.46 mmol). The mixture was heated to reflux and stirred for 12 h. After cooling to room temperature, hexane was added to fully precipitate the product and the solid was collected by filtration and washed with cold ethanol to obtain 607 mg (27%) of **15** as a cream-colored solid; IR (neat) ν_{max} 3198, 3180, 2967, 2932, 1675, 1621, 1597, 1515, 1484, 1353, 1304, 1141, 994, 898 cm^{-1}; ^1H NMR (600 MHz, CD_3OD) δ 1.31 (s, 9H), 2.41 (s, 3H), 4.91 (br s, 2H), 6.88 (s, 1H); ^{13}C NMR (150 MHz, CD_3OD) δ 16.36, 27.20, 40.22, 106.73, 113.08, 131.93, 149.20, 159.55, 172.11, 179.12; MS (ESI) m/z calcd. 296.08, found 297.08 $[M + H]^+$.

5,5-Difluoro-1,3,7,9-tetramethyl-10-(4-(4′-methyl-2′-pivalamido-4,5′-bithiazol-2-ylamino)-4-oxobutyl)-5*H*-dipyrrolo[1,2-*c*:1′,2′-*f*][1,3,2]diazaborinin-4-ium-5-uide (5). According to the general procedure for amide formation, **7** (140 mg, 0.42 mmol), DMF (0.93 mL), CDI (68 mg, 0.42 mmol), and **15** (83 mg, 0.28 mmol) gave crude solid, which was purified by flash column chromatography (1.25:1 hexane/EtOAc) to produce **5** (94 mg, 55%) as a neon orange solid; mp 266 °C dec; IR (neat) ν_{max} 3189, 2960, 1655, 1547, 1509, 2923, 1706, 1546, 1506, 1406, 1197, 1061, 983, 834 cm^{-1}; ^1H NMR (400 MHz, $CDCl_3$) δ 1.30 (s, 9H), 2.01 (m, 2H), 2.36 (s, 6H), 2.50 (s, 6H), 2.51 (s, 3H), 2.53 (m, 2H), 2.97 (m, 2H), 6.03 (s, 2H), 6.91 (s, 1H), 8.91 (br s, 1H), 10.05 (s, 1H); ^{13}C NMR (100 MHz, $CDCl_3$) δ 14.59, 16.49, 16.94, 26.94, 27.26, 27.40, 35.82, 39.24, 108.53, 121.09, 122.02, 131.59, 140.58, 142.19, 143.35, 144.80, 154.39, 155.96, 157.67, 170.02, 176.26; HRMS: Anal. $C_{29}H_{35}BF_2N_6O_2S_2$ m/z calcd. 612.2433, found 613.2405 $[M + H]^+$.

7-Hydroxy-*N*-(4′-methyl-2′-pivalamido-4,5′-bithiazol-2-yl)-2-oxo-2*H*-chromene-3-carboxamide (6). According to the general procedure for amide formation, **8** (209 mg, 1.01 mmol), DMF (2.25 mL), CDI (164 mg, 1.01 mmol), and **15** (200 mg, 0.68 mmol) gave crude solid, which was purified by recrystallization from DMF to yield **6** (56 mg, 17%) as a canary yellow solid; IR (neat) ν_{max} 3376, 2967, 2959, 1698, 1616, 1521, 1505, 1266, 1192, 1129 cm^{-1}; ^1H NMR (400 MHz, DMSO-d_6) δ 1.25 (s, 9H), 6.86 (d, J = 1.8 Hz, 1H), 6.93 (dd, J = 2.1, 8.6 Hz, 1H), 7.29 (s, 1H), 7.88 (d, J = 8.7, 1H), 8.94 (s, 1H), 11.32 (br s, 1H), 11.78 (s, 1H), 11.99 (s, 1H); ^{13}C NMR (100 MHz, DMSO-d_6) δ 16.86, 26.61, 35.75, 102.06, 108.65, 111.21, 111.88, 114.89, 119.51, 132.64, 142.30, 143.20, 149.40, 156.12, 156.42, 156.70, 160.25, 161.17, 164.72, 176.56; MS (ESI) m/z calcd. 484.09, found 485.03 $[M + H]^+$.

Short-Circuit Current Measurements. Fisher rat thyroid (FRT) epithelial cells stably expressing human ΔF508-CFTR were generated as described previously.[19] The FRT cells were cultured on Snapwell porous support for 7−9 days. Test compounds were incubated with FRT cells for 18−24 h at 37 °C prior to measurements. Standard short-circuit current measurement procedures were followed as previously described.[20] The basolateral solution contained 130 mM NaCl, 2.7 mM KCl, 1.5 mM KH_2PO_4, 1 mM $CaCl_2$, 0.5 mM $MgCl_2$, 10 mM glucose, and 10 mM Na-HEPES (pH 7.3). In the apical bathing solution, 65 mM NaCl was replaced by Na gluconate, and $CaCl_2$ was increased to 2 mM. Solutions were bubbled with air and maintained at 37 °C. The basolateral membrane was permeabilized with 250 μg/mL amphotericin B. Hemichambers were connected to a DVC-1000 voltage clamp (World Precision Instruments Inc.) via Ag/AgCl electrodes and 1 M KCl agar bridges for recording of short-circuit current.

Cellular Uptake. FRT cells[19] were cultured on coverglasses and mounted in a perfusion chamber maintained at 37 °C. Cells were incubated with serum-free culture medium containing 10 μM **5** in culture medium. Cells were imaged over 45 min using a laser-scanning confocal microscope (Nikon C1, 100× oil objective, NA 1.49) using appropriate filter sets. Cells expressing endoplasmic reticulum-targeted green fluorescent protein (GFP) were also imaged.

***In Vivo* Metabolic Stability.** All experiments involving live animals were performed according to procedures approved by the Institution of Animal Care and Usage Committee (IACUC) at UCSF. Compound **5** (250 μg/100 μL; 10% DMSO, 10% Tween 80, 40% propylene glycol, 20% ethanol, and 20% H_2O; sterilized through a 20 μm filter prior to injection) or saline was injected intraorbitally in adult CD1 mice. Mice were sacrificed by anesthetic overdose and cervical dislocation at 10 or 30 min. Following perfusion with PBS, organs were harvested and homogenized with PBS (1 mL/g of tissue). An equal volume of cold CH_2Cl_2 was added to extract **5** from the tissue/aqueous layer. Homogenates were centrifuged for 15 min at 4000 rpm and 4 °C. The organic layer was evaporated with nitrogen to 100 μL and the residue was analyzed by TLC. TLC was carried out on precoated glass plates (silica gel 60 F_{254}, 250 μm thickness), using a solvent system of 1:1 ethyl acetate/hexane, and fluorescent images were acquired on a Kodak 4000 mm image station (Eastman Kodak Company, Rochester, NY). TLC plates were imaged with excitation and emission bandpass filters of 465 and 535 nm, respectively, with f-stop at 2.8 and an exposure time of 2 min.

In a separate experiment, **5** was administered by tail vein injection (250 μg/100 μL; 10% DMSO, 10% Tween 80, 40% propylene glycol, 20% ethanol, and 20% H_2O; sterilized through a 20 μm filter prior to injection) in adult mice. Mice were sacrificed by anesthetic overdose and cervical dislocation at 10 or 30 min. Dye-containing extracts (obtained as outlined in the preceding paragraph) were dissolved in eluent (30 μL DMSO and 120 μL 3:1 CH_3CN/H_2O with 0.5% formic acid). Reverse-phase HPLC was carried out using a C18 column (Supelco, 2.1 mm × 100 mm × 5 μm) connected to a solvent delivery system (Waters model 2690, Milford, MA). Elution conditions were as follows: 1 min at 95% CH_3CN/5% H_2O, followed by a linear gradient from 95% CH_3CN/5% H_2O to 0% CH_3CN/100% H_2O over 9 min; 3 min at 0% CH_3CN/100% H_2O; a linear gradient from 0% CH_3CN/100% H_2O to 95% CH_3CN/5% H_2O over 3 min; and a linear gradient from 95% CH_3CN/5% H_2O to 100% CH_3CN/0% H_2O over 2 min (0.2 mL/min flow rate). Mass spectra were acquired to confirm compound identity using a mass spectrometer (Alliance HT 2790 + ZQ) using positive ion detection, scanning from 150 to 850 Da.

Whole-Body Slice Imaging. Optical imaging studies were performed on a reflectance optical scanner (IVIS-50, Caliper Life Sciences, Hopkinton, MA), and data acquisition and processing were performed using the *Living Image* software v

3.2. Compound **5** was formulated in 10% DMSO, 10% Tween-80, 40% propylene glycol, 20% ethanol, and 20% water (2 nmol, 150 μL). The formulated solution was sterilized through a 20 μm filter prior to injection. Male nu/nu mice (Charles Rivers, MA) that had been on a nonfluorescent diet more than 10 days were injected intravenously via tail vein with 150 μL of **5** (2 nmol) or saline. Mice were euthanized 10 min postinjection and immediately frozen and stored at −80 °C. Whole body slices at 40 μm thickness were cut using a cryotome (Hacker-Bright Sledge Microtome, Winnsboro, SC). Coronal slices through the midsection were imaged using excitation and emission bandpass filters of 468 ± 22 nm and 545 ± 30 nm, respectively. Images were collected using the same field of view with binning set at 4, f-stop at 2, and exposure time 20 s. Total photon efficiency is a measure of fluorescent photons from the specimen normalized against the excitation intensity; the resulting efficiency is expressed in units of cm^2.

RESULTS

Chemistry. Synthesis of the BODIPY dye containing a free carboxyl group (**7**) was achieved via a one-pot condensation between 2 equiv of 2,4-dimethylpyrrol and glutaric anhydride followed by the coordination of $BF_3{\cdot}OEt_2$ (Scheme 1).[14,21] The

Scheme 1. Synthesis of Fluorescent Dyes[a]

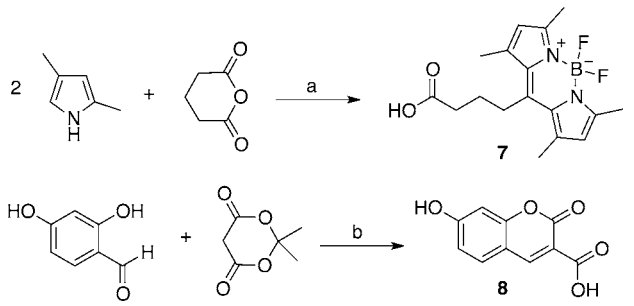

[a]Reagents: (a) i. $BF_3{\cdot}OEt_2$, CH_2Cl_2, reflux, ii. $BF_3{\cdot}OEt_2$, Et_3N; (b) piperidinium acetate, EtOH, reflux.

hydroxy-substituted coumarin-3-carboxylic acid **8** was prepared by Knoevenagel condensation of 2,4-dihydroxybenzaldehyde with Meldrum's acid directly releasing a free carboxyl group in one pot.[15] The percent yield for this one-pot transformation was 76%.

Next, two amino bithiazole intermediates (**12** and **15**) were synthesized (Scheme 2); each intermediate was designed to allow for late stage attachment of the fluorescent dye. Aminobithiazole building block **12** was synthesized by α-bromination of aminothiazole **9** in 86% yield followed by condensation with 1-(2-chloro-5-(dimethylaminophenyl)thiourea **11** in 79% yield. CDI-mediated condensation of **12** with fluorescent acids **7** and **8** provided probes **3** and **4** in modest yields (**3**, 19%, and **4**, 20%, respectively). To synthesize the aminobithiazole precursor **15**, aminothiazole **9** was first treated with CDI-activated pivalic acid to give **13** (83% yield) followed by α-bromination with 30% HBr in AcOH and pyridinium tribromide to produce **14** (49% yield). Bromination of **13** proved to be more difficult than bromination of **9**; therefore, a stronger acidic medium (HBr vs HOAc) was required. Subsequent condensation with thiourea afforded aminobithiazole intermediate **15** (27% yield). Acids **7** and **8** were then activated with CDI and subsequently

Scheme 2. Synthetic Route to Fluorescent Bithiazole Derivatives[a]

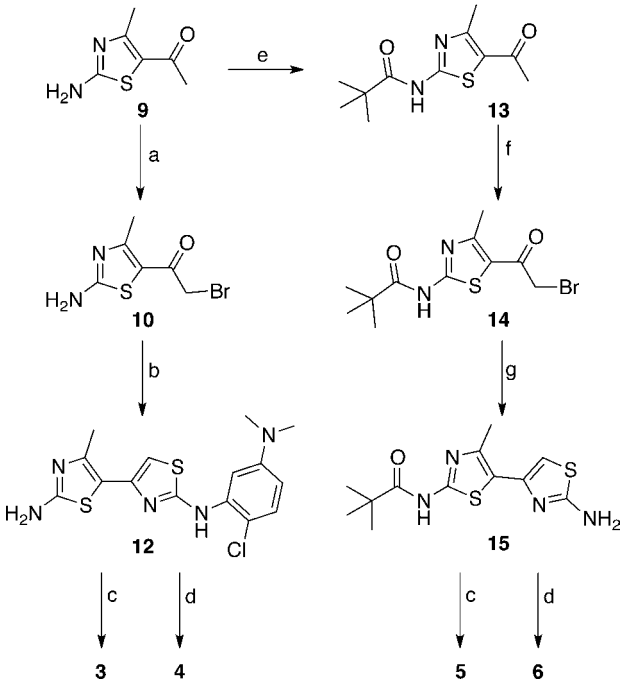

[a]Reagents: (a) Br_2, AcOH; (b) 1-(2-Chloro-5-dimethylaminophenyl)-thiourea (**11**), EtOH, reflux; (c) **7**, CDI, DMF, 80 °C; (d) **8**, CDI, DMF, 80 °C; (e) pivalic acid, CDI, DMF, 80 °C; (f) $PyrH^+Br_3^-$, 33% HBr in AcOH; (g) $NH_2C(S)NH_2$, EtOH, reflux [See Figure 1 for **3**−**6** structures].

treated with **15** to obtain fluorescent compounds **5** and **6** in modest yields (**5**, 55%, and **6**, 17%, respectively).

Corrector Activity. We followed established standard short-circuit current measurement procedures[20] to determine the corrector activity of each fluorescently labeled bithiazole. Apical membrane chloride current was measured in ΔF508-CFTR expressing FRT cells after basolateral membrane permeabilization and in the presence of a transepithelial chloride gradient. Cells were incubated for 18−24 h with 10 μM test compound prior to short-circuit current assay. DMSO vehicle was used as a control. Figure 2A shows minimum apical membrane current with DMSO alone, with a small increase following addition of the cAMP-elevating agent forskolin (20 μM) and the potentiator genistein (50 μM). The increased apical membrane current was inhibited upon addition of the CFTR inhibitor $CFTR_{inh}$-172. While conjugates **3** and **4** (Figure 2A) had little corrector activity at 10 μM, conjugate **6** had moderate activity, and **5** had efficacy comparable to that of 5 μM corr-**4a**. On the basis of its corrector activity, we chose **5** for further studies.

Intracellular Uptake. To assess cellular uptake and localization of conjugate **5**, FRT cells were imaged by confocal microscopy at different times after exposure to 10 μM **5**. Figure 2B shows rapid uptake of **5** within 1 min, which remained stable for >45 min. Fluorescence was observed in an intracellular compartment consistent with a characteristic membrane pattern of the endoplasmic reticulum, which is similar to that in FRT cells expressing ER-targeting GFP (Figure 2B). While not conclusive, the high lipophilicity of **5** would account for its intracellular staining pattern, as endoplasmic reticulum membranes constitute the vast majority of cell membranes.

dx.doi.org/10.1021/bc2004457 | Bioconjugate Chem. 2011, 22, 2593−2599

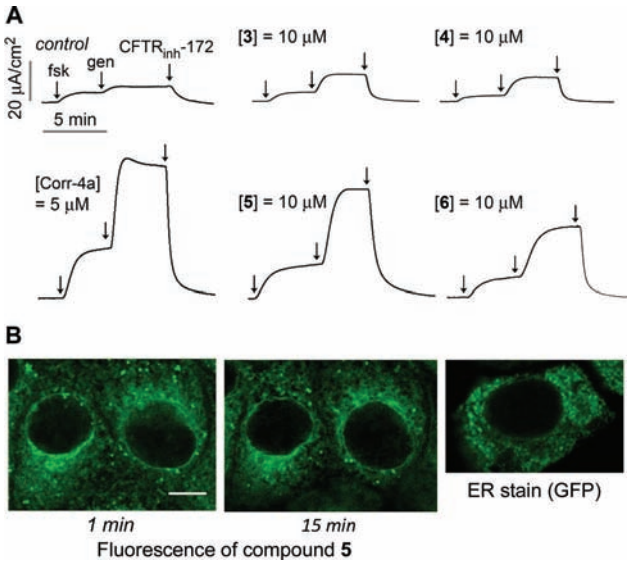

Figure 2. ΔF508-CFTR corrector activity and cellular uptake of **5**. (A) Short-circuit measurements showing apical membrane chloride current after incubation for 24 h at 37 °C with 10 μM of indicated fluorescent bithiazoles. Negative control was incubation with DMSO vehicle alone and positive control was incubation with corr-**4a** (5 μM). Forskolin (20 μM), genistein (50 μM), and $CFTR_{inh}$-172 (10 μM) were added as indicated. (B) Confocal micrographs of live FRT cells after incubation with **5** for 1 or 15 min; for comparison, ER staining shown of FRT cells expressing an ER-targeted GFP. Scale bar, 5 μm.

Metabolic Stability. To determine a suitable time point for whole-body slice imaging of the organ distribution of conjugate **5**, the metabolic stability of **5** was first assessed by fluorescence imaging of TLC plates (see Supporting Information p. S9). By 10 min, **5** was metabolized in liver, but remained largely intact in lung and kidney. By 30 min, **5** was not detected in lung or kidney, and little nonmetabolized compound was seen in liver. Extracts from the lung, liver, kidney, brain, and heart obtained at 10 and 30 min were also analyzed by LC-MS. Rapid uptake and clearance of **5** was found in the liver, lung, kidney, and heart, with no compound seen in brain. Figure 3 shows LC-MS analysis of lung extract at 10 and

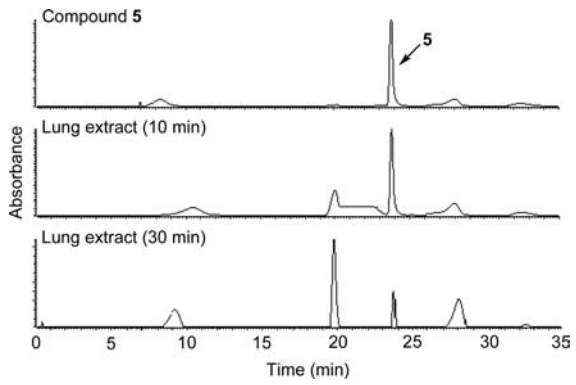

Figure 3. Qualitative LC-MS data for identification of **5** in lung extract. HPLC chromatograms (absorbance, 494 nm) of **5** (A), and lung extract at 10 min (B) and 30 min (C) post injection.

30 min after intravenous injection of **5**. While we have not analyzed the chemical basis of conjugate instability, which would be a major undertaking beyond the scope of the study focused here on a single fluorescent corrector, the detection of intact **5** supports the following imaging studies described below. Chromatograms of liver, kidney, brain, and heart are provided in the Supporting Information (p. S9–S12).

Uptake Measured in Whole-Body Slices. Fluorescence imaging of **5** was done in whole-body slices obtained at 10 min after intravenous administration, in which the above data showed that **5** was largely intact in extrahepatic organs. Coronal slices at the midsection of mice were imaged. Figure 4 shows accumulation of **5** mainly in gastrointestinal organs, including stomach, small and large intestine, and liver, with lesser fluorescence in lung. Little background signal was seen in slices from control mice.

DISCUSSION

In a recent study, we synthesized a focused library of 54 thiazole-tethered pyrazoles that allowed for incorporation of property-modulating functionality (ester, acid, and amide) on C5 of the pyrazole ring (see Figure 5).[18] These pyrazolylthiazoles retained ΔF508-CFTR corrector activity (<1 μM) and improved the experimentally determined log*P* (1.2 log units lower than corr-**4a**). That work also established that the corrector binding site of ΔF508-CFTR affords a fair degree of plasticity with regard to the aniline-moiety binding pocket; compare **16** to corr-**4a** (Figure 5). Building on that insight, we speculated that perhaps the ΔF508-CFTR corrector binding site could accommodate the fluorescent dye moieties shown in analogues **5** and **6** where the dye is attached at the 2-amino position (see Figure 1). SAR insight regarding the plasticity of the presumed amide-binding pocket of ΔF508-CFTR, while less extensive,[7] suggested that dye attachment via the 2′-amino as in analogues **3** and **4** might also retain corrector activity (see Figure 1). We did not attempt to generate conjugates with near-infrared dyes (NIR dyes; for example, a bithaizole modified with a Cy7-based dye[22]) because, while they would offer the advantages of long-wavelength fluorescence and noninvasive imaging, their large size would likely interfere with corrector activity. Positron emission tomography (PET; another noninvasive technique) using an ^{18}F-labeled CF corrector has the potential advantage of only very modestly modifying the small molecule. However, because of the higher costs and complexity, this technique was judged as inappropriate for our initial proof-of-concept work [note: we have synthesized an ^{19}F-labeled analogue of corr-**4a** (4-fluorobenzamide replacing benzamide; refer to Figure 1) that has corrector efficacy comparable to 5 μM corr-**4a**]. On the basis of this analysis, we synthesized fluorescent bithiazole analogues **3**–**6**.

BODIPY and hydroxycoumarin fluorophores were selected for conjugation with bithiazole cores **12** and **15** (see Scheme 2) because each dye is readily generated in one synthetic operation (see Scheme 1), insensitive to changes in pH, affords bright fluorescence and photostability, and has modest molecular size. Also, the preparation of each final substrate (**3**–**6**) closely parallels already developed synthetic protocols.[21]

Of the four bithiazole–fluorophore conjugates **3**–**6**, BODIPY **5** was the most efficacious corrector (see Figure 2A), having comparable corrector activity to that of corr-**4a**. We therefore selected BODIPY **5** for *in vivo* and imaging studies. The activity of **5** further supports the notion that the "analine-binding pocket" of ΔF508-CFTR affords exploitable plasticity.

Small molecular weight therapeutics are desirable in part due to their ability to permeate the cell membrane. An initial concern with the conjugation of a fluorescent dye to the core of corr-**4a** was the possibility of reduced cell plasma membrane

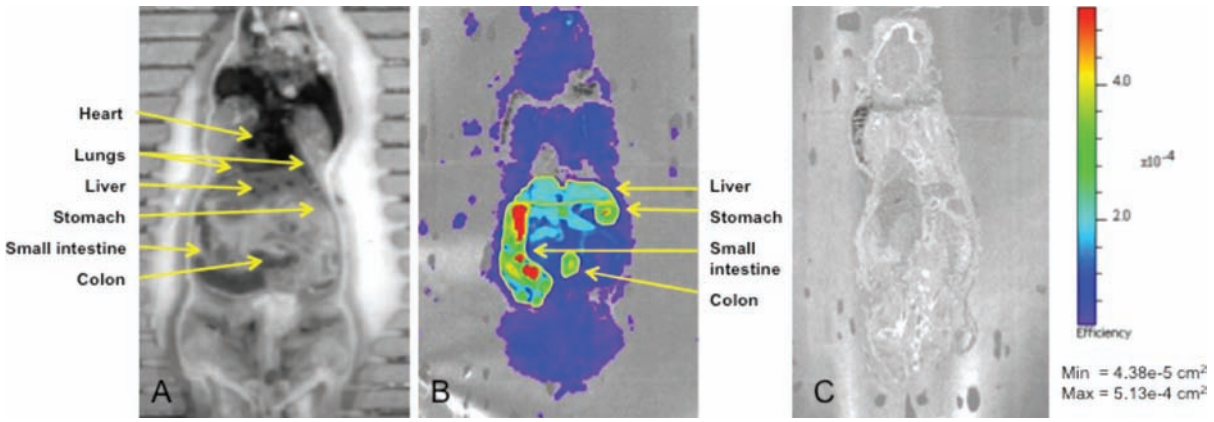

Figure 4. Fluorescence imaging of the coronal slices of mice at 10 min after injection of 2 nmol of **5** or saline. Shown are white light image (A) and fluorescence images of the coronal slice from mice injected with **5** (B) or saline (C).

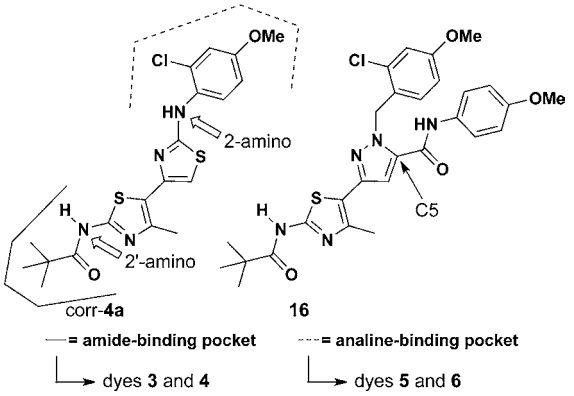

Figure 5. Presumed aniline- and amide-binding pockets of ΔF508-CFTR.

permeability. However, as seen from the rapid appearance of intracellular fluorescence in Figure 2B, conjugate **5** is highly permeable across cell membranes. The rapid uptake and probable ER distribution of **5** is likely a consequence of its lipophilicity at position Y (see Figure 1).

Metabolic stability studies showed that, in the lung, the primary organ of interest in cystic fibrosis, the main fluorescent species at 10 min after intravenous administration was the original compound, allowing unambiguous interpretation of whole-body slice fluorescence images. Unfortunately, however, conjugate **5** is rapidly metabolized by the liver, precluding analysis of its biodistribution at longer times by the methods used here. Interestingly, despite the highly lipophilic nature of the BODIPY moiety at position Y, **5** does not significantly cross the blood-brain barrier at 10 min.

Optical imaging is a sensitive tool to monitor the *in vivo* distribution of exogenous fluorescent agents in animals.[23] Here, the incorporation of BODIPY on the bithiazole core has allowed detection of fluorescence at 510 nm. Because of the limited tissue penetration of light at 510 nm, images were obtained of whole-body coronal slices at 10 min following intravenous administration of **5**. Of relevance to cystic fibrosis, **5** was largely targeted to gastrointestinal organs, where CFTR is expressed, and to lesser extent in lung.

CONCLUSION

In conclusion, our data define the early uptake in mice of a functional, fluorescently labeled bithiazole ΔF508-CFTR corrector. The BODIPY fluorophore did not appear to interfere with the corrector activity of conjugate **5**, but is likely to affect its biodistribution, as lipophilic compounds often accumulate in adipose tissues such as the stomach and intestine. Although the rapid hepatic metabolism and clearance of **5** restricted our analysis of biodistribution to early times after administration, fluorescence imaging of coronal slices has provided information about the uptake of **5**, and hence proof-of-concept for the strategy of fluorescent drug labeling and analysis of biodistribution by whole-body slice imaging.

ASSOCIATED CONTENT

Supporting Information

^{1}H and ^{13}C NMR spectra of all new compounds, fluorescent TLC image, and LC-MS chromatograms of organ homogenates. This material is available free of charge via the Internet at http://pubs.acs.org.

AUTHOR INFORMATION

Corresponding Author

*Phone: 530-554-2145. FAX: 530-752-8995. E-mail: mjkurth@ucdavis.edu.

ACKNOWLEDGMENTS

The authors thank the Tara K. Telford Fund for Cystic Fibrosis Research at the University of California, Davis, the National Institutes of Health (Grants DK72517 and GM089153), and the National Science Foundation [CHE-0910870; grants CHE-0910870, CHE-0443516, CHE-0449845, and CHE-9808183 supporting NMR spectrometers].

REFERENCES

(1) Pilewski, J. M., and Frizzell, R. A. (1999) Role of CFTR in airway disease. *Physiol. Rev. 79*, S215−S255.

(2) Sheppard, D. N., and Welsh, M. J. (1999) Structure and function of the CFTR chloride channel. *Physiol. Rev. 79*, S23−S45.

(3) Denning, G. M., Anderson, M. P., Amara, J. F., Marshall, J., Smith, A. E., and Welsh, M. J. (1992) Processing of mutant cystic fibrosis transmembrane conductance regulator is temperature-sensitive. *Nature 358*, 761−764.

(4) Lukacs, G. L., Mohamed, A., Kartner, N., Chang, A.-B., Riordan, J. R., and Grinstein, S. (1994) Conformational maturation of CFTR but not its mutant counterpart (ΔF508) occurs in the endoplasmic reticulum and requires ATP. *EMBO J. 13*, 6076−6086.

(5) Kopito, R. R. (1999) Biosynthesis and degredation of CFTR. *Physiol. Rev. 79*, S167−S173.

(6) Du, K., Sharma, M., and Lukacs, G. L. (2005) The ΔF508 cystic fibrosis impairs domain-domain interactions and arrests post-translational folding of CFTR. *Nat. Struct. Mol. Biol. 12*, 17−25.
(7) Carlile, G. W., Robert, R., Zhang, D., Teske, K. A., Luo, Y., Hanrahan, J. W., and Thomas, D. Y. (2007) Correctors of protein trafficking defects identified by a novel high-throughput screening assay. *ChemBioChem 8*, 1012−1020.
(8) Becq, F. (2006) On the discovery and development of CFTR chloride channel activators. *Cur. Pharm. Des. 12*, 471−484.
(9) Van Goor, F., Straley, K. S., Cao, D., Gonzalez, J., Hadida, S., Hazelwood, A., Joubran, J., Knapp, T., Makings, L. R., Miller, M., Neuberger, T., Olson, E., Panchenko, V., Rader, J., Singh, A., Stack, J. H., Tung, R., Gootenhuis, P. D. J., and Negulescu, P. (2006) Rescue of deltaF508-CFTR trafficking and gating in human cystic fibrosis airway primary cultures by small molecules. *Am. J. Physiol. 290*, L1117−L1130.
(10) Yang, H., Shelat, A. A., Guy, R. K., Gopinath, V. S., Ma, T., Du, K., Lukacs, G. L., Taddei, A., Folli, C., Pedemonte, N., Galietta, L. J. V., and Verkman, A. S. (2003) Nanomolar affinity small molecule correctors of defective ΔF508-CFTR chloride channel gating. *J. Biol. Chem. 278*, 35079−35085.
(11) Pedemonte, N., Lukacs, G. L., Du, K., Caci, E., Zegarra-Moran, O., Galietta, L. J. V., and Verkman, A. S. (2005) Small molecule correctors of defective ΔF508-CFTR cellular processing identified by high-throughput screening. *J. Clin. Invest. 115*, 2564−2571.
(12) Yoo, C. L., Yu, G. J., Yang, B., Robins, L. I., Verkman, A. S., and Kurth, M. J. (2008) 4′-Methyl-4,5′-bithiazole-based correctors of defective ΔF508-CFTR cellular processing. *Bioorg. Med. Chem. Lett. 18*, 2610−2614.
(13) Yu, G. J. (2009) Golden Bridge to Cystic Fibrosis: Heterocycles. Ph.D. dissertation; pp 93−116, Chapter 3, University of California, Davis.
(14) Li, Z., Mintzer, E., and Bittman, R. (2006) First synthesis of free cholesterol-BODIPY conjugates. *J. Org. Chem. 71*, 1718−1721.
(15) Song, A., Wang, X., and Lam, K. S. (2003) A convenient synthesis of coumarin-3-carboxylic acids via Knoevenagel condensation of Meldrum's acid with ortho-hydroxyaryl aldehydes or ketones. *Tetrahedron Lett. 44*, 1755−1758.
(16) Mizukami, S., Watanabe, S., Hori, Y., and Kikuchi, K. (2008) Covalent protein labeling based on noncatalytic *β*-lactamase and a designed FRET substrate. *J. Am. Chem. Soc. 131*, 5016−5017.
(17) Hantzsch, A. (1889) Thiazoles from thiamides. *Justus Liebigs Ann. Chem. 250*, 257−273.
(18) Ye, L., Knapp, J. M., Sangwung, P., Fettinger, J. C., Verkman, A. S., and Kurth, M. J. (2010) Pyrazolylthiazole as ΔF508-cystic fibrosis transmembrane conductance regulator correctors with improved hydrophilicity compared to bithiazoles. *J. Med. Chem. 53*, 3772−3781.
(19) Yang, H., Shelat, A. A., Guy, R. K., Gopinath, V. S., Ma, T., Du, K., Lukacs, G. L., Taddei, A., Folli, C., Pedemonte, N., Galietta, L. J., and Verkman, A. S. (2003) Nanomolar affinity small molecule correctors of defective Delta F508-CFTR chloride channel gating. *J. Biol. Chem. 278*, 35079−35085.
(20) Sheppard, D. N., Carson, M. R., Ostedgaard, L. S., Denning, G. M., and Welsh, M. J. (1994) Expression of cystic fibrosis transmembrane conductance regulator in a model epithelium. *Am. J. Physiol. 266*, L405−13.
(21) Wang, D., Fan, J., Gao, X., Wang, B., Sun, S., and Peng, X. (2009) Carboxyl BODIPY dyes from bicarboxylic anhydrides: one-pot preparation, spectral properties, photostability, and biolabeling. *J. Org. Chem. 74*, 7675−7683.
(22) Oushiki, D., Kojima, H., Terai, T., Arita, M., Hanaoka, K., Urano, Y., and Nagano, T. (2010) Development and application of a near-infrared fluorescence probe for oxidative stress based on differential reactivity of linked cyanine dyes. *J. Am. Chem. Soc. 132*, 2795−2801.
(23) Mahmood, U., and Weissleder, R. (2003) Near-infrared optical imaging of proteases in cancer. *Mol. Cancer Ther. 2*, 489−496.

Bioconjugate Chemistry

Article

pubs.acs.org/bc

Enhancement of the Growth and Differentiation of Nasal Olfactory Mucosa Cells by the Conjugation of Growth Factors to Functional Nanoparticles

Hadas Skaat,[†] Ofra Ziv-Polat,[†] Abraham Shahar,[‡] and Shlomo Margel*,[†]

[†]Department of Chemistry, Bar-Ilan Institute of Nanotechnology and Advanced Materials, Ramat-Gan 52900, Israel

[‡]N.V.R Research Ltd., Nes-Ziona 74031, Israel

Supporting Information

ABSTRACT: Growth factors are critical components in the tissue engineering approach. Basic fibroblast growth factor (bFGF), a representative growth factor, stimulates the cellular functions of various cells and has been used extensively for the repair and regeneration of tissues. The *in vivo* half-life time of free bFGF is short, about 3−10 min, due to rapid enzymatic degradation. Stabilization of the bFGF was accomplished by the covalent or physical conjugation of this factor to fluorescent maghemite (γ-Fe_2O_3) nanoparticles. In the present study, nasal olfactory mucosa (NOM) cells from adult rats were cultured in suspension on chitosan microcarriers (MCs) in the presence of the nonconjugated or bFGF-conjugated nanoparticles, or the free factor. The floating cells/nonconjugated, conjugated, or free bFGF/MCs aggregates were then seeded in a viscous gel. In this manuscript, we are the first to report that the stabilization of the factor by its conjugation to these nanoparticles significantly improved NOM cell-proliferation properties (migration, growth, and differentiation), compared to the same concentration, or even five times higher, of the free factor. This novel approach may significantly contribute to the advancement of the tissue engineering field.

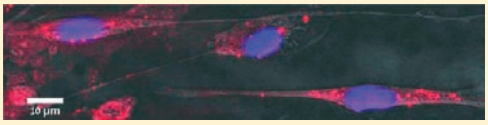

INTRODUCTION

Tissue engineering is an emerging scientific approach to regenerate damaged and diseased tissues.[1] By applying combinations of biomaterials, cells, and bioactive molecules, regeneration of damaged or diseased tissues can be facilitated, ultimately leading to the functional replacement of these tissues.[2] Growth factors are becoming leading therapeutic candidates for tissue engineering approaches.[3] Growth factors are endogenous polypeptides, secreted by a wide range of cell types, which initiate intracellular signals to regulate cellular activities such as adhesion, proliferation, migration, and differentiation. The local delivery of growth factors to the injured tissue site is essential to trigger cellular actions, through binding, to specific receptors on the surface of the target cells, and thereby stimulate the regenerative processes.[4,5]

FGF-2, also known as bFGF, is a representative growth factor which promotes proliferation, differentiation, and numerous other cellular functions of a wide variety of cells, including mesenchymal, neuroectodermal, and endothelial cells.[6] For example, bFGF has been reported to significantly promote NOM cell proliferation and maintain its survival.[7,8] It has also shown a high therapeutic potential for the repair and regeneration of damaged tissues, including skin, blood vessel, muscle, adipose, tendon/ligament, cartilage, bone, tooth, and nerve tissue.[9] For instance, the administration of bFGF to damaged neurons stimulates neurogenesis and provides neuroprotection in different animal models of neurodegenerative diseases, e.g., Parkinson's,[10] Alzheimer's,[11,12] and Huntington's.[13]

The main disadvantage of bFGF is its short *in vivo* half-life time, about 3−10 min, due to rapid enzymatic degradation, leading to loss of biological activity and functions.[6,14] It therefore requires frequent direct injections of the factor in order to maintain its bioavailability necessary for tissue repair. However, repeated administration may lead to undesirable systematic effects and toxicity due to nonspecific distribution and accumulation of the factor throughout the body. To obtain satisfactory performance, growth factors are adsorbed onto, or encapsulated within, nanomaterials to protect their stability and biological activity in a sustained and controllable manner.[15] Recent literature concerning novel biomaterials indicates increasing interest in developing inorganic nanoparticles suitable as growth factor delivery systems mainly by controlled release, such as mesoporous silica nanoparticles,[16] quantum dots,[17] calcium phosphate,[18] and calcium sulfate nanoparticles.[19]

Magnetic iron oxide nanoparticles are particularly promising due to their high surface area to volume ratio, magnetic properties, biocompatibility, relative nontoxicity, and biodegradability. The use of iron oxide magnetic nanoparticles for various biomedical applications, e.g., hyperthermia, diagnosis, cell-labeling and sorting, DNA separation, MRI contrast agents, and drug delivery, have already been demonstrated.[20−26] The combination of magnetic and fluorescent entities may also provide new two-in-one multifunctional nanomaterials with a broad range of both potential diagnostic and therapeutic applications.[27]

For tissue engineering approaches, the use of magnetic nanoparticles is emerging as a potential target, diagnostic, and therapeutic agent. It has been reported that magnetic

Received: August 17, 2011
Revised: October 21, 2011
Published: October 27, 2011

ACS Publications © 2011 American Chemical Society

nanoparticles could be coupled to cells and used to target these labeled cells by an external magnetic field at the desired site in the body.[28] The migration of the labeled cells after implantation can be detected noninvasively using MRI.[29] In addition, various proteins, growth factors, and so forth could be bound to these nanoparticles that might be delivered to the damaged tissue, where they would play a role in tissue development and repair.[30] The use of magnetite (Fe_3O_4) magnetic nanoparticles to enhance cell seeding in tissue engineering scaffolds via a magnetic field has also been reported recently.[31,32] A few studies also investigated the influence of magnetic nanoparticles in the presence and absence of a growth factor on cellular proliferation and differentiation, following long-term incubation. Very recently, Park and co-workers reported that unmodified iron oxide nanopartices in the presence of free nerve growth factor (NGF) synergistically promoted the neurite outgrowth of PC12 cells.[33] Shimizu and co-workers recently demonstrated that glutaraldehyde-activated magnetic beads of 250 nm average diameter covalently bonded to NGF or a brain-derived neurotrophic factor (BDNF) promoted the neurite outgrowth of embryonic chick dorsal root ganglia neurons. In addition, these nanoparticles coated with both NGF and BDNF promoted the neurite outgrowth of PC12h cells. However, in all the cases mentioned above, the observed biological effect was similar, or even lower, than that of the soluble-free NGF, BDNF, or both, respectively.[34]

In the present study, NOM cells were derived from the olfactory mucosa of adult rats. Olfactory mucosa is a potential source of olfactory ensheathing cells and multipotent neural stem cells, which have been used in autologous transplantation therapies for the treatment of degenerative or traumatic conditions of the central nervous system, such as Parkinson's disease or spinal cord injury.[35−37] There are several potential advantages of NOM transplants. These cells are easily obtained through simple nasal biopsies, making them attractive for autologous transplantation and thus eliminating the issue of rejection. Moreover, the neurons and the sustentacular cells within the NOM are able to renew themselves constantly during their life span.

The present article describes a method of preparing new bFGF-conjugated fluorescent maghemite (γ-Fe_2O_3) nanoparticles that induce the significant stabilization of the bFGF through its covalent or physical immobilization to the nanoparticle's surface.[38,39] The NOM cells were cultured in suspension on biodegradable, positively charged MCs in the presence of nonconjugated or bFGF-conjugated nanoparticles, or the free factor. The floating cells/nonconjugated, conjugated, or free bFGF/MCs aggregates were then seeded in a viscous gel (NVR-gel[40]). In this study, we describe the effect of the conjugation of the bFGF to fluorescent γ-Fe_2O_3 nanoparticles on the migration, growth, and differentiation of the NOM cells, compared to the nonconjugated fluorescent nanoparticles and different concentrations of the free bFGF.

MATERIALS AND METHODS

Materials. The following analytical-grade chemicals were purchased from commercial sources and used without further purification: ferrous chloride tetrahydrate, hydrochloric acid (1 M), sodium hydroxide (1 M standard solution), sodium chloride, sodium nitrite, dimethyl sulfoxide (DMSO), gelatin from porcine skin, human serum albumin (HSA), rhodamine B isothiocyanate (RITC), divinyl sulfone (DVS), triethylamine (TEA), Triton X-100, and D-glucose from Sigma (Israel); recombinant human basic fibroblast growth factor (bFGF) from PeproTech (Israel); midi MACS magnetic columns from Miltenyi Biotec GmbH (Germany); bicarbonate buffer (BB, 0.1 M, pH 8.4), phosphate-buffered saline (PBS free of Ca^{2+} and Mg^{2+}, 0.1 M, pH 7.4), Dulbecco's modified eagle medium-nutrient mixture F-12 (DMEM-F12), fetal calf serum (FCS), gentamycine, glutamine, hepes, and trypsin-EDTA solution (0.25%) from Biological-Industries (Israel); human bFGF ELISA kit Quantikine HS from Biotest (Israel); tissue culture plates and 35 cm culture plates from JET BioFiL (Israel); chitosan powder microcarriers (MCs) from Medovent GmbH (Germany). Water was purified by passing deionized water through an Elgastat Spectrum reverse osmosis system (Elga, High Wycombe, UK). NVR-gel was obtained from NVR Ltd. (Neuro-Vascular Reconstruction Laboratories, Ness Ziona, Israel).[40] This gel is composed of 0.7% cross-linked hyaluronic acid enriched with 30 mg/mL laminin (Sigma, St. Louis, MO, USA). The culture medium used in this study was composed of 90% DMEM-F12, 10% FCS, 6 g/L D-glucose, 2 nM glutamine, and 25 μg/mL gentamycine.

Synthesis of γ-Fe_2O_3 Nanoparticles Containing the Fluorescent Probe Rhodamine (R-γ-Fe_2O_3). γ-Fe_2O_3 nanoparticles were prepared by the nucleation and growth of a maghemite layer onto gelatin/iron oxide nuclei, according to the description in ref 24. R-γ-Fe_2O_3 nanoparticles of 15.0 ± 1.1 diameter were prepared by a similar procedure, substituting the gelatin for RITC-conjugated gelatin. Briefly, RITC was covalently conjugated to gelatin by adding 0.5 mL of DMSO containing 5 mg of RITC to 20 mL of aqueous gelatin in solution (1%). The pH of the aqueous solution was then raised to 9.5 by carefully adding a NaOH aqueous solution (1 N). The solution was then shaken for 1.0 h at 60 °C. The RITC-conjugated gelatin solution was then dialyzed at 60 °C against water to remove the excess of unbound RITC. The volume of the solution was then adjusted to 80 mL by adding water, after which the synthesis was continued, as described in our previous publication.[41]

Synthesis of the DVS-Derivatized R-γ-Fe_2O_3 Nanoparticles. R-γ-Fe_2O_3 nanoparticles were functionalized with activated double bonds via the interaction between the primary amine groups of the gelatin coating of the R-γ-Fe_2O_3 nanoparticles and DVS. Briefly, 12 μL of DVS were added to 1 mL of the R-γ-Fe_2O_3 nanoparticles dispersed in BB (3 mg/mL, pH 8.4). TEA was then gradually added until a pH of 10.5 was reached. The reaction mixture was then shaken at 60 °C for 18 h. The formed DVS-derivatized R-γ-Fe_2O_3 nanoparticles were then washed from excess DVS with BB using the high-gradient magnetic field (HGMF) technique.[24]

Covalent Conjugation of the bFGF to the DVS-Derivatized R-γ-Fe_2O_3 Nanoparticles. The covalent conjugation of bFGF to the R-γ-Fe_2O_3 nanoparticles was accomplished via the interaction of the amino and/or hydroxyl groups of the growth factor with the activated double bonds on the nanoparticle's surface, via the Michael addition reaction. Briefly, 125 μL of a bFGF PBS solution (0.4 mg/mL, pH 7.4) were added to 125 μL of the DVS-activated nanoparticles dispersed in BB (4 mg/mL, pH 8.4) at a [Nanoparticles]/[bFGF] weight ratio of 10. The reaction mixture was then shaken at room temperature for 18 h. Blocking of the residual double bonds was then accomplished by adding 1% glycine (w/v) and then shaking for an additional hour. The obtained R-γ-Fe_2O_3-bFGF nanoparticles were then washed from non-magnetic waste with PBS using the HGMF technique. A similar

experiment was also performed substituting the weight ratio [Nanoparticles]/[bFGF] of 10 for 50, by substituting the 125 μL of the bFGF solution for 25 μL.

HSA Coating on the R-γ-Fe_2O_3 Nanoparticles. Coating of the R-γ-Fe_2O_3 nanoparticles with HSA was accomplished by precipitation of this protein onto the surface of the fluorescent maghemite nanoparticles. Briefly, 1 mL of a HSA BB solution (10 mg/mL, pH 8.4) was added to 33 mL of the R-γ-Fe_2O_3 nanoparticles dispersed in BB (4 mg/mL, pH 8.4). The pH was then raised to 9.5 by adding carefully a NaOH aqueous solution (1 N). The reaction mixture was shaken at pH 9.5 and 60 °C for 24 h, and then cooled gradually to room temperature. The obtained HSA-coated R-γ-Fe_2O_3 nanoparticles were then washed with BB from nonmagnetic waste using the HGMF technique.

Physical Conjugation of the bFGF to the HSA-Coated R-γ-Fe_2O_3 Nanoparticles. bFGF was physically conjugated to the HSA-coated R-γ-Fe_2O_3 nanoparticles by adding 125 μL of a bFGF PBS solution (0.4 mg/mL, pH 7.4) to 125 μL of the HSA-coated R-γ-Fe_2O_3 nanoparticles dispersed in BB (4 mg/mL, pH 8.4) at a [Nanoparticles]/[bFGF] weight ratio of 10. The reaction mixture was then shaken at room temperature for 18 h. The obtained R-γ-Fe_2O_3~bFGF (~ is the symbol for the physical conjugation of bFGF to the nanoparticles) were then washed from nonmagnetic waste with PBS using the HGMF technique. A similar experiment was also performed substituting the weight ratio [Nanoparticles]/[bFGF] of 10 for 50, by substituting the 125 μL of the bFGF solution for 25 μL.

Binding Yield and Bound Concentration of the bFGF to the R-γ-Fe_2O_3 Nanoparticles. The concentration of the bFGF conjugated to the fluorescent maghemite nanoparticles was determined by measuring the unbound bFGF with an ELISA kit (Human bFGF Quantikine HS, Biotest Israel) and subtracting it from the initial concentration. The binding yield was calculated by multiplying the ratio between the concentration of the bound factor to the initial concentration by 100. The reported values are an average of at least three measurements of each sample.

bFGF Leakage Extent. The leakage of bFGF, conjugated covalently or physically to the R-γ-Fe_2O_3 nanoparticles, into PBS containing 4% HSA was evaluated using the following procedure: R-γ-Fe_2O_3-bFGF or R-γ-Fe_2O_3~bFGF nanoparticles dispersed in PBS containing 4% HSA (2 mg/mL, pH 7.4) were shaken at room temperature for 24 h. Then, the bFGF-conjugated nanoparticles were removed from the supernatant using the HGMF technique and the concentration of bFGF in the filtrate was measured by the human bFGF ELISA kit.

Characterization of the Functional Nanoparticles. Transmission electron microscopy (TEM) pictures were obtained with a FEI Tecnai C2 Biotwin electron microscope with 120 kV accelerating voltage. Samples for TEM were prepared by placing a drop of the diluted sample on a 400-mesh carbon-coated copper grid. The average size and size distribution of the dry particles were determined by measuring the diameter of more than 200 particles with image analysis software, *AnalySIS Auto* (Soft Imaging System GmbH, Germany). The hydrodynamic diameter and size distribution of the nanoparticles dispersed in the aqueous phase were measured using a submicrometer particle analyzer, model N4 Plus, Coulter Electronics, England. Magnetic measurements were performed at room temperature, by an Oxford Instrument vibrating sample magnetometer (VSM, Oxford Instruments, UK).

Surgical Procedure for the Dissection of Adult Rat NOM. The NOM cells were derived from the olfactory mucosa of Lewis inbred rats (Harlan, Israel). Adult Lewis rats (250 g) were nasally infused with 0.7% Triton X-100 to both nostrils 4 days prior to their scarification. The Triton X-100 caused moderate damage to the neuroepithelium, which enhanced the active NOM tissue reconstruction by basal round and horizontal precursor cells. Prior to the NOM dissection, cardiac perfusion of the rats was made with 60 mL of saline. All the experiments were carried out under the Animals' Care and Use Committee, which is recognized by the Israeli authorities for animal experimentation.

Cultivation of the NOM Cells in the Presence of the Nonconjugated, Conjugated, or Free bFGF. The dissected NOM tissue was fragmented, separated from its bones under a stereomicroscope, and washed several times with an ice-cold culture medium. The NOM fragments were then enzymatically dissociated with a trypsin−EDTA solution (0.25%) for 30 min, washed with a culture medium, and adapted to a 1×10^7 cells/mL culture medium in each 24-well culture plate. Round coverslips were inserted per well, and each well received 0.2 mL of 2% (w/v) chitosan MCs (4 mg) suspended in PBS. Concomitantly, each well received 10 μL (10 μg bound bFGF/well) of the R-γ-Fe_2O_3-bFGF nanoparticles dispersed in PBS (2 mg/mL, pH 7.4). The mixture containing the R-γ-Fe_2O_3-bFGF nanoparticles (0.02 mg) and the MCs (4 mg), [0.5% ($w_{nanoparticles}/w_{MCs}$)], was incubated at 37 °C for 1.0 h. Subsequently, 100 μL of the NOM cell suspension (1×10^6 cells/well) was added and incubated with the R-γ-Fe_2O_3-bFGF nanoparticles/MCs aggregates at 37 °C for an additional 1.0 h. Then, each well received 1.0 mL of culture medium and incubated for additional 5 days. 50 μL of the formed floating cells/R-γ-Fe_2O_3-bFGF nanoparticles/MCs aggregates of each well were then transferred and seeded into 1 mL of the NVR-gel in 35 mm culture dishes. Twenty-four hours after the cultivation, 1.0 mL of the culture medium was added to each culture dish and changed every 4.0 days. Similar experiments were also performed in the presence of the R-γ-Fe_2O_3, R-γ-Fe_2O_3~bFGF nanoparticles and different concentrations of the free bFGF, e.g., the same concentration as the conjugated one, 5 and 10 times higher (0.38, 1.9, and 3.8 μg/well, respectively). The cultures were examined daily under an Olympus IX70 phase contrast microscope (Japan).

The surface morphology of the cells/nanoparticles/MCs aggregates was characterized with a scanning electron microscope (SEM) model FEI Quanta 250 FEG (Oregon, USA). For this purpose, samples were fixed in 2.5% glutaraldehyde in a PBS solution for 1.0 h at room temperature and then washed three times with PBS. The fixed samples were dehydrated in series of 50%, 70%, 80%, 90%, and 100% ethanol/water solutions (v/v) for 10 min each. The residual ethanol was removed using series of 50%, 75%, and 100% (×3) Freon/ethanol solutions (v/v), for 10 min each. Finally, the samples were left for a few seconds to dry at room temperature. The dried samples were mounted on aluminum stubs and sputter-coated with gold in vacuum for 4 min before viewing.

Cellular Uptake Study. The cellular uptake and internalization of the R-γ-Fe_2O_3-bFGF nanoparticles in the NOM cells was studied by acquiring a time series of Z-stacks optical cross-sectional images of the NOM cells. At different time intervals of the cultivation, the cells were washed extensively with PBS and fixed in 4% paraformaldehyde for 15 min at room temperature. After repeated rinsing in PBS, cells in culture on cover glasses

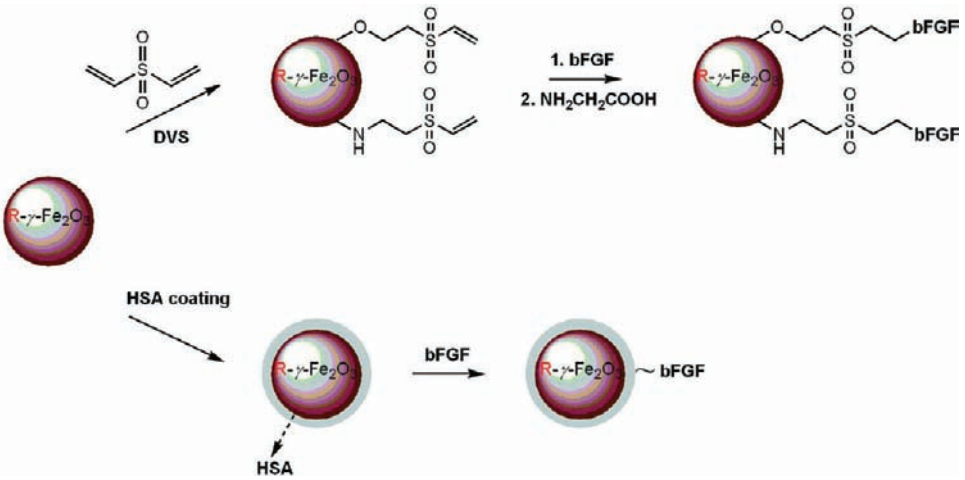

Figure 1. Scheme illustrating the covalent (A) and physical (B) conjugation of bFGF to the R-γ-Fe_2O_3 nanoparticles (− and ~ are symbols for the covalent and physical binding of the bFGF to the nanoparticles, respectively).

underwent nuclear staining and mounting with DAPI-fluoromount-G (catalog #0100−20, SouthernBiotech). The slides were then observed with a LSM 510 fluorescence confocal laser scanning microscope (Zeiss, USA) to obtain the Z-stacks of the cells. Images were captured using the microscope and processed using a computer-based programmable image analyzer *Imaris 6.15* (Zeiss, USA). Each stack focused progressively to a depth of 1.4 μm within the cell and a series of 20 stacks were obtained per cell. The stacks focused on the axial position of the fluorescent tagged nanoparticles, enabling visualization of the location of these particles within the NOM cells. Nuclei are visible in blue due to the DAPI staining (excitation at 359 nm and emission at 457 nm); red fluorescence was derived from the nanoparticles (excitation at 550 nm and emission at 573 nm). Light microscope images were obtained with a Olympus BX60F5 microscope (Eisenberg Bros., Israel).

Immunocytochemistry. Cell cultures were washed three times with PBS, fixed in 4% paraformaldehyde for 15 min at room temperature, and then washed again three times with PBS. The cells were then permeabilized with 0.1% Triton X-100 in PBS for 12 min, and then washed three times with PBS. The cells were then incubated with background buster (to avoid nonspecific staining) for 1.0 h at room temperature. After washing three times with PBS, the cells were incubated overnight at 4 °C with the appropriate primary antibodies in a PBS solution. The following primary antibodies were used: rabbit antitubulin β3, clone EP1331Y (β3Tub, neuronal marker, 1:200, catalog #NB110−576−10, Novus Biologicals); rabbit antineurofilament medium (NF, neuronal marker, 1:400, catalog #NB300−133, Novus Biologicals), mouse anti-S100B (glia marker, 1:80, catalog # DM111−05, Acris Antibodies), and mouse antinestin, clone rat-401 (neurofilament protein, neuronal precursor marker, 1:100, catalog #sc-33677, Santa Cruz Biotachnology). The cultures were subsequently washed three times with PBS and were incubated overnight at 4 °C with the appropriate dye-conjugated secondary antibodies (DyLight 649-conjugated donkey antimouse IgG, 1:200, catalog #715−495−151, Jackson ImmunoResearch; DyLight 488-conjugated donkey antirabbit IgG, 1:200, catalog #711−485−152, Jackson ImmunoResearch), and were washed again three times with PBS. Control experiments were performed similarly, but in the absence of the primary antibodies. Finally, the nuclei of the cells were stained and mounted with DAPI-fluoromount-G. All of the images were observed with a NIKON 90i microscope (Japan) and processed using the *Cell-R* software under the same conditions (exposure time and magnification). To assess the percent of the differentiated cells, we counted only the cells that were stained in both their nuclei and cytoplasm, by DAPI dye and by the specific marker antibodies. The cell % which was positively stained by a specific marker antibody was calculated relative to all the DAPI stained nuclei. The reported values are an average of measurements performed on six randomly, nonoverlapping fields of each triplicate-tested culture.

Statistical Analysis. Statistical analysis was performed by the Student's *t*-test. The results are expressed as a mean ± standard deviation (SD). $P < 0.05$ was considered to be statistically significant.

RESULTS AND DISCUSSION

Characterization of the Nonconjugated and the bFGF-Conjugated R-γ-Fe_2O_3 Nanoparticles. Uniform fluorescent γ-Fe_2O_3 nanoparticles were prepared by nucleation followed by the controlled growth of γ-Fe_2O_3 thin films onto the gelatin-RITC/iron oxide nuclei, as described in our previous publications.[41] The main advantage of these fluorescent nanoparticles is due to the fact that the fluorescent dye is covalently encapsulated within the nanoparticles and not surface bound, as in the common fluorescent nanoparticles. Thus, surface properties such as zeta potential and surface-bound ligand capacity of the nanoparticles are retained.

Figure 1 describes the general approach through which the covalent and physical immobilization of bFGF onto the surface of the R-γ-Fe_2O_3 nanoparticles have been performed. The R-γ-Fe_2O_3 nanoparticles contain gelatin within and on the surface of the nanoparticles.[41] The surface gelatin provides functional groups, e.g., primary amines and hydroxyls, through which functionalization of these nanoparticles with activated double bonds, via the Michael addition reaction, was accomplished with excess DVS. The residual activated double bonds of the DVS-derivatized R-γ-Fe_2O_3 nanoparticles were then used for covalent binding, via the Michael addition reaction of the bFGF to the surface of the R-γ-Fe_2O_3 nanoparticles. Blocking of the remaining double bonds was then performed with glycine. bFGF, besides its covalent binding to the DVS-derivatized

dx.doi.org/10.1021/bc200454k | *Bioconjugate Chem.* 2011, 22, 2600−2610

R-γ-Fe_2O_3 nanoparticles, was also physically attached to the HSA-coated R-γ-Fe_2O_3 nanoparticles. This physical conjugation is based on the fact that the albumin is a carrier protein with high affinity to various exogenous and endogenous compounds, e.g., thrombin, factor VIIa, and so forth.[42,43] Indeed, leakage of both the covalently and physically bound bFGF into PBS containing 4% HSA was not detected by the bFGF ELISA kit.

Figure 2 presents the dry (A) and hydrodynamic (B) diameters and size distributions of the R-γ-Fe_2O_3 nanoparticles

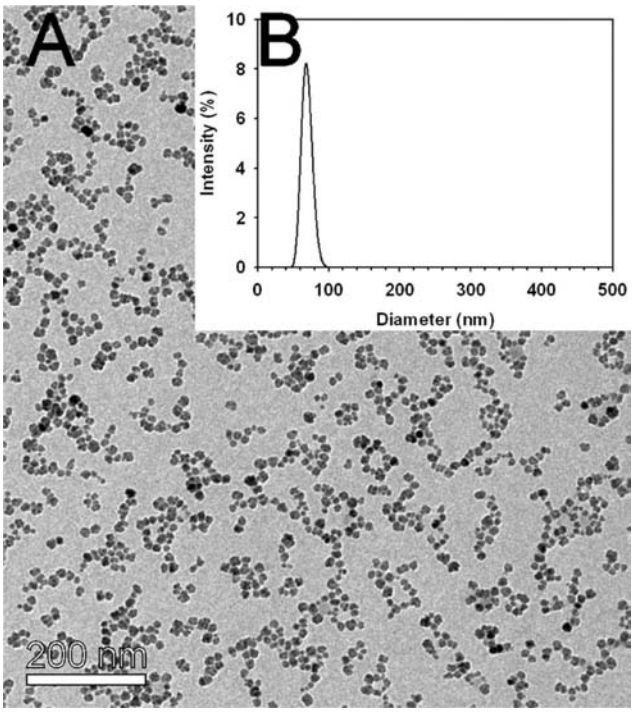

Figure 2. TEM image (A) and size histogram (B) of the R-γ-Fe_2O_3 nanoparticles.

as measured by TEM images and light scattering, respectively. The dry diameter is 15.0 ± 1.1 nm, while the hydrodynamic diameter is 70.0 ± 15 nm. The difference in the diameter measured by TEM and light scattering is due to the fact that the second method also takes into account the surface-adsorbed solvent (water) molecules. The measured dry and hydrodynamic diameters and size distributions of the bFGF-conjugated nanoparticles were slightly higher than those of the nonconjugated ones, e.g., 18.3 ± 1.4 and 22.0 ± 2.1 nm for the dry R-γ-Fe_2O_3-bFGF and R-γ-Fe_2O_3~bFGF nanoparticles, respectively, and 93.0 ± 11 and 106 ± 14 nm for the hydrodynamic R-γ-Fe_2O_3-bFGF and R-γ-Fe_2O_3~bFGF nanoparticles, respectively. Both the nonconjugated and the bFGF-conjugated nanoparticles possess a single population of narrow size distribution, as shown in Figure 2. The immobilization yield of the covalent conjugation of the bFGF to the R-γ-Fe_2O_3 nanoparticles was similar to that of the physical one for both weight ratios of [Nanoparticles]/[bFGF], 10 and 50, as demonstrated in Table 1. For example, for the weight ratio of 10, the covalent and physical immobilization yields were 95.4% and 96.9%, respectively. These high binding yield values may indicate that, in addition to the covalent binding, physical adsorption of the bFGF onto the surface of the nanoparticles may also be involved.[44] Table 1 also shows, as expected, that, for both immobilization types, by decreasing the weight ratio

Table 1. Influence of the Weight Ratio [Nanoparticles]/[bFGF] on the Conjugation Yield and the Concentration of the bFGF Conjugated to the R-γ-Fe_2O_3 Nanoparticles[a]

	conjugation yield (weight %)		[bound bFGF] [$\mu g_{(bFGF)}$/ $mg_{(nanoparticles)}$]	
[nanoparticles]/[bFGF] (w/w)	covalent	physical	covalent	physical
10	95.4	96.9	95.4	96.9
50	92.3	94.4	18.5	18.9

[a]The calculation of the conjugation yield and concentration was accomplished as described in the experimental section.

[Nanoparticles]/[bFGF] the concentration of the bFGF bound to the R-γ-Fe_2O_3 nanoparticles increases, e.g., at the weight ratios of 50 and 10, the covalently bound bFGF concentrations are 18.5 and 95.4 (μg/mg), respectively. On the basis of the above results, we chose to continue this study at [Nanoparticles]/[bFGF] weight ratio of 10.

Characterization of the Interaction Between the Chitosan MCs and the bFGF-Conjugated Nanoparticles. The fluorescence microscope image shown in Figure 3

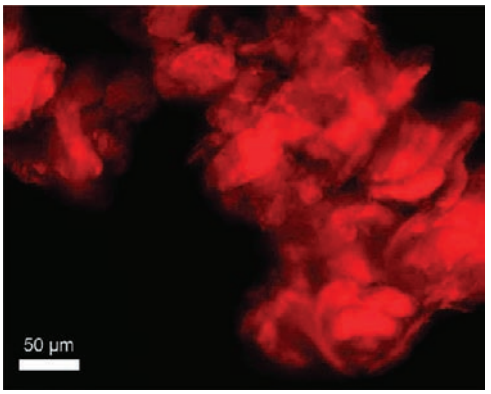

Figure 3. Fluorescence microscopy images of the chitosan MCs interacted with the R-γ-Fe_2O_3-bFGF nanoparticles. Red single staining was obtained by adding the R-γ-Fe_2O_3-bFGF nanoparticles dispersed in PBS to the MCs suspended in PBS, as described in the Materials and Methods section.

illustrates by the red staining the adherence of the R-γ-Fe_2O_3-bFGF nanoparticles to the chitosan MCs. This electrostatic interaction occurs immediately after the addition of the R-γ-Fe_2O_3-bFGF nanoparticles to the MCs suspension. It should be noted that the same behavior was also observed when substituting the R-γ-Fe_2O_3-bFGF nanoparticles for the R-γ-Fe_2O_3~bFGF nanoparticles or the nonconjugated R-γ-Fe_2O_3 nanoparticles.

Our previous study showed that the $M(H)$ curve of the R-γ-Fe_2O_3 nanoparticles has no hysteresis loop, and possesses a saturation magnetization of 55 emu/g.[45] Zero field cooled–field cooled (ZFC-FC) measurements of these nanoparticles exhibit a blocking temperature (T_B) at ca. 275 K, indicating the superparamagnetic behavior of these nanoparticles.[46] Figure 4 presents the magnetization curves at room temperature of the R-γ-Fe_2O_3-bFGF/MCs aggregates containing 0.5 (A) and 0.25 (B) % ($w_{(nanoparticles)}/w_{MCs}$) of the R-$\gamma$-$Fe_2O_3$-bFGF nanoparticles (0.02 or 0.01 mg nanoparticles/4.0 mg MCs). This figure illustrates that both $M(H)$ plots reach magnetic saturation around 2000 Oe. The saturation magnetizations of

dx.doi.org/10.1021/bc200454k | Bioconjugate Chem. 2011, 22, 2600–2610

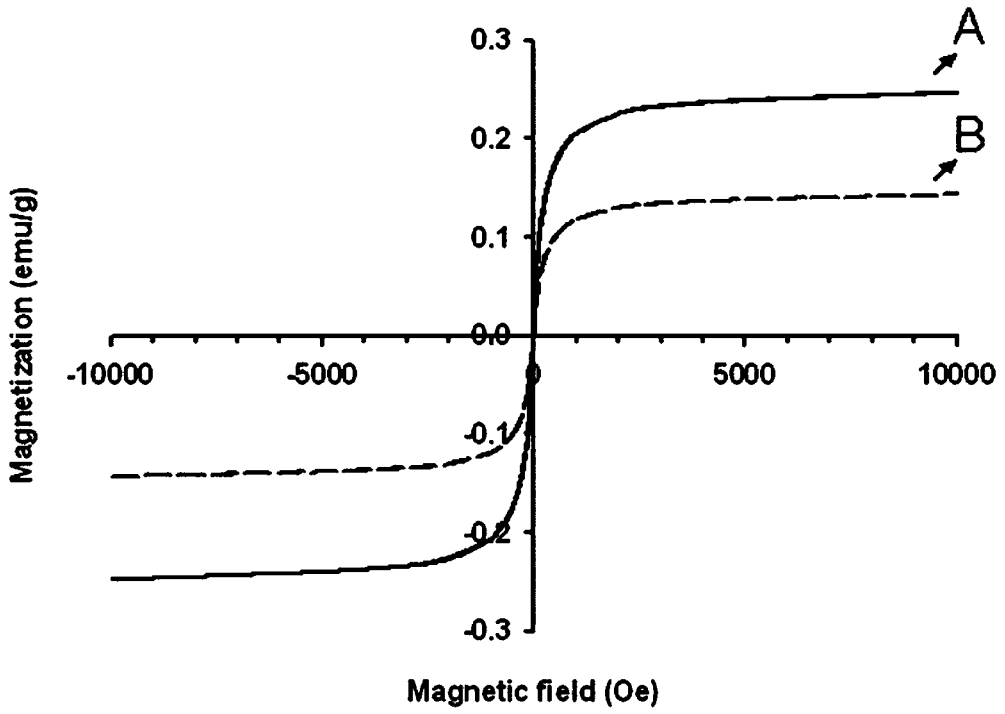

Figure 4. Magnetization curves at room temperature of the R-γ-Fe_2O_3-bFGF/MCs aggregates containing 0.5% (A) and 0.25% (B) ($w_{(nanoparticles)}/w_{MCs}$) of the R-$\gamma$-$Fe_2O_3$-bFGF nanoparticles.

the R-γ-Fe_2O_3-bFGF/MCs aggregates containing 0.5% (A) and 0.25% (B) nanoparticles are 0.26 and 0.14 emu/g, respectively. The difference in the magnetization extent of the R-γ-Fe_2O_3-bFGF/MCs aggregates is probably attributed to the different concentrations of the R-γ-Fe_2O_3-bFGF nanoparticles attached to the MCs. The higher the concentration, the higher the saturation magnetization is. A relatively simple and convenient way to remove the R-γ-Fe_2O_3-bFGF/MCs aggregates from the aqueous PBS continuous phase by a magnetic field is shown in Figure 5. Due to the binding of the R-γ-Fe_2O_3-bFGF nanoparticles to the MCs, the nanoparticles/MCs aggregates become magnetic and easily removed from the aqueous continuous phase by a simple magnet.

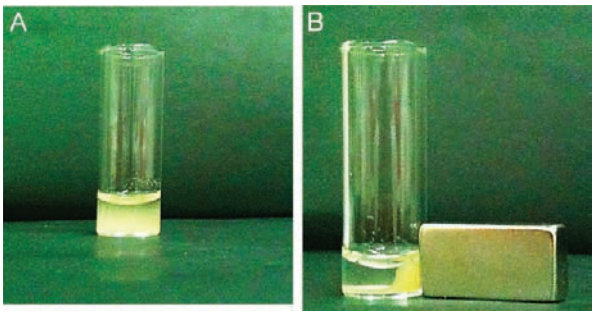

Figure 5. Magnetic MCs dispersed in PBS, before (A) and after (B) applying a magnetic field. The R-γ-Fe_2O_3-bFGF nanoparticles/MCs aggregates were prepared by addition of the R-γ-Fe_2O_3-bFGF nanoparticles to the MCs suspension in PBS, according to the Methods and Materials section.

Influence of the bFGF Conjugation on the Growth of the NOM Cells. In general, the NOM cells were grown in the first stage for a week in suspension attached to the MCs in the presence of the nonconjugated or bFGF-conjugated nanoparticles or the free factor. Subsequently, the formed floating cells/nonconjugated, conjugated, or free bFGF/MCs aggregates were transferred and seeded in the NVR-gel. The cell/MC culture method used in this study mainly served the purpose of establishing a high concentration of NOM cell cultures of long-term viability compared to other standard culture methods.[47,48] The NVR-gel, a transparent and biocompatible semisolid matrix, is composed of cross-linked hyaluronic acid containing the adhesive molecule laminin.[40] This gel has been reported to form a desirable supporting environment for cell attachment, growth, and differentiation, particularly for long-term cultivation.[40] The unique attribute of elasticity of this gel enables its use for clinical applications of tissue engineering, either by its direct implantation or by incorporation into an appropriate scaffold at the site of an injured tissue.[49]

Figure 6 demonstrates by typical phase-contrast microscope images the NOM cell migration and growth from the cells/nonconjugated or bFGF-conjugated nanoparticle/MC aggregates and from the cells/free bFGF/MCs aggregates in the NVR-gel, immediately (A) and 7.0 days after the cultivation in the NVR-gel (B–G). Figure 6A, corresponding to the cells/R-γ-Fe_2O_3-bFGF nanoparticles/MC aggregates immediately after the cultivation in the NVR-gel, reveals only MCs in the background, which means that the migration of the NOM cells to the NVR-gel had not yet occurred. Similar images were also observed when the R-γ-Fe_2O_3-bFGF nanoparticles in the cells/R-γ-Fe_2O_3-bFGF nanoparticles/MC aggregates were replaced with R-γ-Fe_2O_3~bFGF or nonconjugated R-γ-Fe_2O_3 nanoparticles. Figure 6B–D exhibit a significant difference in the amount of the migrated/proliferated NOM cells in the NVR-gel 7.0 days after cultivation. The difference in cell migration and growth depends on the type of R-γ-Fe_2O_3 derivative. The lowest amount of migrated/proliferated NOM cells in the NVR-gel was observed in the presence of the nonconjugated R-γ-Fe_2O_3 nanoparticles (Figure 6B), while a significantly higher amount of migrated/proliferated cells were observed in

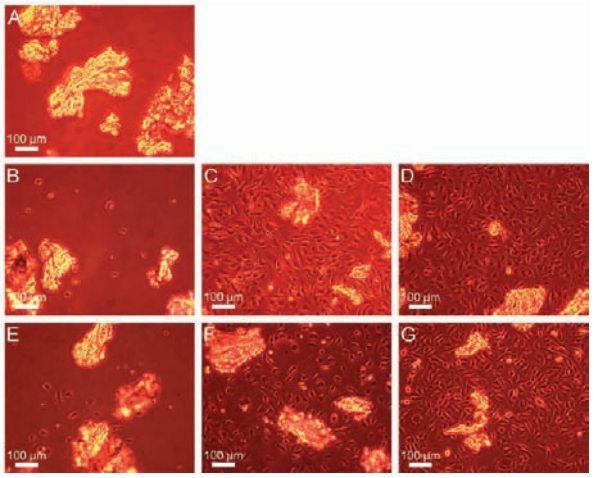

Figure 6. Phase contrast microscope images illustrating the effect of the conjugated and free bFGF on the migration and growth of the NOM cells from the cells/nonconjugated or bFGF conjugated nanoparticles/MC aggregates (A–D) and from the cells/free bFGF of different concentrations/MC aggregates (E–G) in the NVR-gel, immediately (A) and 7 days after cultivation in the NVR-gel (B–G). (A) exhibits the effect of the nonconjugated and bFGF conjugated R-γ-Fe_2O_3 nanoparticles immediately after cultivation, (B) the effect of the nonconjugated R-γ-Fe_2O_3 nanoparticles 7 days after cultivation, (C,D) the effect of the R-γ-Fe_2O_3-bFGF and R-γ-Fe_2O_3~bFGF nanoparticles 7 days after cultivation, respectively. The effect of the same concentration of the free factor as that of the conjugated bFGF, 5 and 10 times higher, 7 days after cultivation in the NVR-gel, is illustrated in images (E,F,G), respectively.

the presence of the R-γ-Fe_2O_3-bFGF (Figure 6C) or R-γ-Fe_2O_3~bFGF (Figure 6D) nanoparticles. These results indicate that the conjugation of the bFGF to the nanoparticles enhances the migration/proliferation rates of the cells in the NVR-gel. It should also be noted that both the covalently (Figure 6C) and the physically (Figure 6D) conjugated bFGF nanoparticles induced a quite similar number of migrated/proliferated cells. The effect of the bFGF conjugation to the nanoparticles on NOM cell migration/proliferation compared to that of the free factor at the same concentration, 5 and 10 times higher, is illustrated in Figure 6E,F, and G, respectively. These figures clearly show that the number of NOM cells that had migrated/proliferated in the NVR-gel was substantially higher in the presence of the conjugated bFGF (Figures 6C,D). Only in the presence of a 10× higher free bFGF concentration (Figures 6G) was the number of migrated/proliferated NOM cells similar to those of the conjugated factor. This observation may due to the fact that the conjugation of bFGF to the nanoparticles increases its stability against inhibitors and proteolytic enzymes present in the culture, and thus prolongs its activity, compared to that of the free factor. A similar stabilization effect was reported previously by us for thrombin,[38] glial cell-derived neurotrophic factor,[39] TRAIL,[50] factor VIIa,[51] and methotrexate[52] conjugated to γ-Fe_2O_3 nanoparticles. Long-term stability of thrombin, TRAIL, and methotrexate conjugated to the γ-Fe_2O_3 nanoparticles compared to the free ones was also previously demonstrated.[38,50,52]

Figure 7 illustrates by SEM images the attached (A) and the migrated/proliferated (B) NOM cells from the cells/R-γ-Fe_2O_3-bFGF nanoparticles/MC aggregates to the NVR-gel, 7.0 days after cultivation in the NVR-gel. This picture presents the NOM cells that remained on the surface of the MCs (A) and those that migrated/proliferated in the NVR-gel, forming a network of bipolar cells (B).

Figure 8 illustrates by typical phase-contrast microscope images the migration/proliferation of the NOM cells from the cells/R-γ-Fe_2O_3 nanoparticles/MC aggregates (A) and from the cells/R-γ-Fe_2O_3-bFGF nanoparticles/MC aggregates (B) 24.0 days after cultivation in the NVR-gel. This figure shows that, in the presence of the nonconjugated R-γ-Fe_2O_3 nanoparticles/MC aggregates (Figure 8A), a relatively small number of the NOM cells migrated/proliferated in the NVR-gel. In addition, the cells that migrated/proliferated in the NVR-gel were flat, resembled fibroblasts, and seemed not to divide intensively. Contrarily, in the presence of the R-γ-Fe_2O_3-bFGF nanoparticles/MC aggregates (Figure 8B), a massive amount of mainly tapered bipolar cells migrated/proliferated in the NVR-gel to form an interconnected network. This excessive increase in the number of the tapered bipolar cells is indicative of their intensive multiplication and differentiation.

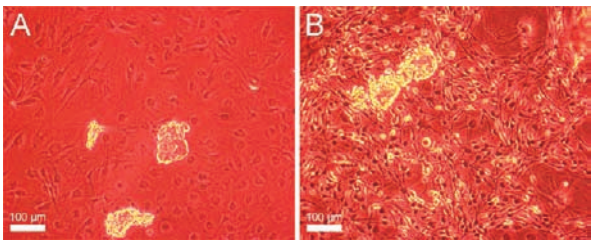

Figure 8. Phase-contrast microscopic images illustrating the migration and growth of the NOM cells from the cells/R-γ-Fe_2O_3 nanoparticles/MC aggregates (A) and from the cells/R-γ-Fe_2O_3-bFGF nanoparticles/MC aggregates (B) 24 days after cultivation in the NVR-gel, as described in the Materials and Methods section.

For a quantitative determination of the effect of the free/conjugated bFGF on the kinetics of the migration/proliferation

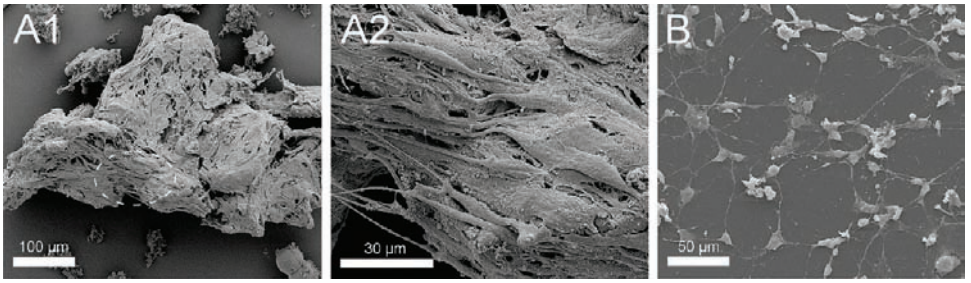

Figure 7. SEM images illustrating the attached (A1,A2) and the migrated/proliferated (B) NOM cells from the cells/R-γ-Fe_2O_3-bFGF nanoparticles/MCs aggregates to the NVR-gel, 7 days after cultivation in the NVR-gel, as described in the Methods and Materials section. A2 represent higher magnifications of the circled region shown in A1.

of the NOM cells in the NVR-gel, the total number of cells dispersed in the NVR-gel was counted, using *ImageJ* software, as shown in Figure 9. This figure presents the total number of

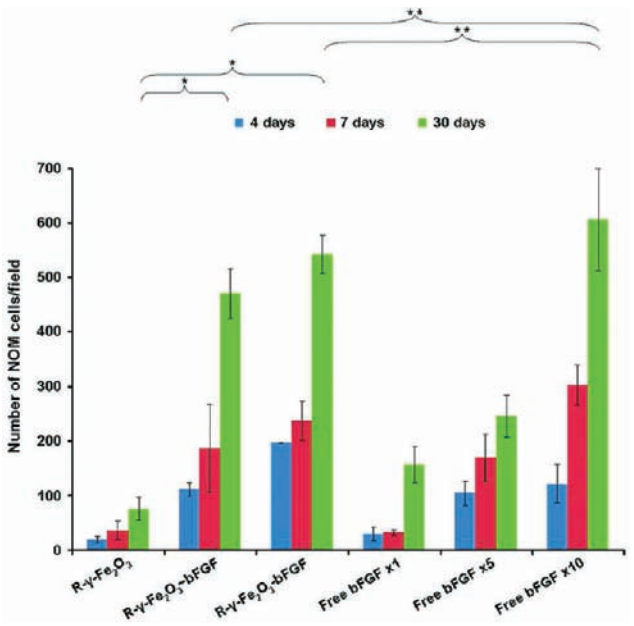

Figure 9. Quantitative analysis of the NOM cells migrated/proliferated from the cells/nonconjugated or bFGF conjugated nanoparticles/MCs aggregates and from the cells/free factor of different concentrations/MC aggregates (i.e., same concentration as the conjugated one, 5, and 10 times higher), 4, 7, and 30 days after cultivation in the NVR-gel, as described in the Materials and Methods section. The reported values are an average of measurements performed on at least three randomly nonoverlapping fields of each triplicate tested culture (* $P < 0.05$; ** $P > 0.05$).

cells migrated/proliferated from the cells/nonconjugated or bFGF-conjugated nanoparticles/MC aggregates and from the cells/free bFGF of different concentrations/MC aggregates to the NVR-gel, 4, 7, and 30 days after cultivation in the NVR-gel. This figure illustrates that the migration/proliferation rates of the NOM cells in the NVR-gel are according to the following order: R-γ-Fe_2O_3-bFGF slightly higher than the R-γ-Fe_2O_3~bFGF ($P > 0.05$), while both are significantly higher than the nonconjugated R-γ-Fe_2O_3 (*$P < 0.05$). For example, 30 days after cultivation in the NVR-gel, the number of cells counted in the presence of the R-γ-Fe_2O_3-bFGF, R-γ-Fe_2O_3~bFGF, and R-γ-Fe_2O_3 nanoparticles was 542 ± 28, 470 ± 37, and 74 ± 14, cells/field, respectively. In addition, Figure 9 also exhibits, as expected, the acceleration in the NOM cell migration/proliferation as the concentration of the free factor increases. However, the cell migration/proliferation rates in the presence of the same concentration of the free factor (free × 1) as the conjugated factor, or even 5 times higher, were lower than that observed for the conjugated factor ($P < 0.05$). Only when the concentration of the free factor was 10 times higher than that of the conjugated factor were similar cell migration/proliferation rates observed (**$P > 0.05$). For example, 30 days after cultivation in the NVR-gel, the number of cells counted in the presence of the covalently conjugated bFGF, free ×1, free ×5, and free ×10 was 542 ± 28, 157 ± 24, 245 ± 31, and 600 ± 67 cells/field, respectively.

Cellular Uptake of the bFGF-Conjugated Nanoparticles by the NOM Cells. Figure 10 demonstrates by

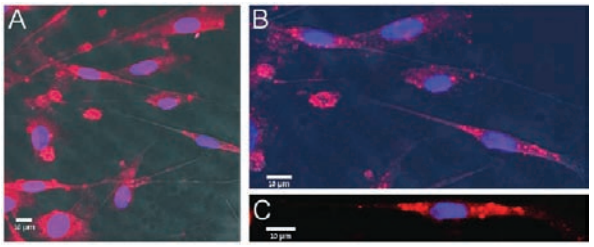

Figure 10. Fluorescence confocal microscopy images showing the cellular uptake and distribution of the R-γ-Fe_2O_3-bFGF nanoparticles in the lysosomes of the migrated/proliferated NOM cells, 7 days after cultivation in the NVR-gel, as described in the Materials and Methods section. (A,B) exhibit combined fluorescence and differential interference contrast (DIC) images; (C) exhibits a fluorescence image. Images (B) and (C) illustrate higher magnification of (A).

fluorescence confocal microscopy images the cellular internalization of the R-γ-Fe_2O_3-bFGF nanoparticles in the migrated/proliferated NOM cells, 7.0 days after cultivation in the NVR-gel. This figure reveals that these nanoparticles were efficiently internalized by endocytosis within the NOM cells, as clearly observed inside the cells as red dots. It is also seen that the nanoparticles were entrapped in the cytoplasm of the cells, mainly in the lysosomes. The internalization of the R-γ-Fe_2O_3-bFGF nanoparticles was also confirmed by Z-stacking confocal microscope images, as shown in the Supporting Information, Figure S1. This figure shows the various sections of a typical NOM cell along its *Z*-axis, and reveals that the majority of the fluorescence from the nanoparticles occurred in the middle of the cell (Figure S1g-l) compared to its top (Figure S1a-f) or bottom (Figure S1m-t), indicating that the nanoparticles are mainly internalized by the cells and not adsorbed on their surface. The bFGF-conjugated nanoparticles were internalized inside the cells, probably via receptor-mediated endocytosis.[53,54] The cellular uptake of these nanoparticles in the NOM cells was also confirmed by Prussian blue iron staining followed by counterstaining with nuclear fast red, as shown in Figure 11.[55] This figure demonstrates by light

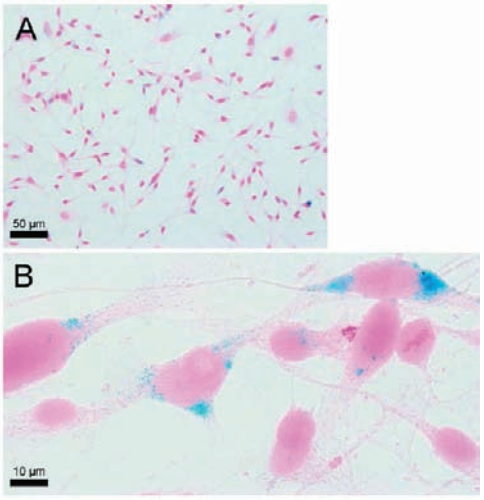

Figure 11. Light microscope images showing the Prussian blue iron staining followed by counterstaining with nuclear fast red of the migrated/proliferated NOM cells from the cells/R-γ-Fe_2O_3-bFGF nanoparticles/MC aggregates to the NVR-gel, 7 days after cultivation in the NVR-gel (A). (B) represents a higher magnification of a specific region shown in (A).

microscopy images the blue granules in the cytoplasm of the cells, indicating the accumulation of the R-γ-Fe_2O_3-bFGF nanoparticles within the NOM cells, 7.0 days after cultivation in the NVR-gel.

Immunofluorescent Staining Illustrating the Effect of the Conjugation of bFGF on the Differentiation of the NOM Cells. Figure 12 illustrates by fluorescent microscopy the immunofluorescent staining images against specific cell markers of the NOM cells migrated/proliferated from the cells/R-γ-Fe_2O_3-bFGF nanoparticles/MCs aggregates (A1,A2,B1,B2) and from the cells/R-γ-Fe_2O_3 nanoparticles/MCs aggregates (C1,C2,D1,D2) to the NVR-gel, 10 days after cultivation in the NVR-gel. The same region of each tested culture was stained with two cell markers, (A:A1,A2) and (C:C1,C2), with anti-S100B and anti-NF, (B:B1,B2) and (D:D1,D2) with antinestin and anti-β3Tub. These figures clearly exhibit that the differentiation and the number of the cells (as illustrated in Figures 6 and 8) migrated/proliferated in the NVR-gel observed in the conjugated bFGF (Figure 12A,B) are significantly higher than that observed for the nonconjugated nanoparticles (Figure 12C,D). Quantitative analysis of the NOM cells grown in the bFGF-conjugated nanoparticles that were stained with anti-S100B and anti-NF (Figure 12A1,A2) revealed that 91.7 ± 3.8% of the cells were positively stained with anti-NF. From these 91.7 ± 3.8% cells, 69.8 ± 3.0% were also positively stained with anti-S100B, while the remaining cells (21.9 ± 3.1%) were not stained by this antibody. 8.3 ± 3.8% of the cells were not stained by any of these two markers. These results indicate that the major part of the cultured NOM cells in the presence of the conjugated bFGF are composed of neuronal cells and/or glia cells. In the parallel cultures (Figure 12B1,B2), which were stained with anti-β3Tub and antinestin, 98.9 ± 1.6% of the cells were positively stained with anti-β3Tub. From these 98.9 ± 1.6% cells, 59.0 ± 2.4% were also positively stained with antinestin, while the remaining cells (39.9 ± 3.9%) were not stained by this antibody. 1.1 ± 1.6% of the cells were not stained with any of these two markers. Altogether, these results demonstrate that the cultured NOM cells on MCs in the presence of the conjugated bFGF are composed mainly from neuronal and/or neuronal precursor cells. On the other hand, Figure 12C1,C2,D1,D2 shows that the number of cells and the differentiation of the NOM cells grown in the presence of the nonconjugated nanoparticles in the NVR-gel were negligible and not suitable for statistical analysis. These results are in good agreement with previous publications showing that bFGF promotes neuronal differentiation of adult and embryonic mouse olfactory epithelium and adult human olfactory epithelium.[56,57]

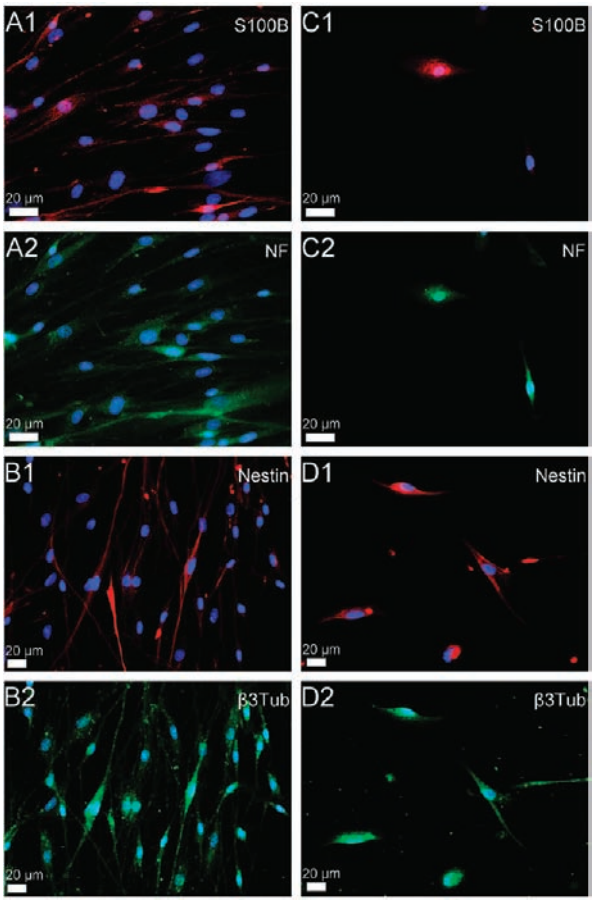

Figure 12. Fluorescence microscopy images illustrating the immunofluorescence staining of the NOM cells migrated/proliferated from the cells/R-γ-Fe_2O_3-bFGF nanoparticles/MC aggregates (A,B) and from the cells/R-γ-Fe_2O_3 nanoparticles/MC aggregates (C,D) to the NVR-gel, 10 days after cultivation in the NVR-gel. Antibodies against the following cell markers: S100B (glia marker, far red, A1,C1), NF (neuronal marker, green, A2,C2), nestin (neuronal precursor marker, far red, B1,D1), and β3Tub (neuronal marker, green, B2,D2) have been used. The nuclei of the NOM cells were dyed with DAPI (blue, A–D). The same region of each tested culture was stained with two cell markers, (A:A1,A2) and (C:C1,C2) with anti-S100B and anti-NF, (B:B1,B2) and (D:D1,D2) with antinestin and anti-β3Tub.

CONCLUSIONS

This manuscript shows that the conjugation of bFGF, either covalently or physically, to the R-γ-Fe_2O_3 nanoparticles significantly enhances the migration, growth, and differentiation of the NOM cells compared to the same concentration, or even 5 times higher, of the free bFGF. These bioactive nanoparticles may therefore be an efficient tool for growth factor delivery. In the future, we plan to extend this study for growth factors other than bFGF, e.g., NGF, VEGF, and so forth, and the use these conjugated factors for *in vivo* tissue engineering. The tissue engineering study will be accomplished, either directly or by incorporation, for the cultured cells/growth factor conjugated R-γ-Fe_2O_3 nanoparticles/MC aggregates into an appropriate scaffold at the site of an injured tissue. The effect of the migrated cells from the MCs on the repair of the examined tissue and the possibility of tracing them noninvasively by MRI will be investigated.

ASSOCIATED CONTENT

Supporting Information

Z-stack fluorescence confocal microscopy images, showing the cellular internalization of the R-γ-Fe_2O_3-bFGF nanoparticles in the migrated NOM cells. This material is available free of charge via the Internet at http://pubs.acs.org.

AUTHOR INFORMATION

Corresponding Author

*E-mail Shlomo.margel@mail.biu.ac.il; Tel 972-3-5318861; Fax 972-3-6355208.

ACKNOWLEDGMENTS

These studies were partially supported by a Minerva Grant (Microscale & Nanoscale Particles and Films). The authors also thank Mrs. Sara Neuman (NVR Research Ltd., Israel) for her

help in this project and Dror Eliaz (Bar-Ilan University, Israel) for his help in obtaining the immunofluorescence images.

REFERENCES

(1) Berthiaume, F., Maguire, T. J., and Yarmush, M. L. (2011) Tissue engineering and regenerative medicine: history, progress, and challenges. *Annu. Rev. Chem. Biomol. Eng. 2*, 403−430.

(2) Ahmed, T. A. E., Dare, E. V., and Hincke, M. (2008) Fibrin: a versatile scaffold for tissue engineering applications. *Tissue Eng., Part B 14*, 199−215.

(3) Lee, K., Silva, E. A., and Mooney, D. J. (2011) Growth factor delivery-based tissue engineering: general approaches and a review of recent developments. *J. R. Soc. Interface 8*, 153−170.

(4) Anitua, E., Sanchez, M., Orive, G., and Andia, I. (2008) Delivering growth factors for therapeutics. *Trends Pharmacol. Sci. 29*, 37−41.

(5) Babensee, J. E., McIntire, L. V., and Mikos, A. G. (2000) Growth factor delivery for tissue engineering. *Pharm. Res. 17*, 497−504.

(6) Bikfalvi, A., Klein, S., Pintucci, G., and Rifkin, D. B. (1997) Biological roles of fibroblast growth factor-2. *Endocr. Rev. 18*, 26−45.

(7) Barraud, P., He, X., Zhao, C., Ibanez, C., Raha-Chowdhury, R., Caldwell, M. A., and Franklin, R. J. (2007) Contrasting effects of basic fibroblast growth factor and epidermal growth factor on mouse neonatal olfactory mucosa cells. *Eur. J. Neurosci. 26*, 3345−3357.

(8) Nishikawa, T., Doi, K., Ochi, N., Katsunuma, S., and Nibu, K. (2009) Effect of intranasal administration of basic fibroblast growth factor on olfactory epithelium. *Neuroreport 20*, 764−769.

(9) Yun, Y. R., Won, J. E., Jeon, E., Lee, S., Kang, W., Jo, H., Jang, J. H., Shin, U. S., and Kim, H. W. (2010) Fibroblast growth factors: biology, function, and application for tissue regeneration. *J. Tissue Eng.* DOI:10.4061/2010/218142. Available from: http://www.sage-hindawi.com/journals/jte/2010/218142/

(10) Timmer, M., Cesnulevicius, K., Winkler, C., Kolb, J., Lipokatic-Takacs, E., Jungnickel, J., and Grothe, C. (2007) Fibroblast growth factor (FGF)-2 and FGF Receptor 3 are required for the development of the substantia nigra, and FGF-2 Plays a crucial role for the rescue of dopaminergic neurons after 6-hydroxydopamine lesion. *J. Neurosci. 27*, 459−471.

(11) Abdipranoto, A., Wu, S., Stayte, S., and Vissel, B. (2008) The role of neurogenesis in neurodegenerative diseases and its implications for therapeutic development. *C.N.S. Neurol. Disord. Drug Targets 7*, 187−210.

(12) Dono, R. (2003) Fibroblast growth factors as regulators of central nervous system development and function. *Am. J. Physiol. Regul. Integr. Comp. Physiol. 284*, 867−881.

(13) Jin, K., LaFevre-Bernt, M., Sun, Y., Chen, S., Gafni, J., Crippen, D., Logvinova, A., Ross, C. A., Greenberg, D. A., and Ellerby, L. M. (2005) FGF-2 promotes neurogenesis and neuroprotection and prolongs survival in a transgenic mouse model of Huntington's disease. *Proc. Natl. Acad. Sci. U.S.A. 102*, 18189−18194.

(14) Shao-hong, L., Shao-xi, C., Bing, L., Kai-wang, M., Zhen-ping, W., and Xiao-kun, L. (2006) In vitro characteristics of poly(lactic-co-glycolic acid) microspheres incorporating gelatin particles loading basic fibroblast growth factor. *Acta Pharmacol. Sin. 27*, 754−759.

(15) Zhang, S., and Uludag, H. (2009) Nanoparticulate systems for growth factor delivery. *Pharm. Res. 26*, 1561−1580.

(16) Zhang, J., Postovit, L. M., Wang, D., Gardiner, R. B., Harris, R., Abdul, M. M., and Thomas, A. A. (2009) In situ loading of basic fibroblast growth factor within porous silica nanoparticles for a prolonged Release. *Nanoscale Res. Lett. 4*, 1297−1302.

(17) Vu, T. Q., Maddipati, R., Blute, T. A., Nehilla, B. J., Nusblat, L., and Desai, T. A. (2005) Peptide-conjugated quantum dots activate neuronal receptors and initiate downstream signaling of neurite growth. *Nano Lett. 5*, 603−607.

(18) Pitukmanorom, P., Yong, T. H., and Ying, J. Y. (2008) Tunable release of proteins with polymer-inorganic nanocomposite microspheres. *Adv. Mater. 20*, 3504−3509.

(19) Park, Y. B., Dziak, R., Genco, R. J., Swihart, M., and Perinpanayagam, H. (2007) Calcium sulfate based nanoparticles. U.S. Patent No. 7767226.

(20) De Vries, I. J. M., Lesterhuis, W. J., Barentsz, J. O., Verdijk, P., Krieken van, J. H., Boerman, O. C., Oyen, W. J. G., Bonenkamp, J. J., Boezeman, J. B., Adema, G. J., Bulte, J. W. M., Scheenen, T. W. J., Punt, C. J. A., Heerschap, A., and Figdor, C. G. (2005) Magnetic resonance tracking of dendritic cells in melanoma patients for monitoring of cellular therapy. *Nat. Biotechnol. 23*, 1407−1413.

(21) Hergt, R., Hiergeist, R., Hilger, I., Kaiser, W. A., Lapatnikov, Y., Margel, S., and Richter, U. (2004) Maghemite nanoparticles with very high AC-losses for application in RF-magnetic hyperthermia. *J. Magn. Magn. Mater. 270*, 345−357.

(22) Scherer, F., Anton, M., Schillinger, U., Henkel, J., Bergemann, C., Kruger, A., Gansbacher, B., and Plank, C. (2002) Magnetofection: enhancing and targeting gene delivery by magnetic force in vitro and *in vivo*. *Gene Ther. 9*, 102−109.

(23) Rudge, S. R., Kurtz, T. L., Vessely, C. R., Catterall, L. G., and Williamson, D. L. (2000) Preparation, characterization, and performance of magnetic iron-carbon composite microparticles for chemotherapy. *Biomaterials 21*, 1411−1420.

(24) Margel, S., and Gura, S. (2006) Nucleation and growth magnetic metal oxide nanoparticles and its use. Israel Patent No. WO9962079.

(25) Perlstein, B., Ram, Z., Daniels, D., Ocherashvilli, A., Roth, Y., Margel, S., and Mardor, Y. (2008) Convection-enhanced delivery of maghemite nanoparticles: increased efficacy and MRI monitoring. *Neuro-Oncology 10*, 153−161.

(26) Shi, X., Wang, S. H., Swanson, S. D., Ge, S., Cao, Z., Van Antwerp, M. E., Lanmark, K. J., and Baker, J. R. (2008) Dendrimer-functionalized shell-cross linked iron oxide nanoparticles for *in vivo* magnetic resonance imaging of tumors. *Adv. Mater. 20*, 1671−1678.

(27) Quarta, A., Di Corato, R., Manna, L., Ragusa, A., and Pellegrino, T. (2007) Fluorescent-magnetic hybrid nanostructures: preparation, properties, and applications in biology. *NanoBioscience I.E.E.E. Transactions 6*, 298−308.

(28) Tran, N., and Webster, T. J. (2010) Magnetic nanoparticles: biomedical applications and challenges. *J. Mater. Chem. 20*, 8760−8767.

(29) Solanki, A., Kim, J. D., and Lee, K. B. (2008) Nanotechnology for regenerative medicine: nanomaterials for stem cell imaging. *Nanomedicine 3*, 567−578.

(30) Gupta, A. K., and Gupta, M. (2005) Synthesis and surface engineering of iron oxide nanoparticles for biomedical applications. *Biomaterials 26*, 3995−4021.

(31) Bock, N., Riminucci, A., Dionigi, C., Russo, A., Tampieri, A., Landi, E., Goranov, V. A., Marcacci, M., and Dediu, V. (2010) A novel route in bone tissue engineering: Magnetic biomimetic scaffolds. *Acta Biomaterialia 6*, 786−796.

(32) Shimizu, K., Ito, A., and Honda, H. (2006) Enhanced cell-seeding into 3D porous scaffolds by use of magnetite. *J. Biomed. Mater. Res., Part B: Appl. Biomater. 77B*, 265−272.

(33) Kim, J. A., Lee, N., Kim, B. H., Rhee, W. J., Yoon, S., Hyeon, T., and Park, T. H. (2011) Enhancement of neurite outgrowth in PC12 cells by iron oxide nanoparticles. *Biomaterials 32*, 2871−2877.

(34) Naka, Y., Kitazawa, A., Akaishi, Y., and Shimizu, N. (2004) Neurite outgrowths of neurons using neurotrophin-coated nanoscale magnetic beads. *J. Biosci. Bioeng. 98*, 348−352.

(35) Escada, P. A., Lima, C., and da Silva, J. M. (2009) The human olfactory mucosa. *Eur. Arch. Otorhinolaryngol. 266*, 1675−1680.

(36) Lima, C., Pratas-Vital, J., Escada, P., Hasse-Ferreira, A., Capucho, C., and Peduzzi, J. D. (2006) Olfactory mucosa autografts in human spinal cord injury: a pilot clinical study. *J. Spinal Cord Med. 29*, 191−206.

(37) Willerth, S. M., and Sakiyama-Elbert, S. E. (2008) Cell therapy for spinal cord regeneration. *Adv. Drug Delivery Rev. 60*, 263−276.

(38) Ziv-Polat, O., Topaz, M., Brosh, T., and Margel, S. (2010) Enhancement of incisional wound healing by thrombin conjugated iron oxide nanoparticles. *Biomaterials 31*, 741−747.

(39) Green-Sadan, T., Kuttner, T., Lublin-Tennenbaum, T., Kinor, N., Boguslavsky, Y., Margel, S., and Yadid, G. (2005) Glial cell line-derived neurotropic factor-conjugated nanoparticles suppress acquisition of cocaine self-adminstration in rats. *Exp. Neurol. 194*, 97−105.
(40) Shahar, A., Nevo, Z., and Rochkind, S. (2006) Cross-linked hyaluronic acid-laminin gels and use thereof in cell culture and medical implants. U.S. Patent No. 0024373.
(41) Skaat, H., and Margel, S. (2009) Synthesis of fluorescent-maghemite nanoparticles as multimodal imaging agents for amyloid-β fibrils detection and removal by a magnetic field. *Biochem. Biophys. Res. Commun. 386*, 645−649.
(42) Azzazy, H. M. E., and Christenson, R. H. (1996) All about albumin: biochemistry, genetics and medical applications (Peters, T. J., Ed) Academic Press Inc., San Diago, CA.
(43) Vernon, R. K., and Spicer, L. J. (1994) Effects of basic fibroblast growth factor and heparin on follicle-stimulating hormone-induced steroidogenesis by bovine granulosa cells. *J. Anim. Sci. 72*, 2696−2702.
(44) Park, K. H., Hyemin, K., and Kun, N. (2009) Neuronal differentiation of PC12 cells on growth factor-loaded nanoparticles coated on PLGA microspheres. *J. Microbiol. Biotechnol. 19*, 1490−1495.
(45) Skaat, H., Shafir, G., and Margel, S. (2011) Acceleration and inhibition of amyloid-β fibril formation by peptide-conjugated fluorescent-maghemite nanoparticles. *J. Nanopart. Res.* DOI:10.1007/s11051-011-0276-4. Available from: http://www.springerlink.com/content/j64v88m876182671/
(46) Boguslavsky, Y., and Margel, S. (2008) Synthesis and characterization of poly(divinylbenzene)-coated magnetic iron oxide nanoparticles as precursor for the formation of air-stable carbon-coated iron crystalline nanoparticles. *J. Colloid Interface Sci. 317*, 101−114.
(47) Martin, Y., Eldardiri, M., Lawrence-Watt, D. J., and Sharpe, J. R. (2011) Microcarriers and their potential in tissue regeneration. *Tissue Eng., Part B 17*, 71−80.
(48) Rochkind, S., El-Ani, D., Nevo, Z., and Shahar, A. (2009) Increase of neuronal sprouting and migration using 780nm laser phototherapy as procedure for cell therapy. *Laser Surg. Med. 41*, 277−281.
(49) Rochkind, S., Shahar, A., Fliss, D., El-Ani, D., Astachov, L., Hayon, T., Alon, M., Zamostiano, R., Ayalon, O., Biton, I. E., Cohen, Y., Halperin, R., Schneider, D., Oron, A., and Nevo, Z. (2006) Development of a tissue-engineered composite implant for treating traumatic paraplegia in rats. *Eur. Spine. J. 15*, 234−245.
(50) Margel, S., Perlstein, B., and Brodie, C. (2009) Polymer nanoparticles coated by magnetic metal oxide and uses thereof. Patent No. WO 2009/040811.
(51) Shafir, G., Galperin, A., and Margel, S. (2009) Synthesis and characterization of recombinant factor VIIa-conjugated magnetic iron oxide nanoparticles for hemophilia treatment. *J. Biomed. Mater. Res., Part A 91*, 1056−1064.
(52) Corem-Salkmon, E., Ram, Z., Daniels, D., Perlstein, B., Last, D., Salomon, S., Tamar, G., Shneor, R., Guez, D., Margel, S., and Mardor, Y. (2011) Convection-enhanced delivery of methotrexate-loaded maghemite nanoparticles. *Int. J. Nanomed. 6*, 1595−1602.
(53) Zhang, Y., Kohler, N., and Zhang, M. (2002) Surface modification of superparamagnetic magnetite nanoparticles and their intracellular uptake. *Biomaterials 23*, 1553−1561.
(54) Reiland, J., and Rapraeger, A. C. (1993) Heparan sulfate proteoglycan and FGF receptor target basic FGF to different intracellular destinations. *J. Cell Sci. 105*, 1085−1093.
(55) Shi, Z., Neoh, K. G., Kang, E. T., Shuter, B., Wang, S. C., Poh, C., and Wang, W. (2009) Carboxymethyl)chitosan-modified superparamagnetic iron oxide nanoparticles for magnetic resonance imaging of stem cells. *ACS Appl. Mater. Interfaces 1*, 328−335.
(56) MacDonald, K. P. A., Murrell, W. G., Bartlett, P. F., Bushell, G. R., and Mackay-Sim, A. (1996) FGF2 promotes neuronal differntiation in explants cultures of adult and embryonic muse olfactory epithelium. *J. Neurosci. Res. 44*, 27−39.
(57) Murrell, W., Bushell, G. R., Livesey, J., McGrath, J., MacDonald, K. P., Bates, P. R., and Mackay-Sim, A. (1996) *Neuroreport 7*, 1189−1194.

Bioconjugate Chemistry

Article

pubs.acs.org/bc

Zn(II)-bis(cyclen) Complexes and the Imaging of Apoptosis/Necrosis

Dorte Oltmanns,[†] Sabine Zitzmann-Kolbe,[‡] Andre Mueller,[‡] Ulrike Bauder-Wuest,[†] Martin Schaefer,[†] Matthias Eder,[†] Uwe Haberkorn,[§] and Michael Eisenhut*,[†]

[†]Department of Radiopharmaceutical Chemistry, German Cancer Research Center, Im Neuenheimer Feld 280, 69120 Heidelberg, Germany

[‡]Global Drug Discovery, Bayer Healthcare, Berlin, Germany

[§]Department of Nuclear Medicine, University Hospital Heidelberg, Im Neuenheimer Feld 400, 69120 Heidelberg, Germany

Supporting Information

ABSTRACT: In vivo cell-death imaging is still a challenging issue. Until now, only ^{99m}Tc-labeled HYNIC-rh-annexin A5 has been extensively studied in clinical trials. In the ongoing search for an alternative imaging agent, we synthesized a series of fluorescent zinc-cyclen complexes as annexin A5 mimics and studied structural variations on the uptake behavior of cells undergoing apoptosis/necrosis. The number of cyclen chelators was varied and the spacer separating cyclen from the central scaffold was modified. Five zinc-cyclen complexes were labeled with fluorescein for flow cytometric studies and one was labeled with ^{18}F for in vivo applications. Jurkat cells were treated with staurosporine to induce apoptosis/necrosis, incubated with the fluorescein-labeled zinc complexes and analyzed them by flow cytometry. Fluorescent annexin A5 and propidium iodide were applied as reference dyes. Flow cytometry revealed greater accumulation of zinc-cyclen complexes in staurosporine treated cells. The uptake was contingent on the presence of zinc and the fluorescence intensity was dependent on the number of zinc-cyclen groups. Confocal laser scanning microscopy showed the {bis[Zn(cyclen)]}$^{4+}$ complex distributed throughout the cytosol different to annexin A5. Owing to the structural similarity of the bis-cyclen ligands with CXCR4 binding bis-cyclam derivatives the zinc-cyclen complex uptake was challenged with the meta derivative of AMD3100. Lack of uptake depletion in staurosporine treated cells ruled out measurable CXCR4 interaction. PET imaging using the ^{18}F labeled zinc-cyclen complex revealed significantly higher uptake in an irradiated Dunning R3327-AT1 prostate tumor as compared to the contralateral control tumor. PET imaging of a HelaMatu tumor model additionally showed an increased uptake after taxol treatment. It could be demonstrated that the fluorescent zinc-cyclen complexes offer potential as new agents for flow cytometry and microscopic imaging of cell death. In addition, the ^{18}F labeled analogue holds promise for in vivo applications providing informations about cell death after radiation therapy and cytostatic drug treatment.

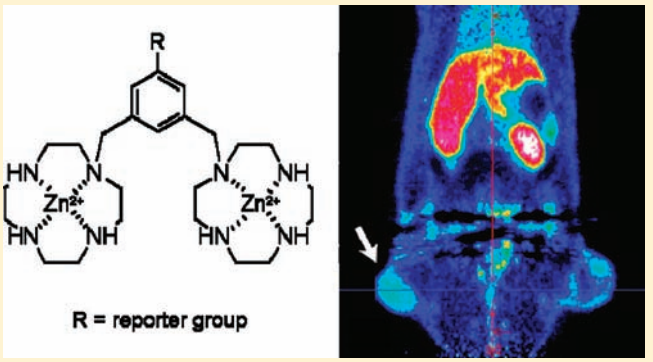

INTRODUCTION

Evading apoptosis is one of the hallmarks of cancer. Overcoming this resistance is important for the success of therapeutic interventions. Apoptosis is accepted as one of the key readouts for early prediction of anticancer treatment response. Imaging apoptosis, therefore, will provide important information to ascertain the effectiveness of anticancer therapies.

Due to the loss of membrane asymmetry at the onset of apoptosis, phosphatidylserine (PS) becomes exposed on the extracellular cell membrane. Annexin A5 (AnxA5), a protein involved in the inhibition of blood coagulation, binds to externalized phosphatidylserine (PS) of apoptotic cells. The binding itself is driven through the formation of a ternary Ca^{2+} complex of AnxA5 with the carboxyl-phospholipid headgroup of PS.[1,2] This concerted interaction results in a considerable strong binding affinity of K_d <10^{-10} M.[3] Owing to this property, fluorescent annexin A5 was introduced as a tool for flow-cytometric detection of apoptosis[4] and is now broadly applied in cell biological research.[5,6] The in vivo imaging of apoptosis was made possible using ^{99m}Tc labeled AnxA5,[7] which was later modified to ^{99m}Tc-HYNIC-rh-annexin A5 and examined in clinical studies.[8]

On the basis of PS selectivity and binding strength of AnxA5, searches for small molecules as annexin mimics have been undertaken to further improve the property of apoptosis imaging. In reference to the role of Ca^{2+} in AnxA5, various Zn^{2+} complexes providing similar cocomplexation characteristics have been investigated as phosphate selective compounds.

Received: August 19, 2011
Revised: October 10, 2011
Published: October 31, 2011

ACS Publications © 2011 American Chemical Society

dx.doi.org/10.1021/bc200457b | Bioconjugate Chem. 2011, 22, 2611–2624

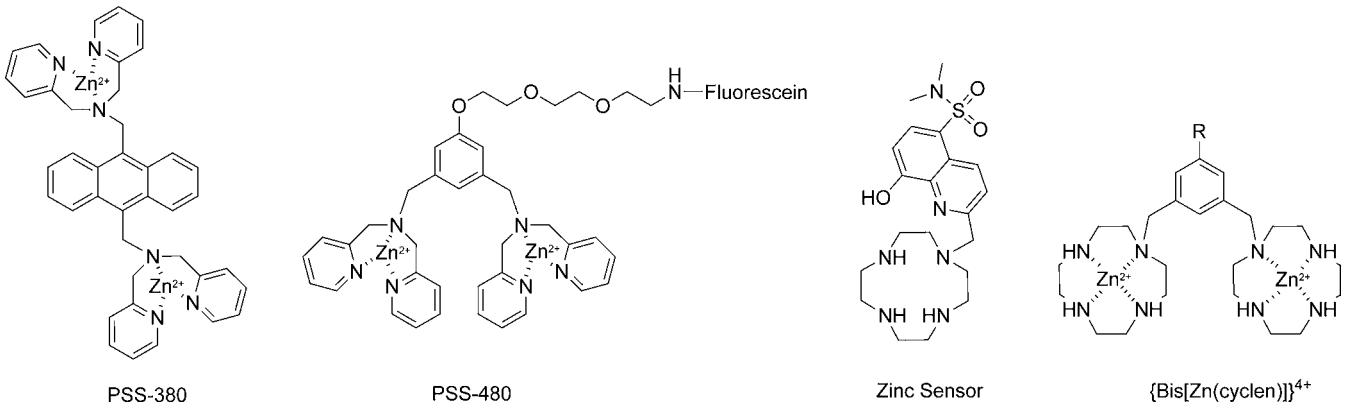

Figure 1. Chemical structures of zinc complexes used as phosphate sensors, a zinc sensor, and the general structure of bis[Zn(cyclen)]$^{4+}$, all designed for apoptosis imaging (R = reporter group).

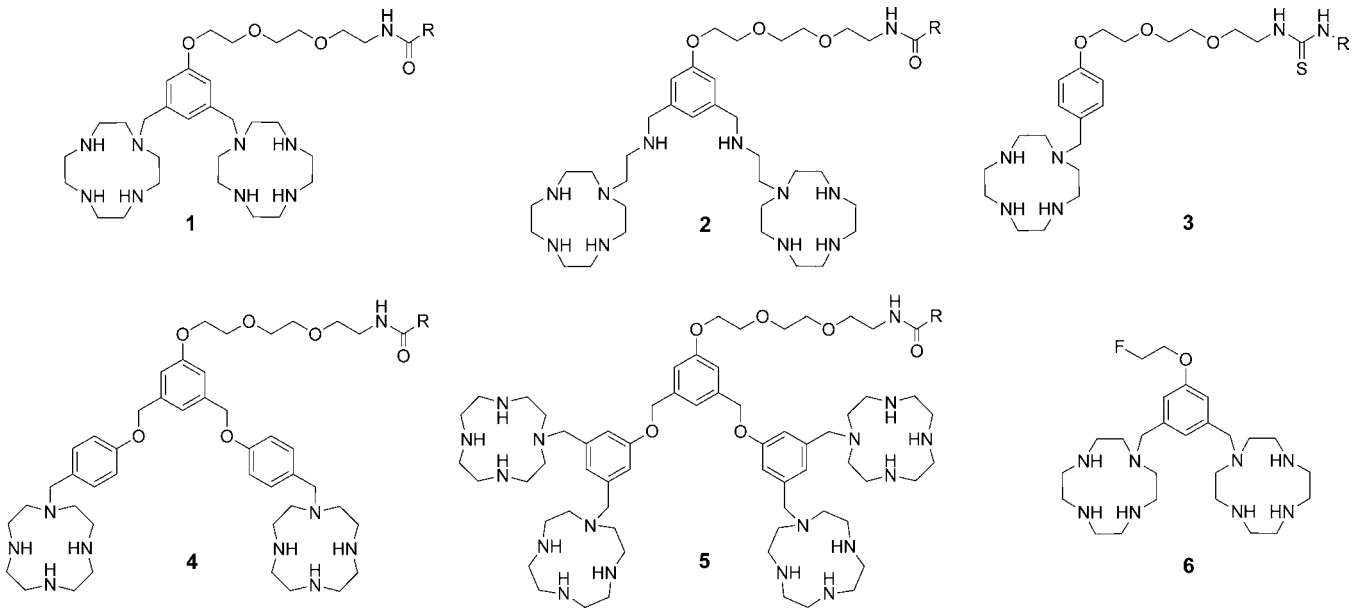

Figure 2. Chemical structures of cyclen derivatives **1**–**6** (R = fluorescein).

The bis(zinc(II)-dipicolylamine) complex PSS-380 shown in Figure1 was described to interact in this way allowing images of apoptotic cells.[9] The bifunctional complex ligand PSS-380 originated from developments of fluorescent chemosensors for phosphorylated peptides.[10,11] Several second-generation bis-(zinc(II)-dipicolylamine) complexes (Figure 1) have been synthesized and tested with artificial phospholipid vesicles[12] and apoptotic cells.[13] Cyclen-based zinc(II) probes were also suggested as microscopic imaging agents for apoptotic cells. The latest development includes the zinc sensor 8-hydroxy-5-*N*,*N*-dimethylaminosulfonylquinolin-2-ylmethyl-pendant cyclen (Figure 1) showing a complexation constant for Zn^{2+} of log K = 22.4 ± 0.1 M^{-1}. The amplified fluorescence was explained with the presence of an increased intracellular zinc concentration during apoptosis which led to complex participation of the chromophore pendant group.[14] The complex stability of the zinc sensor is much higher as compared to dipicolylamine-zinc complexes PSS-380 and PSS-480. The latter stability constants are approximately 10^7 M^{-1} and 10^4 M^{-1} for the first and second Zn^{2+} complex, respectively.[11,15,16]

Therefore, it remains to be examined whether zinc once bound to dipicolylamine stays complexed after the injection into the blood circulation. As indicated above, cyclen derivatives form more stable Zn(II) complexes providing a decent chance to survive complexed in vivo and to bind to the target site (log K[Zn(cyclen)]$^{2+}$ = 15.3 M^{-1}).[17,18] Consequently, the zinc-dipicolylamine complex structure elements were replaced with [Zn(cyclen)]$^{2+}$ to form *m*-phenylene bridged {bis[Zn(cyclen)]}$^{4+}$ derivatives (Figure 1). The ternary complex formation with externalized PS headgroups should similarly proceed as described for the zinc sensor or by the formation of multiple coordination bonds between multinuclear Zn^{2+} complexes and polyanionic compounds.[14,18]

We synthesized six cyclen derivatives, five comprising fluorescein tags and one labeled with ^{18}F (Figure 2). The fluorescent label was chosen for the investigation of structure-related effects on cell binding because of the methodological advantage of flow cytometry. Structural variations of the chelators included methylene (**1**) and 2-azabutylene spacers (**2**) separating cyclen from the central scaffold. In order to study the influence of multimerization, a series of cyclen derivatives with mono-, bis-, and tetra-cyclen structure elements (**3**–**5**) have been included. After complexation with Zn^{2+}, we evaluated these compounds on apoptotic Jurkat cells using flow

dx.doi.org/10.1021/bc200457b | *Bioconjugate Chem.* 2011, 22, 2611–2624

cytometry and confocal laser scanning microscopy (CLSM). To exclude the influence of CXCR4, cell uptake of zinc-cyclen complex $[\mathbf{Zn_2 1}]^{4+}$ was competed with a structurally related biscyclam derivative known to exhibit CXCR4 affinity. CXCR4 is a G-protein coupled chemokine receptor expressed on Jurkat cells and is physiologically involved in, e.g., the homing of metastasizing cells and the T-cell uptake of X4-HIV-1.[19] In addition, the presence of this receptor after induction of apoptosis was studied using a mouse anti-CXCR4 antibody. Furthermore, the in vivo applicability of the radiofluorinated zinc complex of **6** was demonstrated by positron emission tomography (PET) using rats bearing an irradiated Dunning prostate adenocarcinoma and mice carrying HelaMatu tumors treated with taxol.

MATERIALS AND METHODS

General. All chemicals and solvents were purchased from Sigma-Aldrich (Munich, Germany) or Merck (Darmstadt, Germany) and used without further purification. HPLC purifications were performed with Agilent 1100 Series (Agilent, Santa Clara, USA) on a Chromolith SemiPrep RP-18e column (100−10 mm, Merck, Darmstadt, Germany) using a flow of 8 mL/min and a gradient of 100% water (0.1% TFA) to 100% acetonitrile (0.1% TFA). For analytical HPLC, a Chromolith Performance RP-18e column (100−4.6 mm; Merck KGaA, Darmstadt, Germany) was used using a flow of 4 mL/min and the above-mentioned gradient. Analytical HPLC was used to prove the purity of the compounds. ESI mass spectrometry was performed with a Triple Quadrupole mass spectrometer TSQ 7000 (Thermo Fisher Scientific, Bremen, Germany). NMR spectra were measured with a Varian Mercury Plus 300, a Varian NMR System 500 (Varian, Palo Alto, USA), and a Bruker DRX 500 Avance (Bruker BioSpin, Rheinstetten, Germany).

Annexin A5 Alexa Fluor 488 was purchased from Molecular Probes (Invitrogen, Paisley, UK). Anti-hCXCR-4 (fusin) and mouse monoclonal antibody Ig_{2A} clone 12G5 were obtained from R&D Systems (Minneapolis, MN, USA). Cell experiments were conducted with the human T-lymphocyte cell line Jurkat J6, clone E6−1) which was purchased from ECACC (European Collection of Cell Culture, HPA Culture Collections, Salisbury, UK). The cells were cultivated in RPMI 1640 (PAA Laboratories GmbH, Pasching, Austria) containing 1% glutamine and 10% FBS at 37 °C in a 5% CO_2 atmosphere and maintained in log phase.

Flow cytometry was performed with a DAKO Galaxy Flow-Cytometry System (DAKO, Glostrup, Denmark) equipped with *Partec* analysis software (Münster, Germany).

Confocal laser scanning microscopy (CLSM) images were obtained with a LSM 410 microscope (Carl Zeiss Micro-Imaging GmbH, Jena, Germany) and processed with *Advanced Imaging Microscopy Release 4.2* software (Zeiss, Jena, Germany).

The following buffer systems were used for cell experiments. Annexin binding buffer (10 mM HEPES (*N*-(2-hydroxyethyl)-piperazin-*N*′-2-ethane sulfonic acid), 150 mM NaCl, 5 mM KCl, 1 mM $MgCl_2$, 1.8 mM $CaCl_2$) pH 7.4; TES buffer (5 mM TES (*N*-[tris(hydroxymethyl)methyl]-2-amino sulfonic acid), 145 mM NaCl) pH 7.4; PBS buffer (Dulbeccos's PBS without Ca and Mg, PAA Laboratories GmbH, Pasching, Austria).

Analysis and purification of radioactive compounds were conducted on a LATEK P-400 HPLC with a LATEK UV-Detektor (Eppelheim, Deutschland), λ = 220 nm, and a Bioscan radiodetector (Washington, USA). Purification of the radiofluorinated compounds was performed using a Chromolith SemiPrep RP-18e column (100−10 mm, Merck, Darmstadt, Germany) with a gradient of 100% water (0.1% TFA) to 100% acetonitrile (0.1% TFA) in 7 min and a flow of 10 mL/min.

Syntheses. *2-(2-(2-(Tritylamino)ethoxy)ethoxy)ethanol* ***7***. 2-[2-(2-Aminoethoxy)ethoxy]ethanol[20] (1.45 g, 9.72 mmol) and triethylamine (135 μL, 79 μmol, 0.1 equiv) were dissolved under nitrogen in CH_2Cl_2 (20 mL). Tritylchloride in CH_2Cl_2 (15 mL) was added dropwise at room temperature. After 16 h, the solvent was evaporated. The crude product was purified by silica gel column chromatography (EtOAc/petroleum ether = 1:1, 0.1% DIPEA). Yield 1.4 g (38%). ESI-MS: m/z = 392.3, calc. 392.3 $[M+H]^+$. ^{1}H NMR (300 MHz, $CDCl_3$): δ = 7.44−7.37 (m, 6H), 7.24 (m, 6H), 7.14−7.07 (m, 3H), 3.64−3.43 (m, 10H), 2.29 (t, 2H, ^3J = 5.4 Hz) ppm. ^{13}C NMR (300 MHz, $CDCl_3$): δ = 146.03, 128.66, 127.77, 126.24, 72.45, 71.29, 70.66, 70.36, 70.08, 61.78, 43.04 ppm.

2-(2-(2-Bromoethoxy)ethoxy)-N-tritylethylamine ***8***. K_2CO_3 (223 mg, 1.61 mmol, 1.5 equiv) and tetrabromomethane (514 mg, 1.55 mmol, 1.5 equiv) were added under nitrogen to a solution of **7** (400 mg, 1.02 mmol) in CH_2Cl_2 (10 mL). Triphenylphosphine (422 mg, 1.60 mmol, 1.5 equiv) in CH_2Cl_2 (10 mL) was added dropwise. After stirring for 18 h at room temperature, K_2CO_3 was removed by filtration and the solvent was evaporated. Silica gel column chromatography (EtOAc/petroleum ether = 1:2, 0.1% DIPEA) yielded 436 mg (94%). ESI-MS: 456.2; calc. 454.2 $[M+H]^+$. ^{1}H NMR (300 MHz, $CDCl_3$): δ = 7.43−7.37 (m, 6H), 7.23−7.16 (m, 6H), 7.14−7.07 (m, 3H), 3.70 (t, 2H, ^3J = 6.4 Hz), 3.57−3.43 (m, 6H), 3.33 (t, 2H), 2.28 (t, 2H, ^3J = 5.4 Hz) ppm. ^{13}C NMR (300 MHz, $CDCl_3$): δ = 146.09, 128.64, 127.72, 126.18, 71.28, 71.20, 70.61, 70.47, 70.05, 43.00, 30.22 ppm.

O-Alkylation of Phenolic Compounds: General Procedure. The respective phenol (1.2 equiv) and 2-(2-(2-bromoethoxy)ethoxy)-*N*-tritylethylamine **8** (1 equiv) were dissolved under nitrogen in acetonitrile. K_2CO_3 (1.5 equiv) was added and the mixture was refluxed for 20 h. After cooling to room temperature, K_2CO_3 was removed by filtration, and the crude product was purified by silica gel column chromatography.

(2-{2-[2-(3,5-Bis-hydroxymethyl-phenoxy)ethoxy]ethoxy}-ethyl)tritylamine ***9***. 3,5-Di(hydroxymethyl)phenol[21] (170 mg, 1.11 mmol) was reacted with **8** (423 mg, 931 μmol) and K_2CO_3 (193 mg, 1.40 mmol). LC sovents: EtOAc, 0.1% DIPEA. Yield 570 mg (63%). ESI-MS: m/z = 528.4, calc. 528.3 $[M+H]^+$. ^{1}H NMR (300 MHz, $CDCl_3$): δ = 7.43−7.35 (m, 6H), 7.20−7.11 (m, 6H), 7.11−7.02 (m, 3H), 6.81 (s, 1H), 6.71 (s, 2H), 4.51 (s, 4H), 4.01−3.94 (m, 2H), 3.74−3.68 (m, 2H), 3.59−3.54 (m, 2H), 3.52 (t, 2H, ^3J = 5.5 Hz), 3.50−3.44 (m, 2H), 2.25 (t, 2H) ppm. ^{13}C NMR (300 MHz, $CDCl_3$): δ = 159.23, 146.06, 142.15, 128.69, 127.76, 127.62, 117.62, 112.25, 71.27, 70.75, 70.64, 70.15, 69.79, 67.49, 65.10, 43.06 ppm.

[4-(2-{2-[2-(Tritylamino)ethoxy]ethoxy}ethoxy)phenyl]-methanol ***11***. 4-(Hydroxymethyl)phenol (120 mg, 963 μmol) was reacted with **8** (350 mg, 770 μmol) and K_2CO_3 (160 mg, 1.16 mmol). LC sovents: CH_2Cl_2/MeOH = 95:5, 0.1% DIPEA. Yield 345 mg (90%). ESI-MS: m/z = 498.4, calc. 498.4 $[M+H]^+$. ^{1}H NMR (300 MHz, DMSO-d_6): δ = 7.44−7.38 (m, 6H), 7.32−7.24 (m, 6H), 7.23−7.20 (m, 2H), 7.21−7.14 (m, 3H), 6.87−6.82 (m, 2H), 5.05 (t, 1H, ^3J = 5.7 Hz), 4.42 (d, 2H), 4.04−3.98 (m, 2H), 3.74−3.68 (m, 2H), 3.58−3.53 (m, 2H), 3.52 (t, 2H, ^3J = 6.0 Hz), 3.50−3.44 (m, 2H), 2.60 (t, 1H,

^3J = 7.7 Hz), 2.15 (dt ≈ q, 2H) ppm. ^{13}C NMR (300 MHz, DMSO-d_6): δ = 157.20, 145.92, 134.59, 128.23, 127.77, 127.62, 125.99, 113.89, 70.14, 70.05, 69.78, 69.55, 68.90, 66.96, 62.46, 43.02 ppm.

{4-[3-(4-Hydroxymethyl-phenoxymethyl)-5-(2-{2-[2-(tritylamino)ethoxy]-ethoxy}ethoxy)benzyloxy]phenyl}-methanol ***22***. 4-(Hydroxymethyl)phenol (510 mg, 4.10 mmol, 3.5 equiv) was reacted with benzyl bromide **10** (762 mg, 1.17 mmol) and K_2CO_3 (807 mg, 5.84 mmol, 5.0 equiv). LC solvents: EtOAc/petroleum ether (1:1 gradient to EtOAc/0.1% DIPEA). Yield 650 mg (78%). MALDI-MS: m/z = 741.0, calc. 740.4 $[M+H]^+$. ^{1}H NMR (300 MHz, $CDCl_3$): δ = 7.42−7.36 (m, 6H), 7.21−7.13 (m, 10H), 7.11−7.04 (m, 3H); 6.97 (s, 1H), 6.86−6.79 (m, 6H), 4.92 (s, 4H), 4.50 (s, 4H), 4.01−3.94 (m, 2H), 3.75−3.69 (m, 2H), 3.61−3.55 (m, 2H), 3.55−3.50 (m, 2H), 3.49−3.43 (m, 2H), 2.34−2.20 (m, 2H) ppm. ^{13}C NMR (300 MHz, $CDCl_3$): δ = 159.22, 158.11, 146.04, 138.85, 133.44, 128.66, 128.55, 127.74, 126.19, 118.43, 114.89, 112.93, 71.25, 70.71, 70.08, 69.77, 69.59, 69.68, 67.41, 64.87, 43.14 ppm.

{3-[3-(3,5-Bis-hydroxymethyl-phenoxymethyl)-5-(2-{2-[2-(tritylamino)ethoxy]-ethoxy}ethoxy)benzyloxy]-5-hydroxymethyl-phenyl}-methanol ***27***. 3,5-Di(hydroxymethyl)phenol (706 mg, 4.66 mmol, 3.1 equiv) and benzyl bromide **10** (980 mg, 1.50 mmol) were dissolved under nitrogen in acetonitrile. K_2CO_3 (670 mg, 485 mmol, 3.2 equiv) was added and the mixture refluxed for 20 h. LC sovents: ethyl acetate/petroleum ether (2:1), 0.1% DIPEA. Yield 992 mg (84%). MALDI-MS: m/z = 822.2 $[M+Na]^+$, calc. 822.4 $[M+Na]^+$. ^{1}H NMR (300 MHz, $CDCl_3$): δ = 7.47−7.38 (m, 6H), 7.24−7.15 (m, 6H), 7.14−7.06 (m, 3H), 6.85 (s, 1H), 6.71 (s, 2H), 6.64 (s, 6H), 4.73 (s, 4H), 4.30 (s, 8H), 3.92−3.83 (m, 2H), 3.61−3.70 (m, 2H), 3.59−3.49 (m, 4H), 3.48−3.41 (m, 2H), 2.31 (t, 2H, ^3J = 5.0 Hz) ppm. ^{13}C NMR (300 MHz, $CDCl_3$): δ = 158.90, 158.61, 145.96, 142.69, 138.82, 128.63, 127.76, 126.23, 118.61, 117.81, 112.82, 112.14, 71.17, 70.64, 70.56, 69.94, 69.60, 69.35, 67.26, 64.22, 43.55 ppm.

Bromination of Benzyl Alcohols: General Procedure. CBr_4 (1.5 equiv/hydroxyl function) was added under nitrogen to a solution of the respective benzyl alcohol in CH_2Cl_2. Triphenylphosphine (1.5 equiv/hydroxy function) in dichloromethane was added dropwise. After 16 h at room temperature, the solvent was evaporated. The residue was dissolved in ethyl acetate and cyclohexane was added until a white solid precipitated. The precipitate was removed, the filtrate concentrated, and the crude product was purified by silica gel column chromatography.

(2-{2-[2-(3,5-Bis-bromomethyl-phenoxy)ethoxy]ethoxy}-ethyl)tritylamine ***10***. Benzyl alcohol **9** (373 mg, 707 μmol) was reacted with CBr_4 (703 mg, 2.12 mmol) and triphenylphosphine (556 mg, 2.12 mmol). LC sovents: EtOAc/petroleum ether (1:1), 0.1% DIPEA. Yield 426 mg (92%). ESI-MS: m/z = 654.2, 656.2, 652.2, calc. 654.1, 652.1, 656.1 $[M+H]^+$. ^{1}H NMR (300 MHz, $CDCl_3$): δ = 7.43−7.37 (m, 6H), 7.23−7.14 (m, 6H), 7.13−7.06 (m, 3H), 6.91 (t, 1H, ^4J = 1.5 Hz), 6.76 (d, 2H), 4.32 (s, 4H), 4.03−3.97 (m, 2H), 3.77−3.72 (m, 2H), 3.62−3.58 (m, 2H), 3.55 (t, 2H, ^3J = 5.5 Hz), 3.50−3.46 (m, 2H), 2.29 (t, 2H) ppm. ^{13}C NMR (300 MHz, $CDCl_3$): δ = 159.12, 146.04, 139.53, 128.77, 127.77, 126.26, 121.97, 115.34, 71.22, 70.79, 70.13, 69.61 ppm.

(2-{2-[2-(4-Bromomethyl-phenoxy)ethoxy]ethoxy}ethyl)-tritylamine ***12***. Benzyl alcohol **11** (175 mg, 352 μmol) was reacted with CBr_4 (173 mg, 528 μmol) and triphenylphosphine (556 mg, 2.12 mmol). LC sovents: cyclohexane/EtOAc (3:1), 0.1% DIPEA. Yield 121 mg (62%). ^{1}H NMR (300 MHz, $CDCl_3$): δ = 7.52−7.44 (m, 6H), 7.31−7.21 (m, 8H), 7.12−7.21 (m, 3H), 6.86−6.80 (m, 2H), 4.48 (s, 2H), 4.10−4.03 (m, 2H) 3.85−3.78 (m, 2H), 3.70−3.64 (m, 2H), 3.61 (t, 2H, ^3J = 5.4 Hz), 3.57−3.51 (m, 2H), 2.40−2.31 (m, 2H) ppm. ^{13}C NMR (300 MHz, $CDCl_3$): δ = 158.10, 146.01, 136.91, 128.38, 128.10, 127.61, 128.23, 116.48, 70.16, 70.11, 69.69, 69.52, 68.81, 66.89, 48.46, 43.01 ppm.

[2-(2-{2-[3,5-Bis(3,5-bis-bromomethyl-phenoxymethyl)-phenoxy]ethoxy}ethoxy)-ethyl]tritylamine ***28***. Tetrabenzyl alcohol **27** (460 mg, 576 mmol) was reacted with CBr_4 (1.86 g, 5.60 mmol, 9.7 equiv) and triphenylphosphine (1.03 g, 3.93 mmol, 6.8 equiv). LC sovents: petroleum ether/EtOAc (2:1), 0.1% DIPEA. Yield 502 mg (83%). MALDI-MS: m/z = 1082.8, calc. 1084.0 $[M+H]^+$. ^{1}H NMR (300 MHz, $CDCl_3$): δ = 7.51−7.44 (m, 6H), 7.28−7.20 (m, 6H), 7.19−7.12 (m, 3H), 7.19−7.06 (m, 1H), 7.01 (t, 2H, ^4J = 1.3 Hz), 6.95−6.90 (m, 6H), 5.01 (s, 4H), 4.41 (s, 8H), 4.13−4.06 (m, 2H), 3.87−3.80 (m, 2H), 3.71−3.65 (m, 2H), 3.61 (t, 2H, ^3J = 5.0 Hz), 3.58−3.53 (m, 2H), 2.35 (t, 2H) ppm. ^{13}C NMR (300 MHz, $CDCl_3$): δ = 159.32, 159.00, 146.10, 139.66, 138.35, 128.69, 127.78, 126.25, 122.18, 118.61, 115.52, 113.24, 71.29, 70.78, 70.56, 70.15, 69.82, 69.67, 67.54, 43.65, 32.80 ppm.

[2-(2-{2-[3,5-Bis-(4-bromomethyl-phenoxymethyl)-phenoxy]ethoxy}ethoxy)ethyl]tritylamine ***23***. Benzyl alkohol **22** (582 mg, 787 μmol) was reacted with CBr_4 (597 mg, 1.80 mmol) and triphenylphosphine (470 mg, 1.80 mmol). LC sovents: EtOAc/petroleum ether (1:1), 0.1% DIPEA. Yield: 652 mg (95%). ^{1}H NMR (300 MHz, $CDCl_3$): δ = 7.44−7.35 (m, 6H), 7.27−7.13 (m, 10H), 7.13−7.03 (m, 3H), 6.96 (s, 1H), 6.88−6.77 (m, 6H), 4.93 (s, 4H), 4.41 (s, 4H), 4.05−3.94 (m, 2H), 3.77−3.69 (m, 2H), 3.63−3.56 (m, 2H), 3.56−3.50 (m, 2H), 3.50−3.44 (m, 2H), 2.35−2.20 (m, 2H) ppm. ^{13}C NMR (300 MHz, $CDCl_3$): δ = 159.29, 158.67, 146.08, 138.65, 130.44, 130.27, 128.67, 127.76, 126.18, 118.40, 115.10, 113.04, 71.24, 70.69, 70.11, 69.80, 69.59, 69.72, 67.45, 33.34, 43.15 ppm.

N-Alkylation Reaction of Tris(Boc)cyclen and Aminoethyl-tris(Boc)cyclen: General Procedure. Tris(Boc)cyclen or aminoethyl-tris(Boc)cyclen[22] (1.2 equiv/bromide function) and the respective benzyl bromide (1.0 equiv) were dissolved in acetonitrile. K_2CO_3 (1.5−2 equiv) and KI (5 mg) were added. The reaction mixture was heated to 50 °C for 24−72 h. K_2CO_3 was removed by filtration and the solvent evaporated. The crude product was purified by silica gel column chromatography.

[2-(2-{2-[3,5-Bis(1,4,7,10-tetraazacyclododec-1-yl-methyl-1,4,7-tert-butyloxycarbonylester)phenoxy]ethoxy}ethoxy)-ethyl]tritylamine ***13***. Benzyl bromide **10** (150 mg, 230 μmol) was reacted with tris(Boc)cyclen (261 mg, 552 μmol) and K_2CO_3 (95 mg, 690 μmol). After 48 h, the crude product was purified by column chromatography. LC sovents: CH_2Cl_2/MeOH, 0.1% TEA (95:5). Yield 314 mg (95%). MALDI-MS: m/z = 1437.0, calc. 1436.0 $[M+H]^+$. ^{1}H NMR (500 MHz, DMSO-d_6, 343 K): δ = 7.41−7.38 (m, 6H), 7.29−7.24 (m, 6H), 7.18−7.14 (m, 3H), 6.73 (s, 2H), 6.72 (s, 1H), 4.04−4.00 (m, 2H), 3.73−3.69 (m, 2H), 3.69 (s, 4H), 3.58−3.55 (m, 2H), 3.53−3.48 (m, 10H), 3.49 (m, 2H), 3.33 (t, 8H, ^3J = 5.2 Hz), 3.28 (bs, 8H), 2.57 (bs, 8H), 2.22 (t, 2H, ^3J = 5.8 Hz), 1.41 (s, 18H), 1.36 (s, 36H) ppm. ^{13}C NMR (500 MHz, DMSO-d_6, 343 K): δ = 158.03, 154.55, 154.15, 145.61, 137.25, 127.91,

127.16, 125.59, 124.02, 114.85, 78.86, 77.83, 69.98, 69.86, 69.58, 69.30, 68.66, 66.92, 54.94, 53.9, 48.20, 46.43, 46.24, 42.79, 27.87, 27.64 ppm.

{2-[2-(2-{3,5-Bis[4-(1,4,7,10-tetraazacyclododec-1-ylmethyl-1,4,7-tri-tert-butyloxycarbonylester)phenoxymethyl]-phenoxy}ethoxy)ethoxy]ethyl}tritylamine ***24***. Benzyl bromide **23** (285 mg, 329 mmol) was reacted with tris(Boc)cyclen (515 mg, 1.09 mmol) and K_2CO_3 (151 mg, 1.09 mmol) for 72 h. LC sovents: EtOAc, 0.1% DIPEA. Yield 360 mg (67%). MALDI-MS: m/z = 1670.3 $[M+Na]^+$, calc. 1671.0 $[M+Na]^+$. ^1H NMR (500 MHz, DMSO-d_6, 343 K): δ = 7.41−7.35 (m, 6H), 7.30−7.24 (m, 6H), 7.20−7.12 (m, 7H), 7.07 (s, 1H), 6.95−6.89 (m, 6H), 5.04 (s, 4H), 4.09−4.04 (m, 2H), 3.73−3.70 (m, 2H), 3.67 (s, 4H), 3.59−3.55 (m, 2H), 3.55−3.47 (m, 12H), 3.32 (t, 8H, ^3J = 5.3 Hz), 3.26 (bs, 8H), 2.56 (bs, 8H), 2.26−2.19 (m, 2H), 1.41 (s, 18H), 1.35 (s, 36H) ppm. ^{13}C NMR (500 MHz, DMSO-d_6, 343 K): δ = 158.36, 157.19, 154.57, 154.16, 147.37, 138.56, 130.76, 128.55, 127.36, 126.96, 126.10, 118.31, 114.12, 112.66, 78.03, 77.82, 70.81, 69.55, 69.33, 68.59, 68.89, 67.04, 54.54, 53.99, 48.28, 46.56, 46.21, 42.78, 27.90, 27.64 ppm.

10-[4-(2-{2-[2-(Tritylamino)ethoxy]ethoxy}ethoxybenzyl]-1,4,7,10-tetraazacyclododecane-1,4,7-tri-tert-butyloxycarbonyl Ester ***19***. Benzyl bromide **12** (100 mg, 178 μmol) was reacted with tris(Boc)cyclen (101 mg, 214 μmol) and K_2CO_3 (50 mg, 356 μmol) for 72 h. LC sovents: cyclohexane/EtOAc (3:2), 0.1% DIPEA. Yield 136 mg (80%). ESI-MS: m/z = 952.8; calc. 952.7 $[M+H]^+$. ^1H NMR (500 MHz, DMSO-d_6, 343 K): δ = 7.43−7.39 (m, 6H), 7.30−7.25 (m, 6H), 7.20−7.15 (m, 3H), 7.15 (d, 2H, ^3J = 8.6 Hz), 6.85 (d, 2H), 4.04−4.02 (m, 2H), 3.73−3.71 (m, 2H), 3.67 (s, 2H), 3.59−3.56 (m, 2H), 3.54−3.47 (m, 8H), 3.32 (t, 4H, ^3J = 5.3 Hz), 3.27 (bs, 4H), 2.56 (bs, 4H), 2.23 (dt ≈ q, 2H, ^3J = 5.6 Hz), 1.43 (s, 9H), 1.37 (s, 18H) ppm. ^{13}C NMR (500 MHz, DMSO-d_6, 343 K): δ = 158.20, 155.45, 155.06, 146.52, 131.63, 129.11, 128.82, 128.07, 126.50, 114.69, 78.92, 78.71, 70.84, 70.78, 70.46, 70.19, 69.54, 67.82, 55.42, 54.85, 49.20, 47.46, 47.12, 43.69, 28.80, 28.55 ppm.

{2-[2-(2-{3,5-Bis[3,5-bis-(1,4,7,10-tetraazacyclododec-1-ylmethyl-1,4,7-tri-tert-butyloxycarbonylester)benzyl]phenoxy}-ethoxy)ethoxy]ethyl}tritylamine ***29***. Benzyl bromide **28** (460 mg, 437 μmol) was reacted with tris(Boc)cyclen (1.16 g, 2.46 mmol) and K_2CO_3 (495 mg, 3.58 mmol). LC sovents: EtOAc/petroleum ether (2:1), 0.1% DIPEA. Yield 694 mg (61%). MALDI-MS: m/z = 2623.8, calc. 2617.6 $[M+H]^+$. ^1H NMR (500 MHz, DMSO-d_6, 343 K): δ = 7.42−7.35 (m, 6H), 7.28−7.21 (m, 6H), 7.18−7.11 (m, 3H), 7.08 (s, 1H), 6.93 (s, 2H), 6.82 (s, 4H), 6.74 (s, 2H), 4.99 (s, 4H), 4.98−4.04 (m, 2H), 3.75−3.69 (m, 2H), 3.71 (s, 8H), 3.59−3.55 (m, 2H), 3.53−3.48 (m, 18H), 3.48−3.44 (m, 2H), 3.38−3.30 (m, 16H), 3.28 (bs, 16H), 2.56 (bs, 16H), 2.24−2.17 (m, 2H), 1.39 (s, 36H), 1.34 (s, 72H) ppm. ^{13}C NMR (500 MHz, DMSO-d_6, 343 K): δ = 158.41, 157.94, 154.59, 154.15, 145.61, 138.35, 137.31, 127.91, 127.16, 125.59, 124.11, 114.97, 114.78, 112.67, 78.05, 77.83, 69.96, 69.86, 69.57, 69.29, 68.90, 68.60, 67.04, 54.80, 53.90, 48.22, 46.41, 46.20, 42.77, 27.86, 27.64 ppm.

(2-{2-[2-(3,5-Bis{[2-(1,4,7,10-tetraazacyclododec-1-yl-1,4,7-tri-tert-butyloxycarbonylester)ethylamino]methyl}-phenoxy)ethoxy]ethoxy}ethyl)tritylamine ***16***. Benzyl bromide **10** (112 mg, 213 μmol) was reacted with aminoethyl-tris(Boc)cyclen[20] (230 mg, 448 μmol) and K_2CO_3 (135 mg, 980 μmol) for 72 h. LC sovents: $CHCl_3$/2 N NH_3 in EtOH = 95:5. Yield 142 mg (44%). MALDI-MS: m/z = 1523.3, calc. 1523.0 $[M+H]^+$. ^1H NMR (300 MHz, $CDCl_3$): δ = 7.40−7.37 (m, 6H), 7.30−7.24 (m, 6H), 7.16−7.13 (m, 3H), 6.82 (s, 1H), 6.76 (s, 2H), 4.15−4.07 (m, 2H), 3.86−3.78 (m, 2H), 3.71 (s, 4H), 3.73−3.65 (m, 2H), 3.65−3.58 (m, 2H), 3.57−3.43 (m, 10H), 3.41−3.18 (m, 20H), 2.80−2.72 (m, 4H), 2.72−2.57 (m, 2H), 2.31−2.22 (m, 2H), 1.44 (s, 18H), 1.42 (s, 36H) ppm. ^{13}C NMR (300 MHz, $CDCl_3$): δ = 159.03, 155.70, 155.34, 145.61, 141.54, 127.89, 127.14, 120.34, 112.96, 79.48, 79.24, 70.67, 70.23, 69.71, 67.32, 54.19, 55.56, 52.62, 49.93, 48.02, 47.70, 45.01, 42.32, 28.64, 28.46 ppm.

1,3-Bis(1,4,7,10-tetraazacyclododec-1-yl-methyl-4,7,10-tri-carbonyl-tri-tert-butylester)-(5-tert-butyl(methoxy)-dimethylsilan)-benzene ***34***. 3,5-Bis(bromomethyl)phenoxy)-*tert*-butyl-dimethylsilane **33** (610 mg, 1.55 mmol) was reacted with tris(Boc)cyclen (1.83 g, 3.88 mmol, 2.5 equiv) and K_2CO_3 (857 mg, 6.20 mmol, 4 equiv) for 3 d. LC sovents: cyclohexane/EtOAc = 2:1. Yield 1.22 g (68%). MALDI-MS: m/z = 1176.7, calc. 1177.8 $[M+H]^+$. ^1H NMR (500 MHz, DMSO-d_6, 343 K): δ = 6.74 (s, 1H), 6.68 (s, 2H), 3.68 (s, 4H), 3.54−3.47 (m, 8H), 3.35−3.29 (m, 8H), 3.27 (s, 8H), 2.57 (s, 8H), 1.41 (s, 18H), 1.41 (s, 9H), 1.36 (s, 36H), 0.95 (s, 6H) ppm. ^{13}C NMR (500 MHz, DMSO-d_6, 343 K): δ = 154.49, 154.45, 154.12, 137.16, 125.10, 119.99, 78.03, 77.76, 55.02, 54.05, 48.98, 48.17, 46.44, 27.84, 27.63, 25.91, 25.06, −4.96 ppm.

Trityl Deprotection: General Procedure. Procedure A. The trityl protected amine was dissolved in a solution of 1.5% TFA in CH_2Cl_2. 1% water was added. The reaction mixture was stirred 16 h at room temperature. The solvent was removed under reduced pressure and the product purified by silica gel column chromatography.

Procedure B. The trityl protected amine was dissolved in a mixture of hexafluoroisopropanol/CH_2Cl_2 (1:2) and 1% water. After 2−16 h at room temperature the solvent was removed and the product purified by silica gel column chromatography.

[2-(2-{2-[3,5-Bis(1,4,7,10-tetraazacyclododec-1-yl-methyl-1,4,7-tri-tert-butyloxycarbonylester)phenoxy]ethoxy}ethoxy)-ethyl]amine ***14***. Compound **13** (190 mg, 132 μmol) was reacted according to procedure B for 16 h. LC sovents: CH_2Cl_2/7 N NH_3 in MeOH (95:5). Yield 143 mg (78%). MALDI-MS: m/z = 1195.6, calc. 1194.8 $[M+H]^+$. ^1H NMR (500 MHz, DMSO-d_6, 343 K): δ = 6.75 (s, 2H), 6.72 (s, 1H), 4.09−4.05 (m, 2H), 3.78−3.74 (m, 2H), 3.72 (s, 4H), 3.67−3.63 (m, 4H), 3.63−3.60 (m, 2H), 3.51 (t, 8H, ^3J = 5.2 Hz), 3.34 (t, 8H), 3.30 (bs, 8H), 2.97−2.94 (m, 2H), 2.59 (bs, 8H), 1.42 (s, 18H), 1.36 (s, 36H) ppm. ^{13}C NMR (500 MHz, DMSO-d_6, 343 K): δ = 158.00, 154.58, 154.17, 137.25, 124.11, 114.84 78.09, 77.86, 69.45, 69.34, 68.65, 66.89, 66.44, 54.82, 53.90, 48.19, 46.42, 46.24, 38.30, 27.89, 27.66 ppm.

{2-[2-(2-{3,5-Bis[4-(1,4,7,10-tetraazacyclododec-1-ylmethyl-1,4,7-tri-tert-butyloxycarbonylester)phenoxymethyl]-phenoxy}ethoxy)ethoxy]ethyl}amine ***25***. Compound **24** (218 mg, 132 μmol) was reacted according to procedure A. LC sovents: CH_2Cl_2/MeOH (85:15), 0.1% DIPEA. Yield 98 mg (53%). MALDI-MS: m/z = 1407.04, calc. 1406.9 $[M+H]^+$. ^1H NMR (500 MHz, DMSO-d_6, 343 K): δ = 7.19−7.18 (m, 4H), 7.09 (s, 1H), 6.97−6.96 (m, 2H), 6.96−6.92 (m, 4H), 5.05 (s, 4H), 4.14−4.11 (m, 2H), 3.78−3.75 (m, 2H), 3.67 (s, 4H), 3.66−3.62 (m, 4H), 3.62−3.59 (m, 2H), 3.49 (t, 8H, ^3J = 5.3 Hz), 3.31 (t, 8H), 3.26 (bs, 8H), 2.94 (t, 2H, ^3J = 5.4 Hz), 2.55 (bs, 8H), 1.41 (s, 18H), 1.35 (s, 36H) ppm. ^{13}C NMR (500 MHz, DMSO-d_6, 343 K): δ = 158.35, 157.19, 154.56, 154.16, 138.62, 130.79, 128.54, 118.38, 114.12, 112.68, 78.04, 77.83,

69.44, 69.36, 68.89, 68.59, 67.04, 54.46, 53.94, 48.27, 46.55, 46.15, 40.67, 27.89, 27.64 ppm.

10-[4-(2-{2-[2-(Tritylamino)ethoxy]ethoxy}ethoxy)benzyl]-1,4,7,10-tetraaza-cyclododecane-1,4,7-tri-tert-butyloxycarbonylester ***20***. Compound **19** (42 mg, 44 μmol) was reacted according to procedure B for 16 h. LC sovents: $CHCl_3$/7 M NH_3 in MeOH (95:5). Yield 30 mg (99%). ESI-MS: m/z = 710.5, calc. 710.5 $[M+H]^+$. ^1H NMR (500 MHz, DMSO-d_6, 343 K): δ = 7.16 (d, 2H, ^3J = 8.6 Hz), 6.87 (d, 2H), 4.09−4.06 (m, 2H), 3.76−3.73 (m, 2H), 3.67 (s, 2H), 3.64−3.61 (m, 2H), 3.60−3.57 (m, 2H), 3.56 (t, 2H, ^3J = 5.5 Hz), 3.49 (t, 4H, ^3J = 5.5 Hz), 3.31 (t, 4H), 3.27 (bs, 4H), 2.89 (t, 2H), 2.55 (bs, 4H), 1.42 (s, 9H), 1.36 (s, 18H) ppm. ^{13}C NMR (500 MHz, DMSO-d_6, 343 K): δ = 157.31, 154.18, 130.79, 128.28, 113.82, 78.06, 77.85, 69.48, 69.34, 68.66, 68.19, 66.95, 54.43, 53.91, 48.28, 46.55, 46.21, 39.13, 27.91, 27.66 ppm.

2-[2-(2-{3,5-Bis[3,5-bis(1,4,7,10-tetraazacyclododec-1-yl-methyl-1,4,7-tri-tert-butyloxycarbonylester)benzyl]phenoxy}-ethoxy)ethoxy]ethylamine ***30***. Compound **29** (321 mg, 123 μmol) was reacted according to procedure B. LC sovents: CH_2Cl_2/MeOH (85:15). Yield 258 mg (88%). MALDI-MS: m/z = 2377.5, calc. 2375.5 $[M+H]^+$

2-{2-[2-(3,5-Bis{[2-(1,4,7,10-tetraazacyclododec-1-yl-1,4,7-tri-tert-butyloxycarbonylester)ethylamino]methyl}phenoxy)-ethoxy]ethoxy}ethylamine ***17***. Compound **16** (110 mg, 72.2 μmol) was reacted according to procedure A. LC sovents: $CHCl_3$/2 N NH_3 in EtOH (9:1). Yield 88 mg (95%). MALDI-MS: m/z = 1281.5, calc. 1280.9 $[M+H]^+$.

10-(4-{2-[2-(2-{3-[3-Carboxy-4-(6-hydroxy-3-oxo-3H-xanthene-9-yl)phenyl]thioureido}-ethoxy)ethoxy]ethoxy}-benzyl)-1,4,7,10-tetraazacyclododecane-1,4,7-tri-tert-butyloxycarbonyl ester ***21***. Compound **20** (45 mg, 63 μmol) and DIPEA (16 μL, 10 μL/40 μmol) were dissolved in DMF (500 μL). A solution of fluorescein isothiocyanate (isomer 1; 30 mg, 76 μmol) in DMF (500 μL) was added under nitrogen. The solution was stirred for 6 h at room temperature. The solvent was removed under reduced pressure, and a yellow solid was obtained. The crude product was used in the next step without further purification. MALDI-MS: 1099.7, calc. 1099.5 $[M+H]^+$.

Carboxyfluorescein Conjugation: General Procedure. The unprotected amine was dissolved in DMF and, if necessary, the basicity enhanced with DIPEA. A solution of 5(6)-carboxyfluorescein pentafluorophenylester (5(6)-CF-PFP) in DMF was added. The reaction mixture was stirred 1−16 h and the solvent removed under reduced pressure. The crude product was obtained as a yellow solid and not further purified.

N-[2-(2-{2-[3,5-Bis(1,4,7,10-tetraazacyclododec-1-yl-methyl-1,4,7-tri-tert-butyloxycarbonylester)phenoxy]ethoxy}-ethoxy)ethyl]6-(6-hydroxy-3-oxo-3H-xanthene-9-yl)-isophthalic Acid ***15***. Compound **14** (4.4 mg, 3.7 μmol) was reacted with 5(6)-CF-PFP (2.2 mg, 4.1 μmol) for 6 h. MALDI-MS: m/z = 1554.8, calc. 1552.8 $[M+H]^+$.

N-(2-{2-[2-(3,5-Bis{[2-(1,4,7,10-tetraazacyclododec-1-yl)-ethylamino]methyl}-phenoxy)ethoxy]ethoxy}ethyl)6-(6-hydroxy-3-oxo-3H-xanthene-9-yl)-isophthalic Acid ***18***. Compound **17** (24 mg, 18 μmol) was reacted with 5(6)-CF-PFP (11 mg, 20 μmol) for 6 h. R_t (analyt. HPLC, λ = 215, 254 nm): 3.9 min (Δt (isomers) = 0.04 min). MALDI-MS: m/z = 1640.3; calc. 1638.9 $[M+H]^+$.

N-{2-[2-(2-{3,5-Bis[4-(1,4,7,10-tetraazacyclododec-1-yl-methyl-1,4,7-tritert-butyloxycarbonylester)-phenoxymethyl]-phenoxy}ethoxy)ethoxy]ethyl}6-(6-hydroxy-3-oxo-3H-xanthene-9-yl)-isophthalic Acid ***26***. Compound **25** (104 mg, 74.1 μmol) was reacted with 5(6)-CF-PFP (75 mg, 138 μmol) and DIPEA (250 μL) for 1 h. MALDI-MS: m/z = 1765.91, calc. 1764.93 $[M+H]^+$.

N-{2-[2-(2-{3,5-Bis[3,5-bis(1,4,7,10-tetraazacyclododec-1-yl-methyl-1,4,7-tri-tert-butyloxycarbonylester)benzyl]-phenoxy}ethoxy)ethoxy]ethyl}-6-(6-hydroxy-3-oxo-3H-xanthene-9-yl)-isophthalic Acid ***31***. Compound **30** (200 mg, 84.7 μmol) was reacted with 5(6)-CF-PFP (80 mg, 150 μmol) and DIPEA (250 μL) for 1 h. MALDI-MS: m/z = 2759.7 $[M+Na]^+$, calc. 2755.6 $[M+Na]^+$.

Removal of Boc-Protecting Groups: General Procedure. The Boc-protected amine was dissolved in 500 μL CH_2Cl_2/TFA (1:1) and stirred at room temperature for 1−16 h. The solvent was removed under reduced pressure and the crude product purified via semipreparative HPLC.

N-[2-(2-{2-[3,5-Bis(1,4,7,10-tetraazacyclododec-1-yl-methyl)phenoxy]ethoxy}-ethoxy)ethyl]6-(6-hydroxy-3-oxo-3H-xanthene-9-yl)-isophthalic Acid ***1***. Compound **15** (3.5 μmol) was reacted for 2 h with CH_2Cl_2/TFA. Semipreparative HPLC yielded the TFA salt of the product as a yellow solid. Yield 2.4 mg (46%; **1**+5TFA). MALDI-MS: m/z = 953.3, calc. 952.5 $[M+H]^+$. ^1H NMR (500 MHz, DMSO-d_6, 343 K; isomer 5/isomer 6 = 0.6:0.4): δ = 8.91 (t, 0.6H, ^3J = 5.4 Hz), 8.76 (t, 0.4H, ^3J = 5.5 Hz), 8.45 (s, 0.6H), 8.24 (dd, 0.6H, ^3J = 8.1 Hz, ^4J = 1.5 Hz), 8.16 (dd, 0.4H, ^3J = 7.9 Hz, ^4J = 1.3 Hz), 8.07 (d, 0.4H, ^3J = 8.0 Hz), 7.68 (bs, 0.4H), 7.37 (d, 0.6H), 6.89 (s, 1.2H), 6.86 (s, 0.8H), 6.75 (s, 1H), 6.72−6.69 (m, 2H), 6.59−6.51 (m, 4H), 4.15−4.09 (m, 1.2H), 3.79−3.74 (m, 1.2H), 3.74−3.66 (m, 4.8H), 3.64−3.56 (m, 3.2H), 3.56−3.46 (m, 4H), 3.36 (dt, 0.8H), 3.13 (s, 8H), 3.04 (s, 8H), 2.83 (s, 8H), 2.73 (s, 8H) ppm. ^{13}C NMR (500 MHz, DMSO-d_6, 343 K): δ = 159.54, 158.35, 158.10, 154.58, 151.71, 136.43, 136.05, 134.52, 129.06, 128.94, 126.37, 124.01, 123.95, 118.25, 112.71, 112.61, 112.57, 108.91, 102.19, 69.77, 69.67, 69.49, 69.39, 68.91, 68.82, 68.64, 68.45, 66.98, 66.93, 55.06, 46.99, 44.58, 42.01, 38.71 ppm.

N-(2-{2-[2-(3,5-Bis{[2-(1,4,7,10-tetraazacyclododec-1-yl)-ethylamino]methyl}-phenoxy)ethoxy]ethoxy}ethyl)6-(6-hydroxy-3-oxo-3H-xanthene-9-yl)-isophthalic Acid ***2***. Compound **18** (18 μmol) was reacted for 16 h with CH_2Cl_2/TFA. Semipreparative HPLC yielded the TFA salt of the product as a yellow solid. Yield 9.8 mg (34%; **2**+5TFA). MALDI-MS: m/z = 1038.5, calc. 1038.6 $[M+H]^+$. ^1H NMR (500 MHz, DMSO-d_6, 343 K; isomer 5/isomer 6 = 0.6:0.4): δ = 8.36 (s, 0.6H), 8.18 (dd, 0.6H, ^3J = 8.0 Hz, ^4J = 1.3 Hz), 8.10 (d, 0.4H, ^3J = 7.9 Hz), 8.03 (d, 0.4H), 7.58 (s, 0.4H), 7.29 (d, 0.6H), 7.14 (s, 2H), 7.11 (s, 1H), 6.70 (s, 2H), 6.57−6.50 (m, 4H), 4.16−4.08 (m, 5.2H), 4.08−4.04 (m, 0.8H), 3.79−3.74 (m, 1.2H), 3.71−3.67 (m, 0.8H), 3.63−3.56 (m, 3.2H), 3.56−3.40 (m, 4H), 3.37−3.34 (m, 0.8H), 3.18−3.12 (m, 4H), 3.10−3.04 (m, 8H), 3.03−2.99 (m, 8H), 2.89−2.80 (m, 12H), 2.80−2.74 (m, 8H) ppm. ^{13}C NMR (500 MHz, DMSO-d_6): δ = 168.14, 168.02, 165.73, 165.55, 159.93, 159.40, 153.90, 152.20, 137.96, 134.51, 129.25, 128.89, 124.68, 123.97, 123.27, 122.92, 122.21, 116.59, 112.37, 108.61, 102.18, 69.84, 69.88, 69.06, 68.13, 68.78, 68.43, 67.38, 50.15, 47.69, 47.34, 44.54, 42.42, 42.08, 41.72, 39.25, 39.24 ppm.

2-(6-Hydroxy-3-oxo-3H-xanthene-9-yl)-5-{3-[2-(2-{2-[4-(1,4,7,10-tetraazacyclododec-1-yl-methyl)phenoxy]ethoxy}-ethoxy)ethyl]thioureido}-benzoic Acid ***3***. Compound **21** (63 μmol) was reacted for 1.5 h with CH_2Cl_2/TFA. Semipreparative HPLC afforded the TFA salt of the product as a yellow solid. Yield 32 mg (50%; **3**+3TFA). MALDI-MS: m/z =

799.7, calc. 799.4 $[M+H]^+$. ^1H NMR (500 MHz, DMSO-d_6) = 10.27 (bs, 1H), 8.35−8.29 (m, 2H), 7.77 (d, 1H, ^3J = 8.0 Hz), 7.26−7.21 (m, 2H), 7.20−7.15 (m, 1H), 6.92 (d, 2H, ^3J = 8.4 Hz), 6.70−6.67 (m, 2H), 6.62−6.53 (m, 4H), 4.10−4.04 (m, 2H), 3.78−3.73 (m, 2H), 3.72−3.56 (m, 12H), 3.11 (bs, 4H), 3.03 (bs, 4H), 2.82 (bs, 4H), 2.68 (bs, 4H) ppm. ^{13}C NMR (500 MHz, DMSO-d_6): δ = 180.54, 168.44, 159.43, 157.80, 151.79, 146.95, 141.38, 131.12, 129.28, 128.88, 127.02, 126.40, 123.90, 116.17, 114.16, 112.49, 109.61, 102.16, 69.81, 69.60, 68.32, 68.88, 66.97, 54.77, 47.02, 44.50, 43.58, 41.97 ppm.

N-{2-[2-(2-{3,5-Bis-[4-(1,4,7,10-tetraazacyclododec-1-yl-methyl)phenoxymethyl]-phenoxy}ethoxy)ethoxy]ethyl}6-(6-hydroxy-3-oxo-3H-xanthene-9-yl)-isophthalic acid ***4***. Compound **26** (74 μmol) was reacted for 1 h with CH_2Cl_2/TFA. Semipreparative HPLC resulted in a yellow TFA salt. Yield 52 mg (43%; **4**+5TFA). MALDI-MS: m/z = 1165.55, calc. 1164.16 $[M+H]^+$. ^1H NMR (500 MHz, DMSO-d_6, 343 K; isomer 5:isomer 6 = 0.6:0.4): δ = 8.69 (t, 0.6H, ^3J = 5.1 Hz), 8.56 (t, 0.4H, ^3J = 5.1 Hz), 8.44 (s, 0.6H), 8.23 (dd, 0.6H, ^3J = 8.1 Hz, ^4J = 1.5 Hz), 8.15 (dd, 0.4H, ^3J = 7.9 Hz, ^4J = 1.3 Hz), 8.03 (d, 0.4H, ^3J = 8.1 Hz), 7.66 (bs, 0.4H), 7.32 (d, 0.6H), 7.29−7.25 (m, 4 H), 7.11 (s, 2H), 7.03−7.00 (m, 4H), 6.97 (s, 1H), 6.71−6.69 (m, 2H), 6.57−6.54 (m, 4H), 5.07 (s, 4H), 4.15−4.11 (m, 1.2H), 4.08−4.04 (m, 0.8H), 3.80−3.76 (m, 1.2H), 3.71 (s, 4H), 3.71−3.68 (m, 0.8H), 3.66−3.60 (m, 3.2H), 3.56−3.48 (m, 4H), 3.38 (dt ≈ q, 0.8H), 3.13−3.09 (m, 8H), 3.08−3.03 (m, 8H), 2.90−2.85 (m, 8H), 2.78−2.72 (m, 8H) ppm. ^{13}C NMR (500 MHz, DMSO-d_6, 343 K): δ = 167.64, 167.49, 164.53, 164.37, 159.22, 158.43, 157.57, 154.13, 151.57, 138.54, 136.07, 134.10, 130.72, 128.89, 128.53, 128.42, 127.30, 124.25, 123.67, 122.89, 121.88, 118.44, 114.44, 112.85, 112.33, 108.91, 102.04, 69.61, 69.51, 69.29, 69.20, 68.62, 68.45, 68.46, 68.30, 68.93, 67.12, 67.06, 54.95, 47.25, 44.50, 42.15, 41.92, 38.78, 38.79 ppm.

N-{2-[2-(2-{3,5-Bis[3,5-bis(1,4,7,10-tetraazacyclododec-1-yl-methyl)benzyl]phenoxy}-ethoxy)ethoxy]ethyl}-6-(6-hydroxy-3-oxo-3H-xanthene-9-yl)-isophthalic acid ***5***. Compound **31** (84.7 μmol) was reacted for 16 h with CH_2Cl_2/TFA. Semipreparative HPLC gave a yellow TFA salt. Yield 51 mg (24%; **5**+10TFA). MALDI-MS: m/z = 1535.0, calc. 1533.0 $[M+H]^+$. ESI-MS: m/z = 511.9 $[M+3H]^{3+}$, calc. 511.7 $[M+3H]^{3+}$. ^1H NMR (500 MHz, DMSO-d_6, 330 K; isomer 5/isomer 6 = 0.6:0.4): δ = 8.76 (t, 0.5H, ^3J = 5.6 Hz), 8.62 (t, 0.5H, ^3J = 5.6 Hz), 8.44 (s, 0.5H), 8.23 (dd, 0.5H, ^3J = 8.1 Hz, ^4J = 1.5 Hz), 8.15 (dd, 0.5H, ^3J = 7.9 Hz, ^4J = 1.3 Hz), 8.05−8.01 (m, 0.5H), 7.66 (bs, 0.5H), 7.34 (d, 0.5H), 7.13−7.10 (m, 2H), 7.03 (s, 1H), 6.95 (s, 4H), 6.79 (bs, 2H), 6.72−6.70 (m, 2H), 6.57−6.53 (m, 4H), 5.07 (s, 4H), 4.15−4.10 (m, 1H), 4.08−4.03 (m, 1H), 3.80−3.76 (m, 1H), 3.77 (s, 8H), 3.72−3.68 (m, 1H), 3.66−3.40 (m, 7H), 3.40−3.35 (m, 1H), 3.16−3.09 (m, 16H), 3.09−3.03 (m, 16H), 2.90−2.84 (m, 16H), 2.80−2.75 (m, 8H) ppm. ^{13}C NMR (500 MHz, DMSO-d_6): δ = 159.40, 158.44, 158.10, 154.83, 134.07, 128.89, 128.50, 124.36, 123.71, 123.71, 123.64, 121.90, 118.93, 115.17, 113.23, 112.33, 101.97, 69.31, 69.23, 69.06, 68.49, 68.32, 68.97, 68.46, 67.03, 66.77, 54.87, 46.97, 44.51, 41.93, 41.80, 38.69 ppm.

Zn^{2+}-Complexation. The cyclen derivatives **1**−**5** were dissolved in double distilled water (200 μL/500 μg ligand) and adjusted with 0.1 M NaOH to pH 8−10. 0.1 mM $Zn(NO_3)_2$ in H_2O was added to obtain a molar Zn^{2+}/cyclen ratio of 1:1. After heating for 2 h at 50 °C, the complexes were formulated to give 0.5 mM aqueous solutions which were lyophilized for later applications.

1,3-Bis(1,4,7,10-tetraazacyclododec-1-yl-methyl-4,7,10-tri-tert-butyloxycarbonyl ester)-(5-hydroxy)-benzene ***35***. Compound **34** (400 mg, 340 μmol) was dissolved in THF. A 1 M solution of tetrabutylammoniumfluoride in THF (442 μL, 442 μmol, 1.3 equiv) was added at 0 °C. The reaction mixture was stirred for 30 min at 0 °C and 30 min at room temperature. The solvent was removed *in vacuo*; and the product was dissolved in Et_2O, washed with saturated ammonium chloride solution, and dried over $MgSO_4$. Filtration and solvent evaporation yielded **35** as a white solid. Yield 325 mg (90%). MALDI-MS: m/z = 1064.1, calc. 1063.7 $[M+H]^+$. ^1H NMR (500 MHz, DMSO-d_6, 343 K): δ = 9.09 (s, 1H), 6.60 (s, 2H), 6.55 (s, 1H), 3.66 (s, 4H), 3.54−3.47 (m, 8H), 3.35−3.30 (m, 8H), 3.28 (s, 8H), 2.58 (s, 8H), 1.41 (s, 18H), 1.37 (s, 36H) ppm. ^{13}C NMR (500 MHz, DMSO-d_6, 343 K): δ = 156.70, 154.53, 154.16, 136.49, 122.72, 115.82, 78.07, 77.79, 54.57, 53.86, 48.19, 46.46, 46.16, 27.90, 27.67 ppm.

1,3-Bis(1,4,7,10-tetraazacyclododec-1-yl-methyl-4,7,10-tri-tert-butyloxycarbonylester)-(5-(1-fluoro-2-methoxyethane))-benzene ***36***. Compound **35** (57.0 mg, 53.6 μmol) in acetonitrile was reacted with 2-fluoroethyl tosylate (23.4 mg, 107 μmol) and K_2CO_3 (22.2 mg, 161 μmol) under reflux for 18 h. The K_2CO_3 was filtrated and the solvent was evaporated *in vacuo*. Column chromatography on silica gel (cyclohexane/EtOAc = 4:1) yielded 40 mg **36** as a white solid (67%). MALDI-MS: m/z = 1110.3, calc. 1109.7 $[M+H]^+$. ^1H NMR (500 MHz, DMSO-d_6, 343 K): δ = 6.79 (s, 2H), 6.75 (s, 1H), 4.76−4.63 (m, 2H, ^3J = 47.8 Hz), 4.24−4.14 (m, 2H, ^4J = 29.0 Hz), (s, 4H), 3.54−3.48 (m, 8H), 3.37−3.32 (m, 8H), 3.29 (s, 8H), 2.58 (s, 8H), 1.41 (s, 18H), 1.36 (s, 36H) ppm. ^{13}C NMR (500 MHz, DMSO-d_6, 343 K): δ = 157.76, 154.57, 154.16, 137.44, 124.30, 114.89, 82.22, 80.89, 78.07, 77.84, 54.94, 53.95, 48.20, 46.41, 46.29, 27.86, 27.63 ppm.

1,3-Bis(1,4,7,10-tetraazacyclododec-1-yl-methyl)-(5-(1-fluoro-2-methoxyethan))-benzene ***6***. Compound **36** (40 mg, 36 μmol) was dissolved in TFA/CH_2Cl_2 = 1:1 and stirred at room temperature for 1 h. After solvent removal, the TFA salt of the product was obtained as a white solid. Yield 42 mg (100%; **6**+5TFA). ESI-MS: m/z = 255.2, calc. 255.2 $[M+2H]^{2+}$. ^1H NMR (500 MHz, DMSO-d_6): δ = 6.91 (d, 2H, ^4J = 0.9 Hz), 6.77 (s, 1H), 4.82−4.69 (m, 2H, ^3J = 47.8 Hz), 4.30−4.20 (m, 2H, ^4J = 30.0 Hz), 3.72 (s, 4H), 3.14 (s, 8H), 3.09−3.01 (m, 8H), 2.87−2.80 (m, 8H), 2.77−2.71 (m, 8H) ppm. ^{13}C NMR (500 MHz, DMSO-d_6): δ = 158.01, 136.67, 123.79, 115.05, 82.42, 81.08, 55.36, 47.30, 44.50, 42.17, 41.93 ppm.

1,3-Bis-(1,4,7,10-tetraazacyclododec-1-yl-methyl)-(5-(1-[^{18}F]fluoro-2-methoxyethane))-benzene ***^{18}F-6***. The protected precursor **36** (2.5 mg, 2.34 μmol) in 10 μL DMF was reacted with 2-[^{18}F]fluoroethyl tosylate[23] (185 MBq) in 200 μL DMF in the presence of K_2CO_3 (5 mg). The reaction mixture was stirred for 35 min at 120 °C and separated by semipreparative HPLC. The eluate was concentrated on a C18-SepPak-light cartridge and eluted with 2 mL EtOH. Evaporation of the solvent yielded 68 MBq (77% decay-corrected). Deprotection of **^{18}F-36** was performed at ambient temperature with 200 μL TFA in 50 μL acetonitrile. Owing to the HPLC purification of **^{18}F-36**, the specific activity was estimated to >50 GBq/μmol.

After evaporation, the complexation of **^{18}F-6** with Zn^{2+} was carried out in 100 μL PBS for 5 min at 70 °C containing 10 μL of an aqueous 1.5 mM $Zn(NO_3)_2$ solution. For imaging experiments, the zinc complex of **^{18}F-6** was diluted with 400 μL PBS and filtered sterile.

Cell Experiments. *Flow Cytometry.* Apoptosis was induced with 10^6 cells/mL using staurosporine (1 μM) during 4 h. The cells were washed with PBS and split into 1 mL samples containing 10^6 cells. After centrifugation, cells were taken up in 100 μL TES buffer for incubation with complex solutions or in 100 μL annexin binding buffer for annexin experiments. 1.0 μL of a 0.5 mM complex solution was added to the TES buffered cells and 1.5 μL of Alexa Fluor 488 conjugated annexin was added to the cells taken up in annexin binding buffer. After 15 min incubation in the dark, the suspensions were diluted with 300 μL TES or annexin binding buffer. Flow-cytometry measurements were performed with 100 μL cell suspension and 900 μL cold buffer. 6×10^3 cells were counted in each experiment. Where necessary, 10 μL propidium iodide solution (250 μg/mL) was added just before the measurement. Control cells were treated in the same way and measured as a comparison with each experiment.

Evidence of CXCR4. The anti-hCXCR-4 antibody was diluted with cold PBS to a concentration of 10 μg/mL. Control and apoptotic Jurkat cells (approximately 10^6) were suspended in 100 μL antibody solution and incubated for 30 min at 4 °C. The cells were washed three times with cold PBS and taken up in 100 μL PBS solution of FITC-labeled antimouse monoclonal antibody Ig_{2A}. After 30 min incubation at room temperature, the cells were washed again three times with cold PBS and finally dispersed in 400 μL PBS. 100 μL cell suspension was added to 900 μL cold PBS and measured in a flow cytometer.

Competition with meta AMD3100. 1.0 μL of a 50 mM aqueous solution of meta AMD3100, synthesized according to the literature[24] and 1.0 μL of 0.5 mM complex $[\mathbf{Zn_2 1}]^{4+}$ solution was added to 10^6 staurosporine treated Jurkat cells in cold TES buffer. The cells were incubated 15 min at room temperature in the dark. The samples were diluted with TES buffer to 400 μL. 100 μL of the suspension were added to 900 μL cold buffer and measured by flow cytometry.

Confocal Laser Scanning Microscopy (CLSM). Apoptosis induction of Jurkat cells for CLSM experiments was performed as described above. To prevent free floating under coverslips, the cells were immobilized on polylysine precoated slides. After incubation with $[\mathbf{Zn_2 1}]^{4+}$ for 15 min, the cells were transferred to the object slide and placed under the microscope. Images were taken from the midcell *z*-plane.

Animal Studies. The experiments were approved by the governmental review committee on animal care. All animal experiments were performed in compliance with the current version of the German law concerning animal protection and welfare. Animals were kept under standard laboratory conditions at the German Cancer Research Center or at Bayer Healthcare Research Facilities.

Male Copenhagen rats (approximately 180 g) were subcutaneously transplanted on both thighs with 1×10^6 Dunning adeno carcinoma R3327-AT1 cells. Fourteen days after tumor cell implantation, the left tumor was irradiated with a single dose of 50 Gy using an Artiste linear accelerator (Siemens AG, München, Germany). The right tumor served as control. One day before (day 13 after tumor cell inoculation) and six and ten days after irradiation, the rats were imaged using $[\mathbf{Zn_2(^{18}F\text{-}6)}]^{4+}$. 15–25 MBq in 200 μL PBS was injected into the tail vein. For the PET-scan, the animals were anesthetized with sevoflurane and maintained under anesthesia during the scan (2.5% for induction and 1% for maintenance of anesthesia). PET studies were performed with the Siemens Inveon small animal PET scanner (Siemens, Knoxville, USA). A transmission scan was done for 10 min prior to tracer administration with two rotating germanium pin sources to obtain cross sections for attenuation correction. PET data were acquired for 1 h in list mode on an Inveon scanner (Siemens Erlangen Germany) using a matrix of 256 × 256 (pixel size $0.3882 \times 0.3882 \times 0.796$ mm^3). The images were reconstructed iteratively using the space alternating generalized expectation maximization method (SAGE, 16 subsets, 4 iterations) applying median root prior correction.

1.5×10^6 HelaMatu (human cervix carcinoma) tumor cells were inoculated in a volume of 100 μL (medium/matrigel) into the right shoulder of nude mice (NMRI nu/nu, female, ca. 20 g, obtained from Taconic). At day 12 after inoculation, animals were treated with taxol using 18 mg/kg i.v. or vehicle (5% cremophore, 5% ethanol). PET images were acquired using an Inveon small animal PET/CT scanner (Siemens, Knoxville, USA) at 60 min p.i. for 10 min. After the PET study, animals were sacrificed, and tumors were removed and cut into 18 μM slices (Cryostat Fa Leica CM 3050 S). Tumor slices were exposed to a phosphoimager plate (BAS-SR Imaging plate, Fuji, IP-SR 20 × 25) overnight. Analysis was performed using the BAS-5000 Imaging System (Fuji). Cleaved caspase 3 in the tumor samples was detected by immunohistochemistry (IHC) using a polycolonal antibody against cleaved caspase 3 (rabbit, Cell Signaling, # 9661-S). IHC was performed using established standard protocols.

RESULTS

Syntheses. The syntheses of the title compounds essentially followed the preparation strategy applied to obtain bis(dipicolylamine) derivatives.[12] This route offered the possibility of attaching different fluorescent dyes as well as other markers such as radiolabels in the perspective of in vivo imaging. As outlined in Scheme 1, the core structures were obtained as *N*-trityl protected 3,5-bis(bromomethyl)- (**9**) and 4-bromomethyl phenyl (**10**) derivatives.

Scheme 1. Syntheses of Bis(cyclen) Scaffolds

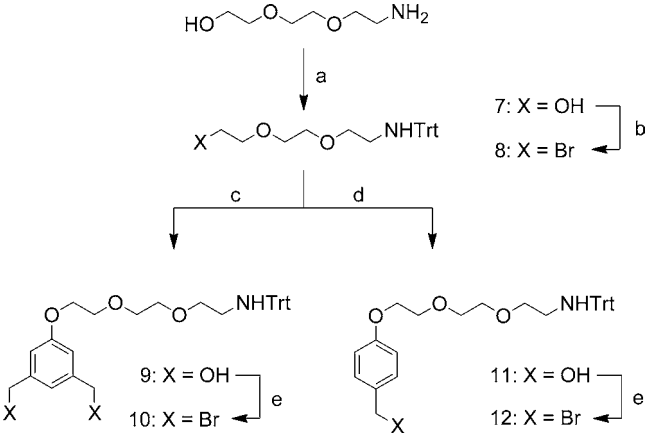

(a) Trityl chloride, Et_3N, CH_2Cl_2; (b) CBr_4, K_2CO_3, Ph_3P, CH_2Cl_2; (c) 3,5-Bis(hydroxymethyl)phenol, K_2CO_3, acetonitrile, reflux; (d) 4-Hydroxymethylphenol, K_2CO_3, acetonitrile, reflux; (e) CBr_4, Ph_3P, CH_2Cl_2.

Tris(Boc)cyclen (Z) was alkylated using precursors **10** and **12** yielding compounds **13** and **19**, respectively (Scheme 2). Selective cleavage of the trityl group with hexafluoroisopropa-

dx.doi.org/10.1021/bc200457b | *Bioconjugate Chem.* 2011, 22, 2611–2624

Scheme 2. Syntheses of Bis(cyclen) Ligands

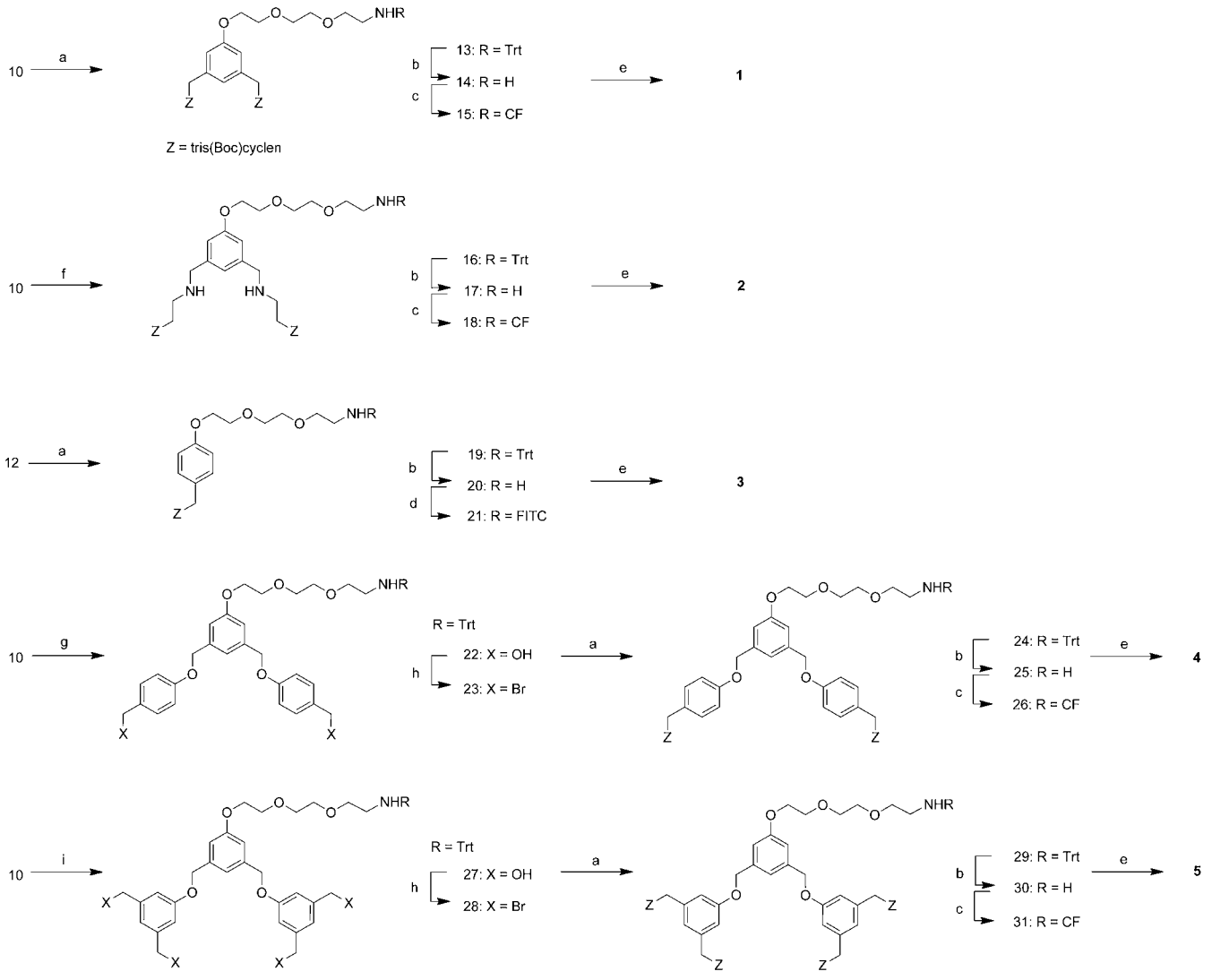

(a) Tris(Boc)cyclen, K_2CO_3, KI, acetonitrile, 50 °C; (b) Hexafluoroisopropanol/1% H_2O, CH_2Cl_2; (c) CF-PFP ester, DIPEA, DMF; (d) FITC, DIPEA, DMF; (e) TFA, CH_2Cl_2; (f) Aminoethyl-tris(Boc)cyclen, K_2CO_3, acetonitrile, 50 °C; (g) 4-Hydroxymethylphenol, K_2CO_3, acetonitrile, reflux; (h) CBr_4, Ph_3P, CH_2Cl_2; (i) 3,5-Bis(hydroxymethyl)phenol, K_2CO_3, acetonitrile, reflux.

nol was followed by the introduction of fluorescent markers carboxyfluorescein pentafluorophenol ester (5(6)-CF-PFP) and fluorescein isothiocyanate (FITC). Deprotection of the cyclen amino functionalities yielded chelator **1** as well as the mono cyclen **3**. In order to introduce a pendant heteroatom into the spacer, tris(Boc)cyclen providing an aminoethyl side arm was alkylated with compound **10**. Removal of the trityl group, conjugation with 5(6)-CF-PFP, and Boc deprotection resulted in chelator **2**. The cyclen multimers **4** and **5** were obtained via elongation of the central scaffold **10** with 4-hydroxymethylphenol and 3,5-di(hydroxymethyl)phenol. Alkylation of tris(Boc)cyclen using the resulting bromo compounds **23** and **28** together with selective trityl deprotection and reaction with 5(6)-CF-PFP gave compounds **26** and **31**, respectively. Final Boc deprotection resulted in the cyclen derivatives **4** and **5** which were then complexed with Zn^{2+} for biological experiments.

The synthesis of the radiofluorination precursor **35** proceeded through alkylation of tris(Boc)cyclen with the TBDMS protected phenol **33** (Scheme 3). After silyl deprotection, compound **35** was reacted with 2-fluoroethyl tosylate and treated with TFA to cleave the Boc groups forming ligand **6**. The radiolabeled congener ^{18}**F-6** was prepared accordingly using HPLC purified 2-[^{18}F]fluoroethyl tosylate.

The final step implied the formation of the Zn^{2+} complexes. Aqueous solutions of the fluorescein-cyclen derivatives were heated at 50 °C with 1 equiv Zn^{2+}/cyclen. The resulting complexes were lyophilized and redissolved in H_2O to form 0.5 mM solutions. The HPLC purified, noncarrier added radiofluorinated bis(cyclen) **6** was transferred into the zinc complex $[\mathbf{Zn_2}(^{18}\mathbf{F\text{-}6})]^{4+}$ by adding Zn^{2+} salt and heating.

Flow Cytometry. The influence of the $\{$bis[Zn(cyclen)]$\}^{4+}$ complexes on cell size and granularity was studied with $[\mathbf{Zn_2 1}]^{4+}$ to exclude cell damaging of untreated Jurkat cells during flow cytometry. The cells were, therefore, analyzed using the flow cytometric sideward (SSC) and forward (FSC) scatter signals which allowed the detection of advanced apoptotic and secondary necrotic cells. The cells were incubated in TES buffer with $[\mathbf{Zn_2 1}]^{4+}$ at concentrations in the range 0−50 μM for up

dx.doi.org/10.1021/bc200457b | *Bioconjugate Chem.* 2011, 22, 2611−2624

Scheme 3. Synthesis of Bis(cyclen) 6 and ^{18}F Labeling

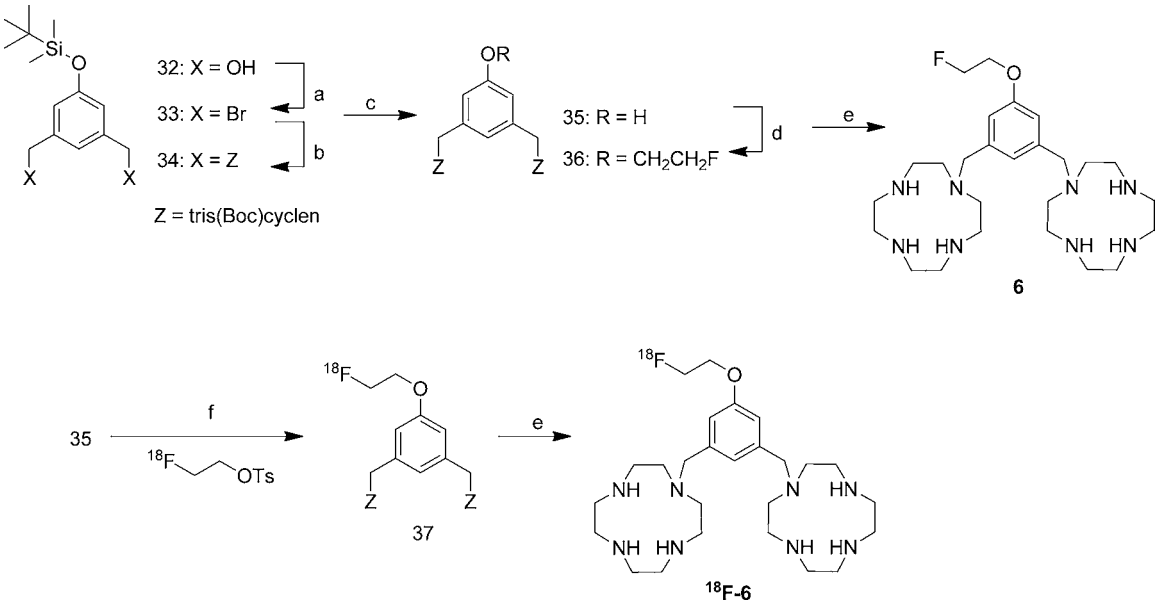

(a) CBr_4, Ph_3P, CH_2Cl_2; (b) tris(Boc)cyclen, K_2CO_3, KI, acetonitrile, 50 °C; (c) $(n\text{-}Bu)_4N^+$ F^-, THF; (d) 2-Fluoroethyl tosylate, K_2CO_3, acetonitrile, reflux; (e) TFA, CH_2Cl_2; (f) K_2CO_3, acetonitrile, sealed reaction vial, 30 min/120 °C.

to 72 h. As demonstrated in the Supporting Information, toxicity against vital Jurkat cells proved negligible.

Apoptosis was induced in Jurkat cells with 1 μM staurosporine for 4 h.[25] Figure 3 shows flow-cytometric density plots (upper row) obtained with Alexa Fluor 488 labeled annexin A5 (AnxA5-AF) and propidium iodide (PI). Cells with high binding of Annexin A5 were found in the rectangle Q1, indicating 4.7% of apoptotic cells for the control cell population vs 38.5% of apoptotic cells after staurosporine treatment. This value varied between 30% and 60%. Simultaneous binding of annexin A5 and propidium iodide are found in Q2, indicating cells which were in the transition of apoptosis to necrosis (late apoptosis and secondary necrosis).[26] Here, 2.5% was obtained for untreated and 19.1% for staurosporine treated cells. Cells in segment Q3 represent unchanged cells and those in Q4 are solely dyed with PI, presumably completely necrotic cells.

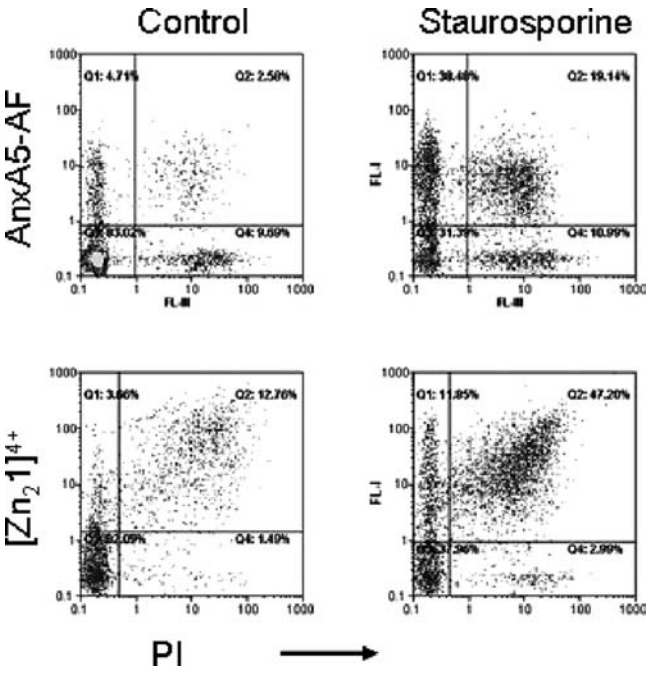

Figure 3. Flow cytometric density plots of Jurkat cells in the presence of AnxA5-AF/propidium iodide (PI) and $[\mathbf{Zn_21}]^{4+}$ (lower panel) after treatment with staurosporine (right). Untreated controls are shown on the left.

Lower row of density plots (Figure 3) illustrates flow cytometry results which were obtained with the same experimental setup as described above but in the presence of $[\mathbf{Zn_21}]^{4+}$. After staurosporine treatment, 11.9% was found in Q1 and 47.2% in Q2. The latter value indicated $[\mathbf{Zn_21}]^{4+}$-binding together with PI accumulation. The sum of Q1 and Q2 was about 60% for both AnxA5-AF and the zinc complex. It appears remarkable that after the addition of $[\mathbf{Zn_21}]^{4+}$ and PI the SSC and FSC signals of the staurosporine treated cells were shifted into the secondary necrosis fraction (arrow in SI) and that these signals can be attributed to Q2. With the exception of $[\mathbf{Zn_22}]^{4+}$, this effect was also observed using the remaining fluorescent zinc-cyclen complexes.

The insertion of a pendant ethylene amino group like in $[\mathbf{Zn_22}]^{4+}$ led to histograms almost indistinguishable between staurosporine treated and control cells. Both the $[\mathbf{Zn_22}]^{4+}$ complex-related fluorescence of treated and control cells appeared in Q1 at 38.2% and 31.9%, respectively, showing similar distribution patterns. The intensity of the green fluorescence of $[\mathbf{Zn_22}]^{4+}$ was, however, strongly reduced as compared with the fluorescence of $[\mathbf{Zn_21}]^{4+}$ in apoptotic cells.

Ligands **3**, **4**, and **5** were synthesized to study the influence of the number of $[Zn(cyclen)]^{2+}$ groups on the fluorescence of staurosporine treated cells. While complex $[\mathbf{Zn_24}]^{4+}$ showed similar results as obtained with $[\mathbf{Zn_21}]^{4+}$, the tetrameric cyclen complex $[\mathbf{Zn_45}]^{8+}$ increased the mean fluorescence intensity (MFI) of the green fluorescence signals of treated Jurkat cells by a factor of 2.3. The monomeric $[\mathbf{Zn3}]^{2+}$ produced in turn a

much smaller MFI, 2 vs 34 of $[\mathbf{Zn3}]^{2+}$ and $[\mathbf{Zn_2 1}]^{4+}$or $[\mathbf{Zn_2 4}]^{4+}$, respectively (SI).

The relevance of zinc(II) in the cyclen complexes, which as outlined in the introduction was thought to be necessary for the ternary interaction with PS, was tested by comparing the complex with the free ligand. The free cyclen derivative **4** produced an unspecific fluorescence of low intensity, whereas the complex $[\mathbf{Zn_2 4}]^{4+}$ showed strong fluorescence of staurosporine treated cells as described above (SI).

All flow cytometric results described so far were obtained in the presence of the respective zinc complexes. Removal of these dyes by two washing steps resulted in the loss of most of the intracellular dye. The reverse result was obtained by increasing the zinc-complex concentration leading to an increase of the mean fluorescence intensity of treated Jurkat cells. Loss and increase of fluorescence intensity indicates reversibility of concentration-dependent accumulation. Figure 4 shows this

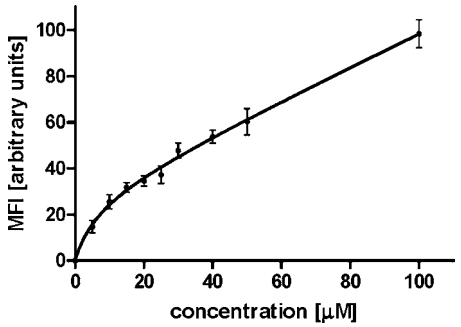

Figure 4. Mean fluorescence intensity (MFI) of staurosporine treated Jurkat cells in the presence of increasing amounts of $[\mathbf{Zn_2 1}]^{4+}$ (Data are expressed as mean ± SD; n = 3.)

dependence, which was obtained with $[\mathbf{Zn_2 1}]^{4+}$ and staurosporine treated Jurkat cells. The mean fluorescence intensity increased within the 0−100 μM range without reaching saturation.

Confocal Laser Scanning Microscopy (CLSM). Clues about the intracellular location of the $\{$bis[Zn(cyclen)]$\}^{4+}$ complexes were obtained using confocal laser scanning microscopy (CLSM). Staurosporine treated Jurkat cells were incubated with a zinc-cyclen complex and placed under the microscope. Figure 5a (and SI) exemplarily shows staurosporine treated cells which deposited $[\mathbf{Zn_2 1}]^{4+}$ throughout the cytoplasm. The membrane binding of AnxA5-AF on the other hand is obvious (Figure 5b).

Influence of the CXCR4 Receptor. The presence of CXCR4 on Jurkat cells was confirmed on control and staurosporine-treated cells using the mouse anti-CXCR4 antibody mAb12G5. Flow cytometry revealed a strong expression of ca. 80% for both cell types. The mean fluorescence intensity was comparable, which means that there is no significant difference in the exposure of CXCR4 on treated and control cells. In addition, competition with the meta derivative of AMD3100 was performed which is known to bind CXCR4 in the low nanomolar range. Even with 100-fold molar excess, no depletion of the $[\mathbf{Zn_2 1}]^{4+}$ fluorescence was observed with apoptotic cells (SI).

PET Imaging. The in vivo behavior of the $\{$bis[Zn(cyclen)]$\}^{4+}$ compounds was studied with $[\mathbf{Zn_2(^{18}F\text{-}6)}]^{4+}$. Male Copenhagen rats bilaterally transplanted with Dunning R3327-AT1 prostate tumors were irradiated on one side with a

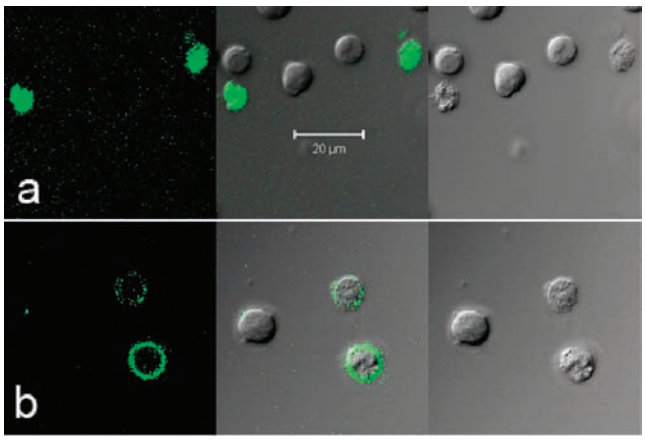

Figure 5. CLSM images (λ_{exc} 488 nm/3%; BP 505−530 nm) of staurosporine treated Jurkat cells incubated with $[\mathbf{Zn_2 1}]^{4+}$ (a) and AnxA5-AF (b). The different locations of both compounds are conclusive: cytoplasmic distribution of $[\mathbf{Zn_2 1}]^{4+}$ (a) and outer membrane accumulation of AnxA5-AF (b).

single dose of 50 Gy. The contralateral tumor served as a control. PET images were obtained one hour after intravenous injection of $[\mathbf{Zn_2(^{18}F\text{-}6)}]^{4+}$ at day six after irradiation (Figure 6a). The irradiated tumor accumulated more radioactivity than the control which showed only faint uptake in the rim area. The time dependence of radioactivity in both tumors indicated modestly elevated initial uptake and retarded washout in the irradiated tumor (SI). With the exception of kidneys and liver, the residual abdominal background activity proved to be low.

In addition, $[\mathbf{Zn_2(^{18}F\text{-}6)}]^{4+}$ was tested with HelaMatu tumor bearing mice 2 days after taxol treatment. PET images were acquired 60 min after injection of $[\mathbf{Zn_2(^{18}F\text{-}6)}]^{4+}$. The treated animal shown in Figure 6b indicated higher tumor uptake as compared to the control tumor (Figure 6d). In comparison to the rat image, the background radioactivity of the mouse (liver, kidneys, intestine) appeared to be higher. In addition, bone joint activity indicated some defluorination. Quantification of tumor radioactivity in the excised tumors confirmed the stronger accumulation in treated tumors (SI). Additional autoradiography of excised tumor slices after the PET-study confirmed this finding in the treated tumors (Figure 7a versus c) and staining for cleaved caspase 3 proved the presence of apoptotic tissue after taxol treatment (Figure 7b versus d).

DISCUSSION

Among other approaches, search for the replacement of the apoptosis imaging agent [^{99m}Tc(HYNIC-rh-annexin A5)] has been focused on metal complexes which were also attractive as phosphate sensors in cell biology. Especially, zinc-cyclen complexes have been found to bind phosphate or other anionic groups.[18] Consequently, a series of mono-, di-, and tetrameric cyclen ligands have been synthesized, capable of stabilizing Zn^{2+} for in vivo applications and of functioning as carriers of fluorescent or radioactive reporter probes. The syntheses of the complex ligands summarized in Schemes 1−3 were followed by zinc complexation as the final reaction step.

Flow cytometry of Jurkat cells which are incubated with fluorescent annexin A5, like AnxA5-AF, represents an established method to determine the degree of apoptosis after contact with cytostatic agents.[4−6] The inhibitory activity of staurosporine on protein kinases of Jurkat cells is known to induce apoptosis.[25] Owing to the disposition of apoptotic cells,

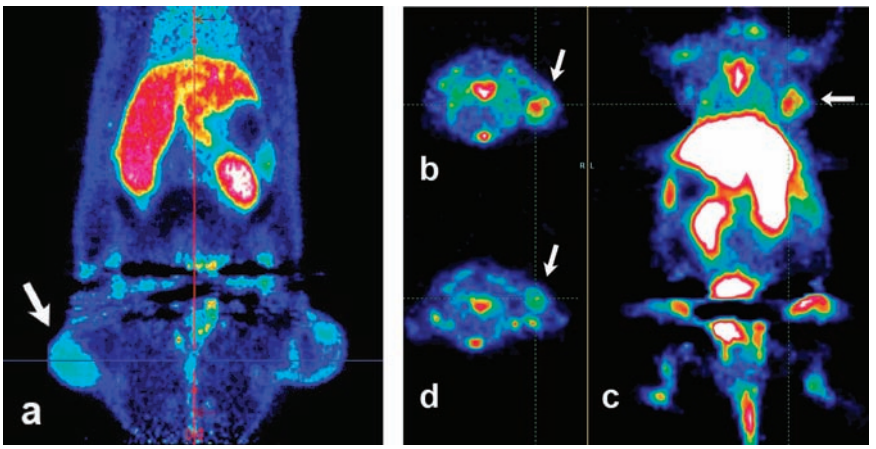

Figure 6. One hour coronal PET image of a rat with a bilaterally transplanted Dunning prostate adenocarcinoma 6 d after 50 Gy radiation therapy (a). The irradiated tumor is indicated by the arrow. One hour PET image of a mouse with HelaMatu tumors (arrows) two days after treatment with taxol (b,c) and the untreated control (d). Transaxial slices are shown in (b) and (d), and a coronal slice is shown in (c).

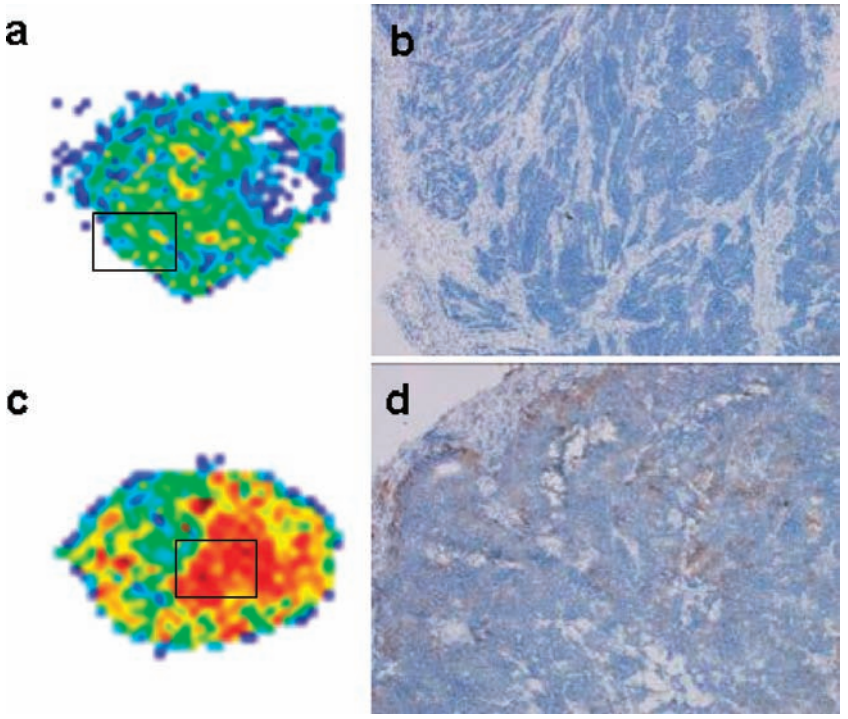

Figure 7. Autoradiography of HeLaMatu tumor slices taken from animals of the PET study (a,c) and IHC images (frames) stained for cleaved caspase 3 (b,d). Upper panel: Tumor samples from control animals. Lower panel: Tumor samples from taxol treated animals. The radioactive uptake (frames) corresponds with the presence of cleaved caspase 3 IHC.

this effect is accompanied by the formation of late apoptotic and secondary necrotic cells.[26]

As illustrated in Figure 3, most staurosporine treated cells were recorded in the Q1 rectangle where cell signals accumulate resulting from annexin A5 binding with externalized PS (see also Figure 5b). In Q2, cell signals from AnxA5-AF and PI binding are collected, which owing to PI uptake indicate leakiness of the damaged cell membrane. This area of flow-cytometric measurements (33% of Q1+Q2) represents the above-mentioned secondary necrosis state of dying cells.

Replacing AnxA5-AF with the bis(cyclen) complex $[\mathbf{Zn_2 1}]^{4+}$, most cells with green fluorescence also showed PI uptake after staurosporine treatment. Although the cell suspensions were taken from the same cell pool, $[\mathbf{Zn_2 1}]^{4+}$ stained the majority of cells in the secondary necrotic population Q2 (80% of Q1+Q2) (Figure 3; lower panel).

The larger Q2 fraction is obviously related to the common permeability of both dyes $[\mathbf{Zn_2 1}]^{4+}$ and PI. Remarkably, these Q2 signals belong to the SSC and FSC signals indicating changes of size and granularity associated with the onset of cell death (arrow in respective SSC/FSC plot, SI). The question whether intracellular accumulating $[\mathbf{Zn_2 1}]^{4+}$ is responsible for this effect can be related to the observation of Kimura et al. that $\{bis[Zn(cyclen)]\}^{4+}$ complexes are able to form ternary complexes with DNA bases like thymidine.[27] This interference is, however, only in effect if apoptosis has been triggered by staurosporine and the zinc complex is internalized. Any cell

dx.doi.org/10.1021/bc200457b | *Bioconjugate Chem.* 2011, 22, 2611–2624

damaging effects of the zinc complex on vital cells were not observed (SI).

As reviewed in the introduction, binding of the zinc complexes on apoptotic cells through the coordination of externalized PS was thought to lead to membrane binding. However, the fluorescence of $[\mathbf{Zn_21}]^{4+}$ was found exclusively in the cytosol of staurosporine affected cells. This finding and the clear membrane fluorescence of AnxA5-AF are apparent in the CLSM images shown in Figure 5. A similar intracellular distribution was reported with bis(zinc(II)-dipicolylamine) complexes.[9,12,13] Microscopic fluorescence images indicate that PSS-480 (Figure 1) stains most prominently those apoptotic Jurkat cells which are also positive with 7-amino-actinomycin, a PI like DNA intercalator, known to dye secondary necrotic cells.[13]

The assumption that zinc-cyclen derivatives can profit from multimerization was demonstrated with $[\mathbf{Zn_45}]^{8+}$. With staurosporine treated cells, this tetramer showed a more than doubled fluorescence intensity as compared to the two comparable dimeric complexes $[\mathbf{Zn_21}]^{4+}$ and $[\mathbf{Zn_24}]^{4+}$. The monocyclen complex $[\mathbf{Zn3}]^{2+}$, on the other hand, produced only signals with reduced intensity. The increase of the fluorescence intensity was obviously mediated by the additional zinc-cyclen functionalities. It may, therefore, be speculated that the uptake initially begins through binding at externalized PS which transports the resulting ternary complexes with the help of aminophospholipid translocase into the cytosol. On the other hand, concentration driven diffusion through a damaged cell membrane may also be conceivable. The absence of zinc, however, inhibits fluorescent signals in Q1 and Q2 (complex ligand **4**, SI) which also points to translocase assisted internalization.

An additional observation supporting this notion is given by the introduction of an exocyclic pendant nitrogen. Complex $[\mathbf{Zn_22}]^{4+}$ contains an extra heteroatom able to coordinate zinc and to compete with PS thereby disturbing PS related membrane penetration. The comparable green, but strongly reduced fluorescences of $[\mathbf{Zn_22}]^{4+}$ in treated as well as in control cells may be explained with unspecific binding (SI).

A saturation experiment was performed with staurosporine treated cells in order to evaluate an uptake limit. Figure 4 illustrates the increase of fluorescence with increasing concentration of $[\mathbf{Zn_21}]^{4+}$. Above 20 μM and up to 100 μM, the uptake of $[\mathbf{Zn_21}]^{4+}$ followed a straight relationship without signs of saturation. It was also evident that the removal of these complexes from the medium resulted in a strong reduction of the intracellular fluorescence. These findings indicate a rather weak intracellular interaction of $\{bis[Zn(cyclen)]\}^{4+}$ complexes.

Owing to the structural similarity of the title compounds, with several bis-cyclam derivatives potential CXCR4 interactions were scrutinized. It is known that the bis-cyclam AMD3100 and its meta derivative including the respective Cu^{2+}, Zn^{2+}, or Ni^{2+} complexes have anti-HIV activity through binding at the chemokine receptor CXCR4.[28] The expression of CXCR4 on Jurkat J6 cells is known and proven to be positive on both staurosporine treated and control cells. Consequently, CXCR4 dependent differences between treated and control cells, which were obtained with the zinc-cyclen complexes, appear to be unlikely. To further exclude the participation of CXCR4 on $[\mathbf{Zn_21}]^{4+}$ uptake, in staurosporine treated cells competition with a 100-fold molar excess of meta AMD3100 was performed. The similarity of flow-cytometry results indicated no involvement of this receptor in the $[\mathbf{Zn_21}]^{4+}$ uptake (SI).

The capacity of $\{bis[Zn(cyclen)]\}^{4+}$ complexes to transport fluorescent dyes into apoptotic and secondary necrotic cells was also investigated using a radiolabeled complex. High-dose radiation therapy was used to induce cell death which is known to force tumors mainly into necrosis. Rats with Dunning prostate adenocarcinoma transplants were, therefore, irradiated using a single gamma dose of 50 Gy. The rats were imaged with $[\mathbf{Zn_2(^{18}F\text{-}6)}]^{4+}$ six days after treatment. As illustrated in Figure 6a, the irradiated tumor clearly showed significant uptake while the untreated control was negative. This was due to the higher initial uptake just after injection of $[\mathbf{Zn_2(^{18}F\text{-}6)}]^{4+}$ and the delayed washout as compared with the contralateral control (SI). The radioactivity of the excretion organs, kidney and liver, was in the expected range, while the residual background activity was low.

The accumulated radioactivity in the Dunning tumor is certainly due to massive cell death after such a high radiation dose.[29] An investigation into the imaging kinetics as a response to therapy has been performed for ten days after the onset of therapy. The data indicate maximal accumulation of $[\mathbf{Zn_2(^{18}F\text{-}6)}]^{4+}$ at day six while decrease of intensity was observed at day ten (SI). The contralateral control tumor meanwhile increased the uptake indicating cell death due to short tumor doubling time of 5.6 ± 0.4 days.[30]

A second imaging experiment using $[\mathbf{Zn_2(^{18}F\text{-}6)}]^{4+}$ was carried out with taxol treated HelaMatu tumor bearing mice. The transaxial PET images of a taxol treated animal (Figure 6b) indicated higher tumor uptake in comparison to the control (Figure 6d). Quantification of the mean tumor uptake values showed an increase by 30% in the treatment group while the tumor size decreased by 15% in comparison to the control group (SI). Autoradiograms of tumor tissue slices shown in Figure 7a,c confirmed the result of the PET study, and immunohistochemistry (Figure 7b,d) validated the presence of apoptotic tissue which corresponded with radioactivity accumulation after taxol treatment.

The perspective of having radiolabeled markers of cell death either produced by apoptosis and/or by secondary necrosis is attractive, because therapy control is one of the main areas of interest during the follow-up of cancer patients. Currently, a series of conventional investigations, including radiography, CT, sonography, and MRI, acquire this information covering the extent and morphology of tumor masses and, to some degree, alterations in tumor perfusion. In contrast, nuclear medicine has at its disposal a series of surrogate markers that are used for the assessment of the therapy response. Radiofluorinated $bis[Zn(cyclen)]^{4+}$ complexes might be more specific for the imaging of therapy response providing information about cell death in treated tumors. Further work is underway to optimize the pharmacokinetics of zinc cyclen complexes and to understand more about the uptake mechanism.

■ ASSOCIATED CONTENT

Ⓢ Supporting Information

Flow-cytometry results, material for the role of CXCR4, additional CLSM data, cytotoxicity, and PET data. This material is available free of charge via the Internet at http://pubs.acs.org.

AUTHOR INFORMATION

Corresponding Author

*E-mail: m.eisenhut@dkfz.de; T +49-6221-422443.

ACKNOWLEDGMENTS

We would like to thank Dr. H. Spring for performing CLSM, Prof. Dr. P. Huber, and Dr. P. Peschke for providing rats with Dunning carcinoma transplants and the radiation experiment, K. Leota for μPET, and U. Schierbaum for animal care, as well as U. Wagner (all DKFZ) for assistance in chemical syntheses. D.O. is grateful for financial support from Bayer Healthcare. There is no other financial conflict of interest dealing with this subject.

REFERENCES

(1) Seaton, B. A. (1996) Annexin V molecular structure, ligand binding and biological function. In *Annexins: Molecular Structure to Cellular Function* (Seaton, B. A., Ed) pp 15−29, R.G. Landes Co., Austin, TX.

(2) Eisenhut, M., and Haberkorn, U. (2006) The molecular position of radiolabels and its impact on functional integrity of proteins. *J. Nucl. Med. 47*, 1400−1402.

(3) Tait, J. F., Gibson, D., and Fujikawa, K. (1989) Phospholipid binding properties of human placental anticoagulant protein-I, a member of the lipocortin family. *J. Biol. Chem. 264*, 7944−7949.

(4) Koopman, G., Reutelingsperger, C. P., Kuijten, G. A., Keehnen, R. M., Pals, S. T., and van Oers, M. H. (1994) Annexin V for flow-cytometric detection of phosphatidylserine expression on B cells undergoing apoptosis. *Blood 84*, 1415−1420.

(5) Schutters, K., and Reutelingsperger, C. (2010) Phosphatidylserine targeting for diagnosis and treatment of human diseases. *Apoptosis 15*, 1072−1082.

(6) Brumatti, G., Sheridan, C., and Martin, S. J. (2008) Expression and purification of recombinant annexin V for the detection of membrane alterations on apoptotic cells. *Methods 44*, 235−40.

(7) Blankenberg, F. G., Katsikis, P. D., Tait, J. F., Davis, R. E., Naumovski, L., Ohtsuki, K., Kopiwoda, S., Abrams, M. J., Darkes, M., Robbins, R. C., Maecker, H. T., and Strauss, H. W. (1998) In-vivo detection and imaging of phosphatidylserine expression during programmed cell death. *Proc. Natl. Acad. Sci. U. S. A. 95*, 6349−6354.

(8) Lahorte, C. M. M., Vanderheyden, J. L., Steinmetz, N., Van de Wiele, C., Dierckx, R. A., and Siegers, G. (2004) Apoptosis-detecting radioligands: current state of the art and future perspectives. *Eur. J. Nucl. Med. Mol. Imaging 31*, 887−919.

(9) Koulov, A. V., Stucker, K. A., Lakshmi, C., Robinson, J. P., and Smith, B. D. (2003) Detection of apoptotic cells using a synthetic fluorescent sensor for membrane surfaces that contain phosphatidylserine. *Cell Death Differ. 10*, 1357−1359.

(10) Ojida, A., Mito-Oka, Y., Inoue, M. A., and Hamachi, I. (2002) First artificial receptors and chemosensors toward phosphorylated peptide in aqueous solution. *J. Am. Chem. Soc. 124*, 6256−6258.

(11) Ojida, A., Mito-Oka, Y., Sada, K., and Hamachi, I. (2004) Molecular recognition and fluorescence sensing of monophosphorylated peptides in aqueous solution by bis(zinc(II)-dipicolylamine)-based artificial receptors. *J. Am. Chem. Soc. 126*, 2454−2463.

(12) Lakshmi, C., Hanshaw, R. G., and Smith, B. D. (2004) Fluorophore-linked zinc(II)dipicolylamine coordination complexes as sensors for phosphatidylserine-containing membranes. *Tetrahedron 60*, 11307−11315.

(13) Hanshaw, R. G., Lakshmi, C., Lambert, T. N., Johnson, J. R., and Smith, B. D. (2005) Fluorescent detection of apoptotic cells by using zinc coordination complexes with a selective affinity for membrane surfaces enriched with phosphatidylserine. *ChemBioChem 6*, 2214−2220.

(14) Aoki, S., Sakurama, K., Matsuo, N., Yamada, Y., Takasawa, R., Tanuma, S., Shiro, M., Takeda, K., and Kimura, E. (2006) A new fluorescent probe for zinc(II): an 8-hydroxy-5-N,N-dimethylaminosulfonylquinoline-pendant 1,4,7,10-tetraazacyclododecane. *Chemistry 12*, 9066−9080.

(15) Hanshaw, R. G., and Smith, B. D. (2005) New reagents for phosphatidylserine recognition and detection of apoptosis. *Bioorg. Med. Chem. 13*, 5035−5042.

(16) Anderegg, G., Hubmann, E., Podder, N. G., and Wenk, F. (1977) Pyridinderivate als Komplexbildner. XI. Die Thermodynamik der Metallkomplexbildung mit Bis-, Tris- und Tetrakis [(Zpyridyl)-methyl]-aminen. *Helvet. Chim. Acta 60*, 123−140.

(17) Kalesse, M., and Loos, A. (1996) Transesterification of phosphodiester by a zinc-containing cyclen derivative: Identification of the active species. *Liebigs Ann.*, 935−939.

(18) Zulkefeli, M., Sogon, T., Takeda, K., Kimura, E., and Aoki, S. (2009) Design and synthesis of a stable supramolecular trigonal prism formed by the self-assembly of a linear tetrakis(Zn2+-cyclen) complex and trianionic trithiocyanuric acid in aqueous solution and its complexation with DNA (cyclen = 1,4,7,10-tetraazacyclododecane). *Inorg. Chem. 48*, 9567−9578.

(19) Raman, D., Baugher, P. J., Thu, Y. M., and Richmond, A. (2007) Role of chemokines in tumor growth. *Cancer Lett. 256*, 137−165.

(20) Hatanaka, Y., Hashimoto, M., and Kanaoka, Y. (1994) A novel biotinylated heterobifunctional cross-linking reagent bearing an aromatic diazirine. *Bioorg. Med. Chem. 2*, 1367−1373.

(21) Ashton, P. R., Anderson, D. W., Brown, C. L., Shipway, A. N., Stoddart, J. F., and Tolley, M. S. (1998) The synthesis and characterization of polyamide dendrimers. *Chem.—Eur. J. 4*, 781−795.

(22) Reichenbach-Klinke, R., Kruppa, M., and König, B. (2002) NADH model systems functionalized with Zn(II)-cyclen as flavin binding site − structure denpendence of the redox reaction within reversible aggregates. *J. Am. Chem. Soc. 124*, 12999−13007.

(23) Wester, H. J., Herz, M., Weber, W., Heiss, P., Senekowitsch-Schmidtke, R., Schwaiger, M., and Stocklin, G. (1999) Synthesis and radiopharmacology of O-(2-[18F]fluoroethyl)-L-tyrosine for tumor imaging. *J. Nucl. Med. 40*, 205−212.

(24) Bridger, G. J., Skerlj, R. T., Thornton, D., Padmanabhan, S., Martellucci, S. A., Henson, G. W., Abrams, M. J., Yamamoto, N., De Vreese, K., Pauwels, R., and De Clercq, E. (1995) Synthesis and structure-activity relationships of phenyenebis(methylene)-linked bis-tetraazamacrocycles that inhibit HIV replication. Effects of macrocyclic ring size and substituents on the aromatic linker. *J. Med. Chem. 38*, 366−378.

(25) Bauer, C., Bauder-Wuest, U., Mier, W., Haberkorn, U., and Eisenhut, M. (2005) Investigation of ^{131}I labelled peptides as caspases substrates for apoptosis imaging. *J. Nucl. Med. 46*, 1066−1074.

(26) Blume, K. E., Soeroes, S., Waibel, M., Keppeler, H., Wesselborg, S., Herrmann, M., Schulze-Osthoff, K., and Lauber, K. (2009) Cell surface externalization of annexin A1 as a failsafe mechanism preventing inflammatory responses during secondary necrosis. *J. Immunol. 183*, 8138−8147.

(27) Kimura, E., Kikuchi, M., Kitamura, H., and Koike, T. (1999) Selective and efficient recognition of thymidylylthymidine (TpT) by bis(ZnII-cyclen) and thymidylylthymidylylthymidine (TpTpT) by tris(ZnII-cyclen) at neutral pH in aqueous solution/macrocyclic ligands/molecular recognition/nucleotides/thymidine/zinc /. *Chem.—Eur. J. 5*, 3113−3123.

(28) De Clercq, E. (2003) The bicyclam AMD3100 story. *Nat. Rev. Drug Discovery 2*, 581−587.

(29) Peschke, P, Karger, C. P., Scholz, M., Debus, J., and Huber, P. E. (2011) Relative biological effectiveness of carbon ions for local tumor control of a radioresistant prostate carcinoma in the rat. *Int. J. Radiat. Oncol. Biol. Phys. 79*, 239−246.

(30) Lohr, F., Wenz, F., Flentje, M., Peschke, P., and Hahn, E. W. (1993) Measurement of the proliferative activity of three different sublines of the Dunning rat prostate tumor R3327. *Strahlenther. Onkol. 169*, 438−445.

Bioconjugate Chemistry

Article

pubs.acs.org/bc

β-Gal Gene Expression MRI Reporter in Melanoma Tumor Cells. Design, Synthesis, and *in Vitro* and *in Vivo* Testing of a Gd(III) Containing Probe Forming a High Relaxivity, Melanin-Like Structure upon β-Gal Enzymatic Activation

Francesca Arena, Jebasingh Bhagavath Singh, Eliana Gianolio, Rachele Stefanìa, and Silvio Aime*

Centro di Imaging Molecolare, Dipartimento di Chimica IFM, Università degli Studi di Torino, Via Nizza 52, 10126 Torino, Italy

Supporting Information

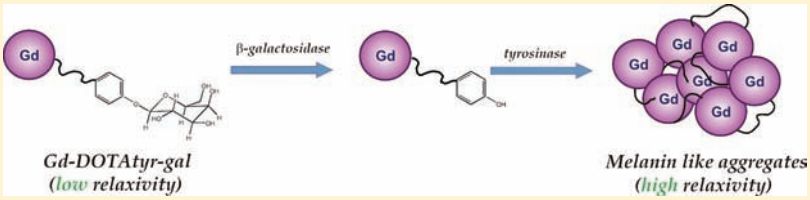

ABSTRACT: The aim of this work is to design and test an MRI probe (Gd-DOTAtyr-gal) able to report on the gene expression of β-galactosidase (β-Gal) in melanoma cells. The probe consists of a Gd-DOTA reporter bearing on its surface a tyrosine-galactose-pyranose functionality that, upon the release of the sugar moiety, readily transforms, in the presence of tyrosinase, into melanin oligomeric/polymeric mixture. The formation of Gd-DOTA-containing melanin oligomers and polymers is accompanied by a marked increase of the water proton relaxation rate. The steps involving the release of the galactose-pyranose group and the formation of the melanin-like structure have been carefully investigated *in vitro* by relaxometric and UV−vis measurements. Cellular uptake studies of Gd-DOTAtyr-gal by melanoma cells have shown that the probe enters the cells, and it appears not to be confined in endosomal vesicles. Using B16−F10*LacZ* transfected cells, the fast formation of paramagnetic melanin-Gd(III)-containing species has been assessed by the measurement of increased longitudinal relaxation rates of the cellular pellets suspensions. The *in vitro* results have been confirmed in *in vivo* MRI investigations on murine melanoma tumor bearing mice. Upon direct injection of Gd-DOTAtyr-gal, a good contrast is observed after 5 h post injection in B16−F10*LacZ* tumors, but not in B16−F10 tumors lacking the β-Gal enzyme. Gd-DOTAtyr-gal in combination with tyrosinase introduces a novel approach for the detection of β-Gal expression by MRI in vivo.

INTRODUCTION

The development of reliable means to follow gene expression *in vitro* and *in vivo* has attracted great interest in recent years. Gene expression is commonly monitored by introducing a marker gene to follow the regulation of the gene of interest.[1] The bacterial *LacZ* gene is a very popular gene reporter, with applications ranging from immunosorbent assays to in situ hybridizations and evaluation of gene distributions. Indeed, *LacZ* has been used in medical trials revealing regions of tissue transfection in biopsy specimens based on hystologic staining. As such, many colorimetric stains and assays have been developed and are in routine use, including reagents such as nitrophenyl-β-D-galactopyranoside, which generates a yellow color, or 4-chloro-3-bromoindole-galactose, which gives a blue stain, and 3,4-cyclohexenoesculetin β-D-galactopyranoside, which yields a black stain, respectively.[2] The application of such methods has various drawbacks such as the need for hystological processing of the region of interest. Magnetic Resonance Imaging offers an alternative to light microscopy, allowing the investigation of intact tissues at the cellular resolution level. The first attempt to tackle the issue of MRI visualization of β-Gal gene expression was carried out by Meade and co-workers by reporting that the relaxivity of a galacto-pyranose-substituted tetraazamacrocycle coordinated to a Gd(III) ion can be specifically "switched on" by removing the sugar with β-galactosidase.[3] Unfortunately, the gain in relaxivity brought about by the activation step is relatively small (for several reasons as elucidated in a successive paper from the same author).[4]

Since Meade's seminal work, MRI detection of β-Gal expression has been under intense scrutiny with the aim of exploring amplification routes that would allow its improved implementation in *in vivo* studies.

Hanaoka et al. reported on the exploitation of the RIME (receptor-induced magnetization enhancement) by using a β-Gal-activated Gd(III) bearing agent which, upon release of the β-galactopyranoside moiety, enhances its relaxivity thanks to the binding to HSA.[5] A similar attempt to amplify the MRI response of a β-Gal responsive Gd(III) complex has been pursued by Yun-Ming Wang et al.[6]

Received: September 8, 2011
Revised: October 24, 2011
Published: October 31, 2011

 © 2011 American Chemical Society dx.doi.org/10.1021/bc200486j | *Bioconjugate Chem.* 2011, 22, 2625−2635

Chart 1. Schematic Representation of the Oligomerization Process Achieved upon the Action of β-Galactosidase and Tyrosinase Enzymes

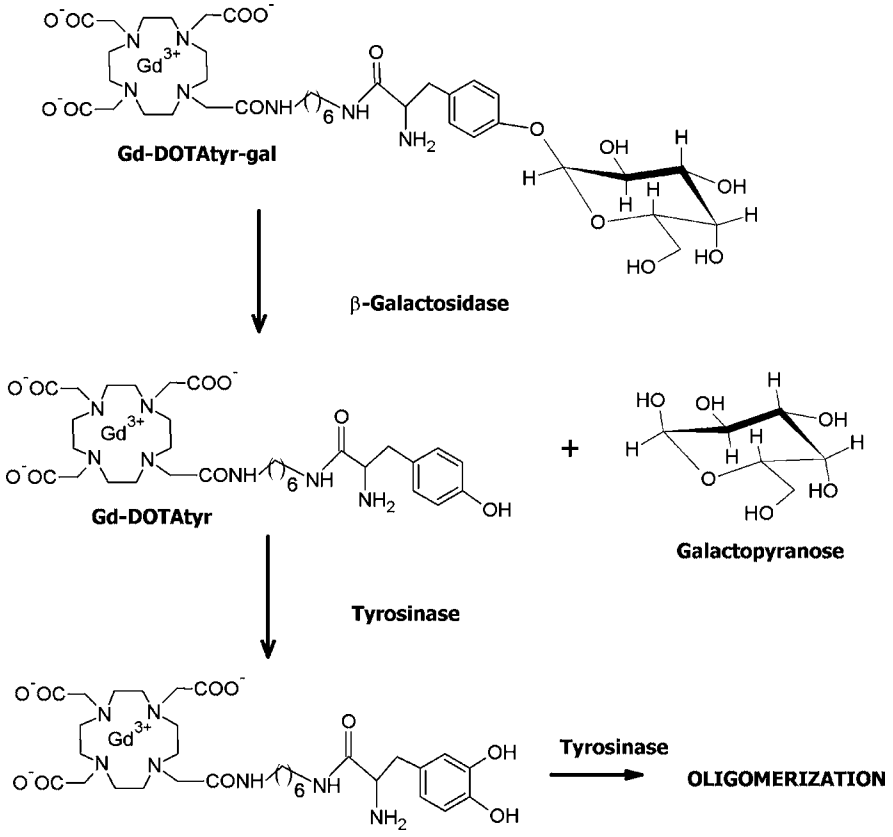

These results represent an interesting proof-of-concept of the RIME approach, but its transaction to cellular and animal applications might be hampered by the fact that β-Gal is in the cytoplasm and HSA is mainly in the extracellular compartments.

As one of the key issues for a successful *in vivo* application deals with the internalization of the probe, Engelmann et al.[7] tackled the problem of penetrating the cell membrane by endowing the surface of a Gd(III) complex with a suitable cationic peptide sequence. The cell-penetrating peptide is bound to a galacto-pyranose moiety and the linkage is selectively cleaved only in β-Gal transfected cells. Thus, the cell accumulation of the MRI agent would be possible only upon β-Gal enzymatic transformation, as the unconverted metal complex could effectively efflux from the cells.

Another efficient method to accumulate a metal complex inside cells relies on the formation of oligo/polymeric structures such as those obtained by Bodganov et al.[8−11] They found that melanin-like macromolecules can form when hydroxo-functionalized Gd(III) chelates are in the presence of tyrosinase or myeloperoxidase.

In the present work, which aims at exploiting the latter route in order to amplify the MRI response at the targeted cells, the designed probe consists of a Gd-DOTA monoamide chelate bearing a tyrosine −OH functionality protected by a galactose moiety (Gd-DOTAtyr-gal). Upon cleavage of the galactose moiety (step activated by the action of β-galactosidase), the tyrosine group, in the Gd-DOTAtyr product, becomes available for the tyrosinase activated melanin polymerization. The formation of the paramagnetic melanin-like macromolecule can be assessed by MRI because the relaxivity of Gd(III)-complexes increases, in the field range 0.5−1.5 T, if they are part of macromolecular systems, as a consequence of the lengthening of their reorientational correlation time (τ_R) (Chart 1).

The β-galactosidase-responsive probe has been tested in B16−F10 and B16−F10*LacZ* murine melanoma cells. Melanoma cells have been used for the enzymatic assays, as these cells possess high tyrosinase activity as witnessed by their natural melanin pigmentation. We also demonstrated the ability of Gd-DOTAtyr-gal to visualize stably expressing *LacZ* melanoma tumors *in vivo* upon its direct intratumoral injection.

EXPERIMENTAL PROCEDURES

Materials. All reagents used for the synthesis of DOTAtyr-gal and DOTAtyr ligands were purchased from Sigma Aldrich Co. β-galactosidase (product no. G5635−5KU isolated from *Escherichia coli*) was purchased from Sigma Aldrich and used without any further purification. β-Gal Staining Kit was purchased from Invitrogen. Tyrosinase isolated from *Mushroom* was obtained from Sigma-Aldrich.

NMR spectra were recorded on JEOL Eclipse Plus400 and Bruker Avance 600 spectrometers operating at 9.4 and 14 T, respectively. ESI mass spectra were recorded on a Waters Micromass ZQ. Analytical and preparative HPLC-MS were carried out on Waters FractionLynx autopurification system equipped with Waters 2996 diode array and Waters Micromass ZQ (ESCI ionization mode) detectors. DOTAMA-$(OtBu)_3C_6NH_2$ was prepared following a reported procedure.[12]

Synthesis of Gd(III) complexes (Scheme 1 and Scheme 2). *Synthesis of N-(9-Fluorenylmethoxycarbonyl)-O-1,1(dimethyl)ethyl-tyrosine pentafluorophenyl Ester*

dx.doi.org/10.1021/bc200486j | *Bioconjugate Chem.* 2011, 22, 2625−2635

Scheme 1. Synthetic Pathway to Gd-DOTAtyr-gal[a]

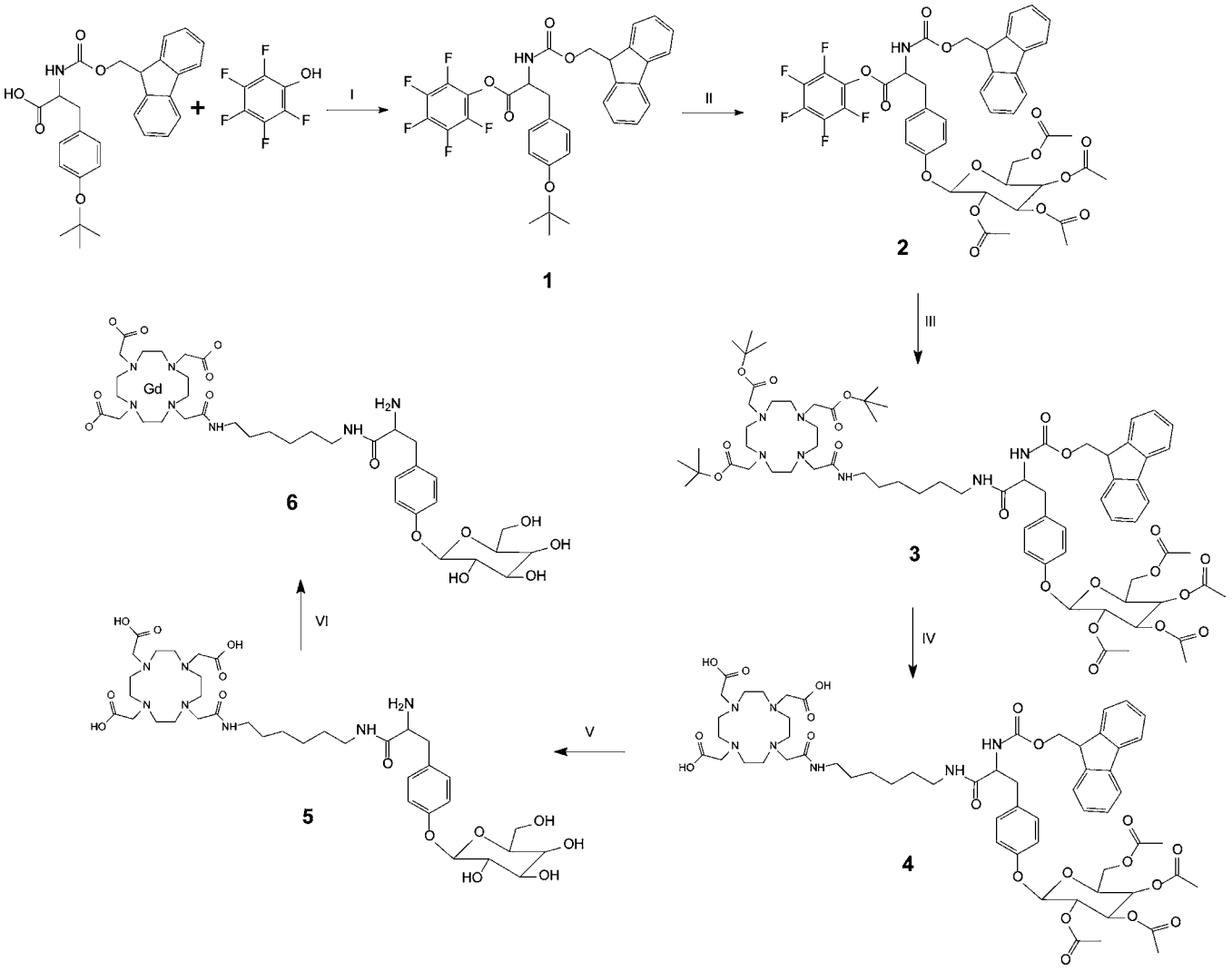

[a](I) EDCI,CH_2Cl_2; (II) Acetobromogalactose, AgOTf, CH_2Cl_2 dry; (III) DOTAMA(O*t*Bu)$_3C_6NH_2$, HOBt, CH_2Cl_2; (IV) TFA,CH_2Cl_2; (V) NaOMe, MeOH; (VI) $GdCl_3$, H_2O, pH 7.

(1). A solution of Fmoc-Tyr-(tBu)OH (2 g, 4.35 mmol), pentafluorophenol (0.8 g, 4.35 mmol) and EDCI (0.834 g, 4.35 mmol) in CH_2Cl_2 (60 mL) was stirred overnight at 0 °C. The solution was transferred to a separatory funnel and washed with water (2 × 10 mL). The organic layer was dried over anhydrous Na_2SO_4, and the solvent was removed under reduced pressure to give the product as a white solid in quantitative yield. ^{1}H NMR (400 MHz, $CDCl_3$): δ 1.33 (s, 9H), 3.21 (m, 2H), 4.21 (t, 1H), 4.43 (m, 2H), 4.98 (m, 1H), 6.96 (d, 2H), 7.01 (d, 2H), 7.31 (m, 2H), 7.38 (m, 2H), 7.54 (d, 2H), 7.77 (d, 2H). ^{13}C NMR (101 MHz, $CDCl_3$): δ 28.89, 37.31, 47.19, 54.77, 67.31, 78.71, 120.11, 124.52, 125.08, 127.17, 127.87, 129.34, 129.89, 136.72, 139.74, 139.90, 141.42, 142.43, 143.78, 155.01, 155.60, 168.16.

*Synthesis of N-(9-Fluorenylmethoxycarbonyl)-O-[2,3,4,6-tetra-O-acetyl-D-galactose-1-(yl)-tyrosine Pentafluorophenyl Ester (**2**).* Compound **1** (2.0 g, 3.2 mmol), AgOTf (1.6 g, 6.4 mmol), and molecular sieves (3 Å, 2.5 g) were placed in a predried flask covered with aluminum foil. After evacuation (0.1 Torr), the flask was filled with argon and dry CH_2Cl_2 (40 mL) was used to suspend the reagents. The suspension was cooled to −10 °C and a solution of the acetyl bromogalactose (1.1 g, 2.6 mmol) in dry CH_2Cl_2 (35 mL) was added. After 120 min at −10 °C, the suspension was neutralized with DIPEA (1 mL, 5.74 mmol) followed by filtration through Celite. The filtrate was concentrated to dryness and the residue was purified by column chromatography (silica gel, CH_2Cl_2: MeOH 95:5, R_f 0.32) to yield a white solid. Yield: 70%. ^{1}H NMR (400 MHz, $CDCl_3$): δ 1.98 (s, 3H), 2.00 (s, 6H), 2.10 (s, 3H), 3.21 (m, 2H), 4.00 (m, 1H), 4.11 (m, 2H), 4.21 (m, 1H), 4.44 (m, 2H), 4.98(m, 1H), 5.09 (m, 1H), 5.30 (m, 1H), 5.40 (m, 1H), 5.51 (m, 1H), 6.97 (d, 2H), 7.13 (d, 2H), 7.28 (m, 2H), 7.38 (m, 2H), 7.50 (d, 2H), 7.75 (d, 2H), 8.31 (broad, CONH, 1H). ^{13}C NMR (101 MHz, $CDCl_3$): δ 20.66, 20.78, 37.21, 47.19, 54.63, 61.42, 66.79, 67.82, 70.81, 71.68, 78.72, 89.80, 120.45, 124.55, 125.05, 127.17, 127.91, 129.39, 129.82, 136.72, 139.74, 139.90, 141.42, 142.40, 143.75, 155.01, 155.61, 168.16, 169.51, 169.92, 170.09, 170.29; $C_{44}H_{38}NO_{14}F_5$ ESI-MS (M+H$^+$) calcd 900.2, found 900.4.

*Synthesis of 1-[2-Oxo-3-aza-9[N-(9-fluorenylmethoxycarbonyl)-O-[2,3,4,6-tetra-O-acetyl-D-galactose-1-(yl)]-tyrosinylamine]nonyl]-1,4,7,10-tetraazacyclododecane-4,7,10-triacetic Acid 1,1(Dimethyl)ethyl Ester (**3**).* To a

dx.doi.org/10.1021/bc200486j | *Bioconjugate Chem.* 2011, 22, 2625−2635

Scheme 2. Synthetic Pathway to Gd-DOTAtyr[a]

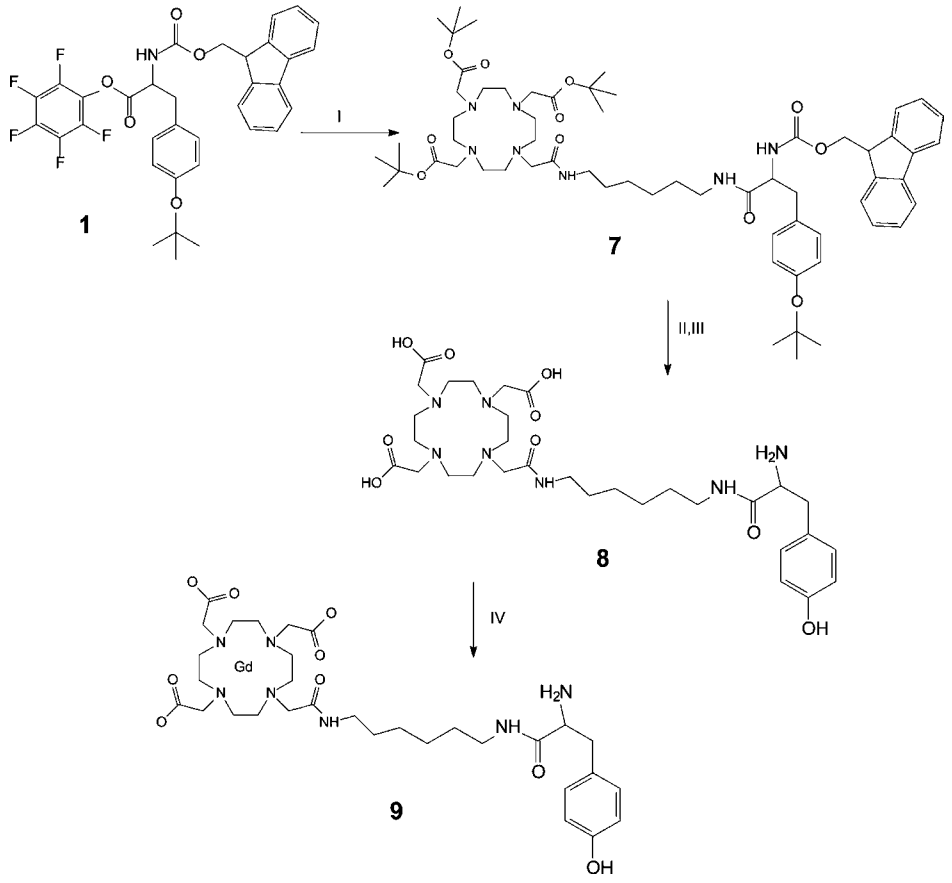

[a](I) DOTAMA(O*t*Bu)$_3$C$_6$NH$_2$, HOBt, CH_2Cl_2; (II) piperidine, CH_2Cl_2; (III) TFA,CH_2Cl_2; (IV) $GdCl_3$, H_2O, pH 7.

solution of DOTAMA(O*t*Bu)$_3$C$_6$NH$_2$ (0.75 g, 1.1 mmol) in CH_2Cl_2 (30 mL) was slowly added **2** (1.0 g, 1.1 mmol) in 30 mL of CH_2Cl_2. After 20 min, HOBt (0.042 g, 0.28 mmol) and DIPEA (0.19 mL, 1.1 mmol) were added to the reaction mixture and stirred at 0−5 °C under argon atmosphere for 3 h, then for another 16 h at room temperature. The reaction mixture was washed with 10 mL of water and dried over anhydrous Na_2SO 4. The filtrate was evaporated to dryness and the white solid was purified by column chromatography (silica gel, elution gradient: CH_2Cl_2/MeOH 95:5 → 9:1 → 8:2) to yield a white solid. Yield: 82%. ^{1}H NMR (600 MHz, $CDCl_3$): δ 1.40 (m, 2H), 1.44 (s, 27 H), 1.50 (m, 2H), 1.60 (m, 2H), 1.85 (m, 2H), 1.98 (s, 3H), 2.02 (s, 6H), 2.10 (s, 3H), 2.70−3.60 (broad, 24H), 3.71 (s, 4H), 4.02 (m, 1H), 4.16 (m, 2H), 4.22 (m, 3H), 4.45 (m, 2H), 4.79 (m, 1H), 5.08 (m, 1H), 5.32 (m, 1H), 5.41 (m, 1H), 5.51 (m, 1H), 6.97 (d, 2H), 7.12 (d, 2H), 7.28 (m, 2H), 7.37 (m, 2H), 7.42 (broad, CONH, 1H), 7.51 (d, 2H), 7.74 (d, 2H), 7.89 (broad, CONH, 1H), 8.21 (broad, CONH, 1H).^{13}C NMR (151 MHz, $CDCl_3$): δ 20.65, 20.72, 25.91, 26.00, 27.90, 28.45, 28.93, 29.66, 37.31, 38.71, 38.81, 47.21, 53.51, 54.54, 55.62, 55.74, 56.17, 54.69, 61.44, 66.72, 67.86, 70.79, 71.65, 78.86, 79.19, 81.6, 89.81, 120.11, 124.41, 125.23, 127.18, 127.82, 129.94, 130.41, 141.42, 143.74, 154.48, 155.89, 155.92, 168.18, 169.57, 169.91, 170.06, 170.31, 171.42, 172.11, 172.23, 172.45, 176, 22; $C_{72}H_{103}N_7O_{20}$ ESI-MS (M +H$^+$) calcd 1386.7, found 1386.9.

*Synthesis of 1-[2-Oxo-3-aza-9[N-(9-fluorenylmethoxycarbonyl)-O-[2,3,4,6-tetra-O-acetyl-D-galactose-1-(yl)]-tyrosinylamine]nonyl]-1,4,7,10-tetraazacyclododecane-4,7,10-triacetic Acid (**4**).* The solution of **3** (1 g, 0.72 mmol) in TFA/CH_2Cl_2 (1:1, 10 mL) was stirred at 0 °C. After 3 h stirring, the reaction mixture was evaporated and the procedure was repeated twice in order to remove all three *t*Bu moieties. Then, the product was precipitated with excess diethyl ether, isolated by centrifugation, washed thoroughly with diethyl ether, and dried in vacuo. The product was used for the next step without further purification: a pale white solid.

*Synthesis of 1-[2-Oxo-3-aza-9[O-[D-galactos-1-(yl)]-tyrosylamido]nonylaminocarbonylmethyl]-1,4,7,10-tetraazacyclododecane-4,7,10-triacetic Acid (**5**).* The solution of **4** (1.2 g, 0.99 mmol) and NaOMe (0.27 g, 4.9 mol) in methanol (26 mL) was stirred under argon atmosphere at 0 °C. After 5 h stirring, the solution was acidified to around pH 7 with Dowex cationic resin. The reaction mixture was filtered and the solvent evaporated to yield a white solid. The crude material was dissolved in water, loaded over an Amberchrom CG161 column and eluted with a water−methanol gradient (100:0 to 0:100). After solvent evaporation, product **5** was collected as a white solid (yield 65%). ^{1}H NMR (600 MHz, D_2O): δ 1.32, 1.42, 1.66 (m, 8H), 2.98−3.16 (broad, 14H), 3.33−3.82 (broad, 22H), 3.93 (m, 1H), 4.99 (m, 1H), 6.87 (d, 2H), 7.12(d, 2H) . ^{13}C NMR (151 MHz, D_2O): δ 25.54, 25.68, 27.97, 28.24, 34.54, 38.51, 38.43, 53.93, 56.05, 56.12, 56.49, 56.75, 65.55, 69.11, 69.77, 71.84, 73.36, 100.91, 117.92, 128.81, 130.91, 156.44, 169.227, 170.01, 171.96, 178.12; $C_{37}H_{61}N_7O_{14}$ ESI-MS for (M+H$^+$) calcd 828.9, found 828.7. For (M+2H^{2+}) calcd 414.9, found 414.7.

dx.doi.org/10.1021/bc200486j | *Bioconjugate Chem.* 2011, 22, 2625−2635

*Synthesis of 1-[2-Oxo-3-aza-9[N-(9-fluorenylmethoxycarbonyl)-O-1,1(dimethyl)ethyl-tyrosinylamine]nonyl]-1,4,7,10-tetraazacyclododecane-4,7,10-triacetic Acid 1,1(Dimethyl)-ethyl Ester (**7**).* To a solution of DOTAMA(O*t*Bu)$_3$$C_6NH_2$ (0.500 g, 0.74 mmol) in CH_2Cl_2 (25 mL) was slowly added **1** (0.46 g, 0.74 mmol) in 30 mL of CH_2Cl_2. After 20 min, HOBt (0.12 g, 0.75 mmol) and DIPEA (0.12 mL, 0.74 mmol) were added and the mixture was stirred for 6 h at 0−5 °C under inert atmosphere. The reaction mixture was then washed with 7 mL of water and dried over anhydrous Na_2SO_4. The filtrate was evaporated to dryness and the residue was purified by column chromatography (silica gel, CH_2Cl_2/MeOH 9:1) R_f: 0.38. Yield: 89%. ^{1}H NMR (600 MHz, $CDCl_3$): δ 1.27 (s, 9H) 1.42 (m, 2H), 1.48 (s, 27 H), 1.49 (m, 2H), 1.62 (m, 2H), 1.87 (t, 2H), 2.07−3.30, 3.40−3.50 (b, 22H), 3.54 (s, 4H), 4.23 (m, 3H), 4.40 (s, 2H), 4.45 (m, 1H), 6.97 (d, 2H), 7.12 (d, 2H), 7.28 (m, 2H), 7.37 (m, 2H), 7.43 (broad, CONH, 1H), 7.51 (d, 2H), 7.74 (d, 2H), 7.91 (broad, CONH, 1H), 8.23 (broad, CONH, 1H). ^{13}C NMR (151 MHz, $CDCl_3$): δ 25.93, 26.01, 28.02, 28.57, 28.88, 28.97, 29.67, 37.41, 38.61, 38.91, 46.67, 47.29, 53.01, 53.24, 54.59, 56.22, 56.57, 58.94, 67.31, 78.76, 120.11, 124.81, 125.13, 127.08, 127.62, 129.98, 130.31, 141.42, 143.84, 155.38, 155.83, 169.42, 172.11, 172.23, 172.45, 174.22; $C_{62}H_{93}N_7O_{11}$ ESI-MS (M+H$^+$) calcd 1112.5, found 1112.7.

*Synthesis of 1-[2-Oxo-3-aza-9[-L-tyrosinylamine]nonyl]-1,4,7,10-tetraazacyclododecane-4,7,10-triacetic Acid (**8**).* The compound 7 (0.91 g, 0.075 mmol) was dissolved in CH_2Cl_2 (25 mL) containing 10% of piperidine and stirred under inert atmosphere at 0 °C. After 3 h stirring, the solvent was evaporated. Upon the addition of diethyl ether, a white solid was obtained. The crude solid was washed with ice-cooled ether and dried. To the white solid, a solution of TFA/CH_2Cl_2 (1:1 *v*/*v*) was added in one step and stirred. After 4 h, the reaction mixture was evaporated, and the procedure was repeated twice in order to remove all three *t*Bu moieties. Then, the product was precipitated with excess diethyl ether, isolated by centrifugation, washed thoroughly with diethyl ether, and dried in vacuo. It was then dissolved in H_2O (4 mL) at pH neutralized by addition of diluted NaOH at 0 °C. The crude product was purified by preparative HPLC-ESI (+)MS by using a Waters Atlantis RPdC18 19/100 column by Method 1 using H_2O/TFA 0.1% (A) and CH_3CN/TFA 0.1% (B) as eluents (see the Supporting Information) .The pure product was obtained as a white powder (Yield 44%). HPLC: Method 2 (see the Supporting Information), retention time 8.90 min, purity 95%. ^{1}H NMR (600 MHz, D_2O): δ 1.39, 1.51, 1.60, 1.85 (m, 8H), 2.70−3.60 (broad, 21H), 3.68 (broad, 6H), 4.23 (m, 4H), 6.76 (d, 2H), 6.98 (d, 2H).^{13}C NMR (151 MHz, D_2O): δ 25.76, 25.92, 28.13, 28.32, 36.34, 38.58, 38.75, 53.82, 46.67, 48.51, 51.11, 53.54, 55.27, 116.00, 126.93, 130.97, 155.32, 168.76, 168.89, 171.24, 171.88; $C_{31}H_{51}N_7O_9$ ESI-MS for (M+H$^+$) calcd 666.4, found 666.3. For (M+2H^{2+}) calcd 333.9, found 333.7.

*Synthesis of Gd-DOTAtyr-gal (**6**) and Gd-DOTAtyr (**9**).* To the solutions of DOTAtyr-gal and DOTAtyr ligands (10 mmol) in water (250 mL), a solution containing $GdCl_3$ (9 mmol) was added. The solution was slowly neutralized to pH 7 with 2 N NaOH. When the pH was constant, the solution was desalted by Sephadex G10 column. The absence of any free Gd(III) ions was checked through the Orange Xylenol spectrophotometric test.[13] Gd-DOTAtyr-gal: $C_{37}H_{58}GdN_7O_{14}$ ESI-MS (M+H$^+$) calcd 983.14, found 983.12. HPLC: Method 2 (Supporting Information), retention time 4.89 min, purity 92%. Gd-DOTAtyr: $C_{31}H_{48}GdN_7O_9$ ESI-MS (M+H$^+$) calcd 821.3, found 821.2. HPLC: Method 3 (Supporting Information), retention time 7.60 min, purity 96%.

Relaxometric Characterization. The longitudinal water proton relaxation rate was measured at 25 °C by using a Stelar Spinmaster (Stelar, Mede, Pavia, Italy) spectrometer operating at 20 MHz, by mean of the standard inversion−recovery technique. The temperature was controlled with a Stelar VTC-91 air-flow heater equipped with a copper constantan thermocouple (uncertainty 0.1 °C). The relaxometric characterization of the field-dependent relaxometry of the paramagnetic Gd(III)-probe solutions was carried out through the acquisition of the NMRD profiles. The proton $1/T_1$ NMRD profiles were measured at 25 °C on a fast field-cycling Stelar relaxometer over a continuum of magnetic field strengths from 0.00024 to 0.47 T (corresponding to 0.01−20 MHz proton Larmor frequencies). The relaxometer operates under computer control with an absolute uncertainty in $1/T_1$ of ±1%. Additional data points in the range 20−70 MHz were obtained on the Stelar Spinmaster spectrometer. The concentration of the solutions used for the relaxometric characterization was determined according to the relaxometric method reported in the Supporting Information section.

***In Vitro* Assessment of Enzyme Activity.** To assess the effect of β-galactosidase enzyme on the r_1 value of Gd-DOTAtyr-gal solution, β-galactosidase isolated from *Escherichia coli* was used. *Escherichia coli* enzyme was reconstituted with 0.1 M sodium phosphate buffer, pH = 7.4 at 25.0 ± 0.1 °C. To assess the effect of tyrosinase enzyme on the r_1 value of Gd-DOTAtyr-gal solution, previously activated by β-galactosidase cleavage, tyrosinase isolated from *Mushroom* was used. *Mushroom* enzyme was reconstituted with 0.1 M sodium phosphate buffer, pH = 7.4 at 25.0 ± 0.1 °C.

Cell Culture. B16−F10 melanoma cells (mouse) were obtained from American Type Culture Collection (ATCC, Manassas, USA), while B16−F10*LacZ* cells were obtained from Riken BRC Cell Bank (Depositor Hamada Hirofumi, Japan). Both cell lines were grown in Dulbecco's modified Eagle's medium (DMEM) containing 10% fetal bovine serum from Lonza (Lonza Sales AG, Verviers. Belgium), 100 U/mL penicillin, and 100 mg/mL streptomycin and maintained at 37 °C under 5% CO_2 conditions. After 3 days of culture, the cells were harvested with trypsine/EDTA, counted with the Trypan-blue exclusion test, and assayed for tyrosinase activity.

Cellular Tyrosinase Activity Assay. The specific activity of tyrosinase was determined by UV/vis spectrophotometry on a Hitachi U2800 spectrometer using L-DOPA as the substrate and was assayed on the basis of the method reported by Tomita et al.[14] Ca. 1 × 10^6 B16−F10 and B16−F10*LacZ* cells were washed with PBS, added to 0.5 mL of a 1 mM L-DOPA solution, sonicated to induce cell lysis, and the absorbance at 475 nm was measured over time by maintaining the temperature of the reaction mixture at 37 °C. An extinction coefficient of 3700 M^{-1} cm^{-1} was used for the quantification of the dopachrome formation.

Functional β-Galactosidase *in Vitro*. Functional expression of β-galactosidase in cells was measured by staining B16−F10*LacZ* cell by the β-Gal Staining Kit according to the manufacturer's instructions. Cells were grown in small dishes (6 cm in diameter) and fixed with 2 mL fixation solution at room temperature for 15 min. The dishes were washed twice with phosphate buffer solution, and 2 mL staining solution (1 mg/mL X-gal) was added at room temperature until the cells were

stained blue. Cells were examined on microscope (Olympus IX70 inverted).

Cell Labeling. The cells were cultured in 75 cm^2 flasks in a humidified incubator at 37 °C and at CO_2/air (5:95 v/v). 8 × 10^5 B16−F10 and B16−F10*LacZ* cells were seeded in 6 cm Petri dishes. Twenty-four hours after seeding, the incubation medium was removed. Cells were washed and incubated in a fresh DMEM medium with different concentrations (10−15−20 mM) of GdDOTAtyr-gal and GdDOTAtyr for 4 h at 37 °C in a CO_2 incubator. After this incubation time, the cells were washed three times with 5 mL ice-cold phosphate-buffered saline (PBS), detached with ethylene diamine tetraacetic acid (EDTA), and, for the T_1 measurement at 1.0 T, collected in 50 μL of PBS, transferred into glass capillaries that were centrifuged at 1500 *g* for 5 min and placed in an agar phantom.

For the electroporation experiment, (3−4) × 10^6 B16−F10*LacZ* cells were detached from the cell culture flask with a trypsin/EDTA solution and placed in an electroporation cuvette containing increasing concentrations of Gd-DOTAtyr-gal in 0.8 mL of PBS. The electroporation was performed using Gene Pulser II electroporation system (Bio-Rad Laboratories, Hercules, CA, USA), applying a single shock at 0.2 V, with 500 or 960 microF capacitance and with a time constant of about 10 ms. Cells were then left in ice for 30 min, washed three times with 10 mL ice-cold PBS, and, for the T_1 measurement at 1.0 T, collected in 50 μL of PBS and transferred into glass capillaries that were placed in an agar phantom. T_1 values were measured on an ASPECT M2 System (Israel) operating at 1 T by using a saturation recovery spin echo sequence (TE = 8.6 ms, 12 variable TR ranging from 40 to 3000 ms, NEX = 4, FOV = 1.7 × 1.7 cm^2, 1 slice, slice thickness = 1 mm).

Determination of Intracellular Gd^{3+}Concentration. At the end of incubation experiments, labeled B16−F10 and B16-*LacZ* melanoma cells were sonicated in order to destroy cellular membranes and obtain cell lysates. Then, cell homogenates were mineralized with HCl 37% (50:50) in sealed vials at 120 °C overnight and the intracellular content of Gd(III) determined according to the method reported in Supporting Informations. The protein content was determined from cell lysates by the Bradford method using bovine serum albumin as standard. One milligram of protein corresponds to 6.1 × 10^6 B16−F10*LacZ* and 6.3 × 10^6 B16−F10 cells.

Adhesion Assay. B16−F10 and B16−F10*LacZ* cells were detached using 2 mM EDTA in PBS, washed with PBS, counted to final concentration of 5 × 10^5 cells/mL and incubated with Gd-DOTAtyr-gal (15 mM) and Gd-DOTAtyr (15 mM) for 4 h at 37 °C in DMEM containing 10% FBS. The cells were then immediately seeded in 3.5 cm Petri dishes. After 30 min, 1 h, 2 h, and 3 h of incubation, the medium and the floating cells were carefully removed by aspiration, and the attached layers were washed twice with PBS. The firmly attached cells were then counted using a cell counting chamber (Burker-Turk chamber) for quantification. Cell adhesion curves were generated after counting triplicate Petri dishes.

Animal Model. 6- to 10-week-old female C57Bl6 mice (Charles River Laboratories, Calco, Italy) were inoculated subcutaneously in the left flank with 0.2 mL of a single suspension containing approximately 1 × 10^6 B16−F10*LacZ* or B16−F10 melanoma cells, respectively. Mice were constantly treated in accordance with European Community guidelines and Ethical Committee Rules of the University of Torino.

MR Images Studies *in Vivo*. To investigate whether β-galactosidase expressing cells could be noninvasively imaged, C57Bl6 mice (n = 6) bearing subcutaneously grown B16−F10 and B16−F10*LacZ* tumors were injected intratumor with 40 μL of Gd-DOTAtyr-gal solution (7.5 mM). MR images were acquired on the Aspect M2 system (Aspect Imaging, Shoam, Israel) operating at 1T equipped with a horizontal bore MRI magnet using a standard T_1 weighted multislice spin echo sequence (TR = 250 ms, TE = 7.0 ms, NEX = 10, FOV = 3.5 cm, 6 slices, slice thickness = 1 mm). Prior to MRI examination, animals were anesthetized by injecting tiletamine/zolepam (Zoletil 100), 20 mg/kg, +xylazine (Rompum), 5 mg/kg.

RESULTS AND DISCUSSION

Design and Synthesis of Gd-DOTAtyr-gal and Gd-DOTAtyr. Gd-DOTAtyr-gal was designed to detect β-galactosidase activity through the conversion into Gd-DOTAtyr that, in the presence of tyrosinase, polymerizes to form melanin-like structures that are characterized by relaxivity values higher than those of the molecular Gd-DOTAtyr-gal and Gd-DOTAtyr complexes. Therefore, Gd-DOTAtyr-gal consists of three moieties: (i) the outer galacto-pyranose unit that acts as masking group and hampers the start of the polymerization; (ii) the phenolic functionality that in the presence of tyrosinase quickly oxidizes to yield polymeric derivatives; and (iii) the Gd(III) complex that acts as the MRI reporting unit.

Gd-DOTAtyr has been synthetized in order to assess its ability to polymerize in tyrosinase containing buffer or cytosol solutions as well as in intact melanoma cells. The melanin-like polymers display a tendency to precipitate as the molecular weight increases. On one hand, this is a limitation because one can exploit only the relaxation enhancement offered by the smaller oligomers. On the other hand, the formation of a polymer implies that the transformed Gd-complexes do not leave the cell and, moreover, their final insolubilization appears as an advantage in terms of limiting the toxicity of the Gd-containing species.

Relaxometric Characterization of Gd-DOTAtyr and Gd-DOTAtyr-gal. The relaxivity of Gd-DOTAtyr and Gd-DOTAtyr-gal in water, at 20 MHz and 25 °C, is 5.8 and 7.8 mM^{-1} s^{-1}, respectively. Their relaxivity profiles in the range of frequencies 0.01−70 MHz (NMRD profiles) have been registered and reported in Figure 1. The relaxivity of Gd-DOTAgal is slightly higher than that of Gd-DOTAtyr at any magnetic field strength because of the higher molecular weight.

The NMRD profiles have been analyzed in terms of the available theory of paramagnetic relaxation, and the main relaxometric parameters have been determined. The two complexes are characterized by similar values for the electronic relaxation time (τ_{so} = 160 ps and 150 ps for Gd-DOTAtyr-gal and Gd-DOTAtyr) and water exchange lifetime (500 ns), while they differ in their reorientational correlation times that were determined to be 192 ps and 125 ps for Gd-DOTAtyr-gal and Gd-DOTAtyr, respectively.

The cleavage of the galactosyl-pyranose moiety operated by the β-galactosidase enzyme (2 μM) has been followed over time at 37 °C by measuring the change in the relaxation rate (at 20 MHz and 25 °C) of the solutions of Gd-DOTAtyr-gal upon addition of the enzyme in phosphate buffer and in serum (Figure 2).

As shown in Figure 2, the transformation of Gd-DOTAtyr-gal into Gd-DOTAtyr, witnessed by the observed decrease of relaxivity, occurs quite readily either in phosphate buffer or in serum.

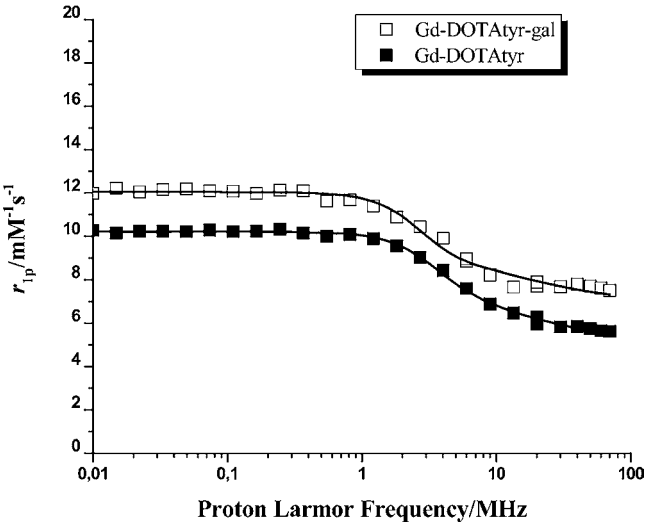

Figure 1. ^{1}H NMRD profiles of Gd-DOTAtyr-gal (□) and Gd-DOTAtyr (■) measured at 25 °C and neutral pH. The data refer to the millimolar concentration of the paramagnetic complexes.

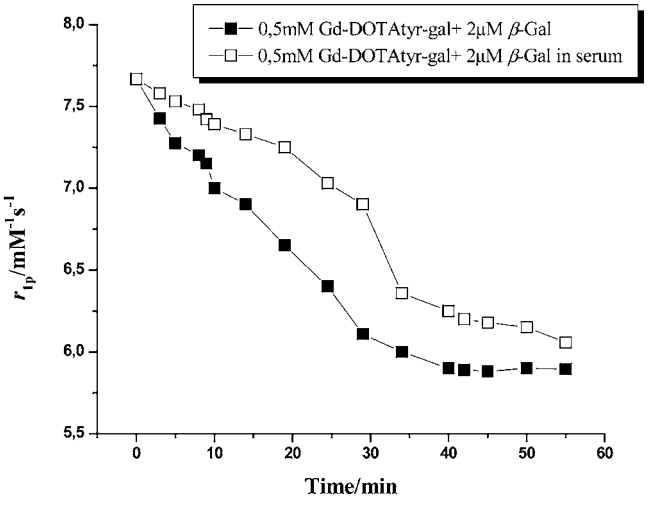

Figure 2. Variation of the relaxivity of Gd-DOTAtyr-gal as a consequence of addition of β-galactosidase enzyme in phosphate buffer (■) and in serum (□).The measurements were carried out at 20 MHz and 25 °C.

Next, the formation of melanin-like polymers from Gd-DOTAtyr in the presence of tyrosinase enzyme has been assessed by either colorimetric and relaxometric measurements. In fact, the formation of melanin-like polymers is characterized by a progressive darkening of the solution (increase of UV absorbance at 475 nm) and by the decrease of the solvent water proton relaxation time (Figure 3).

A similar experiment was also performed on a solution of Gd-DOTAtyr-gal, not activated by β-galactosidase. In this case, no darkening nor any change in the proton relaxation time was observed when the tyrosinase enzyme was added to the solution (Supporting Informations). Having established that Gd-DOTAtyr-gal transforms into Gd-DOTAtyr in the presence of β-galactosidase and Gd-DOTAtyr yields a melanin-like polymer in the presence of tyrosinase, a solution of Gd-DOTAtyr-gal (0.35 mM), β-galactosidase (2 μM), and tyrosinase (3 μM) has been prepared and the change in light absorption and proton relaxation times have been measured.

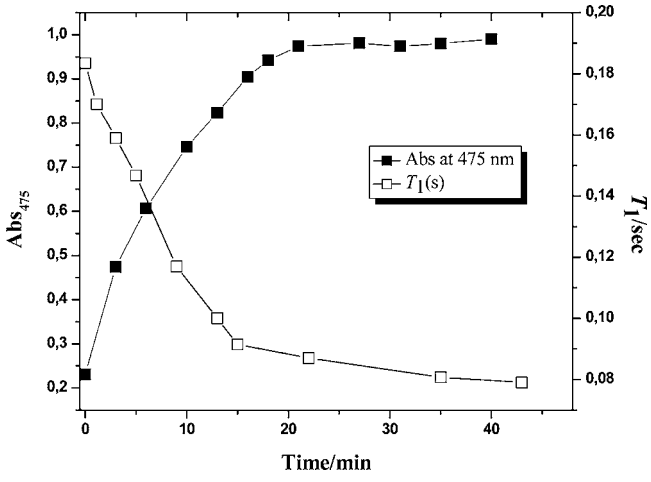

Figure 3. Plot of the spectrophotometric (■) and water proton relaxation time measurements (□) (25 °C, 20 MHz) of a Gd-DOTAtyr (0.35 mM) solution in the presence of tyrosinase enzyme (3 μM) as a function of time.

The obtained results (Supporting Informations) are very similar to those found for the Gd-DOTAtyr in the presence of tyrosinase. This finding clearly shows that the transformation of Gd-DOTAtyr-gal into Gd-DOTAtyr and then the oligomer formation take place in agreement with what was observed for the separated steps of galactose-pyranose release and melanin formation.

Relaxometric Analysis of the Activation Process. An in-depth characterization of the relaxation enhancement for Gd-DOTAtyr-gal solutions upon addition of β-galactosidase and tyrosinase was obtained through the acquisition of the NMRD profiles (Figure 4). As described above, the profile of Gd-

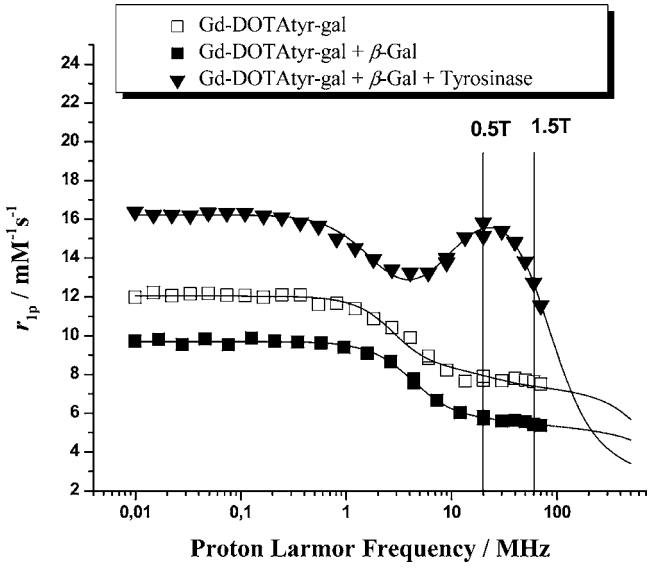

Figure 4. ^{1}H NMRD profiles of Gd-DOTAtyr-gal (□), Gd-DOTAtyr-gal after the addition of β-Gal (■), and Gd-DOTAtyr-gal after the addition of β-Gal and tyrosinase (▼) registered at 25 °C. The data refer to the millimolar concentration of the paramagnetic complexes. The higher r_{1p} values observed in the presence of the two enzymes are due to the formation of paramagnetic melanin-like macromolecules.

DOTAtyr-gal complex (open squares) has the classical shape shown by low molecular weight systems. Incubation of Gd-

dx.doi.org/10.1021/bc200486j | Bioconjugate Chem. 2011, 22, 2625–2635

DOTAtyr-gal complex with β-galactosidase at 37 °C for 40 min (red filled squares) led to a decrease of the relaxivity values along the entire range of investigated frequencies. The lower relaxivity is indicative of the formation of the lower molecular weight system (τ_R = 112 ps) achieved upon the release of the galactose moiety. The obtained profile is in fact almost superimposable with that of the Gd-DOTAtyr complex reported in Figure 1. The successive addition of tyrosinase enzyme (3 μM) to the remaining complex for 40 min leads to the formation of the oligomerized high relaxivity system (filled triangles - τ_R = 5.6 ns). Polymerization is the expected reactivity pathway for the phenolic product (obtained by the action of β-galactosidase) in the presence of tyrosinase, in agreement with the previously reported results for Gd-based tyrosinase and myeloperoxidase responsive agents.[8−11]

Investigation into the shapes of the profiles for the polymeric and monomeric Gd-containing systems reveals that there is a strong dependence of the responsiveness of the Gd-probe from the magnetic field strength at which the experiments are carried out. A marked jump in relaxivity is in fact observed in the field range 0.5−1.5 T (working fields of many clinical MR-scanners). At higher field strengths, the differences in relaxivities of the activated and inactivated systems become less marked.

Enzymatic Activity Assays in B16−F10 and B16−F10*LacZ* Melanoma Cells. In order to evaluate more closely the potential of Gd-DOTAtyr-gal for cellular applications, tests have been carried out in B16−F10 and B16−F10*LacZ* murine melanoma cells. Melanoma cells have been used for the enzymatic assays, as these cells possess high tyrosinase activity as witnessed by their natural melanin pigmentation.[15]

Cellular tyrosinase activity was assayed according to the method of Thomita et al. using L-DOPA as substrate and following the conversion of DOPA to DOPAchrome via DOPA quinone.[14,16] The increase of absorbance with time reports about the DOPAchrome formation and, in turn, on cell tyrosinase activity. Under these conditions, the enzymatic activity of one million B16−F10 and B16−F10*LacZ* cells has been estimated to be ca. 30 U and 3 U, respectively (by using an extinction coefficient for DOPAchrome at 475 nm of 3700 M^{-1} cm^{-1}). One unit of tyrosinase activity is defined as the amount of enzyme that catalyzes the trasformation of 1 μmol L-tyrosine/min. The low tyrosinase activity found for B16−F10*LacZ* fresh homogenates appears to be a frequent phenomenon already reported for other melanoma engineered cells (Figure 5)[14−16] where it has been described as one of the phenotypic variations of cellular differentiation.[18] However when 1×10^6 B16−F10*LacZ* melanoma cells were injected into C57BL/6 mouse, the mouse developed a partially or fully melanotic tumor. This phenomenon, already reported in the literature,[17−19] proved that these cells retained the capacity of producing the pigment, although this capacity appeared not to be well-expressed *in vitro*. Therefore, after being cycled in mice, the B16−F10*LacZ* cells were again assayed *in vitro* by the method of Thomita et al. using L-DOPA as substrate, and a significant resumption of tyrosinase activity was observed (Figure 5).

To assess the enzymatic activity of β-galactosidase in the cells, B16−F10*LacZ* cells were stained with β-Gal Staining Kit and examined under optical microscope as shown in Figure 6.

β-Gal Staining Kit is based on 5-bromo-4-chloro-3-indolyl-β-D-galactopyranoside (X-Gal), a non-inducing chromogenic substrate for β-Gal. The resultant halogenated indigo is a very stable and insoluble dark blue compound (Figure 6).

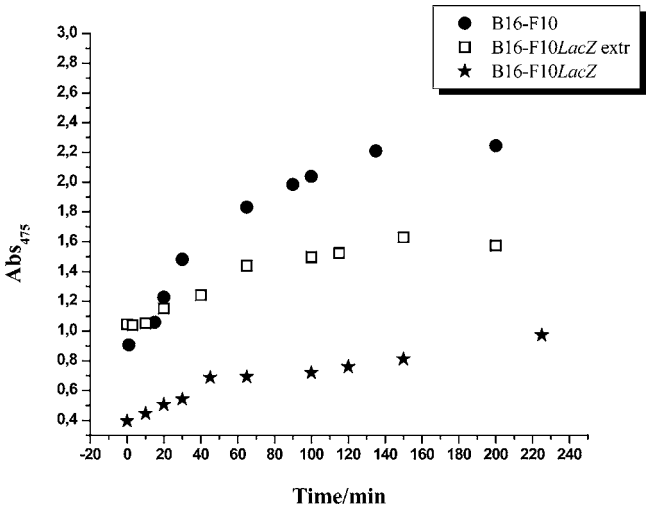

Figure 5. Absorbance at 475 nm as a function of time for B16−F10, B16−F10*LacZ*, and B16−F10*LacZ* (isolated from injected mice) cells homogenates added to a 0.5 mL of a 1 mM L-DOPA solution.

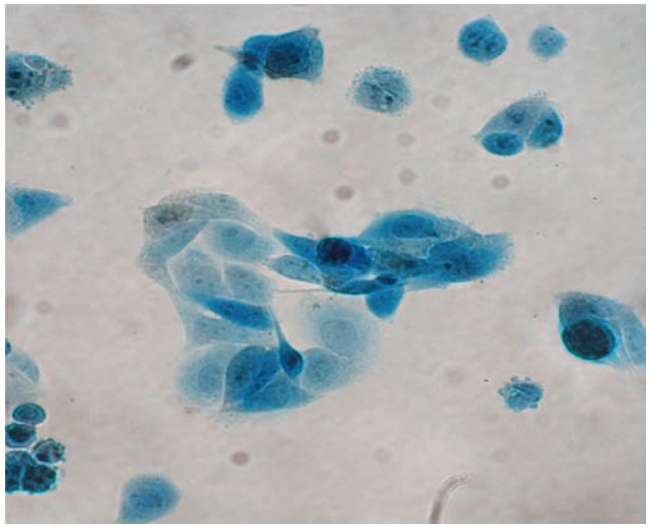

Figure 6. B16−F10*LacZ* cells were stained for β-gal activity by the β-Gal Staining Kit (1 mg/mL X-gal) before examination under the microscope.

Incubation of Gd-DOTAtyr-gal with B16−F10 and B16−F10*LacZ* Cell Homogenates. In each experiment, 8×10^6 B16F10 or a similar number of B16−F10*LacZ* cells were added to 100 μL of a 1 mM Gd-DOTAtyr-gal solution, sonicated to induce cell lysis, and the proton longitudinal relaxation rate at 20 MHz and 25 °C was measured over time while maintaining the temperature of the reaction mixture at 37 °C (Figure 7).

As shown in Figure 7, the relaxivity steadily increases to reach a "plateau" value, after 30 h of incubation. The observed behavior is consistent with the formation of a Gd-incorporated, melanin-like macromolecule. No effect is observed when Gd-DOTAtyr-gal is incubated with B16−F10 cells, lacking the β-Gal enzyme.

Uptake of Gd-DOTAtyr-gal and Gd-DOTAtyr into B16−F10 and B16−F10*LacZ* Cells. Translation of this enzyme-based approach to in vivo applications requires that a sufficient amount of Gd-responsive probe is internalized by the cells to be monitored. The uptake efficiency by melanotic B16−

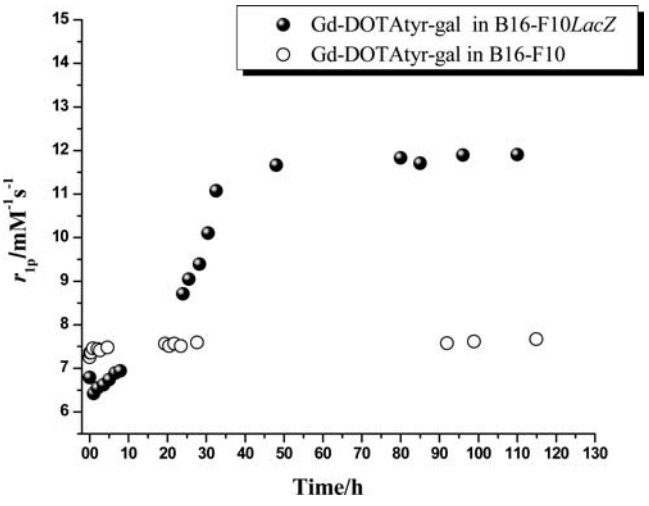

Figure 7. Variation of the relaxivity of Gd-DOTAtyr-gal over time in the presence of B16−F10*LacZ* (●) and B16−F10 (○) cell homogenates. The measurements were carried out at 20 MHz and 25 °C.

F10 and B16−F10*LacZ* cells was assessed by incubating 1 × 10^6 cells in DMEM medium in the presence of different concentrations (10−15−20 mM) of Gd-DOTAtyr-gal and Gd-DOTAtyr, for 4 h at 37 °C (Figure 8).

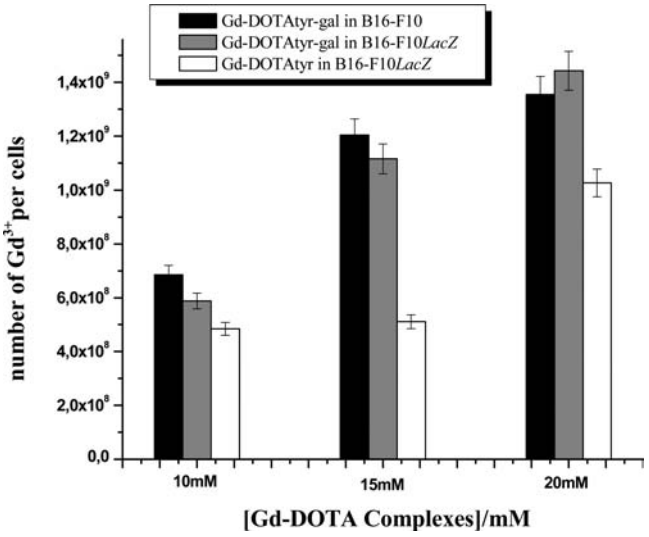

Figure 8. Number of Gd^{3+} units per cell internalized after incubation of Gd-DOTAtyr-gal in B16−F10 (black) and B16−F10*LacZ* (gray) cells and Gd-DOTAtyr in B16−F10*LacZ* cells (white) for 4 h at 37 °C.

The uptake of Gd-DOTAtyr-gal in both *β*-Gal expressing and parent melanoma cells is significantly higher than that of Gd-DOTAtyr. The higher accumulation efficiency of Gd-DOTAtyr-gal may be accounted for the specific recognition of galectin receptors, which are galactose-specific lectins particularly hyperexpressed on B16−F10 cells.[20,22] Support to the specificity of internalization of Gd-DOTAtyr-gal thanks to the recognition of galectins exposed on cell membrane surfaces has been found in measuring the perturbation of the adhesion of B16−F10 cells to fibronectin of culture dishes. It is in fact known that cell−cell and cell−ECM (extracellular matrix) adhesions are mediated not only by integrin−ligand interactions but also by lectin−saccharide interactions.[20,21]

Recently, El-Boubbou et al.[20] demonstrated that galactose-functionalized magnetic nanoparticles strongly interact with B16−F10 cells, and that this interaction is responsible for a reduction of adherent cells by more than 50%.

Upon incubation of B16−F10*LacZ* cells with 15 mM Gd-DOTAtyr-gal, we observed a progressive reduction of the amount of adherent cells increasing the incubation time if compared with control cells (Figure 9). In contrast, a very small

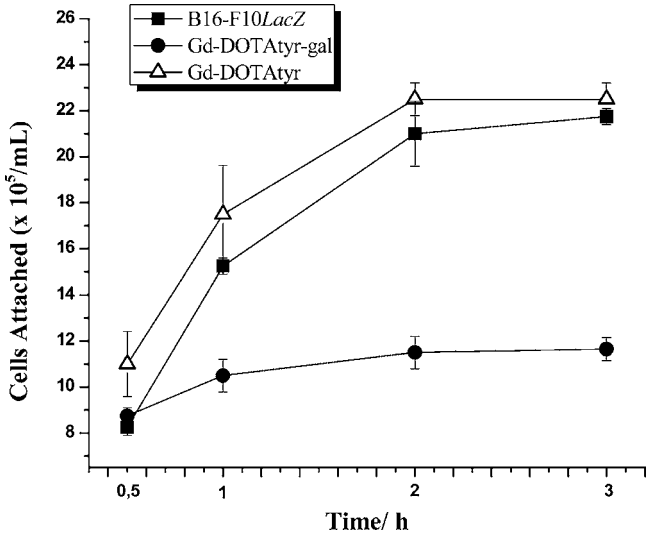

Figure 9. Adhesion of mouse melanoma B16−F10*LacZ* cells to the surface was significantly reduced by incubation with Gd-DOTAtyr-gal (●), while Gd-DOTAtyr (Δ) had no effect on cell adhesion as compared to the cells without any treatment (■).

effect was observed when cells were incubated with Gd-DOTAtyr.

In order to be activated by the cytosolic enzymes, an important issue for the activation of the probe relies on the need to avoid the endosomal compartmentalization of the internalized probe. This issue has been tackled by measuring the variation of observed relaxation rate (at 1T and 25 °C) of the internalized probe as a function of its intracellular concentration (Figure 10). It was recently demonstrated that the occurrence of a linear increase of the observed relaxation rate with the amount of internalized paramagnetic probe is a good reporter of the cytoplasmic localization of the Gd(III)-probe, while a "quenching" effect on the observed relaxation rate is observed in the case of its endosomal entrapment.[23−25] As shown in Figure 10, a linear correlation has been observed, which witnesses that Gd-DOTAtyr-gal, after being internalized by cells, is localized in the cytosol and available for the interaction with *β*-galactosidase and tyrosinase enzymes. Furthermore, in Figure 10 the relaxation rates of cells labeled via their incubation with Gd-DOTAtyr-gal for 4 h at 37 °C are compared with those obtained for cells in which the same Gd(III)-containing probe has been internalized by electroporation (that invariantly leads to a cytoplasmatic localization). The two internalization pathways show the same linear growth of observed relaxation rates as a function of the intracellular Gd(III) complex concentration, to support the view that the same cytoplasmic localization is taking place.

***In Vivo* MRI Experiments.** To assess the *in vivo* capability of the complex Gd-DOTAtyr-gal to discriminate between

dx.doi.org/10.1021/bc200486j | *Bioconjugate Chem.* 2011, 22, 2625−2635

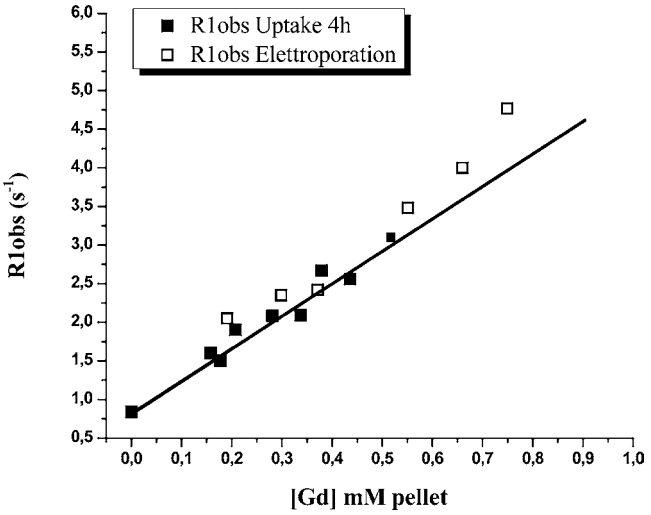

Figure 10. Observed longitudinal relaxation rates of B16−F10*LacZ* cellular pellets, measured at 1 T and 25 °C, as a function of Gd^{3+} concentration in the cellular pellets from uptake experiments (■) and electroporation experiments (□).

melanoma tumors with and without *β*-galactosidase gene expression, an MRI study was carried out on two tumor-bearing animal models, namely, (i) C57Bl6 mice grafted with the murine melanoma cell line B16−F10; (ii) C57Bl6 mice grafted with the murine melanoma cell line B16−F10*LacZ*.

The model was obtained by subcutaneous injection of 1 million of B16−F10 or B16-F10*LacZ* cells, on the right limb of six female C57Bl6J mice. At 10−12 days after implantation, a tumor mass of a 2−3 cm width is clearly detectable in each mouse at the site of injection. At this time, animals received intratumoral injections of the Gd-DOTAtyr-gal (40 *μ*L of 7.5 mM solution) and T_1 weighted multislice MR images were acquired at 1.0 T.

A strong T_1 contrast was detected in the *LacZ* expressing tumors after 4−5 h from contrast agent injection. At the same detection time, no T_1 contrast was observed in the B16−F10 tumor, which was injected with the same amount of contrast agent (Figure 11a). The observed signal enhancement of the B16−F10*LacZ* tumor was an order of magnitude higher than the one observed for B16−F10 tumor (3.5 ± 1.6) (Figure 11b). The intense enhancement clearly indicates that Gd-DOTAtyr-gal is activated by *β*-galactosidase and tyrosinase enzymes both presented in B16−F10*LacZ* tumor.

CONCLUSIONS

The *β*-galactosidase gene *LacZ* is often used as a reporter constructor in eukaryotic transfection experiments due to the proteolytic resistance of the protein product and the easily assayed enzyme activity. In this study, a new Gd(III)-based probe was designed, prepared, and enzymatically tested to be a good *β*-galactosidase substrate in melanoma B16 homogenate. Upon cleavage by *β*-galactosidase, the tyrosine residue can interact with the tyrosinase enzyme in B16−F10*LacZ* melanoma cells with subsequent formation of high-relaxivity Gd-DOTA containing oligomers.

A good relaxation enhancement effect was detected. The slow activation of the probe could be due to a relatively low turnover of the enzyme; therefore, higher loading would allow a larger amount of substrate to be converted by the enzyme, thus giving rise to a larger relaxation enhancement effect.

The ability of Gd-DOTAtyr-gal to enter B16−F10*LacZ* cells following intratumoral injection has been demonstrated.

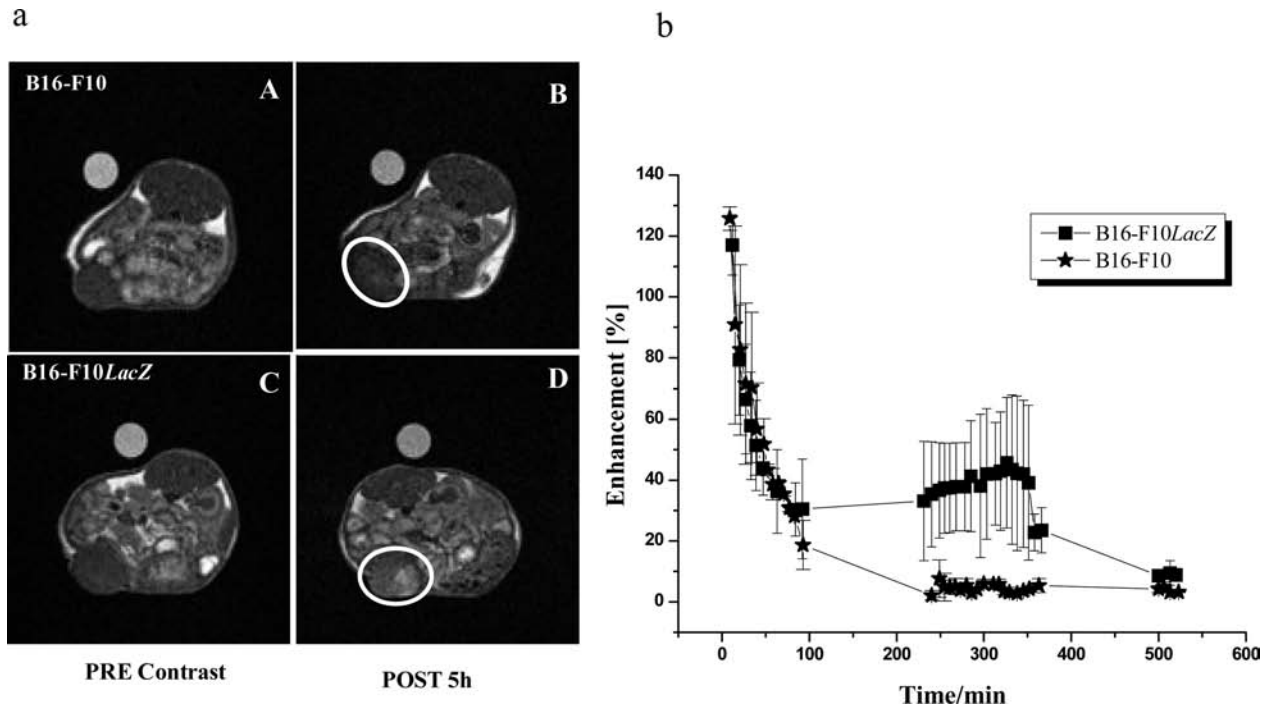

Figure 11. (a) T_1-weighted (TR/TE 250/8.9 ms) MR images of animal model at 1.0 T MR scanner: (A) precontrast image of B16−F10 tumor; (B) at 5 h after intratumoral (IT) injection of 40 *μ*L of Gd-DOTAtyr-gal (7.5 mM) in B16−F10 tumor; (C) precontrast image of B16−F10*LacZ*; (D) at 5 h after intratumoral (IT) injection of 40 *μ*L of Gd-DOTAtyr-gal (7.5 mM) in B16−F10*LacZ* tumor; (b) time−signal enhancement change of the B16−F10 and B16−F10*LacZ* tumor after intratumoral (IT) injection of 40 *μ*L of Gd-DOTAtyr-gal (7.5 mM).

dx.doi.org/10.1021/bc200486j | *Bioconjugate Chem.* 2011, 22, 2625−2635

Besides melanoma cells, Gd-DOTAtyr-gal would be a good gene reporter for any doubly transfected (β-Gal and Tyr) cells. Finally, the importance of working at low magnetic field strength has been shown when the determinant of the relaxation enhancement is represented by the molecular reorientational time.

■ ASSOCIATED CONTENT

Supporting Information

Control enzymatic activity assays on Gd-DOTAtyr-gal and HPLC methods used for the purification of intermediates and final products. This material is available free of charge via the Internet at http://pubs.acs.org.

■ AUTHOR INFORMATION

Corresponding Author

*Fax: +39 0116706487. Tel: +39 0116706451. E-mail: silvio.aime@unito.it.

■ ACKNOWLEDGMENTS

Economic and scientific support from, EC-FP6-project ENCITE (European Network for "Cell Imaging and Tracking Expertise" 201842), EU-COST D38 Action, Regione Piemonte (PIIMDMT and Nano-IGT projects) is gratefully acknowledged.

■ REFERENCES

(1) Daunert, S., Barrett, G., Feliciano, J. S., Shetty, R. S., Shrestha, S., and Smith-Spencer, W. (2000) Genetically engineered whale-cell sensing systems: Coupling biological recognition with reporter genes. *Chem. Rev. 100*, 2705−2738.

(2) Cui, W. N., Liu, L., Kodibagkar, V. D., and Mason, R. P. (2010) S-Gal (R), a Novel (1)H MRI Reporter for beta-Galactosidase. *Magn. Reson. Med. 64*, 65−71.

(3) Moats, R. A., Fraser, S. E., and Meade, T. J. (1997) A "smart" magnetic resonance imaging agent that reports on specific enzymatic activity. *Angew. Chem., Int. Ed. Engl. 36*, 725−728.

(4) Louie, A., Huber, M. M., Ahrens, E. T., Rothbacher, U., Moats, R., Jacobs, R. E., Fraser, S. E., and Meade, T. J. (2000) In vivo visualization of gene expression using magnetic resonance imaging. *Nat. Biotechnol. 18*, 321−325.

(5) Hanaoka, K., Kikuchi, K., Terai, T., Komatsu, T., and Nagano, T. (2008) A Gd3+-based magnetic resonance imaging contrast agent sensitive to beta-galactosidase activity utilizing a receptor-induced magnetization enhancement (RIME) phenomenon. *Chem.—Eur. J. 14*, 987−995.

(6) Chang, Y. T., Cheng, C. M., Su, Y. Z., Lee, W. T., Hsu, J. S., Liu, G. C., Cheng, T. L., and Wang, Y.-M. (2007) Synthesis and characterization of a new bioactivated paramagnetic gadolinium(111) complex [Gd(DOTA-FPG)(H2O)] for tracing gene expression. *Bioconjugate Chem. 18*, 1716−1727.

(7) Keliris, A., Ziegler, T., Mishra, R., Pohmann, R., Sauer, M. G., Ugurbil, K., and Engelmann, J. (2011) Synthesis and characterization of a cell-permeable bimodal contrast agent targeting beta-galactosidase. *Bioorg. Med. Chem. 19*, 2529−2540.

(8) Chen, J. W., Pham, W., Weissleder, R., and Bogdanov, A. A. (2004) Human myeloperoxidase: A potential target for molecular MR imaging in atherosclerosis. *Mag. Reson. Med. 52*, 1021−1028.

(9) Querol, M., Chen, J. W., and Bogdanov, A. A. (2006) A paramagnetic contrast agent with myeloperoxidase-sensing properties. *Org. Biomol. Chem 4*, 1887−1895.

(10) Chen, J. W., Querol, M., Bogdanov, A. A., and Weissleder, R. (2006) Imaging of myeloperoxidase in mice by using novel amplifiable paramagnetic substrates. *Radiology 2*, 473−481.

(11) Querol, M., Bennett, D. G., Sotak, C., Kang, H. W., and Bogdanov, A. A. (2007) A paramagnetic contrast agent for detecting tyrosinase activity. *ChemBioChem 8*, 1637−1641.

(12) Barge, A., Tei, L., Upadhyaya, D., Fedeli, F., Beltrami, L., Stefania, R., Aime, S., and Cravotto, G. (2008) Bifunctional ligands based on the DOTA-monoamide cage. *Org. Biomol. Chem. 6*, 1176−1184.

(13) Barge, A., Cravotto, G., Gianolio, E., and Fedeli, F. (2006) How to determine free Gd and free ligand in solution of Gd chelates. A technical note. *Contrast Media Mol. Imaging 1*, 184−188.

(14) Tomita, Y., Maeda, K., and Tagami, H. (1992) Melanocyte stimulating properties of arachidonic acid metabolites − possible role in post-inflammatory pigmentation. *Pigm. Cell Res. 5*, 357−361.

(15) Petrescu, S. M., Petrescu, A. J., Titu, H. N., Dwek, R. A., and Platt, F. M. (1997) Inhibition of N-glycan processing in B16 melanoma cells results in inactivation of tyrosinase but does not prevent its transport to the melanosome. *J. Biol. Chem. 272*, 15796−15803.

(16) Hearing, V. J., and Ekel, T. M. (1976) Mammalian tyrosinase. A comparison of tyrosine hydroxylation and melanin formation. *Biochem . J. 157*, 549−557.

(17) Silagi, S. (1969) Control of pigment production in mouse melanoma cells in vitro. *J. Cell Biol. 43*, 263−274.

(18) Hiroshi, O., Eiko, F., Ichi, N., and Tsutomu, K. (1982) Induction of pigmentation by continuous X-irradiation of amelanotic tumors of B16-XI mouse melanoma and induced change in chromosomes of amelanotic cells. *Cell. Pathol. 41*, 267−276.

(19) Nishii, R., Kawai, K., Garcia Flores, L. II, Kataoka, H., Jinnouchi, S., Nagamachi, S., Arano, Y., and Tamura, S. (2003) A novel radiopharmaceutical for detection of malignant melanoma, based on melanin formation: 3-iodo-4-hydroxyphenyl-L-cysteine. *Nucl. Med. Commun. 24*, 575−582.

(20) El-Boubbou, K., Zhu, D. C., Vasileiou, C., Borhan, B., Prosperi, D., Li, W., and Huang, X. (2010) Magnetic glyco-nanoparticles: a tool to detect, differentiate, and unlock the glyco-codes of cancer via magnetic resonance imaging. *J. Am. Chem. Soc. 132*, 4490−4499.

(21) Kim, E. Y. L., Gronewold, C., Chatterjee, A., von der Lieth, C. W., Kleim, C., Schmauser, B., Wiessler, M., and Frei, E. (2005) Oligosaccharide mimics containing galactose and fucose specifically label tumour cell surfaces and inhibit cell adhesion to fibronectin. *ChemBioChem 6*, 422−431.

(22) Oguchi, H., Toyokuni, T., Dean, B., Ito, H., Otsuji, E., Jones, V. L., Sadozai, K. K., and Hakomori, S. (1990) Effect of lactose derivatives on metastatic potential of B16 Melanoma cell. *Cancer Commun. 2*, 311−316.

(23) Terreno, E., Geninatti Crich, S., Belfiore, S., Biancone, L., Cabella, C., Esposito, G., Manazza, A. D., and Aime, S. (2006) Effect of the intracellular localization of a Gd-based imaging probe on the relaxation enhancement of water protons. *Magn. Reson. Med. 55*, 491−497.

(24) Strijkers, G. J., Hak, S., Kok, M. B., Springer, C. S., and Nicolay, K. (2009) Cellular compartmentalization of internalized paramagnetic liposomes strongly influences both T(1) and T(2) relaxivity. *Magn. Reson. Med. 61*, 1049−1058.

(25) Gianolio, E., Arena, F., Strijkers, G. J., Nicolay, K., Högset, A., and Aime, S. (2011) Photochemical activation of endosomal escape of MRI-Gd-agents in tumor cells. *Magn. Reson. Med. 65*, 212−219.